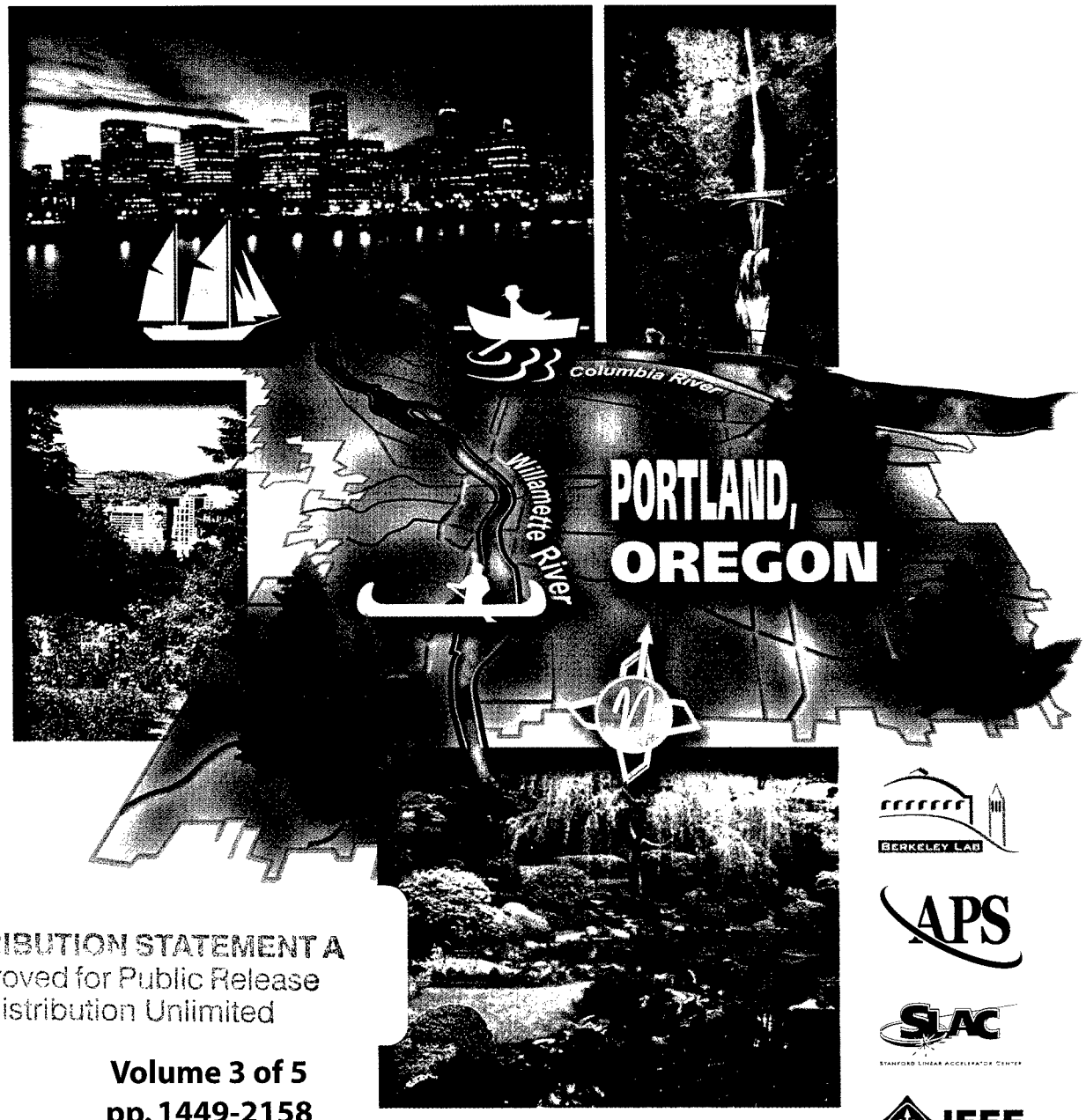
PAC

Proceedings of the

2003 Particle Accelerator Conference



DISTRIBUTION STATEMENT A
Approved for Public Release
Distribution Unlimited

Volume 3 of 5
pp. 1449-2158

BERKELEY LAB

APS

SLAC
STANFORD LINEAR ACCELERATOR CENTER

IEEE

REPORT DOCUMENTATION PAGE

Form Approved
OMB No. 0704-0188

Public reporting burden for this collection of information is estimated to average 1 hour per response, including the time for reviewing instructions, searching existing data sources, gathering and maintaining the data needed, and completing and reviewing the collection of information. Send comments regarding this burden estimate or any other aspect of this collection of information, including suggestions for reducing this burden, to Washington Headquarters Services, Directorate for Information Operations and Reports, 1215 Jefferson Davis Highway, Suite 1204, Arlington, VA 22202-4302, and to the Office of Management and Budget, Paperwork Reduction Project (0704-0188), Washington, DC 20503.

1. AGENCY USE ONLY *(Leave Blank)*	2. REPORT DATE	3. REPORT TYPE AND DATES COVERED
		Final

4. TITLE AND SUBTITLE
2003 Particle Accelerator Conference
Vol. 3

5. FUNDING NUMBERS
G

6. AUTHORS
variou

7. PERFORMING ORGANIZATION NAME(S) AND ADDRESS(ES)
IEEE
445 Hoes Lane, PO Box 1331
Piscataway, NJ 08855-1331

8. PERFORMING ORGANIZATION REPORT NUMBER

9. SPONSORING / MONITORING AGENCY NAME(S) AND ADDRESS(ES)
Office of Naval Research
Ballston Centre Tower One
800 North Quincy Street
Arlington, VA 22217-5660

10. SPONSORING / MONITORING AGENCY REPORT NUMBER
N00014-04-1-0417

11. SUPPLEMENTARY NOTES

12a. DISTRIBUTION / AVAILABILITY STATEMENT
DISTRIBUTION STATEMENT A
Approved for Public Release
Distribution Unlimited

12b. DISTRIBUTION CODE

13. ABSTRACT *(Maximum 200 words)*

The twentieth biennial Particle Accelerator Conference on Accelerator Science and Technology was held May 12 – 16, 2003 at the Hilton Hotel in Portland, Oregon. The Stanford Linear Accelerator Center and the Lawrence Berkeley National Laboratory organized PAC 2003, and it was held under the auspices of the Nuclear and Plasma Sciences Society of the Institute of Electrical and Electronics Engineers and the Division of Physics of Beams of the American Physical Society. The attendance was 1025 registrants from 21 countries. The Program Committee was co-chaired by Alan Jackson and Ed Lee. The program they arranged had opening and closing plenary sessions that covered the most important accomplishments, opportunities, and applications of accelerators. During the remainder of the conference there were parallel sessions with oral and poster presentations. In addition, there was an industrial exhibit during the first three days. The Proceedings present a total of 1154 papers from the invited, contributed orals, and poster sessions.

14. SUBJECT TERMS
Particle Accelerators and Colliders, Beam Dynamics, Magnets, RF Systems, Synchrotron radiation sources, Free Electron Lasers, Energy Recovery Linacs, Instabilities, Feedback Instrumentation, Pulsed Power, High Intensity Beams, Accelerator Applications, Advanced Accelerators.

15. NUMBER OF PAGES
3571

16. PRICE CODE

17. SECURITY CLASSIFICATION OF REPORT	18. SECURITY CLASSIFICATION OF THIS PAGE	19. SECURITY CLASSIFICATION OF ABSTRACT	20. LIMITATION OF ABSTRACT
Unclassified	**Unclassified**	**Unclassified**	

PAC 2003

PROCEEDINGS OF THE 2003 PARTICLE ACCELERATOR CONFERENCE

Portland, Oregon U.S.A.
May 12-16, 2003

Joe Chew, Peter Lucas, and Sara Webber, editors

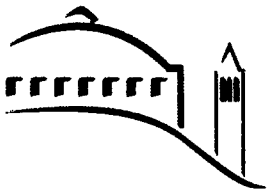
Volume 3 of 5

Organized by
Stanford Linear Accelerator Center
Lawrence Berkeley National Laboratory

Held under the joint auspices of
Institute of Electrical and Electronics Engineers
(Nuclear and Plasma Sciences Society)
American Physical Society
(Division of Physics of Beams)

Sponsored by
U.S. Department of Energy
Office of Naval Research
National Science Foundation








20040311 166

ACKNOWLEDGEMENTS

Cover Design: Terry Anderson

Photographs: Edmund Keene Photographers

Funding for these proceedings was provided under DOE Grant No. DE-FG03-01ER41233 by the following U.S. Department of Energy offices:

- Office of High Energy and Nuclear Physics
- Office of Basic Energy Sciences
- Office of Fusion Energy Sciences

This work related to Department of Navy grant N00014-03-1-0417 issued by the Office of Naval Research. The United States Government has a royalty-free license throughout the world in all copyrightable material contained herein.

Funding for student and postdoctoral associate travel to attend the conference was provided by National Science Foundation Grant No. PHY-0225358.

Proceedings of the 2003 Particle Accelerator Conference

Copyright and Reprint Permission: Abstracting is permitted with credit to the source. Libraries are permitted to photocopy beyond the limit of U.S. copyright law for private use of patrons those articles in this volume that carry a code at the bottom of the first page, provided the per-copy fee indicated in the code is paid through Copyright Clearance Center, 222 Rosewood Drive, Danvers, MA 01923. For other copying, reprint, or republication permission, write to IEEE Copyrights Manager, IEEE Operations Center, 445 Hoes Lane, P.O. Box 1331, Piscataway, NJ 08855-1331. All Rights reserved. Copyright ©2003 by the Institute of Electrical and Electronics Engineers, Inc.

IEEE Catalog Number: 03CH37423

ISBN: 0-7803-7738-9

Library of Congress: 88-647453

Additional copies of this publication are available from
IEEE Operations Center
445 Hoes Lane
Piscataway, NJ 08855-1331 USA
+1 800 678 IEEE
+1 732 981 9667 (FAX)
email: customer.service@ieee.org

Volume 3

Lithium Collection Lens Filling Process for Fermilab Antiproton Source
R. Schultz, P. Hurh (FNAL) 1449

Li Material Testing- Fermilab Antiproton Source Lithium Collection Lens
S. Tariq, K. Ammigan, P. Hurh, R. Schultz (FNAL), P. Liu, J. Shang (University of Illinois) 1452

Beam Study with RF Choppers in the MEBT of the J-PARC Proton Linac
T. Kato, M. Ikegami (KEK), S. Fu, S. Wang (Institute of High Energy Physics, Beijing) 1455

Spallation Neutron Source High-Power RF Transmitter Design for High Availability, Ease of Installation and Cost Containment
J. Bradley III, T. Hardek, M.T. Lynch, D.E. Rees, W. Roybal, P.J. Tallerico (LANL) 1458

Completion of CCL Hot Model for SNS-Linac R&D Program
R. Hardekopf, J. Bernardin, J. Billen, N. Bultman, W. Fox, T. Hardek, S. Hopkins, S. Nath, D. Rej, P.J. Tallerico, L.M. Young (LANL) 1461

Operational Performance of the SNS LLRF Interim System
A. Ratti, L. Doolittle, M. Monroy (LBNL), M. Champion, H. Ma (ORNL) 1464

Beam Dump Window Design for the Spallation Neutron Source
S. Henderson, A. DeCarlo, S.-H. Kim, G. Murdoch, K. Potter, T. Roseberry (ORNL), J. Rank, D. Raparia (BNL) .. 1467

Status of Timing System and Its Upgrade for the PLS Storage Ring
M.H. Chun, Y.J. Han, H.S. Kang, D.T. Kim, S.H. Nam, B.R. Park, J.S. Yang (Pohang Accelerator Laboratory) 1470

Slow-Wave Electrode Structures for the ESS 2.5 MeV Fast Chopper
M.A. Clarke-Gayther (Rutherford Appleton Laboratory) 1473

Electrical Power and Grounding Systems Study and Improvement at TLS
J.C. Chang, J.R. Chen, K.C. Kuo, S.C. Lei, Y.C. Lin (Synchrotron Radiation Research Center) 1476

De-Ionized Cooling Water System Study and Improvement at TLS
J.C. Chang, J.R. Chen, Y.C. Chung, C.Y. Liu, Z.D. Tsai (Synchrotron Radiation Research Center) 1479

Air Temperature Control Improvement for the Storage Ring Tunnel
J.C. Chang, J.R. Chen, C.Y. Liu (Synchrotron Radiation Research Center) 1482

Machine Protection for High Average Current Linacs
K. Jordan, T. Allison, J. Coleman, R. Evans, A. Grippo (Thomas Jefferson National Accelerator Facility) 1485

A Mechanical Tuner for the ISAC-II Quarter Wave Superconducting Cavities
R.E. Laxdal, K. Fong, S. Koscielniak, T. Ries, G. Stanford (TRIUMF) 1488

The Jefferson Lab Quality Assurance Program for the SNS Superconducting Linac Accelerator Project
J.P. Ozelis (Thomas Jefferson National Accelerator Facility) 1491

Utilization of Integrated Process Control, Data Capture, and Data Analysis in Construction of Accelerator Systems.
J.P. Ozelis, V. Bookwalter, B. Madre, C. Reece (Thomas Jefferson National Accelerator Facility) 1494

Study of Coherent Radiation from an Electron Beam Prebunched at the Photocathode
J. Neumann, D. Demske, R. Fiorito, P.G. O'Shea (University of Maryland), G.L. Carr, H. Loos, T. Shaftan, B. Sheehy, Z. Wu (BNL) 1497

A Solid-State Transmitter for the Argonne Advanced Photon Source
I.S. Roth, J.A. Casey, M.P.J. Gaudreau, T. Hawkey, M.A. Kempkes, J.M. Mulvaney, J.E. Petry (Diversified Technologies, Inc.) 1500

Fermilab Booster Beam Collimation and Shielding
N.V. Mokhov, A. Drozhdin, P.H. Kasper, J.R. Lackey, E.J. Prebys, R.C. Webber (FNAL) 1503

Basis for the Reliability Analysis of the Proton Linac for an ADS Program
D. Sertore, D. Barni, P. Michelato, L. Monaco, M. Novati, C. Pagani, R. Paulon, P. Pierini (INFN), L. Burgazzi (Ente Nazionale per le Nuove Tecnologie l'Energia e l'Ambiente) 1506

Beam Commissioning of the J-PARC Linac Medium Energy Beam Transport at KEK
M. Ikegami, S. Anami, S. Arai, J. Chiba, S. Fukuda, Y. Fukui, Z. Igarashi, K. Ikegami, E. Kadokura, N. Kamikubota, T. Kato, M. Kawamura, J. Kishiro, H. Kobayashi, C. Kubota, F. Naito, K. Nigorikawa, S. Noguchi, M. Okada, E. Takasaki, H. Tanaka, A. Ueno, S. Yamaguchi, K. Yoshino (KEK), S. Fu, S. Wang (Institute of High Energy Physics, Beijing), K. Hasegawa, T. Ito, T. Kobayashi, Y. Kondo, Y. Yamazaki, H. Yoshikawa (Japan Atomic Energy Research Institute), J. Qiang, R.D. Ryne (LBNL) 1509

H^- Painting Injection System for the J-PARC 3GeV High Intensity Proton Synchrotron
I. Sakai, Y. Arakida, Y. Irie, T. Kawakubo, S. Machida, I. Sugai, Y. Takeda (KEK), F. Noda, K. Shigaki, T. Shimada, T. Takayanagi, Y. Watanabe, K. Yamamoto (Japan Atomic Energy Research Institute), Y. Ishi (MELCO, Kobe, Japan) 1512

Particle-Beam Behavior in the SNS Linac with Simulated and Reconstructed Beams
S. Nath, J. Billen, J. Stovall, H. Takeda, L.M. Young (LANL), D. Jeon (ORNL), K. Crandall (TechSource, Inc.) 1515

Particle-in-Cell Simulations of the High Current Experiment
C.M. Celata, F.M. Bieniosek, L.R. Prost, P.A. Seidl (LBNL), A. Friedman, D.P. Grote (LLNL) 1518

Design Choices for the Integrated Beam Experiment (IBX)
M.A. Leitner, C.M. Celata, E.P. Lee, B.G. Logan, G. Sabbi, W. Waldron (LBNL), J.J. Barnard (LLNL) 1521

Beam in Gap Measurements at the SNS Front-End
A. Aleksandrov, S. Assadi, W. Blokland, C. Deibele, W. Grice, J. Pogge (ORNL) 1524

ISIS Megawatt Upgrade Plans
C.R. Prior, D.J. Adams, C.P. Bailey, D.W.J. Bellenger, G. Bellodi, J.R.J. Bennett, I.S.K. Gardner, F. Gerigk, J.W. Gray, W.A. Morris, G.H. Rees, J.V. Trotman, C.M. Warsop (Rutherford Appleton Laboratory) 1527

Improvements for the Third Generation Plasma Wakefield Experiment E-164 at SLAC
C.D. Barnes, F.-J. Decker, P. Emma, M.J. Hogan, P. Iverson, P. Krejcik, C.L. O'Connell, R.H. Siemann, D. Walz (SLAC), B.E. Blue, C. Clayton, C. Huang, D. Johnson, C. Joshi, K.A. Marsh, W.B. Mori (University of California, Los Angeles), S. Deng, T.C. Katsouleas, P. Muggli, E. Oz (University of Southern California) 1530

A Slab-Symmetric Dielectric-Loaded Structure for High-Gradient Acceleration at THz
R. Yoder, J.B. Rosenzweig (University of California, Los Angeles) 1533

A Lie Transform Perturbation Scheme for Hamiltonian Averaging in Self Consistent Systems
K.G. Sonnad (University of Colorado at Boulder), J.R. Cary (Center for Integrated Plasma Studies) 1536

Beam Test of a CW Microtron with a 500 MHz RF Cavity for Industrial Applications
H. Tanaka, T.H. Kim, Y. Makita, A. Maruyama, S. Nakamura, T. Nakanishi, Y. Pu, C. Tsukishima, S. Yamamoto (Mitsubishi Corporation) 1539

Commissioning Results of Slow Extraction of Heavy Ions from the AGS Booster
K.A. Brown, L. Ahrens, S. Bellavia, S. Binello, B. Brelsford, D. Du Mont, W. Eng, C. Gardner, D. Gassner, J. Glenn, L. Hammons, J. Hock, L. Hoff, E. Hutchinson, J. Jamilkowski, N. Kling, Y. Kotlyar, A. Krishock, R. Lockey, M. Mapes, I. Marneris, G. Marr, A. Mc Nerney, A. Meyer, J. Morris, C. Naylor, S. Nemesure, D. Phillips, A. Rusek, J. Ryan, T. Shrey, L. Snydstrup, N. Tsoupas, B. VanKuik, S. Zahariou-Cohen, K. Zeno (BNL) 1542

Status of Slow Extraction of High Intensity Protons from Brookhaven's AGS
K.A. Brown, L. Ahrens, J.M. Brennan, J. Glenn, T. Roser, T. Russo, K.S. Smith, N. Tsoupas, K. Zeno (BNL) 1545

LHC Pilot Bunches from the CERN PS Booster
M. Benedikt (CERN) 1548

An 8-GeV Synchrotron-Based Proton Driver
W. Chou (FNAL) 1551

A New Antiproton Beam Transfer Scheme without Coalescing
W. Chou, J. Griffin, J.A. MacLachlan, S. Werkema (FNAL) 1554

Optics of a Proton Driver
L. Michelotti, W. Chou, A. Drozhdin, N. Gelfand, C. Johnstone (FNAL), G.H. Rees (Rutherford Appleton Laboratory), D. Ritson (Stanford University), A.A. Garren (University of California, Los Angeles), S. Ohnuma (University of Hawaii) 1557

Applying Virtual Prototyping to the Innovative Design of Low Energy Accelerators
M. Fan, D. Chen, Shiqui Li, Y. Xiong, T. Yu (HuaZhong University of Science and Technology) 1560

First Tests of a CW RFQ Injector for the IUCF Cyclotrons
V.P. Derenchuk, V. Anferov, D.L. Friesel, W.P. Jones (Indiana University), R.W. Hamm (AccSys Technology Inc.), J. Staples (LBNL) 1563

Longitudinal Tracking Studies for the AHF Booster Synchrotron
L.J. Rybarcyk (LANL) 1566

The Commissioning Plan for the Spallation Neutron Source Ring and Transport Lines
S. Henderson, S. Assadi, S. Cousineau, V. Danilov, G. Dodson, J. Galambos, J. Holmes, K. Reece, T.J. Shea (ORNL), M. Blaskiewicz, Y.-Y. Lee, Y. Papaphilippou, D. Raparia, J. Wei (BNL) 1569

Exploration of Beam Fault Scenarios for the Spallation Neutron Source Target
S. Henderson, S. Cousineau, V. Danilov, J. Holmes, T. McManamy (ORNL), A. Fedotov, Y.-Y. Lee, D. Raparia, J. Wei (BNL) 1572

Superstructures for High Current FEL Application
J. Sekutowicz, K. Beard, P. Kneisel, G. Wu (Thomas Jefferson National Accelerator Facility), C. Thomas (French Atomic Energy Commission), S. Zheng (Tsinghua University, Beijing) 1575

Investigation of Space Charge Effect in TRIUMF Injection Beamline
R. Baartman, Y.-N. Rao (TRIUMF) 1578

Feasibility Studies for a Radioactive-Ion Storage Ring
M.K. Craddock, D. Kaltchev (TRIUMF) 1581

The TRIUMF 500 MeV Cyclotron: Present Operation and Intensity Upgrade
G. Dutto, R. Baartman, P. Bricault, I. Bylinsky, M. Dombsky, R.E. Laxdal, R. Poirier, Y.-N. Rao, L. Root, R. Ruegg, P. Schmor, M. Stenning, G. Stinson (TRIUMF) 1584

Fermilab Booster Orbit Correction
L. Coney, J. Monroe (Columbia University), W.A. Pellico, E.J. Prebys (FNAL) 1587

CRYRING Progress: Weak Beams, Rare Ions and Ordering
A. K_llberg, G. Andler, L. Bagge, M. BjÅrkhage, M. Blom, H. Danared, P. LÅfgren, A. Pa_l, K.-G. Rensfelt, A. Simonsson, F. ˜sterdahl, M. af Ugglas (Manne Siegbahn Laboratory) 1590

Design of a Racetrack Microtron to Operate Outside the Phase Stability Region
M.N. Martins, P.B. Rios, J. Takahashi (Instituto de Fisica da Universidade de Sao Paulo), L.A.A. Terremoto (Instituto de Pesquisas Energeticas e Nucleares) 1593

Beam Transport System for the IFUSP Microtron
M.N. Martins, M.L. Lopes, P.B. Rios, J. Takahashi (Instituto de Fisica da Universidade de Sao Paulo) 1596

Insights in the Physics of the Dynamic Detuning in SRF Cavities and its Active Compensation
M. Doleans, S.-H. Kim (ORNL) 1599

Contruction of User Facilities for the Proton Beam Utilization of PEFP (Proton Engineering Frontier Project)
K.R. Kim, B.H. Choi, H.R. Lee, K.Y. Nam, B.S. Park (Korea Atomic Energy Research Institute) 1602

The Bunching System Based on the Evanescent Oscillations
S.A. Perezhogin, M.I. Ayzatsky, E.Z. Biller, N.G. Golovko, K. Kramarenko, V.A. Kushnir, V.V. Mitrochenko (NSC KIPT) 1605

Pulsed Electron Accelerator for Radiation Technologies
S. Korenev (STERIS Corporation) 1608

The Real-Time System of Electron Beam Dose Measurements for Industrial Accelerators
S. Korenev (STERIS Corporation), I. Korenev (Northern Illinois University) 1611

Target for Production of X-Rays
S. Korenev (STERIS Corporation) 1614

Simulation Tool for Scanning X-Ray Beams Irradiator
G.F. Popov, V.M. Lazurik, V.T. Lazurik, Yu.V. Rogov (Kharkiv National University) 1616

Radiation Processing of Composites for Orthopaedic Implants
G.F. Popov, A. Avilov, V. Deryuga, N. Popova, V. Rudychev (Kharkiv National University) 1619

Design Studies of an Electrostatic Storage Ring
C.P. Welsch, J. Ullrich (Max-Planck-Institut fuer Kernphysik), H. Schmidt-BÅcking (Institut fuer Kernphysik), C. GlÉÙner, K.-U. Kuehnel, A. Schempp (Institut fur Angewandte Physik) 1622

Up-Graded RHIC Injection Kicker System
H. Hahn, W. Fischer, Y.K. Semertzidis, D. Warburton (BNL) 1625

Super-Invar as a Target for Pulsed High-Intensity Proton Beams
H. Kirk, H. Ludewig, L. Mausner, N. Simos, P. Thieberger, R.J. Weggel (BNL), K.T. McDonald (Princeton University) 1628

A High-Field Pulsed Solenoid Magnet for Liquid Metal Target Studies
H. Kirk, M. Iarocci, J. Scaduto, R.J. Weggel (BNL), G. Mulholland (Applied Cryogenics Technology), P. Titus (MIT Plasma Science and Fusion Center), K.T. McDonald (Princeton University) 1631

Moving Solid Metallic Targets for Pion Production in the Muon Collider / Neutrino Factory Project
P. Thieberger, H. Kirk, R.J. Weggel (BNL), K.T. McDonald (Princeton University) 1634

Injection Acceleration and Extraction of High Intensity Proton Beam for the "Neutrino Facility" Project at BNL
N. Tsoupas, J. Alessi, D. Barton, G. Ganetis, A. Jain, Y.-Y. Lee, I. Marneris, W. Meng, D. Raparia, T. Roser, A.G. Ruggiero, J. Tuozzolo, P. Wanderer, W.T. Weng (BNL) 1637

Advancement of the RHIC Beam Abort Kicker System
W. Zhang, L. Ahrens, J. Mi, B. Oerter, J. Sandberg, D. Warburton (BNL) 1640

Final Results on the CERN PS Electrostatic Septa Consolidation Program
J. Borburgh, M. Hourican, A. Prost (CERN) 1643

LHC Beam Dumping System: Extraction Channel Layout and Acceptance
B. Goddard, M. Gyr, J. Uythoven, R. Veness, W. Weterings (CERN) 1646

Performance of Antiproton Injection and Extraction Transfer Lines of the Recycler Ring at Fermilab
A. Marchionni, T.G. Anderson, G.W. Foster, C. Gattuso, M. Hu, D. Johnson, C. Johnstone, C.S. Mishra, A.R. Oleck, H. Piekarz, M. Syphers, M.J. Yang (FNAL) 1649

Initial Operation of the Fermilab MiniBooNE Beamline
C. Moore, J. Anderson Jr., R. Ducar, R. Ford, T. Kobilarcik, E.J. Prebys, A. Russell, R. Stefanski (FNAL), J. Monroe (Columbia University) 1652

Highly Efficient Crystal Deflector for Channeling Extraction of a Proton Beam from Accelerators
V. Guidi (INFN), W. Scandale (CERN), V.M. Biryukov, Y. Chesnokov, V.I. Kotov (Institute of High Energy Physics, Protvino), C. Malagu, G. Martinelli, M. Stefancich, D. Vincenzi (University of Ferrara) 1655

DAÏNE Beam Test Facility Commissioning
G. Mazzitelli, A. Ghigo, M.A. Preger, F. Sannibale, P. Valente, G. Vignola (INFN) 1658

Fabrication of MEBT Chopper for the Spallation Neutron Source
R. Hardekopf, S. Kurennoy, J. Power, R.J. Roybal, D.L. Schrage (LANL), S. Collins, R. Sherwood (Directed Energy, Inc.) 1661

The Mechanical Design of a Proton Microscope for Radiography at 800 MeV
R. Valdiviez, D. Barlow, B. Blind, C. Espinoza, J. Gomez, A. Jason, T. Mottershead, F. Sigler (LANL) 1664

Ionization Cross-Sections in Ion-Atom Collisions for High Energy Ion Beams
I.D. Kaganovich (Princeton University), R.C. Davidson, E.A. Startsev (Plasma Physics Laboratory, Princeton University) 1667

A Proposal for an Additional Beamline to the TRIUMF ISAC Facility
G. Stinson, P. Bricault (TRIUMF) 1670

Electro-Mechanical Design for Injection in the University of Maryland Electron Ring
M. Walter, S. Bernal, T. Godlove, I. Haber, R.A. Kishek, H. Li, P.G. O'Shea, B. Quinn, M. Reiser, A. Valfells, Y. Zou (University of Maryland) 1673

Beam Optics Design on a New Injection Scheme for the University of Maryland Electron Ring (UMER)
H. Li, S. Bernal, T. Godlove, R.A. Kishek, P.G. O'Shea, M. Reiser, M. Walter (University of Maryland) 1676

Beam Extraction of the POP FFAG with a Massless Septum
Y. Yonemura, T. Adachi, M. Aiba, S. Machida, Y. Mori, A. Muto, J. Nakano, C. Ohmori, I. Sakai, Y. Sato, M. Sugaya, A. Takagi, R. Ueno, T. Uesugi, A. Yamazaki, T. Yokoi, M. Yoshimoto, Y. Yuasa (KEK), K. Koba (FNAL), M. Matoba (Kyushu University) 1679

Heavy Ion Beams in the LHC
J.M. Jowett, J.-B. Jeanneret, K. Schindl (CERN) 1682

Abort Gap Studies and Cleaning during RHIC Heavy Ion Operation
A. Drees, L. Ahrens, R. Fliller III, W. Fu, G. Heppner (BNL), V. Kain (CERN) 1685

Results from Vernier Scans at RHIC during the PP Run 2001-2002
A. Drees, B. Fox, Z. Xu (BNL), H. Huang (Yale University) 1688

New Results from Crystal Collimation at RHIC
R. Fliller III, A. Drees, D. Gassner, L. Hammons, G. McIntyre, S. Peggs, D. Trbojevic (BNL), V.M. Biryukov, Y. Chesnokov, V. Terekov (Institute of High Energy Physics, Protvino) 1691

Commissioning of a First-Order Transition Jump in RHIC
J. Kewisch, C. Montag (BNL) 1694

Commissioning Spin Rotators in RHIC
W.W. MacKay, L. Ahrens, M. Bai, E.D. Courant, W. Fischer, H. Huang, A.U. Luccio, C. Montag, F. Pilat, V. Ptitsyn, T. Roser, T. Satogata, D. Trbojevic, J. van Zeijts (BNL) 1697

Design of a Fast Chromaticity Jump in RHIC
C. Montag, D. Bruno, G. Ganetis, J. Kewisch, W. Louie (BNL) 1700

Nonlinear Effects in the RHIC Interaction Regions: Measurement and Correction
F. Pilat, S. Binello, P. Cameron, V. Ptitsyn (BNL) 1703

Commissioning of RHIC Deuteron-Gold Collisions
T. Satogata, L. Ahrens, M. Bai, J. Beebe-Wang, M. Blaskiewicz, J.M. Brennan, K.A. Brown, D. Bruno, P. Cameron, J. Cardona, R. Connolly, A. Drees, W. Fischer, R. Fliller III, G. Ganetis, C. Gardner, J. Glenn, H. Hahn, T. Hayes, H. Huang, U. Iriso-Ariz, W.W. MacKay, A. Marusic, R. Michnoff, C. Montag, F. Pilat, V. Ptitsyn, R. Roser, K.S. Smith, S. Tepikian, D. Trbojevic, N. Tsoupas, S.Y. Zhang, J. van Zeijts (BNL) 1706

Concept Design of the Target/Horn System for the BNL Neutrino Oscillation Experiment
N. Simos, A. Carroll, M. Diwan, S.A. Kahn, H. Kirk, H. Ludewig, D. Raparia, W.T. Weng (BNL), K.T. McDonald (Princeton University), G. Evangelakis (University of Ioannina) 1709

High Luminosity Ù*=0.5m RHIC Insertions
S. Tepikian, H. Huang, W.W. MacKay, F. Pilat, V. Ptitsyn, T. Satogata, D. Trbojevic, J. van Zeijts (BNL) 1712

The RHIC Injector Accelerator Configurations, and Performance for the RHIC 2003 Au-d Physics Run
L. Ahrens, J. Alessi, J. Benjamin, M. Blaskiewicz, J.M. Brennan, K.A. Brown, C. Carlson, T. D'Ottavio, J. DeLong, B. Frak, C. Gardner, J. Glenn, M. Harvey, T. Hayes, H. Hseuh, P. Ingrassia, D. Lowenstein, W.W. MacKay, G. Marr, J. Morris, T. Roser, T. Satogata, G. Smith, K.S. Smith, D. Steski, P. Thieberger, N. Tsoupas, K. Zeno, S.Y. Zhang (BNL) 1715

The LHC Proton Beam in the CERN SPS: an Update
G. Arduini, P. Baudrenghien, T. Bohl, P. Collier, K. Cornelis, W. HÅfle, T. Linnecar, E. Shaposhnikova, J. Tuckmantel, J. Wenninger (CERN) 1718

Protection Devices in the Transfer Lines to the LHC
H. Burkhardt, B. Goddard, V. Mertens (CERN) 1721

PS 13.3-20 MHz RF Systems for LHC
M. Morvillo, R. Garoby, D. Grier, M. Haase, A. Krusche, P. Maesen, M. Paoluzzi, C. Rossi (CERN) 1724

Present Understanding of Electron Cloud Effects in the Large Hadron Collider
F. Zimmermann, G. Arduini, V. Baglin, E. Benedetto, R. Cimino, P. Collier, I. Collins, K. Cornelis, B. Henrist, N. Hilleret, B. Jenninger, J.M. Jimenez, A. Rossi, F. Ruggiero, G. Rumolo, D. Schulte (CERN) 1727

Analysis of the b2 Correction in the Tevatron
P. Bauer, G. Annala, J. DiMarco, R. Hanft, D. Harding, M. Lamm, M. Martens, P. Schlabach, D. Still, M. Tartaglia, J. Tompkins, G. Velev, M. Xiao (FNAL), L. Bottura, F. Zimmermann (CERN) 1730

Beam Loss and Backgrounds in the CDF and D0 Detectors due to Nuclear Elastic Beam-Gas Scattering
A. Drozhdin, V.A. Lebedev, N.V. Mokhov, L.Y. Nicolas, S.I. Striganov, A.V. Tollestrup (FNAL) 1733

Slip Stacking Experiments at Fermilab Main Injector
K. Koba, B. Barnes, T. Berenc, B. Chase, I. Kourbanis, J.A. MacLachlan, K. Meisner, J. Steimel (FNAL) 1736

Observations on the Luminosity Lifetimes and Emittance Growth Rates at the Tevatron
P. Lebrun, V.A. Lebedev, V. Shiltsev, J. Slaughter (FNAL) 1739

Accelerator Related Backgrounds in the LHC Forward Detectors
N.V. Mokhov, A. Drozhdin, I.L. Rakhno (FNAL), D. Macina (CERN) 1742

Mitigation of Effects of Beam-Induced Energy Deposition in the LHC High-Luminosity Interaction Regions
N.V. Mokhov, J.S. Kerby, I.L. Rakhno, J.B. Strait (FNAL) 1745

Energy Deposition Limits in a Nb_3Sn Separation Dipole in Front of the LHC High-Luminosity Inner Triplet
N.V. Mokhov, V.V. Kashikhin, I.L. Rakhno, J.B. Strait, S. Yadav, A.V. Zlobin (FNAL), R. Gupta, M. Harrison (BNL), O.S. BrËning, R. Ruggiero (CERN) 1748

Longitudinal Bunch Dynamics in the Tevatron
R. Moore, V. Balbekov, A. Jansson, V.A. Lebedev, K.Y. Ng, V. Shiltsev, C.Y. Tan (FNAL) 1751

Beam Losses at Injection Energy and during Acceleration in the Tevatron
T. Sen, P. Lebrun, R. Moore, V. Shiltsev, M. Syphers, X.L. Zhang (FNAL), W. Fischer (BNL), F. Schmidt, F. Zimmermann (CERN) 1754

Experimental Studies of Beam-Beam Effects in the Tevatron
T. Sen, Y. Alexahin, V. Shiltsev, M. Xiao, X.L. Zhang (FNAL), F. Schmidt, F. Zimmermann (CERN) 1757

Theoretical Studies of Beam-Beam Effects in the Tevatron at Collision Energy
T. Sen, B. Erdelyi, M. Xiao (FNAL) 1760

Tevatron Run II Luminosity, Emittance and Collision Point Size
J. Slaughter, J. Estrada, K. Genser, A. Jansson, P. Lebrun, J.C. Yun (FNAL), S. Lai (University of Toronto) 1763

Correction Magnets for the Fermilab Recycler Ring
J.T. Volk, G.W. Foster, C. Gattuso, H. Glass, D. Johnson, C.S. Mishra, M.J. Yang (FNAL) 1766

Antiproton Acceleration in the Fermilab Main Injector Using 2.5 MHz (H=28) and 53 MHz (H=588) RF Systems
V. Wu, C.M. Bhat, B. Chase, J. Dey, J.A. MacLachlan, K. Meisner, J. Reid (FNAL) 1769

Tevatron Beam-Beam Simulations at Injection Energy
M. Xiao, B. Erdelyi, T. Sen (FNAL) 1772

Simulations of Octupole Compensation for Head-Tail Instability at the Tevatron
M. Xiao, T. Sen (FNAL), F. Schmidts (CERN) 1775

The Special Applications of Tevatron Electron Lens in Collider Operation
X.L. Zhang, V. Shiltsev (FNAL), F. Zimmermann (CERN), K. Bishofberger (University of California, Los Angeles) 1778

Upgrades of the Tevatron Electron Lens
X.L. Zhang, J. Crisp, J. Fitzgerald, G. Kuznetsov, M. Olson, H. Pfeffer, G. Saewert, A. Semenov, V. Shiltsev, N. Solyak, D. Wildman (FNAL), M. Tiunov (BINP), E. Kashtanov, S. Kozub, V. Sytnik, L. Tkachenko (Institute of High Energy Physics, Protvino), K. Bishofberger (University of California, Los Angeles) 1781

Design Study of 1 MHz Induction Cavity for Induction Synchrotron
K. Torikai, Y. Arakida, S. Inagaki, J. Kishiro, K. Koseki, E. Nakamura, K. Takayama, T. Toyama, M. Wake (KEK), K. Ishibashi (Kyushu University) 1784

Progress in Designing a Muon Cooling Ring with Lithium Lenses
Y. Fukui, D. Cline, A.A. Garren (University of California, Los Angeles), H. Kirk (BNL) 1787

Longitudinal Bunch Rotation Scheme in a Muon Cooling Ring
Y. Fukui (University of California, Los Angeles) 1790

Gaseous Hydrogen for Muon Beam Cooling
R.P. Johnson, R.E. Hartline (Muons, Inc.), C. Ankenbrandt, M. Kuchnir, A. Moretti, M. Popovic (FNAL), M. Alsharo'a, E. Black, D.M. Kaplan (Illinois Institute of Technology) 1792

MICE: The International Muon Ionization Cooling Experiment
Y. Torun (Illinois Institute of Technology) 1795

Muon Cooling Research and Development
M.A.C. Cummings (Northern Illinois University), D.M. Kaplan (Illinois Institute of Technology) 1798

Bench Measurements of Low Frequency Transverse Impedance
A. Mostacci (University of Rome), U. Iriso-Ariz (BNL), F. Caspers, L. Vos (CERN) 1801

A Very Fast Ramping Muon Synchrotron for a Neutrino Factory
D.J. Summers (University of Mississippi), J.S. Berg, R.B. Palmer (BNL), A.A. Garren (University of California, Los Angeles) 1804

A POP Experiment Scenario of Induction Synchrotron at the KEK 12GeV-PS
K. Takayama, Y. Arakida, S. Igarashi, D. Iwashita, J. Kishiro, K. Koseki, E. Nakamura, M. Sakuda, H. Sato, Y. Shimosaki, M. Shirakata, K. Torikai, T. Toyama, M. Wake (KEK), K. Horioka, M. Shiho (Tokyo Institute of Technology) 1807

New RF Design for 11.4GHz Dielectric Loaded Accelerator
W. Gai, C. Jing, R. Konecny, W. Liu, J.G. Power (ANL) 1810

A Compact Wakefield Measurement Facility
J.G. Power, W. Gai, K.-J. Kim, J.W. Lewellen, S.V. Milton, J. Simpson, H. Wang (ANL), H. Carter, D. Finley (FNAL) 1813

FFAG Lattice for Muon Acceleration with Distributed RF
D. Trbojevic, J.S. Berg, M. Blaskiewicz, E.D. Courant (BNL), R. Palmer (CERN), A.A. Garren (LBNL) 1816

Proposal for a Pre-Bunched Laser Wakefield Acceleration Experiment at the BNL DUV-FEL Facility
X.J. Wang, B. Sheehy, Z. Wu (BNL), W. Gai (ANL), A. Ting (Naval Research Laboratory) 1819

Characteristics of Gradient Undulator
A. Mikhailichenko (Cornell University) 1822

Short X and Gamma Production with Swept Laser Bunch
A. Mikhailichenko (Cornell University) 1825

Damping Ring for Generation of Positroniums and Investigation of Fermi-Degeneration in Moving Beams
A. Mikhailichenko (Cornell University) 1828

Longitudinal Dynamics in an FFAG Accelerator under Conditions of Rapid Acceleration and Fixed, High RF
C. Johnstone (FNAL), S. Koscielniak (TRIUMF) 1831

The Integration of Liquid and Solid Muon Absorbers into a Focusing Magnet of a Muon Cooling Channel
M.A. Green (LBNL), R.B. Palmer (BNL), E. Black, M.A. Cummings, D.M. Kaplan (Illinois Institute of Technology), S. Ishimoto (KEK), J.H. Cobb, W. Lau, S. Yang (Oxford University) 1834

Lattices for Milli-eV Neutral Molecules
H. Nishimura, H. Gould, J.G. Kalnins, G.R. Lambertson (LBNL) 1837

Shaping of Pulses in Optical Grating-Based Laser Systems for Optimal Control of Electrons in Laser Plasma Wake-Field Accelerator
C. Toth, J. Faure, C.G.R. Geddes, W.P. Leemans, J. van Tilborg (LBNL) 1840

A Fundamental Theorem on Particle Acceleration
M. Xie (LBNL) 1843

Particle-In-Cell Simulations of Optical Injectors for Plasma Accelerators
D.F. Gordon, R.F. Hubbard, T. Jones, P. Sprangle, A. Ting (Naval Research Laboratory), B. Hafizi (Icarus Research, Inc.) 1846

A Simulation for Electron Trapping and Acceleration in Parabolic Density Profile and Ongoing Experimental Plan
J.U. Kim, N. Hafz, C. Kim, G.H. Kim, H.J. Lee, H. Suk (Korea Electrotechnology Research Institute) 1849

Self-Injection of Electrons from Evolution of Wake Wave

C. Kim, I.S. Ko (Pohang Accelerator Laboratory), G.H. Kim, J.U. Kim, H.J. Lee, H. Suk (Korea Electrotechnology Research Institute) 1852

Photonic Crystal Laser Accelerator Structures

B. Cowan, M. Javanmard, R.H. Siemann (SLAC) 1855

The ORION Facility

R.J. Noble, E. Colby, D.T. Palmer, R.H. Siemann, D. Walz (SLAC), R. Byer (Stanford University), C. Joshi, W.B. Mori, J.B. Rosenzweig (University of California, Los Angeles), T.C. Katsouleas (University of Southern California) 1858

Miniaturization Techniques for Accelerators

J. Spencer (SLAC), J. Mansell (Intellite Inc), W. Ha, T. Plettner, J. Wisdom (Stanford University) 1861

Plasma Wakefield Acceleration of an Intense Positron Beam: Correlation Between Time-Resolved and Time-Integrated Diagnostics

B.E. Blue, C. Clayton, C. Huang, C. Joshi, K.A. Marsh, W.B. Mori (University of California, Los Angeles), F.-J. Decker, M.J. Hogan, R. Iverson, C.L. O'Connell, R.H. Siemann, D. Walz (SLAC), T.C. Katsouleas, P. Muggli (University of Southern California) 1864

Status of the Inverse Free Electron Laser Experiment at the Neptune Laboratory

P. Musumeci, C. Pellegrini, J.B. Rosenzweig, S. Totchisky, G. Travish, R. Yoder (University of California, Los Angeles), S. Tolmachev, A. Varfolomeev, A. Varfolomeev, Jr., T. Yarovoi (RRC Kurchatov Institute) 1867

The UCLA/NICADD Plasma Density Transition Trapping Experiment

M.C. Thompson, W. Lu, W.B. Mori, J.B. Rosenzweig, G. Travish (University of California, Los Angeles), N. Barov (Northern Illinois University) 1870

Acceleration of Injected Electrons in a Laser Beatwave Experiment

S.Ya. Tochitsky, C. Clayton, C.V. Filip, C. Joshi, K.A. Marsh, P. Musumeci, R. Narang, C. Pellegrini, J.B. Rosenzweig, R. Yoder (University of California, Los Angeles) 1873

A Proposal to Experimentally Demonstrate a Novel Regime of Electron Vacuum Acceleration by Using a Tightly Focused Laser Beam

F. Zhou, D. Cline, L. Shao (University of California, Los Angeles), H.K. Ho (Fudan University) 1876

Surface Roughness Effect on a Moving Bunch

S. Banna, L. Sch€chter (Technion - Israel Institute of Technlology), R.H. Siemann (SLAC) 1879

Numerical Study of Interference between Transition Radiation and Cerenkov Wake Field Radiation in a Planar Dielectric Structure

J.-M. Fang, T.C. Marshall (Columbia University), V.P. Tarakanov (ITES, RAS), J.L. Hirshfield (Omega-P, Inc. and Yale University) 1882

Generation of Single Pulse Particle Beams in a Plasma Channel by Laser Injection in Laser Wakefield Accelerators

R. Giacone, J.R. Cary, C. Nieter (University of Colorado at Boulder), E. Esarey, G. Fubiani, W.P. Leemans, C.B. Schroeder (LBNL) 1885

A Method for Tuning Dielectric Loaded Accelerating Structures

A. Kanareykin (Euclid Concepts LLC), W. Gai, J.G. Power (ANL), E. Nenasheva (Ceramics Ltd., St. Petersburg), S. Karmanenko, I. Sheinman (St. Petersburg Electrical Engineering University) 1888

A Tunable Dielectric Structure with Built in Transverse Mode Suppression

A. Kanareykin (Euclid Concepts LLC), A. Altmark, I. Sheinman (St. Petersburg Electrical Engineering University) 1891

Transformer Ratio Enhancement Experiment

A. Kanareykin (Euclid Concepts LLC), W. Gai, J.G. Power (ANL), E. Nenasheva (Ceramics Ltd., St. Petersburg), A. Altmark (St. Petersburg Electrical Engineering University) 1894

A Double-Layered, Planar Dielectric Loaded Accelerating Structure
A. Kanareykin (Euclid Concepts LLC), A. Altmark, I. Sheinman (St. Petersburg Electrical Engineering University) 1897

Generation of an Ultra-Short Relativistic-Electron-Bunch by a Laser Wakefield
A.G. Khachatryan, K.-J. Boller, F.A. van Goor (University of Twente) 1900

Charged Particle Interaction with a Chirped Electromagnetic Pulse
A.G. Khachatryan, K.-J. Boller, F.A. van Goor (University of Twente) 1903

Laser Wakefield Acceleration Experiment at KERI
G.H. Kim, C. Kim, J.U. Kim, H.J. Lee, H. Suk (Korea Electrotechnology Research Institute) 1906

STELLA-II: Demonstration of Monoenergetic Laser Acceleration
W.D. Kimura, L.P. Campbell, C.E. Dilley, S.C. Gottschalk, D.C. Quimby (STI Optronics, Inc.), M. Babzien, I. Ben-Zvi, J.C. Gallardo, K.P. Kusche, I.V. Pogorelsky, J. Skaritka, V. Yakimenko (BNL), R.H. Pantell (Stanford University), D. Cline, F. Zhou (University of California, Los Angeles), L.C. Steinhauer (University of Washington) 1909

Electron Acceleration by Laser Wakefields in Tapered Plasma Densities
H. Suk, C. Kim, G.H. Kim, J.U. Kim, H.J. Lee (Korea Electrotechnology Research Institute) 1912

Focusing of 28.5 GeV Electron and Positron Beams in Meter-Long Plasmas
P. Muggli (University of Southern California) 1915

VORPAL: A Computational Tool for the Study of Advanced Accelerator Concepts
C. Nieter, J.R. Cary (University of Colorado at Boulder) 1918

Towards Realizing Optical Injection of Electrons in Resonantly Excited Plasma Wakefields
N. Saleh, S. Chen, W. Theobald, D. Umstadter, C. Widjaja, V. Yanovsky, P. Zhang (University of Michigan) 1921

Experimental and Numerical Studies of Dielectric Wake Field Acceleration Devices
S.V. Shchelkunov, J.-M. Fang, T.C. Marshall (Columbia University), J.L. Hirshfield (Omega-P, Inc. and Yale University) 1924

Multicavity Proton Cyclotron Accelerator
C. Wang (Yale University), V.P. Yakovlev (Omega-P, Inc.), J.L. Hirshfield (Omega-P, Inc. and Yale University) ... 1927

Stability of Electron Orbits in the Strong Wake Fields Generated by a Train of FSEC Bunches
C. Wang (Yale University), T.C. Marshall (Columbia University), J.L. Hirshfield (Omega-P, Inc. and Yale University) 1930

Modeling of Beam-Ionized Sources for Plasma Accelerators
S. Deng, O. Erdem, T.C. Katsouleas, P. Muggli (University of Southern California), C.D. Barnes, F.-J. Decker, P. Emma, M.J. Hogan, R. Iverson, P. Krejcik, C.L. O'Connell, R.H. Siemann, D. Walz (SLAC), C. Clayton, C. Huang, D. Johnson, C. Joshi, W. Lu, K.A. Marsh, W.B. Mori (University of California, Los Angeles) .. 1933

Magnetic Design of a Superconducting AGS Snake
R. Gupta, A.U. Luccio, W.W. MacKay, G. Morgan, K. Power, T. Roser, E. Willen (BNL), M. Okamura (RIKEN Accelerator Research Facility) 1936

Engineering of the AGS Snake Coil Assembly
M. Anerella, R. Gupta, P. Kovach, A. Marone, S. Plate, K. Power, J. Schmalzle, E. Willen (BNL) 1939

Status of the LHC Main Dipole Pre-Series Production
M. Modena, M. Bajko, M. Cornelis, G. De Rijk, P. Fessia, J. Miles, P. Pugnat, J. Rinn, F. Savary, A. Siemko, E. Todesco, J. Vlogaert (CERN) 1942

The LHC Test String 2: Results from Run 2

R. Saban, E. Blanco-Vinuela, F. Bordry, L. Bottura, D. Bozzini, C. Calzas-Rodriguez, E. Carlier, R. Denz, V. Granata, R. Herzog, Q. King, D. Milani, B. Puccio, F. Rodriguez-Mateos, R. Schmidt, L. Serio, F. Tegenfeldt, H. Thiesen, R. van Weelderen (CERN) 1945

Performance of the First LHC Main Quadrupoles Made in Industry

T. Tortschanoff, K.-M. Schirm, W. Venturini-Delsolaro (CERN), R. Burgmer, H.-U. Klein, D. Krischel, B. Schellong, P. Schmidt, T. Stephani (ACCEL Instruments GmbH), M. Durante, M. Peyrot, J.-M. Rifflet, F. Simon (CE Saclay) 1948

Influence of Azimuthal Coil Size on Skew Multipoles in the LHC Dipoles

I. Vanenkov, C. Vollinger (CERN) 1951

Design Considerations for the CESR-c Wiggler Magnets

J. Crittenden, A. Mikhailichenko, A. Temnykh (Cornell University) 1954

Short Period SC Undulator

A. Mikhailichenko (Cornell University) 1957

Improvements in SC Wiggler Performance

A. Mikhailichenko (Cornell University) 1960

To the Radiation of Particles in a Solenoid

A. Mikhailichenko (Cornell University), E. Bessonov (Moscow FIAN) 1963

Conceptual Design of Large-Bore Superconducting Quadrupoles with Active Magnetic Shielding for the AHF

V.S. Kashikhin, G. Ambrosio, N. Andreev, S. Bhashyam, V.V. Kashikhin, T. Peterson, J. Tompkins, A.V. Zlobin (FNAL), A. Jason, J.P. Kelley, P. Walstrom (LANL) 1966

Field Quality of the LHC Inner Triplet Quadrupoles being Fabricated at Fermilab

G. Velev, R. Bossert, R. Carcagno, J. Carson, D. Chichili, J. DiMarco, S. Feher, H. Glass, V.V. Kashikhin, J.S. Kerby, M. Lamm, T. Nicol, A. Norbrega, D. Orris, T. Page, T. Peterson, R. Rabehl, P. Schlabach, J.B. Strait, C. Sylvester, M. Tartaglia, J. Tompkins, S. Yadav, A.V. Zlobin (FNAL) 1969

Measurements of Field Decay and Snapback Effect on Tevatron Dipole Magnets

G. Velev, G. Annala, P. Bauer, R. Carcagno, J. DiMarco, H. Glass, R. Hanft, R. Kephart, M. Lamm, M. Martens, P. Schlabach, M. Tartaglia, J. Tompkins (FNAL) 1972

Aperture Limitations for 2nd Generation Nb_3Sn LHC IR Quadrupoles

A.V. Zlobin, V.V. Kashikhin, J.B. Strait (FNAL) 1975

Status of LHC Low-Beta Quadrupole Magnets, MQXA, at KEK

N. Ohuchi, Y. Ajima, N. Higashi, M. Iida, N. Kimura, T. Nakamoto, T. Ogitsu, H. Ohhata, T. Shintomi, S. Sugawara, K. Sugita, K. Tanaka, A. Terashima, K. Tsuchiya, A. Yamamoto (KEK), T. Fujii, E. Hashiguchi, T. Kanahara, S. Murai, W. Odajima, T. Orikasa (Toshiba Corporation) 1978

Force Free Design of Super-Ferric Beam Line Magnet

M. Wake, H. Sato, K. Takayama (KEK), H. Piekarz, R. Yamada (FNAL) 1981

Field Quality Analysis of a Second Generation IR Quadrupole for the LHC

P. Ferracin, S. Caspi, L. Chiesa, D.R. Dietderich, S.A. Gourlay, R.R. Hafalia, A.F. Lietzke, A.D. McInturff, G. Sabbi, R.M. Scanlan (LBNL) 1984

Superconducting Solenoids for the MICE Channel

M.A. Green (LBNL), R.B. Palmer (BNL), J.M. Rey (CE Saclay), P. Fabbricatore, S. Farinon (INFN), G. Barr (Oxford University), D.E. Baynham, J.H. Rockford (Rutherford Appleton Laboratory) 1987

Superconducting Focusing Quadrupoles for Heavy Ion Fusion Experiments
G. Sabbi, A. Faltens, M.A. Leitner, A.F. Lietzke, P.A. Seidl (LBNL), R.B. Meinke (Advanced Magnet Lab, Inc.), J.J. Barnard, S.M. Lund, N. Martovetsky (LLNL), C. Gung, J. Minervini, A. Radovinsky, J. Schultz (MIT Plasma Science and Fusion Center) 1990

The Strongest Permanent Dipole Magnet
M. Kumada (National Institute of Radiological Sciences (NIRS)), Y. Iwashita (Kyoto University), M. Aoki, E. Sugiyama (Sumitomo Special Metal Co.,Ltd.) 1993

Superconducting Double-Helix Accelerator Magnets
R.B. Meinke, M.J. Ball, C.L. Goodzeit (Advanced Magnet Lab, Inc.) 1996

Measurements of Beam Driven Hydrodynamic Turbulence
J. Norem (ANL), E. Black (Illinois Institute of Technology), L. Bandura, M.A.C. Cummings (Northern Illinois University), D. Errede (University of Illinois) 1999

Muon Cooling in the RFOFO Ring Cooler
R.C. Fernow, J.S. Berg, J.C. Gallardo, R.B. Palmer (BNL) 2002

Layout and Optics for the RHIC Electron Cooler
J. Kewisch, I. Ben-Zvi, X. Chang, C. Montag, D. Wang (BNL) 2005

Muon Storage Rings for 6D Phase-Space Cooling
H. Kirk (BNL), D. Cline, Y. Fukui, A.A. Garren (University of California, Los Angeles) 2008

Effect of Solenoid Field Errors on Electron Beam Temperatures in the RHIC Electron Cooler
C. Montag, J. Kewisch (BNL) 2011

Lithium Lenses Based Muon Cooling Channel
V. Balbekov (FNAL) 2014

Investigation and Simulation of Muon Cooling Rings with Tilted Solenoids
V. Balbekov (FNAL) 2017

Commissioning of the Fermilab Electron Cooler Prototype Beam Line
S. Nagaitsev, A. Burov, K. Carlson, B. Kramper, T. Kroc, J. Leibfritz, M. McGee, G. Saewert, C.W. Schmidt, A. Shemyakin, A. Warner (FNAL), V. Tupikov (BINP), S. Seletsky (University of Rochester) 2020

Analysis of a Grid Window Structure for RF Cavities in a Muon Cooling Channel
A. Ladran, D. Li, J. Staples, S. Virostek, M. Zisman (LBNL), A. Moretti (FNAL), R.A. Rimmer (Thomas Jefferson National Accelerator Facility) 2023

Longitudinal Cooling of a Strongly Magnetized Electron Plasma
Jinhyung Lee, J.R. Cary (University of Colorado at Boulder) 2026

The Advanced Photon Source Injector Test Stand: Phase Two
S. Berg, T. Barsz, D. Briddick, M. Givens, G. Goeppner, A. Grelick, W. Jansma, J.W. Lewellen, A. Lopez, M. Martens, W. Michalek, S. Wesling (ANL) 2029

A New High Intensity Electron Beam for Wakefield Acceleration Studies
M.E. Conde, W. Gai, C. Jing, R. Konecny, W. Liu, J.G. Power, H. Wang, Z. Yusof (ANL) 2032

Energy-Spread Compensation of a Thermionic-Cathode RF Gun
J.W. Lewellen (ANL) 2035

A Flexible Injector Test Stand Design
J.W. Lewellen, K. Beczek, S. Berg, D. Briddick, R. Dortwegt, M. Givens, A. Grelick, A. Nassiri, S. Pasky, T.L. Smith (ANL) 2038

Ultrashort Electron Bunches with Low Longitudinal Emittance in Multi-Cell Superconducting RF Guns
V.N. Volkov (BINP) 2041

Generation of Sub-Picosecond Electron Bunches in Superconducting RF Photocathode Injector
V.N. Volkov (BINP) 2044

Tests of Niobium Cathode for the Superconducting Radio Frequency Gun
Q. Zhao, T. Srinivasan-Rao (BNL), M. Cole (Advanced Energy Systems) 2047

The Analysis of the Cross-Talk in a RF Gun Superconducting Cavity
Y. Zhao (BNL), M. Cole (Advanced Energy Systems) 2050

Simulation of High Charge Extraction from the ELSA RF Photo-Injector
P. Balleyguier, Ph. Guimbal (French Atomic Energy Commission) 2053

Emittance Growth Study Using 3DE Code for the ERL Injector Cavities with Various Coupler Configurations
Z. Greenwald, D.L. Rubin (Cornell University) 2056

Dipole-Mode-Free and Kick-Free 2-Cell Cavity for the SC ERL Injector
V. Shemelin, S. Belomestnykh, R.L. Geng, M. Liepe, H. Padamsee (Cornell University) 2059

High Brightness, High Current Injector Design for the Cornell ERL Prototype
C.K. Sinclair, I. Bazarov (Cornell University) 2062

Emittance Growth due to the Field Asymmetry in the TTF RF Gun
J.-P. Carneiro (DESY) 2065

Experimental Studies of RF Breakdowns in the Coupler of the TTF RF Gun
J.-P. Carneiro, S. Schreiber (DESY), D. Edwards, I. Gonin (FNAL) 2068

On the Photocathodes Used at the TTF Photoinjector
S. Schreiber (DESY), P. Michelato, L. Monaco, D. Sertore (INFN) 2071

Measurement of the Beam Energy Spread in the TTF Photo-injector
M. HËening (FNAL), H. Schlarb (DESY) 2074

Beam Dynamics Studies for the SPARC Project
M. Ferrario, M. Biagini, M. Boscolo, V. Fusco, S. Guiducci, M. Migliorati, L. Serafini, C. Vaccarezza (INFN), R. Bartolini, L. Giannessi, M. Quattromini, C. Ronsivalle (Ente Nazionale per le Nuove Tecnologie l'Energia e l'Ambiente), C.G. Limborg (SLAC) 2077

Study and Design of Room Temperature Cavities for an RF Compressor Prototype
D. Giove, D. Alesini, F. Alessandria, A. Bacci, C. De Martinis, M. Ferrario, A. Gallo, F. Marcellini, M. Mauri, L. Serafini (INFN) 2080

RF Surface Resistance of Copper-on-Beryllium at Cryogenic Temperatures Measured by a 22-GHz Demountable Cavity
J.-F. Liu, F.L. Frawczyk, S. Kurennoy, D.L. Schrage, A.H. Shapiro, T. Tajima, R.L. Wood (LANL) 2083

An Injector for the Proposed Berkeley Ultrafast X-Ray Light Source
S.M. Lidia, J. Corlett, J. Pusina, J. Staples, A. Zholents (LBNL) 2086

Emittance Compensation Studies of Photoinjector Beams with Angular Momentum
S.M. Lidia (LBNL) 2089

The LBNL Femtosource 10 kHz Photoinjector
J. Staples, S.M. Lidia, S. Virostek (LBNL), R.A. Rimmer (Thomas Jefferson National Accelerator Facility) 2092

Initial Testing of a Field Symmetrized Dual Feed 2 MeV 17 GHz RF Gun
A.S. Kesar, S. Korbly, I. Mastovsky, R.J. Temkin (MIT Plasma Science and Fusion Center), J. Haimson, B. Mecklenburg (Haimson Research Corporation) 2095

Current Nanopulse Generation in RF Electron Gun with Metal-Dielectric Cathode
I.V. Khodak, M.I. Ayzatsky, V.A. Kushnir, V.V. Mitrochenko, V.F. Zhiglo (NSC KIPT) 2098

An Electron Source for a Laser Accelerator
E. Colby, C.D. Barnes, C.M. Sears (SLAC) 2101

Analysis of Slice Emittance Measurements for the SLAC Gun Test Facility
D. Dowell, P.R. Bolton, J. Clendenin, S. Gierman, C.G. Limborg, B.F. Murphy, J.F. Schmerge (SLAC) 2104

Experimental Measurements of the ORION Photoinjector Drive Laser Oscillator Subsystem
D.T. Palmer, R. Akre (SLAC) 2107

Status of the UCLA PEGASUS Laboratory
G. Andonian, P. Frigola, S. Reiche, J.B. Rosenzweig, S. Telfer, G. Travish (University of California, Los Angeles) 2110

The UCLA Pegasus Plane-Wave Transformer Photoinjector
G. Travish, G. Andonian, P. Frigola, S. Reiche, J.B. Rosenzweig, S. Telfer (University of California, Los Angeles) 2112

Experimental Characterization of the Electron Source at the Photo Injector Test Facity at DESY Zeuthen
M. Krasilnikov, K. Abrahamyan, J. B€hr, I. Bohnet, J.-P. Carneiro, K. Floettmann, U. Gensch, H.J. Grabosch, J.H. Han, V. Miltchev, A. Oppelt, B. Petrossyan, J. Rossbach, S. Schreiber, F. Stephan (DESY), M.v. Hartrott, E. Jaeschke, D. Kr€mer (BESSY), D. Lipka (DESY Zeuthen), P. Michelato, C. Pagani, D. Sertore (INFN), I. Tsakov (INRNE Sofia), H. Redlin, W. Sandner, R. Schumann, I. Will (Max-Born-Institute), R. Cee, S. Setzer, T. Weiland (Technische U. Darmstadt) 2114

Velocity Bunching Experiment at the Neptune Laboratory
P. Musumeci, J.B. Rosenzweig, R. Yoder (University of California, Los Angeles) 2117

An Integrated Traveling-Wave Photoinjector
S. Telfer (Xgamma Corporation and UCLA) 2120

Wedge-Shaped, Large-Aperture, Dipole Magnet Design for the Jefferson Lab FEL Upgrade
D. Yu, Y. Luo, D. Newsham, A.V. Smirnov (DULY Research Inc.), G. Biallas (Thomas Jefferson National Accelerator Facility) 2123

Parmela Simulations of a PWT Photoinjector
D. Yu, Y. Luo, D. Newsham (DULY Research Inc.), J. Clendenin (SLAC) 2126

Development of a Polarized Electron Gun Based on an S-Band PWT Photoinjector
D. Yu, Y. Luo, D. Newsham, A.V. Smirnov (DULY Research Inc.), J. Clendenin, D. Schultz (SLAC) 2129

Design of a DC/RF Photoelectron Gun
D. Yu, Y. Luo, D. Newsham, A.V. Smirnov, J. Yu (DULY Research Inc.), J.W. Lewellen (ANL), J. Smedley, T. Srinivasan-Rao (BNL), A. Zholents (LBNL) 2132

Short Multipole Magnet Designs for JLAB FEL Upgrade
D. Yu, Y. Luo, D. Newsham, A.V. Smirnov (DULY Research Inc.), G. Biallas, R. Wines (Thomas Jefferson National Accelerator Facility) 2135

Building a Family of Corrector Magnets for SNS Facility
S.V. Badea, J. Alduino, N. Tsoupas, J. Tuozzolo (BNL) 2138

Design of an Ultra High Vacuum Compatible Copper Septum Magnet
M. Mapes, N. Tsoupas (BNL) 2141

Mechanical Design of a Ferrite-Based Injection Kicker for SNS Accumulator Ring
C. Pai, N. Catalan-Lasheras, W. Eng, H. Hseuh, R.F. Lambiase, Y.-Y. Lee, W. Meng, J. Sandberg, S. Tepikian, J. Tuozzolo (BNL) 2144

Mechanical Design of Fast Extraction Kicker and PFN for SNS Accumulator Ring
C. Pai, D. Davino, H. Hahn, H. Hseuh, Y.-Y. Lee, W. Meng, J. Mi, J. Sandberg, N. Tsoupas, J. Tuozzolo, D. Warburton, W. Zhang (BNL) 2147

Design Considerations for a Lambertson Septum Magnet for the Spallation Neutron Source
J. Rank, Y.-Y. Lee, K. Malm, G. Miglionico, D. Raparia, N. Tsoupas, J. Tuozzolo (BNL) 2150

Magnetic Field Calculations for a Large Aperture Narrow Quadrupole
N. Tsoupas, J. Jackson, Y.-Y. Lee, D. Raparia, J. Wei (BNL) 2153

Design and Manufacturing of SNS Accumulator Ring and Transport System D.C. Magnets
J. Tuozzolo, J. Alduino, S.V. Badea, J. Brodowski, G. Mahler, D. Raparia, S. Seberg (BNL) 2156

LITHIUM COLLECTION LENS FILLING PROCESS FOR FERMILAB ANTIPROTON SOURCE

R. Schultz#, P. Hurh; FNAL*, Batavia, IL 60510, USA

Abstract

The most critical step in fabrication of the lithium collection lens is the introduction of molten lithium into the core of the lens. A preload (hydrostatic compressive stress) of approximately 2500 psi is desired within the solid lithium for proper lens operation. Instrumentation that is accurate at temperatures well above the melting temperature of lithium (180.6 °C) must be used to monitor the pressure during the fill to achieve the desired preload. Measurements from recent lens fills show that as the lens cools, the preload decreases by approximately 50 psi/°C on average. This paper shows that this apparent thermal expansion modulus can be determined analytically as well as numerically. These results are then compared to measured values.

INTRODUCTION

The lithium collection lens[3] used at Fermilab (Figure 1) is a pulsed device with a one-centimeter radius. Operating at up to 1000 Tesla per meter, it is used to focus an 8 GeV antiproton beam coming off of a target. It is cycled approximately once every two seconds and has a life expectancy of between 5-10 million pulses. A positive preload of approximately 2500 psi is necessary to combat the "magnetic pinch" that occurs during each pulse on the lithium during operation. The preload prevents electrical arcing, which can occur if the lithium separates from the titanium septum. There are a few plausible mechanisms that are thought to cause failure. The prevailing theory suggests that the titanium septum fails in fatigue at locations of high stress reversal. Ideally, the preload of the lens should be such that it eliminates the stress reversal and reduces the magnitude of the stress during operation.

Accurately measuring the preload at elevated temperatures has been a problem in the past. The instrumentation experienced large thermal zero-shifts and had a small signal to noise ratio, which resulted in a large uncertainty on the preload. This has hindered the development of any reliable trends that might suggest an optimal preload for future lenses. New advances in pressure transducer technology have made it possible to measure the pressure of solid and liquid lithium up to 400 °C with an accuracy of better than 0.25%. In addition, a more accurate data acquisition system has been implemented, and software was created to show the long-term pressure vs. temperature relationship in real time. This allows us to predict how much the preload will decrease as the lens cools and adjust accordingly during a fill. Better instrumentation along with a better understanding of this phenomenon has made it possible to achieve the target preload within the desired tolerance.

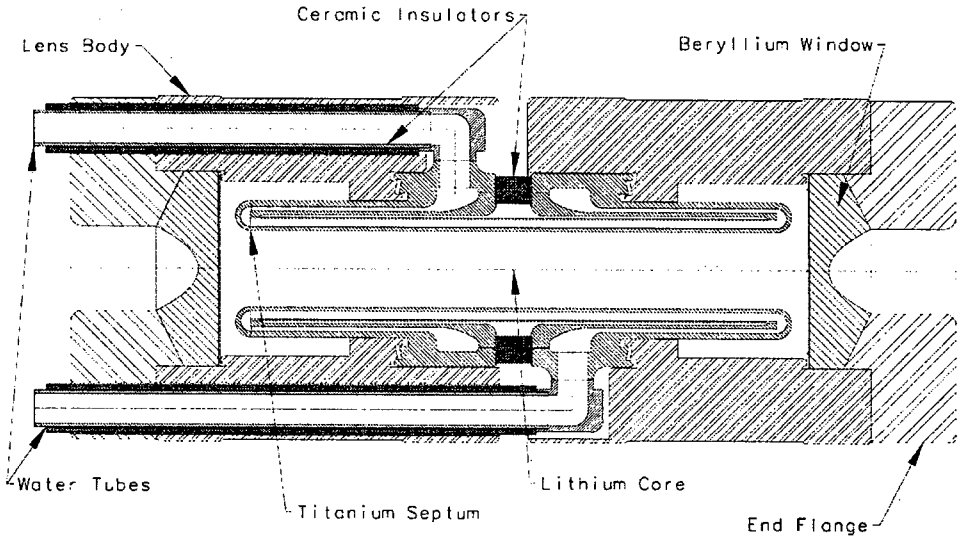


Figure 1. Cross-Sectional View of the Lithium Collection Lens used at Fermilab

* Operated by Universities Research Association Inc. under Contract No. DE-AC02-76CH03000 with the United States Department of Energy.
# rschultz@fnal.gov

0-7803-7738-9/03/$17.00 © 2003 IEEE

THE FILLING PROCESS

The lens is connected to a reservoir of molten lithium through two stop-cocks (metal-on-metal valves), which are open during most of the fill. This allows lithium to flow into or out of the lens. The reservoir of molten lithium is contained within a bellows assembly, which transmits pressure from a hydraulic ram to the lithium. Initially, the lens is injected with molten lithium at a pressure of about 500 psi. As the temperature decreases and the lithium solidifies, the pressure drops dramatically as the lithium thermally contracts. The bellows pressure is adjusted to compensate for the thermal contraction. As the lens temperature drops from the solidus point down to 100 °C, the lithium pressure is slowly increased to 6000 psi. As it continues to cool from 100 °C down to 40 °C, the bellows pressure is adjusted in an attempt to arrive at the desired preload of approximately 2500 psi. The stop-cocks are generally closed at about 40 °C, after which temperature the preload cannot be changed by adjusting the bellows pressure. The lens will continue to cool until it reaches room temperature, when the final preload measurement is made.

INSTRUMENTATION

There have been three forms of instrumentation used to measure the preload. The first involved miniature pressure transducers from Entran®. This transducer was originally specified because it worked well in space-restricted areas. Since it was entirely enclosed in the lens body, the wires could be cut and the transducer would then be left in the lens body for installation into the transformer assembly. The primary limitation of this transducer is that most strain gauge based instrumentation has a realistic temperature limit[5] of between 120–150 °C. Above this temperature, the epoxy bonding the strain gauges to the measurement diaphragm within the transducer begins to break down. Large zero-shifts can occur and have been observed at these elevated temperatures. Zero-shifts of this nature cannot be measured nor compensated for. The uncertainty associated with this type of zero-shift error is on the order of +/- 1000 psi.

The second type of instrumentation used was strain gauges, which measured the circumferential strain on the outside of the lens body. High temperature strain gauges, developed by Vishay Micromeasurements Group, were installed; which are reliable at temperatures up to 260 °C. The internal pressure was calculated by correlating the strain with a pre-determined calibration curve. Since the radius to thickness ratio of the lens body is approximately two, it is considered a thick walled cylinder. Unfortunately, this contributes to a signal to (thermal) noise ratio of approximately one. Ideally, it should be ten or higher. Statistical error analysis[4] suggests an uncertainty for our application on the order of +/- 500 psi for conditions such as this.

Because of the large uncertainties associated with the miniature pressure transducers and the strain gauges, it was necessary to find a better method of instrumentation that could more accurately measure the preload. Dynisco Instruments has developed a variety of robust Melt Pressure Transducers that have been specifically designed for the harsh and rugged environments of the Extrusion and Polymer Processing Industries. Their pressure transducers have a unique design that removes the instrumentation diaphragm from the heat source. The pressure diaphragm can then be exposed to temperatures up to 400 °C without concern of thermal shifts. The design transmits the pressure to the instrumentation diaphragm through a mercury-filled capillary tube. The strain gauges on the instrumentation diaphragm then operate in a much cooler atmosphere. Therefore, the transducer can output a much more accurate signal. The uncertainty is less than 0.25% of the full-scale output, which is generally less than 25 psi.

Our experience has shown that these pressure transducers were not only more accurate, but also more robust during installation. In addition, thermal calibration time is minimal because the thermal output is small and very repeatable. We now conduct the filling process with a total of four Dynisco pressure transducers: one measuring the molten lithium pressure, and one measuring the hydraulic ram pressure, and two measuring the preload.

LITHIUM MATERIAL PROPERTIES

Most metals have a linear coefficient of thermal expansion (α) of between 10-25 μ/°C. Lithium has one of the highest linear CTE's of any metal: α_{Li} = 46-56 μ/°C from 20-180 °C. This contributes to a large loss in preload as the lens cools.

While the thermal properties of lithium are well known and trusted, the mechanical properties are not. Very little data is available; thus, the confidence for that data is low. Lithium is too soft to be used in structural engineering, so there has not been any great need to accurately determine the mechanical properties. Values for the elastic modulus (E_{Li}) have been reported[2,6,7] anywhere from 280 – 1131 ksi at room temperature. There is only one known set of temperature dependant data[7], so that data at 35 °C will be used for the remainder of this discussion.

Given that E_{Li} = 896 ksi and Poisson's Ratio (ν_{Li}) is equals to 0.36, the bulk modulus (K_{Li}) can be calculated, and is equal to 1067 ksi. It is interesting to note that E_{Li} decreases significantly as the temperature increases from 20-180 °C. This is because the homologous temperature ($T_H = T_{abs}/T_{melt}$) is greater than 0.65. Steady state creep that is analogous to viscous flow occurs at $T_H > 0.7$, or $T_{Li} > 45$ °C.

THERMAL EXPANSION MODULUS

The bulk modulus (K) is a relationship that expresses change in pressure with respect to volumetric strain ($\Delta V/V$). Compressibility (X) is then defined as the inverse of the bulk modulus:

$$X \equiv \frac{1}{K} \equiv \frac{\Delta V}{V \Delta P} \quad (1)$$

The volumetric coefficient of thermal expansion (β) is simply three times the linear coefficient of thermal expansion: $\beta_{Li} = 3\alpha_{Li} = 142$ μ/°C at 35 °C.

$$\Delta l = l \alpha \Delta T \qquad \Delta V = V \beta \Delta T \quad (2)$$

By combining equations (1) and (2), a very important material property is derived that is called the Thermal Expansion Modulus (TEM):

$$\frac{\Delta P}{\Delta T} = \frac{\beta}{X} \qquad TEM = \frac{\beta}{X} \quad (3)$$

This is purely a theoretical relationship that describes the increase in pressure of lithium in a completely rigid container. Based on the material properties mentioned before, TEM_{Li} = 151 psi/°C. In practice, though, no container is completely rigid. Because the containment vessel will flex with pressure, the actual loss of preload is a function of the stiffness of the vessel. Therefore, a loss of 151 psi/°C is the theoretical maximum that can be expected at 35 °C.

PRELOAD RATE

The preload rate (PR) describes the change in pressure for lithium in an elastic containment vessel. For a simple cylinder, it can be shown[1] that:

$$PR = \frac{\Delta P}{\Delta T} = \frac{\beta_{Li}}{X_{Li} + \frac{2R}{E\,t}} \quad (4)$$

Here, R is the inner radius of the tube and t is the wall thickness. Test data on a simple titanium tube (E_{Ti} = 16.5 Msi) has confirmed the validity of this relationship. A 7/8" tube with t_{Ti} = 0.061" resulted in a PR of 87-95 psi/°C from 100 °C down to 20 °C. Equation (4) predicts 84 psi/°C at 35 °C.

Because the lithium cavity in the lens is not a simple cylinder, theoretically predicting the lens preload rate is very complicated. For the cylinder part of the septum, equation (4) predicts that PR = 67 psi/°C, given R_{Ti} = 1.0 cm and t_{Ti} = 0.040". Finite Element Analysis has been used to investigate this further. Figure 2 shows a contour plot of the hydrostatic pressure over 1 °C. As one would expect, the preload rate is not uniform throughout the lithium cavity. An axi-symmetric weighted average of the PR in this model is about 71 psi/°C at 35 °C.



Figure 2. Axisymmetric model of the Preload Rate

It is interesting that this model does not agree with the empirical results. After the stop-cocks are closed, the measured PR for the lens is about 46-48 psi/°C.

There are two plausible explanations for this discrepancy. First, it could be caused by a temperature differential between the lithium and the lens body. The effective PR drops sharply if the lithium is cooler than the lens body, by even 1-2 °C. A differential of up to 4 °C has been observed. Secondly, it is also possible that the E_{Li} mentioned is not correct. An E_{Li} of 500-600 ksi would better correlate with the empirical results, and is well within the range of published data. Most likely, it is a combination of both explanations.

The PR as previously discussed is for a constant volume. During most of the filling process, however, the stop-cocks are open; this will be referred to as PR'. Liquid or solid lithium can flow into or out of the lens, depending on the pressure differential between the lens and the bellows. While the nominal PR' during this phase is 50 psi/°C, the short term PR' varies from 20-70 psi/°C. The pressure gradient is necessary to cause the short term PR' to increase or decrease proportionally, in an attempt to achieve the desired preload at room temperature.

CONCLUSIONS

With better instrumentation, we have been able to more accurately measure the preload of the lithium during the filling process. Developing the TEM and PR relationships has helped us to predict, and therefore better control the final preload. Further FEA and a more accurate E_{Li} is necessary to increase our understanding of this phenomenon.

REFERENCES

[1] Bayanov B. et al. (1985). "Study of the Stresses in and Design Development of Cylindrical Lithium Lenses" Preprint BINP 84-168

[2] Brandes, E. (1997). *Smithells Metals Reference Book* (7th ed.)

[3] Chao, A. W. (1999). *Handbook of Accelerator Physics and Engineering*, pg 483-486.

[4] Dieck, R. H. (1997). *Measurement Uncertainty: Methods and Applications* (2nd ed.).

[5] Pierson, J. G. (1999). *The Art of Practical and Precise Strain Based Measurements* (2nd ed.), Chapter 4-52.

[6] Schultz, R. (2002). Lithium: Measurement of Young's Modulus and Yield Strength. Fermilab TM 2191.

[7] Tariq, S. (2003). Li Material Testing. PAC03.

LI MATERIAL TESTING- FERMILAB ANTIPROTON SOURCE LITHIUM COLLECTION LENS*

S. Tariq#, K. Ammigan, P. Hurh, R. Schultz, FNAL, Batavia, IL 60510, USA
P. Liu, J. Shang, University of Illinois, Urbana, IL 61801, USA

Abstract

The lithium collection lens is a high current (greater than 0.5 MA), pulsed device used to focus antiprotons just downstream of the production target. Pre-mature failure of these lenses has led to extensive efforts to understand the cause of the failures. One of the main unknowns is the structural behavior of lithium under such extreme loading conditions. Lithium can be categorized as a soft or "plastic" solid with relatively low modulus of elasticity and yield strength. Very little is available on its nonlinear and viscoplastic (rate dependent) structural properties. Tests were conducted to determine the rate dependent tensile behavior and creep response of lithium at various temperatures. Results of these tests are presented.

INTRODUCTION

The FNAL collection lens operates by passing a large axial current through a solid lithium (Li) cylinder 1 cm in radius. This produces a strong magnetic field proportional to the radius and has the advantage of focusing in both transverse planes. The 1 cm lens was designed for a focusing gradient of 1000 T/m, but due to premature failure it is currently operated at reduced gradients. At a lower gradient of around 745 T/m, the lens can last for millions of pulses and have an operational life greater than six months. The downside is lower antiproton yield due to a reduction in focusing strength. The goal is to develop a lens design capable of 1000 T/m over a 1 cm radius aperture without failing in less than 10E6 pulses [1]. For this, a thorough understanding of the lens electro-mechanical behavior is desired.

The Li cylinder is enclosed in a water-cooled titanium alloy (6Al-4V ELI) jacket called the septum. Its purpose is to contain the Li against the extreme thermal and magnetic loads from the beam and pulse. For proper lens operation, a negative Li hydrostatic stress (preload) of about 2,500psi is required for optimum lens life. This preload is aimed to minimize Li-titanium separation caused by magnetic forces during each pulse.

Mechanical failure of the lens typically occurs in the titanium septum, and although failure theories abound, definitive evidence of a single cause has yet to be identified. A comprehensive finite element model of the lens has been developed using ANSYS® [2,3]. The aim is to better understand the mechanisms leading to failure. One of the main unknowns has been the mechanical behavior of Li at high strain rates. While thermal and electrical properties for Li are well documented, very little mechanical data is available [4]. Basic properties such as modulus of elasticity and plastic behavior have not yet been clearly defined.

*Work supported by the US Department of Energy under contract # DE-AC02-76CH03000
#tariq@fnal.gov

TENSILE TESTS

Dog bone shaped tensile specimens were cast as shown in Fig. 1. Tensile tests were conducted on an MTS 880 servo-hydraulic Material Test System. To minimize interaction with the environment, the samples were immersed in mineral oil inside a cylindrical chamber. The chamber was wrapped with heating tape to heat the oil to the required temperature. The oil was fully stirred before testing to ensure a uniform temperature distribution. To prevent the soft sample from bending or twisting during sample insertion, the upper end of the sample was pinned to the testing machine with a specially designed connecting fixture. Stress-strain curves were obtained by recording the load versus displacement data, calibrated using an extensometer during testing. For small strain measurements, strain gauges were attached to the Li sample using a non-reactive adhesive.

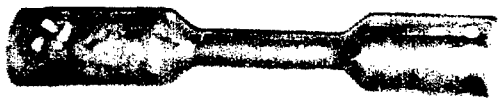


Figure 1: Li tensile specimen.

The samples were pulled at four strain rates ($0.002s^{-1}$, $0.01s^{-1}$, $0.10s^{-1}$, and $1.05s^{-1}$) and three temperatures (room temperature, 50°C, and 75°C). Room temperature plots of true stress versus true strain (σ_T -ε_T) at different strain rates are given in Fig. 2. The modulus of elasticity (E) was calculated from the elastic unloading part of the stress-strain curve ($\sigma_T = E\,\varepsilon_T$). The plastic strain-hardening region can be defined by the equation:

$$\sigma_T = K\varepsilon_T^{\,n} \qquad (1)$$

where K and n are hardening parameters. Table 1 lists these parameters together with E values for the different strain rates and temperatures. The yield strength $\sigma_{0.2}$ was defined as the stress at 0.2% strain offset, and the ultimate tensile strength σ_{UTS} was the greatest load the sample withstood before necking and ultimate fracture.

A rate dependent viscoplastic model can be evaluated which accurately describes the hardening behavior. The Perzyna model [5] was employed which is of the form:

$$\sigma_y = \sigma_o\left[1+\left(\frac{\dot{\varepsilon}}{\gamma^*}\right)^{1/\delta}\right] \qquad (2)$$

0-7803-7738-9/03/$17.00 © 2003 IEEE

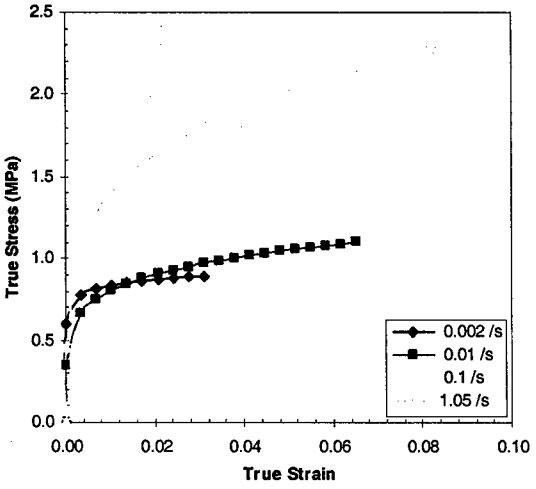


Figure 2: True stress vs. true strain for Li at room temperature and different strain rates.

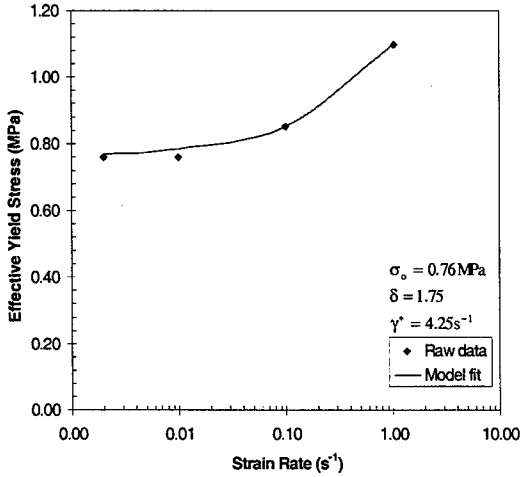


Figure 3: Effect of strain rate on the yield stress of Li at room temperature showing Perzyna model fit.

Table 1: Tensile test results.

Strain Rate /s	0.002	0.01	0.10	1.05
$\sigma_{0.2}$ (MPa)	0.76	0.76	0.85	1.10
σ_{UTS} (MPa)	0.89	1.10	1.69	2.28
n	0.065	0.17	0.19	0.23
K (MPa)	1.12	1.75	2.85	4.03
E (GPa)	7.80	Room Temperature		
$\sigma_{0.2}$ (MPa)	0.42	0.50	0.85	0.92
σ_{UTS} (MPa)	0.51	0.76	1.38	1.75
n	0.069	0.14	0.14	0.20
K (MPa)	0.65	1.16	2.14	3.01
E (GPa)	5.00	50°C		
$\sigma_{0.2}$ (MPa)	0.41	0.45	0.72	0.90
σ_{UTS} (MPa)	0.46	0.60	1.02	1.54
n	0.053	0.098	0.16	0.19
K (MPa)	0.57	0.81	1.64	2.66
E (GPa)	4.00	75°C		

where σ_y is the effective yield stress, σ_o is the static yield stress (σ_{02} at .002s^{-1}), $\dot{\varepsilon}$ is strain rate, γ^* is the material viscosity parameter, and δ is the strain rate hardening parameter. Fig. 3 shows a plot of effective yield stress vs. strain rate at room temperature and the corresponding Perzyna parameters. The effective yield stress rises sharply beyond strain rates of 0.01.

COMPRESSIVE CREEP TESTS

To simulate the behavior of Li in the septum, a test was conducted to study the dynamic response of Li under compression. A titanium alloy tube with similar dimensions to the septum was filled with Li and pressurized at one end while the other end was capped. The resulting pressure distribution in the Li was measured with respect to time using strain gauges mounted on the exterior of the tube as shown in Fig. 4. Six strain gages spaced at varying intervals were used.

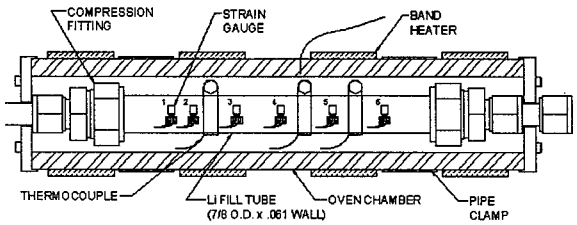


Figure 4: Li fill tube assembly showing (6) strain gauges positioned at 0", ½", 1 ½", 2 ½", 3 11/16", and 4 7/8".

The entire assembly was placed inside a cylindrical oven chamber to heat the Li to the required temperature. Thermocouples mounted on the fill tube monitored the Li temperature. Pressure was applied via a hydraulic system using standard hydraulic oil directly in contact with the Li. Point of load application was close to strain gauge location 1 (SG1). The strain gauge readings were converted to radial stress (preload) values on the tube inner wall (i.e. pressure exerted by the Li on the titanium tube). Tests were conducted at two pressures (2000psi and 4000psi) and four temperatures (room temperature, 50°C, 80°C, and 110°C). Note that the melting point of Li is relatively low at 180.6°C. Results were obtained in the form of preload versus time curves for each strain gage location as shown in Fig.'s 5 and 6.

Creep is a rate dependent material nonlinearity in which the material continues to deform under an applied load, typically accelerated by temperature. From a material viewpoint, creep and viscoplasticity are the same except that the time scales involved are different. Creep, unlike plasticity and Perzyna viscoplasticity, does not involve a yield surface at which inelastic strains occur. Thus, creep strains are assumed to develop at all non-zero deviatoric stresses. Creep strain is typically a function of stress, strain, time, and temperature [6]. Over several pulses in the lens, creep is thought to play an important role as the Li undergoes various loading cycles [2]. Since Li bonds tightly to the titanium surface, a no slip boundary condition is assumed and in the case of the tube test, the

time dependent distribution of pressure across the tube is thought to be primarily by creep.

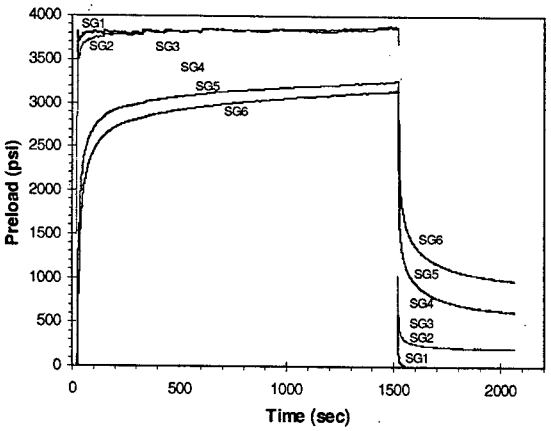


Figure 5: Preload vs. time for Li at 50°C showing relaxation after load removal (4000psi test).

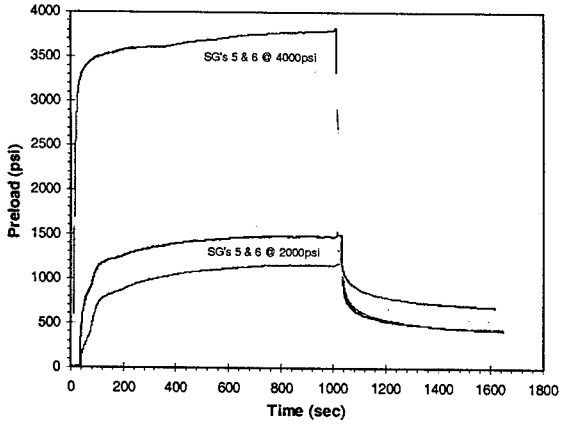


Figure 6: Effect of applied pressure on preload at strain gauge locations 5 and 6 at 80°C.

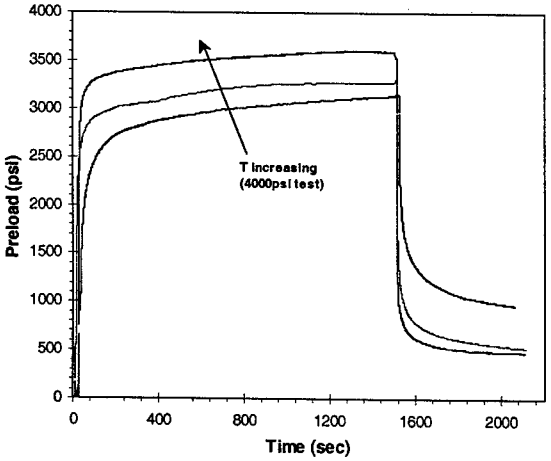


Figure 7: Effect of temperature on preload at strain gauge location 6 (4000psi test).

CONCLUSION

Temperature dependent elastic and viscoplastic properties of Li have been accurately measured in tension. The elastic modulus at room temperature (7.8GPa) was found to be significantly higher than previously published results (2.0-5.0GPa). Li exhibited significant work hardening at higher strain rates with a very small elastic region. The sample stretched considerably with extreme necking before final fracture at a very small cross section.

The compressive creep tests also revealed interesting results. It was seen that Li creeps rapidly especially at higher temperatures as shown in Fig. 7. At lower temperatures, a uniform preload was not achieved across the tube. A drawback of this test was that it did not measure Li creep strain directly. The authors would also like to point out that at the time of writing this paper, data from these tests was still being analyzed and only partial results have been presented. Interested parties should contact the author(s) directly for further information.

Based on the above observations, Li in the lens will most likely undergo some combination of viscoplasticity and creep which will have to be incorporated in the ANSYS® finite element model.

FUTURE WORK

Since Li is almost always in compression in the lens, the tensile tests should be repeated in compression to check for possible differences in material behavior. Higher strain rate tests should also be conducted to see whether Li exhibits further work hardening characteristics, since strain rates in the order of 10^1 and 10^2 are seen in the lens based on finite element analysis [2]. Standard compressive creep tests should also be conducted in which creep strain is measured directly. A temperature dependent comprehensive creep model should be developed from these tests and verified using the tube test results.

REFERENCES

[1] P. Hurh, J. Morgan, & R. Shultz, "The Design of a Diffusion Bonded High Gradient Lens for the FNAL Antiproton Source," TPAG010, PAC 2003, Portland (2003).

[2] P. Hurh, J. Morgan, & S. Tariq, "Comprehensive Electro-Magnetic, Thermal, and Structural Finite Element Analysis of the Lithium Collection Lens at the FNAL Antiproton Source", ROPB011, PAC 2003, Portland (2003).

[3] ANSYS® is a registered trademark of SAS IP Inc.

[4] R. P. Schultz, "Lithium: Measurement of Young's Modulus and Yield Strength," Fermilab TN 2191 (2002).

[5] P. Perzyna, "Fundamental Problems in Viscoplasticity," Advances in Applied Mechanics, Vol. 9, (1966), p. 243.

[6] H. Kraus, "Creep Analysis," John Wiley & Sons, Inc., (1980).

BEAM STUDY WITH RF CHOPPERS IN THE MEBT OF THE J-PARC PROTON LINAC

Takao Kato, Masanori Ikegami, KEK, Tsukuba, Japan

Sheng Wang, Shinian Fu, IHEP, Beijing, China

Abstract

A beam study of the RF fast chopper system in the MEBT of the J-PARC linac was successfully performed up to a beam current of 25 mA. The achieved rise/fall time of the chopped beam was about 10 ns. A beam signal during the chopper-on period, measured at the exit of the MEBT, was less than the noise level of the monitor systems. A flexible pattern of the chopped pulse train was achieved, which is useful for various kinds of operating pulse modes of the J-PARC accelerator.

INTRODUCTION

The J-PARC accelerator consists of three main parts: a 400-MeV proton linac, a 3-GeV rapid cycling synchrotron (RCS) and a 50-GeV synchrotron [1]. The linac accelerates a 50-mA beam of 500 μs in length at a repetition rate of 25 Hz. A fast chopper in the low-energy part of the linac was planned for reducing beam losses in the RCS. An RF chopper [2, 3] was adopted as a deflecting device in the medium-energy beam-transport line (MEBT) between the 3-MeV RFQ and the DTL [4]. In order to satisfy the purpose of the chopper system, it is important to minimize the transient rise/fall time of a chopped beam, since the beam behavior in the transient periods differs from that in the steady period, resulting in additional beam losses along the accelerator. A beam study up to the MEBT was performed [5]. The results of the chopped-beam study are described in this paper.

MEBT LAYOUT

The layout of the MEBT is shown in Fig.1. There are eight focusing magnets, two RF bunchers, two 324-MHz RF chopper cavities (RFD-A and RFD-B), five sets of steering magnets, a beam scraper for chopped beams and several kinds of beam diagnostics. The required time structure of the chopped beam is shown in Fig. 2. The chopping frequency is around 1 MHz in accordance with the RF frequency of the RCS.

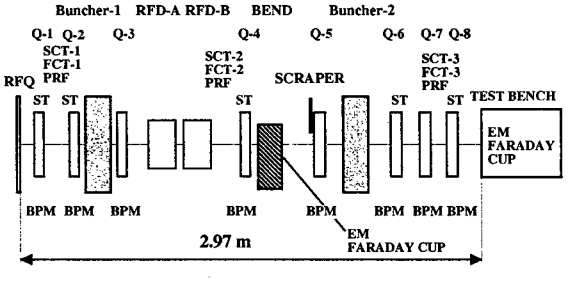


Figure 1: Layout of the MEBT.

RF CHOPPER (RFD) SYSTEM

An RFD is excited with a TE11-like mode. A loaded Q-value was tuned to be as low as about 11 by using two RF input/output couplers having large coupling coefficients. There are five methods to realize a faster transient rise/fall time of a chopped beam: (1) using a coupled RFD system [3] for obtaining a total deflecting-field strength as high as possible within a fixed RF power, (2) optimizing the loaded Q-value for obtaining the fastest rise time on the condition of a limited available RF power, (3) using the phase-reversal method [6] for achieving a faster fall time in the end part of the RF pulse, (4) using excess RF power in order to shorten the required time in which the deflecting field reaches the designed field level, and (5) using a power amplifier with a fast rise/fall time. In our system, two RFDs are connected with a waveguide, making a coupled cavity system and saving the cost of an RF power source. The optimum length of the coaxial waveguide between two RFDs was determined based on an HFSS simulation [7].

We constructed a 30-kW solid-state power amplifier. The amplifier consisted of thirty power modules, each of which produces an RF power of more than 1 kW, resulting in a maximum available power of 36 kW. The transient time of the power amplifier was about 15 ns. The incident wave for the power amplifier was modulated in amplitude by using a diode-switching circuit.

The required RF power of 22 kW for producing a deflecting field of 1.6 MV/m for the coupled RFD system was determined by a TRACE3D simulation under the condition that the chopped beam should be separated from the normal one by 4.4 mm. The deflecting field reached the designed value in nearly half the rise time if the driving power (P_{in}) was increased to 36 kW.

A beam scraper of tungsten was installed 70 cm downstream from the second RFD. The transverse

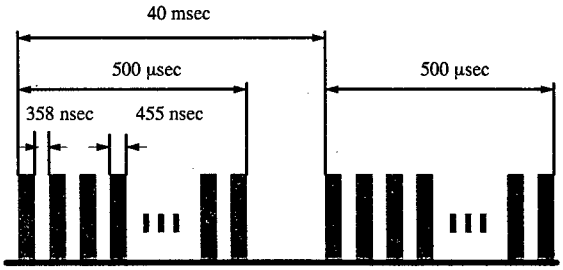


Figure 2: Required time structure of the linac beam pulse. A chopping ratio of 56% and a ring RF frequency of 1.23 MHz are assumed.

0-7803-7738-9/03/$17.00 © 2003 IEEE

position of the scraper could be set with an accuracy of ±0.1 mm over a range of 50 mm. The beam current on the scraper could be measured.

METHOD OF CHOPPED-BEAM MEASUREMENTS

Two kinds of peak currents (5 and 25mA) were used. A low duty factor (repetition rate of 5 Hz and pulse duration of 50 μs) was selected, thus avoiding damage to the scraper surface in the beginning period of the experiment.

The chopped beam experiments consisted of three stages: (1) using a low-intensity beam and a single RFD for studying the fundamental characteristics of the RF chopper system, (2) using a low-intensity beam and a coupled RFD for studying the operation of the coupled RFD system, and (3) using a high-intensity beam and a coupled RFD for studying the characteristics of the total system under realistic conditions. A chopped beam was measured by using several kinds of beam monitors: slow current monitors (SCT), fast current monitors (FCT), beam position monitors (BPM) installed in each Q-magnet, a beam scraper and a Faraday cup. Each beam test consisted of the following steps: (1) eight focusing magnets and some steering magnets were tuned for obtaining both the highest transmission ratio through the MEBT and the allowable transverse emittance growth along the MEBT, (2) the RF amplitude of the first buncher was set to the design value, (3) the RF phase of the first buncher was set so that the average beam energy would be independent of the buncher operation, (4) the beam scraper position was set according to the results of a beam-size measurement, (5) the incident power of the RFD was increased gradually, and (6) the RF phase of the RFD was scanned for searching the optimum phase. Some iterations of the procedures mentioned above were required.

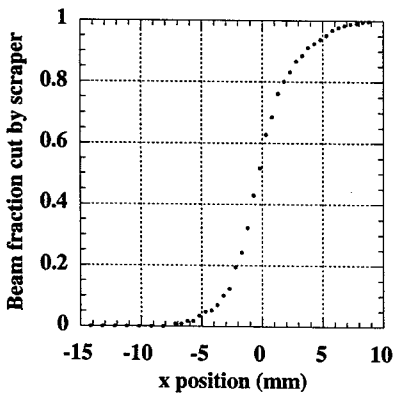


Figure 3: Measured beam fraction cut by the scraper as a function of the scraper position. The beam current was 5 mA. A symmetric transverse profile was assumed in data processing.

EXPERIMENTAL RESULTS

Beam Profile

The profile of a 5-mA beam at the scraper position was determined by measuring the third SCT current as a function of the scraper position (Fig. 3). The measured beam size was smaller than 10 mm, which roughly agrees with the calculated one with TRACE3D. Then, a scraper position of 10 mm away from the beam axis was selected for distinguishing the chopped beam from the normal one. The setting was effective throughout the study with a beam current of up to 25mA.

Deflecting Position

Figure 4 shows the deflecting scheme of a single RFD system. The deviation (Δx) of the chopped beam from the beam axis at the scraper position is expressed as

$$\Delta x = \theta_1 (L_1 + L_2)\left(1 + \frac{qB' L_q}{2mv}\frac{L_1 L_2}{(L_1 + L_2)}\right),$$

where, θ_1 is the deflecting angle in proportional to the deflecting electric field of an RFD, q the electric charge, B' the magnetic field gradient of the quadrupole magnet, m the rest mass of the protons, v the velocity and L_1&L_2 the distances. Figure 5 shows the measured deflecting beam position at the scraper as a function of the

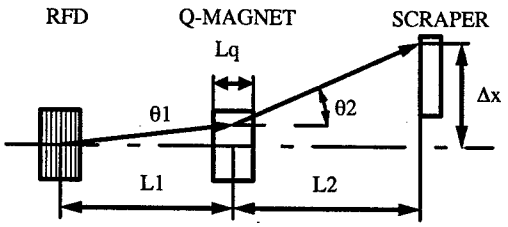


Figure 4: Deflecting scheme of a single RFD system.

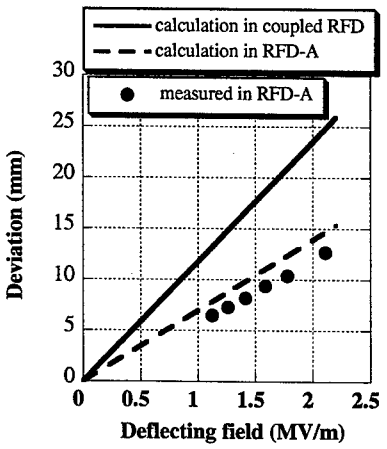


Figure 5: Measured deflecting beam position at the scraper in the single RFD-A system vs. deflecting field of the RFD. The calculated deviation for both the RFD-A and the coupled system are also plotted.

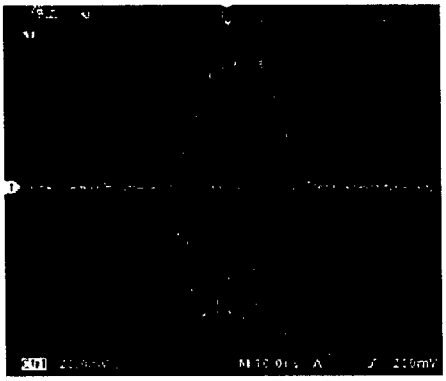


Figure 6: Signal of a chopped beam measured by the eighth BPM. The beam current was 24 mA. P_{in}=36 kW. The phase-reversal switch was turned on. 10 ns/div.

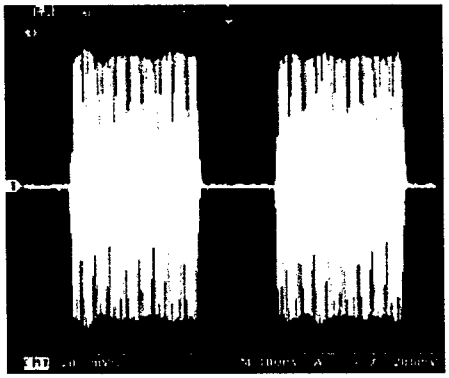


Figure 7: Signal of a chopped beam measured by the eighth BPM. The beam current is 24 mA. P_{in}=36 kW. The phase-reversal switch was turned on. 100 ns/div.

deflecting field of the single RFD-A system. The calculated results for both the RFD-A and the coupled RFD operation are also plotted. The agreement between the measured and calculated results is satisfactory.

Results of Coupled RFD Operation

A beam test with the coupled RFD system was successfully performed. Figure 6 shows a chopped beam pulse measured by the eighth BPM. A very short pulse was produced to clearly observe both transient parts. A transient time of about 10 ns for the rise/fall part was obtained. Figure 7 shows a typical chopped pulse train. The signal arising from the deflected beam, most of which was scraped by the scraper, was less than the noise level at the MEBT exit, indicating that the fraction of the beam at the exit of the MEBT during chopper-on time was negligibly small. The allowable separation between the deflected and normal beams of 23 mA was obtained when the driving power of the coupled RFD system was about 18 kW. However, the measured transient rise time of 15 ns was not so fast that a driving power of more than 18 kW was desirable from the viewpoint of the transient behavior. The tolerance of the allowable RF phase error of the RFD was sufficiently large; the coupled RFD system provided a separation between the chopped and normal beams over a driving RF full phase-range of 96/52 degrees for a driving RF power of 36/18 kW and a beam current of about 5 mA. The method for making any combination of the chopped beam of varied pulse durations or varied repetition rates was established. It was found that the RFD system is very stable in total performance. There were no problems in RFD high-power operation during the beam study period for over one month.

Phase-Reversal Operation

In Fig. 6, the input RF phase was reversed by 180 degrees as fast as possible at a timing of about 12 ns ahead of the RF pulse end. This increased the beam rise time by more than 3 ns.

CONCLUSION

It was proved by the beam study that the RFD chopper system operates very well up to a beam current of 25 mA, satisfying the fundamental requirements for a chopped beam. The achieved rise/fall time (10 ns) of the chopped beam was close to the limit of the RF chopper system, on the condition that a loaded Q-value of 11 and a limited available RF power of 36 kW were used. The beam signal during the chopper-on period measured at the exit of the MEBT was less than the noise level of the monitor systems. A flexible pattern of the chopped pulse train was achieved, which is useful for various kinds of operating pulse modes of the J-PARC accelerator.

ACKNOWLEDGEMENTS

The authors would like to express their thanks to the J-PARC linac group for beam operation of the low-energy part of the linac.

REFERENCES

[1] "Accelerator Technical Design Report for J-PARC," KEK Report 2002-13; JAERI-Tech 2003-044.

[2] T. Kato, "New Design of an RF beam Chopper," Proc. 7th Symp. on Accelerator Science and Technology, 228(1989).

[3] S. Fu and T. Kato, "RF-chopper for JHF linac," Nucl. Instr. And Meth. **A 440**, 296(2000).

[4] S. Fu and T. Kato, "Design Study on a medium-energy beam-transport line for the JHF proton linac," Nucl. Instr. And Meth. **A 457**, 423(2001).

[5] M. Ikegami et al., "Beam Commissioning of the J-PARC Linac Medium Energy Beam Transport at KEK," submitted to this conference.

[6] JHF Project Office, "JHF Accelerator Design Study Report," KEK Report 97-16, Section 4.1 to 4.3, 1998.

[7] S. Wang et al., to be published.

SPALLATION NEUTRON SOURCE HIGH-POWER RF TRANSMITTER DESIGN FOR HIGH AVAILABILITY, EASE OF INSTALLATION AND COST CONTAINMENT *

J. Bradley III, D. Rees, T. Hardek, M. Lynch, W. Roybal, P. Tallerico, LANL, Los Alamos, NM 87545, USA

Abstract

The availability goals and installation schedule for the Spallation Neutron Source (SNS) have driven the availability and installation of the SNS linac's high-power RF systems. This paper discusses how the high-power RF systems' availability and installation goals have been addressed in the RF transmitter design and procurement. Design features that allow RF component failures to be quickly diagnosed and repaired are also presented. Special attention has been given to interlocks, PLC fault logging and real-time interfaces to the accelerator's Experimental Physics and Industrial Control System (EPICS) archive system. The availability and cost motivations for the use of different RF transmitter designs in the normal-conducting and super-conducting sections of the linac are reviewed. Factory acceptance tests used to insure fully functional equipment and thereby reduce the time spent on installation and commissioning of the RF transmitters are discussed. Transmitter installation experience and klystron conditioning experience is used to show how these design features have helped and continue to help the SNS linac to meet its availability and schedule goals.

1 OVERVIEW OF SNS TRANSMITTER SYSTEMS

The Spallation Neutron Source (SNS) is currently under construction at Oak Ridge National Laboratory (ORNL). The RF systems for the 1 GeV proton linac in the SNS are the responsibility of Los Alamos National Laboratory (LANL). Each RF system consists of a Converter /Modulator, a transmitter, one or more klystrons, RF loads, circulators and waveguide to deliver the RF power to the accelerating cavities. Details of the klystrons and Converter/Modulators can be found in other papers at this conference [1], [2].

1.1 Transmitters Types

The transmitters in these systems are divided primarily into two different types. The first type of transmitter accommodates a single 2.5 MW, 402.5 MHz klystron or a single 5 MW, 805 MHz klystron. Eleven of these transmitters are used in the normal conducting (NC) portions of the accelerator and two more in the High Energy Beam Transport (HEBT) systems, as shown in blue in Figure 1. This single-klystron transmitter will be referred to in this paper as an NC transmitter.

The second type of transmitter accommodates up to six 550 kW klystrons and is used exclusively in the superconducting (SC) sections of the linac. This transmitter type will be referred to in this paper as an SC transmitter. Fourteen of these transmitters are used in the current configuration of the SNS linac as shown in blue in Figure 1.

* Work supported by US Department of Energy.

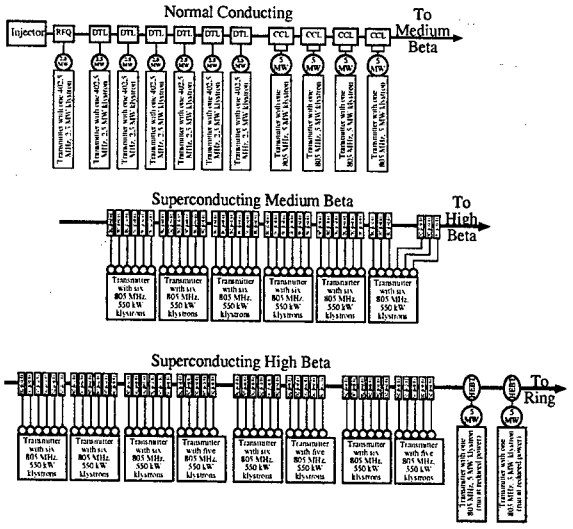


Figure 1: The SNS linac uses 13 single-klystron transmitters and 14 six-klystron transmitters.

1.2 Transmitters Functions

Both types of transmitters provide support and protection for the klystron or klystrons installed within them. This support includes all cooling flow metering and diagnostics for the klystrons, RF loads and circulators. It also provides focus electromagnet power, filament power and vac-ion pump power for the klystron. In addition, the transmitters include a solid state RF pre-amplifier for each klystron and interlocks on all required klystron parameters to shut down the modulator when the klystron is in danger of damage. In the SNS project, the power Converter/Modulator that provides cathode voltage and current to the klystrons is considered as a separate system and is discussed in another paper [2].

Each transmitter consists of three major sub-units: a control rack, a cooling metering cart and a high voltage enclosure. The sub-units for each type of transmitter are shown in Figures 2 and 3. The high voltage enclosures provide support for each klystron and contain the klystron's filament transformer and cathode current monitor. The cooling metering carts contain cooling diagnostics.

The NC transmitter cooling carts also include a blower to provide air cooling for the klystron windows. The control racks contain the interlock circuitry and solid state RF amplifiers to drive the klystrons. The 402.5 MHz version of the NC transmitters contains a 402.5 MHz solid state RF amplifier in the control rack and a separate cooling circuit in the cooling cart for 50% glycol/water cooling of the 402.5 MHz RF loads. The 805 MHz version of the NC transmitter contains an 805 MHz

0-7803-7738-9/03/$17.00 © 2003 IEEE

amplifier in the control rack and no separate glycol/water cooling circuit in the cooling cart. Aside from these characteristics the NC transmitters are functionally identical.

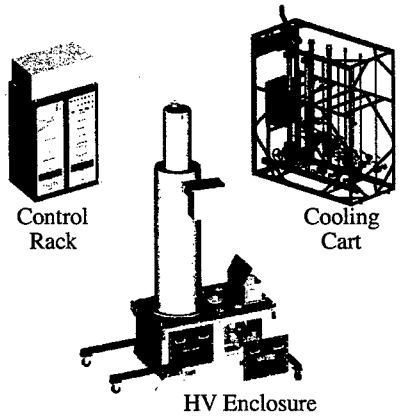


Figure 2: Each NC transmitter supports a single 2.5 MW or 5 MW klystron.

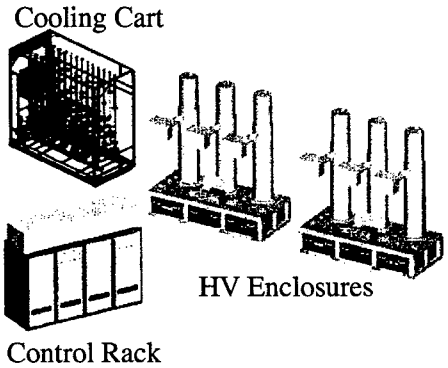


Figure 3: Each SC transmitter supports up to six 550 kW klystrons.

2 DESIGN FOR HIGH AVAILABILITY

2.1 SNS and Transmitter Availability Goals

The availability goals for the SNS transmitters were driven by the availability goal for the total SNS system. The availability goal for the entire SNS system is ≥90% by June 2008 [3]. To achieve this goal, the total availability for all systems within the linac must be greater than 98% [4].

In addition to the transmitters, the linac includes all accelerating cavities, circulators, klystrons and all Converter/Modulator power supplies [3]. For this reason, the transmitters were allocated only a small portion of the allowable down time for the linac. Therefore, the transmitter availability goal was chosen to be >99.5%.

Availability is defined here as the percentage of time that all transmitters are operational during the time that they are being required to be operational. Scheduled maintenance performed during time when the rest of the accelerator is shut down is not included.

A prediction of availability can be calculated using the Mean Time Between Failure (MTBF) and Mean Time To Repair (MTTR) as follows:

$$\text{Availability} = \frac{\text{MTBF}}{\text{MTBF+MTTR}}$$

An availability of 99.6% (>99.5%) implies that the ratio of MTBF to MTTR be 249:1. This value applies to the entire set of 27 transmitters, so the ratio for each transmitter is 27 times greater, or 6723:1.

2.2 MTTR Goal

MTTR includes both the time to diagnose the problem and the time to repair the problem. The LANL high power RF team's past experience with high power RF systems formed the basis of a goal of one hour to diagnose and repair a transmitter component failure. This goal was written into the transmitter specification and the vendor was required to provide calculations to justify their estimate of MTTR. Explicitly requiring a MTTR analysis helped the vendor to keep ease of repair in mind from the very beginning of the design process.

The time to diagnose a failure was minimized by a sophisticated first fault recording system within the transmitter control rack. A fault log with time stamps on each fault and notations on the first fault allow the user to determine the chronology of a multiple stage failure.

The time to repair a failure was minimized by using a very modular design in the transmitter sub-units. Chassis within the control rack included rails to allow for quick chassis change out. Connectors on the back of the chassis in the control rack were clearly labeled and keyed to reduce the chance of a cross connection during a chassis change out. Fully complete drawing packages and schematics were explicitly required in the transmitter statement of work to insure that the transmitter vendor would provide usable documentation.

2.3 MTBF Goal

Once the MTTR goal was established to be one hour, the MTBF goal was implied to be >6723 hours. An MTBF goal of 8000 hours was written into the transmitter specification to allow for a margin of error. The vendor was required to provide calculations to justify their estimate of MTBF.

MTBF calculations were based on published MTBF data for individual components. Preliminary MTBF calculations in the design reviews lead to many design changes that would not have been found otherwise. Design modifications included adding redundancy on components with lower reliability such as cooling fans and power supplies, and additional cooling where it would significantly improve the MTBF. The MTBF calculations took into account the unique characteristics of the klystron gallery at the SNS facility, and the transmitters were designed to maintain their reliability in an ambient temperature of 30 degrees C.

3 DESIGN FOR EASE OF INSTALLATION AND COMMISSIONING

The installation schedule for the SNS linac is aggressive. Conditioning and commissioning of the RF systems near the front of the linac is performed at the same time RF system installation is being done further down the linac gallery. The transmitters were designed to

minimize the amount of labor required to install and commission them.

The high voltage enclosures were provided with air pads to allow them to be moved by hand, even with klystrons attached and while filled with oil. The transmitter sub-units (control rack, water cart and HV enclosure) were delivered fully assembled to reduce the amount of installation labor. Finally, all cables and water hoses were delivered with lengths pre-cut to match the most up-to-date layouts of the klystron gallery and cable trays.

Requirements for complete operating and installation manuals were written into the transmitter contracts from the start of the project. This has produced well done, quality manuals and instructions that have significantly aided in the installation process.

The transmitter contract included an option to require the vendor come on site to assist in the installation process. This proved effective in the first transmitter installation at LANL. Installing the first transmitter as a test stand at LANL helped us work out any problems in the installation process and helped make the first installations at SNS to go more smoothly.

Extensive factory acceptance testing was performed to reduce the frequency of "infant mortality" failures during commissioning. This testing included a 96 hour full power heat run of all solid state RF amplifiers and a 24 hour heat run of the complete integrated transmitter system while operating every sub-system at full rated power.

4 DESIGN FOR COST CONTAINMENT

Warranty requirements for the transmitters were explicitly defined in the statement of work in order to reduce the cost of any transmitter repair in the early stages of SNS operation.

Costs were also reduced as the project developed. The NC transmitters were specified to have a full complement of protective interlocks for the klystrons, RF loads and circulators. When the choice was made to go with a superconducting linac with one klystron per cavity, the number of klystrons in the superconducting section dramatically increased. Eighty one 550 kW, 805 MHz klystrons are now required in the superconducting portion of the linac. Because of the large number of relatively small klystrons, it was decided that fourteen separate transmitters would each support 5 or 6 klystrons, as shown in Figure 1. The single klystron per SC cavity design offered a significant performance advantage, and this performance advantage was traded off against the increased transmitter cost caused by the additional klystrons.

SC transmitter cost was then traded off against functionality. The elimination of transmitter diagnostics such as cooling temperature measurement will make the diagnosis of faults in the RF systems more difficult to determine, increasing MTTR for the RF systems. A comparison of features in the NC an SC transmitters is shown in Table 1.

SC transmitter costs were also reduced by slowing down the specified response time for the transmitter interlocks. Slower interlock systems were less expensive to implement. The tradeoff is that a slower interlock can allow a fault condition to occur for a longer period of time and cause more damage to the component protected by the interlock. Increased damage leads to a decreased MTBF and an increased MTTR. Table 2 compares the specified interlock response times for the NC and SC transmitters.

Table 1: Comparison of Transmitter Features

Feature	NC Transmitter	SC Transmitter
PLC Fault Logging	Y	Y
Cooling Flow Interlocks	Y	Y
Cooling Temp. Interlocks	Y	N
Calorimetric Pwr Interlocks	Y	N
Calorimetric Pwr Recording	Y	N

Table 2: Comparison of Transmitter Response Time Requirements

Fault	NC Transmitter	SC Transmitter
Cathode overcurrent	<1μs	<100 ms
Vac-ion overcurrent	<50 ms	<100 ms
Klystron Magnet Current	<1μs	<100 ms
Klystron Magnet Voltage	<1μs	<100 ms
Klystron Body Temp.	<50 ms	N/A
Klystron Body Flow	<50 ms	<100 ms
Klystron Body Power	<50 ms	N/A
Klystron Collector Temp.	<50 ms	N/A
Klystron Collector Flow	<50 ms	<100 ms
Klystron Collector Power	<50 ms	N/A
RF Interlock fault	<50 ms	<100 ms

5 CONCLUSIONS

The development of the RF transmitter systems for the SNS project has been a challenging endeavor. The balance between reliability, ease of installation and cost shifted over the course of the project. These changes can be seen in the differences in design between the NC and SC transmitters. The performance advantages of the one-klystron-per-superconducting-cavity design and the drive to minimize costs were deemed to outweigh the corresponding decrease in reliability and availability of the transmitters in the superconducting section of the linac.

REFERENCES

[1] D. Rees, "The SNS Linac High Power RF System Design, Status, and Results", PAC 2003, May 2003.
[2] W. Reass, "Design, Status, and First Operations of the Spallation Neutron Source Polyphase Resonant Converter/Modulator System", PAC 2003, May 2003.
[3] N. Holtkamp, "SNS Project Update", 11th ICFA International Mini-Workshop on Diagnostics for High-Intensity Hadron Machines, October, 2002.
[4] B. Miller, "System Requirements Document for WBS 1.4 Linac Systems", SNS Internal Design Document.

COMPLETION OF CCL HOT MODEL FOR SNS-LINAC R&D PROGRAM *

R. Hardekopf†, J. Bernardin, J. Billen, N. Bultman, W. Fox, T. Hardek, S. Hopkins, S. Nath, D. Rej, P. Tallerico, L. Young
Los Alamos National Laboratory, Los Alamos, NM 87545

Abstract

Los Alamos completed the R&D program for the SNS linac in September 2002 with publication of a comprehensive report on the SNS coupled-cavity linac (CCL) hot model [1]. In this paper we summarize the results of this R&D program, including design of the bridge-coupled CCL, refinement of the design through cold models, and fabrication and testing of a hot model. We describe the RF system used to power the model, the prototype water-cooling and vacuum systems, and the experimental tests of these systems, including low-power, high-power, and radiation measurements. The CCL hot-model experiments answered vital questions about design, manufacturability, and stability for this type of RF structure.

INTRODUCTION

The Spallation Neutron Source (SNS) linac consists of four accelerating elements. A radio-frequency quadrupole (RFQ) accelerates the beam from an ion source to 2.5 MeV, a drift-tube linac (DTL) accelerates the beam from 2.5 to 87 MeV, a coupled-cavity linac (CCL) accelerates the beam from 87 to 185 MeV, and a superconducting radio frequency linac (SFF linac or SCL) accelerates the beam from 185 to 1,000 MeV. The linac R&D program at Los Alamos centered on designing and testing a representative segment of the CCL with full RF power. This program effectively tested both the physics and engineering designs of the cavity themselves, as well as prototypes of the vacuum, water-cooling, resonance control, and RF-power systems.

THE CCL HOT MODEL

A "hot model" is a powered section of a linac structure that is usually constructed as a prototype before major funds are committed for full construction. For SNS, the R&D program ran concurrently with much of the final design and procurement. To prove the concepts in time to influence manufacturing, we built a two-segment CCL hot model with prototype vacuum and water systems The purpose of the hot-model was to (1) confirm the physics design and manufacturing of the cavities, (2) verify the vacuum and resonance-control systems, (3) qualify vendors for procurement of CCL components, and (4) examine operational issues such as cold start, multipactoring, cavity conditioning, RF-field distribution under power, and thermal distribution. See [1] for details.

* Work supported by the Office of Basic Energy Science, Office of Science of the US Dept. of Energy, and by Oak Ridge National Lab.
† hardekopf@lanl.gov

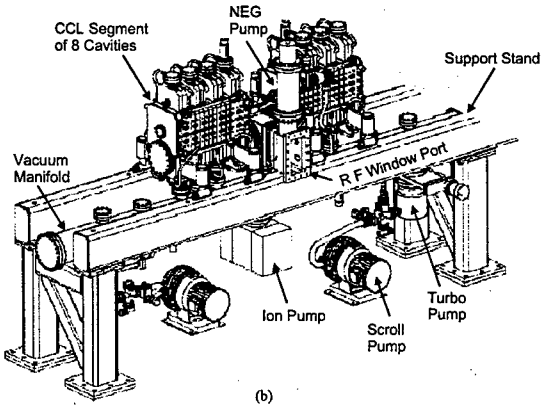


Figure 1. CCL hot model on support stand

CAVITY DESIGN

The SNS CCL requires relatively short accelerating segments compared to some previous CCLs to allow the frequent magnetic focusing required for high-current linacs. This requires resonant coupling (bridge couplers) between a large number of segments for efficient use of RF power. We used the cavity design code *Superfish* to design the shapes of the cavities and to compute surface fields, shunt impedance, and transit-time factors. The field contours shown in Fig. 2 for the TM_{010} mode are lines of constant magnetic field H, which are parallel to the electric field direction.

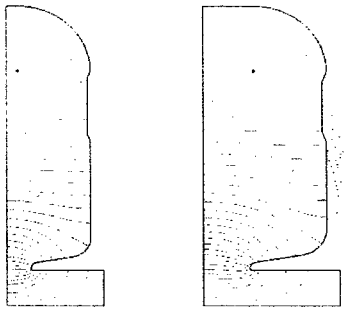


Figure 2. Superfish fields for CCL accelerating cells for $\beta = 0.40$ (left) and $\beta = 0.56$ (right)

In addition to the accelerating cavities, two types of coupling cavities and a bridge coupler cavity, which spans the space between two segments of the CCL structure, were required. One coupling cavity connects two accelerating cavities and the other connects an

0-7803-7738-9/03/$17.00 © 2003 IEEE

accelerating cavity to the bridge-coupler center cavity. To test the physics design, we built several "cold models" to determine the optimum shapes and coupling [2].



Figure 3. Example of cold model with bridge coupler

The mechanical design of the CCL hot-model cavities is described in [3]. The CCL is a multi-cell copper structure comprised of four modules, each made up of twelve segments. Each segment contains eight accelerator cavities or cells (see Figure below). For details of the fabrication process, see [4].

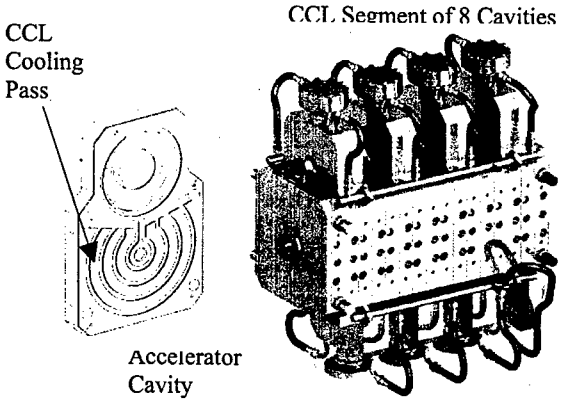


Figure 4. A CCL 8-cell segment with exploded view of the cooling passages

VACUUM SYSTEM

The four main goals of the vacuum experiments on the CCL hot model were (1) Determine if the vacuum system design could satisfy the vacuum pressure requirement of 9×10^{-8} Torr, (2) Measure gas composition of the vacuum environment, (3) Obtain empirical data to benchmark the numerical vacuum model, and (4) Characterize the vacuum conditioning process. To accomplish these goals, we did computer modeling to design the system and compared the experimental results with the model predictions. The results confirmed the design and gave us significant data important to final design of the CCL. See Ref. [1] for details.

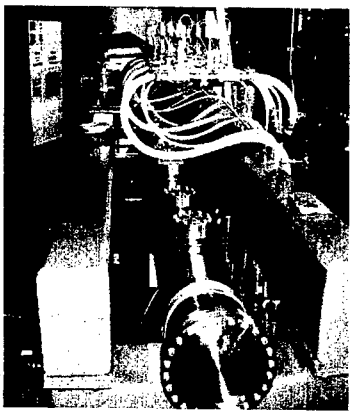


Figure 5. Hot-model vacuum manifold

WATER SYSTEM

The system that supplies the cooling water is equipped with a pump for coolant flow, a heat exchanger to cool the water, a heater to increase cavity temperature if needed, and a three-way valve to divert some of the water returning from the cavities through the heat exchanger while allowing the rest to recirculate [5].

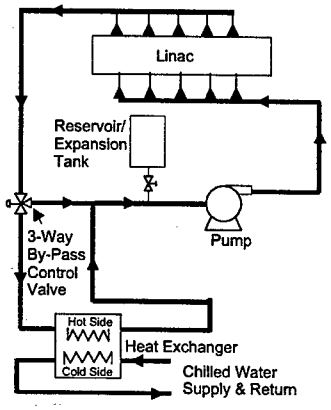


Figure 6. Simplified diagram of water-cooling system

The pump is run at a constant flow, and the flow rate into the cold side of the heat exchanger is also held constant. Many points, including surface temperatures, water temperatures, flow rates, the three-way valve position, forward and reflected RF power, as well as the RF error signal are instrumented and displayed by the control system. Numerical flow network models successfully predicted pressure drops within the CCL RF structure and water-cooling skid. See Ref. [1] for details.

RF POWER SYSEM

The 805-MHz RF system for the SNS linac was initially designed with 2.5-MW peak-power klystrons that used modulating anodes and isolated collectors. For the hot-model testes we initially used an existing modulator to provide power for the klystron, but it was limited in

average power capability. Later in the experiment, we substituted the high-voltage converter modulator (HVCM), providing the initial test bed for this new technology. The 2.5-MW *CPI* klystron used for the hot-model tests exceeded all specifications and produced 2.5 MW within a few minutes of when it was turned on. It performed flawlessly during the hot-model tests. The complete hot-model RF-power system and its calibration are described in [1].

ASSEMBLY AND OPERAION

Following assembly, we made low-power RF measurements to tune the cavities. An axial bead-perturbation measurement showed a constant value of E0 to within ± 0.4% rms. See [1] and [4] for details.

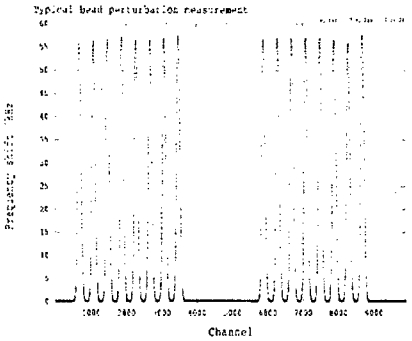


Figure 7. Bead pull measurement on hot-model cavity

We also measured the tilt sensitivity (or stability of the fields against frequency perturbations) by deliberately introducing end-cell perturbations. We raised the cell-1 frequency 160 kHz by pulling the end wall and lowered the cell-16 frequency 160 kHz by inserting a metal tube in the bore. A plot of the percentage difference in field between perturbed and unperturbed measurements showed the expected slope of ~+50 kHz [2].

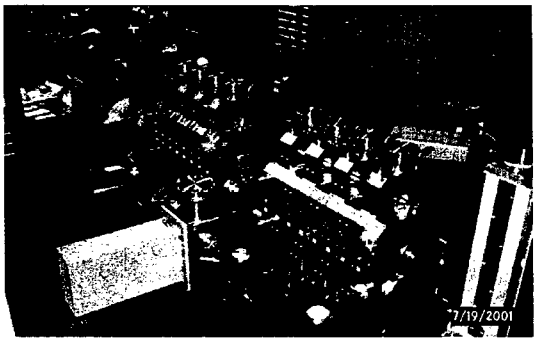


Figure 8. Photograph of the bead-pull measurements being performed on the CCL hot model

An important goal of the hot model testing was to measure the stop-band gap at full RF-power operating conditions. To measure the stop band, we used the last 50 μs of the pulse to switch in a different RF generator whose frequency we could control. By observing the reflected power during this part of the pulse, we measured the frequencies of the two nearest modes to the $\pi/2$ mode. The stop band was slightly more positive at high power than at low power. The fact that these modes remain at very nearly the same frequency at different power levels indicates that cooling of the coupling cavities is well balanced with that of the accelerating cavities and that the stop band in the dispersion curve is not sensitive to the power level. See Ref. [1] for details.

Thermo-luminescence detectors (TLDs) were used to take measurements of the dark-current x-rays at a nominal power level of about 280 kW during a 1-hr run. The TLDs were placed directly above the O-ring on the flange joining the accelerating cavities to the powered bridge coupler. The readings ranged from 1.3 to 3.0 rad/hr. For an estimated SNS 40-year operating life, using 24-hr/day and 300 days/year, the highest reading of 3 rad/hr is equivalent to 0.9-megarad accumulated dose. Since *Viton* O-rings have an estimated radiation tolerance of at least 20 megarad, these measurements indicate that SNS should have no trouble with this use of O-rings in the CCL.

SUMMARY

We met or exceeded our principal goals of demonstrating that the CCL RF structure could be tuned and operated in a stable manner at required power levels. We developed a manufacturing process and a comprehensive tuning plan to be used by industry [4]. We were able to test much of the SNS prototype hardware in an integrated test, including the vacuum system, water-cooling and resonance-control system, the HVCM, the 2.5-MW prototype klystron, and the bridge-coupled CCL structure. This experience has allowed us to anticipate some of the problems that LANL and ORNL will face as we test and commission the CCL at Oak Ridge.

ACKNOWLEDGEMENTS

We gratefully acknowledge the efforts of many Los Alamos engineers, designers, technicians who provided the hot-model hardware. We also acknowledge the support of their group leaders who set priorities and provided leadership during the fabrication and testing.

REFERENCES

[1] R. Hardekopf, editor, "SNS Coupled-Cavity Linac Hot Model," LA-13975, Sept. 2002. Obtain from www.osti.gov/servlets/purl/809551-FCR7Kd/native/.

[2] J. Billen *et al.*, "Room Temperature Linac Structures for the SNS," PAC 2001, Chicago, IL, 1104.

[3] N. Bultman *et al.*, "Mechanical Design of the SNS CCL," PAC 2001, Chicago, IL, 2189.

[4] N. Bultman *et al.*, "Fabrication and Tuning of the SNS CCL Hot Model," PAC 2003, this conference.

[5] J. Bernardin *et al.*, "Resonance Ctrl for CCL and DTL Structures of SNS Linac Using a Closed-Loop Water Cooling System," PAC 2001, Chicago, IL, 1429.

OPERATIONAL PERFORMANCE OF THE SNS LLRF INTERIM SYSTEM*

Lawrence Doolittle†, Alessandro Ratti, Marco Monroy, LBNL, Berkeley, CA 94720, USA
Mark Champion, Hengjie Ma, ORNL, Oak Ridge, TN 37830, USA

Abstract

A new approach has been taken to develop and build the Low-Level RF Control System for the SNS Front End and Linear Accelerators, as reported in a separate paper in this conference[1]. An interim version, based on the proven LBNL MEBT design, was constructed to support short-term goals and early commissioning of the Front End RFQ and DTL accelerators, while the final system[2] is under development. Additional units of the interim system are in use at JLab and LANL for concept testing, code development, and commissioning of SNS SRF cryomodules. The conceptual design of the MEBT system had already been presented elsewhere[3], and this paper will address operational experiences and performance measurements with the existing interim system hardware, including commissioning results at the SNS site for the Front End and DTL Tank 3 together with operational results from the JLab test stand.

INTRODUCTION

The LLRF hardware, firmware, and software described here all involve evolutionary changes from the SNS MEBT design[3]. The hardware in particular was modified to be simpler, easier to assemble, and more rugged and reliable in the field. The 19" rack-mount chassis changed from 4U high × 500 mm (20") deep to 2U high × 350 mm (14") deep.

It takes very little laboratory electronics to turn on a chassis and operate a cavity with it. Besides power and Ethernet, it needs: an external TTL trigger/gate, a +5V interlock permit, and +5 dBm of the relevant LO (e.g., 352.5 MHz). The frequency of operation is 50 MHz above the LO; three passive connectorized filters included in the chassis have to match the RF. The available output power level of +10 dBm will normally need amplification to drive a cavity. The down conversion mixer for the cavity signal is supplied externally; in the SNS installation, that mixer is temperature controlled and matched to a mixer for the phase reference signal.

*This work is supported by the Director, Office of Science, Office of Basic Energy Sciences, of the U.S. Department of Energy under Contract No. DE-AC03-76SF00098. The SNS project is being carried out by a collaboration of six US Laboratories: Argonne National Laboratory (ANL), Brookhaven National Laboratory (BNL), Thomas Jefferson National Accelerator Facility (TJNAF), Los Alamos National Laboratory (LANL), E. O. Lawrence Berkeley National Laboratory (LBNL), and Oak Ridge National Laboratory (ORNL). SNS is managed by UT-Battelle, LLC, under contract DE-AC05-00OR22725 for the U.S. Department of Energy.

† ldoolitt@recycle.lbl.gov

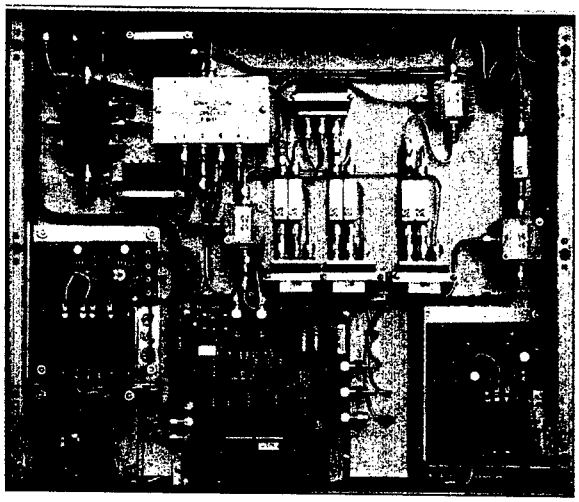


Figure 1: Chassis photograph.

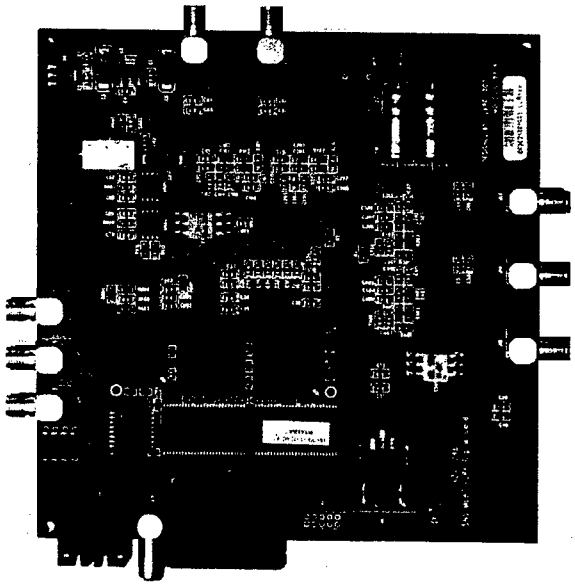


Figure 2: Photograph of main LLRF circuit board.

DESIGN AND CONSTRUCTION

The heart of the chassis is a 137×132 mm circuit board that holds the four 12-bit ADCs (ADS808) operated at 40 MS/s, and a single 12-bit DAC (DAC902) operated at 80 MS/s. A (now obsolete) Xilinx XC2S150 FPGA pro-

0-7803-7738-9/03/$17.00 © 2003 IEEE

vides the signal processing path, and connects to an embedded single board computer, the Bright Star Engineering nanoEngine[4]. Four of that computer's digital I/O pins are used to program the FPGA via its JTAG interface. The FPGA also provides access to housekeeping functions: a phase lock loop, 4 channels of slow DAC, 8 channels of slow ADC, a serial number, and a digital thermometer. The chassis as a whole dissipates 28 Watts, using linear 5V and 15V open frame power supplies.

The phase lock loop circuitry, based on an ADF4001, can lock the on-board voltage controlled crystal oscillator (VCXO, 80 MHz Connor-Winfield UPLD54TE) to an external source. In our case, that source is a 50 MHz phase reference that is used to synchronize cavities across the accelerator site. For most bench testing purposes, that capability can be ignored, and the system free runs at a frequency that is typically 6 kHz low.

Of the four high speed input channels on the board, one was originally labeled "spare." That channel has now been pressed into service recording the input phase reference signal. Measurement of its phase, and performing software corrections based on it, corrects for both the four-fold state held in the PLL, and most of the phase drift involved in bringing the cavity field pickup signal from the tunnel to the control rack[5].

The original SNS MEBT chassis generated its 50 MHz IF output from a distinct 50 MHz source and an analog I/Q modulator. To eliminate the need for that separate (external) signal source, a high speed DAC was pressed into service to directly generate a vector controllable 50 MHz signal. A nominal 30 MHz waveform is updated at 80 MS/s using a DAC with a current rise time of a nominal 1 ns. This raw output has "spurs" at 50 MHz, 110 MHz, 130 MHz, and higher, with power in each line proportional to $1/f^2$. A pair of passive analog filters selects the 50 MHz output for up conversion to the final frequency. We have tested use of DDS (Direct Digital Synthesis) computations inside the FPGA to adjust the output frequency by up to 625kHz. No additional hardware is required to implement this adjustment, which is in concept limited only by the 2.5 MHz bandwidth IF filters used.

Hard-wired interlocks provide positive cutoff of the RF drive in case of external fault conditions. This feature is purposefully independent of, and not over-ridable by, the FPGA and embedded computer.

BENCH CHARACTERIZATION

Careful measurements on the input ADC channel show a white noise spectrum from 0.2 to 5 MHz of 0.22 bits/$\sqrt{\text{MHz}}$ (1.0 bit rms of each sample). Clock jitter adds an additional broadband noise term of 0.0075°/$\sqrt{\text{MHz}}$ (1.3 ps rms on each sample). This noise by itself, integrated over the 300 kHz-ish noise bandwidth of a closed loop cavity system, contributes only about 0.012% and 0.004° of rms cavity field noise. There is additional low frequency noise that doubles the phase noise.

FIRMWARE

The firmware inside the FPGA handles all timing and computation within the 1 ms SNS beam pulse, without intervention from the host computer. Digitized cavity input samples first have their DC offset and the 10 MHz (nominal) output of the setpoint DDS subtracted, to create an error signal. This error is passed through a digital filter

$$(\mathrm{Re}(A_P) + \mathrm{Im}(A_P)z^{-1}) \cdot (1 + A_I/(1+z^{-2}))$$

to generate the output drive signal. The $\mathrm{Re}(A_P) + \mathrm{Im}(A_P)z^{-1}$ term provides gain and phase rotation based on the complex proportional gain coefficient A_P. The $1/(1+z^{-2})$ term is the integrator, and A_I (always real and positive) sets its relative strength. The three multipliers are constructed as dynamic constant coefficient multipliers, for speed and reduced FPGA logic footprint. This filter and the DDS account for most of the 1829 FPGA logic elements used in the design (53% of the chip).

The FPGA only has 48 kbits of on-board RAM, in 12 banks of 4096 bits each. It is allocated as follows:

512×8	Feedforward table
1024×12	Decay wave (reflected or transmitted signal)
1024×11	Forward wave
1024×11	Reflected wave
1024×10	Transmitted wave

Each table is filled half with Real (I) and half with Imaginary (Q) components of the RF waveforms. The latter three history buffers are intended for troubleshooting and operator comfort displays; they have programmable decimation from the raw signal rate, so a full 1 ms pulse can be viewed. Firmware to replace the decimation with 16-bit resolution averaging has been written but not tested. The decay wave data is used by curve fitting routines that determine cavity detune frequency.

With a few exceptions, the signal processing path is expressed as pure synchronous RTL (Register Transfer Level) Verilog in the 40 MHz clock domain. All logic related to the host interface, including support for the low speed housekeeping devices, is expressed as pure synchronous RTL Verilog in the domain of the 25 MHz bus clock provided by the embedded single board computer. Data handoff between these two clock domains happens at the 60 Hz (max) pulse rate, so classic asynchronism issues such as metastability are minimized.

SOFTWARE

Software inside the embedded computer handles all network (100 Mbit Ethernet) traffic, EPICS, and all the computation that happens between beam pulses spaced at least 15 ms apart.

Recent work on EPICS[6] has made it portable to any software environment with POSIX compatibility. We use this capability to run EPICS R3.14.1 on an ordinary Linux

(kernel 2.4) system. We combine about 1600 lines of application and hardware specific C code, with another 900 lines of custom "glue" and the existing EPICS code base, to make the final EPICS server.

A key application specific routine run on this processor is curve fitting to determine the cavity detune frequency. In most cases this information is passed over the network to run a stepper motor or water temperature control, to keep the cavity on resonance.

The 200 MHz StrongARM processor boots Linux from Flash and NFS mounts application-specific files in nine seconds. Four seconds later, the FPGA is programmed and the EPICS server is ready for client connections.

FRONT END BEAM TESTS

This module was first tested with beam on the SNS Front End RFQ in January 2003. During the limited time available, The RF system as a whole had some large (15°), repeatable phase fluctuations, although it could never be isolated to single piece of equipment. No such noise has been seen in the LLRF system before or since. Further tests are planned when this system runs both the RFQ and DTL 1 during the next beam commissioning run.

SRF TEST RESULTS

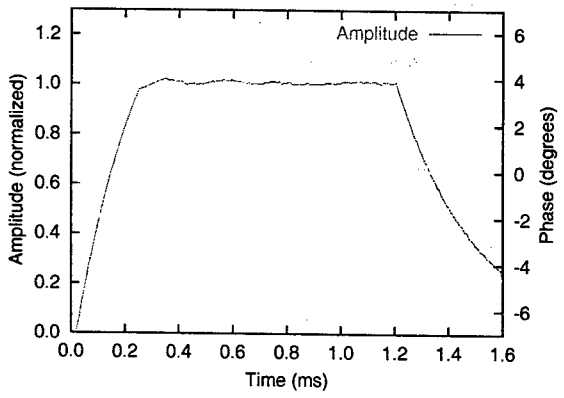


Figure 3: Cavity waveforms from a JLab SRF cavity test.

A prototype SRF cavity was successfully controlled by an interim LLRF system at JLab. An example of such operation is shown in figure 3. The system did an excellent job of removing the phase and amplitude motion within the pulse caused by Klystron power supply droop. The largest error terms were repetitive from pulse to pulse. Careful hand adjustment reduced these terms to $\pm 1\%$ and $\pm 1°$ peak excursion. Plans exist for software to make automated and more flexible adjustments to the feedforward tables to reduce that error further. The pulse-pulse phase fluctuations during these initial tests appeared to be in the $\pm 0.3°$ range.

This hardware was used to demonstrate the following capabilities and features in the SRF environment:

- Control of slow cavity tuners, using curve fits to the trailing edge decay waveform.
- Single shot (burst mode) determination of cavity frequencies detuned by up to 8 kHz (15 bandwidths).
- Fast piezoelectric tuner compensation of Lorentz force detuning.
- Calorimetric (cryogenic) cavity Q measurement.

DTL TEST RESULTS

This system has run SNS DTL (Drift Tube Linac) tank 3 in open loop mode at various duty factors for conditioning the structure. Its resonance calculation was used to track the temperature changes of the tank during warm-up, with the frequency adjusted using an external synthesizer. Work is underway to replace that synthesizer adjustment with the local DDS capabilities.

CONCLUSIONS

Using FPGA technology for low-latency signal processing has immediate benefits for many applications in accelerator electronics, such as instrumentation, interlocks, and controls. Even FPGAs that are relatively small (by today's standards) can do an impressive amount of work, simplifying hardware design enormously.

The implementation presented here has shown the benefits of keeping hardware simple. The combination of an FPGA and a networked computer has made it easy to add new features, test hardware performance, and explore application of this gear to other accelerator development projects. We look forward to collaborating with other labs on further development of this technology.

More documentation on this project is posted online[7].

An ongoing, collaborative effort with ORNL and LANL[2] takes the concepts and architecture demonstrated here and engineers a system that can be fielded in quantity $\sim$100 for the long term needs of the SNS accelerator.

REFERENCES

[1] M. Champion *et al.*, "The Spallation Neutron Source Accelerator Low Level RF Control System," these proceedings.

[2] A. Regan *et al.*, "Newly Designed Field Control Module for the SNS," these proceedings.

[3] L. Doolittle *et al.*, "The SNS Front End LLRF System," Linac 2002, Gyeongju, Korea, August 2002.

[4] Bright Star Engineering, Andover, Mass., USA, http://www.brightstareng.com/arm/nanoeng.htm

[5] H. Ma, "SNS LINAC RF Control: Reference System and Phase Measurement," SNS LLRF Tech Note 3, May 2002.

[6] http://www.aps.anl.gov/epics/

[7] http://recycle.lbl.gov/~ldoolitt/llrf/

BEAM DUMP WINDOW DESIGN FOR THE SPALLATION NEUTRON SOURCE*

G. Murdoch, A. Decarlo, S. Henderson, S. Kim, K Potter, T. Roseberry, Oak Ridge National Laboratory, USA
J. Rank, D. Raparia, Brookhaven National Laboratory, USA

Abstract

The Spallation Neutron Source accelerator systems will provide a 1 GeV, 1.44 MW proton beam to a liquid mercury target for neutron production. Beam tuning dumps are provided at the end of the linac (the Linac Dump) and in the Ring-to-Target transport line (the Extraction Dump) [1]. Thin windows are required to separate the accelerator vacuum from the poor vacuum upstream of the beam dump. There are several challenging engineering issues that have been addressed in the window design. Namely, handling of the high local power density deposited by the stripped electrons from the H- beam accelerated in the linac, and the need for low-exposure removal and replacement of an activated window. The thermal design of the linac dump window is presented, as is the design of a vacuum clamp and mechanism that allows remote removal and replacement of the window.

INTRODUCTION

The SNS linac zero degree beam dump is to be passively cooled dissipating 7.5kW of beam power. The beam flight tube immediately upstream of the dump will be either evacuated or back filled with helium, to separate this medium from the accelerator machine vacuum a beam window is proposed.

DESIGN PARAMETERS

Physics

The window must be able to withstand continuous pulses of 2.1e14 H- particles/pulse with a pulse duration of 1ms at a frequency of 0.2Hz; continuous running is simulated as the worst case scenario. The 2-D gaussian proton beam power density profile for Inconel with the above conditions is given in Figure 1 assuming a window thickness of 2mm [2].

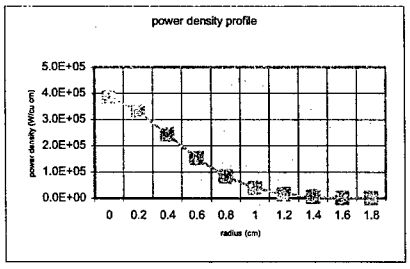


Figure 1

Mechanical

Several criteria must be considered during the mechanical design process. From an operations/maintenance view point a passive window design satisfying the physics parameters above would be the optimum solution i.e. no active cooling apart from convective cooling to air. Also, the window design must be integrated into the overall linac dump beam line design with consideration for subsequent handling issues such as shielding and remote removal and installation.

MECHANICAL DESIGN

A circular domed window 80mm in diameter (beam diameter is 40mm) is adopted as the base design for thermal analysis. Initial runs indicated that the maximum thermal stress can be reduced by ~40% if the beam impinges on the outer surface of the dome instead of the inner surface, it is likely this geometry creates less restriction to thermal expansion of the high temperature surface. Adopting a domed window is also advantageous from a structural integrity point of view. Three radial fins are added to promote convection. Three materials are considered, Aluminum 6061-T6, GlidCop Al-15 & Inconel 718. It is intended to integrate the window design with two EVAC type vacuum flanges, this allows the window and flanges to be designed as an integral component. Also, to aid handling a remote vacuum clamp will be designed.

THERMAL ANALYSIS

The window is modeled as a 2-D axisymmetric running a transient thermal analysis to mimic the pulsed beam parameters. The beam loading is input to the ANSYS solution solver via a text program written to enable the specific beam conditions to be applied. Typical Inconel 718 values for the proton heat generation across a window thickness of 2mm and electron heat generation (across the first 0.5mm for Aluminum and 0.2mm for GlidCop & Inconel [3]) are given in Figure 2, these are derived from Figure 1 using the appropriate material deposition ratios [4]. The incremental values are applied to the model nodes as a function of radius from the center of the window outwards.

Inconel 718

Proton Contrib. power density watts/cu mm	Electron Contrib. power density watts/cu mm	Total p & e Contrib. 0.2mm Deep watts/cu mm	Rad. Lim. mm
2.94E+02	9.23E+02	1.22E+03	0
2.52E+02	7.92E+02	1.04E+03	2
1.85E+02	5.83E+02	7.68E+02	4
1.17E+02	3.68E+02	4.85E+02	6
6.33E+01	1.99E+02	2.62E+02	8
2.93E+01	9.22E+01	1.21E+02	10
1.16E+01	3.66E+01	4.82E+01	12
3.96E+00	1.24E+01	1.64E+01	14
1.15E+00	3.62E+00	4.78E+00	16
2.87E-01	9.03E-01	1.19E+00	18

Figure 2

ANALYSIS RESULTS

Considering the results table of Figure 3, the maximum stress in Aluminum after 45.01s is 158 N/mm^2, which is 80% of the yield strength of the material at 200 C. More

importantly it is ~3 times the fatigue endurance limit. Running the window consistently above the fatigue limit would pose questions on potential crack propagation and consequently lifetime issues.

Material	MaxTemp	M. Point	Stress	Deflection	UTS	Yield	Fatigue
			Von Mises				
	Deg. C	Deg. C	Nmm-2	mm	Nmm-2	Nmm-2	Nmm-2
						(1e7 cycles @ 200 C)	
Alu6061-T	208	582	158	0.11	310	250	75
	(@45.01s)		(@45.01s)			(@ 200C)	(@ 200C)
						(1e7 cycles @ room temp)	
Glidcop-Al	229	1083	229	0.07	269	200	207
	(@45.01s)		(@45.01s)		(@ 200C)	(@ 200C)	
						(1e7cycles @ 540 Deg C)	
Inconel-71	635	1300	486(596)	0.3	965	862	655
	(@195.04s)		(@195.04s)		(@ 650 C)	(@ 650 C)	

Figure 3

The maximum stress seen in the GlidCop after 45.01s is 229 N/mm^2, which is above the yield strength of the material at 200 C. Comparison with fatigue values is difficult as data at elevated temperatures is scarce. Due to the poor diffusivity of Inconel the analysis is run for a longer period of time to achieve near equilibrium conditions, Figures 4 shows the transient analysis plot for Inconel-718. The maximum stress seen in the Inconel window is 596 N/mm^2, (after the first pulse) but tails off to a maximum value of 486 N/mm^2, at 195.04s, shown in Figure 5. This is probably due to the window absorbing heat, slowly warming and consequently causing a reduction in the temperature differential across the window. These stress values compare favorably with a yield strength of 862 N/mm^2, at 650 C and a fatigue endurance limit of 655 N/mm^2, for 1e7 cycles at 540 C.

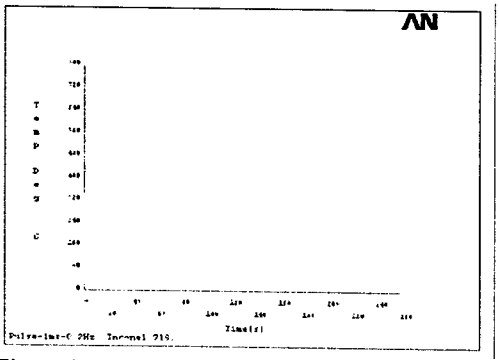


Figure 4

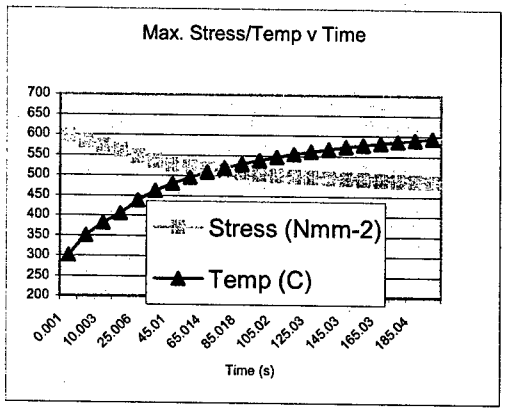


Figure 5

The stress and temperature fringe profiles for Inconel-718 are shown in Figure 6&7 respectively. Consideration of the principal stresses shows a maximum tensile stress value of 213 N/mm^2 and the maximum compressive stress value of 474 N/mm^2, this compressive stress is likely to inhibit crack propagation in the high temperature area.

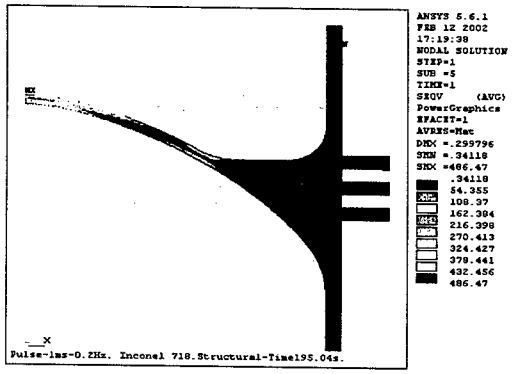


Figure 6

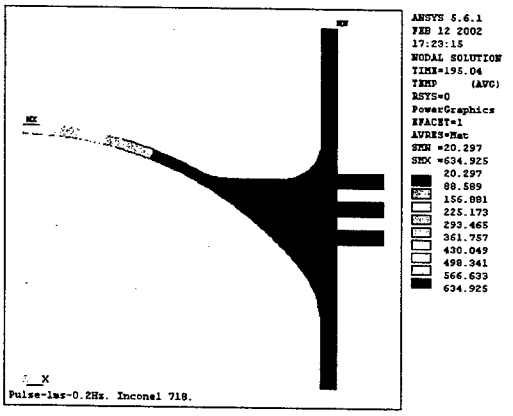


Figure 7

ANALYSIS CONCLUSIONS

For a passively cooled window Inconel-718 is clearly the most robust choice of the three materials analyzed. One concern is continuous running at temperatures in the order of 635 C, although this is localized at beam center. Radiation heat transfer from the window surface has not been considered but basic calculations show that the radiated heat is negligible, being in the order of 1 – 5 watts depending on the emissivity value chosen. The stress values are well within the yield and fatigue limits quoted in the extensive literature available for the material.

Inconel-718 is a recognized quantity from a proton irradiation lifetime point of view, however, it does contain longer half-life isotopes than either GlidCop or Aluminum and consequently will remain more activated. This will have to be taken into consideration in all work planning as an ALARA issue. The choice of a high integrity material such as Inconel-718 should lead to less down time and consequently improved machine availability. A 3-D ProE model of the finalized window design is shown in Figure 8.

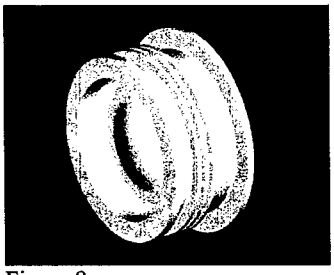


Figure 8

WINDOW REPLACEMENT

In the event of a window failure the window would have to be removed and replaced. It is likely that this could not be done by hands-on maintenance because of high residual radiation dose rates from the window material and surrounding equipment. Consequently, a window change scenario was addressed with many design options studied.

Two remote vacuum clamp designs have been pursued both of which are built and ready for testing. One version of the clamp is shown in Figure 9. The clamp is designed to utilize a standard EVAC type flange.

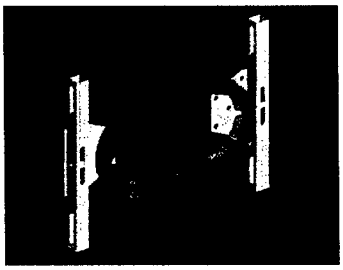


Figure 9

A test rig that will be used to validate the vacuum clamps and mimic a full window change scenario has also been designed and manufactured, this is shown in Figure 10.

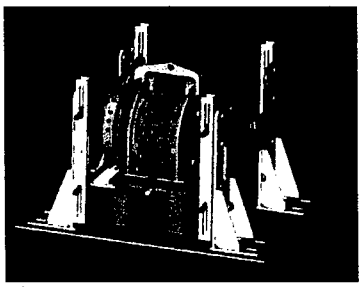


Figure 10

The test rig design is based on the handling concept that the window assembly shown in Figure 11 would be removed each time a window is replaced. A cradle will be lowered into position over the bellows assembly, the vacuum clamps are then opened and the cradle manipulated to compress the bellows. Once the bellows are compressed the window assembly including vacuum seals that are captive to the assembly can be removed. Provision has been made in the design for testing two proprietary vacuum seals, EVAC aluminum diamond and helicoflex delta.

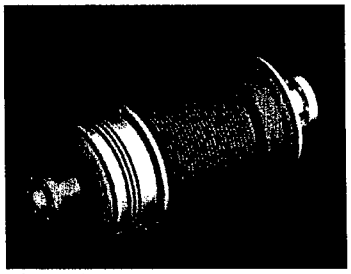


Figure 11

REFERENCES

[1] Deepak Raparia et al., Brookhaven National Laboratory, these proceedings.

[2] Deepak Raparia, Brookhaven National Laboratory, USA Private Communication.

[3] Stuart Henderson, SNS Project, Oak Ridge National Laboratory, Private Communication, Studies in Penetration of Charged Particles in Matter, Nuclear Science Series, Report No. 39.

[4] Franz Gallmeier, SNS Project, Oak Ridge National Laboratory, Private Communication.

*SNS is a collaboration of six US National Laboratories: Argonne National Laboratory (ANL), Brookhaven National Laboratory (BNL), Thomas Jefferson National Accelerator Facility (TJNAF), Los Alamos National Laboratory (LANL), Lawrence Berkeley National Laboratory (LBNL), and Oak Ridge National Laboratory (ORNL). SNS is managed by UT-Battelle, LLC, under contract DE-AC05-00OR22725 for the U.S. Department of Energy.

STATUS OF TIMING SYSTEM AND ITS UPGRADE FOR THE PLS STORAGE RING

M.H. Chun, B.R. Park, J.S. Yang, D.T. Kim, H.S. Kang, Y.J. Han and S.H. Nam
Pohang Accelerator Laboratory, POSTECH
San-31 Hyoja-dong, Pohang 790-784, Korea

Abstract

The timing system for the Pohang Light Source(PLS) storage ring consists of a trigger synchronize module, a fine delay module, a repetition rate pulse generator module, and so on. All the timing modules are installed in the VXI crate and controlled by the 32 bit microprocessors with the host computer. Although the timing system has been operated without any serious problems since commissioning in 1994, there were some minor troubles, and the performances were not so excellent. Therefore, upgrade of the timing system is progressing with a synchronous universal counter and other commercial modules of NIM type for increasing of a reliability, easy maintenance, low timing jitters, and all types of beam filling pattern.

1 INTRODUCTION

The Pohang Light Source (PLS) is a 2.0 to 2.5 GeV, the third generation synchrotron radiation source, which has a full energy linac and a storage ring. The PLS is usually operating at 180 mA storage currents of 2.5 GeV full energy injection with 400 multi-bunch mode[1]. The function of the timing system is to provide the synchronized trigger signals for the linac, the kicker magnet of the injection system, so that a bunch will be fully accelerated in the linac and transported to the injection point at the right time, and injected into the storage ring properly. The PLS timing system was capable of producing trigger pulses for all the pulsed devices that are an electron gun, klystron modulators as well as a kicker[2].

Parameters of present timing system are shown in table 1.

Table 1. Parameters of Present Timing System

Storage Ring RF Frequency	500.082 MHz
Harmonic Number	468
Revolution Frequency	1.068 MHz
Linac RF Frequency	2856 MHz
Repetition rate of Gun	10 Hz
Repetition rate of Modulators	30 Hz
No. of Modulators	12 set
Adjusting Delay range	5 ps to 2 sec
General Delay for Kicker	42.09 us
Jitter between SR and Linac	~200 ps (rms)

2 PRESENT TIMING SYSTEM

The main requirements of timing system is to fill up the required storage ring buckets as well as partial buckets in any pattern and have the small timing jitter so that the beam quality and the transfer efficiency are maintained. For the successful injection, the timing system should provide accurate trigger signals for the gun, klystron modulator in the linac, and injection kicker magnet in the storage ring. For high flexibility and reliability of the timing system, all timing modules are installed in a VXI crate, and fully controlled through the communication network from the upper level computers. The timing trigger pulses are generated with the main modules, such as a trigger synchronizer module(TSM), a repetition rate pulse generator(RRG) and a fine delay module(FDM). Figure 1 shows a block diagram of the present timing system for the PLS storage ring and linac.

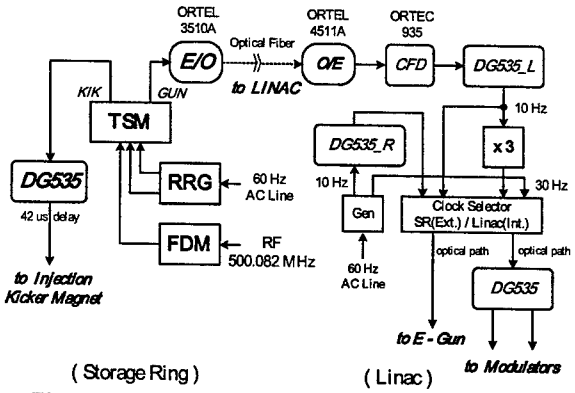


Figure 1 : Block Diagram of Present Timing System

The FDM has two function of dividing the rf frequency by harmonic number and delaying with 2 nanosecond each by the a programmable delay through the computer program. The outputs of the FDM are a storage ring clock and a delayed ring clock of 1.068 MHz revolution frequency. The RRG gives the electron gun and klystron modulators the repetition rate pulse which is synchronized by AC power line. Synchronizing the timing signals to the AC mains is important to minimize the effects of magnet and klystron modulator power supply ripples on the beam [3] The repetition rate pulse is 10 Hz for the gun and kicker, and 30 Hz for the klystron modulators in order to stable operation. The TSM generates timing signals for a gun, modulators and a kicker, which are synchronized on the 500.082 MHz storage ring rf and 1.068 MHz revolution frequency, as well as 60 Hz AC mains.

The DG535 of the Stanford Research Systems(SRS) is a very precise delay and pulse generator providing four precision delays or two independent pulses with 5

0-7803-7738-9/03/$17.00 © 2003 IEEE

picoseconds resolution. The E/O module of the ORTEL is to transfer the timing pulse from electrical signal to optical signal in order to transmit with low jitter to the linac.

3 FUNCTIONS & REQUIREMENTS

The timing system was designed, developed and fabricated in 1994 for the PLS with reference to KEK timing system[2]. The timing system modules was fabricated with VXI standard modules. So far, there were some minor changes to improved the function of the timing system such as the FDM, RRG, TSM, control programming, and optical fibers including linac timing distribution system.

Although the present timing system has been operated without any serious problems since commissioning in 1994, there were some minor troubles, such as a single mode operation, unstable klystron modulators operation with 30 Hz timing pulses, and fan-out signals for diagonasis system. Also there are not sufficient spare parts of the modules to maintenace, and it is difficault to make and improve the modules because of shortage of manpower. Therefore, upgrade of the timing system is progressing with a synchronous universal counter(SUC) [3] and other commercial modules of NIM(Nuclear Instrumentation Module) type for increasing of a reliability, easy maintenance, low timing jitters, and all types of beam filling pattern to users.

There are five important requirements for the upgrade of the present timing system.

First of all, the first is to stable the beam operation for increasing of a reliability with upgrade timing system including klystron modulators operation. The second is to synchronize the 500.082 MHz rf phase between the storage ring and timing signals to control precisely the various beam filling patterns even though to make any arbitrary filling patterns. The third is to decrease the timing jitter as small as possible less than 100 ps especially between the electron gun trigger with respect to the storage ring rf. The fourth is to add the flexibility with bunch by bunch filling for the advanced operation, such as 2.5 GeV top-up mode operations. The fifth is to consider the easy maintenance, modification, expansion with many fan outs, and so on.

To satisfy the requirements with the higher precision, the upgrade will be used the SUC module and commercial modules of NIM which are already proven good qualities.

4 UPGRADED TIMING SYSTEM

The most important module of the upgraded timing system is an SUC which was designed, developed, and operated very well at the SPring-8 in Japan. The SUC works from 450 to 550 MHz rf frequency and has a 30 bit width. Its two main features are a dividing function with an arbitrary positive integer and a digital delay function with a time interval from 2 ns to 2 s. The circuit block diagram is shown in figure 2. The SUC counts the rf bucket number corresponding to the harmonic number (N=468) of the storage ring, and then it provides a pulse corresponding to the revolution frequency of storage ring from '1/N' output. And the output 'M' corresponds to the particular rf bucket within a revolution. Beams from the linac are injected into the addressed rf bucket by setting the number 'M' with control program externally as desired beam filling pattern[4]. The block diagram of the SUC is shown in figure 3.

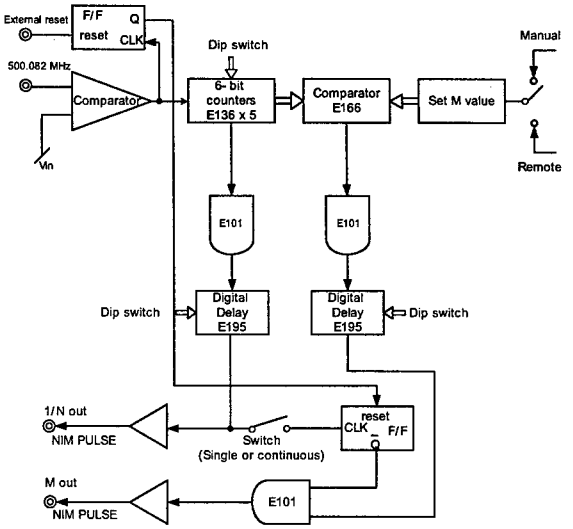


Figure 2 : Block Diagram of the SUC

The block diagram of the upgraded timing system is shown in figure 3.

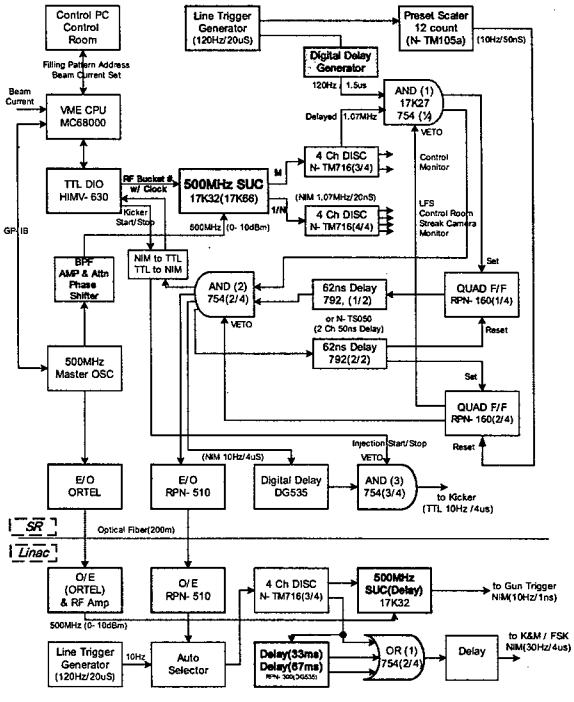


Figure 3 : Block Diagram of Upgraded Timing System

Injection commands with filling pattern are delivered from the central control room via a VME and a computer network. At first address of the rf bucket according to the filling pattern is written on the SUC. The SUC makes '1/N' revolution clock and delayed 'M' revolution clock.

And then, the revolution clock goes to the discriminator for shaping the pulse and adding the fan-outs.

There are two AND gate modules which have two inputs and one veto. An output signal of the AND(1) gate is produced one or two revolution clock about 1 ns period during 10 Hz with about 1.5 us width. Simple coincidence between 1.068 MHz revolution frequency and the 60 Hz AC line may cause an ambiguous output timing depending on the relative timing of the two inputs. Therefore, to avoid the situation of determining the timing by the 60 Hz line pulse, the second coincidence output must be used by ignoring the first output. The AND(1) output enters to AND(2) and a gate generator of the QUAD F/F. The first pulse of AND(1) never triggers the output pulse of AND(2), and the second pulse triggers it because of the veto function with two 62 ns delay modules. A preset scaler counts the 120 Hz by 12 division and produces a reset trigger of the QUAD F/F(2) after every 10 Hz period. And then, AND(1) and AND(2) are reset again for a next new trigger signal of 10 Hz[5].

The 10 Hz gun trigger timing pulse transmit to linac through the E/O (Electrical to Optical translator) and O/E (Optical to Electrical translator) modules to suppress noises and to improve the jitter. At the linac timing system, 30 Hz pulse for the klystron modulators is generated by 10 Hz with delay modules.

Some modules such as line trigger generator and auto trigger selector are developed at a domestic company with ECL technology. A line trigger generator has a function to synchronize with 60 Hz AC line, and to divide input trigger on two stages.

5 SUMMARY

The status of present timing system and its upgrade for the PLS storage ring has been described. The present timing system is usually operating for 400 multi-bunch filling pattern without any serious problems. The upgraded timing system was tested at the laboratory with some NIMs including the SUC, and will be installed this year. Also control group members are developing the control programming by new EPICS with present VME for the better operation of the upgraded timing system. After successfully commissioned, bunch by bunch injection operation to fill same storage current at each buckets will be considered for the top-up injection in the future.

6 ACKNOWLEDGEMENTS

The authors would particularly like to thank Dr. Y. Kawashima of the SPring-8 for information and consultation on the design the upgrade of the PLS timing system. The design scheme is very similar to the timing system of the SPring-8 because of using the same SUC. We would also like to thank ex-colleagues including Dr. S.S. Chang and Ms. M.K. Park for their contribution to the present timing system.

7 REFERENCES

[1] E.S. Kim et al. "Operation Performance in 2.5 GeV Full Energy Injection at PLS", Proc. of in this conference.
[2] S.S. Chang et al. "Timing System for PLS", Proc. of 4th Asia-Pacific Physics (1992).
[3] S. Marques et al. "Upgrade of the LNLS Synchrotron Light Source Timing System", Proc. of PAC'01, Chicago, USA (2001).
[4] H. Suzuki et al. "508.58 MHz Synchronous Universal Counter for Beam Control System of SPring-8", Nuclear Instruments and Methods in Physics Research A 431 (1999) p294-305.
[5] Y. Kawashima. "Timing System at SPring-8", Proc. of 13th Symposium on Accelerator Science and Technology, Japan (2001).

SLOW-WAVE ELECTRODE STRUCTURES FOR THE ESS 2.5 MeV FAST CHOPPER

Michael A. Clarke-Gayther, CLRC RAL, Didcot, United Kingdom.

Abstract

Slow-wave electrode designs for the European Spallation Source (ESS) 2.5 MeV fast beam chopper are described. Broad-band transmission line properties for the initial planar and helical designs have been refined by modelling electromagnetic fields in the Finite Difference Time Domain (FDTD) 'Microwave Studio' code. A compact, radiation hard, vacuum compatible helical structure made from linked strip-line and micro-strip sections has been developed. Simulated characteristics in the frequency and time domain, and the effects of E-field non-uniformity are presented.

INTRODUCTION

The next generation of high power proton drivers for pulsed neutron sources (ESS) [1] and neutrino factories [2], call for significant technical development in many areas of accelerator design. The ESS H^- linac fast beam choppers in the 2.5 MeV medium energy transport (MEBT) lines, must produce the precisely defined gaps in the 280 MHz bunched beam that enable low beam loss operation during accumulator ring injection and extraction. Stringent beam loss requirements in the downstream linacs and rings dictate that the chopping fields should rise and fall within the beam bunch interval of 2.9 ns, to eliminate the possibility of acceleration, and subsequent loss of partially chopped beam. Slow-wave (E-field) transmission line structures have demonstrated field transition times in the nanosecond regime [3, 4], and ESS chopping schemes utilising these structures have been identified [5] and refined [6]. They are designed with the aid of 3D high frequency field modelling codes, where the complex geometry, extended electrical length, and the effects of inter-electrode coupling set a practical limit on the computational accuracy of the broad-band properties. Speed and/or accuracy of computation, have been enhanced by identifying small repetitive structures and modelling their properties in the finite element frequency domain (FEFD) HFSS code, and more recently, in the finite difference time domain (FDTD) 'Microwave Studio' code. Time domain characteristics for the complete structures were analysed in a high frequency SPICE based circuit simulator where the complete structures were modelled by linking the repetitive two-port modules in large series arrays.

SLOW-WAVE ELECTRODE DESIGN

The basic features and function of the proposed slow-wave electrode structures are shown in Figure 1, where partial chopping of beam bunches is avoided by ensuring that the deflecting E-field propagates at the beam bunch velocity.

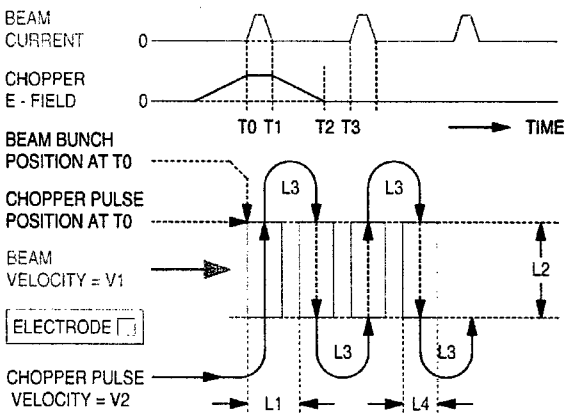


Figure 1: Slow-wave electrode design

In Figure 1:

L2 is the transverse extent of the beam.
T(L1) is the beam transit time for distance L1.
T(L2) is the pulse transit time in vacuum for distance L2.
T(L3) is the pulse transit time in dielectric media for distance L3.
L4 is the electrode width.

For the generalised slow wave structure:
Maximum value for L1 = V1 (T3 - T1) / 2
Minimum Value for L1 = L2 (V1/ V2)
T(L1) = L1/V1 = T(L2) + T(L3)

The relationships for field (E), and transverse displacement (x), where q is the electronic charge, v is the beam velocity, m_0 is the rest mass, z is the effective electrode length, θ is the required deflection angle, V is the deflecting potential, and d is the electrode gap, are:

$$E = \tan\theta \cdot m_0 \cdot \frac{v^2}{q \cdot z}, \qquad E = \frac{V}{d}, \qquad x = \frac{q \cdot E \cdot z^2}{2 \cdot m_0 \cdot v^2}$$

Inspection shows that for given values of m_0, v, and V, large θ and x are obtained when z is large and d is small. The inter-electrode gap shown as L1-L4 in Figure 1, must be made significant if pulse distortion due to inter-electrode coupling is to be minimised.
For a given overall structure length, the effective length (z) will therefore, be maximised, by maximising the electrode width (L4).

0-7803-7738-9/03/$17.00 © 2003 IEEE

ELECTRODE STRUCTURES

Planar slow-wave structure A, helical structure B, and the procedures adopted in their design, have been previously described [7]. Key parameters, common to those designs and to the new helical structure C, are listed in Table 1.

Table 1: Slow-wave structure parameters

Beam velocity	v	2.184e7	$m.s^{-1}$
Mechanical length		400.0	mm
Electrode to beam axis gap	d	6.0	mm
Beam aperture		11.0	mm
Deflection angle	θ	16	mr
Deflection potential (±)	V	1.6	kV
Characteristic impedance	Zo	50 ± 0.5	Ω
Total structure delay		18.04	ns
No. of sections		21	
Section delay	T(L1)	0.87	ns
Pulse transition time (1-90, 90 –1%)		2.9	ns
Structure bandwidth		0 - 500	MHz
Section pitch	L1	19.0	mm
Strip-line width	L4	14	mm
Strip-line thickness		0.45	mm

Helical electrode structure C

A mechanical schematic of structure C is shown in Figure 2. The compact helical structure is formed by strip-line sections near the beam axis, linked by sections of micro-strip. Micro-strip to strip-line transitions, and ceramic strip-line supports, are capacitively compensated by structure and notch dimensioning, respectively.

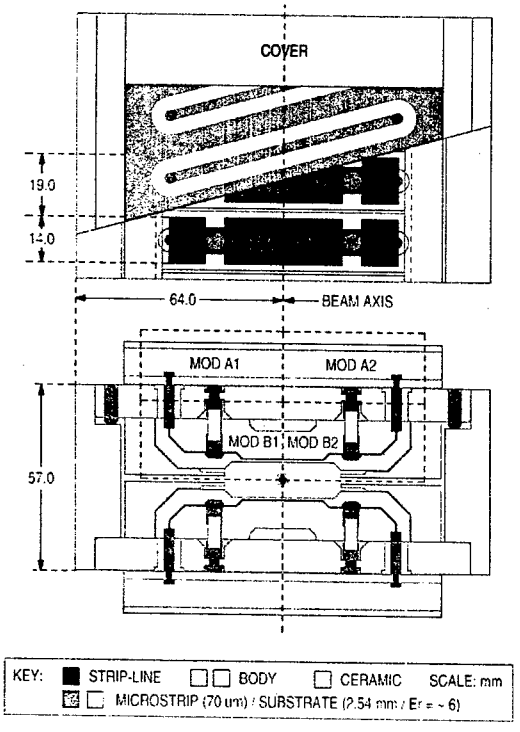


Figure 2: Electrode structure C

Finite element models for two modules, identified as MOD A1/A2 and B1/B2 in Figure 2, were analysed. Simulated S-parameters for the modules are shown in Figure 3.

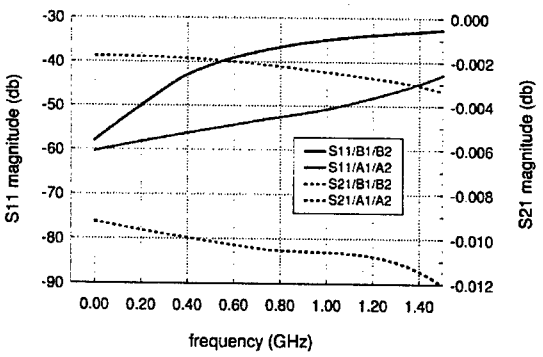


Figure 3: Structure C / Module S-Parameters

Time and frequency domain characteristics for the complete structure were computed by circuit simulation of series connected, two port modules, and lumped element inter-electrode, coupling capacitors, as shown in Figure 4.

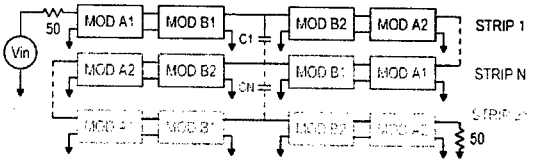


Figure 4: Structure C / Spice model

Simulated reflection and transmission characteristics in the frequency domain are shown in Figure 5. These indicate that the resonant frequencies of the structure are safely above the upper limit of the required bandwidth.

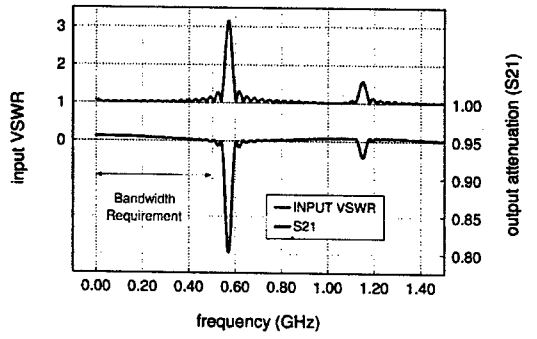


Figure 5: Structure C / Frequency Domain

Simulated pulse transmission characteristics in the time domain are shown in Figure 6. These indicate that structure C may exhibit a higher transmission loss and more pulse shape distortion than structures A or B.

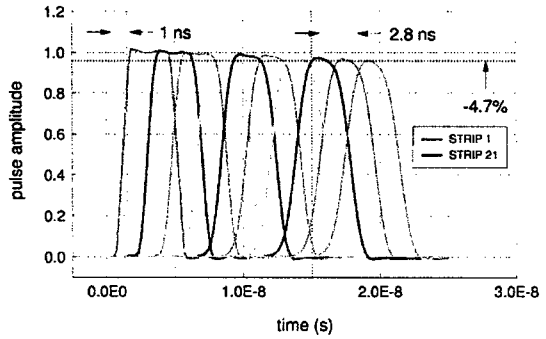


Figure 6: Structure C / Time Domain

E-FIELD UNIFORMITY

Uniformity of the beam-deflecting component of the simulated E field has been analysed. The variation in magnitude of this component as a function of axial position, as shown in Figure 7, exhibits the expected periodicity of the structure. This analysis predicts an average or rms field of ~ 73 % of the equivalent infinite parallel plate field level.

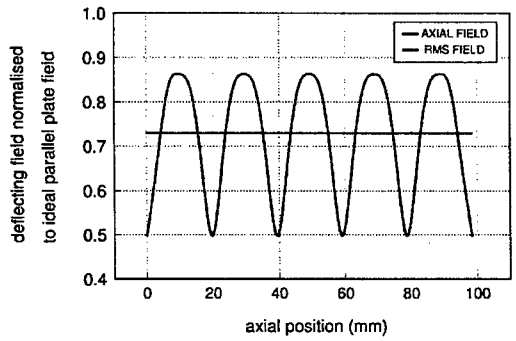


Figure 7: Structure C / Axial field distribution

Variation in the magnitude of the beam-deflecting component of the simulated E field, as a function of transverse position, as shown in Figure 8, indicates that structures A and C exhibit better field uniformity in this plane, than structure B.

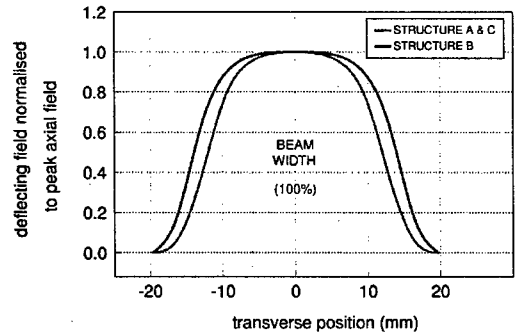


Figure 8: Structure C / Transverse field distribution

SUMMARY

Three slow wave structures for the ESS 2.5 MeV beam chopper have been modelled using finite element and circuit simulation codes. Planar slow-wave structure A, helical structure B, and the procedures adopted in their design, have been previously described [7]. An important common feature of those structures, and of the new helical structure C, is the radiation hard, vacuum compatible, strip-line configuration near the beam axis. Dispersion in the frequency domain, and the resultant pulse distortion due to inter-electrode coupling, have been minimised in these designs, by the introduction of extended inter-electrode ground planes.

Simulated frequency and time domain characteristics indicate that all three of the candidate structures may meet the required ESS specifications for chopper pulse fidelity.

Helical structure C was developed to address the need for a compact structure (more compact than helical structure B), but with the superior transverse field uniformity of planar structure A. These two goals have been achieved, at the expense of a small increase in transmission loss and pulse distortion. Last but not least, the mechanical construction of structure C may well turn out to be the least demanding of the three candidate structures.

REFERENCES

[1] The ESS Accelerator and Beam Lines with the 280/560 MHz Linac, Report No. ESS-01-1A, December 2001.

[2] C. R. Prior, and G. H Rees, 'RAL Proton Driver Studies for a Neutrino Factory', Proceedings of the Neutrino Factory Workshop, NUFACT'00, Monterey, California, June 2000.

[3] S. S. Kurennoy, and J. F. Power, 'Development of Meander-Line current structure for SNS fast 2.5 MeV Beam Chopper', Proc. of the 7th European Particle Accelerator Conference, Vienna, Austria, June 2000, p.336-338.

[4] F. Caspers, A. Mostacci, S. Kurennoy, 'Fast Chopper Structure for the CERN SPL', Proc. of the eighth European Particle Accelerator Conference, Paris, France, 3-7 June, 2002, p. 873-875.

[5] M. A. Clarke-Gayther, 'Modulator Systems for the ESS 2.5 MeV Fast Chopper', Proc. of the 2001 Particle Accelerator Conference, Chicago, USA, p. 4062-4065.

[6] M. A. Clarke-Gayther, 'A Fast Chopper for the ESS 2.5 MeV Beam Transport Line', Proc. of the eighth European Particle Accelerator Conference, Paris, France, 3-7 June, 2002, p. 2136-2138.

[7] M. A. Clarke-Gayther, Yi Nong Rao, Dag Reistad, 'Slow-wave electrode structures for the ESS 2.5 MeV Fast Chopper', Proc. of the eighth European Particle Accelerator Conference, Paris, France, 3-7 June, 2002, p. 2133-2135.

ELECTRICAL POWER AND GROUNDING SYSTEM STUDY AND IMPROVEMENT AT TLS

J.C. Chang, Y.C. Lin, S.C. Lei, K.C. Kuo, and J. R. Chen
National Synchrotron Radiation Research Center
Science-Based Industrial Park, Hsinchu 30077, Taiwan

Abstract

The effect of the electrical power and grounding systems on the beam stability is studied at the Taiwan Light Source (TLS). Based on the study, some major improvements are accomplished at TLS. The electric power SCADA (Supervisory Control And Data Acquisition) system is established to remotely monitor and control the electrical power conditions. The soil resistivity data at TLS is collected and a new grounding system of low impedance (0.18ohm) is constructed. Grounding signals and electric potential are collected at some grounding boxes. Grounding electric potential is observed effected by injection at some specific local grounding boxes. Grounding electric potential difference is also found between the new and old grounding systems. These two grounding systems will be connected as one and rearranged to cope with the grounding related problems.

INTRODUCTION

In order to provide higher electrical power quality, the TLS has implemented some electrical power system upgrading projects [1]. Following the online monitoring and archive systems of the de-ionized water and air condition system established [2], the remote online monitoring and control system of the electrical power system, known as the SCADA system has been set up and upgraded for the past three years. The SCADA system has also been merged into the utility archive system to correlate with beam quality and data of other utility systems and enhance its analysis function.

Beside the electrical power system, grounding system is another crucial but apt to be neglected issue. Providing the safety and electrical reference level function, on the other hand, grounding system also could be a major electrical noise path and even induce EMI problem. Thus, special care must be taken when the grounding system is constructed, employed and maintained. TLS has made many efforts to improve the grounding for these years. One of the major projects is to construct a new low impedance grounding system. In the design phase, the soil resistivity data at three different locations in TLS were collected according to "Four Pole Method" [3]. The soil resistivity values are in the range of 120-180 ohm-meter, depending on location and weather. The grounding resistance of the new grounding system was measured according to the "Fall of Potential Method" [4]. The grounding resistance is 0.18 ohm, which is 10% lower than the designed value. However, the grounding potential difference between the new and old grounding systems is observed. The combination and rearrangement of these two grounding systems is under planning currently.

ELECTRICAL POWER SCADA SYSTEM

The electrical power system at TLS consists of two independent electrical power feeders from the Taiwan Power Company (TPC) of 11.4 KV and 4500 KW contract capacity currently. These two main feeders and its circuit breakers, labeled as CB-U1A and CB-U1B, are located in the Utility building then distributed to each individual building, as shown in Fig. 1. The feeder under the circuit breaker CB-U3A, for the storage ring, is the most loaded and important one. Most of the relays and multimeters of the SCADA system thus are mounted under the feeder.

Totally nine terminal feeders, ABB REF541 high voltage relays, not only served as conventional protect relays, but also are used to control, measure and supervise the high voltage network. Four of such relays are respectively mounted on the CB-U1A, CB-U1B, CB-U3A and CB-U4A in the utility building. Other five relays are mounted in the storage ring building.

Moreover, there are thirty electric power multimeters installed at different local sites in the storage ring and utility buildings respectively. The SCADA system is still kept expanded by means of adding the monitoring sites. For example, the latest electric power multimeter, mounted in January 2003, is used to monitor the feeder for the quadrupole magnet power supply. A new KVA Automatic Voltage Regulator (AVR) of 300KVA was just installed to improve the voltage variation. This AVR can suppress the voltage variation from ±3%, which is the nominal variation specified by the TPC, to ±0.15%, as shown in the Fig. 2.

LOW IMPEDANCE GROUNDING SYSTEM

The old grounding system at TLS was constructed with the storage ring building construction and just for the general safety purpose. A new low grounding system of low impedance is necessary to reduce the noise of signal-sensitive instruments. Thus, TLS had started and design the low impedance grounding system project in 2000.

The original design of the grounding resistance was set as 0.2 ohm. In order to accurately reach this goal, the soil

0-7803-7738-9/03/$17.00 © 2003 IEEE

resistivity collection was necessary. The new grounding system drawing is shown in Fig. 3. The soil resistvity of three locations were measured. According to the "Four Pole Method", as shown in Fig. 4, the distance, L, between the adjacent two electrodes must be changed to obtain the soil resistivity in various depth. The same measuring procedure must be taken twice in two orthogonal directions in one area. The soil resistivity are measured in the range of 120-180Ω -meter. The value will be different as the weather changed. Basically, the soil resistivity will get decrease as L increases. Once the soil resistivity is collected, the grounding resistance can be evaluated.

In the Fig. 3, the new grounding system is composed of nine copper tubes, serving as the electrodes, and a bare copper wire of 650 meters long connecting with the nine electrodes. Each copper tube, 2 inch in diameter and 30 meter long, is buried in a well of 4 inch in diameter and 30 meter in depth, while the bare copper wire is buried in the middle of a 45cm × 30cm ditch. All electrodes and the bare copper wire are covered by Bentonite.

The new grounding system is classified as "clean" and "dirty" subsystem for technical and conventional facility use. There are four locations on the bare copper wire where connected into the storage ring through eight copper wires. These eight copper wires, where four are classified as clean and others as dirty, are connected through two circle buses respectively in the storage ring.

GROUNDING RESISTANCE MEASUREMENT

The grounding resistance is measured by means of "Fall of Potential Method" according to IEEE std81-1983, as shown in Fig. 5. In the Fig. 5, C, E and P represent the current electrode, the electrode of grounding system and the auxiliary electrode, respectively. Referring to Fig. 6, which shows voltage vector relation among V_{23F} ,V_{23R} and V_{23S}, the grounding resistance, R, can be obtained by the following formula

$$R = \sqrt{0.5 \times (V_{23F}^2 + V_{23R}^2 - 2V_{23S}^2)} / I \quad \text{..... .(1)}$$

where V_{23} is the potential difference between electrodes C and E. Subscript F and R represent the cases of the current injection through electrodes C and E respectively. Subscript S is the case of the background stray current existed in the ground. I is the injection current. In the real case, the same measuring procedure was taken three times as current I=0, 10 and 20 A. According to Eq. (1), the grounding resistance R are obtained as 0.18 ohm.

GROUNDING SIGNALS AND ELECTRIC POTENTIAL DATA

There are two equipments to grounding signals. One is a Tektronix TDS3054 oscilloscope equipped with a P60139 voltage probe with 500MHz bandwidth for the transient measurement, while the other is a FLUKE 43B electrical power quality analyzer with 20MHz bandwidth for long tern recording.

Fig. 7 shows the grounding signals of the high frequency power supplies when the beam is shutdown. The maximum frequency is up to 75MHz and the duration between two adjacent pulses is about 5μ s. The signal also appears as the beam is in operation. The source of the signal or noise is still left to be examined.

Fig. 8 is transient potential difference between the new and old grounding systems when the beam is in injection. It shows that beam injection could induce the transient potential difference between the two grounding systems up to 6-8 V. Long-term recording by the FLUKE 43B also shows the similar phenomenon.

CONCLUSION

The electrical power SCADA system has been established and upgraded. The SCADA system consists of nine ABB REF541 relays and thirty multimeters mounted on different local sites and is merged into the utility archive system.

The new low impedance grounding system is constructed and the grounding resistance is measured as 0.18 ohm, which is 10% lower than the designed value.

The grounding signals and the potential difference between the new and old grounding systems are collected. Both transient data and long tern records show 6-8V potential difference due to injection.

ACKNOWLEDGEMENT

The authors would like to thank the electrical power and grounding consultant team led by Prof. S.L. Chen.

REFERENCE

1. Z. D. Tsai, D. S. Lee, C.K. Kuan, C. R. Chen, F. Y. Lin, S. H. Chang, and J. R. Chen, "The Effect of Improving the Temperature Variation at the SRRC Storage Ring", The 7th European Particle and Accelerator Conference (EPAC), June 2000, Vienna, Austria.
2. Z. D. Tsai, D. S. Lee, J. C. Chang, Y. C. Chang and J. R. Chen, "The Status of the Utility System Stability Improvement Study at TLS", The Second Asian Particle Accelerator Conference (APAC'01), September 17-21, 2001, Beijing, China.
3. F. Wenner, "A method of measuring earth resistivity," Bull. National Bureau of Standards, Bulletin 12(4), Paper 258, S 478-496; 1915/16.
4. ANSI/IEEE Std 81-1983, "An American National Standard IEEE Guide for Measuring Earth Resistivity, Ground Impedance, and Earth Surface Potentials of a Ground System".

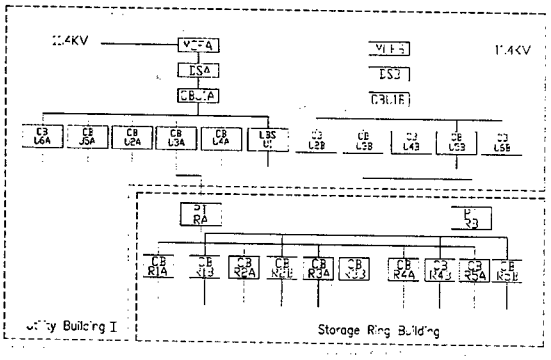


Fig.1: Electrical Power System at TLS.

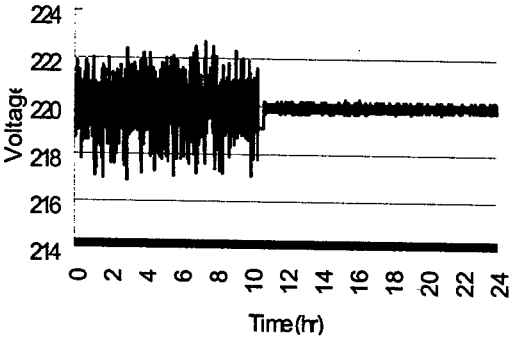


Fig. 2: Voltage variation improvement for the Quadrupole Power Supply.

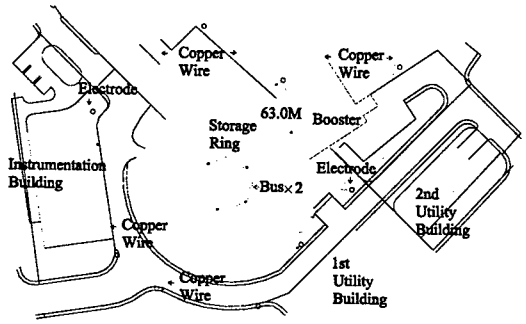


Fig. 3: New grounding system.

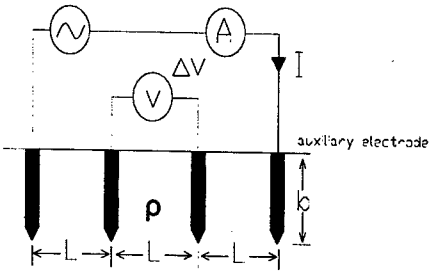


Fig. 4 : Four pole method.

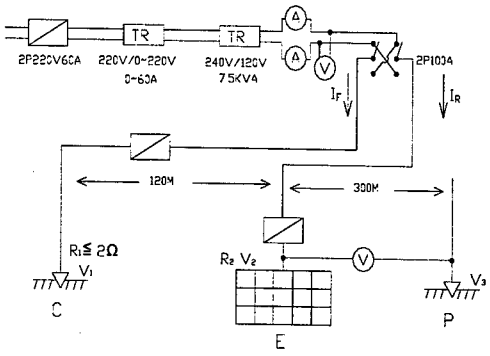


Fig. 5: Fall of potential method.

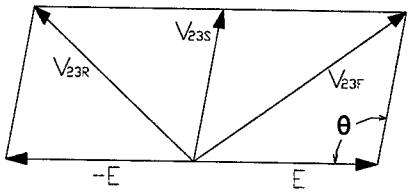


Fig. 6: Voltage vector relation among V_{23F} ,V_{23R} and V_{23S}.

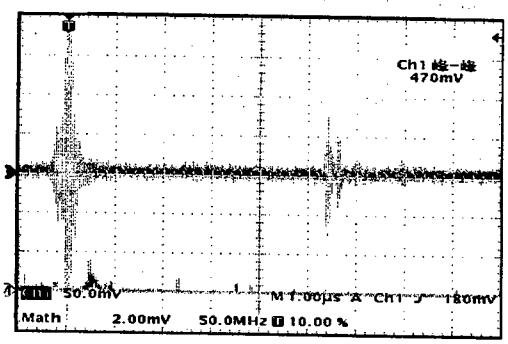


Fig.7: Grounding signals of the high frequency power supply.

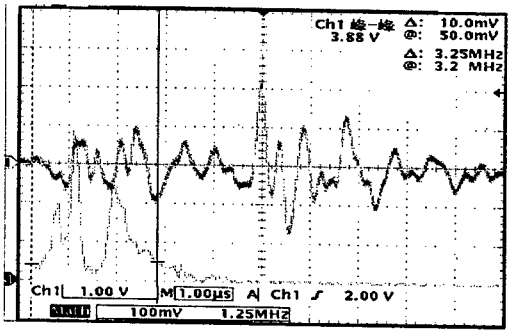


Fig.8: Potential difference between the new and old grounding systems.

DE-IONIZED COOLING WATER SYSTEM STUDY AND IMPROVEMENT AT TLS

J.C. Chang, Z.D. Tsai, Y.C. Chung, C.Y. Liu, J.R. Chen
National Synchrotron Radiation Research Center
Science-Based Industrial Park, Hsinchu 30077, Taiwan

Abstract

In order to promote the stability and quality of the de-ionized cooling water (DIW) system, a series of studies and improvements on the DIW system are accomplished at the Taiwan Light Source (TLS). The total DIW system capacity is increased 400 GPM, where a special subsystem of 150 GPM is for a new superconducting-rf (SRF) system only. The DIW temperature is globally controlled within ± 0.1 °C. A high precision temperature control system of ± 0.01 °C for local DIW supply is also established to meet the critical stability requirements. The water quality has also been improved by upgrading local filters, reverse osmosis, conductivity meters, pH monitors, flow meters and various resins. The conductivity of the water has been maintained above 10 M ohm/cm and the pH at 7± 0.3. Additionally, the dissolution of oxygen, which is another essential water quality factor, has also been much reduced from 5000ppb to 6ppb by new deoxygenating equipment.

INTRODUCTION

Taiwan Light Source (TLS) had started a series of experiments to established the mathematical model [1] and find out the relationships among the beam orbit position and the utility status [2]. The supplied air temperature and cooling water temperature are the main factors. Once the cooling water and the air exceed 1°C and 0.2°C, respectively, the results show the strong correlation between the beam orbit stability and the utility status. Based on the study, TLS has made more efforts to improve the utility system [3] and conduct more precision thermal and mechanical stability studies meet the latest strict requirement of beam intensity variation within 0.1% [4]. The original specification for the temperature fluctuation <±1°C is far from the requirement.

A SRF cavity will be installed into TLS storage ring in 2004. TLS has devoted many efforts in studying the corresponding issues for the SRF system [5]. In order to serve for the oncoming SRF system, the DIW system has been added a new subsystem at TLS. The 2nd Utility Building was constructed and the total DIW system capacity was increased 400 GPM last year. The piping system is also rearranged to meet requirements for each subsystem.

Moreover, a high precision water temperature control experiment is conducted to meet the critical stability requirement. The experimental apparatus has been set up. The test results will be valuable to establish any real local high temperature precision control DIW subsystem.

DIW quality is another crucial but apt to be neglected issue. Although not like the DIW temperature and pressure directly affecting the subsystem operation, the factors of DIW quality, such as conductivity, pH value and dissolution of oxygen deeply influence the DIW system itself, especially for the piping system. For long-term smooth operation, the DIW quality is also studied and improved.

DIW SYSTEM

The DIW system, composed of three subsystems, i.e., the copper (Cu) subsystem, the aluminum (AL) subsystem and the beam line subsystem, has been operated for years at TLS. The Cu DIW subsystem supplies to magnets, power supplies, RF transmitters and cavities. The Al and the beam line DIW subsystems serve for vacuum chambers and beam line devices, respectively. This DIW system had been upgraded by means of two major projects in 2002.

First, the second utility building was constructed. Two sets of chillers of 450 ton were new installed for the DIW and air conditioning systems. The DIW capacity is increased 400 GMP consequently. The forth DIW subsystem, SRF subsystem, of 150 GPM was new established for the oncoming SRF cavity. The capacity of the beam line DIW subsystem was increased from 150GPM to 300 GPM.

Second, redundant frequency inverter systems for each DIW subsystem were established. Originally, there is only one frequency inverter system for each DIW subsystem. It exists the risk of beam trip through the interlock system once the frequency inverter system trips. The redundant frequency inverter system thus is necessary in case of trip of the running inverter system. Two sets of the redundant frequency inverter systems for each Cu and beam line DIW subsystems are ready currently. Other two sets of the redundant frequency inverter system for the Al and SRF DIW subsystems will be installed in Aug. 2003.

There are two phases of heat exchange in each DIW subsystem. The DIW temperature variation is controlled within +/-0.1 °C for the Cu and Al subsystems and +/-0.15 °C for other two subsystems by means of adjusting the flow rate of the chilled water and cooling water. The DIW pressure is control within +/-0.1kg/cm2 by regulating the pumping frequency. The specifications of each DIW subsystems are list in the Tab. 1. The first and second phased Cu and Al DIW temperature is shown in the Fig. 1

0-7803-7738-9/03/$17.00 © 2003 IEEE

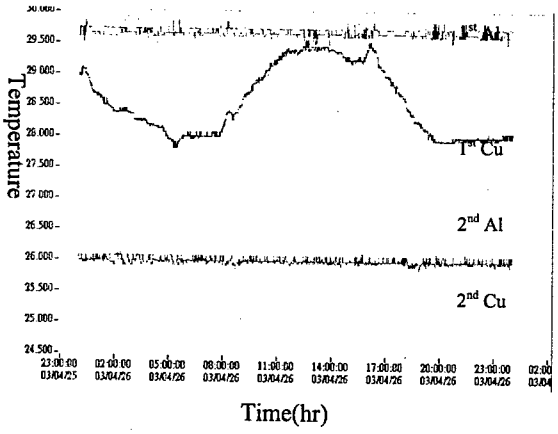


Fig. 1: First and second phased Cu and Al DIW temperature

Table 1: Specifications of each DIW subsystem

	Temperature	Pressure	Flow rate
Cu	25+/-0.1 °C	7.5+/-0.1kg/cm^2	500GPM
Al	25+/-0.1 °C	7.0+/-0.1kg/cm^2	100GPM
SRF	25+/-0.2 °C	7.0+/-0.1kg/cm^2	160GPM
BL	25+/-0.2 °C	7.0+/-0.1kg/cm^2	300GPM

HIGH PRECISION TEMPERATURE CONTROL EXPERIMENT

Beside the primary DIW system upgrading projects abovementioned, the high precision temperature control is a smaller project for local temperature-sensitive equipments. The high precision temperature control experiment has been set up in a laboratory.

Fig. 2 shows of the high precision temperature control experiment. In the experiment, water flows through a 0.5inch stainless pipe. A set of embedded heaters with total 10KW capacity is installed on the upstream of the pipe to control the inlet water temperature. A NI FieldPoint modular distributed I/O system with 16-bit resolution in the range from 4 to 20 Ma serves as the real time controller. A SCR is employed to drive the heater. A heating tape of 220W is coiled on the middle section of the pipe to simulate the heat load.

Two adjustable valves are respectively installed on the upstream and downstream of the embedded heater set to control the flow rate. A flow rate meter with +/- 0.5% accuracy is installed on the downstream.

Three pressure probes with transducers with +/- 0.1kg/cm^2 are installed inlet and the upstream and downstream of the heating tape respectively. The most crucial sensor in this experiment is the thermometer. Three Thermometrics TS8504 thermometers are installed on the upstream and downstream of the embedded heating set and the outlet of the pipe, respectively. The thermometer is accurately calibrated and its accuracy is +/-0.001 °C. The test results show that the water temperature control within +/- 0.01 °C is achievable. The experiment is helpful to set up a real local high precision DIW temperature control system.

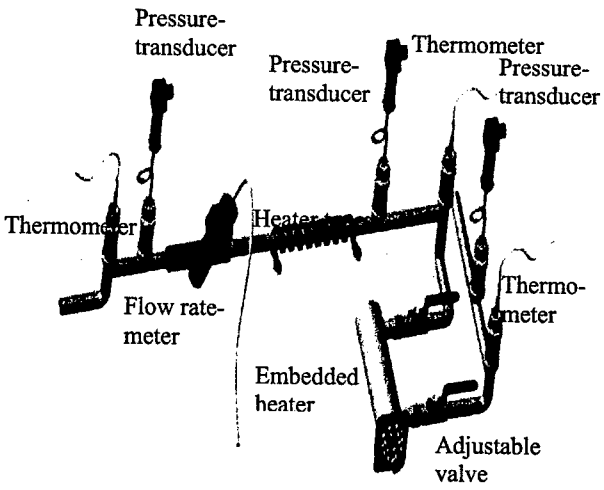


Figure 2: High precision temperature control experiment

DIW QUALITY IMPROVEMENT

Water quality is anther significant issue for the DIW system. There are usually some general impurities in the DIW system after long-term operation, such as suspension, electrolyte, corpuscles, mirco-pranisms, organic substance and gas. There is 5% water entering the recycling loop in the DIW system at TLS. It will flow through 5um filter, resin mixing bed, 1um filter, and ultraviolet sterilizer respectively, as shown in Fig. 3. Once city water is supplied for the DIW system, it will flow through the reverse osmosis (RO) system then into the DIW system. The RO system includes a 10um filter, a set of RO diaphragm, a pressure pump, a medicine tank, a mixing pump, a 8-ton reservoir and a control system.

The water quality has been improved by means of upgrading local filters, reverse osmosis, conductivity meters, PH monitors, accumulated flow meters and various resins. The resistance is kept above 5 Mohm,as shown in Fig.4. The pH value is controlled at 7±0.3, as shown in Fig5. In addition, the dissolve oxygen effect, another important issue of water quality, has also much reduced from 5000ppb to 6ppb through new added deoxygenating equipments.

CONCLUSION

Some major DIW system upgrade projects were implemented in 2002. The DIW capacity was increased 400 GPM. The SRF DIW subsystem of 150 GPM was set up for the oncoming SRF cavity. The capacity of the

beam line DIW system was also increased from 150GPM to 400GPM. Redundant frequency inverter systems for each DIW subsystem were established.

The high precision temperature control experiment was conducted. The critical goal of controlling the water temperature variation within +/- 0.01 °C is achievable. This result will be valuable set up a real local high precision DIW temperature control system.

The DIW quality was improved by means of upgrading some crucial components of the DIW system. The resistance is kept above 5 Mohm, while the pH value is controlled at 7+/-0.3 currently. The dissolve oxygen was reduced from 5000ppb to 6ppb.

REFERENCE

1. H.M. Cheng, J.R. Chen, C.R. Chen, and Z.D. Tsai, "Utility Optimization for the Beam Orbit Stability at SRRC", New York 1999.
2. J.R. Chen, H.M. Cheng, Z.D. Tsai, C.R. Chen, T.F. Lin, G.Y. Hsiung, and Y.S. Hong, "The Correlation between the Beam Orbit stability and the Utilities at SRRC", Proc. of 6th European Particle and Accelerator Conference EPAC98, Stockholm, Sweden, June 22-26, 1998.
3. Z. D. Tsai, D. S. Lee, C.K. Kuan, C. R. Chen, F. Y. Lin, S. H. Chang, and J. R. Chen, "The Effect of Improving the Temperature Variation at the SRRC Storage Ring", The 7th European Particle and Accelerator Conference (EPAC), June 2000, Vienna, Austria.
4. J.R. Chen, D.J. Wang, Z.D. Tsai, C.K. Kian, S.C. Ho, and J.C. Chang, "Mechanical Stability Studies at the Taiwan Light Source", 2nd Int'l Workshop on Mechanical Engineering Design of Synchrotron Radiation Equipment and Instrumentation (MEDSI02), APS
5. W.K. Lau, L.H. Chang, CH. Wang, and M.S. Yeh, "Analysis of the Superconducting RF Cavity Under Heavy Beam Loading at Taiwan Light Source," The 8th European Particle and Accelerator Conference (EPAC), June 2002.

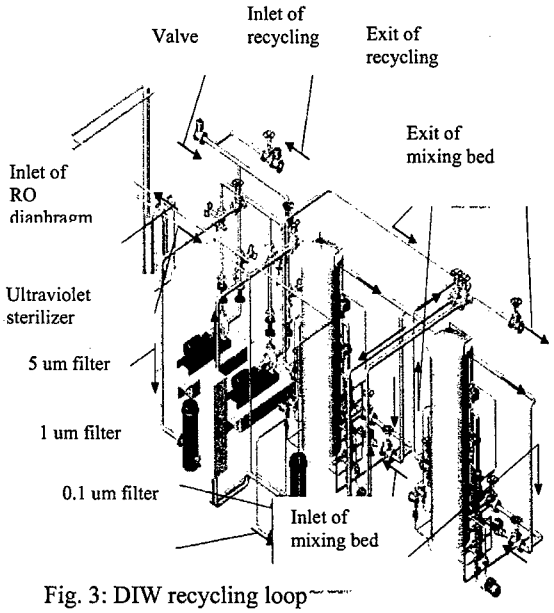


Fig. 3: DIW recycling loop

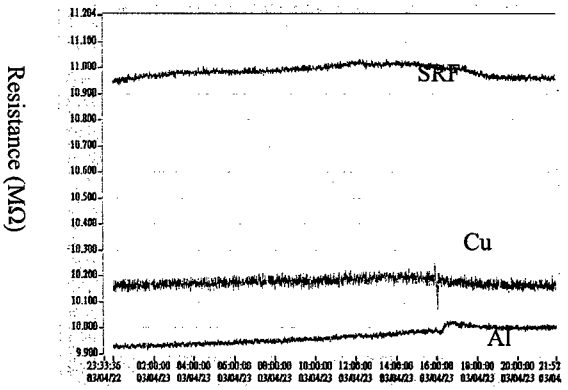


Fig. 4: DIW resistance.

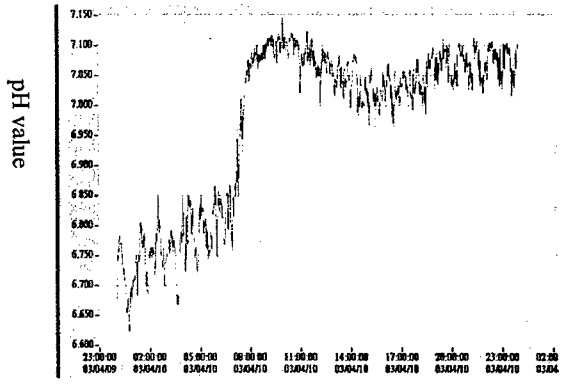


Fig. 5: pH value of Cu DIW.

AIR TEMPERATURE CONTROL IMPROVEMENT FOR THE STORAGE RING TUNNEL

J.C. Chang, C.Y. Liu, and J. R. Chen
National Synchrotron Radiation Research Center
Science-Based Industrial Park, Hsinchu 30077, Taiwan

Abstract

Based on the thermal effects on the beam stability formerly studied, a series of measures are taken to improve the air temperature control for the storage ring tunnel at the Taiwan Light Source (TLS). The cooling capacity is increased about two times by rearranging the Air Handling Units (AHU) and the piping system. The PID parameters are optimised to more effectively suppress the air temperature fluctuation. The global air temperature variation in the storage ring tunnel is currently controlled within ±0.1°C related to time. After successful experience of air temperature control for the elliptical polarization undulator (EPU), the mini environment control is also applied on another insertion device, undulator 5 (U5). The ambient temperature variation of this magnet is controlled within ±0.1 °C related to time. The thermal uniformity is much improved than ever.

INTRODUCTION

In order to enhance the beam operation stability, Taiwan Light Source (TLS) had started a series of experiments to established the mathematical model [1] and find out the relationships among the beam orbit position and the utility status, which includes the cooling air temperature and cooling water temperature [2]. The results show the strong correlation between the beam orbit stability and the utility status as the temperature variation of the cooling water and the air exceed 1 °C and 0.2 °C, respectively. More precision thermal and mechanical stability studies were conducted to meet the latest strict requirement of beam intensity variation within 0.1% [3]. The original specification for temperature fluctuations, <±1°C, is far from the requirement. Many efforts thus have been devoted in the air temperature variation improvement in the storage ring.

Most of the main devices for the beam operation are installed in the storage ring tunnel. The air temperature control in this area thus is the most important air conditioning project. Parts of the AHU and piping system are modified to suppress the air temperature variation.

Besides, following the successful experience of mini environment control for the EPU [4], the similar scheme is also applied on U5. This insertion device, purchased from Danfysik Company, has the same length of 3.9 meter as EPU and with 5 cm magnetic period length. The details of the mini environment control will be described in the later section.

AHU AND PIPING SYSTEM REARRANGEMENT

There had been totally four AHUs serving for the most area of storage ring building, i.e., the tunnel and the experimental hall, since the storage ring was constructed in TLS. The detailed specifications of the AHU are list in Tab. 1. The supplied air from these four AHUs was first mixed through the piping system then ventilated to the tunnel and the experimental hall. However, due to the fast growth of the heat load from the later installed beam lines and instrumentations, the cooling capacity becomes insufficient gradually. Lack of cooling capacity affects the storage ring tunnel more than the experimental hall because the former requires more accurate air conditioning control but shares less cooling capacity than the latter. Therefore, increase of the cooling capacity becomes an imperative for the stable air temperature control in the storage ring tunnel.

Another shortcoming of the air conditioning system for the storage is a long section of supplied air duct exploded under the sunshine. The air temperature could rise up to 2 °C as the air flowed through this section due to solar radiation. Thus, the air conditioning system for the storage ring was modified at two places to cope with the shortcomings abovementioned in 2002. First, the air conditioning system of the storage ring tunnel was separated from that of the experimental hall by rearranging the piping system. Second, the section of the air duct exploded under the sunshine was cut. Currently, two AHUs are independently employed for the storage ring tunnel and the cooling capacity for this area is much increased.

Moreover, The air conditioning system PID control program has also been updated. The program system provides a new function, dead band control logarithm, for reducing the temperature control over or under shooting. The optimum PID parameters are related to the characters of the air condition equipments and the local temperature variation. However, sufficient air conditioning capacity will make optimum PID parameters tuning easier.

AIR TEMPERATURE VARIATIONS IMPROVEMENT

The air temperature of the storage ring tunnel is controlled through four variable air valves (VAVs), labelled as R4A-R4D. Each VAV dominates eight air inlets and two air outlets, as shown in Fig. 1. The opening

0-7803-7738-9/03/$17.00 © 2003 IEEE

of the valves for chilled and heating water are auto adjusted by the controller according to the temperature difference between the setting value and the real inlet air temperature.

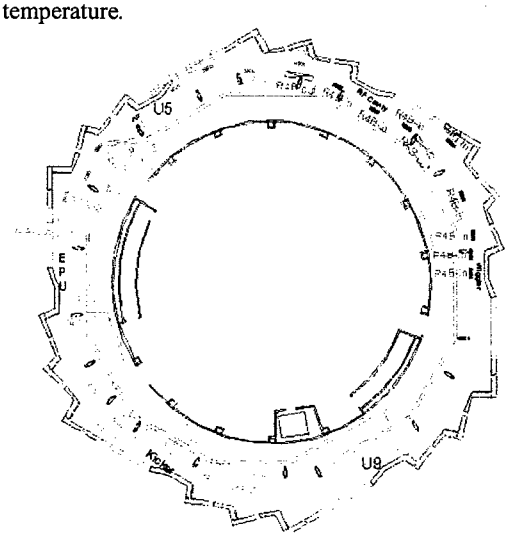


Fig 1: Air conditioning ventilation inlet and outlet distribution in the storage ring tunnel

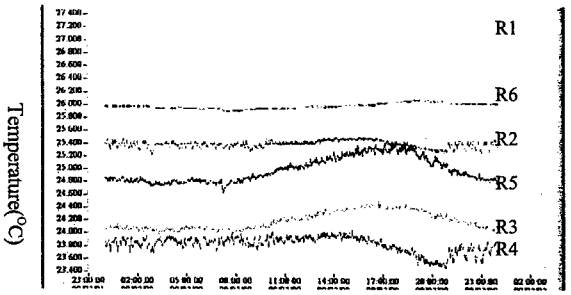
The storage ring tunnel is divided into six sections. There are six thermocouples mounted in each section to remotely monitor and control the air temperature in this area. Fig. 2 (a) and (b) respectively demonstrate the air temperature variation in the six tunnel sections before and after the air conditioning system modification. It is shown from the one day history that the temperature variation is about ±0.2 °C in Fig. 2(a). The apparent rise in the temperature in the afternoon also reflects the insufficient cooling capacity. The valves of the chilled water were usually 100% opened in the summer. This phenomenon almost disappears after modification, as shown in the Fig. 2(b).

Special care is taken to improve the air temperature variation related to time rather than the spatial temperature difference because the former affects the beam stability much more than the latter. Although the temperature differences among each section still exist, the temperature variation during one day is much improved.

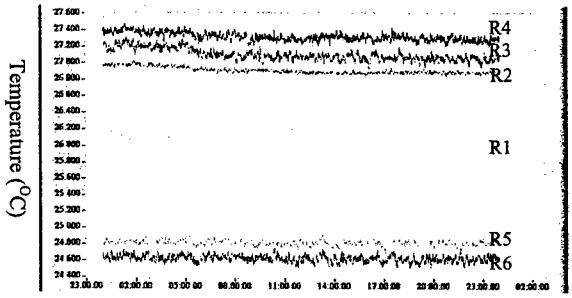
MINI ENVIRONMENT FOR THE U5 AREA

For more accurately and efficiently control the ambient air temperature around U5, isolating this local area and providing the independent air conditioning system, known as the mini environment control, is the best scheme. Fig. 3 shows the isolated U5 area photograph.

U5 is located in the third section in the storage ring tunnel. There are two air inlets supplying sufficient air in the isolated U5 area. There is no air outlet in the isolated area. Accordingly, it can be kept positive pressure in the



(a) Time(hr)



(b) Time(hr)

Fig. 2: Air temperature variation in the six tunnel sections (a) before and (b) after the air conditioning system modification.

area. It is also helpful to keep heat transfer from outside into this area. The surrounding temperature variation can be controlled within +/- 0.1 °C except the beam shut down period.

With sufficient air conditioning capacity in the area, temperature uniformity of the U5 magnet arrays becomes another important issue. Fig. 4 is the sketch of the isolated area of U5. Three cross flow fans are employed to circulate the air around the magnet arrays to achieve the goal of the temperature uniformity. Two small fan units are located on the top in front of the U5 device. One large fan is mounted in the back position. The air flow form the air inlet can be draft down by the top fans and enwrap the U5 magnet arrays, as shown in Fig. 4.

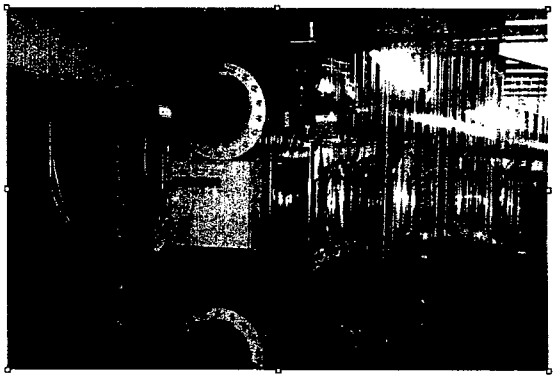


Fig. 3: Photograph of the U5 isolated area.

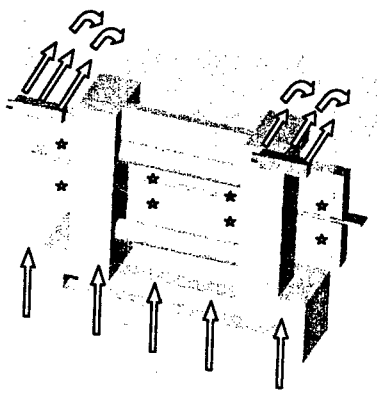


Fig. 4: Sketch of the U5 area.

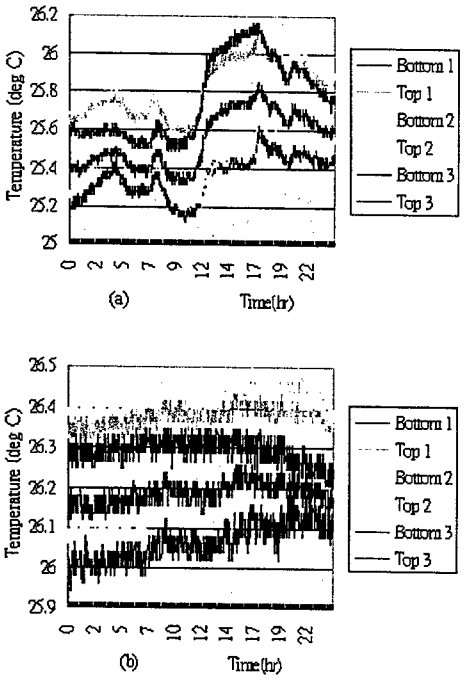


Fig.: 5 Air temperature variation on the U5 magnet arrays (a)before and (b)after the mini environment control.

There are eight thermocouples mounted on the front side of U5 magnet arrays, as shown in Fig. 4. Other eight thermocouples are mounted on the backside. Fig. 5 (a) and (b) respectively show the temperature variation of the U5 magnet arrays before and after the mini environment control is employed. By the forced convection cooling induced by the circulation, the U5 magnet arrays temperature variation of the top magnet arrays can be reduced to 0.2 °C, while the bottom magnet temperature variation can be reduced to 0.15 °C. The temperature variation corresponds to the 23.4 um deformation of the top magnet arrays and 16.7 um deformation of the bottom magnet arrays in the longitudinal direction.

The U5 area temperature variation is kept in +/- 0.1 °C by means of the mini environment control for U5 isolation air conditioning. The circulation air flow can uniform the temperature distribution to 0.2 °C level. The precise temperature control can reduce the thermal effect on the U5 deformation and further improve the beam stability in TLS.

CONCLUSION

The air conditioning system for the storage ring is modified. The cooling capacity for the storage ring tunnel is much increase by means of the rearrangement of the air piping system. The global air temperature variation in the storage ring tunnel is currently controlled within ±0.1 oC during 24-hour operation.

The U5 area temperature variation is kept in +/- 0.1 oC by means of the mini environment control for U5 isolation air conditioning. The circulation air flow can uniform the temperature distribution to 0.2 oC level. The precise temperature control can reduce the thermal effect on the U5 deformation and further improve the beam stability in TLS.

REFERENCE

1. H.M. Cheng, J.R. Chen, C.R. Chen, and Z.D. Tsai, "Utility Optimization for the Beam Orbit Stability at SRRC", New York 1999.

2. J.R. Chen, H.M. Cheng, Z.D. Tsai, C.R. Chen, T.F. Lin, G.Y. Hsiung, and Y.S. Hong, "The Correlation between the Beam Orbit stability and the Utilities at SRRC", Proc. of 6th European Particle and Accelerator Conference EPAC98, Stockholm, Sweden, June 22-26, 1998.

3. J.R. Chen, D.J. Wang, Z.D. Tsai, C.K. Kian, S.C. Ho, and J.C. Chang, "Mechanical Stability Studies at the Taiwan Light Source", 2nd Int'l Workshop on Mechanical Engineering Design of Synchrotron Radiation Equipment and Instrumentation (MEDSI02), APS, U.S.A., Sep 5-6, 2002

4. D.S. Lee, Z.D. Tsai, and J.R. Chen, "Mini Environment Control for the Elliptical Polarization Undulator" 2001 Particle and Accelerator Conference (PAC), June 18-22, 2001, Chicago, USA.

MACHINE PROTECTION FOR HIGH AVERAGE CURRENT LINACS

K. Jordan, T. Allison, J. Coleman, R. Evans, A. Grippo
Thomas Jefferson National Accelerator Facility, Newport News, VA 23606, USA

Abstract

A fully integrated Machine Protection System (MPS) is critical to efficient commissioning and safe operation of all high current accelerators. The Jefferson Lab FEL [1,2] has multiple electron beam paths and many different types of diagnostic insertion devices. The MPS [3] needs to monitor both the status of these devices and the magnet settings which define the beam path. The matrix of these devices and beam paths are programmed into gate arrays, the output of the matrix is an allowable maximum average power limit. This power limit is enforced by the drive laser for the photocathode gun. The Beam Loss Monitors (BLMs), RF status, and laser safety system status are also inputs to the control matrix. There are 8 Machine Modes (electron path) and 8 Beam Modes (average power limits) that define the safe operating limits for the FEL. Combinations outside of this matrix are unsafe and the beam is inhibited. The power limits range from no beam to 2 megawatts of electron beam power. The timing requirements for the BLMs and RF is ~1 microsecond and for the insertion devices (viewers) is ~ 1 millisecond. The entire system is VME based and EPICS compatible. This paper describes the system as it is installed on the JLab 10kW FEL.

SYSTEM DESCRIPTION

The driver accelerator for Jefferson Lab's Free Electron Laser will be capable of producing a 2 MWS electron beam (with the installation of the third cryomodule this fall). The machine can drive either an Infrared Laser (10 kw CW) or Ultraviolet Laser (1 kw CW). In addition to these two primary beam lines there are two diagnostic beam dumps and an insertable dump. There are also a variety of insertion devices that have different maximum average current limits. The MPS system was designed to minimize operator set-up time and confusion with choices of beam paths and power (and the possibility of mistakes). All of the devices that are required to properly accelerate beam and anything that can be inserted into the beam line or Laser is connected to the MPS system. The inputs to the system are organized first by speed (fast or slow) then by major system, and finally by location. The system response times depend on these inputs; the fast inputs are brought into the system on fiber optics, these respond in 1 microsecond to the absence of a 5 MHz square wave on the fiber, the slow inputs (< 1 millisecond) depend on a 24 Volt level for a permit (see adjacent table). Events like the BLM or RF system trips require immediate termination of the electron beam (< 10 microsecond), where the dump water system tripping (< 1 millisecond) is a bit more forgiving! These times are top level requirements and are not imposed by the MPS but rather the inputs in many cases are mechanical switches or relays.

There are three main components to the system; 1. The Machine / Beam Mode Status Cards (MMSC & BMSC), 2. The BLM VME cards, and 3. The Drive Laser Pulse Controller (DLPC).

MACHINE AND BEAM MODES

We have defined 8 Beam Modes and 8 Machine Modes. In both cases the Mode "0" is an invalid setup. Each of the MPS inputs fit into one of more these safe operating modes. The MPS uses magnet switch settings and currents to determine the Machine Modes (MM). The MMs are used internal to the MPS to enable the Drive Laser Pulse Controller (DLPC) which ultimately controls the average current of the electron beam. An example is when the beam viewer ITV3F04 is inserted the MPS sets the DLPC to Beam Mode (BM) 2. This is done by placing a 5 MHz square wave on fiber number 1, 2, and 3 of the 8 fiber optic cables that connect the two systems together. The DLPC allows the operator to select combinations of micropulse frequency and macropulse frequency (or CW) that are valid for the highest beam mode that is permitted. The DLPC *assumes full bunch charge* then calculates allowable combinations of micro and macro pulse width and frequency to conform to the allowable limit. An example is that one could run with this viewer in at 18 MHz micropulse frequency, 10 microsecond width, and 60 Hz repetition frequency, or at 4 MHz micropulse frequency, 400 microsecond macropulse width, and at 2 Hz repetition rate. These are both used depending on operation at hand.

The Machine Mode Status Card (MMSC) takes up to 64 inputs from an optically isolated I/O card through the VME P2 back plane connector. These signals represent interlocks for systems such as the injector gun high voltage power supply status, magnet switch status, and magnet current status. These inputs are used to determine which machine modes are valid. This information is then passed to as many as four Beam Mode Status Cards (BMSC) that are physically the same as the MMSC but differ in functionality.

Each BMSC receives interlock information from systems such as vacuum valves, beam viewers, injector gun, beam dumps, and any other interlocks in the same fashion as the MMSC. They also accept the current valid machine mode from the MMSC through a front panel connector. Each BMSC then determines its allowable beam mode and passes this information to the Machine Protection Driver Card (MPDC).

The MPDC takes in the machine mode and beam mode data from the MMSC and BMSC modules through a front panel connector. The MPDC also monitors a fiber optic

0-7803-7738-9/03/$17.00 © 2003 IEEE

signal from the Fast Shutdown Summation Card that sums interlocks from systems such as RF Control Modules and Beam Loss Monitors. The MPDC then determines the maximum allowable beam mode and transmits this information to the Drive Laser Pulse Controller (DLPC) through 8 fiber optic lines.

All of the aforementioned VME cards use FPGA devices to interpret interlock inputs and determine valid machine and beam modes. The status of all the interlocks, allowable machine modes, and allowable beam modes are available to EPICS from each module through the VME back plane.

Beam Modes

The actual micropulse & macropulse setting are determined by the DLPC

- Beam Mode 0, No Beam Allowed
- Beam Mode 1, Ceramic Viewer Mode
- Beam Mode 2, IR Beam Viewer Mode
- Beam Mode 3, UV Beam Viewer Mode
- Beam Mode 4, High Power Viewer Mode
- Beam Mode 5, IR Laser Alignment Mode
- Beam Mode 6, UV Laser Alignment Mode
- Beam Mode 7, Full Power Mode

Note that modes 4,5, &6 can be used by the Laser Safety System to limit the Laser power

Machine Modes

The Beam Dump location is determined by monitoring the dipole power supply current and the magnet switch positions

- Machine Mode 0, No Beam Allowed; Magnet and Switch Settings Not Valid
- Machine Mode 1, Injector Dumplet
- Machine Mode 2, 2G Strait Ahead Dump
- Machine Mode 3, IR Recirculation Mode
- Machine Mode 4, UV Recirculation Mode
- Machine Mode 5, 6, 7, To Be Determined

BEAM LOSS MONITORING SYSTEM

It is easily understood that we don't want to trip-off the accelerator when using diagnostics since the beam loss produced by the short macropulse is not dangerous to the machine. This is why, in the past, we would have to mask the BLMs in before going into pulsed mode. (An action that must be performed by the operator or software and then the BLM system MUST be unmasked before going back to high power). This new VME based BLM system has the ability to "ignore" the loss detected during a macropulse of restricted size and duty factor. This results in a significant improvement to the systems performance. The new BLM cards (F0151) are configured by EPICS as to what macropulse widths to expect (firmware limited to less than 400us) and will also receive an appropriately delayed beam-sync signal from which to synchronize the window for which the electronics will "ignore" the detected beam loss that would otherwise trip the BLM channel. It is essential to state that after the time window in which the loss is ignored (or vetoed), the BLM interlocking circuit is forced to remain armed for a period of time that is 1250 times longer than the veto pulse. The factor of 1250 comes from the 0.08% duty factor restriction programmed into the firmware. (i.e. 400us * 1250 = 0.5s or 2Hz) This "beam veto" signal cannot be tricked by a failure in the beam-sync source as the timing associated with it is calculated internal to the BLM fault circuit. The result is a system that allows insertion device operation with no procedural steps to ensure that it is done right. The BLM Beam-Veto function allows the operator to use insertion devices with no Interlock masking or changes in its native mode of operation. Finally, a consequence of a BLM system having only a single mode of operation as described above is that this mode of operation must be appropriate for running the machine in high current modes as well. In the normal set-up for full power CW running, the system will continue to receive a beam-sync pulse at 60Hz (or any rep-rate actually). In this case there would exist a short BLM veto pulse lasting approx 13us (16.6ms/1250). This is consistent with a tolerated about of beam loss with a structure at 60Hz of 0.08%. The end result for CW running is that the BLM channel is armed to fault 99.92% of the time and that the 0.08% loss that is not seen is the loss that has been calculated as acceptable under the same line of logic used for Pulsed Mode.

All of the 12 channel BML boards are connected together with a common with a common clock that is initiated by a trip of any of the BLM channels. This clock initiated a shift register which latches the first three channel that trip thus recording the trip history.

DRIVE LASER PULSE CONTROLLER

The DLPC is responsible for enforcing the allowed Beam Mode. A block diagram of the system is show in figure 1. The heart of the system is a scalar board from ConOptics corporation. This has been fitted to a VME mother board and mounted in the VME crate. The laser is a commercial mode locked Nd:YLF that operates at the 20^{th} sub-harmonic of the 1497MHz RF frequency. Elector-optical (EO) cells are used to divide the (~) 75 MHz down by factors of 2 until the desired micropulse frequency is reached. This mode locker must be locked to the accelerator master oscillator for running beam (this is one of the beam mode 0 inputs).

Since the EO cells are not failsafe therefore the DLPC monitors the actual beam current and confirms the average power enabled by a given beam mode is not exceeded. The DLPC uses both the EO cells and a mechanical shutter to stop beam in the event of a fault.

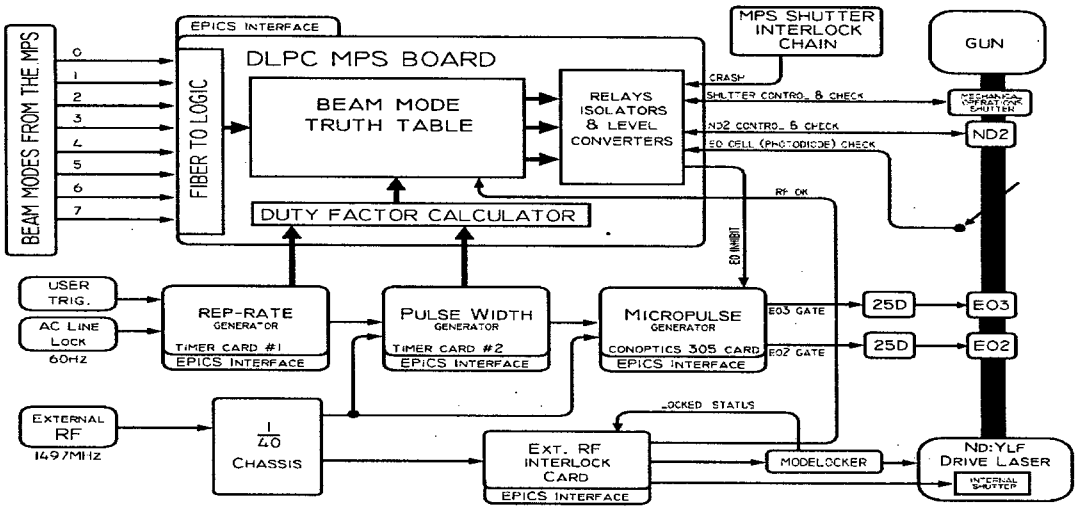


Figure 1: DLPC Block Diagram

SCALABILITY

The design which is based on a single FPGA control board, a common optically isolated input board and a fiber Input/Output board lends itself readily to support nearly any machine configuration.

The system described is configured for the MM/BM VME cards to reside next to each other in a single crate so the 25 pin "D" connector can be strapped with a ribbon cable. In the case one would have multiple locations in a larger facility each remote location would be connected in a serial fashion with 6 fiber optical cables from the 'last' to the 'next' with the final location connecting to the Drive Laser Pulse Controller. The system would able to seamlessly gather the information about the current configuration and status of insertion devices and pass it along to the final gate array which decides which Beam Mode to pass on to the DLPC. As always the status would be monitored in EPICS.

CONCLUSIONS

This system was designed with operability at the forefront of the design considerations. This was accomplished by the following key features; 1. BLM blanking – This allows for easy transition from full power mode to pulsed diagnostic mode, 2. Machine Modes allow for maintenance or commissioning of component in unused beam lines with out impacting operations and eliminates the need for masking of interlocks, 3. Post Mortem information is latched to identify *first fault*, 4. DLPC monitors actual beam current to confirm and enforce allowed beam mode, 5. All status is monitored through EPICS and available to operations staff.

In developing this system we had gone through an iteration with the previous JLab IR Demo machine.

This initial system consisted of VME boards *borrowed* from the Advanced Photon Source at Argonne National Lab and a combination of Programmable Logic Controllers (PLCs) implemented by the CEBAF safety group headed by Kelly Mahoney. This system worked well to protect the machine but had limitations in getting the status of fault conditions cleanly back through EPICS and latching the first offender. This new system was designed to address these shortcomings as well as the challenges faced by an operational laser that may reach powers in excess of 100 kilowatts with planned follow on upgrades.

ACKNOWLEDGEMENTS

I would like to thank the members of the FEL team and in particular George Neil, Steve Benson and Michelle Shinn in providing motivation and insight to provide a system that both protects the accelerator and the laser and eases the operation and commissioning of the various systems. This work was supported primarily by the U.S. Dept. of Energy under contract DE-AC05-84-ER40150 (Thomas Jefferson National Accelerator Facility). The JLab FEL is supported by the Office of Naval Research, the Air Force Research Laboratory, the Commonwealth of Virginia and the Laser Processing Consortium.

REFERENCES

[1] G. R. Neil et al., *Phys. Rev. Lett.*, **84**, (2000) 662.

[2] S. V. Benson et al., "A 10 kW IRFEL Design for Jefferson Lab," PAC'01, Chicago, IL, June 2001, p. 249.

[3] http://laser.jlab.org

A Mechanical Tuner for the ISAC-II Quarter Wave Superconducting Cavities

T.Ries, K. Fong, S. Koscielniak, R.E. Laxdal, G. Stanford,
TRIUMF*, 4004 Wesbrook Mall, Vancouver, Canada, V6T2A3

Abstract

TRIUMF is developing a new mechanical tuner system capable of both coarse (kHz) and fine (Hz) frequency adjustments for maintaining frequency lock on the superconducting quarter wave cavities of the ISAC-II heavy ion linac. A 1 mm thick Niobium plate at the high field end of the cavity is actuated by a vertically mounted permanent magnet linear servo motor, at the top of the cryostat, using a 'zero backlash' lever and push rod configuration through a bellows feed-through. The system resolution at the tuner plate center is $\sim 0.055\mu$m (0.3 Hz) with a dynamic range of 8 KHz and a manual coarse tuning range of 33 kHz. In cold tests with a prototype quarter wave cavity the tuning system's ability to compensate perturbations indicated a bandwidth up to 100 Hz. A large mechanical resonance at 20 Hz should be eliminated in the on-line device. The rf control is based on a self-excited loop with a locking circuit for amplitude and phase regulation. The tuner is fed a position signal integrated from the control loop phase error. Details of the mechanical device and results of open and closed loop cold tests will be given.

1 INTRODUCTION

TRIUMF is installing a superconducting heavy ion linac as part of the ISAC-II upgrade [1] to increase the final energy of the radioactive beam above the Coulomb barrier. A first stage of the project includes the addition of twenty quarter wave, 106.08 MHz, bulk niobium cavities arranged in five cryomodules. A prototype cavity is available for rf testing and development. Four production cavities have recently been delivered to TRIUMF with the remaining sixteen cavities due for delivery in August 2003.

In previous linac installations the tuning of quarter wave cavities has been accomplished with mechanical or pneumatic tuners characterized by slow response, poor resolution and/or large backlash. Detuning by microphonic noise or rapid fluctuations in helium delivery pressure are accomodated by either overcoupling to reduce the loaded Q or with a variable reactive load using a PIN diode network at the cavity. A slow tuner response affects the required Q-loading and may limit the accelerating gradient due to constraints on the stored energy.

The ISAC-II design gradient is 6 MV/m giving a stored energy of $U_o = 3.2$ J. The natural bandwidth of ± 0.1 Hz is broadened by overcoupling. The required forward power is given by $P_f(W) \simeq \pi U_o \Delta f_{\frac{1}{2}}$ for overcoupled systems. A rough rule is to use a loaded bandwidth of six times the microphonic noise plus twice the resolution of the mechanical tuner [3]. The ISAC-II medium beta cavities are outfitted with a passive mechanical damper[2]. Test stand measurements show microphonic noise detuning of the cavity frequency at $\sim$ 0.3Hz RMS due to the main mechanical frequency of 72 Hz. Fluctuations in an on-line accelerator can be several times larger but are not expected to be more than a few Hz RMS. The goal for the ISAC-II cavity tuner is to achieve fine (1 Hz) tuning capability with a response time to control fast helium pressure fluctuations allowing stable operation within a bandwidth of $\Delta f_{\frac{1}{2}} = 20$ Hz. Sensitivity to helium pressure fluctuations is 1 Hz/Torr with expected pressure variations of 10 Torr at rates up to 1 Torr/sec. In addition the tuning range must be adequate to compensate for variability in manufacturing and cooldown. A ± 20 kHz coarse range is a comfortable margin. The tuner described here provides both fine and coarse tuning requirements in a single device.

2 MECHANICAL SYSTEM

2.1 *Tuning Plate*

The tuning plate (see Fig. 1) consists of 1 mm thick RRR Niobium sheet of 240 mm diameter fixed to the bottom Niobium flange by bolts and retaining flange. A flat plate can be used but the deflection force required is parabolic with distance and tends to assume a concave shape upon cooling leading to highly non-linear behaviour. To overcome these problems the ISAC-II tuning plate is spun with a single 'oil-can' convolution and milled with eight radial 1 mm slots. The plate is capable of allowing ± 20kHz (± 3 mm) of tuning range before yielding. Cold tests with the plate give Q and gradient values consistent with the flat plate performance[1].

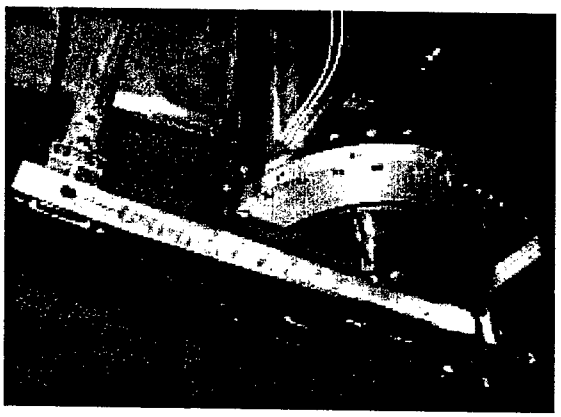


Figure 1: The tuner plate, lever arm, bottom of push-rod and cavity viewed from below.

*TRIUMF receives funding via a contribution agreement through the National Research Council of Canada

0-7803-7738-9/03/$17.00 © 2003 IEEE

2.2 *Tuner*

The tuner diaphragm is actuated by a simple lever arm and push rod arrangement as shown in Fig. 2. The top end of the push rod goes from vacuum to air via an edge welded bellows. The push rod is coupled to a linear direct drive ironless coil servomotor. A low stiffness coil is attached to counteract the effects of air pressure on the bellows. The spring compression is manually adjustable in order to set the mechanically self-seeking equilibrium position before servo startup. The lever arm is specially designed to have a high fundamental frequency, $\simeq$200 Hz, so that it remains decoupled from the position loop bandwidth of $\simeq$200 Hz. The push rod consists of a 25 mm diameter 316 stainless steel tubing with a 0.38 mm thick wall giving less than 0.1 W of heat load. The rotary joints are comprised of anti-backlash, high strength and stiffness pivot bearings. They are limited in rotation to about $\pm 8°$, however, the required motions are well within this range.

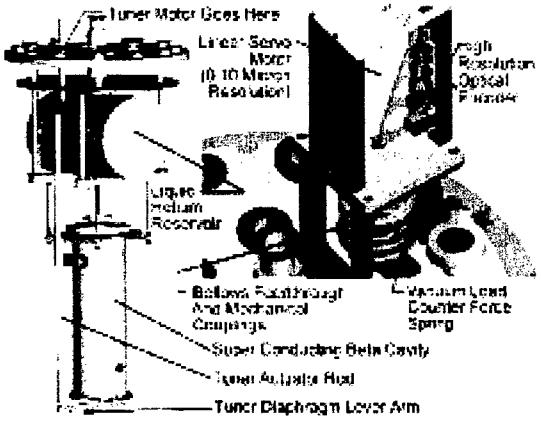


Figure 2: Tuner drive assembly layout.

3 CONTROLS

3.1 *Tuner Drive*

The heart of the supervisory control is the PCI bus digital servo controller. The feedback position of the motor is sent to the controller by the servo amplifier in phase quadrature form. The return command drive error signal is analog in the range ± 10 V but with the "impress" of the previous 12 bit signal.

The position of the motor is sensed by a high resolution sine encoder and fed through special subdividing electronics with an effective control resolution inside the servo amplifier of 0.01μm. The actual system resolution at the plate is about 0.055μm limited only by the analog command signal from the digital servo controller to the amplifier as well as the phase quadrature position signal from the amplifier which can be adjusted to suit. The bandwidth of the current control loop is 600 Hz while the velocity loop can be tuned to better than 200 Hz. The design target for the position loop is 100 Hz to handle possible microphonic control. Fast, precise tuner response is made possible by a stiff high bandwidth velocity loop compensation called PDFF that is immune to overshoot and load disturbances like friction.

3.2 *RF Controls*

The ISAC-II rf control[4] is based on a self-excited loop with a locking circuit for amplitude and phase regulation. The tuner is fed a position signal integrated from the control loop phase error. When a resonant cavity with a natural frequency ω_c and time constant τ is excited at a frequency ω, the phase shift between the input and output is given by $\tan\phi = \tau(\omega - \omega_c)$. This phase shift is measured by an edge-triggered JK flip-flop phase detector. This detector is well suited since it lacks memory when a cycle is skipped and exhibits no reversal behaviour in its output at all phase ranges. The phase shift is processed by a DSP to drive the mechanical tuner and keep the cavity in tune with the external master frequency.

The system response equation is given by

$$\frac{\delta\phi}{\delta x} = \frac{s^2 G_u}{s^3 + s^2\Phi_p(1+T_p) + s(\Phi_i(1+T_p) + \Phi_p T_i) + \Phi_i T_i}.$$

Here $\Phi_{p,i}$ and $T_{p,i}$ are the quadrature loop and tuner loop feedback parameters respectively and G_u is the detuning of the cavity resonance due to deformation of the cavity where $\delta\omega_c = G_u\delta x$. The expression ignores the amplitude loop. An analysis of the equation[4] shows that the tuner response must be slower than the response of the phase quadrature loop in order for the system to remain stable. This fundamental limitation could be avoided if the tuner control was configured to respond to a velocity signal. If the mechanical resonance at 20 Hz is removed (see below) it may be possible to use the tuner to combat detuning from 72 Hz microphonics. However as the results below confirm the present configuration is certainly sufficient to provide accurate compensation for slow (few Hz/sec) frequency fluctuations.

4 COLD TEST RESULTS

The mechanical tuner performance has been characterized over several cold tests from Oct. 2002 to present. Since the tuner plate is linked to the cryostat by the tuner shaft we had concern that tuner or environment noise would feedback to the cavity. Low frequency (0-10 Hz) dithering of the tuner produced no significant coupling to the cavity microphonics. The transfer function from the mechanical tuner modulation signal to the amplitude and phase of the cavity self-excited frequency was recorded. The amplitude is given in Fig. 3. Except for a mechanical resonance at 20 Hz there is good response out to at least 100 Hz. Present thinking is that the mechanical resonance is due to a dogleg in the push-rod that is necessary in the test cryostat but can be eliminated in the on-line system.

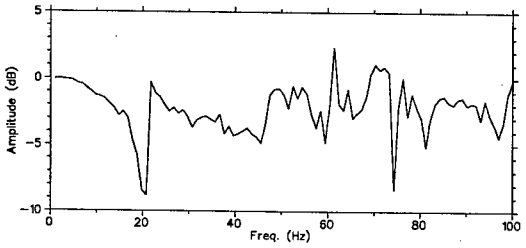


Figure 3: Tuner transfer function.

The tuner on-line performance is measured by altering the cavity frequency by forced variations of the helium pressure with a valve on the vent gas line. The pressure is measured with a transducer located on a flange on the helium space. In general the pressure variations are more extreme than we expect for the on-line system but they allow us to optimize the PID parameters for the control and tuner loops. Data is taken for a variety of cavity field and coupling strength settings. Results for both a low field and a high field case are shown in Fig. 4 and Fig. 5 respectively. The bandwidth for the high field case is limited by the maximum power of the test amplifier. The plots give the pressure change and the associated position drive signal for the tuner. The voltage and phase error are given for each case. Note that the phase error resolution is limited to 1° by the 12 bit ADC. The plots show that the tuner responds accurately to the pressure variation with a resolution better than 0.1μm (0.6 Hz). The regulation in amplitude and phase is within the limits of $\pm 1\%$ and $\pm 1°$ for the low field case. In the high field case due to the limited bandwidth the phase stability goes out of the regulation tolerance during moments of rapid pressure change.

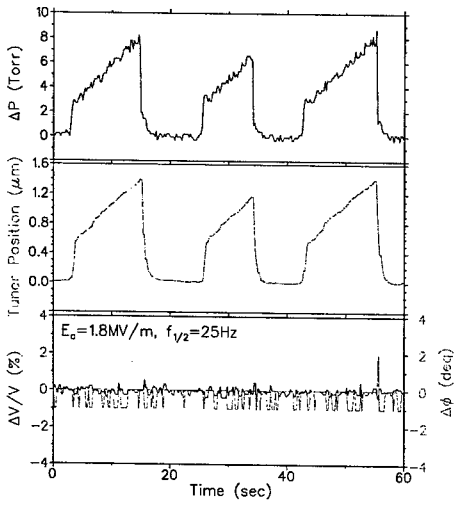


Figure 4: Tuner response to forced helium pressure fluctuation ($\frac{\Delta f}{\Delta P}$ = 1Hz/Torr) and corresponding voltage (blue) and phase (red) errors for low field (E_a=1.8 MV/m) and a bandwidth of $\pm$25 Hz.

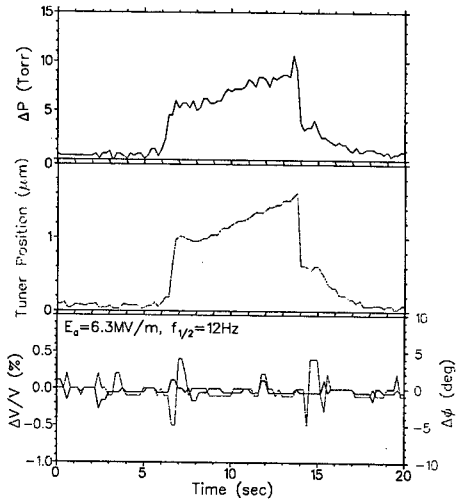


Figure 5: Tuner response to forced helium pressure fluctuation ($\frac{\Delta f}{\Delta P}$ = 1Hz/Torr) and corresponding voltage (blue) and phase (red) errors for high field (E_a=6.3 MV/m) and a bandwidth of $\pm$12 Hz.

The dynamic range of the tuner is limited by the motor strength to $\pm$4 kHz. A threaded position platform for the spring tensioner is used to provide manual coarse frequency adjustments. A tuning range of 33 KHz has been demonstrated and was limited only by mechanical stops on the platform that will be altered to give the full 40 kHz design range.

5 CONCLUSION

The tuner is a significant advance on mechanical tuners presently used on quarter wave structures due to its high precision (0.3 Hz), and response bandwidth (presently limited to 20 Hz). The demonstrated coarse tuning range is 32 kHz. In addition the convoluted lower tuning plate and robust tuner mechanical design allow cold plastic deformation of the plate reducing the tolerance on cavity geometry necessary during cavity fabrication. Assuming that the mechanical resonance at 20 Hz can be eliminated future developments could see the rf controls configured to provide a velocity signal removing the fundamental limit on the tuner speed due to loop stability.

6 REFERENCES

[1] R.E. Laxdal, *et al*, *The ISAC-II Upgrade at TRIUMF: Progress and Developments*, this conference.

[2] A. Facco, *et al*, *Mechanical Mode Damping in Superconducting Low-beta Resonators*, Proc. of the Eighth RF Superconductivity Workshop, Abano, 1997.

[3] J. Delayen, *et al*, *TM_{010} Cavities, RF Control, Tuners, Couplers*, RIA Driver Workshop II, Argonne, May 22-24, 2003.

[4] K. Fong, *et al*, *RF Control System for ISAC-II Superconducting Cavities*, these proceedings.

THE JEFFERSON LAB QUALITY ASSURANCE PROGRAM FOR THE SNS SUPERCONDUCTING LINAC ACCELERATOR PROJECT*

Joseph P. Ozelis†, for the Jefferson Lab SNS Project Team
Thomas Jefferson National Accelerator Facility, Newport News, VA. 23606, USA

Abstract

As part of a multi-laboratory collaboration, Jefferson Lab is currently engaged in the fabrication, assembly, and testing of 23 cryomodules for the superconducting linac portion of the Spallation Neutron Source (SNS) being built at Oak Ridge National Laboratory. As with any large accelerator construction project, it is vitally important that these components be built in a cost effective and timely manner, and that they meet the stringent performance requirements dictated by the project specifications. A comprehensive Quality Assurance (QA) program designed to help accomplish these goals has been implemented as an inherent component of JLab's SNS construction effort. This QA program encompasses the traditional spectrum of component performance, from incoming parts inspection, raw materials testing, through to sub-assembly and finished article performance evaluation. Additionally, process and procedure control, vendor performance and oversight, and design and test program reviews constitute complementary areas where QA involvement contributes to successful production performance.

INTRODUCTION

The superconducting linac of the Spallation Neutron Source (SNS) will consist of 23 cryomodules. Eleven of these cryomodules will each contain 3 medium β superconducting RF cavities, with the remaining twelve each containing 4 high β cavities. In addition to superconducting cavities, the cryomodules contain tuner mechanisms, power couplers, diagnostic and control instrumentation, and cryogenic circuits.

These cryomodules must meet exacting performance requirements. To ensure this, a comprehensive Quality Assurance (QA) program has been developed. This program encompasses a wide array of activities and mechanisms, including:

- inventory control
- incoming component inspection
- component and materials testing
- vendor oversight
- process and procedure control
- process data capture
- process feedback
- sub-assembly test and measurement
- final assembly acceptance testing
- document control
- instrument and device calibration

Each of these independent yet coupled program elements is vital to ensuring that the cryomodules built by Jefferson Lab for the SNS SC linac achieve the required performance and reliability goals.

PROGRAM COMPONENTS

Inventory Control

All parts, components, and subassemblies delivered to JLab from vendors are inventoried, inspected for damage, and entered into a commercial electronic inventory tracking system. Components are identified using in-house generated bar code labels, and stored in a secure location. Access to component storage is restricted to authorized, trained personnel. Components that have not passed incoming inspection requirements (non-conforming parts) are segregated from usable inventory. This inventory control system ensures that accelerator components are carefully tracked, stored, and only acceptable components are used in cryomodule assembly.

Incoming Component Inspection

Where deemed necessary, dimensional inspections are performed upon receipt of a component to verify conformance with required parameters and tolerances. The inspections range from visual inspection to note the condition of surfaces, welds, or finishes, to precise geometric measurements utilizing a coordinate measuring machine (CMM) or surveying apparatus.

All inspections are performed using travelers or officially released drawings, and all inspection data is recorded electronically on-line via the travelers or generic inspection summary reports, using the *Pansophy* system [1], [2]. In the event that a component does not meet the required specifications, a non-conformance report (NCR) is issued and the item is returned to storage, tagged as "Do Not Use", and segregated from usable inventory, pending disposition.

Component and Materials Testing

In many cases, commercially purchased components or raw materials are tested for compliance with specifications. For the SNS medium β cavity production effort, essentially the entire inventory of high RRR Nb disks to be used for half cell fabrication was scanned for

*Work supported by United States Department of Energy under contract DE-AC05-84ER40150
†ozelis@jlab.org.

0-7803-7738-9/03/$17.00 © 2003 IEEE

defects using an eddy current apparatus [4], before being sent to the vendor. Niobium raw material was also tested for mechanical properties not only in the as-received state, but also after representative heat treatments.

Other components have also been tested to ensure adequate performance. High vacuum all-metal gate valves have been leak checked and tested for particulate generation. End cans, thermal shields, and other components of the cryogenic system are routinely leak checked.

Vendor Oversight

Vendor task execution is closely monitored so that uniform levels of quality performance are maintained throughout the production cycle. Vendor-supplied fabrication documentation and test reports are consistently reviewed and compared with in-house testing and verification of parameters to uncover discrepancies or breakdowns in the vendor's QA program. These are immediately addressed with the additional involvement of technical and procurement staff, and are often resolved through the adoption by the vendor of more accurate fabrication or testing procedures.

Process and Procedure Control

Consistent cryomodule performance relies upon the uniform and consistent application of processes and procedures that have been developed and refined through a comprehensive and exhaustive prototyping program. In order to provide this consistency, JLab relies upon process control documents, commonly called travelers, which guide all inspection, fabrication, and testing activities.

These travelers, which are all accessible in electronic form via a standard web browser from a server on the JLab intranet, provide detailed task instructions and links to procedures, reference drawings, and parameter lists, while also serving to provide "shop floor" oversight and review through process "hold-points". Currently there are about 60 unique travelers in use for SNS medium-β cryomodule production, which have been utilized over 1600 times.

Process Data Capture

In addition to process control, the electronic travelers described above also provide a means for easy and efficient process data capture. Accurate and timely capture of inspection, fabrication, and test data is vital to ensuring the integrity and accuracy of data later used in performance analysis and verification.

The travelers are designed to incorporate data fields to accept integer, floating point, and text data, along with direct upload of ASCII or binary data files. The data are then directly entered into an Ingres® database, and immediately available for review and analysis. The production facilities at JLab are equipped with wireless LAN transmitters, so that laptop PC's with wireless network cards can be utilized as mobile workstations to serve the online travelers.

Process Feedback

The electronic travelers provide almost real-time feedback to project staff. Data recorded by the travelers are immediately entered into the supporting database and are available for analysis. The general data field query mechanism of *Pansophy* allows production mangers and engineers to easily mine the traveler data to develop correlations between measured parameters and observed performance.

Furthermore, if a discrepancy is noted during an inspection, assembly, or testing process, a non-conformance report (NCR) can be launched from within the relevant traveler. This NCR is hyper-linked to the traveler, so that the responsible project staff can easily review the source of the NCR and dictate the appropriate corrective action. Once the project staff closes out the NCR, its initiator is notified automatically by e-mail of the disposition.

Sub-Assembly Test and Measurement

At various stages in the production cycle, acceptance testing is performed on sub-systems and larger components. This testing serves to ensure that complicated components that have already undergone significant handling, assembly, or fabrication, are able to meet their performance requirements. Since these systems, once installed in the cryomodule, are usually too complex or difficult to repair or re-configure in-situ, acceptance testing prior to further assembly provides an additional measure of confidence.

For example, before string assembly, all of the superconducting cavities are tested in the JLab Vertical Test Area (VTA) at 2K. Cavities that do not meet the required gradient and Q_o specifications are rejected, re-processed, and re-tested until adequate performance is achieved [4].

Likewise, the 1 MW power couplers are baked and RF conditioned to ensure that they will provide RF power at the required level and duty cycle without experiencing arcing or vacuum degradation. This conditioning also allows the performance of the coupler instrumentation to be assessed [5]. All couplers must pass this acceptance test before being released for use on a cryomodule.

As with other aspects of the SNS QA program, these tests are performed using electronic travelers that provide control of the test and measurement processes and procedures, and integration of the data with the *Pansophy* database.

Final Assembly Acceptance Testing

The ultimate performance verification of the SNS cryomodules is achieved through comprehensive cryogenic RF testing in the JLab Cryomodule Test Facility (CMTF). While cooling the SNS cryomodules to 2K, cryogenic performance and instrumentation is verified and recorded. Each cavity is then powered with the 1MW klystron and RF performance parameters such as gradient, Q_o, Lorentz force detuning, microphonics, HOM damping, etc. are determined and recorded [4].

Again, all test procedures and data are controlled and integrated using the online electronic traveler system.

Final acceptance of the cryomodules by the SNS is contingent upon a successful on-site inspection and verification, where the cryomodules are inspected for shipping damage, including analysis of accelerometer readings taken during shipment, and verification of instrumentation and vacuum system integrity, alignment, and fundamental cavity frequencies.

Document Control

The efforts to fabricate, assemble, and test a complex device such as a cryomodule with exacting performance requirements are necessarily driven by and dependant upon extensive documentation. Be they technical drawings or procedures, process control documents, statements of work, or test results, it is vital that accurate documentation be utilized at all times. Except for engineering drawings, version control and central archival of project documentation is achieved using the Docushare® document management system from Xerox. (Engineering drawings are managed by the JLab Accelerator Division's Mechanical Engineering Department's Document Control Group.) All documents, drawings, graphics, etc., that are hyperlinked to the electronic travelers are therefore managed such that modifications and revisions are uploaded following supervisory mechanisms.

Instrument, Device and System Calibration

Any QA program is only as good as the data that process control and engineering design decisions are based upon. Acknowledging this, the SRF Institute has required that instrumentation, devices, and systems that have been identified as process quality critical be in valid calibration status or removed from service. A tool has been developed as part of *Pansophy* that allows devices to be entered into a database, which tracks their calibration status, notifies the device or system owner when calibrations become due, and provides a means for requesting a device be sent out for calibration. Periodic audits are performed to ensure compliance.

In addition to instrumentation and devices, systems as a whole also are subject to calibration requirements. The RF test facilities are characterized by active and passive components, which can have an effect on measurement accuracy. Therefore, comprehensive calibration routines and procedures are carried out and documented before acceptance testing can begin.

QUALITY PROGRAM IN PRACTICE

While production is still at an early stage, the JLab SNS QA program has already been shown to be effective in several concrete ways.

In some instances, inspections of incoming components revealed lack of compliance with specifications, such as poor adhesion of copper plating on the Fundamental Power Coupler (FPC) outer conductors, incorrect bayonet heights on the cryomodule end cans, warping of the FPC inner conductor, and incorrect positions of the rings on the cryomodule space frame. Each of these issues were corrected by reviewing and revising the fabrication procedures and verification processes employed by the respective vendors.

Raw materials testing has likewise proven beneficial. Early mechanical tests of high-RRR Nb to be used in fabrication of cavities revealed that the hardness and elongation properties of both the as-received and post-heat treatment samples from one of the vendors did not meet the required specifications [6]. Closer analysis indicated that the material had not been fully re-crystallized due to incomplete annealing. The material was sent back to the vendor for re-annealing, and tested satisfactorily upon return. The vendor subsequently modified its annealing procedure.

As a result of the JLab component testing program, leak checking of the LN_2 circuits of the thermal shields eventually revealed leaks that had not been discovered by the vendor's own QA program. Discussions with the vendor and observations of their procedures led to improvements, which then yielded the required sensitivity and reliability. No leaks have been found subsequently.

Continued aggressive adherence to this QA program will prove to be vital in ensuring that the SNS linac project at JLab successfully fulfills its obligations in providing cryomodules that meet the required performance and reliability specifications while also accomplishing cost and schedule goals.

ACKNOWLEDGMENTS

Much as an Environment, Health, and Safety program does, an effective Quality Assurance program relies upon the active contributions of each participating individual. The SNS project at JLab has benefited from the dedicated efforts and cooperation of the staffs of the SRF Institute, Center for Advanced Studies of Accelerators, and Accelerator Division's Mechanical Engineering and Electrical Engineering Support departments. Their contributions are gratefully acknowledged.

REFERENCES

[1] C. Reece et al., "A System for Managing Critical Knowledge for Accelerator Subsystems : *Pansophy*", PAC2001, Chicago, p. 1189

[2] V. Bookwalter et al., "Utilization of Integrated Process Control, Data Capture, and Data Analysis in Construction of Accelerator Systems", paper TPAG029, this conference

[3] Manufactured by BAM 12205 Berlin, Germany, based on a design used at DESY

[4] J. Preble et al., "SNS Cryomodule Performance", paper ROAA001, this conference

[5] M. Stirbet et al., "High Power RF Tests on Fundamental Power Couplers for the SNS Project", EPAC 2002, Paris, p.2283

[6] G. Myneni and P. Knesiel, JLab Internal Notes TN-02-011 and TN-02-001

UTILIZATION OF INTEGRATED PROCESS CONTROL, DATA CAPTURE, AND DATA ANALYSIS IN CONSTRUCTION OF ACCELERATOR SYSTEMS *

V. Bookwalter, B. Madre, J. P. Ozelis, C. Reece +
Thomas Jefferson National Accelerator Facility, Newport News, VA. 23606, USA

Abstract

Jefferson Lab has developed a web-based system that integrates commercial database, data analysis, document archiving and retrieval, and user interface software into a coherent knowledge management product called *Pansophy*. *Pansophy* provides key tools for the successful pursuit of major projects such as accelerator system development and construction by offering elements of process and procedure control, data capture and review, and data mining and analysis. Today, *Pansophy* is used in Jefferson Lab's SNS superconducting linac construction effort as a means for structuring and implementing the QA program, for process control and tracking, and for cryomodule test data capture and presentation/analysis. Development of *Pansophy* continues, with improvements to data queries and analysis functions that are the cornerstone of its utility. In this paper the present configuration and operational environment of *Pansophy* is described, along with future development goals. Additionally, specific examples of its use in an accelerator construction project will be presented.

MOTIVATION AND APPROACH

Pansophy, a web-based system conceived as a vehicle for collecting, managing and exploiting the data from SRF accelerator subsystem development and production efforts, began development in early 2000 [1]. Because data from the construction of the original CEBAF accelerator was saved in paper form, it was cumbersome to search, and trends were difficult to spot. Some electronic files, often in the form of Excel spreadsheets, existed on individual computers, but there was no coherent effort to save data in a searchable electronic format. This resulted in hesitancy to search the archived documentation when data were needed. It was believed that if data could be made immediately available, and trends observed in near real-time, a feed-forward mechanism could then be exploited, and lessons learned could be applied quickly.

To make the most efficient use of development resources, the system was conceived as a custom integration of several commercial software packages.

Since its initial development, *Pansophy* has become a vital resource for documenting and processing data from various SRF Institute accelerator projects. Staff members within the SRF Institute and Accelerator Division have begun making extensive use of its capabilities.

*Work supported by the U. S. Department of Energy contract DE-AC05-84ER40150

+bookwalt, madre, ozelis, reece@jlab.org

GENERAL DESCRIPTION

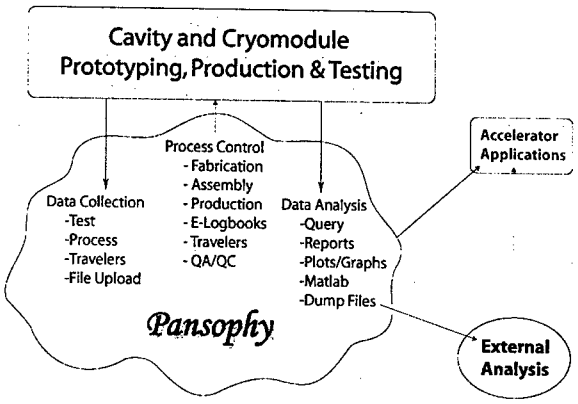


Figure 1: Overview of *Pansophy*

Travelers

The traveler, a central component of *Pansophy*, defines and controls a process while gathering data particular to a part or assembly. It also defines a unit of the database structure. Travelers are initially generated by a scientific or technical staff member using a Microsoft Word® template, while Adobe Acrobat® provides the final format for archival of an electronic version of approved travelers. DocuShare®, a document management software tool from Xerox, manages, archives, and provides controlled access to travelers. The user interface is written using Macromedia's ColdFusion®, and an automated process converts the document from the MS-Word® format to ColdFusion Markup Language (CFML). There are currently over 100 different types of travelers, which have collectively been used about 2000 times. Traveler data, entered online via a web browser, are directly uploaded into an Ingres® database.

Traveler Features

In addition to the process control and data capture functions described above, travelers also incorporate "hold points," a feature that prohibits the completion of a traveler or section of a traveler (and therefore process) until an authorized supervisor reviews the current data. Additionally, the data recorded by the travelers are frozen once the traveler is closed. These features contribute to satisfying quality assurance requirements.

A specialized Non-Conformance Report (NCR) was developed to track situations where inspections, processes, or tests have uncovered deviations from acceptable

0-7803-7738-9/03/$17.00 © 2003 IEEE

parameters. A link is provided on each traveler to initiate an NCR, which is automatically emailed to the responsible engineer for resolution. Upon resolution and close of an NCR, the results are automatically emailed to the NCR initiator and the resident inventory manager. This automated process ensures the appropriate project feedback is achieved [2].

Occasionally activities such as Electron Beam Welding or Niobium Inventory Tracking may require a custom traveler design. This can be easily accommodated.

Access Control and Administration

The SRF Institute at Jefferson Lab has developed a hierarchical, (WBS) project-based traveler naming convention consisting of five components, plus a revision number and a sequence number. Authorized users can use administrative pages to add new traveler components, modify the header information in a traveler, and view current information.

Pansophy is divided into functional areas and tasks are divided into levels. Authorized users are assigned privilege levels, thus providing secured access to the various functional areas. For instance, supervisors can have additional security levels for traveler data approval, while administrators have appropriate security levels for *Pansophy* configurations only. Most *Pansophy* security and administration functions can be performed online.

Logbooks

Pansophy's electronic Logbooks provide a mechanism for recording time-stamped, non-editable, easily searchable entries of experimental setups, procedures, data, and other information. In addition to this customary usage, these e-logs have proven valuable as a source of information for traveler development.

QC/QA functions

As Pansophy usage increased, additional functionality was added to facilitate meeting QC/QA program requirements. A calibration management tool was added which permits users to enter devices into a database with required inspection dates and durations and calibrator information. The tool automatically emails calibration reminders to device owners, as well as allowing owners to track the location of devices and instrumentation.

In addition to the calibration system, a maintenance utility based on similar requirements has been added. It is presently used to track and record maintenance status of vacuum equipment operating in both the accelerator facility (CEBAF) and the SRF Institute.

USE IN ACCELERATOR PRODUCTION

Recent *Pansophy* development has focused on providing and optimizing database query functionality. This functionality provides the essential capability for data mining of the traveler system, a primary motivation for *Pansophy.* Both pre-defined and user-defined queries have been implemented.

Pre-defined queries include simple searches based on Cavity ID, Serial Number, and Vendor ID. Once user input has been entered, all travelers whose data fields contain this label are searched for matches to the user input. A list of travelers is presented to the user with links to the traveler data, allowing the user to quickly find a traveler for a particular cavity and then directly access that cavity's data.

Other pre-defined queries include searches of NCR status (open/closed/all), listings of all instantiations of a selected traveler, and tabular listings of all data fields for all instantiations of a traveler. The NCR search provides an efficient means of tracking NCR status. The data field grids provide overviews of traveler-generated data and allow for initial review of current results from a given production process, which enables feedback to production managers and engineers.

The user-defined query is one of the most powerful, useful features of the *Pansophy* system. Initially, users are presented with a list of travelers from which to select. When a particular traveler is selected, a listing of available data fields for that traveler is displayed, grouped by traveler page number (Figure 2). The user then selects the data of interest, defines the Boolean operators to be used (>, <, =, LIKE, etc.), and selects the operand for the query (Figure 3). The user submits the query to the database interactively and is presented with a spreadsheet-style listing of the requested data. This data can then be transferred to an application such as Excel for further analysis (see Fig. 4). Queries and analyses like those in Figure 4 provide a quick and efficient means for tracking trends and performance during the production run.

FUTURE DEVELOPMENT

The ultimate functionality and utility of Pansophy is explicitly linked to the ability by users to extract, analyze, and benefit from the data captured. Recognizing this, future development of Pansophy will concentrate on developing even more flexible and useful query mechanisms and data output options.

Additionally, the integration of analysis tools such as Matlab® will be pursued. This will enable users to develop semi-custom stored query /analysis suites, so that data can be routinely analyzed in a consistent manner.

In addition to analysis of data resulting from operation of query logic, high-level "views" are planned, where one can chose a component (cryomodule, for example), and then access performance and fabrication data for that component, and some fraction of its subcomponents, using a graphical interface. This interface would allow one to "drill down" to the sub-component level and generate static reports of relevant parameters. Such a feature is expected to be extremely useful in the commissioning phase of installed accelerator components.

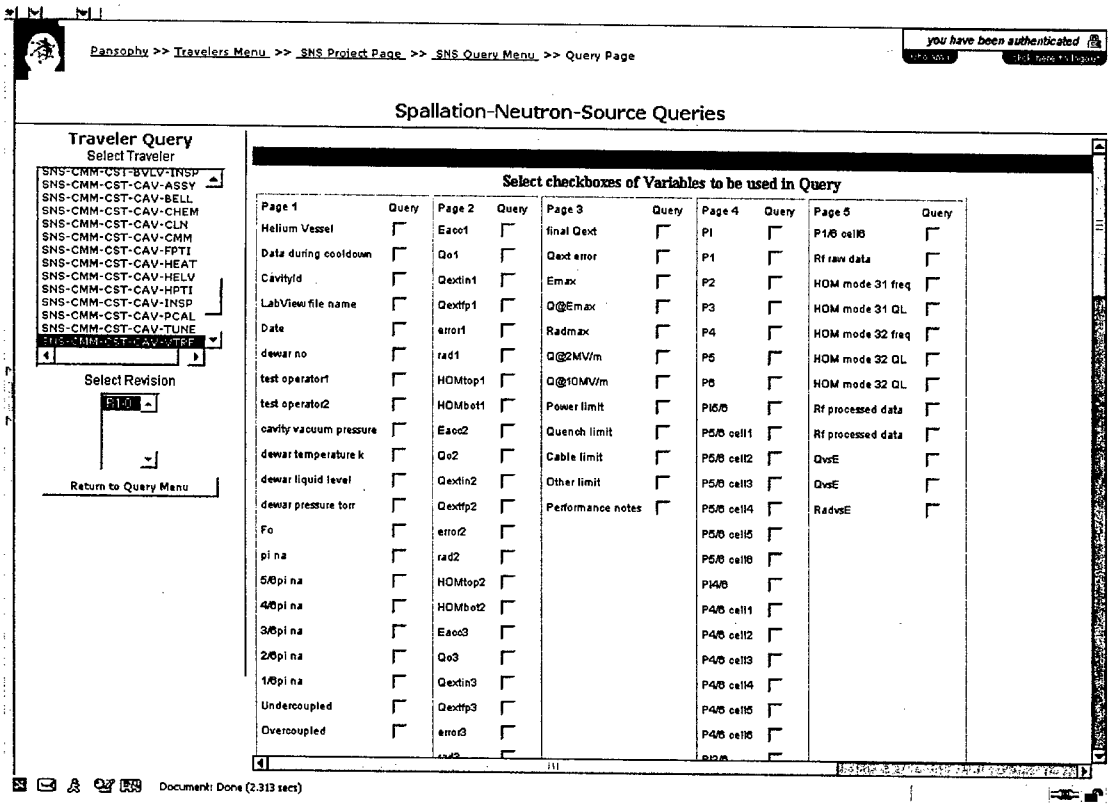


Figure 2. Traveler data field listing used for generating user-defined query.

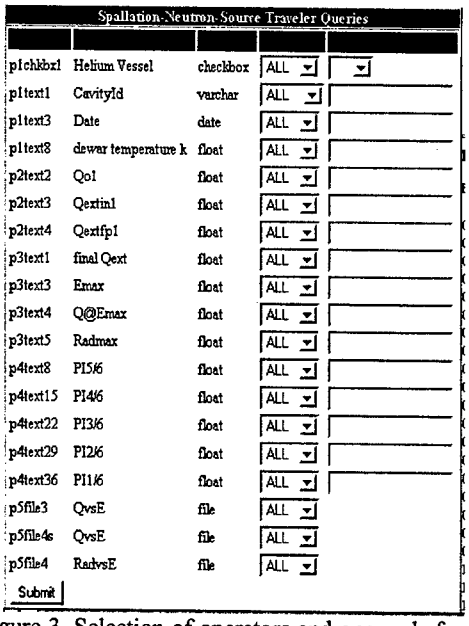


Figure 3. Selection of operators and operands for user-defined query

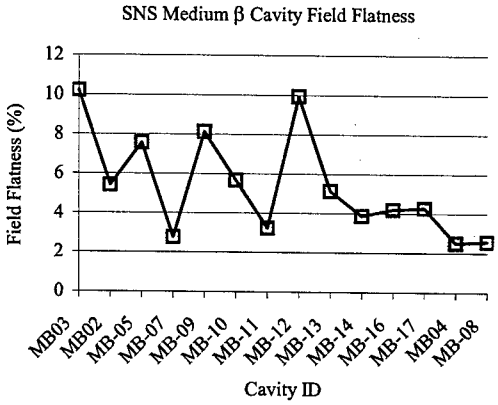


Figure 4. Results of a user-defined query of SNS cavity field flatness %, plotted by cavity.

REFERENCES

[1] C. Reece et al., "A System for Managing Critical Knowledge for Accelerator Subsystems : Pansophy", PAC2001, Chicago, p. 1189

[2] J. P. Ozelis, "The Jefferson Lab Quality Assurance Program for the SNS Superconducting Linac Accelerator Project", paper TPAG028, PAC2003.

STUDY OF COHERENT RADIATION FROM AN ELECTRON BEAM PREBUNCHED AT THE PHOTOCATHODE

J. Neumann*, P. G. O'Shea, D. Demske, R. Fiorito, IREAP,
University of Maryland, College Park, MD 20742, USA
G. L. Carr, H. Loos, T. Shaftan, B. Sheehy, Z. Wu,
Brookhaven National Laboratory, Upton, NY 11973, USA

Abstract

Controlling the longitudinal distribution in an electron beam traveling through an accelerator can enhance system performance in various ways. Prebunching an electron beam in an accelerator can lead to enhanced radiation production from various emitters. Smoothing the shape of the electron beam pulse may suppress instabilities that result in beam breakup. This work, a collaboration between the University of Maryland and the Source Development Laboratory at Brookhaven National Laboratory, uses a Ti:Sapphire drive laser modulated at terahertz frequencies to extract a prebunched beam directly from the photocathode prior to acceleration in a linear RF accelerator. We have demonstrated that prebunched terahertz structure can be maintained after leaving the photocathode and through acceleration to high energy. Through the use of simulation and experiment, this work further explores the characteristics of an electron beam produced in this manner and examines the possibility of using this technology to develop a compact, powerful, narrowband terahertz emitter.

1 INTRODUCTION

During the last year, the University of Maryland has been working with the Source Development Laboratory at Brookhaven National Laboratory to develop a new terahertz light source. In 2002, high-power broadband terahertz radiation at an average power of 20 W was recorded at the Free Electron Laser Facility at Jefferson Laboratory [1]. In contrast, the goal of this collaboration is to develop technology that will lead to a compact, high-power, narrow-band terahertz source. In this case, the photocathode drive laser (a Ti:Sapphire laser frequency tripled to 266 nm) is used as an optical switch to turn the electron beam on and off at terahertz frequencies. The fast switching of the drive laser results in a pre-bunched electron beam. This prebunched electron beam is then accelerated from low energy near the cathode to relativistic velocities and caused to radiate. When an electron beam is prebunched, the radiation emitted near the bunching frequency will be coherent, and the energy will be enhanced by a factor of the number of electrons in the beam above the incoherent energy [2].

A preliminary experiment modulated the 266-nm drive laser at terahertz frequencies by using pulseshaping techniques [3] based on a modified chirped-pulse amplification system. The drive laser was incident on a copper photocathode, which produced a 50-pC electron beam that was also modulated in the terahertz regime. The incident drive laser pulse was measured with a scanning cross-correlator [4] (Fig. 1).

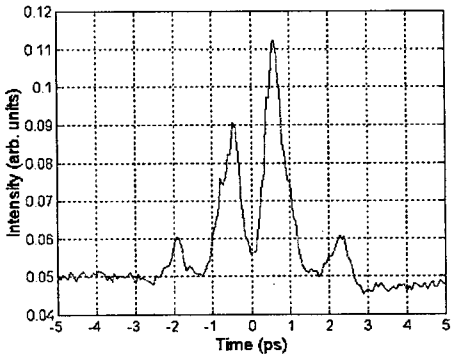


Figure 1: Cross-correlation measurement of 266-nm drive laser pulse incident on photocathode (Head of pulse on right).

The time profile of the electron beam that was generated with the drive laser pulse shown in Fig. 1 was measured using the RF-zero phasing technique (Fig. 2).

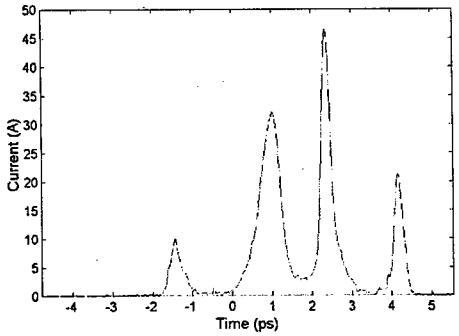


Figure 2: RF-zero phasing measurement of electron beam generated by laser pulse in Fig. 1. (Head of bunch on left).

Currently, a mirror is inserted into the beamline to generate transition radiation. The diagnostic system to

* neumann@glue.umd.edu

0-7803-7738-9/03/$17.00 © 2003 IEEE

measure the energy and spectrum of the light generated by the beam is still being improved. Future experiments will use this system in order to verify coherent radiation production, and demonstrate that the terahertz light is easily tunable by changing the bunching frequency. In order to achieve this goal, terahertz filters are being produced to assist with diagnostics and additional PARMELA simulations help predict the expected high-frequency and high-charge limits of this technique.

2 DIAGNOSTIC IMPROVEMENTS

Spectral information for terahertz radiation can currently be measured using a step-scan Michelson interferometer with a bolometric detector. While the interferometer can be used to collect detailed data, rough spectral content can be measured quickly using various band-pass filters.

The filters were constructed using stainless steel shim stock (each filter is a few hundred micrometers thick) that is chemically etched to produce holes that are fractions of a millimeter in diameter. An example of one of these filters is shown in Fig. 3. When this steel etch is mounted on a fluorogold substrate, reasonable band-pass performance at terahertz frequencies is achieved.

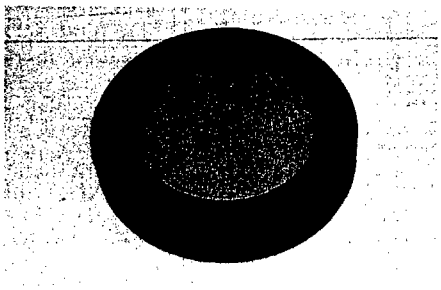


Figure 3: Etched steel terahertz filter.

The frequency characteristics of one filter, tested at the U12IR at the National Synchrotron Light Source, are shown in Fig. 4.

The additional filters still need to be characterized, but the center frequency of each one will be shifted so that various filters could be used in order to estimate the nature of the spectral content of the emitted radiation.

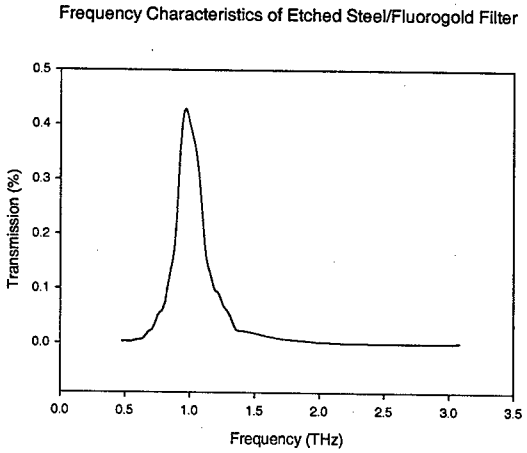


Figure 4: Terahertz band-pass filter.

3 PARMELA SIMULATIONS

The electron beam modulation is introduced at the cathode by modulating the drive laser at terahertz frequencies. Since the electron beam is prebunched at extremely low energies, space charge forces will play a large role in beam dynamics before it is accelerated to relativistic energy. Therefore, it is likely that the modulation on the electron beam will become less pronounced as the frequency of modulation and bunch charge increase.

The acceleration from cathode to gun exit was modeled using the code PARMELA. The input particle distribution at the cathode was considered to be identical to a simulated laser beam envelope because emission at a copper cathode like the one at the Source Development Laboratory is considered to be prompt [5]. For example, one input distribution included four equally sized bunches separated at ~1 THz.

The electron density distribution was examined at the exit of the gun as a function of total charge and frequency of modulation. The degree of modulation, or contrast, is a good measure of how much energy will be radiated by the beam, and is given by

$$Contrast = \frac{N_{max} - N_{min}}{N_{max} + N_{min}} \qquad (1)$$

where N_{max} is the maximum electron density and N_{min} is the minimum electron density in the bunch. The frequency of the density modulation was also obtained at the gun exit.

The Source Development Laboratory is able to produce electron beams that contain up to 1 nC of charge. Although approximately 0.8 THz modulation on a 50 pC

electron beam was achieved in previous experiments, future experiments should explore a broader frequency range and higher charges per bunch. Therefore, the simulations were designed to explore the frequency range between 1 and 4 THz, and at varying charges up to 1 nC. Figure 5 shows preliminary results for the contrast between 1 and 4 THz at 100 pC, 500 pC, and 1 nC.

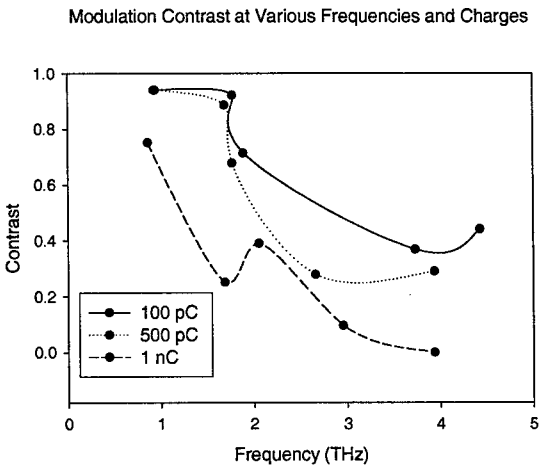


Figure 5: Degree of electron beam modulation as a function of charge and frequency.

The degrading effect of space charge on the modulation contrast at the injector exit is clear in Figure 5. It seems that modulation of the electron beam at the photocathode as a method of prebunching would at least be moderately effective up to a few terahertz at 500 pC and below. As expected, at low charge (~100 pC) and low frequencies, the degree of modulation at the injector exit remains the highest. In contrast, at high charge (~1 nC), or high frequencies there is degradation of the beam envelope even at relatively low frequencies.

4 CONCLUSION

In previous experiments, we were able to demonstrate that modulating the envelope of the drive laser appropriately can modulate an electron beam at terahertz frequencies. The prebunched electron beam can then be used to radiate coherently. Changing the frequency of drive laser modulation will also cause the electron beam modulation frequency to shift. The frequency content of radiation emitted by the electron beam will also shift. Therefore, this method could be used to build a compact, high-power, accelerator based terahertz radiation source.

To proceed toward that goal, we can use terahertz filters to quickly identify the spectral content of radiated light, and can use the PARMELA simulations to help us illuminate some of the limitations of this technique. Further work will also include additional experiments at the Source Development Laboratory to verify the predictions made by the PARMELA simulations.

5 ACKNOWLEDGEMENTS

This work was carried out with the support of the U.S. Department of Energy, Division of Materials Sciences and Division of Chemical Sciences, under Contract No. DE-AC02-98CH10886, in addition to the Joint Technology Office and Army Research Laboratory.

6 REFERENCES

[1] G.L. Carr, *et al, Nature* 420, Nov. 2002. pp 153-155.
[2] G.L. Carr, *et al. Proceedings of the 2001 Particle Accel. Conf.*, 2610 (2001)
[3] A.M. Weiner. *Rev. Sci. Inst.* **71**, 1929 (2000)
[4] H. Loos, *et al. Proc. 2002 Adv. Accel. Concepts*
[5] T. Tsang. *Appl. Phys. Lett.* **63**, 871 (1993).

A SOLID-STATE TRANSMITTER FOR THE ARGONNE ADVANCED PHOTON SOURCE

Ian S. Roth, Jeffrey A. Casey, Marcel P.J. Gaudreau, Timothy J. Hawkey, Michael A. Kempkes, J. Michael Mulvaney, and James E. Petry; Diversified Technologies, Inc. Bedford, MA USA

Abstract

Diversified Technologies has constructed a solid-state transmitter for the Advanced Photon Source at Argonne National Laboratory. The transmitter includes a series opening switch that protects the klystron, a modulating-anode supply, and a filament heater. The opening switch has substantial advantages over a crowbar in protecting RF amplifiers. The mod-anode supply was newly developed for this transmitter.

1 INTRODUCTION

Diversified Technologies has delivered a fully solid-state transmitter to the Advanced Photon Source at Argonne National Laboratory. A photograph of the transmitter is shown in Figure 1.

The high-voltage portion of the transmitter, diagrammed in Figure 2, consists of three major units: an opening switch, a modulating-anode power supply, and a filament heater. The opening switch protects against short-circuit faults in the klystron. The modulating-anode supply corrects for variation in the accelerator current; it operates in linear mode. The filament heater provides DC, rather than AC, to minimize ripple on the beam.

The system also includes power supplies for the ion pump and klystron magnets, and a control system that monitors faults and sends data to the accelerator control room.

This paper discusses the opening switch and the mod-anode supply.



Figure 1. Transmitter for the Advanced Photon Source, with one of the authors (I.R.).

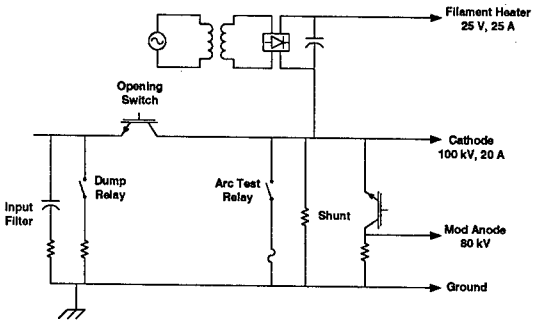


Figure 2. High voltage portion of the transmitter. Not shown are the low-voltage power supplies for the ion pump and magnets.

2 OPENING SWITCH ADVANTAGES

Crowbars are commonly used to protect klystrons from arc damage. When an arc occurs, the crowbar closes, and rapidly discharges the energy-storage capacitor. A typical crowbar circuit that shunts energy from the load is shown in the upper diagram of Figure 3. An alternative way to protect a klystron is to use a switch that opens during an arc, as shown in the lower diagram of Figure 3. Opening switches have substantial advantages over crowbars:

1. No series resistor is required in the circuit, so an opening-switch system has higher efficiency.
2. Opening switches couple less energy into an arc; because of this, they give substantially longer RF tube lifetime.
3. Because the energy-storage capacitor does not

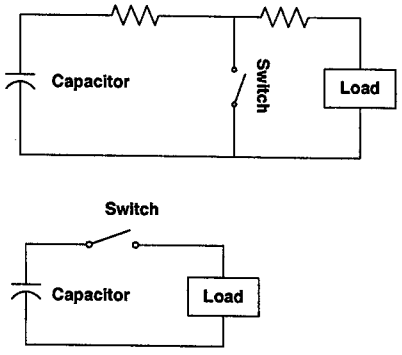


Figure 3. Circuit diagrams for crowbar (upper) and opening switch (lower).

0-7803-7738-9/03/$17.00 © 2003 IEEE

discharge during an arc, high voltage (and RF) can be turned on again immediately after the arc clears.

4. Solid-state opening switches use no mercury, in contrast to the ignitrons typically used in crowbars. Mercury clean-up from an exploded ignitron is time-consuming and costly.

Diversified Technologies has developed opening switches made from series arrays of solid-state IGBTs and FETs. These have much longer lifetimes than vacuum tubes. The forward voltage drop of these opening switches is small, less than 0.5% of the rated switch voltage. DTI solid-state, high-voltage opening switches have been in service for years.

An additional benefit of the series-array opening switch is its redundancy. The switch is made with excess voltage capability, similar to high voltage rectifier stacks. A switch can continue operating even if several devices should fail, since IGBTs always fail shorted.

3 OPENING SWITCHES

3.1 Current Ratings

DTI's opening switches use different components, depending on the current required. The switch built for the Argonne transmitter uses IGBT modules, and is rated for 100 A DC and up to 750 A pulsed. A single switch plate is shown in Figure 4. Some DTI switches use higher-current IGBT modules, at up to 400 A DC and 5 kA pulsed. For lower-current applications, discrete IGBTs are used; these carry currents of up to 25 A DC, and 200 A pulsed. All of these switches require an output current monitor and fast logic that opens the switch when a short-circuit is detected.

3.2 Opening Switch Operation

The typical time between fault sensing and switch opening is 700 ns, depending on the specific switch and controls configuration. This is roughly five times faster than a conventional crowbar system, and dissipates several orders of magnitude less fault energy into the load. Figure 5 shows the response to an arc in a system installed at CPI.

After an arc, the switch can resume normal operation in less than 100 μs- the actual time depends on the load recovery. This fast response may make it possible to retain a circulating beam in an accelerator after a klystron fault. The fast response can also be of high value in a military radar system.

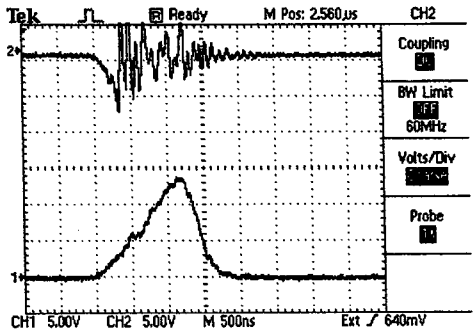


Figure 5. Waveforms of a deliberate opening switch deliberate arc. Upper trace, voltage, 50 kV/division; lower trace, current, 250 A/division.

The current in a pulsed system is typically measured with a current transformer. In a DC system (such as the Advanced Photon Source at Argonne National Laboratory) a current transformer does not work well, because the ferrite saturates. DC systems use a Hall-effect current monitor, which both operates with constant current, and has a pulse response fast enough for fault detection.

Figure 6 shows the logical steps in detecting and responding to a load fault, such as an arc. The key to use of an opening switch is to perform all of these steps, from detection to gate drive output, as quickly as possible.

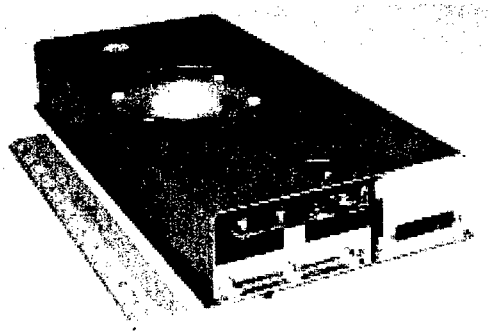


Figure 4. Solid-state switch plate for the Argonne Advanced Photon Source. Each plate is rated at 3.3 kV, 100 A continuous; 36 plates are connected in series to achieve over 100 kV switch capability.

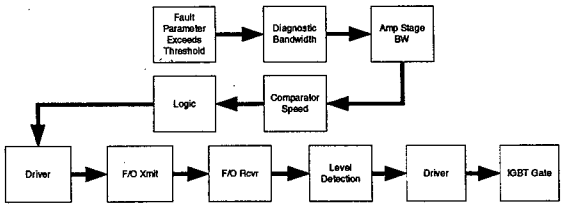


Figure 6. Opening switch fault action.

4 MODULATING ANODE SUPPLY

The modulating-anode (or mod-anode) supply provides feedback from the circulating accelerator beam to the klystron. Previously to this, mod-anode supplies were made using vacuum tubes, which have a limited lifetime. DTI has developed a long-life solid-state mod anode supply.

The mod-anode supply is implemented as a resistor-transistor divider, which has simple controls and no crossover distortion. A simplified circuit diagram[1] is shown in Figure 7. The entire string comprises sixteen circuits, each made of ten IGBTs. Each 10-IGBT array is driven by a single photo-transistor connected to the gate of the bottom IGBT; the phototransistor is driven by a fiber-optic cable. A sample voltage waveform is shown in Figure 8.

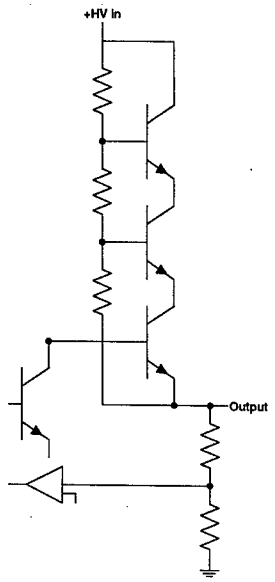


Figure 7. Series linear transistor circuit.

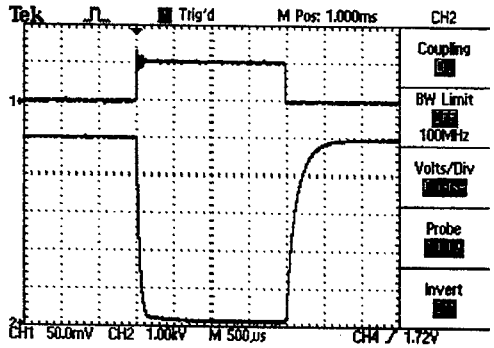


Figure 8. Pulsed waveforms for 10-IGBT linear circuit. Upper waveform: Trigger voltage, 50 mV/division. Lower waveform: Voltage across the array, 1 kV/division. Sweep speed: 500 µs/division. 5 kV was applied across the stack; load resistance was 100 kΩ. The circuit was driven from off to fully conducting.

The full mod-anode supply has a minimum off-voltage of 3.6 kV. The slew rate of supply is limited by the load capacitance, 630 pF, and maximum current that can charge this capacitance without causing an over-current trip, 10 mA. These two quantities give a slew rate of 16 kV/ms in the cathode direction, and 12 kV/ms in the anode direction at a voltage of 30 kV between the mod anode and ground. The slew rates exceed the operational requirements.

5 APPLICATIONS / SUMMARY

Any high voltage system which requires a crowbar for load protection can be upgraded to a fast opening series switch. The advantages of this approach include:

1. Faster arc response
2. Lower energy delivered into the arc
3. Much lower fault currents – by orders of magnitude in many cases
4. Nearly immediate (microseconds) resumption of operation
5. Significantly lower stresses on the upstream power components in the system, such as transformers, circuit breakers, and capacitors

In a pulsed power system, these advantages are essentially free. The same series switch can function as both the pulse modulator and the series opening switch.

Simply adding a series opening switch to a high voltage system can be a highly beneficial path to increased reliability and operability. If a simple 50/60 Hz transformer-rectifier power supply is used, however, the overall system design must also address the *unloaded* voltage of the supply – since opening the series switch essentially presents the supply with an open circuit at its output. If the series resistance of the power supply is high (which is typical in a crowbar system to limit currents into a crowbar), this unloaded voltage may be higher than the typical operating voltage. A switching power supply, capable of responding quickly to changes in load, eliminates this concern.

ACKNOWLEDGEMENTS

This work was supported by the DOE under SBIR grant #DE-FG02-99ER82778. We appreciate the collaboration of Geoff Pile and Doug Horan of Argonne National Laboratory.

[1] See, for instance, Horowitz and Hill, *The Art of Electronics, Second Edition*, pp. 371-2. Cambridge University Press, 1989

FERMILAB BOOSTER BEAM COLLIMATION AND SHIELDING*

N.V. Mokhov†, A.I. Drozhdin, P.H. Kasper, J.R. Lackey, E.J. Prebys, R.C. Webber
FNAL, Batavia, IL 60510, USA

Abstract

The beam power in the upgraded Booster at 8 GeV and 10 Hz will be 64 kW. Beam loss can result in high radiation loads in the ring. The purpose of a new beam halo cleaning system is to localize proton losses in specially shielded regions. Calculations show that this 2-stage collimation system will localize about 99% of beam loss in straight sections 6 and 7 and immediately downstream. Beam loss in the rest of the machine will be on average 0.1 W/m. Local shielding will provide tolerable prompt and residual radiation levels in the tunnel, above the tunnel at the surface and in the sump water. Results of thorough MARS calculations are presented for a new design which includes shielding integrated with the collimators, motors and controls ensuring a high performance and facilitating maintenance.

BEAM COLLIMATION

With the construction of an 8 GeV target station for the 5 Hz MiniBooNE neutrino beam and rapid multi-batch injection into the Main Injector for the NuMI experiment, the demand for Booster protons is increased dramatically at Fermilab. This implies serious constraints on beam losses in the machine. The beam power in the Booster at 8 GeV with 5×10^{12} ppp at 10 Hz will be 64 kW. Assuming that 30% of the beam is lost at injection and 2% at top energy, 0.96 kW (at 0.4 GeV) and 1.28 kW (at 8 GeV) of beam loss are distributed around the ring with a beam loss rate of 13-60 W/m in the RF cavities. The corresponding residual radiation levels inside the tunnel, in sump water and the prompt radiation levels outside the tunnel shielding would substantially exceed tolerable limits.

In order to control beam loss and corresponding radiation levels around Booster so as to avoid radiation damage to sensitive components (cables, connectors etc) and minimize exposures to personnel and environment, particularly in high-maintenance areas (RF stations), one needs to intercept those protons that are doomed to be lost and contain them in a well shielded location. The purpose of the beam halo cleaning system proposed in Ref. [1] is to localize proton losses in sections 6 and 7 which are far from the engineering, support and office buildings.

A 2-stage collimation system is proposed with thin horizontal and vertical carbon or tungsten foils (section 5) followed by secondary collimators (sections 6 and 7). Foils are placed at the edge of the circulating beam after injection. Secondary collimators are positioned with a 0.5σ offset with respect to the foils at phase advances that are optimal to intercept most of particles out-scattered from the foils during the first turn after the halo interaction with the foils (37° and 154° horizontal, and 20° and 127° vertical).

It was shown in Ref. [1] that the highest collimation efficiency is achieved if the scatterer thickness is changed during the cycle from 0.003 mm to 0.1 mm for tungsten or from 0.15 mm to 5.4 mm for carbon. This can be done by rotation of a wedge disk. Currently installed are two 0.3-mm carbon foils. Fig. 1 shows recent measurements of beam loss rates in the Booster ring as a difference between beam loss monitor readings without any collimators and with the vertical primary collimator in. As expected, losses are decreased everywhere except near the L6 section – a location where the secondary collimators will be installed to intercept the protons scattered in the primary collimators.

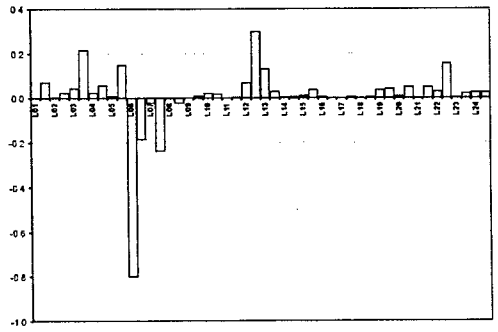


Figure 1: Difference in BLM readings around the ring without and with the L5 vertical primary collimator.

The jaws of the secondary collimators L6A (H), L6B (V+H) and L7 (V+H) are 0.6-m long stainless steel. Such a system would localize about 99% of beam loss in these three regions and immediately downstream. Beam loss in the rest of the machine is on average 0.1 W/m, with several peaks of ~1 W/m. Beam loss rates, calculated for a 5×10^{12} proton beam at 10 Hz as a fraction of the total beam intensity, are

- At 8 GeV: 1% or 5×10^{11} p/s in L6 (two thirds on L6A and one third on L6B), and 1% in L7 and in short regions downstream of L6 and L7.
- At 0.4 GeV: 20% or 10^{13} p/s in L6 (two thirds on L6A and one third on L6B), and 10% in L7 and in short regions downstream of L6 and L7.

These results are based on STRUCT simulations performed for the Booster lattice without injection and extraction bumps. Recent studies reveal that large focusing effects of these rectangular bump magnets change the β-functions and dispersion, and may affect the collimation system efficiency calculated.

* Work supported by the Universities Research Association, Inc., under contract DE-AC02-76CH03000 with the U. S. Department of Energy.

† mokhov@fnal.gov

0-7803-7738-9/03/$17.00 © 2003 IEEE

INTEGRATED SYSTEM

Full-scale Monte Carlo hadronic and electromagnetic shower simulations in the collimators, lattice elements, shielding, tunnel and surrounding soil are done with MARS14 [2] code. The following constraints were taken into account while developing the optimal collimator-shielding system:

- Prompt dose equivalent at peak, 13.5 feet of dirt above the tunnel, is below 0.05 mSv/hr (1 Sv = 100 rem).
- Activation of water in the sumps is within the allowed limits for surface discharge. This corresponds to a star density, averaged over the gravel around the tunnel, of less than 4000 $cm^{-3}s^{-1}$.
- Activation of the outer surfaces that are accessible to personnel allows hands-on maintenance with a residual contact dose rate below 1 mSv/hr after 30-day of irradiation and 1-day of cool off.
- Accumulated absorbed dose in cables, motors, and instrumentation is below the 20-year lifetime limits.
- Air activation and water activation in nearby LCW pipes is low.

The original design [1] consisted of L-shaped copper jaws brazed to a beam pipe. Stands and motors were designed to allow lots of room to stack steel shielding. There were, necessarily, rather large gaps between the jaws and shielding allowing radiation to escape the core, activate air and increasing the shielding dimensions. To access the collimator itself in the event of a catastrophic failure would require removing the shielding and exposing a very hot object. The final solution was an integrated collimator-shielding system. In this design, all failure prone components are outside the shielding. This module is rather compact (approximately $1\times1\times1$ m^3 outside) and uniform, with no cracks and gaps, eliminating the air activation problem. Because of the tight integration of the collimator and shielding steel, both the collimator and the surrounding shielding move as a unit. The actuators are to be sized to move the 11.6 ton block, a typical weight for remotely operated magnet stands.

The mechanical-electrical design took the following mechanical specifications into account:

- The apertures do no occlude any beam when in the garage position.
- They can be remotely translated by 1.5 inches both horizontally and vertically.
- They can be remotely positioned to ±1 mm.
- Their orientation can be remotely corrected for pitch and yaw misalignments of up to ±10 mrad.
- The time required to move them from fully in to fully out should be no longer than a few minutes.
- It should be possible to reliably disable the motion controls.
- All sensitive components should be serviceable without major disruptions to the program.
- It should be possible to completely remove them from the tunnel even after many months of beam.

MARS MODELING AND RESULTS

The system parameters were thoroughly optimized via MARS14 calculations. Fragment of a finalized model are shown in Fig. 2 and 3. All the radiation limits and design constraints of the previous section were taken into account.

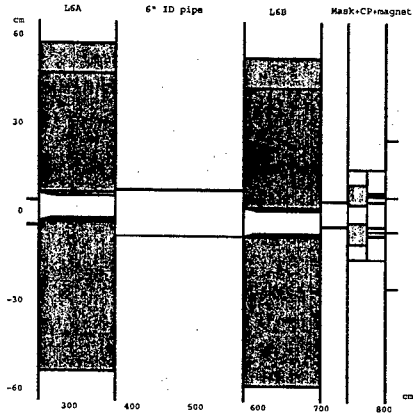


Figure 2: A fragment of the L6 integrated system.

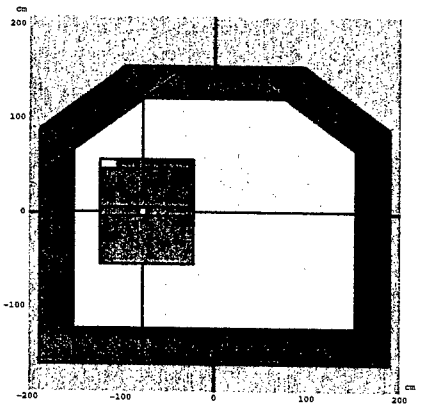


Figure 3: A cross-section of tunnel at L6B.

Based on the calculated 3D energy deposition profiles in the L6A and L6B collimator jaws and shielding, an ANSYS thermal and stress analysis was performed. It was found that no cooling is needed for normal operation and that the maximum steady-state temperature would be 60 $°C$. It was also calculated that there should be no mechanical problems caused by the differential thermal expansion of the jaws and shielding. In an accident case in which the full 8-GeV beam is lost on the collimator, the jaw will withstand 25 pulses over 2.5 s.

Longitudinally, the peak radiation fields were found to occur at the upstream end of the L6B collimator. Fig. 4 shows a vertical profile of prompt dose from 8-GeV beam scraping, in a ± 1 m band located at that peak. The cumulative maximum dose on the surface after 13.5 feet of dirt is 0.0125 mSv/hr, i.e. four times below the limit. Scraping at the injection energy of 0.4 GeV gives 20% of this value. Activation of water in the sumps is caused predominantly by spallation reactions above 50 MeV (*stars*). A horizontal profile of star density from a 8-GeV beam scraping, in a ± 1.6 m band is shown in Fig. 5. The cumulative average star density immediately outside the tunnel walls is 1163 $cm^{-3}s^{-1}$, i.e. 3.5 times below the limit. Scraping at injection gives 30% of this value. In reality, the margin is 2 to 3 times better if one averages over the gravel fill surrounding the tunnel.

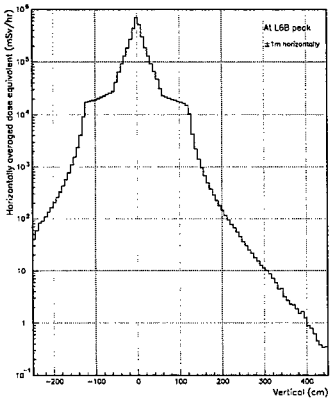


Figure 4: Prompt dose vertical profile.

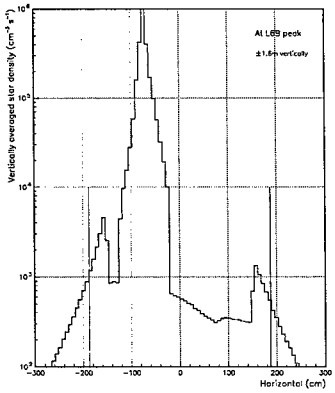


Figure 5: Star density horizontal profile.

Fig. 6 shows a 2D distribution of residual dose at the upstream end of the L6B collimator-shielding for 8-GeV beam scraping. The inner parts are very hot: up to 1 Sv/hr at jaws. Cumulative dose rate on the shielding outside ranges from 0.3 to 1 mSv/hr. Scraping at injection gives 15-25% of these values. The maximum contact dose on the aisle side of the L6B module is right on the limit (Fig. 7). The maximum dose on the 6-inch bare beam-pipes right after L6A and L6B is 40 mSv/hr. The dose on the outside of the correction package (CP) immediately upstream of the main magnet varies azimuthally from 5 to 40 mSv/hr, while on the outside of the first main magnet – from 2 to 10 mSv/hr.

Yearly absorbed dose at the L6B longitudinal peak is about 20 MGy/yr (1 Gy = 100 rad) on the jaws, 40 kGy/yr on shielding outside and up to 10 kGy/yr at walls, ceiling and floor. The maximum absorbed dose in the CP inner coils varies azimuthally from 0.3 to 4 MGy/yr that can reduce their lifetime. It was found that a simple 30-cm long steel mask (7.6 cm ID, 30 cm OD) between L6B and CP reduces the accumulated and residual doses by up to a factor of four.

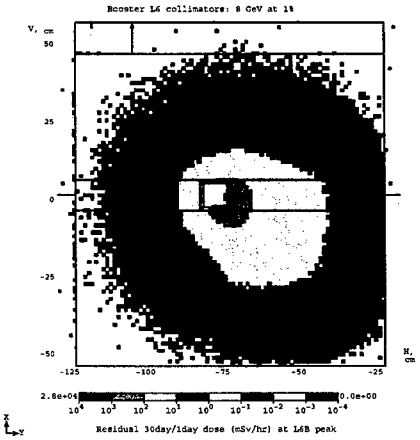


Figure 6: Contact residual dose rate at L6B after 30-day scraping at 8 GeV and 1-day cooling.

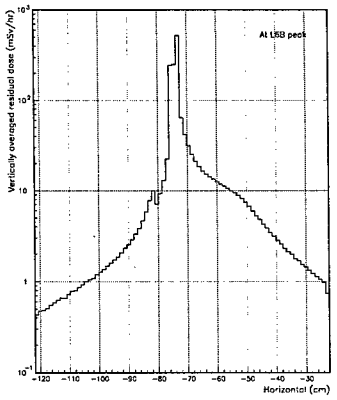


Figure 7: Horizontal profile of residual dose rate at L6B.

REFERENCES

[1] A.I. Drozhdin, P.H. Kasper, O.E. Krivosheev, J.R. Lackey, N.V. Mokhov, M. Popovic, R.C. Webber, *Proc. of the 2001 Part. Accel. Conf.*, Chicago, June 2001, p. 2569.

[2] N.V. Mokhov, "The MARS Code System User's Guide", Fermilab-FN-628 (1995); N.V. Mokhov, "Status of MARS Code", Fermilab-Conf-03/053 (2003); http://www-ap.fnal.gov/MARS/.

BASIS FOR THE RELIABILITY ANALYSIS OF THE PROTON LINAC FOR AN ADS PROGRAM

D. Barni, P. Michelato, L. Monaco, M. Novati, C. Pagani, R. Paulon, P. Pierini, D. Sertore*
INFN Milano – LASA, Via Fratelli Cervi 201, I-20090 Segrate, Italy
L. Burgazzi, ENEA Bologna, Via Martiri di Monte Sole 2, I40129 Bologna, Italy

Abstract

In the framework of the ADS projects (Accelerator Driven System) developing worldwide, a reliability activity is on going to validate and qualify the linac accelerator design with focus on the general operational and design characteristics that shape the accelerator performance. Further quantitative results should be based on estimations mostly deriving from operational surveys at existing accelerator facilities. Currently, a validated accelerator component reliability data base has not yet been assembled, and because of the early stage of the ADS design in which several systems are not established at this time the topic can be addressed by the application of a preliminary FMEA (Failure Mode and Effect Analysis) methodology, helpful in the identification of reliability-critical areas, where modifications to the design can help to reduce the probability of system failures. In this paper, the preliminary results of this activity are presented together with possible solutions to improve the reliability of the reference linac design.

INTRODUCTION

The request of high availability linac, to be coupled to subcritical reactor for waste transmutation and energy production [1,2,3], puts strong demands on future accelerators. Synchrotron light sources lead the state of the art in accelerator availability reaching availability of more than 99% [4]. However, the request of few beam trips longer than few seconds per year of continuous operation requires the development of new strategies and procedures for the design of accelerator. This paper is mainly devoted to assessment of the basis for a linac design where the reliability and availability ('fault tolerance') are the driving guidelines. In the following section, we present tools available for reliability assessment and possible design approaches to implement reliability in linac design, with special care to 'fault tolerance' machine design.

Among the different methodologies for reliability assessment, we found that FMEA (Failure Mode and Effect Analysis) is the more appropriate in early stages of accelerator design when a complete and detailed scheme of the machine is not available. We describe the implementation of FMEA to a possible linac design. Whenever the machine layout reaches a more detailed description, quantitative approaches - based on a formal mathematical approach to reliability - are available and their implementation in the accelerator design is the scope of our future work, as mentioned in the last section.

RELIABILTY TOOLS AND DESIGN APPROCHES

The design of a new system driven by reliability issue usually follows an iterative process. From an initial technical design, one evaluates its possible failure modes, discovers critical parts and may draw a first order estimation on the reliability of the system. The technical design is then reviewed trying to improve the weak areas of the system. This procedure continues till the required reliability and availability goals are reached.

The two main approaches to reliability assessment follow either a "top-down" or "bottom-up" approach. The former is the basis for techniques such as FTA (Fault Tree Analysis) and RBD (Reliability Block Diagram) where the system is analyzed starting from big blocks describing major systems and then going down to the details. If, instead, one follows the system from the details up in the hierarchy to the top ("bottom-up"), techniques such FMEA (Failure Mode and Effect Analysis) or FMECA (Failure Mode and Effect and Criticality Analysis) may be applied.

The "top-down" approach may be difficult for large and complex systems where the knowledge of the single component reliability or the logical connections between different elements of the system may be not precise enough for the assessment of the overall system reliability. This approach can be difficult also in the case of systems in the early stage of the design when a detailed description of the complete system is still missing.

A more valuable approach, specifically for system not fully developed, is the "bottom-up" approach. In this case, even an incomplete description of the system can be used to start a preliminary analysis of the system. In the case of FMEA, its aim is to identify all the possible failure modes of components, analyze their effects on the system performance, and suggest solutions and improvements. In the analysis, it is important to include also severity ranking for the failures and possibly their frequency.

The design of a reliable accelerator, besides the use of reliability tools, can benefit also from some general guidelines, common sense and experience that can valuably drive proper design. Among many of them, the most effective in improving reliability and availability of the system are **part derating** and **redundancy/spares**.

0-7803-7738-9/03/$17.00 © 2003 IEEE

Derating consists in operating a component with a load lower than the maximum rated from its specifications. This solution allows putting less stress on the component - generally guaranteeing a longer lifetime and hence a higher reliability.

Redundancy can be applied to key elements of the system that may induce its failure and it consists in using several identical components (in hot/warm parallelism, depending on the failure rate of the standby component) and/or **spares components** (cold parallelism) to improve the reliability of that particular element.

Although this approach improves the system reliability, it increases the number of components and hence the failure rate, requiring a more complex organization of the system logistic.

Finally a necessary approach in designing a system like a linac for and ADS is the '**fault tolerance**'. By this, we mean the capability of the system to perform its duty within its specifications even if some of its components are defective or are not working at all.

FAULT TOLERANCE

As mentioned previously, 'fault tolerance' is the key element in the design and operation of a linac for an ADS. To guarantee the availability request for coupling a linac to a sub critical reactor, the beam trips have to be about one per month for a 24 h operation in a period of at least three months up to one year - depending on the core details and fuel operation procedures. The possible approaches that can be followed to reach such availability requirements are: demand very high reliability on the single components or design the system to be fault tolerant. In the first case, an enormous technological effort is required to improve the reliability of both newly developed systems and "commercial" components. For example, the Mean Time Between Failure (MTBF) of a klystron is about 50000 h and if 100 of them are in series, the MTFB of the system is 500 h (about 21 days). After that period, the faulty klystron has to be changed and the linac stopped if no fault tolerance is implemented.

A 'fault tolerance' strategy, instead, relies on redundancy and parallelism. However, these are not enough to guarantee that the system will continue to work within specifications with faulty components. Indeed the system has to **detect** the faulty component, **isolate** it and **readjust** itself to provide fault tolerance.

The application of 'fault tolerance' to an accelerator system implies also a strong interaction with the beam dynamics studies. The failure of a component may have different consequences, depending on the component location along the beam line, on the beam parameters on the target and the system has to react properly to deal with it. The reaction time, it is worth to remember, has to be less then 1 second to prevent thermal stresses on the reactor elements. The control system of the accelerator, and the Low Level RF system in particular, have to cope with it and readjust the machine in order to guarantee the beam specifications at the target. This is only possible if a complete analysis of the fault scenarios is done in advance, the impact of the single component fault has been studied regarding beam dynamics effects and improvements on the control system allows reacting time faster then few milliseconds. In other words, the fault tolerance capabilities need to be included in the design of a new generation of accelerator control systems.

THE LINAC CASE

The application of the aforementioned strategies (FMEA and 'fault tolerance') to a linac requires the setup of a reference design. For the ADS case, the accepted scheme foresees a Source, a Low Energy Section, a Medium Energy Section and a High Energy Section. Proper beam transport lines match each of the accelerating sections. A final beam delivery system transports the beam into the reactor vessel.

The proton source is one of the most critical item both for its complexity and because its failure determines the stop of the beam. The same considerations hold also for the Low Energy Section where a Radio Frequency Quadrupole is used. In this first part of the linac is then difficult to implement a complete 'fault tolerance' scheme. Nevertheless, redundancy and derating on critical parts of the system are necessary to increase the reliability of this critical section.

The Medium Energy Section accelerates the beam up to energies about 100 MeV. Also in this case different solutions are possible even if with a larger preference for the SC (superconductive) solution. The same technology is also the preferred one for the High Energy Section. In fact, many advantages characterize SC cavities and among them: high modularity, independent RF feeding and phasing and large bore radius. These features allows a natural implementation of redundancy (modularity), a relaxation of constrains on alignment and beam losses (large bore radius) and the possibility to implement 'fault tolerance' (independent RF feeding and phasing). Moreover, the operation of the structures at cryogenic temperature allows a very stable linac. It is also a general rule to operate the cavities at lower gradients with respect to the maximum achievable, in order to reduce the stress on the cavity operation (part derating).

The 'fault tolerance' of the SC sections mainly relies on the independent feed of the cavities. The failure of a single cavity can be detected by the control system and an automatic procedure can readjust the neighboring elements in order to compensate and maintain the beam within specifications on the target. This procedure implies knowledge of the effect of each single component failure on the beam characteristic on target. A faulty SC cavity on the first part of the High Energy Section has a different impact on the beam in respect of a faulty cavity at the end of the linac. Beam dynamic studies need to help in defining proper procedures to implement 'fault tolerance' during acceleration operation. Moreover, the machine control system and the LLRF system have to react in very short time to keep the machine running.

The reliability of the beam delivery system and beam transport lines for such a machine will be dominated by magnets and their power supplies. Redundancy and fault tolerance in the vacuum system and diagnostics can be planned in advance. The extensive experience at existing facilities shows that magnets usually fail due to water cooling failures (in pipes or connections), to cooling channel clogging or to power supply failures. Preventive maintenance and replacement operations may contribute to solve the majority of these issues.

FAILURE MODE AND EFFECT ANALYSIS

The FMEA analysis provides useful information already in the early stage of the design and even in a qualitative approach.

In order to perform such an analysis, the key systems and components of the accelerator need to be identified. Once they are known, a list of all potential failure modes, corresponding failure frequency and analysis of their effects must be compiled. On the basis of critical components found in the previous analysis, the design of the accelerator has to be reviewed.

The four main systems for the accelerator of an ADS are: the hardware components of the accelerator (cavities, magnets, vacuum connections, etc.), the cryogenic production and distribution plant, the auxiliary infrastructures (water, compressed air, electrical power) and the control system. The vacuum and the RF systems, due to the modularity of the SC solution, are included in the accelerator hardware and are not considered as distinct systems.

Following well-known standards, a WBS (Work Breakdown Structure) hierarchical structure is needed to classify all the components of each system, and based on it the possible failure modes and the detection means are identified. For each failure mode, the effects on the faulty system, on the system upper in hierarchy and on the beam properties, which are our main concern, are highlighted. The effects, at each level of this analysis, are ranked based on their severity. Once the effects of the failures are known, possible corrective or preventive actions are suggested and they should be implemented in the reviewed version of the accelerator design.

The FMEA analysis can also be used as a guideline for addressing the task of preventing undesirable failure modes in a more specific technical and detailed analysis of the components.

At present, activities are ongoing in order to develop a complete FMEA analysis for the reference design of the accelerator designed for the PDS-XADS program of the European Community [5].

FUTURE WORK

The present limitations for a complete and quantitative reliability assessment of linacs for ADS are the lack of a detailed accelerator configuration and the uncertainty in the available reliability data (MTTR, MTBF, etc.).

The absence of a formal reliability database for accelerator components makes difficult to perform a mathematical treatment of the reliability problem for the accelerator. Even if many laboratories have own large datasets of failure modes both at the system and at the component level, there is no common way to store and analyze them, and the effort to unify these databases (in terms of manpower and resources) is so large to hinder the benefit of such an action. Hence **"expert" judgment** is the only way, at the moment, to state reliability figures for accelerator components. The situation is different for "commercial" products where data are available; however the application to the accelerator case requires careful consideration on the different operative conditions.

Concerning the detailed description of a reference linac design, studies are still on going worldwide and decisions have still to be taken mainly concerning the initial part of the linac where different solutions and technologies are currently under consideration.

Once this information will be available, a first quantitative reliability assessment of the accelerator system will be possible.

CONCLUSION

The reliability and availability request for the future accelerator to be coupled to subcritical reactors leads to a new philosophy in approaching linac design. Few trips longer than one second during a period of operation of at least some months can be achieved only if redundancy and 'fault tolerance' capabilities are included in the design and operation of the machine. A valuable tool during the early design stages of the linac to assess the reliability is the FMEA that provides useful information even if applied on qualitative basis and on a not fully developed scheme of the accelerator.

For a quantitative reliability analysis of an accelerator, a common database for accelerator components is still missing. An effort to coherently integrate the dataset present in all the major labs on failure causes is advisable.

The methodology developed for ADS accelerator can be customized to deal with different requests such as future linear colliders [6] or linac for future light sources machines [7].

REFERENCES

[1] AFCI, http://aaa.lanl.gov/
[2] PDS-XADS, Preliminary Design Studies of an Experimental Accelerator Driven System
[3] MYRRHA, http://www.sckcen.be/myrrha/
[4] L. Hardy, "Accelerator Reliability – Availability", *Proceedings EPAC '02*, Paris, p. 149.
[5] Accelerator working group members of PDS-XADS are: ANSALDO (I), CEA (F), CNRS (F), ENEA (I), Framatome ANP (F), Framatome GmbH (D), IBA (B), INFN (I), ITN (P), FZJ (D), University of Frankfurt (D).
[6] TESLA, http://tesla.desy.de/
[7] DESY X-Ray FEL, http://www-hasylab.desy.de/

BEAM COMMISSIONING OF THE J-PARC LINAC MEDIUM ENERGY BEAM TRANSPORT AT KEK

M. Ikegami, T. Kato, Z. Igarashi, S. Yamaguchi, A. Ueno, K. Ikegami, M. Okada
C. Kubota, K. Yoshino, K. Nigorikawa, E. Kadokura, M. Kawamura, Y. Fukui
N. Kamikubota, F. Naito, H. Tanaka, S. Noguchi, S. Fukuda, E. Takasaki,
J. Chiba, S. Anami, S. Arai, H. Kobayashi, KEK, Tsukuba, Ibaraki, Japan
Y. Kondo, T. Kobayashi, T. Ito, K. Hasegawa, H. Yoshikawa,
J. Kishiro, Y. Yamazaki, JAERI, Tokai, Ibaraki, Japan
S. Wang, S. Fu, IHEP, Beijing, China
R. Ryne, J. Qiang, LBNL, Berkley, CA, USA

Abstract

The construction of the initial part of the J-PARC linac has been started at KEK for beam tests before moving to the JAERI Tokai campus, where J-PARC facility is finally to be constructed. The RFQ and MEBT (Medium Energy Beam Transport) has already been installed at KEK, and the beam test has been performed successfully. In this paper, the experimental results of the beam tests are presented together with simulation results with a 3D PIC (Particle-In-Cell) code.

INTRODUCTION

The J-PARC (Japan Proton Accelerator Research Complex) accelerator consists of a 400-MeV linac, a 3-GeV RCS (Rapid Cycling Synchrotron), and a 50-GeV synchrotron [1, 2]. The linac is comprised of a 50-keV negative hydrogen ion source, a 3-MeV RFQ, a 50-MeV DTL, a 190-MeV SDTL (Separate-type DTL), and a 400-MeV ACS (Annular Coupled Structure linac). The construction of the initial part of the J-PARC linac has been started at KEK to develop and establish the linac system before moving to the JAERI Tokai campus, where the J-PARC facility is finally to be constructed. The 324-MHz RFQ and the MEBT (Medium Energy Beam Transport) has already been installed at KEK, and the beam test has been performed successfully from April to July 2002, and January to February 2003. Between these two series of experiments, slight modification of the LEBT (Low Energy Beam Transport) was performed to install a pre-chopper cavity. These beam tests aim to verify the performance of key components of the MEBT. The MEBT has two main roles, namely, to perform transverse and longitudinal matching to the succeeding 324-MHz DTL, and to chop beams with the same frequency with the RCS injection cycle in order to minimize the beam loss at the injection. The schematic layout of the MEBT is shown in Fig.1(a). The MEBT includes eight quadrupole magnets (Q1 to Q8) for transverse matching, two 324-MHz buncher cavities for longitudinal matching, two rf deflection cavities (RFD's) and a scraper for beam chopping, and various beam diagnostic instrumentation for beam diagnosis. We also have five two-plane steering magnets for beam steering. Although various developments have been performed in the experiments, we focus on the emittance measurement results and its comparison with particle simulations in this paper. As for the rf chopper performance which is another key issue on the beam test, we present experimental results in a separate paper [3].

EXPERIMENTAL SETUP

In the beam test, a TBD (Temporal Beam Diagnostic system) is placed at the exit of the MEBT, which will be removed when installing the DTL. The TBD includes a transverse emittance monitor and a Faraday cup. The emittance monitor is double-slit type, and its first slit is located 534 mm downstream from the exit of the MEBT. The slit width and slit interval of the emittance monitor are 0.1 mm and 205 mm, respectively.

In the actual operation, the beam should be strongly focused at the exit of the MEBT to satisfy the matching condition to the DTL. However, the strengths of the last two quadrupoles are weakened in the experiment to enable the emittance measurement at the downstream beam diagnostic system. Figure 1 (b) shows a beam profile for a typical quadrupole setting which satisfies the matching condition to the DTL, and Fig.1 (c) shows a typical beam profile for the experiment, in which only the last two quadrupoles are weakened. In Fig.1 (c), the downstream end of the plot corresponds to the first slit position of the emittance monitor in the TBD. The quadrupole and buncher setting in Fig.1 (c) corresponds to those in Measurement I in the next section.

The transmission ratio through the MEBT is measured with three CT's (Current Transformers), which are located after Q1 (CT1), at the exit of the RFD cavities (CT2), and after Q7 (CT3). We also have three FCT's (Fast Current Transformers), eight BPM's (Beam Position Monitors), and four WS's (Wire Scanners) for beam tuning. Each WS has horizontal, vertical and oblique (45 deg) carbon wires with the diameter of 7μm. As for the detailed layout and specifications for beam monitors, refer to the reference [2].

We use a LaB_6 filament for the ion source in the experiments. The peak current reaches 33 mA at the exit of the

0-7803-7738-9/03/$17.00 © 2003 IEEE

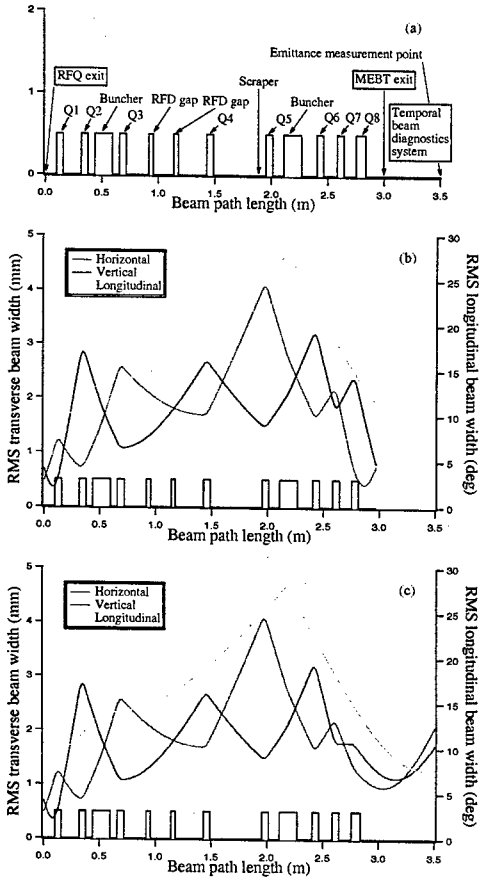


Figure 1: MEBT layout and typical beam profile along the MEBT. (a) Schematic layout of the MEBT. (b) Beam profile along the MEBT for a matched case. (c) A typical beam profile along the MEBT in the experiment.

ion source, and 29 mA at the exit of the RFQ without using cesium seed, which nearly satisfies the design output beam current for the RFQ of 30 mA. We also use a lower beam current of 5 mA for specific beam studies. The duty factor has also been changed from 0.025 % to 0.25 % depending on the purpose of the experiment. We have changed the repetition rate from 5 Hz to 25 Hz, and the pulse width form 50 μsec to 100 μsec. The design duty factor for the first phase of the project is 1.25 % with the repetition rate of 25 Hz and the pulse width of 500 μsec. In the emittance measurement we describe in the next section, we usually use the repetition rate of 12.5 Hz or 25 Hz in order to shorten the measurement time, which is typically about 15 min for one plane.

EXPERIMENTAL RESULTS

The measured normalized rms emittances are summarized in Table 1. Measurement I and II in Table 1 show the emittance at the exit of the MEBT measured with the TBD. Measurement I was obtained in the beam test of January to February 2003, and measurement II was obtained in that of April to July 2002. Measurement III shows the emittance at the exit of the RFQ, which was measured setting up the same TBD after the RFQ before installing the MEBT. As the development of the ion source has been underway in parallel with the beam test, the maximum available beam current was limited to 10 mA when Measurement III was performed. The peak current listed in Table 1 is measured with CT1. Although a certain amount of emittance growth has been observed in increasing the beam current, the obtained normalized rms emittance, which is 0.21 to 0.25 πmm·mrad, is tolerable according to LINSAC end-to-end simulations[2]. LINSAC is a 3D particle-particle code developed at KEK[4].

Table 1: Measured normalized rms emittance

Measurement	I	II	III
Location	MEBT	MEBT	RFQ
Peak curr. (mA)	28.7	24.6	10.0
Hor. (πmm·mrad)	0.252	0.227	0.173
Ver. (πmm·mrad)	0.214	0.220	0.194

Table 2 shows the measured peak current in Measurement I and II. The transmission ratio, which is defined as the ratio of CT3's readout to CT1's, reaches 99.3 % in Measurement I without using steering magnets. In Measurement II, the transmission ratio is limited to 96.3 % while we use the first steering magnet, which is built in Q1, to improve the transmission ratio. Table 2 indicates that slight modification of the LEBT have some effect on the transmission ratio through the MEBT.

Table 2: Transmission ratio of the MEBT

Measurement	CT1	CT2	CT3
I	28.7 mA	28.5 mA	28.5 mA
II	24.6 mA	23.9 mA	23.7 mA

Figure 2 shows the phase-space distribution obtained in Measurement I. In Fig.2, x and y denote the horizontal and the vertical positions, and s is the path length of the design particle. Measured phase-space density is represented by 100k dots (particles) in Fig.2.

Because the emittance monitor in the TBD will be removed when installing the DTL, WS's play an important role in actual beam tuning. Figure 3 shows a typical beam profile measured with WS3, which is located 81 mm upstream from Q4. In the measurement, quadrupole setting is the same with Measurement I, while the bunchers are turned off. The pulse width is shortened to 50μsec to reduce the heat load of the carbon wire. The measurement was done with the repetition rate of 5 Hz.

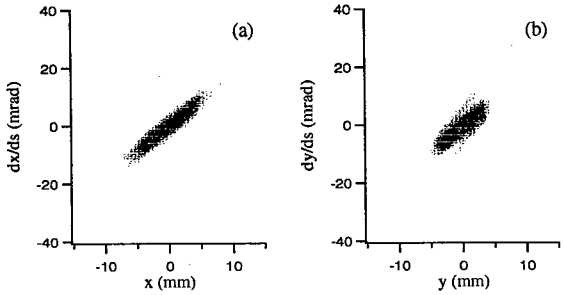


Figure 2: Phase-space distribution measured with the emittance monitor in Measurement I. (a) Horizontal phase-plane. (b) Vertical phase-plane.

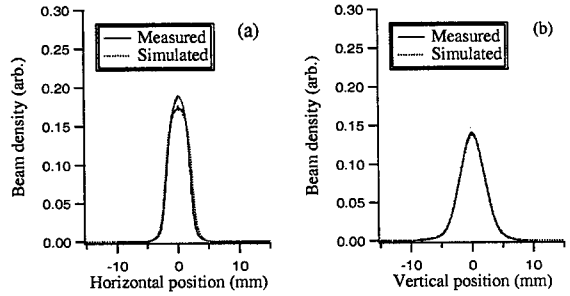


Figure 3: Beam profile measured with WS3 located before Q4. The quadrupole setting is the same with Measurement I, while the bunchers are turned off. (a) Horizontal beam profile. (b) Vertical beam profile. The beam profile obtained in an IMPACT simulation is also shown.

COMPARISON WITH SIMULATION

As a preliminary test on the agreement between experiments and simulations, we have performed 3D PIC (Particle-In-Cell) simulations with IMPACT[5] assuming a 6D Gaussian distribution at the exit of the RFQ. In the simulations, we assume transverse Twiss parameters at the exit of the RFQ which was obtained with Measurement III, and the initial transverse emittances are adjusted to reproduce measured ones at the TBD after the MEBT. We also assume initial longitudinal parameters obtained with PARMTEQm[6] simulations for the RFQ. Figure 4 shows obtained phase-space distribution at the emittance monitor after the TBD, in which we consider the same lattice setting and beam conditions with Measurement I. In the simulation, 1M simulation particles and $64 \times 64 \times 64$ meshes are employed, and the integration step width is set to $\beta\lambda/10$. The assumed initial normalized rms emittances are 0.234 πmm·mrad, 0.193 πmm·mrad, and 0.0822 πMeV·deg in the horizontal, vertical, and longitudinal directions, respectively. In Fig.4, 100k particles out of 1M particles are displayed. Comparing Fig.4 with Fig.2, it is seen that the qualitative agreement between the simulation and the experiment is reasonable, while the shape of the tail portion

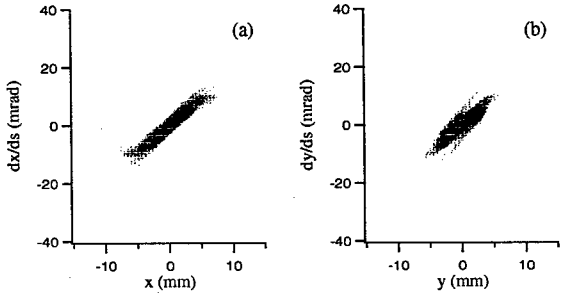


Figure 4: Phase-space distribution at the emittance monitor obtained with an IMPACT simulation for Measurement I. (a) Horizontal phase-plane. (b) Vertical phase-plane.

is slightly different. In Fig.3, we show the beam profile obtained in a similar IMPACT simulation. While the simulated rms beam width is slightly wider in the horizontal direction, the agreement in the vertical direction is excellent. These agreements indicate that the tail portion is already developed to some extent at the exit of the RFQ. Efforts to obtain more realistic initial distribution at the exit of the RFQ is now underway, with which the agreement between experiments and simulations is expected to be improved.

SUMMARY

The beam tests of the RFQ and the MEBT for the J-PARC have been successfully performed at KEK. The peak current of 29 mA is achieved at the exit of the RFQ without using cesium seed. The measured normalized rms emittances are 0.252 πmm·mrad and 0.214 πmm·mrad in the horizontal and the vertical directions, which is tolerable according to LINSAC end-to-end simulations. Preliminary simulation studies are performed with a 3D PIC code, IMPACT, and the agreement between experimental and simulation results is found reasonable.

REFERENCES

[1] Y. Yamazaki, "The JAERI-KEK Joint Project (the J-PARC Project) for the High Intensity Proton Accelerator", in these proceedings.

[2] "Accelerator Technical Design Report for J-PARC", KEK Report 2002-13; JAERI-Tech 2003-044.

[3] T. Kato et. al., "Beam Studies with RF Choppers in the MEBT of the J-PARC Proton Linac", in these proceedings.

[4] T. Kato, "Beam Simulation Code Using Accurate Gap Field Distributions in a Drift Tube Linac", Procs. 1994 Int. Linac Conf., p523-525, 1994.

[5] J. Qiang et al., "An Object Oriented Parallel Particle-In-Cell Code for Beam Dynamics Simulation in Linear Accelerators," J. Comput. Phys., **163**, p434-45, 2000.

[6] K. R. Crandall et al., "RFQ Design Codes", Los Alamos Report LA-UR-96-1836, revised 1998.

H⁻ PAINTING INJECTION SYSTEM FOR THE J-PARC 3-GEV HIGH INTENSITY PROTON SYNCHROTRON

I. Sakai, T. Shimada*, T. Takayanagi*, K Yamamoto*, Y. Arakida, I. Sugai, Y. Takeda, S. Machida, F. Noda*, K. Shigaki*, Y. Watanabe*, Y. Ishi **, T. Kawakubo, Y. Irie,
KEK, Tsukuba, *JAERI, Tokai, ** MELCO, Kobe; JAPAN

Abstract

The J-PARC Project 3-GeV proton synchrotron is designed to accelerate 8.3×10^{13} protons per pulse at a 25Hz repetition rate for the injection energy of 400MeV. The incoming beam emittance of the 400-MeV linac is 4 π mm mrad and the acceptance in the 3-GeV synchrotron is 324π mm mrad in both the horizontal and vertical planes. Painting injection system is designed to fit in the FODO structure, which has rather short drift space. The bump orbit for painting injection is designed to have a full acceptance of the circulating orbit through the injection period. A full-acceptance bump orbit will enable both correlated and anti-correlated painting injection.

INTRODUCTION

The J-PARC Project accelerator complex comprises a 50-GeV main synchrotron, a 3-GeV rapid-cycling synchrotron, and a 180-MeV linac, which is to be upgraded to 400-MeV in the second stage. The accelerators provide high-intensity, high-energy proton beams for various scientific fields. The 3-GeV synchrotron is designed to accelerate 8.3×10^{13} protons per pulse at a 25 Hz repetition rate in the second stage of 400-MeV injection. The hardware of the 3-GeV ring is designed to accept 400-MeV injection beams.

The 3-GeV rapid cycling synchrotron (RCS) has a three-fold symmetric lattice. Each super-period consists of 9DOFO modules, which are assigned to two 3DOFO modules with a missing bend and 3DOFO modules in insertion straights. These insertion straights are designed to be dispersion free. The FODO structure requires modest quadrupole gradients, and the alternating transverse beam amplitude easily accommodates correction systems, but lacks a long uninterrupted drift space for flexible injection.

The injection system for the J-PARC 3-GeV Proton Synchrotron is designed to be constructed in the FODO structure, which has rather short drift space. The injection and collimator system will be in the same straight section. The H⁻ injection system uses the first whole cell and a quarter of the second cell. The collimator system is the latter three quarters of the second cell and the third cell. However, the system is designed to have a full acceptance for the injection bump orbit and to allow independent lattice tuning to obtain a high-intensity beam and low-loss operation.

An outline of the injection system has already been reported [1]. In this paper we mainly describe the challenging issues about the H⁻ injection line, disposal lines for un-stripped H^0& H⁻ ions and the structure of the bump magnets system.

PARAMETERS FOR PAINTING INJECTION

The machine acceptance of the linac and its transport line are designed to have 30π mm mrad, and that of 3-GeV synchrotron has 486π mm mrad. The acceptable momentum dispersion ($\Delta p/p$) in the transport line and 3-GeV ring are $\pm0.3\%$ and $\pm0.1\%$, respectively.

In the beam-transport line from the 180MeV Linac to the 3-GeV RCS (L3BT); the transverse emittance of the H⁻ beam is collimated to 4π mm mrad. In the momentum direction, $\Delta p/p$ is $\pm0.1\%$.

In the case of 400 MeV injection, the painting emittance in the ring is 216π mm mrad for the 3-GeV facilities, and 144π mm mrad for 50-GeV ring injection. The horizontal painting area is controlled by pulse steering magnets located in the injection line and bump magnets in the ring by changing the excitation level in a

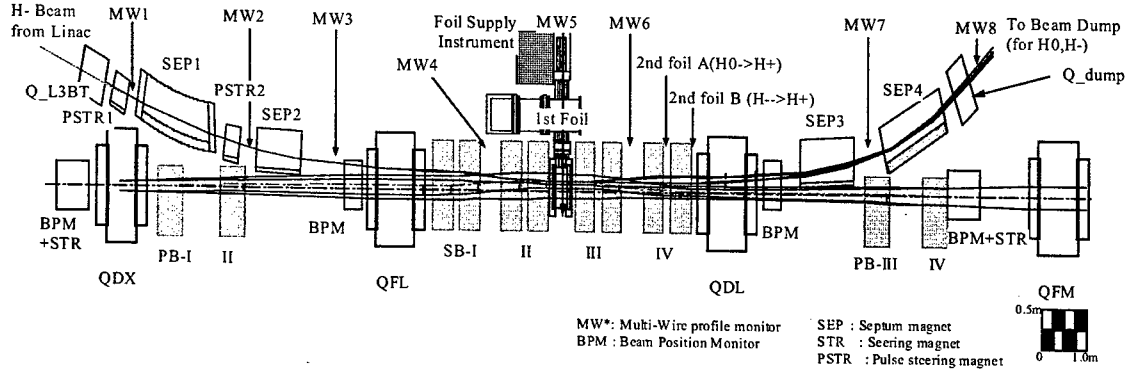


Fig. 1 Outline of the injection system

0-7803-7738-9/03/$17.00 © 2003 IEEE

pulse-to-pulse mode. The vertical painting area can be controlled by changing the excitation level of vertical steering magnets in the injection line.

The collimator acceptance in the 3-GeV ring is 324π mm mrad and the whole ring will have 486π mm mrad needed for the scattered beam by the first collimator to be caught subsequently by the down-stream collimator. The ring will be filled with 308 turn H^- foil-stripping charge-exchange injection. The 500μs pulses from the Linac containing 8.3 x 10^{13} protons will be injected to two-bunch RF buckets in the ring.

DESIGN OF THE MAGNETIC FIELD

The magnetic field must be carefully chosen so as to prevent the Lorentz stripping of H^- and to minimize the stripping of excited H^0.

In the upstream of the stripping foil, the H^- beam will pass through septum magnets, quadrupole magnet and closed orbit bump magnets. The maximum magnetic field is estimated to be 0.55 T for 400-MeV H^- beams. The beam loss rate is less than 10^{-6} for the above magnets. Because the injection beam power is 133 kW, and its losses by Lorentz stripping is less than 1.3 W.

After the H^- beam passes through charge-exchange foil made of 290μg/cm^2 thick carbon, a H^0 beam of 0.4 kW is produced. When a 1MW output is attained, it becomes very important to control the loss of the excited H^0 [2]. In the case that the magnetic field of the bump magnet is set to be about 0.2 T. The excited H^0 with a principal quantum number of $n \geq 6$ becomes the uncontrolled beam loss. Because of the yield of $n \geq 6$ is 0.0136 and the total H^0 beam power is 0.4 kW, the maximum uncontrolled beam loss is about 6 W. On the other hand, the excited H^0 under the condition of $n \geq 5$ reaches second foil without decay to H^+, and is led to the beam dump.

The magnetic field at the foil position is designed to be less than the value at which the bending radius of the stripped electrons is larger than 100mm, which enables a electron catcher to be settled outside of the foil. The foil position is at a distance of 350 mm from the end of the bump magnet SB-III. The trajectory of stripped electrons at the foil is traced by solving 3D differential equations with the Runge Kutta method [3]. The bending radius is estimated to be about 120 mm in the given magnetic field distribution.

CONSTRUCTION OF THE INJECTION SYSTEM IN THE FODO STRUCTURE

An outline of the injection system is shown in Fig.1. The injection system in the horizontal plane is composed of four main orbit bump magnets named "SB" to merge the injection beam with the circulating beam, and four other orbit shift bump magnets named "PB" for painting injection. The "SB" have a split-type structure to insert the second foil for H^0 stripping. Also the vertical painting is performed by vertical steering magnets in the injection beam line.

The incoming beams are injected at the entrance of "SB-I" to obtain a full acceptance for the injection bump orbit. The injection angle of the incoming beams with the circulating beam orbit is expanded by the magnetic field of the upper-stream F quadrupole. The angle of the disposal beam line of un-stripped H^0 and H^- are also expanded by a downstream D quadrupole magnet.

The field of the quadrupole magnets may be changed to meet varieties of operating point of the ring, the injection angles and positions at the quadrupole magnet are adjustable by steering magnets at the up-stream points of the injection line.

Horizontal painting injection is performed by an orbit shift in horizontal plane. Two additional sets of bump magnet pairs for the horizontal painting, named "PB-I, PB-II"and "PB-III, PB-IV", are located in the up-stream of the F quadrupole magnet and downstream of the D quadrupole magnet respectively.

For vertical painting, two small vertical steering magnets, which are not shown in Fig.1 are placed in the transport line at a betatron phase of π up-stream of the stripping foil to vary the injection angle and position. Painting injection in the vertical phase plane is performed by sweeping the injection angle. The phase difference will be compensated by those two vertical steering magnets.

Both correlated and anti-correlated painting injections are available by changing the excitation pattern of the vertical painting magnet

DESIGN OF THE H⁻INJECTION LINE AND H^-, H^0 DISPOSAL LINES

As can be seen in the Fig.1, injection area is so congested that any other focusing magnets can not be inserted in the injection area which has a length of 20 m. Furthermore, the beam needs to be injected vertically off-center for vertical painting. The corner of the F and D quadrupole magnets are thus required to have additional aperture for the injection/disposal beam lines

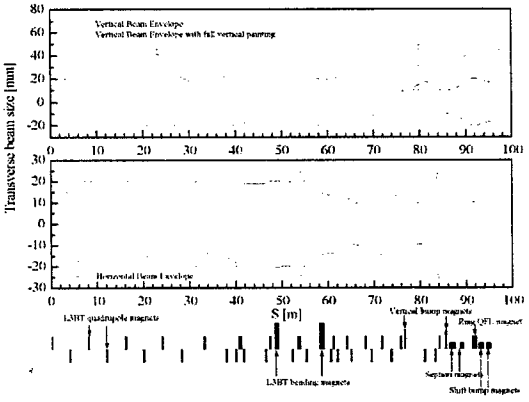


Fig.2 Beam envelope of the injection/disposal beam line

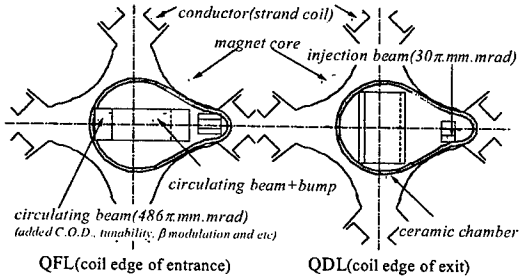


Fig.3 Cross sectional view of the F and D quadrupole

The beam optics of beam transport line from the Linac to RCS is designed to be insensitive to space charge effect. Space-charge effects have been analyzed by simulation on this optical design. The results estimate that the space charge effect is not much of a problem under the designed bunch lengthes of 400 MeV and 180 MeV injection.

APERTURE REQUIREMENT

The vertical aperture at the horizontal edge of the up-stream F quadrupole must satisfy the aperture for the vertical betatron oscillation amplitude by vertical painting. The down-stream D quadrupole is in the same situation concerning the disposal lines for un-stripped H^-, H^0 beams. A cross sectional view of the F and D quadrupole and its beam position is shown in Fig.3.

These ring lattice quadrupoles at the injection region must have a large bore radius of 205 mm. The same large bore radiusis is also required from the extraction region in another super-period of the threefold symmetric lattice, where the kicked beams for extraction pass through the horizontal edge of the D quadrupole.

The mirror symmetrical structure of the super period requires the same large-bore radius as the 12 quadrupoles in the whole ring.

SEPARATION OF THE H^0, H^- AND H^+

In the FODO structure, the beam envelope at the down-stream of F quadrupole, tilts down-stream so that the injection beam line for horizontal painting must be tilted accordingly. The separation angle of the H^0 beams and circulating H^+ beam envelope become tighter than a case of a parallel envelope of the two pairs of quadrupole doublets where $\alpha = 0$.

The separation of the H^0, H^- beams and circulating H^+ beam envelope is one of the challenging issues to design the hardware of the injection system. To solve this problem the split-type bump magnet has been investigated.

The H^0 beams, which are estimated to be 0.3% of the incoming beams, must be converted to H^+ by a second foil to divert to the beam dump. As shown in Fig.1, the second foil "A" is inserted in the middle of the fourth bump magnet, "SB-IV", by a split at the center of the core. The up-stream part of the split core is used to obtain the sufficient clearance of the H^0 and H^+ beam separation

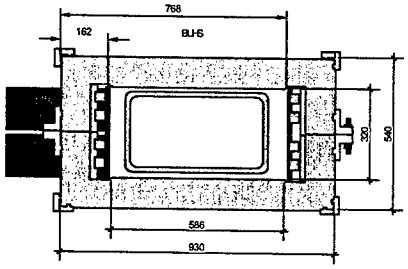


Fig.4 A cross-sectional view of the bump magnet

and the down-stream part kicks the H^+ ions converted from H^0.

H^- beams, which are estimated to be $3x10^{-4}$ % of the incoming beams, are also converted to H^+ by another second foil,"B", set at the entrance of the D quadrupole magnet,"ODK".

THE MAIN BUMP MAGNETS

Four dipole bump magnets named (SB-I~SB-IV), are identical in construction and are powered in series to give a symmetrical beam bump within the straight in an uninterrupted drift space between the focusing magnet and the defocusing one.

A cross-sectional view of the bump magnet is shown in Fig.4. The dipoles are out of the vacuum and a ceramic vacuum chamber is included in the magnet gap. The structure of the magnet is composed of two-turn coils and window frame core made by laminated silicon steel cores of which the thickness is 0.1 mm. The electrical insulation of the coil is achieved by air gap and a ceramic insulator.

The waveform of the magnetic field is trapezoid. A fall time of 100 μs is decided by the hitting probability of proton beams on the stripping foil and the temperature of the foil heated by the beam hit. The maximum temperature of the foil is estimated to be 1500°C at the tip of the foil.

The excitation current is supplied in the middle of the core through the split to form a symmetrical distribution of magnetic field along the longitudinal direction.

SUMMARY

The injection system is designed to be constructed in the FODO structure, which has rather short drift space.

The bump orbit for painting injection has a full acceptance for the circulating beams.

The H^- injection line and the H^0,H^- disposal lines can be designed so as to have a sufficient acceptance for low-loss injection

The painting area is optimized for both 3-GeV users and 50-GeV users in a pulse-to-pulse mode operation.

REFERENCES

[1] I. Sakai et al, EPAC2002, Paris, June 2002
[2] G. Rees, EPAC94, London, June 1994
[3] M. Shirakata et al, EPAC2002, Paris, June 2002

PARTICLE-BEAM BEHAVIOR IN THE SNS LINAC WITH SIMULATED AND RECONSTRUCTED BEAMS*

S. Nath, J. Billen, J. Stovall, H. Takeda, and L. M.Young, LANL, Los Alamos, NM 87545, USA
K. Crandall, Tech Source, Santa Fe, NM, USA, and D. Jeon, SNS/ORNL, Oak Ridge, TN, USA

Abstract

The Spallation Neutron Source (SNS) project is a collaborative effort between Brookhaven, Argonne, Jefferson, Lawrence Berkeley, Los Alamos and Oak Ridge National Laboratories. Los Alamos has designed the entire linac for this accelerator complex. The final design of the SNS linac is comprised of both normal- and super-conducting RF (SRF) structures. The normal-conducting linac section up to 185 MeV, consists of a 2.5-MeV RFQ, a Medium Energy Beam Transfer (MEBT) line, a 402.5-MHz DTL, followed by a 805-MHz CCL. The SRF structure accelerates the beam from a nominal energy of 185 MeV to 1000 MeV. The SRF section consists of two, a medium beta (β= 0.61), and a high beta (β= 0.81) sections. The base-line design of the linac was done with a simulated beam at the input to the DTL. In this paper, we present the behavior of particle-beams originating at different locations upstream of the DTL. Input beams include a simulated beam at the input to the RFQ and a beam reconstructed from measurements.

INTRODUCTION

An earlier paper [1] describes the baseline design and anticipated beam performance of the SNS linac. It is designed to deliver 1.4 MW of circulating beam in the ring at 1 GeV with room for upgrade. The beam from the RFQ at 2.5 MeV goes through a MEBT-chopper section followed by a DTL. At ~87 MeV, the beam from the 402.5-MHz DTL enters the 805-MHz CCL. The major portion of the linac, which accelerates the beam to 1.0 GeV, is a 805-MHz SRF linac that follows the CCL structure. This linac is designed to eventually handle a peak current of 52 mA and deliver 2.65-MW of beam with a 6% duty factor. The current configuration, however, delivers 1.5- MW corresponding to peak beam-current of 38 mA.

In the baseline linac design phase, a simulated beam at the entry to the DTL (case 1) was used to evaluate the performance of the design. All through the changes of the base-line, including final change to the SRF structure for the high-energy portion of the linac, the design was evaluated with this simulated beam. In the next step of the design process, MEBT was included in the evaluation of the beam behavior. The simulated beam started at the beginning of the MEBT section after the RFQ (case2). The MEBT is a transport section where a second and final chopping [2] is performed. Due to constraints imposed by required beam profile in the chopping section, the MEBT design was revisited several times. Finally, it was reconfigured to add slits removing the halo produced in this section and to match the beam to the input to the DTL. This modified MEBT is used for case 3 where simulations are done with a 4-D waterbag distribution at the input to the RFQ. Incidentally, loss and error simulations [3] in the normal conducting section of the linac were done with beam-collimators in the MEBT.

Finally, in case 4, we studied the performance of the linac with beam that was reconstructed from the beam measurement at the end of the LEBT and then transported through the RFQ and the modified MEBT. In the next sections, we present the results for all the four cases. No errors were included in any of the simulations. Beam dynamics code, LINAC was used for all simulation runs.

*Work supported by the Office of Energy Research, Basic Energy Science of the US Department of Energy.

SIMULATION

Modified MEBT

It was recognized very early in the simulation studies that significant halo develops while the beam passes through the MEBT. Some of the halo particles survive through most of the normal conducting linac but get lost primarily near the end of the CCL section. Studies were conducted to mitigate this problem; the MEBT was modified; horizontal (both +x and -x) scrappers were added, in addition to the vertical +y beam chopper target that nominally intercepts and removes 1% of the beam. Details on this modification are reported in an accompanying paper [4].

Matching Through MEBT

The rms-ellipse parameters and emittances at the input to the MEBT were calculated from the case 3 distribution after filtering out the low energy stragglers i.e., looking at the output beam from the RFQ with a simulated 4-D waterbag input. A 6-D waterbag distribution having the same rms properties was generated and was transported to the third buncher cavity in the MEBT. TRACE was used for adjusting the two quads upstream of this buncher cavity to produce a round beam at this cavity. The beam was then transmitted to the beginning of the DTL to get the emittances at the entrance to the DTL. Again TRACE was used to find the match for the beam with these emittances at 38 mA. Finally, the third and fourth cavity and the four quads just upstream of the DTL were adjusted (by using TRACE) to match the beam from the MEBT to the DTL.

Simulation Procedure

In case 1, a 6-D waterbag distribution of 100,000 particles was generated for the matched input to the DTL and run through the linac. For case 2, the simulated beam (6-D waterbag distribution) starts at the beginning of the

0-7803-7738-9/03/$17.00 © 2003 IEEE

MEBT i.e., at the output point of the RFQ. For case 3, we use a simulated 4-D waterbag distribution of 100,000 particles representing 40 mA at the input to the RFQ. The output at the RFQ contains ~0.5% of low energy particles not accelerated by the RFQ. After filtering out the low energy particles the current reduces to ~37.2 mA, somewhat less than 38 mA used for cases 1 and 2. No attempt is made to adjust the MEBT to rematch the beam into the DTL.

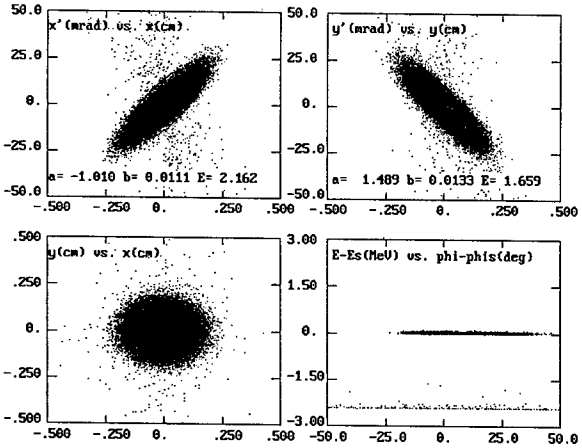


Figure 1. Phase-space plots at the RFQ output for case 4 showing the low energy particles from the RFQ.

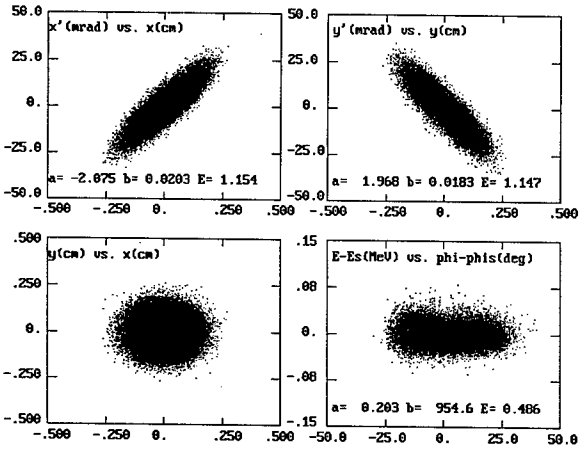


Figure 2. Phase-space plots at the RFQ output for case 4 after filtering out the low energy particles.

For case 4, we start with an initial particle distribution derived from x and y beam emittance measurements [5] made at slightly different longitudinal locations. We transform to the midpoint between the measurements without space charge and construct a numerical particle distribution. This particle distribution continues backward through the LEBT to a reference point upstream of the deflection electrodes. The computer code PARMELA, is used to verify that forward and backward beam transport with 3-D space charge is completely reversible. For our beam simulation studies, we transport the beam starting at this reference point and go through the 3-D fields of the LEBT. A description of the generation of distribution and transport through the LEBT is described in detail in [5].

Figures 1 and 2 show the phase space distributions at the RFQ output point before and after the removal of the low energy particles that made through the RFQ without acceleration. After removal of low energy particles, the beam current reduces to 36.4 mA. As in case 3, no attempt was made to rematch the beam into the DTL. This input distribution should be compared to the simulated input distribution of case 2 shown in Figure 3.

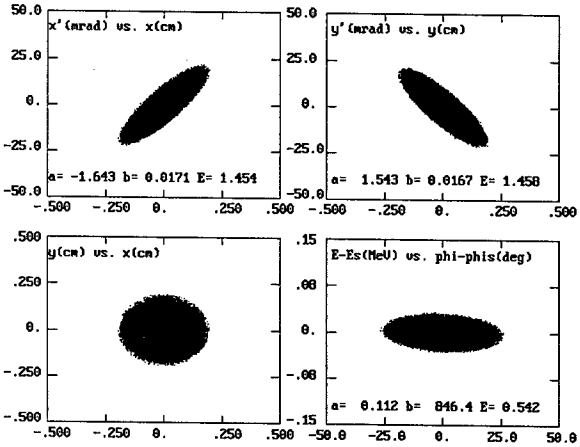


Figure 3. Phase-space plots of the simulated 6-D waterbag distribution at the input to the MEBT for case 2.

RESULTS

Figure 4 shows the normalized rms x- and y-emittance along the length of the entire linac for all the four cases. As can be seen from the plots, for cases 1 and 2, there is virtually no emittance growth in either x or y emittance. The same is true for longitudinal emittance (not shown).

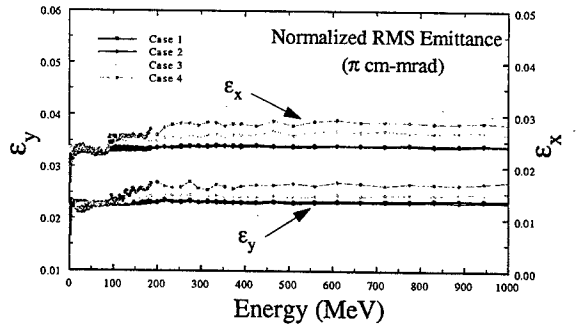


Figure 4. Normalized, rms x- and y-emittance along the length of the linac for four different cases.

Since no attempt is made to adjust the MEBT to rematch the beam coming out of the RFQ for cases 3 and 4, the beam emittance shows growth at the DTL and CCL junctions. Furthermore, there is gradual increase in transverse emittances along the CCL. This is understandable as transverse focusing is gradually

reduced along the CCL to make a smooth transition in focusing strength to the weaker focusing in the SRF section due to longer periodic lattice of the SRF lattice.

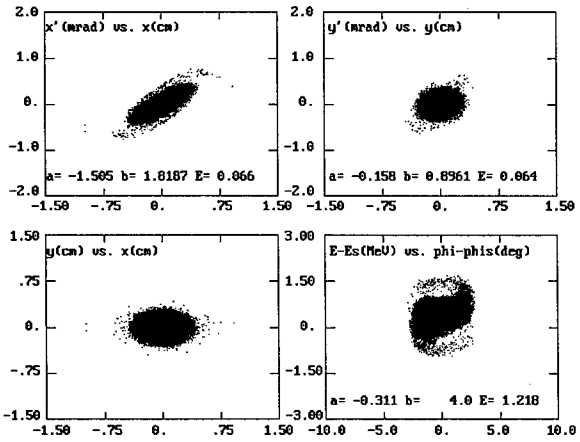


Figure 5. Phase-space projections at the end of the linac for case 2.

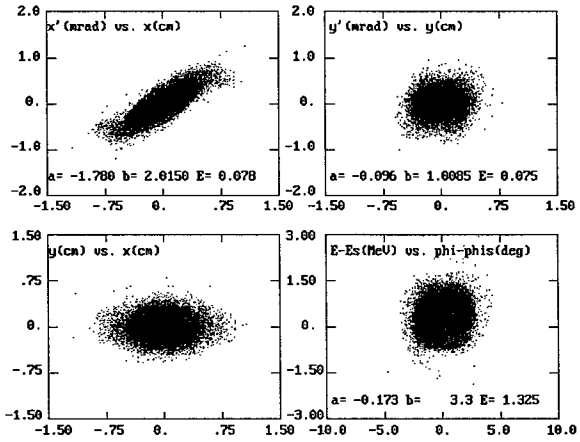


Figure 6. Phase-space projections at the end of the linac for case 4.

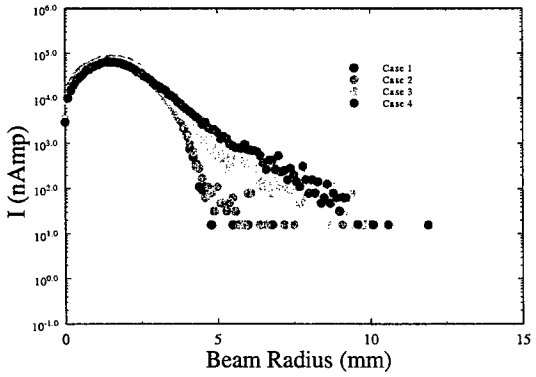


Figure 7. Radial-distribution of particles at the end of the linac for all four cases.

Figures 5 and 6 show phase space projections at the end of the linac (1 GeV) for cases 2 and 4 respectively. As expected, there is considerable growth in the transverse beam extent in case 4 compared to case 2. In addition, there is some halo formation. This is more clearly visible in Figure 7 where the radial distribution of the particles at the linac-end is shown for all four cases. While for cases 1 and 2, the beam virtually does not extend beyond ~5 mm (within statistics), the beam extends to ~10 mm for cases 3 and 4. Also, the beam distributions are more diffused in cases 3 and 4 indicative of halo in the beam.

Finally, the radial dimensions of the beam, both rms as well as 99% beam-size, along the entire length of the linac are shown in Figure 8. Predictably, the beam size gradually increases from the DTL towards the end of the CCL as the transverse focusing slowly decreases in that portion of the linac.

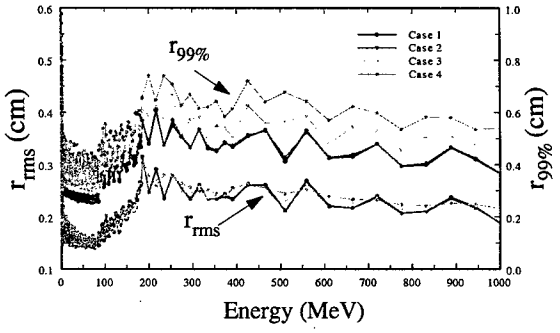


Figure 8. Radial beam-size, both rms and 99% along the length of the linac.

SUMMARY

The MEBT was tuned for a peak current of 38 mA and specific values of transverse and longitudinal emittances. In the examples discussed above, no attempt was made to rematch the beam out of the RFQ to the input of the DTL. Therefore, some mismatch is present in the beam coming out of the RFQ. This would be the case in reality if no dedicated online beam-measurement devices are present at the input to the DTL. In this context, the simulations with beam from the RFQ without rematching the MEBT are representative of realistic operational scenarios.

REFERENCES

[1] J. Stovall et al., "Expected Beam Performance of the SNS Linac," Proceedings of the 2001 Particle Accelerator Conference, p 446, June 18-22, 2001, Chicago, IL, USA.

[2] J. Staples et al., "The SNS Front-end Accelerator Systems," Proceedings of the XIX International Linac Conference, 1998, Chicago, IL, USA.

[3] S. Nath et al., ASAC presentation, October 2001, SNS/ORNL, Tenn., USA.

[4] D. Jeon et al., invited paper to this conference.

[5] S. Nath et al., Proceedings of the XXI International Linac Conference, p 319, 2002, Gyongju, S. Korea.

PARTICLE-IN-CELL SIMULATIONS OF THE HIGH CURRENT EXPERIMENT*

C.M. Celata, F.M. Bieniosek, L. Prost, and P.A. Seidl, Lawrence Berkeley National Laboratory, Berkeley, CA, USA, and the Heavy Ion Fusion Virtual National Laboratory
A. Friedman and D.P. Grote, Lawrence Livermore National Laboratory, Livermore, CA, USA, and the Heavy Ion Fusion Virtual National Laboratory

Abstract

The particle-in-cell code WARP has been used to simulate beam dynamics for the intense ion beam of the High Current Experiment. First a study was done of the dynamic aperture of the alternating-gradient electrostatic quadrupole lattice of the experiment, including nonlinearity due to image forces and imperfections of the focusing lattice field. It was found that particle loss, rather than emittance growth, determined the usable aperture. Simulations of transport in the High Current Experiment were then performed, and the results compared to measured data. We present the results of both of these studies.

INTRODUCTION

The High Current Experiment (HCX) [1], a Heavy Ion Fusion Virtual National Laboratory experiment located at LBNL, employs a driver-scale beam to investigate transport limits for heavy ion inertial fusion induction linac drivers. The beam is a coasting K^+ beam, which is transported through an alternating gradient FODO lattice. At present the current, I, is 185 mA at 1 MeV, and the lattice consists of a ten-electrostatic-quadrupole alternating-gradient system, followed by four magnetic quadrupoles. Expected eventual parameters are 555 mA at 1.8 MeV.

In this report, the dynamic aperture of the HCX electrostatic lattice, which is expected to be similar to an electrostatic-focus section of a driver, is investigated, using the transverse 2D version of the particle-in-cell (PIC) simulation code WARP [2]. The dynamic aperture is an important cost factor for a heavy ion fusion power plant accelerator. In the driver, multiple (~100) beams will be accelerated in parallel through common induction cores. An increase in the aperture necessary for each beam will have a large impact on the radius of the induction core and focusing structures, and thus on the size, weight, and cost of the accelerator.

Two sets of results are reported here. In the first, scaling studies were performed with an initially semigaussian beam, varying the current and undepressed betatron tune of the lattice, in order to find the dynamic aperture of the system for an idealized beam. In the second, the simulation was initialized with a particle distribution function synthesized using data from the upstream end of the HCX experiment, just after the matching section, in order to compare the results with experiment.

* Supported by the Office of Fusion Energy Science, US DOE, contract numbers DE-AC03-76SF00098 and W-7405-Eng-48.

SIMULATION MODEL FOR DYNAMIC APERTURE SCALING STUDIES

We discuss first the calculations made to determine the dynamic aperture of an alternating gradient focusing lattice assumed to consist of the HCX electrostatic lattice, lengthened to 50 lattice periods in order to have sensitivity to longer-length-scale effects. The quadrupole structure is shown in Fig. 1. The quadrupole electrode radius was selected to eliminate the dodecapole field component (i.e., electrode radius = 8/7 x aperture radius). The HCX focusing fields were modelled at each z by means of multipole moments derived from a 3D solution of the Poisson equation for the HCX quadrupoles, which included in the calculation the cylindrical quadrupole electrodes and the charged plates supporting them. Moments giving potential values greater than 1.5% of the quadrupole potential at a radius of 85% of the quadrupole aperture (aperture =2.3 cm, given by the quadrupole electrode surface) were included, with a z resolution of 0.85 mm. Image forces for the same focusing structure, assuming perfect conductors, were calculated at each timestep using a capacitive matrix technique. A square conducting box at 4.9 cm bounded the 512 x 512 cell computational grid. 80 timesteps per lattice period (lattice period = 0.4352 m) were used, giving adequate resolution of the fringe fields.

The simulations followed a transverse slice of the beam through 50 periods of alternating gradient lattice. The beam energy was assumed to be 1.8 MeV. The initial emittance was set to 5 times the thermal emittance of a 0.1 eV, 5 cm radius source for a beam with I=576 mA. It was then scaled with the square root of the current for other values of the current, simulating the effect of changing the source diameter for the same diode/injector. This scaling neglects differences in injector aberrations with beam size. Since ultimately the injector would be designed for the desired current, this approximation seems reasonable. The emittance values used correspond to a space-charge-dominated beam, with phase advance per lattice period, σ, a factor of 7-9 below its undepressed value.

An initially semigaussian distribution function was used for the scaling study because the driver is expected to have a similarly uniform beam. In order to simulate the effect of various aperture filling fractions in the

0-7803-7738-9/03/$17.00 © 2003 IEEE

driver, for each of several values of the focusing strength (as measured by the undepressed betatron phase advance, σ_0) the current was increased until beam quality suffered.

In the HCX it is easier to explore the effect of aperture-filling by decreasing the focusing strength, while keeping the current constant. In the results below, this procedure is compared with the above constant-σ_0 method.

Nonlinear focusing forces and, to a greater extent, image forces, produce a mismatch in the beam, if it is matched assuming linear forces. The PIC code was therefore used to iterate on initial rms beam radii and angles until the beam was rms-matched to +/- ~1-2%.

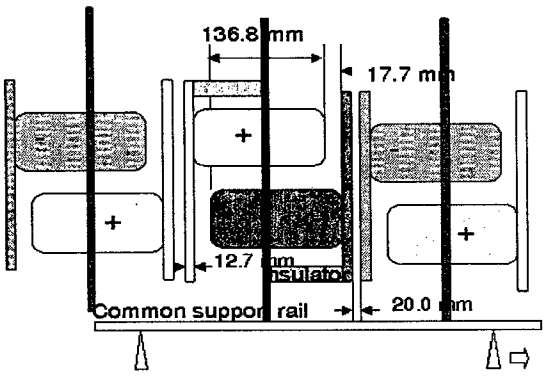


Figure 1: An HCX electrostatic quadrupole

SCALING STUDY RESULTS

Simulations for the scaling studies were performed over 50 lattice periods for σ_0 of 60°, 70°, and 80°, since the focusing strength of the driver is expected to be in this range. At each σ_0 the beam current was increased until beam quality degraded. For each σ_0, particle loss began while emittance was still within acceptable bounds. Therefore the useable aperture is set for this lattice by particle loss, rather than by emittance growth. For 60° and 70° there was no emittance growth. At 80° a few percent growth (0.04 π mm-mrad) was seen over the 50 lattice periods, and the same slow linear growth of emittance continued in 100-period simulations. In all cases the final phase and configuration spaces of the beam particles were unremarkable, except for a slight diamond-shape in configuration space, due to image forces (see Fig. 2 for final phase and configuration space plots).

Particles are lost from the calculation if they reach the radius of the quadrupole electrode surface (0.23 m). The simulation does not generate electrons and gas when particles hit the wall, as would occur in the experiment. Therefore the amount of loss for a given set of conditions is not considered realistic, though it is indicative of the extent of the halo formed and the approximate z position of the beam when particle loss begins. It was found that for σ_0 of 60° and 70°, eliminating particle loss and the attendant electron and gas production required using ≤ 80% of the radial aperture. More aperture must be added if the beam is mismatched, has more halo, or is misaligned. For σ_0 = 80°, loss began when the beam filled 70-75% of the aperture, and was always larger than for the lower σ_0's. This increased particle loss and the slight emittance growth mentioned above are likely to be caused by the same phenomenon seen in the experiments of Tiefenback [3], which may be indicative of the boundary of stability for the envelope mode for space-charge-dominated beams.

In another set of calculations, the beam current was held fixed at 555 mA, while σ_0 was decreased from 60° in order to increase the beam radius. This procedure is the easiest to use in HCX experiments. Again no emittance growth was observed, and particle loss began when the beam major radius was about 80% of the physical radial aperture. Phase spaces were similar to the runs at constant σ_0. This gives confidence that exploring the aperture by decreasing the lattice focusing strength will give information relevant to the driver case.

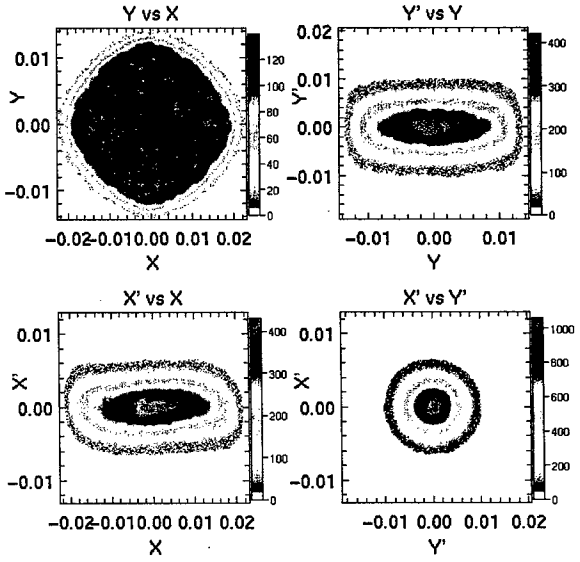


Figure 2: Configuration and phase space contour plots after 50 lattice periods for σ_0=60°, I=849 mA (fills 86% of radial aperture). Units of x and y are meters.

SIMULATIONS OF THE HCX BEAM

The HCX has been used to experimentally explore the dynamic aperture of the electrostatic quadrupole lattice. At this point measurements have been done for radial filling factors, a_{max}/R, (where "a" is the beam major radius and "R" is the quadrupole aperture radius) of 60% and 80% [4]. For both cases, the experiment showed no emittance growth, and particle loss consistent with charge-exchange loss from background gas. This is in agreement with the simulation results discussed above for the semigaussian beam, which for the length of the HCX

10-quadrupole lattice shows no beam loss or emittance growth. Background gas effects are not included in the simulation. However the HCX beam distribution function differs significantly from the semigaussian model. Therefore a simulation was performed for the 60% filling case, using as the initial distribution function a particle distribution determined by measurement.

The distribution function in the x-x', y-y', and x-y phase planes was measured using slit scanners just downstream of the matching section after the HCX injector. Monte Carlo methods [5] were then used to synthesize a distribution function from the data. Note that measurement in these three planes is not sufficient to uniquely determine the distribution function, so additional assumptions about the distribution were required. The choices made are discussed in detail in ref. [5]. A slice near the center of the beam pulse was transported in the simulation (and experiment) through the 10 electrostatic quadrupoles of the HCX lattice. The current was 175 mA with initial measured emittances of 0.43 π mm-mrad for x and 0.37 π mm-mrad for y, and σ_0=65°.

The results are shown in Fig. 3. Though there is rough agreement between simulation and data in final beam size and some features, such as the beam hollowing in configuration space, there is obvious disagreement in distribution function details. As discussed further in Ref. [5], data from a new prototype optical diagnostic [6] (slit + scintillator) indicates that there are distribution function correlations in planes not measured by the slit scanners, which therefore are not reflected in the synthesized distribution function. Optical diagnostics now in the development and design stage will provide these correlations, so that better agreement can be obtained. An important result of the studies reported here is that such previously unmeasured correlations must be included in order to obtain accurate predictions from the simulation.

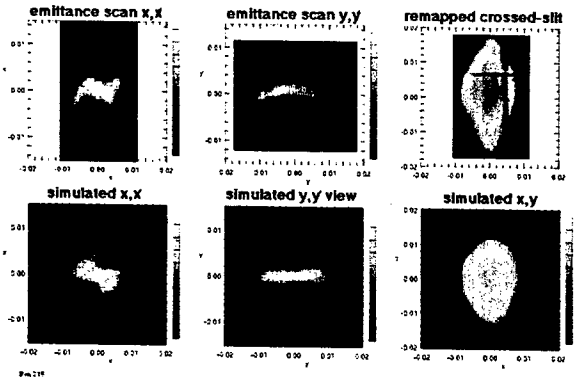


Figure 3: Distribution function in x-x', y-y', and x-y (from left to right) planes after 10-quadrupole transport in the HCX, from measured data (top row) and simulation.

CONCLUSIONS

2D particle simulations for a initially semigaussian distribution indicate that particle loss, rather than emittance growth, defines the dynamic aperture for the HCX electrostatic focusing lattice. For a well-matched centered beam with negligible halo and $\sigma_0 < 80°$, particle loss begins when the ratio of the beam major radius to the radial distance to the quadrupole electrode is approximately 80%. When σ_0 reaches approximately 80°, loss increases, and there is slow emittance growth ~ a few percent in 50 lattice periods. Increasing the beam radius by (1) changing the focusing strength at constant current, and (2) changing the current at constant focusing strength, seem to give similar results for particle loss and dynamics.

A simulation was also done for a distribution synthesized from slitscan measurements of the distribution function in the x-x', y-y', and x-y planes. The results show significant disagreement with experiment. Optical diagnostic data indicates that the possible source of the disagreement is the presence of correlations in planes not measured by the slitscanners. Diagnostics now being designed are expected to provide data needed to resolve the discrepancies.

REFERENCES

[1] P.A. Seidl et al. "Overview of the Scientific Objectives of the High Current Experiment for Heavy-Ion Fusion" Proc. 2001 Part. Accel. Conf. pp. 2932-2934, IEEE #01CH37268C. Piscataway, NJ 08855.

[2] D.P. Grote, A. Friedman, I. Haber, W. Fawley, J-L. Vay, "New Developments in WARP: Progress towards end-to-end simulation", Nucl. Instr. & Meth. **A 415**. 428-432.

[3] M.G. Tiefenback and D. Keefe, "Measurements of Stability Limits for a Space-Charge-Dominated Ion Beam in a Long A.G. Transport Channel" Trans. Nucl. Sci. **ns-32**, 2483 - 2485.

[4] Peter Seidl, D. Baca, F.M. Bieniosek, C.M. Celata, A. Faltens, L.R. Prost, G. Sabbi, W. Waldron, R. Cohen, A. Friedman, S.M. Lund, A.W. Molvik, and I. Haber, "The High Current Experiment for Heavy Ion Fusion, in these proceedings.

[5] Friedman, A., Grote, D.P., Bieniosek, F.M., Celata, C.M., Prost, L.R. and Seidl, P.A., "Simulation Using Initial 4D Beam Particle Distributions Synthesized from Experimental Data", in these proceedings.

[6] Frank Bieniosek, W.B. Ghiorso, and L. Prost, "Beam Imaging Diagnostics for Heavy-Ion Fusion Beam Experiments", in these proceedings.

DESIGN CHOICES FOR THE INTEGRATED BEAM EXPERIMENT (IBX)*

M.A. Leitner#, C.M. Celata, E.P. Lee, B.G. Logan, G. Sabbi, W.L. Waldron
LBNL, Berkeley, CA 94720, USA
J.J. Barnard
LLNL, Livermore, CA 94550, USA

Abstract

Over the next three years the research program of the Heavy Ion Fusion Virtual National Laboratory (HIF-VNL), a collaboration among LBNL, LLNL, and PPPL, is focused on separate scientific experiments in the injection, transport and focusing of intense heavy ion beams at currents from 100 mA to 1 A. As a next major step in the HIF-VNL program, we aim for a complete "source-to-target" experiment, the Integrated Beam Experiment (IBX). By combining the experience gained in the current separate beam experiments IBX would allow the integrated scientific study of the evolution of a high current (~1 A) single heavy ion beam through all sections of a possible heavy ion fusion accelerator: the injection, acceleration, compression, and beam focusing.

This paper describes the main parameters and technology choices of the proposed IBX experiment. IBX will accelerate singly charged potassium or argon ion beams up to 10 MeV final energy and a longitudinal beam compression ratio of 10, resulting in a beam current at the target of more than 10 Amperes. The different accelerator cell design options are described in detail, in particular the induction core modules incorporating either room temperature pulsed focusing-magnets or superconducting magnets.

INTRODUCTION

The U.S. Heavy Ion Fusion program is supporting several key experimental programs to validate the attractiveness of a heavy ion accelerator as a candidate for an inertial fusion energy driver. Over the next few years, the Heavy Ion Fusion Virtual National Laboratory (HIF-VNL) will complete a set of small experiments addressing scientific key questions related to heavy ion fusion drivers [1]. The goal of these experiments is to demonstrate the feasibility of such driver beam manipulations, which can be investigated in separate small-scale experiments as initial step.

As the logical next step, the HIF-VNL proposes a fully integrated beam physics experiment. This intermediate-scale experiment, the Integrated Beam Experiment (IBX), will allow important access to significant areas of heavy ion fusion physics [2]:

The longitudinal properties of a driver-scale beam under induction acceleration, its profile and the manipulation of that profile, and the resultant emittance changes, will be studied for the first time.

Limits of acceleration and longitudinal beam compression can be examined for the first time.

In particular, IBX will be the first experiment to allow exploration of all post-accelerator manipulations of the beam found in a future driver - drift compression, final focus, and chamber transport.

Electron dynamics with acceleration will also be addressed, with the opportunity for the first time to see the effect on beam transport.

The final focus spot size on target depends on the accumulated beam phase-space changes through each region along the accelerator system. The crucial integration role of the IBX will be to test the ability to achieve a high beam brightness (focusability) from source to target.

A key strategic goal in the HIF-VNL theory/simulation program is an integrated and detailed source-to-target simulation capability. The IBX will provide a well-diagnosed experiment to benchmark integrated beam dynamics simulation codes for a single beam through the injection, acceleration, longitudinal drift compression, and final focus, with sufficient beam current to include important gas/electron interactions.

This integrated source-to-target experiment will have a final kinetic energy 10 MeV. The charge-per-unit length will be 1-2 C/m in order to produce the space charge potential necessary for electron dynamics and final transport neutralization studies. The final perveance (measure of the ratio of space charge potential energy to kinetic energy) of the beam after longitudinal compression of a factor of 10 will be ~10^{-3}. The option of such aggressive beam compression will enable exploration of a wide range of final focus transport and final compression alternatives, including the opportunity to employ a variety of schemes to correct geometric and chromatic beam aberrations.

IBX COMPONENTS AND SPECIFICATIONS

The IBX project is currently in a pre-conceptual design stage. As required by the physics program [2] the minimum final beam energy of IBX will be 5 MeV, but depending on funding level should preferably approach 10 MeV. Main performance parameters for a 10 MeV IBX scenario are listed in the following table:

* This work was performed under the auspices of the U.S. Department of Energy by the University of California, Lawrence Berkeley National Laboratory under contract number DE-AC03-76SF00098, Lawrence Livermore National Laboratory under contract number W-7405-Eng-48, Massachusetts Institute of Technology under contract number DE-FC02-93-ER54186, and by the Princeton Plasma Physics Laboratory under contract number DE-AC02-76CH03073.

MLeitner@lbl.gov

0-7803-7738-9/03/$17.00 © 2003 IEEE

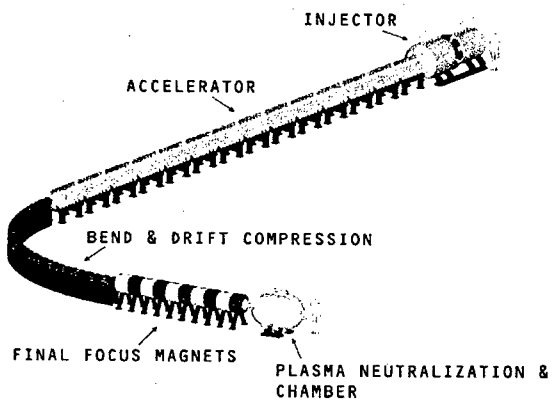


Figure 1: Schematic layout of the Integrated Beam Experiment (IBX).

INJECTOR	
Ion:	K+ or Ar+
Current:	0.6 A
Energy:	1.7 MeV
Pulse Length:	0.25 s
ACCELERATOR:	
Number of Half Lattice Periods:	~ 120
Half Lattice Period Length:	30 cm
Final Energy:	10 MeV
BEND & DRIFT COMPRESSION:	
Number of Half Lattice Periods:	~ 30
Compression Ratio:	10
Beam Pulse Length at End of Drift Compression:	25 ns
FINAL FOCUS & PLASMA NEUTRALIZATION:	
Number of Half Lattice Periods:	~ 10
Final Beam Pulse Length:	~ 15 ns
Final Perveance:	$1.4\ 10^{-3}$
Final Space Charge Density:	1.4 C/m
Final Current:	~ 10 A

Figure 1 shows the mechanical layout of a 10 MeV IBX version. To advance the integrated heavy-ion beam physics program in a time- and cost-effective manner IBX will rely mainly on the use of existing technology, in particular induction core- and superconducting magnet-designs developed in the heavy ion fusion program.

IBX TECHNOLOGY CHOICES

The IBX accelerator is a current-amplifying heavy ion induction linac with an alternating gradient magnetic quadruple transport lattice. The accelerator is built from individual modules as indicated in figure 1. Figure 2 displays schematically the main components of such an IBX accelerator module. A broad range of design alternatives has been examined during IBX pre-conceptual costing studies.

Transport Magnets

IBX has the choice of using either pulsed room-temperature (RT) or steady-state superconducting (SC) quadrupoles for the ion beam transport magnets. Ultimately, for a HIF driver, superconducting magnets will be more effective than RT magnets in terms of field quality, efficiency, and reliability. Furthermore, SC magnets are significantly more cost-effective in large quantity. However, up to today mainly RT pulsed magnets have been used for HIF-VNL experiments because of their significantly lower cost if used in small quantity.

Figure 3 shows a cross-sectional view of a RT and a SC version of IBX acceleration cells. As demonstrated in the figure, the cryostat for the SC case takes up additional radial space leading to larger induction cores and consequently higher costs. IBX will need approximately 100 focusing magnets, which is slightly below the turning point where SC magnets become more cost effective. For this reason present effort is focused on a tradeoff study comparing both technologies.

The use of superconducting magnets in IBX has three major advantages over pulsed RT magnets: First, they are steady state, eliminating eddy current problems. Secondly, the magnet cryostats can provide a cold pumping surface in the beam tube. Third, a HIF driver will also be built with SC cold bore magnets. Therefore, IBX could simulate more closely the vacuum environment seen by the heavy ion beam in a HIF driver.

Having the same vacuum and especially beam-pipe wall conditions compared to a HIF driver allows exploring limitations associated with magnetic focusing, in particular the onset of instabilities or focusing effects due to electrons trapped in the potential well of the ion beam (electron cloud effect).

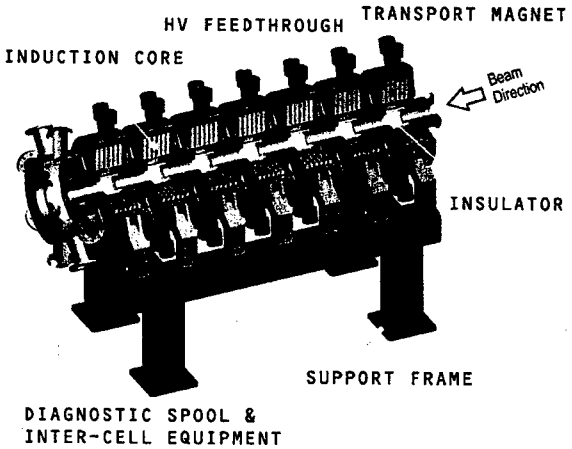


Figure 2: Components of an IBX acceleration module. A half lattice period consists of a quadrupole magnet and an induction acceleration gap. Every several half-lattice periods an induction cell is replaced by a vacuum spool for diagnostics, pumping and auxiliary access.

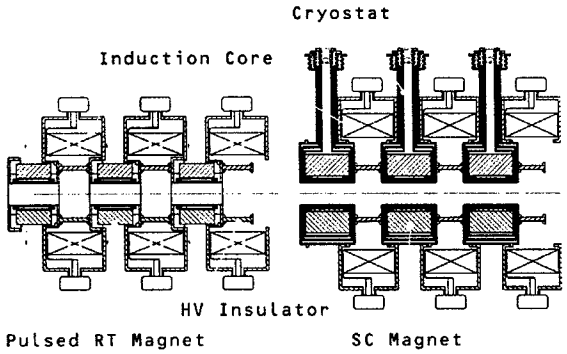


Figure 3: Comparison between a room-temperature (RT) version and a superconducting version (SC) of IBX. The cryostat for the SC case takes up additional radial space, leading to larger induction cores.

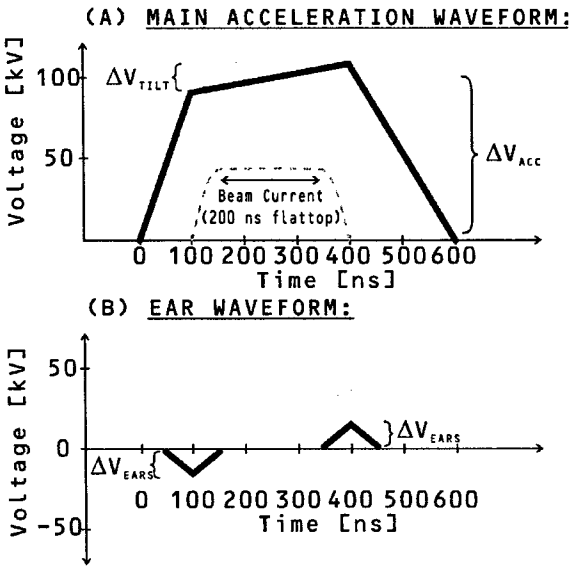


Figure 4: IBX will incorporate agile waveform control utilizing solid-state pulser technology and different core materials to produce flexible pulse waveforms as indicated in this figure.

Induction Cores & Pulsers

Figure 4 shows the different voltage waveforms that have to be generated by a single IBX induction cell. Consequently, the current IBX baseline design integrates three separate induction core types into a single induction cell:

(1): Each half-lattice period (i.e. quadrupole magnet) in IBX will include an induction acceleration gap. The main acceleration pulse (+100 kV/gap) is generated by bulk Metglas cores with a lumped-element pulse-forming network (see figure 4a).

(2): An initial velocity tilt (used for longitudinal bunching), which is applied to the ion beam in the beginning of the accelerator, must be maintained throughout the accelerator by applying a small tilt voltage (~5 kV) on top of the main acceleration pulse (see figure 4a). This tilt voltage will be generated by smaller Finemet cores and linear solid-state amplifiers. Since solid-state pulsers are extremely flexible, the tilt voltage can be modified easily for different longitudinal beam physics experiments. Regulation of the main acceleration waveform to less than 1% can also be achieved using these same cores and pulsers.

(3): Ear voltage pulses (± 5 kV, see figure 4b) confine the head and tail of the high-current bunch from spreading out longitudinally due to space-charge forces. These ear waveforms require the highest magnetization rate. Since the ear voltage pulses are relatively small and short, solid-state pulsers together with a third core component using either Finemet or Ferrite material is utilized.

Solid-state technology (compared to a lumped-element pulse forming network) constitutes an important component of IBX, which will allow enough flexibility for different longitudinal beam physics experiments, each with different high voltage waveform schedules. As a further advantage, solid-state pulsers can be easily integrated into the accelerator control system. Since the waveform is generated by arbitrary waveform generators, feedback loops can correct errors in the applied voltage pulses even during a single beam shot in subsequent cells.

SUMMARY

Main parameters and the most consequential technology choices of the planned Integrated Beam Experiment (IBX) pursued by the Heavy Ion Fusion Virtual National Laboratory (HIF-VNL) have been described. The total project cost including R&D is currently expected to be in the range of 80 M$. Following project approval and a one-year conceptual design effort IBX's first operation could begin after a 5-year design and construction schedule. The unique IBX capability for integrated injection, acceleration, compression and focusing of high-current, space-charge-dominated heavy-ion beams would unfold a completely new field for investigating and exploring heavy ion fusion concepts.

REFERENCES

[1] B.G. Logan, et al.: "U.S. Heavy Ion Beam Science towards Inertial Fusion Energy", to be published Proc. 19th IAEA Fusion Energy Conference, Lyon, France (2002) (http://www.iaea.org/programmes/ripc/physics/)

[2] J.J. Barnard, et al.: "Integrated Experiments for Heavy Ion Fusion", Laser and Particle Beams , in press (2003)

BEAM IN GAP MEASUREMENTS AT THE SNS FRONT-END *

A. Aleksandrov, S.Assadi, W.Blokland, C. Deibele, W. Grice, J. Pogge,
ORNL, Oak Ridge, TN 37830 USA

Abstract

The pulsed beam in the SNS accelerator has a fine time structure which consists of 695ns long mini-pulses separated by 250ns gaps in order to minimize transient beam losses in the accumulator ring which could arise during the ring extraction kicker rise time. This time structure is provided by a two stage Front End chopping system which must reduce the beam current in the gap to a level of 10^{-4} of the nominal current in order to satisfy requirements on the ring extraction losses. A Beam-in-Gap measuring system based on H^- stripping using Nd-YAG laser was developed and tested during the SNS Front-End commissioning period. This paper describes the Beam-in-Gap measurement system design and measured performance.

INTRODUCTION

The SNS accelerator systems are described in details elsewhere [1]. They have to deliver proton beam with average power of 1.44MW to the spallation target. The 1ms long H^- macro pulses are accelerated by the linac to 1GeV energy and injected into accumulator ring. After 1ms accumulation cycle, beam is extracted from the ring in one turn using fast kicker with about 200ns rise time. In order to minimize losses of the partially kicked particles during kicker rise time beam is chopped at the revolution frequency of about 1MHz into 'min-pulses' of 645ns duration with 300ns gaps. The required extinction ratio of about 10^{-4} is provided by two separate chopper systems located in the low energy beam transport section (LEBT) and medium beam transport section (MEBT), respectively. The LEBT chopper with design extinction ratio of about 1% and rise time of 25ns removes most of the beam power during the mini-pulse gaps. The MEBT chopper further reduces extinction ratio to 10^{-4} and sharpens gap's rise/fall edges to 10ns. In order to measure extinction ratio of the chopped beam diagnostic system with dynamic range better than 10^4 is required. Moreover it should have large bandwidth to be capable to measure 10ns rise/fall time of the gap. Beam-in-gap (BIG) measuring system was included in the original base line suit of the SNS diagnostics. The idea was to detach electrons from H^- using pulsed laser beam and measure flux of created neutral H^0 downstream [2]. BIG diagnostics was to be installed in the high-energy beam transport line where dipoles could be used to separate neutral particles from the main beam. This system was rejected later due to budget constraints. Meanwhile decision was made to replace wire scanners in the superconducting part of the linac by laser-based beam profile diagnostics, which is based on the same principle as original BIG diagnostics. Prototype beam profile measuring equipment was installed at the MEBT exit and was successfully tested during front-end system commissioning [3,4]. The same equipment proved to provide BIG measurements with required dynamic range and time resolution as described below.

DESIGN OF THE LASER BASED BEAM-IN- GAP MEASURING SYSTEM

General layout

General layout of the beam-in-gap measuring system is shown in figure 1. The measured beam (1) is intercepted by the overlapping light beam (2) from a high power pulsed laser (3). The electrons removed from the H^-s in photo-detachment process are deflected by dipole magnetic field of a magnet (4) and arrive to the collector (5). Collected charge is measured by data acquisition system. Timing of the laser pulse can be adjusted using variable delay thus allowing scanning H^- density along the macro-pulse. Time resolution is limited by the laser pulse duration.

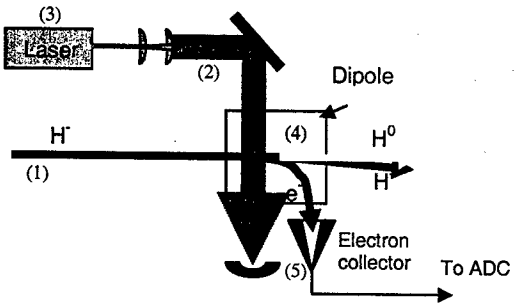


Figure 1. Schematic view of the beam-in-gap measuring system

Signal strength

Signal strength in the detector is defined by ratio of stripped ions in the beam or so called neutralization degree. Neutralization degree due to negative hydrogen ion stripping by overlapping laser beam crossing the ion beam at 90 degrees can be estimated as [5]:

$$\eta_0 \approx \frac{\lambda W_l}{2\pi\hbar c v}\frac{\Sigma_0}{\tau_l \sigma_l},$$

where λ is laser wavelength, W_l is laser pulse energy, Σ_0 is invariant cross-section of photo-detachment, τ_l is laser pulse duration, σ_l is transverse laser beam size (assuming laser beam completely overlaps ion beam), v is ion beam velocity.

0-7803-7738-9/03/$17.00 © 2003 IEEE

Expected neutralization degree in our experiment was close to 100%. Number of stripped electrons and therefore signal in the collector is

$$I_e = k \cdot I_b \cdot \eta_0,$$

where k is collection efficiency, I_b is ion beam current. Collection efficiency is close to 1 in our experiment due to large size of electron collector therefore electron current in the collector is close to the ion beam current. Note that absolute calibration is not required in the beam-in-gap measurements because we are interested in gap cleanness relative to the peak beam current.

Background signal

Two main sources produce a background charge in the collector: H^- stripping on the residual gas upstream of the detector and secondary electrons from beam particles lost in the collector vicinity. Both sources are correlated with the beam but not correlated with the laser pulse therefore time gating of the signal from the collector synchronized with the laser pulse helps to suppress background significantly. For this reason a Faraday cup with large frequency bandwidth was used to collect stripped electrons.

Hardware

We utilized hardware developed for the 'laser wire' profile monitor [5] for the beam-in-gap measurements. Commercial Nd-YAG laser has the following parameters:

Wavelength	1064nm
Max. pulse energy	600mJ
Pulse width	6-8ns
Max. rep. rate	30Hz

Light was transported through a transport line and injected into the vacuum chamber. Laser beam size at the interaction point was enlarged to ~ 2cm in diameter to ensure total overlap with the ion beam.

Stripped electrons were deflected by a 90° electromagnetic dipole and collected to a Faraday cup. The magnetic field required to deflect 1.25kV electrons is about 10Gs and its effect on the ion beam is negligible. The Faraday cup was designed with two important considerations in mind: good isolation from a 402.5 MHz electromagnetic interference from the beam; large frequency bandwidth to allow time gating synchronized with laser pulse for background suppression.

Signal from the Faraday cup was measured with a digital oscilloscope.

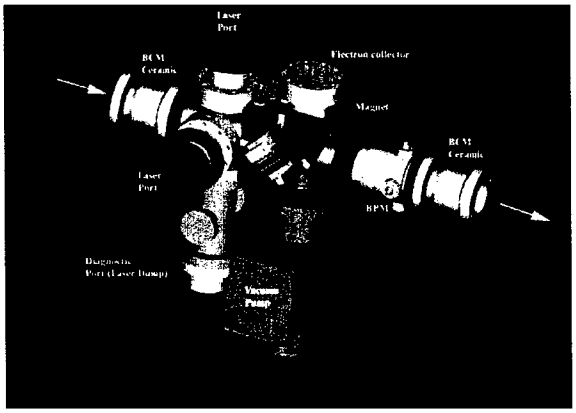


Figure 2. Vacuum chamber layout.

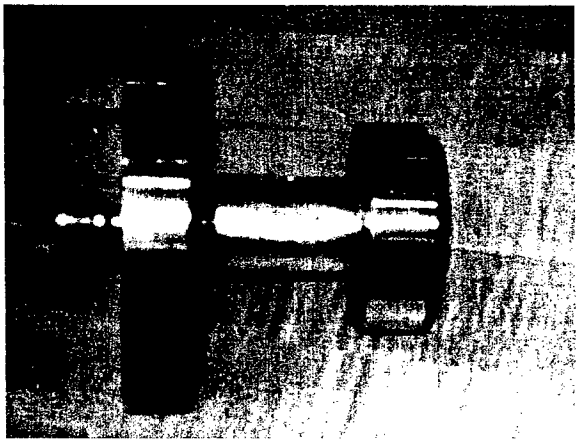


Figure 3. Faraday Cup design

EXPERIMENTAL RESULTS

Beam-in-gap measuring system was installed at the end of the MEBT and tested during the FES commissioning. The chopper system couldn't provide nominal chopping efficiency due to the failure of the high voltage chopper power supply switches. We simulated nominal operation of the chopper using DC deflection in the LEBT with specific goal to check capability of the measuring system itself.

Time resolution

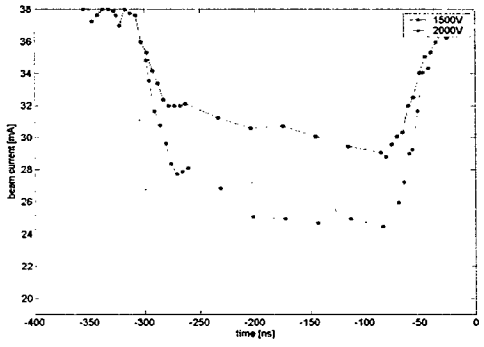


Figure 4. Time profile of a mini-pulse gap measured at different chopper voltage.

Gap of 250ns width was created in the stream of micro-pulses using one remaining operational switch. Nominally there are four switches. The efficiency of the deflector with only one channel operational is about ¼. Therefore depth of the gap couldn't reach design value of 1% but rise and fall edges of the gap were sharp enough to

evaluate temporal resolution of the measuring system as shown in Fig.4. Ion beam density was sampled at various times along the mini-pulse by varying delay between ion beam and laser pulse. Observed temporal resolution of about 5ns is consistent with laser pulse duration.

Dynamic range

Beam-on phase of the mini-pulse was simulated by measurement at full beam current of 32mA. Signal from the electron collector in this case is shown in Fig 5.

In order to simulate full chopping efficiency, shifting beam closer to the edge of the chopper target by applying DC voltage on the deflector compensated lack of pulsed deflecting voltage on the chopper. As a result beam transmission was drastically reduced during both beam-on and beam-off phases. Minimum beam current of 70μA achieved in this configuration is a reasonable simulation of expected beam-in-gap residual current during normal operation of the chopper. Signal from the electron collector is shown in fig 6.

As seen from the Fig.6 beam current of 70μA produces signal in the collector, which is 10 times higher than the background. This represents dynamic range of about $5 \cdot 10^3$. In order to check that dynamic range was limited by the sensitivity of the oscilloscope and not by stripping on the residual gas, we increased residual pressure in the vacuum chamber by factor 2-3. It didn't result on corresponding increase of the background level proving that lack of amplifier gain was the factor limiting the dynamic range. There is no doubt that with additional amplification and filtering dynamic range could reach the required value of 10^4 or better.

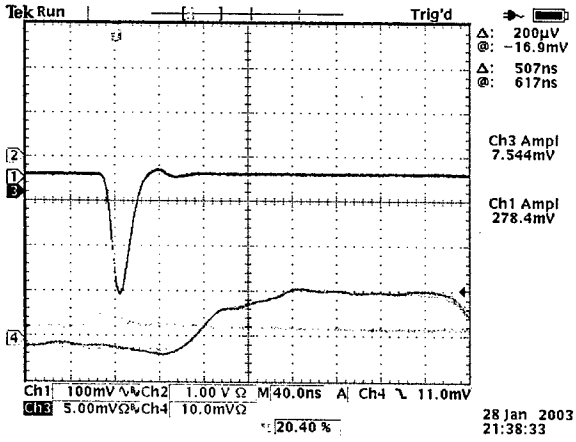


Figure 5. Oscilloscope trace of the signal for full beam current (blue trace). 0 dB amplifier gain. Green trace is laser pulse detected by a photodiode.

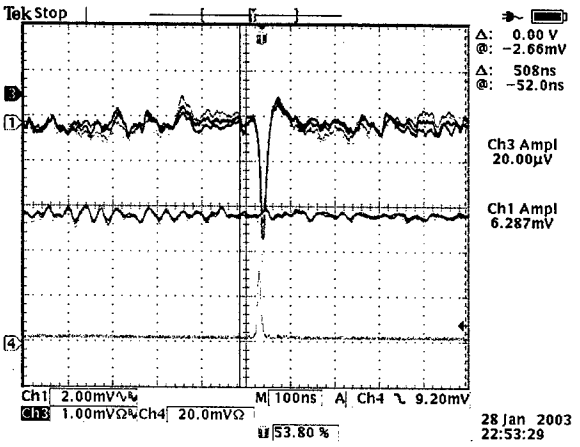


Figure 6. Oscilloscope trace of the signal for beam in the gap (upper blue trace). 20dB amplifier gain. Green trace is laser pulse detected by a photodiode.

CONCLUSION

We have developed a system for the beam-in-gap measurements in the SNS accelerator. Time resolution of 5ns and dynamic range of 10^4 has been achieved experimentally. Demonstrated parameters satisfy the SNS requirements. This system is based on the standard equipment of the 'laser wire' profile monitor therefore beam-in-gap can be measured at any location in the SCL.

REFERENCES

[1] N. Holtkamp, 'Status of the Spallation Neutron Source', these conference proceedings, PAC2003, Portland

[2] R. Shafer, LA-UR 98-2643

[3] A. Aleksandrov, 'Commissioning of the SNS Front End Systems at Oak Ridge', these conference proceedings, PAC2003, Portland

[4] S. Assadi, 'The Spallation Neutron Source diagnostics', these conference proceedings, PAC2003, Portland

[5] A. Aleksandrov, SNS-NOTE-AP-44

* SNS is managed by UT-Battelle, LLC, under contract DE-AC05-00OR22725 for the U.S. Department of Energy. SNS is a partnership of six national laboratories: Argonne, Brookhaven, Jefferson, Lawrence Berkeley, Los Alamos and Oak Ridge.

Proceedings of the 2003 Particle Accelerator Conference

ISIS MEGAWATT UPGRADE PLANS

C.R. Prior. D.J. Adams, C.P. Bailey, D.W.J. Bellenger, G. Bellodi, J.R.J. Bennett, I.S.K. Gardner, F. Gerigk, J.W. Gray, W.A. Morris, G.H. Rees, J.V. Trotman, C.M. Warsop
CLRC Rutherford Appleton Laboratory, Chilton, Didcot, Oxon, U.K.

Abstract

The ISIS spallation neutron source has been running successfully for more than 15 years and at 160 kW remains the most powerful source of its kind in the world. With machines due to operate at or near the megawatt level under construction in the United States and Japan and expected to come on line within the next decade, advances in Europe have not progressed at the same rate. A positive decision on the European Spallation Source (ESS) looks unlikely and one is led to consider the feasibility of alternative options. An ISIS upgrade is one such possibility. The current installation of a radio frequency quadrupole (RFQ) in the linac and a dual harmonic RF system in the synchrotron should lead to an increase in intensity of up to 50%, but plans are also under way to increase the beam power to 1 MW with the possibility of going to 4-5 MW in the longer term. The 1 MW option is based on an increase in energy to 3 GeV by means of a second synchrotron using ISIS as a booster. Details of the new ring and studies of the accelerating system are given in this paper. The ring also has the option of accelerating to 8 GeV at reduced frequency and this could be used as a test bed for the nanosecond bunch compression needed for the proton driver for a neutrino factory (NF). The cost of these proposals is relatively modest compared with a completely new facility. In the longer term, a combination of two such rings with a new synchrotron booster (replacing the existing ISIS) would give several options, for example: 4 MW for neutrons, or 2 MW for neutrons plus 2 MW for neutrino/muon studies, or 4 MW for a neutrino facility.

INTRODUCTION

Based on a 70 MeV linac and an 800 MeV synchrotron, ISIS is an extremely robust, reliable and stable machine. An impressive amount of high quality research has followed since its inception and there have been many important developments over a range of subjects including both physical and biological sciences. Operational experience and technological progress have provided valuable guidance for studies towards future accelerator-based neutron sources. ISIS is increasingly seen as a benchmark not only for neutron production but also as a high power proton accelerator. Many of the ideas behind its design have had a bearing on the US spallation neutron source (SNS) and the Japanese high intensity accelerator facility (J-PARC), and it has had a major influence on plans for a multi-megawatt spallation source in Europe, ESS. While the demand for neutrons in Europe remains strong, a decision over construction of ESS seems increasingly remote. A development of ISIS into a versatile, high power, high intenstity proton driver (ISIS2), therefore seems attractive, and would provide options for a range of fixed-target studies. The proposed upgrade would be in three phases, during each of which ISIS could continue to operate, with changeover made only as construction is completed.

1. Phase 1 involves the construction of a 1 MW proton synchrotron, operating either at 3 GeV and 50 Hz or at 8 GeV and 16.7 Hz, with injection directly from the existing 800 MeV beam from ISIS. The 3 GeV option would provide beam for a 1 MW spallation neutron source, and in 8 GeV mode the machine could be used for bunch compression tests, studies of a pion target and experiments with a prototype muon front-end system, all essential ingredients of a neutrino factory design.

2. Phase 2 sees development of the new synchrotron to 2.5 MW with a new injector comprising a 180 MeV linac and two 1.2 GeV, 50 Hz booster synchrotrons, replacing the ISIS linac and synchrotron.

3. In Phase 3, a second high energy synchrotron would be added, stacked above the first, with both operating at 25 Hz. An energy of ~3 GeV would be used for an enhanced neutron source and acceleration would be to 6 GeV for a 5 MW neutrino factor driver.

PHASE 1: THE NEW SYNCHROTRON

The ISIS synchrotron has a mean radius of 26 m and accelerates two bunches at harmonic number h=2 to an energy of 800 MeV. Installation of a dual harmonic RF system is expected to improve the bunching factor so that pulses of 3.75×10^{13} protons can be accelerated onto the target at a frequency of 50 Hz. Beyond this, the machine is space-charge limited and the simplest way to increase the beam power is through an increase in energy. Bucket to bucket transfer is therefore proposed into a new synchrotron with mean radius 78 m (three times that of ISIS) with h=6, followed by an (approximately) fourfold increase in energy to the MW level of beam power. Since only one third of the circumference is occupied by beam, the peak current remains the same, the average current is reduced by a factor of three, space charge forces are unaltered but, owing to the increased radius, the betatron tune shifts and spreads are trebled. These are allowed for in the design. Similarly

0-7803-7738-9/03/$17.00 © 2003 IEEE

beam scrapers are included in the injection line for assumed (unnormalised) transverse input emittances of 19 π mm.mr (rms), 95 π mm.mr (99%) and 125 π mm.mr (100%).

The synchrotron lattice is based on a racetrack design with superperiodicity two and integer Q_h in the arcs in order to obtain dispersion-free straight sections. Adequate space must be provided for the main and trim magnets and the RF systems, and the straight sections must be sufficiently long to meet the demands of injection, extraction and beam loss collection. Analysis of various models [1] has identified the best option as having 22 cells per superperiod (15 in the arcs, 7 in the straights) with phase shifts per cell close to 96° horizontally and 60° vertically. Arc and betatron tunes are then $(Q_h, Q_v) = (4.0, 2.5)$ and (11.7,7.2) respectively. Trim quadrupoles can be used to raise Q_v so as to avoid the resonances $2Q_v = 14$ and $4Q_v = 28$ under space charge conditions. Chromaticity correcting sextupoles have been evaluated and have been found to give a large dynamic aperture corresponding to a normalised emittance of about 600 π mm.mr. Sector

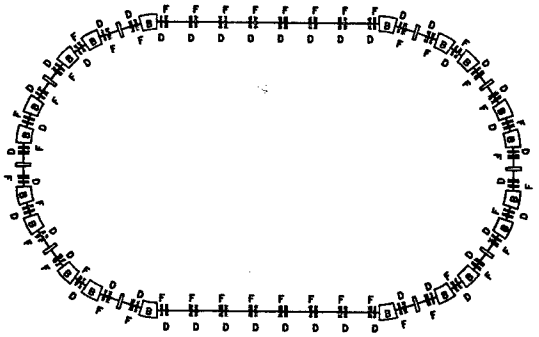


Figure 1: 8 GeV ISIS upgrade synchrotron

dipoles, 5.97 m in length, are preferred to parallel edge units to avoid ripples in the vertical β-function (*c.f.* [2]). Short (1.08 m) central dipoles are included to limit the field to $B \sim 1.44$ T at 8 GeV and assist with dispersion control. The main quadrupoles have field gradients $\lesssim 9.8$ T/m at top energy. The overall dimensions of the lattice, which is shown in Figure 1, are 184 m horizontally × 107 m vertically. The optical parameters are shown in Figure 2.

The accelerating cycle uses a magnetic dipole field of the form

$$B(t) = B_0 - B_1 \cos 2\pi ft + B_2 \sin 4\pi ft.$$

Choosing the higher harmonic amplitude $B_2 = B_1/4\sqrt{2}$ minimises the maximum value of $\dot{B}$ during the cycle and studies show that this leads to a reduction in total RF voltage, $\hat{V}$, in the ring by about 30%. Operation at $f = 50$ Hz, taking the full ISIS pulse from 0.8 to 3 GeV in just under 12 ms, requires $B_0 = 0.4276$ T, $B_1 = 0.1810$ T and $\hat{V} \sim 570$ kV. Parameters for the cycle are listed in Table 1 and some results from longitudinal simulations are shown

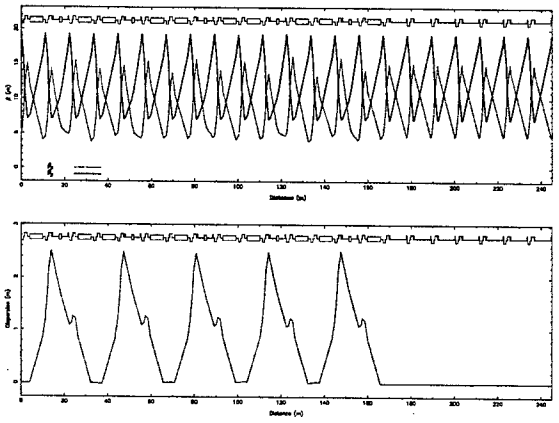


Figure 2: 8 GeV synchrotron optical parameters

in Figure 3. The input beam in these calculations has been taken from ISIS modelling using the dual harmonic RF system currently being implemented and detailed in [3]. The final bunches are 71.5 ns in duration with a momentum spread of $\pm 3 \times 10^{-3}$. In this mode of operation, the

Table 1: Acceleration cycle to 3 GeV

Time (ms)	B (T)	$\dot{B}$	Energy (GeV)	Volts (kV)
-0.95	0.237	0.0	0.8	86.6
0.0	0.247	20.10	0.85	422.4
2.0	0.312	39.63	1.21	571.1
5.0	0.428	36.75	1.87	495.2
7.0	0.504	39.78	2.31	516.3
9.0	0.581	33.83	2.77	432.5
10.95	0.619	0.0	3.0	130.0

machine would be used as a source of spallation neutrons. However, the possibility exists of operating at $f = 16.7$ Hz and accelerating only one pulse in three from ISIS (the others being discarded) to 8 GeV over 30 ms. The aim would be experimental tests of bunch compression to ~1 ns (rms), which is one of the requirements of a proton driver for a neutrino factory. Pion target tests could also be undertaken along with investigations of a prototype pion decay/muon capture channel.

PHASE 2: THE NEW INJECTOR

In Phase 2, the synchrotron would be upgraded to deliver 2.5 MW of beam power, and a new injector would be developed. ISIS as we know it today would be decommissioned. The dual role of a neutron facility with applications to neutrino factory development would be maintained.

The injector would comprise a 180 MeV H^- linac feeding two 1.2 GeV, 50 Hz booster synchrotrons. The choice

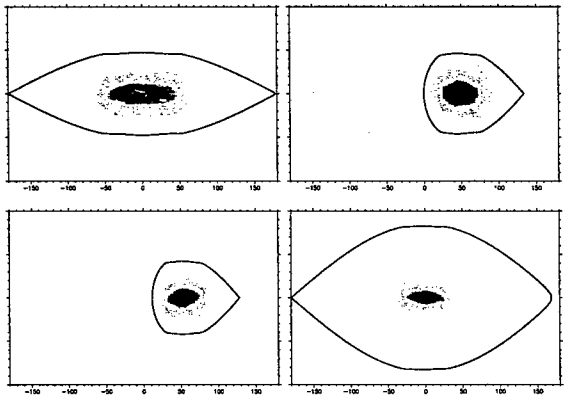


Figure 3: Longitudinal phase space simulation of acceleration to 3 GeV for ISIS2 as a spallation neutron source.

of a low energy linac is based on the need for a small longitudinal emittance (~1 eV.s) to facilitate final bunch compression [4]. The linac is an extension of the design developed for the ESS [5] and comprises a 60 mA H^- ion source, a 280 MHz RFQ, a 2.5 MeV fast beam chopper and a drift tube linac. Beam chopping is necessary to ensure very low levels of particle loss at ring injection and facilitate clean extraction. For both the new linac and ESS, chopping is achieved by deflecting 30% of the train of micro-bunches to a water-cooled collector by means of an electric field. The field has to rise in the inter-bunch gap, which, being of the order of 2 ns, presents severe technological difficulties. A novel two-stage chopper design has been chosen in which two or three microbunches are initially deflected to a collector with voltages $\sim \pm 2$ kV, so creating a larger gap and easing the rise-time requirements for the much stronger deflection of the remaining beam. A prototype is in the early stages of construction and the design is described in [6].

The transfer line to the rings contains a 180° achromatic arc with both positive and negative bends to create a high normalised dispersion $D/\sqrt{\beta_h}$ for momentum collimation within a relatively compact space. Horizontal and vertical betatron collimation will be included, along with momentum ramping cavities for injection painting.

The 1.2 GeV synchrotrons have mean radius 39 m (half the radius of the main synchrotron) and three bunches of protons would be accumulated in each. The rings would be filled one after the other, and all six bunches would then be transferred to the main ring for final acceleration. Using booster synchrotrons allows the task of accumulating the high intensity proton beam to be separated from the NF final compression, which is carried out in the main ring and is addressed with altogether different lattice requirements. H^- injection into the booster rings is by charge exchange through a carbon, or possibly aluminium oxide, stripping foil at a point in the latttice where the normalised dispersion is $\sim$ 1.6. This allows simultaneous longitudinal and horizontal transverse phase space painting in order to help reduce space charge effects. Longitudinal injection will start into a decelerating bucket and end in an accelerating bucket, with the voltages carefully controlled throughout the cycle to maintain losses at the 10^{-4} level. The principles for these rings are similar to those described in [7].

For a compact site layout, the booster synchrotrons could be stacked one above the other and would ideally fit inside the main synchrotron.

PHASE 3: ADDITION OF A SECOND SYNCHROTRON

The final phase of development would see the addition of a second main synchrotron, stacked vertically above the ring built in Phase I, and operating at 25 Hz. The two booster synchrotrons would be filled one immediately after the other, each with 3 bunches of $\sim 1.7 \times 10^{13}$ protons at 50 Hz. Extraction from the two rings needs to be at the same energy, so would be on the falling edge of the B-field from the first ring and the rising edge in the second. All six bunches would be transferred to one of the main synchrotrons; the process would then be repeated to fill the second. After acceleration, extraction would take place on alternate cycles so as to recover the 50 Hz frequency at the target. Of several possible options, a top energy of $\sim$ 3 GeV could be used for a spallation neutron source; at 6 GeV, bunch compression could be carried out for a 5 MW NF proton driver; or one could use the output from each ring for multiple purposes, one ring for neutrino studies, the other for neutrons, for example.

REFERENCES

[1] G.H.Rees: "Lattices for 8 and 30 GeV Proton Drivers." Proceedings of the Neutrino Factory Workshop, NUFACT'02, London, June 2002.

[2] G.W. Foster, W. Chou and E. Malamud (ed): "Proton Driver Study II." Fermilab-TM-2169, May 2002.

[3] C.R. Prior: "Study of Dual Harmonic Acceleration in ISIS." Proceedings of XIIth International Collaboration on Advanced Neutron Sources, ICANS-XII, Abingdon, UK, May 1993.

[4] C.R. Prior and G.H. Rees: "RAL Proton Driver Studies for a Neutrino Factory." Proceedings of the Neutrino Factory Workshop, NUFACT'00, Monterey, California, June 2000.

[5] ESS Accelerator Team: "The ESS Accelerator and Beam Lines with the 280/560 MHz Linac." ESS-01-1A, December 2001.

[6] M.A. Clarke-Gayther: "A fast chopper for the ESS 2.5 MeV beam transport line." Proceedings of the 8th European Particle Accelerator Conference, EPAC'02, Paris, June 2002.

[7] C.R. Prior and G.H. Rees: "Synchrotron-based Proton Drivers for a Neutrino Factory." Proceedings of the 7th European Particle Accelerator Conference, EPAC'00, Vienna, June 2000.

IMPROVEMENTS FOR THE THIRD GENERATION PLASMA WAKEFIELD EXPERIMENT E-164 AT SLAC

C. D. Barnes†, C. O'Connell, F-J. Decker, P. Emma, M. J. Hogan, P. Iverson, P. Krejcik, R. H. Siemann, D. Walz, SLAC, Stanford, CA 94309, USA

B. Blue, C. E. Clayton, C. Huang, D. Johnson, C. Joshi, K. A. Marsh, W. B. Mori, UCLA, Los Angeles, CA, 90095, USA

S. Deng, T. Katsouleas, P. Muggli, E. Oz, USC, Los Angeles, CA 90089, USA

Abstract

The E-164 experiment at the Stanford Linear Accelerator Center is the third in a series investigating Plasma Wakefield Acceleration where the wake is driven by electron bunches. A collaboration between SLAC, UCLA and USC, E-164 has up to $2x10^{10}$ electrons at 28.5GeV in 100 micron long bunches. These bunches enter a 30cm long Lithium plasma with density of $6x10^{15}$ electrons/cm^3, where the transfer of energy from the head of the bunch to the tail takes place. In addition to acceleration, strong focusing, refraction of the electron beam and "betatron X-ray" production are all investigated. E-164 builds on related prior experiments, and its apparatus has evolved considerably. A third Optical Transition Radiator has been added for real time Twiss Parameter measurements which include the effects of scattering. The plasma cell is moved to the focus of the Final Focus Test Beam facility in order to increase bunch electron density. Spectrometry is extended with an upstream chicane in a dispersive region to produce synchrotron X-rays. Performance of these improvements and status of the experiment are discussed.

INTRODUCTION

In the last few years, a series of experiments have been performed at SLAC demonstrating significant energy gain by particles traversing a plasma. In these experiments, known as E-157 and E-162, a single electron or positron bunch both excites the plasma wake and provides the witness particles to observe the large accelerating fields of order 150 MV/m [1]. E-164 will increase these gradients with shorter and more intense electron beams in dense plasmas. The new regime of energy gain requires several changes to the experimental setup and diagnostics, as discussed below.

ELECTRON BEAM

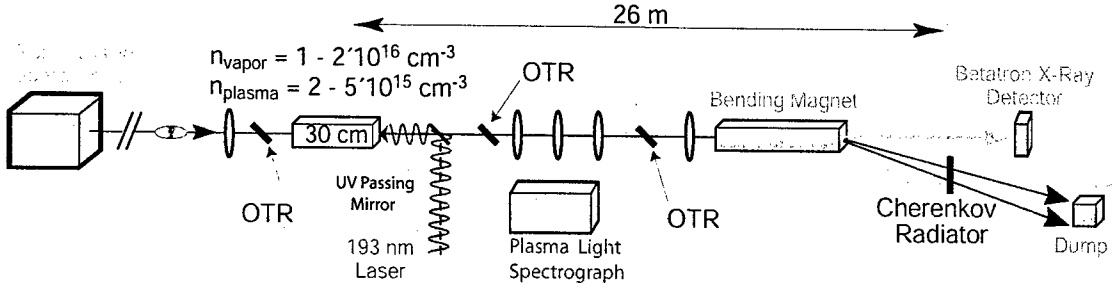
Move of Experimental Setup to IP0

Since the E-157 experiment, the plasma interaction region has been moved to IP0 of the FFTB tunnel at the end of the SLAC linac. This enables the plasma cell to be closer to final quadrupoles and permits smaller spot sizes to be achieved at the plasma entrance. We currently have spot sizes of 20 by 20 microns at the entrance to our plasma cell. The greater electron density in the beam allows the creation of a clean wake in our much denser plasma. In such dense plasma wakes, intense accelerating fields are created. We expect to produce gradients over distances of approximately 30cm that exceed several GeV/meter.

Electron Optics Setup

To verify our small spot sizes, during setup we insert two Optical Transition Radiator (OTR) foils at the locations where the plasma entrance and exit planes will subsequently be. The foils are 25 micron thick Titanium with an optical quality finish on the observed surface. Titanium is resistant to beam damage, but we still observe occasional perforation, and then must move the foil relative to the beam.

These two OTR foils are additionally necessary because, as discussed below, we use an imaging spectrometer to observe the energy spread induced in our electron bunches. Setup of the spectrometer optics to



0-7803-7738-9/03/$17.00 © 2003 IEEE

guarantee an imaging condition requires direct observation of beam spot sizes at the locations for the plasma entrance and exit. When the optics setup is complete, the foils are removed and the plasma oven placed in the beam at the same location.

Single Shot Twiss Parameter Determination

During normal experimental running, we have three OTR foils which can be inserted to help characterize the electron beam. As shown in Figure 1, there is a foil before the plasma cell, one immediately after, and a third foil downstream of a series of quadrupoles. These locations are chosen to have unique betatron phase.

Using MATLAB, we model beam transport including scattering. This code allows single shot determination of the beam Twiss parameters when the plasma is turned off.

The second OTR foil is additionally useful, because it provides a snapshot of the electrons shortly downstream of the plasma cell. As observed in previous experiments at SLAC, [2] we expect a time dependent focusing force on the electron bunch: the plasma wake evolves for various longitudinal positions in the bunch. We believe that the large faint halo in Figure 2 corresponds to the strongly overfocused tail of the electron bunch, while the majority of the electrons are only modestly focused.

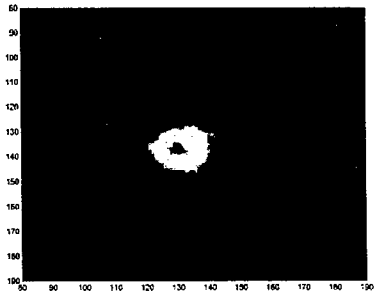


Figure 2: Second OTR Image of Beam

PLASMA SOURCE

Lithium Oven

As shown in Figure 3, the first phase of E164 uses a 30cm long Lithium oven operating at over 800 degrees Celsius with a Lithium vapor pressure of 1 to 3 torr. This temperature and pressure corresponds to a maximum Lithium vapor density of $5x10^{16}$ per cubic centimeter.

Temperature differentials drive a convection cycle in the Lithium to provide a sharp density profile cutoff as the hot vapor encounters the cold Helium buffer gas. [3]

To ionize our Lithium vapor, we use a 100mJ Ultraviolet laser at 193nm, which has good mode quality. This laser enables photoionization of approximately 20% of the lithium atoms illuminated by the laser.

However, preliminary results from the first half of E164 indicate substantial tunnel ionization of the Lithium, in addition to the expected photoionization. This arises because the intense electric fields associated with our tightly focused electron beam can strip the outermost electron from the Lithium atoms. A problem with tunnel ionization is that for our beam parameters, it occurs near the middle of the bunch, when the fields are the largest.

To create a plasma wake useful for acceleration, the gas must already be ionized before the majority of the electron bunch particles arrive to drive the wake. For the second run of E-164, we are considering the use of Cesium, which ionizes more readily. This allows rapid ionization before the main body of the electron bunch arrives. Dispensing with the ionization laser would greatly simplify alignment, but because tunnel ionization ionizes all Lithium atoms in a volume, we cannot change ion density except by adjusting the vapor density, and that is a slow process, making some measurements difficult.

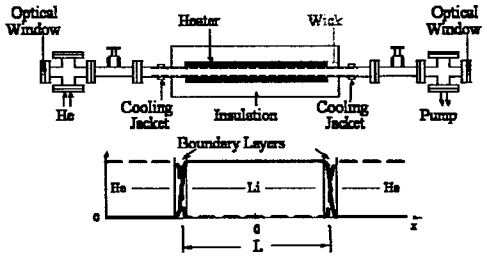


Figure 3: Heat Pipe Oven Layout. L is 30cm.

Plasma Diagnostics

For direct observation of plasma density and plasma decay rate, we use an optical spectrograph to observe the several emission lines of Lithium as the ions recombine.

As discussed above, there appears to be substantial tunnel ionization of the Lithium. We see the Lithium recombination lines when ionizing by the UV laser and also see them under the condition that the laser is turned off, but the electron beam is focused to a tight spot.

Because the plasma acts as a strong lens in X and Y, there is also a possibility that the electron beam will focus to a very small spot inside the plasma. The associated fields of the beam could ionize Lithium a second time, or ionize the Helium buffer gas. Our spectrograph could allow observation of characteristic emission lines in Li^+ and Helium if this effect occurs.

SPECTROMETER

We use an imaging spectrometer which provides a magnified image of the beam as it exits the plasma cell. In the vertical plane, imaging ensures that the spot size is dispersion dominated, giving the best energy resolution.

An aerogel slab approximately 1mm thick is placed at the focal plane of the spectrometer 26 meters downstream of the plasma. The beam produces a bright Cherenkov wake in a cone with opening angle of 7°. Using a standard Nikon 105mm lens, we image a portion of this light cone onto a Princeton Instruments scientific grade CCD camera with 512x512 pixels. This camera digitizes

with 16 bit resolution. The high dynamic range is important, as our acceleration is expected to be seen by a relatively few electrons at the tail of the bunch, and ability to distinguish them is critical.

Dispersion is 10mm at Cherenkov screen and the imaging of the light to the CCD camera used to observe the Cherenkov light is such that the energy resolution is 20MeV per pixel, or 0.07%. A sample spectrometer image is below. Note the large energy spread of 2.5GeV due to strong plasma interaction.

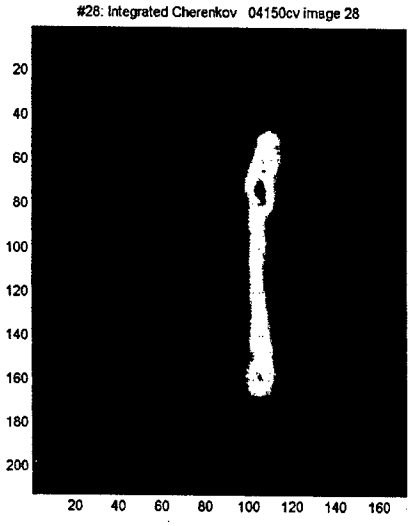


Figure 4: Energy Spectrometer Image

FUTURE ADDITIONS

Synchrotron X-Ray Spectrometer

The short electron bunches used in E-164 mean that the time dependent energy spectrum is impossible to resolve with most techniques. For example, our 150fs bunches cannot be resolved by even the best streak cameras.

To get around this difficulty, we plan to compare the energy spectrum of the beam as it comes into the FFTB with detailed simulations of the linac. Those simulations give full longitudinal phase space, and allow us to infer the bunch profile with confidence.

The main goal is to know the energy spectrum of the bunches before and after the plasma cell for shot-by-shot measurement of energy gain.

Thus for several reasons we desire a non-invasive spectrometer upstream of the plasma cell. There is a region at the beginning of the FFTB with 8cm of dispersion. To do a non-disruptive measurement, we will place a vertical chicane in this dispersive region.

The incoherent synchrotron radiation power produced as the electrons traverse the chicane is in direct proportion to the number of electrons at a given energy, and allows non-invasive measurement of the electron energy spread with expected resolution of 0.2%. This design is adapted from a similar spectrometer at SLAC. [4]

Betatron X-Ray Measurements

The transverse oscillations of the electron beam as it propagates through the strongly focusing plasma lead to intense production by synchrotron radiation of high energy X-Rays. [5]

For E-164 and future experiments, we plan to do spectroscopy on the extremely broadband radiation produced by the electron beam. Theoretical calculations indicate that, for our expected parameters, photons with energies from approximately 100keV to 80MeV will be produced.

There will also be a position-energy correlation in the cone of radiation, so a spectrometer capable of resolving energies at each of a number of positions transverse to the beam is required.

Single photon calorimetry/spectroscopy is well understood, but the extremely intense photon fluxes expected from the synchrotron radiation require special techniques to resolve individual photon energies. Studies of the best setup to achieve this are ongoing, but are expected to use Bragg reflections and surface barrier detectors in conjunction with detectors suited for high energy gamma ray detection such as scintillator crystals connected to photomultiplier tubes.

CONCLUSION

The special requirements of E-164, specifically the dense plasma and very short electron bunches, lead to a need for a number of new diagnostic techniques which are suitable for characterizing the many unusual parameters of the experiment.

Recent and planned improvements are expected to allow the accurate determination of the beam properties in all three dimensions necessary for demonstrating the intense acceleration of our beam in plasma.

ACKNOWLEDGEMENTS

The authors wish to thank Mike Racine and Ron Badger for their help on many time sensitive aspects of hardware production for this experiment, as well as the SLAC linac operators for their patience with our beam containment problems. This work is supported by U.S. DoE Grants No. DE-FG03-92ER40745, No. DE-AC03-76SF00515, No. DE-FG03-98DP00211, and No. DEFG03-92ER40727 as well as NSF Grants No. ECS-9632735, No. DMS-9722121, and No. PHY-00787157.

REFERENCES

[1] P. Muggli *et al.*, Manuscript in preparation.
[2] C. O'Connell *et al.*, Phys. Rev. ST Accel. Beams **5**, 121301 (2002)
[3] C. R. Vidal and J. Cooper, J. Appl. Phys. **40**, 3370 (1969)
[4] J. Seeman *et al.*, SLAC-PUB-3945, (1986)
[5] S. Wang *et al.*, Phys. Rev. Lett. **80**, 13, (2002)

Proceedings of the 2003 Particle Accelerator Conference

A SLAB-SYMMETRIC DIELECTRIC-LOADED STRUCTURE FOR HIGH-GRADIENT ACCELERATION AT THZ*

R. B. Yoder† and J. B. Rosenzweig
Dept. of Physics and Astronomy, UCLA, Los Angeles, CA 90095-1547

Abstract

We present a design for a slab-symmetric accelerating structure to be resonantly excited at terahertz frequencies. The device, consisting of a vacuum gap between dielectric-lined walls, combines the advantages of a slab geometry (including strong suppression of transverse beam wakefields and low power density) with the existence of a resonant mode having phase synchronism with relativistic electrons. Accelerating fields of hundreds of MeV/m are predicted when the structure is powered by a high-power FIR radiation source in development at UCLA. Simulation of the structure fields is described and compared with theory, and an experimental program is discussed.

INTRODUCTION

In all laser-based acceleration concepts, the large transverse fields of a laser pulse must be converted to useful longitudinal fields, a problem solved in the microwave regime by coupling radiation into resonant structures. While this acceleration method is venerable, conceptually simple, and capable of generating very large axial fields, the well-known physical and technical limitations of scaling such structures to near-optical wavelengths have strengthened the cases for plasma-based and far-field optical accelerators, despite the considerable challenges of these latter approaches. However, many of the harmful effects produced by the presence of field-shaping boundaries near the accelerating particles are mitigated if the system is allowed to become very large in one transverse dimension, in effect producing a two-dimensional device. This paper extends and refines previous work on laser-based acceleration in a "slab-symmetric" device, and introduces a new design for a structure driven resonantly at 340 μm, which is to be experimentally investigated at UCLA using a novel high-power terahertz source.

The case for slab structures rests on the inherent translational symmetry of their geometry, which forces the fields of a speed-of-light wave to be invariant in the small transverse dimension; this leads in turn to the suppression of transverse (dipole-mode) wakefields, which otherwise would dominate the beam-structure interaction. A slab-beam can then contain very high charge, acting in effect as a large number of parallel beamlines. The use of dielectric materials (which can withstand surface fields of a few GV/m for pulses of a few picoseconds) [1], coupled with the relatively low Q (100–1000) of a planar structure, allow the production of large gradients (hundreds of MeV/m) before breakdown limitations are reached.

Structure Overview

Fundamentally, our device consists of a pair of parallel dielectric planes, separated by a narrow vacuum gap and bounded above and below by a thin conductive layer. Periodic slots in the conductor provide a means for coupling radiation into the gap and also enforce longitudinal periodicity in the structure fields. When the correct resonant geometry is achieved, the mode pattern is dominated by a longitudinal standing wave having a phase velocity exactly equal to the speed of light. The concept is illustrated in Fig. 1.

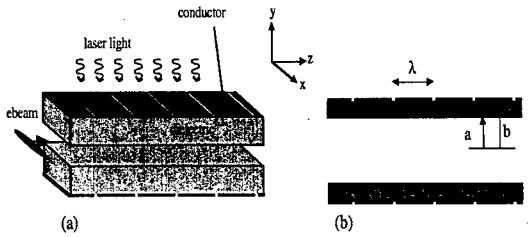


Figure 1: (a) Schematic drawing of the slab-symmetric structure; (b) a cross-section in x, showing the parameter definitions. The 'infinite' dimension (x) extends into the page; electron beam propagation is in $+z$, with radiation (also polarized in z) impinging on the structure from the $+y$ direction.

A number of versions of this concept have been proposed [2, 3, 4], each of which took a slightly different approach to generating the correct longitudinal periodicity in the structure properties. Periodic slots, as used here, represent the optimum choice for coupling power preferentially into the accelerating mode while satisfying the speed-of-light resonance condition. Numerical modeling of the structure, discussed below, is used to optimize the coupling slots for best performance.

Structure Modes

Mode analyses for this class of slab-symmetric structures have been outlined in several recent papers [3, 5]; the solutions hold for any periodically-modulated structure, regardless of the mechanism used for the modulation. We summarize the results briefly here for the fundamental

* Supported by US DoE grant no. DE-FG03-92ER40693
† yoder@stout.physics.ucla.edu

0-7803-7738-9/03/$17.00 © 2003 IEEE

speed-of-light mode, which is the one of interest for acceleration. Using the axes and structure parameters defined in Fig. 1, and assuming initially that the structure is truly infinite in the x direction, we obtain an axial electric field

$$E_z(y,z) = \left\{ \begin{array}{c} E_0 \\ AE_0 \cos[\sqrt{\epsilon-1}\,k_z(b-y)] \end{array} \right\} \cos(k_z z) e^{i\omega t} \quad (1)$$

where the upper line holds within the vacuum gap ($|y| < a$) and the lower within the dielectric ($a < |y| < b$), and where $A = \csc[\sqrt{\epsilon-1}(b-a)k_z]/\sqrt{\epsilon-1}$. The transverse fields are proportional to y and zero on axis. Imposition of boundary conditions at metal and dielectric boundaries gives a resonance condition which specifies allowed values of a, b and ϵ for a given $k_z = 2\pi/\lambda_0$, where λ_0 is the free-space laser wavelength.

The true translational symmetry of the structure is of course broken in any physical device with finite extent. The effect of a non-infinite structure on the accelerating mode has been addressed in [5], where field variation in the x direction is imposed by the addition of conducting walls at $x = \pm L$, where $L \gg a$. It is shown that the axial field in the gap gains a $\cosh(k_\perp y)$ dependence, but with sufficiently large structure aspect ratio (and hence small wavenumber $k_\perp$), the deviation from flatness of the field can easily be kept below 1%.

Optimized Parameters

Starting from a wavelength of 340 μm, we choose $\epsilon = 3$ (close to values for e.g. silicon) and find that the lowest resonance occurs for $a = 115$ μm, $b = 145$ μm, or in other words a vacuum gap of full width 230 μm, bounded by a dielectric layer 30 μm thick. To optimize the coupling of external power into the structure, we can adjust the width of the coupling slots as well as the thickness, or depth, of the conducting layer itself. One must bear in mind that since the drive radiation is not cut off in the coupling slots (they are very long in the x direction), the slots are in effect waveguide sections which can perturb the resonance significantly. The high-Q results presented below are obtained for a slot of width 5 μm and 69 μm deep.

NUMERICAL RESULTS

Field Modeling

Extensive modeling of the ideal slab geometry has been carried out using a two-dimensional finite difference solver to verify the resonance condition and to optimize the coupling of external fields into the structure. In this code, a single structure period is illuminated by a plane wave, with symmetry enforced at the midplane; periodic boundary conditions are used in z. Typical output is shown in Fig. 2. Fig. 3 shows the field within the gap in more detail, where it is clear that the accelerating field is nearly invariant in y, as predicted by (1). The transverse field is zero at the location of the peak accelerating field; see Fig. 3. There is clearly a very strong field in the coupling slot itself; however, in this design the slot acts as a quarter-wavelength transmission line, causing the field to fall to zero at the inner aperture and hardly perturb the accelerating mode. The large slot field indicates that these slots can cause a substantial change to the structure resonant frequency; it also limits the amount of power that can be introduced. Eliminating the quarter-wave condition on the slot length, while mistuning the structure to compensate for the frequency shift, may overcome this problem.

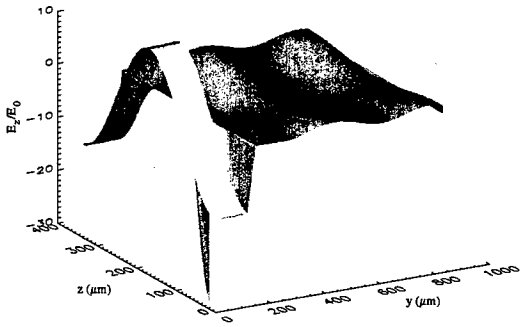


Figure 2: Surface plot showing time snapshot of axial fields, normalized to the amplitude of the incident wave. The field along the z axis shows the accelerating mode, with a field spike in the coupling slot and a plane wave in the space above the structure.

The growth of the accelerating fields in time is shown in Fig. 4, where we see that after a relatively long fill time (on the order of 500 ps) the accelerating field amplitude within the structure reaches a value near 15 times that of the incident wave. The same figure compares the amplitude of the accelerating mode with that of its most important competitor, the so-called 'zero-mode', with fields that are constant in z. As the figure shows, the zero-mode component of the fields remains less than 1% of the accelerating component. The fill time of 600 ps suggests a loaded $Q = \omega\tau$ for the structure on the order of 3000, a relatively high value. For experiments driven with pulsed lasers, it will be important to decrease this fill time while maintaining a reasonable shunt impedance. Nevertheless, the design exhibited here would produce an accelerating gradient of 400 MeV/m when illuminated at 100 MW/cm^2.

Wakefield Stability

The advantageous transverse wakefield properties of the slab-symmetric geometry are one of the reasons for interest in these structures, and our assertion that damaging transverse wakefields vanish for very wide beams has been verified by analysis and simulation. Ref. [5] contains an analytical calculation of the wake potentials in a slab-symmetric structure, and OOPIC simulations of particle wakes in this 340 μm structure were presented in an earlier paper [7]. In both cases, the transverse electric and magnetic forces in

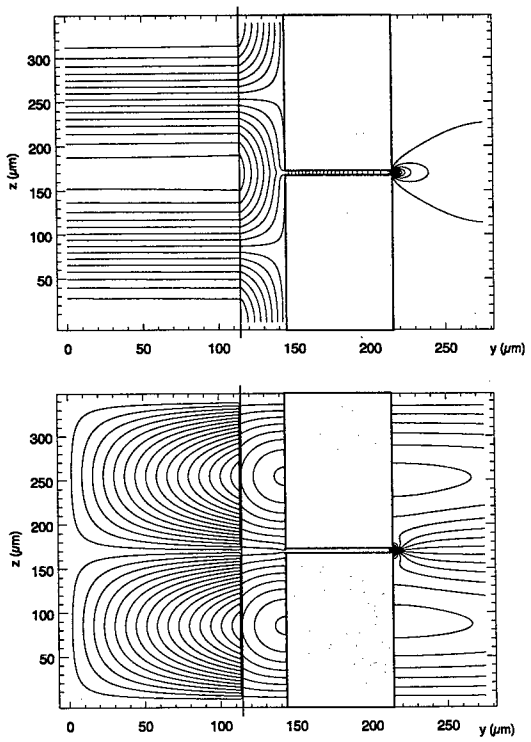


Figure 3: Contour plots showing E_z (above) and E_y (below) over one structure period. The shaded area represents the conductor (with coupling slot), and the dark line shows the dielectric/vacuum boundary.

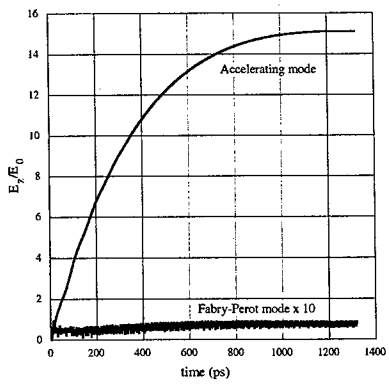


Figure 4: Amplitude of axial electric fields within the vacuum gap vs. time, normalized to amplitude of the incoming wave. The accelerating mode has longitudinal periodicity; the non-accelerating Fabry-Perot mode (multiplied by 10 here) does not.

the vacuum gap canceled within machine precision.

EXPERIMENT

The geometry of the experiment which is planned for the UCLA Neptune facility is dictated by available radiation wavelengths. As mentioned earlier, the accelerator is to be driven with a new terahertz source under development at UCLA. The large resonant vacuum gap in this wavelength range—more than 0.2 mm—makes it feasible to inject the 11–14 MeV beam from the Neptune photoinjector, with normalized transverse emittance in the range of 6–10 π mm mrad, into the structure successfully.

We expect to obtain multimegawatt laser radiation at 340 μm using a difference frequency generation scheme: two frequencies from the Neptune terawatt CO_2 laser will be mixed at high power in a gallium arsenide crystal, with conversion efficiency into the difference frequency near 1%.[6] The two input frequencies, as well as the output radiation, are non-collinear in order to maintain synchronism over a relatively large (several centimeter) interaction length. Output power levels in excess of 100 MW are projected; experimental work is currently in progress.

Diagnosis of the structure can be carried out through cold testing as well as by acceleration experiments and the possible detection of wake radiation. Transmitted light from the lower coupling slots, as shown in Fig. 1, can be used to measure the filling of the structure. Since the design is easily scaleable to other wavelength regimes, it may also be useful to evaluate prototype structures using conventional laser radiation, e.g. at 10.6 μm.

CONCLUSION

We have described a slab-symmetric dielectric-loaded structure which serves as a resonant laser-driven accelerator with advantageous transverse stability for high-charge beams. When such an accelerator is powered by a submillimeter-wave source at 340 μm, the structure dimensions become ample for acceleration of a slab electron beam with achievable transverse size, and with realistic input power levels we calculate acceleration gradients of 400 MeV/m. Experimental investigation of these structures, including cold testing in several wavelength regimes, is planned at the UCLA Neptune facility.

REFERENCES

[1] A. C. Tien, *et al.*, *Phys. Rev. Lett.* **82**, 3883 (1999).

[2] J. Rosenzweig, A. Murokh and C. Pellegrini, *Phys. Rev. Lett.* **74**, 2467 (1995).

[3] J. B. Rosenzweig and P. V. Schoessow, in *Advanced Accelerator Concepts, Eighth Workshop*, 1998, pp. 693–700.

[4] P. V. Schoessow and J. B. Rosenzweig, *Proceedings of the 1999 Particle Accelerator Conference*, pp. 3624–3626.

[5] A. Tremaine, J. Rosenzweig and P. Schoessow, *Phys. Rev. E* **56**, 7204 (1997).

[6] S. Tochitsky, private communication.

[7] R. B. Yoder and J. B. Rosenzweig, in *Advanced Accelerator Concepts, Tenth Workshop*, 2002, pp. 331–340.

A LIE TRANSFORM PERTURBATION SCHEME FOR HAMILTONIAN AVERAGING IN SELF CONSISTENT SYSTEMS

Kiran G. Sonnad and John R. Cary,
CIPS and Department of Physics, University of Colorado, Boulder

Abstract

A periodic focusing system is reduced to an equivalent continuous focusing one for a beam with space charge by averaging over the lattice oscillations. The Lie transform perturbation method is used to canonically transform the laboratory phase space variables to slowly oscillating variables. A similar averaging over the lattice period was performed by R.C. Davidson, H. Qin and P.J. Channell [Phys Rev ST 2, 074401 (1999)] using the Poincare-Von Ziepel perturbation method. The Lie transform method offers certain advantages in that it retains the original form of the Hamiltonian before beginning the process of canonical transformation to a slowly oscillating coordinate frame. On the other hand, the Poincare-Von Ziepel method requires one to make a Taylor expansion of the Hamiltonian in terms of the as yet undetermined expansion terms of the transformed phase space variables. The Lie transform method avoids such a Taylor expansion and so the formulation is less tedious. It will be demonstrated that performing the reverse transformation to the original phase space variables is also straight forward in the Lie transform method.

INTRODUCTION

In many applications of dynamical systems, one is primarily interested in the long time behavior compared to certain fast time scales over which the system evolves. Hamiltonian averaging techniques have been effective in obtaining a set of equations that contain only long-time processes and retain the effects produced by the short time scale processes only up to a desired approximation. The standard procedure is to perform a perturbation canonical transformation to a slowly oscillating reference frame. The Lie Transform perturbation method is more convenient for such a procedure when compared to methods based on the Hamilton-Jacobi transformation. A Lie transformation can be expressed in Poisson bracket notation as an analogy to Hamilton's equation with respect to a continuously varying parameter representing "Time" and a Lie generating function representing the "Hamiltonian". This enables one to develop the whole formulation in Poisson brackets form making inverse transformations at every intermediate stage unnecessary because the results of Poisson brackets are invariant under canonical transformations.

TRANSFORMATION EQUATIONS IN TERMS OF PERTURBATION EXPANSIONS

A Lie Transformation is defined in terms of a Lie generating function w which satisfies the Poisson bracket relation,

$$\frac{dZ}{d\epsilon} = \{Z(z),\ w(z,t,\epsilon)\} \tag{1}$$

This describes a canonical transformation from the phase space vectors z to Z. The transformed variable, Z varies continuously with respect to the time like parameter ϵ with w being analogous to the Hamiltonian. The symplectic structure of the transformation guarantees that the transformation is canonical for all values of ϵ. A Lie operator is defined by $L = \{w,\ \}$. A transformation operator T transforms any function such that $Tf(z,t) = f(Z(z,t),t)$. T is equivalent to the "evolution" operator with respect to the "time" ϵ. For the identity function, this would simply be, $Tz = Z(z,t)$.

To obtain explicit equations for each perturbation term, every physical quantity and operator is expressed as a power series in ϵ known as the Deprit power series [3]. This would be $h(z,t,\epsilon) = \sum_{n=0}^{\infty} \epsilon^n h_n(z,t)$, $H(z,t,\epsilon) = \sum_{n=0}^{\infty} \epsilon^n H_n(z,t)$, $T(t,\epsilon) = \sum_{n=0}^{\infty} \epsilon^n T_n(t)$, $L(w) = \sum_{n=0}^{\infty} \epsilon^n L_n$, $w(z,t,\epsilon) = \sum_{n=0}^{\infty} \epsilon^n w_{n+1}(z,t)$. Where, h represents the original Hamiltonian and H represents the transformed Hamiltonian. Using these expansions, equations for each order of ϵ can be derived to determine the transformed Hamiltonian H with respect to w and h, and the transformation operator T with respect to the operator L. A rigorous derivation of these relationships can be found in Ref. [4] and a more brief one in Ref. [5]. These derivations are based on the work by Dewar [2]. In principle, the relationships can be derived up to any order. We give them here up to third order. In order to perform a time averaging, we need to set $h_0 = 0$ [7]. Using this, equations to determine the transformed Hamiltonian up to third order are,

$$H_0 = h_0 = 0 \tag{2}$$

$$\frac{\partial w_1}{\partial t} = H_1 - h_1 \tag{3}$$

$$\frac{\partial w_2}{\partial t} = 2(H_2 - h_2) - L_1(H_1 + h_1) \tag{4}$$

$$\frac{\partial w_3}{\partial t} = 3(H_3 - h_3) - L_1(H_2 + h_2) - L_2(H_1 + \frac{1}{2}h_1) - \frac{1}{2}L_1^2(h_1) \tag{5}$$

0-7803-7738-9/03/$17.00 © 2003 IEEE

The expansion terms of the inverse transformation operator T^{-1} are given below up to third order. They are,

$$T_0^{-1} = I \tag{6}$$

$$T_1^{-1} = L_1 \tag{7}$$

$$T_2^{-1} = \frac{1}{2}L_2 + \frac{1}{2}L_1^2 \tag{8}$$

$$T_3^{-1} = \frac{1}{3}L_3 + \frac{1}{6}L_1L_2 + \frac{1}{3}L_2L_1 + \frac{1}{6}L_1^3 \tag{9}$$

APPLICATION TO AN INTENSE BEAM IN A LINEAR FOCUSING FIELD

The analysis in this section considers a thin, long nonneutral beam traveling with a constant axial velocity. The charged particles are subjected to a focusing force of the form $-[\kappa_x(s)x\hat{\mathbf{e}_x} + \kappa_y(s)y\hat{\mathbf{e}_y}]$. The axial distance s, is equivalent to time since the beam is assumed to be propagating at constant velocity. In normalized units (see for example Ref. [6]), the Hamiltonian for such a system in the transverse phase space (x, y, x', y') is given by

$$h = \frac{1}{2}(x'^2 + y'^2) + \frac{1}{2}\kappa_x(s)x^2 + \frac{1}{2}\kappa_y(s)y^2 + \psi(x, y, s) \tag{10}$$

The oscillation of the lattice function $\kappa(s)$ is considered to be much faster than the oscillation of the space charge potential $\psi(x, y, s)$. The aim here is to apply the perturbation theory of the previous section to average over the lattice oscillations. As mentioned in the previous section, we to set $h_0 = 0$. The Hamiltonian h is considered to be of the same order as the parameter ϵ. So, we have $h_1 = h$, $h_2 = 0$, and $h_3 = 0$. For this application of a charged particle beam, where the aim is to find an equivalent continuously focusing system, it is sufficient to carry out the procedure up to third order [1, 8].

The given Hamiltonian is now applied to Eqs. (2 - 5). In which everything is expressed in terms of the transformed variables. Equation (2) gives $H_0 = 0$, and Eq. (3) gives

$$\frac{\partial w_1}{\partial s} = H_1 - \frac{1}{2}(X'^2 + Y'^2) - \frac{1}{2}\kappa_x(s)X^2 - \frac{1}{2}\kappa_y(s)Y^2 - \psi(X, Y, s) \tag{11}$$

There are two unknown expressions in this equation. They are, H_1 and w_1 where H_1 needs to be chosen such that it retains only the slowly oscillating terms and cancels terms with a nonzero value when averaged over fast oscillations. This ensures that w_1 averages to zero over fast oscillations which is required in order for the perturbation scheme to be secular [4]. So,

$$H_1 = \frac{1}{2}(X'^2+Y'^2)+\frac{1}{2}\langle\kappa_x\rangle X^2+\frac{1}{2}\langle\kappa_y\rangle Y^2+\psi(X, Y, s), \tag{12}$$

where the angle brackets represent an average over a lattice period S. That is,

$$\langle ... \rangle = \frac{1}{S}\int_0^S ds(...) \tag{13}$$

Hereafter we assume that $\langle\kappa_{x,y}\rangle = 0$ which is true for most practical applications. Since the expansion terms of w appear in the form of derivatives in the transformation equations, it is sufficient to evaluate the indefinite integral with respect to s. Doing this for Eq. (11) gives,

$$w_1 = -\frac{1}{2}\kappa_x^{\mathrm{I}}(s)X^2 - \frac{1}{2}\kappa_y^{\mathrm{I}}(s)Y^2 \tag{14}$$

The Roman numerical superscripts represent an indefinite integral over s. Similarly, a superscript "II" will indicate a double integration over s and so on.

Moving now to the second order perturbation equation which is Eq. (4), we get

$$\frac{\partial w_2}{\partial s} = 2H_2 + 2\kappa_x^{\mathrm{I}}(s)XX' + 2\kappa_y^{\mathrm{I}}(s)YY' \tag{15}$$

Since both the terms on the right side are fast oscillating terms and average to zero, we need to set $H_2 = 0$. Integrating with respect to s yields

$$w_2 = 2(\kappa_x^{\mathrm{II}}(s)XX' + \kappa_y^{\mathrm{II}}(s)YY') \tag{16}$$

We now move to the third order equation which gives,

$$\begin{aligned}\frac{\partial w_3}{\partial s} = {} & 3(\kappa_x^{\mathrm{II}}(s)X\frac{\partial}{\partial X} + \kappa_y^{\mathrm{II}}(s)Y\frac{\partial}{\partial Y})\psi(X, Y, s) \\ & +3H_3 - 3\kappa_x^{\mathrm{II}}(s)X'^2 - 3\kappa_y^{\mathrm{II}}(s)Y'^2 \\ & +2\kappa_x^{\mathrm{II}}(s)\kappa_x(s)X^2 + 2\kappa_y^{\mathrm{II}}(s)\kappa_y(s)Y^2 \\ & -\frac{1}{2}(\kappa_x^{\mathrm{I}}(s))^2X^2 - \frac{1}{2}(\kappa_y^{\mathrm{I}}(s))^2Y^2\end{aligned} \tag{17}$$

Once again, H_3 needs to be chosen so that it cancels terms with nonzero averages over the lattice periods. The second term on the right side of Eq. (17) is a product between slow and fast oscillating terms. Up to the desired order, this product averages to zero over fast oscillations [7].

$$H_3 = \frac{1}{3}\langle\frac{1}{2}(\kappa_x^{\mathrm{I}})^2 - 2\kappa_x^{\mathrm{II}}\kappa_x\rangle X^2 + \frac{1}{3}\langle\frac{1}{2}(\kappa_y^{\mathrm{I}})^2 - 2\kappa_y^{\mathrm{II}}\kappa_y\rangle Y^2 \tag{18}$$

Up to third order, the transformed Hamiltonian given by $H = H_1 + H_2 + H_3$ represents an intense beam with continuous focusing. This can be expressed as

$$H = \frac{1}{2}(X'^2 + Y'^2) + \frac{1}{2}(\mathcal{K}_X X^2 + \mathcal{K}_Y Y^2) + \psi(X, Y, s) \tag{19}$$

where

$$\mathcal{K}_X = \frac{1}{3}\langle(\kappa_x^{\mathrm{I}})^2 - 4\kappa_x^{\mathrm{II}}\kappa_x\rangle \tag{20}$$

and

$$\mathcal{K}_Y = \frac{1}{3}\langle(\kappa_y^{\mathrm{I}})^2 - 4\kappa_y^{\mathrm{II}}\kappa_y\rangle \tag{21}$$

To determine w_3, we need to integrate Eq. (17). Retaining only terms of third order in ϵ, the integration yields

$$\begin{aligned}w_3 = {} & 3\kappa_x^{\mathrm{III}}(s)X\frac{\partial\psi}{\partial X} + 3\kappa_y^{\mathrm{III}}(s)Y\frac{\partial\psi}{\partial Y} \\ & -3\kappa_x^{\mathrm{III}}(s)X'^2 - 3\kappa_y^{\mathrm{III}}(s)Y'^2\end{aligned} \tag{22}$$

To transform back to the laboratory phase space variables, we make use of the operator T^{-1} given by Eqs.(6 - 9). The transformation will be performed up to third order. We may express the transformation in the form of a perturbation expansion as

$$x = T^{-1}X = X + x_1 + x_2 + ... \quad (23)$$

$$y = T^{-1}Y = Y + y_1 + y_2 + ... \quad (24)$$

$$x' = T^{-1}X' = X' + x'_1 + x'_2 + ... \quad (25)$$

$$y' = T^{-1}Y' = Y' + y'_1 + y'_2 + ... \quad (26)$$

The zeroth order terms X, Y, X', Y' represent the fact that $T_0^{-1} = I$, the identity transformation. The first order terms are obtained by operating T_1^{-1} which, from Eq. (7) is simply the operator L_1. So,

$$x_1 = \{w_1, X\} = 0 \quad (27)$$

$$y_1 = \{w_1, Y\} = 0 \quad (28)$$

$$x'_1 = \{w_1, X'\} = -\kappa_x^{\mathrm{I}}(s)X \quad (29)$$

$$y'_1 = \{w_1, Y'\} = -\kappa_y^{\mathrm{I}}(s)Y \quad (30)$$

Similarly, the second order terms can be got from Eq. (8) by operating T_2^{-1} on (X, X', Y, Y'). These are,

$$x_2 = \frac{1}{2}(L_2 + L_1^2)X = -\kappa_x^{\mathrm{II}}(s)X \quad (31)$$

$$y_2 = \frac{1}{2}(L_2 + L_1^2)Y = -\kappa_x^{\mathrm{II}}(s)X \quad (32)$$

$$x'_2 = \frac{1}{2}(L_2 + L_1^2)X' = \kappa_x^{\mathrm{II}}(s)X' \quad (33)$$

$$y'_2 = \frac{1}{2}(L_2 + L_1^2)Y' = \kappa_y^{\mathrm{II}}(s)Y' \quad (34)$$

The third order terms will be determined by the operator T_3^{-1} given by Eq. (9). This gives,

$$x_3 = 2\kappa_x^{\mathrm{III}}X' \quad (35)$$

$$y_3 = 2\kappa_y^{\mathrm{III}}Y' \quad (36)$$

$$x'_3 = \kappa_x^{\mathrm{III}}\frac{\partial\psi}{\partial X} + \kappa_x^{\mathrm{III}}X\frac{\partial^2\psi}{\partial X^2} \quad (37)$$

$$y'_3 = \kappa_y^{\mathrm{III}}\frac{\partial\psi}{\partial Y} + \kappa_y^{\mathrm{III}}Y\frac{\partial^2\psi}{\partial Y^2} \quad (38)$$

The expressions for w_1, w_2 and w_3 have been made use of in the form of Poisson brackets. They carry the transformed variables when performing an inverse transformation. Since Poisson brackets are canonically invariant, w could carry either variables depending on the operation that is being performed.

In this section, we have reduced a general linear focusing system to a continuous focusing system for an intense beam by canonically transforming to a slowly oscillating reference frame. The equivalent continuous focusing system can offer a variety of advantages. It can be solved more efficiently numerically because it can allow larger time steps. The transformed system can also also have symmetries that can reduce its dimensionality, for example, angular momentum is conserved for an alternating gradient focusing system with an azimuthally symmetric charge distribution. The averaged Hamiltonian is time independent, and so it can allow self consistent equilibrium where the phase space density is a function of the transformed Hamiltonian. That is, $F_0(X, Y, X', Y') = F(K)$. This would be a near equilibrium solution in the laboratory frame. In this section, relationships were also derived to transform the system back to the laboratory frame after performing the required calculations in the transformed reference frame,

SUMMARY

This paper demonstrates the use of the Lie transformation perturbation theory to perform a time averaging over fast oscillations for a beam with space charge in a periodic focusing channel. This derivation was previously done using the Poincare - Von Ziepel method Ref [1]. This derivation has the advantage that it does not assume the space charge to satisfy any specific equation like Poisson's or Maxwell's equation unlike those in Refs. [8, 9, 7]. In addition to that, the transformed Hamiltonian and the inverse transformation of phase space variables can be obtained in explicit form. The Lie transformation method greatly simplifies the the algebra especially when the external force term of the Hamiltonian has a complex form having mixed variables like in nonlinear focusing systems. It does not require one to Taylor expand the Hamiltonian and does not require one to perform a reverse transformation at every intermediate stage. Moreover, the reverse transformation needs be done only if required. In conclusion, we state that although the method was applied to an intense beam with linear focusing, its application is more general.

REFERENCES

[1] R. C. Davidson, H. Qin, P. Channel, Phys Rev ST Accel. Beams, "2" p074401(1999)

[2] R. L. Dewar, J. Phys "A9" 2043 (1976)

[3] A. Deprit, Cel. Mech. "1", 12 (1969)

[4] J. R. Cary, Phys. Reports "79", 129 (1981)

[5] Litchenberg and Lieberman 1983 "Regular and Stochastic motion" Springer

[6] R. C. Davidson and H. Qin 2001"Physics of High Intensity Beams in High Energy Accelerators" ICP World Scientific

[7] K. G. Sonnad and J. R. Cary, "Finding a nonlinear lattice with improved integrability using Lie-transform perturbation theory", in preparation.

[8] P. Channell, Phys. Plasmas "6" 982 (1999)

[9] S. Tzenov and R. C. Davidson, Phys Rev. ST Accel and Beams "5" 021001 (2002)

BEAM TEST OF A CW MICROTRON WITH A 500 MHZ RF CAVITY FOR INDUSTRIAL APPLICATIONS

H. Tanaka, T. Nakanishi, Y. Pu, T. H. Kim, Y. Makita, A. Maruyama, C. Tsukishima, S. Yamamoto, and S. Nakamura, Mitsubishi Electric Corp., Advanced Technology R & D Center, 8-1-1 Tsukaguchi-Honmachi, Amagasaki, Hyogo, 661-8661, Japan

Abstract

A CW microtron is made and the first beam test is done. The machine is of a racetrack type. The acceleration energy and the beam power are 5 MeV and 50 kW, respectively. The RF cavity is a conventional normal-conducting 2-cell cavity with coupling slots. The injection energy is 80 keV, and a 500MHz CW gun is used. The bending magnets are divided into two subsections to adjust the acceleration phases of every turn. A beam test of the 500 MHz CW gun shows that a peak current is about 200 mA, and a phase width of the gun emission is about 60 degrees. The beam emittances measured agree well with the calculation results. Injection beam sizes at the center of the RF cavity are about 5 mm and 4 mm in the horizontal and vertical coordinates, respectively.

1 INTRODUCTION

High power electron beams are necessary for industrial applications: X-rays irradiation and electron irradiation. Development of accelerators operated in a continuous wave (CW) mode is of considerable practical interest for industrial applications [1]. The CW microtron with a 500 MHz RF cavity is proposed. The essential interests are compactness and low cost. A key issue of designing the microtron is that the injection energy is as low as 80 keV ($\beta = 0.5$), and the velocity of an electron beam changes with every turn. Hence the energy gain from the RF cavity in each passage changes. A new shaped bending magnet is proposed to adjust beam orbit length of each turn, and appropriate acceleration phases can be adjusted when an electron beam passes the RF cavity. This paper describes manufactured results of the CW microtron. The first beam tests of the CW electron gun and the LEBT are also shown.

2 CW MICROTRON

Basic parameters of the CW microtron are shown in Table 1. Figure 1 shows a schematic drawing of the 5 MeV CW microtron, and Fig. 2 shows a photograph of the CW microtron and the RF power source.

2.1 CW electron gun and LEBT

A 500 MHz CW electron gun and an LEBT are shown in Fig. 3. In order to match an accelerating RF frequency, the 80 keV gun is pulsed at the RF frequency. The gun is a conventional triode type with a 0.5 cm^2 dispenser cathode. A CW emission is modulated by varying a grid voltage in the triode. A signal source of the grid voltage is a pick-up signal of the RF cavity, and the grid voltage is biased to a DC level. The 80 keV electron beam is injected with a chicane magnet from an injection line (LEBT). There are two solenoid magnets and a QF magnet at the LEBT for a transverse beam focusing. The chicane magnet is composed of three bending magnets.

Table 1: Basic parameters of CW microtrons.

	5 MeV Accelerator	**10 MeV Accelerator**
Beam power	50 kW	100 kW
Beam current	10 mA	10 mA
RF frequency	500 MHz	500 MHz
Accelerator dimension	1600 × 3900 × 1100 mm	1600 × 4700 × 1100 mm
Weight	10 ton	11 ton

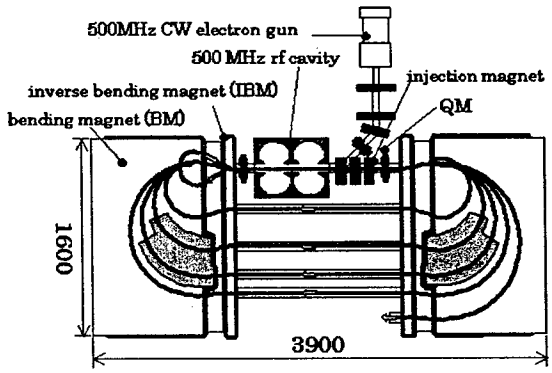


Figure 1: Schematic drawing of the 5 MeV CW microtron.



Figure 2: CW microtron and the RF power source.

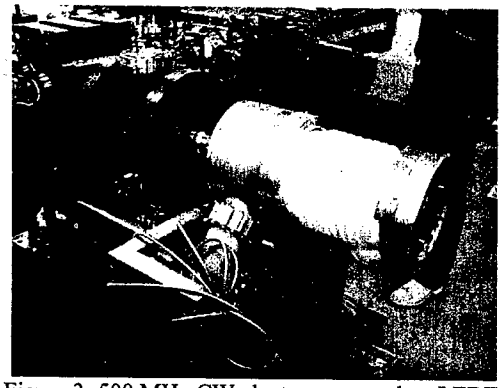


Figure 3: 500 MHz CW electron gun and an LEBT.

2.2 500 MHz RF cavity

The RF cavity is a conventional 2-cell cavity with nose cones and inductive coupling slots as shown in Fig. 4, which is frequently used for an electron storage ring. There are one coupler and two tuners. The frequency is selected around 500 MHz that is determined by a capable input power into the RF cavity and the total size of the microtron. The power supply (100 kW) uses two IOTs (Inductive Output Tube, CPI: K2H50), which are frequently used for broadcasting systems. The RF cavity was designed for a total gap voltage of 1 MV at 40 kW dissipation. A high power test of the cavity has been successfully done, and all measured parameters agree well with the design values.

2.3 Magnets

An electron beam after passing the RF cavity for the first time cannot pass by outside the RF cavity after the first bending magnet (BM). Therefore, an inverse-bending magnet (IBM) is situated near the bending magnet as shown in FIg.1. The electron beam passes the RF cavity for the second time in the inverse direction of the first passing. A transverse beam focusing is obtained with only edge effects of the bending magnets and two QMs near the RF cavity.

In a conventional racetrack microtron, a fixed relation among the magnetic field, the RF frequency, and amplitude of the acceleration voltage is needed for synchronous acceleration under an almost light velocity of a beam [2]. As for the proposed microtron, the electron velocity, however, changes with every turn, and the energy gain from the RF cavity in each passage changes. The RF acceleration phase slip becomes large, when a conventional bending magnet is used. Therefore, we propose a new shaped bending magnet to adjust beam orbit length of each turn [3]. The bending magnet is divided into two subsections described as Fig. 5. The two subsections have different magnetic fields, and the bending angles of the two subsections are adjusted so that beam orbit length of each turn is appropriate for the acceleration. The parameters are optimised with a computer optimisation program so that an electron beam with the widest acceleration phase can be accelerated. Figure 6 shows electron orbits calculated with a numerical integration of exact equations of motion using 3-D magnetic and electric fields. Lines shown in the figure are horizontal beam orbits using calculated 3-D magnetic fields. Dots in the figure are 1000 particles' simulation results using measured magnetic fields. Calculation conditions are as follows: initial acceleration phases are 0, +10, and –10 degrees, and an unnormalized beam emittance is 50 π mm-mrad. The study shows that an electron beam can be accelerated till 5 MeV with practicable beam sizes (x= 18 mm, y= 12 mm).



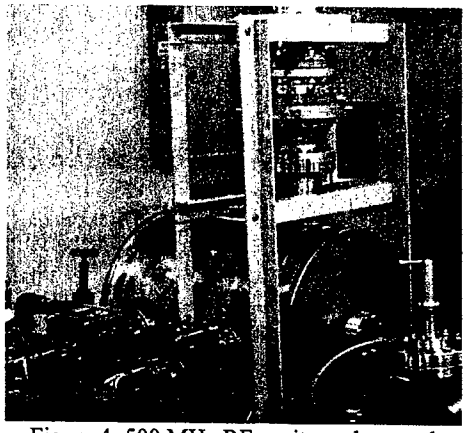


Figure 4: 500 MHz RF cavity and a coupler.

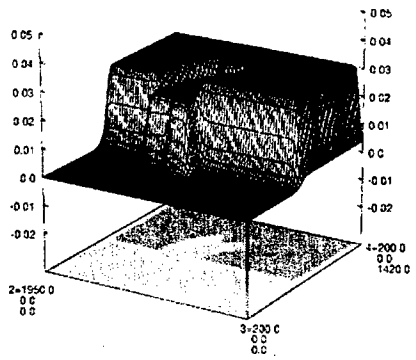


Figure 5: Magnetic field distribution of the bending magnet calculated with TOSCA.

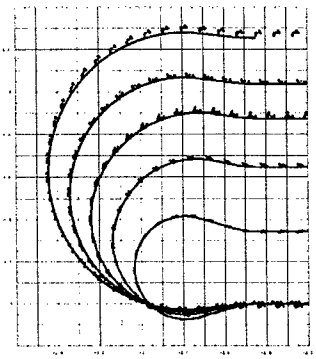


Figure 6: Beam orbits calculated using calculated magnetic fields (lines) and measured magnetic fields (dots). Calculation conditions of the dots: initial acceleration phases are 0, +10, and −10 degrees and an unnormalized beam emittance is 50 π mm-mrad.

3 BEAM TEST

3.1 500MHz CW beam production

The beam test was done with the following diagnostics: 1) a fluorescent screen which is movable along the axis, 2) the Faraday cup which can be measured fast beam signals. Figure 7 shows a beam bunch signal measured by the Faraday cup. The figure shows that a 500 MHz pulsed beam is produced, and the bunch length is about 300 ps (phase width: 60 degrees), that is in good agreement with simulation results.

Figure 8 shows calculated and measured peak beam currents as a function of the grid-cathode voltage. The calculation was done with a beam tracking in consideration of space charge effect. The simulation model was divided into two sections: 1) a section from the cathode to the grid, 2) a section from the grid to an exit of the electron gun, because the former section is a very fine structure as compared with the latter section. A maximum current needed is estimated to be 200 mA on account of attaining an average acceleration current of 10 mA. The figure shows that measured results agree well with the calculation results.

Figures 9 shows unnormalized beam emittances as a function of the grid-cathode voltage (Vgc). The measurement was done with the fluorescent screen and a quadrupole magnet. The measured results agree well with the calculation results, and show that the unnormalized beam emittance is about 60 π mm-mrad.

3.2 Beam injection

An injection beam test was done before an acceleration beam test. The fluorescent screen and the Faraday cup were situated at a position of the RF cavity. The beam test shows that injection beam sizes at the center of the RF cavity are about 5 mm and 4 mm in the horizontal and vertical coordinates, respectively, and beam centering within ± 0.2 mm accuracy can be done.

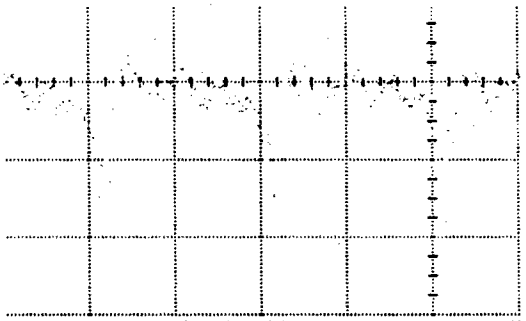


Figure 7: Beam signal with an 80 GHz sampling oscilloscope: (1 ns/div. and 50 mA/div.).

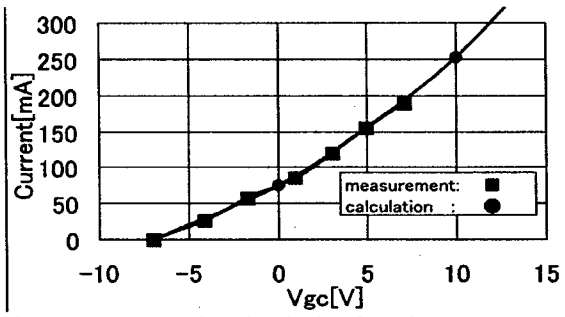


Figure 8: Measured and calculated peak currents as a function of the grid-cathode voltage.

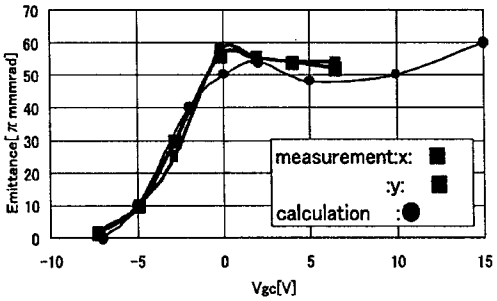


Figure 9: Unnormalized beam emittances as a function of the grid-cathode voltage.

4 SUMMARY

The CW microtron with the 500 MHz RF cavity was made and the first beam test was done. The production of 500 MHz CW beam and the injection into the microtron have been successfully done. Acceleration beam test will be done within this summer.

REFERENCES

[1] J. Pottier, "A new type of RF electron accelerator: the rhodotrin", NIM B 40/41, (1989) 943.

[2] P. Lidbjork, "Microtrons", CERN 94-01, Vol. 2, (1994), 1994.

[3] H. Tanaka, "Beam Dynamics in a CW Microtron for Industrial Applications", EPAC 2000, Vienna, (2000), 1005.

COMMISSIONING RESULTS OF SLOW EXTRACTION OF HEAVY IONS FROM THE AGS BOOSTER*

K.A.Brown†, L. Ahrens, S. Bellavia, S. Binello, B. Brelsford, D. DuMont,W. Eng, C. Gardner, D. Gassner, J.W. Glenn, L.Hammons,J. Hock, L. Hoff, E. Hutchinson, J.Jamilkowski, N. Kling, Y. Kotlyar, A. Krishock, R. Lockey,M. Mapes, I. Marneris, G. Marr, A. McNerney, A.Meyer,J. Morris, C. Naylor, S. Nemesure, D. Phillips, A.Rusek, J. Ryan, T. Shrey, L. Snydstrup, N. Tsoupas, B.VanKuik, S. Zahariou-Cohen, K. Zeno, C-AD Dept., BNL, Upton, NY

Abstract

Brookhaven's AGS Booster has been modified to deliver slow extracted beam to a new beam line, the NASA Space Radiation Laboratory (NSRL). This facility was constructed in collaboration with NASA for the purpose of performing radiation effect studies for the NASA space program. The design of the resonant extraction system has been described in [1]. A more detailed description, which includes predictions of the slow extracted beam time structure has been described in [2]. In this report we will present results of the system commissioning and performance.

INTRODUCTION

The AGS Booster has operated since 1991 as an injector of protons and heavy ions into the AGS. The nominal operating parameters are summarized in table 1. NSRL will employ heavy ion beams of many different ion species and at beam energies ranging from 0.04 to 3.07 GeV/nucleon. Resonant extraction is required in order to deliver a continuous stream of particles. In this report we present results from the commissioning of slow extraction for this facility. The third integer resonant extraction process employs a single thin magnetic septum and a thick septum ejector magnet, with the resonance created by re-configuring 4 of the main horizontal chromaticity sextupoles. The expected extraction efficiency is about 85 %, based on the thin septum thickness and the predicted step size of the resonant beam at the septum.

The maximum kinetic energy of the extracted beams is limited by the maximum Booster rigidity of 17 Tm and by the maximum NSRL transport line rigidity of 13 Tm. Ions are fully stripped at a stripping foil located at the entrance of the thick septum magnet. Intensities of a few 10^8 down to 10^5 ions per pulse or less will be available to experimenters through collimation at the entrance to the D6 septum magnet. Due to the limited range of the Booster quadrupoles at high fields, the design of the resonant extraction system requires moving the operating point in tune space through $\nu_x = 4.5$ and extracting on the 13/3 resonance.

Table 1: AGS Booster Parameters

Parameter	Value
Circumference	201.78 (1/4 AGS) m
Ave. Radius	32.114 m
Magnetic Bend R	13.8656 m
Lattice Type	Separated Function, FODO
No. Superperiods	6
No. of Cells	24
Betatron Tunes,X,Y	4.82, 4.83
Vacuum Chamber	70 x 152 mm Dipoles
	152 mm (circular) Quads
Max. Rigidity	17 Tm
Injection Rigidity	2.2 Tm (200 MeV protons)
	0.9 Tm (1 MeV/nuc Au(32+))
Acceleration Rate	8.9 T/s up to 7.5 Tm (7.5 Hz)
	1 T/s up to 17 Tm (0.7 Hz)

COMMISSIONING RESULTS

The first slow extracted beam from the Booster occurred in October 2002. At that time we demonstrated that we could manipulate the beam in tune space with little or no beam loss while passing through $\nu_x = 4.5$ and that the extraction system worked as designed. After this initial commissioning period we took occasional short periods of time to do various radiation safety beam tests. Our next opportunity for extensive commissioning effort began again at the end March, using polarized protons. This was useful time, since for the proton beams we could observe beam losses on the Booster ion chamber loss monitors. In this period of commissioning we were able to re-establish slow extraction, get beam transported to the target area of the NSRL beam line, commission new instrumentation in the beam line, and begin work on spill control. In addition the beam line itself was commissioned with various studies of the beam optics being performed. These commissioning efforts are discussed in more detail in [3, 4].

* Work performed under Contract Number DE-AC02-98CH10886 with the auspices of the US Department of Energy.

† kbrown@bnl.gov

0-7803-7738-9/03/$17.00 © 2003 IEEE

Booster Main Magnet and Acceleration Configuration

The Booster Main Magnet power supply required significant modifications to allow operation for slow extraction. In addition to modifications in the controls, an active filter was added, to reduce ripple on the extraction flattop. A spill servo system was added including beam abort operations, to disable beam in the middle of the spill through an experimenter supplied interrupt. Details of these changes can be found in [4]. Figure 5 shows the effect of the active filter on the spill structure.

Tune Manipulations

At high field, the Booster quadrupole iron begins to saturate before the dipole iron of the main arc bending magnets. This weakens the strength of the quadrupole relative to the dipole and lowers the machine bare tune. Details on this effect are provided in [5]. For the NSRL project new power supplies were installed to allow the trim windings of the main Booster quadrupoles to operate up to 1100 amp. Previously they could only go up to 700 amp, which was not enough to provide a good operating range for slow extraction at the highest rigidities. Figure 1 shows the regions of tune space that are accessible within ± 1100 amp in the tune trim windings at 14 Tm, the larger region in green, and 16 Tm, the smaller region. For multiturn injection of Fe^{20+} and Fe^{21+}, we use linear coupling to maximize the injection efficiency [6]. The nominal uncoupled tunes for this setup are near the point $\nu_x = 4.757$ and $\nu_y = 4.777$, indicated by the green dot in Figure 1. To get to the proper working point for slow extraction we first shift ν_x down to 4.4 at low energy where we are able to correct the half integer resonance using the normal stop band correctors. The tunes move along the path indicated by the dashed line in the figure, first to the blue point, and then to the black point. Figure 2 shows the effect of these manipulations on the circulating beam current. As can be seen we are able to make these changes in tune space with little or no beam loss.

Extraction Bumps Configurations

For control over step size at the thin septum and beam losses on the thick septum, the equilibrium orbit can be deformed at the thin and thick septum locations using a set of five individually controlled power supplies connected to trim coils on selected Booster Main sector magnets. Figure 3 shows a MAD simulation of the equilibrium orbit (for non-resonant beam) with the locations of the selected bump magnets indicated by the red arrows. The thin septum position and skew can be controlled through a set of motor drives connected to each end of the magnet. The thick septum is not movable, so the beam position at that location must be controlled by the bumps and the amount of excitation in the thin septum. The legend in the figure 3 shows the amount of current in the magnets, required to get the desired bump, for a beam rigidity of about 9.3 Tm. During commissioning we verified that the polarity of these power supplies was correct by exciting them individually and looking at single BPM signals.

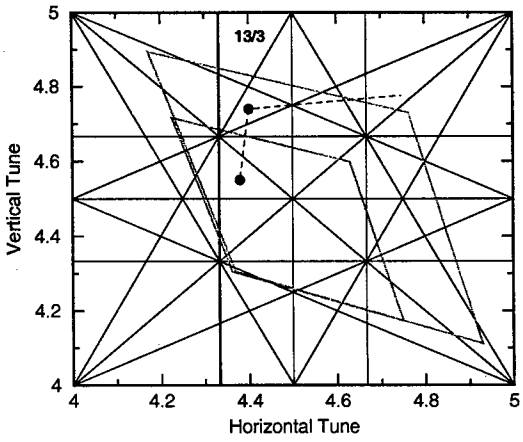


Figure 1: Booster Tune Space manipulations.

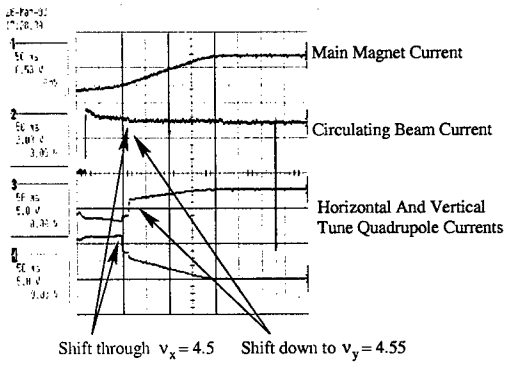


Figure 2: Beam Current Survival during tune manipulations.

Resonance Excitation

To finally extract the beam the resonant sextupoles have to be excited and the beam moved into the resonance by slowly lowering the field of the Booster Main Magnet. This causes the tune of the beam to be slowly shifted down into the resonance and particles enter into non-linear betatron amplitude growth. As the step size increases over many turns the particles eventually either hit the thin septum and are lost or step across it and are deflected across the thick septum and then bent out of the Booster into the NSRL beam line. Figure 4 shows the circulating beam current in the Booster slowly decreasing as beam enters the resonance and is extracted. Figure 5 shows the beam spill as seen on an external ion chamber in NSRL beam line. Finally figure 6 shows the beam as seen on a illumination flag in the beam line.

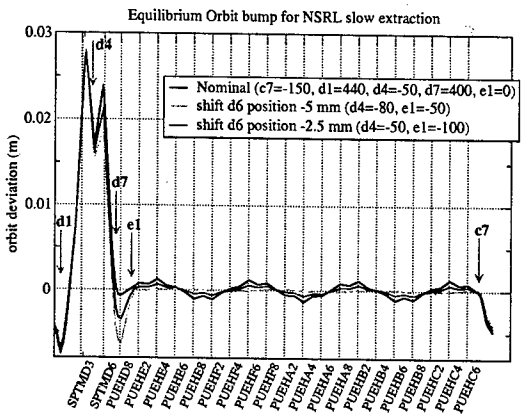


Figure 3: Equilibrium Orbit Deformation for Slow extraction.

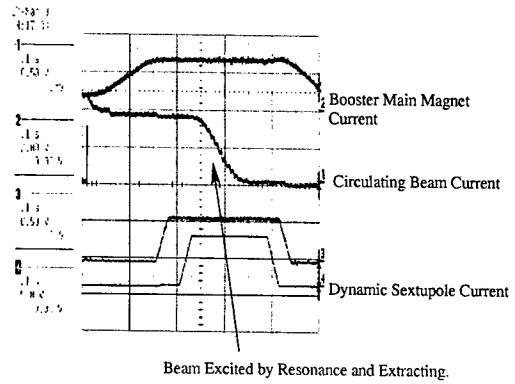


Figure 4: Beam Excited by Resonant Sextupoles and Extracting.

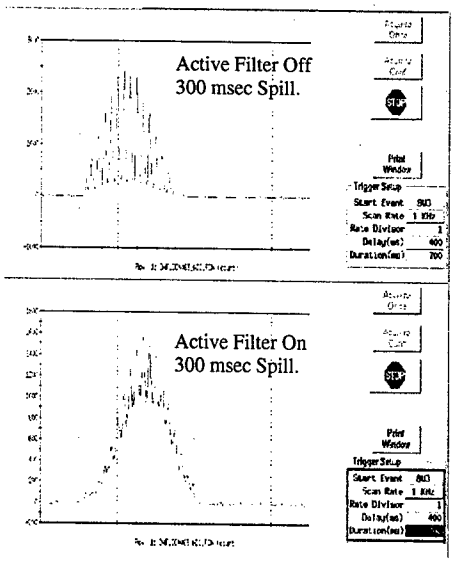


Figure 5: Beam Spill Seen on External Ion Chamber.

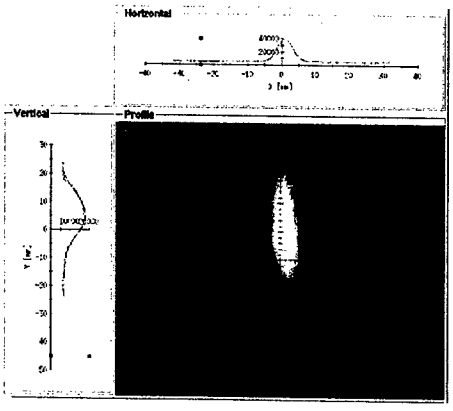


Figure 6: Beam As seen on external flag.

REFERENCES

[1] K.A.Brown, et al, "Design of a Resonant Extraction System for the AGS Booster", p. 1270, Proceedings of the 1999 Particle Accelerator Conference, New York, 1999.

[2] K.A.Brown, et al, "Resonant extraction parameters for the AGS Booster", p. 1571, Proceedings of the 2001 Particle Accelerator Conference, Chicago, 2001.

[3] N.Tsoupas, et al, "Commissioning of the Beam Transfer Line of the Booster Application Facility (BAF) at BNL", These Proceedings.

[4] I.Marneris, et al, "Booster Main Magnet Power Supply Improvements for NASA Space Radiation Laboratory at BNL", These Proceedings.

[5] K.A.Brown, et al, "A High Precision Model of AGS Booster Tune Control", Proceedings of the 2002 European Particle Accelerator Conference, Paris, 2002, p.548

[6] C.J.Gardner, et al, "Injection of Gold Ions in the AGS Booster with Linear Coupling", Proceedings of the 1999 Particle Accelerator Conference, New York, 1999, p.3294

STATUS OF SLOW EXTRACTION OF HIGH INTENSITY PROTONS FROM BROOKHAVEN'S AGS*

K. Brown†, L. Ahrens, J.M. Brennan, J.W. Glenn, T. Roser, T. Russo, N. Tsoupas, K. Smith, K. Zeno
AGS Dept., BNL, Upton, NY

Abstract

The Brookhaven AGS third integer resonant extraction system allows the AGS to provide high quality, high intensity 25.5 GeV/c proton beams simultaneously to four target stations and as many as 8 experiments. With the increasing intensities (over 7×10^{13} protons/pulse) and associated longer spill periods (2.4 to 3 seconds long), we continue to run with low losses and high quality low modulation continuous current beams. We have an active program of high energy physics experiments, including the high precision measurement of the muons magnetic moment [1] and the discovery of the rare Kaon decay, K+ $\rightarrow \pi + \nu\bar{\nu}$ [2] This program is continuing into the future with the rare symmetry violating process experiments [3] currently being designed to operate at the AGS. In this paper we will present results from operation of high intensity slow extraction, the problems we encounter, and our solutions to those problems.

INTRODUCTION

The Brookhaven AGS Resonant extraction system and the beam transport and switchyard systems were designed in the pre-AGS Booster era [5, 6, 7], when the kinetic energy of the injected beam was 200 MeV (50 MeV even further back in time). In the post-Booster era, this energy is now approximately 1.6 GeV. For these two energies the ratio of $\beta\gamma$ is approximately 3.5. Therefore the maximum possible beam emittance is over 3.5 times larger for post-Booster high intensity beams. Even though the emittance is larger, through careful measurements and simulations we have been able to find optics solutions that allow clean extraction and transport of these high intensity beams.

In addition to the larger beams, other factors have changed significantly since the design of the AGS SEB systems. The AGS now uses fast quadrupole magnets to jump the gamma transition point during acceleration. For minimal beam losses to occur during the γ_{tr} jump the momentum spread of the beam has to be minimized. This puts constraints on how large the longitudinal emittance can be. This is due to the highly distorted dispersion function created by the fast quadrupoles, which defines the momentum aperture [8].

Our experiences with extracting high intensity protons has been discussed previously in [4]. In this report we will provide an update on our experiences since that report.

* Work performed under Contract Number DE-AC02-98CH10886 with the auspices of the US Department of Energy.

† Email: kbrown@bnl.gov

SEB HIGH INTENSITY PERFORMANCE

Basic performance parameters are summarized in table 1.

Table 1: AGS SEB Performance Parameters

Parameter	Value	Units
Momentum	25.5	GeV/c
Peak Intensity	71.5	10^{12} proton/pulse
Extract. Eff.	96-98	%
Transport Eff.	90-95	%
Rep. Period	4-8	second
Flattop Length	2-6	second
Spill Length	1.8-5.8	second
Working Point	8.67/8.76	Tune (ν_x, ν_y)
Chromaticity	-2.3/0.2	Chrom. (ξ_x, ξ_y)

Beam Loss Issues

The primary beam loss issues in the past had not been in the extraction process itself, but in the transport of the extracted beam to target stations. Through emittance measurements and simulations we were able to reduce beam losses in the primary transport to very tolerable levels. Back in the extraction systems we find the extraction efficiency drops at the highest intensities. Figure 1 shows the extraction inefficiency as a function of internal beam intensity. At around 5×10^{13} the inefficiency makes a sudden jump up from just under 2 % to about 2.5 %. We operate the AGS with the vertical chromaticity positive above γ_{tr} but we are unable to operate the horizontal chromaticity positive since the current set of sextupoles are not strong enough. We have no direct evidence that the effect is a consequence of operating with a negative horizontal chromaticity. Since the increased beam loss is modest (0.5 %) we tolerate it. There is some cause for concern, though, since we are working towards even higher intensities in the future and at 1×10^{14} this loss becomes significant.

Spill Structure

In the FY98/99 SEB run we ran into a new problem; significant spill structure not associated with power supply ripple. In the FY02 run we observed this effect again. This spill structure was analyzed and found to be random kilohertz oscillations. We found no correlations between these

0-7803-7738-9/03/$17.00 © 2003 IEEE

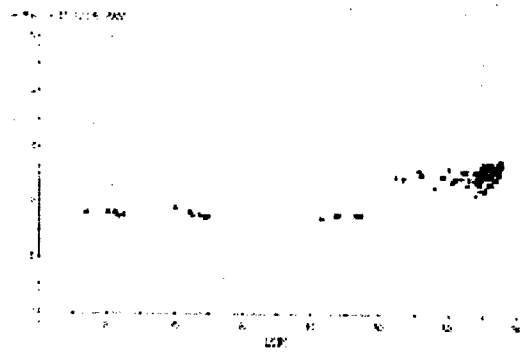


Figure 1: Extracted beam inefficiency vs internal beam intensity

oscillations and power supply ripples. The power supply ripple only accounted for about 20 % of the spill structure. At high intensity the spill was 100 % modulated (intensity dependent). Recall that the spill structure is a consequence of variations in velocities in tune space:

$$S(t) = \frac{dN}{dQ} \cdot \dot{Q}_0(1 + \frac{\dot{Q}_v}{\dot{Q}_0}) \quad (1)$$

$\frac{dN}{dQ}$ is the distribution of particles in tune space. $\dot{Q}_0$ is the rate at which this distribution is pushed into the resonance. $\dot{Q}_v$ is the variations in the rate due to power supply ripple. When there is very little power supply ripple, the remaining structure is a consequence of the rate at which the beam is moved into resonance and the distribution of the particles in tune space. The random kilohertz structure appears to be a direct reflection of the distribution of particles in tune, or more properly, momentum space. Our solution to this problem is to use a 93 MHz RF (VHF) cavity during extraction, placing the 93 MHz buckets between the beam and the resonance, such that the particles are forced between the RF buckets before going into non-linear resonant growth. Since we have a slight negative $\dot{B}$ during extraction the RF buckets will have only a small space between which the beam could pass, breaking up any structure that exists in the beam. This potentially puts 93 MHz structure on the spill, which was not a problem for the experimenters using the beam. Figure 2 shows the beam spill with and without the VHF cavity on during extraction and at different intensities. Although the VHF cavity cures the effect, it is nevertheless unexplained. This phenomena is explored further in [10].

Electrostatic Septum Dark Current

One significant problem which effects our operation is the increasing dark current of the electrostatic septum over the period of a run. Figure 3 shows the septum power supply current as a function of integrated beam intensity during a portion of a physics run. Once the device is drawing the higher currents, it remains drawing those currents indefinitely. To return it to the lowest current levels has required

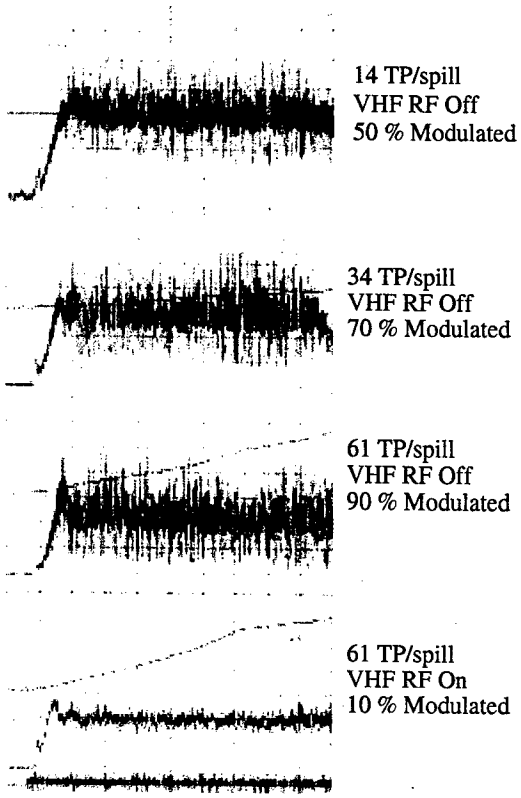


Figure 2: Extracted beam spill as a function of internal beam intensity with and without VHF on

the device to be brought back up to air and cleaned. Attempts to condition the device at higher voltages have not succeeded. This dark current effect has been observed in both our new foil septum and in the older wire septum. A detailed description of the new foil septum is found in [12].

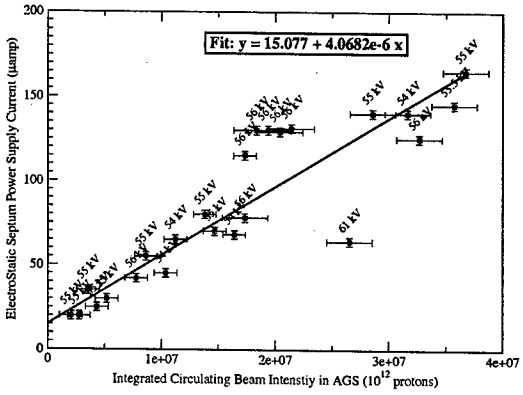


Figure 3: Electrostatic septum power supply current vs integrated beam intensity. Data labels indicate the high voltage as measured at the time.

CONCLUSIONS

The AGS SEB system is able to supply high quality, high intensity proton beams for multiple simultaneous experiments. We are able to contend with instabilities that arise from the high current accelerated beams, as well as unexpected effects, such as spill structure uncorrelated with power supply ripple. For the AGS the VHF cavity has proven to be invaluable for diluting longitudinal phase space and now for smoothing spill structure.

ACKNOWLEDGEMENTS

The authors wish to acknowledge T. Curcio, who kindly collected and provided the data on the electrostatic septum power supply current.

REFERENCES

[1] H.N.Brown et al, "Precise measurement of the positive muon anomalous magnetic moment", Phys. Rev. Lett. 86, 2227 (2001).

[2] S.Adler et al.,"Evidence for the Decay K+ $\rightarrow \pi + \nu\bar{\nu}$" Phys. Rev. Lett. 79, 2204-2207 (1997).

[3] Rare Symmetry Violating Processes Web Link, http://www.bnl.gov/rsvp/

[4] L.A.Ahrens et al., "AGS Resonant Extraction with High Intensity Beams", Proceedings of the 1999 Particle Accelerator Conference.

[5] J.W.Glenn et al., "AGS Slow Extraction Improvements", IEEE NS26,No.3, 3167(1979).

[6] H. Weisberg and J.W. Glenn, "Exploitation of Nonlinear Growth of Betatron Oscillations to Obtain Efficient Slow Extraction at the AGS", Nucl. Inst. & Methods 169, 319(1980).

[7] L. Blumberg et al., "The AGS Slow External Beam Switchyard", BNL 24508R (1979).

[8] L.A.Ahrens et al, "High Intensity Proton Acceleration at the Brookhaven AGS - An Update", Proceedings of the 1997 Particle Accelerator Conference, p.89, http://www.triumf.ca/pac97.html

[9] J.W. Glenn et al, "MICRO-BUNCHING THE AGS SLOW EXTERNAL BEAM", Proceedings of the 1997 Particle Accelerator Conference, p.967, http://www.triumf.ca/pac97.html

[10] J.W.Glenn et al, "Spill Structure in Intense Beams", These proceedings.

[11] Cappi & Steinbach "Improvement of the Low Frequency ..." CERN/PS/OP 80-10 & IEEE NS-28, No 3, June 1981, pp 2806.

[12] J.Hock, "AGS Electrostatic Septum", These Proceedings.

LHC PILOT BUNCHES FROM THE CERN PS BOOSTER

M. Benedikt, CERN, Geneva, Switzerland

Abstract

For the first commissioning phase of the LHC, a single proton bunch is required. The production of this so-called "LHC pilot bunch" will follow a different scheme than the one of the nominal LHC proton bunch train. Both the transverse and the longitudinal LHC bunch characteristics should already be established in the PS Booster. The parameter space for the LHC pilot bunch spans a factor 66 in beam brightness. The intensity should be variable by a factor of 22 from $5.0 \cdot 10^9$ to $1.1 \cdot 10^{11}$, covering the range from the LHC quench limit up to the intensity of a nominal LHC bunch. The transverse emittances (at Booster ejection) should be adjustable in the range $0.85\ \pi\mu m \le \varepsilon_{norm,rms} \le 2.5\ \pi\mu m$, while the longitudinal emittance is kept constant at 0.3 eVs, slightly below the nominal one (0.35 eVs). To cover the whole parameter space, a mixture of several ingredients was required: intensity adjustment with low voltage rf-capture; definition of the transverse emittance with shavers; controlled blow-up followed by longitudinal shaving to define the longitudinal emittance. All beam variants were produced on harmonic two, with only one bunch being sent to the downstream accelerator chain. To cover also the lowest intensity side, the Linac beam was reduced by a factor 5 with a "sieve". The pilot bunches corresponding to the "corners" of the parameter space and a few selected inner reference points were successfully produced in the PS Booster.

INTRODUCTION

The PS-Booster (PSB) is the first circular machine in the LHC proton injection chain. For production of the nominal LHC beam [1], a horizontal three-turn injection is used to accumulate the 50 MeV Linac beam. The multi-turn injection process in the PSB determines the transverse emittances of the beam and therefore the final LHC beam brightness. On the contrary, the longitudinal characteristic of the nominal LHC beam is only fixed at ejection from the PS. Complicated RF gymnastics (triple splitting from harmonics 7 to 21 at injection and two double splittings from harmonics 21 to 42 and 84 before ejection), employing also some controlled longitudinal beam blow-up, are performed in the PS to generate the nominal bunch train for the LHC [2].

The situation is rather different for the first commissioning phase of the LHC, where only a single proton bunch will be required. The production of this pilot bunch will follow a completely different scheme than the production of the nominal LHC proton bunch train. Not only the transverse but also the longitudinal bunch characteristics will have to be established in the PSB thus avoiding all longitudinal gymnastics in the PS. After ejection from the PSB, the pilot bunch should be passed on to the LHC by the downstream machines with the main concerns being to keep the bunch characteristics unchanged and to minimize longitudinal and transverse blow-ups.

Michael.Benedikt@cern.ch

PARAMETER SPACE

At present the various strategies for LHC start-up and the first commissioning phase with beam are still being discussed and consequently no definite specifications for an LHC pilot bunch have been formulated. One of the main goals was therefore to develop a flexible strategy for pilot bunch production that allows a large variation of beam parameters to be best adapted to whatever will be requested by the LHC. For an estimate of the required parameter space some LHC key figures were used:

- Intensity: The number of protons in the bunch should be variable from $5.0 \cdot 10^9$ to $1.1 \cdot 10^{11}$. The lower figure corresponds to the LHC quench limit at injection energy (450 GeV) and the higher is the intensity of a nominal bunch.
- Transverse emittance: Normalised horizontal and vertical rms emittances should be adjustable in the range from $0.85\ \pi\mu m$ to $2.5\ \pi\mu m$ at PSB ejection energy of 1.4 GeV. The $2.5\ \pi\mu m$ correspond to the nominal emittance of the LHC beam ($3.5\ \pi\mu m$ at LHC injection). The emittance variation should allow aperture scans, orbit adjustments and first dynamic aperture studies.
- Longitudinal emittance: This is the only pilot bunch parameter that is foreseen to be kept constant at 0.3 eVs (at PSB ejection), which is just slightly below the nominal longitudinal emittance of 0.35 eVs (in the LHC) thus allowing for some additional blow up in the injector chain.

Combining the above requirements of an intensity variation by a factor 22 and a transverse emittance variation by a factor 3 shows that the parameter space for the LHC pilot bunch spans a factor 66 in beam brightness defined as ratio of protons per bunch and normalized emittance, N_b/ε_n. A graphical representation of the parameter space is given in Figure 1.

The production of the pilot bunches is further complicated by the fact that neither the required low bunch intensities nor the longitudinal emittance of 0.3 eVs correspond to the typical working range of the PSB. In standard operation beams with up to $1 \cdot 10^{13}$ protons per bunch and longitudinal emittances of typically 1.5 eVs are produced.

0-7803-7738-9/03/$17.00 © 2003 IEEE

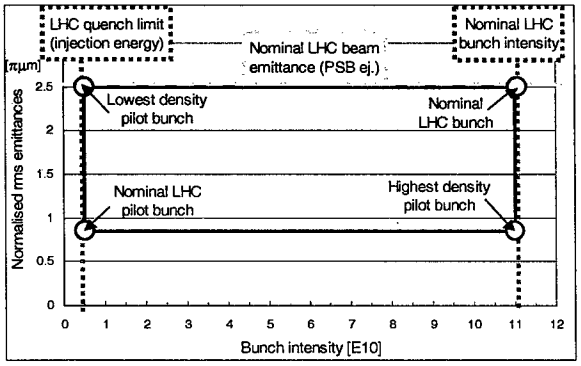


Figure 1: LHC pilot bunch parameter space.

STRATEGY FOR PILOT PRODUCTION

During 2002 several machine development sessions on the subject of LHC pilot bunch production were performed on the PSB. The first step, before any detailed optimization work could start, was to develop a strategy enabling to produce and to change the very different beam variants within a reasonable amount of time. To cover the whole pilot beam parameter space, a mixture of several ingredients was required.

Longitudinal emittance

The control of this parameter is straightforward and the required value of 0.3 eVs was achieved by longitudinal shaving. For this the rf voltage was reduced to limit the bucket acceptance of 0.3 eVs approximately in the middle of acceleration. Afterwards the rf voltage is again raised to the nominal 8 kV required for a correct longitudinal matching with the PS rf system.

Transverse emittances

Independent horizontal and vertical "shavers" are used for emittance control in the PSB. For each plane the system uses a single correction dipole to deflect the orbit towards an aperture limitation where the beam is shaved in betatron amplitudes. This process is applied directly after rf capture at the beginning of acceleration. At this moment, there is almost no adiabatic damping and the physical beam size is still large, improving the precision of the shaving.

Intensity (beam brightness)

Variation of the beam brightness by a factor 66 is the most challenging issue; for every transverse emittance value established by beam shaving, an additional factor 22 in intensity variation is required. For this a combination of three different techniques was used.

1. The longitudinal phase space density was controlled in two steps. Firstly the rf voltage during the bunching process was varied hereby changing the part of the unbunched linac beam that is captured and accelerated. Secondly controlled longitudinal blow up was applied during the first half of the acceleration cycle to depopulate the longitudinal phase space. This was done with a higher harmonic rf system [3]. The final longitudinal emittance is then fixed afterwards by shaving with the principal rf system. Applying more or less blow up gives a good control of the longitudinal density and, since there is quasi no coupling between transverse and longitudinal phase spaces in the PSB, the effect is equivalent to a change of the transverse beam brightness. In this way an intensity (brightness) variation of up to a factor 4 could be achieved.
2. The (transverse) brightness of the beam in the PSB can be influenced by the settings used for the multi turn injection process. The most effective parameters are the steering and the betatron matching of the injection line, the horizontal and vertical tunes of the machine and the fine timing of the "slow" injection bumpers. A brightness variation of a factor 2 was achieved with the different settings.
3. The intensity (brightness) of the linac beam can be changed by a sharp factor 5. This was done with the so-called "sieve" which is a mechanical device installed in the injection line that allows only about 20% of the beam to pass through.

Combining the first two techniques allows continuous variation of the beam intensity by a factor 8, applying the multiplicative factor 5 provided by the "sieve" intensity reduction allows to cover the complete LHC pilot bunch parameter space. The upper part of Figure 2 shows the voltages of second harmonic and blow-up rf systems for generation of the $5.0 \cdot 10^9$-0.85 πμm pilot bunch along the acceleration cycle. The effects of capture voltage, beam blow up, transverse and longitudinal shavings on the evolution of the beam current are shown in the lower part.

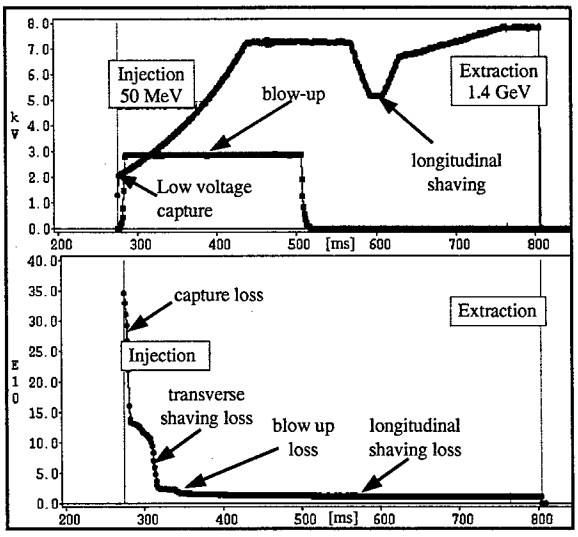


Figure 2: RF voltages and beam intensity along the cycle.

Beam loss issues

The maximum loss when producing pilot bunches with the described strategy amounts to about 10^{12} protons per cycle where most of the loss occurs at injection energy. This is to be compared with beam losses in the order of 10^{13} protons per cycle for day-to-day high intensity operation.

BEAM TESTS

Machine set up

All beam tests were performed in ring 3 of the PSB. A three-turn injection, similar to the one used for the nominal LHC beam, was used as starting point for the set-up. Experience during the last years has shown that this type of injection is best suited for a good reproducibility and stability which is essential for both the nominal LHC and the pilot bunch beams. Resonance compensation and working point optimization are less of an issue because the (vertical) incoherent space charge tune spread at injection is significantly smaller than in the case of the nominal beam where $\Delta Q_v \leq -0.45$. In contrast to the nominal beam all pilot bunch variants were produced with the second harmonics rf system. Obviously this generates two pilot bunches but only one is being sent to the downstream accelerator chain. The use of $h = 2$ for acceleration has two advantages from the operational point of view. The second harmonics rf system is naturally better suited to the production of a relatively small longitudinal emittance (first and second harmonics systems have the same nominal voltage of 8 kV) and by accelerating two bunches, the intensity in the machine is doubled hereby relaxing the demands on the dynamic range of various control loops.

Results

To validate the proposed strategy, pilot bunches corresponding to the corners of the parameter space and a few selected reference points were produced in ring 3 of the PSB. Pilot bunches exist in two flavors: one group, with intensities between $5 \cdot 10^9$ and $2.0 \cdot 10^{10}$ was fabricated by using the sieve for Linac beam intensity reduction, the other group with intensities between $2.5 \cdot 10^{10}$ and $1.1 \cdot 10^{11}$ was based on the nominal Linac beam. Figure 3 shows the LHC pilot bunch parameter space, the reference beams that were produced in 2002 are indicated as large spots.

It is interesting to note that the bunch corresponding to the bottom right corner in Figure 3 features an incoherent space charge tune shift of $\Delta Q_v \approx -0.13$ at SPS injection. This is three times the tune shift of a nominal LHC bunch and might be at the limit of what can be accepted by the SPS.

The intensities were observed to be stable on all bunch variants to better than ±10%, corresponding to LHC demands. It is worth looking at the figures in a bit more detail: ±10% of the lowest intensity pilot bunch corresponds to a fluctuation below $\pm 5 \cdot 10^8$ protons. This is a factor $5 \cdot 10^{-5}$ smaller than the maximum intensity of 10^{13} protons that can be obtained from ring 3, underlining the versatility of the PSB.

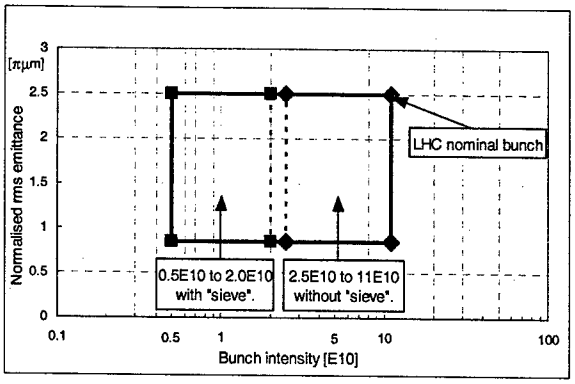


Figure 3: LHC pilot bunches produced in the PSB.

CONCLUSIONS

For the first commissioning phase of the LHC a single bunch will be required. All beam parameters of this pilot bunch should already be defined and fixed at ejection from the PSB in contrast to the production scheme for the nominal LHC beam, where all the longitudinal characteristics is established in the PS. Presently the requirements for the LHC pilot bunch are not fixed; for this reason a relatively large parameter space was defined using critical LHC parameters as input. This parameter space spans a factor 66 in beam brightness and an operational strategy for the PSB was developed in order to produce the different pilot bunch variants and to facilitate the switching between them. As a proof of principle, the most demanding beam variants have been produced during 2002. The observed stability and reproducibility corresponded to the stringent LHC requirements.

REFERENCES

[1] M. Benedikt, R. Cappi, C. Carli, G. Cyvoct, M. Giovannozzi, A. Lombardi, D. Manglunki, M. Martini, E. Metral, G. Metral, K. Schindl, M. Vretenar, "Transverse Performance of the Proton Beam Delivered By The PS Complex For The Future LHC", EPAC 2000, Vienna, June 2000, 1471 (2000).

[2] R. Garoby, S. Hancock, J.-L. Vallet, "Demonstration Of Bunch Triple Splitting In The CERN PS", EPAC 2000, Vienna, June 2000, 304 (2000).

[3] http://psdata.web.cern.ch/psdata/www/icfa9/slides/blas.pdf

AN 8-GEV SYNCHROTRON-BASED PROTON DRIVER*

W. Chou# for the Proton Driver Study Group, FNAL, Batavia, IL 60510, USA

Abstract

In January 2002, the Fermilab Director initiated a design study for a high average power, modest energy proton facility. Such a facility is a possible candidate for a construction project in the U.S. starting in the middle of this decade. The key technical element is a new machine, dubbed the "Proton Driver," as a replacement of the present Booster. The study of an 8-GeV synchrotron-based proton driver has been completed and published [1]. This paper will give a summary report, including machine layout and performance, optics, beam dynamics issues, technical systems design, civil construction, cost estimate and schedule.

INTRODUCTION

A Proton Driver, which is a high average power, modest energy proton facility, offers an interesting future physics program in the U.S. For example, neutrino physics (neutrino superbeam, off-axis neutrino experiments, and a neutrino factory), neutron electric dipole moment (EDM) measurement, neutron-antineutron oscillations, intense cold muon beams, a precision test of CPT, etc. [2]

There have been several iterations on machine studies at Fermilab. Following the completion of a 16-GeV proton driver design [3], the Fermilab Director issued a charge requesting Proton Driver Study II (PD2) on an 8-GeV proton driver. A major objective in the PD2 study is to reduce the up front construction cost.

PD2 explores two possible upgrade options: an 8-GeV high intensity proton synchrotron, or an 8-GeV proton linac. Both options are illustrated in Figure 1. This paper is a summary report of the synchrotron-based design. For details the readers are referred to Ref. [1].

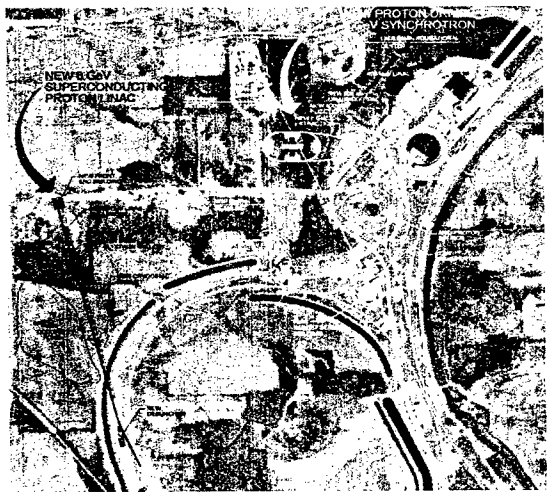


Figure 1: Layout of the two options of an 8-GeV Proton Driver: a synchrotron (yellow), or a linac (red).

LAYOUT AND PERFORMANCE

In Figure 1, the racetrack-shaped machine (in yellow) is a new 8-GeV synchrotron, or the Proton Driver. Also shown (in yellow) are the injection line (from the existing linac) and extraction line (to the existing Main Injector). The Proton Driver has a circumference of 474.2-m, the same as the present Booster.

The main parameters are listed in Table 1. The linac maximum beam energy is increased from 400 MeV to 600 MeV. The required beam intensity is 50 mA, usable pulse length 90 μsec, and repetition rate 15 Hz, all achievable in the present Linac. These numbers correspond to 2.8×10^{13} protons per pulse injected into the Proton Driver. Allowing reasonable beam losses during the cycle (10% at injection, 1% during ramp and at extraction), the design value is 2.5×10^{13} protons per pulse extracted from the Proton Driver. At 15 Hz and 8 GeV, the beam power is about 0.5 MW. With a Proton Driver, the present Main Injector can also be readily upgraded to 2 MW, a would-be most powerful machine in the world [4].

Table 1: Parameters of the Proton Driver

Linac (operating at 15 Hz)	
Kinetic energy (MeV)	600
Peak current (mA)	50
Pulse length (μs)	90
H^- per pulse	2.8×10^{13}
Average beam current (μA)	67
Beam power (kW)	40
Synchrotron (operating at 15 Hz)	
Extraction kinetic energy (GeV)	8
Protons per bunch	3×10^{11}
Number of bunches	84
Protons per cycle	2.5×10^{13}
Protons per hour	1.35×10^{18}
Norm transverse emittance (mm-mrad)	40π
Longitudinal emittance (eV-s)	0.2
RF frequency (MHz)	53
Average beam current (μA)	60
Beam power (MW)	0.5

Compared with the present Booster, the Proton Driver would deliver 5 times more protons per cycle and 10 times more beam power. In order to achieve such an improvement in performance, the following measures are adopted in the PD2 design:

- The linac energy is increased from 400 MeV to 600 MeV. (The space charge scaling factor $\beta\gamma^2$ is increased by ~50%).
- The tunnel is twice as deep (27 ft.).
- The magnets have large aperture. The good field region is 4 in × 6 in.

0-7803-7738-9/03/$17.00 © 2003 IEEE

- The lattice has no transition crossing ($\gamma_t = 13.8$).
- The lattice has smaller beta-functions and dispersion (max $\beta_x = 15.1$ m, max $\beta_y = 20.3$ m, max $D_x = 2.5$ m).
- The RF cavity aperture is increased to 5 inches.
- The lattice has zero-dispersion long straight sections for the RF.
- The injected beam will be painted in transverse phase space to reduce space charge effects.
- The resonant power supply system is dual-harmonic (15 Hz plus a 12.5% 30 Hz component). This reduces the required peak RF power by 25%.
- A carefully designed 2-stage collimator system that will collect 99% of the uncontrolled beam loss.
- There is a perforated metal liner shielding the beam from the magnet laminations.
- The correctors (steering magnets and trim quads) are ac powered and have sufficient strength to make corrections through the full acceleration cycle.
- Space has also been reserved between the linac and the ring for a future linac energy upgrade up to 1.9 GeV. (The 600-MeV beam transport line is 254-m long.)

With these measures, it is believed that the Proton Driver can reach the required beam intensity while keeping the beam loss under control.

OPTICS AND BEAM DYNAMICS

Lattice

Lattice is the foundation of a synchrotron. It is worth making every effort to investigate all possible lattice candidates and choose the best one.

There are two basic requirements on the design: a transition-free lattice, and several dispersion-free straight sections. For high intensity operation in proton synchrotrons, transition crossing is often a major cause of beam loss and emittance blowup. One should avoid it in the first place. Dispersion in the RF, which is placed in one or more straight sections, may lead to synchro-betatron coupling resonance and should also be avoided. Other requirements include small beta and dispersion functions, large dynamic aperture, and ample free space for correctors and diagnostics.

A total of about a dozen lattices have been studied. The chosen one is a doublet 3-cell modular structure with a short dipole in the mid-cell, as shown in Figure 2. It meets all the requirements. The lattice consists of two arcs and two straight sections and has 2-fold symmetry. The details can be found in Ref. [5].

*Work supported by the Universities Research Association, Inc. under contract No. DE-AC02-76CH03000 with the U.S. Dept. of Energy.
#chou@fnal.gov

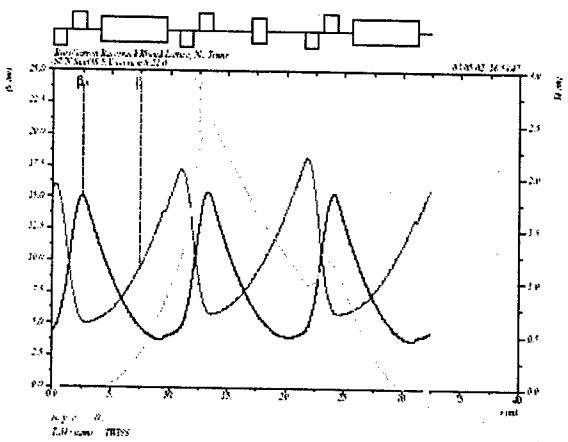


Figure 2: Lattice module of the Proton Driver. Each module has three doublet cells. The dipole in the mid-cell is short. The phase advance per module is 0.8 and 0.6 in the h- and v-plane, respectively. There are five modules in each arc.

Space Charge

Amongst various beam physics issues, the space charge is a major concern. It is often the bottleneck limiting the beam intensity in an intense proton source, in particular, in a synchrotron, because the injection energy is low.

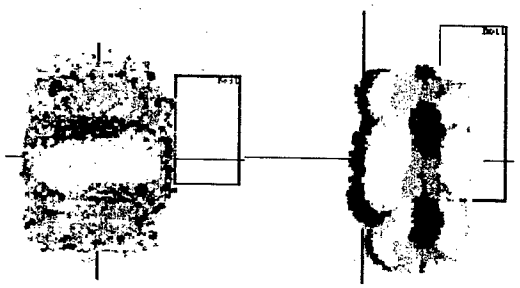


Figure 3: Space charge simulation using Track2D (by C. Prior). It shows the particle distribution after 45 turns injection in the Proton Driver with (left) and without (right) the space charge effect.

Numerical simulation codes Track2D and ORBIT are used in the design. They are particularly useful in helping determine the working point and painting method so that one may avoid resonance and minimize emittance dilution. Figure 3 illustrates how space charge dilutes the beam during multi-turn injection.

TECHNICAL SYSTEMS

All technical systems have been designed. Here is a summary of each system. The details can be seen in the corresponding chapters in Refs. [1] and [3].

RF

The RF system in the present Booster will be reused. Thanks to a dual harmonic magnet power supply (see

below), the peak RF power is reduced from 1.4 MW to 1.06 MW, which the present system can deliver. But the RF cavity bore will be enlarged from 2-1/4 inch to 5 inch.

Magnets

The magnets have a good field region of 4 in × 6 in. The dipole peak field is 1.5 Tesla. The lamination uses M17 silicon steel. There are 12 turns per pole. The copper conductor contains a cooling hole. In order to have a balance between low ac losses and a tolerable voltage-to-ground, three conductors and top/bottom coils are connected in parallel. An ac field measurement facility has been set up at the E4R area for measuring the field at 15 Hz.

Power Supplies

A main feature of the power supplies is that it is a dual harmonic resonant system. On top of 15 Hz there is a 12.5% 30 Hz component in the magnet current. This reduces the peak RF power by 25% and increases the up-ramp time by 14%. A bench test of this system will be performed by using the Booster magnets at the E4R.

Vacuum

The original design uses an external vacuum skin for the magnets and metallic perforated liners to shield the beam from the lamination. However, a new design, which employs a thin metallic pipe reinforced by spiral ribs, looks promising and would be a better choice [6].

Beam Loss and Collimation

The beam loss budget is 10% at injection and 1% during acceleration and at extraction. Among these losses, most would be collected by a 2-stage collimation system, which has efficiency close to 99%, leaving the uncontrolled loss in the rest of the machine below 1 W/m.

Injection

One important advantage of a synchrotron-based Proton Driver is the low injection beam power. This makes the injection much easier compared with a linac-based approach. The stripping foil temperature rise is only about 800 K. A painting scheme has been worked out to obtain a uniformly distributed beam in the phase space with small emittance dilution caused by the space charge.

Extraction

This is an improved version of what is used in the present Booster. In particular, the orbit bumps (doglegs) are longer and weaker in order to minimize the so-called dogleg effect, which was recently found to have a significant impact on the Booster performance [7].

H^- Source and Linac

The H^- source and the linac front end will be upgraded. While the linac beam current will remain about the same (50 mA), the brightness will be increased by a factor of 3, the pulse length increased from 25 μs to 90 μs. The Cockcroft-Walton will be replaced by an RFQ. There will also be a linac extension from 400 MeV to 600 MeV.

Civil Construction and Shielding

The Proton Driver enclosure is 16 ft × 9 ft with 24.5 ft of equivalent earth radiation shielding. It is twice deeper than the Booster tunnel.

COST AND SCHEDULE

A cost estimate to build a Proton Driver at Fermilab has been done by a bottom-up method. Namely, the technical system designs were given to the engineers in each relevant department. They came up with a cost estimate based on their experiences building similar systems before. These costs were summed up, adding to it the EDIA (17%), lab overhead (13%) and contingency (30%). The total estimated cost (TEC) is $235 M in FY02 dollars.

Because this project is yet to be approved by the funding agency, there is an uncertainty on the starting date of construction. The construction would take about four years. In a most optimistic scenario, the groundbreaking could be in 2005. The machine operation would then start around 2009.

ACKNOWLEDGEMENT

A group of accelerator physicists and engineers from Fermilab's Beams Division, Technical Division, and FESS and ES&H sections contributed to this study. A number of physicists from University of California in Los Angeles (UCLA), Oak Ridge National Laboratory, University of Hawaii, Stanford University and Rutherford Appleton Laboratory in England also participated and played important roles. This paper is a report on behalf of this study group. The author expresses his thanks to them for their commitment and contributions to this study.

REFERENCES

[1] "Proton Driver Study II, Part 1," edited by G.W. Foster, W. Chou and E. Malamud, FERMILAB-TM-2169 (May 2002). Also on the web: http://www-bd.fnal.gov/pdriver/8GEV/

[2] G. Barenboim et al., "Physics Potential at FNAL with Stronger Proton Sources," FERMILAB-FN-720 (June 2002).

[3] "The Proton Driver Design Study" edited by W. Chou, C. Ankenbrandt and E. Malamud, FERMILAB-TM-2136 (December 2000). Also on the web: http://www-bd.fnal.gov/pdriver/reports.html

[4] W. Chou et al., "2 MW Upgrade of the Fermilab Main Injector," this conference.

[5] L. Michelotti et al., "Optics of a Proton Driver," this conference.

[6] Z. Tang, W. Chou and A. Chen, "A New Kind of Beam Pipe for Rapid Cycling Proton Synchrotrons," this conference.

[7] W. Chou et al., "Fermilab Booster Modeling and Space Charge Study," this conference.

A NEW ANTIPROTON BEAM TRANSFER SCHEME WITHOUT COALESCING*

W. Chou#, J. Griffin, J. MacLachlan, S. Werkema, FNAL, Batavia, IL 60510, USA

Abstract

An effective way to increase the luminosity in the Fermilab Tevatron collider program Run2 is to improve the overall antiproton transfer efficiency. During antiproton coalescing in the Main Injector (MI), about 10-15% particles get lost. This loss could be avoided in a new antiproton transfer scheme that removes coalescing from the process. Moreover, this scheme would also eliminate emittance dilution due to coalescing. This scheme uses a 2.5 MHz RF system to transfer antiprotons from the Accumulator to the Main Injector. It is then followed by a bunch rotation in the MI to shorten the bunch length so that it can be captured by a 53 MHz RF bucket. Calculations and ESME simulations show that this scheme works. No new hardware is needed to implement this scheme.

INTRODUCTION

To increase the luminosity in the Fermilab Tevatron collider program Run2, one must increase the number of antiprotons (pbars) during collision. Currently the overall pbar transfer efficiency stays around 65%. Where do we lose them? From the pbar intensity plot (Fig. 1), there are two obvious places. One is in the Tevatron, about 20% loss from injection to collision. Another is in the Main Injector, about 10-15% loss during pbar coalescing. It is the latter that we want to get rid of so that the efficiency could be improved. Moreover, the new method would eliminate emittance dilution during coalescing, which also helps increase the luminosity.

The present pbar transfer scheme is as follows. In the Antiproton Accumulator, the pbars are first captured by the 2.5 MHz RF buckets. Then they split to small pieces and re-captured by the 53 MHz buckets. These small pieces are transferred to the MI 53 MHz buckets and accelerated to 150 GeV. Then a reverse process, called the coalescing, occurs. Namely, these small pieces are recombined in the 2.5 MHz buckets to form big bunches and rotated. These rotated bunches are once again captured by the 53 MHz buckets and ejected from the MI to the Tevatron. This complicated beam gymnastics works. However, beam loss and emittance dilution during coalescing have always been a concern. In the following sections, we propose a new scheme that will eliminate coalescing in the process.

NEW SCHEME

We give a step-by-step description of how this new scheme works:

1. The required longitudinal phase space density in the Accumulator is 6-8e10 pbars per eV-s, with the 1st transfer having higher density and the 9th transfer lower density. While this is a modest number compared with what was achieved in Run1b (Fig. 2) [1], we need about 50% increases from where we are now in Run2a (Fig. 3).

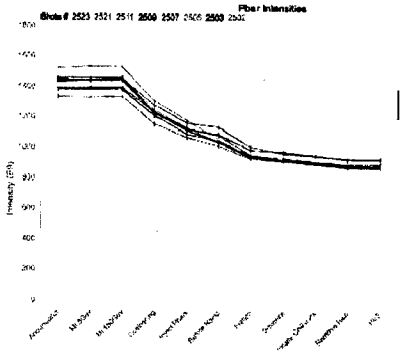


Figure 1: Pbar intensity plot of the 8 most recent shots as of May 9, 2003. The first big drop is the loss during coalescing. The remaining losses are in the Tevatron.

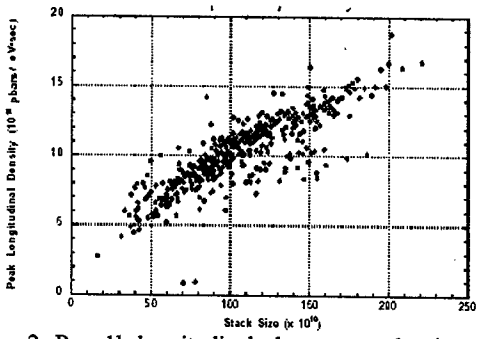


Figure 2: Run 1b longitudinal phase space density at the peak of the antiproton momentum distribution just prior to unstacking as a function of stack size, Ref. [1].

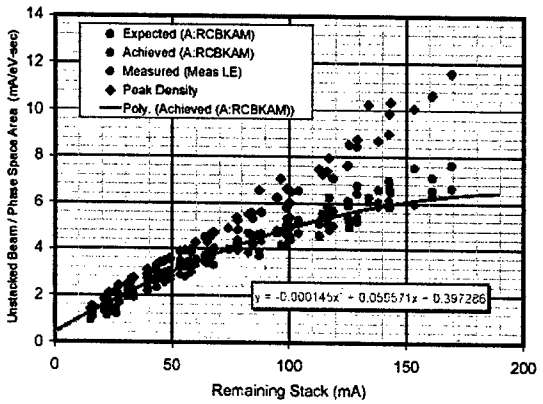


Figure 3: Run2a longitudinal phase space density as a function of stack size.

0-7803-7738-9/03/$17.00 © 2003 IEEE

2. Use ARF4 (h = 4, 2.5 MHz, 9.5 V) to capture 4 bunches from the cooled core. The bucket size is 0.37 eV-s. Each bucket contains 3e10 pbars (Run2a goal). The bucket size will be gradually increased to 0.47 eV-s from the 1st to the 9th transfer while keeping the number of pbars per bucket constant. The corresponding voltage increase is from 9.5 to 15.3 V.
3. Move these bunches to the extraction orbit and increase the RF voltage adiabatically to 100 V for narrowing the bunches.
4. Extract the 4 bunches and inject them into the carefully phase-matched 2.5 MHz RF bucket (h = 28) in the Main Injector.
5. The MI 2.5 MHz RF is set at its maximum voltage (60 kV). A bunch rotation will occur immediately after the injection. The bunch length will be compressed to about ±6 ns. (An alternative approach is to set the MI 2.5 MHz RF at the matched voltage 0.25 kV to receive the bunches prior to bunch rotation.)
6. Capture these bunches by the h = 588 RF in the MI (52.81 MHz, 693 kV). The bunch spacing will be 396 ns.
7. Adiabatically increase the h = 588 RF voltage to 1.8 MV to increase the bucket size and narrow the bunches. Accelerate the 4 bunches to 150 GeV and inject them into the Tevatron.
8. Repeat this process 9 times.

The results obtained from analytic calculations and numerical simulations using ESME are in general agreement. Both show that this scheme works. Fig. 4 are the plots from ESME.

BEAM PHYSICS ISSUES

Longitudinal Density Dilution

The longitudinal density of the antiproton beam will decrease during the 9 transfers. In order to have 3e10 pbars per bunch, we use a bunch area of 0.37 eV-s for the 1st transfer and 0.47 eV-s for the 9th transfer. This implies a 50% increase in longitudinal density from the present operation and requires beam study in the Accumulator.

Momentum Acceptance of the MI

The measured aperture acceptance was $\Delta p/p = \pm 0.7\%$ (i.e., ± 63 MeV) [2]. The bucket height of the 53 MHz RF at 1.8 MV is ± 44 MeV. It can accommodate a 0.75 eV-s bunch. There should not be any problem at the injection.

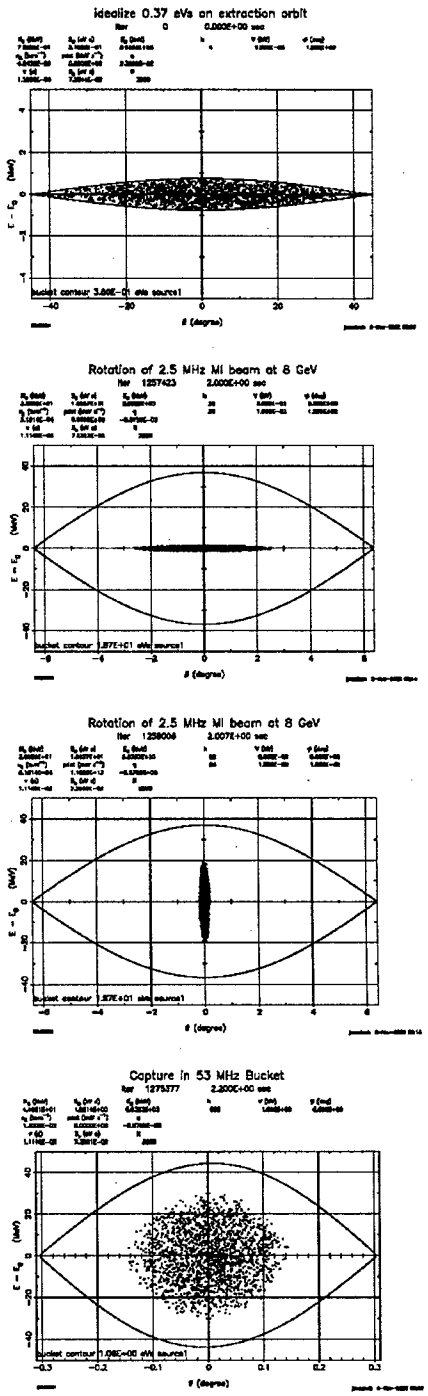


Figure 4: ESME simulation. From top down: (1) h=4 (2.5 MHz) RF capture of 0.37 eV-s pbar bunches in the Accumulator; (2) h = 28 (2.5 MHz) RF capture of pbars in the Main Injector at V_{rf} = 60 kV before the rotation; (3) after the rotation; (4) h = 588 (53 MHz) RF capture of pbars in the Main Injector and V_{rf} adiabatically increased to 1.8 MV.

*Work supported by the Universities Research Association, Inc. under contract No. DE-AC02-76CH03000 with the U.S. Dept. of Energy.
#chou@fnal.gov

Transition Crossing in the MI

The pbar bunches will be 4 times more intense than they are now when crossing the transition. But compared with the proton bunch intensity in \$29 cycle (6e10), pbar bunch intensity (3e10) is only half that value. Furthermore, the longitudinal phase space density of the pbar bunches is much lower than that of the protons.

However, the large pbar bunch emittance (0.37-0.47 eV-s) is a concern. An analysis was done for the transition crossing and found that both the emittance dilution and maximum energy spread were tolerable. They are, respectively, 20% and ± 0.6% for 0.37 eV-s bunches, and 25% and ± 0.7% for 0.47 eV-s bunches.

As a fallback plan, a gamma-t jump system can be readily implemented to improve transition crossing [3].

Another option is to use a third harmonic RF system during transition crossing. The experiment was done on the Main Ring at Fermilab. The hardware exists and can be installed in the Main Injector.

Beam Loading during Bunch Rotation

During bunch rotation using the 2.5 MHz RF in the MI, the beam loading of the 53 MHz RF needs to be compensated. There are two possible solutions: (i) to install a feedback and a feedforward system (which is an on-going activity); (ii) to lower the effective cavity impedance by a factor of 3-4 by lowering the screen voltage from 2 kV to -100 V (a proposal by J. Griffin, which needs to be tested).

HARDWARE AND SOFEWARE ISSUES

An important advantage of this new method is that no new hardware is needed for its implementation. Several issues regarding hardware and software are addressed below:

- Although the maximum voltage of the ARF4 can reach 900 V, we found that the 2.5 MHz bunch rotation and 53 MHz RF capture work better if we use 100 V instead of 900 V.
- A technical challenge is the regulation requirement of the ARF4 to the level of several volts in order to create a 0.37 eV-s bucket. But this is possible. [4]
- There is a slight frequency mismatch between the Accumulator 2.5 MHz RF and the MI 2.5 MHz RF (< 3 kHz). But this can be taken care of. [5]
- The MI 2.5 MHz RF voltage can be jumped quickly from 0.25 kV to 60 kV for bunch rotation [5]. This system has a nominal Q = 100, which gives a field decay time constant τ = 12.7 μs. Measurement shows the actual decay time is shorter. Therefore, it is possible to use the matched RF buckets to receive bunches from the Accumulator prior to the rotation (an option).
- Presently the MI 53 MHz RF cannot operate at its full voltage (4 MV) at injection due to tuner sparking. This will limit the achievable bucket size and need to be discussed with the RF group. We assumed 1.8 MV in this study.

BEAM STUDY PLAN

A two-phase beam study plan is under consideration for testing this new method.

Phase I

2.5 MHz pbar beam transfer, capture and bunch rotation:

- Develop MIRF procedures:
  1) RFI assistance to build and adjust I6 files for the required 2.5 MHz and 53 MHz RF sequence
  2) Use of a 2.5 MHz bunch length monitor
- Develop ARF procedures:
  To build and adjust ARF3 and ARF4 sequence for 2.5 MHz beam transfer to the Main Injector

Phase II

Develop procedures to maximize the pbar longitudinal density extracted from the Accumulator and determine what pbar longitudinal density is achievable:

- New version of VSA software that determines frequency and bucket area for extraction
- Test software on proton beam
- Test software on pbars left over after a shot (abort transfers in MI)
- Verify that the required 50% increase in core longitudinal density can be achieved by doing a shot to the Tevatron with a pbar stack of at least 120 mA.

ACKNOWLEDGEMENT

There have been helpful discussions with K. Koba, B. Chase and D. Perterson on this new method.

REFERENCES

[1] V. Bharadwaj et al., "Fermilab Collider Run 1b Accelerator Performance," FERMILAB-TM-1970 (April 1996).
[2] K. Koba, private communication.
[3] W. Chou et al., "Design of a Gamma-t Jump System for Fermilab Main Injector," Proc. PAC 1997 (Vancouver, Canada), pp. 994-996.
[4] D. Peterson, private communication.
[5] B. Chase, private communication.

Proceedings of the 2003 Particle Accelerator Conference

OPTICS OF A PROTON DRIVER*

L.Michelotti, W.Chou, A.Drozhdin, N.Gelfand, C.Johnstone (FNAL)†
A.Garren (LBL), S.Ohnuma (U.Hawaii), G.Rees (RAL), D.Ritson (SLAC)

Abstract

In a four month study, a design for a Proton Driver was developed as a possible replacement for Fermilab's Booster. Its optical properties are summarized briefly.

1 OVERVIEW

A Proton Driver design (PD2) was developed as a possible replacement for Fermilab's Booster in a four months' study involving more than sixty participants. Constraints that influenced the design, as well as achieved values, are summarized in Table 1; constraints are identified with an asterisk. Based primarily on considerations of available space and the size of lattice functions, a superperiod 2 racetrack configuration was chosen: two 75.44 m straight sections connected by 161.66 m, 180° arcs.[1] Transition is avoided by requiring γ_t to be beyond the reach of the extraction energy.

The racetrack's straight sections will be used for injection, extraction, tuning, and acceleration; collimation and (possibly) tuning will be done in the arcs. Trim quads should be powered symmetrically so as to maintain superperiodicity. It is intended to reuse RF cavities from the current Fermilab Booster in the Proton Driver's straight sections. At least 21 will be needed. The phase advance between kickers and septa as well as lattice functions at various extraction devices were chosen so as to avoid excessive demands on magnets.

In order that quadrupoles and dipoles track well during the ramp, while avoiding both saturation and excessive power loss, it was decided early to limit the maximum field in dipoles to 1.5 T and the peak gradient in quadrupoles to 10 T/m. Because of fabrication requirements for magnet ends and bellows, the minimum space between quadrupoles (in a doublet) was set to 47 cm; the minimum space between a quadrupole and a dipole, to 85 cm.

Phase space painting will flatten the transverse charge distribution, reducing space charge tune spread. The invariant transverse beam emittance, after painting and including space charge effects, is to be no larger than 40 π mm-mr (95%). Dynamic aperture should be *at least* three times that number, for the entire momentum range of $\pm 1\%$. Emphasis was placed on minimizing the maximum values of lattice functions, β_x and β_y, and horizontal dispersion, D. To satisfy physical aperture requirements, a criterion was informally established that set upper bounds of $\beta \leq 20$ m and $D \leq 2.5$ m. Together, these assure a maximum horizontal excursion of $x \approx \pm 5$ cm from the closed orbit, evenly divided between dispersion and emittance, and $|y| < 2.2$ cm.

length	474.2 m *
kinetic energy	600 MeV * to 8 GeV *
revolution frequency	501 kHz $\leq f \leq$ 629 kHz
RF frequency	53 MHz *
RF cavity length	2.35 m *
protons per bunch	$\approx 3 \times 10^{11}$ *
cycling frequency	15 Hz *
transition	$\gamma_t = 13.8 > 9.5$ *
natural chromaticity	(-13.6, -11.9)
momentum acceptance	$\lvert \delta p/p \rvert < 0.01$ *
phase advance	$\Delta\psi_{\rm arc}/2\pi = (n_x, n_y)$ * $= (8, 6)$
tunes	(11.747, 8.684)
dynamic aperture	$> 120\pi$ mm-mr *
magnetic fields	$\leq$ 1.5 T, dipoles, * $\leq$ 10 T/m, quadrupoles *
lattice functions	max (β_x, β_y) $=$ (15.1 m, 20.3 m)
max dispersion	2.5 m
max dipole correction	5 mrad *
element spacing	$\geq$ 47 cm, quad-quad, * $\geq$ 85 cm, quad-dipole *

Table 1: Parameters for a Proton Driver. Asterisks indicate design constraints.

To avoid any possibility of synchro-betatron coupling resonances [1], the PD2 design set to zero (a) chromaticity, using sextupoles in the arcs, and (b) dispersion in the straight sections, where RF cavities will be placed. To assure the latter, horizontal phase advance through an arc was required to be an integer multiple of 2π.

In what follows, we will summarize the optics of the PD2 lattice. Necessarily, this presentation is short, but more information, in greater detail, can be found in the Proton Driver Design Reports [2, 3].

2 LATTICE DESCRIPTION

The PD2 racetrack is partitioned into forty-four 10.777 m cells, 15 in each arc and 7 in a straight section. Each cell contains a defocusing (D) and focusing (F) quadrupole doublet on the main bus and a corresponding pair of independently powered trim quads. The F quad is 1.262 m long, the D quad, 1.126 m; trim quads, positioned just outside the doublet, are 20 cm long. This leaves about 7.1 m of empty space in each cell. In the arcs, it will be

* Work supported by the U.S. Department of Energy
† Operated by the Universities Research Association, Inc. under contract DE-AC02-76CH00300 with the U.S. Department of Energy.

[1] Several possible designs were considered before settling upon one. While the decisions that were made may not be final, they are, nonetheless, the ones under which this study was conducted.

0-7803-7738-9/03/$17.00 © 2003 IEEE

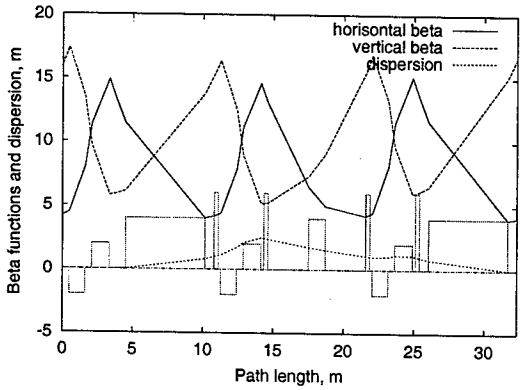


Figure 1: Lattice functions of an arc module, comprising three arc cells, treated as a periodic unit.

filled with dipoles and collimation hardware; in the straight sections, with hardware for injection, extraction, and acceleration. Additional diagnostic and control devices – beam position monitors, orbit correctors, dampers, and the like – must be squeezed into whatever space remains. (PD2's length of 474.2 m, equal to that of the Booster, severely limits space available for utility hardware.)

2.1 *Arc Module*

Each arc is organized into 5 modules of 3 cells, 15 cells in all. Quadrupole lengths were chosen so as to produce a phase advance per module of $(\Delta\psi_x, \Delta\psi_y)|_{\text{module}} = (8\pi/5, 6\pi/5)$ which sets the average phase advance per cell to be $(\Delta\psi_x, \Delta\psi_y)|_{\text{cell}} = (8\pi/15, 2\pi/5) = (96°, 72°)$. A horizontal phase advance close to 90° is convenient for injection and extraction. Because the total phase advance across an arc is $(\Delta\psi_x, \Delta\psi_y)|_{\text{arc}} = (8\pi, 6\pi)$, it is, to first order, optically transparent: its 4×4 transfer matrix is the identity. Thus, the arcs will preserve lattice functions, including zero dispersion, across the straights. If the phase advance per cell were exactly repeated throughout the racetrack, the tunes would be $(\nu_x, \nu_y) = (11.73, 8.80)$.

The two outer cells of an arc module contain a large dipole (5.646 m, 16.2° bend) and the inner cell a small one (1.188 m, 3.4° bend). Their lengths were chosen so as to create a first order achromatic bend, thus zeroing the dispersion between modules. As a stand-alone periodic unit, the lattice functions of a single arc module would be as shown in Figure 1

Four chromaticity correcting sextupoles are placed in each arc module. To conserve space, they replace the four trim quads closest to the short dipole. (They are shown as tall thin elements in Figure 1.) Alternatively, it may be possible, and perhaps preferable, to build a correction package consisting of quadrupole and sextupole. If not, then we must rely on two trim quads (not shown) in the remaining cell to control the phase advance through each module.

2.2 *Straight Section*

The main bus quadrupoles in a straight section cell are identical to their counterparts in the arc cell; dipoles are removed, and trim quads replace the sextupoles. The absence of dipole edge focusing distorts lattice functions (esp., β_y) slightly. Phase advance across a single cell is $(\Delta\psi_x, \Delta\psi_y)|_{\text{cell}} = (8\pi/15, 0.96 \cdot (2\pi/5))$.

3 ANALYSIS

When the straight sections and arcs are attached, a small vertical beta wave is established *but is confined to the arcs*, because of their optical transparency. The tunes associated with the base configuration (trim quads off) are shifted from $(11.73, 8.80)$ to $(11.747, 8.684)$. Space charge will reduce tunes in the core of the beam by an amount that will depend on painting. Protons undergoing large amplitude oscillations will be less affected by space charge, but their tunes will increase (slightly) due to the presence of chromaticity correcting sextupoles. The combined effects of space charge and sextupole fields (and octupole error fields) will spread the tunes away from that point in opposite directions. The single particle "optical tune," the "working point," acts as a reference for this distribution. As the beam's energy increases, the distribution will collapse into it: space charge forces decrease, as $v/c \to 1$, shrinking the distribution from below, and the sextupole/octupole tune spread decrease, as emittances become smaller, shrinking the distribution from above.

Chapter 3 of the Design Study Report [2] contains an optics analysis, including consideration of chromatic properties, tune footprint, field errors, steering magnets, tune adjustment, coupling, resonances, and dynamic aperture. In the following sections we will summarize only the discussions of the $\nu_x + 2\nu_y$ sextupole resonance and dynamic aperture.

3.1 *Sextupole Resonance: $\nu_x + 2\nu_y$*

A phase advance of $(\Delta\psi_x, \Delta\psi_y) = (8\pi/5, 6\pi/5)$ across an arc module means that the sextupoles' contribution to the $\nu_x + 2\nu_y = 29$ resonance driving term will add in phase from one module to the next. This is mitigated by the fact that 29 is an odd number, so that whatever resonance driving term is produced by one of the arcs should be cancelled by the other. Nonetheless, trusting in cancellations across opposite sides of a ring is risky. Superperiodicity of the lattice can be broken by the tuning quads in the straight sections, or simply because of field errors. A phase error between the two arcs will certainly arise. Estimating the effect of this resonance must take that into account.

A (moderately) "safe region" for the $\nu_x + 2\nu_y$ resonance is bounded by the curves [4, pp.233-238]

$$\frac{1}{8}\left(\frac{\delta}{g}\right)^2 = \frac{1}{4}\frac{\epsilon_y}{\pi} + 2\left(\sqrt{\frac{\epsilon_x}{2\pi}} - \frac{1}{4}\frac{|\delta|}{g}\right)^2 ,$$

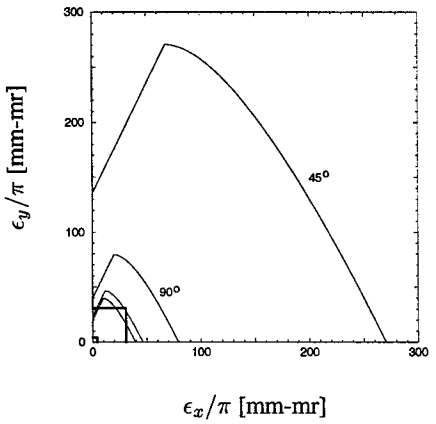


Figure 2: "Safe regions" for the $\nu_x + 2\nu_y$ resonance, in the base configuration, when $\Phi \in \{45°, 90°, 135°, 180°\}$, with invariant emittance of 40π mm-mr shown at injection and extraction. Ignoring space charge and second order sextupole effects, the injected beam is within the boundary provided that $\Phi \ll 105°$.

$$\text{and} \quad -\frac{1}{4}\left(\frac{\delta}{g}\right)^2 = 2\frac{\epsilon_x}{\pi} - \frac{\epsilon_y}{\pi} ,$$

where $\delta = \nu_x + 2\nu_y - 29 = 0.12$ and $g = (\sqrt{2}/8\pi)\times$ $|\sum(B''l/B\rho)\sqrt{\beta_x}\beta_y \exp[i(\psi_x + 2\psi_y - \delta\cdot\theta)]|$. If sextupoles existed in all three of an arc module's cells, the value of g for one module would (almost) vanish, because $\langle\Delta(\psi_x + 2\psi_y)|_{\text{cell}}\rangle = (2/3)\cdot 2\pi$. However, with sextupoles in only two of the three cells, the value of g for one arc module is $\approx 1.36\ \text{m}^{-1/2}$. Let the phase error between the two arcs be $\Phi \equiv \Delta\psi_x + 2\Delta\psi_y$. Then,

$$g_{\text{racetrack}} = 2\,|\sin(\Phi/2)|\,g_{\text{arc}} \approx 14\ \text{m}^{-1/2}|\sin(\Phi/2)| .$$

The "safe regions" are plotted in Figure 2 for $\Phi \in \{45°, 90°, 135°, 180°\}$. Two squares in the lower left corner show the beam emittances at injection and extraction. The boundary crosses the injected beam at $\Phi \approx 105°$. Superperiodicity must be preserved to a value much smaller than that.[2]

3.2 *Dynamic Aperture*

Dynamic aperture was estimated by tracking a single particle within the static magnetic environment produced by dipoles, quadrupoles, and chromaticity sextupoles. Among the effects not considered were space charge, synchrotron oscillations, acceleration, and magnetic field errors. (Details of the procedures used can be found in the Design Study Report [2].) Thus, results obtained should be considered an upper bound on the actual dynamic aperture. They are shown in Figure 3 at the injection energy

[2]This optimistic statement does not take into account the effects of tune spread. A more conservative estimate would restrict Φ to a value four or five times smaller. (See reference [2])

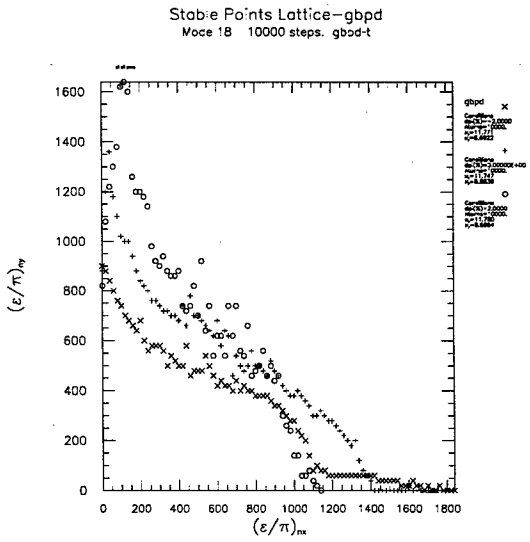


Figure 3: Dynamic aperture: Scatter plot of largest amplitude stable orbits at $\Delta p/p = 0$ and $\pm 2\%$.

of 600 MeV, where dynamic aperture is smallest. Along the diagonal, $\max \epsilon_{\text{inv}} \approx 10 \times 40\pi$ mm-mr. For purely horizontal orbits it increases to $\epsilon_{\text{inv}} \approx 25 \times 40\pi$ mm-mr, and for mostly vertical orbits it is slightly less, $\epsilon_{\text{inv}} \approx 20 \times 40\pi$ mm-mr.

Peaks of the tune spectra for orbits just inside the dynamic aperture were calculated. All but four cluster on the resonance line $4\nu_y = 35$. Chromaticity sextupoles both excite this resonance and provide the necessary tune spread to put it within the reach of very large amplitude orbits.

4 REFERENCES

[1] A. Piwinski. Handbook of Accelerator Physics and Engineering, p.72. Edited by A. Chao and M. Tigner.

[2] Proton Driver Design Study II, Part 1. Technical Report, Fermilab, May, 2002. Fermilab-TM-2169. Available electronically at http://fnalpubs.fnal.gov/archive/2002/tm/TM-2169.html

[3] The Proton Driver Design Study. Technical Report, Fermilab, December, 2000. Fermilab-TM-2136. Available electronically at http://library.fnal.gov/archive/test-tm/2000/fermilab-tm-2136.shtml

[4] Leo Michelotti. *Intermediate Classical Dynamics with Applications to Beam Physics*. John Wiley & Sons, Inc., New York, 1995.

APPLYING VIRTUAL PROTOTYPING TO THE INNOVATIVE DESIGN OF LOW ENERGY ACCELERATORS*

Mingwu Fan, Shiqi Li, Tiaoqin Yu, Dezhi Chen, Yongqian Xiong
Huazhong University of Science and Technology, Wuhan 430074, CHINA

Abstract

Based on the accelerator theory and virtual prototyping technique, an accelerator virtual prototyping system (AVPS) is formulated, implemented for the innovative design of low energy accelerators. The framework of AVPS takes into account the needs of manufacture, assembly/disassembly, operation, and maintenance in a virtual environment during the design phase. In order to guarantee the reliability of AVPS, Augmented Reality (AR) technique is used to integrate the virtual environment and experimental subsystem. Common Object Request Broker Architecture (CORBA) middleware for distributed, object-oriented applications is used to develop and implement the framework. The main components of AVPS include AR subsystem, distributed computing environment and data warehouse.

INTRODUCTION

In 1990s, with the development of Virtual Reality (VR) and CAD/CAM/CAE technologies, a new design method called Virtual Prototyping (VP) has been proposed and used in design of airplanes, cars and other mechanical products. Comparing with CAD/CAM/CAE methods, VP presents an integrated design environment in which the design, manufacture, assembly, operation and maintenance could be discussed before the machine being built. Recur to the use of VR technology, VP provides a friendly interactive interface which allows designers to track and to control the design process. In other words, VP is a development process completely implemented in computer, which can be used to replace or decrease the physical experimental prototype. Consequently, VP is an ideal method to condense time, costless, and risk of product development.

In the field of accelerators, CERN used VR to guide the design of LHC in 1996, and a Virtual Environment Navigation in the Underground Sites system (VENUS) was developed. Using VENUS, engineers can easily to know the work process of LHC and its complex structure. Subsequently, the concept of "virtual accelerators" was proposed by KEK and Jefferson Lab [1-3].

This paper applied VP technique into the research of low energy accelerators. The unique of VP we used is based on augmented reality (AR), which integrates the computing subsystem and experimental subsystem together in the interactive environment. After proposing the framework of AVPS, the key techniques are discussed. A design example of a 30MeV cyclotron is given to show how AVPS system works.

* Supported by National Nature Science Foundation of China

FRAMEWORK OF AVPS

The hiberarchy of AVPS developed by HUST has four layers, namely, the interface layer, the application layer, the data layer, and the support layer, as shown in Figure 1. The interface layer is an augmented reality subsystem made up of virtual environment and experimental subsystem. By using of sensors and actuators, users can interact with AVPS in a natural way. The application layer is a distributed computing environment (DCE) based on CORBA. Programs used for modelling, analysis, manufacture, assembly, debugging and maintenance are encapsulated as a CORBA object. The data layer forms a data warehouse made up of database, knowledge base and corresponding management programs. It provides data information, status information and control information of the system, including the accelerator's performance data, geometry data, and engineering data produced in the process of evolving. The technique standards, criterion and generic data used in the whole produce period are stored in the knowledge base. The support layer is the basis of the AVPS, it includes computer operating system (OS), network, protocol, database management system and knowledge base management system.

TECHNIQUE CHARACTERISTICS

Augmented Reality

As a bridge linking the real object and the virtual reality, the basic idea of an AR system is the mixing of real and virtual images with an enhancement of the user's perceptions of the real world. AR integrates VR environment and real world into an entity, in which they can complement each other. In AVPS, the VR environment is an advanced interface through which users can design, analyze, manufacture, assembly/disassembly, and maintain accelerators in a natural way. Considering that AVPS needs high performance graphics display ability, OpenGL and Performer are used as a develop tool to program the VR environment on SGI graphics workstation. Then CORBA is used to link it with other components. The other important part in the AR system is the experimental system.

Distributed Computing Environment

CORBA has been selected as middleware for building a distributed computing environment, which is a software standard for distributed, heterogeneous, object-oriented applications. It is open, robust, interoperable, multi-platform and multi-user supported. CORBA applications are composed of objects, individual units of running

0-7803-7738-9/03/$17.00 © 2003 IEEE

software that combine functionality and data, and that frequently represent something in the real world. The interface is the syntax part of the contract that the server object offers to the clients invoking it. Any client that wants to invoke an operation on the object must use this IDL interface to specify the operation, and to marshal the arguments that it sends. When the invocation reaches the target object, the same interface definition is used to unmarshal the arguments so that the object can perform the requested operation with them. The interface definition is then used to marshal the results for their trip back, and to unmarshal them when they reach their destination. In AVPS, a typical client and object implementation is virtual reality environment and analysis component such as magnet, cavity, injection et al.

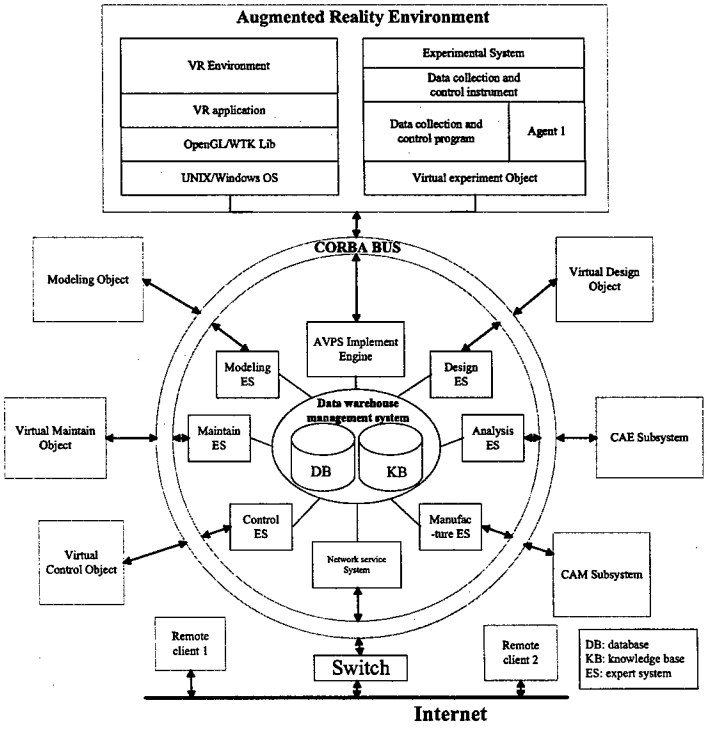


Figure 1: Framework of AVPS

Data Warehouse

The essential of the AVPS is to use an exact digital model to simulate all activities of an accelerator during its lifecycle. Therefore, an efficacious data warehouse is very important. It must include the following models: the structural data, physical property data, environment data, accelerator operation data, interlock and corresponding management system. All these models are integrated into a database and knowledge base. In order to manage and access the complex information in AVPS, data warehousing approach is used, in which the integrated information is available for immediate querying and analysis by clients.

APPLYING AVPS TO SIMULATE THE EVOLVING PROCESS OF ACCELERATORS

AVPS is an integrated solution scheme of accelerator's design, analysis, and simulation of manufacture, assembly, controlling, and maintaining. Through AVPS, engineers can simulate accelerators by using coarse granularity models or refined ones, can test the whole equipment or its subsystem in computer. The fidelity that AVPS can get is decided by the granularities of AVPS model. A refined prototype model can simulate accelerators realistically. It describes accelerator and its subsystem in detail. Fig.2 shows the prototype model of a 30MeV accelerator, CYCIAE-30.

Modelling the Accelerator

Modelling is the base of virtual prototyping. Its purpose is to create virtual prototype of the accelerator. The virtual prototype should include all the geometrical and physical information, such as the geometry shape, the positions and link relations, and physical properties of the parts, and beam information. Management of virtual prototype is the first considerable subject in this stage. Three model libraries, namely, basic library, auxiliary library and custom library, can be built. The basic library stores basic information such as geometry shape, the

position and link relation of the parts. While the auxiliary library stores physical properties, particle beam information, and so on. The custom library is designed for the user's expending.

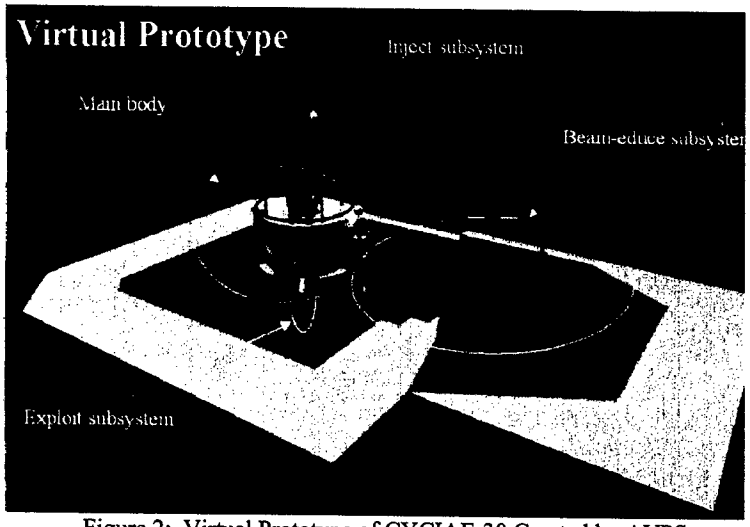


Figure 2: Virtual Prototype of CYCIAE-30 Created by AVPS

Another important subject is the structure of virtual prototype. In AVPS, both graph structure and tree structure methods are used to represent virtual prototype. The relationships among accelerator parts are represented by graph structure method. While the tree structure method is used to describe the hiberarchy of accelerator. In AVPS, engineers can build basic elements firstly, and then organize them into a higher layer, and integrate layers into a uniform system at last.

Virtual Assembly/Disassembly

Virtual assembly/disassembly is the digital mapping of real corresponding process. In order to optimize the path and process of assembly/disassembly, process programing and collision detection technology must be used to handle virtual prototypes created in the modeling module.

The assembly module of AVPS is an interactive, 3D graphic simulation tool, specifically designed for use in developing and documenting assembly processes. Apart from simulating complex assembly/disassembly processes, users can also investigate the assembly feasibility, determine required product design changes, document optimal assembly sequences, and estimate the cycle time involved, with the help of sequence charts. These can also be extended to produce training "movies" for shop floor personnel. Some of the main features of this module are:

- Interactive creation of part trajectory paths.
- Automatic creation of collision-free trajectory paths.
- Interactive creation of process sequences displayed by sequence charts.
- Sequence output in standard spreadsheet formats for integration into assembly process plan documentation.
- A single-pick REVERSE function, which reverses an existing assembly sequence into a disassembly sequence and vice versa.

Particle Motion Simulation

Based on the analysis of main parts, simulation of the accelerator and its subsystems can be carried out in AVPS. These subsystems include the particle injecting system, the accelerating system, the vacuum control system, and the cooling control system, and so on. Integrating parts analysis, subsystem simulation, and model library, AVPS provide the function to simulate the working process and also, AVPS can help engineer to simulate the process of manufacture, control, cooling, and maintain, and change correspond parameters to optimize its performance.

CONCLUSION

A CORBA based virtual prototyping system, AVPS, was proposed, implemented, and used to analysis, design and simulate the evolving process of low energy accelerators. It integrates experimental system, distributed numerical simulation system, and virtual reality environment into a uniform framework. Therefore, AVPS can be applied to condense time, and risk, and to design new type of accelerator.

REFERENCES

[1] J. F. Balaguer, de Gennaro Silvano, "VENUS: A virtual reality project at CERN", Computer Graphics (ACM), 1994, 30(4): 40-43

[2] K. Noriichi, "Virtual accelerator and fundamental guidelines towards sharable software for accelerator control systems", Nuclear Instruments & Methods in Physics Research, 1994, Elsevier Science B V: 497-500

[3] J. L. Anderson, "Technology development for the accelerator production of Tritium", Proc. of PAC 1999, March 27-April 2, New York, v1: 571-573

FIRST TESTS OF A CW RFQ INJECTOR FOR THE IUCF CYCLOTRONS

V. P. Derenchuk*, V. Anferov*, D.L. Friesel*, R.W. Hamm†, W.P. Jones* and J. Staples‡
*Indiana University Cyclotron Facility, Bloomington IN, †AccSys Technology, Inc., Pleasanton CA,
‡Lawrence Berkeley National Laboratory, Berkeley, CA

Abstract

A 750 keV proton injector is being installed in place of a 600 kV Cockroft-Walton high voltage terminal at the Indiana University Cyclotron Facility [1]. The injector features a microwave ion source, a 20 keV to 750 keV CW RFQ and a quadrupole triplet to focus the beam into the 15 MeV injector cyclotron. Two solenoids and one pulsed lens are used to match the 20 keV proton beam to the RFQ and to rapidly change the beam intensity. The injector has been tested offline; the results will be described in this paper.

INTRODUCTION

The Indiana University Cyclotron Facility (IUCF) is in the final phase of an upgrade program of the 210 MeV proton cyclotrons. These accelerators will be used to provide a fixed energy proton beam to the Midwest Proton Radiotherapy Institute (MPRI) for cancer treatment and other applications [2]. Part of this upgrade is to replace the 600 kV Cockroft-Walton high voltage terminal with an AccSys PL-1 20 keV to 750 keV CW radio frequency quadrupole (RFQ) accelerator [3]. This system is expected to operate with at least 95% reliability, should be easy and quick to repair and should have infrequent maintenance requirements.

The cancer clinic requires between 2 nA and 125 nA of 206.5 MeV beam delivered to the entrance of one of three treatment rooms. The intensity should be stable to 5% and have ripple less than 5% for the two minute duration of each treatment plus a several minute setup time. Each treatment will require a unique beam intensity and will typically be different than the intensity the cyclotron operators will use to monitor the beam at a remote beam dump. A pulsed lens is used as a beam intensity modulation system (BIMS) to adjust the level of the beam intensity within 2 ms to 3 ms after a change is requested.

The proton injector, shown in Figure 1, consists of a 2.45 GHz microwave proton source [4] which is a modified version of the LEDA 100 mA CW source [5]. A 20 kV, four-electrode extraction system forms a beam that is then transported by two electromagnetic solenoids which match the beam to the RFQ acceptance parameters. An electrostatic chopper phase locked to one-half of the cyclotron frequency operates at 17.79 MHz to form beam pulses that match the ± 6° RF phase acceptance of the cyclotrons. The BIMS solenoid which adjusts the beam focusing at the entrance of the RFQ has a ferrite gap with return yoke and within 3 ms is changed to any requested current between 0 A and 400 A. The 750 keV beam from the RFQ is focused into the first electrostatic bend of the cyclotron by an NEC built quadrupole triplet [6].

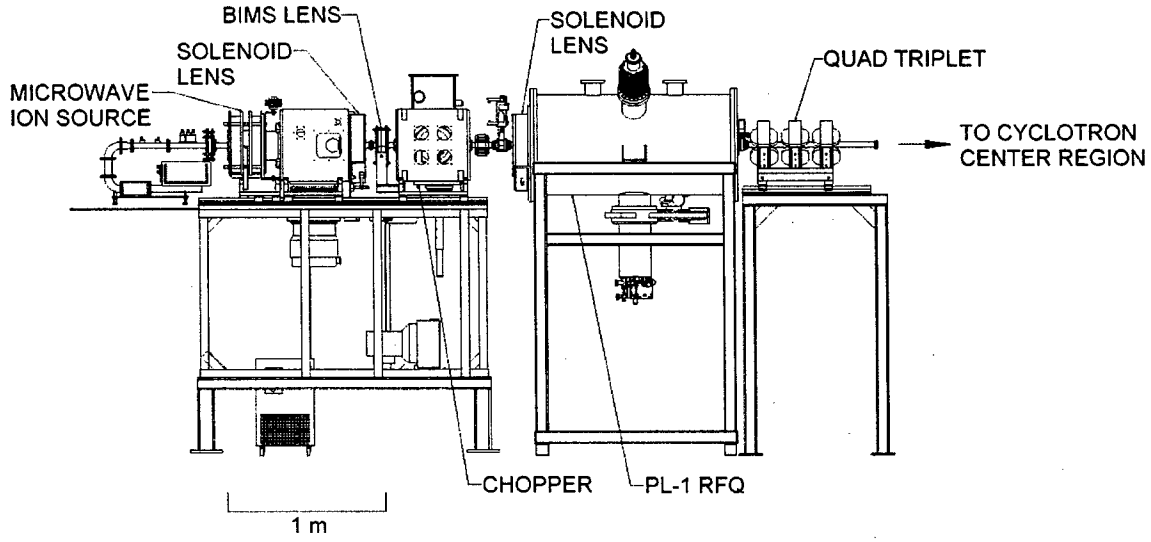


Figure 1: Schematic of the 750 keV proton injector. The beam height and centerline of the injector is 196.4 cm above the floor.

*laddie@iucf.indiana.edu

0-7803-7738-9/03/$17.00 © 2003 IEEE

ION SOURCE

The 2.45 GHz microwave ion source has many similarities to the LEDA source [5] but with much lower intensity and beam energy requirements. A 3D cutaway view in Figure 2 illustrates the primary components of the source. A four electrode 20 kV extraction system forms a proton beam of more than 5 mA. A 2.45 GHz magnetron supplies 1.2 kW of RF power through a circulator to a WR284 waveguide. A directional coupler connected to a three-stub tuner measures the forward and reflected powers. A choke flange coupling with a 3mm thick TFL spacer insulates the three-stub tuner from the source components that are elevated to the 20 kV extraction potential. A double-ridged tapered waveguide between the choke flange and the source body improves the matching of the RF to the source plasma. The microwaves are launched into the source volume through an Aluminum Nitride and Boron Nitride layered vacuum window [5]. A vacuum seal is made with a rectangular shaped metal gasket [7] that requires 5.6 N·m of Torque on the fasteners of a modified WR284 rectangular flange.

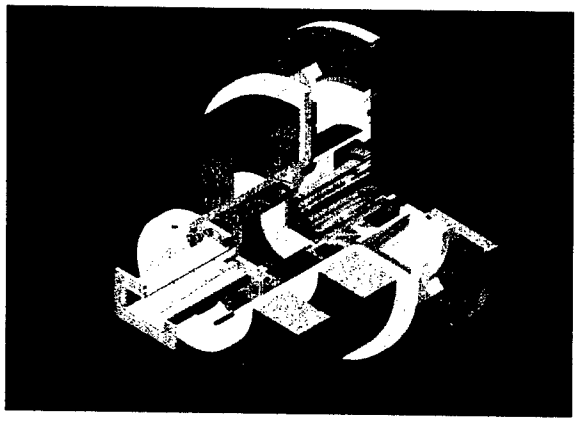


Figure 2: A 3D model of the ion source with a cutaway to show the internal components. The tapered ridged waveguide and source body are insulated from the two solenoid coils by a large nylon insulator and from the vacuum chamber by a ceramic cylinder.

The OFHC copper source body and end flanges are assembled with metal vacuum seals. A pure Boron Nitride (BN) liner covers the two inside ends of the source but the inner diameter of the chamber remains copper. The plasma is extracted via a hole in the BN through a 3.5 mm diameter emission aperture in the plasma electrode. Positive ions are accelerated to a grounded electrode with a 5 mm aperture then pass through a negatively biased electron stopper electrode. A final grounded electrode signals the entrance to the low energy beam transport line (LEBT).

The source has operated for a total of about 26 days including one 14 day period during which the source was vented to add a diagnostic, pumped down and operation recovered in less than 2 hours.

With the H_2 gas flow at 8.9 mbar l/s and the ion source coils set to produce a nominal 900 Gauss field, the plasma self starts at about 300 W of RF power. Nominal operation is with 750 W of RF power with only 10 W to 15 W reflected. Typically, the extraction current is 6 mA and more than 5 mA of beam current is observed 50 cm downstream. The electron stopping electrode operates at negative 150 V.

20 KEV BEAM TRANSPORT

The beam transport and matching section to the RFQ serves three purposes. Two solenoid lenses and Tantalum apertures collimate and focus the beam into the RFQ acceptance. The BIMS solenoid placed between the two matching solenoids is used to modulate the beam intensity according to the needs of the users. A pair of electrostatic plates chops the beam at 17.79 MHz to limit the beam injected outside of the phase acceptance of the cyclotrons.

The RFQ acceptance dictates that at the matching point, the beam must have a spot size of 3.2 mm and a 160 mrad angle of convergence. The symmetrical spot has Twiss parameters of $\alpha = 1.69$ and $\beta = 0.043$ mm/mrad and an emittance of 0.5 π·mm·mrad normalized to $\beta\gamma$ for 90% of the beam. The 20 keV beam emittance was measured upstream of the final solenoid lens and after a 1 cm collimator. At this location the proton emittance falls within an ellipse of 0.40 π·mm·mrad normalized to $\beta\gamma$ for 95% of the 1 mA beam. Heavier ions were clearly separated in phase space and comprised less than 15% of the total beam.

The BIMS solenoid is a 24 turn coil with a ferrite return path. It has an inner diameter of 4.8 cm and length of 7.6 cm with a future plan to install a 1.8 cm long focusing gap. During operation, the strength of the first lens will be lowered to decrease the transmission through the RFQ to the lowest requested level. The BIMS lens will be switched on with a 3 ms rise time at a strength that will give the required beam current out of the RFQ. The beam intensity is adjusted to a ratio of at least 30:1 at the exit of the cyclotrons. Should the lens fail to pulse on or fail off during a patient treatment, it will fail in a low current safe mode. The lens has been tested with 20 keV beam into a stop with a 1 cm aperture 25 cm downstream. As expected, the intensity was modulated by a modest 2:1 at that measurement location.

RADIO FREQUENCY QUADRUPOLE

The 20 keV to 750 keV accelerator is a radio frequency quadrupole (RFQ) built by AccSys Technology Inc. [3] and excited by a 20 kW CW, 213.48 MHz amplifier built by Amplifier Systems Inc. [8]. The basic design of this CW RFQ is described elsewhere [1,9].

Beam was accelerated through the RFQ in DC mode and chopped mode. As much as 0.6 mA of protons was measured after acceleration. The total beam transmission from a stop 30 cm upstream of the RFQ matching point was 70% and the proton transmission calculated to be about 90% after taking into account the 15% heavy ion

fraction at the stop. The optimal transmission through the RFQ occurred with an output power of about 12.5 kW from the amplifier. Figure 3 shows a plot of the output power and relative vane voltage vs. the beam transmission through the RFQ.

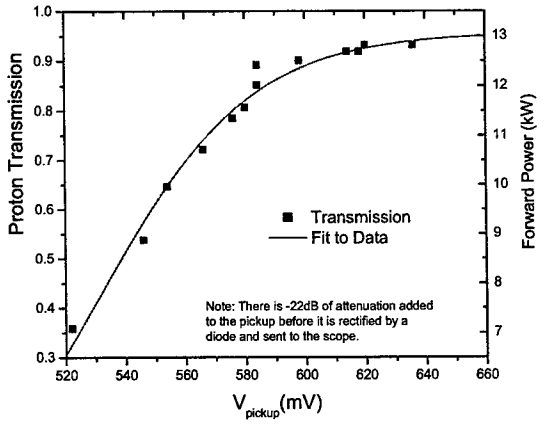


Figure 3: The proton transmission is plotted against a voltage derived from an RF pickup close to a vane. The forward power is plotted on the right-hand side.

The beam chopper was turned on and by adjusting a steerer upstream of the chopper, pulse selection of nearly 1:12 of the RF time structure was obtained. Figure 4 shows the signal of the chopped beam as measured by a gridded pick-up downstream of the quadrupoles and displayed on a 1 GHz bandwidth oscilloscope. The pick-up amplifier is AC coupled so each beam pulse has some undershoot. A 2nd harmonic RFQ RF signal is also observed as background noise.

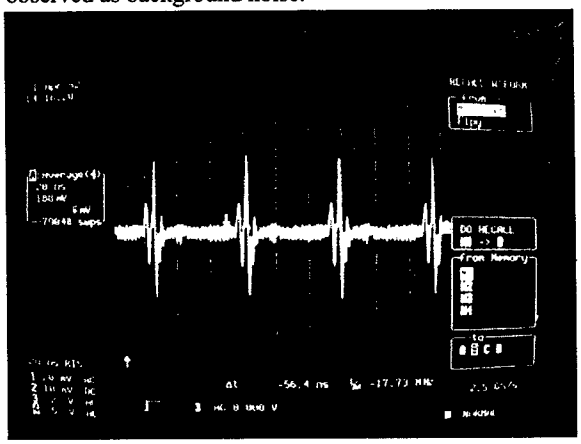


Figure 4: 750 keV chopped beam signal from a gridded pick-up observed on an oscilloscope. The central peak of each bunch falls within the RF phase acceptance of the cyclotrons. The horizontal scale is 20 ns/div.

Development of the RFQ operation will continue after its installation. A water cooled coupling loop will replace an air cooled version in order to improve the reliability of the vacuum window. A circulator is being added to the 50 ohm line between the amplifier and RFQ. Finally, a ± 0.1°C regulated chiller will be used to better regulate the vane temperature and hence the matching to the amplifier.

750 KEV BEAMLINE

The beam exiting the RFQ is strongly divergent vertically and convergent horizontally. A quadrupole triplet refocuses the beam so that it matches the acceptance of the cyclotron. The three quadrupoles are NEC [6] model MQS17L. The pole tips have a diameter of 4.47 cm, a physical length of 7.62 cm and are designed to operate with a pole tip strength of 0.27 T with an excitation of 30 A. The quadrupoles matched these specifications but water cooling had to be added to the coils for long term operation at 30 A.

The quadrupoles operate at their predicted values to bring the beam to a symmetric focus 40 cm downstream of the triplet. A wire scanner at this location is used to measure the beam width while the strength of the third quadrupole is adjusted. The results are used to calculate the area and orientation of the phase space ellipse of the beam at the entrance of the quadrupole. The vertical emittance was measured to have an rms emittance of $\varepsilon_y = 0.14$ π·mm·mrad normalized to $\beta\gamma$ and a horizontal emittance of $\varepsilon_x = 0.12$ π·mm·mrad. This agrees well with the predicted [1] emittances of 0.5 π·mm·mrad normalized for 95% of the beam.

CONCLUSIONS

The 750 keV CW proton injector for the IUCF cyclotrons was tested offline and produces and accelerates the beam as predicted. The injector is being installed at the time of this conference. Development and commissioning will continue after the installation is complete. This work was supported by the State of Indiana, Indiana University, and the DOE (Grant No. DE-FG-02000ER62966).

REFERENCES

[1] D.L.Friesel, et. al., App. of Acc. in Res. and Ind., eds. J.L. Duggan and I.L. Morgan, Denton, 651(2000).
[2] V. Anferov, et. al., FOAA003, these proc., (2003).
[3] AccSys Technology, Inc., 1177 Quarry Lane, Pleasanton, CA 94566-4757.
[4] T. Taylor and J.F. Mouris, NIM **A 336**, 1(1993).
[5] L.D. Hansborough, et. al., Proc. 1997 Particle Accelerator Conf., **IEEE 97CH37167**, 2740(1998).
[6] National Electrostatics Corp., 7540 Graber Rd., P.O. Box 620310, Middleton, WI 53562-0310 .
[7] Garlock-Helicoflex, 2770 The Blvd, Columbia, SC 29290. Custom designed "Delta" seal.
[8] Amplifier Systems, Inc., 18307 Napa St., Northridge, CA 91325.
[9] J.W. Staples, Proc. of the 1994 Linac Conference, Published by the National Laboratory for High Energy Physics, Tsukuba, Japan, 755(1994).

LONGITUDINAL TRACKING STUDIES FOR THE AHF BOOSTER SYNCHROTRON*

L. Rybarcyk†, Los Alamos National Laboratory, Los Alamos, NM 87545, USA

Abstract

The greenfield site option for the Advanced Hydrotest Facility (AHF) contains a 157-MeV H^- linac followed by two synchrotrons, a booster and a 50-GeV main ring. Several different lattice designs are under consideration for the main ring while two different booster designs are presently being studied. The first booster is a 4-GeV synchrotron operating at h=1 with a 5-Hz cycle. The second is a 9-GeV machine operating at h=2 with a 1-Hz cycle. Both designs are required to deliver ~3 x 10^{12} p/bunch. A longitudinal painting scheme was employed during injection to enhance beam quality and capture during the initial portion of the ramp. The longitudinal beam dynamics simulations were performed with the tracking code ESME. The purpose of these studies was to investigate parameter space and obtain estimates for the rf system requirements. This paper presents the results of these studies.

INTRODUCTION

The Advanced Hydrotest Facility as presently envisioned would allow for quantitative proton radiography of dynamic experiments in support of the stockpile stewardship program. The intensity and spatial resolution requirements dictate the charge per bunch and beam energy on target. With twelve axes for 3-D tomography and 1% intensity precision at the target, the 50-GeV Main Ring (MR) will be required to produce ~4.4 x 10^{13} protons per cycle (which includes losses and a safety factor). To fill ~22 rf buckets in the MR, a booster synchrotron will be required to provide ~3 x 10^{12} protons per bunch (ppb). Over the last two years, several MR and booster designs have been under consideration. One of the earlier booster designs was a 4-GeV synchrotron operating at h=1 with a 5 Hz cycle injecting into a MR of either conventional design that crosses transition or one with a negative momentum-compaction factor. The most recent booster design is a 9-GeV machine operating at h=2 with a 1 Hz cycle that would inject beam above transition in a conventional-style MR with a low γ_t.

BEAM DYNAMICS SIMULATIONS

The longitudinal, multi-particle beam dynamics simulations for these studies were performed with the program ESME [1]. In a typical run, 10^4 macroparticles were employed to represent ~4 x 10^{12} protons in a bunch. Space-charge impedance for a perfectly conducting wall was used and all low-level RF feedback was disabled. One handy feature of ESME is that the user can easily integrate additional subroutines into the code. This feature was used to produce several additional calculated quantities during the simulations.

Two new routines were added which calculated the bunching factor, σ_p/p, an estimate of the 95% longitudinal emittance and an estimate for the longitudinal microwave instability threshold using the Keil-Schnell criteria (using σ_p/p and a form factor of 1). Like the standard calculated quantities in ESME, these are calculated for each turn and stored in the history file for plotting or post-processing.

BOOSTER INJECTION

A 157-MeV H^- linac based upon the SNS design was used to provide the requisite beam for the booster. Following the linac are two rf tanks which serve a dual purpose. The first is to reduce the energy jitter of the beam out of the linac while the second is to vary the energy of the beam across a macropulse. This latter function will be combined in synchronous fashion with a beam chopper at the front-end of the linac and the booster rf system to provide a correlated, phase-energy painting scheme.

This longitudinal painting scheme produces a beam that is well matched to an existing rf bucket in the booster. The beam chopper is used to tailor the intensity of the beam through the macropulse and remove particles that would otherwise be outside of the rf bucket. By phase modulating the rf drive to the second post-linac rf tank, the energy of the beam injected into the booster can be varied over the rf bucket height. PARMILA beam dynamics simulations of the linac including the additional rf tanks were performed to create output distributions with 0 and ±1.15 MeV energy offsets. These distributions along with a simple $V_0 Sin\phi$ representation of the energy gain in the second tank and the desired chopping pattern were then used to produce the input beam distribution. An example of the resulting longitudinal distribution following 150-turn injection into the 9-GeV booster is shown in Figure 1.

4 GEV BOOSTER

The 4-GeV Booster is a symmetric, 9-sided lattice with a γ_t of 8.9 and circumference of 261 m. It is designed to operated at h=1 with a repetition rate of 5 Hz. The rf frequency spans the range of 0.592 to 1.128 MHz. The MR requirements for this machine dictate a 95% longitudinal emittance of ~2 eV-s. To accommodate this size beam and a non-zero dP/dt during injection, the rf voltage and synchronous phase were initially set to 8.0 kV and 2 degrees, respectively. Using the correlated phase-energy painting scheme, injection occurs over 150 turns

*Work supported by US DOE, Office of National Nuclear Security Administration

†lrybarcyk@lanl.gov

0-7803-7738-9/03/$17.00 © 2003 IEEE

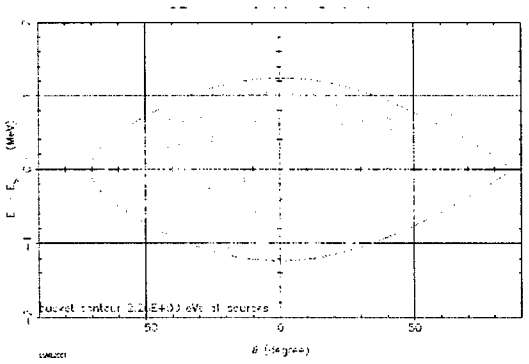


Figure 1: Longitudinal distribution of beam in 9 GeV booster following injection using correlated phase-energy painting scheme.

or 253 μs. The beam energy is swept repeatedly over ±1.15 MeV and the phase width chopped to within ±150 degrees. To inject 4×10^{12} ppb will require a peak (average) beam current from the linac of 5.0 (2.5) mA.

The magnet program is designed to provide the net energy gain in 121 ms. The asymmetry between rising and falling portions of the ramp was chosen to reduce the maximum rf voltage required during acceleration, while keeping the voltage across each main dipole magnet below the maximum available from the programmable power supply. The ramp begins with dP_s/dt constant at 373 MeV/c/s for the first 260 μs. This is immediately followed by a parabolic increase in P_s up through the first 10 ms. During this time the rf bucket area is increased slowly to help limit particle loss. All beam loss occurs during the first few milliseconds. The majority of acceleration occurs during the long linear ramp to ~97% of the final momentum. During the linear ramp, which ends at 113.5 ms into the cycle, the rf voltage and phase are held constant. During the last 7.5 ms of the cycle, dP_s/dt is reduced linearly to zero. The rf voltage is maintained at the maximum value while the synchronous phase diminishes to further reduce the phase-width of the beam for easier extraction.

Curves for P_s and dP_s/dt are shown in Figure 2. Over the cycle V_{rf} reaches a maximum of 64 kV while ϕ_s remains below 32 degrees as shown in Figure 3. The 95% emittance is nearly constant over the cycle at ~2.1 eV-s. The threshold for microwave instability was estimated to be a minimum of ~180 Ω at the end of the cycle. Beam capture and transmission is very good with over 99% of the injected particles reaching extraction.

9 GEV BOOSTER

The 9-GeV Booster is a 16-sided design with a γ_t of 13.87 and circumference of 480 m. It is expected to operate at h=2 and a repetition rate of 1 Hz, although an h=1 option is also being considered. The rf frequency

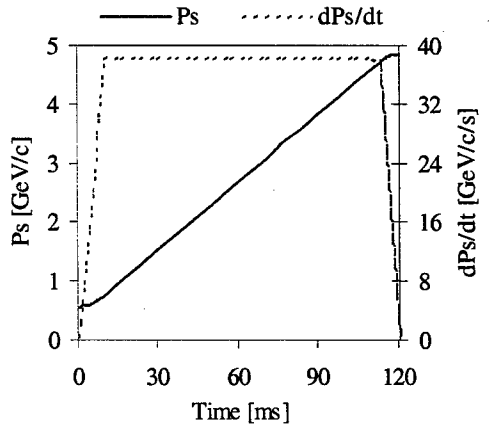


Figure 2: Synchronous momentum (P_s) and dP_s/dt vs. time for the 4 GeV booster.

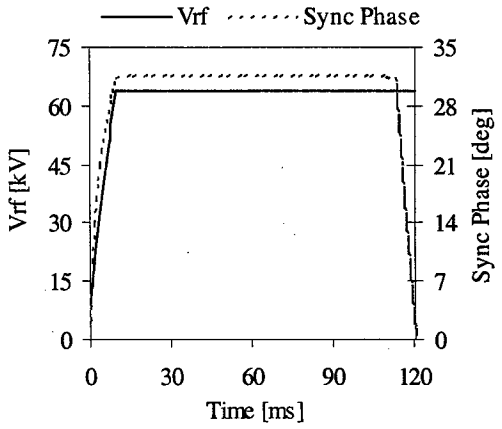


Figure 3: RF Voltage and Synchronous phase (ϕ_s) vs. time for the 4 GeV booster.

covers the range of 0.644 to 1.244 MHz. The main ring fed by this booster also requires a 95% longitudinal emittance of ~2 eV-s. To accommodate this beam, an rf bucket is established with the voltage and synchronous phase at 2.3 kV and 2 degrees, respectively. Using the correlated phase-energy painting scheme, injection occurs over 150 turns or 466 μs. The beam energy is swept repeatedly over ±1.2 MeV and the phase width chopped to within ±73 degrees. To inject 4×10^{12} ppb will require a peak (average) beam current from the linac of 5.5 (2.3) mA.

The magnet program is designed to provide the net energy gain in 600 ms. An asymmetric ramp is used that begins with dP_s/dt at 283 MeV/c/s. P_s increases in a cubic fashion for the first 10 ms. During this time the rf bucket area is kept approximately constant to help limit the rf voltage. The cubic ramp was chosen over a parabolic to help maintain a slightly better bunching factor early in the cycle. All beam loss occurs within the first 10 ms. The

majority of acceleration occurs during the long linear ramp to ~96% of the final momentum. During the linear ramp, which ends at 550 ms into the cycle, the rf voltage and phase are held constant. During the last 50 ms of the cycle, dP_s/dt is reduced linearly to zero. The rf voltage is maintained at the maximum value while the synchronous phase decreases to further reduce the phase-width of the beam for easier extraction and increase $\Delta p/p$ to raise the threshold for microwave instability.

Curves for P_s and dP_s/dt are shown in Figure 4. Over the cycle V_{rf} reaches a maximum of 61 kV while ϕ_s remains below 26 degrees as shown in Figure 5. The 95% emittance is nearly constant over the cycle at ~1.9 eV-s. The threshold for microwave instability was estimated to be a minimum of ~22 Ω at the end of the cycle. Beam capture and transmission is very good with ~99% of the injected particles reaching extraction.

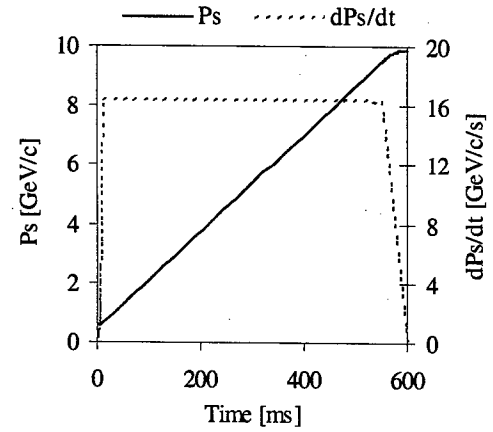


Figure 4: Synchronous momentum (P_s) and dP_s/dt vs. time for the 9 GeV booster.

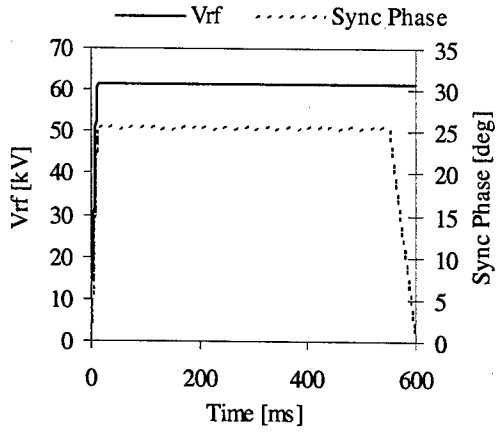


Figure 5: RF Voltage and Synchronous phase (ϕ_s) vs. time for the 9 GeV booster.

SUMMARY

The multiparticle tracking code ESME has been used to develop and study the acceleration process in two different booster synchrotron designs for AHF. A correlated phase-energy injection scheme was used during multi-turn injection to maintain beam quality and reduce losses. The results from the studies show both booster designs exhibit low losses, maintain beam quality and require only modest amounts of rf voltage.

ACKNOWLEDGEMENTS

The author would like to thank J. MacLachlan and F. Ostiguy for their help with the ESME program and T.-S. Wang, B. Prichard, A. Thiessen, J. MacLachlan and S. Koscielniak for valuable discussions on longitudinal beam dynamics in circular machines. The author would also like to recognize the work of R. Garnett who performed the PARMILA simulations to produce the distributions used in the correlated phase-energy painting scheme.

REFERENCES

[1] http://www-ap.fnal.gov/ESME/

THE COMMISSIONING PLAN FOR THE SPALLATION NEUTRON SOURCE RING AND TRANSPORT LINES*

S. Henderson#, S. Assadi, S. Cousineau, G. Dodson, V. Danilov, J. Galambos, J. Holmes, K. Reece, T. Shea, Oak Ridge National Laboratory, Oak Ridge, TN 37830, USA
D. Raparia, M. Blaskiewicz, Y.Y. Lee, Y. Papaphilippou%, J. Wei, BNL, Upton, NY, USA

Abstract

The Spallation Neutron Source (SNS) accelerator systems will provide a 1 GeV, 1.44 MW proton beam to a liquid mercury target for neutron production. In order to satisfy the accelerator systems' portion of the Critical Decision 4 (CD-4) commissioning goal (which marks the completion of the construction phase of the project), a beam pulse with intensity greater than $1x10^{13}$ protons must be accumulated in the ring, extracted in a single turn and delivered to the target. A commissioning plan has been formulated for bringing into operation and establishing nominal operating conditions for the various ring and transport line subsystems as well as for establishing beam conditions and parameters which meet the commissioning goal.

INTRODUCTION

The SNS accelerator complex [1] consists of a 2.5 MeV H^- injector, a 1 GeV linear accelerator, an accumulator ring [2] and associated beam transport lines [3]. The ring and transport line layout is shown in Figure 1. The SNS baseline parameters are summarized in Table 1. The H^- beam from the linac is transported to the ring in the High Energy Beam Transport (HEBT) line. Before the 90 degree bend in the HEBT is a tuning beam dump (the Linac Dump) which will be used for linac commissioning and linac tuneup during operations. The HEBT delivers the beam to the stripping foil for charge-exchange injection into the accumulator ring [4]. Unstripped H^- and partially stripped (H^0) beams are fully stripped in a second foil and transported to the injection dump via the injection dump line [5]. In baseline operation, beam is accumulated in the ring over 1060 turns reaching an intensity of $1.5x10^{14}$ protons per pulse. When accumulation is complete the extraction kicker fires during the 250 nsec gap to remove the accumulated beam in a single turn and direct it into the Ring to Target Beam Transport (RTBT) line, which takes the beam to the liquid-mercury target. Located midway along the RTBT is another tuning beam dump (the Extraction Dump). Both the Extraction and Linac dumps have 7.5 kW beam power capability while the Injection Dump has 200 kW capability.

The commissioning of the accelerator complex will be accomplished in stages as the requisite hardware is delivered and installed on the SNS site. The staged commissioning is already underway with completion of Front-End commissioning [6] in January 2003. After completion of linac commissioning in late 2004, the accumulator ring and transport lines will be commissioned in two separate runs. In the first run, from December 2004 to June 2005, the HEBT, accumulator ring and RTBT to the extraction dump will be commissioned. In the second commissioning run, in December 2005, the remainder of the RTBT is commissioned and beam is delivered for target and instrument commissioning.

The completion of the construction and commissioning phase of the project is accomplished by demonstrating specific performance criteria. The goal for ring commissioning is to demonstrate the accelerator portion of these criteria (the so-called Critical Decision 4, or CD-4, criteria) which include accumulating, extracting in a single turn and delivering to the target a beam pulse of 10^{13} protons at 1 GeV in a machine configuration capable of 1 MW operation. This CD-4 intensity is more than an order of magnitude less than the design intensity of the SNS, corresponding to 100 kW beam power if delivered at 60 Hz repetition rate.

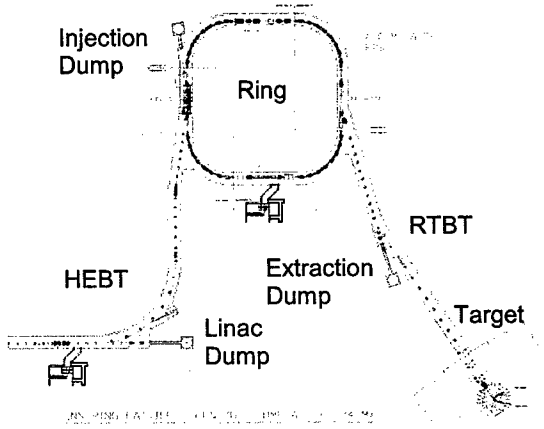


Figure 1: SNS Ring and Transport Line layout

Table 1: SNS Baseline Parameters

Beam Energy	1 GeV
Ring Beam Intensity	$1.5x10^{14}$
Repetition Rate	60 Hz
Accumulated Turns	1060
Accumulation Time	1.0 msec
Beam Power on Target	1.44 MW

*SNS is managed by UT-Battelle, LLC, under contract DE-AC05-00OR22725 for the U.S. Department of Energy. SNS is a partnership of six national laboratories: Argonne, Brookhaven, Jefferson, Lawrence Berkeley, Los Alamos and Oak Ridge.
#shenderson@sns.gov
%present address: ESRF, Grenoble, France

0-7803-7738-9/03/$17.00 © 2003 IEEE

In the target commissioning phase the average beam power must be limited to 3-4 kW in order to maintain radionuclide inventory less than the threshold for a Category 3 Nuclear Facility. Thus, administrative limitations are in place to maintain low average power on the target, although higher-power beams may be delivered over a short duration.

A plan has been formulated for commissioning the ring and transport lines to reach the CD-4 goal and beyond. Central to the success of this plan will be the successful commissioning of key diagnostic systems deployed in the transport lines and accumulator ring [7]. The capabilities of those diagnostic systems that will be most heavily relied-upon during commissioning, the beam position monitors (BPM), beam current monitors (BCM), loss monitors (BLM) and wire scanners are summarized in Table 2.

Table 2: SNS Ring and Transport Line Diagnostics

System	Range	Accuracy/ Resolution
BPM-phase (HEBT)	±180°	±2° / 0.1°
BPM-position	± pipe radius	± 1%/0.5% of radius
BCM (HEBT)	15-52 mA	±1%/0.5%
BCM (Ring/RTBT)	15mA-100A	±1%/0.5%
BLM	1-2.5x10^5 r/hr	±1%/0.5 r/hr
Wire Scanners	± pipe radius	10%/5% on rms width

COMMISSIONING APPROACH

In order to minimize activation of the ring and transport line hardware during commissioning, initial tuning will be performed with a short beam pulse delivered at low repetition rate, typically in a single-shot, "pulse-on-demand" basis. It is expected that linac beam pulse-lengths (controlled by the chopper system in the Front-End injector) in the range 5-20 μsec will be utilized initially, although experience during linac commissioning will provide guidance on the minimum reliably achievable pulse length. The beam intensity can be reduced, if needed, by tuning the ion source, or inserting a current-limiting aperture in the injector beamline.

It is assumed that only the BLMs are functioning on "day-one" as the other systems will need beam to "time-in" and verify proper operation. Initial beam transport in a new section of the ring and transport lines proceeds by tracking the progress with beam loss monitors and minimizing the losses using corrector dipoles. In each case the initial goal is to transport the beam to the appropriate beam dump as rapidly as possible. Once this is accomplished, the basic diagnostics (BCMs, BPMs and profile measuring devices) are commissioned. The transport efficiency is tuned up with BCMs and BLMs. With the beam safely transported to the dump, measurement and correction of the trajectory is performed and beam optics studies and correction commence.

COMMISSIONING SEQUENCE

The following describes the various steps in the commissioning sequence.

HEBT Commissioning

As part of linac commissioning, that portion of the HEBT from the end of the superconducting linac to the Linac Dump is commissioned. A four-wire-scanner array is located in this part of the beamline, allowing measurement of emittance and twiss parameters of the linac output. Several quadrupoles are available for matching the linac beam to the HEBT optics. Proper beamsize at the linac dump window [8] must be verified and adjusted with dump line quadrupoles if necessary. The operability of the dump and bulk shielding are verified up to the beam dump limit of 7.5 kW.

The goals of HEBT commissioning are to bring the HEBT beamline components into operation, commission diagnostics systems, transport a beam to the injection dump and verify the dump's performance, measure and correct the HEBT trajectory and optics and transport a CD-4 pulse (10^{13} protons) to the injection dump. Initial tuning will rely on loss monitors with the goal of transporting the beam to the injection dump, which includes transport through the injection region of the ring lattice. Provision has been made for moving a phosphor screen into place at the injection point (replacing the stripping foil) for visual confirmation of beam parameters.

A number of measurement and correction steps are required to establish proper optical parameters. Achromaticity of the 90 degree bend must be established. Matching of the beam after the achromat to the remainder of the line will be performed using a four-wire-scanner array. The dispersion at the injection point will be measured and corrected if necessary. Finally, two RF cavities, an energy corrector cavity and a momentum painting ("spreader") cavity will be commissioned and their phase and amplitude setpoints established. Once the transport line trajectory and optical parameters have been established, the beam pulse length is increased to transport 10^{13} protons to the Injection Dump.

Ring Commissioning

The objective of this phase of commissioning is to bring the ring hardware into operation, commission key diagnostic systems, measure and correct the ring orbit and optical functions, commission the extraction system, demonstrate accumulation of 10^{13} protons and successfully transport a CD-4 beam to the extraction dump.

The initial commissioning studies focus on transporting a low-intensity beam around the ring to establish the closed-orbit. Initial injection proceeds by powering the dynamic injection bump magnets to place and hold the closed-orbit in the foil while injecting a short pulse of a few ring turns. Initial tuning uses the dipole correctors while observing the beamloss monitors to establish first one, and then several ring turns. The ring BCM is commissioned first and used to tune-up the transport

efficiency. The BPM system is then commissioned and the orbit is measured and corrected. Several closed-orbit correction schemes are envisioned: i) harmonic correction, ii) model-based correction, iii) response-matrix (model-independent) correction and iv) three-bump correction. The chicane and injection bump closure is established.

With the trajectory corrected the optics are measured and corrected. The betatron tunes are measured with the turn-by-turn BPM system, the tune controls are commissioned and the tunes adjusted as necessary. By injecting a beam off-axis and observing the betatron motion on the turn-by-turn BPM system the phase advance between BPMs can be measured. This data will then be used in a model-based correction method to adjust the six main quadrupole power supplies to reproduce the design optics. The chromatieity is measured and the sextupoles are powered to commission the chromaticity correction controls. The dispersion is readily measured by injecting an off-energy beam.

Nominal operating conditions of the RF system are then established. The revolution frequency is measured with a wall current monitor. The cavities are independently powered, and the phase and amplitude loop stability is checked with beam. Cavity relative phase setpoints may be found by injecting an "un-chopped" beam with a single cavity powered. The relative phases of the second and third cavities are adjusted to obtain the same WCM profile as observed on the first cavity. The cavity voltages can be set by observing the synchrotron motion of a beam stored for several msec.

The ring extraction system and RTBT to the extraction dump are then commissioned. Proper operation of the individual extraction kicker modules is confirmed by triggering the kickers individually and observing the betatron motion in the ring. The relative timing of the kicker modules is established. A small beam is extracted and the extraction septum aperture is scanned to establish nominal kicker strengths. Extracted beam is first observed on BLMs and a BCM located in the RTBT. A small beam current is transported to the extraction dump. The extraction efficiency and beam transport efficiency in the RTBT is tuned-up with dipole correctors and loss monitors. The bulk shielding of the dump is verified.

In the next phase of commissioning conditions are established for multi-turn injection by phase-space painting with a goal of transporting 10^{13} protons to the extraction dump. This can be achieved by accumulating 70 turns at the nominal ion source current. The injected beam parameters are characterized (momentum spread, energy jijtter and momentum deviation) and then the injected beam controls (position and angle on the foil) are established. The injection kicker waveforms for phase-space painting are loaded and bump closure is measured and corrected. Pulses of successively greater length are injected to reach the 10^{13} goal with minimization of losses by orbit, tune, chromaticity, injection kicker and extraction tuning. The painted beam profiles are measured with monitors in the RTBT and extraction dump line. If necessary, the settings of the primary collimator may be explored at this point of commissioning.

As each portion of the accelerator is commissioned, the beamloss monitor thresholds (used for input to the Machine Protection System, or MPS) are adjusted, and the MPS performance is checked with intentional controlled loss near each location. Fault studies directed at verifying the bulk shielding are performed as outlined in the SNS Operations Procedures Manual.

Studies for High Intensity Operation

After successful accumulation and extraction of 10^{13} protons, studies related to high-intensity and high-power operation of the ring are planned as time permits. A number of accelerator physics issues central to operation at high-intensity can be studied by accumulating beam intensities above the CD-4 goal at low repetition rate. The topics studied will include i) RF system beam-loading compensation, ii) space-charge studies, iii) exploration of unstable collective modes by delaying extraction, iv) measurement of electron-cloud effects and observation of electron signals on electron detectors, and v) test of a prototype transverse feedback system.

RTBT to Target Commissioning

In this final phase of commissioning, the beamline downstream of the RTBT dipole magnet to the target is commissioned, the proper beamsize demanded by the target is verified with a Harp located just downstream of the last quadrupole magnet, and beam pulses of 10^{13} protons are delivered to the target to satisfy the CD-4 goal.

CONCLUSIONS

A detailed step-by-step plan for commissioning the SNS ring and transport lines has been formulated. This plan focuses on achieving the CD-4 criteria of accumulating, extracting in a single turn and transporting to the target 10^{13} protons at 1 GeV.

REFERENCES

[1] N. Holtkamp, "Status of the Spallation Neutron Source," these proceedings; N. Holtkamp, Proc. EPAC 2002, p. 164.
[2] J. Wei, "SNS Accumulator Ring," these proceedings.
[3] D. Raparia et. al., AIP Conf. Proc. 642, 2002, p. 130
[4] J. Wei et. al., Proc. PAC 2001, p. 2560.
[5] D. Raparia et. al., "Beam Dump Optics for the Spallation Neutron Source," these proceedings.
[6] A. Aleksandrov, "Commissioning of the SNS Front-End," these proceedings.
[7] P. Cameron et. al., "SNS Ring Diagnostics Overview," these proceedings.
[8] G. Murdoch et. al., "Beam Dump Window Design for the Spallation Neutron Source," these proceedings.

EXPLORATION OF BEAM FAULT SCENARIOS FOR THE SPALLATION NEUTRON SOURCE TARGET*

S. Henderson#, S. Cousineau, V. Danilov, J. Holmes, T. McManamy, SNS Project, Oak Ridge National Laboratory, Oak Ridge, TN 37830, USA
D. Raparia, A. Fedotov, Y.Y. Lee, J. Wei, Brookhaven National Laboratory, Upton, NY, USA

Abstract

The Spallation Neutron Source (SNS) accelerator systems will provide a 1 GeV, 1.44 MW proton beam to a liquid mercury target for neutron production. In order to ensure adequate lifetime of the target system components, requirements on several beam parameters must be maintained. A series of error studies was performed to explore credible fault scenarios which can potentially violate the various beam-on-target parameters. The response of the beam-on-target parameters to errors associated with the phase-space painting process in the ring and field setpoint errors in all the ring-to-target beam transport line elements were explored and will be presented. The plan for ensuring beam-on-target parameters will also be described.

INTRODUCTION

The Spallation Neutron Source (SNS) accelerator consists of a 2.5 MeV H- Injector, a 1 GeV Linear Accelerator, an Accumulator Ring and associated transport lines [1]. The linac provides an average macropulse current of 26 mA which is accumulated over 1060 turns by charge-exchange injection in the accumulator ring. The ring intensity reaches 1.5×10^{14} protons at which point the current is extracted in a single turn and transported to the target via the Ring-to-Target Beam Transport (RTBT) line [2]. With a repetition rate of 60 Hz, the SNS provides 1.44 MW average beam power to the liquid mercury target [3] for spallation neutron production. The baseline SNS beam parameters are summarized in Table 1.

Table 1: Baseline SNS Parameters

Parameter	Baseline Value
Beam Power on Target	1.44 MW
Accumulated Protons	1.5×10^{14}
Accumulated Turns	1060
Repetition Rate	60 Hz
Beam Energy	1 GeV
Target Cross-section	404mm x 104 mm
Beam spot width x	200mm x 70 mm

In order to ensure adequate lifetime of target system components, requirements on several beam-on-target parameters must be maintained. These various requirements are summarized in Table 2. At the target shroud face the nominal proton beam spot size is $200 \times 70 mm^2$. For the baseline parameters shown in Table 1, the normal peak single pulse density is 1.9×10^{16} protons/m^2, the time-averaged peak current density is 0.18 A/m^2, the time-averaged beam current density over the nominal spot size is 0.103 A/m^2, and 93% of the beam power is within the nominal footprint. Of primary concern is the peak single pulse proton density. If the peak density increases by more than 25% above nominal (2.3×10^{16} protons/m^2) the beam must be shut off within two 60 Hz pulses. Another requirement demands that 90% of the total beam power remain within the nominal beam spot. In an off-normal condition in which more that half the beam power lies outside the nominal beam spot the beam must be shut off within two 60 Hz pulses. In normal operation, the time-averaged peak current density on the target remains below 0.18 A/m^2. In an off-normal condition in which the time-averaged peak current increases by 10% (0.20 A/m^2), the beam should be shut off within 10 seconds. In addition, tolerances on the beam centroid are noted in the table.

Table 2: Beam on Target Requirements

Requirement	Normal Condition	Off-Normal Condition	Fault Duration
Peak single pulse density	$< 1.9 \times 10^{16}$ proton/m^2	$> 2.3 \times 10^{16}$ proton/m^2	≤ 2 pulses
Peak time averaged current density	≤ 0.18 A/m^2	> 0.20 A/m^2	10 sec
Power within nominal spot	$\geq 90\%$	$< 50\%$	≤ 2 pulses
Centroid tolerance	± 2 mm		

A series of error studies was performed to explore credible fault scenarios which could potentially violate these beam-on-target parameters. The following faults were considered in this study: i) phase-space injection painting errors in the accumulator ring, ii) ring extraction kicker misfires, iii) RTBT dipole errors, iv) RTBT quadrupole errors and v) RTBT dipole corrector errors. These various fault scenarios are discussed in turn.

*SNS is managed by UT-Battelle, LLC, under contract DE-AC05-00OR22725 for the U.S. Department of Energy. SNS is a partnership of six national laboratories: Argonne, Brookhaven, Jefferson, Lawrence Berkeley, Los Alamos and Oak Ridge.
#shenderson@sns.gov

0-7803-7738-9/03/$17.00 © 2003 IEEE

THE RING-TO-TARGET BEAM TRANSPORT LINE

The RTBT is described in [2]. The line begins in the ring extraction region. The extraction system [4] consists of 14 fast kicker magnets to deflect the beam vertically into the extraction septum magnet, which then directs the beam into the RTBT. The RTBT lattice consists of 30 quadrupoles, one dipole and 19 dipole correctors. Two collimators provide protection of the target system from large amplitude particles. The beta-functions are increased in the last quadrupoles to achieve the large beamsize required by the target. A 10m drift takes the beam from the last quadrupole to the target face. Two meters upstream of the target is a 4 mm thick Inconel Proton Beam Window which separates the accelerator vacuum from the target environment.

Central to the discussion of faults and machine errors is the consideration of the aperture throughout the machine. The collimation system [5] in the ring consists of three actively cooled absorbers which form the limiting apertures for the ring with admittance of 300 πmm-mrad in each plane. The collimation system includes an adjustable scraper which is expected to reside at 200 πmm-mrad. The collimators in the RTBT have 300 πmm-mrad horizontal admittance and 400 πmm-mrad vertical admittance.

RING INJECTION PAINTING FAULTS

In order to minimize space-charge and other collective effects in the accumulator ring, phase-space painting is utilized in all three planes [6]. Transverse painting is accomplished by a set of injection bump magnets that sweep the closed-orbit at the injection point during the accumulation cycle.

Several painting faults have been considered, i) injection onto the closed-orbit (corresponding to a failure mode in which the bump magnets are "stuck" at full scale excitation), ii) failure of the horizontal injection bump magnets, iii) failure of the vertical injection bump magnets, and iv) failure of both sets of bump magnets. In each case increasing levels of ring quadrupole gradient errors (up to a maximum of 25% beta function errors) were explored.

The case of injection onto the closed-orbit is potentially dangerous because a high-current-density beam is produced. Particle-in-cell simulations using ORBIT [7] show that indeed the current density on the target can reach 0.47 A/m^2 (or a single pulse density of 4.9x10^{16} protons/m^2) producing an off-normal pulse. However, this fault is accompanied by loss of ~0.5% of the beam in the ring, which is a factor of ~5 greater than nominal conditions. This condition is readily detected with loss monitors that trip the Machine Protection System (MPS). Furthermore, this is an unsustainable fault condition since the closed orbit remains in the injection foil, increasing the foil heating by more than an order of magnitude – a condition that leads to the rapid disintegration of the foil.

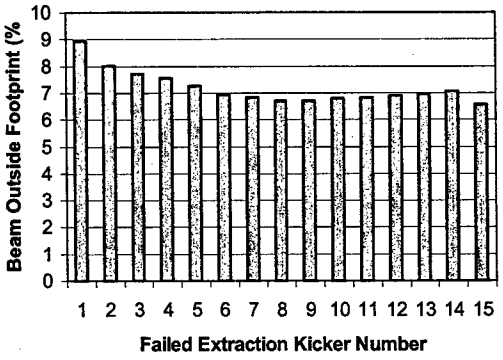


Figure 1: Fraction of beam outside the nominal target footprint for single extraction kicker failures. Number 15 shows the nominal value.

The other faults mentioned are important to consider as they have the potential for painting larger beams which could in principle violate "beam-in-footprint" requirements. It is found that in all the fault scenarios involving failure of the injection bump system the ring losses are orders of magnitude larger than nominal conditions and are therefore readily detected by loss monitors. In the case of horizontal or vertical injection bump failure, ~15% of the beam is lost, whereas for failure of both sets of injection bump magnets ~40% of the beam is lost. In none of these injection-bump failure cases are off-normal target pulses produced. Finally, it should be noted that the injection kicker waveform is monitored for proper operation by the MPS system, providing further protection against this class of failures.

EXTRACTION KICKER MISFIRES

The RTBT transport line optics are designed to achieve an integral multiple of π phase advance between the ring extraction straight and the target in order to minimize the displacement at the target if one or more kickers fails to fire. In addition, the RTBT collimation system is designed to protect the target from faults in which two or more extraction kicker magnets fails to fire. The extraction kicker misfires are not capable of modifying the current density, but may displace the beam centroid.

Figure 1 shows the fraction of beam outside the nominal target footprint as a function of extraction kicker number for single kicker failures. In nominal conditions about 6.5% of the beam lies outside the nominal footprint, whereas all faults respect the 10% requirement, and are therefore incapable of producing off-normal conditions.

DIPOLE ERRORS

There are two high-field dipoles in the transport line, the extraction septum magnet and the 16.8 degree bend magnet. It was found that for 0.1% field errors in either of these dipoles, more than 10% of the beam was lost on the RTBT collimators – a situation which is easily detected by loss monitors. Even for these rather large dipole errors, an off-normal condition is never produced.

The impact of dipole corrector faults has been assessed by investigating the beam-on-target parameters for the case of full-scale powering of single correctors. It is found that single corrector failure is incapable of generating an off-normal condition.

QUADRUPOLE FAULTS

Quadrupole faults have the potential to both increase the current density on the target and place beam outside of the nominal footprint. The RTBT beamline contains 30 quadrupoles, powered by 19 supplies. The impact of quadrupole errors was investigated by transporting the nominal extracted beam distribution through the RTBT to the target (including scattering in the proton beam window) while each quadrupole (or string of quadrupoles as determined by power supply configuration) was swept from zero to 50% higher than its nominal operating gradient. The detailed vacuum chamber geometry was included to accurately model the losses in the beamline. The losses were tallied and the beam-on-target parameters recorded at each quadrupole setting.

Figure 2 demonstrates the results for the "beam-in-footprint" requirement. Shown is the fraction of the beam which is lost in the RTBT at that power supply current for which the "beam-in-footprint" off-normal condition (of 50% of the beam power lying outside the nominal beamspot) is just met. The solid bars show the beam fraction lost up to and including the last quadrupole, and the light bars show the beam fraction lost between the last quadrupole and the target. To generate an off-normal beam pulse requires, in most cases, the loss of much of the beam in the beamline – a condition which is readily detected by loss monitors. Exceptions to this rule are the last few quadrupoles in the line (power supplies 16 through 19), which are capable of violating the "beam-in-footprint" condition without generating losses in the beamline proper. For these cases, dedicated hardware current monitors will be deployed.

Figure 3 shows the maximum target current density achievable by tuning single power supplies from zero to 50% above nominal current with all others at their nominal currents. It is noted that eleven power supplies have the capability of violating the peak single pulse density requirement (which corresponds to 0.22 A/m^2 time averaged current density). In many of these cases detectable beamloss is predicted. Again, some quadrupoles (particularly near the end of the RTBT) do not produce detectable beamloss and so dedicated hardware current monitoring will be used.

FAULT PROTECTION STRATEGY

To ensure required target parameters the following approach will be taken. First, the proper operation of the ring injection painting, extraction and RTBT beamline will be certified by measurement of beam profiles in the RTBT, both in wire scanner arrays as well as at a Harp located immediately downstream of the last quadrupole in the RTBT beamline. Once the beam profiles and trajectory are certified, software current limits will be placed on each RTBT power supply to avoid accidental mistuning. The power supply status is read prior to each 60 Hz beam pulse and factored into the beam permit for the next pulse. In addition, the MPS has power supply status inputs in hardware to ensure that a power supply has not tripped. Critical magnetic elements such as the last quadrupoles in the line will have dedicated current monitoring hardware providing an enable signal to the MPS. As shown above, the beamloss monitoring system, which is also linked to the MPS in hardware, provides protection against most target violating conditions since such conditions are typically accompanied by substantial beamloss in the RTBT.

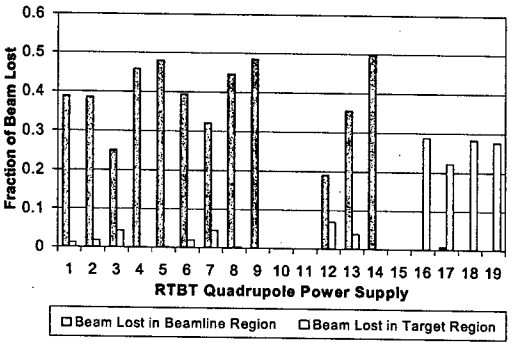


Figure 2: Fraction of beam lost in RTBT at the power supply setting which produces an off-normal "beam-in-footprint" condition.

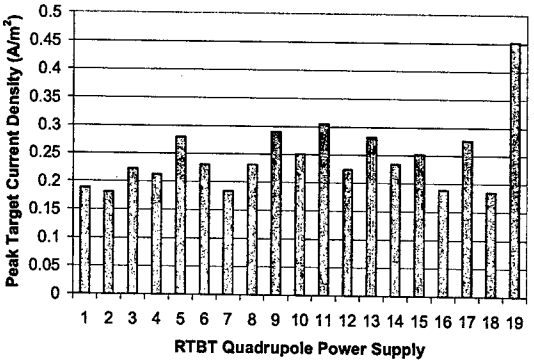


Figure 3: Peak current density achievable by tuning each power supply individually, leaving the others at nominal strength.

REFERENCES

[1] N. Holtkamp, Proc. EPAC 2002, p. 164.
[2] D. Raparia et. al., AIP Conf. Proc. 642 , p.130, 2002
[3] T. Gabriel et. al., Proc. PAC 2001, p. 737.
[4] N. Tsoupas et. al., Proc. EPAC 2000, p. 2270.
[5] S. Cousineau et. al., Proc. EPAC 2002, p. 1019.
[6] J. Wei et. al., Proc. PAC 2001, p. 2560.
[7] J. Holmes et. al., these proceedings.

SUPERSTRUCTURES FOR HIGH CURRENT FEL APPLICATION

J. Sekutowicz, K. Beard, P. Kneisel, G. Wu, TJNAF, Newport News, 23606 VA, USA
C. Thomas, Synchrotron SOLEIL, 91192 Gif-sur-Yvette Cedex, France
S. Zheng, Tsinghua University, 100084 Beijing, China

Abstract

The next generations of FELs at TJNAF will produce coherent light at power levels of 10 kW and 100 kW, respectively [1]. To achieve these power levels, 200 MeV electron beams of 10 mA and 100 mA have to be accelerated in the linear accelerators of the devices. The accelerators will be based on superconducting technology. Stable operation of these machines is only possible if the cavity Higher Order Modes (HOM) excited by the beams can sufficiently be damped. One of the possible accelerating structures which can fulfill this requirement, is a superstructure (SST) made of two weakly coupled subunits and equipped with appropriate HOM couplers. Based on the positive experience at DESY with 1.3 GHz superstructures, we are investigating for possible use similar structures in the linacs for the FEL upgrades. We have built a copper model of the proposed superstructure, based on two copper models of the 5-cell CEBAF cavities. This contribution presents measured results on this model. We are now in the process of fabrication a Nb prototype and hope to perform its cold test by the end of this year.

INTRODUCTION

Two superstructures have been recently successfully used at DESY to accelerate a pulsed 4 mA electron beam to an energy of 47 MeV [2]. The acceleration process was very stable and the measured bunch-to-bunch energy variation was below achievable test accuracy of $2 \cdot 10^{-4}$ [3]. In addition, the experiment at DESY showed that the HOM suppression in two tested 2x7-cell superstructures was very good and no HOM-driven instability was observed.

The proposed superstructure is based on the original CEBAF 5-cell cavities [4]. Two cavities (subunits) couple to each other via a half wave length long interconnecting beam pipe, which provides 0.04 % coupling (Fig. 1). The superstructure features one HOM coupler at each end and two HOM couplers at the interconnecting beam pipe. The couplers are based on the coaxial line technique and are almost identical to TESLA HOM couplers [5]. Their outer diameter is 40 mm. There is still enough space to add more HOM couplers if required.

This SST allows for much better HOM suppression than a standard 10-cell cavity since HOM couplers can be attached to the interconnection in the "middle" of the structure. In addition, a standard waveguide Fundamental Power Coupler (FPC) at one end, as for the CEBAF cavities, is used to feed the RF-power into all 10 cells. A shape modification of the inner end cells is necessary to compensate for the larger inner diameter of the interconnecting pipe and to maintain the right frequency and the field flatness in the accelerating mode. Each 5-cell subunit will be housed in an individual LHe vessel and each will be equipped with a cold tuner. The computed RF-parameters of this SST are listed in Table 1.

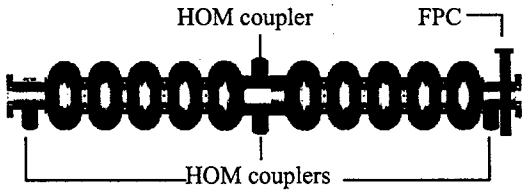


Figure 1: 2x5-cell superstructure equipped with four HOM couplers and only one FPC to feed 10 cells with RF-power.

Table 1. RF-parameters of the 2x5-cell superstructure

Parameter		
Frequency of the accelerating mode	[MHz]	1497
Cell-to-cell coupling, k_{cc}	[%]	3.29
Subunit-to-subunit coupling for, k_{ss}	[%]	$4 \cdot 10^{-2}$
Subunit field instability factor, N^2/k_{cc}	[10^3]	760
(R/Q)	[Ω]	926
Geometric factor, G		275
Distance to the next resonance	[kHz]	335
E_{peak}/E_{acc}		2.64
B_{peak}/E_{acc}	[mT/(MV/m)]	4.74
Active length	[m]	1.0

The field profile of this SST's accelerating mode is very insensitive to frequency errors of an individual cell. It is much less sensitive than in the case of a standard cavity with the same number of cells. This is due to possible frequency correction over each individual 5-cell subunit by means of the cold tuner. Moreover, the field profile within a subunit is very stable, because the cell-to-cell coupling, k_{cc}, is very strong The SST can increase the active length in a cryomodule while the number of input couplers will be reduced. In the standard 8 m long

* Work supported by the U.S.DOE under contract No. DE-AC05-84ER40150.

0-7803-7738-9/03/$17.00 © 2003 IEEE

CEBAF cryomodule, with forty active cells, one could house six SSTs with sixty active cells. By comparison the current upgrade design allows for fifty-six cells (eight 7-cell cavities). The distance between superstructures would be 233 mm, requiring modification of the beam line layout and adaptation of a TESLA-like tuner [6] as well as use of Nb bellows with few convolutions to relax mechanical tolerances and simplify string assembly. The first prototypes of a Nb bellows has been manufactured at JLAB and the engineering work is in progress [7].

MEASUREMENTS ON THE COPPER MODEL

The copper model of the proposed SST has been retrofitted from two existing copper models of 5-cell cavities by modifying the two inner end cells at the interconnection side (Fig. 2). We built this model to verify our prediction of some RF-properties of the accelerating mode. The second purpose was to look at the suppression of HOMs.

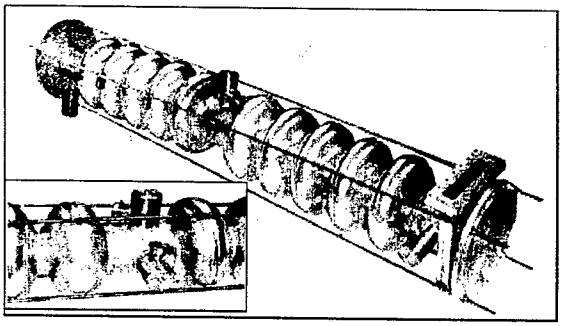


Figure 2: The copper model of the superstructure. The zoomed picture shows the interconnection with two HOM couplers

Accelerating Mode

The measured field profiles of the accelerating mode and its nearest neighbour are shown in Fig. 3 and Fig. 4. Both agreed very well with the theoretical computed profiles. The superstructure FPC is placed at ~90 mm, from the last iris of the end cell. The measured Q_{ext} of the FPC for the accelerating mode is $2.5 \cdot 10^7$. The value of Q_{ext} can be adjusted by means of a waveguide 3-stub tuner and/or by choosing a different position of the end short in the FPC waveguide on the opposite side of the axis.

Damping of HOMs

Parasitic cavity modes, mainly dipoles, can spoil the quality of the beam. The computed frequencies and the (R/Q) values of the high impedance dipoles are listed in Table 2 together with measured values of frequency and Qext. The two last columns show measured data for both polarizations. We measured frequency and Qext of all dipoles up to 3.15 GHz for three different angular positions of the HOM couplers. The best result, shown in Fig. 5, was used for simulation of the FEL 10 kW upgrade with MATBBU [8]. For this, the standard 7-cell upgrade cavities have been replaced with the superstructures, but the whole optics of the beam line remained unchanged. The result was very encouraging (Fig. 6). The threshold beam current (red in Fig. 6) went up to 103 mA (10 mA needed for this upgrade). The current was limited by the dipole mode No. 7 (see Table 2). Additional HOM couplers would further improve the threshold.

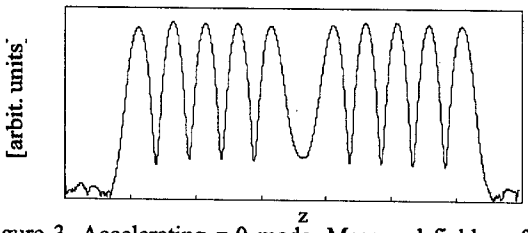


Figure 3. Accelerating π-0 mode. Measured field profile on axis.

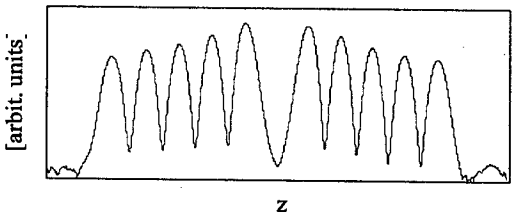


Figure 4: Nearest neighbouring mode π-π. Measured field profile on axis.

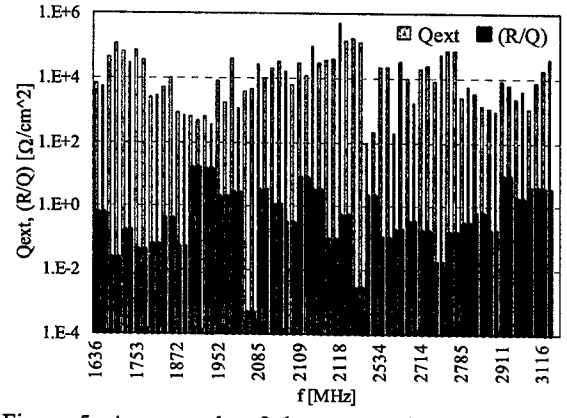


Figure 5: An example of the measured Q_{ext} of dipole modes. The (R/Q) values are shown to illustrate which mode is dangerous for the beam quality.

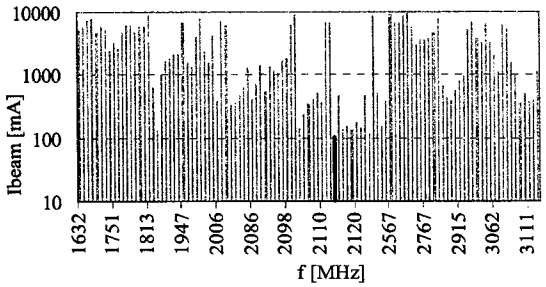


Figure 6: Limitation in the beam current as computed by MATBBU for measured values of frequencies and Q_{ext} of all dipoles up to 3.15 GHz.

Table 2. Computed and measured dipole modes

No. -	$f_{computed}$ [MHz]	(R/Q) [Ω/cm^2]	$f_{measured}$ [MHz]	Q_{ext}
1	1873.96	16.4	1879.79	$6\cdot10^2$
1a	1873.96	16.4	1882.07	$5\cdot10^2$
2	1933.51	14.2	1940.28	$6\cdot10^2$
2a	1933.51	14.2	1941.00	$4\cdot10^2$
3	1950.43	2.1	1952.48	$8\cdot10^3$
3a	1950.43	2.1	1953.07	$2\cdot10^3$
4	2005.28	2.8	2003.56	$4\cdot10^4$
4a	2005.28	2.8	2006.33	$1\cdot10^3$
5	2080.71	3.3	2085.00	$3\cdot10^4$
5a	2080.71	3.3	2086.06	$1\cdot10^4$
6	2110.80	7.8	2108.83	$3\cdot10^4$
6a	2110.80	7.8	2109.09	$1.\cdot10^4$
7	2122.21	3.5	2114.33	$9\cdot10^4$
7a	2122.21	3.5	2114.73	$3\cdot10^4$
8	2201.99	2.2	2189.22	$1\cdot10^2$
8a	2201.99	2.2	2199.74	$2\cdot10^2$
9	2933.19	9.5	2911.38	$8\cdot10^3$
9a	2933.19	9.5	2912.17	$6\cdot10^3$
10	2941.47	2.0	2940.21	$2\cdot10^3$
10a	2941.47	2.0	2940.87	$4\cdot10^3$
11	3063.85	4.1	3065.21	$1\cdot10^3$
11a	3063.85	4.1	3068.26	$7\cdot10^3$
12	3124.27	3.9	3115.54	$2\cdot10^4$
12a	3124.27	3.9	3116.51	$4\cdot10^4$

An important feature of a superstructure is the possibility to change the frequency of a parasitic mode during operation. The subunits' frequencies of a parasitic mode are usually different due to imperfections in the shape of cells. This causes the stored energy in the subunits to be unbalanced (unlike the accelerating mode). Moving the cold tuner of one subunit by an appropriate amount of steps in one direction and the tuner of the other subunit by the same amount but in the opposite direction, one can change the frequencies of all modes which have unbalanced energy, simultaneously keeping the frequency of the accelerating mode constant.

FINAL REMARKS

The Nb prototype of the proposed superstructure is being manufactured. Two spare 5-cell CEBAF cavities have been qualified in cold tests and reshaping of end cells will be performed by the end of July. We plan to test the prototype by the end of this year to verify experimentally the RF-properties of this superstructure. One of the major objectives in this test will be to explore the tuning and possible heating of the HOM couplers attached to the interconnection under cw operation. The test results will be a guide to improve further the HOM suppression, in particular for accelerators with beam currents in the 1 A range. The superstructure and its HOM damping characteristics can relatively easily be re-scaled to a lower frequencies (750 MHz or 500 MHz) and additional damping devices could be added if required.

ACKNOWLEDGMENTS

We would like to express our gratitude to L. Turlington, J. Brawley, S. Manning, B. Manus, S. Morgan and G. Slack for their help in retrofitting of the copper models and modification of the Nb prototypes.

REFERENCES

[1] G. R. Neil et al., "The Jefferson Lab Free Electron laser Program", JLAB-ACC-02-02, TJNAF, 2002.
[2] J. Sekutowicz et al., "Cold- and Beam Test of the First Prototypes of Superstructure for the TESLA Collider", PAC03, Portland, May 2003.
[3] H. Schlarb et al., "Bunch-to-Bunch Energy Stability Test of the Nb Prototypes of the TESLA Superstructure", PAC03, Portland, May 2003.
[4] P. Kneisel et al.; "Development of Superconducting Cavities of Cylindrical Symmetry at Cornell", IEEE Trans. Nucl. Sci., NS-30, 3348, 1983.
[5] J. Sekutowicz, "Higher Order Mode Coupler for TESLA", SRF Works, Newport News, October 1993.
[6] H.-B. Peters, DESY, private communication.
[7] L. Turlington, private communication.
[8] K. Beard et al., "A Tool for Estimating Beam Breakup Due to Higher Order Modes", JLAB-TN-02-044, 2002.

INVESTIGATION OF SPACE CHARGE EFFECT IN TRIUMF INJECTION BEAMLINE

R. Baartman, Y.-N. Rao, TRIUMF, Vancouver, Canada *

Abstract

The TRIUMF cyclotron operates routinely at 200 μA extracted at 500 MeV. Because of growing demands for beam, up to 400 μA is envisaged: this would require $\sim$ 1 mA from the H^- ion source and injection beamline. The phase acceptance of the cyclotron is roughly 36°, so the local peak beam current just before injection would be higher than 4 mA. This leads to large space charge effects on the beam transverse envelope and longitudinal bunching efficiency.

The beam profiles and the bunching efficiency were measured for different currents up to 575 μA. These were used in space charge transport calculations to determine the beam optic properties and the space charge neutralization level. Extending the calculations to higher intensities, it is found that with the present double drift double harmonic bunching system, the bunching efficiency decreases dramatically above a dc current of 600 μA. To enable reaching the envisaged 400 μA from the cyclotron, it requires either raising the cyclotron phase acceptance from the present $\sim$ 36° to 50° by for example increasing the energy gain per turn at injection, or by adding another fundamental harmonic buncher.

1 INTRODUCTION

The TRIUMF cyclotron injection beamline [1] is roughly 35 m in length, and is entirely electrostatic, containing approximately 80 quadrupoles. It has been running routinely with a cw current of $\sim$ 400 μA (H^-) at 300 keV, which results in 200 μA extracted from the cyclotron. In the future, it would be required to transport 1 mA in order to allow up to 400 μA extracted from the cyclotron. With 1 mA average beam current, the bunched beam will have a peak current of $\sim$10 mA. At such high peak currents and low energy level, the space charge effect on the beam transverse size and longitudinal bunching efficiency is large.

The longitudinal space charge effect on the bunching efficiency has been previously discussed [2]. Recently, we performed some measurements of the beam transverse size and bunching efficiency for various currents up to 575 μA. Actual operation of the beamline and calculations including the space charge effect have demonstrated that the high current tune of the beamline still works well for the lower currents; the observed beam spills mainly occur in the vertical section of the beamline (distance > 900 inches in Figs. 1 and 3). Our goal is to find a reasonably standard tune for currents up to 1 mA; we therefore used these measured beam sizes in space charge transport calculations to determine the beam optic properties as well as the space charge neutralization level. Afterwards, we extended the calculations to higher intensities to investigate the bunching efficiency versus current with the present double drift double harmonic buncher system.

*TRIUMF receives funding via a contribution agreement through the National Research Council of Canada

2 TRANSVERSE ENVELOPE

The beam widths were measured with 13 scanning wire profile monitors for various currents. As an example, Fig. 1 shows the beam widths (2σ) measured at dc currents 345 and 575 μA. In the horizontal periodic section, the beam width shows weak dependence on the beam current. It was suspected that there exists some space charge neutralization in the H^- beam due to the ionized positively charged ions captured by the beam's potential well, though the beamline is electrostatic. So, an experiment was made to investigate the space charge neutralization level.

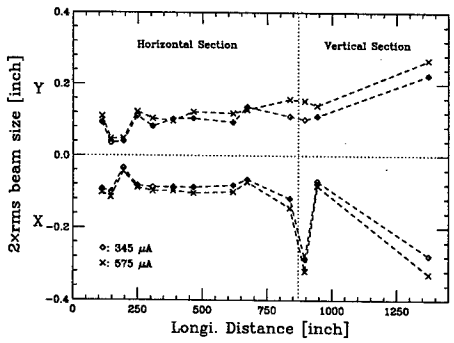


Figure 1: The beam sizes (2σ) at dc currents 345 and 575 μA. The data points are the measurements. The dashed line is only meant to guide the eye.

The first 4 scanning wires in the North-South section of line (250 inches to 500 inches in Fig. 1), are in a section of periodic transport. Each cell is 40 inches, and the phase advance per cell was varied from 30° to 90°. The beam current used was 686 μA, limited by the ion source. The vacuum pressure was 5.0×10^{-7} torr (H_2). For each setting of the quads, we got 6 or 8 parameters of beam size. Repeating this procedure 7 times, we obtained 46 valid parameters in total.

We used the computer code TRANSOPTR [4] to calculate the beam's optic properties in the presence of space charge effect. This code uses the F-matrix approach [3] in the beam transport design and calculation with the linear space charge force included. In the calculations, the code varies 7 parameters (the initial beam in both transverse planes, plus the current) by simulated annealing to achieve best match for the 46 values of beam sizes at the

0-7803-7738-9/03/$17.00 © 2003 IEEE

scanning wire locations.

Typically, the beam size is $2\sigma = 3\,\text{mm}$, with an uncertainty of $\pm 0.15\,\text{mm}$. The uncertainty relates mainly to the difficulty of exactly determining the background noise level. Best fit for the effective current was $580\,\mu\text{A}$, while the actual H^- current is $686\,\mu\text{A}$, so the neutralization factor may be $1-580/686 = 15\%$. The rms deviation of the fitted and measured profile sizes was, however, 0.05 mm, i.e. less than the measurement uncertainty. Fitting with an effective current equal to the actual current resulted in an rms deviation of 0.08 mm; still smaller than the measurement uncertainty. We conclude that the results are consistent with no neutralization. In view of the fact that the beamline is electrostatic and that only a small fraction of the beamline could have external fields which are small compared with the space charge potential of a few volts, this is not surprising.

The KV envelope equation is

$$0 = \frac{d^2a}{ds^2} + k_x a - \frac{\epsilon_x^2}{a^3} - \frac{2K_{sc}}{a+b},$$
$$0 = \frac{d^2b}{ds^2} + k_y b - \frac{\epsilon_y^2}{b^3} - \frac{2K_{sc}}{a+b}.$$

For our parameters, $K_{sc} = 4 \times 10^{-6}$ at 1 mA, 300 keV. For a beam size $a = b = 2.5\,\text{mm}$ and an emittance $\epsilon_x = \epsilon_y = 5.0\,(\pi)$mm-mrad, we see that the emittance term and the space charge term are equal at 1 mA. For our experiment, the beam current was limited by the availability of the current out of the ion source. With $686\,\mu\text{A}$, we were still working in a regime where the beam envelope is dominated by the emittance. Hence the observed beam size shows weak current dependence in the horizontal section as shown in the Fig. 1.

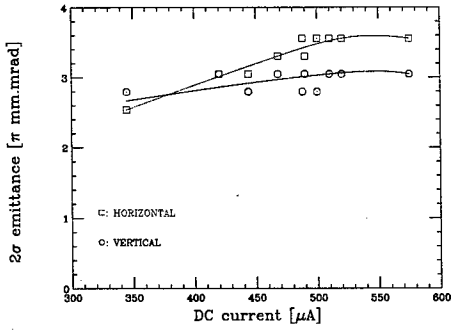


Figure 2: Fitted beam emittance (2σ) vs. current.

In a separate experiment, profiles were taken as a function of beam current. The resulting fitted emittance is shown in Fig. 2.

With bunching, the local space charge density in the beam just prior to the injection is increased by a factor of 5 to 10. (The phase acceptance of the cyclotron is roughly 40°.) This causes space charge to become increasingly dominant as the beam travels along the injection line, leading to a growth in the transverse size of the beam. Shown in Fig. 3 are the calculated bunch dimensions along the injection line. Compare with Fig. 1.

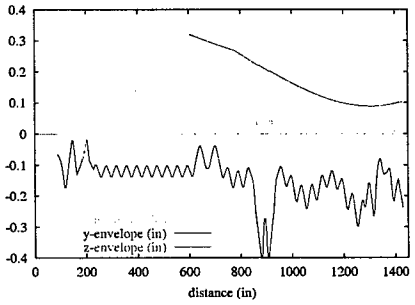


Figure 3: Calculated beam envelope size (inches) at $800\,\mu\text{A}$, showing transverse growth due to decreasing bunch length. The red line represents the bunch length divided by 20.

3 BUNCHING EFFICIENCY

To quantitatively investigate dependence of the bunching efficiency on the beam intensity, we used the computer code SPUNCH [5] to simulate the longitudinal dynamics of the beam with space charge. This code also includes the effect of images in the surrounding vacuum pipe. We assumed an upright elliptic acceptance of $\delta\phi = \pm 18°$ and $\delta p/p = \pm 0.5\%$, and an average pipe radius of 12.7 mm; the beam transverse average radius is 3.0 mm according to above measurements. As an example, Fig. 4 plots a sequence of particle distributions in longitudinal phase space. The calculated bunching efficiency is shown as a function of beam current in Fig. 5, where the machine operational results (approximately equal to the transmission efficiency from the last injection line beam stop to the extraction plus another ~6% loss due to the electromagnetic stripping and gas stripping) are plotted as well. An interesting effect shown in this calculation is that the bunching efficiency begins to drop above $600\,\mu\text{A}$. For instance, at $600\,\mu\text{A}$ injection, the efficiency is decreased to 55%. This yields only $\sim 310\,\mu\text{A}$ at extraction, including a 6% stripping loss. To enable reaching the envisaged $400\,\mu\text{A}$ from the cyclotron, one way is to add another fundamental harmonic buncher situated at 2.4 m from the inflector, as proposed in ref.[2]. In such a way, the bunching efficiency is expected to remain above ~65% (see Fig. 5).

Another way is to increase the phase acceptance of the cyclotron from the present $\sim 36°$ to 50° by raising the energy gain per turn at injection. This was already demonstrated by a late beam development experiment (see the diamond in Fig. 5). The lower dashed line shown in Fig. 5 is the calculated bunching efficiency using a 50° phase acceptance. At $800\,\mu\text{A}$ for example, the 50° phase acceptance would improve the efficiency from 43% to 56%, resulting in the envisaged $\sim 400\,\mu\text{A}$ at extraction.

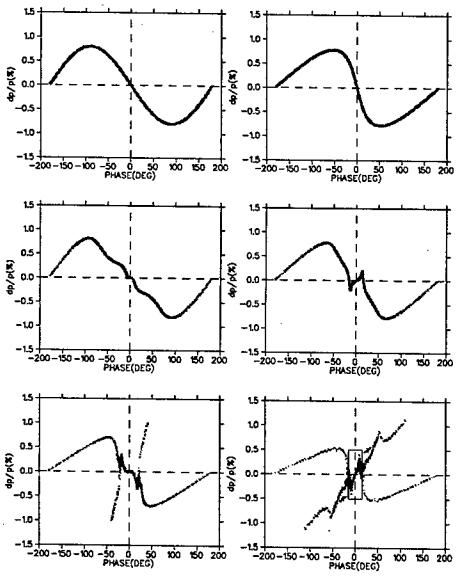


Figure 4: Simulated evolution of particle distribution in longitudinal phase space at 600 μA. From left to right and up to down, windows respectively correspond to the following locations in Fig.3: (1) z=603 inch; (2) z=781 inch; (3) z=902 inch; (4) z=1035 inch; (5) z= 1198 inch and (6) z=1430 inch. Of the 500 particles, 240 are lying inside the $\pm 18°$ phase window in the end.

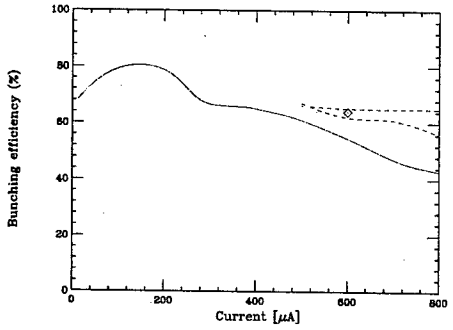


Figure 5: Bunching efficiency vs. beam current. The data points are the machine operational results: the 'diamond' was achieved with $\sim 50°$ phase acceptance due to an increased rf voltage. The solid line is the calculation result with 36° cyclotron phase acceptance. The lower dashed line is the calculation result for a 50° phase acceptance with the present buncher system; the upper dashed line is the calculated performace for the 36° phase acceptance but with the third buncher added.

4 CONCLUSIONS

Machine experiments have indicated that increasing the cyclotron phase acceptance to 50° from the present $\sim$ 36° by raising the energy gain per turn in the central region enables $\sim$ 380 μA extracted from the cyclotron, close to the future goal 400 μA. This encouraging result suggests that the space charge effect in the injection beamline at currents up to 800 μA is handlable. Calculations indicate that with an additional buncher acting as a "rebuncher", 500 μA is achievable. Further work is to model, in more details, the optics in the vertical section just upstream of the inflector as more information about the beam profile becomes available.

REFERENCES

[1] J. Beveridge et al., "INITIAL OPERATION EXPERIENCE WITH THE TRIUMF 300 KeV H^- INJECTION SYSTEM", IEEE Trans. Nucl.Sci.NS-22 No.3 (1975) p.1707.

[2] R. Baartman et al., "THE TRIUMF HIGH EFFICIENCY BEAM BUNCHING SYSTEM", Proc. of 10th Int. Conf. on Cyclotrons and their Applications, East Lansing, (1984), p.158.

[3] F.J. Sacherer,"RMS ENVELOPE EQUATION WITH SPACE CHARGE",IEEE Trans. Nulc.Sci.NS-18, (1971), p.1105.

[4] E.A. Heighway and R.M. Hutcheon,"TRANSOPTR - A Second Order Beam Transport Design Code with Optimization and Constraints",Nucl. Inst. Meth. 187, (1981) p.89.

[5] R. Baartman, "SPUNCH-A SPACE CHARGE BUNCHING COMPUTER CODE", Proc. 11th Int. Conf. on Cyclotrons and their Applications, Tokyo,(1987),p.238.

FEASIBILITY STUDIES FOR A RADIOACTIVE-ION STORAGE RING

M.K. Craddock, University of British Columbia and TRIUMF,
and D. Kaltchev, TRIUMF, Vancouver, B.C., Canada

Abstract

The low intensities of beams of unstable isotopes make it vital to use them efficiently. Their collection in a storage ring would open up a number of possibilities: higher beam intensities, enabling better suppression of background and more accurate measurement of isotopic and ionic properties; higher luminosities, by the use of beam cooling and internal targets; acceleration to higher energies; quasi-simultaneous operation with fixed-target experiments; and colliding- or merging-beam experiments with protons, electrons, muons, etc. The most crucial design aims are rapid accumulation of the beam and avoidance of beam spoilage and loss through interactions with strippers, residual gas and targets. This has led us to study injection by foil stripping and storage of the whole range of charge states produced, in the context of the ISAC radioactive beam facility at TRIUMF.

INTRODUCTION

In line with a recommendation in the Canadian Subatomic Physics Five Year Plan (2001), studies have begun of the scientific potential and technical feasibility of a storage ring for the radioactive ions from ISAC. Such a ring (the ESR) has been successfully built and used at GSI Darmstadt, and others are being built, proposed or considered at IMP Lanzhou, RIKEN, TU Munich, GSI, and CERN (ISOLDE). Some of the attractive possibilities which a storage ring would open up are:

- measurement of otherwise inaccessible interactions;
- cooling of the beam, significantly improving position, time and energy resolution, and allowing the use of internal gas targets and the achievement of higher luminosities than with solid targets in the ISAC-II beam;
- acceleration to higher energies;
- direct measurement of nuclear and ionic properties (mass, lifetime, magnetic moment, ...);
- quasi-simultaneous operation with ISAC-II experiments using the same ions;
- fast extraction of high-intensity pulsed beams for studying interactions with very low cross sections;
- radioactive muonic atom production by merger with a muon beam;
- electron-ion collisions (with the help of an electron storage ring).

ISAC beams

The ISAC-I RFQ and drift-tube linacs currently accelerate light radioactive ions ($A \leq 30$) to 1.5 MeV/u. ISAC-II, now under construction, will add a charge-state booster and further accelerating cavities, extending the mass range to $A \leq 150$) and raising the maximum energy/nucleon E/A to 8 MeV/u for the heaviest ions and 20 MeV/u for the lightest. The superconducting cavities downstream of the second stripper S2 are capable of accelerating several neighbouring charge states in a good quality beam[1]. For ^{132}Sn, for instance, five states q = 29-33, comprising 80% of the beam, can be transmitted within a transverse emittance of 1.5π mmmrad and a longitudinal emittance of 9.6π keV-ns. Figure 1 shows the expected dependence on atomic number Z of various properties of the beam leaving ISAC-II, including $A/\bar{q}$ (where $\bar{q}$ is the average charge), and $n_e = Z - \bar{q}$, the average number of electrons remaining.

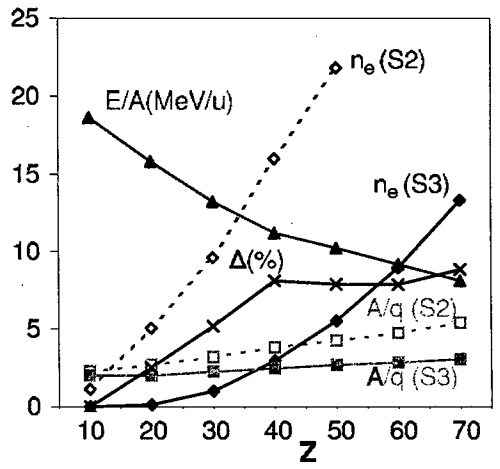


Figure 1: ISAC-II beam properties versus atomic number Z, before (S2) and after (S3) stripping at final energy E/A.

Possible ring scenarios

Three general scenarios might be considered, in order of increasing complexity and cost:

Mini: An accumulator ring, with no provision for cooling or further acceleration (similar in purpose to the 5 MeV/u "Recycler" proposed for the Munich Accelerator for Fission Fragments at the high-flux reactor FRM-II).

Midi: A storage ring with cooling and modest acceleration - say to four times greater energies - 35 MeV/u for the heaviest ions and 80 MeV/u for the lightest.

Maxi: A cooler storage ring capable of handling (say) 100 MeV/u beams delivered by a further ISAC accelerator (linac or cyclotron).

0-7803-7738-9/03/$17.00 © 2003 IEEE

Stable versus radioactive ions

An example of a storage ring for stable ions in a similar energy range is the TSR at MPI Heidelberg, which has a bending power of 1.5 T-m and diameter $\simeq$15 m; ions have been successfully stored over a wide mass range, those that are highly stripped exhibiting lifetimes of many minutes[2]. With a charge (or momentum) acceptance of $\pm 4\%$ it has also demonstrated that multiple charge states can be stored if the dispersion is kept low and the apertures are sufficiently large. Injection into the TSR proceeds by conventional mulititurn betatron and momentum stacking - a relatively complicated process in which batches of tens of turns are successively injected and cooled. The latter process takes almost a second but nevertheless tens of thousands of turns can be accumulated over about 10 minutes. The use of momentum stacking requires finite dispersion at the injection point and so is only compatible with the injection of single charge states.

For radioactive ions the time spent in accumulation is crucial, as is the collection of maximum beam intensity. Focusing on the problems peculiar to storing unstable ions, we have studied the feasibility of injecting by stripping, and of storing the whole range of charge states produced.

Injection by stripping

Advantages: Injecting by stripping in a foil S3 would:
- be simpler and quicker, enabling collection of as many turns in a single batch as can be obtained by stacking many batches with intermediate cooling delays;
- increase the average ionic charge $\bar{q}$, reducing the bending power $B\rho$ and diameter D required for the storage ring;
- reduce the fractional width of the charge-state distribution (CSD), enabling a greater fraction of the beam to be contained;
- make possible capture of the multiple charge states which ISAC-II is capable of accelerating simultaneously.

The significant reductions that can be effected in both n_e and $A/\bar{q}$ by stripping the beam leaving ISAC-II are shown in Fig. 1. Also shown (as a percentage measure of the CSD width) is the parameter $\Delta = (q_+ - q_-)/2\bar{q}$, where q_+ and q_- are the charge states enclosing $\geq$99% of the CSD. These parameters have been calculated following the prescriptions of Shima *et al*[3]. Apparently an acceptance of $\pm 9\%$ would be sufficient to contain 99% of the beam.

Hazards: The basic drawback to injection by stripping is that the stored beam may make further passes through the foil, leading to loss of beam quality and possibly of the ions themselves. The major factors to consider are multiple scattering, energy straggling, energy loss and electron transfer. The estimates below assume a 260 μg/cm^2 carbon foil, sufficiently thick to give an equilibrium CSD.

Multiple scattering, which varies as $Z\sqrt{1+(Z/6)^{2/3}}$, is most serious for heavier ions. For $Z = 65$, though, Meyer's formula[4] predicts an rms angle of only 1.3 mrad, one-third of the maximum acceptable divergence (see below), so losses should be <1%.

Energy straggling is also relatively unimportant. Data from GANIL[5] indicate a HWHM value around 10 keV/u, with very low Z-dependence. The energy loss, however, is important. Although the amounts, 20 keV/u, 150 keV/u and 340 keV/u for Z = 6, 36 and 65 respectively, correspond to only 0.06%, 0.6% and 2.0% momentum offsets, well within the momentum acceptance, it will probably be impossible to provide an rf bucket large enough to contain the decelerated heavy ions. Assuming use of ISAC superconducting cavities at 141 MHz, the minimum voltages required would be 9 kV, 1.2 MV and 13 MV respectively, while the space available would permit only about 5 MV.

Electron transfer is an even more serious threat: on each passage the CSD will re-equilibrate and the empty charge states outside the ring's acceptance will be repopulated. Thus if a certain fraction of the CSD lies outside the charge acceptance, that same fraction will be lost on each pass through the foil. It is clearly vital to maximize the charge acceptance and minimize the number of foil interceptions. The latter can be significantly reduced by painting the incoming beam over the acceptance, as discussed below.

Painting

If the ring's acceptance $A \gg \epsilon$, the incoming beam emittance, and the equilibrium orbit is gradually moved away from the stripping foil, stored ions will only intercept the foil for a short period. Imagining the acceptance to be composed of concentric annuli $i = 1, 2, ..., I$ each as wide as the beam spot, the fraction of interceptions as each is filled is given[6] by a geometrical factor F_i (Fig. 2).

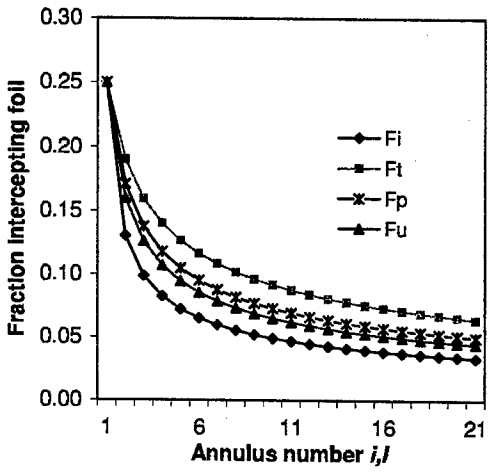


Figure 2: Fraction of foil traversals versus number of annuli.

The figure also shows how the average fraction over the whole acceptance depends on the time spent on each annulus - F_t for equal times, F_p for equal passes through the foil, and F_u for uniform phase space density. In the latter case, $I = 16$ reduces the average foil traversals to 1 in every 20 turns. If this is done in both planes, the average

drops to 1 in 400 turns. Assuming the incoming beam can be focused to half its natural width, $I = 16$ implies a ring acceptance of $16^2 \times 1.5\pi = 384\pi$ mmmrad.

High charge acceptance

The ability to store a wide range of charge states would:
- enable almost the entire beam leaving the stripping foil to be captured rather than just the most populous charge-state;
- strongly reduce the beam loss due to leakage into the tails of the CSD by charge-exchange (as discussed above).

It would also strongly affect the ring design:
- high charge/momentum acceptance requires a low dispersion lattice, large aperture magnets, and careful control of higher-order effects;
- storage of multiple charge states requires zero dispersion at the stripping foil, ruling out momentum painting.

RING PARAMETERS AND LATTICE

The following table shows approximate values for the major ring parameters for each of the scenarios mentioned above, with the TSR for comparison. Injection by stripping, which reduces the A/q for heavier ions from 5 to 3, clearly has a major impact on the bending power $B\rho$ required, and hence on the ring diameter.

Table: Storage Ring Parameters

Ring	Stripping Injn.	Z	A/q	Energy (MeV/u)	$B\rho$ (T-m)
TSR	No		2	30	1.5
Mini	No	6	2	20	1.3
	No	65	5	8	2.0
	Yes	6	2	20	1.3
	Yes	65	3	8	1.2
Midi	No	6	2	80	2.6
	No	65	5	35	4.2
	Yes	6	2	80	2.6
	Yes	65	3	35	2.6
Maxi			2	100	2.9

Lattice design

Initial lattice studies have focused on the Midi ring, which is conceived as being four-sided, with the long straights assigned to injection, cooling, acceleration and experiment. As all these functions require zero dispersion, a natural choice for the arcs has been a double-bend achromat (DBA). The lattice chosen, of the form 0FD0B0F0B0DF0 (Fig.3), restricts the dispersion to a narrow region with a low peak value of 1.24 m and also low β_x - crucial features for realizing a high charge acceptance. The circumference is 57.8 m, the tunes 2.57(x) and 1.84(y), and the transition energy 7.08. Initial tracking studies have shown good behaviour for charge or momentum excursions up to $\pm 4\%$. These studies will be extended to include families of sextupoles and octapoles to see how wide an acceptance can be achieved.

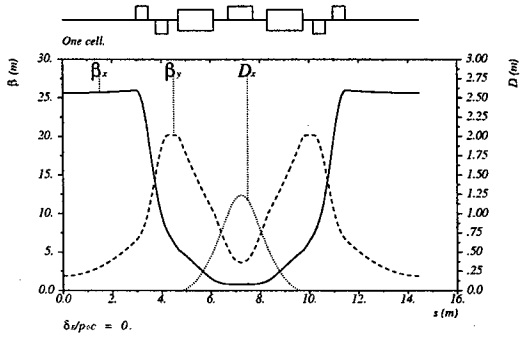


Figure 3: Twiss functions for the lattice under study.

For a beam filling the acceptance $A = 384\pi$ mmmrad specified above, the x envelope has maxima of 10.0 cm in the end F quadrupoles, while the y envelope has maxima of 8.8 cm in their D partners. At the injection point the maximum divergence is 3.8 mrad in x and 10 mrad in y. At the dispersion maximum each charge-state beamlet has a width of 2.4 cm, while a full $\pm 9\%$ CSD will spread across ± 11.2 cm. Magnet apertures consistent with such beams will be required.

CONCLUSIONS

We have attempted to show that foil stripping can not only provide the rapid injection process essential for radioactive ions, but that ion losses can be kept to the $\lambda = 1\%$ level for each traversal if the ring has a high enough charge acceptance, and if Z is not so high that the energy loss is unacceptable. Painting the beam in the x and y planes can reduce the average foil traversal rate per turn $F_x F_y$ to 1/400. If charge Q is injected on each turn, then the stored charge will exponentially approach $Q/\lambda F_x F_y = 40,000Q$, though a more practical aim would be to stop after 40,000 turns ($\simeq$40 ms) with $\simeq$25,000Q. Even if the loss rate were 10 times higher, 2,500Q would be a sizeable improvement over present beam intensities.

ACKNOWLEDGEMENT

The authors would like to thank M. Grieser and M. Lindroos for helpful discussions.

REFERENCES

[1] M. Pasini, R.E. Laxdal, Proc. EPAC 2002, Paris, 933 (2002).

[2] M. Grieser *et al.*, *Cooler rings and their applications*, (World Scientific, 1991) p.190; http://www.mpi-hd.mpg.de/be/tsr/

[3] K. Shima *et al.*, At. Data Nucl. Data Tables, **51**, 173 (1992).

[4] L. Meyer, Phys. Stat. Sol. B **44**, 253 (1971).

[5] E. Baron, Ch. Ricaud, Proc. EPAC'88, Rome, 839 (1988).

[6] D. Raparia, C.W. Planner *et al.*, IEEE Trans. Nucl. Sci. **32**, 2456 (1985).

THE TRIUMF 500 MeV CYCLOTRON: PRESENT OPERATION AND INTENSITY UPGRADE

R. Baartman, P. Bricault, I. Bylinsky, M. Dombsky, G. Dutto, R. Laxdal, R. Poirier,
Y. Rao, L. Root, R. Ruegg, P. Schmor, M. Stenning, G. Stinson
TRIUMF, 4004 Wesbrook Mall, Vancouver, B.C. V6T 2A3, Canada*

Abstract

A new series of experiments (mainly astrophysics) began at TRIUMF in July 2001 when the ISAC-I linear accelerator began delivering up to 1.5 MeV/u radioactive ion beams (RIB) to users. A superconducting linear accelerator extending the RIB energy to 6.5 MeV/u has recently been approved and is now being constructed (ISAC-II). Record RIB intensities are being achieved from different target ion sources with a primary incident proton beam of 500 MeV, up to 50 μA intensity. This will later be increased to 100 μA, compatibly with target acceptance. Furthermore, an additional 100 μA extracted proton beam is being considered for simultaneous (RIB) production from a second target-ion source system. This would significantly enhance the research potential of the laboratory. Four simultaneous high-intensity extracted beams would therefore be required for a total maximum cyclotron accelerated current of about 400 μA. Recently we have been able to deliver 300 μA to the existing three high intensity beam lines at 90% duty cycle. The cw delivery of beam was limited only by the presently available external beam dump capacity. In this paper we will review the present operational experience at 200/250 μA, the future plans for intensity upgrade to 350/400 μA, and the intrinsic factors limiting the total accelerated intensity beyond 400 μA.

INTRODUCTION

ISAC is an ISOL radioactive ion beam facility driven by a 500 MeV proton beam from one of the TRIUMF cyclotron's external beam lines[1]. A layout of the existing ISAC-I and the planned ISAC-II accelerator is shown in Fig. 1 [2, 3].

ISAC-I has been operating since 2001 and consists of a primary beam line (BL2A) capable of delivering up to 100 μA of protons to a target-ion-source mass-separator/LEBT system supplying radioactive beam to either a low-energy experimental area or to a room temperature linac consisting of an RFQ, a stripper, and a DTL in which ions with A $\leq$ 30 are accelerated up to 1.5 MeV/u.

ISAC-II, which is now under construction, will accelerate ions with A $\leq$150 to at least 6.5 MeV/u by 2009[2]. An ECR charge state-booster will produce higher charge-state ions with charge to mass ratios of A/q$\leq$30 for acceleration in the existing ISAC-I RFQ. A new room temperature IH-DTL will accelerate the ions from the RFQ to 400 keV/u where they will be stripped and then injected into a heavy ion superconducting linac[4]. In 2005 the 20 medium β superconducting cavities will begin operating on line. A new beam line will also connect the exit of the ISAC-I DTL to the entrance of the medium β cavities so that the 1.5 MeV/u beam from ISAC-I can be accelerated up to 4.3 MeV/u, permitting higher-energy experiments to begin. In 2007 the high β cavities will be installed, increasing the available energy to at least 6.5 MeV/u. ISAC-II will be completed when the IH-DTL and the low β cavities are added to improve the stripping efficiency and to extend the mass range to A=150.

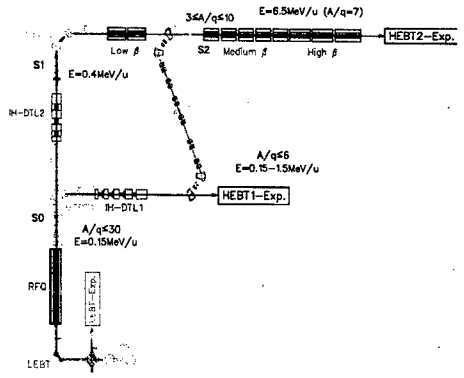


Figure 1: ISAC layout

It is proposed that a new 100 μA extraction line (BL4N) and target station dedicated to target/RIB development be included in TRIUMF's next five year plan. This facility could eventually be reconfigured and used as an additional radioactive ion source for ISAC, allowing at least two experiments to run simultaneously using the proton beams from the TRIUMF cyclotron[3].

As shown in Table 1, using a surface ion source ISAC-I has already produced record intensity radioactive beams downstream of the mass separator. So far, the primary 500 MeV proton beam intensity has been limited to 50 μA. This will eventually increase to 100 μA[5]. An ECR source is now being commissioned in the recently completed east target station[5], and a laser ion source is being developed.

When all of TRIUMF's existing extraction lines are operating simultaneously at their maximum currents (BL1A at 150 μA for pion/muon production, BL2A at 100 μA for

*TRIUMF receives funding via a contribution agreement through the National Research Council of Canada

0-7803-7738-9/03/$17.00 © 2003 IEEE

Table 1: Radioactive Ion Yields

Ion	Target	$I_p(\mu A)$	Yield(P/s)
^{8}Li	Ta	40	8.3×10^{8}
^{9}Li	Ta	35	9.4×10^{7}
^{11}Li	Ta	30	1.2×10^{4}
^{20}Na	SiC	45	2.6×10^{8}
^{21}Na	SiC	45	9.9×10^{9}
^{37}K	TiC	40	6.4×10^{7}
^{38g}K	TiC	40	1.8×10^{10}
^{38m}K	TiC	40	7.4×10^{7}
^{74}Rb	Nb	30	1.3×10^{4}
^{74}Ga	ZrC	45	2.2×10^{6}
^{75}Ga	Ta	40	1.0×10^{6}
^{94}Y	Ta	11	6.0×10^{4}

ISAC, BL2C4 at 50 μA for isotope production), 300 μA will be required from the cyclotron. With the 100 μA BL4N operating, 400 μA will be needed. Because this total current exceeds those so far delivered, a high current development program was begun.

HIGH CURRENT DEVELOPMENT

Over the last 15-20 years TRIUMF has been responding to user demands by simultaneously extracting a total current of up to ≈220 μA down three or four external beam lines. Approximately 5,000 hours of beam time is scheduled each year, and typically 90% of this is successfully delivered. Recently a record total annual extracted beam charge of over 700 mAh was achieved. Our goal is to obtain 350-400 μA simultaneously extracted down the four beam lines shown in Fig. 2.

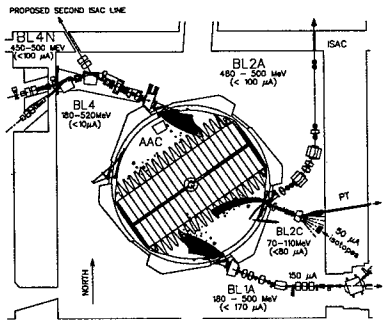


Figure 2: Layout of the TRIUMF cyclotron.

The beam injected into the cyclotron from the ion-source-injection system (ISIS) is normally bunched so that slightly over 70% of it is within the phase acceptance of the cyclotron. The remaining 30% is lost either radially or vertically in the centre region. Radial losses occur when ions that gain too little energy crossing the injection gap spiral into the vertical resonator walls surrounding the centre post. Vertical losses may occur over the first few turns when ions that cross the dee gaps when the rf phase is negative get defocused and hit beam scrapers attached to the dees. Space charge defocussing increases this vertical loss.

A portion of the radially lost beam was being deposited on poorly conducting stainless steel ribs used to reinforce the vertical resonator walls, producing temperature trips at currents higher than ≈220 μA.

In addition to the heating problem, by the end of 2001 it had been discovered while running pulsed beams that the cyclotron transmission dropped from over 60% with equivalent currents of 220 μA or less to approximately 50% with equivalent currents of 300 μA due to increased beam losses in the centre region.

Several improvements were made during the first half of 2002.

1. The correction plates shown in Fig. 3, used for vertical steering on the first few turns, were repaired and realigned after they were found to be beam damaged and misaligned.

2. As shown in Fig. 4, a water-cooled beam stopper was installed in the first quarter turn of the cyclotron to intercept that portion of the beam that previously was being lost radially.

3. The back edge of an r.f. contact was found to be protruding into the beam gap and was trimmed back.

4. Improved ISIS tunes were developed. Running the H^- cusp source at lower arc currents with higher gas flows seemed to improve the transmission through the cyclotron.

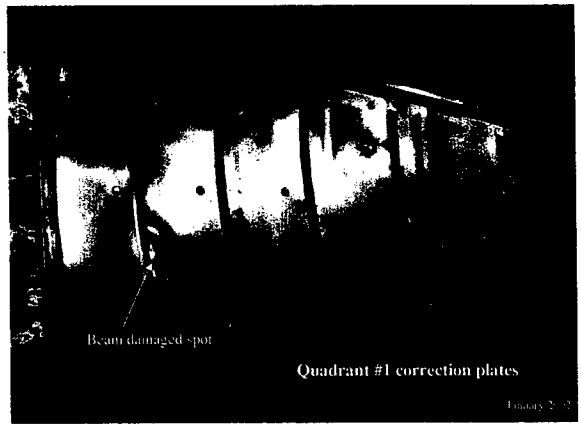


Figure 3: Centre region correction plates showing beam damage.

In July 2002 a new high-current record was established for TRIUMF when 275 μA was accelerated at full duty cycle for 3 hours. As shown in Fig. 5 the stability of the extracted beam was acceptable (the four short beam-off periods were due to rf sparking and to external beam line problems). Extraction of average currents greater than 275 μA

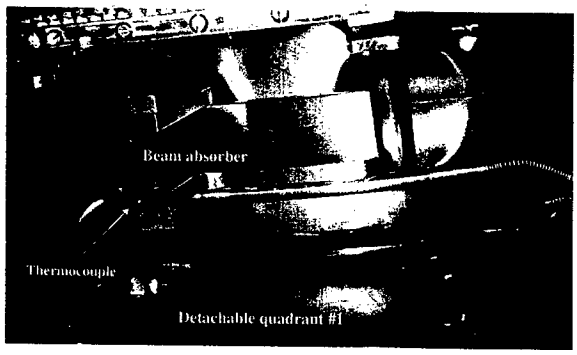


Figure 4: Centre region beam stopper.

was impossible because of external beam dump limitations, however we were able to extract 300 μA equivalent current at 90% duty cycle for two hours without encountering any problems. Cyclotron transmission was better than 60% in both cases while ISIS transmission was ≈90%. No temperature trips occurred during any of these runs. Just before the end of the development shift, 350 μA equivalent was accelerated at 40% duty cycle with 57% cyclotron transmission for half an hour.

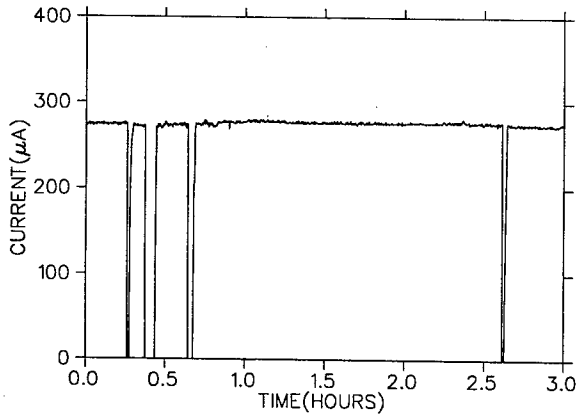


Figure 5: 275 μA extracted current versus time.

During subsequent development shifts we found that although the 300 μA results were easily reproduceable, it was difficult to increase the current much above 300 μA. Near the end of 2002 analysis of the rf power input to the dees and of the time-of-flight between injection and extraction indicated that the calibration of the rf voltage probes had been changing, and the actual rf voltage was ≈10% lower than indicated on the control console, thus limiting the cyclotron's phase acceptance. In December the rf voltage was increased, and equivalent currents of 350 and 380 μA were extracted at 10% duty cycle with over 60% transmission. Time limitations prevented us from trying to decrease the spills and raise the duty cycle or from trying to obtain 400 μA equivalent current. This work will resume in spring 2003 when high current operation resumes after the winter shut down (400 μA equivalent current was previously achieved with a lower transmission using a different ion source in 1988[6]).

Several improvements to facilitate high current development are being implemented or planned.

1. Adjustable emittance-limiting slits are being installed in ISIS to control the emittance of the injected beam.
2. Improved beam diagnostic devices are required in ISIS. An emittance measuring rig as well as additional wire scanners in the vertical section of ISIS are needed.
3. The ion source extraction voltage will be raised from 12 kV to 25 kV, and the source's extraction optics will to be redesigned so that higher currents can be extracted at lower arc currents.
4. The aging lower vertical section of ISIS needs replacing to enhance reliability. In addition, a third buncher may be installed in this section to improve bunching efficiency at higher currents[8].
5. For 400 μA tests and operations a new 200 μA beam dump is required to operate in parallel with the 200 μA acceptance of BL1A. It's proposed that this be installed on BL4N in the vicinity of the ISAC targets.

These projects are proposed for the next five year plan.

The high-current capability of TRIUMF is ultimately limited by space charge and by the spills produced by electromagnetic stripping of the H^- beam at higher energies. TRIUMF's space charge limit has been estimated to be ≈ 500 μA with 100 kV of dee voltage, which comfortably exceeds our 400 μA goal. Stripping losses have been reduced by installing an auxiliary rf booster cavity to increase the energy gain per turn above 450 MeV where most of the stripping loss occurs[7]. This allows us to increase the 500 MeV extracted beam from 170 to 250 μA. The rest of the beam would have to be extracted at 450 MeV or below.

REFERENCES

[1] G. Dutto et al, "Completion of the ISAC-I Accelerator for Radioactive Ions and Extension to ISAC-II", Proc. EPAC 2002, Paris.

[2] R. Laxdal et al, "The ISAC-II Upgrade at TRIUMF - Progress and Developments", this conference.

[3] G. Stinson, P. Bricault, "A Proposal for an Additional Beam line to the TRIUMF ISAC Facility", this conference.

[4] R. Laxdal et al, "Superconducting Accelerator Activities at TRIUMF/ISAC", Proc. 14th Int. Linac Conf., Korea(2002)

[5] P. Bricault, "High Power Targets for ISOL Radioactive Beam Ion Facility", this conference.

[6] G. Dutto et al, "The Upgrading of the TRIUMF Facility to 500 μA Operation", Proc. EPAC 1988, Rome.

[7] G. Dutto et al, "Impact of the Cyclotron RF Booster on the 500 MeV Proton Beam Production", Proc. 16^{th} Int. Conf. on Cyclotrons, East Lansing (2001).

[8] R. Baartman, Y.-N. Rao, "Investigation of Space Charge Effect in TRIUMF Injection Beamline", this conference.

FERMILAB BOOSTER ORBIT CORRECTION

L. Coney, J. Monroe, Columbia University, NY, NY, 10027, USA

W. Pellico, E. Prebys, FNAL, Batavia, IL 60510, USA

Abstract

The Fermilab particle physics program has recently expanded to include the MiniBooNE experiment in addition to the RunII program. As a result, the effective and reliable performance of the Fermilab Booster has become crucial to the lab. The Booster is an 8 GeV proton synchrotron and is a key element of the Fermilab accelerator chain. It must meet increasing demands for proton intensity and high repetition rates. One important requirement placed on the machine is low radiation levels. These levels are highly correlated with losses in the machine, and can limit Booster production. We will describe how a system of ramped dipole corrector magnets are being used to maintain orbital position throughout the acceleration cycle in order to minimize beam losses, maximize proton intensity, and maintain the required repetition rate.

INTRODUCTION

Recently the physics program at Fermilab has grown to include a thriving group of accelerator based neutrino physics experiments. This is in addition to continued RunII operation of the Tevatron as the highest energy proton–antiproton colliding beam accelerator in the world. The neutrino program at Fermilab includes MiniBooNE [1], which began taking accelerator based neutrino data in late summer of 2002, and NuMI/MINOS [2], which is scheduled to come on line in 2005. Both of these experiments depend on massive amounts of protons from the Fermilab accelerator chain. In particular, MiniBooNE generates a neutrino beam that originates as an 8 GeV proton beam from the Fermilab Booster. The MiniBooNE baseline requirement is 5E20 p.o.t. (protons on target) per year; however, the Booster can currently deliver ~2E20 protons/year. This gives MiniBooNE only 40% of its baseline, although it receives roughly 12 times more protons than those used for RunII operations. Clearly, the demand on proton production from the Booster is significantly higher than it has been in the past, and it will continue to rise when NuMI/MINOS begins to take beam. By the year 2006, the Booster may be required to deliver 5 times what it produces now.

THE FERMILAB BOOSTER

The Fermilab Booster [3] was originally built to provide protons to the Main Ring, and it first took beam in 1970. The Booster accepts the 400 MeV proton beam from the Fermilab Linac, accelerates it to 8 GeV, and sends it to MiniBooNE, the Main Injector for RunII, or the Radiation Damage Facility. The Booster is 472 m in circumference with a 24-fold periodic lattice. Each period has a 6 meter long straight and a 1.2 meter short straight drift section, and 4 combined function magnets, two horizontally focusing (F magnet) and two horizontally defocusing (D magnet) [4] (see Fig.1). These magnets cycle in a 15 Hz resonant circuit.

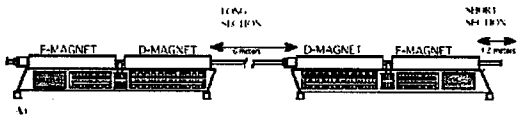


Figure 1: A Booster lattice cell [4], consisting of a focusing magnet, defocusing magnet, long drift, defocusing magnet, focusing magnet, and a short drift (FDOODFO).

In spite of its age, the Booster has been very reliable, maintaining an average uptime of over 90%. However, the machine is being pushed to run at record intensities and repetition rate. At present, the Booster can stably accelerate a *maximum* of 5E12 protons/pulse, and before the MiniBooNE era it typically ran at a repetition rate of ~2 Hz. In order to meet the new demand for protons, the current goal is to run steadily at 5E12 protons/pulse at a repetition rate of 7.5 Hz (5 Hz for MiniBooNE).

High Intensity Running

There are many challenges involved in running the Booster at high intensity, including beam loss and radiation damage issues. Damage or activation of accelerator components in the tunnel is a serious concern. Damage to accelerator elements could increase failure rates, and activation makes it difficult to maintain machine components.

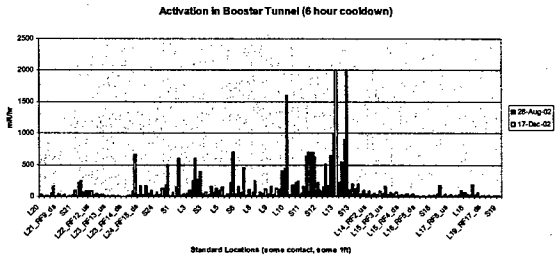


Figure 2: Booster tunnel radiation levels from radiation surveys performed in August 2002 and December 2002. Activation levels were significantly higher in December after MiniBooNE began routinely taking beam.

In December 2002, a radiation survey was done of the Booster tunnel (see Fig. 2). It became clear from the survey data that activation of tunnel components had significantly increased since the turn-on of MiniBooNE. Additionally, the personnel recording the data received a

0-7803-7738-9/03/$17.00 © 2003 IEEE

20 mR radiation dose, and two technicians completing a minor high voltage cable repair in the tunnel received a 30 mR dose. After the survey, some of the beam loss limits in the Booster were lowered to reduce component activation in sensitive locations. Furthermore, reducing beam losses became a high priority in order to facilitate high intensity running of the Booster.

BOOSTER ORBIT CORRECTION

The orbit correction project was designed to reduce beam losses in the Booster by controlling the beam orbit throughout the 33 msec acceleration cycle. This project makes use of the ramped dipole correctors, the BPM (Beam Position Monitor) system, and the extensive array of BLMs (Beam Loss Monitors) in the Booster.

Dipole Correctors

Orbit correction is accomplished using the ramped dipole corrector magnets in the Booster. There are 2 such correctors in each lattice period, one horizontal and one vertical, for a total of 48. Each is located in its respective high beta region, with the vertical correctors in the long straight sections and the horizontal correctors in the short straights (see Fig. 3). We currently manipulate the orbit only in the vertical plane. It is possible to consider orbit correction in the horizontal plane, but there are complications involved in doing so. The Booster RF (Radio Frequency) system uses feedback from the horizontal beam position to determine the RF phase used for acceleration. Any external change to the horizontal beam position would need to accommodate this system in order to keep the machine functioning properly.

Originally, the correctors were run DC and were designed to introduce a separation of 1.4 cm at 10 meters (about half of a period) at the Booster injection energy of 400 MeV [4]. This meant that their impact on the orbit was reduced as the acceleration cycle progressed. Dramatic changes in the orbit position throughout the cycle were not uncommon. Recently, the ability to ramp the magnets was implemented. This enables us to affect the orbit throughout the entire Booster acceleration cycle.

Beam Position Monitors (BPMs)

The Booster BPMs are also crucial to the orbit correction program, since they are used to measure the beam orbit position throughout the cycle. As with the dipole correctors, there are 48 BPMs in the Booster, located in each long and short straight section. These stripline devices measure beam position in both the horizontal and vertical planes with sub millimeter precision. They are also capable of measuring beam intensity.

Beam Loss Monitors (BLMs)

There is an extensive array of BLMs in the Booster. They are located in each long and short straight section, with additional individual loss monitors at key positions around the ring for a total of 60. These ionization loss monitors are in the orbit correction project as a diagnostic. Beam losses with and without the orbit corrections are compared in order to understand how well the correction is working.

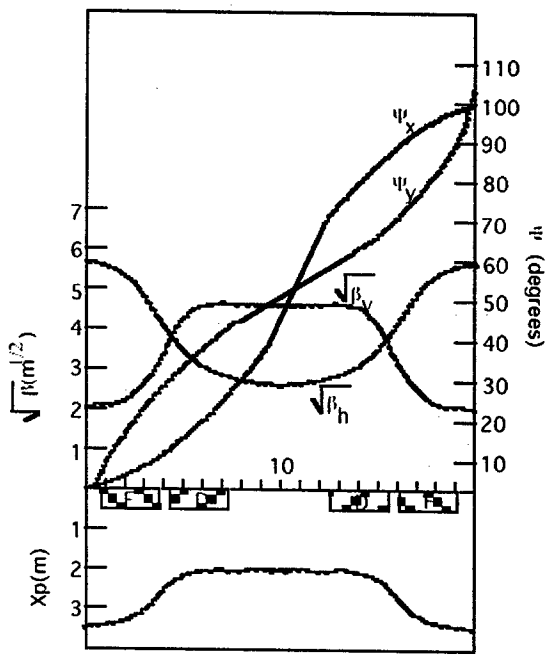


Figure 3: Booster lattice showing the correspondence between focusing and defocusing magnets and the horizontal and vertical beta functions. The vertical high β region is in the long straight section, while the horizontal high β region is in the short straight section [4].

Orbit Correction Procedure

The orbit correction proceeds in several steps. First, the desired orbit is read either from a file or directly from a particular time during an active Booster cycle. In the latter case, an orbit shortly after injection is typically used. The orbit is measured as a function of time using the BPM system, and then the current ramps needed to hold the orbit at the desired point are calculated. There are 12 break points during the 33 msec Booster cycle at which the closed orbit current ramp is calculated. This is complicated by absolute current limits and a 600A/sec slewing limit between each time break for all correctors. The optimum corrections are calculated based on all active correctors, initially without regard to the limits. If any correctors are over the limit, then the quantity (D/L) is calculated for each, where D is the change in current since the last time break, and L is the distance to the limit for that magnet. All of the current changes are then scaled back such that the maximum value for (D/L) is 1, meaning that one corrector is at its limit. That corrector is set to the maximum, removed from the active list, and the orbit is reoptimized using the rest of the correctors. This process is repeated until no additional correctors hit their limits, up to a maximum of 15 iterations for each time break. Once the ramps are calculated, they are sent to the

corrector magnets and implemented in the next accelerator cycle. There is also a steering interface, which enables the user to manipulate the orbit relative to the present desired orbit, and then recalculate the current ramps. This is used to steer the beam at unusual locations, such as extraction points or low aperture regions. Finally, the loss monitors are used to gauge the beam transmission through the machine once the ramps are activated.

Orbit Correction Results

We have run the orbit correction program on Booster beam going to MiniBooNE, and can see a distinct difference in the beam position throughout the acceleration cycle due to the correctors. Figure 4 shows the vertical beam position with and without the ramped correctors at two different locations in the tunnel: long straight sections 13 and 24. At each location, we successfully held the orbit fairly flat throughout the cycle with the correctors. Long 13 is a special case because it is located at an extraction point which forces the beam position to be lower than might be expected.

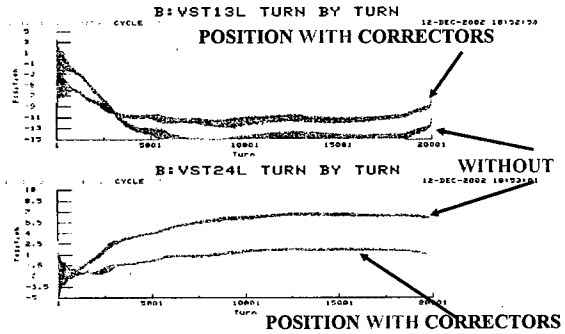


Figure 4: Vertical beam position at long straight section 13 (top) and 24 (bottom) as a function of time in the Booster cycle with and without the correctors.

It is also possible to look at the loss monitor results both with and without the ramped correctors. Figure 5 shows the normalized loss pattern in the Booster as a function of the position around the ring *without* using the ramped correctors. Figure 6 shows the normalized losses *with* the correctors on and actively controlling the vertical beam position. While the overall magnitude of the losses remains similar, the loss distribution was successfully changed. Beam losses at Long 22 and Long 24, where sensitive RF cavities are located, were dramatically improved.

CONCLUSIONS

Demand for proton production at Fermilab has significantly increased, forcing the Booster to run at record intensity and repetition rate. Unfortunately, beam losses create challenges to achieving the new production goals. The orbit correction project has successfully controlled the beam orbit throughout the entire Booster cycle. As a result, beam losses have been significantly improved near sensitive equipment. Work on this project continues in order to reduce overall Booster losses throughout the ring, thus enabling consistent high intensity running of the Booster.

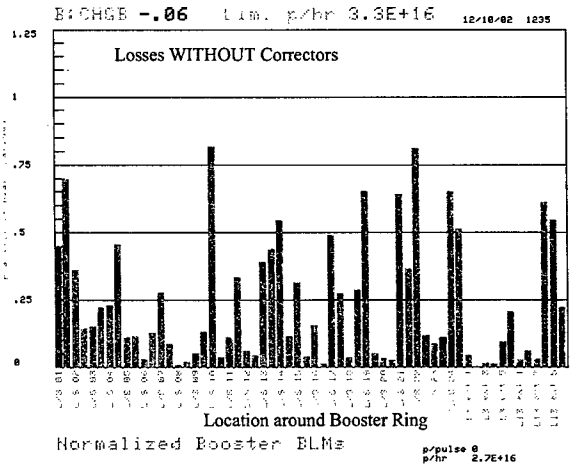


Figure 5: Normalized Booster losses as a function of position around the ring without using the ramped correctors. Note the high losses around L/S 22 and 24 to the right of the plot.

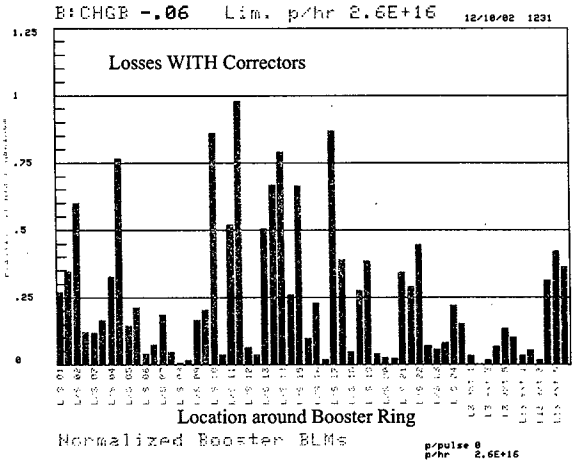


Figure 6: Normalized Booster losses as a function of position around the ring WITH ramped correctors to change the vertical beam position. Note that the losses around L/S 22 and 24 have been significantly reduced.

REFERENCES

[1] E. Church, et al., "A Proposal to Measure $\nu_\mu \rightarrow \nu_e$ Oscillations and ν_μ Disappearance at the Fermilab Booster: BooNE", Fermilab Proposal 898 (1997).
[2] http://www-minos.fnal.gov
[3] Fermilab Technical Memo TM-405 (1973).
[4] B.Worthel, Booster Rookie Book, (1998).

CRYRING PROGRESS: WEAK BEAMS, RARE IONS AND ORDERING

A. Källberg, G. Andler, L. Bagge, M. Björkhage, M. Blom, H. Danared, P. Löfgren, F. Österdahl, A. Paál, K.-G. Rensfelt, A. Simonsson, M. af Ugglas, Manne Siegbahn Laboratory, Stockholm, Sweden

Abstract

Much of the development of the CRYRING facility has been aimed at the production, handling and measurement of weak beams, often of ions that are difficult to produce in the ion sources. Due to the diverse requirements for ions, several different ion source types are in use. To be able to handle and measure the weak beams, the beam diagnostic systems have been improved.

The ECR source is in regular use for single pass experiments and will be used for experiments in the storage ring before the summer of 2003.

The EBIS source has been renovated and upgraded with a new electron gun and will be back in operation in May 2003.

INTRODUCTION

The CRYRING facility consists of a low energy storage ring and a collection of ion sources that can be used for injecting beams into the ring and also for experiments directly at the beam lines from the sources. The available sources are: several types for singly charged ions with different requirements, both positive and negative; an ECR source for ions with moderately high charges and an EBIS source for the production of highly charged ions. The beam line from the ECR source to the ring has been completed, but since the 300 kV platform still requires some work, beams have not yet been transported to the ring. Experiments are planned to use ECR beams in the ring before the summer of 2003. Several experiments have however been using the ECR beam for single-pass experiments at lower energies since 2001. The advantage of the higher currents available have been clear for those experiments that do not need the highest charge states available from the EBIS.

ION PRODUCTION FOR THE RING

Rather exotic requests for ions to be stored in the ring have become a common part of our efforts to run the CRYRING facility. It may be very highly charged ions, like Kr^{33+}, rare organic molecules, like $C_7D_7^+$ and $C_3H_3^+$, or clusters, like $H(H_2O)_6^+$ and D_5^+. Also specially prepared ions are requested, like rotationally or vibrationally cold molecules. Many of the requested ions require careful preparation and sometimes development of methods to produce them in sufficient amounts and in ways that give a reasonable lifetime of the ion sources. For the highly charged ions, the EBIS source has been used exclusively, but for singly charged ions, several different types of ion sources have to be used to comply with all the different ion requirements.

ION SOURCE TYPES

The EBIS source

The EBIS has, to a large extent not been able to deliver beams during the last year. A combination of a much needed renovation and upgrading and a couple of unfortunate technical failures has led to a long period of work on the source while it has not been able to deliver beams to experiments. All this work has just been finished and cooling down of the source has started. Equipped with a new electron gun, it is expected to deliver beams with lower emittance and the transport of the beams will be more efficient. Beams will be delivered to experiments again in May.

Hot cathode source

Several different ion sources are used. The workhorse is a hot filament source with a solenoidal magnetic field [1]. A discharge is created in the source by entering a suitable material from which the desired ion can be created. Quite often a pulsed injection is used, which has the effect both to prolong the lifetime of the source and also often to increase the ion current produced. The substances that are used are gases, liquids as well as solids. Gases are normally straightforward, though special care, of course, has to be taken for gases that are poisonous or explosive. For the liquids, the vapor pressures are regulated by changing the temperatures of the substances. The liquids often have to be cooled to reduce the pressure but in some cases also heating is necessary. In this case also the feed lines into the source, including valves etc., have to be heated to avoid condensing of the liquid in the thin tubes used, which leads to blocking of the tubes and uncontrollable behavior of the source. The solids are heated in an oven that is attached to the source, close to the discharge chamber. If their vapor pressure is sufficient, pure metals is used, e.g. Pb and Ca. More commonly a chloride or fluoride salt has to be used. The oven in use at present is limited to about 900°C and the vapor pressure needed for sufficient ion production is about 10 mtorr. In some cases the use of a noble gas as a carrier gas gives a more stable and reliable operation.

The hot source is suitable for the production of most of the requested ions, also the hydrocarbon ions and ions containing oxygen. The problems associated with these substances in a hot source: internal shortcuts due to soot deposit on the insulators and rapid consumption of the hot filament, respectively, are quite efficiently counteracted by the pulsing mentioned above. At least the need to change source is reduced to at most twice during an experimental week.

0-7803-7738-9/03/$17.00 © 2003 IEEE

Cold cathode source

In some cases, however, a cold cathode source is used. The main reasons for the use of this source are when cluster ions are to be produced and when vibrationally colder ions are needed. The cluster ions are destroyed by the high temperature in the hot source and their formation is also favored by the higher pressure in the cold cathode source. Also with this source pulsing of the vapors that are needed to produce the clusters is used.

Nier type source

Two further ion sources are used when the experimentalists have particular requirements on the vibrational and/or rotational populations of the molecular ions. An electron bombardment source of the NIER type, built at AMOLF, Amsterdam [2], delivers cold ions of symmetric diatomic molecules, such as O_2^+ and N_2^+, with a controlled vibrational population. Since these molecules do not have an electric dipole moment, they do not cool down by emitting infrared radiation while stored in the ring.

Supersonic expansion source

A particular case, ever since it once was the subject of investigation during the first experiment performed in the ring in 1993, is H_3^+. This molecule plays an important role in the production of molecules in interstellar space. To be able to use the measurements of the recombination rates that could be performed in the CRYRING storage ring in calculations of molecular synthesis in interstellar space, the ions have to be produced in a very cold state. With the help of a source utilizing a supersonic expansion technique, developed by the group at the department of chemistry at UC Berkeley led by Richard Saykally, cold H_3^+ molecules with temperatures of 20 – 60 K could be produced. The important results of these measurements in CRYRING have recently been published in Nature [3].

Cesium sputter source

For the production of negative ions, a commercial source of the Cesium sputter type is used. This source is able to produce a wide variety of negative ions by carefully choosing the proper cathode material.

WEAK BEAM DIAGNOSTICS

The success of delivering all these rare ions to the experiments has been made possible due to improvements of the diagnostic equipment, both in the beam lines and the storage ring. In a few cases, beams with currents below 1 nA from the ion source have successfully been transported to the ring, stored, accelerated and electron cooled. Low-noise amplifiers and beam-loss particle detectors have been the main tools for this task. Sometimes the trick of setting up the ring with another ion, which could be produced in larger amounts, and having the same charge-to-mass ratio as the desired one has been used. This procedure helps a lot for the rarest ions. As an example, the use of $^{20}Ne^{2+}$ to prepare the ring for the injection of 0.5 nA D_5^+ can be mentioned. Since many experiments also require a measurement of the stored current in the ring, to be able to measure absolute reaction cross sections, much work has been done to reduce the noise of the AC current transformer. Figure 1 shows an example of a current measurement in the ring. The current transformer used, of the ICT type from Bergoz, has been better adapted to our needs. It now has a noise that is 20 times lower than originally, thus enabling us to measure bunched circulating currents below 1 nA. To obtain this noise reduction, we have replaced the original preamplifier with a higher gain, low-noise one and placed this amplifier close to the detector. Since the current measurement with this type of current transformer has to be performed on a bunched beam, it is done in the beginning of the ring cycle, with the RF voltage on. The count rates of the detectors in the experiments are then normalized to the current measured with the help of a beam-loss detector which measures neutral particles that are lost from the beam at the zero-degree exit after a dipole magnet.

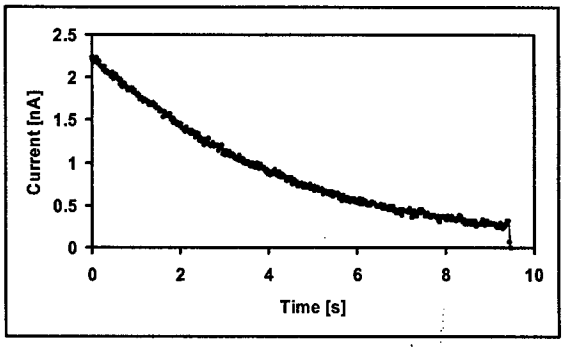


Figure 1: Current of a stored H_2S^+ beam.

ORDERED BEAMS

The phenomenon of a sudden change in the momentum spread of a weak, electron-cooled highly charged ion beam, as seen in the Schottky spectrum, which was originally observed at GSI in Darmstadt, has also been studied in CRYRING. This sudden change of the properties of the beam has been interpreted as a transition to an ordered state and has been observed in weak beams of electron-cooled highly charged ions.

Using coasting beams of 7.4 MeV/u Xe^{36+} ions, we have studied how the particle number at the transition depends on the electron-cooling power (varied by changing the electron current in the cooler). When the cooling is weak it is found that the transition to the ordered state can take place at very low particle numbers—less than 100. Since the circumference of the CRYRING storage ring is 51 m, the particle distance in this case is of the order of 0.5 m. When the strength of the cooling is increased, on the other hand, a kind of saturation is seen, such that ordering with more than about 6000 particles has not been observed. Although this saturation could be due to experimental limitations, there

are reasons to believe that it has to do with the properties of the ordered state.

At CRYRING, indications of ordering have also been seen with a bunched beam, looking at the bunch shape with a longitudinal pickup and an oscilloscope. Using an rf amplitude of only 6 mV, sharp transitions from a broad emittance-dominated bunch to a much narrower, approximately 3 m long space-charge dominated bunch were seen when the bunch contained some 400 Xe^{36+} ions. This bunch length and particle number agree well with theoretical calculations of the bunch length for a one-dimensionally ordered particle configuration, and the line density is quite similar to upper limit for coasting beams. Also in the Schottky spectrum a transition was observed, as shown in fig. 2.

Studying bunched rather than coasting beams gives a possibility to control the linear particle density in the ring by just changing the rf amplitude. Thus one could hope to achieve ordered beams with higher densities than previously observed, and one might also be able to observe their "vaporization". A recent update of our observations can be found in ref. 4.

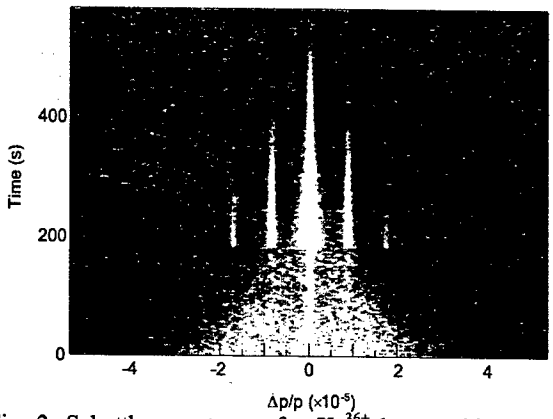


Fig. 2. Schottky spectrum of a Xe^{36+} beam with an rf voltage of 6 mV indicating the observed transition to an ordered state with a bunched beam.

REFERENCES

[1] I. Bergström, S. Thulin, N. Svartholm and K. Siegbahn., Ark. Fys. **1** (1950) 281; K. O. Nielsen, Nucl. Inst. Meth. **1** (1957) 289

[2] C.W. Walter, P.C. Cosby, and J.R. Peterson, J.Chem.Phys. **98**, 2860(1993)

[3] B. J. McCall, A. J. Huneycutt, R. J. Saykally, T. R. Geballe, N. Djuric, G. H. Dunn, J. Semaniak, O. Novotny, A. Al-Khalili, A. Ehlerding, F. Hellberg, S. Kalhori, A. Neau, R. Thomas, F. Österdahl, and M. Larsson, Nature **422**, (2003) 500

[4] H. Danared, A. Källberg and A. Simonsson, J. Phys. B **36** (2003) 1003

DESIGN OF A RACETRACK MICROTRON TO OPERATE OUTSIDE THE PHASE STABILITY REGION

M.N. Martins, P.B. Rios, J. Takahashi, Laboratório do Acelerador Linear, Instituto de Física da Universidade de São Paulo, CP66318, 05315-970 São Paulo, SP, Brazil
L.A.A. Terremoto, Instituto de Pesquisas Energéticas e Nucleares, CNEN-SP, Brazil

Abstract

The beam optics design of a small 5-turn cw racetrack microtron is described. This microtron is the first stage of a two-stage microtron of 31 MeV maximum energy, and 50 μA maximum current. The microtron booster is fed by a 1.8 MeV injector linac. This configuration was chosen in order to maximize the final energy of the system with the available RF power, and, as a result, it was necessary to operate the first stage outside the ideal orbital stability region. The separation between successive return orbits is not constant, and the system presents large phase oscillations from one orbit to another. Nevertheless it was possible to find geometrical and magnetic field strength configurations that allow the extraction of a 4.9 MeV beam, within the design goals for the main acceleration step.

INTRODUCTION

The Physics Institute of the University of São Paulo (IFUSP) is building a 31 MeV continuous wave (cw) racetrack microtron [1,2]. This two-stage microtron includes a 1.8 MeV injector linac feeding a five-turn microtron booster that increases the energy to 4.9 MeV. After 28 turns, the main microtron delivers a 31 MeV cw electron beam. The injector has a capture section and a pre-accelerating section; therefore the complete accelerator has four RF accelerating sections, operating at 2450 MHz. Figure 1 shows an isometric view of the machine in the accelerator building.

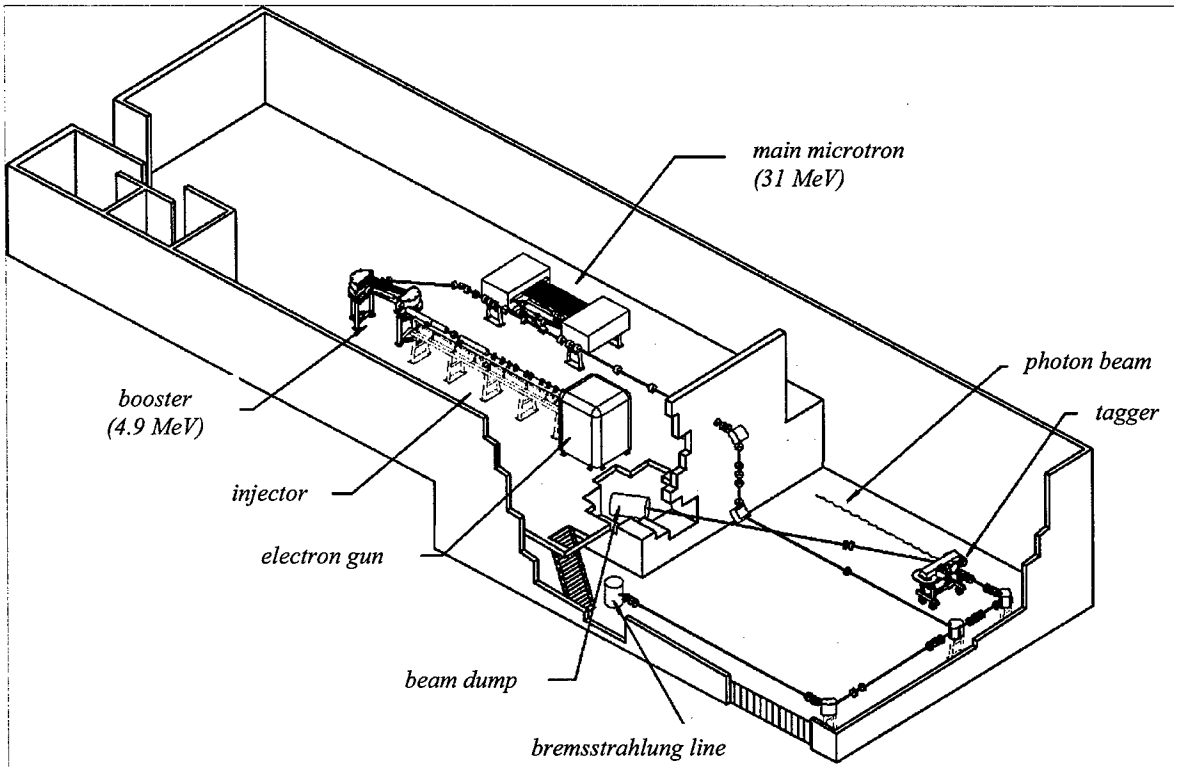


Figure 1 – Isometric view of the accelerator in the accelerator building.

This cascaded configuration was adopted in order to maximize the final energy of the system, keeping costs within our limited budget, what meant powering the whole system with a single RF source, namely a 50 kW cw klystron. Several configurations were tried, with different power distributions, but the one that allowed

0-7803-7738-9/03/$17.00 © 2003 IEEE

achieving the highest final energy, with reasonably conservative parameters, included a microtron booster. This solution allowed increasing the injection energy of the main microtron to close to 5 MeV, reserving enough RF power to push the final beam energy to 31 MeV, approximately 20 % higher than the other configurations.

In this paper we describe the design of the first stage of this configuration, the microtron booster. Due to the low injection energy, 1.8 MeV, the booster operates outside the phase stability region, and so is restricted to a small number of turns.

STABILITY CONDITIONS

The stability conditions of a racetrack microtron are those that allow synchronous acceleration of the electrons and constant spacing between consecutive orbits. They are very well known and identical to those of the conventional microtron [3]:

$$\frac{2\pi r_1 + 2L}{\lambda\beta_1} = \mu \qquad (1)$$

$$\frac{\Delta W}{m_0 c^2}\frac{B_0}{B} + \frac{2L}{\lambda}\left(\frac{1}{\beta_{n+1}} - \frac{1}{\beta_n}\right) = \nu \qquad (2)$$

where μ is the length of the first orbit in integral numbers of wavelength;

r_1 is the first orbit radius;

L is the separation between magnets;

ΔW is the energy gain per turn;

λ is the accelerating RF wavelength;

β_n is the ratio between the electron speed at turn number n and the velocity of light;

B is the magnetic field of the end magnets;

$B_0 = \frac{2\pi m_0 c^2}{e\lambda}$ is the cyclotron field;

ν is the integral increment in the period between two consecutive orbits.

For ultra-relativistic electrons, $\beta_{n+1} \approx \beta_n \approx 1$, and eqn. (2) becomes much simpler. That is the situation in ordinary microtron designs, when the injection into the recirculating path is done with sufficiently high energy. In our case, however, it is not possible to apply the above approximation, and the period increment between orbits is not constant. This clearly prevents phase stability, but we were able to find a reasonably stable condition for a few turns, increasing the beam energy high enough to allow insertion on the second stage. The simulation, using the PTRACE code [4], was divided in two steps: first we simulated a closed RTM (without insertion or extraction magnets) just to look for a possible solution. After finding a reasonable solution, we introduced the insertion and extraction devices and optimized the configuration.

Figure 2 shows some results of the first simulations, namely the phase shift versus energy gain per turn on a hypothetical 10-turn machine.

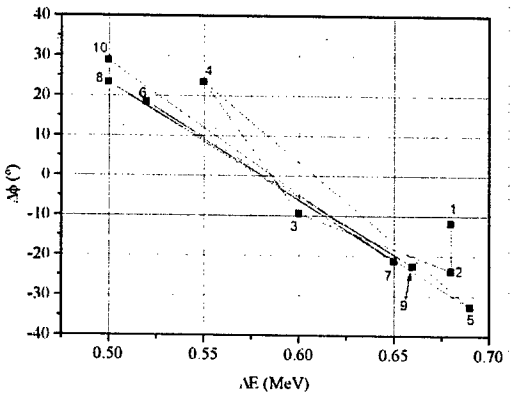


Figure 2 – Phase shift versus energy gain per turn

It is clear from Fig. 2 that a large phase shift oscillation builds up after the fourth turn, but it is also clear that, if one limits the number of turns to five, it is possible to design a stable RTM, that will increase the energy from 1.8 to 4.9 MeV, which is high enough for injection on the main accelerator.

Next step was the simulation of a more realistic machine, including injection and extraction devices. The injection line introduced a new difficulty, due to the proximity between one of the end magnets (N magnet) and a small 15°-dipole (D3) necessary to make the return line of the injected beam parallel to the accelerating structure, as shown in Fig. 3.

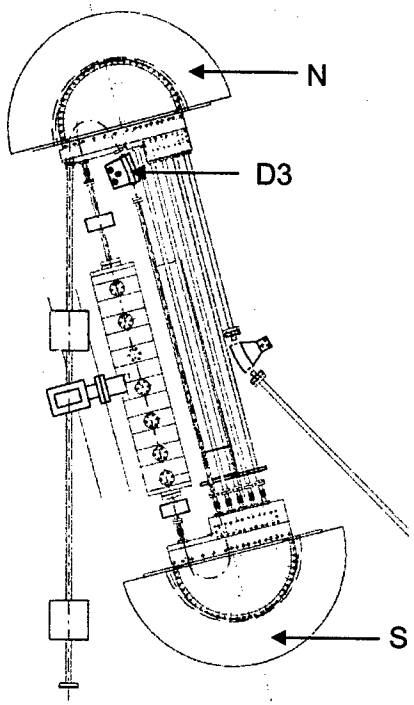


Figure 3 – Schematic drawing of the booster. The distance between the pole faces of the end magnets is 1555.4 mm

The magnetic induction field of the D3 dipole is much smaller than that of the end magnet, and the distance between their pole faces is only about 10 cm, so the field in this region is a combination of their fringing fields. Figure 4 shows the field configuration resulting from the measured fields of both magnets [5,6] and their composition [7].

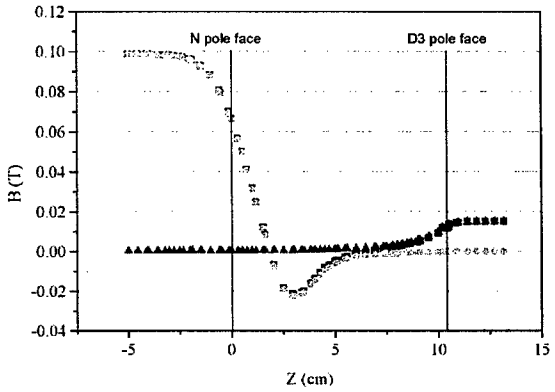


Figure 4 – Field distribution in the region between the end magnet N and the D3 dipole. N end magnet, circles; D3 dipole, triangles; composition, squares.

RESULTS AND CONCLUSIONS

Using the combined field shown in Fig. 4, we optimized the configuration of the booster with the PTRACE code. Table 1 summarizes the main characteristics of the booster, after the optimization process.

As can be seen from Table 1, the path length increment was not constant, nevertheless this configuration is able to boost the beam energy to a level appropriate for injection in the main RTM, with an average energy gain of 0.625 MeV per turn. The mechanical design shown in Fig. 3 was made after the optical design suggested by these simulations.

With this configuration, the RF power from the klystron tube is divided as: 9 kW for each of the structures of the injector linac, 7 kW for the booster and 13 kW for the main stage microtron.

ACKNOWLEDGMENTS

The authors would like to thank the financial support of the Brazilian funding agencies FAPESP, and CNPq.

Table 1 – Main characteristics of the booster

Turn	E (MeV)	β	ν	ΔL (cm)	ΔE (MeV)	Δφ (°)
Injection	1.77	0.9746	0.8816			
1	2.44	0.9849	1.0373	12.643	0.68	-11.81
2	3.12	0.9900	0.9657	13.048	0.68	-23.75
3	3.72	0.9927	0.9066	12.563	0.60	-9.50
4	4.27	0.9943	1.1371	11.444	0.55	23.40
5	4.95	0.9956		13.353	0.69	-32.74

REFERENCES

[1] J. Takahashi *et al.*, in *Proceedings of the EPAC92, Third European Particle Accelerator Conference*, 1992, edited by H. Henke (Editions Frontieres, Gif sur Yvette, France, 1992), p. 429.

[2] J. Takahashi *et al.*, in *Proceedings of the PAC97, Particle Accelerator Conference*, Vancouver, Canada, 12-16 May, 1997, p. 2998.

[3] R.E. Rand, *Recirculating Electron Accelerators*, (Accelerators and Storage Rings V.3), Chur, Switzerland: Harwood Academic Press, 1984.

[4] K.-H. Kaiser, PTRACE code, private communication.

[5] L.R.P. Kassab, P. Gouffon, M.N. Martins and J. Takahashi, Part. Accel. **59**, 75-92(1998); L.R.P. Kassab, P. Gouffon, and M.N. Martins, Nucl. Instrum. and Meth. **A404**, 181-184(1998).

[6] M.L. Lopes, M. Sc. degree dissertation, IFUSP (2002), unpublished.

[7] P.B. Rios, M. Sc. degree dissertation, IPEN-USP (2002), unpublished.

BEAM TRANSPORT SYSTEM FOR THE IFUSP MICROTRON

M.N. Martins, P.B. Rios, M.L. Lopes, J. Takahashi, Laboratório do Acelerador Linear, Instituto de Física da Universidade de São Paulo, CP66318, 05315-970 São Paulo, SP, Brazil

Abstract

This work describes the beam optics design of the two transport lines of the IFUSP cw microtron. The first one links the two stages of the accelerator, while the second one connects them to the experimental hall. Placement of the active elements along the beam line, as well as the optimization of their operational parameters were done by simulation of the beam optics with two different codes.

INTRODUCTION

The Laboratório do Acelerador Linear (LAL) of the Instituto de Física da Universidade de São Paulo is building a continuous wave (cw) electron race-track microtron (RTM) [1-3]. This two-stage microtron includes a 1.8 MeV injector linac feeding a five-turn microtron booster that increases the energy to 4.9 MeV. After 28 turns, the main microtron delivers a 31 MeV electron beam. In order to minimize the background radiation, the experimental hall, with two beam lines, is located 2.68 m below the accelerator room. Figure 1 shows an isometric view of the machine in the accelerator building. In the experimental hall, one of the beam lines will be dedicated to experiments using tagged photons, while the remaining line will be used for high beam intensity experiments, such as nuclear resonance fluorescence (NRF) or production of X-rays by coherent bremsstrahlung [4].

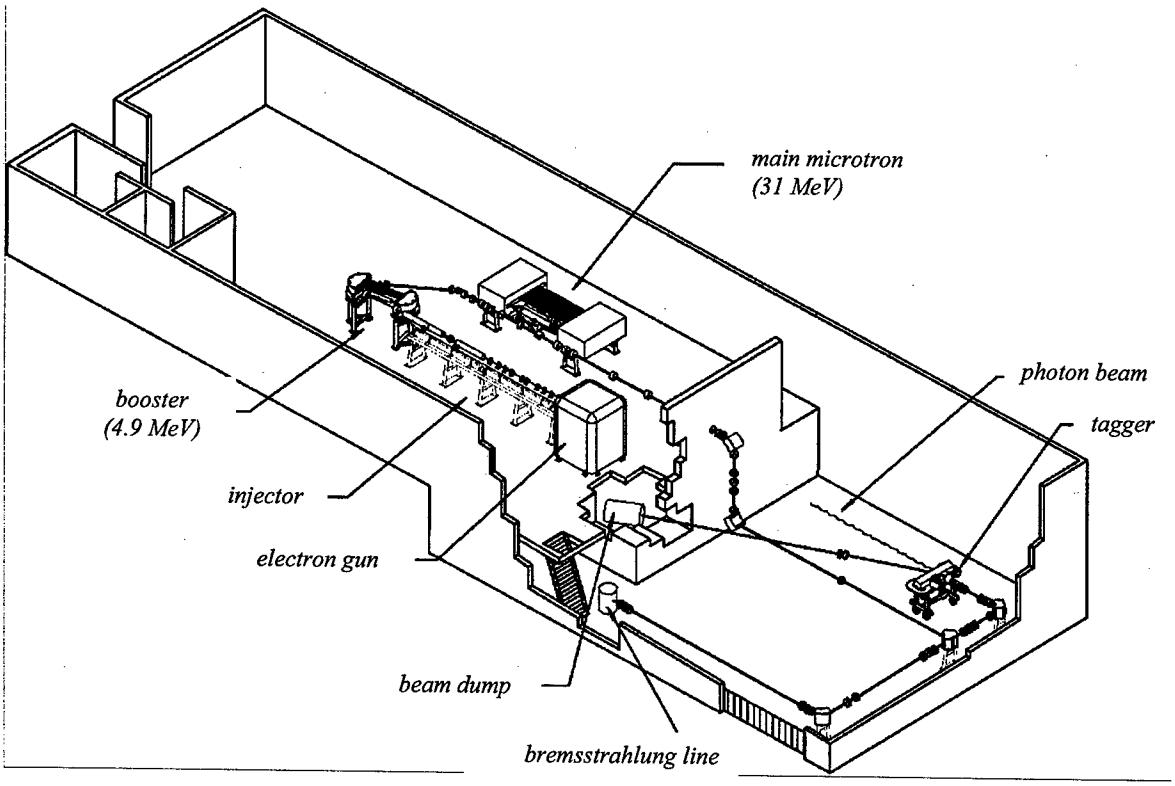


Figure 1 – Isometric view of the accelerator in the accelerator building.

BEAM LINE OPTICS DESIGN

The standard design procedure of beam transport systems includes the following steps:

1. "Zeroth" order calculations, to be used as ansatz to the next step;
2. Envelope simulations to optimize the operational parameters of the active elements and their placement along the beam path;

0-7803-7738-9/03/$17.00 © 2003 IEEE

3. Particle tracking through the obtained transport system.

The first step is usually done by analytical calculations, the last two using computer simulations codes such as TRANSPORT [5,6] and PTRACE [7] respectively.

In this particular project it was not possible to use the TRANSPORT code to simulate the beam characteristics of the microtron booster, due to the low energy of the electron beam, which lead to large accelerating phase slips between consecutive orbits and, consequently, to varying path differences.

PTRACE is a particle tracking code specifically developed to design microtrons, and its main feature is the correct calculation of the phase slip of the electrons, regardless their energy. On the other hand, it presents a severe limitation on the number of simulated tracks per batch (only 10 on the original code). To overcome this limitation we developed a macro to a spreadsheet application that allowed easy simulation of large numbers of electron tracks, as well as determination and visualization of the main characteristics of the beam [8]. This macro was also used as a tool to facilitate the optimization of the operational parameters of the electromagnets of the booster. It allowed the simulation of a large number of electron tracks (typically several thousands) and statistical determination of the beam characteristics.

On the transport lines, *i.e.*, on the lines linking the microtrons and connecting them to the experimental hall, it was possible to use the ordinary designing steps. The main difficulty found was the need of large angular deviations on both vertical and horizontal planes, with small curvature radius, including a switching magnet to select between the two possible experimental lines [9].

RESULTS AND DISCUSSION

Using the methods outlined above, it was possible to obtain a beam of good optical quality along the path.

Figure 2 shows the beam profile along the microtron booster, with marks pointing the last simulation element of each synchronous accelerating turn, as well as the insertion and extraction turns.

As expected, the beam divergence in both horizontal and vertical planes are bigger on the insertion step, since it is not possible to neither introduce correcting elements nor even change the distance between the insertion dipole and the end magnet.

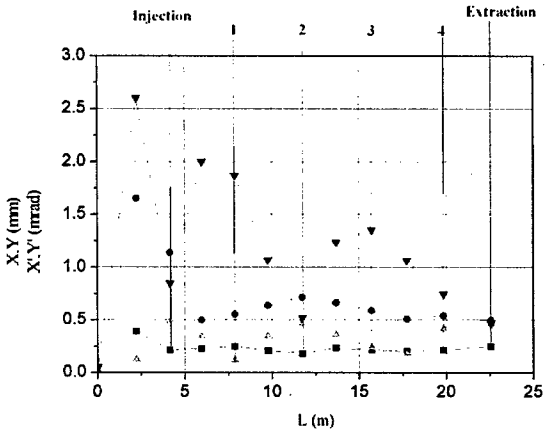


Figure 2 – Beam profile along the microtron booster: horizontal beam size, X (black squares); horizontal beam divergence, X' (red circles); vertical beam size, Y (green triangles); vertical beam divergence, Y' (blue triangles).

Figure 3 shows the beam profile along the transfer line, with its main steps marked.

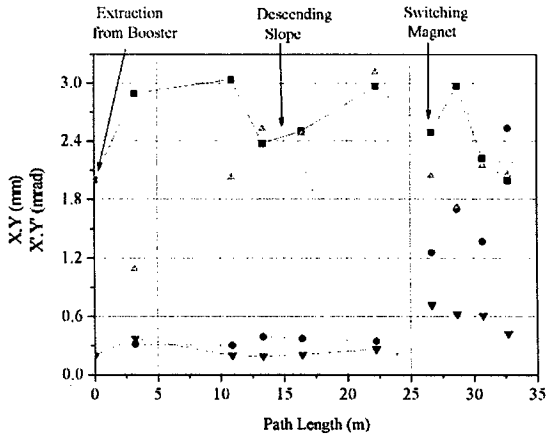


Figure 3 – Beam profile along the transport line: see caption of Fig. 2

We also have space limitations on the extraction line from the booster, where there is not enough room to place correcting elements, and the beam is required to follow two non-symmetrical deviations to (*i*) clear the end magnet, and (*ii*) reach the main transport path, as shown in Fig. 4.

The descending slope is a parallel vertical displacement of 90° with a bending radius of 35 cm, followed by a 6-m long straight section and the switching magnet, where the beam turns horizontally by 90° with an 11-cm radius of curvature. This sharp curve increases the divergence at the end of the trajectory, but the beam still presents characteristics suitable for the intended uses.

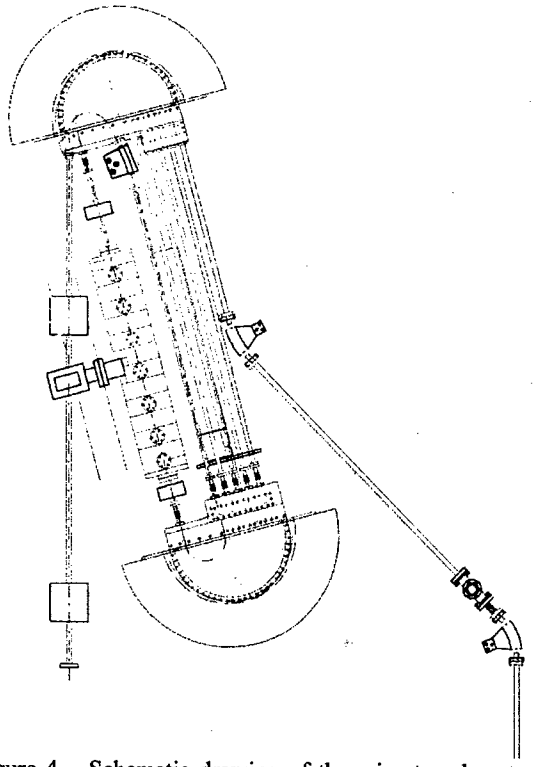


Figure 4 – Schematic drawing of the microtron booster, showing the insertion and extraction lines. The separation between the end magnets is 1.5 m.

CONCLUSIONS

The use of different simulation codes, due to project restrictions, imposed some extra labour but did not introduce any major discrepancies between them.

Spreadsheet applications made the statistical analysis easier and faster, which allowed us to compare results and improve our design. But the need for a dedicated beam transport design tool for low energy microtrons still remains.

ACKNOWLEDGMENTS

The authors would like to thank the financial support of the Brazilian funding agencies FAPESP and CNPq.
The authors would also like to thank the contribution of Mr. P.B. Rios to the development of the macro for the spreadsheet application.

REFERENCES

[1] M.N. Martins *et al.*, in *Proceedings of the PAC03, Particle Accelerator Conference*, TPPE020.
[2] J. Takahashi *et al.*, in *Proceedings of the EPAC92, Third European Particle Accelerator Conference*, 1992, edited by H. Henke (Editions Frontieres, Gif sur Yvette, France, 1992), p. 429.
[3] J. Takahashi *et al.*, in *Proceedings of the PAC97, Particle Accelerator Conference*, Vancouver, Canada, 12-16 May, 1997, p. 2998.
[4] V.B. Gavrikov, V.P. Likhachev, M.N. Martins, V.A. Romanov, Braz. J. Phys. 29, 516-523(1999).
[5] K.L. Brown, D.C. Carey, Ch. Iselin and F. Rothacker: Transport, a Computer Program for Designing Charged Particle Beam Transport Systems. See yellow reports CERN 73-16 (1973) & CERN 80-04 (1980).
[6] *PSI Graphic Transport Framework by U. Rohrer based on a CERN-SLAC-FERMILAB version by K.L. Brown et al., http://people.web.psi.ch/rohrer_u/trans.htm*
[7] K.-H. Kaiser, PTRACE code, private communication.
[8] P.B. Rios, M. Sc. degree dissertation, IPEN-USP (2002), unpublished.
[9] M.L. Lopes *et al.*, in *Proceedings of the PAC03, Particle Accelerator Conference*, WPAB070; and M.L. Lopes, M. Sc. Degree dissertation, IFUSP (2002), unpublished..

INSIGHTS IN THE PHYSICS OF THE DYNAMIC DETUNING IN SRF CAVITIES AND ITS ACTIVE COMPENSATION*

Marc Doleans†, Sang-ho Kim, ORNL/SNS, Oak Ridge, TN 37830, USA.

Abstract

Elliptical SRF cavities operated in pulsed mode experience dynamic Lorentz detuning because of the time varying radiation pressure. Due to the narrow electromagnetic bandwidth of these resonators, the induced detuning can severely affect their matching conditions to the RF feeding system. The active compensation scheme using piezoelectric tuners has proven to be a viable and attractive method to minimize the effects of the Lorentz detuning. To optimize this compensation, mechanical parameters are extracted for the action of the Lorentz forces and the piezoelectric tuner from both measurement and simulation. This process gives insights into the physics of the dynamic detuning, such as the nature of the coupling differences of both detuning sources, the possible settings for the measurement of the dynamic detuning with the methods to deduce mechanical parameters from them, and the origin of possible parasitic effects in the measurements. These issues are reported and discussed along with some ideas for the optimization of the detuning compensation.

DETERMINATION OF THE CAVITY MECHANICAL PROPERTIES

Qualitative modeling by a vibrating string

The modeling of the cavity wall vibrations by a vibrating string is interesting because of its relative simplicity and because it contains various aspects of the physics. Firstly, the amplitude of the vibrations are small which is usually assumed in the vibrating string problem. Secondly, a string of finite length with fixed boundary conditions will produce a modal basis equivalent to the mechanical resonances of the cavity. Thirdly, some mode damping can be added to reproduce the attenuation in time of the cavity mechanical mode vibrations. Fourthly, distributed forcing, like the Lorentz forces, or local forcing, like the piezoelectric tuner action, are both possible. Fifthly, the detuning can be connected to the vibrations by integration of the transverse displacement over the longitudinal dimension of the string. Details of the modeling and of the calculus are presented in [3]. In the end, the model can be reduced to a system of second order ordinary differential equations (ODE) which support other analysis using such a modal approach [4]. In the following, the modal mechanical parameters are written $\{\Omega_m, Q_m, k_m\}$ where the index m refers to the m^{th} mechanical mode. Using the vibrating string model, it can be shown that the usually quoted parameter K for the Lorentz detuning, linking the detuning to the square of the field in the cavity as $\Delta f = -KE^2$, is the sum of all the modal k_m: $K = \sum_m k_m$. Also, it can be shown [3] that the coupling coefficients k_m are, as suggested in [4], the products of the projections of the acting force on the mode shapes by the projections of the frequency sensitivity on the mode shapes. As a direct consequence, it concludes that the coupling coefficients for the Lorentz force action are all of the same sign because the acting force is proportional to the radiation pressure $P_{rad} = \frac{1}{4}\{\mu_0|H|^2 - \epsilon_0|E|^2\}$ whereas, according to the Slater formulation, the frequency sensitivity is locally proportional to $\epsilon_0|E|^2 - \mu_0|H|^2$. This particularity does not hold for other sources of dynamic detuning such as piezoelectric tuners or microphonics because the acting forces do not depend on the cavity fields. In those cases, the coupling coefficients can therefore be of both signs. This fact seems confirmed by measurements as shown in the next section. The system of ODE for the Lorentz forces action and piezoelctric tuner action can therefore be written as

$$\Delta\ddot{\omega}_m + \frac{\Omega_m}{Q_m}\Delta\dot{\omega}_m + \Omega_m^2\Delta\omega_m = -\Omega_m^2 k_{m,L} V^2 \quad (1)$$

$$\Delta\ddot{\omega}_m + \frac{\Omega_m}{Q_m}\Delta\dot{\omega}_m + \Omega_m^2\Delta\omega_m = \Omega_m^2 k_{m,P} V_p \quad (2)$$

where V_P is the input voltage driving the piezoelectric tuner. As mentioned, the coupling coeffients $k_{m,L}$ associated to the Lorentz forces are only expected positive from the model. From Eq. (1) and Eq. (2), it concludes that in CW operation the relevant parameter is K whereas in pulsed operation, the position of the modes with respect to the harmonics of the repetition rate and the width of the resonance peaks are the prime concerns. For this reason, a harmonical analysis of the actions of the Lorentz forces and of the piezoelectric tuner is of direct interest. This can be performed by measuring the transfer functions for both sources of dynamic detuning. In the next section, those measurements and their study using simulations are presented.

Mechanical parameters for the action of the piezoelectric tuner

The amplitude of the transfer function associated to the piezoelectric tuner action was presented in [1]. For the corresponding measurement settings, there is no initial detuning ($\Delta\omega_0 = 0$), the current source is constant through time ($\tilde{I}(t) = \tilde{I}_0$), and the dynamic detuning is sinusoidal ($\Delta\omega(t) = \Delta\omega_{osc}\sin\omega_{osc}t$). The voltage in steady state is periodic, using the parameterization $\theta = \omega_{osc}t$ gives for the normalized voltage $\tilde{v}(\theta) = \frac{\tilde{V}_{SST}(\theta)}{R_L\tilde{I}_0}$

$$\tilde{v}(\theta) = e^{-j\sigma\cos\theta}\sum_n \tilde{P}_n(\sigma)\cos\theta_n\cos(n\theta - \theta_n) \quad (3)$$

where $\tan\theta_n = n\frac{\omega_{1/2}}{\omega_{osc}}$, $\tilde{P}_n$ are polynomials of $\sigma = \frac{\Delta\omega_{osc}}{\omega_{osc}}$ with complex coefficients explicitly given in [3]. Using Eq. (3) it is possible to efficiently reproduce the transfer function of the voltage phase ϕ_V by finding the appropriate mechanical parameters for the piezoelectric tuner action. Particularly, using coupling coefficients of both signs

*SNS is managed by UT-Battelle, LLC, under contract DE-AC05-00OR22725 for the U.S. Department of Energy

† doleansm@ornl.gov

0-7803-7738-9/03/$17.00 © 2003 IEEE

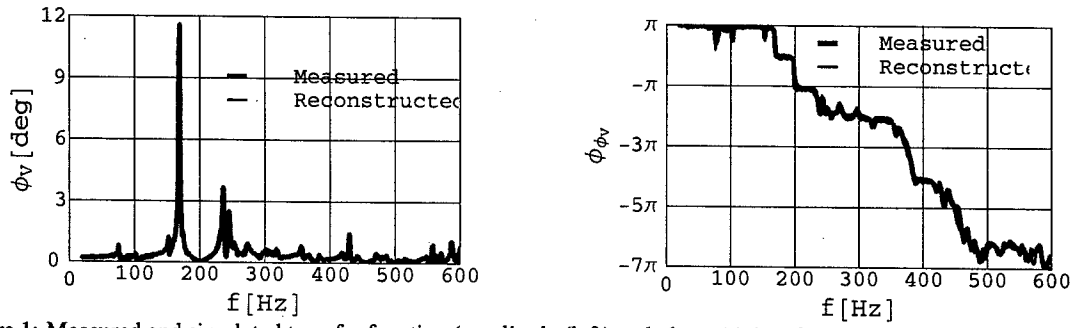


Figure 1: Measured and simulated transfer function (amplitude (left) and phase (right)) for the action of the piezoelectric tuner in the SNS medium beta cavity (Prototype cryomodule cavity #2). The input signal is the sinusoidal modulations of the piezoelectric input voltage $V_P(t)$, the output signal is the voltage phase $\phi_V(t)$.

allows to reproduce correctly the phase of the transfer function as displayed in Fig. 1.

Mechanical parameters for the action of the radiation pressure

A possible way to fill a cavity under dynamic detuning is the phase-lock loop configuration [6]. A phase-lock loop is a feedback loop designed to keep the phase between the forward RF power and the cavity voltage at a given constant value θ_l. As a consequence, the complexity of the coupled system of the voltage differential equations and the mechanical differential equations is greatly reduced because the voltage amplitude is independent of the dynamic detuning. Using this property, it is possible to obtain the transfer function associated to the action of the radiation pressure by exciting the cavity CW with small amplitude modulation on the forward power. The Lorentz transfer function was measured by JLAB in the SNS medium beta prototype cryomodule cavity #1 [5]. The modulated forward RF power $P_{RF} = P_0\{1 + \epsilon \sin \omega_{mod} t\}$, where ϵ is a small parameter, generates a detuning in the m^{th} mechanical mode

$$\Delta\omega_m(t) \approx -k_m V_l^2 \{1 + \epsilon \cos\phi_{mod} \cos\psi_m \\ Q_m \frac{\Omega_m}{\omega_{mod}} \sin(\omega_{mod} t + \phi_{mod} + \psi_m - \frac{\pi}{2})\} \quad (4)$$

where $V_l = \sqrt{8 R_L P_0} \cos\theta_l$, $\tan\phi_{mod} = \frac{-\omega_{mod}}{\omega_{1/2}}$, and $\tan\psi_m = Q_m(\frac{\Omega_m}{\omega_{mod}} - \frac{\omega_{mod}}{\Omega_m})$. Using Eq. (4), it is possible to find adequate mechanical parameters to reproduce the Lorentz transfer function. Doing so, all the coupling coefficients are assumed positive as mentioned previously. The measured and the reconstructed transfer functions are presented in Fig. 2. The fact that all the coupling coefficients are of the same sign translates to a rather large response for the low frequency part of the amplitude of the Lorentz transfer function because the contributions of all the mechanical modes add constructively. In comparison, the low frequency part of the amplitude of the piezoelectric tuner transfer function is not as large because of the interference between modes with positive and negative coupling coefficients. Since all the $k_{m,L}$ are positive, the phase of the Lorentz transfer function remains bounded in $[0; \pi]$. More exactly, in $[-\frac{\pi}{2}; \pi]$ because of an additional $-\frac{\pi}{2}$ shift originating from the parameter ϕ_{mod} which evolves progressively from 0 to $-\frac{\pi}{2}$ as the frequency of the modulations ω_{mod} passes from small values to large values in comparison to the electromagnetic half-bandwidth $\omega_{1/2}$. This transition is the reason for the initial slope of the phase of the transfer function observed in Fig. 2. It is interesting to mention that the value of $\omega_{1/2}$ (and therefore of Q_{ex}) can be determined from this slope.

COMPENSATION SCHEME BASED ON A HARMONIC ANALYSIS OF THE LORENTZ DETUNING

Depending on the profile of the Lorentz detuning in nominal operation, a suited profile $V_P(t)$ has to be found to generate a detuning $\Delta\omega_P(t)$ equal and opposite to the Lorentz detuning $\Delta\omega_L(t)$ (at least during the beam pulse). Based on understanding from modeling, a harmonic analysis of the problem shows that an ideal compensation can be obtained even if the transfer functions for the piezoelectric tuner and for the radiation pressure are not identical in shape (i.e if the sets of coupling coefficients for both detuning sources are not proportional to each other). In the following, this harmonical approach is presented. For SRF cavities operated in pulsed mode, the Lorentz detuning in steady state contains only components of the repetition rate ω_{rep} and its harmonics. The Lorentz detuning can be written $\Delta\omega_L(t) = \sum_{n=0}^{\infty} \Delta\omega_{L,n} \cos(n\omega_{rep} t + \phi_{L,n})$. To obtain an ideal compensation, the detuning associated to the piezoelectric tuner should be such that $\Delta\omega_P(t) = \sum_{n=0}^{\infty} \Delta\omega_{P,n} \cos(n\omega_{rep} t + \phi_{P,n})$, with $\Delta\omega_{P,n} = \Delta\omega_{L,n}$ and $\phi_{P,n} = \phi_{L,n} + \pi$ for each harmonic n. In this prospective, the piezoelectric tuner input voltage must be of the form $V_P(t) = \sum_{n=0}^{\infty} V_{P,n} \cos(n\omega_{rep} t + \theta_{P,n})$. Supposing an infinite number of mechanical modes $m = 1, 2, ..., \infty$, it can be shown [3] that:

$$V_{P,n} = \frac{\Delta\omega_{L,n}}{\sqrt{a_n^2 + b_n^2}} \quad (5)$$

$$\theta_{P,n} = \phi_{L,n} + \pi - \varphi_n \quad (6)$$

where $a_n = \sum_{m=1}^{\infty} c_{n,m} \sin 2\psi_{n,m}$, $b_n = -\sum_{m=1}^{\infty} c_{n,m}\{1 + \cos 2\psi_{n,m}\}$, $c_{n,m} = \frac{k_{P,m} Q_m \Omega_m}{2n\omega_{rep}}$, $\tan\varphi_n = \frac{b_n}{a_n}$, and

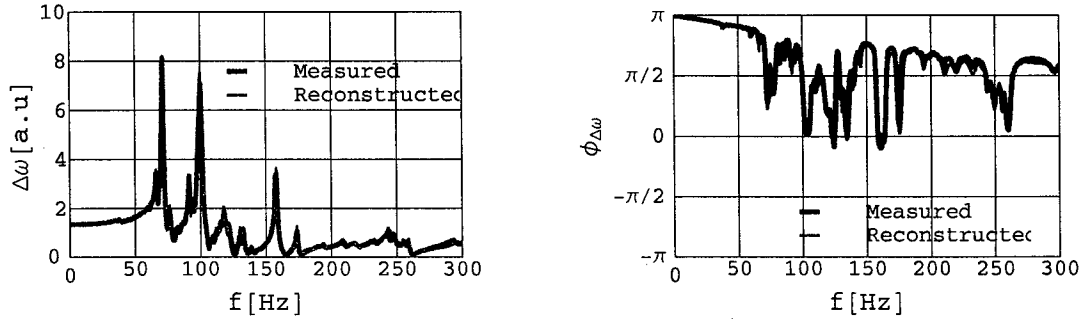


Figure 2: Amplitude and phase of the measured [5] and reconstucted transfer function associated to the Lorentz forces in the SNS medium beta cavity (Prototype cryomodule cavity #1). The input signal is the sinusoidal modulations of the forward RF power, the output signal is the dynamic detuning $\Delta\omega(t)$.

$\tan\psi_{n,m} = Q_m(\frac{\Omega_m}{n\omega_{rep}} - \frac{n\omega_{rep}}{\Omega_m})$. To illustrate this method, the case of the SNS medium beta cavity is considered. An example of a dynamic detuning profile for a cavity operated close to nominal condition was presented in [5] and is used for the illustration of the method. The initial part of the measured Lorentz detuning is caused by a parasitic signal [3] and is therefore suppressed in the analysis. The mechanical basis for the action of the piezoelectric tuner was reconstructed up to 600 Hz, as shown in Fig. 1. Since the repetition rate is 60 Hz, the Lorentz detuning function is truncated to the first ten harmonics as displayed in Fig. 3. The input voltage $V_P(t)$ is calculated using Eq. (5) and Eq. (6). The result is plotted in Fig. 4.

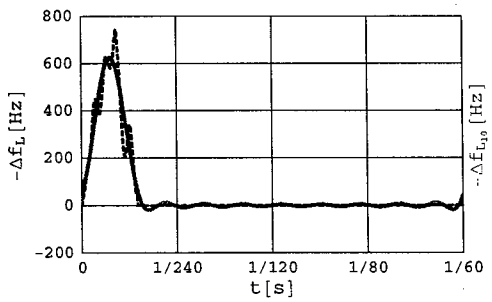


Figure 3: Measured Lorentz detuning function $\Delta f_L(t)$ [5] and its truncation to the 10^{th} harmonic of 60 Hz, $\Delta f_{L_{10}}(t)$. This truncated function constitutes the function compensated by the piezoelectric tuner input voltage $V_P(t)$ of Fig. 4.

CONCLUSION

The modeling effort was beneficial for a better understanding of the coupling of the Lorentz forces and of the piezoelectric tuner action to the cavity. From this understanding, the mechanical basis for both detuning sources could be reconstructed by the use of simulating tools. A harmonic analysis was presented to show the underlying basics of the compensation. The proposed scheme can be further simplified [3] for practical application.

ACKNOWLEDGEMENT

We want to thank our colleagues from ORNL and JLAB for their help, particularly Jean Delayen and Kirk Davis for their support and measurements, and Eugene Tanke for the editing.

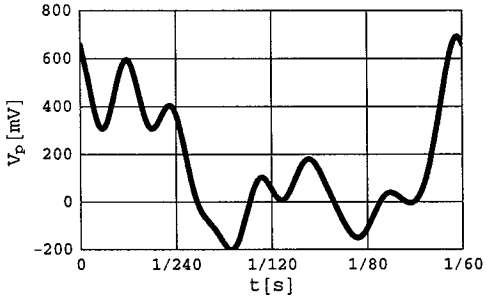


Figure 4: Input voltage function $V_P(t)$ for the piezoelectric tuner (repetitive 60Hz, before amplification) for the compensation of the truncated Lorentz detuning function $\Delta f_{L_{10}}(t)$.

REFERENCES

[1] Marc Doleans and Sang-ho Kim, "Analytical and Semi-analytical Expressions for the Voltage in a Cavity under Dynamic Detuning," Proceedings of Linear Accelerator Conference 2002 (LINAC2002), Gyeongju, 19th-23rd, August 2002

[2] Marc Doleans and Sang-ho Kim, "Analytical and semi-analytical formalism for the voltage and the current sources of a superconducting cavity under dynamic detuning," Nuclear Instruments and Methods in Physics Research A 496 (2003) 51-63

[3] Marc Doleans, "Studies in Reduced-beta Elliptical Superconducting Cavities (General Design Considerations, Dynamic Detuning, and Longitudinal Dynamics)" Thesis, Universite Paris VII, to be published

[4] N. Ouchi, E. Chishiro, C. Tsukishima, and K. Mukugi, "Pulsed SC Proton Linac," Proceedings of Linear Accelerator Conference 2000 (LINAC2000), pp. 683-687, Monterey, California, 21st-25th, August 2000

[5] J. Delayen et al., "Results of the Cryogenic Testing of the SNS Prototype Cryomodule," Proceedings of Linear Accelerator Conference 2002 (LINAC2002), Gyeongju, 19th-23rd, August 2002

[6] J. Delayen, "Self Excited loop," LLRF workshop, JLAB, 25th-27th, April 2001

CONSTRUCTION OF USER FACILITIES FOR THE PROTON BEAM UTILIZATION OF PEFP*

K. R. Kim, H. R. Lee, B. S. Park, K. Y. Nam, and B. H. Choi, KAERI, Daejeon, Korea

Abstract

The PEFP(Proton Engineering Frontier Project) was approved by the Korean government under its 21C Frontier R&D Program last year. Final goals of this project are construction of 100MeV proton linear accelerator, development of beam utilization technologies, and promotion of related industrial technologies [1]. Its major beam utilization areas are new genetic resource development, simulating space radiation environment, SOI(Silicon On Insulator) wafer development using ion-cut technology, and fast switching power semiconductor development. In addition, there are several small research projects concerned with basic science and nuclear physics. In the PEFP, 20MeV proton beam will be supplied to the users for their experiments from the middle of 2007. This paper contains the conceptual design of user facilities and the construction results of 6MeV proton beam test facility for pilot studies of the proton beam utilization experiments in the PEFP.

INTRODUCTION

In the PEFP, there are several research projects concerned with biological technology, nano-technology, space technology, information technology, etc. For basic experiments and pilot studies of the proton beam application projects, some test facilities will be developed and attached to some existing accelerators. In order to understand users' demand, a demand survey was carried out. And on the basis of its result, a development plan of the test facilities has been established and a conceptual design of the 20MeV proton beam utilization facilities of the PEFP has been performed. First of all, a test facility on the 3MV tandem accelerator of SNU(Seoul National University) has been designed and will be installed in a few months.

DEMAND SURVEY

The demand survey for user facilities has been carried out during the period from February 24th to March 15th. 17 researchers who participate in the PEFP replied to the survey suggesting beam specifications and irradiation conditions which they want to apply for their pilot studies of proton beam utilization. They preferred using domestic facilities to foreign ones because of good accessibility and low expenses. The facilities under consideration are 3MV tandem accelerator of SNU, MC-50 Cyclotron of the KIRAMS (Korea Institute of Radiological & Medical Science), and 1MV tandem accelerator of KAERI which is now under development. Some users proposed the irradiation condition of 0.3~50MeV proton energy, 10^7~10^{16} /cm^2 of total dose, and 2cm~15cm diameter of irradiation. On the basis of the survey results, a 6MeV test facility on SNU tandem accelerator has been designed and a design of 20MeV user facilities of the PEFP will follow.

In Korea, several low current proton beam accelerators including industrial ion implanters, tandem accelerators, and cyclotrons have been operated during last 10 years. Two tandem accelerators in KIGAM (Korea Institute of Geo-science and Mineral resources) and KAERI and one cyclotron of KIRAMS are the candidates of PEFP's test facilities. Especially, 1MV tandem accelerator, which is under development in KAERI, has a merit of large current of 10mA. For this reason, it will be utilized as a main test facility for researches with high dose rates.

Proton beam utilization technologies are being developed in the fields of NT, BT, IT, and ST. And several small projects are progressing under a user program development project.

Biological Application

The uses of high LET (Linear Energy Transfer) proton beam have attracted an increasing interest over the last years. In the PEFP, development of new genetic resources using few tens MeV proton beam was the main concern in the field of biological radiation technology. In this research, it is highly important to investigate impacts on biological species through LET of varying proton beam properties [2]. A low flux external beam irradiation facility is essential for the study. The requested energy range is 1~50MeV, with flux density of 10^7~10^9 /cm^2-sec. During irradiation, the temperature of samples has to be maintained below 50 degree centigrade.

Nano Application

A representative theme of nano-technology is SOI wafer development using ion-cut technology. Ion-cut technology was developed by SOITECH and named as Smart-Cut in France in 1994. SOI wafers of several hundreds nanometer thickness are now commercially produced by SOITECH with this technology. Key technologies in manufacturing SOI wafers by ion-cut are uniform ion beam irradiation over whole wafer surfaces of 2~5" size and CMP(Chemical-Mechanical Polishing) technology. The uniformity of dose distribution has to be greater than 95% and the energy difference ΔE has to be less than 3keV regardless of incident energy in the range of 300~600keV. The maximum dose is .5310^{16}/cm^2.

Space Application

The need of electronic devices for space applications has been increasing with the growth of space industry. To evaluate radiation-tolerant characteristics of space devices

0-7803-7738-9/03/$17.00 © 2003 IEEE

is very important in view of operational safety. Proton beam specifications for space applications are similar to those of biological ones. The energy range is 10~50MeV and the flux density is in the range of 10^6~10^{10}/cm^2-sec.

6MEV PRPTON BEAM TEST FACILITY

For pilot studies of proton beam utilization of PEFP, a 6MeV test facility has been designed and will be installed at tandem accelerator in SNU. The beamline is composed of scanning magnets for raster scanning, a beam profile monitor, and an irradiation chamber with a pumping port, a movable target stage and detectors. The schematic drawing of the beamline is shown in Fig. 1. Some manufactured components has been tested.

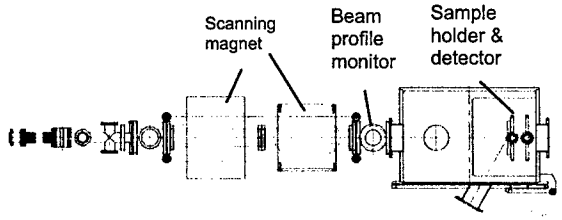


Figure 1: Layout of 6MeV beamline at SNU tandem.

Scanning Magnet

Scanning magnet was designed to irradiate 6MeV proton beam over the area of 6cm36cm with raster scanning method. The pole gap and depth are 110mm and 300mm respectively. As a result of its installation test, the required magnetic field of 1000G has been achieved with 84.2A coil current from 60Hz sine wave power supply as shown in Fig. 2. The magnetic field is linearly proportional to the coil current and the uniformity over the pole area was above 95%. A new power supply of 2~10Hz operation frequency will be installed to improve irradiation uniformity.

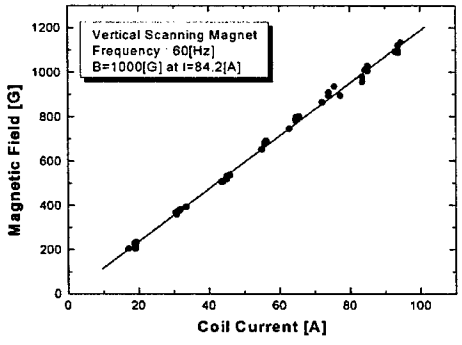


Figure 2: Characteristics of scanning magnet.

Faraday Cup

Small Faraday cup was designed to measure proton beam current. Its material is 99.9% pure Aluminium of 5mm thick and its aperture and depth are 10mm and 60mm respectively. To suppress secondary electrons from cup surface arising through proton beam bombardment, an electrostatic ring with maximum voltage of 1kV and a 830G SmCo permanent magnet are installed, respectively inside and outside of the Faraday cup.

Beam Profile Monitor

Beam profile monitor will be installed to monitor profiles in the middle of the beamline, in the front and back of the scanning magnets to compare beam profile and position changes across the magnets. The beam profile monitor, BPM-NEC83, has an effective scanning area of 7diameter with 1mm diameter Mo-wire.

Irradiation Chamber

Irradiation chamber has a pumping port, movable target stage, detector, etc. To maintain vacuum pressure in the beamline below 2310^{-7} torr, TMP of 800L/sec pumping speed will be installed at the bottom of the chamber. To acquire uniform irradiation performance, the target stage has been designed to allow applications of both raster scanning and spiral scanning methods. For spiral scanning method, the target stage has been designed to have a rotational movement system. For more accurate measurement of dose rates to samples, target and detector will have the same axis of beam. Behind target stage, a kind of 2D detector with high spatial resolution will be installed to measure absorbed dose rates to samples in the radiobiological experiments.

20MEV USER FACILITY

As 20MeV user facilities of the PEFP, 3~4 beamlines will be attached to the main proton linac. The facility for radio biological and space experiments will comprise scanning magnets (wobbler magnets or raster scanning magnets), a scattering foil, a beam monitor, an energy degrader, a modulator, a collimator and a sample changer. The window material of the vacuum chamber for the external beam will be 50μm Kapton or aluminium film of 50mm diameter. In order to obtain a uniform irradiation field, the scanning magnets and a scattering foil of Au with high Z-number will be used. An energy degrader will be used to change LET at irradiation site through reducing proton beam energy. A modulator will be used to make a spread-out Bragg peak. Conceptual design of 20MeV beamline is shown in Fig. 3

A petri dish has been designed for radio biological experiments. Stopping power and lateral straggling of proton beam upon thickness of window material was calculated with TRIM code. The calculation results were illustrated in Table 1. The window material was decided 20μm thick Kapton film. Inner volume of the dish is 80mmϕ335mm and the wall thickness is 4mm. It will be

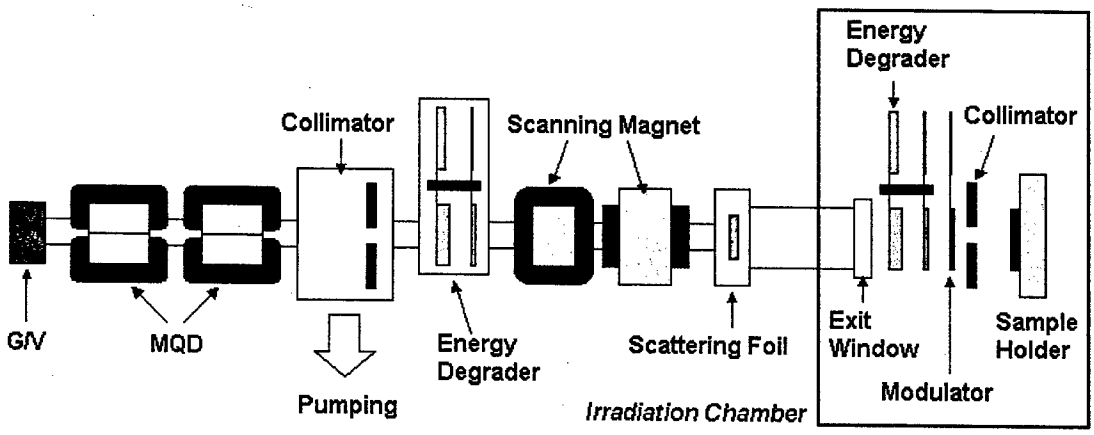


Figure 3: Conceptual design of 20MeV beamline for radio biological experiments.

applied to the experiments for developing new genetic resources using proton beam irradiation.

Table 1: TRIM code calculation results

Material	Stoppimg Power [keV/μm]	Ion Range [mm]	Lateral Straggling [A]
Kapton	3.485	3.17	84.58
Mylar	3.463	3.19	85.04
Polystylene	2.779	3.96	96.42

CONCLUSIONS

Demand survey for user facilities has been carried out and 17 researchers who participate in the PEFP replied to it. On the basis of the survey results, 6MeV test facility for the pilot studies of proton beam utilization technology development at the PEFP has been designed and will be installed at 3MV tandem accelerator in SNU. The magnetic characteristics of scanning magnets of 6MeV beamline have been performed with 60Hz sine wave power supply. To improve irradiation uniformity, a new AC power supply of 2~10Hz will be added. Conceptual design of 20MeV beamline especially for radio biological and space radiation experiments has been performed.

ACKNOWLEDGEMENTS

This paper is a part of the "Proton Engineering Frontier Project" which is sponsored by the Ministry of Science and Technology of Korea under "21C Frontier R&D Program".

REFERENCES

[1] B. H. Choi, et al., LINAC2002, Kyungju, Korea (2002)

[2] T. Kamai, S. Minohara, T. Kohno, et al., "Irradiation of 135MeV/u carbon and neon beams for studies of radiation biology", NIRS-M-91, Japan (1993)

THE BUNCHING SYSTEM BASED ON THE EVANESCENT OSCILLATIONS

M.I. Ayzatsky, E.Z. Biller, N.G. Golovko, K.Y. Kramarenko, V.A. Kushnir, V.V. Mitrochenko, S.A. Perezhogin#, V.F. Zhiglo, NSC KIPT, Kharkov, Ukraine

Abstract

The report presents design and simulated performances of the S-band electron bunching system based on coupled cavity chain in which the on-axis field amplitude changing substantially from the cell to the cell. For realization of such field distribution the operating frequency of the bunching system, which is close to the eigen frequency of the last cell, is higher than frequency of the "π" mode of the rest part of the bunching system. Cell lengths are chosen in the way to get the effective bunching and accelerating of the beam from the initial energy of 25 keV to the energy about 1 MeV with the current of 300 mA. The bunching system can be used in electron linacs both for fundamental researches and for radiation technologies.

INTRODUCTION

An injector substantially defines beam characteristics on a linac exit. It is known, that the increasing of amplitude of an accelerating field on the initial stage of acceleration when phase motion of particles is not frozen allows receiving small phase length of bunches at low energy spread [1]. Bunchers, which use such principle, are described, for example, in [2-4]. Resonant systems of the first and the second of them are a section of non-uniform biperiodic waveguide with magnetic coupling and the third one uses the section of non-uniform dick loaded waveguide (DLW) with the large attenuation of a counter-propagating wave. In [5,6] it was offered to use for this purpose a section of homogeneous DLW exited on the frequency that lies beyond the pass-band of corresponding infinite waveguide. Simulations of longitudinal motion of particles with the self-consisted model of the weakly coupled cavities [5,6] has shown that such system consisting of five cells is able to group low-voltage (25 keV) beam and to accelerate it up to energy, sufficient for injection in accelerating section with constant phase velocity. Besides, it was shown, that in such buncher at beam loading up to 1.5 A the field distribution does not change substantially. Therefore to simulate particle dynamics in the steady state mode it is possible to run the PARMELA program [7] using field distribution obtained with a SUPERFISH group of codes [8]. Intensive study of beam dynamics in the bunching system showed that longitudinal and transversal motion of particles is complicated. In particular, at the large change of energy of particles (from 25 keV to 1 MeV) the efficiency of homogeneous structure decreases. Besides, on the initial stage of bunching particles undergo defocusing action of a RF field that imposes requirements on the transverse characteristics of an input beam. Development of a buncher on the basis of a section of inhomogeneous DLW excited in a stop-band was the result of carried out researches. Design of the buncher, simulated performances of an output beam as well as measured on-axis field distribution of a buncher prototype for "cold" tests are presented below.

#psa@kipt.kharkov.ua

DESIGN AND CHARACTERISTICS OF THE BUNCHER

The buncher consists of a chain of five coupled cavities. The coupling of cavities implemented through central holes for beam passing. The sizes of the holes were selected equal each other. For realization of required on-axis field distribution, the operation frequency of a buncher, which was close to the eigen frequency of the last cell, was selected higher than the frequency of the "π" mode of oscillations of a remaining part of the buncher. In this case the phase advance of a field on a cell remained equal π.

The preliminary calculations of the bunching system were made on the basis of self-consistent model of weakly coupled cavities. Further simulation of the system was carried out with SUPERFISH and PARMELA programs. To do so the configuration of a resonant system obtained as a result of preliminary calculations, was some changed in view of finite width of disks and fringing fields on an entrance and an exit of the buncher that were not taken into account in the preliminary calculations.

As the buncher is intended for bunching and accelerating of a unmodulated beam, to take space charge forces correctly the input beam was represented by bunch with length of $5\beta\lambda$, where β is initial relative speed of particles, λ is operating wavelength. The calculations were conducted for an electron beam with initial energy of 25 keV and current about 300 mA.

The purpose of calculations and simulations was the definition of lengths of the first and the last cells providing the required characteristic of a beam. The period of cells located between the first one and the last one were chosen equal to $0.22\,\lambda$ according to the preliminary calculations. Such choice was stipulated by rather simple adjustment of a resonant system in this case.

To reduce influence of a space charge on a transversal emittance, the electron gun should be placed close to the bunching system as much as possible. Therefore in the developed buncher the inlet opening for injection of a beam is an anode of the gun. Estimations with approximation of a laminar flow on the base of a technique [9] without taking into account action of a RF

0-7803-7738-9/03/$17.00 © 2003 IEEE

field on particle motion have shown that the transporting of a beam on necessary distance can be carried out without application of magnetic lenses. However, for the implementation of calculated parameters of a beam it would be required to increase diameter of a focusing electrode of a gun excessively. Besides, as simulations of particle dynamics in a buncher showed, small radius of a beam in a waist in this case increases value of phase width of bunches because of influence of space charge forces. It has forced us to refuse optimum conditions of transportation and to accept the conciliatory solution taking into account features of longitudinal motion of electrons in the buncher and technical feasibilities of gun manufacturing. The final solution was found by successive running the EGUN [10] and the PARMELA codes. The computational parameters of the gun and characteristic of a beam without taking into account influence of a RF field are listed in Table 1.

Table 1: Computational parameters of a gun and characteristic of a beam

Parameter	Value	Units
Cathode voltage	-25	kV
Cathode radius	2.5	mm
Normalize beam emittance (1 σ)	4.1	π·mm·mrad
Distance from the front cut of the anode aperture to the beam waist	40	mm
The beam radius in the waist	1.2	mm
Beam current	0.3	A

As a result of the carried out researches of particle dynamics in the buncher the optimum distribution of an on-axis field for a case when three middle cells have the identical sizes was determined. This distribution is shown in Fig. 1 by continuous line. Fig. 2 shows the simplified view of the buncher designed on the base of simulations. Buncher characteristics and characteristics of a beam on it exit are listed in Table 2. Fig. 3 shows phase and energy spectra, emittance and transversal profile of a beam. It can be seen, that the designed buncher can be utilized in linacs both for fundamental researches and for radiating technologies.

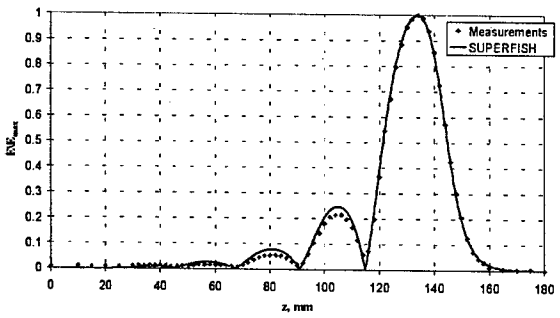


Figure 1: Distribution of on-axis field amplitude: calculated and measured.

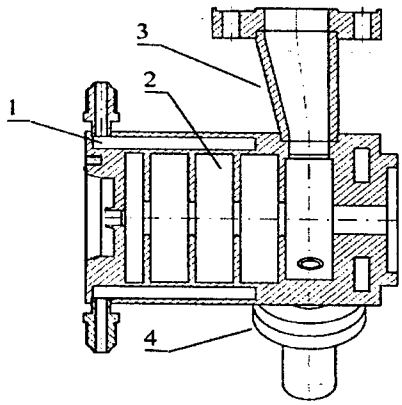


Figure 2: Simplified view of the buncher (1 – cooling ducts; 2 – resonant system; 3 - waveguide; 4 - tuning unit).

Table 2: Characteristics of the buncher

Parameter	Value	Units
Operating frequency	2797.15	MHz
Quality factor	12300	
Power losses in walls	480	kW
Maximum field on the axis	36	MV/m
Current at the injector output	0.28	A
Normalize emittance (1 σ)	18	π·mm·mrad
Δφ (for 70 % of particles)	20	deg
ΔW/W (for 70 % of particles)	7	%
Capture coefficient k_3	93	%
Average energy	767	keV
Maximum energy	863	keV
Beam Ø (for 70 % of particles)	3	mm
$4\sigma_{x,y}$	3.9	mm

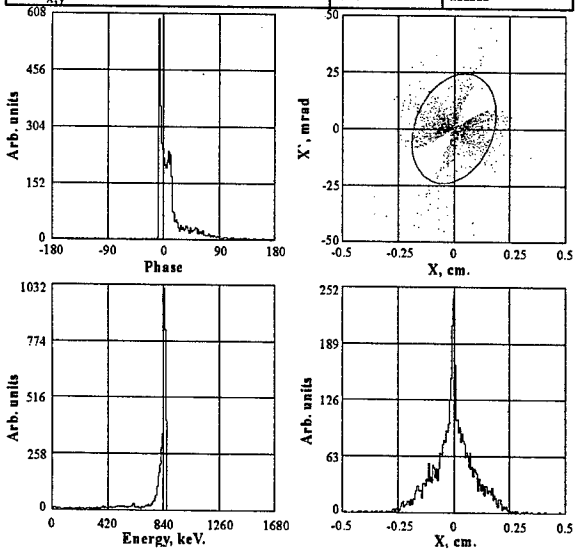


Figure 3: Beam characteristic on an exit of the buncher.

One of the important stages of a buncher creation was the development of a technique of adjusting of a resonant

system for obtaining necessary distribution of the on-axis field on an operating frequency. With this purpose the prototype of a resonant system for "cold" measurements was manufactured and adjusted. The technique of the adjusting consists in following. At first the frequency of the "π" mode of a homogeneous segment of the system (cells number two, three and four) was found by the SUPERFISH. Then the stack of three identical cavities, restricted with cavities of half length, was adjusted to obtain the "π" mode on this frequency taking into account frequency shifts due to brazing, evacuating and difference between the operating temperature and temperature, at which the adjusting is carried out. The cavities were adjusted by lathe boring of their diameter at several steps. After each step the distribution of the on-axis field was checked up by a bead pull method. If it was necessary amplitudes of field in cavities were matching by the additional boring of the cavity with larger amplitude. Then the first half-length cavity of the stack was changed on the first cavity of a buncher and its diameter was adjusted to restore the frequency of the "π" mode of the stack. After that the last half-length cavity was swapped with the fifth cavity of the buncher. By changing its eigen frequency the stack was adjusted on the operating frequency of 2797.15 MHz taking into account the above-mentioned frequency corrections. In such way the required on-axis field distribution on operating frequency was obtained. It is necessary to note, that the measurement of a field distribution in such system has some distinctive because of the amplitude in the fifth cavity exceeds more than 100 times its value in the first one, so the bead should be enough big. The metal cylinder with diameter of 4 mm and length of 6 mm was used. For measurements the technique [11] was used, which allows determining the change of a resonance frequency with a relative mean square error of $6 \cdot 10^{-8}$ at a loaded quality of a cavity about 10000. Simulation of process of measurement with the SUPERFISH showed that errors of the method are –13% for the maximum field in the first cavity and –2,7% for that in the last one. The above-mentioned errors are the best trade between ability of apparatus and influence of the bead on the field distribution. The measured on-axis distribution of the field amplitude of the prototype is shown in Fig. 1 by points.

Encouraged with good performances of the developed buncher we studied possibility of further improvement of beam characteristics by some complicating a resonator system of the buncher. For optimization of electron dynamics in the buncher it is necessary to change length and eigen frequency of each cavity separately, that, however, will not cause essential change of the design of the buncher. Simulations showed that it is possible to get bunches with phase length of 9° and relative energy spread of 5% (for 70% of particles in bunch). Transversal normalized root mean square emittance of a beam is 16 π·mm·mrad in this case. In our opinion, the injector on the basis of such buncher can be used even in infrared free electron lasers. However it is necessary to mark, that the adjustment of the resonant system will be more complicating because of necessity of independent adjustment of each cavity. Now a technique of adjusting of a buncher with the optimized field distribution is under development.

CONCLUSION

Being based on results of research of electron dynamics in bunching systems on evanescent oscillations with self-consistent model of weakly coupled cavities as well as with the SUPERFISH, PARMELA and EGUN codes the design of a S-band buncher and technique of its adjusting were developed. The buncher effectively forms of electron bunches and accelerates them from initial energy of 25 keV to energy about 1 MeV at a current of 300 mA. The buncher can be used in electron linacs both for fundamental researches and for radiation technologies.

REFERENCES

[1] A.N. Lebedev, A.V. Shalnov, "Base physics and techniques accelerators," M.: Energoatomizdat, 1991, (In Russian).

[2] A.A. Zavadtsev, B.V. Zverev, V.E. Kaluzhny, "Manufacturing and adjusting of a buncher of a 5 MeV resonant linac," Uskoriteli, M., Atomizdat, Vol. 17, 1979, p. 93 – 98. (In Russian).

[3] Yu.P. Vakhrushin, A.V. Rjabtsov, V.L. Smirnov, V.V. Terentjev, "Acceleratin structure with optimized many cavity buncher," Proceedings of the conference on charge particle accelerators, Dubna, 1993, Vol. 1, p. 249-251 (In Russian).

[4] M.S. Avilov, A.V. Novochatsky, "Single bunch compression in exponent field," XIV Workshop on charged particle accelerators, Protvino, 1994, Vol. 3, p. 181 – 183. (In Russian).

[5] S.A. Perezhogin, N.I. Ayzatsky, K.Yu. Kramarenko, "Evanescent oscillations in bunching systems," PAC`2001, Chicago, June 2001, p. 2281.

[6] S.A. Perezhogin, N.I. Ayzatsky, K.Yu. Kramarenko, Problems of atomic science and technology, 2001, No. 3, p. 83-85.

[7] L.M. Young, "PARMELA," Los Alamos National Laboratory, LA-UR-96-1835, 1996.

[8] J.H. Billen and L.M. Young, "POISSON/SUPERFISH on PC compatibles," PAC`93, Washington, 1993, p. 790–792

[9] J.R. Pierce, "Theory and design of electron beams," Second edition D.Van Nostrand company, inc. Toronto New York London, 1954.

[10] W.B. Herrmannsfeldt, "EGUN: Electron Optics Program," Stanford Linear Accelerator Center, SLAC-PUB-6729, 1994.

[11] V.A. Kushir, V.V. Mitrochenko, Instruments and Experimental Techniques, Vol. 41, No. 2, 1998, p. 206 – 209.

THE PULSED ELECTRON ACCELERATOR FOR RADIATION TECHNOLOGIES

S. Korenev, STERIS Corporation, Libertyville, IL 60048, USA

Abstract

The design of pulsed electron accelerator for radiation technologies is considered in the report. The pulsed electron source consists from pulsed Marx high voltage generator, vacuum electron source with explosive emission cathode. The measurements system for beam parameters on the basis of PXI system with high-performance National Instruments components and LabVIEW is described.

INTRODUCTION

The radiation technologies include different directions for treatment of materials by electron beams, photons and X-rays. At last time the main focus of radiation technologies was made in the next:

- the modification of materials;
- the food irradiation;
- the sterlization.

The progress of development for pulsed electron accelerators is shown new ideas in this technique. The main principles of design for low energy electron accelerators for applications were considered in papers [1,2]. The main advantage of pulsed electron accelerators is the high efficiency for dissipation of energy for short time in irradiated materials.

This paper is considered a compact pulsed electron accelerator for radiation technologies.

STRUCTURE OF PULSED ELECTRON ACCELERATOR

The pulsed electron accelerator consists from electron source with vacuum chamber and pumping vacuum system and high voltages pulsed Marx generator see Fig. 1. The explosive emission cathodes on the basis of carbon fiber materials [3] and carbon nanotubes [4] are used in this vacuum diode. The two Marx generators with pulse duration 20 and 100 nsec are used for supply of electron source. The high voltage generators have synchronization with real-time system for dose measurements. The variation of gas pressure for gas sparks allows to have regulation of value of accelerating voltage in wide range. Induction elements for charging and discharging circuits in one Marx generator allow to increase repletion of pulses with flow gas to till 100 Hz without special requirements..

The vacuum chamber manufactures from stainless steel. The pressure of residual gas in vacuum chamber is 10^{-5} Torr. The high voltage insulator designed on the basis of new technology of plastic materials from INTECH Corporation. The nylon insulator with central metal electrode has good vacuum and electrical characteristics. Additional vacuum chamber is used for irradiation of samples. This accelerator has additional thin Ti foil window for output electron beam from vacuum chamber to air.

The diagnostic for electron beam is included the current transformer (Rogowski Coils) and Faraday Cups with low induction current shunts. High resistive dividers are used for measurements of acceleration and charging voltage. The block-diagram for measurement system on basis of PXI-1025 is given on Fig. 2,3. The switch, scope and LabVIEW 6.1. from National Instruments were used for design of this system. This system allows to have measurements of stability beam current and accelerating voltage (kinetic energy of electrons) in real-time with following printed protocol. Other variant of measurements of this measurement system permits the measurements the charge of ions from cathode plasma. Last more important for detail turning of plasma cathode with explosive electron emission.

X-rays target [5] presents the structure from Al substrate and deposited layer (target) of material with high atomic number (Ta, W, Au). The thickness of target is 10 – 75 microns. The magnetron method deposition of large thickness of target coating (more 20 microns) has place on the surface of substrate with roughness. This construction of X-rays target allows to have clear X-rays beam without electrons.

MAIN PARAMETERS AND CHARACTERISTICS OF ACCELERATOR

The main parameters of electron accelerator are next:

1. Kinetic energy.....100 – 400 keV.
2. Beam current.....10 – 1000 A.
3. Beam pulse duration .....20 and 100 nsec.
4. Repetition.....0.01 - 100 Hz.

The optimal thickness L_{opt} of an irradiated product is determined by this distribution. The thickness of irradiated product is 0.05 – 20 mm for many materials with density 0.1 – 2.0 g/cc and kinetic energy of electrons 120 – 400 keV. The level of absorbed doses for materials with same thickness is about 50 – 200 kGy/pulse.

The dose distribution for this electron source is presented on Fig. 4. This dose distribution shows the high homogeneous of absorbed doses and high homogeneous of current density for electron beam.

CONCLUSION

The pulsed electron accelerator with considered parameters can be used for broad directions of radiation technologies.

0-7803-7738-9/03/$17.00 © 2003 IEEE

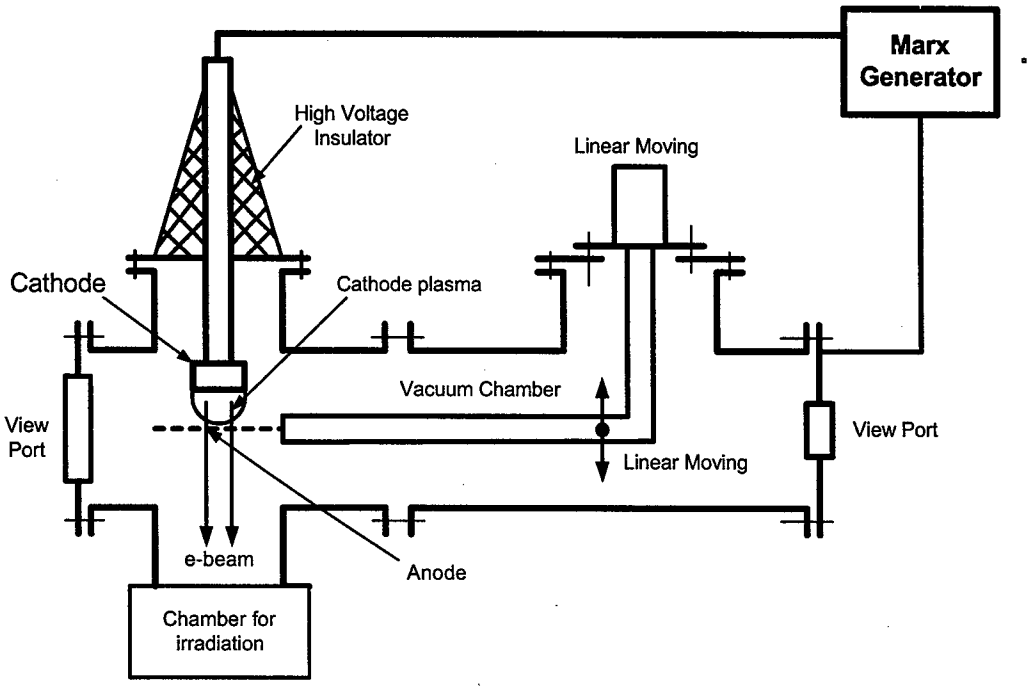


Figure 1: The structure of electron accelerator

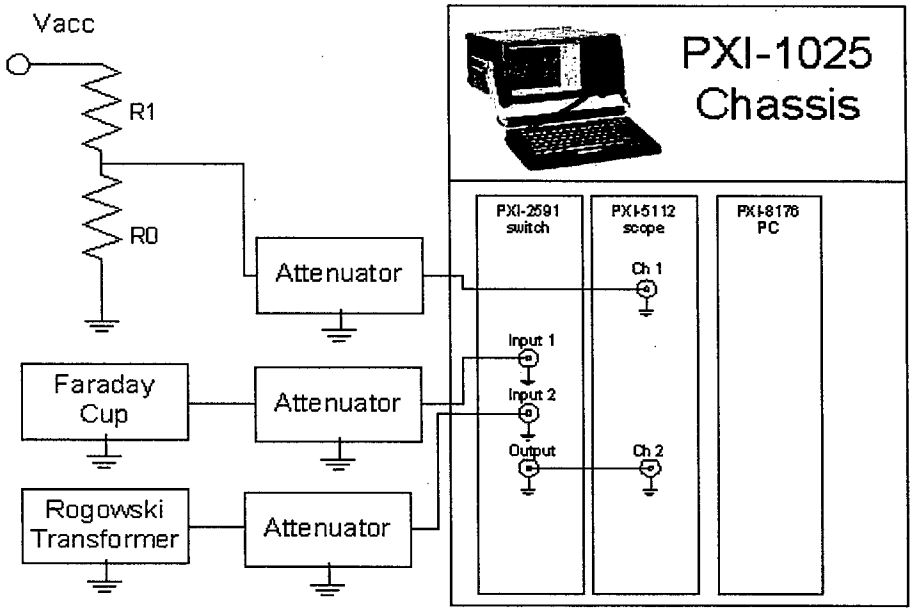


Figure 2: The block diagram for system of beam measurement.

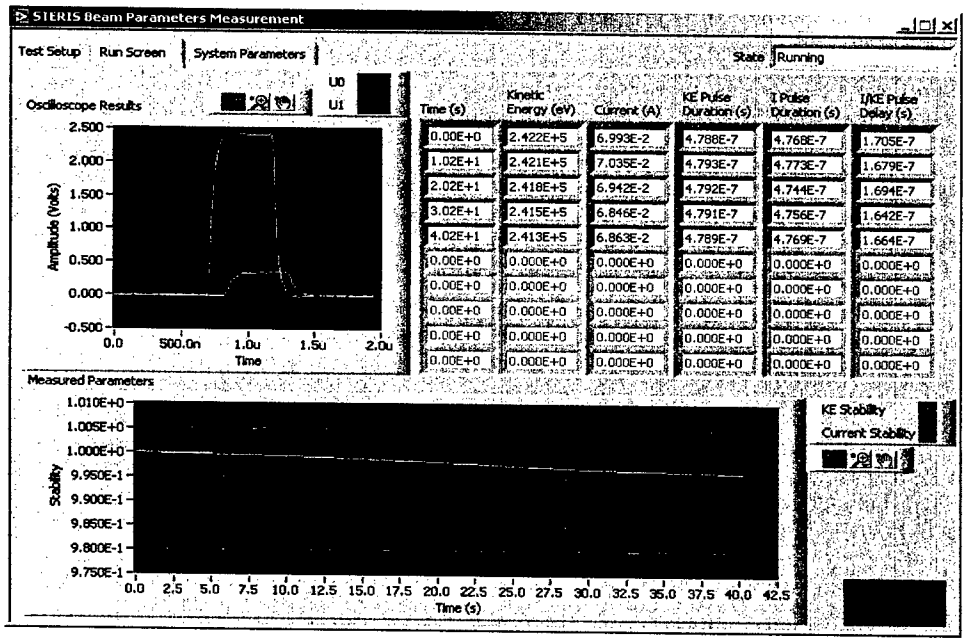
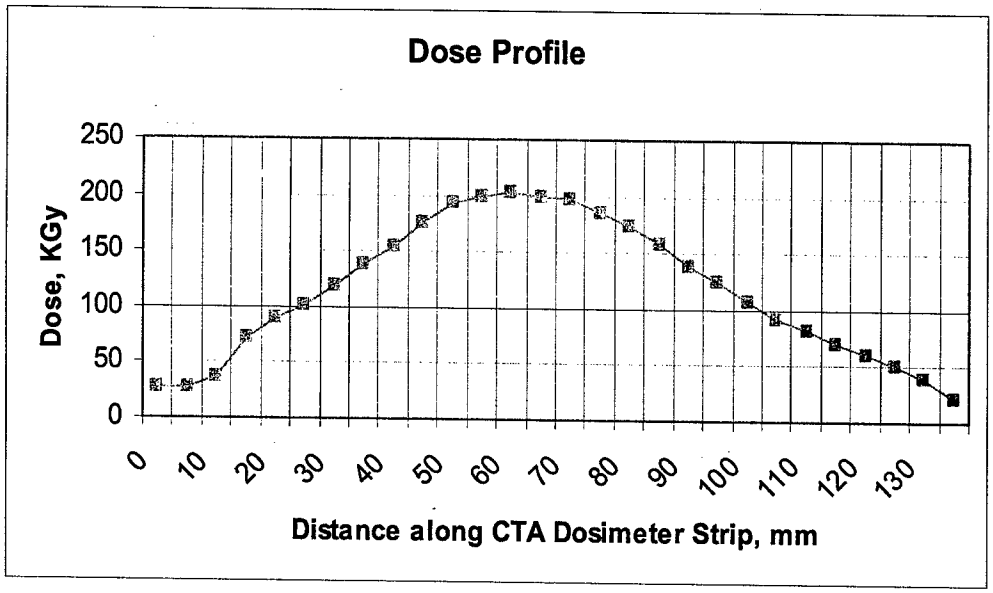


Figure 3: Monitoring Screen for measurements of current and voltage.



REFERENCES

[1] S. Korenev, A. Perry, Vacuum, 47 (1996) 1089.
[2] S. Korenev, Thesis of Doctor of Science, "Design and investigations of pulsed electron and ion sources and their applications", JINR, Dubna, 1994.
[3] S.A. Korenev, A.M. Baranov, S.V. Kostychenko, N.M. Chernenko, Preprint JINR No 13-88-292, Dubna, 1988.
[4] S. Korenev, "The Pulsed Compact Electron Source," ICOP'2002, Alberta, May 2002, p.174.
[5] S. Korenev, Target from Production of X-rays. USA Patent: US 6,463,123

THE REAL-TIME SYSTEM ELECTRON BEAM DOSE MEASUREMENTS FOR INDUSTRIAL ACCELERATORS

S. Korenev, STERIS CORPORATION, Libertyville, IL 60048, USA
I. Korenev, Northern Illinois University, DeKalb, IL 60115,USA

Abstract

The real-time system for electron beam dose measurements for industrial accelerators is considered in the report. The system is acceptable for all types of industrial and research accelerators: CW, DC, RF LINAC and PULSED HIGH CURRENT. The main concept consists in the measurements of beam parameters using partial absorption effect and mathematical treatment of signals from sensors. The 2 modes of operation can be used for this system: manual and full automation. The manual mode includes simple measurements of signals from sensors by oscilloscope with following treatment using simple software. The second mode is used LABView 6.1. for measurements, treatment of signals and presentation on screen PXI-1025 with printed protocol. The system was tested on the pulsed electron accelerator with kinetic energy of electron 400 keV and on the CW accelerator "Rhodotron" for electron with kinetic energy 5 MeV. This system allows to measure the primary kinetic energy of electron beam before product.

INTRODUCTION

The Real-Time (RT) measurements are main component for physical experiment and for radiation process. The RT measurement of absorbed dose in irradiated product for industrial accelerator is serious problem. The standard film dosimeter routine methods [1,2] are difficult for using with RT measurements. The search of new approaches for solution of this problem is very important at present time.

The new method of RT measurement of electron beam absorbed dose on the basis of effect for partial absorption of electron beam in foil and two systems for realization of this method is considered in this paper.

METHOD

The main concept of method for determination of absorbed dose D in irradiated product is based on the main formula [1]:

$$D_{[Gy]} = \frac{W_{[J]}}{m_{[kg]}}, \qquad (1)$$

where: W is dissipated (deposited) energy in the irradiated product, m is mass of this product.

The determination of dissipated energy on product for electrons we suggested to use measurements of kinetic energy and of number of electrons in cross section of collimator. The energy spectra electrons after product determines from beam current measurements on the basis of effects of partial absorption of electrons in foil Fig. 1. The mass of product enters to (1).

The distribution of absorbed doses D in the irradiated product has typical distribution on the Fig. 2.

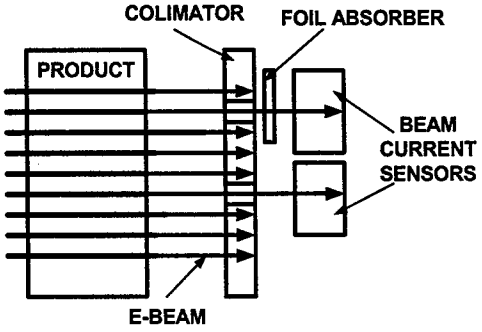


Figure 1: The general principal of method.

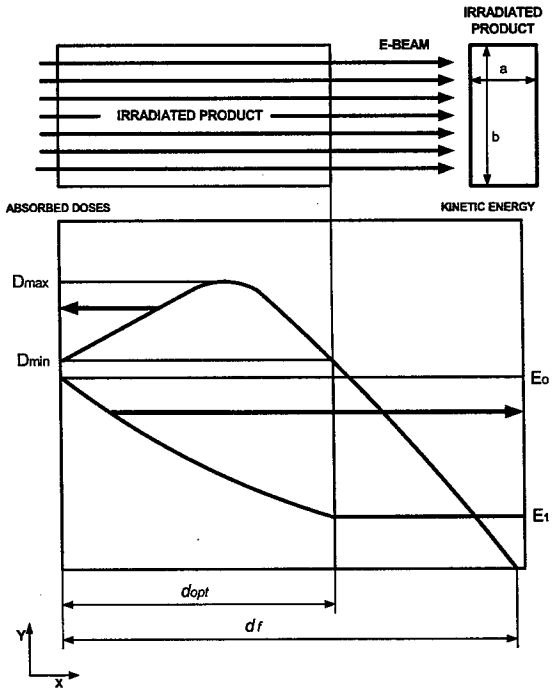


Figure 2: The method of irradiation and distribution of absorbed doses and kinetic energy in irradiated product

The using this parameter we can determine the optimal thickness d_{opt} of product for irradiation (Figure 2).

The value of absorbed dose in irradiated product is determined by formula [1]:

$$D = \frac{E}{m} = \frac{E_k \cdot I \cdot t}{\rho \cdot S \cdot d_{opt}}, \qquad (3)$$

where: E is absorbed energy, m is mass of irradiated product, E_k – kinetic energy (accelerating voltage), I is beam current, t is time of irradiation, ρ is density of irradiated product, S is cross section squire of irradiated product and d_{opt} is thickness of this product.

The kinetic energy E_k can be determines by simple formula:

$$E_k = E_0 - E_1, \quad (4)$$

where: E_0 is primary kinetic energy of electrons, E_1 is kinetic energy after product, (see Fig.1).

The measurements of kinetic energy for electron beam after product can be used for determination of dissipated kinetic energy in irradiated product:

$$E_J = E_k \cdot 1.6 \cdot 10^{-19} \cdot N_e = [J]$$

The absorbed dose D can be calculated in this case by next formula:

$$D = \frac{W}{m} = \frac{E \cdot I \cdot t}{\rho \cdot V} = \frac{\Delta E[eV] \cdot 1.6 \cdot 10^{-19}[J] \cdot N_e}{\rho \cdot d_{opt} \cdot a \cdot b} \quad (5)$$

The effect of partial absorption of electron beam in foil was used for measurements of energy spectra for pulsed electron beams [3,4]. The main idea of this method consists in the measurements of factor of absorption of electron beam in thin foils using the current measurements. The factor of transmission for charge of beam can be calculated from well-known dependence [3]:

$$Q = Q \cdot e^{-(\mu/\rho)d}, \quad (6)$$

where: $\frac{\mu}{\rho}$ is mass absorption coefficient, d is thickness of absorber.

The $\frac{\mu}{\rho}$ determines from empirical formula:

$$\frac{\mu}{\rho} = \frac{[cm^2]}{g} = 17E^{-1.43}, \quad (7)$$

where: E is kinetic energy of electrons [MeV].

The formula for determination of kinetic energy for electron beam before absorber E, after product is next:

$$E = \left[\frac{17 \cdot \rho \cdot d}{\ln\frac{1}{k}}\right]^{0.7} = [MeV], \quad (8)$$

where: d is thickness of absorber (foil), k is factor transmission of beam current in foil absorbed. The k is ratio of beam current after foil absorber (I_1) and beam current (I_0) before foil absorber:

$$k = \frac{I_1}{I_0}. \quad (9)$$

The beam current or number of electrons determines from beam current and time measurements.

SYSTEM DESCRIPTION

The 2 variants of system were designed:

1. Manual system with Tektronix scope with software "MATGEN-2002".
2. Automatic system on the basis electronics and Software "STERIS Dose On-Line" on the basis of LabView 6.1.

The manual system includes the sensors, Tektronix scope with manual enter data from sensors to computer program "MATGEN-2002".

Automatic system includes same absorbed beam energy sensors, measurement instrumentation electronics based on a PXI-1025 Chassis: PC, switch and oscilloscope modules from National Instrument, Fig. 3.

The system allows working with all types of electron accelerators:

1. Direct Current Linear Accelerator
2. Pulsed Radio-Frequency Linear Accelerator.
3. Continuous Wave (CW) Radio-Frequency Accelerator.
4. Pulsed High Current Accelerator.

The program can perform two types of dose measurements and monitoring:

a) accumulated dose for static irradiation, when conveyor is stopped (Fig. 4);
b) current dose for product moving on conveyor.

This system has 3 modes of operations it can perform with data from sensors and electron beam parameters:

1. The Real-Time monitoring of absorbed doses.
2. Calibration of primary kinetic energy of electron beam.
3. Calibration of sensors with an external pulse generator.

In addition to logging measurement results to a file, the developed system features printing a protocol/log of the measured absorbed doses, which also include the main information about the beam and product parameters.

The system was tested with good results on the 2 types of electron accelerators:

1. CW "Rhodotron" Electron Accelerator with power of 80 kW and beam kinetic energy of 5 MeV.
2. Pulsed High Current Electron Accelerator with beam current of 1 kA and beam kinetic energy of 200-400 keV and pulse duration of 300 nsec.

CONCLUSION

The considered method and two systems can be used for monitoring of absorbed doses for the radiation industry.

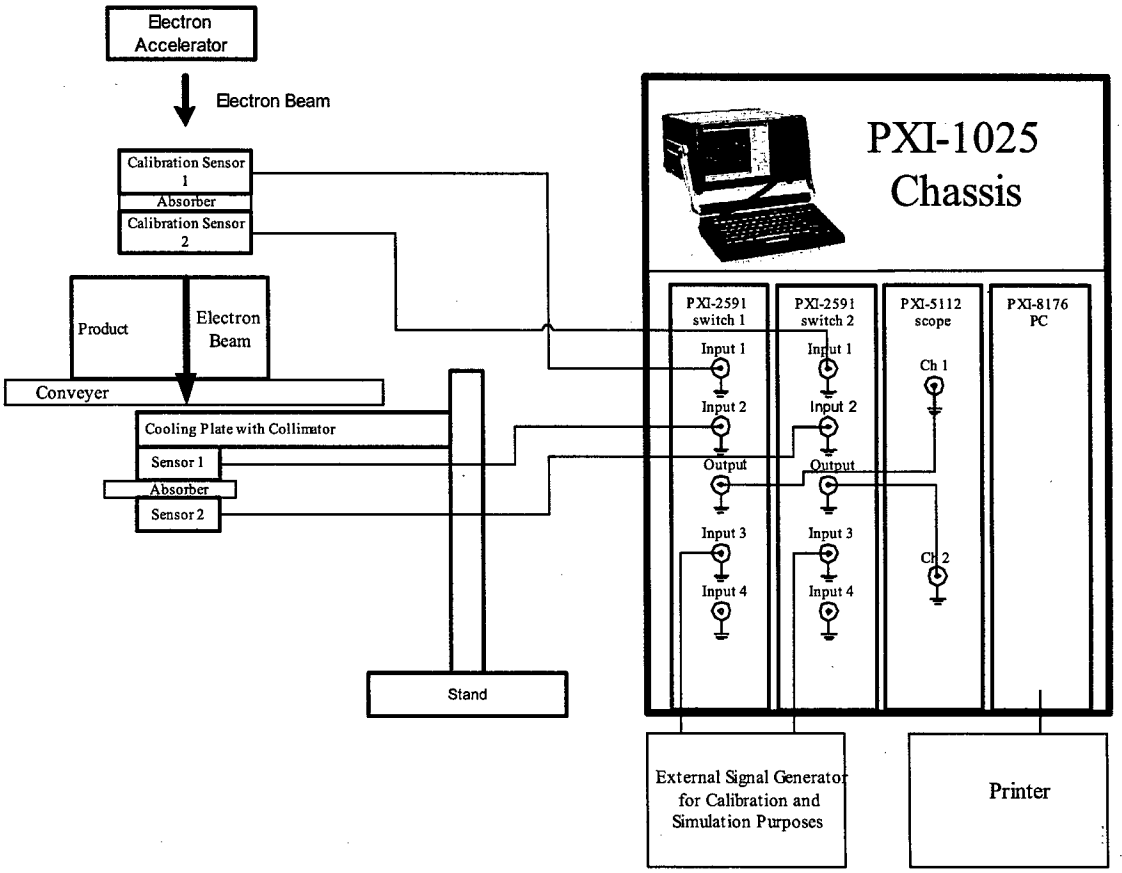


Figure 3: The block-diagram of real-time electron beam absorbed doses monitoring system.

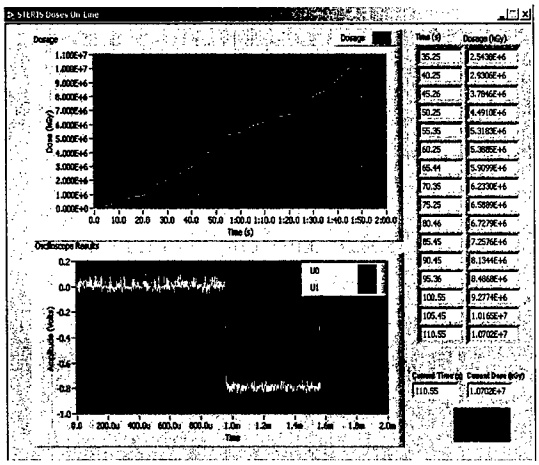


Figure 4: Monitoring screen for accumulated dose measurements.

REFERENCES

[1] W.L. McLaughlin, A.W. Boyad, K.H. Chadwick, J.C.Mcdonald, A. Miller, Dosimetry of Radiation Processing, Teylor and Francis, New York, 1989.

[2] Standard Practice for Dosimetry in an Electron Beam Facility for Radiation Processing at Energies Between 300 keV and 25 MeV, E 1649-94, An American National Standard, pp. 823-841.

[3] E.G. Kratelev, G.O. Meshki, B.N. Yablokov, Pribory I Technika Experienta (1976) No 2, 39 (in Russian).

[4] S.A. Korenev, "Diode with plasma cathode on basis of a sliding surface discharge", Communication of JINR N 9-82-758, 1982, Dubna.

TARGET FOR PRODUCTION OF X-RAYS

S. Korenev, STERIS Corporation, Libertyville, IL 60048, USA

Abstract

The patented new type of X-rays target is considered in the report. The main concept of the target consists in the sandwich structure of deposited coating from materials with high Z on the substrate with low Z, high thermal conductivity and high thermal stability. The target presents multiply layers system. The thermal conditions for X-Rays target are discussed. The experimental results for Ta target on the Al and Cu substrates are presented. This type of target allows improving the cooling system.

INTRODUCTION

The development of X-rays target technology links with high progress in the applications of electron beams and requirements of modern technologies on the basis of X-rays. The main reason of big interest to x-rays target is large depth of penetration of x-rays to condensed matter in comparison with electrons. The standard X-rays target presents Ta or W foil with cooling plate. The optimal thickness of X-rays target can be calculate from empirical formula for electrons with kinetic energy 1-10 MeV [1]:

$$h_{opt} = \frac{0.89 \cdot (E - 0.7)^{0.46}}{\rho \cdot Z^{\frac{0.17}{E^{0.2}}}} [cm] \qquad [1]$$

where: E is kinetic energy of electron [MeV], ρ is density of material target [g/cm^3], Z is atomic number of material target.

According this formula we can see, that variation of optimal thickness for target from Ta has range 0.14 to 0.93 mm and target from W has range 0.12 to till 0.8 mm for this range kinetic energy of electrons.

The conversion factor of electrons to X-rays is small and 2.5 to 12% for Ta target for kinetic energy of electrons 1 to 10 MeV. For kinetic energy of electrons 0.1 –1.0 MeV, this factor is low and has range approximately 0.2 –2.5% for Ta target. The computer simulation of absorbed doses for this range of thickness of target shows, that electron beam can not to converse to X-rays on the 100%. The comparison of these data allows to make conclusions, that two factors lead to partial using of electron beam and after target we have electron beam with low kinetic energy and x-rays with broad energy spectra.

The other problem of target is thermal processes. For low factor of conversion of electron beams to X-rays determines big dissipation of energy.

For example for kinetic energy 1 MeV for Ta target , the factor of conversion is about 2.5%. The present of dissipated energy in the target for optimal thickness 0.2 mm according Monte- Carlo simulation is 70%.

For average power of beam 10 kW we have dissipated power in the target is about 7 kW. The cooling conditions of foil target are difficult and main problem is thermal contact with foil (target) and cooling plate.

The new concept for design of target for produce of X-rays was suggested in U.S.A. Patent [2]. The description of this concept and results of primary tests is considered in this paper.

CONCEPT OF X-RAYS TARGET

The main concept of new X-rays target consists in the coating from material with high atomic number on the substrate with good thermal conductivity and low atomic number. The variant of cooled target for high power accelerator is presented on Fig.1. The variant of target for pulsed accelerator is given on Fig.2.

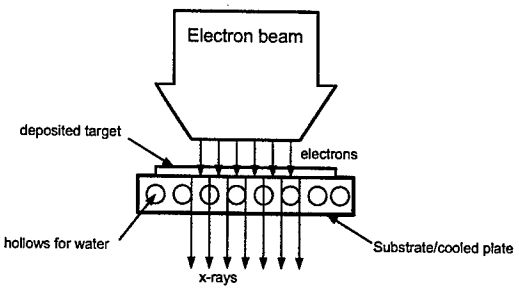


Figure 1: The target for high power beam.

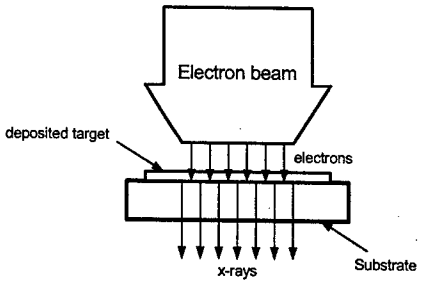


Figure 2: The target for pulsed beam

0-7803-7738-9/03/$17.00 © 2003 IEEE

The thickness of coating depends on kinetic energy of electrons and according (1) is presented in Table 1.

Table 1:

Kinetic energy, MeV	Thickness of Ta target, mm	Thickness of W target, mm
1.0	0.14	0.12
2.0	0.31	0.27
3.0	0.43	0.37
4.0	0.53	0.46
5.0	0.614	0.53
6.0	0.69	0.61
7.0	0.759	0.65
8.0	0.82	0.71
9.0	0.88	0.76
10.0	0.93	0.80

The sandwich multi-structure of target is shown on the Fig 3. The computer simulation of propagation of electrons across the sandwich target gives information about full dissipation of electron beams and decreasing of kinetic energy and decreasing the kinetic energy.

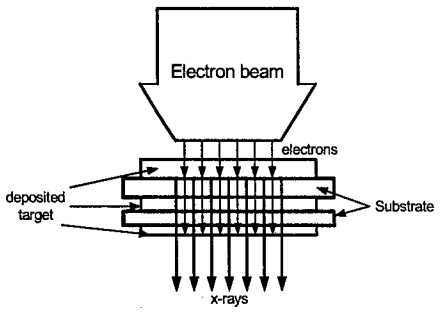


Figure 3: The multi-layers target.

The deposition of large thickness of coating presents complex task which links with adhesion of large thickness of coating with substrate. It is very important for target on the kinetic energy of electrons more 1 MeV. The design of X-rays target for electron with kinetic energy 100 – 500 keV is very simple, because the thickness of target is 5-10 microns from Ta or W. For deposition of small thickness of target can be used all standard methods of deposition of films: Magnetron spattering, lased ablation, electron beam evaporation, cluster deposition using vacuum ion diode. For first case, the preparation of surface for deposition consists in the forming roughness for improving of adhesion of coatings to substrates. The experimental results of deposition of large thickness of coating with roughness of Ta, W coating on the Cu, Al substrates shown, that this effect allows to improving the adhesion of coating to substrate and improving the thermal contact for good cooling. The deposition of large thickness of target also is possible by nano-particles spray method.

EXPERIMENTAL RESULTS

The few samples of X-rays Ta target with thickness 10, 25 and 600 microns were prepared for test experiments. The Ta thin foils with same thickness were used for comparison of data.

The test experiments were conducted on the 2 accelerators: Pulsed electron accelerator with kinetic energy of electrons 200 - 400 keV, and Rhodotron with 5 MeV beam line.

The measurements of temperature is presented on Fig. 5 from Rhodotron with 600 microns targets. The simple experiments with nature air cooling gave results, that gradient of temperature 100°C for power of beam 5 kW for 120 seconds for Ta foil target, and same gradient temperature was received for 450 seconds. These experiments didn't use the water cooling. The simulation of water cooling of target shown decreasing of requirements for water cooling conditions.

The measurements of electron components with electrons and x-rays are gave very important information about decreasing of value of electron after target with Al substrate for thickness about 1-1.5 mm. The energy spectra of X-rays is wide and main average kinetic energy of x-rays has very good correlation with calculated from empirical formula from [3].The substrate allows to decrease the low energy X-rays. Tthe optimal thickness of Al substrate is 1.25 mm for electron with kinetic energy 400 keV.

CONCLUSION

As a results of conducted investigation we can make next conclusions:

1. The suggested concept of X-rays target allows to decrease the requirements on the cooling system.
2. This target is very easy in design.
3. This target with substrate allow improving the energy spectra of X-rays.

REFERENCES

[1] V.I. Ctovbun. "Electron accelerators on energy 0.5–100MeV as a radiation sources" Communication of JINR No 16-7104, JINR, Dubna, 1973.

[2] S. Korenev. Target from Production of X-rays. USA Patent: US 6,463,123

[3] M.P. Svin'in. Calculation and design of high voltage electron accelerators for radiation technology. Moscow, Atomizdat, 1989.

SIMULATION TOOL FOR SCANNING X-RAY BEAMS IRRADIATOR

V. T.Lazurik, V. M. Lazurik, G. F.Popov, Yu.V.Rogov
Kharkov National University, P.O. Box 60, 61052 Kharkov, Ukraine

Abstract

X-ray (bremsstrahlung) produced by high-power electron accelerators are intensively used in different radiation technologies. An electron accelerator, a scanner, an X-ray converter with cooling system, a conveyor line or a turntable chamber, an irradiated product and a package are the major components of the radiation technological lines (RTL) for X-ray irradiator. The detailed physical and geometrical models of the X-ray irradiator were realized in the form of new mathematical software of the "XR-Soft". The program XR-Soft was designed specially for simulation of industrial radiation processes and calculation of the absorbed dose and temperature distribution within products irradiated by scanning X-ray beams on industrial RTL that is based on the pulsed or continuous type of electron accelerators in the energy range from 0.1 to 50 MeV. The motivation for the development of the program XR-Soft is the creation of accurate and easily accessible tool for prediction of the absorbed dose distribution within irradiated materials, for optimization of the irradiation regimes of radiation facility, and for reducing of experimental routine dosimetric measurements in X-ray processing.

1 INTRODUCTION

The conception of the Radiation-Technological Office (RT-Office) was developed by authors. RT-Office realize computer technologies at all stages of works execution on the RTL for electron beam (EB), X-ray and γ-ray processing. It is beginning with the expertise of the consumer order for scientifically–justified definition of the requirements and conditions for realization of an irradiating and ending with a provision of argued report on the fulfilled work.

The RT-Office is the common program shell which provides flexible intellectual interaction between specialized modules and databases for optimal planning of the process of an irradiating and control of its realization. Simulation and calculation modules of the RT-Office are the basis for construction of the specialized software for EB, X-ray and γ-ray processing [1,2,3].

The modules structure, geometrical and physical models of the X-ray irradiator for the program XR-soft that was constructed from the RT-Office modules and is intended for simulation of X-ray processing are considered in the paper more closely.

2 XR-SOFT STRUCTURE

Two geometrical models for X-ray irradiators that were used for simulation X-ray processing are shown in Fig.1 and Fig.2. The first X-ray irradiator includes an electron accelerator, a scanner of electron beam, an X-ray converter with cooling system, and an irradiated product with packaging on moving conveyor (Fig.1). The second one includes an irradiated product placed in turntable cylindrical chamber that is rotating in front of the X-ray beam (Fig.2).

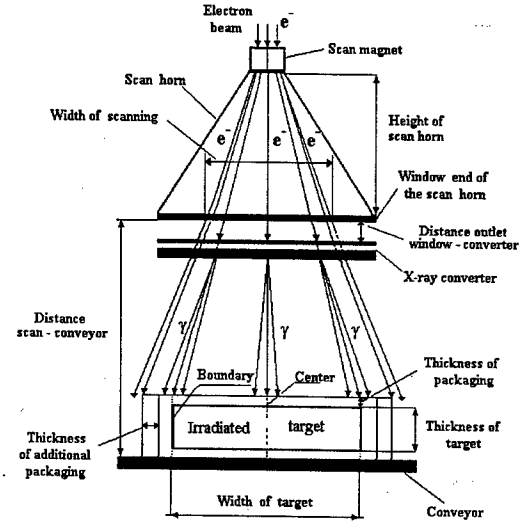


Figure 1. Scheme of radiation facility with X-ray converter for triangular-shaped scan horn and moving conveyor.

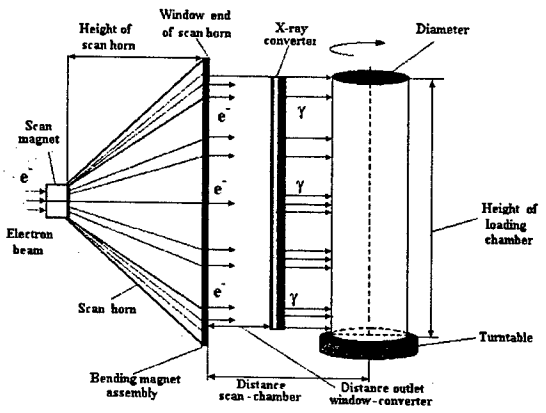


Figure 2. Scheme for X-ray irradiator with turntable loading chamber and non-diverging (parallel ray) EB.

The self-consistent physical models relatively each geometrical models of the X-ray irradiator were constructed on the base of the RT-Office simulation and calculation modules.

These modules are the following:

0-7803-7738-9/03/$17.00 © 2003 IEEE

• Monte Carlo simulation of dose distribution for electron beam into heterogeneous targets.
• Monte Carlo simulation of electron-photon shower in X-ray converter.
• Monte Carlo simulation of dose distribution into heterogeneous targets irradiated by X-ray beam on moving conveyor.
• Monte Carlo simulation of dose distribution for cylindrical turntable target irradiated by X-ray beam.
• Calorimetry. Calculation of spatial distribution of radiation-induced temperature and analytical estimations of integral characteristics of a heat transmission for process of cooling of the irradiated products in a thermostable environment.
• Comparison. Methods of mathematical physics for handling and comparative analysis of depth dose curves obtained by different calculation and experimental methods.
• Dosimetry. Specialized tool for loading and processing of experimental dosimetric data and their transmission to the Comparison module.
• RTL configuration. Loading and saving of the operational characteristics for RTL facility.
• Wizard for control and validation of input data for working regimes of RTL.
• Cognitive visualization of results for 2-dimensional (2-D) and 3-D view of dose distribution.
• The processing technologies database for equipment characteristics and objects used in radiation technologies.

Simulation of X-ray dose mapping in irradiated target materials was conducted by Monte Carlo method in 2-D model. The 2-D dose distribution in the target irradiated by X-ray beam on moving conveyer is represented as function of two coordinates - of the target depth (axis X) and the target width along scan direction (axis Y). The 2-D dose distribution into cylindrical turntable target is represented as function of the target radius (axis X) and the target height (width) along scan direction (axis Y). Such conditions are realized in many practical cases for X-ray beam processing.

Features of realization of a physical model for X-ray processing are the following:
• The use of a forced method for process of producing X-ray on each step of design of electron track in a construction of the X-ray converter.
• The automatic choice of self-consistent parameters is used for simulation of an electron - photon shower. The choice is based on determination a minimum machine time for obtaining given accuracy. These parameters are the following: cutoff energy for modeling of an electron track, threshold energy of catastrophic electron-electron collisions, cutoff energy for modeling of a photon track, threshold angle of grouping electron collisions for modeling of scattering.
• The use of both a simple estimation (collision method) and the special estimation (method of crossing area) for the dose calculation.

These features allow to reduce the running time of Monte Carlo simulation for receiving of the end results in about hundreds time. The program XR-Soft takes into account in detail a construction of the RTL and requirements to regimes of irradiation in each specific radiation-technological process.

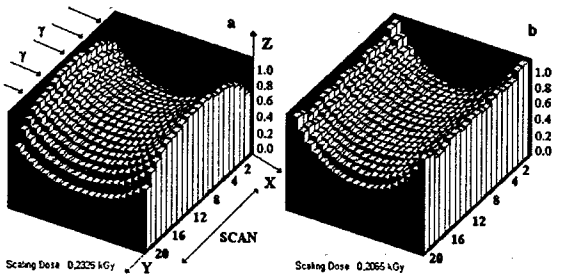
3 SIMULATION OF X-RAY DOSE MAPPING

The processing rate and X-ray absorbed dose distribution within of the irradiated materials depend on a lot of parameters of the radiation facility of RTL and characteristics of target material. *Input data* for the program XR-Soft are the following: *Parameters of electron beam*: average beam current, or pulse duration and repetition frequency in pulsed accelerators, electron spectrum, beam diameter and spatial distribution of the beam intensity. *Parameters of scanning system*: modes of operation, the triangular or non-diverging irradiation treatment field in target material; form of current in magnet of scanning system; repetition frequency of scanning; angular distribution of electron beam at the outlet of a scanning system; parameters of the exit window for electron beam. *Parameters of the X-ray converter with cooling system:* geometrical characteristics of the X-ray converter with cooling system, thickness of plates (layers) and cooling agent, materials composition, distance between exit window and X-ray converter. *Parameters of conveyor line*: speed and geometrical characteristics of the line. *Parameters of irradiated product*: geometrical characteristics of the irradiated product; elemental composition of the target; material and size of the covering for irradiated product. *Regimes of target irradiation*: one-, two-sided irradiation on moving conveyer, and irradiation of turning target.

For searching optimum solution, the program XR-Soft calculates and represents an X-ray energy spectrum, an absorbed dose distribution within irradiated products, a dose uniformity ratio, an optimum product thickness, an X-ray utilization efficiency in the irradiated products, an electron beam power utilization, and other important characteristics for economic evaluation of X-ray processing.

X-ray dose mapping within compound (wood of aspen + 70% polymethylmethacrylate (PMMA)) with density 0.8 g/cm^3 for optimal target thickness at double-sided irradiation for saw-tooth and special forms of current in scan magnet are shown in Fig. 3 (a) and (b) respectively. X-ray beam was generated by scanning electron beam with electron energy 5 MeV in a tantalum converter. The optimal converter construction includes the tantalum target plate with thickness 1.2 mm, the cooling water channel - 3mm and the aluminum backing plate - 5.0 mm. The X-ray yield in the forward direction for 5 MeV electron is 8.71%. Regimes irradiation: electron beam energy - 5 MeV; beam current – 1 mA; triangular scanning; width of target - 100cm; width of scanning -100cm; conveyer speed - 1cm/s. Target has not cover box. The optimal thickness for maximum X-ray

power utilization is 38.5cm relatively of dose distribution at the center of a target. X-ray beam power utilization in this case is 58%.



Figures 3 (a) and (b). X-ray dose mapping within compound for optimal target thickness and for the saw-tooth form of current (a) and the special form of current (b) in scan magnet. Statistical deviations: 2.2 % for center target and 2.5% for boundary target. (Running time is about 8 minutes on PC AMD-K7, 750 MHz).

For each product to be treated in the X-ray irradiation facility, there will usually be a minimum dose limit $D_{min\text{-}lim}$ to obtain the desired effect and a maximum dose limit $D_{max\text{-}lim}$ to avoid product degradation. As is seen from Fig. 3(a), the X-ray depth-dose distribution within compound has minimal value on the boundaries of a target along direction of the scanning X-ray beam and maximal value at plane that cross the target center. From standpoint of the dose limits, the minimum dose limit $D_{min\text{-}lim}$ must be chosen as a minimum dose value $D_{min\text{-}bound}$ on the boundaries of an irradiated target, the maximum dose limit $D_{max\text{-}lim}$ - as a maximum dose value $D_{max\text{-}center}$ in the target center. In this case the dose uniformity ratio will be determined for all irradiated volume as $DUR_V = D_{max\text{-}center}/D_{min\text{-}bound}$.

For the center of a target the dose uniformity ratio $DUR = D_{max}/D_{min}$ is 1.51. For the target boundary the DUR is 1.94. The value DUR_V is 2.91. Significant dose gradient in volume of irradiated target in direction of X-ray scanning can be decrease by the choice of the special shape of current in scan magnet [2,6]. By the use the program XR-Soft, the special shape of current in scan magnet which provide the maximum uniformity for X-ray dose distribution in the irradiated compound was determined (see Fig. 3(b)). In this case X-ray beam power utilization is 53% and the value DUR_V is 2.1 and also is greater than DUR in the target center.

Further decreasing of the target thickness at double sided X-ray treatment results in decreasing both the value DUR_V and the X-ray power utilization. For example, for compound thickness h=30cm the DUR_V is 2.0 for saw-tooth shape of current and the DUR_V is 1.6 for the special shape of current in scan magnet. The X-ray power utilization is 48%.

Most effectively X-ray processing can be realized by treatment of turning loading chamber with irradiated materials which is placed in front of scanning X-ray beams [7]. In this case at given value DUR_V an optimal material thickness for X-ray processing will be greater than for double-sided irradiation. The program XR-Soft allows to simulate a dose mapping in turning cylinder chamber with materials irradiated by scanning X-ray beam. The direction of scanning X-ray beam is in parallel with a cylinder axis. For above compound and X-ray parameters, for the value $DUR_V = 1.54$, the optimal thickness (diameter) for the treated material is 60 cm.

The testing and verification of the results simulated by the program XR-Soft were carried out in compare with theoretical calculated data, with results obtained by the universal packages such as ITS, EGS4 and PENELOPE, and experimental data set in published works [4,5]. The comparison investigations indicated that the developed physical and mathematical models are reliable and correct, and the program XR-Soft is accurate, easily accessible for all users with a different level of background in an area of computer technologies.

4 CONCLUSION

X-ray dose mapping must be conducted with consideration of the dose non-uniformity in the target center as well as on the boundaries of an irradiated target along direction of the scanning X-ray beam. A non-uniformity equalization for X-ray dose distribution along a direction of scanning can be done by the choice of the special shape of current in scan magnet, with help of the special filters, or with special methods of irradiation [2]. As a minimum, the 2-D simulation model for X-ray dose mapping must be used for correct analysis of the optimum product thickness, X-ray power utilization, max/min dose ratio, and X-ray processing capacity. The program XR-Soft can be used as predictive tool for X-ray dose mapping, for determination of location D_{min} and D_{max} in target irradiated by scanning X-ray beams on RTL, and for optimization of regimes X-ray irradiation to receive the maximum processing capacity with the minimum for dose uniformity ratio.

5 REFERENCES

[1] V.T. Lazurik, V.M. Lazurik, G.F.Popov, Yu.V. Rogov and S.A Korenev. Proc. of the PCaPAC, 2000, DESY, Hamburg, Germany, p.4. CD-Rom.

[2] V.T. Lazurik, V.M. Lazurik, G.F.Popov, Yu.V.Rogov Abstract book of the ICAP-2002 Conference, p.49, East Lansing, MI, USA. (Paper in press).

[3] V.T. Lazurik, V.M. Lazurik, G.F.Popov, Yu.V. Rogov Abstract Book of the PCaPAC 2002, P.32, Frascaty, Italy. (Paper in press).

[4] M.Cleland, and G.Pageau. Nuclear Instruments and Methods in Physics Research. 1987. B24/25, 967-972.

[5] J.Meissner, M. Abs, M.Cleland , A.Herer, Y. Jongen, F. Kuntz, A.Strasser. Radiation Physics and Chemistry. 2000. Vol. 57, 647-651.

[6] S. Pismenesky, G.Popov, V.Rudychev. Radiation Physics and Chemistry. 2002. Vol. 63, 601-602.

[7] Y.Jongen Abstract book of the 6th Gamma Processing Seminar. 2002. Ottawa. Canada.

RADIATION PROCESSING OF COMPOSITES FOR ORTHOPAEDIC IMPLANTS

G. Popov, A.Avilov, V.Deruga, N.Popova, V.Rudychev,
Kharkov National University, P.O. Box 60, 61052 Kharkov, Ukraine

Abstract

Prime task for orthopedists and traumatologists is the development of new artificial materials for replacement of osseous tissue and cartilage defects, for functional rehabilitation of the injured locomotorium tissue after traumatic fractures and surgical interventions. Electron beam (EB) processing of polymer composites with bioactive ceramics was used for manufacture of new artificial materials for orthopedic implants. Experimental approaches and problems of EB processing for composites formation are discussed in the paper.

1 INTRODUCTION

The materials for reconstructive-restorative surgery of human locomotor ligaments must satisfy severe conditions about impermissibility of carcinogenic, blastomogenic, and allergenic effect on organism. They have not to be toxic or electrolytically active ones. Their mechanical properties must correspond to those for natural osseous tissue and cartilage. They have to stimulate the process of osteogenesis.

Now there is no artificial materials that completely satisfy all demands of medicine. The mechanical properties of human osseous tissue are very different from those of inert metal alloys currently used in artificial joints. This large mismatch in mechanical properties causes bone resorption or loss around the implant, as well as loosening of the artificial joint stem in the medullar cavity. Ultra high-molecular weight polyethylene (UHMWPE) used as a substitute for gristle is also rigid, it is not of sufficient wear-resistance, it has little adhesion to bone cement, that causes both increasing of volume of surgical operations and decreasing of a service life of the product.

All previously mentioned puts a task for searching of new materials for replacement of natural osseous and gristle tissues. Polymeric composites with bioactive ceramics are considered as the most appropriate candidates to this role. Our investigations deals with research and engineering studies of the use of EB processing of artificial materials for orthopedic implants. The investigations were performed in three main problem directions.

- Development of technological methods and processes of new composite materials formation for osseous tissue implants. The problem is the receiving of materials which have to possess mechanical and operating characteristics closed to those of natural osseous tissue and cartilage.
- Development of composite material (CM) for elastic elements of prosthesis that are simultaneously the elements of friction couple. The problems are the decreasing the friction coefficient in artificial joint and reducing the wearing rate of ultra high-molecular weight polyethylene (UHMWPE) construction element for endoprotheses.
- Radiation induced graft copolymerization of methylmethacrylate (MMA) monomer on surface of UHMWPE and composites based on it. The decided problem is the increasing adhesion of UHMWPE to bone cement.

2 EB PROCESSING OF COMPOSITES

The candidate CMs for implants were designed on a basis of reinforced polymers by various fibers and bioactive ceramics, which were treated by EB. The radiation-induced polymerization was fulfilled in compounds reinforced with various fibers such as carbonic, glassy, nylon, metallic ones, or their mixtures. As binding agents, vinyl monomers and oligomers, polyester and thermosetting resins were used. The following monomers and oligomers as well as their mixtures constitute the base of polymer matrices: MMA, ethyl methacrylate, butyl methacrylate, polyacril acid, oligomers on the base of unsaturated polyesters kind of TGM-3, PN-609-21M, Palatal A430, as well as the UHMWPE powder.

The EB irradiation of compounds in all processes was carried out by pulsed electron accelerator with energy range from 4 to 7 MeV, beam power up to 5 kW and absorbed dose in the range from 1 to 200 kGy [1, 2]. The spatial profile of electron beam intensity on the target surface was measured by an one-dimensional wire acoustic dosimeter. The absorbed dose distribution of electron beam into compound was measured by one dosimetric film inserted in parallel with EB between two contacted compounds. An equalization of electron depth dose distribution into one- and double sided irradiated compounds was conducted with help of simulation tools ModeRTL [3]. To provide the dose distribution with enhanced uniformity ~ 5 to10% special semitransparent filters for beam electrons were designed [4]. These filters partly overlapped the electron beam directed on irradiated samples, which mixed up transversally to electron beam

0-7803-7738-9/03/$17.00 © 2003 IEEE

direction. Radiation treatments and subsequent postradiation thermal treatment of composite materials were carried out in vacuum or in argon atmosphere. The postradiation treatment of polymer composites comprises artificial aging in thermostat at temperatures of 60 to 160 ^{0}C.

Detailed research of the radiation-induced polymerizing kinetics of monomer/oligomer systems in compounds was performed by measuring the following parameters: the coefficient of conversion K of monomer–oligomer system in compound, the temperature increase ΔT_P due to radiation induced heating, and the temperature increase ΔT_{PX} due to heat liberation in the course of exothermic radiation–induced by reaction of polymerization. The investigations of characteristics K, ΔT_P, ΔT_{PX} were performed depending on electron dose rate, absorbed dose of EB in compounds, type and concentration of reinforcing elements of compound, and external conditions of irradiation (temperature, pressure, irradiation environment –vacuum, air, inert gas).

It was experimentally shown:

- In the presence of reinforcing elements, the reaction of radiation-stimulated polymerization of monomer–oligomeric systems in compounds flows with increased rate as compared with block polymerization of pure monomers/oligomers.
- Molecular mass of polymer matrix in compound is in 1.5 to 2 times higher as compared with the case of block polymerization.
- Integral dose to be necessary for full completion of compound polymerization is in 1.5 to 4 times less as compared with the case of block polymerization.
- Process of radiation-induced polymerization is easy controlled and regulated by selection of mode of irradiation.

The technological modes of polymer composite materials formation were experimentally elaborated. By varying either the composition of the reinforcement and matrix polymer and EB processing regimes, we managed to obtain materials with modules of elasticity ranging from 10 to 40 GPa, bending strength 200 MPa and more, compressive strength 150 MPa and more, which satisfy the strength criteria of supporting elements of joints. These materials were experimentally tested as intraosseouse fixative devices.

3 EB PROCESSING OF UHMWPE

At present, the most of endoprotheses are using UHMWPE and metal alloys as materials for friction couple. Disadvantages of these materials are more high friction coefficient of hinged couple as compared with natural joint and a high value of wearing rate of elements made of UHMWPE. The wearing debris initiated an osteolysis which leads to implant loosening.

The production technique of material for elastic elements of prostheses to be simultaneously the elements of friction couples was elaborated. Cylinder and plate samples were made by hot molding or by shaping under pressure of UHMWPE powder (Tomsk, Russia) with molecular weight distribution 2.5-4.7 million grams/mole. The samples were made of pure UHMWPE and of UHMWPE reinforced by carbon, glass fiber, cord, and textile.

The radiation-induced crosslinking creates a 3-D network (gel phase) in the structure of UHMWPE as well as it is accompanied by occurrence of long term free radicals in bulk of PE. Free radicals can lead to destruction of UHMWPE due to oxidation processes which reduce the molecular weight of PE.

To reduce free radicals, EB processing of compound was carried out by two methods. In the first method, the radiation crosslinking of end samples of pure UHMWPE and of UHMWPE - based composite was conducted by pulsed EB, followed by the thermal annealing and slow cooling. In the second one, the hot samples in the temperature range 100-160 ^{0}C were treated by EB. The radiation treatment of compounds was conducted by EB with energy 6 MeV and absorbed dose in the range from 1 to 300 kGy. EB processing of UHMWPE was performed in vacuum, in medium of the air or an inert gas.

Crosslink density was determined by placing irradiated samples in hot xylene and measuring of gel and sole phases as well as by the use of Fourier Transform Infrared Spectroscopy (FTIR) technique [5]. In accordance with FTIR technique crosslink density was measured by a spectrophotometer as the ratio of trans-vinylene peak area at 965 cm^{-1} to the irradiation stable peak area at 2022 cm^{-1}. Presence of free radicals was determined by measuring of oxidation index as the ratio of carbonyl peak area at 1717 cm^{-1} to the stable peak area at 1370 cm^{-1}.

Wear rate was investigated on a stand for long-term examination which imitates work of hip joint. A friction couple consisting of a spherical insert of radiation-modified composite and a highly polished ball of stainless steel with diameter 32 mm was immersed in physiological solution or bovine serum and worked under cyclic loading up to 100 kg. The inserts were examined on wear in cyclic loading in the range of $5\cdot10^5$– $3\cdot10^6$ cycles by gravimetric method.

The investigations of variation of structural characteristics, friction coefficient, wear rate of polymer composite materials based on radiation crosslinking UHMWPE were carried out depending on the dose rate and an absorbed dose. As a result of investigations it was shown, that the minimum of oxidation index into irradiated samples is observed at a maximal dose rate and respectively at minimal irradiation time. The minimum gravimetric wear rate about 2 mg/(million cycles) and absence of free radicals had the pure crosslinked UHMWPE, which was irradiated by electron dose of 90 to 120 kGy at sample temperature of 120 to 150 ^{0}C in vacuum or in noble gas with subsequent thermal

annealing. This value of wear rate is more than 20 time less in comparison with unirradiated samples.

4 GRAFTING OF MMA ON UHMWPE

In restorative surgery of joints many artificial implants are fixed to osseous tissue by bone cement. The basis of composition of bone cement is polymethylmethacrylate (PMMA) or other acrylic polymers. Implants from UHMWPE to be also used in restorative surgery have weak adhesion to bone cement. For increasing adhesion of UHMWPE to bone cement, the investigation and elaboration of operating regimes of radiation grafting of MMA monomer on surface of UHMWPE samples were performed.

The radiation induced graft copolymerization of MMA was carried out on the surface of UHMWPE plates to be preliminarily irradiated by 6 MeV EB in the air with subsequent heating in contact with solution of MMA monomer in methanol. This is so-called the graft copolymerization on the base of the post-effect. In this case, the copolymerization in a boundary layer on UHMWPE surface occurs at heating due to radicals. These ones are generated in the course of decomposition of peroxides and hydroperoxides appearing at irradiation. To prevent homopolymerization of MMA monomer, saline $Fe_2SO_4 \cdot 7\ H_2O$ was added in MMA solution.

The values of degree of the radiation grafting $\eta(mg/cm^2)=(P_{gr}-P_0)/S_{sample}$ were obtained experimentally in the range from 1 to 50 mg/cm^2. Where P_{gr} is the weight of the sample with grafted MMA after irradiation, P_0 is the weight of the initial sample of UHMWPE, S_{sample} is the full area of UHMWPE plate. Free radicals were extracted from UHMWPE plates after radiation grafting by artificial aging of heated samples.

The adhesion properties of UHMWPE samples with radiation induced graft copolymerization of MMA were tested by measurement of tensile bonding strength between UHMWPE and PMMA samples, which were connected together by bone cement "PALACOS R", GmbH Germany. The bone cement "PALACOS R" on 90% consists of PMMA. The tensile bonding strength between bone cement and UHMWPE samples with radiation-induced grafted MMA increased up to 80 time in comparison with samples without radiation grafting.

One of the features of new composites is the inclusion in their structure of biologically active ceramics in the form of powder or granules. The bioactive ceramics is introduced into a composite as the constituent on all volume or by in form of coatings. Calcium phosphate compounds - hydroxyapatite (HA) and tricalcium phosphate (TCP) were used as bioactive ceramics. HA and TCP are the basic inorganic components of the hard tissues of an organism. HA and TCP show excellent biocompatibility and are well integrated with bone tissues due to interactions at the interface and growing of new tissues into its pore structure. The inclusion of biologically active ceramics in structure of composites leads to effective osteointegration of composite material with living tissue and creation of firm biomechanical interface.

All new composite materials were *in vitro* and *in vivo* examined on biocompatibility, cytotoxicity and carcinogenicity. For these purposes, an express method of cultivation of cellular culture was used. The osteointegration of composite materials with living tissue, the process of bone tissue formation on the surface and into composite materials were investigated on small animals - rats and rabbits.

5 CONCLUSION

EB processing was used for radiation modification and manufacture of new CMs for orthopedic implants. CMs were made on a basis of reinforced polymers by various fibers and bioactive ceramics. CMs with modules of elasticity ranging from 10 to 40 GPa, bending strength 200 MPa and more, compressive strength 150 MPa and more which satisfy the strength criteria of supporting elements of joints were designed. The wear rate of crosslinked UHMWPE is more than 20 time less in comparison with unirradiated samples. EB-induced graft copolymerization of MMA on the surface of UHMWPE samples significantly increase its adhesion to bone cement.

6 ACKNOWLEDGMENTS

The work was supported by the STCU, Kyiv, project #957. The authors wishes to express gratitude to Prof. N.Dedukh, Dr. S.Malushkina, and Prof. V.Radchenko, SJPI, for conducting of *in vitro* and *in vivo* testing of new composite materials on biocompatibility.

REFERENCES

[1] G. Popov, A. Avilov, V.Deryuga, V.Rudychev, and I.Zalyubovsky. Proceedings of the 18th Particle Accelerator Conference., New York, USA, 2000, Vol. 4, p. 2549-2551.

[2] A.Avilov, V. Deryuga, S.Korenev, and G. Popov. Sixth International Conference on Electron Beam Technologies, EBT 2000, Varna, Bulgaria, p. 86-87.

[3] V.T.Lazurik, V.M. Lazurik, G. Popov , Yu. Rogov. Abstract book of the ICAP-2002 Conference, p.49, East Lansing, MI, USA. (Paper in a press).

[4] A.Lisitsky, S. Pismenesky, G.Popov and V.Rudychev. Radiation Physics and Chemistry Vol. 63, 2002, p. 591-594.

[5] W. Johnson, B.Lyons, Radiation Physics and Chemistry Vol. 46, 1995, p. 829-832.

DESIGN STUDIES OF AN ELECTROSTATIC STORAGE RING

C. P. Welsch[1], J. Ullrich, MPI-K, Heidelberg
C. Gläßner, K.-U. Kühnel, A. Schempp, IAP, Goethe University, Frankfurt
H. Schmidt-Böcking, IKF, Goethe University, Frankfurt
Germany

Abstract

Electrostatic storage rings combine a number of very interesting characteristics that make them an attractive tool in the low energy range. In contrast to magnetic rings, all of the fields in an electrostatic storage ring are completely mass independent. At the same particle energy and charge state, ions from light protons to heavy biomolecules can in principal be stored with identical field setups.

A small ring for ions of energies up to 50 keV is planned to be build up at Goethe University in Frankfurt. Different designs have been calculated and the results are presented in this contribution. Furthermore, prototypes of the necessary optical elements have been manufactured and are described as well.

1 INTRODUCTION

In 1997 the first electrostatic storage ring began operation at ISA, Denmark [1]. Many different types of ions could be stored in the ring ELISA since and the expected flexibility of the machine with respect to storable ions could be proven.

Operating at energies of some 10 keV, electrostatic rings can be seen as a cross between 'classical' magnetic rings and electrostatic traps. They offer easy access to all their elements, a wide range of possible experiments at relatively low costs.

In order to improve the resolution in existing experimental setups and to cover new fields, a small machine for total energies up to 50 keV is planned in Frankfurt.

2 POSSIBLE LAYOUTS

From the point of view of particle dynamics and because of practical reasons, the symmetry of a storage ring should be chosen as high as possible. This reduces calculations to small fractions of the whole circumference and takes advantage of the structure's periodicity.

Optical elements can be manufactured and utilized several times and the straight sections give plenty of room for experiments. An overview of such a design is shown in Fig. 1.

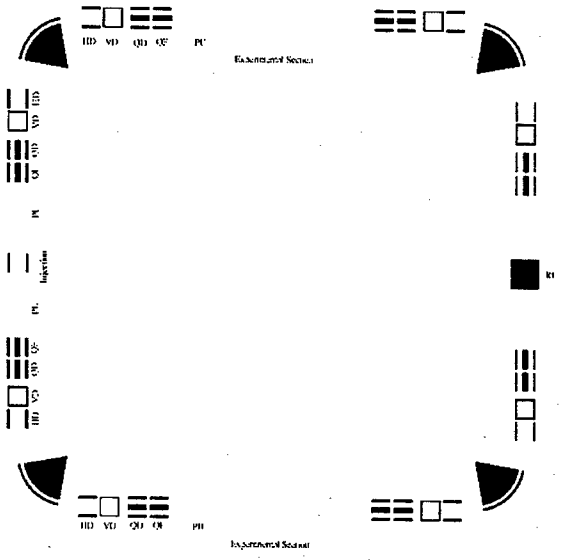


Figure 1: classical "ring" shape

The distances between the different elements are not drawn to scale in order to facilitate a first overview.

Injection into the machine can be done in two different ways: Either the beam enters the ring at a small electrostatic inflector, that bends the beam on axis and is switched off after half the ring's circumference is filled, or it enters along one of the straight section, where one of the corner deflectors would have to be switched off at the beginning.

Another reason for splitting the 90° corner sections up into three elements is the possibility of bringing e.g. laser or electron beams into the machine and thus enabling interaction experiments.

The beam envelope corresponding to this first design is shown in Fig. 2. A symmetry point lies in the middle of the cylindrical deflector and a smooth propagation through the system is reached. It should be pointed out that in the cases (3) and (4), the beam is focused in this bend in both planes and higher space charge forces occur.

[1]carsten.welsch@mpi-hd.mpg.de

0-7803-7738-9/03/$17.00 © 2003 IEEE

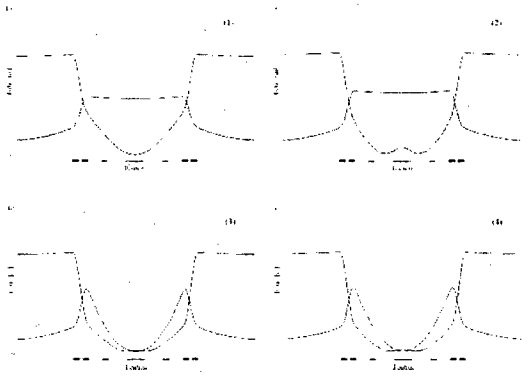


Figure 2: Beta-function for a classic shape

A racetrack shape design as given in Fig. 3 reduces the size of the whole machine even further at the cost of a lower symmetric lattice.

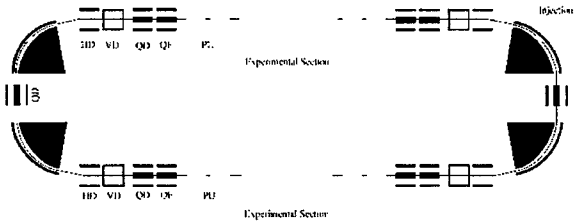


Figure 3: racetrack shaped ring

In this example, the width of the whole machine could be reduced below 2 meters, which would make the complete ring transportable.

The size of the elements was kept identical in order to use the results of previous calculations. The tune values for two different points of stable operation are given in Table 1.

Table 1: Tune values for a racetrack design

parameter	*value*
Q_x	2.248
Q_y	0.295
Q_x	2.82
Q_y	0.266

Direct comparison of the beta functions in a circular and racetrack like machine show that in the latter case, the beam dimension can be reduced even further.

3 OPTICAL ELEMENTS

3.1 Deflecting elements

For the different reasons mentioned above, the 90° bend in the corners of the ring is split up into three elements.

A first small angle deflection is done in a parallel plate deflector. A set of two bends is put in one cavity as shown in Fig. 4. One of electrode pairs is rotated by 90° and is used for closed orbit correction.

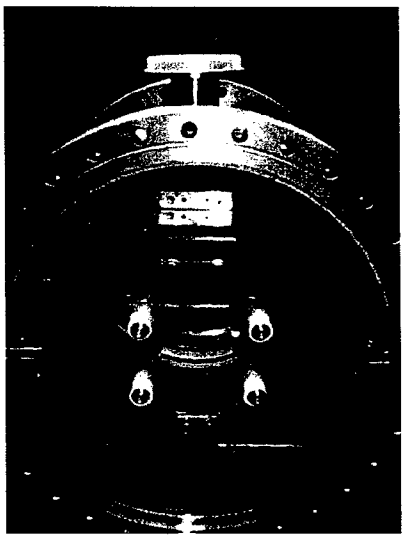


Figure 4: 10° parallel plate deflector

Necessary voltages are about ± 4.5 kV per electrode at plate distances of 100 mm.

The main bending of 70° is done in a cylindrical deflector as shown in Fig. 5. At the entrance and exit of this element grounded shields are placed in order to reduce the effects of fringe fields [3].



Figure 5: 70° cylindrical deflector

3.2 Transverse Size

It is only possible to cover the requirements of different experiments if the beam size and shape can be changed within a wide range. For that purpose, several pairs of quadrupole lenses are foreseen. From a strongly focussed to a parallel beam, many shapes are possible.

Each electrode is 10 cm long and the inner aperture is roughly 2.5 cm.

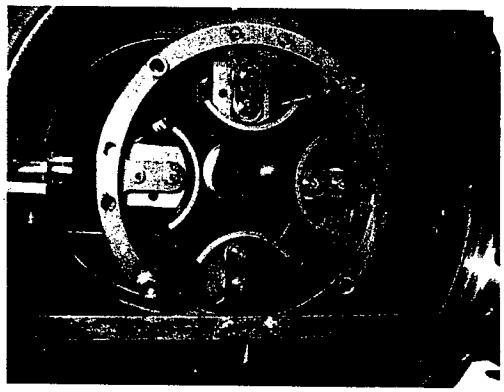


Figure 6: 70° cylindrical deflector

A list of the latest design parameters for a circular layout is given in Table 2.

Table 2: List of design parameters

General Parameters	
Maximum energy	50 keV
Circumference	17.91 m
Revolution time	3.5 µs (p)
10° deflectors	
Plate area	200 mm x 70 mm
Plate distance	100 mm
Voltage	+/- 4.5 kV
70° deflectors	
Height	70 mm
Radii	235 mm and 265 mm
Voltage	+/- 6 kV
Quadrupoles	
Length	100 mm
Aperture Radius	25 mm
Voltage	+/- 1 kV

4 OUTLOOK

In order to study all the different elements necessary for a complete ring, a quarter ring section has been build up in Frankfurt, Fig. 7. Special focus was put on practical aspects.



Figure 7: Overview of the quarter ring section

At present, vacuum measurements are made with these cavities and the next step will be to test the diagnostic [4] and optical elements with a test beam.

5 ACKNOWLEDGEMENTS

The authors would like to thank Søren Pape Møller for the many discussions and fruitful cooperation – nihundrede tak for Hjaelp !

6 REFERENCES

[1] S.P. Møller, "ELISA, an electrostatic storage ring for atomic physics"
NIM A **394**, 281 (1997)

[2] C.P. Welsch, "An electrostatic storage ring at IAP"
PAC, Chicago, IL, USA, 2001

[3] C.P. Welsch et al, „Analysis of Field Perturbation due to Electrode Errors in an Electrostatic Storage Ring"
EPAC, Paris, France, 2002

[4] C.P. Welsch et al, „A Flexible Control System for an Electrostatic Storage Ring"
EPAC, Paris, France, 2002

UP-GRADED RHIC INJECTION KICKER SYSTEM*

H. Hahn#, W. Fischer, Y. K. Semertzidis, D. S. Warburton, BNL, Upton, NY, 19793, USA

Abstract

The design of the RHIC injection systems anticipated the possibility of filling and operating the rings with a 120 bunch pattern, corresponding to 110 bunches after allowing for the abort gap. Beam measurements during the 2002 run confirmed the possibility, although at the expense of severe transverse emittance growth and thus not on an operational basis. An improvement program was initiated with the goal of reducing the kicker rise time from 110 to ~95 ns and of minimizing pulse timing jitter and drift. The major components of the injection system are 4 kicker magnets and Blumlein pulsers using thyratron switches. The kicker terminating resistor and operating voltage was increased to reduce the rise time. Timing has been stabilized by using commercial trigger units and extremely stable dc supplies for the thyratron reservoir. A fiber optical connection between control room and the thyratron trigger unit has been provided, thereby allowing the operator to adjust timing individually for each kicker unit. The changes were successfully implemented for use in the RHIC operation.

INTRODUCTION

Beam injection into the RHIC is done vertically by means of four kicker systems per ring, each consisting of a magnet connected to a Blumlein pulser using thyratron switches [1,2]. The pulsers are located outside the RHIC tunnel and are connected to the magnets by ~75 m of high voltage cables. The Blumlein pulser [3,4] consists of rigid, oil-filled transmission lines in a folded triaxial configuration. The magnet was originally conceived as a transmission line magnet with 25 Ω characteristic impedance to match the two parallel 50 Ω feeding cables. Using a conceptual SLAC design [5], the first version of the magnet was build with a "C" cross section formed of interspersed ferrite and high-dielectric constant bricks [6]. The kicker operates in air and thus requires a ceramic beam tube with the dimensions of 47.6 mm o.d. and 41.3 mm i.d., presenting the smallest aperture at injection. Voltage breakdown in the dielectric loaded kickers suggested their replacement by the present all-ferrite magnets [7].

Beam transfer from the AGS into RHIC is done in box-car fashion. The bunches created in the AGS are transferred individually in order to form a nominal 60-bunch pattern to yield collisions at the six interaction points, implying 55 × 55 bunches after allowing for the dump gap. The revolution frequency in RHIC is 78.196 kHz and the RF harmonic of the acceleration system is 360, so that every sixth bucket can be filled. The bunch spacing is 213 ns and the bunch length at transfer is 20 ns, thus requiring an injection kicker rise time of 190 ns, well within the capabilities of the injection system. Increasing the luminosity by doubling the bunch pattern to 120 corresponding to 110 × 110 injected bunches was part of the original design but requires a kicker system rise time of better than 95 ns [8]. Beam based measurements of the dielectric-loaded kickers showed a rise time clearly below this value [9], whereas the operational all-ferrite magnets during the 2002 run had a ~110 ns rise time [7]. Injection of 110 bunches was possible although with severe transverse emittance growth. Based on this experience, a system rise time of 95 ns without timing jitter or drift became the goal of the up-grade program discussed in the present paper.

SYSTEM UPGRADES

The original concept of the injection system with a transmission line kicker magnet is in principle capable of satisfying these requirements. However voltage breakdown problems forced the mismatched termination of the kicker magnet. Nevertheless, the following hardware modifications achieved 110 bunch operation in the 2003 run:

- the injection kicker magnets are terminated with 25 Ω instead of the previous 16 Ω, thereby raising the operating voltage from 31 to ~38 kV.
- the home-grown thyratron trigger system consisting of a DC power supply and two hard tube trigger units are replaced by a commercial solid state trigger unit. The new unit eliminates the sensitivity to ac power fluctuations and reduces the short term pulse jitter to ~3 ns peak-to-peak.
- the thyratron reservoir ac supply is replaced by a dc power supply, highly regulated to better than 0.01 V, thereby minimizing drift.
- a fiber optical connection between control station and the thyratron trigger unit allows the operator to adjust slow drifts due to temperature changes affecting the system immediately before injection.

ALL-FERRITE KICKER MAGNET

In the conversion of the dielectric-loaded into the all-ferrite magnet the ceramic bricks were replaced by ferrite, but in order to minimize the cost, the overall geometry and in particular the magnet frame was retained [7]. The magnet length is 1.12 m and the core cross section is shown in Fig.1.

It is not obvious that the converted all-ferrite magnet would retain transmission line characteristics rather than adopt those of a lumped magnet. However, a direct measurement of the magnetic field confirmed the transmission line properties. The time dependent magnetic

*Work performed under contract DE-AC02-98CH10886 for the U. S. Department of Energy
#hahnh@bnl.gov

0-7803-7738-9/03/$17.00 © 2003 IEEE

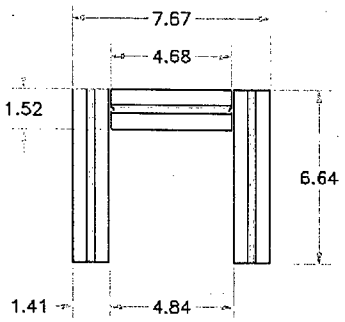


Figure 1: Kicker magnet core cross section (in cm)

field of the all-ferrite kicker was measured using the Faraday effect (1846), which describes the phenomenon that the polarization of a light beam traversing a crystal is changed by an applied magnetic field. In the present setup, a green Ar laser light was used together with an artificially grown TGG crystal which has a large Verdet constant.

The rise time of the magnetic field, measured at two positions in the magnet, ~ 80 cm apart, with one ~20 cm down-stream from the input and the second ~20 cm up-stream from the 25 Ω terminating resistor is shown in Fig. 2. The incoming pulse from the pulser has a rise time of ~33 ns. The transit time to cover the 80 cm is 24 ± 2 ns in both cases. Since the propagation velocity equals the light velocity times the ratio of characteristic impedance / Z_0, one finds a characteristic impedance of ~40 Ω. The effective rise time of the all-ferrite kicker with matched termination would be <50 ns.

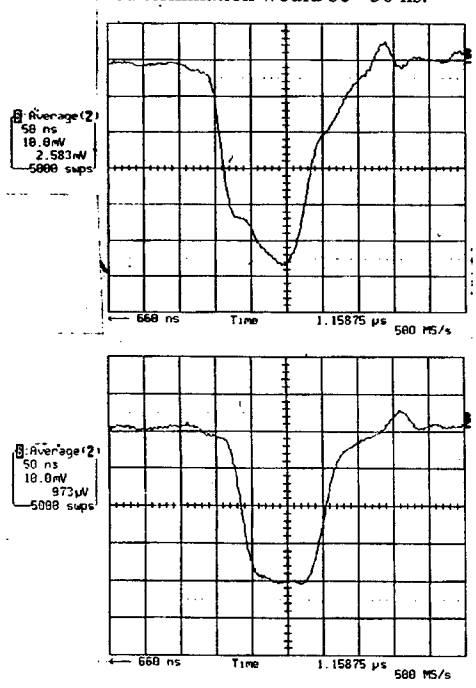


Figure 2: Magnetic field pulse at input (top) and output (bottom) of kicker magnet

The response of the kicker to a step function was also measured with the network analyzer in the time domain mode. The time dependent current or magnetic field at the kicker for different terminations is shown in Fig. 3. Note that the smaller mismatch between instrument, 50 Ω and the magnet yields only a qualitative comparison.

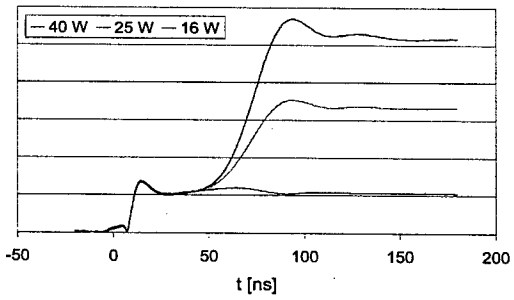


Figure 3: Kicker response to step function

The effective rise time of a mis-matched transmission line magnet consists of the rise time of the incoming pulse plus twice the transit time in the kicker. For RHIC operation, the magnet is mismatched with a low impedance to gain current and magnetic field at a lower voltage. The voltage required to achieve the necessary current is given by

$$U_B = \left[\frac{2}{Z_K + Z_0}\left(1 + \frac{Z_K - Z_L}{Z_K + Z_L}\right)\right]^{-1} I_K$$

where U_B represent the Blumlein source voltage and Z_0, Z_K, Z_L is the impedance of the source, of the kicker, and of the terminating load respectively. The total deflecting current is required to be ~1.15 kA at the reduced injection energy of 8.86 GeV/u for gold. During the 2002 run, the magnets were terminated with 16 Ω requiring ~31 kV. The voltage requirement with a matched termination of 40 Ω becomes ~46 kV, a level not yet tested. In the 2003 run, the kicker with 25 Ω termination runs conservatively at ~38 kV.

BLUMLEIN PULSER

Beam injection in the 2002 run was hampered by timing jitter and drifts of the pulser units. The switch tube in the Blumlein Pulser is a two-gap deuterium-filled thyratron, EEV 1168C (70 kV, 4 kA specs).

Trigger Unit

Proper operation of the thyratron requires triggers, 500 V on G1 and 1.5 kV on G2, as well as a negative 150 V to hold-off the anode voltage, which are now provided by a commercial trigger unit EEV MA2709A (a.k.a. "black box). The timing jitter of the thyratron is quoted as 1 ns typical, with 5 ns maximum. The trigger timing shift of the commercial trigger unit was tested to be less than 1 ns against line changes of 10 % (i.e.105 - 120 V) Implementation of the changes reduced the jitter to ~3 ns peak to peak.

Reservoir Voltage Power Supply

The reservoir voltage is the most critical parameter in the quest for trigger stability, both jitter and drift. The dependence of current timing on the dc reservoir voltage is shown in Fig. 4. The data sheet recommends that the reservoir voltage be stabilized to $\pm$ 0.05 V, which according to our measurements corresponds to typically $\pm$ 3 ns. New DC power supplies (Mid Eastern Ind. HWD 10-15B) 10 V & 10 A with 0.01 V regulation will be used

Achieving the full anode current rise time determines the minimum reservoir voltage. Operation at the highest level compatible with maintenance of the anode voltage hold-off is recommended. The kicker system runs at a low voltage, well below its design, so that the reservoir voltage can go to the manufacturer's limit of 6.5 V.

Changing the heater voltage by 10 % has no short term effect on the trigger time, but may contribute to a temperature induced drift. The heater is stabilized by a Solatron transformer.

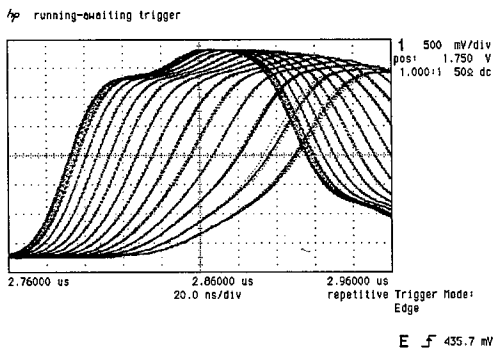


Figure 4: Anode Current change with reservoir voltage from 5.0 to 6.3 V

Anode Current Rise Time

The thyratron data sheet gives a nominal rate of rise of anode current of better than 150 A/ns but the actual value depends on the external circuit. The rate of rise in the Blumlein pulser as measured by the magnetic field in Fig. 2 is ~38 A/ns at operating conditions. However, the full rate of current rise is only reached after the anode delay time, defined as 0 to 25 %, which is typically ~100 ns. Allowing a 2% of full current delay adds ~65 ns to the time between the G2 trigger and bunch arrival. Since predictable, the effective pulse rise time is not affective by these delays. Simultaneous triggering of the four pulsers takes advantage of these delays and minimizes the overall kicker rise time.

Fiberoptic Controls

To accommodate the individual turn-on delays and time drift of the four thyratrons the bunch synchronized trigger drives a Stanford Research Systems DG535 4 channel delay generator with each channel remotely variable to 5ps resolution through an IEEE buss controller. Each of the 4 output channels is connected to an Agilent 1404 fiberoptic transmitter and then through a 30M light cable to the E2V MA2709A trigger unit input. This system was found to contribute <1 ns jitter to the system.

BEAM BASED MEASUREMENTS

The kicker rise time and flattop were measured with beam for the all-ferrite kickers with 16 and 25 Ω terminations. For the measurement beam was injected and the kicker timing was shifted. The rise time with 25 Ω was reduced from ~110 to ~95 ns as seen in Fig. 5.

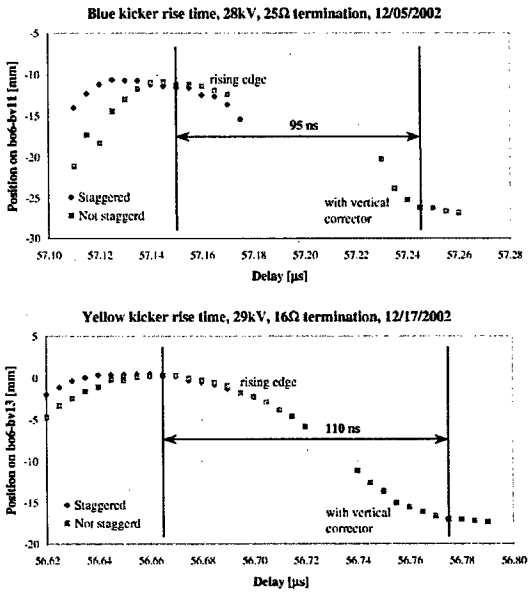


Figure 5: Beam based rise time measurements

REFERENCES

[1] E. B. Forsyth, Report AD/RHIC/RD-85 (BNL 1995)
[2] E. B. Forsyth, G. C. Pappas, J. E. Tuozzolo, & W. Zhang, Proc. 1995 PAC, Dallas, TX, p. 1921.
[3] G. N. Glasoe & J. V. Lebacqz, *Pulse Generators*, (McGraw-Hill, New York, 1948) p.463.
[4] W. Zhang, R. Sanders, W. Fischer, & L. Hoff, Proc. 1999 PAC, New York, NY, p. 1261
[5] F. Bulos & A. Odian, Report SLAC-PUB-3453, CN-279, (1984) and R. Cassel (private communication)
[6] H. Hahn, N. Tsoupas, & J. E. Tuozzolo, Proc. 1997 PAC, Vancouver, BC, p. 213.
[7] H. Hahn, W. Fischer, V. I. Ptitsyn, & J. E. Tuozzolo, Proc. 2001 PAC, Chicago, IL, p. 3705
[8] H. Hahn, Nucl. Instr. & Methds, **A499**, p.245 (2003)
[9] W. Fischer, H. Hahn, W. W. MacKay, T. Satogata, N. Tsoupas, & W. Zhang, Proc. 1997 PAC, Vancouver, BC, p. 210

Proceedings of the 2003 Particle Accelerator Conference

SUPER-INVAR AS A TARGET FOR A PULSED HIGH-INTENSITY PROTON BEAM

Harold Kirk*, Hans Ludewig, Leonard Mausner,
Nikolaos Simos, Peter Thieberger, Robert Weggel, BNL, Upton, NY 11973, USA
Kirk McDonald, Princeton University, Princeton, NJ 08544, USA

Abstract

We describe measurements performed on samples consisting of the alloy Super-Invar, which is a candidate material for a robust solid target used in conjunction with an intense pulsed proton beam. A low coefficient of thermal expansion is the characteristic property which makes Super-Invar an attractive target candidate. We have irradiated our samples at the Brookhaven Linac Isotope Producer facility. Tests for variations of the thermal expansion coefficient as a function of inflicted radiation damage are described. The high radiation dose is severely detrimental to its low coefficient of thermal expansion.

INTRODUCTION

Increasing the power of proton accelerator facilities will generate new physics opportunities. This is especially true in the fields of high-energy physics where intense secondary beams of pions, muons and neutrinos are of great interest. Material sciences can greatly benefit from the production of intense pulsed neutrons. A key issue to realize these possibilities is the development of new target systems which can function with proton beams at power levels of 1 MW or more. The target must withstand very elevated values of both peak and average power. We discuss in this paper a study of two candidate materials for a high-peak power target.

We have previously reported studies[1] in which rods of carbon were exposed to intense proton pulses and the amplitude of the generated pressure waves recorded. The results showed a very clear reduction in the pressure wave amplitude for carbon-carbon, as compared to ATJ carbon. We attribute the difference to the extremely low value of the coefficient of thermal expansion (CTE) of the carbon-carbon rod.

We are led to consider other materials which also have a low coefficient of thermal expansion (CTE). Invar is a metal alloy which predominantly consists of 62% Fe, 32% Ni and 5% Co. The form of Invar which we have tested is Super-Invar, which is heat treated so as to have a particularly low CTE. The CTE for Super-Invar at room temperature is typically at 0.6×10^{-6}/°K, but its variation after radiation damage from an intense proton beam is unknown.

*hkirk@bnl.gov

EXPERIMENTAL LAYOUT

The irradiated Super-Invar samples consisted of 28 3/16″ rods each 1.688″ long. Half of the samples were necked down to a diameter of 0.08″ in the center region The necked-down samples were used for post-irradiation mechanical tensile testing. In addition, 8 Inconel rods were used as fillers in the target stack. Fig. 1 depicts the configuration of the samples within the target holder. In addition, 16 1mm diameter nickel wires were placed between sample cylinders, half each at the target entrance and exit. These were used as horizontal and vertical profile monitors for the proton beam.

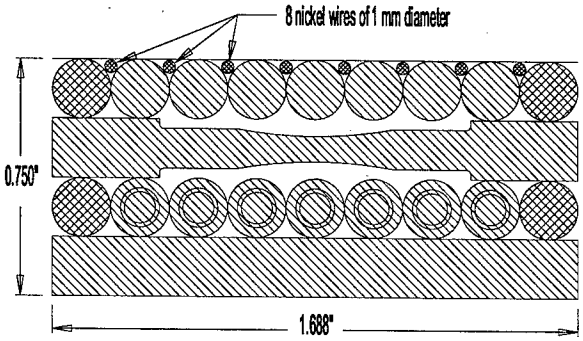


Figure 1: Target sample layout. Cross-hatched samples are Inconel. The proton beam enters from the top.

The irradiation was done at the Brookhaven Linac Isotope Producer (BLIP) facility with a 200 MeV proton beam from the linac which also serves as an injector for the AGS booster. The integrated beam current over a two week period was 24 mA-hrs which corresponds to a total of 5.4 $\times 10^{20}$ protons on target. The proton fluence at the target center was 1.3×10^{20} protons/cm^2. The beam energy after attenuation in the water surrounding the target was 190 MeV at our sample entrance.

The samples, with holder, were immersed in a water tank for target cooling purposes. In addition, water was directed to flow through each sample holder. The unobstructed water flow rate is 11 GPM. We estimate that the actual water flow rate through the sample was reduced to the order of 2 GPM. Given this flow rate and the peak proton current of 108 μA experienced during the exposure, we calculate that the peak temperature within the interior of a sample

0-7803-7738-9/03/$17.00 © 2003 IEEE

rod was on the order of 200° C.

After exposure, the target sample was removed and placed in a lead shielded enclosure for seven months to allow for the radio-activity to decline to more manageable levels for the subsequent measurements. Nonetheless, our measurements of the CTE and tensile properties had to be performed within the confines of a hot cell equipped with remote handling capabilities.

Upon removal of the samples from the target holder, the individual cylinders were washed in an acid bath to remove corrosion from the rods. Samples were then sorted by position in the the target, making use of identifying marks on each cylinder and nickel wire.

MEASUREMENTS

Activation Measurements

The samples were placed individually into an ATOMLAB 100 dose calibrator in order to measure the integrated activation levels. The first (entrance) plane (Fig. 1) consisted of straight cylindrical rods and wire positioned in a horizontal orientation, while the the fourth (exit) plane had a similar arrangement but with a vertical orientation. The activation levels of the front plane could then be used to extract information as to the vertical profile of the incident proton beam, while the exit plane could be used for obtaining the horizontal profile of the proton beam (Fig. 2). The nickel wire and Invar rods have different volumes as well as composition, hence overall normalization for each data set differ. However, the beam rms widths extracted from each set of material agree well.

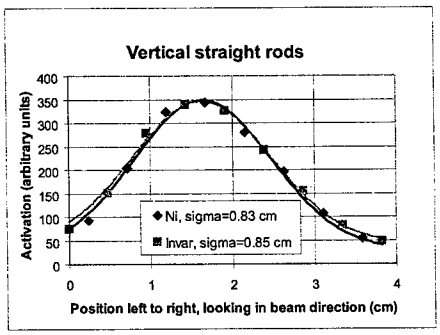


Figure 2: Measured specimen activity as a function of target position. The lines are Gaussian fits.

This measured beam profile, along with the total proton flux and incident energy, served as input into the code MCNPX[2] which calculated the atomic displacements within each sample. Results of the activation measurements of each sample correlate well with the calculated values for the atomic displacements averaged over each rod.

Thermal Expansion Measurements

Measurement of the coefficient of thermal expansion utilized an L75 dilatometer purchased from LINSEIS, Gmbh. This device was specifically fabricated to allow ease of remote operation since the measurements were confined to a hot cell where remote manipulation of the equipment as well as the mechanical insertion of the samples was required. Measurement of non-irradiated samples demonstrated that the stock material had the expected CTE of 0.6×10^{-6} /°K at room temperature while the base line for the temperature range of 50°C to 150°C was an average CTE of 1.0×10^{-6} /°K (see Fig. 3). This figure also demonstrates that irradiation dramatically alters the thermal expansion properties of Super-Invar. The results for all fourteen straight irradiated specimens are shown in Fig. 4.

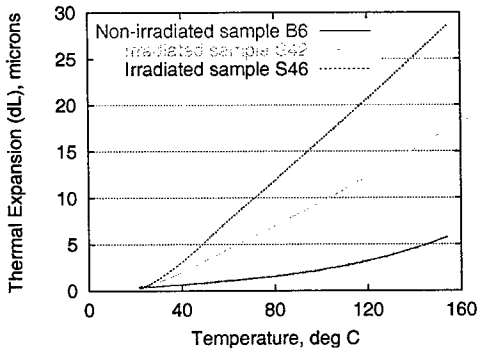


Figure 3: Measured thermal expansions for three different Super-Invar specimens.

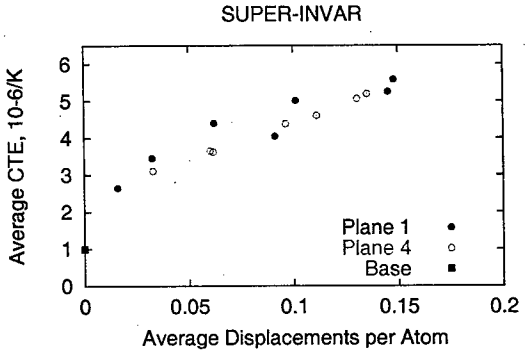


Figure 4: Measured average coefficients of thermal expansion as a function of calculated average atomic displacements per atom.

It should be noted that the average CTE values reported here correspond to a temperature interval from 50°C to 150°C and are also averaged over the length of each sample. Auxiliary measurements of un-irradiated samples heat treated to temperatures up to 400°C indicate that most of the observed effect is due to radiation damage, but some

contribution from heating during irradiation and from possible effects of thermo-mechanical shock caused by the pulsed beam can not be excluded.

We also measured the average CTE of the eight Inconel rods as well as two non-irradiated Inconel specimens. Since the Inconel rods were used as spacers at the edges of the target, their levels of activation and atomic displacement are typically less than for the Super-Invar samples. Nonetheless, we do observe a small change in the CTE for Inconel (see Fig. 5).

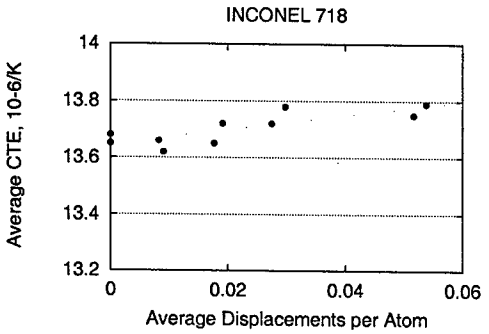


Figure 5: Measured average coefficients of thermal expansion of the Inconel samples as a function of calculated average atomic displacements per atom.

Tensile Measurements

The effect of different levels of irradiation on the mechanical properties of Super-Invar was assessed by performing a tensile test on specimens that have been specially designed for that purpose. In particular, the two middle planes of the target were formed by specimens which had been necked-down to a diameter of 80 mils. The maximum irradiation levels reached during the exposure to the beam has been calculated to be 0.25 dpa.

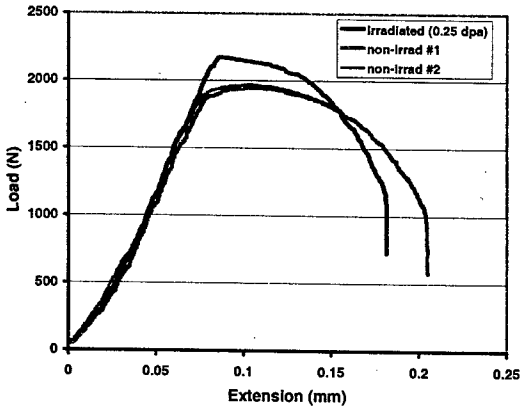


Figure 6: Load-displacement curves for irradiated and non-irradiated invar specimens.

The load-displacement curves of virgin as well as irradiated specimens from the same block of material were obtained. Particular care was taken to maintain the same parameters of tensile test in order to avoid scattering of the data. As a result very similar load-displacement curves were achieved for the non-irradiated specimens. This provided a reference for the mechanical properties (such as the yield strength, the ultimate strength and the modulus of elasticity) that are evaluated as a function of the irradiation.

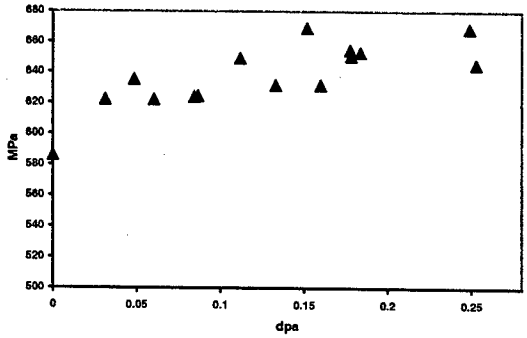


Figure 7: Yield vs atomic displacement for irradiated and non-irradiated invar specimens.

While no effect was observed for the modulus of elasticity, irradiation effects are apparent. Specifically, the material becomes stronger but brittle. A 15% increase in tensile strength was observed. The irradiated material, however, lost its post-yield strength (no ultimate strength) and fractured at smaller displacement (strain) levels.

SUMMARY

Our results indicate that selecting a target material based on it's attractive coefficient of thermal expansion should be preceded by a consideration of the effects that radiation damage can impart on this property. Super-Invar can be considered a serious target candidate for an intense proton beam only if one can anneal the atomic displacements followed by the appropriate heat treatment to restore its favorable expansion coefficient. On the other hand, the more modest influence of radiation damage on the Inconel samples suggests that targetry material selection based on yield strength rather than low thermal expansion coefficient may lead to a more favorable result.

REFERENCES

[1] H.G. Kirk, *TARGET STUDIES WITH BNL E951 AT THE AGS*, Proceedings of the 2001 Particle Accelerator Conference, Chicago, Il., March 2001, p.1535.

[2] MCNPX Users Manual-Version 2.1.5, L.S. Waters, ed., Los Alamos National Laboratory, Los Alamos, NM. TPO-E83-G-UG-X-00001. (1999)

A HIGH-FIELD PULSED SOLENOID MAGNET FOR LIQUID METAL TARGET STUDIES

H.G. Kirk*, M. Iarocci, J. Scaduto, R.J. Weggel, BNL, Upton, NY 11973, USA
G. Mulholland, Applied Cryogenics Technology, Ovilla, TX 75154, USA
P. Titus, MIT, Cambridge, MA 02139, USA
K.T. McDonald, Princeton University, Princeton, NJ 08544, USA

Abstract

The target system for a muon collider/neutrino factory requires the conjunction of an intense proton beam, a high-Z liquid target and a high-field solenoid magnet. We describe the design parameters for a pulsed solenoid, including the magnet cryogenic system and power supply, that can generate transient fields of greater than 10T with a flat-tops on the order of 1 second. It is envisioned to locate this device at the Brookhaven AGS for proof-of-principle testing of a liquid-jet target system with pulses of 10^{13} protons.

THE TARGETRY CONCEPT

A muon collider or a neutrino factory based on a muon storage ring [1] require intense beams of muons, which are obtained from the decay of pions produced in proton-nucleus collisions. To maximize the yield, pions of momentum near 300 MeV/c should be captured. For proton energies above 10 GeV, the pion yield per unit of proton beam energy is larger for a high-Z target. For proton beam energies in the MW range, beam heating would melt or crack a stationary high-Z target, so a moving target must be used. A mercury jet target is the main focus of BNL E951 [2], although R&D is also being conducted on a carbon target option as might be suitable for a low-energy proton source, and conceptual studies have been carried out for rotating-band targets, a tantalum/water target, and a liquid-lithium target.

The low-energy pions are produced with relatively large angles to the proton beam, and efficient capture into a decay and phase-rotation channel is obtained by surrounding the target with a 20-T solenoid magnet, whose field tapers down to 1.25 T over several meters [3], as sketched in Fig. 1. Pion yield is maximized with a mercury target in the form a 1-cm-diameter cylinder, tilted by about 100 mrad with respect to the magnetic axis. To permit the proton beam to interact with the target over 2 interaction lengths, the proton beam is tilted by 33 mrad with respect to the mercury jet axis.

The use of a mercury jet target raises several novel issues. The rapid energy deposition in the mercury target by the proton beam leads to intense pressure waves that can disperse the mercury. Further, as the mercury enters the strong magnetic field eddy currents are induced in the mercury, and the Lorentz force on these currents could lead to distortion of the jet. On the other hand, the magnetic pressure on the mercury once inside the solenoid will damp mechanical perturbation of the jet. To address these issues an R&D program is now underway.

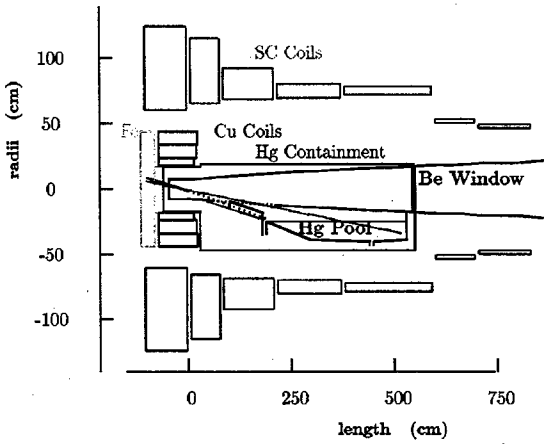


Figure 1: Concept of targetry based on a mercury jet and proton beam at 100 mrad and 66 mrad, respectively, to the axis of a 20-T solenoid magnet.

THE TARGETRY R&D PROGRAM

In the USA, R&D on targetry for a neutrino factory and muon collider has been formalized as BNL experiment 951 [2]. This project maintains close contacts with related efforts in Europe [4] and in Japan [5].

The broad goal of E951 is to provide a facility that can test all the major of a liquid or solid target in intense proton pulses and in a 20-T magnetic field.

Present E951 activities focus on the interaction of intense proton pulses with targets in zero magnetic field. European targetry studies have emphasized the interaction of mercury jets with a magnetic field, the operation of rf cavities near high-power targets, and target material evaluation.

Mercury Jet + Proton Beam

The present R&D program on mercury jets is an outgrowth of work at CERN in the 1980's in which a prototype mercury jet was prepared, but never exposed to a beam.

Experiment 951 is conducted in the A3 beamline of the BNL AGS into which a single bunch of up to 5×10^{12}

*hkirk@bnl.gov

0-7803-7738-9/03/$17.00 © 2003 IEEE

24-GeV protons can be extracted and brought to a focus as small as 0.6×1.6 mm^2. The dispersal of both static and moving mercury targets by the proton beam was observed via two high-speed cameras using shadow photography. The principal results obtained thus far are summarized elsewhere [6]. Figure 2 shows results from a mercury target that was exposed to pulses of $2\text{-}4 \times 10^{12}$ 24-GeV protons. Dispersal velocities of up to 15 m/s were observed. A key result is that the dispersal of mercury was confined to that part of the jet directly intercepted by the proton beam.

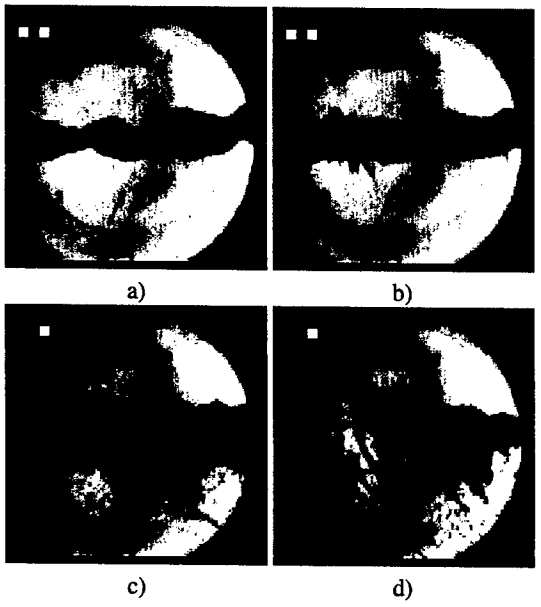


Figure 2: Hg jet interaction with 3.8×10^{12} 24-GeV protons; $t =$ a) 0 ms; b) 0.75 ms; c) 10 ms; d) 18 ms.

Thus, it appears that the dispersal of mercury by a proton beam is dramatic, but not violent, and that the dispersal will be a relatively modest issue for a target facility that operates at 15 Hz.

Mercury Jet + 15-T Magnet

A 4-mm-diameter mercury jet of velocity 12 m/s has been injected int a 15-T magnet [6] with typical results as shown in Fig. 3. By placing the nozzle of the jet well into fringe field of the magnet, disruptive effects of eddy currents are avoided. Furthermore, the high magnetic pressure of the central field suppresses the Rayleigh instability of the jet, in comparison to the case of zero field.

Mercury Jet + Proton Beam + 15-T Magnet

Having conducted successful tests of the separate interaction of a mercury jet with a proton beam, and with a 15-T magnet, the next step is a combined test of mercury jet plus intense proton beam plus a 15-T magnet, in a configuration

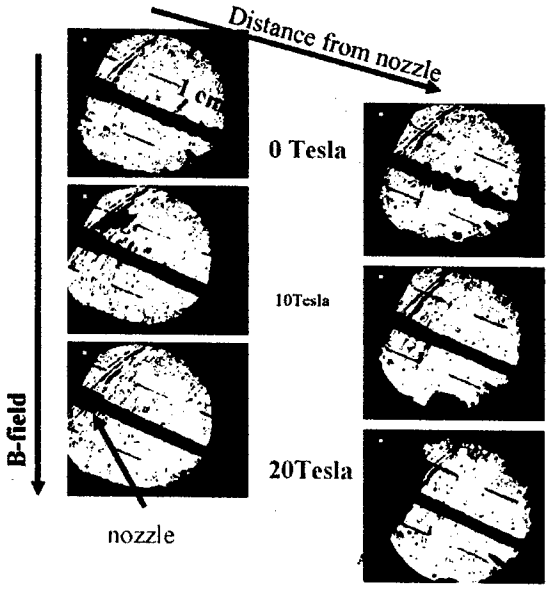


Figure 3: The Rayleigh instability of a mercury jet is suppressed by high magnetic fields.

prototypical of that suitable for a neutrino factory or muon collider.

A design of a 15-T pulsed solenoid magnet for this purpose has been completed [3, 7], as illustrated in Figs. 4-7. The copper coils are cooled by liquid nitrogen to reduce their resistance, and hence the power requirements [8]. The time dependence of key magnet parameters during pulse are illustrated in Fig. 4.

The magnet consists of 3 concentric copper coils, mounted inside a common cryostat, as shown in Fig. 5. Extensive ANSYS simulations have been made of the mechanical and thermal performance of the magnet [7], some of which are summarized in Fig. 6. The cooling scheme for the coils is illustrated in Fig. 7.

The pulsed magnet system is intended to be operated for less than 1,000 pulses, including checkout as well as data taking with proton beams. As such, it appears most cost effective to provide the 4.5-MW pulsed power with an array of batteries, rather than a rectified DC power supply.

Construction of this magnet system is expected to begin later this year, and could be completed in 3 years.

REFERENCES

[1] M.M. Alsharoa *et al.*, "Recent Progress in Neutrino Factory and Muon Collider Research within the Muon Collaboration", submitted to Phys. Rev. ST Axial. Beams. (April 22, 2003), http://www.cap.bnl.gov/mumu/pubs/prstab-030422/prstab.pdf

[2] J. Alessi *et al.*, "An R&D Program for Targetry at a Muon Collider", proposal to the BNL AGS" (Sept. 1998);

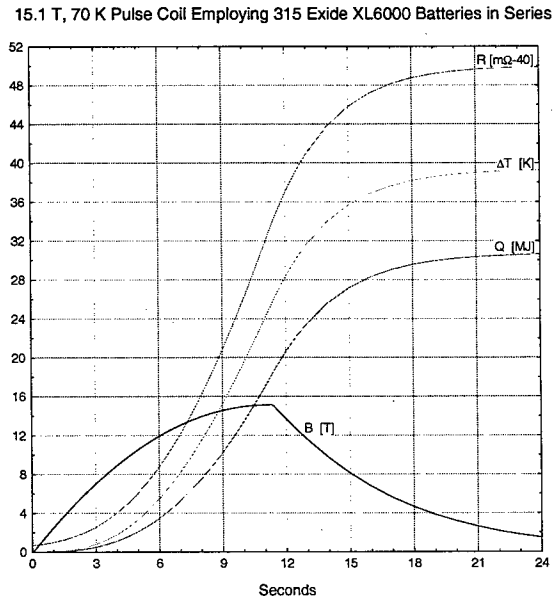


Figure 4: Behavior of the 15-T magnet during a pulse. The peak current is 7200 A at a peak voltage of 600 V. Approximately 30 MJ of energy is dissipated in the magnet, which raises its temperature from 70 to 110K.

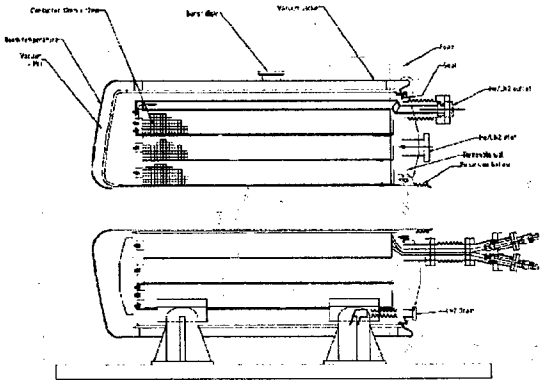


Figure 5: Longitudinal cross section of the 15-T pulsed magnet, showing the 3 coil packages and cryostat [7].

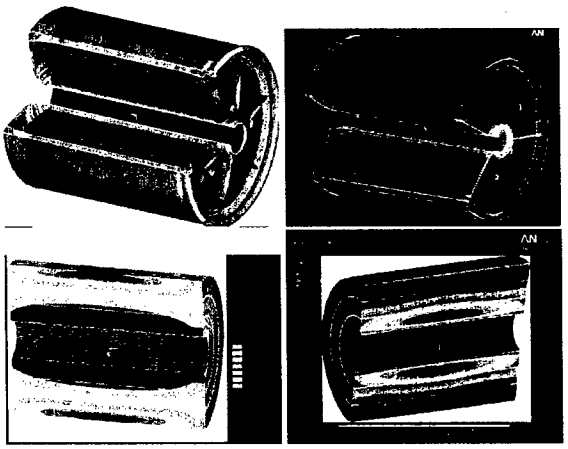


Figure 6: Top: structural analysis of the cryostat. Bottom: thermal and structural analysis of the coils. From [7].

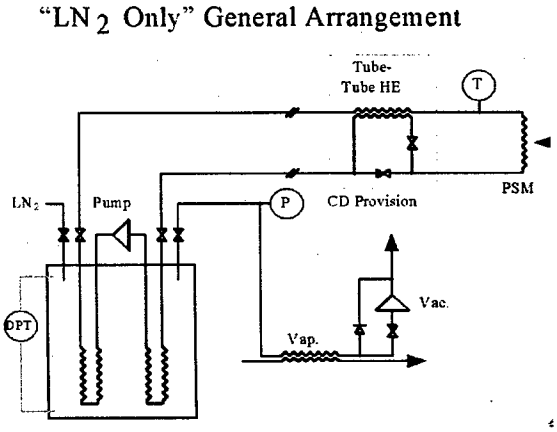


Figure 7: Scheme for cooling the pulsed magnet via flow of He gas that passes through a LN_2 heat exchanger [8].

http://puhep1.princeton.edu/mumu/target/targetprop.PBS

[3] R.J. Weggel, "A Three-Stage Cryogenic Pulse Magnet Program for BNL Targetry Experiment" (Feb. 2002), http://www.hep.princeton.edu/mumu/target/weggel/chicago_020902.pdf

[4] A. Blondel, "Report from the European Muon Collider Oversight Group", (Jan. 15, 2003), http://www.cap.bnl.gov/mumu/collab/030114/MUTAC03-blondel2.pdf

[5] K. Yoshimura, "A Study of a Neutrino Factory in Japan" (Jan. 15, 2003), http://www.cap.bnl.gov/mumu/collab/030114/MUTAC03-yoshimura.pdf

[6] A. Fabich, "High Power Proton Beam Shocks and Magnetohydrodynamics in a Mercury Jet Target for a Neutrino Factor", Ph.D. thesis, U. Vienna (Nov. 2002), http://www.hep.princeton.edu/mumu/target/thesis-2002-038.pdf

[7] P. Titus, "E-951 15-T Pulsed Magnet for Mercury Target Development" (Sept. 6, 2002), http://www.hep.princeton.edu/mumu/target/MIT/desrev_090602.pdf

[8] G.T. Mulholland, "E-951 Cryogenics for Pulsed Solenoid Magnet" (Sept. 6, 2002), http://www.hep.princeton.edu/mumu/target/mulholland/E951_ESR_Pres_090602.pdf

MOVING SOLID METALLIC TARGETS FOR PION PRODUCTION IN THE MUON COLLIDER / NEUTRINO FACTORY PROJECT

P. Thieberger*, H.G. Kirk, R.J. Weggel, BNL, Upton NY, USA
and K. McDonald, Princeton University, Princeton, NJ, USA

Abstract

The production of large fluxes of pions and muons using high-energy, high-intensity proton pulses impinging on solid or liquid targets presents unique problems which have not yet been entirely solved. We investigate the possibilities of using solid targets by choosing a metal of either extremely low thermal expansion coefficient or exceptionally high mechanical strength. Candidates are respectively Super-Invar and Vascomax 350 or Inconel 718. Moving targets in the form of chains or cables would be required for cooling purposes. These materials seem easily capable of surviving the beam pulses required for the largest beam power contemplated. Questions regarding radiation damage effects are being investigated.

INTRODUCTION

The new frontier of multi-megawatt accelerators offers important new physics opportunities as well as interesting technical challenges. In particular, the production of large fluxes of pions and muons using high-energy, high-intensity proton pulses impinging on solid or liquid targets [1, 2] presents unique problems which have not yet been entirely solved. The large required power and power density deposited in the material as well as the short pulse duration produce large, almost instantaneous local heating, and the resulting sudden thermal expansion can result in damage-causing stresses in solids and in the violent disruption of liquid jets. We concentrate on solutions based on solid metallic targets which, through their motion, carry the deposited power from the interaction region to a cooling bath.

The conditions created by the short beam pulses (rms width ~50 ns during recent experiments [3] and <5 ns for a final system [1, 2] are very unusual. Intense, almost instantaneous, beam heating causes a fraction of the target volume to suddenly be in a highly compressed, inertially confined state. Subsequently this volume expands initiating strong vibrations in the material. The amplitude of these oscillations is such that large negative pressures (tensile stresses) or shear stresses can be generated exceeding the strength of the material and thus causing mechanical failure.

For a preliminary screening of possible materials, we assume that tensile and sheer stresses will arise in the oscillations which are similar in magnitude to the initial compression. In fact, the natural tendency in most cases will be for the energy initially concentrated in a fraction of the target volume to rapidly spread over the entire volume thus reducing subsequent peak values. However, vibration focusing effects can lead to unexpected stress concentrations. Computer modeling will be required once a candidate material is selected, and target geometries can then, if necessary, be modified.

CANDIDATE MATERIALS

Two possible approaches to avoid stress induced failures are to either select extremely strong materials that may withstand the large stresses, or materials with extremely low coefficient of thermal expansion for which the thermal shock stresses will be minimized. In the present study we consider the alloys Vasco Max C-350 and Inconel 718 in the first category and Super Invar in the second one. For comparison, we also include data for pure iron. Table 1 lists the thermal and mechanical properties of these materials.

For all these materials and for target radii ranging down to a few mm, the radial sound transit times are orders of magnitude larger than the energy deposition times of nanoseconds or even tens of nanoseconds. Heat diffusion times are longer still by several orders of magnitude. The initial compression is therefore inertially confined to good approximation and the subsequent oscillations are nearly adiabatic.

STRESS ESTIMATES

To determine the initial compression we must first find maximum values of the energy density deposited by the beam. This was done by using the MARS code [4] for a number of different target radii, and by assuming a proton beam rms radius, σ, 2.5 times smaller than the target radius in each case. An example of such a calculation for iron is shown in Fig. 1 for a target radius of 7.5 mm, a beam rms radius of 3 mm and a 24 GeV proton pulse of 16×10^{12} protons. Table 2 lists maximum energy density values for a range of radii. Once the maximum value ε_{max} of the energy density (per unit mass) is found from these calculations for each case, we calculate the corresponding maximum compression P_{max} for each material:

$$P_{max} = 3 \times \varepsilon_{max} \times B \times \alpha / c_v$$

where B is the bulk modulus, α the linear expansion coefficient, and c_v the specific heat at constant volume. The factor 3 is, for an isotropic material, the ratio between volumetric and linear relative expansions. These stress values are then appropriately scaled for the 1 MW and the 4 MW options of the Muon Collider/ Neutrino Factory project [1, 2] the first of which calls for 15 pulse per second with 17.3×10^{12} protons per pulse, with both these numbers doubled for the second one.

* PT@BNL.GOV

0-7803-7738-9/03/$17.00 © 2003 IEEE

Table 1. Mechanical and thermal characteristics.

	Density	Linear Exp. Coeff.	Young Modulus	Bulk Modu-lus	Poisson Ratio	Specific Heat @ constant pressure	Thermal Conducti-vity	Yield Stren-gth	Fatigue Endu-rance Limit
Symbol	ρ	α	Y	B	μ	C_P	λ	$\sigma_{0.2}$	σ_{-1}
Unit	g/cm^3	10^{-6} / ^{0}K	G Pa	G Pa		J/(g ^{0}K)	W/(m ^{0}K)	M Pa	M Pa
Iron	7.87	12.5	205	171	0.30	0.478	80	170	~85
Inconel 718	8.19	13.1	200	158	0.29	0.435	11.2	1034	586
VascoMax C-350	8.08	15.0	200	167	0.30	0.450	25.2	2242	758
Super Invar	8.15	0.63	144	88.9	0.23	0.515	10.5	276	~138

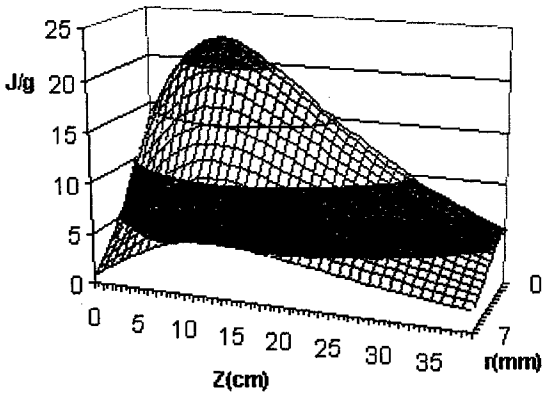


Fig. 1 Three-dimensional view of energy deposition MARS values for a 3 mm rms radius 24 GeV, 16×10^{12} proton beam pulse on a 7.5 mm radius iron target.

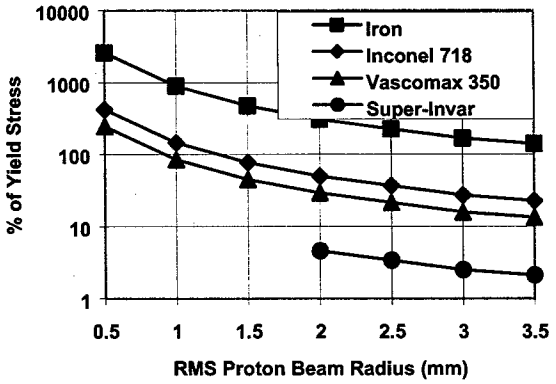


Fig. 2 Maximum initial stress as % of yield stress for the 24 GeV, 17.3×10^{12} proton beam pulses required for the 1 MW option.

In Figs. 2 and 3, we apply our criterion to both options of the Muon Collider/Neutrino Factory proposal [1, 2] by plotting these maximum stresses as percentages of the respective yield stresses for the different materials and for

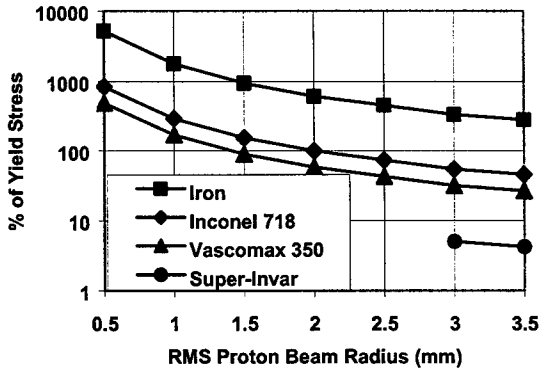


Fig. 3 Maximum initial stress as % of yield stress for the 24 GeV, 34.7×10^{12} proton beam pulses required for the 4 MW option.

a range of rms beam radii, with target radii 2.5 times larger. We see, for example, that for Vascomax 350 our criterion wouldn't be exceeded even for the 4 MW option down to a ~4 mm radius target which is smaller than envisaged. Super-Invar, while being further from reaching the yield stress is limited to larger radii due to the fact that its low expansion coefficient characteristic disappears at temperatures higher than ~120 °C. Also, results from radiation damage studies, reported elsewhere in these proceedings [5], indicate that Super-Invar may not be an appropriate choice.

A somewhat more stringent criterion for estimating the resiliency of these materials is to compare the maximum initial stresses to the fatigue limit instead of the yield stress. In that case the results for Vascomax 350 and for Inconel 718 become similar, and indicate that target radii equal or larger than 4.5 mm and than 7.5 mm would be viable for the 1 MW and the 4 MW option respectively. Using fatigue limits is probably overly conservative since these limits, which are specified at low repetition rates, are known to increase substantially with frequency. We also see that iron or other alloys much weaker than the ones considered here would be inadequate even for the 1 MW option using either criterion.

Table 2. Maximum energy densities deposited by 16×10^{12} 24 GeV proton beam pulses in iron targets. Values for the other materials considered here will be nearly identical.

Proton beam rms radius [mm]	.5	1	1.5	2	2.5	3	3.5
Target radius [mm]	1.25	2.5	3.75	5	6.25	7.5	8.75
Maximum energy density [J/g]	305	105	55.6	36.0	26.5	22.1	16.5

POSSIBLE IMPLEMENTATIONS

Finally we show some schematic representations of possible chain configurations for moving targets as alternatives to the previously proposed "Band Saw" system [6] or the use of a metallic cable [7].

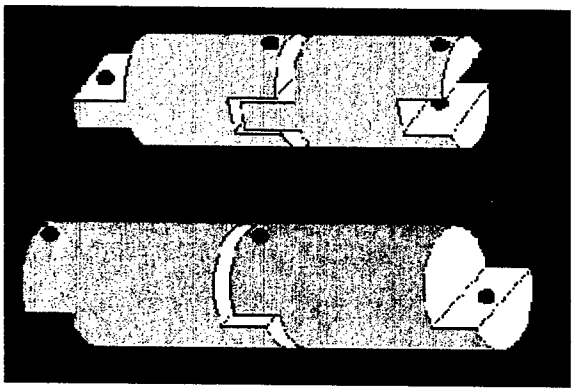


Fig. 4 Examples of metallic chain links configurations showing rather compact designs with large metal to gap volume ratios.

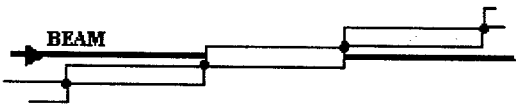


Fig. 5 Schematic of a chain with long links which, if surrounding hardware such as magnet coils permit, would allow each beam pulse to be coaxial with the target.

Cooling requirements dictate in each case the minimum velocity as well as the length for a chain of a given material and a given geometry. An estimated required velocity for a Vascomax C-350 chain for the 4 MW option would, for example, be 3 m/s and the total length would be ~35 m to transfer the power deposited by the beam to a 20 °C cooling bath without exceeding an internal target temperature of 300 °C and thus largely preserving the strength of the material.

DISCUSSION AND CONCLUSIONS

We conclude that solid moving metallic targets with very large tensile strength are viable candidates for a 1 MW and even a 4 MW Muon Collider/Neutrino Factory system and should therefore also be considered for other multi megawatt high energy proposals. It was also shown that more conventional solids such as iron can not be expected to work.

The choice between Vascomax C350 and Inconel 718 (or perhaps Inconel 750) may be influenced by the fact that Inconel isn't ferromagnetic and will therefore not be subjected to the rather large forces Vascomax chains will experience when entering and exiting a high solenoidal field. A disadvantage of Inconel is its low thermal conductivity which makes cooling slower and will thus require longer chains. It may be possible to improve this situation by providing cooling channels through the chain links.

The present stress and temperature estimates are thought to be conservative since no credit was taken for the advantageous frequency dependence of fatigue tolerance, nor for the possibility of using non-Gaussian beam profiles to reduce the peak energy density if necessary. Uncertainties about the survival of high-temperature stationary carbon targets and about the possibility of rapidly clearing large quantities of dispersed mercury for liquid jet targets [8] makes these moving solid targets a safer choice.

REFERENCES

[1] N. Holtkamp and D. Finley, eds., A Feasibility Study of a Neutrino Source Based on a Muon Storage Ring, Fermilab-Pub-00/108-E (2000), http://www.fnal.gov/projects/muon_collider/nu-factory/nu-factory.html}.

[2] S. Ozaki, R. B. Palmer, M. S. Zisman, and J. Gallardo,Editors, Feasibility Study-II of a Muon-Based Neutrino Source, BNL-52623 (June 2001); http://www.cap.bnl.gov/mumu/studyii/FS2-report.html.

[3] H. G. Kirk, et.al. Target Studies with BNL E951 at the AGS, Proceedings of the 2001 Particle Accelerator Conference, Chicago, Il., March 2001, p.1535.

[4] N. V. Mokhov et.al., Fermilab-Conf-98/379LANL Report LA-UR-98-5716(1998); http://www-ap.fnal.gov/MARS/

[5] H. G. Kirk et.al., SUPER-INVAR AS A TARGET FOR A PULSED HIGH-INTENSITY PROTON BEAM}, Proceedings to this Conference, PAC03, Portland, OR., May 2003.

[6] B. J.King et.al. A Rotating Metal Band Target for Pion Production at Neutrino Factories and Muon Colliders, Proceedings of the 2001 Particle Accelerator Conference, Chicago, Il., March 2001, p.1532.

[7] R. B. Palmer, Private Communication.

[8] P. Thieberger, MUC note # 212: http://www-mucool.fnal.gov/mcnotes/public/pdf/muc0212

INJECTION ACCELERATION AND EXTRACTION OF HIGH INTENSITY PROTON BEAM FOR THE "NEUTRINO FACILITY" PROJECT AT BNL *

N. Tsoupas, J. Alessi, D. Barton, G. Ganetis, A. Jain, Y. Lee, I. Marneris, W. Meng, D. Raparia, T. Roser, A. Ruggiero, J. Tuozzolo, P. Wanderer, B. Weng , BNL, Upton, NY 11973 USA

Abstract

The proposed "neutrino-production" project[1,2] to be built at the Brookhaven National Laboratory (BNL) requires that the neutrino-production target be bombarded by a high intensity proton beam-pulse of ~$90x10^{12}$ protons of 28 GeV in energy and at a rate of 2.5 Hz, resulting in a 1 MW power of proton beam deposited on the target for the production of the neutrinos. In this paper we investigate the possibility of producing this high intensity proton beam, using as the main accelerator the Alternating Gradient Synchrotron (AGS) at the Brookhaven National Laboratory (BNL).

The following aspects of the project are reported in this paper: a) The beam injection into the AGS synchrotron of 1.2 GeV H^- beam produced by a super-conducting LINAC[3]; b) The effect of the eddy currents induced on the vacuum chamber of the circulating beam during the "ramping" of the main magnets of the AGS. c) The method of the beam extraction from the AGS and the optics of the 28 GeV beam extracted from the AGS.

1 H^- BEAM INJECTION INTO AGS

The AGS synchrotron was operating in early years [5] with protons being injected from a 200 MeV H^- beam produced by a LINAC. In this section we discuss the proposed injection into the AGS, of an H^- beam produced by a 1.2 GeV Supercoducting LINAC, (SC_Linac).

1.1 Layout of H- Injection region in AGS

Figure 1 is a schematic diagram of the accelerators system involved in the production of the 28 GeV proton beam. Namely the 200 MeVLinac, the SC_linac, and the AGS. The H^- injection region has been chosen to be the location of the B20 straight section of the AGS. A schematic diagram of the injection region is shown in Fig. 2. In this diagram the following components of the injection region are shown:

a) Three of the main magnets (B19,B20,C01) of the AGS.
b) The stripping foil, shown inside the magnet C01.
c) The closed beam orbits which is "locally-bumped" during the time period for H^- beam injection [2].
d) The closed orbit of the circulating proton-beam with no beam bumps (labeled as "Circulating p-beam" in Fig. 2)
e) The trajectory of the injected H^- beam. The direction of the injected H^- is defined by the coordinate point (x,x') shown in Fig. 2 [2]. The coordinate x is the distance from the center point of the straight section SS_B19 and x' is the angle between the direction of the central particle of the H^- beam and the direction of the straight SS_B19.
f)The trajectories of the H^- beam which is not stripped by the stripping foil. The trajectory of the partially stripped H^- beam (H^0) and the trajectories of the electrons (e) emanating from the stripping foil. All these particles must be collected downstream of the stripping foil into various "beam-dumps".

* Work Performed under Contract No. DE-AC02-98CH10886 with the U.S. Department of Energy.

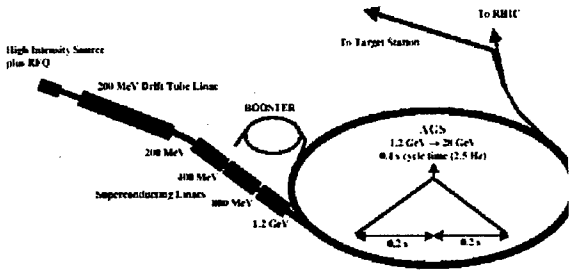


Figure 1. Schematic diagram of the accelerators for the "neutrino production".

1.2 Generating the "local beam" bumps for the H-beam injection.

In order to make the circulating proton beam collinear with the H^- injected beam at the injection point ("stripping foil" in Fig. 2), the circulating proton beam is "locally bumped" by using two horizontal "bump-magnets" [2].

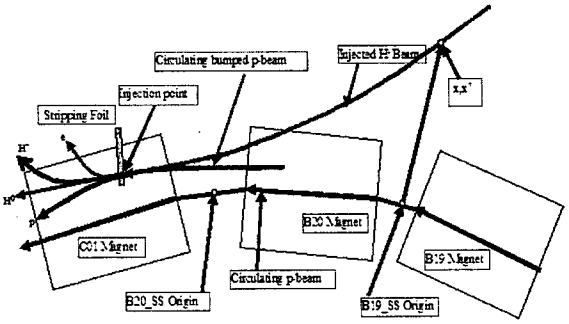


Figure 2. Schematic diagram of injection region in AGS.

Figure 3 plots the closed beam orbit in AGS with the "local bump" turned OFF (red line) and turned ON (blue line). Figure 4 shows a section of the bumped orbit of the beam at the location of the C01 main-magnet (see fig. 2) The maximum displacement of the closed orbit (~56 mm) occurs at the center of the 75 inches long C01 magnet.

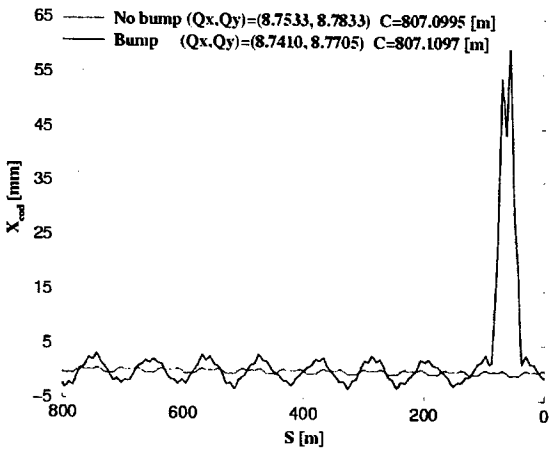


Figure 3: Closed orbits in the AGS. The red and blue curves corresponds to bumps OFF, and ON

Each of the other lines shown in Fig. 4, are trajectories of the H^- injected beam corresponding to a different (x,x') location and direction of the H^- injected beam. The values of (x x') that were used to generate the trajectories shown in figure 4 are shown also on the same figure 4. Each of the H^- trajectories is tangent to the "bumped-closed orbit" (black line) and this has been achieved by adjusting the initial conditions (x,x') of the H^- injected beam.

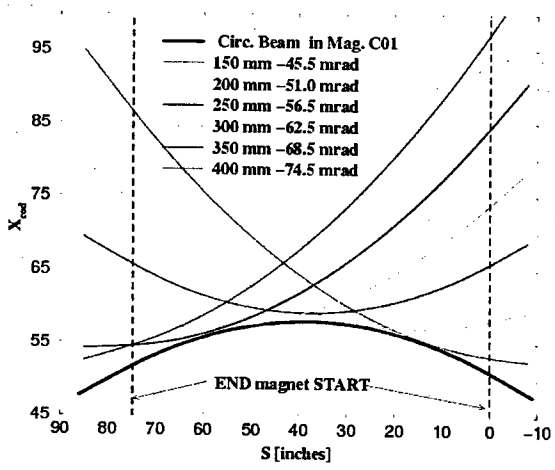


Figure 4. A section of the "Bumped Closed Orbit" (black line) inside the C01 magnet of AGS.

From all the possible H^- trajectories shown in Fig. 4, the H^- trajectory with (x,x')=(250 mm,-56.5 mrad) has been selected as the "injection trajectory" (blue line in Fig 4).
The various H^- trajectories shown in figure 4 have been calculated using the code AGS_BATE[4].
In addition to the "local-bump" of the closed orbit discussed above, a set of two fast time varying bumps (horizontal and vertical) of the closed orbit may also be superimposed to help optimize the "beam painting" of the AGS phase space.

1.3 Calculations of the beam parameters at the injection point of the H^- beam.

In order to minimize the emittance blow-up of the H^- injected beam into the AGS, the beam parameters of the injected H^- beam must match those of the circulating beam in AGS at the "injection point" (Fig. 2). In this write-up the 'injection-point" is the point where the H^- injected beam and the circulating beam intersect the plane of the stripping foil. The beam parameters of the circulating beam in AGS at the "injection point" have been calculated, for an injection beam energy of 1.2 GeV, using the computer code AGS_BATE[4]. The calculated beam parameters appear in Table 1. The proximity of the H^- injection line to the AGS main magnets requires that the fringe field of the AGS magnet is taken into account for the calculations of the H^- trajectories and the beam parameters at the injection points. In order make the matching calculations easier, we have selected another point "Matching point" (point x,x' in Fig. 2). The beam parameters at this point were calculated using the beam parameters at the "Injection_point" and the first order transfer Matrix (R) between matching and injection point. The R-matrix was calculated by tracing the H^- beam in the fringe field of the B20 and C01 main magnets of AGS.

TABLE 1: The beam parameters at the "Injection point" and "Matching point" (see text).

Loc.	β_x[m]	α_x	η_x[m]	η'_x	β_y[m]	α_y
INJ.	28.0	-1.00	-1.25	-0.05	8.00	0.43
MAT.	26.6	-1.32	-1.00	-0.10	16.10	1.75

1.4 Handling of the H^- H^0 and e^- beams.

The H^- injected beam will not be stripped totally of its electrons by the stripping foil, therefore the emerging beam from the foil will also consists of: H^- ions, H^0 particles and electrons (e). Except for the fully stripped H^- (protons) the rest of the particles must be "dumped" into a material which can absorb the deposited energy. The different rigidity of these three particles species, may require specially designed beam dumps[5].

2 ACCELARATION OF PROTONS

The proposed main-magnet cycle, of frequency 2.5 Hz. for the "neutrino production" operations, requires a time interval of ~90 msec between the beam injection and extraction . This fast ramp rate of the AGS main magnets will generate eddy currents in the following materials: a) the coils that power the magnet, b) the 1.9 mm thick vacuum chamber, and c) the iron of the main magnet. The eddy currents will generate Ohmic heating in the coils of the magnets, in the wall of the vacuum chamber, and in

the iron of the magnet which consists of laminations 3.2 mm thick and held together by two 2.5 cm thick plates at each end of the magnet. The eddy currents in the wall of the vacuum chamber will also generate time varying magnetic multipoles at the region of the circulating beam. The Ohmic effects on the materials mentioned above and the multipoles generated by the eddy currents have been studied theoretically and appear in ref.[2]. Figure 5 is a plot of the measured temperature in the wall of the vacuum chamber, when the coils of one of the AGS magnets is powered at a frequency of 2.5 Hz.

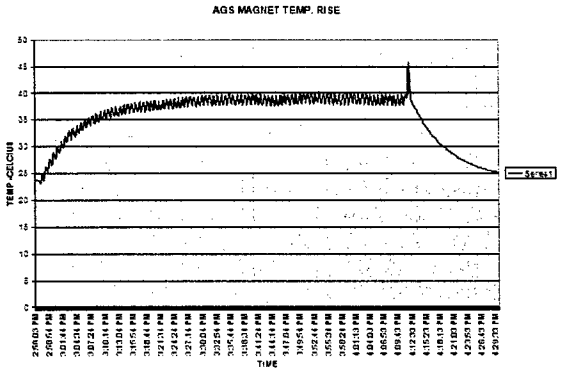


Figure 5. Temperature in the wall of the vacuum chamber as a function of time. The temperature levels at ~40 °C.

3 BEAM EXTRACTION FROM AGS

At present the AGS synchrotron is equipped with a Fast Beam Extraction (FEB) system[6] which is used to extract the circulating bunched beam in AGS to the AtR beam transfer line[7] for beam injection into RHIC[7] and to the g-2 experiment[6]. This FEB system will be used for the extraction of the 28 GeV high intensity proton beam which will irradiate the "neutrino production" target. A section of the AtR beam transfer line, which is used to transfer the extracted beam from AGS into the Relativistic Heavy Ion Collider (RHIC), will also be used to transport the 28 GeV proton beam to the "neutrino production" target [2]. Description of the FEB system has been written in ref. [4,6].

3.1 Layout of the AGS Fast Extracted Beam (FEB)

A schematic diagram of the Fast Extracted Beam (FEB) in AGS is shown in Fig. 6. During beam extraction the circulating beam is "locally bumped" at two locations along the AGS ring, one location is the fast extraction kicker (FK) and the other location is the septum magnet (H10) both shown in Fig. 6. The bunched beam is then extracted (dotted line in fig 6) upon the firing of the fast extraction kicker (FK) shown in Fig. 6. Finally the H10 septum magnet extracts the beam into the AtR transfer line.

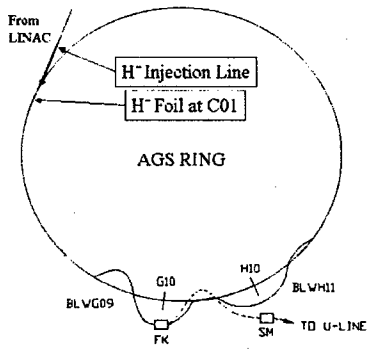


Figure 6. Schematic diagram of the Fast Extracted Beam in AGS.

3.2 Beam Parameters at the AGS Extraction Point

The beam transport line to the neutrino target is discussed in ref [2]. The beam parameters which are used in the optics of the transport line from the AGS to the neutrino production target have been calculated [4] and measured experimentally[7] and appear in Table 2.

TABLE 2: Theoretical (Theo.) and measured (Meas.) beam parameters at the "Extraction point" of the AGS.

Loc.	β_x m	α_x	η_x m	η'_x	β_y m	α_y
EXT. Theo.	37.5	-4.1	-1.5	-0.13	6.5	0.85
EXT. Meas.	36.7	-4.5			7.7	1.2

4 CONCLUSIONS

The results of the present study show that it is feasible to inject an H^- beam at 1.2 GeV into AGS at a frequency of 2.5 Hz, accelerate it to 28 GeV and extract it to the neutrino production target.

5 REFERENCES

[1] "Report on the BNL Neutrino Working Group" BNL-69395 Informal Report Oct. 2002
[2] BNL-71228 Informal Report
[3] A. Ruggiero et. al. These Proceedings
[4] N. Tsoupas, et. al. "Closed Orbit Calculations in AGS and Beam Parameters at Extraction" AD/RHIC/RD-75
[5] D.S. Barton "Charge Exchange Injection at the AGS" BNL Int. Rep. 32784 PAC, Santa Fe NM, March 3 1983
[6] N. Tsoupas et. al. "Fast Extracted Beam (FEB) for the g-2 Experiment" CA/AP/54
[7] N. Tsoupas et. al. "A computer code to measure the Beam Emittance and Beam Parameters of the AtR Line" C-A/AP/42

ADVANCEMENT OF THE RHIC BEAM ABORT KICKER SYSTEM *

W. Zhang, L. Ahrens, J. Mi, B. Oerter, J. Sandberg, D. Warburton
Brookhaven National Laboratory, Upton, NY 11973-5000

Abstract

As one of the most critical system for RHIC operation, the beam abort kicker system has to be highly available, reliable, and stable for the entire operating range. Along with the RHIC commission and operation, consistent efforts have been spend to cope with immediate issues as well as inherited design issues. Major design changes have been implemented to achieve the higher operating voltage, longer high voltage hold-off time, fast re-triggering and redundant triggering, and improved system protection, etc. Recent system test has demonstrated for the first time that both blue ring and yellow ring beam abort systems have achieved more than 24 hours hold off time at desired operating voltage. In this paper, we report on the system status and improvements.

INTRODUCTION

Each RHIC Beam Abort System has five high voltage modulators located inside tunnel directly connected to their corresponding magnet sections. There are two identical systems, one for each of the RHIC Blue and Yellow Ring. The kicker system charging voltage tracks the beam energy during beam injection, acceleration, and storage. Its operation range is from 4 kV to 27 kV. At top beam energy, a pulsed current of 18 kA per module is required to clear the circulating beams from the superconducting ring. The charging voltage is about 27 kV for this pulsed output current level. During beam storage, all capacitor banks of the high voltage modulators will maintain at commanded voltage level for up to ten hours until being discharged.

The discharging event is usually a normal beam abort at the end of store, or an urgent request due to any ring system pulled beam permit. Along with the effort to increase instantaneous and integrated beam luminosity, the improvement and advancement of the existing modulator systems has been continuing.

In operation, if one of the thyratrons prematurely conducts, the beam will be lost around the ring. With high energy and high intensity beam, this beam loss can quench the superconducting magnet and damage valuable and sophisticate detectors used by RHIC experiment. Like many other complicated issues, multiple factors contributed to the RHIC Abort Kicker instability. Besides the known high voltage problems there are other phenomena that seem to be related to the beam energy, beam intensity, beam loss level, and possibly beam coupling, etc. With engineering design and construction issues and physics issues tangled together, the analysis of a particular event is often inconclusive. The first step is to solve inherited engineering issues, such as high voltage break down, thyratron reverse arcing, and to build a fast re-trigger system to reduce beam spreading in event of premature discharge.

* Work performed under Contract Number DE-AC02-98CH10886 with the auspices of the US Department of Energy.

HIGH VOLTAGE HOLD-OFF IMPROVEMENT

The high voltage modulator of the RHIC Beam Abort Kicker consists of a Pulse-Forming-Network in series with a thyratron switch. Each capacitor bank has a capacitance of 8.3 μF; it stores 3kJ of energy at 27 kV. Its high voltage section had a history of arcing but difficult to locate. Usually, a corona discharge would trigger the thyratron to discharge the PFN. Occasionally, a very loud sparking noise can be heard.

A series of test was performed on the prototype modulator to identify problem area. Eventually, a large conductor plate made of sharp copper sheet and several insulators with metallic inserts, hiding behind an aluminum extrusion for structure support and front panel mounting, were found to be the main problem. They were improperly designed and constructed. The removed conductor plate was badly discolored and showed clear corona marks and arcing signs along its edges. It was located right beneath the thyratron anode connection, and its corona discharge current can easily set off the thyratron. The removed insulating material and high voltage standoffs were found to have had internal discharges due to closely spaced metallic inserts from end to end. It was necessary to redesign the conductor plate and high voltage standoffs that can fit into the existing place and to eliminate the corona discharges for higher voltage hold-off.

After design modification, the prototype unit voltage hold off level was largely improved. It was DC tested at 30 kV and 35 kV for eight hours continuously for several days. All ten high voltage modulators in the RHIC ring were modified accordingly to gain higher voltage hold-offs. The RHIC Beam Abort Kicker high voltage modulators was tested for high voltage DC hold-off at desired operating reference voltage of 27kV for more than 36 hours continuously at Yellow Ring, and for more than 60 hours continuously at the Blue Ring. The DC tests were successful, and no acing or corona discharges were observed during these tests.

FAST RE-TRIGGER SYSTEM

A temporary fast re-trigger system using kicker output current read-back signals through a multi-channel RF combiner to re-trigger the trigger and delay generator was adopted for a quick fix during 2001-2002 operation. This has a delay of 2.5 μs between the first and rest channels

0-7803-7738-9/03/$17.00 © 2003 IEEE

due to transmission time of lengthy signal and trigger cables between the service building and the modulators located in the ring. A re-trigger system with less delay and wider response range was designed and implemented later during 2001-2002 operation. However, the partial beam loss was still big enough to cause experimenters concern for the detectors.

Prior to the 2003 operation, the re-trigger system together with the redundant high voltage trigger generators and power supply were moved into ring to shorter cable length caused delays. This helps reducing partial beam loss to an acceptable level to the experiments. However, the semiconductor devices used in the present version is not intended for application in the radiation area, and a new design with better noise immunity and radiation hardened is underway.

SWITCH EVALUATION

The hollow-anode thyratrons are used as main switch in the RHIC Beam Abort Kicker modulators. Two different models, CX1575C and CX3575C, are being used in operation. To reverse conduct several kilo-Amperes of current for 30 μS requires a large amount of plasma, which well exceeds the capability of any hollow anode thyratrons. The thyratrons can be damaged due to reverse arcing, and their degradation of high voltage hold-off has been reported [1] [2]. Each year, several thyratrons have to be replaced. Some of them can be reconditioned and some are permanently damaged. CX 1575C was the version used in the original design, and the CX3575C is a larger version of CX1575C with higher voltage and current capability. It performed better than CX1575C in the test stand during evaluation [2]. Therefore, all the thyratrons in the Yellow Ring system were changed to CX3575C during 2002 operation. However, this change did not stop the misfire situation of the Yellow Beam Abort System, and two CX3575C had to be replaced soon after their installation.

Many attempts were made to stabilize the thyratrons in operation. The reservoir voltages of several thyratrons have to be reduced to lower the gas pressures in hope to lessen their sensitivities to beam operation. Although reverse arcing is a damaging factor to thyratron, but this is usually a gradual degradation of the voltage hold-off capability. The damage patterns from recently replaced thyratrons suggest the damage induced by the misfire without sufficient plasma ionization ruins thyratron much faster and drastic than under normal operation condition. The Blue Ring Beam Abort Kicker System has a much lower rate of misfiring, and the thyratrons are lasting much longer.

The premature discharge problem during this run has some association to the re-triggering system moved into the ring. The output current read-back cables bring the beam signal and other noises into the re-trigger system inputs. The large amplitudes of noises and beam signal can cause trigger misbehavior or induce output oscillation. Several modifications were made to improve its noise susceptibility, and filters were added to the thyratron grids inside high voltage modulators.

To further improve the switch performance, a new gas switch HX3002 developed by E2V has been recommended as a possible candidate for RHIC Beam Abort Kicker application. This switch is capable of high reverse current conduction. It is designed for low repetition rate, high-energy pulser applications, such as crowbar switch [3]. Figure 1 shows both CX1575C thyratron and HX3002 gas switch.

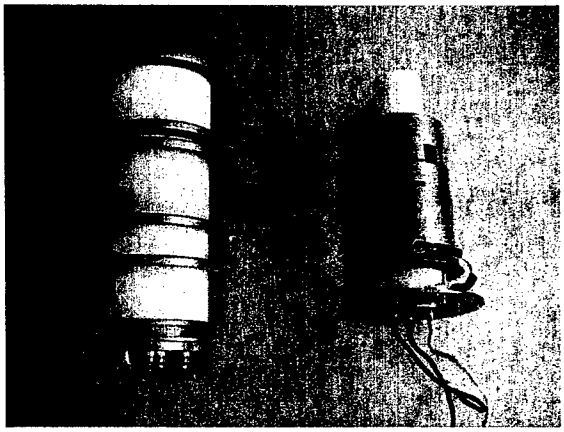


Figure 1: A CX1575C thyratron and a HX3002 gas switch

The HX3002 gas switch is rated for 38 kV, 20 kA peak forward conduction. Its reverse current capability was factory tested to 17 kA. The RHIC Beam Abort Kicker operation range is from 4 kV to 27 kV. The required output current at 27kV is about 18kA. We tested the HX3002 with a low energy pulser from 5kV to 35 kV, with 3500 pulses, and hi-potted it at 38 kV for more than 20 hours after the pulse test. The full energy pulse test in the RHIC Beam Abort prototype module was performed up to 30 kV, with 5kV increments, for about 2000 pulses. At 30 kV, the current reached 21.69 kA peak. The waveform obtained from this switch tube is identical to the one with thyratron. A single-shot L-C oscillation test was done at 30 kV level, the current swing between +/- 14 kA, as shown in figure 2. Again, no damage or degradation was observed. This bi-direction capability is far superior to a thyratron.

It has been installed in one of the Yellow ring high voltage modulators recently to test under real operation environment. The Base mounting dimensions of hollow anode thyratron CX1575C, CX3575C, and HX3002 are identical. The HX3002 is slightly shorter than the thyratrons, therefore easy to fit in the thyratron mounting position. To reduce the chance of gas breakdown under high voltage, a double trigger pulsed ionization scheme is selected. In this method, no DC pre-ionization is provided, and is assumed to be less likely to self-conduct. A 30 Amperes current trigger is provided to drive the gas tube, and the anode delay time is around 0.7 μs. This current was found to saturate the existing high voltage isolation pulse transformer used for thyratron triggering,

and a coaxial trigger transformer made of high voltage cable and ferrite ring was constructed to replace it.

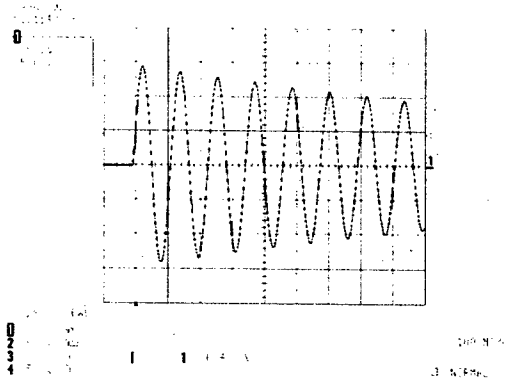


Figure 2: HX3002 oscillating current waveform at 30kV, +/- 14 kA operating condition.

CONCLUSION

Consistent performance improvement has been achieved in RHIC Beam Abort Kicker systems. The future investigation will focus on the following issues:

The Blue and Yellow Ring Beam Abort Kicker System are assumed to be identical, and no apparent difference has been found. But, the Blue Ring Beam Abort Kicker System is much more stable than the Yellow one.

The beam passing through the kicker aperture couples to the kicker magnet. The kicker magnet pulse current transformers show clear beam current signals. There is a signature that can be detected on all kicker current transformers prior to each misfire. The kicker will usually respond to it in a few hundred nanoseconds to a microsecond dependant on its magnitude. The threshold of the kicker response has been increased, but with higher beam energy and higher intensity the struggle continues. This signature is common to all units, and is therefore assumed to associate with structures such as beam chamber, grounding, beam property, etc. Figure 3 shows a typical misfire situation, where a sudden change in channel 4 signal followed by the kicker current rise. In this setup the channel 4 is set at very high gain to detect the event. The currents in two other channels, with lower scope gain, and a beam bunch pick up signal are also shown. The sweep time is about 5 μs. Since all beam loss monitors in the RHIC ring around sector 9 and downstream of it are integrator type, the response time is too slow to detect it. The time resolution of vacuum pressure change sampling is in millisecond domain, there is no fast detection available to diagnose transient event in vacuum. Meanwhile, the kicker itself is the device fast enough to detect the phenomenon. Twelve PIN diodes detectors are to be installed around the beam abort kickers to assist diagnostics.

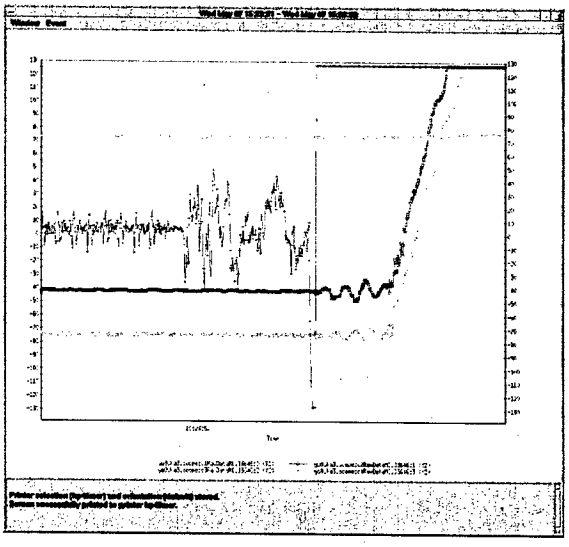


Figure 3: A typical premature discharge following a signature event detected by the pulse current transformer

To use a resonant charge power supply to charge up the capacitor banks in a few milliseconds upon receiving the beam abort command has been suggested. In this way, the main switch of the high voltage modulators will be unstressed most time during beam operation, and only under high voltage stress for a few milliseconds right before beam abort. This shall provide better operation stability and is being studied.

ACKNOWLEDGEMENT

We would like to thank Dr. H. Hahn of BNL, Dr. R. Sheldrake and Dr. C. Pirrie of E2V for their expert advice and to Mr. J. Addessi, Mr. K. Hartmann, Mr. S. Perlstein, and Mr. R. Zapasek for their technical support and contribution.

REFERENCE

[1] H. Hahn, A. Dunbar, C. I. Pai, R. T. Sanders, N. Tsoupas, J. E. Tuozzolo, " THE RHIC BEAM ABORT KICKER SYSTEM", IEEE Proceedings of The 1999 Particle Accelerator Conference, 1999, pp. 1100-1102.

[2] H. Hahn, "Test Results CX3575C #1460", BNL C-A internal communication, Nov. 1999.

[3] C. A. Pirrie, and C. A. Roberts, "A new Discharge Switch for Discharging high Energy Capacitor Banks", Digest of Technical papers of the Eleventh IEEE International Pulsed Power Conference, 1997, pp. 334-339.

FINAL RESULTS ON THE CERN PS ELECTROSTATIC SEPTA CONSOLIDATION PROGRAM

J. Borburgh, M. Hourican, A. Prost, CERN, Geneva, Switzerland

Abstract

The CERN PS electrostatic septum consolidation program is coming to completion after almost 4 years of development. The program was started to fulfil the increased requirements on vacuum performance and the need to reduce the time necessary for maintenance interventions. The new design of septum 31, used for the so-called 'continuous transfer' 5-turn extraction, and the related construction issues will be presented together with the operational experience gained during the PS 2002 run. In addition, the experience of two years of operation with the new generation septum 23, used for a resonant slow extraction, will be briefly discussed. The continued development undertaken since its installation in the PS ring in 2001 will also be described.

INTRODUCTION

A consolidation program was started for the electrostatic septa in the CERN PS accelerator 4 years ago. In 2001 redesigned and newly constructed for septum 23 was put into operation [1], and is used for a resonant slow extraction towards the East Hall experimental area [2]. Septum 31, constructed almost 20 years ago, is used for the so-called 'continuous transfer' (CT) 5-turn extraction towards the SPS. This septum used technology for its vacuum and displacement systems that is now outdated. It was decided to consolidate this high performance electrostatic deflector 31, analogue to the new design of septum 23, keeping in mind the high operational and maintenance constraints. Parallel to this effort, a development based on the existing anode design has checked the possibility to construct the septum 23 bakeable up to 100 °C.

OPERATIONAL EXPERIENCE

The new version of septum 23, installed in the PS ring in 2001, remained in the accelerator for a period of two years without any failures. Previously, the septum would have been removed from the machine after one year, stored for one year to allow radiation levels to decay and then been subjected to an overhaul procedure to restore its full operational capacity. With the new generation septa, the increased operational lifetime has now significantly reduced the maintenance required and hence the radiation exposure of personnel. The maintenance requirements have now been reduced to a 3-monthly oil change on the high-voltage feedthrough followed by a short period of reconditioning. The short HV cable between the cathode and the resistance is changed annually.

Due to the improved vacuum, as the pressure in the main vessel has now reached levels of approximately 2×10^{-9} mbar, with even 1.7×10^{-10} mbar recorded after operating the titanium sublimators, virtually no dark current (< 2 μA) has been recorded during the accelerator runs.

The new septum 31, used for continuous transfer, to the SPS [3], has been installed for the 2002 physics run. Throughout this run, a pressure of 8×10^{-9} mbar was normal and even pressures of 5.4×10^{-10} mbar were measured following sublimation, better than one order of magnitude compared with the previous generation of septa.

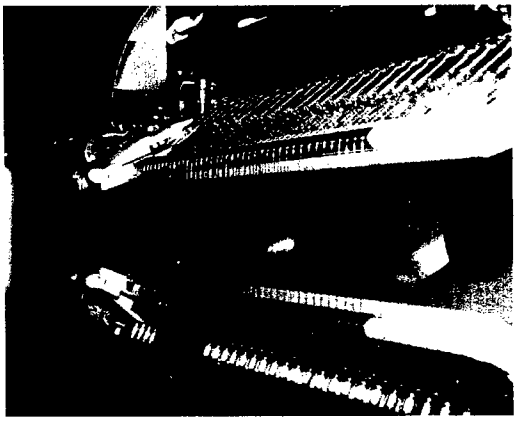


Figure 1: Septum 31 diffuser array at beam entry point of aluminium septum support

Due to the beam slicing nature of the extraction method, the septum foil is susceptible to overheating and warping from the direct impact of the beam. To reduce this effect, a diffuser is fitted to the upstream side of the septum. This diffuser consists of an array of tungsten-rhenium wires, of diameter 100 μm, spaced by 5 mm (see fig. 1), which creates a localised beam blow up and has a diluting effect in the region of the foil.

In the future, septum 31 might benefit from a new extraction method which will reduce even further the direct beam losses on the foil [4]. In the meantime the septum will continue to be replaced at yearly intervals.

Following installation in the accelerator the septa undergo a conditioning period when the voltage is increased progressively to a maximum of 250 kV for the large gap (30 mm) and 235 kV for the small gap (20 mm). The upper voltage limit is imposed by the condition of the main HV cables in the accelerator. The cable insulation properties have been deteriorated due to the effects of ageing and ionising radiation in the accelerator.

Prior to installation in the accelerator, the septa are conditioned in the test laboratory, at 280 kV for the large gap, and 250 kV for the small gap.

0-7803-7738-9/03/$17.00 © 2003 IEEE

NEW GENERATION SEPTUM 31

The septum 31 uses the same proven high voltage technology as septum 23, with the main parameters shown in table 1.

Table 1: Main parameters of septum 31

Cathode length	1850	mm
Operational gap width	26	mm
Theoretical beam deflection	1	mrad
Beam momentum	14	GeV/c
Operational voltage	178	kV
Septum foil thickness	0.1	mm

The aluminium 'C' shaped septum support holds a 100 μm thick molybdenum foil which is pre-tensioned to provide a flat surface. The molybdenum sheets are hand polished using an average grain size ceramic powder of between 2-3 μm, which results in a mirror finish. Mounted above the aluminium support is a hand polished deflector which provides protection against titanium sublimation on the active parts of the high voltage assembly (see fig. 2).

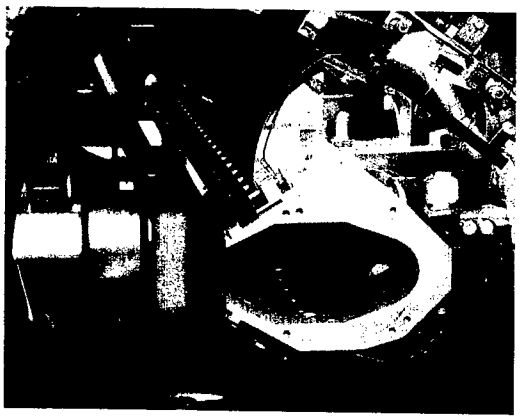


Figure 2: Septum prior to installation in PS

The high voltage feedthrough, rated at 300 kV, uses Shell Diala B oil for insulation purposes and is fitted with Peralumam PRE 30 (Peral) deflectors which are anodised in a sulphuric acid solution. A ceramic tube, connected to a wire-wound ceramic resistance, forms the main supporting structure for the feedthrough. The resistance decouples the cathode from the supply cable, to limit the energy discharged when sparking occurs between the cathode and septum.

The polished Peral cathode is anodised in a chromic acid solution which increases its voltage breakdown limit. The cathode is supported on ceramic rods fitted with Peral and stainless steel deflectors. The ceramic rods are cleaned by powder blasting, using ceramic powder of 100 μm average grain size. The deflectors are dry hand polished, mirror finished for the stainless steel type, whilst the Peral deflectors are polished and then anodised in a sulphuric solution.

The positioning systems for septum 31, being of a similar modular nature to septum 23, allow for precise movements in the radial and angular directions for the septum, and radial displacement for the cathode. The radial positioning system provides a resolution of 0.1 mm, with a 0.01 mrad resolution in the angular system. The supporting mechanical bearings for septum 23 are installed in the vacuum tank, but for septum 31 they have been externally mounted, to further improve the vacuum. The vacuum tank is UHV compatible, and equipped with "Wheeler" type flanges at each end. All vacuum joints are made of silver plated copper and are bakeable.

In the event of a failure, the high voltage feedthrough can be removed from the tank in situ, without the need to remove the complete tank from the accelerator, as was the case with the previous generation septa. This was facilitated by the addition of an intermediate flange on the vacuum tank.

To ensure RF impedance continuity, multi-contacts have been installed between the entry and exit points of the vacuum tank and the septum support. The contacts have been fitted to stainless steel plates to allow for rapid dismantling, thus reducing radiation exposure of personnel, see figure 3. The addition of the improved contact array has successfully eliminated parasitic resonances which were found on the previous generations of septa. The septum support is equipped with a slot, allowing insertion of a beam pick-up. This slot was found to be generating two major resonances. The slot has now been fitted with a cover with RF spring contacts, successfully eliminating the dangerous resonances.

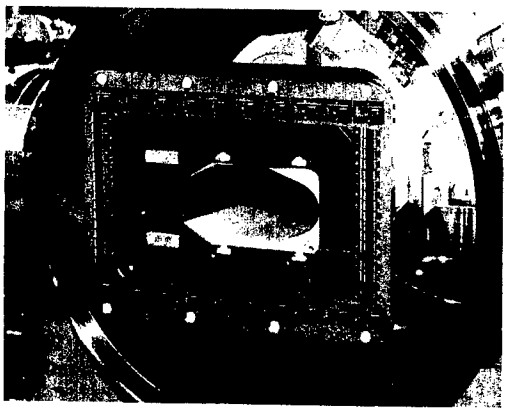


Figure 3: RF multi-contacts for impedance continuity

SEPTUM 23 BAKEABLE SUPPORT

Investigations were carried out to assess the suitability of the aluminium septum support as a bakeable system, to achieve even better vacuum levels. The main problem is thermal expansion of the complete tensioned assembly during bakeout, resulting in warping of the molybdenum foil. Due to the difference in thermal expansion

coefficients between aluminium, stainless steel and molybdenum, the resulting stress levels in the sheet exceed the elastic limit of the material. During cooling the tension is reduced and the sheet adopts a corrugated profile. To reduce these thermal effects, the tensioner was rebuilt using titanium and stainless steel and the original stainless steel rods were replaced by molybdenum rods. Slits have been chemically etched into the molybdenum foil to reduce the effect of differential expansion. Figure 4 shows a cross-section of the bakeable septum support.

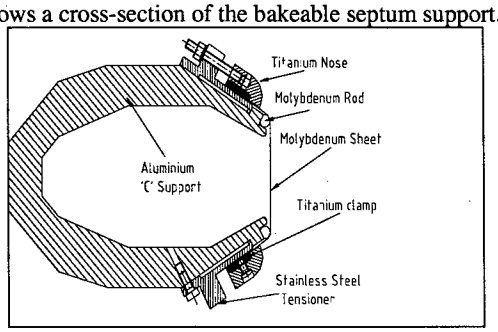


Figure 4: Cross-section of bakeable septum

A finite element analysis of the electric field was carried out and the results show that although the good field region is more uniform it is reduced in the vertical direction to 40 mm compared to 42 mm in the operational septum, see figure 5.

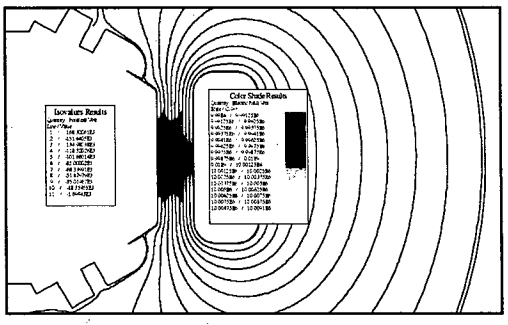


Figure 5: Electric field of bakeable septum

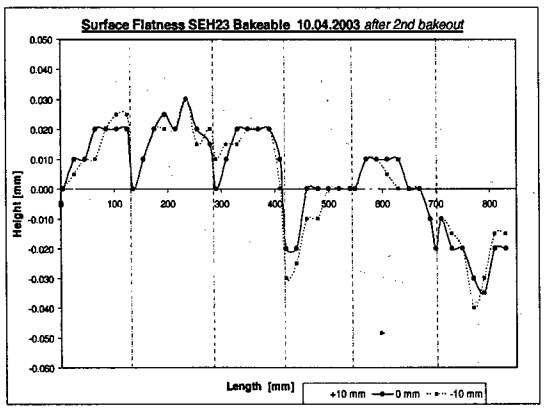


Figure 6: Surface flatness after 2nd bakeout at 100 °C

The prototype septum was assembled and underwent two bakeout cycles at 100 °C, each followed by venting with nitrogen and verification of the condition of the foil. It was found that after the second bakeout cycle, the foil retained its tension and the flatness of the sheet over the entire length of the septum remained well within the nominal limit of 100 μm (see fig. 6). High voltage testing is currently underway to verify the geometry of the titanium nose parts (see fig. 4), which have been installed closer to the foil in order to mask the slits from the cathode.

FUTURE DEVELOPMENTS

Further development of a bakeable septum 23 will be postponed due to manpower shortage. The next step should be the continuation of the development of a stainless steel septum support. The use of Invar may be considered due to its extremely low coefficient of thermal expansion. A 2.3 m bakeable support for septum 31 will also be studied at a later stage.

The adoption of 3M Fluorinert as a replacement insulation medium for the high voltage feedthrough is also planned. This would comprise a permanent system of regeneration of the liquid and thus reduce the possibilities of breakdowns, eliminate the need for the current 3-monthly oil change and reduce the risk of contamination of the PS vacuum system in case of a feedthrough failure.

A suitable high voltage cable to replace the existing type in use in the PS is presently being sought.

CONCLUSIONS

Through the application of advancing technology the vacuum levels in the septa tanks were improved by more than one order of magnitude. The performance and reliability of septum 23 has permitted its operational lifetime to be increased from one to two years. This results in lower radiation exposure for the personnel and extended cooling time for the reserve septum. There have been no high voltage breakdowns registered, the dark current is negligible and the de-conditioning effect has become noticeably lower.

The adoption of standard modular displacement systems reduces the necessary amount of reserves to be kept in stock. All electromagnetic septa in the PS are equipped with similar displacement systems, thus providing for easy interchange between septa.

REFERENCES

[1] J. Borburgh, M. Hourican, M. Thivent, "Consolidation project of the electrostatic septa in the CERN PS ring", Proc. PAC'01, Chicago, June 2001.

[2] Ch. Steinbach, H. Stucki, M. Thivent, "The new slow extraction system of the CERN PS", Proc. PAC'93, Washington, May 1993.

[3] A. Pace et J. Cl. Cendre, Mise à jour: M. Gourber-Pace, (Feb. 2000). "Le Transfert Continu pour la Physique à Cible Fixe du SPS"CERN PS/OP note 97-39.

[4] R. Cappi, M. Giovannozzi, "Novel Method for Multi-turn Extraction", Phys. Rev. Lett. 88 (2002) 104801.

LHC BEAM DUMPING SYSTEM: EXTRACTION CHANNEL LAYOUT AND ACCEPTANCE

B.Goddard, M.Gyr, J.Uythoven, R.Veness, W.Weterings, CERN, Geneva, Switzerland

Abstract

The LHC beam dumping system must safely abort the LHC beams under all conditions, including those resulting from abnormal behaviour of machine elements or subsystems of the beam dumping system itself. The extraction channels must provide sufficient aperture both for the circulating and extracted beams, over the whole energy range and under various beam parameters. These requirements impose tight constraints on the tolerances of various extraction channel components, and also on the allowed range of beam positions in the region of these components. Operation of the beam dumping system under various fault states has been considered, and the resulting apertures calculated. After describing briefly the beam dumping system and the extraction channel geometry, the various assumptions made in the analysis are presented, before deriving tolerance limits for the relevant equipment and beam parameters.

INTRODUCTION

The beam dumping system is a vital element of the LHC, where 340 MJ of energy is contained in each circulating beam and where a single nominal intensity high energy bunch could melt or damage a metallic surface [1]. The concept of the beam dumping system is to fast-extract the beam in a loss-free way from each ring of the collider and to transport it to an external dump, positioned sufficiently far away to allow for appropriate beam dilution. This requires a particle-free gap in the circulating beam for the rise time of the extraction kicker.

The layout of the system under construction in straight section 6 of the LHC is shown in Figure 1. It comprises for each ring 15 extraction kicker magnets MKD (3 μs rise time, 0.27 mrad horizontal deflection), 15 steel septum magnets MSD (2.4 mrad vertical deflection) and 10 modules of dilution kicker magnets MKB. The beam dump proper, situated in a cavern 750 m from the centre of the septum magnets, comprises the TDE core and shielding (total weight about 1000 tons).

BEAM PARAMETERS

The beam dumping system must be able to accept LHC beams with nominal parameters up to ultimate intensity (e.g. during a planned abort at the end of a physics run) and also beams with off-normal parameters (e.g. as arising from an equipment failure or beam instability), in addition to variations imposed by optical effects (e.g. beta-beating, tuning range). The beam characteristics are well known for the LHC nominal beam; however, the characteristics of the planned commissioning and early years beams are also taken into account, as for completeness is the ultimate beam. The relevant worst-case beam characteristics (LHC V6.4) to be expected at point 6 have been presented [2] and are given in table 1.

Table 1. Maximum assumed LHC beam characteristics.

Beam	Max ε_n 450 GeV μm	Max ε_n 7 TeV μm	Total Orbit mm	Beta variation %	Total p+ 10^{14}
Commission	6.0	12.0	±4	42	0.3
Early Years	6.0	12.0	±4	42	0.8
Nominal	7.5	15.0	±4	42	3.1
Ultimate	7.5	15.0	±4	42	5.3

FAILURE MODES

The beam dumping system acts at the request of the machine protection system, which collects the status and messages from all critical machine subsystems. Although great effort is undertaken in maximising the reliability of the dumping system (e.g., appropriate margins, redundancy, autonomy, failure tolerant signal transmission, and by monitoring of all vital parameters), failures cannot be totally excluded [3].

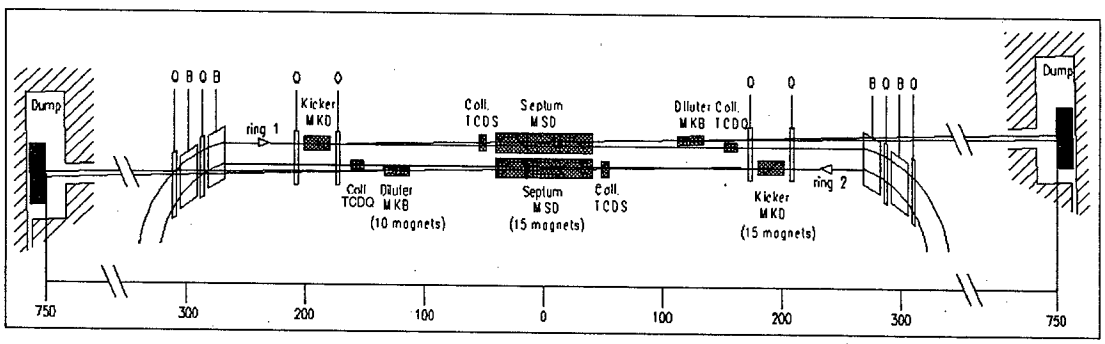


Figure 1. Schematic layout of beam dumping system elements.

0-7803-7738-9/03/$17.00 © 2003 IEEE

One serious failure is an unsynchronised firing of the extraction kickers [4], which would damage the steel septum and vacuum chamber. Protective elements (TCDS and TCDQ), are therefore placed in front of the septum and the Q4 quadrupole downstream of the septum [5].

The other relevant internal beam dumping system failure mode is the 'missing module' case, where only 14 out of the 15 MKD modules trigger.

The effects of off-normal operating conditions arising from the LHC machine proper are grouped together and treated under local orbit excursions and emittance growth.

APERTURE FOR CIRCULATING BEAM

From [6], for the normal machine the specification to be met is $n_1 \geq 7.0$. For this analysis an extra factor 1.17 is added to the β for variations in the LHC tune.

At TCDS

The TCDS is positioned as far in as possible to the circulating beam axis. Assuming mechanical and alignment tolerances $\delta_{xT} = \pm 1$mm for the TCDS, with a maximum orbit of +2 mm, the curve of available aperture versus orbit is shown in Figure 2.

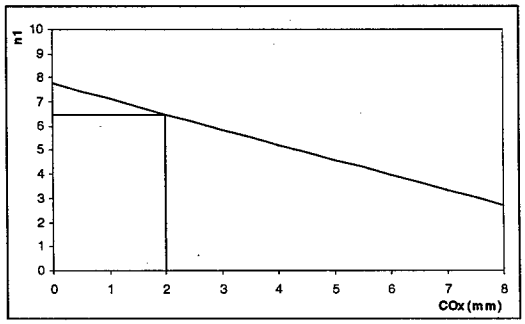


Figure 2. Aperture at TCDS for circulating beam as a function of local beam position.

At MSDC vacuum chamber

The outside position of the chamber is +28.2mm (-20.2 inside), which provides a fairly comfortable aperture for the circulating beam, where at an orbit excursion of +4 mm the aperture remains above n1 = 6.5.

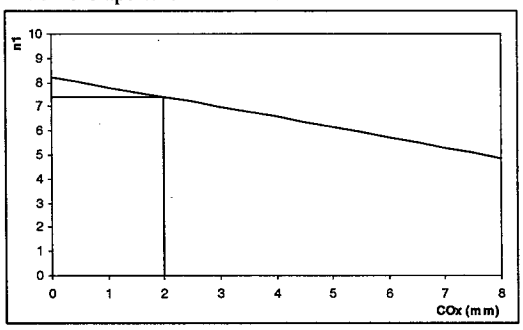


Figure 3. Circulating beam aperture at MSDC5 vacuum chamber as a function of local horizontal beam position.

APERTURE FOR EXTRACTED BEAM UNDER NORMAL CONDITIONS

The width of the MSD septum and the assumed closed orbit errors define the geometrical shape of the TCDS protection element. The total width of the MSDC septum and vacuum chambers (including tolerances) is 28.3 mm. The static closed orbit is assumed to be held to ±2 mm. For the aperture calculation the total overshoot of the MKD kicker waveform is taken to be 10% [7].

Nominal case - 15/15 MKD

The extracted beam is centred in the septum gap for the nominal case. The same kick is imposed from 450 GeV to 7 TeV beam energy. The available apertures as a function of orbit are shown in figures 4 and 5. Assuming that for 'loss free' extraction an aperture of 4 σ is sufficient at 450 GeV, and 6 σ at 7 TeV, the respective maximum orbit excursion should stay within about ±4.2 and ±7.5 mm.

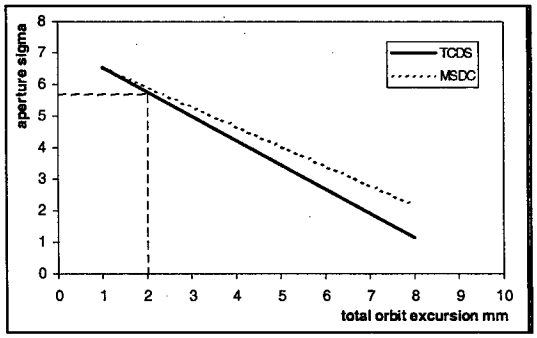


Figure 4. Aperture at 450 GeV for extracted beam as a function of the orbit in the nominal 15/15 MKD case.

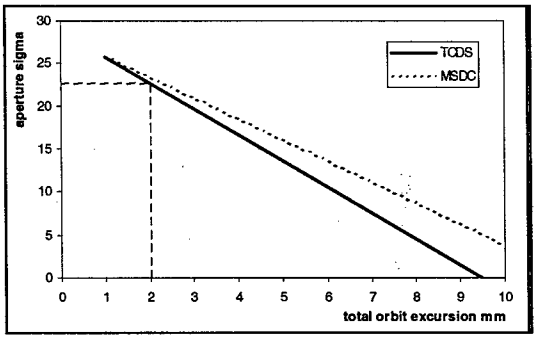


Figure 5. Aperture at 7 TeV for extracted beam as a function of the orbit in the nominal 15/15 MKD case.

Missing module case - 14/15 MKD

The worst missing MKD module is the MKD1; in this case the deflection at the TCDS is 91.96% of the total, and the beam approaches the TCDS. The available apertures at 450 GeV and 7 TeV as a function of orbit are shown in figures 6 and 7. Here, for even moderate orbit excursions, the TCDS will receive beam in the event of an MKD missing, with the attendant risk of quenches in downstream super-conducting magnets or TCDS damage.

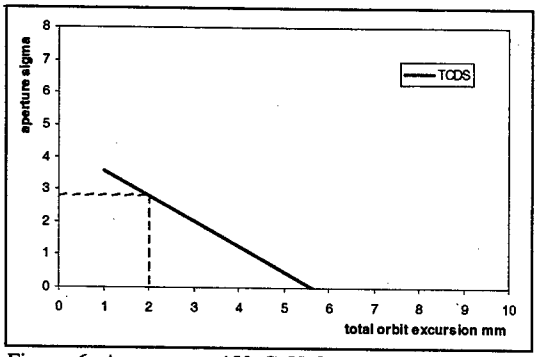


Figure 6. Aperture at 450 GeV for extracted beam as a function of the orbit in the 14/15 MKD case.

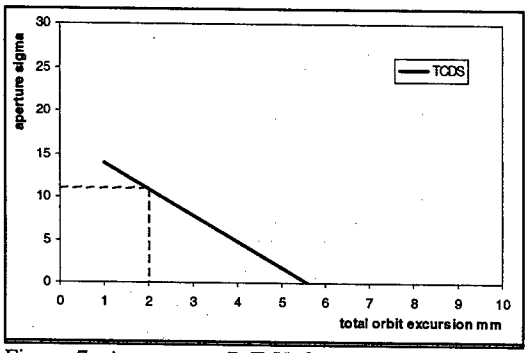


Figure 7. Aperture at 7 TeV for extracted beam as a function of the orbit in the 14/15 MKD case.

APERTURE FOR EXTRACTED BEAM FOR OFF-NORMAL LHC OPERATION

The dump channel must also accept off-normal LHC operating conditions, manifested as fast orbit excursions and/or an emittance increase. These events are certain to occur during the LHC lifetime, and dump actions are highly likely to be associated with unstable or off-normal beam conditions, so the possible range of parameters must not result in damage to the LHC, including the dumping system itself. Ideally these failures should also not result in any losses in the extraction channel.

TCDS damage limits

For the various parameters described in table 1, together with the nominal and 14/15 MKD case, the aperture of the dump channel was evaluated and the resulting impacting number of protons on the TCDS calculated and compared to the assumed damage limit. Full details can be found in [2]; the main results are:

- Orbit excursions of up to ±4 mm should be tolerable without damage, up to nominal intensities,
- Emittance increases of x2 / x4 are safe at 450GeV / 7TeV respectively, but may produce Q4 quenches at low energy for large orbit excursions,
- The 14/15 MKD case will produce losses on the TCDS and a quench of the Q4 magnet.

FURTHER SYSTEM IMPROVEMENTS

The scope for low-cost improvement is limited since the extraction channel design is essentially finished, tunnelling is completed and hardware construction well advanced. However, the possibility of an increase in the aperture of the MSDC magnets via a new vacuum chamber design is still being pursued.

CONSEQUENCES

The aperture of the dump channel is limited, especially for off-normal operating conditions of the dump system itself or of the LHC machine. The limits have been quantified at different energies and under various realistic failure scenarios. The following points should be retained:

1. Orbit control (feedback) will be needed to achieve sufficient aperture for the circulating beam of n1 = 6.5,
2. Operation during commissioning and 'early years' is not expected to be limited by the dump aperture,
3. For normal operation, with realistic failure cases, orbit excursions of up to ±4 mm should be tolerable without damage, up to nominal intensities,
4. Emittance increases of x2 / x4 are safe at 450GeV / 7TeV respectively, but may produce Q4 quenches at low energy for large orbit excursions,
5. The 14/15 MKD case will produce losses on the TCDS and Q4 quench.
6. Reliable interlocking at about ±4 mm of the local beam position in point 6 is absolutely necessary.

ACKNOWLEDGEMENTS

The work described in this paper has been carried out in close and productive collaboration with many colleagues involved in the LHC project. Particular thanks are due to E.Weisse, V.Mertens, J.M.Jimenez, M.Sans, R.Schmidt, J.B.Jeanneret, E.Vossenberg, J.Wenninger and N.Mokhov.

REFERENCES

[1] G.R. Stevenson, CERN/TIS-RP/IR/93-10.
[2] B.Goddard, Proc. XIIth Chamonix Workshop on LHC Performance, 2003.
[3] J.H. Dieperink *et al.*, LHC Project Report 113.
[4] R.Assmann *et al.*, LHC Project Note 293.
[5] A. Drozhdin, Fermilab Project Note FN-0724, 2002.
[6] J.B.Jeanneret, R.Ostojic, LHC Project Note 111.
[7] J.Uythoven, E.Vossenberg, private communication.

PERFORMANCE OF ANTIPROTON INJECTION AND EXTRACTION TRANSFER LINES OF THE RECYCLER RING AT FERMILAB

A. Marchionni, T.G. Anderson, G.W. Foster, C. Gattuso, M. Hu, D.E. Johnson, C.J. Johnstone, C. S. Mishra, A.R. Oleck, H. Piekarz, M. Syphers, M.J. Yang, FNAL, Batavia, IL 60510, USA

Abstract

The Recycler Ring, an 8 GeV antiproton accumulator, is being commissioned at Fermilab. Antiproton transfers in and out of the Recycler Ring take place through two transfer lines connecting the Recycler to the Main Injector. Transfer line layout and operation of beam transfers will be described. Particular attention has been paid to injection mismatch effects, in order to limit emittance growth during transfers. A considerable improvement has been achieved by removing vacuum windows, previously present in both transfer lines.

INTRODUCTION

The Recycler is a fixed 8 GeV kinetic energy antiproton storage ring [1], which makes use of permanent gradient and quadrupole magnets for the ring lattice. It is located in the Main Injector tunnel at a distance of 57" above the Main Injector ring and with the same basic cell geometry. Two transfer lines, MI-22 and MI-32, connect the Recycler to the Main Injector [2]. The MI-22 line is used to transfer antiprotons from the Main Injector into the Recycler, following a clockwise trajectory, and to extract protons from the Recycler into the Main Injector in the counterclockwise direction. Conversely the MI-32 line serves as antiproton extraction line from the Recycler into the Main Injector and as proton injection line into the Recycler for commissioning and tune-ups.

TRANSFER LINE LAYOUT

The MI-22 and MI-32 lines are positioned on either side of the MI 30 straight section in the Main Injector, where a single kicker at the 304 location is used for both transfer lines. Details on the positioning of the kickers and associated injection and extraction Lambertson magnets in both Main Injector and Recycler rings are summarized in Fig.1.

At extraction time the circulating beam is kicked horizontally by 1 mrad to enter the magnetic field region of the corresponding Lambertson magnet, which provides a 22 mrad vertical bend of the appropriate sign to initiate the transfer between the two rings. All the Lambertsons follow a same design (4 m long, 1.68 kG) which makes use of permanent magnet material [3]. Approximately an odd multiple of 90 degree phase advance is mantained between kickers and Lambertsons. The Main Injector Lambertsons are placed in the short (three half-cells) straight sections, while the Lambertson magnets in the Recycler fit easily even in the bend sections.

The distance between each kicker and the associated Lambertson magnet is of the order of 200 m. To reduce the amplitude of the orbit oscillation, induced by the kicker, between the kicker and the Lambertson, an oscillation of approximately half the amplitude and shifted by 180 degrees in phase is created with a time bump. This oscillation is referred to as a counterwave and

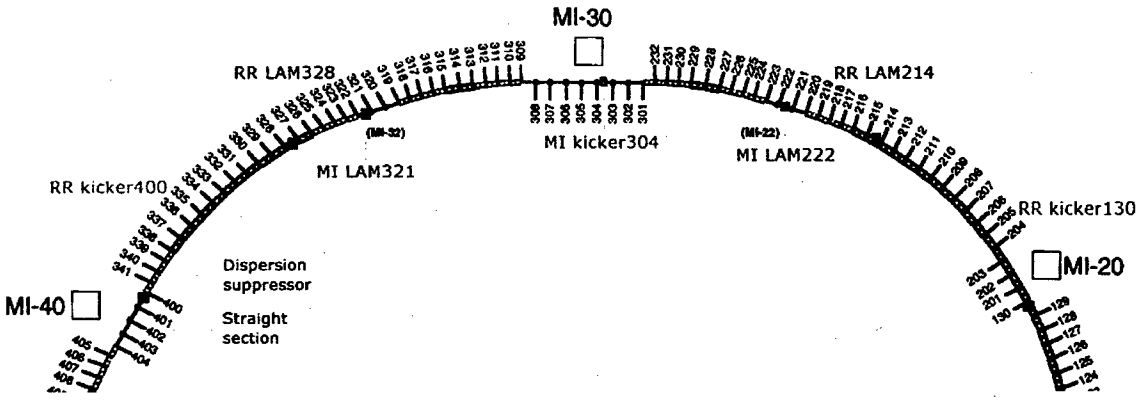


Figure 1: Sketch of locations of kickers and Lambertson magnets in Main Injector (MI) and Recycler (RR) rings. The MI-22 transfer line extends from MI LAM222 to RR LAM214 for approximately 8 half-cells, and the MI-32 line from MI LAM321 to RR LAM328 over about 7 half-cells.

Work supported by the U.S. Department of Energy under contract No. DE-AC02-76CH03000

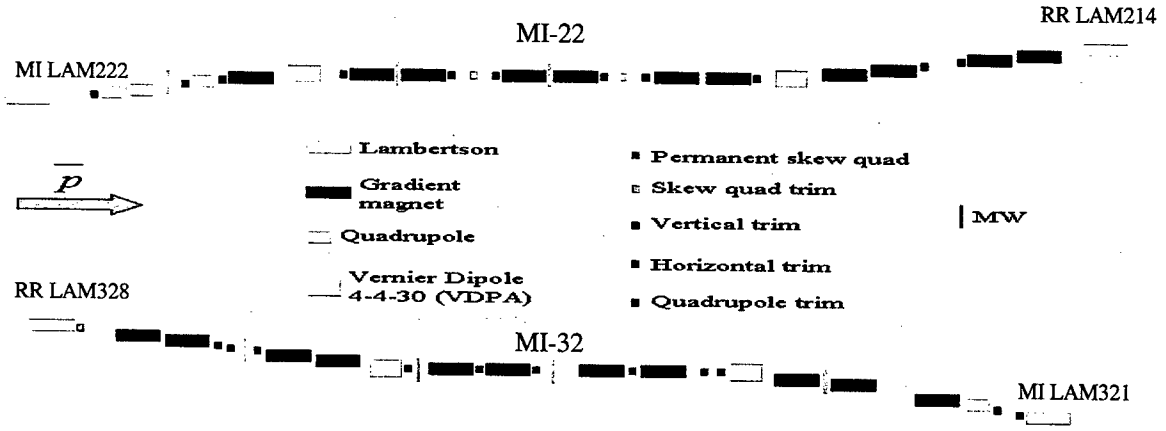


Figure 2: schematic of MI-22 and MI-32 transfer lines

intended to optimize the available horizontal aperture. The resulting orbits of circulating and injected/extracted beams have orbit excursions, opposite in sign, up to a maximum of about 25 mm.

Both MI-22 and MI-32 transfer lines match closely the lattice functions of the Recycler ring and make use of the same quadrupole and gradient permanent magnets of the ring. The use of the gradient magnets is required because the transfer lines for the most part are placed in an arc cell region. The detailed layout is shown in Fig. 2. In addition to the vertical bends provided by the injection and extraction Lambertsons, which are of equal strengths and opposite sign, two additional bends of the same strength and opposite sign are required. They are provided by electromagnets (named VDPA in Fig. 2), which are also used as safety critical devices.

BEAM TRANSFER OPERATION

Beam is transferred in and out of the Recycler in 2.5 MHz bunches. All beam transfer operations are driven by clock events. Hardware devices are pre-loaded with all the required settings for manipulations needed to inject or extract antiprotons (or protons for tune-ups). A specific set of clock events are generated to indicate to the hardware which operation to perform. The extraction process begins when the hardware components decode these clock events. Trim dipoles in both rings set the extraction/injection counterwaves just prior to the transfer time.

The transfer line devices generally run in DC mode as they only see single pass beam. Trim dipoles in the transfer lines are used to steer the beam onto the closed orbit of the downstream accelerator to minimize emittance dilution due to steering errors. An automated procedure, which uses a turn by turn beam position detector present in both Recycler and Main Injector rings, extracts position and phase of the injection oscillation and computes new settings of the trim dipoles in order to minimize dilution. Steering adjustments down to a quarter of a mm are routinely achieved. Powered quadrupoles were installed in each transfer line for aid in matching lattice functions between transfer lines and both accelerators. These are currently kept off.

Injection and extraction efficiencies larger than 95% are achievable for beams of about 10 π mm-mrad in 95% normalized transverse emittance and with 10^{-3} fractional momentum spread.

EMITTANCE DILUTION

During commissioning, beam transfers between Recycler and Main Injector have been showing transverse emittance dilution effects. Emittance dilution measurements were performed with protons injected into the Recycler through the MI-32 line and then transferred back into the Main Injector through the MI-22 line. The emittance of the proton beam was measured in the Main Injector before injection into the Recycler and just after extraction from the Recycler, using the same flying wire system installed in the Main Injector. Measurements showed a cumulative growth, after injection closure, of about 6 π mm-mrad, in 95% normalized transverse emittance, for both planes.

An emittance dilution of this size is unacceptable for antiproton operation. The expected 95% normalized transverse emittance of cool antiprotons from the Accumulator is about 10 π mm-mrad and that of cold antiprotons from the Recycler should be less than this. The cumulative emittance growth for each transfer, due to all sources, should be kept below 1 π mm-mrad.

There are four sources of emittance dilution during transfers that need to be considered [4]: betatron function and dispersion mismatch between the transfer line and the ring, steering error into the ring and scattering from vacuum windows, if present. In the following formulae we will always refer to 95% normalized transverse emittance.

To get an estimate of the magnitude of the expected dilution due to a betatron function mismatch,

$$\Delta\varepsilon_N = \left[\tfrac{1}{2}(\beta\gamma_0 + \beta_0\gamma - 2\alpha\alpha_0) - 1\right]\cdot\varepsilon_0,$$

we compare the design and measured Recycler lattice functions. For an initial 95% normalized emittance of 10 π mm-mrad, we get less than 1/2 π mm-mrad growth.

The dilution due to a dispersion mismatch,

$$\Delta\varepsilon_N = 3\pi(\gamma\beta)\frac{(\Delta D_{eq})^2}{\beta}(\sigma_p/p)^2,$$

does not depend on the initial emittance, but rather on the momentum spread, σ_p/p. Assuming a σ_p/p of 10^{-3} and a measured dispersion wave of about 0.5 meter, the growth is predicted to be less than 1/2 π mm-mrad.

Currently, we close the injection orbit onto the closed orbit to better than 1/4 mm, which produces negligible growth, given by

$$\Delta\varepsilon_N = 3\pi(\gamma\beta)(\Delta X_{eq})^2/\beta.$$

Vacuum windows were present in both transfer lines in order to protect the 10^{-10} Torr vacuum in the Recycler from the few 10^{-8} Torr vacuum in the Main Injector and transfer lines. Due to safety considerations, the Beryllium windows in the original design were replaced by 0.003" Titanium windows. They were positioned just upstream of the last gradient magnet before injection into the Recycler ring, at a location of maximum vertical betatron function, where β_{Vlatt}=50 m and β_{Hlatt}=15 m.

When an irreducible emittance growth was observed during beam transfers to and from the Recycler, the Titanium windows were reconsidered as a possible cause. Each vacuum window was computed to contribute to a 95% normalized emittance growth of [5]

$$\Delta\varepsilon_N = 3\pi(\gamma\beta)\beta_{latt}\vartheta_{rms}^2,$$

where θ_{rms} is the projected rms scattering angle due to multiple Coulomb scattering through the material. This gives a growth of 4.2 π mm-mrad in the vertical plane for each window, which explains most of the measured effect. The observed horizontal/vertical symmetry in emittance growth is likely due to betatron coupling in at least one of the rings or transfer lines.

It was decided to replace the vacuum windows with a differential vacuum pumping system, which was installed in the transfer lines during the January '03 shutdown [6]. This system has to deal with a gas load of about 5×10^{-6} Torr-l/s from the Main Injector side of the transfer lines and was designed to fit in an available free space extending over a length of about 15 m in the upper part of the transfer lines, close to the Recycler ring. Pumps are placed with significant lengths of beam pipe between them so that the resulting conductance between pumps is much less than the pumping speed of the pumps. The result is that a relatively small fraction of the gas load at each pump is allowed to flow to the next pump. Three 150 l/s ion pumps, spaced about 1.4 m apart, were installed in a 3 m long section of the transfer lines closest to the Main Injector. Moving towards the Recycler ring, as the gas load gets reduced, a 150 l/s titanium sublimation pump (TSP) was placed at about 7.3 m from the last ion pump. Two more TSPs, 88 l/s each, were placed 5.6 m further away, just upstream of the Recycler Lambertson. Next to each TSP small ion pumps of 30 l/s are mounted. Automatic gate valves protect the Recycler vacuum in the case of vacuum accidents in the Main Injector or transfer lines. The system has been proven to work reliably since installation, providing two orders of magnitude differential pressure, from 10^{-8} to 10^{-10} Torr.

Emittance growth measurements for the round trip of protons in the Main Injector were taken in this new configuration without vacuum windows. A substantial improvement is observed, as shown in Fig. 3. The residual growth is probably due to betatron function and dispersion mismatch, residual steering errors and kicker waveform defects.

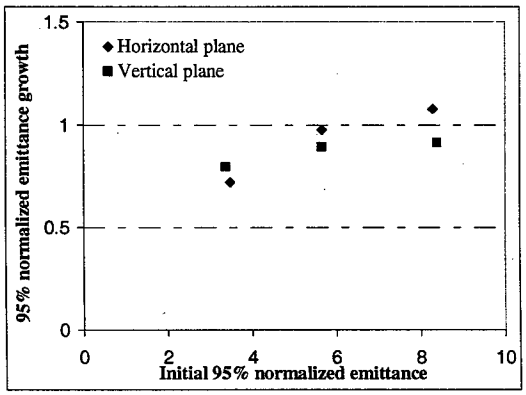


Figure 3: cumulative 95% normalized transverse emittance growth after vacuum windows were removed

REFERENCES

[1] G. Jackson, "The Fermilab Recycler Ring Technical Design Report", FERMILAB-TM-1991

[2] D. Johnson, "Revised Recycler pbar transfer lines", Main Injector note 161, December 1997.

[3] M.P. May et al., "The Design and Construction of the Permanent Magnet Lambertson for the Recycler Ring at Fermilab", Proceedings of PAC'97, Vancouver, Canada, 1997.

[4] M.J. Syphers, "Injection Mismatch and Phase Space Dilution", Fermilab note FN-458, June 1987.

[5] M.J. Syphers and C.J. Johnstone, "Vacuum windows in Recycler Transfer Lines", Main Injector note 286, Fermilab Beams-doc-375-v1, September 2002.

[6] T.G. Anderson, A.R. Oleck, H. Piekarz, "Main Injctor-Recycler windowless vacuum system". Report in preparation.

Proceedings of the 2003 Particle Accelerator Conference

INITIAL OPERATION OF THE FERMILAB MINIBOONE BEAMLINE*

C. Moore, J. Anderson Jr., R. Ducar, R. Ford, T. Kobilarcik, E. Prebys, A. Russell, R. Stefanski, FNAL, Batavia, IL 60510, USA

J. Monroe, Columbia University, N.Y, N.Y

Abstract

The MiniBooNE neutrino experiment is projected to take more intensity in a single year than was delivered during the seventeen years of running the Fixed Target Program. The experiment will require almost continuous running (18,000 pulses/hour) at full intensity (5E12 protons per pulse). In order to safely handle this intensity various measures have been instituted. The design of the beamline ensures sufficient clearance between the beam and apertures. A MiniBooNE Beam Permit System has been installed that is able to check various digital and analogue information against nominal values on a pulse by pulse basis. An automated total beam loss monitoring system (electronic berm) measures any beam loss between the beginning and end of the line. An automated correction system (Autotune) finds and corrects minor beam wandering. A description of the beamline design and relevant instrumentation is given.

INITIAL DESIGN

The first consideration in the design of the very high intensity proton beamline was to make the size of the beam pipe large with respect to the size of the beam. Figure 1 shows the beam envelope and the apertures along the beamline. There were two major obstacles to achieving this goal. First, the beamline passes underneath an existing service building. Typically, a FODO channel is used to keep the beam tightly focused, but in this case the beam had to pass through a 43 m. berm pipe. The second consideration was that for a tight focus, the beam should be large in the final focus quadrupoles. Using elements with large apertures (6-3-120 dipoles, LEP trims, and LEP quadrupoles) ameliorated both problems.

OPTICS MEASUREMENTS AND COMPARISON TO THEORY

Dipole Measurements

To measure the quadrupole gradients, each dipole trim magnet was varied, and the change in beam position at each BPM was recorded. The optics program TRANSPORT was used to find the quadrupole gradients that gave the best fit to the data. Figure 2 shows a representative trajectory.

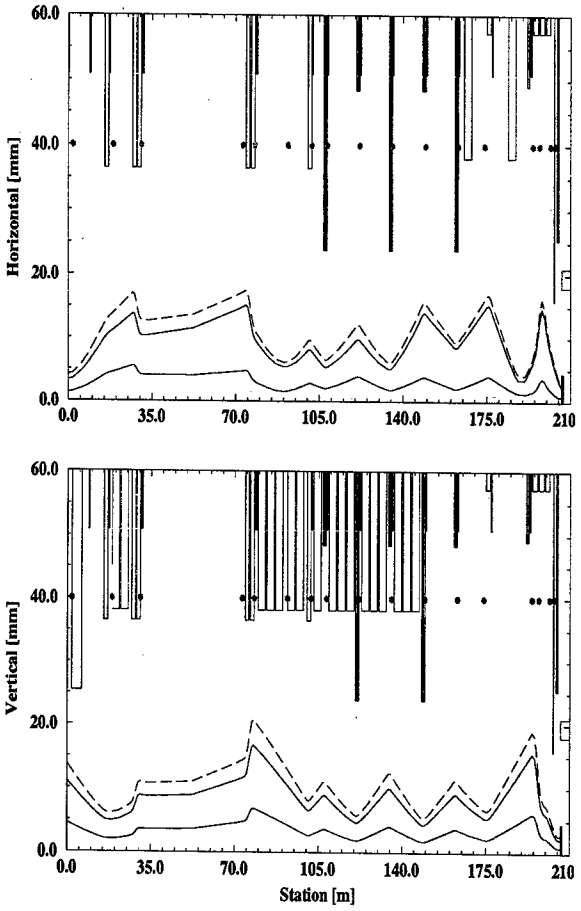


Figure 1. Beam envelope and apertures. The lower beam envelope is the one sigma and the two upper traces are the 95% and 99% with momentum folded in. The assumed emittances were 20 PI and a dp/p of .1%. The line indicates the total loss monitor coverage and the dots indicate the location of individual loss monitors.

Beam Profile Measurements

To measure the input lattice parameters, each profile monitor was inserted into the beam, one at a time to reduce scattering, and the beam size was recorded.

*Operated by Universities Research Association, Inc. under contract number DE-AC02-76CH03000 with United States Department of Energy.

0-7803-7738-9/03/$17.00 © 2003 IEEE

TRANSPORT was used to vary the initial beam parameters to find the best fit to the measured profiles. The calculated beam sizes are compared with the measured profiles in Figure (3).

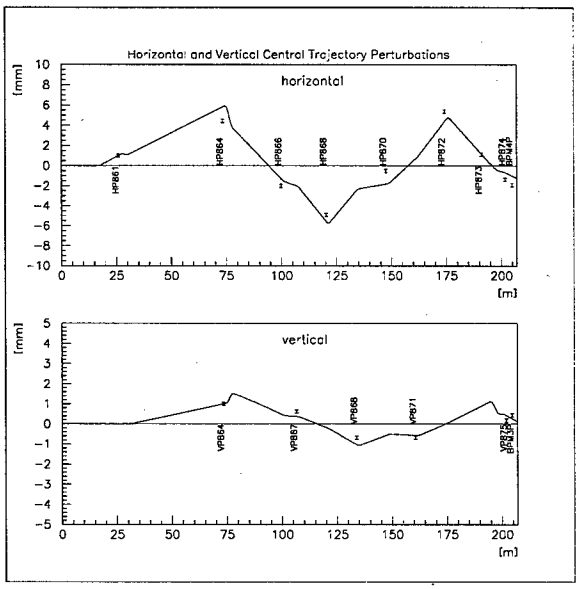


Figure 2. Example horizontal and vertical dipole changes

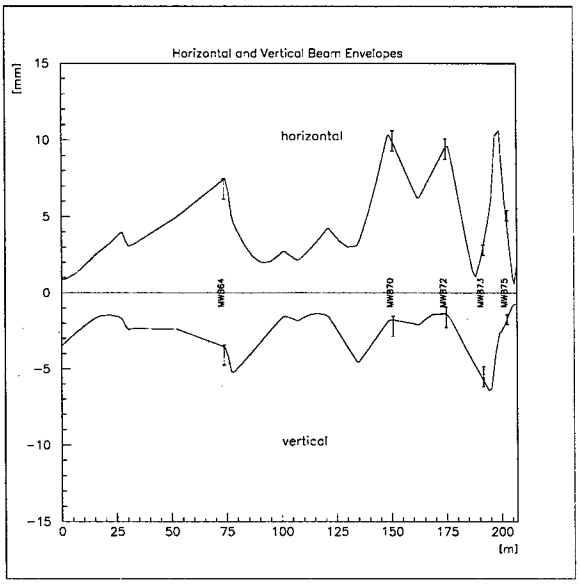


Figure 3. Beam sizes compared to prediction

Dispersion Measurements

To measure the dispersion, three foils of different thicknesses were inserted into the beam, one at a time, at the same location. For a given foil thickness, the energy loss, and hence the momentum change caused by the foil, is known. The changes in positions at the downstream BPMs were recorded for each foil to make a direct measurement of dx/(dp/p). The measurement was modeled in TRANSPORT and the comparison between the measured data and predicted dispersion wave is shown in Figure (4), with the error bars indicating the spread in measurements from the three foils

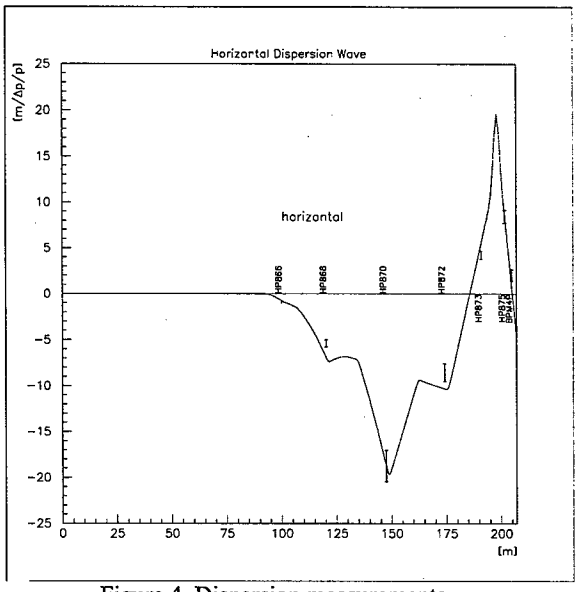


Figure 4. Dispersion measurements

Local Bumps and Target Mults

Local bumps were developed to perform aperture scans during commissioning. Nominal beam positions were defined by centering the beam in the apertures. Position and angle mults were developed for target scans, and were used in conjunction with a 90 degree monitor to center the beam on target.

AUTOTUNE

An automatic beamline correction program, Autotune, was developed to aid in keeping the proton beam on the nominal trajectory [1]. The procedure of the program is as follows: for every trim magnet in the beamline, the current is changed by a small amount and the change in position at every BPM is measured. The measurements are used to solve the linear equations relating the change in current to the change in position. The trim magnets and BPMs are chosen such that the matrix can be inverted. Once the transfer matrix is found, Autotune finds the trim currents needed to correct deviations of the beam from the nominal trajectory.

BEAM PERMIT SYSTEM

Beam Permit Systems have long been implemented for various accelerators and beamlines at Fermilab, with inputs generally in the class of simple go/no-go status. The new MiniBooNE Beam Permit System hardware consists of a supervisory micro-controller sampling multiple analogue and digital inputs in accord with programmed state logic and delays sensitive to accelerator clocks. Limits or allowable ranges are downloaded to the

micro-controller via the Accelerator Controls Network (ACNET). Sampled results are compared to these limits, and out of limit inputs effect a trip of the beam permit system, thereby preventing transfer of beam until the limit situation is corrected. Up to eight different sampling times are accommodated, with the process of sampling, determination, and trip taking less than 100 microseconds.

The Beam Permit System, currently in use, successfully prevents beam transport when monitored conditions are not proper, and inhibits repetitive transport of beam when beam losses or other conditions are abnormal. Monitored quantities include analogue representations of magnet power supply ramped outputs, sampled both before and during beam extraction to the MiniBooNE beamline, and all of the beamline loss monitors (with different signal time constants), which are sampled immediately after beam transport. There is complete coverage of the beamline with long loss monitors and spot coverage with short loss monitors (shown as the dots in Figure 1). Loss monitor readings taken during the dispersion measurements (described above) also demonstrated that the total loss monitor trip points are set to a level corresponding to a 0.02% beam loss.

E-BERM

To minimize air and groundwater activation and radiation in areas outside the overburden, a total beam loss monitoring system termed an Electronic Berm (E-Berm) was developed. The E-Berm, shown in Figure 5, consists of two Pearson 3100 toroids, associated integrating electronics, a resistive wall monitor, and a comparator module, used in conjunction with two toroid calibration modules. The toroids are located at the beginning and end of the beamline. The comparator module calculates the difference between the two toroids for each pulse, and for the sum of the previous ten pulses. The instantaneous and integrated losses are designed to be output to the radiation safety interlock system, which automatically inhibits the next beam pulse if the per-pulse losses are greater than 6%, or if the average losses are greater than 2%.

In addition to the total beamline losses, the E-Berm checks for other abnormal conditions on each pulse. The timing of the toroid signal in the integrator gate is verified to be within an acceptable envelope by comparison with the timing signal from a nearby resistive wall monitor. The beam-off readings of the two toroid integrators are also measured and checked against a reasonable interval, to guard against integrator failure. Finally, the relative calibration of the toroids is measured for each beam pulse. The calibration sequence consists of a series of 10 current pulses that are sent through a toroid calibration loop and read back through an integrator. The calibration occurs simultaneously for both toroids, over the full dynamic range (0.5E11 to 5E12 protons per pulse) of the beam intensity. A linear regression is performed on the measured and ideal values of the integrated toroid output in the calibration module. Gain and pedestal corrections are obtained for each toroid, and are compared with an acceptable range. If any of the monitored quantities are abnormal, the system is designed to trip the radiation safety interlock system.

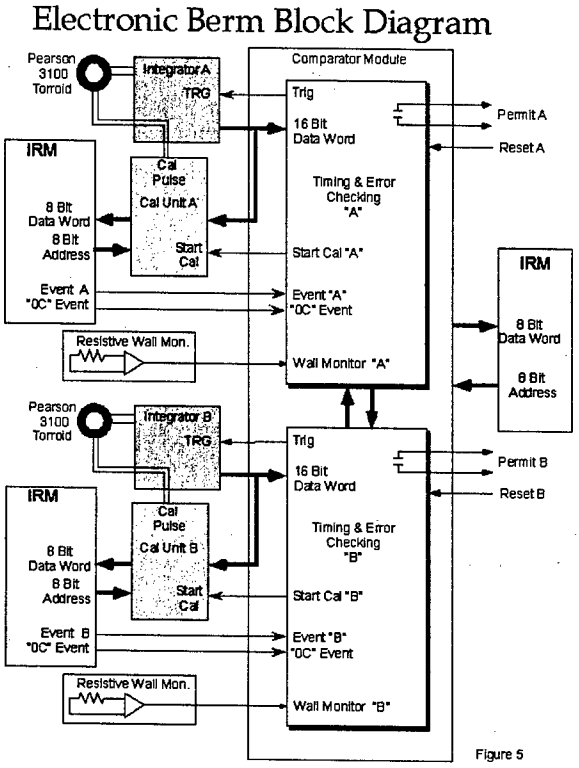


Figure 5: Electronic berm block diagram

CONCLUSION

The beamline has worked very well. The limitation on MiniBooNE intensity has been Booster losses; however up to 60% of the design intensity has been transported to the target with minimal losses until the final horn protection collimator. The highest contact reading before the final focus region is less than 10 millirem/hour. The highest contact reading in the final focus region is 200 millirem/hour on the horn protection collimator.

REFERENCES

[1] T. Kobilarcik, J. DeVoy, C. Moore, "Automatic Beamline correction", This Conference

HIGHLY EFFICIENT CRYSTAL DEFLECTOR FOR CHANNELING EXTRACTION OF A PROTON BEAM FROM ACCELERATORS

V. Guidi, C. Malagù, G. Martinelli, M. Stefancich, D. Vincenzi, *Univ. Ferrara, INFM-INFN, Italy*; V.M. Biryukov, Yu.A. Chesnokov, V.I. Kotov, *IHEP Protvino, Russia*; W. Scandale, *CERN, Switzerland*

Abstract

The design and performance of a novel crystal deflector for proton beams are reported. A silicon crystal was used to channel and extract 70 GeV protons from the U-70 accelerator in Protvino with an efficiency of (85.3±2.8)%, as measured for a beam of ~10^{12} protons directed towards crystals of ~2 mm length in spills of ~2 s duration. Experimental data agree with the theoretically predicted Monte Carlo results for channeling. The technique allows one to manufacture a very short deflector along the beam direction (2 mm). Consequently, multiple encounters of circulating particles with the crystal are possible with little probability of multiple scattering and nuclear interactions per encounter. Thus, drastic increase in efficiency for particle extraction out of the accelerator was attained. We show the characteristics of the crystal-deflector and the technology behind it. Such an achievement is important in devising a more efficient use of the U-70 accelerator and provides crucial support for implementing crystal-assisted slow extraction and collimation in other machines, such as the Tevatron, RHIC, the AGS, the SNS, COSY, and the LHC.

INTRODUCTION

The use of bent crystals for beam extraction in accelerators is under development at several laboratories. [1,2,3]. The advantages of this method are the ease of its realisation, feasibility of its simultaneous work with collider regime or with internal targets, and the absence of intensity pulsations because no resonant blow-up of the beam is needed to direct the beam onto the crystal for extraction. The crystal has a minimal "septum width", and is very convenient even for application in a beam-loss localisation system as a coherent scatterer [4].

A collaboration of researchers working at the 70-GeV accelerator of IHEP has recently achieved a substantial progress in the parameters of crystal-assisted beam deflection: an extraction efficiency larger than 85% has been obtained up to such an high intensity as 10^{12} protons [4]. A major feature of such reaching was the usage of very short crystals for extraction; the crystals were selected to the minimal value foreseen by the physics of channeling [5,6]. Thereby, the circulating particles encountered the crystal many times and suffered negligible divergence at each pass due to reduced scattering and nuclear interactions in the crystal. Multiple passage of particles allowed the protons to be eventually channeled by the crystal planes, leading to the experimentally recorded high efficiency.

Fig. 1 shows the theoretical prediction [7] made for the extraction efficiency at 70-GeV proton accelerator, and the figures measured in the campaign of measurements through 1997-2001 with crystals of different size and design. The trend is clear from both theory and experiments: the shorter the crystal, the higher the efficiency. The theoretical plot indicates the optimal crystal length for the conditions of the 70-GeV experiment, i.e. slightly less than 1 mm. Indeed such a short crystal deflector is very difficult to obtain. In this paper, we discuss the design and manufacturing of the crystal deflectors that led to the successful execution of experiments.

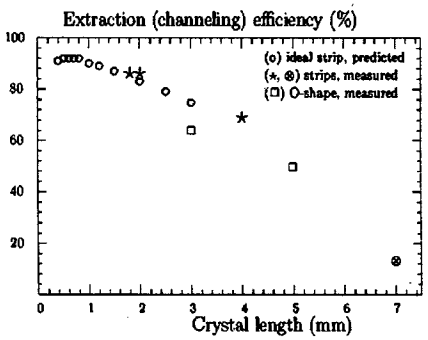


Fig.1 Crystal extraction efficiency as measured and as predicted for 70-GeV protons.

CRYSTAL BENDING SYSTEM

The first designs of short crystals appeared in literature in 1998 [3]. It consisted of an "O-shaped" deflector cut from a monolithic piece of oriented silicon. Here the bending was obtained by compressing the crystal at its middle part. Indeed, this method is not suitable for an efficient deflection with a crystal shorter than 5 mm. Any attempt to reduce this length resulted in poor bending efficiency as it is clear in Fig. 1 with the "O-shaped" 3-mm long sample.

Therefore, a new design to produce suitably short sample is needed. A possibility is the use of the anisotropic properties of a crystal lattice. From the theory of elasticity it is known (see e.g.[8]) that bending a crystal plate in the longitudinal direction causes some "anticlastic

0-7803-7738-9/03/$17.00 © 2003 IEEE

bending" or twists appear in the orthogonal direction. In that case, a crystal plate obtains the shape of a saddle, barrel, or a pure cylinder depending on the concrete anisotropic properties of the material. The surface equation for the crystal plate in the ideal case of the method of moments discussed in [9] is:

$$y = \frac{1}{2R_{II}} z^2 - kx^2$$

Where y is the direction of the incident beam, x and z are the longitudinal and transversal coordinates, and k is a coefficient depending on the concrete anisotropic properties of the material (see Fig. 2). For $k>0$ this is the equation of a hyperbolical paraboloid (saddle), $k<0$ gives the equation of an elliptical paraboloid (barrel), and $k=0$ is for a parabolic cylinder. It turns out that the first case applies to Si (111), therefore the crystal plate obtains the shape of a saddle as sketched in Fig.2. The orthogonal bending of a narrow crystal plate was used for beam deflection.

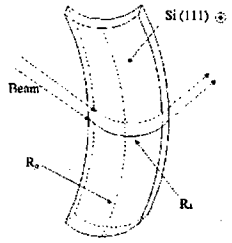


Fig. 2 Scheme of the bent crystal plate.

In our case, a crystal plate of silicon may be shaped like a saddle for the purpose (Fig. 2). The technical advantages of such a deflecting system are that it may be easily made shorter along the beam, has no straight sections in bending, and needs no additional material around the "legs".

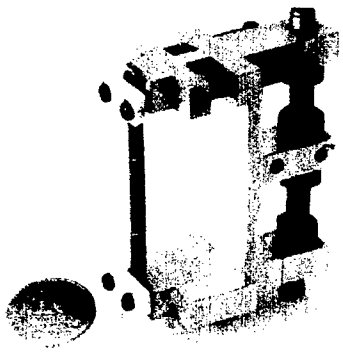


Fig. 3 Photo of crystal bending device (on the left is a narrow crystal strip).

The crystals were manufactured at the Semiconductors and Sensors Laboratory of the University of Ferrara as narrow strips, about 2 mm along the beam. The metal holder showed in Fig. 3 imparts the right curvature to the samples. A strip of monocrystalline silicon was bent in the longitudinal direction by an angle of about 100 mrad in the orthogonal direction: as a consequence the strips were bent in the orthogonal direction of about 1 mrad. The quality of the strip bending was preliminary checked by the laser system described in Ref. [8]. Then the crystals were tested directly in the experiments on high-energy accelerator.

SAMPLE'S PREPARATION

The starting material consisted of prime-grade, (111) oriented, 525-μm-thick silicon wafers. The crystals were sliced to form 0.5×50×2 mm^3 (thickness, height, and length, respectively) by means of a mechanical dicing saw. The length of 2 mm was chosen to be exposed to steer the protons in the collider and was determined according to the previous considerations. The (111) crystalline direction was intended for alignment toward the radial direction in the accelerator.

A crucial methodology for the achievement of high-performance crystal extractors was the chemical treatment of the samples as explained in next section. The preparation of the sample herewith described is suitable to remove the defects induced by the saw at the beam entry and exit facets of the silicon crystals. Indeed, mechanical slicing of the samples induces a large amount of scratches, dislocations, line defects and anomalies that would reduce the overall channelling efficiency of the crystal. According to the experience gained through previous runs at the accelerator, it came out that a 30 μm superficial layer was ineffective for channeling. We attributed this effect to the presence of in-depth lattice imperfections induced during the slicing.

Thus, we attempted the removal of such a layer by a sequence of room-temperature chemical treatments to the surfaces [10]. To avoid an unwanted sample thinning, the largest surfaces were protected by Apiezon wax while the others were left uncoated. The prime treatment was a wet planar etching (HF, HNO_3 and CH_3COOH (3:5:3)) and the timing was such to obtain an etching depth of about 30 μm. The samples were prepared and treated in clean-room environment (class 100) to avoid material contamination, which would locally modify the etch rates and the finishing of the etch ground.

Preliminary, the first process stages were aimed at the removal of pollutants such as greasy or metallic compounds. The wafers were degreased in trichloro-ethylene, acetone and then isopropanol. A two-stage cleaning procedure was, then, carried out to remove organic and metallic impurities from the surface of the wafers. The samples were cleaned in solution of water, hydrogen peroxide and ammonium hydroxide (5:1:1) at 75 °C for 10 min. After a short dipping in diluted HF (10% in weight) the wafers were washed in water,

hydrogen peroxide and hydrochloric acid (4:1:1) at 75 °C for 10 min. The specimens were cut from the coated wafer through a diamond-blade saw avoiding any alignment with major crystalline axes.

Finally, the entry and exit facets were ready for the prime chemical etching to remove the mechanical damages induced by the blade. The wax coating was eventually removed according to standard procedure and the resulting samples were once more subject to a complete cleaning process.

TESTS WITH HIGH-ENERGY PROTONS

The new crystal-deflectors were first tested in an external beam of 70 GeV protons. Fig. 4 shows a schematic of the experimental set-up. The incident proton beam was monitored by scintillation counters S1, S2. The crystal holder in the beam line may be tilted through a goniometer around the axis orthogonal to the proton beam and to the (111) orientation of the crystal. The rotation of the goniometer can be imparted as steps of 5 μrad each. The optimum crystal orientation was obtained by tilting the sample through a goniometer to determine the maximum counting rate of the remote scintillation counters S3, S4.

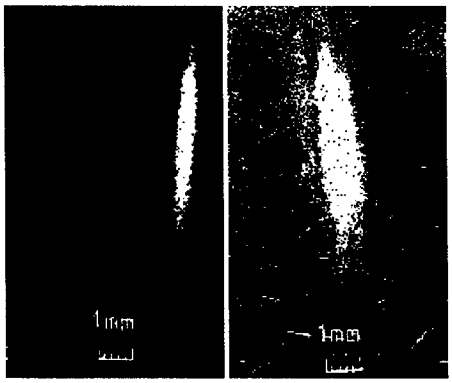


Fig.4 Image of the beam deflected with chemically polished crystal (left) and mechanically treated (right).

The precise measurement of the profiles of the bent beam has been done with nuclear photo-emulsions placed outside the vacuum chamber, 7 m far from the crystal.

Fig. 4 shows the results of the tests for the chemically polished deflectors compared to the deflectors having mechanical treatment of end faces. As seen from the picture, the profile of the beam bent by a chemically polished crystal is more uniform and sharp. Its width corresponds to the crystal thickness once the beam divergence within the critical angle of channeling (equal to 20 μrad for 70 GeV protons) has been taken into account. At the same time, the beam bent by a mechanically polished crystal has irregularities corresponding to an angular distortion of the order of 100 μrad.

After testing in an external beam, the crystals were installed in the IHEP U-70 accelerator ring to extract the circulating beam. The crystals with chemically polished faces have shown the best efficiency for beam extraction — up to a value larger than 80% [4]. New crystals can be applied for beam extraction and collimation of beams at accelerators in a broad range of energies as shown in Ref.[4,11]. One of the major applications would be the use in large colliders such as the LHC as a collimation system.

ACKNOWLEDGEMENTS

This work was supported by INTAS-CERN Grant No. 132-2000, RFBR Grant No. 01-02-16229, and by the "Young Researcher Project" of the University of Ferrara.

REFERENCES

[1] H. Akbari, X. Altuna, S. Bardin et al *Phys. Lett. B* 313, 491(1993)
[2] R.A.Carrigan, Jr., et al. *Phys. Rev. ST Accel. Beams AB* **1**, 022801 (1998)
[3] A.A.Arkhipenko, A.G.Afonin, B.I.Baranov et al. *Phys. Lett. B* **435**, 240 (1998)
[4] A.G. Afonin et al. *Phys. Rev. Lett.* **87**, 094802 (2001)
[5] V.Biryukov, *Nucl. Instr. and Meth. B* **53**, 202 (1991)
[6] A.M. Taratin, S.A.Vorobiev, M.D. Bavizhev et al, *Nucl. Instr. and Meth. B* **58**, 103 (1991)
[7] V.I. Kotov et al., *Proc. of the Seventh European Particle Accelerator Conference*, ed. M. Regler (EPAC, Vienna, 2000) p. 364; CERN-LHC-2000-007-MMS.
[8] V.M. Biryukov, Yu.A. Chesnokov and V.I. Kotov, *"Crystal Channeling and its Application at High Energy Accelerators"* (Springer, Berlin, 1997). See also http://crystalbeam.narod.ru
[9] V.M. Samsonov, *LNPI* Preprint N. 278, Leningrad, 1976
[10] Brida et al. *Microelectronic Engineering* **53**, 547 (2000)
[11] A.G. Afonin et al. EPAC 2002 Proceedings (Paris), p.2511

Proceedings of the 2003 Particle Accelerator Conference

DAΦNE BEAM TEST FACILITY COMMISSIONING

G. Mazzitelli*, A. Ghigo, M.A. Preger, F. Sannibale, P. Valente, G. Vignola
Laboratori Nazionali di Frascati dell'INFN, Frascati, Italy

Abstract

The DAΦNE Beam Test Facility (BTF) is a beam transfer line optimized to produce single electrons and positrons mainly for high-energy detectors calibration in the energy range between 20 and 800 MeV. The BTF has been successfully commissioned in February 2002, and started operation in November. The scheme of operation, the commissioning results, as well as the first users' experience are presented.

DESCRIPTION OF THE DAΦNE BTF

The Beam Test Facility (BTF) has been designed [1] to provide a defined number of particles in a wide range of multiplicities and energies, mainly for detector calibration purposes, such as energy calibration and efficiency measurements (in single electron mode), and also for beam diagnostics devices and detector aging (at higher intensities).

The BTF is part of the DAΦNE accelerator complex, consisting of a double ring electron-positron collider, a high current linear accelerator (LINAC), an intermediate damping ring (Accumulator) and a system of 180 m transfer lines connecting the four machines. The LINAC delivers electrons with energy up to 800 MeV, with a typical current of 500 mA/pulse, or positrons with energy up to 550 MeV, with a typical current of 150 mA/pulse; the pulse duration can be adjusted in the range $1 \div 25$ ns with a maximum repetition rate of 50 Hz. When injecting for operation of the main rings at the ϕ resonance, the beam energy is 510 MeV.

The minimum LINAC beam current that can be conveniently measured by the DAΦNE current monitors is $I \approx 1$ mA, corresponding to $\approx 10^8$ electrons/pulse, so that it is thus necessary to strongly reduce the number of particles to reach the few particles range. The reduction of the particle multiplicity can be achieved with different methods, the one chosen for the BTF operation is the following[2]: first the LINAC beam is intercepted by a (variable depth) target in order to strongly increase the energy spread of the primary beam; then the outcoming particles are energy selected by means of a bending magnet and slit system. The energy selector only accepts a small fraction of the resulting energy distribution, thus reducing of the number of electrons by a large and tunable factor. The target is shaped in such a way that three different values of depth can be selected by inserting it into the beam-pipe, corresponding to $1.7, 2.0, 2.3\ X_0$.

The attenuated beam is transported by a ≈ 12 m transfer line to the BTF hall, where the experimental set-ups can be installed; at the end of the BTF line a second bending magnet allows to use two separate test lines: one directly from the straight section, the other from the magnet at 45°. A schematic view of the BTF layout is shown in Fig. 1.

Due to the momentum dispersion introduced by the bending magnet, the relative energy spread $\Delta E_{\rm sel}/E_{\rm sel}$ is essentialy determined by the magnet/collimators configuration[1]; in the standard BTF operation for a wide range of slit apertures a resolution better than 1% can be obtained.

The number of transported electrons (or positrons) can be adjusted in a wide range, down to single particle, and is well below the sensitivity of any standard beam diagnostics device, so that many different particle detectors have been used to monitor the beam characteristics.

The experimental area extendes over a 100 m^2 area hall, surrounded by shielding walls of (movable) concrete blocks; a 20 ton crane and a remotely controlled, motorized trolley are available. A number of coaxial cables are stretched between the experimental hall and a dedicated control room, where the BTF beam (and user apparata) can be fully steered. The facility is fully equipped with a complete DAQ, both VME and CAMAC, with NIM electronics and HV modules available for the users.

BEAM COMMISSIONING

During 2002 the BTF has been successfully commissioned and started operation, delivering beam to the first user experiments, from Nov. 2002 to May 2003[3]. Two different operation modes of the facility have been successfully implemented:

- "parasitic": when the DAΦNE collider is working for the main experiments, the LINAC can deliver electron/positron beams to the BTF only between two injection cycles for the main rings. The LINAC setting was optimized to provide a 510 MeV energy, $4 \div 5$ mA intensity beam, with a repetition rate of 24 Hz (+1 shot to the spectrometer line for LINAC energy measurement), and the pulse duration was the same as for injection in the accumulator, ≈ 10 ns. With a typical collimator setting of 2 mm total aperture, both for the upstream and downstream slits and with the target depth set to $1.7\ X_0$, only a few electrons reach the diagnostic detectors.

- "dedicated": when there are no collisions in the DAΦNE main rings the LINAC beam can be continuously delivered to the BTF. In this case is possible to change the LINAC energy in order to optimize the

* giovanni.mazzitelli@lnf.infn.it

0-7803-7738-9/03/$17.00 © 2003 IEEE

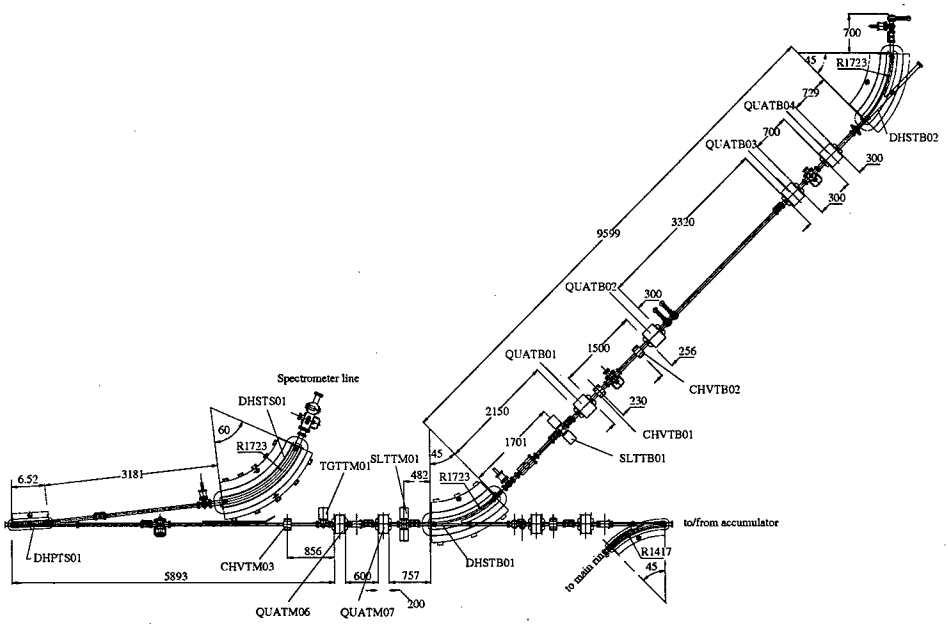


Figure 1: Layout of the Beam Test Facility.

energy/multiplicity of the BTF beam; moreover, the pulse duration can be also changed.

The facility has been operating both in the single electron production scheme and in the high multiplicity operation mode, according to the different user requirements. At low multiplicity a calorimeter has been used as main diagnostic device. The detector is a lead/scintillating fibers calorimeter (developed for the KLOE experiment[4]), with single side photomultiplier readout, with good energy resolution (7% at 500 MeV).

Due to the good energy resolution of the calorimeter (anyhow still worse than the intrinsic beam-line energy acceptance) the number of produced electrons can be counted simply by measuring the total deposited energy E: $n = E/E_1$, where E_1 is the energy deposited by a single electron. An example of ADC spectrum (pedestal subtracted) is shown in Fig. 2, for a selected energy of $E_{\rm sel} = 442$ MeV: the individual peaks corresponding to $0, 1, \ldots, n$ electrons can be easily identified.

The most effective way to change the average number of particles in the beam is to change the selected energy $E_{\rm sel}$; in particular, at the **same** LINAC energy and intensity and with the **same** collimator settings, the multiplicity increases by decreasing the chosen $E_{\rm sel}$. In addition, the multiplicity can be tuned by changing the aperture of the upstream and/or downstream collimators. In this case the energy resolution of the selector will be also affected by a relatively small amount, in any case well below the intrinsic resolution of our calorimeters. In particular, the measured multiplicity increases by increasing the slits aperture until the intrinsic beam spot size is exceeded.

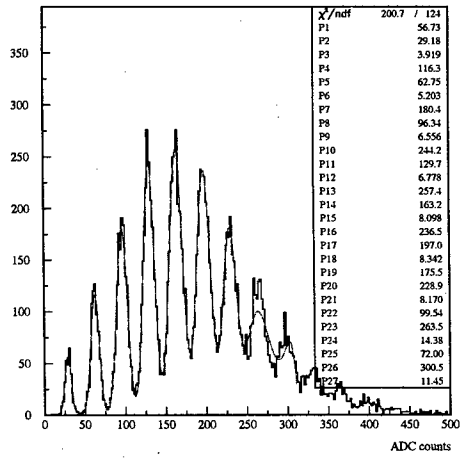


Figure 2: Counting electrons in the calorimeter: charge spectrum for $E_{\rm sel} = 442$ MeV.

Above $\approx$ 20 particles the calorimeters are no longer effective due to saturation effects. In order to have a diagnostics device in the $\overline{n}$ = 100-1000 range (and higher), a detector has been developed and tested in collaboration with the AIRFLY group [5, 6], based on the Cerenkov radiation emission.

Another important parameter is the beam energy, that can be chosen by changing the current of the energy selector dipole magnet. The average measured energy of the single electron signal in the calorimeter is proportional to the incoming beam energy $E_{\rm sel}$ as shown in Fig. 3.

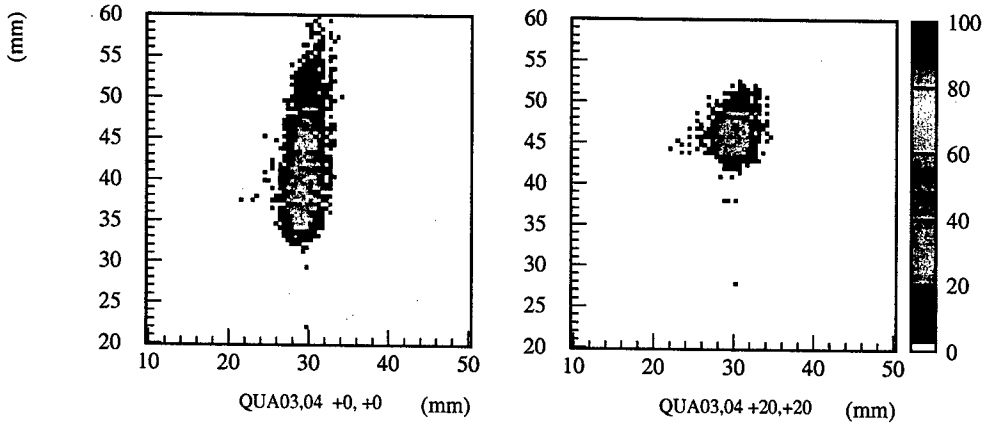


Figure 4: Beam spot measured by the AGILE silicon tracker: on the left for defocussed beam (last vertical and horizontal quadrupoles off); on the right for optimized optics ($\sigma_x \approx \sigma_y \approx 2$ mm).

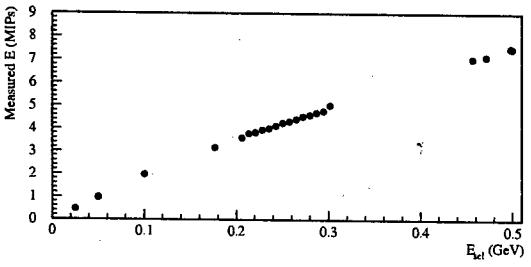


Figure 3: Total energy deposited in the calorimeter by a single electron as a function of the selected beam energy $E_{\rm sel}$.

The single electron beam spot size has been measured profiting of the high spatial resolution of the silicon microstrip tracker of the AGILE gamma-ray experiment [7]. An example of the beam spot measured by the silicon microstrip monitor is shown in Fig. 4: a $\sigma_x \approx \sigma_y \approx 2$ mm spot has been measured with an optimized optics, defocussed optics have been also studied for detector efficiency testing purposes.

Many user experiments were carried out since Nov. 2002, both in single electron mode and at high multiplicity. The single electron mode has been mainly used for testing particle detectors, while the AIRFLY experiment (measuring the air fluorescence yield) has been the main user of the high multiplicity beam: a wide range of particle multiplicity has been exploited, spanning from 10 to more than 1000 electrons/pulse. In both cases the full energy range of the BTF beam has been spanned, up to the maximum LINAC energy ($\approx$ 800 MeV), and also at very low energy (as low as 25 MeV).

Many different settings for BTF beam, for various energy/multiplicity/beam-size configurations have been optimized. The desired beam characteristics were in general easily tunable and the settings showed a very good reliability. Moreover, some diagnostic devices have been integrated in the DAΦNE control system in order to provide an easy user interface.

CONCLUSIONS

The BTF has been operational during the second half of year 2003, both in parasitic and dedicated mode, giving beam to a number of experimental users in a wide range of energy and particle multiplicity. It demonstrated to be easily tunable and very reliable both from the point of view of the desired particle number (from single electron mode to $\approx$ 1000) and energy setting. In order to overcome the present limitations imposed by the DAΦNE collider experiments operation and to largely improve the duty-cycle, we plan to upgrade the facility [8]; a complete separation between the DAΦNE transfer lines to the Main Rings and the BTF channel will allow to operate in the BTF mode with the only limitations of the LINAC switching time and the time spent for filling the Main Rings. An upgrade of allowed dose, up to 10^{10} particles/s, will also permit to use the BTF for testing of standard beam diagnostic devices.

REFERENCES

[1] F. Sannibale, G. Vignola, DAΦNE Techical Note **LC-2** (1991).

[2] L. Rinolfi *et al.*, *Single electron beams from the LEP preinjector*, in Proceedings of PAC 89, Chicago (1989) 298.

[3] G. Mazzitelli, P. Valente, *Commissioning of the DAΦNE Beam Test Facility*, LNF-03-003(P).

[4] M. Adinolfi *et al.*, Nucl. Instrum. Meth. **A482** (2002) 364.

[5] P. Privitera *et al.*, *AIRFLY Letter of Intent*, INFN Gr. V, unpublished.

[6] G. Mazzitelli *et al.*, *Beam Instrumentation for the Single Electron DAΦNE Beam Test Facility*, DIPAC 2003.

[7] M. Prest *et al.*, Nucl. Instrum. Meth. **A501** (2003) 280.

[8] G. Mazzitelli *et al.*, DAΦNE Techical Note **BTF-1** (2003).

FABRICATION OF THE MEBT CHOPPER SYSTEM FOR THE SPALLATION NEUTRON SOURCE *

R. Hardekopf†, S. Kurennoy, J. Power, R. Roybal, D. Schrage,
Los Alamos National Laboratory, Los Alamos, NM 87545
and
R. Sherwood, S. Collins, Directed Energy, Inc., Ft. Collins, CO 80526

Abstract

Los Alamos completed design, fabrication, procurement, and initial testing (without beam) of the SNS medium-energy beam-transport (MEBT) chopper, including the meander-line traveling-wave structure and the electrical-pulser system. This report reviews the design parameters and discusses the fabrication process for the chopper structures, including measurements of the impedance and rise time. (The MEBT vacuum system and chopper-target beam stop were developed at and reported by LBNL.) We discuss the specifications for the pulse generator and its fabrication and testing at Directed Energy, Inc. of Ft. Collins, CO. Experimental tests of the chopper system are currently being performed at the SNS site at ORNL and will be reported separately.

INTRODUCTION

The SNS linac will accelerate a 1-2 mA (average) H^- beam to 1 GeV for injection into an accumulator ring for bunch compression. Beam chopping is required to provide a gap in the beam, which is maintained during the accumulation process and allows extraction from the ring with minimal losses. A beam chopper in the low-energy beam transport (LEBT) between the ion source and the RFQ pre-chops the beam, and a fast traveling-wave chopper in the medium-energy beam transport (MEBT) provides the final clean up of the chopping gap. The physics design of the MEBT chopper meander-line deflecting structure has been described previously [1,2]. It is a folded, notched stripline that matches the electric wave velocity along the beam axis to the beam particle velocity, thus providing a rise and fall time determined mainly by the rise and fall times of the electric pulse.

Table 1. MEBT Chopper Specifications

Parameter	Value	Comments
Beam energy	2.5 MeV	ß=0.073
Length	35 cm	
Gap	1.8 cm	Adjustable
Pulser voltage	±2350 V	Max. ±2500 V
Deflection angle	18 mrad	
Chopping period	945 ns	
Duty factor	32 %	68 % beam on
Rise / fall time	10 ns	2-98 %

* Work supported by the Office of Basic Energy Science, Office of Science of the US Dept. of Energy, and by Oak Ridge National Lab.
† hardekopf@lanl.gov

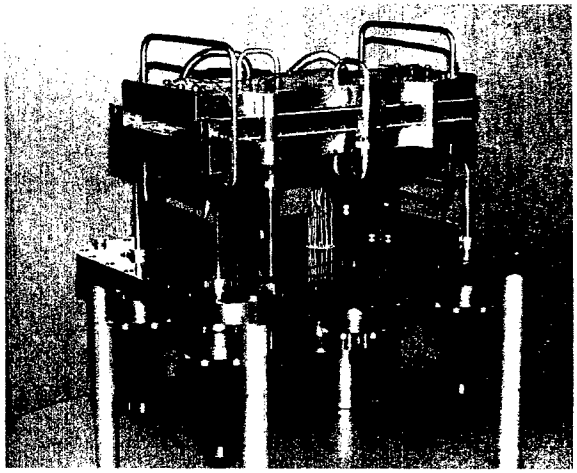


Figure 1. One of two completed MEBT-chopper structure assemblies. The unit is upside down from the normal mounting position on the beamline.

The MEBT chopper is suspended from the lid of a vacuum box located just downstream of the RFQ [3]. There is space in the MEBT for an identical structure called the "antichopper" located downstream of the chopper beam stop. If required, the antichopper could restore partially deflected beam on the leading and trailing edges of the pulse to the MEBT axis prior to entering the DTL. Beam simulations of the chopper systems were reported at a previous conference [4].

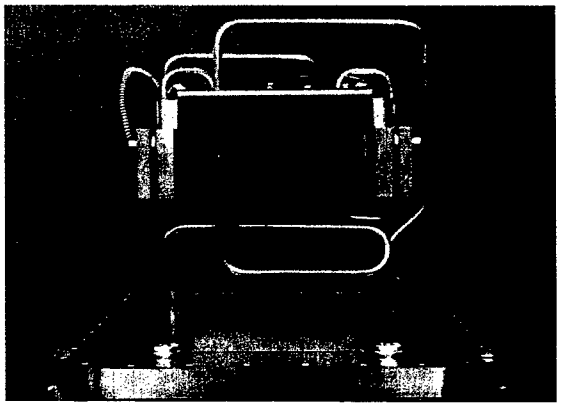


Figure 2. End view of the chopper structure

0-7803-7738-9/03/$17.00 © 2003 IEEE

DEFLECTING STRUCTURE

The meander line required a material with high electrical conductivity on a substrate with a low dielectric constant. We chose a composite material commonly used in the manufacture of printed circuit boards, Rogers Corp. RT6002, which is 0.100-inch thick with a .020-inch thick copper back plate. The profile of the meander stripline was drawn in AutoCAD and translated to a machine that made a mask of the notched meander pattern. The vendor for the etched circuit boards was Multi-Plate Circuits, Inc. Although not extremely difficult, the entire process was tedious and time consuming. The first step was to fabricate sample pieces that could be used to measure critical dimensions. We determined that an "etch factor" was needed in the artwork to achieve our final specifications. The next step was to etch the raw material to the desired thickness. Then a photo-image resist was applied to the boards, and they were run through a developer. About 350 microns of tin/lead was applied to the boards, and they were then run through an ammonia etcher. The boards were measured on an optical comparator after each pass until desired dimensions were achieved. Finally, the tin/lead was stripped, the boards were run through a dryer, and then routed to the final dimensions (See Figure 3).

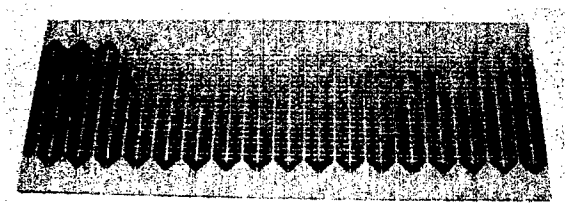


Figure 3. Etched circuit board prior to machining

After the machining of the substrate was complete, it was impossible to maintain the flatness tolerance on the copper surface because of the removal of the dielectric material on the underside of the substrate. A solution to this problem was to epoxy the substrate to the base plate. Eccobond 45 Catalyst 15 epoxy was used for this process. Several tests to determine the bonding strength of the epoxy were conducted prior to actually gluing the assembly together. A thin layer of epoxy (.003"-.004") mixed with a "rigid" mix ratio yielded the best results. It was also determined that a "weighted" cure time of 48 hours with 100 lbs./sq. in. would be necessary. To ensure uniform weight distribution over the entire length of structure, a precision fixture was placed over the epoxied assembly. Approximately 2000 lbs. of weight were then placed over the entire assembly, and the epoxy was allowed to cure for over two days. As part of the manufacturing process we performed in-process testing to ensure that the glue joint had been properly made. Glue-joint specimens were fabricated simultaneously with the gluing of the meander line to the ground plane using the same procedure (epoxy from the same mixed batch, thickness of epoxy applied, joint loading, and cure time). The specimens were tested to affirm that the glue joint had achieved strength greater than that of the meander-line substrate material. The full strength of the epoxy is specified as 2.5X the ultimate strength of the substrate material. The strength test determined whether the glue joint would fail in the epoxy or in the meander-line assemblies.

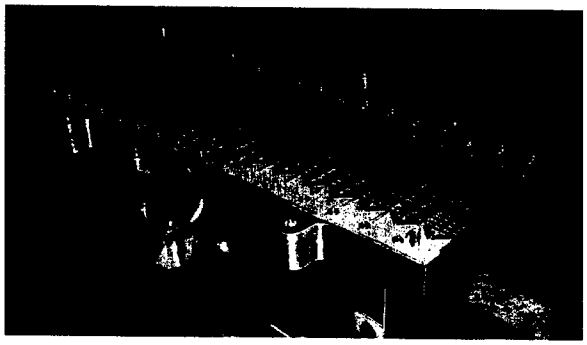


Figure 4. Finished circuit board glued to ground plane

Following fabrication, the structures were electrically tested and found to have an impedance of nominally 51±0.5 ohms. One could adjust the impedance to exactly 50 ohms with tuning tabs along the structure, but this was unnecessary in our case. The structures were hi-potted to 4.5 kV under vacuum, along with all of the high voltage cable assemblies. We measured the structure risetime to be 1.5 ns (see Fig. 5), substantially faster than that of the pulser (about 10 ns). The delay through the structures varies from 22.07 to 22.24 ns, including the 7-16 DIN to N to SMA adaptors required for the measurement.

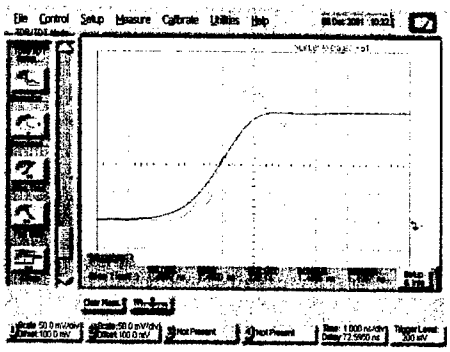


Figure 5. The risetime of a complete assembly is 1.5 ns, including the interconnections and vacuum feedthrough connectors. Data are in green, a 2-ns risetime filter in red.

DEFLECTING PULSER

The 50-ohm deflecting pulser was designed and built by Directed Energy, Inc. (DEI) to specifications provided by Los Alamos. The specification for two pulsers to drive the top and bottom meander lines is ± 2500 V with 10-ns (2 to 98%) risetime. Development of the 1-ns risetime, 1-kV MOSFET for this application was done by DEI under a separate R&D contract.

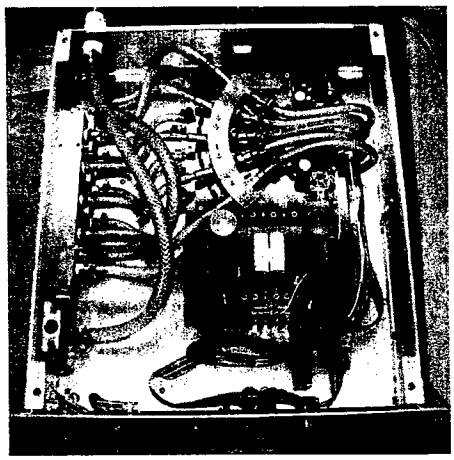


Figure 6. Chassis layout of the DEI positive polarity pulser

The PVX-3125 pulse generator is a half-bridge (totem pole) design, providing fast rise and fall times. It uses five of DEI's patented power MOSFET transistors in each leg of the bridge, configured in a series transmission line format, to provide the pulse generator's voltage and current requirements.

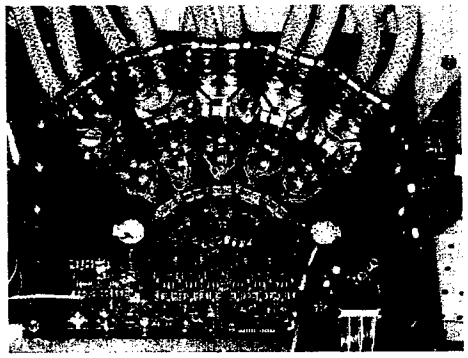


Figure 7. One-half of the MEBT chopper pulser output-switch assembly

The amplitude of the external DC power supply controls the output voltage. The efficiency of the pulse generator is about 90%; therefore a DC power supply setting of 3.3 kV yields an output voltage of about 3 kV. Two versions are required, a positive pulser and a negative pulser. A TTL input gate controls the output pulse width and frequency. Pulse width and frequency are constrained to preset limits suitable for our application. The maximum pulse width is 100 to 905 nanoseconds and the maximum frequency is 1.05 MHz.

This pulse generator features a high-speed overcurrent protection circuit. The main energy storage capacitor bank is isolated from the output stages by an IGBT switch assembly. A much smaller and faster capacitor is integral to the main switch assembly. If a peak over-current condition is detected, the IGBT is opened, the output pulse is truncated, and the output is tied to ground. This circuit protects the pulse generator, load and cabling from potential damage due to an arc or short in the cable or load. The following figures show examples of the output.

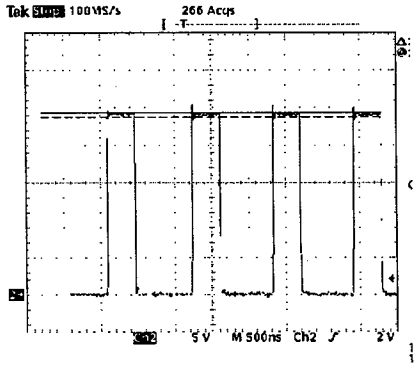


Figure 8. String of four pulses (out of ~1000 during a 1-ms SNS macropulse)

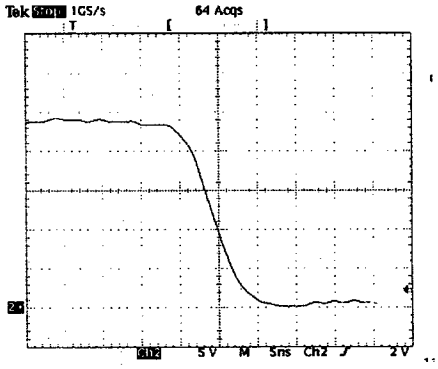


Figure 9. Expansion of trailing edge of typical output pulse showing fall-time of about 8 ns at 2350 volts

ACKNOWLEDGEMENTS

The authors acknowledge the close collaboration with LBNL personnel who designed and built the SNS Front-End system, in particular, D. Oshatz. We also acknowledge the vital contributions of T. Wright for mechanical fabrication and T. Cote for layout of the circuit boards, selection of material, and translation of the AutoCAD file to the format required by the vendor.

REFERENCES

[1] S. Kurennoy and J. Power "Meander-Line Current Structure Development for SNS Fast Chopper," Proc. of the XX Intl. Linac Conf., 2000, Monterey, CA.

[2] S. Kurennoy et al., "Progress with SNS Fast Beam Chopper," Proc, of the 2001 PAC, Chicago, IL, 1435.

[3] D. Oshatz et al., "Mechanical Design of the SNS MEBT," Proc. of the 2001 PAC, Chicago, IL, 70.

[4] S Nath et al., "Beam Behavior Through the SNS Chopper System," Proc. of the XXI Intl. Linac Conf., 2002, Korea.

THE MECHANICAL DESIGN OF A PROTON MICROSCOPE FOR RADIOGRAPHY AT 800 MEV[1]

Robert Valdiviez, Floyd Sigler, David Barlow, Barbara Blind, Andrew Jason, Tom Mottershead, John Gomez, Camilo Espinoza
Los Alamos National Laboratory

Abstract

A proton microscope has been developed for radiography applications using the 800-MeV linear accelerator at the Los Alamos Neutron Science Center (LANSCE). The microscope provides a magnified image of a static device, or of a dynamic event such as a high-speed projectile impacting a target. The microscope assembly consists primarily of four Permanent Magnet Quadrupoles (PMQ's) that are supported on movable platforms. The platform supports, along with the rest of the support structure, are designed to withstand the residual dynamic loads that are expected from the dynamic tests. This paper covers the mechanical design of the microscope assembly, including the remote positioning system that allows for fine-tuning the focus of an object being imaged.

1 INTRODUCTION

Figure 1 shows the microscope assembly installed on the beam line in Area C of LANSCE. The beam direction is left to right. Area C is the experimental area where proton radiography is performed on a variety of experiment types. The experiments that have been imaged range from the shock propagation through high-explosive configurations to the flow pattern of liquids through coolant channels in industrial equipment.

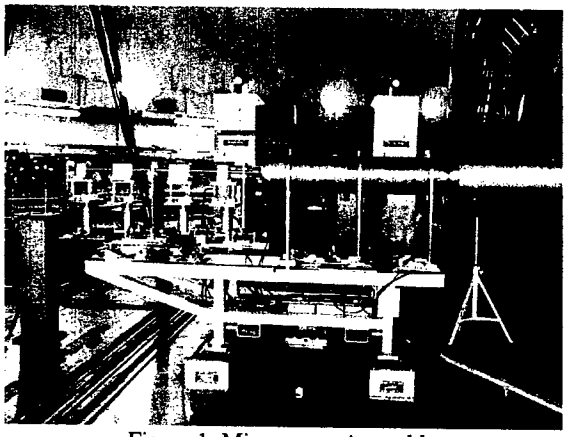


Figure 1: Microscope Assembly

The magnetic lattice of the proton radiography beam-line consists mainly of two magnetic sections [1]. The first section is an illumination section that is up-stream of the object or event being imaged, contains dipole and quadrupole magnets along with beam diagnostic assemblies, and provides for beam conditioning for the imaging task at hand. The second section is a focusing section that consists of four nominally 12-inch-diameter bore quadrupole magnets and a beam collimator. The focusing section provides for transport of the scattered proton beam to the imaging plane. A second focusing section and imaging plane that is located down-stream of the first focusing section is available if necessary for a given imaging experiment.

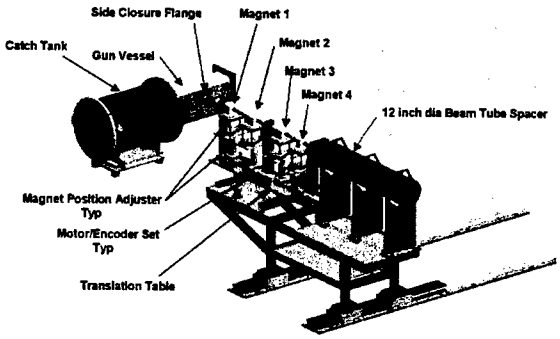


Figure 2: Microscope Assembly

The proton microscope assembly and PMQ lattice [2], shown in Figure 2, replaces the first focusing section of the proton radiography lattice. Two of the large electromagnetic quadrupole magnets are physically rolled off of the beam line via tracks on the floor, and the microscope assembly is rolled into their place for magnified imaging tasks. The other two electromagnetic quadrupole magnets remain in place, but are not powered. In this magnified imaging configuration the four PMQ's of the microscope assembly provide all of the down-stream beam focusing. An image magnification of approximately seven times is possible with the microscope. A small beam collimator is contained in the beam tube of the microscope assembly for controlling the image contrast.

[1] This work sponsored by the U.S. Department of Energy, NNSA

0-7803-7738-9/03/$17.00 © 2003 IEEE

2 THE MECHANICAL DESIGN OF THE PROTON MICROSCOPE

The microscope assembly consists of a main support structure, a transition beam tube that consists of a 1.25-inch-diameter and a 12-inch-diameter tube that are joined in series, a magnet lattice support plate that provides for lateral translation of the entire magnetic lattice off of the beam-line, the four individual magnet support bases, and the four sets of PMQ's. Remote positioning of three of the PMQ sets is also included in the design. The three down-stream PMQ sets can have their longitudinal, or Z position varied over approximately +/- 3.0 inches to allow for focusing adjustments. This positioning is done by using motor and encoder sets that communicate to a Personal Computer (PC) in the counting house for the experimental area. The motor and encoder sets move the support bases of the PMQ's.

The main support structure of the microscope is a welded structural steel frame, and is shown in Figure 3.

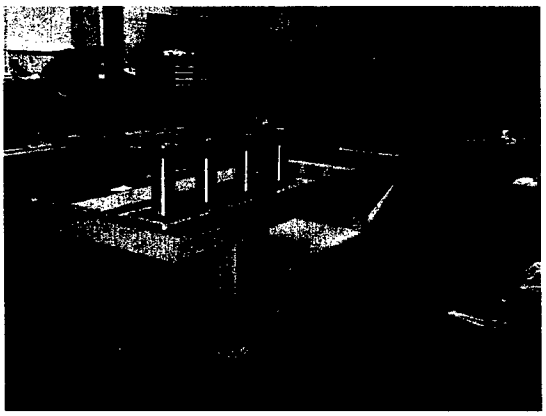


Figure 3: Microscope Assembly Support Stand

The structure is designed to resist the residual shock loads that it can experience from dynamic tests. Dynamic tests that the microscope would image would be limited to small high-explosive-mass quantities, thus producing low residual dynamic loads on the support structure. However, since the microscope could be parked in storage near much higher energetic tests being conducted, the design considered higher shock loadings, in the range of 2g, to prevent inadvertent damage to the microscope. The support frame is also designed to resist seismic loads for personnel safety considerations. The support structure also has its center of gravity biased to the low center region using thick steel plates. This center of gravity design has been used to provide static stability regardless of the microscope's configuration. Magnets and beam tubes can be removed without producing a tipping hazard. The weight of the support structure is 2377 pounds. The total weight of the microscope assembly is 3400 pounds.

The transition beam tube allows for coupling into the gun or test vessel on one end, and the existing lattice beam tube on the downstream end. The 1.25-inch-diameter tube, with a 0.12-inch-wall thickness, couples into the test vessel. Since high-speed material impact tests (velocities of approximately 6100 feet/sec) are conducted in the vessel the adjoining beam tube has a thick wall to resist penetration damage from shrapnel of the impact experiment. The 1.25-inch diameter beam tube can be removed and replaced without having to disassemble the microscope assembly. The 1.25-inch-diameter tube couples into the 12-inch-diameter tube using a flange and a transition piece. The 12-inch-diameter tube has a 0.5-inch-thick wall.

The magnet support bases are mounted on a main support plate. This support plate is mounted on rails that are aligned laterally to the beam line. The main support plate translates the four magnet sets, support bases, and 1.25-inch diameter beam tube off of the beam line. This feature is included to allow for quick replacement of a beam tube. Beam tube replacement will be necessary when the tube inside surface has significant damage done to it, or when the beam collimator is to be changed in a given imaging set-up. The beam collimator is integral to the beam tube.

The magnet support bases provide for the support of the PMQ sets, and their alignment. Figure 4 shows two PMQ sets and their respective support bases. Each PMQ set support base provides five degrees of freedom for magnet alignment. The sixth degree of freedom, longitudinal, or Z, position is provided manually for the first PMQ set, and remotely for the other three.



Figure 4: PMQ's and Support Bases

The PMQ sets are made by combining single PMQs into a set of two or four. A single PMQ has an average measured quadrupole gradient-length (GL) product of approximately 2.81T. By combining two or four PMQ's the necessary magnet strength is obtained for each set. Each PMQ has an inside bore of 1.375 inch, leaving a nominal gap of 0.062 inch between the magnet bore and the outside of the 1.25-inch diameter beam tube. The gap

is needed to prevent the beam tube from impacting the magnet bore during dynamic testing.

3 ASSEMBLY OF THE PMQ SETS

The PMQ sets are assembled by separating the individual PMQ's beyond their field-influence distance on a rail assembly. Alignment rods are placed through two of the clamping holes in the PMQ bodies, and a clamping assembly is used to draw the magnets together. At a separation distance of approximately 0.008 inch the repulsive force between two PMQ's is approximately 350 pounds. The PMQ's are drawn together to where no axial gaps are present, permanent alignment rods and bolts installed and tightened, and the PMQ set is then removed from the clamping fixture. The PMQ set is then ready for installation onto the microscope assembly.

4 THE MAGNET MOTION CONTROL SYSTEM

The remote-motion control for the three down-stream PMQ sets of the microscope is accomplished by having each of the magnet support bases mounted on one common rail. A motor-encoder set is used on each magnet support base to change its longitudinal, or Z, position. The support bases are held in place with the use of an electrically deactivated brake that is an integral part of the motor assembly. A clutch assembly is also placed in-line with the drive shaft. If the drive components meet too much drive resistance, then the clutch slips and prevents damage to any of the components.

The motors communicate with the control PC via the RS232 communication protocol. The encoders communicate in the RS485 communication protocol. The encoder RS485 signal is converted to the RS232 protocol via an in-line converter device. All signals are converted from the RS232 protocol to a fiber optic signal for the transmission length between the PC in the counting house and the experimental area. A fiber-optic signal is used for the majority of the control transmission length of 425 feet in order to eliminate possible electrical interference from other cabling.

A user interface program on the PC enables the microscope user to query the encoders to view their current Z positions, and make any positional changes. The control software performs the limit checking and other control guard functions to prevent running magnet support bases into each other. If the control software limit checking were to fail the clutch assemblies would prevent hardware damage should two support bases make contact.

The encoders are the optical type with 1024 steps per revolution. The encoders are also absolute, meaning that they maintain their positional information through power off-on cycles. The lead screws that are used to convert rotational motion to linear translation have a pitch of eight threads per inch. This produces a theoretical minimum translation distance of 0.00012 inch. The lead screws use zero-backlash design drive nuts. Even with this zero-backlash design the minimum translation distance is likely slightly greater than 0.00012 inch

5 TESTING THE MECHANICAL FUNCTION OF THE MICROSCOPE

Testing of the mechanical systems took place prior to the beam line installation. The system hardware and software performed as designed. PMQ support bases were moved in increments as small as 0.0005 to 0.001 inch with proper placement and positional tracking by the motion control hardware and software. The displacements were measured using auxiliary mechanical gages that were mounted to the lattice support plate.

6 MECHANICAL AND IMAGING PERFORMANCE OF THE MICROSCOPE

In October of 2002 the microscope assembly was installed onto the LANSCE Area C beam line. The PMQ sets were aligned to the global beam line coordinate system. Drive system communication checks were made on the microscope assembly. After the preliminary work was completed a static target was placed in the temporary test vessel up-stream from the microscope. A proton beam pulse was sent through the radiography lattice, and an image with good resolution and contrast of the static target was obtained at an approximate seven times magnification. Further tuning of the microscope resolution by slight longitudinal repositions of the PMQ sets adjusted the resolution of the static image. The inclusion of a beam collimator in the small beam tube of the microscope provided a small improvement in the resolution of the image. The microscope assembly performed well, and as designed in its first imaging experiment.

7 CONCLUSIONS

The ability to obtain magnified images in the approximate seven times range at heightened resolution will enable new classes of experiments to be conducted with proton radiography. Also, because the microscope magnetic lattice itself is rather compact a similar design could be used in other radiography beam lines for providing magnified images.

8 REFERENCES

[1]Gary Hogan, et al, "Proton Radiography", PAC99 proceedings, April, 1999.

[2]Tom Mottershead, et al, "Design and Operation of a Proton Microscope for Radiography at 800 MeV", these conference proceedings.

IONIZATION CROSS SECTIONS FOR ION-ATOM COLLISIONS IN HIGH ENERGY ION BEAMS

Igor D. Kaganovich*, Edward A. Startsev and Ronald C. Davidson,
Plasma Physics Laboratory, Princeton University, Princeton, New Jersey, 08543 USA

Abstract

Knowledge of ion-atom ionization cross sections is of great importance for many accelerator applications. When experimental data and theoretical calculations are not available, approximate formulas are frequently used. Based on experimental data and theoretical predictions, a new fit for ionization cross sections by fully stripped ions is proposed. The Born approximation and classical trajectory calculations are frequently used to estimate the cross sections. Neither approximation is expected to be valid over the entire range of projectile ions and target atoms. Aspects of both models must be included in order to address the shortcomings in the underlying assumptions. A large difference in cross section, up to a factor of six, calculated in quantum mechanics and classical mechanics, has been obtained for 3.2GeV I^- and Cs^+ ions. Because at such high velocities the Born approximation is well validated, the classical trajectory approach fails to correctly predict the stripping cross section at high energies for electron orbitals with low ionization potential.

INTRODUCTION

Ion beams lose electrons when passing through a background gas in accelerators, beam transport lines, and target chambers. As a result, the ion confinement time and beam focusability are decreased. An unwanted electron population, produced in ion-atom collisions, may also lead to the development of collective two-stream instabilities. Therefore, it is important to assess the values of ion-atom ionization cross sections. In contrast to the electron and proton ionization cross sections, where experimental data or theoretical calculations exist for practically any ion and atom, the knowledge of ionization cross sections by fast complex ions and atoms is far from complete [1]. While specific values of the cross sections for various pairs of projectile ions and target atoms have been measured at several energies [2-5], the scaling of cross sections with energy and target or projectile nucleus charge has not been experimentally mapped. When experimental data and theoretical calculations are not available, approximate formulas are frequently used.

The most popular formula for ionization cross section was proposed by Gryzinski [6]. The "web of science" search engine shows 457 citations of this paper, and most of the citing papers use Gryzinski's formula to evaluate the cross sections. In this approach, the cross section is specified by multiplication of a scaling factor and a unique function of the projectile velocity normalized to the orbital electron velocity. The popularity of Gryzinsky's formula is based on the simplicity of the calculation, notwithstanding the fact that the formula is not accurate at small energies.

Another fit, proposed by Gillespie, gives results close to Gryzinski's formula at large energies, and makes corrections to Gryzinski's formula at small energies [7]. Although more accurate, Gillespie's fit is not frequently used in applications, because it requires a knowledge of fitting parameters not always known *a priori*. In this paper, we present a new fit formula [8] for the ionization cross section which has no fitting parameters and is correct at small energies. The formula is checked against available experimental data and theoretical predictions.

The typical scale for the electron orbital velocity with ionization potential I_{nl} is $v_{nl} = v_0\sqrt{2I_{nl}/E_0}$. Here, n, l is the standard notation for the main quantum number and the orbital angular momentum quantum number, and $v_0 = 2.2 \cdot 10^8 cm/s$ is the atomic velocity scale [9]. The collision dynamics is very different, depending on whether v is smaller or larger than v_{nl}.

We first summarize the scaling of ionization cross section by the fully stripped ions. More than a century ago, Thompson calculated the ionization cross section in the limit $v >> v_{nl}$ [1]. This treatment neglected the orbital motion of the target electrons and assumed a straight-line trajectory of the projectile, which gives [1]

$$\sigma^{Bohr}(v, I_{nl}, Z_p) = 2\pi Z_p^2 a_0^2 \frac{v_0^2 E_0}{v^2 I_{nl}}, \qquad (1)$$

where $a_0 = 0.529 \cdot 10^{-8} cm$ is the Bohr radius. Subsequent treatments accounted for the effect of finite electron orbital velocity. The most complete and accurate calculations were done by Gerjuoy, by averaging the Rutherford cross section over the phase space of the atomic electrons leading to ionization. The result of the calculations can be expressed as

$$\sigma^{GGV}(v, I_{nl}, Z_p) = \pi a_0^2 Z_p^2 \frac{E_0^2}{I_{nl}^2} G^{GGV}\left(\frac{v}{v_{nl}}\right). \qquad (2)$$

Here, the scaling function $G^{GGV}(x)$ is defined in [8].

Bethe made use of the Born approximation of quantum mechanics to calculate cross sections [9]. The Born approximation is valid for $v/v_0 > 2Z_p$ and $v >> v_{nl}$ [9]. This yields the relation

$$\sigma^{Bethe} = \sigma^{Bohr} \times \left[0.566 \ln\left(\frac{v}{v_{nl}}\right) + 1.26\right]. \qquad (3)$$

Note that for $v >> v_{nl}$, the logarithm term on the right-hand side of Eq.(3) contributes substantially to the cross

* ikaganov@pppl.gov

0-7803-7738-9/03/$17.00 © 2003 IEEE

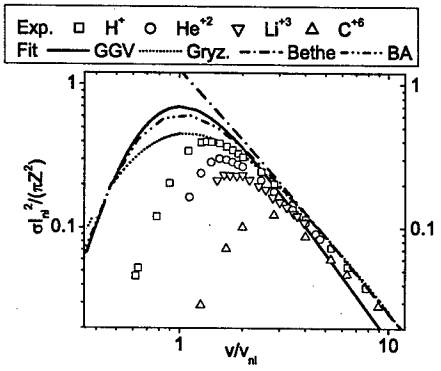


Figure 1: Ionization cross sections of atomic hydrogen by fully stripped ions showing both experimental data and theoretical fits. GGV stands for the classical calculation by Gerjuoy using the fit of Garcia and Vriens. Gryz denotes the Gryzinski approximation. Bethe stands for Bethe's quantum-mechanical calculation in the Born approximation, limited to $v > v_{nl}$ in Eq.(3). Finally, BA denotes the Born approximation in the general case. All values are in atomic units. For hydrogen, the ionization potential is $I_{nl} = 1/2$, $v_{nl} = v_0 = 2.19 \cdot 10^8 cm/s$, and the cross section is normalized to $a_0^2 = 0.529^2 \cdot 10^{-16} cm^2$.

section, and as a result the quantum mechanical calculation in Eq.(3) gives a larger cross section than the classical trajectory treatment in Eq.(1) (see Fig.1).

Gryzinsky attempted to obtain the ionization cross section using only classical mechanics, similar to Gerjuoy. But, in order to match the asymptotic behavior of the Bethe formula in Eq.(3) at large projectile velocities, Gryzinsky assumed an artificial electron velocity distribution function (EVDF) instead of the correct EVDF. After a number of additional simplifications and assumptions, Gryzinsky suggested an approximation for the cross section in the form given by Eq.(2) with another function $G^{Gryz}(x)$, which is specified in [6, 8]. The Gryzinsky formula can be viewed as a fit to the Bethe formula at large velocities $v >> v_{nl}$ with some rather arbitrary continuation to small velocities $v < v_{nl}$.

Figure 1 shows the experimental data for the cross sections for ionizing collisions of fully stripped ions colliding with a hydrogen atom,

$$X^{q+} + H(1s) \rightarrow X^{q+} + H^+ + e, \qquad (4)$$

where X^{q+} denotes fully stripped ions of H, He, Li, C atoms, and $(1s)$ symbolizes the ground state of the hydrogen atom. The experimental data are taken from the data of Shah *et al.* (see details in [8]).

From Fig.1 it is evident that the Bethe formula describes well the cross sections for projectile velocities larger than the orbital velocity $v >> v_{nl}$. At large energies, the GGV formula underestimates the cross section whereas, Gryzinsky's formula gives results close to the Bethe formula and the experimental data. Both, the GGV and Gryzinsky formulas disagree with the experimental data at small energies, because they assume free electrons, neglecting the influence of the target atom potential on the electron motion during the collision. To account for the difference between the Born approximation results and the experimental data for $v < v_{\max}$, Gillespie proposed to decrease the results of the Born approximation at low velocities by an exponential factor [7]. Although Gillespie's fit proved to be very useful, the fitting parameters are not available for most target atoms. Based on the results of the classical trajectory approximation, Olson developed a scaling for the total electron loss cross section [10], which includes both the charge exchange cross section and the ionization cross section. Unfortunately, application of the scaling to the ionization cross sections does not yield good agreement [8].

NEW FIT FORMULA FOR THE IONIZATION CROSS SECTION

We propose the following scaling [8]

$$\sigma^{ion}(v, I_{nl}, Z_p) = \frac{\pi a_0^2 N_{nl} Z_p^2}{(Z_p+1)} \frac{E_0^2}{I_{nl}^2} G^{new}\left(\frac{v}{v_{nl}\sqrt{Z_p+1}}\right), \qquad (5)$$

where

$$G^{new}(x) = \frac{\exp(-1/x^2)}{x^2}\left[1.26 + 0.283\ln\left(2x^2+25\right)\right]. \qquad (6)$$

The resulting plots of the scaled cross sections are shown in Fig.2. Comparing Fig.1 and Fig.2, it is evident that all of the experimental data merge close together in the scaled plot based on Eqs.(5) and (6).

We have also applied the new fit formula in Eqs. (5) and (6) to the ionization cross sections of helium [8]. Again, all of the experimental and theoretical results merge close together on the scaled plot. The new proposed fit in Eq.(5) with the function in Eq.(6) gives very good results for both hydrogen and helium [8].

STRIPPING CROSS SECTIONS AT LARGE PROJECTILE VELOCITIES

We have investigated theoretically and experimentally the stripping of 3.4 Mev/amu Kr^{+7} and Xe^{+11} in N_2; and 10.2 MeV/amu Ar^{+6}, 19MeV/amu Ar^{+8}, 30 MeV He^+, and 38 MeV/amu N^{+6}, all in He, N_2, Ar and Xe [5]. Both the Born approximation and the classical trajectory calculation give very good estimates, except for the case of Xe. This is not expected to be the case for fully stripped target ions and/or low ionization potentials of the projectile ions. Tables 1 and 2 show the stripping cross sections for only one electron from the outer electron shell for different projectile ions with the same velocity $v = 32v_0$ $(25MeV/amu)$ colliding with a nitrogen atom (N) or bare nitrogen nucleus (N^{+7}).

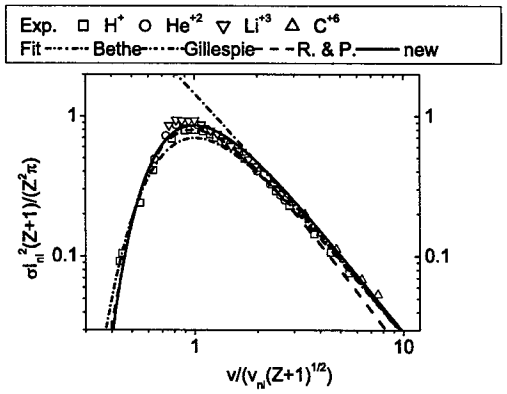


Figure 2: Ionization cross sections of hydrogen by fully stripped ions showing the scaled experimental data and the theoretical fits. BA denotes the Born approximation. Gillespie denotes Gillespie's fit. R.&P. symbolizes the fit proposed by Rost and Pattard [11]. "New" denotes the new fit given by Eq. (6).

$\sigma, 10^{-16} cm^2$	Cs^+	I^-	H^- ions
N	0.045	0.08	0.10
N^{+7}	0.32	2.5	12.5

Table 1. Stripping cross sections of $3.35GeV$ Cs^+, $3.2GeV$ I^- and $25MeV$ H^- by N or N^{+7} calculated making use of the Born approximation in quantum mechanics (stripping of only one electron from the outer electron shell is considered here with ionization potentials: $22.4eV$ for Cs^+; $3.06eV$ for I^-; and $0.75eV$ for H^-).

$\sigma, 10^{-16} cm^2$	Cs^+	I^-	H^- ions
N	0.10	0.47	1.34
N^{+7}	0.17	1.29	5.05

Table 2. The same stripping cross sections as in Table 1 but calculated making use of the classical trajectory approximation.

The result of cross sections calculations using Eq.(1) with a factor $5/3$, and the result in Eq.(3), coincide with the results in Tables 1 and 2 for the stripping cross sections by a fully stripped nitrogen ion calculated in the classical trajectory approximation and the Born approximation of quantum mechanics, respectively. The stripping cross sections calculated in the classical trajectory approximation for Cs^+ and I^- ions by fully stripped nitrogen ions is only factor 2-3 larger than the stripping cross sections by neutral nitrogen atoms, which is in qualitative agreement with the observations in [3]. However, there is a large difference, up to a factor 100 (for H^-), in the same stripping cross sections calculated in the Born approximation of quantum mechanics. It is evident that the stripping of Cs^+ ions by N^{+7} decreases by a factor of $22.4eV/3eV = 7.5$ compared with I^- ions, which is in agreement with the Bohr [Eq.(1)] and Bethe [Eq.(3)] formulas. However. the stripping cross sections for Cs^+ and I^- ions by a neutral nitrogen atom differ by only a factor of 2 in the Born approximation.

CONCLUSIONS

The new scaling formulas in Eqs. (5) and (6) for the ionization and stripping cross sections of atoms and ions by fully stripped projectiles has been proposed. We have recently investigated theoretically and experimentally the stripping of more than 18 different pairs of projectile and target particles in the range of 3-38 MeV/amu to study the range of validity of both the Born approximation and the classical trajectory calculation. In most cases both approximations give similar results [2, 5]. However, for fast projectile velocities and low ionization potentials, the classical approach is not valid and can overestimate the stripping cross sections by neutral atoms by an order-of-magnitude [13].

ACKNOWLEDGMENT

This research was supported by the U. S. Department of Energy.

REFERENCES

[1] R. K. Janev, L. P. Presnyakov and V. P. Shevelko, *Physics of Highly Charged Ions* (Springer, Berlin, 1999).

[2] D. Mueller, L. Grisham, I. Kaganovich, R. L. Watson, V. Horvat and K. E. Zaharakis, Physics of Plasmas **8**, 1753 (2001).

[3] R. E. Olson, R. L. Watson, V. Horvat and K. E. Zaharakis, J. Phys. B: At. Mol. Opt. Phys. **35**, 1893 (2002).

[4] R. L. Watson, Y. Peng, V. Horvat, G. J. Kim and R. E. Olson, Phys. Rev. A **67**, 022706 (2003).

[5] D. Mueller, L. Grisham, I. Kaganovich, R. L. Watson, V. Horvat, K. E. Zaharakis and Y. Peng, Laser and Particle Beams **20**, 551 (2002).

[6] M. Gryzinski, Phys. Rev.A **138**, 322 (1965).

[7] G. Gillespie, J. Phys. B: Mol.Phys. **15**, L729 (1982); G. Gillespie, Phys. Lett. **93A**, 327 (1983).

[8] I. D. Kaganovich, E. A. Startsev and R. C. Davidson, "Scaling cross sections for ion-atom impact ionization", to be submitted to Phys. Rev. A (2003); and to http://arxiv.org/abs/physics/.

[9] L. D. Landau and E. M. Lifshitz, *Quantum Mechanics* (Addison-Wesley Publishing Co., 1958).

[10] R. E. Olson, Phys. Rev. A **18**, 2464 (1978).

[11] J. M. Rost and T. Pattard, Phys. Rev. A **55**, R5 (1996).

[12] V. P. Shevelko, I. Yu. Tolstikhina and Th. Stoehlker, Nucl. Instr. Meth. Phys. Res. B **184**, 295 (2001).

[13] I. D. Kaganovich, E. A. Startsev and R. C. Davidson, "Comparison of quantum mechanical and classical trajectory calculations of cross sections for ion-atom impact ionization of negative- and positive-ions for heavy ion fusion applications", submitted to Phys. Rev. A (2003); and http://arxiv.org/abs/physics/0304112.

A PROPOSAL FOR AN ADDITIONAL BEAMLINE TO THE TRIUMF ISAC FACILITY

Glen Stinson and Pierre Bricault
TRIUMF, 4004 Wesbrook Mall, Vancouver, B.C., Canada, V6T 2A3

Abstract

The present ISAC facility at TRIUMF is fed by one beamline, beamline 2A, that can direct beam to one of two target locations. One of these targets has been in use since ISAC was commissioned; the second is currently being commissioned. The number of proposals for experiments at ISAC are such that we feel the need to deliver more simultaneous radioactive ion beams. A proposal has been made for an another beamline to ISAC so as to make additional beams available. Through partial extraction by H^- stripping, this proposed line would extract a 450-500 MeV beam from extraction port 4 of the TRIUMF cyclotron. A fast switching system would be used to feed an additional two target stations, each equipped with its own mass-separator system. These new target stations will allow target and ion-source development, and also at least three simultaneous experiments at ISAC. In addition to these two target stations, provision for a 200 μA beam dump has been made.

INTRODUCTION

ISAC at TRIUMF is a radioactive ion beam facility that uses the isotope separation on line (ISOL) technique to produce radioactive ion beams (RIB). The ISOL system consists of a primary production beam, a target/ion source, a mass separator, and a separated-beam transport system. These systems together act as the source of radioactive ion beams to be provided to the accelerator or the low-energy experimental areas. We utilize the 500 MeV - 100 μA primary proton beam extracted from the H^- cyclotron[1]. A new beamline has been built to transport this beam to one of the two target stations followed immediately by a residual proton beam dump.

Before discussing the proposed new beamline we present an overview of the beamlines that are presently in operation at TRIUMF. Figure 1 shows a layout of the TRIUMF cyclotron and the existing beamlines. Beamline 1A (BL1A), running to the east of the cyclotron, is the high-current beamline that feeds experiments in the meson experimental hall. Although capable of extracting beams in the energy range from 180 to 500 MeV at a maximum intensity of 170 μA, it is normally run at 500 MeV at a beam current of $\sim$150 μA. Beamline 2C is used for proton therapy (PT) and for isotope production. The latter accepts beam in the energy range of 70 to 110 MeV with a typical beam current of 50μA (maximum 80 μA). To the west of the cyclotron, beamline 4 (BL4) feeds beams to experimenters in the proton experimental hall. The energy range of this beamline is 180 to 500 MeV at a maximum intensity of 10 μA.

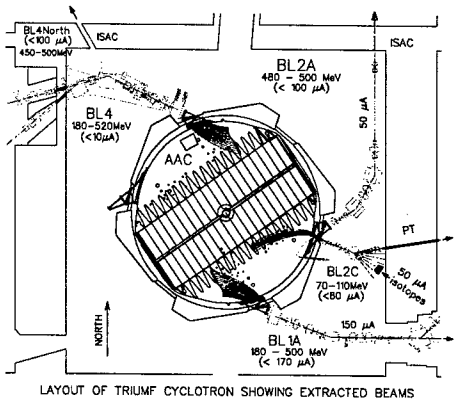


Figure 1: Beamlines in the cyclotron vault.

The TRIUMF ISAC facility is now fed by one beamline, beamline 2A, that delivers extracted beam in a northerly direction. This beamline is designed for extraction energies between 480 and 500 MeV and an intensity of 100 μA. Currently, the typical operating intensity of 50 μA is limited by the targets. The primary proton beam can be directed to one of two targets: the west target that has been in operation since ISAC was commissioned, and the east target to which the proton beam has been delivered just recently. Because of the demand for experimental beam, provision of additional beamlines to ISAC is considered imperative.

THE PROPOSED BEAMLINE 4N

Historically, extraction port 4 of the TRIUMF cyclotron has been used for beam delivery to the TRIUMF proton experimental hall. There the demand for beam time for experiments has been declining. Consequently, it is proposed to install another beamline from this extraction port such that this new beamline could be used to provide the additional lines to the ISAC facility. The vault portion of this beamline is seen in the upper left corner of figure 1. An overview of the proposed facility is shown in figure 2.

This new beamline, called beamline 4N (N for North), more-or-less parallels BL2A and runs north to deliver beam to another set of targets and mass analyzing systems. Thus, in principle, three beams of radioactive ions—one from beamline 2A and two from beamline 4N—could be delivered to ISAC.

0-7803-7738-9/03/$17.00 © 2003 IEEE

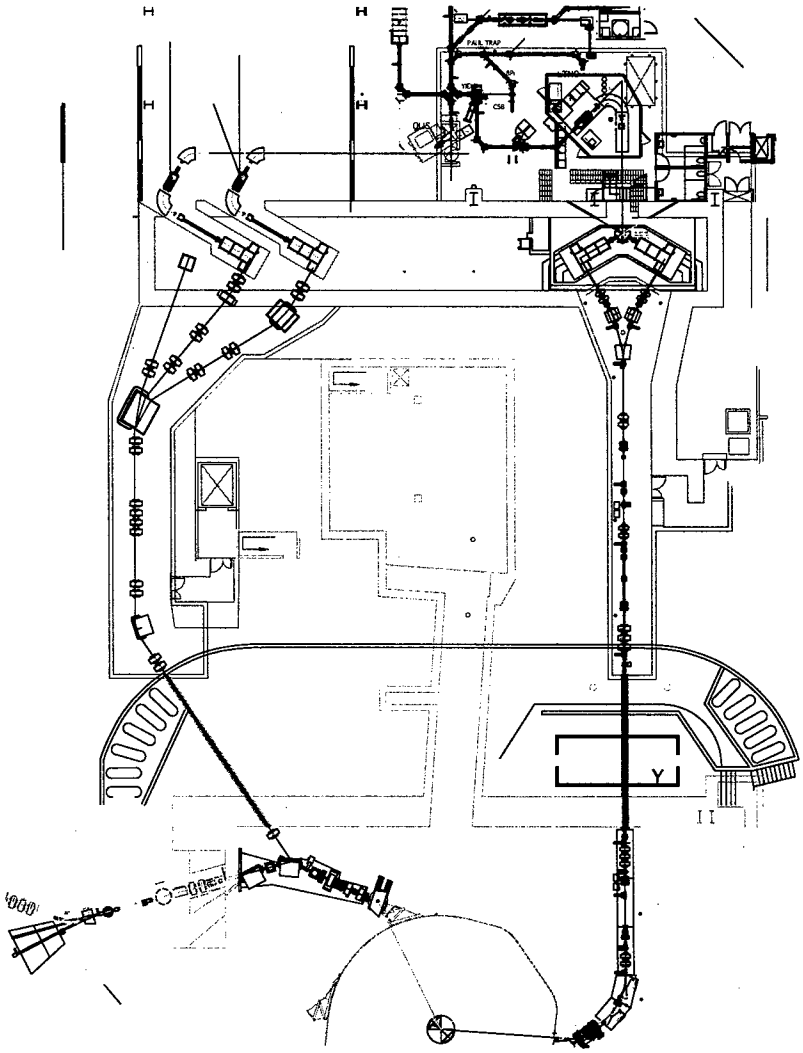


Figure 2: Beamlines to the ISAC facility: existing BL2A (right) and proposed BL4N (left).

Optics of the beamline

The vault section of BL4N utilizes the first three quadrupoles of BL4. Because we wish to leave the beamlines to the proton experimental hall intact, the existing 40° dipole is replaced with a switching magnet that bends 40° left and 32.6° right with respect to the direction of the extracted beam. A quadrupole doublet is also added in this vault section. There follows a long 16 m drift through the (existing) shielding berm of the cyclotron to the tunnel that encloses the remaining portion of the beamline. In the tunnel a quadrupole doublet, another 32.6° dipole, and another quadrupole doublet are the first transport elements encountered by the beam. These elements are used to produce a dispersed double waist at the midpoint of the long drift through the berm and a doubly-achromatic double waist downstream of the last dipole.

A four-quadrupole matching section follows to produce another double waist with a beam size of ± 2 mm in each of the horizontal and vertical directions.

A quadrupole doublet and a switching magnet follow. The switching magnet directs beam to the two targets. The east target is reached through a bend (relative to the beam direction at the entrance of the switching magnet) of 60° to the right followed by one of 30° to the left. Similarly, the west target is reached by a bend of 40° to the right followed by one of 10° to the left. Beam size at each target is designed to be a double waist of dimensions ± 2 mm in each of the horizontal and vertical directions. Because any targets will be relatively thick, double achromaticity at a target is not required. However, the beamline is designed to be spatially achromatic ($R_{16} = 0$ in TRANSPORT notation) only at a target.

Figure 3 shows the beam half-widths along the beamline leading to the east target. Note that the vertical half-width is plotted as negative.

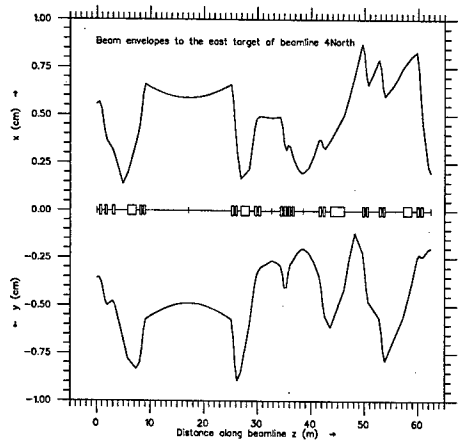


Figure 3: Beam envelopes along the beamline leading to the east target.

With all beamlines operating at their full intensities (BL1A at 150 μA, BL2C at 50 μA, BL2A at 100 μA, and BL4N at 100 μA), a beam-dump capacity of 400 μA will be required in order that the cyclotron be tuned for extraction of that amount of beam. Consequently, another beamline bending 20° degrees to the right (relative to the beam direction at the entrance of the switching magnet) is proposed to direct beam to a 200 μA beam dump. This, in conjunction with the BL1A beam dump, provide the required beam-dump capacity.

NEW TARGET STATIONS FOR THE ISAC FACILITY

The ISAC target stations are located in a sealed building serviced by an overhead crane. The target maintenance facility includes a hot cell, warm cell, decontamination facilities, and a radioactive storage area. The target area is sufficiently shielded so that the building is accessible during operation at the maximum proton beam current.

Beamline elements near the target are installed inside a large T-shaped vacuum chamber surrounded by close-packed iron shield. This general design eliminates the air activation problem associated with high-current target areas by removing all the air from the surrounding area. The design breaks naturally into modules; an entrance module containing the primary beam diagnostics, an entrance collimator and a pump port; a beam dump module containing a water cooled copper beam dump; a target module containing the target/ion source, extraction electrodes and first steering component and heavy ion diagnostics; and two exit modules containing the optics and the associated diagnostics for the transport of heavy ion beams.

The actual ISAC facility comprises two target stations. They share the same proton beam and the same mass separator. We can swap from one to the other by reversing the magnetic field in the Y-magnet in beam line 2A. This mode of operation does not permit target and new ion beam development and simultaneous delivery of RIB to experiments.

Development of new RIB is crucial because each element can take up to 2 years before it can be delivered to experiments. On the other hand, ion-source development in the harsh environment of the target is even more crucial.

In order to allow target and ion source developments for the future program at ISAC we are planning to build new target stations on the new beam line 4N. The actual target hall will be expanded to the west to include room for the two new target stations. The idea is to use as much of the actual infrastructure that we have developed over the last 10 years for the remote handling, nuclear ventilation, waste storage, etc. Furthermore, the new target station will use the same technology we have successfully developed for our actual RIB operation. Figure 2 shows a layout of the actual and proposed target stations. Each of the new stations will have its own mass separator in order to be able to switch from development work to RIB delivery in a very short time.

Eventually, we will be able to deliver more beams by the addition of a new switch-yard in the diagnostic box like the ISOLDE GPS design [2]. This design allows the selection of three ion beams within the mass range of $\pm 15\%$ from the central ray. This setup will eventually allow us to serve three experiments at the same time.

ACKNOWLEDGEMENT

This work has been funded under a contribution from the National Reseach Council of Canada.

REFERENCES

[1] P. G. Bricault, M. Dombsky, P. W. Schmor, and G. Stanford, Radioactive ion beams facility at TRIUMF, Nuclear Instruments and Methods, B126 (1997) p. 213.

[2] E. Kugler et al. NIM B70 (1992) 41.

ELECTRO-MECHANICAL DESIGN FOR INJECTION IN THE UNIVERSITY OF MARYLAND ELECTRON RING*

M. Walter#, S. Bernal, T. Godlove, I. Haber, R. A. Kishek, H. Li, B. Quinn, A. Valfells, Y. Zou, M. Reiser, P.G. O'Shea, Institute for Research in Electronics and Applied Physics (IREAP), University of Maryland, College Park, MD 20742

Abstract

Closure of the University of Maryland Electron Ring (UMER) is anticipated in May 2003. An initial prototype of the injection "Y" has been completed. Electro-mechanical aspects of the design and test results of this prototype are presented. The design incorporates an offset quadrupole and a pulsed dipole to achieve the 10-degree bend required from the injection line. To accommodate penetration of the pulsed dipole magnetic field a glass gap has been inserted at the point of injection. A fixture was used to align the sections of the assembly and serves as a permanent mount plate. A similar method will be used for extraction of the beam after the electron ring has been closed.

INTRODUCTION

The University of Maryland Electron Ring (UMER) is a low energy (10 kV), high intensity (100 mA), recirculating electron ring designed to explore the physics of space charge dominated beams [1,2]. Closure of the ring is anticipated in May 2003. In order to close the ring, a "Y" shaped section must replace the 10° bend that is currently installed on UMER at the point where the injection line intercepts the ring.

Design of the injection Y was dependent upon the method adopted for beam injection. Two design schemes are still in competition for the final experimental setup. The first utilizes electrostatic steering of the beam using an applied voltage on parallel capacitive plates in a custom-made vacuum chamber. This scheme would require several components to be precisely placed within the chamber and electrical feed-throughs on custom flanges for connections to the plates and any diagnostics. Due to limited space, the quadrupole magnets may also need to be placed within the vacuum. It was assumed that all these requirements would significantly increase the size, cost, and difficulty of the assembly.

The second method is magnetic steering of the beam using pulsed coils to create an orthogonal magnetic field component. This injection scheme eliminates the requirements for large chambers as all magnetic components may be mounted outside the vacuum boundary. Components may be adjusted, repaired, or even upgraded without breaking vacuum. The latter design was chosen for our first attempt and is described in this presentation. Work done by H. Li [3] describes in detail the magnetic components of this injection scheme. The work presented in this paper is primarily concerned with the mechanical design of this complicated assembly.

*This work is funded by US Dept. of Energy grant numbers DE-FG02-94ER40855 and DE-FG02-92ER54178.
#mwalter@ireap.umd.edu

DESIGN PROCEDURE

The design of the injection Y is centered (both physically and mathematically) on the point where the injection line meets the electron ring. Figure 1 shows an overview of the complete assembly. In this figure the beam is injected from the upper left (Arm #1), enters the ring to the right (Arm #2), and returns through the lower left arm (Arm #3).

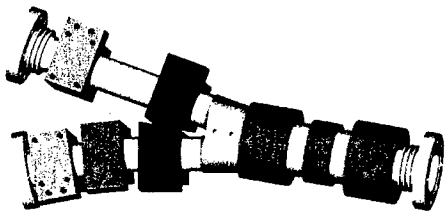


Figure 1: Injection Y assembly with magnets installed.

Glass Gap

The pulsed dipole is centered on the point of injection therefore a nonmagnetic material is required in this region. A glass gap of approximately 10 cm was constructed by Larson Electronic Glass. We wished to minimize disturbances to the magnet field in the region of injection, therefore the glass is joined to one inch of 316 series stainless steel at each end by the use of a "housekeeper" detail in which the steel is tapered down to approximately 0.002 inches of thickness where it meets the glass. This taper accommodates the differences in thermal expansion between the steel and glass. Weld reliefs were cut at the outer edge of the steel to facilitate connection at both ends to the vacuum structure. This bonding method eliminates any magnet material in the joint, but because the steel is so thin, it places limitations on structural strength at the same time. Details of this construction may be seen in Figure 2.

The minimum diameter of the cylinder is limited by its overall length and the fact that it must incorporate a

0-7803-7738-9/03/$17.00 © 2003 IEEE

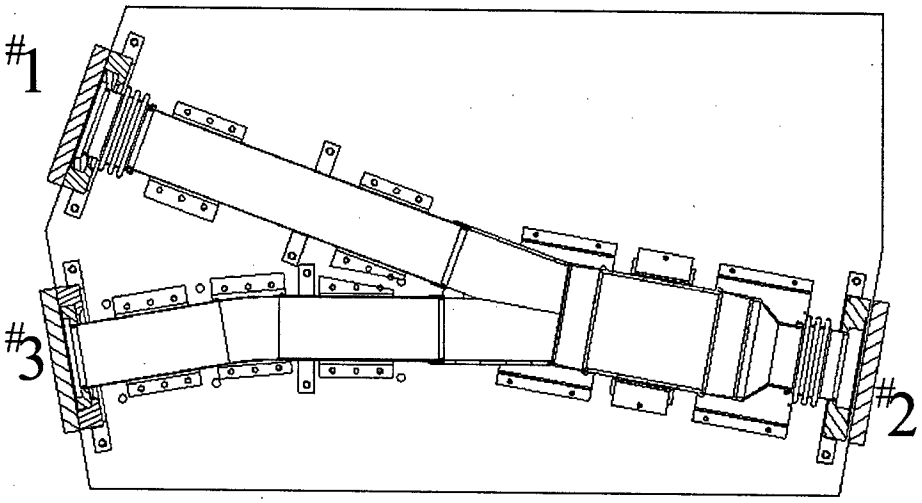


Figure 2: Cutaway view of injection Y assembly.

connection to the 2.0 inch pipes from both the injection line and ring return, each offset by plus and minus 10° respectively from the center line of the cylinder. When the length is fixed at 10 cm, these restrictions yield a diameter slightly larger than 3 inches. Since glass this large is commonly manufactured in 0.25 inch incremental diameter, we were forced to step up to outer diameter of 3.25 inches.

Finally, a thin coating of conducting material was required to prevent any possibility of charge buildup and damage to the glass or glass-steel joint. The coating also had to be thin enough to permit the fast pulsed magnetic field penetration. According to Faltens [4] the thickness of a thin coating is related to the field penetration time for a dipole by

$$dR = {ct\rho}/{200R} \qquad (1)$$

where dR is the thickness, c is the speed of light, t is the penetration time, ρ is resistivity, and R is the radius. For field penetration times on the order of 5 ns and using aluminium ($\rho=2.4\times10^{-8}\,\Omega$–m), Eqn. 1 yields very thin coating thicknesses of approximately 20 to 30 nm. It was found however, that the resistivity of the coating increases greatly with the formation of an oxide layer over the aluminium. The measured resistance of several prototype aluminium coated cylinders varied from 10 to 30 ohms, an order of magnitude better than needed. The resistance of the final assembly was not measured due to the risk associated with damaging the coating. All the vapor deposition was done within IREAP.

The pulsed dipole has been fabricated from #18 magnet wire wrapped on a plastic cylinder with a diameter of 88 mm. The pulsed dipole's axial length is 44 mm. Initial tests of the dipole indicate that the magnetic field rise time is on the order of 20 ns.

Junction

The three branches of the Y section are welded to one junction piece. The junction has been cut from a solid piece of 316 series stainless steel. Counterbores have been included to facilitate weld reinforcement rings required on arms #1 and #3. A weld relief was cut around the right end to minimize weld stresses when connecting to the glass gap assembly.

An oversized, offset quadrupole mounts over the junction. This quadrupole has been designed to bend the beam approximately 5° and ease the demands placed on the pulsed dipole.

Arm #1

The injection line mates to Arm #1 by means of a 4.5 inch rotatable Conflat flange. A set of formed bellows has been added to allow for small adjustments and connection to the downstream end of the injection line. The length of this arm was determined by the spacing of the focusing quadrupoles mounted over it. Weld support rings were added at both ends of the thin-walled stainless steel pipe to prevent damage during final assembly.

Arm #2

The injection Y mates to the electron ring at Arm #2. Formed bellows were incorporated again to allow for small adjustments and connection of the vacuum flanges. Arm #2 also reduces the diameter of the vacuum boundary back down to the standard diameter throughout the ring (d=1.96 inches). The reduction is done in a tapered section over 1.0 inch axial distance.

Arm #3

The return path of the beam is through Arm #3. No bellows were required because the downstream end of the last ring chamber has bellows. Arm #3 has a 10° bend as determined by the uniform spacing of the ring's 36 bending dipoles. Weld support rings were added at both ends of this arm again to prevent damage. Quadrupole mount blocks placed on both Arm #1 and Arm #3 near the junction will require modification as shown by the tapered cut in Figure 2.

Support plate

All the previously described components must be positioned within tolerances acceptable for UMER. To achieve this, a pair of support plates were manufactured at IREAP. The separate pieces were sandwiched between the two plates, held in position by brackets, and welded. The support plate simplifies alignment of the completed assembly within the electron ring because precision holes were bored under the injection point and the bend in Arm #3. Finally, the support plate provides physical protection to the very fragile glass gap and prevents compression forces on the glass-steel joint. A photograph of the completed assembly with the top plate removed is presented in Figure 3.

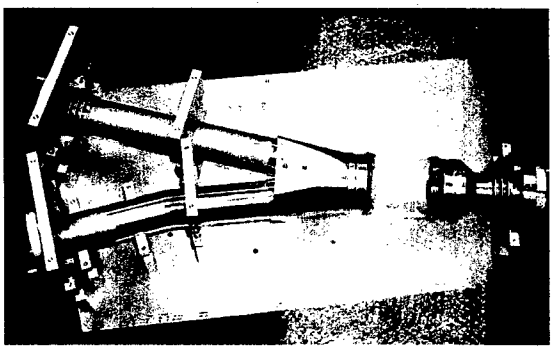


Figure 3: Completed assembly of the injection Y.

CONCLUSIONS

The pulsed magnetic beam steering version of the injection Y has been built. A glass gap with a thin conductive coating permits fast penetration of the pulsed dipole magnetic field. A prototype pulsed dipole has been built and successfully tested. Initial beam tests are scheduled for the next phase of experimentation when we will install the injection Y at the end of the beam line. Lessons learned in the design and construction of the injection Y will be used in development of the extraction Y.

REFERENCES

[1] http://www.ireap.umd.edu
[2] S. Bernal, et. al., "Beam Transport Experiments over a Single Turn at the University of Maryland Electron Ring", these proceedings.
[3] H. Li, et al., "Beam Optics Design on a New Injection Scheme for the University of Maryland Electron Ring (UMER)", these proceedings.
[4] personal conversation, T. Godlove and Andrew Faltens, LBNL, 20 June 1988.

BEAM OPTICS DESIGN ON A NEW INJECTION SCHEME FOR THE UNIVERSITY OF MARYLAND ELECTRON RING (UMER)*

H. Li†, R.A. Kishek, S. Bernal, T. Godlove, M. Walter, P.G. O'Shea, M. Reiser
Institute for Research in Electronics and Applied Physics, University of Maryland,
College Park, MD 20742

Abstract

A new optics design for beam injection into the University of Maryland Electron Ring (UMER) is proposed for multi-turn operations. We review the previous method where two pulsed and physically overlapped Panofsky quadrupoles (one is centered on the injector and the other is centered on the ring) are employed. The new design with only one DC quadrupole reduces both the mechanical and electrical complexities. The DC quadrupole is located symmetrically relative to the injector ($+10^0$) and the ring (-10^0). The beam's centroid motion as well as space-charge-dominated beam matching is studied to evaluate the new design. Some relevant beam issues such as stability and experimental considerations are also discussed for the multi-turn operations.

INTRODUCTION

The biggest challenge for the completion of the University of Maryland Electron Ring (UMER) [1] is the design of the beam optics for the injector region. This includes several quadrupoles and dipoles in a very stringent space. We had planned initially to use two pulsed Panofsky quadrupoles [2] as well as a pulsed dipole. As illustrated in Figure 1, the Panofsky Quad 1 (PQ1), replacing one of the regular ring quadrupole, is centered on the ring for multi-turn operation, while Panofsky Quad 2 (PQ2) is centered on the injector to provide focusing for the injected beam. However, by using this method, complex mechanical and electrical issues arise despite the simplicity in the beam optics. First of all, the two Panofsky quads must physically overlap. Furthermore, PQ1 has to be squeezed between PQ2 and the pulsed dipole. Thus, we have two quads of slightly different sizes over a very stringent space. Secondly, one of the PQs must be switched on (off) while the other is off (on) to avoid field overlap. Since we are planning to use wire magnetic quadrupoles, the number of conductors has to be reduced to achieve the desired fast switching, which means we must make a compromise between field quality and circuit inductance. In order to overcome the disadvantages stated above, we have chosen a simpler scheme, which reduces both the mechanical and electrical complexities, but also makes the beam optics more complicated than in the original design. As shown in Figure 2, one large DC quad is centered on the bisector of the injector legs and the ring, making $\pm 10^0$ angles with the pipe axes. When the injected and return beams pass through the large quadrupole with an angle and an axis-offset, the beams see a dipole field as well as a quadrupole field. The extra dipole term will be beneficial to assist the bending. In order to adjust the beam centroid exactly into the injection point, two extra short dipoles (SD1 and SD2) are required to steer the beam towards the quadrupole axis. Further, the large quadrupole must be a defocusing one horizontally so that the beam is bent outward of the injection point. We will describe here the relevant optics of beam centroid motion and envelope matching for injection of a space-charge-dominated beam.

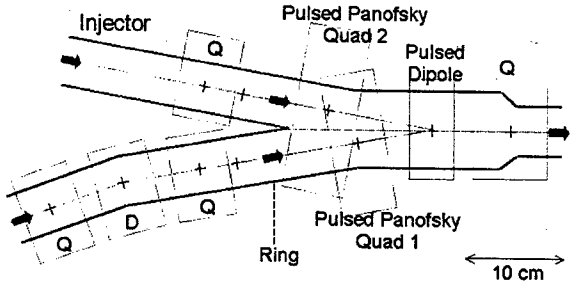


Figure 1: UMER injection design, scheme 1

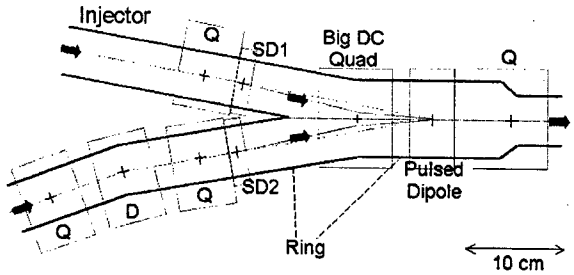


Figure 2: UMER injection design, scheme 2

BEAM CENTROID CONTROL

The deflection angle by SD1 must be precisely calculated so the beam centroid can move along the pipe

* Research supported by the U.S. Department of Energy.
† lihui@eng.umd.edu

axis after passing through the injection dipole. We have derived a first order solution for the simplified model shown in Figure 3. If we assume that the short dipole and pulsed dipole are both thin lenses, and the big DC quad is modeled with a hard-edge gradient profile and an effective length l, the overall transfer matrix can be written as $M_d \cdot M_l \cdot M_s$, where M_s, M_d and M_l are the matrices for the drift regions s, d and the quad, respectively. The matrix analysis yields the deflection angle θ (at the short dipole), and the bending angle β (at the pulsed dipole), required for zero injection error. Equations (1) and (2) give θ and β in terms of geometrical parameters and the quadrupole strength.

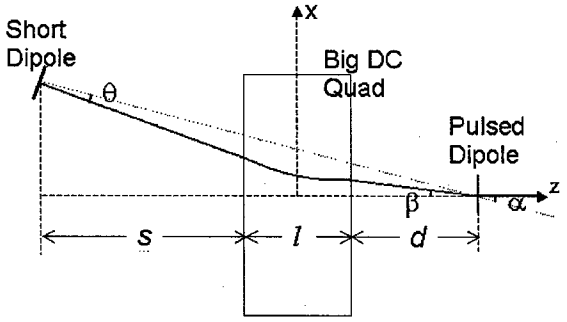


Figure 3: Simple injection model

$$\theta = \tan^{-1}\left(\frac{(a+kdb)(s+d+l)}{a(s+d)+b(1/k+ksd)}\tan\alpha\right)-\alpha, \quad (1)$$

$$\beta = \tan^{-1}\left(\frac{(s+d+l)}{a(s+d)+b(1/k+ksd)}\tan\alpha\right), \quad (2)$$

where $a=\cosh(kl)$, $b=\sinh(kl)$, $k^2=eG/(m\gamma\beta c)$, and G is the quad field gradient. For the UMER injector, given $\alpha = 10^0$, s = 6.66 cm, d = 4.69 cm, l=6.37cm and k = 11.63 m^{-1}, we get the required deflection angle $\theta \approx 2.43^0$ and $\beta \approx 7.26^0$ from Eqs. (1) and (2).

In reality, there are several factors that lead to deviations from the above results for θ and β. First, the big DC quad has a wide fringe field; second, the short dipole and the pulsed dipole are not thin lenses either; third, UMER is often operated in the strong space-charge-dominated regime. In order to reflect all these effects, we performed a more realistic simulation with accurate 3D magnetic fields in the particle-in-cell (PIC) code WARP [3]. In this stage, we chose a typical UMER operation point: E = 10 keV, I = 24 mA, ε = 30 μm, ν_0 = 7.6 and $k/k_0 \approx 0.30$ (tune depression). The simulation yielded the exact solution $\theta \approx 2.58^0$ and $\beta \approx 7.23^0$, which agrees very well with the approximate solutions from Eqs. (1) and (2).

Another important issue besides the correct θ and β settings is the stability of the scheme. If an initial error $\Delta\theta$ is introduced by SD1, an error at the injection point will occur. The matrix analysis give the injection errors caused by errors in θ.

$$\Delta x \approx -[a(s+d)+b(1/k+ksd)]\cdot\Delta\theta, \quad (3)$$

$$\Delta\beta \approx -(a+ksb)\cdot\Delta\theta. \quad (4)$$

where Δx is the location error and $\Delta\beta$ is the angle error at the injection point. For example, if the short dipole SD1 introduces an error of 1%, the induced injection errors are about 0.1 mm and 0.05^0. If the error in θ is 5%, the resultant injection errors are about 0.5mm and 0.23^0. These injection errors seem small for beam transport over short distances, but it's important to understand the effect for multi-turn operation. Clearly the largest potential errors may occur at SD2 and the big quad (see Fig. 2) on the beam return.

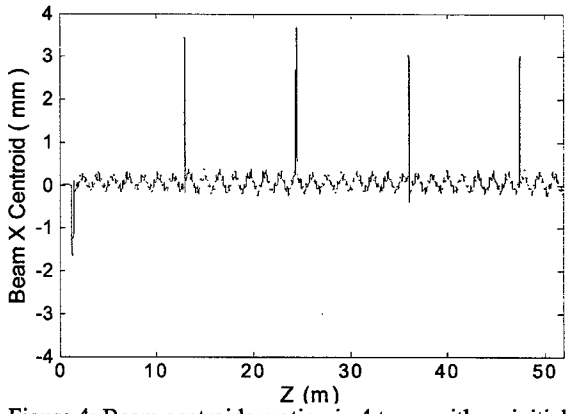


Figure 4: Beam centroids motion in 4 turns with an initial angle error 1% by SD1.

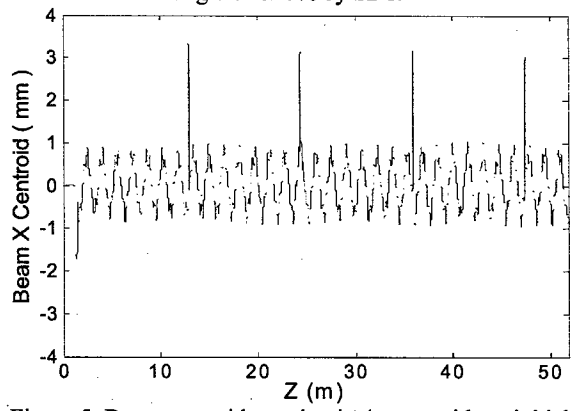


Figure 5: Beam centroids motion in 4 turns with an initial angle error 5% by SD1.

Figure 4 and 5 show the beam (x)centroid motion in 4 turns with 1% and 5% errors ($\Delta\theta/\theta$) in SD1, respectively. The bending angle by the pulsed dipole and the deflection angle by SD2 are set correctly. The beam centroid is measured relative to the reference trajectory of the ring lattice. In both Figs. 4 and 5, the first negative spike reflects the beam centroid deviation from the injector's

pipe center when passing though SD1 and the big quad. The positive spikes downstream happen exactly when the beam travels back to SD2 and the big quad in the following turns. From Fig. 4, the centroid oscillation (ripple) due to the 1% initial error is quite small. From Fig. 5, the centroid oscillations due to the 5% initial error do not grow in the following turns. The centroid ripples within 1 mm, which may be corrected with additional steering.

The mechanical design of the new injection scheme has been completed [4]. Since the magnet fields involved are small, we also need the means to balance the vertical component of the Earth's field. Equations (1) and (2) will be our starting point or guideline for future experiments. Refinements should be possible by changing the strengths of SD1 and pulsed dipole iteratively to reduce the injection errors, using a similar procedure as in the simulation. The injection errors (Δx, $\Delta\beta$) can be measured with the beam-position monitor (BPM) in the first diagnostic chamber in the ring.

BEAM MATCHING

Beam matching is an important topic besides the centroid control. The new injection scheme makes the optics design of the matching section more difficult than before. The reasons can be summarized as follows: (I) the beam will experience a changing quadrupole gradient (though the changes are small) through the big quad because of the curved trajectory. (II) The integrated field gradients along the beam trajectory for the x and y directions will be slightly different. This introduces a small asymmetry in the focusing. (III) The big quad has a much larger effective length and longer fringe fields than the regular ring quadrupoles, which impair the periodic FODO structure around the injection region. Despite these drawbacks, we can still work on a solution with the envelope sizes and slopes to do rms envelope matching. Unfortunately, we could not use the KV envelope equations to solve this problem because of the difficulties to build an accurate quadrupole model along the curved trajectory. We chose the same PIC code beam parameters as in the previous section. The beam matching is performed by varying the quadrupole strengths in the injector and observing the rms beam sizes and slopes (x, y , x', y') at a specific location in the periodic lattice after the injection region, where the desired beam sizes and slopes are known. The result is plotted in Figure 6 for the injector region and the first half turn. The beam displays a slight mismatch (~0.5mm) that does not grow for the following turns (not shown in the figure). It is an acceptable result considering the above effects. In the bottom part of Fig. 6, we also plotted the corresponding beam centroid motion. The negative spike occurs around the injection region, while the small ripples downstream correspond to effects from the ring bending dipoles.

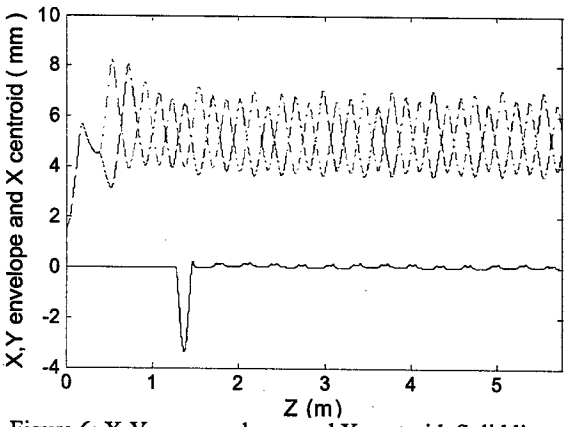


Figure 6: X-Y rms envelopes and X centroid. Solid line: x-y envelope; bottom line: x-centroid.

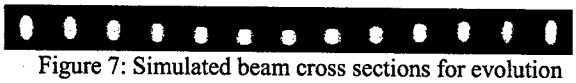


Figure 7: Simulated beam cross sections for evolution through the injection region.

Figure 7 shows the evolution of a matched beam through the injection region, starting 12 cm upstream of the large DC quad. The picture in the middle represents the beam at the center of the large DC quad. The beam centroid shift is clearly observed.

CONCLUSIONS

We have presented calculations and simulations for a new injection scheme for multi-turn operation in the University of Maryland electron Ring (UMER). The great advantage of the new scheme lies in its simplicity both mechanically and electrically: one large DC quadrupole is used instead of the two pulsed quads of the original design. In studying the beam optics, we have developed a simple model to calculate the deflection angles of the involved magnets, which can be used as the starting point for the experiments. We have also tested the stability of the system and found it to be acceptable. Furthermore, beam matching calculations with the new elements show slight mismatches that can be reduced by refinements in the design of the injection quad.

We would like to thank Tom Shea who gave us the initial idea for the injection scheme.

REFERENCES

[1] P.G. O'Shea et al, Experiments with space-charge-dominate beams for heavy ion fusion applications, Laser and Particle Beams, 20, 599-602, 2002.

[2] Y. Li, et al, Design, Simulation And Test of Pulsed Panofsky Quadrupoles, 1999 Particle Accelerator Conference (PAC'99), New York City, NY, 1999.

[3] D.P. Grote, et al, Fus. Eng. & Des. 32-33, 193-200, 1996.

[4] M. Walter et al, Electro-Mechanical Design for Injection in UMER, TPPB025, these proceedings.

BEAM EXTRACTION OF THE POP FFAG WITH A MASSLESS SEPTUM

Y. Yonemura*, T. Adachi, M. Aiba, S. Machida, Y. Mori, A. Muto, J. Nakano,
C. Ohmori, I. Sakai, Y. Sato, M. Sugaya, A. Takagi, R. Ueno, T. Uesugi,
A. Yamazaki, T. Yokoi, M. Yoshimoto, Y. Yuasa, KEK, Ibaraki, Japan
M. Matoba, Kyushu University, Fukuoka, Japan
K. Koba, FNAL, Batavia

Abstract

We propose a new extraction scheme with a massless septum magnet in FFAG accelerator, with which the DC beam can be extracted. The system consists of a combination of massless and ordinary septa without kickers. After passing through the massless septum, the beam tail is stretched by the field gradient of the massless septum magnet, and that can be extracted with an ordinary septum. From the result of the tracking simulation, the principle of the extraction scheme is verified. The result of the performance test of the massless septum indicates that the magnet works well as designed, and this scheme is feasible.

INTRODUCTION

After the first proton acceleration of the Proof of Principle (PoP) FFAG synchrotron, we have been studying the scheme of the beam extraction from it.

Due to the fast beam acceleration of FFAG accelerator, fast extraction with high repetition kicker magnet is ordinary adopted as the beam extraction scheme of FFAG. Therefore he development of kicker with high repetition rate is a technical challenge. On the other hand, the slow extraction scheme using the resonance of horizontal betatron oscillation requires complicated control system. Here, by making use of the characteristics of FFAG accelerator, a novel slow extraction scheme is proposed.

BEAM EXTRACTION WITH A MASSLESS SEPTUM MAGNET

The proposed scheme employs so called "massless septum" which is proposed by LANL group [1] [2]. Typical configuration of the magnet is shown in Figure 1, and the generated field is typically as shown in Figure 5. The field of the massless septum is divided into two types. One is flat field region and the other is the region with field gradient. The region with the field gradient is the key of the proposed scheme.

The principle of the extraction schemes is as follows. As the beam is accelerated, the orbit approaches to the region with field gradient. Finally, when a part of the beam traverses the region, the beam tail is stretched by the field gradient (Figure 1 (a)). The beam tail is scraped with ordinary septum, and extracted (Figure 1 (b)). It is the basic idea of the proposed extraction scheme. After that, the beam tail is returned to the closed orbit in the secondary massless septum magnet (Figure 1 (c)).

Similar to the case of slow extraction, the high efficiency of the beam extraction is expected when the extraction scheme with massless septum magnet is employed. Because the tail of the beam that is developed with massless septum magnet is sufficiently long compared to the thickness of the coil or wire. the efficiency of beam extraction with a massless septum magnet can be obtained as below:

$$\epsilon = 1 - \frac{t}{\Delta X / \cos\alpha} \qquad (1)$$

ϵ, t and ΔX are the efficiency of the extraction, the thickness of the electric septum and the moving distance after the acceleration, respectively. α is an acute angle between the beam and it's tail.

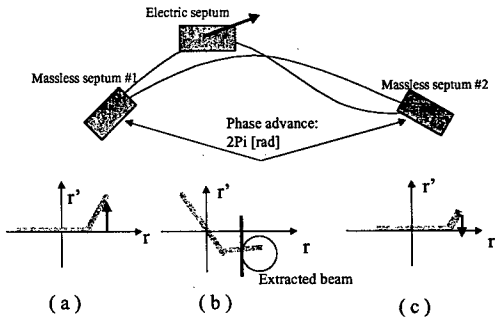


Figure 1: Extraction scheme with massless septum magnet (a) beam tail is developed (b) beam is extracted with an electric septum (c) beam tail returned to the closed orbit

TRAKING SIMULATION OF THE BEAM EXTRACTION WITH MASSLESS SEPTUM

To examine the feasibility of the extraction scheme with the massless septum magnet, single-particle tracking simulation using Runge-Kutta method was carried out in the PoP FFAG synchrotron. For the simplicity of the simulation, the beam is assumed to be linealy distributed (See Figure 1).

Figure 2 shows that the configuration of the extraction system for the simulation. Since the phase advance per one

* yonemura@post.kek.jp

0-7803-7738-9/03/$17.00 © 2003 IEEE

cell of the PoP FFAG is nearly equal to 90 degree, two massless septum magnets are separated by 4 cells in this extraction scheme. The result of the simulation is shown in Figure 3 As the result of the tracking simulation, the principle of the extraction scheme is verified.

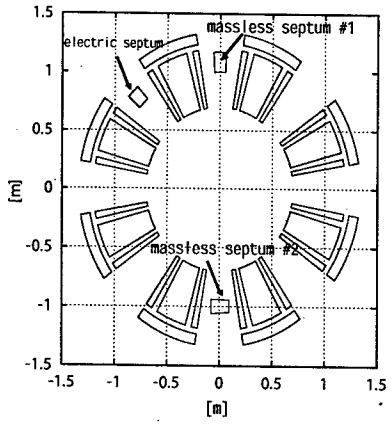


Figure 2: Configuration of the extraction system.

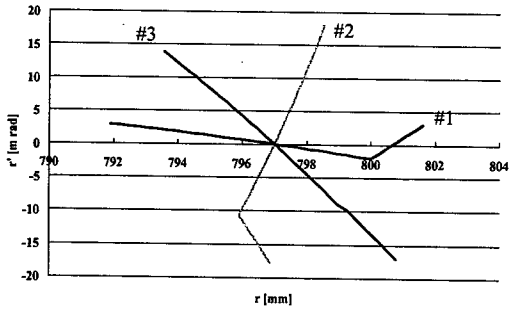


Figure 3: Shape of the beam in the phase space at the first masless septum magnet (#1), electrostatic septum (#2) and the second massless septum magnet (#3).

DESIGN OF THE SEPTUM MAGNET

A septum magnet has been designed for the purpose to examine the feasibility of use the massless septum magnet. the calculation of magnetic field were carried out with the computer code POISSON. The upper half of the designed magnet is shown in Figure 4. The calculated field lines are also presented in the same figure.

The horizontal size and vertical size are 17cm and 4.5cm respectively. A pair of shims is put on the pole edges to pump the magnetic field. The gap height from the medium plane is 5mm in the extracted beam region. When the coil currents are 1000AT, the magnetic flux density in the

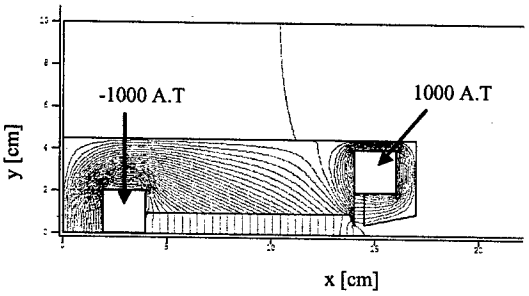


Figure 4: Upper half of the designed magnet. The calculated field lines are also presented in this figure.

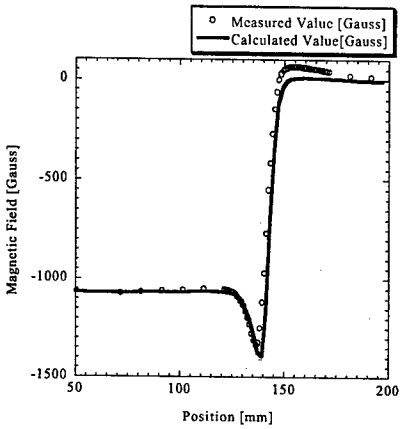


Figure 5: Magnetic flux density at the median plane plotted as a function of the horizontal position.

extracted region is 0.1 T. In Figure 5, the magnetic field strength at the median plane is plotted as a function of the horizontal position from left edge of magnet.

We made have built a model of the massless septum magnet based on the field calculation, and The measurement of the magnetic field was carried out. The result of the measurement also is shown in Figure 5. This figure indicates that the calculation result and the experiment result show well agreement. The picture of the magnet is shown in Figure 6.

EXPERIMENT WITH THE PROTOTYPE MAGNET

Using the PoP FFAG synchrotron, the perfomance of the prototype magnet was investigated. The aim of the experiment was confirming the effect that the beam tail is stretched by the field gradient of the magnet. The massless septum magnet was installed in the chamber of straight section (Figure 2 #1). The ring Faraday cup was installed at the exit of the magnet to observe of the beam. In this experiment, we have compared the beam oscillation when the magnet was excited and not excited. The typical exper-

imental result is shown in Figure 7. In this figure, when the magnet is not excited, the rising edge of the signal is sharp. The signal of the faraday cup is rising gradually, and the rise time becomes fast when the magnet is excited. This result indicated that the beam traversing inside of the massless septum has been successfully extracted.

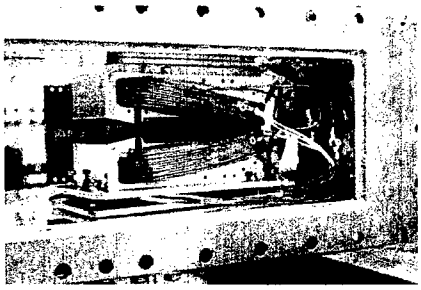


Figure 6: Picture of the massless septum magnet.

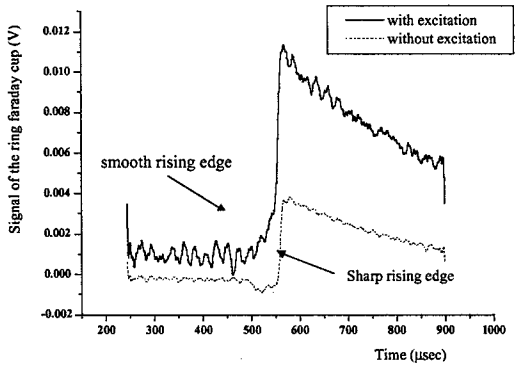


Figure 7: Signal of the faraday cup with excitation magnet and without

SUMMARY

We have proposed a new extraction scheme with massless septum magnet, and the feasibility of the scheme is examined. From the result of the tracking simulation, the principle of the extraction scheme is verified. The result of the performance test of the massless septum indicates that the magnet works well as designed, and the extraction scheme is feasible.

To realize the scheme, the additional simulation in detail and experiment are now going on.

REFERENCES

[1] J. Liu et al., Proc. of the Advanced Hadron Facility Accelerator Design Workshop, 1988.

[2] H. S. Butler et al., Proc. of the advanced Hadron Facility Accelerator Design Workshop, 1988.

[3] Eugene P. Colton, Slow Extraction At LAMPF II, IEEE Trans. on Nucl. Scie., Vol. NS-32, No.5, 2439(1985)

[4] M. Aiba et al., "Beam Injection And Extraction in 150MeV FFAG", Proc. of European Particle Accelerator Conference, 1076(2002)

[5] M. Aiba et al., "DEVELOPMENT OF A FFAG PROTON SYNCHROTRON", Proc. of 7th European Particle Accelerator Conference, 581 (2000)

[6] M. Yoshimoto et al., "RECENT BEAM STUDIES OF THE POP FFAG PROTON SYNCHROTRON", Proc. of Particle Accelerator Conference, 3254 (2001)

HEAVY ION BEAMS IN THE LHC

J.M. Jowett, J.-B. Jeanneret, K. Schindl, CERN, Geneva, Switzerland

Abstract

In addition to protons, the LHC will collide beams of heavy ions. The beam intensity in the LHC ring is tightly constrained from below by beam instrumentation (visibility on the beam position monitors in particular) and from above by magnet quench limits, the capabilities of the injectors and beam lifetime. We summarise current plans for beams of lead ions with emphasis on nuclear electromagnetic interactions, commissioning strategies and the differences from operation with protons.

INTRODUCTION

The LHC experiments have requested collisions between pp, Pb-Pb, p-Pb and p-A beams, where 'A' denotes one of a few possible species of light ion. Soon after start-up of the collider, Pb-Pb collisions will be provided to the heavy-ion detector ALICE and one or both of the general-purpose detectors CMS and ATLAS. The design of the chain of injectors, including the new LEIR accumulator ring, is described elsewhere [1,2].

Given that the nominal emittance of the ions corresponds to beams of the same size as the nominal protons at the same magnetic field, many considerations for protons [3] can be applied quite directly to the ions. In this paper, we concentrate on collisions between fully stripped $^{208}Pb^{82+}$ ions, highlighting some of the main issues in the main LHC ring itself. Earlier studies on the beam parameters for ions are summarised in [4].

Recall that the momentum of a fully-stripped ion of charge Z and mass number A (in AMU) in a ring with magnetic field and radius appropriate for a proton of momentum p_p is Zp_p while its momentum per nucleon is Zp_p/A. Table 1 shows some main parameters for lead ions at the nominal collision energy corresponding to $p_p = 7\,\text{TeV}$.

NUCLEAR INTERACTIONS OF IONS

Besides the hadronic nuclear interactions

$$^{208}Pb^{82+} + {}^{208}Pb^{82+} \xrightarrow{\text{nuclear}} X, \qquad (1)$$

nonlinear QED effects come into play in the peripheral collisions of heavy ions at LHC energies [5]. Cross-sections for electromagnetic interactions, notably those involving e^+e^- pair production, are very large. These processes include the familiar Rutherford elastic scattering:

$$^{208}Pb^{82+} + {}^{208}Pb^{82+} \xrightarrow{\gamma} {}^{208}Pb^{82+} + {}^{208}Pb^{82+} \qquad (2)$$

and free pair production:

$$^{208}Pb^{82+} + {}^{208}Pb^{82+} \xrightarrow{\gamma} {}^{208}Pb^{82+} + {}^{208}Pb^{82+} + e^+ + e^- \qquad (3)$$

Table 1: Parameters for Pb-Pb collisions in the LHC common to all performances scenarios given later.

Energy per nucleon	E_u	2.76	TeV
Crossing angle	ϕ	~80	μrad
Transverse (RMS) normalised emittance	ε_n	1.5×10^{-6}	m
Longitudinal emittance	ε_z	2.5	eV s/charge
Bunch length (RMS)	σ_z	0.075	m
No. of experiments	n_{exp}	2 / 3	

Although copious, these two processes are harmless because the momentum changes of the ions are small.

Electron Capture by Pair Production (ECPP)

This process is closely related to (3) but the final state electron is captured by one of the ions

$$^{208}Pb^{82+} + {}^{208}Pb^{82+} \xrightarrow{\gamma} {}^{208}Pb^{82+} + {}^{208}Pb^{81+} + e^+ \qquad (4)$$

The cross section for ECPP has been discussed in numerous works; among them the extrapolation from measurements in fixed-target experiments at the SPS [6] and recent QED calculations [7]. Table I of [7] provides the best currently available estimate of the Pb-Pb ECPP cross-section at LHC energies. Summing the partial cross-sections for a few of the lowest bound states gives $\sigma_{ECPP} \approx 281\,\text{barn}$, significantly higher than in earlier discussions.

The magnetic rigidity of the ion is increased by the capture of the electron and the equivalent fractional momentum deviation is

$$\delta_p = \frac{1}{Z-1} = 0.012 \quad \text{for Pb} \qquad (5)$$

This shifts the momentum right outside the acceptance

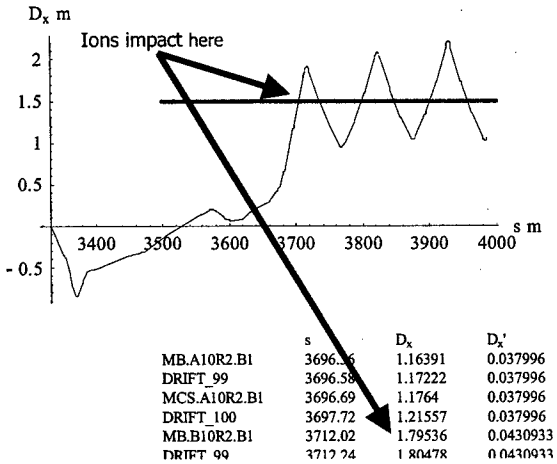
$$|\delta_p| > \delta_p^{max} \approx 6\times10^{-3} \qquad (6)$$

and the lost ion will follow a dispersive trajectory from the interaction point towards the downstream arc until it strikes the beam screen at a point where the horizontal dispersion function satisfies the condition

$$x_\delta(s) \approx D(s)\delta_p \approx R_{\text{eff}} = 18\,\text{mm} \Rightarrow D(s) \approx 1.5\,\text{m} \qquad (7)$$

The angle of incidence at the point of impact $x'_\delta(s) \approx D'(s)\delta_p$. To see where this point is, we inspect the example of the ions of Beam 1, travelling away from an interaction point to the right (Figure 1). Impact on the

0-7803-7738-9/03/$17.00 © 2003 IEEE



	s	Dx	Dx'
MB.A10R2.B1	3696.[illegible]	1.16391	0.037996
DRIFT_99	3696.58	1.17222	0.037996
MCS.A10R2.B1	3696.69	1.1764	0.037996
DRIFT_100	3697.72	1.21557	0.037996
MB.B10R2.B1	3712.02	1.79536	0.0430933
DRIFT_99	3712.24	1.80478	0.0430933

Figure 1: Identification of ion impact in the first magnet of the dispersion suppressor. The plot starts at the collision point in the ALICE detector.

beam pipe occurs inside the first superconducting dipole magnet of the dispersion suppressor (MB.B10R2.B1). A similar situation prevails for ions of Beam 2 travelling to the left and at every interaction point where ions collide.

Thus, ECPP creates secondary beams of $^{208}Pb^{81+}$ ions emerging in both directions from each collision point and hitting the beam pipe in well-defined locations [8]. The beam-pipe heating may be strong enough to quench superconducting magnets. The distance over which this secondary beam's energy is diluted, can be estimated as

$$l_d = \frac{2\sqrt{\varepsilon\beta_x + D_x^{\,2}\sigma_\delta^{\,2}}}{D'(s)\delta_p} \approx 1.4\,\mathrm{m} \qquad (8)$$

Note that this estimate assumes that the full energy is distributed over a distance corresponding to $\pm 1\sigma$ of the beam distribution in the horizontal plane. On one hand this is pessimistic because the real distribution is somewhat wider. On the other, the energy density at the peak of the distribution in the centre will be higher so the present estimate seems reasonable. The shower length, also of the order of 1 m, further dilutes the energy. Adding this "in quadrature" leaves us with $l_{deff} \approx 1.7\,\mathrm{m}$.

Assuming rather complete fragmentation of the ions in the material, the quench limit for Pb ions at 7 TeV,can be inferred from that of protons by dividing by the charge

$$f_q(\mathrm{Pb}) = \frac{1.7\times10^{7}\ \mathrm{p/m/s}}{Z} = 8\times10^{4}\ \mathrm{Pb/m/s} \qquad (9)$$

Equating this to the flux of $^{208}Pb^{81+}$ ions from the ECPP process,

$$f_q(\mathrm{Pb}) = \frac{L\,\sigma_{\mathrm{ECPP}}}{l_{deff}} \qquad (10)$$

Table 2: Cross sections (barn) for collisions of protons, Argon (for comparison) and Lead ions at LHC energy.

	σ_H	σ_{EMD}	σ_{ECPP}	σ_{tot}
p	0.1	0	4×10^{-11}	0.1
Ar	3.1	1.7	.04	4.8
Pb	8	225	281	514

shows that the luminosity is limited to $L \approx 0.5\times10^{27}\,\mathrm{cm^{-2}s^{-1}}$, a factor 2 below the nominal [4].

The cross section increases only weakly with energy, $\sigma_{ECPP} \approx A\log\gamma_{col} + B$. Possible cures (e.g., collimation) and various safety factors and uncertainties in this calculation will be clarified by more detailed study.

Electromagnetic Dissociation (EMD)

One nucleus can make a transition to an excited state that subsequently decays by emitting a neutron:

$$^{208}Pb^{82+} + {}^{208}Pb^{82+} \xrightarrow{\gamma} {}^{208}Pb^{82+} + (^{208}Pb^{82+})^* \downarrow {}^{207}Pb^{82+} + n \qquad (11)$$

The change in mass number is a decrease in magnetic rigidity of the ion equivalent to a momentum deviation

$$\delta_p = -\frac{1}{A-1} = -4.8\times10^{-3} \text{ for Pb} \qquad (12)$$

from the nominal momentum. Comparing this with the momentum acceptance δ_p^{max},

$$|\delta_p| + \sigma_\delta = 4.8\times10^{-3} + 0.8\times10^{-3} < \delta_p^{max} \approx 6\times10^{-3} \qquad (13)$$

These off-momentum ions should be intercepted by the momentum collimation system. A small fraction of them, which have large enough betatron amplitude, will be lost in the nearby dispersion suppressor. Their longitudinal loss map will be large, thus making them harmless.

LUMINOSITY AND BEAM LIFETIME

The total cross-section for removal of an ion from the beam is $\sigma_{tot} \approx \sigma_H + \sigma_{EMD} + \sigma_{ECPP}$ (see values in Table 2). Nuclear electromagnetic processes dominate the beam loss rate. Rather than discussing the non-exponential decay during a fill, we limit ourselves here to quoting the *initial* beam (intensity) lifetime due to beam-beam interactions for a configuration in which beams collide at n_{exp} interaction points:

$$\tau_1 = \frac{k_b N_b}{n_{exp} L\,\sigma_{tot}} = \frac{22.4\,\mathrm{hour}}{n_{exp}} \left(\frac{10^{27}\,\mathrm{cm^{-2}s^{-1}}}{L}\right) \qquad (14)$$

and the initial luminosity half-life is $\tau_{L1/2} = (\sqrt{2}-1)\tau_1$.

But the luminosity may be limited by the experiments or by the ECPP quench limit. Given that

$$L = \frac{k_b N_b^{\,2} f_0}{4\pi\sigma^{*2}} = \frac{k_b N_b^{\,2} f_0}{4\pi\beta^* \varepsilon_n}\gamma \qquad (15)$$

the decay could be offset by varying $\beta^* \propto N_b^{\,2}$ as the intensity decays. This "β^*-tuning" [9] would be very valuable during collision to maximise integrated luminosity—especially if we can find some scope for increasing the initial value of N_b, whose value is limited by injection from the SPS [2]. It is not expected to be a straightforward operational procedure in the LHC as the beams will have a tendency to move apart by distances comparable with the beam size at the IP.

A higher initial value of β^* would also increase the margin for the ECPP quench limit if necessary and further increases the interest in β^*-tuning.

A further operational complication is that the beam position monitors (BPMs) in the LHC require a minimum charge per bunch in order to function properly. Even with recent improvements, this corresponds to $N_b \approx 2\times10^7$ for Pb ions in the arc BPMs, little more than a factor of 3 less than the nominal intensity, implying a very narrow gap between "commissioning" and "design" values. With the full complement of 592 ion bunches, commissioning would also be dangerously near the ECPP quench limit.

These and other reasons related to the project schedule, led to the recent proposal [2] of an additional "Early" mode of operation of the injector chain, leading to about 10 times fewer bunches in the LHC. In this scheme, which we envisage using in an initial period of ion running, N_b and β^* (and hence the beam lifetime) could have their nominal values but the ECPP quench limit would be far away, the bunches would be visible on the BPMs, the injector scheme would be simplified and some interesting heavy ion physics would be accessible with the reduced luminosity. If necessary, the initial value of β^* could be raised to increase the beam lifetime.

Although the present estimate of ECPP gives serious cause for concern, we would like to emphasise that the uncertainties and safety margins still in hand do not allow the design luminosity of $L \approx 10^{27}\,\mathrm{cm^{-2}s^{-1}}$ to be definitively excluded.

The *initial* performance parameters in various operational scenarios are summarised in Table 3.

The relative importance of the various physical effects limiting performance can be quite different with ions other than lead.

Other issues remaining to be studied for ions include the optimum crossing-angles, collimation and a review of the beam instrumentation.

Finally we mention that a full design report for the "Ions for LHC" project is due in the coming months.

ACKNOWLEDGEMENTS

We thank numerous colleagues in the I-LHC and LHC projects for many helpful discussions.

REFERENCES

[1] M. Chanel, *LEIR: The Low Energy Ion Ring At CERN* in Proc. EPAC2002, Paris.
[2] Various authors in Proc. Workshop on LHC Performance – Chamonix XII, CERN-AB-2003-008.
[3] L.R. Evans, paper MOPA001, this conference.
[4] D. Brandt, LHC Project Report 450, 2000.
[5] S.R. Klein in *Proc. 18th Advanced ICFA Beam Dynamics Workshop on Quantum Aspects of Beam Physics*, Capri, 2000, World Scientific.
[6] P. Grafström et al, Proc. PAC99, New York.
[7] H. Meier et al, Phys. Rev. A, **63**, 032713 (2001).
[8] S. R. Klein, Lawrence Berkeley National Laboratory Report No. LBNL-45566, e-print physics/0005032
[9] A. Morsch, ALICE-INT-2001-10.

Table 3: Initial performance in various running scenarios.

		Nominal	**Intensity quench-limited**	**Quench-limited, β*-tuning**	**Early scheme**	**Units**
Number of bunches	k_b	592			~60	
Bunch spacing (typical)	S_b / c	99.8			1350	ns
Twiss function at IP $(x = y)$	β^*	0.5		1.0	0.5	m
Number of Pb ions/bunch	N_b	7×10^7	5×10^7	7×10^7		
Beam size at IP	σ^*	16		22.5	16	μm
Luminosity half-life for $n_{exp} = 2,3$	$\tau_{L1/2}$	4.6 / 3.1	9.2/6.2		4.6 / 3.1	hour
IBS growth time	τ_{IBS}	15	21	15		hour
Initial luminosity	L	1.0	0.5	0.5	0.1	$10^{27}\,\mathrm{cm^{-2}s^{-1}}$

ABORT GAP STUDIES AND CLEANING DURING RHIC HEAVY ION OPERATION*

A. Drees†, L. Ahrens, R. Fliller III, W. Fu, G. Heppner, BNL, Upton, NY 11973
V. Kain, CERN, Geneva, Switzerland

Abstract

Since the RHIC Au-Au run in the year 2001 the 200 MHz cavity system was used at storage and a 28 MHz system during injection and acceleration. The rebucketing procedure causes significant debunching of heavy ion beams in addition to amplifying debunching due to other mechanisms. At the end of a four hour store, debunched beam can account for more than 30% of the total beam intensity. In order to minimize the risk of magnet quenching due to uncontrolled beam losses at the time of a beam dump, a combination of a fast transverse kicker and copper collimators were used to clean the abort gap. This report gives an overview of the upgraded gap cleaning procedure and the achieved performance. The upgraded procedure in conjunction with a new application allows to measure properties of the debunched beam routinely.

INTRODUCTION

While a 28 MHz cavity is used for injection and acceleration in RHIC,thus defining the total number of buckets in RHIC to be 360, a 200 MHz storage system for Au-particles is in use since the 2001 run. Beam debunching of heavy ions is due to a combination of RF failure, rebucketing and IBS [1] and can account for as much as 50% of the total beam. In addition, any species beam can debunch due to RF cavity failures. The two rings, blue and yellow respectively, and the six interaction regions (IR) of RHIC with the four experiments are sketched in figure 1. The abort gap is needed to make sure that the circulating beam is cleanly removed by the abort system [2]. Any significant beam in this abort gap will not be dumped properly and can therefore cause magnet quenches and background peaks for the experiments.

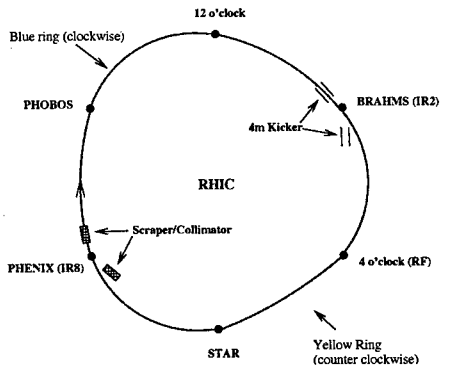


Figure 1: *Location of the kicker and collimators in the RHIC rings.*

HARDWARE

To attack these problems, the existing hardware of the transverse collimators [3] and the transverse kickers used for the tune measurement system [4] are combined. Any beam in the abort gap is excited transversely by the kickers while the collimators are positioned such that they are the limiting aperture in the rings. Figure 1 shows their location in the RHIC ring.

Each ring has one kicker module with four stainless steel striplines, each of which can be powered independently. The pulse voltage cannot be changed. For this application, the kickers are setup to excite beam within the abort gap, buckets 331-360. By selecting a kick frequency close to the horizontal and vertical betatron frequency the beam is kicked resonantly enhancing the effect on the beam significantly if compared with a single or non-resonant kicks. Finding the resonant frequency is crucial for the gap cleaning application and a set point equal to or very close to the betatron frequency was shown to kick bunched beam at storage out of the ring after a few dozens of turns. Typically 300 turns per trigger were used. The horizontal kicks are about 5 times more efficient than the vertical ones due to the different β-functions.

The RHIC collimators [3] consist of 45 cm long L-shaped copper scrapers placed downstream of the PHENIX detector in each ring allowing a positioning resolution of 0.5 μm horizontally and vertically. Four dedicated PIN diode loss monitors and four ion chamber beam loss monitors downstream of each scraper monitor beam losses caused by the collimator.

THE APPLICATION

The new cleaning application supports the two steps of the abort gap cleaning procedure:
(1) excite the debunched beam transversely and
(2) collimate the excited beam with the scrapers.

(1) In order to excite the debunched beam, the tune meter kickers are triggered such that in place of an occupied bucket beam in the abort gap is excited. The kicker is pulsed for 300 turns/trigger with a trigger repetition rate of 1 or 0.25 Hz. To enhance the cleaning efficiency, the frequency has to be as close as possible to the betatron tune of the debunched beam. The new Gap Cleaning application allows a tune scan in the range of suspect, 0.2 to 0.25,

* Work performed under Contract Number DE-AC02-98CH10886 with the auspices of the US Department of Energy.
† drees@bnl.gov

0-7803-7738-9/03/$17.00 © 2003 IEEE

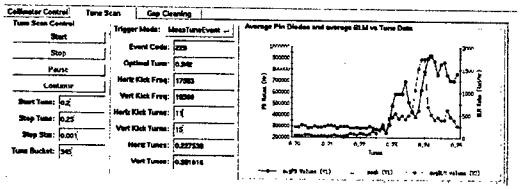


Figure 2: *The application panel to start a tune scan and to find the best resonant tunes for cleaning.*

where the losses at the collimator are recorded as a function of the kicking frequency in terms of betatron tune. Only the horizontal tune is scanned. An example is given in Fig. 2. To monitor the losses we use two independent loss monitor systems, PIN diodes and ion chambers. Once a resonant frequency is found, the application loads it into the gap cleaning procedure. The gap cleaning panel (Fig. 3)

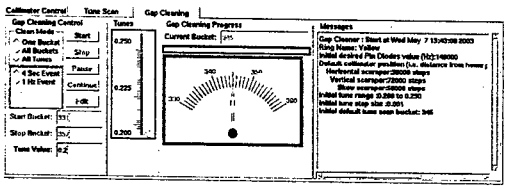


Figure 3: *The application panel to setup the gap cleaning process.*

allows three modes: (i) constant excitation tune and constant bucket, (ii) constant excitation tune but trigger timing is changed to step thru all gap buckets and (iii) constant bucket but excitation tune is varied in a variable range with a variable step size.

(2) At the beginning of the procedure, the scrapers are moved to a predefined position using the collimator control panel of the application (Fig. 4). For fine adjustments, a

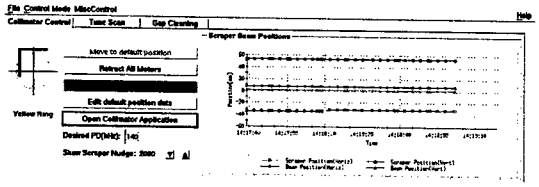


Figure 4: *Collimator control panel of the gap cleaning application.*

"wanted" rate from the PIN diodes, sensitive to scattered particles from the scraper jaw, are used to determine the 'good' location for gap cleaning. To keep high cleaning efficiency, the scraper position typically has to be adjusted a few times during the procedure which lasts approximately 30 minutes.

Regardless of the panel one is working with the application includes a set of convenience graphs as shown in Fig. 5. PIN diodes (top, left) and loss monitors (top, right) are both located downstream of the collimator. Also shown is the amount of debunched current in the blue or yellow

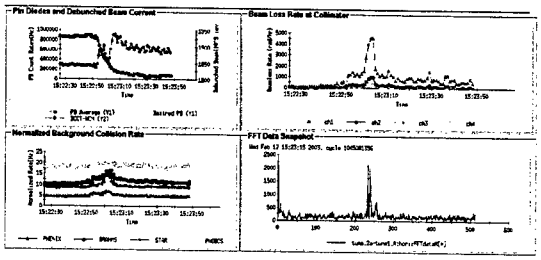


Figure 5: *The convenience graphs as shown in the gap cleaning application during a cleaning procedure on Feb. 12, 03.*

ring in units of 10^9 ions. Note that the tune spectrum (bottom, right) is obtained from debunched beam during the process. Experimental background rates allow monitoring of background increases due to the cleaning procedure while it is in progress. While PHOBOS is unaffected and PHENIX is mildly affected, STAR and BRAHMS see an increase of about 50% during parts of the cleaning.

THE DATA

Table 1 summarizes the magnet quench during the Au run in January and February of 2003. Note that, without RF failures, there is typically no debunching of the blue

Table 1: *RHIC magnet quenches between Jan 01 and Feb. 28 03, caused by either beam dump or aborts involving significant debunched beam I_{deb}.*

fill	**Ring**	$I_{deb.}$		**cause**
		Blue	**Yellow**	
		[10^{11} d]	[10^9 ions]	
2640	Y	-	2	abort kicker
2736	Y	-	2	beam losses
2766	Y	-	2	beam losses
2769	B/Y	9	12	permit
2780	Y	2	6.7	permit
2803	Y	-	6.6	normal dump
2840	Y	-	42	permit
2852	Y	-	3	abort kicker
2859	B	14.5	1	permit
2884	Y	-	9.5	permit (cryo)
2911	B	0.5	3	abort kicker
2930	Y	-	3.6	abort kicker
2945	Y	-	3.5	abort kicker
2955	B/Y	0	8	abort kicker
2982	Y	-	5.5	permit
3006	B	3.5	4.3	permit
3011	Y	-	3.5	beam losses
3061	Y	-	20	permit

beam since it corresponds to deuterons. Accordingly there are much less blue quenches recorded. There are mainly three conditions under which debunched beam can lead to

magnet quenches: (i) **abort kicker** prefires, (ii) **normal dumps** and (iii) **permit** pulls for any reason related or unrelated to the debunched beam. Note that abort kicker prefires will, if out of time, lead to quenches without any debunched beam present. In addition to this, high bunched **beam losses** will cause magnet quenches regardless of the amount of debunched beam in the machine.

With one exception (2955) all abort kicker prefires happened at times when the amount of debunched beam alone would not have caused a quench. However, the abort kicker not only prefired but also missed the gap, thus causing an enormous amount of beam losses in certain areas. In fills 2736, 2766 and 3011, the cause of the magnet quenches is most likely the bunched beam loss itself since $I_{deb} \leq 3.5\ 10^9$ Au ions in all three cases. There are 10 candidates left during a period of 2 months were the presence of debunched beam is most likely responsible for the quench. This corresponds to 30% of all recorded real magnet quenches in the two months and to about 10% of all stores during that period. One fill, 2803, ended with a quench because of a regularly initiated dump, ignoring the amount of debunched beam. In fill 3006 the blue magnet quench happened due to a gap cleaning procedure failure. The remaining 8 fills ended with a magnet quench because the permit tripped prematurely before the debunched beam could be removed. $I_{deb} \geq 5.5\ 10^9$ Au ions in all these fills. It should be discussed if loss monitor trip levels could be either disabled or increased significantly if $I_{deb} \geq 5.0\ 10^9$ Au ions. However, there were fills (for instance 2801) which ended without a magnet quench although they had a little more debunched Au beam than this limit. For deuteron beam the statistic is very small since deuteron beams mainly debunch due to RF failures. There is no quench case recorded with $I_{deb} < 9\ 10^{11}$ d but at least one case (fill 2801) where $I_{deb} = 8\ 10^{11}$ d without causing a quench. Therefore, the sustainable limit for debunched deuteron beam seems to be higher, around $I_{deb} = 8\ 10^{11}$ d.

Figure 6, bottom, shows the RHIC yellow beam currents at the end of store 2887. The difference between the total beam, measured by the DCCT [5] and the bunched beam current,measured by the WCM [6], corresponds to the debunched beam. It amounts to 17.5 10^9 Au ions or 63% when the cleaning procedure is started around 17:20. The procedure is stopped after about 35 minutes. Every tune measurement (top of fig. 6) indicates a trigger event for the beam excitation in the abort gap. Note that during the beginning of the procedure, tunes can actually be measured by coherent oscillations of the debunched beam. Tunes are in the order of 0.23 during this example. The cleaning rate here is a record of 0.4410^9 ions/minute. After pausing for about one hour gap cleaning is resumed and the beam is dumped without problems around 19:00. In general, cleaning rates in 2003 were around 0.22 10^9 for Au ions and around 0.15 10^{11} for d. The rates vary from fill to fill and depend strongly on the cleaning efficiency. However, the average for heavy ions could be increased by a factor of about 1.8 compared to the last Au-Au run [7].

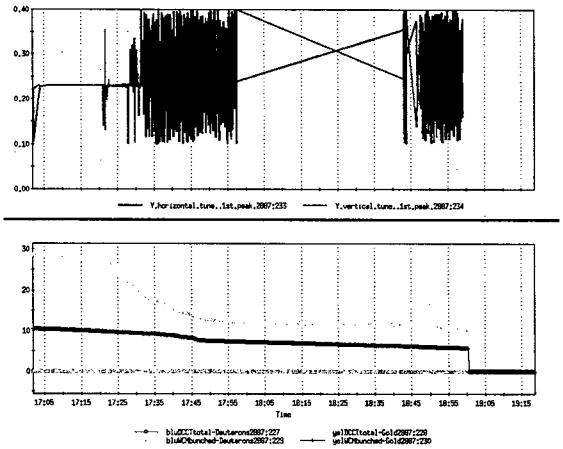


Figure 6: *Top: Tune measurements as a function of time during the end of store 2887, Feb. 03 03. Bottom: Bunched and total yellow beam current as a function of time during the same store.*

CONCLUSION

With the new gap cleaning application the efficiency of the procedure could be almost doubled compared to last year and is found to be 0.22 10^9 Au ions/minute and 0.15 10^{11} d/minute on average. Still, a total of 10 fills, i.e. about 10% of all stores in the examined period of dAu running, ended by a magnet quench due to debunched beam. This number corresponds to 30% of all recorded real magnet quenches. However, 7 of them were caused by premature loss monitor permit trips and disabling or increasing the loss monitor trip level could help avoiding these cases. The sustainable limit for debunched Au beam could be confirmed to be 5.0 10^9 and a preliminary limit for deuterons was found to be 8 10^{11}.

REFERENCES

[1] W. Fischer, R. Connolly, S. Tepikian, J. van Zeijts, K. Zeno "INTRA-BEAM SCATTERING MEASUREMENTS IN RHIC" Proceedings of EPAC, Paris, 2002.

[2] H. Hahn et al., "The RHIC Beam Abort Kicker System", Proceedings of the 1999 Particle Accelerator Conference, New York.

[3] R. Fliller, A. Drees et al., "The Two Stage Crystal Collimator for RHIC", Proceedings of the 2001 Particle Accelerator Conference, Chicago (2001).

[4] A. Drees, R. Michnoff,M. Brennan, J. DeLong, "ARTUS: The Tune Measurement System at RHIC",Proceedings BIW2000, Boston, 2000.

[5] Bergoz Beam Instrumentation, http://www.bergoz.com/

[6] P.R. Cameron et al., "The RHIC Wall Current Monitor System", Proceedings of the Particle Accel. Conf. 1999, p. 2146.

[7] A. Drees et al., "Abort Gap Cleaning in RHIC", Proceedings of the EPAC 2002 conference, Paris, 2002.

RESULTS FROM VERNIER SCANS AT RHIC DURING THE PP RUN 2001-2002*

A.Drees†, Zhangbu Xu, Brendan Fox, BNL, Upton, NY 11973
Haibin Huang, Yale University, New Haven, CT

Abstract

Using the Vernier Scan or Van der Meer Scan technique, where one beam is swept stepwise across the other while measuring the collision rate as a function of beam displacement, the transverse beam profiles, the luminosity and the cross section can be measured. Data and results from the polarized proton run in the year 2001/02 are presented.

INTRODUCTION

The cross section observed by the experimental trigger counters is one of the necessary ingredients to absolutely normalize experimental data in heavy ion and proton collisions such as data on π^0 production. During the Au-Au runs ZDCs [1] are used for minimum bias triggering because of their large cross section. The ZDCs are common to all experiments . During pp runs, however, those detectors are not suitable for triggering because of their small cross section when protons collide. Instead, experiments use individual beam beam counters (BBC), which are of different type, shape, location and acceptance. In general, a BBC consists of two identical parts at a certain distance on either side of the vertex location at an Interaction Point (IP). Collision rates are typically measured by a coincidence of particle detection on both sides. In order to determine the cross section observed by those detectors, Vernier Scans at the individual IPs were performed collecting data from the local BBCs. In this report, we describe the method of Vernier Scans to measure the absolute cross section of pp collisions at $\sqrt{s_{NN}} = 200$ GeV at the STAR and PHENIX experiment at the Relativistic Heavy Ion Collider (RHIC).

VERNIER SCANS

The Vernier Scan technique was invented by S. van der Meer in 1968[2] who showed that it is possible to measure the effective height h_e of the colliding ISR beams by observing the counting rate R in a suitable monitor system while sweeping the two beams vertically through each other. A Gauss-shaped curve results with its maximum at zero displacement. The interaction rate observed by a BBC detector, R_{BBC}, is defined as the total number of beam particles (N_{blu} and N_{yel}) going through each other in some area A with cross section σ_{BBC}:

$$R_{BBC} = \frac{N t_{blu} N t_{yel}}{A} \sigma = \mathcal{L} \sigma_{BBC} \qquad (1)$$

For two beams with Gaussian distribution in both, horizontal and vertical directions, the luminosity is given by [3]:

$$\mathcal{L} = \frac{k_b f_{rev} N_1 N_2}{2\pi \sqrt{(\sigma_{x1}^2 + \sigma_{x2}^2)(\sigma_{y1}^2 + \sigma_{y2}^2)}}. \qquad (2)$$

with i=1,2 for blue and yellow beams respectively and N_i the number of particles per bunch assuming all bunches in one beam are of the same intensity. Bunch-to-bunch variations will be discussed below. In the case of non-centered beams, consider the case of one beam displaced by d, the luminosity $\mathcal{L}(d)$ as a function of d is:

$$\mathcal{L}(d) = \frac{k_b f_{rev} N_1 N_2 \exp\left[-d^2/2(\sigma_{x1}^2 + \sigma_{x2}^2)\right]}{2\pi \sqrt{(\sigma_{x1}^2 + \sigma_{x2}^2)(\sigma_{y1}^2 + \sigma_{y2}^2)}} \qquad (3)$$

The terms $\sqrt{\sigma_{i1}^2 + \sigma_{i2}^2}$, where $i = x, y$, in Eq.3 and Eq.2 correspond to the beam profile derived from the width of the distribution measured by the Vernier Scan. The result for the horizontal plane is:

$$\sigma_{Vx} = \sqrt{\sigma_{x1}^2 + \sigma_{x2}^2}. \qquad (4)$$

Vernier Scans measure the effective beam profile over the

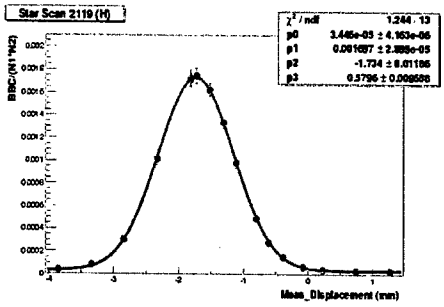


Figure 1: *Vernier Scan in STAR in the horizontal plane.*

whole longitudinal interaction area between the two halfs of a BBC, i.e. approximately +/- 0.75 m (PHENIX) and +/- 3.5 m (STAR), instead of measuring the beam transverse size at the center of the IP only. However, the collision rates we get from those detectors do correspond to the number of events originating from the entire effective beam area as well. Therefore, applying a Gauss-fit+constant to the normalized collision rate = $R_{BBC}/N t_{blu} N t_{yel}$ as a function of beam displacement yields the effective beam size as well as the maximum achievable normalized rate R_{max}, the optimal position and the background. Fig. 1 shows an example of a typical data set and the applied Gauss fit. From this

* Work performed under Contract Number DE-AC02-98CH10886 with the auspices of the US department of Energy.
† drees@bnl.gov

0-7803-7738-9/03/$17.00 © 2003 IEEE

the cross section σ_{BBC} can be derived:

$$\sigma_{BBC} = 2\pi\ R_{max}\ \sigma_{Vx}\ \sigma_{Vy}\ k_b / f_{rev} \qquad (5)$$

where f_{rev} is the revolution frequency and k_b the number of bunches per ring.

DATA ANALYSIS

Table 1 lists the available vernier scans from the pp_fy02 run at the STAR and PHENIX IRs respectively. The data

Table 1: *List of vernier scans performed at STAR and PHENIX during the year 2002 RHIC pp run. All scans were done at a β^* of 3m.*

fill	IP	beam	comment
2136	8	blue	$\sigma_{vtx} = 80cm$
2161	8	yellow	$\sigma_{vtx} = 80cm$
2277	8	yellow	$\sigma_{vtx} = 60cm$
2119	6	blue	1/2 scan
2161	6	yellow	
2193	6	yellow	no BPM
2277	6	yellow	

needs to be corrected for several effects: for the beam displacement in the other plane during a scan, for the actual bunch pairing at the given IR taking into account the bunch-to-bunch intensity variation and for the crossing angle between the two colliding beams (if any). The precision of the measured beam displacement and the bunched beam current add to the systematic errors.

Beam Position Measurements

When a vernier scan is performed, the beam displacements are not necessarily minimized. Thus the maximum achievable rate could be reduced by a certain amount depending on the offset from the optimal position in the other plane. In addition, beam position changes in one plane are induced by doing a scan in the other due to coupling. Therefore the beam position is recorded in both planes while doing a scan in one. The measured collision rates are then corrected for the deviation from the optimal position. Accurate beam position measurements (here from the BPMs at the DX magnets) are hence crucial to the procedure. Fig. 2 shows the RMS of the typically 14 beam position measurements per data point, corresponding to 60 sec of data taking per position. The average RMS is of the order of 5 μm but about a factor of 2 higher in the horizontal plane. The BPM scatter is taken into account by adding a 3% point-to-point systematic error. The uncertainty in the absolute scale of the BPM measurement [6] is considered by adding an absolute systematic error of 2%.

Fill Pattern

The collision rates during a scan is normalized by the total bunched beam current in the ring during the 60 seconds

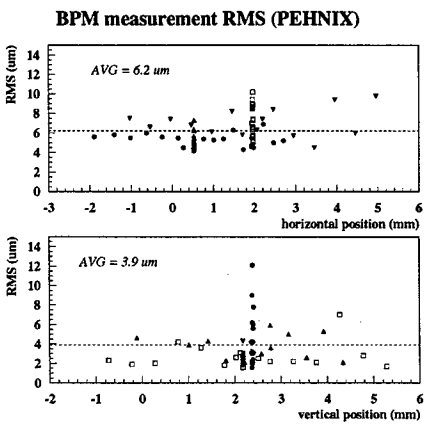


Figure 2: *RMS of beam position measurements from two vernier scans in PHENIX, 2136 and 2161.Each value corresponds to the RMS of 14 measurements which are included in one data point for the scans.*

of the data taking. The bunched current is measured by the Wall Current Monitor (WCM) [4]. The WCM readings are calibrated with the DCCT [5] measurements at the end of the ramp when only bunched current can be present. A systematic point-to-point error of 1-2% is assigned to the uncertainty of the WCM measurements after this calibration. Since bunch-to-bunch intensities vary and the colliding bunch pairs depend on the IR, the R_{max} value from the Gauss-fit has to be corrected for the actual measured intensity of colliding pairs. Fig. 3 shows the colliding blue-yellow pairs for the PHENIX vernier scans. Taking the fill

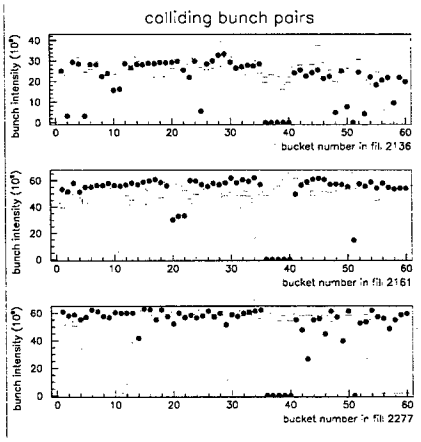


Figure 3: *Bunch intensity for blue and yellow beams as a function of bunch number during the PHENIX vernier scans. Note that blue bunches are shifted by +41 corresponding to actual pairing in PHENIX. The abort gap does not line up in PHENIX.*

pattern into account, the product of the total beam currents needs to be corrected by factors from 0.9 to 0.97, depending on IR and fill.

Crossing Angle

In case a crossing angle between the colliding beams in the horizontal plane is present the achievable luminosity has to be corrected by a factor R [7]:

$$R = \sqrt{1 + (\frac{\sigma_z}{\sigma_x^*} tan\phi)^2} \qquad (6)$$

(vertical plane accordingly). For an average beam size of σ_x^* = 360 μm and a typical bunch length of about 1m, R amounts to 1% for an angle of ϕ = 0.1 mrad and 4% for ϕ = 0.2 mrad. From the BPM measurements we derived the crossing angles for the vernier scan fills (only PHENIX so far). Fig. 4 shows the extrapolated beam trajectory between the DX BPMS at +/- 8m. Since the data is taken

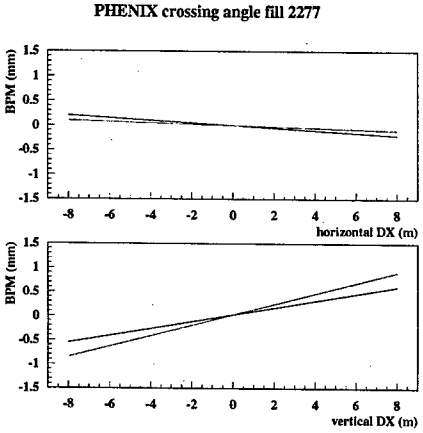


Figure 4: *Beam trajectories at IR8 in fill 2277 in the horizontal plane (top) and vertical plane (bottom). The angle between the two lines corresponds to the crossing angle ϕ.*

after a vernier scan no transverse offset between the beam is present. However, due to digital offsets in the electronics the BPM readings for the two beam were not identical although the DX BPM are recording positions for both beams. The two trajectories were vertically shifted by a few 100 μm so they would cross at 0. The angle between the trajectories reached 0.1 mrad in one case and was significantly smaller in all other. By applying the same shift on one side only one would create a larger angle ϕ. This value was found to be 0.1 mrad on average and used to determine a systematic point-to-point error of 1%.

SUMMARY

The cross sections and point-to-point errors are listed in tab. 2. A common absolute error for the uncertainty of the BPM scale of 2% and for the beam blow up due to the scan itself of 1% has to be added to the statistical and systematic errors. A weighted fit of the available measurements is shown in fig. 5. Thus the final value for the BBC cross section is found for
STAR: $\sigma_{BBC} = 21.6 \pm 0.2 \pm 1.0 \pm 0.8$ mbarn and for

Table 2: *Cross sections (Xsec) and statistical and systematic errors obtained from the individual vernier scans. All values are given in units of mbarn.*

fill	IP	Xsec	stat.	sys.
2136	8	12.3	0.2	1.3
2161	8	13.0	0.2	1.4
2277	8	12.8	0.1	1.0
2119	6	25.6	0.4	2.8
2161	6	27.5	0.5	1.8
2193	6	26.7	0.4	1.9
2277	6	24.6	0.4	1.5

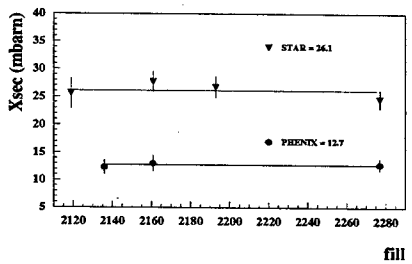


Figure 5: *Final cross sections of the STAR and PHENIX beam beam counters (BBC). Error bars include statistical and point-to-point systematic errors.*

PHENIX: $\sigma_{BBC} = 12.7 \pm 0.1 \pm 0.3 \pm 0.4$ mbarn.

Note that the PHENIX value is arbitrarily normalized to a vertex distribution σ_{vtx} of 80 cm and the third scan (2277) was scaled by the ratio $\frac{60cm}{80cm}$. In order to normalize the cross section to the entire interaction region, data from the PHENIX experiment is necessary, which was outside of the scope of this report. Since the STAR BBC covers the full interaction region, no further correction is necessary.

It could be shown that the Vernier Scan method is a powerful tool not only to determine the absolute instantaneous luminosity but also to provide the experiments with a valuable and independent measurement of the cross section seen by their BBC.

REFERENCES

[1] C. Adler, et al., nucl-ex/0008005.

[2] S. van der Meer, ISR-PO/68-31, KEK68-64.

[3] P. Castro-Garcia, CERN SL/96-70, KEK97-01-158.

[4] P. Cameron et al., "The RHIC Wall Current Monitor System", Proceedings of the 1999 PAC, p. 2146 (1999).

[5] Bergoz Instrumentation, "http://bergoz.com", Beam Charge Monitors

[6] P. Cameron et al. "RHIC beam position monitor characterization", Proceedings of the Particle Accelerator Conference, Piscataway, p 2458, 1995.

[7] "Handbook of Accelerator Physics and Engineering", edited by A. Chao, M. Tigner, World Scientific, p. 248 ff. (1999).

NEW RESULTS FROM CRYSTAL COLLIMATION AT RHIC *

R. P. Fliller III†, A.Drees, D.Gassner, L. Hammons, G. McIntyre, S. Peggs, D. Trbojevic,
BNL, Upton, NY, 11793, V. Biryukov, Y. Chesnokov, V. Terekhov, IHEP, Protvino, Moscow Region

Abstract

In this paper, we discuss new results from the use of the crystal collimator from the 2003 run. The yellow ring of the Relativistic Heavy Ion Collider (RHIC) has a bent crystal collimator. By properly aligning the crystal to the beam halo, particles entering the crystal are deflected away from the beam and intercepted downstream in a copper scraper. The purpose of a bent crystal is to improve the collimation efficiency as compared to a scraper alone. We compare these results to previous data, simulation, and theoretical predictions.

1 INTRODUCTION

A typical collimation system for a collider consists of moveable jaws that are positioned to be the primary machine aperture. Particles with low impact parameters have a finite probability of scattering out of the collimator jaw and forming a secondary halo [1]. This secondary halo can have a significant effect on machine performance [2]. Secondary jaws are used to contain the scattered particles and proper placement of these jaws is necessary for optimal performance.

Finding novel ways to collimate the halo can greatly simplify collimator design. By using bent crystal channeling, a properly aligned crystal will channel the entering particles away from the beam and produce very little halo from scattering. A secondary jaw intercepts the channeled particles with large impact parameters. This secondary jaw can be placed further away from the beam in comparision to a traditional system. This paper discusses our experiences with a bent crystal collimator in the yellow ring of the Relativistic Heavy Ion Collider (RHIC) during the year 2003 run.

2 CRYSTAL CHANNELING

Crystal channeling is a phenomena by which ions entering a properly aligned crystal will follow the crystal planes, even if the crystal is mechanically bent [3]. This makes it possible to give a large angular kick to the channeled ions in a short distance . For proper alignment, the incident particles must be aligned to the crystal planes with an angle less than the critical angle,

$$\theta_c = \sqrt{\frac{2U(x_c)}{pv}}. \qquad (1)$$

where the maximum interplanar potential is given by $U(x_c)$, where x_c is the transverse location where the incident ion enters the electron cloud of the lattice atoms; the momentum and velocity of the ion are p and v respectively. $U(x_c)$ is approximately $Z_{ion}16$ eV for silicon. For RHIC energies, $\theta_c = 37$ μrad at injection and 11 μrad at storage energy. At incident angles greater than θ_c the ion will no longer be channeled but scatters through the crystal as if it were an amorphous solid.

3 LAYOUT

The RHIC crystal collimation system is shown in Fig. 1. It consists of a 5 mm long crystal and a 450 mm long L-shaped copper scraper placed downstream of the PHENIX detector in the yellow (counter-clockwise) ring. The crystal is an O-shaped silicon crystal with the (110) planes placed at a slight angle with respect to the normal of the input face, and a bend angle $\theta_b = 0.34$ mrad. This crystal is different from the one used during the 2001-2 RHIC run, but is of the same design. There are eight PIN diode loss monitors between the crystal and the scraper (the upstream PIN diodes), and four PIN diodes downstream of the scraper (the downstream PIN diodes) to look for scattered particles from the crystal and scraper respectively. In addition, two scintillators forming a hodoscope aligned to the crystal surface look at particle scattered at large angles. Four ion chamber beam loss monitors are located downstream of the scraper as well [4].

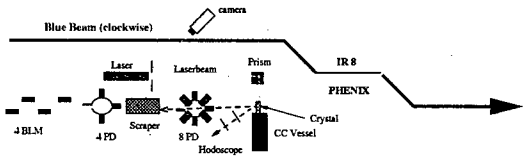


Figure 1: The RHIC Crystal Collimation system

4 THEORY

As previously reported in Ref. [4], the channeling efficiency of the crystal is about one half of the initial expectation [5]. In response, we developed a simple model of the first turn particle distribution on the crystal. We assume an initial distribution of

$$f(J,\delta) = \frac{1}{\sqrt{2\pi\sigma_\delta\epsilon}} \exp\left[-\frac{\delta^2}{2\sigma_\delta{}^2}\right] \exp\left[-\frac{J}{\epsilon}\right] \qquad (2)$$

where J is the particle action, ϵ is the unnormalized rms emittance, δ is the momentum deviation, σ_δ is the rms mo-

* Work performed under the auspices of the U.S. Department of Energy
† rfliller@bnl.gov

mentum deviation. This distribution is then transformed into positions and angles, (x, x') by integrating over all momenta to obtain the phase space distribution of all particles at the crystal. Calculating the average angle of all of the particles that will hit the crystal surface, and assuming that the particles have low impact parmeters with respect to the rms beam size, or the crystal is far from the beam core one derives

$$\theta = x_{crystal} \frac{-\alpha\epsilon + DD'{\sigma_\delta}^2}{\beta\epsilon + D^2{\sigma_\delta}^2}. \quad (3)$$

The crystal edge is at $x_{crystal}$ from the center of the beam, the dispersion and its slope are given by D and D', and α and β are the Twiss parameters at the crystal. For RHIC, the crystal is at a high β, low dispersion region and Eq. 3 reduces to

$$\theta \approx x_{crystal} \frac{-\alpha}{\beta} \quad (4)$$

The expression for the angular spread of the beam that hits the crystal face, σ_θ, is quite lengthy, but it is sufficient to say that σ_θ is strongly proportional to α, β, $D\sigma_\delta$, and the rms impact parameter, and is weakly affected by ϵ, and $x_{crystal}$ [6]. For this RHIC run, $\sigma_\theta = 23\mu$rad, assuming that particles hit over the entire face of the crystal.

Knowing the angular spread of the particles hitting the crystal, one can estimate the channeling efficiency of a perfectly aligned crystal using Eq.12.12 from Ref. [7], and neglecting the small (4%) effect of the bending of the crystal

$$e \approx \frac{2x_c}{d_p} \frac{\pi}{4} \frac{\theta_c}{\sigma_\theta}. \quad (5)$$

where d_p is the distance between the crystal planes. This formula is only valid as long as $\sigma_\theta > \theta_c$. For this RHIC run $e = 32\%$, and averaging over the data for this run gives an efficiency of $< e >= 26\%$.

5 SIMULATION OF 2001 RUN

It was found during the 2001 RHIC run that the beta function at the crystal did not agree with the model [8]. Measurements with the crystal collimator further showed that $-\alpha/\beta$ did not agree with the model and the channeling dip was wider than expected [4]. In fact, it was found that the measured α based on the channeling dip angle verus crystal position is consistant with $\alpha = 1.5\alpha_{model}$ and the measured beta function.

To simulate the action of the crystal in RHIC we used the CATCH (Capture And Transport of CHarged particles in a crystal) code [9]. For computing speed, a 6×6 matrix was used to track the ions around the ring. Particle distributions are gaussian in momentum deviation, δ, and exponential in action, J, with a 15π mm-mrad normalized rms emittance. Only particles that hit the crystal are tracked in the horizontal plane, so as to avoid tracking uninteresting particles in the core. In the vertical plane, the phase ellipse is filled.

Fig. 2 shows simulations of the number of scattered particles verus the crystal angle with the measured and model Twiss parameters and data for the $\beta^* = 1$m local PHENIX

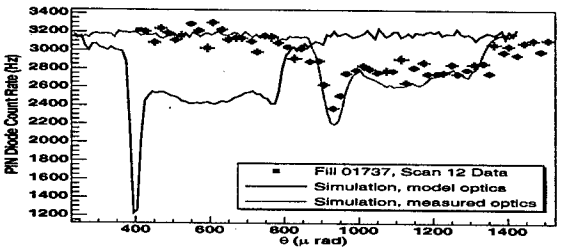


Figure 2: The effects of the modeled (blue) and measured (red) Twiss parameters compared with a typical crystal angular scan. Simulations are shifted -365 μrad to account for survey offsets.

optics during the 2001 run. The large dip is when the crystal planes are aligned with the beam. The effect on the position and width of the dip due to changing α/β is quite clear. The rms width of the large dip is equal to the quadrature sum of σ_θ and θ_c. Efficiency is defined as maximum depth of the large dip divided by the background rate. For the measured optics, $\sigma_\theta = 24$ μrad and $e = 30\%$, according to the theory. This is in good agreement with the simulation and the data in Fig. 2. For the model optics, $\sigma_\theta = 8.9$ μrad which is in good agreement with simulation. Formula 5 does not apply in this case because $\sigma_\theta < \theta_c$.

The subsequent structure to the right of the large dip shows channeling of particles that scatter through a fraction of the crystal into a crystal plane and then channel the remaining distance. This is known as volume capture [7]. Fig. 3 shows the effect of multiple turns on the channeling shape. The depth of this subsequent structure is dominated by the number of encounters that particles can have with the crystal. The angular width of the volume capture region and the channeling dip is equal to the bend angle of the crystal.

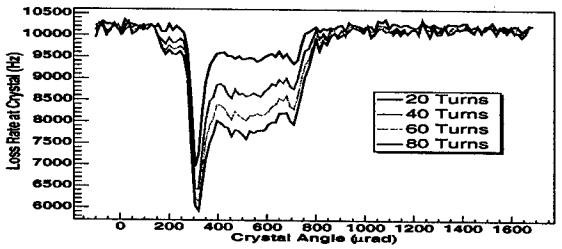


Figure 3: The Effect of multiple turns of the channeling signal.

6 CRYSTAL CHANNELING

Experiments with the crystal collimator have been performed with gold and polarized proton beams in RHIC. The crystal angle was moved through a range of angles for a variety of different crystal positions, scraper positions, and

lattices. Beam losses were recorded by the PIN diodes, hodoscope, and beam loss monitors. Signals from the RHIC experiments were also logged to monitor their background rates. Table 1 lists the available data samples.

Table 1: Tabulation of Angular Scans

Species	β^* @ IR8	No. of Scans	$< \sigma_\theta >$	$< e >$
Au	5 m	27	45 μrad	20%
Au	2 m	24 (2001 Run)	105 μrad	28%
Au	2 m	20 (2003 Run)	37 μrad	26%
Au	1 m	109	69 μrad	16%
p	3 m	119	70 μrad	26%

The $\beta^* = 1$ m is at the PHENIX interaction region only, all the other experimental IRs were kept at $\beta^* = 2$m. The 2003 Run data is taken during deuteron-gold operations.

Fig. 4 shows a typical angular scan from the 2003 RHIC run. All of the data is averaged over 20 μrad, the resolution of the angular readback. The fit is to two gaussians on a sloping background with a sloped line connecting them [4]. For each set of data, approxiately 40% of the data can be fit. The remaining data is a combination of data that contains incomplete scans due to technical problems, scans with low signal because the crystal was not close enough to the beam or was shielded by the scraper, scans where the beam has an oscillation due to the AGS Booster cycle, or scans that are well outside of the angular acceptance of the crystal. Of the data that can be fit, the fit function tends to return widths that are wider and efficiencies that are smaller than the data and the simulations show.

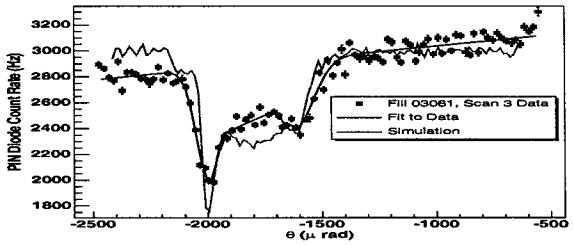


Figure 4: Data from Fill 03061. The simulation is done with the measured machine optics[10].

The values in Table 1 are averages over all of the fits for each RHIC configuration. The average efficiency over all runs is 23%. The average width of the channeling dip over all runs is 68.5 μrad as measured from the upstream PIN diodes. The hodoscope was not used in the averages because in the FY2001-2 run, it was not properly configured, and had a low signal to noise ratio. This was improved for the 2003 run by increasing the gain and improving the relative timing of the phototubes. The $\beta^* = 5$m and $\beta^* = 2$m averages have a large variation because of the low number of angular scans taken.

7 CONCLUSIONS AND FUTURE PLANS

We have shown that the channeling efficiency of the crystal, and hence its ability to be an efficient collimator is dominated by the phase ellipse at the collimator entrance. If one were to place a collimator at a location where $\alpha \approx 0$, such as in a quadrupole, the channeling angle would be independant of crystal position, and one may be less sensitive to optical errorr, since changes in α should be small. Placing the crystal at a large β location has the further advantage that the beam has a very small angular divergence so efficiency is increased. In RHIC, the largest high β location is in the IR triplets. Unfortunately, the β function changes so rapidly outside these quadrupoles, that α quickly becomes large. In places where α does not pass quickly though zero, β is quite small. Unfortunately, because of lattice and space constraints, and the need to improve our collimation efficiency for the upcoming high luminosity run, the crystal collimator will be removed in favor of a conventional two stage collimation system.

Crystal channeling in RHIC could be achieved and is consistant with simulation and theoretical results. Crystal collimation was unsuccessful because of the low efficiency, however, crystal channeling still might be a promising way to collimate beams in future accelerators, provided the position can be chosen appropriately.

8 REFERENCES

[1] T. Trenkler and J.B. Jeanneret., "The Principles of Two Stage Betatron and Momentum Collimation in Circular Accelerators" CERN Note: SL/95-03 (AP), LHC Note 312;

[2] R. Aßman *et. al.* "Requirements for the LHC Collimation System" Proceeding of the 2002 European Particle Accelerator Conference, Paris, France (2002).

[3] J. Lindhard. *K. Dan. Vidensk. Selsk. Mat.-Fys. Medd.* **34**, No. 14 (1965).

[4] R. P. Fliller III, *et. al.* "Crystal Collimation at RHIC" Proceeding of the 2002 European Particle Accelerator Conference, Paris, France (2002).

[5] V. M. Biryukov,*et. al.*,"Optimization of the Parameters in the RHIC Single Crystal Heavy Ion Collimation" Proceeding of the 1999 Particle Accelerator Conference, New York, New York (1999).

[6] R. P. Fliller III, Ph. D. thesis, State University of New York at Stony Brook (to be published).

[7] V. M. Biryukov, Y. A. Chesnokov, and V. I. Kotov. *Crystal Channeling and Its Application at High Energy Accelerators.* Springer–Verlag, Berlin, Heidelburg, 1997.

[8] T.Satogata,*et. al.* "Linear Optics During the RHIC 2001-2 Run",Proceeding of the 2002 European Particle Accelerator Conference, Paris, France (2002).

[9] V. Biryukov, "Crystal Channeling Simulation - CATCH 1.4 User's Guide", SL/Note 93-74(AP),CERN 1993.

[10] T.Satogata,*et. al.* "Linear Optics Measurement and Correction in the RHIC 2003 Run" These Proceedings; M. Bai *et. al.* "Measurement of Betatron Functions and Phase Advances in RHIC with AC Dipoles" These Proceedings.

Proceedings of the 2003 Particle Accelerator Conference

COMMISSIONING OF A FIRST-ORDER TRANSITION JUMP IN RHIC *

Jörg Kewisch†, Christoph Montag,
BNL, Upton, NY 11973, USA

Abstract

When accelerating gold ions in the Relativistic Heavy Ion Collider (RHIC) the transition energy must be crossed. RHIC uses a set of special quadrupoles and power supplies which can reverse polarity in less than 40 milliseconds.

These quadrupoles are used to produce dispersion bumps which increase the transition energy as the beam approaches transition. The change of polarity will then jump the transition energy across the beam energy. This paper describes the commissioning of the RHIC transition crossing system.

INTRODUCTION

The Relativistic Heavy Ion Collider (RHIC) was built in the tunnel constructed for the ISABELLE accelerator. RHIC has two super-conducting storage rings, intersecting in six interaction points. Each ring is alternating on the inside and outside, so RHIC has a tree-fold symmetry. Besides recycling the tunnel the over 30 year old Alternating Gradient Synchrotron (AGS) is used as an injector for protons at 27 GeV, deuterons at 12 GeV/u and gold ions at 10.2 GeV/u. Gold ions are the accelerated to an energy of 100 GeV/u, protons to 250 GeV.

For each storage ring there is an energy where the revolution frequency of an ion around the ring is independent of its energy deviation. The change of frequency caused by the change in the ions speed with energy is canceled by a change of the ions path length around the ring. At this so called "transition energy" there is no longitudinal focusing and the energy spread in the beam becomes infinite. Crossing the transition energy in storage rings is normally avoided by injecting the beam above the transition energy.

The transition gamma is defined as

$$\frac{1}{\gamma_t^2} = \frac{1}{L}\int \frac{D(s)}{\rho(s)} ds$$

In approximation the dispersion can be expressed as a function of the bending radius R and the dipole length l (assuming a phase advance per arc cell):

$$\gamma_t = l\sqrt{\frac{RL}{2\pi}}$$

To avoid transition in RHIC the transition energy must be below 10 GeV. With a Ring length of 3833 m and a bend radius of 242 m this would require a dipole length of 27 m. The resulting beta function is then approximately 90 m and the maximum dispersion is 4.5 m. Instead of dealing with such large beam and magnets it was decided to use a transition crossing scheme described in [2]. The transition gamma is now 23.1, above the ion injection energies but below the proton injection energy. The maximum beta function in the arcs is 45 m and the maximum dispersion is 2 m.

POWER SUPPLIES

The transition crossing scheme uses a set of quadrupoles with a special power supply which is able to reverse polarity within 40 milliseconds. The power supply [1] uses Insulated Gate Bipolar Transistors (IGBT) to switch the polarity and a charged capacitor to supply high voltage during the jump. Figure 1 shows the principle.

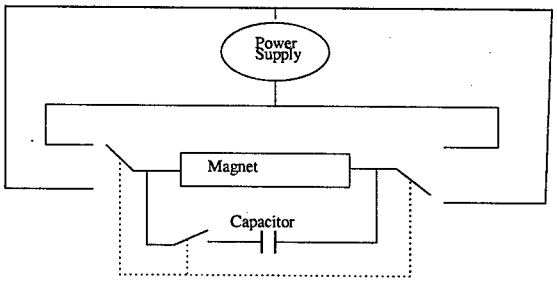


Figure 1: Function of the jump supply. The polarity of a low voltage supply is switched using IGBTs. Simultaneously a charged capacitor is connected to supply a high voltage which determines the duration of the jump.

The program interface shown in figure 2 is used to control the γ_t power supplies currents and jump time. It also arms the Multiplexed Analog-Digital Converters to measure the currents with a sample frequency of 10 kHz and displays the result after the jump.

OPTICS CONSIDERATIONS

The placement of the jump quadrupoles is illustrated in figure 3. In the ideal case the betatron function is the same in all quadrupoles and phase advance between the all quadrupoles is 90 degrees. Four quadrupoles are placed in the arc where the dispersion has its maxima.

* Under contract with the United States Department of Energy, Contract Number DE-AC02-98CH10886

† jorg@bnl.gov

0-7803-7738-9/03/$17.00 © 2003 IEEE

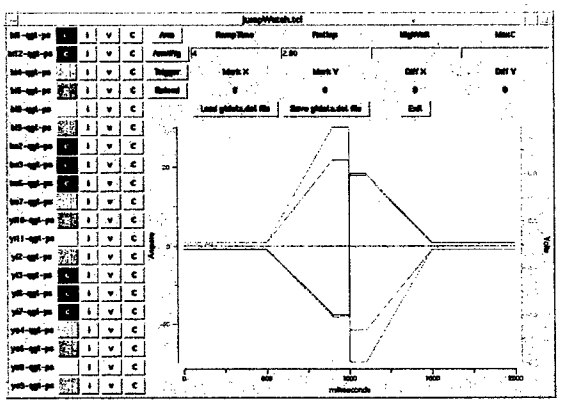


Figure 2: The γ_t Control program is used to set the power supply currents, capacitor voltage and the jump timing. The power supply currents (set point and read back) and the power supply voltage and capacitor voltage is displayed.

The quadrupole pairs gt1/gt3 and gt2/gt4 create two overlapping dispersion bumps, thus changing γ_t. Since these four quadrupoles have the same polarity they also produce a large change in the tunes. Four additional quadrupoles in the straight sections of RHIC (where the dispersion is small) compensate this tune change. Finally, each quadrupole generates a change of the beta function which is compensated by its direct neighbor.

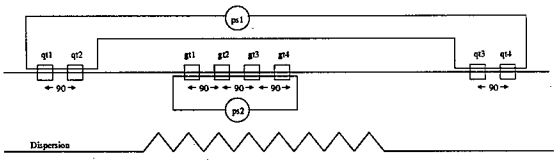


Figure 3: Placement of the γ_t quadrupoles.

In RHIC the beta functions the γ_t quadrupoles vary by about 10% and the phase advance in only about 72 degrees. Therefore the ideal RHIC optics is significantly distorted by the γ_t quadrupoles. Figure 4 shows the beta function.

Since the beta beat generates a strong quadratic component of the tune during the jump the twelve power supplies are set in four logical families using two families in the inner arcs and two in the outer arcs. The remaining tune variation is shown in figure 5.

When RHIC was first turned on a short was discovered in one of the γ_t power supplies. The short could not be fixed without opening the cryostat. The power supply for the tune compensation in the same arc was turned off too and the set points were adjusted to the new situation. The resulting tune variation is not significantly different.

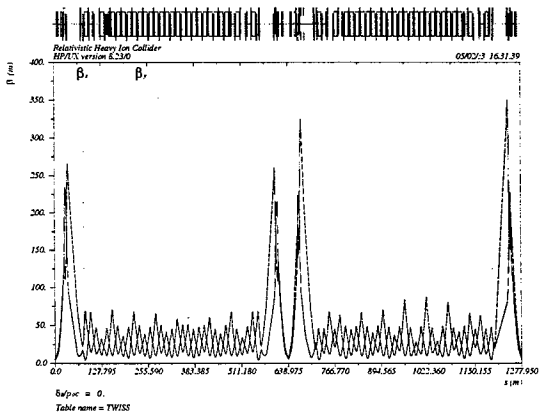


Figure 4: Distortion of the RHIC beta functions by the γ_t quadrupoles. In the undistorted optics the maximum beta function is 270 m in the interaction point quadrupoles and 45 m in the arcs.

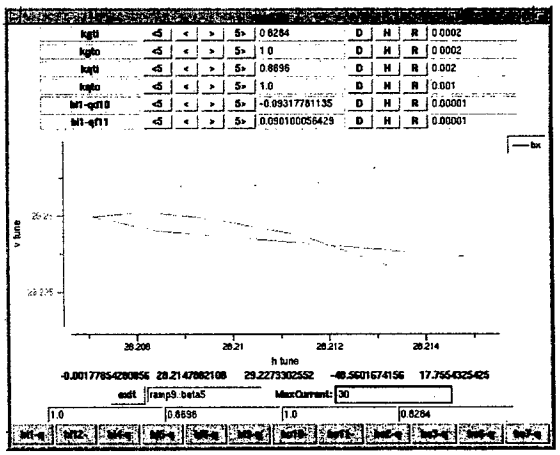


Figure 5: Tune variation during the jump.

COMMISSIONING

The first test of the system where performed at injection energy. Using the RHIC tune measurement system the magnet polarities where checked which revealed one miss-wired quadrupole. After the repair the measured tune variation during the jump was $\Delta\nu_x = 0.008$ and $\Delta\nu_y = 0.003$ as predicted. With a tune change of 0.7 caused by the GT-families alone this is a very good cancellation.

Initially, the beam loss during the jump was in the order of 5%. A vast improvement was the beam based alignment which was also performed at injection energies. By changing a single power supply current (with four quadrupoles) at a time and measuring the orbit difference around the machine the offset in the quadrupoles was determined and cor-

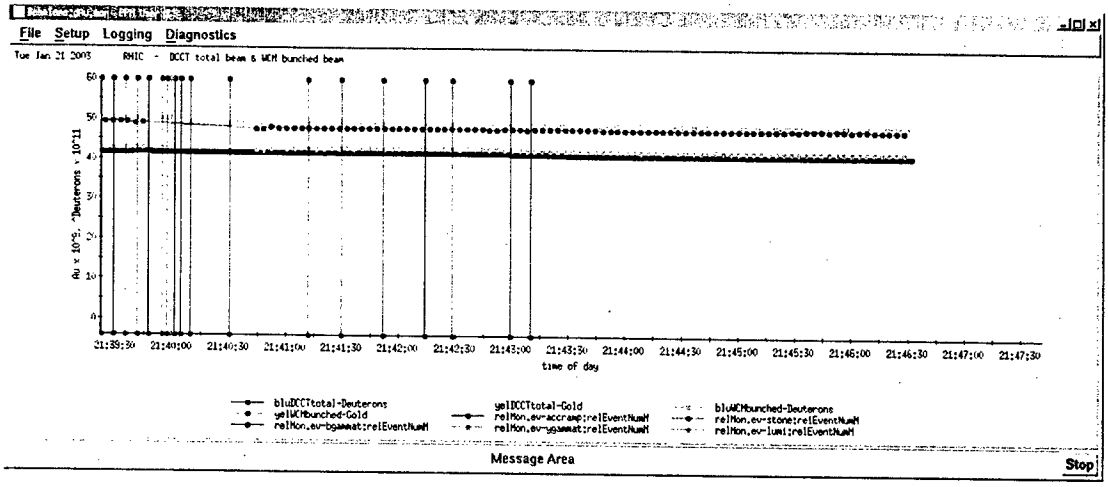


Figure 6: Beam currents during the ramp after beam based alignment in the blue ring.

rected using dipole correctors. The resulting orbit was measured with the beam position monitors and declared to be the "golden orbit". The orbit at the time of the jump was then corrected to these values. Figure 6 shows the beam currents during a ramp with such correction in the "blue" ring, but uncorrected in the "yellow" ring.

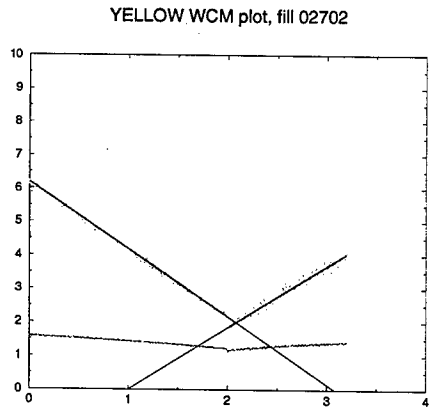


Figure 7: Bunch length (red) in nanoseconds vs. time in seconds. the transition jump is at $t = 2$ sec. Also shown is the 4th power of the bunch length (yellow) and lines to guide the eye to find the zero crossing of σ_s^4.

The jump timing is another parameter that was carefully optimized is the jump timing. The tool used was the measurement of the bunch length using a Wall Current Monitor (WCM). Figure 7 shows the bunch length as the function time. Also shown is the forth power of the bunch length. Close to the transition the bunch length is $\sigma_s \propto |\gamma - \gamma_t|^{\frac{1}{4}}$ and the acceleration is constant: $\gamma \propto t$ The forth power of the bunch length vs. time is a straight line and γ_t is can be measured by finding the intersection of this line with zero. The jump timing is set where the two lines intersect. This way the slip factor $\eta = \frac{1}{\gamma^2} - \frac{1}{\gamma_t^2}$ does not change with the jump. During the jump the phase of the RF is also changed from ϕ_s to $180^o - \phi_s$. The timing of this phase flip is optimized to minimize coherent oscillations after the jump.

INSTABILITIES

After increasing the beam current in RHIC head-tail instabilities where observed slightly before or after the transition jump, leading to fast beam loss. These instabilities could be fought using octupoles to increase the Landau damping in the machine. Most likely the instabilities coincide with the crossing of the chromaticity through zero. It is proposed [3] to add a sextupole jump scheme to avoid these problems.

CONCLUSIONS

The transition jump system in RHIC was designed to adapt to the given dimensions of the accelerator. After careful commissioning this system works well and is no limitation to the performance of the accelerator.

REFERENCES

[1] J. Mi et al: RHIC Gamma Transition Jump Power Supply Prototype Test, PAC2001

[2] T. Grisselada: Design of Quadrupole Schemes to modify Gamma Transition, CERN PS/90-51 (PA)

[3] C. Montag et al: Design of a fast Chromaticity Jump in RHIC, this conference

Proceedings of the 2003 Particle Accelerator Conference

COMMISSIONING SPIN ROTATORS IN RHIC*

W. W. MacKay†, L. Ahrens, M. Bai, E. D. Courant, W. Fischer, H. Huang, A. U. Luccio, C. Montag, F. Pilat, V. Ptitsyn, T. Roser, T. Satogata, D. Trbojevic, J. van Zeijts,
BNL, Upton, NY 11973, USA
and the PHENIX Collaboration[1]

Abstract

During the summer of 2002, eight superconducting helical spin rotators were installed into RHIC in order to control the polarization directions independently at the STAR and PHENIX experiments. Without the rotators, the orientation of polarization at the interaction points would only be vertical. With four rotators around each of the two experiments, we can rotate either or both beams from vertical into the horizontal plane through the interaction region and then back to vertical on the other side. This allows independent control for each beam with vertical, longitudinal, or radial polarization at the experiment. In this paper, we present results from the first run using the new spin rotators at PHENIX.

INTRODUCTION

The Relativistic Heavy Ion Collider (RHIC) has the capability of colliding polarized protons[2, 3] in the energy range of $\sqrt{s}$ from 50 to 500 GeV. In each of the collider rings there are a pair of Siberian snakes to maintain polarization during the energy ramps. The stable spin direction in each ring is vertical with spin up between snakes in one half of the ring and spin down in the other half.

This year we have been running (Run 3) with 55 bunches of polarized protons in each ring at 100 GeV per beam. Individual bunches are injected with either spin-up (+) or spin-down (−). In one ring the pattern alternates $+-+-\cdots$, and in the other ring the pattern is $++--\cdots$ to allow for all four possible incident polarization combinations.

Each ring has a Coulomb Nuclear Interference (CNI) polarimeter which measures the transverse asymmetry of carbon nuclei recoiling from a thin carbon filament which can be moved into the beam.[4]. The asymmetry is due to an interference of the Coulomb and nuclear parts of the cross section. The STAR and PHENIX detectors are between snakes in the same half of the rings, and CNI polarimeters are in the opposite half; so for a bunch of protons with spin up as measured by the CNI polarimeter, STAR and PHENIX would measure spin down.

There are four spin rotators (Fig. 1) around each of the STAR and PHENIX interaction regions[3]. With the four rotators around each experiment we can rotate the polarization locally to obtain longitudinal and radial polarization at the collision point without affecting the spin dynamics in the rest of the rings. For longitudinal polarization the incoming rotator rotates the spin from vertical into the horizontal plane. Between the end of the rotator and the interaction point are two horizontal bends (D0 and DX) for bringing the beams into collision. There is an energy-dependent net rotation of the polarization about the vertical axis: about 10° at injection (24.3 GeV), 40° at 100 GeV, and 100° at full energy 250 GeV. On the outgoing side of the collision point, the DX, D0, and rotator magnets reverse the spin precession so that from rotator to rotator, the interaction region (IR) is transparent to spin.

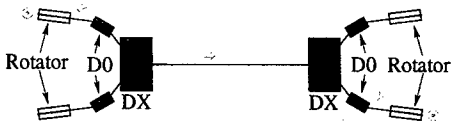


Figure 1: Layout of rotators around PHENIX (or STAR) interaction region.

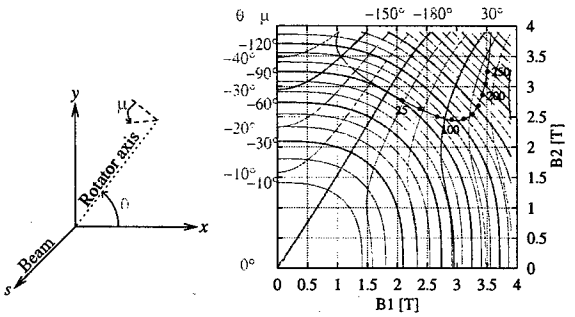


Figure 2: The helical rotators rotate the spin by an angle μ about an axis transverse to the beam as shown in the left diagram. The plot on the right shows contours of μ and θ, the angle of the rotation axis from the x-axis for various settings of fields in the inner and outer pairs of helices.

PHENIX LOCAL POLARIMETER

In order to have a verification of polarization direction at the experiments, both PHENIX and STAR developed local polarimeters for measuring transverse components of the polarization. When the polarization is longitudinal the local polarimeters show no transverse components while the CNI polarimeter measures a nonzero vertical component on the other side of the ring.

The PHENIX Local Polarimeter was based on experi-

* Work performed under the auspices of the U. S. Department of Energy (contract # DE-ACO2-98CH10886) and RIKEN of Japan.
† waldo@bnl.gov

0-7803-7738-9/03/$17.00 © 2003 IEEE

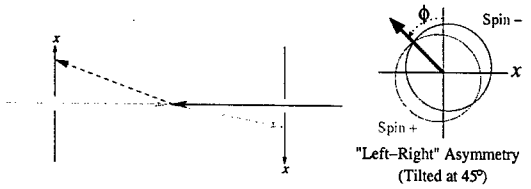


Figure 3: Left: Layout of the local PHENIX polarimeters around the interaction region. The y-axis (vertical) is out of the page; each local polarimeter has a right-handed Cartesian system with z-axis pointing along the corresponding beam direction. Right: definition of the left-right asymmetry indicating a polarization tipped away from the vertical axis by an angle ϕ.

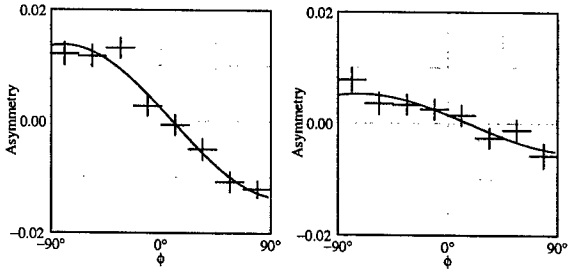


Figure 4: PHENIX local polarimeter measured asymmetries with the rotators off: left is for the Blue ring, and right is for the yellow ring. The curves are fits of a cosine function to the measured asymmetries. The positive peak at $\phi = -\pi/2$ corresponds to a spin-down polarization.

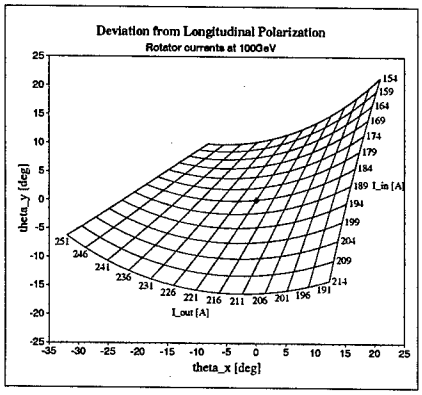


Figure 5: Sensitivity of polarization direction to rotator settings at 100 GeV. The angles θ_x and θ_y are defined in terms of the polarization components by the equations $\tan\theta_x = P_x/P_z$ for horizontal and $\tan\theta_y = P_y/P_z$ for vertical.

mental evidence from a test experiment performed at IP12 in Run 2[5] which showed that there is a left-right asymmetry in very forward neutron production from collisions of protons with one transversely polarized beam.

Each PHENIX local polarimeter consists of the Zero Degree Calorimeters (ZDC) and a Shower Maximum Detectors (SMD) inserted between the first and the second modules of the three-module ZDC units on both sides of the PHENIX IR. The ZDCs sampled the neutron energy through the hadronic shower development within its volume. The SMDs consist of 8 horizontal and 7 vertical 1.5 cm strips of plastic scintillator read by a 16 channel photomultiplier tube (Hamamatsu M16). Based on the energy observed in each strip, we reconstructed the energy-deposited profile, and hence deduced the hit position of the neutron which was then used to reconstruct the left-right and up-down asymmetries. Both these types of asymmetries were further combined to show a ϕ distribution of asymmetry (defined in Fig. 3), $\phi = 0$ starting from the vertical direction, increasing in the counter-clockwise direction. To minimize the effect of different bunch intensities, the asymmetry was calculated by the formula

$$A_{\rm LR} = \frac{\sqrt{L^+R^-} - \sqrt{L^-R^+}}{\sqrt{L^+R^-} + \sqrt{L^-R^+}}, \qquad (1)$$

where $L^\pm$ corresponds to the number of neutrons detected to the left of the ϕ-line, and a $R^\pm$ the number on the right for spin-up (+) and spin-down (−) bunches.

ROTATOR CALIBRATION

Fig. 4 shows the asymmetry measured by the local polarimeters at PHENIX for both rings with the rotators turned off. The phase of the cosine distribution indicates vertical polarization (spin-down) opposite to the CNI polarimeter measurement (spin-up) on the other side of the snakes.

Each rotator consists of four superconducting helical dipole magnets – alternating right and left-handed helices[2]. The outer pair of helices are connected in series to one power supply, and the inner pair to a second. With the two snakes at full strength in a given ring at 100 GeV, longitudinal polarization is obtained when $I_{\rm in} = 184$ A and $I_{\rm out} = 221$ A. Fig. 5 shows the sensitivity of transverse polarization components to changes in rotator currents at 100 GeV.

When we first turned on the rotators around PHENIX the polarization measured by the local polarimeters showed nonzero zero asymmetries corresponding to a large negative radial component in both rings (see Fig. 6). The amount of precession through the D0 and DX magnets at 100 GeV is about 40° degrees. In our earlier calculations we inadvertently missed a sign, and had the power supplies to all rotators wired backwards. With the wrong polarity, the spin in the rotator is rotated by an angle $-\mu$ about the same axis so that after the rotator, the spin is rotated to the other side of the longitudinal by $-40°$. The additional precession through the D0 and DX magnets then rotates the polarization to $-80°$ from the longitudinal. This was verified by spin tracking through all rotators in both rings. After correcting the polarity of the rotator power supplies, the

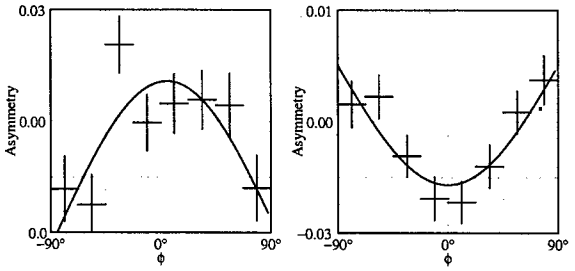


Figure 6: PHENIX asymmetries measured after first turning on the rotators at PHENIX with reversed currents ($I_{\rm in} = -184$ A and $I_{\rm out} = -221$ A): left is for the Blue ring, and right is for the Yellow ring.

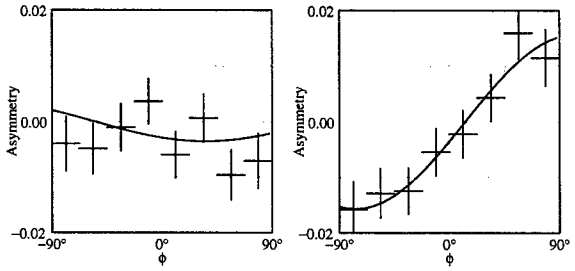


Figure 7: PHENIX asymmetries measured after correcting the polarities of the power supplies. Both sets of rotators were set to the currents: $I_{\rm in} = 184$ A and $I_{\rm out} = 221$ A. The negligible asymmetry in the Blue ring (left plot) is consistent with longitudinal polarization at PHENIX. The Yellow ring measurement (right plot) still shows a sizable vertical component due to the weak snake as discussed in the text.

measurements showed a negligible transverse component in the Blue ring (see Fig. 7).

During the initial startup a helical dipole in one of the snakes in the Yellow ring failed with an opening of the superconductor. We reconfigured this snake to run as a partial snake using a single pair of helices; the amount of spin rotation in this snake was only 158° rather than a full 180°. We were able to operate the Yellow ring with one full snake and the weaker snake maintaining polarization by keeping the spin tune close to 0.5 during the ramps for energy, beta-squeezes, and rotators. With this weak snake the stable spin direction is not vertical, but tilts away from the vertical by about 11°. This tilt is also translated through the rotators into a spin which is not quite longitudinal as shown in the right side of Fig. 7.

A correction may be made according to Fig. 5 from an estimate of the direction of the polarization away from the longitudinal and the orientation of the transverse components. From the Yellow ring measurements of the local polarimeter in Fig. 7 and the CNI polarimeter, a crude estimate determined that the spin was pointing as much as 40° away from the longitudinal with a transverse component about 12° away from the vertical. A first estimate was made for the correction shown in the left of Fig. 8 went in the wrong direction. Compensating in the opposite (correct) direction (Fig. 8 right) nulled the transverse components to yield longitudinal polarization.

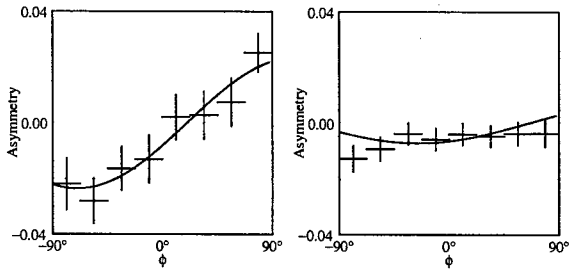


Figure 8: Further PHENIX asymmetries for the Yellow ring with rotator adjustments. A setting of $I_{\rm out} = 198$ A and $I_{\rm in} = 229$ A shown at left increased the transverse component. At right the setting with currents $I_{\rm out} = 244$ A and $I_{\rm in} = 138$ A eliminated the transverse component.

RHIC is now the first collider with longitudinal polarization in both beams. The STAR rotators were successfully commissioned later during the conference.

REFERENCES

[1] http://www.phenix.bnl.gov

[2] I. Alekseev et al., *Polarized proton collider at RHIC*, NIM **A 499** (2003), 392.

[3] W. W. MacKay et al., "Spin Dynamics in AGS and RHIC", These Proceedings.

[4] O. Jinnouchi et al., Proceedings of SPIN2002, Upton NY (to be published).

[5] Y. Fukao for the IP12 Local Polarimetry Collaboration, Proceedings of SPIN2002, Upton, NY (to be published).

DESIGN OF A FAST CHROMATICITY JUMP IN RHIC *

C. Montag†, J. Kewisch, D. Bruno, G. Ganetis, W. Louie, BNL, Upton, NY 11973, USA

Abstract

During transition crossing in the Relativistic Heavy Ion Collider (RHIC), chromaticities have to change sign. This sign change is partially accomplished by the γ_t quadrupole jump; however, the resulting chromaticity jump is only $\Delta\xi_x = 2.1$ in the horizontal and $\Delta\xi_y = 2.4$ in the vertical plane. To increase the jump height, a dedicated chromaticity jump scheme has been designed, consisting of fast power supplies connected to six sextupoles per ring, which is capable of providing a chromaticity jump of $\Delta\xi = 6$.

INTRODUCTION

The Relativistic Heavy Ion Collider (RHIC) consists of two superconducting storage rings installed side-by-side, which intersect at six interaction points. Therefore, each ring consists of three inner and three outer arcs. Ions other than protons are injected into RHIC from the Alternating Gradient Synchrotron (AGS) below transition energy, at γ in the range of 10 to 15. When accelerated to storage energies of 100 GeV/nucleon, which corresponds to $\gamma = 107$ for fully stripped gold ions, for example, the transition energy has to be crossed at $\gamma_t = 23.2$. This is accomplished by a dedicated set of γ_t-quadrupoles which are equipped with special power supplies capable of switching the sign of the magnetic field within some 30 msec.

This sign flip modifies the horizontal dispersion D_x, leading to a change in the transition energy as

$$\alpha = \frac{1}{\gamma_t^2} = \frac{1}{C}\int_0^C \frac{D_x(s)}{\rho(s)}\,\mathrm{d}s, \qquad (1)$$

where C is the circumference of the ring, and $\rho(s)$ designates the local bending radius. Figure 1 shows the resulting horizontal dispersion function D_x before and after the transition jump.

Since the arcs are equipped with regular sextupoles to control the chromaticities of the machine, the modified dispersion function within these sextupoles slightly changes the chromaticities. In the case of RHIC, the associated chromaticity change due to the γ_t-quadrupole sign change is $\Delta\xi_x = 2.1$ horizontally and $\Delta\xi_y = 2.4$ vertically for a γ_t jump height of $\Delta\gamma_t = 1.0$.

The positive sign of this chromaticity change provides the necessary sign flip when crossing transiton. However, operational experience shows that the magnitude of this chromaticity jump may not be sufficient, because chromaticites have to be kept around $\xi_{x,y} = -1$ before transition to ensure a symmetric jump with $\xi_{x,y} = +1$ after γ_t. Keeping

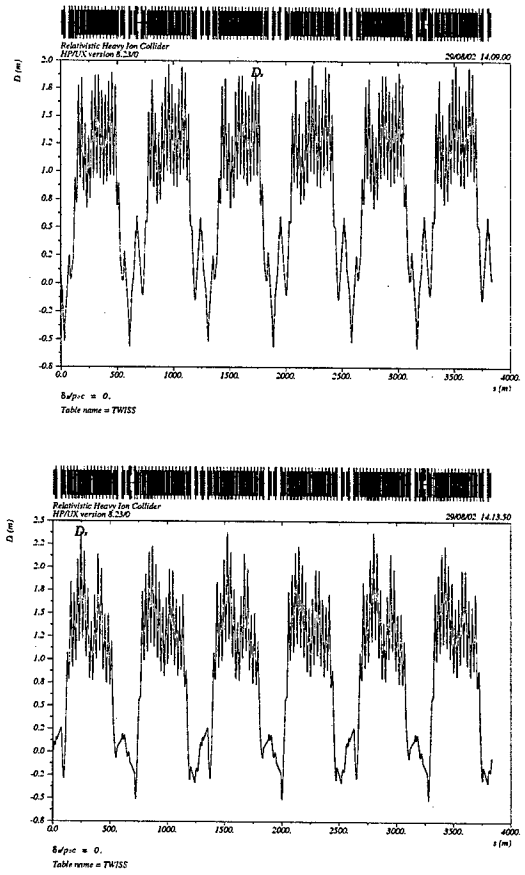


Figure 1: Horizontal dispersion function D_x before (top) and after (bottom) crossing transition for $\Delta\gamma_t = 1.0$.

chromaticites that close to zero can lead to transverse instabilites around transition, as it was observed during RHIC operations.

To improve this situation, a dedicated chromaticity jump scheme was developed [1]. This scheme consists of two sextupoles at one end of each outer RHIC arc, which are jumped from zero to their final strength within 30 msec at transition. Since this leads to an uneven sextupole distribution around the ring, we performed extensive dynamic aperture studies to ensure the feasibility of this scheme. This paper presents the results of these studies.

* Work performed under contract number DE-AC02-98CH10886 with the auspices of the US Department of Energy

† montag@bnl.gov

0-7803-7738-9/03/$17.00 © 2003 IEEE

RESULTS

Dynamic apertures where calculated by MAD [2] for three different values of $\Delta p/p$: -0.002, 0.0, and $+0.002$. At injection and transition, $\Delta p/p = 0.002$ corresponds to roughly one σ_p, while it corresponds to about two σ_p at store. Tunes were set to $Q_x = 28.21$ horizontally and $Q_y = 29.23$ vertically, and the b_2 component of the dipoles was included in the tracking according to magnetic field measurements [3].

At injection with a *beta*-function of $\beta^*_{x,y} = 10\,\mathrm{m}$ at all IPs the jump sextupoles are off, as well as the γ_t-quadrupoles. The remaining regular arc sextupoles correct the chromaticities in both planes to $\xi_{x,y} = -2$. Figure 2 shows the resulting dynamic aperture in the $(x - y)$ plane, together with the result for the existing regular sextupole scheme. The two schemes do not differ significantly.

Right before the transition jump, the jump sextupoles are

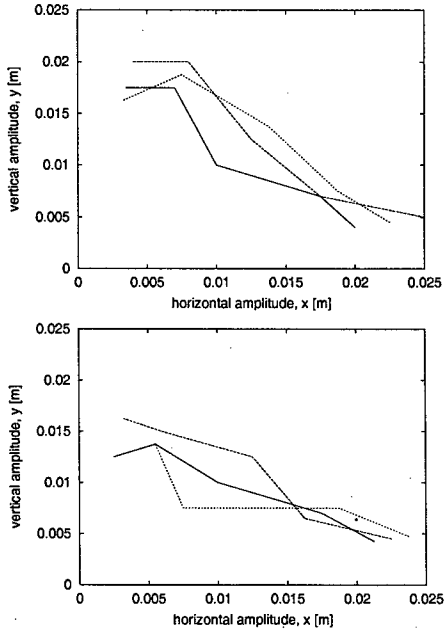


Figure 2: Dynamic aperture at injection in the $(x - y)$ plan e, for $\Delta p/p = 0.0$ (solid), 0.002 (dashed) and -0.002 (dotted). The β-function in all IPs is set to $\beta^* = 10\,\mathrm{m}$. One σ corresponds to 1.25 mm in both planes for an emittance of $\epsilon = 10\pi$ mm mrad. The top graph shows the situation with the new jump sextupole configuration, while the lower plot exhibits the dynamic aperture for the regular sextupole scheme.

still off, and the remaining regular arc sextupoles provide chromaticities of $\xi_{x,y} = -2$ in both planes. Additionally, the γ_t-quadrupoles are on and provide an increased $gamma_t$ value, with $\Delta\gamma_t = 0.5$. The resulting dynamic aperture is significantly smaller than for the regular scheme (see Figure 3), but since it is still at least $12\sigma_{x,y}$ it is considered sufficient.

Right after the transition jump, the γ_t-quadrupoles have

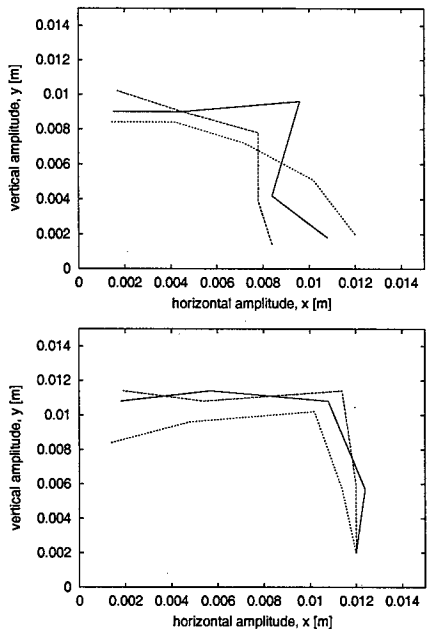


Figure 3: Dynamic aperture just before the transition jump, for $\Delta p/p = 0.0$ (solid), 0.002 (dashed) and -0.002 (dotted). The β-function in all IPs is $\beta^* = 5\,\mathrm{m}$. One σ corresponds to 0.6 mm in both planes for an emittance of $\epsilon = 10\pi$ mm mrad. The top graph shows the situation with the new jump sextupole scheme, while the lower plot depicts the dynamic aperture for the regular scheme.

flipped sign. The jump sextupoles are turned on now and set the total chromaticities to $\xi_{x,y} = +2$, while the strength of the remaining regular arc sextupoles remains unchanged. This results in a dynamic aperture that is practically the same as for the regular sextupole scheme, Figure 4.

At store the γ_t quadrupoles are off again, while the jump sextupoles are set to the maximum strength the fast power supplies are capable of providing, which corrresponds to roughly the same strength as the remaining sextupoles in the horizontal plane and about half of the regular sextupole strength vertically. The resulting dynamic aperture for a β-function of $\beta^*_{x,y} = 2\,\mathrm{m}$ at all IPs is shown in Figure 5. As a comparison with the existing regular sextupole scheme shows, the dynamic aperture is practically the same for both configurations.

CONCLUSION

Dynamic aperture studies have been performed to ensure the feasibility of a fast chromaticity jump to improve transition crossing performance in RHIC. Comparison with the existing regular sextupole configuration showed sufficient dynamic aperture in spite of the resulting irregular

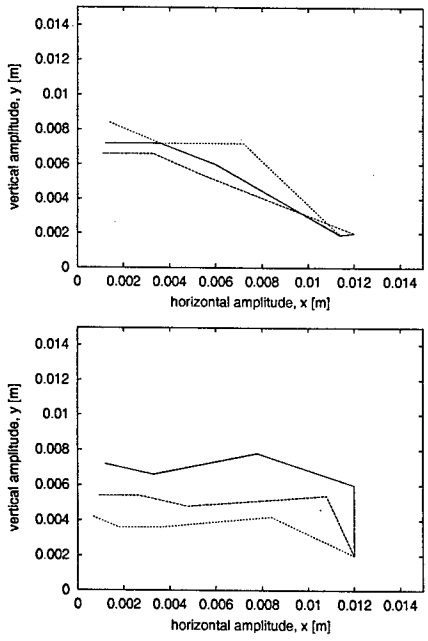


Figure 4: Dynamic aperture just after the transition jump, f or $\Delta p/p = 0.0$ (solid), 0.002 (dashed) and -0.002 (dotted), for $\beta^* = 5$ m in all IPs. One σ corresponds to 0.6 mm in both planes for an emittance of $\epsilon = 10\pi$ mm mrad. The top graph shows the situation with the jump sextupoles, while the lower plot exhibits the dynamic aperture for the regular scheme.

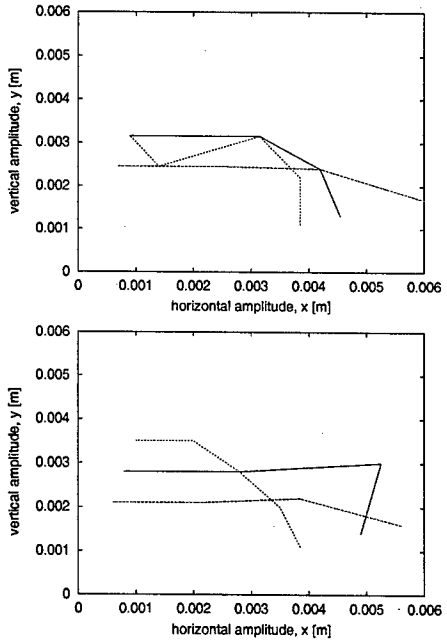


Figure 5: Dynamic aperture at store, for $\Delta p/p = 0.0$ (solid), 0.002 (dashed) and -0.002 (dotted), for $\beta^* = 2$ m in all IPs. The jump sextupoles are ON, providing 87% of the regular sextupole strength in the horizontal direction, and 44% in the vertical plane. One σ corresponds to 0.35 mm in both planes for an emittance of $\epsilon = 40\pi$ mm mrad (end of store). The top graph depicts the situation with jump sextupole configuration, while the lower plot shows the dynamic aperture for the regular sextupole scheme. Note that at the end of the store, the emittance is assumed to be blown up to $\gamma\epsilon = 40\pi$ mm mrad, resulting in an rms beam size of 0.35 mm at the IP.

sextupole distribution. This scheme will therefore be implemented for the upcoming RHIC run.

REFERENCES

[1] C. Montag, J. Kewisch, Dynamic aperture studies towards a γ_t sextupole jump in RHIC, BNL C-A/AP/84

[2] H. Grote, F. C. Iselin, The MAD program, CERN/SL/90-13 (AP)

[3] S. Tepikian, private communication

NON-LINEAR EFFECTS IN THE RHIC INTERACTION REGIONS: MEASUREMENT AND CORRECTION*

F. Pilat, S. Binello, P. Cameron, V.Ptitsyn, BNL, Upton, USA

Abstract

A technique for measuring and correcting locally non-linear effects arising from field errors and feed-down from the interaction region (IR) triplets has been developed at RHIC. After a brief review of the method, we will compare measurements taken with different IR optics configurations, with beta at the interaction point ranging from 3 to 1m. The beam data are compared with results from a realistic RHIC model, which includes measured field errors in the magnets, and simulates operational effects and corrections. A control room application has been developed for the RHIC run 2003 that allows faster measurements of non-linear effects, online plotting and fitting of non-linear terms from measurements of tune shift as a function of orbit bump amplitude. Results for local non-linear correction during run 2003 are presented.

INTRODUCTION

The IR bump method allows the determination and correction of triplet errors from beam data by measuring rms orbit and tune shift as a function of the amplitude of closed orbit bumps centred on the IR triplets [1]. This technique has been used during RHIC run 2000 to correct the triplet linear coupling effects [2]. Refinement of linear corrections and test of non-linear corrections were achieved during run 2001 [3].

During the RHIC run 2003, ended in May, a control room application has been developed that speeds up data taking and facilitates the online data analysis and setting of the correctors. That allowed the systematic correction of sextupole effects at all low beta IR's, for optics with β^*=2m (d-Au run) and β^*=1 with (polarized p run). We also tested octupole correction in IR8 and the use of the the application for measuring the beam-beam tune shift vs. crossing angle in IR6. In Section 4 we will address the comparison of beam data with model predictions. Finally we will draw conclusions and discuss planning for the next RHIC run.

THE IR BUMP APPLICATION

The IR bump application interface is shown in Figure 1.

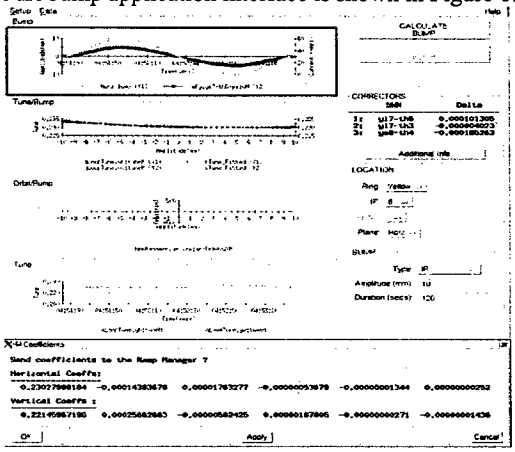


Figure 1. IR bump application interface and functionality.

The application allows us to select, calculate and set orbit bumps centred on a single triplet or spanning the entire IR. Bumps are ramped from zero to the chosen maximum amplitude in a set amount of time, typically 1-2 minutes. Tune values and dipole corrector power supply currents are monitored on the bump. Tunes and rms orbits are plotted as a function of bump amplitude and polynomial fitting up to 5th order is available to quickly quantify the non-linear effects and to aid in the determination of corrector settings.

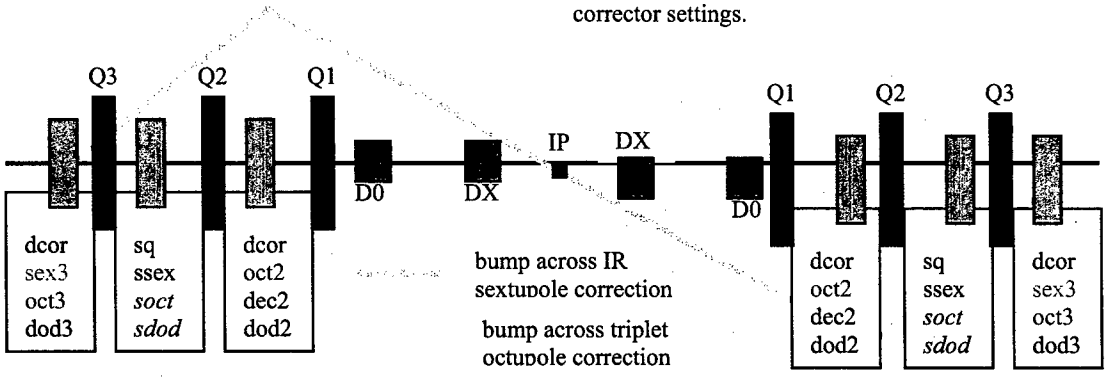


Figure 2. Schematics of a RHIC IR, with the IR correction system and IR bumps used for the correction

*Work performed under the auspices of the US Dept. of Energy

Orbit data proved valuable for linear correction. The feasibility of measuring accurately non-linear effects however resides in the high resolution (~10^{-5}) of the PLL (Phase Lock Loop)[4] tune measurement system used for this application in its highest resolution mode. The application greatly enhanced the speed of non-linear IR measurements and allowed the operational correction of low order non-linear effects.

MEASUREMENT AND CORRECTION

The RHIC IR's are schematically described Figure 2. The beams are horizontally separated first, so there are 2 triplets per ring at every crossing. Nested in each triplet there are 3 multi-layer correction packages, hosting correctors from dipole to dodecapole. Dipole and skew quadrupoles are powered at every IR, while power supplies for non-linear correctors are presently available only at the IR's designed as low β^* (IR6 and IR8). Local coupling correction at all triplets was accomplished in run 2000 and 2001. The goal for 2003 was the operational correction of low-order non-linear effects in IR6 and IR8. The motivation is 2 folded: simulation evidence that correction of triplet field errors increases the dynamic aperture at store from 3.5 to ~5σ, and operational. IR sextupole errors cause the IP orbit and angle bumps used for collision steering not to be perfectly closed, thus operationally coupling IP's.

Prerequisite for non-linear measurements and correction is a well corrected machine: good overall orbit correction (rms < 2mm), with beams well centred in the triplets (<2mm); chromaticity adjusted, coupling corrected to ΔQ_{min} <0.002 with enough tune separation (>0.006) to insure independence of horizontal and vertical dynamics; beams anti-cogged by 3 buckets to insure no interference from beam-beam effects.

Sextupole corrections at β^*=2m IR's

In each IR there are 2 sextupole correctors (sx3 in Figure 2) at high β_x and β_y locations given the anti-symmetry of the IR optics.

IR	pl	sextupole BC	sextupole AC	octupole BC	octupole AC
Yir8	H	0.22209	0.01347	0.00535	0.00093
	V	-0.33559	0.00595	-0.00388	0.00119
Yir6	H	-0.23338	-0.02673	-0.00968	-0.00051
	V	0.41028	-0.00042	-0.00745	-0.00251
Bir8	H	-0.03204	no correct.	-0.00557	-0.00557
	V	0.07865	no correct.	0.00646	0.00646
Bir6	H	-0.06853	0.02713	0.00536	-0.01491
	V	0.12877	0.01121	-0.00176	0.00015

Table 1. Sextupole and octupole coefficients (in units of 10^{-3}) of the tune vs. bump amplitude, before (BC) and after (AC) local sextupole correction, β^*=2m optics.

For sextupole correction we used a horizontal 10mm bump spanning the 2 triplets. The 2 sextupole correctors are independently adjusted on the basis of the fitted sextupole coefficients. Before and after correction tune dependence at all IR's is summarized in Table 1. Since the effect in Blue IR8 was small, it has been left uncorrected. Figure 3 shows the tune dependence vs. bump amplitude before and after sextupole correction at IR8 in the yellow ring.

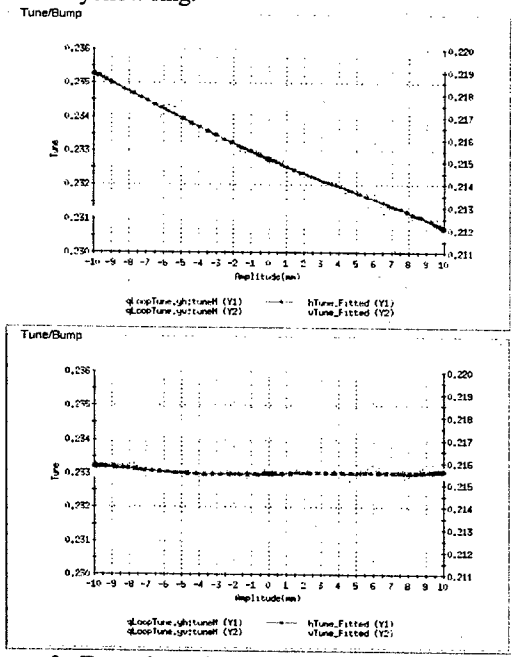


Figure 3. Tune dependence vs. bump amplitude before and after correction, IR8, β^*=2m optics.

Sextupole corrections at the β^*=1m IR's

In the d-Au run IR8a and IR6 have been operated at β^*=2m, while the optics has been squeezed at the same IP's to β^*=1m in the polarized proton run. Measurements and sextupole correction were repeated in the new configuration. Results are summarized in Table 2 and displayed in Figure 4.

IR	pl	sextupole BC	sextupole AC	octupole BC	octupole AC
Yir8	H	-0.09225	-0.00717	0.00714	0.00187
	V	0.19926	-0.00351	0.00013	0.00228
Yir6	H	-0.00446	0.09622	-0.00080	-0.00713
	V	0.19372	0.08155	0.00666	0.00634
Bir8	H	-0.03177	-0.00343	-0.00444	-0.00669
	V	0.17317	-0.00344	-0.00076	0.00043
Bir6	H	-0.10395	-0.00241	0.00044	0.00057
	V	0.10728	0.00399	-0.00514	-0.00461

Table 2. Coefficients (in units of 10^{-3}), before (BC) and after (AC) local sextupole correction, β^*=1m optics.

The measured tune shift vs. bump amplitude are on average larger for the β^*=2m configuration than for β^*=1m. This counter-intuitive result is explained by the fact that for d-Au (1m optics) the magnets were ramped to 4500A (Au 100 GeV/u, d 250 GeV), while for pp to 1800A (p at 100 GeV) and the dependence of field errors on the current offsets the β^* dependence.

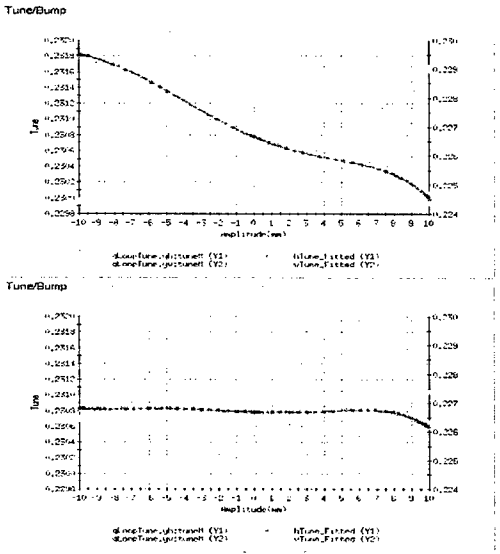


Figure 4. Tune dependence vs. bump amplitude before and after correction, IR8, β*=1m optics.

Octupole correction at IR8

Local octupole correction has been tested in yellow IR8. Since we have 2 octupoles correctors per triplet, we used horizontal 3-bump centred at the individual triplets. Results are summarized in Table 3.

triplet	bump	Octupole BC	Octupole AC
Yi7	10mm	0.00750	0.00153
		-0.00867	-0.00059
Yo8	7 mm	0.00399	-0.00397
		-0.00941	-0.00188

Table 3. Octupole coefficients (units 10^{-3}) before and after correction at the IR8 triplets, yellow ring, β*=2m.

The octupole correction was not retained for operations since feed-down from octupoles degraded the pre-existing sextupole correction. Conceptually, octupole correction should be performed first followed by sextupole, to avoid feed-down, but sextupole correction had higher priority.

Measurements at the β=3m IR's*

IR	bump	plane	sextupole	octupole	decapole
Yir10	10 H	H	-0.04798	-0.00829	0.00059
		V	0.04262	-0.00092	-0.00111
Yir10	10 V	H	-0.03633	0.00121	0.00085
		V	-0.02066	0.00159	0.00060
Yir2	10 H	H	-0.09138	-0.00856	0.00133
		V	0.13084	0.00553	-0.00116
Yir2	10 V	H	-0.03863	0.00137	-0.00013
		V	0.20178	0.00656	0.00656

Table 4. Measurements at β*=3m interaction regions.

Measurements were taken at the experimental high β IR's (3m) to explore the possibility of further β-squeeze in these locations, where we do not have non-linear correctors. At 3m the effects are large, especially in IR2, not surprisingly since the high field quality triplets were installed in IR6 and IR8 (low β* IR's)

Test measure of beam-beam effects at IR6

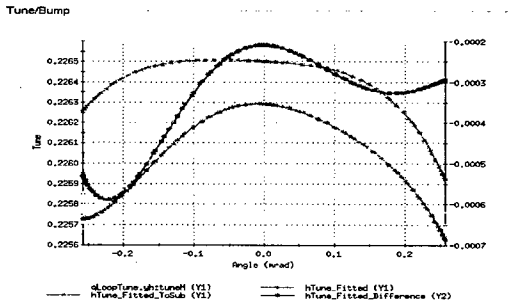


Figure 5. Tune shift vs. crossing angle: difference between cogged and un-cogged beam.

The bump amplitude is proportional to the crossing angle at the IP. By comparing data with colliding beam (cogged) and not colliding (un-cogged) the IR bump application has been tested to determine the tune shift due to the beam-beam effect as a function of crossing angle [5], an interesting operational beam-beam parameter.

COMPARISON WITH THE MODEL

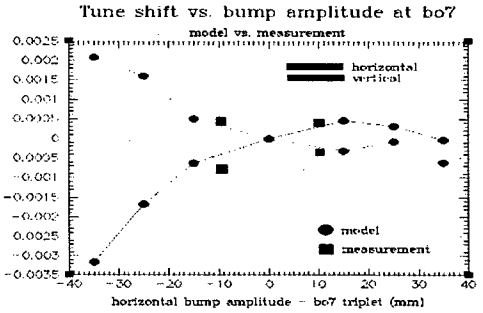


Figure 5. Comparison of model and measurement at bo7

Realistic modelling of the IR bumps with individual measured field and alignment errors in the triplet cold masses has started. Preliminary results for IR8 show good correlation between measured and simulated tune shifts.

CONCLUSIONS AND PLANS FOR 2004

The development of the IR bump application enabled the operational correction of local IR sextupole effects in run 2003, for β*=2m and β*=1 optics, and to prove the feasibility of octupole correction. The plan for 2004 is to make the octupole correction operational, and to more precisely correlate, via measurements and modelling, machine performance to the quality of IR corrections.

REFERENCES

[1] J-P. Koutchouk, F. Pilat, V. Ptitsyn, "*Beam-based measurements of field multipoles in the RHIC low beta insertions and extrapolation of the method to the LHC*", PAC 2001

[2] V. Ptitsyn, J. Cardona, J-P. Koutchouk, F. Pilat, "*Measurement and correction of the linear effects in the RHIC IR's*", PAC 2001

[3] F. Pilat, P. Cameron, J-P. Koutchouk, V. Ptitsyn, *"Linear and non-linear corrections in the RHIC Interaction Regions"*, EPAC 2002

[4] P. Cameron, *"RHIC third generation PLL tune system"*, PAC 2003

[5] W. Fischer, *Private Communication*

COMMISSIONING OF RHIC DEUTERON-GOLD COLLISIONS

T. Satogata *, L. Ahrens, M. Bai, J. Beebe-Wang, M. Blaskiewicz, J.M. Brennan, K.A. Brown, D. Bruno, P. Cameron, J. Cardona, R. Connolly, A. Drees, W. Fischer, R.P. Fliller III, G. Ganetis, C. Gardner, J.W. Glenn, H. Hahn, T. Hayes, H. Huang, U. Iriso-Ariz, W.W. MacKay, A. Marusic, R. Michnoff, C. Montag, F. Pilat, V. Ptitsyn, T. Roser, K. Smith, S. Tepikian, D. Trbojevic, N. Tsoupas, S.Y. Zhang, J. van Zeijts
Brookhaven National Laboratory, Upton, NY 11973–5000, USA

Abstract

Deuteron and gold beams have been accelerated to a collision energy of $\sqrt{s}$ = 200 GeV/u in the Relativistic Heavy Ion Collider (RHIC), providing the first asymmetric-species collisions of this complex. Necessary changes for this mode of operation include new ramping software and asymmetric crossing angle geometries. This paper reviews machine performance, problems encountered and their solutions, and accomplishments during the 16 weeks of ramp-up and operations.

INTRODUCTION

After productive p-p and Au-Au collider physics runs in 2000–1 with collision energies of $\sqrt{s}$ =130–200 GeV/u, RHIC experiments reported early high-p_t jet quenching results [1]. To compare Au-Au results with cold nuclear matter probes, 16 weeks of operations time were spent commissioning and operating $\sqrt{s}$ = 200 GeV/u deuteron-gold (dAu) collisions in RHIC, from late November 2002 to late March 2003. This was the first operation of a asymmetric-species heavy hadron collider, and an important demonstration of RHIC's flexibility to probe hot and cold nuclear matter at the 200 GeV energy scale.

A summary of machine performance goals and achievements for this run are listed in Tables 1 and 2. Almost all run goals were either met or exceeded. The only unachieved primary goal was gold per-bunch beam intensity, limited by injector and injection performance.

Table 1: RHIC 2002–3 dAu Run Parameters

Machine Performance	goal	achieved
Setup/Ramp-up time [weeks]	2/3	2.5/3
Storage energy [GeV/u]	100	100
Number of bunches	55	110/55
β^* [m]	2	2/3/4
Diamond length σ [cm]	20	15
Peak luminosity [$\times 10^{28}$ cm^{-2} s^{-1}]	4.0	6.2
$\langle L \rangle$(store) [$\times 10^{28}$ cm^{-2} s^{-1}]	1.6	2.8
$\langle L \rangle$(week) [nb^{-1}/week]	4.0	4.6

*Work performed under Contract Number DE-AC02-98CH10886 under the auspicies of the US Department of Energy; author email satogata@bnl.gov

RUN PREPARATION

With limited run time, an early consensus among experiments was reached to focus on a single run configuration with deuterons in the blue ring and gold ions in the yellow ring. This setup required reversal of DX power supply shunts to maintain unipolar constraints on these power supplies at injection and through the acceleration ramp[2]. These machine constraints could also only be satisfied by including a 1 mrad crossing angle at injection and, more importantly, a 1 mrad common angle for head-on collisions at storage energy, as shown in Fig. 1. Zero-degree neutron calorimeters (ZDCs), used for luminosity monitoring, were moved by 10 mm in the appropriate direction to maintain necessary signal levels[3]. Power supply and ZDC work required two days of run-specific setup time.

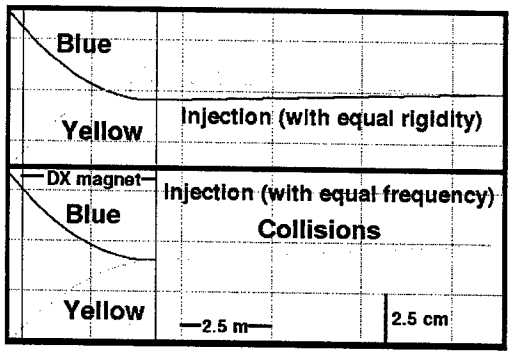


Figure 1: dAu collision geometries at injection and store

Both Tandems were used and had excellent uptime: Tandem MP7 supplied gold beam and MP6 supplied deuteron beam. All injectors (Tandems, Booster, AGS and transfer lines) were required to "mode-switch" between both species for every RHIC fill with a typical species change time of 3–5 minutes[4]. Production injection always started with deuterons, to minimize IBS-driven gold beam emittance dilution on the injection porch. Overall injector setup time and development were a concern throughout the run due to division of effort between setup of both species.

Run preparation also included demonstrations by controls and instrumentation to gracefully handle two beams of significantly different character and intensities. Logging, instrumentation, and control systems easily demonstrated the flexibility to handle separate species in each RHIC ring.

0-7803-7738-9/03/$17.00 © 2003 IEEE

Table 2: RHIC 2002–3 dAu Stored Beam Parameters

Storage Parameter	Au, Yellow Ring		d, Blue Ring	
	goal	achieved	goal	achieved
Intensity/bunch	1.0×10^{9}	0.7×10^{9}	0.8×10^{11}	1.2×10^{11}✓
Total Intensity (55/110 bunches)	55×10^{9}	38 / 60×10^{9}✓	45×10^{11}	57 / 69×10^{11}✓
Transverse Emittance [95%, $\pi\mu$rad]	10–40	10–30✓	15	12 ✓
Bunch Length [ns] (200 MHz RF)	5	5✓	5	5✓

RUN CHRONOLOGY AND ISSUES

At the 2002 RHIC Retreat, a goal was set of 14 days of set-up time (time to initial collisions) and 21 days of ramp-up time (time to develop collisions and lifetime to physics production) for every new species configuration[5]. This run guidance, based on experience during gold and polarized proton commissioning, was reasonably close, with 18 days from first beam in the blue ring to first collisions. 20 days after first collisions, minimum goals were met for the start of dAu physics.

As in previous RHIC Au runs, injection was performed with β^*=10 m at all interaction points (IPs). The initial acceleration ramp also squeezed to β^*=5 m at all IPs to optimize optics for independent transition jumps, and then squeezed to final collision optics in the last half of the acceleration ramp. Collision optics were β^*=10 m at non-experimental IPs, and β^*=2–4 m at experimental IPs, depending on experiment background issues. Beams were vertically separated with ±5 mm bumps at all IPs through the acceleration ramp to avoid all but long-range beam-beam effects.

Initial setup was injecting beams with equal rigidities, minimizing transfer line mode switching requirements and maintaining species symmetry between both rings for injection setup. However, collisions required equal frequencies between the two beams, and in this condition modulated long-range beam-beam forces created untunable beam loss during the acceleration ramp. On Jan 2 we changed ramp conditions to equal frequencies from injection to collision (see Fig. 1), minimizing beam-beam modulation, producing more efficient acceleration ramps, and enabling study of ring-to-ring RF locking during acceleration[6]. Ramp recommissioning took less than two days.

Table 3: Short RHIC 2002–3 dAu Run Chronology

11/1	Start of RHIC cooldown
12/13	Both rings at 4K
12/22	First ramps of d/Au to collision energies
12/24	First d/Au collisions at all experiments
12/27	Start of routine detector commissioning
1/2	Injection: equal rigidity to equal frequency
1/9	Routine 110 bunch ramping
1/12	Start of 2003 d/Au Physics Run
2/21	Low-noise storage RF driver
2/22	Deuteron transverse instability fixed
	First production store to hit goal levels
2/26	Return to 55 bunch operations
	Routine goal operations
3/24	End of 2003 d/Au Physics Run

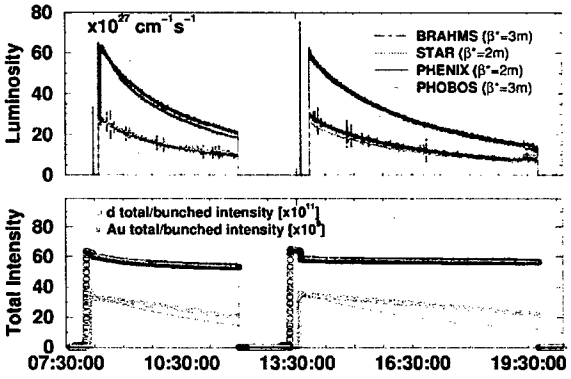


Figure 2: Two typical RHIC FY03 dAu stores, showing beam current ($\times10^{9/11}$ Au/p, total and bunched) and luminosity lifetime. Luminosity lifetime was dominated by gold beam lifetime and IBS-driven debunching and emittance growth. Time between stores was about 1 hour.

RUN PERFORMANCE DETAILS

Fig. 3 shows single-bunch and total beam intensity evolution through the course of the run, measured at the end of every acceleration ramp. To meet performance goals, the number of bunches in each ring was doubled from 55 to 110 at the beginning of January. Though this produced reasonable physics, pressure rises created intolerable backgrounds and beam lifetime issues[7], and required a return to 55 bunch stores on Feb 26. Single-bunch intensity development was limited by RHIC development time and mode switching, though deuteron intensities were improved in late Feb with RF bunch merging in the Booster[4]. RHIC ramp efficiencies averaged 95% after the startup period.

Fig. 4 shows the total integrated luminosity for the run, with final totals well above the minimum required for physics. This plot correlates only roughly with Fig. 3; on Feb 22 an emittance-diluting instability in the deuteron acceleration ramp was diagnosed and cured, improving emittance and raising luminosity by almost a factor of two.

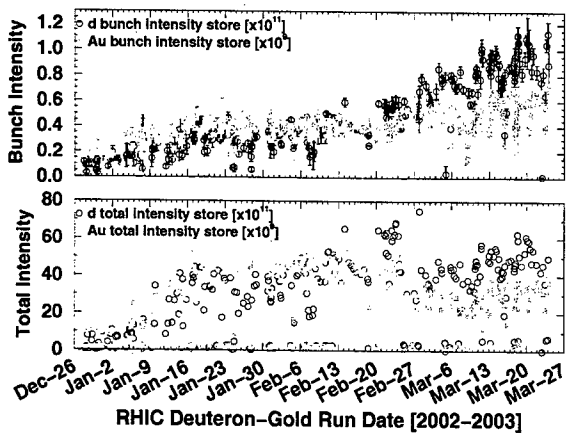


Figure 3: RHIC dAu run intensity evolution, as measured at the end of every acceleration ramp. Small total intensities are indicative of 6-bunch setup or beam study ramps. Error bars in the top plot are over all bunches in the store. Unsuccessful ramps are excluded.

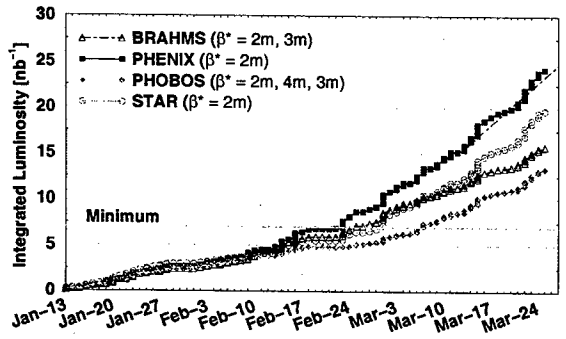


Figure 4: dAu run integrated luminosity. PHENIX integrated luminosity averaged 4.6 nb^{-1}/week near run end.

RUN HIGHLIGHTS

A new transverse injection damper system was commissioned[9] early in the run, successfully limiting emittance growth due to bunch-by-bunch injection variations. The addition of 720 Hz digitizers in February also added the capability of coherence monitoring to this system. Signals during production acceleration ramps showed a clear deuteron beam transverse instability (see Fig 5) near transition, leading to large emittance dilution and backgrounds. Using the coherence monitor, this instability was avoided by careful chromaticity adjustments[8].

The RHIC PLL tune system[10] was commissioned to routine use during this run, and there were several ramps with successful tune feedback that constrained limited tune variations to 10^{-3}, though with more beam loss than without tune feedback. Feed-forward ramp coupling corrections were also performed in both rings, using a new method for coupling correction based on N-turn maps[11].

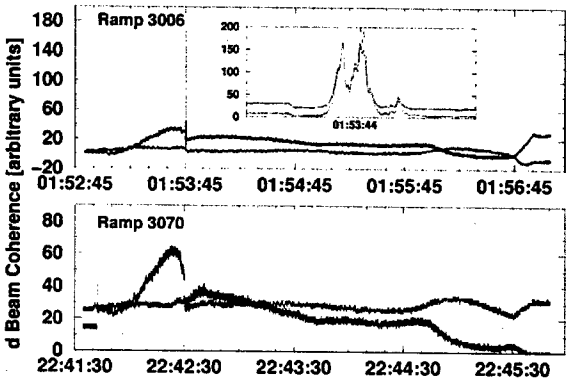


Figure 5: Blue transverse coherence monitor readings for ramps 3006 (Feb 16) and 3070 (Feb 27), showing the effects of chromatic instability correction. The inset shows details of the near-transition instability over one second.

With injection kicker improvements, this was the first RHIC run to demonstrate routine 110-bunch injection, part of the RHIC-II luminosity upgrade. 110-bunch ramping sometimes created pressure rise within the PHOBOS IR region, creating destructive radiation for an experiment that is dominated by radiation-sensitive Si detectors. Returning to 55-bunch operations eliminated these pressure rises[7].

ACKNOWLEDGEMENTS

The authors thank Steve Peggs and Phil Pile for productive discussions, and the RHIC/AGS operations staff for successful physics operations of this run.

REFERENCES

[1] P. Levai *et al.*, "Discovery of Jet Quenching at RHIC and the Opacity of the Produced Gluon Plasma", Nucl.Phys. A698 (2002) 631–634.

[2] J. van Zeijts *et al.*, "Ramp Design and Implementation for the RHIC d/Au Run", TPPB048, these proceedings (May 2003).

[3] A. Drees *et al.*, "Luminosity Monitoring at RHIC with Various Species", TPPB031, these proceedings (May 2003).

[4] L. Ahrens *et al.*, "RHIC Injector Configurations for the RHIC d/Au Run", TPPB047, these proceedings (May 2003).

[5] `http://www.c-ad.bnl.gov/RHIC/retreat2002/`

[6] J.M. Brennan *et al.*, "Operation of the RHIC RF System", ROAA006, these proceedings (May 2003).

[7] S.Y. Zhang *et al.*, "RHIC Pressure Rise and Electron Cloud", MOPA010, these proceedings (May 2003).

[8] M. Blaskiewicz *et al.*, "Transverse Instabilities in RHIC", RPPB007, these proceedings (May 2003).

[9] A. Drees *et al.*, "RHIC Transverse Injection Damping", WPPG044, these proceedings (May 2003).

[10] P. Cameron *et al.*, "RHIC Third Generation PLL Tune System", ROAB009, these proceedings (May 2003).

[11] W. Fischer *et al.*, "Linear Coupling Correction from N-Turn Maps", WPAB078, these proceedings (May 2003).

CONCEPT DESIGN OF THE TARGET/HORN SYSTEM FOR THE BNL NEUTRINO OSCILLATION EXPERIMENT*

N. Simos[a♣], H. Kirk[a], S. Kahn[a], A. Carrol[a], H. Ludewig[a], W. T. Weng[a], M. Diwan[a], D. Raparia[a]
K. McDonald[b], G. Evangelakis[c]
[a]Brookhaven National Laboratory, Upton, NY 11973, USA
[b]Princeton University, Princeton, NJ 08544, USA
[c]University of Ioannina, Greece

Abstract

The design concept for the integration of the target and the focusing horn system for the proposed BNL neutrino oscillation experiment is described in this paper. Also presented are issues associated with the functionality and thermo-mechanical response of the selected target intercepting the 28 GeV protons of the 1 MW upgraded AGS beam, the loading and mechanical response of the focusing horn subjected to high currents and energy deposited due to beam/target interaction, the integration of the two systems, and the heat removal schemes. The proposed target intercepts the 8.9×10^{13}, 28 GeV protons with a 2.5 Hz cycle time over a spot that encloses the 3σ of the beam. In the baseline design the inner conductor of the aluminum horn encloses the target while allowing for an annular space for forced cooling. Approximately 250 kA pulse of current of 20μs duration will flow through the horn at 2.5 Hz repetition rate inducing high compressive forces, vibration and heat. The paper addresses these issues of horn mechanical response, heat removal scenario, and useful life estimation including radiation damage.

1 INTRODUCTION

To achieve the 1 MW beam power for the proton driver at BNL serious consideration must be given to both the selection of target material and the horn configuration. Assessment studies indicate that a solid target is a viable option for the proposed 1 MW beam. As a result, low- and high-Z materials have been investigated both in terms of material endurance as well as feasibility of the target/horn configuration. A carbon-carbon composite, formed by a special weaving of carbon fibers, has been selected as the target baseline. Specifically, this carbon-carbon composite exhibits very low thermal expansion between room temperature and approximately 1000°C. Such property leads to small generated thermo-mechanical stresses due to beam-target interaction and will extend the useful life of the target. Experiments performed on this target material as well as other common graphite-based targets verified the advantage of the carbon-carbon composite in the way it responds to short-duration proton beam pulses. Long-term irradiation effects on the properties of this carbon composite, such as thermal expansion, thermal conductivity, strength, etc., are to be experimentally assessed. The pion-focusing horn is to be made out of an aluminum-based material. Candidate materials are the 3000-series and 6061-T6 aluminum.

Parameters controlling the horn material selection are the low resistivity, the high strength and the resistance to corrosion and micro-cracking. The pulsed nature of the machine, combined with irradiation effects that lead to material embrittlement, can potentially limit the useful life of the focusing horn if micro-cracking is allowed to develop. In order to enhance the corrosion resistance of the horn conductor, especially the surfaces exposed to water used for heat removal, special surface treatments in the form of nano-structured films are being explored.

2 INTEGRATED SYSTEM

Figure 1 is a conceptual description of the target and horn integrated system being considered for this experiment. The 12mm diameter, 80cm long carbon-carbon composite target considered in this study is fully inserted into the inner horn conductor while allowing for a 1mm annular gap between the target and inner horn surface for forced coolant flow. Shown in the front of the target is a beam "collimator" or baffle that has a dual role. Specifically, it provides the upstream target support and accommodates the special channels that provide coolant into the annular space. It also plays the role of beam diffuser in the event the proton beam strays off the beam axis. In addition to the above two functions, the front end of the target will be maintained at a low temperature which will help in removing heat deposited on the target by conducting into the mass of the baffle. At the downstream end of the target a special fin-like end support allows the forced coolant to leave the annular space. The horn, made out of an aluminum alloy, has a diameter in its narrowest section of 1.4cm and a thickness over that section of 2.5mm. The thickness of the inner horn conductor reduces to ~ 1mm downstream of the neck-down section where the captured pions pass through on their way to the decay pipe. The overall horn length is 217 cm.

♣ work performed under the auspices of the US DOE
♣ simos@bnl.gov

0-7803-7738-9/03/$17.00 © 2003 IEEE

The baseline design requires a 250 kA peak current with a repetition rate of 2.5 Hz. One of the options being considered assumes a 20μs half-sine current pulse. Results of horn response with such current pulse structure are presented in this paper. Under such short current pulse most of the flowing current will be within one skin depth of the conductor. The magnetic pressures and joule heating generated in the conductor control the mechanical design of the horn. While heat generated in the narrowest section of the horn by both current and secondary particles is partly removed by the fluid flowing in the annular space, the balance will be removed by the spraying of coolant through a set of optimally positioned jets against the current-side of the inner conductor. Two coolant options are being considered, namely, the spraying of water and of cold helium. The schematic of Figure 1 depicts the water-cooling option.

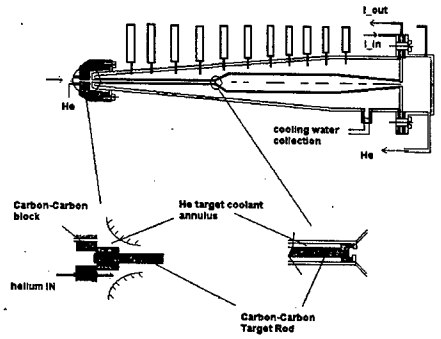


Figure 1: Horn/Target Configuration

Also under consideration is a downstream thin window whose role is to hold the target coolant in a closed system. The coolant is thus collected, cooled and returned to the target upstream to be re-ejected into the annular space. The key issue with such window is the fact that it will see a significant portion of the incoming beam power and will be subjected to high thermo-mechanical stress conditions. Further, the presence of additional material in the flight path of pions generated and focused by the horn represents an additional impediment. However, since the only role of such window is to prevent the coolant from escaping from the closed envelope, a low-Z material (for minimal interaction with secondary particles or heat generation from intercepting the beam protons) such as carbon-carbon composite can provide the required boundary.

2.1 Energy Deposition and Heat Removal

Energy generated in the target/horn system is due to the target/proton interaction and the current flowing in the horn. Energy is also deposited in the horn from secondary particles generated in the target. Different mechanisms, namely heat convection, conduction and radiation heat exchange between target and horn are responsible in removing the deposited heat. The heat balance of the overall system, as it reaches an operating temperature, is addressed by utilizing a sophisticated finite element analysis.

Target Heat Deposition

Energy depositions for two different beam spots on two target diameters have been estimated using hadron interaction codes. Specifically, 1mm and 2mm rms proton beams are interacting with 6mm and 12mm diameter targets respectively effectively capturing 3σ of the beam. $8.9\text{x}10^{13}$, 28 GeV protons are delivered on target with a 2.5 Hz cycle time. The integrated energy deposited on carbon-carbon target per $8.9\text{x}10^{13}$ protons is 5.1 kJ and 7.3 kJ respectively resulting in temperature rises of 1000 °C and 280 °C in the target. While the 1mm beam deposits less energy, thus easing the heat removal capacity required, the temperature rise is high making the 2mm beam more preferable.

Horn Joule Heating

For a 20μs half-sine current pulse (effective frequency of 0.025 MHz) the current is expected to flow over a skin depth of the inner surface of the inner conductor. The skin depth δ for a horn made out of 3000-series aluminum, for example, with resistivity $\rho = 4.2$ mohm-cm, is calculated based on the following relations:

$$\delta = (6.61/f^{1/2})\, k_1 \;\; ; \;\; f = 0.025 \text{ MHz}$$
$$k_1 = [\rho/\rho_c]^{1/2} \;\; ; \;\; \rho_c = 1.724 \text{ mhoms-cm}$$

leading to a skin depth of $\delta_{Al} = 0.06525$ cm.
In the narrow section of the inner conductor which surrounds the target and is subject to peak joule heating, the heat generated per unit length is derived from

$$JH_{\text{pulse-cm}} = \int_0^{20\mu s} \int_A J^2(z,t)\, \rho \; dA \; dt = 3.88 \text{ Joules}$$

where $J(z,t) = J(z)\sin(\pi t/20\mu s)$, $J(z) = J_o\, e^{-z/\delta}$ and $J_o = 689$ kA/cm^2 is the current density at the conductor surface. The peak temperature rise in the horn, induced by joule heating alone is estimated to be ΔT=7.4°C.

Secondary Particle Heating

Based on the simulation results of different hadron interaction codes, a significant amount of heat is deposited on the horn from secondary particles produced in the target. The heat deposited in the inner conductor of the horn is estimated to be ~ 8.4 kW.

Heat Removal Scheme

The deposited heat in both the target and horn is removed by forced flow. In this study the target and the horn have been decoupled. Specifically, forced helium is used in the 1mm annular space between the target and horn to remove the heat from the target which amounts to

18.25 kW for the 2mm rms beam. Forced convection heat transfer calculations were performed to assess the required convection capacity for removing the heat from the target. To maintain the base temperature of the carbon-carbon composite target in a safe regime, a value of 840°C was assumed with a beam induced ΔT~280 °C.

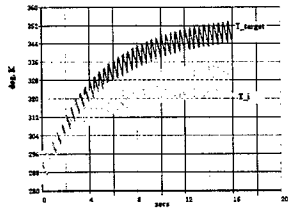


Figure 2: Transient temperatures in the horn conductor

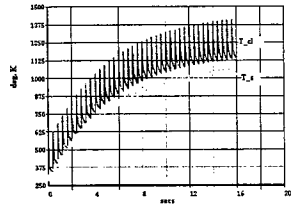


Figure 3: Transient temperatures in the C-C target

The inlet temperature of the helium in the annulus is assumed to be 5°C. In the integrated system the target exchanges heat with the inner conductor of the horn through radiation which, based on an allowable surface temperature of the horn of 90°C (the goal is to maintain the aluminum temperature below 100°C whenever it is in contact with water), amounts to ~1.36 kW. Heat from the target is also being removed through conduction to the baffle block upstream of the target that is maintained at a low temperature. It is estimated that helium with a bulk velocity of ~40m/s is required to remove the deposited heat from the target.

The heat deposited on the horn (current, secondary particles and radiation exchange) is being partially removed by the helium in the annulus and mainly by coolant spraying on the surface of the horn where current flows. While re-circulating water is the baseline choice, the option of forcing cold helium is being also explored. Preliminary heat transfer calculations show that there is significant margin of heat removal capacity using water and just enough capacity using helium. The use of helium will reduce corrosion issues of the horn conductor and extend its useful life. Using detailed finite element analysis [3] incorporating the entire heat transfer scheme and the transient nature of the two inputs (protons and current) the "steady-state" temperatures in the target and horn were calculated and shown in Figures 2 and 3.

2.2 The Thermal Stress Problem

The rapid temperature rises induced by the beam/target interaction and the intensity of the proton beam pulse will induce very high thermal stresses in solid targets. The carbon-carbon composite was selected for its low thermal expansion that in turn leads to low thermal shock stresses. Figure 4 depicts the von Mises stresses generated in the target and their attenuation between pulses. The calculated stresses are within the mechanical strength of the material. Figure 5 is a comparison of the response of an ATJ graphite and a carbon-carbon composite target to the same proton beam intensity obtained experimentally. The results clearly show significant stress reduction. Preliminary stress calculations for the horn due to current and secondary particle heating pulses as well as magnetic pressures indicate that the horn can operate safely under the required parameters.

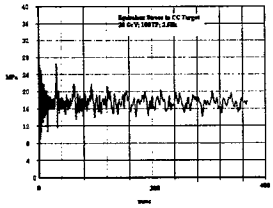


Figure 4: Beam-induced von Mises stresses on target

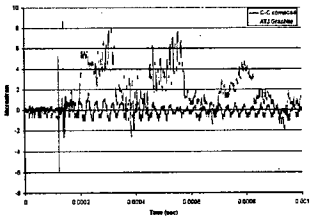


Figure 5: Experimental strains (CC vs. ATJ graphite)

2.3 Radiation Damage and Surface Treatment

High levels of irradiation along with thermal fatigue and potential corrosion are anticipated when operating a 1 MW system. The effects of long-term irradiation on the key properties of the target material, such as thermal expansion and conductivity, are not yet known and will be assessed through irradiation studies. In addition, innovative surface treatments for the horn material, such as nano-structured films and plating, are being explored to help extend the useful life of the component.

REFERENCES

[1] D. Burgreen, "Thermoelastic Dynamics of Rods, Thin Shells and Solid Spheres", Nucl. Sc. And Eng., 12, 203-217, 1962

[2] S. Kahn, et al., "Focusing Horn System for the BNL Very Long Baseline Neutrino Oscillation Experiment", PAC2003 Proceedings.

[3] ANSYS, Swanson Analysis Systems Inc., 1999

HIGH LUMINOSITY β^*=0.5m RHIC INSERTIONS*

S. Tepikian, H. Huang, W. MacKay, F. Pilat, V. Ptitsyn, T. Satogata, D. Trbojevic, J. van Zeijts
BNL, Upton, Long Island, New York

Abstract

An increase in RHIC collision luminosity is possible by reducing the beam size at the interaction point (IP). We present a method for reducing the IP beta function, β^*, from the design minimum of $1m$ to $0.5m$. We demonstrate that this β^*=$0.5m$ configuration is achievable with existing RHIC power supplies for $100GeV$ protons. We discuss the correction of the higher order IR multi-poles and the second order chromaticity.

INTRODUCTION

RHIC consists two rings, each ring has 6 interaction regions (IRs). At the center of each IR is the IP, where collisions can occur. Each IR consists of 9 quadrupoles on each side of the IP organized anti-symmetrically. These quadrupoles can be further subdivided into a dispersion suppressor and telescope. Our goal is to reduce the beam size at the IP. This is achieved by reducing the beta function and dispersion at the IP. A schematic is shown in Fig. 4. In the next section, we discuss the β^* squeeze.

β^* SQUEEZE

We will find the quadrupole strengths shown in Fig. 4 to produce a lattice with a given β^* at the IP. With this design we have 12 parameters to vary. The procedure used requires meeting these 14 constraints:

- $\beta_x^* = \beta_y^* = \beta^*$ (2 constraints).
- $\eta^* = 0$ and $\alpha_x^* = \alpha_y^* = 0$ (3 constraints).
- $\beta_{max_x} = \beta_{max_y}$ in the triplets (1 constraint).
- Matching the Insertion to the arcs (6 constraints).
- Getting the correct tunes (2 constraints).

Using the MAD program [1], the optics were fit from $\beta^* = 1m$ to $\beta^* = 0.5m$. Additionally, the strengths for the quadrupoles are calculated from the power supply currents by using a 5th order polynomial fit to the measured transfer function (averaged over all quadrupoles of the same type). Fig. 1 gives the resulting penalty function. Fig. 2 gives the final power supply currents for $100GeV$ protons. This is after some additional smoothing with the ends fixed. Fig. 3 shows the beta function plot for a RHIC insertion at $\beta^* = 0.5m$.

Shunt and Trim Supplies

Each half of the insertion is controlled by 3 trim power supplies for the trim quadrupoles next to Q4, Q5 and Q6.

* Work performed under Contract Number DE-AC02-98CH10886 with the auspices of the US Department of Energy

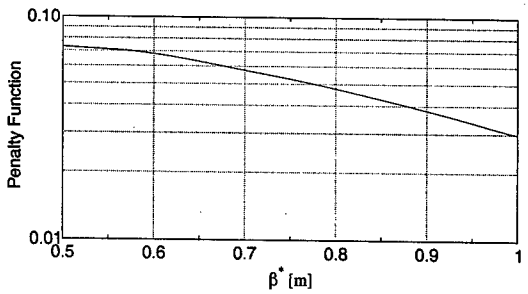


Figure 1: The final penalty function vs β^*

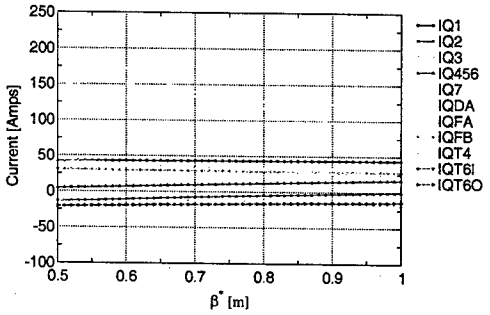


Figure 2: The shunt and trim supplies for the RHIC insertion as a function of β^*. Note, IQT4 = IQT4I = IQT4O = -IQT5I = -IQT5O and IQ456 is fixed to a function of β^*.

Furthermore, the inner and outer trim supplies can be independently controlled. On the QF main bus there are 5 shunt supplies for the main quadrupoles from Q1 through Q7. The QD bus has two shunt supplies per half insertion for controlling QFA(B) and the QDA quadrupoles. One is common between inner and outer, while two others can be independently controlled. The following tables gives the limits on these power supplies:

A comparison of the required currents given in Fig. 2

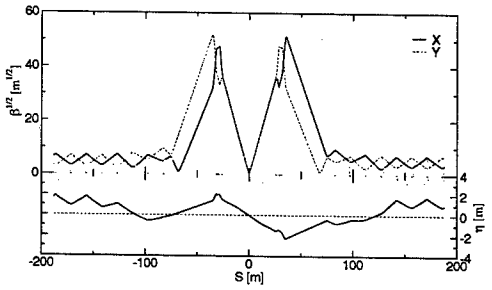


Figure 3: The RHIC insertion optics with $\beta^* = 0.5m$.

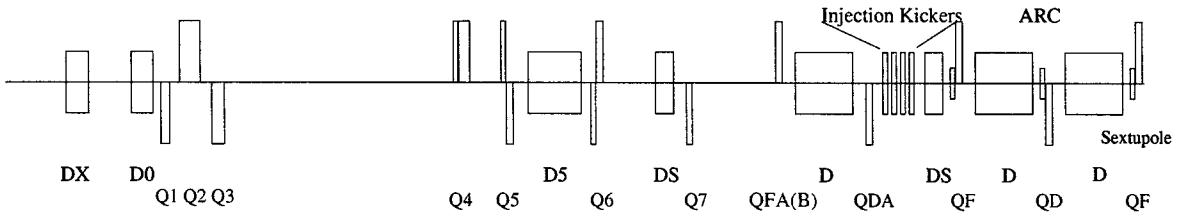


Figure 4: A schematic for half of the RHIC insertion. The quadrupoles Q4, Q5 and Q6 have associated trim quadrupoles. Q4 and Q5 trims are set to the same, but opposite strengths. Antisymmetry is broken for the trim quadrupole at Q6 and the quadrupoles at QFA(B). This leads to 12 adjustable parameters (including QF and QD).

Table 1: Shunt and Trim power supplies

Supply	Minimum [Amps]	Maximum [Amps]
Trim	-150	150
IQFA(B)	1	200
IQDA	-300	300
IQ7	1	600
IQ456	1	450
IQ3	1	300
IQ2	-150	150
IQ1	1	200

with the power supply limits given in Table 1 shows that the required currents are within the power supply limits.

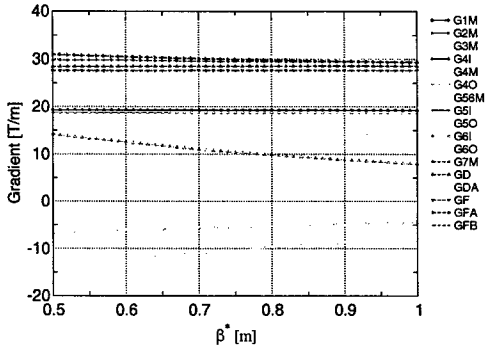


Figure 5: The gradient strengths for protons at $100GeV$ vs. β^*.

Matching to Existing Squeeze

RHIC squeezes from β^* of $10m$ to $1m$ with an existing solution. A lot of effort went into optimizing the tunes, chromaticity, orbit, coupling, etc. with this squeeze. A smooth transition in the power supply currents from the new squeeze of $1m$ to $0.5m$ to the existing squeeze is required. To create a ramp with a β^* squeeze, a function $\beta^*(time[sec])$ must be carefully chosen so that the changes to the power supply currents remain smooth throughout the squeeze. This is accomplished with the quadrupole strength values $K(\beta^*)$ (see Fig. 5) for each quadrupole, along with the values of $dK(\beta^*)/d\beta^*$. Furthermore, some smoothing may be necessary to achieve the final goal. Finally, modeling from MAD does not necessarily agree with the machine model due to differences in the MAD description and the real machine. One example: all focusing quadrupoles do not have the same strength even when connected to the same current bus due to differences in the integrated strengths of these magnets.

NONLINEAR CORRECTION

The large $\beta_{max} = 2.66km$ in the triplets leads to some undesirable effects that must be corrected. Additionally, if the beams 95% normalized emittance is $20\pi mm\text{-}mrad$, the triplet's beam size is $\sigma = 9mm$ for $100GeV$ protons. Since the triplet aperture is $56.5mm$, this is quite tight. Furthermore, the dispersion in the triplets is $\pm 2m$, which is affected by the momentum spread. This creates aperture constraints in the triplets, high order chromatic effects, triplet multi-pole problems, etc. We start with the multi-poles effects and correction.

IR Multi-Pole Correction

In two of the IR's, we have high order correctors to improve dynamic aperture for the low β^* insertions. There is an operational tool [2] to measure the effect of the triplet multi-poles on the tune spread and calculate the corresponding corrector strengths. An orbit bump is applied through the triplets and the tune variations is measured with the PLL tune-meter [3]. We obtain a data set of the tune versus orbit bump amplitude. This data is then fit to polynomial. From the polynomial coefficients, the multi-pole correction strengths can be determined. Furthermore, the bump can be horizontal or vertical so that the skew multipoles can be corrected as well. Next we discuss chromatic effects.

Nonlinear Chromatic Correction

Besides transverse effects there are longitudinal effects as well. A beam with a momentum spread produces a tune spread from chromatic effects. The most significant contribution to chromatic effects are the triplets in RHIC. The large β_{max} exasperates the problem. Using the MAD

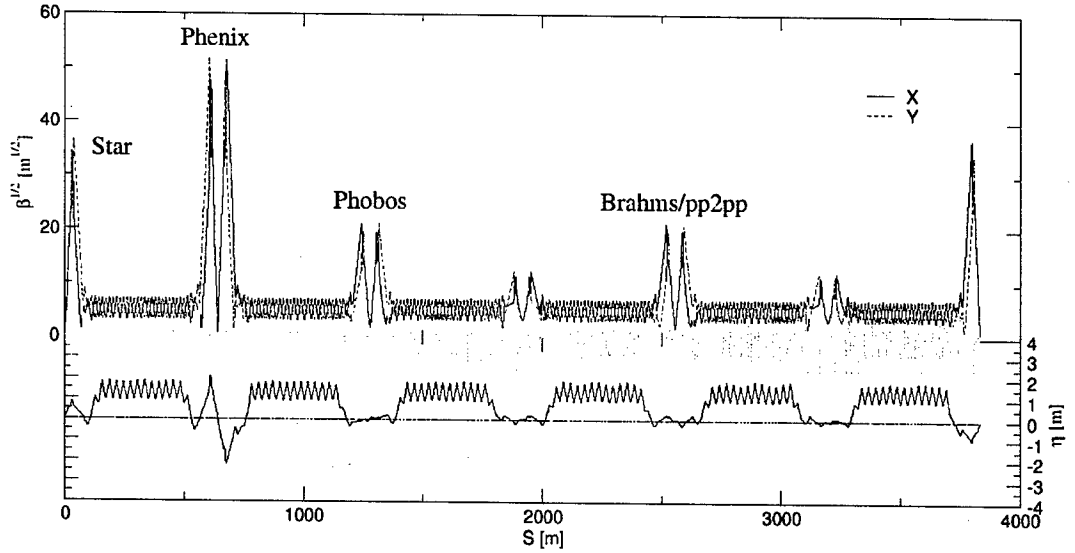


Figure 6: The RHIC optics parameters. The Star insertion is set to $\beta^* = 1m$, Phenix has $\beta^* = 0.5m$, Phobos and Brahms are at $\beta^* = 3m$ and the remaining insertions have $\beta^* = 10m$

model with the design optics Fig. 6, the amplitude and chromatic terms can be calculated as:

$$\nu_x = \nu_{x_0} - 644\epsilon_x - 1753\epsilon_y + 2\delta - 623\delta^2 - 211100\delta^3$$

$$\nu_y = \nu_{x_0} - 1753\epsilon_x + 390\epsilon_y + 2\delta + 1727\delta^2 + 80400\delta^3$$

Both the second and third order terms become significant when $\Delta p/p \simeq 0.003$ in the horizontal plane and the second order term becomes significant when $\Delta p/p \simeq 0.001$ Compare this with the chromatic terms if we set the Phenix insertion to $\beta^* = 1m$ (this is the current optics in RHIC for the Run 2003 polarized proton operation) instead:

$$\nu_x = \nu_{x_0} - 447\epsilon_x - 1203\epsilon_y + 2\delta + 209\delta^2 - 134000\delta^3$$

$$\nu_y = \nu_{x_0} - 1203\epsilon_x + 269\epsilon_y + 2\delta + 977\delta^2 - 31500\delta^3$$

A preliminary measurement of the second order chromaticity has produced numbers similar in magnitude to those above. A more detailed analysis of these results needs to be done.

The second order chromaticity can be corrected in RHIC by either using four families of sextupoles [4] or using four families of octupoles which are organized as two families in high dispersion regions and two families in low dispersion regions. The two families in the high dispersion regions correct the second order chromaticity while the two families in the low dispersion region are used to correct the tune spread from the first two families. Since, the octupoles are wired in this fashion, we would correct second order chromaticity by this method.

SUMMARY

We presented a design for the RHIC insertion that achieves a $\beta^* = 0.5m$ at the IP. This design works with the existing power supplies for protons at $100GeV$. We discuss how to implement this solution with the existing β^* squeeze ramp. Furthermore, correction of the triplet multipoles and second order chromaticity is discussed as well. Further studies for dynamic aperture should be done due to the tight space available in the triplets. We plan to have beam studies with this insertion in the future.

REFERENCES

[1] H. Grote, F. C. Iselin, "The MAD Program User's Reference Manual", CERN/SL/90-13(AP) (1995)

[2] F. Pilat, P. Cameron, V. Ptitsyn, J. P. Koutchouk, "Nonlinear Effects in the RHIC Interaction Regions: Modeling, Measurement Correction", these proceedings (TPPB041)

[3] P. Cameron, J. Cupolo, W. Dawson, C. Degen, A. DellaPenna, M. Kesselman, A. Marusic, J. Mead, C. Schultheiss, R. Sikora, K. Vetter, "RHIC Third Generation PLL Tune System", these proceedings (ROAB009)

[4] W. Scandale, S. Tepikian, "Chromatic Correction of RHIC when One or Two Insertions is at $\beta^* = 0.5m$", RHIC/AP/45 (November, 1994)

THE RHIC INJECTOR ACCELERATOR CONFIGURATIONS, AND PERFORMANCE FOR THE RHIC 2003 Au-d PHYSICS RUN*

L. Ahrens†, J. Alessi, J. Benjamin, M. Blaskiewicz, J.M. Brennan, K.A. Brown, C. Carlson, J. DeLong, T. D'Ottavio, B. Frak, C.J. Gardner, J.W. Glenn, M. Harvey, T Hayes, H-C Hseuh, P. Ingrassia, D. Lowenstein, W. Mackay, G. Marr, J. Morris, T. Roser, T. Satogata, G. Smith, K.S. Smith, D. Steski, N. Tsoupas, P. Thieberger, K. Zeno, S.Y. Zhang, BNL, Upton, NY 11973, USA

Abstract

The RHIC 2003 Physics Run [1] required collisions between gold ions and deuterons. The injector necessarily had to deliver adequate quality (transverse and longitudinal emittance) and quantity of both species. For gold this was a continuing evolution from past work [2]. For deuterons it was new territory. For the filling of the RHIC the injector not only had to deliver quality beams but also had to switch between these species quickly. This paper details the collider requirements and our success in meeting these. Some details of the configurations employed are given.

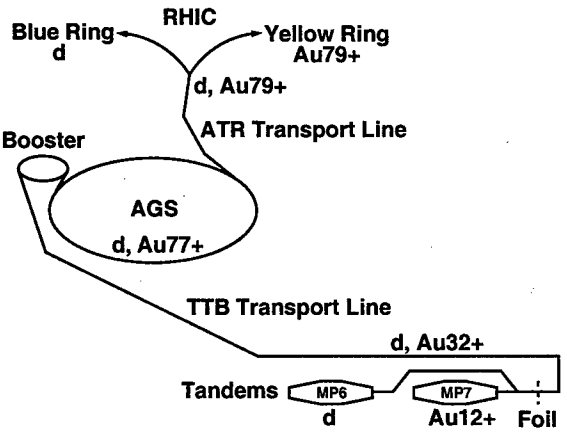


Figure 1: Acceleration of Deuterons and Gold for RHIC.

INTRODUCTION

The RHIC injector complex, shown schematically in Figure 1, comprises two Tandem Van de Graaffs (MP6 and MP7) [3], the Tandem-to-Booster (TTB) transfer line, the Booster synchrotron, the Booster-to-AGS (BTA) transfer line, the AGS synchrotron, and the AGS-to-RHIC (ATR) transfer line. This paper will describe how these pieces were configured for the 2003 RHIC Au-d physics run. The performance goals for the run were defined during the winter of 2002 in order for the RHIC experiments to optimize their configurations. For the gold beam, goal specification was a simple extension from the past several RHIC runs. For deuterons, expectations again derived largely from experience with gold and protons but necessarily required assumptions about this new beam species coming from the Tandem. The goals worked out required that the injector complex provide gold bunches of 1×10^9 ions, deuteron bunches of 8×10^{10} ions, transverse emittances of about 15π mm mradians in both planes and for both beams, and longitudinal emittances consistent with allowing rebucketing into the RHIC 200 MHz RF system [4] at store.

GOLD ACCELERATION

The goals for gold were to be back where we had ended the previous run. The essential acceleration strategy did not change from that of the 2001 Au run [2]. Historically the intensity, and particularly the efficiency for the multiturn injection and early acceleration in the Booster, improves slowly over the months of the run. To the extent that this improvement is a result of the Booster beam tube surfaces being slowly "scrubbed" clean by gold beam particles that end up outside the machine acceptance at injection and during RF capture, such improvement could suffer from time spent learning to optimize the deuteron acceleration. In addition for this run there would not be a "back-up" Tandem set up for gold; the second Tandem (MP6) would be for deuterons. The possibility of switching to the other Tandem to e.g. replenish the essential and short-lived stripping foils in the terminal would be more costly to the run. Foil consumption rates were an issue. These concerns were qualitatively correct, but managed to stay off the run "critical path".

The gold acceleration strategy [2] involves accelerating on RF harmonic $h = 6$ in the Booster, boxcar transferring four Booster loads into an AGS whose RF runs at $h = 24$, debunching this beam at the AGS injection energy and rebunching into four bunches (in an $h = 12$ RF structure) and accelerating to RHIC injection energy. Transfer into RHIC through the ATR line is done one bunch at a time. The longitudinal emittance demands from RHIC constrain this dance. In particular an additional merge to double the intensity per bunch but also the longitudinal emittance is ruled out. As in the past, achieving the 1×10^9 gold ions per bunch RHIC goal was possible but difficult, and not routine. One evolution during this run relevant here involved the stripping foil between Booster and AGS which

*Work supported by the U.S. Department of Energy under contract number DE-AC02-98CH10866.

† ahrens@bnl.gov

0-7803-7738-9/03/$17.00 © 2003 IEEE

takes Au^{32+} to Au^{77+}. The standard 23 mg/cm^2 carbon foil was replaced for two weeks of the run by a 23 mg/cm^2 fused silica foil. The silica foil, because of its better uniformity produced a beam with a longitudinal emittance less than half that obtained from the carbon foil. The average energy loss from both foil passages were by design very comparable; the percentage of the beam ending in the 77+ charge state was empirically found to be about 10% lower for the Silica. This intensity cost was too much for this run when the intensity crunch came, but the result opens up serious planning for an additional merge in the future.

DEUTERON PRODUCTION AND ACCELERATION

Production and acceleration of deuterons generated many new challenges, and the beam performance provided feedback to correct the flaws in our initial assumptions. The setup evolved rapidly throughout the run. The intensity design was based on having a 100 μA deuteron beam available coming into the Booster. The multiturn injection process was expected (from gold experience) to allow at most 45 turns to be accumulated, and with 50% overall efficiency explains the intensity goal. First the radiation issues associated with accelerating this proton and its loosely bound neutron in the relatively lightly shielded Tandem and TTB lines had to be dealt with. The "Access Control" system for the Tandem and beam line was upgraded. Shielding was added where necessary. A fail-safe system to limit beam intensity was installed. Because the potential amount of prompt radiation from scraping the beam increases rapidly with beam kinetic energy, a maximum (intensity) $\times$ (kinetic energy) constraint follows from this.

Several other factors come in to determining the optimal energy for the TTB transfer, and indeed two solutions were worked through. The first began with deuterons from Tandem at a kinetic energy of 6 MeV per nucleon. These were transported to Booster, injected, adiabatically captured at RF harmonic $h = 6$, and accelerated to the maximum frequency of the RF system as is done in the canonical gold setup. However, the magnetic rigidity of the deuteron beam at the top frequency is only 3.7 Tm compared to 9.2 Tm for gold (Au^{32+}) which means that the current required in the Booster extraction septum magnet is less than half that required for gold. Since the power supply does not regulate well at this reduced current, one is forced to operate at a higher current with beam extracted on the rising portion of the half-sine wave output of the supply. This makes the trajectory of the extracted beam sensitive to timing jitter of the power supply pulse. (The pulse was not RF locked.)

The jitter problem was eventually resolved, but in the mean time another scheme was worked out. The RF system has enough range to capture and accelerate the 6 MeV per nucleon deuterons on harmonic $h = 3$ which allows for acceleration to a much higher magnetic rigidity (7.3 Tm). Although this eliminates the problem of operating the extraction power supply at low current, another problem arises at AGS injection. Here the injection kicker magnet has two modes of operation, a "long pulse" mode and a "short pulse" mode, which deliver pulse widths of 1400 and 500 ns respectively. For the $h = 6$ setup, the required pulse width of the kicker is 1350 ns which is just accommodated by the long pulse mode. However, for the $h = 3$ setup, the required pulse width is reduced to 640 ns which is too short for the long pulse mode and too long for the short pulse mode. If one uses the long pulse, three transfers of three bunches to AGS are possible. Debunching these and rebunching into four bunches as per the canonical gold setup gives a single bunch intensity equal to three fourths of one Booster fill. On the other hand if the short pulse is used, only two of the three bunches in each Booster fill can be transferred to AGS, but six transfers are possible. This gives a total of 12 bunches which, after debunching and rebunching into four, gives a single bunch intensity equal to one Booster fill. This is the scheme that was adopted for the first part of the run.

The next step in the evolution of the deuteron setup required increasing the kinetic energy of deuterons from Tandem to 8.7 MeV per nucleon. This allowed for capture in Booster at even lower harmonic $h = 2$ and helped the Tandem transmission efficiency (which was marginal at the lower kinetic energy). The captured beam could be accelerated to top energy at $h = 2$, but well before this, the revolution frequency of the beam is high enough (some 800 kHz) for a merge of two bunches into one using the available proton RF system. After the merge, acceleration continues to top energy at $h = 1$ with the proton RF system. Due to the very low RF voltages required, the merge is a delicate process that required some time and new gear to perfect. Figure 2 shows a turn-by-turn "mountain range" of the process. (Time moves up in the figure.)

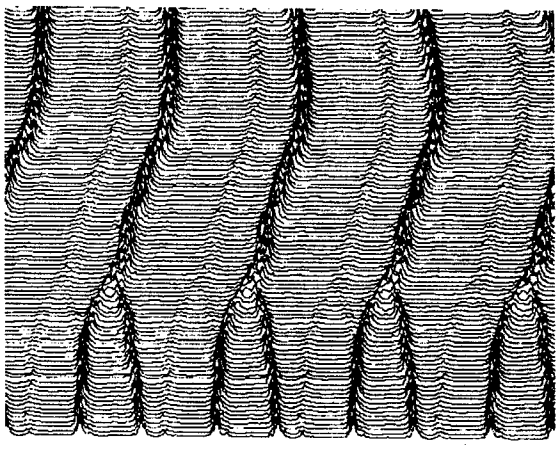


Figure 2: Merging of Two Bunches into One in Booster.

Having just one bunch in Booster effectively eliminated the constraint imposed by the pulse width of the AGS injection kicker and opened up the possibility of transferring up to eight Booster fills per AGS cycle. Initially the con-

trol system could deal with only enough Booster cycles for seven transfers but eventually controls modifications allowed for eight. The eight bunches were debunched and rebunched into four (in an $h = 8$ RF structure) on the AGS injection porch giving a single bunch intensity equal to two Booster fills. This scheme was used for the remainder of the run and easily met the initial goal of 8×10^8 deuterons per RHIC bunch.

Getting sufficient numbers of negative ions of deuterium (D^-) from the source that feeds the Tandem (MP6) also proved to be a challenge. Both the Au^- and D^- ions were generated using a PSX-120 cesium sputter ion source [5] operating in a pulsed mode. Initially TiD_2 powder was used in the D^- source but this produced a large amount of O^- ions which created significant space charge forces and lowered the transmission efficiency. Eventually the powder was replaced by a solid TiD_2 cathode which minimized the production of other negative ions. With pulsed currents as high as 496 μA at the source output, currents as high as 188 μA were seen at the Tandem output with 144 μA transported to the end of the TTB line.

MODE SWITCHING

The blue RHIC ring is filled with 56 deuteron bunches and then the yellow RHIC ring with 56 gold bunches. Doing this as quickly as possible is required. Besides the time lost the beam emittances somewhat deteriorate while circulating at RHIC injection energy. Most of the injector accelerator controls have built-in the capability to follow one of four different sets of commands–there are four "Users" predefined. Changing from one User to another is fast relative to the 5 second AGS cycle. This now familiar business is referred to as "pulse-to-pulse modulation", PPM. For the change from deuterons to gold several major systems that are not PPM must also be switched. All of the three transfer lines ended up having different rigidities for the two species. Many of the magnets in these lines are inherently slow to change. The TTB magnets with large bends and small fields have to be very carefully controlled. Further there are mechanical systems–foils to insert or remove, and kicker systems that need pulse-forming networks adjusted–which must be allowed to switch. All of this process, which is referred to as a "mode switch" was orchestrated using a software program to do the "sequencing". The execution followed similar programs used at RHIC for example for quench recovery. The actual application to Au-d mode switching was the responsibility of the Operations group. A goal for this switching of 5 minutes was met gradually but easily once confidence in all of the steps was established.

REFERENCES

[1] T. Satogata, et al, "Commissioning of RHIC Deuteron-Gold Collisions", TPPB043, these proceedings (May, 2003).

[2] C.J. Gardner, et al, "Status and Recent Performance of the Accelerators that Serve as Gold Injector for RHIC", PAC01, Chicago (2001) 3326–3328.

[3] D.B. Steski, et al, "Upgrade and Operation of the BNL Tandems for RHIC Injection", PAC01, Chicago (2001) 2545–2547.

[4] J.M. Brennan, et al, "Operation of the RHIC RF Systems", ROAA006, these proceedings (May, 2003).

[5] Distributed by Peabody Scientific, Peabody, MA, 01960, USA

THE LHC PROTON BEAM IN THE CERN SPS: AN UPDATE

G. Arduini, P. Baudrenghien, T. Bohl, P. Collier, K. Cornelis, W. Höfle, T. Linnecar, E. Shaposhnikova, J. Tückmantel, J. Wenninger

CERN, Geneva, Switzerland

Abstract

During the 2001 run the beam-induced electron-cloud, generating dramatic vacuum pressure increases and fast transverse instabilities, was the main limitation in the achievement of the nominal LHC beam intensity in the SPS. Nominal longitudinal and transverse parameters at the extraction energy (450 GeV) could be achieved only with a single batch and with a maximum bunch population of 0.5×10^{11} p. In 2002 the threshold for the onset of the electron cloud in the arcs could be increased from 0.4×10^{11} p/bunch to 0.9×10^{11} p/bunch by means of a dedicated 10-day 'scrubbing' run with the LHC beam. At the end of this period four LHC batches with design bunch population (1.1×10^{11} p) could be injected for each SPS cycle, as foreseen for the nominal filling scenario, without provoking vacuum interlocks. After a series of machine development sessions the LHC beam with nominal intensity could be accelerated to 450 GeV with nominal longitudinal emittance and with transverse emittances close to the design values for the first three batches. The problems encountered with this high brilliance beam and the solutions developed are presented.

LHC PROTON BEAM IN THE SPS

The SPS is the last element of the LHC injector chain accelerating 26 GeV/c protons delivered by the PS to 450 GeV/c before extraction to the LHC. The main parameters of the nominal LHC beam are presented in Table 1 [1].

Table 1: Main parameters of the LHC beam in the SPS

Momentum [GeV/c]	26	450
Tunes (H/V)	26.18/26.13	
Max. n. of batches	4	
n. bunches/batch	72	
Bunch population[10^{11} p]	1.1	
Bunch spacing [ns]	24.97	24.95
Full bunch length [ns]	4	1.74
Batch spacing [ns]	224.7	224.6
r.m.s. $\varepsilon^{*}_{H,V}$ [μm]	3	3.5
ε_L [eV s]	0.35	< 0.7

Since 1999, when the first LHC-type beams were available from the SPS injectors, electron multipacting was observed as a consequence of the bunch intensity and spacing of the LHC beam [2]. Beam Induced Multipacting (BIM) generates important pressure rises and an electron-cloud develops along the bunch train inducing transverse beam instabilities [3]. In the vertical plane these manifest themselves as a single bunch head-tail instability as a result of the interplay of the electron cloud and of the machine impedance in coupling the motion of the head and the tail of the bunch. The only cure found so far is to run at high positive vertical chromaticity. In the horizontal plane low order coupled bunch instabilities are observed and can be cured by the transverse feedback which has a bandwidth of 20 MHz designed to damp all coupled bunch modes up to the highest (the bunch spacing is 25 ns, see Tab. 1).

In 2001, though cures could be found to control the beam instabilities induced by the cloud, the intensity continued to be limited by the dramatic vacuum pressure rise triggering the beam abort system and preventing stable operation with more than one batch at 0.6×10^{11} p/bunch. Nominal longitudinal and transverse parameters at the extraction energy could be achieved only with a single batch and with a maximum bunch population of 0.5×10^{11} p, i.e. half the nominal population [4].

SCRUBBING RUN

The Secondary Emission Yield (SEY) of the surface of the stainless steel vacuum chambers is the main parameter affecting multipacting for given beam characteristics. Measurements performed both in the laboratory and in the machine indicated that the electron bombardment resulting from multipacting produces a reduction of the SEY ('scrubbing' effect) [5]. In order to confirm that observation, the SPS was operated continuously for ten days with LHC beam at the beginning of the 2002 run. At the end of the 'scrubbing' period the dynamic pressure increase was suppressed by four orders of magnitude and the threshold bunch population for the onset of the electron cloud was doubled from 0.4×10^{11} p to 0.8×10^{11} p in the SPS arcs, corresponding to a reduction of the SEY from 2.2 to 1.6 [6]. This allowed the nominal intensity to be injected without vacuum interlocks.

The success of the scrubbing run was also due to the excellent performance of the transverse feedback in the horizontal plane after the upgrade of its power protection circuits during the shutdown 2001-2002 which allowed running this system at high gain in a reliable way. The reduction of the SEY and the corresponding increase of the multipacting threshold allowed the chromaticity required to stabilize the beam vertically to be reduced.

Subsequent vacuum measurements indicated that de-conditioning occurs when the machine is not operated with the LHC beam but the re-conditioning time is shorter (about 18 hours). 'Scrubbing' is a local phenomenon and the location of the processed area is determined by the

0-7803-7738-9/03/$17.00 © 2003 IEEE

beam position. The effectiveness of the conditioning depends also on the electron energy that in turn depends on the beam transverse size and in particular on bunch length and bunch charge. An ulterior reduction of the SEY to 1.5 was observed during dedicated machine studies with acceleration to 450 GeV/c when the beam size and the bunch length are getting shorter.

THE WAY TO THE NOMINAL LHC BEAM

Transverse plane

Though the conditioning increased significantly the multipacting threshold, this remained inferior to the nominal intensity and electron cloud transverse instabilities were observed. Particular care was taken to minimize injection errors to allow operation of the transverse feedback system at high gain while avoiding saturation of the amplifiers at injection, where the feedback acts also as an injection damper. It proved to be particularly important to minimize the bunch-to-bunch injection errors affecting the second, third and fourth batches as a consequence of the non-nominal rise time of the injection kicker. At the beginning of the 2002 run the rise-time was larger than 300 ns (0-100%), instead of the nominal 220 ns (the batch spacing is 225 ns – Tab. 1). The injection kicker system [7] consists of sixteen magnets, powered in pairs by eight Pulse Forming Networks (PFN). Twelve out of the sixteen magnets have an impedance of 16.67Ω while the remaining four have an impedance of 12.5Ω and are the slowest elements in the chain. The temporal evolution of the kick delivered by each pair of magnets could be measured in dedicated experiments by kicking the circulating beam. The fine synchronization of the eight PFNs could be measured and adjusted with particular attention to the slowest magnets reducing the kicker rise time to about 250 ns (0-100%). With this configuration only the first bunch of the injected batch and the last bunch of the circulating beam are affected. The damper can effectively damp the oscillation of these bunches in a few tens of turns at least for the first three batches while the damping efficiency appears to be marginal for the fourth batch.

One of the undesired effects of the electron cloud is the baseline distortion of the position signal provided by the electrostatic pick-ups used to drive the transverse feedback. In order to avoid such a phenomenon the Δ-signal from the pick-up is band-pass filtered at 120 MHz (±20 MHz) and mixed with a 120 MHz reference derived from the beam synchronous 200 MHz. This configuration eliminates disturbances due to the electron cloud but is quite sensitive to phase oscillations of the beam, which occur particularly at injection. It was significantly reduced by the implementation of a longitudinal damper.

At the end of the 2002 run the normalised r.m.s. transverse emittances at extraction energy for a beam with nominal bunch population were $\varepsilon^*_{H,V}$ = 2.2(H)/2.2(V) μm for one batch and $\varepsilon^*_{H,V}$ = 3.0(H)/4.1(V) μm for three batches, close to the nominal values (Tab. 1). The values quoted above for three batches correspond to the emittance of the trailing bunches of the last batch where the blow-up due to the electron cloud is larger and very likely are overestimated by 10-20% due to a problem found in the software reconstructing the wire scanner position during the scan. No measurement with four batches was possible because of the breakage of the wire scanner discussed in the next section.

Longitudinal plane

2002 was an important milestone for the acceleration of the full LHC beam in the SPS since, following eight years of preparatory work, nominal longitudinal parameters at extraction energy were obtained for the first time. Indeed the impedance reduction program was completed [1], [8], each of the four 200 MHz Travelling Wave Cavities were equipped with a feedforward and feedback pair [9] and the 800 MHz system was back in operation, ready to provide extra Landau damping. The steps taken are described in detail in [10].

A single batch with intensity three times below the nominal and an emittance of 0.35 eVs develops a coupled bunch longitudinal instability towards the end of the acceleration cycle. This can be cured for nominal intensity if the emittance is intentionally increased above 0.5 eVs and the 800 MHz is used for Landau damping. As a result, the final emittance has been measured in the range 0.52-0.56 eVs, well below the initial target (< 0.7 eVs) [10].

Notwithstanding the campaign to shield the vacuum ports, signals above 2.8 GHz were still visible [8]. These signals were proved recently to be due to pick-up resonances and not due to line density modulation (no change in frequency during debunching). Note that the pick-up cut-off frequency is 2.8 GHz.

Even with the significant reduction of inductive impedance, at least a factor 2.5, the residual impedance (~ 5 Ω) is sufficient to cause loss of Landau damping for single bunches with population above 0.5×10^{11} p. This was verified last year by observation of the Schottky spectrum. Undamped quadrupole oscillations are observed on the flat bottom after injection into an unmatched voltage, in the absence of emittance blow-up due to the microwave instability that we had in the past. These oscillations are not observed for bunch trains of 72 bunches, but could be a problem for the pilot or intermediate beam (12 bunches) required for LHC operation.

In machine studies it was observed [11] that during the normal injection procedure satellite bunches, at 5 ns spacing from the main bunches, were created. This seems to be due to uncaptured particles at injection drifting around the ring and then being recaptured. The situation is worse when the injection voltage is raised from 700 kV to 2 MV. These satellite bunches would remain and be injected into the LHC where the requirements on their intensity from the experiments are very strict.

The longitudinal damping system needed to cure a low frequency (<2 MHz) dipole mode coupled-bunch

instability on the flat bottom [10] is also used to damp the phase and energy error at the injection of the second, third and fourth batch. This is essential to keep the emittance constant for all bunches. Its gain was programmed during the ramp in order to get the best compromise between the damping rate needed and the slow blow-up caused by the noise injected by the electronics.

New ideas for synchronizing the SPS beam onto the LHC reference were tested. The LHC bucket reference is used to synchronize the CPS-SPS transfer so that, at 450 GeV/c, the SPS beam is in correct position for transfer to LHC, thereby minimizing the rephasing in the SPS [12]. The method was tested and the rephasing angle is now less than 4 RF buckets (20 ns). It is hoped to reduce it to less than 1 RF bucket in 2003.

SUMMARY, PRESENT LIMITATIONS AND POSSIBLE CURES

By the end of 2002 LHC beam with nominal intensity was accelerated to extraction energy with nominal longitudinal emittance and with transverse emittances close to the design values for the first three batches. Operation with nominal LHC beam revealed some hardware problems that will require attention and additional investigations in the future:

- marginal injection kicker rise-time. Faster thyratron switches will be installed for the PFNs powering the slowest magnets and a further reduction of the rise time by several ns is expected.
- breakage of the carbon wires in the wire scanners even when in parking position [13]. RF measurements conducted in the laboratory on a wire scanner tank showed high impedance modes at around 700 MHz. The beam-induced RF power is absorbed by the carbon wire and is responsible for the observed failures. Ferrite tiles have been installed in the wire scanner housing to reduce the impedance of the cavity modes and SiC wires have replaced some of the carbon wires providing a larger resistivity and therefore lower dissipation.
- heating of the ferrites of the kickers. Measurements confirmed that the time constant for such phenomena is of the order of a day as already anticipated. This should not be problematic for operation with LHC beam interleaved with other modes as expected in the future.
- instantaneous outgassing of the graphite beam dump absorber. This occurs not only when the beam is dumped onto the absorber at the end of each cycle but also during the ramp. The short time constant (seconds) of the latter phenomenon points to a surface phenomenon like multipacting or surface heating due to RF modes induced by the beam.
- instantaneous outgassing of the beam dump and tune measurement kickers. Here again, the short time constant seems to favour the hypothesis of multipacting or surface heating as being responsible for such phenomena.

A scrubbing run including acceleration to 450 GeV/c is foreseen also for the 2003 run. Attempts will be made to increase the bunch population well above nominal with the aim of increasing the multipacting threshold above the nominal bunch population.

Future studies will focus on consolidating the procedures and the cures found for the LHC beam, on ensuring quality control of the nominal beam before extraction and to provide the low intensity test beams required for the LHC.

ACKNOWLEDGEMENTS

We would like to thank our colleagues in the PS division for the excellent quality of the LHC beam delivered to the SPS, and those of the LHC/VAC group for their good collaboration during the scrubbing run.

REFERENCES

[1] P. Collier ed., 'The SPS as Injector for the LHC – Conceptual Design', CERN/SL/97-07 DI.

[2] G. Arduini et al., 'Electron Cloud Effects in the CERN SPS and LHC', Proceedings of EPAC 2000, Vienna, p. 259.

[3] G. Arduini et al., 'The Electron Cloud Instability of the LHC Beam in the CERN SPS', these Proceedings.

[4] G. Arduini et al., 'Status of the LHC Proton Beam in the CERN SPS', Proc. of EPAC2002, Paris, p. 206.

[5] N. Hilleret et al., 'The Variation of the Secondary Emission Yield and of the Desorption Yield of Copper during Electron Bombardment: Origin and Impact on the conditioning of LHC', Proceedings of EPAC2002, Paris, p. 2553.

[6] J.-M. Jimenez et al., 'Electron Clouds – Results from SPS and Experiments for 2003', these Proceedings.

[7] J. Bonthond et al., 'The future of the SPS Injection Channel', Proc. of PAC'99, New York, p. 1228.

[8] T. Bohl, et al., 'Impedance Reduction in the CERN SPS as seen from Longitudinal Beam Measurements', Proceedings of EPAC 2002, Paris, p. 1446.

[9] P. Baudrenghien, G. Lambert, 'Control of strong beam loading. Results with beam'. Proc. of the XI Chamonix Workshop, CERN-SL-2001-003 DI, p. 63.

[10]P. Baudrenghien et al., 'Nominal Longitudinal Parameters for the LHC Beam in the CERN SPS', these Proceedings.

[11]T. Bohl et al., 'Observation of Parasitic Beam and Cleaning with Transverse Damper', CERN AB-Note-2003-021 MD.

[12]P. Baudrenghien, 'Beam Control for Protons and Ions', Proceedings of IX Chamonix Workshop, Chamonix, CERN-SL-99-07 DI, p. 116.

[13]F. Roncarolo et al., 'Cavity Mode Related Wire Breaking of the SPS Wire Scanners and Loss Measurements of Wire Materials', these Proceedings.

PROTECTION DEVICES IN THE TRANSFER LINES TO THE LHC

H. Burkhardt, B. Goddard, V. Mertens, CERN, Geneva, Switzerland

Abstract

Beams will be transferred from SPS to LHC through two transfer lines, each of over 2.5 km length, equipped with conventional resistive magnets with relatively small apertures. Beam energy densities will be roughly 4 orders of magnitude above the LHC quench limit and about one order above damage level. Possible failures of the various elements in the transfer lines and the SPS machine are discussed, together with results from tracking studies. The benefit from installing protection devices in the transfer lines is discussed, along with related layout aspects and the required protection performance.

1 INTRODUCTION

Beams will be injected from the SPS into the LHC through the two transfer lines TI 2 and TI 8 [1], see Fig. 1.

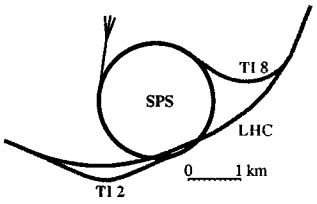


Figure 1: Schematic view of the LHC injection transfer lines.

Protection devices in the transfer lines should be safe for nominal beam intensities and also survive the impact of beams of ultimate intensities, which will be about 50 % above the nominal intensities. Parameters are summarized in Table 1.

Table 1: Nominal beam parameters for LHC injection.

Proton momentum	450 GeV/c
Normalized emittance	$\epsilon_N = 3.75\,\mu$m
Emittance	$\epsilon = 7.82$ nm
Protons per bunch	1.1×10^{11}
Bunches per batch	72
Number of batches	3 or 4
Nominal intensity	$4 \times 72 \times 1.1 \times 10^{11}$ $= 3.2 \times 10^{13}$

The batches are extracted in $4/11$ of an SPS turn or $7.86\,\mu$s. The damage level for fast losses is about 2×10^{12} protons and the quench level in the LHC of the order of 10^9 protons [2]. An attenuation by at least a factor of 20 and better by a factor of 100 should be achieved to prevent damage by the injected beam [3].

Primary collimators in the LHC will be set to $6 - 7\,\sigma$ at injection and secondary collimators to $7 - 8.2\,\sigma$. This reduces the tertiary halo of the circulating beams to below the quench level at physical apertures (at $> 10\,\sigma$). Wrongly injected beams could however do damage before they even arrive at the collimation sections in the LHC.

Cleaning of the injected beams is best done as early as possible. A 'shaving' to $3.5\,\sigma$ (corresponding to less than 0.05 % loss for Gaussian beams) is foreseen in the SPS.

The combined effect of closed orbit errors, SPS extraction and transfer lines ripple and drifts corresponds to an increase by $1.5\,\sigma$ [1]. This adds up to a $5\,\sigma$ envelope for the injected beams in the LHC.

Injection steering will be done with low intensity (pilot) beams, well below the damage level. When everything is well adjusted and a pilot circulates in the LHC, the injection of high intensity batches can start.

2 POSSIBLE FAILURES AND PROTECTION

Protection against mis-firing of the extraction kickers in the SPS is foreseen. The septum MSE which follows the extraction kicker MKE will be protected by the septum diluter (TPSG, about 4 m of C + Al, [4]). Protection against mis-firing of the MKI kickers at the end of the transfer lines into the LHC is provided by the injection beam stopper TDI, the D1 shielding TCDD and the TCL injection collimators. They will be set to about $8.5\,\sigma$ vertically. There is at present no passive horizontal protection for the injected beams in the LHC.

The transfer lines are pulsed, use warm magnets and are turned off when no injection is needed. The beam is horizontally extracted from the SPS (MKE kicker). The lines are several kilometres long with many horizontal and some vertical bending magnets. Wrong bending fields could result in local loss of the full intensity. Active protection based on monitoring of the currents of the magnets in the transfer lines is planned. Large injection oscillations could still be caused for example by problems with corrector settings in the transfer lines or timing faults [5].

Most critical is the end of the line with the tight septum (MSI) aperture and the injection region in the LHC. Passive protection for the septum is needed, which at the same time can be used to limit injection oscillations in the LHC.

Fig. 2 shows the septum MSI in TI 8 as seen from the side. It consists of five (two MSIA and three MSIB) each 4 m long steel septum magnets. The aperture available for the injected beam is indicated by dotted lines. It reduces from effectively 17 mm on the right to 13 mm on the left, which leaves $7\,\sigma$ in both planes to the beam.

0-7803-7738-9/03/$17.00 © 2003 IEEE

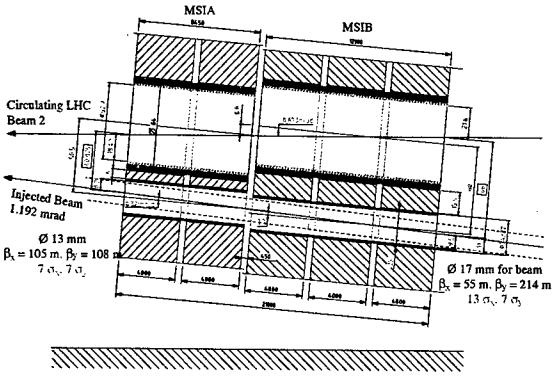


Figure 2: Septum MSI in TI 8, seen from the side.

3 OPTICS AND POSSIBLE POSITIONS OF COLLIMATORS

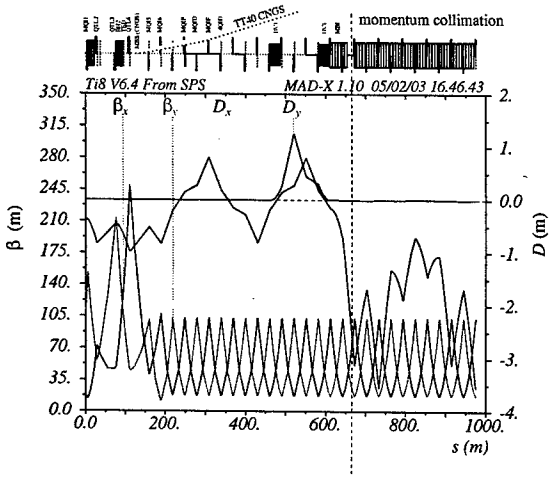


Figure 3: Optics at the beginning of TI 8 and proposed position for momentum collimation.

The optics of the first kilometre of the transfer line TI 8 is shown in Fig. 3. The beam energy is constant through the transfer line. Momentum collimation can be done in the first available space with high dispersion. The betatron collimation should be able to protect the tight septum aperture and the injection region against any bending errors upstream. It should therefore be placed towards the end of the line. As a first proposal to be looked at more closely, we will follow the following strategy to place collimators "TCDI" in the transfer line:

- Momentum collimation in the first available place with large dispersion (which is in the horizontal plane).
- Vertical collimation at about 90° phase advance upstream of the septum (and about 180° in H).
- Horizontal collimation at about 90° upstream of the septum.
- Septum protection, combined in H and V.

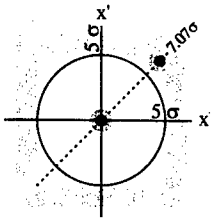


Figure 4: Illustration of the phase space with two collimators at 90° set to 5 σ.

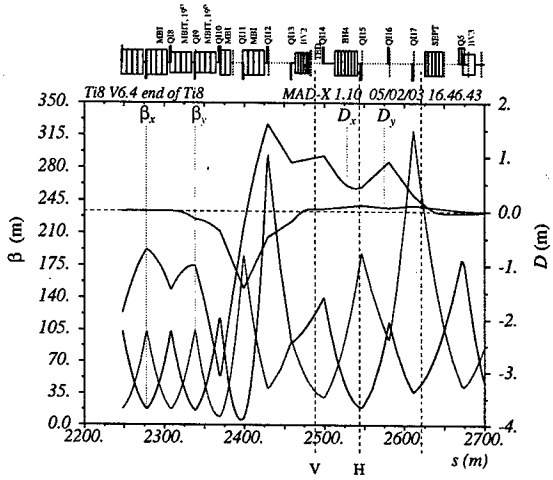


Figure 5: Optics at the end of TI 8 and proposed positions for betatron collimation.

The phase space limits obtained from collimation at 5 σ with 90° phase difference are sketched in Fig. 4. The beam spots of a centred beam and the worst case of a displaced beam are also sketched.

A first detailed proposal for positions of collimators has been worked out for the line TI 8. The numbers are given in Table 2. The end of the line with the proposed positions for betatron collimation is also shown as Fig. 5. The table gives s positions in the transfer lines, the optics parameters β and dispersion and the phase advance relative to the beginning of the septum.

5 σ settings would imply rather narrow settings, ± 2.3 mm at QI15 in H and ± 2.8 mm in V. To allow for injection steering, the collimators at QI14 and QI15 should be retractable. The first betatron collimator COLLQI14 has been placed close to the beam stopper TED at a phase advance of 90° in the vertical plane from the septum. The β_x in this place is relatively large and the horizontal phase advance to the septum not too far from 180°. Adding also horizontal collimation in this position is considered and would allow to limit the aperture in both planes to reduce losses close to the septum.

4 PERFORMANCE ESTIMATE

The critical impact parameter b_c, below which scattering from the collimator edge is significant, is about $b_c = 12\,\mu$m

Table 2: Optics at transfer line collimators.

Name	s, m	β_x, m	D_x, m	σ_x, mm	$\Delta\mu_x$ to MSI	β_y, m	D_y, m	σ_y, mm	$\Delta\mu_y$ to MSI
COLLMOM	671	102	-3.08	1.69	$-20°$	18.2	-.001	0.38	117°
COLLQI14	2487	122	0.99	1.08	163°	38.4	0.042	0.55	87°
COLLQI15	2546	19.8	0.44	0.45	97°	186	0.11	1.20	29°
COLLMSI	2627	54.3	0.11	0.65	0°	218	0.09	1.31	0°

at 450 GeV/c [6]. For a uniform impact over a distance d, there will be roughly a fraction of d/b_c protons scattered back in the beam pipe.

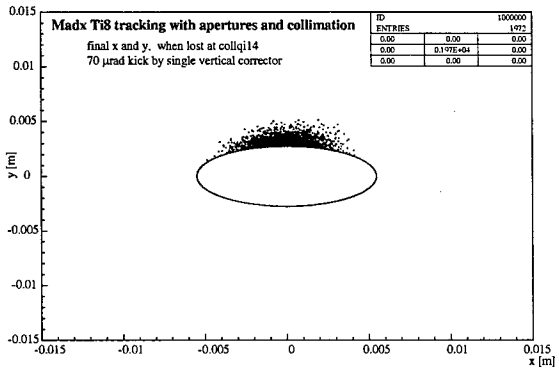


Figure 6: MAD-X TI 8 tracking with apertures.

Impact distributions for the proposed transfer line collimators have been studied using MAD-X [7] tracking for the transfer line TI 8 with apertures and collimators. In the most favourable case, losses are distributed homogeneously in the available aperture, resulting in a flat loss distribution over 5 mm on the collimator. For this case, we estimate an attenuation by a factor or $5\,\mathrm{mm}/12\,\mu\mathrm{m} \approx 400$. A result for the least favorable case, in which the beam impacts directly without any blow-up is shown in Fig. 6. The attenuation based on the r.m.s beam size $\sigma = 0.5\,\mathrm{mm}$ is then $5\,\mathrm{mm}/12\,\mu\mathrm{m} \approx 40$. Not all particles scattered back elastically into the beam pipe will be lost in critical places. The scattering angle can be estimated from multiple scattering:

$$\theta_0 = \frac{13.6\,\mathrm{MeV}}{\beta cp}\sqrt{x/X_0}\,[1 + 0.038\log(x/X_0)] \qquad (1)$$

Numerical estimate for graphite: one nuclear interaction length is $\lambda \approx 26\,\mathrm{cm}$ and one radiation length $X_0 \approx 19\,\mathrm{cm}$. The effective distance x before absorption is estimated as 2λ. The result for the average scattering angle is $\theta_0 \approx 50\,\mu\mathrm{rad}$. This is about 2 or 3 times more than the beam divergence. It implies that the back-scattered proton losses will be rather distributed. Together with the attenuation of 40 estimated above, there are good reasons to believe that the performance of the transfer line collimators would in fact be sufficient to prevent damage. This should be verified by tracking with simulation of the interactions in the collimators.

The proposed setting at $5\,\sigma$ at two phases separated by 90° will limit oscillations to below $\sim 8\sigma$ at any phase. This still leaves some margin for tolerances up to the LHC physical aperture of about $10\,\sigma$ in the LHC.

Whether the momentum collimation at the beginning of the line is really needed will depend on the reliability of the quality check/interlock system planned for the extraction from the SPS. The passive protection proposed here would reduce the momentum aperture in the line from about $\pm 0.8\,\%$ (estimated with $r = \pm 3.2\,\mathrm{cm}$ aperture and $D_x = 3.5\,\mathrm{m}$ dispersion in the transfer line arc) to about $\Delta E/E \pm 0.24\,\%$, as estimated for momentum collimation at $D_x = 3\,\mathrm{m}$, $\beta_x \approx 100\,\mathrm{m}$, $1\,\sigma = 1.7\,\mathrm{mm}$ with a setting at $5\,\sigma$ or $\pm 8.5\,\mathrm{mm}$. This is sufficient to prevent localized losses due to energy errors.

5 SUMMARY AND OUTLOOK

A collimation at $5\,\sigma$ in the transfer line will be important to protect the LHC injection regions against serious damage and to limit injection oscillations in the LHC. Issues presently under study include

- fixed or mobile apertures,
- attenuation performance,
- exact positioning,
- necessity of momentum collimation.

In parallel, work leading to a detailed technical design has started.

6 REFERENCES

[1] A. Hilaire, V. Mertens, and E. Weisse, "Beam Transfer to and Injection into LHC", LHC Project Report 208 and Proc. EPAC 1998, pp.2117-2119.

[2] J. Jeanneret, "Collimation schemes and Injection protection Devices in LHC", Proc. Chamonix XI , CERN SL/2001-003 (DI) (2001), p. 298.

[3] H.Burkhardt, "Do we need collimation in the transfer lines ?", Proc. Chamonix XII, CERN AB/2003-008 (ADM) (2003).

[4] B. Goddard, R. Guinand, A. Herrera-Martinez, Y. Kadi, and S. Marque, "Transient Thermo-Mechanical Analysis of the TPSG4 Beam Diluter", CERN-SL-2002-060 ECT.

[5] M. Jonker, "Reliable Timing Controls for Safe Operation of the LHC", Proc. Chamonix XII, CERN AB/2003-008 (ADM)

[6] N. Catalan Lasheras *et al.*, "Proton collimation in TeV colliders", CERN-LHC-PROJECT-REPORT-156, Oct 1997.

[7] H. Grote, F. Schmidt,"MAD-X", this conference

THE PS 13.3-20 MHZ RF SYSTEMS FOR LHC

M. Morvillo, R. Garoby, D. Grier, M. Haase, A. Krusche, P. Maesen, M. Paoluzzi, C. Rossi,
CERN, Geneva, Switzerland

Abstract

As part of the preparation of the PS as an injector for the LHC, a prototype 20 MHz rf system has been used, to demonstrate that the nominal longitudinal performance of the proton beam for LHC can be obtained using multiple bunch-splittings. Based on these successful results obtained during 2000, the development of the operational rf system began in 2001. To allow the preparation of bunch trains with a bunch spacing of 25 or 75 ns, this system must operate either at 20 or 13.3 MHz respectively. Two new ferrite cavities and their associated amplifiers have been designed and built. Each one can provide a maximum voltage of 20 kV peak during 200 ms with a 10% duty cycle. The cavities are equipped with fast (~20 ms) gap shorting relays, and rf feedback reduces their Q below 10 at both frequencies. A single system is sufficient to generate the nominal beam for LHC. The second one will then be both a "hot spare" and a very valuable performance enhancement providing the possibility of handling a larger than nominal emittance or generating bunch trains with different spacings in the same PS supercycle. The design and the results measured on the final device are described and discussed.

INTRODUCTION

This project is part of the preparation of the PS complex as injector for the LHC. During the year 2000 a new scheme for producing the LHC beam structure was successfully tested, using a prototype 20 MHz rf system installed during the 1999 PS shutdown. Making use of rf systems operating at 10, 20, 40 and 80 MHz, bunches are split in 12 without debunching/rebunching, and a nominal bunch spacing of 25 ns is finally obtained [1, 2]. In 2001, 75 ns bunch spacing was proposed for the early stage of LHC operation, to limit electron cloud induced heating of the vacuum chamber and maximise luminosity for a limited total beam intensity [3]. To make both bunch spacings feasible, the operational rf systems have then been specified to be able to operate either at 13.3 or 20 MHz. A first system was finished in 2002 and installed during the winter shutdown in the PS ring. The second one is under construction and will be installed one year later.

GENERAL SYSTEM SPECIFICATION

Each system is made-up of a power amplifier driving one cavity and occupies a single short straight section in the PS. It is tunable at 13.3 and 20 MHz and it can deliver the full voltage (20 kV) during 200 ms with a 10% duty cycle. When not in use, high voltage relays short-circuit the resonators. When in use, the relays are open and rf feedback reduces the quality factor to 10 and the shunt impedance accordingly. A single system is sufficient to generate the nominal beam for LHC, either with 25 or 75 ns bunch spacing. The presence of two systems will make both types of beam available within the same PS supercycle, without activating excessively the mechanical devices used for tuning.

CAVITY DESIGN

The request for a maximum peak rf voltage of 30 kV, together with the space constraint imposed by the PS short straight section (1.5 m), have led to the decision of installing two identical systems. The cavity mechanical layout is shown in fig. 1. The resonator is made of two sections, each of them with its own ceramic gap. Splitting the rf voltage between two gaps is imposed by the safe voltage holding limit of the gap relays (10 kV).

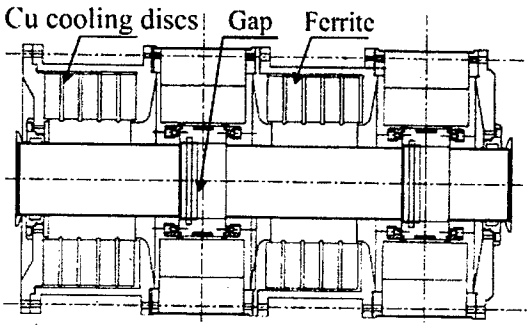


Figure 1: Cavity mechanical layout

Compared to a single resonator solution, more ferrite rings are used and losses are lower. The two sections are driven in parallel by the common tube amplifier with two short transmission lines. The cavity is shown in Fig. 2.

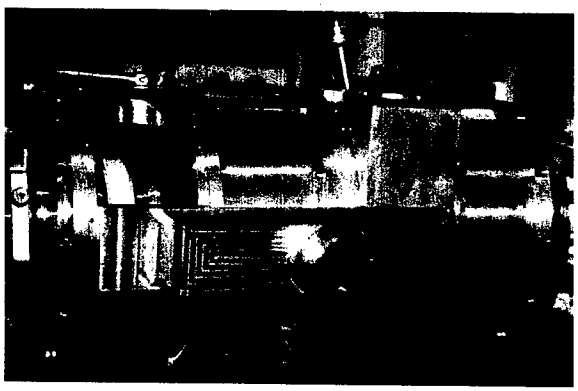


Figure 2: The ferrite cavity. The end part of the transmission lines and the ceramic gap are visible

The ferrite rings are Philips (now Ferroxcube) standard grade 4E1, and heat is removed by water-cooled copper disks. This grade has been chosen for its low permeability

0-7803-7738-9/03/$17.00 © 2003 IEEE

(~14) and low loss at 20 MHz. The ferrite ring size is 440x250x33.3 mm. Each cavity has ten rings in total. During the development, the cavity characteristics have been estimated with multiple measurements on small size ring samples. Since only two fixed resonant frequencies are required, magnetic bias has not been selected and, instead, tuning is achieved with two variable vacuum capacitors connected in parallel with the gaps. The cavity being very close to the PS main magnets (see Figure 3), a magnetic shield surround the ferrite rings to avoid unwanted detuning due to the fringe field. Its main characteristics are summarized in Table 1.

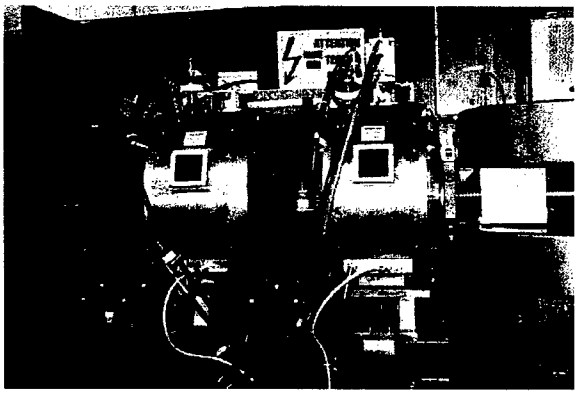


Figure 3: The cavity installed in the PS ring. The magnetic shield and the PS magnets are visible.

Table 1: Main characteristics of a 13 – 20 MHz cavity

Parameter \ Frequency [MHz]	**13.3**	**20**
Quality factor at 20 kVp	82	63
Quality factor at 100 Vp	163	100
Nominal V_{RF} [kVp]	15	15
Maximum V_{RF} [kVp]	20	20
Shunt resistance at 20 kVp [kOhm]	1.7	2
Power dissipation at 20 kVp [kW]	25	30
RF magnetic flux density at 20 kV [mT]	9.7	6.7
Peak power density at 20 kVp [mW/cm^3]	860	730

AMPLIFIER CHAIN

A grounded cathode tube power amplifier has been developed, based on a water cooled tetrode RS1084CJ (THALES), driven by a 400 W solid state amplifier. Feedback from the cavity gap provides reduction of the cavity impedance seen by the beam. Both amplifiers are kept as close as possible to the cavity resonator in order to keep the group delay low. A low Q (~2.5) resonator is implemented in the grid of the tetrode. A coaxial rf switch selects between two shorted coaxial cables to tune the grid resonator at the two frequencies. Fine tuning is obtained using a coaxial line stretcher. The anode dissipation of the tetrode is minimised by pulsing to 4 A the DC current only during operation (10 % maximum duty cycle). The CERN-made driver amplifier has a gain of 54 dB, a group delay of only 30 ns, and a 3 dB bandwidth extending from 0.15 to 80 MHz. The presence of the two transmission lines generates high frequency resonances that limit the overall loop gain. At 20 MHz the unwanted resonance is located at 56 MHz while at 13.3 MHz it is at 71 MHz. The 56 MHz resonance is especially dangerous, because the gain is only 24 dB below the value at 20 MHz. Two notch filters, connected directly to the feedback probe, are used to filter out the two resonances. The main characteristics of a complete rf system are summarized in Table 2.

Table 2: Main characteristics of a 13–20 MHz system

Parameter\Frequency [MHz]	**13.3**	**20**
Feedback gain at 100 Vp [dB]	25	21
Feedback gain at 20 kVp [dB]	20	17
Open Loop Bandwidth [kHz]	75	176
Closed Loop Bandwidth [MHz]	2.6	4.5
Forward Path Gain [dB]	94	95

TUNING

Four different components have to be adjusted as a function of the operating frequency: the grid circuit of the power amplifier, the cavity, the rf feedback loop (gain and phase) and the servo control of the rf voltage amplitude (AVC). The cavity tuning is obtained by changing the capacitance in parallel with the two gaps. That method has two disadvantages. First of all, the variation of the resonant frequency with the amplitude (~85 kHz in both cases) cannot be compensated. This affects the closed loop transfer function (modulus and phase) of the system. The phase is amplitude dependent and it changes by 4.5° at 13.3 MHz and 3° at 20 MHz. The amplitude of the frequency response becomes tilted (see next paragraph). The second disadvantage is the slowness: changing the operating frequency requires about two minutes. A single stepping motor monitored by a 12 bit encoder drives the variable capacitors. The other three elements are adjusted by means of four rf coaxial switches. All these operations are performed by a programmable logic controller (PLC). The PLC, together with hard-wired logic, blocks the system during the frequency change and detects and signals any fault in the switching elements. To ensure stability during the process, the open loop gain is kept low by disabling the grid pulser of the tetrode and blanking the driver.

EXPERIMENTAL RESULTS

Measurements of the cavity and of the closed loop frequency responses at 20 kVp are shown in Figures 4 and 5. Low voltage results (100 Vp) are given in Figures 6 and 7.

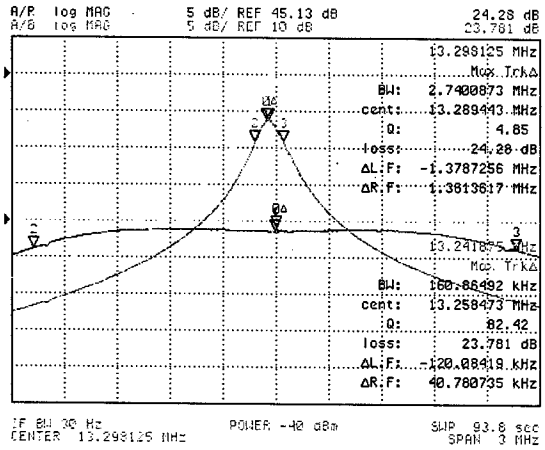


Figure 4: Response of the system at 13 MHz and 20 kVp.

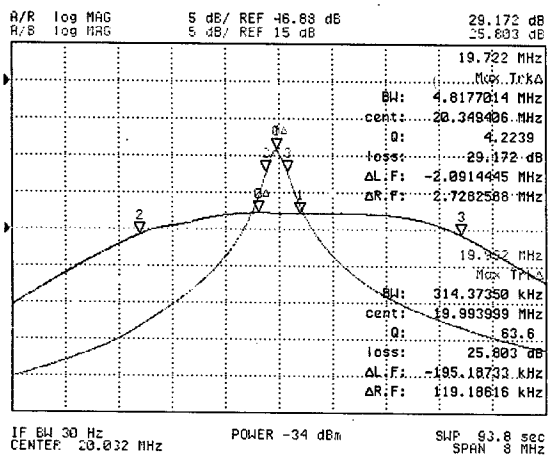


Figure 5: Response of the system at 20 MHz and 20 kVp.

The maximum voltage has been obtained with a duty cycle of 15% and 300 ms rf pulse length. The limiting factor is the gap heating. The feedback is adjusted at maximum and the measured bandwidths exceed the specifications by a factor two. At such high feedback gains, the frequency response is deformed and the ratio of closed loop over open loop bandwidth is greater than the amount of feedback introduced. Because of the change of the tune of the resonators with amplitude, the frequency responses are different at low and high voltages, and feedback adjustment is a compromise.

The system now installed in the PS will start being used with beam in June 2003. The first goal will be to check the performance of the gymnastics leading to 75 ns bunch spacing. The second system, presently in construction, will benefit from this experience and it will be installed during the next winter shut-down.

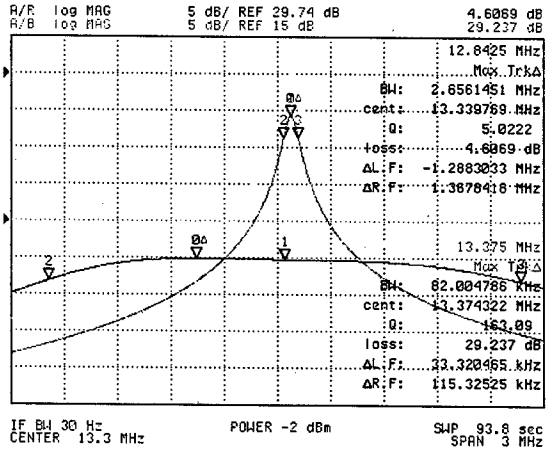


Figure 6: Response of the system at 13 MHz and 100 Vp.

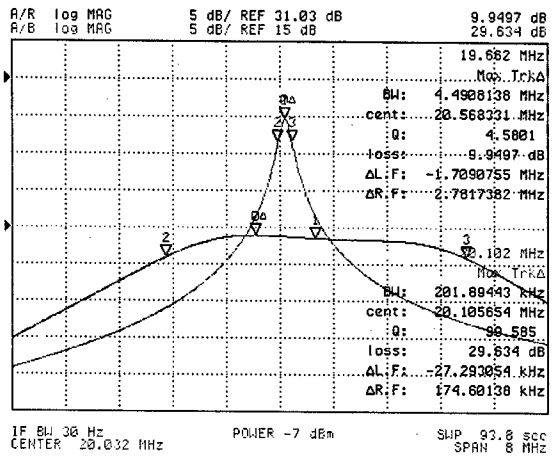


Figure 7: Response of the system at 20 MHz and 100 Vp.

ACKNOWLEDGEMENTS

We are in debt to the numerous members of the PS/RF (now AB/RF) group who contributed to the development of this new system, and especially A. Marmillon, C. Rougemont and R. Monnin. Staff from the workshop and drawing office also deserve our thanks.

REFERENCES

[1] R. Garoby, *Status of the nominal proton beam for LHC in the PS*, CERN/PS 99-013 (RF).

[2] M. Benedikt et al, *The PS complex as proton pre-injector for the LHC design and implementation report*, CERN-2000-03, Feb 2000.

[3] R. Garoby, *Multiple Splitting in the PS: Results and Plans*, CERN/PS 2001-004 (RF).

PRESENT UNDERSTANDING OF ELECTRON CLOUD EFFECTS IN THE LARGE HADRON COLLIDER

G. Arduini, V. Baglin, E. Benedetto, R. Cimino, P. Collier, I. Collins, K. Cornelis, B. Henrist, N. Hilleret, B. Jenninger, M. Jimenez, A. Rossi, F. Ruggiero, G. Rumolo*, D. Schulte, F. Zimmermann, CERN, Geneva, Switzerland

Abstract

We discuss the predicted electron cloud build up in the arcs and the long straight sections of the LHC, and its possible consequences on heat load, beam stability, long-term emittance preservation, and vacuum. Our predictions are based on computer simulations and analytical estimates, parts of which have been benchmarked against experimental observations at the SPS.

1 INTRODUCTION

An electron cloud and its effets are observed in the CERN SPS, when operated with LHC-type beams. The electrons are created by a beam-induced multipacting process [1]. A similar electron build up in the LHC might complicate its commissioning and early operation. Simulations for the LHC can be benchmarked against SPS measurements.

2 INSTABILITIES

Instabilities due to electron cloud have been seen in the SPS with the LHC beam since 1999 [2, 3]. In the horizontal plane, we observe a coupled-bunch instability, whose wave length is comparable to the length of a 72-bunch train (called 'batch'). The growth time is about 1 ms (50 turns) and nearly independent of the bunch population. We believe that the coupled bunch wake in the horizontal plane is caused by the spatial structure of the electron cloud, which is concentrated in the form of two vertical stripes on either side of the beam, slowly following the beam motion. The coherent and incoherent components of the flat-chamber impedance can add to the electron-cloud wake [4]. In the vertical plane a single-bunch instability is observed. Its growth time is about 2 ms (100 turns) at the nominal LHC intensity, and it changes strongly with beam current. Countermeasures that were taken include the transverse damper system, which acts against the coupled-bunch instablity, and a high chromaticity, up to 20 units, suppressing the single-bunch effect. Most successful, however, was a dedicated 10-day scrubbing run in 2002, initially accompanied by an extensive electron-cloud activity and a high vacuum pressure, in the course of which the secondary emission yield of the vacuum chamber decreased substantially. However, at the end of the scrubbing run, the electron-cloud threshold was still about 20% lower than the nominal LHC intensity.

We can translate these observations to the LHC, by applying simplified scaling laws. The growth rate for the coupled bunch instability is roughly approximated by [5] $1/\tau \approx 2\pi r_p \beta c \rho_{\rm el}/\gamma$. Taking an SPS beta function of $\beta_{\rm SPS} \approx 40$ m and a beam momentum of $p_{\rm SPS} \approx 26$ GeV/c, the 1 ms growth time at injection into the SPS corresponds to an average electron density of $\rho_{\rm el} \approx 3 \times 10^{11}$ m^{-3}. Assuming the same value of $\rho_{\rm el}$, $\beta_{\rm LHC} \approx 100$ m, and $p_{\rm LHC} \approx 450$ GeV/c, at injection into the LHC the growth time would be 5 ms (50 turns). This number is comparable to the LHC feedback damping time. The TMCI-like single-bunch instability has a threshold [6]

$$N_{b,\rm thr} \approx \frac{\gamma Q_s h_x h_y}{\beta C} \frac{2L_{\rm sep}}{r_p} . \qquad (1)$$

Inserting the synchrotron tunes $Q_{\rm SPS} \approx 0.003$ or $Q_{\rm LHC} \approx 0.006$, the circumferences $C_{\rm SPS} \approx 6.9$ km or $C_{\rm LHC} \approx 27$ km, the bunch spacing $L_{\rm sep} \approx 7.5$ m, the chamber half apertures $(h_x h_y)_{\rm SPS} \approx 1.3 \times 10^{-3}$ m^2 or $(h_x h_y)_{\rm LHC} \approx 4 \times 10^{-4}$ m^2, the beta functions $\beta_{\rm SPS} \approx 40$ m or $\beta_{\rm LHC} \approx 100$ m, and the momenta $p_{\rm SPS} \approx 26$ GeV/c or $p_{\rm LHC} \approx 450$ GeV/c, we find a threshold bunch population of $N_{\rm thr,SPS} \approx 4 \times 10^9$ for the SPS, and $N_{\rm thr,LHC} \approx 1 \times 10^{11}$ for the LHC. Thus, the LHC beam is expected to be 25 times more stable vertically than the SPS beam, for the same electron line density. In the worst possible case, with strong multipacting all around the entire LHC circumference, the threshold will be reached close to the LHC design intensity. The actual threshold observed in the SPS is the threshold for multipacting and not the instability threshold for a saturated (or constant) electron cloud density calculated above.

Some uncertainties however remain. Direct simulations of the single-bunch instability in the LHC using the code HEADTAIL [7] yield the emittance growth rate as a function of electron density. The result is illustrated in Fig. 1. The emittance growth steeply increases with the electron density. However, even the smallest growth rates in Fig. 1 represent a significant emittance dilution over the time scale of the LHC injection plateau (20 minutes) or in collision (24 hours). It is peculiar that there is no threshold. The origin of the simulated emittance growth is presently under study, and it is further discussed in a companion paper [9].

3 VACUUM

While in the SPS the electron cloud manifests its presence by a large pressure increase [10], the situation may be the opposite in the warm sections of the LHC (about 20% of the circumference), where the vacuum chambers are coated by TiZrV getter, with a sticking coefficient of 1 for ions. The reason is that not only ionization by the beam can contribute to the pumping of the residual gas [11], but, more importantly, ionization by the low-energy electron. At saturation, the average number of electrons roughly equals that of the protons [12]. Then the linear pumping speed

* present address: GSI Darmstadt, Germany

0-7803-7738-9/03/$17.00 © 2003 IEEE

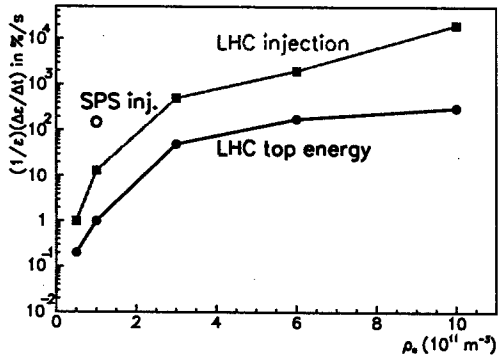


Figure 1: Simulated LHC emittance growth rates in %/s vs. average cloud density [8].

of the electron cloud is $S_{\mathrm{lin,e^-}} \approx \sigma_e I_b/e$, where I_b denotes the beam current and the ionization cross section σ_e for the low-energy electrons is two orders of magnitude larger than that of the ultra-relativistic protons (100–400 Mbarn instead of 0.4–2 Mbarn). The estimated electron pumping is $S_{\mathrm{lin,e^-}} \approx 20\,\mathrm{ls^{-1}m^{-1}A^{-1}}$ for H_2 and $130\,\mathrm{ls^{-1}m^{-1}A^{-1}}$ for methane, which will reduce the pressure.

4 BUILD UP AND HEAT LOAD

The build-up of an electron cloud along an LHC bunch train (batch) has been simulated using the ECLOUD code [13]. Results for different bunch intensities both in dipoles and field-free regions are displayed in Figs. 2 and 3. At first the electron density increases as a function of bunch intensity; it reaches a maximum for bunch intensities between about 8×10^{10} and 10^{11}; for even higher bunch intensities it decreases again. This non-monotonic dependence might be related to the 'lock-out' regime of S. Heifets [14].

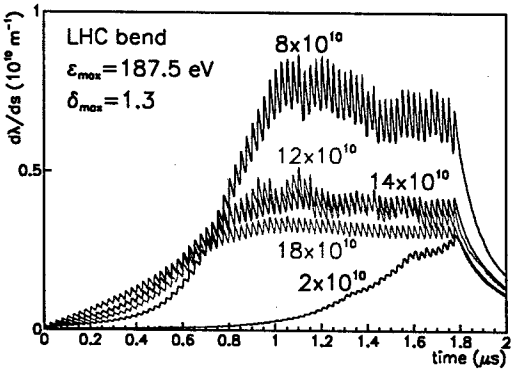


Figure 2: Electron line density as a function of time during the passage of a batch in an LHC dipole, for $\delta_{\max} = 1.3$, $\epsilon_{\max} = 187.5$ eV and different bunch intensities.

A firm commissioning constraint for the LHC is the heat load deposited on the cold bore of the arc chamber. Figure 4 shows the simulated average LHC arc heat load as a function of the bunch intensity for two different values of $\delta_{\max}$. Also indicated is the available cooling capacity, which decreases for higher intensities due to the enhanced heating by synchrotron radiation and image currents. For a maximum secondary emission yield $\delta_{\max} = 1.1$, the

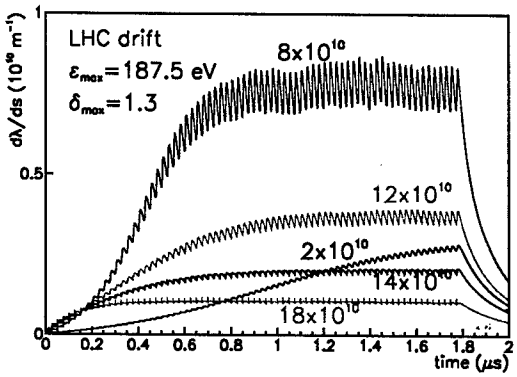


Figure 3: Electron line density as a function of time during a batch passage in an LHC field-free arc region, for $\delta_{\max} = 1.3$, $\epsilon_{\max} = 187.5$ eV and different bunch intensities.

threshold at which the simulated heat load surpasses the cooling capacity is equal to the ultimate LHC intensity of $N_b \approx 1.7 \times 10^{11}$. For $\delta_{\max} = 1.3$ the simulated threshold drops to $N_b \approx 5 \times 10^{10}$, about half the nominal design intensity. These numbers agree to within about 20% with earlier simulations [8].

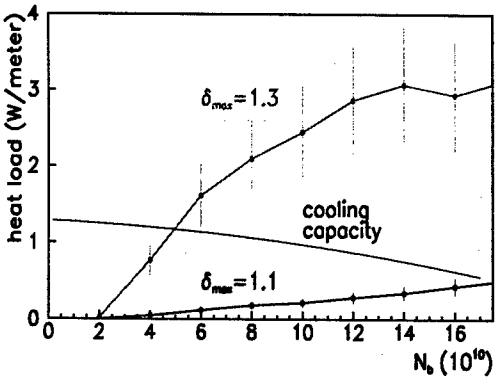


Figure 4: Average LHC arc heat load simulated in 2003 and cooling capacity as a function of bunch population N_b.

The exact modelling of the elastic electron reflection between 0 and 10 eV is still uncertain. Recent measurements [15] indicate that the probability of elastic reflection may approach 1 in the limit of 0 incident energy, while in our present parametrization this probability varies roughly between 0.2 and 0.6 depending on the value of $\delta_{\max}$. Modifying the low-energy reflectivity would increase the predicted heat load and could enlarge the simulated survival times.

5 SPS BENCHMARKS

In 2002, a discrepancy between the measured and simulated location of the electron-cloud stripes in a dipole field has been a major concern. The stripes occur in the region with maximum multipacting, and their position is sensitive to details of the secondary emission. After a revision of the ECLOUD code, we now obtain a satisfactory agreement, at the 10–15% level. A comparison of the measured [10] and newly simulated horizontal stripe position as a function of bunch intensity can be found in [8, 16]. Figure 5 unveils the

sensitivity of the electron position to rather small changes in the dipole magnetic field, and also the effect of changing the maximum secondary emission yield. The latter does not affect the position of the stripes, but alters the overall electron flux to the wall.

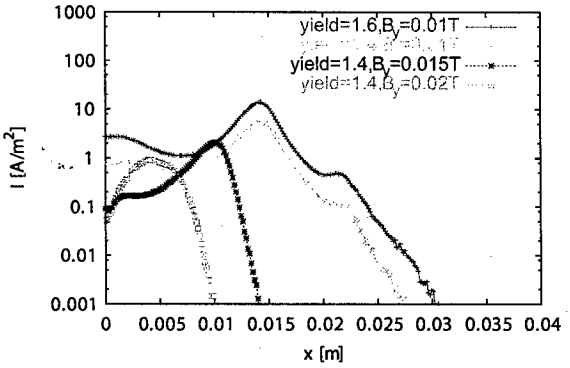


Figure 5: Simulated electron flux vs. horizontal position x in the SPS for an intensity of $N_b = 1.2\times10^{11}$, two different magnetic fields and yields $\delta_{\max}$. The beam is at $x = 0$.

The simulated energy distribution of electrons impinging on the chamber wall is shown in Fig. 6. For a field of 100 G the distribution has a maximum at 200 eV, in good agreement with observations [10]. Simulated and measured energy spectra above 30 eV also agree well without magnetic field [8, 10]. Electrons at energies below 30 eV have not been measured and are not included in Fig. 6. However, in the simulation the overwhelming majority of the incident electrons are at these low energies.

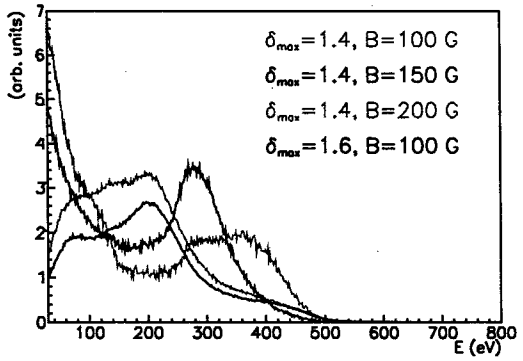


Figure 6: Simulated electron energy distribution at the wall for a dipole field in the SPS.

The measured and simulated absolute flux of electrons onto the chamber wall was compared, considering only the electrons of energy larger than 20 eV, for the passage of 1–3 batches [8]. For any number of batches, in a dipole field the measured flux is about 6 times lower than simulated. This difference may be due to the limited energy and momentum acceptance of the strip detector. In a 100-G field the cyclotron radius is $\rho \approx 750$ μm at 5 eV and 3.4 mm at 100 eV. These values are comparable to the chamber hole radius of 1 mm. Also the partial suppression of the cloud build up by the detector itself could contribute to the discrepancy. However, in the case without magnetic field the difference between simulations and measurement is much larger, about a factor 35. This could indicate that we do not model the field-free case correctly.

For the successful commissioning of the LHC a reliable prediction of the heat load in the cold part of the machine is important. Several warm and cold calorimeters were installed in the SPS [17], whose purpose is to measure the actual heat load for different apertures, temperatures, and beam conditions. Their results serve as a benchmark for the simulations. Extensive measurements were performed for different numbers (1–4) of LHC batches. The measured heat loads [17] span a wide range, extending from 30 mW/m for 1 batch in a warm large-aperture calorimeter to 8 W/m for 3 batches in a cryogenic environment. Within the large scatter of the experimental data points, the measurements are consistent with the simulations for all the cases compared. However, the exact value of the secondary emission yield in the calorimeters is not precisely known and can rapidly change during beam operation, so that in some cases the experimental data fluctuate by a factor of 10. Measurements and simulations disagree on the effect of a magnetic field. The simulated heat load is maximum without field, while the observed one is two times higher at 100 G. Further benchmarking studies are planned for 2003.

6 CONCLUSIONS

Over the last three years an enormous progress has been made at CERN in electron-cloud diagnostics, beam measurements, and simulations. In general, the observations and simulations appear consistent. The successful suppression of the electron cloud in the SPS lends further confidence that we will be able to cure it in the more challenging environment of the LHC, with a cold vacuum system, a reduced clearing gap, and, at higher beam energies, a large number of primary photo-electrons from synchrotron radiation. Most open questions are under investigation.

7 REFERENCES

[1] O. Gröbner, Xth HEACC, Serpukhov (1977).
[2] G. Arduini, EPAC 2002, Paris, La Villette (2002).
[3] K. Cornelis, Proc. ECLOUD'02, CERN, Geneva, April 15-18, CERN-2002-001 (2002).
[4] K. Cornelis, CERN Mini-Workshop *http://sl.web.cern.ch/-SL/sli/Scrubbing-2002/Workshop.htm* (2002).
[5] F. Zimmermann et al., APAC'01, CERN SL-2001-057 (AP).
[6] K. Ohmi et al., PRL 85, p. 3831 (2000).
[7] G. Rumolo et al., SL-Note-2002-036 (2002).
[8] F. Zimmermann et al., Proc. Chamonix XII (2003).
[9] E. Benedetto et al., these proceedings.
[10] M.J. Jimenez, et al., Proc. Chamonix XII, 2003.
[11] C. Benvenuti, M. Hauer, ISR-VA/CB/sm (1976).
[12] A. Rossi et al., Proc. ECLOUD'02, CERN, Geneva, April 15-18, CERN-2002-001 (2002).
[13] G. Rumolo et al., SL-Note-2002-016 (AP) (2002).
[14] S. Heifets, Proc. ECLOUD'02, CERN, Geneva, April 15-18, CERN-2002-001 (2002).
[15] I. Collins, R. Cimino, private communication (2003).
[16] L. Evans, "Beam Physics at LHC," these proceedings.
[17] V. Baglin, B. Jenninger, CERN Mini-Workshop *http://sl.-web.cern.ch/SL/sli/Scrubbing-2002/Workshop.htm* (2002).

ANALYSIS OF THE B2 CORRECTION IN THE TEVATRON

P. Bauer†, G. Annala, J. DiMarco, R. Hanft, D. Harding, M. Lamm, M. Martens, P. Schlabach, D. Still, M. Tartaglia, J. Tompkins, G. Velev, M. Xiao, FNAL, Batavia, IL, USA
L. Bottura, F. Zimmermann, CERN, Geneva, Switzerland

Abstract

Beam loss and emittance dilution during ramping from injection to collision energy is observed in the Tevatron, now in its collider run-II stage. It is well known that the sextupole (*b2*) components in the superconducting dipole magnets decay during the injection plateau and snap back rapidly at the start of the ramp. These so called dynamic effects, which were originally discovered in the Tevatron, are compensated with the chromaticity correctors, distributed around the ring. Imperfect control of the chromaticity during injection and snapback can contribute to the beam loss. Therefore a thorough investigation of the *b2* compensation in the Tevatron was launched, including beam chromaticity measurements and offline magnetic measurements on Tevatron dipoles. This paper reports the status of this investigation. A companion paper describes in detail the results of the magnet measurements [1]. This work was partly conducted as a collaboration between FNAL and CERN.

1 TEVATRON B2 COMPENSATION

Sextupole, *b2*, (and other) magnetic components are present in the 774 Tevatron dipole magnets at a level of several units of 10^{-4} of the main field. This is a well known feature of accelerator magnets. In fact, one differentiates between geometric, hysteretic and dynamic *b2* contributions. The simple, compact ends of the Tevatron dipoles have a strong negative *b2*, which is compensated by a built-in, positive *b2* of ~14 units in the body section, such as to give zero average geometric *b2* [2]. The hysteretic *b2* loop evolves around the geometric *b2*. The loop shape is more or less invariant (depending only weakly on magnet temperature and ramp-rate). During constant excitation such as at injection the *b2* drifts and snaps back rapidly whenever the ramp starts. These dynamic effects in superconducting magnets are the result of (slowly) changing current distributions among the superconducting strands forming the Rutherford cable from which the coils are wound. These changing current distributions cause local magnetic field changes that in turn cause changes in the magnetization response of the superconductor. The current imbalances within the cable also affect the bore field directly, producing a sinusoidal field pattern along the magnet, with the cable twist pitch as period. This, however, is believed to be irrelevant to the beam, because the cable pitch is short (~6.4cm).

*Supported by the Universities Research Association, Inc., under contract DE-AC02-76CH03000 with the U.S. Department of Energy
†pbauer@fnal.gov

The chromaticity (ξ) correctors in the Tevatron compensate for all of the above effects as well as the natural chromaticity of the ring and provide a chosen ξ set-point (~8-20 units). They are placed next to the arc quadrupoles, therefore referred to as defocusing (SD) or focusing (SF). According to recent measurements 1 unit of *b2*, left uncompensated, produces 26.22/-23.92 units of horiz./vert. chromaticity, ξ_x/ξ_y [3]. The dynamic *b2* compensation has been fine-tuned over many years. It retained, however, the characteristic logarithmic time dependence of the drift amplitude during the injection porch, (1), where the offset and slope depend on the pre-cycle parameters (the time on the back-porch, t_{BP}, and the flat-top, t_{FT}). The beam-less pre-cycle is necessary to homogenize the ramping history of all magnets and hence bring the machine into a reproducible state that allows to use (1). A schematic of the pre-cycle is shown in Fig. 1.

$$b_2^{drift}(t,t_{FT},t_{BP}) = b_{2,ini}(t_{FT},t_{BP}) + m(t_{FT},t_{BP})\ln(t) \quad (1)$$

The *b2* drift amplitude increases with shorter pre-cycle back-porch and longer pre-cycle flat-top. Further details regarding the trends of the *b2* drift parameters with the pre-cycle conditions can be found in [1]. During the first seconds of the ramp, the snapback occurs, which, on the basis of magnetic measurements performed in 1996, [4], is calculated for the Tevatron *b2* algorithm with (2),

$$b_2^{SB}(t) = b_2^{drift}(t_{IP},t_{FT},t_{BP})\left(1-\left(\frac{t}{t_0}\right)^2\right)^2 \quad (2)$$

where b_2^{drift} is computed with (1) for $t=t_{IP}$, the injection porch duration and t_0, the snapback duration (now 6 sec). Note that the dynamic *b2* correction in the Tevatron plays out on top of that for the geometric and hysteretic *b2* components. It is therefore customary to present the *b2* drift and snapback without the other contributions. This implies the removal of the small (~0.1 unit) change of hysteretic *b2* during the snapback phase (150-156 GeV).

2 MEASUREMENTS ON MAGNETS

Fig. 1 shows recent rotating coil measurements at Fermilab's Magnet Test Facility of the *b2* in the body of several Tevatron dipoles as a function of beam energy (transfer function: 980 GeV = 4332.57 A = 4.306 T). The measurements were taken after the same pre-cycle as for a usual Tevatron shot setup (t_{FT}=*20 min* "dry-squeeze" ,

0-7803-7738-9/03/$17.00 © 2003 IEEE

t_{BP}=*1 min*, see insert in Fig. 1). The dynamic effects during the injection and back-porch plateaus are clearly visible (and they are shown more explicitly in Fig. 2). To be representative of the Tevatron the geometric *b2* for each magnet shown in Fig. 1 was removed and replaced by the average geometric *b2* of all Tevatron dipoles, as derived from the archived measurements performed during magnet production [5]. The average *b2* of all Tevatron dipoles installed, according to the archive data was calculated to be 1.47 units. Fig. 1 also shows the average hysteretic *b2* for all magnets installed as derived from the magnetic measurement archive. Note, however, that the measurements at production were performed only at 0.66/150, 2/452 and 4/905 kA/GeV, after stopping of the ramp. This resulted in an unknown amount of *b2* drift such that the archive data are expected to underestimate the width of the *b2* loop, especially at injection (150 GeV). The *b2* data in Fig. 1,2 were corrected, where needed, for temperature such as to be representative of the 4 K average Tevatron magnet temperature. The temperature correction consisted in removing the geometric and scaling the entire loop with an experimentally derived scaling factor (~-15%/°K, [1]).

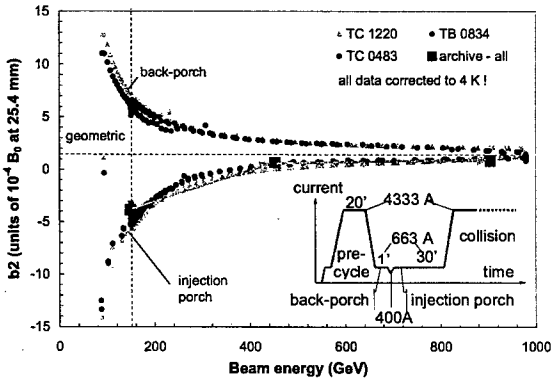


Figure 1: b2 loops measured in Tevatron dipoles and average b2 loop as expected from archive data.

Fig. 2 contains the same data as Fig. 1, except that it shows the *b2* drift during a 30 min injection porch, followed by the snapback together with the Tevatron *b2* fit (equations 1,2). In one case the measurement was obtained with Hall-probes, which were introduced through the other end of the magnet. The Hall-probe array, which reads data at 10 Hz, was supplied by CERN. All snapback data were baseline corrected, i.e. the geometric and hysteretic *b2* were removed from the data such as to show the pure snapback.

It is important to note that both Fig. 1 and Fig. 2 show a significant magnet-to-magnet spread in the *b2* characteristics. Magnetic measurement data from a small number of magnets are therefore not representative of the accelerator. A separate study of the *b2* using beam based methods is required to obtain the average *b2* characteristics of the machine. Such measurements will be discussed next. Fig. 2 indicates, however, that the snapback fit used in the Tevatron appears to underestimate

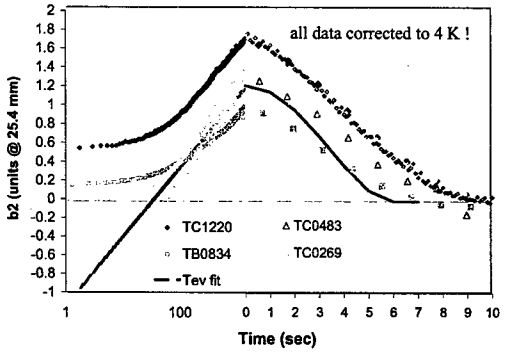


Figure 2: b2 drift and snapback measured in Tevatron dipoles after a standard pre-cycle. Note that the time for the drift data is on a log scale. For TC1220 both rotating coil and Hall probe snapback data are shown.

the duration of the snapback. As discussed in [1] a Gaussian would fit better. The discrepancy of magnet data and the logarithmic fit at the start of the drift, however, is irrelevant for accelerator operation (and can easily be adjusted by shifting the time scale in the ln-function).

3 BEAM BASED MEASUREMENTS

The following describes beam based chromaticity measurements performed recently, not only during the injection porch, but also during the ramp [3]. The derivation of the average magnet *b2* from the beam chromaticity assumes that the measured chromaticity (ξ_{meas}) is given as the sum of the natural chromaticity (ξ_{nat}), the *b2* in the dipole magnets (ξ_{b2mag}) and the (compensating) *b2* supplied by the sextupole correctors (ξ_{b2corr}) as in (3).

$$\xi_{tot,i} = \xi_{meas,i} = \xi_{nat,i} + \xi_{b2mag,i} + \xi_{b2corr,i} \quad i = x, y \qquad (3)$$

The natural chromaticity was calculated with a MAD Tevatron lattice model (-29 units). The *b2* corrector currents were converted to *b2* with: 1 unit of *b2* = ~-0.496 / -0.765 A in the SF / SD correctors [3]. The chromaticity measurements were performed with an un-coalesced proton beam on the center orbit. The Tevatron was prepared with a standard pre-cycle (20 min flat-top, 1 min back-porch). After injecting the beam, tunes were measured as a function of time during the injection porch as well as up the ramp with the Schottky pick-up. A sec-time resolution was obtained using a fast buffer digital oscilloscope in the time capture mode. This measurement (including the beam-less pre-cycle) was performed for different RF frequency settings (Δf=-20, 0, +20 Hz from nominal). The derivative of the tunes as a function of RF frequency gives the instantaneous chromaticity. Therefore each measurement required three Tevatron cycles (including the pre-ramp).

Fig. 3 shows the results of different chromaticity measurements performed during the ramp to collision. Note that the first part of the beam derived *b2*-curve is the

snapback, which is shown again in Fig. 4 in the case of the Dec 4th data. The drift amplitude in the Sept 18th case is larger, presumably due to a longer dwell at injection (this parameter was not recorded in this measurement). The average hysteretic up-branch as derived from the Tevatron magnetic measurement archive (such as in Fig 1) is shown also. The brackets ascribed to each point represent the σ of the width-distribution of the *b2* loops of all dipoles installed. One can see that the average magnet *b2* predicted on the basis of the ξ measurement is close to the expected. Also note that the measurement performed on Sept 18th did not use the oscilloscope time capture mode to record the tune data, but the tunes were read from the oscilloscope display, therefore introducing a larger error (estimated at ± 0.5 *b2* units).

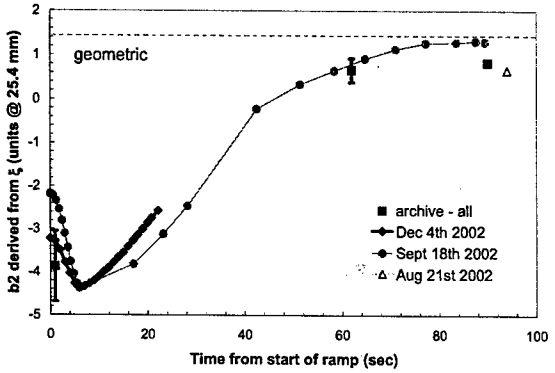


Figure 3: *b2* up the ramp as derived from beam chromaticity measurements and expected average of all magnets installed derived from magnetic measurement archive (brackets represent σ of loop width distribution).

Fig. 4 shows the *b2* snapback measured during one of the beam studies presented in Fig. 3, for 2 different injection porch (IP) durations (20, 120 min). As with the magnet data the hysteretic and geometric *b2* were removed from the data by extrapolation of the 160 and 200 GeV data to the lower energy snapback phase. These tests were performed to see the effect of different drift amplitudes on the Tevatron *b2* compensation (in the 120 min IP case the *b2* drifts 25% more than in the 20 min case). A correlation between drift amplitude and the field (current, beam energy) at which the snapback is complete is expected on the basis of the existing dynamic effect models and was observed in the LHC dipoles. In fact this correlation allows for a novel approach in b2 compensation, which consists of predicting the snapback on the basis of *b2* measurements just before ramping. Fig. 4 indeed shows that the snapback takes slightly longer in the 120 min IP case. The difference is not as distinct as the difference in drift amplitude because the parabolic current ramp time-compresses the end of the snapback. A plot of the snapback in terms of magnet current reveals that the 120 min IP case takes 25% more current to snap back [5]. The two curves in Fig. 4 also show a difference between the fit and the data for the drift amplitude.

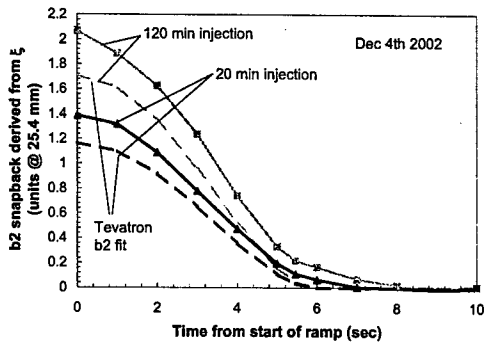


Figure 4: b2 snapback derived from chromaticity measurements after a 20 min and a 120 min IP. Dashed lines: Tevatron b2 compensation algorithm (equation 1,2).

4 SUMMARY AND OUTLOOK

The comparison of magnetic measurements on some Tevatron dipoles, the expected average Tevatron magnet characteristics derived from the magnetic measurement archive and beam based *b2* measurements have so far shown that the current Tevatron *b2* compensation works reasonably well in what refers to the geometric and hysteretic *b2* components. There is, however, experimental evidence suggesting that the dynamic *b2* compensation can be improved. In particular magnet measurements indicate that the *b2* snapback is better described by a Gaussian function than the polynomial that is currently in use and that today's fit under-estimates the snapback duration. It is hoped that the implementation of an improved functional form of the *b2* compensation will reduce emittance growth and beam loss. The measurements also confirmed that the *b2* drift amplitude and the snapback time are correlated as observed in LHC dipoles. This allows for a novel *b2* compensation scheme, which was actually proposed for the LHC, and which uses on-line chromaticity measurements during injection to predict the snapback. Such an approach could also be of interest for the Tevatron, making use of the recently developed head-tail chromaticity monitors, [6].

5 ACKNOWLEDGMENTS

The continued encouragement and support of R. Kephart, V. Shiltsev and V. Lebedev is gratefully acknowledged.

6 REFERENCES

[1] G. Velev et al., WPAE016, this conference
[2] P. Bauer et al., Fermilab, Technical Division, Internal Note TD-02-040, Jan. 2003
[3] M. Martens et al., Fermilab, Beams Division Internal Note Beams Doc-478, March 2003
[4] G. Annala et al., http://www-bdnew.fnal.gov/tevatron/adcon/magnets.html
[5] P. Bauer et al., Fermilab, Technical Division Internal Note TD-03-008, March 2003
[6] P. Ivanov et al., RPPB021, this conference

Proceedings of the 2003 Particle Accelerator Conference

BEAM LOSS AND BACKGROUNDS IN THE CDF AND DØ DETECTORS DUE TO NUCLEAR ELASTIC BEAM-GAS SCATTERING

A.I. Drozhdin, V.A. Lebedev, N.V. Mokhov, L.Y. Nicolas, S.I. Striganov, A.V. Tollestrup
* FNAL, Batavia, IL 60510, USA

Abstract

Detailed simulations were performed on beam loss rates in the vicinity of the Tevatron Collider detectors due to beam-gas nuclear elastic interactions. It turns out that this component can drive the accelerator-related background rates in the CDF and DØ detectors, exceeding those due to outscattering from collimation system, inelastic beam-gas interactions and other processes [1, 2]. Results of realistic simulations with the STRUCT and MARS codes are presented for the interaction region components and the CDF and DØ detectors. It is shown that a steel mask placed upstream of the detectors can reduce the background rates by almost an order of magnitude.

INTRODUCTION

Even in good operational conditions in an accelerator, some particles leave the beam core producing a beam halo. This happens because of beam-gas interactions, intra-beam scattering, proton-antiproton collisions in the interaction regions (IP), and particle diffusion due to RF noise, ground motion and resonances excited by the accelerator magnet nonlinearities and power supplies ripple. As a result of halo interactions with limiting apertures, hadronic and electromagnetic showers are induced in accelerator and detector components causing excessive backgrounds in the detectors. A two-stage collimation system has been developed for the Tevatron Run II [3] to reduce uncontrolled beam losses in the machine to an allowable level. About 0.1% of primary particles hitting the collimators are scattered back into the beam pipe causing collimation system inefficiency. These particles are lost mostly in the high β regions producing the CDF and DØ detectors backgrounds.

The main process of beam-gas interaction, a multiple Coulomb scattering, results in slow diffusion of particles from the beam core causing emittance growth. These particles increase their betatron amplitudes gradually during many turns and are intercepted by collimators. Nuclear elastic beam-gas scattering may increase particle betatron amplitude at one interaction to an amount which exceeds the Tevatron aperture. Many of these particles are lost in the accelerator before they reach collimators located at $5 - 6\sigma_{x,y}$. It turns out that 25% of them are lost in the vicinity of the IPs adding to the detector background.

A multi-turn particle tracking through the accelerator with elastic beam scattering on the residual gas and halo interactions with the collimators is conducted with the STRUCT code [4]. All the accelerator components with their real strengths and aperture restrictions are taken into account. Using the beam loss distributions calculated this way in the vicinity of the Tevatron's IPs, detailed hadronic and electromagnetic shower simulations with the MARS14 code [5] are performed in the machine, detector and tunnel components. It is found that short steel collimators/masks in the IPs would substantially reduce detector backgrounds induced by nuclear elastic beam-gas scattering.

* drozhdin@fnal.gov

PROTON-NUCLEUS ELASTIC SCATTERING

The products of inelastic interactions of the beam with residual gas nuclei are lost within tens of meters after such interactions. At the same time, scattering angles in nuclear elastic beam-gas interactions are small enough for protons to travel much larger distances in the accelerator and – if not intercepted by collimators – resulting in their loss on limiting apertures. A differential cross section of proton-nucleus (pA) elastic scattering can be parameterized as

$$d\sigma/dq^2 = \sigma_{el} B_{el} e^{-B_{el} q^2} + \sigma_{qel} B_{qel} e^{-B_{qel} q^2}, \quad (1)$$

where $q = p\theta$, p is a proton momentum, θ is a scattering angle, σ_{el} and B_{el} are a total cross section and slope of the coherent pA elastic scattering from the nucleus as a whole, σ_{qel} and B_{qel} are a total cross section and slope of the incoherent pA elastic scattering (scattering which excites or breaks up the nucleus). Total cross sections of these processes are calculated using the Glauber model with inelastic corrections. For a 1-TeV proton on nitrogen, σ_{el} = 115 mb and σ_{qel} = 25 mb. The slope of the coherent scattering is almost independent of energy and can be taken from [6] as $B_{el} = 12.85 * A^{2/3}$ GeV^{-2}. The slope of the incoherent scattering is the same as in the pp elastic scattering: $B_{qel} = 11.0$ GeV^{-2} at 1 TeV. Differential cross section of proton-nitrogen elastic scattering at 1 TeV is shown in Fig. 1 (top) along with a Coulomb scattering contribution calculated from the Rutherford cross section with a Gaussian nuclear form-factor. Note that a total macroscopic cross section of the later process is 8478 cm^2/g, i.e. about 100 times larger than the corresponding elastic cross section. The quality of this formalism is demonstrated in Fig. 1 (bottom) where one can see a good agreement with data [6]. Using the above formulae, one can calculate a probability for proton to scatter elastically on nitrogen to an angle larger than θ_{min} due to strong interactions

$$W_{\theta \geq \theta_{min}} = 0.0011(e^{-11.0 q^2_{min}} + 4.6\, e^{-74.5 q^2_{min}}) \cdot \rho t, \quad (2)$$

0-7803-7738-9/03/$17.00 © 2003 IEEE

where $q^2_{min} = (p\theta_{min})^2$, p is a proton momentum (GeV/c), θ is a scattering angle (radian), ρ and t are a density (g/cm^3) and thickness (cm) of a nitrogen target. Formula (1) was implemented into the STRUCT code for studies of beam-nitrogen elastic scattering described in the rest of this paper with gas pressure given in a nitrogen equivalent.

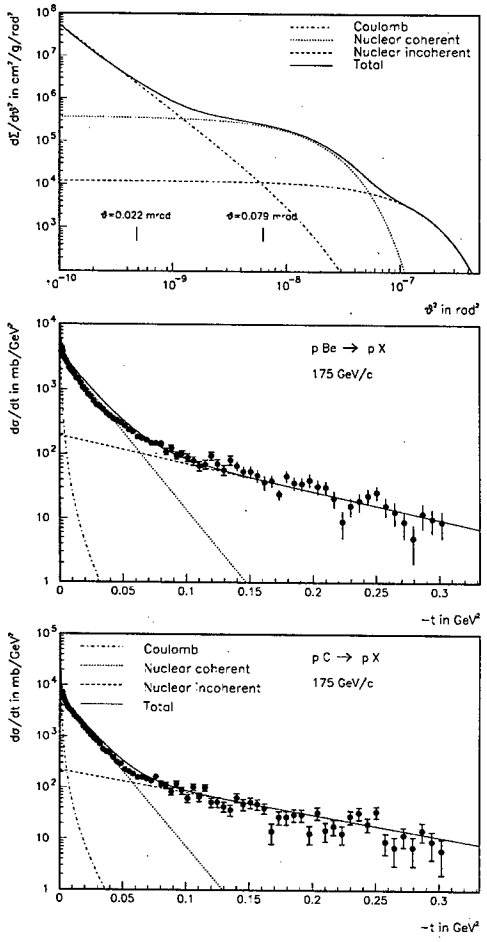


Figure 1: Components of the proton-nitrogen elastic differential cross section at 1 TeV (top) and comparison to experimental data [6] at 175 GeV/c (middle and bottom).

The simulations show that the beam loss rate in the detector regions depends linearly on the gas pressure. Beam loss rate upstream of DØ and BØ as a function of an average gas pressure is shown in Fig. 2. A nuclear elastic beam-gas scattering at a gas pressure $\geq 2\times 10^{-10}$ torr exceeds the beam loss in the IPs created by tails from the main collimators. Most of the particles are lost in the separators and in the three dipoles preceding the IPs.

Fig. 3 shows the measured [7] residual gas pressure distribution in the Tevatron Run II along with a calculated beam loss distribution in the ring.

We found that a shadow collimator placed at $13\sigma_x$ ($\pm$11 mm) and $20\sigma_y$ ($\pm$6.3 mm) immediately upstream of the last three dipoles preceding the IPs would allow to suppress the

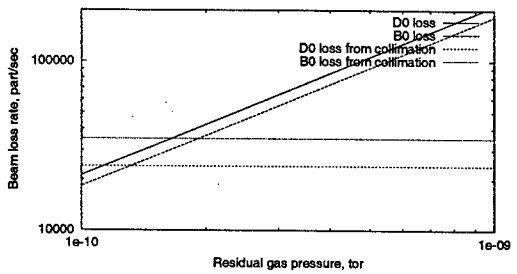


Figure 2: Beam loss rate upstream of DØ and BØ as a function of an average gas pressure. Also shown are beam losses upstream of DØ and BØ originated by the collimation system.

beam-gas induced particle loss in the IPs by an order of magnitude. Details of beam loss distribution in the DØ and BØ regions are shown in Fig. 4 with and without shadow collimator.

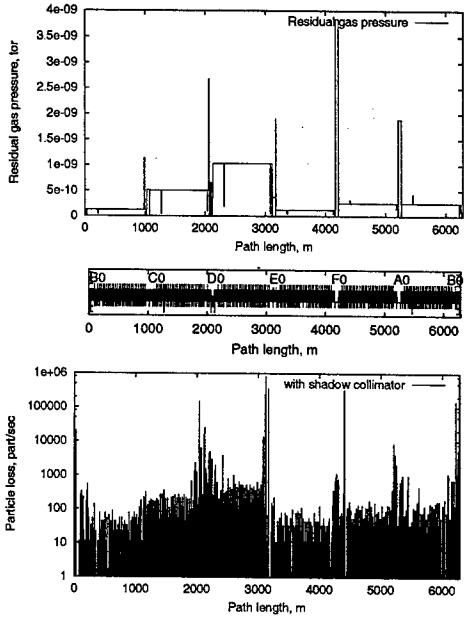


Figure 3: Measured residual gas pressure (top) and beam loss distribution in the Tevatron ring from nuclear elastic beam-gas scattering (bottom).

BEAM LOSS PARTITION

Beam loss rates in the DØ and BØ regions due to nuclear elastic beam-gas scattering and large angle Coulomb scattering – both at the average gas pressure in the ring of 10^{-9} torr – are presented in Table 1 in comparison with those due to elastic $p\bar{p}$ interactions at the two IPs. As shown in Fig. 1 (top), at angles responsible for beam loss in the interaction regions ($\theta \geq 0.079$ mrad), the nuclear elastic scattering cross sections are more than an order of magnitude larger than the Coulomb scattering cross section. As a result, the beam loss rates originated directly from the beam-gas Coulomb scattering and elastic $p\bar{p}$ interactions are two orders of magnitude less compared to the coherent

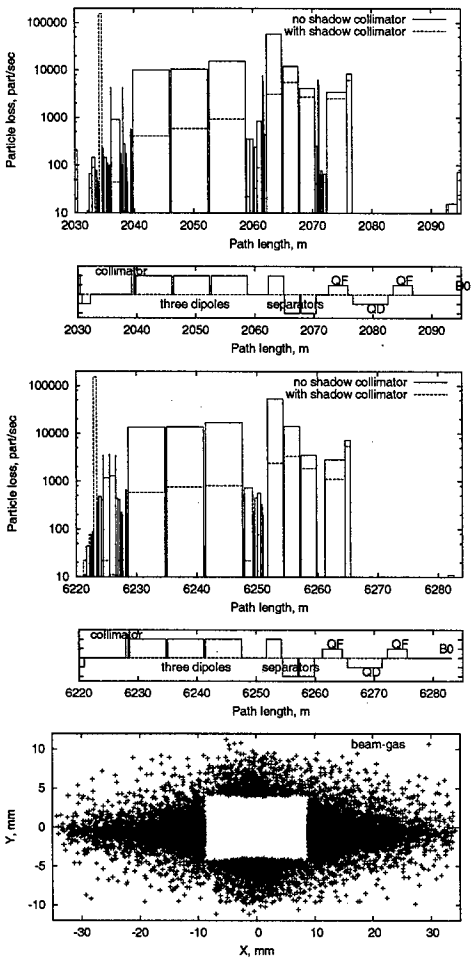


Figure 4: Beam-gas induced loss distributions in the DØ (top) and BØ (middle) regions with and without shadow collimator, and proton hits at the shadow collimator (bottom).

and incoherent beam-gas nuclear scattering.

Table 1: Beam loss rates upstream of DØ and BØ for three sources of particle scattering.

Source	Beam loss rate, s^{-1}	
	DØ	BØ
Nuclear elastic beam-gas	2.04×10^{5}	1.87×10^{5}
Large angle Coulomb beam-gas	2.72×10^{3}	1.40×10^{3}
Elastic $p\bar{p}$ at two IPs	1.44×10^{3}	1.05×10^{3}

BACKGROUNDS IN CDF AND DØ

Fig. 5 (top) shows MARS-calculated charged particle flux in the CDF beam halo monitor (BHM) with and without collimator. The calculations were done with an average pressure of 10^{-10} torr. One sees that the collimator reduces the rates up to one order of magnitude.

The shielding efficiency of a shadow collimator for representative CDF subdetectors is shown in Fig. 5 (bottom) as a function of a distance from the IP for elastic beam-gas scattering as a source. One sees that such a mask reduces

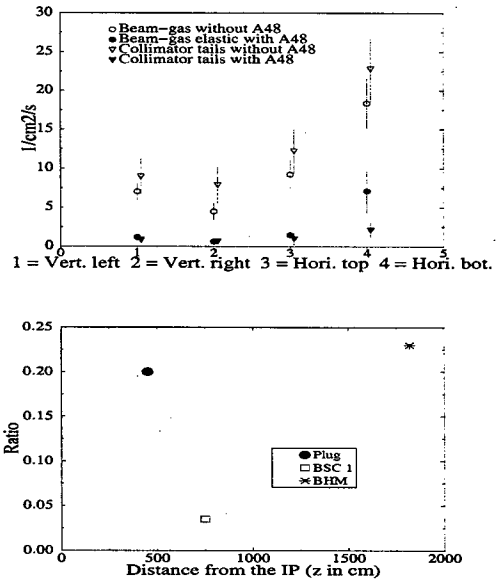


Figure 5: CDF BHM hit rate (top) and the main detector absorbed dose ratio with/without shadow collimator as a function of a distance from the IP (bottom).

the backgrounds in the main detector by a factor of 4.5 to 25. The Beam Shower Counters (BSC) are about a few centimeters to the beam pipe, whereas BHM is at 0.6 m and Plug at 1 m from the beam axis.

CONCLUSIONS

A nuclear elastic beam-gas scattering in the Tevatron generates beam loss in the interaction regions not intercepted by the main collimation system designed for cleaning of slow growing beam halo. This beam loss – and additional background in the DØ and CDF detectors – is proportional to the residual gas pressure. These backgrounds are comparable at an average gas pressure in the machine of about 2×10^{-10} torr to the backgrounds due to tails from the collimation system. A proposed shadow collimators placed in a small phase advance upstream of the last three dipoles preceding the IPs would suppress the beam loss and corresponding backgrounds in the main detectors caused by beam-gas interactions by an order of magnitude.

REFERENCES

[1] A.I. Drozhdin et al. FERMILAB-FN-734, April 2003.

[2] L.Y. Nicolas et al. DØ-Note-4129, CDF-Note-6407 (2003).

[3] M.D. Church et al. Fermilab-Conf-99/059 (1999).

[4] A.I. Drozhdin et al. "STRUCT Program User's Reference Manual", http://www-ap.fnal.gov/~drozhdin/

[5] N.V. Mokhov, "The MARS Code System User's Guide", Fermilab-FN-628 (1995); Fermilab-Conf-00/181 (2000); http://www-ap.fnal.gov/MARS/.

[6] A. Schiz et al. *Phys. Rev.*, **D21**, 3010 (1980).

[7] B. Hanna, Residual Gas Pressure Measurements, Aug.02.

SLIP STACKING EXPERIMENTS AT FERMILAB MAIN INJECTOR

K. Koba, T. Berenc, B. Barnes, B. Chase, I. Kourbanis, J. MacLachlan, K. Meisner, J. Steimel
FNAL, Batavia, IL 60510, USA

Abstract

In order to achieve an increase in proton intensity, Fermilab Main Injector will use a stacking process called "slip stacking"[1]. The intensity will be doubled by injecting one train of bunches at a slightly lower energy, another at a slightly higher energy, then bringing them together for the final capture. Beam studies have started for this process and we have already verified that, at least for a low beam intensity, the stacking procedure works as expected[2][3][4]. For high intensity operation, development work of the feedback and feedforward systems is under way[5][6][7].

INTRODUCTION

The Fermilab Main Injector (MI) accelerates protons and extracts them to a target to produce antiprotons. In the operation cycle for the antiproton production, 84 bunches are injected from Booster to MI. Bunches are accelerated from 8GeV to 120GeV and extracted to hit the production target. The total beam intensity is $4.5*10^{12}$ particles per pulse (ppp) with a cycle of 1.5 sec. The Main Injector parameters are listed in Table 1.

Run IIb will follow Run IIa and has a luminosity goal $4.1*10^{32}$ $cm^{-2}sec^{-1}$ requiring $9.634*10^{12}$ total antiprotons in the Tevatron. In order to achieve this goal, we need $9.0*10^{12}$ protons in 84 bunches in the Main Injector for antiproton production. Higher proton intensities are required to get more antiprotons and higher stacking rates in the accumulator. In order to achieve this, we are planning to use a scheme called "slip stacking". With slip stacking, the intensity of the bunches can be doubled by injecting one bunch train at slightly lower energy, another train at slightly higher energy and bringing them together.

Beam studies of the slip stacking process have started and we have already established that the stacking procedure works as expected.

Table 1: Main Injector parameters on stacking cycle

RF frequency @ injection	52.811400Hz
Proton energy @ injection	8GeV
Proton energy @ extraction	120GeV
Harmonic number	588
Transition gamma	21.6
Mean radius	528.3m

* Work supported by the Universities Research Assoc., Inc., under contract DE-AC02-76CH03000 with the U.S. Dept. of Energy.

RF PARAMETERS

For slip stacking, we use three different radio frequency (RF) systems and follow four steps. Step 1: The first bunch train is injected from the Booster on the central orbit and captured by the first RF system. To make a room for the second bunch train, the first bunch train is then decelerated until it circulates on the inside of the central orbit. Step 2: The second bunch train is injected on the central orbit and captured by the second RF system. Step 3: As the two bunch trains have slightly different energies, they can move relative to each other. Both bunch trains are accelerated till they are separated by the same amount from the central energy. Step 4: When the two bunch trains coincide at the same longitudinal location, they are captured by the third RF system.

Since two bunch trains have different energies, MI must have an enough momentum aperture to accept both. The momentum aperture of MI is +/-0.7% at injection, corresponding to the frequency separation of +/-3000Hz from the central value of 52.8114MHz.

MI cavities and Injection Matching

MI has eighteen 53MHz cavities. These are separated into the two groups, each with 9 cavities. Low level RF (LLRF) signals go to two groups of cavities individually. For the slip stacking, we are using one out of 9 cavities in each group at injection. The RF voltage at injection is adjusted so that one cavity produces 62 kV in order to achieve a low momentum spread.

At extraction, the Booster RF voltage is 380kV, which matches to a MI injection voltage of 1MV for normal operation. Since the MI injection RF voltage is 62 kV for the slip stacking, a bunch rotation is carried out in Booster before extraction so that the bunch shape will be matched to the RF bucket of MI at injection. As the Booster RF voltage is rapidly reduced, the bunch starts to rotate in the phase space. After a quarter of synchrotron period, the bunch is injected into MI.

Frequency Curve

The frequency as a function of time is shown in Figure 1 for the first and the second RF systems. The frequency separation was kept at 1200Hz which is enough to keep the bunch shape unchanged.

The first bunch train was injected on the central orbit with nominal frequency at 0.13msec and captured by the first RF system of 62kV. At this time, the frequency of the second RF system was 1200Hz higher than the first RF system. The first bunch was then decelerated to a frequency 1200Hz lower than the original value. After

0-7803-7738-9/03/$17.00 © 2003 IEEE

one Booster cycle of 66.7msec, the second train was injected on the central orbit and captured by the second RF system. After slipping, both bunch trains were captured by all 18 cavities with 800kV and 0 frequency separation.

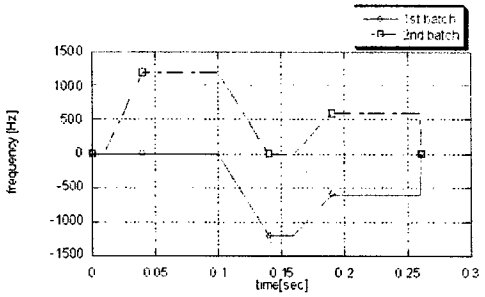


Figure 1: Frequency for first bunch train and second bunch train as a function of time.

PREVIOUS BEAM STUDY

Two bunch trains, each with 82 bunches, were injected into MI. The total intensity for two trains was low, $0.8*10^{12}$ppp, in order to reduce beam loading effects.

Figure 2, a mountain range picture of the signals from the wall current monitor (WCM), reveals the progress of slip stacking from the beginning to the end. The WCM had a resolution of 0.5ns/sample. The data were obtained every 1.42ms for 0.18s. There was no beam loss during the slip stacking process.

The length of the first bunch of the first bunch train shown in Fig. 2 was used to calculate the emittance. Figure 3 shows the calculated 95% emittance during 0.18s. Since there was an empty space between upper and lower bunches, there should be an emittance growth. The emittance growth expected from simulation is a factor of 3.2. From the plot, we see that there is no emittance growth before the two batches are recaptured by one RF bucket but there is a factor of 4.0 emittance growth after the recapture.

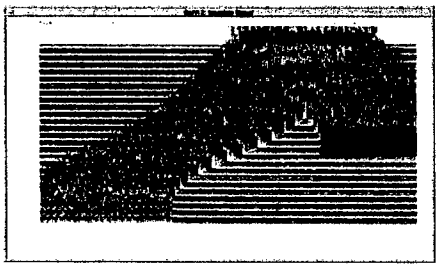


Figure 2: Mt range plot. The signal came from WCM with a resolution of 0.5ns/sample. The data were obtained every 1.42ms for 0.18s.

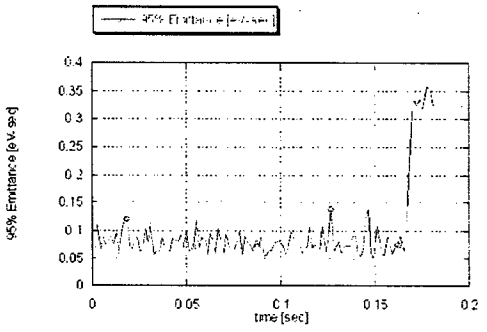


Figure 3: The 95% emittance calculated by bunch length shown in Fig.2.

SLIP STACKING PHASE VARIATION

Frequency curves (Fig.1) applied to the beam are calculated assuming that, at the time of recapture, two bunch trains are sitting exactly on the same longitudinal location, that is, two cavities are in phase. However, MI slip stacking studies revealed cycle to cycle variation in the RF system phase slip. This produced an unreliable RF voltage for recapture.

The largest phase variation was traced to timing jitter on the 720Hz line locked Tevatron Clock event. A MI LLRF system Digital Signal Processor (DSP) generates the frequency curves from user tuned tables. The frequency curves are a function of time and are integrated by the DSP to apply phase modulation to the RF systems that slip the bunch trains. The DSP processes run at 720Hz, 23*720Hz, and 138*720Hz via a scheduler that is synchronized with the Tevatron Clock event by a phase lock loop (PLL). As the PLL input jitters and the DSP follows the jitter, the frequency curves output and its integral (RF phase) varies.

The RF phase variation was reduced to 0° by changing the frequency curve generation from the Tevatron Clock time base to accurate LLRF internal time.

SIMULATION FOR RECAPTURE

To understand what caused the emittance growth at recapture, simulation studies were carried out using the code ESME[8]. In the simulation studies, the time and voltage to recapture bunches were varied to match the observed RF phase variation.

The delay was changed from 0 to 250 μsec causing a +/-60 degrees phase variation and the 95% bunch length after 15msec was measured. The emittance plotted in Fig. 4 was estimated from the bunch length. It increased by a factor of 3.2 to 7.0 with increasing delay. Since the RF phase variation produced errors as large as 45 degrees, it could cause the emittance growth.

The recapture voltage was changed from 0.5 to 1.0MV because the voltage is changing from 0.8 to 1.0MV after the time to recapture. The 95% emittance plotted in Fig. 5 shows the emittance growth by a factor of 3.2 to 3.6.

By the two simulation studies, it was verified that the emittance growth was mainly due to the RF phase variation produced by the time error of Tevatron Clock event.

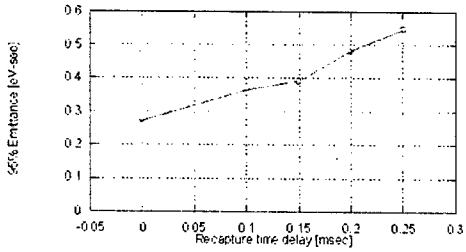


Figure 4: The estimated 95% emittance vs. recapture delay time.

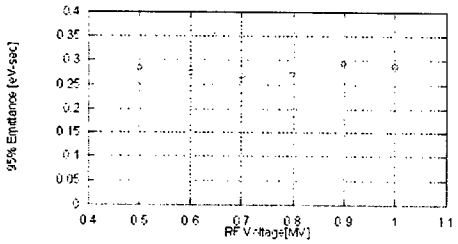


Figure 5: The estimated 95% emittance vs. recapture RF voltage.

BEAM STUDY

Previous beam studies have reported that there is an emittance growth when two bunch trains are recaptured. Simulation studies have indicated that the emittance growth is caused by variation in the final RF system phase. The phase variation was eliminated and the 95% longitudinal emittance was measured again. A factor of 3.2 in the observed emittance growth is the same as simulation results and there is no unexpected emittance growth during slip stacking.

ACCELERATION

Acceleration was also tried. Figure 6 shows the beam intensity during beam acceleration. Approximately $1.0*10^{12}$ total particles were injected, slip stacked and accelerated to 120GeV. There was a beam loss of ~2% at the beginning of acceleration.

The emittance at 120GeV was measured. The observed value of 0.24eV-sec is less than the one we currently have in the normal operation cycle.

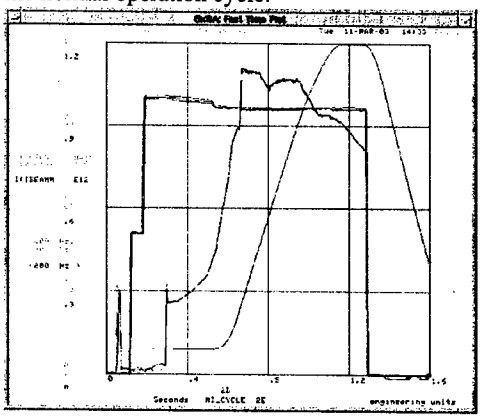


Figure 6: RFSUML: RF voltage[MV], MMNTUM: momentum[GeV/c], IBEMM: total beam intensity [E12 ppp]

CONCLUSION

Beam studies have stared for the slip stacking process, and we have already verified that, at least for low beam intensity, the stacking procedure works as expected.

There was no beam loss during the process, but there was emittance growth when two bunch trains were recaptured. Simulation studies have indicated that the emittance growth is caused by RF phase variation.

The RF phase variation was eliminated and the emittance was measured again. No undesirable emittance blow up has been observed.

Beam has been accelerated to 120GeV with a beam loss of ~2% at the beginning of acceleration.

For higher intensity operation, development of the feedback and feedforward system is under way.

REFERENCES

[1] J. A. MacLachlan, "The Beam Dynamics of Slip Stacking", Fermilab FN-0711, November 2001.

[2] K. Koba, "Slip Stacking," ICFA2002, April 2002.

[3] K. Koba," Emittance measurement and acceleration – Revision of MI-0294", MI-0294

[4] K. Koba," Slip Stacking at Low Intensity – Status of the Beam Studies", MI-0296

[5] J.Dey, J. Steimel and J. Reid, "Narrowband Beam Loading Compensation in the Fermilab Main Injector Accelerating Cavities", 2001 PAC, p. 876, Chicago, June 2001.

[6] J. Dey, et al, "53 MHz Feedforward Beam Loading Compensation in the Fermilab Main Injector," PAC '03, These proceedings.

[7] J. Steimel et al," Beam Loading Compensation for Slip Stacking", PAC '03, These proceedings.

[8] J. A. MacLachlan, "Users Guide to ESME", 2000.

Proceedings of the 2003 Particle Accelerator Conference

OBSERVATIONS ON THE LUMINOSITY LIFETIMES AND EMITTANCE GROWTH RATES AT THE TEVATRON

P. Lebrun*, V. A. Lebedev, V. Shiltsev, J. Slaughter
FNAL, Batavia, IL 60510, USA

Abstract

A record luminosity of $4.2\,10^{31}$ has been reached at the Fermilab $p-\bar{p}$ collider. The lifetime of this luminosity at the beginning of the store is about 10 hours. This lifetime can be explained by the measured loss of anti-protons and protons due to collisions and emittance growths. We report on transverse emittance growth rates based on our Synchrotron Light Monitor. Longitudinal emittance growth rate measurements are based on the TeV Sampled Bunch Display data. It is shown that Intra Beam Scattering is a significant source of emittance growth rates. We comment on other possible factors for these observed emittance growth rates. Finally, we comment on future luminosity lifetimes, as we hope to further increase our peak luminosity.

INTRODUCTION & INSTRUMENTATION

The luminosity lifetime is a critical factor in reaching high integrated luminosity at any collider[1]. In this paper, we summarize the results based on various Tevatron instruments and on the various factors determining the luminosity lifetime for the $p\,\bar{p}$ Tevatron collider.

The luminosity is measured by the CDF Cerenkov Luminosity Counter(CLC)[2]. The bunch intensities are measured by the Fast Bunch Integrator (FBI) connected to a wall current monitor[3]. Although this is not the optimum way to determine the bunch intensity due to uncertainties in the measured offsets coming from the non-uniform beam structure, the precision of this device is adequate to establish the correlations shown below. The Sampled Bunch Display (SBD)[4] is used to measure the longitudinal profile of every bunch in the Tevatron ring. This device samples at 2 GHz, performs Gaussian fits and reports a measurement of the bunch length for the 2×36 bunches every 3 seconds or so. The transverse emittances are measured at the beginning of the High Energy Physics phase (e.g., when the beam collides) with the Flying Wires (FWs)[5]. These wires create background at the experiments, so we do not fly them during the stores. Instead, we use the Synchrotron Light Monitor (SL)[6], which measures the transverse beam profile in each plane without perturbing the beams. This device reports each bunch transverse size every 15 seconds. The emittances reported by FWs and the SL are reproducible with a typical rms of a few percent. However, the systematic error, or absolute scale uncertainty, is much larger (on the order of 30%), as indicated by the effective emittance measurement deduced from the luminosity counters[7]

The data is collected via the Sequenced Data Acquisition (SDA) system. The stores we consider here are from August 2002 through May 2003.

LUMINOSITY LIFETIME

The Luminosity $\mathcal{L}$ recorded by the collider detectors (CDF and D0) can be compared to the computed ones based on bunch intensities and emittances [1, 7]. For a given $p\,\bar{p}$ pair of bunches, this Luminosity is

$$\mathcal{L} = \frac{f\,N_p\,N_{\bar{p}}(6\beta_l\gamma_l)}{4\,\pi\,\beta^*\,\epsilon_{eff}}\,\mathcal{H}(\sigma_z/\beta^*)$$

where f is the revolution frequency (47.713 KHz), $N_p\,N_{\bar{p}}$ the proton and anti-proton bunch intensities, $\beta_l\gamma_l$ are the Lorentz boost factor (1,045 at 980 GeV) and β^* is the beta function at the interaction point (IP). $\mathcal{H}$ is the hourglass factor, derived from the SBD bunch length measurements. The effective emittance ϵ_{eff} is expressed in terms of the 95%, normalized beam emittances $\epsilon_p\,\epsilon_{\bar{p}}$ as

$$\epsilon_{eff} = 1/2\,\sqrt{(\epsilon_p + \epsilon_{\bar{p}})_x\,(\epsilon_p + \epsilon_{\bar{p}})_y}$$

Therefore, the normalized collision rate change vs time for a given pair of bunches (or the inverse of the luminosity lifetime) can be expressed as the following sum:

$$1/\mathcal{L}\,d\mathcal{L}/dt = 1/\lambda_a + 1/\lambda_p + 2/\sigma_a(d\sigma_a/dt)/(1.+\epsilon_p/\epsilon_a) +$$

$$2/\sigma_p(d\sigma_p/dt)/(1.+\epsilon_a/\epsilon_p) + 1/\mathcal{H}d\mathcal{H}/dt$$

where λ_a, λ_p are the anti-proton and proton bunch intensity lifetimes, respectively. σ_a and σ_p are the beam widths, averaged over both transverse planes[1].

Each of these terms can be determined from data. The proton lifetime can be much shorter than the inverse collision rate at the interaction points. The cause for such occasional short proton lifetimes is not known for certain (slightly incorrect closed orbits, betatron tunes, or nonlinear resonance whose effects are possibly amplified by beam-beam forces). For other "good stores", the proton lifetime is the smallest component in determining this luminosity lifetime: the $\bar{p}$ lifetime is typically 16 hours against $\approx>$ 100 hours for the proton beam. The emittance terms contribute to $\approx$ 25 hours for all three planes. The self-consistency of this simple derivation has been checked by comparing the measured luminosity lifetime to the sum of

[1]We assume here that the horizontal and vertical emittance are not too different from each other, which is the case.

0-7803-7738-9/03/$17.00 © 2003 IEEE

these other quantities, as shown in figure 1. Although reasonably good agreement is obtained (5 to 15%, relative, on the luminosity lifetime), the effective emittance growth rate is significantly different than the measured (SL) emittance growth rate. This is shown for a good store in figure 2.

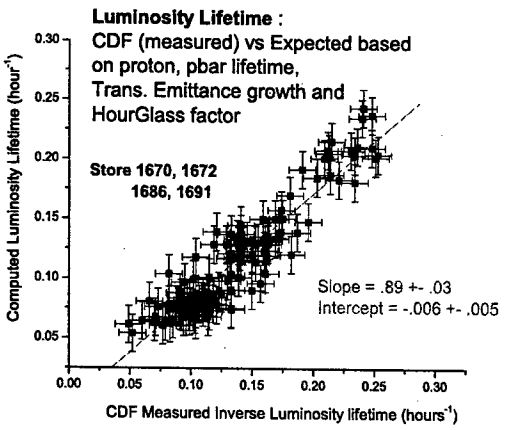


Figure 1: Correlation plot showing the predicted (based on various emittance and intensity detectors) vs measured luminosity lifetime. One data point corresponds to one $p\bar{p}$ bunch in a given store. This data was taken during August 2002. Similar results have been obtained on recent stores.

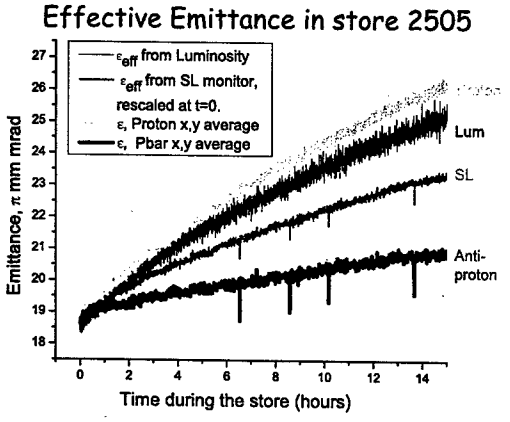


Figure 2: The effective emittance deduced from Luminosity measurement, averaged over all 36 bunches is shown as a function of time during the store. Also shown is the average proton and anti-proton emittances, reported by the SL front-end, re-scaled by a fixed factor, and the effective emittance deduced from this SL data. Data was taken May 3, 2003.

EMITTANCE GROWTH PHENOMENOLOGY

We now concentrate on the emittance growth rate factors. Such growth rate $r_\epsilon = 1/\epsilon\, d\epsilon/dt = 2r_\sigma = 2/\sigma\, d\sigma/dt$ [2] is typically a few percent per hour, in all three planes, at the beginning of the store. r_ϵ itself decays with an approximate half-life of 5 hours. Note that, to first order, these growth rates are insensitive to fixed scale factors in the bunch size measurements. Various sources of emittance growth have been considered. We list them here in order of decreasing importance, starting with the proton beam:

- Based on modeling, Intra-Beam scattering (IBS) plays a leading role. Tentative evidence from the SL and SBD data is shown in the latter part of the paper.
- Poor vacuum in the Tevatron: The un-coalesced (small longitudinal emittance bunches) proton beams have a lifetime of about 500 hours. From this and direct pressure measurements, we concluded that the beam heating from multiple scattering on residual gas is small compared to IBS predictions.
- We measured the low-level phase noise in the r.f. system and wrote a simple numerical simulation model of the longitudinal dynamics with such noise. There is satisfactory agreement between measured noise spectral density and this model, once IBS is taken into account[8]
- Other possible sources such as non-linear resonances or beam-beam effects have also been considered. However, we do not have firm quantitative results, due to the inherent complexity of such simulation. The longitudinal dampers stabilize the bunches during the stores. They do not affect such slow diffusion processes.

For the anti-proton beam, IBS is less intense because the bunch intensity is about 6 to 10 times smaller than for the proton beam. However, we strongly suspect that beam-beam effects plays a leading role[9]. In any event, the transverse emittance growth for the anti-proton beam is typically less pronounced than for the proton beam. In some cases, beam-beam effects in conjunction with a slightly wrong betatron tune causes beam losses instead of emittance growth, given the tight dynamical aperture.

We now show that these observed $r_{\epsilon(x,y,z)}$ growth rates, for the proton bunches are qualitatively and semi-quantitatively consistent with IBS predictions. The grow rates reported from now on have been measured for the first 2.5 hours of the stores, where such effects are maximized. The correlation between the horizontal and longitudinal growth rates shown on figure 3 is statistically significant, although there is a lot of fluctuation bunch to bunch and store to store. A similar correlation between the vertical and horizontal growth rates has also been observed.

[2] in absence of dispersion

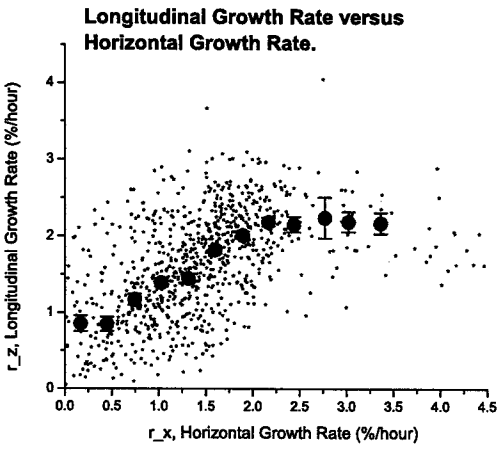


Figure 3: Correlation plot showing the longitudinal vs horizontal relative bunch size growth rates. Out of 15 stores, all but two stores showed some correlations. For each of these 13 stores, there is a probability of only a few percent that the apparent correlation is not real.

The comparison of data vs the IBS model is shown in figure 4. The correlation between predicted and measured values is statistically significant, once we reject the stores or bunches for which the proton loss rate is anomalously high compared to the expected loss due to collisions at B0 and D0. Semi-quantitative agreement is also observed in the transverse planes. In the absence of betatron coupling, IBS predicts no growth rate in the vertical plane. Since we are running with significant betatron coupling, emittance growth is indeed observed in both transverse planes. Despite the reduction of the growth rate in the horizontal plane due to this coupling effect, the IBS prediction for most of the stores are significantly above the measured values, in the horizontal and longitudinal plane. We suspect that residual beam losses could account for this discrepancy. Note also that we still have an unresolved discrepancy between the effective emittance growth rates and the measured (SL) emittance growth rates (see above) .

CONCLUSION

The Luminosity lifetime at the beginning of good stores (i.e., small unknown beam losses) is about 10 hours, and increases to 15 to 20 hours at the end of the store. This lifetime is quantitatively ($\approx$ 15%, relative) understood in terms of beam losses and emittance growth. We compared these emittance growth rates with the IBS prediction and found semi-quantitative agreement. ($\approx$ 50%). This work allows us to have a degree of confidence in the model describing various luminosity upgrade scenarios[1]. We are planning to operate the collider at a peak luminosity of 3.3 10^{32} by raising both proton and anti-proton beam in-

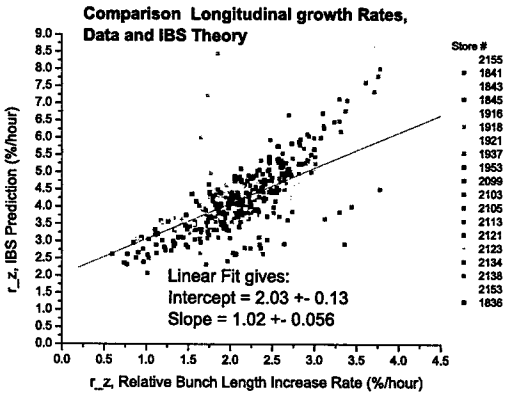


Figure 4: Correlation plot between the measured and IBIS-predicted longitudinal relative bunch size growth rates.

tensities, while preserving the current emittances. Under these circumstances, IBS is significant for both beams. The luminosity lifetime will then be $\approx$ 6 hours.

We thank Jim Patrick, Timofey Bolshakov and Kevin Cahill from the Fermilab Beam Division and Suzanne Panacek, Krzysztof Genser and Nikolai Kouropatkine from the Computing Division for their dedicated support in carrying out this analysis via the SDA project. This work is supported under US DOE under Contract no DE-AC02-76CH03000

REFERENCES

[1] V.A. Lebedev, *et al* "Beam Physics at the Tevatron", this conference, ref # MOPA003. See also The RunII Handbook, at http://www-bd.fnal.gov/runii/index.html

[2] D. Acosta *et al.*, Nucl. Instrum. Meth. A **494**, 57 (2002).

[3] G. Vogel, *et al*, A multi-Batch Fast Bunch Integrator for the Fermilab Main Ring, Beam Instrumentation Workshop 98.

[4] S. Pordes, *et al*, "Measurements of Proton and Antiprotons beam intensities in the Tevatron" this conference, ref. WPPB038

[5] W. Blokland, *et al*, "A new Flying Wire System for the Tevatron" PAC97, Proceedings of the 1997 Particle Accelerator Conference, Vol. 2, p. 2032.

[6] H.Cheung, *et al*, "Performance of a Beam Monitor in the Fermilab Tevatron Using Synchrotron Light", this conference, Ref # WPPB036

[7] J. Slaughter, *et al*, "RunII Tevatron Luminosities and Collision Point Sizes", this conference, Ref # TPPB070

[8] J. Steimel, *et al*, "Effect of RF noise on the Longitudinal Emittance Growth in the Tevatron" Collision Point Sizes", this conference, Ref # MOPA008

[9] X.L.Zhang, *et al*, "Experimental Studies of Beam-Beam Effects in the Tevatron", this conference, Ref # TPPB068

ACCELERATOR RELATED BACKGROUNDS IN THE LHC FORWARD DETECTORS*

N.V. Mokhov†, A.I. Drozhdin, I.L. Rakhno, FNAL, Batavia, IL 60510, USA
D. Macina, CERN, Geneva, CH-1211, Switzerland

Abstract

Detailed Monte Carlo simulations are performed on radiation environment in the LHC IP5 interaction region at the locations of the TOTEM Roman Pots proposed to detect particles produced at very small angles in the elastic scattering and diffraction dissociation processes at the LHC. Radiation loads on these detectors are calculated with the MARS14 code both of the *pp*-collision origin and beam loss related (beam-gas and tails from collimators).

INTRODUCTION

The TOTEM Roman Pot (RP) detectors will measure the total *pp*-interaction cross section, elastic scattering, and diffractive processes at the LHC [1]. These detectors consist of tracking devices placed into special units mounted on the vacuum chamber of the accelerator in the very forward region of the IP5: at 145 to 220 m from the CMS detector. Radiation doses and background particle rates at the RP locations are fundamental inputs to their design. The TOTEM will run at a luminosity not to exceed 10^{33} cm^{-2} s^{-1}, i.e., ten times lower than nominal. Results of comprehensive studies of energy deposition effects due to *pp*-collisions are described in Ref. [2]. Accelerator related background in the CMS detector was calculated in Ref. [3]. Here we present results of detailed calculations of radiation effects in the forward detectors due to both *pp*-collisions and beam loss for the extended model based on the current version 6.4 lattice [4]. Operational beam loss rates in the vicinity of the detectors are studied taking into account both realistic vacuum distribution and apertures in the entire machine.

MODELING IN IP5

A new detailed calculation model is based on the current LHC lattice, IP5 component description of Ref. [2], latest advanced version of the MARS14 code system [5], and upgraded STRUCT code [6]. The MARS model of a 300-m long section includes all the essential components from the IP5 through the first two MB dipoles (Fig. 1). The RP stations (Fig. 2) are located at 145, 149, 180, 220, and 220.28 m from the IP. The last detector, RP5, is placed immediately after RP4 and rolled by 90° around the z-axis.

Calculations are performed for the IP5(R) section for the *pp*-collisions at 10^{33} cm^{-2} s^{-1} with their products moving in the Beam 1 direction. The TCL collimator in front of the Q5 quadrupole is in its garage position. Beam loss, calculated both for Beam 1 and 2, are induced by interactions of a 3.1×10^{14} proton beams with collimators in the IP3 and IP7 and residual gas. A realistic vacuum distribution and both elastic and inelastic beam-gas interactions are taken into account. Note that a simplified pressure model and inelastic beam-gas interactions only were considered in Ref. [3]. The residual gas density distributions in strait warm and cold sections as well as in cryogenic arcs were recently estimated for the IP1 and IP5 [7]. The residual gas is represented as a mixture of four molecules (H_2, CH_4, CO, and CO_2). The element concentration distribution in the IP5 is shown in Fig. 3. For the purpose of this study,

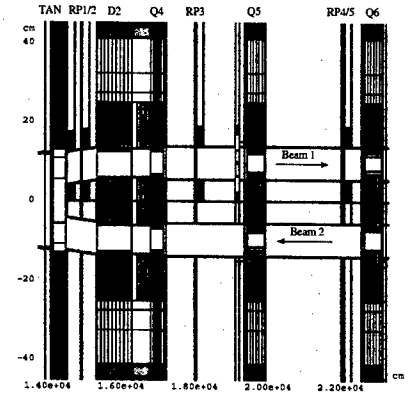


Figure 1: A fragment of the IP5 MARS model with five RPs.

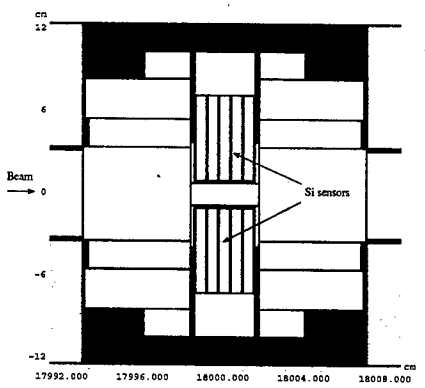


Figure 2: Elevation view of the RP MARS model.

* Work supported by the Universities Research Association, Inc., under contract DE-AC02-76CH03000 with the U.S. Department of Energy.
† mokhov@fnal.gov

0-7803-7738-9/03/$17.00 © 2003 IEEE

the vacuum distribution in other regions is assumed to be the same as that in the IP5. A corresponding beam loss rate due to inelastic beam-gas interactions is presented in Fig. 4. The lowest pressure and, therefore, beam loss rate is observed in the warm sections. The value of estimated residual gas pressure in the warm sections of about 10^{-11} torr is unusually low when compared to that for other accelerators (10^{-10} - 10^{-9} torr). The main difference between the LHC warm sections and those for other machines is in a coating material for the vacuum chamber. For the LHC most of the warm vacuum chamber will be coated with TiZrV NEG. This coating has, after activation at low temperatures, a very high pumping speed for the components of the residual gas. Static pressures of about 10^{-13} torr were measured at laboratory conditions [7].

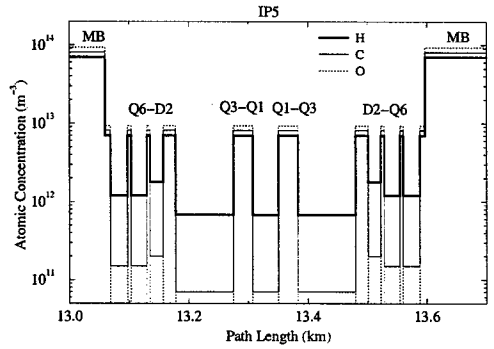


Figure 3: Residual gas concentration in the IP5.

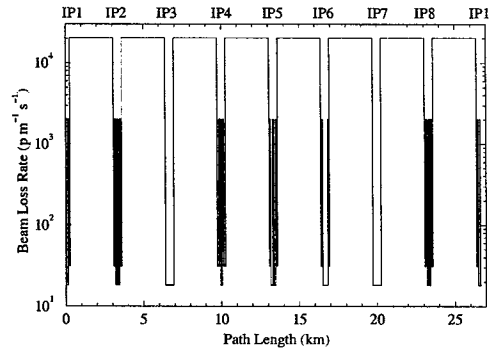


Figure 4: Estimated beam loss rate in the LHC lattice due to inelastic beam-gas interactions.

Beam loss due to the elastic beam-gas scattering [8] represents a "long-range" contribution in the region of interest because of very small scattering angles involved. On the contrary, inelastic beam-gas scattering gives rise to a "short-range" contribution. Therefore, calculation schemes for the two beam loss mechanisms are different. For elastic scattering, the first stage consists of a multi-turn STRUCT simulation of propagation of halo along with scattered protons (E>5 TeV) through the entire collider ring, similar to modeling the IP3 and IP7 collimator contribution. Scattered protons, lost on the LHC limiting apertures, form the source for the second stage – full shower simulation with the MARS code. Sample tracks of protons lost on the IP5 outer triplet apertures and picked up with MARS are shown in Fig. 5 for Beam 2. Most of the protons shown are lost on the Q4 and Q5 apertures and the tapered beam-pipe between the TAN and D1. For inelastic beam-gas interactions, large scattering angles are involved and, therefore, rather short regions (a few hundred meters) in the vicinity of the IP5 are considered in single-stage MARS runs.

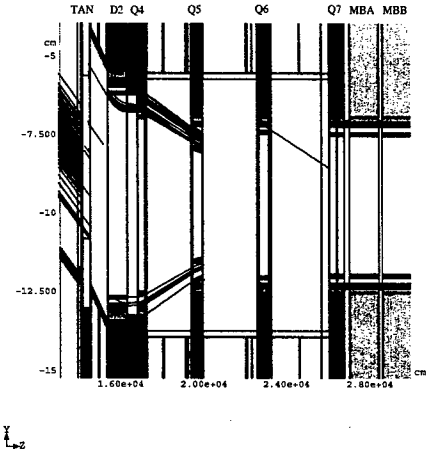


Figure 5: Sample tracks of the Beam 2 protons elastically scattered on residual gas around the ring and lost at z = 140-270 m from the IP5.

RADIATION LOADS IN TOTEM

At normal operation conditions and nominal luminosity, the radiation resulting from colliding beam interactions dominates over all other sources. However, beam loss induced effects may play a role at a reduced luminosity. Fig. 6 shows beam loss distributions in the IP5 region calculated with STRUCT for Beam 1 interactions with the IP3 collimators [3] and residual gas (elastic) around the ring. The rates in the RP vicinity are of the order of hundredth of W/m (on L-side) and are comparable for the two sources. The MARS calculated dynamic heat loads to the separation dipole and outer triplet quadrupoles on the R-side are shown in Fig. 7 for *pp*-collisions at 10% of the nominal luminosity (Beam 1) and beam-gas elastic and inelastic interactions for Beam 2 (contribution from Beam 1 is negligible here). One sees that at the TOTEM conditions, *pp*-collisions are still the dominant source of radiation, although at some spots the total accelerator related load is comparable. A relatively small contribution of the beam-gas inelastic component here can be understood if one takes into account a very high vacuum (low pressure) in this short region (dominant for inelastic interactions) compared to the rest of the machine starting at the MB dipoles (elastic interactions) as shown in Fig. 3.

Full-scale MARS simulations of showers induced in the TOTEM region are performed for all the sources described

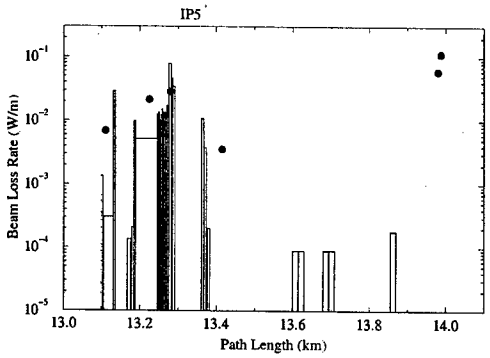


Figure 6: Beam loss rate in the IP5 caused by tails from collimators (symbols) and beam-gas elastic scattering (histogram).

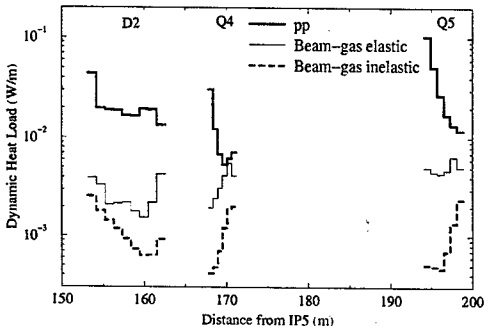


Figure 7: Dynamic heat load on the IP5(R) D2, Q4 and Q5 magnets due to *pp*-collisions at 10^{33} $cm^{-2}s^{-1}$ and beam-gas elastic and inelastic interactions.

above. Calculated are particle fluxes above 0.1 MeV, absorbed dose, energy and angular distributions at the RP silicon sensors as well as radiation loads to accelerator and other components at larger radii in this region. The results revealed that the *pp*-collisions dominate significantly even at the TOTEM luminosity of 10^{33} cm^{-2} s^{-1}. Backgrounds induced by tails from the collimators and beam-gas elastic and inelastic scattering are of the order of 0.1-1% of the total rates at the RPs. An example of a 2D distribution of neutron flux is shown in Fig. 8 for the RP5. Table 1 gives the particle fluxes and absorbed dose on the silicon sensors of all the RP detectors calculated at 10^{33} cm^{-2} s^{-1}. Also shown is a distance $d_{Si} = 10\sigma+0.5$ mm between the inner edge of the RP sensor and beam axis.

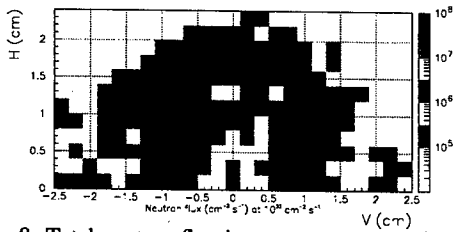


Figure 8: Total neutron flux isocontours averaged over the six RP5 silicon sensors.

Table 1: Total particle fluxes ($10^5 cm^{-2}s^{-1}$) averaged over silicon sensors and peak and average absorbed doses (10^4 Gy/yr).

Item	RP1	RP2	RP3	RP4	RP5
Charged hadrons	7.5	2.9	1.0	0.58	6.7
Neutrons	3.7	1.3	0.61	0.37	1.4
Electrons	115	28	23	12	18
Photons	1410	279	187	81	147
D_{max}	12	10	20	1.9	55
D_{av}	3.4	1.1	0.69	0.37	1.2
d_{Si}	10.36	10.33	8.77	5.97	2.10

CONCLUSIONS

Detailed calculations performed for the TOTEM Roman Pots in the IP5 region with the up-to-date lattice, detector parameters, MARS model, and realistic vacuum distribution reveal the high background rates on the silicon sensors, exceeding $10^{12} cm^{-2}$ of charged hadrons per year with the peak dose of about 100 kGy/yr. We found that the *pp*-collisions dominate even at 1/10 of the nominal luminosity, with backgrounds induced by tails from the collimators and beam-gas elastic and inelastic scattering contributing 0.1-1% to the above values.

Authors thank J.-B. Jeanneret and A. Rossi of CERN for information on the LHC apertures and newest vacuum model.

REFERENCES

[1] G. Matthiae, TOTEM Technical Proposal, CERN/LHCC 99-7 (1999).

[2] N.V. Mokhov, I.L. Rakhno, J. S. Kerby, J. B. Strait, "Protecting LHC IP1/IP5 Components Against Radiation Resulting from Colliding Beam Interactions", Fermilab-FN-732 (2003); LHC Project Report 633, CERN, Geneva (2003).

[3] A.I. Drozhdin, M. Huhtinen, N.V. Mokhov, Nucl. Instr. and Methods in Phys. Research, **A 381** (1996), 531-544.

[4] http://proj-lhc-optics-web.web.cern.ch/proj-lhc-optics-web/V6.4/.

[5] N. V. Mokhov, "The MARS Code System User's Guide", Fermilab-FN-628 (1995); N.V. Mokhov, "Status of MARS Code", Fermilab-Conf-03/053 (2003); http://www-ap.fnal.gov/MARS/.

[6] I.S. Baishev, A.I. Drozhdin, N.V. Mokhov, "STRUCT Program User's Reference Manual", SSCL-MAN-0034 (1994); http://www-ap.fnal.gov/~drozhdin/.

[7] A. Rossi, N. Hilleret, CERN Memo, March 2003.

[8] A.I. Drozhdin, V.A. Lebedev, N.V. Mokhov et al., Fermilab-FN-734 (2003).

MITIGATION OF EFFECTS OF BEAM-INDUCED ENERGY DEPOSITION IN THE LHC HIGH-LUMINOSITY INTERACTION REGIONS*

N.V. Mokhov†, I.L. Rakhno, J.S. Kerby, J.B. Strait, FNAL, Batavia, IL 60510, USA

Abstract

Beam-induced energy deposition in the LHC high luminosity interaction region components is one of the serious limits for the machine performance. The results of further optimization and comprehensive MARS14 calculations in the IP1 and IP5 inner and outer triplets are summarized for the updated lattice, calculation model, baseline pp-collision source term, and for realistic engineering constraints on the hardware design. It is shown that the optimized layout and absorbers would provide a sufficient reduction of peak power density and dynamic heat load in the superconducting components with an adequate safety margin. Accumulated dose and residual dose rates in and around the region components are also kept below the tolerable limits in the proposed design.

LHC IP1 AND IP5 REGIONS

The Large Hadron Collider (LHC) under construction at CERN, will produce *pp* collisions at center-of-mass energy $\sqrt{s}$=14 TeV and luminosity $\mathcal{L}$=10^{34} cm^{-2}s^{-1}. The interaction rate of 8×10^8 s^{-1} represents a power of almost 900 W per beam, the majority of which is directed towards the low-β insertions. Studies [1, 2, 3] have identified this as a serious problem and proposed the ways to mitigate it. Here a brief summary of extensive studies of the IP1 and IP5 high luminosity insertions are presented based on the up-to-date LHC optics (version 6.4), better understanding of practical possibilities with quadrupole cooling and shielding, and upgraded MARS14 [4] modeling. Ref. [3] describes these studies in great details.

To protect SC magnets against debris generated in the *pp* collisions and in the near beam elements, a set of absorbers in front of the inner triplet, inside and between the low-β quadrupoles, and in front of the D2 separation dipole was designed on the basis of energy deposition MARS14 calculations. Fig. 1 shows the inner triplet configuration with the absorbers in. The two curves show the approximate "n1 = 7" beam envelope for injection and collision optics, including closed orbit and mechanical tolerances.

All essential components situated in the tunnel of the IP1(R) and IP5(R) regions of 215-m long are implemented into the MARS14 model with a detailed description of their geometry, materials and magnetic field distributions. The model includes all the beam line, cryogenic and protection elements, tunnel, first meters of rock (molasse) outside the tunnel, as well as near beam components and solenoid magnetic fields of the ATLAS and CMS detectors for the IP1 and IP5, respectively. Fig. 2 shows the interaction region beam elements and their placement in the tunnel as modeled in the code.

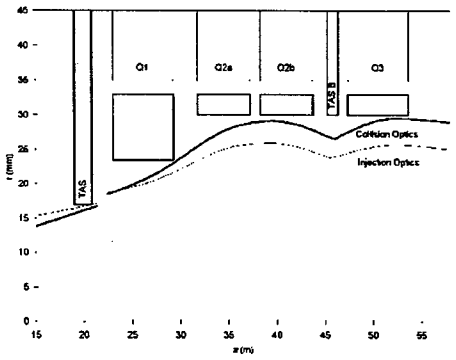


Figure 1: The LHC low-β insertions including absorbers: schematic view with the beam envelopes.

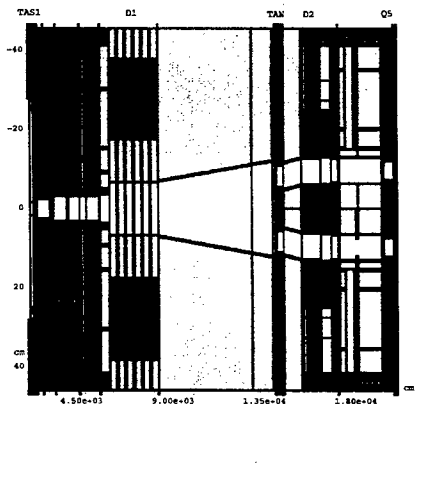


Figure 2: A fragment of the IP5 MARS model.

DESIGN CONSTRAINTS

The protection system design constraints used in the study are as follows:

1. Baseline luminosity of 10^{34} cm^{-2}s^{-1}.
2. Keep *geometrical aperture larger than "n1 = 7"* for injection and collision optics, including closed orbit and mechanical tolerances.

* Work supported by the Universities Research Association, Inc., under contract DE-AC02-76CH03000 with the U. S. Department of Energy.

† mokhov@fnal.gov

0-7803-7738-9/03/$17.00 © 2003 IEEE

3. *Quench stability:* keep peak power density ϵ_{max}, which can be as much as an order of magnitude larger than the azimuthal average, below the quench limit with *a safety margin of a factor of 3.*

4. Use *1.6 mW/g as a quench limit.* For many years, the estimated quench limit for the LHC high-gradient quadrupoles was 1.2 mW/g. Tests of porous cable insulation systems and recent calculations concerning the insulation system to be used in the Fermilab-built LHC IR quadrupoles (MQXB) have shown that up to about 1.6 mW/g of heat can be removed while keeping the coil below the magnet quench temperature.

5. Rely on *radiation-hard materials.* With the above levels, the estimated lifetime will exceed 7 years at the baseline luminosity even in the hottest spots.

6. Keep *dynamic heat loads below about 10 W/m.*

7. *Hands-on maintenance:* keep residual dose rates on the component outer surfaces below about 0.1 mSv/hr.

8. Always obey *engineering constraints.*

PROTECTION SYSTEM

A protection system on each side of the IP1 and IP5 has been designed over the years on the basis of comprehensive MARS calculations. It includes:

- The TAS front copper absorber at L=19.45 m (1.8 m long, 34-mm ID, 500-mm OD).
- A 7-mm thick stainless steel (SS) liner in Q1.
- The SS absorber TASB at L=45.05 m (1.2-m long, r=33.3-60 mm). Proposed in earlier studies a TASA absorber at L=30.45 m (1.1-m long, r=25-60 mm) is eliminated from the design.
- A ~3-mm thick SS liner in the Q2A through Q3.
- 40-cm long SS masks at L=23.45 m, r=250-325 mm to protect the Q1 slide bearings.
- The neutral particle copper absorber TAN at 140 m.
- The 1-m long TCL SS collimator at 191 m from IP.

The TAS absorbers in front of the first low-β quadrupoles are designed as a front-line system to protect the inner triplet by catching the particles originating from the IP and the cascades initiated by them. TAS's parameters were optimized over years. Currently the TAS are at 19.45 m from the IP in the IP1 and IP5, made of copper, 1.8-m long and 1.7 cm inner and 25 cm outer radii. At design luminosity, they catch 184 W of collision power on each side of the IP, allowing only 5% of the incoming energy (outside TAS aperture) to penetrate through the absorber body.

It was shown in Ref. [1] that a ~7-mm thick liner in the Q1 quadrupole is needed to bring ϵ_{max} at the Q1 non-IP end below the design limit (see Fig. 3). The same exponential shielding effect in a material preceding the SC coils dictates a thicker beam pipe in the Q2A through Q3 region. An intermediate absorber TASB protects the Q3 quadrupole, as do the masks inside the cryostat for the Q1 slide bearings. A neutral particle absorber TAN at 140 m on each side of the IP, was designed to protect the separation dipoles D2 and the outer triplet quads against the neutral component from the IP (neutrons and photons predominantly) and charged and neutral particles generated in the near beam components on the 140-m way from the IP. An instrumented copper core (21×26×350 cm) with two 5 cm diameter beam holes is surrounded by massive steel shielding with a 30-cm steel / 30-cm marble albedo trap.

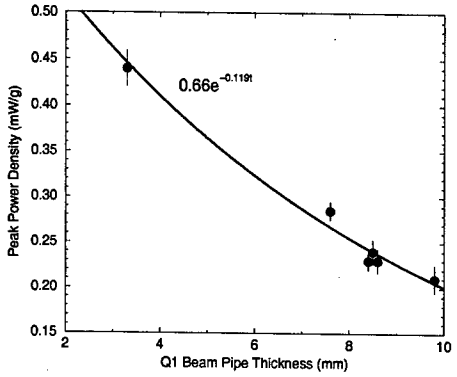


Figure 3: Peak power density in the Q1 layer *vs* liner thickness (beam screen together with cold bore).

POWER DENSITY AND HEAT LOAD

As a result of optimization of the above system parameters, it became possible to meet the design constraints. For quench stability, it was essential to perform a detailed 3D analysis of power density ϵ in the quadrupole coils, which varies strongly in longitudinal radial and azimuthal directions. There are pronounced peaks in the horizontal and vertical planes, with a difference between maximum and minimum values reaching a factor of 10 and between the peaks and azimuthally averaged values of a factor of 2.5 to 5.5. A longitudinal distribution of an azimuthal peak in the first radial bin of the SC coils (35<r<46.5 mm) is shown in Fig. 4. In the IP5, for the baseline horizontal crossing, the power density reaches its maximum ϵ_{max} = 0.45 mW/g at the Q2b non-IP end, a factor of 3.5 below the quench limit. In the SC separation dipole and outer triplet quadrupoles, the protection system provides a safety margin of 10 to 100.

Integral power dissipation distribution in components of the IP5 inner triplet is presented in Fig. 5, while Table 1 gives integral values for the the components in the entire 215-m region studied. Statistical uncertainty for each of the values in the Table does not exceed 1%. The integration with respect to radius for all the components was per-

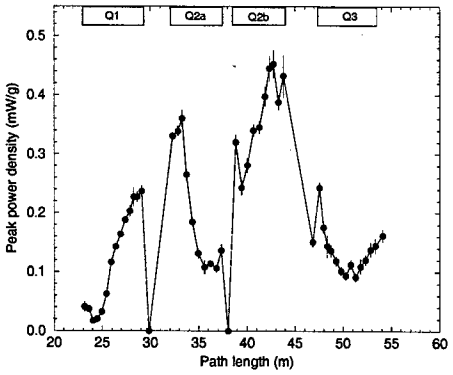


Figure 4: Longitudinal distribution of peak power density in the first radial bin of the IP5 SC coils in the IP5 quadrupoles.

formed from 0 up to 45.72 cm, *i.e.* through the vacuum vessel. Results for the IP1 are quite similar. The table also gives hadron fluxes and prompt dose on the vessel, useful for a beam loss monitor system design, and an estimate of radiation environment in the tunnel near the cryostat.

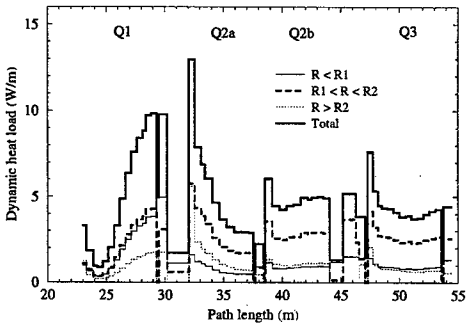


Figure 5: Power dissipation in the baseline IP5 inner triplet components. R_1=35 mm, R_2=81 mm in Q1 and Q3 and R_2=67 mm in Q2a and Q2b.

UNCERTAINTIES

Based on numerous international benchmarkings on micro and macro levels, status of the current event generators, thorough sensitivity analysis in the inner triplet over eight years (event generators, other physics input, geometry, materials, fields, crossing etc), numerous discussions and analyses of the results by the community over the same eight years, understanding of the Monte Carlo aspects, we believe that we predict the maximum power density in the coils with an accuracy better than 30%. This is true for the innermost layers of the coils (just a beginning of showers) for a particular configuration. The results, especially for local peak power deposition, can be quite sensitive to configuration changes, however. The uncertainty is higher at larger radii and larger distances from the IP, often because of statistics. Integral energy deposition and integral flux values such as azimuthal average, power dissipation (dynamic heat load) are predicted with about 10-15% accuracy. Residual dose rates are estimated within a factor of two to three.

Table 1: Dynamic heat load P (W) on the IP5 components, and prompt dose equivalent DE (Sv/hr) and hadron flux Φ ($10^4 cm^{-2}s^{-1}$ at E>14 MeV) on the vessel at longitudinal peaks at the nominal luminosity.

Element	P	DE	Φ
Absorber TAS	184		
Absorber TASB	5.7	18.12	91.84
Quadrupole Q1	30.7	12.44	92.72
Quadrupole Q2a	28.8	22.09	133.4
Quadrupole Q2b	26.6	5.184	40.91
Quadrupole Q3	27.7	12.61	93.76
Corrector MCBX1	6.9	17.55	144.6
Corrector MCBX2	1.6	4.202	32.67
Corrector MQSXA	2.0	15.85	106.0
Corrector MCBXA	3.1	4.712	41.58
Feedbox DFBX	6.92	6.670	39.31
Dipole D1	50		
Absorber TAN	189		
Dipole D2	1.96	2.079	11.08
Quadrupole Q4	0.39	0.243	1.696
Quadrupole Q5	1.79	1.466	9.104

CONCLUSIONS

The system described in this paper and developed under realistic engineering constraints will protect the LHC IP1/IP5 region components against luminosity-driven short- and long-term deleterious energy deposition effects with a good safety margin, at least at the design luminosity of 10^{34} $cm^{-2}s^{-1}$.

REFERENCES

[1] N.V. Mokhov, J.B. Strait, "Optimization of the LHC Interaction Region with Respect to Beam-Induced Energy Deposition", EPAC96 and Fermilab-Conf-96/136 (1996).

[2] N.V. Mokhov, J.B. Strait, Proc. of the 1997 Part. Accel. Conf., Vancouver, B.C., Canada, May 1997, p. 124.

[3] N.V. Mokhov, I.L. Rakhno, J.S. Kerby, J.B. Strait, "Protecting LHC IP1/IP5 Components Against Radiation Resulting from Colliding Beam Interactions", Fermilab-FN-732 (2003), LHC Project Report 633 (2003).

[4] N.V. Mokhov, "The MARS Code System User's Guide", Fermilab-FN-628 (1995); N.V. Mokhov, O.E. Krivosheev, "MARS Code Status", *Proc. of Monte Carlo 2000 Conf.*, p. 943, Lisbon, October 23-26, 2000; N.V. Mokhov, "Status of MARS Code", Fermilab-Conf-03/053 (2003); http://www-ap.fnal.gov/MARS/.

ENERGY DEPOSITION LIMITS IN A Nb_3Sn SEPARATION DIPOLE IN FRONT OF THE LHC HIGH-LUMINOSITY INNER TRIPLET*

N.V. Mokhov†, V.V. Kashikhin, I.L. Rakhno, J.B. Strait, S. Yadav, A.V. Zlobin, FNAL, Batavia, USA
R. Gupta, M. Harrison, BNL, Upton, NY 11973, USA
O.S. Brüning, F. Ruggiero, CERN, Geneva, Switzerland

Abstract

Interaction region inner triplets are among the systems which may limit the LHC performance. An option for a new higher luminosity IR is a double-bore inner triplet with separation dipoles placed in front of the first quadrupole. The radiation load on the first dipole, resulting from pp-interactions, is a key parameter to determine the feasibility of this approach. Detailed energy deposition calculations were performed with the MARS14 code for two Nb_3Sn dipole designs with no superconductor on the mid-plane. Comparison of peak power densities with those in the baseline LHC IR suggests that it may be possible to develop workable magnets for luminosities up to 10^{35} cm^{-2} s^{-1}.

DIPOLE FIRST IR

After the LHC operates for several years at a nominal luminosity $\mathcal{L} = 10^{34}$ cm^{-2} s^{-1}, it will be necessary to upgrade it for higher luminosity. An interesting option for a new interaction region (IR) is a double-bore inner triplet with separation dipoles placed in front of the quadrupoles [1, 2]. Compared with the baseline design consisting of single-bore quadrupoles shared by both beams, this layout substantially reduces the number of long-range beam-beam collisions, allows the beams to pass on-axis through the quadrupoles, and permits local correction of triplet field errors for each beam. However, β_{max} is considerably larger for the same β^*. Increasing the LHC luminosity by an order of magnitude creates a hostile radiation environment resulting from colliding beam interactions [3], with most of the power of almost 9 kW per beam directed towards the IR magnets. The problem is particularly severe for the dipole-first layout, since most of the charged secondaries will be swept into the dipole by its large magnetic field.

Detailed MARS14 [4] energy deposition calculations have been performed to determine the feasibility of this approach. Fig. 1 shows the layout considered. The D1 dipole starts at 23 m, allowing space, as in the current IR, for a 1.8-m long TAS absorber, and there are 5 m between the D1 and D2 to allow for a TAN neutral particle absorber. The orbits shown are for a horizontal crossing angle of ± 0.212 mrad, scaled up from the baseline ± 0.15 mrad to allow for reducing β^* to 25 cm. In view of the reduced number of long-range collisions, such a crossing angle provides sufficient beam separation for operation with a 12.5 ns bunch spacing at the ultimate bunch intensity of 1.7×10^{11} p/bunch. A vertical crossing can be generated by rolling the D1 and D2 by several degrees, or with strong correctors placed in front of the D1 (~8 T-m) and behind the D2 (~3 T-m). The dipole strengths shown are for a horizontal crossing plane; they both go to 15 T for a vertical crossing plane. The transverse size and positions of the dipole and quadrupole boxes correspond to the required coil apertures, which are 130 mm, 100 mm and 100 mm for the D1, D2 and quadrupoles, respectively, assuming that all the quads have the same coil bore. Although desirable, it would be difficult to include a hole through the yokes to allow the neutral beam to pass through the D2 and the triplet to a downstream TAN. Therefore, for the purpose of this study, the TAN is assumed to be between D1 and D2.

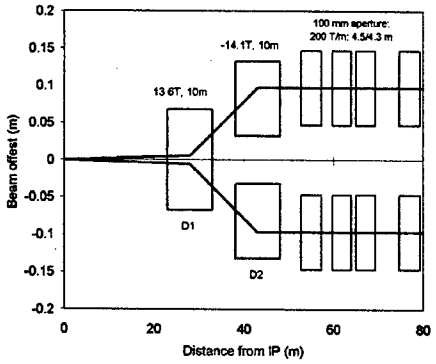


Figure 1: Interaction region layout.

The required physical aperture at the non-IP end of the D1 is shown in Fig. 2. The radial clearance about each beam (incoming and outgoing) is [2] $1.1\times9\sigma$ + 8.6 mm = 23.5 mm, where the factor 1.1 allows for 20% β-function errors, σ = 1.5 mm, and 8.6 mm is the sum of various orbit and alignment errors. At the non-IP end of the D1, the orbits in Fig. 1 are offset by $\pm$36 mm, giving rise to a racetrack shaped aperture.

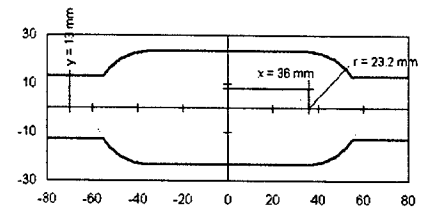


Figure 2: Required physical aperture at the D1 non-IP end.

* Work supported by the Universities Research Association, Inc., under contract DE-AC02-76CH03000 with the U. S. Department of Energy.
† mokhov@fnal.gov

0-7803-7738-9/03/$17.00 © 2003 IEEE

Horizontal channels are shown along the mid-plane outside of this aperture, which could allow much of the collision debris to exit the coil region (see Fig. 4). The height of the channels must take into account divergence of the beam and the combined tolerances on orbit and alignment and the crossing angle, since the forward collision debris peak follows the outgoing beam. The dimension shown in Fig. 2 is 3σ + 8.6 mm = 13 mm. The channel dimensions, if such a design were adopted, would be subject of optimization based on energy deposition and the mechanical constraints on the magnet design.

TWO DESIGNS FOR D1

In this paper, calculations are done for D1 of two types, whose parameters are summarized in Table 1. Both designs are based on a Nb_3Sn superconductor (SC). The first one, shown Fig. 3, is a traditional cos-theta design with a 4-layer graded coil of inner radius 65 mm and a cold iron yoke. High field quality is achieved by optimizing the azimuthal sizes of each layer and of the wedges in the innermost layer. Copper spacers of half-height 10, 6, 4 and 4 mm are placed at the mid-plane, where the peak power deposition from collision fragments occurs.

Table 1: Magnet parameters

Parameter	Units	$\cos\theta$	Block
Coil aperture ID	mm	130	84
No. of layers	-	4	4
Quench bore field	T	15.8	15
Quench peak field	T	16.8	16.7
Conductor x-sec. area	cm^2	119.1	174.4
Yoke inner radius	mm	145	305
Yoke outer radius	mm	500	500

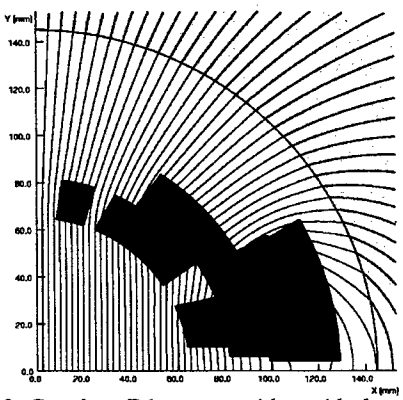


Figure 3: Cos-theta D1 magnet with a mid-plane spacer.

The second dipole design uses block type coils (Fig. 4). The iron can be either warm or cold depending on the details of the design. The required field quality (not yet optimized) is achieved by adjusting the size and position of coil blocks. All material is removed from the mid-plane region, so that the first material encountered by the dominantly horizontal spray of particles is outside the coil region. This approach, however, presents significant challenges to the magnetic and structural design. The dipole has a clear circular aperture of 70 mm and horizontal slots of height ±6 mm. The coils have a minimum vertical separation of 33.5 mm. The maximum stress in stainless steel collar is about 700 Mpa. The maximum horizontal and vertical coil deflections at 15 T are less than 0.2 mm. The magnitude of the vertical deflections can be reduced by incorporating *stress intercepts* within the coil structure that directly transfer load from the coil to collar. The magnitude of the horizontal deflections can be reduced by further strengthening the collar by increasing its size, etc.

The block-coil dipole design is very preliminary, and its aperture is smaller than the required one shown in Fig. 2. However, the MARS model discussed sets to zero all tolerances on alignment and orbit errors, which are a significant component of the aperture requirement. As a consequence the studies here allow a valid first comparison of magnet designs with and without material on the coil mid-plane, which is the main result of this paper.

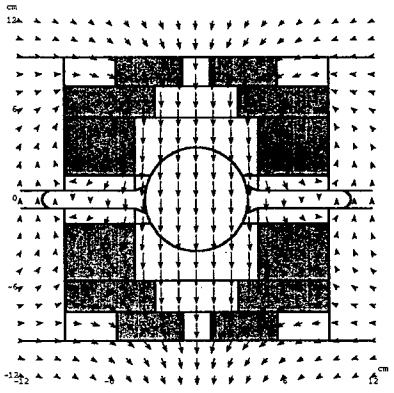


Figure 4: A MARS model fragment block coil D1 magnet with open mid-plane.

ENERGY DEPOSITION RESULTS

The MARS runs were performed for the LHC IP5 region with the layout of Fig. 1 at $\mathcal{L} = 10^{35}$ cm^{-2} s^{-1} and horizontal crossing. The CMS detector with its 4-T solenoid field is assumed here. A copper 1.8-m long TAS at z=19.45 m has a 21-mm radius round aperture (compared to the baseline's 17-mm) and 450-mm outer radius. A simple interconnect between TAS and D1 is assumed with a 240-mm ID beam pipe. The D1 dipole in both designs is 10-m long with 13.6-T bore field. A 120-mm ID and 124-mm OD stainless steel beam pipe is implemented in the cos-theta design, with no pipe in the block-coil dipole case. A copper 5-m long TAN with two corresponding apertures sits at z=33 m immediately downstream of the D1.

As in the baseline [3], the TAS protects the upstream end of the first magnet against severe energy flux from the IP, absorbing a power of 1.75 kW. The peak power den-

sity ϵ_{max} at shower maximum is 89 mW/g. The power dissipated in the TAN is about 2 kW, depending on which dipole is used in the study, and ϵ_{max} = 870 mW/g. Active cooling will be required for both absorbers.

The strong magnetic field in the D1 deflects charged particles horizontally left and right, concentrating power deposition in the mid-plane, which reaches its maximum at the non-IP end of the dipole. The power density 2D distributions at the longitudinal maximum are shown in Fig. 5 and 6 for the two dipoles. One clearly sees the local peak on the left (closer to the outgoing beam): in the SC coils for the cos-theta dipole and deep in the "trap" for the block coil type magnet. The peak power density in the copper spacers on the mid-plane of the cos-theta magnet is 49 mW/g. The maximum power density in the SC coils is 13 mW/g, as shown in Fig. 7, more than 20 times the peak power in the quadrupoles in the baseline LHC IR at $\mathcal{L} = 10^{34}$ cm^{-2} s^{-1} [3]. Dealing with this will present a significant challenge to the magnet designers.

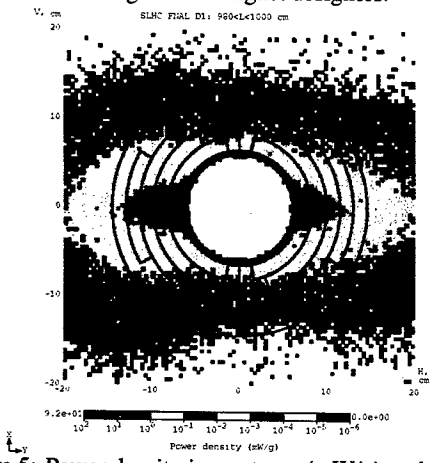


Figure 5: Power density isocontours (mW/g) at the non-IP end of the cos-theta dipole.

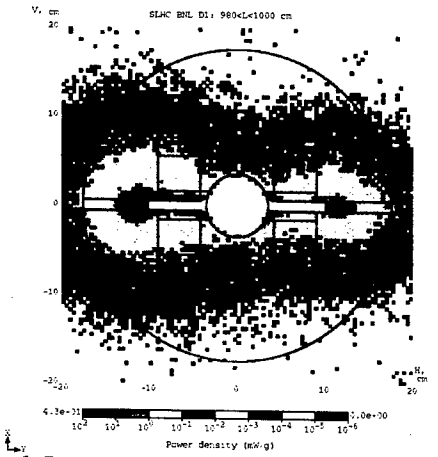


Figure 6: Power density isocontours (mW/g) at the non-IP end of the block-coil dipole.

In contrast, ϵ_{max} in the coils of the block-type dipole with no material on the mid-plane is only 1.1 mW/g, about

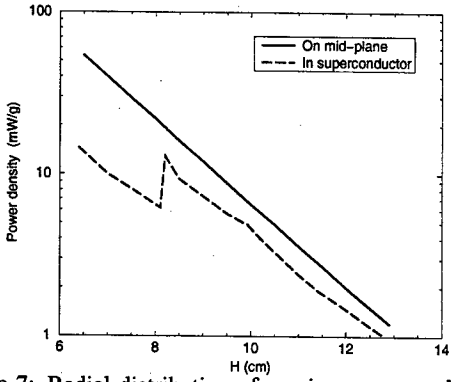


Figure 7: Radial distribution of maximum power density in the cos-theta dipole coil: on the mid-plane and in the superconductor.

twice the peak power in the quadrupoles in the baseline LHC IR at the baseline luminosity. While this is an encouraging result, it must be emphasized that such a design has never been tried, and substantial R&D must be done before the feasibility of a magnet of this type can be demonstrated.

The total power dissipated in the dipole is about 3.5 kW in either design. Efficient removal of such a power from the cryogenic system is also a major challenge for implementing this IR design as part of an LHC upgrade.

CONCLUSIONS

The radiation environment for a dipole-first IR is quite severe: the peak power density at $\mathcal{L} = 10^{35}$ cm^{-2} s^{-1} is up to two orders of magnitude larger than in the baseline inner triplets at 10^{34} cm^{-2} s^{-1}. The dipole-first layout is attractive because it reduces number of long-range beam-beam collisions and allows more robust correction of triplet errors, encouraging us to find a solution for the energy deposition problem. The preliminary results presented here show that the power deposited in the coil can be reduced to a level comparable to that in the baseline LHC in a dipole with no material on the coil mid-plane. However, much work remains to be done to demonstrate that a dipole of such a design can be made to reach high field, maintain good field quality, and meet all other requirements for use in a very high luminosity IR.

REFERENCES

[1] T. Taylor et al., "Towards a New LHC Interaction Region Design for a Luminosity Upgrade," these proceedings.

[2] O.S. Brüning et al., "LHC Luminosity and Energy Upgrade: A Feasibility Study," LHC Project Report 626 (2002).

[3] N.V. Mokhov, I.L. Rakhno, J.S. Kerby, J.B. Strait, "Protecting LHC IP1/IP5 Components Against Radiation Resulting from Colliding Beam Interactions," Fermilab-FN-732 (2003), LHC Project Report 633 (2003).

[4] N.V. Mokhov, "The MARS Code System User's Guide," Fermilab-FN-628 (1995); N.V. Mokhov, "Status of MARS Code," Fermilab-Conf-03/053 (2003).

LONGITUDINAL BUNCH DYNAMICS IN THE TEVATRON

R. Moore, V. Balbekov, A. Jansson, V. Lebedev, K.Y. Ng, V. Shiltsev, C.Y. Tan
Fermi National Accelerator Laboratory, Batavia, IL, USA 60510

Abstract

We present our observations of the longitudinal bunch dynamics in Tevatron for uncoalesced proton bunches at 150 GeV and coalesced proton bunches at 150 GeV and 980 GeV. We have observed long-term (>15 minutes) coherent oscillations of uncoalesced protons that preserve already existing oscillations from upstream accelerators. A single-bunch instability in large intensity protons bunches at 980 GeV has also been observed.

UNCOALESCED PROTONS AT 150 GEV

Table 1 provides some relevant parameters of the Tevatron. A resistive wall monitor and a 2 GS/s digital oscilloscope are used to gather longitudinal profiles of the beam. Coherent synchrotron oscillations, originating in upstream accelerators, can be maintained for many (> 15) minutes in the Tevatron without an increase in longitudinal emittance. Uncoalesced protons are a train of 30 consecutive radiofrequency (RF) buckets populated with typically 10 E9 protons per bunch; this beam is used for machine tune-up, not colliding beam physics. Figure 1 illustrates the synchrotron oscillations of 3 bunches of uncoalesced protons over time at 150 GeV. We refer to this phenomenon as "dancing bunches" [1].

Table 1: Tevatron Parameters

Parameter	Value
Average radius	1000 m
Injection, Collision Energy	150, 980 GeV
RF frequency (period)	53.1 MHz (18.8 ns)
RF Voltage	1.1 MV
RF harmonic	1113
Synchrotron Freq. (150, 980 GeV)	86 Hz, 34 Hz
RF Bucket Area @ 150, 980 GeV	4.5, 11 eV-sec

Figure 2 shows a typical Fast Fourier Transform (FFT) of a typical bunch in an uncoalesced train. The sharp peak corresponds to a dipole oscillation at the synchrotron frequency of 86 Hz. There are no visible correlations in the amplitude or phase of the individual bunch oscillations (see Figure 3). Nevertheless, a weak coupling of the bunches probably exists since there is a slow amplitude modulation of the oscillations, as seen in Figure 1. The second, broader peak in Figure 2 with frequency about 260 Hz is not fully understood. We do know that this motion is coupled among all the bunches; Figure 4 shows the amplitude of this higher frequency oscillation is essentially the same for all bunches over the measurement period. In addition, the bunches oscillate in phase at this higher frequency, and this frequency actually decreases slowly over time. We believe this motion may be a driven oscillation, but the source of the driving force has not been identified.

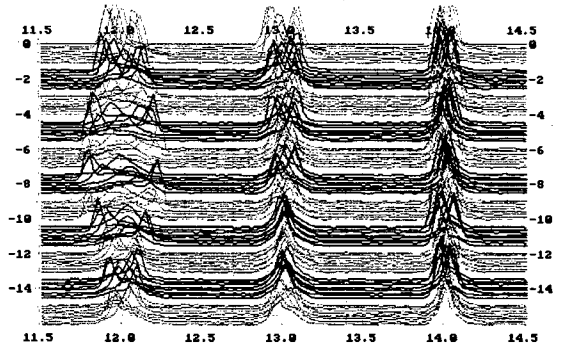


Figure 1: Longitudinal profile of bunches 12-14 of an uncoalesced proton train. Time (vertical axis, in minutes) progresses downward. Each colored band represents 0.9 sec of data; 40 turns (≈0.85 μs) separates individual traces. Each band is separated in time by 1.5 min.

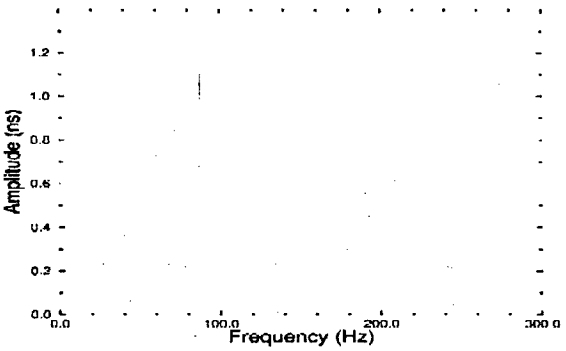


Figure 2: FFT of an oscillating proton bunch centroid.

An inductive impedance Z/n = i * const can explain how coherent synchrotron oscillations can survive for so long with little coupling among the bunches [2]. It does not affect coherent oscillations of a bunch centroid, but it does shift the oscillation frequency of individual particles around the center incoherently by an amount $\Delta\Omega$ which is proportional to $|Z/n|$. The condition when "dancing" should be observed can be expressed as $\Delta\Omega > \delta\Omega$ where $\delta\Omega$ is a synchrotron frequency spread. For the Tevatron at 150 GeV, the longitudinal impedance threshold allowing "dancing bunches" is $|Z/n|\ (\Omega) \sim 2*10^{11}\varphi^5/N \approx 1\Omega$, where $N = 10^{10}$ (number of protons per bunch), and $\varphi = 0.5$ (bunch half-length in RF radians). This impedance agrees well with the estimated longitudinal impedance value based on transverse impedance measurements [3].

0-7803-7738-9/03/$17.00 © 2003 IEEE

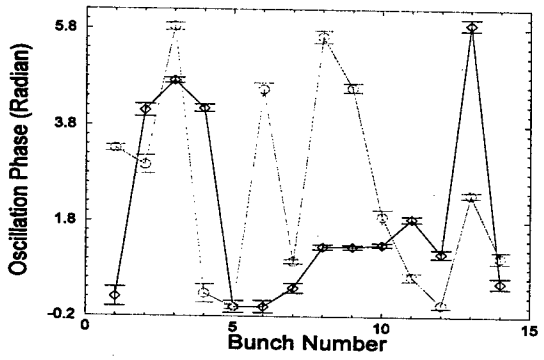


Figure 3: Oscillation phase of uncoalesced proton bunches. Black diamonds are 90 sec after injection; green triangles are 180 sec after injection; red circles are 820 sec after injection.

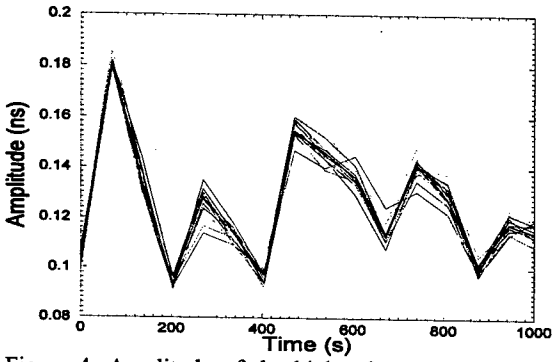


Figure 4: Amplitude of the higher-frequency oscillation versus time. Each color represents a different bunch.

COALESCED PROTONS AT 150 GEV

For colliding beam physics operation, the Tevatron is loaded with 36 coalesced proton and antiproton bunches. Coalescing occurs in the Main Injector at 150 GeV prior to injection into the Tevatron [4]. Typically 7 proton bunches are coalesced into a single bunch of 250-290 E9 protons. As seen in Figure 5, coalesced protons essentially fill a Tevatron RF bucket at 150 GeV. Typical RMS proton lengths in the Tevatron at injection are 3.1-3.3 ns; there is ~10% bunch length growth between the Main Injector and Tevatron, as shown in Figure 6. However, we observe longitudinal shaving in the Tevatron at 150 GeV; Figure 7 shows how the average RMS bunch length of the 36 proton bunches decreases.

One can also see in Figure 5 how coalesced protons can oscillate. These oscillations are remnants of the coalescing process, and they can persist for minutes in the Tevatron like the dancing uncoalesced bunches. Figure 8 depicts the longitudinal phase space distribution of the bunch shown in Figure 5; the distribution was reconstructed with longitudinal tomography code from CERN [5]*. The oscillating peaks seen in Figure 5 are also evident in Figure 8 as the off-center "hot spots" in the phase space distribution. An active, wideband longitudinal damper system [6] helps reduce these proton oscillations; the damper system is enabled only after all 36 proton bunches are injected.

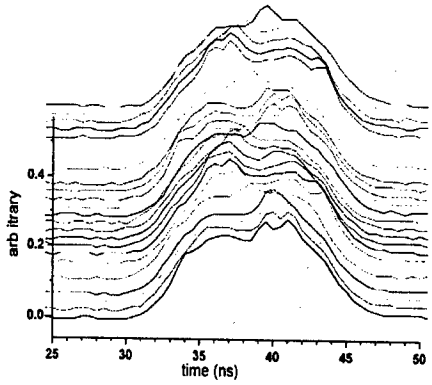


Figure 5: Profile of a coalesced proton bunch at injection in the Tevatron. Traces are separated in time (from bottom to top) by 40 Tevatron turns.

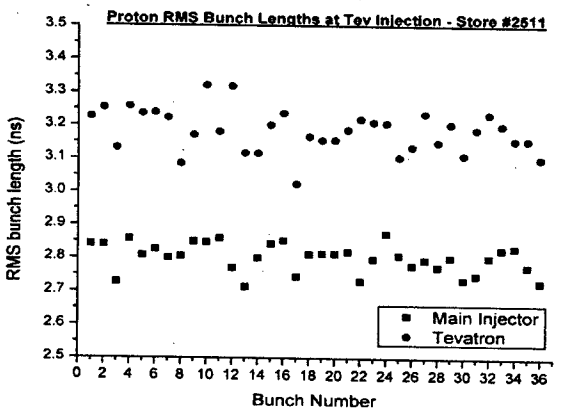


Figure 6: RMS bunch lengths of coalesced protons prior to extraction from the Main Injector (black squares) and after injection into the Tevatron (red circles).

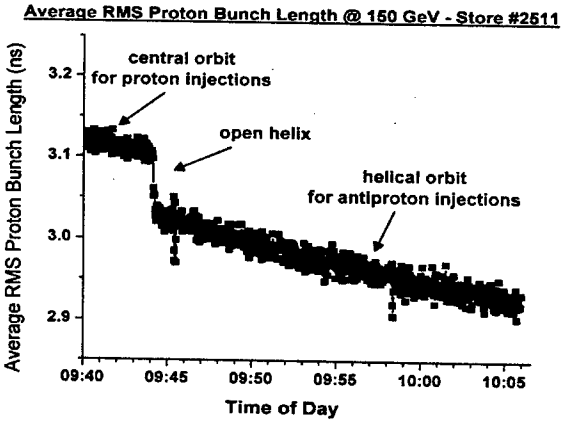


Figure 7: Coalesced protons experience longitudinal shaving while at 150 GeV.

* Although the code can handle space charge effect, this option was turned off for the reconstructions presented here.

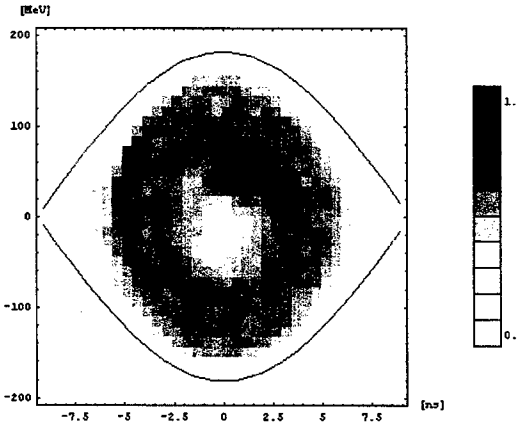


Figure 8: Reconstructed longitudinal phase space distribution of the coalesced proton bunch shown in Figure 5. Darker colors mean higher phase space density.

COALESCED PROTONS AT 980 GEV

After acceleration to 980 GeV, coalesced proton bunches are quite Gaussian and have no off-center "hot spots" in their longitudinal phase space distribution (See Figure 9 and Figure 10.) Once typical proton bunch intensities at 980 GeV reached ~150 E9, we began to observe single-bunch instabilities which would cause spontaneous bunch length growth with minimal beam loss in many, but not necessarily all bunches. However, the colliding beam luminosity would decrease as a result of the bunch length growth. (See Figure 11.) The previously mentioned longitudinal damper system has effectively eliminated this instability [6]. During HEP stores, the average proton RMS bunch length is 1.9-2.0 ns at the start of a store and grows at a rate of 0.03-0.06 ns/hr. Additional details about Tevatron emittance lifetimes in general can be found in [7].

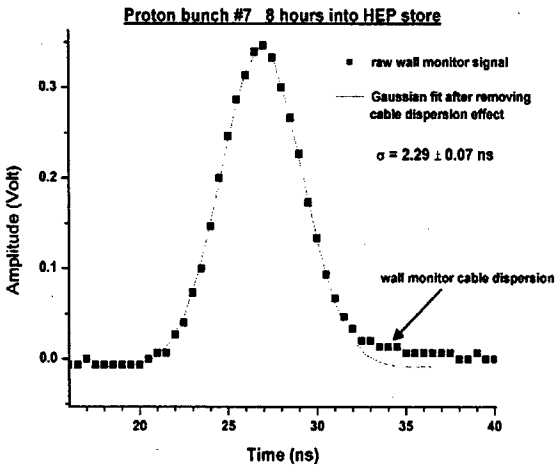


Figure 9: Longitudinal profile of a coalesced proton bunch at 980 GeV in the Tevatron.

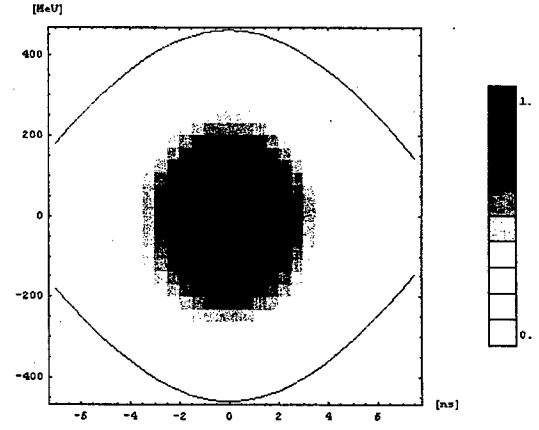


Figure 10: Reconstructed longitudinal phase space distribution of a coalesced proton bunch at 980 GeV.

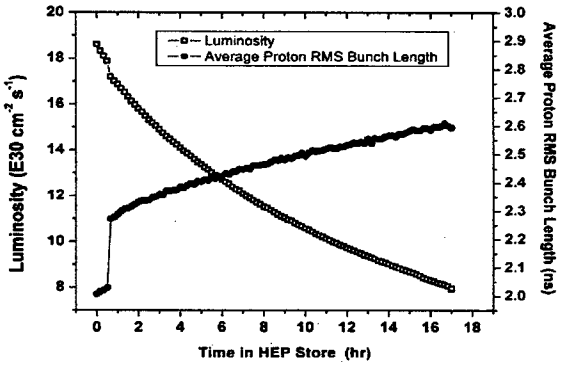


Figure 11: Illustration of proton bunch length blow-up and resulting decrease in luminosity during a high-energy physics (HEP) store in the Tevatron before longitudinal damper system was commissioned.

REFERENCES

[1] W. Guo, R. Moore, K. Y. Ng, S. Y. Lee, "Dancing Bunches at the Tevatron", Fermilab Technical Memo TM-2203, 2003.

[2] V. I. Balbekov and S. V. Ivanov, "Thresholds of Longitudinal Instability of Bunched Beam in the Presence of Dominant Inductive Impedance", IHEP-91-14, Protvino, 1991.

[3] P. Ivanov et al, "Head-Tail Instability at Tevatron", these proceedings (RPPB021).

[4] I. Kourbanis et al, "Performance of Main Injector Bunch Coalescing during Fermilab's Current Collider Run", these proceedings (RPAG021).

[5] S. Hancock, S. Koscielniak, M. Lindroos, Phys Rev ST-AB, Vol. 3, 124202 (2000).

[6] C.Y. Tan and J. Steimel, "The Tevatron Bunch By Bunch Longitudinal Dampers", these proceedings (RPPB024).

[7] P. Lebrun et al, "Observations on the Luminosity Lifetimes, Emittance Growth Factors and Intra-Beam Scattering at the Tevatron", these proceedings (TPPB062).

BEAM LOSSES AT INJECTION ENERGY AND DURING ACCELERATION IN THE TEVATRON

T. Sen, P. Lebrun, R. Moore, V. Shiltsev, M. Syphers, X.L. Zhang (FNAL);
W. Fischer (BNL), F. Schmidt, F. Zimmermann (CERN)

Abstract

Protons and anti-protons circulate on helical orbits in the Tevatron. At injection energy (150 GeV) the lifetimes of both species are significantly lower on the helical orbits compared to lifetimes on the central orbit but for different reasons. There are also significant beam losses in both beams when they are accelerated to top energy (980 GeV)- again for different reasons. We report on experimental studies to determine the reasons and on methods of improving the lifetimes and losses for both beams.

INJECTION ENERGY

Higher proton intensities at injection in recent stores have not increased the proton intensities at low-beta and have therefore not had an impact on the luminosity. Proton losses at 150 GeV appear to grow proportionately to the intensity. The coalescing process in the Main Injector leads to larger transverse and longitudinal emittances with increasing intensity and is the likely cause for the increase in losses.

Typically proton lifetimes on the proton helix are about 2 hours, as seen in Figure 1 which shows the beam bunched intensity (FBIPNG) after protons are moved to the helix. The sharp drop at the beginning occurs when protons are moved from the central orbit to the helix. This jump is also seen in calculations of the dynamic aperture (DA). Figure 2 shows the DA (without beam-beam effects) of protons as a function of the momentum deviation. The DA drops by at least 3σ for all values of $\delta p/p$ from the central orbit to the proton helix. This figure also shows the strong dependence of the DA on the momentum spread. The DA of uncoalesced bunches (typically $\delta p/p < 2 \times 10^{-4}$) is about 2σ greater than for coalesced bunches which have momentum spreads $\delta p/p > 5 \times 10^{-4}$. Uncoalesced bunches are in fact observed to have better lifetimes both on the central orbit and the helix.

The importance of losses due to the longitudinal emittance was also seen during a study on December 3rd, 2002. When 12 bunches of coalesced protons were injected onto the proton helix, the bunch length decay lifetime was $\sim$ 5.4hrs while the intensity lifetime was $\sim$ 2.5hrs. Longitudinal scraping accounts for a significant fraction but not all of the observed intensity loss. Losses were found to increase sharply when the chromaticity was increased by 1 to 2 units in either plane - again emphasizing the importance of the momentum spread.

During this same study we also injected a single coalesced proton bunch on the anti-proton helix. The intensity evolution is seen in Figure 3. The intensity has a rapid decay at the start followed by a more gradual decay. This

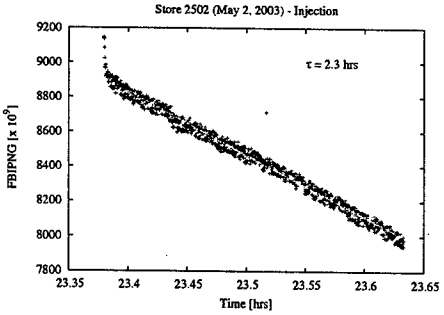


Figure 1: Proton bunched beam lifetime in Store 2502 (May 2, 2003).

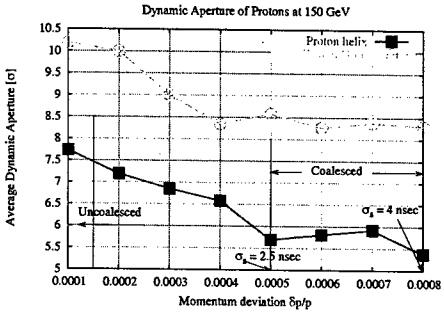


Figure 2: Dynamic aperture of protons on the central orbit and helix vs $\delta p/p$.

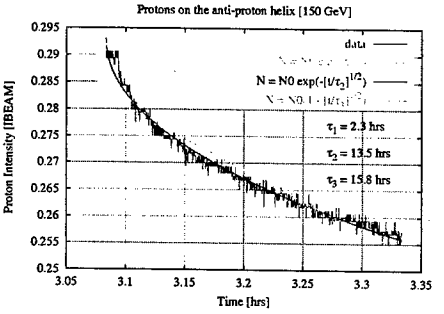


Figure 3: Beam intensity on the anti-proton helix (Dec 3, 2002).

decay is also typical of the anti-proton intensity decay in stores before the vertical damper was recommisioned. This decay is not well described by a single exponential decay law but heuristically found to be well described by a square root in the exponential $N(t) = N_0 \exp[-\sqrt{t/\tau}]$.

A simple model of constant phase space diffusion suffices to explain this behaviour. From the evolution of the

0-7803-7738-9/03/$17.00 © 2003 IEEE

particle intensity over time, it is evident that the extent of the antiproton distribution closely resembles the available aperture, whether it is physical or dynamic. For diffusion in one degree-of-freedom, the problem can be cast in terms of dimensionless variables $\tau \equiv (R/W_a)t$ and $Z \equiv W/W_a$, where R is the rate of change of the Courant-Snyder invariant, W, of a particle and W_a is the value of W corresponding to the limiting aperture (i.e., the admittance). The solution to the diffusion equation is[1]

$$N(\tau) = 2\sum_n \frac{c_n}{\lambda_n} J_1(\lambda_n) e^{-\lambda_n^2 \tau/4} \qquad (1)$$

where the λ_n are the zeroes of the Bessel function $J_0(z)$, and the c_n are given by

$$c_n = \frac{1}{J_1(\lambda_n)^2} \int_0^1 f_0(Z) J_0(\lambda_n \sqrt{Z}) dZ \ , \qquad (2)$$

$f_0(Z)$ being the initial particle phase space distribution (assumed to be radially invariant). In order to match the observed shape of the antiproton intensity variation in the Tevatron, the initial distribution needs to have an rms size comparable to the available aperture ($\sigma \approx a$). Once the correct shape has been established, the ratio of emittance growth rate to initial emittance sets the time scale: $\tau = 2(\dot{\epsilon}/\epsilon)(\sigma/a)^2 t$. In the Tevatron, the observed shape of the antiproton intensity curve over 15 minutes suggests that this time scale corresponds to $\tau \approx 0.04$ and that $a \approx \sigma$, or a rather uniform distribution in the available phase space. The antiproton beams coming from the Main Injector have transverse emittances (95%, normalized) of about 20π mm-mrad, are rather Gaussian, and the available transverse aperture is approximately 3σ or so. Also, the necessary emittance growth rate would have to be $\dot{\epsilon} \approx 16\pi$ mm-mrad/hr, exceedingly large. However, if we apply the same type of analysis to the longitudinal degree-of-freedom we find much more reasonable numbers. Namely, for an approximately uniform beam (after coalescing) entering a 4 eV-sec bucket, and a growth rate of 1/3 eV-sec/hr – all very consistent parameters for the Tevatron – then we get $\tau \approx 2$ (0.33 eV-sec/hr/4 eV-sec)(0.25 hr)) = 0.042. This suggests that the behavior of the beam lifetime at injection is governed more by longitudinal effects. Using Eq. 1 and taking differing numbers of terms in the sum, we plot $N(\tau)$ over the range of interest of τ as well as $e^{-\sqrt{\tau}}$ in Fig. 4 . For this plot, we assume a uniform initial distribution within the aperture. The fact that we need to keep several terms ($n > 4$) in the expansion shows that several time scales are important.

More recently with the vertical dampers recommisioned, the vertical chromaticity has been dropped to 4 units at injection. At this lower chromaticity, the anti-proton intensity decays as a simple exponential.

Beam study with anti-protons only

In an anti-protons only study on September 10, 2002, we observed that these antiprotons were indeed much more

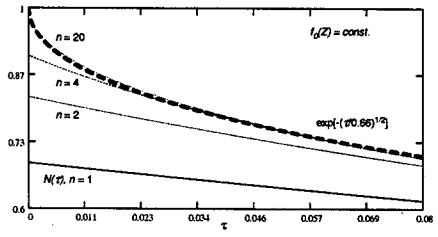


Figure 4: $N(\tau)$ using 1, 2, 4, and 20 terms in the sum. Also plotted is $e^{-\sqrt{\tau/0.66}}$.

stable than with protons present. A detailed study for all 36 bunches on the front porch showed that the lifetime is quite high, i.e. between 10.6hrs and 25hrs. We found a significant correlation of the lifetime with the vertical emittance seen in Figure 5. At that time there was a vertical aperture limitation due to a Lambertson magnet at C0. This was removed during the January shutdown.

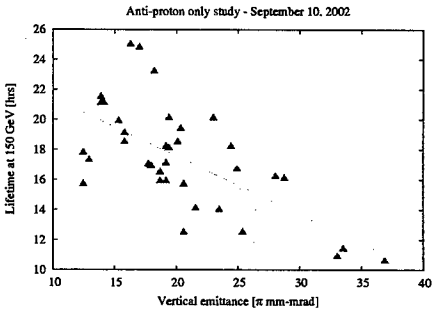


Figure 5: Anti-proton lifetime vs vertical emittance in an anti-proton only study.

ACCELERATION

Beam losses on the Tevatron ramp have been significant since the beginning of Run II (March 1, 2001). In the last year they have become the most significant contributor to the Tevatron inefficiency. Several phenomena take place - e.g., losses due to shaving on a physical aperture, limited DA due to machine nonlinearities and to beam-beam effects, loss of the DC beam, reduction of RF bucket area, etc. Figure 6 shows the variation of several parameters on the ramp in store 2328 (March 16, 2003, initial peak luminosity 40.6×10^{30} cm^{-2}s^{-1}).

Two dedicated experiments were done to identify the mechanisms that cause protons to be lost during the ramp. In both experiments, only proton bunches were injected and ramped. The conditions in the Booster and the Main Injector were adjusted so that the bunches had different intensities and emittances.

In the first experiment of September 24, 2002 we found that the losses were most strongly dependent on the lon-

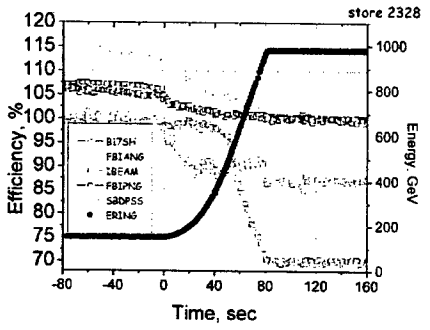


Figure 6: Transfer efficiencies during the ramp in store 2328.

gitudinal emittance. For example, uncoalesced bunches which had the smallest longitudinal emittance lost less than 2% of their intensity during the ramp. At the other extreme, coalesced bunches with the largest longitudinal emittance lost about 12% of their intensity and furthermore their longitudinal emittance decreased by about 20% after the ramp. This implies that particles from the longitudinal tails were lost. We found a weaker dependence of the loss on bunch intensity and vertical emittance. In the second experiment on January 6, 2003 we attempted to isolate the dependence of the loss on the individual parameters in a controlled fashion. This time we also obtained the longitudinal profiles of the bunches at 150 GeV both on the central orbit and on the helix and again at 980 GeV. The longitudinal dampers were not turned on so the longitudinal oscillations of the bunches were not damped. We found that the most rapid loss occurs during the first 10 seconds of the ramp when the bucket area is decreasing - see Figure 7.

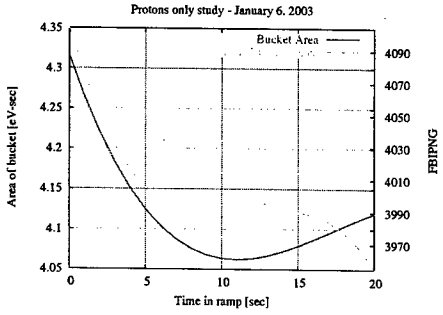


Figure 7: The bucket area and the beam intensity during the initial stages of the ramp. A large portion of the beam loss occurs while the bucket area is shrinking.

We found that the loss during the ramp was determined overwhelmingly by the longitudinal emittance and the longitudinal profile. Figure shows the loss during the ramp as a function of the rms bunch length. The correlation is significant. Short coalesced bunches with nearly Gaussian profiles had the smallest losses ($< 2\%$) while long oscillat-

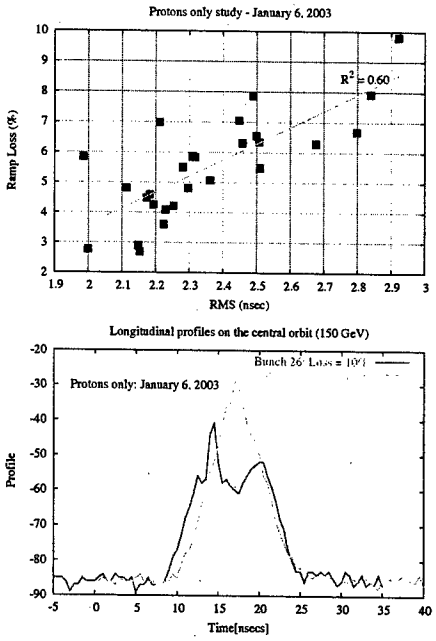


Figure 8: Longitudinal profiles of two bunches with nearly the same intensity and rms bunch length but very different losses during the ramp. The non-Gaussian oscillating bunch had greater losses during the ramp.

ing bunches had losses around 10%, seen in Figure 8. We found very little dependence on the bunch intensity. The same was true when we accelerated two proton bunches on the anti-proton helix.

During the anti-proton only study on September 10, 2002, we accelerated the 36 bunches to flat top. We found that there was some loss (8.5%) of DC beam from the machine but the bunched beam current losses were very small ($< 2\%$) and within the noise of the measurement. Analysis of stores when both species are present shows a strong correlation of the anti-proton loss during the ramp with the anti-proton vertical emittance. These are due to the beam-beam interactions which have a larger impact on the larger amplitude anti-protons.

Beam losses during the ramp can be minimized if the longitudinal and transverse emittances are as small as possible. This would require better coalescing in the Main Injector, perhaps with the addition of longitudinal dampers. It might also help to turn on the longitudinal dampers during the ramp in the Tevatron.

REFERENCES

[1] D.A. Edwards and M.J. Syphers, *An Introduction to the Physics of High Energy Accelerators*, Section 7.2, Wiley, New York (1993).

EXPERIMENTAL STUDIES OF BEAM-BEAM EFFECTS IN THE TEVATRON

Xiaolong Zhang, Tanaji Sen,Vladimir Shiltsev, Meiqin Xiao,Yuri Alexahin, FNAL, Batavia, IL 60510, USA
Frank Schmidt, Frank Zimmermann, CERN, Geneva, Switzerland

Abstract

The long-range beam-beam interactions limit the achievable luminosity in the Tevatron. During the past year several studies were performed on ways of removing the limitations at all stages of the operational cycle. We report here on some of these studies, including the effects of changing the helical orbits at injection and collision, tune and chromaticity scans and coupling due to the beam-beam interactions.

GENERAL OBSERVATIONS

The Tevatron is currently colliding 36 proton against 36 antiproton bunches, where either beam consists of 3 equally spaced trains of 12 bunches in a common single vacuum chamber. The two beams are separated by a helical orbit except at the two locations of High Energy Physics (HEP) experiments, where they collide head on. The beam-beam effect gains more and more importance as the Tevatron beam intensity continues to increase in the quest for higher luminosity [1]. Recently, the total beam intensities injected into the Tevatron has been slightly over 10×10^{12} protons and 1.2×10^{12} antiprotons, which, subsequently, yielded a peak luminosity of $43\times10^{30}cm^{-2}s^{-1}$ with over 8×10^{12} protons and 0.9×10^{12} antiprotons in collision. Intensive studies were carried out in recent months to understand and quantify limitations from beam-beam effects.

Beam Loss Through Shot

The typical beam loss through the shot setup is shown below in Figure 1. The red curve is the energy of the Tevatron, the green curve is the proton total bunch intensity, and the black is the total antiproton bunch intensity. The poor proton lifetime is caused by a limited dynamic aperture.

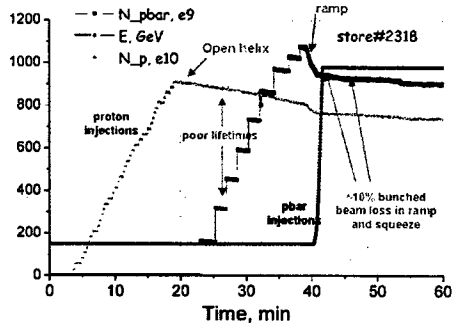


Figure 1: Beam intensity and loss during injection, ramping and squeeze

During ramping, there are about 10~12% antiproton loss and about 5~7% proton loss. There also is about 5% combined beam loss during low beta squeeze and halo removing process.

The losses are smaller for shorter bunches (~30% of longitudinal emittance reduction will reduce losses to ~ 3-4%) and for smaller transverse emittance (almost no losses occur if the transverse emittances are less than 12 pi mm mrad, while typical emittances are 20-25 pi mm mrad). Antiproton losses are much higher in case of insufficient separation.

Antiproton Only

A study with antiprotons only proved that the antiproton loss on the ramping is caused by the beam-beam effect. Figure 2 shows the antipron intensity during ramping and squeezing. No bunched beam loss (red curve) is observed; some DC beam (black curve) is lost during ramping.

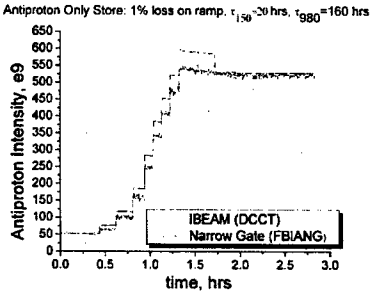


Figure 2: Beam intensity during antiproton only store.

Comparing the antiproton losses in Figures 1 and 2, we conclude that the loss is mainly caused by the presence of strong proton bunches.

Inproving Sequence #13

The antiproton loss due to insufficient separation was also a problem at the initial stage of Tevatron Run II operation as shown in Figure 3.

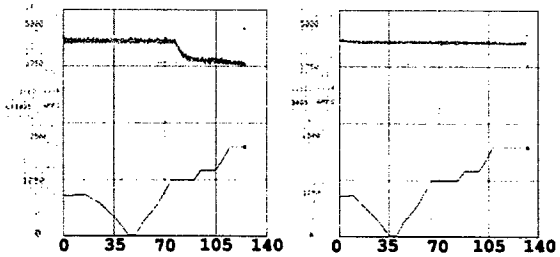


Figure 3: The antiproton losses due to the insufficient beam separation (left) and its solution (right).

0-7803-7738-9/03/$17.00 © 2003 IEEE

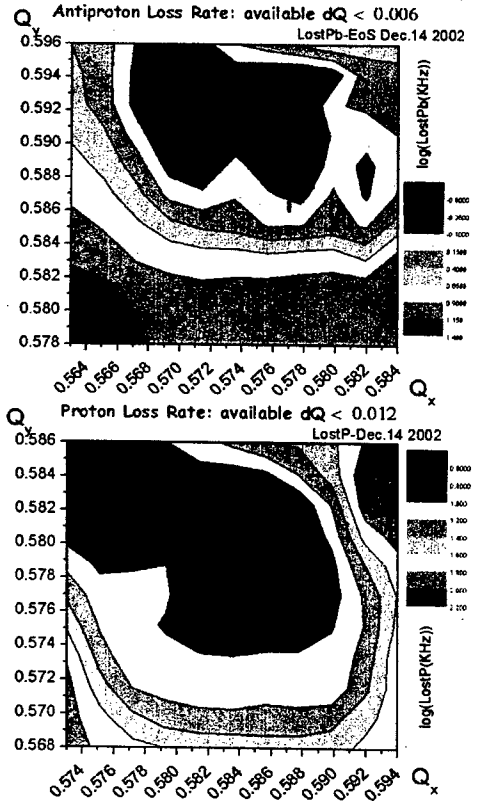
There was a huge antiproton loss during the ramp when the Tevatron energy was greater than 500 GeV in ramping sequence #13, which is illustrated by the cyan curve (C:FBIANG) on the left of Figure 3. After painstaking studies, the problem was identified as an insufficient beam separation. The solution was one more ramping break point with increased beam separation, which was added between ramping sequences #13 and #14. After this improvement, the loss due to beam-beam effects was eliminated as shown in the similar graph on the right of Figure 3.

TUNE MEASUREMENT

There are basically 3 systems for tune measurement in the Tevatron [2]. These include two Schottky systems, an old one at 21MHz and a new one at 1.75GHz, and the tune meter which measures the beam betatron oscillation frequency by FFT and is able to measure the tune bunch by bunch. The beam can be excited using either a stripline kicker or the Tevatron electron lens [3].

Tune Scan

One can find the best working point for protons and antiprotons by a tune scan. Figure 4 is the result of one of the tune scans carried out at the end of a HEP store.



The tune scan shown in the figure above displayed the loss versus the working point. The proton and antiproton losses were measured by the CDF detector. The top figure shows the loss rate of protons and the bottom one that of antiprotons. The blue color in the above graph indicates small losses and the crosses stand for the initial nominal working point at the time of the tune scan study. It indicates that there is some room for daily operational optimization of the working point.

Tune Diagram

By exciting or gating individual bunches, we can measure the bunch by bunch tune of the 36×36 bunches. The graph below shows the tunes of the 36 antiproton bunches at the end of the store.

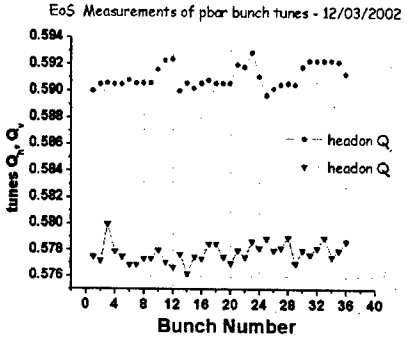


Figure 5: The bunch by bunch tune of the antiproton bunches

For this study, we 'tickled' each antiproton bunch and measured the tune spectrum by the Schottky signal monitor. We found that the vertical tune of the first bunch in the train of 12 bunches was lower and a few bunches at the end of the train had higher tune. The magnitudes of the the tune shifts and the fact that leading and trailing bunches are strongly affected agree with the simulations[1][4]. The first bunch had a lower tune because it missed one long range beam-beam collision and the higher tune was due to the fact the last few bunches had smaller emittances.

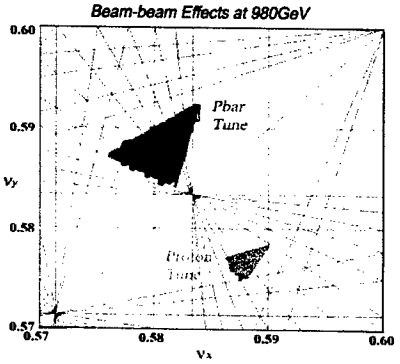


Figure 6: The tune diagram of the proton and antiproton bunches

The Figure 6 shows the usual working points of the Tevatron for proton and antiproton bunches. The tunes of both beams overlap 12th order resonance lines.

Emittance Scallops

Another beam-beam effect observed in the Tevatron is that occasionally antiproton emittances blow up when the tunes of the antiproton bunches are not optimized. The emittance blows up slowly, over about 5~15min. Afterwards we observe an enhanced emittance variation from bunch to bunch, which is shown in Figure 7, and is called the emittance scallop effect.

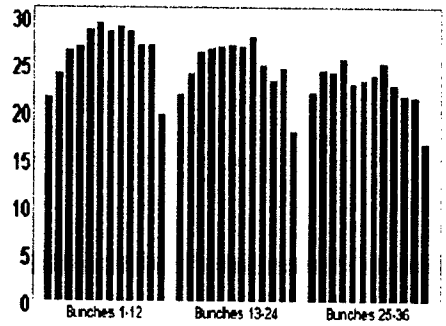


Figure 7: Emittance scallops of Antiproton bunches measured by Tevatron Fly wire.

The emittance blow up degrades the luminosity. Thus, some studies were carried out trying to use the TEL as beam-beam compensation to eliminate these emittance blow ups [5]. Moreover, we must be careful in choosing the Tevatron working point. Unfortunately, the tunes and coupling, etc. are drifting in time [6]. It takes a lot of effort to re-optimize the Tevatron in every other week.

EFFECTS OF HELIX SIZE

One of the most direct studies on long range beam-beam effect was carried out by investigating the effects of the helix size on the colliding beams. Figure 8 below shows the proton and antiproton losses versus the helix sizes of the Tevatron beam orbit for 980GeV at the end of HEP store.

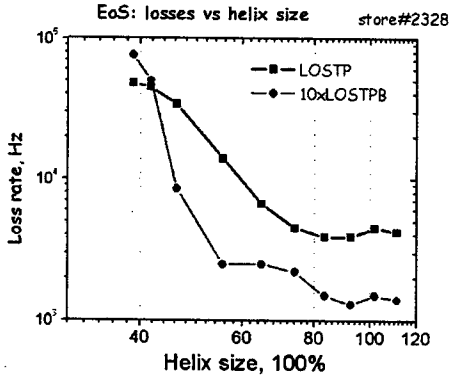
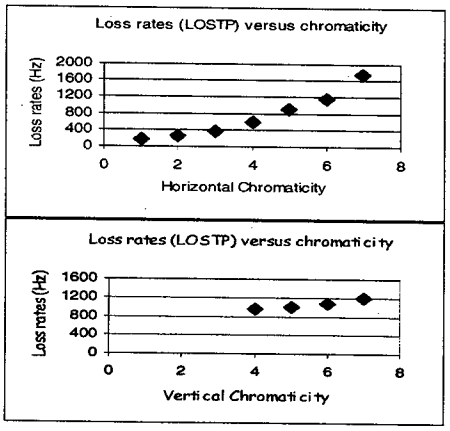


Figure 8: The beam losses versus the beam separation.

The loss rates are low and approximately flat within 82~110% of the nominal helix size, and they went up as the helix size is decreased, which agrees with theoretical expectations, since much stronger long range beam-beam effects cause larger beam-beam tune shifts and shift the more of the beam onto nonlinear resonances, as the beam separation gets smaller.

EFFECTS OF THE CHROMATICIY

The chromaticity is the main factor which causes proton beam losses during injection at 150GeV when the proton



beam is on the helical orbit. Generally, the lower the chromaticity, the less is the proton loss. The Figure 9 above shows a chromaticity scan at injection energy on the proton orbit for coalesced bunches. One can see that when the horizontal chromaticity was lowered to 1 unit, we had minimum losses. However, we could lower the vertical chromaticity onuly down to 4 units, where the head-tail instability occurred. For normal Tevatron operation, we now apply transverse beam feedbacks, in order to be able to lower the chromaticity to improve the proton lifetime at injection.

SUMMARY

Beam-beam effects are the key to further Tevatron Run II upgrades. Intensive studies were carried out on beam separation scheme, working points, beam emittance control, etc. We have plans and a schedule for further beam-beam studies aimed at improving the Tevatron performance with increasing beam intensity, so as to provide a higher luminosity and stable operation.

REFERENCES

[1] Tanaji Sen et al., this conference, TPPB069 and TPPB067.
[2] Cheng-Yang Tan, this conference, WPPG052
[3] X. Zhang et al., this conference, TPPB076
[4] Alexahin Yuri, FERMILAB-Pub-00/120-T(2000)
[5] K. Bishofberger et al., this conference, TPPB083 and MOPA011
[6] Mike Martens, this conference, FPAB031

THEORETICAL STUDIES OF BEAM-BEAM EFFECTS IN THE TEVATRON AT COLLISION ENERGY

T. Sen*†, B. Erdelyi and M. Xiao

Abstract

The dynamics due to the long-range beam-beam interactions depends on several beam parameters such as tunes, coupling, chromaticities, beam separations, intensities and emittances. We have developed analytical tools to calculate, for example, amplitude dependent tune shifts and chromaticities, beam-beam induced coupling, and betatron and synchro-betatron resonance widths. We report on these calculations and dynamic aperture calculations with long-term tracking. These theoretical results are compared with observations at collision energy and used to predict performance at design values of beam intensities and emittances.

1 INTRODUCTION

Beam-beam phenomena have limited the beam currents and the luminosity achievable in the Tevatron. Injected proton currents are about 10 times larger than the anti-proton currents so beam-beam effects have largely acted on the anti-protons at all stages of the operational cycles. At collision of Tevatron Run IIa , 36 anti-proton($\bar{p}$) bunches in three trains of twelve bunches collide with 36 proton(p) bunches. Each bunch will experience two head-on interactions at B0 and D0 and seventy long-range interactions. These long-range are distributed over the entire ring with differing beam separations and differing phase advances from one interaction to the next. Fig. 1 shows the beam separations (in unit of the $r.m.s.$ beam size) at all the seventy-two locations of beam-beam interactions for bunch 1, 6 and 12. The simulation of long-term tracking shows that long-range beam-beam interactions, in particular, these nearest interactions have the dominant effects on the dynamic aperture. It is well known that the long-range beam-beam force generates amplitude dependent tune shift, which in turn implies that the chromaticity shift is also amplitude depedent. These amplitude dependencies induce the familiar tune footprint, and also coupling and chromaticity spread within a bunch.

We have developed analytical tools to calculate, for example, amplitude dependent tune shifts and chromaticities, beam-beam induced coupling, and betatron and synchro-betatron resonance widths. In this paper, we report on these calculations.

2 BEAM-BEAM TUNE SHIFT

For details on the derivation of the formulae see [1]. The expression for the horizontal amplitude dependent tune shift is

$$\Delta\nu_x = \frac{4\pi C}{\varepsilon_x}\int_0^1 \frac{e^{-(p_x+p_y)}}{v\left[v\left(r^2-1\right)+1\right]^{1/2}}\sum\nolimits_x\sum\nolimits_y dv, \quad (1)$$

where

$$\sum\nolimits_x = \sum_{k=0}^{\infty}\frac{\left(\frac{a_x}{d_x}\right)^k}{k!}\Gamma\left(k+\frac{1}{2}\right) \times\left[I_k\left(s_x\right)\left(\frac{2k}{a_x^2}-v\right)+I_{k+1}\left(s_x\right)\frac{s_x}{a_x^2}\right], \quad (2)$$

$$\sum\nolimits_y = \sum_{l=0}^{\infty}\frac{\left(\frac{a_y}{d_y}\right)^l}{l!}\Gamma\left(l+\frac{1}{2}\right)I_l\left(s_y\right). \quad (3)$$

As shorthand notations we introduced the ratio of rms beam sizes $r=\sigma_y/\sigma_x$, and dimensionless variables for the amplitudes and separations according to $a_x=\sqrt{2\beta_x J_x}/\sigma_x$, $d_x=D_x/\sigma_x$ and similarly defined a_y and d_y. Using these notations, the following relationships have been used in (1): $p_x=v\left(a_x^2+d_x^2\right)/2$, $r_x=va_x^2/2$, $s_x=va_xd_x$, $p_y=fv\left(a_y^2+d_y^2\right)/2$, $r_y=fva_y^2/2$, $s_y=fva_yd_y$,where $f=\frac{r^2}{v(r^2-1)+1}$. The vertical amplitude dependent tune shift is derived analogously, due to symmetry in x and y.

For example, the tune footprint shown in Figure 2 includes all beam-beam interactions acting on $\bar{p}$ bunch 6, and the analytical results are superimposed on the footprint obtained by tracking.

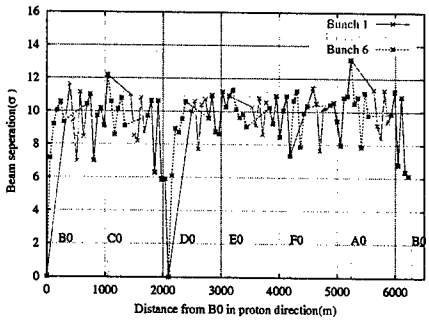


Figure 1: Separations at beam-beam encounters for pbar bunch 1, 6 and 12

3 BEAM-BEAM CHROMATICITY

To provide a formula for the computation of the chromaticities, we split the separation into two parts: one due to the closed orbits of on-momentum particles, the other due to dispersion for off-momentum particles. Denoting

* tsen@fnal.gov

† Work supported by the U.S.Department of Energy under contract No.DE-AC02-76CH03000.

0-7803-7738-9/03/$17.00 © 2003 IEEE

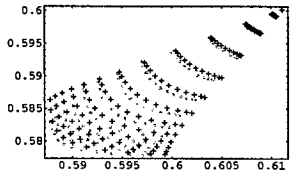


Figure 2: Tune footprints corresponding to all 72 interactions. Shown is a superposition of the analytical results with the tune footprints obtained by FFT of tracking data.

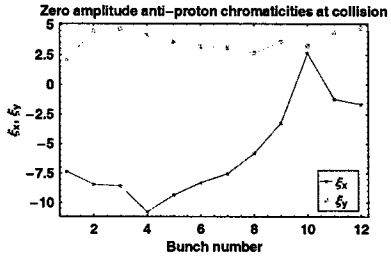


Figure 3: Zero amplitude chromaticities of a train of 12 anti-proton bunches.

the dispersion (in units of rms beam size) at the location of the interaction by η, first we make the following replacements in (1): $d_x \mapsto d_x + \eta_x\delta$, $d_y \mapsto d_y + \eta_y\delta$, where δ is the relative momentum or energy deviation. The horizontal zero amplitude chromaticity is given by

$$\xi\frac{4}{d^6}\left(d_x^3\eta_x + 3d_x^2d_y\eta_y - 3d_xd_y^2\eta_x - d_y^3\eta_y\right). \quad (4)$$

The vertical chromaticity can be calculated similarly.

Figure 3 shows the zero amplitude chromaticities of a train of 12 $\bar{p}$ bunches. Notice the large variations in the bunch-to-bunch horizontal chormaticities.

4 BEAM-BEAM INDUCED COUPLING

The minimum tune split is a measure of the global coupling and is given by the amplitude of the complex term driving the difference resonance $(\nu_x - \nu_y) = p$ [2]. This driving term due to beam-beam interaction at a location s in the ring is given by

$$F(a_x, a_y) = -\frac{N_p r_p\sqrt{\beta_x\beta_y}}{2\pi\gamma_p}\frac{r}{\sigma_x^2}(a_x + d_x)(a_y + d_y)$$
$$\times \exp\left\{i(\psi_x - \psi_y - (\nu_x - \nu_y - p)\frac{s}{R})\right\} \times$$
$$\int_0^1 dv \frac{v}{[v(r^2-1)+1]^{3/2}}$$
$$\cdot\exp\left\{-\frac{v}{2}[(a_x^2 + d_x^2) + f(a_y^2 + d_y^2)]\right\} \quad (5)$$

Fig. 4 shows the minimum tune splits of zero amplitude particles for 12 bunches in a train. Bunch to bunch difference in coupling can be identified.

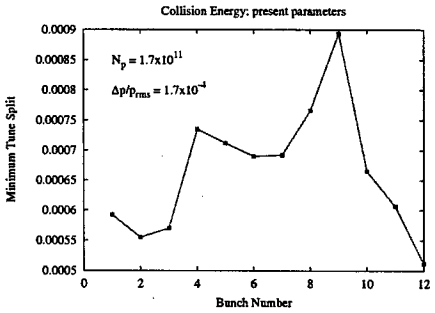


Figure 4: Small amplitude beam-beam coupling at collision

5 RESONANCE STRENGTHS

Resonance driving terms have been computed by the normal form method in the code Cosy Infinity. Their normalization along the diagonal at an amplitude of 2σ and summation over the subresonances are shown in Figure 5. The two pictures show the resonance strengths of the resonances driven by the lattice nonlinearities, and by the addition of the beam-beam interactions. The largest strength is always scaled to 1. Clearly, the lattice drives mostly third order resonances while the beam-beam effects drive the seventh and fifth order ones. There is no single dominating resonance. This makes active beam-beam compensation harder. We are looking into current wire correction of the resonance strengths, and as a first step we are investigating whether with a few appropriately placed wires the same type of resonance structure could be excited. In case of affirmative answer the beam-beam driven resonances could be significantly reduced.

6 FOOTPRINT COMPENSATION

Since at collision the nearest parasitics dominate the nonlinear dynamics, we attempted to minimize the footprints, by compensating for the aspect ratios or dispersions, as shown in [1]. Compensation of aspect ratios clearly reduces both the shift and the spread of the tunes, as can be seen in the left plot of Figure 6. On the other hand, compensation of aspect ratios does not have a dramatic effect on the chromaticity footprint. Perhaps more importantly, aspect ratio compensation does not harm the chromaticity footprint. The chromaticity footprint is mainly affected by compensation of the dispersions; there is a significant reduction in the size of the footprint. The result is contained in right plot of Figure 6. Unfortunately, by tracking with the conditions corresponding to the compressed footprints we concluded that the compensations have a marginal effect on the DA, increasing the average DA by up to ≈ 0.5 σ and the minimum by 1 σ, but fail to show the dramatic effects similar to the footprint size reduction.

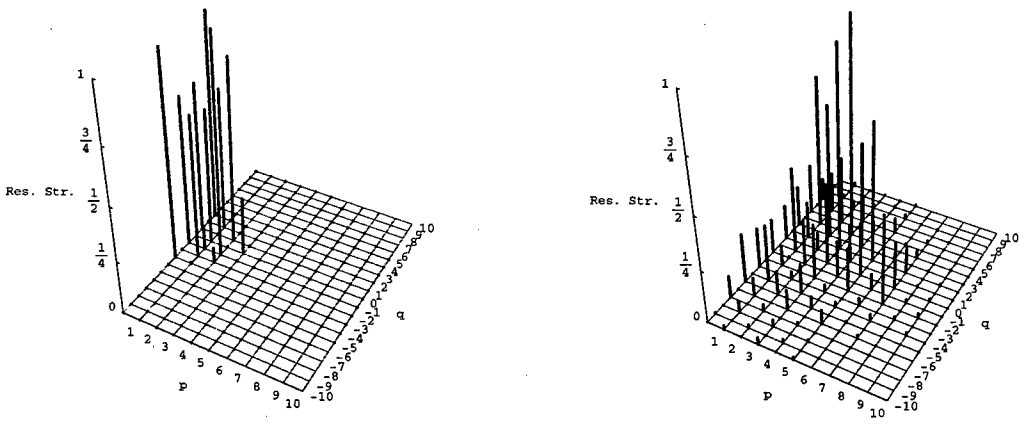


Figure 5: Resonance strengths at collision a) without and b) with beam-beam effects.

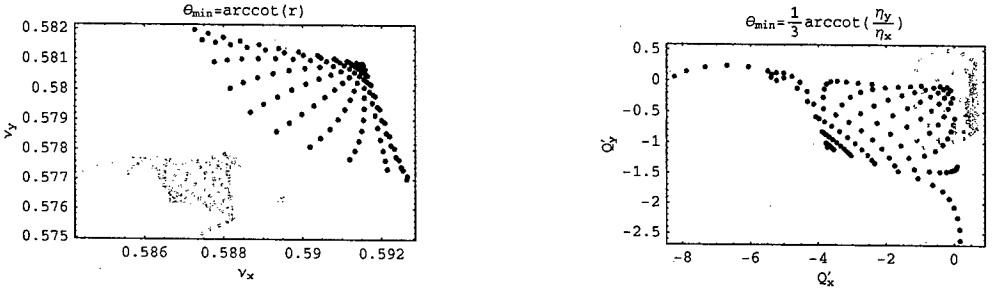


Figure 6: Left:Tune and Right: Chromaticity footprint compensation of the nearest parasitic beam-beam interactions.

7 NONLINEAR EFFECTS ON DYNAMIC APERTURE

We have calculated DA(Dynamic Aperture) due to the beam-beam effects by long-term tracking [3]. Due to the large proton bunch length(comparable to β^*=0.35m) and the rapidly varying betatron phase at the IPs, the anti-protons experience these kicks over a range of phases. For head-on interactions, we divided a proton bunch into 9 slices, taking the bunch length effects into account. These effects include hour glass effects (assuming a Gaussian beam distribution longitudinally) and phase variations (propagation between slices).The long-range interactions are modeled by delta function kicks. Fig. 7 gives the dynamic aperture in function of proton bunch intensities for $\bar{p}$ bunch 1, 6 and 12. Particles are tracked for 100,000 turns. We can see that DA of $\bar{p}$ bunch 1 is better than that of $\bar{p}$ bunch 6 except at one point. DA of $\bar{p}$ bunch 12 is also better than that of $\bar{p}$ bunch 6 at most of the intensities.

8 CONCLUSION

We have developed analytical tools for the computation of the amplitude dependent tune shifts, linear chromaticities and couplings due to beam-beam interactions. The expressions can be used for efficient numerical evaluation at any amplitude, separation, dispersion and aspect ratio.

At collision, the DA is largely dependent on proton intensity, and different from bunch to bunch. We found that

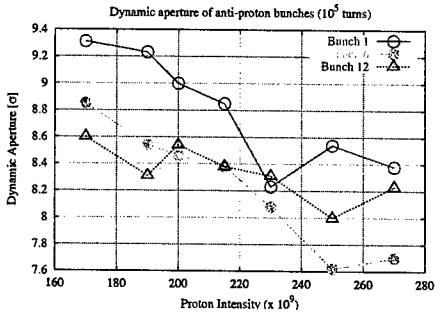


Figure 7: Dynamic aperture $vs.$ proton beam intensity

the DAs are determined by the long-range interactions. The tune footprint is largely determined by the head-on collision, but head-on collision have very little effect on the DA.

9 REFERENCES

[1] B. Erdelyi and T. Sen, Analytic studies of the long-range beam-beam tune shifts and chromaticities, FNAL-TM-2171

[2] T.Sen, unpublished notes

[3] T.Sen and M. Xiao, Beam-beam interactions in RUN IIa, Beams Division Document 217 [http://beamdocs.fnal.gov/DocDB/0002/000217/001/tsen.pdf]

[4] T.Sen, The Beam beam interaction of finite length bunches in hadron colliders, Fermilab-Pub-00-93(2000)

TEVATRON RUN II LUMINOSITY, EMITTANCE AND COLLISION POINT SIZE

J. Slaughter, J. Estrada, K. Genser, A. Jansson, P. Lebrun, J. C. Yun,

Fermi National Accelerator Laboratory, Batavia, IL 60510,

S. Lai,

University of Toronto, Toronto, Canada M5S 1A7

Abstract

We compare the Tevatron luminosity as measured by the CDF and D0 experiments with that computed from machine characteristics. We also compare the CDF measurements of the size of the interaction region with that predicted by machine parameters. Although these results are still preliminary, they show promise as a useful crosscheck of the instrumentation and our understanding of the Tevatron machine characteristics.

INTRODUCTION

Understanding the behavior of the Tevatron depends on understanding the instrumentation and the lattice parameters. The experiments D0 and CDF provide independent measurements of the luminosity[1] and of the size of the luminous region. The luminosity (10^{30}cm^{-2}sec^{-1}) can also be calculated from lattice parameters and beam measurements in the Tevatron, as

$$L = \frac{10^{-5} f B N_p N_{\bar{p}} (6\beta_r\gamma_r)}{2\pi\beta^* \sqrt{(\varepsilon_p + \varepsilon_{\bar{p}})_x (\varepsilon_p + \varepsilon_{\bar{p}})_y}} H(\sigma_l/\beta^*). \quad (1)$$

Here, N_p and $N_{\bar{p}}$ are the numbers of protons and anti-protons per bunch (~10^9), B is the number of bunches (36), f is the revolution frequency (47.7 KHz) and $\beta_r\gamma_r$=1045 is the relativistic factor, β^* is the beta function at the interaction point (measured in cm, and assumed equal in x and y). H is the hourglass factor, a function of the bunch length σ_l and β^*, and finally ε_p and $\varepsilon_{\bar{p}}$ are the proton and anti-proton 95% normalized emittances in π-mm-mr. Comparing the calculated luminosity to the measured one provides a crosscheck between the Tevatron beam instrumentation and the detectors.

The experiments very accurately measure the size of the luminous regions at the interaction points as a function of z (distance along the beam axis) from the distributions of primary vertices as measured by the silicon vertex detectors. In the simplest model,

$$\sigma(z) = \sqrt{\varepsilon(\beta^* + (z-z_0)^2/\beta^*)}, \quad (2)$$

where σ is the rms beam size, $\varepsilon = (\varepsilon_p \varepsilon_{\bar{p}})/((\varepsilon_p + \varepsilon_{\bar{p}})$ is a pseudo-emittance and z_0 is the z location where β is a minimum. Note that if the p and pbar emittances are equal, the pseudo-emittance is half the equivalent beam emittance.

Although not discussed in this paper, CDF can measure the bunch lengths of the p and pbar bunches separately by using the Central Outer Tracker (COT) information in conjunction with the time of flight (TOF) system[2].

SIZE OF THE LUMINOUS REGIONS

CDF has fit for ε, β^* and z_0 in Equation 2 for 20 runs in 14 stores from the last 6 months of 2002. Figure 1 shows typical distributions for one run with fits to Equation 2. The average values of the parameters are given in Table 1. The average β^* is 38 cm, 9% larger than the nominal 35 cm and the minimums are displaced with respect to the center of CDF. It is expected that β^* and z_0 are the same store to store, but not ε. Fixing β^* to the average β^*, 38.6 cm in x and 38.0 in y, and then refitting improves the fits, while fixing β^* to the nominal 35 cm gives slightly worse fits. The average over 20 runs of the run-by-run ratio of x and y pseudo-emittances is 1.01±.04. If the proton and anti-proton emittances are assumed to be the same*, then the pseudo-emittances imply that their values are 15.7±1.5 π-mm-mr in the horizontal plane and 15.8±1.5 π-mm-mr in the vertical plane. The largest uncertainties in the vertex measurements are, first, that they integrate over a significant time period, ranging from 4 to 15 hours with an average of 8 hours, in which the emittances are changing, and, second, they rely on proper subtraction of the measurement resolution. In this preliminary analysis the experimental resolution that is subtracted in quadrature from the uncorrected beam width is about equal to the resulting beam width.

* The flying wires give a ratio of anti-proton to proton emittance of 1.00±.22 in the horizontal plane and 1.03±.13 in vertical plane, based on data from 95 stores.

This works was supported by Department of Energy of the U.S. under contract no DE-AC002-76CH03000 and by the Natural Sciences and Engineering Research Council of Canada.

0-7803-7738-9/03/$17.00 © 2003 IEEE

Table 1 Luminosity weighted averages over 20 runs from fits to Equation 2. The errors are the weighted standard deviations. The emittances ε_x and ε_y are pseudo-emittances as defined in the text. The column labeled equivalent emittance is obtained by inverting $\varepsilon = (\varepsilon_p \varepsilon_{\bar{p}})/2(\varepsilon_p + \varepsilon_{\bar{p}})$, assuming the proton and anti-proton emittances are the same.

	β_x (cm)	β_y (cm)	ε_x π-mm-mr	ε_y π-mm-mr	Z_{0x} (cm)	Z_{0y} (cm)	equivalent emittance π-mm-mr
β_x, β_y free	38.6±2.5	38.0±3.0	7.9±1.1	7.8±1.0	14.2±1.6	-9.2±1.7	15.7±1.5
β_x, β_y fixed	38.6	38.0	8.0±1.1	7.9±1.1	14.3±3.1	-9.2±1.4	15.8±1.5
β_x, β_y fixed	35.0	35.0	8.3±1.2	8.1±1.2	13.3±1.1	-8.5±1.4	

LUMINOSITY DETERMINATIONS

Using Equation 1, we compare the luminosities as measured by CDF and D0 with the calculated luminosities. The intensities are measured using the FBIs (Fast Bunch Integrator)[3], The hourglass factor is calculated using the bunch length σ_l from the SBD (Sampled Bunch Display)[4] and the emittances are measured by either the flying wire system (FW)[5] or the synchrotron light (SL) system[6]. Since the flying wires cause background for the experiments, they are only flown once at the beginning of the store and then again at the end, just before terminating the store. The SL measurements are made continuously throughout the HEP store.

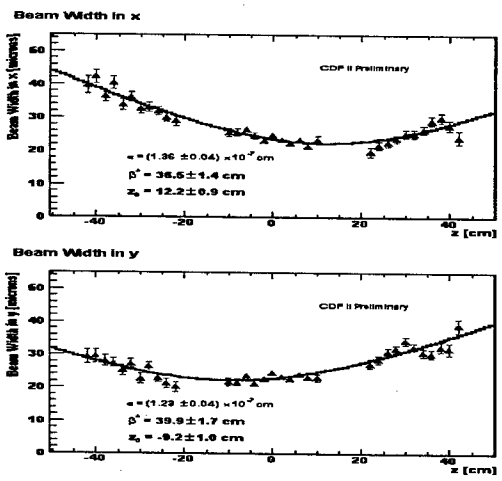


Figure 1 Example plot for one run of 20 runs showing luminous region size versus z and the fits to Equation 2. Typical correlation coefficients of the fits are about -0.8 for (β^*, ε), 0.5 for (β^*, z_0), and -0.6 for (ε, z_0)

Figure 2 plots the ratio of the bunch-by-bunch calculated luminosity to the CDF luminosity at the beginning of the store as a function of CDF luminosity for a sample of 52 recent stores. The calculated luminosity uses the FW emittances. Figure 3 shows the same ratio but for D0, using 5 stores. Each store has approximately 100 measurements taken every 10 minutes. The calculated luminosity uses the SL emittances and assumes that the horizontal emittance equals the vertical one for p and pbar respectively. The main characteristic of the plots is a systematic scale factor that is a function of luminosity, although with different intercepts and slopes. In Figure 2 the slope is -0.22±0.03 and the intercept is 0.92±.02(Fit 1). In Figure 3, the slope is –0.0634±0.0002 and the intercept is 0.7702±0.0003(Fit 2). The equivalent analysis but for CDF, gives –0.0826±0.0012 and 0.7455±0.0008(Fit 3).

We now investigate possible explanations for both the dependences on measured luminosity and the differences in the fit parameters. Note that multiplying the calculated luminosity by a constant factor changes both the intercept and the slope of the fits to the ratio.

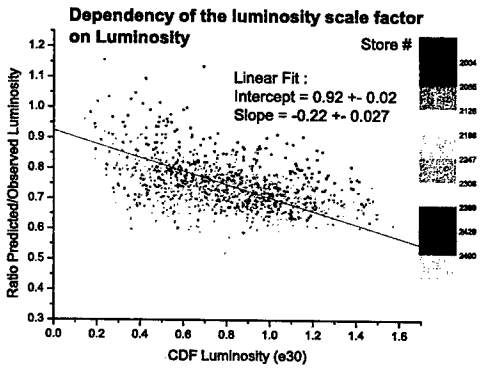


Figure 2 Ratio of calculated to measured CDF per bunch luminosity at the beginning of the store for a sample of 52 stores versus CDF luminosity.

We first consider the measured luminosities. Both CDF and D0 quote statistical errors of less than 1% and systematic errors of about ±5%. The ratio of the total D0 measured luminosity to that of CDF versus CDF luminosity is linear, with an intercept of 0.984±.001 and a slope of –0.00194±.00005. (At CDF luminosities of 20 and 40 10^{-30} cm^{-2} sec^{-1}, the ratio is 0.95 and 0.91 respectively.) This difference is enough to account for the difference between the D0 and CDF versions of the fits to the data in Figure 3 quoted above. Although there are significant store-to-store variations, within errors the

measured luminosities for CDF and D0 are linear with proton and anti-proton intensities, with no offset.

N_p and $N_{\bar{p}}$ have been calibrated to ±2%. H is not very sensitive to errors in σ_t and is quite constant for the data in Figures 2 and 3. For the data in Figure 2, the average H is .48±.02, and the average σ_t is 2.4±.4 ns for anti-protons and 2.5±.5 ns for protons. By definition, the β^* dependence is independent of luminosity. A larger than nominal β^* as indicated by the luminous region measurements reported above makes the disagreement slightly worse. If β^* were different at D0 than at CDF, it could help explain the differences between Fits 2 and 3. Most Tevatron experts believe the lattice parameters are only know to ±10%. These two factors could explain an intercept and slope factor of the order of ±10%.

The final factor in Equation 1 is the combination of emittances $F_{emit} = \sqrt{(\varepsilon_p + \varepsilon_{\bar{p}})_x (\varepsilon_p + \varepsilon_{\bar{p}})_y}$. A major difference between the data sets in Figures 2 and 3 is that the calculated luminosity uses the flying wire emittances in the first case and the synchrotron light emittances in the second case. There is direct evidence of a difference between the flying wire emittances and those measured by synchrotron light. Both measurements of emittances are recorded simultaneously at the beginning of each store. Comparing the ratios of emittances bunch by bunch over a large number of stores gives the relationships between the two methods shown in Table 2. However, this study gives no information as to whether either of them is correct. Preliminary beam scraping results give good agreement with proton vertical emittances and show significant discrepancies for the anti-proton vertical emittance measurements, in agreement with Table 2, indicating that the flying wire emittances are somewhat more reliable than the synchrotron light measurements. However, there is also evidence that the lattice parameters at the synchrotron light and flying wire locations are different from what is assumed in these calculations and could explain some of the inconsistencies.

The effective emittance is defined by solving Equation 1 for the factor F_{emit}. This can then be directly compared to F_{emit} evaluated with FW emittance measurements. For the same data as in Figure 2 averaged over all 36 bunches in the machine, the ratio of the FW F_{emit} to the effective emittance is linear in measured luminosity with an intercept of 0.97±0.03 and a slope of –0.004±.001 For luminosities of 20 and 40 $10^{30}cm^{-2}sec^{-1}$, this translates into ratios of effective emittance to F_{emit} of .84-.94 and .74-.88 respectively. This result is very consistent with the ratio (.85) of the average effective emittance 19.6±2.9 and the average flying wires emittance factor 23.0±3.2 π mm mr evaluated for the same data.

DISCUSSION AND CONCLUSIONS

In this paper we have summarized current, as yet preliminary, understanding of the agreement between accelerator performance numbers as measured by Tevatron instrumentation compared to what is seen by the experiments. While there is qualitative agreement, much remains to be done. The different aspects of the comparisons need to be done on the same data sets. D0 is doing a luminous region study similar to that of CDF and both experiments are working on another method[7] of measuring the size of the luminous region in which the measurement resolution factors out, providing an important crosscheck. More scraping studies and better knowledge of the lattice parameters will help calibrate the flying wires and the synchrotron light. *We thank all members of the Sequenced Data Acquisition team for their dedicated support.*

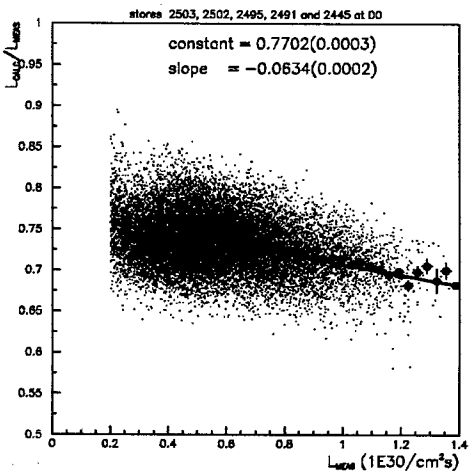


Figure 3 Ratio of calculated to measured D0 bunch-by-bunch luminosity during 5 stores versus D0 measured luminosity.

Table 2. Coefficients for the best linear fit formula for synchrotron light emittances (SL) in terms of the flying wire (FW) emittances (SL = Intercept + Slope*FW).

Quantity	Slope	Intercept
ε_x for protons	1.12±0.14	8.9±2.0
ε_y for protons	1.28±0.17	-0.5±4.7
ε_x for anti-protons	0.65±0.21	34.2±4.3
ε_y for anti-protons	0.64±0.21	14.1±6.5

REFERENCES

1 D0 Collaboration, Fermilab_Conf-98/395-E, and for CDF, D. Acosta *et al.*, Nucl. Instrum. Meth. A **494**, 57 (2002).
2 M. Jones *et al,* Fermilab TM-2172.
3 G. Vogel *et al,* A Multi-Batch Fast Bunch Integrator for the Fermilab Main Ring
4 S. Pordes *et al,* Measurements of Proton and Antiproton beam intensities in the Tevatron' these proceedings
5 W. Blokland *et al,* A new Flying Wire System for the Tevatron, PAC'97.
6 H. Cheung, Performance of a Beam Monitor in the Fermilab Tevatron Using Synchrotron Light, these proceedings
7 L. Ristori *et al,* CDF Note 4189.

CORRECTION MAGNETS FOR THE FERMILAB RECYCLER RING

GW Foster, HD Glass, C Gattuso, DE Johnson, CS Mishra, JT Volk, M-J Yang
FNAL, Batavia, IL 60510, USA

Abstract

In the commissioning of the Fermilab Recycler ring the need for higher order corrector magnets in the regions near beam transfer lines was discovered. Three types of permanent magnet skew quadrupoles, and two types of permanent magnet sextupoles were designed and built. This paper describes the need for these magnets, the design, assembly, and magnetic measurements.

1 INTRODUCTION

The Fermilab recycler[1] is an 8 GeV anti-proton storage ring. The magnets for this storage ring are made of combination gradient magnets and quadrupoles[2]. All main magnets are hybrid permanent magnets with low carbon steel pole pieces and strontium ferrite to provide the field[3]. As operational experience with the Recycler has been gained, the need for higher order correction elements became apparent. Beam measurements revealed a skew quad component in the field region of the Lambertsons[4] used for extraction and injection between the Main Injector and Recycler. To minimize the resultant x-y coupling, a pair of skew quads were installed in the transfer line. The transverse placement of the Lambertsons in the Recycler ring dictated that the closed orbit must be offset (~25 mm) through the field free region of the Lambertson and the adjacent ring gradient magnets. The ring gradient magnets have built in sextupole that feeds down into a quadrupole field due to the orbit offset. This feed down disturbs the focusing properties of both the injection and circulating lattice. A set of three permanent magnet sextupoles were installed to cancel the integrated sextupole component of the adjacent gradient magnets

2 SKEW QUADRUPOLES

The Lambertson magnets use strontium ferrite to generate the required field. The field free region is made by gun boring a hole through the Lambertson base plate. Due to the variation of the residual B field in the ferrite, a skew quadrupole moment is induced in the bend field region of the Lambertson. To compensate this skew quad, several different types of corrector magnets were developed. Although each met the integrated gradient requirement of 0.39 Tesla-meter/meter, the rectangular (2b) design was installed in each Recycler to Main Injector transport line due geometrical constraints.

Submitted May 2003
volk@fnal.gov
Work supported by the U.S. Department of Energy under contract No. DE-AC02-76CH03000

2a. Panofsky Quad

The use of current sheets to make a quadrupole focusing lenses was first suggested W. K. H. "Pief" Panofsky. These current sheets can also be realized by the use of permanent magnet material. For the panofsky

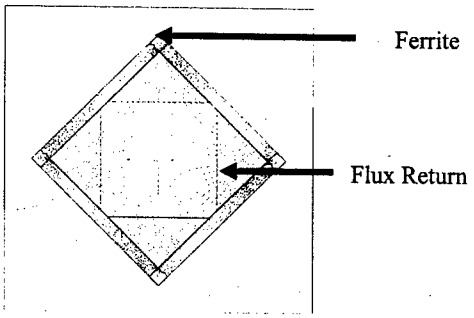


Figure 1: PANDIRA model of Panofsky quadrupole

style quad a 101.6 mm square steel flux return was built and triangular shaped grade 8-strontium ferrite magnets were put in the corners (Figure 1). The open aperture of the magnet, 101.6 mm by 50.8 mm, was set by the size of the beam pipe. A two dimensional magnetic model was made in PANDIRA. A Br of 3800 Gauss and Hc of 3500 oersteds were used in the PANDIRA file. The field was predicted to be 4.96 Tesla/m, with an integrated field of 0.5 Tesla-meter/meter predicted for bricks 0.1 m long. The magnet was measured at Fermilab's Magnet Test Facility using a tangential coil. The integrated field was found to be 0.471 Tesla-meter/meter or 5.8% low. This may be explained as loss of field through the ends, which is not modeled in the 2-D codes.

To adjust the integral gradients, triangular pieces of steel in the same cross-section as the upper and lower magnets (101.6 mm x 50.8mm) and 0.9 mm thick were added at both ends top and bottom to reduce the field. Figure 2 shows the relation between integral gradient versus the total number of steel shims.

The simple linear relationship shows that the magnet can be tuned over a range of 0.1 Tesla-m/m. Beyond that range a clear saturation of the steel shims sets in.

One of the requirements for these magnets is that the Recycler vacuum not be opened to air during installation. This required that the magnet be split to install around the beam pipe. To accomplish this the upper and side magnet material was glued to the upper flux return using Loctite Depend™. The magnet was mounted on the test stand the top was removed and re-installed multiple times. Each time the magnet was measured. After the first opening the field change from

0-7803-7738-9/03/$17.00 © 2003 IEEE

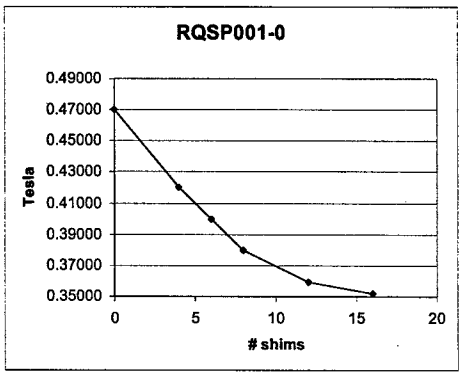


Figure 2: Trimming the integrated skew quad strength as a function of the total number of shims added

0.4711 Tesla-m/m to 0.4700 Tesla-m/m. Successive changes showed a variation of 0.0002 Tesla-m/m or 4 parts in 10^4. There was no attempt to provide precision alignment between the top and bottom parts of the magnet.

2b. Rectangular Skew Quadrupole

A variation of the skew quadrupole was designed. This magnet required no angle cutting of the Strontium Ferrite magnets. It did require more machine work on the flux returns. Figure 3 shows the PANDIRA output for this magnet. The corners were clipped to allow closer positioning of the magnet to the adjacent beam line. This magnet was 152.4 mm in length with a gradient of 4.2 Tesla per meter. This magnet was also designed to be split apart and installed around the vacuum pipe of the recycler. Similar studies were using shorting steel were done on this type of magnet yielding similar results. The rectangular quad was the final design installed in the Recycler.

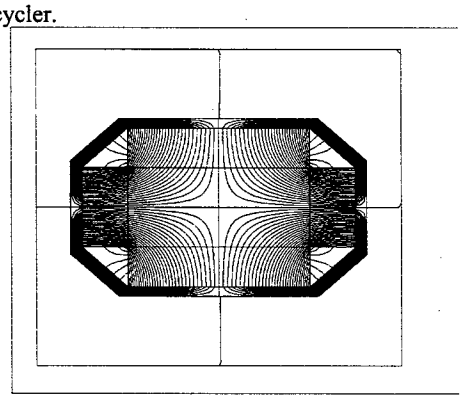


Figure 3: Skew Quad with Rectangular Bricks

2c. Halbach array quad

A third type of skew quad was made using a Halbach array this is a simple two magnet style skew quad as shown in figure 4. A 50.8 mm by 25.4 mm thick strontium ferrite center brick and two 25.4 by 25.4 mm side bricks were used to build the array. The predicted strength was 0.51 Tesla-m/m. The measured strength was0.60 Tesla-m/m. The higher measured strength was due to variation in the Br of the ferrite. Similar strength tuning was used as the previous two styles of magnets.

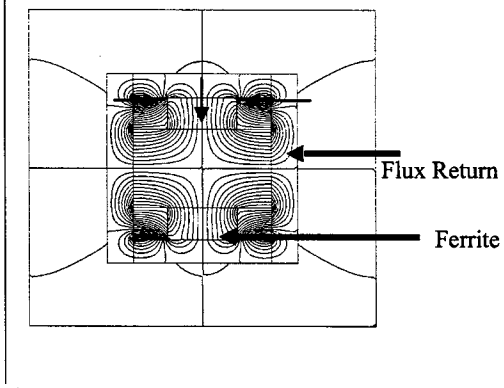


Figure 4: Halbach array skew quad arrows indicate direction of the field array

3 SEXTUPOLES

The required integrated sextupole strength to cancel the sextupole component in each pair of gradient magnets was determined by minimizing the lattice function distortion due to the design orbit offset through the pairs of gradient magnets. The design integrated strengths, B''L/2, ranged from 1.5 to 2.5 Tesla/m, depending on lattice location. The basic design selected was a Halbach array rolled around the pipe. For the sextupole a total of 12 pieces of permanent magnet material were used. The direction of the field rotated by 90 degrees for each magnet. Figure 5 shows a PANDIRA output of the sextupole.

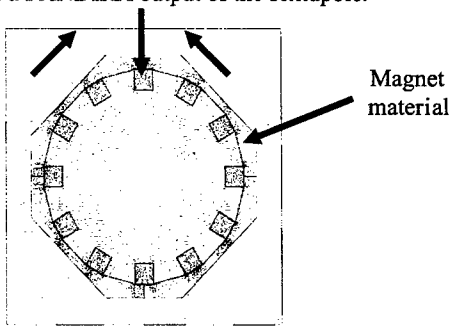


Figure 5: Sextupole field map with typical direction of Br shown

Aluminum spacers were used to separate each of the segments of magnetic material. A hole was drilled the length of each spacer to provide a place to install steel washers. These washers were used to adjust the strength of the sextupole to the desired strength. Figure 6 shows a plot of the total number of washer versus the strength of the sextupoles. A total strength change of 83% was possible by adding washers in all the holes.

Some adjustments of the higher harmonics were possible by asymmetric loading of washers. This was not necessary for these sextupoles.

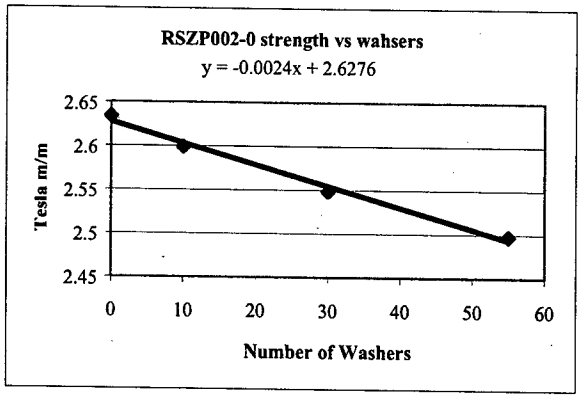


Figure 6: Trimming the integrated sextupole strength as a function of the total number of shims added

The sextupoles were designed to clamp around the beam pipe. This eliminated the need to disturb the Recycler vacuum. It did require that two different internal diameter magnets to be designed. One type fit around the 10.16 by 5.08 cm elliptical beam pipe and the other type fit around the 15.24 cm diameter bellows. Studies were done to assure that the field did not change when the magnets were disassembled and reassemble.

To achieve the required fields the small diameter sextupole used grade 8 strontium ferrite. Each of the 12 channels used 66 mm of ferrite to achieve the desired gradient of 2.3 Tesla /meter.

The larger diameter sextupole use Neodymium Iron Boron magnets with a Br of 11800 Gauss and Hc of 16000 Orsteads part number HS 30 CV. Hitachi metals of Edmore Michigan supplied the material.

Figure 7 shows the PANDIRA prediction of the field at the mid plan along with a hall probe scan of the magnet. The offset in the hall probe data is due to differences in the Br of the magnet material.

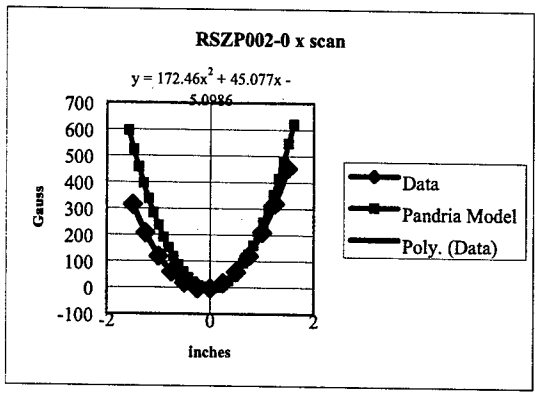


Figure 7: Hall probe scan of sextupole with Pandira model data

The authors would like to thank Dr. B C Brown for help with preparation of this paper and Mark Thompson of the Fermilab Magnet Test Facility for help with measurements.

REFERENCES

1) Stephen D Holmes "Status of the Fermilab Main Injector and Recycler" 1997 Particle Accelerator Conference Conf 97-46
2) H.D Glass, "Permanent magnets for beam lines and the recycler ring at Fermilab", 17th International Conference on High-Energy Accelerators
3) B. C. Brown et al., "Hybrid Permanent Magnet Gradient Dipoles for the Recycler Ring at Fermilab", Proceedings of 15th International Conference on Magnet Technology, 161, 1998.
4) M.P. May et al., "The Design and Construction of the Permanent Magnet Lambertson for the Recycler Ring at Fermilab," Proceedings of PAC'97, Vancouver, Canada, 1997.

ANTIPROTON ACCELERATION IN THE FERMILAB MAIN INJECTOR USING 2.5 MHZ (H=28) AND 53 MHZ (H=588) RF SYSTEMS

V. Wu, C. M. Bhat, J. A. MacLachlan, B. Chase, K. Meisner, J. Dey and J. Reid
FNAL, Batavia, IL 60510, USA

Abstract

During the Run II era at Fermilab, the Recycler stores antiprotons at 8 GeV and the Main Injector accelerates the antiprotons and the protons from 8 GeV to 150 GeV for Tevatron injection. The Recycler injects antiprotons to the Main Injector in 2.5 MHz rf buckets. This report presents an acceleration scheme for the antiprotons that involves a slow ramp with initial 2.5 MHz acceleration and subsequent fast acceleration with 53 MHz rf system. Beam acceleration and rf manipulation with space charge and beam loading effects are simulated using the longitudinal simulation code ESME [1]. Simulation suggests that one can expect about 15% emittance growth for the entire acceleration cycle with beam loading compensations. Preliminary experimental results with proton beam will also be presented.

1 INTRODUCTION

In Run II, four antiproton bunches from the Recycler will be accelerated in the Main Injector from 8 GeV to 150 GeV. Antiproton transfer from the Recycler to the Main Injector is envisioned as 2.5 MHz bucket to bucket transfer to eliminate injection mismatch. An acceleration scheme with a slow ramp (2.5 MHz acceleration) followed by a fast ramp (53 MHz acceleration) was previously developed. (See references [2, 3, 4].) The simulations in this report follow a similar track as those of reference [3] and [4] with the inclusions of space charge and beam loading effects.

2 SIMULATIONS

The Main Injector accepts antiproton bunches from the Recycler with the following initial beam and rf parameters:

- Total beam energy: 8.938 GeV
- Rf frequency: 2.5 MHz
- Rf voltage: 2 kV
- Invariant 95% longitudinal emittance per bunch: 1.5 eVs
- Number of particles per bunch: 6×10^{10}.

The maximum accelerating rf voltages are 60 kV for the 2.5 MHz system and 4 MV for the 53 MHz system.

The ramp curve is shown in Fig. 1. The minimum ramp time is determined primarily by the maximum available 2.5 MHz rf voltage and the heating of the ferrite loaded 2.5 MHz cavities. The parabolic ramp begins at 0.5 second (8 GeV) and stops at 6.2 second (27 GeV front porch) where

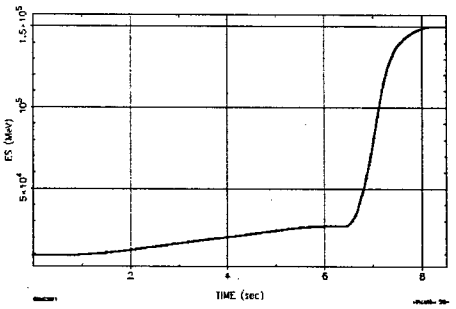


Figure 1: Ramp curve. The slope of the ramp increases to 4 GeV/s at 2 second and remains constant until 5.2 second where it ramps down to zero at 27 GeV. dP/dt during 53 MHz acceleration is about 190 GeV/c/s.

the transfer to 53 MHz system occurs. After 53 MHz capture, the beam is accelerated to 150 GeV in about 1.8 seconds.

The rf programs for the 2.5 MHz and the 53 MHz accelerations are shown in Fig. 2 and 3, respectively. For

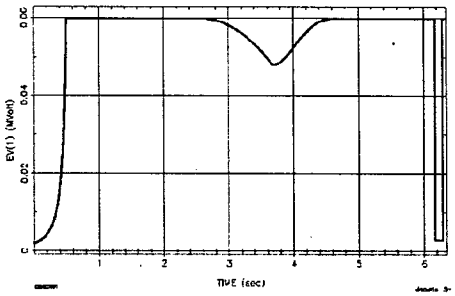


Figure 2: Voltage program for 2.5 MHz acceleration.

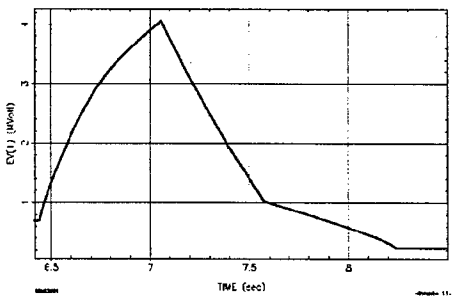


Figure 3: Voltage program for 53 MHz acceleration.

0-7803-7738-9/03/$17.00 © 2003 IEEE

the first 0.5 second, the bunches are adiabatically shrunk by increasing the rf voltage to 60 kV. Because of the lack of phase focusing at transition, the rf voltage is lowered before transition to reduce the energy spread. This maneuver eases the problem of emittance dilution due to transition crossing. The rms emittance dilution for crossing transition is about 3%. At the 27 GeV front porch, the rf voltage drops to 3 kV (or 4 kV) and the bunches are rotated to minimum height with a second harmonic linearizing voltage. Then the h=28 and h=56 voltages are jumped to 60 kV and 10 kV respectively for a quarter period rotation to minimum width. The bunches are captured with the h=588 buckets of 700 kV voltage.

The acceleration and rf manipulation are first simulated without space charge and beam loading for a single bunch. Some pictures of the time evolution of the phase space distribution are shown in Fig. 4. The overall 95% emittance

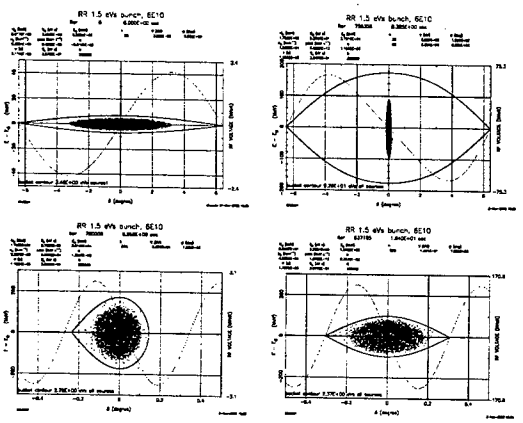


Figure 4: Time evolution of phase space distribution. Top left: Initial distribution. Top right: At the end of quarter synchrotron rotation. Bottom left: Accelerating bunch (53 MHz). Bottom right: Final distribution.

growth is 4% and no particles are lost.

The antiproton bunch intensity is about a factor of 10 smaller than typical Main Injector operation. However, because of the unusually long ramp, simulation with space charge is carried out to check emittance dilution. The effects of beam space charge and coupling impedance between the beam and the beam pipe are simulated with the following input parameters:

- Assume circular beam pipe as a broadband resonator (Q=1) with 1.7 GHz cutoff frequency
- Z_{ll}/n = 1.6 (MI longitudinal impedance per harmonic [5, 6])
- Single bunch intensity = 6×10^{10}.

(See reference [7] for the theoretical basis.) Simulations are also carried out with Z_{ll}/n = 3.2, 4.8, 6.4, 8 and 24×10^{10} (total intensity for 4 bunches). The longitudinal emittance growth verse Z_{ll}/n is shown in Fig. 5. The space charge voltage ranges from 20 to 300 V during the 2.5 MHz acceleration and 3 to 8 kV during the 53 MHz acceleration.

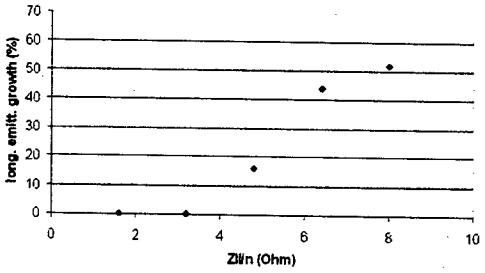


Figure 5: Longitudinal emittance growth vs. Z_{ll}/n.

Within a factor of three of Z_{ll}/n = 1.6, there is no significant emittance growth. For the case of bunch intensity 24×10^{10} and Z_{ll}/n = 1.6, the emittance growth is less than 5% and particle loss is less than 1%.

For the simulation with beam loading of the 2.5 MHz fundamental mode, four bunches and a single cavity are modelled in ESME. The quality factor and the shunt impedance of the 2.5 MHz cavity are 112.5 and 45000 Ω, respectively. To simulate the total beam loading voltage of five cavities, the shunt impedance is increased by a factor of five.

Simulations show that beam loading causes significant emittance dilution and phase shift to the bunch distribution. The peak beam loading voltage for the entire cycle and an instantaneous beam loading voltage are shown in Fig. 6. The maximum beam loading voltage during the cy-

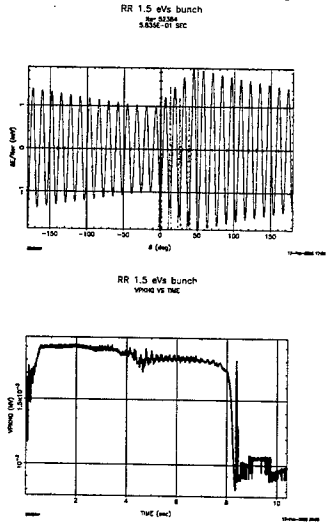


Figure 6: Top plot: Instantaneous beam loading voltage at a particular time along the ring. Bottom plot: Peak beam loading voltage during the entire cycle. Ignore voltage after 8.2 second at which 53 MHz acceleration takes over.

cle is about 1.9 kV. Beam loading problem is most severe at the beginning of the rotation at 27 GeV where the beam loading voltage is 1.4 kV and the cavity voltage is 3 to 4 kV. The bunches are shifted from their bucket centers by about 45 to 50 degrees. Large emittance growth (over a factor

of 2) and significant particle loss are observed after the 53 MHz capture. In conclusion, beam loading compensation is needed for the 2.5 MHz acceleration scheme.

3 EXPERIMENTAL TEST OF 2.5 MHZ ACCELERATION IN MI

Preliminary test of the 2.5 MHz acceleration scheme is conducted using proton beam from the Fermilab Booster. As a first experiment, the Booster beam is used to produce 2.5 MHz bunches in the Main Injector and the bunches are accelerated from 8 GeV to 27 GeV. Since the 2.5 MHz radial and phase control systems are currently under development, the experiment is carried out with open loop conditions–no active radial feedback and phase feedforward controls.

Figure 7 represents a typical data sample taken during the proton acceleration. Four Booster batches are injected

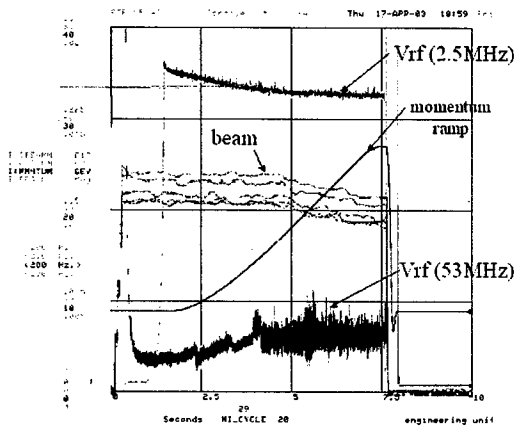


Figure 7: Beam–MI beam intensity in units of E12, Vrf (2.5 MHz)-rf voltage on 2.5 MHz rf system (kV), momentum (GeV), Vrf (53 MHz)-rf voltage on 53 MHz rf system (MV) as a function of time (sec).

into the Main Injector in succession and then are adiabatically debunched into four 2.5 MHz buckets. Once the beams are captured in 2.5 MHz buckets, the 2.5 MHz voltage is adiabatically raised to accelerate the beam. In the meantime, the 53 MHz voltage is paraphrased below 10 kV to minimize the 53 MHz component of the beam. There is 100% transmission up to transition (around 5.2 second). After transition, about 12% of the beam is lost. Since transition crossing is performed manually by moving (realigning) the 2.5 MHz buckets, transition loss is expected. In normal operation, transition phase jump will be controlled by the LLRF phase control system.

Figure 8 shows a sample of mountain range data for the early part of the cycle. The bunches exhibit oscillations and beam loss which are presumably due to the lack of radial and phase controls. These effects can also be due to the fact that the beam loading compensation systems are not yet effectively applied during the acceleration.

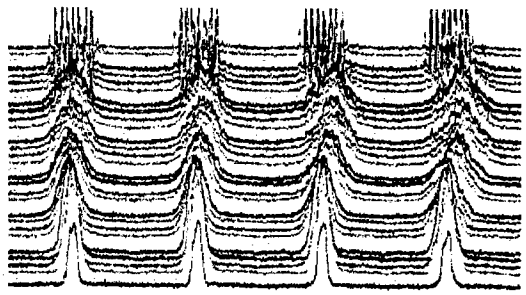


Figure 8: Mountain range bunch data. Four Booster batches of 7 bunches each are adiabatically debunched into four 2.5 MHz buckets. The 2.5 MHz bunches are subsequently accelerated to 27 GeV.

During the acceleration, the transverse emittance was measured using the MI flying wires. Data shows that there are no emittance growths in the transverse directions.

In summary, we have demonstrated 2.5 MHz acceleration up to 27 GeV with open loop operation as a proof of principle. The experimental results are consistent with our longitudinal beam dynamics simulations. In the future, with the operation of the radial and phase control systems, the issues of longitudinal emittance growth, beam loss and beam loading will be carefully examined.

REFERENCES

[1] J. A. MacLachlan, User's Guide to ESME 2002, November 2002.

[2] G. Jackson, The Fermilab Recycler Ring Technical Design Report, FERMILAB-TM-1991, November 1996.

[3] C. M. Bhat, Pbar Acceleration in the MI using 2.5 MHz RF System and RF Specification, MI note 260, January 2000.

[4] J. A. MacLachlan, Antiproton Acceleration in the Main Injector with RF at Harmonic Number h=28 or h=84, FERMILAB-TM-2177, June 2002.

[5] M. A. Martens and K. Y. Ng, Impedance and Instability Threshold Estimates in the Main Injector I, Fermilab internal note.

[6] W. Chou, Intensity Limitations in Fermilab Main Injector, June 1997.

[7] J. A. MacLachlan, Longitudinal Phase Space Tracking with Space Charge and Wall Coupling Impedance, February 1987.

TEVATRON BEAM-BEAM SIMULATIONS AT INJECTION ENERGY

M. Xiao*†, B. Erdelyi and T. Sen, FNAL, Batavia, IL 60510, USA

Abstract

Major issues at Tevatron injection are the effects of 72 long-range beam-beam interactions together with the machine nonlinearity on protons and anti-protons. We look at particle tracking calculations of Dynamic Aperture(DA) under present machine conditions. Comparisons of calculations with observations and experiments are also presented in this report.

1 INTRODUCTION

In Run IIa the Tevatron is operating with 36 proton and anti-proton ($\bar{p}$)bunches, both are distributed in 3 trains of 12 bunches [1]. The Tevatron is initially filled with three trains of twelve proton bunches. The bunches are spaced 21 rf buckets apart. They are injected onto the central orbit and subsequently moved to a helical orbit before anti-protons are injected. The anti-protons are injected four bunches at a time into the abort gaps between the proton bunches, we call this stage Cog0. After the leading four bunches in each train is injected, the anti-protons are cogged by 84 rf buckects to make room for the next four bunches in the abort gap, we call this stage Cog1. The leading eight bunches in each train are cogged again by 84 buckets to allow the injection of the last four bunches in each train. After each train is full, which we call stage Cog2, the two beams are accelerated to top energy, the optic keep unchanged during the ramp. The main beam parameters of the machine conditions at injection are listed in Table 1

Table 1: Beam parameters at injection energy

Parameter	present ($p/\bar{p}$)	Design ($p/\bar{p}$)
Bunch intensity (E11)	2.2/0.13	2.7/0.3
Emittance (95 %) (πmm-mrad)	25/20	20/15
Momentum spread (r.m.s.,σ_p)	$7.\times10^{-4}$/ 4.5×10^{-4}	4.3×10^{-4}/ 4.3×10^{-4}
Chromaticities	(8,8)	(8,8)
working point	(0.583,0.575)	(0.585,0.575)

2 DYNAMIC APERTURE OF PROTONS

One of the key observations at injection is that the lifetime of the protons drops substantially when they are moved from the central orbit to the helical orbit. Fig. 1 shows the DAs(Dynamic Aperture,in unit of beam size σ) of coalesced and uncoalesced protons on center orbit and on proton helix orbit. Particles are tracked for 100,000 turns (2 seconds in the Tevatron). Chromaticity and feed-down sextupoles and measured field errors of all the magnets in the ring were included in this calculation. It is evident that the nonlinearities have a major impact since the DA of uncoalesced protons(dp/p<1.E-4) on central orbit and on helix is larger than 6σ, while the DA of coalesced beam is about 8σ on central orbit and about 5σ on the helix. The physical aperture is (4 - 6 σ), limited at C0. In a typical store, we observed proton lifetime on the central orbit is 4-6 hrs, but 1.5-2 hrs on the helix.

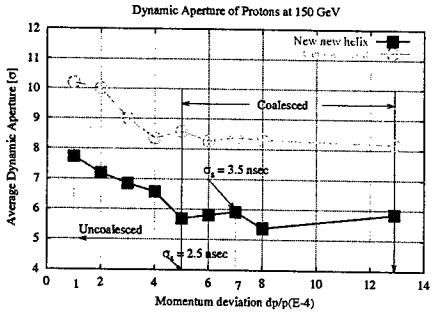


Figure 1: Dynamic aperture of protons.

3 BEAM-BEAM EFFECTS ON ANTIPROTONS

Each anti-proton bunch experiences 72 long-range interactions during injection(after 2nd cogging). Totally there are 138 interaction points in the ring. Fig. 2 shows the separations of all 138 interaction points in the ring after 2nd cogging. The separation follows dispersion pattern since currently the momentum spread of the beam is large. The minimum separation is about 3σ. Beam-beam effects are different for each anti-proton bunch in a train and at different cogging stages since the sequence of long-range interactions is different for each of them.

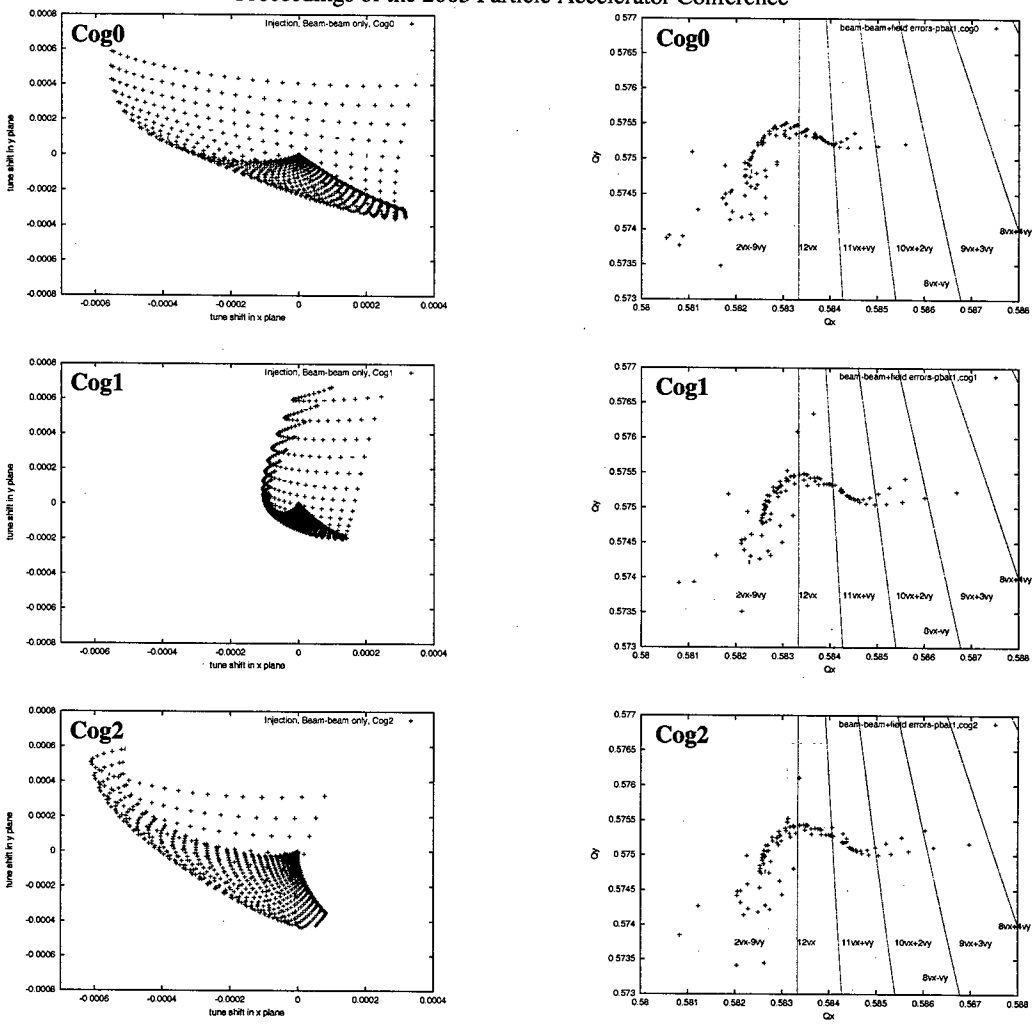
The left column of Fig. 3 shows the tune footprints of anti-proton bunch 1 with only beam-beam effects. Folds can be identified in these figures, at the folds resonance widths are large. When tune shift crosses zero, the beam-beam force has a maximum.

Long rang beam-beam force in the Tevatron creates an additional amplitude dependent chromaticities [2], the source of this chromaticity is the hotizontal and vertical dispersion at the parasitic collisions which makes

* meiqin@fnal.gov

† Work supported by the U.S.Department of Energy under contract No.DE-AC02-76CH03000.

0-7803-7738-9/03/$17.00 © 2003 IEEE



Only Beam-beam

Beam-beam and field errors

Figure 3: Footprint of $\overline{P}$ bunch 1 at three cogging stages.

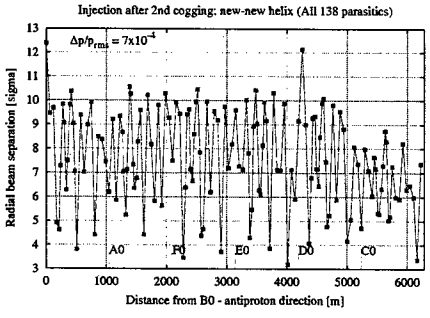


Figure 2: Radical beam separations at 138 interaction points in the ring.

the beam separation depend on the momentm deviation δp/p.Chromaticies due to beam-beam force can be calculated analytical for small amplitude particles. Fig. 4 gives the chromaticities of 12 anti-proton bunches in a train. This additional chromaticities will enhance the synchro-betatron resonances. bunch to bunch difference can be indentified too.

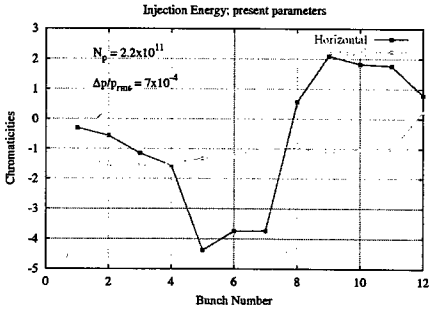


Figure 4: small amplitude beam-beam chromaticities at injection.

Beam-beam force also introduces additional coupling on

anti-protons.Coupling due to Beam-beam force can be calculated analyticaly. Like the tunes and the chromaticities, the strength of the coupling is an amplitude dependent quantity. Fig. 5 shows small amplitude beam-beam coupling for 12 anti-proton bunches in a train. Bunch to bunch diference in coupling can be indentified.

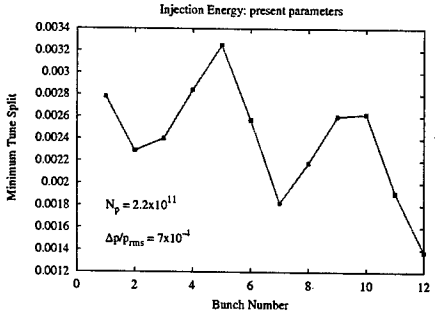


Figure 5: small amplitude beam-beam coupling at injection.

4 DYNAMIC APERTURE OF ANTI-PROTONS

Anti-proton's helical orbit is almost symmetric to the proton helical orbit. In addition to beam-beam effects from the protons, anti-protons are also subject to the machine nonlinearities. The right column of Fig. 3 gives the footprints of anti-protons at three cogging stages wiht beam-beam effects and field errors. The pink rectangular box in each plot indicates the range of the tune shift due to only beam-beam. Tune shifts of the particles due to field errors are much larger than those due to only beam-beam, footprints are dominated by field error.The footprints in three stages look similar.

The calculations of DA by tracking were done for anti-protons. It was found the average DAs are about 4 σ, and the same at three cogging stages. Fig. 6 gives DAs of $\overline{p}$ in function of proton intensities at stage Cog2. It was also found that the DAs of $\overline{p}$ are about 2 σ less than those of protons due to beam-beam effects. The difference between the bunches can be indentified. DAs of the first and the last bunch in a train($\overline{p}1$ and $\overline{p}12$) is better than those of the bunches in the middle of the train ($\overline{p}$ 6 as a representative).

DA tracking at injection has received experimental confirmation.We extracted stores (10) with low anti-proton emittance lifetimes for the first 4 bunches (10 FW measurements in each store). From the asymptotic emittance, we calculated the DA. Fig. 7 shows the average DA from these stores for the 4 bunches. For one of the stores, we calculated the intensity reduction from assuming that the bunch occupies the final 3D DA. That agrees nicely with the observed intensity loss for all the 4 bunches.

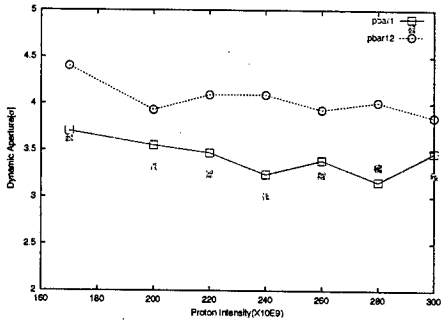


Figure 6: DA of $\overline{p}$ vs. proton intensities at Cog2, 10^5 turns

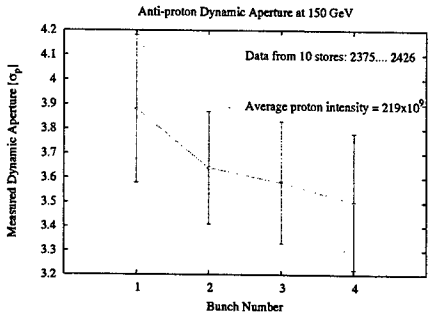


Figure 7: Measure Dynamic apeture at injection

5 CONCLUSION

At injection for uncoalesced beam, the DA of protons on the central orbit and proton helix is much larger than physical aperture at C0. For coalesced beam, the DA of protons on the helix is baout $6\sigma(\varepsilon_x=\varepsilon_y= 25\pi$mm·mrad). Decreasing proton bunch length to design value(momentum deviation wil reduced from 7.e-4 to 4.3e-4) would increase the lifetime significantly.

The average DA of anti-protons at injection is about 4σ, and the minimum DA is about 3σ, this value is the same at all 3 Cogging stages.

Anti-Proton lifetime at injection needs significantly improvement. It requires

- Change in the helicalseparations
- beter control of machine nonlinearities(aligment)
- better working point
- smaller anti-proton emittamce
- bema-beam compensation(under study)
- understanding of how lifetime scales with proton intensity

6 REFERENCES

[1] http://www-bd.fnal.gov/lug/runII_handbook/RunII_idex.html

[2] Y. Alexahin,http://www-ap.fnal.gov/meiqin/beam-beam01/beambeam01.html.

SIMULATIONS OF OCTUPOLE COMPENSATION OF HEAD-TAIL INSTABILITY AT THE TEVATRON

M. Xiao*† and T. Sen, FNAL, Batavia, IL 60510, USA
F. Schmidt, CERN, Geneva, Switzerland

Abstract

The proton lifetime in the Tevatron depends sensitively on chromaticities. Too low chromaticities can make the beam unstable due to the weak head-tail instability. One way to compensate this effect is to introduce octupoles to create a larger amplitude dependent betatron tune spread. However, the use of octupoles will also introduce additional side effects such as second order chromaticity, differential tune shifts and chromaticities on both proton and anti-proton helices. The non-linear effects may also reduce the dynamic aperture. We report on a simulation study to find the best combinations of polarities and strengths of the octupoles.

1 INTRODUCTION

In the Tevatron at injection energy, the transverse weak head-tail phenomenon drives proton beam unstable if it is not damped. Before the transverse dampers were commissioned, the damping was done by setting the chromaticities to relatively high values of 8 units in both planes. On the other hand, the beam lifetime at injection energy depends sensitively on chromaticity. In principle, a lower chromaticity would help to decrease the growth of higher order modes of instability, and improve the DA(Dynamic Aperture), and consequently the beam lifetime. However, too low chromaticities can make the beam unstable [2]. Currently, the Tevatron is running with tranverse and logitudinal dampers. Better beam lifetime is observed when the chromaticity decreased from 8 units to 2 units. Another way to compensate the instability of the protons is to introduce octupoles to create larger amplitude dependent betatron tune spread. If the shifted coherent tunes due to wake fields is within the width of the incoherent betatron tune spread or spread in synchrotron tunes, all unstable higher order modes can be damped by Landau damping.

Table 1 lists the number and the average beta function and the dispersion of two octupole families we used for the simulations. The use of octupoles will also introduce additional side effects on both proton and anti-protons. These effects are second order chromaticity, addtional coupling and non-linearty. Octupoles will also produce differential tune shift and linear chromaticities on both proton and pbar helices.The purpose of this simulation is to find the best combinations of polarities and strengths of the octupoles.

* meiqin@fnal.gov
† Work supported by the U.S.Department of Energy under contract No.DE-AC02-76CH03000.

Octupoles	Number	$<\beta_x>$, $<\beta_y>$[m]	$<D_x>$, $<D_y>$[m]
TOZD	24	93.6,30.2	3.67,-0.02
TOZF	12	30.5,92.5	2.07,-0.01

Table 1: Octupoles in the Tevatron used in this simulation

2 THE AMPLITUDE-DEPENDENT TUNE SHIFT DUE TO OCTUPOLES

The field due to an octupole in terms of the multipole components (b_3, a_3) is

$$B_y + iB_x = \frac{B_o(b_3 + ia_3)}{R_{ref}^3}[x^3 - 3xy^2 + i(3x^2y - y^3)] \quad (1)$$

The octupole strength parameter k_3 is defined as

$$k_3 = K_n L = \frac{n!}{(R_{ref}^n \rho)} b_n L = \frac{1}{(B\rho)} \frac{\partial^n B_y}{\partial x^n} . L \quad (2)$$

Introducing the action angle coordinates $x = \sqrt{2\beta_x J_x} cos\phi_x$, $y = \sqrt{2\beta_y J_y} cos\phi_y$ and assuming the phase and the beta functions are nearly constant over the length of a single octupole, we can find the action-dependent tune shift as follows [1]

$$\begin{aligned} \Delta\nu_x &= a_1 J_x + a_2 J_y \\ \Delta\nu_y &= a_2 J_x + a_3 J_y \end{aligned} \quad (3)$$

where

$$\begin{aligned} a_1 &= \frac{1}{16\pi} \sum_n k_3(n) \beta_{x,n}^2 \\ a_2 &= -\frac{1}{8\pi} \sum_n k_3(n) \beta_{x,n} \beta_{y,n} \\ a_3 &= \frac{1}{16\pi} \sum_n k_3(n) \beta_{y,n}^2 \end{aligned}$$

$J_{x,y}$ is the action,and related to the amplitude by $J_{x,y} = \frac{(a_{x,y})^2}{2} \cdot \varepsilon_{nx,y}$, and $a_{x,y}$ is the amplitidue im units of beam size σ, $\varepsilon_{nx,y}$ is the normalized emittance (1σ)in x or y plane.

Let $k_3(F)$ be TOZF's strength, $k_3(D)$ be TOZD's strength. At Tevatron injection, the action-dependent tune-shifts due to octupoles are obtained as follows:

$$\begin{aligned} \Delta\nu_x &= 2091.5251([k_3(F) + 0.2124k_3(D)]J_x \\ &\quad -0.6444[k_3(F) + 1.9961k_3(D)]J_y) \quad (4) \\ \Delta\nu_y &= 1349.6594(-[k_3(F) + 1.9961k_3(D)]J_x \\ &\quad +3.0269[0.0533k_3(F) + k_3(D)]J_y) \quad (5) \end{aligned}$$

0-7803-7738-9/03/$17.00 © 2003 IEEE

At present machine conditions, the proton emittance is 25πmm- mrad(95%). For the particle with initial amplidute of 5σ, we can get the expression for the octupole's strengths which are needed to compensate the decrease of tune spread due to lowering the chromaticities as follows:

$$k_3(F) = -4.5726 \times 10^3[0.6194 \times \Delta\nu_x + \Delta\nu_y] \quad (6)$$

$$k_3(D) = -2.3044 \times 10^3[\Delta\nu_x + 0.6570 \times \Delta\nu_y] \quad (7)$$

3 QUANTITIVE CALCULATION FOR THE OCTUPOLE STRENGTH

All unstable higher order modes of the weak head-tail effect can be damped if the spread of betatron frequency which has the incoherent tune shift included,or the spread of synchrotron frequency are larger than the coherent tune shift due to the impedance [2].

The growth rate of head tail modes measured at 150 GeV is about 110/*sec*, and the coherent tune shift is $\Delta\nu_{coh}$=$-1.\times 10^{-3}$ [3]. On the other hand, the synchrotron tune spread at 150 GeV is calculated to be $\Delta\nu_s$= 2.2×10^{-4}. The incoherent linear tune shifts in both x and y planes due to the space charge for the particle near the center of the proton bunch with 3-D Gaussian density distribution are also calculated, and they are $(\Delta\nu_x)_{SC} = -0.36 \times 10^{-3}, (\Delta\nu_y)_{SC} = -0.70 \times 10^{-3}$.

Therefore, in order for the landau damping to work, the betatron tune spread should be

$$\begin{aligned}(\Delta\nu_x)_\beta &= [\Delta\nu_{coh} - (\Delta\nu_x)_{SC} - \Delta\nu_s] \\ &= -0.42 \times 10^{-3} \quad (8)\\ (\Delta\nu_y)_\beta &= [\Delta\nu_{coh} - (\Delta\nu_y)_{SC} - \Delta\nu_s] \\ &= -0.08 \times 10^{-3} \quad (9)\end{aligned}$$

Then, the octupole strengths calculated from Eq. 7 for TOZF and TOZD are

$$k3(F) = 1.55, \quad k3(D) = 1.09 \quad (10)$$

At tevatron injection,

$$k3 = K_3 L = 1.2267506/m^3/Amps \times I \quad (11)$$

I is the magnet currents of octupoles.

4 DYNAMIC APERTURE TRACKING WITH AND WITHOUT OCTUPOLES

Before the octupoles were introduced into the lattice, we calculated the dynamic aperture at different chromaticities. Fig. 1 shows DAs of protons and pbars in function of momentum deviation at different chromaticities. The particles were tracked 100,000 turns by code MAD. We can see that the DAs of pbars at chromaticity of 2 units are 0.5σ larger than those of 8 units, although the DAs of protons seems not much improved.

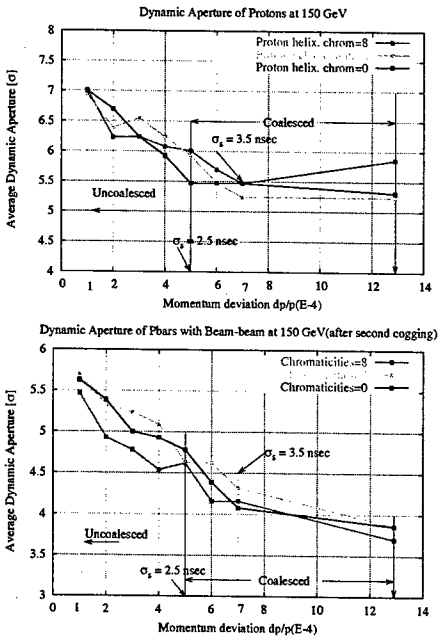


Figure 1: DA of protons and anti-protons vs. momentun deviations at different chromaticities

Using the code SIXTRACK we have also calculated the chaotic border which separates regular librator motion from fast amplitude growth. Table 2 lists DAs and chaotic borders at different chromaticities, calculated using code SIXTRACK. The momentum deviation in this calculation is dp/p=4.3e-4. Small chromaticities help to improve long term dynamic aperture since chromaticity sextupole strength are reduced, and synchro-betatron resonances are weaker.

Table 2: Dynamic aperture and chaotic border of protons(p) and anti-protons ($\bar{p}$) at injection

Chromaticities		(8,8)	(2,8)	(2,2)	(0,0)
p	Chaotic border(σ)	4.8	5.0	5.2	5.4
	DA (σ)	6.4	6.9	6.8	6.9
$\bar{p}$	Chaotic border(σ)	2.9	4.5	4.6	4.7
	DA (σ)	5.1	5.4	5.4	5.3

In the machine, when we reduce the both or one plane chromaticities from 8 units to 2 units, pbar lifetime was observed significately increased(from 2hrs to 12hrs), while proton lifetime of protons increased not so much. This may be because the proton beam is tickled by the damper kicker.

We used octupole strength $|k_3(F)|$=2, $|k_3(D)|$=1 with different combinations of polarities to test their impact on the Dynamic Aperture. These values are closed to the estimated values in Eq. 10. The results are listed in Table 3. From Table 3 we can see that if TOZF is positive, the dynamic aperture and chaotic border are larger than the other

chromaticities	(ξ_x=2, ξ_y=2)				(ξ_x=2,ξ_y=2)	(ξ_x=8,ξ_y=8)
octupole strength (k_3(F),k_3(D))(m^{-2})	(+2,+1)	(+2,-1)	(-2,+1)	(-2,-1)	(0,0)	(0,0)
$a_1 = \frac{\partial \nu_x}{\partial (a_x^2)}$ (10^{-5})	-15.38	-8.15	-4.29	10.60	-23.21	-4.29
$a_3 = \frac{\partial \nu_y}{\partial (a_y^2)}$($10^{-5}$)	6.34	- 5.04	- 4.05	-14.91	2.82	- 5.29
$a_2 = \frac{\partial \nu_x}{\partial (a_y^2)}$ or $\frac{\partial \nu_y}{\partial (a_x^2)}$ (10^{-5})	5.00	- 0.03	- 5.29	-12.36	6.69	- 4.05
Average DA (σ)	7.0	7.1	6.6	6.2	6.8	6.4
minimum DA (σ)	6.2	6.3	5.9	5.4	6.3	6.0
Chaotic border (σ)	5.8	5.5	4.5	4.4	5.2	4.7

Table 3: Dynamic Aperture and chotic boder with/without octupoles

combinatons. We also analyzied the coefficents a_1,a_2,a_3 in Eq. 5 for each combination. We expect that a_1 and a_3 must be much larger than a_2, so that the tune spread will be less dependent on the coupling term. On the other hand, a_1 and a_3 increase with octupole strength. It was found that both a_1 and a_3 are increasing but a_2 is decreasing if TOZD is also positive. This implies that the tune spread will be increased for larger amplitude particles, while the coupling effects will be lower.

With $k_3(F)$=2, $k_3(D)$=1, and chromaticity set at (ξ_x=ξ_y=2), we calculated the dynamic aperture and chaotic border of the anti-protons. It was found that the average DA is 5.6σ, the chaotic border is 5.1σ.

The machine study of octupoles at the Tevatron injection energy has been done by P. Ivanov in Tevatron department. A single coalesced proton bunch with relative higher intensity was injected onto the central orbit, and then two octupole families TOZF and TOZD were introduced to suppress the tranverse coherent instability while reducing the chromaticities in both x and y planes. Different combinations of polarities of two octupole families have been tested, and it was found positive polarity for both families are the best, which confirmed our calculations by simulation. So far, high intensity proton beams(N_p=280-300e9 per bunch) have been successfully injected onto the central orbit with small(zero) chromaticity setting and octupole settings $k_3(F)$=1.6, $k_3(D)$=4.1. Nevertheless, beam loss occured while going from injection bump to the proton helix - probably because of significant tune changes and strong coupling due to orbit motion. Further study in the machine is in progress.

5 CONCLUSION

The optimized combination is found by Dynamic Aperture tracking that both octupole families need to be posotive, it was confirmed by machine studies at the Tevatron.

Stronger octupole streangths have been tried and it's found that they are not better for the compensation. Besides, the tune shifts feeddown from octupoles on the helices are larger, and it is more difficult to make feeddown sextupoles work.

6 ACKNOWLEDGEMENTS

Petr Ivonov in Tevatron department provided the information needed for the simulations. I(Meiqin Xiao) would like to thank K.Y.Ng and C.Y.Tan for their useful suggestions and discussions.

7 REFERENCES

[1] T.Sen, "Octupole for differential chromaticity settings in the Tevatron, Tevatron Note, http://www-bd.fnal.gov//

[2] K.Y.Ng "Physics of Intensity Dependent Beam Insteabilities", USPS, Long Beach, CA.January 14-25,2002

[3] P.Ivanov "Tevatron Beam insteability studies". Private notes.

THE SPECIAL APPLICATIONS OF TEVATRON ELECTRON LENS IN COLLIDER OPERATION

X.Zhang, V.Shiltsev, FNAL, Batavia, IL 60510, USA
F.Zimmermann, CERN, Geneva, Switzerland
K.Bishofberger, UCLA, Los Angeles, CA 90095-1547

Abstract

Besides the Tevatron Electron Lens (TEL) runs as a R&D project for Tevatron Beam-Beam Compensation [1], it is used daily as a Beam Abort Gap Cleaner for collider operations. It can also serve as beam exciter for beam dynamics measurements and as a slow proton or antiproton bunch remover. This report describes all these applications and related observations.

TEL AS DC BEAM CLEANER

DC Beam and Abort Gap Loss

Currently in the Tevatron, the protons are injected with a large longitudinal emittance, filling the RF bucket. And some of the DC beam coming from the Main Injector Coalescing Process is also injected. In addition, the protons slowly leak out of the buckets and migrate into the abort gap due to noise sources, which are not well understood [4]. The DC beam component usually reaches a level of about 200×10^9 during injection. These uncaptured protons are lost at the beginning of the ramp. At the end of a High Energy Physics (HEP) store, the DC beam amounts to 6×10^9 protons and antiprotons, which is enough to cause a quench in the Tevatron. When these numbers of protons are lost suddenly, their loss is evidenced by spikes in the CDF detector, which prevent the CDF from working properly. The detector may even be damaged. The Tevatron itself also quenches occasionally, if there are high losses at abort or on the ramp, due to the DC beam.

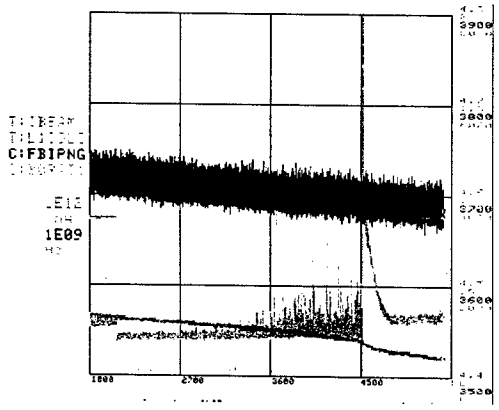


Figure 1: Beam intensity and loss during HEP store.

Figure 1 shows such a typical case for High Energy Physics Store. In this figure, the T:IBEAM is the total beam current in the Tevatron, C:FBIPNG is the total bunch current, the T:L1COLI is the average current of the electron beam and C:B0RATI is the abort gap loss counter from the CDF detector. When the TEL was shut off (red trace), the abort gap loss started to grow after about 10min and the high spikes appeared.

DC Beam Cleaning

To clean out of the DC beam in the abort gap, the dipole beam-beam kick is used to excite the multipole resonance of particle oscillation to increase its oscillation amplitude, until the particles get lost at a limited aperture. Therefore, when the TEL was turned on, a significant amount of DC beam was lost, which is seen on T:IEBAM (green curve), while the bunched-beam lifetime T: FBIPNG did not change. A huge spike on the abort gap loss signal indicates that the DC beam in the abort gap was cleaned out by the TEL. Later the loss in the abort gap was stabilized without any loss spikes. By introducing the TEL for DC beam cleaning, we accelerate the loss of the DC beam and also distribute these losses over the warm section, which eliminates the big spikes in the detector, so that it is able to work properly, and we also reduce the quench likelihood during beam ramping and beam abort. Moreover, the slightly higher smooth baseline loss rate does not have any harmful effect. In DC beam cleaning operation, the electron beam of the TEL is placed about 2.5mm beside the proton beam orbit horizontally and 1.5mm below, as is shown in Figure 2.

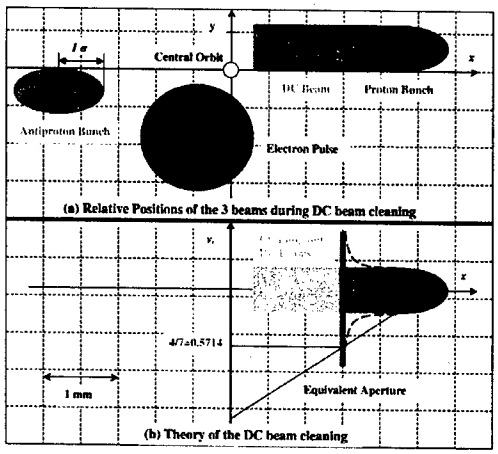


Figure 2: DC beam cleaning: (a) Beam postions (b) Physical mechanism of cleaning.

In Tevatron operation, we found that the most effective beam removal by TEL is to apply the electron beam kick of the TEL in every 7^{th} turn or 3^{rd} turn, which excites the $4/7^{th}$ order or $2/3^{rd}$ order resonance respectively. Figure 3 (below) shows a 1-turn snapshot taken when the TEL was

0-7803-7738-9/03/$17.00 © 2003 IEEE

operated in Abort Gap Cleaning State with 3 electron pulses pulsed in all 3 abort gaps on every 7th turn. The blue trace is the electron gun cathode current. The pulse width is about 1μs and the peak amplitude is about 400mA. The green trace is the intensity signal of the TEL BPM, where the big upright spikes are the proton bunch signals (the proton pulse length is only 20ns). The downward pulses are electron pulses timed in the abort gap. The intensity of the antiproton bunches was 10 times less than that of the proton bunches. So they are the barely seen small downward spikes in between the proton bunches. The TEL excites the 7th resonance of the protons in the abort gap and drives them out quickly.

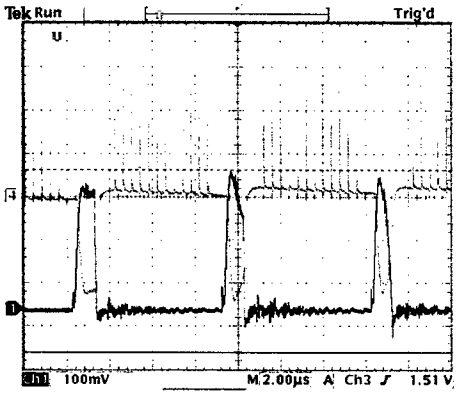


Figure 3: TEL for DC beam cleaning at 3-pulse every 7th turn.

Mechanism of DC Beam Cleaning

For normal Tevatron operation, the fractional part of the tune was chosen as 0.583 horizontally and 0.575 vertically. The most harmful resonance lines for the Tevatron are $4/7^{th}$=0.5714 and $2/3^{rd}$=0.667. When the particles in the DC beam lose energy by synchrotron radiation, their transverse oscillation amplitudes also increase, their tunes change, and, finally, they fall into the resonance band, where their oscillation amplitudes get larger and larger, until the particles hit the aperture and are lost. Usually it takes about 40 min for them to get lost with collimators open, while with the collimators closed at the beam and aperture restricted, it takes about 15 min. However, with TEL excitation, this process takes only about 20sec. When the TEL is on, the tune of the DC beam particles is roughly described by:

$$\nu = \nu_0 + C_V \frac{x}{D_x} + \Delta\nu(x^2) + \Delta\nu_{TEL} \qquad (1)$$

where ν_0 and ν are the tune of the on-momentum particles and DC-beam particles respectively; and $\Delta\nu_{TEL}$ the DC-beam particle tune change due to the electron beam. The tune also varies with the beam orbit[5], and $\Delta\nu(x^2)$ is the tune changes due to the particle orbit x; C_V is the vertical chromaticity and D_x the dispersion function at the TEL location which indicates the tune variation with particle momentum.

The DC beam cleaning mechanism is also shown in Figure 2(b). As the electron beam kicks the DC beam particles, their betatron oscillation amplitudes increase. The tune changes linearly with the particle position due to the chromaticity and quadratically due to high order field errors of the Tevatron. When the tune falls into the $4/7^{th}$ resonance, their oscillation amplitudes increase very fast until they hit the aperture and get lost. The equivalent aperture is the smallest aperture restricted by the collimation system transferred to the TEL location, which is about 3 mm from the helical beam orbit. Figure 4 shows the simulation results of the maximum particle oscillation amplitude for the linear lattice. The maximum amplitude is determined from the nonlinear force of the electron beam. Normally about 1/3 of the DC beam is cleaned out of the abort gap, since the electron beam roughly occupies 1/3 of the beam abort gap.

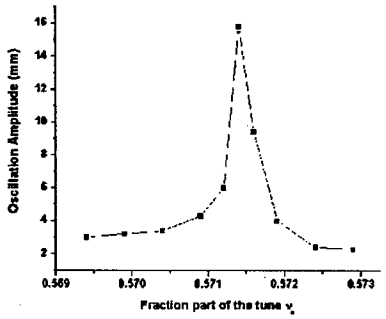


Figure 4: The oscillation amplitude of the particles near the 4/7th resonance line

AS BEAM TICKLER

The electron beam of the TEL can also be used as a beam 'tickler' for beam-dynamics measurements. To do so, we only need to modulate the electron beam current or position to produce the desired dipole kicks, and measure the beam response. Figure 5 (below) shows the method by which we modulated the electron current using white noise. The TEL was timed to specific pbar bunches to measure their tunes and emittance growth versus the noise strength.

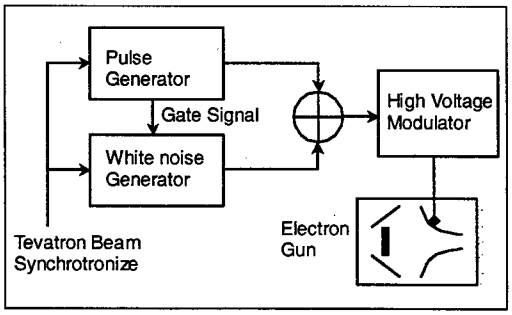


Figure 5: The scheme of TEL electron-current modulation.

Figure 6 shows the waveform of electron current modulated by the white noise. The modulation depth was 70%. This modulation was used to excite individual antiproton bunches for measuring bunch-to-bunch tunes.

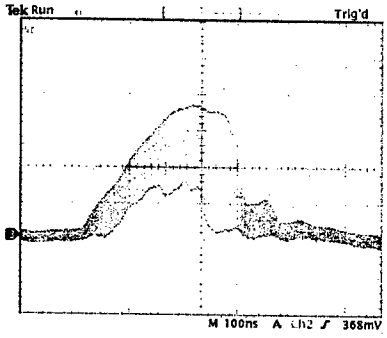


Figure 6: The waveform of the white noise modulated electron current.

The emittance growth due to the noise modulated electron beam kick was also observed [1]. It exhibits a quadratic dependence, which agrees with the theoretical prediction.

Pbar Tune Measurement

During the High Energy Physics store of Tevatron operation, normally the proton intensity is over ten times larger than the pbar intensity. The Schottky signal, which we are using now for tune measurement, is dominated by the proton signal. In order to detect the tune of the individual pbar bunches, we have to tickle the pbar beam.

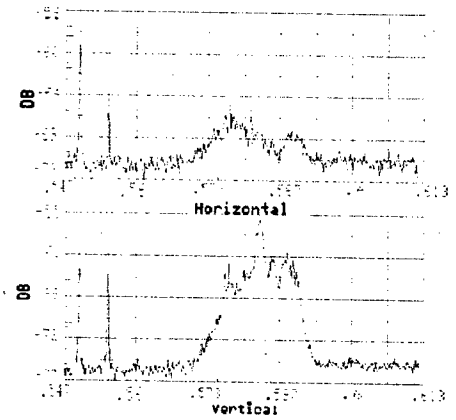


Figure 7: Tune signal from Schottky spectrum detector.

Figure 7 shows the Schottky spectrum of the beam without the TEL. It mainly shows the coalesced proton tune signal, which is about 0.575 in vertical and 0.59 in horizontal. By contrast, in Figure 8 the antiproton beam is excited by the TEL and we can infer the antiproton signal from the split peaks. For this measurement, we have controlled the modulation strength carefully in order not to blow up the pbar emittance too fast.

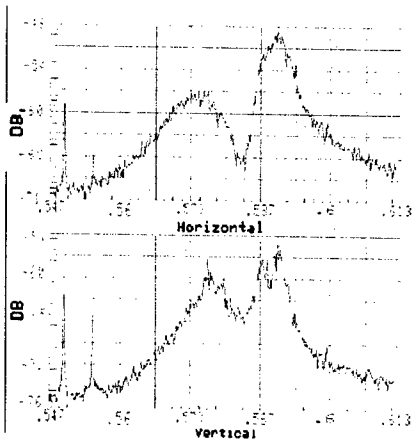


Figure 8: Tune signal with TEL excitation

AS BEAM REMOVER

The TEL acted as a controllable proton beam remover as shown in Figure 9. We can remove unwanted proton bunches one by one in a controlled way so that the loss in the Tevatron is kept below the dangerous level. During this operation, the electron beam is operated every 3rd or 7th turn to optimize the proton shaving speed.

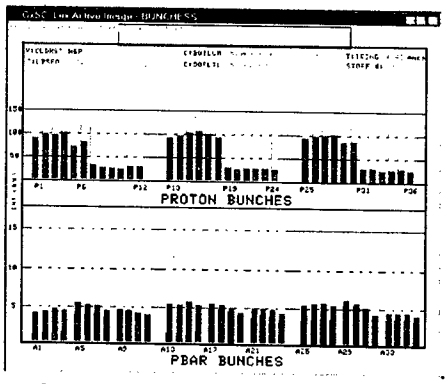


Figure 9: Tevatron display of bunch intensities during the removal of 18 proton bunches by the TEL.

ACKNOWLEDGEMENT

We thank the operations crew for their kind help and patience during our studies.

REFERENCES

[1] K. Bishofberger et al., this conference, TPPB083 and MOPA011
[2] X. Zhang et al., Beam Instrumentation Workshop 02, pp. 483-490
[3] V. Shiltsev et al., Phys. Rev. ST Accel. Beams **2**, 071001 (1999)
[4] Alvin Tollestrup et al., this conference, WPPB040
[5] Mike Martens et al., this conference, FPAB031

UPGRADES OF THE TEVATRON ELECTRON LENS

X.Zhang, J.Crisp, J.Fitzgerald, G.Kuznetsov, M.Olson, H.Pfeffer, G.Saewert, A.Semenov,
V.Shiltsev, N.Solyak, D.Wildman, FNAL, Batavia, IL 60510, USA
K.Bishofberger, UCLA, Los Angeles, CA 90095-1547
E.Kashtanov, S.Kozub, L.Tkachenko, V.Sytnik, IHEP, Protovino, Russia
M.Tiunov, BINP, Novosibirsk, Russia

Abstract

This paper will describe the main upgrades of the Tevatron Electron Lens (TEL) during the year 2003. The bending angle of the electron beam entrance and exit to the main solenoid will be decreased from 90 degrees to 53 degrees and three more solenoids will be added to each of the two bends, which will allow us to control the electron beam size more freely. A new gun will also be installed which will give us a Gaussian transverse beam distribution in addition to the flat beam with much smoother edge to minimize the nonlinear effect of the beam-beam force. In addition, a new BPM system will be installed to let us have more precise beam position measurements for proton, antiproton and electron beams. A knife-edge beam profile measurement system will replace the space-consuming scanning wires. We expect that these upgrages will improve the ability to increase the lifetime of the (anti)proton beam during beam-beam compensation operation.[1]

ELECTRON GUN UPGRADE

The structure of the old electron gun is shown below. It has a cathode, an anode, and an additional control electrode to change the transverse electron beam

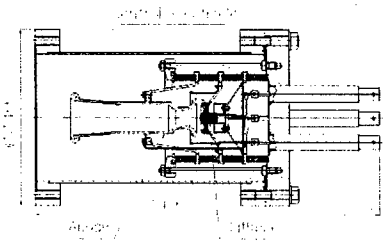


Figure 1: Electron gun structure

distribution. It was designed to provide several amps of beam current with a rectangularly uniform distribution of

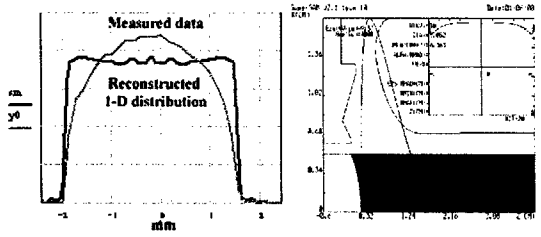


Figure 2: The measured electron distribution (left) and the designing of (right) for the old gun

electron beam and a measured perveance of about 5.8 μP. The measured value is 6.0. The perveance of an electron gun relates the beam current to the applied anode voltage, and is defined as the following:

$$I(A) = PV^{\frac{3}{2}}$$

Where the I is the electron beam current and the V is the voltage between the anode and the cathode of the electron gun. The P is the perveance, typically in units of micro-perveance (μP).

Figure 2 shows the wire scan of the beam transverse distribution, which is the magenta curve. The blue curve is the reconstructed beam transverse profile. Inaccuracies in the measurements are the likely cause of the three central bumps. Since this gun has a sharp edge, which produces a large nonlinear force, the beam acts as a soft collimator and causes the high loss and shorter lifetime for the proton beam. It provided a smaller tune region that obtained good proton beam lifetime. The maximum lifetime achieved was only 70hrs. [2]

To resolve this problem, a new gun was built and

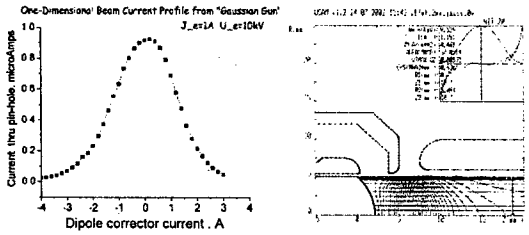


Figure 3: The measurement (left) and the designing of the new Gaussian gun

installed. The distribution-control electrode was changed as in Figure 3. The electron beam profile can be changed from Gaussian to uniform by adjusting the voltage on this electrode. For typical use as a Gaussian beam, the perveance was designed to be 1.2 μP. The reason for the lower perveance is due to the fact that the distribution-control electrode effectively suppresses current from the beam edge. The measured perveance was 1.8 μP in pulsed mode and 1.3 μP in DC mode. The reason for this difference is currently being explored.

The tune scans for the Gaussian gun showed that it provided a larger area with low proton losses. The maximum lifetime of the proton beam was 160hrs for same tuneshift as the flat-distribution gun, which is a significant improvement[2].

0-7803-7738-9/03/$17.00 © 2003 IEEE

ELECTRON BEAM BENDS

The bending angle of the electron beam is 90 degrees for the present layout of the TEL[1]. The electron beam path through the bends and the final beam size are both determined by the ratio between gun solenoid and the main solenoid; therefore, the field combinations of gun/collector solenoid and the main solenoid for electron beam to pass without scraping the walls are limited. Also, there is not much freedom to vary electron beam sizes to adapt to the larger-than-designed (anti)proton beam sizes. In addition, the electron beam size is larger in the bends due to the weak magnetic fields in the bending section. The gradient of the magnetic field also causes small vertical beam orbit drift.

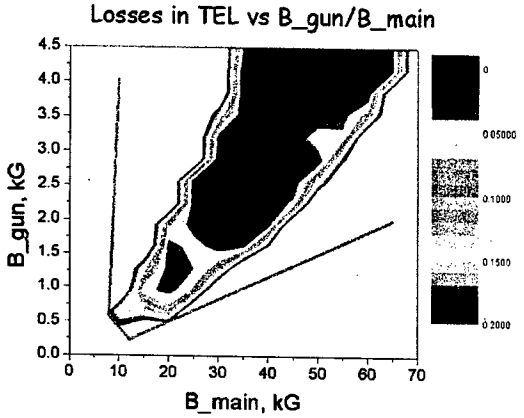


Figure 4: Electron losses in the path

Figure 4 shows the measured transmission rate for above configuration. In this measurement, the average electron beam current was 0.2mA. So the color code of 0.2 represents the electron beam was totally lost in the path.

Decreasing of the electron bending angle (see Figure 5) with additional solenoids in the bending path expect to at east double the transmission region of Figure 4 between the magenta lines. The magnetic field simulations show that this will allow 60% larger e-beam size variation than present system. Figure 5 shows the future layout of the TEL with 53 degrees of bending angle. The new support with additional solenoids in the bending section (three for gun side and three for collector side) is already built and tested. These solenoids will be used to strengthen the magnetic field in the bends to keep the electron size smaller and the beam path more controlled.

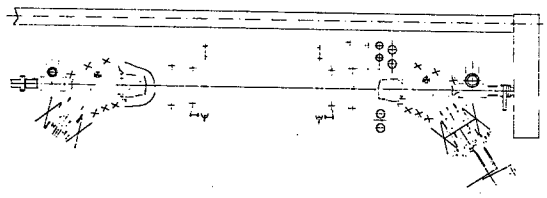


Figure 5: New layout of the TEL

The results of the magnetic measurements are shown in Figure 6. The three red rectangular represent the solenoids in the gun bend and the green box represents the aperture limit for the electron beam. The blue line is the designed trajectory and the magenta line shows the electron beam trajectory deduced from the magnetic field measurement. The maximum difference is about 1cm at the exit of the last solenoid, which can easily be compensated by adjustments in various solenoid currents and correctors.

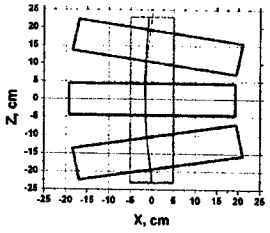


Figure 6: The path of the electron beam in the bends: designed (magenta) and measured (blue)

BPM UPGRADE

The BPM pickups installed in TEL are a diagonally cut cylinder type shown in Figure 7. This kind of BPM gives good linear measurements of positions. For TEL operation, we want to measure electron beam position relative to proton or pbar beam positions very precisely. However, offsets arise from the different BPM impedances for electron beam and proton beam signals, since for proton-like signal the main frequency

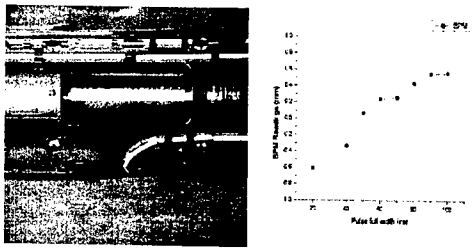


Figure 7: The diagonally cut TEL BPM system

component is about 53MHz while for electron beam the main frequency component is less than 2MHz. The cross-talking between different electrodes can also contribute to the offset.[3] The maximum measured offset with a fixed position wire for main signal frequency from 50MHz to 10MHz is over 1mm as shown in Figure 7.

A new BPM system with four plates has been designed and is under testing (see Figure 8 left). It's compact and has built-in electromagnetic shields between neighboring plates to minimize crosstalk. The measured response versus the signal frequency for this BPM is shown in Figure 8. This BPM has a maximum offset of only 0.065mm, compared to 1mm for the old BPM.

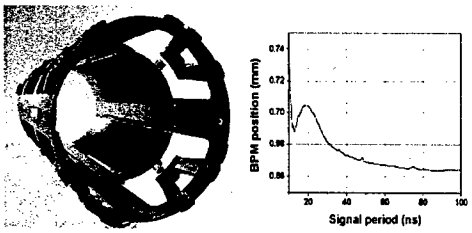


Figure 8: The prototype of new TEL BPM

MODULATOR UPGRADE

A pulse modulator is used to apply the short high-voltage pulse to the anode in order to produce the necessary pulsed current for beam-beam compensation. To obtain a tune shift of 0.01, we need a peak current of 2A from the uniform-profile electron gun[1]. The traces in Figure 9 show the electron pulse shape seen at the cathode, collector, and a BPM plate. On the left graph, the blue trace is the cathode current, cyan trace is the collector current, and the magenta is the BPM signal. The BPM signal shows the spikes of proton bunch signals and an additional 30MHz ripples caused by the circuit resonance of the modulator.

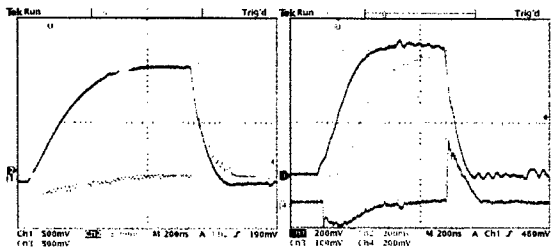


Figure 9: Electron beam pulse shape

The 30MHz problem was solved by changing the inductor and resistor in the modulator circuit. In addition, we also improved the pulse rise time by the adjusting the modulator circuits. The graph on the right shows the traces after this upgrade: the blue and magenta were the cathode and collector current signals; the cyan and green were BPM intensity and position signals respectively. We can see that the rise time is shorter and the 30MHz ripple is gone.

Another problem was the pulse-to-pulse current fluctuations at 15Hz, 60Hz and 120Hz, which were caused by the ripple from the power line feeding into the RF tube in the modulator. Changing the modulator's filament power supply to DC and adding 60Hz and 120Hz RF compensation to the screen and grid power supplies greatly minimized the ripple. Figure 10 shows the 120Hz ripple before and after compensation. With all these efforts, the electron beam pulse-to-pulse stability now is better than 0.1%. We also decreased the timing jitter for electron pulse to less than 1ns.

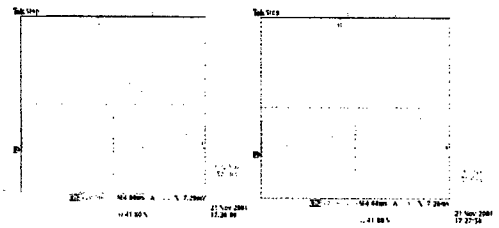


Figure 10: The 120Hz ripple before (left) and after adding the compensation (right)

The present modulator can only output about 7kV pulse, which can only produce 600mA peak electron current from the new Gaussian gun. This current is not enough for beam-beam compensation. In addition, the modulator produces an undesired trailing pulse, shown as in Figure 11, which excites proton bunches during Tevatron abort gap cleaning operation[4]. Therefore, we have to set offset voltage of about -500V in order to eliminate this trailing pulse, which further decreases the available voltage to produce electron current. A new modulator is needed to provide 14kV pulses and not have any trailing pulses.

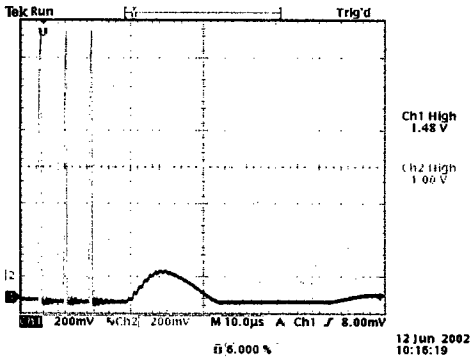


Figure 11: The trailing pulse in 3-pulse of every 7 beam revolution for Tevatron DC beam cleaning operation.

ACKNOWLEDGEMENTS

The authors thank Dave McGinnis and David Peterson for their advice on the upgrade of our BPMs. We also thank Lucy Nobrega and Derek Plant for their mechanical expertise and George Krafczyk for his power supplies which were used for testing the new solenoids. Finally we thank the control room operators for their help during all of our studies.

REFERENCES

[1] http://www-bd.fnal.gov/lug/tev33/ebeam_comp /reports/BBC_TDR_v5.doc
[2] K.Bishofberger *et al.* This conference. MOPA011
[3] X. Zhang *et al.* Beam Instrumentation Workshop 2002, pp. 483-490
[4] X. Zhang *et al.* This conference. TPPB076.

DESIGN STUDY OF 1MHZ INDUCTION CAVITY FOR INDUCTION SYNCHROTRON

Kota Torikai, Yoshio Arakida, Shigemi Inagaki, Kunio Koseki, Eiji Nakamura, Takeshi Toyama, Masayoshi Wake, Junichi Kishiro, Ken Takayama, KEK, Oho1-1, Tsukuba City, Ibaraki, Japan,
Kenji Ishibashi, Kyushu University, Hakozaki 6-10-1, Fukuoka, Japan

Abstract

An induction cavity was designed for the POP experiment of induction synchrotron using the KEK 12GeV PS. It must be operated at a repetition rate of 667-882 kHz for acceleration from the injection energy to the flat-top energy. Design issues include handling of heat deposit, minimization of voltage droop and coupling impedance, and tolerable jitter. Its Q-value on the cavity assembled following the design was obtained from the longitudinal coupling impedance measurement. Effects of the droop in the acceleration voltage on the synchrotron motion, which has been estimated from the circuit parameter measurement on R, C, and L, was analysed from a longitudinal beam dynamics point of view. The effect of the droop is given by the square of phase delay.

INTRODUCTION

A novel idea of the induction synchrotron, which was proposed by Ken Takayama and Junichi Kishiro [1], enables us to have an extremely long bunch, called a super-bunch [2]. Employing this novel technique, it seems to be possible to multiply the beam intensity without increasing the line density. A POP experiment of the induction synchrotron is scheduled in 2003 [3]. For super-bunch production a long and flat accelerating voltage and a short-pulse barrier bucket are crucial instruments. Important issues to realize the induction cavity are among (1) heat deposit and cooling, (2) high voltage shielding in the cavity, (3) ceramic accelerating gap, (4) longitudinal and transverse coupling impedances, (5) droop. It depends on a chosen magnetic material and a repetition rate how serious the first issue is. Since the issue (1) and (2) have been discussed in another place [4], they are not mentioned much here.

INDUCTION ACCELERATING SYSTEM

The Induction accelerating system including a diver is represented as an equivalent parallel LCR circuit within a certain range of frequency. Such an equivalent circuit model is schematically shown in Fig.1. In this model, L stands for the inductance of the magnetic core, C for the stray capacitance of the cavity, R for the effective loss of the core, respectively. Responses of the cavity to a rectangular-shape input-pulse are characterized by a delay in the rise time and a voltage droop, as shown in Fig. 1. A rise time of the voltage is proportional to a factor 1 / CR, and the voltage droop is determined by L / R. The cavity is connected with a pulse modulator [5] through a coaxial cable so as to keep its semiconductors away from the radiation in the accelerator ring. Therefore, the pulse operation requires wideband matching to suppress the reflection from the cavity.

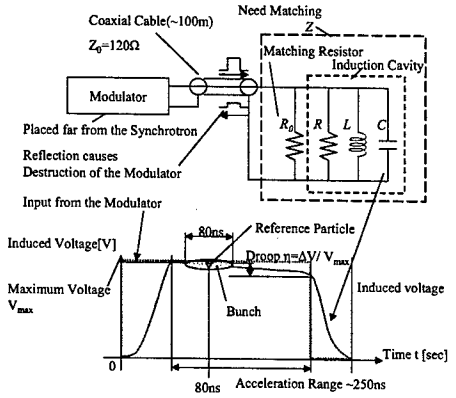


Figure 1: Induction Acceleration Setup

LONGITUDINAL IMPEDANCE MEASUREMENT

A measurement of longitudinal impedance of the cavity was made within the frequency range of 300 kHz - 1 GHz by employing the S-matrix technique [6]. The assembled cavity and longitudinal impedance measurement setup are shown in Fig. 2, and the measurement composition is shown in Fig. 3. The results are given in Table 2. Resonant structures at 289MHz and 578MHz were found to be a quality factor of 66 and 68. These resonances are understood to result from the length of the primary current loop (0.5m). Each of other resonances has a much lower Q-value.

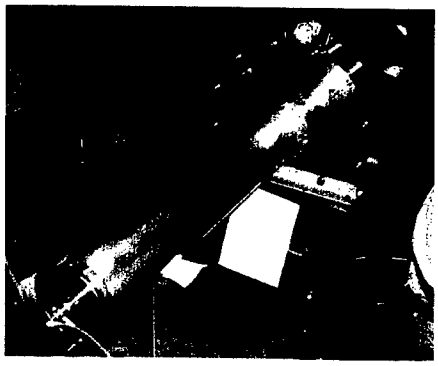


Figure 2: Induction Cavity with Transmission Lines

0-7803-7738-9/03/$17.00 © 2003 IEEE

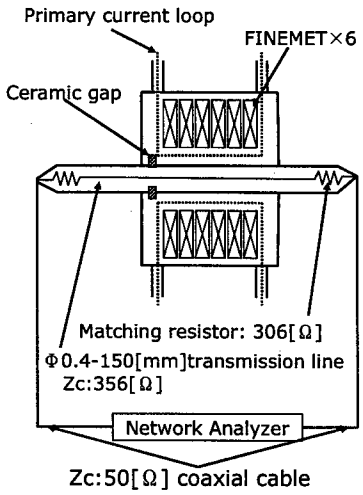


Figure 3: Measurement Composition

Table 1: Longitudinal Impedance of the Induction Cavity

Freq.[MHz]	Long. Imp. [Ω]	Freq. Width[MHz]	Q-value
203	24	46	4
289	4	4	66
299	18	6	50
386	25	14	27
431	24	23	19
578	37	9	68
830	21	61	14

L, C, R OF INDUCTION CAVITY

An impedance of the cavity Z_{cavity} is measured as an equivalent circuit expression of RLC-series,

$$Z_{cavity} = R_s + j\left(\omega L_s - \frac{1}{\omega C_s}\right) = R_s + jX_s$$

where R_s and L_s is expressed by the complex permeability of the donut-shaped core $\mu = \mu' + j\mu''$,

$$R_s = \frac{\mu'}{2\pi} D \ln\frac{b}{a}, L_s = \frac{\mu''}{2\pi} D \ln\frac{b}{a}$$

where D, a and b represent the thickness, the inner diameter and outer diameter of the core, respectively. In general, each of μ', μ'' has frequency dependence, not a constant. The step voltage input consists of many higher-order frequencies. Therefore, the measurement of $\mu'(\omega), \mu''(\omega)$ is required.

Consequently, a transformation of equivalent parallel RLC circuit is performed by

$$R_p = \frac{Z_{cavity}^{\ 2}}{R_s}, L_p = \frac{Z_{cavity}^{\ 2}}{\omega^2 L_s}, \frac{1}{C_p} = \omega^2 C_s Z_{cavity}^{\ 2}.$$

For consideration of the impedance matching, a reflection ρ is related as the function of impedance between the cavity Z_{cavity} and the transmission line Z_{line},

$$\rho = \frac{Z_{line} - Z_{cavity}}{Z_{line} + Z_{cavity}}.$$

The real part and the imaginary part of impedance are measured for certain frequency range by network analyzer. In this measurement, the inductance and the capacitance are determined by employing Q-value at a resonance frequency.The frequency dependence of the L and R of the cavity can be obtained by changing the resonant frequency by adding a capacitor of known value to the measurement setup. The frequency dependence of the inductance and the resistance is measured to compare the equivalent L, R of the naked core with that of the assembled cavity. The results are shown in Fig.4.

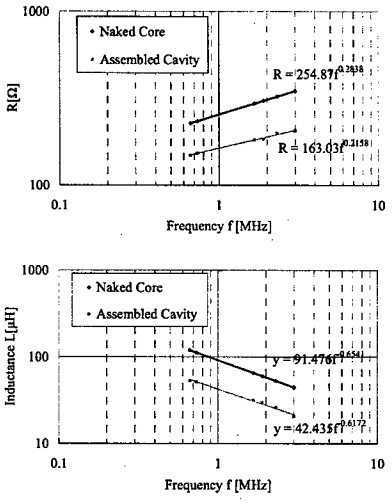


Figure 4: Comparison of Naked Core and Cavity

Design parameters of the required induction cavity are listed in Table 2. The frequency dependence of the inductance and resistance has considerable effect on impedance matching between the induction cavity and the power modulator. Consequently, the repetition rate change of synchrotron operations induces an acceleration voltage error and an additional feedback system will be needed to satisfy the stability criteria.

Table 2: First Plan of the Design Parameters for an Induction Synchrotron POP Experiment at KEK-PS

Induction Voltage	2500V
Repetition Rate (injection)	667kHz
Resistive Component of a core	46Ω
Inductive Component of a core	20μH
Capacitance of the Cavity	300pF
Core Stacks	6
Impedance of the Cavity	267Ω
Matching Resistor	215Ω
Impedance of Coaxial Cable	120Ω
Loss of the Cavity (50% Duty)	11.4kW
Loss of Matching Resistor (50% Duty)	14.5kW
Required Total Power (50% Duty)	25.9kW

VOLTAGE DROOP 'S EFFECTS ON RF BUNCH CONFINEMENT

The induced voltage, shown in Fig.1, is expressed as a function of the synchrotron phase ϕ, maximum induced voltage V_0 and voltage droop V_{drp},

$$V_{ind}(\phi) = V_0 - V_{drp}\frac{\phi}{2\pi}.$$

In the POP experiment step-I, an RF confined bunch is accelerated with induction voltage. Therefore, the applied total voltage is given by

$$V_{total}(\phi) = V_{RF}\sin\phi + V_0 - V_{drp}\frac{\phi}{2\pi}$$

Consequently, the potential well $U(\phi)$ is written in the form of

$$U(\phi) = \frac{heV_{RF}}{2\pi}(-\cos\phi - A\phi^2), A \equiv \frac{V_{drp}}{4\pi V_{RF}}.$$

The voltage droop changes the RF potential and modifies the RF buckets as shown in Fig.5. In the droop effect, a ratio of $\frac{V_{drp}}{4\pi V_{RF}}$ becomes an important parameter representing the RF bucket distortion.

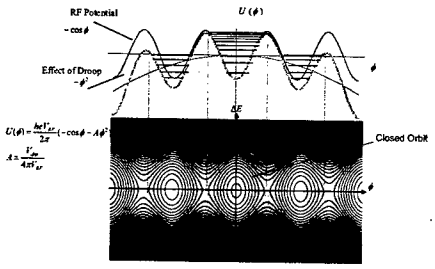


Figure 5: Effect of Voltage Droop in Potential Well

Changes in the phase-space as a function of structure the ratio A are shown in Fig.6. In the POP experiment, V_{RF} = 92kV, and V_{drp} ≈400V. The parameter A is an order of 10^{-4}. A modification in the phase space should be negligibly small; RF bunch confinement can be performed well.

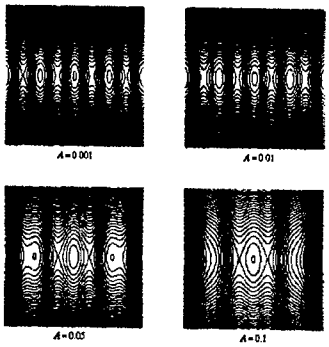


Figure 6: Effect of Voltage Droop in Phase Space

CONCLUSIONS

From the comparison of the naked core and the whole cavity, the cage reduces effective permeability to 1/2. Therefore, an induction cavity for the POP experiment is designed with that effect. As for an induced electric field, a sufficient gap distance and a narrowed primary loop are effective to reduce the structural capacitance. 4-68 Q-values were obtained from a longitudinal coupling measurement. Mode specifications of the resonances are now being made. From the acceleration voltage analysis, voltage droop distort the potential well and decreases the stable area as a function of ϕ^2 and $\frac{V_{drp}}{4\pi V_{RF}}$.

REFERENCES

[1] Ken Takayama and Junichi Kishiro, Nucl. Instrum. Methods Phys. Res., Sect. A, **451**, 304 (2000).
[2] Ken Takayama et al., Phys. Rev. Lett., 88, **14** (2002).
[3] Ken Takayama et al., "A POP Experiment Scenario of Synchrotron at the KEK 12-GeV PS", in this proceedings.
[4] K.Torikai, "High Repetition Rate Induction Cavity", in Proceedings of RPIA2002.
[5] Kunio Koseki, "R&D Works on 1 MHz Power Modulator for Induction Synchrotron" in this proceedings.
[6] for instance "Handbook of Accelerator Physics and Engineering", edited by Alexander W. Chao and Maury Tigner, World Scientific Pub., p570-572, 1999.

Proceedings of the 2003 Particle Accelerator Conference

PROGRESS IN DESIGNING A MUON COOLING RING WITH LITHIUM LENSES

Y. Fukui*, David B. Cline, Alper A. Garren, University of California at Los Angeles, CA
Harold G. Kirk, Brookhaven National Laboratory, NY

Abstract

We discuss particle tracking simulations in a storage ring with lithium lens inserts designed for the six-dimensional phase space cooling of muons by the ionization cooling. The ring design contains one or more lithium lens absorbers for transverse cooling that transmit the beam with very small beta-function values, in addition to liquid-hydrogen wedge-shaped absorbers in dispersive locations for longitudinal cooling. Such a ring could comprise the final component of a cooling system for use in a muon collider. The beam matching between dipole-quadrupole lattices and the lithium lenses is of particular interest.

OVERVIEW

The ionization cooling is one of the most promising method to reduce the 6 dimensional phase space of muon beam, where both transverse and longitudinal momenta are reduced due to the energy loss in absorbers, and only longitudinal components of the muon momenta are restored through the accelerating fields of RF cavities. The multiple Coulomb scattering contributes to heat the transverse phase space. And the dE/dx straggling through absorbers contributes to heat the longitudinal phase space. Wedge absorbers in dispersive region in bending cells perform the emittance exchange between the longitudinal emittance and the horizontal emittance. [1]

Lithium lens is an active focusing element with energy absorber function at the same time. With β at 1 cm with high current density Lithium lenses, the equilibrium normalized transverse emittance can be at around 100 mm · mrad, which is necessary for a $\mu^+\mu^-$ collider. [2]

In the muon cooling ring with Lithium lenses, Lithium lenses with the β function as low as 1.0 cm is placed in a straight section with matching solenoid magnets. Figure 1 shows a schematic view of a muon cooling ring with a Lithium lens. Circumference is 37.5 m, the straight section is 5.9 m long each, and the radius of the bending section is 4.6 m.

MUON COOLING IN STRAIGHT CHANNELS WITH LITHIUM LENSES

We designed muon cooling rings with a Lithium lens which is made of 2 matching higher β Lithium lenses sandwiching the central lower β Lithium lens. β at the inner 22 cm long Lithium lens is 1.0 cm . The matching Lithium rod with the length of 6.3 cm each, which sandwich the central

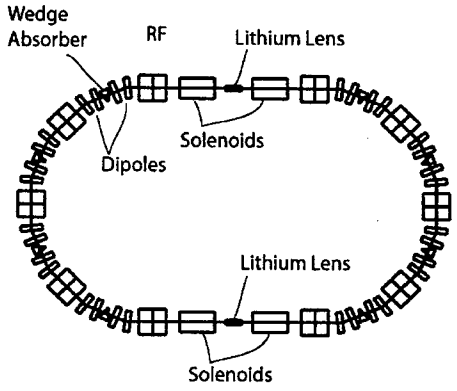


Figure 1: A schematic diagram of a muon cooling ring with Lithium lenses in straight sections.

Lithium lens, has an equilibrium β at 4.0 cm, which swings the β function from the β at 16 cm at the outer end to the β at 1 cm at the inner end of the matching Lithium rod. The solenoids has 6 Tesla B_z field where the B_z direction of solenoids is opposite to each other, and each solenoid is 1.3 m long Figure 2 shows a schematic diagram of a Lithium lens and straight section which is made of 2 matching solenoids and a set of Lithium lenses. Figure 3 shows the β as a function of z in the Lithium lens and matching cells with solenoids.

In order to study the muon beam dynamics through a Lithium lens and matching solenoid lattices which sandwich the Lithium lens, we performed tracking simulation with ICOOL tracking code. [3] Original model was designed by using the SYNCH [4] which generates the input date for the tracking code ICOOL.

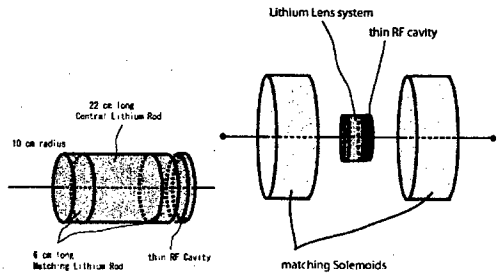


Figure 2: A schematic diagram of a Lithium lens(left) and straight section(right).

Figure 4 shows the development of the normalized transverse emittance as a function of z through 33 sets of 5.9 m

* fukui@slac.stanford.edu

0-7803-7738-9/03/$17.00 © 2003 IEEE

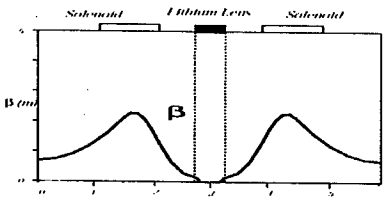


Figure 3: β as a function of s in the Lithium lens and matching cells with solenoids.

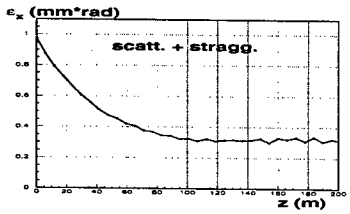


Figure 4: Normalized transverse emittance as a function of z through 33 sets of straight sections.

long straight channel. In this simulation, the loss of muon p_z due to the dE/dx energy loss through the Lithium lens is recovered through a thin RF cavity by adding average p_z kick. The equilibrium normalized transverse emittance is around 0.3 mm · rad. Figure 5 and 6 show the development of the normalized longitudinal emittance, $\Delta p/p$ and Δz as a function of z, and the transmission as a function of z, respectively.

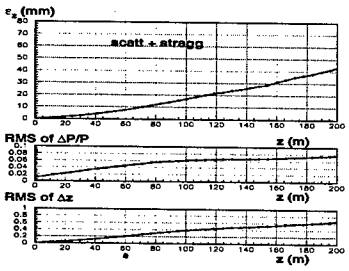


Figure 5: Normalized longitudinal emittance, $\Delta p/p$ and Δz as a function of z through 33 sets of straight sections.

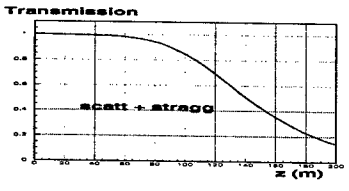


Figure 6: Muon transmission as a function of z through 33 sets of straight sections.

MUON COOLING IN A COOLING RING WITH LITHIUM LENSES

We designed a 45 degree bending cell by using two sets of zero-gradient dipole magnets with edge focusing. Wedge absorbers of liq. H_2 are placed in dispersive regions in the bending cells. RF cavities are placed wherever the space is available.

Figure 7 shows β vs. z and D vs. z in a muon cooling ring with Lithium lenses in straight sections. The β vs. z and D vs. z in a 45 degree bending cell is shown in Figure 8 We placed 1.7 cm long liq.H_2 wedge absorbers at the center of dispersive regions in the bending cells.

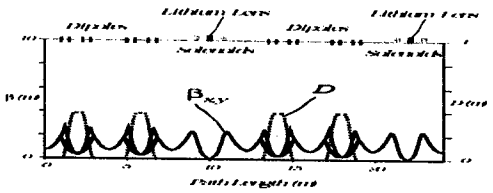


Figure 7: β vs. z and D vs. z in a muon cooling ring with Lithium lenses in straight sections

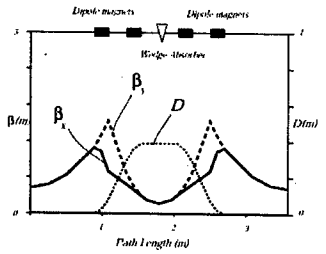


Figure 8: β vs. z and D vs. z in a 45 degree bending cell

Table 1 lists parameters of the muon cooling ring with two Lithium lenses in straight channels.

Table 1: Parameters of a muon cooling ring

muon momentum	250 MeV/c
Circumference	37.5 m
straight section length	5.9 m (× 2)
Structure of half cell	2 dipoles with edges
number of bending cells	8
bend cell length	3.6 m
length of Lithium lens	34.5 cm (× 2)
lowest β in Lithium lens	1.0 cm
energy loss	35 MeV/turn
dipole bend angles	44.2, -21.7 degree
dipole edge angles	30/-3, -11/-11 degree
dipole magnetic field	6.5, -3.2 tesla
Cell tunes bend cell	0.72/0.70
Cell tunes straight cell	4.0

Figure 9 shows the development of the normalized transverse emittance as a function of z through 8 turns of the muon cooling ring in Figure 1. channel. In this simulation, the loss of muon p_z due to the dE/dx energy loss through the Lithium lens or Liq. H_2 wedge absorbers is recovered through a thin RF cavity by adding average p_z kick. The figure indicates the transverse cooling in the muon cooling ring with Lithium lenses. Figure 10 and 11 show the development of the normalized longitudinal emittance, $\Delta p/p$ and Δz as a function of z, and the transmission as a function of z, respectively.

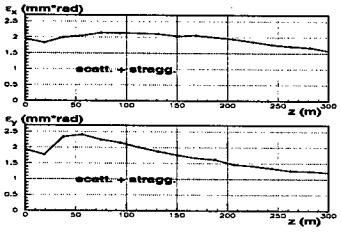


Figure 9: Normalized transverse emittance as a function of z through 8 turns of a muon cooling ring.

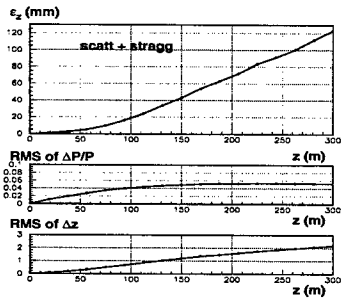


Figure 10: Normalized longitudinal emittance, $\Delta p/p$ and Δz as a function of z through 8 turns of a muon cooling ring.

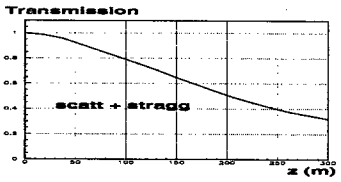


Figure 11: Muon transmission as a function of z through 8 turns of a muon cooling ring.

CONCLUSION

We designed a race track muon cooling ring with 35 cm long Lithium lenses in straight channels with β at 1 cm. Bending cells have zero-gradient dipole magnets with edge focusing, and wedge absorbers in dispersive regions. Study is in progress to obtain the 6 dimensional muon cooling in this cooling ring.

ACKNOWLEDGMENTS

The authors wish to thank R. B. Palmer, R. Fernow, A Sessler, M. Zisman, J. Wurtele, D. Neuffer, and V. Balbekov, for useful discussions, and their help and encouragement.

REFERENCES

[1] H. G. Kirk, D. B. Cline, Y. Fukui, A. A. Garren, *Progress Toward A Muon Ring Cooler*, SNOWMASS-2001-M101, Jun 2001. 5pp., Prepared for APS / DPF / DPB Summer Study on the Future of Particle Physics (Snowmass 2001), Snowmass, Colorado, 30 Jun - 21 Jul 2001.

[2] C. M. Ankenbrandt, et., al., the NuMu Collaboration, *Status of Neutrino Factory and Muon Collider Reasearch and Developmemt and Future Plans*, Phys. rev. ST Accel. Beams 2 (1999) 081001

[3] R. Fernow, *A Simulation Code for Ionization Cooling of Muon Beams*, Part. Accel. Conf., Edts., A. Luccio and W. MacKay, Proc. 1999, p. 3020.

[4] A. A. Garren, A. S. Kenney, E. D. Courant, A. D. Russel, and M. J. Syphers. *SYNCH - A Compueter System for Synchrotron Design and Orbit Analysis, User's Guide*, SSCL-MAN-0030, 1993

LONGITUDINAL BUNCH ROTATION SCHEME IN A MUON COOLING RING

Y. Fukui*, University of California at Los Angeles, CA

Abstract

We present an idea of achieving better longitudinal phase space cooling in a muon cooling ring with the RF cavity configuration which generate short bunch length and large energy spread at the energy absorbers in a low momentum muon cooling ring. In this scheme, the heating terms in the longitudinal phase space, the slope of the dE/dx as a function of muon momentum and the dE/dx straggling through absorbers, are relatively small compared to the energy spread of the muon beam in the absorber.

INTRODUCTION

The Muon Ring Cooler, a muon cooling ring with conventional (non-solenoidal) magnet elements, has demonstrated emittance exchange from the longitudinal phase space to the horizontal transverse phase space by using a wedge absorbers in dispersive region.[1] The source of the 6 dimensional phase space cooling is the ionization cooling, where muons lose magnitude of momentum by the ionization energy loss through absorbers, and then only p_z is recovered by the RF cavities, which gives the net effect of the transverse phase space cooling. The transverse heating factor is the multiple Coulomb scattering through absorbers, which effect can be minimized by placing absorbers where the β is small, and hence the beam angles, dx/dz or dy/dz are relatively large compared to the scattering angle. The longitudinal heating factors are, the dE/dx straggling through an absorber, and the non-zero slope of dE/dx as a function of muon momentum. In the same way as in the transverse phase space, those heating terms in the longitudinal phase space can be relatively small compared to the energy spread of the muon beam in the absorber in this scheme.

Table 1 lists a comparison of an electron damping ring and a muon cooling ring on elements of damping, excitation, and the partition numbers in the transverse phase space and in the longitudinal phase space.

CONTROLLING THE LONGITUDINAL PHASE SPACE PARAMETERS

In the transverse phase space, the (transverse) strong focusing FODO lattice system [2] allows us to have a large Δx' (transverse angle) and a small Δx (transverse beam size) at the absorbers where the effect of the multiple scattering (transverse phase space heating) on the Δx' is minimized, due to the large Δx' there. The magnetic elements used here is the focusing/defocusing quadrupole magnets.

* fukui@slac.stanford.edu

Table 1: Comparison of an electron damping ring and the Muon Cooling ring

	e **Damping Ring**		
phase space	x	y	z
Damping	x' synch.rad. +RF	y' synch.rad. +RF	synch.rad. $\Delta E \propto E^4$
Excitation	x-x' orbit change		quantum fluct. $\propto E^{3.5}$
Partition #	$(1-\mathcal{D})$	1	$2+\mathcal{D}$

	μ **Cooling Ring with Wedge Absobers**		
phase space	x	y	z
Damping	x' Ion.Cooling	y' Ion.Cooling	$\Delta E \propto$ E in Wedge
Excitation	x-x' orbit change mult.scat.	mult.scat.	$\frac{dE}{dx}$ struggling $\propto E^2$
Partition #	2-d	2	d

In the exactly the same way as the transverse phase space, we can think about setting a FODO lattice structure with a *Longitudinal Strong Focusing* which is based solely on the longitudinal phase space.

Figure 1 shows schematics of the transverse and longitudinal strong focusing. UFP(Unstable Fixed Point) and SFP(Stable Fixed Point) in the $\Delta p/p$ - ϕ(RF phase) phase space are used to expand or contract the bunch length of muon beam in a longitudinal strong focusing lattice. The length of the longitudinal strong focusing lattice is allowed to be different from the length of the transverse strong focusing lattice.

In order to realize the longitudinal strong focusing lattice, one or multiple of the following conditions need to be met:

1) muon momentum is low enough or the RF gradient is large enough in order to generate $\Delta c \Delta t$ in going from an absorber to another absorber,

2) the magnitude of the energy straggling in the dE/dx energy loss through an absorber is smaller than the total energy spread of the muon bunch at the absorber location.

SUMMARY

The longitudinal strong focusing lattice can be used to minimize the normalized equilibrium longitudinal phase space of the muon beam, combined with the use of a wedge absorber in a dispersive region in a muon cooling ring. The longitudinal heating factors, the dE/dx straggling through

0-7803-7738-9/03/$17.00 © 2003 IEEE

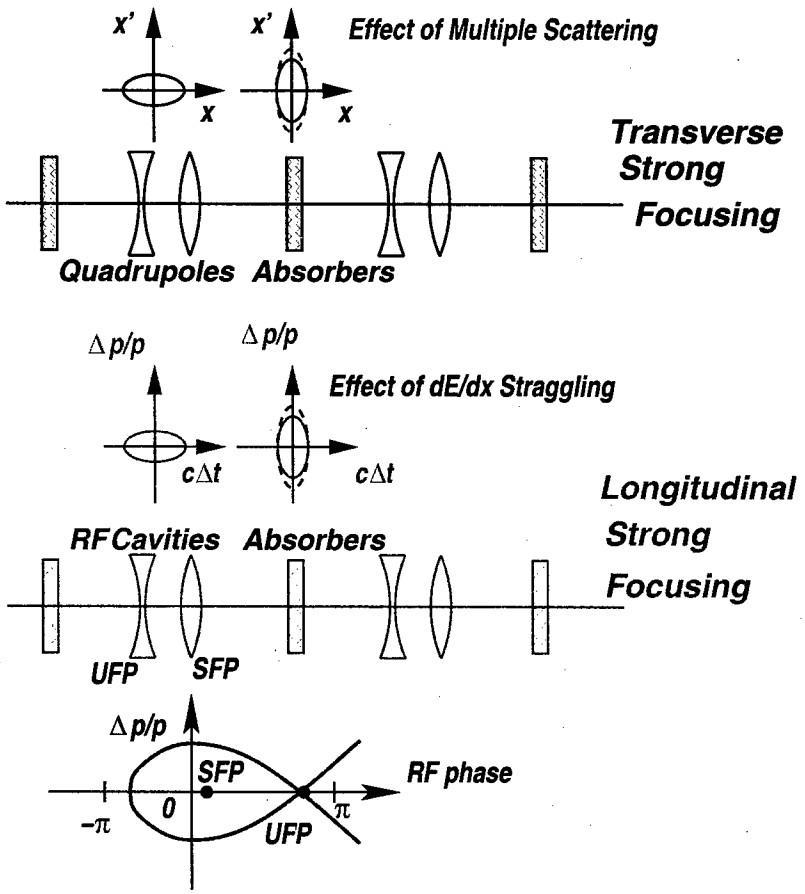


Figure 1: Schematic diagrams of the transverse and longitudinal strong focusing lattices

an absorber, and the non-zero slope of dE/dx as a function of muon momentum, can be made relatively small compared to the energy spread of the muon beam in the absorber in this scheme. This scheme corresponds the scheme of the transverse cooling through the ionization cooling where the low β is required to achieve the low transverse normalized equilibrium emittance.

REFERENCES

[1] H. G. Kirk, D. B. Cline, Y. Fukui, A. A. Garren, *Progress Toward A Muon Ring Cooler*, SNOWMASS-2001-M101, Jun 2001. 5pp., Prepared for APS / DPF / DPB Summer Study on the Future of Particle Physics (Snowmass 2001), Snowmass, Colorado, 30 Jun - 21 Jul 2001.

[2] E. D. Courant and H. S. Snyder, *Theory of Alternating-Gradient Synchrotron*, Annals of Physics, 3, 1-48 (1958)

GASEOUS HYDROGEN FOR MUON BEAM COOLING[1]

R. P. Johnson, R. E. Hartline, Muons, Inc., Batavia, IL 60510
C. M. Ankenbrandt, M. Kuchnir, A. Moretti, M. Popovic, Fermilab, Batavia, IL 60510
M. Alsharo'a, E. L. Black, D. M. Kaplan, Illinois Institute of Technology, Chicago, IL 60616

Abstract

Muons, despite their short lifetime, have an advantage in that they can be accelerated through matter without suffering appreciable scattering as do strongly interacting protons or electromagnetic showering as do less massive electrons. Thus RF cavities filled with dense gas to suppress electrical breakdown can provide high gradients for relatively short muon ionization-cooling channels for Neutrino Factories and Muon Colliders. Hydrogen gas, with large dE/dx, radiation length, and heat capacity, also acts as the perfect energy absorber having several engineering advantages. The progress of a DOE STTR grant project to develop high-pressure high-gradient RF cavities is described. First measurements of RF breakdown curves are reported, where stable operation was achieved with surface gradients of 50 MV/m for hydrogen and 28 MV/m for helium.

INTRODUCTION

The development of liquid hydrogen energy absorbers and RF cavities for ionization cooling of muon beams has been underway for some years by members of the Neutrino Factory and Muon Collider Collaboration, NFMCC [2]. These efforts will lead to a Muon Ionization Cooling demonstration Experiment, MICE [3]. Last year a new initiative started to study an alternative to the NFMCC-MICE technique for ionization cooling [4]. Muons, Inc, in partnership with IIT, has been funded by a Small Business Technology Transfer (STTR) grant to develop high gradient RF cavities that are filled with a dense gaseous energy absorber that also suppresses RF breakdown as described by Paschen's Law [5].

A dense gaseous energy absorber enables an entirely new technology to generate high accelerating gradients for muons by using the high-pressure region of the Paschen curve. Electrical breakdown is suppressed in this case because the mean free path for an ion in a dense gas is so short that collisions prevent acceleration to high-enough energy to create an avalanche. This idea of filling RF cavities with gas is new for particle accelerators and is possible only for muons because they do not scatter as do strongly interacting protons or shower as do less-massive electrons. Multiple Coulomb scattering is important, though, so a long scattering length is beneficial.

In this application, hydrogen gas is twice as effective as helium, the next best gas [4]. The use of a gaseous absorber presents other practical advantages [6] that make it a simpler and more effective cooling method compared to the liquid hydrogen flasks used in the NFMCC and MICE designs. Also, a new idea for six-dimensional cooling using gaseous hydrogen has been proposed [7].

LAB G TEST CELL

Phase I of the STTR grant was to build an 805 MHz RF test cell (TC) and to use it at Lab G at Fermilab to measure breakdown characteristics of helium gas at high pressure and at liquid nitrogen temperature. Figure 1 shows a cross section schematic of the prototype TC used for the initial tests at Lab G. The top and bottom discs of the pillbox design are standard 12" diameter stainless steel (SS) Conflat blanks commonly used for vacuum applications. These are strong and relatively inexpensive, with replaceable copper gaskets that did not work in this high-pressure application. Instead, the gaskets were replaced with rings of lead-tin solder in special grooves.

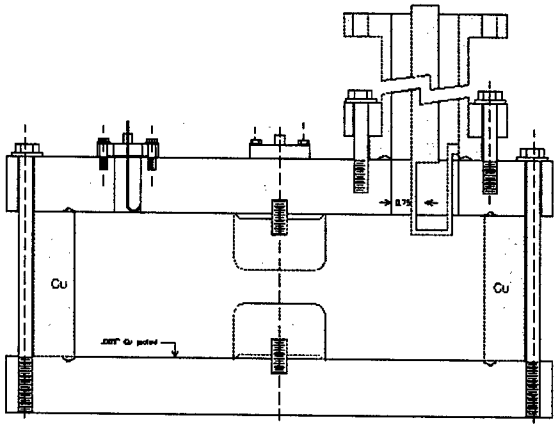


Figure 1. Test Cell Schematic. The ID is 9 inches, the internal height 3.2 inches, and the electrode gap is 2 cm.

The cylindrical wall of the pillbox is made of copper to ensure good thermal conductivity between the contained gas and a liquid nitrogen bath surrounding the TC. Stainless steel bolts hold the copper cylinder between the two SS disks. Stainless steel and copper are used in this application because they have almost identical coefficients of thermal expansion. This feature reduces the design complications, making the interfaces effectively static problems and the bolt tensions almost independent of temperature.

The 30-inch long SS coaxial RF feed shown in figure 1 allowed the pressure barrier to be well above the LN2 bath where it did not suffer thermal variations. This allowed a simple barrier design where the central conductor was epoxied in place. The power feed and probe used for the measurements described below were

0-7803-7738-9/03/$17.00 © 2003 IEEE

not loop-couplers as shown in the schematic, but capacitive stubs.

A network analyzer was used to measure the Qo and calibrate the pickup probe at room temperature and at liquid nitrogen temperature. Calibrated directional couplers were used to measure the forward and reflected RF power. The program SuperFish was used to calculate the ideal Qo and shunt impedance of the cavity from which the power for a given gradient was calculated. One could easily determine the TC resonant frequency by maximizing the amplitude of the signal from the probe as a function of the klystron pulse generator frequency.

The TC had a measured Q_o of 25,300 at 77 K and 13,600 at room temperature. The calculated room temperature Q_o for the TC was 19,200. The measured room temperature Q_o is about 30 % lower than calculated. This, however, is within the expected normal range for cavities that are bolted together. One normally comes within 5 % of calculation with high purity copper cavity brazed or electron-beam welded together and with only a few small ports.

The Q_o improved a factor of 1.86 at 77 K compared to room temperature. The resistance ratio for pure copper over this temperature range is 8. This corresponds to an expected Q_o improvement factor of 2.82 for highly purified copper since Q is inversely proportional to the square root of the resistivity. However, the TC was not constructed solely of high purity copper. The outside cylinder of the TC was made of high purity copper but the end plates were made of copper plated stainless steel. The lead-tin solder seal between the copper plated disks and the copper cylinder may have had a larger effect on the Q than the plating material, however, but remains to be investigated.

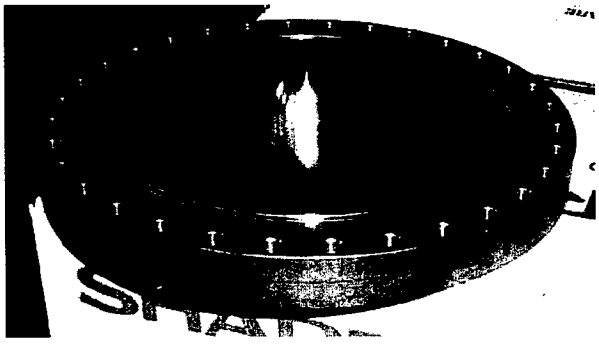


Figure 2. Twelve-inch-diameter Copper-plated stainless-steel Conflat disk and electrode.

Figure 2 shows a picture of the bottom disk and one doorknob electrode just before the TC was assembled to measure hydrogen breakdown for the first time. The shape of the electrode was made more hemispherical than shown in the schematic to match the TC frequency to that of the klystron. All internal SS surfaces were plated with copper to improve the cavity quality factor and reduce RF heating. At 800 MHz, the skin depth is 2.7 microns so that any plating of at least 10 microns is sufficient.

Because of the use of high-pressure hydrogen, safety issues were a major concern. The Test Cell Document [8] prepared for the Fermilab Liquid Hydrogen Target Safety Panel contains the required engineering note, flammable gas analysis, and oxygen deficiency analysis.

HELIUM DATA

Figure 3 shows the breakdown voltages for the test cell with helium gas at liquid nitrogen temperature as a function of pressure. The dark diamonds were obtained by first raising the klystron power until breakdown occurred, then slowly lowering the power until the pulses were clean, with no breakdown over a few minute period. The light squares show the resonant frequency of the cavity (MHz). The RF frequency is a sensitive measure of the pressure. A close examination of the frequency point at 315 PSIG shows the pressure is set incorrectly and the actual pressure was 345 PSIG, which explains why that gradient point seems high.

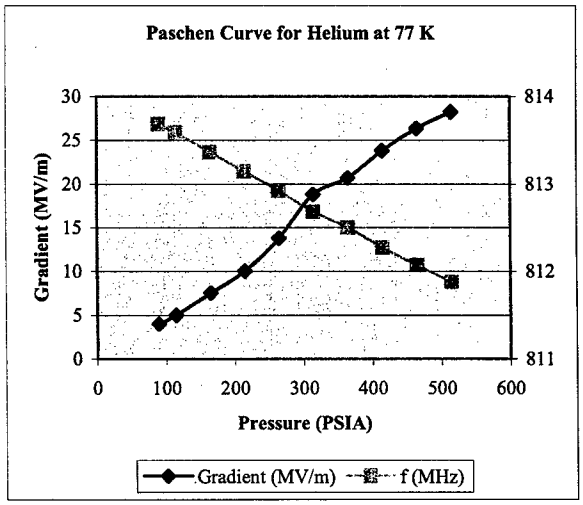


Figure 3. Maximum stable RF gradient (dark) for helium at liquid nitrogen temperature and cavity frequency (light) as a function of pressure. The dark Paschen curve was the proof of principle goal of the STTR phase I project.

The data seem to follow the linear increase with gradient expected by Paschen's Law up to a value useful for muon cooling applications.

HYDROGEN DATA

On April 11, the use of hydrogen gas in the Lab G environment was authorized. After 3 hours of conditioning at 450 PSIG at 77 K the maximum gradient increased from 35 MV/m to over 55 MV/m. Another 5 hours of conditioning did not improve the maximum gradient and may have made it worse. At that point the

dark points in figure 4 were taken. After raising the voltage until breakdown occurred, the dark colored diamonds were obtained by then slowly lowering the power until the RF ran stably, without sparking.

The previous data measured in 1948 [9], shown in figure 4 as light colored squares, have a maximum of 28 MV/m at 23 atmospheres at room temperature and DC conditions. In figure 4 the pressures of these data have been scaled to 77 K for comparison.

The new data show the same Paschen's Law behavior as the helium data, where the maximum stable gradient increases almost linearly with pressure, up to 170 PSIA. In the hydrogen case, however, the rate of increase of the maximum gradient diminishes once the gradient reaches 50 MV/m, presumably due to breakdown at the electrode surface.

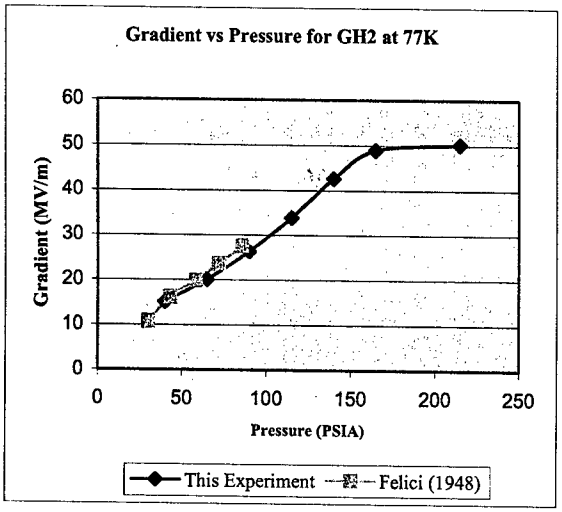


Figure 4. Measured maximum stable RF gradients for hydrogen gas at LN2 temperature compared to the DC breakdown gradients of Felici and Marchal (1948).

The pressurized test cell required RF conditioning that is usual for evacuated cavities. That is, the application of many breakdown discharges usually allows higher and higher voltages to be attained. The breakdown above 170 PSIA in figure 4 is dominated by gradient at the surface of the electrodes and the qualities of the electrodes rather than the gas itself. One possibility is that above 50 MV/m the power in the discharges is sufficient to cause damage to the electrodes rather than the polishing action seen in most RF conditioning. Examination after this run of the TC electrodes, initially prepared with 1500 grit sandpaper and cleaned with alcohol, showed no visible surface imperfections. However, it may be difficult to see the difference between a surface that holds off 55 MV/m and one that holds off 50 MV/m. In the future we will examine the detailed behavior of the breakdown above 170 PSIA, where the maximum gradient seemed to deteriorate with conditioning time rather than improve.

CONCLUSIONS

This study has extended the range of possibilities for muon cooling. Measurements have been made of high-gradient RF in dense gases near 805MHz, a viable frequency for muon ionization cooling. A cryogenic technique has been used to achieve high gas density.

RF breakdown and stability levels for hydrogen gas have been measured at the highest density to date. The maximum stable gradients of 50 MV/m for hydrogen and 28 MV/m for helium are high enough to be very interesting for cooling channels with these continuous gaseous absorber materials.

REFERENCES

[1] This work is supported in part by US DOE grant DE-AC02-ER86145 and by the Illinois HECA grant to the Illinois Consortium for Accelerator Research.

[2] M. Alsharo'a et al., Status of Neutrino Factory and Muon Collider Research and Development and Future Plans, submitted to Phys. Rev. ST Accel. Beams, e-Print Archive: hep-ex/0207031 (2002).

[3] Proposal to the Rutherford Appleton Lab: An International Muon Ionization Cooling Experiment (MICE), The MICE Collaboration. January, 2003 http://hep04.phys.iit.edu/cooldemo/micenotes/public/pdf/MICE0021/MICE0021.pdf

[4] R. P. Johnson et al., Gaseous Hydrogen and Muon Accelerators, in International Workshop on Hydrogen in Materials and Vacuum Systems, Edited by G. Myneni and S. Chattopadhyay, AIP Conference Proceedings 671, Melville, New York, 2003.

[5] Sanborn C. Brown, Basic Data of Plasma Physics, The Fundamental Data on Electrical Discharges in Gases, American Vacuum Society Classics, AIP Press, 1993, p 149.

[6] R. P. Johnson and D. M. Kaplan, A Gaseous Energy Absorber for Ionization Cooling of Muon Beams.MUC/NOTE/COOL_EXP/PUBLIC/195 March, 2001.

[7] Ya. Derbenev and R. P. Johnson, Six-dimensional muon beam cooling in a continuous, homogeneous, gaseous hydrogen absorber, COOL03, May 2003, RIKEN, Japan. To be published in NIMA.

[8] R. E. Hartline et al., Lab G RF Test Cell Construction, Operation, Safety, and First Results, munote-001 5/06/03. http://members.aol.com/muonsinc/TC.pdf

[9] Meek and Craggs, "Electrical Breakdown in Gases", John Wiley & Sons, 1978, p. 557.

Proceedings of the 2003 Particle Accelerator Conference

MICE: THE INTERNATIONAL MUON IONIZATION COOLING EXPERIMENT

Y. Torun*, Illinois Institute of Technology, Chicago, IL 60616, USA
for the MICE Collaboration

Abstract

The MICE Collaboration has designed an experiment in which a section of an ionization cooling channel is exposed to a muon beam. This channel includes liquid-hydrogen absorbers providing energy loss and high-gradient rf cavities to re-accelerate the particles, all tightly packed in a solenoidal magnetic channel. It reduces the beam transverse emittance by >10% for muon momenta between 140 and 240 MeV/c. Spectrometers placed before and after the cooling section perform the measurements of beam transmission and emittance reduction with an absolute precision of ±0.1%.

INTRODUCTION

A Neutrino Factory based on a muon storage ring is the ultimate tool for studies of neutrino oscillations, including possibly the discovery of leptonic CP violation [1, 2]. It is also the first step towards a $\mu^+\mu^-$ collider. Ionization cooling of muons has never been demonstrated in practice but has been shown by end-to-end simulation and design studies to be an important factor for both performance and cost of a Neutrino Factory. This motivates an international program of R&D, including an experimental demonstration. The aims of the International Muon Ionization Cooling Experiment are:

- To show that it is possible to design, engineer and build a section of cooling channel capable of giving the desired performance for a Neutrino Factory
- To place it in a muon beam and measure its performance in various modes of operation and beam conditions, thereby investigating the limits and practicality of cooling

A proposal [3] has been submitted to Rutherford Appleton Laboratory (RAL) to mount the experiment at ISIS.

EXPERIMENT LAYOUT

The main components of MICE are outlined in Fig. 1. Cooling is provided by one lattice cell from the 201 MHz cooling channel of "Study-II" [4] with some components modified for cost savings and compliance with RAL safety requirements. The incoming muon beam first encounters diffusers to generate a large tuneable input emittance. In this section, a precise time measurement and particle identification are performed. Next comes an input spectrometer consisting of tracking devices within a uniform-field solenoid to measure the phase space coordinates of each particle. This is followed by the cooling section, with hydrogen absorbers, rf cavities and superconducting coils. One additional absorber finishes the cooling section, both for symmetry and to protect the trackers against dark currents emitted by the rf cavities. The momentum, position and angles of the outgoing particles are measured in a second spectrometer, identical to the first one. At the downstream end of the experiment, another time-of-flight (TOF) measurement is performed, and particle identification by means of a Cherenkov counter and a calorimeter eliminates muons that have decayed in the apparatus. To avoid emittance growth, the magnets in these two cells are matched to the spectrometer solenoids using two sets of matching coils.

MEASUREMENT TECHNIQUE

To allow precision measurement of transmission and emittance, one muon at a time will be tracked through the apparatus and detected using standard particle-physics techniques, which are much more precise than those typically used in beam instrumentation. A "virtual bunch" formed in offline analysis will be used to demonstrate how an actual bunch would have behaved had the beam intensity been orders of magnitude higher.

Momentum measurement requires a magnetic spectrometer. Ease of matching into and out of the cooling section and the need to keep a large-emittance beam in a small physical volume has led to the choice of solenoid magnets on each side of the cooling channel.

Each detector measures, at given z positions, the coordinates x and y of every incident particle, and the time. Momentum and angles are reconstructed by using several measurement planes. For the experimental resolution not to affect the emittance measurement significantly, the rms resolution of the measurements must be better than about 10% of the rms beam size at the equilibrium emittance in each of the six dimensions. An essential aim of MICE is to measure the equilibrium emittance precisely. For each incident particle it will be possible to determine whether it was lost in the channel or went through successfully. Therefore, losses can be separated clearly from cooling. Except for possible collective effects such as space charge, this technique is equivalent to full-beam measurements, but offers several advantages. Correlations between parameters can be easily measured. The role of each beam parameter (energy, transverse momentum, rf phase, etc.) can be studied using selection cuts in the ensemble of tracks without mak-

* torun@iit.edu

0-7803-7738-9/03/$17.00 © 2003 IEEE

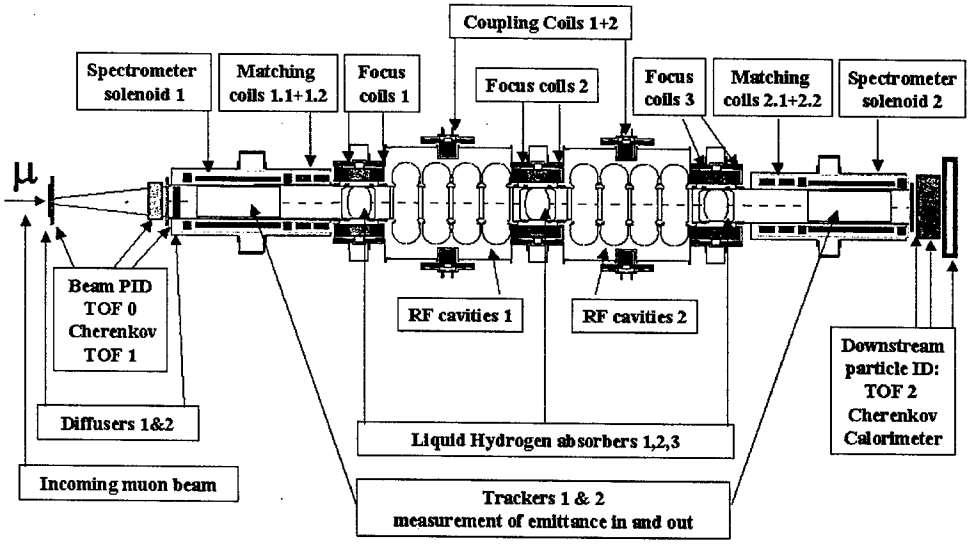


Figure 1: MICE layout.

ing changes to the beam parameter settings. Software cuts based on the incoming beam make it possible to derive a variety of results with different input beam conditions from a single data set. Any desired input beam conditions can be reconstructed by appropriate weighting or culling of the observed particles.

RF BACKGROUND

The layout described above has one major drawback: the detectors will be exposed to a large dark current and x-ray background generated by the nearby high-gradient rf cavities. The understanding of this problem is well underway [5]. Several factors contribute to protect the tracking detectors: i) the rf cavities will be operated at a moderate gradient of 8.3 MV/m, due to the limited availability of rf power; ii) most dark-current electrons are deflected by the field flips [6]; iii) the electrons must also pass through the liquid-hydrogen absorbers, which are thick enough to absorb them completely, letting through x-rays only; iv) the detectors are built of low-Z material and are well able to distinguish muon hits from those generated by x-rays. Thus, it appears that the performance of the detectors will not be affected.

POSSIBLE EXPERIMENTS AND TIMELINE

Many different cooling experiments can be performed with the proposed apparatus. First, beam momentum can be varied since the magnets have been designed to allow exploration of momenta as high as 240 MeV/c. The Super-FOFO lattice used here has the property that the beta function at the absorber can be changed by adjusting the currents in the focusing and coupling coils. Different rf voltages and phases can also be used. Another important part of the experimental program will be testing various absorbers. It will be straightforward to replace the liquid hydrogen with liquid helium. The mechanical assembly of the liquid hydrogen absorbers will also allow replacement of one of the absorber windows by a structure supporting solid absorbers [7].

Since all detectors and parts of the equipment will not be ready at the same time, one can foresee a development of the experiment in time, to allow a number of preparatory stages. This leads to the scenario presented in Fig. 2. First (step I), the beam can be tuned and characterized using a set of TOF and particle ID detectors. In step II, the first spectrometer solenoid allows a first measurement of 6D emittance with high precision and comparison with the beam simulation. This should allow a systematic study of the tracker performance. In step III, the two spectrometers work together without any cooling device in between which allows the study of systematic errors. Step IV, with one focusing pair between the two spectrometers, should provide experience with operating the absorber and a precise understanding of energy loss and multiple scattering in it. Several experiments with varying beta-functions and momenta can be performed with observation of cooling in normalized emittance. Starting from step V, the real goal of MICE, which is to establish the performance of a realistic cooling channel, will be addressed. Only with step VI will the full power of the experiment be reached.

COOLING CHANNEL

The MICE magnetic channel consists of seven magnet assemblies composed of eighteen superconducting solenoid coils spread over a length of nearly 11.5 m. The baseline MICE channel operates with muons at an average

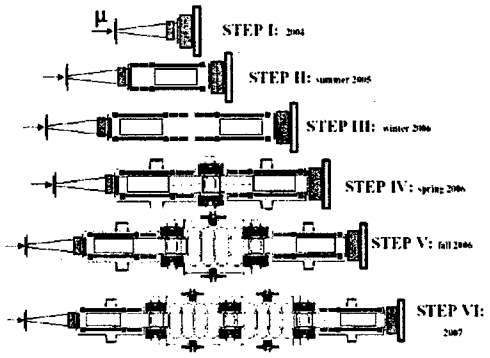


Figure 2: Six possible steps in the development of MICE

momentum p=200 MeV/c and β=42 cm at the center of the absorber. Eight 201-MHz rf cavities, in two 4-cavity assemblies, are needed in the cooling section. Due to the (financial) limitation of having only 8 MW of rf power available, the MICE cavities will operate at a gradient of about 8 MV/m (compared with the 16 MV/m specification for Study-II). The cavity shape chosen is based on a slightly reentrant rounded profile with a large beam aperture and a small nose cone [8]. To achieve high shunt impedance, the beam aperture is terminated electromagnetically using thin beryllium foils or thin-walled Al tubes. Hydrogen was chosen as the most suitable absorber material because of its large ionization energy-loss rate ("cooling") and small probability of multiple scattering ("heating").

DETECTORS

The driving design criteria for the MICE detector systems are robustness, in particular of tracking detectors, to potentially severe background conditions in the vicinity of rf cavities and redundancy in particle identification (PID) to keep contamination below 1%. Three TOF stations equipped with fast scintillators are foreseen. The first two, upstream of the cooling section and separated by about 10 m, will provide the basic trigger for the experiment, in coincidence with the ISIS clock. These have precise timing (around 70 ps) and will provide muon identification as well as the muon timing (relative to the rf phase) necessary for the measurement of the input longitudinal emittance. The coincidence with a third station of similar nature, downstream of the second measuring station, will select particles traversing the entire cooling section. The baseline design for the tracking detectors is five sets of scintillating fiber planes per spectrometer, deployed in three stereo views, with the fibers individually read out using cryogenic VLPC photodetectors. An alternative design is also under investigation in which each spectrometer contains a time projection chamber with triple-GEM readout (TPG). Additional detectors will provide redundant particle identification to eliminate from the sample any residual pions in the incoming beam or muons that decay within the apparatus. These include time-of-flight scintillation counters, Cherenkov detectors and a calorimeter. While these are standard ingredients for particle-physics experiments, measuring an emittance ratio with 0.1% precision has never been done and will require careful design of diagnostics and attention to system integration and calibration.

STATUS

The MICE Collaboration has brought together 141 physicists and engineers from the world's accelerator and particle physics communities to tackle the technical challenges of ionization cooling. Together, they have designed an experiment to demonstrate the feasibility of muon cooling and, with enthusiastic support from the UK particle physics community, shown that it can be carried out at Rutherford Appleton Laboratory. By measuring the parameters of each muon individually, MICE will measure the transverse emittance in each transverse plane with an absolute precision of 0.1%. The proposed cooling section will be operable with a variety of optical settings and absorber materials, allowing the cooling performance to be mapped out for a range of cooling-channel parameters and beam momenta and compared with the predictions of detailed simulations. By demonstrating that the technology of muon ionization cooling is not only technically feasible, but that its cost and performance are well understood, MICE will pave the way for the start of a Neutrino Factory construction project and will point the way to muon colliders in the longer term. The proposed schedule for the commissioning and operation of MICE will establish the technical feasibility of muon ionization cooling by 2007; we are seeking funding from agencies around the world to realize this schedule.

ACKNOWLEDGEMENTS

The author's work was supported by the US Department of Energy and the Illinois Board of Higher Education.

REFERENCES

[1] C. Albright *et al.*, arXiv:hep-ex/0008064, May 2000

[2] M. Lindner, arXiv:hep-ph/0209083, Sept. 2002

[3] Proposal to the Rutherford Appleton Laboratory, An International Muon Ionization Cooling Experiment, MICE-Note 21, http://www.mice.iit.edu/mnp/MICE0021.pdf

[4] Feasibility Study-II of a Muon-Based Neutrino Source, S. Ozaki *et al.*, BNL-52623, June 2001

[5] J. Norem *et al.*, Dark Current and X-Ray Measurements of an 805 MHz Pillbox Cavity, this conference

[6] P. Gruber and Y. Torun, A Technique for Imaging Dark Currents, this conference

[7] M. Green *et al.*, The Integration of Liquid and Solid Muon Absorbers into a Focusing Magnet of a Muon Cooling Channel, this conference

[8] D. Li *et al.*, A 201 MHz RF Cavity Design with Non-stressed and Pre-curved Be Windows for Muon Cooling Channels, this conference

MUON COOLING RESEARCH AND DEVELOPMENT

M.A.C. Cummings*, Northern Illinois University, Dekalb, IL 60115, USA
Daniel M. Kaplan, Illinois Institute of Technology, Chicago, IL, 60616, USA

Abstract

The MuCool Collaboration is engaged in a program of research and development on hardware for ionization cooling of a muon beam. The aim of MuCool is to develop the key pieces, including high-gradient normal-conducting RF cavities and high-power liquid-hydrogen energy absorbers. This effort will lead to a more detailed understanding of the construction and operating costs of such hardware, as well as to optimized designs that can be used to build a Neutrino Factory or Muon Collider. This work is being undertaken by a broad collaboration including accelerator and particle physicists and engineers from many national laboratories and universities in the U.S. and abroad. The intended schedule of work will lead to ionization cooling being well enough established that a construction decision for a Neutrino Factory could be taken before the end of this decade based on solid technical foundations.

INTRODUCTION

The concept of a muon collider has been given serious consideration in recent years to extend the energy reach of particle physics machines. The larger muon mass, compared to electrons, suppresses bremstrahlung and synchrotron radiation, resulting in high-resolution mass and energy measurement. The challenges of muons are their short lifetime (~10^{-6} s) and their production into a diffuse phase space from pions. The phase space can be reduced via ionization cooling sufficiently within the muon lifetime to store a muon beam.

Cooling is based on the principle that the density of a beam can be increased only by non-conservative interactions such as ionization energy loss, as phase space is otherwise conserved by Liouville's Theorem. The evolution of transverse beam emittance ε_n within matter is given by [1]:

$$\frac{d\varepsilon_n}{ds} \approx -\frac{1}{\beta^2}\frac{dE_\mu}{ds}\frac{\varepsilon_n}{E_\mu} + \frac{1}{\beta^3}\frac{\beta_\perp (0.014)^2}{2E_\mu m_\mu L_R}, \qquad (1)$$

where s is path length, E_μ is beam energy in GeV, $\beta = v/c$, L_R is the radiation length of the absorber material and $\beta_\perp$ is the betatron function describing the focusing strength of the lattice. The two terms of Eq. 1 reflect the competition between multiple scattering of the muons within the absorber (a heating effect) and the ionization loss. The second, "heating" term is minimized when absorbers are placed in a strong focusing field (low $\beta_\perp$) and consist of material of low atomic number (high L_R), the optimal choice being hydrogen.

*macc@fnal.gov

IONIZATION COOLING CHANNELS

In an ionization-cooling channel, the dE/dx ionization loss of the muons in the medium decreases all three of their momentum components without changing the size of the beam. The longitudinal momentum of the beam is then restored through RF cavities placed between the absorbers. These have to achieve sufficient accelerating gradients so that the muons go through the cooling channel before a significant fraction of them decay. It is also desired that the maximum acceleration of the cavities exceed that required to restore the longitudinal momentum to allow "off-crest" operation; this results in continuous rebunching so that even with large momentum spreads the beam can remain captured in the RF bucket. The cooling effect can be rotated between transverse and longitudinal phase space by inserting wedge-shaped absorbers into dispersive regions of the cooling channel lattice ("emittance exchange"); longitudinal ionization cooling as such is impractical due to energy loss straggling.

COOLING CHANNEL R&D

An effective ionization cooling channel will require low-Z absorbers with sufficient cooling capacity to handle heat loads on the order of hundreds of watts. These absorbers need to be placed in low beta regions, requiring high magnetic fields or large field gradients, with sufficient accelerating gradient to achieve cooling in the shortest practical distance. The MuCool Collaboration is engaged in R&D on all three technology fronts.

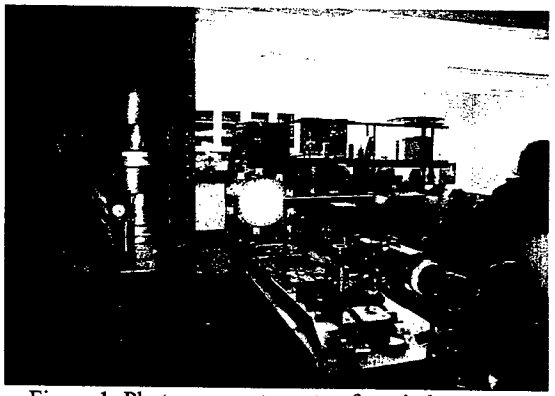


Figure 1: Photogrammetry setup for window tests..

0-7803-7738-9/03/$17.00 © 2003 IEEE

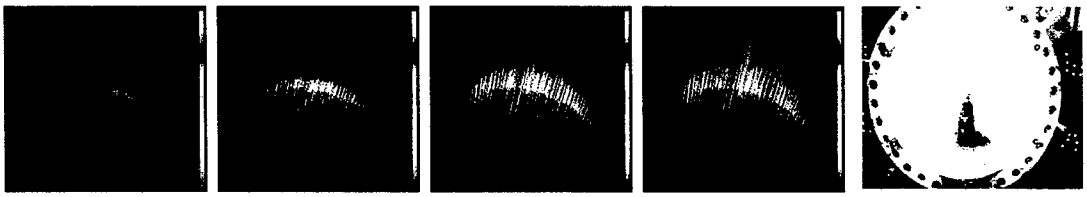


Figure 2: Successive photogrammetry measurements for a window pressure test to bursting (the far right-hand picture). Hundreds of points can be measured without coming into contact with delicate window surfaces.

High-Power Hydrogen Absorbers

The development of high-power liquid-hydrogen (LH_2) absorbers has been a critical goal in the MuCool program. The driving issues are to minimize the multiple scattering (beam heating) and to handle large heat loads while maintaining uniform temperature, and hence density, within the absorber volume. To handle the former requirement, we have developed new shapes for the ends of the hydrogen flasks that allow for significant reductions in their thickness (particularly near the center where the beam intensity is maximum) [2]. We have successfully fabricated tapered, curved windows out of disks of an aluminum alloy (6061-T6) using a numerically controlled lathe. We also devised novel means to test these non-standard windows and demonstrate that they meet design specifications and satisfy applicable safety requirements. By optimizing the maximum stress as a function of volume pressure, one of our designs, the inflected "thinned bellows" window, was able to achieve a minimum central thickness one fourth that of the ASME-standard "torispherical" window of equivalent strength and diameter [2].

We developed photogrammetric techniques to measure the shape of the windows and their performance in pressure tests. The advantages of photogrammetry are the non-contact nature of the measurement (projected points of light, with parallax calculations to determine the space points within a calibrated coordinate system), and that ~1000 points could be measured simultaneously. This represents almost 2 orders of magnitude improvement over CMM measurements (about 30 discrete points) for shape measurement and strain gages (about 16 measurements) for the pressure tests [2].

We have completed manufacture and pressure tests of the first series of non-standard window, the "tapered torispherical" design, establishing testing and certification procedures, including finite element analysis (FEA) predictions for window performance [2]. Fabrication of the next series non-standard window type, of the "thinned bellows" design, is now underway, including windows for the vacuum vessels surrounding the absorber (mandated by the Fermilab safety code). We will be considering the use of lithium-aluminum alloys, such as the 2195 alloy used in the Space Shuttle; the resulting thinness could challenge the current fabrication technique, and any new alloy will have to be certified for machinability and high-radiation application.

The power to be dissipated in these absorbers in the cooling channel designs considered so far is within the limits of what has been achieved in LH_2 targets developed for and operating within the high-power environments of current experiments. However, the highly turbulent fluid dynamics involved in the heat-exchange process necessitates R&D for each new configuration. We are pursuing two approaches to heat extraction: a conventional flow-through design with an external heat exchanger, similar to that used for high-powered LH_2 targets, and a convection-cooled design with an internal heat exchanger built into the absorber vessel. The convection design has desirable mechanical simplicity and minimizes the total hydrogen volume in the cooling channel (a significant safety concern), but is expected to be limited in the amount of power it can handle compared to the flow-through design. To study and optimize the fluid mixing and heat transfer properties of these designs, we have been exploring ways to visualize the flow patterns and temperature distributions within the fluid [3].

High-Gradient Normal-Conducting RF Cavities

An ionization-cooling channel requires insertion of high-gradient RF cavities into a lattice employing strong solenoidal magnetic fields. This precludes using superconducting cavities. The cooling channels under consideration will use normal-conducting 201-MHz cavities, but the R&D is more readily carried out with smaller, higher-frequency devices.

Radio-frequency cavities normally contain a minimum of material in the path of the beam. However, the penetrating nature of muons allows the use of closed-cell ("pillbox") cavities, provided that the cell closures are constructed with thin material of long radiation length. Eq. 1 implies that this material will have little effect on cooling performance as long as its thickness L per cooling cell (at the $\beta_\perp$ of its location in the lattice) has $\beta_\perp L/L_R$ small compared to that of the absorber. Closing the RF cells approximately doubles the on-axis accelerating gradient for a given maximum surface electric field, allowing operation with less power and less "dark

current" emission. Two alternatives have been considered for the design of the cell closures: thin beryllium foils and grids of gas-cooled, thin-walled aluminum tubing.

The tests of a 6-cell open cavity, designed at Fermilab, and a closed, single-cell cavity, designed at LBNL, both at 805 MHz, are being carried out in Fermilab's Laboratory G. The dedicated test area includes a high-power 805-MHz klystron transmitter (12-MW peak pulsed power with pulse length of 50 μs and a repetition rate of 15Hz), an x-ray-shielded cave, remote-readout test probes, safety-interlock systems, and a control room and workshop area for setup of experiments [4]. The cave also contains a high-vacuum pumping system and water cooling for the cavity. To allow tests of the cooling-channel RF cavities and absorbers in a high magnetic field or high field gradient, a superconducting 5 Tesla solenoid with a room-temperature bore of 44 cm was constructed by LBNL and installed in the Lab G cave, with two separate coils that can be run in "solenoid" mode (currents flowing in the same direction) or "gradient" mode (currents flowing in opposite directions).

A primary challenge in high-gradient RF cavity development is the suppression of dark currents (electrons emitted from the cavity surface via quantum tunnelling as described by the Fowler-Nordheim formalism) and their associated x rays. Our tests show that exposed copper surfaces appear to be problematic at high field [5]. A variety of window and cavity surface preparations and coatings remain to be explored, including TiN-coated copper at the locations of maximum surface field. Alternatives to flat, pre-stressed foils are receiving attention, and we expect to prototype and test several solutions at 805 MHz; the 805 MHz pillbox-cavity prototype was designed with just this type of test program in mind. Design studies indicate that both pre-curved Be foils and grids of gas-cooled, thin-walled Al tubes should be feasible and may be cheaper and induce less scattering than flat foils.

The design of the 201 MHz closed-cell cavity for muon cooling is complete [6]. We intend to build a first prototype in the next year.

MuCool Test Area at Fermilab

In order to rigorously test the heat capability and radiation hardness of our cooling channel components, we are building a MuCool Test Area (MTA) off the end of the Fermilab Linac. This location combines the availability of multi-megawatt RF power at both 805 and 201 MHz, and a 400 MeV proton beam at high intensity. Cryogenic facilities are being constructed for LH_2 absorber and superconducting magnet operation. The underground enclosure will provide the needed radiation shielding for a high-power beam test of a single prototype cooling cell. We anticipate the first stand-alone LH_2 absorber test towards the end of 2003, and tests for the 201-MHz cavity when it becomes available. Beam tests will happen within the next three years, to explore the possible effects on cavity breakdown and absorber power-handling. This is only a high-power engineering test, and not a cooling demonstration. A complementary cooling experiment (MICE) has been approved and will operate at Rutherford Appleton Laboratory in England [7].

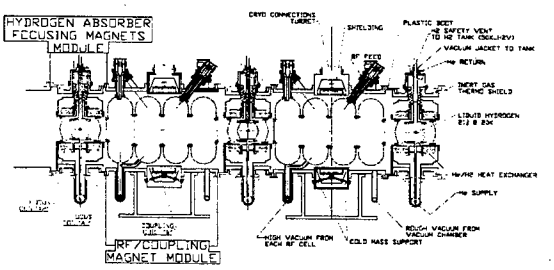


Figure 3. Cooling channel design: Absorbers between 201 MHz RF cavities, surrounded by high-field solenoidal coils.

Acknowledgements

This work was supported in part by the U.S. Dept. of Energy, the National Science Foundation, the Illinois Board of Higher Education, the U.S.-Japan Agreement on High Energy Physics and the UK Particle Physics and Astronomy Research Council.

REFERENCES

[1] D. Neuffer, Part. Acc. **14** 75 (1983).
[2] M.A.C. Cummings *et al*, "Current LH_2 Absorber Research in MuCool", NuFact '02, Imperial College, London, UK, 2002.
[3] J. Norem *et al*, "Measurement of Beam Driven Hydrodynamics" , these proceedings.
[4] D. Li *et al*, "RF Tests of an 805 MHz Pillbox Cavity at Lab G of Fermilab", these proceedings.
[5] J. Norem *et al*, "Dark Current and X Ray Measurements of an 805 MHz Pillbox Cavity", these proceedings.
[6] D. Li *et al*, "A 201 MHz RF Cavity Design with Non-Stressed and Pre-Curved Be Windows for Muon Cooling Channels", these proceedings.
[7] Y. Torun *et al*, "MICE: Muon International Cooling Experiment", these proceedings.

Proceedings of the 2003 Particle Accelerator Conference

BENCH MEASUREMENTS OF LOW FREQUENCY TRANSVERSE IMPEDANCE

A. Mostacci, Univ. di Roma "La Sapienza", Rome, Italy,
F. Caspers, L. Vos, CERN, Geneva, Switzerland,
U. Iriso, BNL, Upton, New York, 11973, USA.

Abstract

For frequencies below 10 MHz the classical two wire transmission line method is subject to difficulties in sensitivity and measurement uncertainties. Thus for evaluation of the low frequency transverse impedance properties of the LHC dump kicker a modified version of the two wire transmission line has been used. It consists, in the present case, of a 10 turn loop of approximately 1 meter length and 2 cm width. The change of input impedance of the loop is measured as a function of the surroundings and by using a proper reference (metallic beam pipe) these changes are converted into a meaningful transverse beam coupling impedance. Measurements of several calibration objects have shown close agreement with theoretical results.

INTRODUCTION

A beam that oscillates from side to side with amplitude $\pm\Delta$ induces differential currents and charges on the walls of the vacuum chamber. These in turn produce a transverse magnetic field and an electric field which further deflects the beam. The threshold for beam instability and the growth rates depends on the so called transverse coupling impedance Z_T.

Transverse impedances are well known in literature and they can be theoretically calculated for a number of particularly simple structures or in general, they are numerically computed with codes. In this paper we are interested on bench measurements techniques, in particular at low frequencies (below few kHz). At those frequencies a better sensitivity can be obtained by using a loop [1], instead of the classical two wire technique [2].

The interest for very low frequencies is directly related to the low transverse oscillation frequencies of future large machines (like LHC). To validate the bench measurement technique, measurements were carried out on a stainless steel pipe (with conductivity σ =1.3 10^6 S/m) for which theoretical results are available. The radius of the pipe is b =50 mm, its wall thickness is t =1.5 mm and its length is L =50 cm. This paper reports those preliminary measurements and asseses a measurement recipe to be applied later to the more complex geometries of LHC devices.

TRANSVERSE IMPEDANCE BENCH MEASUREMENTS

Being I the beam current, the source of the differential wall current is the dipole $I\Delta$ per unit length of the beam. The same wall currents and magnetic (deflecting) field result if the beam is replaced by two parallel wires or more simply by a loop of length L, width Δ and current I. The magnetic field induces a voltage in the loop which increases its impedance (the current I is constant). This additional impedance is simply the variation of the loop impedance when inserted in the Device Under Test (DUT) with respect to the loop impedance. Assuming that the loop is coiled N times, the transverse coupling impedance can be obtained from

$$Z_T = \frac{c}{\omega}\frac{Z^{DUT} - Z^{f.s.}}{N^2\Delta^2} \qquad (1)$$

where Z^{DUT} is the (measured) impedance of the loop when inserted in the DUT and $Z^{f.s.}$ is the (measured) impedance of the loop far away from any perturbing object (i.e. in free space).

In general, when measuring a very small impedance (as pointed out in [1]), one should also subtract the radiation resistance from the loop measurements in free space. This is appreciable unless the loop is very short compared with the wavelength. Alternatively one could place the loop in a circular perfectly conducting pipe (a copper or brass one is enough), for which the added impedance is easy to calculate.

MEASUREMENT SET-UP

The coil used in the measurement was L_w =1.25 m long and Δ =22.5 mm wide. To reduce the signal to noise ratio (particularly important in our case since the measured signals are very small), the loop was coiled N =10 times. In this way, one can increase the useful signal with a factor N^2 with a drawback of lowering the frequency of loop self resonances: the chosen number of turns is a compromise to keep the lowest self resonance above 1 MHz.

The loop input impedance (much lower than 50 Ohm) was measured with an Agilent Vector Network Analyser (VNA4395A) using two different S-parameters test sets, according to the two different frequency ranges of the measurement. In the higher frequency range (10 kHz–1 MHz), a standard transformer type directional coupler (provided with the instrument as an impedance measurement test set) could be safely used. For lower frequencies (100 Hz–10 kHz), a resistive coupling network has been used: the RF output signal from the instrument is split and partly used for reference (the **A** signal in Fig. 1) and partly directed to the measurement coil (the DUT in Fig. 1). The reflected signal (**B**) is then measured and a 20 db attenuator

0-7803-7738-9/03/$17.00 © 2003 IEEE

(corresponding to dashed white line in Fig. 1) prevents the signal from the DUT from affecting the reference.

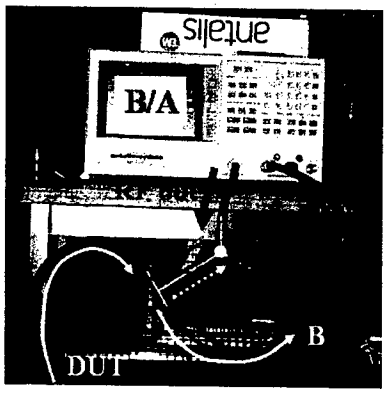


Figure 1: Set up for the low frequency measurements.

CIRCULAR STEEL TUBE

The transverse impedance of a circular pipe is well known and closed formulae are available, at least in the most significant limits. In the following we report the ones used to compare to the experimental data.

Being $\delta = \sqrt{2/(\omega\mu\sigma)}$ the skin depth, L the length of the structure (which in our case is L =50 cm), the transverse impedance for a circular beam pipe is for the "thick wall" case (see for example [3])

$$\frac{Z_T}{L} = \frac{1+j}{\pi}\frac{c}{\omega\sigma b^3\delta} \quad \text{for} \quad \delta \ll t, \tag{2}$$

where c is the speed of light. For wall thickness smaller than the skin depth, a better approximation for the real transverse impedance can be obtained by using the wall thickness t instead of δ in Eq. (2); anyway both formulae are not suited for very low frequencies where they diverge.

At low frequencies such that the skin depth is greater than the wall thickness, the interaction between the loop and a cylindrical resistive pipe can be described with an equivalent circuit model and the resulting transverse impedance is

$$\frac{Z_T}{L} = \frac{c}{\pi b^3\sigma\omega t\Delta^2}\frac{1+j\omega_c/\omega}{1+(\omega_c/\omega)^2} \quad \text{with} \quad \omega_c = \frac{2}{\pi\mu b\sigma t} \tag{3}$$

which is a corrected version of the result in Ref. [1].

An interesting derivation of the transverse impedance of a circular pipe with arbitrary surface impedance has been recently published in [4].

A field matching approach has been proposed to describe the impedance of a vacuum chamber with wall thickness smaller than the skin depth, in the framework of the VLHC studies. The results for a circular beam pipe are reported in Ref. [5] and the interested reader can find the closed analytical formulae in Ref. [6].

The measurement results on the steel pipe are compared to the theoretical expectation in Fig. 2. The thick wall formula ($\delta \ll t$) of Eq. (2) is a reasonable approximation only above 85 kHz (light blue line); a good agreement over the whole range is achieved with an analytical model (brown line) and with the field matching of Ref. [6] (green diamonds). At low frequencies also the equivalent circuit model of Eq. (3) gives reasonable results (red line). In conclusion all the theoretical expectations for the real transverse impedance agree in their different validity ranges and the measurement (dark blue line) is coherent with them.

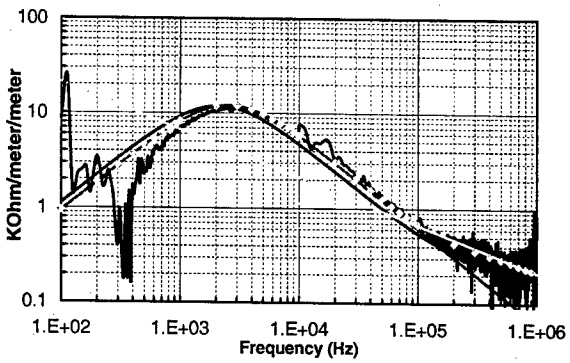


Figure 2: Transverse impedance per unit length (real part) of a steel circular pipe.

On the contrary for the imaginary part, the theoretical expectation are all in agreement, but they substantially differ from the measured values. In particular the measurements give a negative the immaginary part, while the theories predicts positive values. The results are shown in Fig. 3, with the same notation of Fig. 2.

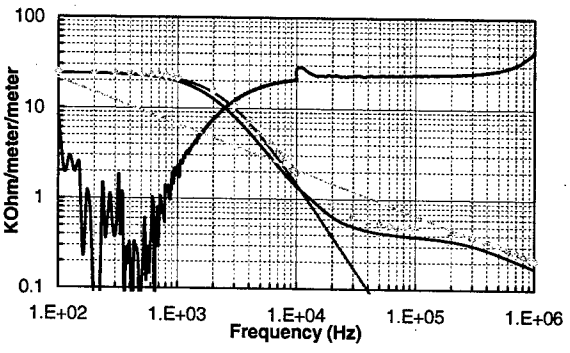


Figure 3: Transverse impedance per unit length (imaginary part, absolute value) of a steel circular pipe.

REFERENCE MEASUREMENT ON A BRASS PIPE

From the measurement shown above there is a clear contradiction between the expected imaginary transverse impedance (which saturates for very low frequencies) and

the measured one (which vanishes at low frequencies). This controversy is important to solve since a consistent measurement recipe is needed for transverse impedance measurements on real LHC devices. For the moment the transverse impedance is obtained from the added loop impedance on the coil in the the DUT compared to a reference (lossless) case, i.e. the free space.

The inductance of two wires (at a distance Δ) is different if they are placed in the free space or inside a cylindrical conductor of radius b. The difference between the inductances in the two cases is independent from the conductor properties (in particular from its conductivity) and it is proportional to $(\Delta/b)^2$. Therefore one can show [1, 4] that, according to Eq. (1), the (imaginary) transverse impedance of a perfectly conducting pipe (of radius b) is different from zero and equal to the "magnetic image transverse impedance" [4]

$$Z_T^{p.c.} = -j\frac{Z_0}{2\pi b^2}. \qquad (4)$$

For the brass pipe used in measurement (of the same geometry of the steel pipe, i.e. b =50 mm), one gets $Z_T^{p.c.} = -j24\,\mathrm{k}\Omega$. The measurements shown in Fig. 4 agree (within the measurement uncertainties) with that prediction: the real part is mostly zero while the imaginary part is about -23 kΩ in the plateau. The low frequency deviations are due the measurement difficulties while at high frequency (above 200 kHz) the effect of the loop self resonance becomes not negligible.

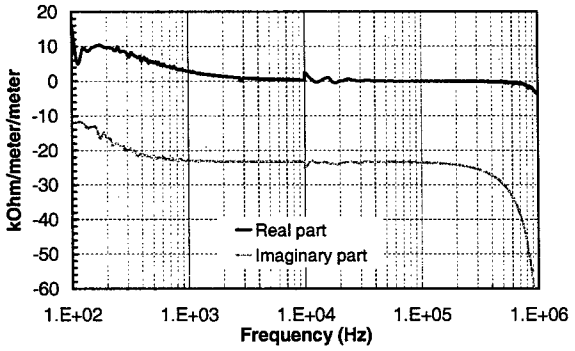


Figure 4: Transverse impedance per unit length of a brass circular pipe, according to Eq. (1).

In conclusion, to properly measure the transverse impedance, one should compute the added loop impedance with respect to the perfectly conducting pipe, i.e.

$$Z_T = \frac{c}{\omega}\frac{Z^{DUT} - Z^{p.c.}}{N^2\Delta^2} \qquad (5)$$

must be used instead of Eq. (1). $Z^{p.c.}$ is the impedance of the loop inside a perfectly conducting pipe with the same geometry of the DUT.

By applying Eq. (5) to the steel cylindrical pipe, the real transverse impedance is not substantially modified, while the imaginary part saturates for low frequencies (as one should expect from theory). Figure 5 shows the measurement results, with the same notation of Fig. 2.

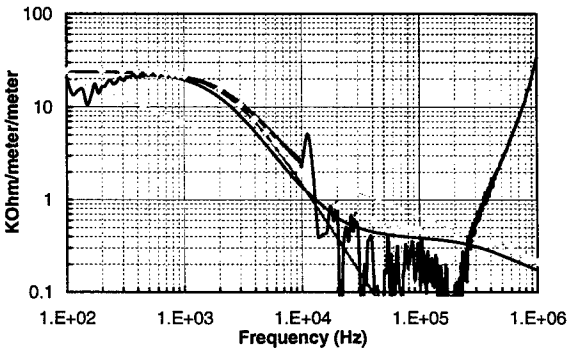


Figure 5: Transverse impedance per unit length (imaginary part) of a steel circular pipe after comparison with a brass tube.

CONCLUSIONS

A practical method to evaluate the transverse impedance of accelerator components at low frequencies has been reported. A modification of the classical two wire method which is running into sensitivity problems below a few MHz has been successfully tested and compared with theoretical expectations. This modified method, which uses essentially a loop with a certain number of turns, is better matched to the transverse impedance to be evaluated (at least in some practical cases of interest for LHC) than the normal two wire technique. Also it can be used from a few Hz onwards while the upper operational frequency is limited to the first loop resonance. To asses the validity of the method, measurements on a lossy circular beam pipe have been checked against theoretical results.

ACKNOWLEDGMENTS

The authors are grateful to H. Hahn (BNL) for interesting and stimulating discussions.

REFERENCES

[1] G. Nassibian, F. Sacherer, CERN, PS-BR 77-40, 1977.

[2] A.W. Chao, M. Tinger (Eds.), *Handbook of Accelerator Physics and Engineering* (World Scientific, 1999).

[3] B. Zotter, A. Kheifets, *Impedance and Wakes in High-Energy Particle Accelerators* (World Scientific, 1998).

[4] L. Vos, CERN-AB-2003-005 ABP, 2003.

[5] A. Burov, V. Lebedev, *Proc. of EPAC 2002*, Paris, France, pp. 1452 (2002).

[6] V. Lebedev, *Multi-Bunch Instabilities in VLHC*, presented in VLHC Workshop, SLAC, March 2001.

A VERY FAST RAMPING MUON SYNCHROTRON FOR A NEUTRINO FACTORY

D. J. Summers*, University of Mississippi–Oxford, University, MS 38677, USA
J. S. Berg, R. B. Palmer, Brookhaven National Laboratory, Upton, NY 11973, USA
A. A. Garren, University of California, Los Angeles, CA 90095, USA

Abstract

A 4600 Hz fast ramping synchrotron is studied as an economical way of accelerating muons from 4 to 20 GeV/c for a neutrino factory. Eddy current losses are minimized by the low machine duty cycle plus thin grain oriented silicon steel laminations and thin copper wires. Combined function magnets with high gradients alternating within single magnets form the lattice. Muon survival is 83%.

Historically synchrotrons have provided economical particle acceleration. Here we explore a very fast ramping muon synchrotron [1] for a neutrino factory [2]. The accelerated muons are stored in a racetrack to produce neutrino beams ($\mu^- \rightarrow e^- \overline{\nu}_e \nu_\mu$ or $\mu^+ \rightarrow e^+ \nu_e \overline{\nu}_\mu$). Neutrino oscillations [3] have been observed at experiments [4] such as Homestake, Super–Kamiokande, SNO, and KamLAND. Further exploration using a neutrino factory could reveal CP violation in the lepton sector.

This synchrotron must accelerate muons from 4 to 20 GeV/c with moderate decay loss ($\tau_{\mu\pm}$ = 2.2 μS). Because synchrotron radiation goes as m^4, muons radiate two billion times ($(105.7/.511)^4$) less power than electrons for a given ring diameter and lepton energy. Grain oriented silicon steel (3% Si) is used to provide a high magnetic field with a high μ to minimize magnetic energy ($B^2/2\mu$) stored in the yoke. Magnetic energy stored in the gap is minimized by reducing its size. Cool muons [5] with low beam emittance allow this. The voltage needed to drive a magnet is $-L\,di/dt$. Voltage is minimized by shrinking the volume of stored energy to reduce the inductance, L.

Acceleration to 4 GeV/c might feature fixed field dogbone arcs [6] to minimize muon decay loss. Fast ramping synchrotrons [6, 7] might also accelerate cold muons to higher energies for a $\mu^+ \mu^-$ collider [8].

We form arcs with sequences of combined function cells within continuous long magnets, whose poles are alternately shaped to give focusing gradients of each sign. A cell has been simulated using SYNCH [9]. Gradients alternate from positive 20 T/m gradient (2.24 m long), to zero gradient (.4 m long) to negative 20 T/m gradient (2.24 m) to zero gradient (0.4 m), etc. Details are given in Table 1.

It is proposed to use 5 such arc cells to form an arc segment. These segments are alternated with straight sections containing RF. The phase advance through one arc segment is 5 x 72^0 = 360^0. This being so, dispersion suppression between straights and arcs can be omitted. With no dispersion in the straight sections, the dispersion performs one full oscillation in each arc segment, returning to zero for the next straight as shown in Fig. 1. There will be 18 such arc segments and 18 straight sections, forming 18 superperiods in the ring. Straight sections (22 m) without dispersion are used for superconducting RF, and, in two longer straights (44 m), the injection and extraction. To assure sufficiently low magnetic fields at the cavities, relatively long field free regions are desirable. A straight consisting of two half cells would allow a central gap of 10 m between quadrupoles, and two smaller gaps at the ends. Details are given in Table 2. Matching between the arcs and straights is not yet designed. The total circumference of the ring including combined functions magnets and straight sections adds up to 917 m (18 × 26.5 + 16 × 22 + 2 × 44).

Table 1: Combined function magnet cell parameters. Five cells make up an arc and 18 arcs form the ring.

Cell length	m	5.28
Combined Dipole length	m	2.24
Combined Dipole $B_{central}$	Tesla	0.9
Combined Dipole Gradient	T/m	20.2
Pure Dipole Length	m	0.4
Pure Dipole B	Tesla	1.8
Momentum	GeV/c	20
Phase advance/cell	deg	72
beta max	m	8.1
Dispersion max	m	0.392
Normalized Trans. Acceptance	π mm rad	4

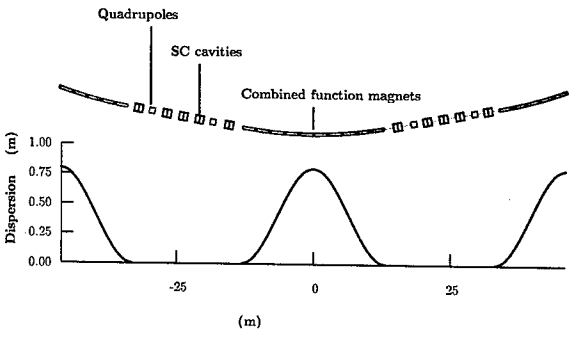


Figure 1: Combined function magnets bend the muons in the arcs. Superconducting RF cavities accelerate muons in the straight sections. Two quadrupoles per straight section provide focusing. The straight sections are dispersion free.

* summers@relativity.phy.olemiss.edu

0-7803-7738-9/03/$17.00 © 2003 IEEE

Table 2: Straight section lattice parameters.

ϕ	$L_{cell}/2$	L_{quad}	dB/dx	a
77^0	11 m	1 m	7.54 T/m	5.8 cm
β_{max}	σ_{max}	B_{pole}	U_{mag}/quad	
36.6 m	.0195 m	0.44 T	≈ 3000 J	

The RF (see Table 3) must be distributed around the ring to avoid large differences between the beam momentum (which increases in steps at each RF section) and the arc magnetic field (which increases continuously). The amount of RF used is a tradeoff between cost and muon survival. Survival is somewhat insensitive to the fraction of stored energy the beam removes from the RF cavities, because the voltage drop is offset by time dilation.

The muons accelerate from 4 to 20 GeV. If they are extracted at 95% of full field they will be injected at 19% of full field. For acceleration with a plain sine wave, injection occurs at 11^0 and extraction occurs at 72^0. So the phase must change by 61^0 in 37 μsec. Thus the sine wave goes through 360^0 in 218 μsec, giving 4600 Hz.

Estimate the energy stored in each 26.5 m long combined function magnet. The gap is about .14 m wide and has an average height of .06 m. Assume an average field of 1.1 Tesla. The permeability constant, μ_0, is $4\pi \times 10^{-7}$. $W = B^2/2\mu_0$[Volume] = 110 000 Joules. Next given one turn, an LC circuit capacitor, and a 4600 Hz frequency; estimate current, voltage, inductance, and capacitance.

$$B = \frac{\mu_0 NI}{h} \rightarrow I = \frac{Bh}{\mu_0 N} = 52\,\text{kA} \quad (1)$$

$$W = .5\,L\,I^2 \rightarrow L = 2\,W/I^2 = 80\,\mu\text{H} \quad (2)$$

$$f = \frac{1}{2\pi}\sqrt{\frac{1}{LC}} \rightarrow C = \frac{1}{L\,(2\pi f)^2} = 15\,\mu\text{F} \quad (3)$$

$$W = .5\,C\,V^2 \rightarrow V = \sqrt{2W/C} = 120\,\text{kV} \quad (4)$$

Table 3: Superconducting RF parameters.

Frequency	201	MHz
Gap	.75	m
Gradient	15	MV/m
Stored Energy	900	Joules
Muons per train	5×10^{12}	
Orbits (4 to 20 GeV/c)	12	
No. of RF Cavities	160	
RF Total	1800	MV
ΔU_{beam}	110	Joules
Energy Loading	.082	
Voltage Drop	.041	
Muon Acceleration Time	37	μsec
Muon Survival	.83	

Separate coils might be put around each return yoke to halve the voltage. The stack of SCRs driving each coil might be center tapped to halve the voltage again. Four equally spaced 6 cm coil slots could be created in each side yoke using 6 cm of wider laminations to cut the voltage by five, while leaving the pole faces continuous. 6 kV is easier to insulate than 120 kV. It may be useful to shield [1] or chamfer [10] magnet ends to avoid large eddy currents where the field lines typically do not follow laminations. A DC offset power supply could be useful [1]. Neutrino horn power supplies look promising.

Grain oriented silicon steel is chosen for the return yoke due to its high permeability at high field at noted in Table 4. The skin depth [11], δ, of a lamination is 160 μm from eqn. 5. ρ = resistivity.

$$\delta = \sqrt{\rho\,/\,\pi\,f\,\mu} = \sqrt{47 \times 10^{-8}\,/\,\pi\,4600\,1000\,\mu_0} \quad (5)$$

Take $\mu = 1000\mu_0$ as a limit on magnetic saturation and hence energy storage in the yoke. Next estimate the fraction of the inductance of the yoke that remains after eddy currents shield the laminations [12]. The lamination thickness, t, equals 100 μm [13]. $L/L_0 = (\delta/t)\,(\sinh(t/\delta) + \sin(t/\delta))\,/\,(\cosh(t/\delta) + \cos(t/\delta)) = 0.995$. So it appears that magnetic fields can penetrate 100 μm thick laminations at 4600 Hz. Thicker 175 μm thick laminations [14] would be half as costly and can achieve a somewhat higher packing fraction. $L/L_0(t = 175\ \mu\text{m}) = 0.956$.

Calculate the resistive energy loss in the copper coils. There are four 5 cm square copper conductors each 5300 cm long. R = 5300 (1.8 $\mu\Omega$-cm) / (4) (5^2) = 95 $\mu\Omega$. So, $P = I^2R\int_0^{2\pi}\cos^2(\theta)\,d\theta$ = 130 000 w/magnet. Eighteen magnets give a total loss of 2340 kw. But the neutrino factory runs at 30 Hz. Thirty half cycles of 109 μsec per second gives a duty factor of 300 and a total I^2R loss of 8000 watts. Muons are orbited in opposite directions on alternate cycles. If this proves too cumbersome, the duty cycle factor could be lowered to 150. See if .25 mm (30 gauge) wire is usable. From eqn. 6, the skin depth, δ, of copper at 4600 Hz is 0.97 mm.

$$\delta = \sqrt{\rho\,/\,\pi\,f\,\mu_0} = \sqrt{1.8 \times 10^{-8}\,/\,\pi\,4600\,\mu_0} \quad (6)$$

Now calculate the dissipation due to eddy currents in this w = .25 mm wide conductor, which will consist of

Table 4: Permeability ($B/\mu_0 H$). Grain oriented silicon steel has a far higher permeability parallel ($\|$) to than perpendicular ($\perp$) to its rolling direction [14, 15]. T = Tesla.

Material	1.0 T	1.5 T	1.8 T
1008 Steel	3000	2000	200
Grain Oriented ($\|$)	40000	30000	3000
Grain Oriented ($\perp$)	4000	1000	

transposed strands to reduce this loss [10, 16]. To get an idea, take the maximum B-field during a cycle to be that generated by a 0.025m radius conductor carrying 26000 amps. The eddy current loss in a rectangular conductor made of transposed square wires .25 mm wide (Litz wire [17]) with a perpendicular magnetic field is as follows. $B = \mu_0 I/2\pi r = 0.2$ Tesla.

$$P = [\text{Volume}]\frac{(2\pi f B w)^2}{24\rho} \quad (7)$$

$$P = [4\ .05^2\ 53]\ \frac{(2\pi\ 4600\ .2\ .00025)^2}{(24)\,1.8\times 10^{-8}} = 2800\,\text{kw} \quad (8)$$

Multiply by 18 magnets and divide by a duty factor of 300 to get an eddy current loss in the copper of 170 kw. Stainless steel water cooling tubes will dissipate a similar amount of power [6]. Alloy titanium cooling tubes would dissipate half as much.

Do the eddy current losses [16] in the 100 μm thick iron laminations. Use eqn. 7 with a quarter meter square area, a 26.5 m length, and an average field of 1.1 Tesla.

$$\text{P} = [(26.5)\ (.5^2)]\ \frac{(2\pi\ 2600\ 1.1\ .0001)^2}{(24)\,47\times 10^{-8}} = 5900\,\text{kw} \quad (9)$$

Multiply by 18 magnets and divide by a duty factor of 300 to get an eddy current loss in the iron laminations of 350 kw or 700 watts/m of magnet. So the iron will need some cooling. The ring only ramps 30 time per second, so the $\int \mathbf{H}\cdot d\mathbf{B}$ hysteresis losses will be low, even more so because of the low coercive force (H_c = 0.1 Oersteds) of grain oriented silicon steel. This value of H_c is eight times less than 1008 low carbon steel.

The low duty cycle of the neutrino factory leads to eddy current losses of less than a megawatt in a 4600 Hz, 917 m circumference ring. Muon survival is 83%. The high permeability of grain oriented silicon steel permits high fields with little energy stored in the yoke. Gradients are switched within dipoles to minimize eddy current losses in ends. Time dilation allows extra orbits with little muon decay at the end of a cooling cycle. This allows one to use more of the stored RF energy. Much of the magnetic field in our lattice is used for focusing rather than bending the muon beam. More muon cooling would lead to less focusing, more bending, and an even smaller ring.

This work was supported by the U. S. DOE and NSF. Many thanks to K. Bourkland, S. Bracker [18], C. Jensen, S. Kahn, H. Pfeffer, G. Rees, Y. Zhao, and M. Zisman.

REFERENCES

[1] D. J. Summers *et al.*, NuFact 02, hep-ex/0212041; Berg, Garren, Palmer, Rees, Summers, Zhao, http://www-mucool.fnal.gov/mcnotes/public/pdf/muc0259/muc0259.pdf.

[2] D. Cline and D. Neuffer, AIP Conf. Proc. **68** (1980) 846; D. Neuffer, IEEE Trans. Nucl. Sci. **28** (1981) 2034; D. Ayres *et al*, physics/9911009; A. Blondel *et al.*, Nucl. Instrum. Meth. **A451** (2000) 131; R. Palmer, C. Johnson, and E. Keil, NIM **A451** (2000) 265; N. Holtkamp, D. Finley, *et al*, "A feasibility study of a neutrino source based on a muon storage ring," (2000) FERMILAB-PUB-00-108-E; S. Ozaki, R. Palmer, M. Zisman, J. Gallardo, *et al*, "Feasibility study II of a muon based neutrino source," (2001) BNL-52623.

[3] V. Barger *et al.*, Phys. Rev. Lett. **45** (1980) 2084; S. Geer, Phys. Rev. **D57** (1998) 6989; S. M. Bilenky *et al.*, Phys. Rev. **D58** (1998) 033001; V. Barger *et al.*, Phys. Rev. **D62** (2000) 073002; 013004; A. De Rujula *et al.*, Nucl. Phys. **B547** (1999) 21; A. Romanino, Nucl. Phys. **B574** (2000) 675; A. Cervera *et al.*, Nucl. Phys. **B579** (2000) 17; M. Koike and J. Sato, Phys. Rev. **D61** (2000) 073012; K. Kodama *et al.* (DONUT), Phys. Lett. **B504** (2001) 218; C. Albright, hep-ex/0008064; Waltham, physics/0303116.

[4] R. Davis *et al.* (Homestake), PRL **20** (1968) 1205; B. T. Cleveland *et al.*, Astrophys. J. **496** (1998) 505; Y. Fukuda *et al.* (Super-K), Phys. Rev. Lett. **81** (1998) 1562; Q. R. Ahmad *et al.* (SNO), Phys. Rev. Lett. **89** (2002) 011301; **89** (2002) 011302; **87** (2001) 071301; H. H. Chen, Phys. Rev. Lett. **55** (1985) 1534; K. Eguchi *et al.* (KamLAND), PRL **90** (2003) 021802.

[5] A. Skrinsky and V. Parkhomchuk, Sov. J. Part. Nucl. **12** (1981) 223; D. Neuffer, Part. Accel. **14** (1983) 75; R. Fernow and J. Gallardo, Phys. Rev. **E52** (1995) 1039; V. Balbekov and A. Van Ginneken, AIP **441** (1998) 310; G. Penn and J. S. Wurtele, Phys. Rev. Lett. **85** (2000) 764; C. Wang and K. Kim, Phys. Rev. Lett. **88** (2002) 184801; M. M. Alsharo'a *et al.*, hep-ex/0207031.

[6] D. J. Summers, Snowmass 2001, hep-ex/0208010.

[7] D. Summers, D. Neuffer, Q. S. Shu, and E. Willen, PAC 97, physics/0109002; D. Summers, Snowmass 1996, physics/0108001; Bull. Am. Phys. Soc. **39** (1994) 1818.

[8] D. Neuffer, AIP Conf. Proc. **156** (1987) 201; D. Cline, NIM **A350** (1994) 24; D. Neuffer, *ibid.*, 27; V. Barger *et al.*, Phys. Rev. Lett. **75** (1995) 1462; R. Palmer *et al.*, Nucl. Phys. Proc. Suppl. **51A** (1996) 61; R. Raja and A. Tollestrup, Phys. Rev. **D58** (1998) 013005; C. M. Ankenbrandt *et al.*, PRSTAB **2** (1999) 081001; V. Barger, hep-ph/9803480; M. Berger, hep-ph/0110390.

[9] A. Garren *et al.*, AIP Conf. Proc. **297** (1994) 403.

[10] N. Marks, "Conventional Magnets – I and II," CERN Jyväskylä Accelerator School, CERN 94-01, **II**, 867–911.

[11] P. Lorrain, D. Corson, and F. Lorrain, "Electromagnetic fields and waves," 3rd edition (Freeman, 1988) 537–42.

[12] K. L. Scott, Proc. Inst. Radio Eng. **18** (1930) 1750–64.

[13] Arnold Eng. (Marengo, IL) http://www.grouparnold.com.

[14] http://www.aksteel.com/markets/electrical_steels.asp.

[15] R. Bozorth, "Ferromagnetism," (Van Nostrand, 1950) 90–1.

[16] H. Sasaki, "Magnets for fast-cycling synchrotrons," Conf. Synchro. Rad. Sources (Indore, 1992) KEK 91-216.

[17] http://www.mwswire.com/litzmain.htm.

[18] B. M. Lasker *et al.*, Publ. Astron. Soc. Pac. **85** (1973) 109.

A POP EXPERIMENT SCENARIO OF INDUCTION SYNCHROTRON AT THE KEK 12GEV-PS

K.Takayama, J.Kishiro, K.Koseki, K.Torikai, E.Nakamura, T.Toyama, Y.Arakida, M.Wake, H.Sato, M.Shirakata, S.Igarashi, and Y.Shimosaki, M. Sakuda, D. Iwashita, KEK, Tsukuba, Ibaraki 305-0801, Japan
K. Horioka and M. Shiho, Tokyo Institute of Technology, Nagatsuda, Kanagawa 226-8502, Japan

Abstract

A scenario for the first POP experiment and crucial issues of accelerator operation with induction acceleration are discussed.

INTRODUCTION

This is a plan to demonstrate the concept of the induction synchrotron [1] in the KEK 12GeV PS. In this proof-in-principle experiment, the acceleration and longitudinal beam confinement will be performed by employing induction accelerating devices instead of conventional RF devices. The induction device unit, consisting of DC power-supply, pulse-modulator with solid-state switching elements, and 2.5kV induction accelerating cavity, has been developed at KEK since 2000 [2]. A required number of units will be installed along the beam line. Experiments will be done sharing the machine time with the K2K experiment and other fixed target experiments during the time period of 2003-2008. As a first step, a single RF bunch will be accelerated with induction acceleration.

SCENARIO OF INDUCTION ACCELERATION

A proton bunch, which is accelerated in the 500MeV booster synchrotron, is injected into the 12GeV main ring, which is waiting for the bunch with the RF buckets. The RF bucket captures the bunch. This RF bunch is accelerated with induction voltage, which is synchronized with the lumping pattern of guiding magnetic fields. A super-imposed induction voltage of 10kV is generated in the four induction gaps, each of which is capable of generating 2.5kV. At the transient stage of the beginning of acceleration, the magnetic fields have a parabolic lumping pattern. The four induction devices are independently triggered following a programmed trigger pattern with a constant output voltage of 2.5kV. During the constant acceleration stage, these four induction devices are simultaneously triggered. A finite droop in the induction voltage is inevitable because of finite inductance and circuit resistance. From a point of longitudinal beam dynamics, the droop takes a role of an additional gradient force in the RF confinement. In the other word, the droop leads to a parabolic potential in the longitudinal phase space; the resulting confinement force is a super-impose of the sinusoidal wave force and this linear gradient force. Before the transition energy, the few percent droop gives an additional confinement force, while it somewhat reduce the focusing beyond the transition.

HARDWARE

Four induction cells are installed in the short-straight section of IV-3D. Each of cells is energized with a corresponding pulse modulator through a matching high voltage cable. The induction cell is estimated to generate heat of approximately 15kW assuming the operation cycle of 4 sec (acceleration period of 2sec). The magnetic core is forcibly cooled with insulation oil. The induction cell is connected with a ballast resistance of 200 Ω to minimize reflection due to mismatching. All deposited heat on the devices is removed with pure cooling water. The modulator connected with a DC power supply is placed in the power-supply yard on the ground level. Since the device is essentially a pulse device, noise shield should be crucial.

SCHEDULE

The POP experiment will be performed in the following schedule. Beyond the first step, the second and third step are scheduled, where a super-bunch trapped in the induction barrier bucket will be accelerated to 12 GeV.

Table1: Road map of the POP experiment

Year	'03	'04	'05	'06	'07
Step 1					
Step 2	→		super-bunch (SB) handling		
Step 3	acceleration of SB	→			

The POP experiment is supported by Grant-In-Aid for Creative Scientific Research (KAKENHI 15GS0217).

REFERENCES

[1] K.Takayama and J.Kishiro, "Induction Synchrotron", *Nucl. Inst. and Meth.* **A451**, 304-317(2000).
[2] http://www-accps.kek.jp/Superbunch/index.html
[3] K.Koseki et al., "R&D Works on 1MHz Power Modulator for Induction Synchrotron", to be presented in PAC2003.
[4] K.Torikai et al., "Design Study of 1 MHz Induction Cavity for Induction Synchrotron", to be presented in PAC2003.

0-7803-7738-9/03/$17.00 © 2003 IEEE

NEW RF DESIGN FOR 11.4GHz DIELECTRIC LOADED ACCELERATOR*

W. Liu, C. Jing, W. Gai, R. Konecny, and J. G. Power
High Energy Physics, Argonne National Laboratory, Argonne, IL, 60439, USA

Abstract

In this paper we present a new solution for externally RF coupled dielectric loaded accelerator. In this scheme, a separate TE-TM converter is used for RF coupling and a short tapered section is used for matching the RF into the dielectric accelerating structure. Advantages of this new design are there is no dielectric presented near the coupler, thus less prune to premature breakdowns; and it can be made into separate modules of coupler, matching and accelerating structures, this will simplified the dielectric structure development because only one set of couplers is required for a defined RF frequency but with many different dielectric structures. An example of X-band 11.424 GHz coupler and dielectric accelerating structure is obtained via EM simulations. Based on the simulation results, a set of coupler, matching and dielectric structures were fabricated. We present bench measurement results and its comparison with the design.

INTRODUCTION

Dielectric based accelerating structures were proposed and studied as a practical accelerator in the past decades [1-5]. The advantages and potential problems of using dielectric material are discussed in the above references and summarized in [5]. An implementation is also described in [5]. However, the high power experiments could not demonstrate high power and high field characteristics of dielectric accelerating structures because the RF coupler designed to convert TE-mode from rectangular waveguide to TM-mode in the accelerating structure could not support very high power transmissions. The failure of high power capabilities was suspected due to the presence of dielectrics near the coupling slots [6] that has field enhancement effect, thus causing breakdown near the slot.

In order to eliminate any field enhancement near the coupler due to the presence of dielectrics, we have adopted a new coupling scheme that separate the coupler from the accelerating section as suggested by Tantawi and Nantista[7] and Syratchve[8]. As shown in Figure 1, this new scheme of the dielectric loaded accelerator is consists of 3 modules: 1) Coupler section; 2) Dielectric tapered matching section and 3) Dielectric accelerator section. The coupling section is used to convert the rectangular TE10 mode to circular TM01 mode. The tapered dielectric section is used to provide matching between TM01 modes in coupler and dielectric accelerator. This scheme separates the dielectric loaded accelerator from the coupling structure by a tapered matching section and thus makes the coupler independent of the dielectric properties. Also because the coupling slot is located in a section of circular metallic waveguide, the area of the coupling slots are much bigger than in the previous scheme[5] and this makes the peak value of the EM field much smaller than that of the old scheme under the same input power. Another advantage of this modular scheme is that it simplifies the experimental implementations of high power tests because only one set of input and output coupler needs to be made for different dielectric accelerators. Once the couplers have been proved to have high power capability, we can reuse them in other dielectric loaded accelerators working in the same band provide that we have redesigned and implemented the dielectric taper section accordingly. Because properties of the accelerator section were studied in details previously [1-5], we will concentrate our efforts on coupler and dielectric taper designs. First, we will study the RF

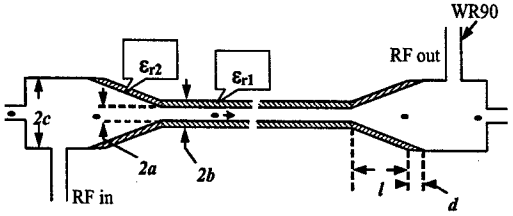


Figure 1: Illustration of the scheme dielectric accelerator, coupler and also the taper section

coupler and, then a tapered matching section is optimized accordingly for a given dielectric structure. For the coupling section, we have multiple choices: symmetric two ports structure and single port structure. By using symmetric two ports structures, one can eliminate field asymmetry in the coupler region and also minimize the beam break up (BBU) effects. By using the single side coupler structure, we can simplify the testing facilities and carry out the experiment easily. Both symmetric two ports structure and single side structure have been designed but only single side structure has been made and used in our tests.

In this paper, we did all the EM simulation by using Microwave Studio[9]. Both simulation results and test results are given and compared.

11.424G RF COUPLING SYSTEM DESIGN AND EM SIMULATIONS

In this section, we have considered designs for coupler and dielectric taper. Due to the availabilities of X-band high power RF sources at SLAC and Naval Research Laboratory, we concentrate our designs at 11.424 GHz center frequency so the modeled structure can be high power tested.

For the coupler, we have designed both symmetric two ports coupler and single side coupler, but only design of

* This work is supported by DOE, High Energy Physics, Advanced Technology branch.

the single side coupler is presented here because of the space limit. As mentioned before, two ports design can eliminate field asymmetry in the coupler region and also minimize the beam break up (BBU) effects. But it is much more convenient to test a structure with only a single RF coupling port. Although it is difficult to implement single port design for practical high energy linear colliders, but this would satisfy our requirements on high power test of dielectric based accelerators because field asymmetry and wakefield induced instabilities are not concerns here. The scheme of single side coupler is given in figure 2. A set of parameters were found to give maximize the efficiency of mode conversion from rectangular TE10 to circular TM01 mode as illustrated in figure 2. By optimizing these parameters, we obtained the optimized coupling structure. The S parameters of the optimized single side structure are given in figure 3. As shown in figure 3, S21 is almost 0 dB in the region of 11.424GHz, which means that nearly 100% of energy from rectangular TE10 has been converted into circular TM01. Peak electrical fields around the corners

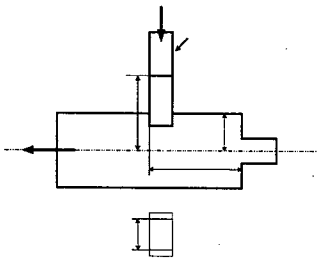


Figure 2: Scheme of the single side coupler

(blended at a radius of 2mm) of the coupling slot are to be less than 40 MV/m for 100 MW RF power, which is well below the copper surface breakdown threshold.

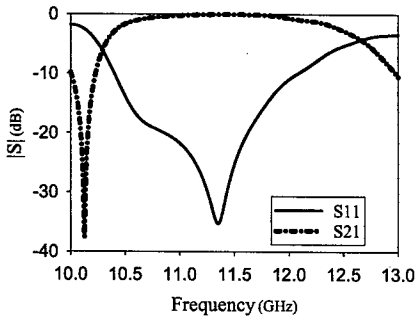


Figure 3: S parameters of optimized single side coupler, optimized for 11.424GHz

So far, we have only discussed the RF coupler that is dielectric material independent. Next we will consider a design of dielectric taper section, which will be determined by the dielectric constant of dielectric accelerating section. Purpose of the dielectric taper section is to match the wave impedance between the dielectric loaded circular waveguide (dielectric loaded accelerator section) and the regular circular waveguide where the RF coupling structure is implemented, thus achieve high transmissions. As shown in figure 1, the geometry of taper section is determined by its length l when the diameters of both dielectric loaded waveguide and the regular waveguide are predetermined. The dielectric constant of the taper can be somewhat different from the dielectric in accelerating section. The parameter d is determined by $d = \frac{b-a}{c-b} l$. The goal of taper section design is to find out a proper length l with acceptable S11, which is a measure of reflection coefficient. The real material we chose for our simulation and experiments are Alumina (ε_r=9.4) and MCT20 (ε_r=20). Figure 4 gives the S11 of a taper section for a dielectric accelerating structure with ε_{r1}=9.4 where a=5mm, b=7.185mm and c=12.079mm. Theoretically, every minimum value point in the S11 vs l curve could be selected for our purpose, but a shorter l will results in a tighter tolerance on machine errors because the bandwidth is narrower for shorter l as shown in figure 4. In our final drawing, the length l is chosen to be 40mm with which the expected S11 would be -19dB for alumina material ε_{r2}=9.4.

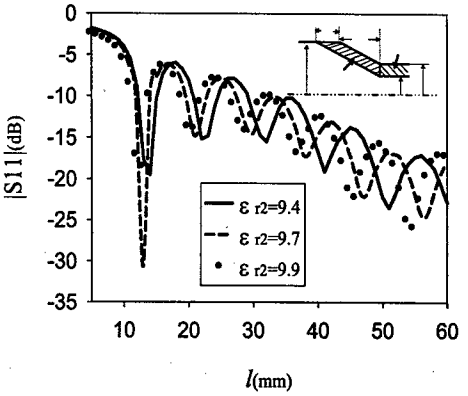


Figure 4: S11 vs l curves of alumina dielectric taper section

Next, we considered MCT 20. This is the same dielectric materials we used in the previous high power test [6]. For MCT20, the geometrical parameters for the dielectric loaded accelerator are determined as a=2.96mm, b=4.53mm. As the taper scheme for alumina does not work well in MCT20 based structure because of the much higher permittivity and much smaller dielectric accelerating tube, an alternative scheme is adopted for designing MCT20 taper section. As shown in figure 5, the alternative scheme has three independent parameters. Changing any one of these 3 parameters could change the properties of the taper section. In our final design for MCT20 taper section, t_1 is chosen to be 39mm and t_3 is

chosen to be 5mm. By optimizing t_2 with Microwave studio for minimized S11 at 11.424GHz, t_2 is found out to be 17.8mm. Figure 5 also gives the S11 vs *frequency* for MCT20 taper section with parameters given above. Figure 5 shows that the S11 at the working frequency, 11.424GHz, of this MCT20 taper section is about -25dB and the bandwidth where S11 bellow -10dB is about 200MHz. This MCT20 taper section will be made and tested soon.

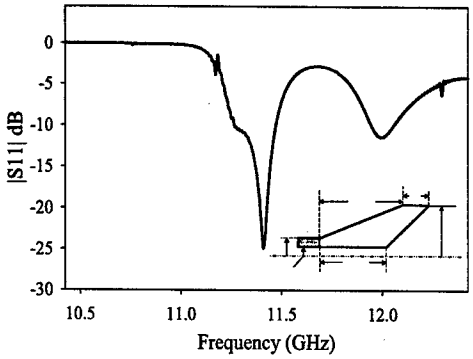


Figure 5: Scheme of the MCT20 taper and it's S11 of structure optimized for 11.424GHz

EXPERIMENTAL VERIFICATIONS

Based on the dimensions obtained from EM simulation via Microwave Studio, two single side couplers and tapered matching section have been made. A set of tests have been carried out using HP8510 network analyzer. Figure 6 is the coupler to coupler tests result comparing with its EM simulation result and shows good agreement between them. Machine errors have been guessed and included in the EM simulation. From figure 6, we could say that the design and implementation of the couplers is a success.

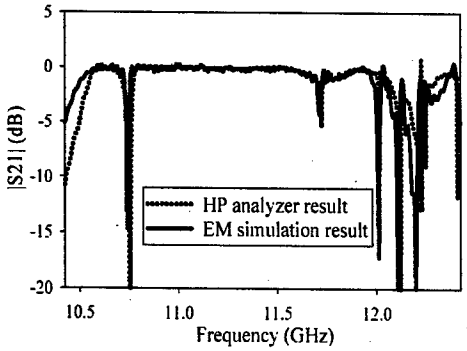


Figure 6: Comparing S21 of Coupler to coupler HP analyzer test result and EM simulation result

Besides the implementation of couplers, several pieces of alumina dielectric taper and a pair of copper jack are also made based on the simulation results given before. The permittivity of alumina used for the taper is 9.7 according to the catalog, which is different from the permittivity of the alumina dielectric accelerator tube, 9.4. By assemble them together with couplers and dielectric accelerating tube, a testing alumina dielectric loaded accelerator is made. The NRL high power test on this testing alumina dielectric loaded accelerator assured that this RF coupling system design has a very good high power capability[10].

SUMMARY

A new RF design for dielectric loaded accelerating structure has been implemented and tested. This new design separates the coupler from the dielectric loaded accelerating structure by a tapered transition section. This has successfully eliminated the arcing problems observed during previous high power tests of our old design. Both symmetric two ports and single port couplers have been investigated. We found that both type are capable of converting the rectangular TE10 mode into circular TM01 mode with efficiency above 99% over a relatively wide bandwidth. For the simplicity of the high power experiments setting at NRL, we used the single side coupler. A testing alumina structure has been made and tested at NRL, and has been proved to have the high power capability.

This work is supported by DOE, High Energy Physics, Advanced Technology branch. We acknowledge the useful discussion with S. Gold, S. Tantawi, C. Natista, I Syratchev and D. Yu during this work.

REFERENCES

[1] G. Flesher and G. Cohn, AIEE Trans. 70, 887 (1951)
[2] R. Kenigs, M. Jones, and W. Gai, Particle Accel. **24,** 223 (1989) and W. Gai et al, Physical Rev. Lett, **61,** 24, p2756 (1988)
[3] T-B Zhang, J. Hirshfield, T. Marshall, and B. Hafizi, Phys. Rev. E **56,** 4447(1997) and T. B. Zhang, T. C. Marshall, M. A. LaPointe, J. L. Hirshfield, and A. Ron, Phys. Rev. E **54,** 1918-1929 (1996)
[4] W. Gai, R.Konecny, and J. Simpson, in Proceedings of Particle Accelerator Conference, edited by M. Comyn, M.K. Craddock, M. Reiser and J. Thomson, pp. 636-638, 1997
[5] P. Zou, W.Gai, R. Konecny, X.Sun, T. Wong and A. Kanareykin, Rev. Of Scientific Instruments, **71,** 2301-2304(2000)
[6] J.G. Power, et al, in Advanced Accelerator Concepts, AIP Conference Proceedings 647, pp. 156-164 (2002).
[7] S. Tantawi and C. Nantista, private communications
[8] I. Syratchev, CLIC Note 505, CERN 2001, unpublished
[9] Microwave Studio, Version 4.0 CST America, http://www.cst-america.com
[10] J.G. Power et al, High power testing of x-band dielectric-loaded accelerating structure, in this conference.

A COMPACT WAKEFIELD MEASUREMENT FACILITY*

J. G. Power, W. Gai, J. Lewellen, S. Milton, K.-J. Kim, J. Simpson, H. Wang,
ANL, Argonne, IL 60439, USA
D. Finley, H. Carter, FNAL, Batavia, IL 60510, USA

Abstract

The conceptual design of a compact, photoinjector-based, facility for high precision measurements of wakefields is presented. This work is motivated by the need for a thorough understanding of beam induced wakefield effects for any future linear collider. We propose to use a high brightness photoinjector to generate (approximately) a 2 nC, 2 mm-mrad drive beam at 20 MeV to excite wakefields and a second photoinjector to generate a 5 MeV, variably delayed, trailing witness beam to probe both the longitudinal and transverse wakefields in the structure under test. Initial estimates show that we can detect a minimum measurable dipole transverse wake function of 0.1 V/pC/m/mm and a minimum measurable monopole longitudinal wake function of 2.5 V/pC/m. Simulations results for the high brightness photoinjector, calculations of the facility's wakefield measurement resolution, and the facility layout are presented.

INTRODUCTION

A fundamental concern for the NLC is the beam-induced wakefield effect. In general, the short-range wake acts back on the beam and degrades its quality, while the long-range wake deleteriously affects subsequent bunches. Wakefield effects, such as those due to RMS structure misalignment and schemes to suppress these effects (e.g. emittance bumps), have been studied mainly with numerical calculations and with previous machines, such as the SLC. These techniques, however, will work at the NLC only if the structure wakefields are below certain thresholds. For example, the RMS structure misalignment must be less than 20 μm to avoid resonant instabilities. For quality control reasons, it would be beneficial if the wakefield characteristics of the NLC structures were accurately measured before being installed into NLC accelerating modules. We propose to characterize these structures by directly mapping their wakefields [1].

Direct mapping of the wake function of NLC structures was previously made at the AATF [2], with moderate precision using approximately 10 MeV beams, and also at ASSET [3], with high precision using approximately 1 GeV beams. In this paper, we present a zeroth order design study that shows that direct-wakefield measurements can be made with high precision using 10 MeV beams if the facility is based on high-brightness RF photocathode guns [4]. Such a facility could then be used as the basis of an NLC quality control center.

FACILITY OVERVIEW

A compact, collinear, direct-wakefield measurement facility [Fig. 1] can be made using a high-brightness, 20 MeV, 2 nC drive beam to excite the wakefields and a high-brightness, 5 MeV, 0.1 nC witness beam to probe the wakefields. For wakefield measurements, a beamline is designed to transport the drive and witness beams collinearly through the structure. The longitudinal location of the witness beam with respect to the drive beam can be continuously varied from a time delay t of one nanosecond ahead of the drive to tens of nanoseconds behind it. This is accomplished by varying the optical delay path of the laser pulse generating the witness beam in conjunction with an adjustment to the phase of the RF into the witness gun.

The drive beam is matched from the output of the drive gun and linac (not shown) to the drive beam lattice (quad (Q) triplet and dipole (D) chicane) and through the NLC structure. In a similar fashion, the witness beam is delivered through a dog-leg section and into the NLC structure. Initial alignment of the drive (witness) beam through the structure is done while blocking the witness (drive) beam and centering the drive (witness) beam on the *straight-through zeroing BPM*.

Measurement of the Longitudinal Wake

Upon exiting the structure, the drive and witness beams are separated by a horizontal dipole magnet (*H*) that bends the beams by approximately 2.5^0 and 10^0 respectively. With the witness beam running in front of the drive beam, the horizontal dipole magnet, *H*, is adjusted until the witness beam is centered in the horizontal direction on the *witness-beam zeroing BPM (WB-ZBPM)*. To measure the monopole longitudinal wake function the structure is centered (zero offset with respect to the beams) and the witness beam is positioned at a time t behind the drive beam. The longitudinal wakefield is proportional to the longitudinal momentum kick received by the witness beam,

$$\Delta\theta_z(t) = \frac{\gamma}{\gamma+1}\left(\frac{\Delta E_z(t)}{E}\right) \qquad (1)$$

where γ is the relativistic energy factor, E is the energy of the witness beam (5 MeV), and ΔE_z is the longitudinal energy change of the witness beam centroid. After exiting *H*, the drive beam is dumped and the witness beam is directed towards a weak vertical dipole magnet (*V*) and the *WB-ZBPM*. Conceptually, one could simply measure the horizontal offset at *WB-ZBPM* to infer the energy change (ΔE_z) of the witness beam centroid. However, from the point of view of beam optics and BPM resolution, it is better to use *H* to center the witness beam centroid on *WB-ZBPM* and then use this change to the magnetic field of *H* to calculate the change in energy, ΔE_z.

0-7803-7738-9/03/$17.00 © 2003 IEEE

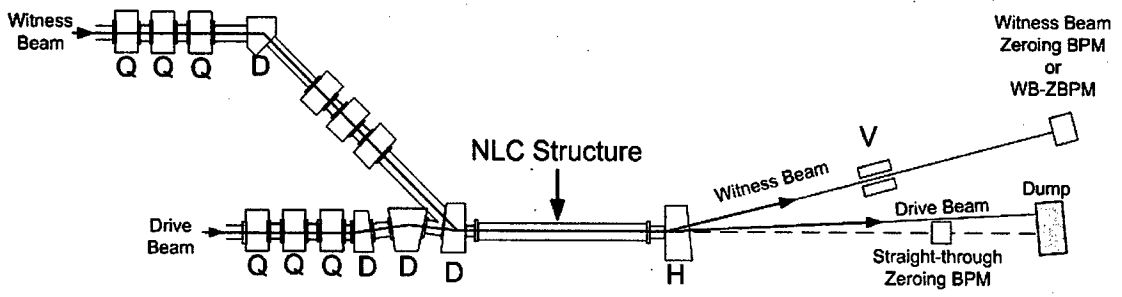


Figure 1: Block Diagram of the Compact Wakefield Measurement Facility.

Measurement of the Transverse Wake

To measure the dipole transverse wake function the structure is displaced 1 mm in the vertical direction relative to the collinear drive and witness beams. The witness beam is then placed at time t behind the drive bunch, which causes the trailing witness beam to receive a vertical deflection,

$$\Delta\theta_y = \frac{\gamma}{\gamma+1}\left(\frac{\Delta E_y}{E}\right) \qquad (2)$$

where ΔE_y is the transverse energy change of the witness beam centroid. To compensate for the longitudinal wake, the magnet H is again used to horizontally center the witness beam on *WB-ZBPM*. The vertical deflection of the witness beam ($\Delta\theta_y$) will cause the beam to be displaced in the vertical direction (out of the plane in Figure 1) at *WB-ZBPM*. Once again, conceptually, we could measure this vertical offset, at *WB-ZBPM*, to infer the strength of the transverse wake, but for practical purposes it is better to use the vertical dipole magnet V, to center the witness beam on *WB-ZBPM* and use the change in magnetic field strength of V to infer $\Delta\theta_y$.

Machine Functions

The machine functions for matching the drive and witness beams through the structure and into the measurement area were found with COMFORT [5]. The results are shown in Figure 2 and Figure 3.

HIGH BRIGHTNESS ELECTRON SOURCE

A new 1 ½ Cell L-band (1.3 GHz) RF photocathode gun at the Argonne Wakefield Accelerator (AWA) facility has recently been commissioned. The primary purpose of this gun is to generate high-intensity beams, with a nominal bunch charge of 100 nC, for studying wakefield acceleration schemes. The beam produced by the gun in this *high-intensity mode* is not suitable for characterization of NLC structures due to the large normalized beam emittance of approximately 100 mm-mrad.

In order to determine if this gun can be operated in a *high-brightness mode* to generate the drive beam, we first spend a moment to discuss the requirements of the drive beam. The maximum allowable emittance of the electron source is estimated by examining the dimensions of an NLC structure and then requiring that the beam be able to pass through it. Typical NLC structures currently under consideration are about 1 meter long with an inner radius of the iris near 3 mm. We choose a comfortable safety margin by requiring that the beam's one-sigma radius be about an order of magnitude less than the iris radius, or $\sigma_{x,y} \approx 300$ μm. Assuming that: (1) the beam is focused to a waist at the center of the structure; (2) the beta function is one meter, or $\beta =$ 1 m; and (3) the normalized energy of the beam is γ = 40; then the maximum allowable normalized emittance from $\sqrt{\varepsilon\beta} = 300\mu m$ is ε_n^{max} = 3.6 mm mrad.

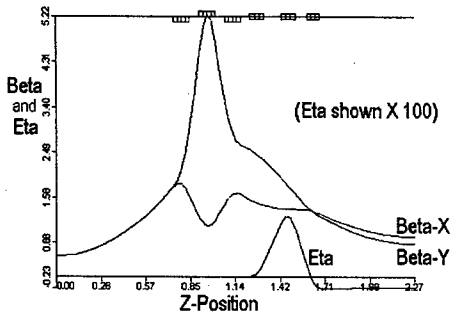


Figure 2: Drive beam machine functions from the end of the drive linac to the center of the NLC structure.

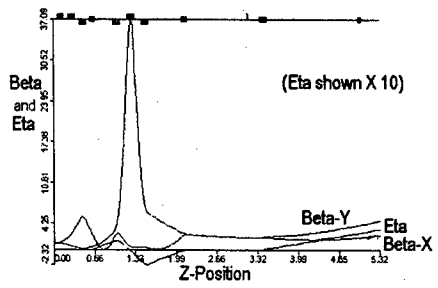


Figure 3: Witness beam machine functions from the end of the witness gun to WB-ZBPM.

Table 1: High-Brightness Gun Operating Mode

Charge (nC)	2
Laser spot radius (mm)	1.6
Laser pulse length (psec)	8
RF launch phase (^{0})	40
Energy (MeV)	10.4
Energy spread (%)	0.5%
Normalized r.m.s. emittance (mm mrad)	1.9

Our second requirement is to operate the drive gun at the highest possible charge to increase our wake function measurement sensitivity. Recent Parmela [6] simulations indicate that the gun can indeed be operated in a *high-brightness mode*. The beam parameters produced by the AWA gun operating in high-brightness mode are summarized in Table 1. It is worth pointing out that this operating point uses a drive beam charge of 2 nC that easily satisfies the drive beam requirements.

RESOLUTION OF THE WAKEFIELD MEASUREMENT SYSTEM

In this section we put all the previous sections together and make an estimate of our measurement resolution.

Longitudinal Wakefield Resolution

The longitudinal momentum kick (see Eq. 1) is related to the longitudinal wake function by,

$$\Delta\theta_z(t) = \frac{\gamma}{\gamma+1}\left(\frac{-eQ_d L_s W'_{\|,0}(t)}{E}\right) \qquad (3)$$

where Q_d is the drive bunch charge in pC, L_s is the structure length in meters, E is the witness beam energy in units of eV, $W'_{\|,0}(t)$ is the monopole (m=0) longitudinal wake function [7] per unit length in units of V/pC/m, and the prime stands for differentiation in the z direction. From this equation we can see that we will achieve good sensitivity to the wake function (i.e. a large kick) if Q_d is large and E is small. Since Q_d and E are fixed at 2 nC and 5 MeV, respectively, then the resolution depends on the accuracy to which we can measure the energy change, $\Delta E_z/E$.

If the witness beam charge is 10 pC, we can estimate a normalized r.m.s. emittance of 0.1 mm mrad and a momentum spread of 1%. From figure 3, we see that the horizontal beta function of the witness beam is β_x = 2.6 m and the dispersion is η_x = 0.2 m at *WB-ZBPM*. The width due to the beta function (σ_β = 0.5 mm) is added in quadrature with the width due to the momentum spread and dispersion function (σ_η = 2.0 mm) to give the total width (σ_{tot} = 2.1 mm). We now assume that the accuracy of WB-ZBPM is about 1/10th of the one sigma beam width, or 210 μm. Since H bends the witness beam by 10^0, then a 0.1% change in longitudinal momentum over a 2 m drift will produce a horizontal offset of the witness beam centroid at WB-ZBPM of 350 μm, comfortably larger than the resolution of WB-ZBPM. Finally, combining equations 1 and 3, and solving for $W'_{\|,0}(t)$ gives a minimum measurable monopole longitudinal wake function per unit length of 2.5 V/pC/m.

Transverse Wakefield Resolution

The transverse momentum kick (see Eq. 1) is related to the transverse wake function by,

$$\Delta\theta_y(t) = \frac{\gamma}{\gamma+1}\left(\frac{-eQ_d L_s W'_{\perp,1}(t)}{E}\right)\Delta y_d \qquad (4)$$

where $W'_{\perp,1}(t)$ is the dipole (m=1) transverse wake function per unit length in units of V/pC/m/mm, Δy_d is the offset of the drive beam relative to the center of the structure measured in mm, and all other variables have been previously defined.. Once again, good sensitivity to the transverse wake function is obtained when Q_d is large and E is small.

From figure 3, we see that the vertical beta function of the witness beam is β_y = 4.6 m leading to a vertical beam size of σ_β = 0.4 mm at *WB-ZBPM*. Once again, we assume that our BPM resolution is 1/10th of the spot size, so that the vertical BPM resolution is 40 μm. Next, we estimate the minimum angular kick ($\Delta\theta_y$) that our system can detect. Since the drift length is 2 m, a 20 μrad kick produces an offset of 40 μm at *WB-ZBPM*, an amount equal to our resolution. Finally, solving Equation 4 for $W'_{\perp,1}(t)$ gives a minimum measurable dipole transverse wake function per unit length of 0.1 V/pC/m/mm.

CONCLUSION

We have presented a conceptual, zeroth order design for a compact wakefield measurement facility. This facility can measure both the longitudinal and transverse wake functions with state of the art precision. Our estimates show that we can measure a minimum measurable monopole longitudinal wake function of 2.5 V/pC/m and a minimum measurable dipole transverse wake function of 0.1 V/pC/m/mm. The Argonne Wakefield Accelerator facility at ANL could be used to build a prototype version of this facility to prove the validity of this concept.

REFERENCES

[1] H. Figueroa et al., Phys. Rev. Lett., 60, No. 21 (1988)
[2] J. W. Wang, et al., Proc. PAC 1991, pp. 3219-3221.
[3] C. Adolphsen, SLAC-PUB-6629 (1994)
[4] M. E. Conde et al., Phys. Rev. ST Accel. Beams 1, 041302 (1998)
[5] M.D. Woodley, et al., IEEE Transactions on Nuclear Science, NS-30, No. 4, (1983)
[6] L.M. Young, Physics of Particle Accelerators, AIP-184, p. 1245, New York, (1989)
[7] A. W. Chao, "Physics of Collective Beam Instabilities in High Energy Accelerators," John Wiley & Sons, New York, 1993

FFAG LATTICE FOR MUON ACCELERATION WITH DISTRIBUTED RF*

D. Trbojevic, J.S. Berg, M.Blaskiewicz, E.D. Courant, R. Palmer, BNL, Upton, New York
A. Garren, LBL, Berkeley, California, USA

Abstract

A future muon collider or neutrino factory requires fast acceleration to minimize muon decay. We have previously described an FFAG ring that accelerated muons from 10 to 20 GeV in energy. The ring achieved its large momentum acceptance using a low-emittance lattice with a small dispersion. In this paper, we present an update on that ring. We have used design tools that more accurately represent the ring's behavior at large momentum offsets. We have also improved the dynamic aperture from the earlier design.

1 INTRODUCTION

Fixed field alternating gradient (FFAG) lattice designs [1] have been extensively used and studied in recent years [2]. Fast acceleration of large emittance muon beams, is essential for either neutrino factory or muon collider projects because of the short muon lifetime. The KEK feasibility study in 2001 had chosen the standard FFAG lattice design for the muon acceleration and "cooling". In addition, a small "proof of principle" 50-500 *KeV* FFAG proton ring was built and commissioned [2]. The advantages of this design are: the large momentum acceptance, fixed magnetic field during acceleration, relatively large energy gain per turn, transition energy above the output energy, etc. The standard design is a so-called "scaling" synchrotron where the betatron tunes are constant during acceleration, giving zero chromaticity. Particles at different energies follow orbits parallel to each other during acceleration. A disadvantage of this "scaling" FFAG designs is that it has a large required aperture with a large circumference ratio due to required negative bending. The present report follows the basic principle of the FFAG described by Symon [1] but with a non-scaling FFAG using the minimum emittance lattice design [3]. The disadvantages of the scaling FFAG design are dramatically reduced. A relatively small FFAG synchrotron with a circumference of ~300 m can be designed to accelerate muons from energy of 10 *GeV* up to 20 *GeV* in about ~20 turns. It is assumed that the magnets and the RF are super-conducting.

Organization of the Report:

The next section presents the basic idea of the design. The lattice properties calculated at the central momentum of E_o=15 *GeV* are described in the third section. The lattice function dependence on momentum is described in the fourth section (the amplitude functions, tunes, orbits, momentum compaction, circumference). The acceleration is described in the fifth and the section 6 is aconclusion.

2 LATTICE PROPERTIES OF A CELL

The basic idea of accelerating muons with the FFAG scaling synchrotron using the minimum emittance lattice has been described in detail earlier. To allow a large momentum acceptance and large energy change a small dispersion minimum emittance lattice is employed. The amplitude of the normalized dispersion function is defined as the square root of the dispersion emittance function H [3]:

$$H=\xi^2+\zeta^2, \quad \xi=\eta'\sqrt{\beta}+\frac{\alpha\cdot\eta}{\sqrt{\beta}}, \zeta=\frac{\eta}{\sqrt{\beta}}.$$

where η is the dispersion function. The minimum emittance lattice is one that minimizes the function H [3]. This is achieved having the minimum of the horizontal amplitude β_x and dispersion function η_x occur at the center of the bending element. If the bending element is a combined function magnet, the conditions are more favorable. This update of the previous designs includes three major simplifications: the necessary space for the accelerating cavities has been enlarged by removal of one of the magnets, and the basic cell betatron tune changes during acceleration are kept between half integer values, permitting the removal of sextupole magnets. A small opposite bend has been added to the focusing quadrupole; this improves the tune acceptance over the large momentum range of the basic cell.

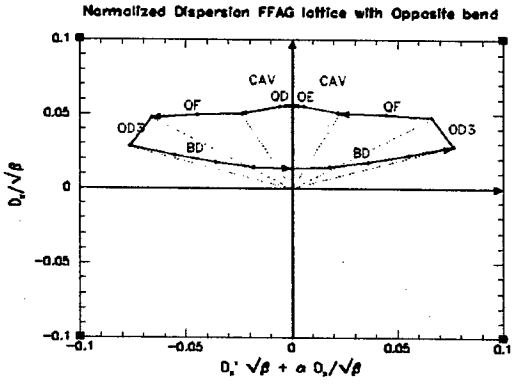


Figure 1: Normalized dispersion space: the opposite bend at QF quadrupole, while the major bend is at BD.

The square root of the H function is presented by the red lines in Fig. 1. The opposite bend is in the focusing quadrupole labeled as QF. The normalized dispersion

*Work performed under Contract Number DE-AC02-98CH10886 with the auspicies of the US Deparment of Energy.

0-7803-7738-9/03/$17.00 © 2003 IEEE

vector changes for a $D'\sqrt{\beta_x} = \theta\sqrt{\beta_x}$ at the bending elements. Due to the larger betatron function β_x at the focusing quadrupole, the vector $\theta_{QF}\sqrt{\beta_{x_QF}}$ is almost the same size as the one for the major bend $\theta_{BD}\sqrt{\beta_{x_BD}}$. This reduces the overall value of the H function and allows large momentum acceptance. In Fig. 1 a drift, space or non-bending element is presented as a part of a circle. The circumference of the machine is C~300 m; it consists of sixty identical cells ~5 meters long.

3 THE BASIC CELL

The basic FFAG minimum emittance cell is made of only two type of magnets: the central bending element is a combined function magnet, l_d ~ 1.6 m long, with a defocusing gradient;, the two focusing quadrupoles, l_{QF}~0.55 m long, have equal but opposite focusing gradients and a negative bending field. As in the previous design the minimum of the horizontal betatron and dispersion functions are at the center of the dipole as presented in Fig. 2.

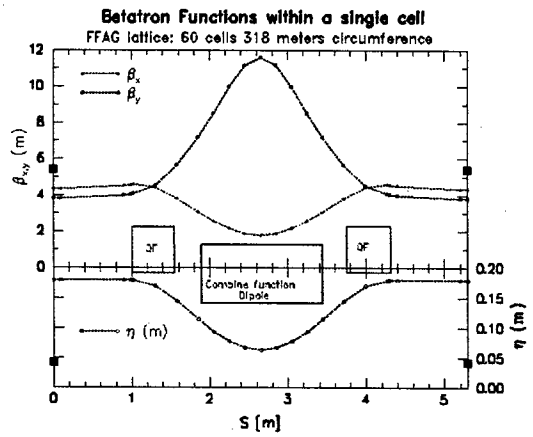


Figure 2: The betatron functions in the basic cell. The dispersion function is labeled as η.

The energy range for muon acceleration considered is between 10–20 *GeV*. The lattice functions are presented at the central energy equal to E_c=15 *GeV*. The lattice design tool used for this example is SYNCH [4]. Because it has been found [6] that other lattice programs [MAD, TEAPOT, COSY] have limitations at large momentum deviations. The betatron functions are calculated for the required momentum range of $\delta p/p = \pm 33$ %. The magnets have sextupole strengths of ¼ of the strength that would make the chromaticity zero at the central momentum (stronger sextupoles would entail an unacceptably small dynamic aperture). A comparison of the calculations of the lattice function dependence on momentum for large momentum offsets obtained by four different lattice tools is presented at this conference [6]. The betatron functions (closed orbit offsets x_{co}, β_x, β_y, ν_x, and ν_y) are presented without ¼ sextupoles strength, while they were used to study the influence on the orbit circumference and in longitudinal tracking.

4 BETATRON FUNCTIONS DEPENDENCE ON MOMENTUM

The incorporation of opposite bend in the focusing quadrupole allows tune changes during acceleration within the basic cell to be within a range which avoids integer and half integer resonances ($0.1 < \nu_{x,y} < 0.4$). This is a necessary condition for a stable particle motion. The dependence of the tunes on momentum within the basic cell is shown in Fig. 3.

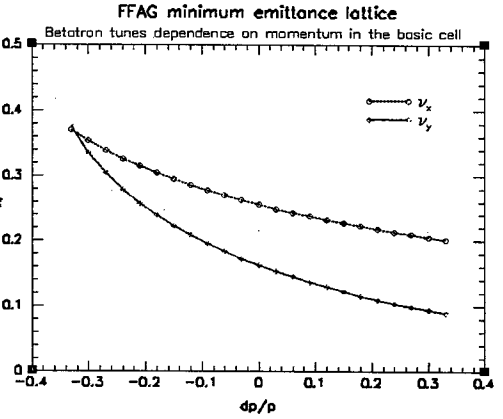


Figure 3: Betatron tunes, ν_x and ν_y, dependence on a large range of momentum in the basic cell.

The betatron functions β_x and β_y should have moderate values over the required momentum range. When the vertical tune comes close to an integer or half-integer the maximum of the vertical betatron function becomes larger, as shown in Fig 4.

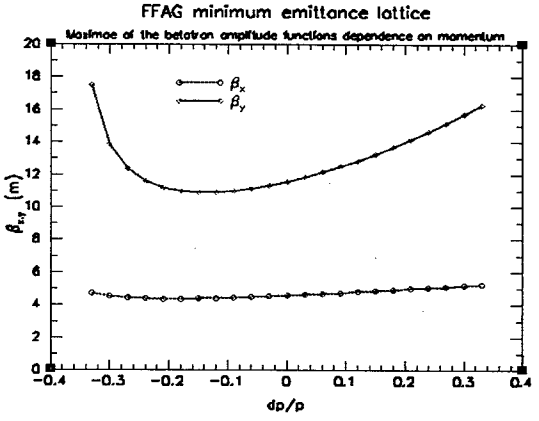


Figure 4: Betatron functions dependence on momentum.

The particle orbits during acceleration through a single cell are the most important aspect of this lattice design, as shown in Fig. 5. Some important details from this figure need to be emphasized: at the start of acceleration particles move through the basic cell on the inside of the aperture and have mostly negative closed orbit offsets (x_{co}< 0). The largest orbit offsets at the lower energy side in this example are of the order of x_{co}~50 *mm*. As the particles are accelerated from E_o=10 *GeV* up to E_m=20

GeV, the orbits move towards the outside of the magnets' aperture with a zero closed orbit for the central energy of E_c=15 *GeV*. The closed orbit offsets at the maximum energy reach values of x_{co}~58 *mm*. These closed orbit offsets may be compared to offsets of the order of x_{co}~500 mm, for the same energy range 10 –20 GeV, in the scaling FFAG [2].

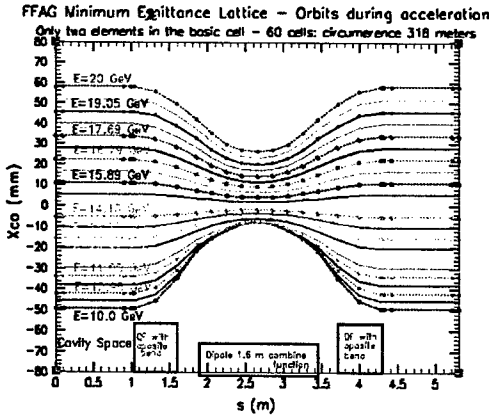


Figure 5: Closed orbit offsets during acceleration from the muon energy of 10 GeV to 20 GeV, in the basic cell.

Acceleration Parameters: α_c – the Momentum Compaction and a Difference in the Path Length

The dependence of the momentum compaction α_c on energy is approximately linear. At the lowest energy the lattice has imaginary γ_t, and as the energy crosses the central energy γ_t becomes real. The path length difference during acceleration, as calculated by SYNCH, is shown in Fig. 6.

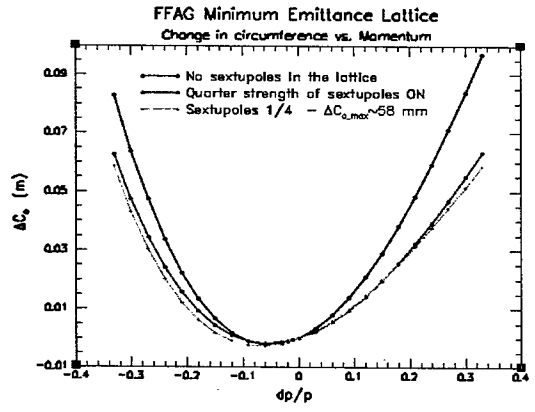


Figure 6: Change in circumference during acceleration.

5 ACCELERATION

A simulation of the longitudinal motion as presented in Fig. 7, was performed with the assumption that the path difference is the same as presented in Fig. 6 with quarter strength of sextupoles. More details about this simulation have been previously presented [7]. Parameters used for the simulation are: 10 bunches, 0.1 *μC/bunch*, initial bunch half length *1.6 ns*, initial half energy spread 4 *MeV*, initial 200 *MHz* RF voltage 650 *MV/turn*, final vs. initial emittance = 1.125, and a for the beam loading a fraction of stored cavity energy absorbed by the beam, 45%.

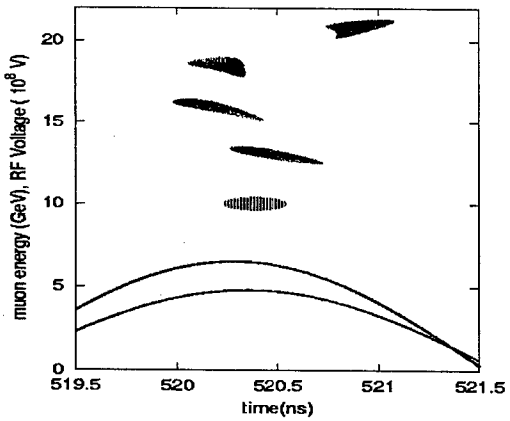


Figure 7: Longitudinal simulation of acceleration.

6 CONCLUSIONS

We have described an example of the non-scaling FFAG lattice and its advantages with respect to the standard scaling FFAG concept. When compared with the scaling examples the aperture size is significantly smaller as well as the circumference. The super-conducting combined function magnets are within a reasonable size and strength. The muon acceleration, the major cost item in the neutrino factory feasibility studies, is becoming more realistic and less costly.

7 REFERENCES

[1] K. R. Symon, "The FFAG Synchrotron – MARK I", MURA-KRS-6, November 12, 1954, pp. 1-19.

[2] R. Ueno et al, "Multi Orbit Synchrotron with FFAG Focusing For Acceleration of High Intensities Hadron Beams", PAC 99, New York, 1999, 2271-2273.

[3] D. Trbojevic and D. Courant, E., "Low emittance lattices for electron storage rings revisited", 4th European Particle Accelerator Conference, London, England, June 27-July 1, 1994, pp. 1000-1002.

[4] A. Garren, A. S. Kenney, E. D. Courant, A. D. Russell, and M. J. Syphers, SYNCH-A Program for Design and Analysis of Synchrotrons and Beam Lines, User's Guide 1993.

[5] F.C. Iselin and H. Grote, MAD, "Methodical Accelerator Design", CERN/SL, 90-13 (12991).

[6] E.D. Courant, J. S. Berg, A. Garren, R. Talman, and D. Trbojevic, "A Comparison of several lattice tools for Computation of orbit functions of an accelerator", this conference, EPAG010.

[7] D. Trbojevic, M. Blaskiewicz, E. D. Courant, and A. Garren, "Fixed field alternating gradient lattice design without opposite bend", Proceedings of EPAC2002, Paris, France,pp.1199-1201.

PROPOSAL FOR A PRE-BUNCHED LASER WAKEFIELD ACCELERATION EXPERIMENT AT THE BNL DUV-FEL FACILITY*

X.J. Wang, B. Sheehy and Z. Wu, NSLS, BNL, Upton, NY 11973, USA
W. Gai, HEP Division, ANL, Argonne, IL 60439, USA
A. Ting, Plasma Physics Division, NRL, Washington, DC 20375, USA

Abstract

We propose a pre-bunched Laser Wakefield Acceleration (LWFA) experiment in a plasma channel at the BNL DUV-FEL Facility. BNL DUV-FEL facility is uniquely qualified to carry out the proposed experiment because of the high-brightness electron beam and RF synchronized TW Ti:Sapphire laser system. The DUV-FEL is a 200 MeV linac facility equipped with a photocathode RF gun injector, a 100 fs Ti:Sapphire laser system and a magnetic bunch compressor. The proposed LWFA will inject a 150 MeV, 10 fs electron bunch into a centimeters long plasma channel. Simulation and preliminary experiment showed that, high-brightness 10 fs electron bunch with 20 pC charge could be produced using the technique of longitudinal emittance compensation. The initial experiment will be performed using the existing Ti:Sapphire laser system (50mJ, 100 fs) with 30 μm spot and 4 cm channel, the maximum energy gain will be about 15 MeV. We propose to upgrade the existing SDL laser output to 500 mJ with a shorter pulse length (50 fs). For an electron beam spot size of 20 um, the expected energy gain is about 100 MeV for a 5 TW, 50 fs laser pulse.

INTRODUCTION

The ultra-high acceleration gradient and renewable acceleration structure are the major attractive features of the plasma based accelerators [1-2]. Acceleration gradient over 100 GV/ m has been observed in many labs [3-4]. The challenges now facing the laser plasma accelerator community are to produce and preserve the electron beam quality in the plasma accelerators, and to extend plasma acceleration length.

Plasma channel is being explored to extend the interaction length of the laser plasma accelerators. Though other laser plasma accelerators has demonstrated higher acceleration gradient, standard laser plasma wake field accelerator (LWFA) holds most promise for future applications because of its controllability and quality of the electron beam. Studies showed the optimized LWFA required laser pulse length ranges from 10 fs to 100fs, plasma density $10^{17} - 10^{19}$ cm^{-3} with several centimetres long plasma channel [5-6]. The quality of the electron beam to inject into such LWFA is one of the major challenges to realize GeV plasma accelerator. To reduce the energy spread due LWFA, the injected electron beam bunchlength should be much shorter than the plasma wavelength. The plasma wavelength and channel size also put the stringent requirement on the transverse emittance of the electron beam.

We propose a plasma channel LWFA experiment at the NSLS DUV-FEL facility to demonstrate the feasibility of pre-bunched beam injection and phase lock. The DUV-FEL facility is uniquely qualified for the proposed experiment because of high-brightness electron source and synchronized femto-second TW laser system. In the following sections, we first describe the BNL DUV-FEL facility and possible laser upgrade for the LWFA, followed by ultra-short (10 fs) electron beam generation using the longitudinal emittance compensation technique; then we will describe the proposed LWFA experiment. We will also discuss the phase lock (timing jitter) between the laser and injected electron beam, it is feasible to control the jitter below 10 fs.

THE BNL DUV-FEL

The BNL DUV-FEL facility is a dedicated platform for future light source technology R&D and applications. The main focus at the DUV-FEL is to develop and explore the laser seeded high gain harmonic generation (HGHG) FEL technology.

The major components of the DUV-FEL are high-brightness photocathode RF gun injection system (fig.1), a TW Ti:sapphire laser system, four sections of SLAC type travelling wave linac, a four magnets chicane bunch compressor installed in the middle of the linac, and HGHG free electron laser (fig.2).

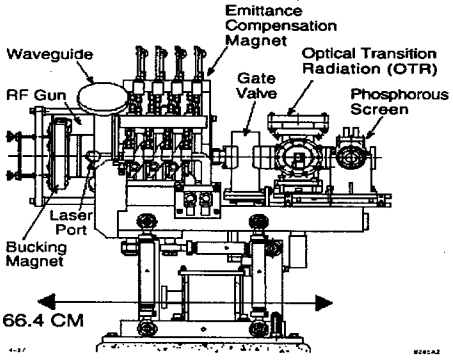


Figure 1: The BNL photoinjector.

The DUV-FEL Ti:sapphire laser system is capable of delivering 100fs 50 mJ output at the 10 Hz. It consists of a Millenium pumped Tsunami oscillator, a single grating

*Work supported by US DOE under the contract NO. DE-AC02-98CH10886
#xwang@bnl.gov

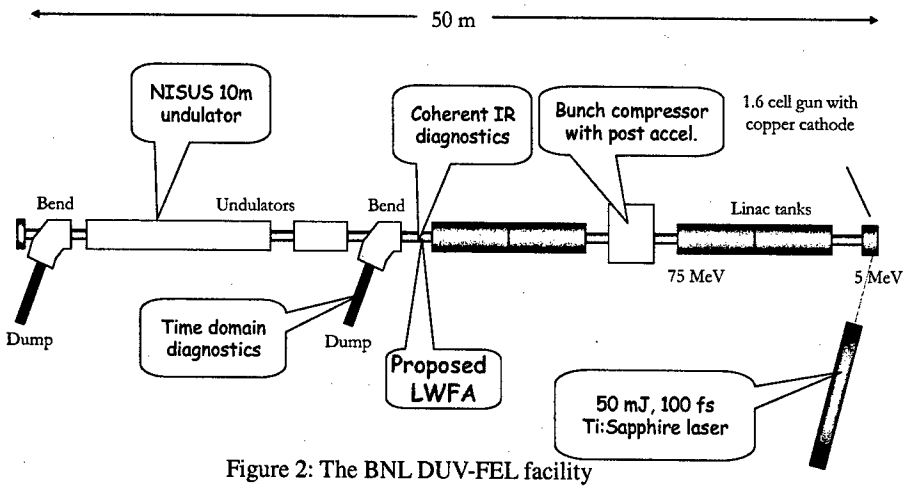


Figure 2: The BNL DUV-FEL facility

stretcher, two grating compressors. Two frequency doubled Nd:YAG pump lasers (GCR150 and GCR170), a regen and two-stages of double-pass amplifier.

The oscillator generate 80~100fs, 8nJ pulse train with 81.6 MHz. The oscillator is synchronized with the RF system of the linac. The laser pulses pass a Faraday isolator before they are sent to stretcher. After the stretcher, the pulse is 200ps, 4nJ. The pulses are then sent to the regen. In the regen, two Pockels cells are used to trap and dump the laser pulse in a repetition rate of 10Hz. The pulse energy is about 2.5 mJ after the regen. The output after the two-stages of double pass amplifier is about 70 mJ. The amplified output is divided into two beams, compressed separately with two independent compressors. One compressor's output is used to drive the photocathode RF gun, and the other is used for high gain harmonic generation (HGHG) FEL, or other laser based experiments, such as proposed LWFA here.

Initially, the proposed LWFA experiment will be performed using the present laser system. We also examine the possible laser upgrade for 100 MeV to 1 GeV LWFA experiment. The proposed upgrade will take place in two steps. First we would like to upgrade the present oscillator with shorter output pulse length, reducing the pulse length from 100 fs down to 50 fs. To minimize the cost, the oscillator pump laser and RF synchronization system will be re-used. The second part of the upgrade will increase the output energy to 500 mJ or more. A vacuum based compressor will also be added.

ULTRA-SHORT ELECTRON BEAM GENERATION

To keep the accelerated electron beam energy spread on the order of a few percent, the electron beam bunch length less than one tenth of the plasma wavelength is required. That means a the injected electron beam should have a few fs long bunch length.

Though optical laser injectors [4] have been explored for LWFA. Large energy spread and relative low energy make it challenging to preserve both transverse and longitudinal emittance before injected into the LWFA. We propose an alternative technique to generate 10 fs electron bunch at 150 MeV for 20 pC charge based on the longitudinal emittance compensation techniques [7].

Our previous study shows that, 10 fs electron bunch can be generated at 40 MeV [8] using the longitudinal emittance compensation. To minimize the space charge effect and generate proper energy chirping, the electron beam is produced using a relative long laser (8ps FWHM) in the photocathode RF gun at the near zero crossing phase (12°). Electron beam first compressed in the RF gun as it is rapidly accelerated. The beam produce by the RF gun will be continually compressed if the first section of the linac after the RF gun is operating at the off-crest (70°). The basic idea of the longitudinal emittance compensation is the bunch compression is accompanied by the acceleration simultaneously. The photoinjector (fig.1) is ideal suit for this purpose, the solenoid magnet for the transverse emittance compensation is now used to control the beam bunch lengthening due to the divergence.

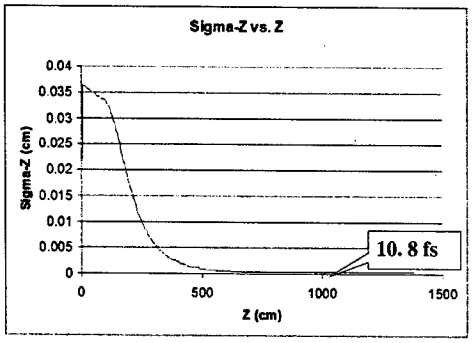


Figure 3: Electron beam bunch length as the function of the distance along the linac.

Fig.3 shows the electron beam bunch length evolution along the linac. The last three sections of the linac are used to accelerate the electron beam and minimize the energy spread. The energy spread at the 150 MeV is about 0.1%.

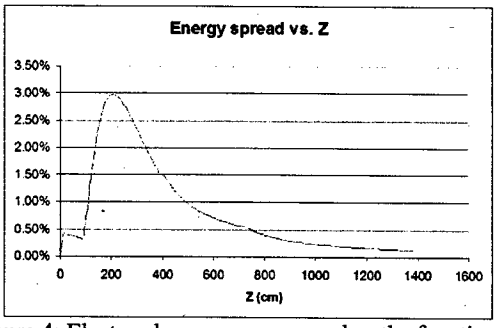


Figure 4: Electron beam energy spread as the function of the distance along the linac.

Using longitudinal emittance compensation technique will also allows us to minimize the transverse emittance because of the coupling between the transverse and longitudinal emittance. Fig.5 shows the emittance as the function of the distance along the linac, the oscillation of the emittance inside the linac is due to the lack of focusing. The final emittance ε_n <0.5 mm-mrad.

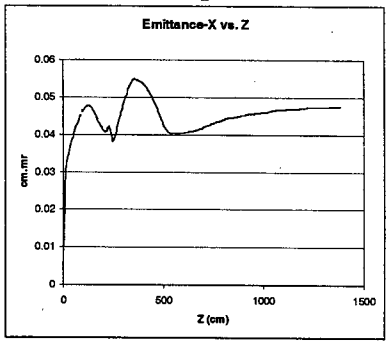


Figure 5: Transverse emittance as the function of the distance along the linac.

PRE-BUNCHED LWFA

The combination of femtosecond TW laser and ultra-short electron beam at the BNL DUV-FEL facility will make it extreme attractive to perform the pre-bunched LWFA experiment.

The proposed LWFA will use the pre-formed plasma channel developed at the NRL [9]. Table I summarize the laser and plasma channel parameter for the experiment. For 4 cm long interaction and 0.5 TW laser power, 15 MeV energy gain is expected (fig.6).

Many fundamental issue of GeV LWFA can be studied in our initial experiment, such as emittance growth, plasma stability and phase locking between the laser and electron beam.

We have recently investigated the phase locking (jitter) between the laser and electron beam [10]. Since the electron is generated by the same laser, the jitter is mainly caused by the electron beam energy fluctuation. Presently technologies existing to reduce this jitter below 10 fs.

Table 1: Summary of the parameters of LWFA.

Laser power (TW)	0.5
laser spot size radius (μm)	30
Laser pulse length (FWHM, fs)	50-100
Input electron beam Energy (MeV)	150
Electron Beam Bunch length (rms,fs)	10
Channel radius (μm)	60
Plasma density on axis (1/cm^3)	$8x10^{17}$
Rayleigh length (cm)	0.35
Interaction length (cm)	4
Maximum Energy gain (MeV)	15

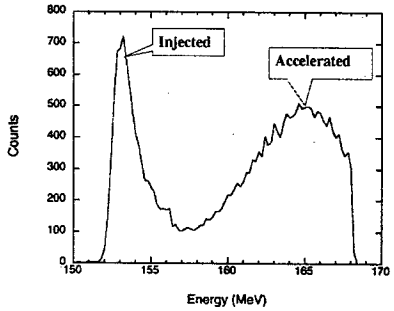


Figure 6: Electron beam energy spectrum before and after the LWFA.

REFERENCES

[1] T. Tajima and J. Dawson, Phys. Rev. Lett. **43**, 267 (1979).

[2] E. Esarey, P. Sprangle, J. Krall and A. Ting, IEEE Trans. Plasma Sci., 24, 253-288(1996).

[3] V. Malka *et al*, **Science**, 298, 1596-1600 (2002).

[4]Proceeding of the 10th AAC Workshop, AIP Conference Proceedings 647, Edited by C. Clayton and P. Muggli.

[5] W.P. Leemans et al, IEEE Trans. Plasma Sci., 24, 331- 341 (1996).

[6] R. F. Hubbard, P. Sprangle and B. Hafizi, IEEE Trans. Plasma Sci., 28, 1159 - 1169 (2000).

[7] X.J. Wang et al, Phys. Rev. E 54, R3121 -R3124 (1996).

[8] X.J. Wang and X.Y. Chang, " Femto-seconds Kilo-Ampere Electron Beam Generation", to be published in NIM A.

[9] D. Kaganovich *et al.*, Phys. Rev. E, 59, R4769 (1999)

[10] X.J. Wang, "Timing Jitter Issues for Photocathode RF gun Based Linac System", to be presented at the FEL'03.

CHARACTERISTICS OF GRADIENT UNDULATOR[1]

A. Mikhailichenko, Cornell University, LEPP, Ithaca NY 14853, USA

Abstract

Undulator/wiggler having the same polarities of magnetic field in opposing though medial plane poles can be used for generation radiation which intensity is a function of the beam size and displacement. Characteristics of such device analyzed here analytically and by tracking.

INTRODUCTION

Utilization of quadrupole wiggler is an interesting option for broadening the bandwidth of pick-ups in fast feedback systems [1] and for beam alignment [2]. Such a wiggler, which is a sequence of ordinary focusing and defocusing quadrupoles, generates a radiation, which depends on the beam shape and position.

Although in such system radiation for two transverse coordinates can be easily distinguished by polarization, desire to have sensitivity to one coordinate only is always an option. In [3] a device, called *gradient undulator,* was described for the first time. Practical utilization of this device suggested in [4].

Here we will concentrate our attention on practical aspects of design and properties of magnetic fields in gradient undulator. The test was also included trajectories analyses, which was carried out numerically on the basis of real 3D model. Knowing the real trajectory allows finding radiated field instantly in principle.

ANALYTICAL CONSIDERAIONS

Let us consider first some simple aspects of symmetry of gradient undulator/wiggler in comparison with usual dipole wiggler; both are represented in Fig.1.

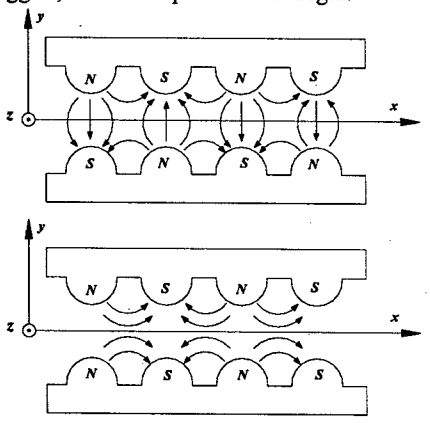


Figure 1: Dipole wiggler, upper one and gradient undulator/wiggler, lower. Beam is moving along x –axis. Normal to the drawing's plane is z –direction.

In *gradient wiggler*, the longitudinal field $B_z(y)$ has nonzero value at the plane $\{x, z\}$, but now wiggling amplitude linearly increasing with y coordinate following $B_y(y)$.

Using Maxwell's equation $div\vec{B}=0$ and $rot\vec{B}\big|_z=0$ after some algebra one can obtain analytical field expression for gradient wiggler with wide poles as the following [5, 6]

$$B_x(x,y)=\sum_{k=0}^{\infty}\frac{(-1)^k y^{2k}B^{(2k)}(x)}{(2k)!},$$
$$B_y(x,y)=-\sum_{k=0}^{\infty}\frac{(-1)^k y^{2k+1}B^{(2k+1)}(x)}{(2k+1)!} \quad (1)$$

For demonstration, fields (1) can be represented in lowest order as the following

$$B_x(x,y)=B(x)-\frac{y^2}{2}B''(x)+\frac{y^4}{2\cdot 12}B^{(IV)}(x)-\ldots \quad (2)$$
$$B_y(x,y)=-y\cdot B'(x)+\frac{y^3}{2\cdot 3}B'''(x)-\frac{y^5}{5!}B^{(V)}(x)-\ldots$$

One can see from here, that gradient in y direction associated with $B'(x)$. For example if dependence in x direction is periodic, $B(x)=B_0 Cos\frac{x}{\lambda_w}$, the last determines the gradient in y direction as

$$G(x)\equiv\frac{\partial B_y}{\partial y}=-B'(x)=\frac{B_0}{\lambda_w}Sin\frac{x}{\lambda_w} \quad (3)$$

So we are coming to fundamental conclusion for this type of wiggler, that the gradient is proportional to the longitudinal field and reciprocally proportional to the period.

If the field is time dependent, then the following substitution needs to be done in all formulas [6]

$$\frac{\partial^{2k}B(x)}{\partial x^{2k}}\to\left(\frac{\partial^2}{\partial x^2}-\frac{1}{c^2}\frac{\partial^2}{\partial t^2}\right)^k B(x,t),$$

where c stands for the speed of light. Odd derivative obtained by taking integral over x in this combination.

HARDWARE ASPECTS

Let us consider now more or less realistic model of such a wiggler. Orientation of the poles is represented in Figures 1 and 2. This model has not associated with any specific project, but taken for example only.

[1]Extended version is available at http://www.lns.cornell.edu/public/CBN/2003/CBN03-1/CBN03_1.pdf . Work supported by NSF.

0-7803-7738-9/03/$17.00 © 2003 IEEE

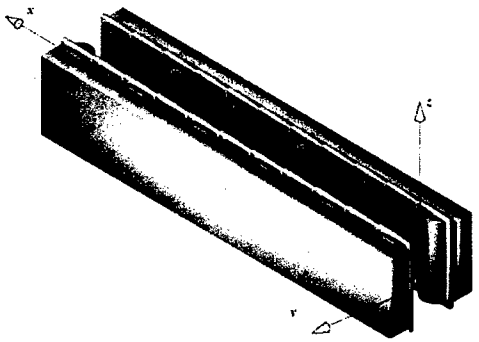


Figure 2 (Color): View to the gradient wiggler model.

Particles are moving along x. Pole size in z direction is $\pm$ 15 cm (=30cm), radiuses of cylinders 4 cm, coil cross-section is 2×2.3 cm^2, period $\lambda_w = 24.84$ cm, gap between poles ± 3.5 cm. Coil cross section is a rectangle with dimensions $\{x \times y\} = \{2 \times 2.5\} cm^2$. Yoke plate ends at y=15 cm from medial plane y=0.
This wiggler is not sensitive to z- position of the particle, giving linear dependence in radiated field across y direction. Radiation in this wiggler is polarized along z – axis. Yoke modeled by soft Steel 1010. Total current running in central coil is 60 kA-Turns, what suggests utilization of SC windings. All field calculation done with 3D code MERMAID.

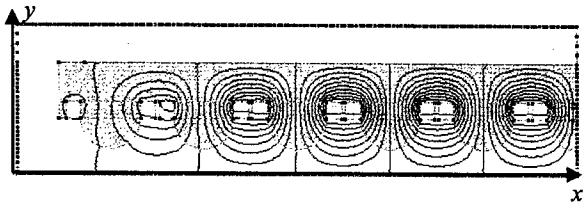


Figure 3 (Color): Lines of magnetic field in central plane of wiggler, z=0. Half of the wiggler is shown; right side of the plot is a plane of symmetry along x. Radiuses of the poles are 4 cm, period -25 cm. Gap between coils 0.5 cm. Length of the pole in z direction is $\pm$ 15 cm. Particles are moving from the left side. {xz, y=0} represents medial plane.

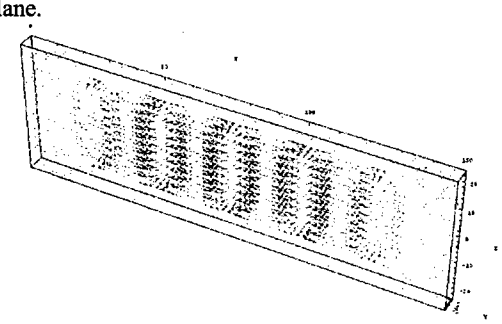


Figure 4 (Color): Vectorial representation of the fields in the gap of 11-pole gradient wiggler inside the 3D volume {x=0-150;y=$\pm$ 3;z=$\pm$ 24} cm. Medial plane of the wiggler {x, z} runs at y=0.

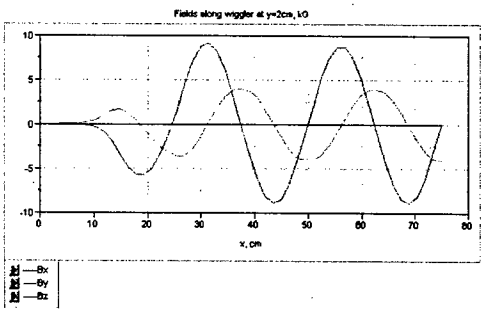


Figure 5 (Color): Field graphs for y=+2 cm, z=0. Half wiggler is shown as in Figure 3. Center is at the right side of the plot at 75 cm. B_y comes to it's maximum, B_x, indeed comes to zero. Basically B_z=0 along this axis as it must be according to symmetry properties.

Wiggler is focusing towards medial plane {x, z} in y – direction. This focusing is typical for any wiggler and is proportional to the associated angle of wiggling $\alpha \cong K/\gamma$, with K–factor depending on vertical position itself.

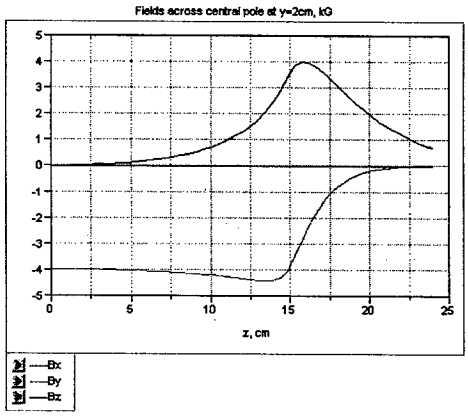


Figure 6 (Color): Fields across central pole, starting from z=0, y=2 cm. Material of yoke St1010. Points at {x=75, y=2, z=0-24} cm.

The increase in B_y component (lower curve in Fig.6) at the side of the pole explained by the flux concentration here. The flux expelled from central region escapes from the sides. This effect also generates B_z component.

TRAJECTORIES

Formally, as formulas for magnetic field is known, (5), it is possible to make analytical calculations of particle's trajectory. We will continue here our numerical exercises, however. Trajectories calculated numerically by using code UMKA [7] on the basis of MERMAID 3D field calculations.

One can expect, as the field in vertical direction is linearly varying, trajectories with zero angle and displacement at output for one vertical input will have different resulting kicks and angles for other vertical input.

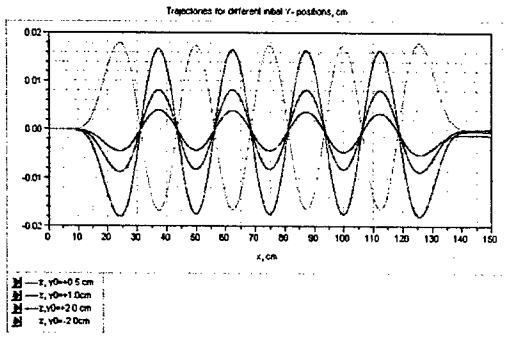


Figure 7 (Color): Trajectories for different initial positions in Y direction. There are shown ones for $y_0 = +0.5$ cm, +1.0 cm, +2.0 cm, -2.0 cm. The last one corresponds the start point below median plane. Beam energy 2 GeV.

One can see, that this type of wiggler can also be used for fine-tuning of dynamic aperture of damping ring for linear collider, typically overloaded by dipole wigglers.

RADIATION AND ACTION TO THE PARTICLE

As trajectory $z(x)$ is known, this allows calculation of second derivative $\dot{\vec{v}} \cong \ddot{z}(x = ct)$ and hence, electric field. Basically to obtain time structure at the observation point one needs to take second derivative with graph in Fig.7 and shrink this curve by Doppler factor. One can see that a single particle spectrum is the same as in a dipole wiggler with the same trajectory and formulas are the same (see for example [4]).

Evidently, the frequency of radiation

$$\omega = \frac{c/\lambda_w}{1-\vec{n}\vec{v}} \cong \frac{2\gamma^2 \cdot c/\lambda_w}{1+\gamma^2\vartheta^2 + K^2/2} \qquad (4)$$

is a function of magnetic field through $K = 93.4 \cdot B_y(y)[Tesla] \cdot 2\pi\lambda_w[m]$, ϑ is an angle to observer (from x-direction). So with variation of y, K factor also changes. If one restricts the width at the level ~50% from maximal, then $K^2/2 \le 1$, and hence, $K \le \sqrt{2}$. This limits either B_0 for given amplitude y or amplitude, if B_0 is given. For the wiggler with given field at the axis B_0 the broadening will be less than 50% for amplitudes

$$y \le \sqrt{2} \cdot \frac{mc^2}{eB_0} \equiv \sqrt{2} \cdot \lambda_w \frac{mc^2}{eB_0\lambda_w} = \frac{\sqrt{2} \cdot \lambda_w}{K_0}, \qquad (5)$$

where $K_0 = eB_0\lambda_w / mc^2$. For the wiggler considered above, $B_0 \sim 0.8T$, $2\pi\lambda_w \cong 0.25$ m, $K_0 \cong 18.7$ and amplitude must be $y \le 0.3cm$ i.e. below 3 mm. For narrower width, the amplitude must be restricted proportionally.

In Optical Stochastic Cooling, OSC, dependence of frequency of radiation on amplitude, might be useful for specific tuning for cooling the particles with large amplitudes only. Period of the wiggler must be adjusted properly, together with angle of observation.

For OSC, implementation of quadrupole like devices might be interesting for reduction of radiation from cold central part of the bunch. This device, similarly to the quadrupole wiggler, provides the energy shift as a function of particle displacement at location of kicker.

$$\Delta E = \frac{eE_0L}{2}\frac{K}{\gamma} \cong \frac{eE_0L}{2}\frac{K_0}{\gamma}\frac{y}{\lambda_w}, \qquad (6)$$

where E_0 stands for electric field strength in co-directionally propagating electromagnetic wave, the length of wiggler is L. One can see that action is also linearly dependent of position of particle in the gradient undulator or in quadrupole wiggler.

CONCLUSIONS

The device analyzed –gradient undulator/wiggler can be interesting not only for the purposes of beam size measurements, but also for nonlinear correction of magnetic properties in the damping ring or in a transport channel, acting in one particular direction only. Minimal number of poles for this purposes –three–give closed bump.

Device can be interesting for implementation into OSC, serving as a pickup and/or a kicker linearly (re)acting to the particle's instant position in one direction.

REFERENCES

[1] A. Mikhailichenko, M. Zolotorev, "Optical Stochastic Cooling", Phys.Rev.Lett.71: 4146-4149, 1993.

[2] E.G. Bessonov, A.A. Mikhailichenko, "Alignment of the Linac With the Help of Radiation from the Quadrupoles of the Linear Collider", 4th European Particle Accelerator Conference (EPAC 94), London, England, 27 Jun - 1 Jul 1994: Proceedings Edited by V. Suller and Ch. Petit-Jean-Genaz. River Edge, N.J., World Scientific, 1994, vol. 3, p. 2579-2581.

[3] E.G. Bessonov, J. Pflüger, G.-A. Voss, N.J. Walker, Internal DESY report M96-18, September 1996.

[4] E.G. Bessonov, N.J. Walker, S.G. Wipf, "Beam size measurements in Linear Collider using Gradient Undulator and off-axis Detection", TESLA 97-18, November 1997.

[5] K. Steffen, "High Energy Beam Optics", Interscience Publishes, 1965.

[6] A.A.Mikhailichenko, "3D Electromagnetic Field: Representation and Measurements", Cornell CBN-95-16, 1995. 42pp.

[7] G.Dudnikova, V.Vshivkov, K.Vshivkov, UMKA-VG, Institute of Computation Technologies, Lab. of Plasma Physics, Siberian Branch of RAN.

SHORT X AND GAMMA PRODUCTION WITH SWEPT LASER BUNCH

A. Mikhailichenko, Cornell University, LEPP, Ithaca NY 14853, USA

Abstract[1]

We described here the new way of production of ≤ 100 fs bursts of X and gamma radiation by Compton back-scattering of a laser bunch which have been swept along the electron trajectory. In the method described the time duration of the secondary radiation does not depend on electron bunch length and is shorter than duration of the primary laser bunch by factor $1/N_R$–the number of resolved spots of sweeping device (up to 1/ 1000). The method of the laser bunch sweeping is also helpful in obtaining short electron bunches from a photo cathode.

INTRODUCTION

An idea on generation of X-rays and gammas by Compton back-scattering was developed many years ago [1] ,[2] and used well in a framework of gamma-gamma collider activity [3]. This idea was applied to a circular machine also [4], [5]. In this method accommodated to a circular machine the short laser bunch interacts with a passing electron bunch with 90° across the laser's ray trajectory. In this case the time duration of the secondary radiation defined by the time duty of primary laser radiation $\tau \cong \sigma_b / c$, or by the length of the laser bunch σ_b, or by the length of the electron bunch. In any case the method requires either short primary laser bunch and/or short electron bunch in some modification of the method.

SCHEME

In contrast to this method mentioned above, in our publication [6] we described so called laser undulator installed in Tabletop accelerator. This accelerator developed as a side product in a framework of high-energy linear collider [7-9]. Main difference of our proposal from others is that here we used ***swept*** laser bunch, having slope of 45 degree to direction of propagation in the region of interaction between laser and electron bunches. The laser bunch of this shape can be generated by appropriately designed sweeping device used in [7-9] for high-energy accelerator.

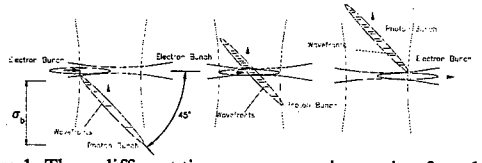


Figure 1: Three different times sequences increasing from left to the right. Laser bunch slope with respect to direction of propagation is 45 degrees. Volume with electrons that radiate does not depend on the electron bunch length at all.

[1] Extended version is available at http://www.lns.cornell.edu/public/CBN/2002/CBN02-11/cbn0211.pdf.

In our method the time duration of the secondary radiation is defined by instant transverse size of the primary laser bunch at location of electron beam trajectory, Fig.1 and Fig.2. Meanwhile the total number of radiated secondary particles defined by full length of the laser bunch. With implementation to any damping ring X and gamma ray production with the time duty of the order of 100 fs or even better can be obtained now with routinely operational laser having bunch of ~30 ps.

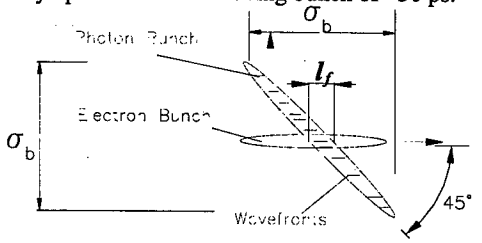


Figure 2: Scaled view of central part from Fig.1.

Despite the primary laser bunch has the length σ_b, the length of interaction (radiation) region is l_f which defined by the number of resolved spots of sweeping device (see lower). One can see that the number of electrons effectively interacting with the photon bunch is lower than the bunch population in factor l_f / σ_b, namely this moving length l_f describes radiating electrons. This active region is moving with re-radiated photons.

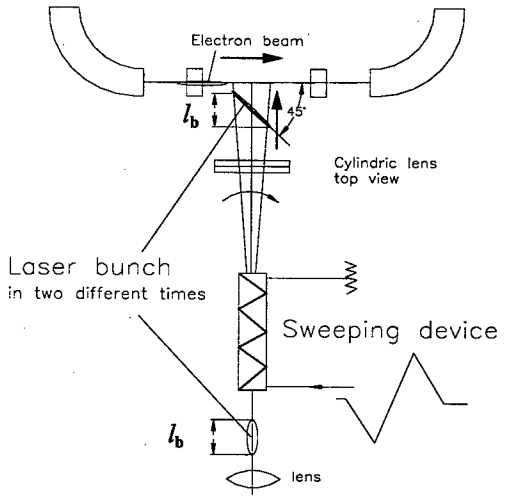


Figure 3: General scheme.

The arrangements of the scene are represented in Fig. 3. Sweeping device deflects the front of laser bunch to the left on the picture plan; the tail of the laser bunch is deflected to the right of the plan. Lens at the lower edge of the figure focuses the primary laser bunch onto the

0-7803-7738-9/03/$17.00 © 2003 IEEE

interaction region. As far as cylindrical lens, in can be mentioned that it is working with broadband radiation. Utilization of optical materials with appropriate frequency bandwidth is not a problem however. Scaled view on cylindrical lens is shown in Figure 4.

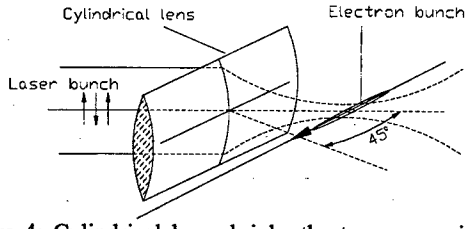


Figure 4: Cylindrical lens shrinks the transverse size of the laser bunch in vertical direction. Low dispersion material of the lens allows proper focusing of short bunch

Circular or elliptical polarization could be obtained also if the primary laser beam has circular or elliptical polarization.

YIELD OF SECONDARY PHOTONS

The photon generation in laser undulator could be treated also as Compton back-scattering. The number of photons, radiated at first harmonic by every particle, could be written as

$$N_\gamma \cong \sigma_b \sigma_\gamma n_\gamma, \qquad (1)$$

where $\sigma_\gamma \cong \frac{8\pi}{3} r_0^2$ is Thomson cross section of photon-electron scattering, $n_\gamma \cong H^2 / \hbar\omega$. This introduces the length of interaction as usual $l_\gamma \cong 1/\sigma_\gamma n_\gamma$, so the number of photons per initial particle is simply $N_\gamma \cong \sigma_l / l_\gamma$.

The energy of the backward scattered photon is [3,10]

$$\hbar\omega' = \frac{mc^2 \gamma \cdot x}{1+\gamma^2 \vartheta'^2 + x} \qquad (2)$$

where $x = \frac{2\gamma^2 \hbar\omega_0}{mc^2\gamma} = \frac{2\gamma\hbar\omega_0}{mc^2}$.

For a primary laser radiation with a wavelength around micrometer, $\hbar\omega_0 \cong 1eV$, parameters and energy of secondary photons are represented in Table 1.

Table 1

E, GeV	x	$\hbar\omega'$, MeV
0.1	0.00077	0.077
1.0	0.0077	0.77
10.	0.077	711
100.	0.77	43370

All secondary photons are moving in the same sample having the longitudinal length of l_f in Fig.2. Namely this distance defines the duty time for secondary radiation.

For a micrometer level of the primary wavelength the number of resolved spots N_R~100 can be expected. Vertical size of the laser radiation defined by cylindrical lens and can be estimated as ~5 μm. So the effective volume of interaction for single particle with this 30ps-laser flash could be estimated as $V \cong 1cm \times 100\mu m \times 5\mu m \cong 5 \cdot 10^{-6} cm^3$. The number of primary photons can be calculated as $N_{0\gamma} \cong E_{flash} / \hbar\omega_0$. The photon density and the length of interaction go respectively $n_\gamma \cong N_\gamma / V$ and total number of secondary photons goes to

$$N_\gamma \cong N_{eff} \sigma_b / l_{eff}, \qquad (3)$$

where $N_{eff} \cong N \cdot l_f / \sigma_b \cong N / N_R$, N is the bunch population. For the laser flash with, say $E_{flash} \cong 1mJ$, $\hbar\omega_0 \cong 1eV$, each electron radiates in average $N_\gamma \cong \sigma_l / l_\gamma \cong 8.3 \cdot 10^{-4}$ photons per pass. For $N \cong 10^{10}$ this brings the photon number to $N_\gamma \cong 8.3 \cdot 10^4$ /bunch/pass. Suggesting repetition rate 100kHz one can expect the photon flux $\dot{N}_\gamma \cong 8.3 \cdot 10^7 s^{-1}$. Total power from laser goes to $10mJ \times 10^5 \frac{1}{s} = 100W$. These numbers gave an idea of the possibilities of the method proposed.

The brightness of the source can be evaluated as the following

$$B \cong \frac{\dot{N}_\gamma}{(\gamma\varepsilon)\cdot(\beta/\gamma)\gamma^{-2}} = \frac{\gamma^3 \cdot \dot{N}_\gamma}{(\gamma\varepsilon)\cdot\beta} \qquad (4)$$

If we suggest that the electron beam emittance be $\gamma\varepsilon \cong 3 \cdot 10^{-3} cm \cdot rad$, envelope function in the region of interaction as $\beta \cong 1cm$, then one can estimate for $\gamma \cong 10^4$

$$B \cong 8.3 \cdot 10^{24} photons / cm^2 / rad^2 / \sec.$$

Duty time for these bursts of radiation is about 100 fs, despite the primary length of laser bunch is ~30ps.

SWEEPING DEVICE

The devices types suitable for the sweeping were collected in [8]. Each sweeping device uses controllable deflection of the laser radiation in time. Any deflecting device could be characterized by a deflection angle ϑ and the angle of natural diffraction $\vartheta_d \cong \lambda / a$, where a —is the aperture of the sweeping device, λ is a wavelength. The ratio of deflection angle to diffraction angle is a fundamental measure of quality for any deflecting device. This ratio defines the number of resolved spots (pixels) along the sweeping line, $N_R = \vartheta / \vartheta_d = inv$. As one can see, N_R value gives the number for the duty time reduction.

Electro-optical sweeping device uses controllable dependence of refractive index on electrical field strength and direction applied to some crystals. When a voltage $V(t)$ applied to the metallization, the refractive index

changes $\Delta n = \Delta n(V(t))$. To increase the numbers N_R, $\Delta\vartheta$, *multiple-prism* deflectors were developed, see Fig.5.

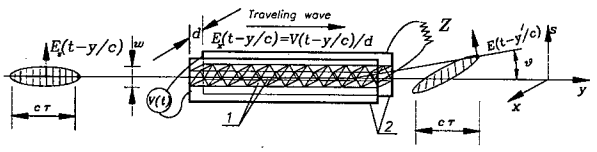


Figure 5 [8]: Prisms 1 with *oppositely directed optical axes* installed in series between two parallel strip–line electrodes 2, *d*–is the distance between them. *Z*– is matching impedance. Lines across the laser bunch schematically show the wave fronts. $E_x(t-y/c)$–is a driving electrical field.

We suggested a *traveling wave* regime here to be able to sweep the short laser bunch. Here neighboring prismatic crystals have oppositely oriented optical axes. These crystals positioned between strip–line electrodes. To be able to sweep short laser bunches, the voltage pulse *V* (*t*) is propagating along this strip-line as a *traveling wave* together with the laser bunch to be swept, [8]. This gives the necessary voltage profile along the laser pulse at *cm* distances.

Deflection angle and the number of resolved spots become

$$|\Delta\vartheta| \cong \Delta n \frac{2L_d}{w} \cong \frac{L_d}{w \cdot d} n_0^3 \cdot r_{ij} \cdot V \,,\; N_R \cong \Delta n \frac{2L_d}{\lambda} \,, \quad (5)$$

where L_d stands for full length of deflecting device, *w*–is the laser beam width (along direction of deflection). The broad band traveling wave deflector could be obtained also if the same crystals located in the middle of a waveguide shortened from both sides [8]. In Table 2 we summarized general parameters of electro optical deflectors.

Table 2

Wavelength	Materials	ϑ, *rad*	N_R
$\lambda \cong 10\mu$	*GaAs, ZnTe, ZnS, CdS, CdTe, CuCl*	0.01-0.02	10
$\lambda \cong 5\mu m$	*$LiNbO_3$, $LiTaO_3$, CuCl*	0.01-0.02	20
$\lambda \cong 1\mu m$	*KDP, DKDP, ADP, KDA, $LiNbO_3$*	0.01-0.02	100

Mechanical deflection system is also possible here [8].

The same idea can be applied to the electron bunch production with help of photocathod, Fig. 6. The shortage of illumination time increases with increase of illumination angle θ in Fig. 6. So one can see that practically any existing scheme can be equipped with this sweeping device.

CONCLUSIONS

The method proposed allows generation of short bunches of secondary photons practically with ordinary equipment. Secondary radiation duty is shorter, than primary laser duty in ~ 300 times for visible light. Electro-optical sweeping device is available on the market. The photon flux of ~30-100 fs of X or gamma radiation is big enough to satisfy the broad variety of user's needs.

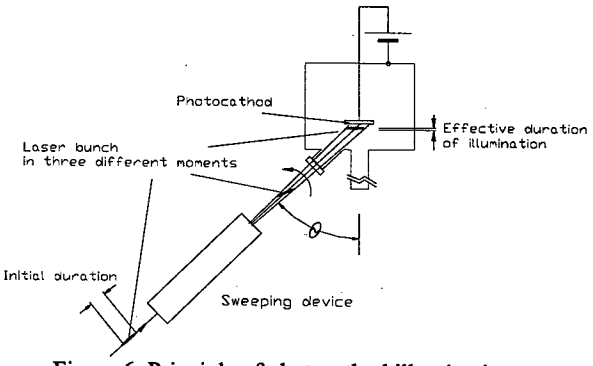


Figure 6: Principle of photocathod illumination.

The scheme is not sensitive to a jitter of laser or electron beam as the only a small length of electron bunch radiates and this duration time does not depend on the bunch length at all. Laser with synchronized modes can generate necessary sequence of primary laser bunches.

Work supported by NSF.

REFERENCES

[1] F.R. Arutynian, V.A. Tumanian, Phys. Lett., 4(1963), 176.
[2] E. Feinberg, H. Primakoff, "Interaction of Cosmic Ray Primaries with Sunlight and Starlight", Phys. Rev. 73(1948) 449-469.
[3] I.F.Ginzburg, G.L.Kotkin, V.G.Serbo, V.I.Telnov, NIM 205:47,1983. JETP Lett. 34:491-495, 1981. Pisma Zh. Exp.Teor. Fiz. 34: 514-518, 1981.
[4] K.-J Kim et al., NIMA 341, 351 (1994).
[5] W. Leemans et al., AIP Proc. 1994 Workshop on Advanced Accelerator Concepts, Lake Geneva, LBL –36369.
[6] A. Mikhailichenko, "Table-top accelerator with extremely Bright Beam", 9th Advanced Accelerator Concept Workshop (AAC2000), Santa Fe, New Mexico, 10-16 Jun., Published in AIP Conf. Proc.569, 2000, pp.-881-889.
[7] A.Mikhailichenko, "Parameters of $2\times200GeV$ Linear Collider with Microstructures Excited by Laser Radiation", ibid., 365-373.
[8] A. Mikhailichenko, "Particle Acceleration in Microstructures Excited by Laser Radiation", CLNS 00/1662, Cornell 2000, 89 pp.
[9] A. Mikhailichenko, "Particle Acceleration in Microstructures", SNOWMASS-2001-T401, Jun 2001, 32pp.
[10] V.B. Berestetskii, E.M. Lifshits, L.P. Pitaevskii, "Quantum Electrodynamics", Pergamon Press, Second Edition, 1982.

DAMPING RING FOR GENERATION OF POSITRONIUMS AND INVESTIGATION OF FERMI DEGENERATION IN MOVING BEAMS

A. Mikhailichenko, Cornell University, LEPP, Ithaca NY 14853, USA

Abstract

Kayak-paddle look-like damping ring developed as injector for a laser driven linear accelerator with microstructures [1], allows beam emittance, which is defined by quantum effects in electron-positron gas of particles in the bunch. Utilization of co-directionally moving congruent electron and positron bunches allowing production of positronium beam with $\sim 10^{10}$ para-positroniums per second. This arrangement might be a step toward investigation of the nature of Fermi-degeneration in moving beams.

INTRODUCTION

The question about lowest possible emittance for moving bunch was initiated in [1], [2]. This subject has crucial importance for acceleration in microstructures, scaled down to the laser wavelengths. Here also might be a chance for enhancement for all linear collider schemes, however. One can see, that for every scheme of LC remaining under development now, utilization of beams with smaller transverse and longitudinal emittances allows to have smaller beam size at IP. So even with lowered bunch population, luminosity can be kept at the same level if emittance reduced. Lowering the number of particles in the bunch makes the beam more stable during acceleration. Lowering the bunch population also reduces a problem with intra-beam scattering phenomena in damping ring-injector.

Extreme among coolers was so called Kayak-paddle cooler first described in [3] and accommodated for laser driven linac business in [4]. It was found, that, formally, minimal phase volume occupied by single particle is limited by opening angle of radiation only and might be very close to the $\lambda\!\!\!^{-}_c = \hbar/mc$. Namely this fact forced us at this point to investigate quantum limitations associated with Fermi nature of electron gas.

MINIMAL NUMBER OF PARTICLES

Minimal number of particles required for collision can be defined as the following. In a moving frame the minimal uncertainty in definition of transverse position can be estimated as a $\lambda\!\!\!^{-}_c = \hbar/mc$ –Compton wavelength, leaving uncertainty for transverse momentum as mc. Meanwhile spread of transverse momentum for colliding beam at IP is $p_\perp \cong mc\gamma\sqrt{\gamma\varepsilon/\gamma\beta_0}$. For typical emittance value $\gamma\varepsilon \cong 10^{-4} cm\cdot rad$, $\gamma \cong 10^6$, $\beta_0 \cong 10^{-2} cm$ -beta function at IP, $p_\perp \cong mc\cdot 10^2$, i.e. much more than defined by uncertainty. Minimum number of particles N can be found from luminosity required $N^2 \geq 4\pi\lambda\!\!\!^{-2}_c L/nf$, where f is a repetition rate, n is a number of bunches per train. For $L \cong 10^{34}$, f=100Hz, n=10, $N \geq 4\cdot 10^5$. So only half of a million particles is enough for successful operation. With such amount of particles all collective phenomena vanished. We also mentioned in [4] that the lowered emittance with reduced number of particles can be obtained by scrapping all extra particles obtained from usual beam injectors. Phase density will remain the same however.

RF structure-to beam energy transfer reduction is not a problem as the productivity of equipment estimated by resulting luminosity. Lowering the bunch population increases effective accelerating gradient due to lower RF loading and less phase shift required by BNS mechanism.

FERMI-DEGENERATION

Naturally, electron gas when it is cooled will be crystallized if it is not neutralized. There are two ways for neutralization. First is neutralization by ions, second one – usage of co-directionally moving electron-positron bunches. In last case creation of positroniums is the main process accompanying the cooling.

For neutralization by ions for bunch with electron density $n_b \cong N/\pi\sigma_\perp^2 l_b$, l_b is the bunch length, $\sigma_\perp$ is transverse dimension, ion density n_i, must be $Z_i n_i \gamma = n_b/\gamma$, eZ_i - ions charge. It yields that ion density small value as $n_i = n_b/\gamma^2/Z_i \cong 10^{-7} n_b$ for $\gamma \cong 10^3$, $Z_i \cong 10$. This defined by emittance dilution as a result of collisions during damping time.

Ideal electron gas defined as a having no interactions between particles [6]. As the collisions do not change distributions as far as they are elastic, they just equalizing the temperature among degrees of freedom. That is why Fermi-degeneration of electron gas can be described so as the electrons have no interactions.

It was shown in [1] for the first time, that there exists a strong quantum limitation for the lowest emittances in the beam like

$$(\gamma\varepsilon_x)(\gamma\varepsilon_y)(\gamma\varepsilon_s) = (\gamma\varepsilon_x)(\gamma\varepsilon_y)(\gamma l_b(\Delta p/p_0)) \geq \tfrac{1}{2}(2\pi\lambda\!\!\!^{-}_C)^3 N, \quad (1)$$

where $(\gamma\varepsilon_s) = \gamma l_b(\Delta p/p_0)$–is an invariant longitudinal emittance, $\Delta p/p_0$ –is a relative momentum spread in the bunch, $\gamma\varepsilon_x$ and $\gamma\varepsilon_y$ –are the transverse horizontal and vertical emittances. Formula (1) describes the electron gas trapped in limited space volume and each particle can reach every point in the phase space. Electron gas temperature T in case of disperse motion can be written similar to as it was done in [1]

$$\tfrac{3}{2}Nk_B T \cong N\cdot mc^2\gamma\left[\frac{\gamma\varepsilon_x}{\beta_x}+\frac{\gamma\varepsilon_y}{\beta_y}+\gamma\left(\frac{1}{\gamma^2}-\eta\right)\left(\frac{\Delta p_\parallel}{p_0}\right)^2\right]. \quad (2)$$

Basically the difference connected with the fact that

0-7803-7738-9/03/$17.00 © 2003 IEEE

longitudinal mass is $m_{\parallel}^{-1} = \frac{1}{m\gamma}\left(\frac{1}{\gamma^2} - \eta\right)$, $\eta = \frac{\gamma}{l}\frac{\partial l}{\partial \gamma}$. One can easily recognized here invariants introduced in [7]. So, these invariants are just temperature of moving bunch.

What is important here is that 3D case can be convolved in 2D one by operation *at critical energy only*, when $\eta = 1/\gamma^2$. In this case longitudinal temperature formally becomes equal to zero. As the auto-phasing is not working here, stability can be arranged by feedbacks. Linear motion like in pure focusing channel formally also cannot be treated like 2D, due to $\alpha \neq 0$ in this case. For a two-dimensional phase space emittances now limited by

$$(\gamma\varepsilon_x)(\gamma\varepsilon_y) \geq (1/2)(2\pi\lambda\!\!\!^{-}_C)^2 N. \qquad (3)$$

The last also could be obtained from (1) supposing $\Delta p \cong \hbar / l_b$. For equal emittances this comes to $\gamma\varepsilon_x \geq 2\pi\lambda\!\!\!^{-}_C\sqrt{N/2} = 1.7\cdot 10^{-1}\sqrt{N}$. For $N=10^{10}$, $\gamma\varepsilon_x \geq 1.7\cdot 10^{-6}$ cm rad. We will see lower, that Kayak-Paddle cooler has adequate emittances. Fermi energy is [6]

$$E_F = \frac{p_F^2}{2m} \cong (3\pi^2)^{2/3}\frac{\hbar^2}{2m}\rho^{2/3} \quad \text{or} \quad E_F = cp_F = (3\pi^2)^{1/3}\hbar c\rho^{1/3}, \qquad (4)$$

where $\rho = N/\sigma_\perp^2 / l_b$ is the bunch density. The last works if the particles in the rest frame are relativistic. So for degeneration as the temperature must be $k_B T \leq E_F$. Fermi energy must be small compared with Coulomb's energy of interaction between particles, so $e^2/\rho^{1/3} << E_F$. Substitute here (4) one can obtain that $\rho >> (\alpha/\lambda\!\!\!^{-}_C)^3$, $\alpha = e^2/\hbar c \cong 1/137$. The last condition well satisfied at high densities.

KAYAK-PADDLE COOLER

This type of cooler was introduced in [3] and described in [4]. Here we will give more details on its hardware. Specific shape of this cooler naturally gave its name.

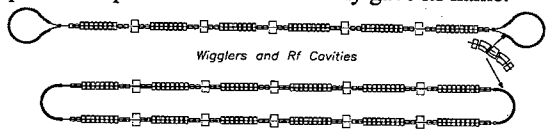


Figure 1: Top: A Kayak-paddle cooler [3]. At the lower part the sketch of more conservative design is represented.

In Fig. 1 straight sections are the same. Two of these sections joint by (semi) arcs. Straight sections made as a sequence of wigglers and accelerating structures, installed along straight line and having the bends at the end. Bends made with many short period divisions to prevent emittance dilution. Conservative scheme is more expensive, but, probably, is easy in tuning.

The cooler gives emittances obtained after considerations of radiation dynamics for a single electron in plane wiggler as [3]

$$(\gamma\varepsilon_x) \cong (1/2)\cdot\lambda\!\!\!^{-}_C\overline{\beta}_x(1+K_x^2/2)K_x/\lambda\!\!\!^{-} \qquad (5)$$

$$(\gamma\varepsilon_y) \cong (1/2)\cdot\lambda\!\!\!^{-}_C\overline{\beta}_y K_x/\lambda\!\!\!^{-}, \qquad (6)$$

where $\overline{\beta}_{x,y}$ –are averaged envelope functions in the wiggler. $K = eH_\perp\lambda_w/2\pi mc^2$, $H_\perp$ –is the magnetic field in the wiggler, λ_w –is the wiggler period. The last formulas together with the cooling time

$$c\tau_{cool} \cong (1/2)\cdot(\lambda\!\!\!^{-2}_w/r_0K^2\gamma), \qquad (7)$$

defines the cooling dynamics under SR. Substitute for estimation $\overline{\beta}_{x,y} \approx 1\,m$, $\lambda\!\!\!^{-} \cong 5cm$, $K \cong 1$, one can obtain for *quantum emittances* the following

$$(\gamma\varepsilon_x) \cong 0.5\cdot 10^{-8} cm\cdot rad, \quad (\gamma\varepsilon_y) \cong 2\cdot 10^{-10} cm\cdot rad.$$

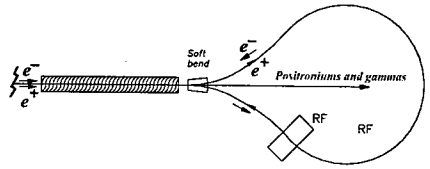


Figure 2: Bending area for co-directionally moving electrons and positrons. RF moved in arcs.

One can see that quantum limitations for the lowest emittance are important here. We also conclude, that coupling is allowable for the cooling business.

Motion in straight section filled with wigglers and RF cavities defined by specific lengthening is $\cong K^2$ times higher, than for free space,

$$\kappa = \gamma\frac{\partial ct}{\partial\gamma} = \frac{(1+K^2)\cdot s}{4\gamma^2}, \qquad (8)$$

So the RF phase shift variation due to deviation of energy from equilibrium while passing the distance *ds* is

$$\delta\varphi = 2\pi\frac{\delta l}{\lambda} = \frac{2\pi}{\lambda}\kappa\frac{\Delta\gamma}{\gamma}\cdot ds, \qquad (9)$$

where λ is the wavelength of accelerating RF structure. As a result one can obtain the pendulum equation for energy deviation in terms of accelerating wavelength

$$\frac{d^2(\Delta\gamma/\gamma)}{d^2(s/\lambda)} = -\frac{2\pi\, eE\lambda\, Sin\varphi_0}{mc^2\gamma}\cdot\frac{1+K^2}{\gamma^2}\cdot\left(\frac{\Delta\gamma}{\gamma}\right). \qquad (10)$$

By this procedure (wigglers and RF) longitudinal frequency can be kept high, so longitudinal motion can act on scene.

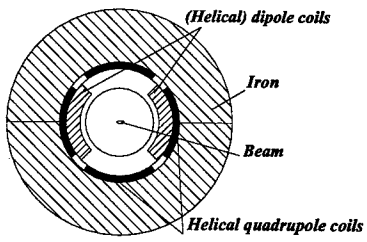


Figure 3: Elements of helical wiggler and helical quadrupole core cold mass. Beam is moving in vacuumed chamber. Windings done with SC wires.

In addition to the helical dipole windings, the core contains the helical quadrupole windings too, Fig.3.

Proposal to use helical quadrupole for particle confinement has a long history and was mostly in use in plasma business. Utilization of helical magnets for particle accelerators described in [8]. Usage of helical quadrupole and dipole is preferable due to simplified technology. Even in absence of artificial coupling there is a coupling by IBS like $(1+K_x^2/2)\varepsilon_y\beta_x=\varepsilon_x\beta_y$, [4]. That is why full coupling allowed here.

GENERATION OF POSITRONIUMS

Cross section for para-positronium has dependence like $\sigma_{\uparrow\downarrow}\cong\pi r_0^2 c/v_{rel}$, where v_{rel} is relative velocity of particles [6]. Ortho-positronium decays in three gammas and has suppression factor as fine structure constant $\sigma_{\uparrow\uparrow}\cong\alpha\sigma_{\uparrow\downarrow}$, $\alpha=e^2/\hbar c$. Transverse velocity in Lab frame is $v_\perp\equiv cK/\gamma$, where K is undulatority factor defined earlier. So the cross section goes to

$$\sigma_{\uparrow\downarrow}\cong\pi r_0^2\gamma/K. \qquad (11)$$

The luminosity for single bunch intrabeam collisions in a cooler could be estimated like [4]

$$L\cong\frac{N^2\cdot c}{4\pi l_b\lambda_w\sqrt{(\gamma\varepsilon_y)\beta_y/\gamma}}. \qquad (12)$$

For parameters considered above, (7) $L\cong10^{31}\mathrm{cm}^2\mathrm{s}^{-1}$. This defines the number of positroniums $\sim10^6\mathrm{s}^{-1}$.

Lifetime of the beam for gamma decay defined by lifetime of positroniums and by direct reaction of two-photon annihilation. The ratio between last ones defined by $\psi^2(0)/n_b$, where $\psi(r)=1/\sqrt{\pi a}\,exp(-r/a)$ is a psi-function of ground state of positronium, and n_b stands for electron-positron density, $a=2\lambda_c/\alpha$ is the Bohr's radius of positronium. Lifetimes of positroniums $\tau_{\uparrow\downarrow}\cong2\hbar/mc^2/\alpha^5\approx1.23\,10^{-10}$ s (para, two gammas), $\tau_{\uparrow\uparrow}\cong1.4\cdot10^{-7}$ s, (ortho, three gammas).

If positronium is not decayed and coming to splitting magnet it can simply continue straight motion out of the ring or be split for electron and positron. The field value in soft bend (Fig.2) must satisfy condition $H\gamma\le e/a^2$. This gives $H\le4.4\cdot10^6/\gamma$ [G]. Otherwise magnetic field of magnet will pull apart electron and positron.

EXTREME RING

Now we are ready to introduce some extreme configuration dedicated exclusively for the purposes of positronium generation Fig. 4. This is basically the same straight sections as in Fig.1 arranged, however for electrons and positrons have individual channels.

Operation of this ring is clear from described above, however. In helical wiggler (undulator) positrons and electrons are rotating in the same direction, what gives same preference with solenoid.

For injection usual hardware can be used. Positrons and electrons obtained in external accelerators, not shown here for simplicity and trivial nature (the same for Fig. 1).

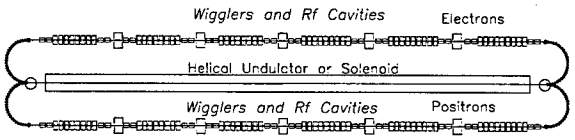


Figure 4: Extreme ring for demonstration of Fermi-degeneration and positronium generation.

This ring gives one ray of gammas and positroniums. Interest for positronium generation is shown in [9] also.

CONCLUSION

In this publication we introduced a plan for dedicated ring construction for investigation of Fermi degeneration in moving beams. This is a part of big scheme for obtaining the ultra-cold beams allowing drastic decrease of number of particles required for collision and/or reduction of the acceleration wavelength.

The work supported by NSF.

REFERENCES

[1] A. Mikhailichenko, "On the physical limitation to the lowest emittance (toward colliding electron- positron crystalline beams)", 7th Advanced Accelerator Concepts Workshop, 12-18 October 1996, Lake Tahoe, CA, AIP Conference Proceedings 398, p.294: CLNS 96/1437, Cornell, 1996.

[2] A. A. Mikhailichenko, "To the quantum limitations in beam physics", CLNS99/1608,March 23, 1999; a paper at PAC99, Proc., vol. 4, pp. 2814-2816.

[3] A.A. Mikhailichenko, "Damping Ring for VLEPP linear collider", III international Workshop on linear Colliders LC91, Protvino, September 17-27, 1991. Proceedings, Edited by V.E. Balakin, S. Lepshokov, N.A. Solyak, Serpukhov, (IFVE). 1991. Serpukhov, USSR: BINP (1991).

[4] A. Mikhailichenko, "Injector for a Laser Linear Collider", CLNS 98/1568, a Talk on 8th Advanced Accelerator Concepts Workshop, Baltimore, Maryland, July 5-11, 1998, pp.891-900..

[5] L.D. Landau, E.M. Lifshitz, "Statistical Physics", Pergamon Press, 1985.

[6] V.B. Berestetskii, E.M. Lifshits, L.P. Pitaevskii, "Quantum Electrodynamics", Pergamon Press, Second Edition, 1982.

[7] A. Piwinsky, "IBS", Proc. 9th Intern. Conf. on High Energy Acc., Stanford, CA, 2-7 May, 1974, SLAC, 1974, p.405.

[8] A.S. Artamonov, Ya.S. Derbenev, N.I. Inozemtsev, "Helical achromatic focusing of a charged particle beam", Zh.Tekh. Fiz. **60**, 156-159 (1990). Transl.: Sov. Tech. Phys. **35**(4) 1990.

[9] I.N.Meshkov, A.N. Skrinsky, NIM A391(1997) 205-209.

Proceedings of the 2003 Particle Accelerator Conference

LONGITUDINAL DYNAMICS IN AN FFAG ACCELERATOR UNDER CONDITIONS OF RAPID ACCELERATION AND FIXED, HIGH RF

S. Koscielniak*, TRIUMF, Vancouver, B.C., Canada
C. Johnstone, FNAL, Batavia, IL 60510, USA

Abstract

A signature of fixed-field acceleration is that the orbit of the beam centroid unavoidably changes with energy. The corresponding change in pathlength results in phase slip relative to the fixed-frequency accelerating waveform. Nevertheless, depending on the location of the fixed-points of the motion, synchronous or asynchronous cross-crest acceleration is possible for a limited number of turns. The possibility of asynchronous rf can be understood simply by realizing that for acceleration in a single pass, the initial cavity phases can be set to exactly compensate for the phase slip. The present work explores the influence of the path-length fixed points and of rf manipulations on the longitudinal dynamics in FFAGs.

INTRODUCTION

In a regime where acceleration is completed in a few turns or tens of turns, cost/technology constraints imply that both the magnetic field and the radio frequency are fixed and that the particle beam transits the radial aperture during acceleration. The fastest acceleration and the most effective use of voltage arises during on- or cross- crest operation. If one abandons the constraint of isochronous orbits, as is inevitable for highly-relativistic beams, there is much range for creativity in design of the magnet lattice and the phase-slip profile. However, simplifying concepts such as rf buckets and phase stability, etc., no longer apply.

A very important feature of fast acceleration is the freedom to cross betatron resonances. In a non-scaling Fixed-Field Alternating Gradient (FFAG) accelerator, the optics change slowly with energy, crossing resonance tunes, and the orbit pathlength is parabolic as a function of energy. Variable optics allow the machine lattice to be built from linear magnetic elements only with a corresponding large dynamic aperture. The nonscaling FFAG is of particular interest because it provides an opportunity to consider the nature and location of fixed points of a strong nonlinear oscillator as the model for the longitudinal dynamics.

DIFFERENCE EQUATIONS

On the "central orbit" accelerating cavities are spaced a distance L_0 apart and are driven at angular frequency ω with peak voltage V. In the ultra-relativistic limit, non-isochronism results only from path length dependence on energy $\Delta L(E)$. We define $T_0 = L_0/c$ and $\Delta T = \Delta L/c$ with the speed of light c. Let the iteration index be n. We introduce a relative time coordinate $T_n = t_n - nT_s$ where $T_s = 2m\pi/\omega$ and $m = \text{Integer}[\omega T_0/2\pi]$. In the moving frame, the energy E and arrival times are

$$\begin{aligned} E_{n+1} &= E_n + eV\cos(\omega T_n) \\ T_{n+1} &= T_n + \Delta T(E_{n+1}) + (T_0 - T_s)\,. \end{aligned} \quad (1)$$

In the *synchronous* case L_0 is the only free variable; apart from the choice of a harmonic number, ω (and hence T_s) is determined uniquely from L_0. In the *asynchronous* case both L_0 and ω retain the status of free variables.

Realistic equations

Equations (1) are *toy* equations. They apply either to a linac of indefinite length, or to the interaction with a single cavity in a cyclic accelerator. However, the condition of periodicity in a cyclic accelerator (equipped with a string of cavities) alloyed with near-sychronism allows for greater sophistication in the choices for the rf.

Let $\omega T_s = (2m + q)\pi$ where m is an integer and q is a fraction. Let the N_c cavities each have some initial phasing ϕ_n on the first turn. The energy increment is $\propto \cos[\omega T_n + (nq\pi + \phi_n)]$. If we set $\phi_n = -nq\pi$ then the simple form of equation (1) is recovered. At the end of the first turn, the beam starts to return through the same cavities a second time. Maintaining synchronism has two consequences. Firstly, for the continued cancellation between $(N_c + k)q\pi$ and ϕ_k it follows that $N_c q = 2M$ with integer $M = 0, 1, 2, \ldots$. Secondly, if one is to avoid a jumping of the phase between turns then $\text{Modulo}[N_c\delta\phi, 2\pi] \approx \delta\phi = \omega(T_0 - T_s)$.

In the *synchronous* case with zero inter-turn phase jumps these conditions lead to a discrete set of frequencies ω. The usual condition is to set $T_s = T_0$. Typically the reference energy does not rise linearly, and the reference phase varies in a roughly sinusoidal fashion. This approach has the advantage that phase deviation moduli never exceed $\pi/2$ and negative energy increments are not encountered.

However, it can be advantageous to break the condition of zero inter-turn phase jump, and to loosen the stricture on q and ϕ_k. In this *asynchronous* case, each line ω is broadened into a narrow continuum. Careful choice may narrow the excursions about the crest of the wave and facilitate a reference orbit for which $\cos(\omega T_n + \phi_n) = 1 \;\forall n$. (2)

Best frequency and initial phases

Suppose acceleration is to be accomplished in two turns. One may fake an exact (2) by (i) setting the fixed radiofre-

*TRIUMF receives federal funding via a contribution agreement through the National Research Council of Canada

0-7803-7738-9/03/$17.00 © 2003 IEEE

quency to the ideal value for the second turn, and (ii) by adjusting the initial phases at injection so that cavity phases are correct during the first-turn passage of the reference particle. When acceleration extends over more than two turns one may hope to share the deviations from (2) more or less equally among the turns by careful choices. This ambition becomes less achievable, the larger is the number of turns N_t. "Best frequency and phases strategy" refers to maximising $\mathcal{S} = \sum_{n=1}^{N_t \times N_c} \cos[\omega T_n^{\rm ref} + \phi_k]$ with respect to ω and ϕ_k under the *assumption* that we attempt to force the reference particle to arrive at $\cos(\phi) = 1$. This is accomplished in a statistical sense; although many terms are close to unity others will deviate. Generally, as the number of turns is increased so the distribution grows until zero or even negative terms appear in the sum $\mathcal{S}$ (i.e. phase deviation moduli exceed $\pi/2$).

INFLUENCE OF FIXED POINTS

To what degree equations (1) are useful for acceleration depends on the nature and location of the sets of first-order fixed points which are the solutions of $E_{n+1} = E_n$ and $T_{n+1} = T_n$. In what follows, we shall describe how the algebraic form $\Delta T(E)$ influences cross-crest acceleration. Manipulation of $\Delta T(E)$ is really a matter for the magnet lattice designer, so part of the discussion is hypothetical.

Synchronous and asynchronous rf are equally valid. However, for examples we adopt the synchronous case because the absence of inter-turn phase-jumps will generate a simpler and more continuous phase space. Nevertheless, the influence of the $T_{n+1} = T_n$ fixed points is equally important to the asynchronous case.

Linear path dependence

In the case of a scaling, radial-sector FFAG, orbits are staggered radially outward as a function of momentum and the orbital change can be approximately linear with energy. For linear path dependence $\Delta T = \alpha(E - E_c)$, equations (1) correspond to motion within a stationary r.f. bucket. E_c is the energy of the central orbit. A beamlet injected at bucket bottom will be accelerated to the bucket top during one half synchrotron oscillation. The beam twice crosses the crest of the voltage waveform; and those moments correspond to the maximal acceleration rate. The minimum voltage occurs when bucket height is set equal to the difference of extraction and injection energies.

Quadratic path dependence

The case of quadratic path length dependence on energy is important since it corresponds to that of the non-scalling FFAG type accelerator, which is considered for rapid acceleration of muons[1, 2, 3]. Figure 1 show the phase space generated by the model equations $y \propto (E - E_c)$ and

$$dy/ds \propto \cos(x\pi/2)\ ,\ dx/ds \propto y^2 - 1\ . \qquad (3)$$

There are two elliptic and two hyperbolic fixed points. There is libration and rotation, as in the linear case, but a striking new feature of the phase space is a serpentine libration that flows along $y = +2, -2, +2, -2, \ldots$ while x increases without limit. This meander feature, emphasised in figure 2, can be used to augment the range of acceleration. A beamlet introduced at $(x, y) = (-1, -2)$ may be later extracted at to $(1, 2)$. Because there are two $T_{n+1} = T_n$ fixed points, there are two reversals of the phase-slip direction. Thi is an advantage because it allows the beam to cross the waveform crest three times before the phase slips to values where the beamlet is decelerated. The width of the meander varies weakly with the voltage.

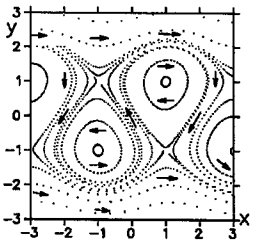


Figure 1: Phase space of quadratic pendulum

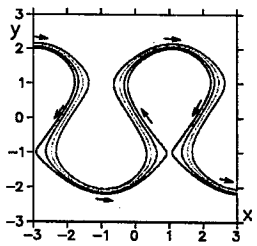


Figure 2: Manifold of serpentine libration

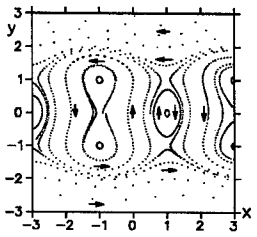


Figure 3: Phase space of cubic pendulum, $\alpha = 1$

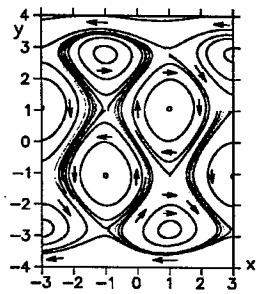


Figure 4: Phase space of quartic pendulum, $\alpha = 1/3$

Cubic path dependence

Consider the model equations:

$$dy/ds \propto \cos(x\pi/2)\ ,\quad dx/ds \propto y(1 - \alpha^2 y^2)\ . \qquad (4)$$

As the cubic parameter α is increased, the $y \neq 0$ fixed points come to dominate the motion. For example $\alpha = 1$ in figure 3. The acceleration range diminishes but some of the phase-space paths become almost vertical which facilitates faster acceleration. Moreover, there are some phase profiles which cross the crest four times which implies more effective use of the accelerating voltage.

Quartic path dependence

Consider the model equations:

$$dy/ds \propto \cos(x\pi/2)\ ,\quad dx/ds \propto y^2(1-\alpha^2 y^2) - 1\ . \qquad (5)$$

As α approaches $\simeq 1/3$, the quartic fixed points (i.e. at large $|y|$) begin to dominate the phase space motion; and a bi-serpentine libration emerges with twice as many manders, as shown in figure 4. The beamlet injected at

$(x, y) = (1, -3.5)$ is extracted at $(-1, 3.5)$. The phase profile crosses the crest of the waveform five times, and the acceleration range is extended to $y = \pm 3.5$. Thus four reversals of phase-slip direction is advantageous; because it allows the beamlet to cross the crest five times before the phase slips to values where deceleration occurs.

From these examples we have seen the general features: (i) number of crest crossings equal to one plus the order of the polynomial, and (ii) meanders only occur for even orders.

PARTICLE TRACKING

As a particular example, we take a non-scaling FFAG of 2 km circumference and path length variation $\Delta L(E)$ up to 50 cm (120° of rf phase). The machine has 300 cells and 200 MHz rf cavities. Particle tracking was completed both for asynchronous and synchronous rf for acceleration completed in a number of turns ranging from two to ten. Figures 5,6 and figs. 7,8 show the beam centroid motion for the asynchronous and synchronous cases, respectively.

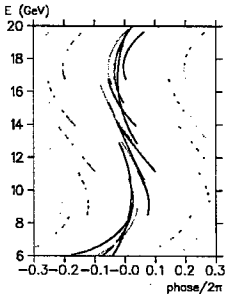


Figure 5: Phase portrait for 2–5 turns acceleration.

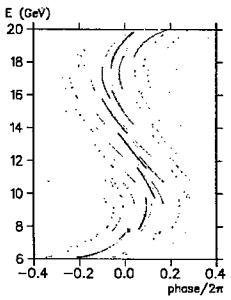


Figure 6: Phase portrait for 6–9 turns acceleration.

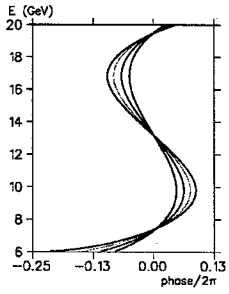


Figure 7: Phase portrait for 3–6 turns acceleration.

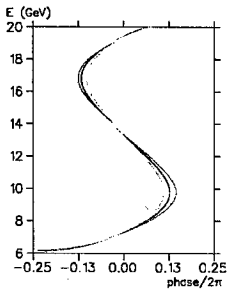


Figure 8: Phase portrait for 7–10 turns acceleration.

Table 1 captures the variation of output emittance with voltage per turn and number of turns. The table is unable to indicate the emittance quality; to what degree the phase space is distorted, whether there are voids or tails, etc. However, an indication of relative quality is given in figures 9,10 and 11,12 for asynchronous and synchronous rf, respectively.

For five or less turns, the output emittance for the asynchronous scheme is superior. For six and seven turns, the emittance quality is comparable for the two schemes. For eight or more turns, the output emittance is superior for the synchronous rf scheme.

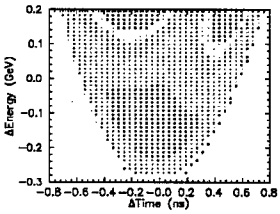


Figure 9: Input emittance

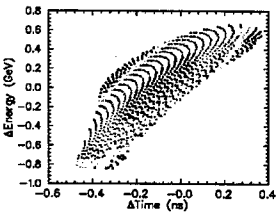


Figure 10: Output emittance

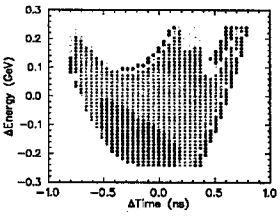


Figure 11: Input emittance

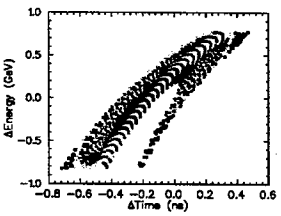


Figure 12: Output emittance

Table 1: Comparative performance

Turns #	over factor	volts GV	emittance eV.s [Asynk]	emittance eV.s [Synk]
4	1.10	3.850	0.2590	0.3150
5	1.15	3.220	0.5114	0.3520
6	1.15	2.683	0.4701	0.4580
7	1.20	2.400	0.4646	0.4518
8	1.25	2.187	0.1479	0.2962
9	1.30	2.022	0.1806	0.2684
10	1.30	1.820	–	0.1017

CONCLUSION

The "fast regime" in a fixed-field accelerator opens a new frontier of beam dynamics in which non-linear pathlength variation with energy and fixed radio-frequency combine to give a longitudinal phase space that is both useful for acceleration and rich in new physics. We have categorized the motion in terms of its fixed points; and we have developed a context for the "best frequency and phases" rf strategy that emphasises the distinction between synchronous and asynchronous rf. Finally, for the quadratic pathlength dependence in a non-scaling FFAG we have compared the relative performance, in identical machines, of synchronous and asynchronous rf schemes.

REFERENCES

[1] C.Johnstone and S.Koscielniak: *Recent Progress on FFAGs For Rapid Acceleration*, proceedings of Snowmass 2001, 30 Jun-21 Jul 2001, Snowmass Village, CO.

[2] J.S. Berg: *Longitudinal Reference Particle Motion in Nearly Isochronous FFAG Recirculating Accelerators*, ibid.

[3] C.Johnstone and S.Koscielniak: *FFAGs for Rapid Acceleration*, accepted for publication NIM-A Nov. 2002.

THE INTEGRATION OF LIQUID AND SOLID MUON ABSORBERS INTO A FOCUSING MAGNET OF A MUON COOLING CHANNEL *

M. A. Green, Lawrence Berkeley National Laboratory, Berkeley CA, USA; E. L. Black, M. A. Cummings, and D. M. Kaplan, Illinois Institute of Technology, Chicago IL, USA; S. Ishimoto, KEK, Tsukuba, Ibaraki, Japan; J. H. Cobb, W. Lau and S. Yang, Oxford University, Oxford, UK; R. B. Palmer, Brookhaven National Laboratory, Upton NY, USA

Abstract

This report describes how one can integrate the muon absorber with the focusing coils of a SFOFO muon cooling channel [1]. The absorber material must be a low Z material that reduces the muon momentum with minimum scattering. The best materials to use for muon ionization cooling absorbers are hydrogen, helium, lithium hydride, lithium, and beryllium. Hydrogen or helium in an absorber would normally be in the liquid state. Lithium hydride, lithium, and beryllium would normally be in the solid state. This report limits the absorber materials discussed to hydrogen, helium, lithium, and beryllium. In order to achieve the same level of ionization cooling with a solid absorber as a liquid hydrogen absorber, the beta of the muon beam must be reduced more than a factor of two. This affects both the designs of the absorber and the magnet around it. Reducing the beam beta reduces the momentum acceptance of the channel. Integration of a liquid hydrogen absorber and solid absorbers with a superconducting focusing solenoid is discussed. The choice of absorber material affects the design of the superconducting focusing magnet and the superconductor that is used to generate the magnetic field.

MUON IONIZATION COOLING

Ionization cooling has been selected as a cooling method, because stochastic cooling, electron cooling and laser cooling take a long time (>1 sec) compared to the life of a muon (2.1 μs for a muon at rest). When a muon enters a material, energy is lost along the track. This means that both longitudinal and transverse momentum are lost as the muon passes through the cooling material. If the muon is re-accelerated in the longitudinal direction, the loss of transverse momentum is retained and beam cooling has been achieved. Coulomb scattering of the muon beam in the material counters the effect of cooling. If the emittance lost is greater than emittance gained due to scattering, net ionization cooling results.

An equation that describes ionization cooling can be stated as follows [2]:

$$\frac{d\varepsilon_{x,N}}{dz} = -\frac{1}{\beta^2}\frac{\varepsilon_{x,N}}{E}\left[\frac{dE}{dz}\right] + \beta_\perp \frac{(0.014GeV)^2}{2\beta^3 E m_\mu L_R} \quad (1)$$

where $\varepsilon_{x,N}$ is the muon emittance; $\beta = v/c$; E is the muon energy; $\beta_\perp$ is the transverse beam beta, m is the mass of a muon and L_R is the radiation length of the absorber.

The term with the minus sign on the right hand side of Equation 1 is the cooling term; the term on the right hand side of Equation 1 with the plus sign is the coulomb scattering term. For rapid ionization cooling one needs strong focusing in order to achieve a low value of $\beta_\perp$ and on wants to have a high value of L_R, which implies that one wants to use a low Z material for doing the cooling. In general, cooling is proportional to the number of electrons in the atom. Coulomb scattering is proportional to the number of charged nucleons in the atom squared. Thus hydrogen is the best material to use for ionization cooling. Table 1 compares the properties of a number of liquid and solid absorbers.

Table 1. A Comparison of the Properties of Various Absorber Materials

Material	dE/dx (MeV g-1 cm^2)	L_R (g cm^{-2})	Density (g cm^{-3})	Length for 10 MeV of Absorption (cm)	Equilibrium Cooling Factor
Liquid. Hydrogen	4.12	61.3	0.0708	34.28	1.000
Liquid Helium	1.94	94.3	0.125	41.24	0.524
Lithium Hydride	1.89	79.3	~0.78	6.78	0.352
Lithium	1.65	82.8	0.534	11.35	0.268
Beryllium	1.61	85.2	1.848	3.36	0.172
Aluminum	1.62	24.3	2.70	2.28	~0.05

0-7803-7738-9/03/$17.00 © 2003 IEEE

Table 1 compares various liquid and solid materials that can be used for muon ionization cooling. The last column in Table 1 compares the relative emittance reduction to the equilibrium value (the value where coulomb scatting exactly matches the cooling term). From Table 1, one can see that hydrogen should be twice as good as any other cooling material. This is not completely true because liquid hydrogen must in a leak tight container. Helium must also be contained.

Safety requirements dictate that a hydrogen absorber must have two sets of windows, the primary hydrogen-windows, and safety-windows. The two windows are separated by a vacuum space that is directly connected to a volume that is at least 50 times the absorber volume. Safety standards dictate that both windows must be designed to have a burst pressure that is four times the design pressure for the windows. Safety standards require the hydrogen absorber to have a design working pressure of 0.17 MPa (25 psig). If the hydrogen and safety windows are fabricated from 6061 aluminum, their thickness will be of the order of 300 μm. If an alloy in the 2090 or 2190 series can be used, the window thickness can be reduced to about 130 μm. There are two question concerning the 2090 and 2190 aluminum alloys. Can they be machined to a thickness of 130 microns and can they alloy be welded to 6061 aluminum? For an absorber that is 300 mm thick, the 6061 windows will reduce the relative cooling factor from 1.000 to 0.693. If the 2190 series of aluminum windows can be used the cooling effectiveness is increased to 0.815.

If helium is used to cool the muons, the total window thickness can go down a factor of four. The effectiveness factor for helium absorbers with 6061 and 2190 windows would be 0.447 and 0.478 respectively. Testing an absorber with liquid helium is an option in an experiment such as MICE [3], but the use liquid helium absorber are limited by the transfer of heat from the absorber to a cooling medium of two-phase liquid helium [4]. Table 2 compares the thermal conductivity k and the available ΔT for heat transfer out of the absorber for five candidate absorber-materials [5]. The product of ΔT and k is the heat transfer potential for the absorber. The higher this product the better. In general, a helium absorber is not viable for a high power cooling channel or a ring cooler.

Of the materials shown in Table 1, only lithium hydride is questionable in its application for absorbers. Lithium hydride is not as reactive as lithium, but it produces more hydrogen when it reacts with water. Lithium hydride generally comes in pellet form, which can be a safety hazard. Lithium hydride melts at 680 C decomposes at about 745 C. Lithium hydride would be difficult to handle in the molten state. It also may be difficult to encase lithium hydride in aluminum because of its tendency to form lithium-aluminum-hydride. Pellets of lithium hydride have poor thermal conductivity. The thermal conductivity is variable depending on the hydroxide content. Lithium hydride should not be ruled out without more study, but it has not been included in the list of absorber materials shown in Tables 2 and 3.

Lithium and beryllium both appear to be viable materials for ionization cooling. Lithium must be encased to prevent oxidation and reaction with water. Thin aluminum windows (say 50 μm) can protect the lithium absorber from the air. The case around the absorber can carry coolant for the absorber. (Oil is a recommended coolant for lithium.) Lithium in the molten state (melting T = 180.5 C) can be used as an absorber. Molten lithium is used in lithium lenses, which cool the beam while reducing the beam beta.

Beryllium, while toxic in the form of dust, can be handled safely in block form. The melting temperature of beryllium is 1553 K (1278 C), which means that radiation cooling is an option for many absorbers. Water-cooling pipes can be attached a copper sheath around a beryllium absorber. No absorber windows are needed.

The use of solid absorbers is only attractive if one can reduce the transverse beam beta $\beta_\perp$. A strong focusing solenoid is needed to reduce the beam beta in a solid absorber. A small beta in one part of a cooling cell implies that there will be a large beam beta in another part of the cooling cell. The large beam beta in another part of the cooling cell (such as the RF cavity iris) will limit the momentum acceptance of the cooling channel. This suggests that the use of solid absorbers would be more attractive in later cooling stages of a cooling channel.

COOLING IN MICE

The proposed Muon Ionization Cooling Experiment (MICE) allows one to compare the cooling performance of various absorber materials. The predicted cooling for the MICE channel with an average momentum of 200 MeV/c and a beam beta of 420 mm in the absorber is shown in the first column of Table 2. The MICE channel cooling channel cools far from the equilibrium emittance. This is apparent when one compares hydrogen and helium cooling. Note: the beam beta in the MICE channel is too large for any cooling to occur with an aluminum absorber. MICE should be able to demonstrate cooling using hydrogen, helium, and low Z solid absorbers.

Table 2. A number of Material Parameters For Five Absorber Materials

Material	MICE Cooling Factor (%)	k ($W\ m^{-1}\ K^{-1}$)	ΔT (K)
LH_2	-12.9	~0.113	~5.0
LHe	-11.0	~0.029	~0.7
Li	-9.5	85.9	~120
Be	-6.0	218	>800
Al	+13.4	236	>400

Table 3. Focus Coil Current Density, Focus Coil Peak Induction, and the MICE Channel Momentum Acceptance as a function of Beam Beta at the Absorber Center

$\beta_\perp$ (mm)	Focus Coil J (A mm^{-2})	Coil B_p (T)	$\Delta p/p$ (±%)
420	107	6.27	25
255	127	7.44	20
160	141	8.26	17
103	156	9.14	14
55	177	10.37	8

Average muon momentum = 200 MeV/c

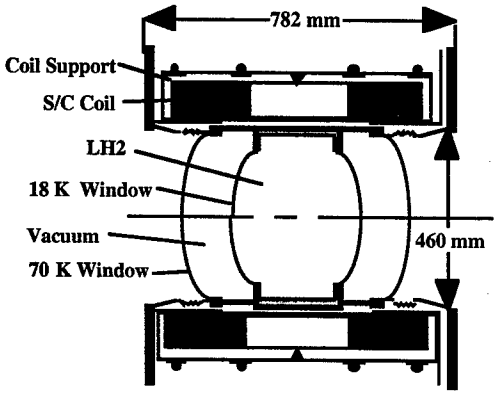


Figure 1. A Cross-section of a MICE Focusing Magnet around a Liquid Hydrogen Absorber

Simulations of the MICE channel have been made for various cases where the beam beta is changed in the absorber [6]. Table 3 shows the MICE focusing coil current density and peak induction in the windings for various values of the absorber beam beta for a muon beam with an average momentum of 200 MeV/c. The final column shows the momentum acceptance of the MICE channel as a function of beam beta at the center of the absorber within the focusing magnet.

Since the MICE coils shown in Figure 1 are made from niobium titanium, the average coil current densities and peak induction in the windings shown in Table 3 are not realistic for beam betas less than 250 mm. In order to do the lowest beam beta experimental cases in MICE, the average momentum of the MICE beam must be reduced. The case where the transverse beam beta is 55 mm, will have an average beam momentum of 140 MeV/c.

Figure 2 illustrates how one might modify the MICE magnets so that solid absorbers can be used. Figure 2 shows a niobium tin insert magnet installed in the niobium titanium MICE coils. The current density in the niobium tin winding can be as high as 150 A mm^{-2}, for a peak induction in the niobium tin coil as high as 11 T.

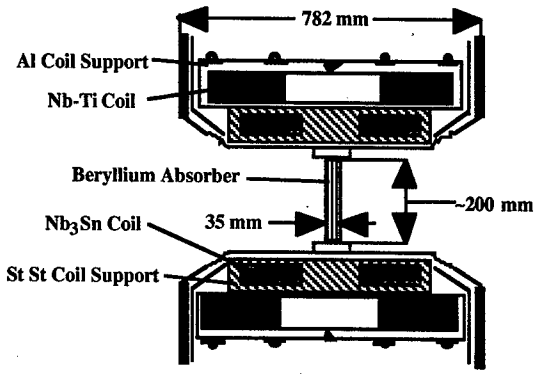


Figure 2. A Cross-section of the MICE Focusing Magnet with a Nb_3Sn Insert Coil and a Beryllium Absorber

Figure 2 illustrates the kind of magnet design that must be considered in order to utilize solid absorbers in the later stages of a muon cooling channel, where a lower momentum acceptance can be tolerated.

CONCLUDING COMMENTS

Hydrogen is the best material to use for ionization cooling of muons. The use of liquid hydrogen is advised in the first stages of a muon cooling channel or ring cooler. Solid absorbers can be used to effectively cool muons, provided one is willing to operate the focusing magnets at higher fields and tolerate a lower momentum acceptance. The focusing magnet around the absorber can be smaller than the magnet proposed for the level II study and MICE. The inner focus coils will probably have to be made from niobium tin.

ACKNOWLEDGEMENT

This work was supported by the Office of Science, United States Department of Energy under DOE contract number DE-AC03-76SF00098.

REFERENCES

[1] S. Ozaki, R. B. Palmer, M. S. Zisman and J. Gallardo Eds, "Feasibility Study II of a Muon Based Neutrino Source," BNL-52623, June 2001

[2] D. M. Kaplan, "MuSat and MICE Experimental Verification of Ionization Cooling Techniques," presented at the First International Neutrino Factory Summer Institute, Cosner's House, Abingdon UK 29 June 2003

[3] "A Proposal to the Rutherford Appleton Laboratory, an International Muon Ionization Cooling Experiment (MICE)," proposed by the MICE Collaboration, 15 December 2002

[4] M. A. Green, "Comments on Liquid Hydrogen Absorbers for MICE," Lawrence Berkeley Lab Report LBNL-52082, Jan. 2003

[5] J. H. Cobb, "Thermal Transients in Absorber Materials," Oxford University, August 2002

[6] R. B. Palmer, and R. Fernow "200 MHz Cooling Experiment Design Version 4," October 23, 2002 version of the MICE channel

LATTICIES FOR MILLI-eV NEUTRAL MOLECULES *

H.Nishimura, G.Lambertson, J.G.Kalnins, and H. Gould, LBNL, Berkeley, CA94720, USA

Abstract

An electric dipole moment of neutral polar molecules interacts with non-uniform electric field; therefore it is possible to design electrodes that replace magnets for charged particles and a lattice that is a series of electrodes to circulate such molecules. We describe our recent result of designing a ring for CH_3F in comparison with our previous design for ND_3.

STARK POTENTIAL

The interaction between the dipole moment of a neutral polar molecule and an external electric field is defined by the Stark potential W. As a dipole always lines up to the field direction, the potential W is a function of the field strength $E = |\vec{E}|$ of the external field $\vec{E}$. The x force is given by: $F_x = -\partial W/\partial x = -dW(E)/dE \cdot \partial E/\partial x$ and similarly for y and z. The molecule is called strong-seeking if $dW(E)/dE > 0$, or weak-seeking if $dW(E)/dE < 0$. ND_3 is an example of the weak-seeking case with the following potential:

$$W = \sqrt{C_1 + C_2 E^2} - C_3 - C_4 E^2 \qquad (1)$$

where $E = |\vec{E}|$, $C_1 = 2.77 \cdot 10^{-49}, C_2 = 6.35 \cdot 10^{-60}, C_3 = 5.26 \cdot 10^{-25}$ and $C_4 = 1.78 \cdot 10^{-38}$.
CH_3F is an example of the strong-seeking case with the following potential:

$$W = \frac{C_1 w_a^2 R}{1 + C_2 w_a} \qquad (2)$$

where $w_a = d_e E/R, d_e = 1.86 \times 3.36 \cdot 10^{-30}, R = 0.85 \times 1.99 \cdot 10^{-23}, C_1 = -0.2085$ and $C_2 = 0.2445$.

ELECTRODE

There are 3 kinds of static electrodes shown in Fig.1. The type 1 and 2 electrodes are lenses to focus or defocus the beam in the transverse planes. For weak-seeking molecules, Type 1 is horizontally defocusing, 2 is focusing, and 3 deflects towards the right. For strong-seeking molecules, the forces are reversed. The fields from these electrodes are gradients of the following potential:

$$\begin{aligned}\Phi(x,y) = \; & -E_0(y + A_2 y + A_3(x^2 y - \tfrac{1}{3}y^3) \\ & + A_5(x^4 y - 2x^2 y^3 + \tfrac{1}{5}y^5))\end{aligned} \qquad (3)$$

* Work on the synchrotron storage ring is supported by the Director, Office of Science, of the U.S. Department of Energy, and work on the linear decelerator is supported by the Director, Office of Science, Office of Basic Energy Sciences, of the U.S. Department of Energy; both under Contract No. DE-AC03-76SF00098.

In Type 3, $E_0 A_2$ determines the bending radius and A_3 becomes a knob to adjust the focusing forces. In arc sections we use cylindrical geometry for calculations and the potential differs slightly from Eq.3.[2]. There is also focusing in

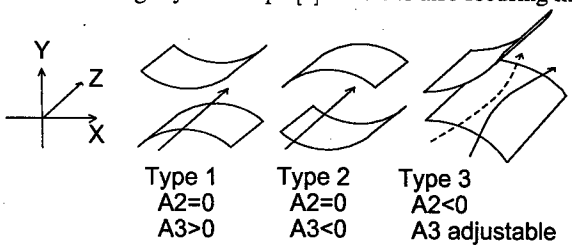


Figure 1: Electodes

the direction of the the fringe field at each longitudinal end of an electrode. It is approximated for small excursions, numerically integrated and replaced by a thin lens on or near the edge. It acts as a vertically focusing lens for weak-seeking molecules and defocusing for strong-seeking ones. See [2] and [3] for details.

STORAGE RING

Design Principles

Requirements We require the lattice to provide the following.
(1)Dispersion-free long straight sections for injection, RF bunchers and beam experiments.
(2)Adjustable betatron tunes and beta functions.
(3)Tolerance for the effect of the gravity force.

Solutions Solutions we have adopted are:
(1)Achromatic arc: Adjusting the horizontal betatron phase advance in each arc to be a multiple of 2π, the straight sections become dispersionless. The vertical phase advance is also tuned in the same manner to keep the vertical closed-orbit distortion(COD) due to the gravity in a reasonable range.
(2)A triplet of focusing/defocusing straight electrodes on each end of long straight sections to adjust betatron tunes and beta functions.
(3) Vertical orbit correction to compensate the effect of gravity if needed.

Storage Ring for ND_3

In case of a weak-seeking molecule, the bending electrode can be focusing in both horizontal and vertical planes. Therefore, it is possible to design a storage ring lattice with arc electrodes that bend the beam through a large angle [1]. The ring has the racetrack shape shown in Fig.2. Straight

0-7803-7738-9/03/$17.00 © 2003 IEEE

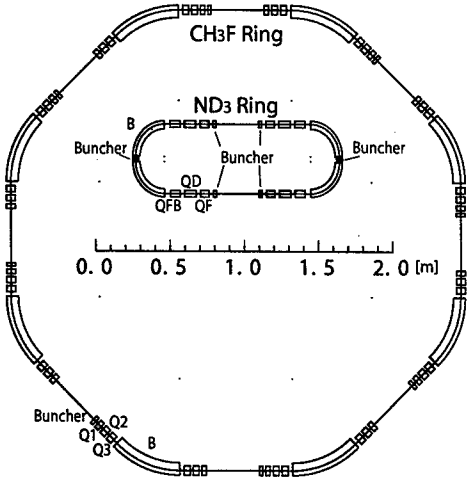


Figure 2: Storage Ring Lattices

sections are 40 cm long. Acceptances are 35 mm · mrad horizontal and 71 mm · mrad vertical at its nominal velocity of 90 m/sec. Other ring parameters are listed in Table.1. Simple adjustments allow one to reduce the velocity to 60 m/sec [2].

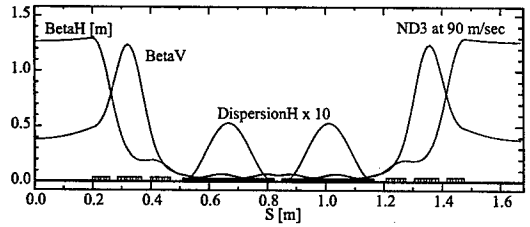


Figure 3: Beta and Dispersion of the ND3 Ring

Storage Ring for CH_3F

For the strong seekers, a bending electrode can not focus in both planes simultaneously. Therefore, the arc must be an alternating sequence of focusing(BF) and defocusing(BD) bending electrodes; four cells with 90 ° phase advance make up a 45 ° arc sector with radius 60 cm. Parameters listed in Table.(2). As a result, the CH_3F ring becomes much larger than the ND_3 ring as shown in Fig.2.

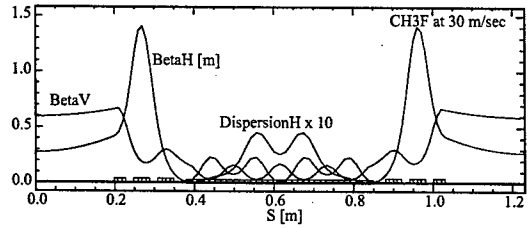


Figure 4: Beta and Dispersion of the CH3F Ring

The horizontal beta becomes large at Q2 which would cause strong amplitude-dependent tune shift. Therefore, the A_5 component is introduced to Q2 to reduce the amplitude-dependent tune shift and increase the dynamic aperture.

Table 1: Ring Parameters

Paramter	ND_3	CH_3F
Circumference (m)	3.357	9.850
Circulation period (s)	0.0380	0.3121
Velocity in free space (m/s)	90.0	30.0
Symmetry of the ring	2	8
Bending radius (m)	0.20	0.60
Long Straight Section (m)	0.40	0.40
Beta horizontal [1]:β_x (m)	1.264	0.274
Beta vertical [1]: β_y (m)	0.513	0.596
Horizontal dispersion[1] (m)	0.001	0.000
Horizontal tune: ν_x	5.250	13.368
Vertical tune: ν_y	5.200	10.398
Chromaticity - H: ζ_x	-0.0885	-73.8
Chromaticity - V: ζ_y	-0.0942	-38.1
Momentum compaction: α	-0.99	-0.899
Dynamic aperture - H: a_x (mm)	6.5	1.75
Dynamic aperture - V: a_y (mm)	6.0	3.50
Acceptance - H: ϵ_x (mm - mr)	35	11
Acceptance - V: ϵ_y (mm - mr)	71	21

Table 2: Bending Electrode Parameters for CH_3F Ring, E_0 in MV/m, R and L in cm, T in degree.

	Eo	A_2	A_3	R	T	L
BF	4.00	-10.55	-2296	60	5.625	7.85
BD	4.00	-10.55	2343	60	5.625	7.85

The effect of gravity becomes an issue because of the lower velocity of the molecule. In case of the ND_3 ring, a small 0.17 mm displacement of the closed orbit did not require orbit correction. Note that in the CH_3F ring, the sequence inside the triplets is changed to D-F-D as listed in Table 3. This reduces the effects of edge focusing but the vertical displacement still becomes as large as 2.6 mm and the dynamic aperture is completely killed. A vertical kick is needed, one choice is to shift Q2 downwards 0.24 mm to reduce the orbit distortion to 0.26 mm as shown in Fig.5. The dynamic aperture in Fig.6 is then unaffected by gravity.

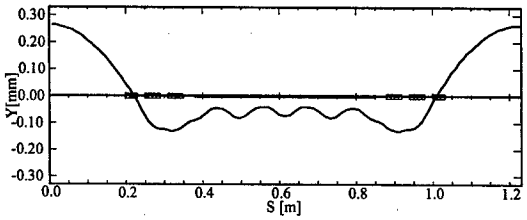


Figure 5: Corrected Vertical COD of the CH3F Ring

A buncher is a pair of parallel plates with field pulsed in an offset triangular waveform that sweeps between zero

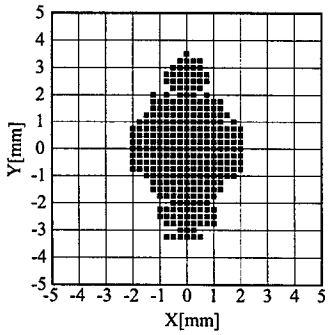


Figure 6: Dynamic Aperture of the CH3F Ring

Table 3: Parameters of Straight Electrodes for CH_3F Ring, E_0 in MV/m and L in cm.

	Eo	A_2	A_3	A_5	L
Q1	3.34	0	2000	0	3.0
Q2	3.71	0	-2000	-1.283E+6	4.0
Q3	2.85	0	2000	0	4.0

and 1.4 MV/m at the bunch frequency, 625 Hz. Eight bunchers in the ring (see Fig.2), each 1 cm long, provide 205 longitudinal buckets to capture bunches that have $\pm 1.2\%$ velocity spread.

Source and Intensity

Molecules from a source, typically at 310 m/s, must be decelerated for injection into a ring. A linear decelerator array for this purpose consists of a series of pulsed field regions. A molecule of CH_3F will enter each region at zero field and decelerate upon exit at full field. This sequence is reversed for ND_3. An a.g. pattern of static focusing lenses must be added to confine the beam transversely; for CH_3F these must also overcome the vertical defocusing from fringe fields. 120 pulsed decelerator electrodes and an equal number of lenses are required making an array of 15.1 meter length. Bunches that emerge from this are 8 mm long spaced 48 mm. They are injected into 205 buckets formed by the bunchers in the ring. The injection kicker electrode is a section of arc guide fields that is turned off rapidly after the buckets in the ring are filled. In the deceleration process, emittances of the bunches in the three orthogonal momentum-displacement spaces are conserved. These become the acceptances for molecules at the source and are amply filled by a typical xenon-seeded source. A CH_3F bunch will have 1×10^7 molecules. At the 625 Hz bunch rate this gives a circulating current of 6×10^9 molecules/sec.

DISCUSSION

Designing a storage ring lattice for a strong-seeking molecule is far more complex than that for a weak-seeking one. The arc sectors must have an alternating-gradient structure. The higher-order component in a lens field, A_5 in this case, plays a crucial role in attaining a reasonable dynamic aperture. The vertical closed orbit due to gravity has to be corrected. However, in this initial effort, solutions are found.

ACKNOWLEDGEMENTS

We thank Swapan Chattopadhyay and Ying Wu for early assistance with this work, and David Robin for useful discussions.

REFERENCES

[1] H. Bethlem, G. Berden, and G. Meijer,"Decellerating Neutral Dipolar Molecules" Phys. Rev. Lett. 83, 1558 (1999).

[2] H. Nishimura, G. Lambertson, J. G. Kalnins, and H. Gould, "Feasibility of a synchrotron storage ring for neutral polar molecules" to be published in Rev. Sci. Instr. Preprint:LBNL-51597, http://arxiv.org/abs/physics/0212044

[3] G. Lambertson, "Beam Dynamics in a Storage Ring for Neutral (Polar) Molecules" in this proceedings, Portland, May 2003.

SHAPING OF PULSES IN OPTICAL GRATING-BASED LASER SYSTEMS FOR OPTIMAL CONTROL OF ELECTRONS IN LASER PLASMA WAKE-FIELD ACCELERATOR*

Cs. Tóth#, J. Faure, C. G. R. Geddes, J. van Tilborg, and W. P. Leemans, L'OASIS Group,
Accelerator and Fusion Research Division, Lawrence Berkeley National Laboratory,
BLDG 71R0259, 1 Cyclotron Rd., Berkeley, CA 94720 USA

Abstract

In typical chirped pulse amplification (CPA) laser systems, scanning the grating separation in the optical compressor causes the well know generation of linear chirp of frequency vs. time in a laser pulse, as well as a modification of all the higher order phase terms. By setting the compressor angle slightly different from the optimum value to generate the shortest pulse, a typical scan around this value will produce significant changes to the pulse shape. Such pulse shape changes can lead to significant differences in the interaction with plasmas such as used in laser wake-field accelerators. Strong electron yield dependence on laser pulse shape in laser plasma wake-field electron acceleration experiments have been observed in the L'OASIS Lab of LBNL [1]. These experiments show the importance of pulse skewness parameter, *S*, defined here on the basis of the ratio of the 'head-width-half-max' (HWHM) and the 'tail-width-half-max' (TWHM), respectively.

INTRODUCTION

The details of the time-envelope function of ultrashort light pulses ('pulse shape') plays a crucial role in many nonlinear optical phenomena. Two light pulses with the same full-width-half-maximum (FWHM), but having different rise- and fall-time characteristics, or amplitude modulation, can lead to vastly different results in processes where the excitation in the medium depends strongly on the instantaneous light intensity. An example is the yield and energy spectrum of accelerated electrons in a laser wake-field accelerator operating in the self-modulated (SM-LWFA) regime [1,2], where a driving pulse with a sharp leading edge will result in faster growth of the plasma wake-field, and consequently, higher energy electrons after acceleration. There are several methods of actively controlling the shape of ultrashort light pulses, such as frequency-domain filtering and spectral-to-time domain envelope transfer by using liquid crystal phase modulators [3] and acousto-optic phase and amplitude control [4]. Here we investigate the intrinsic pulse shaping behavior of the most widely used optical pulse compressor – the grating pair – with special emphasis on the pulse skewness.

* This work was supported by DOE Contract No. DE-AC-03-76SF0098. C.G.R.G. acknowledges the Hertz Foundation.
#ctoth@lbl.gov

SHAPE OF ULTRASHORT LIGHT PULSES

The conventional description of the propagation and phase evolution of ultrashort light pulses is based on the Taylor series expansion of the optical phase around the center laser frequency, ω_0. The properties of ultrashort (sub-100 fs duration) optical pulses strongly depend on the higher order phase terms beyond the second order; the presence of higher order components (such as 'cubic' third order, or 'quartic' fourth order) modifies the shape of the pulse, resulting in modulation, and may even lead to the appearance of pre- or post-pulses [5-9].

Definition of Skew

In order to characterize quantitatively the shape of the pulse, it is worthwhile to introduce the skewness parameter, *S*. The simplest, self-explanatory definition of *S* is based on the ratio of the 'tail-width-half-max' (TWHM) and the 'head-width-half-max' (HWHM) of the laser intensity, as, for example, *S*=(TWHM/HWHM)-1. In addition to this heuristic definition of the skewness, a variety of more rigorous analytical expressions involving more features of the envelope function, *I(t)*, can be used. In the particular case of laser-plasma accelerators, the following definition of skew based on second and third order moments [10] proved to be useful:

$$S = m_3/m_2^{3/2},\ m_k = \int_{t_a}^{t_b}(t-t_0)^k I(t)dt \Big/ \int_{t_a}^{t_b} I(t)dt \quad (1)$$

In practical cases the limits of integration, t_a and t_b, can be set according to the meaningful amplitude level of the retrieved pulse shape just above the noise level of the measurement. S=0 corresponds to symmetric pulse shape, S<0 describes a pulse with a slowly increasing front part and suddenly dropping tail, while S>0 represents a fast increase and long tail.

Skew-flips

In a typical chirped pulse amplification (CPA) system, the final pulse-forming device is the grating pair pulse compressor. In contrast to the most simplistic view, by scanning the grating separation the experimenter changes not only the pulse length and the linear chirp, but also modifies all the higher order terms [7-9], and consequently the pulse shapes. The effects on the pulse

0-7803-7738-9/03/$17.00 © 2003 IEEE

shape become negligible at settings far from the shortest compression. On the other hand, when the pulse duration is in the range of a few times the minimum and the compressor angle is set slightly off from the optimum, or when the pulse contains not fully compensated higher-order terms, then a typical scan around the shortest pulse will produce significant changes to the pulse shape. For example, by compressing stretched pulses with a positive bias third-order phase component, the pulse shape in the course of a compressor separation scan initially will be skewed toward the head of the pulse (S>0), then flips to become a skewed pulse at the tail (S<0), and finally flips back again to the original asymmetric one (S>0) as the solid curve shows in Fig. 1a. It must be emphasized, that these changes of the pulse envelope are fundamentally different from the well-known and widely used mapping of the spectral amplitude to the time domain for strongly chirped pulses, where only the dominant, second-order phase coefficient plays any role [3].

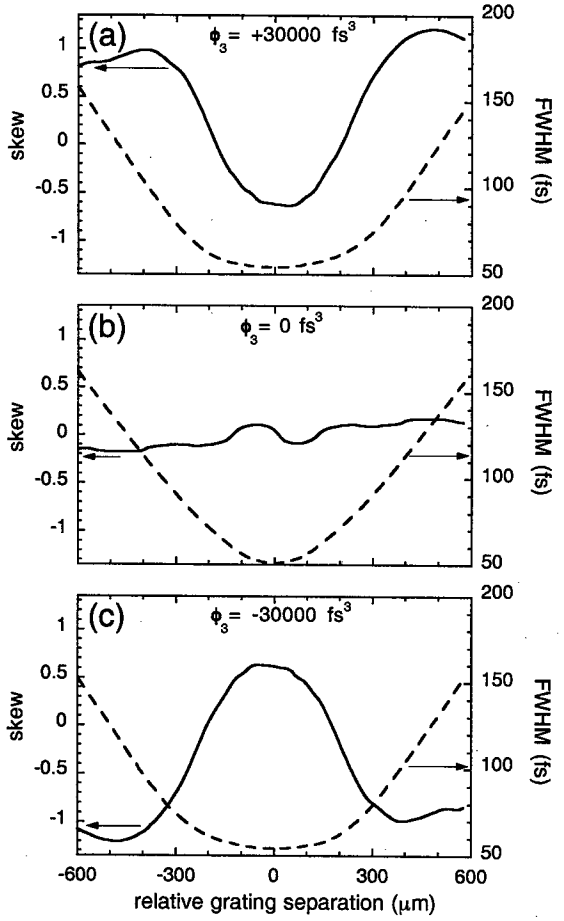


Figure 1: Pulse width, Full-Width-Half-Maximum, FWHM (dashed curve) and skew, S, (solid curve) of ultrashort pulses in a CPA system plotted around the best compression in the function of the grating separation for three cases of third order bias phase components

Further details of this 'skew-flip' behavior can be examined in the three panels of Fig. 1, which show the simulated pulse shape dependence for ~20 nm spectral bandwidth during a compressor scan around the shortest pulse for three specific third order bias values. The grating parameters are: groove density = 1480 mm^{-1}, angle of incidence = 50.0 deg, grating separation at the shortest pulse = 323 mm, and λ = 795 nm.

EXPERIMENTS

In a real laser system, however, the situation is complicated by the non-negligible presence of even higher order, generally uncompensated, phase terms beyond the third, associated again with the material dispersion in the components of the laser system. The solid curve in Fig. 2 shows the results of a full simulation of the pulse shape evolution in our Ti:sapphire CPA laser. The squares correspond to measured data, averaged for 5 laser shots. The pulses were fully characterized by retrieving the amplitude and phase functions from Polarization-Gate Frequency Resolved Optical Gating (PG-FROG) images [11,12]. The two inserts in Fig. 2 show example retrievals at the positive chirp side (a) and at the negative chirp side (b), respectively. While both pulses have the same FWHM pulse duration (76 fs), the pulse at the positive chirp side has sharper rising edge than the pulse with negative chirp – in good agreement with the simulation results and the skew definitions above.

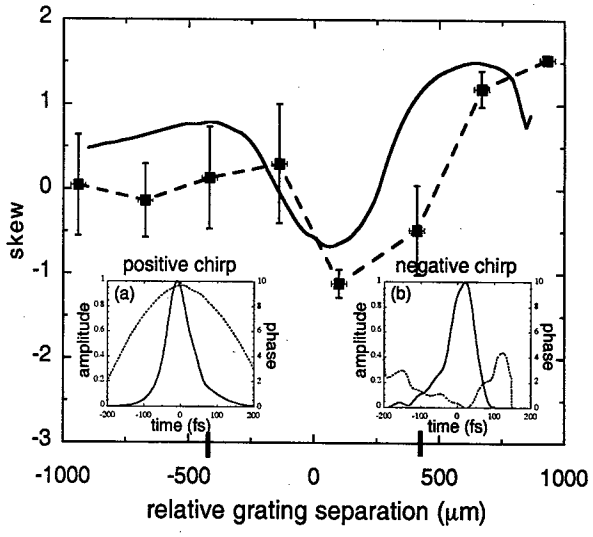


Figure 2: Simulated (solid curve) and measured (squares) skew of pulses in a CPA system around the best compression plotted in the function of the grating separation. Inserts show retrieved amplitude and phase functions in the time domain at the marked relative grating separations. (a): -420 μm, positive chirp side, (b): +410 μm, negative chirp side.

The modulations at the rising edge of the negatively chirped pulse indicate the presence of unbalanced third and higher order phase terms. These unbalanced terms are eventually responsible for the seemingly general 'chirp/shape' relationship of 'positive chirp = faster rise time and slower fall time; negative chirp = slower rise time and faster fall time' observed in our laser setup.

It should be noted, however, that for other experimental parameters (e.g., different mismatch of the stretcher/compressor or different stretcher/amplifier chain designs), balanced compression could manifests itself differently at 'off-shortest' pulse durations (off-shortest compressor settings), leading to different 'chirp/shape' combinations. The above analysis shows the possibility of laser pulse shape control by the simple method of grating alignment and change of separation without the insertion of sophisticated pulse shapers. For example, by decreasing the angle of incidence on the gratings by 0.6 degree, the effect of the added $\phi_3 = +30000$ fs^3 third order phase component makes possible to generate positively- or negatively-skewed pulses at different positions along the grating scan.

SELF-MODULATED LWFA

To illustrate the practical importance of the skewness of ultrashort laser pulses, we describe a strongly nonlinear experiment: the acceleration of electrons by laser produced plasma wakes in the SM-LWFA regime. In laser plasma acceleration experiments at the L'OASIS Lab of LBNL (Ti:sapphire CPA laser system, ~0.5 J compressed energy in >45 fs pulses, He gas target excited by ~1.5×10^{19} W/cm^2 peak intensity), we observed strong asymmetry in the yield of electrons and neutrons produced by the accelerated electrons of multiple-tens of MeV energy as a function of the compressor scans [1,2]. The total charge of the emitted electrons has been found to depend strongly, and asymmetrically, on the position of the grating separation relative to the optimum pulse compression setting. Analytic modeling and simulation indicate that the effect of the intrinsic frequency chirp is less important and itself can not explain the observed anomaly [13]. On the other hand, taking into account the shape dependence, it is possible to explain the observed asymmetric enhancement; according to Raman instability analysis, faster rise times generate larger plasma wakes underneath the laser pulse envelope, resulting in larger plasma waves and eventually larger electron yield.

SUMMARY

In conclusion, we have shown that appropriate knowledge and control of the pulse shapes in grating-based CPA systems can be used for optimization of a laser wake-field accelerator. The interplay of pulse shapes, skewness, and sign of chirp can lead to an enhanced growth of the plasma wake responsible for electron acceleration. In the experiments, pulse shaping is achieved with a conventional grating compressor scan by intentionally offsetting the higher order phase components. This method of higher order phase control is a simple alternative to the recently developed acousto-optic phase modulation devices such as the DAZZLER [4,14], and can conveniently be used at arbitrarily high power and energy levels limited only by the damage threshold of the compressor gratings.

REFERENCES

[1] W. P. Leemans, P. Catravas, E. Esarey, C. G. R. Geddes, C. Toth, R.Trines, C.B. Schroeder, B.A. Shadwick, J. van Tilborg, and J. Faure, Phys. Rev. Lett. **89**, 174802 (2002)

[2] W. P. Leemans, D. Rodgers, P. E. Catravas, C. G. R. Geddes, G. Fubiani, E. Esarey, B. A. Shadwick, R. Donahue, and A. Smith, Phys. Plasmas **8**, 2510-2516 (2001).

[3] A. M. Weiner, D. E. Leaird, J. S. Patel, and J. R. Wullert, IEEE J. Quantum Electron. **28**, 908-920 (1992).

[4] F. Verluise, V. Laude, Z. Cheng, C. Spielmann, and P. Tournois, Opt. Lett. **25**, 575-577 (2000).

[5] D. N. Fittinghoff, B. C. Walker, J. A. Squier, C. Tóth, C. Rose-Petruck, and C. P. J. Barty, IEEE J. Sel. Top. Quantum Electron. **4**, 430-440 (1998).

[6] S. Backus, C. G. Durfee, III, M. M. Murnane, and H. C. Kapteyn, Rev. Sci. Inst. **69**, 1207-1223 (1998).

[7] A. Sullivan and W. E. White, Opt. Lett. **20**, 192-194 (1995).

[8] J. Squier, C. P. J. Barty, F. Salin, C. Le Blanc, and S. Kane, Appl. Opt. **37**, 1638-1641 (1998).

[9] Cs. Tóth, D. N. Fittinghoff, B. C. Walker, J. A. Squier, and C. P. J. Barty, in Ultrafast Phenomena XI, Eds.: T. Elsaesser et al., (Springer, Berlin, 1998) pp.109-111.

[10] CRC Standard Mathematical Tables, Ed.: W. H. Beyer, (CRC Press, Inc., Boca Raton, FL, 1981) p. 508.

[11] D. J. Kane and R. Trebino, Opt. Lett. **18**, 823-825 (1993).

[12] R. Trebino, Frequency-Resolved Optical Gating (Kluwer Academic, Boston, 2002), p. 101.

[13] C.B. Schroeder, E. Esarey, B.A. Shadwick, and W. P. Leemans, Phys. Plasmas **10**, 285-295 (2003)

[14] K. Ohno, T. Tanabe, and F. Kannari, J. Opt. Soc. Am. B **19**, 2781-2790 (2002)

Proceedings of the 2003 Particle Accelerator Conference

A FUNDAMENTAL THEOREM ON PARTICLE ACCELERATION

Ming Xie, Lawrence Berkeley National Laboratory, Berkeley, CA 94720, USA

Abstract

A fundamental theorem on particle acceleration is derived from the reciprocity principle of electromagnetism and a rigorous proof of the theorem is presented. The theorem establishes a relation between acceleration and radiation, which is particularly useful for insightful understanding of and practical calculation about the first order acceleration in which energy gain of the accelerated particle is linearly proportional to the accelerating field.

INTRODUCTION

Near Field and Far Field.– Electromagnetic fields may be separated into two classes, near fields and far fields. By this separation, we define all radiation fields as far fields for they are capable of carrying electromagnetic energy far away from their sources, and all the rest, therefore, as near fields. In all conventional accelerators near fields have been used for particle acceleration. However, for laser driven particle acceleration, which is characterized by the use of electromagnetic fields with exceedingly smaller wavelengths, it is becoming imperative to make far fields our primary choice.

Linear Acceleration and Nonlinear Acceleration.– Energy coupling between a far field and a charged particle, and hence the mechanisms of laser acceleration, may be separated into two classes, first order or linear accelerations and nonlinear accelerations. By this separation, we define all acceleration processes in which energy gain of the accelerated particle is linearly proportional to the accelerating field as linear accelerations, and all the rest, therefore, as nonlinear accelerations. In all conventional accelerators linear accelerations have been used and proved effective and practical. For this reason, significant efforts of research on laser acceleration in the past have been dedicated to the understanding and implementation of linear accelerations with far fields. Through this collective experience a few rules of thumb on linear acceleration have been accumulated [1] and later summarized by Palmer [2].

Energy Conservation for Linear acceleration.– According to Palmer, linear acceleration is possible only if a particle would radiate in the absence of an accelerating field since the energy gain of the particle in the presence of an accelerating field, by energy conservation, should be proportional to the interference or cross-term between the accelerating field and the field radiated by the particle. Palmer argued by pointing out that all known mechanisms of linear acceleration are in one way or another based on inverse processes of radiation. From this point of view, it appears evident that linear acceleration is not possible in a field free vacuum since a particle moving at a constant velocity in vacuum would not radiate.

Objective of This Article.– Although the point of view of Palmer is physically insightful and the argument empirically compelling, a rigorous proof in a general and useful form, despite earnest effort by Zolotorev et al. [3], remains elusive. Earlier, I pointed out [4] that the apparently intimate relationship between acceleration and radiation can be established fundamentally and rigorously from the reciprocity principle of electromagnetism. In this article, I present the proof.

Reciprocity Principle.– The reciprocity principle of electromagnetism is rooted in a symmetry in the Maxwell's equations, a symmetry between two different solutions. The principle has been formulated into reciprocity theorems in many different forms for a wide range of applications. Of these the most well-known are perhaps the theorem derived by Lorentz and another one often attributed to Rayleigh-Carson. An extensive references on reciprocity theorems in electromagnetism can be found in [5].

Unique Situation of Particle Acceleration.– Yet, despite the great variety of reciprocity theorems in existence, none is applicable to the situation of particle acceleration that we are about to consider, for in which we have to deal with a current source of a point charge which in time spans over an infinite region of space. This intrinsic difference and its influence on the ways we establish a new reciprocity theorem will become self-evident later on.

Conclusions and Acknowledgments.– A comprehensive user instructions with examples on the reciprocity theorem proved here will be published elsewhere. Stimulating discussions with Max Zolotorev are acknowledged. This work was supported by the U.S. Department of Energy under contract No.DE-AC03-76SF00098.

PROOF OF THE THEOREM

Formulation of Reciprocity Relations.– Consider two independent solutions for a given system, field $\{\mathbf{E}_a, \mathbf{H}_a\}$ generated by source $\{\mathbf{J}_a, \rho_a\}$ and field $\{\mathbf{E}_p, \mathbf{H}_p\}$ generated by source $\{\mathbf{J}_p, \rho_p\}$, each satisfying the Maxwell's equations, respectively

$$\nabla \times \mathbf{E}_a = -\frac{\partial \mathbf{B}_a}{\partial t}, \quad \nabla \times \mathbf{H}_a = \frac{\partial \mathbf{D}_a}{\partial t} + \mathbf{J}_a \qquad (1)$$

$$\nabla \times \mathbf{E}_p = -\frac{\partial \mathbf{B}_p}{\partial t}, \quad \nabla \times \mathbf{H}_p = \frac{\partial \mathbf{D}_p}{\partial t} + \mathbf{J}_p \qquad (2)$$

0-7803-7738-9/03/$17.00 © 2003 IEEE

Using identity $\nabla \cdot (\mathbf{A} \times \mathbf{B}) = \mathbf{B} \cdot \nabla \times \mathbf{A} - \mathbf{A} \cdot \nabla \times \mathbf{B}$, a relation between the two solutions in differential form can be obtained from Eq.(1) and Eq.(2)

$$\begin{aligned} &\nabla \cdot (\mathbf{E}_a \times \mathbf{H}_p + \mathbf{E}_p \times \mathbf{H}_a) \\ &+ P_{ap} + \mathbf{E}_a \cdot \mathbf{J}_p + \mathbf{E}_p \cdot \mathbf{J}_a \;=\; 0 \end{aligned} \tag{3}$$

where $P_{ap} = P_e + P_m$

$$P_e = \mathbf{E}_a \cdot \frac{\partial \mathbf{D}_p}{\partial t} + \mathbf{E}_p \cdot \frac{\partial \mathbf{D}_a}{\partial t} \tag{4}$$

$$P_m = \mathbf{H}_a \cdot \frac{\partial \mathbf{B}_p}{\partial t} + \mathbf{H}_p \cdot \frac{\partial \mathbf{B}_a}{\partial t} \tag{5}$$

Integrating Eq.(3) over a volume V from which $\mathbf{J}_a$ is excluded and over time, we obtain an integral relation

$$\begin{aligned} &\int_{-\infty}^{\infty} dt \int_S dS \hat{\mathbf{n}} \cdot (\mathbf{E}_a \times \mathbf{H}_p + \mathbf{E}_p \times \mathbf{H}_a) \\ &+ \int_{-\infty}^{\infty} dt \int_V dV P_{ap} + \int_{-\infty}^{\infty} dt \int_V dV \mathbf{E}_a \cdot \mathbf{J}_p = 0 \end{aligned} \tag{6}$$

where S is a surface enclosing V with a unit normal vector $\hat{\mathbf{n}}$ pointing outward from the enclosed region.

Four Conditions Defining the System.– In order to describe a situation that is generally applicable to particle acceleration, we shall make the following specifications and assumptions about the system. (I): Take $\mathbf{J}_p$ as the current density of a charged particle

$$\mathbf{J}_p = q\mathbf{v}_p(t)\delta[\mathbf{r} - \mathbf{r}_p(t)] \tag{7}$$

where $\mathbf{r}_p$ and $\mathbf{v}_p$ are the position and velocity of the particle along a trajectory which, by our assumption of the two solutions being independent, describes the motion unperturbed by the electromagnetic accelerating fields $\{\mathbf{E}_a, \mathbf{H}_a\}$. (II): Separate the unperturbed trajectory into three segments: for $t = \{-\infty, t_1\}$, $\mathbf{v}_p(t) = \mathbf{v}_1$; for $t = \{t_1, t_2\}$, $\mathbf{v}_p(t)$ may vary; and for $t = \{t_2, \infty\}$, $\mathbf{v}_p(t) = \mathbf{v}_2$; where $\mathbf{v}_1$ and $\mathbf{v}_2$ are constant velocities with which the particle enters and leaves a spatial region V_s within which the particle may interact with a passive environment of the system and radiate spontaneously as a result. (III): Assume that the interaction between the particle and the accelerating fields is confined in a finite region V_f beyond which the magnitude of the fields $\{\mathbf{E}_a, \mathbf{H}_a\}$ scales inversely proportional to the distance measured from within V_f. (IV): Define an interaction volume by $V_{int} = \max(V_s, V_f)$ and take the integration volume V to be sufficiently larger than V_{int}. Under these four conditions, Eq.(6) can be transformed into a transparent and convenient form in four steps.

Step 1: Relating the Third Term to Energy Gain.– Given Eq.(7), the third term in Eq.(6) becomes

$$\int_{-\infty}^{\infty} dt \int_V dV \mathbf{E}_a \cdot \mathbf{J}_p = q \int_{T_1}^{T_2} dt \mathbf{E}_a[\mathbf{r}_p(t), t] \cdot \mathbf{v}_p(t) \tag{8}$$

where T_1 and T_2 are the times at which the particle enters and leaves the volume V, respectively. Under the conditions (III) and (IV) that the accelerating fields diminish with sufficiently large V, Eq.(8) approaches the value of the accumulated energy gain or loss of the particle along the entire unperturbed trajectory

$$\Delta W_p \equiv q \int_{-\infty}^{\infty} dt \mathbf{E}_a[\mathbf{r}_p(t), t] \cdot \mathbf{v}_p(t)$$

Step 2: Eliminating the Second Term.– The second term in Eq.(6) can be eliminated altogether. Upon rewriting P_e and P_m in Eq.(4) and Eq.(5) as

$$P_e = \frac{\partial(\mathbf{E}_p \cdot \mathbf{D}_a)}{\partial t} + \mathbf{E}_a \cdot \frac{\partial \mathbf{D}_p}{\partial t} - \frac{\partial \mathbf{E}_p}{\partial t} \cdot \mathbf{D}_a \tag{9}$$

$$P_m = \frac{\partial(\mathbf{H}_p \cdot \mathbf{B}_a)}{\partial t} + \mathbf{H}_a \cdot \frac{\partial \mathbf{B}_p}{\partial t} - \frac{\partial \mathbf{H}_p}{\partial t} \cdot \mathbf{B}_a \tag{10}$$

it is noticed that the first terms on the RHS of Eq.(9) and Eq.(10) vanish after time integration, since $\mathbf{E}_p \cdot \mathbf{D}_a = 0$ and $\mathbf{H}_p \cdot \mathbf{B}_a = 0$ within V at $t = \pm\infty$, long before and after the particle enters and leaves the region. In addition, the second terms would cancel the third terms if the constitutive relations take the following form

$$\mathbf{D}(\mathbf{r}, t) = \epsilon(\mathbf{r})\mathbf{E}(\mathbf{r}, t), \quad \mathbf{B}(\mathbf{r}, t) = \mu(\mathbf{r})\mathbf{H}(\mathbf{r}, t)$$

which hold in vacuum and in isotropic but nondispersive medium. For more general situations with dispersive medium, consider the relations in frequency domain

$$\mathbf{D}_\omega(\mathbf{r}) = \epsilon(\mathbf{r}, \omega)\mathbf{E}_\omega(\mathbf{r}), \quad \mathbf{B}_\omega(\mathbf{r}) = \mu(\mathbf{r}, \omega)\mathbf{H}_\omega(\mathbf{r})$$

where the Fourier transform is defined by

$$F_\omega(\mathbf{r}) = \frac{1}{\sqrt{2\pi}} \int_{-\infty}^{\infty} dt e^{i\omega t} F(\mathbf{r}, t)$$

Then, it follows

$$\int_{-\infty}^{\infty} dt P_e(t) = i \int_{-\infty}^{\infty} d\omega\omega(\epsilon^* - \epsilon)\mathbf{E}_{\omega a} \cdot \mathbf{E}^*_{\omega p}$$

$$\int_{-\infty}^{\infty} dt P_m(t) = i \int_{-\infty}^{\infty} d\omega\omega(\mu^* - \mu)\mathbf{H}_{\omega a} \cdot \mathbf{H}^*_{\omega p}$$

For lossless medium, we have $\epsilon^* = \epsilon$ and $\mu^* = \mu$, thus

$$\int_{-\infty}^{\infty} dt \int_V dV P_{ap} = 0$$

Step 3: Removing a Singularity in the First Term.– The first term in Eq.(6) depends on the values of two sets of fields on the surface S far away from the interaction region V_{int}. The fields due to the particle have two parts, $\{\mathbf{E}_p, \mathbf{H}_p\} = \{\mathbf{E}_r, \mathbf{H}_r\} + \{\mathbf{E}_c, \mathbf{H}_c\}$, i.e., the fields spontaneously radiated within V_s by the particle interacting with the passive system, and the Coulomb fields of a point charge. Our goal is to prove that at any time t

$$\int_S dS \hat{\mathbf{n}} \cdot (\mathbf{E}_a \times \mathbf{H}_c + \mathbf{E}_c \times \mathbf{H}_a) = 0 \tag{11}$$

As the Coulomb fields are short ranged, $\{\mathbf{E}_c, \mathbf{H}_c\}$ have significant value on the surface only in the region near

the points where the particle traverses the surface. Hence, without loss of generality, we define a local Cartesian coordinate system with its origin chosen at the point where the trajectory of the particle moving along the z-axis with a constant velocity $\mathbf{v}$ intersects the surface in the xy-plane.

The second term in Eq.(11) can be expressed as

$$\int_S dS\mathbf{E}_c \cdot (\mathbf{H}_a \times \hat{\mathbf{n}}) \tag{12}$$

where $\mathbf{H}_a \times \hat{\mathbf{n}} = H_a^s\,\hat{\mathbf{s}}$, H_a^s is the tangential component of the magnetic field and $\hat{\mathbf{s}}$ is a unit vector on the surface. Since the accelerating fields in the far zone must form a local plane wave which is either linearly or elliptically polarized, we may choose $\hat{\mathbf{s}} = \hat{\mathbf{x}}$ for the linearly polarized case, and treat $\hat{\mathbf{x}}$ and $\hat{\mathbf{y}}$ components in $\hat{\mathbf{s}}$ separately but similarly for the elliptically polarized case.

Assuming, for simplicity, that the charge passes through the origin at $t = 0$ and noting that $\epsilon = \epsilon_0$ and $\mu = \mu_0$ beyond V_s, as required by the condition (II) that no radiation, including Cherenkov and transition radiation, occurs beyond V_s, the Coulomb fields of a moving charge in vacuum are given explicitly by [6]

$$\mathbf{E}_c = \frac{q\gamma[x\hat{\mathbf{x}} + y\hat{\mathbf{y}} + (z - vt)\hat{\mathbf{z}}]}{4\pi\epsilon_0[x^2 + y^2 + \gamma^2(z - vt)^2]^{3/2}}, \quad \mathbf{H}_c = \epsilon_0\mathbf{v}\times\mathbf{E}_c$$

where γ is the Lorentz factor.

It is noted that the surface integral Eq.(12) becomes singular at the moment the point charge passes through the origin on the surface. To remove this singularity, we separate the integral into two parts, $S = S_1 + S_2$, and assume that the area of S_1 is so small that over which H_a^s is a constant. As a result, the principal value of the integral over S_1 exists and vanishes in the following sense

$$\int_{S_1} dSH_a^s\mathbf{E}_c \cdot \hat{\mathbf{x}} = H_a^s \int_{-a}^{a} dx \int_{-b}^{b} dy\mathbf{E}_c \cdot \hat{\mathbf{x}} = 0$$

Having removed the singularity over S_1, it is easy to see

$$\int_{S_2} dSH_a^s\mathbf{E}_c \cdot \hat{\mathbf{x}} \sim \frac{1}{R} \to 0$$

as required by the conditions (III) and (IV), where R is the distance measured from within V_f. Similarly, it can be shown that the first term in Eq.(11) vanishes as well.

Step 4: Separating Incoming and Outgoing Waves.– The first term in Eq.(6) can be further simplified noting that the accelerating fields constrained by the condition (III) must have a focal point within V_f. Hence on a remote surface we may separate the fields by $\{\mathbf{E}_a, \mathbf{H}_a\} = \{\mathbf{E}_i, \mathbf{H}_i\} + \{\mathbf{E}_o, \mathbf{H}_o\}$ with the incoming and outgoing local plane waves satisfying $\mathbf{E}_i = Z_0(\hat{\mathbf{r}} \times \mathbf{H}_i)$, $\mathbf{H}_i = -(\hat{\mathbf{r}}\times\mathbf{E}_i)/Z_0$ and $\mathbf{E}_o = -Z_0(\hat{\mathbf{r}}\times\mathbf{H}_o)$, $\mathbf{H}_o = (\hat{\mathbf{r}}\times\mathbf{E}_o)/Z_0$, respectively, where $\hat{\mathbf{r}}$ is a unit vector pointing outward from a reference point within V_f, and $Z_0 = \sqrt{\mu_0/\epsilon_0}$ is the vacuum impedance. Noting that the radiation fields by definition are outgoing waves and using identity $\mathbf{A}\times(\mathbf{B}\times\mathbf{C}) = (\mathbf{A}\cdot\mathbf{C})\mathbf{B} - (\mathbf{A}\cdot\mathbf{B})\mathbf{C}$, we have

$$\int_S dS\hat{\mathbf{n}} \cdot (\mathbf{E}_i \times \mathbf{H}_r + \mathbf{E}_r \times \mathbf{H}_i) = 0$$

and finally, the surface integral is reduced to

$$\int_S dS\hat{\mathbf{n}}\cdot(\mathbf{E}_o\times\mathbf{H}_r+\mathbf{E}_r\times\mathbf{H}_o) = \frac{2}{Z_0}\int_S dS(\hat{\mathbf{n}}\cdot\hat{\mathbf{r}})(\mathbf{E}_o\cdot\mathbf{E}_r)$$

Reciprocity Theorem on Particle Acceleration.– Collecting all steps proven above, we obtain

$$\begin{aligned}\Delta W_p &\equiv q\int_{-\infty}^{\infty} dt\mathbf{E}_a[\mathbf{r}_p(t), t]\cdot\mathbf{v}_p(t) \\ &= -\frac{2}{Z_0}\int_{-\infty}^{\infty} dt\int_S dS(\hat{\mathbf{n}}\cdot\hat{\mathbf{r}})(\mathbf{E}_o\cdot\mathbf{E}_r)\end{aligned} \tag{13}$$

The theorem states that the accumulated energy gain of a charged particle in the presence of an accelerating field along an unperturbed trajectory is equal to the overlapping integral in space and in time of the outgoing accelerating field with the field radiated by the particle in the far zone on a surface enclosing the interaction region. Q.E.D.

Theorem Expressed in Frequency Domain.– Although the reciprocity theorem is conditioned and proved in time domain, once established, however, it can be evaluated in frequency domain if it is convenient. Substituting into Eq.(13) the Fourier transforms of the fields, we have

$$\Delta W_p = \int_0^{\infty} d\omega\Delta W_{\omega p} \tag{14}$$

where for each frequency component

$$\begin{aligned}\Delta W_{\omega p} &\equiv q\sqrt{\frac{2}{\pi}}\int_{-\infty}^{\infty} dt\, Re\{\mathbf{E}_{\omega a}[\mathbf{r}_p(t)]e^{-i\omega t}\}\cdot\mathbf{v}_p(t) \\ &= -\frac{4}{Z_0}Re\int_S dS(\hat{\mathbf{n}}\cdot\hat{\mathbf{r}})(\mathbf{E}_{\omega o}\cdot\mathbf{E}^*_{\omega r})\end{aligned}$$

Alternatively, Eq.(14) can also be derived following the similar steps of proof, but starting from the conjugated pairs of Maxwell's equations in frequency domain

$$\nabla\times\mathbf{E}_{\omega a} = i\omega\mathbf{B}_{\omega a}, \quad \nabla\times\mathbf{H}_{\omega a} = -i\omega\mathbf{D}_{\omega a} + \mathbf{J}_{\omega a}$$
$$\nabla\times\mathbf{E}^*_{\omega p} = -i\omega\mathbf{B}^*_{\omega p}, \quad \nabla\times\mathbf{H}^*_{\omega p} = i\omega\mathbf{D}^*_{\omega p} + \mathbf{J}^*_{\omega p}$$

Nevertheless, it is in time domain that we observe and enjoy nature in its unobstructed clarity and simplicity.

REFERENCES

[1] AIP Proc. for AAC Workshops in the past two decades.

[2] R. Palmer, AIP Conf. Proc. for AAC, **335** (1995) 90.

[3] M. Zolotorev, S. Chattopadhyay, K. McDonald, *A Maxwellian Perspective on Particle Acceleration*, unfinished note, (1999), (http://www.hep.princeton.edu/~mcdonald/accel/).

[4] M. Xie, PAC01 Conf. Proc. (2001) 3876.

[5] C. Baum and H. Kritikos, *Electrodynamic Symmetry*, Chapter 1 (Taylor & Francis, 1995).

[6] P. Lorrain and D. Corson, *Electromagnetic Fields and Waves*, 2nd edition, Chapter 6 (Freeman, 1970).

Proceedings of the 2003 Particle Accelerator Conference

PARTICLE-IN-CELL SIMULATIONS OF OPTICAL INJECTORS FOR PLASMA ACCELERATORS

D.F. Gordon, A. Ting, T. Jones, B. Hafizi*, R.F. Hubbard, P. Sprangle
Naval Research Laboratory, Plasma Physics Division, Washington, DC 20375 USA
**Icarus Research, Inc., P.O. Box 30780, Bethesda, MD 20824-0780 USA*

Abstract

Two possible methods of optically injecting electrons into a plasma accelerator are the self-modulated laser wakefield accelerator (SMLWFA) and laser ionization and ponderomotive acceleration (LIPA). A magnetic selection scheme is proposed to select a narrow band of energies from the intrinsically broad beam produced by the SMLWFA. The scheme is analyzed using 2D particle-in-cell (PIC) simulations and 3D ray tracing. The effects of space charge on the ideal LIPA distribution are examined using full 3D PIC simulations.

INTRODUCTION

Plasma based accelerators use the large fields possible in an electrostatic plasma wave to accelerate electrons. Optical injection [1, 2] is a set of methods utilizing a high power laser to produce electrons with enough energy to be trapped and accelerated by the plasma wave. The use of optical injection has two important advantages. First, in experiments where a laser drives the plasma wave a portion of the drive beam can be split off and used for the injector. This solves the problem of timing the injector with the drive beam and eliminates the need for expensive RF equipment. Second, most optical injection schemes produce a very short electron pulse which leads to higher beam quality in the accelerator.

In this paper, we use two and three dimensional particle-in-cell (PIC) simulations to evaluate two possible optical injection schemes. The first scheme is the self-modulated laser wakefield accelerator (SMLWFA) [3, 4, 5, 6] with magnetic selection. The SMLWFA utilizes an instability mechanism to drive a large amplitude plasma wave which also modulates the laser intensity. The instability saturates via wavebreaking which traps and accelerates large numbers of background electrons. The electrons typically emerge as a thermal distribution with a temperature of a few MeV. Initially, the electrons are bunched to within about 100 fs. This beam is not suitable as an injector because of the large energy spread. We propose a scheme to select a narrow band of energies from the distribution.

The second scheme is laser ionization and ponderomotive acceleration (LIPA) [2]. In this scheme, use is made of the momentum space distribution resulting from tunneling ionization. It can be shown that for tunnel ionized electrons in a plane wave, the axial and transverse momenta are related by [2]

$$\frac{u_\perp}{u_\parallel} = \pm\sqrt{\frac{2}{\gamma - 1}} \tag{1}$$

where $u_\perp$ is the momentum perpendicular to the laser axis, $u_\parallel$ is the momentum parallel to the laser axis, and γ is the relativistic Lorentz factor. Thus, in the ideal case there is a one to one relation between the angle of emission and the energy of the electrons. By placing an aperture at a suitable angle to the laser axis, a particular narrow band of energies can be selected. The electron pulse is also short because of the small focal region from which the electrons originate. Using detailed 3D PIC simulations, we study the limitations of this scheme due to collective plasma effects and tight focusing.

MAGNETICALLY SELECTED SELF-MODULATED LASER WAKEFIELD ACCELERATOR

The scheme for magnetically selecting a narrow band of energies from the broad range range of energies expected from a SMLWFA is illustrated in Fig. 1. The electrons are focused by a solenoid lens through a hole in a parabolic mirror. The drive laser is focused by the parabolic mirror onto a target. A second solenoid between the parabolic mirror and the target refocuses the electrons onto the target. The energy selection arises from chromatic aberration in the lenses.

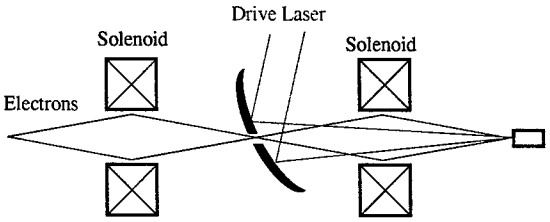


Figure 1: Magnetic Selection Scheme

Evaluation of this scheme proceeds in two stages. First, we use fully explicit 2D PIC simulations to obtain the full phase space information on the beam emerging from the SMLWFA. Second, we use those particle states as an input into a 3D ray tracing program to follow the particles through the system of lenses and apertures shown in schematically in Fig. 1.

0-7803-7738-9/03/$17.00 © 2003 IEEE

The PIC simulations were carried out using turboWAVE [7], a fully relativistic and electromagnetic code that can be run in 1, 2, or 3 dimensions. The code has an option for averaging over the laser cycles, but that mode of operation was not utilized for any of the work presented here. In the simulation, a 2 TW laser pulse with wavelength 1 μm and pulse length 300 fs was focused into a slab of helium about 1 mm long. The density of helium atoms was 10^{19} cm^{-3}. Ionization of the helium was modeled using the ADK tunneling ionization rate [8]. In the course of the simulation, the laser pulse self-modulates and drives a large plasma wave which traps background electrons. The high energy electron states at the end were written to disk for use in the ray tracing model.

The spectrum produced by the SMLWFA for three collection cones is shown in Fig. 2 for energies between 1 and 10 MeV. As expected, the distribution is approximately thermal. A best fit over all energies gave a temperature of 5 MeV. The electron macro-pulse width was about 70 fs for the higher energy particles. The simulation exhibited axial electric fields of about 200 GV/m. The laser intensity exhibited significant hosing in addition to axial modulation.

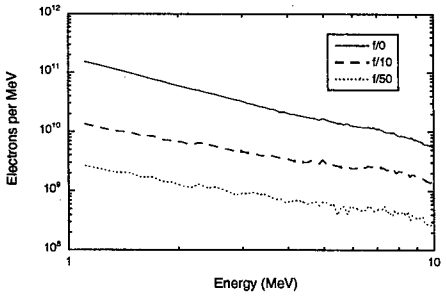


Figure 2: SMLWFA Spectrum generated by 2 TW laser

The particle states were taken from the PIC simulation and run through the optical setup shown in Fig. 1. The consecutive distances between the source, the first solenoid, the mirror, the second solenoid, and the target were all 20 cm. The diameter of the hole in the mirror was 1 mm. The diameter of the target was 60 μm. Both solenoids had the same focusing strength in any given run. Several runs were made for different values of the focusing strength. An example of the spectrum produced by one such run is shown in Fig. 3. For this case, the field was 7 kG. As was typical of all the cases, there is a main population and a secondary population at a higher energy. The energy spread in the main population was always about 1% and the pulse length was always a few ps. By varying the solenoid field between 3 and 20 kG the mean energy in the main population could be varied between 1 MeV and 11 MeV. The number of particles on target was in every case near 3×10^7.

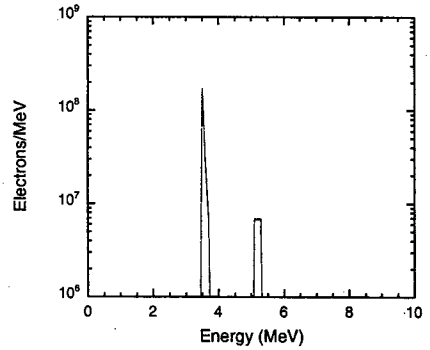


Figure 3: Magnetically Selected Spectrum for solenoid fields of 7 kG

LASER IONIZATION AND PONDEROMOTIVE ACCELERATION

We now turn to simulations of LIPA. In this case, a 10 TW laser was focused to an rms spot size radius of 3 μm into a half space of nitrogen. The laser was focused to a point 30 μm inside the gas. The laser intensity was strong enough to ionize all 7 atomic shells according to the ADK model used in the simulation.

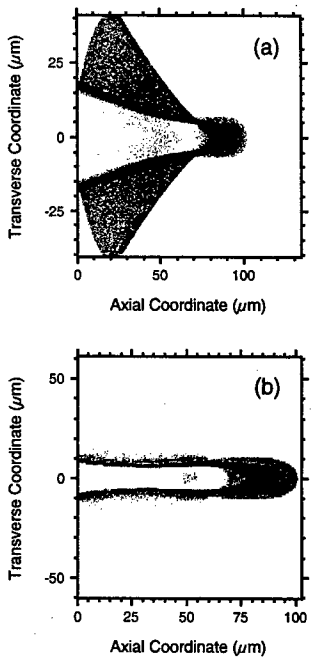


Figure 4: Electron density after 100 μm propagation of 10 TW beam into nitrogen densities of (a) $n_g = 1.1 \times 10^{11}$ cm^{-3} (b) $n_g = 1.1 \times 10^{16}$ cm^{-3}

Intensity plots of the electron density after 100 μm of

propagation are shown in Fig. 4. The case of extremely low density is shown in Fig. 4(a), which was taken from a 2D simulation. Here, the density is so low that the ejected electrons feel almost no restoring force from the ions. Fig. 4(b) shows the results of a 3D simulation at higher density. Comparison with the low density case illustrates clearly that the ions strongly inhibit the electron's ability to escape the laser focus.

The effect of the space charge forces on the prospects for injection are illustrated in Fig. 5. In the 3D simulation considered here, a circularly polarized 2 TW laser with 50 fs pulse length was focused to a 3 μm radius. To study the prospects for injection, the particles from the PIC simulation were propagated via ray tracing through a 60 μm diameter aperture placed at various angles with the laser axis at a distance of 1 mm from the laser focus. The properties of the beam transmitted through the aperture were recorded. In Fig. 5(a), the mean energy is plotted along with the theoretical energy implied by Eq. (1). Because of the space charge forces, the actual energy is reduced. Furthermore, Fig. 5(b) reveals that the energy spread can be substantial, reaching 25% in the worse case. Fig. 5(c) shows the pulse length, which is only about 10 fs for smaller angles, but increases to 100 fs for larger angles. Finally, Fig. 5(d) shows the number of particles collected, which peaks at about 32° at a value of 10^5 electrons. Thus, for these parameters, the number of particles is very small.

CONCLUSIONS

A magnetically selected SMLWFA produces about 10^7 particles in a few ps pulse with a 1% energy spread. The quality of the beam produced by LIPA depends strongly on the density. A tradeoff must be made between beam quality and number of particles. For a nitrogen density of 10^{16} cm^{-3}, the beam quality is acceptable but the number of particles is only 10^5.

REFERENCES

[1] D. Umstadter, J.K. Kim, and E. Dodd, Phys. Rev. Lett. **76**, 2073 (1996).

[2] C.I. Moore, A. Ting, T. Jones, E. Briscoe, B.Hafizi, R.F. Hubbard and P. Sprangle, Phys. Plasmas **8**, 2481 (2001).

[3] A. Modena, Z. Najmudin, A.E. Dangor, C.E. Clayton, K.A. Marsh, C. Joshi, V. Malka, C.B. Darrow, C. Danson, D. Neely, and F.N. Walsh, Nature (London) **377**, 606 (1995).

[4] C.I. Moore, A. Ting, K. Krushelnick, E. Esarey, R.F. Hubbard, B. Hafizi, H.R. Burris, C. Manka, and P. Sprangle, Phys. Rev. Lett. **79**, 3909 (1997).

[5] R. Wagner, S.-Y. Chen, A. Maksimchuk and D. Umstadter, Phys. Rev. Lett. **78**, 3125 (1997).

[6] K.-C. Tzeng, W.B. Mori and T. Katsouleas, Phys. Rev. Lett. **79**, 5258 (1997).

[7] D.F. Gordon, W.B. Mori and T.M. Antonsen, Jr., IEEE Trans. Plasma Sci. **28**, 1224 (2000).

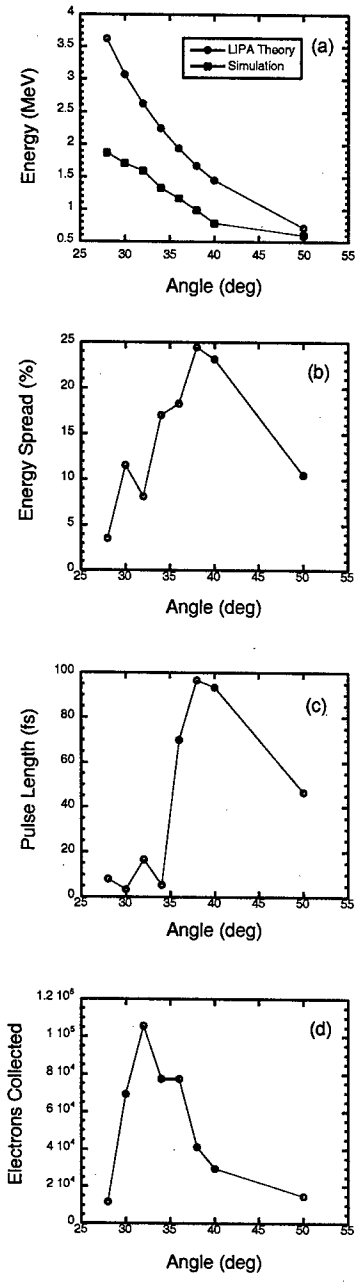


Figure 5: Characteristics of LIPA beam as a function of angle with laser axis

[8] M.V. Ammosov, N.B. Delone, and V.P. Krainov, Zh. Eksp. Teor. Fiz. **91**, 2008 (1986) [Sov. Phys. JETP **64**, 1191 (1986)].

A SIMULATION FOR ELECTRON TRAPPING AND ACCELERATION IN PARABOLIC DENSITY PROFILE AND ONGOING EXPERIMENTAL PLAN*

J. U. KIM,# C. KIM, G. H. KIM, N. HAFZ, H. J. LEE, H. SUK
Korea Electrotechnology Research Institute
Center for Advanced Accelerators
28-1, Seongju dong, Changwon, 641-120 South Korea

Abstract

It is known that as a laser wakefield passes through a downward density transition in a plasma some portion of the background electrons are trapped in the laser wakefield and the trapped electrons are accelerated to relativistic high energies over a very short distance. In this study, by using a two-dimensional particle-in-cell (PIC) simulation, we suggest an experimental scheme that can manipulate electron trapping and acceleration across a parabolic plasma density channel, which is easier to produce and more feasible to apply to the laser wakefield acceleration experiment. Also, we present a brief ongoing experimental research plan by using the newly developed high power femtosecond laser in KERI.

INTRODUCTION

The plasma-based accelerators such as laser wakefield accelerators (LWFA) have shown much interest in both theory [1-2] and experiment.[3-4] In the conventional LWFA scheme, for acceleration of electrons they should be injected externally by using an external injection accelerator or high-power lasers for optical injection.[5-6] However, in the self-injection cases,[7-9] some background electrons in a plasma can be self-injected and the electrons can be accelerated by the laser wakefield to relativistic high energies over a very short distance. Therefore, the major advantage of the self-injected LWFA is that it may be built with very compact tabletop size because it does not require auxiliary heavy facilities that most conventional accelerators do. That is why people in the advanced accelerator community have shown much interest in the self-injection LWFA method in recent years.

In this study, we propose an experimental scheme with a parabolic plasma density channel, which may be easily obtained experimentally by an intense laser and gas jet interaction. There were some previous LWFA studies performed in a preformed parabolic density channel,[10-11] but most of the works were conducted along the axis of the channel in which electron density is minimum to provide optical guiding of an intense laser pulse. In the current study, however, we report a preliminary simulation result of electron trapping and acceleration in a plasma when a short and intense laser pulse passes across a parabolic plasma channel, For this purpose, a 2-dimensional (2-D) particle-in-cell (PIC) simulation has been performed and fully relativistic and electromagnetic OSIRIS code [11] were employed. The simulation box (i.e., moving window) was assumed to propagate with the speed of light, c, in free space.

PLASMA DENSITY MODEL & SIMULATION PARAMETERS

The density profile modelled in the simulation has a typical parabolic shape of $n(r) \approx n_0 + \Delta n r^2/r_{ch}^2$. Here, n_0 and Δn are the minimum density on axis and density change, respectively and r_{ch} is the channel radius. The full width of the plasma channel (r) and the width of the parabolic density region were set to 3,140 k_0^{-1} ($\approx$ 400 μm) and 2,512 k_0^{-1} ($\approx$ 320 μm), respectively. The edges of the plasma channel were set to 314 k_0^{-1} ($\approx$ 40 μm) for the upward and downward density transitions, respectively. Here, k_0 is the wave number of laser in free space. Assuming the cylindrical symmetry of the plasma channel the density profile shows a density minimum on axis (i.e., r = 0) and it increases with r and reaches the highest value at the edge where it decreases to zero with relatively short scale length, L_s of $\approx$ 40 μm. 2-D PIC simulations were performed using this parabolic density channel assuming that the peak and minimum plasma density were n_e = 5×10^{18} cm^{-3} and 2.1×10^{18} cm^{-3}, respectively and a fully ionized plasma channel was assumed. Also, a short (= 50 fs, i.e., pulse length L = cτ ≈15 μm), intense laser pulse (i.e., peak power, P = 10 TW and wavelength λ_0 =1.064 μm) was assumed to pass through the plasma channel. The normalized vector potential a_0 was set to 2.27 and the laser beam was focused at the centre of the channel to a spot size of 10 μm.

RESULTS & DISCUSSIONS

In the simulation it was observed that some background electrons are trapped at the first node of wakefield as the plasma wakefield passes just down rim ($\approx$ 57 μm) of the parabolic density channel. At further elapsed time, the trapped electrons were injected into the acceleration phase of the wakefiled and accelerated further [Fig. 1] until they reach the minimum density position (i.e., $\Delta Z = 1571\ k_0^{-1}$ (i.e., $\approx$ 200 μm) of the parabolic density channel. In general, accelerated electrons are highly relativistic so its velocity is faster than the phase velocity (v_{ph}) of the

*Part of the work was submitted to APL April, 2003.
#jukim@keri.re.kr

0-7803-7738-9/03/$17.00 © 2003 IEEE

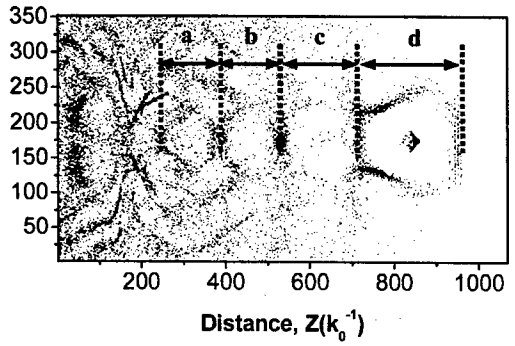


Figure 1: Further acceleration of the trapped electrons at the downward density transition of the parabolic density profile (i.e., $n(r) \approx n_0 + \Delta n r^2/r_{ch}^2$). Where a<b<c<d.

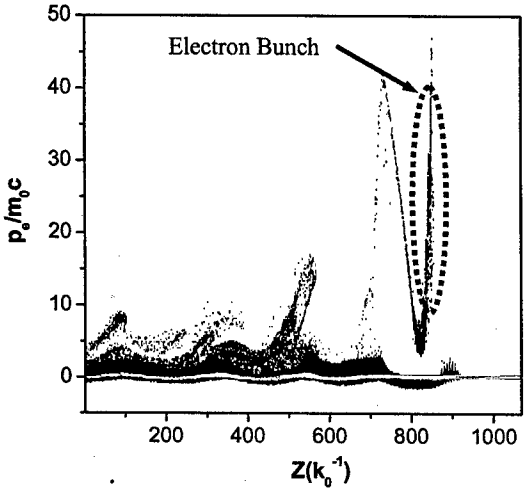


Figure 2: A simulation result of the momentum phase space (p_z, z) of the plasma electrons at the propagation distance $\Delta Z = 2{,}940\ k_0^{-1}$ (≈ 375 μm in plasma).

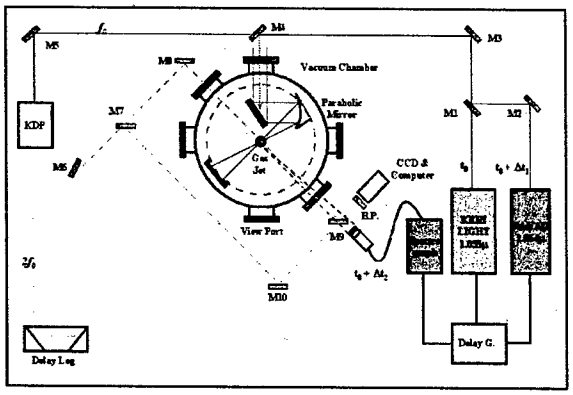


Figure 3: Future experimental schematic for diagnostics of the laser induced plasma.

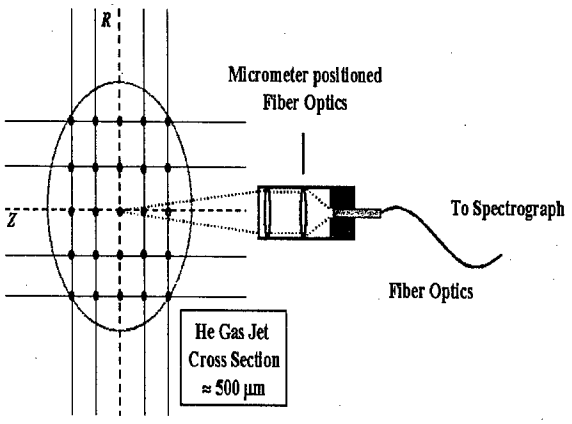


Figure 4: Detailed schematic diagram of the electron density and temperature measurement by using optical emission spectroscopy of seeded copper.

wakefield, which is nearly equal to the group velocity (v_g) of the driving laser.[12] Therefore, it is anticipated the trapped electrons would reach the deceleration phase of the wakefield. However, this is not the case as long as we consider the downward density transition in the parabolic density channel in which increased plasma wavelength can keep the trapped electrons effectively in the acceleration phase of the wakefield.

In Fig. 1, it is clearly seen that the wavelength of the wakefield increases continuously from "a" (≈16 μm) to "d" (≈25 μm) as the wakefield passes through the downward density regions of the parabolic density profile. While being accelerated, the trapped electrons have shown so-called "betatron" motion [13] in which their transverse amplitude is continuously changing from maximum to minimum in the wakefield. On the contrary, as the laser wakefield passes through the upward density transition of the parabolic density profile, situations are quite reversed. Since the plasma wavelength, λ_p, decreases the very front portion of the accelerated electrons are gradually laid in deceleration phase (i.e., slippage or detuning) [12] of the wake field. It should be noted that, however, except for the very few front part of the electron beam most of the electrons are still in the acceleration phase of the wakefield, thus gaining more energy from the field.

Figure 2 shows a typical simulation result of the momentum phase space (p_z, z) of the plasma electrons at propagation distance of $\Delta Z = 2{,}940\ k_0^{-1}$ (i.e., ≈ 375 μm). The results show that the accelerated electron bunch (denoted as a doted circle in Fig. 2) has momenta in the ranges of 5 and 20 MeV/c and the beam pulse width of approximately $\approx 31\ k_0^{-1}$ (i.e., ≈ 4 μm). However, it should be pointed out that the accelerated electron bunch shows large energy spread, which is due to the dephasing of the electron beams to the laser wakefield,[12] and it is commonly observed elsewhere.[9]

Figure 3 shows an ongoing experimental schematic for diagnostics of laser-induced plasmas produced in high-density gas jet and high power laser (~2 TW) interaction. The planned research is to study the characteristics of waveguides formed as subsequent two laser pulses are focused in the gas jet with appropriate time delay. For this purpose two lasers will be employed. One of which will be a high power laser, whose peak power, pulse duration, and wavelength are 2 TW, 700 fs, and 1.053 μm, respectively, and the other is a long pulse (7 ns FWHM) Nd:YAG laser. Plasma channels will be imaged by Mach-Zehnder and Schlieren visualization methods. Temporal and spatial evolutions of the electron density as well as electron temperature will be obtained by using optical emission spectroscopy as shown in Fig. 4. Usually, two typical methods in optical emission spectroscopy may be employed in the measurement of electron temperature in plasmas. One of which is the "Boltzmann plot method" and the other is so called "two-line method". Particularly, for this purpose, either a thin copper wire of approximately 20 μm will be installed in the centre of the gas jet or very fine copper powders (i.e., nano or micro-scale copper powders) will be seeded in the gas jet. Since the spectroscopic parameters such as spontaneous emission rate, degeneracy, and lower and upper level electronic energies are well known for the specific copper emission lines, therefore, only relative intensity measurements of copper emission lines are required in order to deduce electron density and temperatures in the plasma.

In conclusion, we presented on-going experimental plan in KERI by using a recently developed high power femtosecond laser system. The planned research is to study the characteristics of waveguides as subsequent two laser pulses are focused in the gas jet with appropriate time delay and the detailed experimental procedures were introduced. Also, a 2-D PIC simulation study was performed in this study to investigate the electron trapping and acceleration in plasma by using a simple parabolic density model, which may be easily obtained experimentally by a laser and gas jet interaction. The scale length of the density transition used in this simulation is larger than Suk's scheme [9] but smaller than Bulanov's.[8] Despite the large momentum spread the trapped electrons can be effectively accelerated with momenta in the range of 5 – 20 MeV/c, which is similar to the previous results that used sharp downward density transition.[9] It is anticipated that the current work proposes an experimentally easier and more feasible method for the electron trapping and acceleration in a plasma.

This work was supported by the Korean Ministry of Science and Technologies through the Creative Research Initiative Program.

REFERENCES

[1] S. V. Bulanov, V. I. Kirsanov, and A. S. Sakharov, JEPT Lett. **50**, 198 (1989).
[2] P. Sprangle, E. Esarey, and A. Ting, Phys. Rev. Lett. **64**, 2011 (1990).
[3] H. Hamster, A. Sullivan, S. Gordon, W. White, and R. W. Falcone, Phys. Rev. Lett. **71**, 2725 (1993).
[4] J. R. Marques, J. P. Geindre, F. Amiranoff, P. Audebert, J. C. Gauthier, A. Antonetti, and G. Grillon, Phys. Rev. Lett. **76**, 3566 (1996).
[5] D. Umstadter, J. K. Kim, and E. Dodd, Phys. Rev. Lett. **76**, 2073 (1996).
[6] E. Esarey, R. F. Hubbard, W. P. Leemans, A. Ting, and P. Sprangle, Phys. Rev. Lett. **79**, 2682 (1997).
[7] K. Nakajima et al., Phys. Rev. Lett. **74**, 4428 (1995).
[8] S. V. Bulanov, N. Naumova, F. Pegoraro, and J. Sakai, Phys. Rev. E **58**, R5257 (1998).
[9] H. Suk, N. Barov, J. B. Rosenzweig, and E. Esarey, Phys. Rev. Lett. **86**, 1011 (2001).
[10] R.N. Agarwal, V.K. Tripathi and P.C. Agarwal, IEEE Trans. Plasma Sci. **24**, 143 (1996).
[11] R. G. Hemker, Ph. D. Thesis, UCLA 2000.
[12] E. Esarey, P. Sprangle, J. Krall, and A. Ting, IEEE Trans. Plasma Sci. **24**, 252 (1996).
[13] E. Esarey, B. A. Shadwick, P. Catravas, and W. P. Leemans, Phys. Rev. E **65**, 056505 (2002).

Proceedings of the 2003 Particle Accelerator Conference

SELF-INJECTION OF ELECTRONS FROM EVOLUTION OF WAKE WAVE

C. Kim*†, G. H. Kim, J. U. Kim, I. S. Ko†, H. J. Lee, and H. Suk
Center for Advanced Accelerators
Korea Electrotechnology Research Institute, Changwon, 641-120, Korea
†Department of Physics, POSTECH, Pohang, 790-784, Korea

Abstract

Self-injection mechanisms of plasma electrons in the self-modulated laser wakefield acceleration (SM-LWFA) are investigated. Two-dimensional (2-D) particle-in-cell (PIC) simulations show that a significant amount of plasma electrons can be self-injected into the acceleration phase of a laser wakefield by a dynamic increase of the wake wavelength in the longitudinal direction. In addition, a merging of the wake wave is observed and a large amount of electrons are self-injected to high energies. In this paper, injection phenomena are studied with 2-D simulations and a brief explanation of a new self-injection mechanism is presented.

INTRODUCTION

The laser wakefield acceleration (LWFA) has been highlightened since it is known that they can accelerate electrons to a relativistic high energy over a distance of the plasma wavelength λ_p [1]. For example, a maximum available electric field by the laser wakefield is on the order of 100 GV/m when a plasma density of $n_0 = 10^{18}$ cm^{-3} is used. This electric field is three orders of magnitude stronger than that of conventional radio frequency (RF) accelerators. So far, various acceleration schemes have been studied, such as the plasma wakefield accelerator (PWFA) [2], the plasma beat wave accelerator (PBWA) [3, 4], the self-modulated laser wakefield accelerator (SM-LWFA) [5], and wakefield accelerators driven by multiple electron or laser pulses [6, 7].

Among those schemes, the SM-LWFA has been widely studied because of its simplicity. In the SM-LWFA, a long ($> \lambda_p$) ultrahigh-intensity ($\geq 10^{18}$ W/cm^2) laser pulse is used to generate a laser wakefield in a homogeneous plasma. When the long laser pulse passes through the plasma, the laser pulse is modulated into many shorter pulses due to the Raman forward scattering instability. In this case, the modulated pulse width is equal to the plasma wavelength λ_p. These laser pulse train excites the wakefield resonantly and the amplitude of the wakefield grows up. The shape of the wakefield changes from a sinusoidal wave to a steep one as the wave grows, and eventually the transverse and the longitudinal wave breakings occur [8]. Due to this effect, some electrons are self-injected into the wakefield and they are accelerated to high energies. Some other effects are also known to be a source of the self-injection in the SM-LWFA and the beam quality of self-injected electrons are high enough to make an accelerator without any additional injection linac. Thus the SM-LWFA is considered as a strong candidate for the table top accelerator owing to its simple structure.

Even though the SM-LWFA has been deeply studied and great progresses has been made, large parts of the SM-LWFA study remains uncovered area. For example, various dynamical processes of wake wave evolution and electron self-injections can be observed in the simulation of the SM-LWFA. As mentioned previous paragraph, a laser pulse, which is longer than the plasma wavelength, is modulated to train of short laser pulses. The interaction continues until the modulated laser pulses get out of the plasma and the energy of the laser pulses shrink down as they pass through it so that the shape of the laser wake wave changes continuously. The self-focusing effect of the laser gives significant changes to the wake wave, as well. The transverse envelope oscillation of the laser after the self-focusing [9] increase or decrease the wavelength of the wake wave transversely. Moreover, during this process, a dynamic self-injection of electrons can be observed. During the evolution of the wake wave, it is noticed that there are sudden self-injections of electrons with dynamic changes of wake wave. These sudden electron injection is hard to be explained with previously known mechanisms of the SM-LWFA and it seems that there are a couple of other injection mechanisms. In this paper we describe the evolution of the wake wave and a dynamic self-injection of electrons. In addition, we propose a new mechanism of an electron self-injection which explains these dynamic self-injections of electrons.

SELF-INJECTION OF ELECTRONS BY EVOLUTION OF LASER WAKE WAVES

2-D PIC Simulation

As mentioned in the previous section, a laser wake wave changes dynamically in the longitudinal direction as it propagates in a plasma and this process leads to self-injection of some background plasma electrons in the laser wakefield. In order to investigate the longitudinal self-injection mechanism in SM-LWFAs, we performed 2-D PIC simulations with the OSIRIS code [10]. The OSIRIS code employs a moving window to simulate a laser plasma interaction with limited computing power. The moving

* chbkim@postech.ac.kr

0-7803-7738-9/03/$17.00 © 2003 IEEE

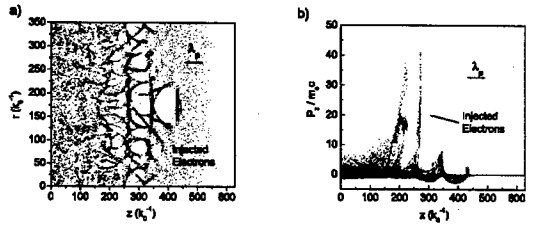


Figure 1: Electrons distribution of the plasma (a) and the phase space (b) when the laser propagates 0.76 mm (=$6300\omega_0^{-1}$). The vector potential a_0 of the laser is 3.0 and the density of the plasma is 2×10^{19} cm^{-3}. The horizontal axis scale is $628k_0^{-1}$ ($= 80$ μm) and the vertical axis scale is $351k_0^{-1}$ ($= 45$ μm). The generated wake wave and self-injected electrons are shown. Note that the wavelength of wake wave is longer than the plasma wavelength λ_p.

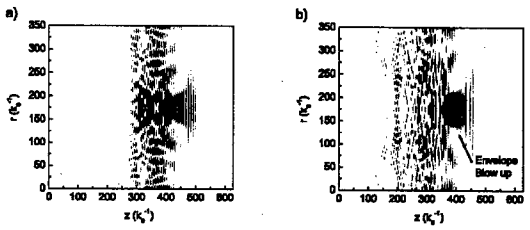


Figure 2: Transverse electric field at (a) $4200\omega_0^{-1}$, (b) $6300\omega_0^{-1}$ of Fig. 1 simulation. Note that there are a transverse oscillation of laser envelope and a serious longitudinal dispersion. These transverse oscillation and longitudinal dispersion can make an evolution of the wake wave.

window is on the frame of the laser pulse and advances with the speed of light. The electric and the magnetic fields are calculated only within the moving window. The values of fields are shifted by on mesh grid when the laser advances the distance $l > \Delta x$, where Δx is the grid size. Total simulation grid cell number is 1200×400 and 16 grid cells are used to resolve the laser wavelength. A periodic boundary condition is used for the r direction and the Lindman open-space boundary condition is used for the z direction. In the simulation, the plasma density is increased along the z axis from 0 to 2×10^{19} cm^{-3} over a distance of 0.25 mm, and then a homogeneous plasma density continues to the position of $z = 1$ mm. The plasma wavelength λ_p in the non-relativistic cold fluid regime is calculated to be 7.4 μm when the plasma density is 2×10^{19} cm^{-3}. The wavelength of the laser pulse is 1.064 μm and the pulse width is 40 μm (0.135 ps long), which is 5 times longer than the plasma wavelength λ_p. The direction of the laser is from left to right and the linear polarization is used. The laser pulse is focused in the plasma right after the plasma reaches its maximum density and the spot size at the focal point is 10 μm. The vector potential of the laser a_0 is 3.0 so that this simulation is in the relativistic self-focusing regime.

Self-Injection of Electrons

Figure 1 (a) shows the electron distribution when the laser propagates $6300\omega_0^{-1}$. The typical D shape of the wake wave and ion cavities are observed. Fig. 1 (b) is the phase space of Fig. 1 (a). Self-injected electrons are clearly seen and the bunch length of the electron beam is extremely short. Note that the wake wavelength (a distance between two electron peaks) is little longer than the plasma wavelength. As the laser propagates inside the plasma, it is observed that the wavelength of the wake wave is increased and electrons are self-injected simultaneously. Especially, the self-injection of electrons is enhanced as the longitudinal wavelength increases and it suddenly disappears when the wavelength shrinks down. In addition to the longitudinal development of the wavelength, the wake wave experiences the severe transverse modulation. The transverse size of the wake wave shrinks down straight forwardly until the laser pulse reaches its focal point and it shows a complex motion after the focal point. In one time the wake wave blows up and it is torn out into several pieces at the other time. From these longitudinal and transverse motion, the laser wake wave evolves dramatically and it seems that this evolution is closely related to the self-injection of electrons.

Mechanism of Electron Self-Injection

The wake wave evolution seems to be caused by two effects. One is the transverse oscillation of the self-focused laser pulse and the other is its dispersion in the longitudinal direction. Fig. 2 is the transverse electric field at different moving window positions. In the beginning (Fig. 2 (a)), laser pulses experience the self-focusing and the transverse size of the envelope is small. As the laser propagates into the plasma, the laser envelope blows up by the transverse oscillation of the self-focused laser pulse. The expanded transverse size of the laser pulse in Fig. 2 (b) is exactly matched with the wake wave in Fig. 1 (a) and it is clear that the transverse oscillation of the self-focused laser pulse causes the transverse modulation of the wake wave.

On the other hand, the longitudinal wavelength increase comes from the dispersion of the laser in which the group velocity of a laser pulse in a plasma is given by $v_g = c\sqrt{1 - \omega_p^2/\omega_0^2}$. In this equation, c is the velocity of light in free space, ω_p is the plasma oscillation frequency, and ω_0 is the laser oscillation frequency. This equation tells us that the laser pulse width increases when it passes through the plasma because the laser spreads its frequency spectrum by energy losing.

As a result of the transverse oscillation and the dispersion effect, the self-modulated short laser pulses change to

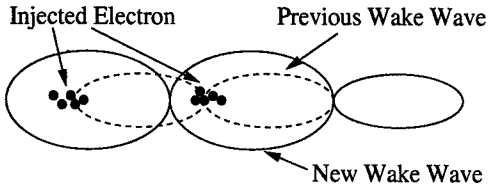


Figure 3: Schematic diagram of the electron self-injection mechanism. When the wavelength of the wake is increased, electrons in the previous nodes can be injected into the wakefield owing to their transverse momentum.

larger ones and this in turn increases the wake wavelength. When the laser envelop blows up, boundary electrons of the wake are pushed out so that the wavelength is increased and the strong self-injection of electrons occurs. This process can be explained in the schematic diagram in Fig. 3. When the evolution of the wake wave is happened, there is a mismatching between a previous wave and a new one so that most of electrons are pushed out to the new boundary. However, some electrons in previous nodes are injected into the acceleration phase of the wakfield owing to their strong transverse momentum. It should be noted that the increasing rate in λ_p is nonlinear. Hence, initial periods of the wake wave can be merged together (see Fig. 4) and this leads to a sudden self-injection of electrons as well.

Merging of Wake Wave

Fig. 4 is the phase space plot at different times of a simulation, which shows the merging of the wake wave. The density of the plasma is 5×10^{19} cm^{-3} and the vector potential a_0 is 2.0. At first, it starts from a typical phase diagram of the SM-LWFA. The wavelength of the wake wave is given by the plasma wavelength λ_p, even though wavelengths of first two periods are longer than that. As the laser propagates into the plasma, dramatic changes are observed (see Fig. 4 (b)). A large amount of electrons are injected strongly into the wakefield and accelerated to high energies. The wavelength of the third period is increased 2 times longer than the plasma wavelength λ_p and this means that two wake periods is merged into one. The merging of the wake wave is also confirmed with the expanded boundary of the wake wave. Below the zero momentum, the boundary of the wake wave blows up two times bigger than before.

SUMMARY

PIC simulation studies have been performed to investigate the self-injection mechanisms in the SM-LWFA. These studies show that a significant amount of plasma electrons can be self-injected into a wakefield when the laser wake wave evolves dynamically in the longitudinal direction. The transverse oscillation and the longitudinal dispersion of the laser envelope cause this evolution of wake wave. This injection is so severe that it seems to be a dominant self-injection source in some cases. In addition to the increase of longitudinal wavelength, the merging of two period is observed and this merging causes the self-injection of a large number of electrons as well.

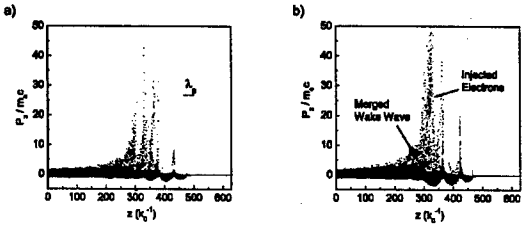


Figure 4: Phase space plot at (a) $2772\omega_0^{-1}$, (b) $3024\omega_0^{-1}$ when the vector potential is 2.0 and the density of the plasma is 5×10^{19} cm^{-3}. Scales of the horizontal and the vertical axes are same with Fig. 1. Note that there is a merging of wake wave so that a large number of electrons are accelerated to high energies.

REFERENCES

[1] T. Tajima and J. M. Dawson, Phys. Rev. Lett. **43** 267, (1979).

[2] J. B. Rosenzweig, D. B. Cline, B. Cole, H. Figueroa, W. Gai, R. Konecny, J. Norem, P. Schoessow, and J. Simpson, Phys. Rev. Lett. **61** 98, (1988).

[3] Y. Kitagawa, T. Matsumoto, T. Minamihata, K. Sawai, K. Matsuo, K. Mima, K. Nishihara, H. Azechi, K. A. Tanaka, H. Takabe, and S. Nakai, Phys. Rev. Lett. **68** 48, (1992).

[4] C. E. Clayton, M. J. Everett, A. Lal, D. Gordon, K. A. Marsh, and C. Joshi, Phys. Plasma **1** 1753, (1993); M. Everett, A. Lal, D. Gordon, C. E. Clayton, K. A. Marsh, and C. Joshi, Nature **868** 527, (1994).

[5] K. Nakajima, D. Fisher, T. Kawakubo, H. Nakanishi, A. Ogata, Y. Kato, Y. Kitagawa, R. Kodama, K. Mima, H. Shiraga, K. Suzuki, K. Yamakawa, T. Zhang, Y. Sakawa, T. Shoji, Y. Nishida, N. Yugami, M. Downer, and T. Tajima, Phys. Rev. Lett. **74** 4428, (1995).

[6] Y. B. Fainberg, V. A. Balakirev, I. N. Onishchendo, G. L. Sidelnikov, and G. V. Sotnikov, Fizika Plazmy **20** 647, (1994); Plasma Phys. Rep. **20** 606, (1994).

[7] K. Nakajima, Phys. Rev. A **45** 1149, (1992).

[8] S. Bulanov, N. Naumova, F. Pegoraro, and J. Sakai, Phys. Rev. E **58** R5257, (1998).

[9] J. Krall, A. Ting, E. Esarey, and P. Sprangle, Phys. Rev. E **48** 2157, (1993).

[10] R. G. Hemker, K.-C. Tzeng, W. B. Mori, and C. E. Clayton, Phys. Rev. E **57** 5920, (1998).

Proceedings of the 2003 Particle Accelerator Conference

PHOTONIC CRYSTAL LASER ACCELERATOR STRUCTURES

B. Cowan*, M. Javanmard, R. Siemann, SLAC, Stanford, CA 94309, USA

Abstract

Photonic crystals have great potential for use as laser-driven accelerator structures. A photonic crystal is a dielectric structure arranged in a periodic geometry. Like a crystalline solid with its electronic band structure, the modes of a photonic crystal lie in a set of allowed photonic bands. Similarly, it is possible for a photonic crystal to exhibit one or more photonic band gaps, with frequencies in the gap unable to propagate in the crystal. Thus photonic crystals can confine an optical mode in an all-dielectric structure, eliminating the need for metals and their characteristic losses at optical frequencies.

We discuss several geometries of photonic crystal accelerator structures. Photonic crystal fibers (PCFs) are optical fibers which can confine a speed-of-light optical mode in vacuum. Planar structures, both two- and three-dimensional, can also confine such a mode, and have the additional advantage that they can be manufactured using common microfabrication techniques such as those used for integrated circuits. This allows for a variety of possible materials, so that dielectrics with desirable optical and radiation-hardness properties can be chosen. We discuss examples of simulated photonic crystal structures to demonstrate the scaling laws and trade-offs involved, and touch on potential fabrication processes.

INTRODUCTION

The extraordinary electric fields available from laser systems make laser-driven charged particle acceleration an exciting possibility. Practical vacuum laser acceleration requires a guided-mode structure capable of confining a speed-of-light (SOL) mode and composed entirely of dielectric materials, and photonic crystals provide a means to achieve this capability. A photonic crystal is a structure with permittivity periodic in one or more of its dimensions. As described in [1], optical modes in a photonic crystal form bands, just as electronic states do in a crystalline solid. Similarly, a photonic crystal can also exhibit one or more photonic band gaps (PBG's), with frequencies in the gap unable to propagate in the crystal. Confined modes can be obtained by introducing a defect into a Photonic Crystal lattice. Since frequencies in the bandgap are forbidden to propagate in the crystal, they are confined to the defect. A linear defect thus functions as a waveguide.

A significant benefit of photonic crystal accelerators is that only frequencies within a bandgap are confined. In general, higher order modes, which can be excited by the electron beam, escape through the lattice. This benefit has motivated work on matallic PBG structures at RF frequencies [2]. In addition, an accelerating mode has been found in a PBG fiber structure [3]. After discussing 2D planar structures we consider the fiber geometry in more generality.

* benc@slac.stanford.edu

2D PLANAR PHOTONIC CRYSTAL ACCELERATOR STRUCTURES

Structure Geometry

The geometries we consider in this section are two-dimensional: we take them to be infinite in the vertical (y) direction, while the electron beam and the accelerating optical field copropagate in the z-direction, transverse to the direction of symmetry. While such structures are not immediately suitable for charged particle acceleration, 2D structures can be analyzed with much less CPU time than can 3D structures, thereby allowing rapid exploration of multiple sets of geometric parameters. The computational technique is discussed further below.

Our underlying photonic crystal lattice is a triangular array of vacuum holes in a silicon substrate. Assuming an operating wavelength of $1.5\,\mu$m in the telecom band, silicon has a normalized permittivity of $\epsilon_r = \epsilon/\epsilon_0 = 12.1$ [4]. Such a lattice exhibits a wide TE bandgap, as desired since the accelerating field component is transverse to the direction of symmetry. For lattice constant a the nearest-neighbor center-to-center hole spacing, we choose the hole radius $r = 0.427a$ to maximize the relative width of the bandgap.

The accelerator structure consists of a vacuum guide in this lattice, as shown in Fig. 1. The guide width w is defined such that the distance between the centers of the holes adjacent to the waveguide are $w + a$. Also, dielectric material can be added to the sides of the guide, and we let δ denote the total width of the dielectric "pad" added to both sides of the guide. Fig. 1 also shows an accelerating mode of this geometry, i.e. E_z is nonzero on axis and $\omega = ck_z$. In fact, for a general selection of w and δ, there will be a k_z for which this waveguide mode is synchronous. This is because the dispersion properties of this PBG waveguide are similar to a metallic guide in that $\omega/k_z > c$ throughout most of the bandgap, but at the upper edge of the gap the dispersion curve reduces in slope and meets the SOL line. The padding can be added in order to bring the SOL frequency into the center of the gap where the dispersion curve is more linear.

0-7803-7738-9/03/$17.00 © 2003 IEEE

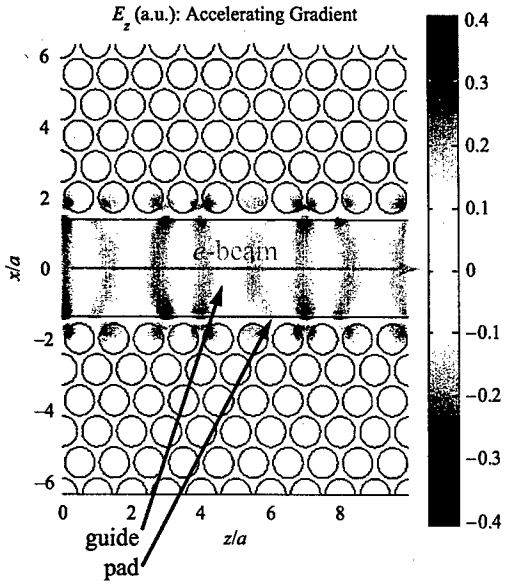


Figure 1: An accelerator structure geometry with a waveguide mode. The shading indicates the electric field component in the direction of e-beam propagation. Here the guide width is $w = 3.0a$, the pad width is $\delta = 0.25a$, and the wavelength is $\lambda = 2.78a$.

Accelerating Mode Parameters

Several parameters characterize the performance of an accelerating mode. The relationship between the input laser power and the accelerating gradient is described by the characteristic impedance [5]. Since our 2D structures only confine modes in one transverse dimension, we normalize the impedance to that of a structure one wavelength high, so $Z_c = E_{\rm acc}^2 \lambda / P_h$, where $E_{\rm acc}$ is the accelerating gradient and P_h is the laser power per unit height. We find an empirical power-law scaling of the impedance, with $Z_c \propto (w/\lambda)^{-3.55}$.

Next, there is the *damage factor* $f_D = E_{\rm acc} / |\mathbf{E}|^{\rm mat}_{\rm max}$, where $|\mathbf{E}|^{\rm mat}_{\rm max}$ is the maximum electric field magnitude anywhere in the dielectric material. Since laser power is ultimately limited by the damage threshold of the material, the damage factor is an important measure of the maximum possible accelerating gradient a structure can sustain.

The damage threshold exhibits a dependence on laser pulse width which becomes favorable at very short pulse widths, as examined in [6] and paramaterized in [5]. Thus these accelerator structures are transmission-mode, and a high group velocity v_g is desired so that short pulses may be used. The qualitative behavior of these parameters presents a trade-off. As the guide is widened, the damage factor decreases. On the other hand, the group velocity increases, allowing shorter laser pulses to be used, for which the material damage threshold is at a higher field. To find the optimum parameters we plot the maximum possible accelerating gradient taking both effects into account in Fig. 2.

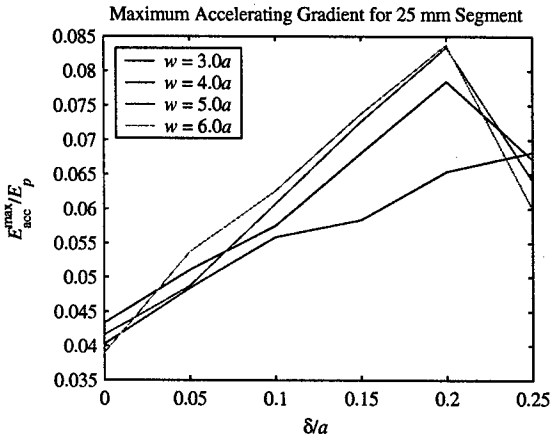


Figure 2: The maximum accelerating gradient sustainable by each structure geometry, normalized to the material damage threshold E_p for 1 ps pulses.

PHOTONIC CRYSTAL FIBER STRUCTURES

The geometry of this structure is again a triangular array of vacuum holes, this time in silica ($\epsilon_r = 2.13$). Here the structure is considered to be a fiber drawn infinitely in the beam propagation direction, with the electrons and laser pulse copropagating along the fiber. For these structures $r = 0.35a$, and the defect consists of a larger central hole. Modes were found for three different mode radii, and are shown in Fig. 3. The frequencies of the three modes are given by $\omega a/c$ of 8.20, 8.12, and 8.20 and group velocities $0.60c$, $0.654c$, and $0.59c$ (left to right).

The structure was simulated using periodic boundary conditions, and the fields in the lattice region are due to crosstalk between neighboring defects. By increasing the size of the supercell, this crosstalk can be minimized, however the computational time significantly increases. Also, the 6-fold azimuthal symmetry of the structure implies that SOL modes in vacuum contain only $m = 6n$ azimuthal modes for n an integer, reducing the emittance blowup from higher-order modes. Finally, we find that the characteristic impedance decreases with guide radius, as is the case with metallic waveguide structures.

COMPUTATION TECHNIQUES

We use the MIT Photonic Bands (MPB) package, a public-domain code using an iterative eigensolver technique [7]. For a given geometry and Bloch wavevector, MPB computes frequencies and field configurations of supported modes. MPB can compute group velocities of

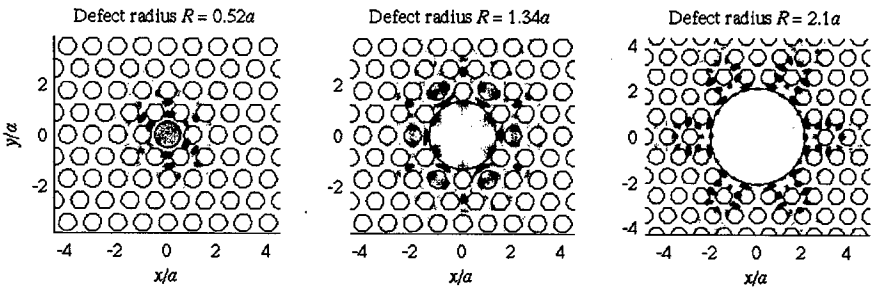


Figure 3: Accelerating modes of several photonic crystal fiber configurations. The shading indicates the axial electric field, which is also the direction of propagation of the mode.

modes as well by applying the Feynman-Hellmann theorem [8, 9].

Using the frequencies and group velocities, we can inductively converge on the longitudinal wavenumber for which a speed-of-light mode exists. Having found a mode for a particular wavenumber, we can use its frequency and group velocity to obtain a linear approximation for its dispersion curve near that wavenumber. The intersection of that approximation with the SOL line gives the wavenumber for the next computation, which yields a mode whose phase velocity is closer to c. Since the iterative eigensolver for each step can be seeded with the field configuration from the result of the previous step, successive steps are quite fast, and convergence to an SOL mode is a computationally light task once the initial mode has been found.

FABRICATION POSSIBILITIES

The 2D structures discussed above are amenable to photolithography, with 50 : 1 apect ratios available from current reactive ion etching equipment. Some investigation into fabrication of these structures has taken place in the past [10]. Fabrication of 3D photonic crystals with omnidirectional bandgaps, such as the "woodpile" structure [11], is an active area of research. A number of techniques are being developed, including multilayer lithography, wafer fusion, stacking by micromanipulation, self-assembly, and others [12]. PCF manufacturing is a large and growing area of research in industry, since photonic crystals allow for tailoring optical properties to specific applications, from nonlinearity for wavelength conversion in telecommunications to large mode area for materials processing [13].

CONCLUSION

Photonic crystals have great promise as potential laser accelerator structures. Not only do they support accelerating modes, but such modes exist for a wide range of geometric parameters. While the basic accelerator parameters have been examined, much remains to be done to understand the properties of these structures. Wakefield computations as well as coupling structure design have yet to be explored. In addition, there are many photonic crystal lattices for which accelerating modes have not been computed, including 3D geometries. However, manufacturing technology, numerical simulation capability, and theoretical understanding continue to progress at an extraordinary rate, driven by industry forces. We therefore expect a bright future for photonic crystals as an accelerator technology.

REFERENCES

[1] J. D. Joannopoulos, R. D. Meade, and J. N. Winn, *Photonic Crystals: Molding the Flow of Light* (Princeton University Press, Princeton, NJ, 1995).

[2] M. A. Shapiro et al., Phys. Rev. ST Accel. Beams **4**, 042001 (2001).

[3] X. E. Lin, Phys. Rev. ST Accel. Beams **4**, 051301 (2001).

[4] D. F. Edwards, in *Handbook of Optical Constants*, edited by E. D. Palik (Academic Press, 1985), vol. 1, p. 547.

[5] L. Schächter, R. L. Byer, and R. H. Siemann, in *Advanced Accelerator Concepts: Tenth Workshop, Mandalay Beach, CA, 2002*, edited by C. E. Clayton and P. Muggli, U.S. Department of Energy (American Institute of Physics, Melville, NY, 2002), no. 647 in AIP Conference Proceedings, pp. 310–323.

[6] B. C. Stuart et al., Phys. Rev. Lett. **74**, 2248 (1995).

[7] S. G. Johnson and J. D. Joannopoulos, Optics Express **8**, 173 (2001).

[8] See for instance J. J. Sakurai, *Modern Quantum Mechanics*, Rev. ed. (Addison-Wesley, Reading, MA, 1995)

[9] S. G. Johnson et al., Phys. Rev. E **65**, 066611 (2002).

[10] Wendt et al., J. Vac. Sci. Technol. B **11**, 2637 (1993).

[11] S. Y. Lin et al., Nature **394**, 251 (1998).

[12] S. G. Johnson, *Fabrication of Three-Dimensional Crystals: Those Clever Experimentalists*, from lecture series *Photonic Crystals: Periodic Surprises in Electromagnetism*, `http://ab-initio.mit.edu/photons/tutorial/`

[13] René Engel Kristiansen, *Guiding Light with Holey Fibers*, OE Magazine June 2002, p. 25.

Proceedings of the 2003 Particle Accelerator Conference

THE ORION FACILITY*

R.J. Noble#, E.R. Colby, D.T. Palmer, R.H. Siemann, D. Walz, SLAC, Stanford, CA, USA
R. Byer, Stanford University, Stanford, CA, USA
C. Joshi, W. Mori, J. Rosenzweig, UCLA, Los Angeles, CA, USA
T. Katsouleas, USC, Los Angeles, CA, USA

Abstract

ORION will be a user-oriented research facility for understanding the physics and developing the technology for future high-energy particle accelerators, as well as for research in related fields. The facility has as its centerpiece the Next Linear Collider Test Accelerator (NLCTA) at the Stanford Linear Accelerator Center (SLAC). The NLCTA will be modified with the addition of a new, high-brightness photoinjector, its drive laser, an S-band rf power system, a user laser room, a low-energy experimental hall supplied with electron beams up to 60 MeV in energy, and a high-energy hall supplied with beams up to 350 MeV. The facility design and parameters are described here along with highlights from the 2nd ORION Workshop held in February 2003.

INTRODUCTION

ORION will be a user-oriented research facility for understanding the physics and developing the technology for future high-energy particle accelerators, as well as for research in related fields [1]. The facility has as its centerpiece the Next Linear Collider Test Accelerator (NLCTA) at SLAC. The NLCTA will be modified with the addition of a new, high-brightness photoinjector, its drive laser, an S-band rf power system, a user laser room, a low-energy experimental hall supplied with electron beams up to 60 MeV in energy, and a high-energy hall supplied with beams up to 350 MeV. Facility construction is anticipated to start in October 2003, contingent upon funding approval, and first beam is planned for 2005. Notably, the first experiment, E163, "Laser Acceleration at the NLCTA", has been approved by SLAC. In February 2003, about 90 participants attended the 2nd ORION Workshop, and new suggestions were received regarding possible experiments and the facility design [2].

FACILITY DESIGN

The general parameters for the ORION Facility are given in Table 1, and the conceptual layout is shown in Figure 1. The parameters have evolved from the input of many potential users, and various anticipated experiments are tabulated in the ORION Technical Design Study [3]. User requests indicate the need for bunch charges of 2 pC to 4 nC, 1 to 2 bunches (drive-witness), normalized rms emittances of <2 to 40 mm-mrad, rms bunch lengths of 0.1 to 2 psec, and minimum relative energy spreads $\leq 10^{-3}$. For certain plasma wakefield acceleration experiments, a drive bunch with greater than 1 nC charge and a witness bunch up to 0.3 nC will be desired, and this can be accommodated by splitting the laser pulse energy to produce two bunches from the photoinjector. The Mg cathode and specified laser energy at ORION are sufficient to produce several nC of total charge. Beam dynamics studies [3] have shown that a single bunch of 4 to 5 nC can clear the aperture of the NLCTA X-band prebuncher cavity, which is the limiting device of the injector. Overall the parameters in Table 1 are consistent with experimental needs anticipated in the first years of ORION operation.

Table 1. Parameters of the ORION Facility

Beam Energies	7 MeV (Source); 7-67 MeV (LE Hall); 67-350 MeV (HE Hall)
Charge per Bunch	0.25 nC optimum, adjustable up to a nominal maximum of 1 nC
Number of Bunches	1 or 2 (split charge)
Transverse Emittance	$\leq 2\times10^{-6}$ m, normalized rms (0.25 nC)
Bunch Length	1.8 psec, rms (0.25 nC)
Charge Stability	±2.5%, pulse-to-pulse
Timing Jitter	0.25 picosec, rms
Repetition Rate	10 Hz
Average Beam Power	0.67 W at 67 MeV; 3.5 W at 350 MeV (1 nC bunches)
Electron Source	1.6 cell, S-band (2.856 GHz) Photoinjector, Mg cathode
Drive Laser	Commercial Ti:Sapphire, 266 nm wavelength, 1 mJ output
Source RF System	SLAC 5045 Klystron; Solid-State, NLC-type Modulator
Injector Linac	Two X-band (11.4 GHz), 0.9 m, 30 MV, NLC structures
High-Energy Linac	Four X-band, 1.8 m, 72 MV, NLC structures

ORION modifications to the NLCTA consist of the S-band photoinjector, its drive laser, the radio-frequency power system, the beamlines to the experimental halls, the drive laser room, user laser room, and the low-energy and high-energy experimental halls.

*Work supported by DOE contract DE-AC03-76SF00515.
#noble@slac.stanford.edu

0-7803-7738-9/03/$17.00 © 2003 IEEE

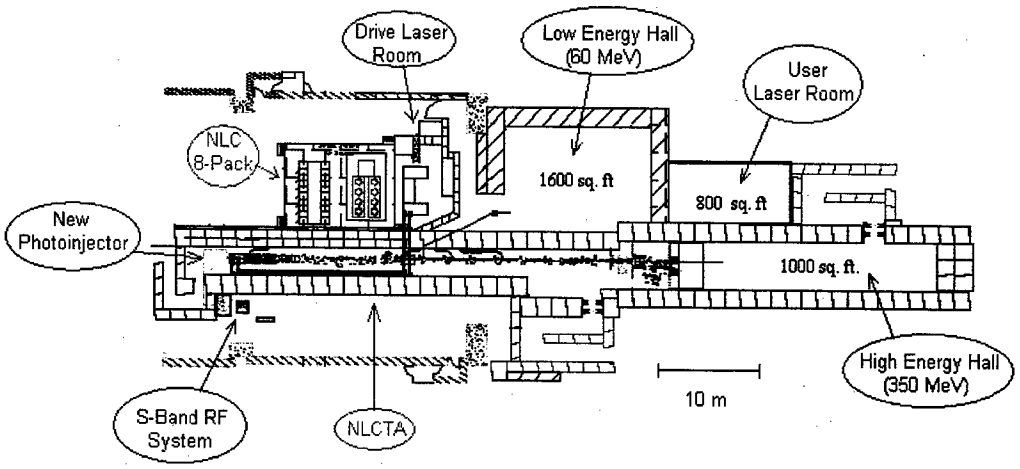


Figure 1. Conceptual layout of the ORION Facility at the NLCTA.

The S-band rf gun for ORION is the standard 1.6 cell design used at BNL, ANL and UCLA. The gun was fabricated by J. Rosenzweig's group at UCLA and brazed at SLAC (Figure 2). Power conditioning of the gun is in progress at SLAC. Prior to actual use on ORION, an Mg cathode will be installed in place of the temporary Cu cathode plate. With its higher quantum efficiency (photoelectrons per laser photon), Mg will permit the use of a less expensive, low-power laser for E163, the first experiment planned for the ORION facility, while also providing 1 nC bunches for NLC cavity phase shift measurements. The use of Mg cathodes on these guns is well established, including several years of operation at the BNL Accelerator Test Facility.

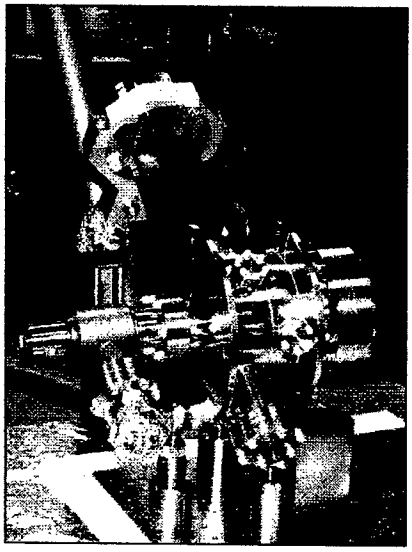


Figure 2. ORION rf gun after the final braze at SLAC.

BEAM DYNAMICS STUDIES

The production and successful transport of a wide variety of beams is essential to the flexibility of the ORION facility. Detailed simulations of the beam dynamics for the NLCTA with the rf gun installed have been completed using the computer codes Parmela [4] and Elegant [5] through the NLCTA beamlines into the low- and high-energy halls. With many experiments calling for high charge, high brightness beams, the production and preservation of these beams has been carefully studied [3]. The beamlines pose several challenges unique to the ORION facility: injection from an S-band gun into an X-band accelerator requires the production of higher density bunches than is typically optimal to suppress rf-induced emittance growth in the accelerator; the present NLCTA chicane is a 3π design permitting wide variation of the temporal dispersion (R_{56}), but at the expense of strong second-order aberrations in the horizontal plane; beamlines leading to the low energy hall are connected via a 25° dogleg with rather inflexible optics, requiring careful matching and second-order temporal dispersion (T_{566}) control to preserve the profile of high charge bunches. Each of these challenges is soluble, and will provide ample opportunity for exploring injector operation in a new range of parameter space.

ORION WORKSHOP HIGHLIGHTS

The Second ORION Workshop was held in February 2003 at SLAC to revisit the anticipated experiments at ORION, invite new experimental ideas, discuss the on-site needs of potential users, and to generate input on the facility design. There were about 90 participants and 54 papers were published in the proceedings [2]. The four

working groups were Beam-Plasma Physics (chair T. Katsouleas, USC), Laser Acceleration (co-chairs R. Byer, Stanford Univ., Yen-Chieh Huang, National Tsinghua Univ.), Laboratory Astrophysics (chair P. Chen, SLAC), and Particle and Radiation Sources (chair J. Rosenzweig, UCLA). Each working group generated a final summary report, and the interested reader can find those documents in the proceedings.

The Beam-Plasma group made a significant effort to specify the needs for experiments probing the details of plasma wakefields, to investigate efficient energy extraction by an accelerated bunch (the beam-loading issue), and to characterize the tunnel-ionization of gases by intense drive beams, which would eliminate the need for laser-ionization. Plasma wakefield accelerators driven with 10 μm bunches hold the promise of 10 to 100 GeV/m gradients, but dedicated studies of wake phenomena will be required to design a prototype accelerator. Participants concluded that witness bunches ranging from 0.1 to 0.3 nC and sub-picosecond duration are essential for ORION wakefield experiments. The higher charge witness beam has the advantage of "flattening" the wakefield locally, leading to uniform energy gain across the bunch and the associated reduced energy spread essential for colliders. Beam-plasma experiments are very demanding in terms of ultra-fast diagnostics and the need for physics simulations. This group discussed the hardware and software for real time computer modeling of experiments to permit users to perform essential end-to-end simulations from source to the experimental diagnostics.

The Laser Acceleration group explored in detail the beam and facility requirements for seven distinct experiments, providing important input for the facility design. Today laser acceleration is at a stage analogous to where copper-cavity acceleration was in the 1940's. Participants agreed that commercial terawatt peak-power lasers (the analog of klystrons) have now opened a path toward realizing an all-optical accelerator with 1 GeV/m gradients limited only by the surface damage threshold. Optical accelerators based on periodic metal or dielectric arrays, planar waveguides, fiber structures and photonic band-gap devices were all considered at the workshop. Initial calculations of shunt impedances and accelerating efficiencies for some generic structures were presented, and experiments to measure these at ORION were proposed.

The LabAstro group was a new addition to ORION for this workshop, and enthusiastic participants explored possible experiments to calibrate cosmic ray measurement techniques, to investigate the dynamics of cosmic acceleration in the lab, and to use laser and particle beams as probes for fundamental astrophysics. The availability of large area halls with electron energies from less than an MeV to hundreds of MeV was seen as a new opportunity for calibrating cosmic-ray, air fluorescence and radio emission detection methods. Six experiments were suggested to investigate the dynamics of astrophysical processes, including Alfven shock particle acceleration, hybrid-mode excitation and particle trapping in beam-driven, magnetized plasmas (jet physics), beam interactions with magnetosonic solitons and shocklets, diamagnetic pulse acceleration, the behavior of positron-electron plasmas produced via laser-matter interaction, and the simulation of electroweak, neutrino-plasma instabilities (relevant to supernova energy transport) with conventional electron-plasma instabilities. Electron and laser beams can be used to both excite and diagnose simulated astrophysical plasma phenomena. Participants recognized that with the space available for lasers at ORION, the opportunity to use both lasers and particle beams at *one facility* would be unique for lab-astro experiments, enabling rapid progress in the field.

The Particle and Radiation Sources group hosted a wide variety of talks on the electron source and diagnostic requirements needed for the proposed ORION experimental program. The NLCTA chicane with its second-order aberrations and lack of diagnostics is not well suited to transport the high-brightness, short bunches for ORION plasma wakefield experiments, and replacement with alternate transport was recommended. Velocity bunching at the source was suggested for further study to achieve short ORION bunches with small energy spread. Dedicated diagnostic systems for longitudinal beam measurements after the injector and after the transport line to the low-energy hall were also suggested.

The basic ORION facility design with two experimental halls and one user laser room has remained the same in light of the 2nd ORION Workshop. The option for expanding the High Energy Hall to roughly 5000 square feet in the future needs serious consideration given the list of new high-energy experiments suggested at the workshop. For beam-plasma and lab-astro experiments, the option for electron beams up to 700 MeV is attractive for studying the energy dependence of various instabilities and beam-wakefield interactions. With the completion of the so-called NLC 8-Pack klystron/modulator array this year, such higher energy beams will be achievable once new NLC cavities are perfected and installed permanently at the NLCTA.

Originally envisioned for advanced accelerator work, the ORION concept is now evolving to serve researchers in plasmas, lasers and astrophysics as well. ORION's greatest returns are likely to be the many unanticipated discoveries from its multidisciplinary group of users.

REFERENCES

[1] http://www-project.slac.stanford.edu/orion/
[2] Presentations from the Second ORION Workshop, February 18-20, 2003, Stanford, CA, R. Noble and R. Reitmeyer, editors, SLAC-WP-026, at web address: http://www.slac.stanford.edu/cgi-wrap/pubpage?SLAC-WP-026
[3] ORION Research Facility Technical Design Study, April 12, 2002, available at the ORION website [1].
[4] H. S. Deavon, *et al,* LA-UR-90-1766, p. 137 (1990).
[5] M. Borland, APS LS-287, Sept. (2000).

MINIATURIZATION TECHNIQUES FOR ACCELERATORS

Wonill Ha*, Justin Mansell†, Tomas Plettner, Jeffrey Wisdom, Stanford University, Stanford, CA, USA
James Spencer, SLAC, Menlo Park, CA 94025, USA

Abstract

The possibility of laser driven accelerators[1] suggests the need for new structures based on micromachining and integrated circuit technology because of the comparable scales. Thus, we are exploring fully integrated structures including sources, optics (for both light and particle) and acceleration in a common format – an accelerator-on-chip (AOC). Tests suggest a number of preferred materials and techniques but no technical or fundamental roadblocks at scales of order 1μm or larger.

INTRODUCTION

The exponential growth in the complexity of high energy accelerators and colliders dictates techniques that leverage infrastructures such as those being developed for optical telecommunications (MEMS) and integrated circuit electronics (SOC). Acceptable materials (and wavelengths) must allow velocity synchronism between many laser and electron pulses with optimal efficiency in high radiation and intense laser fields.

Tests related to deep etching, fabrication and radiation damage on candidate amorphous and crystalline materials shows Si to be ideal from 1.2-10 μm but other candidates exist[2]. We have made micro-planar electron optics and wigglers on Si capable of pulsed currents of >1 A without failures and etched micro structures in Si having aspect ratios on a wall's height-to-thickness of 500:1 with surfaces that were flat, parallel and smooth to <10 nm. Also, we have made optical structures such as gratings and matrices of pyramidal structures for field emission and alignment at different μm level scales.

Representative examples are discussed to suggest that there are IC analogs for essentially *all* particle and light sources as well as their respective optics. To date, we have found no technical nor fundamental roadblocks to building such integrated systems on scales consistent with infrared lasers. The need for many parallel beams of both light and particle implies useful applications in other fields.

Still, many questions remain that need answering when even the circuit board equivalent seems beyond reach but this is roughly equivalent to the terawatt table top laser (T^3) and SLAC linac that was used to do photon acceleration by electron beams[3] – the inverse process. Now, everyone takes the T^3 laser for granted. Thus, our goal is to show the possibility of an AOC by showing that it is consistent, or not inconsistent, with microelectronic/photonic integration technologies that should provide incredible leverage.

* Now at Novallux, Inc
† Now at Qynergy, Inc

GENERAL TYPES OF STRUCTURES

In many regions, the mean directions of both laser and particle will be the same. In such cases, it is then useful to impose an axis or plane of symmetry i.e. cylindrical or planar structures. In either case, tensor beams are possible[4] although they appear easier to implement in a multiplanar form. For several reasons, we will consider only planar structures below.

Within this class, several possibilities can be considered for integrated systems including: 1) In-Plane, 2) Out-of-Plane, 3) 3-Dimensional and hybrids such as 4) Multi-Planar as opposed to typical, off-chip, discrete components. Types 1), 2) and 3) are *single* wafer structures with 1) and 2) distinguished by the number of fab steps required to get more than one active layer whereas 3) can have true 3D open structures. For OP type, we include structures made on top of other structures or ones fabricated on opposite faces of a wafer but still planar or ones using layer transfers to a single wafer. MP includes the possibility of more than one wafer e.g. stacked, OP wafers requiring precise alignment with high relative placement accuracy.

Basic Examples

We have made many etching tests to verify and understand previous work and to extend it to our applications. Our masks usually include several structures over a range of scales to test different etchant and mask conditions. While it is usually possible to visually discriminate out-



Figure 1: A 500 μm period grating etched on (100) Si.

0-7803-7738-9/03/$17.00 © 2003 IEEE

comes with an SEM, it is difficult to capture good photos of the smaller, deeper feature sizes, e.g., 5-20 μm slits in a 500 μm thick wafer. We note that the fastest to slowest etch directions in Si are [211], [110], [100] and [111].

Reflective and Diffractive Optics elements (DOE) are wavefront transformers that can *replace* or improve (via some hybrid form) classical optical elements. Of interest is the use of reticulated steps (binary optic approximation) to correct both spatial and color aberrations in lenses or any optical system. Fig. 1 shows a large period (d=500 μm) grating with mirror surfaces, etched to a depth of $\sim$290 μm along the (111) planes of a (100) Si wafer. The edge angle with the top surface is 54.6°. This grating is intended for reflective optics but has many refractive-diffractive uses.

In refractive mode, for monochromatic light below the bandgap, arrays of beamlets can be produced with angles, relative to the incident beam, and relative separation from one another calculable from:

$$m\lambda = d\,sin(\theta_m)\,. \qquad (1)$$

m is the order. Our source example[4, 5] uses two DOEs.

With decreasing d, angles increase and for d< λ, an AR surface superior to AR coatings can be generated using such patterns with differing index. An array of line sources (Fig. 1) or points (Fig. 2) are practical since subwavelength binary features < 50 nm have been produced.

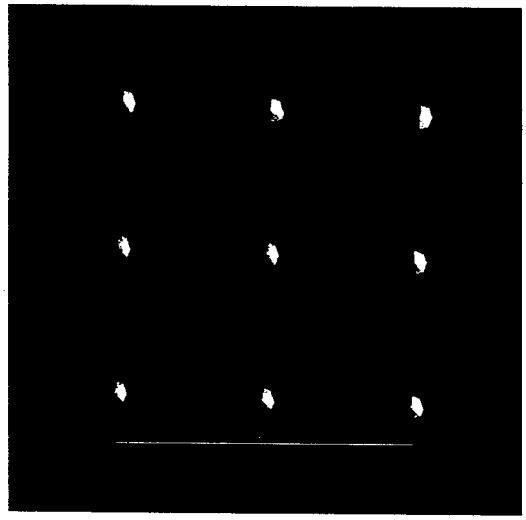


Figure 2: A 500 μm period matrix etched on (100) Si[6].

Planar Undulators and Optics for particles exist for all of the above structure types and it is straightforward to write down coil-dominated fields for their many physical expressions. The hardest aspect is to assemble and measure their fields without a test beam. Using gold, many undulator patterns were produced on both quartz and Si wafers. By scaling the line width and length for 20, 50 and 100 μm periods they have the same resistance R and have been driven with 1 ns pulse currents up to several amps without failure by conditioning to higher currents while carefully monitoring and constraining R. To accommodate particle beams, periodic trenches and slits are needed that can also be used as pattern generators. An important question is whether they can be made deep enough to accommodate a true tensor beam structure. In Fig. 3 we demonstrate the possibility of etching a single, thick wafer **or** stack to give accurate registration between wafers. IR light does not provide sufficient resolution.

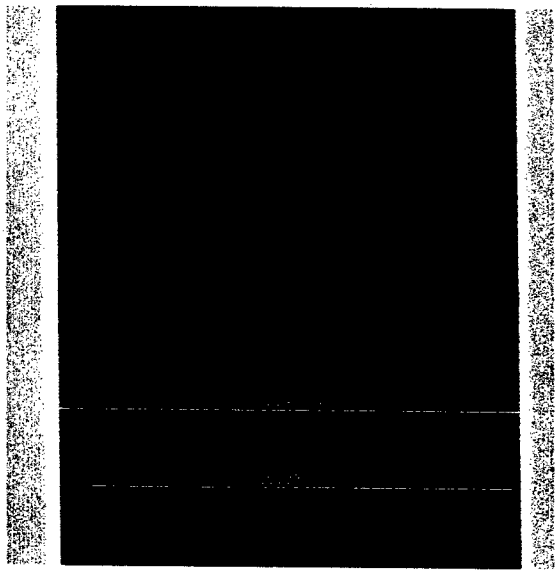


Figure 3: View of a 50 μm slit etched along the [111] lines in a 500 μm thick, (110) Si wafer. The wall height-to-thickness ratio is 500:1. Thinner slit widths are harder to view and thicker ones have worse resolution.

In this and similar SEM pictures, we showed that it is possible to go from an unknown [111] orientation on a (110) wafer to make small accurate slits with length-to-width ratios of 250:1 and wall height-to-width ratios of 500:1. We also demonstrated that the surface of the walls were flat, parallel and smooth to better than $\approx$10 nm by finding and focusing on particles < 100 nm in size on the wall surfaces. Although we have achieved 15-2000 μm slits on one wafer with a single etch it is clear that at least two or more etching steps are needed for such cases.

High Q Examples

Solenoids/Helical Undulators are difficult elements. Most standard electronic components are in-plane but some components such as the inductors used in VCOs could be improved (Q, parasitic effects, etc.) by 3D versions. Today, pancake coils are used whose axis is perpendicular to the wafer surface. By requiring some form of in-plane coil e.g. a spiral, both area and feature size are increased inefficiently because the line width only needs to be a few μm (skin depth at 1 GHz)[7]. Such coils also drive the field into the material which increases the frequency dependent impedance via eddy currents through the substrate and other nearby impedances. Improvements are clearly possible. Chua et al.[8] developed a 3D coil with a higher Q by

balancing compressive and tensile stress in lithographically defined, deposited material. This demonstrates a direct IC analog for the solenoid in magnetic optics and by extension the helical undulator.

Microcavity, Optical Resonators are one of the more important optical systems one needs to integrate with other photonic components. The laser AOC itself is a resonator but needs to integrate an active medium with other such elements. The semiconductor diode is one example while spherical or ellipsoidal "microspheres" are another.

The Alignment Problem

For perspective, Si transmits only IR light >1.1 μm for normal incidence[2] which is not adequate for wafer-to-wafer matching or aligning top-bottom masks. Wafer flats and notches are often rounded to improve breakage but quoted accuracy of $\pm$ 1° is a problem. Improvements in the original boule x-ray measurement and transfer with optical polishing of the flats is possible since the original batches undergo good control and labeling.

Tensor Source and Laser Driver

For conventional radio frequency accelerators, the rf gun was a major improvement that was well matched to the rf accelerator. Increasing rf frequency improves things because it allows higher gradients that increase the inertial resistance to space charge blowup out of the cathode as well as helps to avoid bunching systems. However, if a buncher is required, for laser based frequencies employing conventional rf guns, then space charge debunching and transverse blowup appears difficult to avoid. This remains true even when the microbunch charge is considerably reduced. Thus, laser acceleration schemes require new source techniques compatible with the wavelength regime.

A generic drive laser system is suggested in Fig. 4 where the laser depends on the system to be driven. It could be used, in various forms, to drive a pin-cushion cathode to produce tensor beams or as a power source for the accelerator where Ti:Sa, Er:YAG and Cr:ZnSe are possible candidates. Notice that several elements in this Fig. 4 could be DOEs in trenched Si or Silica.

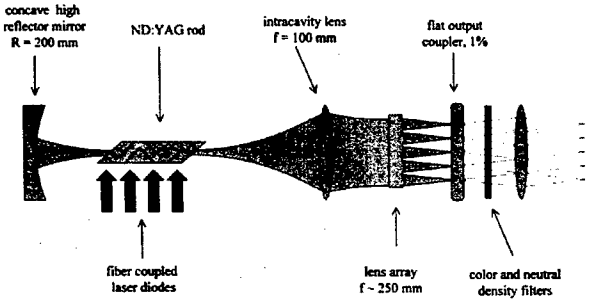


Figure 4: Laser driver for multibunch source & accelerator.

Fig. 5 shows a gun illuminated from the output of Fig. 4. Tips may not be necessary for some materials such as GaAs and this may well be advisable for stability and lifetime but these characteristics depend on the applied voltages, wavelengths and intensities. Polarized beams can be generated using circularly polarized light. STM probes produce about 4 pA/V of ballistic electrons from GaAs with no laser light in a technique called ballistic electron emission.

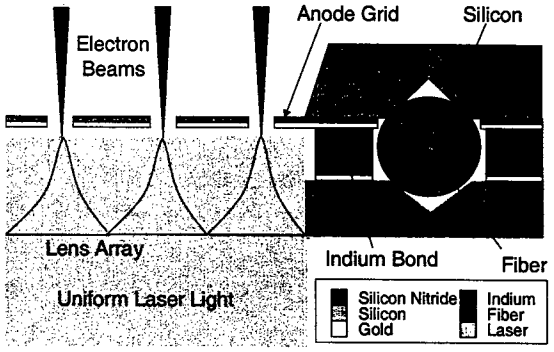


Figure 5: Schematic for a backlit, gated photocathode[5].

ACKNOWLEDGMENTS

We thank Bob Kirby and Frane Marcelja of SLAC's Physical Electronics Group for the SEM work, Vincent Speiring of Kymata, Inc for some deep etching experiments and our colleagues on the LEAP experiment – especially Prof's. Byer, Harris and Siemann for their various support of this work under U.S. Dept. of Energy contracts DE-FG03-97ER41043 and DE-AC03-76SF00515.

REFERENCES

[1] R.L. Byer et al., "Progress of the Laser Electron Accelerator Project at Stanford University", PAC'01, Chicago, June 2001.

[2] Eric Colby, Gary Lum, Tomas Plettner and James Spencer, "Gamma Radiation Studies on Optical Materials", *IEEE Trans. Nucl. Sci.* 49(2002)2857.

[3] C. Bamber et al., "Studies of Nonlinear QED in Collisions of 46.6 GeV Electrons with Intense Laser Pulses", *Phys. Rev.* D60(1999)092004.

[4] J.E. Spencer, "Limitations Imposed by Beam-Beam Effects and Their Remedies ", *Intl. J. Mod. Phys.* 13(1998)2479 and also: *Intl. J. Mod. Phys.* 15(2000)2543.

[5] J.E. Spencer, "The Silicon Lattice Accelerator", to be published in *Intl. J. Mod. Phys.*.

[6] One might expect a four sided pyrimidal structure but 8, as shown here, and 16 was discussed in Neil A. Cade et al., *IEEE Trans. Elect. Dev.* 36(1989)2709. A sharper, possibly more acceptable, tip is possible using (110) wafers and coating.

[7] This is clearly inadequate for many applications such as optical computers. Semiconductor lasers have operated at rates > 1 THz. At 29 GHz, several pJ pulse energies in ps pulses have been demonstrated: Krainer et al., "29 GHz modelocked miniature Nd:YVO_4 laser", *Elect. Lett.* 35(1999)1160.

[8] C.L. Chua, D.K. Fork, K.F. Van Schuylenbergh, J.P. Lu, "Self-assembled out-of-plane high Q inductors", Solid State Sensor, Actuator and Microsystems Workshop, Hilton Head, SC, June 2002.

PLASMA WAKEFIELD ACCELERATION OF AN INTENSE POSITRON BEAM: CORRELATION BETWEEN TIME-RESOLVED AND TIME-INTEGRATED ENERGY DIAGNOSTICS

B.E. Blue,*†# P. Muggli,§ M.J. Hogan,‡ C.L. O'Connell,‡ C. Clayton,* F.-J. Decker,‡ C. Huang,* R. Iverson,‡ K.A. Marsh,* W.B. Mori,* D. Walz,‡ T.C. Katsouleas,§ R. Siemann,‡ C. Joshi*

* University of California Los Angeles, Los Angeles, CA 90095
§ University of Southern California, Los Angeles, CA 90089
‡ Stanford Linear Accelerator Center, Menlo Park, CA 94025

Abstract

The E162 experiment at the Stanford Linear Accelerator Center was the first experiment in which a positron beam gained energy in a plasma wakefield accelerator [1]. A single positron bunch both excited (gave energy to) and witnessed (extracted energy from) the plasma wakefield. The energy dynamics within the single positron bunch were measured in a dispersive section of the beamline with both time-resolved (1 ps streak camera) and time-integrated (CCD camera) diagnostics. This paper will correlate the energy gain and loss measurements from both diagnostics.

MOTIVATION

The bunch length (σ_z/c=2.4 ps) used in the E162 experiment was long enough to be temporally resolved using current state of the art streak cameras. However, streak cameras do not exist to temporally resolve the dynamics within the beam as the bunch length is shortened in future experiments (E164: σ_z/c ~300 fs; E164X: σ_z/c ~30 fs). Therefore, the use of time-integrated diagnostics is mandated and a methodology must be generated in order to extract the accelerated particles from the back of the bunch from data that contains both the accelerated and decelerated particles in the entire bunch.

E162 EXPERIMENT

The experimental setup has been described in detail elsewhere [2], but the salient features will be briefly introduced. A 730 μm long, 40 μm round positron bunch containing $1.2\text{x}10^{10}$ particles was propagated through a 1.4 meter long plasma of density $0\text{-}2\text{x}10^{14}$ cm^{-3}. Upon exiting the plasma, the beam was imaged onto a 1 mm thick aerogel Cherenkov radiator using a magnetic imaging spectrometer with 291 MeV/mm of dispersion in the vertical plane. The visible Cherenkov radiation was imaged onto the slit of a streak camera and onto a CCD camera. By measuring the change in position of individual beam slices in the dispersive plane with the streak camera, the energy distribution in a single bunch could be measured. This paper will address how the energy gain in the back of the positron bunch and energy loss by the core of the bunch can be measured on the CCD camera at the expense of losing temporal information.

† Present Address: Lawrence Livermore National Laboratory, Livermore, CA 94550
# Email: blue3@llnl.gov

TEMPORALLY RESOLVED ENERGY CHANGE OF A SINGLE POSITRON BUNCH

As a ultrarelativistic positron beam propagates through an underdense plasma, the highly mobile plasma electrons are pulled in towards the beam by the beam's space charge field. As these plasma electrons from various radii arrive on the axis of the beam at various times and overshoot, they create a wakefield structure that has complex longitudinal and transverse electric field components [3]. The energy change induced on a positron bunch by the plasma wakefield is shown in Figure 1. The main body of the beam loses 52±16 MeV driving the plasma wave, while the back of the beam extracts energy from the wave and in turn gains 79±19 MeV.

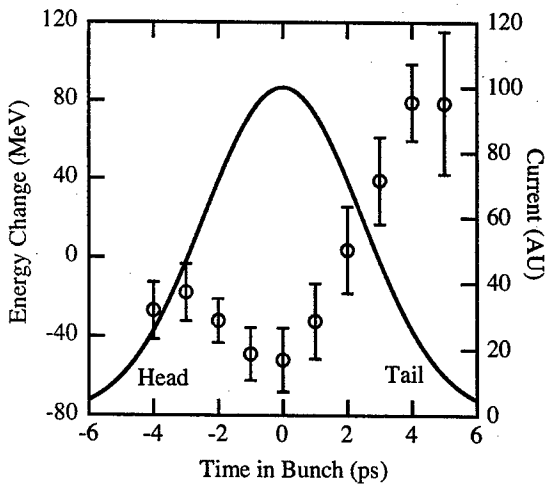


Figure 1: Time slice analysis (red circles) of the energy dynamics imparted on a single positron bunch (blue line) after it passed through 1.4 m of $1.8\text{x}10^{14}$ cm^{-3} plasma. The front half of the beam losses energy driving the plasma wave, while the back of the beam is accelerated by the plasma wave.

0-7803-7738-9/03/$17.00 © 2003 IEEE

METHOD OF MEASURING ENERGY GAIN FROM A TIME-INTEGRATED CCD DIAGNOSTIC

The time-resolved streak camera diagnostic allowed us to measure the energy of 1 ps slices within a single positron bunch. Furthermore, the energy of each slice could be measured independently from the energy and/or spot size fluctuations of other beam slices. However, when a time integrated diagnostic is used, the energy dispersed profile will contain the superimposed contributions of spot size (focusing and defocusing) and energy gain/loss of each beam slice. In an ideal design, the dispersion would be much greater than the undispersed spot size and therefore spot size fluctuations could be neglected. Due to hardware constraints in our experiment, the spot size was on the order of the dispersion. This implies that the measured energy gain will consist of a shift in the distribution of particles whose contribution to the overall energy dispersed profile will be partially masked by other particles which were not accelerated.

With a general overview of measuring the energy gain on a time-integrated diagnostic now introduced, the specific method used in our measurement will now be introduced. The first step was in determining the extent of the focusing/defocusing of the positron beam. Although the complex wakefields setup non-uniform focusing and defocusing along the length of the bunch [4], the overall extent of the focusing for the entire bunch can be measured. This is shown in Figure 2. The plasma off RMS spot size at the Cherenkov radiator plane is about 210 μm, while at the density of interest for our analysis (1.8×10^{14} cm^{-3}), the spot size has blown up by ~10 % to 230 μm. In energy space this width corresponds to an energy width of ~70 MeV.

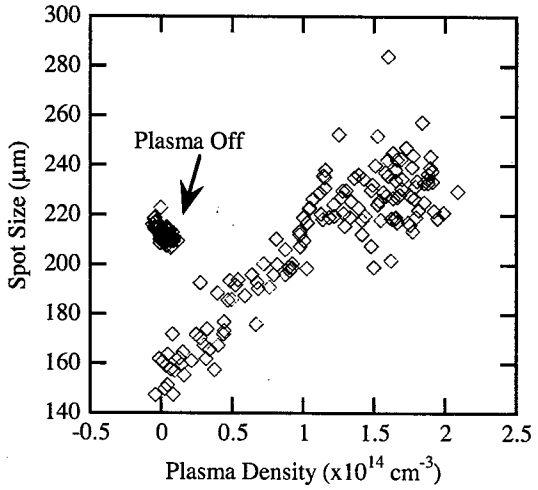


Figure 2: Plasma focusing of the positron beam.

The next step is to look at the profiles of the beam in the energy dispersed plane. These profiles were generated by acquiring a time-integrated CCD image of the positron beam at the Cherenkov plane. The image was integrated in the non-dispersive plane to remove ambiguity about which part of the beam was sampled by the profile. Figure 3 shows the acquired profiles for both the plasma off (dashed blue line) and plasma on (solid red line) cases. The peak of the plasma off case was normalized to 28.5 GeV since we are interested in changes to the beam energy. Since the contributions to the profiles are from both spot size and energy change, the x-axis is labeled with both units. We know that an energy change in the beam is distorting the profile because the profile is not symmetric about the origin, a fact confirmed from the time-resolved streak camera data. Focusing and defocusing will symmetrically expand or contract the distribution, while a change in energy will shift the distribution towards the left (energy loss) or right (energy gain). As shown in Figure 3, at a density of 1.8×10^{14} cm^{-3}, the beam losses energy driving the plasma wave, and additionally, part of the beam has gained energy.

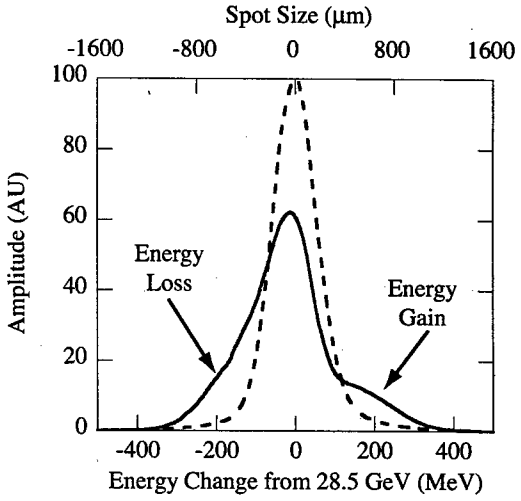


Figure 3: Profile of positron beam in the dispersive plane. The profile of the beam sans plasma (dashed blue line) is due to the spot size of the beam. The profile of the beam after propagating through 1.4 m of plasma (solid red line) includes the effect of focusing/defocusing and energy gain/loss.

To extract the magnitude of the energy gain, a Gaussian was fit to the energy gain distribution of Figure 3. This fit is shown as a dashed black line in Figure 4. Since the dispersion induced shift in position is on the order of the beam RMS spot size, part of the Gaussian fit will be masked by the rest of the beam. This is shown in Figure 4 as the dashed black line shown inside of the beam profile (solid red line). The measured energy gain of 90 MeV was determined from the mean position of the Gaussian fit. This is in reasonable agreement with the streak camera data which measured an average energy gain of 79 MeV over the last two slices of the beam as seen in Fig. 1.

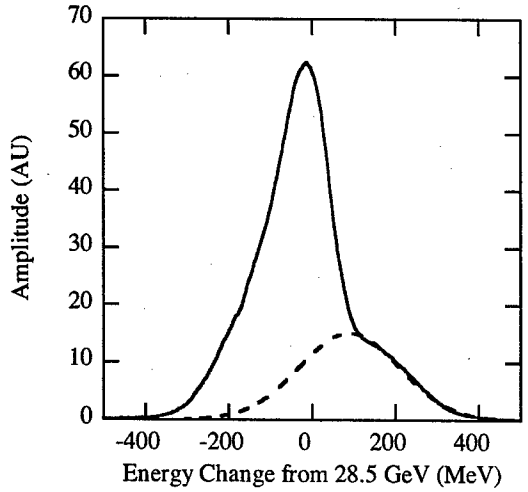


Figure 4: Profile of the plasma modulated positron beam in the dispersive plane (solid red line) and a Gaussian fit to energy gain (dashed black line) in the back of the positron bunch. An energy gain of 90 MeV was measured.

To determine the average energy loss of the beam, a center-of-energy (similar to center-of-mass) calculation was made on the energy dispersed profile. To remove the energy gain contribution to the profile, the Gaussian fit to the energy gain was subtracted from the profile. The resultant "energy-loss" profile is shown as a dashed black line in Fig. 5. The center-of-energy calculation resulted in an average energy loss by the bulk of the beam of 63 MeV. This is in reasonable agreement with the time-resolved streak camera data that measured an energy loss by the centroid of the beam (0 ps slice) of 52±16 MeV.

We are currently attempting more sophisticated fitting routines to cases where the beam size in the dispersion plane is dominated by initial energy spread, not focusing or defocusing effects. This will be extremely important for the ultra-short beam cases of E164 (σ_z~100 μm) and E164X (σ_z~10 μm) where no comparison with a time-resolved diagnostic will be possible.

CONCLUSIONS

We have used two different methods to measure the energy gain and loss induced on a positron beam in the plasma wakefield accelerator. The time-resolved diagnostic measured an energy gain of 79±19 MeV and the time-integrated diagnostic measured an energy gain of 90 MeV. The time-resolved diagnostic measured an energy loss of 52±16 MeV of the beam centroid, while the time-integrated diagnostic measured an average energy loss of 63 MeV. These two diagnostic measurements are in reasonable agreement with each other, therefore future plasma wakefield acceleration experiments will be able to use time-integrated diagnostics in order to measure energy loss and gain.

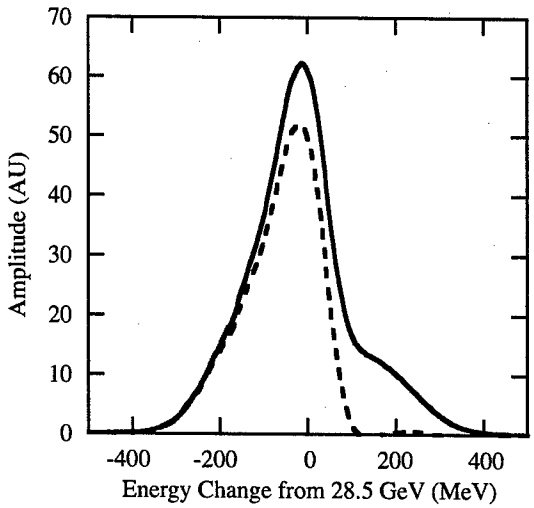


Figure 5: Profile of the plasma modulated positron beam in the dispersive plane (solid red line) and the distribution of charge with the contribution of energy gain subtracted (dashed black line). An average energy loss by the bulk of the beam of 63 MeV was measured.

ACKNOWLEDGEMENTS

This work is supported by U.S. DoE grant numbers DE-FG03-92ER40745, DE-AC03-76SF00515, DE-FG03-98DP00211, and DE-FG03-92ER40727 and by NSF grant numbers ECS-9632735, DMS-9722121, and PHY-00787157.

REFERENCES

[1] B. Blue *et al.*, Accepted for Publication in *Physical Review Letters.*
[2] C. Joshi *et al.*, Phys. Plasmas **9**, 1845 (2002).
[3] S. Lee *et al.*, Phys. Rev. E **64**, 045501 (2001).
[4] M.J. Hogan *et al.*, Accepted for Publication in *Physical Review Letters.*

STATUS OF THE INVERSE FREE ELECTRON LASER EXPERIMENT AT THE NEPTUNE LABORATORY

P. Musumeci, C. Pellegrini, J. B. Rosenzweig, S. Tochitsky, G. Travish, R. Yoder
University of California at Los Angeles, CA 90095, USA
A. Varfolomeev, S. Tolmachev, A. Varfolomeev Jr., T. Yarovoi, RRCKI, Moscow, Russia

Abstract

We report on the status of the Inverse Free Electron Laser accelerator experiment under construction at the UCLA Neptune Laboratory. This experiment will use a 400 GW CO_2 laser to accelerate through a tapered undulator an electron beam from 14.5 MeV up to 55 MeV. The scheme proposed is the diffraction dominated IFEL interaction where the Rayleigh range of the laser beam is 3.5 cm, much shorter than the interaction length (the undulator length is 50 cm). The undulator is strongly tapered in both field and period. The present status of the experiment is reported.

INTRODUCTION

Inverse Free Electron Laser schemes to accelerate particles have been proposed as advanced accelerators for many years [1, 2]. Recent successful proof-of-principle IFEL experiments have shown that along with high gradient acceleration this scheme offers the possibility to strongly manipulate the longitudinal phase space of the output beam [3]. The Inverse Free Electron Laser is in fact, a strong candidate for microbunching and phase-locking electrons at the optical scales. Up to now, though, only modest energy gain has been achieved mostly because of the limitations in the peak radiation power available.

The purpose of the UCLA experiment is to achieve a substantial energy gain and to investigate the longitudinal structure of the electron beam. This experiment addresses problems common to other advanced accelerator schemes like the issue of increasing the interaction length of a laser-driven accelerator dealing with the limitations of radiation diffraction and to increase the final energy gain by tapering of the structure to maintain phase synchronism with the accelerating particles.

At the Neptune Laboratory [4] at UCLA there is the unique opportunity of having a 10.6 μm high power laser and a relativistic high brightness electron beam in the same experimental facility. In the Neptune scheme, the 14.5 MeV electron beam from the split photoinjector linac system, interacts inside an undulator magnet with the high power CO_2 laser focused by a lens (f/25) with focal distance of 2.6 m to a tight spot of few hundreds microns. Because the Rayleigh range of the laser is much shorter than the undulator length, the interaction is diffraction dominated [5]. The fundamental element of the Neptune IFEL experiment is the undulator magnet that provides the coupling between photons and electrons. Strong tapering of both period and magnetic field amplitude is needed for high-gradient acceleration.

In this paper, after a brief status report, we devote a section to the solutions of the problems of spatial alignment and time synchronization of the electron and the photon beam. In the last section we describe the diagnostics setup to analyze the results of the experiment. A Browne-Buechner pole spectrometer is used to get single shot spectrum of accelerated electrons and a Coherent Undulator Radiation based diagnostic to detect microbunching of the electrons down to 3 fs is presented.

INVERSE FREE ELECTRON LASER ACCELERATOR

In the table we summarize the design parameters for the Neptune 10.6 μm IFEL experiment.

Table 1: IFEL at Neptune parameters

Initial beam energy	14.5 MeV
Final beam Energy	55 MeV
Electron beam microbunch size	3 fs
Electron beam emittance	10 μm
Electron beam size at focus	150 μm
Electron beam charge	300 pC

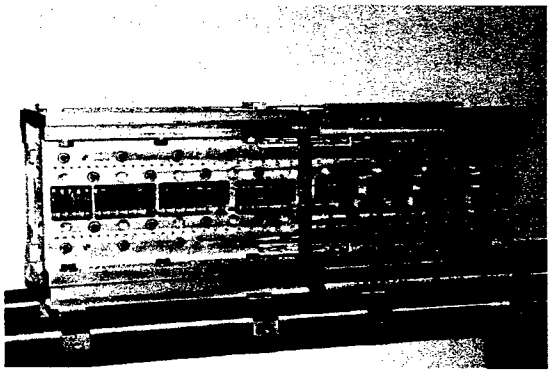


Figure 1: Double tapered 0.5 m long Kurchatov undulator

The undulator is shown in fig.1. It has been designed and built at the Kurchatov Institute of Moscow [6]. In order to

0-7803-7738-9/03/$17.00 © 2003 IEEE

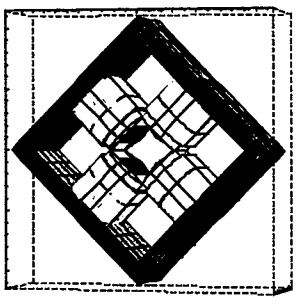


Figure 2: 2.5 inches gap quadrupole magnet. Maximum gradient at 10 amps excitation current = 6.5 T/m

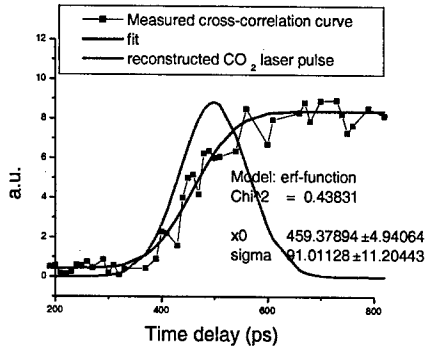


Figure 3: Cross correlation of CO_2 pulse and electron beam.

maintain phase synchronicity and preserve the accelerating bucket along the accelerator, the undulator is strongly (non adiabatically) tapered in period (from initial 1.5 cm to final 6 cm) and magnetic field amplitude (from 0.1 T to 0.6 T). It is 50 cm long and has a constant gap of 12 mm. The construction phase has been completed and the installation in the beamline is scheduled for the next month.

A TW CO_2 laser system capable of generating 100 J in 100 ps pulse is used in the experiment. To match into the 0.5 m long 12 mm gap undulator with the 10.6 μm beam the f/25 geometry will be used. The spot size at the focus has $w_0 \simeq 350$ μm so that the Rayleigh range is 3.5 cm is matching the tapering design. To ensure clipping-free propagation of the focused beam in the vacuum pipe (diameter of the pipe larger than $4w_0$), we designed new quadrupole magnets with large aperture. These magnets have a gap ≥ 2.5 inches and tapered coils to maintain the field gradient ($\simeq 6.5$ T/m) required to focus the electron beam to 150 μm spot size. They have been designed with the help of the 3D magnetostatic code RADIA [7] (fig.2).

The energy of the NEPTUNE LINAC has been upgraded to the design value 14.5 MeV replacing the old klystron. The available S-band RF power is now 22 MW. To improve the high power handling capabilities of the dielectric filled waveguide, a recycling system for the SF_6 is being implemented to purify the gas after any breakdown occurred. Also, the electric field gradient inside the 1.6 cell gun has been limited in the past by severe arcing inside the standing wave cavity. For this reason, a new 1.6 cell gun has recently been installed and it is now in the conditioning stage.

INPUT DIAGNOSTIC

We describe in this section the experimental setup to ensure the spatial and temporal overlapping of the photon and electron beam inside the undulator.

Spatial alignment

To ensure overlapping of the photon and electron beam inside the undulator the alignment is performed on a screen in the middle of the undulator at the common waist. A phosphorous screen fluorescent to the electrons and with a graphite layer coating so that unamplified CO_2 pulse can produce a visible spark, will be used for the alignment of the two beams. A combination of two such screens separated by ~ 0.5 m provides a very small angle misalignment ($\sim$ 1 mrad). The precision of the alignment is limited by the spot sizes and the spatial jitters of the two beams to 50 μm. The acceptance window of the IFEL accelerator has been estimated with the help of three dimensional simulations [?] to be 2 mrad and 100 μm well above the expected values of alignment errors.

Temporal synchronization

A deterministic synchronization of 10 μm and e-bunches is possible because the same 1 μm laser pulse is used for the production of electrons on the photocathode (after frequency quadrupling) and to switch the short CO_2 laser pulse. A first order temporal synchronization is reached by synchronizing at the ns level, the photocathode drive laser and the CO_2 laser system using fast photodiodes. To break the barrier of ns resolution, optical techniques have to be used. The effect we exploit is the electron-beam-controlled transmission of 10 μm radiation in semiconductors [9]. A cross correlation timing technique based on this effect, has already been successfully applied at the Neptune laboratory in the context of the Plasma Beat Wave accelerator [10]. One of the cross-correlation curves is shown in fig. 3.

CO2 laser pulses and 10-ps electron bunches (FWHM) can be deterministically synchronized with a total uncertainty of ~ 20 ps. The tolerance on the error on the temporal synchronization for the IFEL accelerator depends on the laser pulse length. The accelerator performances seriously degrade when the peak power driving the interaction falls below a threshold value. In the Neptune case, the window of acceptance is 30 ps.

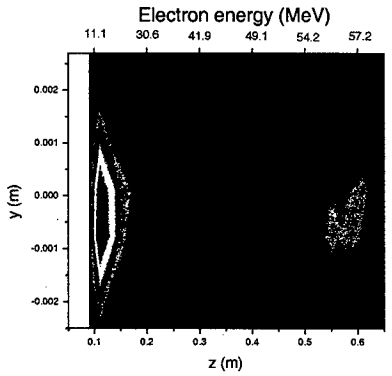


Figure 4: Simulated image at the output slit of the Browne Buechner spectrometer.

OUTPUT DIAGNOSTICS

Browne-Buechner spectrometer

The electron spectrometer consists of a pair of pole pieces energized by a "C-shaped" water-cooled electromagnet and a vacuum box[11]. The gap between the pole pieces is set to 1.5" by the requirement of dumping the high power CO_2 beam after the interaction. Browne-Buechner [12] pole pieces are chosen to maximize the dispersion and the energy coverage. An additional edge entrance angle of 10 degrees provides additional vertical focusing. The tilted exit plane of the vacuum box is made so that the different energies are in focus along the length of the exit plane. The radius of the circular boundary of the magnetic field is 9.3 cm and with 40 amp excitation in the main coils of the spectrometer, the field inside the gap is 1.1 T. With this magnetic field amplitude, electrons of energy up to 65 MeV can be focused on the output slit the spectrometer. The electron beam dynamics through the spectrometer has been simulated with the three dimensional code TREDI [8]. In the fig. 4, we show the image on the output slit of the spectrometer obtained from a "start-to-end" simulation of the Inverse Free Electron Laser accelerator.

Coherent undulator radiation bunching diagnostics

The output beam is microbunched with 10.6 μm period so that any radiation generated by the beam has a spectrum peaked at this wavelength [13]. On the other hand it is not possible to distinguish between beam generated radiation and the driving high power CO_2 laser beam. Moreover a transition radiation screen cannot be inserted in the beam line too close to the exit of the undulator because it would be damaged by the high power driving laser. The proposed solution to detect the microbunching is to look at coherent undulator radiation harmonics. Debunching of the electrons in the drift space following the accelerator is not important, because the radiation source is inside the undulator where the bunching reaches the maximum. The light can be collected few meters downstream with the advantage that the fluence level of the high power CO_2 beam is strongly reduced by diffraction. To further attenuate 10.6 μm light with respect to the harmonics level a SF_6 damping cell can be inserted. SF_6 has a peak in the absorption spectrum at 10.6 μm but it is transparent at the harmonics 5.3 μm and 3.15 μm. An optical grating can then disperse the different wavelengths to selectively measure the power in the radiation harmonics. For 300 pC bunch charge, we calculated an energy of 10 nJ at 3.15 μm in a 3 mrad collection cone, 3 m downstream of the exit of the undulator. Studying how the power radiated in the harmonics changes as a function of the electron charge injected in the accelerator should give a quantitative measurement of the beam bunching [14].

ACKNOWLEDGEMENTS

The authors wish to thank S. Telfer for the help in designing the large aperture quadrupole magnets and C. Clayton for a number of fruitful discussion. This work is supported by U.S. Dept. of Energy grant DE-FG03-92ER40693

REFERENCES

[1] R. Palmer, J.Appl.Phys. **43**, 3014, 1972.

[2] E. D. Courant, C. Pellegrini and W. Zakowicz, Phys. Rev. A **32**, 2813 (1985).

[3] W. D. Kimura *et al.* Phys. Rev. Lett. **86**, 4041 (2001)

[4] C. E. Clayton *et al.*, Proceedings of PAC 1997, Vancouver, CA (1997)

[5] P. Musumeci and C. Pellegrini, AIP Conf. Proc. **569**, 249 (2000).

[6] A. A. Varfolomeev, S. V. Tolmachev, T. V. Yarovoi, P. Musumeci, C. Pellegrini, J. B. Rosenzweig Nucl. Instr. Meth **483**, 377 (2002)

[7] P. Elleaume *et al.*, PAC 97 Proc., 3509 (1997)

[8] L. Giannessi *et al.*, Nucl. Instr. Meth., **393**, 434 (1997)

[9] P., Corkum *et al.*, Journal of Applied Physics, **50**, 3079 (1979)

[10] S., Tochitsky *et al.*, in these proceedings

[11] C. E. Clayton *et al.*, Proc. of PAC 95, Dallas, Texas, 1-5 May 1995

[12] C. P. Browne and W. W. Buechner Rev. Sci. Instr. **27**, 899 (1956) 15.

[13] Y., Liu *et al.*, Phys. Rev. Lett. **80**, 4418 (1998)

[14] A. Tremaine *et al.*, Phys. Rev. E **66**, 3 (2002)

THE UCLA/NICADD PLASMA DENSITY TRANSITION TRAPPING EXPERIMENT*

M. C. Thompson†, W. Lu, W. Mori, J. B. Rosenzweig, G. Travish,
UCLA, Los Angeles, CA 90095, USA
N. Barov, NIU, DeKalb, IL 60115, USA

Abstract

Plasma density transition trapping is a recently purposed self-injection scheme for plasma wake-field accelerators. This technique uses a sharp downward plasma density transition to trap and accelerate background plasma electrons in a plasma wake-field. Two and three dimensional Particle-In-Cell (PIC) simulations show that electron beams of substantial charge can be captured using this technique, and that the beam parameters such as emittance, energy spread, and brightness can be optimized by manipulating the plasma density profile. These simulations also predict that transition trapping can produce beams with brightness $> 5\text{x}10^{14}$ Amp/(m-rad)^2 when scaled to high plasma density regimes. A proof-of-principle plasma density transition trapping experiment is planned for the near future. This experiment is a collaboration between UCLA and Northern Illinois University (NICADD). The goal of the experiment is to capture a $\sim$ 100 pC, 1.2 MeV beam with $\sim$ 4% rms energy spread out of a $2\text{x}10^{13}$ cm^{-3} peak density plasma using a $\sim$ 6nC, 14 MeV drive beam. Status and progress on the experiment are reported.

1 INTRODUCTION

In a plasma wake field accelerator (PWFA) a short, high density electron beam is used to drive large amplitude plasma waves. Accelerating gradients in these systems scale with the non-relativistic plasma frequency $\omega_p = (4\pi n_0 e^2/m_e)^{1/2}$, where n_0 is the plasma density, e is the electron charge, and m_e is the electron mass. It follows that high gradient PWFAs have very short period waves. Accelerating a second beam in such a system and maintaining its energy spread and emittance requires injecting a sub-picosecond beam into the drive beam's wake with well sub-picosecond timing accuracy. This is often referred to as witness beam injection, which has never been fully achieved experimentally. All experiments to date that have injected external electrons into accelerating plasma waves have used either continuous electron beams or beam pulses that were long compared to the plasma wave [1, 2, 3, 4, 5]. As a result the accelerated electrons had an induced energy spread equivalent to the acceleration, which would eventually result in 100% energy spread.

The difficulty of witness beam injection makes it desirable to develop a system in which charge is automatically loaded into the accelerating portion of the wake by the drive beam's interaction with the static plasma environment. This approach allows timing concerns to be eliminated entirely. Bulanov et al. have suggested such a scheme for laser wake-field accelerators (LWFA) in which a region of gradually declining plasma density is used to produce plasma electron trapping through gentle conventional wave breaking [6]. Suk et al. [7] recently proposed a new self-trapping system for the use in the blow out regime of PWFAs where $n_b > n_0$ (underdense condition). In this scheme the beam passes though a sharp drop in plasma density where the length of the transition between the high density in region one (1) and the lower density in region two (2) is smaller than the plasma skin depth $k_p^{-1} = v_b/w_p$, where $v_b \cong c$ the driving pulse's velocity. As the drive beam's wake passes the sudden transition there is a period of time in which it spans both regions. The portion of the wake in region 2 has lower fields and a longer wavelength than the portion in region 1. This means that a certain population of the plasma electrons at the boundary will suddenly find themselves rephased into an accelerating portion of the region 2 wake. When the parameters are correctly set, these rephased electrons are inserted far enough into the accelerating region to be trapped and subsequently accelerated to high energy.

The plasma density transition trapping scheme originally proposed by Suk et al., like the one presented by Bulanov et al., provides very short injection pulses that are phase locked to the plasma wave, but suffers from a lack of beam quality, as defined by energy spread and transverse emittance. These beam quality issues are shared to a significant extent by the optically stimulated injection systems [8, 9], which also have challenging timing requirements due to the multiple interacting laser pulses. We have found, however, that beam quality, as measured by beam brightness, can be greatly enhanced in the plasma density transition trapping system by tailoring the density profile of the plasma and scaling to higher plasma density. The beam brightness benefits of scaling to higher plasma density are quantified by a set of scaling laws that we have developed following similar work concerning rf acceleration in photoinjector sources [10]. From this work we conclude that the beam brightness B obeys the relation

$$B \propto \frac{I}{\varepsilon^2} \propto n_0, \qquad (1)$$

where I is the beam current, ε is the beam emittance, and n_0 is the plasma density [11]. This scaling law has been verified through simulation.

*Work Supported by U.S. Dept. of Energy grant DE-FG03-92ER40693
† mct@physics.ucla.edu

0-7803-7738-9/03/$17.00 © 2003 IEEE

We have planned and constructed a proof-of-principle transition trapping experiment that will use an order 10^{13}cm^{-3} peak density plasma with a density profile optimized to maximize charge capture and minimize energy spread. The predicted brightness of the beam produced in this experiment is about 5x10^{10} Amp/(m-rad)^2. Scaling laws and simulations predict that the same system scaled up to 10^{17}cm^{-3} will produce a beam of brightness 5x10^{14} Amp/(m-rad)^2, which rivals the brightness specified for the LCLS photoinjector [12].

2 PARTICLE-IN-CELL CODE SIMULATIONS

The development of an experimental plan for the transition trapping experiment has evolved through extensive PIC code simulations, primarily with the two dimensional PIC code MAGIC [13]. The majority of this work has centered on the original experimental case model [14] which uses the plasma density profile labelled number 1 in Fig. 1 and has the parameters listed in Tables 1 and 2 under Profile 1. The two dimensional simulation results for this case have been verified using the three dimensional PIC code OSIRIS [15]. Our recent efforts have focused on substantially improving the simulations to reflect the real experimental conditions as accurately as possible.

Profile 1, as seen in the lower trace in Fig. 1, is an idealized plasma density profile composed of linear segments and a step function transition. This idealization, especially the perfect step function transition, is clearly not realistic. Simulations have shown that a finite length density transition is acceptable as long as it is shorter than the plasma skin depth $k_p^{-1} = v_b/w_p$ of the high density region [14]. We produce plasma density transitions by using a perforated metal foil to partially block the flow of a plasm column. An electron beam passing through the column on the far side of the obstruction sees a sharp transition in the plasma density as it passes the foil edge. This process has been studied extensively in simulation [11]. The results of these studies, as well as preliminary experiments, indicate that metal screen barriers can be used successfully to produce transition trapping at our target density in the mid 10^{13}cm^{-3}.

It is exceedingly difficult to produce a plasma density profile with the smooth linear dependencies shown in the lower curve in Fig. 1. A more realistic option is to alter the natural profile of the plasma column as little as possible. As can be seen from Fig. 2, the raw plasma column produced in our plasma source has a gaussian profile with a higher peak density than we originally anticipated. If we use a simple screen of uniform open area to reduce the amplitude of half the gaussian distribution we produce the profile labelled number 2 in Fig. 1. The gaussian based profile is qualitatively similar to the linear profile and preserves most of its features including the gradual decline in density after the transition. This gradual density decline is critical for enhancement of charge capture and the reduction of energy spread [11]. Simulations using this new cut-off gaussian profile indicate that its performance is superior, especially in terms of captured charge, to that of the original linear density profile. This is primarily do the higher peak plasma density. The drive and captured beam parameters from these simulations are presented in Tables 1 and 2, respectively, under Profile 2.

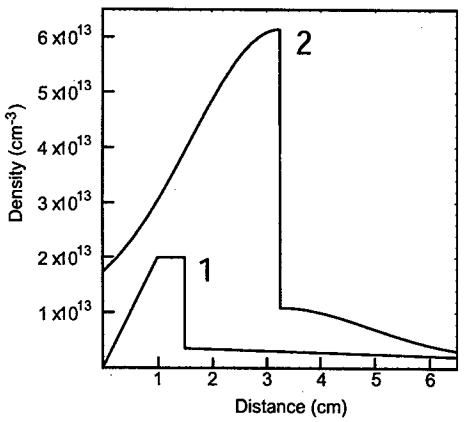


Figure 1: Plasma Density Profiles

There are several factors which will be present in the actual experiment, but which we cannot simulate simultaneously, that will lead to reductions in the captured charge. The value for the captured charge give in Table 2 should therefore be taken as an upper bound. The first of these factors are the finite transition length and effects due to the transition creation mechanism. As indicated above, the first two of the factors have been simulated extensively and should only lead to minor loss of captured charge. An-

Table 1: Driving Beam Parameters

	Profile 1	Profile 2
Beam Energy	14 MeV	14 MeV
Beam Charge	5.9 nC	5.9 nC
Beam Duration σ_t	1.5 ps	1.5 ps
Beam Radius σ_r	362 μm	362 μm
Normalized Emittance	15 mm-mrad	15 mm-mrad
Peak Beam Density	4x10^{13} cm^{-3}	4x10^{13} cm^{-3}

Table 2: Captured Plasma Electron Beam Parameters

	Profile 1	Profile 2
Beam Energy	1.2 MeV	1.5 MeV
Beam Charge	100 pC	470 pC
Beam Duration σ_t	1.7 ps	0.3 ps
Beam Radius σ_r	250 μm	100 μm
Normalized Emittance	24 mm-mrad	16 mm-mrad
Energy Spread (rms)	4%	4%

other important factor is the three dimensional effects associated with the drive beam interacting with the plasma confinement field. A magnetic field on the order of 100 gauss is necessary to confine the plasma in the region where the drive beam will encounter the density transition. This field must be oriented perpendicular to the drive beam path so that the drive beam will actually be steered by the plasma confinement field during the trapping process. This steering is a disruption to the trapping process that may lead to loss of captured charge. In order to investigate this effect we have started a series of simulations with the three dimensional PIC code OSIRIS. Initial indications are that bending during the trapping process may have a significant detrimental effect, but further study is needed.

3 PLANNED EXPERIMENT

This experiment will be performed at the Fermilab NICADD Photoinjector Laboratory (FNPL) as part of an ongoing collaboration with UCLA. This collaboration has centered on PWFAs and has recently yielded interesting new results in the field of witness beam injection [16].

3.1 Photoinjector and Linac

The FNPL accelerator is a 18 MeV electron linac [17]. The system consists of a normal conducting L-band RF gun with a cesium telluride photo-cathode and a 9-cell superconducting accelerating cavity. Bunches with charge in excess of 8 nC can be produced and compressed to durations of 1.6 ps rms using magnetic compression. All the beam parameters necessary for the plasma density transition trapping experiment have already been demonstrated at FNPL.

3.2 Plasma Source

By modifying an existing pulse discharge plasma source [18] we have created a plasma column with a peak density of $6x10^{13}cm^{-3}$. As shown in Figure 2 the raw plasma column has a gaussian transverse density profile and over 6 cm of the plasma has density greater than $2x10^{13}cm^{-3}$, ensuring that we have sufficient plasma to form either of the density profiles in Fig 1.

We have made preliminary measurements of plasma density transitions produced using obstructing screens. These initial measurements lack fine resolution, but were consistent with our understanding of the density transition production mechanism. High resolution measurements of the density transition are planned for the near future.

4 PRESENT STATUS AND CONCLUSIONS

Preparations for the transition trapping experiment are near completion. The plasma source and associated diagnostics are assembled and in the final stages of testing at UCLA. Once testing is complete the apparatus will be moved to FNPL and integrated into the existing beamline.

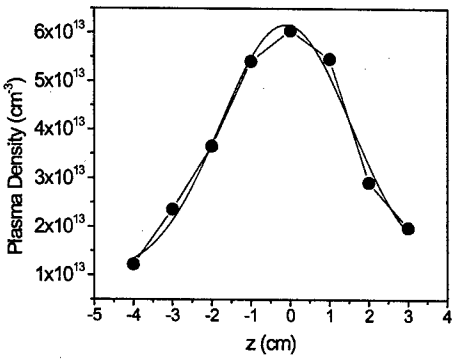


Figure 2: Measured Transverse Density Profile of the Plasma Column

We expect to perform the plasma density transition trapping experiment during the summer of 2003.

5 ACKNOWLEDGEMENTS

The authors would like to thank T.C. Katsouleas and L. Ludeking for their assistance with the MAGIC PIC simulations.

REFERENCES

[1] J. B. Rosenzweig, *et al.*, *Phys. Rev. Lett.*, **61**, 98 (1988).

[2] C. E. Clayton, *et al.*, *Phys. Rev. Lett.*, **70**, 37 (1993).

[3] F. Amiranoff, *et al.*, *Phys. Rev. Lett.*, **81**, 995 (1998).

[4] N. Barov, *et al.*, *Phys. Rev. Special Topics - Accel. Beams*, **3**, 011301 (2000).

[5] M. J. Hogan, *et al.*, *Physics of Plasmas*, **7**, 2241 (2000).

[6] S. Bulanov, *et al.*, *Phys. Rev. E*, **58**, R5257 (1998).

[7] H. Suk, *et al.*, *Phys. Rev. Lett.*, **86**, 1011 (2001).

[8] D. Umstadter, *et al.*, *Phys. Rev. Lett.*, **76**, 2073 (1996).

[9] E. Esarey, *et al.*, *Phys. Rev. Lett.*, **79**, 2682 (1997).

[10] J. B. Rosenzweig and E. Colby, in *Advanced Accelerator Concepts*, 1995, vol. 335 of *AIP Conf. Proc.*, p. 724.

[11] M. C. Thompson and J. B.Rosenzweig, in *Advanced Accelerator Concepts*, 2002, vol. 647 of *AIP Conf. Proc.*, p. 600.

[12] M. Ferrario, *et al.*, in *Proc. EPAC 2000*, Austrain Acad. Sci. Press, 2000, p. 1642.

[13] B. Goplen, *et al.*, *Computer Physics Communications*, **87**, 54–86 (1995).

[14] M. C. Thompson, *et al.*, in *Proc. PAC 2001*, IEEE, 2001, p. 4014.

[15] R. A. Fonseca, *et al.*, in *Computational Science - ICCS 2002*, Springer, 2002, LNCS 2331, pp. 342–351.

[16] N. Barov, *et al.*, "High-Gradient Plasma Wakefield Acceleration of a Witness Beam," in *Proc. PAC 2003.*

[17] J.-P. Carneiro, *et al.*, in *Proc. PAC 1999*, IEEE, 1999, p. 2027.

[18] H. Suk, *et al.*, in *Proc. PAC 1999*, IEEE, 1999, p. 3708.

ACCELERATION OF INJECTED ELECTRONS IN A LASER BEATWAVE EXPERIMENT*

S. Ya. Tochitsky[1#], R. Narang[1], C.V. Filip[1], P. Musumechi[2], C.E. Clayton[1], R. Yoder[2], K.A. Marsh[1], J.B. Rosenzweig[2], C. Pellegrini[2], and C. Joshi[1], Department of Electrical Engineering[1], Department of Physics[2], UCLA, 405 Hilgard avenue, Los Angeles, CA, 90095, USA

Abstract

A 10-ps beam of 12 MeV electrons was loaded in a 1-cm long plasma beat wave accelerator driven by a TW CO_2 laser pulse. CO_2 laser pulses and electron bunches were deterministically synchronized with an uncertainty of 20 ps. At the resonant electron plasma density of ~10^{16} cm^{-3} the electrons have been accelerated to 22 MeV with a gradient of ~1 GeV/m.

INTRODUCTION

Laser-plasma accelerators of particles, which have a potential to become next-generation high-gradient accelerators, rely on laser excitation of large amplitude relativistic plasma waves (RPWs) for acceleration. Two main considerations drive a significant interest to this type of devices: availability of laser power sources producing multi GV/m electric fields and the fact that plasmas can sustain these very strong fields. Since the interaction length of a focused laser beam is limited fundamentally by diffraction, multistage acceleration is required to achieve the kinetic energy of interest for high-energy physics. In this context it is important to inject a well-characterized electron beam into a pre-formed plasma accelerating structure and explore methods for extracting and characterizing a high-quality beam.

Here we report on a high-gradient acceleration of externally injected electrons in a plasma beatwave accelerator (PBWA) driven by a CO_2 laser. RPWs are excited by beating electromagnetic waves where difference between the laser frequencies, $\Delta\omega=\omega_1-\omega_2$, is equal to the plasma frequency, ω_p [1,2]. The energy gain reached 10 MeV for approximately a 1-cm long PBWA. The interaction length and intensity is strongly limited by ionization-induced refraction of the laser beam [3]. Possible ways to overcome this limitation in the PBWA's length are discussed.

EXPERIMENTAL SET-UP

The experiment is being done at the Neptune Laboratory at UCLA. The layout of the PBWA set-up is shown in Fig. 1. A TW CO_2 laser system producing two-wavelength pulses at 10.3 μm and 10.6 μm was used to drive the plasma beatwave. This pair of lines determined value of the resonant electron plasma density of $n_e \approx 9.4 \times 10^{15}$ cm^{-3}. The laser beam was focused by a F/18 lens giving a spot size $w_0 \approx 200$ μm and a Rayleigh range of $2Z_R \approx 26$ mm. A 12 MeV electron beam with parameters listed in Table 1 was focused down to 150 μm

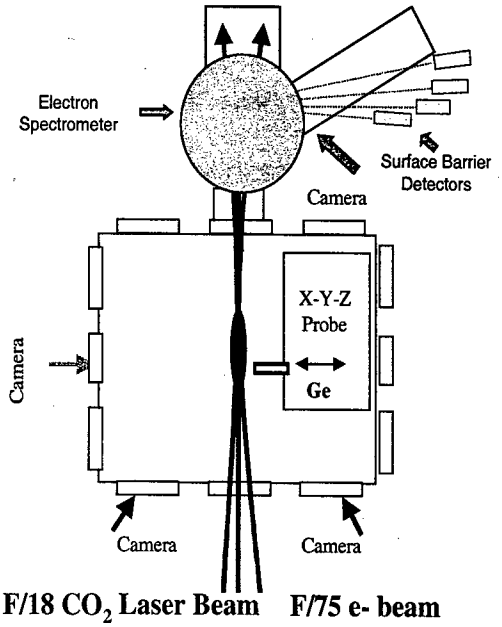


Figure 1: Layout of the PBWA set-up.

(σ_{rms}) and injected into the plasma. The energy spectrum of electron beam was analyzed using a Browne-Buechner spectrometer in combination with a fluorescer screen (for energies E=12-15 MeV) and a set of Si surface barrier detectors (E>15 MeV). With the current set-up 3-5 electrons with maximum energy up to 50 MeV were detectable.

Table 1: Electron Beam Parameters

Bunch Length (FWHM)	10 ps
Emittance	12 mm-mrad
Energy	12 MeV
Charge	100 pC

Synchronization

In order to inject a 10-ps electron bunch at the very maximum of the plasma wave amplitude driven by a 160-ps CO_2 laser pulse, they must be synchronized on a picosecond scale. Synchronization is possible because the same 1 μm pulse is used to produce electrons on a photocathode and to switch a short 10-μm pulse for amplification in a MOPA CO_2 laser system [4]. A two-step technique was used for synchronization: cross-correlation between 10 μm photons and electrons

#sergei12@ucla.edu

0-7803-7738-9/03/$17.00 © 2003 IEEE

measured with an unamplified laser pulse followed by compensation of a constant time delay gained in active medium of the final CO_2 amplifier.

Electron-beam-controlled transmission of 10-μm radiation in Ge [5] was utilized for the cross-correlation measurement. For this purpose the pulse was sent through a 1-mm thick germanium plate at the laser focus and time dependence of the 10-μm transmission was recorded. The latter was realized by a computer controlled optical delay line. A typical result of cross-correlation measurement is presented in Fig. 2. There is a part in the dependence corresponding to a time window when an e-bunch reaches

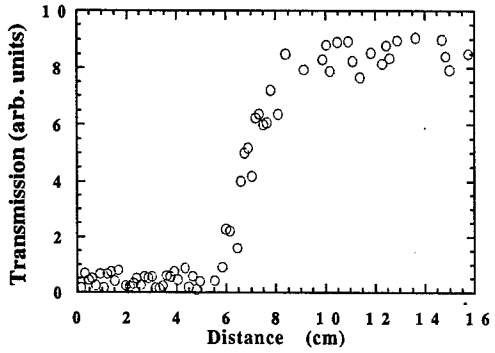


Figure 2: Cross-correlation measurement.

the Ge plate first and 10-μm radiation is fully attenuated. The plasma formation happens on a time scale similar to the duration of the plasma creating electron-bunch. Therefore, accuracy of the cross-correlation measurements is limited by a 10-ps bunch length. A total width of the recorded cross-correlation curve is ~ 270 ps, which agrees very well with a CO_2 laser pulse length measured by a streak camera.

These measurements were done with a 10- μm laser pulse propagating through a 3 X 2.5-m long multiatmosphere CO_2 amplifier with no inversion of population. It is known that the resonant behavior of the refractive index (n) in the vicinity of a homogeneously broadened molecular transition results in an increase of n in the inverted medium. This leads to decrease of the group velocity of the laser pulse with gain in comparison with no-gain conditions. Series of measurements revealed that a 120±20 ps pulse delay was gained in our case [6]. In the experiment we compensated for the delay after the cross-correlation measurement. Thus a total uncertainty of 20 ps is achieved in synchronization of CO_2 laser pulses and electron bunches, which was adequate for a 160-ps laser pulse.

PLASMA BEATWAVE PRODUCTION AND CHARACTERIZATION

A typical 2.5-cm long plasma, generated in a backfill of H_2 at resonant density of ~10^{16} cm^{-3} is shown in Fig. 3.

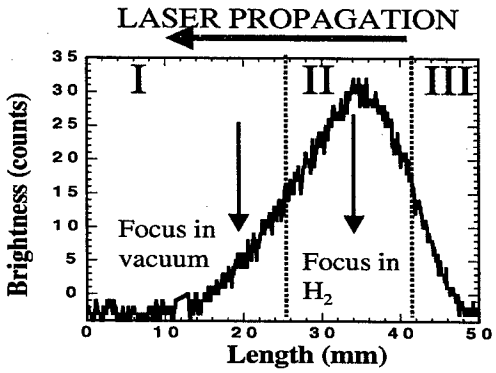


Fig 3: Lineout of H_2 plasma at 160 mTorr.

The plasma was produced at a distance larger than Z_R from the focus in vacuum. Note, that position of focus in vacuum for a high-power beam was determined by ionizing Ar with a fraction of the total power corresponding to an appearance intensity of 2.5×10^{14} W/cm^2. The plasma lineout in Fig.3 clearly demonstrates asymmetry caused by ionization-induced refraction [3]. Optimal peak power of the laser beam in the experiment was 0.5 TW. This power did not exceed the field ionization threshold for H_2 (1.37×10^{14} W/cm^2) by a factor of two. Increasing both the laser power and plasma density resulted in shifting the plasma further upstream, making losses caused by refraction more severe.

RPW's driven by a two-wavelength CO_2 laser pulse were detected and characterized by a collinear Thomson scattering (TS) technique using a green probe beam [7]. An F/4 optic was used for focusing the 532.1 nm probe beam. This allowed to sample only approximately 1 mm of the 2.5-cm long plasma and, by scanning the sampling point, to map the RPWs longitudinally. The latter information was very important for the asymmetric plasmas distorted by ionization-induced refraction of the laser beam. TS signal resolved both in frequency in time for the zone II in Fig. 3 is presented in Fig.4. A short, ~

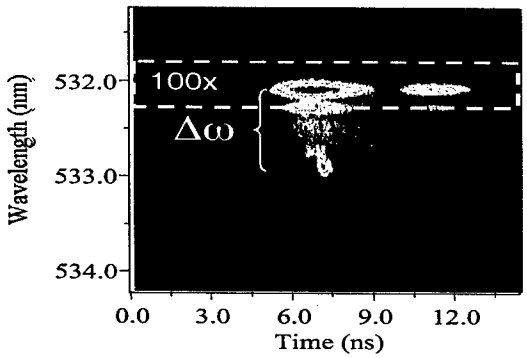


Figure 4: Streak camera image of the TS signal.

100 ps sideband shifted by 8.1 Å from the wavelength of the probe light was the result of scattering from the RPW. The 8.1 Å shift of the scattered light corresponds exactly to the Δω separation between the two frequencies of the CO_2 laser beatwave. Another conclusion drawn from

these measurements is that TS signal and, therefore, the wave amplitude is a strong function of the plasma brightness. It is not a surprise, since the plasma beatwave efficiently couples energy of an electromagnetic wave of the laser field into an electrostatic plasma wave with almost zero group velocity, additionally increasing heating of the plasma. The amplitude of the RPW $\varepsilon=\Delta n_e/n_e$, where Δn_e is the magnitude of the perturbation of the electron density associated with the wave, was estimated from the absolute amount of scattered light to be ~0.1 around focus in H_2 (zone II). However, the plasma wave amplitude dropped to 0.01-0.02 in both peripheral zones I and III limiting the effective length, where a large amplitude RPW was excited, to ~1 cm.

ELECTRON ACCELERATION

One of the main difficulties of measuring ionizing radiation and electrons in particular is that the commonly employed detectors are sensitive to a variety of radiation sources. To decrease the background caused by stray hard X-rays produced by bremsstrahlung, each surface barrier detector was placed in a thick lead housing with an aperture equal to 8 mm (detector size). Detectors were also shielded by 1-3 mm of Cu cutting off all X-rays below 0.1 MeV at the peak of SBD's sensitivity. A series of null tests were performed under various conditions, which could, in principle, produce false signals on our detectors. They are transverse blowing of the e-beam by the laser beam or plasma producing scattered 12 MeV electrons, acceleration of electrons by a Raman instability in the plasma rather than the beatwave, and the acceleration of background plasma electrons rather than the injected electrons from the photoinjector. All null tests using both single- and two-wavelength laser pulses confirmed that detected above the noise signal is result of acceleration in the PBWA. As seen in Fig. 5, the highest energy gain was ~10 MeV. In the experiment the e-beam was not matched both longitudinally and transversely to the plasma wave, therefore 100% energy spread was obtained.

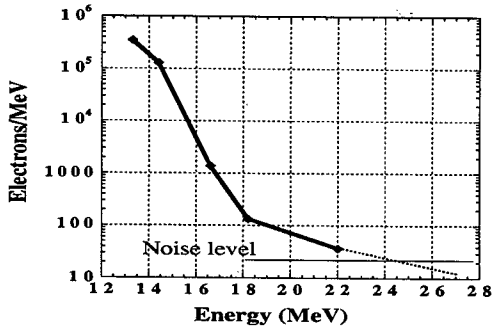


Fig 5: Single-shot electron spectrum.

The diameter of the accelerating structure was larger than the plasma wavelength of 340 μm making the longitudinal contribution of the electron density perturbation at least three times larger than the radial contribution [8]. In this case a 1-D formalism based on Gauss's law can be applied to estimate the maximum energy gain $W_{max}=0.96\varepsilon(n_e)^{0.5}L$, where L is the efficient beatwave length. For a beatwave length of 1 cm and the wave amplitude $\varepsilon=0.1$, the energy gain W_{max} =10 MeV. This energy gain is in a good agreement with one obtained in the experiment. Thus it is ionization-induced refraction of the laser beam by the plasma that limits the beatwave length and, therefore the net energy gain.

We consider several possible solutions for the refraction problem. One can try to guide the laser pulse in a gas filled hollow waveguide [9] in order to confine the laser beam in the focal region. Another solution is to create an ion channel by using a longer laser pulse with a duration longer than the characteristic time of ion motion, thus initiate a self-guiding process [10,11]. Experimental results on enhanced acceleration by laser beatwave in a self-induced ion channel will be reported elsewhere [12].

ACKNOWLEDGEMENTS

This work was supported by US. Department of Energy contract DE-FG03-92ER40727.

REFERENCES

[1] C. Clayton et al., Phys. Rev. Lett. 70 (1993) 37.
[2] E. Esarey in Handbook of Accelerator Physics and Engineering, edited by A. Chao and M. Tigner (World Scientific, Singapore, 1999).
[3] W.P. Leemans et al., Phys. Rev. A 46 (1992) 1091.
[4] S.Ya. Tochitsky et al., Optcs Lett.24 (1999) 1717.
[5] P.B. Corkum et al., J. Appl. Phys. 50 (1979) 3079.
[6] S.Ya. Tochitsky et al., IEEE J QE (to be submitted).
[7] C.V. Filip et al., Rev. Sci. Instr. (to be published).
[8] F. Dorchies et al., Phys. Plasmas 6 (1999) 2903.
[9] B. Cross et al., IEEE Trans. Plasma Sci. 28 (2000) 1071.
[10] P.E. Young et al., Phys. Rev. Lett. 75 (1995) 1082.
[11] V. Malka et al., Phys. Rev. Lett. 79 (1997) 2979.
[12] S.Ya. Tochitsky et al., Phys. Rev. Lett. (to be submitted).

A PROPOSAL TO EXPERIMENTALLY DEMONSTRATE A NOVEL REGIME OF ELECTRON VACUUM ACCELERATION BY USING A TIGHTLY FOCUSED LASER BEAM*

F. Zhou, D.Cline, UCLA, Los Angeles, CA 90095, USA
H.K.Ho, L.Shao, Fudan University, Shanghai, China

Abstract

The trajectory of most vacuum laser acceleration schemes is a straight line and the electron beam can obtain a small net energy gain only within two times of laser-Rayleigh length. A novel regime of electron beam dynamics trajectories in intensive laser field has been studied recently [1-2]. The most prominent feature of those dynamics trajectories is that the incident electron beam can be captured into an intensive laser field region in a curved trajectory, rather than expelled from it as predicted by the ponderomotive potential mode. A proposal to demonstrate a proof-of-principle experiment at Brookhaven Accelerator Test Facility (ATF) is presented. The key parameters to meet the experiment requirements are discussed. The preliminary simulation results using existing ATF laser and electron beam are presented.

1 INTRODUCTION

Current laser driven particle acceleration schemes can be divided into two categories: one with a medium and the other without a medium in the electron acceleration path. The one with a medium includes the plasma-based laser acceleration [3] and the Inverse Cherenkov Acceleration (ICA) [4]. The one without a medium includes inverse free-electron laser (IFEL) acceleration [5] and the structure-loaded vacuum laser acceleration [6-7]. The acceleration schemes adopting media along the particle acceleration path often comprise with material properties, including scattering and stability. The IFEL acceleration suffers from excess radiation loss when scaled to high energies. In recent years there has been a renewed interest in the possibility of accelerating electrons by laser field in vacuum [8-12], where the laser acceleration of electrons in vacuum can be realized using the non-linear or ponderomotive forces associated with the laser-electron interaction. The use of ponderomotive forces can result in a very limited net energy gain by using the lower laser energy even in the limit of a finite interaction region truncated by using the optical components.

In the recent years, a new mechanics has been invented to accelerate the electrons in vacuum by using high-intensity tightly focused laser [1, 13]. Unlike the straight electron beam dynamics trajectory in most vacuum laser acceleration, the most prominent feature of this vacuum laser acceleration is its curved electron dynamics trajectory. The electron beam has an incident angle to the laser when injecting into the laser region. The incident electron beam can then be captured into this intensive laser field region, rather than expelled from it as predicted by the conventional ponderomotive potential model. Immense acceleration to energies in excess of 1 GeV in few centi-meters has been observed in the simulation with high intensity focused laser beam. The demonstration for the first proof-of-principle experiment at Accelerator Test Facility (ATF) Brookhaven National Laboratory is proposed by using the novel vacuum laser acceleration mechanics. In the next sections, we will briefly review the theory, and then the possibility to obtain some critical parameters to realize the acceleration experiment is discussed. The schematic layout of the experiment at ATF is presented.

2 THEORETICAL BASIS

For most vacuum laser accelerations, the electron dynamics trajectory is a straight line. A major difficulty in using lasers in vacuum to accelerate electrons is that the phase velocity of the electric field in the direction of the accelerated electrons is greater than the speed of the light for straight electron beam trajectory, $v_p / c \sim 1 + 1/(kZ_l)$, k is the laser wave number, Z_l is the laser Rayleigh length, $z_l = \pi w_0^2 / \lambda$. This results in no net energy gain over the infinite interaction length, but a small finite net energy gain can be obtained by placing optical components near the laser focus to limit the interaction length. Actually, this mechanics can be described with the Ponderomotive potential model (PPM), which is typically valid in cases in which an electron experiences many quiver oscillations in the laser field such that a time averaging over the fast quiver motion can be justified. The motion to describe the interaction between the electrons and laser beam in this model can be simplified. The longitudinal and transverse electric field component in a focused Gaussian laser beam in PPM can be given by:

$$E_r = E_0 \frac{r w_0}{w^2} \exp(-\frac{r^2}{w^2}) \sin\psi \qquad (1)$$

$$E_z = E_0 \frac{2 w_0}{k w^2} \exp(-\frac{r^2}{w^2}) \times [(1 - \frac{r^2}{w^2}) \cos\psi - \frac{z r^2}{z_l w^2} \sin\psi] \qquad (2)$$

where

0-7803-7738-9/03/$17.00 © 2003 IEEE

$w = w_0[1+(z^2/z_l^{\,2})]^{1/2}$ is the laser beam radius, w_0 is the beam radius at the focal waist, ω is the laser frequency, E_0 and ϕ_0 are constants. Thus, the energy gain is the integral of the E_z from z_1 to z_2, z_1 and z_2 are interaction region, which is determined by phase velocity:

$$V_\varphi \approx c[1+\frac{1-f_\varphi}{kZ_R(1+z^2/Z_R^{\,2})}] \qquad (3)$$

where

$$f_\varphi = \frac{r^2(1-z^2/Z_R^{\,2})}{w_0^{\,2}(1+z^2/Z_R^{\,2})}$$

In order to make V_φ <c, both conditions must be met, i.e.:

$-Z_R < z < Z_R$, and $r > w_0$

In this case, the electron trajectory is completely parallel to the Z-axis, i.e., a straight line, and the electrons can be accelerated within the laser Rayleigh length. In addition, this conclusion is only limited within the low laser energy. However, when the electrons move in a curved trajectory, the phase velocity can be smaller than the speed of the light in a significant length [13] and thus results in a significant net energy gain over a longer distance. When the electron beam has a small incident angle to the laser electric field, the phase velocity along the trajectory is:

$$V_{\varphi e} \approx c[1+\frac{1-f_\varphi}{kZ_R(1+z^2/Z_R^{\,2})} - \frac{rz\theta_i}{Z_R^{\,2}(1+z^2/Z_R^{\,2})} + \frac{\theta_i^2}{2}] \qquad (4)$$

where θ_i is the electron beam incident angle to the laser beam axis. Usually θ_i is smaller. It is obvious that when the electron is incident to the laser field and thus the phase velocity is not a constant at each point. However, the key point is the phase velocity is smaller than speed of the light. Thus, contribution from term $v \times B$ in Lorentz force becomes noteworthy. Since the phase velocity is smaller than the speed of the light in such curved trajectory, the electron can be accelerated over a significant distance and thus obtain a significant net energy gain.

3 BEAM PARAMETERS AT BROOKHAVEN ATF

Based on the simulations, the electron beam can be captured and significantly accelerated by focused laser beam with higher accelerating gradient when the a_0 specifying the laser energy is greater than 8 [1], which corresponds to 8×10^{17} W/cm^2 of the laser intensity for 10.6 micron CO2 laser. The conversion of the laser intensity into laser peak power for different laser spot size is given in Table 1.

The sensitive role played by the injection energy is considered. On the one hand, an initially slow electron will not be able to penetrate the high intensity regions of the beam and may be reflected with little or no energy gain. On the other hand, an initially fast electron may pass through undeviated and gain or lose a small amount of energy. Simulations show that the optimum electron injection energy is in range of 5-20 MeV. To achieve a significant net energy gain, basically three requirements need to be met:

- strong intensity laser at least in Terra Watt level
- incident injection angle, ~5 degrees.
- low injection momentum (5-20 MeV)

Table 1: Laser peak power vs laser spot size

Laser spot size (microns)	Peak power (TW)
10	0.8
30	7
50	20

The ATF electron accelerator system consists of a photocathode based RF gun, two SLAC type S-band linac sections and three dedicated beam lines. At the exit of the RF gun, the energy is around 4 MeV. For most experiments, the electron beam energy at the end of the linac is about 40 MeV, where two linac sections provide 35 MeV. As mentioned in the above, this novel vacuum laser acceleration experiment favors the low electron beam momentum to injection the laser channel, ~20 MeV. This lower energy is readily achieved after lowering the RF power for two linac sections. The electron beam performance at this energy, energy spread, emittance pulse length, may become a little worse, but not severely. The simulations show that the emittance and energy spread are ~2 mm.mrad, 0.1%, respectively for 0.3 nC and 20 MeV beam. The small electron incident angle to the laser beam, ~ 5 degrees, is easily met.

Compared with existing beam parameters at the ATF, the most challenging parameter for this experiment is the laser peak power. At the ATF, we use the CO2 laser (wavelength is 10.6 microns) to synchronize and interact with the electron beam. Presently, with a high-pressure, big-aperture booster amplifier, the ATF CO2 laser system can operate up to 30 GW of the peak power in longer pulse, 180 ps with FWHM, as shown in Figure 1.

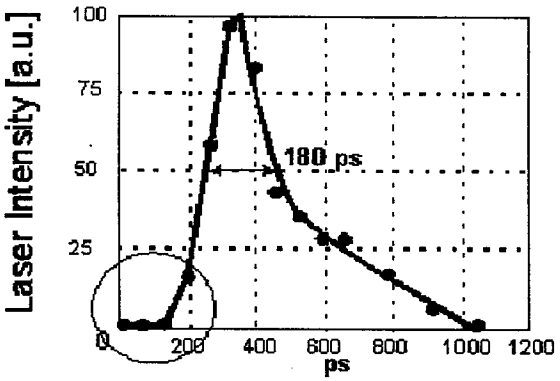


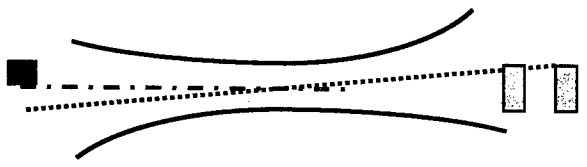
Figure 1: Measured time profile of the CO2 beam after the preamplifier

The relatively long pulse duration is due to the narrow bandwidth of the preamplifier, 4 atm and 1 liter with 1/200 ps^{-1} bandwidth. In this year, CO2 laser upgrade for high peak power is being carried out at the ATF. Main steps of the on-going upgrade is [14]:

a. To generate 1 ps second harmonic of YAG laser in KD*P crystal for slicing CO2 laser
b. Gate ~ 1 ps CO2 pulse Kerr switch controlled by YAG second harmonic.
c. Use 10-atm preamplifier 0.15 littter to match the present booster amplifier in bandwidth, 9 atm and 9 liter with 1 THz bandwidth.

In this summer, ATF can have the capability to provide intensive laser with ~1 ps pulse duration and the peak power in 1 TW level with these upgrades. The ultra small laser beam size can be achieved with strong focusing mirrors. To match the small laser beam size, electron beam size need to be focused down to several tens of microns, which has been obtained in the beam line with miniature permanent quads [15]. According to the simulations, the expected energy gain is in order of MeV with 1 TW laser peak power.

The proposed experimental elements can be accommodated in an existing vacuum chamber with many ports. The CO2 laser has an incident angle to the electron beam. The schematic layout for the experiment is shown in Figure 2.



Green line: CO2 laser
Dot green line: CO2 laser axis
Red line: injected electron beam axis
Black brick: mini permanent quad to focus the electron beam size down to several tens of microns.
Yellow bricks: steering magnets to steer the electron beam back to the original electron beam axis.

Figure 2: The schematic layout of the experiment

As mentioned in the above, electron beam trajectory is curved in the laser field region. The electron beam can be steered back to the original line (red straight line) with steering magnets after the electron beam obtains the energy and exit the laser field region.

4 SUMMARY

A novel vacuum laser acceleration that is different from the most vacuum laser acceleration described with ponderomotive potential model is discussed. The prominent characteristic is that the electron beam dynamics trajectory is not a straight line, but a curved trajectory in the laser region relative to the Z-axis. In such mechanics, the phase velocity can be kept below the speed of the light for significant distance although it is not a constant. To meet this condition, the injected electron beam is incident to the laser, and its incident momentum is about 20 MeV and the laser peak power is at least in TW. An experiment to conduct the first proof-of-principle of this vacuum laser acceleration is proposed at Brookhaven Accelerator Test Facility. The possibility to realize these important beam parameters, incident angle, initial momentum and laser peak power in TW level, is discussed. It is shown that the requirement of the electron injection angle and momentum can be readily met. The CO2 laser peak power in TW level can hopefully be achieved with the on-going CO2 laser upgrades. Energy gain in order of MeV is observed in the simulations using 1 TW laser power.

*) Work done under the auspices of the US Department of Energy under grant No. DE-FG03-92ER40695.

5 REFERENCES

[1] P.X.Wang, Y.K.Ho, *et al.*, J. App. Phys. 91, 856 (2002).
[2] Y.Salamin, *et al.*, Phys. Rev. ST-AB, 5, 101301 (2002).
[3] See for example T.Tajima and J.M.Dawson, Phys. Rev. Lett. 43, 267 (1979).
[4] See for example, W.D.Kimura *et al.*, Phys. Rev. Lett. 74, 1995.
[5] A.van Steenbergen, *et al.*, Phys. Rev. Lett. 77, 2690 (1996).
[6] V.Yakimenko, *et al.*, PAC01, Chicago, 2001.
[7] Y.C.Huang, et al., ATF user meeting, 2002.
[8] E.J.Bochove, *et al.*, Phys. Rev. A 46, 6640 (1992).
[9] L.Steinhauer and W.Kimura, J. Appl. Phys. 72, 3237 (1992).
[10] Y.Liu, *et al.*, PAC'99, 1999.
[11] Y.Huang, *et al.*, Appl. Phys. Lett., 68 (6), 1996.
[12] E.Esarey, *et al.*, Phys. Rev. E 52, 5443 (1995).
[13] P.X.Wang, Y.K.Ho, *et al.*, App. Phys. Lett. 78, 2253 (2001).
[14] I.Pogorlesky and M.Babzien, ATF user meeting, 2002.
[15] V.Yakimenko, *et al.*, to be published at NIM A, 2002.

SURFACE ROUGHNESS EFFECT ON A MOVING BUNCH

S. Banna and L. Schächter, Electrical Engineering Department, Technion, Haifa 32000, ISRAEL

Abstract

The effect of surface roughness on a moving electron bunch is considered by resorting to a model of a metallic structure with random perturbations on its surface. Based upon this model analytic expressions have been developed for both the average energy emitted per groove as well as for its standard-deviation. For a relativistic bunch both quantities are shown to be virtually independent of the momentum. Moreover, it has been found that the standard-deviation of the energy emitted per groove is proportional to the standard-deviation of the roughness parameter to the power of 1/4.

1 INTRODUCTION

The acceleration structure of a linear collider designed to operate at X-band is manufactured within an accuracy of about $1\mu m$. These four orders of magnitude difference between the operating wavelength and the typical surface roughness will be difficult to maintain in case of a vacuum *optical* accelerator operating at $1\mu m$ since such a difference implies engineering at the atomic level $1\mathring{A}$. In fact, both the size of the bunch as well as the roughness of the structure are anticipated to be of the same order of magnitude, leading to a significantly different regime of operation when compared to that of a machine driven by a *microwave* source. It is the purpose of this paper to put forward the main results of a study aimed to the investigation of the impact of the surface roughness upon the wake-field of a moving bunch of a size comparable to the dimensions of the surface roughness.

Several studies have been conducted in the past in order to investigate the surface roughness effects upon wake-fields by considering either single obstacles or periodic structures. For example, Kurennoy et al. [1] have developed a general theory of beam interaction with small discontinuities of the vacuum chamber of an accelerator. The analysis was extended [2] to obstacles protruding inside the drift pipe of an accelerator for wavelengths larger compared to the obstacle's typical size. Further, an evaluation of the coupling-impedance has been presented by Stupakov [3] employing the so-called *small-angle approximation.*

2 FORMULATION OF THE PROBLEM

In the framework of our investigation a quasi-analytic analysis facilitating a relatively simple evaluation of the wake-field due to surface roughness of arbitrary size has been developed. It relies on an approach published about a decade ago in the context of quasi-periodic traveling output structures for high-efficiency, high-power microwave sources [4,5]. The model relies on a cylindrical waveguide of constant internal radius to which a series of grooves are attached; their geometric parameters i.e. width, height and location, are assumed to be *randomly* distributed, and in principle, these grooves can be large on the scale of the typical wavelength of the radiation driving the system. Details of this study will be published separately [6].

In order to analyze the wake-field generated by the surface roughness, consider a metallic structure consisting of a random number (N) of grooves attached to a cylindrical waveguide of constant internal radius (R_{int}), as illustrated in Fig. 1. The center of the n^{th} groove is denoted by z_n, its width by d_n and its external radius by $R_{\text{ext},n}$. An electron bunch of radius R_b, length L_z and a total charge Q, is moving along the symmetry axis of the structure at a constant velocity v_0, generating a current density denoted by $J_z(r,z;t)$.

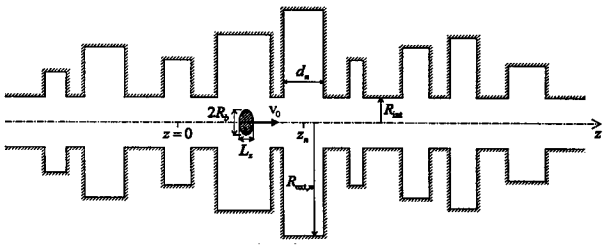


Figure 1: A finite-size bunch moving in vacuum along the axis of a structure with random size grooves.

As the only component of the current density is parallel to the z-axis, it is sufficient to consider only the longitudinal magnetic vector-potential A_z satisfying the non-homogeneous wave equation. Its solution has two components: the so-called *primary* field determined by the current density in the absence of the metallic structure and the so-called *secondary* field accounting for the impact of the structure. Taken together, these fields satisfy the boundary conditions, establishing the unknown amplitudes. Once these amplitudes have been established all the field components may be determined; in particular the longitudinal component of the secondary electric field $E_z^{(s)}(r,z;t)$. As the bunch traverses the structure, the emitted power may be expressed in terms of this field component as

$$P(t)=2\pi\int_0^{R_b} rdr\int_{-\infty}^{\infty} dz J_z(r,z;t)E_z^{(s)}(r,z;t). \qquad (1)$$

Moreover, the emitted energy is given by

$$W=\frac{Q^2}{4\pi\varepsilon_0 R_{\text{int}}}\text{Re}\left[\int_0^{\infty} d\Omega\, S(\Omega)\right]\equiv\frac{Q^2}{4\pi\varepsilon_0 R_{\text{int}}}\bar{W} \qquad (2)$$

$S(\Omega)$ representing the normalized spectrum and $\bar{W}$ the normalized energy. As already indicated, the geometrical

0-7803-7738-9/03/$17.00 © 2003 IEEE

parameters of each groove are random and of the same order of magnitude. Explicitly, they are given by

$$\bar{R}_{\mathrm{ext},n} \equiv \frac{R_{\mathrm{ext},n}}{R_{\mathrm{int}}} = 1 + \bar{g}_n, \quad \bar{d}_n \equiv \frac{d_n}{R_{\mathrm{int}}} = \bar{g}_n, \qquad (3)$$

where $\bar{g}_n$ is a random variable that is uniformly distributed between 0 and $\bar{\delta}$; $\bar{\delta}$ will be referred to as the *normalized roughness parameter*. The center of the first groove ($\bar{z}_1 \equiv z_1/R_{\mathrm{int}}$) is being chosen as a point of reference ($\bar{z}_1 = 0$) and accordingly, the center's location of the n^{th} (n=2,3,...,N) groove is given by $\bar{z}_{n+1} = \bar{z}_n + 0.5\bar{d}_n + 0.5\bar{d}_{n+1} + \bar{g}_n$.

3 DISCUSSION

Although, the analysis is valid for a large variety of values of $\bar{\delta}$, the discussion that follows is limited to relatively small values of $\bar{\delta}$ since if R_{int} is of the order of $0.5\mu m$ the typical roughness is not expected to be larger than $0.1\mu m$ therefore, we consider $0 \le \bar{\delta} \le 0.2$. Moreover, the accelerated bunch is expected to be of the order of $30^\circ \div 45^\circ$ (namely about $0.1\mu m$), and as a result, $0.15 \le \bar{L}_z \equiv L_z/R_{\mathrm{int}} \le 0.30$; the normalized radius of the bunch is chosen to be $\bar{R}_b \equiv R_b/R_{\mathrm{int}} = 0.5$. In order to determine the characteristics of the emitted energy (average and standard-deviation), a series of simulations has been performed where each data point is a result of averaging over 80 *different distributions* for a given $\bar{\delta}$.

In both frames of Fig. 2 the spectrum of the emitted energy is illustrated. The left frame shows the maximum and minimum values of the normalized spectrum, its average value, its average value plus the standard-deviation and its average value minus the standard-deviation; in all five cases $\bar{R}_b = 0.5$, $\bar{L}_z = 0.25$, $\bar{\delta} = 0.1$ $\gamma = 10^4$. Evidently, all the curves overlap for high frequencies and the deviation from the average values for low frequencies is less than 25%. Furthermore, as illustrated in the right frame of Fig. 2, the first zero of the spectrum remains virtually unchanged when varying $\bar{\delta}$. In fact, this zero is related to the cut-off frequency of the cylindrical waveguide i.e $\Omega \equiv \omega R_{\mathrm{int}}/c = p_1 = 2.4048$, where c is the speed of light in vacuum, p_1 being the first zero of Bessel function of zero order and first kind. Other simulations indicate that the normalized spectrum is weakly dependent on γ and in fact, for the ultra-relativistic case the spectrum is virtually independent of γ.

After examining the properties of the spectrum, our focus moves towards the *total energy* emitted, establishing its dependence on the roughness parameter ($\bar{\delta}$) with $\bar{L}_z$ as a parameter. The left frame of Fig. 3 illustrates the average value of the normalized energy per groove versus $\bar{\delta}$; $\left(\bar{L}_z = 0.15, 0.20, 0.25, 0.30,\ \bar{R}_b = 0.50\right)$ and $\gamma = 10^4$. Two facts are evident: firstly, the average as well as the normalized energy per groove ($\tilde{W} \equiv \bar{W}/N$) increases with the increase of $\bar{\delta}$. Secondly, $\tilde{W}$ increases when reducing the length of the bunch ($\bar{L}_z$). Simulations reveal that the impact of γ for relativistic energies is virtually negligible. According to these simulations the average emitted energy may roughly be approximated by

$$\frac{\langle W \rangle}{\frac{Q^2}{4\pi\varepsilon_0 R_{\mathrm{int}}} \times N} \approx 0.57 \tanh\left(\frac{45\frac{\langle g \rangle}{R_{\mathrm{int}}}}{1 + 20.72\frac{L_z}{R_{\mathrm{int}}}}\right) + \frac{1.429}{1 + 20.72\frac{L_z}{R_{\mathrm{int}}}} \qquad (4)$$

A second important feature of the emitted energy is its normalized standard-deviation given by the expression $\Delta\bar{W}\bar{\delta}^{-0.25} \equiv \sqrt{\langle \bar{W}^2 \rangle - \langle \bar{W} \rangle^2} \Big/ \left(\langle \bar{W} \rangle \bar{\delta}^{0.25}\right)$. The latter is shown in the right frame of Fig. 3 versus $\bar{\delta}$, with $\bar{L}_z$ as a

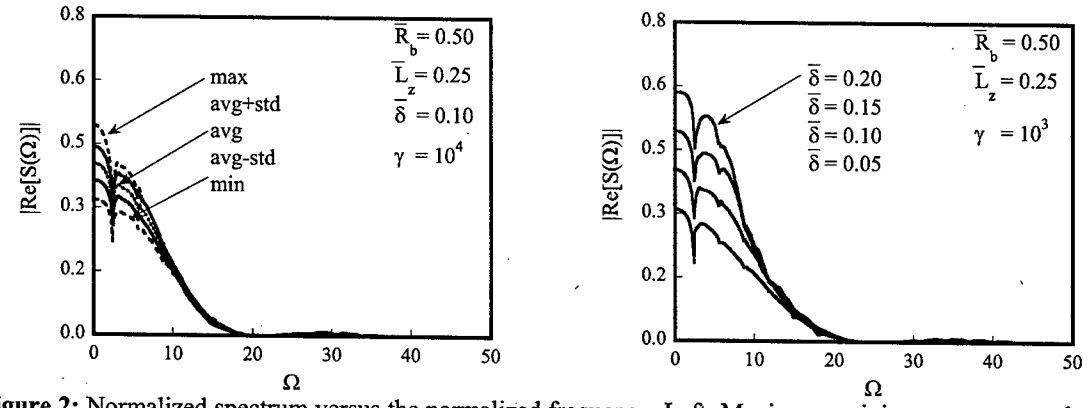


Figure 2: Normalized spectrum versus the normalized frequency. Left: Maximum, minimum, average value for the normalized spectrum and average value plus/minus one standard deviation. Right: Average value of the normalized spectrum for different values of $\bar{\delta}$.

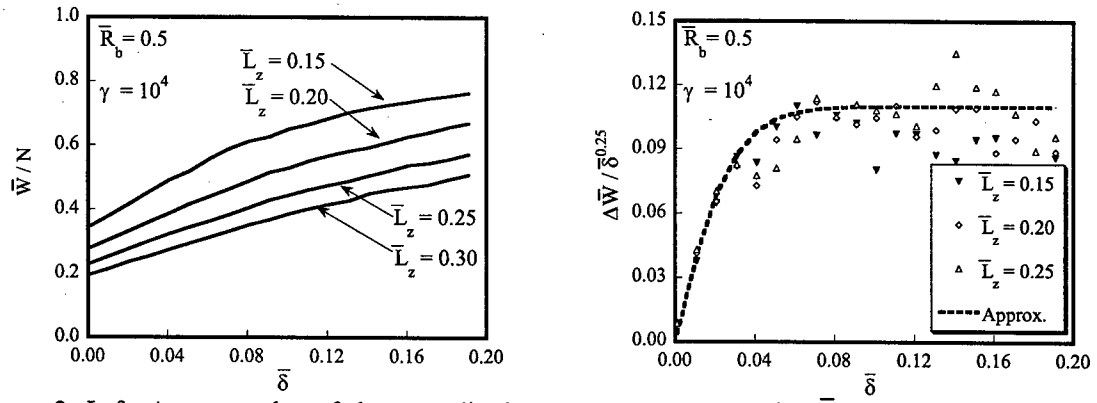


Figure 3: Left: Average value of the normalized energy per groove versus $\bar{\delta}$. Right: Normalized standard-deviation of the energy out of 80 different distributions versus $\bar{\delta}$.

parameter. A best fit of the simulation results reveals that the standard-deviation may be approximated by

$$\frac{\sqrt{\langle W^2\rangle - \langle W\rangle^2}}{\frac{Q^2}{4\pi\varepsilon_0 R_{\text{int}}}\times N} \approx 0.15\left(\frac{\Delta g}{R_{\text{int}}}\right)^{0.25}\tanh\left(121.2\frac{\Delta g}{R_{\text{int}}}\right) \times\left[0.57\tanh\left(\frac{45\frac{\langle g\rangle}{R_{\text{int}}}}{1+20.72\frac{L_z}{R_{\text{int}}}}\right)+\frac{1.429}{1+20.72\frac{L_z}{R_{\text{int}}}}\right]. \quad (5)$$

Simulations indicate that the last approximation is adequate for variety of values for $\bar{R}_b$, $\bar{L}_z$ and γ. The expression in Eq. (5) constitutes a generalization of the conditions imposed in Eq. (3) since based on the latter the roughness parameter $\bar{\delta}$ determines both $\langle\bar{g}\rangle$ as well as $\Delta\bar{g}$. In order to identify the role of each one of the last two parameters, the simulation was repeated for fluctuations in the parameters of a periodic structure e.g. $\bar{R}_{\text{ext},n} = \bar{R}^{(0)}_{\text{ext},n} + \bar{g}_n$, $\bar{d}_n = \bar{d}^{(0)}_n + \bar{g}_n$ and $\bar{z}_{n+1} = \bar{z}_n + 0.5\bar{d}_n + 0.5\bar{d}_{n+1} + \bar{g}_n$.

4 CONCLUSIONS

The characteristics of the electromagnetic energy emitted by a bunch traversing a number of grooves of random geometry were established. Of special interest are the average and the standard-deviation of the emitted energy per groove in terms of the average roughness $\langle\bar{g}\rangle$ and its standard-deviation $\Delta\bar{g}$. The main result of the present study may be expressed in terms of these two quantities as given in Eqs. (4) and (5). These relations are valid for relativistic energies ($\gamma > 50$) and independent of the radius of the bunch provided $R_b \le R_{\text{int}}/2$. For a point-charge ($L_z = 0$) and for practical structures where $\delta \approx 0.1R_{\text{int}}$ the expression for the average energy per groove reads

$$\frac{\langle W\rangle}{N} \approx \frac{Q^2}{4\pi\varepsilon_0 R_{\text{int}}}\times 2. \quad (6)$$

It should be pointed out that the expression for the average energy per groove is identical to that developed for the case of a point-charge moving in a cylinder of radius R_{int} bored in a dielectric or metallic medium [7], and is almost equal to that obtained for the case of a point-charge moving in a cylindrical wave-guide with a periodic wall of arbitrary, yet azimuthally symmetric geometry [8].

5 ACKNOWLEDGEMENT

This study was supported by the Israel Science Foundation and the United States Department of Energy.

6 REFERENCES

[1] Sergey S. Kurennoy et al.; "Coupling Impedances of Small Discontinuities: A General Approach ", Phy. Rev. E 52, pp. 4354-4360 (1995).

[2] Sergey S. Kurennoy; "Beam Coupling Impedance of Obstacles Protruding into a Beam Pipe", Phy. Rev. E 55, pp. 3529-3532 (1997).

[3] G.V. Stupakov; "Impedance of Small Obstacles and Rough Surfaces", Phys. Rev. ST Accel. Beams 1, pp. 064401-1:10 (1998).

[4] L. Schächter and J.A. Nation; "Analytic Method for Studying a Quasiperiodic Disk Loaded Waveguide", Appl. Phys. Lett. 63, pp. 2441-3 (1993).

[5] L. Schächter; *Beam-Wave Interaction in Periodic and Quasi-Periodic Structures*, Springer-Verlag, Berlin, (1997).

[6] S. Banna and L. Schächter; "Electromagnetic-Wake due to Surface Roughness", submitted for publication.

[7] L. Schächter and D. Schieber; "On the Characteristics of the Cherenkov and Ohm Forces", Nucl. Instrum. Methods Phys. Res. A 388, pp. 8-16 (1998).

[8] L. Schächter and D. Schieber; "Decelerating Field on a Bunch Moving in a Periodic Symmetric Structure", Phys. Lett. A 293, pp. 17-22 (2002).

NUMERICAL STUDY OF INTERFERENCE BETWEEN TRANSITION RADIATION AND CERENKOV WAKE FIELD RADIATION IN A PLANAR DIELECTRIC STRUCTURE*

J.-M. Fang†, T.C. Marshall, Columbia University, New York, NY, USA
V.P. Tarakanov, ITES, RAS, Moscow, Russia
J.L. Hirshfield, Yale University and Omega-P Inc, New Haven, CT, USA

Abstract

The PIC code KARAT is used to study the interference between transition radiation and Cerenkov wake field radiation, set up by the passage of a bunch of charge through a dielectric structure of finite length. An example studied is a tall, dielectric-lined rectangular wake field microstructure, recently proposed as a stageable element of an advanced linear accelerator, which would use a train of femtosecond duration bunches. These bunches would be chopped out of a longer bunch using a powerful CO_2 laser and formed into a rectangular-profile bunch by a quadrupole. The bunches set up a periodic wake field which can be built up to as much as 600 MV/m using ten 3-fs bunches each containing a charge of 1-pC. Of interest is the difference in relative propagation speeds of the transition radiation and the Cerenkov radiation (which advances almost at c), and the relative magnitudes of the fields.

INTRODUCTION

Acceleration of electrons in wake fields set up by a series of driving bunches in a dielectric structure has shown promise as a linear accelerator in which large gradient electric fields might be possible [1, 2]. Such wake fields are appealing because they do not require power injected into the structure from an external source, but rather use fields set up by bunches obtained from a conventional rf linac. Recently, we have studied the use of tall, planar dielectric wake field structures having micron-scale dimensions [3]. Such structures are capable of precision manufacture using microcircuit technologies, and have the capability of achieving very high field gradients: indeed, a series of ten, 3-fs, 1-pC charge bunches has recently been shown to set up a wake field of $\sim$ 600 MV/m in a structure 20 μm $\times$ 150 μm in cross section [4]. The bunches are 10 μm wide, and dielectric slabs a few μm thick line the structure (see Fig. 1). Planar dielectric structures offer the attraction of improving the stability of the bunch motion and the amount of charge carried compared with a cylindrical structure of comparable size, and the small transverse dimension permits a large wakefield to be developed.

The bunches could be obtained initially from a 500 MeV rf linac-type source, and are processed using a LACARA accelerator "chopper" [3], or possibly an IFEL [5] used as a "pre-buncher", so as to obtain a sequence of bunches a few fsec in duration. A TW CO_2 laser is used as a "modulator" [3] of the original psec, nC bunch provided by the linac to form such a sequence of short bunches, periodically spaced, each having charge in the pC range. These *drive* bunches, the energy of which can be recycled, would be followed by an *accelerated* bunch which is situated in the accelerating component of E_z which follows the drive bunch train. In this way fields comparable with those achieved in laser plasma wake field accelerators can be set up, yet the energy is obtained largely from the rf linac source rather than a laser. We have found that it is possible to distort the original circular cross section of the input bunches into a near rectangular profile, using a quadrupole, and that the rectangular profile is maintained for a distance $>$ 10 cm of travel [3].

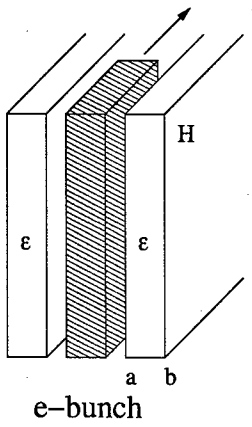


Figure 1: Schematic of slab bunch within a planar dielectric wake field structure.

Transverse fields set up by the bunch have been calculated, and an estimate has been made of how far a drive bunch might travel without additional focusing [6] ($\sim$ 7.1 cm). Also, studies have been made of fields in 3D using the PIC code KARAT [7], and show that the E_z component of wake field is rather uniform across the structure. In the structure under study, the wake fields are dominated by two modes having nearly the same periodicity.

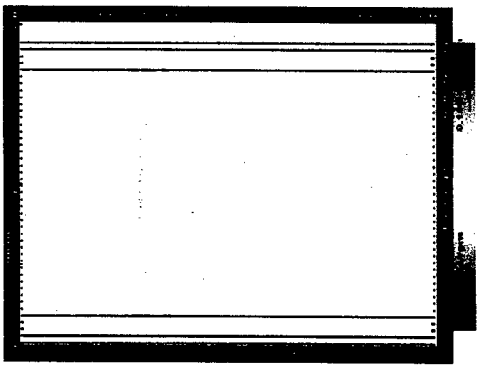
FIELDS FROM A SINGLE BUNCH

The transition radiation which is emitted when the bunch enters or leaves the structure is typically omitted in analytic

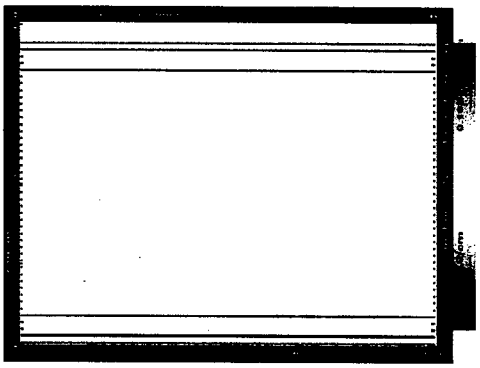
* work supported by the Department of Energy
† fang@beamer8.physics.yale.edu

0-7803-7738-9/03/$17.00 © 2003 IEEE

theoretical treatments of the wake fields. The transition radiation effect was remarked upon in [4, 8] and was recently treated analytically using a simplified model by Onishchenko, *et al* [9]. Qualitatively, the transition radiation emitted by the entry of the bunch into the structure interferes with the wake field radiation in a certain region. This region extends from the point where the bunch enters the structure to a front which expands with the group velocity of waves in the structure. As the bunch and its wake field move with nearly the speed of light, the expanding region between the transition zone and the bunch fills with wake field radiation which resembles that emitted by the bunch in an infinitely long structure. However, the group velocity depends on the mode frequency, so in cases of multimode operation (see e.g. [8]) the transition radiation zone would not be very clear. It shows up more clearly in the example of wake field structures in which mainly one mode is excited [9], which is the case studied here. The planar dielectric structure studied here is 18.8 μm $\times$ 30 μm $\times$ 120 μm long. The dielectric slab is 1.9 μm in thickness and has a dielectric constant of 3. The vacumn channel is 15 μm wide. The microbunch has a charge of 0.2-pC and its pulse duration is 3.3-fs long. The transverse profile of the bunch is 10 μm $\times$ 26 μm.



(a) at 150 femtosecond



(b) at 350 femtosecond

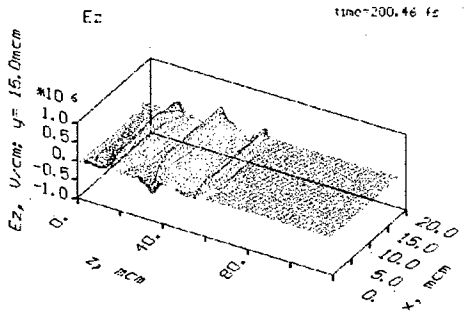
Figure 2: Transition radiation and wake field from a single bunch.

Figure 2 shows the axial field E_z pattern in the x-z plane at the midway y-plane, at 150-fs and 350-fs after the entry of the first bunch into the structure. [These are color figures. The color scale indicates the magnitude of the field and the color itself represents the field's polarity (red for positive polarity and blue for negative).] The excited wake field alternates its polarity, thus the color in the figures too, periodically. In Fig. 2(a), the electron bunch has just entered the structure for a short period of time (150-fs), such that the transition radiation dominates and only one wake field period is seen following the electron bunch. As the electron bunch traverses into the structure further (Fig. (2b)), the wake field radiation pulls away from the transition radiation, due to the difference in their propagation speeds, and several wake field periods are formed. The period of the wake field is close to 20 μm. We also see the region where the transition radiation intereferes with the wake field radiation gradually expands, as the electron bunch propagates further. The propagation speed of the head of the wake field radiation is that of the bunch, whereas the propagation speed of the transition radiation front is estimated at about 1.7×10^{10} cm/sec, close to c $\surd$ (further study is needed to determine the propagation speed of the transition radiation). The magnitude of the wake field (E_z) is $\sim$ 40 MV/m, whereas the magnitude of the transition radiation is weaker, at $\sim$ 10 MV/m, an decrease which is consistent with the simplified analytic model by Onishchenko, *et al* [9].

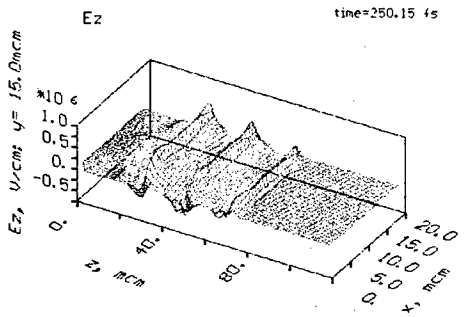
FIELDS FROM THREE BUNCHES

For the excitation of the wake field in a dielectric structure, a high gradient accelerating field can be obtained by using a train of bunches, carefully spaced at the wake field's period [1, 2].

For the dielectric structure in which mainly one mode is excited, transition radiation has an effect on the build-up of the wake field generated by a train of bunches. The dielectric structure we studied here is such a structure. For the PIC code Karat simulation, the bunches are placed 20 μm apart to match the wake field period of this planar structure and to permit the build-up of the wake field by coherent superposition. All other parameters are the same as the simulation for a single bunch. Figure 3 shows the axial field E_z in the x-z plane at mid y-plane at 200-fs and 250-fs. The build-up of the wake field is evidenced for the first 2 bunches of Fig. 3(a). The third bunch in Fig. 3(a), is still in the transition radiation zone and the wake fields of the three bunches don't add up linearly because of the interference between the transition radiation and the Cerenkov wake field radiation. As the bunches advance further away from the transition radiation region (Fig. (3b)), the build-up of the wake field is evidenced for all three bunches. Figure 4 is the E_z *vs* z plot along the center of the planar structure and gives a clear reading of the magnitude of the wake field. The intereference effect of the transition radiation is clearly seen in Fig. 4(a), as the magnitude for 2nd and 3rd wake field is nearly the same.

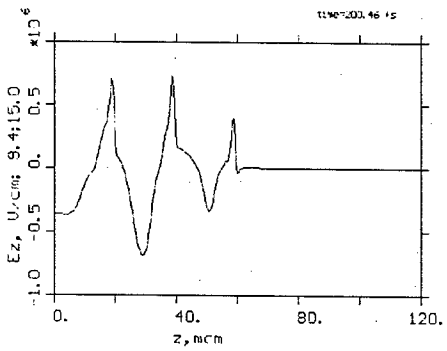


(a) 200 femtosecond

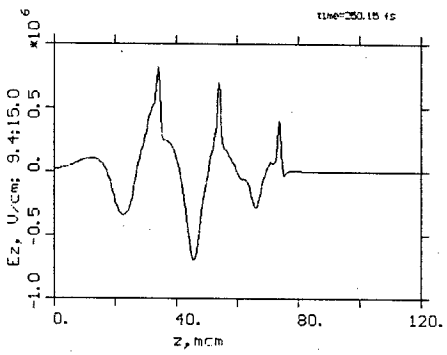


(b) 250 femtosecond

Figure 3: Transition radiation and wake field from three bunches.



(a) 200 femtosecond



(b) 250 femtosecond

Figure 4: E_z *vs* z along the center of the planar structure from three bunches.

CONCLUSIONS

We have studied the interference effect between the transition radiation and the Cerenkov wake field radiation in a planar dielectric structure using the PIC code Karat. We have chosen a structure where mainly one mode is excited. The transition radiation is important when the bunch has just entered the structure. Due to the difference in propagation speed between the transition radiation and the wake field radiation, a train of periodic wake fields is excited as the bunch advances further into the structure. The transition radiation also has an effect on the build-up of the wake field by a train of bunches. This is a problem for system that uses a very long train of drive bunches to build up the accelerating wake field in a short structure [10].

REFERENCES

[1] T.-B. Zhang, J.L. Hirshfield, T.C. Marshall, and B. Hafezi, Phys. Rev. **E56**, 4647 [1997]

[2] J.G. Power, M.E. Conde, W. Gai, R. Konecny, P. Schoessow, and A.D. Kanareykin, Phys. Rev. ST AB **3**, 10132 [2000]

[3] T.C. Marshall, C. Wang, and J.L. Hirshfield, Phys. Rev. ST AB **4**, 121301 [2002]

[4] T.C. Marshall, J.-M. Fang, J.L. Hirshfield, C. Wang, V.P. Tarakanov, S-Y. Park, "Wake Fields Excited in a Micron-Scale Dielectric Rectangular Structure by a Train of Femtosecond Bunches", p. 361, AIP Conference Proceedings **647** [2002]

[5] Y. Liu, et al., Phys. Rev. Lett. **80**, 4418 [1998].

[6] S-Y. Park, C. Wang, and J.L. Hirshfield, "Theory for Wake Fields and Bunch Stability in Planar Dielectric Structures", p. 527, AIP Conference Proceedings **647** [2002]

[7] V.P. Tarakanov, "Users' Manual for Code KARAT", BRA Inc., VA, USA [1992]

[8] T.C. Marshall, J.-M. Fang, J.L. Hirshfield and S-Y. Park, "Multi-mode, Multibunch Dielectric Wake Field Resonator Accelerator", p. 316, AIP Conference Proceedings **569**, [2000]

[9] Onishchenko, I.N., Sidorenko, D. Yu, and Sotnikov, G. V., Phys. Rev. **E65**, 066501 [2002]

[10] Onishchenko, I.N., Sidorenko, D. Yu, and Sotnikov, G. V., Ukrainian Physical J. **48**, 17 [2003]

GENERATION OF SINGLE PULSE PARTICLE BEAMS IN A PLASMA CHANNEL BY LASER INJECTION IN LASER WAKEFIELD ACCELERATORS

R. E. Giacone, J. R. Cary and Chet Nieter
Center for Integrated Plasma Studies- University of Colorado at Boulder
E. Esarey, W. Leemans G. Fubiani and C. Schroeder
Lawrence Berkeley National Laboratory

Abstract

A laser injection mechanism that generates a single pulse, high quality beam is described. In the past, different all-optical injection schemes for the generation of ultrashort electron bunches were proposed. A very promising scheme proposed by E. Esarey [1] uses the collision of two counterpropagation laser pulses to inject particles. However, the results of ours 2D particle-in-cell (PIC) simulations have shown that in addition to the bunch created by pulse collision, a train of pulses is also generated by a different mechanism. In this paper we show that is possible to achieve a single pulse, high quality beam if the generation of the plasma wakefield takes place in a channel and particles are injected by a phase-kick mechanism [J. Cary at this conference]. We have performed 2D PIC simulations of our proposed injection scheme using the code VORPAL [C. Nieter at this conference]. We have obtained a high quality 11 MeV., 6 fs. single electron bunch with energy spread of4% and emittance of $0.01\pi - mm - mrad$.

INTRODUCTION

Plasma-based accelerators [2] - [3] have received much theoretical and experimental attention in the last decade due to the large longitudinal electric fields that can be excited in a plasma without the limitations found in conventional accelerators. One widely investigated and very promising concept is the laser wakefield accelerator (LWFA) [6], in which a laser drives a wake field in the plasma and the wake field then accelerates electrons. Self-trapping and acceleration of electrons have been demostrated through many experiments [6] - [7] in the self-modulated (long pulse) LWFA. In this case the wake field grows through the modulation instability to the point where wave-breaking occurs. The resulting electron beams typically have 100% energy spread. In the short pulse regime, where the length of the laser pulse is of the order of the plasma wavelength c/ω_p, one can create clean wake fields, but then one has the problem of injecting electron bunches into those accelerating fields. Such bunches would have to be extremely short, with length of the order of the laser pulse length, i.e., multiple femtoseconds. These requirements are beyond current technology including that of photocathode radio-frequency electron guns. The rest of the paper is organized as follows: in Sec. 2 we describe our injection scheme and give a brief description of the VORPAL code. In Sec. 3 we present the results of the simulations, and summary and conclusions are presented in Sec. 4.

PARTICLE INJECTION SCHEME IN A PLASMA WAKE FIELD

The accelerating electric field (or gradient) in conventional radio frequency linear accelerators is limited to around 100 MV/m, partly due to heating or breakdown on the walls of the structures. In order to accelerate electrons to very high energies (greater than 1 TeV), it is necessary to develop new acceleration concepts providing a higher electric field. Plasmas can support large high longitudinal electric fields. More precisely, ionized plasmas can sustain electron plasma waves (EPW) with longitudinal electric field on the order of the nonrelativistic wave-breaking field [5], $E_0 = cm_e\omega_p/e$. For an electron density of $n_e = 10^{18}cm^{-3}$ the electric field is $E_0 \approx 100GV/m$ (which is approximately three orders of magnitude greater that obtained in conventional RF linacs) with a phase velocity close to the speed of light.

In the laser wakefield accelerator (LWFA), a single short ($\leq 1ps.$), ultrahigh intensity ($\geq 10^{18}W/cm^2$) laser pulse injected in an underdense plasma excites an EPW behind the pulse. The plasma wake is excited by the ponderomotive force created by the photons. A correctly placed trailing electron bunch can be accelerated by the longitudinal electric field and focused by the transverse electric field of the plasma wake.

For this reason, all-optical injection schemes have been proposed. Recently E. Esarey and coworkers [1] proposed a colliding laser pulses scheme that uses three laser pulses. An intense pump pulse generates a fast ($v_{p0} \approx c$) wake field. A forward going and a backward going injection pulses collide at some distance behind the pump pulse generating a slow ponderomotive beat wave with phase velocity $v_{pb} \approx \Delta\omega/2k_0$. During the time in which the two injection pulses overlap, the slow beat wave injects plasma electrons into the fast wake field for acceleration to high energies.

In any of the optical injection schemes, one beamlet of electron is supposed to be generated. However our 2D PIC simulations of the colliding pulses scheme and phase-kick injection show that multiple beams are generated instead of a single beamlet (see Fig. 1).

In all these schemes the wake field has to be high enough

0-7803-7738-9/03/$17.00 © 2003 IEEE

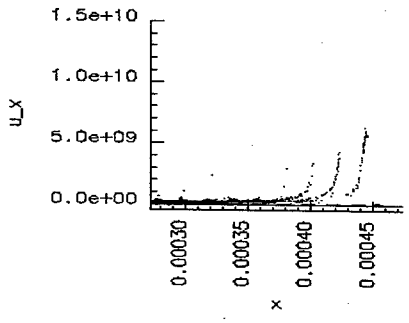


Figure 1: Particles in $x - v_x$ phase-space phase-kick injection. We observed that a train of beamlets is formed.

that transverse wakebreaking takes place and we get particles injected in each accelerating bucket. We propose to modify the structure of the wake field such that only one wavelength has high intensity (therefore, only one accelerating bucket will be suitable for injection). In order to reduce the wake field the pump pulse is propagated in a plasma channel. With the right plasma parameters, the wakefield will be rapidly dumped and only one beamlet will be generated. Particle injection is conducted by a second conterpropagating laser pulse which will beat with the pump and kick particles into an invariant curve that is accelerated, longitudinal trapped and transversely focused.

To carry out our simulations, we have made use of the VORPAL simulation code [10]. VORPAL is a fully relativistic fluid/PIC code that can be run in 1, 2, or 3 dimensions. (The work presented here consists of 2-D simulations). Among other situations, the VORPAL code can be used to simulate the self-consistent dynamics of relativistic particles in electromagnetic fields. Because only the region of the plasma near the pulse is of interest, it is possible to implement a moving window algorithm [9],such that the simulation follows the small region of interest and ignores the rest of the device. The code is also implemented in parallel through the Message Passing Interface(MPI). Parallel computation is critical for these computationally intensive simulations. The laser pulses used in the simulation were modeled as linearly polarized Gaussian in the transverse direction and have an amplitude variation that at the focus is longitudinally a half-sine pulse,

$$E_i = \frac{m_e c \omega_i a_i}{e} \cos\left(\pi(x - x_0 - v_{gi}t)/L_i\right) exp\left(-y^2/2w_i^2\right) \cos(k_i x + \omega_i t) \quad (1)$$

For $|x - x_0| \leq L_i/2$, where the subscript i is either p, f for the pump or the forward pulse (with the - sign in the argument of the last cosine), or b for the backward pulse (with the + sign in the argument of the last cosine). The amplitude a_i is in units if $m_e c$. The length of the pulse is L_i, and w_i is the rms width of the pulse.

SIMULATIONS RESULTS

The electron plasma density was $n_{e0} = 2.78 \times 10^{17} cm^{-3}$ which corresponds to a wavelength of $\lambda_p = 20\mu m$ and to a plasma frequency $\omega_p = 9.4 \times 10^{13} s^{-1}$. The laser pulses were linearly polarized with transverse Gaussian profile. The minimum laser spot size was $20\mu m$ and the Rayleigh length was about $31\lambda_p$. The laser pulse length was chosen to be about $\lambda_p/2$. The pump laser intensity was $I_L = 5.8 \times 10^{17} W/cm^2$ and the laser wavelength $\lambda_0 = 2.0\mu m$. the backward pulse had $\lambda_2 = 2.0\mu m$ and intensity $I_L = 5.8 \times 10^{17} W/cm^2$ and pulse length was λ_p. The plasma channel radius is $8.0\mu m$.(see Fig. 2).

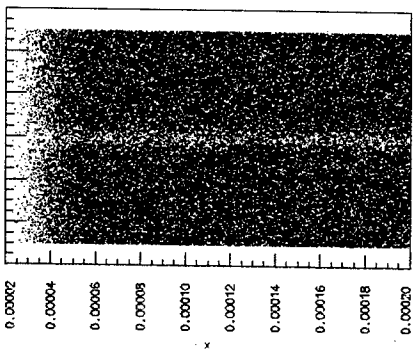


Figure 2: Electron density distribution at $t = 0$ shown in $x - y$ phase-space

The length of the simulation box was $L_x = 200\mu m$ in the X and $L_y = 100\mu m$ in the Y direction. The computational mesh consisted of 1200 cells in the X direction and 200 cells in the Y direction. The simulation used about 1,200,000 computational particles.

The pump pulse is launched into a vacuum region of 20 μm. It follows a (1 - cosine) rise density of 40 μm, and then a flat density region of 120 μm. At $ct = 195\mu m$, the moving window is turned on. The pulses collided at $ct = 155\mu m$.

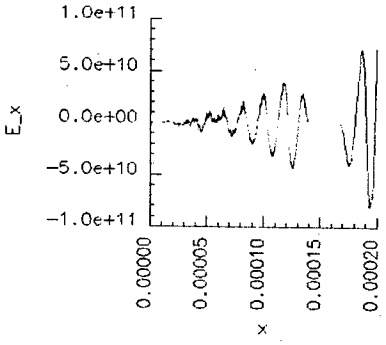


Figure 3: Longitudinal Electric field as a function of distance of propagation right before collision takes place. Notice the fast decay of the plasma wake field due to the channel.

Figure 3 shows the longitudinal electric field on axis before collision takes place. We observe the pump pulse propagating to the right and behind the wake field that creates. We clearly see the rapid decay of in the wakefield intensity due to the propagation in the channel.

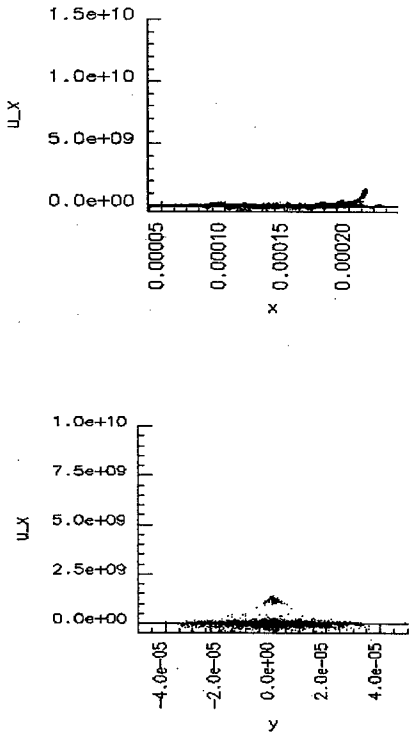


Figure 4: (a) Snapshot of electrons in $X - V_x$ phase-space. (b) Snapshot of electrons in $Y - V_x$ phase-space right after collision.

Figures 4 and 5 are snapshots of electrons in $X - V_x$ and $Y - V_x$ phase-space at right after collision occurs and after close to one Rayleigh length of propagation respectively. We observe that after close to one Rayleigh length of propagation a high quality, single beam is obtained. The beam pulse length is 6.6 fs., while the relative rms energy spread p_x / p_x is 4%. The faster particles are at a relativistic factor of $= 22$ in about $600\mu m$, which corresponds to an accelerating gradient of $24GeV/m$. The quality of the beam is also good. The transverse emittance is $0.01\pi - mm - mrad$, which implies a normalized emittance of $0.33\pi - mm - mrad$.

CONCLUSIONS

We have shown 2D PIC simulations performed with the code VORPAL of a new particle injection into a plasma wakefield scheme. PIC simulations of previous all-optical injection schemes produced a train of beamlets instead of a single beam. We have managed to avoid the multiple beam injection by propagating the pump laser pulse in a plasma channel to allow a rapid dacay of the plasma wake field. A

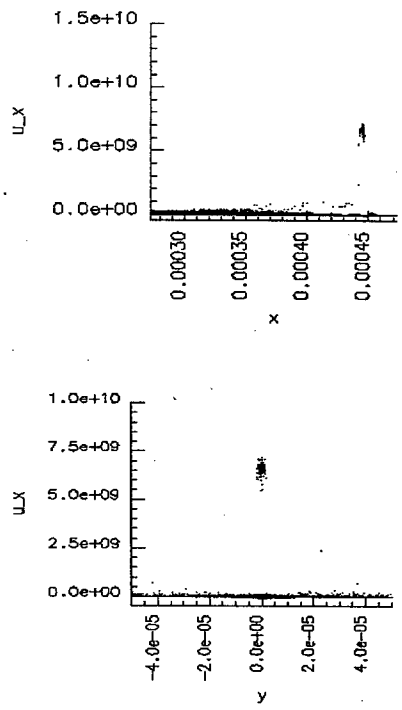


Figure 5: (a) Snapshot of electrons in $X - V_x$ phase-space. (b) Snapshot of electrons in $Y - V_x$ phase-space after about one Rayleigh length of propagation.

second counterpropagating laser pulse is used to inject particles into the first accelerating bucket through a phase-kick mechanism. After almost one Rayleigh length of propagation a high quality, single beam is obtained. The beam pulse length is 6.6 fs, with rms energy spread of 4% and normalized transverse emittance of $0.33\pi - mm - mrad$

REFERENCES

[1] E. Esarey, R. F. Hubbard, W. P. Leemans, A. Ting and P Sprangle, " Phys. Rev. Lett 79, 2682 (1997).

[2] T. Tajima and J. Dawson, Phys. Rev. Lett. 43, 267 (1997).

[3] P. Sprangle et. al., Appl. Phys. Lett. 53, 2146 (1998), E. Esarey et. al., Comm. Plasma Phys. Controlled Fusion 12, 191 (1989), S. Bulanov, V. Kirsanov and A. Sakharov, JETP Lett. 50, 198 (1980).

[4] C. K. Birdsall and A. B. Langdon, "Plasma Physics via Computer Simulations" (Adam Hilger, Bristol, 1991).

[5] E. Esarey, P. Sprangle, J. Krall and A. Ting, "IEEE Trans. Plasma Sci." 24, 252 (1996).

[6] K. Nakajima, "Phys. Rev. Lett." 74, 4428 (1995).

[7] A. Ting, "Phys. Plasmas" 4, 1889 (1997).

[8] C. B. Schroeder, P. B. Lee, J. S. Wurtele, E. Esarey and W. P Leemans, "Phys. Rev. E" 59, 6037 (1999).

[9] C. D. Decker and W. Mori, Phys. Rev. Lett. 72, 490 (1994).

[10] C. Nieter and J. R. Cary, submitted to Journal of Comp. Phys.

A METHOD FOR TUNING DIELECTRIC LOADED ACCELERATING STRUCTURES

A. Kanareykin Euclid Concepts LLC, Solon, OH 44139, USA
W. Gai, J.G. Power ANL, Argonne, IL, 60439, USA
E. Nenasheva Ceramics Ltd., St. Petersburg, 194223, Russia
S. Karmanenko, I. Sheinman, Electrical Engineering University, St. Petersburg, 197376, Russia

Abstract

We present a method to vary the resonant frequency of a *dielectric loaded accelerating* **(DLA)** structure driven by either the wakefield of a beam or an external rf source. The structure consists of a thick ceramic layer backed by a thin layer of ferroelectric. The overall frequency of the DLA structure is tuned by applying a DC bias voltage to the ferroelectric layer in order to vary its permittivity. This scheme is needed to compensate for frequency shifts in DLA structures due to machining imperfections and dielectric constant heterogeneity. We have identified BST ferroelectric-oxides compounds as a suitable material for this application; it has a relative dielectric constant that can be tuned from 300 to 500. From this, we calculate that the overall frequency of the structure can be tuned over a range of (2÷4)% for an X-band DLA structure. In this paper, a detailed model of the DLA structure is given and an experimental test is proposed. We present cold test measurements for an 11.424 GHz planar tunable DLA structure.

INTRODUCTION

Frequency control of any accelerating structure is a fundamental issue. Synchronization between the electron beam velocity and the phase velocity of the accelerating field must be maintained in order for the bunch to gain energy. A frequency error in the accelerating structure will result in a change in the phase velocity of the accelerating field and thus a loss of synchronization between the beam and field. Lack of frequency control also causes problems for multistage accelerators where one has to match the accelerating field frequencies between adjoined sections. One can see that the capability of tuning the accelerating structure is a basic necessity for acceleration.

The frequency spectrum of a conventional, metallic accelerating structure is defined by the geometry of the waveguide. In addition to geometry, the frequency spectrum of a DLA structure is also affected by the ceramic loading inside the conducting walls. For example, if we design it for 11.424 GHz, choose a ceramic material with the dielectric constant of 16, and an inner radius of 5mm, then the outer radius is 6.647 mm. For this particular structure, the phase velocity of the accelerating mode will be mismatched to the electron beam speed by 7.03% if the outer radius of the structure increases by 0.1%, or 6.7 μm. One can see that the dispersion curves of the waveguides are very sensitive to the geometry. We also point out here that the dielectric constant homogeneity along the waveguide has technological limitations due to the manufacturing techniques used for the ceramic tubes e.g. particle size dispersion and firing temperature variation inside the furnace. Thus, the DLA structure requires a method of tuning to avoid an overly stringent machining tolerances and expensive ceramic material manufacturing processes.

BASIC CONCEPTS: HOW TO VARY THE PERMITTIVITY.

There are two classes of materials that can be tuned, in other words, materials with electromagnetic properties that can be controlled by external fields: **ferrites**, controlled by magnetic fields, and **ferroelectrics**, controlled by electric fields. Ferrite material does not appear to be a practical solution for high frequency, high gradient accelerators because of its extremely high loss factor and also because the magnetic field will interfere with the electron beam optics. The use of ferroelectrics for tuning purposes would appear to be a natural solution, except for the fact that ferroelectrics are very lossy in the > 10 GHz frequency range. The typical loss factor for $Ba_xSr_{1-x}TiO_3$ (BST) ferroelectric, commonly used at room temperature, is $(1\div3)\times10^{-2}$ near 10 GHz frequency range. However, a new scheme involving ferroelectrics [1,2] allows control of the dielectric constant (and consequently the frequency spectrum) for the dielectric waveguides by incorporating ferroelectric layers., while simultaneously having low loss. For example, the loss factor for a good linear microwave ceramic is $(0.5\div5)\times10^{-4}$.

We propose to use a combination of ferroelectric and ceramic layers to permit tuning of a composite ceramic–ferroelectric waveguide while keeping the overall material loss factor in the $(4\div5)\times10^{-4}$ range. It will be shown that the losses in our composite structure are comparable to the losses in conventional DLA structures that consist of a single dielectric cylinder inserted into a conductive copper jacket.

The most notable feature of the tunable DLA is the replacement of a single ceramic by a composite of 2 layers as shown in Fig. 1. The inner layer is ceramic, with permittivity ε_1, typically in the range of 4÷36. The outer layer is a thin film made of BST ferroelectric, of permittivity ε_2, placed between the ceramic layer and the copper sleeve. The DLA structure tuning is achieved by varying the permittivity, ε_2, of the ferroelectric film by applying an external DC electric field across the ferroelectric. This allows us to control the effective

0-7803-7738-9/03/$17.00 © 2003 IEEE

dielectric constant of the composite system and therefore, to control of the structure frequency during operation.

The basic design of the cylindrical geometry is shown in Fig. 2. The relative depths of the layers in this figure are not to scale; the ferroelectric layer is actually 10 times thinner than the ceramic layer.

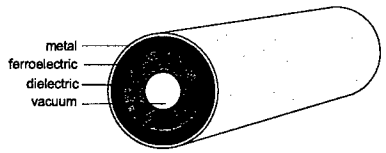


Figure 1. Basic designs of tunable dielectric accelerating structures, cylindrical geometry, outer layer is ferroelectric, inner layer is ceramic.

The typical thickness is (2÷3) mm for the ceramic layer and (200÷300) μm for ferroelectric film. It should be mentioned that this geometric ratio of 10 plays an important role for this structure design. The dielectric constant of the BST ferroelectric is typically within 1000÷2000, and we have reduced this by using a composition of BST and oxides to 300÷500 to avoid any extra magnetic loss at the conducting walls. A DC field can vary this dielectric constant in the range of (20÷30)% or about 100 units. Thus the primary ceramic layer with the dielectric constant of (4÷20) and (2÷3) mm in thickness, will be tuned by the comparatively thin (200÷300) μm ferroelectric layer. The loss factor of this composite DLA structure will be about the same as the ceramic-only structure due to the geometric ratio, since the volume of high loss ferroelectric material is much smaller than that of the basic ceramic.

Numerical Simulations

We have simulated the radial dependence of the electric field components for the 11.424 GHz dielectric loaded cylindrical waveguide with the ferroelectric layer of 200 μm and dielectric constant of 500 excited by the high current beam of 100 nC, $\sigma_z = 2$ mm. The accelerating gradient of 30 MV/m is flat inside the vacuum channel and decays rapidly inside the ceramic layer. The ferroelectric tunability depends on the ratio between the DC and RF axial field magnitudes. The DC field inside the ferroelectric layer does not exceed 10 V/μ. Our simulations show that the maximum longitudinal RF field inside the ferroelectric layer for the 11.424 GHz structure is $E_z = 0.23$ MV/m and therefore Ez_{vacuum}:$Ez_{ferro} = 166$ and E_{DC}:$Ez_{ferro} = 43.5$. These ratios mean that the ferroelectric layer remains tunable since the effect of the beam and RF field is negligible in comparison with the DC field between the microstrip contacts. It should be mentioned that transverse field magnitude is much less than the longitudinal inside the ferroelectric as well, $Ez_{ferro} >> Er_{ferro}$.

Microstrips

One has to supply a dc field into the ferroelectric layer to vary the dielectric constant of the structure loading. We have developed a technique to deposit copper microstrip (using a photolithography) on substrate samples in order to measure the tunability and loss tangent of an 11.424 GHz planar structure. The microstrip geometry configuration used for supplying the bias field to the ferroelectric layer also suppresses the transverse dipole wakefield suppression. This is discussed in [A. Kanareykin et al, TPPG041, these Proceedings].

FERROELECTRIC PROPERTIES

A promising principle to tune microwave devices is the use of the nonlinearity of a ferroelectric material. A ferroelectric crystal or ceramic is a material with a spontaneous dielectric polarization below a Curie temperature T_c. A representative ferroelectric material is a $BaTiO_3$ - $SrTiO_3$ solid solution (BST). Above T_c, the ferroelectric is in a paraelectric phase and does not show spontaneous polarization, but still has the dielectric nonlinearity. The BST solid solution can be synthesized in the form of a polycrystalline or ceramic layer on the dielectric substrate.

As stated above, we seek a DLA structure design for the frequency range f = (10÷13) GHz with a tunability of (2÷3)% or ~ 200 MHz. In this section, we describe the properties of our BST ferroelectric and present cold test results of the 11.42 planar GHz DLA structure.

Ferroelectric Composition

The ferroelectric properties we need to produce for the DLA structure are: (1) dielectric constant in the range of 200÷800; and (2) loss tangent of $(1÷6)\times10^{-3}$ at the 10÷13 GHz frequency range. Available materials are made of a BST matrix with oxides doping. For room temperature applications the $Ba_xSr_{1-x}TiO3$ (BST) ferroelectric is typically made with $x < 0.7$. Normally, BST thin films for high frequency applications have Ba:Sr ratio of 50:50 or 60:40. For our application we require a bulk ferroelectric material or thick film ferroelectric on a ceramic substrate.

Loss Factor

A typical loss factor for a thin (1μ) ferroelectric film is ~ $(1÷5)\times10^{-2}$ for the 10 GHz band [2]. Recently, we have obtained an encouraging result that showed the loss factor of 4×10^{-3} at 35 GHz for the dielectric constant of 495 and DC field variation from 2.8 V/μm to zero [3,4]. The expected loss factor for our BST-oxides composition is $(2÷5)\times10^{-3}$ for the 11 GHz frequency range.

We have chosen the tunability of the structure not to exceed 3% to allow us to adjust for a maximum 200 MHz frequency shift. The 11.42 GHz cylindrical structure (Fig. 1) parameters are: vacuum channel radius of 0.5 cm, dielectric radius of 0.633 cm, ferroelectric layer thickness of 230 μ, dielectric constants of ceramic and ferroelectric

are 16 and 250 respectively. Lines 3 and 4 show ratios between the wall and ferroelectric losses, and line 5 shows the ratio of the loss factor of the 11.42 GHz tunable structure and equivalent DLA (no extra layer) structure designed for the same 11.42 GHz frequency [2].

Table 1. The 11.424 GHz tunable DLA structure loss factor ratios. Tunability factor is of 2.22%.

1	Thickness of ferroelectric	230 μ
2	Loss factor of ferroelectric	5×10^{-3}
3	Ferroelectric losses,%	26.6
4	Wall losses, %	63.9
5	Loss ratio	1.632

It should be noticed that we have to take into account the increase in the losses of the conducting walls if we use the tuning ferroelectric between the ceramic layer and the metal. However, the total ratio of losses in the tunable structure to the same frequency structure made only with ceramic is in the range of (1.7÷1.8), $W_{diel}/W_{ferr} < 2$. (line 5 of the table, "Loss ratio"). It means that our price for tunability is the increase of energy loss by (1.5÷2.0) dB for the double layer 3% tunable accelerating structure in comparison with a (non-tunable) dielectric loaded waveguide.

Planar Tunable DLA Structure Demonstration

A BST ferroelectric doped with the oxides composition, with loss factor of 4×10^{-3}, and dielectric constant of 500 has been synthesized [3,4]. Tunability measurements of the ferroelectric developed have been done at 9÷11 GHz by the cavity "open wall" resonator method. The basic idea is shown in Fig. 2: in the wall of the waveguide of the required frequency we cut out windows on opposite sides. We made a "landing" place of 20×30 mm into the waveguide wall for the testing substrates. A set of 2 substrates has been used for this demonstration: (1) a ceramic inner substrate, with the dielectric constant of 100 and thickness of 2 mm; and (2) a ferroelectric outer layer of 500 μm and dielectric constant of 495. We used a photolithography deposition to put the microstrip contacts onto the substrate surface. The negative group was grounded and the positive group was connected to a high voltage DC power supply. The best result we achieved, using an electric field of 1400 V DC, corresponds to 2.8 V/μm dc field applied to the ferroelectric sample. We measured a **106 MHz** shift, or 1.1% at 9.5 GHz with the ferroelectric material tunability factor of 9.5%. Recently, we have fabricated the samples with a tunability factor of 15% for the same biasing field of 2.8 V/μ. We did not observe any sign of saturation and we expect a tunability factor in the range of (22÷25)% for the new samples tuned by the bias filed of 5 V/μm. The overall planar structure tunability factor will be in the range of **(2.1÷2.4)%** that corresponds to **228 MHz** frequency shift.

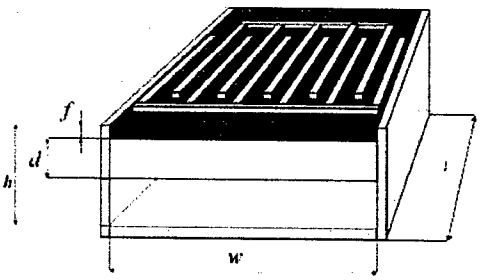


Figure 2. Tunable planar 11.424 GHz structure with open walls. One can see the ferroelectric substrate with the microstrip contacts (interdigital configuration) to supply bias voltage into the ferroelectric material.

SUMMARY

A new scheme for the tuning of DLA accelerating structures is proposed. The basic idea is to use a double layer of dielectric. The outer layer, made of ferroelectric material with permittivity controlled by an applied DC field, will tune the whole accelerating structure to the desired frequency. The (9÷11) GHz tunable DLA structure has been tested with a ferroelectric layer 500 μ thick with a dielectric constant of 495, tunability of 9.5%,a loss factor of 4×10^{-3}, and a peak applied DC bias field of 2.8 V/μ. The overall structure tunability of **1.1%** or **106 MHz** was demonstrated. This tuning effect is fast and programmable in real time (< 1 μsec) during operation of the accelerator.

The multi-layer tunable technology can also be extended to many other high frequency, high power devices.

This work is supported by the US Department of Energy, grant SBIR DE-FG02-02ER83418. The ferroelectric samples have been fabricated for the Omega-P, Inc. project [V.P. Yakovlev et al, TPAE031, these Proceedings], the project that initiated the research of our ferroelectric group under support to Omega-P, Inc. through DoE SBIR Phase I grant DE-FG02-02ER83537.

REFERENCES

[1]. A. Kanareykin, I. Sheinman, A. Altmark, Technical Physics Letters, Vol. 28, N. 11, pp. 916-918, 2002.

[2]. A. Kanareykin, W. Gai, J. Power, A. Altmark and I. Sheinman, AIP Conference Proceedings, N 647, pp. 565-575, 2002.

[3]. E. Nenasheva, A. Kanareykin, N. Kartenko, S. Karmanenko, International Conference on Electroceramics, MIT, Cambridge, MA, USA, 2003. (To be published).

[4]. S. Karmanenko, A. Kanareykin, E. Nenasheva, A. Dedyk, A. Semenov, The 10th European Meeting on Ferroelectricity. Cambridge, UK, 2003. (To be published).

A TUNABLE DIELECTRIC LOADED STRUCTURE WITH BUILT IN TRANSVERSE MODE SUPPRESSION

A. Kanareykin, Euclid Concepts LLC, Solon, OH 44139, USA
A. Altmark, I. Sheinman, Electrical Engineering University, St. Petersburg, 197376, Russia

Abstract

Recently, a method for tuning dielectric-loaded accelerating (DLA) structures has been proposed [1,2]. In these structures, a ferroelectric layer backs a conventional ceramic layer, thus allowing the effective dielectric constant of the waveguide to be varied by applying a DC electric field to the ferroelectric layer. In this paper, we present a design for a cylindrical version of this multilayered, tunable DLA structure that has the additional benefit of suppression of transverse deflecting modes [3,4] due to the axially segmented conducting wall. This structure consist of a layer of conventional ceramic, surrounded by a thin layer of a ferroelectric, that is in turn surrounded by axially-oriented, insulated microstrip electrodes and a layer of absorbing material (ferrite). The axial orientation of the microstrips means that transverse deflection modes are suppressed, since they require an azimuthal current, while longitudinal accelerating modes are allowed, since they only require axial currents. We will present calculations of the relevant accelerator parameters for a cylindrical DLA structure.

INTRODUCTION

A new method of wakefield acceleration of the charged particles, using wakefields generated by the short high charge electron bunches passing through dielectric loaded accelerating structure, now is the object of intensive experimental and theoretical study. Commonly a dielectric loaded accelerating structure (DLA) is the single-layered dielectric (ceramic) tube with an inner vacuum channel for the passing electron beams. A dielectric cylinder is inserted into a conductive copper jacket.

Wakefield acceleration assumes the energy transfer from a high-current low-energy electron beam (driver) to a low-current high-energy accelerating beam of charged particles (witness). While passing the ceramic waveguide the driver beam generates Cherenkov electromagnetic waves (wakefields) with the longitudinal fields up to 100 MV magnitudes to be used for the witness beam acceleration.

Large amplitude longitudinal wakefields also imply that strong transverse deflecting forces will be generated if the drive beam in the structure is misaligned. This deflection field can have serious detrimental effects on the accelerated beam from the head - tail single bunch break up instability of the accelerated beam, resulting from the leading particles in an offset bunch driving HEM modes that in turn deflect the electrons in the tail of the bunch. The deflected tail electrons will eventually be driven so far off axis that all or most of the particles will be lost by scraping on the inner walls of the dielectric waveguide. On the other hand, synchronization between the electron beam velocity and the phase velocity of the accelerating field must be maintained in order for the bunch to gain energy. For some applications DLA structure requires an unachievably tight machining tolerance of the waveguide geometry and extremely expensive ceramic material manufacturing process. Recently, a method for tuning DLA structures has been proposed [1,2]. A combination of ferroelectric and ceramic layers have been used to permit tuning of a composite ceramic–ferroelectric waveguide while keeping the overall material loss factor in the $(4\div5)\times10^{-4}$ range. It was shown that the losses in the composite structure are comparable to the losses in conventional DLA structures that consist of a single dielectric cylinder inserted into a conductive copper jacket. Dielectric permeability variation allows adjusting of the phase-beam matching between the longitudinal wakefield and the witness beam position for acceleration mechanism efficiency. [6].

Tunable DLA Structure

The DLA structure with ferroelectric layer tuned by an external DC electric field is shown in Fig. 1. The inner layer is ceramic, with permittivity typically in the range of 4÷36. The outer layer is a film made of BST ferroelectric, dielectric constant of 200÷500, placed between the ceramic layer and the copper sleeve. The DLA structure tuning is achieved by varying the permittivity, ε_2, of the ferroelectric film by applying an external DC electric field across the ferroelectric. One can use the well-developed technology based on photolithography and microstrip contact deposition to supply a DC field to the ferroelectric film. This technology has been widely used in the field of high frequency phase-shifters and tunable filters design based on thin ferroelectric films. The main problems to be addressed in order to apply this technology for our particular design are:

- The configuration has to match the desired set of guiding modes
- DC field penetration into the ferroelectric layer with the field magnitude for the maximum tuning range (10 V/μm for the material to be used)
- Satisfy conditions of minimum insertion losses.

0-7803-7738-9/03/$17.00 © 2003 IEEE

Fig. 1 shows our current preferred geometry for the configuration of the bias field microstrips for the ferroelectric-ceramic tunable DLA structure. Figure 2 shows the particular dimensions of the microstrips structure for (10÷13) GHz accelerating waveguide. One has to find an appropriate microstrip width for the particular layer. Our simulations showed that for the (180÷220) μm layer that corresponds to 11 GHz average frequency the optimal ratio is $h = 3 \times d$, where h is the layer thickness and d is the strip width.

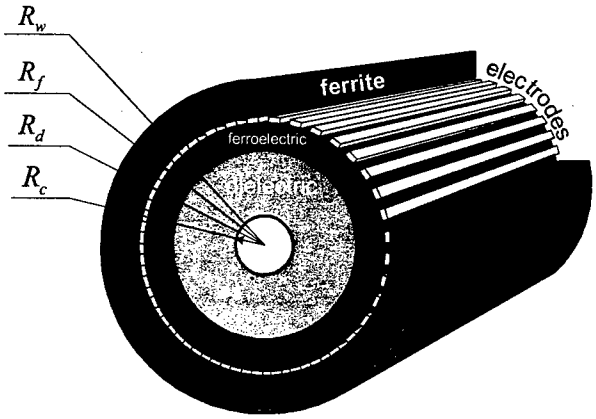


Figure 1. Tunable dielectric loaded accelerating structure with transverse deflecting modes suppression.

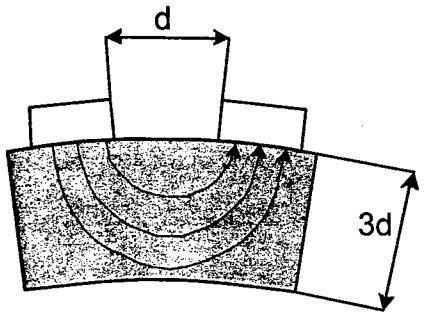


Figure 2. Microstrip profile. The ferroelectric layer thickness is within 3d, where d is a microstrips gap.

The microstrip separation is approximately d as well. For the (10÷13) GHz frequency range $d = (50 \div 60)$ μ. A DC bias of (0.5÷1) KV is applied across this gap to provide the (5÷10) V/μ biasing field.

Transverse Biasing

It should be mentioned that the biasing field is transverse relative to the accelerating field for the microstrip configuration in Fig. 1. The ferroelectric material we plan to use is to be formed in a polycrystalline paraelectric phase [5] and does not show any significant anisotropy. One can refer here to the measurements of the 106 MHz shift of the TM_{01} fundamental frequency of the 11.42 GHz planar ceramic loaded waveguide with BST ferroelectric layer with the dielectric constant of 500 supplied with the *transverse biasing* field [5]. Microstrip configuration gap was 300 μ for the bias DC field of 2.8 V/μ.

Transverse Modes Suppression

The deflection modes cause BBU effects resulting in particle loss and consequently in acceleration distance limitation. An rf slow wave structure that supports accelerating modes while having damped the deflecting modes then be desirable. Such a device was proposed and experimentally tested in [3,4], where the uniform outer copper sleeve was replaced by axial, closely spaced, insulated wires that allow only axial wall currents of the system. This anisotropic copper metallization provides very low Q factor selectively for the deflecting transverse modes while maintaining high Q for the accelerating mode. The axial orientation of the microstrips means that transverse deflection modes are suppressed, since they require an azimuthal current, while longitudinal accelerating modes are allowed, since they only require axial currents. The direct wakefield measurements showed the attenuation was consistent with the 246 pcs e-folding time bench test and therefore the BBU effects can be greatly reduced in the DLA structures [3].

One can see in Fig. 1 and Fig. 2 that the microstrip configuration completely satisfies the transverse mode suppression design discussed above. It is fortunate we have all-in-one transverse mode suppressor and tunable accelerating structure providing with the same microstrip configuration.

Fig. 3 presents HEM11 and HEM12 transverse mode magnitude vs. the distance behind the bunch of 100 nC charge, $\sigma_z = 0.4$ cm, the offset of $r_0 = 0.03$ cm. The three various thickness of absorbing ferrite Δ is shown. Parameters of the waveguide, Fig. 1, are: $R_c = 0.5$ cm, $R_d = 0.6$ cm, $R_f = 0.623$ cm, $R_w = R_f + \Delta$, dielectric constant of the ceramic layer $\varepsilon_d = 16$, dielectric constant of the ferroelectric layer $\varepsilon_f = 200$, ferrite conductivity $\sigma_{ferro} = 0.1$ $(ohm \times m)^{-1}$, $\mu_{ferro} = 5$, $\varepsilon_{ferro} = 1$. One can see the deflecting field magnitude is almost flat for the relatively thin ferrite layer of 0.4 cm and it is damping dramatically for the ferrite layer of 0.8 cm thickness. The transverse field suppressor parameters are extremely sensitive to the right choice of the absorbing sleeve geometry due to the redistribution of the wakefields power over the waveguide boundaries.

Fig. 4 shows the transverse field superposition of HEM_{11} and HEM_{12} modes for the offset of 0.25 cm, the beam is deflected significantly. The repetitive rate frequency of the AWA photoinjector is 1.3 GHz that corresponds to 22÷23 cm available spacing between the bunches. One can see that the transverse field magnitude will be damped down by that distance.

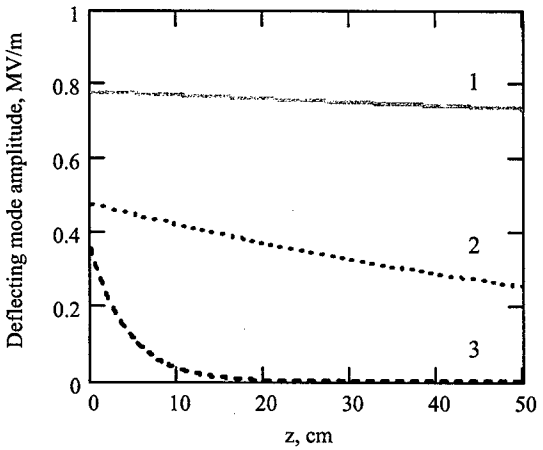


Figure 3. Magnitude of a radial deflecting field of the first transverse mode vs. the distance z behind the bunch for the 13.625 GHz accelerating structure. Three thickness of ferrite have been studied, 1 – Δ = 0.4 cm, 2 – Δ = 0.5 cm, 3 – Δ = 0.8 cm. 100 nC beam offset is 0.03 cm.

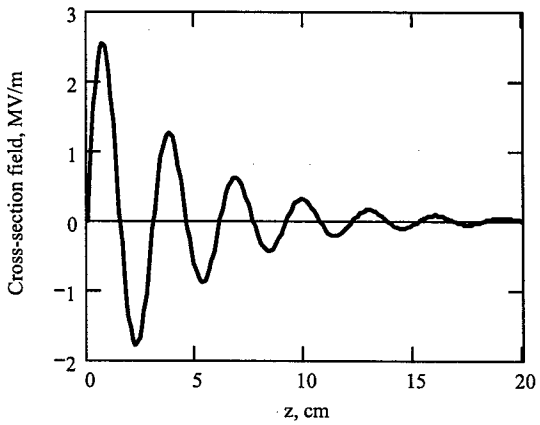


Figure 4. Deflecting field magnitude vs. the distance z behind the bunch, offset is of 0.25 cm, the beam is deflected off the half of the vacuum channel radius.

The beam misalignment will cause the azimuthal field between the microstrips embedded into the ferroelectric layer [7]. Figure 5 shows that the magnitude of this field is in the range of 0.5÷0.6 MV/m for the critically deflected beam with the offset is 0.25 cm and almost negligible for the initial offset of 0.03 cm. The DC bias field that we have used for the ferroelectric layer tuning [5] was in the range of 2.8 MV/m for the 300÷500 μm gap between the microstrips in comparison with 0.5 V/μm rf field at the same point.

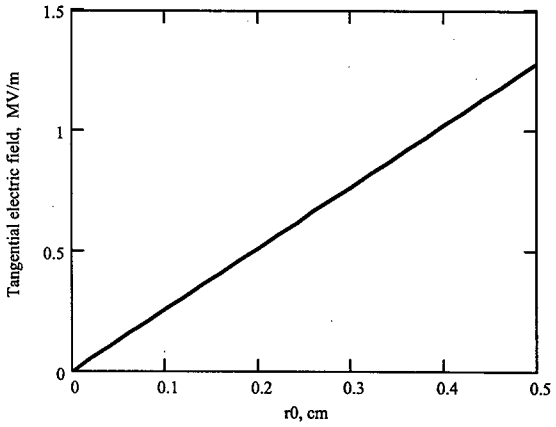


Figure 5. Azimuthal field magnitude between the microstrips vs. offset of the 100 nC electron beam passing through the 13.625 GHz accelerating structure. The beam rms length is 0.4 cm.

SUMMARY

The microstrip configuration for the tunable dielectric loaded accelerating structure fabricated with the double-layer ferroelectric technology will support the accelerating modes of the waveguide while the transverse deflecting modes can be damped. It should be noticed that the frequency tuning during the experiment favorably distinguishes the dielectric loaded accelerating structures from the conventional accelerators and opens a variety of applications for the systems with the "wave-beam" precise matching requirements.

ACKNOWLEDGMENTS

This work is supported by the US Department of Energy, Grant SBIR DE-FG02-02ER83418.

REFERENCES

[1] A. Kanareykin, I. Sheinman, A. Al'tmark. Technical Physics Letters, Vol. 28, N 11, pp. 916-918, 2002.

[2] A. Kanareykin, W. Gai, J. Power, A. Altmark and I. Sheinman. AIP Conference Proceedings No 647, AAC 2002, pp. 565-575, 2002.

[3] E. Chojnacki et al., Jorn. Appl. Phys., 69, 6257, 1991.

[4] W. Gai, Ching-Hung Ho., Jorn. Appl. Phys., Vol. 70. N 7, pp. 3955–3957, 1991.

[5] S.F. Karmanenko, A.D. Kanareykin, E.A. Nenasheva, A.I. Dedyk., A.A. Semenov. The 10th European Meeting on Ferroelectricity. Cambridge, UK, 2003. (To be published)..

[6] J.G. Power, W. Gai, A.D. Kanareykin., AIP Conference Proceedings 569, New York, American Institute of Physics, p.605-615, 2001.

[7] J. Simpson. Private communication.

TRANSFORMER RATIO ENHANCEMENT EXPERIMENT

A. Kanareykin, Euclid Concepts LLC, Solon, OH 44139, USA
W. Gai, J. G. Power. ANL, Argonne, IL, 60439, USA
E. Nenasheva, Ceramics Ltd., St. Petersburg, 194223, Russia
A. Altmark, Electrical Engineering University, St. Petersburg, 197376, Russia

Abstract

Recently, a multibunch scheme for efficient acceleration based on dielectric wakefield accelerator technology was outlined in [1]. In this paper we present an experimental program for the design, development and demonstration of an Enhanced Transformer Ratio Dielectric Wakefield Accelerator (ETR-DWA). The principal goal is to increase the transformer ratio R, the parameter that characterizes the energy transfer efficiency from the accelerating structure to the accelerated electron beam. We present here an experimental design of a 13.625 GHz dielectric loaded accelerating structure, a laser multisplitter producing a ramped bunch train, and simulations of the bunch train parameters required. Experimental results of the accelerating structure bench testing and ramped pulsed train generation with the laser multisplitter are shown as well. Using beam dynamic simulations, we also obtain the focusing FODO lattice parameters.

INTRODUCTION

There has been tremendous progress in ceramic structure-based acceleration schemes in the past few years. One of the most critical issues for dielectric wakefield acceleration is the improvement of the transformer ratio R, commonly defined as R = (Maximum energy gain behind the bunch) / (Maximum energy loss inside the bunch). It is crucial that methods be found to increase R in order to fully realize this technique as a practical option for high energy accelerators. According to the *wakefield theorem* [2] the accelerated beam cannot gain more than twice the energy of the drive beam, or in other words, R is less than 2 for collinear acceleration. Several schemes have been proposed to obtain $R > 2$ in collinear wakefield accelerators, but no experimental results have been obtained due to the inherent difficulties of these experiments. One proposed scheme operates with the driver beam having an *asymmetric* axial current distribution [2]. Using a similar idea, another scheme tailors the profile of a train of individually symmetric drive bunches [3] into a triangular ramp to produce $R > 2$. In this paper we consider the latter, here termed the *ramped bunch train* (RBT) method of transformer ratio enhancement. Experimental implementation of the proposed method [1] allows an enhancement of the transformer ratio by up to a factor of 4 compared to a conventional collinear accelerating scheme. The Enhanced Transformer Ratio (ETR) Experiment is under commissioning at Argonne National Laboratory's Argonne Wakefield Accelerator (AWA) facility, in cooperation with Euclid Concepts LLC.

ENHANCED TRANSFORMER RATIO EXPERIMENT

We plan to experimentally demonstrate ETR-DWA in 2003 - 2004. Our initial proof of principle demonstration will use a ramped bunch train (RBT) of 4 bunches, with charge ratio of 2-6-10-14 nC and bunch length of $_z = 0.4$ cm we predict an R pf 7.8. Simulations also show that both high gradient and high R can be obtained by using an RBT parameters of 10-30-50-70 nC to achieve R = 7.6 and E = 104 MV/m. Experimental design includes a laser multisplitter, producing a ramped train of laser pulses for the AWA photoinjector, and a 13.625 GHZ dielectric loaded accelerating structure supplied with a focusing FODO lattice to minimize BBU effects for RBT. The accelerating structure is to be installed into the AWA beamline [4]. This transformer ratio enhancement technique based on ceramic waveguide design will result in a highly efficient accelerating structure for future generation wakefield accelerators.

EXPERIMENTAL DESIGN

Accelerating Structure Fabrication

A ceramic composition based on $MgTiO_3$-Mg_2TiO_4 systems have been sintered using the solid-phase synthesis method [5]. This material is characterized by a unique homogeneous fine-grained structure and minimum porosity, with a dielectric constant of 16. The dielectric loss factor has been measured with the dielectric loaded resonator method. Measurement of the witness samples at 9 GHz frequency showed the following results: $Q \times f = (6.0 \div 7.7) \times 10^4$, loss factor of $(1.12 \div 1.17) \times 10^{-4}$.

Table 1. Bench measurements of the dielectric loaded accelerating structure.

#	Structure parameters	Bench test
1.	TM_{01} frequency	13497.6 MHz
2.	Inner radius	0.4999 cm
3.	Outer radius	0.6345 cm
4.	Dielectric constant	16.038

The set of 5 waveguide sections tuned for 13.625 GHz TM_{01} mode have been designed and fabricated of the ceramics composition discussed above. The dielectric tubes were formed with a specially developed two-stage

0-7803-7738-9/03/$17.00 © 2003 IEEE

technology: hydraulic and isostatic pressing. The special press-form for the 13.625 GHz ceramic waveguide fabrication has been designed and produced. The accelerating structure bench test parameters are presented in Table 1.

Mechanical tolerances and dielectric constant heterogeneity along the accelerating structure have been studied intensively due to the critical impact of structure imperfections on the Transformer Ratio to be measured. We found the maximum deviation of the dielectric constant was within 0.055.

It was shown that the mechanical tolerances did not exceed $3 \div 10$ m and the dielectric constant deviation measured at the bench test appeared within 0.2% of the average and 0.35% of the maximum deviation. It should be noticed that one can obtain the maximum transformer ration in the range of $7.5 \div 7.8$, Fig. 2.

Ramped Bunch Train Generation.

An Enhanced Transformer Ratio can be demonstrated if a RBT is generated with the required charge distribution and interbunch distances. Maximal R is achieved by requiring that all bunches lose energy at the same rate. Our simulations show that this happens when the bunch train has a charge ratio of (2-6-10-14) nC.

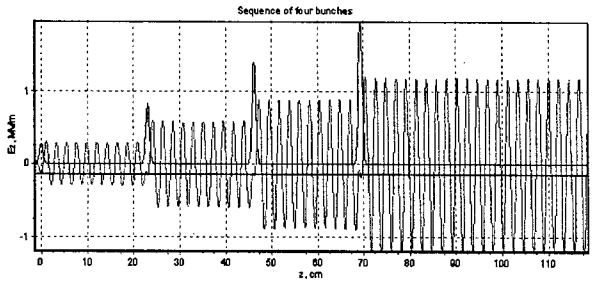


Figure 1. Single mode 13.625 GHz structure, 4 bunch (2-6-10-14) nC Ramped Bunch Train $_z = 0.4$ cm, Structure parameters are presented in Table 1.

We studied the interbunch distance adjustment for the transformer ratio enhancement as well. The repetition frequency of the AWA corresponds to the interbunch distance variation in the range of $22 \div 23$ cm that in turn relates to $d = (10 + 1/2)$. The optimal RBT parameters for the proof-of principal experiment are (2-6-10-14) nC. Wakefields and charge distribution for this case are presented in Fig. 1, while the accelerating structure parameters are presented in Table 1. We have studied the impact of tolerances and dielectric heterogeneity on the R value to be measured in the experiment. It was shown that the imperfection factors effect discussed above can be compensated with the laser multisplitter system by intensity and interbunch distance adjustments.

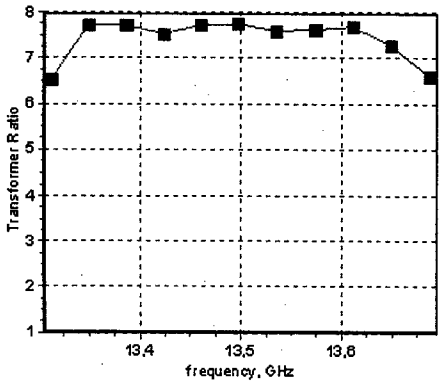


Figure 2. Transformer Ratio R vs. the TM_{01} mode frequency shift caused by the dielectric constant heterogeneity and mechanical tolerances. Interbunch distances adjustments are within 0.7 cm.

The average Transformer Ratio of 7.45 and maximum of 7.8 can be demonstrated with mechanical tolerances of 10 m and dielectric constant deviation of 0.35% if the interbunch distances adjusted within 0.7 cm, Fig. 2. We studied the multimode and single mode cases and demonstrated the method of transformer ratio optimization for the multimode structure parameters.

It was shown that one can perform high gradient acceleration with the wakefield gradient exceeding 100 MV/m and at the same time to provide an enhanced transformer ratio up to 7.27 with the following parameters of the drive bunch and the structure (the "target" case): inner radius of $a = 0.1$ cm, outer radius of $b = 0.268$ cm, dielectric constant of $= 16$, bunch length of $_z = 0.15$ cm charge distribution of 15, 39, 67 and 93 nC, Transformer Ratio **R = 7.27,** accelerating gradient of **E = 104.3 MV/m.**

Laser Multisplitter Design and Testing

The laser beamsplitting system is a critical issue for the success of the project. To generate the electron bunch-train, a laser pulse train is injected into the AWA drive photoinjector. This laser train is made by optically splitting a single laser pulse into four separate pulses with a combination of mirrors and beam splitters [6]. We have modified the original multisplitter at the AWA to create a Ramped Pulse Train required for the RBT generation. We installed and tested this beam splitting system at the AWA facility. The 4 output laser pulses have been generated and measured with an energy meter and streak camera. We measured the energy ratio of the pulse train, and have made a detailed study of each individual mirror. Based upon measured reflection coefficients, the energy ratios matched the expected ones for the 2nd, 3d and 4th bunches. We investigated the origin of the 1st bunch energy deviation and found out that the mirrors did not match the vendor's specification. Since then we have corrected this problem and are confident that we can make the required Ramped Laser Pulse train.

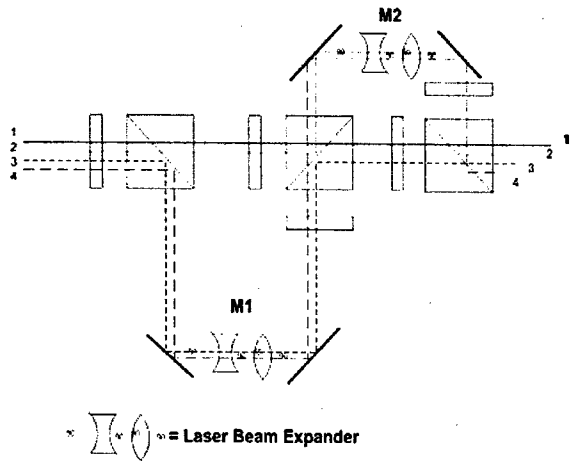


Figure 3. Adjustable and Variable Pulse Radius laser multisplitter design.

The measured laser pulse length was 8 ps and the interbunch spacing was 780 ps, just as anticipated.

We have recently redesigned the multisplitter so that one can adjust the pulse intensities as well as interbunch distances. Fig. 3 presents an Adjustable Laser Multisplitter design that is able to vary the laser pulse intensity and therefore to compensate for mechanical tolerances and other imperfections in the value of transmission and reflection coefficients. The adjustable multisplitter uses a half-wave retardation plate and a polarizing cube beamsplitter to continuously vary the pulse intensities.

The RBT introduces different space charge defocusing for the differing bunch intensities. We accommodate this by including a Variable Beam Radius option for the Laser Beamsplitter [6]. In order to generate different laser pulses with variable radius one can use a beam expanding telescope in the 2 legs of magnification M1 and M2 (Fig. 3) and clipping iris after the multisplitter. Thus we can determine the bunch train radii required for a periodic FODO channel. In general, we have designed the optical multisplitter system and performed preliminary tests on the laser beam splitting required for the Ramped Bunch Train generation.

RBT Transportation Beam Dynamic Simulations

We have studied BBU related effects for the beam train and accelerating beam both passing through the 13.625 GHz accelerated structure. The head-tail instability caused by the misalignment of the RBT can be controlled by using BNS damping [7], with the additional complication that the focusing channel has to control the drive bunch train of different charges passing through the same accelerating structure.

We have studied the beam dynamics of the most interesting and optimal beam that we plan to use in the ETR proof-of–principle experiment; a charge distribution of (2-6-10-14) nC. Our simulation showed that one can control the "optimal" bunch train in the structure up to 52÷60 cm without any FODO lattice, with no significant particle loss, and that the average transformer ratio still exceeded 7.0. At the same time, we studied the propagation in the structure with the FODO lattice applied as well; the "optimal" beam traversed 90 cm, Fig. 4 shows this RBT at 60 cm distance passed, no particle loss, beam is under control.

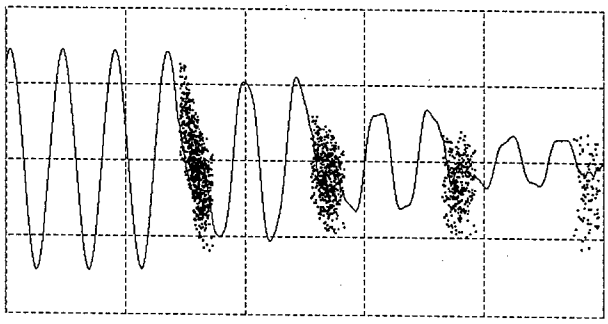


Figure 4. Beam dynamics simulations of the optimal (2-6-10-14) nC RBT, FODO focusing applied, 60 cm passed.

SUMMARY

The proposed Enhanced Transformer Ratio experiment is based upon the Ramped Bunch Train (RBT) technique. The 13.625 GHz accelerating structure has been manufactured and the uniformity of dielectric properties is in the range of 0.35%. We have installed and tested a prototype laser beam splitter to produce a ramped bunch train of 4 bunches, predicted to achieve a transformer ratio of R=7.8. RBT parameters have been simulated and optimized. Numerical simulations of the beam dynamics of the RBT have been presented and the appropriate FODO lattice parameters have been calculated.

This work is supported by the US Department of Energy, Grant # SBIR DE-FG02-02ER83418.

REFERENCES

[1] J.G. Power, W. Gai, A. Kanareykin, X. Sun. PAC 2001 Proceedings, pp. 114-116, 2002.
[2] P.B. Wilson, SLAC Report No296, p.273, 1983, K.L. Bane, P. Chen, P.B. Wilson, IEEE Trans. Nucl. Scien, 32, 3524, 1985.
[3] P. Schutt, T. Weiland, V.M. Tsakanov, Nor Amberb Conf. Proc., Armenia, 7(15) pp.12-17, 1989.
[4] www.hep.anl.gov/pmalhotr/AWA/docs/2p041.pdf
[5] E. Nenasheva et al. The 9th Int. Conference "Physics of Dielectrics", St.Petersburg, Russia, 2000, p.142.
[6] http://www.hep.anl.gov/pmalhotr/AWA/pubs.htm WF-198, WF-213, WF-215.
[7] W. Gai, A.D. Kanareykin, A.L. Kustov, J. Simpson, Phys. Rev. E, v. 55, N 3, pp. 3481-3488, 1997.

A DOUBLE-LAYERED, PLANAR DIELECTRIC LOADED ACCELERATING STRUCTURE

A. Kanareykin, Euclid Concepts LLC, Solon, OH 44139, USA
I. Sheinman, A. Altmark, Electrical Engineering University, St. Petersburg, 197376, Russia

Abstract

Recently, a method to tune *dielectric-loaded accelerating (DLA)* structures has been proposed [these proceedings]. In these structures, a ferroelectric layer backs a conventional ceramic layer, thus allowing the effective dielectric constant of the waveguide to be varied by applying a DC electric field to the ferroelectric layer. In this paper, we present a design for a planar version of this double-layered, tuneable DLA structure. The advantage of the planar waveguide is its spectral uniformity, ease of frequency tuning, and its simplicity of fabrication. The dispersion equation for the structure and the accelerating wakefield exited by a planar electron bunch has been calculated. Based on this work, we present simulation results for 13, 20 and 35 GHz structure parameters including tunability factor. The transverse deflecting wakefields caused by the beam offset have been studied as well. In addition, we present the results of cold test measurements for an 11.4 GHz, double-layered, ceramic-ferroelectric test device, including tuning range and Q measurements.

INTRODUCTION

The field of advanced accelerators is in search of novel revolutionary technologies to allow progress in particle accelerators for high-energy physics experiments. Techniques based on the Dielectric Wakefield Accelerator (DWFA) [1] concept are some of the most promising to date in terms of their potential to provide high gradient accelerating structures for future generation linear colliders. These structures may be excited by a high current electron beam or an external high frequency high power RF source and have been under intensive study in recent years [1]. The basic RF structure is very simple — a cylindrical, dielectric loaded waveguide with an axial vacuum channel is inserted into a conductive sleeve. A high charge, (typically 20÷40 nC), short, (1÷4 mm) electron *drive* beam generates TM_{01} mode electromagnetic Cherenkov radiation (wakefields) which, propagating through the waveguide vacuum channel, is used to accelerate a less intense beam pulse following at an appropriate distance.

The planar accelerating structures can produce a high accelerating gradient and can easily be fabricated. It is desirable to operate accelerating structures at high frequencies to overcome breakdown limits of the structure. Simply scaling cylindrical geometry to low wavelengths limits the accelerator luminosity. It should be noticed that high frequency dielectric structures also require tight mechanical tolerances and their fabrication becomes difficult. In [2], the slab type of dielectric structure has been studied using a normal mode analysis. Previously, the planar boundless structures have been studied in [3] and the structure excitation by the short beam were presented in [4] a rectangular dielectric-lined structure having micron-scale dimensions presented in [5] Experimental demonstration of the high frequency planar structure has been done in [6]. Recently, a method for tuning the DLA structures has been proposed [7]. The ceramic loading covered by the relatively thin ferroelectric film allows for tuning the entire structure due to the dielectric material nonlinearity. In this paper, we present a planar *tunable dielectric loaded accelerator* mode analysis, design, and cold test results.

TUNABLE PLANAR DLA STRUCTURE

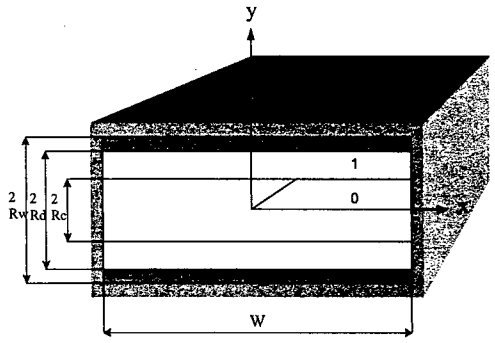


Figure 1. Double-layer Tunable Planar DLA structure. Inner layer is a ceramic substrate, the outer one is made of BST ferroelectric.

DLA structures, in comparison with vacuum ones, have an important parameter that determines the frequency spectrum - the dielectric constant of the loading material. In [7] a new scheme was proposed allowing control of the dielectric constant (and consequently the frequency spectrum) for the dielectric waveguides by incorporating ferroelectric layers. The most notable feature of the tunable DLA is the replacement of a single ceramic by a composite of 2 layers. The outer layer is a film made of BST ferroelectric placed between the ceramic layer and the copper wall. The DLA structure tuning is achieved by varying the ferroelectric permittivity by applying an external DC electric field across the ferroelectric. The design shown in Fig. 1 is not the only one possible; the positions of the layers can be swapped so that the ferroelectric film will form the inner layer. The advantage of this configuration would be the reduction of the magnetic loss on the conducting copper walls, while the disadvantages would be high gradient RF fields on the ferroelectric material surface, scattered electrons and increased heating. We consider the outer layer is a

0-7803-7738-9/03/$17.00 © 2003 IEEE

ferroelectric one, dielectric constant of 500, loss factor of 4×10^{-3} at 11.424 GHz, the inner layer is made of ceramic, dielectric constant of 20÷30, loss factor of $(1\div3)\times10^{-4}$. The normal modes in dielectric loaded guides are LSM and LSE modes that have no H or E components normal to the dielectric/ ferroelectric interface. In each slab, the fields for LSM/LSE modes were derived from the electric/magnetic Hertz potential and satisfied the boundary conditions at the interface between ferroelectric/dielectric and dielectric/vacuum.

The electron beam passes the vacuum channel along an axis waveguide with an initial offset. The wakefield is generated behind the bunch if the dielectric material satisfies the Cherenkov radiation terms:

$$V=\beta c \quad \text{and} \quad \beta>\varepsilon^{-1/2}.$$

Solving the equations for E_z and H_z, substituting them to boundary conditions and equating zero determinants of the turned out systems, one can obtain the dispersive equations for antisymmetric and symmetric solutions corresponding to:

$$\Delta_{odd}(k,k_x)=0,\ \Delta_{even}(k,k_x)=0, \qquad (1)$$

where $k_x=2n\pi/w$ for antisymmetric solutions and $k_x=(2n+1)\pi/w$ for symmetric ones.

The expressions for longitudinal components of electric and magnetic fields E_z and H_z can be written as:

$$E_z(x,y,\zeta)=\sum_{n,m=0}^{\infty} E_{z\,m,n_p}(x,y,k_{n,m})\cos(k_{z\,n,m}\zeta), \qquad (2)$$

$$H_z(x,y,\zeta)=\sum_{n,m=0}^{\infty} H_{z\,m,n}(x,y,k_{n,m})\cos(k_{z\,n,m}\zeta), \qquad (3)$$

where $k_{n,m}$ are roots of the dispersive equations (1), $\zeta=z-Vt$, $E_{z\,m,n}(x,y,k_{n,m})$ and $H_{z\,m,n}(x,y,k_{n,m})$ are defined by the boundary conditions. Other field components of electrical and magnetic fields can be written through E_z and H_z.

The Planar DLA Structure Parameters

Table 1. Tunable rectangular waveguide parameters.

№	w, cm	R_c, cm	d, μm	R_w, cm	ε_1	ε_2	$\delta\varepsilon_2$	f, GHz	δf %
1	4	0.5	150	0.6048	16	500	25%	13.625	2.0
2	4	0.5	90	0.5639	16	500	25%	20	2.2
3	4	0.3	55	0.3355	16	500	25%	35	2.9

Table 1 shows the Tunable DLA structure parameters corresponding to planar geometry presented in Fig. 1. for the 13, 20 and 35 GHz frequency range. The ferroelectric layer thickness of d decreases for the high frequencies, $\delta\varepsilon_2$ is the dielectric permittivity variation of the ferroelectric layer, $\delta\varepsilon_2=\Delta\varepsilon/\varepsilon$. One can see the ferroelectric dielectric constant variation within 25% causes $\delta f=(2\div2.9)\%$ overall frequency adjustment of the planar DLA structure.

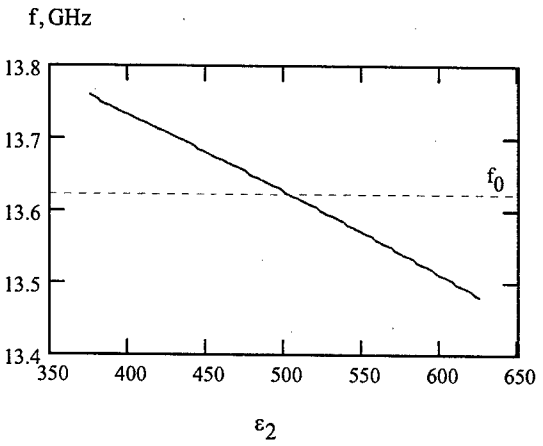


Figure 2. 13.625 GHz frequency variation vs. dielectric constant of the ferroelectric layer. The waveguide parameters correspond to line 1 of Table 1.

Fig. 2 shows the 13.625 GHz structure frequency shift caused by the dielectric constant variation of the ferroelectric layer, tunability factor of the ferroelectric material was of 20÷25%.

Wakefields

In Table 2, the parameters of the electron beams that will be used in the planning experiments are presented. The first line of the table corresponds to the beam passing the structure almost along the central axis, offset is 0.03 cm. The beam is misalignment at line 2, the offset is 0.5 cm off the x and 0.2 cm off the y respectively.

Table 2. Electron bunch parameters.

№	q, nC	W, MeV	x_0, cm	σ_x, cm	y_0, cm	σ_y, cm	z_0, cm	σ_z, cm
1	100	150	0.03	0.49	0.03	0.12	0	0.4
2	100	150	0.5	0.375	0.2	0.075	0	0.4

Accelerating longitudinal gradient is shown in Figure 3, peak magnitude is 22 MV/m. It should be noticed that the similar cylindrical (11÷13) GHz accelerating structure supports the single mode wakefields for the 0.4 cm long bunches [7] At the same time, wakefields excited by the 0.4 cm long bunch passing through the 13 GHz planar structure show multimode properties of the structure, Fig.3.

Fig. 4 and 5 present a 3D picture of the wakefields, Fig. 4 corresponds to the beam position slightly deflected off the z ax, line of Table 2, the accelerating gradient is flat at the cross section of the structure. Fig. 5 present the worse case where the beam is deflected, line 2 of Table 2, the peak gradient is deflected as well. The magnetic field H_z magnitude increases near the wall boundary as expected due to the high value of the ferroelectric dielectric constant, thus one can predict significant wall losses for this kind of structure.

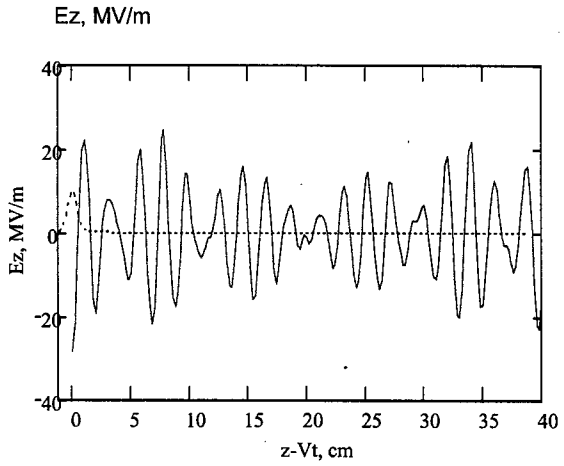


Figure 3. Accelerating field E_z vs. the distance behind the bunch $\zeta = z - Vt$ excited by the 100 nC beam. Beam parameters are presented in Table 2, line 1.

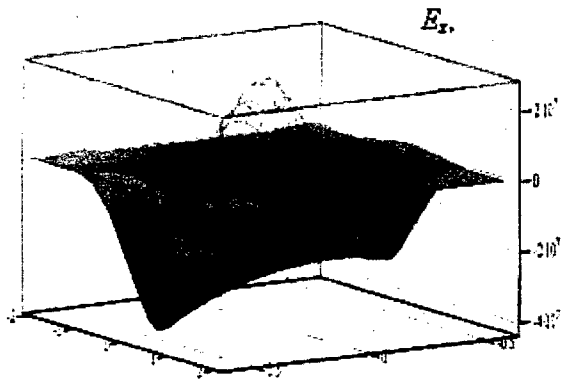


Figure 4. Longitudinal accelerating gradient at the cross section of the planar DLA structure. Beam parameters are presented in Table 2, line 1.

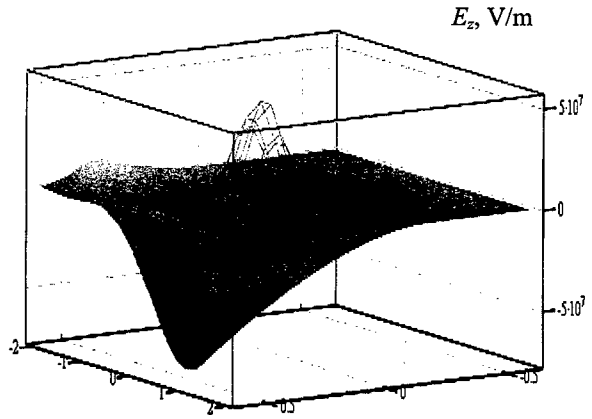


Figure 5. Longitudinal accelerating gradient at the cross section of the planar DLA structure. Beam parameters presented in Table 2, line 2. The beam is misaligned and the peak gradient is deflected as well.

Cold Test Measurements

Tunability measurements have been done at 9.5 GHz by cavity □open wall□resonator [8] Dielectric constant of the ceramic substrate was 100. Electric field of 1400V applied to BST sample (dielectric constant of 495) that corresponds to 2,8 V/μ bias field. We measured the 106 MHz frequency shift, tunability factor of the material was 9.5%.

SUMMARY

A planar tunable dielectric loaded accelerating structure was presented and the frequency tunability factor was calculated. Accelerating gradient dependence on the beam misalignment was studied and the cold measurement results were presented.

This work is supported by the US Department of Energy, Grant □ SBIR DE-FG02-02ER83418.

REFERENCES

[1] http://www.hep.anl.gov/pmalhotr/AWA/pubs.htm
[2] L. □iao, W. Gai, and □. Sun. PAC 2001 Proceedings p. 3963.
[3] S.□.Park et al., Phys Rev. E 62, 1266, 2000.
[4] A.Tremaine et al., Phys. Rev. E 56, 7204, 1997.
[5] T.C.Marshall et al. AIP Conference Proceedings 569, 316, 2001.
[6] M.Hill, et al., PRL, 87,094801-1, 2001.
[7] A. Kanareykin, W. Gai, □ Power, A. Altmark and I. Sheinman, AIP Conference Proceedings, □ 647, pp. 565-575, 2002.
[8] S. Karmanenko, A. Kanareykin, E. □enasheva, A. Dedyk, A. Semenov, The 10th European Meeting on Ferroelectricity. Cambridge, UK, 2003. (To be published).

GENERATION OF ULTRA-SHORT RELATIVISTIC-ELECTRON-BUNCH BY A LASER WAKEFIELD*

A. G. Khachatryan, K.-J. Boller, and F. A. van Goor,

Laser Physics & Nonlinear Optics Group, Dept. of Applied Physics, University of Twente, P.O. Box 217, 7500 AE Enschede, The Netherlands

Abstract

The possibility of the generation of an ultra-short (about one micron long) relativistic (up to a few GeVs) electron-bunch in a moderately nonlinear laser wakefield excited in an underdense plasma by an intense laser pulse is investigated. The ultra-short bunch is formed by trapping, effective compression (both in longitudinal and in transverse directions) and acceleration of an initially nonrelativistic (with kinetic energy of a few hundreds keVs) e-bunch that is injected in front of the laser pulse. The initial bunch may be of poor quality, may have a duration in the order of the laser pulse length or longer and can be generated by a laser-driven photo-cathode RF gun. Our 1D and 3D calculations predict that the accelerated ultra-short bunch will show a low energy spread of less than one percent and a low transverse emittance in the order of a nanometer. An energy gain in the GeV-range is feasible at an accelerating distance of a few centimetres. The total number of accelerated electrons is restricted by the beam loading effect only and can reach a value of 10^8–10^9.

INTRODUCTION

Electron bunches with the length in the order of a hundred microns have been produced using a photo-cathode radio-frequency (RF) gun [1], a thermionic RF gun [2], and a magnetic bunch compressor [3]. However, many applications, such as laser wake-field acceleration, inverse Cherenkov acceleration, inverse free electron laser (FEL), x-ray FEL, high energy physics and other applications, require much shorter electron bunches with a length in the order of a micrometer. Generation of such a short electron bunch is a difficult technical problem, new approaches to which are required. Recently, a new scheme of a laser wake-field accelerator (LWFA) has been proposed [4,5], which allows the generation of an ultra-short, ultra-relativistic, high quality electron bunch. The scheme utilizes a non(weakly)-relativistic bunch of electrons which is injected in front of a high-intensity laser pulse generating a nonlinear wake wave in an underdense plasma (see Fig. 1). Our results [4,5] showed that the electron bunch runs through the pulse, is trapped in the first accelerating maximum in the wake, essentially compressed both in longitudinal and transverse directions, and accelerated to an ultra-relativistic energy. Here we show that the trapped electron bunch length is much less than the plasma wavelength. We also show that the generation of ultra-short relativistic bunches by our scheme is possible even when the initial bunch length is much longer than the plasma wavelength.

*This work is supported by Fundamenteel Onderzoek der Materie (FOM, The Netherlands) under "Laser Wakefield" project.

ONE-DIMENSIONAL (1D) THEORY

Because the trapped electrons are concentrated close to the axis, their longitudinal dynamics are well described by a 1D theory [5]. The 1D theory also allows a more detailed description of the problem. Suppose that an electron is initially ahead of the laser pulse (see Fig. 1) and moves with a velocity v_0 less than the group velocity

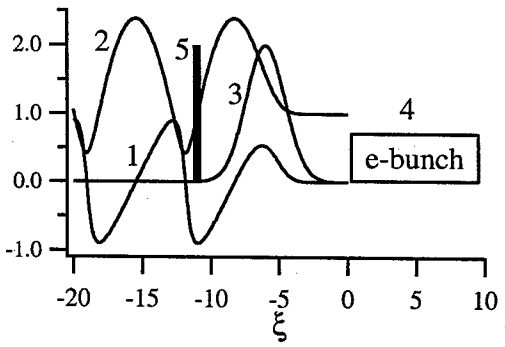


Figure 1: The laser wakefield scheme: the wake electric field E_z (1), the potential Φ (2), the laser pulse amplitude a (3), the initial (4) and trapped (5) bunches as a function of the position in a moving frame. a_0=2, σ_z=2, γ_g=50.

of the pulse v_g, which, in turn, is equal to the wake phase velocity. From the well known integral of motion $\gamma-\beta_g p-\Phi$=const (see, e.g., [4]; where γ and p are the gamma factor and the momentum of the electron normalized to $m_e c$, $\beta_g=v_g/c$, $\Phi(\xi)=1+e\varphi/m_e c^2\equiv 1+\phi$ is the normalized wake potential, $\xi=k_p(Z-v_g t)\equiv z-\tau$, $k_p=\omega_p/v_g$, $\omega_p=(4\pi n_p e^2/m_e)^{1/2}$ is the plasma frequency, and n_p is the unperturbed plasma electron concentration) one can obtain an expression for the initial momentum of the trapped electron [4,5]:

$$p_0=\gamma_g^2[\beta_g S-(S^2-\gamma_g^{-2})^{1/2}], \qquad (1)$$

where $S=1/\gamma_g+1-\Phi_{tr}$, Φ_{tr} is the wake potential at the trapping point ξ_{tr}, at which $p=\beta_g\gamma_g\equiv p_g$, $\gamma_g=(1-\beta_g^2)^{-1/2}$. One

can see that the initial momentum of the trapped electron has a minimum, p_{min}, corresponding to the minimum of the wake potential, Φ_{min}; at this trapping point the wake electric field $E_z=-(1/\beta_g)^2 d\Phi/d\xi$ (normalized to $m_e c\omega_p/e$) is zero. The maximum value $p_{max}=p_g$ corresponds to the point in the wake where $\Phi=1$ ($E_z=-E_{z,max}<0$). In the nonlinear wakefield the longitudinal space interval, in which electrons can be trapped, decreases with the wake amplitude $E_{z,max}$ (though the nonlinear wake wavelength increases) and is less than a quarter of the linear wake wavelength $\lambda_p=2\pi/k_p$. Figure 2 shows numerical results for the minimum trapping momentum and the wakefield amplitude in dependence on the peak amplitude a_0 of a Gaussian laser pulse: $a=a_0\exp[-(\xi-\xi_c)^2/\sigma_z^2]$. As usual, the electric field amplitude a of the pulse is normalized to $m_e c\omega_L/e$, where ω_L is the laser frequency. In this paper values of $a_0=2$, $\gamma_g=50$, $\sigma_z=2$, and $\xi_c=3\sigma_z$ are used in the numerical calculations.

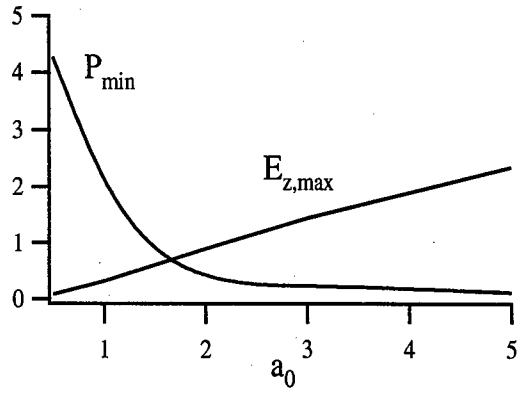


Figure 2. Calculated dependence of minimum initial momentum of trapped electrons, p_{min}, and wakefield amplitude, $E_{z,max}$, on the peak laser pulse amplitude, a_0.

For a moderately nonlinear wakefield with an amplitude much less than the wave-breaking field $[2(\gamma_g-1)]^{1/2}$, $|1-\Phi_{tr}|=|\phi_{tr}|>>1/\gamma_g<<1$. In this case, supposing that p_0 is not close to p_g, one can obtain from (1):

$$p_0 \approx (\phi_{tr} - 1/\phi_{tr})/2, \qquad (2)$$

where $-1<\phi_{tr}<0$. Then $p_{min}\approx(\phi_{min}-1/\phi_{min})/2$. In the linear wakefield $|\phi|<<1$, so $p_{min}\approx 0.5/|\phi_{min}|>>1$. Thus, in the linear wakefield, only relativistic electrons can be trapped. However, for an initially relativistic electron, the trapping time increases proportional to γ_0^2.

The trapping time, τ_{tr}, which is the time interval, that is necessary for an electron to reach the trapping point $\xi_{tr}(p_0)$, depends on the initial momentum p_0 and on the initial position ξ_0:

$$\tau_{tr}(\xi_0, p_0) = \tau_{tr0}(p_0) + \xi_0/(1-\beta_0/\beta_g), \qquad (3)$$

where τ_{tr0} is the trapping time of an electron which is initially at $\xi=0$. The dependence $\tau_{tr}(p_0)$ is shown in Fig. 3 for $a_0=2$ and $\gamma_g=50$; in this case $E_{z,max}\approx 0.9$ (see Fig. 1), the nonlinear plasma wavelength is $\Lambda_p\approx 1.144\lambda_p$, and $p_{min}\approx 0.53$. The trapping time has a minimum, which corresponds to $p_0\approx 1$, or to a kinetic energy of about 200 keV. For the trapping time of an electron bunch, in which the electron momentum changes in the range $p_1\le p_0\le p_2$, and, supposing that the tail of the bunch is at $\xi=0$, we can write:

$$\Delta\tau_{tr} \approx (\tau_{tr,max} - \tau_{tr,min}) + L_0/(1-\beta_2/\beta_g), \qquad (4)$$

where $\tau_{tr,max(min)}$ is the maximum (minimum) value of τ_{tr0} for electrons in the range $p_1\le p_0\le p_2$, and L_0 is the initial bunch length.

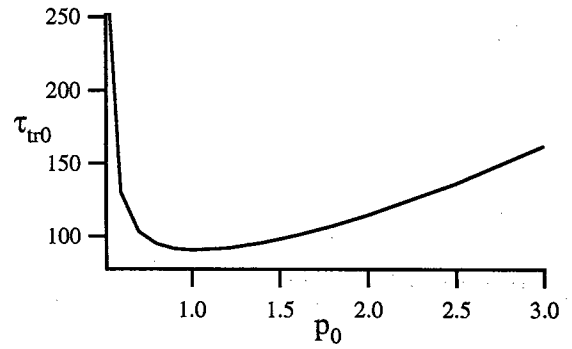


Figure 3. The trapping time, τ_{tr0}, as a function of the initial electron momentum, p_0.

As the trapped electron has reached a relativistic energy ($\gamma>>1$) in the wakefield, its dynamics becomes slow, and its spatial position in the wake changes on a normalized time scale of $\tau_{acc}=2\pi\gamma_g^2$. So, another electron, with the same p_0 but different ξ_0 will be trapped very close to the first one if $\Delta\tau_{tr}<<\tau_{acc}$. Test particle simulations showed that the trapped bunch length is much less than the plasma wavelength and undergoes practically no change during acceleration. One can see that the absolute and relative energy spread in the trapped bunch are $\delta\gamma\approx\Delta\tau_{tr}|E_z(\xi_{tr})|$ and $\varepsilon=\delta\gamma/\gamma\approx\Delta\tau_{tr}/(\tau-\Delta\tau_{tr})$ respectively [4,5]. In the case of finite momentum spread δp_0 in the initial bunch, electrons with different p_0 will be trapped at different trapping points. From Eq. (2) $\phi_{tr}\approx p_0-\gamma_0$. Then, for an electron bunch $\delta\phi_{tr}=\phi_{tr}(p_2)-\phi_{tr}(p_1)\approx|E_z|L\approx\delta\gamma_0-\delta p_0$, where E_z is some value of the wake electric field in the region occupied by the trapped bunch, L is the trapped bunch length. So, the trapped bunch length can be estimated as $L\approx(\delta\gamma_0-\delta p_0)/|E_z|$ when the effect of the finite initial bunch

length is less than the effect of the initial momentum spread.

In Fig. 4 the energy of trapped electrons is shown for the case of an initially mono-energetic bunch (in this case the trapped bunch length and the absolute energy spread are approximately proportional to the initial bunch length), p_0=1, and L_0=10λ_p. For example, at an acceleration length l=400λ_p (corresponding to 2 cm for λ_p=50 μm), the trapped bunch length is about $7\times10^{-3}\lambda_p$ (≈0.35 μm in the case of λ_p=50 μm) when L_0=10λ_p and 10 times less when L_0=λ_p; the trapped bunch length change is insignificant during acceleration. The energy of the electrons is about 1 GeV at l=400λ_p, the relative energy spread is ≈0.93% for L_0=λ_p and ≈9.5% when L_0=10λ_p. The generation of good quality ultra-short relativistic e-bunches in the case of large initial momentum spread and L_0~λ_p is also possible [4,5]. The initial bunch can be generated for example by a laser-driven photo-cathode RF gun.

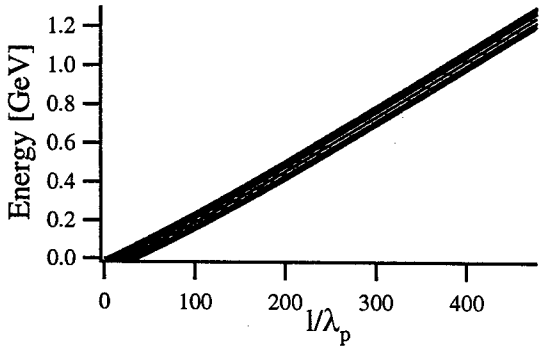


Figure 4. Energy of accelerating electrons, p_0=1, L_0=10λ_p.

THREE-DIMENSIONAL (3D) CASE

In a 3D linear wakefield, generated in an uniform plasma, the transverse force is defocusing in the trapping region. Fortunately, in the nonlinear wakefield and in the wake generated in a plasma channel the near-axis wakefield can be focusing over the entire accelerating region [5,6], so that our scheme can "work" in 3D as well. The trapped electrons are concentrated near the axis due to the focusing force. An example of the radial motion of the electrons with different initial radial positions is shown in Fig. 5 for the case of a laser wakefield excited in a plasma channel by a pulse with a Gaussian (~$\exp(-r^2/\sigma_r^2)$) radial profile. For these initial bunch parameters and L_0=λ_p, the trapped bunch length is L≈$3.5\times10^{-3}\lambda_p$, the relative energy spread is ε ≈3% at the acceleration distance l=400λ_p, and L≈0.01λ_p and ε ≈10% when L_0=10λ_p. In the case of finite momentum spread in the initial bunch, namely, $0.9\le p_{z0}\le1.2$, $-0.02\le p_{r0}\le0.02$ ($1.35\le\gamma_0\le1.56$), and L_0=0.8λ_p, the trapped bunch length is about 0.02λ_p during acceleration. The average energy and the relative energy spread in the accelerated bunch are ≈1.07 GeV and ≈4.5% respectively, at l=400λ_p. The longitudinal dynamics and energy of the trapped electrons in 3D are approximately the same as in the 1D case.

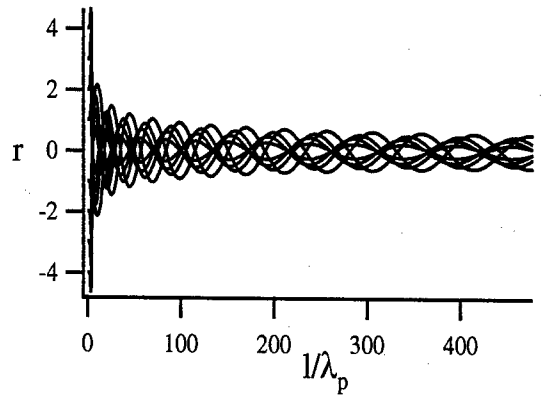


Figure 5. Transverse dynamics of trapped electrons, p_{z0}=1, p_{r0}=0, a_0=2, σ_z=2, σ_r=5.

In 3D, the normalized emittance was calculated to be ε_n~$(R^2\Omega/4\pi^2)\lambda_p$ [5], where Ω=$(|\partial f_r/\partial r|/\gamma)^{1/2}$ is the betatron frequency, R<<σ_r is the trapped bunch radius (Ω and R are in the normalized units), and is in the order of a nanometer in the ultra-relativistic regime. For example, ε_n~3 nm for the case presented in Fig. 5 (initially mono-energetic bunch) when L_0=10λ_p, l=400λ_p and λ_p=50 μm; in the case of the finite initial momentum spread considered above, the emittance is approximately the same.

The total number of accelerated electrons is restricted by the beam loading effect, N_{tot}<<$3\times10^7\lambda_p$[μm] [5]. One can see that this number can reach a value of ~10^8 when the plasma wavelength is in the order of tens of microns (that is typical for laser pulses with λ_L~1 μm) and ~10^9 for λ_p in order of hundreds microns (that is typical for CO_2 laser pulses, λ_L≈10 μm). The scheme can also be applied to the self-modulated LWFA case.

REFERENCES

[1] X. J. Wang, X. Qiu, and I. Ben-Zvi, Phys. Rev. E **54**, R3121 (1996).
[2] P. Kung, H.-C. Lihn, H. Wiedemann, and D. Bocek, Phys. Rev. Lett. **73**, 967 (1994).
[3] B. E. Carlsten and S. J. Russell, Phys. Rev. E **53**, R2072 (1996).
[4] A. G. Khachatryan, JETP Letters **74**, 371 (2001).
[5] A. G. Khachatryan, Phys. Rev. E **65**, 046504 (2002).
[6] N. E. Andreev, L. M. Gorbunov, V. I. Kirsanov, K. Nakajima, and A. Ogata, Phys. Plasmas **4**, 1145 (1997).

CHARGED PARTICLE INTERACTION WITH A CHIRPED ELECTROMAGNETIC PULSE*

A. G. Khachatryan, K.-J. Boller, and F. A. van Goor,

Laser Physics & Nonlinear Optics Group, Dept. of Applied Physics, University of Twente, P.O. Box 217, 7500 AE Enschede, The Netherlands

Abstract

It is found that a charged particle can get a net energy gain from the interaction with an electromagnetic chirped pulse. Theoretically, the energy gain increases with the pulse amplitude and with the relative frequency variation in the pulse.

INTRODUCTION

Modern high-intensity lasers can generate electromagnetic (EM) pulses with the electric field amplitude E_0[TV/m]$\cong 3.2a_0/\lambda_L[\mu m]$ in order of 10 TV/m (here $a_0=E_0/(m_e c\omega/e)$ is the normalized peak amplitude and λ_L is the laser wavelength). However, it is not easy for a charged particle to get a net energy gain of even 10 MeV after interaction with such laser pulses. In the laser pulse field, a free charged particle experiences the ponderomotive force. In the one-dimensional (1D) case the acceleration in front of the pulse is followed by deceleration in the descending part of the pulse, so that the net energy gain is zero. However, in a laser pulse of finite transverse extension an electron can leave the pulse before the decelerating field will compensate the acquired energy (see, e. g., recent articles [1] and references therein). Acceleration of free electrons to MeV energy, after interaction with a high-intensity ($I_0\approx 10^{19}$ W/cm^2, $a_0\approx 3$) laser pulse in vacuum, has been observed experimentally [2]. Free electrons can also acquire energy from the laser field if they are "born" inside the pulse (where $a\neq 0$) due to tunnelling ionisation [3].

In this article we show that a charged particle can get a net energy gain after interaction with an electromagnetic pulse with the carrier frequency changing from head to tail (chirped pulse) even in the one-dimensional case. Presently, high-intensity ($I_0\sim 10^{19}$ W/cm^2) short chirped laser pulses are available [4]. A chirped pulse can be generated as a result of reflection from a relativistic mirror when the gamma factor, γ_m, of the mirror changes during reflection. Computer simulations showed that γ_m of an electron mirror produced by a high-intensity femtosecond laser pulse focused on a thin solid target can increase from $\gamma_m\sim 1$ to the value of $\sim 10^3$. So, the carrier frequency of the reflected EM pulse $\omega_r\approx 4\gamma_m^2\omega_{in}$ (where ω_{in} is the incidence frequency) will increase considerably. The plasma electron density spike in a nonlinear laser wakefield can also serve as a relativistic mirror with changing velocity if the group velocity of the laser pulse, which is equal to the wake phase velocity, changes. This can take place, for example, in a non-uniform plasma. Below we consider the interaction of a charged particle (here–an electron) with a one-dimensional chirped EM pulse. This approach is valid when the particle remains close enough to the pulse axis, so that we can neglect the change of the EM field in the transverse direction.

*This work is supported by Fundamenteel Onderzoek der Materie (FOM, The Netherlands) under "Laser Wakefield" project.

DYNAMICS OF AN ELECTRON IN AN ELECTROMAGNETIC FIELD

Suppose that the EM pulse propagates in the Z direction and is linearly polarized in the x direction. For a one-dimensional chirped pulse we can write $E_x=E_0(\zeta)\cos[\omega(\zeta)\zeta]$, $\zeta\equiv Z-ct$, $\mathbf{B}=\mathbf{e}_y B_y=\mathbf{e}_y E_x$, where $\omega(\zeta)$ is the carrier frequency and $\mathbf{B}$ is the magnetic field of the pulse. In the pulse field ($\mathbf{E}(E_x,0,0)$, $\mathbf{B}(0,B_y=E_x,0)$), we have for the electron's momentum components:

$$dp_x/d\tau = -(1-\beta_z)E_x, \tag{1}$$

$$dp_y/d\tau = 0, \tag{2}$$

$$dp_z/d\tau = -\beta_x E_x. \tag{3}$$

Here $\mathbf{p}=\mathbf{P}/m_e c$ and $\beta=\mathbf{v}/c$ are the dimensionless momentum and velocity, $\tau=\omega_0 t$ is the dimensionless time, $\omega_0=\omega(0)$, the spatial variables are normalized to c/ω_0 and the electric and magnetic fields are, as usual, normalized to $m_e c\omega_0/e$. According to Eq. (2), the y-component of the momentum is conserved: $p_y(\tau)=p_y(\tau=0)\equiv p_{y0}=$const. From Eqs. (1)-(3) we find the well-known integral of motion [1]

$$\gamma(\tau)-p_z(\tau)=\gamma_0-p_{z0}\equiv C=const \tag{4}$$

where $\gamma=(1+\mathbf{p}^2)^{1/2}$ is the relativistic factor. Equation (1) gives us the expression for the transverse momentum:

$$p_x = p_x(\xi_0)+\int_{\xi_0}^{\xi} E_x(\xi)d\xi \equiv p_{x0}+A, \tag{5}$$

where $\xi=(\omega_0/c)\zeta\equiv z-\tau$, $\xi_0=\xi(\tau=0)$. With known p_x and $p_y=p_{y0}$ one can find the longitudinal momentum p_z and γ from Eq. (4):

$$\begin{pmatrix} p_z \\ \gamma \end{pmatrix} = \begin{pmatrix} p_{z0} \\ \gamma_0 \end{pmatrix} + f(A,\vec{p}_0), \tag{6}$$

0-7803-7738-9/03/$17.00 © 2003 IEEE

where $f=A(A+2p_{x0})/2C$. When an electron is initially non-relativistic ($\gamma_0\sim1$), $C\approx1$ and $f=A^2/2+Ap_{x0}$. For an initially relativistic electron with the longitudinal momentum prevailing, $(p_{x0})^2,(p_{y0})^2<<(p_{z0})^2>>1$, we have from (6):

$$\begin{pmatrix} p_z \\ \gamma \end{pmatrix} \approx \begin{pmatrix} p_{z0} \\ \gamma_0 \end{pmatrix}\left[1 + A(A+2p_{x0})\begin{cases} \gamma_{\perp 0}^{-2}, & p_{z0}>0, \\ \mp 1/4\gamma_0^2, & p_{z0}<0 \end{cases}\right], \quad (7)$$

where $\gamma_{\perp0}=[1+(p_{x0})^2+(p_{y0})^2]^{1/2}$. When initially the transverse motion dominates ($(p_{y0})^2,(p_{z0})^2<<(p_{x0})^2>>1$, $|p_{x0}|\approx\gamma_0$) then:

$$\begin{pmatrix} p_z \\ \gamma \end{pmatrix} \approx \begin{pmatrix} p_{z0} \\ \gamma_0 \end{pmatrix} + \frac{A(A+2p_{x0})}{2\gamma_0}. \quad (8)$$

LINEARLY CHIRPED PULSE

Thus, the dynamics of an electron are determined by the initial momentum and the value of $A(\xi_0,\xi)$. Let us consider the interaction of an electron with a chirped EM pulse over an infinite interaction region $\xi_0=+\infty$, $\xi=-\infty$. For simplicity we choose a linearly chirped Gaussian pulse, $E_x=a_0\exp(-\xi^2/\sigma^2)\cos(\Omega\xi)$, where $\Omega(\xi)=\omega/\omega_0=1+\Delta\Omega\xi/2\sigma$ is the normalized carrier frequency, $\Delta\Omega=\Omega(\sigma)-\Omega(-\sigma)$. So, for the linear chirp we obtain:

$$A=\int_{+\infty}^{-\infty}E_x d\xi = -\frac{\pi^{1/2}a_0\sigma}{(1+\nu^2)^{1/4}}\exp\left[-\frac{\sigma^2}{4(1+\nu^2)}\right]\times \cos\left[\frac{arctg(\nu)}{2}-\frac{\sigma^2\nu}{4(1+\nu^2)}\right], \quad (9)$$

where $\nu\equiv\Delta\Omega\sigma/2$. According to expression (9), when $\sigma^2/4(1+\nu^2)>>1$, the momentum (energy) acquired by the electron is negligibly small. For a non-chirped pulse ($\nu=0$) the value of A is maximum for $\sigma=2^{1/2}$: $A=-(2\pi)^{1/2}\exp(-1/2)a_0$. This case of a sub-cycle EM pulse was studied in Ref. [6]. For a multiple-cycle pulse considering here, momentum (energy) transferred to an electron after interaction with such a pulse can be considerable when $\nu^2>>1$. In this case:

$$A\approx -a_0\left(\frac{2\pi\sigma}{\Delta\Omega}\right)^{1/2}\exp\left(-\frac{1}{(\Delta\Omega)^2}\right)\cos\left(\frac{\sigma}{2\Delta\Omega}-\frac{\pi}{4}\right). \quad (10)$$

We see that for a non-chirped pulse $A\to0$ (known result) and that $A\neq0$ for a chirped pulse (new result) due to the change in the carrier frequency. One can see also that A is a periodic function with an amplitude and "frequency" depending on the chirped pulse parameters. The value of A is equal to zero when $\sigma/\Delta\Omega=\pi(1/2\pm m)$, m=1,3,5,... Fig. 1 shows the dependence $A(\Delta\Omega)$ for different lengths of the pulse. Thus, the energy of an electron can be changed

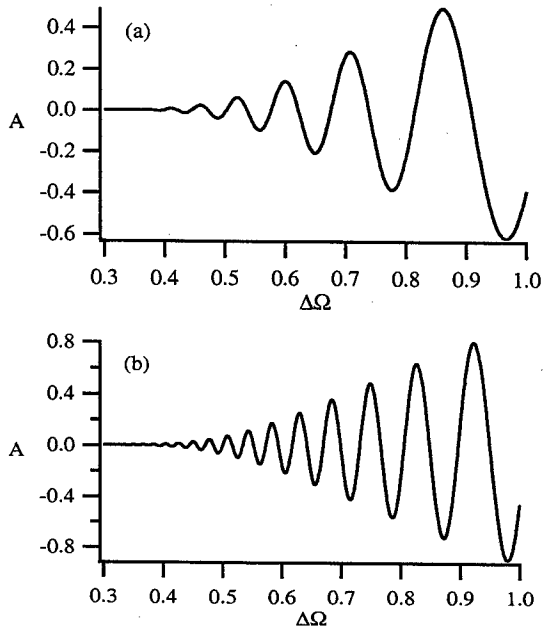


Figure 1: Electron's transverse momentum gain A after interaction with a chirped EM pulse, a_0=0.1, σ=50 (a) and σ=100 (b).

considerably, after interaction with a chirped EM pulse, by proper choice of the pulse parameters. For example, $A\approx2$ for $\Delta\Omega=0.5$, $a_0=3$, and $\sigma=100$. The latter two values approximately correspond to the experimental conditions of Ref. [2].

ELECTRON ACCELERATION

The effect found can be used to accelerate charged particles. For non-relativistic electrons the energy gain is $\Delta\gamma=\gamma-\gamma_0=A(A+2p_{x0})/2$ and the absolute energy spread in an electron bunch after interaction with the chirped pulse will be $\delta\gamma=\delta\gamma_0+\delta f=\delta\gamma_0+A\,\delta p_{x0}$, where $\delta\gamma_0$ (δp_{x0}) is the energy (transverse momentum) spread before interaction. In the relativistic case, according to (7), when $p_{z0}>0$, energy gain is proportional to the initial energy and can be considerable even for small value of A.

Assume initially $p_{x0}=p_{y0}=0$ and that the electron co-propagates with the pulse (for which $A=A_1$) with relativistic velocity. After interaction with the pulse, according to (5) and (7), $p_{z1}=p_{z0}(1+A_1^2)$ and $p_{x1}=A_1$. To compensate the transverse momentum, p_{x1}, acquired, a second pulse can be sent along p_{x1}, so that p_{x1} (p_{z1}) will be the longitudinal (transverse) momentum with regard to the second pulse. Then, after interaction with second

pulse, according to (7) and (8), $p_{z2}=p_{z1}+A_2$ and $p_{x2}=p_{x1}+A_2(A_2+2p_{z1})/2\gamma_1$; here the signs of p_{x1} and p_{z1} in the frame of second pulse should be taken into account. So, by proper choice of the parameters of the pulses one can make p_{x2} equal to zero. This occurs, for example, when $A_1=A_2>0$, $A_2<<2p_{z0}$, and $p_{x1}<0$ and $p_{z1}>0$ in the frame of the second pulse. This two-step acceleration process can be repeated. The interaction time with the first pulse is $\Delta\tau\sim\tau_L/(1-\beta_{z0})$, where τ_L is the duration of the pulse. So, for large enough γ_0 the diffraction broadening of the pulse, which takes place on a time scale $\tau_d\sim Z_R/c$ ($Z_R=\pi r_0/\lambda_L$ is the Rayleigh length, r_0 is the focal spot size), can restrict the interaction time.

When a relativistic electron moves across a chirped pulse, the transverse momentum (energy) can be increased, $p_x=p_{x0}+A$. A second pulse propagating in parallel with the first one can accelerate the electron further, so that the longitudinal momentum acquired after interaction with the first pulse will be compensated.

Equations (1)-(3) were solved numerically. Figure 2 shows the dynamics of electron, which is initially at rest,

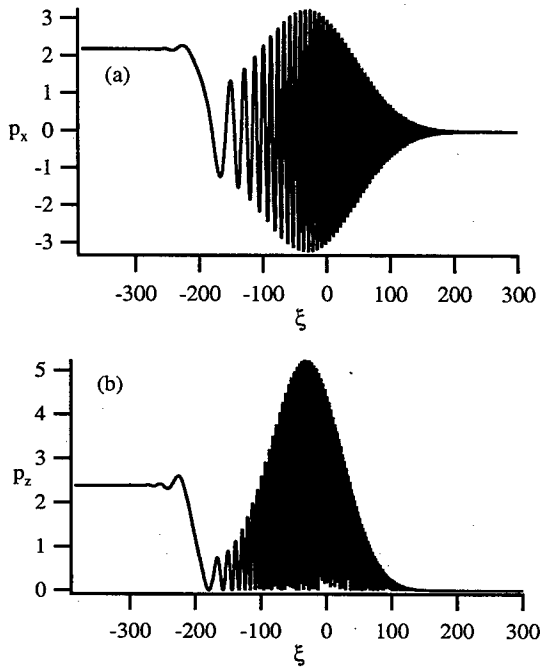


Figure 2 Dynamics of an electron interacting with a chirped pulse, $\mathbf{p}_0=0$, $a_0=3$, $\sigma=100$, and $\Delta\Omega=0.51$.

in the chirped pulse field. The electron momentums are $p_x=A\approx2.19$ and $p_z\approx2.39$ after interaction. In this case $\gamma=1+p_z$ (see equation (4)) and the interaction time is in the order of the pulse duration. When initially $p_{z0}=3$, the transverse momentum dynamics are the same, but the final longitudinal momentum is much higher, $p_z\approx17.71$ (see Fig. 3), in a good agreement with formula (9), $\gamma\approx p_z$. In this case the interaction takes place, in the laboratory frame, over a distance of about $4544\lambda_L\approx172l_{FWHM}$, where $l_{FWHM}=2(\ln2)^{1/2}\sigma$ is the full width at half maximum of the pulse. For comparison, the Rayleigh length is $\approx7854\lambda_L$ for a laser pulse with $r_0=30$ μm and $\lambda_L=1$ μm. For non-chirped pulses the electron momentum was found to be unchanged, so that $\mathbf{p}=\mathbf{p}_0$.

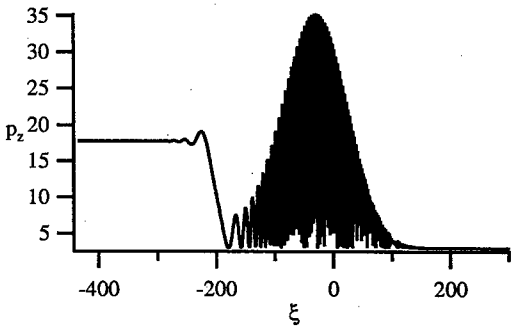


Figure 3: The calculated longitudinal momentum of an electron. All parameters are the same as those in Fig. 2 excepting initial longitudinal momentum, $p_{z0}=3$.

CONCLUSION

It has been shown that free charged particles can undergo a net energy gain after interaction with a chirped electromagnetic pulse. This new effect can be applied for particle acceleration as well as for diagnostic purposes – to measure the chirp in a pulse. The phenomena found can play an important role in chirped laser pulse–plasma interactions which are currently under intensive theoretical and experimental investigations. (see, e. g., [4,7]).

REFERENCES

[1] Y. I. Salamin, G. R. Mocken, and C. H. Keitel, Phys. Rev. ST Accel. Beams **5**, 101301 (2002); P. X. Wang et al., J. Appl. Phys. **91**, 856 (2002).

[2] G. Malka, E. Lefebvre, and J. L. Miquel, Phys. Rev. Lett. **78**, 3314 (1997).

[3] C. I. Moore, A. Ting, S. J. McNaught, J. Qiu, H. R. Burris, and P. Sprangle, Phys. Rev. Lett. **82**, 1688 (1999).

[4] J. Faure et al., Phys. Rev. E **63**, 065401 (2001).

[5] S. Il'in, V. V. Kulagin, and V. A. Cherepenin, Plasma Phys. Rep. **27**, 1048 (2001).

[6] Rau, T. Tajima, and H. Hojo, Phys. Rev. Lett. **78**, 3310 (1997).

[7] T.-W. Yau et al., Phys. Plasmas **9**, 391 (2002); C. B. Schroeder, E. Esarey, B. A. Shadwik, and W. P. Leemans, *ibid.* **10**, 285 (2003).

LASER WAKEFIELD ACCELERATION EXPERIMENT AT KERI*

G. H. Kim, C. Kim, J. U. Kim, H. J. Lee, H. Suk
Center for Advanced Accelerators, Korea Electrotechnology Research Institute (KERI),
Changwon 641-120, Republic of Korea

Abstract

Laser wakefield have been well-known as a method to accelerate particles, including electrons, ions, and even photons. At KERI in Korea, a TW Ti:sapphire/Nd:glass hybrid laser system is established recently. In this paper, the performance of the TW laser system will be presented. And the experimental topics scheduled at KERI will be presented.

1 INTRODUCTION

The studies on intense laser-plasma interactions have been an interesting research subject after the development of the CPA (chirped pulse amplification) technology [1]. Multi-TW laser pulse can be focused to intensities of $I \geq 10^{18}$ W/cm^2, that is strong enough to cause nonlinearity in even unbound (free) electrons. Acceleration of electrons by a plasma wakefield showed the possibility of application to small-scale accelerators because the acceleration gradient of a plasma wakefield is much larger by three or four orders of magnitede than that of conventional RF linacs. Several methods to generate ultra-high field were proposed, including the plasma wakefield accelerator, the plasma beam-wave accelerator (PBWA), the laser wakefield accelerator (LWFA), and the self-modulated laser wakefield accelerator (SM-LWFA) and so on [2]. With the development of the laser technology LWFA and SM-LWFA attract much attention.

All-optical acceleration schemes with self-injection of electrons becomes an important issue since it does not need any external accelerator or lasers for electron injection and we need not to worry about timing problems [3-5]. Recently Suk *et al* proposed a new self-injection scheme that background plasma electrons are self-injected and trapped by a plasma wakefield when an electron beam passes through an underdense plasma with a sharp downward density transition [5]. Similar results were observed in the 2-D PIC simulations with the OSIRIS code when an electron beam is replaced by an intense laser pulse [6]. We are going to verify this scheme experimentally. As a preliminary step, in this paper, we report the installation of TW laser system at KERI, Korea. In Sec. 2, the TW laser system is described in detail. Future experiment plans will be presented in Sec. 3.

2 TW LASER SYSTEM

Figure 1 and 2 are the picture and layout of the TW laser system of Ti:sapphire/Nd:glass hybrid type installed in KERI, respectively. According to CPA technology, the system consists of four parts mainly: oscillator, stretcher, amplifier, and compressor. A diode-pumped solid-state Nd:glass laser (model GLX-200) is used as oscillator. Figure 3 shows the performance of the TW laser system at each step, including the pulse energy, pulse repetition rate, pulse temporal width, pulse spectral width and average power. The laser produce a train of mode-locked, transform-limited femtosecond pulses at the center wavelengths ranging from1050 nm to 1070 nm. To achieve rock-solid ultrafast pulses, the laser relies on diode pumping of the laser crystal and the use of a semiconductor saturable absorber mirror (SESAM) to start and stabilize the pulse-forming process. A beam cutter is used to tune the center wavelength of the laser and is fixed to the wavelength of 1054 nm with the average power of 220 mW (equal to the pulse energy of 3 nJ) and pulse repetition rate of 76 MHz. In a pulse stretcher, the input beam is incident on a single diffraction grating that is multi-passed to reduce complexity. And the beam passes the grating four-times to ensure that the stretched laser beam is spatially reconstructed. The pulse is stretched to 1.4 ns.

The amplifier system consists of two parts depending on the laser crystals: a regenerative amplifier using a Ti:sapphire laser rod and multi-step linear amplifier using

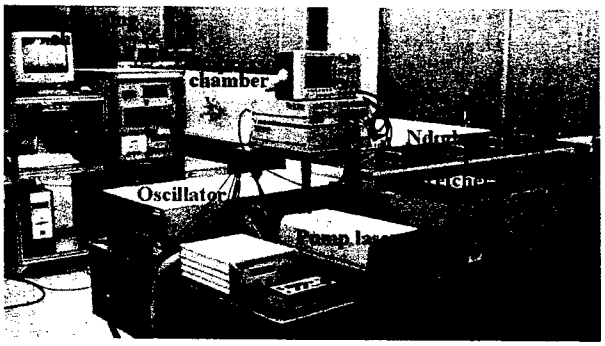


Figure 1: TW laser system at KERI

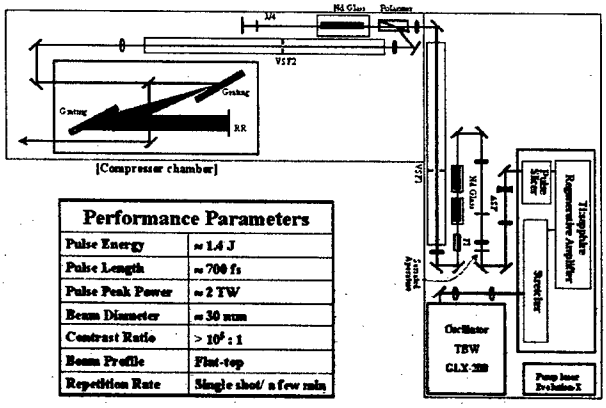
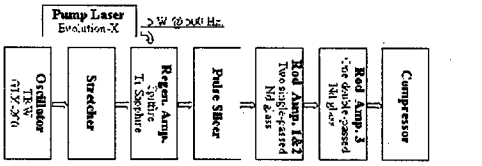


Figure 2: Layout of TW laser system at KERI

0-7803-7738-9/03/$17.00 © 2003 IEEE



Pulse Energy	3 nJ	-	-	0.4 mJ	24 mJ	2 J	1.4 J
Pulse Repetition Rate	76 MHz	76 MHz	500 Hz	500 Hz	single	single	single
Pulse Temporal Width	~350 fs	-	-	1.4 ns	-	-	700 fs
Pulse Spectral Width	4.7 nm	-	Unseeded:9.7 nm Seeded: 4.1 nm		-	-	-
Average Power	220 mW	-	-	200 mW	-	-	-

Figure 3: Performance of TW laser system

Nd:glass laser rods. Optical excitation of the regenerative amplifier is achieved by pumping with a frequency doubled Q-switched Nd:YLF laser with the pulse repetition of 500 Hz and pulse energy of 10 mJ at the wavelength of 527 nm. After a number of round trips, the pulse is ejected by activating Pockels cells with the pulse repetition rate of 500 Hz and pulse energy of 0.4 mJ (gain $> 10^5$). A synchronization and delay generator is used between the mode-locked oscillator and the regenerative amplifier in order to fire Pockels cells in the regenerative amplifier and the pulse slicer. The generator also serves as a protection device to the amplifier system by disabling the triggers to the Pockels cells in the event that the spectrum collapses due to failure of the mode-locked laser or clipping of the spectrum by adapting the bandwidth detection.

At any individual amplifier stage, the maximum energy is limited by the damage threshold of the optical elements. In order to extract the maximum possible energy, it is desirable to fill the rod with the laser beam in case of side pumping. But, diffraction can cause rings and strong intensity modulation (hot spots in some cases) that can cause optical damage. So, before sending to Nd:glass amplifiers, the beam is incident on the serrated aperture with the inner diameter of 3.5 mm and outer diameter of 4.0 mm to cut the edge part of a Gaussian beam. The beam size at the serrated aperture is adjusted to produce a spatial profile that compensates for the radial gain profile of the Nd:glass rods in the linear amplifiers. This insures a flat-top profile at the output of the laser system.

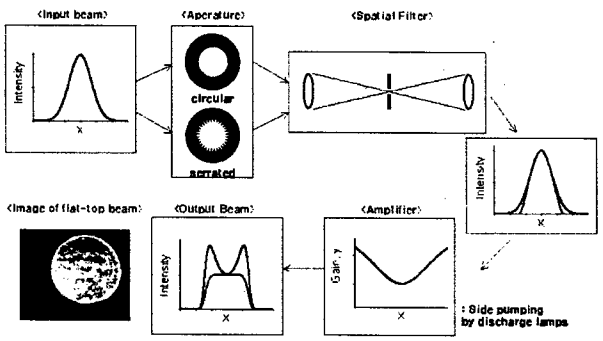


Figure 4: Relay imaging in Nd:glass amplifiers

Figure 4 shows the principle of this relay imaging technique in rod amplifier system. There is some energy loss at the serrated aperture due to the clipping. This is not a problem because there is sufficient gain in the amplifiers to make up for this loss. Following the serrated aperture the beam is transmitted through a spatial filter with the pinhole of 10 times the diffraction limit of the focused spot size, where the overall flat-top bema profile will be retained. However, any high spatial frequencies from the aperture, or from diffraction rings in the beam, are filtered. Then, the beam is transmitted through two laser rods as a pair in series with the dimensions of 9.5 mm × 115 mm and single-passed. The gain of two rods is around 100 when pumped at ~2.5kV. Each rod is pumped by four discharge lamps with the maximum pump energy of 500 J. Following the 9.5 mm amplifiers there is a Faraday isolator. A vacuum spatial filter is used to relay the first image located after the second 9.5 mm amplifier to the next image plane located just after the 1" amplifier double pass. The pulse energy after this vacuum spatial filter is 24 mJ. The vacuum system for this and another vacuum spatial filter in the system is a dry type scroll pump capable of pumping down to ~300 mTorr. The final double-pass laser rod has the dimensions of 25.4 mm × 304.8 mm and produces a gain of ~80 when pumped at ~7kV. The rod is pumped by eight discharge lamps with the maximum energy of 12 kJ. Another vacuum spatial filter is used to relay the second image plane just after the 25.4 mm amplifier to the first grating in the compressor chamber. The pinhole size is approximately 10 times diffraction limited at 1.2 mm diameter. The beam is expanded to the diameter of 30 mm after the vacuum spatial filters to limit the beam energy to 125 mJ/cm^2 that is lower than the damage threshold of the compressor gratings of 250 mJ/cm^2. Finally the beam is transmitted to the compressor chamber. Compressor consists of two diffraction gratings (1740 lines/mm) and one retro-reflecting mirror assembly. It is designed to compress pulses from the Nd:glass amplifier chain to 700 fs with the efficiency of 70 %. Compressor is placed inside a vacuum chamber with the dimensions of 60"×27"×20". Figure 5 shows the autocorrelation measurement of the compressed pulse with the pulse width of 700 fs.

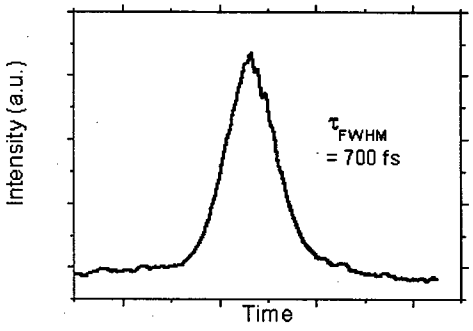


Figure 5: Autocorrelation measurement

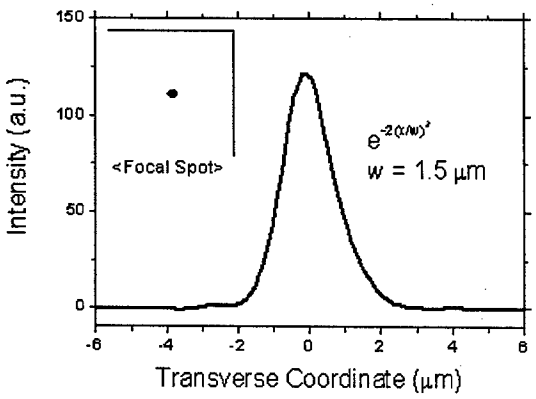


Figure 6: Focal spot measurement.

And then, the beam is transmitted to the interaction chamber that is coupled with the compressor chamber to study the laser-plasma interactions. The beam is focused to a focal spot just above a gas nozzle using an off-axis parabolic mirror. An energy analyser to obtain energy distribution of accelerated electron beam is installed inside the interaction chamber. The charge of the electron beam is measured with the ICT beam charge monitor (Bergoz).

All required electronics to synchronize lasers, operate and fire laser amplifiers, and provide the laser cooling are contained in the 19" rack.

3 FUTURE EXPERIMENT PLAN

Before main experiments, we checked the beam quality of focused beam using an off-axis parabolic mirror with the focal length of 50 mm. An objective lens with the magnification of 60 times was used. In order to avoid the damage of the objective lens the pulse energy was attenuated with anti-reflecting mirrors and neutral density filters. Figure 6 shows the beam profile of focal spot and the inset shows the two-dimensional image of focal spot. It shows that the beam quality of focal spot is very good with the beam diameter of 3 μm.

We are now considering two approaches to achieve local density transition to verify Suk's self-injection scheme [6]. One is the density transition produced using thin wires. Characterization of density distribution after a thin wire above the gas nozzle is under study using an interferometer. The other is the density transition at the boundary of plasma channel. This will be discussed in details in another paper [7].

4 SUMMARY

TW laser system of Ti:sapphire/Nd:glass hybrid type is installed at KERI successfully. TW laser pulses are with the pulse energy of 1.4 J, pulse length of 700 fs, and then the peak power is 2 TW. Experiments of the particle acceleration are scheduled on various scheme, e.g. gas jet with density transition and so on.

REFERENCES

[1] T. Tajima and J. M. Dawson, Phys. Rev. Lett. **43**, 267 (1979).

[2] E. Esarey, P. Sprangle, J. Krall, and A. Ting, IEEE Trans. Plasma Sci. **24**, 252 (1996).

[3] S. Bulanov, N. Naumova, F. Pegoraro, and J. Sakai, Phys. Rev. E **58**, R5257 (1998).

[4] K. Nakajima et al., Phys. Rev. Lett. **74**, 4428 (1995).

[5] H. Suk, N. Barov, J. B. Rosezweig, and E. Esarey, Phys. Rev. Lett. **86**, 1011 (2001).

[6] H. Suk, C. Kim, G. H. Kim, J. U. Kim, H. J. Lee, and W. B. Mori, in *Advanced Accelerator Concepts: Tenth Workshop*, AIP Conf. Proc. No. 647 (AIP, New York, 2002), pp. 710-716.

[7] J. U. Kim, C. Kim, G. H. Kim, H. J. Lee, N. Hafz, H. Suk, to be appeared in *Proceedings of the 2003 Particle Accelerator Conference.*

STELLA-II: DEMONSTRATION OF MONOENERGETIC LASER ACCELERATION

W. D. Kimura,* L. P. Campbell, C. E. Dilley, S. C. Gottschalk, and D. C. Quimby
STI Optronics, Bellevue, WA 98004-1495, USA

M. Babzien, I. Ben-Zvi, J. C. Gallardo, K. P. Kusche, I. V. Pogorelsky, J. Skaritka, and V. Yakimenko, Brookhaven National Laboratory, Upton, NY 11973, USA

F. Zhou and D. B. Cline, UCLA, Los Angeles, CA 90095, USA

L. C. Steinhauer, Redmond Plasma Physics Laboratory, Redmond, WA 98052, USA

R. H. Pantell, Stanford University, CA 94305, USA

Abstract

Monoenergetic laser acceleration of trapped microbunches has been demonstrated for the first time. An inverse free electron laser (IFEL) is used to create microbunches, which are then accelerated by a second IFEL using a tapered undulator. An adjustable magnetic field chicane is located between the two IFELs and is used to control the phase of the microbunches with respect to the laser field in the second IFEL. The IFELs are driven by a single laser beam from a high peak power CO_2 laser. During the experiment, the trapped portion of the microbunch electrons had an energy gain of >16% with an energy width of ~0.86% (full width at half-maximum).

BACKGROUND

Laser acceleration of relativistic electrons offers the potential for very high acceleration gradients. Staging of these laser accelerator devices, in which the laser acceleration process is repeated many times, is important for eventually reaching a high net energy gain. However, this staging process must also preserve the electron beam (*e*-beam) quality so that a useful high-energy *e*-beam is produced.

Staging between two laser-driven acceleration devices was first demonstrated during the Staged Electron Laser Acceleration (STELLA) Experiment [1] located at the Brookhaven National Laboratory (BNL) Accelerator Test Facility (ATF). During this experiment an inverse free electron laser (IFEL), driven by a high peak power CO_2 laser at a wavelength of 10.6 μm, was used to modulate the energy of the *e*-beam passing through the device. The *e*-beam was allowed to drift downstream from the IFEL. During this drift, the fast electrons caught up with the slow ones, resulting in bunching of the electrons into a train microbunches. Each microbunch had a length of <1 μm and was separated from the other microbunches by the laser wavelength, i.e., 10.6 μm. Thus, this first IFEL served as a "buncher." It used a permanent-magnet (PM) uniform gap undulator.

The microbunches then entered a second IFEL, which acted as an "accelerator." It used an identical PM undulator as the buncher. Staging of these two laser-driven devices required rephasing the microbunches with the laser field in the accelerator IFEL.

Separate laser beams were used during STELLA to drive the two IFELs. A relatively weak laser beam (~24 MW) modulated the electrons by ≈±0.5% in the buncher, and a stronger laser beam (~200 MW) accelerated the microbunches in the accelerator. A passive optical delay line was used to control the phase of the laser beam driving the accelerator with respect to the microbunches entering the second device.

With the ±0.5% buncher modulation, the electrons needed to drift by 2 m before they optimally bunched. Hence, the accelerator IFEL was located 2 m downstream from the buncher IFEL.

While successful at demonstrating staging, the accelerated microbunches during STELLA were not truly trapped in the ponderomotive potential well of the laser field in the accelerator IFEL and, hence, the accelerated electrons had a fairly broad energy spread and were not well separated in energy from the other background electrons.

Therefore, the goal of the STELLA-II experiment was to improve on the quality of the staging process by separating the accelerated microbunch electrons from the background electrons and at the same time maintaining a narrow energy spread of the accelerated electrons. This latter characteristic is important for efficient acceleration of the accelerated microbunches in subsequent acceleration stages.

DESCRIPTION OF EXPERIMENT

STELLA-II improves upon the basic scheme used during STELLA. A diagram of the experiment is shown in Fig. 1. Two IFELs are still used, but a single laser beam is used to drive both devices. This eliminates phase jitter between the two laser beams, which was evident

*Electronic address: wkimura@stioptronics.com

0-7803-7738-9/03/$17.00 © 2003 IEEE

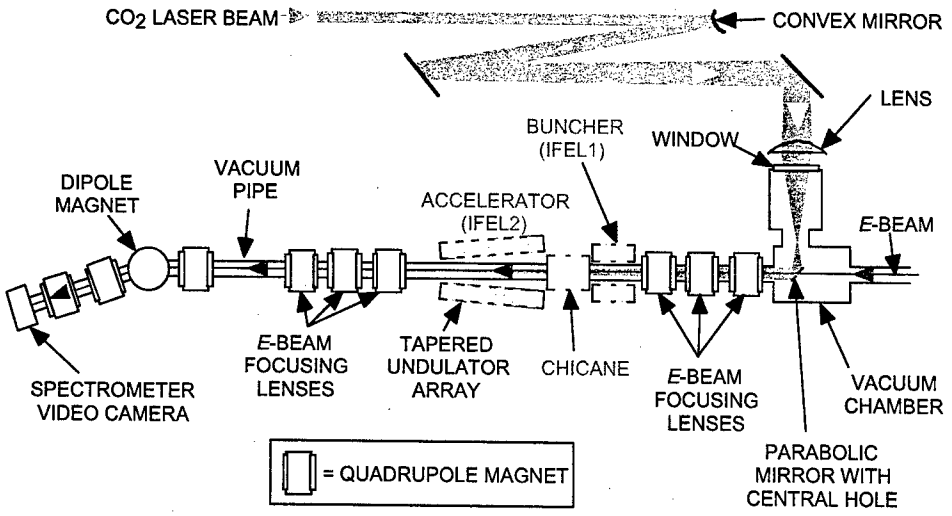


Figure 1. Diagram of STELLA-II experiment.

during the STELLA experiment. In order to use a single laser beam, the two IFELs must also be located close to each other. Therefore, the 2-m drift space between the devices was eliminated and replaced with a magnetic chicane.

The buncher still uses a PM undulator; however, it was redesigned to provide a small amount of modulation when a large amount of laser intensity travels through it since the high-power laser beam driving the accelerator IFEL must also pass through the buncher IFEL.

The chicane is a hybrid permanent magnet/electromagnet (EM) device that makes the modulated electrons bunch at its output by causing the faster electrons to take a shorter path than the slower electrons. The constant PM field provides the nominal curved trajectory for this process while the adjustable EM field allows a fine adjustment on the length of the trajectory. Thus, the EM field serves the same role as the optical delay line during STELLA and provides the phase delay adjustment needed during the experiment.

Another key difference between STELLA-II and STELLA is the usage of a tapered undulator for the accelerator IFEL. STELLA used an untapered undulator; STELLA-II uses an 11% gap tapered undulator. Using a tapered undulator is critical for achieving higher energy gain, but it requires a minimum amount of laser power to drive the device. Upgrades made to the ATF CO_2 laser have greatly increased its available peak power.

The high energy gain provided by a tapered undulator enables the microbunch electrons to be separated away from the unbunched background electrons. As mentioned earlier, this was one of the goals of the STELLA-II experiment.

EXPERIMENTAL RESULTS

Table 1 lists the basic experimental values during the STELLA-II experiment.

Figure 2 gives an example of the modulation energy spectrum produced by the PM buncher. The chicane is designed to provide optimum bunching when the buncher produces ±0.5% energy modulation on the *e*-beam. Thus, the modulation seen in Fig. 2 is close to the desired amount. During the experiment it was found there was considerable variation from shot-to-shot of the amount of the modulation and the shape of the modulation spectrum. We believe this may be due to shot-to-shot variations in the laser intensity distribution at the buncher location.

Table 1: STELLA-II experimental parameters.

Parameter	Value
E-beam energy	45.6 MeV
E-beam intrinsic energy spread	~0.04%
E-beam normalized emittance	1.5 mm-mrad
E-beam charge	~0.1 nC
E-beam pulse length	~3 ps
Laser wavelength	10.6 μm
Laser pulse length	~180 ps
Laser pulse energy	>5 J

It was also noted during the experiment that the modulation was often considerably larger than the desired ±0.5%. This would lead to overmodulation of the electrons, which meant they would optimally bunch before they entered the accelerator IFEL.

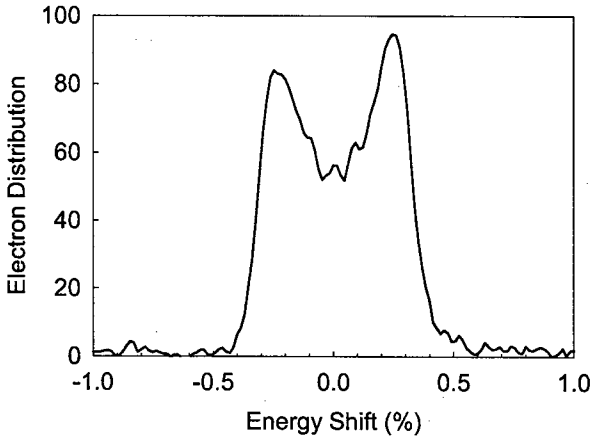


Figure 2: Example of energy modulation spectrum produced by the PM buncher.

In addition, the modulation spectrum did not always display clean double-peaks as seen in Fig. 2, which implied less than ideal modulation. This would lead to less than optimum bunching of the electrons, i.e., the electrons in the microbunches would be spread over a wider phase. We believe this may help explain some of the results seen in energy spectra generated by the tapered undulator.

Figure 3 shows the energy spectrum from the tapered undulator after the electrons pass through the PM buncher and chicane. The EM field on the chicane was adjusted so that the phase delay between the microbunches and the laser field in the accelerator IFEL yielded approximately maximum acceleration.

A narrow spike of accelerated electrons can be clearly seen on the right of the spectrum centered at approximately 16% energy gain (>7 MeV net energy gain). The energy width of the peak is ≈0.86% full-width-at-half-maximum (FWHM). The amount of acceleration and width of the peak is consistent with our model simulations for this experiment [2]-[3].

The apparent sharp dips in the spectrum (indicated in red) located at roughly 1% and 14% energy shift are due to fiducial marks on the spectrometer phosphor screen that are seen by the video camera. We believe the actual electron energy spectrum continues across these dips in a smooth fashion.

There are electrons in the middle of the spectrum between the narrow peak on the right and the smaller peak on the left. The model predicts with optimal bunching that there should be insignificant electrons between these two peaks. The presence of these electrons between the peaks may be evidence of less than optimal bunching occurring. In other words some of the electrons in the microbunch may be spread out in phase and, therefore, are not trapped as well as the electrons in the right-most peak.

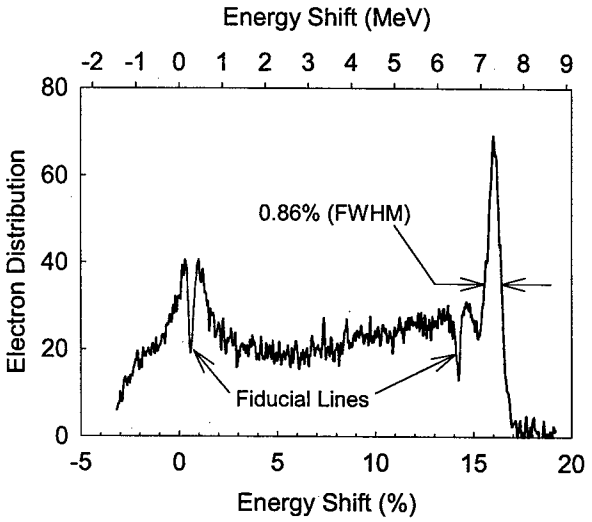


Figure 3: Example of energy modulation spectrum produced by the accelerator IFEL. The fiducial lines indicated in the figure are lines that are on the spectrometer phosphor screen seen by the video camera.

CONCLUSION

Monoenergetic laser acceleration has been demonstrated for the first time. Trapped electrons in microbunches produced by an IFEL were accelerated by 16% representing an energy gradient of >22 MeV/m. The energy width of these trapped electrons is ~0.86%, which is consistent with model predictions.

This accomplishment is an important step towards the goal of eventually realizing practical accelerators based upon laser acceleration.

ACKNOWLEDGEMENTS

This work was supported by the U.S. Department of Energy, Grant Nos. DE-FG03-98ER41061, DE-AC02-98CH10886, and DE-FG03-92ER40695

REFERENCES

[1] W. D. Kimura, *et al.*, Phys. Rev. Lett. **86**, 4041-4043 (2001).

[2] W. D. Kimura, *et al.*, Phys. Rev. ST Accel. Beams **4**, 101301 (2001).

[3] W. D. Kimura, *et al.*, *Advanced Accelerator Concepts*, Jun. 23-28, 2002, Mandalay Beach, CA, AIP Conference Proceedings No. 647, C. E. Clayton and P. Muggli, Eds., (American Institute of Physics, New York, 2002), p. 269-277.

ELECTRON ACCELERATION BY LASER WAKEFIELDS IN TAPERED PLASMA DENSITIES

H. Suk,* C. Kim, G.H. Kim, J.U. Kim, and H.J. Lee
Center for Advanced Accelerators, KERI, Changwon, Korea

Abstract

When a laser wake wave passes through a sharp downward density transition in plasmas, a significant amount of plasma electrons are self-injected into the acceleration phase of the wakefield and accelerated to relativistic high energies over a very short distance. We report that the energies of the injected plasma electrons can be increased a few times if an upward density tapering is used. Although space-charge effect of the trapped electrons deforms the accelerating wakefield severely, it is demonstrated that density tapering is a very effective way to enhance the trapped electron energies.

INTRODUCTION

Laser and plasma-based acceleration methods[1] can provide very high acceleration gradients on the order of 100 GeV/m. So far various acceleration methods based on different injection schemes[2-5] have been investigated. One of them is the self-injection and acceleration method of background plasma electrons at a sharp downward density transition.[5] Originally this self-injection method was devised for an electron-beam-driven plasma wakefield acceleration (PWFA), but we found that a superficially similar self-injection and acceleration phenomenon could happen for a laser-driven wakefield acceleration (LWFA).

In the case of using a short intense laser pulse, however, there are some differences from that of using a high-energy electron beam pulse. One of them is that the group velocity v_g of a laser pulse in a plasma is significantly smaller than that of an ultrarelativistic electron beam pulse as $v_g = c(1-\omega_p{}^2/\omega_0{}^2)^{1/2} < c$. Here, c is the velocity of light in free space, ω_p and ω_0 are the plasma oscillation frequency and laser frequency, respectively. Since the phase velocity v_{ph} of a laser wakefield is almost equal to v_g, v_{ph} becomes smaller than the accelerated electron speed in the highly relativistic regime. Hence, the trapped electrons and the laser wakefield become out of phase as the trapped electrons are accelerated to highly relativistic energies. This phase slippage effect limits the maximum available electron energy before the diffraction effect of a drive laser pulse is significant. Calculation of Sprangle *et al.*[6] showed that an externally-injected single test particle can gain a significantly higher energy when it is placed in a density-tapered plasma channel. In their calculation, however, the space-charge effect was not taken into accounted as only a single test particle was used. In their case, furthermore, the diffraction effect of a drive laser pulse was cancelled by a focusing effect in a preformed parabolic plasma channel so that only 1-dimension-like treatments were done. In this paper, we report 2-D simulation results, in which trapped plasma electrons by the self-injected laser wakefield acceleration using a sharp density transition can gain significantly higher energies when the trapped particles are accelerated in a tapered plasma density.

*Email address: hysuk@keri.re.kr

SIMULATION RESULTS

In order to investigate the energy enhancement effect of the trapped plasma electrons in the self-injected laser wakefield acceleration, we performed 2-D particle-in-cell (PIC) simulations as a satisfactory 2-D theory does not exist yet. For this purpose, we used the fully relativistic and electromagnetic OSIRIS code[7] that employs a moving simulation window. Two different cases shown in Fig. 1 were simulated, in which one (Case-I) is without density tapering and the other (Case-II) has upward density tapering. In both cases, the plasma densities have $n_0 = 5\times10^{18}$ cm^{-3} and $n_0{}^{II} = 0.6n_0{}^{I}$, respectively, and $n_0{}^{III}$ in Case-II is varied to change the tapering slope. Here, the superscripts II and III denote parameters for $n_0{}^{II}$ and $n_0{}^{III}$, respectively. In the simulations, the laser pulse length L is slightly smaller than $\lambda_p{}^{II}$, the plasma and laser frequency ratio $\omega_p{}^{II}/\omega_0$ is 0.04, and the normalized vector potential a_0 defined by $a_0 = p_0/m_e c$ is 2.5 at the laser beam waist. Here, p_0 is the electron oscillation momentum due to the laser electric field and m_e is the electron rest mass. For the given laser and plasma parameters, simulations have been

0-7803-7738-9/03/$17.00 © 2003 IEEE

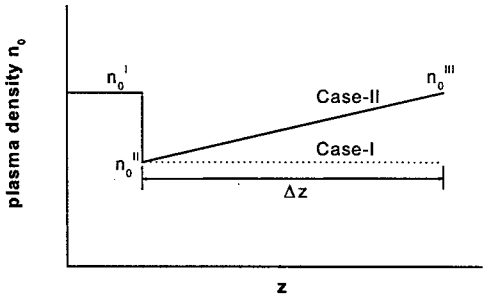


Figure 1: Plasma density profiles for untapered and tapered cases.

performed with $n_0^{II} = n_0^{III} = 0.6n_0^{I}$ in Case-I and the result is shown in Fig. 2. Figure 2 illustrates the trapping and acceleration phenomenon by the self-injected laser wakefield acceleration. In this simulation, the laser beam is focused to a minimum diameter of 19 μm around the sharp downward density transition (shown as a vertical line in the top figure of (a)), and then the laser beam size increases due to diffraction as it propagates in the plasma. When the laser wake wave passes the density transition, λ_p increases suddenly so that some background plasma electrons are self-injected into the acceleration phase of the first period of the laser wake wave (see the top figure of (a)). The injected plasma electrons are trapped by the wakefield and accelerated to high energies, as shown in Fig. 2(b). As mentioned above, however, the accelerated particles outrun the laser wakefield, which is evidently shown in the bottom figure of Fig. 2(a). As a result, the particles eventually arrive in the deceleration phase of the wakefield and can not gain energy any more.

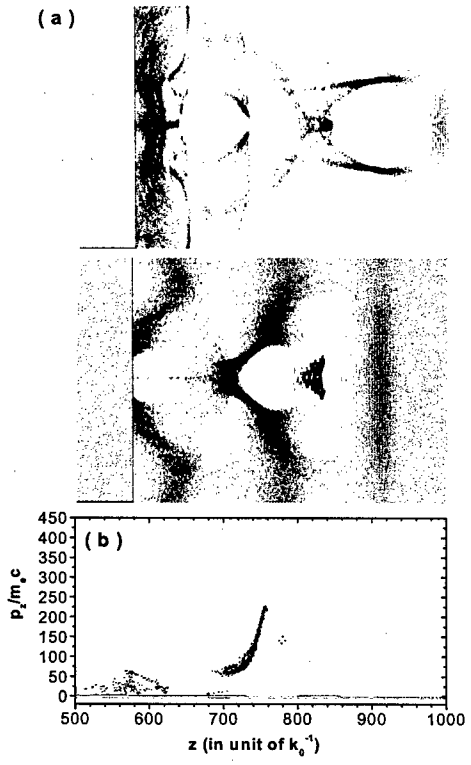


Figure 2: Simulation results for the untapered density profile (Case-I): (a) phase space plots (y,z) of plasma electrons at two different positions (the distance is $8421\,k_0^{-1}$) and (b) momentum phase space plot (p_z, z) for the bottom in Fig. 2(a).

Energy saturation of the self-injected particles due to the detuning effect may be overcome by using upward density tapering. To investigate the tapering effect, a linearly tapered density (Case-II in Fig. 1) was used in simulations, in which the density increases from $n_0^{II} = 0.6n_0^{I}$ to $n_0^{III} = 1.3n_0^{II}$ over a distance of $\Delta z = 9300k_0^{-1}$. Here, k_0 is the wavenumber of laser light in free space. In this case, the simulation result indicates that the laser wakefield wavelength decreases gradually as the wake wave propagates along the upward density tapering, so the trapped particles stay in the acceleration phase over a longer propagation distance, compared to the untapered case. In other words, the initial phase velocity v_{ph}^{II} of the first node in the wake wave is gradually increased to $v_{ph}^{III} \cong v_{ph}^{II} + (\lambda_p^{II} - \lambda_{III})/\Delta t > v_{ph}^{II}$, where Δt is the time that is taken for the wake wave to propagate the distance Δz. Due to the increased phase velocity of the wakefield, therefore, the detuning effect can be reduced. Of course, it should be pointed that the increased density leads to a smaller v_g, but this effect is minor as $v_g \cong c$ for $\omega_p/\omega_0 << 1$. Instead, the increasing v_{ph} effect is much more significant as $\lambda_p^{III}/\lambda_p^{II} = (n_0^{II}/n_0^{III})^{1/2}$. Comparison of Fig. 3(a) and Fig. 2(a) clearly shows the reduction in detuning (slippage). As a result, significantly higher energies for the trapped plasma electrons can be produced, as shown in Fig. 3(c). However, it should be pointed out that the self-injected plasma electrons deform the laser wakefield severely, which leads to deterioration and reduction of the accelerating wakefield. This results from the strong space-charge effect of the tightly focused {\it plasma electron beam}, in which the focusing force is provided by the background ions and remnant electrons in the wake wave. The superstrong radial focusing force is given by

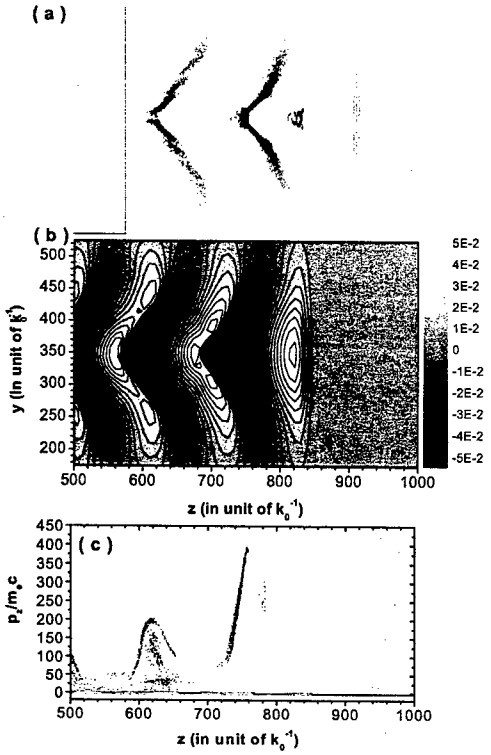


Figure 3: Simulation results for the upward density tapering (Case-II) : (a) phase space plot (y,z) of the plasma electrons, (b) longitudinal electric field E_z in the plasma, and (c) momentum phase space (p_z, z) of the plasma electron.

$F_r = (n_0 - \Delta n_0)e^2 r / 2\varepsilon_0$, where Δn_0 is the remnant electron density in the wake wave, r is the radial distance from the axis, and ε_0 is the permittivity of free space. Due to the strong focusing, the plasma electron beam density n_b is larger than the background plasma density so that the beam space-charge force expels almost all ambient plasma electrons transversely and generates another small plasma wake wave behind the beam, as shown in Fig. 3(a) (note that an electron-free ion cavity is produced behind the beam).

In the tapering case, degree of slippage is dependent on the upward density gradient. Figure 4 shows comparison of two tapered cases and untapered case. It shows that tapered cases increase the detuning distance noticeably and higher energies can be achieved. Figure 3 implies that there is more room for energy enhancement with density tapering. Hence, it is expected that higher energies can be obtained if steeper density gradients are used.

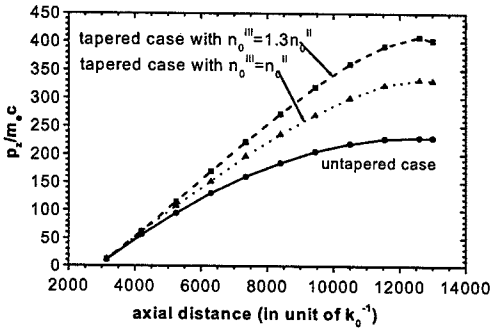


Figure 4: Comparison of momentum gains for untapered and tapered cases.

SUMMARY

It was demonstrated that electron energies by the self-injected laser wakefield acceleration can be enhanced a few times by using an upward density tapering in 2-D cases. Although space-charge force of the self-injected plasma electrons deforms the wakefield severely, the electron energies can be increased effectively before the diffraction effect of a laser pulse eventually limits the energy gain. This kind of self-injection and energy enhancement scheme with a density tapering may be demonstrated with a special-shaped gas jet in relatively low densities (e.g. $n_0 = 10^{16} \sim 10^{17}$ cm^{-3}).

ACKNOWLEDGEMENTS

One of the authors (H. S.) would like to express deep thanks to Prof. W. Mori for sharing the OSIRIS code.

REFERENCES

[1] T. Tajima and J. M. Dawson, Phys. Rev. Lett. **43**, 267 (1979).
[2] D. Umstadter, J. Kim, E. Dodd, Phys. Rev. Lett. **76**, 2073 (1996).
[3] E. Esarey, R. F. Hubbard, W. P. Leemans, A. Ting, and P. Sprangle, Phys. Rev. Lett. **79**, 2682 (1997).
[4] S. Bulanov, N. Naumova, F. Pegoraro, and J. Sakai, Phys. Rev. E **58**, R5257 (1998).
[5] H. Suk, N. Barov, J. B. Rosenzweig, and E. Esarey, Phys. Rev. Lett. **86**, 1011 (2001).
[6] P. Sprangle et al. Phys. Plasmas **9**, 2364 (2002).
[7] R. G. Hemker, K. C. Tzeng, W. B. Mori, C. E. Clayton, and T. Katsouleas, Phys. Rev. E. **57**, 5920 (1998).

FOCUSING OF 28.5 GEV ELECTRON AND POSITRON BEAMS IN METER-LONG PLASMAS

Patric Muggli*
University of Southern California, Los Angeles CA 90089, USA

Abstract

Plasmas can focus both electron and positron beams. However, while the incoming Gaussian transverse profile of an electron beam is preserved upon focusing, the focusing of a positron beam by a long, high-density plasma results in a tightly focused core with the formation of a charge halo. The plasma acts on the positron beam as focusing element with transverse and longitudinal aberrations. The analysis of the focused positron beam transverse profiles is presented here.

INTRODUCTION

Plasma-based accelerators are characterized by their large accelerating gradient, one or more order of magnitude larger than those in today's state of the art radio-frequency base accelerators. Laser-driven plasma accelerators have demonstrated extremely high gradients, in excess of 100 GV/m [1]. However energy gains have been limited to ≈200 MeV [2], because the TW laser beam needs to be focused to an extremely tight focal spot to achieve the large intensity (>10^{18} W/cm^2) necessary to drive the large amplitude plasma wave. As a result the acceleration distance is limited to a few Rayleigh length of the laser beam, i.e., less than one millimeter. In particle beam driven plasma accelerators [3] or Plasma Wakefield Accelerators (PWFAs), gradients in the 1-10 GV/m range are expected. However, particle beams are focused by he plasma and can be channeled over long distances, therefore allowing in principle for multi-GeV energy gains to be achieved in meters-long plasmas [4]. Present experiments are performed in the very nonlinear regime of the PWFA, reached when the beam density n_b is larger than the plasma density n_e. Focusing of both electron and positron beams is predicted and observed experimentally. However differences are expected since an electron bunch expels the plasma electrons from the bunch volume, while a positron beam, attracts them toward the bunch volume. Electron bunches can be focused by an ideal, aberration-free plasma focusing element. For a positron bunch the plasma acts as a focusing element with transverse (spherical) and longitudinal aberrations. Previous results showing the dynamics of the focusing of positrons by low-density (n_e<10^{12} cm^{-3}) plasmas have been published [5]. Focusing of a positron beam by a short, dense plasma has also been observed previously [6].

FOCUSING OF ELECTRONS

A dense (n_b>n_e) electron bunch is sent into an initially neutral plasma expels all the plasma electrons from the bunch volume (blow-out), a short distance behind the bunch front. The remaining pure ion column partially neutralizes the space charge field of the core of the bunch, and the bunch is therefore focused by its self-magnetic field. The density of a Gaussian cylindrical bunch with radius σ_r, length σ_z, and N particles, is given by $n_b=N/\sigma_r^2\sigma_z(2\pi)^{3/2}$. For a highly relativistic electron bunch the pure ion column focusing field can be calculated using Poisson's equation and is given by:

$$E_r = \frac{1}{2}\frac{n_e e}{\varepsilon_0} r \qquad (1)$$

The plasma is initially neutral, and the ion column density n_i is equal to n_e. Alternatively, the focusing strength of the pure ion column is given by:

$$\frac{B_\theta}{r} = \frac{E_r}{rc} = \frac{1}{2}\frac{n_e e}{\varepsilon_0 c} \qquad (2)$$

and amounts to 6 kT/m for n_e=2×10^{14} cm^{-3}. Previous works [7] have shown that the focusing of narrow ($k_{pe}\sigma_r$<<1) electron bunches in this blow-out regime (n_b>n_e) is well described by a beam envelope model [8] for the beam transverse size σ_r: $\sigma_r''+K\sigma_r=\varepsilon^2/\sigma_r^3$. The plasma restoring term is given by: $K=(1/\gamma mc^2)(F_r/r)=(1/\gamma mc^2)(eE_r/r)=\omega_{pe}^2/2\gamma c^2$. Here $k_{pe}=\omega_{pe}/c$ is the relativistic plasma wave wavenumber, $\omega_{pe}=(n_e e^2/\varepsilon_0 m_e)^{1/2}$ is the plasma pulsation, and ε is the beam emittance. The incoming Gaussian beam (in the transverse dimensions x and y) is focused to a nearly Gaussian spot, as seen on Fig. 1. In this blow-out regime, most of the bunch charge is focused by the pure ion column, which acts on the beam as an essentially aberration-free focusing element. The formation of the pure ion column, and access to the blow-out regime within a single bunch has also been studied [9].

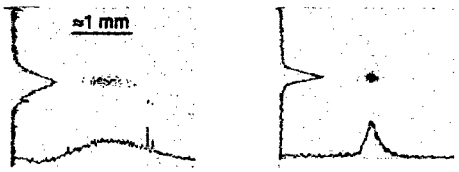


Figure 1: OTR images of the electron bunch without plasma (n_e=0 left), and with n_e≈10^{14} cm^{-3} (right) with the x (horizontal) and y (vertical) beam profiles. Without plasma the beam size is asymmetric because the beam emittances are different in the x and y planes.

FOCUSING OF POSITRONS

A positron bunch sent into an initially neutral plasma, attracts the plasma electrons toward, rather than expels them from the bunch volume, and they stream through it. As a result no blow-out condition exists. The neutralizing plasma electron density has a radial maximum on axis,

0-7803-7738-9/03/$17.00 © 2003 IEEE

and varies along the entire bunch length. The positron bunch is partially neutralized and is therefore focused by the plasma. However, the focusing field varies nonlinearly both along r and z, and the plasma acts on the positron bunch as a focusing element with strong spherical and longitudinal aberrations [10].

An experiment known as E-162 [11] has been performed at the Stanford Linear Accelerator Center (SLAC) to study the acceleration of 28.5 GeV electrons and positrons [12] in a 1.4 m-long plasma. The 1.4 m long plasma with n_e in the 0-2×10^{14} cm^{-3} range is obtained by photo-ionization of a lithium vapor by a ultra-violet laser pulse [13]. The particle beam is $\sigma_z \approx 700$ μm long, has $N \approx 2\times10^{10}$ particles, and is focused at the plasma entrance to a round spot with $\sigma_x \approx \sigma_y \approx 25$ μm. In this experiment the focusing of the beam by the plasma is monitored by recording the beam size at a distance of ≈1 m downstream from the plasma. At that location the backward optical transition radiation (OTR) emitted by the particle beam when traversing a thin titanium foil is imaged onto a CCD camera to obtain time integrated transverse images of the beam on a shot-to-shot basis.

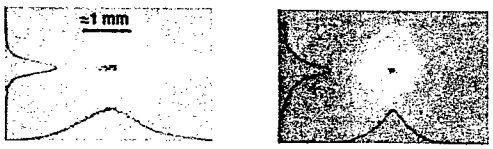


Figure 2: OTR images of the positron bunch without plasma (n_e=0, left), and with $n_e \approx 10^{14}$ cm^{-3} (right) with the x (horizontal) and y (vertical) beam profiles. Without plasma the beam size is asymmetric because the beam emittances are different in the x and y planes.

Experimental results show that the incoming Gaussian positron beam acquires non-Gaussian transverse profiles after the high-density plasma ($n_e > 10^{13}$ cm^{-3}), as seen on Figs 2. The focused beam shows a focused core surrounded by a charge halo, and the transverse profiles have a narrow triangular core profile sitting on a broader triangular pedestal (the halo). A simple bi-triangular profile fitting routine has been developed to describe the focused positron x and y beam profiles. The routine is initiated with linear fits to the experimental profiles in the 20% and 80% amplitude range for the triangular pedestal and core, respectively. The routine then minimizes the difference between the area under the experimental beam profile and the fit profile shape, assuming left-right symmetric profiles for each image. The beam size is obtained from the full width at half maximum (FWHM) of the core triangle fitted to the data, while the relative halo size is described by the ratio between the charge in the triangular core to the charge in the triangular halo, as shown on Fig. 3. Note that the profiles of the beam in absence of plasma are nearly Gaussian, with a root mean square width σ. Fig. 3 shows that in the case of a test Gaussian profile, the width of the profile obtained by using σ_{FWHM}=FWHM/$2(2ln2)^{1/2}$=22.3 is in very good agreement with the input Gaussian width σ=24. Note that in this bi-triangular description, the best fit to a Gaussian profile has a halo that contains <4% of the Gaussian curve area.

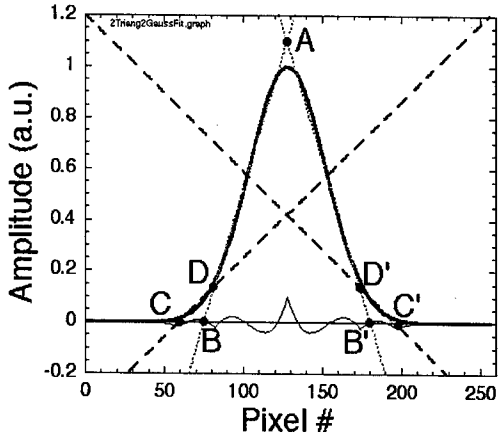


Figure 3: result of the bi-triangular fit to a test Gaussian profile. The fit to the core is represented by the dotted purple lines (area ABB'), while the fit to the halo is represented by the dashed green line (area BCD and B'C'D'). The thin blue line is the difference between the fit and the Gaussian curve.

This bi-triangular shape fitting is applied to the x- and y-profiles of the positron beam measured in the E-162 experiment. On Fig. 4 the result of the bi-triangular fit applied to the x-profile of the plasma off case of Fig. 2 is shown. The Gaussian fit result is also shown for comparison. From the bi-triangular fit results, the bunch core size σ_{FWHM} is ≈69 pixels or ≈622 μm. The "halo" contains ≈10% of the total charge. Figure 5 shows the same results for the plasma on case of Fig. 2. The core sizes σ_{FWHM} are ≈303 μm and ≈181 μm, and the halos contain ≈14% and ≈54% of the total charge in the x and y direction, respectively. These results show both focusing of the beam by a factor ≈2 In the x direction, and the formation of a significant halo in the y-direction. Complete results showing the focusing of the positron beam and the size of the beam halo as a function of the plasma density will be published later. Preliminary results indicate that, at the OTR screen location, a reduction in beam core size by a factor of three or more is observed. In the electron beam case, oscillation of the beam size as a function of n_e were observed [7], reflecting the betatron oscillation of the beam envelope along the plasma length. However, in the case of a positron beam no such size oscillation is observed. In the blow-out regime reached with electrons, the pure ion column focusing force is linear with radius (Eq. 1) and constant along the bunch, therefore allowing for the preservation of the emittance of the beam charge reaching the blow-out. This emittance preservation is very important for future PWFA, in which a driver bunch with $n_b > n_e$ will drive the wake, loose energy, and experience a significant emittance growth, while the witness bunch trailing the driver bunch will gain

energy, and preserve its emittance. The study of emittance preservation for electron and positron beams in the PWFA will be the subject of a future publication.

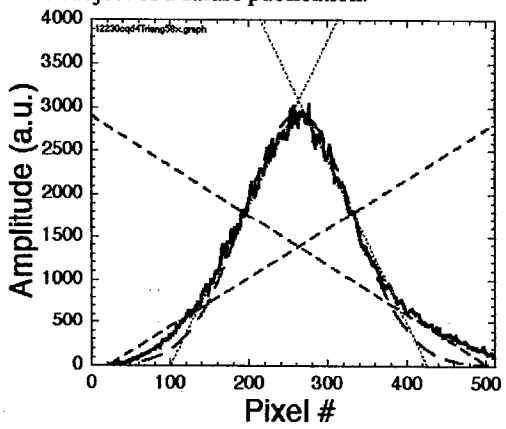


Figure 4: The x beam profiles (red line) from the beam on Fig. 2 with plasma off, and its fits: Gaussian (blue line), and bi-triangular core.(purple dotted lines) and halo (green dashed lines).

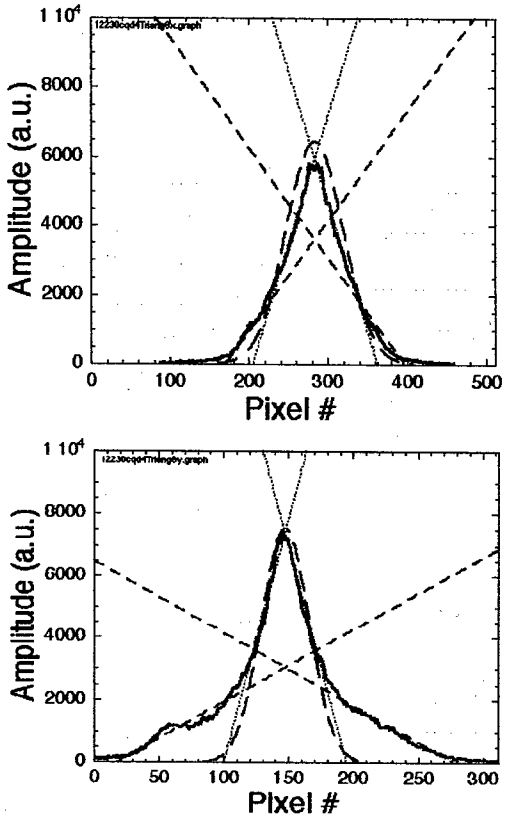


Figure 5: The x (top) and y (bottom) beam profiles (red lines) from the beam on Fig. 2, and their fits: Gaussian (blue line), and bi-triangular core.(purple dotted lines) and halo (green dashed lines). The halo is larger in the y-profile.

CONCLUSIONS

The focusing of electron and positron beams a distance of ≈1 m downstream from a 1.4 m-long plasma has bee observed experimentally. The incoming Gaussian bunch (in the transverse dimension) is focused to a Gaussian shape in the case of an electron bunch. In the case of a positrons beam, the bunch is focused to a tight core surrounded by a charge halo. The focused beam profiles are accurately described by a bi-triangular distribution for the bunch core and halo. The beam core size as well as the relative amount of charge contained in the halo are derived from the fitting parameters.

ACKNOWLEDGEMENTS

This work is supported by the US DoE and NSF grants.

REFERENCES

[1] D. Gordon *et al.*, Phys. Rev. Lett. **80**, 2133 (1998), C.I. Moore *et al.*, Phys. Rev. Lett. **79**, 3909 (1997); R. Wagner *et al.*, Phys. Rev. Lett. **78**, 3125 (1997); A. Modena, *et al.*, Nature **377**, 606 (1995).
[2] V. Malka *et al.*, Science **298**, 1596 (2002).
[3] P. Chen, *et al.* , Phys. Rev. Lett. **54**, 693 (1985).
[4] S. Lee *et al.*, Phys. Rev. STAB **5**, 011001 (2002).
[5] M.J. Hogan et al., Phys. Rev. Lett. **90**, 205002 (2003).
[6] J.S.T. Ng *et al.*, Phys. Rev. Lett. **87**, 244801-1 (2001).
[7] C.E. Clayton *et al.*, Phys. Rev. Lett. **88**, 154801 (2002).
[8] K.G. Steffen, in *High Energy Beam Optics* (John Wiley, New York, 1965), p. 173.
[9] C.L. O'Connell *et al.*, Phys. Rev. ST Accel. Beams 5, 121301 (2002)
[10] S. Lee *et al.*, Phys. Rev. E **64** , 045501(R) (2001).
[11] M. Hogan *et al.*, Phys. Plasmas **7**, 2241 (2000).
[12] B.E. Blue *et al.*, Phys. Rev. Lett. **90**, 214801 (2003).
[13] P. Muggli *et al.*, IEEE Trans. on Plasma Sci. **27** (3), 79 (1999).
*muggli@usc.edu

VORPAL: A COMPUTATIONAL TOOL FOR THE STUDY OF ADVANCED ACCELERATOR CONCEPTS

C. Nieter* and J.R. Cary, University of Colorado at Boulder, Boulder, CO 80309, USA

Abstract

VORPAL, a fully object-oriented, dimension-free plasma simulation code, now has matured and is being used to study advanced accelerator concepts, particularly Laser Wake Field Acceleration. Both fluid and PIC models exist in the code and they can be used independently or in conjunction to perform hybrid simulations. VORPAL has a moving window and the ability to launch laser pulses from boundaries or initialize pulses in the plasma. VORPAL can accommodate a variety of different issues in LWFA, including chirped pulses, propagation of pulse in plasma channels, and optical injection of particle beams.

THE VORPAL FRAMEWORK

The VORPAL code framework make strong use of object oriented design to provide a variety of features included the ability to set the dimension of the simulation at run time, a general domain decomposition, and the the availability of multiple models for both the electromagnetic fields and the plasma. A full description of the code and the methods used in its development can be found in reference [1].

Multi-Dimensional

By templating most of the classes in the VORPAL libraries over dimension and floattype we are able to support simulations of one, two, and three dimensions and of either float or double precision with one code base. One of the principal challenges in writing a multi-dimensional code is the field updates. Normally the fields would be stored as multi-dimensional arrays and the updates would be done with nested loops. This can not be done for an arbitrary dimensional code since the dimension and hence the number of nested loops is not known at the outset.

To solve the problem of field updates, a combination of recursion and template meta-programming is used. The field data is stored internally in a one dimensional array. A generalization of an iterator is used which understands how the one dimensional index of the field data relates to the corresponding position in the multi-dimensional grid. These iterators have methods to bump their position on the grid in any direction. Updater classes are then created which consist of a collection of iterators, usually representing a stencil for a finite difference approximation of the relevant differential equation. These updater classes have a *updateCell()* method which updates the field at that point. These updater classes are then "walked" across the grid by what are referred to as walker classes. The walker classes are templated over dimension and they call the next lowest dimension recursively. The walker class for the lowest dimension is then specialized to actually call the *updateCell()* method of the updater class.

* nieter@colorado.edu

Domain Decomposition

VORPAL is designed to run as both a serial code on stand alone workstations and as a parallel code on systems that run MPI. As part of our general philosophy of flexibility, we have developed a general three dimensional domain decomposition for VORPAL. Any decomposition that can be constructed from a collection of bricks is possible. With this general domain decomposition static load balancing can be and dynamic load balancing is in the final stages of development. To minimize overhead, VORPAL overlaps communication with computation as much as possible.

To achieve this general domain decomposition, we use the idea of a slab. A slab is an object whose sides are straight lines and whose corners are all right angles. So in one dimension a slab is a straight line, in two dimensions a slab is a rectangle and in three dimensions a slab is a brick. The intersection of any two slabs of the same dimension is another slab. Each domain is described by two slabs, one which is referred to as the physical region is all the cells for which the processor is responsible for updating. The other, which is referred to as the extended region is the physical region plus one layer of guard cells in each direction. The cells that a domain needs to send to a neighboring processor is simply the slab that is the intersection of the sending processors physical region with the receiving processors extended region.

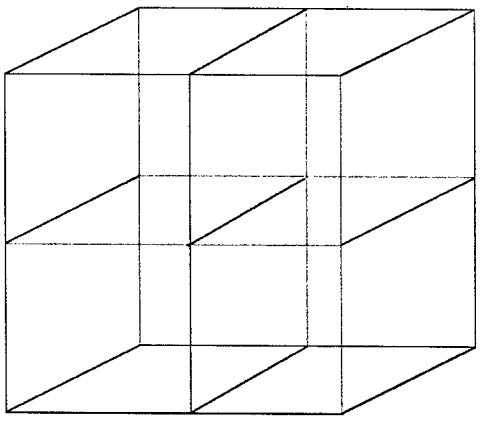


Figure 1: Standard 2D decomposition of a 3D cubic region.

This general domain decomposition allows for full load balancing. In Fig. 1 we see a standard 2D decomposition of a 3D cubic region. This decomposition is determined by

0-7803-7738-9/03/$17.00 © 2003 IEEE

the two planes that cut across the region. To balance the load between the three different domains, the relative times between the first domain and the remaining three must be balanced. This requires three degrees of freedom but the position of the two planes only provide two. In Fig. 2 a more general decomposition that is possible using VORPAL has three movable planes providing the required number of degrees of freedom for load balancing to be done.

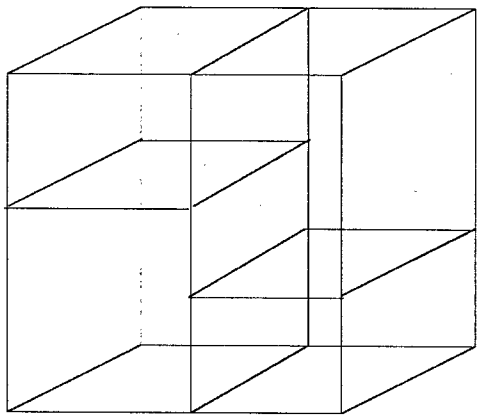


Figure 2: General 2D decomposition of a 3D cubic region.

Available Models

VORPAL flexible object oriented framework makes it possible to have multiple models for both the electromagnetic fields and the plasma in the same code. By interacting with the rest of the code through standard interfaces, different models can be used depending on the relevant physics being studied. Hybrid simulations can be done by using multiple models to represent different regions of the plasma or different species.

VORPAL has a finite difference finite time domain Maxwell solver for the electromagnetic fields based off the Yee mesh. Externally applied fields can be modeled using classes that produced profiles that varying in time or space according to some functional description. The Yee field can be combined with any number of externally applied fields. An electrostatic solver is currently under development.

The plasma particles can currently be modeled with either a cold fluid model or a particle-in-cell (PIC) model. The cold fluid model directly advects the fluid velocity rather than using flux transport to find the fluid momentum. This allows for regions of zero plasma density. The PIC model uses policy classes to provide for a variety of different particle dynamics, including a full relativistic Boris push, a non-relativistic electrostatic push, and free streaming particles.

APPLICATIONS TO LWFA

Several different features have been incorporated into VORPAL to make a useful tool in the study of Laser Wake Field Acceleration (LWFA) [4]. The laser wake field acceleration concept involve sending a high intensity short laser pulse into a plasma. The pondermotive force from the laser pulse blows out the plasma electrons creating a charge separation in the plasma. The electrons are pulled back by the ions and a plasma oscillation is created. This produces a wake field behind the laser pulse. These wake fields can generate field gradients on the of 100 GeV/m.

To study the propagation of the laser pulse and the generated wake field, the simulation region would have to be long enough to follow the pulse as it propagates through the plasma. This can become very expense computationally depending on long the pulse must be followed. However, the interesting physics occurs only in the region around the laser pulse itself. Therefore by including a moving window [2] [3] into VORPAL we can achieve considerable saving in compute time.

Since the various optical injection schemes that have been proposed required one or more pulses besides the pump pulse that generates the wake field, VORPAL has pulse launching boundaries that can launch multiple pulses of various polarizations and chirp from multiple boundaries. Plasma channels are one method of keeping the laser pulse collimated beyond the Rayleigh length in LWFA. VORPAL has the capacity to initialize a variety of plasma channels to study there effects on LWFA.

HYBRID SIMULATIONS

The LWFA is an example of a situation where a hybrid PIC/fluid simulation would be useful, since the beam and the plasma oscillations that generate the accelerating wake field are in some sense separate entities. The beam itself is best modeled by a collection of macro-particles, but by modeling the wake field with a fluid one can avoid the noise that is associated with modeling the bulk plasma with PIC and reduce the computational requirements of the simulation.

In the beat-wave (or colliding-pulse) injection scheme [5] for Laser Wake Field Acceleration (LWFA), three laser pulses are fired into the plasma. The first pulse, referred to as the pump pulse, is responsible for generating the wake field. The remaining two pulses are used to kick particles up to an energy that that puts them traveling in phase with the wake field for subsequent acceleration. This injection works by firing two counter propagating pulses with polarization perpendicular to the pump pulse. One pulse trails the pump pulse at a distance that puts it in the accelerating region of the wake field. The second injection pulse is launched from the other side of the plasma. Since injection pulses have a polarization perpendicular to the pump pulse, the second injection pulse passes through the pump pulse with minimal nonlinear interaction due to the plasma. When it reaches the other injection pulse the two pulses beat. This generates a short lived large electric field and a beat potential that inject the beam particles into the wake field.

To perform a hybrid simulation of this situation we model the front of the plasma with a collection of particles long enough that injection occurs with this region. Past this region the plasma is then modeled by a fluid. After injection the beam particles are traveling near the speed of light so they will remain in the simulation after the moving window is active. The remaining particles will leave the simulation as the window shifts the plasma, moving the wake field into the region where it will be modeled by the fluid. Although initially the computational cost of such a hybrid simulation is greater than a simple PIC simulation, once the moving window moves the bulk of the particles out of the simulation, only the beam particles are being updated. So the hybrid simulation reduces computational cost for long runs and reduces the noise in the simulation since the bulk of the plasma is being modeled by a fluid.

A simple hybrid simulation shows that VORPAL's ability to use multiple models to represent the plasma gives it the capacity to perform these hybrid simulations. The pump pulse and the right traveling colliding pulse are launched into vacuum from the left boundary in what we refer to here after as the x-direction and the right traveling pulse is created adiabatically within the plasma. All the pulses have a half cosine profile in the direction of propagation and are Gaussian in the transverse direction.

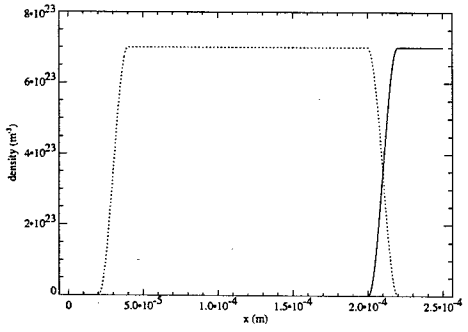


Figure 3: The initial distribution of particle and fluid densities used for a hybrid LWFA simulation. The dashed line is the density profile of the particles and the solid line is the density distribution for the fluid.

We take the rms length of the pump pulse, L_p to be half the plasma wavelength and the lengths of the two colliding pulses to be half a plasma wavelength. The wavelength of the two colliding pulses are slight detuned so they will beat. The forward moving pulse trails the pump by 55 μm measured center to center. This ensures that injection will occur at an accelerating and focusing region in the wake field. Fig. 3 shows the initial plasma density distribution. The plasma starts at zero and rises as a half cosine to the bulk density over 80 μm. The plasma is represented by particles for the next 100 μm so the injection pulses collide in within particles.. At this we have transition region of 20 μm where the particle density drops as the fluid density rises. After we have a constant fluid density.

In Fig. 4 we see the x-component of the relativistic velocity (γv) of the particles plotted against their x positions. A beam has clearly been formed and accelerated to an energy of approximately 14 MeV in less than half a millimeter. At this point in the simulation the initial particle region has been moved out of the simulation by the moving window, and only the particles traveling near the speed of light are present.

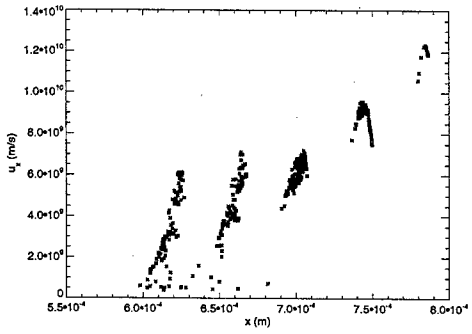


Figure 4: The relativistic velocity in the x-direction of the particles for the hybrid colliding pulse simulation plotted in the x-direction.

While such hybrid simulations are possible, we have found that they do not yet work well for highly asymmetric cells, as are required for laser pulses containing a large number of wavelengths. Asymmetric cells are known to be problematic in fluid numerics. Thus, the use of hybrid simulations for extreme cases appears to require algorithm development.

CONCLUSIONS

VORPAL is well suited as a computational code for studying LWFA. It has several features specificly developed with this problem in mind and due to its highly object oriented design it can change to accomodate new directions in research. A hybrid simulation of the colliding pulse injection scheme highlights some of ways that VORPAL can used to study LWFA.

REFERENCES

[1] C. Nieter, J. R. Cary, "VORPAL: a versatile plasma simulation code", to be published in J. Comp. Phys.

[2] Y. Pemper and B. Fidel and E. Heymana and R. Kastner and R. W. Ziolkowski, "Study of absorbing boundary conditions in the context of the hybrid ray-FDTD moving window solution" in The Thirteen Annual Review of Progress in Applied Computational Electrodynamics, ACES Symposium, 1997, pg. 17.

[3] C. D. Decker and W. B. Mori, *Phys. Rev. Lett.* **72**, 490 (1994).

[4] T. Tajima, J. M. Dawson, *Phys. Rev. Lett.* **43**, 267 (1979).

[5] E. Esarey, R. F. Hubbard, W. P. Leemans, A. Ting, P. Sprangle, *Phys. Rev. Lett.* **79**, 2682 (1997)

TOWARDS REALIZING OPTICAL INJECTION OF ELECTRONS IN RESONANTLY EXCITED PLASMA WAKEFIELDS†

N. Saleh, P. Zhang S. Chen, C. Widjaja, W. Theobald, V. Yanovsky, D. Umstadter
FOCUS Center, University of Michigan, MI 48109, USA

Abstract

The concept of optical injection of plasma background electrons into resonantly driven laser wakefields has been extensively studied theoretically [1]. It was shown that when a strong 1-D wakefield is ponderomotively excited by an ultra-short laser pulse comparable in duration to the plasma wave and a similar transverse laser pulse, but otherwise tightly focused onto the wakefield, is introduced, a relativistic electron bunch with a very narrow (a few %) energy distribution, and very short duration (10's fs) is produced. This concept is actively being investigated experimentally using the University of Michigan's Hercules laser system. We report our progress toward experimentally realizing this concept.

1 INTRODUCTION

Plasma-based laser wakefield accelerators (PBLWFA) have exhibited superiority over conventional RF-based accelerators primarily due to their high field gradients and compactness. Despite the wide array of applications (PBLWFA) have spurred [2][3], they continue to fall short of meeting some modern demanding application. There are two major shortcomings of (PBLWFA) realized so far; first, their acceleration schemes depend on plasma instabilities like Raman scattering [4]. Second, the electron bunches produced have undesirably large longitudinal emittance. To mitigate these shortcomings, a number of schemes were proposed [5-10], some of which are being experimentally investigated [11], and some have reported promising results [12-14]. The general principle of these schemes suggests that a short, intense laser pulse, called pump, with duration comparable to the plasma wave period can resonantly excite a wakefield in the plasma. The short duration of the pump pulse makes the excited plasma wave resilient to laser-plasma instabilities that require several plasma periods to grow. This process merely generates an accelerating structure but does not load the plasma wave with particles. This is so because the electrons carrying the plasma wave oscillate in a certain phase that results in null net motion. In order to load the plasma wave with electrons, either external or internal injection is required. The scheme we experimentally pursue [1], LILAC (Laser Injected Laser Accelerator), utilizes internal injection by means of another equally short intense laser pulse, called injection pulse, synchronized with the pump. The femtosecond synchronization required has been demonstrated in numerous recent pump-probe experiments using ultrafast lasers. This injection method eliminates the jitter problems encountered frequently in RF-accelerators. The injection of the electrons occurs over a duration of a single plasma period and is achieved by the ponderomotive or ionization "kick" of the injection pulse which causes the oscillating electrons to be dephased from the plasma wave and become trapped then accelerated by the excited wakefield.

† Supported by the Division of High Energy Physics, Office of Science, U.S. DOE, award DE-FG02-98ER41071. Lasers are supported by NSF.

2 EXPERIMENTAL SETUP AND PROCEDURE

2.1 Laser System

The experiment we describe will use the University of Michigan HERCULES laser system at the FOCUS center [15]. It is a 100-TW class, Ti:Sa CPA-based laser system, whose output wavelength is centered at $\lambda = 810$ nm. The 12 fs seed pulse coming out of the system main oscillator is contrast-enhanced, stretched then injected in to a novel large-ring-cavity regenerative amplifier [16]. Two downstream amplification stages increase the final power to a nominal level of 100 TW when parasitic transverse lasing in the amplifiers is subdued. The final amplified beam is split by a 50:50 beam-splitter before compression, each beam is sent to a different compressor. This allows for controlling the pulse durations independently. The final beam diameter is 50 mm, and polarized upward, making all horizontal transport mirrors in S-polarization configuration suitable for the high-damage-threshold, broad-band dielectric mirrors used in the compressors and experiment, and also makes possible producing interference fringes to study interesting physical phenomena like stochastic heating [13].

2.2 Experimental Setup

The experimental setup is illustrated in Fig. 1. After the beam is split, the primary compressor houses the pump pulse, while the secondary compressor houses the injection pulse. The experiment layout has been designed so that the pulses overlap with zero delay in the 1 mm He gas jet target inside the experimental chamber. The pump pulse is focused onto the gas target by an f/10 15°-off axis gold-coated parabolic mirror, this provides a good approximation to the 1-D focusing geometry desired. The injection pulse is focused tightly by an f/3 90°-off axis parabolic mirror. The injection parabolic mirror is mounted on a micron-precision 3-D translation stage that permits fine tuning of the spatial overlap of the two pulses. The gas target density can be varied up to 5×10^{19}

0-7803-7738-9/03/$17.00 © 2003 IEEE

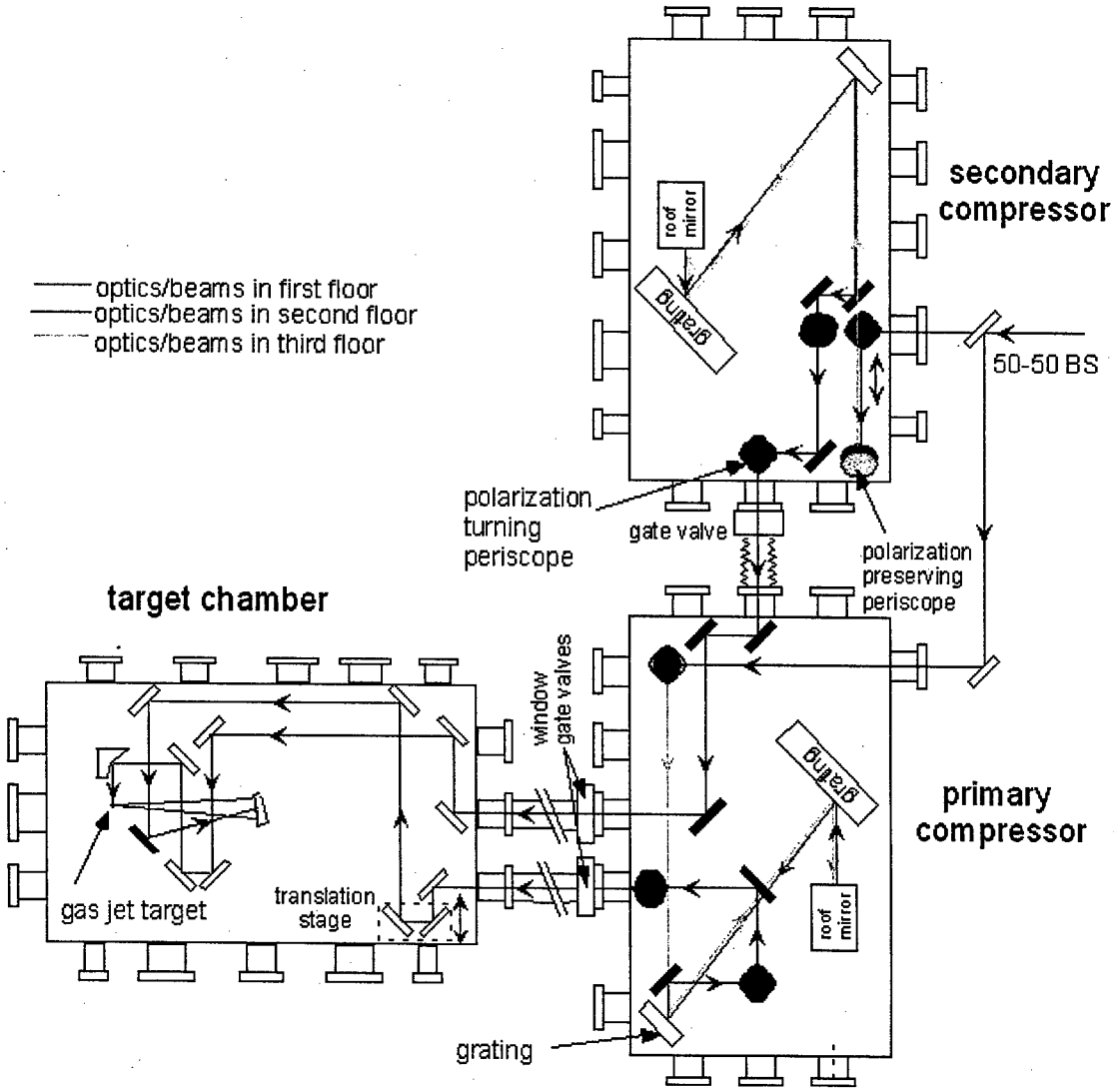


Figure 1: Layout of the LILAC experiment.

electrons/cm^3 by changing the backing pressure of the solenoid-activated supersonic nozzle assembly. The produced e^- beam is diagnosed by an integrating coil transformer for the charge measurement, and a Kodak LANEX scintillating screen for transverse spatial profile and the emittance measurement (using the pepper pot technique [17]), this screen is imaged with a 12-bit CCD camera. The spatio-temporal overlap of the two pulses is monitored from the top through the observation of the Thomson scattering of the fundamental laser wavelength. The e^- beam momentum is measured by inserting a dipole sector magnet between the source (nozzle) and the scintillating screen, and imaging the dispersed trace of the e^- beam.

2.3 Experimental Procedure

In order to determine the proper point of injection in the phase space, the parameter space of the experiment should be set at the threshold of the pump beam self-trapping, where the dark current (the electron signal from the pump alone before injection) diminishes. This should occur close to the resonant regime, $\tau_{laser} \sim 2\pi / \omega_{plasma}$. A target density scan will be performed to achieve that. At the optimum injection point, the injection beam is turned on and further fine-tuning of the beams overlap is performed if needed. The effect of injection beam on pump e^- is then studied.

3 PRELIMINARY RESULTS

A preliminary run with only one beam was taken at 10 TW and peak intensity in excess of 10^{19} W/cm^2. Fig. 2. shows the electron beam profile measured with the laser pulse off-resonance at $\tau_{laser} \approx 2.5\ \tau_{plasma}$. The electron beam measured has a superior divergence solid angle of about 15 μSr, (~ 0.25°). To our knowledge is the smallest divergence angle achieved with laser accelerators to date.

Fig. 3 shows the target density scan up to the density corresponding to a few plasma periods. Full characterization of the electron beam from the pump alone is actively underway.

4 CONCLUSION AND FUTURE WORK

We have developed a 100 TW class CPA laser system and setup the LILAC experiment including successfully overlapping two laser pulses to within 30 fs and a few microns. Preliminary data of the one beam alone show that the dark current diminishes close to the resonance regime, while off-resonance an electron beam with superior divergence is obtained. Further characterization of the electron beam before injection is underway. The laser power level is being maximized by further subduing the parasitic transverse lasing in the amplifier media. The effect of the injection beam on the pump electron beam will be studied in the immediate future. Full characterization of the electron beam obtained with optical injection will be performed and compared to theory and simulation.

5 ACKNOWLEDGEMENT

The authors acknowledge the contribution to the laser system development by V. Chvykov, G. Kalintchenko, S-W Bahk, and G. Mourou.

6 REFERENCES

[1] D. Umstadter *et al.*, Phys. Rev. Lett. **76**, 2073 (1996).
[2] N. Saleh *et al.*, Rev. Sci. Instr. **71**, 2305 (2000).
[3] D. Umstadter, J. Phys. D **36** R151-R165 (2003).
[4] P. Bertrand *et al.*, Phys. Rev. E. **49**, 5656 (1994).
[5] E. Esarey *et al.*, Phys. Rev. Lett. **79**, 2682 (1997).
[6] B. Rau *et al.*, Phys. Rev. Lett **78**, 3310 (1997).
[7] G. Hemker *et al.*, Phys. Rev. E. **57**, 5920 (1998).
[8] C. Moore *et al.*, Phys. Rev. Lett. **82**, 1688 (1999).
[9] S. Bulanov, Plasma Phys. Rep. **25**, 468 (1999).
[10] H. Suk *et al.*, Phys. Rev. Lett. **86**, 1011 (2001).
[11] Kaganovitch *et al.*, these proceedings.
[12] W. Leemans *et al.*, in the 44th Annual Meeting of the Division of Plasma Physics www.aps.org/meet/DPP02/baps/abs/S1800110.html
[13] N. Saleh *et al.*, AIP conf. Proc., **647**, 690 (2002).
[14] P. Zhang *et al.*, submitted to Phys. Rev. Lett.
[15] V. Yanovsky *et al.*, Technical Digest of CLEO 2000, 288 (2000).
[16] V. Yanovsky *et al.*, App. Phys. B **74**, 181 (2001).
[17] P. Ostroumov *et al.*, Rev. Sci. Instr. **73**, 56 (2002).

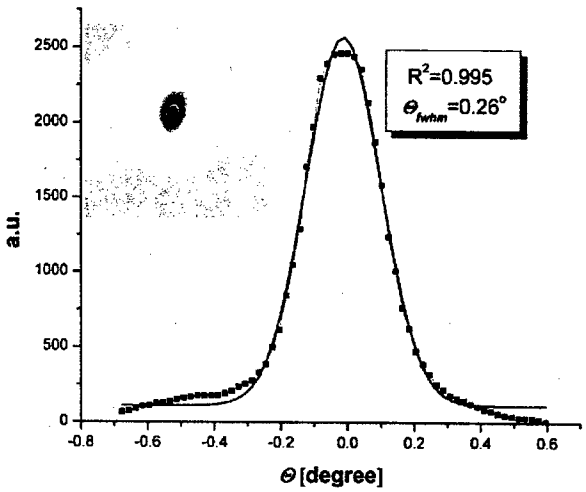


Figure 2: Lineout of the e⁻ beam produced by the one laser beam off-resonance. Inset is the corresponding LANEX image.

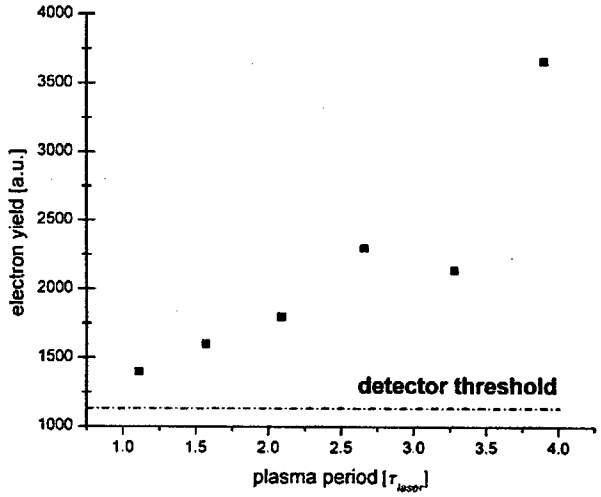


Figure 3: e⁻ beam yield from the pump alone vs target density measured in plasma periods.

EXPERIMENTAL AND NUMERICAL STUDIES OF DIELECTRIC WAKE FIELD ACCELERATION DEVICES*

S.V. Shchelkunov#, J.-M. Fang, T.C. Marshall, Columbia University, New York, NY 10027
J.L. Hirshfield, Yale University, and Omega-P, Inc., New Haven, CT 06511

Abstract

Results are reported from experiments, and numerical analysis of wake fields set up by electron bunches passing through a cylindrical dielectric liner made of alumina. The bunches excite many TM- modes, and the *Ez* component of wake field is sharply localized on the axis periodically behind the bunches. The experiment is at ATF Brookhaven, and uses up to three 50 MeV bunches spaced by one wake field period (*21* cm) to study the superposition of wake fields by measuring the energy loss of each bunch after it passes through the 53-cm long dielectric element. The millimeter-wave spectrum of radiation excited by the passage of bunches is of interest too. The numerical analysis was aimed not only to simulate the behaviour of our device, but in general to predict dielectric wake field accelerator (DWA) parameters. It is shown that one needs to match the radius of dielectric channel with the bunch longitudinal rms-length to achieve optimal performance.

INTRODUCTION

In a dielectric wake field accelerator, a dielectric loaded waveguide supports wake fields radiated by the passage of an electron bunch (e-bunch), which travels at a speed exceeding that of light in the structure. Our studies here relate to a cylindrical structure, consisting of a thick cylindrical shell of alumina (high dielectric constant $\kappa \sim 9.6$) having a small bore hole (radius $A = 1.5$ mm) and an outer radius ($R = 1.9$ cm), all contained within a close-fitting conducting cylinder, which serves as a vacuum wall. The waveguide dimensions and dispersion free dielectric with large κ will favour the coherent superposition of many waveguide modes [1,2,3]. In this, we describe a multi-bunch experiment, with the purpose to measure the energy loss of a short drive bunch train. Very short bunches will be employed to favour wake fields of high amplitude, also shown by micrometer scale rectangular structures excited by fsec driving bunches [4,5].

A variety of numerical studies having to do with DWA performance is presented. We assume that the wake fields interact with Gaussian- shaped bunches (commonly produced by RF- guns) with the head- half width σ_1, tail half- width σ_2, and negligible (mostly) transversal features. If not specified otherwise, κ=9.65, $A = 1.5$ mm, $R = 1.931$ cm, $\sigma_1 = 1$ ps, $\sigma_2 = 2.5$ ps, initial energy = 50 MeV.

NUMERICAL STUDIES

Many recently conducted theoretical studies consider only the interaction between wake fields and infinitely thin electron bunches, but only by taking into account the real longitudinal features of an electron beam, can one predict the efficiency, energy spread, and acting accelerating gradient on a test bunch, which comes after the train of N driving bunches. Describing the wake fields inside of a circular waveguide through the decomposition into the normal eigen-modes [3], and advancing this approach toward computation of the energy exchange between electron bunches and the electromagnetic fields one finds that the power radiated by a train of e-bunches is:

$$P = \frac{Q_0^2 \cdot \beta \cdot c}{16\pi \cdot \varepsilon_0 \cdot A^2} \sum_m \left(\Omega_m \cdot \sum_{i,j} q_i \cdot q_j \cdot \cos\left(\frac{\omega_m \cdot (z_i - z_j)}{\beta \cdot c} \right) \right)$$

where Q_0 – reference charge; $q_i = Q_i/Q_0$ with Q_i - charge of ith bunch; ω_m – eigen frequencies of the structure;

$$\Omega_m = \frac{f_m^2(0)}{\alpha_m} \cdot \left(\left(\Gamma_c^m\right)^2 + \left(\frac{\Gamma_s^m}{2}\right)^2 \right)$$

with f_m – eigen functions, α_m – normalization coefficients, and Γ_c^m, Γ_s^m are given by:

$$\Gamma_c^m = \frac{\sigma_1}{\sigma_1+\sigma_2} \exp\left(-\left(\frac{\omega_m \cdot \sigma_1}{2 \cdot \beta \cdot c}\right)^2\right) + \frac{\sigma_2}{\sigma_1+\sigma_2} \exp\left(-\left(\frac{\omega_m \cdot \sigma_2}{2 \cdot \beta \cdot c}\right)^2\right)$$

$$\Gamma_s^m = \frac{\sigma_1}{\sigma_1+\sigma_2} \exp\left(-\left(\frac{\omega_m \cdot \sigma_1}{2 \cdot \beta \cdot c}\right)^2\right) - \frac{\sigma_2}{\sigma_1+\sigma_2} \exp\left(-\left(\frac{\omega_m \cdot \sigma_2}{2 \cdot \beta \cdot c}\right)^2\right)$$

Every bunch is located along the z- axis at z_i, moves at the speed of $\beta \cdot c$, and has the same shape, but different charge.

Deploying this expression for the case where the first N- bunches, spaced at $z_i = L \cdot (1-i)$, pump energy into the wake, and the very last bunch, located at $z_T = L \cdot (1-N-1/2)$ is accelerated, one derives the expressions for the set of parameters which should be used to describe a wake field apparatus as an accelerator device (L = wake field period):

- enhancement of the wake field due to its amplification by the train of N bunches:

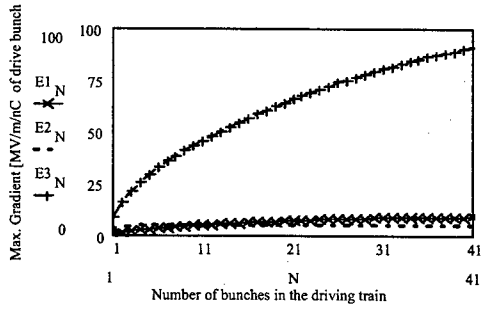
$$\xi = \left(\sum_{m,i,j}^{\infty,N,N} \Omega_m \cdot \cos\left(\frac{\omega_m \cdot L \cdot (i-j)}{\beta \cdot c}\right) \right) \Big/ \sum_m^{\infty} \Omega_m$$

- structural ratio (we are introducing now as)

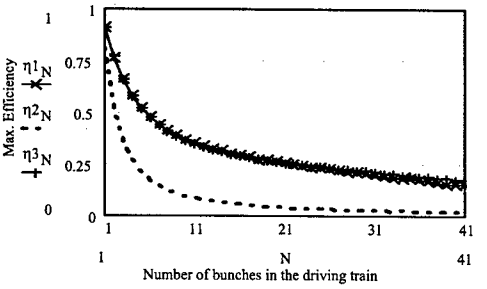
$$\chi_\rho = -\left(\sum_m \Omega_m \cdot \sum_i^N \cos\left(\frac{\omega_m \cdot L(N-i+1/2)}{\beta \cdot c}\right) \right) \Big/ \sum_m \Omega_m$$

*Supported by US DOE.
#shchelkunov@bnl.gov

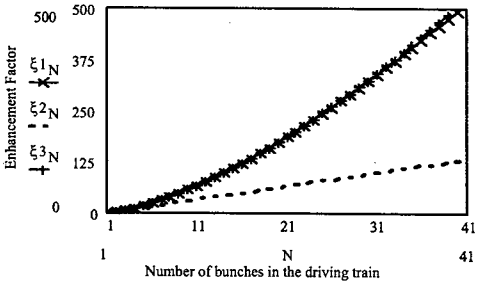
0-7803-7738-9/03/$17.00 © 2003 IEEE



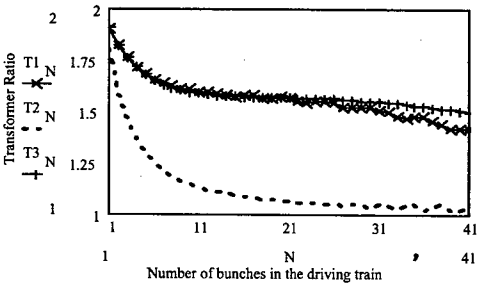
a) maximum possible accelerating gradient acting on a test bunch (given per [nC] of a driving bunch); the upper ($E3_N$) curve corresponds to the narrow bunch + small channel radius in the dielectric slab



b) maximum possible efficiency of energy transfer



c) enhancement of the wake field due to its coherent amplification by the train of N bunches



d) transformer ratio

Figure 1: Parameters of DWA are shown for the different bunch length and dielectric hole radius (σ_1, σ_2, A).
#1 – (1 ps, 2.5 ps, 1.5 mm) – solid, marked by "X",
#2 – (1 ps, 2.5 ps, 0.5 mm) – "dot",
#3 – (0.33 ps, 0.83 ps, 0.5 mm) – "dash", marked by "+"

- efficiency of energy transfer from the N- bunch train to a test bunch of charge $Q_T = q_T \cdot Q_0$

$$\eta = \frac{2 \cdot q_T \cdot \chi_\rho - q_T^2}{\xi}$$

with its maximum value of

$$\eta_{MAX} = \frac{\chi_\rho^2}{\xi}$$

- acceleration gradient acting on the test bunch:

$$E_T = \frac{Q_0}{16 \cdot \pi \cdot \varepsilon_0 \cdot A^2} \sum_m \Omega_m \cdot \left(2 \cdot \chi_\rho - q_T\right)$$

- customarily used transformer ratio [2] is expressed as:

$$TR_N = 2 \cdot \eta_{MAX} \frac{N}{\chi_\rho}$$

One sees that maximum efficiency occurs when a test charge equals χ_ρ, while the accelerating gradient drops down by 2 times from its possible maximum. Only a test charge less than $2 \cdot \chi_\rho$ can experience acceleration.

Fig. 1 gives examples of performances for several cases. The maximum gradient of 256 MV/m will be achieved after 20 narrow driving bunches each with charge Q_0 = 4 nC (see the #3 case.) One can increase significantly the accelerating gradient by reducing the channel radius in a dielectric only if it is accompanied by bunch shortening. The reason for this is that both the wake field peak where acceleration/ deceleration occurs and an e-bunch are features of almost the same longitudinal dimensions. When one reduces the channel radius the wake field can become narrower than the bunch, which leads to reduction of all performances (see the case #2 in Fig. 1, b), c), d). Fig. 2 demonstrates that when mismatching between the bunch length and the channel radius happens, almost all driving bunches (N≥ 4) cannot lose energy above some limit.

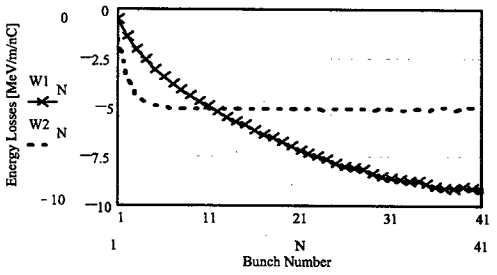


Figure 2: Energy lost by every consecutive driving bunch for different (σ_1, σ_2, A):
#1 – (1 ps, 2.5 ps, 1.5 mm) – solid, marked by "X";
#2 – (1 ps,2.5 ps, 0.5 mm) – "dot"

In considering narrowing the driving bunches to improve performance, one should keep in mind that excessive narrowing may lead to an increment in the test bunch energy spread when a few drive bunches are used. The only reliable way to prevent it is to narrow the test

bunch. For drive (σ_1, σ_2) ≈ (1 ps; 2.5ps), and test (σ_1, σ_2) ≈ (0.3 ps; 0.8ps) the energy spread does not exceed 15 %.

The accuracy of bunch spacing (between any bunch and the reference bunch) must be better than 425 μm to avoid any performance decrease larger than 15 %. This also means that our model is valid when the time slippage of a bunch is within this range after interaction with the wake field. Thus, the DWA length must not exceed some limit, or, equivalently the acceleration gradient should be sufficiently high.

The Tab. 1 shows the lowest limit on gradient $E_{lim,min}$ when one plans to have gross energy losses/gain of W.

Table 1: Lowest gradient vs. planned energy gain/losses to use this numerical model

W [MeV]	0.1	1	10	50
$E_{lim,min}$ **[KV/m]**	0.05	4.8	375	4600

For the structure at ATF- BNL with the drive (σ_1, σ_2) ≈(1ps; 2.5 ps), Q0 ≈300 pC the decelerating/accelerating gradient is at least 500 times larger than the limit. The energy losses are: 1st bunch – 78; 2nd – 212; and 3rd – 315 KeV. The maximum accelerating gradient is 716 KV/m (after N= 3 drive bunches), and the acting gradient on a test charge of 150 pC will be 537 KV/m.

Should another set of (σ_1, σ_2, Q_0, κ, A, etc) occur, the model allows the "quick-to-predict" computation of energy losses/gains and any other relevant parameters (ξ, η, E_T, etc)

EXPERIMENTAL STUDIES

Oversize alumina castings were obtained from LSP Industrial Ceramics (Lambertville, NJ). Since no sample 53 cm in length had the straightness of bore hole that was required, it was decided to use two selected shorter sections smoothly butted together and fitted into a metal-walled cylindrical vacuum jacket and waveguide. Initial measurements of the spectrum of TM_{0n} modes (after a single bunch) were made on a slightly oversized sample [6], which was then ground to the correct dimension (Fig. 3) for this experiment. A new measurement (Tab. 2) of the TM_{0N} frequencies shows that the wake field period is 21 cm.

The apparatus is installed on the 2nd beamline of the ATF- BNL, which was redesigned to meet the experimental (Fig. 4) requirements. New focusing triplets were introduced, together with beam profile monitors (BPMs) to produce the small e-beam transverse size and a suitable alignment to pass the bunch down the hole in the dielectric. The HeNe laser-and-optical system was employed to check the alignment on every assembling and operational step. The transport dynamics of the redesigned line has been studied intensely to insure matching between the ATF rf- linac and the apparatus.

The three driving bunches are obtained by splitting an optical pulse into three precisely delayed pulses, which impinge on the rf- photocathode gun within 30° of the peaks of 2.8 GHz field to generate the compressed electron bunches that are suitable for the excitation of multiple TM- mode wake fields. The spacing between drive bunches (equal to the wake field period L) will be adjusted to maximize energy losses of every individual bunch. Since in this test experiment no large bunch charge is available, the energy losses can be comparable with the energy jitter of the diagnostic apparatus, and a technique is being developed to maintain the same energy over a significant period of time.

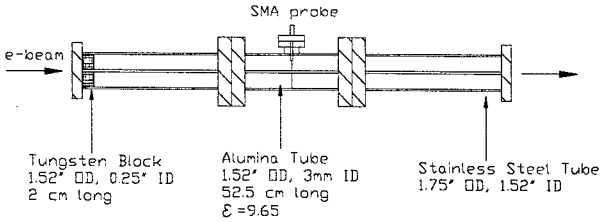


Figure 3: Apparatus drawing and dimensions

Table 2: Spectrum for $TM_{01} - TM_{06}$*

M#	1	2	3	4	5	6
Exp.	2.04	4.70	7.45	10.14	12.99	15.68
Th.	2.03	4.72	7.45	10.21	13.02	15.83

* *(frequencies in [GHz], M# - mode number, Exp. – experimental data, Th. – theoretical prediction ± 1% which results from κ =9.65 + 1%, R= 19.31 mm ± 0.3%, A= 1.5 mm ± 1%·R (the best manufacturing accuracy)*

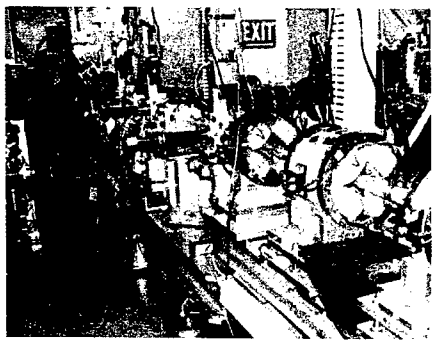


Figure 4: DWA experiment at ATF

REFERENCES

[1] T.B. Zhang et al, Physical Rev. E56, 4647 (1997).
[2] J.G. Power et al, PRST AB 3, 10132 (2000).
[3] S.Y. Park, J.L. Hirshfield, Physical Rev. E62, 1266 (2000).
[4] T.C. Marshall et al, PRST – Accelerators and Beams 4, 121301 (2002).
[5] T.C. Marshall et al., Advanced Accelerator Concepts Tenth Workshop, AIP Con. Proc. #647, p. 361.
[6] J.-M. Fang et al., Proc. of the PAC 1999, Vol. 5, p. 3627 (1999).

MULTICAVITY PROTON CYCLOTRON ACCELERATOR*

Changbiao Wang[1], V. P. Yakovlev[2], and J. L. Hirshfield[1,2]
[1]Department of Physics, Yale University, New Haven, CT 06520-8120, USA
[2]Omega-P, Inc., 199 Whitney Ave., New Haven, CT 06511, USA

Abstract

Analysis is presented for a multicavity proton cyclotron accelerator in which a 122 mA, 1 MeV proton beam is accelerated to 954 MeV using a cascade of eight cavities in an 8.1 T magnetic field, with effects of finite beam radius and velocity and energy spreads taken into account. The first cavity operates at 120 MHz, and successive cavities have resonance frequencies lower in increments of 8 MHz. For this example, average acceleration gradient exceeds 37.9 MV/m, average effective shunt impedance is 207 MΩ/m, but maximum surface field in the cavities does not exceed 7.2 MV/m. Such an accelerator might be suitable for driving a high-power neutron spallation source.

INTRODUCTION

Intense proton beams are needed in a wide variety of applications in high-energy physics, including production of elementary particles such as kaons, pions, muons, and neutrinos [1]. A 10-30 GeV proton accelerator with mA-level current will be required for a future muon collider [2]. 0.5-2.5 GeV high intensity proton beams could also be required with beam powers exceeding 100 MW for neutron production by spallation for several critical applications, such as accelerator production of tritium [3] and accelerator-driven transmutation of nuclear waste [4]; current machines operate at about 1 MW [5].

The multi-cavity proton cyclotron (MCPC) has been proposed and analyzed for high-efficiency, high-gradient acceleration of a high-current proton beam in a normal conducting structure [6-8]. It has been shown that a proton beam can be accelerated in the MCPC from 1 MeV to ~1 GeV with more than 100 MW beam power [8]. The new concept is based on use of a cascade of rotating-mode normal conducting TE_{111} cavities in a strong nearly-uniform static magnetic field. Cyclotron-resonance acceleration in each cavity provides energy gain for the protons. The cavity resonance frequencies f_n decrease from f_1 for the first cavity, with a fixed frequency interval Δf between each of the N cavities; thus $f_n = f_1 - (n-1)\Delta f$ and $f_1 = l\Delta f$, with the integer $l \geq n$, and $1 \leq n \leq N$. Proton pulses are injected into the first cavity at intervals $\Delta T = 1/\Delta f$ or integer multiples thereof.

Based on the previous study [8], an example is presented below with the effects of beam spreads in velocity, energy, and radius taken into account. The effect of drift tunnels between cavities is also included and the phase angle of injection of proton beam is optimized. Simulations show that a 122-mA, 1-MeV proton beam is accelerated to 954 MeV using a cascade of eight regular TE_{111} cavities in an 8.1 T magnetic field and the performance of the MCPC is not so significantly affected by these effects for a beam with reasonable spread parameters. It is also found that this acceleration mechanism can be sustained for an exceptionally wide injection phase angle in the first cavity, e.g., two rf cycles (16.7 ns), compared to 0.3 of an rf cycle (2.5 ns) in the previous work [8]. This feature is highly significant, in that it allows operation with high duty factor (~13%) and low peak proton current (<1 A), thereby mitigating against issues that can arise from high beam space charge.

In addition, the effect on proton dynamics of the apertures and drift tunnels for a beam traversing cavities is also examined by use of realistic rf fields in place of analytic field forms for idealized cavities.

SIMULATION ANALYSIS

The cascade of eight TE_{111} cavities in the MCPC example has a frequency separation of $\Delta f = 8$ MHz and resonant frequencies of 120, 112..., and 64 MHz. Thus 15, 14..., and 8 full rf cycles pass in these cavities, respectively, between proton bunches when they are injected every 125 ns (i.e., at an 8 MHz rate). Average beam current is chosen to be 122 mA, injected in 16.7 nsec bunches (two rf cycles in the first cavity), and thus with a peak current of 0.915 A (duty factor = 1/7.5); the energy of the injected proton beam is taken to be 1 MeV.

In simulations, 20-cm drift tunnels between cavities are added to isolate cavity fields from one another; an injected proton beam with finite spreads in energy, velocity and radius is introduced. The parameters for the spreads are chosen by reference to those for an ideal solid Brillouin beam of radius r_b [m] with the specified peak current I [A] in the specified magnetic field B_z[T]. Here the magnetic field B_z (7.9 T) can be obtained from the gyro-resonant condition for the first cavity, and the beam radius is chosen to be 0.9 mm from Brillouin beam condition, given by $r_b B_z = (240 I U_p/\gamma\beta c^2)^{1/2}$, where U_p is the particle rest energy expressed in eV (938.2×10^6 eV for proton), γ and β are the relativistic energy factor and normalized velocity on the axis for the beam, and c is the speed of light in m/s. For the solid Brillouin beam, the across-beam voltage depression caused by space charge is given by $30I/\beta$, and it is 0.6 kV for a beam with energy 1 MeV and peak current 0.915 A. The beam energy spread is chosen to be 1.2 keV (=0.37 keV in rms spread), double the above beam energy depression. The normalized transverse velocity spread can be estimated from $\Delta\beta_\perp \approx (2\Delta\gamma/\langle\gamma\rangle)^{1/2}/\langle\gamma\rangle \approx (2\Delta\gamma)^{1/2}$ with $\langle\gamma\rangle$ the average energy factor; it is chosen to be 1.3×10^{-3}, corresponding to rms spread 6.5×10^{-4}. According to

*Work supported by US DoE.

0-7803-7738-9/03/$17.00 © 2003 IEEE

$30I/\beta[1+2\ln(R_w/r_b)]$ where R_w is the first cavity radius (92 cm), the full voltage depression is 8.8 kV, much less than the beam voltage 1 MV, and the space charge effect on particle dynamics is negligible. Beam parameters in simulations are listed in Table 1.

Table 1: Proton Beam Parameters in Simulations

initial beam energy	1 MeV
initial beam velocity	$0.0461c$
peak beam current I	0.915 A
average beam current $\langle I \rangle$	0.122 A
pulse period	125 nsec
pulse duration	16.7 nsec
duty factor	1/7.5 = 13.3%
beam radius r_b	0.9 mm
beam energy spread	1.2 keV
rms perpendicular velocity spread	$6.5\times10^{-4}c$

Analytic field expressions for TE_{111} mode [8] are used and the intrinsic (ohmic) quality factors Q_0 for the cavities are calculated assuming copper construction. Simulations show that the peak surface electric fields range from 3.9 to 7.2 MV/m, well below breakdown. Specific cavity parameters and mean acceleration energy gains for each of the eight stages are given in Table 2.

Fig. 1 shows the dependence of average energy factor and axial magnetic field on axial distance. The magnetic field traversing the cavities varies mildly in the range 7.9-8.2 T for optimum energy gain, and the average energy factor is increased from 1.0011 (1 MeV) to 2.0164 (953.7 MeV). The final beam power is 116.2 MW, rf-to-beam power efficiency is 66.8%, and average effective acceleration gradient is 37.9 MV/m, as compared with 40.4 MeV/m for a zero-spread beam without drift tunnels [8]. Most of this decrease is due to the 140-cm increase in machine length from adding the drift tunnels.

Fig. 2 shows the dependence of rms γ- and β_z-spreads on axial distance z. The energy factor spread is increased from initial 3.9×10^{-7} (0.37 keV) to 0.0063 (6 MeV) at the end of the device, and the axial velocity spread is increased from $9.2\times10^{-6}c$ to $0.0040c$, compared with 0.0026 (2.4 MeV) and $0.0012c$ at the end respectively for the zero-spread beam example [8].

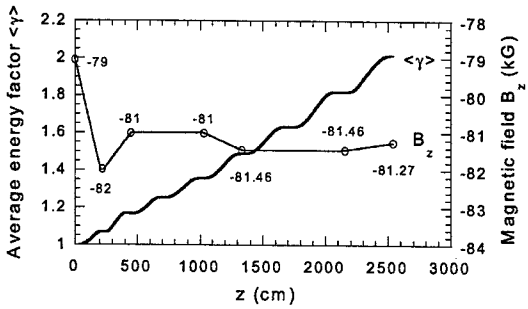


Figure 1: Dependence of average energy factor $\langle\gamma\rangle$ and axial magnetic field B_z on axial distance z. In the 20-cm drift regions the magnetic field is uniform.

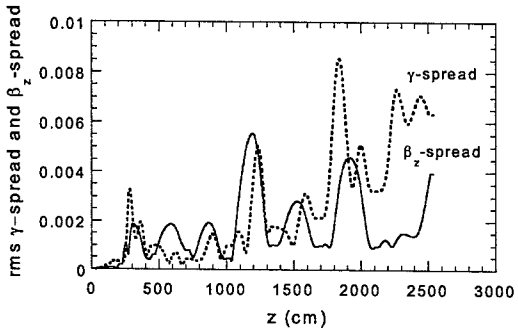


Figure 2: Dependence of rms energy factor and normalized axial velocity spreads on axial distance.

INFLUENCE OF APERTURES AND TUNNELS ON PARTICLE DYNAMICS

Although the effect of protons drifting through tunnels between cavities is considered in the above analysis, the modification of rf fields by the apertures on cavity end walls and by the tunnels is not included. Proton dynamics will be influenced by this modification. To gauge this influence, a study that uses realistic fields was done for the first three stages with a 122-A, 1-MeV zero-spread proton beam, for comparison with a study that uses analytic field expressions for idealized cavities. Table 3 shows the simulation results for the two cases: *case a* corresponds to analytic field expressions used and *case b*

Table 2: Parameters for a 122 mA, 8-Cavity Proton Cyclotron

stage #	cavity frequency (MHz)	cavity radius (cm)	cavity length (m)	rf power input (MW)	relative rf phase	beam-loaded cavity Q_L	intrinsic cavity Q_0 (copper)	peak surface field (MV/m)	mean energy gain (MeV)
1	120	92	2.06	18.0	0	6.25×10^4	1.1×10^5	7.2	63.6
2	112	98	2.23	15.0	1.40π	2.68×10^4	1.1×10^5	4.0	92.9
3	104	106	2.39	15.5	1.45π	4.36×10^4	1.2×10^5	4.8	80.9
4	96	110	2.81	18.5	1.85π	4.39×10^4	1.2×10^5	4.9	96.1
5	88	120	3.07	24.0	0.50π	4.41×10^4	1.2×10^5	5.1	124.3
6	80	132	3.38	23.0	1.70π	3.67×10^4	1.3×10^5	4.1	135.3
7	72	144	3.92	30.0	0.15π	3.65×10^4	1.3×10^5	4.2	177.0
8	64	172	3.89	30.0	0.55π	3.85×10^4	1.5×10^5	3.9	182.7
total			25.15	174.0					952.7

Table 3: Simulation Results for the First Three Cavities for *Case a* and *Case b*

	120 MHz cavity		112 MHz cavity		104 MHz cavity	
	case a	*case b*	*case a*	*case b*	*case a*	*case b*
energy gain (MeV)	63.6	64	92.9	93	80.9	80
maximum $E_\perp$ (MV/m)	11.3	11.3	6.3	8.14	7.6	9.4
unloaded quality factor	110,000	109,000	110,000	111,000	120,000	11,600
power applied (MW)	18	18	15	17	15.5	19
power dissipated (MW)	10.2	10	3.7	6	5.6	9.5

corresponds to realistic fields used [9].

In simulations, the energy gains are adjusted to be the same for the two cases. From Table 3, it is seen that almost nothing is affected for the first cavity. Compared to *case a*, the input rf power for *case b* is increased by 13.3% for the second cavity while 22.6% for the third, with more power lost to the walls.

Fig. 3 shows the dependence of energy E and radial coordinate R on axial distance z for individual particles for *case b*, with cavity and drift outlines shown to scale. It is seen that all the particles go through the cavities without hitting any walls.

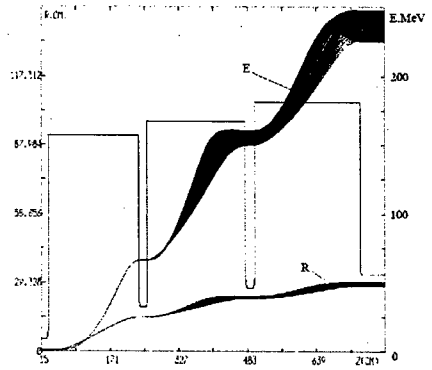


Figure 3: Energy and radius *versus* z for accelerated protons in a zero-velocity-and-radius-spread beam for *case b*. Peak current I = 915 mA, and duty = 1/7.5. Cavity and drift tunnel outlines are shown to scale.

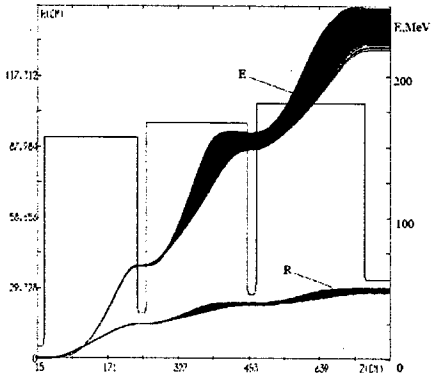


Figure 4: Energy and radius *versus* z for accelerated protons in a beam with velocity, energy, and radius spreads for *case c*. Peak current I = 915 mA and duty = 1/7.5. Cavity and drift tunnel outlines are shown to scale.

Case c is an example where realistic rf fields like *case b* are employed for a beam with parameters given by Table 1 except the energy spread is 0.6 keV. The results are shown in Fig. 4, for comparison with the above zero-spread beam *case b*. It is seen from Fig. 4 that the energy curves for individual particles spread wider than *case b*, leading to a bigger energy spread, but their average energy is almost the same, about 238 MeV.

REMARK

The new proton accelerator concept MCPC presented here could form the basis for an alternative to a superconducting linac for production of high-intensity proton beams, either for a K-factory or a Π-factory, in a muon collider, or in a neutron spallation source such as that needed for driving a sub-critical reactor for accelerator-based transmutation of nuclear waste.

REFERENCES

[1] J. L. Laclare, "CONCERT a high power proton accelerator driven multi-application facility concept," IEEE NSS-MIC, Lyon, France, Oct. 15-20, 2000.

[2] C. M. Ankenbrandt et al., Phys. Rev. ST Accl. Beams 2, (1999) 081001.

[3] J. L. Anderson, P. W. Lisowski, W. P. Bishop, J. T. McCormack, and J. G. Angelos, "Status of the accelerator production of Tritium (APT) project," in Proc. of the 3rd Int. Conf. on ADTTA, Praha (Pruhonice), Czech, June 7-11, 1999.

[4] G. P. Lawrence, "High-power proton linac for transmuting the long-lived fission products in nuclear waste," in Proc. of PAC'1991, p. 2598.

[5] W. Chou, "Spallation neutron source and other high intensity proton sources," A lecture at the 3rd OCPA Int. Accel. School, Singapore, Jul. 25-Aug. 3, 2002.

[6] J. L. Hirshfield, C. Wang, and R. Symons, in AAC: 9th Workshop, AIP Conf. Proc. 569 (AIP, New York, 2001), p. 833.

[7] C. Wang and J. L. Hirshfield, in Proc. of PAC'2001, p. 3389.

[8] J. L. Hirshfield, C. Wang, and V. P. Yakovlev, Phys. Rev. ST Accel. Beams 5, (2002) 081301.

[9] V. P. Yakovlev, O. A. Nezhevenko, O. V. Danilov, D. G. Myakishev, and M. A. Tiunov, in AAC: 10th Workshop, AIP Conf. Proc. 647 (AIP, New York, 2002), p. 421.

STABILITY OF ELECTRON ORBITS IN THE STRONG WAKE FIELDS GENERATED BY A TRAIN OF FSEC BUNCHES*

Changbiao Wang[1], J. L. Hirshfield[1,2], and T. C. Marshall[3]
[1]Physics Department, Yale University, New Haven, CT 06520 USA
[2]Omega-P, Inc., New Haven, CT 06520 USA
[3]Applied Physics Department, Columbia University, New York, New York 10027, USA

Abstract

A tall, dielectric-lined rectangular wake field microstructure is being analyzed as a possible stageable element of an advanced linear wake field accelerator, to be driven by a train of fsec microbunches. These microbunches would be chopped out of a longer bunch using a powerful CO_2 laser and formed into a rectangular-profile bunch using a quadrupole. The fsec bunches set up a periodic wake field in the microstructure that can be built up to 600 MV/m, for example, using ten 3-fsec bunches each containing 2 pC of charge. Results are described from computations of test particle electron orbits in the longitudinal and transverse wake fields excited by these fsec bunches. It is found that test electrons in drive bunches will be well confined within the structure for a travel distance of ~10 cm and test electrons located in an accelerated bunch will have stable motion for at least 50 cm.

INTRODUCTION

Acceleration of electrons in wake fields set up by a series of driving bunches in a dielectric structure has shown promise as a linear accelerator in which large gradients might be possible [1,2]. Such wake fields are interesting because they do not require power injected into the structure from an external source, but rather use fields set up by bunches obtained from a conventional rf linac. Recently, we have studied the use of tall, planar dielectric wake field structures having micron-scale dimensions [3]. Such structures are capable of precision manufacture using microcircuit technologies, and have the capability of achieving very high field gradients: indeed, a series of ten, 3-fsec 1-pC charge bunches has recently been shown to set up a wake field of ~500 MeV/m in a structure 18.8×150 μm in cross section [4]. The bunches are 10 μm wide, and dielectric slabs a few μm thick line the structure. Planar dielectric structures offer the attraction of improving the stability of the bunch motion and the amount of charge carried compared with a cylindrical structure of comparable size, and the small transverse dimension permits a large wakefield to be developed.

The bunches could be obtained initially from a 500 MeV rf linac-type source, and are processed using a LACARA accelerator "chopper" [3], or possibly an IFEL [5] used as a "pre-buncher", so as to obtain a sequence of bunches a few fsec in duration. A TW CO_2 laser is used as a "modulator" [3] of the original psec, nC bunch provided by the linac to form such a sequence of short bunches, each having charge in the pC range. These *drive* bunches, the energy of which can be recycled, would in practice be followed by an *accelerated bunch* which is situated in the accelerating component of E_z which follows the drive bunch train. In this way fields comparable with those achieved in laser plasma wake field accelerators can be set up, yet the energy is obtained largely from the rf linac source rather than the laser. We have found that it is possible to distort the original circular cross section of the input bunches into a rectangular profile, using a quadrupole, and that the rectangular profile is maintained for several centimeters of travel [4].

Transverse fields set up by the bunch have been calculated, and an estimate has been made of how far a drive bunch might travel without additional focusing [6] (several cm). Also, studies have been made of fields in 3D using the PIC code KARAT. The E_z component of wake field was found to be rather uniform in cross section. In the structure under study, the wake fields are dominated by two modes having nearly the same periodicity (about 21 μm in the chosen geometry). In this paper, we study the motion of *test particles* which are situated initially in a grid of loci at the location of any drive or accelerated bunch (see Fig. 1). Our findings show that adequate stability of the drive bunches can be obtained by choosing a tall structure (300 μm), and that a certain group of test particles can be accelerated for a distance of ~1/2 m or more without external focusing, maintaining a nearly stable profile and gaining energy of 300 MeV in that distance.

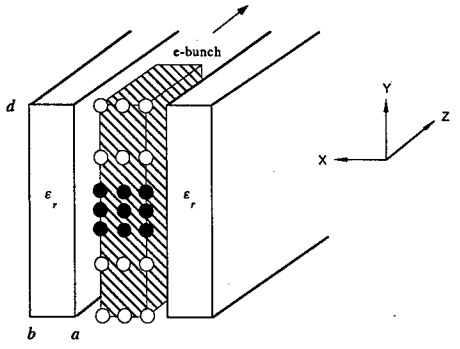


Figure 1: Schematic slab bunch within a planar wake field structure. Circles stand for test particles in the (decelerated) drive bunch while dots stand for test particles in the accelerated bunch.

*Work supported by US DoE.

0-7803-7738-9/03/$17.00 © 2003 IEEE

NUMERICAL PROCEDURE AND MODEL

A complete theory for excitation of wake fields in 3D planar dielectric-lined waveguides, similar in structure to a theory for cylindrical waveguides [7], has been formulated [6]. Park wrote a code [8] based on his theory [6] to calculate distributions of wake field forces excited by a train of rigid electron bunches moving at a constant velocity. In this paper, the code is used to calculate dynamics for test particles by adding a routine solving the Lorentz force equations, in which the wake field forces are as in Ref. 6.

The dielectric structure is shown in Fig. 1, with the beam channel width $2a$ = 15 μm, the dielectric thickness b-a = 1.9 μm, and the dielectric (channel) height $2d$ = 300 μm, and the relative dielectric constant ε_r = 3. The rigid drive bunches are 10 μm wide, 300 μm high, and 1 μm (3 fsec) long, each containing 2 pC of charge. The initial velocity of test particles is assumed to be the same as that of drive bunch, which has a relativistic energy factor of γ = 1000 (510.5 MeV). The self-field effect and the reaction on the drive bunch are neglected. The test particles in the drive bunch are initially uniformly distributed within a 10×300−μm rectangle while the test particles in the accelerated bunch are located within a 10×40−μm rectangle. In simulations, 861 computational particles are used to calculate the interaction between wake fields and test particles.

The place of injection of the accelerated bunches can be optimized. At a place behind the last drive bunch appropriate for acceleration, the transverse wake fields are small while the axial field is large. Since the axial slippage between the wake fields and accelerated particles is quite small, one can estimate what wake field peaks are potentially good for acceleration using only the initial field distributions. Therefore, we first find the possible positions and then do dynamic simulations one by one to obtain the best one favoring stable motion.

MOTION OF DRIVE BUNCH

Coherence of wake fields from different drive bunches requires a fixed bunch spacing. The first dive bunch is set at z = 1200 μm and the 10th drive bunch is at 1009.2 μm, with a spacing of 21.2 μm. The stability of the 10th drive bunch is examined by initially setting test particles at z = 1009.2 μm, where the axial wake field force on the axis is −210.2 MeV/m, excited by first 9 drive bunches.

Fig. 2a shows the dependence of F_x on y at z = 1009.2 μm for x = 0, 1, 3, 5 μm (F_x is anti-symmetric with respect to x). It is seen that the magnitude of F_x increases nearly linearly with x, and F_x is focusing or defocusing, depending on y. F_x is focusing around y = -95, -25, 25, and 95 μm while defocusing around y = -135, -60, 0, 60, and 135 μm. Fig. 2b shows the distributions of the test particles at z = 1009.2 μm, 4 cm, 7 cm, and 10 cm under the influence of the wake fields. The four x-direction focusing locations can be easily identified from the z = 4-cm distribution. Because of a strong defocusing force in the region of 115 μm < |y| < 150 μm (two y-ends), particles there get lost to walls (see the z = 10-cm distribution). Fig. 2c shows the dependence of average relativistic energy factor and percentage of surviving particles upon axial distance. All the particles go ~2 cm without hitting any walls, and finally more than 70% arrive at z = 10 cm. The particles are decelerated from <γ> = 1000 (510.5 MeV) to 955.2 (487.6 MeV).

Simulations show that 94% of the test particles at the second drive bunch survive traveling 10 cm while 77% at the fifth and 73% at the eighth.

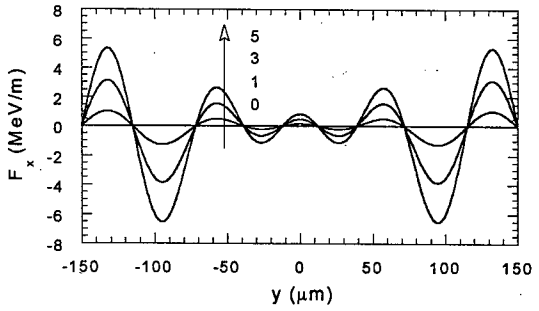


Figure 2a: Dependence of F_x on y for x = 0, 1, 3, and 5 μm. F_x is focusing when F_x < 0, while F_x is defocusing when F_x > 0.

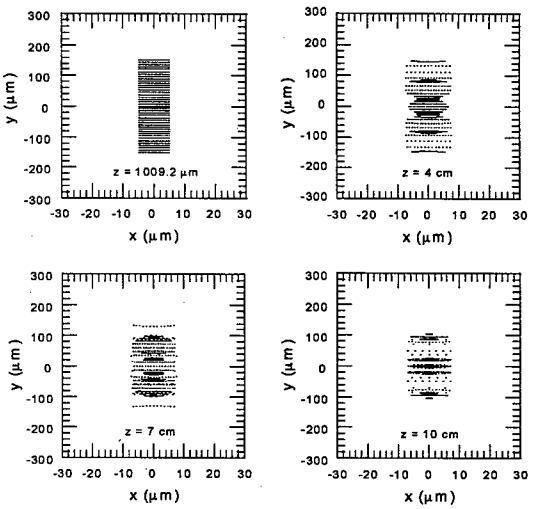


Figure 2b: Drive bunch test particle distributions at z = 1009.2 μm, 4 cm, 7 cm, and 10 cm.

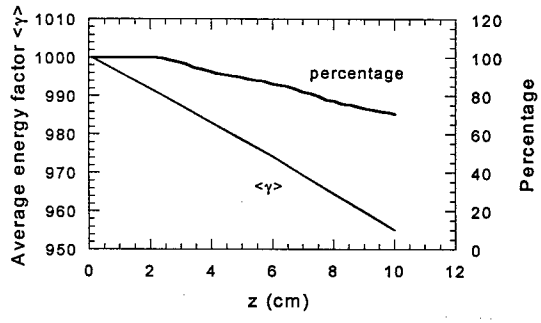


Figure 2c: Dependence of average energy factor and percentage of surviving particles on axial distance.

MOTION OF ACCELERATED BUNCH

The accelerated bunch comes from a different source than the drive bunch. The stability of accelerated particles depends on positions in the wake field and the size of the region the particles take up. Simulations show that the test particles in the accelerated bunch following a train of 10 drive bunches should to be situated at z = 60.5 μm, where the transverse wake field forces are small and focusing in a rectangular region of $|x| < 5$ μm and $|y| < 20$ μm while the axial wake field force on the axis reaches its peak, 618.1 MeV/m, as shown in Fig.3a. F_x and F_y are focusing when less than zero, since they are plotted at $x > 0$ and $y > 0$ respectively.

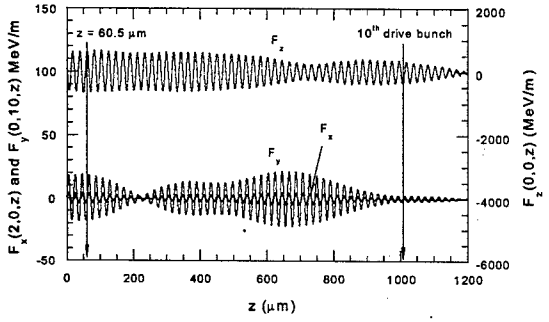


Figure 3a: Dependence of wake field forces $F_x(2,0,z)$, $F_y(0,10,z)$, and $F_z(0,0,z)$ on axial distance z, excited by 10 drive bunches. The stability of the accelerated bunch is examined by setting test particles at z = 60. 5 μm.

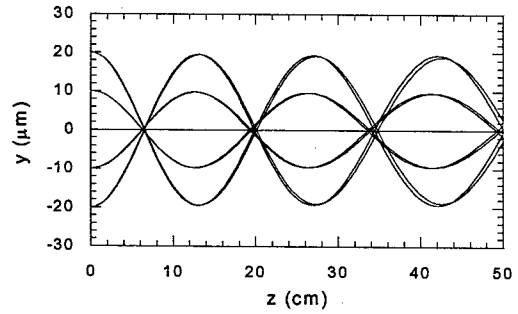


Figure 3b: Orbits on the y-z plane for 15 sampled accelerated particles.

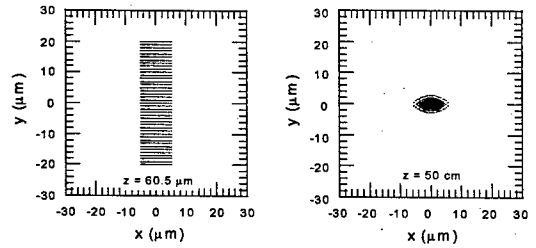


Figure 3c: Test particle distributions on the x-y planes at z = 60.5 μm where 861 electrons are initially distributed and at 50 cm where they are all well focused again.

Simulations show that during the course of acceleration, the particles experience focusing and defocusing alternatively, and they are well confined within a rectangular region of $|x| < 7.5$ μm and $|y| < 20$ μm. Fig. 3b shows the orbits on the y-z plane for 15 sampled accelerated particles. Fig. 3c shows the initial distribution (z = 60.5 μm) and final distribution (z = 50 cm).

It is found that the bunch of particles is accelerated from $\langle\gamma\rangle$ = 1000 (510.5 MeV) to 1589.1 (811.5 MeV) in a 50-cm distance.

DISCUSSION

In the analysis, the electron bunch is assumed to be cold. A rough estimation of effect of finite emittance can be made as follows. Suppose we take a 500 MeV electron beam with a radius of 50 μm and a normalized emittance of 1 mm-mrad as an example. The maximum normalized transverse velocity is 2×10^{-5} and the maximum transverse displacement caused by the emittance is 7.5 μm after a 37.5-cm travel. From this it follows that the emittance effect is not so important for a 10-cm interaction between decelerated test particles and the wake fields. For accelerated test particles, the emittance effect will be reduced because both F_x and F_y are nearly linearly focusing forces in the whole region the particles take up. Of course, a more sophisticated code is needed to better understand emittance effect on the stability.

We have also studied a 1-pC bunch 150 μm tall (half the height and charge as the example) inside the same structure, and find nearly the same acceleration gradient and similar stability behavior.

We have shown that both drive and accelerated bunches can enjoy comparatively stable motion whilst traversing many centimeters through the structure, permitting a very large gradient to be exploited for particle acceleration.

REFERENCES

[1] T.-B. Zhang, J.L. Hirshfield, T.C. Marshall, and B. Hafezi, Phys. Rev. E56 , (1997) 4647.

[2] J.G. Power, M.E. Conde, W. Gai, R. Konecny, P. Schoessow, and A.D. Kanareykin, Phys. Rev. ST Accel. Beams 3, (2000) 101302.

[3] T.C. Marshall, C. Wang, and J.L. Hirshfield, Phys. Rev. ST Accel. Beams 4, (2002) 121301.

[4] T. C. Marshall, J.-M. Fang, J. L. Hirshfield, C. Wang, V. P. Tarakanov, and S. Y. Park, "Wake Fields Excited in a Micron-Scale Dielectric Rectangular Structure by a Train of Femtosecond Bunches," in Advanced Accelerator Concepts: tenth Workshop, edited by C. E. Clayton and P. Muggli, AIP Conf. Proc. No. 647 (AIP, New York, 2002), p. 361.

[5] Y. Liu, X. J. Wang, D. B. Cline, M. Babzien, J. M. Fang, J. Gallardo, K. Kusche, I. Pogorelsky, J. Skaritka, and A. van Steenbergen, Phys. Rev. Lett. 80, (1998) 4418.

[6] S-Y. Park, C. Wang, and J.L. Hirshfield, "Theory for Wake Fields and Bunch Stability in Planar Dielectric Structures," in Ref. [4], p. 527.

[7] S-Y. Park and J.L. Hirshfield, Phys. Rev. E62, (2000) 1266.

[8] S-Y. Park , Private communications.

MODELING OF BEAM-IONIZED SOURCES FOR PLASMA ACCELERATORS

S. Deng[1], C. D. Barnes[3], C. E.Clayton[2], C. O'Connell[3], F. J. Decker[3], P. Emma[3], O. Erdem[1], C. Huang[2], M. J. Hogan[3], R. Iverson[3], D. K. Johnson[2], C. Joshi[2],T. Katsouleas[1], P. Krejcik[3], W. Lu[2], K. A. Marsh[2], W. B. Mori[2], P. Muggli[1],R. H. Siemann[3], D. Walz[3]

[1]University of Southern California, Los Angeles, CA 90089
[2]University of California, Los Angeles, CA 90095
[3]Stanford Linear Accelerator Center Stanford, CA 94309

Abstract

When considering intense particle or laser beams propagating in dense plasma or gas, ionization plays an important role. Impact ionization and tunnel ionization may create new plasma electrons, altering the physics of wakefield accelerators, creating and modifying instabilities, etc. Here we describe the addition of an ionization package into the 3-D object-oriented fully parallel PIC code OSIRIS [1]. Using intense beams to tunnel-ionize neutral gas may become a new source of plasma. For the beams whose electrical fields are right above threshold, the optimal gas density for maximize electrical field is about 7 n_0 (n_0 is the optimal density according to linear theory $\omega_p\sigma_z/c=2^{1/2}$ [2]). We apply the simulation tool to the parameters of the current E164 [3] Plasma Wakefield Accelerator experiment at the Stanford Linear Accelerator Center (SLAC). We find that tunnel ionization affects the wakefield and energy gain of E-164 experiment.

INTRODUCTION

Following the success of recent plasma-based accelerators (peak accelerating gradients on the order of 200 MeV/m for E157/E162 [4]), experiments are underway to achieve yet higher gradients with shorter and more intense drive beams. For these, ionization the working gas by the beam becomes important. In future experiments and concepts such as E164X and the afterburner, a high-density short bunch is used to drive nonlinear (blowout regime) plasma wakes, and multi-GeV peak accelerating gradients are achieved. The need for long homogeneous plasma sources of high density (up to 10 meters of $2*10^{16}$ cm^{-3}plasma for the afterburner) makes the possibility of a plasma self-ionized by the drive beam attractive.

In this paper, we study the optimal gas density at which the plasma wakefield is maximized for a self-ionized plasma wakefield accelerator. Simulation results for the E164 experiment and E164X experiment are presented.

PIC CODE OSIRIS AND IONIZATION MODELS

OSIRIS is a fully relativistic PIC code with newly added ionization package which includes 2D and 3D impact ionization and tunnel ionization.

The probability [6] for a particle to impact-ionize the gas is

$$P_i = n_g\sigma(v_i)|v_i|\Delta t$$

Here n_g is gas density, σ: is gas cross-section, and v is the velocity of the incident particle.

For tunnel ionization, the Ammosov-Delone-Krainov(ADK)[7] model is used to calculate the tunneling ionization probability. According to the ADK formula, the ionization rate for Li is give by the following equation:

$$\omega(t) = \Delta t*3.46*10^{21}\exp(-85.5/E)/E^{2.18}$$

Here E is the amplitude of the applied electrical field, with unit GV/m.

OSIRIS is an object-oriented program. It enables us to add an ionization module without changing other existing modules. The ionization module can interact with other modules freely.

IONIZATION AS A NEW PLASMA SOURCE

. Using short bunch with high density to tunnel-ionize neutral gas is a possible way to create plasma. In Fig. 1, newly created electrons are pushed away by the driving beam and form a wake.

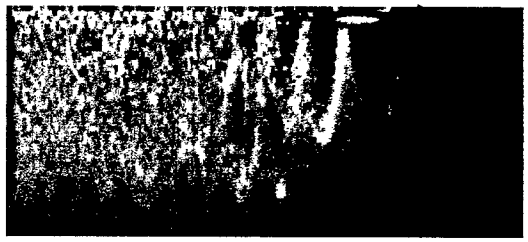


Fig 1. Real space of new electrons

We did two runs to check the amplitude of the wakefield: run 1 is for a short beam with electric fields far above threshold, and run 2 is for a beam with electric field just above threshold.

0-7803-7738-9/03/$17.00 © 2003 IEEE

The physical parameters are shown in table 1.

Table 1: physical parameters

	Run 1	Run 2
Beam Energy (GeV)	30	50
N	2e10	2e10
$\sigma_z(\mu m)$	20	63
$\sigma_r(\mu m)$	20	14.1
$n_0(cm^{-3})$	$4.41*10^{16}$	$1.4*10^{16}$
$n_{gas}(cm^{-3})$	$1.25*10^{17}$	$4.2*10^{16}$

n_0 is the optimal density according to linear theory $\omega_p\sigma_z/c=2^{1/2}$.

In both case, n_{gas} is around 3 times n_0. As one sees in Fig. 2, the wakefield created in the self-ionization case is comparable to that in the pre-ionization case for far above threshold case --case 1(the pre-ionized plasma density is set to equal to gas density). For the case just above threshold --case 2 (pre-ionized plasma density is set to equal to n_0) the wakefields are smaller. This is because for a beam with field just above threshold, the head of the beam cannot ionize gas until its electric field reaches the threshold value. The rapidly ionized plasma then "sees" an effectively shortened beam, because it does not see the head of the beam. A higher gas density is needed to match the plasma period (wavelength) to the effective pulse length.

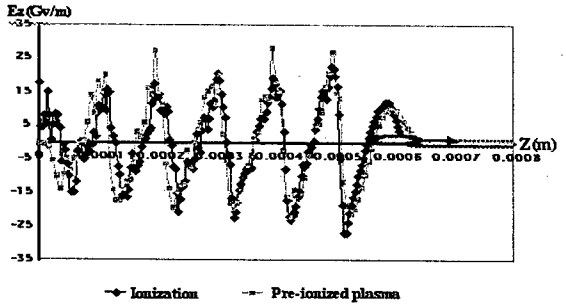


Fig 2a). Comparison of longitudinal E field of pre-ionized case and self-ionized cases for run 1

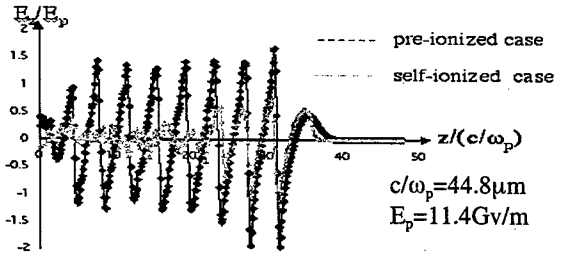


Fig 2b). Comparison of longitudinal E field of pre-ionized case and self-ionized cases for run 2

Parameter search results to find the optimal gas density at which the wakefield are maximized for run 2 are shown in Fig 3. As we expected, the electrical fields peak at higher density (7 n_0) for self-ionied case than pre-ionized case ($3n_0$). Even in the pre-ionized case, the optimal density is larger than the linear theory optimal density n_o because the non-linear wake drives the plasma electrons relativistically, increasing their mass and decreasing the plasma frequency. The density needs be higher to compensate this frequency decrease.

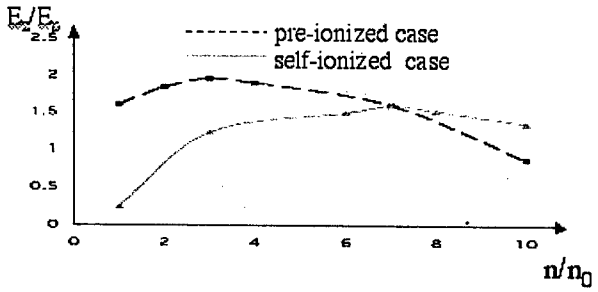


Fig 3. Peak longitudinal E field vs. gas or plasma density

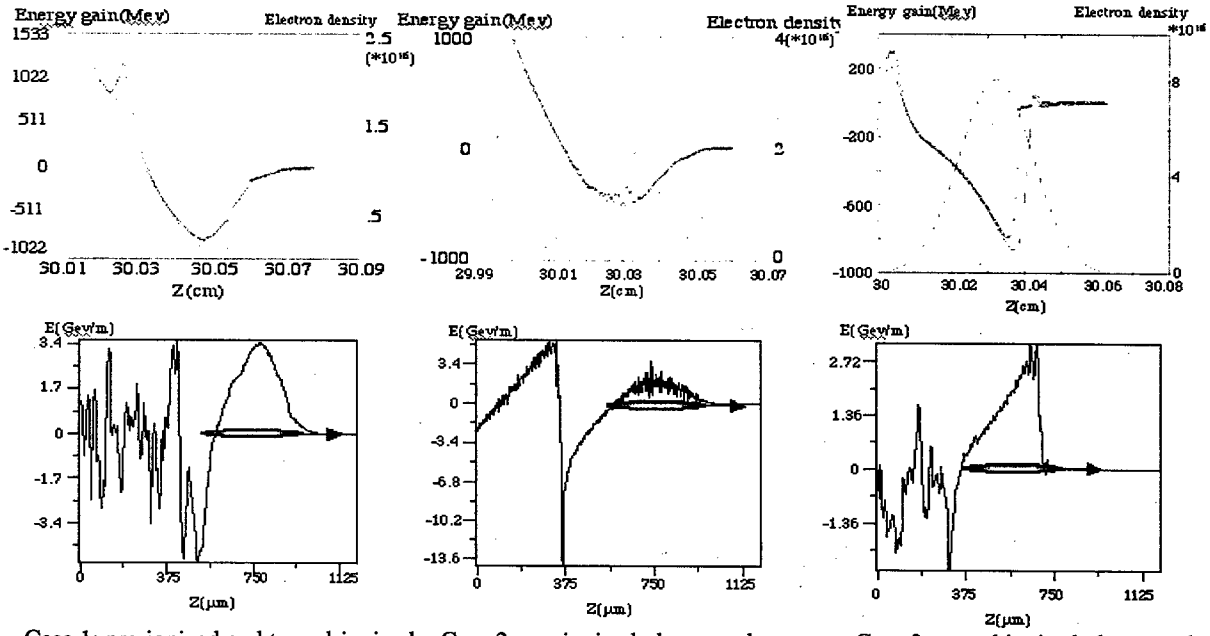
SIMULATION FOR E 164

3 comparison runs are done for E164 parameters. Case 1 is for with both pre-ionized plasma and tunnel-ionized plasma. Case 2 is for pre-ionized plasma only. Case 3 is for tunnel-ionzed plasma only. The physics parameters are shown in table 2.

Table 2: physical parameters for e164 runs

	Case 1	Case 2	Case 3
Beam Energy (GeV)	30	30	30
N	2e10	2e10	2e10
$\sigma_z(\mu m)$	100	100	100
$\sigma_r(\mu m)$	25	25	12.5
$N_{plasma}(cm^{-3})$	$5*10^{15}$	$5*10^{15}$	0
$N_{gas}(cm^{-3})$	$4.5*10^{16}$	0	$2.5*10^{16}$

Fig. 4 shows the Energy gain and the lineout of longitudinal electrical wakefield for each case. The increased plasma density due to new created electrons makes the wakefield wavelength shorter (see the comparision diagram for case 1 and case 2. For E164 parameters, the wakefield are close to threshold of tunnel ionisation; the magnitude of wakefield and energy gain for case 3 is much less than the pre-ionized case.



Case 1: pre-ionized and tunnel-ionized Case 2: pre-ionized plasma only Case 3: tunnel ionised plasma only

Fig 4. Comparision results for E164 (x's represent maximum energy gain, blue line represents average gain; The Gaussian shows the beam profile)

SIMULATION FOR E164X

In E164X, even shorter beams (10-20μm) are used than in E164 (100μm). In this case, the electrical field of the beam is far beyond the threshold. As one can see in Fig, 5, 25GeV/m peak acceleration fields can be achieved, and the peak average energy gain is around 25MeV for a 2mm run. These results support the thesis that self- ionization can be used as a way to create plasma sources for plasma wakefield accelerators and the beam wakefield can be made comparable to the pre-ionized plasma case.

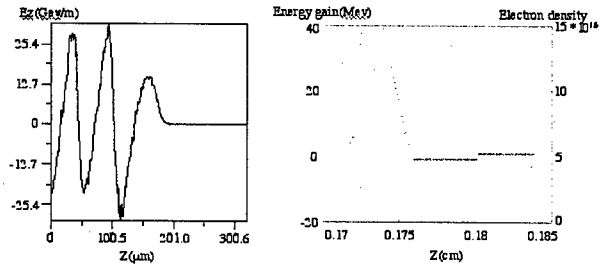


Fig 5. E164X simulation results

CONCLUSION

Tunnel ionization cannot be neglected when very short beams are driving the plasma wakefield. The new created electron can shorter the wavelength and yield similar or smaller wakefields, depending on how short the beam is. For very short beams (like E164X), the wakefields are comparable to the pre-ionzed case, while for beams whose fields are near threshold (like E164), higher density is required to optimally match. More work will be done to study the optimal density.

ACKNOWLEDGMENTS

The authors gratefully acknowledge helpful conversations with David L. Bruhwiler. This work is supported by U.S. Department of Energy, under Contracts No. DE-FG03-92ER40745,DE-FC02-01ER41192, DE-FC02-01ER41179, DE-FG03-92ER40727, and NSF PHY-0078508.

REFERENCES

[1] R. G. Hemker, F. S. Tsung, V. K. Decyk, W. B. Mori, S. Lee, and T..Katsouleas, Development of a parallel code for modeling plasma based accelerators, IEEE Particle Accelerator Conference 5 , 3672-3674 (1999).

[2] E164 proposal, unpublished.

[3] R. Keinigs and M.E. Jones, Phys. Fluids 30, 252 (1987)

[4] David L. Bruhwiler, Rodolfo E. Giacone, Physical Review Special Topics, vol. 4, pp. 101302 (2001)

[5] E164X proposal, unpublished.

[6] V. Vahedi and M. Surendra, Comput. Phys. Commun. 87, 199(1995)

[7] M.V. Ammosov, N.B. Delone and V.P.Krainov, Sov. Phys. JETP 64, 1191 (1986)

MAGNETIC DESIGN OF A SUPERCONDUCTING AGS SNAKE*

R. Gupta#, A. Luccio, G. Morgan+, W. Mackay, K. Power, T. Roser, E. Willen,
Brookhaven National Laboratory, Upton, NY 11973 USA
M. Okamura, RIKEN, Saitama, Japan

Abstract

Brookhaven National Laboratory plans to build a partial helical snake for polarized proton acceleration in the AGS. It will be a 3 Tesla superconducting magnet having a magnetic length of 1.9 meter. AGS needs only one magnet and currently there is no plan to build a prototype. Therefore, the first magnet itself must function at the design operating field and provide the required field quality, spin rotation and deflections on the particle beam. New software have been developed that exchanges input/output between the OPERA3d field design program, the Pro-Engineering CAD model and the software that drives the machine to make slots in aluminum cylinders where blocks of 6-around-1 NbTi wires are placed. This new software have been used to carry out a number of iterations to satisfy various design requirements and to assure that the profile that is used in making field computations is the same that is used in cutting metal. The optimized coil cross-section is based on a two layer design with both inner and outer layers having five current blocks per quadrant. The ends are based on a design concept that will be used for the first time in accelerator magnets.

INTRODUCTION

At present there is a significant loss of polarization in accelerating polarized protons from 5 GeV to 25 GeV in Brookhaven AGS (Alternating Gradient Synchrotron). The proposed 30% partial Siberian Snake can overcome both imperfection and intrinsic resonaces [1]. Drawing on our previous experience with superconducting helical magnets for RHIC [2], a 203.2 mm (8 inch) coil aperture helical dipole is being designed and built for AGS. The basic design parameters are listed in Table 1. The dipole field rotates with a pitch of 0.2053 degrees/mm for 786 mm in the center and a pitch of 0.3920 degrees/mm for 577 mm in each end. In order to minimize the residual deflections and offsets of the beam on its orbit through the Snake, a careful balancing of the coil parameters is necessary. This required the development of new software that apart from doing various calculations can also generate appropriate input/output for other 2d and 3d field calculations programs and for various CAD programs. Similarly a significant effort was also invested in developing and automating CAD based design techniques [3]. A good design for the coils was found after several iterations where the coil pitch and length of helical sections were optimized while retaining the cross section and ends. In addition to the main helical coils, a solenoid winding is planned inside the main coils to compensate for the axial component of the field that is experienced by the beam when it is off-axis in this helical magnet. Also, the magnet system will have several corrector coils placed on the same tube on which the solenoid is placed. The engineering design of this magnet is presented elsewhere [3].

Table 1: AGS Helical Magnet Design Parameters.

Superconductor Parameters:	
Filament diameter	10 micron
Wire diameter	0.33 mm
Cu to Non-Cu ratio	2.5:1
Cable type	6-around-1
Cable diameter, bare	0.99 mm
Cable diameter, insulated	1.09 mm
Cable I_c @ 5T, 4.2 K	530 A
Coil Parameters:	
No. of coil layers	2
Coil inner radius for inner layer	101.6 mm
Coil inner radius for outer layer	127.8 mm
Current blocks per quadrant	10 (5 per layer)
No. of turns in 9 blocks	12 X 9 = 108
No. of turns in inner-pole block	12 X 5 = 60
Other Parameters:	
Design field	3.0 T
Quench field	~4.1 T
Operating current	~350 A
Quench current	~500 A
Operating temperature	4.5 K
Stored energy @3T	0.4 MJ
Inductance	6.5 H
Pitch in the middle (786 mm)	0.2053 deg/mm
Pitch in the ends (577 mm each)	0.3920 deg/mm
Slot size, width/depth	13.6/13.1 mm
Warm bore tube id/od	152.4/156.5 mm
Cold bore shield id/od	165.2/167.7 mm
Cold bore tube id/od	176.5/181.6 mm
Inner Aluminum tube id/od	195.6/229.6 mm
Outer Aluminum tube id/od	248/281.8 mm
Iron yoke id/od	300.4/685.8 mm
Shell id/od	685.8/687.1 mm
End plate thickness	12.7 mm
Magnetic length	1.9 m
Aluminum tube length	2.27 m
Vacuum vessel length	2.57 m

2-D MAGNETIC DESIGN

The cross section of a helical coil may be specified in a plane that is perpendicular to the helix and with a pitch by

* Work supported by the U.S. Department of Energy under Contract No. DE-AC02-98CH10886 and by RIKEN of Japan.
#gupta@bnl.gov.
+Retired from BNL.

which the field is required to rotate. The design of AGS snake requires the pitch to be different in the middle of the dipole as compared to that in the two ends (see Table 1).

The design procedure developed here is such that the initial coil cross section is optimized for a good field quality in a straight dipole magnet. In this procedure the size of conductor blocks in this straight dipole is assumed to be the same as that in the plane perpendicular to the helix in an helical dipole. This means that in a plane perpendicular to the beam axis the subtended block size in an actual helical dipole will be different for two pitches and also for the two layers. In this straight magnet (see cross-section in Fig. 1), the physical separation between the blocks is much larger than that it is in the helical magnet (see 3-d model in Fig. 2), however, the relative angular separation of each block remains the same.

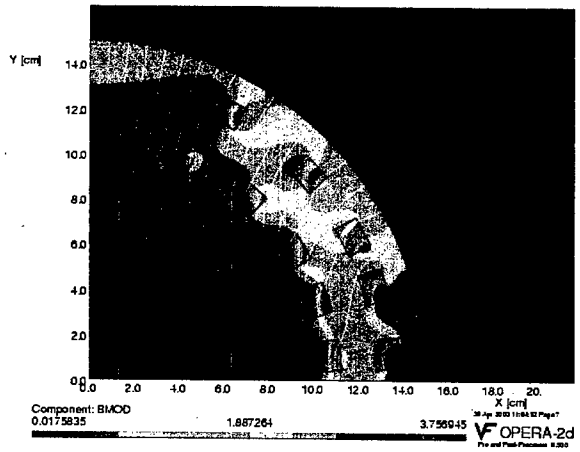


Fig. 1: Cross section of the straight magnet with the identical block size as in helical section.

The optimized coil cross section consists of five conductor blocks per quadrant in each of two layers. To minimize the design effort and the magnet cost, the coil is optimized such that all slots in the two aluminum cylinders have an identical cross section in the plane perpendicular to the helix. In addition, all blocks, except the pole block in the inner layer, consist of nine layers each of 12 turns (a total of 108 turns per block). To reduce the peak field on the conductor, the pole slot in the aluminum tube for the inner layer is filled with five instead of nominal nine layers. The above adjustment in the number of layers in a block can also be used to partially iterate the field quality without changing the detailed design even after the slots have been machined in the aluminum tube. This method was first used successfully in RHIC helical dipole magnet [2].

In a straight magnet with no axial component of the field, the field quality is expressed in terms of the normal and skew harmonics, b_n and a_n, defined in the following expansion of horizontal and vertical components of field (B_x, B_y):

$$B_y + iB_x = 10^{-4} \times B_o \sum_{n=0}^{\infty} (b_n + ia_n)[(x+iy)/R]^n$$

where x and y are the horizontal and vertical coordinates, B_o is the dipole field strength and R is the "reference radius" that is chosen to be 65 mm here. The magnitude of the nth harmonic is called c_n which is related to the skew and normal harmonic by the relation $c_n^2=a_n^2+b_n^2$. The computed normal harmonics in this straight magnet at 1.0 T and 3.0 T are given in Table 2.

Table 2: Computed values of normal harmonics (b_n) at 1 T and 3 T in a 2-d model where the coils are straight.

Harmonic No.	2	4	6	8	10
Harmonics@1T	0.0	-0.1	-0.4	-3.1	1.3
Harmonics@3T	1.4	-1.0	-0.5	-3.1	1.3

3-D MAGNETIC DESIGN

Fig. 2 shows the OPERA3d model of the coils (yoke not shown for clarity) with the magnitude of field superimposed on the surface of conductor blocks for a field of 3.12 T at the center of the magnet. The peak field, which is used in computing the quench field in Table 1, is 3.86 T.

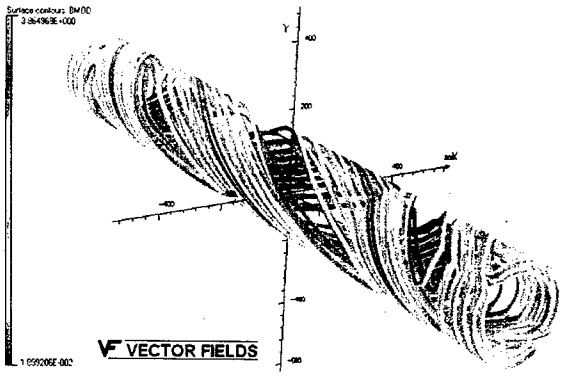


Fig. 2: OPERA3d model of the coils with the magnitude of the field superimposed on the conductor surface (the iron yoke is not shown for clarity). The field at center is 3.12 T.

The conventional 2-d field harmonics description for a straight magnet is not valid in the case of helical fields. Those harmonics become dependent on integration radius and on helical pitch. The harmonic computation, however, can still be used in describing fields in limited sense, when properly used. In Fig. 3, the sextupole harmonics are plotted as a function of axial position by integrating B_y at a radius of 65 mm. The field in the center of the magnet is 3.12 T.

The end design is based on the formalism developed by G. Morgan [4]. As compared to RHIC snake [2], we have improved the end design as (a) the helical rotation of the coil continues through the end and (b) the bend radius is significantly reduced to increase the effective field generated for a specified coil length. The prescription by Morgan minimizes harmonic content by a judicious choice of angles of the current blocks as they traverse side-to-side in the ends. An end design similar to that used in the RHIC helical magnets was also developed [5].

However, the current Morgan end design was preferred for its harmonic content and efficiency.

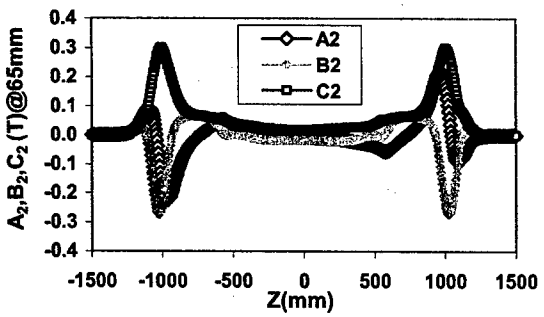


Fig. 3: The sextupole harmonic along the magnet axis computed by integrating B_y at a radius of 65 mm and using the harmonic definitions appropriate for 2-d fields.

The magnitude of the field and the field components on the magnet axis are shown in Fig. 4. The change in the magnitude of the field in the magnet center and near two ends is caused by the difference in the pitch by which the magnetic field is required to rotate.

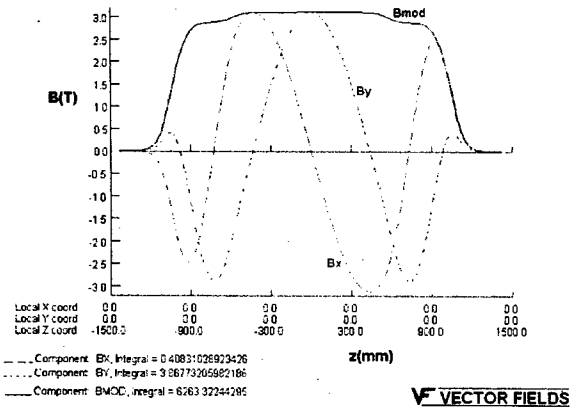


Fig. 4: The magnitude and the components of field on the magnet axis.

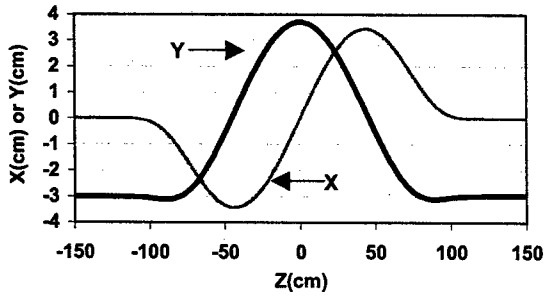


Fig. 5: The nominal horizontal and vertical position of the beam as function of axial position inside the helical magnet.

The actual beam is injected 3 cm off-axis in the horizontal plane to maximize the use of available aperture. The field inside the helical magnet must satisfy some stringent requirements. Apart from satisfying the spin dynamics requirements, the beam must exit the helical magnet with nearly the same position and angle by which it entered the magnet. This requirement was satisfied after a number of involved iterations. This iteration process benefited by the development of various in-house software packages and techniques. The final results are shown in Fig. 5 where the horizontal and vertical position of the beam is plotted as the function of axial position in the helical magnet.

The beam experiences an axial component of the field when it is away from the magnet axis. In the present design, the net integral of this axial component, as experienced by the beam along the path shown in Fig. 5, has a significant non-zero value. One way to compensate this is by introducing an additional solenoidal coil in the middle of the magnet. This is shown in Fig. 6. The other corrector windings will be placed on the same tube near the ends.

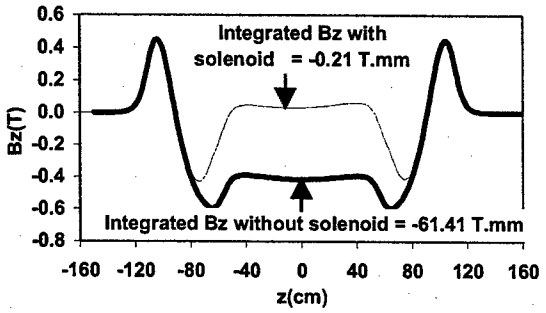


Fig. 6: The axial component of the field along the nominal beam path. The integral value is made zero with the help of a solenoidal winding on the beam tube in the middle of the magnet.

SUMMARY

The design and analysis of a partial helical snake for AGS has been completed. A number of software techniques have been developed to obtain a design that satisfies the basic requirements.

ACKNOWLEDGMENTS

We would like to thank M. Anerella, M. Harrison, P. Kovach, A. Marone and S. Plate for their constant support and encouragement.

REFERENCES

[1] T. Roser, et al., "Acceleration of Polarized Beams using a Strong Partial Siberian Snake", this conference.
[2] E. Willen, et al., "Performance Summary of the Helical Magnets for RHIC", this conference.
[3] M. Anerella, et al., "Engineering of AGS Snake coil Assembly", this conference.
[4] G. Morgan, "Private Communication".
[5] M. Okamura, et al., "Design Study of A Partial Snake for AGS", Proceedings of EPAC 2002.

ENGINEERING OF THE AGS SNAKE COIL ASSEMBLY*

M. Anerella#, R. Gupta, P. Kovach, A. Marone, S. Plate, K. Power, J. Schmalzle, E. Willen,
Brookhaven National Laboratory, Upton, NY 11973 USA

Abstract

A 30% Snake superconducting magnet is proposed to maintain polarization in the AGS proton beam, the magnetic design of which is described elsewhere [1]. The required helical coils for this magnet push the limits of the technology developed for the RHIC Snake coils. First, fields must be provided with differing pitch along the length of the magnet. To accomplish this, a new 3-D CAD system ("Pro/Engineer" from PTC), which uses parametric techniques to enable fast iterations, has been employed. Revised magnetic field calculations are then based on the output of the mechanical model. Changes are made in turn to the model on the basis of those field calculations. To ensure that accuracy is maintained, the final solid model is imported directly into the CNC machine programming software, rather than by the use of graphics translating software. Next, due to the large coil size and magnetic field, there was concern whether the structure could contain the coil forces. A finite element analysis was performed, using the 3-D model, to ensure that the stresses and deflections were acceptable. Finally, a method was developed using ultrasonic energy to improve conductor placement during coil winding, in an effort to minimize electrical shorts due to conductor misplacement, a problem that occurred in the RHIC helical coil program. Each of these activities represents a significant improvement in technology over that which was used previously for the RHIC snake coils.

A PROCESS FOR MODELING AGS SNAKE HELICAL COILS

Previously, helical coil grooves or blocks were created through a time-consuming process using CAD software. After defining the helical path of each groove, numerous cross-sections of the groove were constructed at intervals along the paths. All cross-sections were manually oriented normal to their helical path during construction. Surfaces were then lofted through these cross-sections and used to perform the cuts necessary to produce the grooves in the basic cylindrical part. This process made changes quite difficult. Where variable pitch helixes were required, separate helixes were constructed and joined.

With the use of Pro/Engineer, the process of creating variable pitch helical grooves changed dramatically. Using PTC's Advanced Surfacing module with the Pro/E Foundation module, the complex helical cuts are produced in a more efficient manner. Also, since Pro/E can easily construct variable pitch helixes (see Figure 1) the process of creating the helical paths was greatly simplified. The paths produced in this manner were parametric, meaning they could easily be changed without the need to reconstruct them as the design evolved.

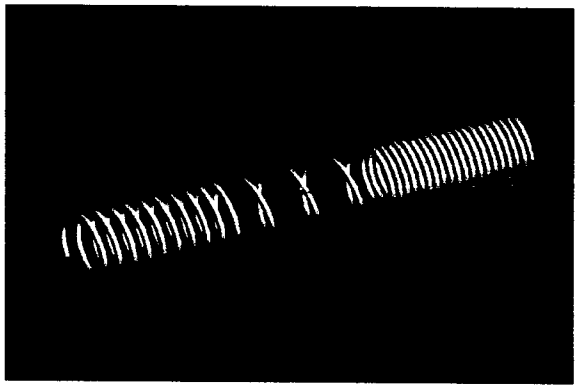


Figure 1.

A technique was developed to construct the variable pitch cuts in the tube. Helical surfaces were constructed normal to a cylindrical surface and then intersected with that surface to produce the curves that define the helical portions of the grooves' paths. Various techniques were used to develop the paths of the coil ends. The end curves along with the helical curves define the basic paths of the grooves (see Figure 2). These basic curves were then projected onto a larger cylindrical surface to produce the remaining curves required to define the variable cross-section sweeps. The completed cuts were then produced using the Pro/Engineer variable section sweep cut functionality (see figure 3).

In the coil models all grooves were defined and created in this manner. A typical, completed coil tube produced using this process is shown in Figure 4. Since most of the geometry created using this process is parametric, design changes that would normally require extensive geometry modifications could frequently be accomplished by changing a single parameter, resulting in all subsequent geometry being automatically updated. In an evolving, iterative design such as this, considerable time has been saved as a result of these capabilities.

*Work supported by the U.S. Department of Energy under Contract No. DE-AC02-98CH10886.
#mda@bnl.gov

0-7803-7738-9/03/$17.00 © 2003 IEEE

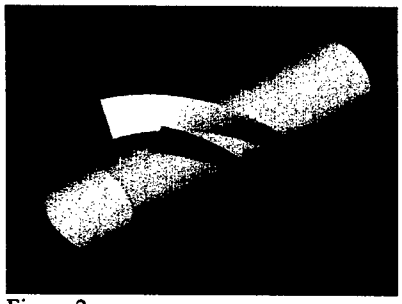


Figure 2.

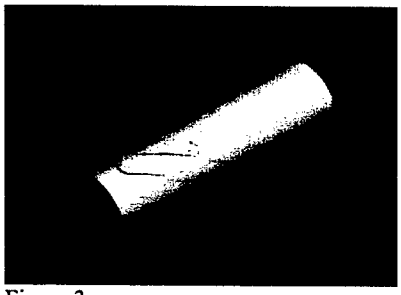


Figure 3.

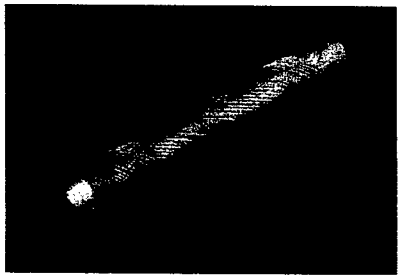


Figure 4.

Once the final magnetic and mechanical designs had been established and verified, the models of the two coil support tubes were sent electronically to the machine tool, using NC programming software and post processors developed by both PTC and MasterCam. In this way, tool paths were developed directly from the engineering surfaces, and not as interpreted by IGES or other graphics translation software. Parts were subsequently machined using a 4-axis CNC machine tool and inspected to be within 0.25 mm of desired surface position along all locations of the helices. The inner coil support tube in the machine tool is shown below in figure 5.

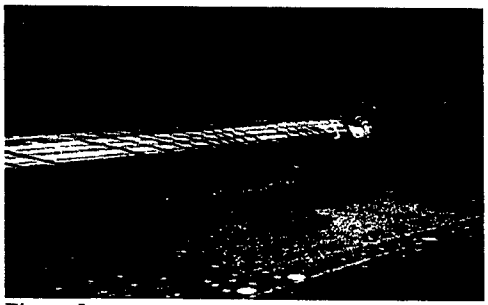


Figure 5.

AGS SNAKE COIL TUBE ANALYSIS

A three-dimensional finite element structural analysis was done on the inner and outer coil support tubes for the AGS snake magnet to determine the stress and deflections in each tube under the Lorentz forces. A 30 inch long section from the center of each tube was used for the analysis. The calculated azimuthal pressures exerted by each coil block were scaled based on the percentage of the groove depth occupied by the coil windings. The resulting pressure for each block as indicated in Table 2 was applied the full sidewall of the groove. Both ends of the tube were completely constrained and the outside diameter of the tube was constrained in the radial direction. Material was assumed to be aluminum with a Young's modulus of 10e6 psi. Results shown in figures 6 through 9 indicate a peak stress of 34000 psi for the inner tube and 13000 psi for the outer tube with maximum deflections of .0020 inches and .0016 inches respectively.

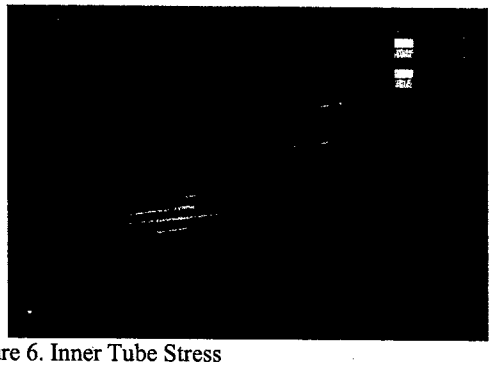


Figure 6. Inner Tube Stress

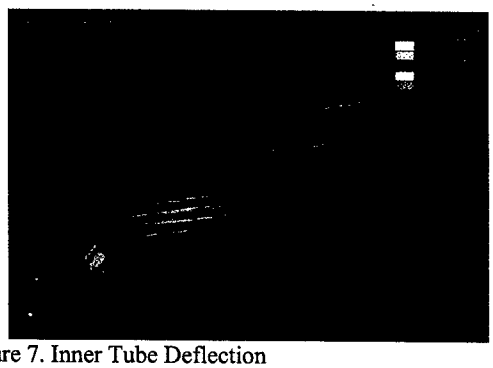


Figure 7. Inner Tube Deflection

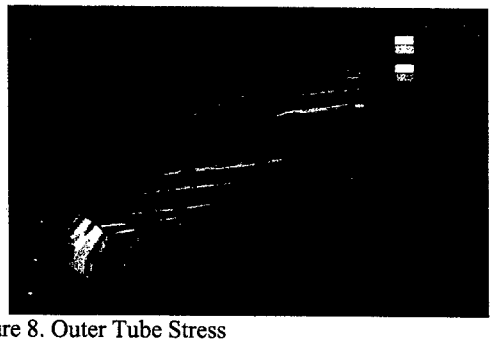


Figure 8. Outer Tube Stress

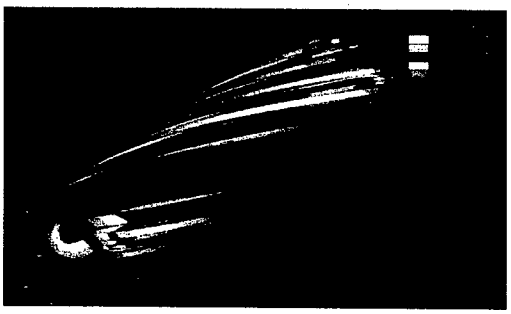


Figure 9. Outer Tube Deflection

Table 1. Tube Dimensions (in.)

Tube	ID	OD	t	slot depth
Inner	7.70	9.04	.67	.512
Outer	9.76	11.10	.67	.512

Table 2. Lorentz Force Loads

Block Number	Coil Azimuthal Pressure (psi)	Coil Block Height	Load Applied to Slot Wall (psi)
Inner			
1	350	0.422	288
2	900	0.422	742
3	1650	0.422	1360
4	2239	0.422	1845
5	2777	0.239	1296
Outer			
1	331	0.422	273
2	607	0.422	500
3	1176	0.422	969
4	1404	0.422	1157
5	1324	0.422	1091

Slot depth = 0.512 in all cases

A METHOD TO USE ULTRASONIC ENERGY TO IMPROVE CONDUCTOR PLACEMENT DURING COIL WINDING

AGS Snake coils are arranged in blocks of windings within the machined tube grooves. These winding blocks are arrays of round cable, twelve rows wide and nine layers high as shown in Figure 10. Between each vertical layer is a b-stage epoxy impregnated fiberglass substrate. After winding, the cables are compressed into the substrate during an elevated temperature and pressure cure cycle. The cure cycle seats the conductors into the substrate while the epoxy flows to eliminate voids, thereby providing suitable support for the conductors.

Inherent in the helical winding pattern and the inward shift in radial position described above is a surplus of wire placed into the grooves during winding. It was found during production of the RHIC helical coils that this excess conductor led to electrical shorts in several instances due to the resulting incorrect positioning of conductor, as is seen in Figure 11. In the AGS Snake application this problem would become more severe. Therefore, a method was developed using a 500-watt hand-held ultrasonic welder to seat the conductors into the substrate below during the winding process. This process was used after each of the nine layers of conductors was placed into the grooves. Measurements of the height of conductor layers in the block were made after each layer was wound and ultrasonically seated. Tests conducted using this method, the results of which are shown in Figure 13, indicate that each conductor layer was successfully seated 0.15 mm into the substrate. Electrical hypot testing at 2KV potential was performed afterwards, between adjacent wires and between all wires and the grounded groove, to verify that the insulation was not damaged by the ultrasonic welding process.

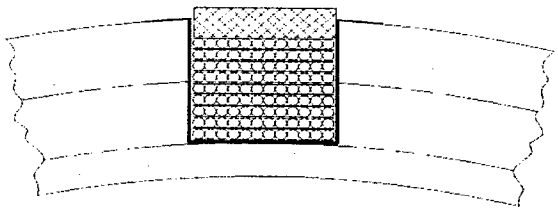


Figure 10. Coil Block cross-section

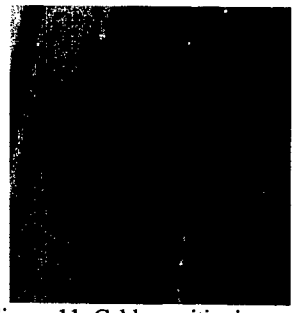


Figure 11. Cable positioning error

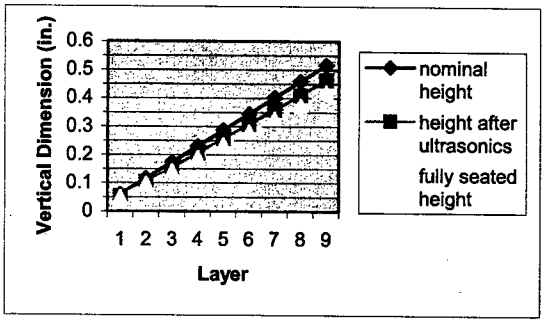


Figure 12. Comparison of Cable Seating Depths

SUMMARY

Improved methods and tools are being utilized for the design, engineering, and assembly of the AGS Snake magnet coils. These methods and tools will ensure that the coils meet all magnetic, electrical, and mechanical requirements.

REFERENCES

[1] R.Gupta, et al, "Magnetic design of a Superconducting AGS Snake," this conference.

STATUS OF THE LHC MAIN DIPOLE PRE-SERIES PRODUCTION

M. Modena, M. Bajko, M. Cornelis, P.Fessia, J. Miles, P. Pugnat, J. Rinn,
G. de Rijk, F. Savary, A. Siemko, E. Todesco, J. Vlogaert,
Accelerator Technology Division, CERN, Geneva, Switzerland

Abstract

The procurement of a pre-series of 90 Main Dipole was decided as the first step towards the series production of 1232 Arc Main Dipoles within the LHC magnet program. The pre-series production is already completed at one Contractor's site and is approaching the completion at the other two companies. Technical aspects: manufacturing tolerances, manufacturing difficulties, first evaluation on Non-Conformities appearing during production and a short overview of magnet performance are presented.

THE LHC DIPOLE "PRESERIES" AND "SERIES" CONTRACTS

The 1232 LHC Arc Dipoles (also called Main Bending Magnets or MB) will be the "backbone" of the LHC now under construction at CERN in Geneva-Switzerland. The final design R&D phase (1996-1999) was completed in Nov 1999 and subsequently orders were placed with three European Companies: (Consortium Alstom/Jeumont-F, Ansaldo Superconduttori -I, and BNN-D) for the manufacture of 30 MB cold masses (c.m.) per contract. This initial production was called the "Pre-series". In Nov 2001 CERN placed the contracts (for the same number of MB per Company) for the remaining 1158 cold masses with the same three Companies. Today, (May 2003), the status for the 6 contracts is the following: The Consortium Alstom-Jeumont has completed the Pre-series Contract (complete delivery of the 30 c.m.) and have at their premises several Series c.m. in different phases of production up to N. 46 (16th of the "Series" Contract). 7 c.m. of Pre-series have been delivered by Ansaldo Superconduttori, and production is advancing up to c.m. 12 of the Series. BNN has delivered 13 c.m. of Pre-series and has up to c.m. 10 of the Series in progress.

Although the "steady state" production rate has not yet been achieved, the Manufacturers are coming out of the "learning phase", and it is now possible to make some conclusion about the performance of the Pre-series production during start-up, about the changes adopted during this phase and about the results obtained (see also [1]).

THE PRESERIES MANUFACTURING

Design Changes

Since the signature of the Pre-series contract and the start of manufacturing activities, the design of the C.M. (including the Technical Specification) has evolved [2]. The Pre-series c.m. manufacturing was proceeding following "on line" these changes, in order to have the changes applied ASAP limiting so the number of C.M. of "first generation".

Some changes concerned the c.m. configuration "as delivered at CERN". These changes are not relevant for the magnet final configuration (as installed in the LHC). The c.m. are delivered to CERN ready to be fully test at 1.9 K, but this configuration is later changed to prepare them for the final installation in the LHC tunnel.

The most relevant changes concerned the 2D cross section in the straight part and the geometrical configuration of the conductor blocks and end spacers in the coil ends.

Since the Final Prototype phase on, the coil-straight parts have proved to be thermally extremely stable, since no training quenches originate there. The training quenches all originate in the coil heads. In particular the first and second turn of the outer layer coil have been identified as the locations where the majority of the training quenches are triggered.

In order to optimize the field margin to quench of the coils heads, it was decided to introduce an additional end spacer after the second turn of the second layer in the coil heads in both ends (Fig.1: the additional end spacers are the two marked with digits).

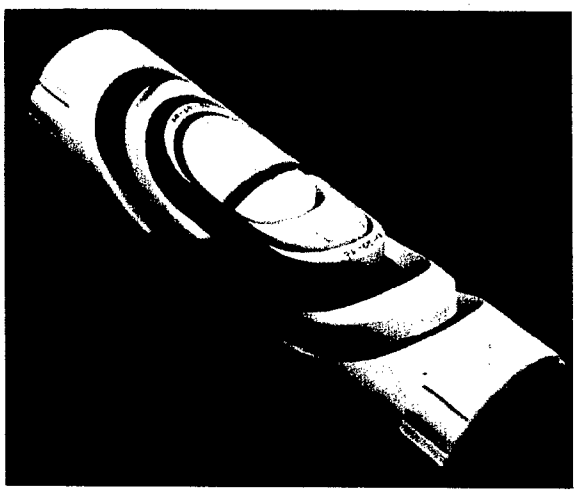


Fig. 1: Complete "final configuration" set of LHC Dipole outer layer end spacers.

A 3D electromagnetic model was used to compute the peak field along the cable width (15.1 mm) in order to follow the evolution of the field value along the path of the conductor around the spacer. Graph (Fig.2) shows the peak field in the first and second turn of the second layer before and after introducing of the additional spacer, which separates the first and second turn from the third.

The computed effects of the change are clearly visible: the peak field experienced by the 1st and 2nd turn

0-7803-7738-9/03/$17.00 © 2003 IEEE

decreases as soon as the 2nd cable is separated from the 3rd, starting from 25 mm inside the head.

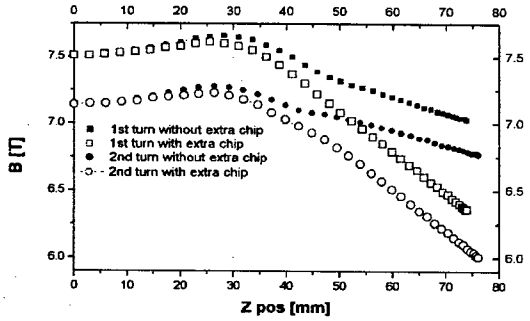


Fig. 2: The peak field in the first and second cable of the second layer with and without the extra end spacer.

The peak field reduction on the apex of the turn is about 0.6 T. With the 3D model it was possible to verify that this change in conductor position did not significantly (<0.1T) increased the field on any other conductor of the coil.

Thanks to this modification it was possible to achieve better compaction of the cable stack in the heads, resulting in a significant reduction in the number of training quenches, as will be presented below.

Corrective actions following indication from magnetic field quality measurements

At the beginning of the pre-series production, a too high value of b3 and b5 was observed [3]. A corrective action was taken based on the measurement of 9 collared coils at 300 K and 2 cryomagnets. Due to the organization of the production, where some components are assembled in parallel, the corrective action was implemented on the 30th produced magnet of the pre-series. The action consists of a small modification on the copper wedge profile (maximum 0.4 mm) of the inner layer, keeping the same overall shape of the coil to avoid any change in the adjacent collared coil components nor coil manufacturing tooling. The change was aiming at maintaining the same value of the main field, whilst reducing the b3 and b5 [3]. The effect on main field was in good agreement with simulation, and the correction on b3 and b5 was between 60% and 80% of what was expected. This cross-section correction has brought b3 and b5 to values that are now close to the optimal ones for beam dynamics.

Magnetic measurements policy and status

Magnetic measurements are carried out first of all at the Manufacturers premises at room temperature at two different moments during production: on the collared coil and on the completed cold mass. Measurements are performed with a 750 mm long rotating coil at 20 consecutive positions along the magnet axis to cover 15 m. The magnetic measurement is a contractual obligation and therefore all the magnets will be tested. Furthermore, special measurements have also been requested for critical cases (change of measuring device, analysis on anomalies in field quality, test of assembly procedures).

By early March 2003, 81 collared coils and 43 cold masses have been measured. Only one measurement of a c.m. was skipped for scheduling reasons at the initial stage of the pre-series production.

Magnets are measured later after cryostating at CERN at the normal operation condition (1.9 K). The present average delay between collared coil and cold test is one year (Fig.3) and the minimum reached so far is 7 months. This delay should be reduced to a few months during the full speed production.

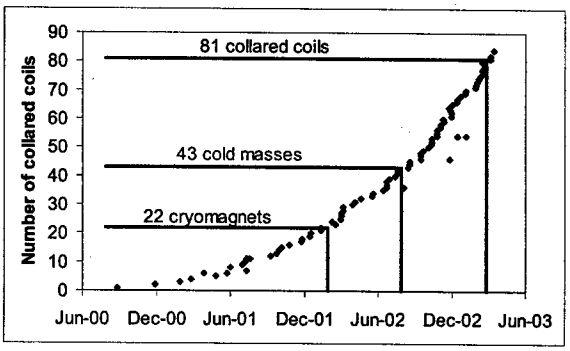


Figure 3: Measured collared coils versus time, and delay in cold mass and cryomagnet measurements.

The results of the magnetic measurements are used for two different purposes:

- the steering of the field quality towards the beam dynamics targets [4],
- the quality control of the assembly.

Their usefulness relies on the correlations between measurements at room temperature and at 1.9 K. The correlation is rather good in general and will be carefully monitored during production [5].

Assembly quality control by magnetic measurements, example of detected Non Conformities

Magnetic measurements are a powerful and economic tool to detect Non Conformities (NC) such as: assembly problems and faulty components, signatures of the tooling and trends in the production (see for instance [6] for the experience at RHIC). In over 81 collared coils, 2 cases of bad assembly procedures have been found: a double coil protection sheet (0.5 mm thick) in collared coil 2002 and a missing collaring shim in the outer layer (0.8 mm thick) in collared coil 1027. It is important to note that, in both cases the NC concerned only a short length of the magnet (1-2 meters) and therefore it would not have affected the integral field in a significant way. Nevertheless, assembly faults of this type induce discontinuities in the magnet structure that may cause performance limitations (quenches) or other serious problems. For this reason it is important to identify and correct these errors at an early

stage when the correction can still be carried out in an economic and fast way. In both cases the collared coils were decollared and the defect removed. The analysis of the measurement is based on automatic filters [7] that signal alarms whenever drift of anomalies in field quality are observed.

Outline of present status for field quality and future actions

Systematic components of skew and even normal multipoles are currently within beam dynamics targets. For b3, b5 and b7 the values are close to optimal values to within a fraction of unit, being in all cases larger than the targets. If the target values would be met at the end of the production, the machine would have a good field quality. Indeed, being at the edge of the allowed ranges, trends can drive the production to values far from the optimal ones and therefore an additional corrective action should be taken. More details are given at this Conference [5].

A proposed change is to increase the midplane insulation thickness by about 0.1 mm on both layers. This would slightly increase the pre-stress within the allowed range and would push b3, b5 and b7 down towards safer values. A negligible effect is expected on the integrated main field. A test on short models has been completed [8].

Random components are within specifications with the exception of the b3, which is presently around 70% larger than the specification. This high value of the b3 spread is due to a positive trend in the first part of the production and to the correction of the cross-section. The last 50 collared coils show a much lower value of random b3.

The integrated main field [9] exhibits a systematic difference between firms of up to 20 units. This effect can be due to a variation of coil geometry of the same order of magnitude as the tolerances (some tens of microns). The magnetic length will be fine tuned through ferromagnetic laminations in the ends to reduce these differences. The final aim is to have an installation scenario where mixing between different firms is possible.

Other important design changes

An important change proposed in the last months and now under discussion with the Manufacturers concerns an eventual revision (relaxation) of the geometric tolerances of the cold masses. These tolerances were completely re-checked and revised by all specialists concerned in their definition and achievement (i.e. accelerator physics, c.m. procurement, c.m. reception and cryostating, installation in the tunnel). If confirmed, this relaxation of tolerance would significantly help the Manufacturers to speed-up and simplifying the manufacturing process.

THERMAL PERFORMANCES OF THE FIRST PRESERIES PRODUCTION

The thermal performance (also called "quench performance") is evaluated by measuring the number of quenches necessary to reach Nominal (8.33 T) and Ultimate (9 T) magnetic field level. The provisional acceptance criteria require that the Nominal field be exceeded after no more than the 2nd quench and the Ultimate field after no more than the 7th quench. To date, 28 cryodipoles have been fully tested at CERN. All cryodipoles except one reached the Nominal field of 8.33 T after at most a 2nd quench (Fig.4). The ultimate field level after thermal cycle was reached within: 0 quenches for 15 in 28 magnets, 4 quenches for 4 magnets and 2 and 4 quenches for one magnet. A detailed presentation on the performance achieved by the first 12 cold masses can be found in [10].

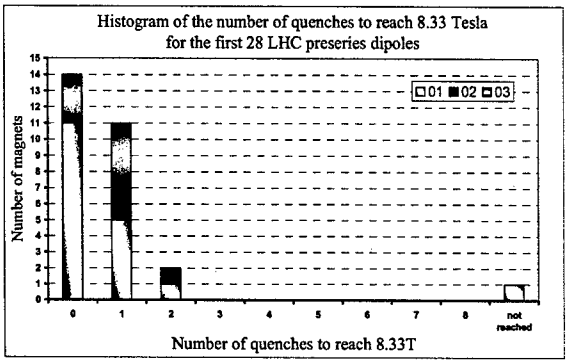


Figure 4: Thermal (quench) performance of the first 28 cryomagnets to reach Nominal field of LHC (8.33 T).

In total three c.m. have shown unrecoverable Non Conformities (appeared during tests at CERN). In one case this was due to a non conforming superconducting cable which escaped the QA controls at the cable manufacturer's premises In the other two cases the problems were affecting the electrical integrity of the c.m. In one case it was the cable insulation (a short circuit appeared during energization) and in the other case it was the integrity of the connection of the quench heaters (the element that guarantees the safe discharge of the magnet's electromagnetic energy in the case of a quench). In all three cases immediate corrective actions were taken, but these problems can be considered part of the inevitable "learning phase" of the component manufacturers (cable problem) and cold mass manufacturers (electrical problems).

REFERENCES

[1] L.Rossi, Invited talk at this Conference.
[2] M.Modena et al. PAC 2001 proceedings.
[3] E.Todesco et al, EPAC 2002 proceedings.
[4] S.Fartoukh and O.Bruning, LHC Project Report **501**.
[5] W. Scandale, et al, presented at this Conference.
[6] R. Gupta et al., MT-15 proceedings (1997) 110-3.
[7] S.Pauletta, Master Thesis, Univ. of Torino (2002).
[8] cern.ch/lhc-div-mms/MMSPAGES/MA/mid_ins.html
[9] cern.ch/lhc-div-mms/MMSPAGES/MA/bdl.html.
[10] L.Bottura et al, ASC 2002 Proceedings.

THE LHC TEST STRING: RESULTS FROM RUN 2

R.Saban, E.Blanco-Viñuela, F.Bordry, L.Bottura, D.Bozzini, C.Calzas-Rodriguez, E.Carlier, R.Denz, V.Granata, R.Herzog, Q.King, D.Milani, B.Puccio, F.Rodriguez-Mateos, R.Schmidt, L.Serio, F.Tegenfeldt, H.Thiesen, R.van Weelderen, CERN, Geneva, Switzerland

Abstract

After the commissioning and the first powering of the main circuits in autumn 2001 in its shorter version, the facility was completed to a full cell of LHC in the regular part of an arc and commissioned in July 2002. During this second run, which accumulated more than 4000 hours below 2 K, a very dense experimental program was carried-out to validate the final versions of the technical systems and design choices such as the bus-bar cables running along the magnet cold masses inside the cryostats. The program included the investigation of thermo-hydraulics of quenches, quench propagation, power converter controls and tracking between power converters. The cryogenic process dynamics were studied in length; predictive control techniques were tested and their performance assessed.

During a short shutdown starting in December 2002, the facility was stripped of all instrumentation contributing to increased heat loads and heat load measurements will be performed in a last run during the first half of 2003.

The paper describes the facility and details the results obtained during the experimental program.

THE STRING PROGRAMME

String 2 [1] was assembled in two phases starting in January 2000. It follows the final design of LHC with the cryogenic helium distribution line running alongside the magnets. During the first phase, the facility, which comprised an electrical feed box, a half-cell and an additional short straight section, was assembled using exclusively prototype components specially instrumented for the experimental programme. The three dipoles, which were added during Phase 2 [2], are machine worthy pre-series magnets. During Phase 2, 19 quenches in the dipole circuit were provoked and one training quench was observed. The dipoles were ramped to nominal current (11850 A) 15 times. No natural quench was observed in neither of the quadrupole circuits which were powered to nominal current 6 times and quenched 9 times.

VALIDATIONS AND MEASUREMENTS

Quench Propagation

The extent of the propagation in LHC-like decay times on a full cell was measured by a decay time constant of 100 s like for the dipole circuit in an LHC arc; for this, the power converter was programmed to continue supplying an exponentially decaying current after the first magnet was quenched. This was possible because of the robustness of the converter current loop (RST): the time constant during the event varied from 1280 s to 200 s. The extent of the propagation confirms that it will be limited to a full cell.

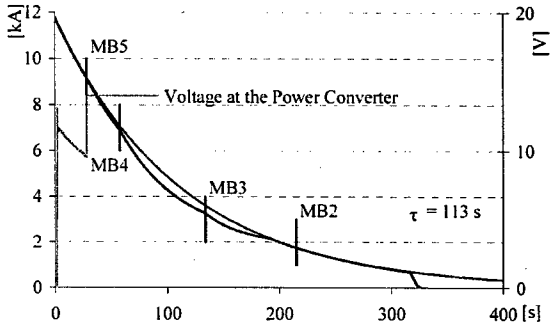


Figure 1: Quench propagation experiment. The quench heaters were fired on the last dipole (MB6) and helium forced towards the neighbouring dipoles. The propagation stops before the last dipole (MB1).

Pressure in the Cold Mass Following a Quench

The quench recovery procedure using one (out of the two) relief valve confirmed that a complete cell could be discharged within the pressure design limits of the helium vessels.

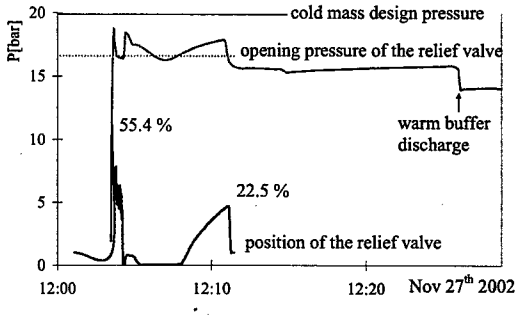


Figure 2: Evolution of the pressure in the cold mass after a full house quench. The quench heaters were fired on all dipole and quadrupole magnets simultaneously.

Cryogenic Process Control

The highly non-linear nature of the 1.9 K cooling loop dynamics, which exhibits variable time length delay and inverse response, required the use of a more advanced regulator than the standard PID controller to maintain the magnet temperatures at the desired value.

The tuning of the PID controller was done with the objective of avoiding undesired oscillations and

0-7803-7738-9/03/$17.00 © 2003 IEEE

instabilities. The PID performance was observed to be inefficient in terms of cancellation and recovery of magnet temperature perturbations from varying heat loads.

The implementation of a hybrid model-based predictive controller (MBPC) with an internal state estimator [3] optimized the heat load effect treatment in both excursion and recovery of the magnet temperatures. The use of an estimator gave additional valuable information on the unmeasured He II mass present in the heat exchanger and the dynamic heat load at any moment. Also, the use of an explicit model of the process allowed the controller to adapt itself to the new heat load condition increasing the robustness of the regulator.

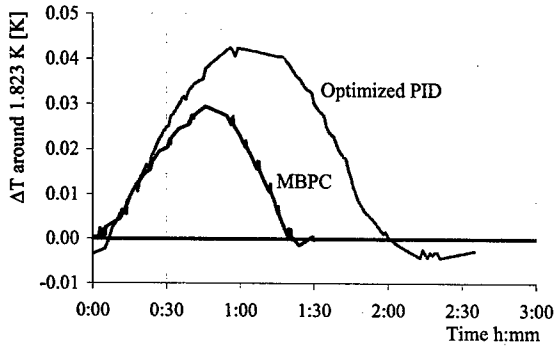


Figure 3: Hybrid model-based predictive controller versus optimized PID control with a 0.2 W/m heat load

In Figure 3, the performance of the MBPC controller is compared with an optimized PID when a heat load of 0.2 W/m was applied in a step. In both cases the unavoidable temperature excursion is seen but MBPC cancels it earlier and also recovers more rapidly.

Bus bar cables

One 42 × 600 A and three 3 × 6 kA superconducting cables were installed in a 50 mm Ø tube attached to the shrinking cylinders of the main dipole and quadrupole magnets to evaluate similar configurations in the LHC. There, the cables will conduct current to corrector magnets next to the quadrupoles and to individually powered quadrupoles in the insertion regions.

In a first series of tests the currents in six out of the nine 6 kA conductors and six 600 A conductors were ramped to nominal current while the voltage on the conductors was continuously monitored for spikes hinting at conductor movement. It was feared that Lorentz forces between conductors in neighbouring cables could lead to conductor movement and subsequent quenches, but during five ramps to maximal current no such event was observed.

Measurements on the expansion of a normal zone after a quench triggered by a spot heater revealed that the behaviour of the cables in the limited space inside the tubes is similar to the behaviour of such cables in a cryostat [4, 5]. However, transversal quench propagation to conductors in adjacent cables was observed for 6 kA cables, indicating that the heating of a normal zone does substantially change the helium environment in the tube.

The extensive tests (43 provoked quenches) on the installed cables gave us final and positive results for the design, installation and quench protection of the cables in the LHC machine.

EMC of all the components (power converters, quench detection, PLCs, signal conditioners)

A kicker power supply and a dummy load were installed in the area crowded with power converters, electronics for the interlock system, the quench protection, the control of the switches, the signal conditioning and the cryogenic process control. During a one week run, kicker pulses of varying number and voltage were fired and the performance of the other systems was monitored to detect eventual perturbations. The tests performed with one generator at full voltage in the String represent correctly (di/dt and dv/dt) the operational conditions of 15 generators at injection, which is the most critical situation in terms of signal to noise ratio. This experiment confirmed the electromagnetic compatibility of all the equipment and their interconnections.

Tracking between the three main circuits

The main result of the tracking measurement campaign is reported in Figure 4 which show the instantaneous value of the ratio B_2/B_1 obtained for all runs performed as compared to maximum bounds for the feed-back to lock.

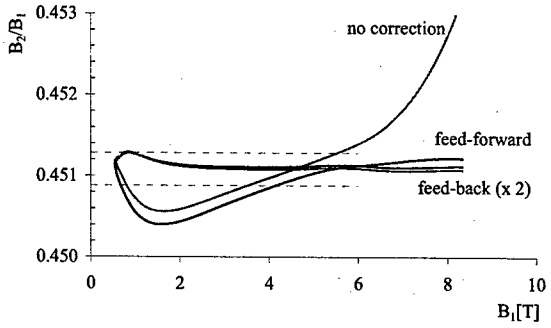


Figure 4: The ratio B_2/B_1 for the focussing quadrupole plotted as a function of the dipole field along the reference current ramp.

The curve marked *feed-forward* uses the knowledge of the transfer functions as established on the test benches. This correction compensates well the difference in the high field saturation, but leaves a substantial deviation at low and intermediate field. This deviation is mostly due to a systematic measurement artefact. Irrespective of its nature however, and because this is a systematic effect,

the deviation is well corrected by iteration on the measured B_2/B_1 ratio as shown by the curves marked *feed-back*. In this case the tracking error on the B_2/B_1 ratio is definitely inside the range to be achieved for the tune feed-back system to lock, and in fact quite close to the range necessary to maintain the maximum allowed tune variation to within 3×10^{-3} as dictated by the nominal LHC performance.

The optimised current ramp was sent unchanged in a second cycle, with the aim to verify the reproducibility of the ramp. The result demonstrates that the reproducibility is excellent.

Quench protection

String 2 Phase 2 offered the unique occasion to test, for the first time, an LHC like quench protection system on the scale of an LHC full cell. During installation, commissioning and operation a variety of subjects like feasibility of the installation, required functionality as well as reliability and maintainability of the system were critically revised. The outcome confirmed the validity of the basic designs and the functionality of the system. Nevertheless a number of minor problems were identified and already successfully implemented into the latest designs for the LHC quench protection system. For example, the improved designs of quench detection boards and acquisition and monitoring controllers now offer an enhanced functionality and require a significantly lower level of maintenance than those currently installed

The values chosen for thresholds and discrimination time for the main bus-bars, the corrector magnets and their connecting bus bars were sound and only needed little corrections over the commissioning phase. They confirmed the calculations of the quench velocities.

COMMISSIONING

Procedures, which are expected to become the basis for the commissioning of the LHC sectors, were developed and tested for both the cryogenic system and the electrical system as a whole.

The tests preceding the powering of the circuits [6, 7] involved two phases: during the first phase the magnets and the power converters were not electrically connected and were tested separately. The former, involving the magnet side, were aimed at electrical insulation tests at different temperature levels during the cool down. Before the two sides were electrically connected, they were linked together by the interlock system (Powering Interlock System in LHC); the power converters were turned on and tested on a short circuit while the quench protection system was fired to verify the sequence of events. This was repeated for every circuit before the power converter was connected to the current leads on the electrical feed box. While this gradual powering is safe, it proves to be lengthy.

The final tuning of the systems took place following observation of faults induced by the operation in unison with other systems (e.g. false quench signals on the global detectors during converter turn-on and ramp-up).

The optimisation of operation by adapting procedures to particular cases also took place during this phase (e.g. avoiding full quench recovery procedures when auxiliary circuits trip).

The importance of the timing of the commissioning procedures and their dependence on temperature did not go unnoticed: the commissioning of the quench detectors across the superconducting part (few tens cm) of a current lead was found to be very tricky (!) after the lead had been cooled down.

A better understanding of the issues related to operating a particular system and observing the effects it can have on other systems took place during this phase. This stimulated the exchange of information between specialists.

CONCLUSIONS

The String has proven to be a valuable test bed where the validations of the technical systems required before series production and installation could be found. It is the experimental setup where the interplay of the different technical systems could be observed and a variety of measurements carried-out.

It is thanks to the String programme that the actors who will be involved in the hardware commissioning of LHC approach this difficult task with self confidence and enthusiasm.

REFERENCES

[1] The LHC Prototype Full-Cell: Design Study, LHC Project Report 170, March 1998.

[2] R.Saban et al., First Results and Status of the LHC Test String 2, EPAC '02, June 2002, Paris, France.

[3] E. Blanco et al. Nonlinear Predictive Control in the LHC Accelerator, ADCHEM 03: International Symposium on Advanced Control of Chemical Processes.

[4] R. Herzog, M. Calvi and F. Sonnemann: Quench propagation and heating in the superconducting 600 A auxiliary busbars of the LHC Advances in Cryogenic Engineering, Vol. 47 p575.

[5] R. Herzog, M. Calvi, F. Sonnemann and J.M. Pelegring-Carcelen: Quench propagation in the superconducting 6 kA flexible busbars of the LHC, Advances in Cryogenic Engineering, Vol. 47 p583.

[6] R.Saban et al., First Powering of the LHC Test String 2, 17th International Conference on Magnet Technology, September 2001, Geneva, Switzerland.

[7] R. Saban, What Have We Learnt from the String Programme (Design, Assembly, Experiments And Measurements)? Workshop on LHC Performance, Chamonix, March 2003.

PERFORMANCE OF THE FIRST LHC MAIN QUADRUPOLES MADE IN INDUSTRY

R. Burgmer, H.-U. Klein, D. Krischel, B. Schellong, P. Schmidt, T. Stephani,
ACCEL Instruments GmbH, Bergisch-Gladbach, Germany
M. Durante, M. Peyrot, J.-M. Rifflet, F. Simon, CEA-Saclay, France
K.-M. Schirm, T. Tortschanoff, W. Venturini-Delsolaro, CERN, Geneva, Switzerland

Abstract

After the creation of a new dedicated factory and a period of technology transfer, ACCEL Instruments has constructed and delivered the first LHC main quadrupole magnets to CERN. The design of these magnets had been the subject of a close collaboration between CEA-Saclay and CERN. Thus, CEA ensures also the technology follow-up for the fabrication of 400 quadrupole magnets and their cold masses. The two quadrupoles delivered to CERN were bare magnets, i.e. magnets not integrated into their cold masses. The purpose was to verify their performance before fabricating full cold masses. The two magnets were tested at 1.9 K in a vertical cryostat at CERN. For both magnets the current could be ramped up to well above their nominal level before a quench occurred. The second powering provoked on one of the magnets a quench at the ultimate level of excitation and in the other magnet no quench, even after the ultimate current value had been well exceeded. The field quality measurements, as far as possible in the vertical cryostat, confirmed the multipole content already found during the warm field measurements made in the factory.

INTRODUCTION

The development and prototyping of the main quadrupole magnets for the LHC has been treated in earlier publications. [1], [2], [3]. It had been the subject of a close collaboration between CERN and CEA-Saclay in France. After the signature of the contract with the German Company ACCEL Instruments GmbH, CEA ensures together with CERN the technology transfer and follow up of the series fabrication in a newly created factory in Troisdorf near Bonn.

Before integrating any of the main quadrupoles into their cold masses, two bare magnets, fabricated according to the factory established procedures, were shipped to CERN for undergoing training and field quality measurements in a dedicated test facility. These measurements were thought to provide further confirmation of the soundness of design, which had already been shown by the performance of the prototypes constructed by CEA-Saclay and tested in both laboratories, CERN and CEA [4], [5]..

DESIGN FEATURES

The main parameters of the twin aperture quadrupoles are recalled in table 1.

Table 1:Main parameters of the LHC quadrupole

	Value	Unit
Injection field gradient (0.45 TeV beam energy)	14.5	T/m
Nominal field gradient (7 TeV beam energy)	223	T/m
Nominal current	11'870	A
Operating temperature	1.9	K
Magnetic length at 1.9 K	3.1	m
Stored energy (both apertures) at 7 TeV	0.79	MJ
Ultimate operational field gradient	241	T/m
Gradient at short sample field limit	278	T/m
Distance between aperture axis at 1.9 K	194.00	mm
Inner coil diameter at 293 K	56.00	mm
Outer coil diameter at 293 K	118.60	mm

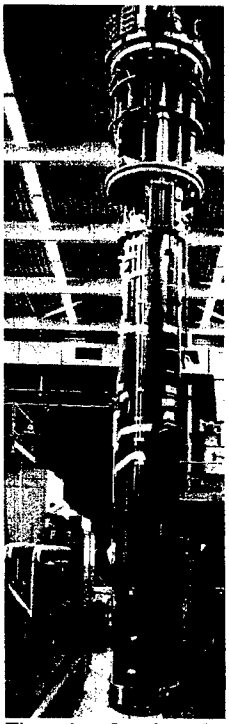


Fig. 1: Quadrupole suspended before being inserted into its vertical test cryostat.

Contrary to the main LHC dipole magnets, the electromagnetic forces are taken only by the coil collaring system and no pre-stressing function is provided by the yoke. ACCEL has made a number of computations and mock-up tests to simplify the collar keying system from a three piece one, as used for the prototypes, to a single piece keying. ACCEL could show that with this simplified way of keying no degradation, i.e. overstressing during the keying in the press and no loss of final pre-stress has to be expected.

While ACCEL took over the concept of most of the prototype tools they developed an own highly efficient and versatile collaring press. In its final configuration the bare quadrupole magnet together with the corrector magnets on both ends of it, are assembled inside an inertia tube which functions as the helium vessel and as the stiffening and alignment element.

0-7803-7738-9/03/$17.00 © 2003 IEEE

For transporting and testing the bare magnets, dedicated structures had to be used which ensured the solidity of the magnet, both in vertical and horizontal position and allowed to suspend it into the vertical test cryostat at CERN.

The first of the two magnets was delivered to CERN in July 2002 and was tested in August. The second one arrived in August and was tested in October 2002.

QUENCH PERFORMANCE

First quadrupole, MQ001

The first quench of the MQ001 occurred at 12631A, corresponding to a gradient of 237 T/m. Analysis of the voltage tracks showed unambiguously that the quench had been initiated in one of the external cables and not in the coils. In the light of this, it was decided to modify the test program by reducing the current ramp rate of the next training quench. That was meant to give hints on the quench mechanism, as the first quench had occurred in a very low field region, an anomalous location due to its high superconductor margin. The second current ramp was at 2 A/s and the magnet quenched at 12808 A, corresponding to 240.8 T/m. The third current ramp was at 1 A/s and the quench current was 12758 A, 239.9 T/m. All the three quenches were localized in the same spot of cable, between the outermost voltage tap and the current lead end.

In case of overheating of the bottom end of the vapour cooled current leads, a slower ramp should have lowered the quench current. On the contrary, a slight improvement of the quench current was observed. The possibility of cable degradation was put to the test by performing quenches at 4.5 K. It appeared that the critical current of the cable was not degraded, and this excluded one possible cause of the quenches at 1.9 K in the external cables. Actually, from the available evidence it was not possible to conclude whether the quench origin was in the current lead or in the cable itself. Moreover, due to the geometrical constraints the lower end of the current leads had been slightly modified. Therefore, for future tests, it was decided to add an intermediate voltage tap to the quench detection setup.

Second quadrupole MQ002

At the first current ramp to quench, at 10 A/s, there was a quench at 12476 A. It was localized in the series connection between the two apertures. The second current ramp was set at 20 A/s and the magnet reached the ultimate current of 12860 A without quenching. Then the current could be kept constant at the ultimate value for 300 s, which allowed excluding joule heating as the source of the first quench. Again the only quench had occurred outside the magnet coils. After a thermal cycle to room temperature, the magnet reached again the ultimate current without quenching, showing 100% memory effect. As in the LHC the MQ magnets will have to withstand current ramp rates up to 400 A/s, this mode of functioning was also tested on the MQ002. For both decay rates of up to 400 A/s no quench occurred between 50 and 12850 A. Finally, the quench current at 4.5 K was 11439 A, which compares well with the 11446 A at 4.43 K of the MQ001.

MAGNETIC MEASUREMENTS

The set up for magnetic measurements on MQ002 did not cover all the magnetic length of the main quadrupole. Therefore all the measurements hereafter are representative only of the 2D field quality in the straight part of the magnet.

The magnetic field was measured, after training, as a function of the magnet current between 50 A and 12500 A. As customary, geometric values are averages of the ramp up and down branches of the main hysteresis loops, evaluated at 5000 A.

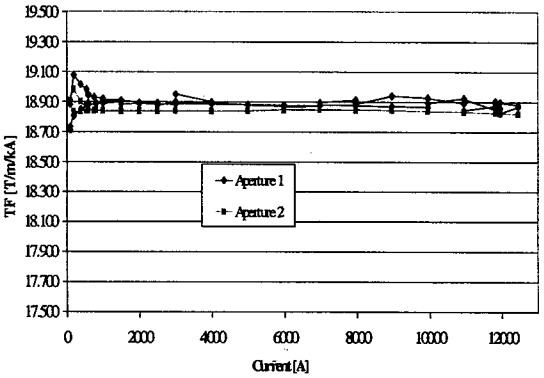


Fig. 2: Quadrupole transfer function

The values at injection current 760 A and at 12500 A are representative of the persistent currents and of the iron saturation contributions respectively. All measurements are corrected for feed-down by zeroing the dipolar component of the magnetic field.

-The measured quadrupole transfer function is shown in Fig. 2.

-The multipole components at 5000 A and at collision current are given in Tables 2 and 3.

- The variation of the normal dodeca-pole component, b6, with the current is shown in Fig.3.

CONCLUSIONS

Quench performance

The power performance of the two MQ magnets was excellent, both having reached the ultimate gradient without any training quench. The cable critical current at 4.5 K was found to be comparable to the corresponding values measured in prototypes.

After thermal cycle the current of the MQ 002 magnet could be ramped to the ultimate value without quench. The magnet withstood current ramp rates up to 400A/s at 12500 A without quenching.

Table 2: Multipole components in terms of relative field errors at 17 mm in left aperture

MQ_002	FIRST RUN		SECOND RUN	
Aperture1	5 kA	11870 A	5 kA	11750 A
b3	0.91	1.25	0.97	1.26
a3	2.50	2.42	2.70	2.49
b4	0.10	0.09	0.07	0.06
a4	-0.14	-0.02	-0.23	-0.08
b5	-0.42	-0.17	-0.62	-0.27
a5	1.16	1.07	1.14	1.08
b6	3.35	3.48	3.33	3.48
a6	0.34	0.24	0.39	0.29
b7	0.25	0.29	0.28	0.29
a7	0.14	0.13	0.11	0.13
b8	0.05	0.06	0.05	0.06
a8	-0.09	-0.04	-0.13	-0.05
b9	-0.02	0.00	-0.03	0.00
a9	0.09	0.07	0.09	0.08
b10	-0.13	-0.11	-0.13	-0.12
a10	0.01	-0.01	0.01	-0.01
b11	0.02	0.02	0.03	0.03
a11	0.02	0.02	0.02	0.02
b12	-0.01	-0.01	-0.01	-0.01
a12	-0.01	-0.01	-0.01	-0.01
b13	-0.01	-0.01	-0.02	-0.01
a13	0.01	0.01	0.01	0.00
b14	-0.18	-0.18	-0.18	-0.18
a14	-0.01	-0.01	-0.01	-0.02
b15	0.00	0.00	0.00	0.00
a15	0.00	0.00	0.00	0.00

Table 3: Multipole components in terms of relative field errors at 17 mm in right aperture

MQ_002	FIRST RUN		SECOND RUN	
Aperture 2	5 kA	11870 A	5 kA	11750 A
b3	-0.99	-1.20	0.94	1.18
a3	-1.30	-1.05	1.46	1.12
b4	1.31	0.93	1.52	1.05
a4	0.33	0.13	0.71	0.30
b5	0.20	0.36	-0.06	-0.30
a5	0.20	0.14	-0.11	-0.13
b6	3.59	3.45	3.68	3.53
a6	0.35	0.23	0.49	0.29
b7	-0.11	-0.14	0.07	0.12
a7	-0.08	-0.01	0.09	0.03
b8	-0.09	-0.12	-0.08	-0.11
a8	0.11	0.07	0.12	0.07
b9	-0.04	-0.01	0.07	0.03
a9	0.11	0.10	-0.11	-0.10
b10	-0.05	-0.06	-0.04	-0.05
a10	-0.02	-0.04	0.00	-0.03
b11	-0.01	-0.02	0.01	0.02
a11	0.01	0.02	-0.01	-0.02
b12	0.00	0.00	0.00	0.00
a12	0.01	0.00	0.01	0.00
b13	0.00	0.00	0.00	0.00
a13	0.02	0.01	-0.02	-0.02
b14	-0.17	-0.18	-0.17	-0.17
a14	-0.01	0.00	-0.01	-0.01
b15	0.00	0.00	0.00	0.00
a15	0.00	0.00	-0.01	0.00

Field quality

In general the field multipole components are small. The first allowed term, b6, the dodecapole, has a value of 3.5 units, very near to the value needed to compensate the effect of persistent currents at injection.

The results of these tests provide the confidence that the design is sound and the series fabrication in the new factory of ACCEL Instruments can be ramped up in order to fabricate all 400 main quadrupole magnets of LHC.

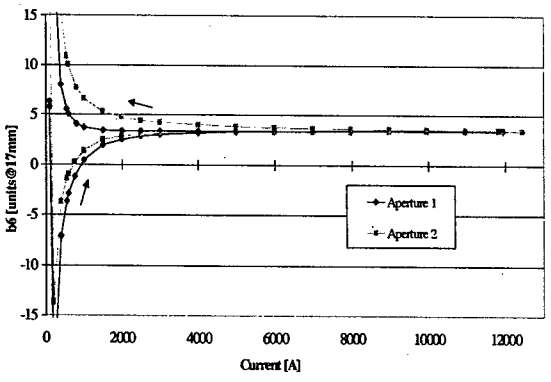


Fig. 3: Normal dodeca-pole in MQ002, b6, versus current

REFERENCES

[1] T. Tortschanoff V. Parma, P. Rohmig, M. Peyrot, J.-M. Rifflet, P. Védrine, D. Vincent, "The Short Straight Sections for the LHC", Proc. PAC97 Conference, Vancouver, Canada. 1997.

[2] M. Peyrot, J.-M. Rifflet, F. Simon, T. Tortschanoff, P. Vedrine, "Construction of the New Prototype of Main Quadrupole Cold Masses for the Arc Short Straight Sections of LHC", Proc. MT-16, Ponte Vedra Beach, Florida, USA, 1999.

[3] L. Nielsen, V. Parma, T. Renaglia, P. Rohmig T. Tortschanoff, J.-B. Bergot, Ph. Dambre, E. Roy, D. Vincent, M. Peyrot, J.-M. Rifflet, F. Simon, "A Modular Design for the 56 Variants of the Short Straight Section in the Arcs of the Large Hadron Collider (LHC)", Proc. EPAC-2000, Vienna, 2000.

[4] T. Tortschanoff, J. Billan, L. Bottura, V. Remondino, A. Siemko, M. Peyrot, J.M. Rifflet, F. Simon, "Performance of Series-design Prototype Main Quadrupoles for the LHC", Proc. EPAC-2000, Vienna, 2000.

[5] J. Billan, V. Remondino, A. Siemko, T. Tortschanoff, M. Peyrot, J.-M. Rifflet, F. Simon, "Performance of prototypes and start up of series fabrication of the LHC arc quadrupoles," Proc. PAC2001 Conference, Chicago, Illinois, USA. 2001.

INFLUENCE OF AZIMUTHAL COIL SIZE ON SKEW MULTIPOLES IN THE LHC DIPOLES

Iouri Vanenkov, Christine Vollinger, CERN, Accelerator Technology Division, Geneva, Switzerland

Abstract

The field quality in superconducting accelerator magnets is strongly influenced by the azimuthal dimension of the superconducting coil. Asymmetries between the upper and lower poles steer skew harmonics that can endanger the beam dynamics stability. We present dimensional measurements of a large number of coils that have been carried out in one of the three manufacturers of the main LHC dipoles. A magneto-static model is then used to work out the influence of coil non-nominalites on field harmonics. Comparison to magnetic measurements carried out at room temperature shows that skew harmonics can be partly traced back to azimuthal coil dimensions. We focus on harmonics, which are more critical with respect to the beam dynamics limits (a_2 and a_4). Finally some strategies are presented, like the sorting of individual coil poles in order to reduce the detrimental effects on these multipoles.

INTRODUCTION

The Large Hadron Collider (LHC), a superconducting proton-proton accelerator, is made of about 8400 superconducting magnet units of different types. Among them, one has 1232 main dipoles, whose 15 m long coils are held in place by austenitic stainless steel collars. The collars are surrounded by an iron yoke, which is contained in a stainless steel shrinking cylinder [1].

The magnetic field components integrated along the dipole length are described through the two-dimensional multipolar expansion at a reference radius R_{ref}:

$$B_y + iB_x = B_1 \sum_n (b_n + ia_n) \frac{(x+iy)^{n-1}}{R_{ref}^{n-1}}, \quad (1)$$

where R_{ref} = 17 mm and the b_n and a_n are the multipolar coefficients. They are usually expressed in 10^{-4} units relative to the main field B_1. Even normal multipoles b_2, b_4, ... and skew components $a_2, a_3, a_4, \ldots$ arise due to left-right and top-bottom asymmetries of the coil geometry with respect to the aperture centre. Since an extremely high field quality is needed for the storage of a particle beam for many hours, the relative deviation from the ideal field in the aperture of a magnet should be of the order of 10^{-4} or less [2]. In superconducting magnets, the field quality is determined by the coil arrangement and the position of the conductors. Manufacturing tolerances of the order of 0.05 mm result in a non-nominal azimuthal coil size, thus producing an up/down asymmetry, e.g., a shift and a tilt of the magnet mid-plane. In the warm magnetic measurements, such a mid-plane shift can be seen as a non-zero value of the skew quadrupole a_2 whereas a tilt produces a skew sextupole a_3. While there is a larger margin for a_3, the LHC beam dynamic limits are rather tight for a_2: therefore, we restrict our analysis on this multipole. Measured data on coils sizes show that a shift of the mid-plane of up to 0.15 mm is to be expected. One possibility of reducing the overall spread of the coil sizes is a sorting of the poles to minimize the up/down asymmetry. In this paper we first present the statistical analysis carried out on the mechanical and magnetic measurements data taken on the pre-series dipoles of one manufacturer [3,4]. We then discuss a magneto-static model used to give the dependence of a_2 on the mid-plane shift and the correlations between mechanical and magnetic measurements. Finally, results from optimized coil sizes that could be achieved by applying the sorting algorithm are presented.

AZIMUTHAL COIL SIZE MEASUREMENTS

The measurements of the azimuthal coil sizes and of the equivalent modulus of elasticity give important information for the analysis of the dipole field quality. The size of the coil could vary due to dimensional tolerances of the individual coil components (see for instance [5] for copper wedges analysis) or tolerances in the tooling and they are measured with a precision of ± 0.01 mm. At the dipole manufacturers, coils are measured by means of the so-called Pole Measuring Machines (PMM). Since each one of three dipole contractors is equipped with a different type of PMM, no direct cross-analysis is carried out. However, during the dipole manufacturing each coil layer or pole is measured in several longitudinal positions delivering a large amount of raw data, which is treated in a standard way for all the companies before it is transferred into the CERN database.

In order to standardize the data post-processing and speedup the data exchange between companies and CERN, the Collared Coil Database software package (CCD) was developed at CERN and installed at each dipole manufacturer site. The core of CCD package is a database (MS Access) that includes a facility to exchange the data with CERN via e-mail. For each PMM, the package includes a post-processor application (LabVIEW 6i), which treats the raw data on coil size measurements and does an automated upload of the treated data into the database. The CCD package also includes a data-viewer (LabVIEW 6i) that allows a follow-up to be carried out by the project engineers either at the companies or at CERN. The viewer also includes an optimization tool to do a

0-7803-7738-9/03/$17.00 © 2003 IEEE

pairing of the magnet poles for a minimization of the unwanted up/down asymmetry.

The coil size measurements of the pre-series magnets showed that due to the tolerances on the coil components, mostly the insulation of the cable, the coil size varies in the range of +/- 0.2 mm (see fig.1). This coil size variation is random and thus can induce large differences in the azimuthal dimensions of the upper and lower pole within one aperture. As an example, in figure 1 the inner layer coil size in the collared coil no. 15 shows a difference between the size of the upper pole (pole 1) and the lower pole size (pole 2) of 0.15 mm! A similar bad case is observed for the collared coil no. 17. In this graph, each point is the average of coils size measured in 18 positions along the coil, 4 points is a set of poles that belong to one collared coil.

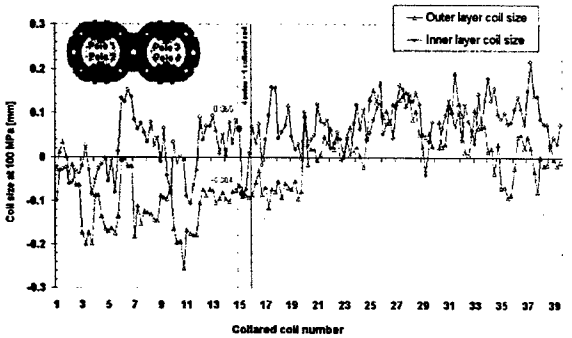


Figure 1: Azimuthal coil size deviation with respect to the nominal size for a set of 40 magnets built by manufacturer 1.

MAGNETIC MEASUREMENTS

All the LHC dipoles will be tested for magnetic field quality at 300 K: a first test is carried out after the collaring and a second one after the yoke assembly is completed and the outer cylinder welded. The magnetic measurement of the collared coils is an essential tool for the control and the steering of the dipole field quality during the mass production [4]. Results are screened to detect assembly errors and are then compared to beam dynamics targets to check if corrective actions are necessary.

Beam dynamics targets are based on the integrated values along the magnet axis, since local variations are negligible for circulating particles. These values are given in terms of systematic (average over 1232 dipoles) and random (standard deviation over 1232 dipoles). The systematic must fit within a range, and the random must be lower than the target. The values are summarized in Table 1.

One can observe that random components are within targets in all cases, a_2 being the case in which we are closer to the tolerance. Moreover, the measured random of a_2 (1.9 units) in the aperture 1 of the pre-series magnets of manufacturer 1 is larger then the random target. Therefore, for this company the analysis of the influence of coil size tolerances on the skew quadrupole are carried out and an improvement is proposed.

Table 1: Measured skew multipoles versus beam dynamics targets.

	a_2	a_3	a_4
Random target	1.6	0.7	0.50
Random measured	1.3	0.4	0.28
Systematic Max	1.3	1.9	0.13
Systematic Min	-0.8	-1.6	-0.16
Systematic Meas.	0.0	-0.1	0.02

MAGNETOSTATIC MODEL

The coils of the LHC main dipole magnet are wound of a Rutherford type cable, containing 28 and 36 wires on the inner and the outer coil layer, respectively. Between the coil blocks, copper wedges are inserted to produce a sufficient field quality in the magnet aperture, since the trapezoidal shape of the cable is not sufficient to build a circular inner alignment, when wound on a mandrel (see fig. 2). Compared to the superconducting cable and the cable insulation, these wedges are rather rigid and define the coil cross-section. At the same time, the outer coil shape is determined by the inner contour of the collars. Although collar deformations take place, since they are up/down symmetric and they do not contribute to skew multipoles, we can neglect them for our analysis.

The influence of different azimuthal coil sizes on skew multipoles has been modelled applying the above quoted approximations using a magneto-static code [6]. Due to the hypothesis on the rigidity of the collars, points 1-4 in fig. 2 are fixed, and the inner and the outer width of the cable (W_i and W_o) are varied to produce a difference between the upper and lower pole azimuthal size. The shape of the copper wedges is also preserved.

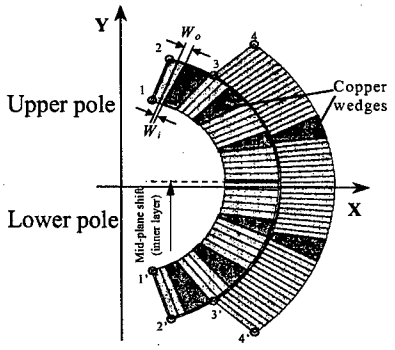


Figure 2: Inner layer mid-plane shift due the coil size difference between upper and lower pole.

Table 2 shows the calculated changes of the skew multipoles a_2 and a_4 due to shifts in the mid-plane of 0.05, 0.10 and 0.15 mm. The values correspond to a smaller upper pole, which means that the mid-plane is shifted upwards. One finds a linear dependence of the multipoles on the mid-plane shift. The inner and the outer layer have been calculated separately: as expected, in general, the

multipoles are more sensitive to shifts on the inner layer. The total effect can be obtained by superposition of the contribution of the individual layers.

Table 2: Calculated effect of a mid-plane shift on skew multipoles.

Mid-plane shift	Inner layer		Outer layer	
	δa_2	δa_4	δa_2	δa_4
0.05 mm	-2.67	-0.38	-1.56	-0.11
0.1 mm	-5.30	-0.77	-3.16	-0.20
0.15 mm	-7.95	-1.07	-4.69	-0.36

CORRELATIONS

From cross-analysis of data on magnetic and coil size measurements, some correlation between the expected a_2 due to coil mid-plane shift and the measured values can be observed (see fig. 3).

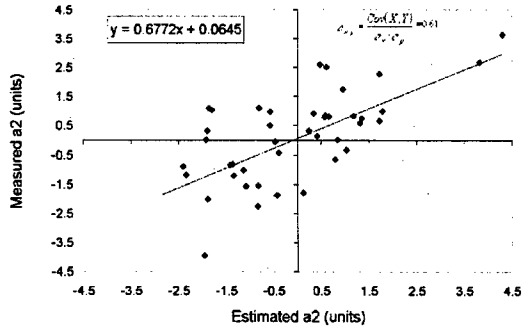


Figure 3: Measured and estimated a_2 resulting from the expected coil mid-plane shifts in the magnets of manufacturer 1.

In this graph the data belongs to the magnets, which are collared without sorting of their poles. The fact that the correlation factor is only 0.61 indicates that not only the difference in coil sizes but also other factors (such as a re-distribution of the current density within a coil arc due to tolerances of coil components) is contributing to these harmonics. For the last 9 magnets the manufacturer 1 has applied the sorting of poles within one set of poles and this already reduced the sigma on a_2 from 1.9 to 1.5 (see fig. 4). This was sufficient to reach the target value of 1.6. At the time of writing this paper, more magnets were assembled following coils sorting procedure and the sigma on a_2 was decreased even more. It is clear that if a bigger stock of poles is used, a safety margin could be added. In case of a stock with 12 poles, which becomes realistic when the companies move into series production scale, the effect on sorting becomes even more efficient (see fig.5). It should be noticed, that the sorting of the poles might be limited in some cases due to constraints in the mix of the cables produced by different manufacturers. This could limit the pole pairing only if the stock of poles is small.

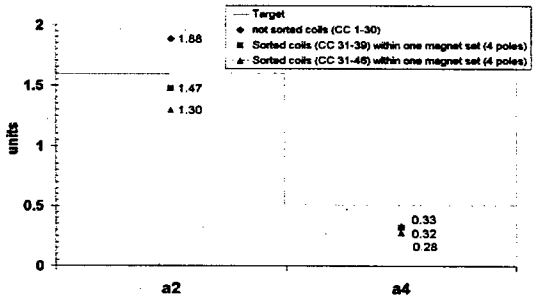


Figure 4: Effect of poles sorting on random of a_2 and a_4.

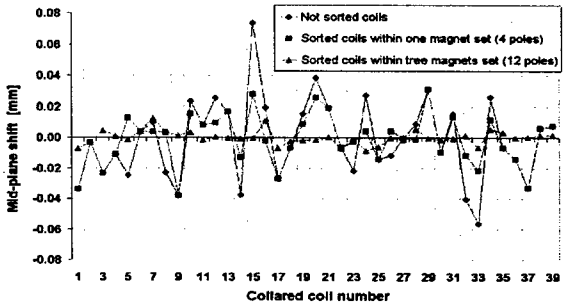


Figure 5: Effect of poles sorting on mid-plane shift value.

CONCLUSIONS

A model was developed to compute the effect of azimuthal coil size variation on the skew qudrupole and skew octupole of superconducting LHC dipole. The model was applied to the data on coil sizes of one dipole manufacturer. Some correlation was observed between measured and expected multipole coefficients.

A sorting of coils procedure, introduced at one of the dipole manufacturer, shown that it is a good method to reduce the random of a_2 mutipole. Dedicated software was developed and introduced to the dipole manufacturer to follow the coil size trends and simplify the procedure of sorting the poles.

ACKNOWLEDGEMENTS

We wish to thank L. Rossi for support, discussions and help given in this work. We thank the project engineers of the AT-MAS group for the constant support in the analysis and for providing assembly data.

REFERENCES

[1] L.Rossi, these proceedings.
[2] S. Fartoukh et al, *LHC Project Report* 501 (2002).
[3] M. Modena et al, these proceedings.
[4] W. Scandale et al, these proceedings.
[5] B. Bellesia, *LHC Project Report* 630 (2003).
[6] S. Russenschuck, ROXIE: Routine..., CERN 99-01, Geneva, 1999

DESIGN CONSIDERATIONS FOR THE CESR-c WIGGLER MAGNETS *

J. A. Crittenden†, A. Mikhailichenko, A. Temnykh
Laboratory for Elementary-Particle Physics, Cornell University, Ithaca, NY 14853-8001

Abstract

The damping-dominated beam dynamics of the CESR storage ring modified to operate in the 1.5–3 GeV energy range impose unique and stringent design specifications on the 1.3-m-long superconducting wiggler magnets which provide the necessary damping. A superferric 7-pole wiggler magnet which meets these design specifications has been designed, built and tested *in situ*. Studies of finite-element models and particle-tracking simulations have shown that that an 8-pole model of similar design will provide improved consistency in transfer functions when operated at peak fields which differ from the primary design value.

INTRODUCTION

The e^+e^- collider CESR at Cornell University is presently undergoing an upgrade which will permit studies of charmed hadron decays with unprecedented statistical accuracy [1]. The requisite luminosity at the beam energy of 1.5–3 GeV relies on control of the emittance and on the reduction of damping time afforded by the introduction of superconducting wiggler magnets with peak fields reaching 2.1 Tesla. Over the past several years, the CESR operations group has undertaken extensive engineering studies [2, 3]. During the past year, six wiggler magnets have been built and tested [4, 5]. One wiggler has been installed in CESR, and a beam-based characterization of its properties has been carried out [6]. Lattice designs based on symplectic particle-tracking algorithms [7] have been developed. We report here on the accuracy obtained with finite-element-based field calculation algorithms, comparing the results to field measurements. We also discuss wiggler design considerations in relation to calculated transfer functions.

FIELD CALCULATIONS

The wiggler magnets are 1.3 m long, 23.8 cm wide, with a vertical gap of 7.62 cm which accommodates a beam pipe with horizontal and vertical apertures of 9 and 5 cm. The horizontal uniformity of 2×10^{-3} in the vertical field component over ± 4 cm is obtained via 6-cm-wide rectangular cutouts in the pole faces with depths ranging from 3.5 mm to 5.5 mm depending on the pole length and its field strength. Two 7-pole wigglers with slightly different coil types and four 8-pole wigglers have been built and tested. Detailed information on the three wiggler designs is given in Table 1. The longitudinally symmetric field of the 7-pole model uses the two 15-cm-long end poles to cancel the kick of the 20-cm-long central pole, while the asymmetry of the 8-pole design ensures zero kick to within construction tolerances. Trim coils in the end poles allow adjustment of the first and second field integrals. The wiggler field calculations were performed using the MERMAID 3D package and the magnetostatics portion of the OPERA (version 8.5 size 3) [8] software package. Exploiting the three-fold symmetry of the ideal geometry, 1/8 models were used for the highest accuracy fields. Full 3-dimensional models were used in the study of geometrical construction errors. The finite-element mesh size was limited to a maximum of 1 cm the magnet steel. The more detailed permeability data available in MERMAID for 1010 steel was ported to the OPERA software for these calculations. During the model development stage of the project, contributions to the field from the magnetized iron were calculated via finite-element interpolation, while the current contributions were obtained from integrals over the current elements. The final accuracy of the calculation was obtained by using the integral method for each contribution. Each of the two contributions makes up about half of the peak field in these superferric magnets.

FIELD MEASUREMENTS

Detailed field map measurements providing information on field uniformity at a level better than 10 G for the vertical field component were obtained using a motor-driven Hall probe. Flip-coil measurements [5] were used to obtain accurate information on the horizontal and vertical field components integrated along straight lines over the length of the wiggler. The integrals of the vertical field component for several excitation levels for the second of the two 7-pole wiggler magnets are shown in Fig. 1. Figure 2 shows these integrals for the first of the four 8-pole wigglers. The greater dependence on excitation exhibited by the 7-pole design results from the fact that the end pole fields compensate the central pole field. Since the peak field in the end poles is smaller, saturation effects result in such a dependence. The asymmetric field of the 8-pole design avoids this dependence. However, since a single current source is used for the end-pole trim coils in both models, this first integral cannot be controlled with the trim current in the 8-pole design, and depends critically on construction tolerances. The value of the first integral for all four of the 8-pole wigglers was measured to be less than 3 G-m. The 8-pole design employs the trim coils to adjust the second integral, which is related to beam displacement. The trim current in the 7-pole design can be used to minimize the first integral and the kick. Construction tolerances then

* Work supported by the National Science Foundation
† critten@lns.cornell.edu

0-7803-7738-9/03/$17.00 © 2003 IEEE

Table 1: CESR-c wiggler geometrical parameters and operating currents for 2.1 T peak field

Pole Length (cm)	Nr	Main Current (Amp-turns)	Main Turns	Main Width (cm)	Trim Current (Amp-turns)	Trim Turns	Trim Width (cm)
Wiggler #1 (7-pole)							
20	5	95.00k	588	2.540	—	—	—
15	2	61.07k	378	1.631	0.86k	663	0.909
Wiggler #2 (7-pole)							
20	5	95.00k	660	2.540	—	—	—
15	2	57.00k	396	1.532	4.569k	684	0.965
Wigglers #3 – #6 (8-pole)							
20	4	95.00k	660	2.540	—	—	—
15	2	95.00k	660	2.540	—	—	—
10	2	50.67k	352	1.354	0.993k	836	1.186

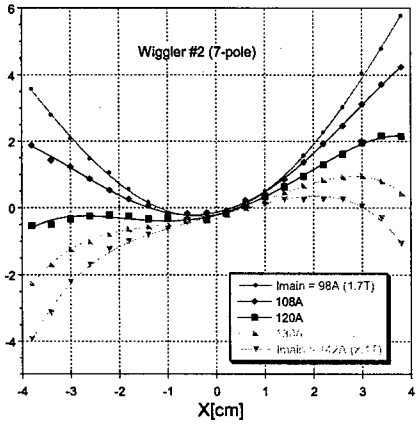


Figure 1: Flip-coil measurements of the integral of the vertical field component for the second of the two 7-pole wigglers as a function of horizontal entrance position in units of Gauss-meters.

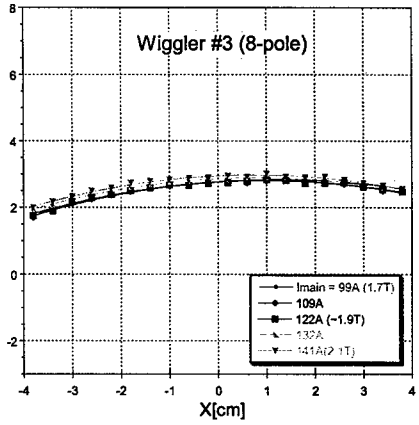


Figure 2: Flip-coil measurements of the integral of the vertical field component for the first of the four 8-pole wigglers as a function of horizontal entrance position in units of Gauss-meters.

determine the value of the second integral. The second integral for the two 7-pole wigglers was measured to be less than 3 G-m^2, which corresponds to a displacement of approximately 0.05 mm for a 1.8 GeV beam. In either design, the dynamic effect on the beam displacement can be reduced to well below 0.1 mm, and so did not influence design decisions.

The flip-coil measurements also quantified the residual integral of the horizontal field component, which has the effect of a skew quadrupole field in the case of a linear horizontal dependence. Figures 3 and 4 show the measurements for the 7- and 8-pole wigglers. Field calculations of geometrical errors within fabrication tolerances showed effects of this magnitude must come from a combination of sources. The combined effect was small enough that a small skew quadrupole magnet sufficed to provide the desired correction during CESR operation with the first wiggler installed in the ring. Space for additional skew quadrupole magnets has been provided for in the final CESR-c design if they turn out to be needed. It is interesting to note that the effect is much smaller in the 8-pole design, even though the excitation dependence observed in Fig. 3 for the 7-pole design is quite weak.

CALCULATED TRANSFER FUNCTIONS

The relationship between the field integrals and the transfer functions is complicated by the dynamic effect of the wiggling trajectory, which results in vertical focusing and horizontal kicks which depend on particle energy and entrance position. The horizontal kick for normal incidence in the horizontal symmetry plane as a function of entrance position for 1.8 GeV electrons as calculated with the OPERA tracking algorithm is shown in Fig. 5. The results are consistent with the MERMAID tracking algorithm tracking through the MERMAID-calculated field to an accuracy better than 10 μrad over $\pm$ 3.0 cm. This level of accuracy was also obtained with Runge-Kutta, symplectic integration and Taylor-tracking as described in Ref. [7]. The variation of the horizontal kick with horizontal entrance position is observed to be equal within 10 μrad for the 7- and

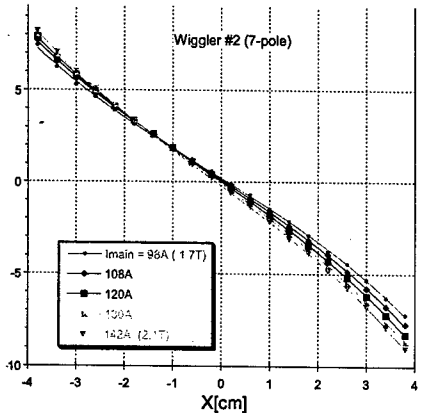


Figure 3: Flip-coil measurements of the integral of the horizontal field component for the second of the two 7-pole wigglers as a function of horizontal entrance position in units of Gauss-meters.

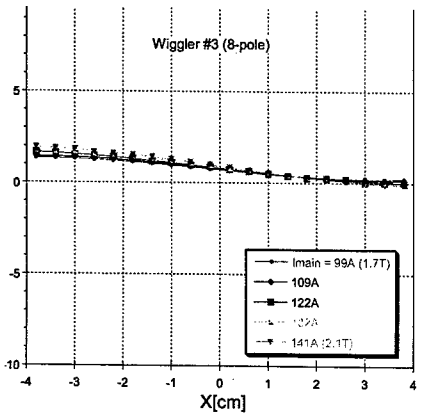


Figure 4: Flip-coil measurements of the integral of the horizontal field component for the first of the four 8-pole wigglers as a function of horizontal entrance position in units of Gauss-meters.

8-pole models. The 8-pole model shows less dependence on excitation, consistent with the flip-coil measurements described above.

The transverse motion of the wiggling trajectory through the longitudinal component of the wiggler field results in a vertical focusing effect. The tracking calculations showed the cubic term in the vertical dependence of the vertical kick to be stronger in the 8-pole design than in the 7-pole design by 2.2% for a peak field of 1.7 T, 4.2% for 1.9 T and 5.5% for 2.1 T.

Beam-based measurements of tune as a function of beam position in the wiggler proved consistent with these calculated transfer functions for peak fields of 1.9 T and 2.1 T [6].

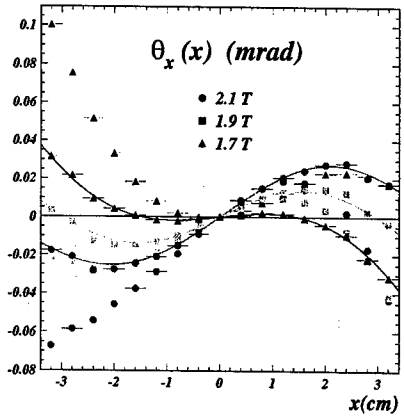


Figure 5: Horizontal kick as a function of horizontal entrance position for 1.8 GeV electrons of perpendicular incidence. Results for peak fields of 1.7 T, 1.9 T and 2.1 T are shown for the first 7-pole wiggler design and the 8-pole design. Curves connect the points for the 8-pole model.

CONCLUSIONS

Six superconducting wiggler magnets that meet the design specifications of the CESR-c upgrade have been designed, built and tested. Field maps and transfer functions of sufficient accuracy have been obtained independently with various software packages and computational algorithms. Such construction uniformity was achieved as to allow an 8-pole model to be implemented without necessitating a second trim coil power supply. The 8-pole model exhibits a smaller skew quadrupole component and will allow an increased range of excitation adjustment for tuning purposes during CESR-c beam studies and luminosity optimization. Ten more wigglers of the 8-pole design will be built during the coming year with the goal of installing eight of them in CESR in 2004.

REFERENCES

[1] D. Rice *et al.*, *Parameters for Low-Energy Operation of CESR*, proceedings of PAC2001

[2] A. Mikhailichenko, *Optimized Wiggler Magnet for CESR*, Proceedings of PAC2001, Chicago, IL, June 18-22, 2001

[3] Y. He *et al.*, *Design and Operation of the Cryostat for the CESR-c Wiggler Magnets*, these proceedings,

[4] D. Rice *et al.*, *Production and Testing Considerations for CESRc Wiggler Magnets*, these proceedings

[5] A. Temnykh, *Vibrating Wire and Flipping-Coil Magnetic Measurements of a CESR-c 7-pole Wiggler Magnet*, these proceedings

[6] A. Temnykh, J.A. Crittenden, D. Rice and D. Rubin, *Beam-based Characterization of a New 7-Pole Super-conducting Wiggler at CESR*, these proceedings

[7] D. Sagan, J.A. Crittenden, D. Rubin and E. Forest *A Field Model for Wigglers and Undulators*, these proceedings

[8] Vector Fields, LTD. `http://www.vectorfields.com`

SHORT–PERIOD SC UNDULATOR

A. Mikhailichenko, Cornell University, LEPP, Ithaca NY 14853, USA

Abstract[1]

We describe here design of short period helical undulator with SC windings. 2mm period, K~0.12 undulator can be used in positron production scheme. Results of test of 6 in-length prototype cold mass is represented also.

INTRODUCTION

Polarization in future linear collider recognized as a factor increasing collisions rate, effective polarization and as an instrument for drastic reduction of background especially if both electron and positron bunches are polarized. Method for polarized positron production was suggested many years ago [1]. At first stage circularly polarized high-energy gammas generated in a short period helical undulator by (used) high-energy beam after collision. At second stage these circularly polarized gammas converted into positrons/electrons in a thin target. *Energy selection* of secondary particles delivers polarization to the beam as a result of transferring polarization of gammas to the secondary particles at high-edge of energy spectrum. Polarization with this method can reach 65-70% with ~130 m long undulator.

Cold mass of undulator with superconducting coils having period of 1 cm, ~30 cm-long with ~6 mm aperture clearance, was successfully tested in a framework of VLEPP linear collider activity [2], [3]. Field of ~0.5 T was measured at the axis. The design was recommended for future LC application practically without any changes required.

New growing interest to this subject was indicated at last LC02 [4], [5]. Publication [4] now grew up into proposal for E-166 experiment at SLAC [6], carried by international community. One other potential utilization of polarized positrons –arrangement collisions in SLAC B-factory is also connected with undulator-based positron generation. Here ~4-m long undulator allow generation necessary amounts for normal operation of B-Factory [7]. SC can be used in future Linear Collider full-scale project. Nice advantage of SC undulator is that its functionality does not depend on repetition rate.

Main point of concern for small aperture undulator is operational stability of SC coil while few kW high-energy beams is running within 2mm from cold walls. So in this case manufacturing and testing *section* of SC undulator is necessary.

For successful operation of conversion system, undulator-having $\geq 1-1.3\times10^4$ periods required. In any case this undulator will be manufactured as relatively short sections of ~2-m long.

[1] Extended version is available at http://www.lns.cornell.edu/public/CBN/2003/CBN03-4/CBN03_4.pdf .

CRYOSTAT

Cryostat serves as housing for cold mass core. The cryostat sketch is represented in Fig.1. 2-meter long module will be able to work with cryocooler having 1.5W power at LHe temperature and ~40 W at 50°K. It also allows operation with filling by LHe directly trough the input 9 in fig.1. In this case cryocooler can operate too or can be replaced by LN cylindrical container.

Main support of long cold mass, having ~1" in diameter and length ~4 m, is going with suspension elements shown in Fig.2. As the cold mass is light weighted this solution allows good control of position of axis.

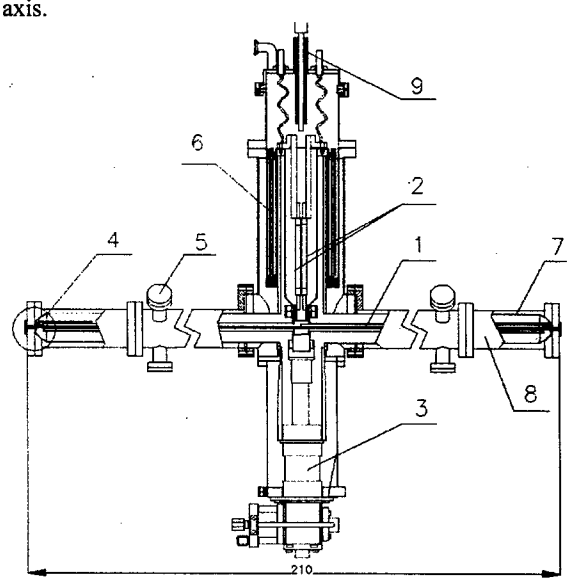


Figure 1: Cryostat for 2 m-long module. 1-is a cold mass, 2-HTS leads, 3-Cryocooler, 4-end region, see Fig.2, 5-is suspension elements, Fig.2, 6-are coaxial Al-StSteel cylinders, 7-is intermediate 50°K temperature shield, 8-is a vacuumed corps, 9-is filling tubing for operation with filled liquid He. All responsible spaces interlaced by superinsulation. Full height of cryocooler is 21.91".

These suspension straps made from composite glass fibers impregnated and cured with epoxy (Fiberglass). These straps are commercially available in broad variety of sizes.

Central support unit made with few coaxial cylinders with two Al ones among them. For the heat flow all the length is working in series. For the lengthening the thermal expansion coefficients of Al and StSteel are working one against other, like in gridiron pendulum.

Total heat losses calculated remains formally below 0.5W, however to get some operational margins the cryocooler with 1.5W at 4.2°K and 40 W at 50°K chosen for testing device (Model RDK-415D from Janis Co.).

0-7803-7738-9/03/$17.00 © 2003 IEEE

Maintenance interval ~10kHours is big enough to accomplish any experiment. As it was mentioned full-scale undulator will work with LHe supply.

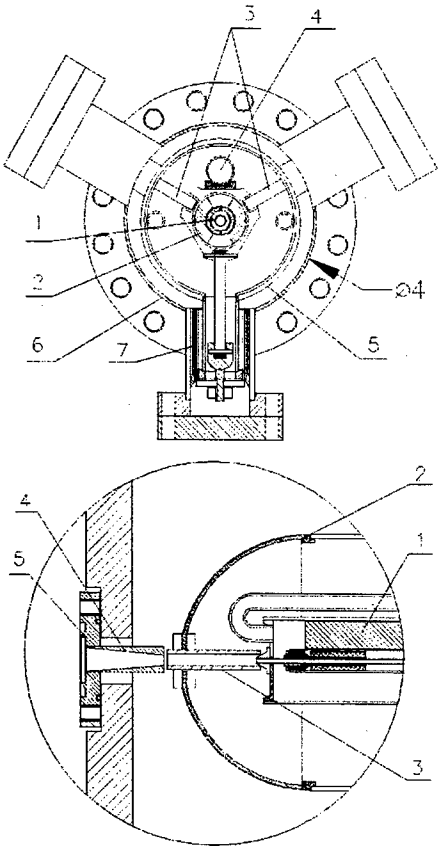


Figure 2: Suspension system and end of cryostat, circled in Fig.1. Left: 1-is a cold mass, 2-is a copper collar, 3-are suspension straps, 4-is two phase He tube, 5-is a 50°K shield, 6-is a vacuumed corpus, 7-is a stretching mechanism and heat lock. Right: 1-is a cold mass, 2-is a 76°K-shield, 3-is an aligning cylinder, 4-tapered diameter transformer, 5-is a flange.

COLD MASS WITH 1-cm PERIOD

As we mentioned in introduction the cold mass was tested in framework of VLEPP activity. Suggested that cooling can be arranged by flow of LH in gaps between yoke.

Yoke helix was machined in ~10-cm long sections. After trimming these pieces soldered by Indium to the tube, so it is going without brakes.

Heat losses due to imaginary currents can be evaluated for $N=10^{10}$, bunch length σ_b=0.001≡1mm one can obtain $\hat{W} \cong 3.27 \cdot 10^{-6}$ *J*. For repetition rate *f*, Hz and for the number on bunches in train *n*, average power dissipation will be $P \cong \hat{W} \cdot f \cdot n$ *Watts*, remaining within *mW* level. As the chamber has temperature of liquid He, this resistance must be lowered at least ~100 times.

It was shown in [2] that thermal relaxation of core cooled by flowing Helium could be described by space and time parameters $\kappa \cong 10cm$, $\tau \cong 22.4s$.

Measurement in this model was carried with a help of Hall probe moved along the axis in liquid Helium. Maximal current was ~6 *kA* × *turns* (marked by *). With present day wires available on market all parameters for total current above 6 *kA* × *turns* in Table 1can be guaranteed.

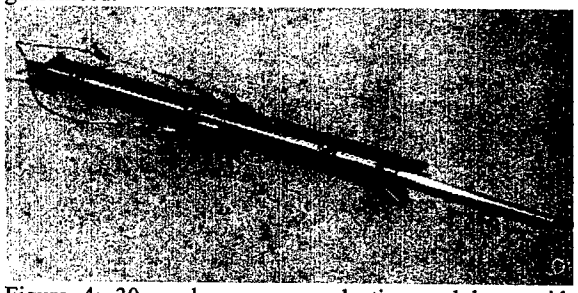


Figure 4: 30 cm-long superconducting undulator with period 10 mm and the axis field ~ 5 kG. Diameter of StSteel chamber is 6 mm, wall thickness 0.1mm.

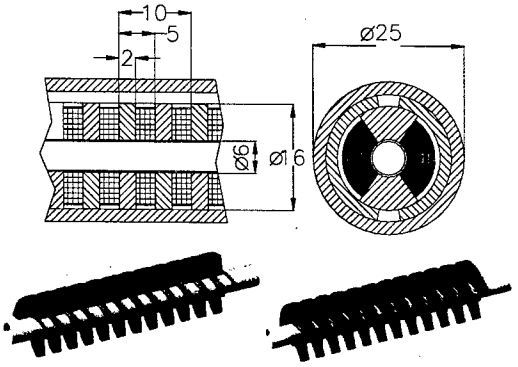


Figure 3: (Color) Yoke of 6 mm in aperture, 10-mm period of undulator with SC wires [2]. At the left vertical cut made for better look inside. Colored red and blue helical yokes made from soft steel. Half cylinders, covering yoke are not shown.

2.4 mm PERIOD MODEL TEST

Technology tested can be scaled down to a shorter period required for possible test (or implementation, [7]) at SLAC. A ~six inches long model prototype with period 2.42 mm having all peculiarities of full length one was tested [9].

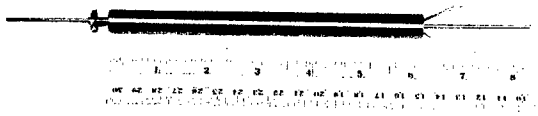


Figure 4: SC undulator model. Iron cylindrical shield for end trimming and ring jumper are visible here. One end of undulator has Copper jacket of ~12mm in diameter hides soft iron semi-cylinders having diameter ~9.8 mm.

We used here the stainless steel tube of 1.5 mm in diameter with the wall thickness of 0.3 mm as a vacuum

chamber. The goals of the work done were to see if technology can be useful for scaling down all dimensions and to investigate if any sign of degradation of the wire is present, as the bending radius is small.

The winding done with pair of SC wires interlaced by soft-steel ones with the help of cylindrical director made on G10. SC wire has 0.6mm in diameter- standard OXFORD 54 filament wire insulated by Formvar. Undulator model was tested in a Dewar filled for the Cornell LEPP wiggler coil test set in parasitic mode [9].

Field measurement in such small aperture is a problem. However the axis field module is a constant along the undulator. Measuring integrated value with *scalar* probe will give the value of axis field. So here the magneto-resistive sensors as a Bismuth wire can be used [10].

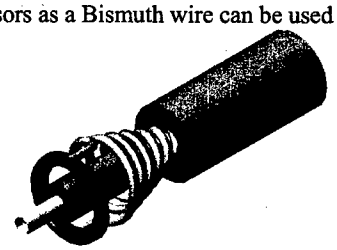


Figure 5: (Color) End commutation. Red ring is a SC wire circled and soldered with Indium to the Copper ring. Green cylinder at the right made with two halves.

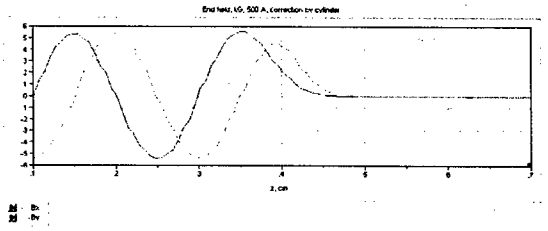


Figure 6: (Color) End field with conical expansion and trimming magnetic cylinder. Period –2mm.

In Dewar tests we reached the current ~510A which is close to the short sample limit. The field at the axis, according to calculations, reaches ~0.34T, K parameter, respectively, goes to ~0.08. The field amplitude between SC wires reaches ~2.3T in specific points inside the wire. The field was calculated with 3D code MERMAID.

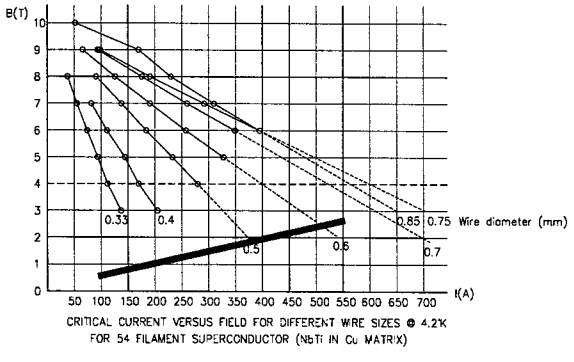


Figure 7: Properties of the SC wire. Loading curve for the points with highest field is represented as a solid line.

With the tube having OD=1.0668 mm, as planned, parameters we expect to reach with current 500 A current the field at the axis~0.54T and $K \cong 0.12$. In final design we also are considered utilization of soft steel wire with rectangular shape, giving additional 10% to the field at the axis. Filling epoxy mixed with iron-like powder (ferrite), can also give additional ~10% percent in field strength at the axis.

CONCLUSIONS

The cryostat described can accommodate any core with short-period undulator. Utilization of such SC undulator might bring significant relief in operational cost of linear collider.

Cold mass of helical SC undulator having 1-cm period and 6 mm aperture clearance was successfully tested years ago. No doubt, that technology can be successfully used for full-scale wiggler with 0.8-1 cm period and ~100-130 m long.

Six-inch long model of undulator cold mass with 2.4 mm period was manufactured and tested in Dewar.

There are no apparent limitations in scaling this technology even more down with appropriate tube and wire diameters down to period of 0.1*mm* and K~0.05 .

REFERENCES

[1] V.E. Balakin, A.A. Mikhailichenko, "Conversion System for Obtaining Highly Polarized electrons and positrons", Preprint INP 79-85, Novosibirsk 1979.

[2] A.A. Mikhailichenko, Dissertation, BINP, Novosibirsk, 1986, Translation: CBN 02-13, Cornell 2002.

[3] T.A. Vsevolojskaya, A.A. Mikhailichenko, E.A. Perevedentsev, G.I. Silvestrov, A.D. Cherniakin, XIII International Conference on High Energy accelerators, August 7-11, 1986, Novosibirsk.

[4] R.Pitthan, J.Sheppard, "Use of Microundulators to Study Positron Production", LC02, Proceedings, SLAC-WP-21.

[5] A. Mikhailichenko, "Optimized parameters of the Helical Undulator for test at SLAC", LC02, Proceedings, SLAC-WP-21.

[6] See: http://www.slac.stanford.edu/~achim/positrons/.

[7] A.A. Mikhailichenko, "The feasibility of polarized e^+e^- collisions at SLAC B-factory", CLNS 99/1645, CORNELL U., 1999.

[8] H. Lierl, P.Shmüser, "Cooldown of a HERA Octant Equipped cold Dipoles", DESY, HERA, 84/16, 1984.

[9] A. Mikhailichenko, T. Moore, "First test of short period helical SC undulator prototype", Cornell *CBN* 02-6, June 3, 2002

[10] A.Mikhailichenko, "Low aperture magnetic element measurements", (Novosibirsk, IYF). IYF-89-94, Jun 1989, 12pp. See: http://ccdb3fs.kek.jp/cgi-bin/img/reduced_gif?198911230+1+14).

IMPROVEMENT OF SC WIGGLER PERFORMANCE

A. Mikhailichenko, Cornell University, LEPP, Ithaca NY 14853, USA

Abstract[1]

Described is a methodology of improvement for good field region in a SC 2.1 T CESR's wiggler as example. The method includes a tapering, shimming and pole face winding with active field distribution correction. This technology can be applied to any wiggler, however.

INTRODUCTION

Development of SC wigglers at Cornell LEPP was initiated by proposal considered to modernize the CESR for the low energy operation [1]. About 16 meters total of ~2.1 T wigglers will bring CESR-c to 10^{32} level in luminosity. With installation and testing the first wiggler in CESR, the job started more than 2 years ago [2, 3] came to its end. In first run luminosity $L \geq 10^{31}$ achieved at Ψ, gives assurance, that program can be accomplished.

Here the goal is to increase emittance in contrast to the goal clamed for the damping-ring in LC: as low emittance as possible.

It was shown in [3], that physical nature of appearance of octupole (and higher) type dependence of kick versus vertical displacement is in *wiggling with angle in the pole fringe* field.

The methods found might be interesting to others and now everyone can apply them to his own wiggler design.

OPTIMAL DIMENSIONS

Wiggler for CESR operation at 2 GeV was described in [2, 3]. All calculations carried with 3D code MERMAID. Period was chosen $\lambda_w = 40cm$. For $y_0 = 2cm$, $\lambda_w \cong 6.37cm$, the ratio of cubic term to linear one goes to be ~0.0164 or 1.6%. Quadrupole lenses typically designed with this ratio ~ ten times better, however.

The height was chosen equal to $\cong 14.5$ cm. It is slightly below the saturation, but saved about one inch of steel, lowering field on ~5% only.

Loading curve is chosen so that designed current is ~half corresponding crossing with the wire property one. Technology is described in [5]. To prevent coil destruction initiated by quench, passive resistors attached to each coil was suggested [2] as simplest solution.

Wiggler acts in one direction mostly, providing vertical focusing. That is why it is difficult to keep orbit closed, as the wiggling amplitude is also changes with vertical position. Maximal field corresponds to the coil which width is twice the height. Finally the coil cross section was chosen with cross section $\cong 1'' \times 0.75''$ for simplicity of winding.

[1] Extended version is available at http://www.lns.cornell.edu/public/CBN/2003/CBN03-3/CBN03_3.pdf. Work supported by NSF.

Evolution of temperature inside the coil defined by heat-skin layer depth, which for ~1cm thickness gives time constant τ ~100ms, mostly defined by parameters of epoxy.

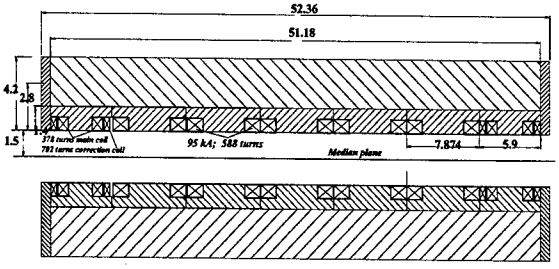


Figure 1: Dimensions of 40-*cm* period 7-pole wiggler #1. Wiggler #2 and all others have 660 turns of 0.8-mm OXFORD wire in main coil. A-turns remain the same.

TAPERING

Tapering, or variation in field strength along the wiggler, used when there is a desire to have zero (or any) average displacement of trajectory in a wiggler. Although it is likely evident, it was mentioned first in [6] however, that end poles with fields integrals ¼, -¾, +1 of regular one gives zero displacement of trajectory. If periods are the same these numbers reflect the field strengths at each pole.

This is not the only solution, however. Let us consider the series of odd numbers with reversing signs as

$$1, -3, +5, -7, +9, \ldots (-1)^k (2k-1),\ k=0,1,2,3,\ldots \quad (1)$$

Let these numbers will represent now the nominators of fractions of the field integrals for each pole normalized to the maximal one in regular part of wiggler. So the next pole after *m,* supposed to be a main one, must have the value counted as (2*m*+1)+1, just one unit more, and opposite sign. Now one can obtain, that full integral over all wiggler will be

$$S(m) = 2\sum_{k=0}^{m} (-1)^k (2k+1) - (-1)^m (2m+2) \equiv 0.$$

One can also find that $\sum_{m=0}^{k} S(m) \equiv 0$. This means that the field first and second integrals over all wiggler are zero. For example series as +1/8, – 3/8 , +5/8, – 7/8, +1, [n(–1,+1)], – 7/8, +5/8, – 3/8, +1/8 , where fractions stand normalized to central pole integral, will also give zero angle and displacement. One can easily find the sequence of tapering for 6, 8, 10, 12, 14, 16,... , Fig. 2, and so on poles.

We called this ***adiabatic entrance.***

Once particle entered into wiggler with such tapering and began its oscillations following ~sinusoidal trajectory, there are two ways out. First is a symmetrical exit, when the sign of deflection in the last pole is the same as during

0-7803-7738-9/03/$17.00 © 2003 IEEE

entrance, and the second one is asymmetric one, when the kick is going in opposite direction. Obviously in first case the total number of poles is odd, in second case it is even.

One disadvantage associated with tapering is a necessity to have few different types of coils. However adiabatic entrance is useful for helical undulators having very short period for example, as exact managing the pole strength at the end is not an easy task.

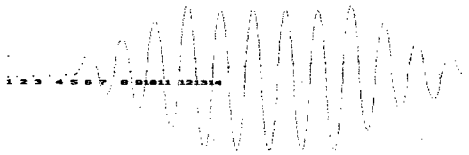


Figure 2: Trajectory of particle in a wiggler with tapering ~1/16, -3/16,+5/16, -7/16, +9/16, -11/16, +13/16, -15/16, +1. Doublet of quadrupoles envelops wiggler from each side. Same period.

Seven-pole wiggler was made with tapering ½, -1. This gives displacement $\Delta \cong \lambda_w K/\gamma$ what is amplitude of wiggling but this, first, supposed to reduce the coil types to two only and to have maximal period for reduction of nonlinearities. For eight-pole wiggler tapering is ¼, ¾, 1. Knowing the fields and having tracking code in hand one can investigate properties of wiggler model *dynamically by tracking*. For tracking special code was used [4]. This code used the field map obtained from MERMAID. Kicks, obtained by particles running across aperture with different x – coordinate remain in $\pm 50\mu$rad for all fields and *not correlated* with integrals along straight lines.

SHIMMING

To reduce nonlinear effects the pole top field must be as flat as possible. The old fashion way as shimming is also working here, despite the iron is deeply saturated.

Poles having length 20 cm, 15cm and 10 cm were developed during these years, Fig. 3. The 10 cm poles successfully used in 3-pole model [5] and are in use in 8-pole one. Width of the deeps was chosen as a half of all pole width and with simplest shape.

POLE FACE WINDINGS

Next step in flattering is active correction. So if one puts a coil on the pole surface it will generate the dipole, sextupole... field with the same symmetry. So as adjusting main current can neutralize the dipole field change, this coil can be considered as a source of sextupole. Lowering at the center is an ideal place for positioning this correction coil.

For winding the SC wire with 0.017" diameter was used. This dimension includes Capton tape wrapping and Bonadll impregnation. After winding form with coil was heated ~200°C and after cool down a solid coil obtained. The coil having 100 turns will require the feeding current of 400/100=4 A only. Poles with coils wounded and cured on the pole attached to the steel plate (Fig.1) enveloped by stainless steel cover.

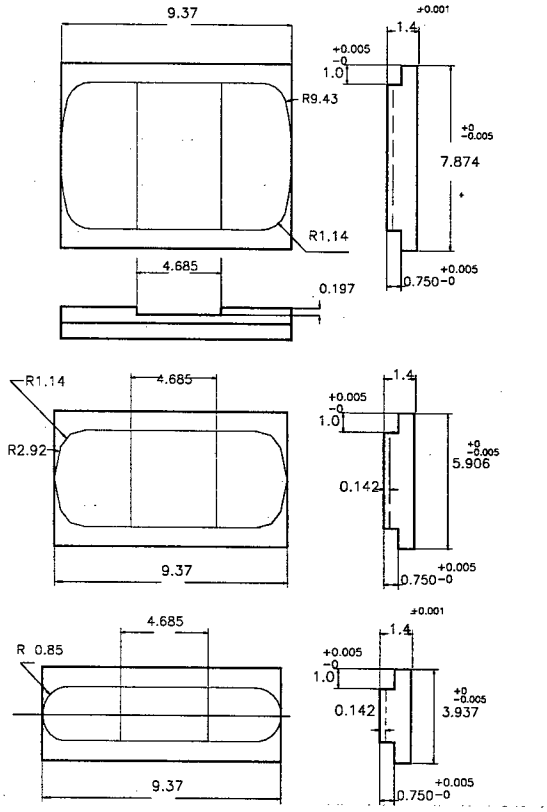


Figure 3: 20 cm, 15 and 10 cm poles developed for wigglers.

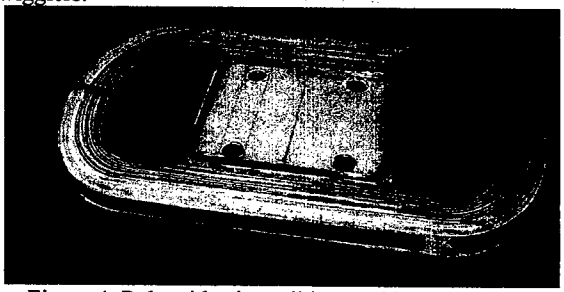


Figure 4: Pole with trim coil inserted into the lowering in groove made in G10 insertion.

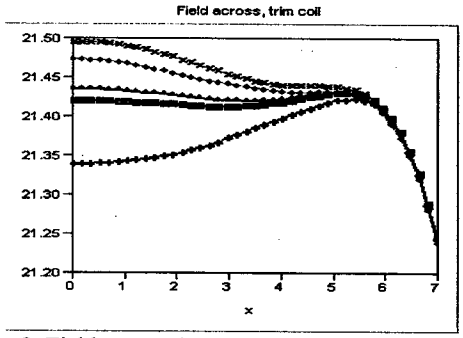


Figure 5: Field across the pole as a function of current in trim coil.I=0(up);0.1;0,4;0.5;1 kA Main feeding current is 95 kA/pole. Material of the pole is annealed Steel 1010.

MEASUREMENTS

To the moment six wigglers total were measured so far. Two of theses have seven-pole structure, four others eight-pole ones. Measurements were carried with Hall probe device F.W.Bell 6010 series. The difference in readings at the same points are less that 5G during the time of measurements. The readings stay within $\leq 1.25 \cdot 10^{-3}$ for all measurements.

Number of longitudinal points is 1060, going through 1/16". Signal acquired at every point becomes written to the file (having 1060 data rows). Each of these files marked in association with transverse position of Hall probe in cartridge, direction of motion of the cartridge, data, when taken. Slots in cartridge have transverse period 0.625 cm, so mostly deflected from center ones running at $\pm$ 3.75 off central line.

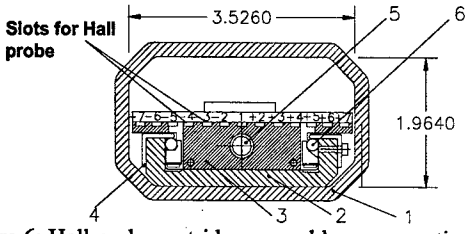


Figure 6: Hall probe cartridge assembly cross-section. 1 is the warm copper vacuum chamber with dimensions in inches, 2 is aluminum rail, 3 is a cartrige with slots for Hall probe, 4 is holding profile, 5 is a shaft with 1/16" thread, 6 represent alignment fixtures. Slots are numbered as they appear in the file descriptor.

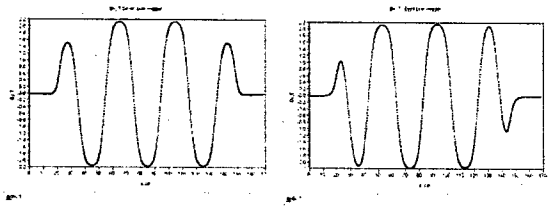


Figure 7: Measured longitudinal distribution for seven and eight pole wigglers.

According to formulas [3] the eight-pole wiggler generates 7.68/6.3 $\cong$ 1.22 times more strong integrated cubic vertical nonlinearity than a seven-pole one. The difference between calculated and measured values can be estimated as 50G *in absolute value*. Measurements conclude with a series of files with measured data along lines defined by position of Hall probe in a cartridge.

CONCLUSIONS

MERMAID demonstrated excellent possibilities for optimization and wiggler design.

Tapering in a wiggler allows having zero displacement of trajectory. It might be vital for wigglers with even number of poles, as trajectory sweeps only ~half of transverse coordinate swept without tapering. This king of procedure can be recommended for TESLA damping ring, as one can see from publications, that they use even number of poles without proper tapering.

We represented here for the first time the possible tapering laws for zero displacement of orbit in a wiggler.

Flatness of the poles need to be kept as plane as possible. This can be done either with profiling iron, either with active pole face winding.

Measurements with long coils can be considered as indicative only, as they are not related directly to dynamic properties of the wiggler. Mapping with Hall probe can be considered acceptable within accuracy ~10^{-3}. With special probes having microchip with calibration, this can be lowered in half. Such probes are available on the market now.

Implementation of *trim coils* integrated with end poles of wiggler is extremely useful for fine-tuning.

Nonlinearities in a wiggler strictly correlated with period, reversibly proportional to its square and proportionally to the square of magnetic field.

In CESR wigglers the width of poles, 24 cm were made maximal possible and was defined by the diameter of Dewar, available at that moment.

Pole face windings can be recommended for widening dynamic diapason.

Steel properties for room temperature deliver rather good approximation for such ones at liquid Helium temperature.

REFERENCES

[1] CLEO-c AND CESR-c: A new Frontier of Weak and Strong Interactions, CLNS 01/1742, Cornell 2001.
G.Codner, et al, "Parameters for Low Energy operation of CESR", PAC2001, Chicago, IL June 18-22, 2001, Proceedings pp.374-376.

[2] A. Mikhailichenko, "Wiggler for CESR operation at 2 GeV", Internal report, Cornell, http://cesrelog.lns.cornell.edu/documents/charm/param/am010122.pdf, Cornell U., 2000.

[3] A. Mikhailichenko, "Optimized Wiggler Magnet for CESR", PAC2001, Chicago, IL, June 18-22, 2001, Proc., pp. 3648-3650.
A. Mikhailichenko, "The Wiggler for a Damping Ring", LC02, Feb. 4-8, SLAC, Stanford, CA, 2002.

[4] G.Dudnikova, V.Vshivkov, K.Vshivkov, UMKA-VG, Institute of Computation Technologies, Lab. of Plasma Physics, Siberian Branch of RAN.

[5] A. Mikhailichenko, T. Moore, "Lessons from 3-pole wiggler test", CBN 01-18, Cornell, LEPP, 2001.

[6] A. A. Mikhailichenko, V.V. Parkhomchuk, "Damping Ring for a Linear Collider", BINP Preprint 91-79, Novosibirsk, 1991.

TO THE RADIATION OF PARTICLES IN A SOLENOID

A. Mikhailichenko, Cornell University, LEPP, Ithaca NY 14853, USA
E. Bessonov, FIAN, Moscow, Russia

Abstract

We attract attention that the well known law of radiation during motion in solenoid, allowing transverse momentum loss independently from its longitudinal one, can be used effectively for cooling of charged particles beams practically not dependently of theirs energy.

INTRODUCTION

It is well known that the force due to radiation reaction to the particle directed along the instant particle's velocity and can be expressed as the following [1]

$$\vec{F}_{rad} = \frac{2}{3}\frac{e^4}{m^2c^4}\left(F_{kl}u^l\right)\cdot\left(F^{km}u_m\right)\cdot\vec{n}, \qquad (1)$$

where e and m are the electron charge and mass respectively, c is a speed of light, $\vec{n}$ is unit vector directed along the instant particle's velocity $\vec{n}=\vec{v}/|\vec{v}|$, $F_{kl}(x^i)=\partial_k A_l-\partial_l A_k$ (with A_k as components of 4–vector of potential) are components of 4–tensor of electromagnetic field, $u^i=\{c,\vec{v}\}$ is 4–vector of particle's velocity. This expression (1) can be represented in 3–components as the following

$$\vec{F}_{rad} = -\frac{2}{3}\frac{e^4\gamma^2}{m^2c^5}\left\{\left(\vec{E}+\frac{\vec{v}\times\vec{H}}{c}\right)^2-\frac{\left(\vec{E}\cdot\vec{v}\right)}{c^2}\right\}\cdot\vec{v}, \qquad (2)$$

where $\vec{E},\vec{H}$ are electric and magnetic fields respectively. One can see that in absence of electric field the force $\vec{F}\neq 0$ only if $\vec{v}\times\vec{H}\neq 0$, or only for transverse to the speed components.

The circumstance that the particle's friction force opposes the instant velocity yields the requirements of radiation particle's energy in full to reduce the transverse momentum while longitudinal one is compensated by RF cavity. By this way the temperature of electron beam associated with transverse moment is lowering in a damping ring at the cost of radiation the full energy of particle. Even in extreme case of energy losses in a single act, the transverse emittance might be reduced on expense of full energy loss [2].

One other important circumstance associated with the fact that devices supposed to force the radiation process installed in the damping ring are likely with transverse dipole fields, such as wigglers or bending magnets. They still force the radiation with the same rate even for the beams having zero transverse temperature.

Meanwhile the energy associated with transverse momentum itself is much less, than the full one. So desire to operate somehow only with transverse component of full momentum was a subject of interest since the synchrotron radiation limit in synchrotron was predicted in [3].

In [4] an attempt was made to consider radiation in focusing channel of linear collider. In [5] more fundamental consideration of the radiation in focusing channel was made. As the focusing channel is a system of focusing/defocusing quadrupoles having gradient $\pm G(z)$ installed with period $2\pi\lambda\!\!\!^{-}_u$, the radiation here have all peculiarities of undulator radiation with undulatority factor $K=eH_\perp\lambda\!\!\!^{-}_u/mc^2$ where local magnetic field $H_\perp\cong G\cdot x$ defined by instant amplitude $x(z)$ of oscillations in the channel. Radiation is going on harmonics defined by period of focusing/defocusing lenses shrunken by Doppler effect in factor $1/(1-\vec{n}\vec{\beta})$ [6]. The length of formation of radiation with wavelength λ as always $l_f\cong 2\lambda\gamma^2\cong 2\pi\lambda\!\!\!^{-}_u$. In this focusing channel radiation is absent for particles running at the axis (having low transverse temperature). The particle here must radiate however it's all energy as the focusing field is transverse. As the amplitude is decreasing, the power of radiation drops significantly.

All these considerations are important in attempt to reach extreme temperatures, in particular temperatures when the beam trapped in focusing channel can be considered as degenerated Fermi-gas [7].

Meanwhile in [8,9] there were considered radiation in a solenoidal field as example in each case. In both cases was indicated, that particle could lose its transverse moment without affecting its longitudinal one. In this sense the solenoidal field in any circumstances cannot be considered as a limit of any kind of focusing system with quadrupoles.

In this publication we are investigating briefly this peculiarity from the point of possible utilization for the cooling beams for lowering temperature. We found that the rates of cooling might be interesting.

LOW OF MOTION IN MOVING SYSTEM OF REFERENCE

Let us remind first the radiation law for relativistic particle in solenoidal field.

In the coordinate system moving with average velocity of an electron, particles move along helical trajectory with instant radius $R=\beta'\varepsilon'/eH$ (Fig.1).

The intensity of radiation by electron is

$$I=\frac{2}{3}\frac{e^4H^4v'^2\gamma'^2}{m^2c^5}=\frac{2}{3}cr_e^{\,2}H^2\beta'^2\gamma'^2, \qquad (3)$$

where primes denote quantities calculated in the moving system of reference: v' is the electron's velocity,

0-7803-7738-9/03/$17.00 © 2003 IEEE

$\beta' = v'/c$, $\gamma' = \varepsilon'/mc^2 = 1/\sqrt{1-\beta'^2}$, ε' is the electron's instant energy. It was substituted here also $r_e = e^2/mc^2$ –classical electron radius. For ions an evident substitution need to be done: $e \to Ze, m \to AM$, where Z -is the charge of ion and A- it's atomic number.

The time dependence of the electron energy is described by the equation $d\varepsilon/dt = -I$, which can be represented in the form [1]

$$\frac{d\gamma'}{dt} = -\frac{2}{3}\frac{r_e^2 H^2 \beta'^2 \gamma'^2}{mc} = -\frac{2}{3}\frac{r_e^2 H^2}{mc}(\gamma'^2 - 1), \quad (4)$$

This equation has the solution

$$\gamma' = \frac{\sinh[\alpha\cdot(t-t_0)] + \gamma_0' \cosh[\alpha\cdot(t-t_0)]}{\cosh[\alpha\cdot(t-t_0)] + \gamma_0' \sinh[\alpha\cdot(t-t_0)]} \quad (5)$$

where $\alpha = \frac{2}{3} r_e^2 H^2/mc \cong 1.94\times10^{-8} H^2[G]$. One can see that at the initial moment $t = t_0$ the energy $\gamma = \gamma_0$. In the limit $t - t_0 \to \infty$ the value $\gamma' \to 1$.

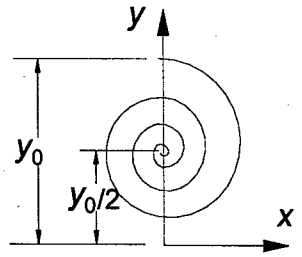


Figure 1: Projection of the particle's trajectory to the transverse plane.

Time dependence of the gamma for two different initial values is represented in Fig.2. The damping of the energy and amplitudes of electron oscillations in the magnetic field in the non-relativistic case described by exponential function. In the ultra relativistic case $\gamma_0 >> 1$, according to (3) they decay independently on theirs initial energy as

$$\gamma'\big|_{\gamma_0>>1,\ t-t_0>>0} \cong ctgh[\alpha\cdot(t-t_0)].$$

One can see, that equilibrium value reaches practically independently of its initial values. In the non-relativistic case kinetic energy $T = mc^2(\gamma' - 1)$ changes according to (5) as

$$T \cong T_0 e^{-2\alpha(t-t_0)}. \quad (6)$$

So the damping time according to (6) goes to

$$\tau' = \frac{1}{2\alpha} = \frac{3mc}{4r_e^2 H^2} \cong \frac{2.58\cdot10^8}{H^2[G]}. \quad (7)$$

We have considered the process of the energy loss in the moving system. In the laboratory system the damping time will be higher, $\tau = \tau'\gamma_\parallel$, where $\gamma_\parallel = 1/\sqrt{1-\beta_\parallel^2}$, $\beta_\parallel$, $\gamma_\parallel$ are the relative longitudinal velocity and relative longitudinal relativistic factor in the laboratory coordinate system.

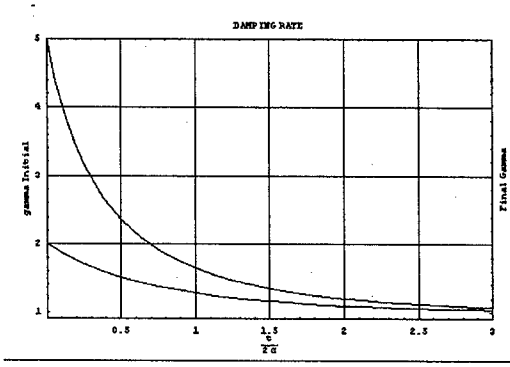


Figure 2: γ' as a function of normalized time $t/(2\alpha)$ for two different initial values $\gamma_0' = 2$ and $\gamma_0' = 5$.

Usually the relative energy γ and the transverse relative velocity $\beta_\perp$ are given in the laboratory coordinate system. That is why the relative longitudinal velocity $\beta_\parallel$ and relativistic factor $\gamma_\parallel$ can be expressed through these values, $\gamma_\parallel = \gamma/\sqrt{1-\beta_\perp^2\gamma^2}$. The velocity $\beta_\perp = \beta'/\gamma_\parallel$.

This yields the damping time in the laboratory coordinate system to be

$$\tau = \frac{3mc}{4r_e^2 H}\frac{\gamma}{\sqrt{1+\beta_\perp^2}}. \quad (8)$$

In the laboratory coordinate system the electron moves along special drill spiral of the radius

$$R = R' = \frac{mc^2\sqrt{\gamma'^2-1}}{eH}\Big|_{\gamma'-1<<1} \cong \frac{\sqrt{2}mc^2}{eH} e^{-\alpha(t-t_0)}. \quad (9)$$

Let us estimate the damping times however. For longitudinal field in solenoid as high as 100 kG, (7) yields $\tau' \cong 2.58\cdot10^{-2}$ s in the rest frame. For a 50 MeV beam the time constant goes according to (8) to $\tau \cong 2.6$ s. If we suggest that the solenoid has the length L_{sol} ~100m and the rest length of the ring $L_{rest} \cong L_{sol}$ is about the same length, one can obtain that the number of turns for cooling will need to be

$N_{turns} \cong c\tau/(L_{sol} + L_{rest}) \cong 2c\tau/L_{sol} \cong 2.3\cdot10^6$ turns.

ENTERING CONDITIONS

Let us say a little about possible adjustment of the injection into solenoidal field. The trajectory of the electron drawn at the Fig.1 corresponds to the case when the electron enters the solenoid with zero initial polar angle with some vertical deviation from the axis. In more general axisymmetrical case let us first mention that equation $div\vec{B} = 0$ yields

$$H_r(z) = -\frac{1}{r}\int_0^r r'\frac{\partial H_z(r',z)}{\partial z}dr' \quad (10)$$

So the angular momentum defined simply by Bush's theorem

$$\Delta p_\vartheta(z) \cong \frac{e}{c}\int_{-\infty}^{z} \dot{z}\cdot H_r dt = -\frac{e}{c}\int_{-\infty}^{z} H_r dz = \frac{e}{cr}\int_0^{y_0} r'\cdot H_z(r',z)dr' \equiv \frac{e}{c}\frac{\Phi(y_0)}{2\pi r}$$

The same formula describes the change of the transverse momentum at the out end of solenoid, but with y_{out} in formula for flux. Without radiation the total change of transverse momentum is zero. As the dipole radiation carries polarization the particle will decrease some transverse momentum. This is a sequence of the fact that the center of helix is shifted from radial position required by $<\rho>=\rho/2$ for exit without angular moment. The coil of solenoid will accept the angular momentum arising at the entrance and the exit of solenoid.

The final position of the electron corresponds to the case when its deviation from the axis of solenoid is equal to the half of the initial one. If we will focus the electron beam on the axis of the solenoid then the initial conditions of all electrons will be such that they will rotate relative the solenoid axis and will tend to its axis.

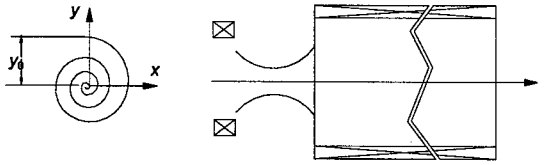


Figure 3: Entrance into solenoid. Short solenoid has focal point in front of the main one. Manipulating by polarity, location and strength of short trim pre-solenoid one can adjust the entering conditions.

For the initial values as the entrance of the solenoid in Lab system as $x_0, \dot{x}_0, y_0, \dot{y}_0$ one can obtain the trajectory averaged values as [10]

$$<x>=\frac{x_0}{2}+\frac{\dot{y}_0}{\omega_H}, \qquad <y>=-\frac{\dot{x}_0}{\omega_H}+\frac{y_0}{2}, \quad (12)$$

where $\omega_H = eH/\gamma mc$. So for shrinkage to the central axis the right parts of these expressions must be zero. So with arrangement of crossover in the focal point of solenoidal edge one can expect that the beam will shrink to the axis line. This condition is not important in the terms of damping rate and principle described, however.

From the technical point of view the transferring envelope function from the part with focusing quads the symmetrical values required by solenoid can be easily arranged by shifting the last quad to the half of period, for example.

In publication [11] described a ring for electron cooling of positrons. This ring has long solenoids and particle dynamics considered there. However SR is not included into consideration.

CONCLUSION

In general the problem under discussion is a problem of thermal relaxation near temperature of degeneration for relativistic beam with radiation and collisions in solenoidal field. We considered here only a small fraction of the problem. Even so the utilization of long solenoids in damping rings has visible potential.

High magnetic field required can be generated with the help of SC coil. Low emittance of the beam allows smaller diameter of the clearance, so the energy stored in solenoid can be made not high.

One can cool the beams having low energy proportionally decreasing the damping time in Lab system.

Cooling in solenoidal field allows natural solution to the cooling of polarized particles. This is in contrast to usual scheme with dipole wigglers, which destroys polarization if adequate measures are not applied; say by arrangements a transverse orientation of the spin in the region of the wiggler, or using asymmetric wigglers.

Natural orientation of spin along axes of solenoid preserves it during cooling.

Damping times remain in second range, so the few bunches must circulate in the ring. The lowest temperature in the cooler with solenoid can reach extremes required for degeneration however.

REFERENCES

[1] L. D. Landau, E.M.Lifshits, "Field Theory", 1973.
[2] V. Telnov, "Laser Cooling Electron Beams for Linear Colliders", Phys. Rev. Lett., 78: 4757-4760, 1997.
[3] D. Ivanenko, I. Pomeranchuk, Phys. Rev. 65, 343 (1944).
[4] M. M. Karliner, S. I. Man'kov, B. M. Fomel, V. P. Yakovlev, "The growth of Energy Spread of a Beam due to the Synchrotron Radiation in Magnetic Focusing System of High Energy Linear Collider", Budker INP Preprint 86-94, Novosibirsk, 1994.
[5] Z. Huang, R. Ruth, "Suppression of Radiation Excitation in Focusing Environment", 7th Advanced Acc. Concepts Workshop, Lake Tahoe, CA, 13-19 Oct 1996, AIP Proceedings 398, pp. 254-262.
[6] E. G. Bessonov, A. A. Mikhailichenko, "Alignment of the Linac with the help of radiation from the Quadrupoles of the Linear Collider", EPAC 94, London, June 27- July11, 994, Proceedings, p.2579.
[7] A. Mikhailichenko, "On the Physical Limitations to the Lowest Emittance. (Toward Colliding Electron Positron Crystalline Beams)", Cornell U., LNS, CLNS-96-1436, Oct 1996, 7pp.
[8] V. N. Bayer, V. M. Katkov, V. S. Fadin, "Radiation of Relativistic Electrons", Moscow, Atomizdat, 1973.
[9] V. L. Ginzburg, "Theoretical Physics and Astrophysics", Moscow, Science Publishing (Nauka), 1981.
[10] I. N. Meshkov, "The Charged Particles Transport", Moscow, Science Publishing (Nauka), 1991.
[11] I. N. Meshkov, A. O. Sidorin, A. V.Smirnov, E. M. Syresin, "Particle Dynamics in a Storage Ring with a Longitudinal Magnetic Field", NIM A427(1999) 58-62.

CONCEPTUAL DESIGN OF LARGE-BORE SUPERCONDUCTING QUADRUPOLES WITH ACTIVE MAGNETIC SHIELDING FOR THE AHF

V.S. Kashikhin, G. Ambrosio, N. Andreev, S. Bhashyam, V.V. Kashikhin,
T. Peterson, J. Tompkins, A.V. Zlobin, FNAL, Batavia, IL 60510, USA
A. Jason, J.P. Kelley, P. Walstrom, LANL, Los Alamos, NM 87544, USA

Abstract

The Advanced Hydrotest Facility, under study by LANL, uses large-bore superconducting quadrupole magnets. In the paper we discuss the conceptual design of such quadrupoles using active shielding. The magnets are specified to achieve gradients of up to 24 T/m with a 28-cm warm bore and to have 0.01% field quality. Concepts for quench protection and the magnet cryosystems are also briefly discussed to confirm the viability of the proposed design.

INTRODUCTION

The LANL Advanced Hydrotest Facility (AHF) [1] uses large-bore superconducting (SC) quadrupole magnets to image protons for radiography of fast events [2]. Since 12 imaging lines converge on the object to be radiographed [3], size limitations are an important consideration as is magnetic coupling between lines. The pre-conceptual magnetic analysis of warm yoke, cold iron-core and active shield versions was described in [4]. In this paper we investigate an active shielding version, a very promising approach for this application. The quadrupoles have two concentric windings connected in series and configured so that the outer winding effectively eliminates the outer fringing magnetic field. This design also eliminates problems connected with a warm or cold ferromagnetic core. The active shielding eliminates fringing fields and Lorentz forces between adjacent quadrupoles and reduces magnet weight and size.

Imaging lenses consist of several large-bore quadrupoles, which can either be wired in series using common current leads, or be powered separately. With the large number of magnets in the system, Hi-Tc current leads are preferred [5]. Cold masses might be cooled with forced-flow supercritical helium [6], or alternatively with pool-boiling helium [7]. The first approach is widely used in accelerators, the second one in MRI, SC spectrometers, etc. Brief discussion of both options, and a preliminary quench analysis is presented in this paper.

QUADRUPOLE DESIGN

Specification and Parameters

In order to meet the imaging system requirements for AHF, the focusing quadrupole magnets should satisfy the criteria presented in Table 1 [8]. In addition, due to the limited space, the magnets should generate a minimum fringe field outside to avoid interaction between magnets in the doublets and adjacent strings.

Table 1. Magnet parameters

Parameter	Small-bore	Large-bore
Operating gradient, T/m	24.15	13.18
Magnetic length, m	3.0	4.3
Reference radius R_{ref}, mm	113.4	241.3
Field quality at R_{ref}	$<10^{-4}$	$<10^{-4}$
Main coil inner radius, mm	170.0	322.0
Screen coil inner radius, mm	276.0	513.5
Iron screen inner radius, mm	345.0	595.0
Iron screen thickness, mm	10.0	10.0
Number of turns in the main coil	232	508
Number of turns in the shield coil	104	220
Coil area, cm^2	174.4	378.0
Operating current, kA	14.10	11.77
Quench gradient with NbTi, T/m	28.25	15.80
Quench current with NbTi, kA	16.49	14.11
Peak field in the coil, T	6.1	6.3
Inductance, mH/m	9.91	49.41
Nominal stored energy, kJ/m	985.4	3420.7
Max. field in the iron screen, T	0.4	0.2

Design Concept

The quadrupole design is based on the active shielding concept, in which the return flux from the main winding is suppressed using another winding carrying an opposite current. The cross-section of the large aperture quadrupole based on this concept is shown in Fig.1. This approach suppresses nearly all leakage flux and avoids the interaction between the cold mass and iron screen inherent in the warm iron yoke concept. It also avoids iron saturation effects, which cause field distortions.

A simple estimate shows that limiting the magnet current to reasonable values of 15-20 kA leads to several hundreds of turns in the windings for the given apertures and gradients. A traditional shell type coil with that number of turns would suffer from stress accumulation at the midplane and large random field harmonics coming from the variation of individual cable positions within the shells. Thus it was imperative to split the shells into a number of mechanically decoupled blocks, providing the stress management and individual positioning and support for each block.

In order to accomplish this task, winding into the support structure approach was chosen. The winding mandrel is a cylinder with rectangular slots machined in longitudinal direction. For easier stacking and prestressing inside the slots, the cable is wound in the "hard bend"

0-7803-7738-9/03/$17.00 © 2003 IEEE

way with the long edge tangential to the mandrel. In addition, to simplify the manufacturing, all slots in the mandrel are oriented radially. After the coil is wound and cured, the mandrel serves as the mechanical support structure for the coil.

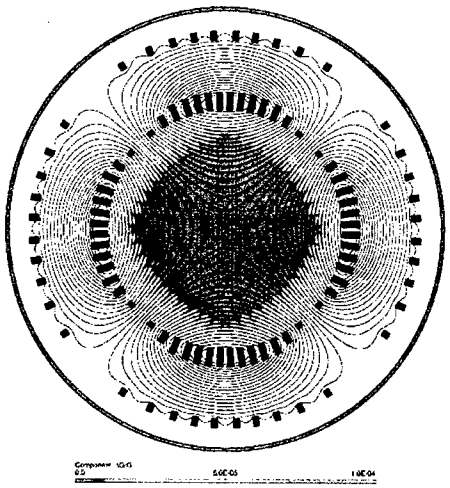


Fig. 1 Large-bore quadrupole field quality and flux lines

As opposed to the traditional shell-type magnet, the cable width in the proposed design concept does not drive the shell thickness and therefore the maximum gradient. It offers an opportunity of tuning the operating parameters by simply changing the number of turns in the blocks and neither the cable dimensions nor the number of layers. However, the cable width does drive the number of blocks and thus cost of the support structure, which should obviously be minimized. From this viewpoint, the maximum cable width acceptable for winding in the hard-bend direction should be chosen. Simple bending experiments demonstrated that a Rutherford type cable with 28 (1 mm in diameter) strands can be hard-bent around ~50-mm round mandrel without loss of stability. Given that the cable mechanical stability will be additionally enhanced by support from the mechanical structure during winding, the number of strands was fixed at 32.

Superconducting Cable

Both magnets are based on the same 32-strand cable with either NbTi or Nb_3Sn strands. The strand and cable parameters are summarized in Table 2. The higher critical current density and lower Cu:nonCu ratio in Nb_3Sn strands allows replacing significant amount of SC strands in Nb_3Sn cable with pure Cu strands while preserving the required field gradient.

Field Quality

Field quality in an air core magnet with large number of conductor blocks can be rather easily optimized to values of two orders of magnitude better than specified field harmonics 10^{-4}. Table 3 presents results of the optimized cross sections shown in Figures 1 and 2. Hence, the manufacturing accuracy will define the final field quality.

Table 2: Cable parameters

Parameter	**NbTi**	**Nb_3Sn**
Strand diameter, mm	1.000	
Number of strands	32	
Cable bare width, mm	16.214	
Cable bare thickness, mm	1.772	
Number of SC strands	32	8
Number of Cu strands	0	24
Copper to non-copper ratio	1.6	0.85
J_c(5T,4.2 K), A/mm^2	3000	-
J_c(12T,4.2 K), A/mm^2	-	2200

Table 3: Body field harmonics

n	**b_n, 10^{-4}**	
	Small-bore	**Large-bore**
6	-0.0012	-0.0002
10	0.0005	-0.0001
14	-0.0035	-0.0001
18	0.0005	0.0002

Random field harmonics were calculated as standard deviations among a large number of cases assuming +/-50 μm random block displacements from the nominal position. With these tolerances, the small bore will meet the field quality requirements for individual harmonics at the one σ level. However, due to the larger number of blocks, the large bore magnet with the same positioning tolerances will meet the field quality requirements at greater than the 3σ level or one can relax the tolerances to +/-140 μm to get the same probability.

A similar tolerance is placed on the end field harmonics. Three dimensional analysis and careful adjustment of the winding ends must be accomplished.

Quench Margin

The maximum field gradient was calculated for the quadrupoles made of NbTi and Nb_3Sn conductors with the properties shown in Table 2. Both the large and small quadrupoles using NbTi conductor achieve the maximum operating gradients with a 15-20% critical current margin. Using Nb_3Sn cable in these magnets increases the operating gradients by a factor of 1.5 with the same Ic margin.

Radiation losses in magnet coils will produce an extra heat load of 0.3–1.0 mJ/g. Fig. 2 shows the quench limit for NbTi and Nb_3Sn coils vs the magnet critical current margin. For operation at a heat deposition of 1.0 mJ/g, the critical current margin with NbTi coils has to be more than 25% while Nb_3Sn coils can operate with a margin of only 10%.

Quench Protection

Magnets will be protected with an active quench protection system based on the internal quench heaters as used in modern SC accelerators. Analysis shows that for a quench-detection time of ~50 ms and 50% coil volume

quenched by the heaters, the coil maximum temperature does not exceed 300 K and maximum voltage between the coil and ground during a quench is less than 100 V.

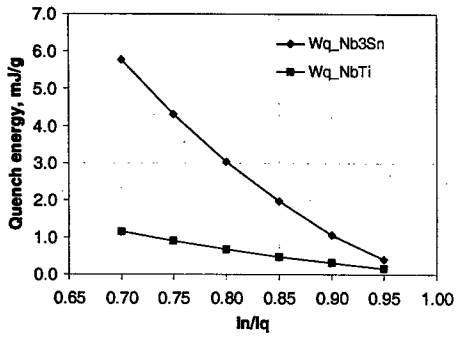


Fig. 2 Quench energy vs. coil critical current margin for NbTi and Nb_3Sn quadrupoles.

Cryosystem

The 12 intersecting lens-lines severely limit space for the cryo-distribution system. Also, unlike the simple end-to-end arrangement of magnets in RHIC or the Tevetron, the lens lines' arrangement does not lend itself to a simple flow through solution for cryogens as would be desired for a supercritical cooling approach. Initially, a pool-boiling approach was considered [5,6]. Supercritical flow is provided by a cryoplant located on the surface through a complex distribution system to JT valves on lens-line-magnet cryostats (Fig 3), nominally 50-m below grade. Flash and boiloff gas is returned to the cryoplant by a parallel route, possibly boosted by a cold compressor. Similar routing is used for thermal shield cooling (40-K, 4-atm helium), with some of this gas directed to Hi-Tc lead gas-cooled stages.

One potential problem with large heat loads in pool-boiling systems is the large volumetric flow rate required for removing vapor generated in tight spaces, particularly with density-gradient-driven flows (natural convection). Especially in non-vertical spaces of less than 1 mm, heat fluxes that can be removed by boiling and natural circulation start to drop off. Our extensive experience with pool-boiling cooled magnets in vertical test dewars may not be relevant, since heat loads there are typically minimal and local heat fluxes are very low. In spite of the geometric difficulties presented by the radial magnet arrangement, supercritical forced-flow cooling, which has been used successfully in long accelerator magnet strings such as RHIC, might have to be developed for the AHF system as an integral part of the magnet design.

Supercritical cooling is accomplished either with warm-compressor or cold-pump driven flow. High flow rates and recoolers are required to keep the helium temperature sufficiently below magnet-stability margins. Warm-compressor-driven flow cases were found to have prohibitive operating and capital costs [7]. With a single cold-pump driving the flow serially through the lens lines, 24 recoolers (two per line), and a pump-box, the purchase order cost of a supercritical-flow cryosystem (plant + distribution) is roughly 20% more ($5 M) than for a pool-boiling system, and consumes 23% (0.62 MW) more power. These differences are attributed to the additional equipment and associated heat load. Further studies are needed prior to finalizing the cooling approach.

Forced-flow liquid-helium cooling was not considered. This approach could lead to vapor trapping in magnets and jumpers, and density-wave type flow instabilities.

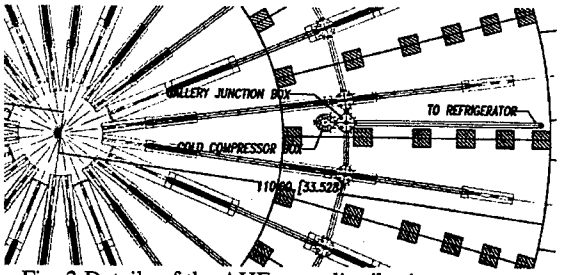


Fig. 3 Details of the AHF cryo-distribution system.

SUMMARY

Conceptual design of the AHF SC quadrupoles confirmed feasibility of the design based on the active shielding approach. The results, from this analysis, are:

- the specified field quality 10^{-4} can be achieved;
- quadrupole windings can be made from NbTi or Nb_3Sn superconductor;
- a proposed mechanical structure with adequate stress management;
- a quench protection system is viable;
- cryosystem concepts have been developed.

REFERENCES

[1] P.W. Lisowski and J.A. Paisner, "An Advanced Hydrotest Facility for the Stockpile Stewardship Program", Proc. of the 4th Int. Meeting on Nuc. App. of Accel. Tech., November 12-15, 2000, Washington D.C., p. 13.

[2] G.E. Hogan et al., "Proton Radigraphy", Proc. of the 1999 Part. Accel. Conf., 1999, p.579.

[3] C.T. Mottershead, J.D. Zumbro, "Magnetic Optics for Proton Radiography", Proc. of the 1997 Part. Accel. Conf., Vancouver, 1997, p.1397.

[4] N. Andreev et al., "Magnetic Design of Large-Bore SC Quadrupoles for the AHF", ASC 2002.

[5] J.P. Kelley, "The Impact of High Tc Leads on the AHF Lens Cryosystem of Firing Site 2," LANL Tech. Note, LA-UR-02-2692, Feb. 13, 2002.

[6] J.P. Kelley, "Cooling the FS-2 Lens System with Supercritical Helium – Cryosystem Considerations," LANL Tech. Note, LA-CP-02-516, Oct. 18, 2002.

[7] J.P. Kelley and G.T. Mulholland, "AHF Magnetic Lens Cryosystems," Adv. Cryo. Eng. Vol. 47, AIP Press, Melville, NY (2002), p. 60.

[8] P.W. Walstrom, "Magnetic Field Quality Specifications for the AHF Magnetic-Lens SC Quadrupoles", LANSCE-1 Tech. Note, LANSCE-1: 01-063, Aug. 23, 2001.

FIELD QUALITY OF THE LHC INNER TRIPLET QUADRUPOLES BEING FABRICATED AT FERMILAB *

G.V. Velev†, R. Bossert, R. Carcagno, J. Carson, D. Chichili, J. DiMarco, S. Feher, H. Glass, V.V. Kashikhin, J. Kerby, M. Lamm , T. Nicol, A. Nobrega, D. Orris, T. Page, T. Peterson, R. Rabehl, P. Schlabach, J. Strait, C. Sylvester, M. Tartaglia, J.C. Tompkins, S. Yadav, A.V. Zlobin
FNAL, Batavia, IL 60510, USA

Abstract

Fermilab, as part of the US-LHC Accelerator Project, has designed and is producing superconducting low-beta quadrupole magnets for the Large Hadron Collider (LHC). These 70 mm bore, 5.5 m long magnets operate in superfluid helium at 1.9 K with a maximum operating gradient of 214 T/m. Two quadrupoles, combined with a dipole orbit corrector, form a single LQXB cryogenic assembly, the Q2 optical element of the final focus triplets in the LHC interaction regions. Field quality was measured at room temperature during fabrication of the cold masses as well as at superfluid helium temperature in two thermal cycles for the first LQXB cryogenic assembly. Integral cold measurements were made with a 7.1 m long rotating coil and with a 0.8 m long rotating coil at 8 axial positions and in a range of currents. In addition to the magnetic measurements, this paper reports on the quench performance of the cold masses and on the measurements of their internal alignment.

1 INTRODUCTION

Superconducting low-beta quadrupole magnets (MQXB) for the Large Hadron Collider have been fabricated at Fermilab. These magnets are required to provide a maximum operating gradient of 214 T/m over a 70 mm coil bore, and to operate in superfluid helium at 1.9K [1]. Two 5.5 m long MQXB magnets are combined with a dipole orbit corrector (MCBX) to form a single cryogenic assembly (LQXB).

To date half of cold MQXB masses have been built. Four of them (MQXB01-04) were selected for assembling in the first two LQXB cryogenic units. In this paper we present the results of the warm field measurements of magnets MQXB01-09 in the production stage. The quench performance and field measurements of the first LQXB01 (MQXB01-02 quadrupoles) are described as well. A comparison with the results from the model magnet program [2] and the full scale prototype [3] is included. The results of the relative alignment of the first two cold masses inside the LQXB cryogenic assembly are also presented, including warm to cold correlations.

2 QUENCH PERFORMANCE

LQXB01 was tested at Fermilab Magnet Test Facility in superfluid helium at LHC operational temperature at 1.9 K in two thermal cycles (TC1 and TC2). Figure 1 summarizes the quench performance for the HGQ05-09 model magnets [2] together with the result from the prototype MQXP01 [3]. The outstanding performance of the first two MQXB01-02 magnets is pointed out by the large squares and the triangle around the horizontal solid line. MQXB01 achieved 230 T/m without any training. MQXB02 needed one training quench to reach the acceptance criteria of 230 T/m. Also it is important to note that magnets do not need to be retrained on TC2.

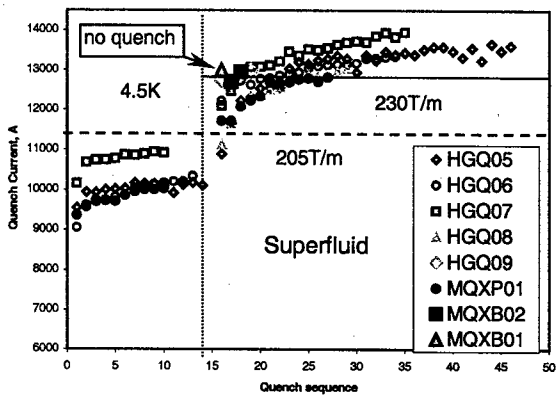


Figure 1: Quench training history for the model magnets HGQ05-09 and first prototype MQXP01. The horizontal dashed line corresponds to 205 T/m field gradient. The solid line corresponds to 230 T/m field gradient which is the acceptance criteria for MQXB magnets

3 MAGNETIC MEASUREMENTS

4.1 Measurement system

Magnetic measurements were performed using a horizontal drive rotating coil system. A long drive shaft, assembled from 1.5 m sections, is used to transfer the rotation to the probe. The shaft sections are supported in gates. They are controlled by photo-eyes and cycled open-closed by pneumatic cylinders when the probe is inserted or extracted from the magnet. Details on the magnetic measurements readout system are reported elsewhere [3].

The probes used have a tangential winding for measurement of higher order harmonics as well as specific dipole and quadrupole windings for measurement of the lowest order components of the field. The warm

*Work supported by the U.S. Department of Energy
†velev@fnal.gov

0-7803-7738-9/03/$17.00 © 2003 IEEE

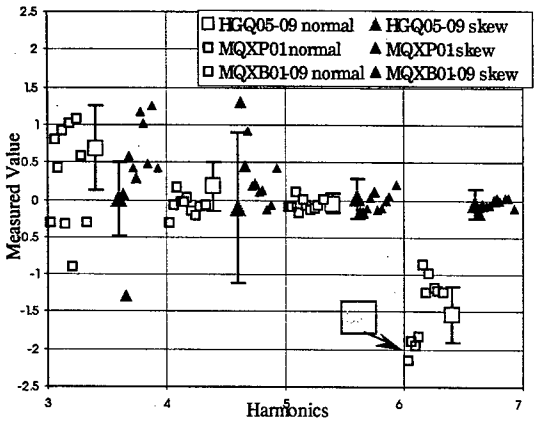


Figure 2: Measured collared coil harmonics in the body of MQXB01 through MQXB09. The large squares and triangles represent the average harmonics derived from the model magnet program. The error bars are one sigma. The arrow points at a systematically larger dodecapole than in the model magnets.

measurements are made with a coil of 31.8 mm nominal radius and 91.2 cm long. For the cold measurements we used two probes. The integral harmonics are obtained using a 7.1 m long rotating coil assembled from three independent probes connected in series. In addition to the integral measurements a DC cold scan was done with a 81 cm long probe.

4.2 Results of the warm measurements

In the process of production of every MQXB magnet two measurements are performed to ensure magnet quality. In the first one an integral z-scan of the collared coil is executed. This measurement checks the quality of the coil assembly and of the collaring process.

The second z-scan is done after yoking is complete. The measurement probe is placed at the same z-positions as for the collared measurements. This allows us to compare the harmonic changes due to the process of the yoking.

Fig. 2 shows the harmonics up to the dodecapole for the average of the last five HGQ model magnets, for the MQXP01 prototype, and for the MQXB01-09 production cold masses after. An acceptable but systematic deviation from the average harmonics of short model magnet tests is observed in the normal dodecapole for the first three cold masses MQXB01-03 (Fig.2).

The similar result for b_6 is obtained for the yoked cold masses. A performed accelerator simulation pointed to the possibility that in some configuration b_6 could be too large to be compensated with the available corrector strength. An effort was made into the production to decrease the normal dodecapole deviation. The result of the field calculation was implemented first in the MQXB04 cold mass [4]. 50 μm of Kapton insulation were removed from the midplane of each inner coil octant, and 25 μm were added to each inner pole. This caused each inner coil octant to be shifted toward the midplane by 25-50 μm. A decrease of 1 unit in b_6 is

Table 1: Integral field harmonics (in units at 17 mm) in MQXB01-02 at 11.9 kA field (214 T/m) compared to the acceptance criteria defined in Reference table v.3.2 [2]

n	Reference table v.3.2	MQXB 01	MQXB 02	Reference table v.3.2	MQXB 01	MQXB 02
	$\langle b_n \rangle \pm \delta(b_n)$	b_n	b_n	$\langle a_n \rangle \pm \delta(a_n)$	a_n	a_n
3	0.00±1.66	0.75	0.15	0.00±1.34	-0.82	-0.88
4	0.00±1.25	0.64	-0.65	0.00±1.29	-0.06	0.29
5	0.00±0.65	0.09	-0.24	0.00±0.65	-0.47	-0.13
6	0.21±0.97	-0.37	-0.23	-0.03±0.19	-0.02	0.10
7	0.00±0.12	-0.02	-0.05	0.00±0.10	-0.02	-0.02
8	0.00±0.08	0.02	0.01	0.00±0.05	0.02	-0.01
9	0.00±0.04	0.04	0.02	0.00±0.04	-0.03	-0.03
10	-0.01±0.04	-0.01	-0.02	0.00±0.04	-0.04	-0.04

observed which is somewhat larger than the expected 0.85 units from the field calculation. Following the result of the warm measurements the shim pattern was slightly modified in MQXB05 to decrease the change. This shim pattern was used in the production of MQXB07-09.

4.3 Cold measurements.

Harmonic measurements in the superconducting state have been performed on the MQXB01-02 cold masses connected in a single cryogenic unit LQXB01 at 1.9 K. The integral harmonics at 11923 A (214 T/m) are presented in Table 1. They are compared with the field quality values from the reference table v3.2 [2] which are derived from the model magnet program. The uncertainties assigned to the reference means, $\langle b_n \rangle$ and $\langle a_n \rangle$ in Table 1, correspond to $\delta(b_n,a_n) = d(b_n,a_n) + 3\sigma(b_n,a_n)$, where d and σ are the uncertainties in mean and standard deviation respectively. One may conclude that the magnet harmonics are inside the accelerator required limits.

To check for possible dynamic effects during the injection plateau, measurements were performed with an accelerator cycle similar to the one used in the LHC arc dipole tests [4]. The duration of the plateau is 15 min at 669 A (12.3 T/m). The decay and snap-back of the normal dodecapole at for MQXB01-02 is presented in Fig.3. The average decay amplitude is 0.55 units after 15 min. followed by the snap-back time of ~8.5 s.

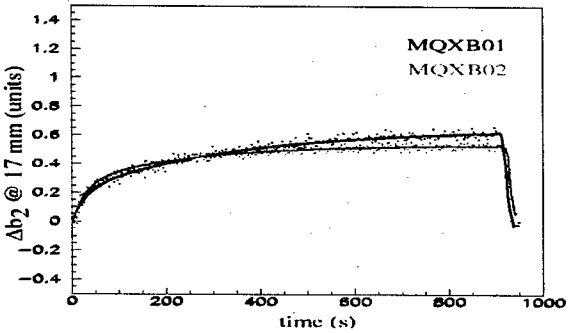


Figure 3: Decay and snap-back of the dodecapole component for a plateau at injection of 15 min.

Table 2: Hysteresis width (in units) of the dodecapole at 6kA.

Ramp Rate A/s	HGQ models					MQXB	
	05	06	07	08	09	01	02
10	-0.1	0.2	0.1	0.1	-0.1	-0.3	0.1
40	-0.1	1.1	0.6	0.7	-0.1	-0.4	-0.3
80	-0.1	2.1	1.1	1.5	-0.1	-0.6	-0.4

Current loops at 10, 40 and 80 A/s for MQXB01-02 have been performed. Table 3 summarizes the width ($b_6^{\text{up ramp}} - b_6^{\text{down ramp}}$) of the dodecapole hysteresis at 6 kA. One can conclude that MOXB01-02 have a similar behavior to the model magnets and that the Eddy current contribution to b_6 is relatively small.

The integral quadrupole field over the 5.5 m magnetic length was measured with a single stretched wire system (SSW) [5] and found to be 101.07±0.02 T/kA at injection and 98.86 ±0.02 T/kA at collision.

4 ALIGNMENT OF THE COLD MASSES FOR LQXB

Alignment measurements of the LQXB magnets consist of measuring the average magnetic axis of the two cold-mass system and transferring its location to the external fiducials. The survey data are reported to CERN and will be used in the absolute positioning of the LQXB assembly with respect to the LHC beamline axis.

The relative alignment of the MQXB cold masses inside the LQXB was carefully monitored for changes during TC1 and TC2 on the cold test stand using SSW. Table 3 summarizes, in chronological order, measurements performed in TC1 and TC2 at 4.5 K as well as warm measurements between the thermal cycles. The average ΔX, ΔY center offsets, the yaw, pitch and roll angles of MQXB01-02 are presented relative to the final alignment measurement labeled "cold TC2", when the magnetic centers of the cold masses are positioned on x,y=0,0.

Based on the TC1 results, small mechanical adjustments were made between the "After TC1" and "Before TC2", using the adjustment logs of the cold mass supports. The cold mass positions changed predictably with changes of the logs. The changes seen during the thermal cycles, warm-cold-warm, are reproducible, for each TC, and similar in TC1 and TC2 despite the mechanical adjustments between them.

Table 3: Measured changes in average ΔX, ΔY center offsets, yaw, pitch and roll angles relative to the cold TC2 measurement

Measu-rement	Magnet	ΔX (mm)	ΔY (mm)	Yaw (mrad)	Pitch (mrad)	Roll (mrad)
Before TC1	01	-0.32	0.88	0.05	-0.15	-0.37
	02	-0.16	0.60	-0.04	0.03	0.47
Cold TC1	01	-0.36	0.54	0.06	-0.03	-0.33
	02	0.03	0.14	0.08	-0.06	0.47
After TC1	01	-0.29	0.65	0.07	-0.17	-0.36
	02	-0.06	036	-0.05	0.07	0.56
Before TC2	01	0.06	0.25	0.16	-0.30	-0.56
	02	-0.08	0.38	-0.05	0.07	0.33
Cold TC2	01	0.0	0.0	0.20	-0.27	-0.50
	02	0.0	0.0	0.03	-0.04	0.50
After TC2	01	0.16	0.15	0.14	-0.33	-0.55
	02	-0.01	0.26	-0.07	0.10	0.44

The final cold SSW measurement, labeled "Cold TC2", confirmed that the relative yaw, pitch and roll angles between the MQXB01-02 cold masses are within alignment tolerances required from the accelerator beam optic studies [6].

5 CONCLUSIONS

The first LQXB cryogenic unit for the LHC interaction region has been tested.

Both magnets in the LQXB01 cryogenic assembly showed outstanding quench performance. They reached the acceptance criterion of 230 T/m with minimal training quenches.

The quality assurance warm magnetic measurements after collaring and yoking of the cold masses were described. As a whole the field harmonics are quite small and consistent with those measured in the last five short model magnets and in the first full scale prototype

Cold magnetic measurements were performed on the MQXB01-02 cold masses assembled in the cryogenic unit (LQXB01). Integral field are quite small and they are consistent with the acceptance criteria. The effect of the cable Eddy currents is small and similar to that seen in the model magnets. The decay and snap-back at injection plateau was studied and the average change in b_6 was found to be relatively small (0.55 units after 15 min).

The alignment of the first two cold masses inside LQXB01 assembly has been completed. Field alignment measurements, performed with the SSW system, confirmed that the placement errors of the cold masses are within the required limits.

6 REFERENCES

[1] "The Large Hadron Collider, Conceptual Design", CERN/AC/95-05 LHC

[2] N. Andreev et al., "Field quality in Fermilab-built models of quadrupole magnets for the LHC interaction region", IEEE Trans. Appl. Supercond., Vol. 11, No. 1, March 2001.

[3] R. Bossert et al., "Production and Test of the First LQXB Inner Triplet Quadrupole at Fermilab", EPAC 2002, Paris, FERMILAB-CONF- 02/115, June 2002.

[4] L. Bottura, P. Burla, R. Wolf, "LHC Main Dipoles Proposed Baseline Current Ramping", LHC Project Report 172, 1998.

[5] J. DiMarco et al., "Field alignment of quadrupole magnets for the LHC interaction regions", IEEE Trans. Appl. Supercond., Vol. 10, No. 1, March 2000.

[6] Private Comunication by T. Sen. See also "Alignment tolerances of IR quadrupoles in the LHC", FERMILAB-CONF-99/304, November, 1999.

MEASUREMENTS OF FIELD DECAY AND SNAPBACK EFFECT ON TEVATRON DIPOLE MAGNETS *

G.V. Velev†, G. Annala, P.Bauer, R. Carcagno, J.DiMarco, H. Glass, R. Hanft, R. Kephart, M.Lamm, M. Martens, P.Schlabach, M. Tartaglia, J. Tompkins
FNAL, Batavia, IL 60510, USA

Abstract

The performance of Fermilab's Tevatron accelerator, currently in its Run II stage, is degraded by beam loss and emittance dilution during ramping from injection to collision energy. This could be related in part to insufficient compensation of dynamic effects such as the decay of the magnetic field in the dipoles during the dwell at injection and the following so-called snapback during the first few seconds of the energy ramp. The two effects are closely related and depend on the powering history of the magnets. Dynamic effects, which were originally discovered at the Tevatron [1], were investigated on Tevatron magnets in various past measurement campaigns in the 1980s and later in 1996 [2]. This paper reports on the most recent measurements performed on an additional set of Tevatron magnets.

1 INTRODUCTION

At injection energy the sextupole field errors from persistent currents can be significant due to their large amplitude and time dependence. It was found that their change during injection is unacceptable for the Tevatron operation and corresponding corrections were developed (for example see ref. [1][3]).

The Run II Tevatron corrections were obtained from 1996 magnetic measurements [2] and are later optimized using beam based measurements. However up to 10% beam losses at injection and at the beginning of the acceleration is still observed in the Tevatron.

A systematic series of measurements for an additional optimization of the existing correction algorithm was carried out. In this paper we present the first results from measurements of b_2 decay and snapback on four Tevatron dipoles (TC1220, TB0834, TC0483, TB0269) which have been extensively tested at the Fermilab Magnet Test Facility.

2 MAGNETIC MEASUREMENTS

2.1 Measurement system

Magnetic measurements were performed using a horizontal drive rotating coil system. A 1.8 m long drive shaft is used to transfer the rotation to the probe in the body of the magnet. The shaft and the probe are supported by bearings inside the warm bore.

The probe in use, a 81.7 cm long coil with a 19.6 mm nominal radius, has a tangential winding for measurement of higher order harmonics as well as specific dipole and quadrupole windings for measurement of the lowest order components of the field.

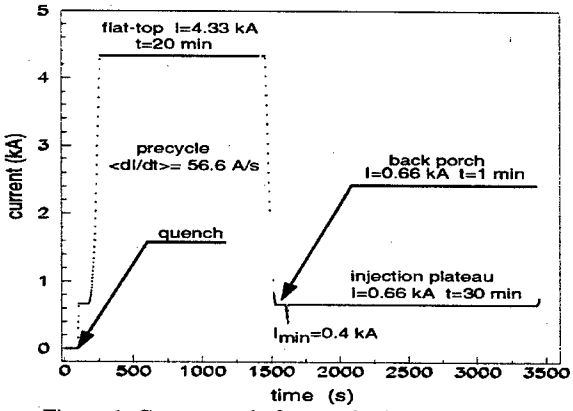


Figure 1: Current cycle for standard decay and snap-back measurements.

Coil winding voltages are read out by Metrolab PDIs. The PDIs were configured first to read and store data in the internal buffers (active time) and next to transfer them to the VME computer (passive time). More details on the readout system are reported elsewhere [4].

To achieve good sensitivity on the rapidly changing dynamic effects in the magnets, like a snap-back which typically occurs within an interval of 5-10 s in the case of the Tevatron, the shaft rotational speed was set to 5 Hz. To decrease the effect of the mechanical vibration and to increase the signal to noise ratio we used an analog bucking technique providing a cancellation of the main dipole field term with a simple addition of signals from the tangential and dipole coils.

2.2 Current cycle

In our measurements we used current profiles which are as close as possible to the real Tevatron operation cycles. The nominal current profile is shown in Fig. 1. Its parameters are: a 20 min. flat-top (FT) at 4.3 kA (980 GeV beam energy), a 1 min. back porch (BP) duration and a 30 min. injection plateau (IP). Additionally we varied the duration of FT (1,10, 20 and 60 min., in some cases up to 12h), the duration of the BP (1,10 and 30 min.), the duration of IP (30, 60 and 120 min.), as well as number of the flattops (NF) (1,2,3 and 6) and the maximum flat-top current (3.5, 4.0 and 4.3 kA). The variation of the last parameter has no direct impact on Run II Tevatron operation since the maximum current is held constant at 4.3 kA.

*Work supported by the U.S. Department of Energy
†velev@fnal.gov

0-7803-7738-9/03/$17.00 © 2003 IEEE

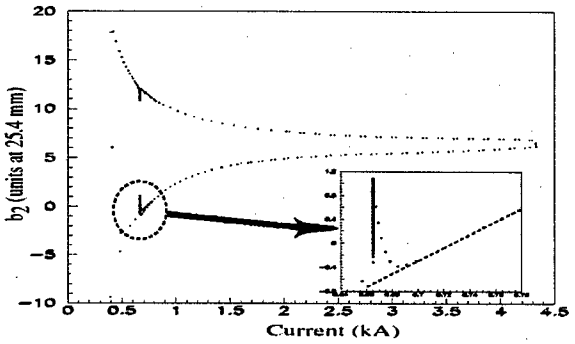


Figure 2: Hysteresis loop of the sextupole component. The insert shows the snap-back and the line approximation of the loop at the snap-back's region

3 DECAY AT INJECTION PLATEAU

The magnets of our sample have different quench performances. Therefore they have been measured at different temperatures, from 3.9 to 4.5 K. We normalized all measurements to 3.9K, using corrections which vary from magnet to magnet from 13% to 16% per 1K.

The typical b_2 hysteresis loop from the nominal measurement is shown in Fig. 2. In the Tevatron operational scheme its sextupole correctors have to be controlled in such a way that they compensate for decay and snap-back of the b_2 harmonic at injection time. Therefore we need to extract only the effect of the dynamic processes. To subtract the underling sextupole loop we linearly parametrized b_2 as a function of the current in the region of 0.7-0.78 kA and extrapolated its value to the injection plateau at 0.66 kA (see the insert in Fig.2).

Two different functional forms have been used in the past to model decay processes in superconducting accelerator magnets. The behavior of Tevatron and HERA magnets could be modeled as a logarithmic decay [3],[5]

$$\Delta b_2 = b_{2,0} + b_{2,1} \cdot \log(t / t_0). \quad (1)$$

The behavior of RHIC magnets was parametrized by two superimposed exponentially decaying terms [6]

$$\Delta b_2 = b_{2,0} + b_{2,1} \cdot e^{-t/t_1} + b_{2,2} \cdot e^{-t/t_2}. \quad (2)$$

In our case we used a logarithmic function to parametrize the b_2 decay. Fig. 3 shows the b_2 decay for different durations of FT. It was found that t_0 is close to 1 s as in the HERA magnets thus $t_0 = 1$ s was fixed in our fits. To describe the interval below 100 s we slightly modify the logarithmic form (1) adding a time offset parameter t_s

$$\Delta b_2 = b_{2,0} + b_{2,1} \cdot \log(t + t_s). \quad (3)$$

The parameters $b_{2,0}$, $b_{2,1}$ and t_s were fitted with different functional forms, either polynomial or exponential or superposition of both, depending on the duration of IP, BP and FT. These one dimensional functions are the first step towards a new multiparameter correction form for the Tevatron b_2 correction at injection.

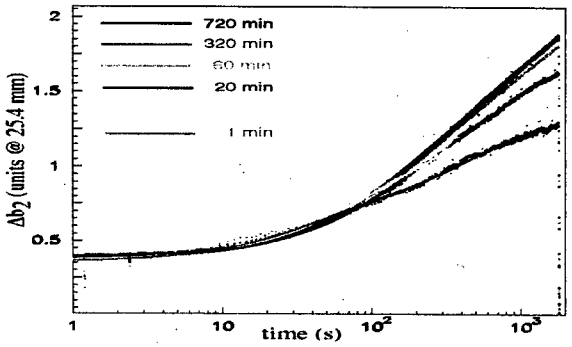


Figure 3: Decay of the sextupole component for a plateau at injection of 30 min. and different duration of the flat-top (magnet TC1220). After one hour duration of flat-top, the b_2 decay shows similar behavior

We also tried to model the b_2 decay with a double exponential form according to (2). In two of the four measured magnets the fit returned a very large time constant of order of 10^6. In the other two magnets the double exponential form (2) performed slightly better than (3). The attempt to find the best parametrization for the decay part was not conclusive and will be continued in the future experiments. In addition we are trying to understand if there is a reason for the different parametrization behavior (for example, different cable characteristics).

4 MEASUREMENTS OF THE SNAP-BACK

At the Tevatron the snap-back compensation is done according to

$$\Delta b_2 = b_{2,0} \cdot (1 - t^2 / t_0^2)^2, \quad (4)$$

where $b_{2,0}$ is the initial amplitude and t_0 is the snap-back time [2]. Although the polynomial form (4) was found in general to work for snap-back compensation, we determined that a gaussian form

$$\Delta b_2 = b_{2,0} \cdot \exp(-t^2 / t_0^2), \quad (5)$$

describes our measurements with a high probability (χ^2/ndf ~1). Some of the snap-back fits are shown in Fig. 3. The time scale is set to zero when the acceleration ramp is started and the snap-back is initiated. Note that t_0 has a different meaning in formulae (4) and (5): in the first case it is the value where the functional form is zeroed, in the second case, it is the standard width of the gaussian distribution.

We parametrized the snap-back amplitude $b_{2,0}$ and time t_0 as a function of the duration of the current cycle intervals (IP, BP, FT). An exponential dependence according to

$$b_{2,0}, t_0 = p_1 \cdot \exp(-t / p_2) + p_3 \quad (6)$$

where t is the duration in minutes of the varied cycle interval is proposed. Fig.4 shows a parametrization of $b_{2,0}$ and t_0 for different duration of the flat-top. The dashed line represents the average fit to the four measured

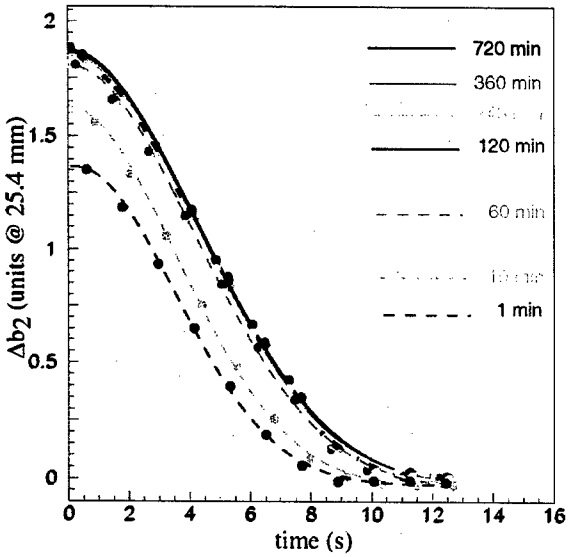


Figure 3: Snapback of the sextupole component for a plateau at injection of 30 min. and different duration of the flat-top (magnet TC1220). The dashed lines represent the snap-back for short flat-top durations.

magnets.

Table 1 summarizes the fit output for the p_1-p_3 parameters. When we vary NF the data are fit to a constant. This is because the fit returns a negligible slope in case of linear approximation. In addition one can observe that after 60 min. of FT the snap-back amplitude and time are practically independent of its duration (see fig. 3 and fig 4).

These two results are important for the optimization of the Tevatron operation. In fact one can propose to remove the precycle after the end of a successful store and to start the injection directly after ending a collision. On the other hand if the store is ended abnormally, for example by a quench, data suggest that the number of precycles may be reduced from 6 to 3 or either 2.

The effect of the BP duration shows opposite tendency comparing to the FT duration. The snap-back amplitude and time decrease exponentially with the BP duration and converge to Δb_2=0.8 units and t_0=3.54 s at large values of the BP durations (Table 1, BP column).

Table 1: Results from the fits describing $b_{2,0}$ and t_0 with the exponential form (6). The parameters represent the average fit from the sample of four measured magnets.

Par	IP	BP	FT	NF
Snap-back amplitude				
p_1	-0.7±0.1	0.78±0.1	-0.5±0.1	0
p_2	52.±5.1	7.1±0.5	7.9±0.2	0
p_3	2.0±0.2	0.8±0.1	0.2±0.1	1.5±0.2
Snap-back time				
p_1	-1.1±0.2	2.1±0.1	-2.6±0.6	0
p_2	66.±28.	5.91±0.7	0.9±0.2	0
p_3	6.4±0.1	3.54±0.1	5.2±0.1	5.3±0.2

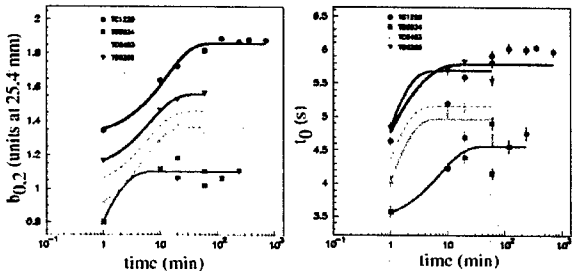


Figure 4: The snap-back amplitude and time parametrized with (6) as a function of the flat-top duration time. The dashed line represents the average fit for the sample of four magnets.

6 CONCLUSIONS AND PLANS

The sextupole decay and snap-back effects at Tevatron injection ware studied on four Tevatron dipoles. It was confirmed that the durations of IP, BP and FT have a major impact on the b_2 decay amplitude and snap-back time. Other possible variations of the current cycle, like the number of flattops and the maximum flat-top current were found to have small or no impact on the dynamic processes at injection.

A new type of the snap-back parametrization was proposed. Is was found that gaussian distribution, instead of polynomial form (4), fits better the magnet data.

The data shows that b_2 decay amplitude and the snap-back time reach saturation after 60 min. FT. This result supports the proposal of removing the precycle after the end of successful stores.

A set of functions describing the sextupole decay and snap-back are obtained. These functions are the first step towards a new multidimensional correction form for the Tevatron operation at injection.

We are planning to extend the measurements to more dipoles and to refine them in order to develop a detailed set of measurements in the relevant parameter space for Tevatron operation.

6 REFERENCES

[1]D.A.Finley et al., "Time dependent chromaticity changes in the Tevatron", Proceeding of Part. Acc. Conf., Washington, DC, 1987.

[2] G. Annala et al., "Tevatron Dipole Measurements at MTF", http://www-bdnew.fnal.gov/tevatron/adcon/magnets.html, P. Bauer et al., "Analysis of the b2 Correction in the Tevatron", These Proceedings

[3] D.E. Johnson and D.A. Herrup "Compensation of time Varying Field in the Tevatron Superconducting Magnets", Proceedings of PAC 1989.

[4] G. Velev, "Field Quality of the LHC Inner Triplet Quadrupoles at Fermilab", These Proceedings

[5] K.-H.Mess and P. Smchmüser, "CERN Accelerator School on Superconductivity in Particle Accelerators", CERN Report 89-04, 1989.

[6] W.Fisher, A. Jain and S.Tepikian, "Beam-Based Measurements of Persistent Current Decay in RHIC", Phys. Rev. ST Accel. Beams 4, 2001.

APERTURE LIMITATIONS FOR 2ND GENERATION Nb_3SN LHC IR QUADRUPOLES[1]

A.V. Zlobin*, V.V. Kashikhin, J.B. Strait, FNAL, Batavia, IL 60510, USA

Abstract

One of the straightforward ways towards the higher luminosity in the LHC is a replacement of the present 70-mm NbTi quadrupoles with Nb_3Sn quadrupoles which would provide the same field gradient but in a larger aperture. Conceptual designs of such magnets with 90 mm aperture have been developed and studied. This paper discusses the possibilities and limitations of further increasing the aperture of Nb_3Sn low-beta quadrupoles , and shows that an aperture up to 110 mm is possible.

INTRODUCTION

Present optics of two LHC interaction regions (IR) is based on single-bore inner triplets consisting 70-mm NbTi quadrupoles with a nominal field gradient of 205 T/m operating at T=1.9 K. These magnets were designed to provide β^*=50 cm for a nominal LHC luminosity of 10^{34} $cm^{-2}s^{-1}$ [1]. Replacing them with higher performance magnets will be a major component of the LHC luminosity upgrades.

The future LHC luminosity upgrade plans being discussed at present time require new low-beta quadrupoles with higher field gradient, larger operation margin and larger magnet aperture [2,3]. Preliminary analysis shows that large-aperture quadrupoles based on Nb_3Sn superconductor meet these basic requirements [4,5]. This paper continues the studies with the goal to determine the aperture limitations for Nb_3Sn IR quadrupoles.

MAGNET DESIGN

The conceptual design of 90-mm Nb_3Sn quadrupole magnets based on 2-layer shell-type designs has been recently developed and analyzed [6,7]. The 90-mm aperture is close to the limit for a 2-layer design due to the large cable aspect ratio. Therefore 4-layer designs were considered for quadrupoles with 100-mm and 110-mm aperture. Both magnets consist of two double-layer shell-type coils and cold iron yoke. The goal was to achieve a nominal field gradient of 205 T/m with a 20% margin and the best field quality with one wedge in the innermost layer. The current density in the coil layers was graded, providing a noticeable contribution to the field gradients. The circular iron yoke was set 15 mm beyond the coil to provide space for the collars. The magnetic permeability of the iron was constant and equal to 1000. The 4-layer 100 and 110 mm coil cross-sections as well as 2-layer 90 mm quadrupole coil optimized with ROXIE code are shown in Figure 1.

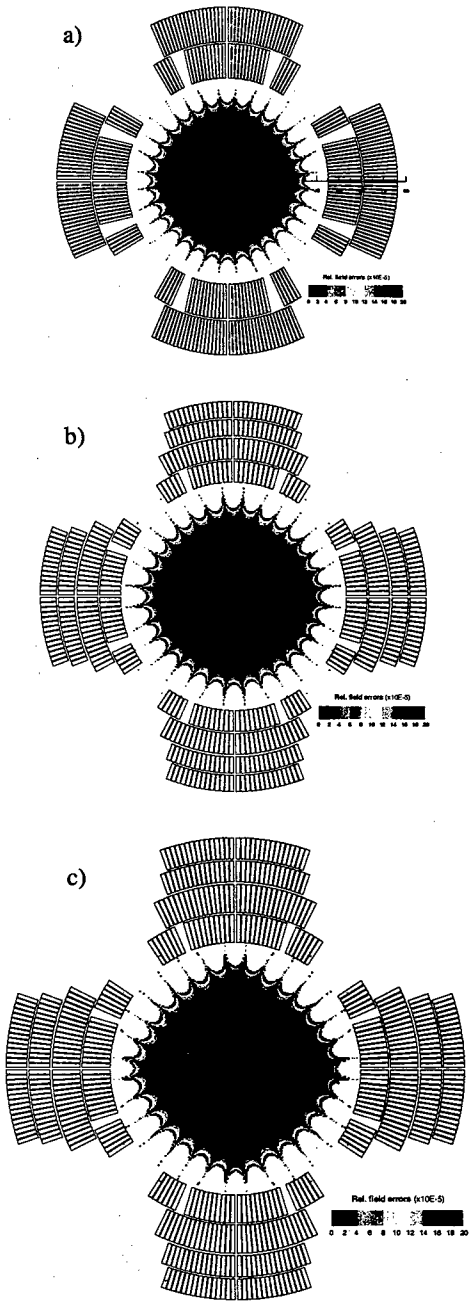


Figure 1: Quadrupole coil cross-sections with 90-mm (a), 100-mm (b) and 110-mm (c) apertures.

[1] Work supported by the U.S. Department of Energy
* zlobin@fnal.gov

0-7803-7738-9/03/$17.00 © 2003 IEEE

The coil parameters for all the three quadrupole designs are summarized in Table 1. The coil width and volume required to reach the target field gradient increase dramatically in the 110-mm aperture quadrupole design.

Table 1: Coil parameters.

Parameter	Aperture		
	110 mm	100 mm	90 mm
Number of layers	4		2
Number of turns	248	228	144
Coil width, mm	45.5	34.5	31.5
Coil area, cm^2	84.9	59.3	48.1

Table 2 summarizes the final cable parameters for the all three designs. Two different cables are used in each 4-layer quadrupoles in order to increase the efficiency of magnet design. The cables are based on the same 1-mm Nb_3Sn strand. The cable dimensions including insulation were determined in an iterative optimization process in order to achieve maximum gradients with minimum coil areas. The cable keystone angle was set to ensure the radial position of each turn in the coil. The 2-layer 90-mm quadrupole uses one cable based on the 0.7 mm Nb_3Sn strand in both layers.

All the cables have the same packing factor of 89% and Cu:nonCu ratio of 1.2. Practical experience shows that the cables used in the 4-layer designs are simpler for manufacturing and have better mechanical and electrical properties than the cable used in the 2-layer design due to the smaller aspect ratio.

Table 2: Cable parameters.

Parameter	Aperture				
	110 mm		100 mm		90 mm
Coil layer	1-2	3-4	1-2	3-4	1-2
Number of strands	24	18	18	14	42
Strand D, mm	1.0				0.7
Cable width, mm	12.33	9.23	9.23	7.17	15.14
Inner edge, mm	1.59	1.66	1.61	1.67	1.08
Outer edge, mm	1.94	1.87	1.92	1.86	1.39
Keystone angle, deg	1.7	1.3	1.9	1.5	1.18
Aspect ratio	7	5	5	4	12

MAGNET PARAMETERS

Field quality

Table 3 presents the systematic geometrical harmonics at the reference radius equals to the half of the coil bore radius for the 100-mm and 110-mm designs and also for the 2-layer 90-mm quadrupole. For comparison the field harmonics of present 70-mm NbTi LHC IR quadrupoles (MQXB) at the reference radius of 17 mm (which as well corresponds to the half bore radius for this magnet) are also presented.

The first allowed geometrical harmonics, b_6 at $R_{ref}=R_{bore}/2$ is almost the same for 90, 100 and 110 mm designs and it is noticeably better than the b_6 in present 70-mm design. The higher order geometrical harmonics, b_{10} and b_{14}, are almost the same in 90, 100 and 110 mm designs and slightly higher than in MQXB. If required, the geometrical harmonics can be further optimized by introducing additional wedges in the coil.

Table 3: Systematic field harmonics b_n @$R_{ref}=R_{bore}/2$.

n	Aperture			
	110 mm	100 mm	90 mm	70 mm
6	0.0002	0.0005	0.0006	-0.013
10	0.0033	0.0029	0.0045	-0.001
14	0.0118	0.0046	0.0069	-0.0011

Short sample limit

Figure 2 shows the calculated quench gradient for 110, 100 and 90 mm quadrupoles as a function of the critical current density in the non-copper area of the superconducting cable. The Nb_3Sn strands with J_c(12T,4.2K) more than 3 kA/mm^2 allow a quench gradient above 250 T/m to be reached in all the designs. An R&D program in the U.S., aimed at the development of high J_c Nb_3Sn strands for a new generation of SC accelerator magnets, has been launched few years ago. Based on the results achieved in the framework of this program, strands with the critical current density >3 kA/mm^2 will be available in 2-3 years. The Jc(12T,4.2K) of 2.9 kA/mm^2 has been reached in short samples. However, more work has to be done on reduction of strand magnetization and improvement of their stability.

The data presented in Figure 2 and Table 1 confirm that the efficiency of the magnet design decreases with aperture increasing. In order to reach the same field gradient wider coils with higher critical current density are required.

The maximum quench field in the coil of the 110, 100 and 90 mm quadrupoles reaches 15.3, 14.5 and 13.5 T respectively with cable critical current density of 3 kA/mm^2 at 12 T and 4.2 K. The maximum field in the 110 mm quadrupole exceeds the maximum field achieved in the Nb_3Sn high field accelerator magnets at present time.

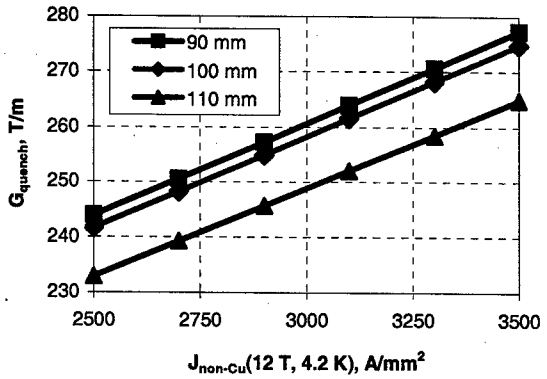


Figure 2: Quench gradients at 4.2 K as functions of the critical current density in the coil.

Lorentz forces and coil stress

Table 4 presents the calculated horizontal and vertical components of the Lorentz force applied to one octant of the coil at the nominal field gradient of 205 T/m, and the maximum stress in the coil associated with these forces. Analysis shows that the level of Lorentz forces in the 90-mm quadrupole reaches the same level as in the LHC arc dipoles. In the quadrupole with 110 mm aperture the expected Lorentz forces are higher than the forces in the Nb_3Sn high field dipole models being developed at the present time for different applications.

The level of mechanical stresses in the coil of the 110 mm quadrupole approaches to 100 MPa. To provide the coil pre-stress of this level at operating temperature, the coil prestress during fabrication increases to the level at which significant irreversible Nb_3Sn strand degradation may occur. Clearly, the robust mechanical structure capable of providing an adequate coil support during operation and avoiding coil over-compression during fabrication is a key element for these quadrupole designs.

Table 4: Lorentz forces and maximum coil stress.

Parameter	Aperture		
	110 mm	100 mm	90 mm
Fx(205T/m), MN/m	3.44	2.38	1.5
Fy(205T/m), MN/m	-3.42	-2.39	-1.92
Maximum coil stress, MPa	99	90	73

Quench protection

All superconducting accelerator magnets have large stored energy and require a special quench protection system in case of quench. Magnet inductance and stored energy at the nominal field gradient of 205 T/m for the 110, 100 and 90 mm quadrupoles are presented in Table 5. Quench protection of these magnets can be provided using the traditional approach based on internal quench protection heaters, which distribute the stored energy in the coil, thereby preventing coil overheating and reducing the voltages between the coil and ground as well as mechanical shock in the coil during quench. The acceptable coil maximum temperature for accelerator magnets is 300-400 K. The results of calculation of the maximum coil hot spot temperature, T_{hs}, in the region where the quench occurred and the maximum temperature under the quench heaters, T_{blk}, are reported in Table 5 for the fractions of coil volume quenched by the heaters, F_{qh}, of 50% and 25%.

Table 5: Quench protection parameters.

Parameter		Aperture		
		110 mm	100 mm	90 mm
L, mH/m		17.46	14.71	4.86
W(205 T/m), kJ/m		1181	703	468
T_{hs}, K	F_{qh}=50%	230	225	230
	F_{qh}=25%	335	320	315
T_{blk}, K	F_{qh}=50%	150	140	127
	F_{qh}=25%	220	200	180

For the redundancy of quench protection system the parameter F_{qh} that provides safe coil protection, should be less than 50%. In this case two parallel sets of heaters could be installed in the magnet. Calculations show that even for F_{qh}=25% the coil maximum temperature in all the quadrupole designs is within 315-335 K. With F_{qh}=50% the maximum temperature does not exceed 250 K which is more comfortable for brittle Nb_3Sn coils.

CONCLUSION

The studies presented here show that a 110-mm aperture quadrupole magnet using Nb_3Sn strand can provide a maximum field gradient of 250 T/m (20% above the present nominal gradient of 205 T/m) with acceptable field quality. Quench protection of these magnets can be provided using the traditional approach based on internal quench heaters.

Single-aperture inner triplets with these magnets can reduce β^* by a factor of 3, from 50 cm to 17 cm leading to a potential luminosity increase by a factor of 3.

However, the following parameters make the 110 mm quadrupoles quite challenging:

- the critical current margin of 20% requires high-performance Nb_3Sn strands with the critical current density Jc(12T,4.2K)>3 kA/mm^2;
- the peak field in the coil at quench exceeds the state-of-the-art level of 15 T for Nb_3Sn accelerator magnets;
- the maximum stress in the coil, induced by Lorentz forces, reaches 100 MPa approaching the level of stress which may cause significant degradation or even damage of brittle Nb_3Sn coils.

The risks associated with the above factors have to be analyzed and taken into account while choosing the final quadrupole aperture.

REFERENCES

[1] "The Large Hadron Collider" Conceptual Design, CERN/AC/95-05 (LHC), 20 October 1995.

[2] T. Taylor, "Superconducting Magnets for a Super LHC", EPAC 2002, Paris, France, p.129.

[3] J.B. Strait et al., "Towards a New LHC Interaction Region Design for a Luminosity Upgrade", presented at PAC 2003, Portland, OR, May 2003.

[4] T. Sen, J. Strait, A.V. Zlobin, "Second Generation High Gradient Quadrupoles for the LHC Interaction Regions", PAC 2001, Chicago, IL, June 2001, p.3421.

[5] T. Sen et al., "Beam physics issues for a possible 2nd generation LHC IR", EPAC2002, Paris (France), June 2002, p.371.

[6] A.V. Zlobin et al, "Large-Aperture Nb_3Sn Quadrupoles for 2nd generation LHC IRs", EPAC2002, Paris (France), June 2002, p.2451.

[7] A.V. Zlobin et al., "Conceptual design study of Nb_3Sn low-beta quadrupoles for 2nd generation LHC IRs", Proceedings of 2002 Applied Superconductivity Conference, Houston, TX, August 2002.

STATUS OF LHC LOW-β QUADRUPOLE MAGNETS, MQXA, AT KEK

N. Ohuchi#, Y. Ajima, N. Higashi, M. Iida, N. Kimura, T. Nakamoto, T. Ogitsu, H. Ohhata, T. Shintomi, S. Sugawara, K. Sugita, K. Tanaka, A. Terashima, K. Tsuchiya, A. Yamamoto, KEK, Tsukuba, Ibaraki, Japan; T. Fujii, T. Kanahara, E. Hashiguchi, S. Murai, W. Odajima, T. Orikasa, Toshiba-corp., Yokohama, Kanagawa, Japan

Abstract

KEK has developed a superconducting quadrupole magnet, MQXA, for the LHC interaction region. This magnet is required to generate an operating field gradient of 215 T/m in the magnet bore of 70 mm and have an effective magnetic length of 6.37 m. For the accelerator operation, sixteen MQXA magnets will be installed in total for four interaction regions, and the cold tests of ten MQXA magnets of them have been completed. These ten magnets had good quench performance and satisfactory field quality for the requirement of beam optics. This paper describes the production quality and the magnet performance of the MQXA magnets.

INTRODUCTION

Under the cooperative program between CERN and KEK, KEK has developed a superconducting low-beta quadrupole magnet, MQXA, for the LHC interaction region [1], and KEK will provide eighteen MQXA magnets in total, including two spare magnets. These MQXA magnets will operate in the final focus system (low-β triplet) with the MQXB magnets developed by FNAL [2]. The MQXA magnets are designed to have a magnet bore of 70 mm and generate an operating field gradient of 215 T/m along the effective magnetic length of 6.37 m in the superfluid helium at 1.9K [3, 4]. As the peculiar points in this design, the magnet has a four-layer coil configuration with current grading, however, mechanically the magnet has a two-layer coil configuration. The horizontal split iron yokes have a function of mechanical support against the electro-magnetic force. The main parameters are summarized in Table 1.

After the R&D studies with two full-scale proto-type magnets [5], the series production of MQXA was launched in 2001 [6]. Presently, the construction of eleven MQXA magnets was completed and ten of these magnets were tested at 1.9 K. We report the production and performance of these ten MQXA magnets in this paper.

PRODUCTION

Coil Size Control

In order to minimize the difference from magnet to magnet in the mechanical characteristics and field quality, the dimension of each coil is controlled during the curing process. To confirm manufacturing quality in this process, the coil sizes were measured at six points along the straight section for each octant of the inner or outer two layer coils. In Figs. 1 (a) and (b), the average coil sizes of MQXA-1 to 10 under the pressure of 53MPa are shown. The error bars correspond to the standard deviation of 1σ for the 48 measured values. The coil size is described by the deviation from the design dimension. The coil sizes of the inner layers varied from –74 μm for MQXA-5 to –5 μm for MQXA-10, and the standard deviation of 1σ for ten magnets is 23 μm. For each magnet, the deviation of 1σ is in the range from 15 μm to 23 μm. For the outer layers, the variations of the coil size are smaller than those of the inner layers. The 1σ for ten magnets is 7 μm. The 1σ in each magnet is in the same range as the inner layers. The 1σ of the measured Young's moduli for ten magnets are 0.11 GPa and 0.22 GPa for the inner and outer layers, respectively. From those measured results, the variations are within the production tolerance, and the ten magnets showed a good reproducibility.

Table 1: Main Parameters of LHC-MQXA

Field gradient=215T/m	Coil
Current=7149A	inner radius=35mm
Peak field=8.63 T	outer radius=81.3mm
Load line ratio	Yoke
inner=80%	inner radius=92mm
outer=78%	outer radius=235mm
Stored energy=352kJ/m	Yoke length=6.51m
Inductance=13.8mH/m	Effect. mag. length=6.37m

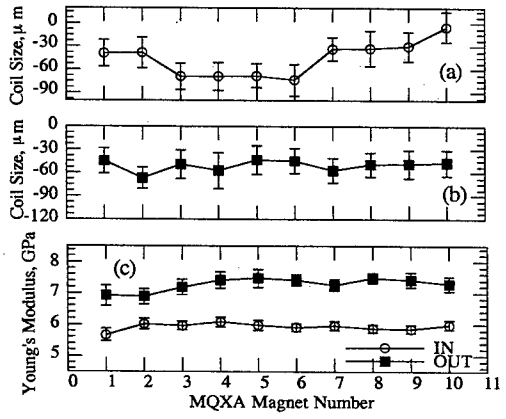


Figure 1: Coil size (a,b) and Young's Modulus (c) of MQXA-1 to 10.

Cold Mass Geometry

The deformation (bending) of the magnet cold mass was measured after welding the magnet-shell, and before and after the cold test. In Fig. 2, the deformations after the cold test are shown. The magnets were aligned on the supports at the axial positions of plus and minus 2100 mm

norihito.ohuchi@kek.jp

0-7803-7738-9/03/$17.00 © 2003 IEEE

for these measurements. In the early MQXA magnets, the large vertical deformations from 0.8 mm to 1.1 mm were measured. Presently, it is understood that these deformations were induced by welding caps of the holes on the shell for the assembly and the magnet sag. In the recent magnets, the welding scheme was improved and this vertical deformation was reduced. The horizontal deformations of ten magnets were within plus or minus 0.3 mm. These deformations were within the mechanical tolerance.

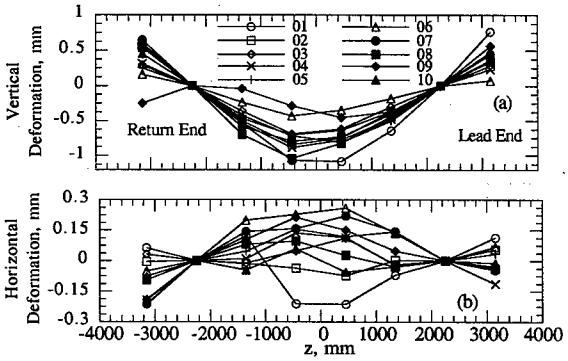


Figure 2: Vertical (a) and horizontal deformations (b) of ten magnets. The position of z=0 mm corresponds to the magnet center.

QUENCH PERFORMANCE

In order to evaluate the quench performance of the magnets, all magnets are scheduled to be tested at 1.9 K in the vertical cryostat at KEK. The test scheme is as follows: (1) Training quench up to 230 T/m with a ramp-rate of 10 A/s. (2)Full energy dump test at 215 T/m (LHC operating point) induced by a quench protection heater. (3)Re-excitation up to 220 T/m without a quench.

Fig. 3 shows the training quench history of MQXA-1 to 10. All magnets reached 230 T/m after their training quenches. For these ten magnets, the total number of quenches was 72 times including the quenches during the second thermal cycle. The ratios of the quench locations are 60%, 28% and 11% in the lead end, the return end and the straight section, respectively. Fig. 4 shows the distribution of the quench locations for each magnet. From the MQXA-1 to MQXA-7, the locations of the quench origin concentrated in the both ends, especially in lead end. However, the MQXA-10 showed different characteristics, i.e. four quenches in the magnet straight section, the largest number of training quench (during the first thermal cycle) and the lowest current at the first quench. We will watch this quench behavior for the successive magnets.

In the full energy dump test at 215 T/m, it was confirmed that the measured MIITs ranged from 11.1 to 11.5 and the coil temperature was less than 350 K in the adiabatic assumption. After this dump test, all magnets were energized to 220 T/m without a quench.

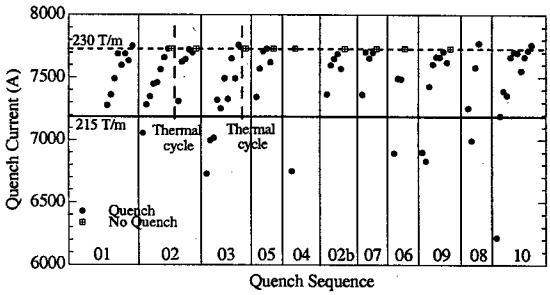


Figure 3: The training history of the MQXA-1 to 10.

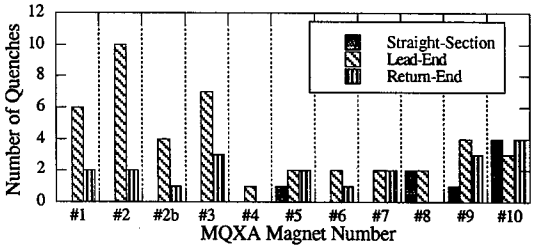


Figure 4: Distribution of the quench location.

MAGNETIC FIELD PERFORMANCE

Field Gradient and Effective Magnetic Length

The magnetic field measurements were performed using a 600 mm long harmonic coil of which nominal coil radius was 21 mm [7]. In order to obtain the integral magnetic field, the harmonic coil was moved stepwise along the magnet length, *z*-scan measurements, in a warm bore of a vertical anti-cryostat. For six excitation currents, the *z*-scan measurements were performed. The measured field gradient, G, and the effective magnetic length, L_{EFF}, were summarized in Table 2. G and L_{EFF} are the average of ten magnets and 1σ is its standard deviation. The G values of 12.366T/m and 216.24 T/m are close to the field gradients at the injection porch and the flat top of the accelerator cycle, respectively. Four data between these two currents were taken to obtain the current dependence of G. For each current, 1σ was in the level of 3×10^{-4} with respect to each field gradient. The effective magnetic lengths were in the range of from 6.365 m to 6.3686 m and 1σ was less than 1 mm. From these results, the differences from magnet to magnet in G and L_{EFF} are quite small for these magnets.

Table 2: Field Gradient and Effective Magnetic Length

I	G, T/m		L_{EFF}, m	
kA	average	1σ	average	1σ
0.392	12.366	0.004	6.3650	0.0008
2.011	63.278	0.016	6.3648	0.0008
3.208	100.68	0.026	6.3647	0.0007
6.134	185.87	0.049	6.3676	0.0008
6.677	200.97	0.047	6.3681	0.0008
7.228	216.24	0.058	6.3686	0.0008

Field Quality

The measured error field components are described as the multipole coefficients on the reference radius of 17mm by Eq. 1,

$$B_y + iB_x = 10^{-4} B_2 \sum_{n=1}^{\infty} (b_n + ia_n) \left(\frac{x+iy}{R_{ref}} \right)^{n-1} , \quad (1)$$

where B_2 is the quadrupole strength, R_{ref} is the reference radius. The coefficients b_n and a_n are the normal and skew $2n$-pole coefficients. These coefficients are expressed in *units*, which are normalised with respect to B_2 and scaled by a factor 10,000.

For the production of MQXA magnets, the reference error components at 215 T/m were defined from the R&D studies with five 1m-model magnets and field calculations. The reference systematic and random error components are shown in Table 3. For the MQXA-1 to 10 magnets, the error components in the straight section of 5.4 m at the current of 7.228 kA are shown in Table 4. In this sec-tion, the averaged b_4 was 1.23 *units*, and it was beyond the systematic error in Table 3. This b_4 is still controllable in the beam optics because the b_4 corrector, which will be installed in the triplet system, has a capacity to cancel two times larger b_4 than 1.23 *units*. The other harmonic com-ponents was in very low values compared to the sys-tematic errors in Table 3. Especially, averaged b_6 was 0.16 *units* while the allowed systematic b_6 error was 0.94 *units*.

Table 3: Reference Error Field for MQXA

n	b_n			a_n		
	design	sys. err.	rand. err.	design	sys. err.	rand. err.
*Straight Section (L_{eff}=5.8 m)						
3	0.0	0.50	0.99	0.0	0.50	0.99
4	0.0	0.67	0.54	0.0	0.27	0.54
5	0.0	0.13	0.26	0.0	0.13	0.26
6	+0.134	0.94	0.48	0.0	0.07	0.13
7	0.0	0.03	0.06	0.0	0.03	0.06
8	0.0	0.02	0.03	0.0	0.03	0.03
9	0.0	0.01	0.02	0.0	0.01	0.02
10	+0.001	0.06	0.03	0.0	0.01	0.01
*Lead End (L_{eff}=0.31 m)						
6	4.65	0.25	0.12	0.0	0.03	0.03
10	-0.129	0.03	0.03	0.0	0.03	0.03
*Return End (L_{eff}=0.19 m)						
6	-0.53	0.42	0.20	0.0	0.05	0.05
10	-0.16	0.05	0.05	0.0	0.05	0.05

Table 4: Multipole Coefficients in Straight Section

n	b_n		a_n	
	average	1σ	average	1σ
3	0.03	0.36	0.22	0.36
4	1.23	0.12	-0.07	0.36
5	-0.00	0.04	0.02	0.05
6	0.16	0.10	-0.04	0.03
7	-0.00	0.01	-0.00	0.01
8	0.01	0.00	0.00	0.01
9	-0.00	0.01	-0.00	0.00
10	-0.01	0.01	-0.01	0.00

Table 5: Multipole Coefficients in Ends

n	*Lead End*				*Return End*			
	ave. b_n	1σ	ave. a_n	1σ	ave. b_n	1σ	ave. a_n	1σ
3	0.08	0.45	0.86	0.64	-0.02	1.47	-0.01	1.18
4	2.13	0.24	0.04	0.48	1.12	0.24	0.20	0.28
5	0.00	0.26	-0.16	0.22	-0.01	0.19	0.06	0.17
6	2.66	0.13	0.09	0.06	-0.49	0.12	-0.06	0.04
7	-0.02	0.02	0.03	0.02	0.00	0.01	-0.01	0.02
8	0.12	0.01	0.00	0.02	0.01	0.01	-0.00	0.01
9	-0.00	0.01	0.00	0.01	-0.00	0.02	0.00	0.02
10	-0.06	0.01	-0.00	0.01	-0.09	0.01	-0.00	0.01

The variations from magnet to magnet in the multipole components were very small, and 1σ of each multipole coefficient was within the range of the random error.

The multipole components in both ends at the current of 7.228kA are summarized in Table 5. From the constraint of the measurement system, the measured effective lengths for the lead end and the return end are 0.63m and 0.34m, respectively, and they are different from the values in Table 3. In the both ends, the large multipole components are b_4 and b_6. In the lead end, b_6 of 2.66 *units* is almost same as the design value for this effective magnetic length. The coefficient b_4 of 2.13 *units* corresponds to the integrated b_4 of 1.34 *units*·m, and the value is one fifth of b_4 in the straight section. It can be cancelled by the corrector. In the return end, b_6 is slightly larger than the design in the negative sign. Since b_6 in the straight section and the lead end has a positive sign, b_6 in the return end reduces the integral b_6 in the whole magnet.

CONCLUSION

The ten production MQXA magnets for the LHC interaction regions were manufactured and tested at 1.9 K. All magnets reached 230 T/m after the training quenches, and they were re-excited up to 220 T/m without a quench following the full energy dump at 215 T/m.

The variations, 1 σ, of the field gradient and the magnetic length were 3×10^{-4} with respect to their gradient and less than 1mm, respectively. As for the field errors, b_4 was the major component and the integral b_4 in the straight section was 1.23 units. The b_4 was still within a capacity of the b_4 corrector. All other harmonics were satisfactory below the beam optics requirements.

ACKNOWLEDGMENT

The authors would like to appreciate the support of T. Taylor and R. Ostojic at CERN. We also wish to thank J. Strait, J. Kerby and the Technical Division at FNAL for their cooperation.

REFERENCES

[1] R. Ostojic, *IEEE Trans. Appl. Superconduct.*, Vol. 12, No. 1, pp.196-201, 2002.
[2] G. Velev *et al.*, WPAE015 presented in this conference.
[3] K. Tsuchiya *et al.*, *IEEE Trans. Appl. Superconduct.*, Vol. 10, No. 1, pp.135-138, 2000.
[4] A. Yamamoto *et al.*, *IEEE Trans. Appl. Super-conduct.*, Vol. 10, No. 1, pp.131-134, 2000.
[5] T. Ogitsu *et al.*, *IEEE Trans. Appl. Superconduct.*, Vol. 12, No. 1, pp.183-187, 2002.
[6] T. Nakamoto *et al.*, "Production and Performance of the LHC Interaction Region Quadrupoles at KEK," to be published in *IEEE Trans. Appl. Superconduct.* 2003.
[7] N. Ohuchi *et al.*, *IEEE Trans. Appl. Superconduct.*, Vol. 12, No. 1, pp.188-191, 2002.

FORCE FREE DESIGN OF SUPER-FERRIC BEAM LINE MAGNET

M. Wake, H. Piekarz*, R. Yamada*, H. Sato and K. Takayama
KEK, Tsukuba, 305-0801 Japan, FNAL*, Batavia, IL 60510, USA

Abstract

A force free design of super-ferric beam line magnet is proposed. Super-ferric magnets use induction efficiently to produce magnetic field. The problem of super-ferric magnet has been the electromagnetic force that increases the heat load of the magnet and eliminates the advantage of the energy saving of superconductivity. This design balances out the electromagnetic force works on the conductor and realizes the very light support of the conductor resulting a very small cold mass and heat load. Beam line magnet can be much more economical both in construction and operation. Shifting of conductor position, asymmetric pole width and adjusting holes in the pole piece are the major force balancing techniques. Testing is planned using VLHC test facility at Fermilab

INTRODUCTION

Beam line magnet has been an attractive application area of superconducting magnet. High ramp rate that generate transient loss of superconductor is not required in most of the beam lines. Power saving of super-conducting magnets in DC operation is very large. However, construction cost of superconducting magnets and operation cost of cryogenic system has been expensive enough to hesitate the use of superconducting magnets unless the requirement of the bending field is very high.

One of the solutions to use suprconducting magnet efficiently at low field is the use of iron yoke. Super-ferric magnet should be very economical because it uses much less superconductor. The problem of superferric magnet is the cryogenics. Cryostat containing whole iron is costly and lossy. Warm iron design has a problem of large electro-magnetic force between iron and conductors. Heavy-duty spacers to support coils in a vacuum insulation easily give a very large heat load to the cryogenic system. Cost down merit of super-ferric magnet is difficult to achieve in both case.

The design presented in this paper balances out the electro-magnetic field by two gaps of iron. Since support system is very simple and light, cryogenic load is small and construction cost is very low. The principle of the force balance is similar to the VLHC Pipetron magnet but the construction of the magnet is made asymmetric so that it becomes suitable for single bore beam line magnets.

DESIGN PRINCIPLE

The electromagnetic force on the magnet conductor is the vector product of field and current. For example, 20 turns of 5kA in 2T field results in 200,000N. It easily becomes very large. This is the reason why we need to design magnets with very rigid supporting structure to prevent quenches due to conductor motions. However, if the direction of the field is opposite at both sides of a conductor, the total force working on the conductor could be balanced out. This is automatically achieved in a symmetric structure having a single conductor in the center of the collider geometry. The pipetron magnet, or transmission line magnet, in the VLHC phase I design, is based on this principle [1]. Although it requires 100kA class high current, 2T magnetic field in a 2 cm iron gap was successfully achieved by a single conductor. Support structure of the conductor of this magnet was very simple and light with small heat load.

Two-aperture geometry of pipetron magnet requires twice large current to generate field. Therefore, it is not ideal to use such two-aperture magnet for a beam line, which uses only one aperture. Because most of beam lines require larger pole gap, typically 40mm, operation current will become too large to operate. Although we have solution for it, high current is the major disadvantage of this design. Since the electro-magnetic force on the conductor is generated by the leakage field comes from the pole gap, one gap which is not used for beam can be smaller than other gap if the conductor position is shifted closer to the smaller gap. The basic geometry of this magnet is shown in Fig.1. Conductor is the only cryogenic part of the magnet. It is supported in a vacuum jacket covered by super-insulations and cooled by the liquid helium flow in the conductor. Other parts all stay at room temperature. Therefore, the cold mass of the magnet is very small.

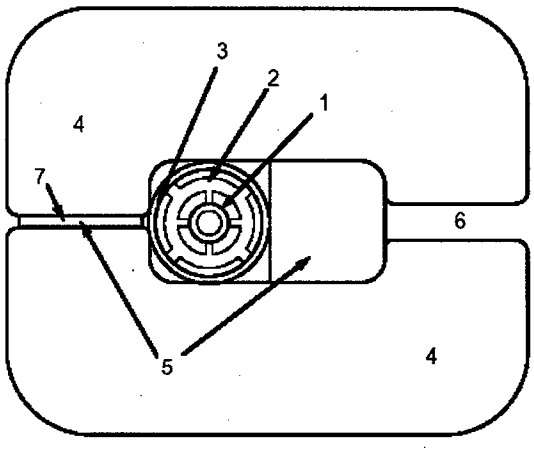


Fig. 1: Asymmetric force balance structure.

1:Superonducting cable 2:Conductor support 3:Vacuum tube for thermal insulation 4:Iron yoke 5:Iron support structures made of non-magnetic stainless steel. 6:Beam gap 7:Dummy gap to generate counter force

0-7803-7738-9/03/$17.00 © 2003 IEEE

The conductor is made of superconducting braid sandwiched between two invar pipes so that the thermal contraction is avoided. The beam tube is placed in the large gap. The small gap works as the dummy gap to generate the force balance field.

FORCE BALANCING

The problem of the asymmetric construction is the saturation of iron. In a symmetric geometry, force balance can be maintained no matter how iron is saturated but the force balance can not be automatically maintained in asymmetric geometry when both side of iron saturate differently. The calculation of magnetic field and the force on the conductor has to be made using finite element code with non-linear iron permeability. We used ANSYS 6.2. The optimum design should be determined by looking at the force as a function of the current.

Figure 2 is the plot of the force on the conductor as a function of the central field of the beam space. Curves are plotted for different dummy gaps. Apparently, the force balance changes with the current. Forces are not completely eliminated. However, the level of the force is in the order of several hundred Newton's if the gap is adjusted to the optimum for the field of up to 1.5 Tesla. This is not large and practically acceptable for a light spacer system. Since conventional magnets are excited often to the saturation level, it is desired to go to higher field to compete with conventional magnets in the construction of beam lines.

There is a way to control the saturation of iron to some extent. The force calculation result after saturation control is shown in Fig.3. If the width of pole piece is wide, the saturation starts at higher current. If a hole is made at the edge of the pole piece, local saturation of iron provide counter electro-magnetic force at lower level of excitation.

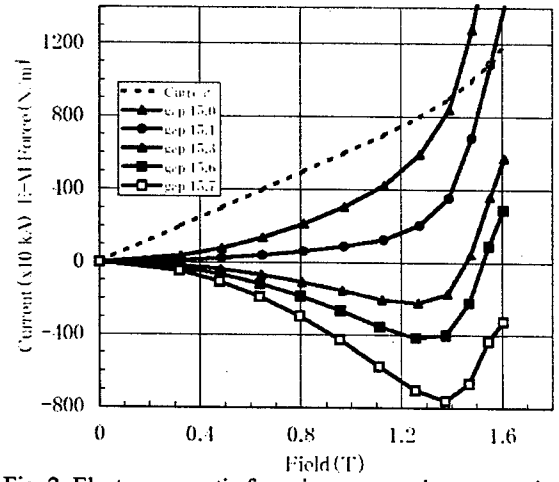


Fig. 2: Electro-magnetic force in asymmetric construction

Forces for different dummy gaps are plotted. Half gap 15.3 mm provides optimum force balance up to 1.5T with maximum force –200 N.

Combining such techniques, one can design a no-force magnet for a single aperture beam line magnet. Figure 4 is the cross section of the design example. Flux line pattern in the optimised geometry is also shown in the figure. It is shown that the force balance is well maintained even after a severe saturation of iron started at 1.5T. Essentially there is no force up to 1.7T. The vertical force is zero if the conductor is in the vertical center but this is an unstable balance. De-centering force of 2kN/mm works on the conductor. Therefore, vertical alignment of less than 0.1 mm is required to stay within 200N, although the field quality is not much affected by the position of the conductor. The conductor support can achieve this accuracy [1]. The beam gap of the magnet in Fig.4 is 140mm x 40mm. Operation current is 129.2 kA at 1.7T. Most of beam line requirement is satisfied by this design. For example, a beam line of 50GeV proton with bending radius 110m needs 1.514 T in the average. If magnetic field of 1.7T is provided in the magnet, 20cm spaces are available between every magnet of length 2m. Monitors and other instrumentation can be installed in these spaces. One side of beam tube is opened and accessible in this magnet and the necessary spaces in between magnets are not as much as H shape magnets. Since the field of this magnet is generated by single-conductor cable, quadrupole magnet of this type is not possible. Alternate gradient configuration is necessary to make magnet combined with the focusing capability.

OTHER ADVANTAGES

By moving the conductor from the center to the asymmetric position, the space for the structure to connect top and bottom iron became available.

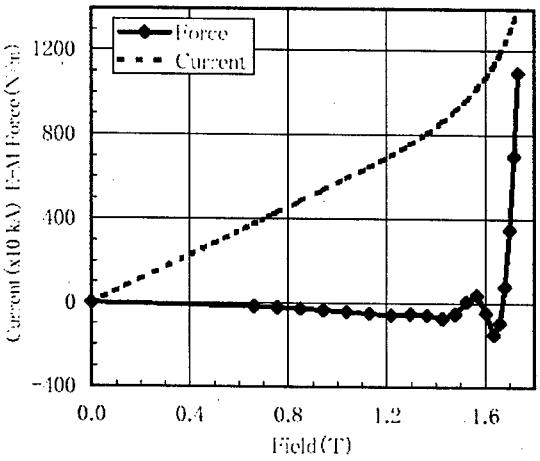


Fig. 3: Electro-magnetic force in adjusted construction

Pole width 200mm and half gap 13.2mm with 5mm diameter hole in the dummy pole piece gave optimum.

With the combination with the spacer in the dummy gap, both iron yokes can be firmly connected. Since the field quality of this magnet is dependent on the iron shape, and the force between two irons is very large, such structure is helpful to achieve the field quality.

It is important to reduce unnecessary field in produced by the current at the spaces in between magnets. If we use symmetric two gap magnet, it is difficult to shield the beam tube from the field coming from the conductor. Beam tube is too close to the conductor. In this design, the distance between the beam tube and the current provide the space for shielding. Even just rotating the iron structure by 90 degree would provide a nice magnetic shield with no-force on the conductor.

The connecting structure of iron also works as the radiation shield. Since conductors are exposed to the beam space in usual magnet design, beam induced quenches are serious problems for superconducting magnets. Magnets are often designed with extra large aperture to avoid beam induced quenches and this causes high cost of production and operation. But this magnet hide superconductor behind the thick stainless steel block and there is no problem of beam induced quenches.

OPERATIONAL

To operate this magnet in a beam line, we need to set up the vacuum insulated conductor along the beam line just like a power transmission line. Iron yokes covering this transmission line will simply make the magnet strings. The return current bus has to be made separately. There is a possibility to use return current but the contribution of the return current to the single aperture magnet is very little [2].

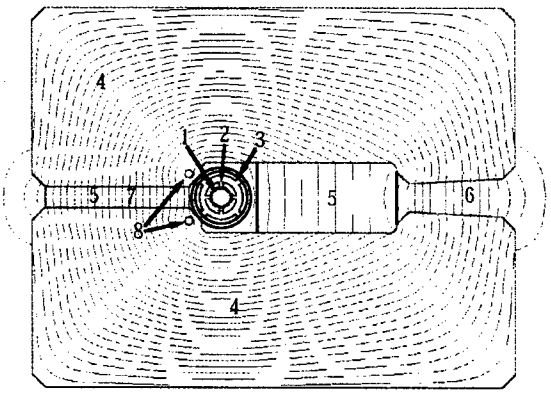


Fig. 4: No-force cross-section.

1:Superonducting cable 2:Conductor support 3:Vacuum tube for thermal insulation 4:Iron yoke 5:Iron support structures made of non-magnetic stainless steel. 6:Beam gap 7:Dummy gap to generate counter force 8:Holes in the dummy pole piece to control the saturation of iron

Very simple structure of the magnet makes the construction cost very reasonable. However, the operation of this magnet requires a very large current. At low field, 100kA is not a very large current for superconductor. The current carrying capacity of superconductor increases very much at low field. A test of conductor operation for pipetron was successfully made including joints at Fermilab [1]. In case of very long beam line, Nb3Sn can be used to run the system with elevated temperature [3].

Thermal contraction in thick straight line is difficult to handle but the transmission line conductor uses invar pipes both for liquid helium channel and the pressure pipe so the contraction effect is minimized to the level that mechanical stresses resulting from contraction/expansion can be well controlled. A 100kA power supply is technically not difficult but costly if it is done in conventional way. We have introduced a special power supply system. Even the current is high, the voltage required to excite this magnet is very low. Recent development of IGBT chopper and shotky diode enables us to build low voltage high current power supply. A 100kA power supply was already built at Fermilab. KEK demonstrated feasibility of such a power supply using a smaller version [4]. Current leads to supply 100kA into the conductor have been fabricated at Fermilab and will be tested soon. The cryogenic heat load of the current lead is about 1kw including the helium flow in the leads and this is the main part of the heat load. Still total heat load is not as much as the usual superconducting magnet if the length of the beam line is sufficiently long.

CONCLUSION

The force free design of superferric beam line magnet was successfully performed. A test operation of this magnet is being prepared using the VLHC test bench at Fermilab. Detailed force balance characteristics will be studied in the test operation. If this design is applied in some of the accelerator beam line, it becomes a good performance proof of the VLHC phase I superconducting magnet system for the operation economy and long term reliability.

REFERENCES

[1] "Design Study for a Staged Very Large Hadron Collider", Fermilab-TM-2149, 2001.

[2] M.Wake and R.Yamada, "New Types of Superconducting Magnet Designs for High Energy Collider", Proc. MT-15 p.47-50, Science Press, Beijin, 1998.

[3] E.Barzi, G.W.Foster, E.Malamud, P.O.Mazur, H.Piekarz, M.Wake, K.Hayashi, M.Koganeya, "Nb3Al Prototype Conductor for the Transmission Line Magnet", proc.1999 Particle Accelerator Conf. 3330-3332,1999.

[4] M.Wake, H.Sato, K.Suda, "A Battery-Powered High-Current Power Supply for superconductors (in Japanese)" Teion-kogaku, 37 783-786,2002.

FIELD QUALITY ANALYSIS OF THE NEXT GENERATION IR QUADRUPOLE FOR THE LHC*

P. Ferracin#, S. Caspi, L. Chiesa, D.R. Dietderich, S.A. Gourlay, R.R. Hafalia, A.F. Lietzke, A.D. McInturff, G. Sabbi, R.M. Scanlan, LBNL, Berkeley, CA 94720, USA

Abstract

Lawrence Berkeley National Laboratory (LBNL) is carrying out a conceptual design study of a Nb_3Sn quadrupole for the next generation LHC Interaction Region (IR). The choice of a gradient of 205 T/m and an increased bore size of 90 mm represents a promising strategy towards increasing the luminosity up to an ultimate goal of 2.3×10^{34} $cm^{-2}s^{-1}$. At the present time Nb_3Sn is the only conductor with sufficient current density for this application. Coil designs with either two or four layers are being considered. Previous studies have examined cable and coil parameters, systematic harmonics, support structure and quench protection system. In this paper the issue of field quality is further discussed.

INTRODUCTION

NbTi quadrupoles for the Interaction Regions of the Large Hadron Collider (LHC) are being fabricated at KEK (MQXA) [1] and at FNAL (MQXB) [2]. An aperture of 70 mm with an operating gradient of 205 T/m allow for a luminosity of 10^{34} $cm^{-2}s^{-1}$. During the past year, conceptual design studies were carried out by LBNL [3], FNAL [4] and BNL [5] to analyze a second generation Nb_3Sn LHC IR quadrupole magnet capable of increasing the luminosity of the machine up to an ultimate goal of 2.3×10^{34} $cm^{-2}s^{-1}$ [6]. In this paper, further design studies are reported focusing in particular on field quality issues. Iron saturation, random errors and impact of yoke misalignments on field harmonics are considered. Different strategies of correcting both allowed and non-allowed multipoles are discussed, and future plans of the magnet R&D are outlined.

MAGNET DESIGN

The magnet cross-section is shown in Fig. 1. Nb_3Sn superconducting cables are wound around bronze poles and supported during assembly by four bolted stainless steel pads (30 mm thick). A 5 mm gap separates the pads from a four-piece iron yoke, contained within an aluminum shell 18 mm thick. The outer diameter of the shell is limited to 500 mm, the same as in MQXA, and therefore compatible with the existing cryostat.

From a structural viewpoint, the main characteristic is the absence of supporting collars. The assembly is done by means of the key and bladder technology [7], implemented here for the first time in a cos(2θ) magnet.

* This work was supported under contract DE-AD03-76SF00098 by the Director, Office of Energy Research, Office of High Energy Physics, U.S. Department of Energy.

pferracin@lbl.gov

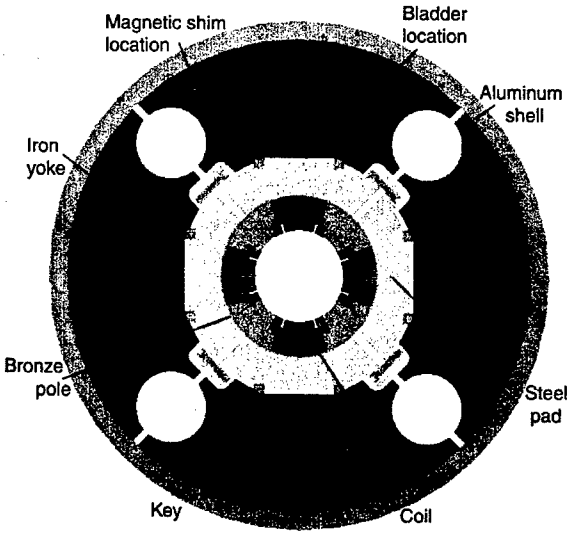


Figure 1: Cross-section of the quadrupole magnet.

The bladders are inserted and inflated in the gap between pads and yokes, providing an initial pre-stress to the coil. Interference keys are then used to lock in the pre-stress and allow bladder removal. During assembly, this technology provides about half of the required coil pre-stress, with little spring back. During cool-down, the different thermal contraction between aluminum and iron increases the coil pre-stress. Preliminary computations with an aluminum pad have shown that it could replace the stainless steel pad still maintaining sufficient pre-compression. A detailed study of the stresses inside the magnet during assembly, cool-down and excitation was presented in Ref. [3].

With respect to the previous analysis, some design modifications were implemented. The pad material was changed from iron to stainless steel. The inner radius of the yoke was reduced by 10 mm and the G10 spacer was removed. The yoke includes four 70 mm diameter holes for longitudinal heat transfer within the cold mass. We point out that the gaps between the pads and the yokes, and between the four pads provide additional space for cooling. A reference coil aperture of 90 mm was chosen for the analysis. However, changes in the coil aperture can be easily accommodated in this design concept.

Superconducting coil

The baseline design of the quadrupole features a four-layer cos(2θ) coil (Fig. 2, left). For consistency with previous analyses, we have assumed a critical current density of 2.4 kA/mm^2 at 12 T and 4.2 K, a conservative

0-7803-7738-9/03/$17.00 © 2003 IEEE

value compared to the current carrying capacity of recent Nb_3Sn strands. The short sample gradient at 1.9 K is 267 T/m (30 % design margin). At an operational temperature of 4.2 K, the short sample gradient decreases to 249 T/m (20 % design margin). Details on the magnetic parameters are given in Ref. [3].

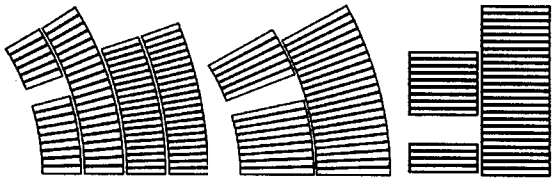


Figure 2: Coil cross-sections: four-layer cos(2θ) (left), two-layer cos(2θ) (center) and block-type (right).

The proposed four-layer coil design was based on magnetic efficiency and cable design considerations [3]. However, alternative designs of both shell-type and block-type coils are being developed. A two-layer cos(2θ) design (Fig. 2, center) reduces the number of parts and the magnet inductance, but requires the development of a new fully-keystoned cable with a special keystone-shaped core. It provides a short sample gradient of 247 T/m at 1.9 K, with a margin of 20 %. Block-type geometries have advantages in terms of conductor compatibility, separation between high field and high stress points, reduction of peak stress, simplification of support structures and assembly techniques [8]. In fact, a block coil was originally proposed for the LHC inner triplet [9]. The design (Fig. 2, right) consists of two layers of a flat cable with 35 strands. One potential issue of this coil is the minimum-bending radius of the cable in the ends. This issue will be addressed in future R&D magnet programs. This design generates a short sample gradient of 230 T/m at 1.9 K with a margin of 12 %. A less conservative critical current density in the superconductor, an increase of the conductor area and the use of a four-layer graded coil can push the margin above 20 %.

FIELD QUALITY ANALYSIS

The three coil geometries, optimized with ROXIE [10], limit the geometric harmonics to 0.05 units at a reference radius of 22 mm. For an effective filament diameter of 100 μm, the magnetization effect on b_6 during the start-up of the second excitation cycle is about + 30 units at 400 A (about 1/15 of I_{op}), decreasing to a minimum of – 12 units at 1400 A. A reduction of the filament diameter by at least a factor of two is being pursued by the DOE Conductor Development Program. A correction scheme such as the one based on a ferromagnetic ring [11] can also be used to reduce magnetization above 1200 A. It should be noted that the field quality of the IR quadrupoles at injection is not critical for the machine. In the present yoke and pad design the effect of iron saturation on b_6 (evaluated with OPERA-2d [12]) was reduced to less than 0.1 units from injection to short sample.

Random harmonics

To estimate the multipole errors produced by fabrication tolerances, random displacements of the conductor blocks with respect to the design geometry were applied in the range of ± 50 μm. The calculated errors for the four-layer design and for the MQXB design were compared (Fig. 3), considering for both cases a reference radius of half the magnet aperture (22 and 17 mm respectively). The amplitude of the displacements is about 2.5 times greater than the one observed in the short models of the first generation MQXB quadrupoles [13]. This conservative assumption takes into account the difficulties of controlling Nb_3Sn coil dimensions during the high-temperature reaction phase.

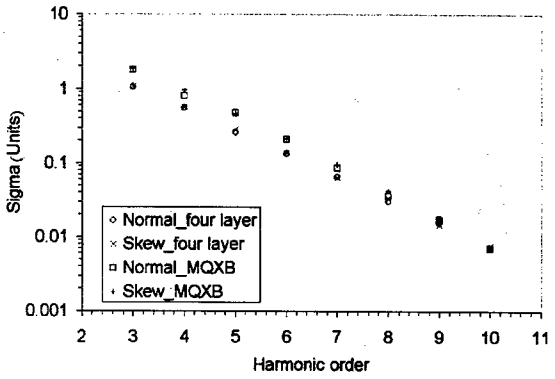


Figure 3: Numerical estimates of the geometric random multipoles (10^{-4} units) due to a random block displacement of 50 μm for the four-layer design (at R_{ref} = 22 mm) and the MQXB (at R_{ref} = 17 mm).

As pointed out in Ref. [14], the numerical estimates present a very regular pattern and can be well fitted by second order polynomials on a semi-logarithmic scale. The small discrepancy observed for the low-order harmonics can be explained by the different block sizes in the two designs.

Yoke misalignments

During assembly, the inflation of the bladders creates an interference gap between the pad and the yoke of about 0.5 mm. This interference is defined by the key thickness and is maintained during cool-down and through excitation, providing the required coil pre-stress. A sensitivity analysis of the effect of radial and azimuthal displacements of the yoke on field harmonics with respect to the nominal position was performed for the four-layer design. A positive radial displacement of one yoke quadrant by 0.1 mm produces a b_3 of – 0.08 units and a b_4 of – 0.02 units. On the other hand, the effect of a similar azimuthal displacement will produce only negligible harmonics. The impact of yoke misalignments on field quality seems therefore significantly lower than the effect of fabrication tolerances (Fig. 3).

FIELD QUALITY CORRECTION

In order to achieve the level of field quality required in the IR quadrupole, methods for correction of field errors will be tested in prototypes. Systematic deviations of the allowed harmonics will be corrected by simple modifications to the coil cross-section. Correction of the low-order non-allowed harmonics can be obtained with magnetic shims, as successfully demonstrated in previous IR quadrupole R&D programs [15-16].

Allowed harmonics

Systematic variations of b_6 can be corrected by changing the coil shim patterns at the pole and mid-plane, with little or no impact on coil pre-stress [13]. In Tab. 1 the variations of b_6 corresponding to a variation of the mid-plane insulation for the four-layer design are reported. The corresponding change in b_{10} is very small.

Table 1: Variation of allowed harmonics at nominal current (10^{-4} units at R_{ref} = 22 mm) due to an increase of 100 μm of the mid-plane insulation thickness.

Mid-plane shim	Inner layer		Outer layer	
[μm]	Δb_6	Δb_{10}	Δb_6	Δb_{10}
+ 100	-1.44	-0.01	-0.34	0.00

For correction of systematic deviation of b_{10} from the design values, the proposed coil design features a copper wedge at the optimal position in the innermost layer. A change in the wedge azimuthal dimension of + 100 μm results in a change in b_{10} of + 0.05 units. The corresponding change of b_6 is well within the range that can be corrected by pole/mid-plane shims.

Low-order non-allowed harmonics

The quadrupole design incorporates magnetic shims for correction of low-order non-allowed harmonics generated by conductor positioning errors. The magnetic shim location is indicated in Fig. 1. In Tab. 2 the changes of the low-order non-allowed harmonics produced by a single shim are given.

Table 2: Variation of sextupole and decapole at nominal current (10^{-4} units at R_{ref} = 22 mm) vs magnetic shim thickness.

mm	Δb_3	Δa_3	Δb_4	Δa_4
- 5	-0.49	0.22	-0.07	0.11
+ 5	0.96	-0.45	0.12	-0.22

Relative to the expected RMS spread σ (Fig. 2), independent corrections of b_3/a_3 in the range ± 4 σ and of b_4/a_4 in the range ± 2 σ are possible with 8 tuning shims at operational conditions [16]. Due to saturation effect, the field errors at injection cannot be reduced with this method. However, the field quality of the IR quadrupoles at injection is not critical for the machine.

FUTURE PLANS

In order to test the assembly procedure and to check the stress distribution at full pre-compression after cool-down, a mechanical model of the quadrupole loading structure will be fabricated (Fig. 4). The model will incorporate the components of the proposed quadrupole design; an aluminum tube will replace the coil. This inner tube and the outer shell will be instrumented with strain gauges. The recorded data will be compared to the computed stresses.



Figure 4: Mechanical model of the quadrupole.

CONCLUSIONS

An analysis of the field quality in the next generation LHC IR quadrupole has been performed. The study focused on field errors that may arise from fabrication tolerances of the components and from misalignments of the yoke. Changes in coil cross-section and magnetic shims were proposed as a correction strategy for the allowed and low-order non-allowed harmonics.

REFERENCES

[1] N. Andreev et al., IEEE Trans. Appl. Superconduct., Vol. 11, no. 1, March 2001, p. 1558.
[2] T. Shintomi et al., IEEE Trans. Appl. Superconduct., Vol. 11, no. 1, March 2001, p. 1562.
[3] G. Sabbi et al., "Nb_3Sn quadrupole magnets for the LHC IR", ASC 2002, Houston (TX), August 2002.
[4] A. Zlobin et al., "Conceptual design study of Nb_3Sn low-beta quadrupole for 2nd generation LHC IRs", ASC 2002, Houston (TX), August 2002.
[5] R. Gupta et al., "Next generation IR magnets for hadron colliders", ASC 2002, Houston (TX), August 2002.
[6] T. Taylor, EPAC 2002, Paris, June 2002, p. 129.
[7] S. Caspi et al., IEEE Trans. Appl. Superconduct., Vol. 11, no. 1, March 2001, p. 2272.
[8] G. Sabbi, *IEEE Trans. Appl. Supercond.*, Vol 12, no. 1, March 2002, p. 236.
[9] W. Scandale et al., PAC 1991, San Francisco, May 1991, p. 2260.
[10] S. Russenschuck, Proceeding of the 1st International Roxie Users Meeting and Workshop, Geneva, March 1998, p. 5.
[11] S. Caspi, LBNL Internal Note, SC-MAG-691, October 1999.
[12] OPERA-2d, by Vector Fields Limited, Kidlington, Oxford OX5 1JE, England.
[13] P. Schlabach et al., "Field Measurement of Fermilab-built Quadrupole magnets for the LHC Interaction Region", ASC 2002, Houston (TX), August 2002.
[14] P. Ferracin et al., Phys. Rev. STAB, Vol. 11, 2000, 122403.
[15] R. Gupta et al., IEEE Trans. Magnetics, Vol. 32, 1996, p. 2069.
[16] G. Sabbi et al., IEEE Trans. Appl. Superconduct., Vol. 10, no. 1, March 2000, p. 127.

SUPERCONDUCTING SOLENOIDS FOR THE MICE CHANNEL*

M. A. Green, Lawrence Berkeley Laboratory Berkeley CA, USA; G. Barr, Oxford University, Oxford UK; D. E. Baynham, and J. H. Rockford, Rutherford Appleton Laboratory, Chilton-Didcot UK; P. Fabbricatore and S. Farinon, INFN Genoa, Italy: R. B. Palmer, Brookhaven National Laboratory, Upton NY, USA; J. M. Rey, CEN Saclay, Gif sur Yvette, France

Abstract

This report describes the channel of superconducting solenoids for the proposed international Muon Ionization Cooling Experiment (MICE). MICE consists of two cells of a SFOFO cooling channel that is similar to that studied in the level 2 study of a neutrino factory[1]. MICE also consists of two detector solenoids at either end of the cooling channel section. The superconducting solenoids for MICE perform three functions. The coupling solenoids, which are large solenoids around 201.25 MHz RF cavities, couple the muon beam between the focusing sections as it passes along the cooling channel. The focusing solenoids are around the liquid hydrogen absorber that reduces the momentum of the muons in all directions. These solenoids generate a gradient field along the axis as they reduce the beta of the muon beam before it enters the absorber. Each detector solenoid system consists of five coils that match the muon beam coming to or from an absorber to a 4.0 T uniform solenoidal field section that that contains the particle detectors at the ends of the experiment. There are detector solenoids at the beginning and at the end of the experiment. This report describes the parameters of the eighteen superconducting coils that make up the MICE magnetic channel.

THE MICE CHANNEL

MICE is a channel of superconducting solenoids. The magnets in MICE are around the RF cavities, absorbers (liquid or solid) and the primary particle detectors [1], [2]. The MICE superconducting solenoid system consists of eighteen coils that are grouped in three types of magnet assemblies. The two cell cooling channel is 5.50-m long. Each cell consists of a focusing coil pair around an absorber and a coupling coil around the RF cavity that re-accelerates the muons to their original momentum. At the ends of the experiment are uniform field solenoids for the particle detectors and a set of matching coils used to match the muon beam to the cooling cells. Three absorbers are used instead of two in order to shield the detectors from dark currents generated by the RF cavities at high operating acceleration gradients. A layout of the full version of MICE is shown in Figure 1 below.

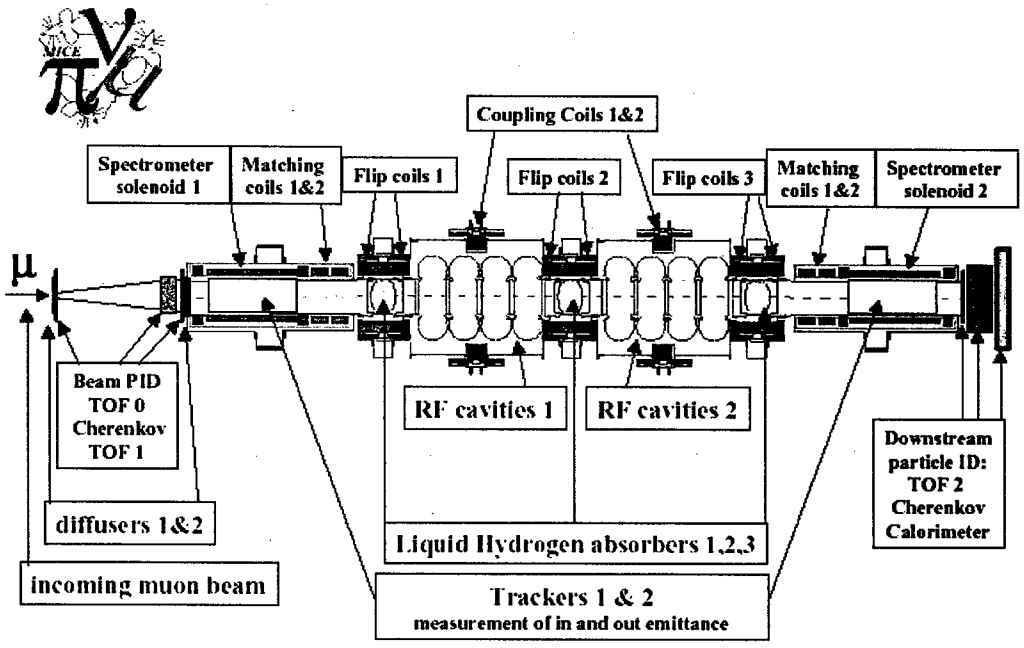


Figure 1. A Schematic Representation of MICE. (The solenoid coils are shown in dark red.)

0-7803-7738-9/03/$17.00 © 2003 IEEE

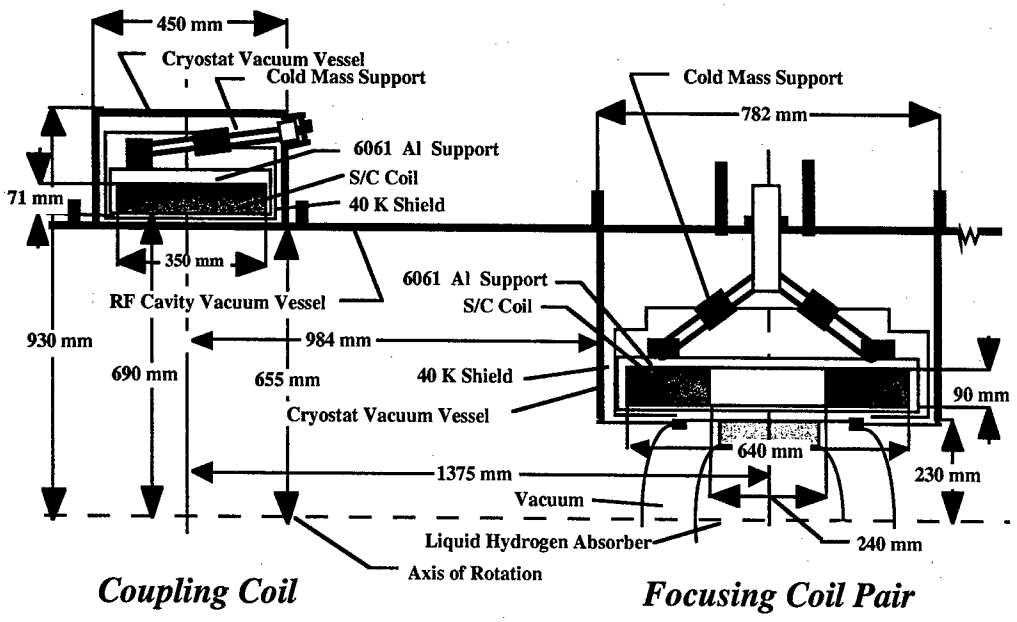


Figure 2. A Quarter Section of a MICE Cooling Cell Showing the Coupling Coil and Focusing Coil Pair

Figure 2 shows a quarter section of a MICE cooling cell. The inner diameter of the coupling coil cryostat is large enough to permit it to be installed around a four cell 201.25 MHz copper RF cavity. The coupling coil controls the beam beta within the RF cavity and matches the muon beam from focusing coil to focusing coil. When the beam beta is low in the center of the focusing coil pair, the current in the coupling coil is low (the beam beta in the RF cavity is large). By varying the current in the focusing coil pair and the coupling coil one can vary the beam beta in the absorber.

The focusing coils (on the right side of Fig 2.) produce a cusp shaped field, with zero field at the center. The design momentum of the MICE channel is 200 MeV/c. The MICE channel average muon momentum is limited by the peak field in the focusing coils. The focusing coil design permits the channel to operate with an average momentum of 240 MeV/c without quenching the magnet. The cusp shaped field in the focusing coils produces large magnetic forces (up to 240 metric tons) that push the coils apart. The focusing coils will have separate leads so that they can be operated either in the solenoid mode or the gradient mode (the cusp field case). The three focusing magnets will be powered using a single power supply. Both coupling coils will be powered using a second power supply. Both supplies produce 10 V and 300 A.

The basic parameters for the focusing coils and the coupling coils are presented in Table 1. The focusing and coupling coils are wound with a MRI superconductor with the following parameters; insulated dimensions 1.0 by 1.65 mm, Cu to S/C ratio = 4, copper RRR = 75, twist pitch = 12.7 mm, filament diameter 78 μm, and J_c(5T,4.2K) = 2940 A mm^{-2}.

Table 1. Focusing and Coupling Magnet Parameters

Parameter	focusing	Coupling
Inner Cryostat R (mm)	230	655
Outer Cryostat R (mm)	668	930
Cryostat Length (mm)	782	500
Inner Coil R (mm)	255	690
Coil Thickness (mm)	90	71
Coil Length (mm)	200	360
D between Coils (mm)	240	-NA-
No. layers per Coil	66	52
No. turns per Coil Layer	121	218
Design Current (A)*	240.3	238.2
Coil Average J (A mm^{-2})*	106.7	105.6
Self Inductance (H)	~45	~230
Peak B in Coil (T)*	6.27	5.45
Temperature Margin (K)*	~1.1	~1.6
Inter-coil Force (MN)	1.82	-NA-

* For channel with p = 200 MeV/c and β = 420 mm

THE DETECTOR MAGNET

At each end of the experiment is a superconducting detector magnet module. The detector magnet module consists of three coils that produce a uniform field (to 3 parts in 1000) of 4 T over a length of 1000 mm and a diameter of 300 mm. Also included in the detector magnet module are two solenoids that match the muon beam to the adjacent focusing magnets. Figure 3 shows a cross-section of the detector solenoid module. Figure 4 shows the field profile on axis as one goes down the MICE channel from one end to the other.

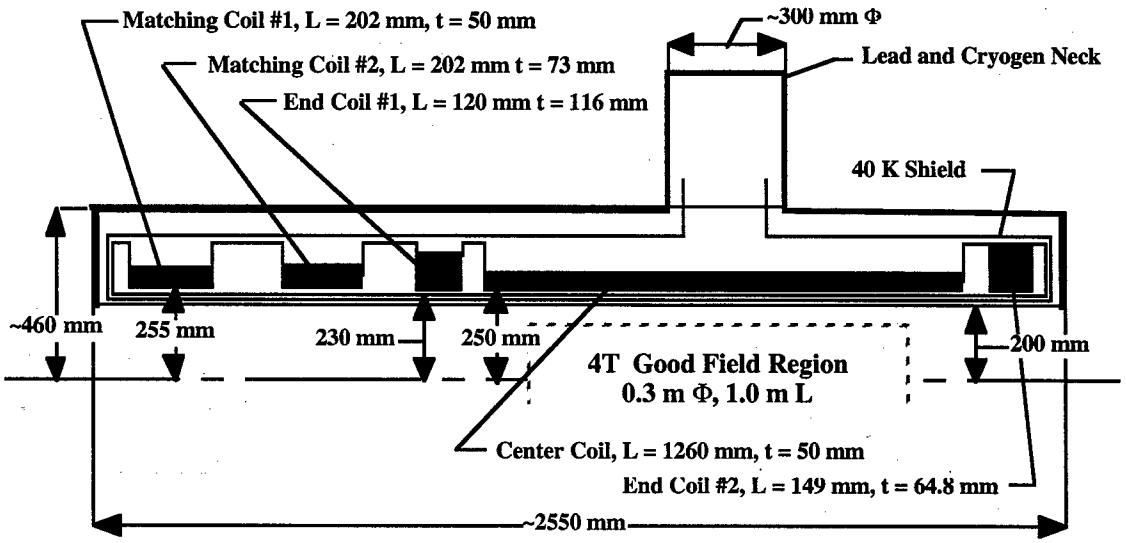


Figure 3. The Upper Half of the INFN Genoa Detector Solenoid Module

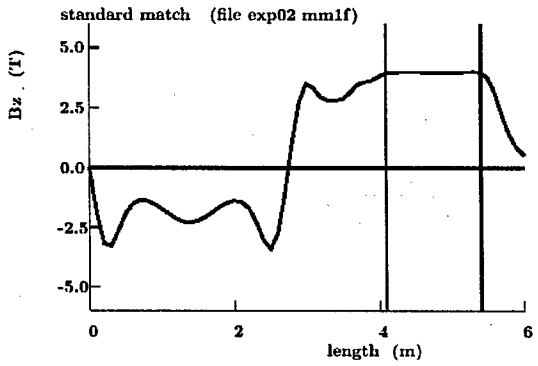


Figure 4. Magnetic Induction on Axis from the center of MICE to the End. B(-x) = -B(x).

In addition, upstream from the first detector there are two low-field muon capture solenoids. These magnets may be conventional or superconducting. These magnets are not shown in Fig.1 nor is their magnetic induction included in Fig. 4.

FORCES BETWEEN COILS

The MICE channel shown in Fig. 1 consists of eighteen superconducting coils. These coils are coupled inductively and mechanically. The cold mass supports for the coupling coils must be designed to carry a longitudinal force of at least 200 kN. The cold mass supports for the focusing coils and the detector coil module must be designed for a force of at least 600 kN. The cold to warm force on the two outer focusing magnets and the detector magnet modules appears to be strongly dependent on the spacing between the outer focusing coils and the first matching coil. The net force on the focusing magnet module will pull the focusing magnet toward the detector module. The net force on the detector magnet module will pull the detector module toward the focusing magnet.

Further work is needed to determine the forces on the cold-mass support system of all of the magnet modules during the various operating modes of the experiment. The magnetic forces that act on the cold mass supports must be calculated for the magnet currents that occur during a magnet system quench.

ACKNOWLEDGEMENT

This work was supported by the Office of Science, United States Department of Energy under DOE contract number DE-AC03-76SF00098.

REFERENCES

[1] S. Ozaki, R. B. Palmer, M. S. Zisman and J. Gallardo Eds"Feasibility Study II of a Muon Based Neutrino Source," BNL-52623, June 2001

[2] R. B. Palmer, and R. Fernow "200 MHz Cooling Experiment Design Version 4," October 23, 2002 version of the MICE channel

[3] M. A. Green and J. M. Rey, "Superconducting Solenoids for an International Muon Cooling Experiment," to be published in IEEE Transactions on Applied Superconductivity 13, No. 2

[4] S. Farinin and P. Fabbricatore, "First Thoughts about the Design of the Spectrometer Solenoids for the MICE Experiment," a Power Point presentation by S. Farinon at the MICE workshop at LBNL, 23 to 25 October 2002

[5] M. A. Green, "Superconducting Solenoid Magnets for MICE," LBNL-51910, December 2002

SUPERCONDUCTING FOCUSING QUADRUPOLES FOR HEAVY ION FUSION EXPERIMENTS*

G. Sabbi#, A. Faltens, M. Leitner, A. Lietzke, P. Seidl, LBNL, Berkeley, CA
J. Barnard, S. Lund, N. Martovetsky, LLNL, Livermore, CA
C. Gung, J. Minervini, A. Radovinsky, J. Schultz, MIT-PSFC, Cambridge, MA
R. Meinke, Advanced Magnet Lab, Palm Bay, FL

Abstract

The Heavy Ion Fusion (HIF) Program is developing superconducting focusing magnets for both near-term experiments and future driver accelerators. In particular, single bore quadrupoles have been fabricated and tested for use in the High Current Experiment (HCX) at Lawrence Berkeley National Laboratory (LBNL). The next steps involve the development of magnets for the planned Integrated Beam Experiment (IBX) and the fabrication of the first prototype multi-beam focusing arrays for fusion driver accelerators. The status of the magnet R&D program is reported, including experimental requirements, design issues and test results.

INTRODUCTION

The HIF program is progressing through a series of physics and technology demonstrations leading to an IFE power plant [1]. A set of scaled experiments carried out during the past several years has confirmed theoretical calculations of space charge dominated beam transport. In order to determine if these results can be extended to the power levels required by HIF targets, experiments with high current beams are currently underway in the areas of injection, transport and final focus. The next phase will involve source-to-target experiments to demonstrate that all beam manipulations required by the driver can be carried out in an integrated manner, thus setting the basis for a demonstration power plant.

Efficiency requirements determine the use of superconducting quadrupoles for beam transport in most of the driver accelerator [2]. Superconducting magnets are also preferred for near term experiments, to gain operational experience and to better simulate the beam environment in a fusion driver. Magnet development for HIF is carried out by a collaboration of Lawrence Berkeley National Laboratory (LBNL), Lawrence Livermore National Laboratory (LLNL), MIT Plasma Science and Fusion Center, and Advanced Magnet Lab (AML). In this paper, the experimental requirements are discussed, and the magnet R&D status and plans are presented.

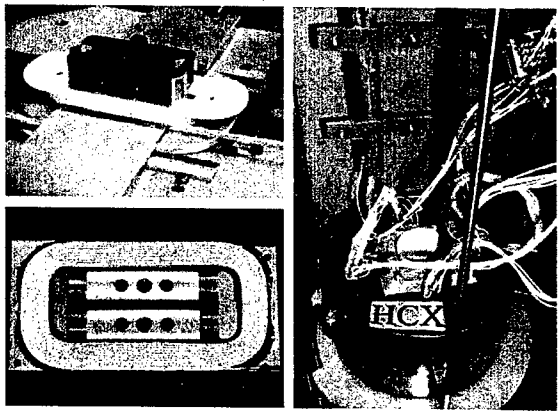


Fig. 1: Left: HCX optimized quadrupole coil fabrication. Right: Completed magnet undergoing test preparations.

HIGH CURRENT EXPERIMENT

HCX is designed to explore the physics of intense beams with driver-scale line-charge density (0.2 μC/m) and pulse duration ($\tau \geq 4$ μs) [3]. Magnetic transport experiments in HCX will primarily investigate the effects due to electrons trapped in the potential well of the ion beam. A quadrupole gradient of 84.2 T/m over a magnetic length of 10.1 cm and a coil aperture of 70 mm are required [4]. Following analysis and comparison of several design concepts, prototype quadrupoles of two different types were fabricated and tested [5]. A 2-layer racetrack design, developed by LLNL [6], was finally selected and further improved [7]. A prototype of the optimized design has been fabricated by AML and is ready for testing at LBNL (Fig 1). The coil ends were modified from continuous arcs to tight bends followed by straight segments. This layout improves the magnetic length relative to the physical coil length, and gives better field quality. However, some difficulties were encountered in winding the cable around the 6 mm radius. To address this problem, cable optimization studies were performed and a slight increase of the minimum bending

* Supported by the Office of Energy Research, US DOE, at LBNL and LLNL under contract numbers DE-AC03-76SF00098, W-7405-Eng-48, and at MIT under contract number DE-FC02-93-ER54186.
# Tel: 510-495-2250, e-mail: GLSabbi@lbl.gov

0-7803-7738-9/03/$17.00 © 2003 IEEE

radius is planned for future models. A change of the coil holder material from stainless steel to aluminum was also incorporated. The projected cost of aluminum holders in production is significantly lower than for stainless steel. However, experience with magnet fabrication showed that some design improvements are required to take into account larger deflections of the aluminum holder after applying pre-stress to the coils. Ultimately, the choice between the two materials will depend on the magnet test results. The structural tube used in the bore of previous prototypes to provide internal support to the coils was eliminated, to increase the space available to the beam for a given coil aperture. The superconducting strand was changed from SSC-outer to SSC-inner type, with lower copper fraction. The strand was redrawn from 0.808 mm to 0.648 mm for compatibility with the previous cable dimensions. The calculated short sample gradient is 132 T/m, with an effective magnetic length of 105.4 mm for a coil physical length of 125 mm.

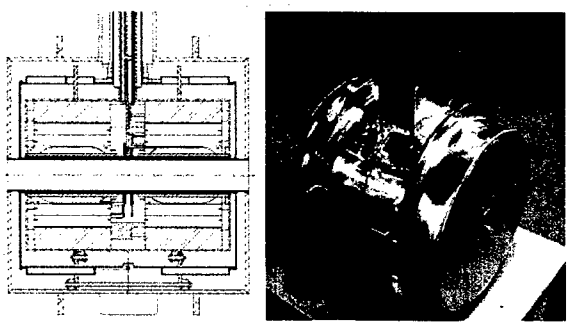


Fig 2: HCX focusing doublet design and fabrication.

A compact focusing doublet prototype, designed by LLNL, was fabricated by MIT and CVIP Inc. using two of the first-generation quadrupoles (Fig. 2). The cryostat design is compatible with the HCX lattice period of 45 cm, and provides a warm axial gap between cryostat tanks, as required for induction acceleration, diagnostics and pumping ports. The coil leads and cryogen supplies are provided through a central chimney, to maximize the space for induction acceleration cores surrounding the beam transport line. In order to minimize the radial space between the beam pipe and the LHe vessel in the magnet bore, special low-emissivity aluminized stainless steel foils are used for radiation shields [8]. However, high vacuum and low surface contamination are required for the foil to work properly. This excludes the combined use of MLI superinsulation in the same vacuum space, due to outgassing. Application of the foil in all areas of the cryostat, and in particular close to welds, proved labor intensive. The use of separate vacuum chambers has been proposed to address this problem. The first cryostated unit will be cold tested at MIT to check quench performance and measure the heat loads in different configurations before installation in HCX. Based on this experience, a second focusing doublet will be designed and fabricated using optimized HCX magnets.

INTEGRATED BEAM EXPERIMENT

The purpose of the IBX is to integrate in a single experiment all beam manipulations required in a driver, including injection, acceleration, compression, bending and final focus, at significant line-charge density [9]. The beam will be accelerated to an energy of about 10 MeV in a magnetic transport section consisting of 50 lattice periods (100 quadrupoles). The machine design is in progress, and the magnet parameters have not yet been finalized. In particular, the option of using resistive (pulsed) quadrupoles or steady state superconducting quadrupoles is still being evaluated. The magnet parameter range being considered is: clear bore 40-80 mm, operating gradient 40-120 T/m, magnetic length 8-14 cm. For a given integrated strength, high gradients over a short magnet length are preferred, to increase the space for accelerating gaps, cryostat terminations and beam diagnostics. The design must accommodate dipole steering coils and may include a cold beam pipe (at 4.5 K) with a 77 K baffle-like beam screen [10].

The HCX racetrack quadrupole is well matched to IBX requirements with simple modifications. For a clear bore of 80 mm and a gradient of 60-70 T/m, a design based on a single coil layer has been proposed, allowing significant cost savings (Fig. 3). The coil parameters are very similar to the HCX outer coils. The short sample gradient is in the range of 70-80 T/m, depending on the conductor properties (critical current density, packing and copper fraction). With respect to the dimensions quoted in Fig. 3, the gradient could be increased by reducing the radial space allocations. The thickness of the cold bore tube could be decreased, pending demonstration of the coil performance in the absence of internal mechanical support (HCX prototype test). Some aperture gains can also be obtained with more efficient designs of the beam screen and the dipole steering coils.

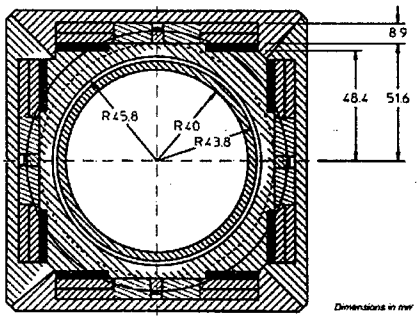


Fig. 3: Racetrack design for IBX (dimensions in mm).

An alternative two-layer coil of the HCX type would satisfy IBX magnet designs aiming at small aperture and very high gradient. Assuming some optimization of the radial space allocation in the magnet bore, the coil aperture corresponding to a 40 mm clear bore is 60 mm, a small extrapolation with respect to the HCX. For a 60 mm coil aperture, a short sample gradient of 160-170 T/m can be achieved.

While the HCX racetrack design appears well suited to IBX, other approaches may be considered. Possible alternatives include a simple shell ($\cos 2\theta$) design of the RHIC type [11]. A significant difference in magnetic efficiency between shell and racetrack coils is not expected for very short magnets, but shell-type coils are radially more compact in a single-bore configuration. A compact magnet results in a more effective acceleration system. The RHIC arc quadrupole is close to the IBX aperture and gradient specifications, and is already optimized for low cost and robust performance. However, contrary to IBX, no strong constraint on the coil end design was present in RHIC (1.1 m magnetic length). In order to obtain very compact ends and meet gradient specifications, the magnet would have to be redesigned using a two-layer coil with a narrow cable. The development of a new shell design requires expensive tooling and experimental verification of the magnet performance by fabrication and test of several prototypes.

MULTIPLE BEAM EXPERIMENTS

Following IBX, experiments with multiple beams will be performed, to study magnetic coupling effects at high energy and provide the basis for a high average fusion power Engineering Test Facility (ETF). Superconducting quadrupole arrays must be developed for this application. The design challenges include minimization of the transverse size (to limit the size and cost of the induction accelerator cores), implementation of special edge coils to adjust the field in outer cells and terminate the magnetic flux, and maximization of the quadrupole gradient [12].

Since a very large number of cells is required in the fusion driver, economy of fabrication is also a primary consideration. Racetrack coils are simple to fabricate and well suited to the square cell layout of the array. They can be arranged back-to-back improving flux sharing, and they require less structural support since the outwards components of the magnetic force are balanced between cells. Neighboring coils can in fact be combined with reduction of the number of parts, conductor joints, and inductance. However, further R&D is required to simplify the fabrication methods with respect to those presently used for HCX. Cost reductions may result from the use of kapton insulation without epoxy impregnation, and by applying the bladders and keys technology [13] to prestress to the entire array in a single step.

Other innovative approaches to magnet design are being considered. Coil designs using round cables individually supported by grooved cylinders or plates have been actively explored by AML [14]. Although the first prototypes did not perform as well as the racetrack coils, with further R&D these issues may be resolved, and ultimately result in very cost-effective magnets. A new concept, again based on a round cable and grooved supports, but with a helical winding geometry, is also being developed [15].

Special edge coils are required to adjust the field in the boundary cells and terminate of the magnetic flux within the shortest radial distance from the array, avoiding magnetic coupling between the quadrupole array and the surrounding induction cores. While several 2D studies have been performed in the past, recent analysis has shown that finding acceptable solutions is significantly more difficult if end effects are considered. Preliminary results show that the use of an iron yoke may be beneficial in addressing these issues [16].

SUMMARY

Accelerators for fusion energy production will require arrays of superconducting quadrupoles to transport multiple beams in the accelerator and focus them on the target. The development of superconducting magnets for both near term experiments and the ultimate driver application is being actively pursued by the U.S. Heavy Ion Fusion Program. The main parameters and requirements have been discussed, and the R&D status and plans have been presented.

REFERENCES

[1] J. Barnard et al., "Progress in Heavy Ion Driven Inertial Fusion Energy: from Scaled Experiments to the Integrated Research Experiment," Proceedings of the 2001 Particle Accelerator Conference, Chicago, June 2001.

[2] W. Meier et al., "A 3.3 MJ, Rb+1 Driver Design based on an Integrated Systems Analysis," Nucl. Instr. and Meth. A 464 (2001) 433-439.

[3] P. Seidl et al., "The High Current Transport Experiment for Heavy Ion Inertial Fusion", this conference.

[4] S. Lund et al., "Characterization of Prototype Superconducting Quadrupoles for the High Current Experiment," HCX Magnet Note 01-0222-01, February 2001.

[5] A. Lietzke et al., "Development of Superconducting Quadrupoles for Heavy Ion Fusion", Proceedings of the 2001 Particle Accelerator Conference, Chicago, June 2001.

[6] N. Martovetsky, B. Manahan, "Focusing Magnets for HIF based on Racetracks," IEEE Trans. Appl. Superconductivity, 11 (1), pp. 1506-1509, March 2001.

[7] A. Faltens et al., "Progress in the development of superconducting quadrupoles for heavy ion fusion", Laser and Particle Beams (2002), 20, 617-620.

[8] M. Larin et al., "Liquid Helium Cryopumps with low-emissivity Al film coatings and low helium consumption," J. Vac. Sci. Tech. A(13)5, 1995

[9] J. Barnard et al., "Integrated Experiments for Heavy Ion Fusion," Laser and Particle Beams, accepted for publication (2003).

[10] M. Leitner et al., "Technology Choices for the Integrated Beam Experiment (IBX)", 15th Topical Meeting on the Technology of Fusion Energy, Washington, November 2002. To be published in *Fusion Science and Technology*.

[11] M. Anerella et al., "The RHIC Magnet System", NIM A 499 (2003) 280-315.

[12] G. Sabbi et al., "Parameters and Requirements of Superconducting Focusing Quadrupoles for Heavy Ion Fusion", Proccedings of the 2002 Applied Superconductivity Conference, Houston, TX, August 2002.

[13] S. Caspi et al., "The Use of Pressurized Bladders for Stress Control of Superconducting Magnets", *IEEE Trans. Appl. Supercond.* Vol. 11, No. 1, March 2001.

[14] R. Meinke et al., "Development of Quadrupole Arrays for Heavy Ion Fusion", IEEE Trans. Appl. Supercond. 10 (1), March 2000.

[15] R. Meinke et al., "Modulated Double-Helix Quadrupole Magnets", Proccedings of the 2002 Applied Super-conductivity Conference, Houston, TX, August 2002.

[16] A. Radovinsky, "Four Quad Double Helical Array with an Iron Yoke. Proof of Principle", HCX-MIT-031703-01, March 2003.

THE STRONGEST PERMANENT DIPOLE MAGNET

M. Kumada, NIRS/JST/Lviv Polytechnic, Chiba, Japan
Y. Iwashita, Kyoto University, Kyoto, Japan
M. Aoki, E. Sugiyama, Sumitomo Special Metals, Osaka, Japan

Abstract

The authors have been developing very strong permanent magnets. In the past, our magnets could generate a 4.45 Tesla dipole field. We are now in a process of reaching much higher fields by a special magnetic circuit. We will present our latest results of the strongest permanent dipole magnet ever built.

INTRODUCTION

An everlasting desire of magnet builder is to pursue to produce a magnetic field strength as high as possible. The strongest manmade magnetic field must be the one made by Terawatt level of Laser. It is an equivalent magnetic field. Duration of the field is short as the laser pulse. One of the author(Kumada) proposed the magnetic field can be used as a Laser wiggler for a compact X ray Laser FEL but has not been constructed. A very strong magnetic field is generated by flux compression mechanism by theta pinch plasma or metallic cylinder by implosion but they are single shot and destructive. A rather practical strongest field must be the one by hybrid magnet where it is made of a combination of a superconducting magnet and a pulsed magnet. Again the duration of pulse is not very long as the pulsed magnet is made of copper conductor.

The field strength of permanent magnet is rather modest compared with those magnets. Residual field strength of the strongest permanent magnet material is at a level of 1.3 Tesla. And in most cases, the magnetic field strength made by these materials is half of the residual field. But using the permanent magnet is still attractive as it provides us almost eternal field without energy consumption. The permanent magnet is especially attractive to the application of small gap size magnet or magnet having short period. Successful applications to a wiggler or undulator are widely accepted.

Extensive efforts to get higher field with wiggler of undulator with permanent magnet have been made. By using permendur, which is a material of high saturation field, 3 Tesla field was achieved at SPRING 8 by a group of University of Tokyo. The working mechanism of the undulator is due to Halbach. The field strength of this magnet is stronger than the residual field. Halbach had invented a novel magnetic circuit of Rare Earth Cobalt(REC) magnet where the maximum increase can be factor of 2 for the case of his REC quadrupole magnet.

Then a motivation of designing a medical accelerator as compact as possible one of the authors (Kumada) then invented an extended Halbach dipole magnet. A concept of saturated iron and flux compression is developed. Dipole magnet is designed and constructed. A method of increasing the field by cooling the magnet is also shown to work. World record of 4.45 T in 8 mm gap was reached in this way[1,2,3,4]. The increase of the field can also be applied to the permanent multipole magnets. Straight application is to a final focus quadrupole of the linear collider[5,6].

Encouraged by the result of the 4.45 T dipole the authors proposed a project of permanent magnet based cyclotron and got a grant from Japan Science Technology. The magnet consists of hill and valley. The maximum field of the hill is about 2.2 T and the average field is 1.4 T. A new concept of flux compression is invented in it. The details with full of new ideas will be presented in a forthcoming 18-th Magnet technology conference (MT18) in Japan this fall.

Cugart and Block of ESRF of Grenoble broke this record shortly. They recorded a 5 Tesla inside a tiny gap of 0.15mm[7].

Applying similar magnetic compression scheme of the cyclotron magnet, we have designed and manufactured a 6 T dipole magnet. While we broke the new record again, we only reached 5.16 T with a gap height of 2mm where a Grenoble group reached 5 T with a gap height of 0.15mm. In this paper, we will present our data of 5.16 T dipole magnet in more detail.

SIX TESLA PERMANENT MAGNET DIPOLE

To go beyond 5 T, we took a different approach from a previous 4.45 T dipole magnet. In the previous design, we had an extended Halbach type magnetic circuit. To increase the field strength than this, one either need to make the gap small as possible or has to make outer size as large as possible. ESRF group took an approach of a small gap. It has a variable gap length and 5 Tesla was reached with a very small gap of only 0.15 mm. In extended Halbach type magnet, to make a small gap is mechanically difficult. Its assembling accuracy is poor too. This time, we took a small gap approach and chose a magnetic circuit as shown in Fig. 1 and Fig. 2. It is a combination of Halbach type and our flux compression type magnet. Although its effect is not much, we used a permendur as a central pole this time. Permanent magnets surround the pole. Direction of permanent magnet blocks are directing to the centre in order to compress flux[8]. In Table 1, parameters of this magnet are shown.

Three kinds of material are used. The photos of the magnet are shown in Fig. 3. The small radius permendur rod is inserted vertically. As the plots of B vector shows in Fig. 4 and Fig. 5, field direction changes in a middle of

0-7803-7738-9/03/$17.00 © 2003 IEEE

the vertical location in the permendur pole as shown in Fig. 6. This shows that the permendur is not used properly. This choice is accepted in the design as its effect is small.

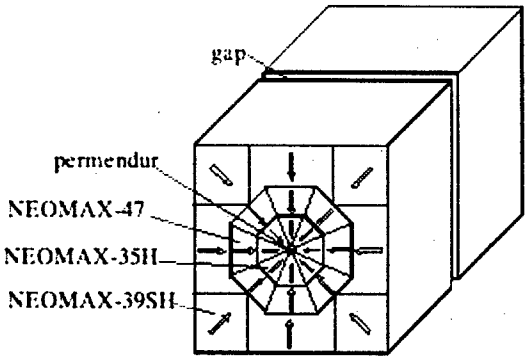


Fig. 1 6 T magnet cut out view.

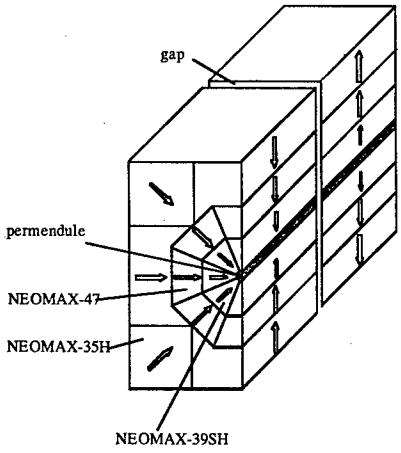


Fig. 2 Cut-out view of the 6 Tesla magnet showing magnetization directions inside.

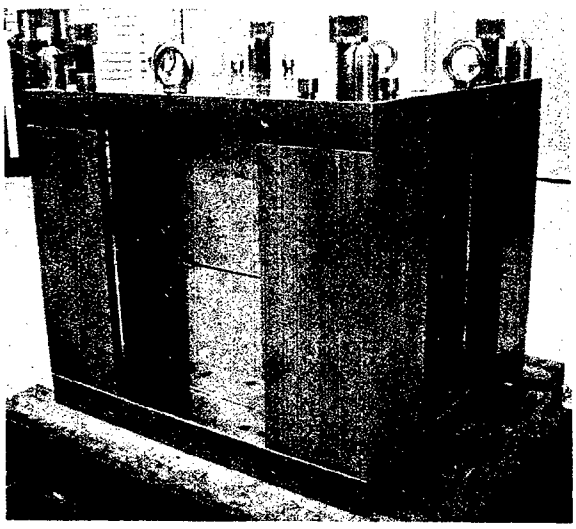


Fig. 3 Photos of the 6 Tesla magnets

Table 1 Specification of the 6 Tesla magnets

Central field strength (T)	
Calculated	6.29 (g=2mm)
Measured	5.16 (g=2mm)
Variable gap size g (mm)	2,5,10
Outer dimension (magnetic part (mm^3))	340x340x390
Weight of the magnet material (kg)	340
Outer dimension (with supporting structure (mm^3)	570x570x490
Total weight(with supporting structure (mm^3))	900

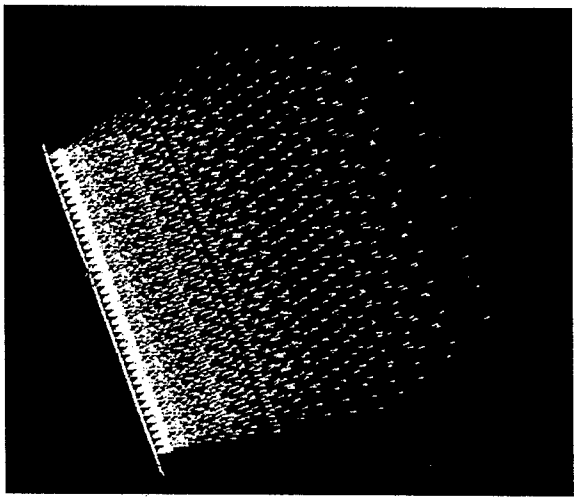


Fig. 4 Plot of B vector inside magnet.

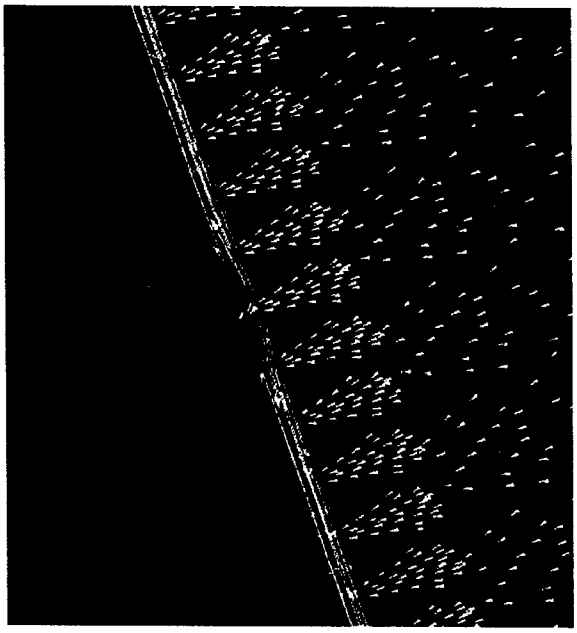


Fig. 5 Enlarged view of the centre of a permendur pole.

Although we have reached the world strongest field strength of 5.16 Tesla in the aperture of 2 mm by a permanent magnet, the design field of 6 Tesla could not be reached. The reason is under investigation. The higher field could be reached by reducing the gap when thinner magnetic sensor is available. Fig. 7 shows the comparison of the calculation and the measurement. The discrepancy between them become larger as the field increases. To see the reason of discrepancy between the calculation and the measurement, Fig. 8 was plotted at a relatively low field level of 3.7 Tesla. The field distribution of the measurement shows a broader distribution than that of the calculation. This indicates an important feature is missing in the calculation model. Understanding the mechanism of the discrepancy may lead us to go one step beyond.

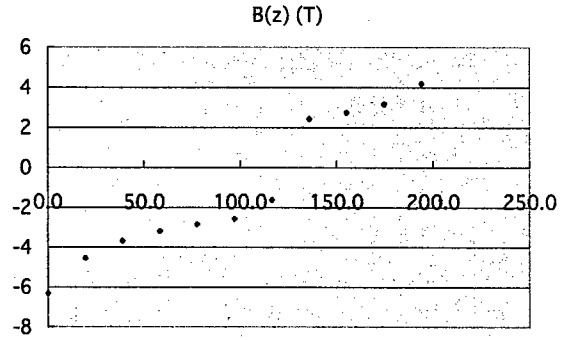


Fig. 6 Field distribution inside the permendur pole on a vertical direction

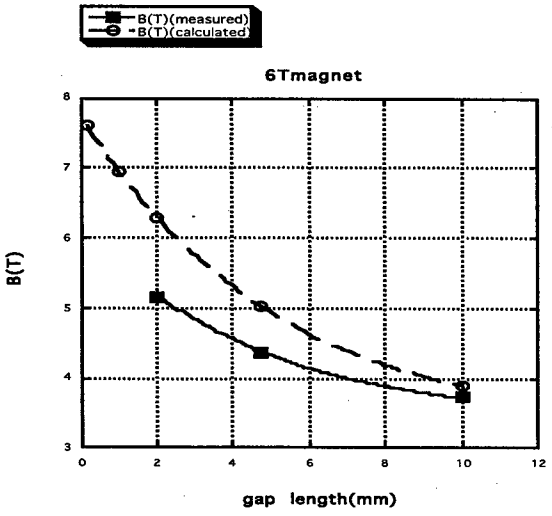


Fig. 7 Comparison of field strength between those of computation and measurement.

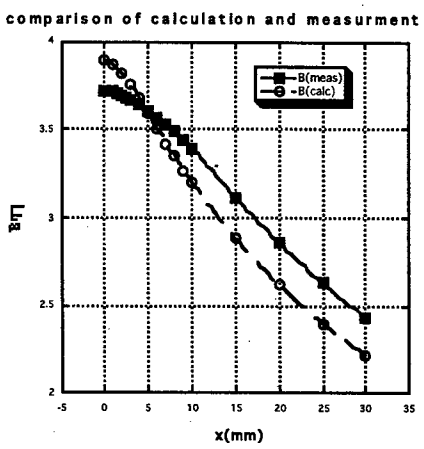


Fig. 8 Comparison of a field distribution between that of calculation and measurement.

CONCLUSION

We have achieved the world strongest magnetic field of 5.16 Tesla in a 2 mm gap in a permanent dipole magnet at a room temperature. The designed field value of 6.29 Tesla could not be reached. There is still an indication that an important feature is missing in a design of the magnet.

REFERENCES

[1] CERN Courier (International journal of high energy physics), "Magnet becomes more compact", volume 41,number 7, September 2001,page 9

[2] M.Kumada, T.Fujisawa, Y.Hirao, M.Endo, M.Aoki, T.Kohda, Y.Iwashita, I.Bolshakova, R.Holyaka, "Development of a model 4 Tesla dipole magnet", PAC2001、June,18-22,2001,Chicago

[3] M. Kumada, T. Fujisawa, Y. Hirao, M. Endo, M. Aoki, T. Kohda, Y. Iwashita, I. Bolshakova, R. Holyaka, "Development of high field permanent magnets", MT17(International magnet technology conference), 9/24-28, 2001, Geneve

[4] M.Kumada, T.Fujisawa, Y.Hirao, M. Endo, M. Aoki, T. Kohda, Y. Iwashita, I. Bolshakova, R.Holyaka, "Challenge to a high field permanent magnet of variable field strength", Japan accelerator Conference, 2001, 29-31 May Symposium on Accelerator Science and Technology, Osaka University, Oct 28-31

[5] Y.Iwashita, T.Mihara, E.Antokhin, M.Kumada, M.Aoki, "Permanent magnet quadrupole for Final Focus for Linear Collider", contribution in this conference PAC03, Portland.

[6] http://icfa-nanobeam.web.cern.ch/icfa-nanobeam/paper/kumada.pdf

[7] http://www.cerncourier.com/main/article/42/3/5

[8] Y.Iwashita, "Axial Magnetic Field Lens with Permanent Magnet", Proc. of the 1993 Particle Accelerator Conference, May 17-20, 1993, Washington, D.C., p.3154

SUPERCONDUCTING DOUBLE-HELIX ACCELERATOR MAGNETS*

R. B. Meinke#, M. J. Ball, C. L. Goodzeit, Advanced Magnet Laboratory, Palm Bay, FL, USA

Abstract

We describe an important contribution to accelerator magnet technology based on the concept of modulating the helical turns of solenoid coils to produce pure multipole fields of any order. Calculations show that these configurations inherently produce virtually error free fields of the desired multipole order in a large fraction of the aperture in the two dimensional cross section without the presence of iron. The characteristics of one such configuration, the double-helix dipole (DHD), are described. It is also explained how the novel geometry of the double-helix coils simplifies the manufacturing, eliminates complex coil parts, and thus significantly reduces the cost of the magnets in comparison to the conventional cosine theta (racetrack design) coils. This has been demonstrated by the design and construction of a prototype dipole that produces a 4T field in an 80 mm aperture (without iron).

FOREWORD

The double helix coil configuration represents a significant advance in accelerator magnet technology over the conventional cosine theta type (racetrack design) coils. The performance of virtually any type of accelerator magnet is improved while the cost of manufacture is substantially reduced with this magnet configuration.

The double-helix dipole and higher multipole magnets have been previously described [1,2,3]. They achieve pure multipole fields by the sinusoidal modulation of the axial position of the turns of a solenoid wound coil. For example, in the case of the dipole, the axial position of the conductor path is described as shown in Figure 1 and Figure 2 shows a 2-layer double helix dipole magnet (DHD).

Each turn of the coil can be well approximated as an ellipse tilted at an angle α with respect to the axis of the coil. This produces a transverse field component superimposed on a solenoid field component. When pairs of such windings with opposite tilt angles are assembled concentrically, the solenoid field components cancel and the dipole components add to produce a pure dipole field.

Higher order multipole fields can be obtained by modulating the axial position z of the winding according to the relation $z = h + A_n \sin(n\theta)$, where h is the helical advance and A_n is the amplitude of the modulation. Using a modulation frequency of $n = 2$, the result is a magnet with a pure quadrupole field. Similarly, $n = 3$ produces a sextupole, $n = 4$ produces an octupole, and so forth.

Combined function magnets are also possible by modulating the conductor path at 2 frequencies. For example, $z = h + A_0 (\sin\theta + 0.01 \sin 3\theta)$ will produce a dipole with a small amount of sextupole.

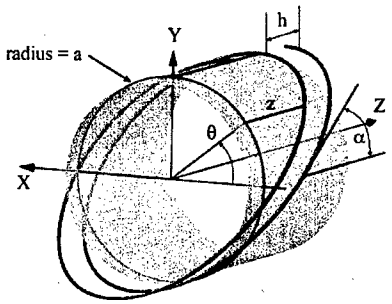


Figure 1: For the case of the dipole, the z coordinate of the conductor path is given by $z = h + A_0 \sin\theta$ with $A_0 = a / \tan\alpha$, where a is the radius of the coil aperture, α is the tilt angle of the winding with respect to the horizontal axis, and h is the helical advance per

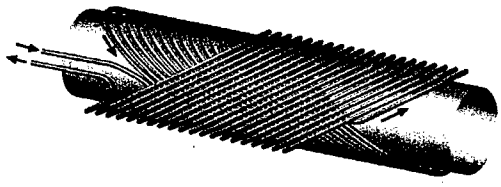


Figure 2: Double helix dipole (DHD) concept uses pairs of layers with opposite tilt and current direction. Aperture may be circular or elliptical. High field values can be obtained by using multiple pairs of layers with the transition between layers as shown.

The high magnetic fields required for future accelerators can only be achieved with Nb_3Sn, or other A15 or HTS type superconductors, which are brittle and sensitive to mechanical strain. The traditional cosine-theta racetrack dipole and quadrupole configurations make it difficult and expensive to employ such conductors. The double helix design, however, facilitates the use of pre-reacted, brittle conductors for such applications.

In this paper we describe some of the characteristics of double-helix magnets for accelerator applications and show how a double-helix dipole model magnet (DHD002) was designed and constructed.

*Work partially supported by U.S. Department of Energy under SBIR grant DE-FG02-02ER83360.
Email for R.B.Meinke is rmeinke@magnetlab.com or C.L. Goodzeit is mjbcarl@attbi.com

0-7803-7738-9/03/$17.00 © 2003 IEEE

CHARACTERISTICS OF DOUBLE-HELIX DIPOLE MAGNETS

Field Strength and Multipole Content

The dipole field (without iron or end effects) contributed by current I in each layer of a DHD is given by $B_y = I\ (\mu_0/2d)\ \cos\alpha$ where d is the effective width of the conductor. Theoretically there are no higher order multipoles created in the ideal double-helix configuration. Actual coil geometry with helicity and finite sized conductors produces a very low level of harmonic content in a large portion of the coil aperture. Table 1 shows the multipole fields computed at the center of the model magnet DHD002.

Table 1: DHD002 multipole fields in gauss at 9238 A, computed with AMPERES at the magnet longitudinal center and R_{ref} = 25 mm (~2/3 of coil aperture).

Multipole order	Skew	Normal	Multipole Units
0	0.0055	-40320.0000	10000
1	0.0019	-0.4100	0.101687
2	-0.0003	-0.1940	0.048115
3	-0.0006	-0.2240	0.055556
4	0.0005	-0.2580	0.063988
5	0.0007	-0.0580	0.014385
6	0.0001	0.0960	-0.02381
7	0.0002	-0.0440	0.010913
8	0.0000	-0.1320	0.032738
9	-0.0001	0.0240	-0.00595

End Fields

Three-dimensional magnetic analysis was performed using AMPERES. The graph in Figure 3 shows the normal multipoles present in the ends (final ~200 mm) of the 1500 mm long DHD002. The graph for skew multipoles is similar. Although end field harmonics are present, the integral of those harmonics tends to vanish.

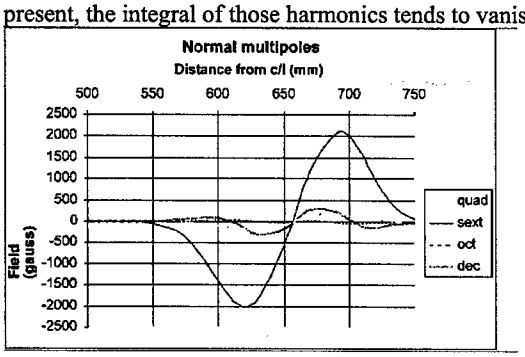


Figure 3: Normal Multipoles in the End Region

Comparison with Conventional Accelerator Magnet Technology

Although the conventional Rutherford style cosine theta racetrack coils can produce a given magnetic field with perhaps the least mass of superconductor, the unique coil geometry of the double-helix configuration enables a relatively simple and inexpensive method of making accelerator magnets. While the conventional method of coil fabrication uses flat insulated cable, wrapped with adhesive and molded under heat and pressure, in comparison the manufacture of DH coils is remarkably simple. Furthermore the conventional coils require many precise and expensive parts, while DH coils use only five types of components:

- Stainless steel support / bore tube
- Round multi-strand conductor
- Cylindrical composite tubes for placement of the conductor turns
- Cryogenic grade epoxy for impregnating the assembled coils
- Aluminum alloy cylinders that are thermally shrunk on the completed coil assembly to provide structural reinforcement.

Another significant difference of the DHD design is the elimination of the requirement for applying azimuthal pre-stress to the coils. Therefore, very high field magnets can be made using the DHD configuration and adequately reinforced by using thermally-shrunk aluminum cylinders on a completed impregnated coil assembly.

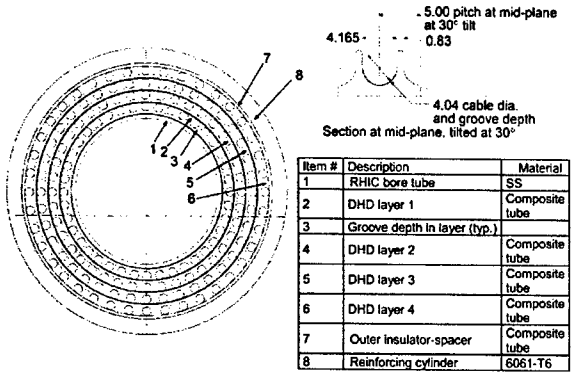
Also, the double helix design facilitates the use of pre-reacted brittle superconducting materials. The mechanical strain induced in the strands of the cable can be kept to less than 0.4% in the manufacture of DHD coils. This is accomplished by using small strand conductor (typically 10 –12 mil diameter) in the pre-reacted cable and controlling the change in radius of curvature of the conductor from the reacted state to the placement on the coil form. This is enabled by the relatively large minimum bend radius in the DHD geometry and the identical geometry of each turn in the coil.

THE DHD MODEL MAGNET DHD002

Parameters

A DHD model magnet was designed and constructed under a DOE Phase I SBIR grant. An objective was to demonstrate the simplicity of the design, ease of manufacture, and performance of this technology. The completed magnet assembly was delivered to Brookhaven National Laboratory in early April and will be tested in June or July.

This model has an 80 mm coil aperture and a length of 1.5 m. It has 4 coil layers, which were wound with a round cable composed of 19 strands of NbTi material of the type that was used for the SSC inner coils. The bare cable diameter was 4.04 mm and the effective width including insulation between the turns was 5 mm. The magnet cross section is shown in Figure 4.



Item #	Description	Material
1	RHIC bore tube	SS
2	DHD layer 1	Composite tube
3	Groove depth in layer (typ.)	
4	DHD layer 2	Composite tube
5	DHD layer 3	Composite tube
6	DHD layer 4	Composite tube
7	Outer insulator-spacer	Composite tube
8	Reinforcing cylinder	6061-T6

Figure 4: Cross section of DHD002. Helical turns of cable are represented by a series of circles; however, the circles do not represent actual conductor cross section/position.

The calculated performance of DHD002 with α=30° and operating current = 9238 A is central field = 4.02 T, peak field = 4.19 T. At an operating temperature of 4.35 K, the quench current is 11,311 A giving a current margin of 22.4%. Current densities in the SC and copper at operating conditions are J(NbTi,operating) = 2181 A/mm^2 and J(Cu,operating) = 1678 A/mm^2. The current density in the copper is rather high for this application, but the use of 1.3:1 SSC inner strand was dictated by its availability. The magnet inductance is 3.66 mH.

Magnet Fabrication Procedure

Composite tubes of appropriate diameter for each of the coil layers were obtained and grooves having the tilted helical geometry (and also the lead and layer transition path) were machined in them using a computer-controlled milling machine. The base cylinder was bonded on the RHIC bore tube that was supplied by BNL and bare conductor was placed in the grooves using a simple fixture with adjustable tension.

The additional composite tubes were added sequentially and the conductor placed in the pre-machined grooves without splices between the layers. The type of continuous layer transition shown in Figure 2 was used between layers.

The completed coil assembly was covered with a thin composite tube barrier and vacuum impregnated with cryogenic grade epoxy. A sample section of coil used to evaluate the vacuum impregnation procedure is shown in Figure 5.

The assembly was completed by sliding pre-heated segments of aluminum alloy cylinders over the completed coil assembly to provide radial pre-compression to the coil for reinforcement. Note that the double helix construction technology uses a modular approach that easily enables the construction of very long magnets.

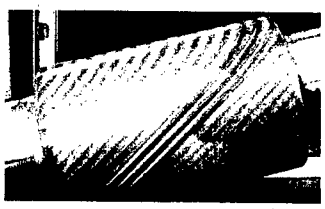


Figure 5: A few turns of epoxy impregnated coil, with a Lexan cover, show typical turn geometry. Insulation is provided by the web of the coil support grooves and the epoxy impregnation.

SUMMARY

The principle of obtaining pure multipole fields by modulating the axial position of the turns in helically wound (solenoid) coils can be applied to accelerator magnets to yield a simple design that is easy to manufacture and significantly less costly than conventional coil designs. We have shown how this technology can produce a high field quality, low cost design that can be fabricated using standard machine tools and simple fixtures rather than expensive dedicated tooling. The method of using bare, round multi-strand cable placed in pre-machined grooves in composite cylinders produces a precisely-wound, splice-free coil assembly. When impregnated with epoxy and reinforced with thermally-shrunk aluminum cylinders, the result is a self-supporting coil assembly that is adequately reinforced for very high Lorentz force without the requirement of applying high azimuthal pre-stress to the coils.

ACKNOWLEDGMENT

The authors would like to acknowledge the contribution and help of Brookhaven National Laboratory that supplied the surplus RHIC bore tube for DHD002 and has agreed to perform cryogenic testing and multipole measurements. This work is scheduled to be undertaken in June -July 2003.

REFERENCES

[1] C. L. Goodzeit, R. B. Meinke, and M. J. Ball, "The Double-Helix Dipole – A Novel Approach to Accelerator Magnet Design", Paper 4LC07, ASC2002, Houston, TX, August 2002; to be published, *IEEE Transactions on Superconductivity,* June 2003.

[2] R. B. Meinke, C. L. Goodzeit, and M. J. Ball, "Modulated Double-Helix Quadrupole Magnets", Paper 4LC08, ASC2002, Houston, TX, August 2002; to be published, *IEEE Transactions on Superconductivity,* June 2003.

[3] AML has Patents Pending on the use of the double helix configuration for accelerator magnets and other applications.

MEASUREMENT OF BEAM DRIVEN HYDRODYNAMIC TURBULENCE

J. Norem*, ANL, Argonne, IL 60439, USA
E. Black, IIT, Chicago IL 60439, USA
L. Bandura, M. A. C. Cummings, NIU, DeKalb, IL 60115 USA
D. Errede, UIUC, Champaign IL 60510, USA

Abstract

Cooling intense muon beams in liquid hydrogen absorbers introduces kW of heating to the cold fluid, which will drive turbulent flow[1]. The amount of turbulence may be sufficient to help cool the liquid, but calculations are difficult. We have used a 20 MeV electron beam in a water tank to look at the scale of the beam driven convection and turbulence. The density and flow measurements are made with schlieren and Ronchi systems. We describe the optical systems and the turbulence measured. These data are being used to calibrate hydrodynamic calculations of convection driven and forced flow cooling in muon cooling absorbers.

INTRODUCTION

The schlieren method was discovered in 1864 by August Toepler[2]. This qualitative test allows one to see density fluctuations in a fluid. The general setup involves an objective lens or mirror, point light source, and a knife edge at the focus of the lens or mirror. The object to be visualized is placed between the objective and knife edge. The image can be directed onto a screen or into a camera. This is a highly sensitive test, allowing for precision measurements. The image obtained consists of a light and dark pattern corresponding to the density fluctuations. The placement of the knife edge determines whether a higher density region appears light or dark compared to the average background. A vertical knife edge is used to view density variations in the horizontal direction and a horizontal knife edge shows vertical density variations.

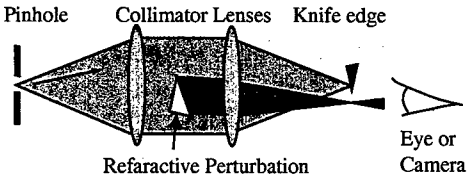


Figure 1. The Schlieren principle

In schlieren refraction, optical perturbations refract light in proportion to the gradients of refractive index in a direction perpendicular to the optical path. When the directly transmitted light is entirely or partially blocked, as in Fig. 1, the optical perturbations can be seen either with the eye or a camera.

The Ronchi method is an extension of the schlieren technique that can make quantitative measurements.

* norem@anl.gov

Unlike the schlieren system, the Ronchi method is quantitative. Instead of a knife edge at the focus, a glass slide with closely spaced, parallel lines (ronchi ruling) is used. By knowing the spacing of these lines on the Ronchi ruling and the deflection of the lines in the image, it is possible to measure the magnitude of the refraction, and thus the density gradient in the sample.

EXPERIMENTAL PROCEDURE

The electron linac used in this experiment is located at Argonne National Laboratory in the Chemistry Division. It delivers a beam of approximately 20 MeV. In our experiment, we used 50-200 pulses with approximately 30 nC per pulse. Pulse lengths ranged from 4-40 ns. During this experiment, we were the only users of the linac. The beam intensity was primarily a function of the pulse length, and the total beam power depended on the pulse repetition rate. Most of the data were taken at 30 to 60 Hz, which produced the scale of turbulence we needed for tuning up.

We used two setups, the first one with the beam perpendicular to the optical path and the second one with the beam close to colinear with the optical path. The collinear geometry was most relevant to checking the

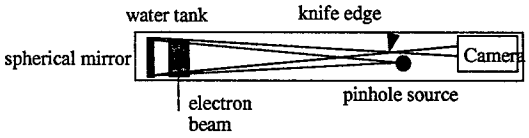


Figure 2, Transverse optical path and beam

computational fluid dynamics models.

In our first setup, we used a spherical mirror with a focal length of one meter, a knife edge, pinhole light source, and a digital camera to record the data, (Fig. 2). The water was placed in a rectangular tank with two optically flat 10 cm x 10 cm pieces of glass for the front and back windows. The optical depth was 5 cm and the sides were 0.8 mm thick aluminum. The top was open, but covered with a layer of G10, because evaporation at the surface produced eddies in the water after a period of a few minutes. The electron beam was directed into the tank through one of the aluminum sides. Behind the water tank was the spherical mirror. The placement of the knife edge and light source varied in different runs of this experiment but were always approximately one meter in front of the spherical mirror. The camera was placed about one and a half meters away from the mirror.

0-7803-7738-9/03/$17.00 © 2003 IEEE

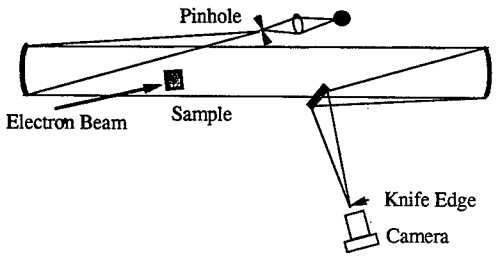


Figure 3, Colinear optical path and beam.

In the second setup, two spherical mirrors with focal length 91 cm were mounted two meters apart, as shown in Fig. 3. A 5 cm diameter. cylindrical tank with 5 mm thick fused quartz windows was placed between the spherical mirrors. A pinhole light source was placed slightly off-axis and pointed toward one of the mirrors. A small flat mirror was used to direct light away from the axis of the spherical mirrors toward the knife edge, and the camera was set directly behind. When two paraboloids are used off axis in this way, the dominant aberration, coma, is minimized.

In this experiment, we used the SILICON VIDEO® 2112 CMOS digital camera for data acquisition. The software used in conjunction with this camera is XCAP (V2.1.010611) from EPIX, Inc. The initial frame for each run was triggered manually. After this, the software took additional frames automatically at regular time intervals ranging from 1-5 seconds each. These frames were initially stored as binary files in the frame buffer and later converted via XCAP to JPEG file format.

The primary experimental complication was due to electrical pickup in the camera from the charge in the beam. When the apparatus was carefully grounded with low impedance conductors, this problem disappeared. We also saw significant Cherenkov light from the beam in the second setup. The Cherenkov light can be minimized or eliminated by a mask in front of the camera lens, since all schlieren or Ronchi data would pass through an aperture of mm dimensions, as was done in the first setup.

Figures 4, 5 and 6, show the beam power, beam profile at the entrance window to the target cell, and the beam radius as it passed through the cell. The beam radius increased due to the initial divergence of the beam, and multiple scattering in the water and windows.

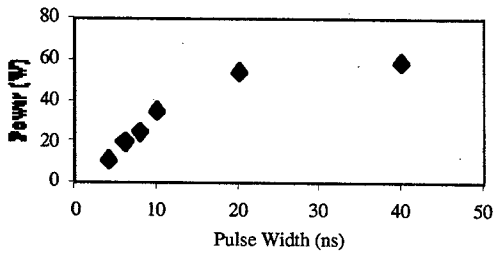


Figure 4, Beam power vs pulse length, at 30 Hz.

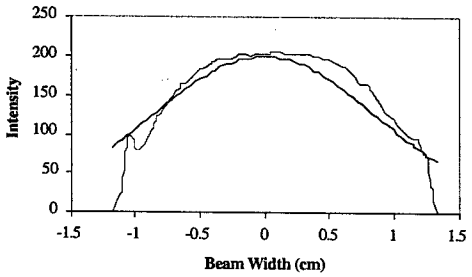


Figure 5, Beam profile.

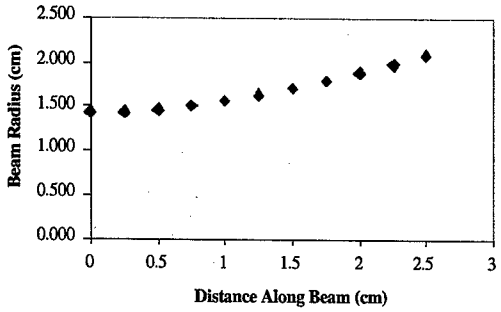


Figure 6, The beam size in the test cell

The second setup is shown in Fig. 7, which shows the two mirrors, test cell, camera and light source structure near the beam exit window of the linac.

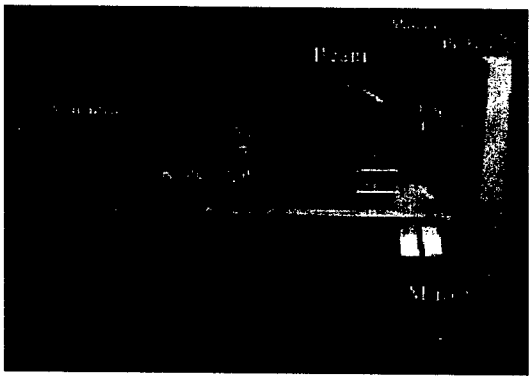


Figure 7, The colinear setup.

RESULTS

The data presented here are preliminary, since we have just begun to process the graphics, and have not had a chance to fully understand the density and velocity gradients in the cell. We have looked at perpendicular and colinear geometries, horizontal and vertical knife edge data which produces vertical and horizontal density gradients. We have also produced horizontal and vertical Ronchigrams which can be used to generate numerical estimates of the density fluctuations. This data were taken with time intervals between pictures of 0.5 to 2 s, and

using a range of beam powers. We will show some example data. Fig. 8 and 9 show vertical and horizontal gradients viewed from the side, and Fig. 10 and Fig. 11 show vertical and horizontal colinear gradients. Fig 12 is taken with a vertical Ronchi grid.

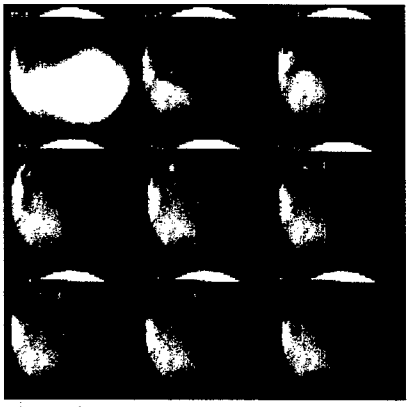


Figure 8, Transverse image, horizontal gradients

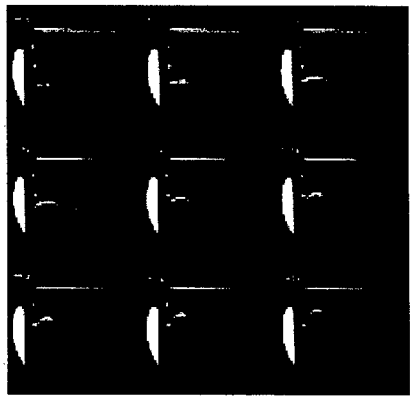


Figure 9, Transverse image, vertical gradients

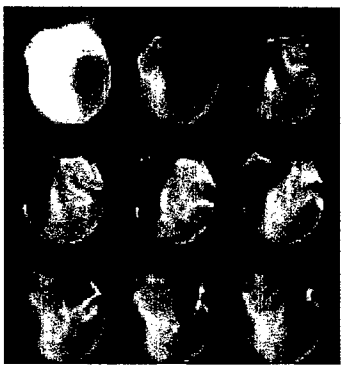


Figure 10, Colinear image, vertical gradient



Figure 11, Colinear image, vertical gradients



Figure 12, Colinear image, Ronchi pattern

This initial test of schlieren and Ronchi methods shows that density gradients in liquid targets are easily accessible. We plan to extend this work to quantitative comparison with predictions of computational fluid dynamics for high power beams in water and liquid hydrogen.

ACKNOWLEDGEMENTS

C. Jonah and S. Chemerisov of the Argonne Chemistry Division have been very helpful operating the linac and giving useful advice. W. Lau and S. Yang of Oxford and K. Cassel, of IIT, have provided useful insight about comparison with theoretical models. This work was done as part of the MUCOOL experimental program, and was supported in part by the US Dept of Energy and the State of Illinois.

REFERENCES

[1] M. A. Cummings, et. al., in *Proceedings of NUFACT02*, London, (2002)

[2] Settles, G. S., *Schlieren and Shadograph Techniques* Springer-Verlag, New York, (2001)

MUON COOLING IN THE RFOFO RING COOLER

R.C. Fernow, J.S. Berg, J.C. Gallardo*, R.B. Palmer, BNL, Upton, NY 11973, USA

Abstract

The performance of the ring described here compares favorably with the linear cooling channel used in the second U.S. Neutrino Factory Study[1]. The 6D phase space density of an idealized ring is increased by a factor of 238, compared with the linear channel's factor of only 15. The simulations make use of fully realistic magnetic fields, and include absorber and rf cavity windows, and empty lattice cells for injection/extraction.

INTRODUCTION

In the present U.S. Neutrino Factory design [2] the muon beam 6D phase space volume must be reduced in order to be able to accelerate it and inject into the storage ring pointing to a long distance neutrino detector. Ionization cooling is currently the only feasible option for cooling the beam within the muon lifetime ($\tau_0 = 2.19\,\mu$s). If muons alternately pass through a material absorber, and are then reaccelerated, and if there is sufficient focusing at the absorber, then the muon's transverse phase space is reduced, *i.e.* the muons are cooled in the transverse dimension. A consequence of the transverse cooling is an increase of the longitudinal phase space caused by energy straggling in the material. The consequent momentum spread can be reduced if dispersion is introduced and a wedge absorber placed such that high momentum particles pass through more material than low momentum particles. However, in this process the beam width is increased. The process is thus primarily an exchange of emittance between the longitudinal and transverse dimensions, but when combined with transverse cooling in the material, all three dimensions can be cooled.

The ring design parameters are given in Tb. 1. All cells are strictly identical, and the presence of an integer betatron resonance within the momentum acceptance is eliminated.

Figure 1 shows a detailed view of three cells of the lattice, in plan (a) and side (b) views. The solenoids are not evenly spaced; those on either side of the absorbers are closer in order to increase the focusing at the absorber. The longitudinal field on-axis has an approximately sinusoidal dependence on position. The beam axis is displaced laterally with respect to the coil centers (as shown in Fig. 1a) to minimize horizontal fields that cause vertical beam deviations.

The bending field for the ring, and the required dispersion, are provided by alternately tilting the solenoids by 3.0°.

* Correspondent: gallardo@bnl.gov

Table 1: RFOFO Basic Ring Parameters

Circumference (m)	33
Cells	12
Max B_z (T)	2.77
Coil Tilts (deg.)	3.0
Ave Momentum (MeV/c)	220
Min Trans. Beta (cm)	38
Max. Dispersion (cm)	8
Momentum Compaction	0.0037
Wedge Absorber Material	H_2
Wedge Thickness on axis (cm)	25.4
Wedge Angle (°)	90
Wedge Vertex position (cm)	12.7
Wedge Azimuthal angle (°)	230
Frequency (MHz)	201.25
Gradient (MV/m)	12
Phase (°) from 0-crossing	25

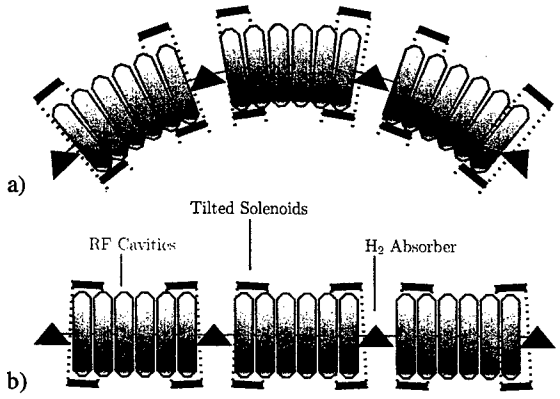


Figure 1: Three cells of the RFOFO lattice; a) plan view; b) side view. Notice that the coils have been displaced radially by 10 cm.

MODELING THE RING

The RFOFO ring was modeled using the ICOOL code[3]. The magnetic field from the tipped solenoids was calculated in an independent code that found the resultant field by summing the fields from a system of current sheets[4, 5]. The field of a solenoidal current sheet can be written analytically in terms of elliptic integrals. The resultant field components were shown to satisfy the 3D Maxwell equations to a high level of accuracy and agreed with independent calculations[6, 7]. The solenoidal field on-axis was approximately sinusoidal with a peak magni-

0-7803-7738-9/03/$17.00 © 2003 IEEE

tude of 2.7 T. The solenoids were tipped to produce an average vertical dipole field of 0.125 T on-axis. The circle containing the centers of the solenoids was displaced 10 cm outwards radially from the nominal beam axis in order to minimize the horizontal dipole field on the axis.

The rf cavities were modeled using cylindrical pillboxes running in the TM010 mode. The cavities are located in a dipole field in this design. Since we are accelerating muons, the cavities can be enclosed with metallic end windows in order to produce the maximum electric field on-axis for a given amount of rf power. The rf windows were stepped in thickness radially, in order to provide minimum thickness near the beam axis and still control the temperature increase due to rf heating.

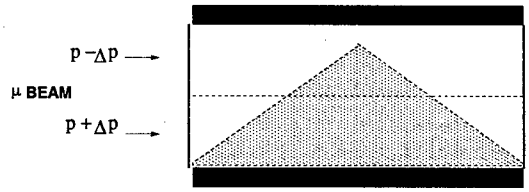


Figure 2: Wedge absorber used in the simulations.

The *wedge* absorbers are house-shaped, as shown in Fig. 2. The wedge only extends part way across the gap, such that a particle on the reference orbit always loses the same amount of energy crossing the wedge. The absorber windows were planar and located axially just in front of and behind the wedge itself. This is likely a worst case because the whole beam is forced to cross the window regardless of its transverse position. In reality the window shape will conform to the absorber and the effect on the beam of scattering in the window should be lessened.

We use a Gaussian input beam[6] in the simulations with a normalized transverse emittance of 12 mm and a normalized longitudinal emittance of 18.4 mm. The reference momentum is 203 MeV/c. This value was chosen to make the circulation time around the ring on a closed orbit equal to the 25th harmonic of 201.25 MHz. The initial beam has a correlation between the axial momentum and the transverse amplitude, to minimize the tendency for the particles in the bunch to spread out longitudinally in the solenoidal field. The initial *rms* bunch length is 8 cm, so this ring is not compatible with the bunch train assumed in Study-2. The use of compact cooling rings will likely also require the use of a preceding bunch compression ring.

The mean transverse position of the starting bunch was displaced by -10 mm in x and 18 mm in y to put the reference momentum particle on a closed orbit.

SIMULATION RESULTS

Three merit factors have been widely used in the discussion of cooling ring performance. The quantity **M-factor**, defined by $M = \frac{\epsilon_6(\text{initial})}{\epsilon_6(\text{final})} \times$ Transmission, is most useful for collider applications. Another figure of merit, which is local in character, is the **Q-factor** defined by $Q(s) = \frac{\frac{d\,\epsilon_6(s)}{ds}}{\frac{d\,N(s)}{ds}} \frac{N(s)}{\epsilon_6(s)}$; if $Q(s)$ is constant, then $< Q >= Ln(\frac{\epsilon_6(s)}{\epsilon_6(0)})/Ln(\frac{N(s)}{N(0)})$. The third merit factor, and the one most directly useful for neutrino factories, is the muon density into a fixed accelerator acceptance volume. If N is the number of muons and V is a fixed acceptance volume in phase space, then we define the **D-factor** at any location s along the ring to be $D(s) = \frac{N(s)/V}{N(0)/V}$.

We first consider the performance of an idealized ring before the introduction of windows around the absorbers and rf cavities and before the introduction of empty cells for injection/extraction. Figure 3 shows the three emittances, transverse, longitudinal and 6D, merit factor M and transmission plotted on a logarithmic scale versus distance traveled. Table 2 summarizes the performance. The **Q-factor** is 8.7. After a distance of 400 m ($\approx$ 12 turns), the

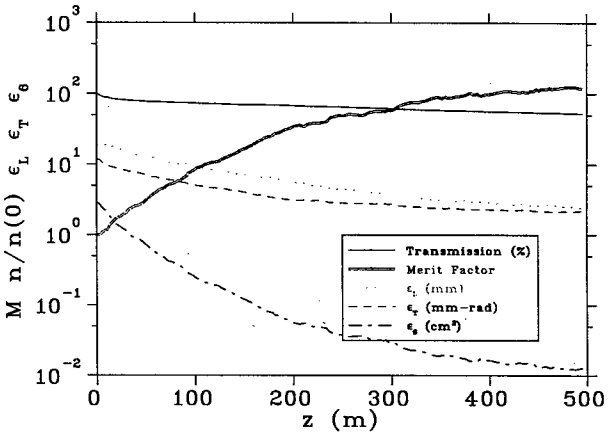


Figure 3: Performance of RFOFO Ring. Transmission, normalized transverse emittance, normalized longitudinal emittance, normalized 6-dimensional emittance, and the merit factor M, as a function of distance.

6D emittance has fallen by a factor of 238, with a transmission of 53% (66% without decay). The **M-factor** is 125. The same factor for the Study-2 cooling lattice, also without windows, is 15.

Table 2: RFOFO Ring Performance

	Before	After	ratio
$\epsilon_\perp$ (πmm^2)	11.87	2.14	5.5
$\epsilon_\parallel$ (πmm)	18.64	2.53	7.4
ϵ_6 (π^3cm^3)	2.86	0.012	238
N/N_0, inc. decay	1	0.53	0.53
M-factor	1	125	**125**
D-factor	1	8.57	**8.57**

We next show the idealized ring behavior in terms of the

muon density. Figure 4 shows the total muon transmission together with the muon density into two fixed acceptance volumes. These volumes could correspond to the acceptance of a linear accelerator that follows the cooling ring at a neutrino factory.

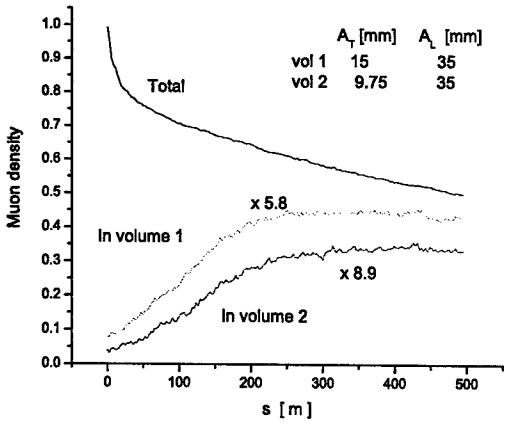


Figure 4: Performance of RFOFO Ring. Transmission and muon density into two fixed acceptance volumes. These results were obtained using a 100° wedge.

The idealized ring increases the muon density into the smaller acceptance volume by a factor of almost 9 in 250 m, which corresponds to about 8 turns. The density in the larger acceptance volume increases by about a factor of 6.

The introduction of windows around the absorbers or rf cavities introduces new sources of scattering and degrades the cooling performance. In addition a real ring needs space for injection/extraction. This is treated here by leaving the rf and absorbers out of two of the 12 lattice cells. The empty cells have the same pairs of solenoids however, so the magnetic field periodicity is preserved. Table 3 shows the result of a) adding absorber windows, b) adding rf cavity windows, and c) leaving empty cells in the lattice.

The absorber window used in Study-2 was 360 μm of aluminum. We see that windows of this thickness degrade the performance by about 30%. For safety reasons it may be necessary to use an additional window that increases the total amount of aluminum. On the other hand the use of other materials or optimized window shapes could reduce the amount of material. Another possibility would be to replace the liquid H_2 absorber with a solid material. LiH is one possible candidate, although Tb. 3 shows there is a 45% loss of performance with this option.

The rf Be windows degrade the performance by about 35%. One possibility to get around this problem is to operate the cavities at liquid nitrogen temperature. The lower operating temperature and the reduced rf gradient of 12 MV/m versus 16 MV/m in Study-2 allow the thickness of the windows to be decreased by a factor of 20 and the performance loss is only 13%. Alternatively, one could eliminate the rf cavity windows altogether and use an open cavity. This has the disadvantage that four times more power is required to produce the same E_z on axis.

Table 3: Perturbations on the idealized ring performance. FS2 stands for Study-2 used windows; FS2/20 stands for windows used in Study-2 with thicknesses reduced by a factor of 20.

absorber	abs win	rf win	empty cells	D
LH	none	none	0	8.93
LH	250μm AL	none	0	7.50
LH	360μm AL	none	0	6.60
LH	500μm AL	none	0	6.08
LiH	none	none	0	4.88
LH	none	FS2	0	5.88
LH	none	FS2/20	0	7.80
LH	none	none	2	6.73
LH	360μm AL	FS2/20	2	4.25

Introducing empty cells for injection/extraction reduces the performance by 25%.

Finally, we consider an example that combines all of these effects. We choose liquid H_2 as the absorber with Study-2 like windows, assuming we can use this effective amount of aluminum because of improved alloys or window shape. We assume operation at liquid nitrogen temperature and use the thinner Be rf windows and leave empty cells in the lattice for injection/extraction. This realistic ring model still gives an impressive increase in the muon density of a factor of 4.25

REFERENCES

[1] S. Ozaki, R. Palmer, M. Zisman, J. Gallardo, Editors, *Feasibility Study II of a Muon Based Neutrino Source*, BNL-52623, June, 2001.

[2] The MC Collaboration, *Recent Progress in Neutrino Factory and Muon Collider Research within the Muon Collaboration*, to be published. (http://www.cap.bnl.gov/mumu/pubs/prstab-030422/prstab.pdf)

[3] R. Fernow, *ICOOL: a simulation code for ionization cooling of muon beams*, Proc. 1999 Particle Accelerator Conference, p. 3020-3022.

[4] R. Fernow, J. Gallardo, *Realistic on-axis fields for the RFOFO cooling ring*, MUC-NOTE-COOL-THEORY-265, Nov. 2002. This series of technical notes can be found at (http://www-mucool.fnal.gov/mcnotes/)

[5] R. Fernow, J. Gallardo, *Calculation of RFOFO fields using the off-axis expansion in ICOOL*, MUC-NOTE-COOL-THEORY-268, Jan. 2003.

[6] V. Balbekov, *Simulation of RFOFO ring cooler with tilted solenoids*, MUC-NOTE-COOL-THEORY-264, Nov. 2002.

[7] S. Bracker, *Magnetic field maps for the RFOFO muon cooling ring*, MUC-NOTE-COOL-THEORY-271, Mar. 2003.

Proceedings of the 2003 Particle Accelerator Conference

LAYOUT AND OPTICS FOR THE RHIC ELECTRON COOLER*

Jörg Kewisch†, Xiangyun Chang, Dong Wang, Christoph Montag, Ilan Ben-Zvi,
BNL, Upton, NY 11973, USA

Abstract

As part of a luminosity upgrade it is planned to add an electron cooling section to the RHIC accelerator. Existing electron coolers operate at low beam energies and use a continuous electron stream. The ion energy of 100 GeV/u in RHIC requires an electron energy of 55 MeV. Therefore the RHIC cooler uses a linac with energy recovery for the electron acceleration. Short bunches exiting the linac section are stretched longitudinally to reduce the momentum spread and space charge effects in the cooling section, and compressed afterwards for deceleration and energy recovery in the linac. This report describes the design of the electron beam transport and simulation results.

INTRODUCTION

The RHIC accelerator provides collisions of ions from protons to gold. The particles are injected through a chain of pre-accelerators including a Tandem accelerator for ions and a linac for (polarized) protons, a booster and the AGS synchrotron. The normalized transverse emittance in RHIC is 10 mm mrad for ions. Future extensions of the accelerator complex include a pair of electron coolers (for the "blue" and "yellow" rings) which will be used to fight the degradation of the bunch length and emittance due to intra beam scattering over the duration of a fill and even increase the luminosity by decreasing the transverse emittance.

To achieve this task the RHIC electron coolers have to work at storage energies of 100 GeV/u. This corresponds to an electron energy of 55 MeV. The usual techniques of generating such electron beams (like a Pelletron) cannot be used. Instead, a super-conducting linac is appropriate and energy recovery is used to reduce the resulting beam power of 5 MW to manageable levels before dumping the beam.

A first study was performed in collaboration of BNL and Budker Institute of Nuclear Physics [1]. The design laid out in this study has since been improved, the biggest change being the replacement of a DC electron gun by a photo-cathode RF gun.

This report presents the improvements to the layout and optics of the RHIC Electron Cooler.

OVERVIEW

The layout of the cooler is shown in Figure 1. The electron beam is created in the photo-cathode RF gun shown in red in the picture. A bunch charge of 10 nC is assumed and the energy after the gun is 2.5 MeV. Using a pair of dipole magnets with a deflection angle of 3 degrees each the beam is injected into the super-conducting linac, consisting of four 5 cell 700 MHz cavities and two 2100 MHz cavities. The beam is accelerated to 55 MeV. It passes a weak dipole magnet which will extract the beam after energy recovery. A matching section with six quadrupoles is used to achieve the required phase advances for the transport of magnetized beam. The "stretcher" increases the bunch length from 1.5 cm to 7 cm, with a 200 MHz cavity at the end to reduce the energy spread of the beam. This cavity needs to be in a location with zero dispersion to maintain magnetization and emittance of the beam. The electron beam is then injected into the cooling section where it merges with the ion beam. The cooling section includes two 13 m long solenoids with a matching section between them to maintain magnetization. A second 200 MHz cavity introduces the opposite energy spread, so that the following "compressor" section (identical to the stretcher) reduces the bunch length to 1.8 cm. The beam passes the 3 degree magnet mentioned above, however, the beam energy is now 25 times higher so that the beam is only deflected by a tenth of a degree. The path length is adjusted so that the beam is shifted by 180 degrees relative to the accelerating phase of the cavity and is therefore decelerated while passing through the cavities. With a beam energy of now 2.5 MeV the dipole magnet mentioned above deflects the beam into the beam dump.

DETAILS

Injection into the cavities

At the entrance of the linac the low energy beam and the high energy beam must be merged. This is accomplished by a dipole magnet that deflects the low energy beam by 3 degrees while the high energy beam is not effected significantly. The dipole creates dispersion which reduces the magnetization of the beam. Since the momentum distribution of the electrons is changed in the linac the dispersion must be compensated locally. Therefore a pair of dipoles is used with solenoid focusing to create a 180 degree betatron phase advance between them. In order to avoid coupling the focusing is done with a so called Stabenov magnet: two solenoid coils with opposing fields.

*Under contract with the United States Department of Energy, Contract Number DE-AC02-98CH10886

†jorg@bnl.gov

0-7803-7738-9/03/$17.00 © 2003 IEEE

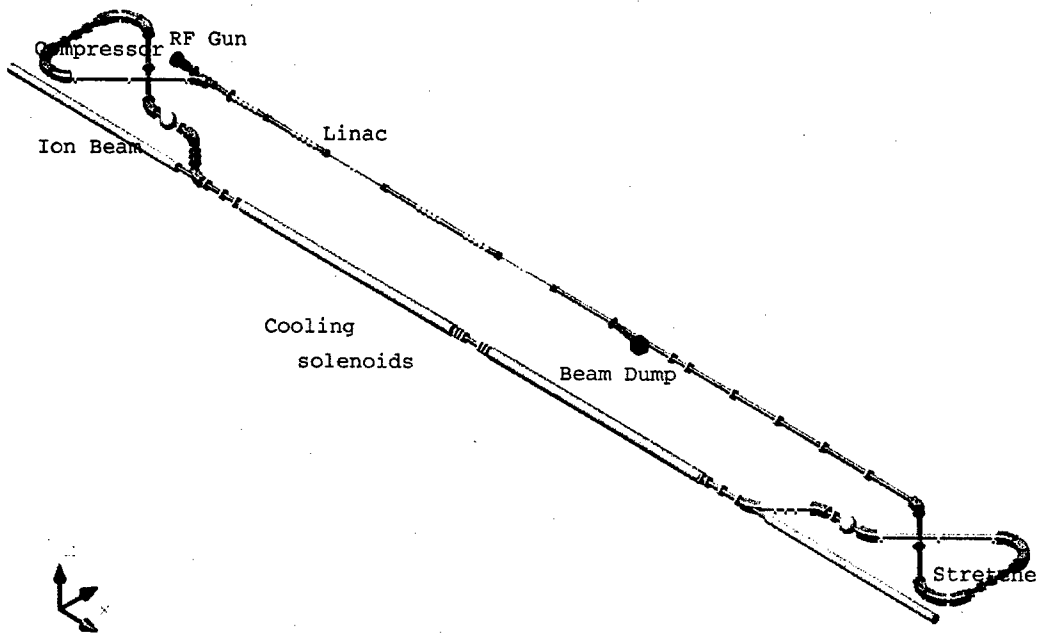


Figure 1: Schematic overview of the RHIC electron cooler. The magnetized electron beam is accelerated in a recirculating super conducting linac and stretched to the required bunch length in an extra loop in the arc that also serves as a transfer line into the solenoid. At the exit of the solenoid a second arc reduces the bunch length to its original value and transports the beam back to the linac for energy recovery. (graphic by S. Bugros)

Harmonic energy correction

The bunches have a length of ± 15 degrees in the 700 MHz system. The head and the tail therefore see a smaller acceleration field than the center of the bunch. In order to flatten the energy spread in the electron beam two 2100 MHz cavities decelerate the beam and do so much more in the middle than in the head and tail. The system also minimizes energy spread due to space charge.

Stretcher/Compressor

The stretcher lengthens the electron beam which has two purposes: First, together with a 200 MHz cavity it rotates the bunch in longitudinal phase space to reduce the energy spread of the electron bunch. For such rotation the path length in the stretcher should be only a function of the momentum deviation of the electrons. The path length deviation through the stretcher is:

$$\Delta L = \int \frac{x_\beta(s) + \frac{\Delta(s)p}{P} D}{\rho(s)} ds$$

where $x_\beta(s)$ is the betatron motion of the particle, $D(s)$ is the dispersion function and $\rho(s)$ is the bending radius in the dipoles. By using a mirror symmetric layout with 180 degrees phase advance between the inner dipoles the contribution of x_β to the integral is zero The optics of the stretcher is shown in figure 2

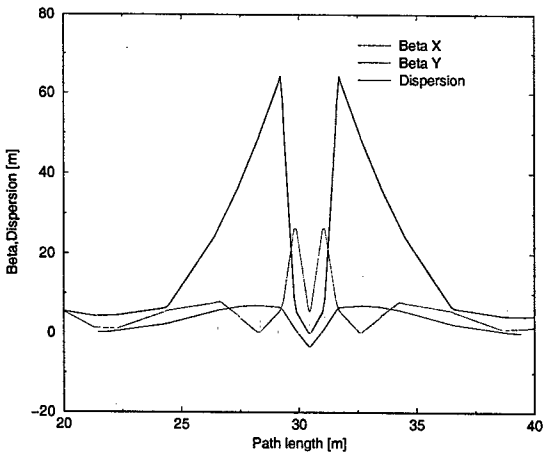


Figure 2: Optics of the stretcher/compressor

The second function of the stretcher is to reduce the density of the electron beam and therefore to reduce the space charge effect of the electron beam on the ion beam.

Cooling solenoid and coupling compensation

The length of the cooling section is approximately 30 meters. For engineering reasons the cooling solenoid is split into two parts. To preserve electron beam magne-

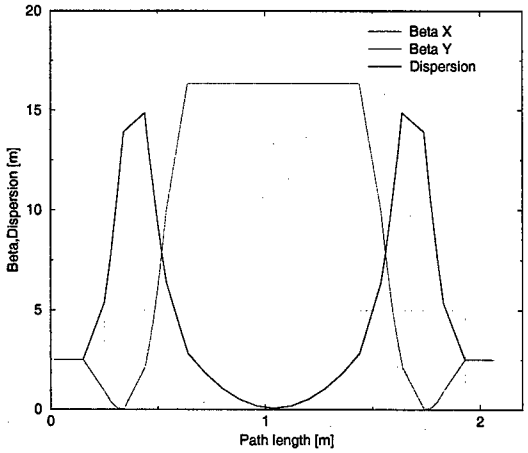


Figure 3: Optics of the matching section between the cooling solenoids

tization an appropriate matching section between the two solenoids is required. In reference [2] this matching is accomplished by a short focusing solenoid in the middle of the gap.

Using a solenoid for the focusing preserves axial symmetry and requires that the field of the two cooling solenoids have the same direction. This is a source of coupling for the ion beam and rotates the spin if RHIC accelerates polarized protons. To avoid these detrimental effects an alternative scheme has been developed consisting of a quadrupole matching section between the solenoids. Using quadrupoles for focusing allows having opposing fields in the cooling solenoids. The matching section must provide a phase advance of 180 degrees in the horizontal direction and 360 degrees in the vertical direction. Figure 3 shows the optics for the matching section. Figures 4 and 5 show the difference of the two methods.

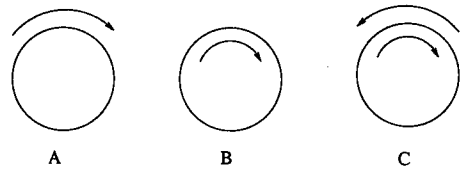


Figure 4: Maintaining beam magnetization across solenoid gaps. Focusing with solenoid: A - the fringe field of the first cooling solenoid creates a vortex. B - Focusing with a short solenoid reproduces the same vortex at the entrance of the second cooling solenoid. C - the fringe field stops the vortex.

PARMELA RESULTS

The electron optics has been checked with the tracking program PARMELA [3]. PARMELA includes the space

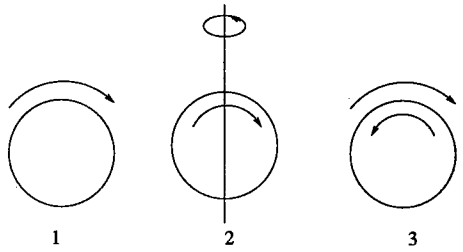


Figure 5: Maintaining beam magnetization across solenoid gaps. Focusing with quadrupole: 1 - the fringe field of the first cooling solenoid creates a vortex. 2 - A quadrupole section rotates the vortex around the vertical axis. 3 - the fringe field of the second cooling solenoid stops the vortex.

charge forces at low energies and is used to optimize the beam parameters. Without alignment error PARMELA predicts inside the cooling solenoid a transverse temperature of 1500 eV and an energy spread of $8 \cdot 10^{-5}$. None of the tracked particles was lost before reaching the beam dump.

CONCLUSION

The design of the RHIC electron cooler is still "work in progress". A transverse temperature to less than 1000 eV should be achieved to obtain the desired cooling rates. We are confident that this goal can be reached by careful emittance compensation. Also, a careful study of field and alignment errors is necessary.

REFERENCES

[1] V. Parkhomchuk, I. Ben-Zvi: Electron Cooling for RHIC, C-A/AP/47

[2] A. Burov et al.: Optical principles of beam transport for relativistic electron cooling, Phys. Rev. Special topics - Accelerators and Beams, Vol 3, 094002 (2000)

[3] K. R. Crandall, L. Young, H. Billen, LANL

Proceedings of the 2003 Particle Accelerator Conference

MUON STORAGE RINGS FOR 6D PHASE-SPACE COOLING

Harold Kirk*, BNL, Upton, NY 11973, USA
David Cline, Yasuo Fukui, Al Garren, UCLA, CA 90095, USA

Abstract

We describe several storage ring designs for reducing the 6-dimensional phase space of circulating muon beams. These rings utilize quadrupole and dipole magnets as well as wedge-shaped, liquid-hydrogen, energy-loss absorbers and energy compensating rf cavities. We obtain evaluations of their cooling performance by particle tracking simulation. Such rings are potentially useful for future Neutrino Factories or Muon Colliders as well as for existing facilities in which cooled, intense muon beams could enhance their physics programs.

INTRODUCTION

Two key components of a future collider complex based on counter-circulating muon beams [1] are the target/capture system [2] and the cooling system[3]. In addition, cooling systems[4] are envisioned for Neutrino Factory complexes[5, 6] which are based on the collection and storage of circulating muon beams.

Attempts to reduce the cooling infrastructure, thereby reducing costs of the cooling system, have led to a consideration of cooling rings as a possible simplifying approach to achieve 6D cooling of the muon beam phase space. Whereas linear cooling systems are useful for cooling the transverse emittance of muon beams, cooling rings have the additional advantage of generating momentum dispersion in the circulating beam thus providing the opportunity to insert wedge absorbers into the beam in order to also reduce the longitudinal beam emittance. We discuss in this paper one such approach in which the ring structure is composed of quadrupole and dipole magnets along with the inclusion of energy-loss absorbers and rf cavities which are required to restore the energy of the muon beam [7].

RING LATTICES

In general, our approach has been to obtain linear lattice solutions using the code SYNCH [8] and then transferring the lattice parameters to the code ICOOL [9] where the effects of energy loss in absorbers and the subsequent energy recovery in rf cavities can be modeled.

The system can cool both transversely and longitudinally, but the longitudinal cooling, which is proportional to the product of the absorber wedge angle and beam dispersion, causes a reduction of the cooling in the transverse bend plane[10]. The cooling, together with heating from scattering and straggling in the absorbers, results in a minimum achievable equilibrium emittance[11]. The expression for the transverse equilibrium emittance is given by

$$\epsilon_{N,eq} = \frac{\beta_\perp {E_s}^2}{2\beta m_\mu c^2 L_R (dE/ds)} \qquad (1)$$

where $\beta_\perp$ is the Courant-Snyder focusing parameter, E_s is the characteristic scattering energy ($\sim$ 13.6 MeV), β is the Lorentz velocity, m_μ is the muon mass, c is the velocity of light, L_R is the material radiation length, and dE/ds is the energy loss rate of the beam in the absorbing material. The equilibrium emittance sets the minimum achievable emittance and is directly proportional the beam parameter $\beta_\perp$.

Each cell is designed to obtain beam waists at the centers of both the absorbers and rf cavities. We seek a β_{min} in the absorber which will yield a small equilibrium emittance. We also attempt to minimize the β_{max} of the lattice, thus maximizing the transverse acceptances.

A Quadrupole-dipole lattice

This 32 meter circumference ring has eight symmetric cells (Fig. 1) . The 22.5° dipoles and the adjacent center

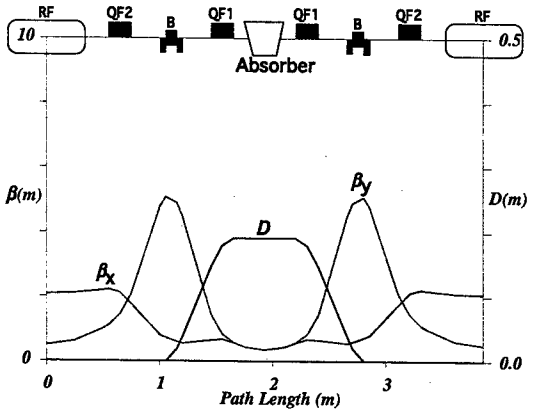


Figure 1: A quadrupole-dipole 8-cell ring lattice with β_{min} and dispersion values in the wedge absorbers chosen to produce 6D cooling.

*hkirk@bnl.gov

0-7803-7738-9/03/$17.00 © 2003 IEEE

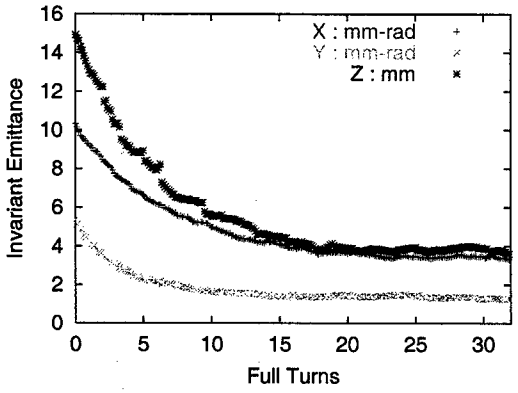


Figure 2: History of the normalized emittance for each plane as a function of full-ring turns in the dipole-quadrupole ring of Fig. 1

quadrupoles create finite dispersion in the absorber with zero dispersion in the rf cavities. The gradients in the quadrupoles and dipoles are adjusted to give β_{min}=25 cm at the cell center. We set the length of the absorber equal to the value of β_{min} so that the $\beta_\perp$ parameter of the beam remains nearly constant within the absorber. For computational convenience in the simulations, the gradient dipole was replaced by a zero-gradient dipole bordered by two thin quadrupoles. Fig. 2 shows the performance of the ring in terms of the evolution of the normalized beam emittances. Note that an emittance reduction is achieved for all three planes.

Dipole-only lattice

A particularly simple lattice design, shown as a 4-cell, 10-meter ring (Fig. 3), has only a single dipole magnet in each half cell. The desired orbit functions are obtained with the aid of edge focusing. In this case, the dispersion is non-zero everywhere, including in the rf cavities. The compactness of the ring and the low beta values give good beam acceptance and high cooling efficiency. Similar rings with three and two cells have also been designed and simulated, with comparable results in cooling performance. The performance of this ring (Fig. 4) is characterized by a merit factor, which is defined as the ratio of the initial 6D normalized emittance to the final emittance times the survival rate of the circulating muons (see Eq. 2). Muon losses are incurred both from dynamical losses in transit around the ring and losses from the decay of the muons.

$$Merit = Transmission \times \frac{\epsilon_{x_i}}{\epsilon_{x_f}} \frac{\epsilon_{y_i}}{\epsilon_{y_f}} \frac{\epsilon_{y_i}}{\epsilon_{y_f}} \qquad (2)$$

We observe, for this lattice design, a merit factor increase of ~100 which corresponds to an increase in the muon beam phase-space occupation density by 2 orders of magnitude.

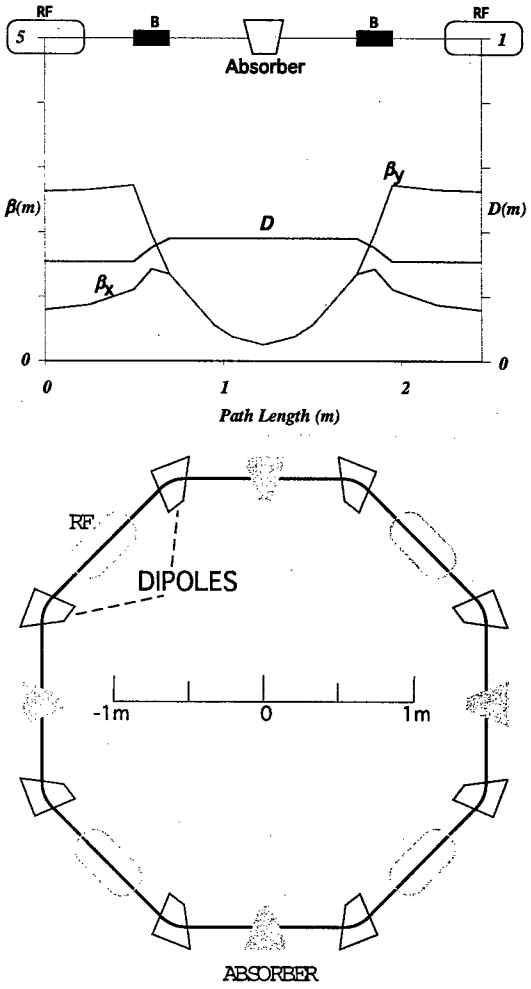


Figure 3: A dipole-only 4-cell ring lattice. The required focusing is accomplished by adjusting the dipole entrance and exit pole-face angles.

Reverse-bend dipoles

The eight cells of this 29 meter ring each contain four dipoles, the center two of which have reverse bending (Fig. 5). The dipoles have zero gradient but strong edge focusing. The dispersion is zero at the ends of the cell. The main advantage of this feature, as in the previously described quadrupole-dipole lattice case, is that it allows for the inclusion of straight sections to the ring thus providing for the possibility of injection and extraction sections. Another potential advantage is that the circumference of the ring is increased thereby allowing for the injection and extraction of longer bunch trains.

The cooling performance (Fig. 6) of this ring, as measured by the merit factor (Eq. 2) is comparable to the previously considered dipole-only lattice with no reverse bends.

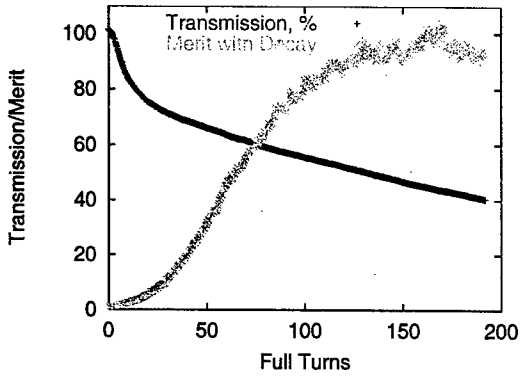


Figure 4: Performance (see Eq. 2 for Merit definition) of a 500 MeV/c circulating muon beam in the 4-cell, dipole-only ring of Fig. 3.

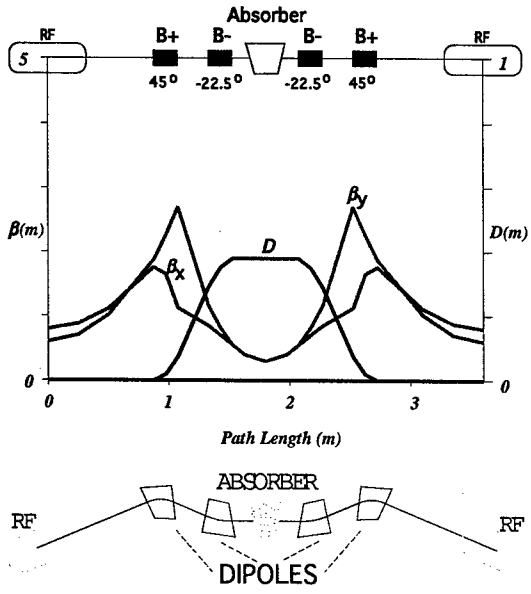


Figure 5: A dipole-only, 8-cell ring lattice including reverse bends. The pole-face angles and the reverse bending give 6D cooling as well as zero dispersion in the rf drift spaces.

SUMMARY

We have demonstrated that the cooling of muon beams in 6D phase space can be achieved with storage ring containing magnetic elements consisting only of quadrupoles and dipoles and in some cases only dipoles. This can result in a significant simplification of the muon cooling system component of future muon colliders and/or neutrino factories. Our analysis is valid for linear optic designs. In the future we will extend these results to consider the non-linear effects of magnetic elements.

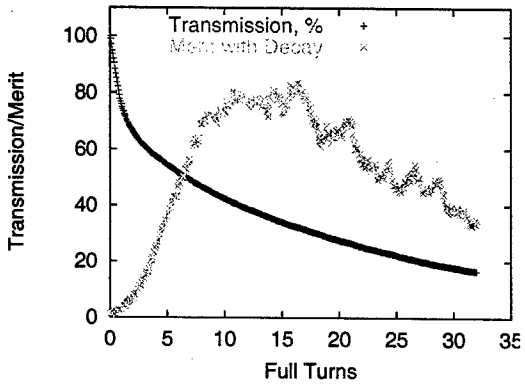


Figure 6: Performance of a 250 MeV/c beam circulating in the 8-cell, reverse-bend dipole ring of Fig. 5

REFERENCES

[1] *Muon-Muon Collider: A Feasibility Study*, BNL-52503, Fermilab Conf-96/092, LBNL-38946 (1996).

[2] H.G. Kirk, *Targetry for a $\mu^+\mu^-$ Collider*, Proceedings of the 1999 Particle Accelerator Conference, New York, NY, March 1999, p.3029.

[3] J.C. Gallardo *et al.*, *An Ionization Cooling Channel for Muon Beams Based on Alternating Solenoids*, Proceedings of the 1999 Particle Accelerator Conference, New York, NY, March 1999, p.3032.

[4] J.C. Gallardo *et al.*, *Ionization Cooling Scenario for a Neutrino Factory*, Proceedings of the 2001 Particle Accelerator Conference, Chicago, Il., March 2001, p.3861.

[5] N. Holtkamp and D. Finley, eds., *A Feasibility Study of a Neutrino Source Based on a Muon Storage Ring*, Fermilab-Pub-00/108-E (2000), http://www.fnal.gov/projects/muon_collider/nu-factory/nu-factory.html.

[6] S. Ozaki, R. Palmer, M. S. Zisman, and J. Gallardo, Editors, *Feasibility Study-II of a Muon-Based Neutrino Source*, BNL-52623 (June 2001); http://www.cap.bnl.gov/mumu/studyii/FS2-report.html.

[7] H. Kirk, D. Cline, Y, Fukui, and A. Garren, *Progress Toward a Muon Ring Cooler*, Accelerator M1 Working Group Report, Snowmass 2001 Workshop, Snowmass, Colorado, 2001. http://www.slac.stanford.edu/econf/C010630/papers/M101.PDF

[8] A.A. Garren, A.S. Kenney, E.D. Courant, A.D. Russel, and M.J. Syphers, *SYNCH, A program for Design and Analysis of Synchrotrons and Beamlines*, LBL-34668, BNL-49925, FNAL-PUB-94/013 (1993).

[9] R.C Fernow, *ICOOL: A Simulation Code for Ionization Cooling of Muon Beams*, Proceedings of the 1999 Particle Accelerator Conference, New York, NY, March 1999, p.3020.

[10] D. Neuffer, *$\mu^+\mu^-$ COLLIDERS*, CERN **99-12**, (1999), p.25.

[11] Ibid. p.26.

EFFECT OF SOLENOID FIELD ERRORS ON ELECTRON BEAM TEMPERATURES IN THE RHIC ELECTRON COOLER *

C. Montag†, J. Kewisch, BNL, Upton, NY 11973, USA

Abstract

As part of a future upgrade to the Relativistic Heavy Ion Collider (RHIC), electron cooling is foreseen to decrease ion beam emittances. Within the electron cooling section, the "hot" ion beam is immersed in a "cold" electron beam. The cooling effect is further enhanced by a solenoid field in the cooling section, which forces the electrons to spiral around the field lines with a (Larmor) radius of 10 micrometers, reducing the effective transverse temperature by orders of magnitude. Studies of the effect of solenoid field errors on electron beam temperatures are reported.

INTRODUCTION

To improve the luminosity of the Relativistic Heavy Ion Collider (RHIC) as well as as essential part of the electron-ion collider eRHIC currently under study, electron cooling at high beam energies of $\gamma \approx 100$ is being foreseen [1]. The RHIC electron cooler consists of a superconducting energy-recovery linac to accelerate electrons to energies up to some 55 MeV, thus matching the Lorentz factor of the stored ion beam. To enhance the cooling effect, a magnetized beam and a solenoidal field in the cooling section is foreseen [2]. Figure 1 shows a schematic drawing of the RHIC electron cooler.

Table 1 shows some key parameters of the RHIC electron cooler.

However, to preserve low electron emittances from the gun through the linac and transfer line and through the solenoid, exact optics matching as well as high magnetic field quality is required. Simulation studies were performed to identify the effect of transverse magnetic field components in the cooler solenoid on electron beam temperatures. The goal was to determine the required field quality as a function of the wavelength of the transverse field distortion, which in turn defines the optimum spacing of correction coils.

* Work performed under contract number DE-AC02-98CH10886 with the auspices of the US Department of Energy

† montag@bnl.gov

γ_{max}	110
$B_{\parallel}$	1 T
solenoid length	30 m
cathode temperature	20000 K
$\Delta p/p$	$1 \cdot 10^{-4}$
bunch charge	10 nC
transv. rms beam size in cooler	2 mm
electron bunch length	5 cm
cooling time	30 min

Table 1: Parameters of the RHIC electron cooler

SIMULATION RESULTS

To study the effect of transverse field errors on electron beam temperatures, an ensemble of particles was tracked through a 30 m long 1 T solenoid with an additional transverse field component of

$$B_x(z) = \hat{B}_\perp \cdot \sin(k \cdot z), \quad (1)$$

$$\hat{B}_\perp = a \cdot B_{\parallel}, \quad (2)$$

where $B_{\parallel} = 1\,\mathrm{T}$ is the main solenoid field, z is the longitudinal coordinate along the solenoid, and $k = 2\pi/\lambda$ is the wave number for an error field wavelength λ. The coefficient a has been scanned to determine the magnetic field error tolerances for a given temperature increase.

The electrons are assumed to have been created at a cathode with temperature $T = 20000\,\mathrm{K}$. This beam is accelerated to $\gamma = 107$ to match the storage energy of gold ions in RHIC. The longitudinal momentum spread is assumed as $\Delta p/p = 1 \cdot 10^{-4}$, the design value of the RHIC electron cooler.

Tracking within the solenoid is performed by application of the Lorentz force equation,

$$\vec{F} = \frac{\mathrm{d}\vec{p}}{\mathrm{d}t} = m\frac{\mathrm{d}\vec{v}}{\mathrm{d}t} = e \cdot (\vec{v} \times \vec{B}), \quad (3)$$

which is integrated using a fourth-order Runge-Kutta method.

To calculate temperatures, all velocities are transformed to the moving beam frame according to

$$v_{\parallel} = \frac{v_{\parallel}^* - v_0}{1 - v_{\parallel}^* \cdot \frac{v_0}{c^2}} \quad (4)$$

and

$$v_\perp = \frac{v_\perp^*}{\gamma_0 \cdot \left(1 - v_{\parallel}^* \cdot \frac{v_0}{c^2}\right)}. \quad (5)$$

Here, $v_{\parallel}$ and $v_\perp$ are the longitudinal and transverse velocity of one particular electron, respectively, while v_0 and γ_0 are the velocity and Lorentz factor of the bunch center-of-mass. An asterisk denotes the laboratory frame. Using the

0-7803-7738-9/03/$17.00 © 2003 IEEE

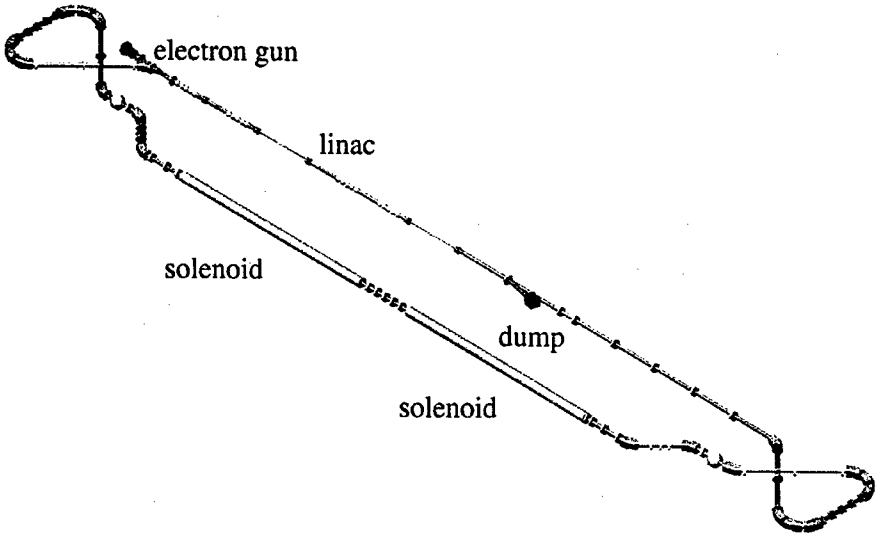


Figure 1: Schematic overview of the RHIC electron cooler. The magnetized electron beam is accelerated in an energy-recovery superconducting linac and stretched to the required bunch length in in an extra loop in the arc that also serves as a transfer line into the solenoid. At the exit of the solenoid a second arc reduces the bunch length to its original valueand transports the beam back to the linac for energy recovery. For easier manufacturing, the 30 m long superconducting solenoid is split into two parts with an appropriate matching section in between that preserves beam magnetization and thus low beam temperatures.

velocities in the moving frame, temperatures are calculated from the respective rms values as

$$T_{\parallel} = \frac{m \cdot \langle v_{\parallel}^2 \rangle}{2k} \tag{6}$$

and

$$T_{\perp} = \frac{m \cdot \langle v_{\perp}^2 \rangle}{2k}, \tag{7}$$

where $k = 1.3806 \cdot 10^{-23}\,\mathrm{J/K}$ is the Boltzmann constant. Figure 2 shows the ratio of longitudinal electron beam temperatures at the entrance, $T_{\parallel}(z = 0\,\mathrm{m})$, and at the exit of the solenoid, $T_{\parallel}(z = 30\,\mathrm{m})$, as a function of the transverse field wavelength for different values of the coefficient a, corresponding to relative transverse field errors in the range of $\hat{B}_{\perp}/B_{\parallel} = 1 \cdot 10^{-6} \ldots 5 \cdot 10^{-5}$. The longitudinal electron beam temperature increase shows a significant resonant behavior when the wavelength of the transverse field component is in the vicinity of the Larmor wavelength of the electrons,

$$\lambda_{\mathrm{Larmor}} = \frac{2\pi\gamma mc}{eB_{\parallel}} \approx 1.14\,\mathrm{m}, \tag{8}$$

where m and e are the electron rest mass and charge, while c and γ denote the speed of light and the Lorentz factor, respectively.

In contrast to this, the transverse temperature $T_{\perp}$ stays practically constant, independent of the wavelength of the

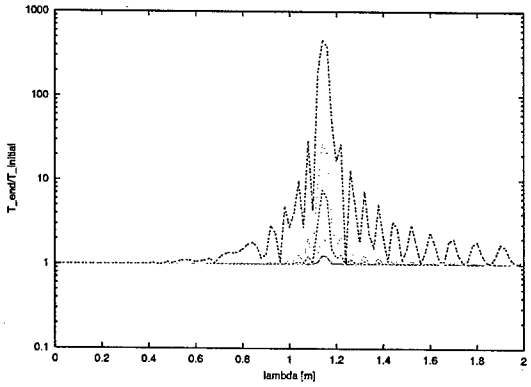


Figure 2: Longitudinal electron beam temperature increase $T_{\parallel}(z = 30\,\mathrm{m})/T_{\parallel}(z = 0\,\mathrm{m})$ at the end of the 30 m long cooler solenoid, as function of the wavelength λ of the transverse field component. The lowest, red line corresponds to a transverse field amplitude of $\hat{B}_{\perp} = 1{\cdot}10^{-6}{\cdot}B_{\parallel}$, while the top line (black) shows the relative temperature increase for the case $\hat{B}_{\perp} = 5 \cdot 10^{-5} \cdot B_{\parallel}$. Lines in-between correspond to $\hat{B}_{\perp} = 2{\cdot}10^{-6}{\cdot}B_{\parallel}$ (green), $\hat{B}_{\perp} = 5{\cdot}10^{-6}{\cdot}B_{\parallel}$ (blue) $\hat{B}_{\perp} = 1 \cdot 10^{-5} \cdot B_{\parallel}$ (purple), and $\hat{B}_{\perp} = 2 \cdot 10^{-5} \cdot B_{\parallel}$ (turquoise), respectively.

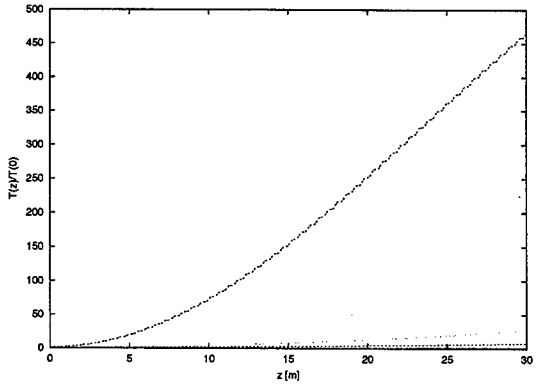


Figure 3: Relative longitudinal temperature increase $T_{\|}(z)/T_{\|}(z = 0\,\mathrm{m})$ in the resonant case with $\lambda = \lambda_{\mathrm{Larmor}} \approx 1.14\,\mathrm{m}$ as function of the longitudinal position along the solenoid. The lowest, red line shows a transverse field amplitude of $\hat{B}_{\perp} = 1 \cdot 10^{-6} \cdot B_{\|}$, while the top line (black) corresponds to the relative temperature increase for the case $\hat{B}_{\perp} = 5{\cdot}10^{-5}{\cdot}B_{\|}$. Lines in-between correspond to $\hat{B}_{\perp} = 2{\cdot}10^{-6}{\cdot}B_{\|}$, $\hat{B}_{\perp} = 5{\cdot}10^{-6}{\cdot}B_{\|}$, $\hat{B}_{\perp} = 1{\cdot}10^{-5}{\cdot}B_{\|}$, and $\hat{B}_{\perp} = 2 \cdot 10^{-5} \cdot B_{\|}$, respectively.

transverse magnetic field. The increase in longitudinal electron beam temperature $T_{\|}$ can therefore be explained as coupling of transverse electron motion into the longitudinal direction, thus effectively increasing the longitudinal energy spread $\Delta p/p$ and hence the longitudinal temperature $T_{\|}$.

The relative longitudinal temperature increase as function of the longitudinal position within the cooler solenoid in the resonant case with $\lambda = \lambda_{\mathrm{Larmor}} \approx 1.14\,\mathrm{m}$ is depicted in Figure 3. As this picture reveals, the longitudinal electron beam temperature increases approximately linearly along the cooler solenoid.

CONCLUSION

The effect of a transverse sinusoidal field component on electron beam temperatures inside the solenoid of the RHIC electron cooler has been studied. The longitudinal temperature shows a significant resonant effect when the wavelength λ of the transverse magnetic field equals the Larmor wavelength $\lambda_{\mathrm{Larmor}} = 1.14\,\mathrm{m}$, while the transverse temperature remains unchanged over a large range of transverse field amplitudes $\hat{B}_{\perp}$. To preserve the small longitudinal electron beam temperature, transverse magnetic field components must not exceed $\hat{B}_{\perp} = 1 \cdot 10^{-6} \cdot B_{\|}$ for wavelengths close to the Larmor wavelength $\lambda_{\mathrm{Larmor}}$ of the electrons inside the solenoidal magnetic field. Therefore, dipole correctors should be placed at distances of $\lambda_{\mathrm{Larmor}}/4$ to enable effective suppression of transverse magnetic fields with these wavelengths.

REFERENCES

[1] I. Ben-Zvi, J. M. Brennan, X. Chang, J. Kewisch, W. Mackay, C. Montag, S. Peggs, T. Roser, T. Srinivasan-Rao, D. Trbojevic, D. Wang, R&D towards Cooling of the RHIC Collider, this conference.

[2] J. Kewisch, I. Ben-Zvi, X. Chang, C. Montag, D. Wang, Layout and Optics for the RHIC Electron Cooler, this conference

LITHIUM LENSES BASED MUON COOLING CHANNEL

V. Balbekov, FNAL, Batavia, IL 60510, USA *

Abstract

A linear ionization cooling channel for neutrino factory or muon collider is considered. It includes short Li lenses, matching solenoids, and 201 MHz RF cavities. The basic challenge is a suppression of chromatic effects in a wide energy range typical for muon beams. A special lattice is proposed to reach this, and methodic of an optimization is developed to minimize the chromatic aberrations by suppression of several betatron resonances. The most engineering constraint is a high field of matching solenoids. A channel with less of 10 T field is considered in detail. It is capable to cool transverse emittance of a beam from 2-3 mm to 0.5 mm at the channel length of about 130 m. Because there is no emittance exchange, longitudinal emittance increases in the process from 10 to 20 mm at transmission of about 90%.

INTRODUCTION

Lithium lens is probably the most promising cooling device for a final stage of muon ionization cooling for a $\mu - \mu$ collider [1]. However, design of matching sections between the lenses is a big problem because of a huge energy spread of muon beam and a strong modulation of beta-function. In such conditions, chromaticity is a crucial point for performances of the channel. Two ways to mitigate this effect was discussed. First of them is to create a system with synchrotron phase advance as a multiple of 2π per cell, obtaining about the same average energy of all the particles. As is shown in Ref. [2], high accelerating frequency and gradient are required to reach this (e.g. 805 MHz and 36 MeV/m). However, even at such ultimate parameters, length of the cooling cell and Li lens should be very large: 10-12 m and 1.6-1.8 m correspondingly. At 201 MHz/15 MeV/m accelerating system accepted nowadays as a baseline for muon cooling system [3], the length would be 2-3 times more. Another method was proposed in Ref. [4], and is developed in this paper. The idea is (i) to use as small betatron phase advance per cell as possible to get a maximal energy space between linear stop-bands, and (ii) to suppress several of them by a special design of cooling cell. An additional optimization of the system with more realistic magnetic field is performed here.

LAYOUT AND PARAMETERS

The cooler is a linear periodical system consisting of cells shown in Fig.1. The cell includes Li lens, 3 solenoid coils, and 6 cavities. Parameters of the equipment are presented in Table 1.

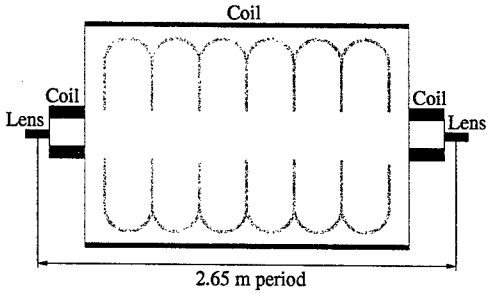


Figure 1: Schematic of a cooling channel with Li lenses, matching, and acceleration sections.

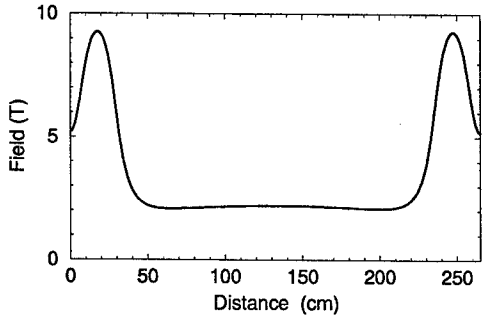


Figure 2: Axial magnetic field of the period .

Axial magnetic field of the cell is plotted in Fig.2. It penetrates into Li lens considerably increasing its focusing

Table 1: Parameters of the Cell

Period length	265 cm
Li lens length	13.46 cm
Li lens radius	3 cm
Li lens gradient	2.624 T/cm
Length of any short coil	22.45 cm
Inner radius of short coil	6 cm
Outer radius of short coil	14 cm
Current density	99.53 A/mm^2
Length of long coil	206.64 cm
Inner radius of long coil	69 cm
Outer radius of long coil	71 cm
Current density	96.09 A/mm^2
Radio frequency	201.25 MHz
Reference energy (total)	250 MeV
Accelerating gradient	12 MeV/m
Synchronous phase	30°

* Work supported by the Universities Research Association, Inc., under contract DE-AC02-76CH03000 with the U. S. Department of Energy.

0-7803-7738-9/03/$17.00 © 2003 IEEE

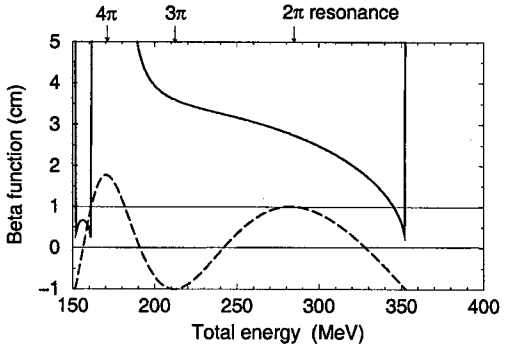


Figure 3: Solid line: beta-function in the center of Li lens *vs* total energy of muon, dashed - 1/2 of spur of transfer matrix ($\cos\mu$).

power. Proper transverse field of the lens is taken in hard edge approximation i.e. it drops sharply at the ends.

The cell is designed to maximize width of resonance-free energy interval by a suppression of linear resonances with phase advances 2π and 3π per period. Method of the tuning is thoroughly described in Ref. [4], and the result is presented in Fig.3, where beta-function in the center of Li lens is plotted *vs* total energy of muon. It is seen that the resonance-free region is significantly broader of 100 MeV what is certainly sufficient to accept and cool muon beam.

The parameters are chosen to get the stable region centered approximately at 250 MeV of total energy. However, any other choice is also possible by scaling of the field proportionally to central momentum at the same geometry.

Dependence of beta-function of the cell on longitudinal coordinate is plotted in Fig.4 where total energy of muon is taken as a parameter. Maximum of beta-function does not exceed 2 m at $200 < E < 300$ MeV, and 1.3 m for the center of this interval. We are going to consider the cooling of a beam with initial unnormalized transverse r.m.s. emittance about 1000 mm-mrad. It is enough to have windows of radius about 10 cm in the high radius solenoids to accept this beam. Beta-function in Li is plotted in Fig.5 (only right hand part of this symmetric plot is shown). It does not exceed 12.3 cm what corresponds r.m.s. beam size about 11 mm, so that the lens radius 30 mm is sufficient. Average value of beta-function is 5 cm approximately, corresponding an equilibrium normalized beam emittance about 0.4 mm.

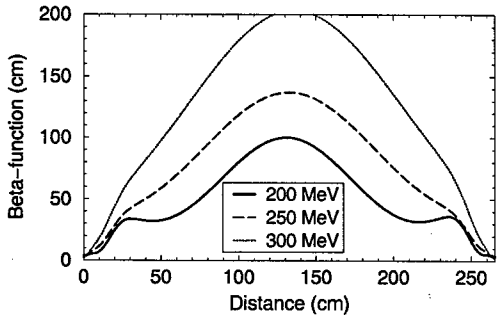


Figure 4: Beta-function of the period *vs* distance.

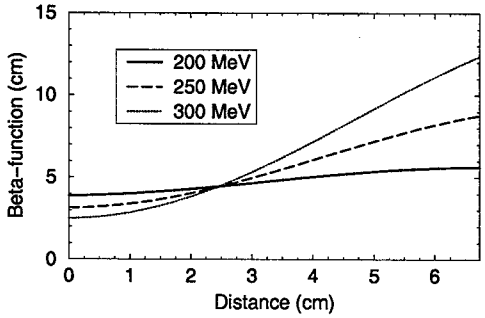


Figure 5: Beta-function in Li lens *vs* distance.

COOLING SIMULATION

Muon bunch with Gaussian distribution and initial parameters listed in Table 2 is taken for the simulation. A beam with such emittance would be provided e.g. by a ring cooler described in Ref. [5], We take an injection point at the center of Li lens where ratio of transverse size to momentum of the beam should correspond to beta-function of about 3 cm (see Fig.5). [1]

Table 2: Parameters of Injected Beam

Normalized transverse r.m.s. emittance	2.0 mm
Transverse r.m.s size in any direction	5.2 mm
Transverse r.m.s. momentum	40 MeV/c
Normalized longitudinal r.m.s. emittance	9.3 mm
R.m.s. bunch length (ct)	70 mm
R.m.s. energy spread	14 MeV
Normalized 6D emittance	37 mm^3

To take into account a dependence of longitudinal velocity on transverse momentum, the following correlation was applied after random generation:

$$E = E_{ref}\left[1+\left(\frac{cp_t}{316\ \mathrm{MeV}}\right)^2+\left(\frac{r}{14\ \mathrm{cm}}\right)^2\right]_{rn}+\Delta E_{rn}$$

Numerical coefficients are determined empirically to get maximal transmission of the channel. Note that this correlation is excluded by the inverse transformation at the calculation of emittance of the cooled beam. The only aperture restriction is applied by Li lens of radius 3 cm.

Evolution of the beam emittance and transmission is shown in Fig.6 Enough effective transverse and 6D cooling takes place approximately on 50 cooling cells that is 132.5 m long. After that, the beam obtains the parameters

[1] We take a periodical channel and do not consider a problem of matching of the beam in the beginning.

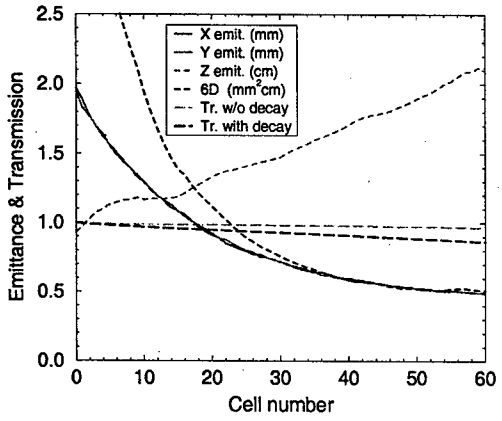


Figure 6: Evolution of the bean emittance and transmission (Gaussian distribution, 10000 muons).

listed in Table 3 where cooling factors are also given in a brackets.

Table 3: Beam Parameters after 50 Cooling Cells

Transverse r.m.s. emittance	0.52 mm	(3.8)
Transverse r.m.s size	2.7 mm	(1.9)
Transverse r.m.s. momentum	20 MeV/c	(2.0)
Longitudinal r.m.s. emittance	19 mm	(.49)
R.m.s. bunch length (ct)	100 mm	(.70)
R.m.s. energy spread	18 MeV	(.78)
Normalized 6D emittance	5.2 mm^3	(7.1)
Transmission with decay	0.89	
Transmission without decay	0.97	

Equilibrium transverse emittance of about 0.4 mm is really not achievable, first of all because of longitudinal heating resulting both from straggling and negative derivative of energy loss dE/dx in the used energy interval. The effect is readily illustrated by Fig.7 where the longitudinal phase space of the beam is shown before the cooling and after 60 cooling cells. There is a considerable lengthening of the bunch resulting a violation of initial Gaussian distribution, and diffusion of some particles through the separatrix. An attempt to continue the cooling results an acceleration of the diffusion and fast growth of the particle loss.

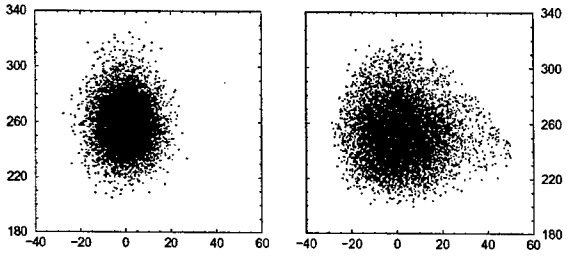


Figure 7: Longitudinal phase space of the beam at injection (left) and after 60 cooling cells (right). Horizontal axis – ct (cm), vertical – E (MeV).

CONCLUSION AND DISCUSSION

It is shown that a short periodical cooling channel with Li lens and specially tuned solenoids has enough large energy acceptance to be used for transverse cooling of muon beams. A channel of length 132.5 m provides a decrease of transverse emittance from 2 mm to 0.5 mm at transmission of about 89%. Emittance exchange should be introduced to overcome longitudinal heating and to continue the cooling without an additional particle loss. Another obstacle is a high field of matching (small radius) solenoid which reaches 9.3 T in this design. It is more then own (transverse) field on the surface of Li lens which is only 7.9 T. Solenoid field penetrating to the lens does not exceed 6.8 T, that is maximal total field is 10.4 T. A using for the matching of another Li lens with less gradient and more aperture is really impossible because of multiple Coulomb scattering. As is seen from Figs. 2 and 4, both length and beta-function of such lens should exceed corresponding parameters of the main lens by factor about 3. Therefore its contribution in the scattering and equilibrium emittance would be order of magnitude more that is inadmissible.

Distinguishing feature of the channel is a great quantity ($\sim$ 50) of very short ($\sim$ 13 cm) Li lenses. It results from an aspiration to get as large energy acceptance as possible. However, about 3 times longer lens ($\sim$ 40 cm) and the lattice period (6-7 m) could be used if desirable energy acceptance would as small as 40-50 MeV. It was shown recently that muon beam with similar energy spread can be obtained by means of so called RFOFO ring cooler [6].

REFERENCES

[1] Charles M. Ankenbrandt et al. "Status of Muon Collider Research and Development and Future Plans", Phys.Rev.ST Accel.Beams 2, 081001 (1999).

[2] V.Balbekov. "Ionization Cooling of Muon Beam by Multistage System of Li Lenses with Matching Sections", In Proc. of the 1999 PAC, V.5, p.3146.

[3] "Feasibility Study-II of a Muon-Based Neutrino Source", Editors S. Ozaki, R. Palmer, M. Zisman, and J. Gallardo, BNL-52623, June 2001; http://www.cap.bnl.gov/mumu/studyii/FS2-report.html.

[4] V.Balbekov. "Achromatic Cooling Channel with Li Lenses", FNAL MCNote 245, April 2002.

[5] V.Balbekov, S.Geer, et al. "Muon Ring Cooler for the MUCOOL Experiment", In Proc. of the 2001 PAC, V.5, p.3867.

[6] V.Balbekov. "Simulation of RFOFO Ring Cooler with Tilted Solenoids", FNAL MCNote 245, November 2002. R.C.Fernow, J.S.Berg, J.C.Gallardo, R.B.Palmer. "Muon Cooling in the RFOFO Ring", FNAL MCNote 273, April 2003.

INVESTIGATION AND SIMULATION OF MUON COOLING RING WITH TILTED SOLENOIDS

V. Balbekov, FNAL, Batavia, IL 60510, USA *

Abstract

Alternating solenoid focused muon cooling ring without special bending magnets is considered and investigate in detail. Both fringe field between solenoid coils with opposite directed current, and an inclination of the coils in vertical plane are used to provide a bending and closing of the particle trajectories. Realistic (Maxwellian) magnetic field is calculated and used for a simulation. Methodic is developed and applied to find closed orbit at any energy, dispersion, region of stability, and other conventional accelerator characteristics. Earlier proposed RFOFO cooling ring with 200 MHz RF system and liquid hydrogen absorbers is investigated in detail. After an optimization, normalized 6D emittance about 20 mm^3 and transmission 57% are obtained.

INTRODUCTION

So called RFOFO ring for an ionization cooling of muon beams was proposed and simulated for the first time in Ref. [1]. Only solenoids was used in this design to get magnetic field, presuming that the vertical (bending) component can be obtained by tilting of the solenoid coils. Actually bending field in Ref. [1] was generated by a truncated Fourier decomposition of the field from a bent solenoid. The real coils to generate the axial field, in the presence of bending field, was not considered then.

Simulation with realistic field produced by vertically tilted coils was performed for the first time in Ref. [2]. Both fringe field between solenoids with opposite directed current, and an inclination of the coils in vertical plane are used to bend the particle trajectories and to get closed orbits in a wide energy interval. This report is a further development and optimization of this cooler. [1]

LATTICE

Following Ref. [1], the ring consisting of 12 periods is considered, each providing turn angle 30°. The period shown in Fig.1 includes 2 solenoid coils with opposite direction of currents, 5 cavities, and liquid hydrogen wedge absorber. Period length is 275 cm along the centerline of the coils that is a circle of radius $R_0 = 275 \times 12/(2\pi) \simeq 525.21$ cm. Therefore circumference of the ring is 33 m along this line. Space between the centers of an absorber and nearest solenoid coils is 55 cm. Another parameters of the equipment are taken from Ref. [1] and listed in Table 1.

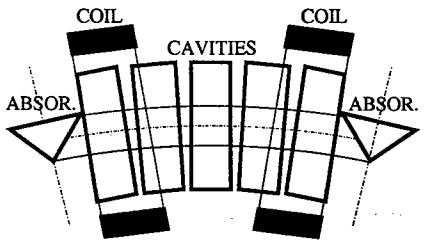


Figure 1: Layout of the cooling ring (one period, schematically).

Table 1: Parameters of the Cooler

Inner radius of coils	77 cm
Outer radius of coils	88 cm
Coil length	50 cm
Current density	± 95.27 A/mm^2
Tilting angle of the coil	± 52 mrad
Accelerating frequency	199.2 MHz
Accelerating gradient	16 MeV/m
Synchronous phase	33°
Absorber thickness at the center	28.5 cm
Energy loss at the center	12.52 MeV
Gradient ox energy loss dE/dy	0.7 MeV/cm

MAGNETIC FIELD

We will work in a cylindrical frame $r\theta y$; however, more conventional variables $x = r - R_0$ and $z = R_0\theta$ are actually used ($R_0 = 525.21$ cm). Magnetic field in this frame is obtained in several stages:

- Flat field map of single coil is generated in its natural frame $r_{coil}z_{coil}$ for the region $0 \le z_{coil} \le 540$ cm, $r_{coil} \le 480$ cm.
- Grid is prepared in the cylindrical xyz frame for the area: $-36\,\text{cm} \le x \le 14\,\text{cm}$, $-23\,\text{cm} \le y \le 27\,\text{cm}$, $-770\,\text{cm} \le z \le 770\,\text{cm}$, at the step of 1 cm in any direction.
- Position of each node of the grid is transformed to the frame of a positive coil with its inclination taken into account. Field in this point is calculated in $r_{coil}z_{coil}$ frame using the coil field map and linear interpolation.
- Obtained field components are transformed to the cylindrical frame xyz resulting field map of single tilted coil with positive current centered at $x = y = z = 0$. Field of the coil with opposite current and inclination is generated using properties of symmetry.
- Centers of positive and negative coils are moved to $z = \mp 82.5$ cm correspondingly, and their fields are added resulting field of the coil pair.

* Work supported by the Universities Research Association, Inc., under contract DE-AC02-76CH03000 with the U. S. Department of Energy.

[1] Note at edition: Recently analogous investigation is done and similar results are derived in Ref. [3].

0-7803-7738-9/03/$17.00 © 2003 IEEE

• Fields of central pair and 2 pairs shifted to the left and right with a step of 275 cm are added resulting field map of the period at -137.5 cm $\leq z \leq 137.5$ cm.

Components of periodical magnetic field are plotted against longitudinal coordinate in Figs. 2 and 3 at different transverse coordinates. The longitudinal field almost does not depend on transverse coordinates, radial field depends mostly on x (and z), and vertical field – on y (and z).

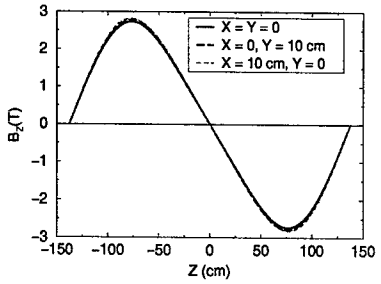


Figure 2: Longitudinal magnetic field at different transverse coordinates.

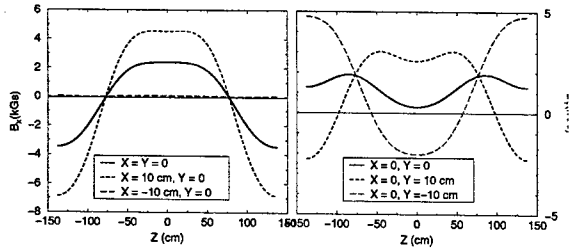


Figure 3: Transverse magnetic field at different transverse coordinates (left – radial, right – vertical).

CLOSED ORBIT AND DISPERSION

A search of closed orbit is not a trivial problem in such complicated magnetic field. Symmetry of the field facilitates it, because deviations of closed orbit from centerline should be even function of z at any energy. The results are presented in Fig.4 at total energy from 190 MeV to 270 MeV with step 10 MeV. Swing of the orbit is minimal at reference energy $E_{ref} = 220$ MeV at chosen inclination angle 52 mrad. The orbit is shifted on about 11 cm to the

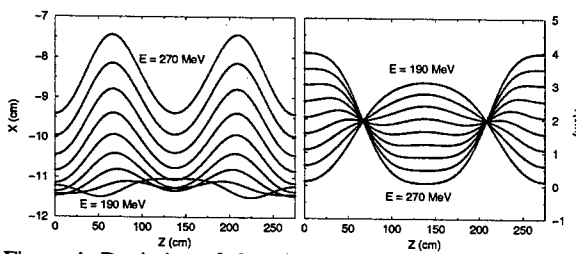


Figure 4: Deviation of closed orbit from centerline *vs* distance at different energy. (left – radial, right – vertical).

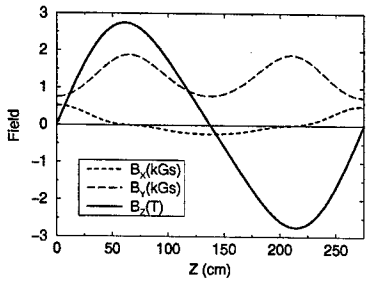


Figure 5: Magnetic field *vs* longitudinal coordinate on 220 MeV closed orbit.

ring center. where the particle is kept both by transverse and longitudinal fields. Magnetic field on this orbit is plotted in Fig.5.

Dispersion, that is deviation of closed orbit from reference one, is shown in Figs.6. Left plot shows dependence of dispersion at the absorber center on total energy. The vertical dispersion is surprisingly linear, however radial one is nonlinear at all. Therefore only vertical wedge absorbers will be used in the ring for emittance exchange. Right Fig.6 represents dispersion function *vs* distance at E = 220 MeV. Vertical dispersion is about 8 cm at the absorber center.

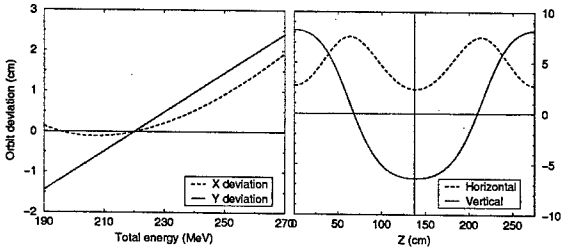


Figure 6: Left: dispersion at the absorber center *vs* total energy. Right: dispersion function at 220 MeV *vs* distance.

REGION OF STABILITY

4D transfer matrix was calculated for small deviations of a particle with arbitrary energy from corresponding closed orbit. Its eigenvalues are plotted in Fig.7. It is seen that region of stability extends from 185 to 265 MeV, end eigenvalues are almost equal in pairs (there is conjugated pair). Long-dashed line on this plot represents beta-function the same rectilinear channel, which has almost the same region of stability. It means, probably, that this 2D beta-function can be used for estimations of equilibrium emittance, etc. By such a consideration, equilibrium transverse emittance of a cooled beam should be about 1.5 mm without an emittance exchange.

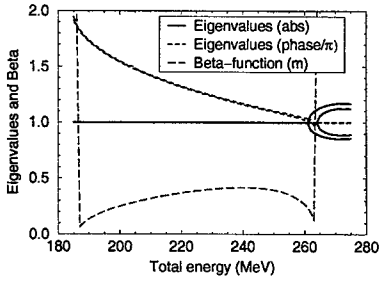


Figure 7: Eigenvalues of the transfer matrix and beta-function at the absorber center *vs* total energy.

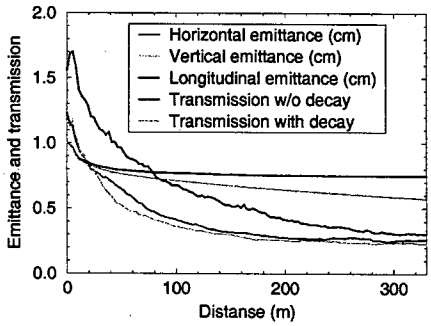


Figure 8: Evolution of the beam parameters at the cooling.

COOLING SIMULATION

2000 particles are used for the cooling simulation of Gaussian beam with the parameters listed in Table 2 (3rd column is commented later). After random generation, the following correlation has been applied to take into account linear dispersion

$$x = x_{random} + D_x(\Delta p/p)_{random},$$

and similar expression for y where $D_x = 2.69$ cm and $D_y = 8.15$ cm (see right Fig.6). Then a correlation due to dependence of revolution frequency on transverse momentum is included by the formula:

$$E_{total} = \Delta E_{random} + E_{ref}\sqrt{1 + (p_{t,random}/mc)^2}.$$

Note that all the correlations are excluded by inverse transformations at the emittance calculation of the cooled beam. The beam is injected in the absorber center at transverse coordinates: $x_c = -11.36$ cm, $y_c = 1.57$ cm corresponding to closed orbit at reference energy 220 MeV.

Evolution of the beam emittance and transmission at the cooling is shown in Fig.8. Parameters of the beam after 10 turns (330 m) are presented in 3rd column of Table 2. Merit factor is defined as

$$M = T\frac{\epsilon_{6,initial}}{\epsilon_{6,final}}$$

where T is transmission with decay, $\epsilon_6 = \epsilon_x\epsilon_y\epsilon_z$ is 6D beam emittance.

Transverse and longitudinal phase space of the beam before and after 10 turns cooling are representer in Figs. 9 and 10.

Table 2: Parameters of injected and cooled beams

	Inject	10 turns
Horizontal emittance (cm)	1.2	.26
Vertical emittance (cm)	1.2	.23
Longitudinal emittance (cm)	1.6	.31
Horizontal r.m.s. size (cm)	5.0	2.3
Vertical r.m.s. size (cm)	5.0	2.1
Horiz. r.m.s. momentum (MeV/c)	25	12
Vertical r.m.s. momentum (MeV/c)	25	12
R.m.s. bunch length (ct) (cm)	11	4.7
R.m.s. energy spread (MeV)	15	6.9
Transmission without decay	1	.75
Transmission with decay	1	.57
Merit factor	1	68

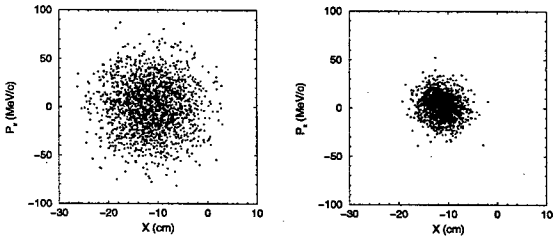


Figure 9: Projection of phase ellipsoid on $x - p_x$ plane before (left) and after the cooling (right)

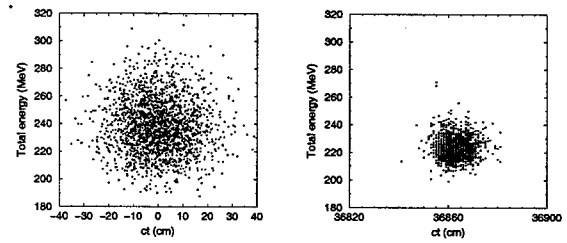


Figure 10: Projection of phase ellipsoid on $ct - E$ plane before (left) and after the cooling (right)

REFERENCES

[1] J.S.Berg, R.C.Fernow, R.B.Palmer. "An Alternating Solenoid Focused Ionization Cooling Ring". FNAL McNote 239, March 2002.

[2] V.Balbekov. "Simulation of RFOFO Ring Cooler with Tilted Solenoids", FNAL McNote 264, November 2002.

[3] R.C.Fernow, J.S.Berg, J.C.Gallardo, R.B.Palmer, "Muon Cooling in the RFOFO Ring", FNAL McNote 273, April 2003.

COMMISSIONING OF THE FERMILAB ELECTRON COOLER PROTOTYPE BEAM LINE

S. Seletsky, University of Rochester, Rochester, USA; A.V. Burov, K. Carlson, J. Leibfritz, B. Kramper, T. Kroc, M. McGee, S. Nagaitsev, G. Saewert, C.W. Schmidt, A. Shemyakin, and A. Warner, FNAL, Batavia, USA; V. Tupikov, Budker INP, Novosibirsk, Russia

Abstract

A prototype of a 4.3-MeV electron cooling system is being assembled at Fermilab as part of the ongoing R&D program in high energy electron cooling. This electron cooler prototype will not demonstrate the actual cooling but it will allow determining if the electron beam properties are suitable for antiproton beam cooling. An electron beam is accelerated by a 5-MV Pelletron (Van de Graaff type) accelerator and transported to a prototype cooling section. The cooling will take place in a 20-m long solenoid flanked on both sides by a delivery and return beam-line – a total of 60 meters of transport channel. This paper describes the first results of commissioning this novel beam line as well as the status of the electron cooling R&D program.

INTRODUCTION

The application of electron cooling to 8.9 GeV/c antiprotons in the Recycler ring is a part of the program aimed to increase the collider luminosity. The Recycler Electron Cooling system (REC) is expected to counteract various beam heating mechanisms and to aid beam stacking in the Recycler [1]. The technical parameters of the REC system are summarised in Table 1.

Table 1: Electron Cooling System Parameters

Parameter	Design value	Achieved or installed	Units
Electrostatic Accelerator			
Terminal Voltage	4.34	4.34/3.5	MV
Electron Beam Current	0.5	0.5/1.0	A
Terminal Voltage Ripple	500	500	V
Cathode Radius	2.5	2.5	mm
Gun Solenoid Field	≤ 600	600	G
Cooling Section			
Length	20	18	m
Solenoid Field	≤ 150	150	G
Vacuum Pressure	0.1	wip (work in progress)	nTorr
Electron Beam Radius	6	wip	mm
Electron Beam Divergence	≤ 80	wip	μrad

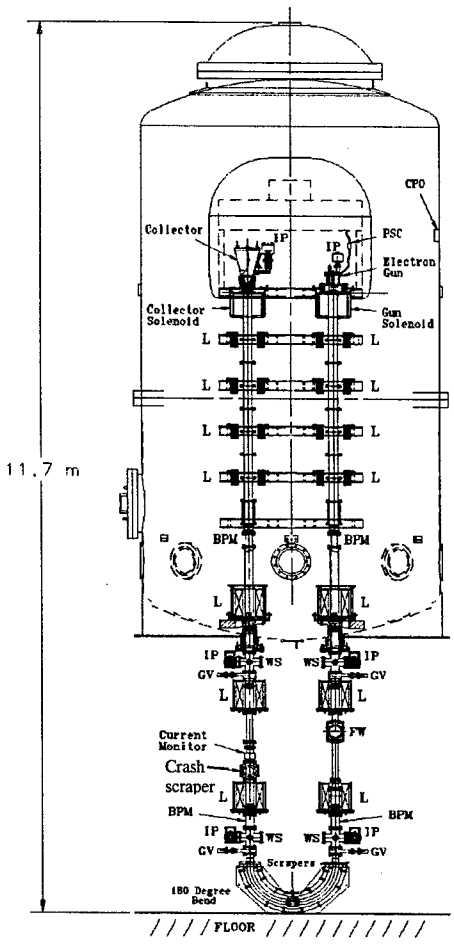


Figure 1: Mechanical schematic of the U-bend test stand. Symbols denote: IP- ion pump, L- lens, GV- gate valve, WS- wire scanners, FW - flying wire, BPM – beam-position monitor.

At present, the test of beam recirculation in the short beam line (Figure 1) has been completed. The magnetic field measurements of the cooling section solenoid have been carried out. The full-scale prototype beam line assembly and installation is nearing completion. Beam is expected to be tested though a complete cooling line in June, 2003.

0-7803-7738-9/03/$17.00 © 2003 IEEE

BEAM RECIRCULATION EXPERIMENT

The recirculation experiment at Fermilab was performed in 2001 – 2002 within the framework of the REC project with a system, which included (see Fig. 1) an electrostatic accelerator, Pelletron, and a short beam line (U-bend). After attainment of a 0.5-A, DC electron beam at the kinetic energy of 3.5 MeV in December, 2001 [2], the main efforts on the final stage of the experiment, in May-November, 2002 were devoted to improving of the beam operational stability.

Estimations made for the future electron cooler has shown that infrequent short-duration processes in the Pelletron, like beam interruptions or discharges, would not deteriorate the performance of the Recycler ring. A weak interaction (i.e. cooling) between the electron and antiproton beams makes heating of the antiproton beam during electron current interruptions negligible. Long beam lines between the Pelletron and the cooling section preserves the high vacuum in the Recycler ring in cases of pressure bursts in the accelerating tubes. Therefore, the figure of merit for electron beam stability is the average duty factor of the electron beam operation.

Several processes affected the duty factor in the recirculation experiment. First, a stable recirculation of a DC beam can be interrupted by sudden jumps in current losses, which forces the protection system to shut the electron gun off. Second, full acceleration tube discharges can result in large changes of the residual gas pressure and tube's high voltage stability. Third, the full discharges sometimes result in a cold emission from the gun control electrode, which has to be conditioned away before restoring the beam recirculation. These issues are described in detail in Ref. [3]. The cold gun emission was nearly completely eliminated by a proper choice of the gun electrode materials.

As for the beam interruptions and tube discharges, the system behaved differently at a Pelletron voltage of 3.5 MV and 4.34 MV. We found that without any beam the accelerating gradient can be as high as 16 kV/cm (corresponding to 5 MV), with the dc electron beam in excess of 10 mA the stable operating gradient drops to 12 kV/cm. This prompted us to plan an upgrade for the Pelletron from 5 to 6-MV maximum rating by extending the acceleration tube length by 20%. This upgrade will be implemented when the Pelletron is moved to its final location. With this upgrade the accelerating gradient at the design voltage of 4.34 MV will be very close to that of the present machine at 3.5 MV. Table 1 shows the achieved results for two voltages – 4.34 and 3.5 MV. While at 4.34 MV we were able to demonstrate the design current of 0.5 A, the stable beam operation was frequently interrupted by beam-induced tube discharges (every 4 minutes or so) with eventual high-voltage de-conditioning such that the Pelletron was no longer capable of holding 4.34 MV. At a lower 3.5-MV voltage and the best beam line settings we did not see any full-tube discharges, while the beam interruptions occurred on average every 20 minutes (with a 0.5-A beam) and did not cause any de-conditioning to the accelerating tube. Figure 2 shows a 4-hour run with a 0.5 A beam at 3.5 MV.

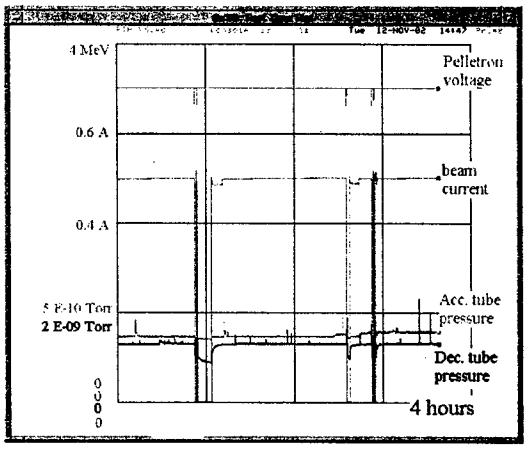


Figure 2: Pelletron voltage, ion gauge readings, and the beam current recorded over 4 hours of running at 3.5 MV, 0.5 A. An interruption in the first hour was caused by a computer glitch.

In all beam interruptions the Pelletron voltage drops by no more than 200 kV. This prompts the computer control system to shut the electron gun off. The Pelletron voltage then returns to its nominal value in several seconds and the recirculation at the nominal current is restored in 20 seconds by the control system without any operator interference. Figure 3 shows the beam recovery process on a shorter time scale.

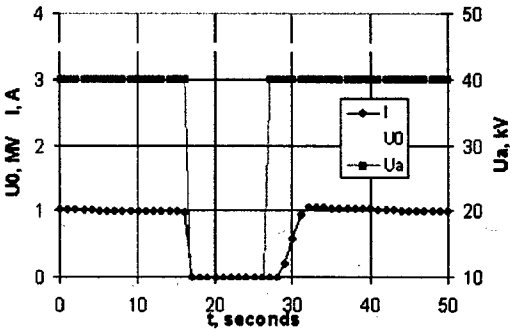


Figure 3: Beam recovery after an interruption of a 1-A beam recirculation. The electron gun was operated with a 40-kV anode voltage (Ua curve).

Putting aside mechanical and electronics failures, at 3.5 MeV, 0.5 A, and the best conditions, only short beam interruptions were present, and the duty factor was better than 99%. While a current of 0.5 A has been achieved at the energy of 4.34 MeV, multiple interruptions led to full discharges and loss of tube conditioning. The necessity to recondition the tubes makes such a regime intolerable. The level of the beam current at 4.34 MeV, at which the duty factor is above 95%, is 0.1 A or less.

FIELD QUALITY IN THE COOLING SECTION SOLENOID

The cooling section solenoid consists of ten solenoid modules, gaps between the modules and magnetic field correctors [4]. The transverse field in the cooling section is measured by a dedicated compass-based magnetic sensor, while the longitudinal field is measured by a Hall probe.

For successful cooling it is necessary to keep the electron beam angles (with respect to the anti-proton beam) below 0.1 mrad inside the cooling section (see Table 1). This requirement in turn sets several restrictions on the magnetic field quality: the longitudinal field at any point in the cooling section shouldn't differ too much from the field averaged over the whole cooling section and the absolute value of a running integral of the transverse field should be below 1G·cm at any point inside the cooling section [4].

The measured transverse field of an un-corrected solenoid does not satisfy these requirements. Indeed, the simulation of the electron motion in this field showed that the acquired angles are as large as 5 mrad.

To improve the field quality an algorithm of compensation was suggested [5]. Initially, it was tested in a 4-meter prototype of the cooling section. It was found that the algorithm works reliably and gives a field of the proper quality.

The field of the full-scale 18-m long cooling section was measured and served as an input for the algorithm. The calculated currents of the transverse correctors were used to predict the compensated field. Figure 4 gives the electron trajectory in this expected field. It shows that the angle of an electron beam is below the threshold value in 95% of the cooling section, which is more than enough for successful cooling.

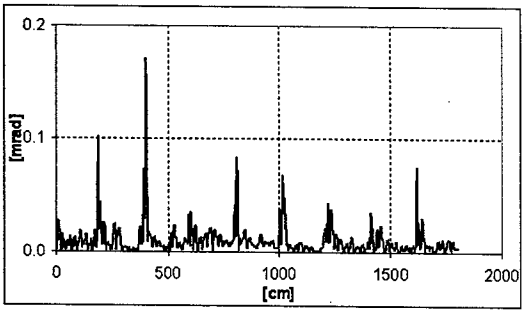


Figure 4: Simulation of electrons motion (electrons angle) in the predicted magnetic field (electron enters the solenoid at 5mm off axis).

A more careful analysis of the compensated field showed it to be unsatisfactory although it was approximately 10 times better than the initial field (see Figure 5).

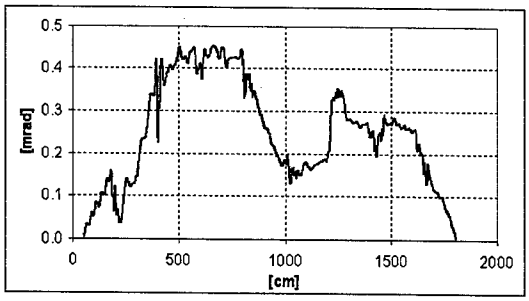


Figure 5: The total electron angle simulated in the fields obtained after the adjustments of field correctors (electron enters the solenoid at 5mm off axis).

Such a situation is related to a problem with the long-term stability of the measurement. At the present time significant work is being done to improve the measurement stability. Repeated adjustments and measurements are planed for this summer.

ACKNOWLEDGMENTS

The authors are thankful to A. C. Crawford for his work on this project.

REFERENCES

[1] S. Nagaitsev et al, NIM A441(2000), 241.
[2] J. Leibfritz et al, "Status of the Fermilab Electron Cooling project", Proc. of EPAC'02, Paris, 3-7 June, 2002.
[3] A. Shemyakin, "Attainment of an MeV-range, dc electron beam for the Fermilab cooler", to be published in COOL 03 workshop proceedings.
[4] S. Nagsitsev et al, "Fermilab Electron Cooling Project: Estimates for the Cooling Section Solenoid", FERMILAB-FN-689, March 2000.
[5] S. Nagaitsev et al, "Field measurements in the cooling section solenoid for the Recycler cooler", Proc. of EPAC'02, Paris, 3-7 June, 2002.

ANALYSIS OF A GRID WINDOW STRUCTURE FOR RF CAVITIES IN A MUON COOLING CHANNEL**

A.Ladran*, D. Li*, A.Moretti#, R. Rimmer†, J. Staples*, S. Virostek* M. Zisman*
* LBNL, Berkeley, CA. One Cyclotron Road, Berkeley, CA 94720, USA
† Jefferson Lab, Newport News, VA. 23606, USA
# FNAL, Batavia, IL 60510, USA

Abstract

We report on the electromagnetic and thermal analysis of a grid window structure for high gradient, low frequency RF cavities. Windows may be utilized to close the beam iris and increase shunt impedance of closed-cell RF cavities. This work complements previous work presented for windows made of solid beryllium foil. An electromagnetic and thermal analysis of the thin wall tubes in a grid pattern was conducted using both MAFIA4 and ANSYS finite element analyses. The results from both codes agreed well for a variety of grid configurations and spacing. The grid configuration where the crossing tubes touched was found to have acceptable E-Fields and H-Fields performance. The thermal profiles for the grid will also be shown to determine a viable cooling profile.

1 INTRODUCTION

It was postulated that windows for closed-cell high gradient RF cavities could be improved by using a grid of thin wall round tube construction to replace a solid window. Closing the beam iris increases the shunt impedance. [1] The advantage of the grid over a window is that it could provide similar, or better performance to the beryllium window (Field attenuation, low scattering mass and low field distortion) but at a lower cost.

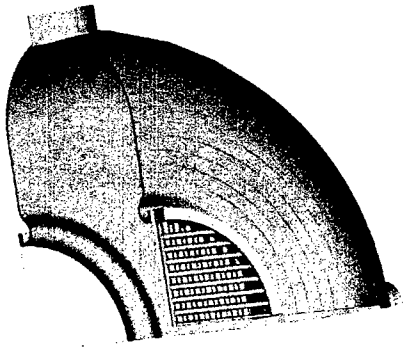


Figure 1: ¼ symmetry cutaway of 201MHz RF Cavity with closed irises using a beryllium window and a grid window.

** This work was supported by the director, Office of Science, Office of High Energy and Nuclear Physics, Division of High Energy, U.S. Department of Energy under contract DE-AC03-76SF00098.

A concern is that even with relatively low heat flux the thin wall tube is insufficient to dissipate the heat. The tube radii will cause local heating from surface field concentration and may be subject to thermal distortion and stresses. Gaseous helium cooling will be provided to minimize the undesired affects from the heat loads. Using Finite element tools such as MAFIA4 [2] and ANSYS [3] several grid configurations were modelled to find the optimum geometry for heat dissipation, E-field attenuation and field uniformity in the cavity. The analysis showed that certain grid geometries had electromagnetic performance similar to a solid beryllium window. Using MAFIA4 simulations to tests these configurations, the 15x15 tube array with the tubes touching was selected as a viable option. This configuration was then modelled in ANSYS using High Frequency EMAG elements and a mesh density sufficient to solve for the grid thermal profile.

2 DESCRIPTION OF A GRID WINDOW

The basic non-touching grid window is shown in Fig. 2. It consists of a criss-cross pattern of 12.8 mm (0.5 inch) diameter thin-wall tubes, <0.25 mm (0.010 inch), either aluminium, or a low z material. The tubes will be brazed to an annular ring that provides both structural support and the cooling gas distribution channels. The base design for the grid uses a 15x15 tube pattern. The parallel tubes are coplanar with a centerline spacing of 25.4 mm. The two planes of parallel tubes are oriented orthogonal to each other with a gap sufficient to prevent arcing between tubes and terminate the field. The gap shown is 25 mm on centers, but the final design is with the tubes touching.

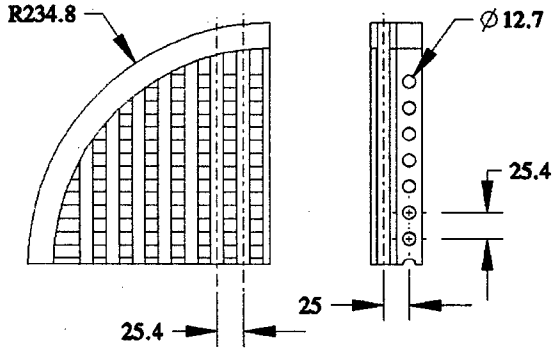


Figure 2: Layout of baseline grid window ¼ symmetry. Orthogonal grid tubes are spaced apart [units: mm]

Several configurations of grids were investigated. As shown in Fig. 3, case 1 is a 15x15 array of orthogonal grids not touching, case 2 is the same with the tubes touching and case 3 is a lower density (4x4 array) of larger diameter tubes. Three alternative concepts are shown in Fig. 4, two with non-orthogonal patterns and the third is a 15x15 fully overlapped tubes array on a single plane. Analysis had low field penetration for the fully overlapped grid configuration, but it is not apparent how to build it using conventional (low cost) methods.

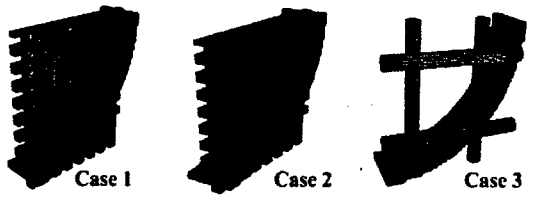


Figure 3: Gridded windows configurations modelled in MAFIA4. Left to Right: Case 1 - 15x15 grid spaced, Case 2 - 15x15 grid touching, Case 3 - 4x4 grid touching.



Figure 4: Other gridded windows configurations modelled in MAFIA4. Left to Right: Spider, "L" (HILAC), 15x15 grid fully overlapped.

3 RF ANALYSIS

The grid geometries shown above were evaluated using MAFIA4, a finite-integration code that simulates electromagnetic fields. The models were 1/8 cut with z and y-symmetry. Each of the models were built with a closed boundary behind the grid to provide an anteroom to model the amount of field that leaked past the grids. The field in the anteroom region has strong coupling to H_{phi}.

The MAFIA4 results give the E-field distortion in the main cavity body, the grid region and the anteroom region. The power density was also determined for the walls and grids. MAFIA4 generates a diagonalized rectangular mesh and cannot represent round tubes precisely, so the initial evaluation models were done with square tubes. A round tube model was tested and although it was modelled with fewer mesh points it gave electromagnetic results similar to the square tube simulations, which validate the square tube model.

The simulations for cases 1 to 3 demonstrated promising performance from each of the geometries. Case 1 shown in Fig. 5, the non-touching grid had good field quality, but had some field leakage past the grid. Case 2 shown in Fig. 6, the touching grid minimized the field leakage and had good field quality. An indication of the magnitude field leakage beyond the grid is given in results from a MAFIA4 solution for a touching round tube and was $2x10^{-5}$ along $E_z(0)$. The large tube lower density geometry given in case 3 also had promise as a window with good attenuation and good field quality in the cavity. A non-touching version of case 3 was also modelled, but had significant field penetration. The E field results for the non-orthogonal configurations given in Fig. 4 also showed significant field penetration past the grid.

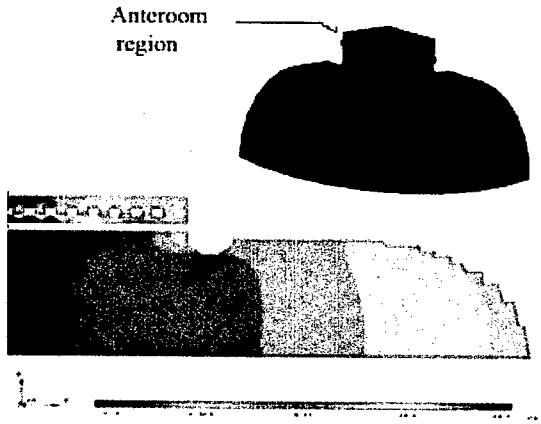


Figure 5: E_z field for case 1 15x15 array, grids not touching. Note the strong field past the grid in the "anteroom" region.

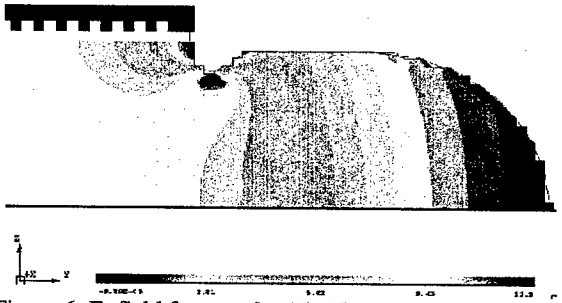


Figure 6: E_z field for case 2 - 15x15 array, grids touching. Excellent attenuation of fields past grid, excellent field quality near grids in cavity.

4 FEA THERMAL MODEL

The touching grid design had the best field attenuation with low distortion and seemed to be an excellent candidate for a window structure. A thermal model was the next step in characterizing its temperature profile.

The case 2 grid window was modelled using ANSYS and solved for both electromagnetic solutions and the temperature profile, Fig. 7. This technique has been used previously to model the thermal profile of the solid beryllium windows under RF heating. [4,5]. The grid geometry model provided some unique challenges due to the mesh density required to model the grid features.

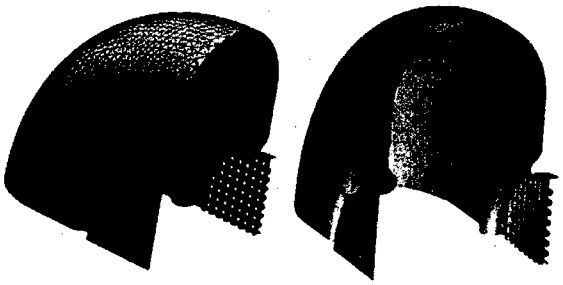


Figure 7: ANSYS FEA mesh and Heat flux results

The large RF tank and small grid tube features in the touching grid had a wide range of length scales. The areas of interest regarding the grid, such as the tube intersections, were on the order of a millimeter while the scale of the cavity itself was on the meter scale. The difference in length scale as well using a ¼ cut, z-symmetry cavity model required large regions within the cavity and grid and wall regions to be meshed with very small elements to get good heat flux results. Good results that matched well with the MAFIA4 solutions were achieved using element lengths of between 1 mm to 1.5 mm at the grids, which is about a 10:1 ratio to the tube diameter. Fully meshed the 201 MHz RF cavity model with a case 2 grid had over $1x10^6$ Degrees of Freedom. To run an ANSYS high frequency analysis of this size required more computer memory than the ~ 1.7 GB memory limit associated with ANSYS using 32-bit processors. This model was run successfully using a UNIX based computer with multiple 64-bit processors, 4 GB ram, 10 GB hard disk swap and the ANSYS default memory model and multiple processor options turned on.

5 THERMAL ANALYSIS

The MAFIA4 solution (Hf = <0.04 watts/cm^2) for power density on the cavity walls and grids shown in Fig. 8 was in good agreement with the ANSYS solutions (Hf = 0.03 watts/cm^2).

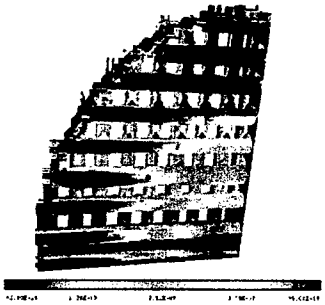


Figure 8: Power density for case 2 touching tubes using MAFIA4 Hf = <0.04 watts/cm^2.
Field gradient: 16 MV/m at $E_z(0)$, duty factor of $1.9x10^{-3}$

Using ANSYS, the heat flux distribution in the cavity and grid was solved for an average power of 10 kW. The heat flux was then applied to a thermal model to solve for the thermal profile of a helium gas cooled grid The model includes the water-cooling of the RF cavity body and the helium gas cooling of the grid tubes. Respectively, the film coefficients used for cooling were 15,000 watts/m^2 and 250 watts/m^2. The result of the thermal analysis shown in Fig. 9 gives a temperature rise in the tubes to be less than 8° C. The thermal stress and deformation will still need to be completed to determine if this temperature rise is undesirable, but it is apparent that further refinements to the model to match actual operation could reduce the temperature rise. One example to enhance the model would be to include the active cooling provided to the grid annular support ring by the cooling gas supply channels.

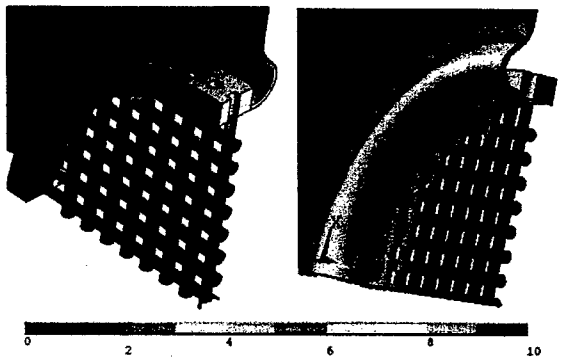


Figure 9: Temperature (°C) profile of grid using ANSYS.

6 CONCLUSION

It was shown that a touching grid geometry would be the preferred geometry over the non-touching in a high gradient closed cell RF cavity. The heat flux results from both MAFIA4 and ANSYS had good agreement. ANSYS high frequency and thermal FEA can be used for developing the electromagnetic model and thermal models provided an adequate mesh density is applied. The temperature results are important for determining if the RF heating of the tubes could be sufficiently cooled using a gas. Further studies will examine the structural affect of non-uniform heating on the grid tubes. The development of a cost effective grid design will be facilitated by the ability to model the geometries adequately.

7 REFERENCES

[1] R.A. Rimmer, et. al., Closed-Cell 201.25 MHz RF Structures for a Muon Ionization Cooling Experiment, EPAC 2002
[2] MAFIA, http://www.cst.de/
[3] ANSYS, http://www.ANSYS.com
[4] N.Hartman, D. Li, J.Corlett, Thin Beryllium Windows - Analysis and Design Status, LBNL MUCOOL 180.
[5] N. Hartman, R.A. Rimmer, Electromagnetic, Thermal, and Structural Analysis of RF Cavities using ANSYS, PAC 2001

LONGITUDINAL COOLING OF A STRONGLY MAGNETIZED ELECTRON PLASMA

Jinhyung Lee* and John R. Cary†
CIPS‡ and Department of Physics, University of Colorado, Boulder, CO

Abstract

The optimal values of Q and $(\omega - \Omega_r)$ for cooling a pure electron plasma with a microwave bath have been calculated. An electron plasma which has no internal degree of freedom, cannot be cooled down below a heat bath temperature. However, the longitudinal cooling can be achieved by energy transfer from the poorly cooled parallel degree of freedom to the well cooled (by synchrotron radiation) perpendicular degree of freedom. To do this, we introduce a microwave bath to the electron plasma. A microwave tuned to a frequency below the gyrofrequency of the electron forces an electron moving towards the microwave to absorb a photon and then to move up one in Landau state. The electron loses longitudinal momentum in this process, so that the longitudinal energy can be reduced. On the basis that most of the electrons are in the ground or first excited state, we set up a transition equation and develop a FEM code. With an appropriate condition for B-field and intensity of the microwave, the cooling times for several values of Q and $(\omega - \Omega_r)$ are calculated and the optimal values are found. Applying the optimal values at appropriate times in a cooling process, the best cooling can be obtained. For an electron plasma magnetized with 10T B-field, cooling to the solid state can occur within 2 hours. Without this optimization, times were always several hours, longer than the life time of the plasma in real system.

INTRODUCTION

The concept of crystalline non-neutral plasma, regarded as a new state of matter, has been studied for a variety of fundamental and applied physics areas, including the study of space-charge-dominated beams, the study of Coulomb crystals, the realization of high luminosity ion colliders, the application to ultra-high resolution nuclear experiments and to the atomic physics research, etc. Crystallization occurs as non-neutral plasmas and beams are cooled below the transition temperature. In fact, as seen in many Penning trap experiments, the non-neutral plasmas has three different phases: fluid, fcc, and bcc[1]. The Crystallization in one dimension has been observed in the beams at the Aarhus accelerator[2], in agreement with calculations[3], and crystallization in three dimension has been observed in the ion Penning trap at NIST[4] and in dusty plasmas[5].

In high energy physics, Penning traps and antiparticle storage rings have been used for experimental tests of the CPT theorem, which predicts equivalence of various physical parameters such as masses, charge-to-mass ratio, magnetic moments, and gyromagnetic ratio for particles and antiparticles. Charged particles can be confined perfectly in an ideal cylindrically symmetric trap with a uniform axial magnetic field, which is the basic setup of the Penning trap. This approach, the use of Penning trap, has been favored and widely used because the particle can be cooled down to a temperature of the order of tens of mK. Penning traps at CERN have been used to capture antiparticles for high-resolution measurements for proton mass and for mass spectrometry of nuclei[6].

Recently, laser cooling has been the primary approach towards obtaining such ultra cool beams and plasmas. A laser that is tuned to a frequency below the resonant frequency of the ion is directed at the ionic plasma. Ions moving towards the laser beams see an upshifted laser beam, and thus can absorb the light. Subsequently they spontaneously emit a photon isotropically. Thus, in the full process, they lose momentum by recoil. This leads to cooling. Such a method naturally works only for ions, not electrons or protons, as they have the internal resonances needed for narrow absorption. For non-ionic beams, electron cooling has been used, but such cooling has not produced ultra cool beams[7].

For this reason we already investigated phase transition of strongly magnetized electron plasmas in Penning traps and we concluded that the phase transition can occur on the condition that longitudinal temperature is below a certain value irrespective of transverse temperature. Now the question is how to decrease the longitudinal temperature to the critical value. As one of the possible ways we suggest a microwave cooling method. Applying a tuned microwave into the longitudinal direction, the longitudinal energy can be reduced and then the temperature can be dropped down below the critical value. This means that the electron plasma crystallization can be achieved. In the following sections we suggest how to reduce the longitudinal temperature and the result is shown.

MICROWAVE COOLING

Two Level Equations

In the low transverse temperature limit, the longitudinal energy can be reduced by the microwave radiation. Absorption of a microwave photon in Penning trap by an electron, thus moving it up one in Landau state, can reduce the parallel energy, just as laser cooling works for ionic plasma and equilibria. Then the spontaneous radiation reduces the transverse energy, so that the transverse state move back to the original Landau state and finally the transverse temperature is the same to the heat bath temperature. From

* Email: jinhyung@Colorado.edu
† Email: cary@Colorado.edu
‡ Center for Integrated Plasma studies

0-7803-7738-9/03/$17.00 © 2003 IEEE

the entire process only the longitudinal temperature can be decreased.

The longitudinal velocity distributions during the process can be described by Master equations. With an assumption that most of particles are in the ground or first excited state, the equations are

$$\frac{\partial f_0(u_z)}{\partial t} = \sum_{k_{||}=\pm k_0} [f_1(u_z+\frac{\hbar k_{||}}{m})D(u_z+\frac{\hbar k_{||}}{m},u_z) - f_0(u_z)W(u_z,u_z+\hbar k_{||})] \quad (1)$$

$$\frac{\partial f_1(u_z)}{\partial t} = \sum_{k_{||}=\pm k_0} [f_0(u_z-\frac{\hbar k_{||}}{m})W(u_z-\frac{\hbar k_{||}}{m},u_z) - f_1(u_z)D(u_z,u_z-\hbar k_{||})] \quad (2)$$

where $f_n(p_z)$ is the distribution of transverse quantum number n. The spontaneous and the stimulated transition probabilities are defined as

$$P_{||} = \frac{2e^2\omega^2}{3c}\frac{\hbar\Omega}{mc^2} \quad (3)$$

$$w_{||} = \frac{I\sigma}{\hbar\omega_R}\frac{(\gamma/2)^2}{(\gamma/2)^2+\Delta^2(\omega,k_{||},u_z,v_z)} \quad (4)$$

$$D_{||} = \frac{P_{||}}{\hbar\Omega}+w_{||} \quad (5)$$

$$W_{||} = \frac{P_{||}}{\hbar\Omega}exp[\frac{-\hbar\Omega}{k_BT_\perp}]+w_{||} \quad (6)$$

with resonance conditions,

$$\Delta \equiv \omega-\omega_R \quad (7)$$

$$\hbar k_{||}(=\pm\hbar k_0) = m(v_z-u_z) \quad (8)$$

$$\hbar\omega_R = \hbar\Omega+\frac{m}{2}(v_z^2-u_z^2). \quad (9)$$

Cooling Condition of Nonneutral Plasmas

The problem we should consider is that the cooling is very effective as long as the width is smaller than the standard deviation of the velocity profile. When a microwave with a frequency ω_R and a wave number $k_{||}$ propagates along the magnetic field in the plasma, an electron with longitudinal momentum p_z along the magnetic field experiences, because of the usual Doppler effect, a shifted frequency

$$\omega' = \omega+k_{||}\frac{p_z}{m}. \quad (10)$$

If ω' coincides with the electron cyclotron frequency Ω, then the resonant absorption of the wave energy by electrons will take place. This phenomenon is effective in the vicinity of the resonance frequency. The particles near the resonance in velocity space lose their momenta so that they move into the lower velocity space. From the resonance conditions the entire particles near the resonance are shifted into the lower velocity space. Moreover, if the resonance frequency is well-chosen, then the particles can almost lose their momentum. Thus the width of final distribution can be almost the same as the width of microwave, which means that the lowest temperature of particles can be determined by the width of microwave. This gives a condition of microwave applied to the particles. The initial width of microwave should be less than the standard deviation of initial velocity distribution[8]. The condition in mathematical form

$$\frac{\delta\omega}{k_{||}} < \frac{\sqrt{\langle p_z^2\rangle}}{m} \quad (11)$$

where $\delta\omega = \gamma/2$ is the width of microwave, implies that the smaller width of microwave gives the lower temperature of final distribution. However if the initial width of microwave is too small, the number of particles involved with the microwave is so small that cooling time can be too long. So, in order to find the fastest way to cool the particles we should take a larger width initially. In that case the temperature is still too high to reach the critical temperature at which $\Gamma_{||} \approx 170$. Then it is necessary to take a smaller width at the moment to continue to cool the electrons down to the critical temperature.

RESULTS

Taking appropriate conditions about the initial state, the longitudinal temperature can be estimated after the state reaches an equilibrium. Our system is supposed to be immersed in a liquid helium heat bath, so that the initial temperatures (transverse and longitudinal temperatures) can be 4.2K, the temperature of liquid helium. We apply 10T as its magnetic field, $0.7\times10^9/cm^3$ as its number density to the plasma in the trap, and at least 10^4 as the Q factor of microwave cavity. For the number density ($0.7\times10^9/cm^3$), the critical temperature which gives $\Gamma_{||}=170$ is approximately 14mK.

In order to find the best way to cool the electron plasma, we have applied various values of Q and $\Delta\omega$ ($\Delta\omega\equiv\Omega-\omega$) to the plasma. For the set of (Q,$\Delta\omega$), the cooling rates and transverse temperatures are calculated. For convenience of calculation we take the $\Delta\omega$ as

$$\Delta\omega \equiv P\frac{\gamma}{2}. \quad (12)$$

With the aid of the definition the cooling rates and transverse temperature are calculated as functions of two variables, Q and P.

The cooling rates that the plasma takes as long as Eqs. (11) is valid are calculated for various values of Q, P, and the microwave intensity $I\sigma$. From our simulations, the cooling rates are maximized at $Q=4.0\times10^4$ for $P=3.0$, $Q=5.0\times10^4$ for $P=4.0$, and $Q=6.0\times10^4$ for $P=5.0$. In table 1 the cooling rates for the three sets of (P,Q) by changing the intensity $I\sigma$ are shown.

As expected, the stronger microwave gives the faster cooling. However, the transverse temperature becomes

Table 1: The cooling times (sec) for various values of the microwave intensity $I\sigma$ and P.

	$(P, Q/10^4)$		
$I\sigma(\times\hbar\Omega)$	(3.0,4.0)	(4.0,5.0)	(5.0,6.0)
5.0	13488.4	21783.1	33791.8
10.0	7881.5	12028.4	18037.0
15.0	6014.8	8784.8	12795.2
20.0	5082.0	7167.1	10179.3
25.0	4522.2	6198.9	8612.9
50.0	3400.5	4273.1	5496.8
75.0	3023.8	3636.2	4469.2
100.0	2833.8	3318.8	3959.9

higher as the microwave becomes stronger. Then the number of particles in the second excited state is not so small that our two level assumption will not be valid any more. Therefore, the maximum intensity of microwave should be determined by the two level assumption. For 10T as its magnetic field strength, the maximum intensities are $25\hbar\Omega$ for (3.0,4.0) as $(P, Q/10^4)$, $50\hbar\Omega$ for (4.0,5.0),and $75\hbar\Omega$ for (5.0,6.0).

With the best values of P, Q, and $I\sigma$ to cool the plasma, however, it still takes too long to have the critical temperature. From the result of our simulation the cooling time is almost 6 hours for any of three cases. The time is unrealistic in experiments. The plasma profile in Penning trap with the high magnetic field cannot stand for the long time. The reason why it takes too long is explained as follows. The plasma is cooled so rapidly that the temperature reaches the value at which breaks Eqs. (11), and then the cooling becomes much slower because the high peaked central frequency of applied microwave is too far from the plasma profile. The real intensity of microwave to apply to the plasma is too weak to cool it as rapidly as before its temperature reaches the value.

For this reason we take the other way to cool the plasma more rapidly. At the moments whenever the plasma breaks the Eqs. (11), we change the central frequency and microwave width in the velocity space. This can be achieved by changing P and Q. As done initially, the best sets of P, Q, and $I\sigma$ to get a cold plasma rapidly can be chosen in the same way. In our results the P and $I\sigma$ are not changed during the whole simulation, but the Q is changed at the moments whenever the plasma breaks the condition. The best Qs are satisfied that $\sqrt{T_{||}} \times Q$ for the different values of Q and $T_{||}$ is always the same to the initial at the moments. Applying this method, we calculate the cooling times for various cases. The result is shown in table 1 where the initial Qs are picked up 4.0×10^4, 5.0×10^4, and 6.0×10^4 for their Ps. The successive Qs are determined during the simulations by the condition that $\sqrt{T_{||}} \times Q$ is the same.

In Fig 1, time evolutions are shown for $P = 3.0, Q = 4.0 \times 10^4$ and $I\sigma = 25\hbar\Omega$. Also, in table 2 the times when the Qs are determined.

As we expected, the cooling times can be reduced as much as we wanted. The fastest cooling times is more than 1 hour and less than 2 hours which is very realistic in Penning trap experiments.

Table 2: The times when Qs should be changed for various values of the microwave intensity $I\sigma$ and $P = 3.0$.

	$P = 3.0, I\sigma = 25.0$			
t (sec)	Q	α	$T_{||}$	$T_{\perp}$
0.0	40000	0.92999	4.2	4.2
2539.5	85129	1.97910	0.927294241	10.167975
3732.9	181180	4.21617	0.204713972	10.167198
4293.1	385614	9.04924	0.045192312	10.163583

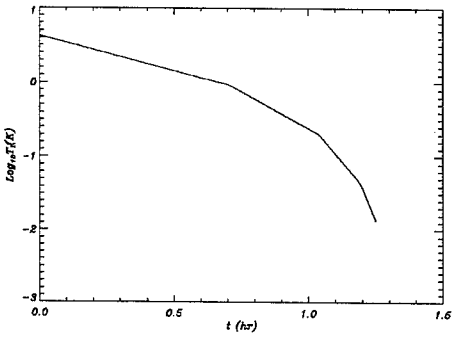


Figure 1: Time evolution of the longitudinal temperature for $P = 3.0$ and $I\sigma = 25\hbar\Omega$.

DISCUSSION

Applying microwaves into the longitudinal direction, the temperature can be decreased below the critical temperature by exchange of energy between two degrees of freedoms. With the condition that an appropriate low temperature heat bath reduces the transverse energy of the plasma continuously, the electron plasma crystallization can be achieved in Penning traps in 2 hours.

REFERENCES

[1] S. Hamaguchi, R. T. Farouki, and D. H. E. Dubin, Phys. Rev. E **56**, 4671(1997).

[2] M. Steck, K. Beckert, H. Eickhoff *et al.*, Phys. Rev. Lett. **77**, 3803(1996).

[3] R. W. Hesse, Phys. Rev. Lett. **83**, 3430(1999).

[4] W. M. Itano *et al.*, Science **297**, 686(1998).

[5] E. Morfill *et al.*, Phys of Plasma **6**, 1769(1999).

[6] G. Gabrielse *et al.*, Phys. Rev. Lett. **57**, 2504(1986).

[7] G. Baur, G. Boero, W. Oelert *et at.*, Phys. Lett. **B 57**, 2504(1986).

[8] S. Stenholm, Rev. Mod. Phys. **58 (3)**, 699(1986).

THE ADVANCED PHOTON SOURCE INJECTOR TEST STAND: PHASE TWO*

S. Berg, T. Barsz, D. Briddick, M. Givens, G. Goeppner, A. E. Grelick , W. Jansma, J. Lewellen, A. Lopez, M. Martens, W. Michalek, S. Wesling
Advanced Photon Source, Argonne National Laboratory, Argonne, IL 60439, USA

Abstract

The high-power S-band feed subsystem and the versatile method of beamline construction have been combined to provide for further testing of a unique gun that incorporates three cavities and requires three separate S-band feeds. Completed in December 2002, this configuration of the injector test stand is intended to investigate performance of the ballistic bunch compression gun [1]. If this gun proves to be desirable for injection at the APS, then the ballistic bunch compression gun together with the S-band feed subsystem and portions of the beamline will be relocated in the APS linac tunnel.

INTRODUCTION

The injector test stand (ITS) began to take shape shortly after the APS commissioning in 1996. The north wall of the room is the original poured concrete wall that was once a part of the linac tunnel, while the south wall is constructed from 8″ × 8″ × 16″ density-enhanced concrete shielding blocks, effectively separating the 116″ × 219″ test room from the gun end of the linac tunnel. In 2001, the test stand was used to commission the third-generation thermionic-cathode rf guns that are used for normal storage ring injection at the APS and which incorporate an improved cathode design [2]. The commissioning of these two guns plus a third unit was quickly achieved with little difficulty because it was facilitated by first-phase design features built into the ITS. These features included quick-disconnect magnets and power supplies, a single rf-port waveguide installation, a 10′ by 44″ slab-style leveled table with ample room for diagnostics, water-cooling provisions [3], and the integration of the diagnostics and controls into the EPICS-based control system. The latter 'helps ensure that the "look and feel" and response of the ITS control system is similar to that of the rest of the APS' [4].

This paper discusses the second phase of the test stand installation involving investigation into performance of the prototype ballistic bunch compression (BBC) gun.

NEW BEAMLINE

The new beamline is presented in Figure 1. Shown are the BBC gun, the modular beamline assembly, the laser port, spectrometer/filter line, and experimental area, which are further described in [3]. Rebuilding the beamline from the previous ITS configuration involved reusing a majority of the previous phase beamline components aligned only to a different lattice and the fabrication of two new breadboards. The use of these breadboards and the versatile method of beamline construction led to quick construction of the new assembly [5]. The beamline components are common linac elements: five quadrupoles, two steering correctors, one gate valve, two dipoles, two current monitors, two Faraday cups and viewscreens, and four 20-l/s ion pumps (two for the beamline and two for the three-chambered BBC gun). Future plans include installation of a beam position monitor (BPM) to permit the testing of new BPM electronics, a Golay-cell-based bunch length monitor, and a pepperpot-based emittance measurement system.

The incorporation of linear bearing rails in the ITS simplifies the alignment of these beamline components. The alignment of the X and Y axes is controlled by the fit between the rail and the mount that interfaces the beamline component to the rail, whereby the rails themselves have been installed and aligned on the breadboards to within 25 microns (0.001″) of nominal. The beamline component assemblies are guided in the Z axis along a master rail, and they are fixed in the X and Y axes to a degree commensurate with the manufacturing tolerance of the machined portion of the mount that mates the master rail. Upon installation to the rails, shims are sometimes employed between the mount and the beamline component to correct for the Y alignment. The more critical adjustments to achieve lattice are in the Z axis, where optical tooling methods are employed. The APS Survey and Alignment (S&A) group maintains a permanent tooling bar setup capable of precise measurement in two perpendicular axes.

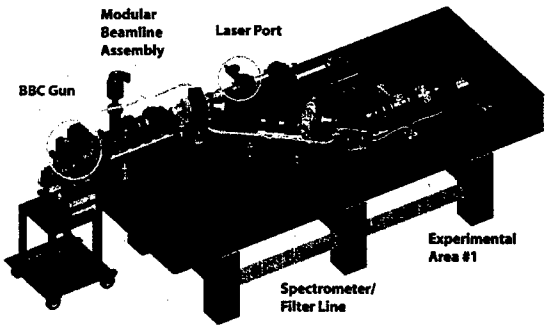


Figure 1: New beamline.

*Work supported by U.S. Department of Energy, Office of Basic Energy Sciences, under Contract No. W-31-109-ENG-38.

0-7803-7738-9/03/$17.00 © 2003 IEEE

For example, one constraint was that the distance from dipole 1 to breadboard 2, quad 2 be equal to the distance from quad 2 to dipole 2. This was achieved to three decimal places, noting that typically alignment tolerances of ±0.001″ are achieved with the S&A setup. Placement of other components was not as critical. The rail system has saved much time and effort in alignment of test stand components.

THREE-PORT FEED WAVEGUIDE

A list of the key components incorporated into the feed subsystem and a corresponding block schematic diagram of these components are described in [6]. The majority of the waveguide is pressurized to 32 psig and is constructed of oxygen-free high-conductivity copper, WR-284-sized, extruded rectangular tubing. This is furnace brazed to stainless steel flanges, yielding vacuum-grade waveguide to connect the commercially available pressurized key components. This system uses seven commercially manufactured pressurized key waveguide components to provide isolated rf power feeds to three separate ports of the BBC gun: two variable power dividers, two phase shifters, and three circulators. Three circulators have been purchased from two different manufacturers, while the variable power dividers and phase shifters have been purchased from a third manufacturer.

We had problems during installation of the variable power dividers and phase shifters. In 1996 we encountered similar difficulties when installing this manufacturer's 6061-T6 aluminum ribbed waveguide. Upon applying torque to the aluminum flanges during assembly or leak checking, the flanges became stressed and the leak-tight braze joint opened via a mechanism of micro-cracking to the extent that SF_6 pressure could not be maintained. During the ITS installation, the manufacturer became personally involved with the repair of sub-components for the phase shifters and variable power dividers, such as panty-adapters. This cooperative exercise between the manufacturer and the APS produced a successful installation and uncovered many factors and observations.

1) The manufacturer indicated that the aluminum dip-brazed WR-284 waveguide's 0.2″ nominal wall construction is approaching a pressure limit at 45 psig, not with regard to safety but with regard to seal integrity of the joint. 2) The integrity of the joint sometimes relies on a micro-seal variety epoxy; this is pulled under vacuum during the repair process into microcracks of the braze joint. 3) The manufacturer cautions that a rotational and gradual application of torque to the flange bolts during installation is easiest on the fragile nature of the braze joint. 4) The application of pressure testing at the APS to monitor the integrity of the dip-brazed joints proved to be very valuable. 5) At the APS, pressurization with argon gas both with and without water immersion was employed to investigate the time degradation of pressure over several days. 6) The pressure used during testing should be representative of the maximum value used in service; for the APS pressurized waveguide and switching system this is 35 psig. 7) This investigation should be begun as early as possible in preparation for installation. 8) Professional and persistent communication between the QA representative and the manufacturer may be needed to secure repaired subassemblies qualified for installation.

The isometric view in Figure 2 depicts the three WR-284-size windows that separate the pressurized system from three short legs of the WR-284 waveguide under vacuum. The elevation view in Figure 2 shows these three vacuum legs directed to the BBC gun.

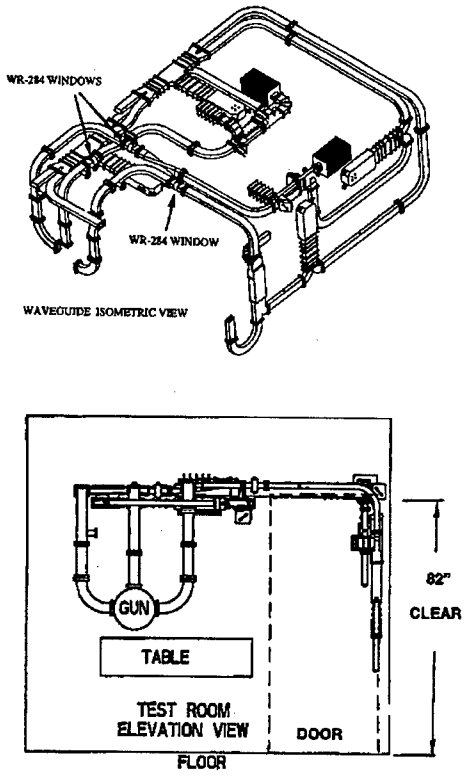


Figure 2: Waveguide isometric and elevation view.

LIMITED VOLUME IN ROOM

The three-port feed subsystem in the injector test room is fed by the pressurized waveguide switching system, as described in [7]. Figure 3 shows how the WR-284 waveguide feeds from the linac tunnel through a penetration in the south wall of the test room to WR-284 switch no. 6. This is the reference point from which the three-port feed and the previous ITS waveguide configuration were constructed.

Ceiling-mounted fluorescent lights were relocated to the south wall, and a unistrut grid was installed on the ceiling and north wall to support the waveguide layout. This schematic called for three separate loops, as shown in Figure 2, and the layout resulted in the following linear lengths: the loop from switch 6 to the BBC gun center port measures 23 feet, the loop from switch 6 to the cathode port of the BBC gun measures 46 feet, and the

loop from switch 6 to the forward port of the BBC gun measures 45 feet. Many alternate layouts were considered.

The three-layer proposal described in [5] placed all of the waveguide against the ceiling. Considering the overall loop lengths of that denser layout, crowding the key components offered no clear advantage regarding the impact of waveguide length on overall return loss. Even in that more compact layout, the loop lengths were calculated to be 23 feet, 36 feet, and 33 feet.

CURRENT STATUS

The waveguide layout now installed in the test room maximizes access to key components for the purpose of serviceability. Figures 2 and 3 illustrate how efficient planning has optimized aisle passages, making the injection test area a more practical area in which to work.

Commissioning has begun on the BBC gun; first beam was achieved on 11 March 2003. Efforts are presently focused on high-power conditioning and improving the beam performance of the gun.

REFERENCES

[1] J.W. Lewellen and S.V. Milton, "Preliminary Calculations of Ballistic Bunch Compression with Thermionic Cathode RF Guns," Proc. SPIE – Int. Soc. Opt. Eng (Coherent Electron Beam X-Ray Sources: Techniques and Applications) Vol. 3154, pp. 162-171 (1997).

[2] K.J. Beczek et al., "A Rationalized Approach to Thermionic Gun Design," Proceedings of the 2001 Particle Accelerator Conference, Chicago, IL, pp. 2206-2208 (2001).

[3] J.W. Lewellen et al., "The Advanced Photon Source Injector Test Stand," Proceedings of the 2001 Particle Accelerator Conference, Chicago, IL, pp. 2212-2214 (2001).

[4] J.W. Lewellen, S. Pasky, "An Operator Training Facility at the Advanced Photon Source," these proceedings.

[5] K.J. Beczek, "A Versatile Method of Beamline Construction," Proceedings of the 2001 Particle Accelerator Conference, Chicago, IL, pp. 1462-1464 (2001).

[6] A.E. Grelick, "The High Power S-Band Feed Subsystem for the Advanced Photon Source (APS) Injector Test Stand," Proceedings of the 2001 Particle Accelerator Conference, Chicago, IL, pp. 1393-1395 (2001).

[7] S. Berg et al., "Rebuilding WR-340 and WR-284 Waveguide Switches to Meet Higher Power at the Advanced Photon Source," these proceedings.

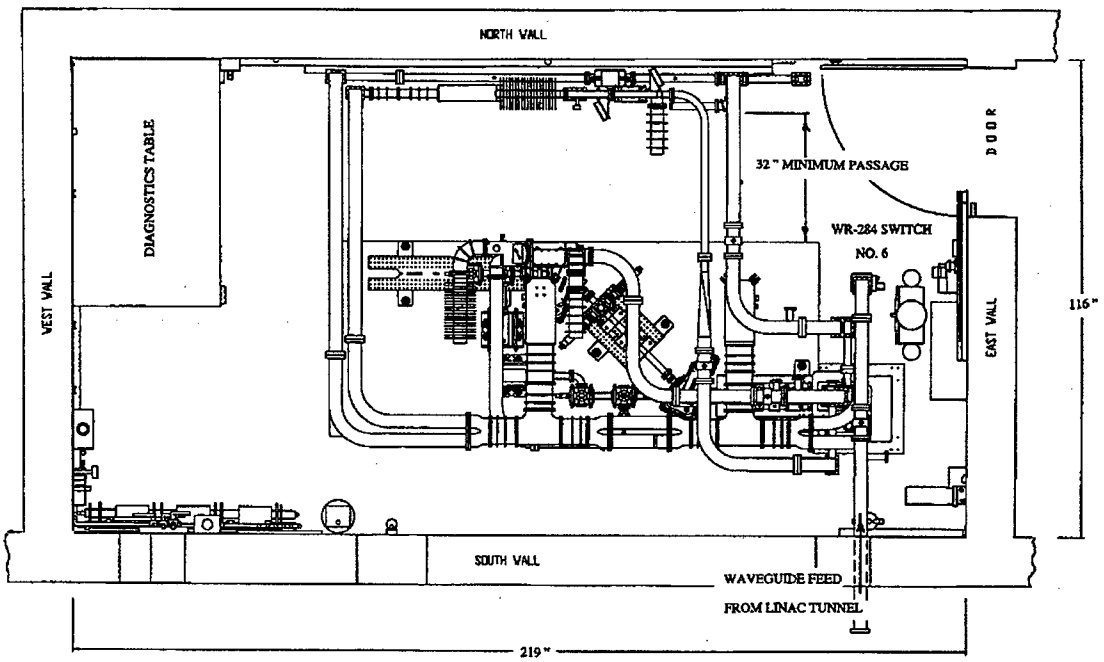


Figure 3: Test room plan view.

A NEW HIGH INTENSITY ELECTRON BEAM FOR WAKEFIELD ACCELERATION STUDIES*

M.E. Conde#, W. Gai, C. Jing, R. Konecny, W. Liu, J.G. Power, H. Wang, Z. Yusof
ANL, Argonne, IL 60439, USA

Abstract

A new RF photocathode electron gun and beamline have been built for the study of electron beam driven wakefield acceleration. The one and a half cell L-band gun operates with an electric field on the cathode surface of 80 MV/m, and generates electron bunches with tens of nanocoulombs of charge and rms bunch lengths of a few picoseconds. The beam diagnostics include a Cherenkov radiator and streak-camera for bunch length measurements, YAG screens for beam profile, integrating charge transformers (ICTs) for bunch charge, an energy spectrometer, and a pepper-pot plate for measurement of the transverse emittance. Measurements of the beam properties at various bunch charges are presented.

INTRODUCTION

The Argonne Wakefield Accelerator (AWA) has been successfully used for conducting wakefield experiments in dielectric loaded structures [1] and plasmas [2]. Although the initial wakefield experiments were successful, higher drive beam quality would substantially improve the wakefield accelerating gradients. For this reason we have built a new L-band photocathode RF gun [3]. This gun will generate high charge bunch trains which will be used in high gradient wakefield acceleration experiments and other high intensity electron beam applications.

FACILITY UPGRADE

The new AWA photocathode RF gun produces high charge electron bunches with shorter bunch length and lower emittance, in comparison with the previous AWA drive gun [4]. The new AWA laser system also presents superior performance in terms of beam profile, energy per pulse and stability.

New Electron Gun and Beamline

The new one and a half cell RF gun operates with a focusing solenoid and a bucking solenoid to cancel the magnetic field on the plane of the cathode. These two solenoids are exactly next to each other, with the photocathode plane as their plane of symmetry. A third solenoid is located at the exit of the gun. There is a vacuum pumping port in the full cell, located diametrically opposite to the RF coupler, both being at the equator line of the full cell. The initial photocathode consisted of a small disc of copper inserted through an opening on the back wall of the half cell. Recently, the photocathode material was replaced by a magnesium disc, which has a higher quantum efficiency. The cathode holder can also function as a tuning plunger, allowing us, in conjunction with the gun temperature, to adjust the parameters of the two cells, in order to achieve the right resonance frequency for the π mode and field balance in the cavity.

The measured value of the unloaded quality factor (Q_0) of the gun is 20300. The gun cavity is somewhat overcoupled (S_{11} = −10 dB), but the installation of a tuning post in the waveguide will improve the coupling. The new gun has been conditioned up to 13 MW of power, with a corresponding accelerating gradient on the cathode surface of 80 MV/m.

The beamline (Fig. 1) has an ICT for measurement of bunch charge at the exit of the gun, and another one downstream of the future wakefield structures to diagnose possible beam scraping. The beamline includes several insertable YAG screens for observation of the beam profile, a pepper-pot plate for measurement of the transverse emittance, and a quartz plate as a Cherenkov radiator for bunch length measurement in conjunction with a streak camera. A quadrupole triplet and an energy spectrometer are also installed in the beamline.

New Laser System

The new laser system consists of a Spectra Physics Tsunami oscillator followed by a Spitfire regenerative amplifier and two Ti:Sapphire amplifiers (TSA 50). It produces 1.5 mJ pulses at 248 nm, with a pulse length of 6 to 8 ps FWHM and a repetition rate of up to 10 pps. A final KrF Excimer amplifier is optionally used to increase the energy per pulse to 14 mJ.

BEAM MEASUREMENTS

Measurements of beam parameters are presented in this section. Some of the parameters are plotted as a function of the accelerating gradient on the cathode. This number was calculated from the value of the input RF power into the gun, using the measured value of the Q_0 of the cavity. In the near future a field probe will be installed in the gun cavity allowing for a more direct measurement of the field intensity.

* Work supported by DOE, High Energy Physics Division, Advanced Technology Branch, under Contract No. W-31-109-ENG-38.

#conde@anl.gov

0-7803-7738-9/03/$17.00 © 2003 IEEE

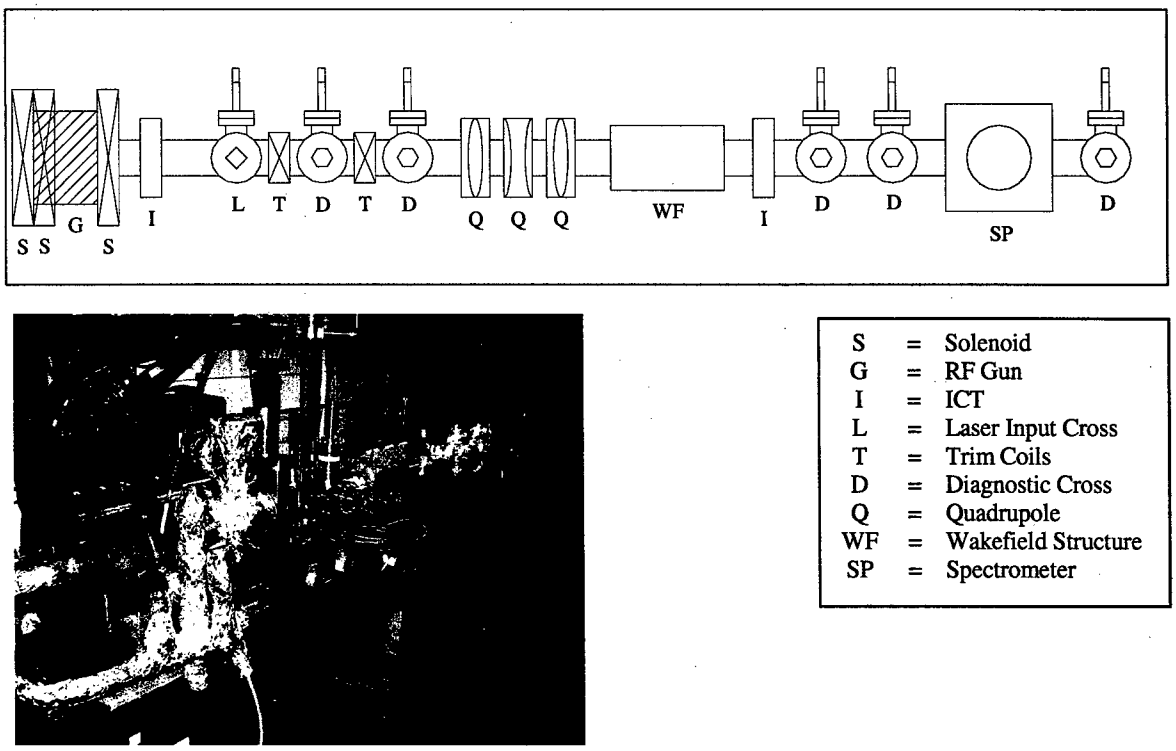


Figure 1: Schematic and picture of the new AWA beamline.

Dark Current

A Faraday-cup consisting of a ceramic DC break and an aluminum block was installed in the beam line for the measurement of dark current. An RC circuit with a time constant of 5 seconds connected to the Faraday-cup allowed an ammeter to measure the average dark current when the machine was operating at a rate of five pulses per second. Figure 2 shows a plot of the charge collected by the Faraday-cup per RF pulse as a function of the accelerating gradient on the cathode surface. We observe the expected rapid increase of dark current as the accelerating gradient in the gun is increased.

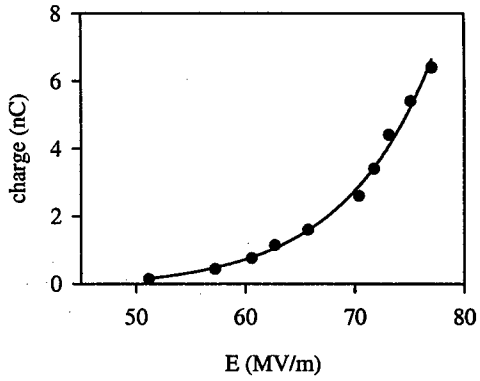


Figure 2: Dark current measurement. Average charge collected by the Faraday-cup during one RF pulse (about 6 μs long), as a function of the accelerating gradient on the cathode surface.

Bunch Charge

Using an ICT (Bergoz ICT-178-070-20:1), we have measured the bunch charge as a function of the laser pulse energy (Fig. 3a) and also as a function of the injection phase at the gun (Fig. 3b). The quantum efficiency of the magnesium cathode (presently about 1×10^{-4}) will improve when we implement the procedure for the laser cleaning of the cathode surface [5]. At the highest laser beam energies there is clear indication of space charge effects on the cathode, preventing the extracted charge from reaching much beyond 100 nC (Fig. 3a).

Beam Energy

The spectrometer at the end of the beamline was used to measure the energy of the electron beam. Figure 4 shows a plot of the beam energy as a function of the accelerating gradient on the cathode surface. This is in good agreement with numerical simulations (PARMELA) [6].

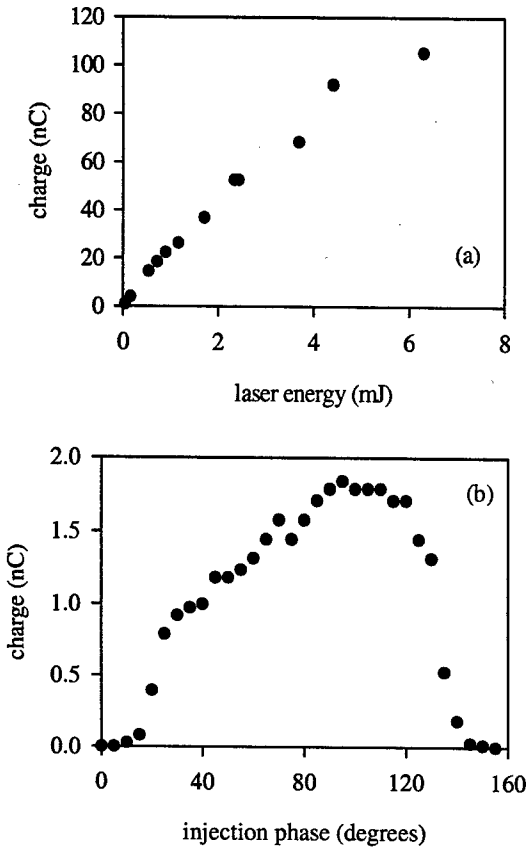


Figure 3: Measured bunch charge: (a) as a function of the laser pulse energy; (b) as a function of the injection phase.

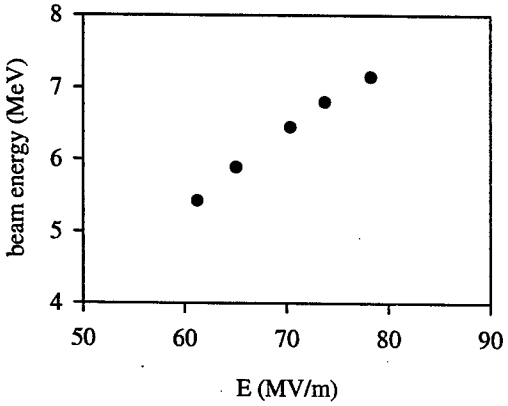


Figure 4: Electron Beam energy as a function of the accelerating gradient on the cathode surface.

Bunch Length

A 1.5 mm thick quartz plate was used as a Cherenkov radiator for bunch length measurements with a Hamamatsu C1587 streak camera. Initial measurements showed bunch lengths spanning from about 13 to 17 ps FWHM, for bunch charges up to 70 nC.

Transverse Emittance

A tungsten pepper-pot plate was used for transverse emittance measurements. The plate was 0.5 mm thick with 0.2 mm diameter holes spaced by 5.6 mm in a cross pattern. The profiles of the resulting beamlets are analyzed on a YAG screen. Preliminary data indicate a normalized emittance of 40 mm-mrad for 20 nC bunches.

IMMEDIATE NEXT STEPS

The splitting of the laser pulses into pulse trains, and the subsequent generation of electron bunch trains will be implemented right away.

A dielectric loaded wakefield structure has been built and will be installed in the new beamline very shortly. It will allow us to test the high power handling capability of the dielectric material.

CONCLUSION

The initial measurements of the beam parameters indicate good agreement with the design values, and confirm the tremendous improvement that the new AWA drive beam represents in comparison with the old drive beam. Some of the beam diagnostics will be further refined, allowing for more precise beam characterization and optimization of the operating parameters. The present magnesium photocathode will soon be replaced by a high quantum efficiency cesium telluride cathode, enabling the generation of long high charge bunch trains (16 or more bunches of 40 nC). A one meter long linac structure will be added to the beamline to increase the beam energy to about 18 MeV, lowering the physical emittance of the beam and facilitating studies of higher gradient wakefield structures.

REFERENCES

[1] Gai, W. et al., "Experimental Demonstration of Two Beam Acceleration Using Dielectric Step-Up Transformer" in *Particle Accelerator Conference-2001*, edited by P. Lucas and S. Webber, Chicago, 2001, pp. 1880-1882.

[2] Barov, N. et al., *Phys. Rev. ST Accel. Beams* **3**, 011301 (2000).

[3] M.E. Conde *et al.*, Proceedings of Particle Accelerator Conference, p.3957, 2001.

[4] M.E. Conde *et al.*, Phys. Rev. ST Accel. Beams **1**, 041302 (1998); M.E. Conde *et al.*, Proceedings of Particle Accelerator Conference, p.1996, 1997.

[5] X.J. Wang and T. Srinivasan-Rao, private communication.

[6] W. Gai *et al.*, Nucl. Instr. and Meth. A 410, p.431, 1998; W. Gai *et al.*, Proceedings of Advanced Acceleration Concepts Workshop, Baltimore, 1998.

ENERGY-SPREAD COMPENSATION OF A THERMIONIC-CATHODE RF GUN*

J.W. Lewellen†, ANL, Argonne, IL 60439, USA

Abstract

The Advanced Photon Source (APS) ballistic bunch compression (BBC) gun was designed as a prototype injector to explore the technique of drift-space compression of a high-brightness beam [1]. It is constructed from three independently powered S-band rf cells, one cathode half-cell, and two full cells, and is designed to operate with both thermionic cathodes and photocathodes; this flexibility allows the gun to be operated in modes other than for ballistic compression.

In particular, appropriate choices of rf power and phase can be used to reduce the energy spread of the beam produced by the gun. With a thermionic cathode, simulations indicate that a 1% FWFM energy spread can contain at least 90% of the emitted beam charge. This operating mode demonstrates many of the capabilities required for ballistic bunch compression, but allows verification of the basic gun performance via a much easier measurement. Also, such a beam is of interest as a source for other experiments, e.g., low-cost, compact, free-electron lasers.

INTRODUCTION

The APS ballistic bunch compression (BBC) gun was built to demonstrate the principle of ballistic compression for high-brightness beams. This is accomplished by placing a positive chirp on the electron beam as it transits the gun, thereby inducing the beam to self-compress in the drift space between the gun and a capture linac section. An analogy would be the operation of a highly relativistic klystron with no output coupler.

To allow full exploration of the parameter space, the rf field gradient and phase is independently adjustable in each cell of the gun. This allows the gun to be readily operated in modes other than ballistic compression.

The BBC gun was designed to operate with either a thermionic cathode or a photocathode [2]. The thermionic cathode offers the advantages of simplicity, robustness, and high average beam currents. Disadvantages typically include beams with large energy spreads and lower per-bunch charge than is possible with a photocathode. The remainder of this paper assumes a thermionic cathode.

When operating with a thermionic cathode, the energy-compression mode is of particular interest. The BBC gun can generate a beam with most of the beam in a very narrow relative energy spread, making the gun more efficient as a driver for devices such as compact, far-infrared free-electron lasers. Also, as the performance of the gun in this mode is easily measured with a simple electron spectrometer, it provides a ready check of the operation of the gun.

* This work is supported by the U.S. Department of Energy, Office of Basic Energy Sciences, under Contract No. W-31-109-ENG-38.

† Lewellen@aps.anl.gov

PRINCIPLES OF OPERATION

Beams from thermionic-cathode rf guns typically suffer the disadvantage of very large energy spreads [3]. Even given that charge is concentrated at the head of the bunch, typically no more than 10 – 20% of the beam charge is within a 1% FWFM energy spread. Figure 1 shows the simulated momentum spectrum of the BBC gun running in π-mode, thereby mimicking the operation of a conventional thermionic-cathode rf gun.

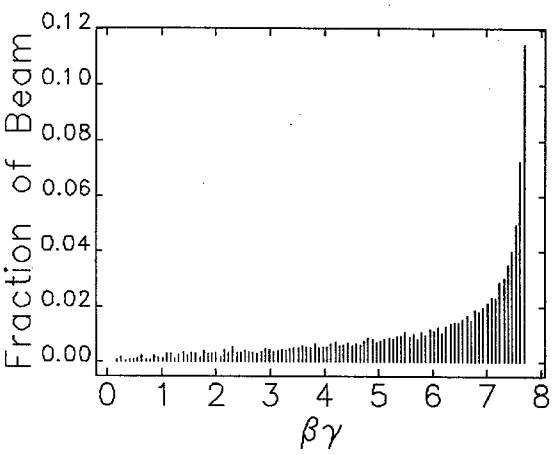


Figure 1: Momentum spectrum of BBC gun operating in π-mode. Bin widths are 1% of the maximum momentum.

A somewhat greater fraction of the bunch charge can be moved into the uppermost 1% of beam energy by increasing the gradient in the gun, specifically the cathode cell. This is not an especially desirable mode of operation for several reasons, including the possibility of gun damage and the requirement for running at relatively high beam energies.

The ballistic compression gun offers an alternative mode of operation. By appropriate selection of the gradient and phase in the full cells, a much greater amount of the beam charge can be compressed into the uppermost 1% beam energy. This method has been proposed before [4] but not yet physically demonstrated.

One-Dimensional Model System

The model system for energy compression consists of a thermionic-cathode source in a cathode cell, followed by full cells. The length of the full cells is taken to be ½ of the free-space wavelength corresponding to the resonant frequency of the gun–in other words, a typical gun design.

0-7803-7738-9/03/$17.00 © 2003 IEEE

To a reasonable approximation, the energy of the beam as a function of the time it exits the cathode cell can be represented by a quadratic equation, i.e.,

$$P_0(t) = a + b \cdot t + d \cdot t^2, \quad (1)$$

where $P_0(t)$ is the normalized momentum ($\beta\gamma$) as a function of time; t extends over a range of typically -20/+40 ps; and a, b, and d are constants depending on the particular gun in question. For the BBC gun with a typical gradient of 50 MV/m in the cathode cell, a = 1.529, b = $-1.68 \cdot 10^{10}$ sec^{-1}, and d = $-5.95 \cdot 10^{19}$ sec^{-2}.

The beam is, at the exit of the cathode cell, not fully relativistic and has a large velocity spread as well as a large energy spread. Treating the full cells as true pillbox cavities and ignoring the change in particle velocity while within the cell, the normalized momentum at the end of the nth full cell can be approximated as

$$P_n(t_i) = P_{n-1}(t_i) + \Delta P_n \cdot \cos\left(\pi \frac{\sqrt{1 + P_{n-1}^2(t_i)}}{P_{n-1}(t_i)} + \omega t_i + \phi_n \right), \quad (2)$$

where t_i is the time the ith particle leaves the cathode cell, ΔP_n is the maximum momentum gain through the nth full cell for a relativistic particle, ω is the angular frequency of the cavity, and ϕ_n is the phase of the field in the nth cavity. Finally, a weighting function $\rho(t_i)$ can be defined as the normalized longitudinal charge density at the exit of the cathode cell. This explicitly takes into account the bunching that naturally occurs in the cathode cell of most rf guns; in effect, it places more emphasis upon the head of the bunch.

Figure 2 shows the momentum at the exit of the cathode and full cells as a function of cathode cell exit time relative to a reference particle, generated using Eqs. (1) and (2). For this plot, $\omega = 2\pi \cdot 2856$ MHz, ΔP_1 = 1.9, ΔP_2 = 3.0, ϕ_1 = 230 deg, and ϕ_2 = 135 deg. The weighting function $\rho(t_i)$ is shown in Figure 3 and was derived from a simulation of the beam at the exit of the BBC gun cathode cell. In this calculation, 46% of the beam was within 1% of the maximum beam momentum.

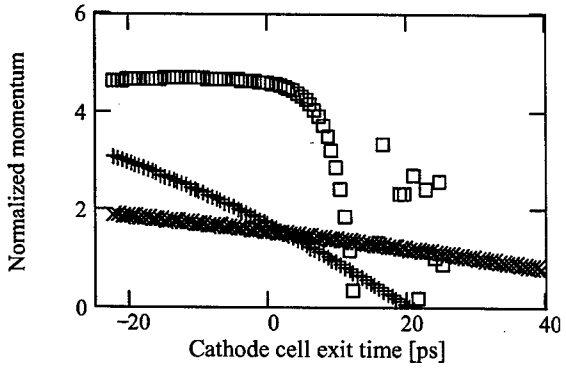


Figure 2: Momentum spectra at the exit of the cathode cell ("X"), first full cell ("+"), and second full cell ("□").

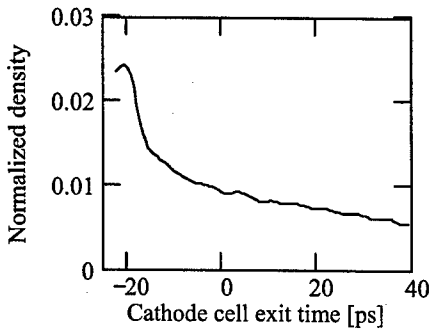


Figure 3: Normalized longitudinal beam density at the exit of the cathode cell. The exit time is relative to the PARMELA reference particle exit time.

THREE-DIMENSIONAL SIMULATION

The computer code PARMELA [5] was used to simulate the energy-compression process using the actual BBC gun field profiles, assuming a 3-mm-radius thermionic cathode and small bunch charge (e.g., the built-in space-charge routines were not used).

A downhill simplex optimizer was used to automatically vary the phase and field gradient in the full cells; the number of beam particles within 1% of the peak beam energy served as the figure-of-merit for the optimization process.

The optimized beam momentum spectrum is shown in Figure 4. Approximately 96% of the particles are within 1% of the maximum momentum, and the great majority of the beam is within the top 3%. (Compare this result to Figure 1, the same gun running in a π-mode.) Figure 5 shows the longitudinal phase space at the exit of the BBC gun for π-mode and ballistic compression as well as energy compression settings.

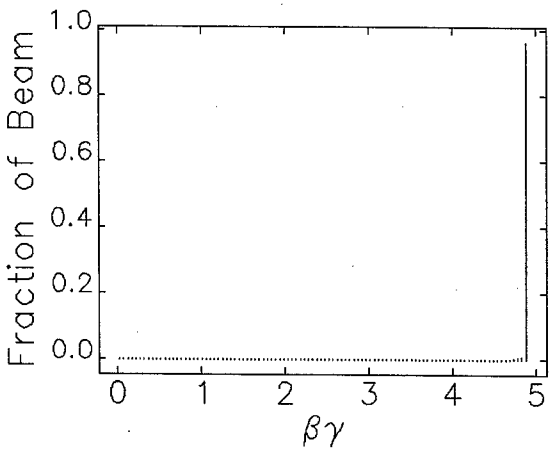


Figure 4: Momentum spectrum of the BBC gun operating in energy-compression mode. Bin widths are 1% of the maximum momentum.

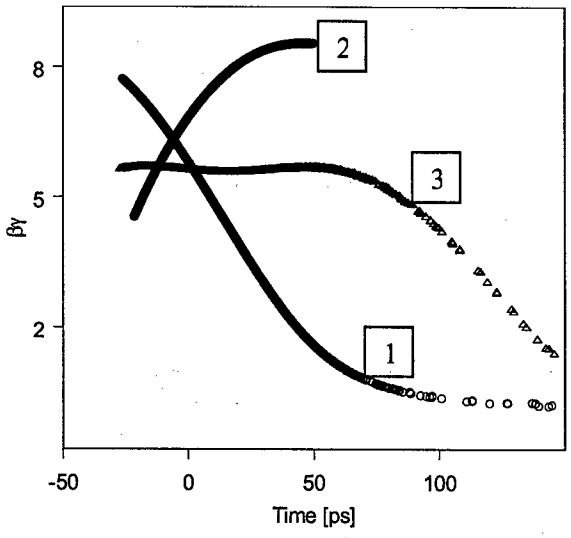


Figure 5: Longitudinal phase space for various operating modes. π-mode is Curve 1, ballistic compression is Curve 2, and energy compression is Curve 3.

The maximum beam energy in the simulation is somewhat lower than for the π-mode; this is an expected result, as one can think of the gradient in the full cells being used more to rotate the longitudinal phase space than to raise its mean value. The simulation's much better result, as compared to the analytic expression, is due to several factors. First, there are fewer approximations made in terms of the particle transport through the full cells. Second, the simulation is a 3-d calculation, and particles with very low beam energies tend to be lost on walls or cell nosecones. This has the result of automatically winnowing some low-energy particles from the beam before they can exit the gun and be included in the analysis. If the lost particles are also counted, the result is in better agreement with the analytic calculation.

The calculated transverse normalized emittance for this simulated beam, excluding particles outside of a 1% FWFM energy window and including only particles which exit the gun, was 35 μm. While not a spectacular emittance, in itself this would be a suitable beam for devices with modest emittance requirements, such as far-infrared free-electron lasers [6]. If the beam is divided longitudinally into 10-ps-long slices, the leading three slices–all consisting of particles within a 1% FWFM momentum spread–contain 66% of the beam and have an average emittance of about 1.5 μm. The emittance grows towards the tail of the beam, where the particle density becomes much lower and the energy spread begins to increase.

RESULTS AND DISCUSSION

Both the one-dimensional analytic approximation and the three-dimensional simulation demonstrate that the APS ballistic compression rf gun can operate in an energy-compression mode, generating a beam with very low energy spread from a thermionic cathode. Operating in such a mode will verify the basic beam dynamics of the gun via an easily measured quantity, the fraction of the beam charge within a small energy spread. This will prove to be an important step towards operation of the gun in the ballistic-compression mode.

The projected emittance of the low-energy-spread beam as a whole indicates that the gun should be suitable as the sole-source driver for devices such as far-infrared free-electron lasers, which often have modest beam quality and energy requirements. The slice emittance at the head of the beam is considerably better than the projected whole-beam emittance.

ACKNOWLEDGEMENTS

The author wishes to thank John Schmerge (SLAC/SSRL), John Power (ANL/AWA), and Stephen Milton (ANL/XFD) for various discussions and ideas. This work is dedicated to the memory of Kevin Beczek.

REFERENCES

[1] J.W. Lewellen and S.V. Milton, "Preliminary Calculations of Ballistic Bunch Compression with Thermionic Cathode RF Guns," Proc. SPIE – Int. Soc. Opt. Eng (Coherent Electron Beam X-Ray Sources: Techniques and Applications), Vol. 3154, pp. 162-171 (1997).

[2] J.W. Lewellen et al., "The Advanced Photon Source Injector Test Stand," Proceedings of the 2001 Particle Accelerator Conference, pp. 2212-2214 (2001).

[3] J.W. Lewellen et al., "A Hot-Spare Injector for the APS Linac," Proceedings of the 1999 Particle Accelerator Conference, Vol. 3, pp. 1979-1981 (1999).

[4] J.W. Lewellen, Ph.D. Thesis, Stanford University, 1997.

[5] J.H. Billen and L. Young, "Poisson Superfish," Los Alamos document LA-UR-96-1834 (user's guide for Version 6).

[6] J.F. Schmerge, Ph.D. Thesis, Stanford University, 1996.

A FLEXIBLE INJECTOR TEST STAND DESIGN*

J.W. Lewellen† K. Beczek, S. Berg, D.A. Briddick, R. Dortwegt, M. Givens, A. Grelick, A. Nassiri, S. Pasky, T.L. Smith
Argonne National Laboratory, Argonne, IL 60439, USA

Abstract

The Advanced Photon Source (APS) has constructed an injector test stand (ITS) for high-brightness electron beam research. The test stand includes three rf ports with independent phase and power control, beamline supports designed for rapid reconfiguration, and a control and diagnostics system based on the design of the APS linac. The beamline design features a high-resolution electron spectrometer that includes provision for operation as a dispersion-free dogleg, and a rapidly reconfigurable gun-to-spectrometer transport line. Picosecond and nanosecond photocathode drive lasers are available; the room shielding is also adequate for the high average beam powers typically produced by thermionic-cathode rf guns.

The initially installed gun is a ballistic-compression gun, which requires all three rf ports to be connected to the gun. Plans include the installation of a higher-order mode photoinjector, requiring one rf connection; this will free the other ports to provide power to a small TW linac section and deflector cavity for bunch-length measurements. The test stand is also capable of being used as an operator training facility, and serves as a validation facility and test bed for the APS main injector rf guns.

INTRODUCTION

Rf electron guns, in various forms, are key elements of many current and projected accelerators. Typically, rf guns are split into two distinct categories: those using thermionic cathodes to generate electrons and those using photocathodes. The choice of cathode and other design features such as the number of cavities in the gun, cavity coupling schemes, and cavity interior geometry, is heavily influenced by the task the gun is designed to address.

Photocathode rf guns use an external drive laser to cause electrons to be emitted from the photocathode. This type of gun is generally selected for tasks requiring high-brightness beams, single-bunch or widely-spaced bunch operation, and relatively high charge per bunch. Although there are exceptions, these guns are typically used for experimental purposes, as distinguished from "operational" systems; this is often due to the maintenance issues frequently associated with the drive laser and photocathode.

Thermionic-cathode rf guns use a heater to generate thermal electron emission from the cathode surface. This type of gun produces beam as long as rf is applied to the cavity, and can generate very high average beam currents. This is usually the gun type of choice when high-charge, single-bunch operation is not important, and when beams of only moderate transverse brightness are required. Due to their high reliability and simplicity of operation, they are often chosen for "operational" roles such as beam sources for electron storage rings; this type of gun has also been used for long-wavelength free-electron laser experiments.

The APS presently has installed two thermionic-cathode guns to serve as sources for filling the storage ring and one photocathode gun to serve as the beam source for a single-pass FEL experiment and nascent user program. Thus, we have a need for an injector test and repair facility that can accommodate both types of injectors in use at the APS. In addition, the APS injector test stand is intended to facilitate the testing of new injector designs, to provide for an operational test bed for new diagnostics or hardware intended for installation in the APS injector complex, and to act as a training facility for accelerator operators when the storage ring is running in top-up mode.

PRESENT CONFIGURATION

The APS ITS is effectively an independent accelerator enclosure from the rest of the APS, in terms of personnel access and beam permit. Rf power can be delivered to the room as long as the APS linac rf system is enabled.

A ballistic bunch compression (BBC) rf gun is presently installed in the ITS. This gun generated first beam, using a thermionic cathode, on 11 March 2003. The rf power feed system provides independently phased high-power rf to the three independent ports on the BBC gun and is more fully described in [1]. The waveguide network was specifically designed for the BBC gun, but can also be used to power up to three independent rf elements, e.g., a gun, small linac section, and transverse deflection cavity.

The beamline, shown in Figure 1, includes a branch line that can be operated as either a dispersion-controlled dogleg or a spectrometer with a dispersion of 0.5 m. The beamline downstream of the second dogleg dipole is intended for use as a low-energy experimental area. Diagnostics include current monitor toroids, Faraday cup / viewscreen monitors, a dipole field Hall probe, and energy slits in the dispersive beamline. These are commissioning diagnostics and are appropriate for an exploration of the BBC gun operation in energy-compression mode [2]. Other diagnostics, for example an emittance-measurement pepperpot screen or a Golay cell-based bunch length monitor, will be installed as required by the experimental program.

The picosecond drive laser for the APS photoinjector is located adjacent to the ITS enclosure. The optical trans-

* This work is supported by the U.S. Department of Energy, Office of Basic Energy Sciences, under Contract No. W-31-109-ENG-38.
† Lewellen@aps.anl.gov

0-7803-7738-9/03/$17.00 © 2003 IEEE

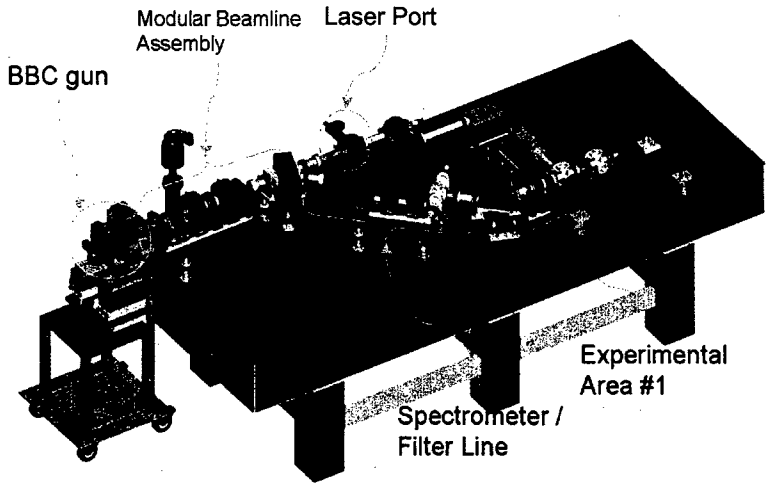


Figure 1: Present layout of the APS injector test stand; the waveguide network is omitted for clarity.

port path to the ITS was removed to facilitate the waveguide installation, but will be restored shortly. In addition, a nanosecond drive laser has been purchased and will shortly be installed in the ITS. An optical switchyard will allow either laser to be used with an installed gun.

All of the quadrupole and corrector power supplies are on quick-disconnect assemblies. This allows the beamline to be rapidly reconfigured or a malfunctioning magnet or power supply to be replaced. The rail support system is modular also; more details can be found in [3]. The entire beamline is built on a standard 1m × 3m optical table, allowing the rapid addition of either beamline or diagnostic elements.

Finally, the ITS control system uses the same architecture as the rest of the APS. This not only allows the ready use of the entire APS data acquisition and control toolkit, but also allows the room to be used for prototyping new hardware and software before general deployment throughout the APS.

A more thorough discussion of the development history of the ITS and the methods and techniques used in its construction may be found in [4].

INITIAL OPERATION

The BBC gun generated its first beam on 11 March 2003, following conditioning of the waveguide network into high-power loads. The initial operation revealed some interesting and unexpected behaviors of the gun, not surprising in a brand-new gun; subsequent efforts have been focused on improving the performance of the gun and waveguide network.

FUTURE PLANS

Short- and Mid-Term

In the immediate future, the experimental program will focus on four topics: ballistic bunch compression, energy compression, operation of the long-pulse drive laser as an injector gate, and DC/rf photoinjector studies [5].

In the ballistic bunch compression process, the longitudinal phase space of a moderate-energy electron beam is prepared such that the beam will self-compress in the field-free drift region between the exit of the beam source and the entrance of a linear accelerator [6]. As the compression is accomplished without magnetic elements, the beam is not subject to effects such as coherent synchrotron radiation [7]. The APS BBC gun will permit the exploration of the ballistic compression process with both thermionic and photocathodes.

Thermionic-cathode rf guns can serve as the sole accelerators for such devices as compact, far-infrared free-electron lasers [8]. The large energy spread produced by typical guns of this type, however, requires the use of an energy filter and results in much of the beam charge being discarded. By suitable manipulation of the longitudinal phase space, however, the energy spread can be dramatically reduced [2]. This has the effects of simplifying the beamline design as well as improving overall efficiency. The APS BBC gun is suitable for exploring this concept also.

One future requirement for the APS injector complex is the ability of the linac to generate shorter bunch trains at higher total charge levels, in support of enhanced top-up operation, and to reduce the requirement for a low-energy damping / accumulator ring. The use of a nanosecond Q-switched drive laser offers a promising method of gating the beam from a thermionic-cathode rf gun. The APS BBC gun, operating in a π-mode, can mimic the operation of the main injector rf guns. This will allow a thorough exploration and characterization of this technique before installation in the linac tunnel. This is not a physics experiment per se, rather, it is leveraging the use of the ITS as a benefit to APS operations in general.

Future Topics and Possibilities

Longer-term plans include the addition of a 1.6-m, SLAC-type, traveling-wave constant-gradient linac section; fabrication and testing of a higher-order-mode photoinjector; photocathode research; and emittance evolution studies. Also, the ITS will serve as a development platform for long-wavelength radiation production, characterization, and use as a measurement tool. Depending on the desired mode of operation, this may use an energy-compressed beam to drive a compact free-electron

laser or a time-compressed beam to generate a broadband pulse via a wiggler or dipole.

The ITS will also start to function as an operator training facility on a more regular basis, as well as providing a means of testing new components with beam. These tasks, while not specifically experimental in nature, will provide a needed service to the operation of the APS and will help to involve more of the APS Operations staff in injector research and development.

Finally, proposed changes in the APS storage ring injector complex will require a significant redesign of the linac electron gun region. The ITS will allow the prototyping and characterization of proposed changes in a timely fashion, with no risk to the operation of the APS linac.

CONCLUSIONS AND SUMMARY

The Advanced Photon Source injector test stand is currently undergoing commissioning. The initial series of experiments will capitalize on the ITS to study topics relating to APS performance enhancement as well as fundamental injector physics. Future upgrades, including the addition of a capture linac section, will significantly increase the range of capabilities of the ITS. Finally, the ITS will also provide service as a training facility for APS accelerator operators and as a means for increasing the involvement of Operations staff in ongoing accelerator physics research projects.

ACKNOWLEDGEMENTS

Many people have contributed to the design, construction and initial operation of the APS injector test stand. Special thanks go to John Schmerge, David Dowell, John Power, Stephen Milton, Wayne Michalek, Aaron Lopez, and William Yoder for their suggestions, thoughts, and efforts.

REFERENCES

[1] A.E. Grelick et al., "The high-power S-band feed subsystem for the Advanced Photon Source injector test stand," Proceedings of the 2001 Particle Accelerator Conference, Chicago, IL pp. 1393-1395 (2001).

[2] J.W. Lewellen, "Energy spread compensation of a thermionic-cathode rf gun," these proceedings.

[3] K. Beczek and J.W. Lewellen, "A Versatile Method of Beamline Construction," Proceedings of the 2001 Particle Accelerator Conference, Chicago, IL, pp. 1462-1464 (2001).

[4] S. Berg et al., "The Advanced Photon Source Injector Test Area," these proceedings.

[5] D. Yu et al., "Design of a DC/rf Photoelectron Gun," these proceedings.

[6] J.W. Lewellen and S.V. Milton, "Preliminary Calculations of Ballistic Bunch Compression with Thermionic Cathode rf Guns," Proc. SPIE – Int. Soc. Opt. Eng (Coherent Electron Beam X-Ray Sources: Techniques and Applications), Vol. 3154, pp. 162-171 (1997).

[7] A good starting point for obtaining information on coherent synchrotron radiation is the Web site for the 2002 CSR Workshop held at DESY-Zeuthen, http://www.desy.de/csr/.

[8] J.F. Schmerge et al., "The free-electron laser as a laboratory instrument," IEEE Journal of Quantum Electronics, Vol. 31, no. 6, pp. 1166-71 (1995).

ULTRASHORT ELECTRON BUNCHES WITH LOW LONGITUDINAL EMITTANCE IN MULTI-CELL SUPERCONDUCTING RF GUNS

V.N.Volkov, Budker Institute of Nuclear Physics, Russia

Abstract

Ultra short bunches with low longitudinal emittance obtained using multi-cell superconducting RF gun having a longitudinally shorted first cell (down to 0.15 lambda) with a divergence of an accelerating RF field pattern near the photocathode are discussed. The optimised RF gun parameters and bunch characteristics computed by PARMELA are presented. Such 10 MeV ultra short electron bunches with low longitudinal emittance compatible for additional longitudinal compression scheme having RF buncher cavity and drift space or magnetic chicane downstream of them [1].

This work was financially supported by Forschungs Zentrum of Rossendorf.

INTRODUCTION

Recently we have found out an unique opportunity of superconducting multi-cell RF guns shown in figure 1 to produce electron bunches with very small transversal emittance [2, 3]. This relies on transversal focusing configuration of RF electric field pattern constructed near the photocathode by spherical surface of the cathode stem tip and displacements of it into the back wall of first cell as shown in figure 2a.

There is still other unique ability of such RF guns to produce ultra short electron bunches with very small longitudinal emittance. This relies on inverse of the first configuration of a field with defocusing or divergence of RF electric field pattern near the cathode (as shown in figure 2b) and significantly shorted length of the first cell.

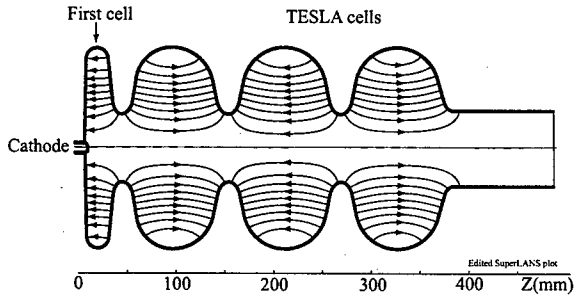


Figure 1. The geometry of superconducting RF gun cavity for producing of ultra short bunches with small longitudinal emittance or bunches with small transversal emittance.

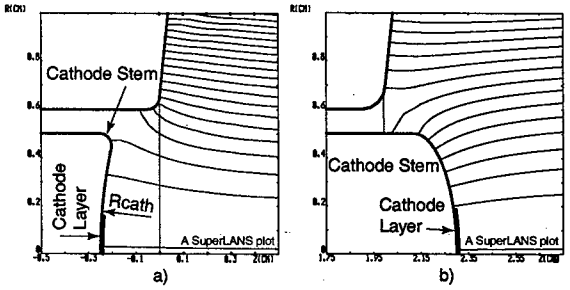


Figure 2. Configuration of part of RF gun geometry near the cathode producing RF electric field pattern with two different operations: a) to produce a bunch with small transversal emittance; b) to produce ultra short bunch with small longitudinal emittance.

BASIC

The effect of bunch compression in a multi-cell superconducting RF gun was described in [4]. A short electron bunch injected from laser driven photocathode is being accelerated by the electric field in the first cell and then enters to the second cell. The RF field in the second cell at that instant has a negative strength and change the sign later because of very short accelerating gap of first cell. Therefore the bunch at the beginning of the second cell decelerates and then accelerates again in the second cell and then only accelerates in the other cells. The head of the bunch enters to the second cell earlier when strength of electric RF field is more negative. Therefore the bunch head accelerates less than the tail and exposes to longer delay. I.e. compressing effect lies on phase-dependent delay of particles. The electron bunches in this compression method obtain a very low energy spread and low longitudinal emittance.

We have to note the phase-dependent delay play an important role to obtain the low longitudinal emittance of a bunch also. The particles launched from centre of the cathode enter to the second cell earlier than those launched from periphery of the cathode because of divergence of RF electric field pattern (defocusing) near the cathode. Therefore the periphery trajectories of the particles are directed under some angle to the axis and have therefore more length. The periphery particles have obtained more energy in second cell but the central particles have obtained more energy in the other cells because the RF electric field is greater at the axis (more strongly it occurs in a beam pipe of a final cell). As a result all the particles from centre and periphery obtained the same accelerating energy downstream of the cavity. This fact is the cause of low longitudinal emittance of bunches.

0-7803-7738-9/03/$17.00 © 2003 IEEE

SIMULATIONS

Incoming data

The energy gain in 3.3* RF gun cavity is 25 MV/m. The laser pulse length (FWHM) is 3 ps. Laser time intensity was modeled by a Gaussian distribution. We have found the minimal value of bunch length at a distance of 400 mm from exit of the cavity. Bunch charge: 1 pC, 10 pC and 100 pC. The RF field in RF gun cavity has calculated by SuperLANS cod. Bunch dynamic has computed by PARMELA for 10000 particles.

Optimizing of the launch RF phase and the laser spot size to minimize bunch length

The spline interpolated results for bunch length with charge of 1, 10, 100 pC are shown in figures 3, 4 and 5.

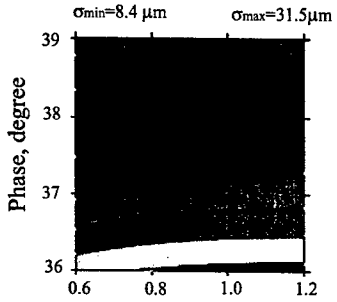


Figure 3. The bunch length as dependence of launch RF phase and laser spot size for bunch charge of 1 pC (spline interpolated data). The optimal RF phase is 38.288° and optimal spot size is 0.734393 mm. The minimal bunch length is σ_{L1} = 8.3952 μm.

$$\sigma_{L1}\,[\eta m] = 8.395 + 17.483798 \cdot \delta D^2 + 8.4371 \cdot \delta\varphi inj^2 - \\ - 9.292102 \cdot \delta D \cdot \delta\varphi inj$$

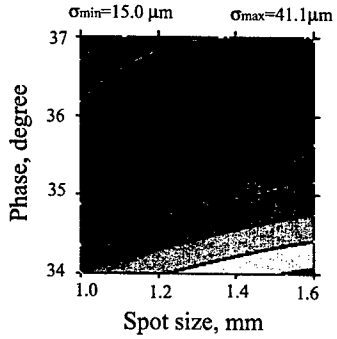


Figure 4. The bunch length as dependence of launch RF phase and laser spot size for bunch charge of 10 pC (spline interpolated data). The optimal RF phase is 36.448° and optimal spot size is 1.35 mm. The minimal bunch length is σ_{L10} = 15.013 μm.

$$\sigma_{L10}\,[\eta m] = 15.013 + 37.928679 \cdot \delta D^2 + 7.449166 \cdot \delta\varphi inj^2 \\ -14.319715 \cdot \delta D \cdot \delta\varphi inj$$

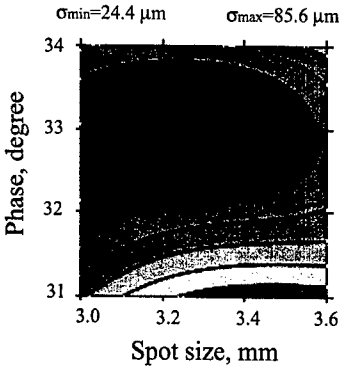


Figure 5. The bunch length as dependence of launch RF phase and laser spot size for bunch charge of 1 pC (spline interpolated data). The optimal RF phase is 33.281° and optimal spot size is 3.251 mm. The minimal bunch length is σ_{L100} = 24.373 μm.

$$\sigma_{L100}\,[\eta m] = 24.37 + 109.2551 \cdot \delta D^2 + 21.173782 \cdot \delta\varphi_{inj}{}^2 - \\ -12.26148 \cdot \delta D \cdot \delta\varphi_{inj}$$

The minimal bunch length and optimal injection phase and optimal laser spot size for three different bunches are shown in table 2.

Table 2. The minimal bunch length and optimal pair of launch phase and laser spot size.

Bunch charge, pC	1	10	100
Launch phase, deg.	38.28	36.44	33.28
Laser spot size, mm	0.734	1.350	3.250
Minimal bunch length (rms), μm	8.39	15.01	24.37

Dynamic results

In the table 3 bunch characteristics computed by PARMELA are shown.

Table 3. The bunch dynamics characteristics.

Charge, pC	1	10	100
Bunch rms length, μm	8.39	15.01	24.37
Bunch energy, MeV	6.16	6.13	6.12
Energy spread, %	0.225	0.207	0.36
Longitudinal rms emittance, KeV·mm	0.11	0.189	0.54
Transv. norm. emittance (rms), mm·mrad	0.184	0.644	6.51

* The whole part of this numerical designation displays an amount of complete (unit) cells in RF gun cavity, and fractional (.3) testifies that length of the first short cell makes 30 % from complete length.

Minimum of longitudinal emittance

There are a minimum of bunch longitudinal emittance at other optimal pairs of injection phase and laser spot size shown in table 4. But this pair is close to the previous one.

Table 4. The minimal bunch longitudinal emittance at optimal pair of launch phase and laser spot size.

Q, pC	1	10	100
$\varepsilon_{\parallel}$[KeVmm]	0.105	0.16	0.364
$\varphi_{inj\text{-}opt}$, deg.	39.25°	34.25°	32.23°
D_{opt}, mm	0.6	1.6	2.82

REFERENCES

[1] V.Volkov, D.Janssen. Generation of sub-picoseconds electron bunches in superconducting RF photocathode injector (these conference).

[2] D.Janssen, V.Volkov, RF focussing – an instrument for beam quality improvement in superconducting RF guns, Nucl. Instr. And Meth. In Phis. Res. A452 (2000) 34-43.

[3] RF Focussing - an Instrument for Beam Quality Improvement in Superconducting RF Guns, V.Volkov,D.Janssen, 7th European Particle Accelerator Conference, Austria Centre Vienna, June 2000, p.2055-2057.

[4] Generation of sub-picoseconds electron bunches from superconducting 5.3 cell rf gun and coherent wiggler radiation, V.N.Volkov, D.Janssen, PAC2001, June 18-22, 2001, Chicago, Illinois, USA.

[5] X.J.Wang, I.Ben-Zvi, *Longitudinal emittance compensation in a photocathode rf gun injector*, PAC97, 1997, 2793-2795.

[6] L.Serafini, R.Zhang, C.Pelegrini, *Generation of sub-picosecond electron bunches from RF photo injectors*, Nucl. Instr. And Meth. In Phis. Res. A387 (1997) 305-314.

[7] K.J.Kim, *RF and Space-Charge Effects in Laser-driven RF Electron Guns*. Nucl. Instr. And Meth. In Phis. Res. A275 (1989) 206.

GENERATION OF SUB-PICOSECOND ELECTRON BUNCHES IN SUPERCONDUCTING RF PHOTOCATHODE INJECTOR

V.N.Volkov, Budker Institute of Nuclear Physics, Russia

Abstract

A multi-cell superconducting photocathode laser driven RF gun having a longitudinally shorted first cell (the length of the first cell is 0.15 lambda instead of 0.25 lambda) can generate shorted electron bunches with very low longitudinal emittance [1]. These bunches could be considerably longitudinally compressed by additional compressing scheme having a buncher cavity and drift space after them or four dipole achromatic chicane placed just after the buncher cavity. The first scheme with drift space is longer on two meters but has appreciably better effectiveness to compress a bunch. The buncher is composed from 3900 MHz multi-cell TESLA like cavity. Chicane has a modernised geometry to compensate transversal emittance dilution of a bunch. Bunch dynamic calculations in two such compressing schemes (optimized at 10 MeV of bunch energy) show that a bunch rms length down to 7 micrometers (0.02 picoseconds, the laser pulse FWHM duration is 2.5 picoseconds) with a peak current of 1500 A can be reached. The optimised characteristics of two compressing schemes with two different RF injectors (with 3.3 and 5.3 cells) are presented.

This work was financially supported by Forschungs Zentrum of Rossendorf

INTRODUCTION

Development of a simple and reliable source of short electron bunches is an essential problem. Short electron bunches of a sub-picosecond length may be used in free electron lasers for obtaining the light spontaneous radiation with very short wave length (from crystalline undulator for example) and high radiation power because of CW operation of superconducting RF injector.

There are very important for longitudinal compressing initially to have a short electron bunches with low longitudinal emittance. Such bunches may be obtained in multi-cell superconducting RF gun having a very short first cell with convex photocathode attractive on itself electric field pattern. The phase-dependent delay in such RF gun plays an establishing role in forming short bunches with low longitudinal emittance [1, 2].

Two compressing scheme having TESLA like buncher multi-cell superconducting cavity with 3900 MHz frequency are used in dynamic calculations: first - with drift space up to distance of 5 meters from the cathode, and four dipole achromatic chicane placed just after the buncher cavity – second one.

Though the first scheme with drift space is much easier and more cheaply, and besides is more effective than second one (it gives 7 microsecond bunch length instead of 9), however second one was optimized with all carefulness, as in a sequence of time it was first and, as then it seemed, unique. Therefore it seems it is useful to show these calculations too.

SUPERCONDUCTING RF GUN

To perform the simulations we used two different variants of RF gun – with 3.3* and 5.3 cells [1] shown in figure 1 and 2. The energy gain is: 25 MeV/m with 6.14 Mev of bunch energy in first variant and 20 MeV/m and 9.77 MeV in second one. Electron beam downstream RF gun has a divergence of 0.8 and 0.6 mrad/mm correspondingly. Both variants have given approximately identical results of bunch characteristics downstream of the drift space (see table 3).

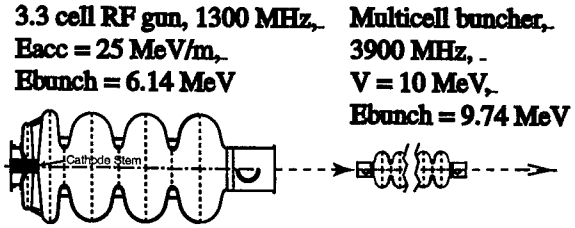


Figure1: The variant of first compressing scheme having a higher accelerating gradient E_{acc} of 3.3 cell RF gun and buncher with acceleration of bunch energy up to 9.74 MeV.

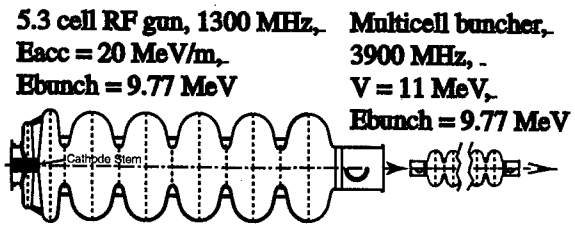


Figure 2: The variant of first compressing scheme having a lower accelerating gradient E_{acc} of 5.3 cell RF gun and unaccelerating buncher (V – cavity RF acc. voltage).

BUNCHER

The buncher in these compressing schemes plays a double role. The basic one is increase of an energy spread of a linear bunch energy distribution (energy of particles linearly increases lengthways on the bunch from its head

* The whole part of this numerical designation displays an amount of complete (unit) cells in RF gun cavity, and fractional (.3) testifies that length of the first short cell makes 30 % from complete length.

0-7803-7738-9/03/$17.00 © 2003 IEEE

to a tail). To reduce the drift space length, it is necessary to increase the energy spread at the expense of increase of cavity voltage. Other important role of buncher cavity is to compensate divergence of electron beam so that all trajectories of particles downstream of the cavity were parallel to an axis. There is transverse focusing action in the multi-cell cavity, and to the compensation of divergence of 0.6 or 0.8 mrad/mm of incoming electron beam about 10 MV cavity RF voltages is required.

To perform the simulations we used the geometry of TESLA 1300 MHz cavity scaled as 3:1 for the buncher 3900 MHz cavity. The number of cells in such cavity can be more than 9 to reduce RF field amplitude in the cavity because RF power almost is not transmitted in a beam. The dynamic calculations with number of cells 9, 11 and 13 have shown the same results. Peak RF electric field at the axis of the cavity with 9, 11, 13 cells are correspondingly 55, 45, 38 MV/m.

Our choice of 3900 MHz was essentially motivated by the fact that at lower frequency the intensity of transverse focusing effect will be higher therefore cavity voltage will less to compensate beam divergence, and drift space length will become inadmissible large.

RESULTS

To obtain the shortest electron bunch in compressing scheme the effect of following parameters to this length was studied: laser spot size, launch RF phase (or laser jitter), laser pulse duration, RF voltage and RF phase of buncher cavity. In figure 3 the example of optimization of together laser spot size and launch RF phase for scheme of figure 2 is shown. Dynamic calculations launched 16 times for 4 different values of each parameter, and then spline interpolation of the results is made to find the optimum. The optimized parameters of compressing schemes of figure 1 and figure 2 together and their bunch characteristics are presented in tables 1, 2, 3.

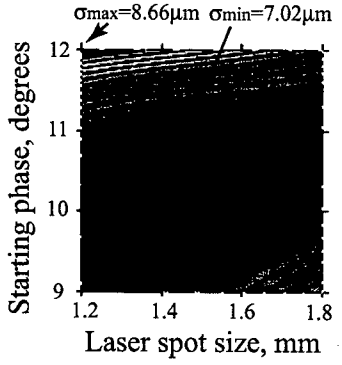


Figure 3: The spline interpolated results of 16 calculations of rms bunch length (σ) for the scheme of figure 2.

The sensitivity of rms bunch length to main parameters of figure 2 scheme can be written as follows:

$$\sigma\,[\mu m] = 7.02 + 2.94\cdot\Delta\sigma_L^2\,[mm] + 0.31\cdot\Delta\varphi_L^2\,[^\circ] - 0.68\cdot\Delta\sigma_L\cdot\Delta\varphi_L + 8.08\cdot\Delta V^2\,[MeV] + 4.59\cdot\Delta\Phi^2\,[^\circ] + 9.13\cdot\Delta V\cdot\Delta\Phi$$

Where σ – rms bunch length, μm; σ_L – laser spot size, mm; φ_L – Launch RF phase, degree; V – buncher cavity voltage, MV; Φ – operation RF phase of buncher cavity.

Table1: The optimized parameters of the compressing schemes.

Injector	Fig.1	Fig.2
Acceleration gradient in RF gun, MeV/m	25	20
Launch RF phase, degree	37.0	11.09
Laser spot size, mm	1.0	1.72
Laser pulse duration (FWHM), ps	3.0	5.6
RF voltage of buncher cavity, MV	10.11	10.77
RF phase of buncher cavity, degree	17.18	0.0
Target distance from cathode, m	5.1	5.04

Table 2: Bunch characteristics downstream of RF gun.

Injector	Fig.1	Fig.2
Bunch charge, pC	50	50
Bunch rms length, μm	131.0	173.4
Bunch energy, MeV	6.14	9.76
Energy spread, %	0.56	0.46
Longitudinal rms emittance, KeV·mm	0.663	0.843
Transversal normalized emittance (rms), mm·mrad	1.13	1.34
Beam divergence, mrad/mm	0.797	0.595

Table 3: Bunch characteristics at target distance.

Injector	Fig.1	Fig.2
Bunch rms length, μm	6.28	7.02
Max. bunch radius, mm	7.14	7.93
Bunch energy, MeV	9.74	9.77
Energy spread, %	1.05	1.70
Longitudinal rms emittance, KeV·mm	0.645	1.169
Transversal normalized emittance (rms), mm·mrad	2.43	3.97
Peak current, A	1445	1266

CHICANE SCHEME

In this compressing scheme a four dipole achromatic chicane is placed just after the buncher cavity. The sketch of the chicane geometry is shown in figure 4.

The elements of the geometry specified in the figure play the following role for optimization:

- By curvature radiuses of extreme dipole magnets (R1, R2) the transverse emittance dilution has compensated.
- By curvature radiuses of the central magnet tips (R) a curvature of a bunch front in horizontal and in a vertical plane has leveled.
- By inclination (β1) of the first dipole magnet tip the convexity of a bunch front has corrected.
- By inclination (β2) of the second dipole magnet tip the convergence dilution in a horizontal plane of a beam has compensated.

The optimized values of geometry elements are presented in table 4.

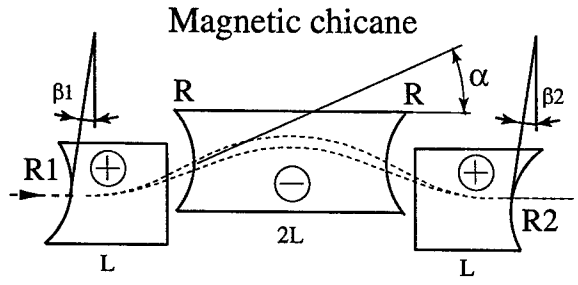


Figure 4: Sketch of magnetic chicane geometry. The fringe magnetic field taken in account in the simulation.

Table 4: The optimized elements of chicane geometry.

α	L	β1, β2	R1, R2	R
4.97°	250 mm	9°	200 mm	207 mm

The bunch characteristics computed by PARMELA for 10000 particles has shown in table 5.

Table 5: The bunch characteristics of magnetic chicane scheme.

The bunch downstream of...	Fig.2 gun	Chicane
Bunch rms length, μm	111.6	8.425
Max. bunch radius, mm	7.2	8.1
Bunch energy, MeV	9.72	9.305
Energy spread, %	0.319	1.224
Longitudinal rms emittance, KeV·mm	0.78	0.96
Transversal normalized emittance (rms), mm·mrad	1.41	4.1

REFERENCES

[1] V.N.Volkov, D. Janssen" Ultra short electron bunches with low longitudinal emittance in a multi-cell superconducting RF guns ," these conference.

[2] Generation of sub-picoseconds electron bunches from superconducting 5.3 cell rf gun and coherent wiggler radiation, V.N.Volkov, D.Janssen, PAC2001, June 18-22, 2001, Chicago, Illinois, USA.

TESTS OF NIOBIUM CATHODE FOR THE SUPERCONDUCTING RADIO FREQUENCY GUN

Qiang Zhao, Triveni Srinivasan-Rao, BNL, Upton, NY 11973, USA
Mike Cole, Advanced Energy Systems, Medford, NY 11763, USA

Abstract

For the superconducting all-niobium photocathode radio frequency gun project, we have studied the surface preparation techniques of the niobium cathode material. The quantum efficiency (QE) of high purity niobium (RRR=250) has been intensively measured at room temperature on a dedicated DC system. After buffer chemical polishing or electrolytic polishing, the initial QE is in the order of 10^{-7} range tested by a 266 nm picosecond laser beam. However, the QE could be improved by more than two orders of magnitude after appropriate in situ laser cleaning. Both 266nm ps-YAG and 248nm ns-excimer laser beams have been used in the process of cleaning. The thresholds of the laser cleaning intensity were also experimentally determined to keep the morphology of the superconducting cavity surface.

INTRODUCTION

For the development of a continuous wave (CW) high brightness electron source, one of the direct and simple approaches is to use the niobium surface of the superconducting (SC) cavity itself as the photocathode [1]. However, without appropriate treatment, the quantum efficiency (QE) of niobium was found to be too low to be of practical use [2,3] at the laser wavelength of interest (e. g. 266nm). Previous experimental results showed that QE of niobium could reach up to 10^{-4} by a special preparation technique of a series of diamond mechanical polishing followed by laser cleaning [1]. Since the laser cleaning technique has been successfully applied to the copper and magnesium cathode [5,6], we systematically investigated the laser cleaning effect on the buffer chemical polished (BCP) or electrolytic polished (EP) niobium surface irradiated by the fourth harmonic of a picosecond Nd:YAG laser or a nanosecond KrF excimer laser beam. The cleaning laser energy density should be high enough to effectively remove the contamination on the niobium surface. It, however, could not be beyond the damage threshold. Otherwise the morphology of the surface in the cleaned area will be completely changed, which will increase the field emission and thus degrade the performance of the SC cavity. From experiments, we found the effective laser cleaning energy density is around $0.3 mJ/mm^2$ for a 15ps, 266nm laser beam while about one order higher for a ~20ns, 248nm excimer laser.

EXPERIMENTAL APPARATUS AND TECHNIQUES

The picosecond pulses were produced by a 10-Hz mode-locked Nd:YAG laser (Quantel YG 501 DP). The 1.063 μm laser out of oscillator is limited to the TEM_{00} mode by a 1-mm-diameter intracavity pinhole. A single laser pulse is selected from the train and amplified by an Nd:YAG laser amplifier through two passes. Two KDP (potassium dihydrogen phosphate) crystals are used one after the other to generate 266nm (hν=4.66eV) radiation via harmonic conversion. It can produce about 1mJ/pulse ultraviolet (UV) beam with pulse duration of about 15 ps. This UV beam was utilized for both laser cleaning and QE measurements on the DC system.

The excimer laser (Lambda-Physik LPX-100) operating with KrF gas mix is capable of producing a ~20ns pulse beam with energy of about 250mJ/pulse at wavelength of 248nm (hν=5.0eV). This laser can run at 10 Hz repetition rate, and was also used for laser cleaning.

The UV beam from laser system was directed onto the cathode by UV mirrors via various optical elements. A He-Ne reference laser and two irises were used to define the trajectory of the UV beam to repeatedly align the beam on the cathode. A half wave plate and a polarizing cube acted as a variable attenuator to control the laser energy. A pyroelectric detector (Molectron J3-09) was used to measure the UV pulse energy entering the vacuum chamber. The laser beam size on the cathode can be adjusted by the variation of the lens position or the irises' apertures. The spatial profile of the UV beam was determined at the equivalent site of the cathode by using a CCD camera system (Spiricon LBA-100A). Figure 1 is the schematic layout of the beam optics for the QE tests.

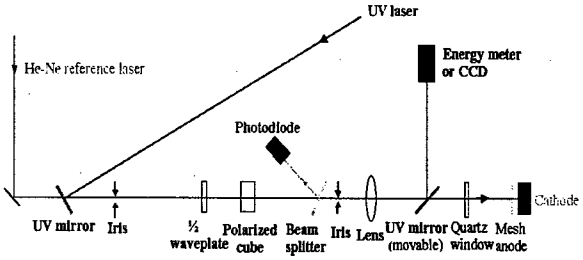


Figure 1: Layout of beam optics for QE test

A 2-3/4 inch stainless steel cubic cell with three fused silica windows was used as the vacuum chamber. The chamber was mounted on an x-y translation stage so that it can be remotely moved both horizontally and vertically with a 1μm resolution. This feature was used to scan the cathode for a uniform laser cleaning with the ps laser. A rotary stage with a high voltage and a charge signal feed-through was placed attached to the cube. The anode and cathode were installed parallel to each other on two aluminum rods attached to the high voltage and the charge signal feed-through, respectively. Thus anode and cathode can be rotated together in vacuum at any angle.

0-7803-7738-9/03/$17.00 © 2003 IEEE

After the introduction of new samples into the chamber, the system was initially evacuated down to approximately 10^{-6} Torr by the successive use of two liquid nitrogen cooled sorption pumps. This pressure was further reduced to around 5×10^{-9} Torr after appropriate baking by using a Varian Star-Cell ion pump. The vacuum level in the chamber was monitored by an ionization gauge.

We tried to simulate the SC cavity treatment procedures to prepare the cathode. The niobium cathodes were machined directly from a high purity grade of bulk sample into a cylinder with 9mm diameter and 9 mm thickness. The niobium has the same quality as that used for the SC cavity with residual resistivity ratio (RRR) value of 250 provided by Wahchang Company. All cathodes were then initially cleaned with detergent water. Most of the cathodes were further treated to buffer chemical polishing with the mixture of Fluoric (48%), Nitic (65%) and Phosphoric (85%) acids in a ratio of 1:1:2 by volume. A few samples were cleaned by electropolishing at TJNAL, and some were further mechanically polished after BCP or EP. A compact etching station was established for BCP purpose. The niobium sample was attached on a Teflon holder and immersed into the acids solution with cathode surface facing up. A 50ml Teflon beaker holding the solution was dipped into an ice-cooled water bath so that the temperature of the solution could be maintained during etching. To facilitate the heat exchange and dislodge any buildup of dissolved material around the sample, the acids mixture was agitated by a magnetic stirrer in the course of BCP etching. The cathodes were typically etched for 15-60 minutes at temperature of 12-15 degrees centigrade and then rinsed with deionized (DI) water (18MΩ) and cleaned in an ultrasonic DI water bath. This was followed by high purity of nitrogen drying the sample in a cleaned environment and transport into the vacuum chamber immediately.

In the normal QE measurement, a positive DC high voltage of up to 10KV was applied to the anode across the diode gap of about 1.5mm. In order to obtain a uniform field between the anode and cathode, a thin copper mesh (70 lines/inch) was used to cover the anode hole on the cathode side. The charge signal from the cathode was successively amplified by a low noise, charge sensitive pre-amplifier and a shaping main amplifier, and then recorded by a digital oscilloscope (Tektronics 2440) with a 50Ω termination. The charge measurement system was calibrated by applying a known voltage to a calibrating capacitor in the preamplifier. During QE measurement, photoelectrical charge must be kept low enough to avoid space charge domination and to ensure the charge amplifiers operating at their linear ranges. The laser energy irradiating the cathode was continuously monitored and measured by a fast photodiode calibrated against an energy meter (Molectron J3-09) before and after QE test. To reduce the background from the scattering light in the room, the window of the photodiode was always covered by a UG11 filter. Care was also taken to make sure the photodiode was always working within the linear response range. QE can, therefore, be deduced by simultaneously recording the laser signal from the photodiode together with the charge signal from the cathode on the same scope.

EXPERIMENTAL RESULTS

When we started to test a newly prepared cathode on the DC system, the initial QE of Niobium was 10^{-7} for BCP and EP samples and 10^{-6} for a MP sample. We first used the UV beam from the ps-YAG laser to clean the surface. Tests indicated that QE could be significantly improved when the incident laser energy density was excess of 0.2 mJ/mm^2 for about 50 minutes. Although the QE increased with further increase of energy density, the morphology of cathode surface was totally changed even before QE arrive at its maximum. Such a surface modification would not be acceptable for the SC cavity, since it could induce severe field emission and thus limit the performance of the cavity. Our experiments showed that the optimal energy density was around 0.3 mJ/mm^2 for ps-YAG beam. Figure 2 illustrates the cathode surfaces before and after laser cleaning with different laser energy densities observed under optical microscopes. Some of the samples were also inspected under scanning electron microscopes for higher magnifications.

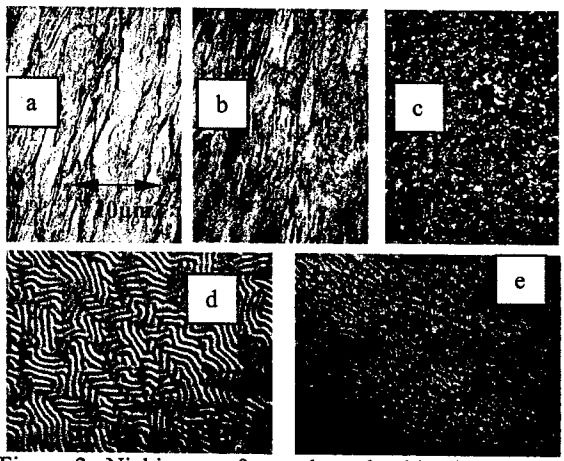


Figure 2: Niobium surfaces cleaned with different ps-YAG laser energy densities, observed under optical microscope. BCP sample: a) before laser cleaning, b) laser energy density 0.25mJ/mm^2, c) laser energy density 0.67mJ/mm^2 EP sample: d) before cleaning; e) laser energy density 0.45mJ/mm^2

UV beam from excimer laser also demonstrated the capability of cleaning cathode to increase the QE. Since the output energy of excimer laser is more than 200 mJ and the spatial profile is uniform, it is more efficient to clean a large area without the need of beam scanning. The optimized energy density for this laser was in the region of 3.5 mJ/mm^2.

Since the photoemission of the niobium from the UV laser is a one-photon effect, there was a linear relationship between the energy of incident laser and the charge of the

emitted electrons as shown in Figure 3. The different intercepts on the log-log graph express different QE. Similar behavior was also observed on cleaning with YAG laser.

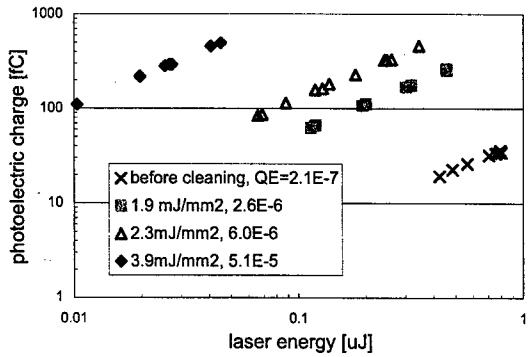


Figure 3: QE of BCP Niobium sample cleaned by 248nm, measured by 266nm

Figure 4 is the summary of the typical QE of niobium with different surface treatment. All the measurements were conducted by the 266nm YAG laser. BCP, MP+BCP and EP samples were laser cleaned with energy density around 0.3mJ/mm^2, and BCP(HV) was cleaned with much lower energy density prior to measurements. Althogh BCP(HV) cleaning is more effective, extreme care is required since the cathode surface could easily be damaged due to the formation of plasmas. The red bar in BCP data in Figure 4 corresponds to a heavier BCP cleaning that resulted in doubling of QE.

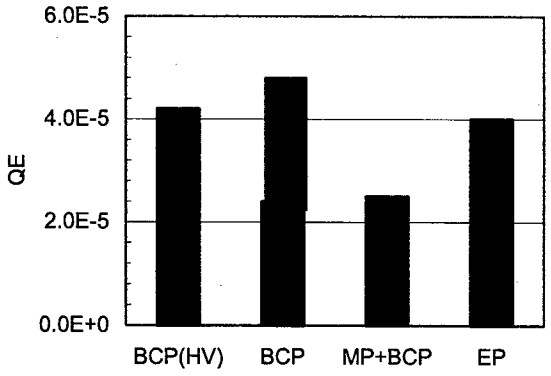


Figure 4: Summary of QE. Laser cleaning energy density was around 0.3 mJ/mm^2 by ps-YAG (266nm) for all samples except BCP(HV). Field on the cathode during measurement was about 1.5MV/m. BCP (HV): high voltage of 5KV applied across 1.7mm gap during cleaning at 0.1mJ/mm^2. Red BCP: cathode was heavily BCP cleaned with total remove of ~60um.

Since the gradient on the cathode was lower in the DC system than in the gun cavity, QE was measured as a function of field gradient to take account of the Schottky effect. A typical result is seen in figure 5. By extrapolating this data to 35MV/m in the gun cavity, QE of nearly 10^{-4} could be achieved.

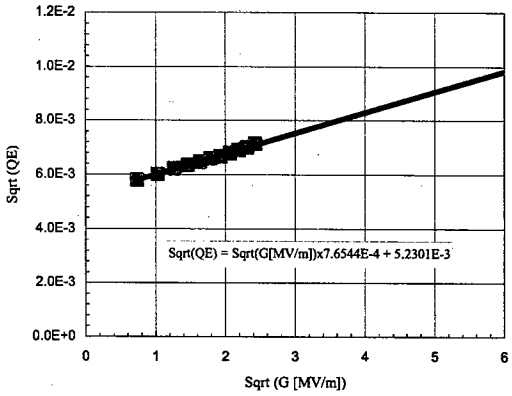


Figure 5: QE vs. field gradient for a BCP sample

SUMMARY

The QE of BCP and EP Niobium samples increased more than two orders of magnitude after appropriate in situ laser cleaning. Both the UV beams from the ps-YAG and ns-excimer can be used to clean the niobium cathode. The cleaning laser energy densities were determined to avoid the damage of surface. The real QE of niobium in SC cavity at cryogenic temperature will be tested soon.

ACKNOWLEDGMENTS

The authors would like to thank I. Ben-Zvi for the support and advice. We wish to thank T. Tsang, J. Smedley and R. Geng for the valuable discussions. We acknowledge the expert technical assistance of M. Montemagno and J. Walsh. We also appreciate J. Warren and R. Sabatini for their assistance in performing SEM analysis and JLAB for electro polishing the Nb samples. This research is supported by the U.S. Department of Energy under Contract No. DE-AC02-98CH10886, DE-AC02-98CH10886DOE, and SBIR grant DE-FG02-99ER82724.

REFERENCES

[1] M. Cole, et al., "Development of a Novel SC RF photocathode electron gun", LINAC'2k, p116.

[2] L.N. Hand and U. Happek, "Photoelectric quantum efficiency of niobium for 193nm and 248 nm", Nucl. Instr. & Meth. A372 (1996) 335.

[3] A.R. Fry and A.C. Melissinos, "Electron Emission From Metallic Surfaces by Picosecond Laser Pulses", Univ. of Rochester Preprint UR-1340/ER-40685-789, Jan. 1994.

[4] T. Srinivasan-Rao, et al., "Performace of Magnesium Cathode in the S-band RF gun", PAC'97, p2790.

[5] T. Srinivasan-Rao, et al., "Photoemission studies on metals using picosecond UV laser pulses", J. Appl. Phys. 69(1991)3291

THE ANALYSIS OF THE CROSS-TALK IN A RF GUN SUPERCONDUCTING CAVITY

Yongxiang Zhao, BNL, Upton, NY-11973-5000
Michael D Cole, Advanced Energy System Inc.

Abstract

A project to develop an all Niobium Superconducting RF Gun is underway at Brookhaven National Laboratory in collaboration with Advanced Energy Systems. The geometry of the gun requires that the power input and the pickup probes are on the same side of the cavity, which causes direct coupling between them, or crosstalk. At room temperature, the crosstalk causes serious distortion of the RF response. This paper addresses the phenomenon, the analysis and the simulation results as well as the measurements. A method is provided on how to extract the desired information from the confusing signal and allow accurate measurements of the coupling between the probes and the cavity.

INTRODUCTION

Superconducting cavities (SCC) have been used in many accelerator facilities. The great success of the superconducting technology has encouraged many other applications like microwave guns. For example, DESY has applied it for a microwave gun.[1,2] In Brookhaven National Lab, an "Electron Cooling" project is underway[3]. As a first experiment, a microwave gun with superconducting cavity is employed [4,5].

A SCC in an accelerator usually has its input antenna (or launcher) on one side and the pickup probe on the other side. The coupling between them is only through the cavity cells, and has a perceivable coupling only near the resonant frequency. For a cavity of a microwave gun, one end must be the cathode; thus, both launcher and pickup may be on the same side, as is the case here. We found there was strong cross-talk between the launcher and the pick-up in room temperature measurement [6]. Fig. 1 shows a typical response of S21 by virtue of a network analyzer. Obviously, it is too much distortion from a typical resonant curve. How to extract the useful information from the undesirable signal is a challenge.

To this end, we had to make a model for simulation. Analyses are also necessary in order to understand the relationship between parameters and the responses in the measurements. Fortunately, we found the crosstalk is not important when the cavity is cooled down to the superconducting status.

This article summarizes the results of the analysis and the measurements. It also provides a method to deal with crosstalk in case it is not negligible.

MODELING AND SIMULATION

We chose the equivalent circuit model as shown in Fig. 2, where C_0-L_0-R_0 represents the cavity. C1 and C2 represent the input and pickup couplers, respectively, with each connected to a 50 ohm cable. A capacitance C12 is added to represents a direct coupling between input and pickup and introduces crosstalk.

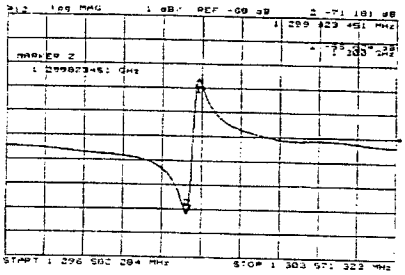


Fig.1 A typical phenomenon of crosstalk

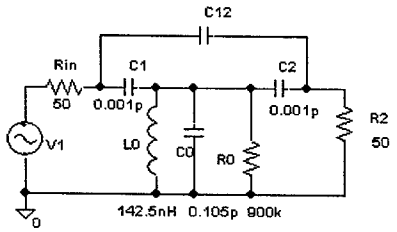


Fig.2 The equivalent circuit

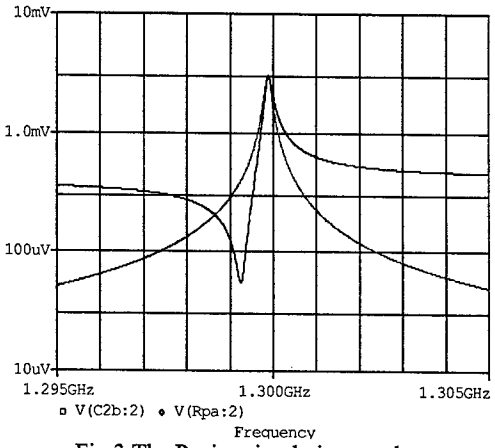


Fig.3 The Pspice simulation result

Here all the couplings are attributed to capacitance, because the probes are of rod shape and located in the electric field area.

Fig. 3 shows the results from PSpice. Evidently, without direct coupling, the curves display normal resonance (symmetric green curve). The phase changes 180 degrees when the frequency crosses the resonance (not shown). When C12 is added (C12 = 0.001pF is

0-7803-7738-9/03/$17.00 © 2003 IEEE

chosen in this curve), both the magnitude and phase display are distorted, exactly as we measured.

The dip frequency is due to the interference of two signals. One is the normal coupling through the cavity, of which the phase is very frequency sensitive. The other is due to the direct coupling, which is not sensitive to frequency. When the two signals have opposite phases, the signals cancel each other and thus form a dip.

The simulation also demonstrates that if one increases the Q of the cavity by cooling it down from room temperature to its superconducting state, in the vicinity of the resonant frequency the coupled signal through the cavity becomes much stronger than that through C12, and the crosstalk becomes less important.

ANALYSIS

The simulation gives a clear response, but doesn't give an explicit relationship between its parameters. Therefore, it is necessary to analyze the equivalent circuit. Fig. 4 gives a generalized form, which resembles a bridge circuit.

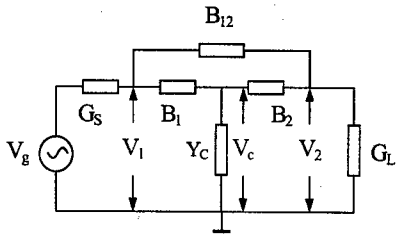


Fig. 2. The generalized circuit

Applying Kirchhoff law, after algebraic manipulation one obtains the following matrix equation.

$$\begin{pmatrix} Y_1 & -B_{12} & -B_1 \\ -B_{12} & Y_2 & -B_2 \\ -B_1 & -B_2 & Y_0 \end{pmatrix} \begin{pmatrix} V_1 \\ V_2 \\ V_C \end{pmatrix} = \begin{pmatrix} G_S \\ 0 \\ 0 \end{pmatrix} V_g \quad , \qquad (1)$$

where $Y_1 = Gs + B_1 + B_{12}$

$Y_2 = G_L + B_2 + B_{12}$

$Y_0 = Yc + B_1 + B_2$.

Y_0 is the total admittance of the cavity including the coupling capacitance. In our special case, $G_S = G_L = G_0 =$ 1/ 50(ohm), and the couplings are very weak such that B_1, B_2 and B_{12} are negligible in comparison with G_0. Then approximately, $Y_1 = Y_2 = G_0 = 0.02$ *mho*.

Solving the equation (1), one obtains:

$$\frac{V_2}{V_g} = \frac{Y_0 B_{12} + B_1 B_2}{G_0 Y_0 - B_1^2 - B_2^2} . \qquad (2)$$

The coupling coefficient related to the coupling capacitance is:

$$\beta_2 = Q_0^2 \frac{R_2}{R_C} \frac{C_2^2}{C_C^2} \quad , \quad \beta_1 = Q_0^2 \frac{R_S}{R_C} \frac{C_1^2}{C_C^2} . \qquad (3)$$

Note that $R_S = R_2 = 1/G_0$, and $R_c \omega_0 C_c = Q_0$.

Note that only Y_0 is frequency sensitive. The other parameters can be regarded as approximately constant. The fraction (2) includes a pole and a zero. Without crosstalk (i.e. $B_{12} = 0$), its numerator becomes constant and thus has no zero, corresponding to a simple resonance.

Substituting the parameters $B_1 = j\omega C_1$, $B_2 = j\omega C_2$, $B_{12} = j\omega C_{12}$, formula (2) can be rewritten in the form:

$$\frac{V_2}{V_g} = \frac{j\omega C_{12}}{G_0(1+\beta)} \cdot \frac{1 + jQ_z \cdot 2(f - f_z)/f_0}{1 + jQ_L \cdot 2(f - f_0)/f_0} , \qquad (4)$$

where $\beta = \Sigma\beta_i$, $Q_L = Q_0/(1+\beta)$, $Q_Z = Q_0(1+\delta_Z)$, $f_z = f_0(1 - \frac{1}{2}\delta_Z)$, $\delta_z = C_1C_2/C_0C_{12}$

Evidently a pole is at $f = f_0$, and a zero at $f = f_Z$. This verifies what we have observed in the measurement. If the crosstalk is serious, that is δ_Z is small, then f_Z is close to f_0, and the resonant curve is so distorted that the peak frequency f_{max} is not exactly at f_0, f_{min} is not exactly at f_Z, the measured Q from 3 dB bandwidth is not exact Q_L.

The introduced "crosstalk parameter" δ_Z, is also a measure of relative frequency separation of f_Z and f_0.

$$\delta_Z = \frac{2(f_0 - f_Z)}{f_0} \qquad (5)$$

The closer the two frequencies, the more the distortion of the resonant curve, implying more serious crosstalk.

The agreement with observation once again verifies the circuit model. In order to make a further normalization, Let's define

$$\delta = \frac{2(f - f_0)}{f_0} , \text{and } F = Q_0 \delta, \; F_Z = Q_0 \delta_Z . \qquad (6)$$

δ is the relative frequency deviation. F is the normalized frequency deviation, such that $F = 1$ corresponds to a frequency at the edge of the 3-dB bandwidth. F_Z is the normalized crosstalk parameter that measures the deviation of the dip frequency from the resonant frequency.

Substituting (3) and (6), then (4) can be rewritten as

$$\frac{V_2}{V_g} = \frac{j\sqrt{\beta_1\beta_2}}{1+\beta} \cdot \frac{1}{1 + jk_L F} \cdot \frac{1 + jk_Z(F + F_z)}{F_Z} \qquad (7)$$

where $k_Z = 1+\delta_Z \approx 1$, $k_L = 1/(1+\beta) \approx 1$.

Equation (7) has a clear physical meaning. On the RHS, the first two fractions represent the response in the absence of crosstalk. The first one is the magnitude of the coupling at resonant frequency. The second manifests the resonant performance. The third fraction involving F_Z manifests the effect of the direct coupling or the crosstalk. It approaches unity for $F_Z \to \infty$, i.e. whenever either Q_0 or δ_Z is very large. Just like parameter δ_Z, F_Z is also a measure of crosstalk.

At room temperature, F_Z is in a range that the crosstalk must be taken into account. When cooled down to the superconducting state, Q_0 increases a few orders of

magnitude, such that the condition $F_Z >> 1$ is realized, and the crosstalk vanishes.

THE RELATIONSHIP TO THE TESTED PARAMETERS

Using the analyses above, we now can calculate the parameters we want from the parameters that we can measure.

The parameters we want to know are the resonant frequency f_0, Q_0, coupling coefficient β, and external Q.

Refer to Fig.1, the measurable parameters are f_{max}, f_{min} and corresponding $S21_{max}$, $S21_{min}$. $S21_{min}$ usually is very weak that may not be read out precisely. Instead, we can measure a middle point f_M and its $S21_M$. From network analyzer, one may also read out Q_{read}, which is not the real loaded Q due to distortion.

From (7) we obtain:

$$S21 = 10\log\left\{\frac{4\beta_1\beta_2}{(1+\beta)^2}\cdot\frac{1}{1+k_L^2F^2}\cdot\frac{1+k_z^2(F+F_z)^2}{F_z^2}\right\} \quad (8)$$

Note that both k_L and k_Z are very close to unity and $\beta = \beta_1 + \beta_2 << 1$. Obviously, if crosstalk is negligible (i.e., $F_z >> 1$), the maximum S21 occurs at resonance or $F = 0$, one obtains $\beta_1\beta_2$ by testing $S21_{max}$.

$$S21_{max} = 10\log(4\beta_1\beta_2). \quad (9)$$

If the crosstalk is not negligible, then

$$10\log(4\beta_1\beta_2) = S21_{max} - \Delta S_0, \quad (10)$$

where

$$\Delta S_0 = = -20\cdot\log\left(1-\frac{1}{C^2}\right) \quad (11)$$

$$C = 10^{\Delta S_{0M}/20} \quad (12)$$

$$\Delta S_{0M} = S21_{max} - S21_M \quad (13)$$

In order to determine each coupling coefficient, one has to use an extra probe C. Combing with the input probe A and pickup B, one can measures three products $\beta_A\beta_B$, $\beta_A\beta_C$, and $\beta_C\beta_B$. Then it is ready to find each individual β value by

$$\beta_A = \sqrt{\frac{(\beta_A\beta_B)\cdot(\beta_A\beta_C)}{(\beta_C\beta_B)}} \quad (14)$$

The loaded is:

$$Q_L = G_q\, Q_{read}, \quad (15)$$

Where

$$G_q = \sqrt{2\left(\frac{C^2-1}{C^2-2}\right)^2 - 1} \quad (16)$$

The deviation of the resonant frequency is:

$$f_{max} - f_0 = \frac{f_0}{2Q_0}\cdot\frac{\sqrt{F_z^2+4}-F_z}{2} \quad (17)$$

where

$$F_Z = C - \frac{1}{C} \quad (18)$$

SUMMARY

The frequency response with an asymmetric was found due to crosstalk. A model with direct coupling along with PSpice simulation successfully demonstrated this phenomenon. A detail analysis gives the formulas, from which one can calculate the coupling parameters, although the frequency response is serious distorted.

This work was aimed to solve the crosstalk problem in a superconducting gun. But of course, this method is also applicable for any crosstalk phenomena.

ACKNOWLEDGEMENT

This work was supported by the U.S. DOE., Office of Basic Energy Sciences, under Contract Nos. DE-AC02-98CH10886DOE, SBIR grant DE-FG02-99ER82724, and under CRADA No. BNL-C-01-08. This work is a part of the project of "Electron Cooling" headed by Ilan Ben-Zvi, in cooperation with AES. The cavity experiment is managed by Triveni Srinivasan-Rao and Mike Cole of BNL and AES, respectively.

REFERENCES

[1]. D. Janssen etc., "The Development of a Superconducting RF Gun: Status of the Drossel Collaboration", PAC97, p.2838.

[2]. E. Barhels etc., "On the way to a superconducting RF-gun: first measurement with the gun cavity." Neclear Instrument and Methods in Physics Research A 445 (2000) 408-412.

[3]. Ilan Ben-Zvi, etc., "Electron cooling for RHIC", Proceedings, 2001 Particle Accelerator Conference, Chicago IL. June 18-22, 2001. BNL-68727

[4]. M. Cole, H. Bluem, J. Rathke, T. Schultheiss (AES.), I. Ben-Zvi, T. Srinivasan-Rao (BNL), "Progress Toward an All Niobium Superconducting RF Photocathode Electron Gun", Presented at the 2001 Particle Accelerator Conference in Chicago Illinois.

[5]. M. Cole, H. Bluem, J. Rathke, T. Schultheiss (AES), I. Ben-Zvi, T. Srinivasan-Rao (BNL), "Development of a Novel Superconducting RF Photocathode Electron Gun", Presented at the 2000 LINAC Conference in Monterey, California.

[6] Yongxiang Zhao, "Analysis and measurement of cross-talk in a superconducting cavity", BNL-69422, Sep. 2002.

SIMULATION OF HIGH CURRENT EXTRACTION FROM THE ELSA RF PHOTO-INJECTOR

P.Balleyguier, Ph.Guimbal CEA/DPTA Bruyères-le-Châtel, France

Abstract

Extracting a high-charge bunch from a photo injector is a real challenge, because of space charge effects. Our goal is to extract a 100-nC bunch from our 144-MHz photo-injector, and to keep it a low emittance. The effect of HOM excitations has also to be considered for our a long term goal, which is to extract a burst of ten consecutive such bunches. This paper presents some simulations of basic phenomena (image charges, space charge limitation, RF mode excitation ...), that we carried out to validate the tool that we use (the MAFIA-TS2 2D PIC solver), and the results of global simulations.

INTRODUCTION

The intensity of electron emission is a critical issue in flash X-ray machines like AIRIX [1]. The ELSA unique low frequency (144 MHz) photoinjector [2] is a good tool to explore the domain of space charge limited emission. Such experiment requires improvements on the photo-injector, components (photo cathode, drive-laser, RF power...). An important work on the drive laser stabilization is underway. Boosting the RF power by +50% is also considered. We present here some simulations validating the principle of high charge emission. We use the MAFIA time-domain particle-in-cell (PIC) solver TS2 in a 2D axisymetrical simulation (r,z). Next subsections shows some of the simple tests that we made in order to check if basic phenomena were treated correctly by this code.

Image charge

Unlike the classical code PARMELA working with image charges, MAFIA-TS2 solves the Maxwell equations directly with the limit condition (metallic wall). We first checked the equivalence of the two formalisms.

A single particle is emitted at low speed ($\beta_0 \ll 1$) from a metallic cathode without external field. In the non relativistic limit, the limit condition on the cathode is equivalent to an image charge moving backward from the cathode, symmetrically with the real particle. This image charge acts on the real particle by decelerating it along its trajectory. As the total energy of the real particle (kinetic plus potential) remains constant, we have:

$$\frac{mc^2}{2}\beta(z)^2 - \frac{qe}{16\pi\varepsilon_0}\frac{1}{z} = cte,$$

the second term on the left hand side being the potential energy created by the image charge on the real particle.

With MAFIA, we simulated such a case, and computed the particle speed along its trajectory. As expected, the total energy (from MAFIA's speed and position) is indeed constant, after the first half mesh step (fig.1). The energy drop ΔE between initial and asymptotic-final kinetic energy is about the potential energy of the particle at the distance of one mesh step. We conclude that the so-called "image charge" effects are correctly simulated (as long as the initial energy is higher than ΔE).

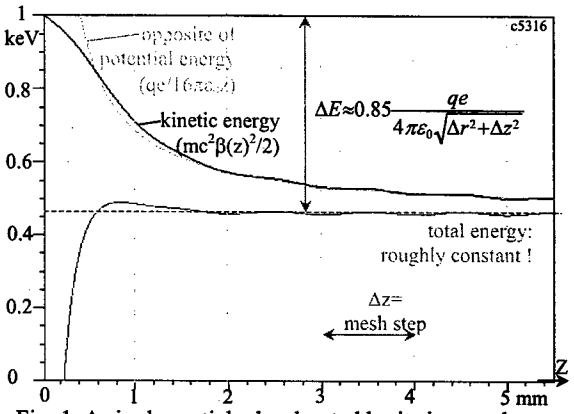


Fig. 1. A single particle decelerated by its image charge.

Space charge limitation

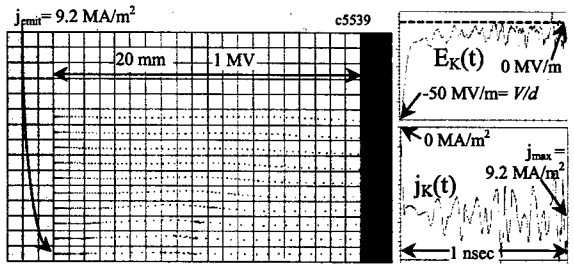


Fig. 2. Transient behaviour at the space charge limit value: electron motion gets turbulent.

In a planar diode with a uniform external field, the density of emitted electrons cannot exceed the value for which the external field is cancelled by the space-charge field. When this occurs, the particle motion becomes turbulent (fig. 2). If an attempt is made to emit a higher density current, the turbulence grows and some particles roll back to the cathode. Simulations show that the current limitation indeed coincides with the cancellation of the cathode field (fig. 3). The density limit, according to Child Langmuir's (CL) law, is proportional to $U^{3/2}/d^2$:

$$j_{cl} = \frac{4}{9}\varepsilon_0\sqrt{\frac{2e}{m}}\frac{U^{3/2}}{d^2} = \frac{\varepsilon_0 mc^3}{e}\frac{1}{d^2}\frac{4\sqrt{2}}{3}u^{3/2}, \text{ with } u = \frac{Ue}{mc^2}.$$

For voltages U>0.5 MV, the agreement is still good with the relativistic CL law [3] (fig. 4):

0-7803-7738-9/03/$17.00 © 2003 IEEE

$$\hat{j}_{clr} \approx \frac{\varepsilon_0 mc^3}{e} \frac{1}{d^2} 2(\sqrt{u+1}-0.85)^2$$

But the absolute MAFIA current limit is higher than CL's value by a factor (about 1.8 here) decreasing with mesh size. The residual discrepancy factor (which tends to 1.4 as mesh size tends to zero) results from the finite radial extension of the beam that permits a higher current density than in the CL's 1D model.

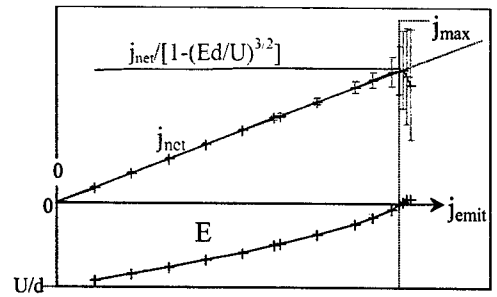


Fig. 3. For given voltage and distance, the cathode field (E_K) drops as the current density (j_{emit}) increases.

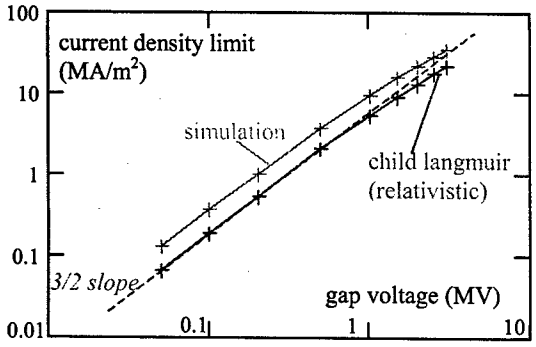


Fig. 4. Despite a 1.8 discrepancy factor, the voltage dependence of the density limit is OK.

Immersed cathode

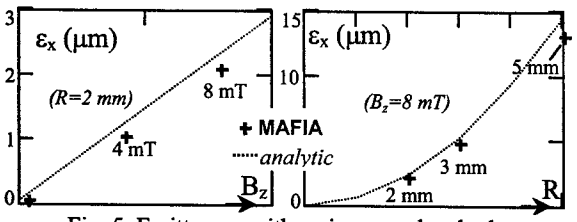


Fig. 5. Emittances with an immersed cathod .

Immerging a cathode in magnetic field B_z creates some azimuthal emittance. For a short bunch of radius R [4]:

$$\varepsilon_x = \frac{e}{mc^2} \frac{B_z c R^2}{8}.$$

A 1-pC bunch, 25-ps rms (gaussian) long, was simulated in the geometry of the ELSA photoinjector (see below). An additional coil in the cathode nose creates a longitudinal magnetic field on the cathode. From $r'=v_r/v_z$, *and* $\theta'=v_\theta/v_z$, MAFIA/TS2 computes the normalized rms emittance:

$$\varepsilon_x = \beta\gamma(\langle x^2\rangle\langle x'^2\rangle - \langle xx'\rangle^2)^{1/2}$$

$$= (\beta\gamma/2)(\langle r^2\rangle\langle r'^2+\theta^2\rangle - \langle rr'\rangle^2)^{1/2}.$$

Results are in good agreement with the analytical value (fig 5).

ELSA PHOTO INJECTOR

RF Modes

Excitation of the photoinjector cavity by a short bunch of charge q has been simulated in time domain with the TS2 solver. After a Fourier transform, the spectrum shows the same frequencies than the modes computed by the eigenmode solver in frequency domain (fig. 6). Moreover, at 144 MHz, the amplitude of the accelerating mode is within 1% of the expected value: $U = q\omega R/Q$.

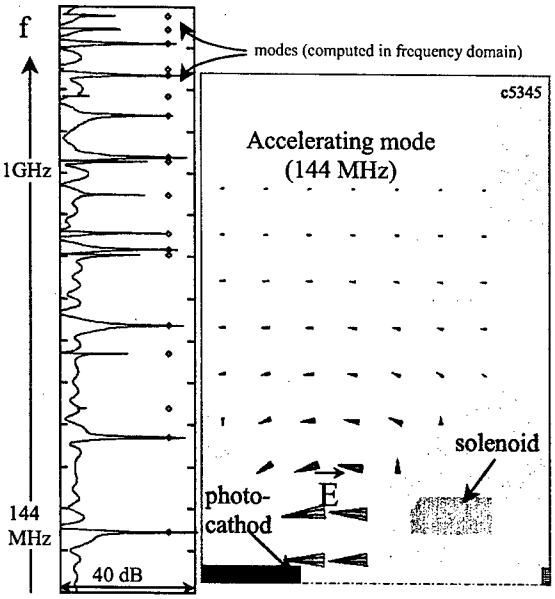


Fig. 6 Response of the ELSA photoinjector cavity computed in time and frequency domains.

Charge extraction

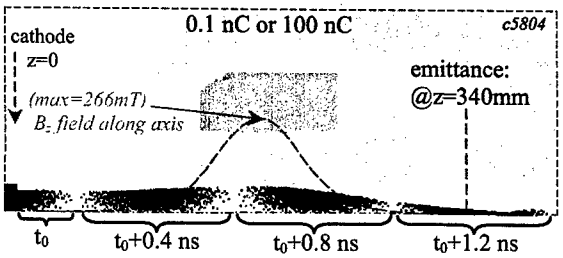


Fig. 7. 0.1 or 100 nC extracted from ELSA's photoinjector. The middle of the bunch is extracted at t_0.

A gaussian bunch (65 ps-rms) of 100 nC is extracted uniformly from a 15-mm radius photocathode. The RF voltage is U=2.7 MV, the gap length is d=100 mm.

According to MAFIA, such a bunch can be accelerated without major perturbation on the particle dynamics (fig. 7): the plots look exactly the same either for a low charge (0.1 nC) or a 100 nC charge. However, at 100 nC, a few particles (5.5 %) are lost on the wall tube: the photoinjector parameters (cathode radius, focusing magnetic field...) have not been optimized yet. As the emittance is dominated by non-linear radial effects due to the wide extraction area, the charge has only a slight influence on it: ε_x is 174 μm at 0.1 nC, and 181 μm at 100 nC (fig. 8).

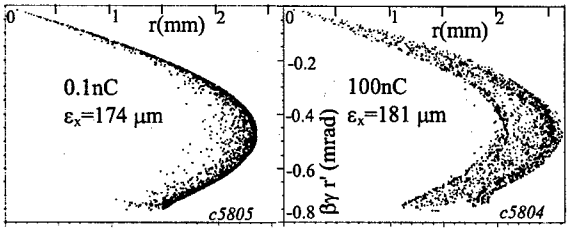


Fig. 8. Phase plane (r r') and emittance @z=340 mm.

Wakefields effects

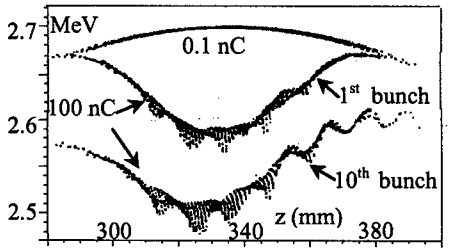


Fig. 9 Energy dispersion for different bunches.

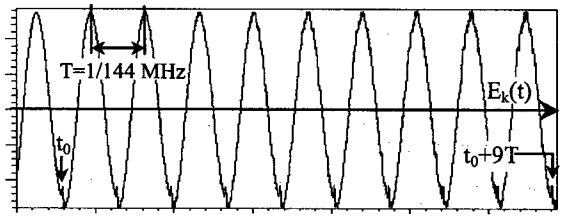


Fig. 10. Photocathode E-field for a 10×100nC bunch train.

The charge has also some influence on the output energy of the bunch (fig. 9). Wheras a low charge bunch is almost uniform in energy (apart from the top curvature due to the RF sine dependence of the fields), the wakefield of a 100-nC charge causes an energy drop in the bunch center. In addition, the global energy further decreases in case of multibunch operation because of cavity filling out: -0.27 Joule at each bunch out of 45 Joules initial energy. Each successive pulse emission causes a bump on the photocathode field, and some higher frequency noise gradually emerges (fig. 10).

Overloading

As no major consequence was observed so long, we tried to push the charge until bunch explosion: it occurred above 500 nC. As an example, an attempt to extract a charge of 1000 nC is displayed (fig. 11). This simulation clearly shows a particle lack on axis in the bunch center, a high number of lost particles (caused by radial excursion), and eventually, a split residual bunch coming out from the cavity. The number of particle is 1000, and the mesh step is 0.9 mm in the gap. Other mesh size and number of particle were tried: results were qualitatively equivalent.

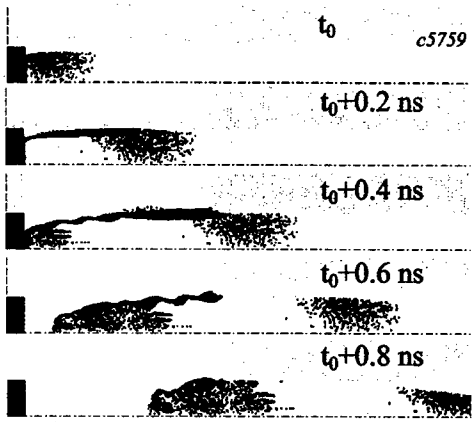


Fig. 11. At 1000 nC, the bunch explodes.

CONCLUSION

According to MAFIA simulations, a bunch charge of 100-nC can be extracted and correctly accelerated in the ELSA photoinjector. Apart from an acceptable energy degradation, no major consequence was observed on the beam dynamics. Multibunch operation can be considered for a few bunches.

REFERENCES

[1] E. Merle et al., "Transport optimization and characterization of the 2kA AIRIX electron beam", LINAC2000, Monterey, August 2000, p. 494.

[2] JG.Marmouget et al. "Present performance of the low emittance high bunch charge ELSA photoinjected linac", EPAC'2002, Paris, June 2002, p. 1795.

[3] H.Jory, W.Trivelpiece, Journ.Appl.Phys., 40, p.3294 (1969)

[4] JP.Carneiro, "Etude expérimentale du photo-injecteur de Fermilab", PhD memorandum, Université de Paris XI-Orsay, May 2001, p.145.

EMITTANCE GROWTH STUDY USING 3DE CODE FOR THE ERL INJECTOR CAVITIES WITH VARIOUS COUPLER CONFIGURATIONS *

Z. Greenwald †, D. L. Rubin, Cornell University, Ithaca, NY

Abstract

We compute emittance growth in electron bunches in high gradient accelerating cavities due to field nonlinearities and phase dependence associated with the finite bunch length. The determination of the emittance is based on tracking of individual particles through tabulated, 3-dimensional, electromagnetic fields. No symmetry is assumed. The fields for the structure, including input coupler, are calculated using MAFIA or MWS[1]. We examine particle trajectories RF focusing and emittance growth of injector cavities with various coupler configurations under study for Cornell Energy-Recovery-Linac proposal [2].

INTRODUCTION

A study of beam emittance growth in ERL injector cavities [2] was done using the new code 3DE[3]. The study was done for four different coupler configurations over the particle energy range of $0.5\ MeV - 10\ MeV$. All four structures have two identical RF cells. The input and output beam pipe dimension of the first structure is slightly different than the pipe dimensions of the other three structures. The arrangements of the couplers in each structure is listed below:

- **Structure I** : Two cells cavity - NO couplers
- **Structure II** : Two cells + ONE vertical coupler at the bottom of the output pipe located at $z = 0.281\ m$ from the input, see Figure 1.
- **Structure III** :Two cells + TWO vertical symmetric couplers at the bottom and top of the output pipe located at $z = 0.281\ m$ from the input, See Figure 2.
- **Structure IV** :Two cells + TWO vertical asymmetric couplers, the same as structure III, axcept there is a 1 mm vertical shift of the bottom coupler relative to the top one.

The top coupler in structures III & IV was added in order to compensate the effect of the transverse kick of the bottom coupler on the emittance. In structure IV a 1 mm shift was added to simulate practical imperfection in manufacturing.

THREE DIMENSIONAL ELECTROMAGNETIC FIELD

The three dimensional Electromagnetic field for all the structures were calculated using the code MWS[1]. The fields were calculated for both electric and magnetic wall

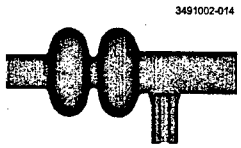


Figure 1: A two cells with one vertical coupler structure.

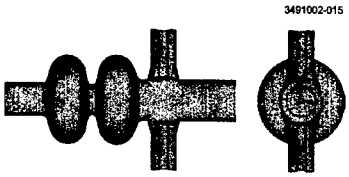


Figure 2: A two cells TWO symmetric vertical couplers structure.

boundary conditions and were combined, in order to simulate propagating waves, using the following expressions [4]:

$$E = (-E_e + j \cdot k_n \cdot E_m)\, \epsilon^{-j \cdot \omega \cdot t + \varphi} \quad (1)$$

$$H = (H_e - j \cdot k_n \cdot H_m)\, \epsilon^{-j \cdot \omega \cdot t + \varphi} \quad (2)$$

E_e, H_e, are fields calculated with the electric wall boundary condition

E_m, H_m, are fields with calculated the magnetic wall boundary condition

k_n is a normalization coefficient. The value of k_n is determined from the characteristic impedance of the coaxial line of the RF couplers. The sign of k_n is chosen to satisfy the a condition for a propagating waves into the structure.

TRACKING

The 3DE code calculates the new kick on the particle due to the RF field at each coordinate and calls $BMAD's$ tracking routine [5], which uses a Runge - Kutta algorithm, to calculate the new particle location. Using the new location 3DE code calculates the new angles and particle energy. A comparison of the trajectories of three particles with vertical displacement of $y = -2,\ 0,\ 2\ mm$

* Work supported by the National Science Foundation.
† Email: zipi@cesr10.lns.cornell.edu

0-7803-7738-9/03/$17.00 © 2003 IEEE

and horizontal displacement of $x = 0,\ 0,\ 0\ mm$ entering structure II (two cells with ONE vertical coupler) and structure IV (two cells with TWO, 1 mm shifted, vertical couplers) is seen in Figure 3. The particles traveling in the ONE coupler structure are being kicked in the $-y$ direction after passing the location of the coupler at $z = 0.281\ m$, due to the transverse kick.

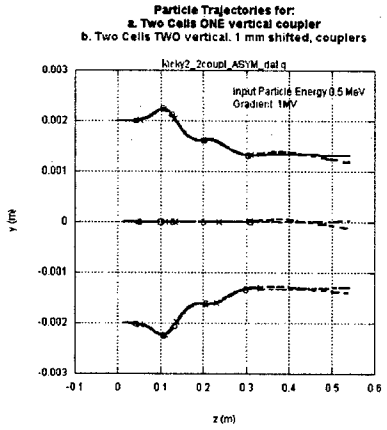


Figure 3: Particles trajectories in structures II (dashed line)& IV (solid line) (These are the one-coupler & two-asymmetric-couplers structures)

RF FOCUSING

We observe the expected trasverse focusing[3], and compute its strength as $\frac{\Delta y'_{out}}{\Delta y_{in}}$. A comparison of the RF focusing versus Input-Particle-Energy for all four structures can be seen in Figure 4. The RF phase was optimized to get maximum acceleration at each input energy. The RF focusing of structures II, III, IV (two cells WITH couplers) is essentially identical and about 90% of the focusing with no couplers. When the gradient in the structure was raised from 1 MV/l to 3 MV/l ($l = 0.54\ m$, *total length of the structure*), the RF focusing strength was increased by a factor of 3.4 for Input-Particle-Energy of 1 Mev in the structure of two cells and ONE coupler.

EMITTANCE

The emittance obtained for structure I with two cells, NO coupler for a bunch with a uniform square distribution, at input particle energy of 0.5 MeV gradient of 1 MV/l with $\sigma_{yin} = 1\ mm$, $\sigma_{y'in} = 0$ is $2.833410^{-9}\ m - rad$. Note that the input emittance is nominally zero where the output emittance ϵ is:

$$\epsilon_{RMS} = \sqrt{\sigma_y^2 \cdot \sigma_{y'}^2 - \sigma_{y,y'}^2} \qquad (3)$$

y and y' are the vertical displacement and angle, and σ_y and $\sigma_{y'}$ are the rms beam sizes. The corresponding phase

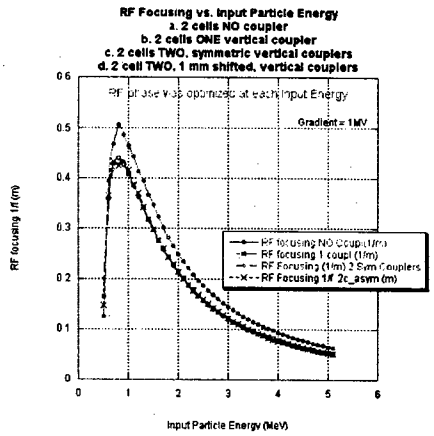


Figure 4: RF focusing versus Input-Particle-Energy for all four structures

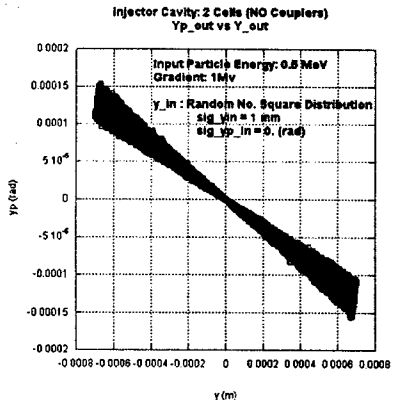


Figure 5: Phase space of a 1 mm transversely squared bunch

space distribution is seen in Figure 5. The emittance growth calculated for a bunch with Gaussian distribution $\sigma_{yin} = 2\ mm$, $\sigma_{y'in} = 0$, at input energy of 0.5 MeV and Gradient of 1 MV/l, are summarized in Table I. The output phase space for bunch with Gaussian distribution for structures II (ONE coupler) & IV (TWO asymmetric couplers) are shown in Figure 6 and a histogram of the transverse angle, y'_{out}, of the particles at the output are shown in Figure 7.

Calculation of emittance versus energy for II (ONE coupler) & IV (TWO asymmetric couplers) is shown in Figure 8. At low energy where the emittance is dominated by the RF focusing there is not much difference between one coupler and two couplers. At high energy, where the non uniformity of transverse kick due to the coupler is the dominant contribution, we can see the effect of the cancellation in structure IV due to the second opposite coupler.

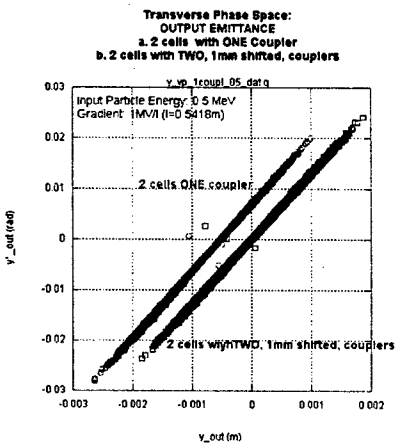


Figure 6: Phase space of structures II (ONE coupler) & IV (TWO asymmetric couplers) at the output

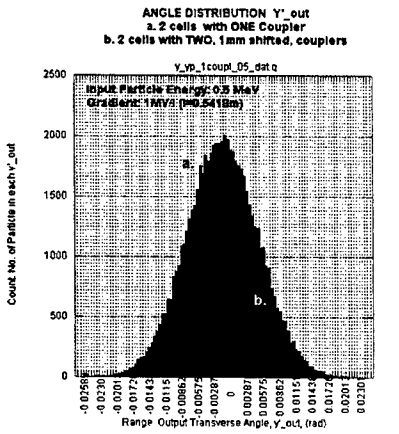


Figure 7: Distribution of the angle, y', at the output of structures II (ONE coupler) & IV (TWO asymmetric couplers)

CONCLUSIONS

Calculation of the emittance (not including space charge effect) shows that the highest emittance obtained in these structures will be $4.74 \cdot 10^{-8}\ m - rad$ for the first cavity after the gun (input particle energy of $0.5\ MeV$). At this energy the different arrangements of couplers makes very little effect. On the other hand, when the particle input energy increases the non uniformity of the transverse kick is dominant. At input energy of $2\ MeV$ the output emittance of structure IV (TWO asymmetrical couplers) is $\frac{1}{16}$ of the emittance of structure II (ONE coupler). See Figure 8. Having two couplers also keeps the bunch along the center of the beam pipe, where in the case of one coupler the bunch is displaced by $0.5\ mm$ in the $-y$ direction of the center, as seen in Figure 6. Also note, transversely displacing the beam by $1\ mm$ in structure IV compensated for

Table 1: Emittance Growth calculated by the Code 3DE for a Gaussian bunch. Input Particle Energy $0.5\ MeV$. The Gradient in the Cavity is $1\ MV/l$. (l=0.5418m)

Structure	ERL Injector Cavities Study	
	Emittance m-rad	Notes
II	$4.397 \cdot 10^{-8}$	*Two cells ONE coupler*
II off center	5.35410^{-8}	*bunch is 1 mm displaced in y*
III	$4.6916 \cdot 10^{-8}$	*Two cells – TWO symmetric couplers*
IV	$4.74 \cdot 10^{-8}$	*Two cells – TWO asymmetric couplers*
IV off center	$4.34 \cdot 10^{-8}$	*bunch is 1 mm displaced in y*

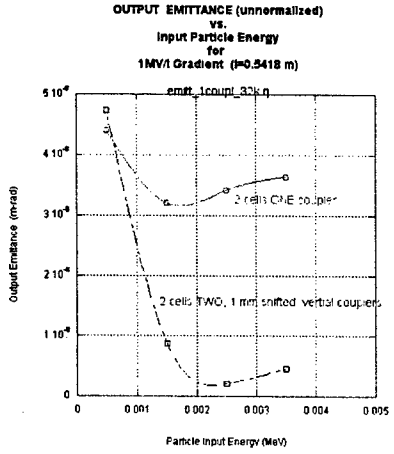


Figure 8: Emittance vs. Particles-Input-Energy of structures II (ONE coupler) & IV (TWO asymmetric couplers)

the asymmetry between the couplers, causing to a decrease in the emittance growth as seen in Table 1.

ACKNOWLEDGEMENTS

I would like to thank D. Sagan for his help with the BMAD tracking routine. Many thanks to S. Peck for being very helpful with programing.

REFERENCES

[1] CST Microwave Stodio, User Guide, CST GmbH, Budinger Str. D-64289 Darmstadt, Germany

[2] V. Shemelin, SRF notes 021028-08

[3] Z. Greenwald, "Three Dimension Emittance Calculation Code - 3DE " SRF 021203-10

[4] V. Shemelin, I. Bazarov, SRF minutes October 2002

[5] D. Sagan, Tracking subroutine ODIENT.F90

DIPOLE-MODE-FREE AND KICK-FREE 2-CELL CAVITY* FOR THE SC ERL INJECTOR

V. Shemelin#, S. Belomestnykh, R. L. Geng, M. Liepe, H. Padamsee

Laboratory for Elementary-Particle Physics, Cornell University, Ithaca, NY 14853

Abstract

For the ERL injector, superconducting cavities are needed to deliver to the beam a 100 kWCW RF power. With a beam current of 100...33 mA, gap voltage of 1...3 MV, the coupler must have an external Q-factor in the range of $4.6\times10^4...4.1\times10^5$. The cavity shape and coupler design presented provide the possibility of working in the range of parameters without substantial transverse kick to the beam and HOM-losses in the system. In order to preserve field flatness while the dipole mode is driven out, the 2-cell cavity has a protruding iris between the cell and the larger beam pipe. A twin-coaxial coupler has high coupling but low kick because of its symmetry. Calculation and optimization of the coupler-cavity system are performed with a 2D SLANS and 3D Microwave Studio® codes.

1 INTRODUCTION

A multi-GeV Energy Recovery Linac (ERL), proposed by Cornell University in collaboration with Jefferson Lab, is a low emittance, high average beam current CW accelerator for X-ray science [1]. An injector and a main linac of the ERL are based on the superconducting RF technology.

One of driving ideas behind this machine is to create a low emittance beam using a high-brightness photoemission electron gun and then to preserve the emittance while the beam is accelerated in the injector and in the main linac. The goal is to have the beam with the normalized emittance of 2 mm·mrad in undulators. An extension of existing technology in several directions is required to achieve this ultimate goal. Development of a 100 MeV, 100 mA average current ERL prototype is in progress at Cornell University [2].

One of the possible sources of emittance dilution is a kick caused by non-zero on-axis transverse electromagnetic fields of fundamental power couplers in superconducting cavities. This effect is especially strong in the injector cavities, where a high average RF power per cavity must be coupled to a vulnerable low-energy beam. The requirements here are far more demanding than in any existing system. Our design goal is to allow a maximum emittance growth of no more than 10% total for five injector cavities out of the initial emittance of 1 mm·mrad [3].

The five injector cavities are superconducting 2-cell niobium structures. They provide a total of 500 kW of RF power to the beam. Consequently, the permitted beam current depends on the injector energy and varies from 100 mA at 5 MeV to 33 mA at 15 MeV. The injector cavity coupler has to deliver to the beam $P_{beam} = 100$ kW of RF power and provide matching conditions for a cavity gap voltage of $V = 1$ through 3 MV. In accordance with the formula

$$Q_{ext} = \frac{V^2}{R/Q \cdot P_{beam}},$$

where R/Q is the characteristic impedance of the cavity, the coupler must be adjustable with the external Q factor overlapping the range from 4.6×10^4 to 4.1×10^5. Such small values of Q_{ext} may demand a deep insertion of the antenna into the beam pipe that adds to the problem of the kick.

There are several possibilities to completely or partially suppress the transverse kick from the fundamental RF power coupler and associated with it emittance growth. They were analyzed in detail in [4]. We settled on the twin-coaxial coupler as a more practical option.

Another source of the emittance dilution is an interaction of the beam with high Q transverse higher-order modes (HOMs). Especially dangerous are lowest dipole modes whose frequencies can be below cut-off frequency of the beam pipes. However, it is possible to find a cavity shape so that the frequency of the lowest dipole mode is high enough to propagate into the beam pipe. In this case its impedance becomes small as well as its impact on the beam. Examples of such shapes are single-cell superconducting cavities developed at Cornell [5] and at KEK [6].

In this paper we present the 2-cell superconducting cavity shape with propagating dipole modes in the presence of the twin-coaxial coupler. 2D codes SLANS and SLANS2 [7] were used to optimize the cavity shape. The 3D MWS 4.0 code was used to verify the obtained results, to optimize the coupler and to study the dipole modes in the presence of the coupler. More details about the optimization can be found in [8].

2 CELL SHAPE OPTIMIZATION

Having the same frequency as in the TESLA project [9] and planning to use TESLA-like multi-cell cavities in the main linac of the ERL, we first chose the shape of the 2-cell cavity also TESLA-like (Fig. 1a). However, it turned out that this geometry has a trapped dipole mode. In order to allow this mode to propagate into the beam pipe we decided to use the KEK approach by enlarging one of the beam pipes. We chose the inner radius of one of the beam pipes and the radius of the iris equal to these of TESLA.

*Supported by Cornell University
#vs65@cornell.edu

0-7803-7738-9/03/$17.00 © 2003 IEEE

Scaling of the KEK single-cell dipole-mode-free cavity gave us bigger inner radii. A decrease of the inner iris radius increases the frequency of the dipole mode significantly, so we stayed at the TESLA value for the inner iris radius. The larger beam pipe, right-hand one on the Figs. 1b and 1c, serves for propagating the dipole mode out from the cavity. The right iris (Fig. 1c) secures identity of fields in both cells but does not preclude the coupling of the dipole mode with the beam pipe.

We analyzed the influence of different cavity dimensions on the TE11-mode frequency, on the maximal values of the surface fields, electric and magnetic, and on the value of R/Q of the fundamental mode.

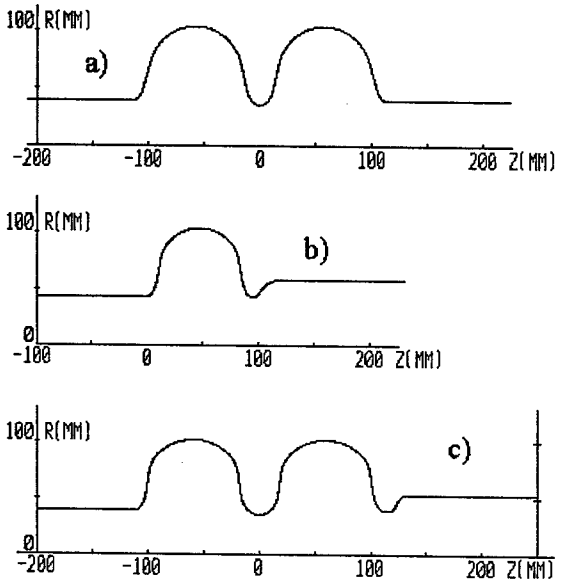


Fig. 1. a) Geometry with a trapped dipole mode (TESLA-like), b) KEKB geometry with a propagating dipole mode, c) Optimized geometry for the ERL injector with a propagating dipole mode.

The frequency of the dipole (TE11-like) mode was kept at least 10 MHz higher than the cut-off frequency of the beam pipe. The right iris has the same inner radius as the left pipe. The bigger right-hand beam pipe radius causes negligible asymmetry of the fundamental mode

Even having strong restrictions upon the frequency of the dipole mode, we have found main cavity parameters being not much different from those of the TESLA cavity. This can be explained by an additional freedom: we have no limitations to the cell length. As one can see (Fig. 1), the injector cavity has a thicker iris than in TESLA. This is connected with the quest for higher frequency of the dipole mode. The cell-to-cell coupling is weaker (0.7 %) but still sufficient for 2 cells.

The simulation code MultiPac [10] is used to check multipacting characteristic of the optimized cavity. This cavity shape is free of multipacting according to the criteria of this code. Though the resonant motion of electrons can take place at peak surface electric fields of 30 – 40 MV/m, the impact energy is about only 26 eV, which is too low to warrant electron multipacting. For the original TESLA shape, resonant trajectories also exist with an average impact energy of 32 eV that also is taken as a low value.

3 COUPLER SHAPE OPTIMIZATION

Fig. 2 shows the geometry of the cavity with a twin-coaxial coupler and some details of the coupler. Because the ERL injector cavity coupler has to transfer an average power of 100 kW, we have decided to use a 60 mm diameter outer conductor [4]. To minimize losses in the inner conductor we chose an impedance of 60 Ohm. A shape of the antenna tips presents a bended elliptic disc. Parameters of this disc were found from two requirements: to keep the dipole mode frequency as high as possible, and provide necessary coupling with the cavity. The bending of the disc, for example, increases coupling by 20 % as compared with a flat disc.

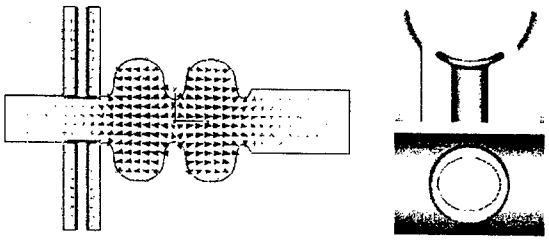


Fig. 2. Geometry of the cavity with the fundamental mode excited in it and details of the coupler.

The coupling is adjustable by changing the depth of penetration of the antenna tip (Fig. 3). The edges of the cross-sections between the outer tube of the coaxial line and the beam pipe are rounded with a radius of 4 mm. This helps to exclude high values of electric field on the surface and increases coupling, but decreases the dipole mode frequency. Finally (see Fig. 2), the smaller radius of the elliptic cross-section and the ratio of its half-axes were used for optimization.

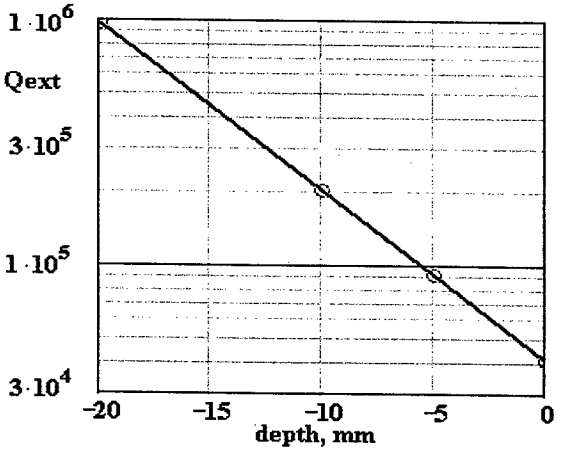


Fig. 3. Dependence of Q_{ext} on the depth of antenna penetration measured relative to the inner cavity iris.

The final value $Q_{ext} = 4.08\times 10^4$ satisfies the specified requirements. The value of the R/Q obtained with MWS is 218 Ohm.

The value of the transverse kick is recalculated in comparison with the previous estimation [4], because the position of the coupler had changed from the large beam pipe to the narrow one, and geometry of the antenna tip had changed as well. For geometric asymmetry Δl in penetration of the antenna tip when the penetration is maximal, the kick is

$$\left(\Delta p_t/\Delta p_l\right)_{geo} = \left(-0.2-2.2i\right)\cdot 10^{-4}\ \ \Delta l/\text{mm},$$

where Δp_t is the change of the transverse momentum, and Δp_l is the change of the longitudinal momentum of particles after passing the cavity along its axis. For phase asymmetry $\Delta\varphi$ between two antennas the kick is

$$\left(\Delta p_t/\Delta p_l\right)_{phase} = \left(1.1-0.7i\right)\cdot 10^{-4}\ \ \Delta\varphi/\text{degree}.$$

The kick now is about 3 times bigger than in the previous calculation but still quite tolerable.

4 PROPERTIES OF THE DIPOLE MODE

We maintained the condition

$$\Delta f(\text{TE11}) = f(\text{TE11}) - f_{\text{cut-off}} \geq 10\,\text{MHz}$$

for the dipole mode by optimizing the cavity shape to secure adequate propagation. Calculation with both SLANS2 and MWS code gave $\Delta f(\text{TE1}) = 10.0$ MHz for the final shape.

When two coaxial couplers are added to the geometry, degeneracy of the dipole mode is cancelled, and the mode splits into 2 modes: parallel and transverse mode (with the electric field in the cavity parallel or perpendicular to the coaxial line). Their frequencies changed from the original one but still stayed high enough over the cut-off frequency. These frequencies depend on the coupler geometry, and on the boundary condition at the end of the larger beam pipe. The frequency of the parallel mode depends also on the boundary condition at the ends of the coaxial line. This means that the parallel mode is excited not only in the larger beam pipe but in the coaxial line also and thus has all the more low external Q. With the method described in detail in [4] and extended for circular waveguides, the value of Q_{ext} of the parallel dipole mode was found as $Q_{ext,\,p} = 250$. The transverse dipole mode has lower frequency than the initial value (without input coupler) but still propagates into the beam pipe and has $Q_{ext,\,t} \sim 1000$.

5 CONCLUSIONS

Optimization of the superconducting 2-cell cavity-coupler system for the ERL injector was performed using the MWS 4.0 and SLANS software packages to produce dipole-mode-free and kick-free cavity. Main parameters of the cavity are presented in Table. The completion of calculations allows us to begin production of the injector cavity with the twin-coaxial coupler.

Table. Calculated parameters of the 2-cell cavity with the twin-coaxial coupler.

Fundamental π-mode frequency	1300 MHz
E_{pk}/E_{acc}	1.94
H_{pk}/E_{acc}	42.8 Oe/(MV/m)
Coupling cell to cell	0.7 %
R/Q, fundamental mode (FM)	218 Ohm
Q_{ext}, FM, required range	4.6×10^4...4.1×10^5
Q_{ext}, FM, penetration *depth* of the antenna = 0...-15 mm	4.1×10^4...4.6×10^5
$Q_{ext,p}$, dipole mode, parallel	250
$Q_{ext,t}$, dipole mode, transverse	1000

6 REFERENCES

[1] Study for a proposed *Phase I Energy Recovery Linac (ERL) Synchrotron Light Source at Cornell University*, ed. by S. Gruner and M. Tigner, CHESS Technical Memo 01-003 and JLAB-ACT-01-04 (July 4, 2001).

[2] I. Bazarov, et al., "Phase I Energy Recovery Linac at Cornell University", *Proceedings of the 8th European Particle Accelerator Conference*, Paris, France, June 2002, pp. 644-646.

[3] S. Belomestnykh, et al., "High Average Power Fundamental Input Couplers for the Cornell University ERL: Requirements, Design Challenges and First Ideas," Cornell LEPP Report ERL 02-8 (September 9, 2002).

[4] V. Shemelin, S. Belomestnykh and H. Padamsee, "Low-kick Twin-coaxial and Waveguide-coaxial Couplers for ERL", Cornell LEPP Report SRF 021028-08 (November 28, 2002).

[5] H. Padamsee et al., "Accelerating Cavity Development for the Cornell B-Factory, CESR-B", *Proceedings of the PAC'91*, pp. 786-788.

[6] S. Mitsunobu et al., "Superconducting RF Activities at KEK", *Proceedings of the 5th Workshop on RF Superconductivity*, Hamburg, Germany, 1991, pp. 84-94.

[7] D. G. Myakishev, V. P. Yakovlev. "The New Possibilities of SuperLANS code for Evaluation of Axisymmetric Cavities", *1995 Particle Accelerator Conference and International Conference on High-Energy Accelerators*, Texas, May 1995, pp. 2348-2350.

[8] V. Shemelin, H. Padamsee, S. Belomestnykh, "HOM-free 2-cell cavity with strong input coupler for the SC ERL injector", Cornell LEPP Report SRF 030219-01 (February 19, 2003).

[9] B. Aune et al., "Superconducting TESLA Cavities", *Phys. Rev. ST Accel. Beams* 3 092001 (2000).

[10] P. Ylä-Oijala et al. MultiPac 2.1. Rolf Nevanlinna Institute, Helsinki, 2001.

HIGH BRIGHTNESS, HIGH CURRENT INJECTOR DESIGN FOR THE CORNELL ERL PROTOTYPE*

I.V. Bazarov† and C.K. Sinclair, Wilson Laboratory, Cornell University, Ithaca, NY 14850

Abstract

Cornell University, in collaboration with Jefferson Laboratory, has proposed the construction of a 100 MeV, 100 mA CW Energy Recovery Linac (ERL) prototype, to study and resolve the many accelerator physics and technology issues of this type of machine. The long term goal of this work is the construction of a state-of-the-art 5 to 7 GeV ERL-based synchrotron light source. A key element of this machine is a high brightness injector with every bunch filled (77 pC/bunch at 1300 MHz). We report the design of a versatile injector for the prototype ERL which also meets the requirements for a full energy light source. The injector uses a very high voltage DC photoemission electron gun with a GaAs photocathode and a conventional bunching cavity. A cryomodule with five two-cell superconducting RF cavities allows energies between 5 and 15 MeV to be delivered, with an average beam power of 500 kW limited by the installed RF power. Thorough simulations, using realistic particle distributions at the photocathode, indicate this injector should provide a normalized rms transverse emittance approaching 1 mm-mrad, and an rms longitudinal emittance of 10 keV-degrees. Operation at reduced bunch charge will provide a smaller transverse emittance, until aberrations and the time dependence of the RF fields impose limitations.

INTRODUCTION

There is considerable current interest in developing ERLs as driver accelerators for the production of synchrotron radiation. The transverse and longitudinal emittances of the full energy beam in such accelerators are not limited to the equilibrium values that prevail in similar energy storage rings, but rather are determined by the emittances produced in the injector and any growth during subsequent acceleration and transport. In principle, an ERL-based light source should deliver high flux X-ray beams with beam brightness much higher, and pulse durations far shorter than those available from storage rings.

Many accelerator physics and technology issues must be quantitatively understood before the construction of a full scale ERL light source can be responsibly proposed. To address and resolve these issues, Cornell, in collaboration with Jefferson Lab, has proposed the construction of a low energy, full current ERL prototype [1]. The injector is a key element of this small accelerator. It must deliver a high average current beam with very small transverse and longitudinal emittances, at a sufficiently high energy that space charge effects are under control. Since our proposal was written, we have developed a complete design for this injector. The performance of this design has been modeled in detail. The code ASTRA [2] was used to model the beam propagation from the photocathode through the injector cryomodule. Since bend magnets are not included in ASTRA, PARMELA [3] was used to model through the magnets that merge the injector beam with the full energy recirculated beam at the main linac entrance. Coherent synchrotron radiation (CSR) effects in the merger magnets were modeled with `elegant` [4]. We present here the detailed injector design, and various simulation results. These indicate that this injector design will deliver a 100 mA average current beam with very low transverse and longitudinal emittances. The emittance is significantly improved at reduced bunch charge.

INJECTOR DESIGN

The ERL will use the established TESLA SRF technology at 1300 MHz. 100 mA average current corresponds to 77 pC/bunch. We will use a DC photoemission gun operating at 500 to 750 kV to deliver this current. The cathode electrode has a 20° cone angle for transverse focusing. A negative electron affinity GaAs photocathode offers high quantum efficiency and a low thermal emittance. The cathode is illuminated by a 780 nm, harmonically mode-locked Ti:sapphire laser providing a 1300 MHz train of $\sim$ 45 ps FWHM duration pulses [5]. The optical beam at the photocathode will be shaped to a near-flattop transverse profile by refractive optics [6], and will have a Gaussian longitudinal profile.

The center of the first solenoid is located $\sim$ 29 cm downstream of the photocathode, after an RF shielded gate valve. A single cell buncher cavity, adapted from the PEP-II cell design [7], is used for conventional drift bunching. The center of this cell is 50 cm from the center of the first solenoid. A second solenoid follows the buncher cavity.

Acceleration to the full injector energy is provided by a cryomodule containing five two-cell SRF cavities [8]. The center of the first cavity is 1 m downstream from the center of the buncher cavity. These two-cell cavities were carefully designed to assure that harmful dipole higher-order modes propagate through the beam pipe to ferrite HOM loads [9]. Beam energy is not recovered in the injector. With an energy gain of 5 MeV in the injector cryomodule, each cavity delivers 100 kW of average beam power. Each cavity has two coaxial couplers, to minimize the coupler kick and keep the power delivered per coupler at a con-

* Work supported by Cornell University
† bazarov@cornell.edu

0-7803-7738-9/03/$17.00 © 2003 IEEE

servative 50 kW. The couplers are variable, allowing the external Q to be changed. This feature allows operation at higher injector energy and reduced average current, subject only to the limitation imposed by the 500 kW of installed injector RF power. We will explore injector performance over an energy range of 5 to 15 MeV.

Three sector dipoles with equal bend angles merge the injected beam with the full energy single pass recirculated beam. We have calculated the effects of space charge and CSR through these merger magnets, to completely characterize the injector beam at the entrance to the main linac. Fig. 1 gives a schematic view of the full injector.

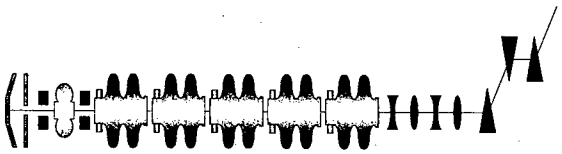


Figure 1: Injector schematic.

PARAMETERS AND MODELING

We have explored a broad range of operating parameters for the injector elements, but have not yet done a final optimization. Rather, we have sought to demonstrate a modeled performance significantly better than required for the proposed ERL, as a solid proof-of-principle that our performance requirements can be met.

Initial ASTRA modeling was done with a small number of macroparticles, and a "tophat" transverse distribution and zero thermal emittance at the cathode, to quickly

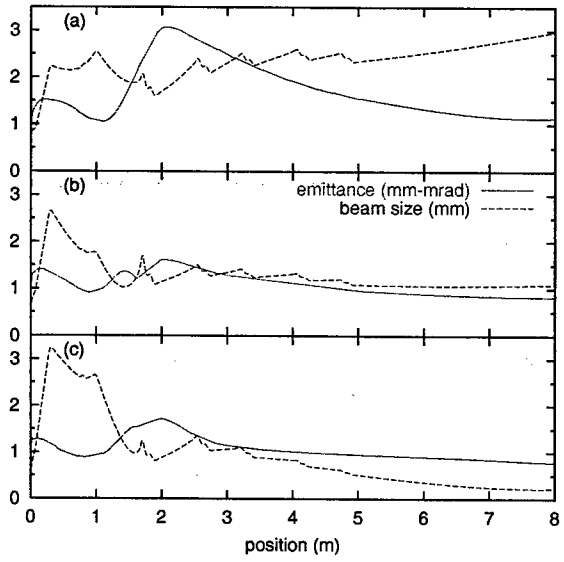


Figure 2: Rms normalized emittance and rms beam size for 77 pC/bunch for different kinetic energies at the end of the injector: a) 6 MeV, b) 11 MeV, and c) 15 MeV

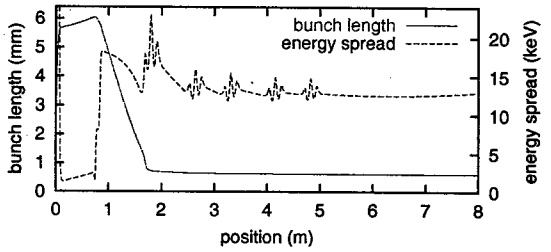


Figure 3: Rms bunch length and rms energy spread in the injector for 77 pC/bunch, 11 MeV final energy.

determine the best value ranges for the fields of the two solenoids and the buncher. Modeled fields were used for the gun, solenoids, and buncher and accelerator cavities.

Following the survey runs, detailed ASTRA solutions were developed at several different injector energies, using 5000 macroparticles. For these cases, the Fermi-Dirac distribution of Ref. 6 with a β value of 15 was used for the transverse distribution at the cathode. The thermal emittance due to an effective cathode temperature of 35 meV, as measured for GaAs photocathodes, was used in all cases [10].

ASTRA modeled beam from the photocathode to 3 m after the cryomodule. As the superconducting cavity energy gain increases, the RF focusing in the first cavity also increases. To obtain solutions with reasonable behavior of the beam envelope, the illuminated spot size at the cathode was decreased as the energy was increased. We found well-behaved solutions from 6 to 15 MeV, with normalized transverse emittances below about 1 mm-mrad and longitudinal emittances about 10 keV-degrees. Three such solutions are shown in Fig. 2. Typical bunch length and energy spread in the injector are shown in Fig. 3.

Emittance growth due to space charge through the merger magnets was modeled with PARMELA. The Twiss

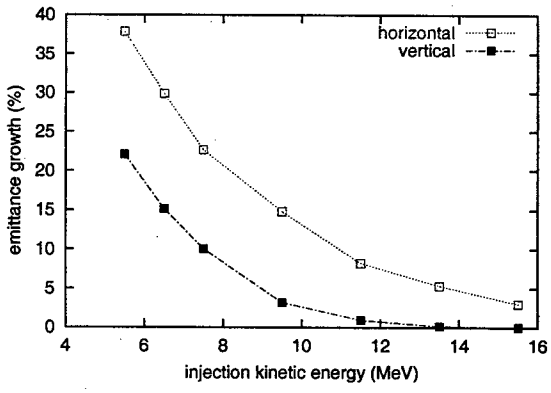


Figure 4: Emittance growth in the merger due to space charge for different injection energies. Initial rms normalized emittance is taken to be 1 mm-mrad.

parameters at the entrance to the merger were selected to obtain reasonable beam envelopes in the main linac, where the initial RF focusing is very strong due to the very high (20 MV/m) accelerating gradient, particularly at the lowest injector energy. The results are given in Fig. 4. Reducing the gradient in the first main linac cavity, or operating at higher injection energies will reduce the emittance growth through the merger system.

CSR effects through the merger magnets were modeled with `elegant` for a 15 MeV, 0.6 mm long bunch as a function of the bend angle of the merger dipoles. No shielding effects were included. The results are shown in Fig. 5. We will use a 15° bend angle for the merger magnets. The emittance growth depends strongly on the bunch length at the entrance of the merger system. The bunch length for these simulations, as determined from the previous ASTRA runs, varied between 2 and 3 ps. The optimum bunch length for a full scale ERL has not yet been determined. The simulations here apply to the case where the synchrotron radiation critical wavelength is much shorter than the bunch length. Some reduction in the effect is possible at the lowest injector energy, where the critical wavelength is the longest.

Operation of the full energy ERL with reduced emittance, obtained by reducing the bunch charge, will be important for some applications. By reducing the bunch charge a factor of ten, we have obtained a significantly smaller final emittance, as shown in Fig. 6. While the thermal emittance of the cathode is a noticeable contribution in this case, space charge remains the major source of emittance growth. We plan to conduct further optimizations for the low emittance, reduced bunch charge case.

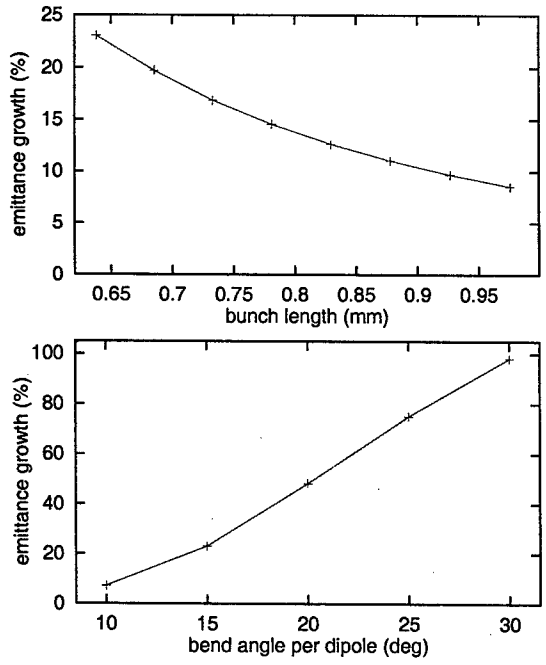


Figure 5: Emittance growth in the merger due to CSR for 77-pC bunch as a function of rms bunch length (top) and dipole bend angle for 0.6-mm bunch (bottom). Initial rms normalized emittance is taken to be 1 mm-mrad.

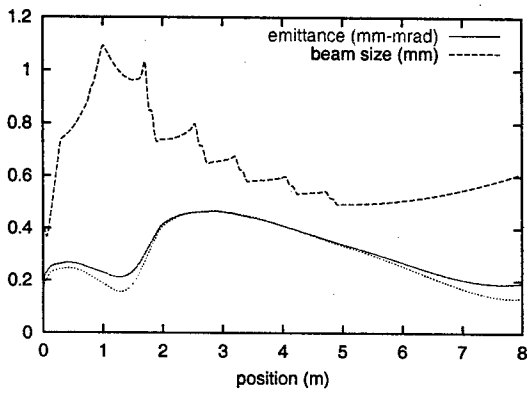


Figure 6: Rms normalized emittance and rms beam size for 8 pC/bunch. Dotted line shows emittance in case of zero thermal emittance at the photocathode. Kinetic energy at the end of the injector is 6 MeV.

CONCLUSIONS

Based on the simulations we have conducted to date, we are confident that our ERL injector design will deliver a beam with rms normalized transverse and rms longitudinal emittances of about 1 mm-mrad and 10 keV-degrees. The strong RF focusing in the initial cavity of the injector, and again in the first cavity of the main linac, complicates finding the optimum parameters. We plan to conduct a more complete exploration of all parameters using computer-aided optimization routines.

REFERENCES

[1] S.M. Gruner, M. Tigner (eds.), CHESS TM 01-003, available at http://erl.chess.cornell.edu/papers/ERL_Study.pdf

[2] K. Flöttmann, *ASTRA User Manual*, September 18, 2000.

[3] L. Young, *PARMELA Reference Manual*, LA-UR96-1835, January 8, 2000.

[4] M. Borland, *elegant: A Flexible SDDS-Compliant Code for Accelerator Simulation*, APS LS-287, September 2000.

[5] C. Hovater and M. Poelker, NIM A **418**, 280 (1998).

[6] J. Hoffnagle and C. Jefferson, Appl. Opt. **39**, 5488 (2000).

[7] V. M. Vescherevich and S. Belomestnykh, *Buncher Cavity for ERL*, Proceedings of PAC'03.

[8] H. Padamsee et al., *Overview of the Cornell ERL Injector Cryomodule*, Proceedings of PAC'03.

[9] V. Shemelin et al., *Dipole-Mode-Free and Kick-Free 2-cell Cavity for the SC ERL Injector*, Proceedings of PAC'03.

[10] B.M. Dunham et al., *Emittance Measurements for the Illinois/CEBAF Polarized Electron Source*, Proceedings of PAC'95.

EMITTANCE GROWTH DUE TO THE FIELD ASYMMETRY IN THE TTF RF GUN

J.-P. Carneiro*, DESY, Hamburg, Germany

Abstract

This paper reports the effect on the transverse emittance of the multi-pole field components due to the input coupler of the TTF RF gun. ASTRA simulations with 3D fields from CST MicroWave Studio (MWS) are presented for a typical operation of the Fermilab photo-injector at 1 nC.

INTRODUCTION

The Tesla Test Facility (TTF) RF gun has been developed by Fermilab as a contribution to the TTF collaboration. The gun consists in a 1.625 cells cavity resonating in the $TM_{010,\pi}$ mode at a frequency of 1.3 GHz. It is feed through a waveguide connected to the full cell by a coupling slot. Previous studies [1], [2] reported that this side coupling into the full cell induces a field asymmetry which deteriorates significantly the transverse emittance.

In the studies presented in this paper, we used the new implementation of the ASTRA code ([3], [4]) which allows 3D electric fields to be read instead of the usual 2D fields. In this case, the 6 components of the electric field are taken every millimeter around and along the longitudinal axis (+/- 10 mm in X and Y, and 250 mm in Z). In order to cross-check this new implementation, we compared first, for a symmetric RF gun (without coupler), the ASTRA beam dynamics using 2D fields from Superfish [5] and 3D fields from CST MicroWave Studio (MWS) [6]. Then, we developed a MWS version of the RF gun including the coupler and the waveguide and exported the 3D fields into ASTRA. As a benchmark, we considered a typical FNPL photo-injector operation at 1 nC. This photo-injector is a duplicate of the one that was installed at DESY Hamburg for the phase I of TTF.

SYMMETRIC RF GUN

A symmetric model of the RF gun has been first built using Superfish and is represented in Figure 1(a). Several iterations have been necessary in order to determine the diameters of the hall and full cells (resp. Θ^{HC} and Θ^{FC}) which lead to a frequency of the π-mode (f^{π}) close to 1.3 GHz with a field flatness ($\alpha = E_z^{HC}/E_z^{FC}$) near unity. In the model showed in Figure 1(a), $\Theta^{HC} = 178.387$ mm and $\Theta^{FC} = 178.47$ mm were used leading to $f^{\pi} = 1300.009$ MHz and $\alpha = 0.99$. The cavity internal quality factor was $Q_0 = 23665$.

* Jean-Paul.Carneiro@desy.de

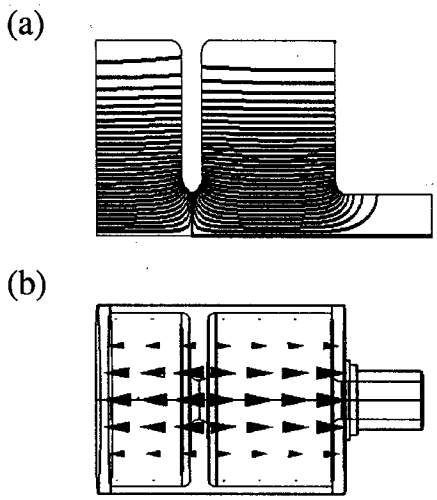


Figure 1: Symmetric model of the RF gun using (a) Superfish and (b) MicroWave Studio.

In order to compare the MWS fields with the ones produced by Superfish, a MWS model of the symmetric RF gun has been built (Figure 1(b)) using the same dimensions than those used with Superfish. The comparison is shown in Figure 2. As we will discuss in Figure 6, the fields and electrical characteristics of the cavity (f^{π}, α, Q_0) produced by MWS were found to be strongly dependant with the size of the quadratic mesh used for the runs. Here a fine mesh has been used in MWS ($\Delta_x = \Delta_z \cong 4$ mm, $\Delta_y \cong 2$ mm), leading to $f^{\pi} = 1299.82$ MHz , $\alpha = 0.99$ and $Q_0 = 22082$, close to the Superfish results.

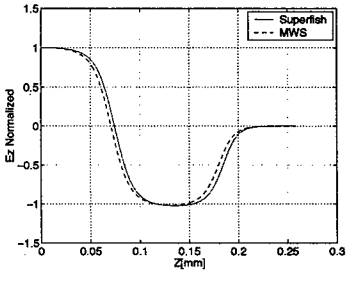


Figure 2: Comparison between Superfish and MWS of the longitudinal electric field on axis for the symmetric model of the RF gun

0-7803-7738-9/03/$17.00 © 2003 IEEE

RF GUN WITH COUPLER

A layout of the MWS model of the RF gun with the coupler and waveguide is shown in Figure 3. A description of the coupler is presented in [7].

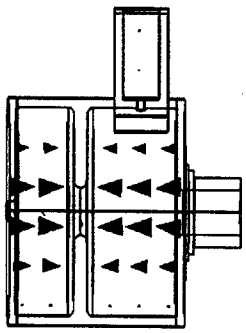


Figure 3: MWS model of the TTF RF gun with coupler.

Computation of the external Q

We tuned the asymmetric RF gun by slightly decreasing the diameter of the cells with MWS in order to obtain a resonant frequency of 1.3 GHz, with a field flatness $\alpha = 1$ and a coupling $\beta = Q_0/Q_{ext} = 1$. The internal quality factor Q_0 was computed directly by MWS and we used the Kroll-Yu method [8] to compute the Q external (Q_{ext}) of the cavity. In this method, a resonant curve of the phase shift along the waveguide vs. the frequency of the π-mode is mapped out, as shown in Figure 4. The slope of the curve multiplied by one half of the resonant frequency results in Q_{ext}. After several iterations, we obtained: $f_\pi = 1300.054$ MHz, $\alpha = 1.03$ and $\beta = 1.7$ for a fine mesh ($\Delta_x = \Delta_z \cong 4$ mm, $\Delta_y \cong 2$ mm), the RF gun being slightly overcoupled.

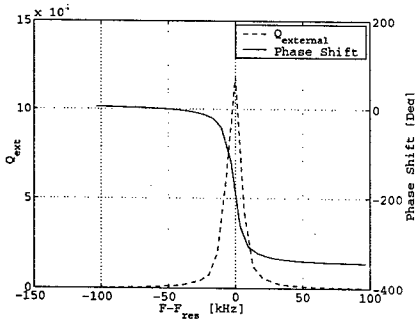


Figure 4: Phase shift vs. frequency (F_{res}=1.3 GHz).

Figure 5 compares the longitudinal component of the electric field E_z taken along the Y axis (axis of the coupler), at $z = 138.5$ mm and $x = 0$ (middle of the coupler) for the case of a symmetric and asymmetric RF gun. Both

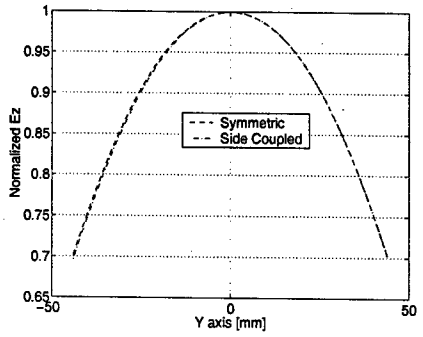


Figure 5: Longitudinal electric field on the coupler axis.

simulations were done with a fine mesh. From these simulations, we can see that the coupler does not induce a shift of the electric field E_z.

IMPACT ON BEAM DYNAMICS

In the FNPL photo-injector setup, the RF gun is surrounded by 3 solenoids (a primary, a secondary and a bucking to zero the magnetic field on the cathode) and is followed by a 9-cell superconducting cavity. We stopped our simulations at $z = 3.8$ m, i.e at the exit of the 9-cell. A description of the entire FNPL beam line is presented in [9]. In the ASTRA simulations presented here, we considered a typical operation of the FNPL photo-injector at 1 nC. We used a uniform transverse and longitudinal distribution of the laser beam of 5000 macro-particles with respectively a diameter of 3 mm diameter and a length of 11 ps. The three solenoids were set at 260 A, implying a peak magnetic field of $\sim$ 1321 Gauss and a residual magnetic field on the photo-cathode of $\sim$ 62 Gauss. In the case of a symmetric RF gun using the Superfish electric fields (ASTRA-2D), the peak field at the cathode was 40 MV/m resulting in a kinetic energy of the beam at the exit of the booster of $E_k = 17.27$ MeV for a launch phase of 40°. The accelerating field on the 9-cell cavity was 12 MV/m with a phase of $\sim 10°$ off-crest to minimize the energy spread ($\sim$ 26 keV). In the case of ASTRA-3D simulations using the 3D electric fields from MWS, the peak field on the cathode was lowered ($E_0 = 38.7$ MV/m for the symmetric RF gun and $E_0 = 39.0$ MV/m for the RF gun with coupler) in order to match the energy given by ASTRA-2D.

Case symmetric RF Gun

Figure 6 shows that in the case of a symmetric RF gun using the 2D electric fields from Superfish (Figure 1(a)), the transverse emittance of the beam at $z = 3.8$ m is symmetric at $\epsilon_x = \epsilon_y = 2.3$ mm-mrad. It is interesting to notice that when using the 3D fields from MWS, the emittance converges with the size of the mesh used for the MWS simulations to reach a very good agreement with the ASTRA-2D simulation. In fact, for the same geome-

try (Figure 1(b)), the emittance lowers from $\epsilon_x = \epsilon_y \cong 18$ mm-mrad to $\epsilon_x = \epsilon_y = 2.3$ for a mesh size in MWS of resp. $\Delta_x = \Delta_z \cong 10$ mm, $\Delta_y \cong 5$ mm and $\Delta_x = \Delta_z \cong 4$ mm, $\Delta_y \cong 2$ mm. A smaller mesh size in MWS leads to a better accuracy of the electric field but at a price of a much longer simulation run.

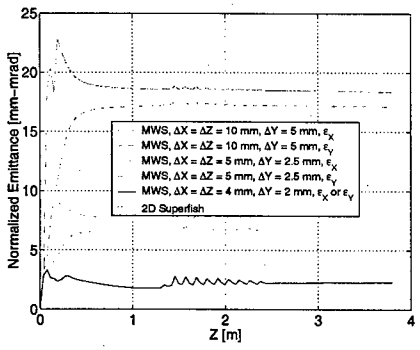


Figure 6: ASTRA simulation for a typical 1 nC operation of the FNPL photo-injector with a symmetric RF gun using 2D electric fields from Superfish and 3D electric fields from MWS (for different mesh sizes).

Case RF Gun with coupler

In the case of an RF gun with coupler, we had no time to do a convergence study of the emittance with respect to the mesh size in the MWS runs. We used a mesh size of $\Delta_x = \Delta_z \cong 4$ mm, $\Delta_y \cong 2$ mm in the same order of the one that showed a good convergence in the case of the symmetric RF gun. In this case, Figure 7 reports an emittance $\epsilon_x = 2.5$ mm-mrad and $\epsilon_y = 2.45$ mm-mrad when using 3D fields from MWS. For comparison, we reported also in Figure 7 the ASTRA-2D simulation using the symmetric RF gun. These simulations show an increase of the emittance in the case of an RF gun with coupler compared to the symmetric RF gun of $\Delta\epsilon_x = 0.2$ mm-mrad and $\Delta\epsilon_y = 0.15$ mm-mrad. We suspect this increase of the emittance to be due either from the coupler kick or from the mesh used in the MWS runs. A study of the convergence of the emittance for finer mesh size in MWS runs in the case of an RF gun with coupler is necessary to solve this dilemma.

CONCLUSION

ASTRA simulations showed an increase of the emittance of $\sim 10\%$ for a typical operation of the FNPL photo-injector at 1 nC in the case of an RF gun with coupler compared to a symmetric RF gun. These simulations have been done using the new feature of the ASTRA simulation code that allows the use of 3D electric fields. These fields were obtained using MicroWave Studio and it has been shown

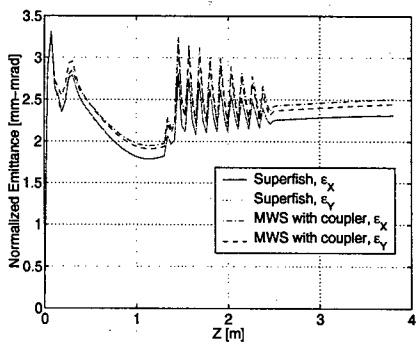


Figure 7: ASTRA simulation for a typical 1 nC operation of the FNPL photo-injector using 2D electric fields from Superfish (symmetric RF gun) and 3D electric fields from MWS (RF gun with coupler).

that the higher the accuracy (i.e the finer mesh) on the electric field the smaller the emittance.

More work needs to be done to determine if this increase of 10% comes from the coupler kick or from the accuracy of MWS on the electric field. If it comes from the coupler kick, then this increase will be 5 times smaller than the one presented in reference [2].

ACKNOWLEDGMENT

The author would like to thank M. Dohlus for helpful discussions, M. Krassilnikov for supplying the first MWS version of the RF gun, S. Schreiber and D. Edwards for a careful reading of the paper.

REFERENCES

[1] D. T. Palmer *et al.*, "Microwave measurements of the BNL/SLAC/UCLA 1.6 cell photo-cathode RF gun", Proceedings of the PAC 1995, Dallas.

[2] M. Krassilnikov *et al.*, "Impact of the RF-GUN Power Coupler on Beam Dynamics", Proceedings of the EPAC 2002, Paris.

[3] K. Floettmann, "ASTRA User Manual", available at http://www.desy.de/mpyflo/Astra_dokumentation/.

[4] S. Lidia *et al.*, "Recent Improvements to the ASTRA Particle Tracking Code", these proceedings.

[5] POISSON/SUPERFISH group of codes, Version 4.28 for PC, Los Alamos, 2002.

[6] CST MicroWave Studio, Version 4.0, Darmstadt, 2002.

[7] J.-P. Carneiro *et al*, TESLA note 0313, to be published.

[8] N. M. Kroll and D. U. Yu, "Computer Determination of the External Q and Resonant Frequency of Waveguide Loaded Cavities", Particle Accelerators, 34(231), 1990.

[9] J.-P. Carneiro *et al.*, "Transverse and longitudinal beam dynamics at the FNPL Photoinjector", to be submitted to PR-STAB.

EXPERIMENTAL STUDIES OF RF BREAKDOWNS IN THE COUPLER OF THE TTF RF GUN

J.-P. Carneiro*, S. Schreiber, DESY, Hamburg, Germany
D. Edwards, I. Gonin, FNAL, Batavia, USA

Abstract

During the TTF-FEL Phase I, the RF gun of the TESLA Test Facility (TTF) has been operated with long RF pulses (up to 0.9 ms) and high RF peak power (up to 3 MW). RF breakdowns have been observed and localized in the RF input coupler. In this report we will present statistics of RF breakdowns for different RF pulse length, peak power and repetition rates from 0.1 Hz to 2 Hz. We will also discuss the origin of these breakdowns.

INTRODUCTION

Fermilab has developed and delivered to DESY two RF guns for the operation of phase 1 of the TESLA Test Facility (TTF) linear accelerator. The first RF gun (designated *G3* in the following) has been operated in TTF from October 1998 to April 2002. *G3* presented a reliable behavior with short RF pulses ($< 300\ \mu s$). However, for longer RF pulse lengths, the gun suffered more and more from RF breakdowns reducing the effective beam time. At the point, where the breakdown rate was not acceptable for the test of TESLA accelerating structures, a second RF gun (*G4*) has been installed in June 2002. Gun *G4* has been operated at the Fermilab/NICCAD photoinjector test stand from 1999 to March 2002 with short RF pulses (typically $30\ \mu s$) and at DESY until November 2002 with long RF pulses ($900\ \mu s$). The forward power was usually 2.8 MW with a repetition rate of 1 Hz. For this study, different pulse lengths and repetition rates ranging from 0.1 Hz to 2 Hz have been used. In contrast to the operation at Fermilab, breakdowns have also been observed with *G4* at DESY, fortunately with a much lower rate than *G3*. This paper will describe the dependence of the breakdown rate on the RF pulse length, forward power, and repetition rate. The origin of these breakdowns will be discussed as well.

RF GUN DESCRIPTION

The Fermilab RF gun consists of a 1 1/2-cell (1.625) OFHC copper structure resonating in the $TM_{010,\pi}$ mode at 1.3 GHz. It is a high duty cycle RF gun designed to handle $800\ \mu s$ long RF pulses with 4.5 MW of peak power and at 10 Hz repetition rate. In this regime, an average power of 36 kW is dissipated in the cavity walls. This heat is removed by water flowing in cooling channels machined in the cavity walls. The cooling system allows a water flow of 4 l/s at a pressure of 6 bars.

* Jean-Paul.Carneiro@desy.de

The RF is fed into the cavity through a sideways mounted waveguide at the full cell by a coupling slot. A layout of the RF gun and the coupling slot is shown in reference [3].

BREAKDOWNS OBSERVATION

A layout of the RF system of the gun is presented in Fig. 1. It consists mainly in an oscillator (1.3 GHz), a vector modulator, a pre-amplifier, and a klystron. Details about the feedback loop can be found in [2] and [3].

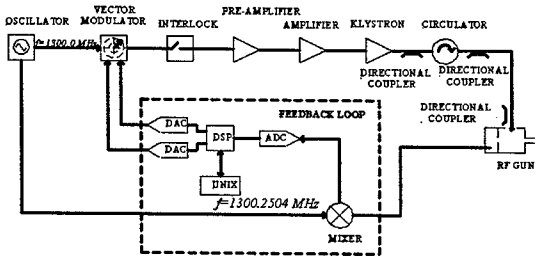


Figure 1: Layout of the RF distribution system.

As indicated in Fig. 1, an interlock module is installed at the exit of the vector modulator. In case of an interlock this module stops the RF immediately within the pulse. Fast interlock channels are: a photo-multiplier mounted at the vacuum side of the RF input coupler, an electron detector at the SF_6 side of the RF window, reflected RF power from the gun measured with a diode through a directional coupler. Other slower interlocks are: vacuum pressure, SF_6 pressure, RF window temperature.

If a breakdown occurs, the reflected RF power increases rapidly. An interlock is triggered at a threshold of 150 kW, which inhibits RF within a μs. This prevents further development of the breakdown event and limits damage to the gun. This interlock does not block the next or further RF pulses to reduce dead time.

Breakdown statistics is acquired by a script interfacing the TTF control system. It stores the RF pulse shape sampled by a 1 MHz ADC. An example of the collected statistics over 600 pulses is shown in Fig. 2. It shows a histogram of the distribution of the time of breakdown in respect to start of the RF pulse. In this example, 10 % of the 600 RF shots had a breakdown, which mostly occurred within 30 μs.

0-7803-7738-9/03/$17.00 © 2003 IEEE

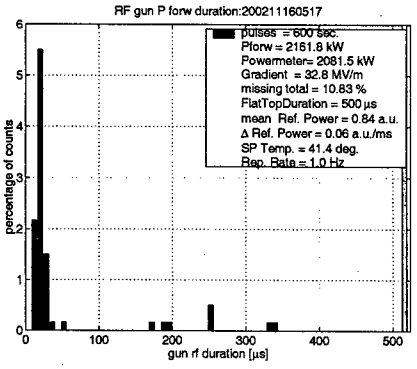


Figure 2: Example of breakdown statistics. The histogram shows the distribution of the time of breakdown in respect to start of the RF pulse. In this example, 10 % of the shots had a breakdown, which mostly occurred within 30 μs.

BREAKDOWNS STATISTICS

We measured the dependence of the breakdown probability as a function of forward power, RF pulse length, and repetition rate.

Figure 3 shows the percentage of breakdowns in respect to the number of RF pulses, measured as a function of the forward power. In this experiment, the RF pulse length is 500 μs, the repetition rate 1 Hz. In Fig. 3(a), a sharp rising edge and in (b) a smooth rising edge of the RF pulse is used. A sharp edge is achieved, when the RF pulse from the klystron is not modified, the amplitude and phase feedback is switched off. The fill time of the gun is approx. 3 μs. A smooth rising of 75 μs is obtained by modeling the forward power with the low level RF system, feedback loops closed. Each point of measurement in Fig. 3(a) is the average of two sets of measurements, each set having a statistics of 600 RF pulses. The arrows in Fig. 3(b) indicate the direction of measurement. From this data, we deduce that the breakdown events appear at a forward power of $\sim$1 MW. In the case of a sharp rising edge, the probability of breakdowns increases with the forward power: from $\sim$13 % at 2.2 MW to $\sim$24 % at 2.8 MW. In the case of a smooth edge, we see a similar percentage of breakdowns up to 2.3 MW (about 20 %), but then a decrease to $\sim$14 % occurs for higher forward powers. From this measurements we deduce, that operating the gun with a sharp or smooth rising edge of the RF pulse does not impact the breakdown probability at least up to 2.3 MW. The decrease of breakdowns for higher forward power is probably due to further conditioning of the gun. This is supported by the observation, that while reducing the RF power, much less breakdowns occurred (circles following the arrows in Fig. 3(b)).

Figure 4 shows the breakdown probability as a function of RF pulse length for a constant forward power of 2.2 MW and a repetition rate of (a) 1 Hz and 2 Hz, and (b) 0.1 Hz. Each point represents a statistics of 5 measurements, each

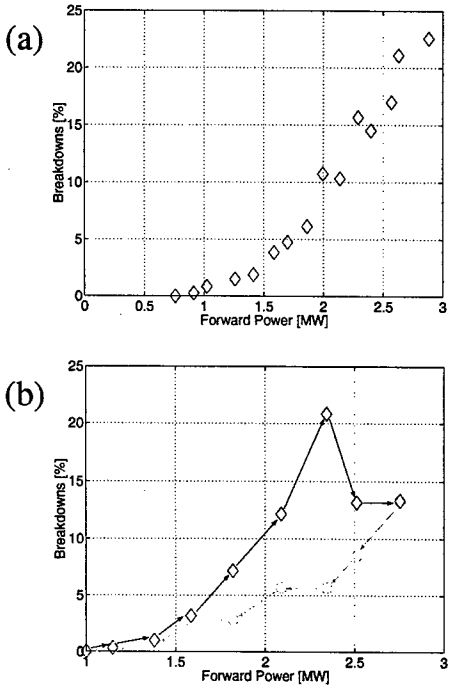


Figure 3: Breakdowns statistics versus forward power for an RF pulse length of 500 μs, a repetition rate of 1 Hz and a (a) sharp and (b) smooth RF pulse rising edge.

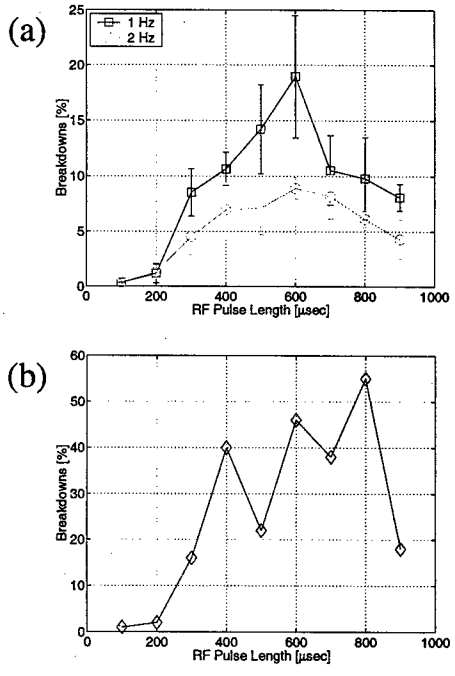


Figure 4: Breakdowns statistics versus the RF pulse length for a forward power of 2.2 MW and at (a) 1 Hz and 2 Hz (b) 0.1 Hz repetition rate.

measurement being a statistics over 600 RF pulses.

Breakdown starts to show up at an RF pulse length of more than 100 μs. The breakdown probability reaches a maximum at 600 μs. This behavior has been observed in different measurements; it is therefore not due to a conditioning effect. Comparing the breakdown rate for different repetition rates (Fig. 4(a) and (b)), it is interesting to notice, that the breakdown rate is inversely proportional to the repetition rate.

ORIGIN OF BREAKDOWNS

Piezo-electric ultrasonic sensors are used to locate the breakdowns in the RF gun [1]. The breakdowns generate an acoustic signal. Their amplitude and arrival time is measured with several sensors spread out over the outer surface of the gun and waveguides. The breakdowns have been located in the RF coupling slot, between the waveguide and the full cell.

Statistics on the breakdowns observed during the experiments presented in the previous section show (Fig. 2 as an example), that independently of the repetition rate, the forward power, the pulse length or the sharpness of the RF pulse, the breakdowns occur mainly between the 10th and the 30th μs of the RF pulse.

In the following, we try to explain this behavior. During the tuning of the RF gun, the coupling slot edges have been kept sharp. We estimate the roundness of these edges to be in the order of 0.1 mm. HFSS simulations show, that in the presence of RF power in the gun cavity, the edges facing the interior of the cavity are exposed to a strong surface magnetic field in the order of 375 kA/m (for 2.2 MW of RF power, 900 μs pulse length). This magnetic field induces eddy currents which induces heat. It is dissipated into the metal and induces stresses. Figure 5 shows ANSYS [4] simulations of the temperature and corresponding stress distribution in the coupling slot (part facing the interior of the cavity; RF 2.2 MW, 900 μs). The peak temperature is 420°C with a stress of 170 MPa. We think that the abrupt increase of the surface temperature of the copper and its associated stress is the most probable reason for the breakdowns. In fact, we suspect field emission created at surface cracks opened due to the repetitive stress. Multipactoring or sparks develop, which then led to a reflection of the incident power. Similar effects have been observed at copper RF structures at SLAC and are presented in details in [5].

A new design of the coupling slot with more round edges and using tungsten [6] could cure the breakdown problem. The melting point of tungsten is three times higher than copper.

CONCLUSION

RF breakdowns have been observed in the Fermilab RF gun for RF powers of more than 1 MW and RF pulse length of more than 100 μs. These breakdowns have been located in the coupling slot between the waveguide and the full cell. They are most probably caused by RF pulse heating inducing an abrupt temperature rise and the development of local stress. The breakdown probability increases sharply with the RF power and does not depend significantly on the sharpness of the rising RF pulse edge. The breakdown rate is inversely proportional to the repetition rate, going from 20 % at 0.1 Hz to 8 % at 2 Hz. After the end of the TTF phase 1 runs, both RF guns have been sent back to Fermilab, where these studies will be continued.

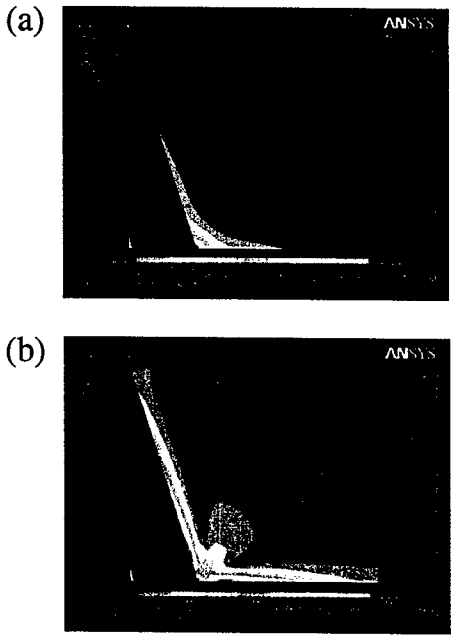


Figure 5: ANSIS simulation of the (a) temperature (°C) and (b) stress (Pa) distribution around the coupling slot edge. Forward RF power = 2.2 MW, RF pulse length = 900 μs.

ACKNOWLEDGEMENT

We thank M. Ross and J. Nelson for tracking down the breakdown location with their microphone system and H. Schlarb for scripting the breakdown statistics program.

REFERENCES

[1] J. Nelson and M. Ross, TESLA note 2001-35, Nov. 2001.

[2] G. v. Walter, Diploma Thesis, RWTH Aachen 1999.

[3] J.-P. Carneiro, TESLA note 2003-13, to be published.

[4] See http://www.ansys.com .

[5] D.P. Pritzkau, SLAC-Report-577, Dec. 2001.

[6] H. H. Braun, CLIC Note 535, Sep. 2002.

ON THE PHOTOCATHODES USED AT THE TTF PHOTOINJECTOR

S. Schreiber*, DESY, Hamburg, Germany
P. Michelato, L. Monaco, D. Sertore, INFN-LASA, Milano, Italy

Abstract

Since the start-up of the laser driven rf gun based photoinjector at the TESLA Test Facility (TTF) late 1998, several cathodes have been used. We report on the properties of Cs_2Te and KCsTe cathodes under operating conditions, their quantum efficiency and lifetime. Darkcurrent emitted by the RF gun or the cathodes have been a major concern in the first year of operation. Meanwhile, new cathode production techniques and a conditioning effect of the RF gun has reduced the darkcurrent significantly.

INTRODUCTION

Since December 1998, the TESLA Test Facility (TTF) at DESY operates a laser-driven RF gun based photoinjector. It has been used for TESLA related experiments and to drive the TTF-FEL free electron laser[1]. The TTF accelerating structures are based on superconducting technology, which allows acceleration of long pulse trains. At TTF, trains of up to 800 μs length with four different bunch frequencies have been generated: 100 kHz, 1 MHz, 2.25 MHz, and 54 MHz. Beam parameters used in different experiments or running conditions are summarized listed in Table 1.

Table 1: Electron beam parameters as produced by the TTF RF gun during the last runs.

Parameter		TESLA (CDR)	TESLA FEL (TDR)	HOM
RF frequency	GHz	1.3		
Repetition rate	Hz	1		
Pulse train length	μs	1 to 800		
gradient on the cathode	MV/m	40 MV/m		
Pulse train current	mA	8	9	2
Bunch frequency	MHz	1	2.25	54
Bunch charge	nC	1 to 8	1 to 4	0.04
Nb bunches per train		1 to 30	1 to 1800	20000
Bunch length (rms)	mm	≈ 4	≈ 3	
Laser spot diameter	mm	10	3	6

Producing a large number of bunches per train is only possible with a high quantum efficiency cathode. Cesium telluride photocathodes have been chosen, since a quantum efficiency above 1 % has been first achieved at CERN[3]. The required laser energy in the UV reduces to be only a few μJ for a bunch charge in the nC range. This makes a laser system producing thousands of laser pulses per pulse train feasible. The quantum efficiency of metals like copper are three orders of magnitude smaller and thus would require a large kW-scale laser system. In the following, we report our experience with the various cathodes used at TTF.

* siegfried.schreiber@desy.de

CATHODE SYSTEM AND PREPARATION

A sketch of the the cathode system attached to the RF gun is shown in Fig. 1. The RF gun built by FNAL is an

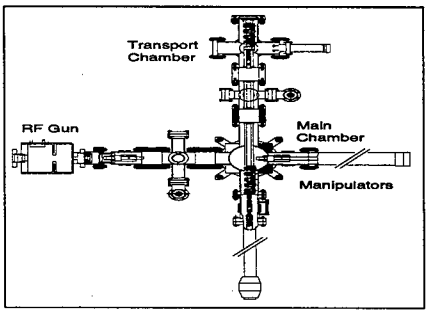


Figure 1: Schematic overview of the cathode system attached to the TTF RF gun.

L-band 1 1/2-cell RF gun operated with a 5 MW 1.3 GHz klystron. The RF pulse length is up to 900 μs with a forward RF power of 3 MW, corresponding to a gradient of 40 MV/m on the cathode, and a repetition rate of 1 Hz. A Cs_2Te or KCsTe cathode is illuminated by a train of UV (262 nm) laser pulses. The laser, a mode-locked solid-state laser system based on Nd:YLF, is synchronized with the gun RF.[4] The laser pulse length measured with a streak camera is 7 ± 1 ps.

To maintain their quantum efficiency, Cesium telluride cathodes have to stay allways in ultra-high vacuum. Therefore, a load lock system has been developed.[5] It is a split function system, where the cathodes are not prepared in the system attached to the gun, but off-site. Cathodes are first prepared at INFN-LASA in Milano. A stack of up to four cathodes is transported in a transportation chamber to DESY. During the transport, an ion pump powered by a battery keeps the vacuum level stable around $1 \cdot 10^{-10}$ mbar. The transport chamber is then attached to the load lock system of the RF gun. Two vacuum manipulators are used to pick a cathode from the stack and to insert it into the gun. Figure 2 shows the cathode plug inserted into the backplane of the gun. The RF contact is assured by a Cu-Be spring.

The cathode plug is made out of pure Molybdenum. The surface is cleaned and polished with optical quality. Thin layers of Tellurium and Cesium are then deposited in UHV onto the polished plug surface. Tellurium and Cesium react to produce Cs_2Te. It has an energy gap of 3.2 eV and an electron affinity of 0.5 eV [6]. It is blind to visible radi-

0-7803-7738-9/03/$17.00 © 2003 IEEE

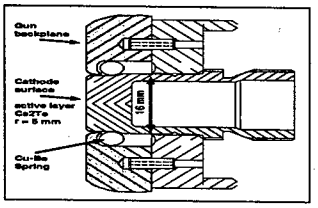


Figure 2: Detail of the cathode plug inserted to the RF gun backplane. The Cu-Be spring asuring RF contact is indicated.

ation, UV light is required for photoemission.

Cathodes have been operated in the RF gun from December 1998 to November 2002. During this four years of running, 12 different cathodes have been used, 10 Cs_2Te and 2 KCsTe cathodes (Tab. 2). In total for 1192 days, cathodes have been operated in the gun. The reason to remove a cathode has never been a low quantum efficiency. Only during the period of strong dark current, cathode have been changed frequently.

Table 2: Cathodes used during TTF phase. Cathodes not otherwise indicated are Cs_2Te.

cathode	days in use	
1	89	
13	234	
12	92	
22	9	
23	29	
21	27	
33	26	
36	145	
50	139	KCsTe
11	317	
51	85	
54	0.1	KCsTe
sum	1192	

QUANTUM EFFICIENCY MEASUREMENTS AND LIFETIME

The quantum efficiency (QE) measured with a Hg lamp after growing of the emissive film is usually very high, up to 10% for Cs_2Te and 20% for CsKTe. The spectral response shows a plateau which is reached at a wavelength of 260 nm. The measured uniformity of the QE is a few percent with respect to the maximum.[5]

Transportation

To evaluate the effect of the 24 hour long transportation, we measured the QE just before leaving Milano and just after arrival at DESY. To keep ultra-high vacuum conditions, the pumping system of the transportation chamber is powered by a battery through a DC/DC converter. This keeps the vacuum pressure in the $1 \cdot 10^{-10}$ mbar range. In Table 3, measurements performed for the first set of cathodes are reported. The measurement shows no QE degradation during the transportation.

Operation in the RF gun

The quantum efficiency of the cathodes has been measured several times during their operation in the gun. The laser energy is measured with a calibrated ($\pm$ 5%) joulemeter (Molectron). The charge is measured at the exit of the gun with an integrated current transformer (Bergoz). Figure 3 shows an example for cathode 13. From the slope of a straight line fit to the data we obtain a quantum efficiency of 0.6 %. The estimated measurement error is 10 %. The QE after the production of cathode 13 was 10 % with uniformity near to 5 %. It remained three months in the transport system before it was installed into the gun. Immedeately after its installation, we measured a QE of 5.6 %. After 5 months of usage in the RF gun, the QE decreased by a factor of 10 to 0.6 %. During this period, the pressure at the pump near the gun was stable at $3.5 \cdot 10^{-11}$ mbar. Since the gun has never been baked, we expect a water partial pressure of some $1 \cdot 10^{-10}$ mbar. In other words, the cathode has been exposed to some $1 \cdot 10^{-3}$ mbar s of water. The harmful effect of water is at least comparable to oxygen. This explains the rather low, but stable QE in our case.

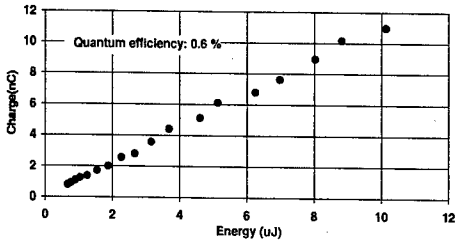


Figure 3: Measured charge output of the RF gun as a function of laser energy on cathode 13. The laser spot diamter was 10 mm.

Table 3: Quantum efficiency (QE) measured before and after transportation from Milano to DESY, after 3 month of storage, and after operating in the RF Gun for 5 months.

QE (%)	Milano	DESY	3 month storage	5 month operation
stack 1 cathode nb 13	6.1 $\pm$ 0.2 10	6.0 $\pm$ 0.3	5.6	0.6

DARKCURRENT

During operation in the RF gun, the cathode is exposed to a very high electric field of 40 mV/m. Field emission from the cathode and the gun backplane form dark current emitted by the RF gun. To understand the origin of the darkcurrent and to find ways how to suppress it has been

one of the major concerns at the beginning of the RF gun operation.

Darkcurrent values quoted here are measurd with a Faraday cup at the RF gun exit, with nominal solenoid fields which are used for beam, and for a field of 35 MV/m on the cathode surface.

In the first two years of operation, we observed frequently a sudden on-set of strong field emission. Fig. 4 shows the history of the darkcurrent measured for all cathodes operated in the RF gun. After an initial 'eruptive' period of one year, we observed suddenly a very strong emitter on the gun backplane close to cathode 21, which leads to a darkcurrent of several mA. Once this emitter has been conditioned, the darkcurrent decreased slowly, until – after another year – the darcurrent almost vanished. During

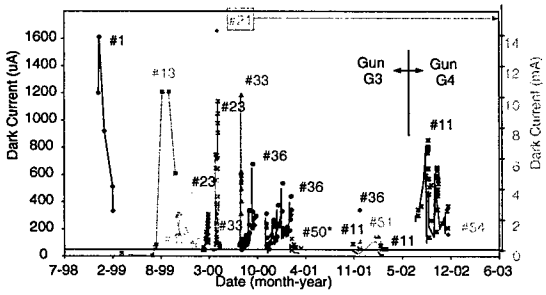


Figure 4: History of the darkcurrent of all cathodes used during TTF phase 1.

the 'hot' period, we studied the dependance of the darkcurrent on the finishing of the cathodes. The coated substrate shows always a higher dark current then uncoated Mo substrates. At the beginning, all substrate surfaces have been finished with a tooling machine, they were not mirror-like and an inspection with an optical microscope revealed deep scratches at the surface. For these reasons, the next sets of cathodes have been prepared with a better surface polishing. We used diamond grinding powder with size down to 50 nm to obtain a mirror like surface. The first Cs_2Te cathode with this new surface finishing was tested in March 1999. A significant reduction of darkcurrent has been achieved: from 300 μA to 16 μA. However, also with this cathode a sudden increase in darkcurrent after 3 month of usage has been observed.

Only after two years of operation, the darkcurrent stablized with cathode nb. 11 to a very low and for us acceptable value of 20 to 25 μA. For this reason, cathode 11 has been left in the gun from July 2001 – with some interruptions – up to the end of TTF1 mid November 2002.

Since the darkcurrent has now been low and stable, checks with a former high darkcurrent cathode could be made. We reinserted cathode 36 with which 200 μA of darkcurrent have been measured earlier. Indeed, after reinsertion to the gun, the darkcurrent increased again to 200 μA. After putting cathode 11 back, the current fell back down to the 25 μA level. At least in this case, the cathode is responsible for the darkcurrent, not the gun, nor the RF contact spring, since both have not been changed.

However, later-on we made a different observation. In May 2002 we replaced the RF gun G3 with gun G4 from FNAL. Now the darkcurrent with cathode 11 inserted 200 μA again and even increasing. This gun has been operated at the NICAAD photoinjektor test facility in FNAL with short RF pulses of only 30 μsat 1 Hz. Gun G3 has been operated at TTF most of the time with long RF pulses of 500 to 900 μs, with 1 Hz and around the clock.

The darkcurrent measured at TTF with G4 is very similar to the values obtained FNAL.[7] On the other hand, the small value of darkcurrent has now moved with G3 to FNAL. This is a strong indication, that a conditioning effect of the gun during operation significantly reduced the darkcurrent.

To summarize, both, gun and cathode contribute to the dark current phenomena and have to be attact both. This explains also partly the confusing picture we got from the data for different cathodes. Only with a clean gun, effects of the cathode induced darcurrent can be evaluated correctly.

DISCUSSION AND CONCLUSION

At TTF we have been operating various cathodes from December 1998 to November 2002. The quantum efficiency drops during gun operation presumably due to residual water in the vacuum down to a stable 0.5 % level. This is sufficient to allow to produce bunchs trains of 9 mA as required.

We have been suffering by strong darkcurrent emission in the order of mA during the first two years, until its level stabilized at a reduced and acceptable level of 25 μA. This is on the one hand due to a conditioning effect of the RF gun itself, and on the other due to improved finishing techniques of the cathode surface. From our understanding, the RF contact spring does not contribute significantly to the dark current.

REFERENCES

[1] S. Schreiber et al., "Performance of the TTF Photoinjector for FEL Operation", Proc. of the workshop "The physics and applications of high brightness electron beams", Chia Laguna, Sardinia, July 1-6, 2002.

[2] J. Andruszkow *et al.* [TESLA Collaboration], Phys. Rev. Lett. **85**, 3825 (2000) [arXiv:physics/0006010].

[3] E. Chevallay, J. Durand, S. Hutchins, G. Suberlucq and M. Wurgel, Nucl. Instrum. Meth. A **340** (1994) 146.

[4] S. Schreiber, D. Sertore, I. Will, A. Liero and W. Sandner, Nucl. Instrum. Meth. A **445** (2000) 427.

[5] D. Sertore, S. Schreiber, K. Flottmann, F. Stephan, K. Zapfe and P. Michelato, Nucl. Instrum. Meth. A **445** (2000) 422.

[6] E. Taft and L. Apker, J. Opt. Soc. Am 43 (1953), 81.

[7] W. Hartung *et al.*, "Studies of photo-emission and field emission in an RF photo-injector with a high quantum efficiency photo-cathode," PAC2001 and FERMILAB-CONF-01-215-E

MEASUREMENT OF THE BEAM ENERGY SPREAD IN THE TTF PHOTO-INJECTOR

M. Hüning, *FNAL*, Batavia, IL 60510, USA
H. Schlarb, *DESY*, 22607 Hamburg, Germany

Abstract

At the TESLA Test Facility (TTF) linac the required high peak current for FEL operation is achieved by compressing the beam longitudinally in a magnetic chicane. The peak current after the chicane is determined by the residual energy spread of the electron bunch which is produced by an rf photo-injector. By residual energy spread we refer to the energy spread of a temporal slice of the bunch which can not be compensated by any time dependent energy modulation. To determine the energy distribution, an improved optical system has been implemented to image the beam at an OTR-station after a spectrometer dipole. In this paper the results of the beam profile measurements are presented and compared to particle tracking simulations. It is shown that the residual energy spread in the injector on in order of a few keV only, even at bunch charges of 4 nC.

INTRODUCTION

Most existing and future designs of linac driven Self-Amplified Spontaneous Emission Free-Electron Lasers (SASE-FELs) use high brightness photo-injectors to meet the tight requirements on the transverse and longitudinal beam quality. In a photo-injector, the electrons are produced by impinging a short-pulse laser on a photo-cathode installed in a radio frequency gun which is operated at high gradients. The rapid acceleration in the RF gun is necessary to overcome the strong repulsive space charge forces. Several optimisation steps are required in the design and during operation of a photo-injector to minimise the transverse projected emittance growth. In addition to the transverse emittance, the longitudinal phase space distribution also has major impacts on the linac design and the possibilities to operate a SASE-FEL.

Unlike other sources, such as conventional thermionic injectors or damping rings, the energy of electrons produced in a photo-injector is correlated in time and spread only in a very narrow energy band. The time-energy correlation is mainly caused by the RF curvature and thus is non-linear. In general, the correlation can be linearised by accelerating the beam at higher harmonic frequencies before it is compressed in length [1, 2]. If the correlation is eliminated, the residual energy spread determines the achievable peak current while maintaining an energy spread small enough to operate a SASE-FEL.

At the TESLA Test Facility (TTF), a photo-injector has been used to drive a SASE-FEL operating in the VUV-wavelength range between 80 nm and 180 nm [3]. A detailed description of the experimental facility can be found in [4]. The TTF-FEL consists of a linear accelerator producing bunches with an energy up to 300 MeV and a 14.1 m long undulator magnet. The bunches exit the photo-injector with an energy of 16 MeV. At 2.8 nC bunch charge, the rms width of longitudinal charge density is 3.6 mm. The main accelerator contains two superconducting acceleration modules which are separated by a magnetic bunch compressor.

As a consequence of the fairly long bunch length in comparison with the RF wavelength of 23 cm, the rf-induced curvature downstream of the bunch compressor causes a strongly non-Gaussian charge distribution with a narrow leading peak and a long tail (no linearisation). From the experimentally observed FEL, radiation the photon pulse duration τ_{rad} has been determined to be less than 50 fs FWHH [5]. The observations are in agreement with particle tracking simulations and numerical simulations of the SASE process. Of the 2.8 nC bunch charge, only the 0.1-0.2 nC contained in the leading spike with a peak current of 1.3 kA contributes to the FEL radiation. The current of trailing electrons is insufficient to initiate the SASE process. The key beam parameter determining the width of the spike $\sigma_{z,spike}$ is the residual (slice) energy spread $\sigma_{E,s}$. Tracking simulations of the photo-injector predict a residual energy spread below 5 keV. However, investigations in the past could only set a lower threshold of 22.1±2.7 keV[6] for the slice energy spread, much too large and in disagreement to the numerical results. To close the gap in understanding, the optical setup and the experimental condition have been improved to yield high precision measurements of the beam energy distribution.

EXPERIMENTAL CONDITIONS

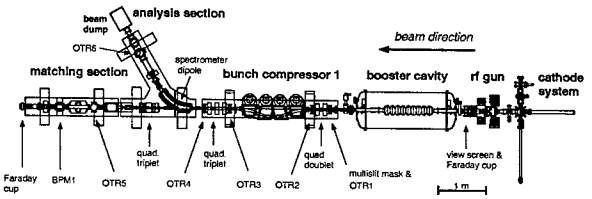


Figure 1: Scheme of the photo-injector.

Figure 1 shows a scheme of the TTF photo-injector. Beam and injector parameters for the experiment and during FEL operation are listed in Tab. 1. The UV-drive laser operates at a wavelength of 262 nm with a pulse energy of 100 μJ. With an ultra-fast streak camera (FESCA-200, Hamamatsu Photonics, Japan) a pulse duration of 7±0.5 ps rms has been measured. The laser pulse shape is Gaus-

0-7803-7738-9/03/$17.00 © 2003 IEEE

sian. The laser spot on the cathode is radially uniform with a diameter of 6 mm. For the experiment, a bunch charge of 4 nC has been adjusted. The 1.3 GHz, 1 1/2-cell room-temperature copper gun has been operated at a gradient of 35 MV/m accelerating the beam to an energy of 3.8 MeV. The nominal gun phase is 40°. A superconducting 9-cell booster cavity rises the beam energy to 16 MeV. Bunch compressor 1, after the booster has been switched off. Using the quadrupole triplet located upstream of the

Table 1: Photo injector and beam parameters

parameter	symbol	value	unit
bunch charge	Q	4	nC
gun gradient	G_{gun}	35	MV/m
gun phase	ϕ_{gun}	30-50	deg.
laser diameter	d	6	mm
laser pulse	σ_t	7	ps
booster gradient	$G_{booster}$	11.5	MV/m
booster phase	$\phi_{booster}$	131-155	deg.
dispersion at OTR6	η_x	1.367	m
beam energy	E	15.4-16.3	MeV
x/y norm. emittance	ϵ_x/ϵ_y	10.6	μm
x/y norm. slice emit.	$\epsilon_{x,s}/\epsilon_{y,s}$	4-14	μm
slice beta-func. OTR6	β_x	7-17	cm
FEL operation			
bunch charge	Q	2.8	nC
gun gradient	G_{gun}	40	MV/m
laser diameter	d	3	mm

spectrometer dipole, the beam is focused onto an optical transition screen (OTR6) situated in the spectrometer beam line. The horizontal dispersion at the screen amounts to 1.37 m. The OTR-screen is rotated by 45° with respect to the y-axis. To correct the depth of field on the entire screen, a shift-tilt objective has been used to image the OTR-light on a 12-bit CCD camera. With horizontal and vertical wires on the screen the magnification is determined to be 32.3 (36.4) μm per CCD-pixel in x (y). By measuring the point spread function of the optical setup a resolution of 44 μm rms has been derived. The exposure time of the CCD camera has been set at its minimum (10 μs) to reduce the counts on the image due to X-rays. Figure 2 shows a typical image of a single bunch. The peak width is proportional to the residual energy spread while the long low energy tail is mainly determined by the phase of the booster cavity. For the measurement, gun and booster cavity phase have been varied. For each new phase setting, the focusing strength of the quadrupole triplet has been corrected to minimize the rising edge of the peak in the energy profile. Phase, amplitude, and charge jitter significantly change the peak profile on shot-to-shot basis. For each setting, 10 images are stored. Altogether about 270 pictures are analyzed.

Simulations

The particle tracking code ASTRA [7] is used to simulated charge distribution produced in the injector. Per run, 4000 macro-particles are tracked providing a sufficiently accurate result within reasonable computation time. Figure 3 shows the longitudinal phase space at the entrance of the spectrometer dipole. The two cases, 4 nC (blue) and 0.01 nC (green), demonstrate the difference between a bunch with high space charge force and one without (thermal emittance is set to zero).

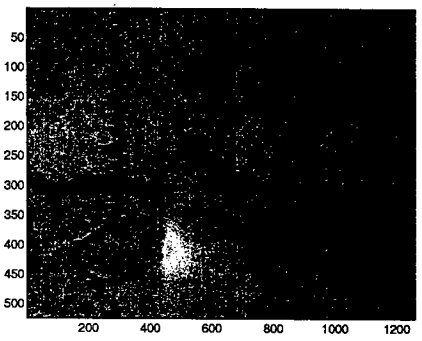


Figure 2: Image of bunch at OTR6.

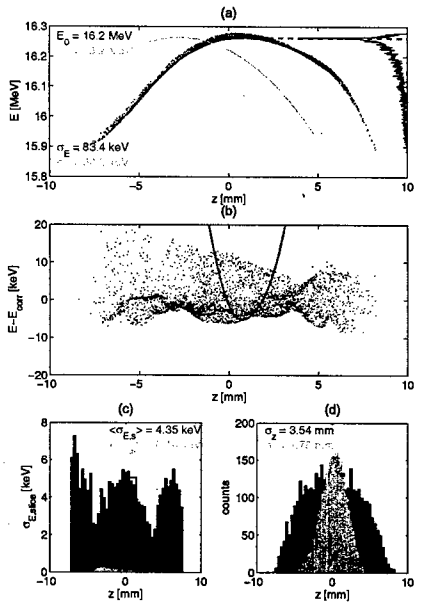


Figure 3: Longitudinal phase space distribution (σ_t =7 ps, ϕ_{gun} =40°, $\phi_{booster}$ =145°).

The rf-induced correlated energy spread is typically 2 orders in magnitude larger than the slice energy spread (see Fig.3(b) and Fig. 3(c)). The cosine-like distribution projected on the energy axis produces a spike at high energies (see Fig. 3(a)). The smaller the residual energy spread, the more pronounced and narrow the spike will be. For the later analysis, we use only the particles with the energies above the peak value of energy spike indicated by a red

dashed line in Fig. 3(a). Due to the RF curvature, particles within the parabolar-like curve plotted in Fig. 3(b) contribute to shape and width of the rising edge of the spike. For the example shown, the longitudinal rms width of these particles is 670 μm or $0.2 \cdot \sigma_z$. Figure 3(c) shows that the residual energy spread calculated for particles located in different bunch slices (blue) agree well with the one we are able to measure (red bar). Because the residual energy spread changes with the position z (Fig. 3c) the phase of the booster cavity has been varied in steps of 2°. This allows observation of the residual energy spread at various positions along the bunch.

Image processing and data analysis

The first step in the image processing is the removal of single, high intensity pixels caused by x-rays hitting the CCD. Then, an average of 100 CCD background pictures, showing a small deviation in the read out per pixel, is subtracted. To further improve the quality of the horizontal projection, only the image in a band of $\pm 4\sigma_y$ obtained by fitting a Gaussian to the vertical projection is used. The profile is then filtered using wavelets (sym-lets of 8^{th} order). By filtering that is based on spatial frequency as well as scale, wavelet-filters can significantly reduce noise without obscuring narrow features of the profile, especially the steep rising edge seen at high energies.

The simulation data are treated similarly, only that in this case 0^{th} order wavelets (Haar wavelets) are used to avoid negative values in the profile. Filtering of the simulation data is necessary because of the limited number of particles used for the tracking.

To find the phase offset of the booster cavity, which is a priori unknown, the simulated profiles are fitted to the measured ones by allowing a horizontal and vertical shift as well as vertical scaling. The simulations cover a number of laser pulse lengths and phases. The most likely parameters are found when the sequence of simulated profiles best agrees with the measured ones. The best agreement was found with a laser pulse length of 7 ps. Note that for determining the phase offset, the whole profile is taken into account with a special focus on the low energy tail which is dominated by the rf-curvature and hence best reveals the absolute phase. The residual energy spread is quantified by fitting a Gaussian function to the high energy edge of the profile, where position and height of the maximum are fixed, and only the σ can vary. The results are shown in Fig. 4.

Agreement between measurement and simulations

Figure 4 shows the compilation of the measured and simulated residual energy spread. Besides statistical fluctuations from bunch to bunch, the measurements are influenced by a number of systematic errors. The broadening influence of the rf curvature is present both in the measurement and in the simulation. No significant impact from the optical resolution of the system is to be expected, whereas the beam optics allow for a resolution slightly below 2 keV. Only for two phase values, 133° and 135°, has a resolution of 2.5 keV been found. The intensity of the beam images was very limited. After digitisation, even the most intense images deliver pixel readings of only up to three counts above the pedestal of about two counts. This leads to distortion of the results, especially for weaker images. On one hand the height of the profile appears even smaller, which is reflected by the scaling factors needed in the fits that match the expectations. On the other hand this causes much steeper edges in the measured profile than there are in the original distribution. This significantly increases the measurement error towards the ends of the bunch. Taking these effects into account, the simulations reproduce the measurements very nicely.

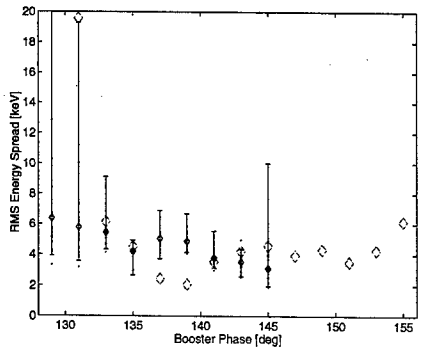


Figure 4: Slice energy spread measurement (points) and simulation (large diamonds).

CONCLUSION

The residual energy spread in a photo injector has been measured with a resolution down to 2 keV ($\sigma_E/E = 1.3 \cdot 10^{-4}$). Utilising the cosine-curvature of the accelerating rf-fields, slice energy spread could be measured. The results are consistent with simulations. The values are close to and below 5 keV. This matches observations made with the TTF SASE-FEL radiation indirectly confirming predicted values.

REFERENCES

[1] Ph. Piot et.al., DESY Report No. TESLA-FEL-01-06

[2] "LCLS CDR", SLAC Report No. SLAC-R-593, 2002

[3] J. Rossbach, NIM A, Vol. 475, Dec. 21, 2001.

[4] J. Andruszkow et.al., Phys. Rev. Lett. 85, 3825 (2000).

[5] V. Ayvazyan et.al., Phys. Rev. Lett. 88, 104802 (2002).

[6] S. Schreiber, "Performance Status of the RF-gun based Injector of the TESLA Test Facility Linac", Proc. of EPAC00, Vienna, 2000.

[7] K. Flöttmann, www.desy.de/~mpyflo/Astra_documentation

BEAM DYNAMICS STUDIES FOR THE SPARC PROJECT

M. Biagini, M. Boscolo, M. Ferrario, V. Fusco, S. Guiducci, M. Migliorati, Vaccarezza,
INFN-LNF, Frascati, ITALY
L. Serafini, INFN-Mi, Milan, ITALY
R. Bartolini, L. Giannessi, M. Quattromini, C. Ronsivalle, ENEA-Frascati, ITALY
C. Limborg, SLAC, Stanford, USA, J. B. Rosenzweig, UCLA, Los Angeles, USA

Abstract

The aim of the SPARC project, is to promote an R&D activity oriented to the development of a high brightness photoinjector to drive SASE-FEL experiments. We discuss in this paper the status of the beam dynamics simulation activities.

INTRODUCTION

The SPARC photoinjector has to drive a SASE FEL experiment at 530 nm [1]. To meet the FEL requirements a high brightness electron beam has to be generated, accelerated up to 155 MeV and transported up to the entrance of the undulator, minimizing the emittance and energy spread degradation due to correlated space charge and wake field effects. In order to saturate the FEL radiation in the planned 15 m long undulator, and to additionally allow generation of higher harmonics, the design beam parameters are very rigorous: normalized emittance $\varepsilon_n < 1$ μm, relative energy spread $\Delta\gamma/\gamma < 0.1$ % and peak current $I \sim 90$ A. Fortunately, such parameters have to be reached only on the scale of the FEL cooperation length, which in our case is less than 300 μm.

START TO END SIMULATIONS

The accelerator consists of a 1.6 cell RF gun operated at S-band with a peak field on the cathode of 120 MV/m and an incorporated metallic photo-cathode followed by an emittance compensating solenoid and three accelerating sections of the SLAC type (S-band, travelling wave). A transfer line made with two triplets allows the matching with the undulator optics (see Fig. 1). A start-to-end simulation of the beam dynamics from the injector through transfer line and undulator system has been performed by means of the codes PARMELA [2] and GENESIS [3].

We take as our example the most conservative system that is to be encountered, one with no velocity bunching [1], and a relatively low energy of 155 MeV (consistent with either low gradient, three TW section operation, or high gradient, two TW section operation). The temporal profile of the bunch has been taken uniform over 11.5 ps with a rising time of 1 ps, a laser spot on the cathode of 1 mm and a 1 nC charge, with a 35 degree launch phase in the gun, 0.27 T of solenoid field and on-crest acceleration in the linac. We decided to place a set of coils around the first accelerating structure (700 G), to provide additional flexibility in the choice of the accelerating gradient (25 MV/m in the simulations).

The transverse emittance compensation process is visible in figure 2: the emittance reaches an absolute maximum in the centre of the solenoid and it is reduced to a minimum in the drifting section, then begins again to increase. The booster entrance is located at the envelope laminar waist corresponding to an emittance relative maximum [4]. The emittance oscillation is driven by a properly matched accelerating field [5] down to an absolute minimum (~0.6 μm) at the linac exit where the average bunch energy is 155 MeV, high enough to damp space charge forces. The estimated thermal emittance (0.3 μm), included in the simulation, results to be in the present design the main contribution to the total emittance.

As expected, the emittance along the transfer line and in the undulator is not anymore affected by space charge effects even when the beam has to be focused to a very small spot (~55 μm) to meet the undulator matching conditions.

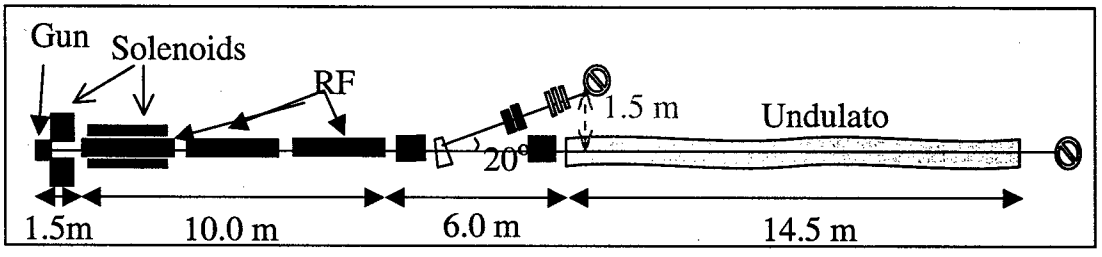


Figure 1: Schematic layout of SPARC phase 1

Transverse and longitudinal phase spaces at the entrance of the undulator are shown in figure 3. Despite some halo observed in the transverse phase space related to the bunch tails mismatch, the core of

0-7803-7738-9/03/$17.00 © 2003 IEEE

the bunch is very good behaved, having a 0.6 μm rms normalized emittance in both planes.

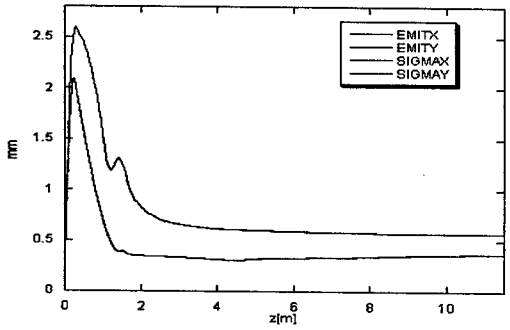


Figure 2: PARMELA simulation of the rms normalized emittance and bunch envelope evolution along the SPARC injector up to 11.5 m.

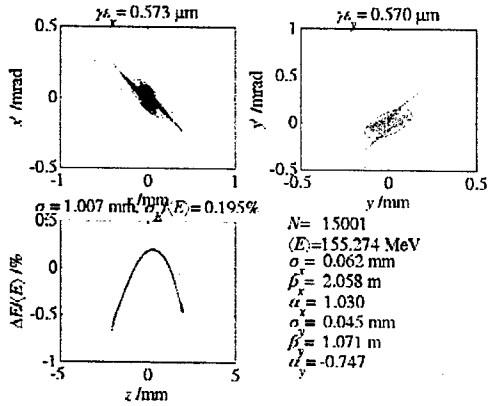


Figure 3: Transverse and longitudinal phase spaces at the entrance of the undulator.

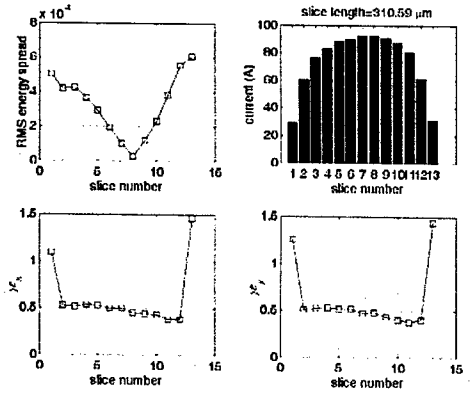


Figure 4: Slice analysis of beam properties at the undulator entrance.

The longitudinal phase space shows the typical energy phase correlation induced mainly by the RF field, with little contribution from longitudinal space-charge, having relative rms energy spread lower than 0.2% as required. The slice analysis performed at the undulator entrance is shown in figure 4. Slice emittance and energy spread are well below the nominal design values for more than 85% of the bunch length. The slice peak current is above 60 A in the same region.

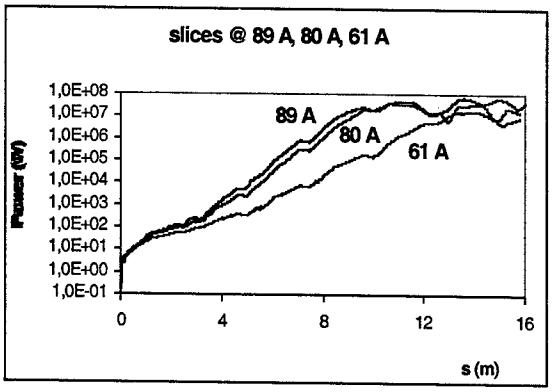


Figure 5: GENESIS simulations of the FEL for three representative slices along the bunch.

The analysis of the FEL performance has been performed with the code GENESIS, taking in to account three representative slices along the bunch provided by PARMELA, showing that even the radiation emitted by the slices closer to the tails that contain a lower local value of the current (61 A) can reach saturation as shown in figure 5.

SENSITIVITY STUDIES

Once the nominal parameters are set we have to provide also stable operation and tolerate some jitter in the nominal value of the parameters . In this section we discuss only two selected topics of such studies performed thus far, in which cathode emission uniformity, laser beam ellipticity, laser centroid offset, laser time structure, and solenoid field errors have been explored.

The effects of cathode's dishomogeneities [6] have been tested by simulating, using the code TREDI [7], a zone on the cathode with reduced quantum efficiency QE. We have assumed a circular QE "hole" with a surface 10% of the nominal bunch spot, centered half-way of the bunch radius. The results suggest that localized inhomogeneities do not dramatically degrade the emittance, growing by $\Delta\varepsilon_{x(y)} \approx 10\%$ (15%) for QE $\approx$ 70% as reported in figure 6. This analysis will be further extended to the cases of randomly distributed ("spotty") inhomogeneities, which better describe the behavior of real cathodes.

Flat top laser pulses with rise times shorter than1 ps are required in order to avoid emittance degradation [8], as shown in figure 7.

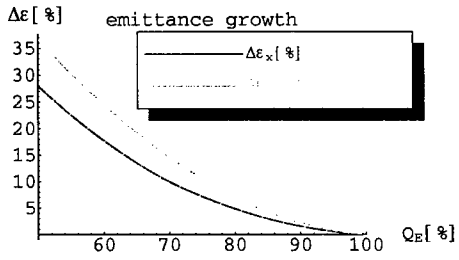


Figure 6: Emittance growth as a function of Q_E.

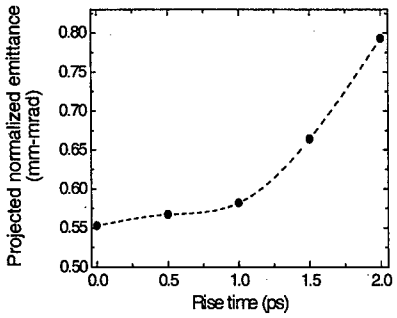


Figure 7: Norm. rms emittance versus rise time.

But laser pulse shaping with short rise time may result in the formation of longitudinal ripples. Therefore, the effect of a laser pulse with longitudinal ripples has been investigated. The beam is assumed to be transversely uniform in these studies. The striking result is that even with a 30% of longitudinal irregularity the beam emittance degradation is limited to 6%. This result can be interpreted as if the space-charge force induces a compensation of the longitudinal irregularity. This hypothesis is justifed by PARMELA simulation results. In figure 8 the evolution of longitudinal beam distributions are displayed. At the cathode the temporal spectrum has a 30 % ripple overlapped on a square pulse, the relative energy spread is zero. As the beam goes through the gun and drifts the temporal oscillations transform in energy oscillations. At the entrance of the first acceleration structure (at z=150 cm) the beam has lost the temporal ripples, which have converted into energy variations through a fractional plasma oscillation. These energy ripples do not have any notable effect to the rms energy spread at the end of the linac, as they are soon suppressed inside the first accelerating structure. These results indicate that the shape of the laser pulse should be square with a very small rise time, whether a smooth temporal profile is not a stringent requirement.

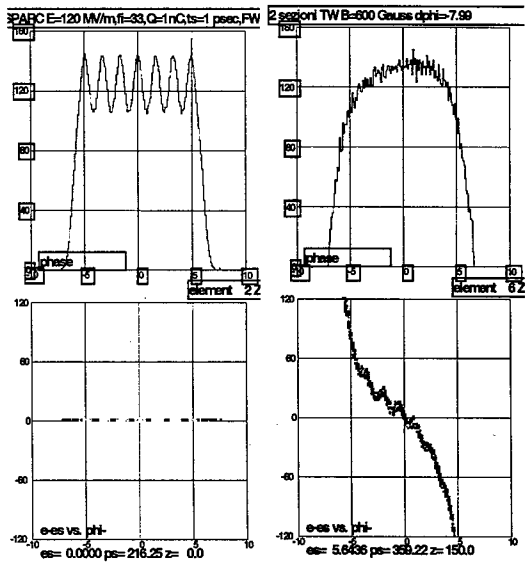


Figure 8: Longitudinal beam distribution: phase and energy spectrum in the upper and lower plots, respectively. Left plot: initial distribution at cathode (z=0 m); right plot: beam at z=1.5 m.

CONCLUSIONS

Start to end simulation of the optimal SPARC working point have shown that we can meet the FEL requirements with a reasonable parameter set. The requirements on the longitudinal and transverse profile of the laser pulse, the phase jitters, the laser pointing stability have been set. Preliminary sensitivity studies have not shown dramatic concerns about the possibility of stable operation. A more systematic [9] study is in progress .

REFERENCES

[1] L. Palumbo et al., "The SPARC Project: A High-Brightness Electron Beam Source to Drive a SASE-FEL Experiment at LNF", this conference.
[2] J. Billen, "PARMELA", LA-UR-96-1835, 1996.
[3] S. Reiche, Nucl. Instrum. & Meth. A429,243 (1999).
[4] M.Ferrario et al., "HOMDYN Studies for the LCLS RF Photoinjector", Proc. of ICFA Workshop on the Physics of High Brightness Beams, UCLA, Nov. 1999
[5] L.Serafini,J.Rosenzweig,*Phys. Rev. E* **55**(1997) 7565
[6] F. Zhou et al.,PRST-AB, V. 5, 094203 (2002).
[7] L. Giannessi, M. Quattromini, Submitted to PRST AB (2003).
[8] J. Yang, J. of Appl. Phys., V. 92, N. 1, (2002)
[9] C. Limborg, "New optimization for the LCLS photo-injector", Proc. Of EPAC-02, Paris 2002.

STUDY AND DESIGN OF ROOM TEMPERATURE CAVITIES FOR AN RF COMPRESSOR PROTOTYPE

David Alesini[+], Franco Alessandria[*], Alberto Bacci[*], Carlo De Martinis[*], Massimo Ferrario[+], Alessandro Gallo[+], Dario Giove[*], Fabio Marcellini[+], Marco Mauri[*], Luca Serafini[*]

[+]*INFN-LNF-Frascati*, [*]*INFN-Milan and University of Milan*

Abstract

The generation of high brightness electron beams with sub-ps bunch lentgh at kA peak currents is a crucial requirement in the design of injectors for Linac based X-Ray FEL's. In the last years the proposal to use a slow wave RF structure as a rectilinear compressor in this range of interest, to overcome the difficulties related to magnetic compressors, has been widely discussed in the accelerator physics community. In this paper the results in the design and study of a 3 GHz model structure will be presented.

INTRODUCTION

The need to produce high brightness electron beams delivered in short (sub picosecond) bunches has been driven recently by the demands of X-Ray SASE FELs, which require multi-GeV beams with multi-kA peak currents and bunch lengths in the 100-300 fs range, associated to normalized transverse emittances as low as few mm mrad. The strategy to attain such beams is based on the use of RF Linacs in conjunction with RF laser driven photo-injectors and magnetic compressors. The formers are needed as sources of low emittance high charge beams with moderate currents, the latter are used to enhance the peak current of such beams up to the design value of 2-3 kA by reduction of the bunch length achieved at relativistic energies (> 300 MeV). Nevertheless the impact of magnetic compressors on the beam dynamics is quite relevant, with tendency to reduce the performances of the whole system in terms of the final beam brightness achievable [1].

In the last years, developing a previous work about a plasma buncher scheme, alternative option of compression based on slow wave RF fields has been proposed [2]. The basic idea is to develop a rectilinear RF compressor that works indeed as a standard accelerating structure which simultaneously accelerates the beam and reduces its bunch length.

RF RECTILINEAR COMPRESSOR THEORY

The great advantage of a rectilinear scheme is obviously the absence of curved path trajectories, in addition to the fact that compression is applied at moderate energies (from 10 to 100 MeV) leaving the Linac free from any further beam manipulation.

We briefly report the basic elements of the theory of RF compressor as outlined in ref.2.

The interaction between an electron and the longitudinal component E_z of the RF field in a RF travelling wave structure is described by the Hamiltonian

$$H = \gamma - \beta_r \sqrt{\gamma^2 - 1} - \alpha \cos\xi$$

where $\gamma = 1 + \frac{T}{mc^2}$ is the normalized energy of the electron, $\xi = (\omega t - kz - \psi_0)$ is the phase of the wave as seen by the electron (ψ_0 is the injection phase) and $\alpha = \frac{eE_0}{2mc^2 k}$ is a dimensionless parameter which represents the accelerating gradient.

If we consider a wave whose phase velocity is slightly lower than c, we have that $k = k_0 + \Delta k = \frac{\omega}{c} + \Delta k$ (where the detuning parameter is small i.e. $\Delta k << k_0$) and we can write for the resonant beta and gamma the expressions $\beta_r = 1 - \frac{c\Delta k}{\omega}$ and $\gamma_r = \sqrt{\frac{\omega}{2c\Delta k}}$.

The behaviour of the RF compressor may be easily understood looking at the phase contour plots in the [γ,ξ] phase space. As an example we have considered a wave of amplitude α = 0.65 and resonant gamma γ_r = 24. This corresponds to a wave phase velocity of β_r=0.999.

In fig. 1 we plot a phase-space diagram showing that particles injected with a phase equal to –π/2 and an energy smaller than the resonant one, will slip back in phase while accelerated up to $\gamma = \gamma_r$. Due to the nature of phase lines the bunch will have a phase spread (i.e. a bunch length) smaller than the initial one. For the same reason a further acceleration would clearly tend to de-compress the bunch.

The figure of merit for the compression process may be defined as the ratio between the initial phase spread and the final one at the extraction. Values in excess of 10 may be reached in such a scheme. A proper matching of the beam into the accelerating section and an additional focusing provided by external solenoids has been shown by simulation to obtain a proper preservation of the transverse emittance as discussed in Ref. [3]

0-7803-7738-9/03/$17.00 © 2003 IEEE

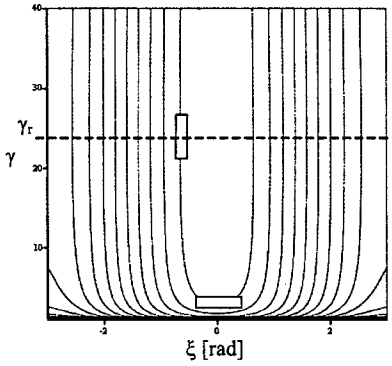


Fig. 1 Phase space plots of a slow RF wave

DESIGN OF CELLS FOR A SLOW WAVE RF COMPRESSOR

In the last year preliminary experimental investigations have been carried out using speed of light linac sections, which showed the validity of the velocity bunching concept[3]. In such a frame our group started an experimental activity aimed at the development of cells for the construction of a slow wave TW structure which can be used as a RF compressor. Table 1 shows the main parameters which we took as a reference for our investigations.

Table 1 Reference parameters for the study of the RF compressor

Parameter	Value
Frequency of the wave structure	2856 MHz
Linac structure	TW
Accelerating gradient	20 MV/m
Initial energy	6 MeV
Extraction energy	16 Mev
Compression factor	7
RF pulse repetition rate	1÷10
Bunch length	10 ps

The required compression factor calls for the availability of a structure able to control the phase velocity in the range between 0.999 c and c. In an iris loaded TW structure the equation:

$$(dvf/vf) = (df/f)\ (1 - vf/vg)$$

shows that the v_f can be controlled by changing the excitation frequency or, in a equivalent way, by detuning the structure. A suitable approach may be that to use a thermal control process that change the v_f at a fixed exciting frequency. The feasibility of such an approach has been initially studied referring to the typical parameters of a SLAC structure. The results obtained show that a change of the order of 1‰ of the phase velocity is equivalent to a variation of the order of 0.6 °C in the temperature of the structure. This calls for a system able to control in real time the temperature with a resolution of the order of 0.06°C under a RF power load of the order of ~ 1.5 kW. We evaluated that it would be too much difficult to achieve such a performance and we tried to approach the problem with a new cell design. The goal was to obtain a structure able to decrease of a factor of 3 the thermal sensitivity, so that the required phase velocity modulation will ask for a temperature variation of the order of 2 °C. The fact that the required accelerating gradient is lower with respect to a standard SLAC structure gave us a certain degree of freedom in the design as far as the shunt impedance figure is involved. Table 2 shows the main parameters of the new structure (referenced as ALMA 3) which we propose for the RF compressor.

Table 2 Main parameters of the Alma 3 TW structure

	SLAC Mark IV	Alma 3
Cell radius (mm)	41.24	42.60
Iris radius (mm)	11.30	15.40
Disk thickness (mm)	5.84	5.90
Cell length	35	35
Frequency (MHz)	2856	2856
Mode	2π/3	2π/3
Q	13200	13084
Shunt impedance (MOhm/m)	53	41
Vg/c	0.0122	0.0341
ΔT (equivalent to 1‰ Vf)	0.6 °C	2.0 °C
Tuning ring capability (MHz)	-	18
Tuning rod capability (kHz)	-	200

The mechanical design of the cell has been carried out in a complete fashion taking into account the requirements due to the cooling system and to the brazing process to join cells to give the final structure.

At the same time, at least for the first prototypes, we add frequency control capabilities to the cells both during the mechanical machining (using a tuning ring) and after the brazing (using a set of tuning rods). Such a feature has been foreseen to allow to control the influence of the achievable mechanical tolerances on the frequency response of the cells (a tolerance of 0.01 mm in the cell diameter gives an uncertainty of 370 kHz in frequency) and to provide a tuning tool for field adjustment.

The thermal control of this structure will be obtained using 8 channels for water flow. These channels have been machined within the cells body to provide a better heat exchange. The behaviour of this design has been verified under the expected RF power load using the finite element code Ansys. The results of this analysis show that the system will be suitable to match our requirements (fig. 2). The so far obtained thermal sensitivity allows to use a refrigeration unit with a control capability of the order of 0.1°C@45°C operating point. Such units are commercially available and we plan to use one of these as the basic building block of the thermal control setup.

To prove the reliability of the design and to gain experience on such a structure we machined a 4 cells aluminum prototype. The cells were stacked together using stainless steel threaded rods.

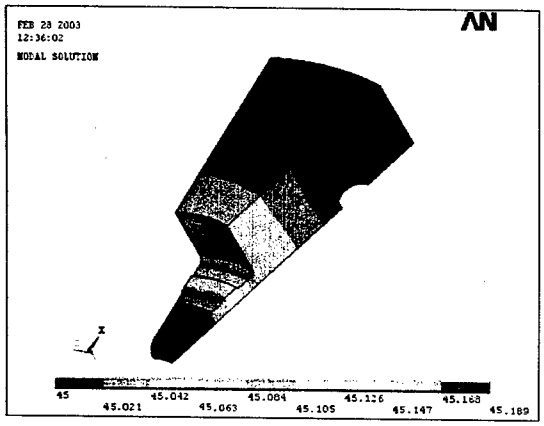


Fig. 2 Ansys simulation of the thermal behaviour of the ALMA 3 structure

The machining of these cells was simplified with respect to the final ones removing the cooling channels and the brazing grooves. The mechanical tolerances obtained were quite close to those required and this allowed to carry out significant measurements both on the single cell and on the set of the four cells.

The resonant frequency measurements on the single cells were in very good agreement with the expected values obtained with the code Superfish and confirmed the influence of the mesh value adopted in the numerical analysis (0.15 mm which gave us a frequency accuracy of the order of 100 kHz). For the sake of simplicity we started considering this assembly as a SW structure giving us the opportunity of sampling the dispersion curve at 4 points and to check field profile (Fig. 3).

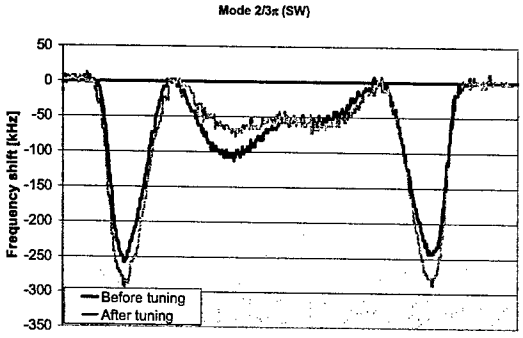


Fig.3 Measurements of the ALMA 3 structure accelerating field

The dispersion curve as a function of the cells temperature was measured using a test bench based on a laboratory oven. The internal size of the oven allows to position the 4 cells stack along with RF probes and temperature sensors to characterize the oven behaviour and to measure the cells temperature. Measurements were carried out in the range between 25 and 45 °C. The oven stability was of the order of 0.1 °C. The results (Fig. 4) proved a good agreement with the predicted behaviour of the phase velocity and gave the final validation of the whole design.

At the same time that we carry out the above described measurements, the OFHC copper to be used for the machining of a new 9 cells prototype has been forged by an Italian company according to our specifications. Great care has been taken to the control and measurement of the grain size of the bulk material (< 100 μm) in order to match the requirement for the brazing procedure. This process will be carried out at CERN and the whole cycle has been defined in agreement with CERN specialists.

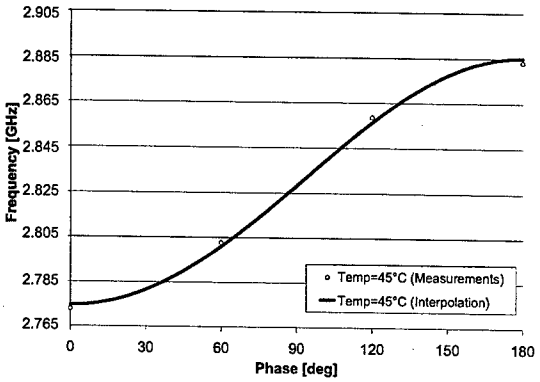


Fig. 4 Measurements of the ALMA 3 structure dispersion curve

CONCLUSIONS

The design of a new cell for a RF compressor working in the S-band has been completed and the measured performances of a first aluminum prototype have proven the feasibility of such an approach.

At this time the machining of the copper cells has been started and we plan to have a 9 cells brazed structure within the end of June 2003.

ACKNOWLEDGEMENTS

We would like to acknowledge very helpful discussions with M. Vretenar and S. Mathot (CERN), R. Boni (INFN-LNF) and the valuable support received in the experimental work by Luigi Gini and Carlo Uva (INFN-Milan) and Luciano Grilli (University of Milan).

REFERENCES

[1] P.Emma "Accelerator Physics Challenges of X-Ray FEL SASE Sources", EPAC2002, Paris, June 2002, p. 49

[2] L. Serafini et al. "Ultra-short Bunch Generation with a Rectlinear Compressor", PAC2001, Chicago, June 2001, p. 2242.

[3] M. Ferrario et al. "Recent Advances and Novel Ideas for High Brightness Electron Beam Production Based on Photo-Injectors" INFN-LNF 03/06P– 5 May 2003

RF SURFACE RESISTANCE OF COPPER-ON-BERYLLIUM AT CRYOGENIC TEMPERATURES MEASURED BY A 22-GHZ DEMOUNTABLE CAVITY

J.-F. Liu†, F. L. Krawczyk, S. S. Kurennoy, D. L. Schrage, A. H. Shapiro, T. Tajima, R. L. Wood,
Los Alamos National Laboratory, Los Alamos, NM 87545, USA

Abstract

A 22-GHz demountable cavity on the cold head of a compact refrigerator system was used to measure the RF performance of several copper-plated Beryllium samples. The cavity inner surface was treated by chemical polishing and heat treatment, as well as an OFE copper coupon to provide a baseline for comparison. The measured surface resistance was reasonable and repeatable during either cooling or warming. Materials tested included four grades of Beryllium, OFE copper, alumina-dispersion strengthened copper (Glidcop®), and Cu-plated versions of all of the above. Two coupons, Cu-plated on Beryllium O-30 and I-70, offered comparable surface resistance to pure OFE copper or Cu-plated Glidcop. The RF surface resistance of Cu-on-Beryllium samples at cryogenic temperatures is reported together with that of other reference materials.

INTRODUCTION

Beryllium material offers extremely low thermal expansion plus very high thermal conductivity at cryogenic temperatures. High-purity Be also has high electric bulk conductivity at cryogenic temperatures, which suggest that RF performance of bare Beryllium should be high. Past efforts to produce high-performance Be RF surface have failed to meet expectations, whereas measurements of copper on Be at cryogenic temperatures have proven effective. This attempt [1,2] to produce Cu-plated RF surfaces on Be substrate aims to combine the excellent bulk thermal properties of the Be substrate with the good RF properties of copper. If successful, this material should tolerate very high surface power densities and thus can be used in the production of high power RF cavities that do not exhibit thermal distortion. Work with small coupons was performed to allow confirmation of the desired RF performance and development of plating, fabrication, and brazing processes.

EXPERIMENTAL SETUP

The experimental setup is shown in Fig. 1. The cavity itself consists of two components: one is machined out of a block OFE copper, with a cylindrical cavity and a small annular groove on the flat end wall. The other is a replaceable endplate. The dimensions of the cavity are 20.138 mm diameter and 12.454 mm length. The detailed calculation of the cavity modes can be found elsewhere [3] and the typical values are as follows. At room temperature ($\rho = 1.72 \times 10^{-8}$ Ωm), the working mode of the cavity is TE_{011} at 21.75 GHz, and the skin depth is 0.448 μm for both TE_{011} and TM_{111}. The groove serves to shift its frequency down from that in an exact pillbox, where TE_{011} mode would be degenerate with two TM_{111} modes. At the middle of the height, the cylinder has two RF ports with loop couplers made of a 50 Ω coaxial line. The couplings are fixed around 1% at room temperature. TM_{111} modes are unexcited by adjusting the loop direction. The advantage of working with TE_{011} mode is that there is no surface current across the annular contact between the test coupon and the cylinder, so that the quality of the contact is not crucial.

The cavity was evacuated with a turbo-molecular pump station through four small holes of 2 mm diameter on the top surface. The typical vacuum was around 10^{-6} Torr before cooling down. The temperature of cavity was monitored with a silicon diode. The resonant frequency was defined as the frequency at which the transmitted power of the network analyzer took the maximum value of the S_{21} coefficient in the scattering matrix. The quality factor Q_L was determined through the half-power points of the S_{21} coefficient. From the S_{11} and S_{22} coefficients, the coupling factors β_1 and β_2 were calculated. The cavity was placed on the cold head of a compact refrigerator system. The lowest temperature achieved was ~12 K. A LabView software was developed to automate the

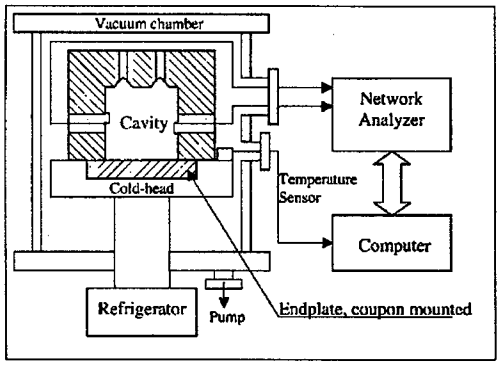


Figure 1: Schematic diagram of experimental setup with a 22 GHz demountable cavity. The network analyzer automatically measured the transmission S_{21} and the reflections S_{11} and S_{22} during either cooling down or warming up.

†jfliu@lanl.gov

0-7803-7738-9/03/$17.00 © 2003 IEEE

measurement, i.e., the unloaded quality factors Q_0 were obtained continuously during cooling down or warming up.

The cavity inner walls and one reference OFE copper coupon were chemically polished (CP) with a mixture of phosphoric acid (85 %), nitric acid (69.8 %) and acetic acid (99.9 %) in a volumetric ratio of 11:4:5. They are then heat treated in a hydrogen furnace at 790 °C for a few minutes. The $Q_{0,Cu}(T)$, or, in the form of $R_{s,Cu}(T)$, as a function of temperature was measured as reference for later comparison. Then the endplate was replaced by the various test coupons.

The surface resistance of the test coupons $R_{s,S}(T)$ at temperature T can be obtained from,

$$\frac{R_{s,S}(T)}{R_{s,Cu}(T)} = k\left(\frac{Q_{0,Cu}(T)}{Q_{0,Cu+S}(T)} - 1\right) + 1, \qquad (1)$$

where k, 4.7737, is the geometrical factor of the cavity.

COUPON PREPARATION

Four different grades of Beryllium substrate have been prepared, S-200FH, S-65, I-70, and 0-30. The primary differences between these grades were a) oxide content, and b) means of preparation of the "powder" from which the larger pieces were made (using HIP). For instance, the O-30 was made from "spherical atomized" powder, and I-70 from "impact ground" powder. At least one coupon of each Be substrate candidate was given a 2.5 – 5 μm thick "strike" of Nickel (diffusion barrier) and then plated 100-200 μm with high-purity copper. Bare Be coupons and copper-plated coupons were made from each of these substrate materials.

Table 1. A summary of coupons prepared for testing.

Sample Ser.#	
C1	Pure OFE-copper, chemical polished (CP) and heat treatment
C2	Pure OFE-copper
S1	Stainless steel 304
G1	Cu-plated Glidcop
G3	Glidcop
O-30SN1	Cu-coated on Beryllium
O-30SN3	Bare beryllium
I-70SN1	Cu-coated on Beryllium
I-70SN3	Bare beryllium
S-200FHSN1	Cu-coated Beryllium
S-200FHSN3	Bare Beryllium
S-65SN1	Cu-coated Beryllium
S-65SN3	Bare Beryllium

For baseline comparison, we made coupons from a) 300-series stainless steel, b) OFE copper, and c) Glidcop with and without copper plating.

"OFE copper, ASTM F68 class 2 or better" is specified by LANL for hydrogen furnace brazed RF structures. The relevant factors were that it had to be 99.99% copper and less than 5ppm oxygen. The low-bulk oxygen content was necessary in order for the material to survive the brazing process without blistering. The hydrogen atmosphere is able to reduce oxides within a short distance of the copper surface without damage to the copper. Therefore, the plating probably does not need to meet the < 5 ppm oxygen specification. Nonetheless, every effort was made to approach the 99.99% purity level in order to obtain acceptable RF surface resistance.

Two Glidcop coupons were prepared with and without copper plating, just for comparison. Cyanide-copper plating was used rather than the typical "bright-acid" type, since the former exhibits fewer problems in hydrogen-furnace brazing. The RF performance of cyanide-copper plating was previously unknown.

The details of the coupon fabrication are reported elsewhere [1]. All coupons we measured are listed in Table 1.

RESULTS

In order to calculate the RF surface resistance of the test coupons, the reference OFE copper endplate C1 was measured first. Figure 2 shows the Q_0 and R_s in the function of temperature. The curves during cooling and warming were consistent with each other.

We repeated the measurement for each of the coupons, as shown in Fig. 3. The surface resistance for G1, Cu-plated Glidcop, was comparable to that of OFE-copper C2 without chemical polishing and heat treatment.

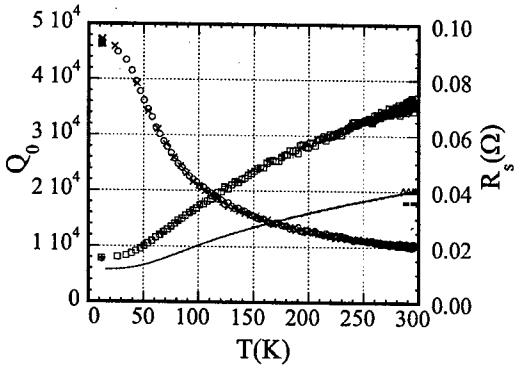


Figure 2. The unloaded quality factors Q_0 and the surface resistance R_s of the reference OFE copper sample as a function of temperature. The crosses (×) and circles (o) show the data during cooling down and warming up, respectively, and the corresponding R_s are shown with plus (+) and rectangular (□) markers. The solid line shows the surface resistance measured with a mirror-finished cavity at 13.6GHz [4] (the data is scaled to 21.75 GHz by $f^{1/2}$ law). The dashed line near the right vertical axis is the expected Q_0 by calculation, the corresponding surface resistance is indicated by the triangles (Δ).

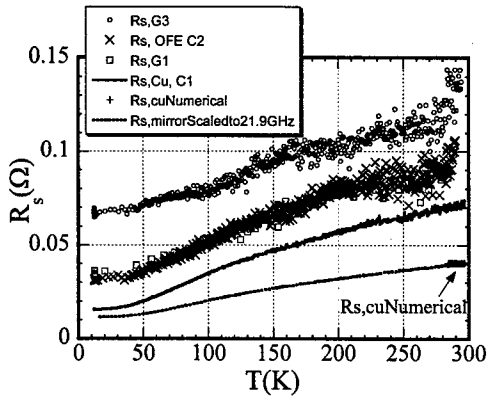


Figure 3. The R_s for C1, C2, G1, and G3 as a function of temperature together with data of a mirror-finished OFE copper measured elsewhere [4].

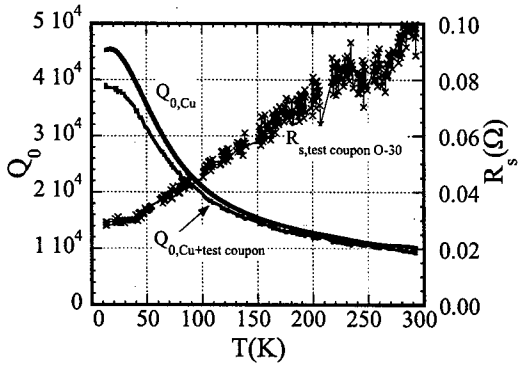


Figure 4. The R_s of the Cu-plated on O-30 Beryllium substrate as a function of temperature.

Four pairs of Cu-plated Be and bare Be samples have been measured. One example is shown in Fig. 4. The test coupon is Cu-plated on O-30 Be substrate, and the surface resistance is comparable to OFE copper (C2) over the full temperature range. At 22 GHz, the RF skin depth is less than or equal to the oxide layer thickness on bare Beryllium. Thus, though we tried to measure the bare Be coupons, we were unable to measure the RF properties of metal Be. The measured R_s were erratic and was much worse than the value that would be predicted from the DC electrical bulk resistivity.

EFFECT OF SURFACE ROUGHNESS

We found that the roughness of test coupons has a very significant effect at 22 GHz. The roughness of 8 coupons has been measured, and the average values are listed in Table 2. A typical value of RF skin depth for pure OFE copper at 22 GHz is about 0.448 μm. Although the coupon C1 surface was treated very carefully with chemical polishing and heat treatment, its average roughness was still 0.163 μm, not small enough if compared to 0.448 μm skin depth. This may explain why the unloaded quality factor was lower than the expected value.

Table. 2: Roughness and surface resistance of measured coupons.

Sample Ser.#	Roughness R_a(μm)	R_s(Ω) @ 73 K	R_s(Ω) @ 293 K
C1	0.163	0.026	0.070
C2	0.83	0.043	0.100
S1		0.347	0.388
G1	0.586	0.044	0.096
G3	0.155	0.078	0.133
O-30SN1	0.632	0.041	0.101
I-70SN1	1.238	0.042	0.109
S-200FHSN1	0.988	0.087	0.208
S-65SN1	0.644	0.168	0.287

The roughness of C2 was much worse than C1. It was clearly shown that the chemical polishing and heat treatment were effective to improve the surface roughness.

SUMMARY

The RF surface resistance as a function of temperature down to ~ 12 K was measured using a 22-GHz TE_{011} mode cavity.

Among four Cu-plated Be coupons, two coupons Cu-plated on Be O-30 and I-70 showed a comparable RF performance to that of the pure OFE copper and the copper-plated Glidcop over the full temperature range. The "cyanide copper" plating method was shown to be acceptable.

Our next step is to perform heat treatment of the copper-plated Be coupons to investigate the stability and RF performance degradation caused by Be/Cu diffusion during braze heat.

ACKNOWLEDGEMENT

We would like to express our thanks to Lloyd Young for his comments and discussion, to ETL for machining of the cavity and heat treatment, and to Randy Edwards for the cavity chemical polishing.

REFERENCES

[1] R. Wood, Memo LANSCE-1:02-058, August 2002.
[2] D. Schrage, Memo AT-1:91-384, September 1991.
[3] S. Kurennoy, Memo LANSCE-1:02-042, September 2002.
[4] J.-F. Liu, J. Appl. Phys. **87**, 3912, (2000).

AN INJECTOR FOR THE PROPOSED BERKELEY ULTRAFAST X-RAY LIGHT SOURCE*

S. Lidia#, J. Corlett, J. Pusina, J. Staples, A. Zholents, Lawrence Berkeley National Laboratory, Berkeley, CA 94720, USA

Abstract

Berkeley Lab has proposed to build a recirculating linac based x-ray source for ultra-fast dynamic studies [1]. This machine requires a flat electron beam with a small vertical emittance and large x/y emittance ratio to allow for compression of spontaneous undulator emission of soft and hard x-ray pulses, and a low-emittance, round electron beam for coherent emission of soft x-rays via the FEL process based on cascaded harmonic generation [2]. We propose an injector system consisting of two high gradient high repetition rate photocathode guns [3] (one for each application), a ~120 MeV superconducting linear accelerator, a 3rd harmonic cavity for linearization of the longitudinal phase space, and a bunch compressor. We present details of the design and the results of particle tracking studies using several computer codes.

INTRODUCTION

The proposed Linac-based Ultra-fast X-ray source ('LUX') facility [1] requires a high-brightness, high duty factor, and highly reliable electron beam injector to produce both hard x-rays by spontaneous emission in undulators and wigglers and soft x-rays in cascaded harmonic generation free-electron lasers. Two rf photoinjector guns produce electron beams with very different emittance profiles, albeit with similar brightness, for the different x-ray production modes. The parameters for the injector are listed in Table 1.

Energy at rf gun exit	~ 10	MeV
Energy at compressor entrance	~ 120	MeV
Bunch charge	1-3	nC
Flat beam injector (1 nC):		
Horizontal emittance	~ 20	mm-mrad
Vertical emittance	< 0.4	mm-mrad
Total emittance	< 3	mm-mrad
Round beam injector (1 nC):		
Emittance	< 2	mm-mrad
Uncorrelated energy spread	± 15	keV
Correlated energy chirp	± 600	keV
Bunch length at compressor entrance	~ 20	ps
Bunch length at compressor exit	2	ps
Repetition rate	~ 10+	kHz

Table 1: LUX photoinjector parameters.

The dual-gun injector complex is shown schematically in Figure 1. Two rf photoinjector guns [3] provide time-interleaved beams at the 10kHz repetition rate. One gun utilizes a magnetized cathode configuration for flat beam production [4], while the other gun produces a typical 'round' beam from an unmagnetized cathode. The beams from the two guns are both injected into the super-conducting linac and from there follow an identical beamline. The magnetized beam follows a linear trajectory to the linac, while the unmagnetized beam is transferred via an achromat transfer line from a gun situated off-axis.

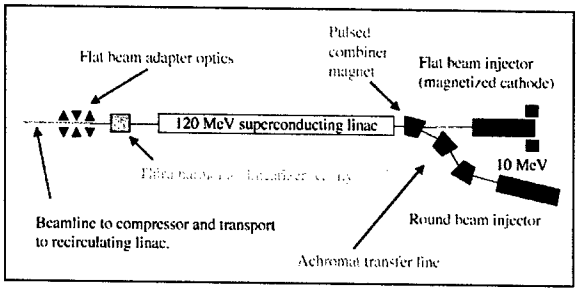


Figure 1: LUX dual-gun injector complex.

Following the linac, a 3rd harmonic (3.9GHz) cavity (3HC) acts to linearize the longitudinal phase space of the beam, and to impose the requisite correlated energy chirp prior to injection to the compressor beamline and transfer to the main recirculating linac of LUX. Between the 3HC and the compressor is the 'Adapter' beamline of skew quadrupoles followed by normal quadrupoles. The skew quadrupole lattice removes the angular momentum carried by the magnetized ('flat') beam, producing a beam with large (~50) ratio between horizontal and vertical emittance. The normal quadrupoles then match the beam to the compressor.

BEAMLINE OPTIMIZATION

We have optimized the generation, transport, acceleration, and manipulation of the electron beams using the 2.5D particle tracking code *Astra* [5]. Optimization seeks to find beamline parameters that simultaneously produce both sets of beams ('flat', 'round') which satisfy the performance requirements (Table 1). Considerable effort has been spent on studying emittance compensation [6] for beams carrying significant canonical angular momentum. The evolution of the magnetized beam is shown in Figure 2, and that of the unmagnetized beam in Figure 3. Figure 2 shows the evolution of several various normalized RMS 'emittances' projected over the full 20ps bunch length: the total 4D emittance (ε_{4D}); the usual radial emittance (ε_r); and the two uncoupled, normal mode

*This work was supported by the Department of Energy under Contract No. DE–AC03–76SF00098.
Electronic mail: SMLidia@lbl.gov

0-7803-7738-9/03/$17.00 © 2003 IEEE

emittances (ε_{drift}, $\varepsilon_{cyclotron}$). For eventual application of the flat beam where an ultra-low vertical emittance is required, the cyclotron emittance is minimized. For quasi-laminar beams, the circular (normal) mode emittances are related to the radial emittance and canonical angular momentum ($M=xp_y-yp_x$) via

$$2\varepsilon_{\pm} = \pm\langle M\rangle + \sqrt{(2\varepsilon_r)^2 + \langle M^2\rangle}\,. \qquad (1)$$

The drift and cyclotron (i.e. circular modes) emittances correspond to the (+) and (-) angular momentum modes in Equation (1).

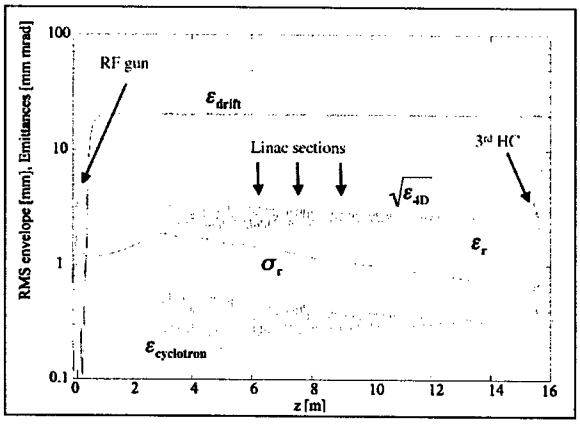


Figure 2: RMS spot and normalized emittance evolution from the cathode (z = 0m) to the entrance of the Adapter (z = 16m) for the magnetized ('flat') beam.

Until the symmetry of the beamline is broken in the skew-quadrupole Adapter lattice, the canonical angular momentum of the beam is conserved. Hence, emittance compensation in this beamline can be monitored by observing the evolution of the radial emittance. Figure 2 illustrates that compensation of the cyclotron emittance through the linac tracks along with the radial emittance. The total 4D emittance (conserved for linear forces) remains essentially constant along this entire portion of the beamline, and at ~2.5 mm-mrad meets the injector specifications with some overhead.

The evolution of the unmagnetized beam up to the Adapter lattice is shown in Figure 3. The gun-to-linac drift length has been increased from 3m to 5m to match the phase of the emittance oscillation. In so doing, the radial emittance is compensated at the linac exit, also with some overhead compared to specifications.

FLAT BEAM ADAPTER OPTICS

Following the 3rd harmonic cavity is the Adapter lattice consisting of 3 skew quadrupoles. The spacing and excitation strength of the skew quadrupoles are determined [7] to cancel the correlations induced by the canonical angular momentum and decouple the horizontal and vertical phase spaces. When this is done properly, the residual angular momentum is removed and, most importantly, the drift and cyclotron emittances are mapped to the horizontal and vertical, producing a flat beam. The evolution of the horizontal and vertical beam emittances and spot sizes are shown in Figure 4.

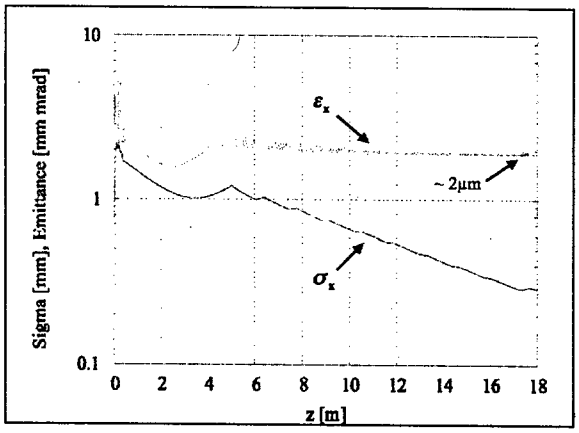


Figure 3: RMS spot and normalized emittance evolution from the cathode to the entrance of the Adapter for the unmagnetized ('round') beam.

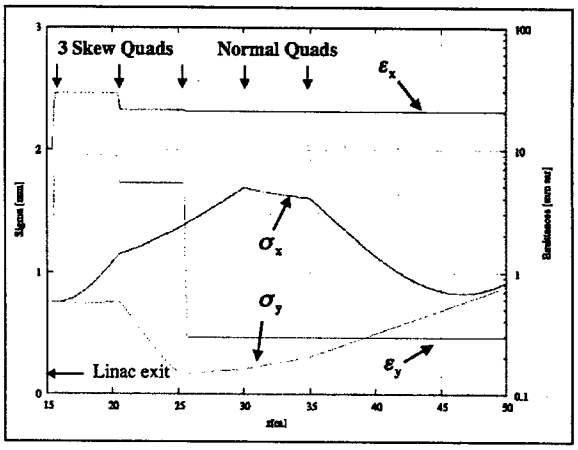


Figure 4: Horizontal and vertical RMS spot size and normalized emittance evolution in the Adapter.

LONGITUDINAL DYNAMICS AND BUNCH COMPRESSION

Manipulation of the longitudinal phase space is another essential duty of the injector. To offset intense space-charge forces at low energy, the beam is generated at the cathode with a bunch length ~20 ps. The launch phase and cell-to-cell phasing in the rf guns are adjusted to produce a low emittance beam with small uncorrelated energy spread. The linac produces a nonlinear correlation over the bunch length, which is removed with the 3rd harmonic cavity. The evolution of the longitudinal phase space from the 1st rf gun cell to the gun exit to the linac exit and the 3rd harmonic cavity exit is shown in Figure 5. As shown, the longitudinal phase space at the entrance to the compressor has an uncorrelated energy spread within specifications.

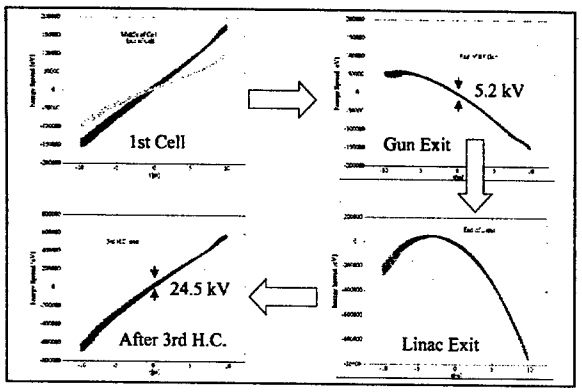


Figure 5: Development of longitudinal phase space from the rf gun to the compressor entrance.

After the flat beam adapter the electron beam executes a 180° turn before it merges the recirculating linac in the bending magnet of the injection chicane (see Figure 6). We use this 180° turn to compress the electron bunch from ~20-30 ps to approximately 2 ps. The design is largely affected by considerations regarding detrimental effects of CSR (coherent synchrotron radiation). Following [8] we split the actual bunch compressor into two parts and separate them by $-I$ transport lines. The idea is to use the CSR in the downstream bunch compressor to compensate for the CSR induced excitation of the horizontal emittance in the upstream bunch compressor. This will give us only a limited success because of the difference in bunch lengths in the upstream and downstream bunch compressors. Therefore to improve compensation we choose bending radii for bend magnets in the downstream compressor to be 1.5 times larger than in the upstream compressor.

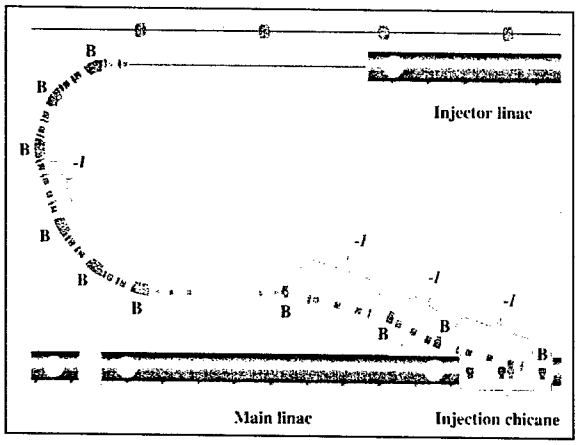


Figure 6: Compressor beamline.

The effect of CSR on horizontal emittance is strongest in the final bend. This is because of the large beta-function in the recirculating linac at the injection point. Compensation of CSR in this magnet requires more complicated arrangements for injection than just a bend. We found that we can have a fairly effective compensation using four bend magnets and separate them by $-I$ transport matrix. In this setting, the two upstream bends have the opposite polarity to the two downstream bends. An additional benefit is that the overall arrangement is achromatic.

To analyze this design we performed particle tracking through the entire bunch compressor and injection lattice using *elegant* [9]. An initial particle distribution was loaded that is uniform both transversely and longitudinally. Tracking through the compressor beamline shows a relative horizontal emittance gain less than 25%, with no discernable increase in energy spread.

CONCLUSIONS

We have produced an injector design for LUX that exceeds performance specifications. There are still several areas that need additional study. We must predict any emittance growth in the low energy achromat line, as well as incorporate its optics into the general emittance compensation scheme for the unmagnetized beam. The Adapter beamline has been optimized for the production of low vertical emittance flat beams using a simple skew quadrupole triplet configuration. This beamline must perform this duty while also matching both the flat and round beam into the compressor. A more complicated beamline may be required to perform this job, and must be studied further.

REFERENCES

[1] J. Corlett, *et. al.*, "A Recirculating Linac-Based Facility for Ultrafast X-ray Science", *Proc. 2003 Part. Accel. Conf.*, Portland, 2003.

[2] W. Fawley, *et. al.*, "Simulation Studies of an XUV/Soft X-Ray Harmonic-Cascade FEL for the Proposed LBNL Recirculating Linac", *Proc. 2003 Part. Accel. Conf.*, Portland, 2003.

[3] J. Staples, *et. al.*, "The LBNL Femtosource 10 kHz Photoinjector", *Proc. 2003 Part. Accel. Conf.*, Portland, 2003.

[4] R. Brinkmann, Y. Derbenev, and K. Floettmann, TESLA Note 99-09, April 1999. A.Burov, Y. Derbenev, S. Nagaitsev, Phys. Rev. E **66**, 016503 (2002).

[5] Astra executables and documentation may be obtained at http://www.desy.de/~mpyflo.

[6] B.E. Carlsten, NIM A **285**, 313 (1989). L. Serafini and J.B. Rosenzweig, Phys. Rev. E **55**, 7565 (1997). S. Lidia, "Emittance Compensation Studies of Photoinjector Beams with Angular Momentum", *Proc. 2003 Part. Accel. Conf.*, Portland, 2003.

[7] E. Thrane, *et. al.*, "Photoinjector Production of a Flat Electron Beam", *Proc. XXI Int'l. Linear Accel. Conf.*, Gyeongju, Korea, 2002.

[8] Linac Coherent Light Source, Conceptual Design Report, SLAC-R-593, UC-414, (2002).

[9] M. Borland, "elegant: A Flexible SDDS-Compliant Code for Accelerator Simulation", *Proc. Int'l. Comp. Accel. Physics Conf.*, Darmstadt, Germany, 2000.

EMITTANCE COMPENSATION STUDIES OF PHOTOINJECTOR BEAMS WITH ANGULAR MOMENTUM*

S. Lidia, LBNL, Berkeley, CA 94720, USA

Abstract

Beam dynamics studies on the FNPL photoinjector that seek to optimize the transport of intense electron beams with large values of canonical angular momentum have been performed. These studies investigate the effect of solenoid emittance compensation on beams that evolve under the combined influence of intense space charge forces and large angular momentum. We present details of experimental measurements and supporting simulations of beam envelope evolution.

INTRODUCTION

Flat beams generated in rf photoinjectors have been proposed for the generation of short-pulse hard x-rays [1] based on earlier studies for linear collider applications [2]. The flat beams are generated by a technique that uses a magnetized cathode to create strong coupling between the horizontal and vertical phase spaces. The coupling is removed downstream by a skew quadrupole lattice which produces a beam with large ratio between the vertical and horizontal emittances.

Emittance compensation techniques [3][4] are now widely used in the design and operation of photoinjectors to minimize the normalized emittance of the beam as it is transported from the injector. Here, we study the modifications of the technique for beams that carry large amounts of angular momenta .

THEORETICAL DEVELOPMENT

Emittance

In an azimuthally symmetric system, the normalized 4-D transverse emittance can be expressed as [5]

$$\varepsilon_{4D} = \frac{1}{4}(\gamma\beta)^2\left[\langle r^2\rangle\langle r'^2+(r\theta')^2\rangle - \langle r\cdot r'\rangle^2 - \langle r^2\theta'\rangle^2\right] \quad (1)$$

where $r' = dr/dz$ and $\theta' = d\theta/dz$. This emittance measures the volume of the full 4-D transverse phase space. Photoinjector beams can be classified as rigid rotators such that θ is constant over all radii. In this case, the normalized radial emittance

$$\varepsilon_{nr} = \frac{1}{2}(\gamma\beta)^2\left[\langle r^2\rangle\langle r'^2\rangle - \langle r\cdot r'\rangle^2\right] \quad (2)$$

provides the full measure of the beam phase space.

Beam Envelope Evolution

The envelope equation of the RMS radial beam spot size ($\sigma_r = \sqrt{\langle r^2\rangle}$) can be expressed as [5]

$$\sigma_r'' + \sigma_r'\left(\frac{\gamma'}{\gamma\beta^2}\right) + k_{eff}^2\sigma_r - \frac{\kappa_s}{\sigma_r} - \frac{\varepsilon_{nr}^2}{\sigma_r^3\gamma^2\beta^2} - \left(\frac{\langle p_\theta\rangle}{mc\gamma\beta}\right)^2\frac{1}{\sigma_r^3} = 0 \quad (3)$$

The effective linear restoring force

$$k_{eff}^2 = \frac{\gamma''}{2\gamma\beta^2} + \left(\frac{qB_z}{\gamma\beta mc}\right)^2 \quad (4)$$

depends on both the external magnetic focusing as well as acceleration. The normalized, radial emittance (5th term) and angular momentum (6th term) contribute similarly to the envelope evolution so that an effective emittance can be defined as

$$\varepsilon_{eff}^2 = \varepsilon_{nr}^2 + \langle p_\theta\rangle^2/(mc)^2 . \quad (5)$$

The (conserved) canonical angular momentum for a single electron at the point of emission from the cathode is

$$p_\theta = -\frac{1}{2}eB_{z0}r_0^2 \quad (6)$$

and the perveance term describing space charge defocusing is

$$\kappa_s = \frac{I_b/I_0}{(\gamma\beta)^3} . \quad (7)$$

Typically, the local thermal emittance in a photoinjector beam is much smaller than the projected emittance that incorporates longitudinal (slice) variations. In our case, we assume that the effective emittance is dominated by correlated angular momentum and that the thermal contribution is completely negligible.

In the absence of acceleration, an equilibrium (laminar) solution to equation (3) is readily found,

$$\sigma_{eq}^2 = \left(\frac{\kappa_s}{2k_{eff}^2}\right)\left[1+\left(1+\mu^2\right)^{1/2}\right], \quad (8)$$

where

$$\mu = 2\frac{k_{eff}\varepsilon_{eff}}{\gamma\beta\kappa_s} \quad (9)$$

measures the relative influence between the perveance and the effective emittance in describing the envelope dynamics. For space-charge dominated beams μ approaches zero, while for emittance dominated beams μ approaches infinity.

The evolution to the envelope equation linearized about the laminar envelope admits oscillatory solutions with characteristic wavenumber

$$k_{eq}^2 = k_{eff}^2\left\{1+\frac{2}{\left[1+\left(1+\mu^2\right)^{1/2}\right]}+\frac{3\mu^2}{\left[1+\left(1+\mu^2\right)^{1/2}\right]^2}\right\}. \quad (10)$$

This wavenumber takes the limiting forms for space-charge dominated and effective-emittance dominated beams,

$$k_{eq}^2 \Rightarrow \begin{cases} 2k_{eff}^2 , & \mu^2 \to 0 \\ 4k_{eff}^2 , & \mu^2 \to \infty \end{cases} . \quad (11)$$

*This work was supported by the Department of Energy under Contract No. DE–AC03–76SF00098.

0-7803-7738-9/03/$17.00 © 2003 IEEE

When acceleration is included, these same formulae apply to describe new equilibria, provided that the envelope parameters are scaled as

$$\left.\begin{matrix}\sigma_r \\ k_{eff}^2 = \dfrac{\gamma^*}{2\gamma\beta^2} + \left(\dfrac{qB_z}{\gamma\beta mc}\right)^2 \\ \varepsilon_{eff}^2 \\ \kappa_s\end{matrix}\right\} \Rightarrow \left\{\begin{matrix}(\gamma\beta)^{1/2}\sigma_r \\ K^2 = \dfrac{(\gamma^2+2)(\gamma')^2}{4(\gamma\beta)^4} + \left(\dfrac{qB_z}{\gamma\beta mc}\right)^2 \\ (\gamma\beta)^{3/2}\varepsilon_{eff}^2 \\ (\gamma\beta)^{1/2}\kappa_s\end{matrix}\right. \quad (12)$$

Emittance Compensation

It has been shown previously [4] that the projected emittance oscillates with the same spatial frequency as the beam envelope. On emission from the photocathode, the beam will contain small fluctuations in equilibrium radius along its length. The different longitudinal beam slices will have different initial phases of the emittance oscillation. For small variations from a nominally matched laminar beam the slices will oscillate together coherently such that the total emittance projected over all the slices has a sinusoidal variation down the beamline [4]

$$\varepsilon_{nr} \approx \frac{\gamma\beta}{2\sqrt{2}} k_{eq}\sigma_0\sigma_{eq}\left(I_{peak}\right)\frac{\delta I_{rms}}{I_{peak}}\left|\sin\left(k_{eq}z\right)\right|. \quad (13)$$

From equation (11), it is seen that the projected emittance minima occurs periodically along the beamline. As the beam accelerates, the emittance value is eventually 'frozen' in. Focusing and acceleration profiles for photoinjectors can be determined so that the projected emittance passes through a minima as the beam energy increases to the point that space-charge induced emittance oscillations are negligible.

We study solutions to the envelope equation by parameterizing with respect to the initial angular momentum. The RF gun design may then be considered optimized for a particular value of the initial angular momentum when the effective radial emittance is minimized.

Parameterizing With Cyclotron Phase Advance

We have used HOMDYN [6] to evaluate possible operating points of a flat beam injector. The degree of emittance compensation provided by solenoid focusing can be measured against the cyclotron phase advance, θ_c,

$$\theta_c\left(t_{final}\right) = \int_0^{t_{final}} dt \frac{eB_z}{m\gamma}. \quad (14)$$

This parameter is useful when comparing simulations or experimental data sets when the initial beam spot is held constant. When the spot size varies, the Larmor phase advance,

$$\theta_L\left(t_{final}\right) = \int_0^{t_{final}} dt\left(\frac{p_\theta}{m\gamma}\frac{1}{r^2} + \frac{eB_z}{2m\gamma}\right), \quad (15)$$

is the appropriate measure of single particle azimuthal motion. The utility of the cyclotron phase advance is such that it only depends on the solenoid tune and the beam energy. It provides a measure independent of the beam envelope dynamics, including space charge and emittance effects.

EXPERIMENTAL STUDIES AT FNPL

Experimental studies of flat beam production has been underway at the FNPL (Fermilab-NICADD Photoinjector Laboratory) facility [7]. The layout of the FNPL beamline is shown in Figure 1.

The FNPL photoinjector consists of a 1.6 cell, 1.3 GHz RF gun with a high quantum efficiency Cs_2Te photocathode driven by a frequency-quadrupled Nd:glass laser, followed by a 9-cell superconducting booster cavity resulting in an 14-15 MeV electron beam. A dipole chicane is present to provide magnetic bunch compression. As shown in Figure 1, three of the normal quadrupoles have been rotated about their axis to become skew quadrupoles. During flat beam production, these skew quadrupoles are energized.

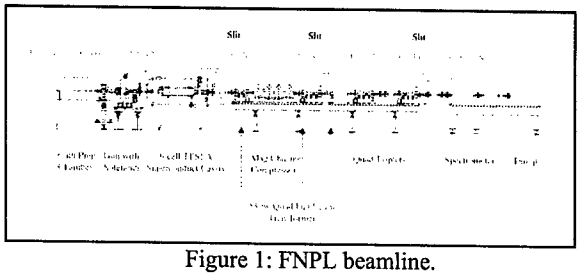


Figure 1: FNPL beamline.

Emittance Optimization Studies

Parametric studies were performed to examine the effect of solenoid focusing on flat beam final emittance and emittance ratio. The main solenoid provides the field on the cathode and defines the initial canonical angular momentum on the beam. The secondary solenoid controls the matching into the booster accelerator and tunes for emittance compensation.

The cyclotron phase advance at the entrance to the booster module has been calculated using HOMDYN. Figure 2 shows the cyclotron phase advance (in units of π) as the secondary solenoid current is varied over its full range, for different values of the main solenoid current. By varying the current in both the main and secondary solenoids a usable range of cyclotron phase advance from ~0.8π to ~1.5π radians can be explored.

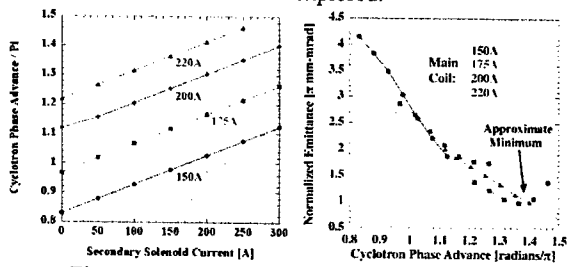


Figure 2: HOMDYN simulations: (left) Cyclotron phase advance (in units of π) vs. secondary solenoid current, (right) Normalized emittances at the booster exit.

Beam envelopes and radial emittances from HOMDYN simulations for four distinct cyclotron phase advances (0.88 π, 1.1 π, 1.35 π, 1.46 π) are shown in Figure 3.

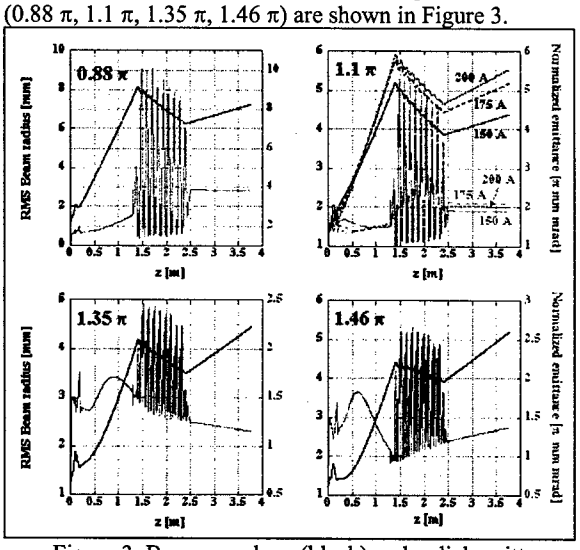


Figure 3: Beam envelope (black) and radial emittance (red) for cyclotron phase advances of 0.88π, 1.1π, 1.35π, and 1.46π (HOMDYN).

In the first two regions (cyclotron phase advance of 0.88π and 1.1π) the beam is under-compensated, the emittance increases through the booster. In the second region (1.1 π), the emittance at the exit of the booster is reduced by a factor ~2 compared to the previous case.

We see here the utility of cyclotron phase as a measure of emittance compensation. The results of three separate simulations, with different values of angular momenta, but with equal cyclotron phase advance (1.1π) are overlaid. The beam envelopes show some difference, but the emittance evolution is identical for the three cases.

The third (1.35 π) case shows the emittance compensated case, while the fourth (1.46 π) cases shows the over-compensated case in which the emittance oscillation has already passed through a minimum before exiting the booster.

Experimental Vertical Emittance Measurement

The vertical emittance at the entrance to the skew quad channel has been measured using the horizontal slit analyzer at the booster cavity module exit and the imaging the beamlets on downstream OTR foils. The measured values are shown in Figure 4. Over the range of parameters scanned, and by comparison with Figure 2 above, we see that the individual emittance minima occur for nearly equal values of the cyclotron phase advance as calculated by HOMDYN.

The absolute values of the emittance are properly to be recognized as upper bounds, as they reflect the projected emittance averaged over approximately 20 bunches with varying bunch charge (~0.5-1.2 nC per bunch), and hence varying compensated emittance values. These studies will continue with more stringent control over the bunch train charge profile.

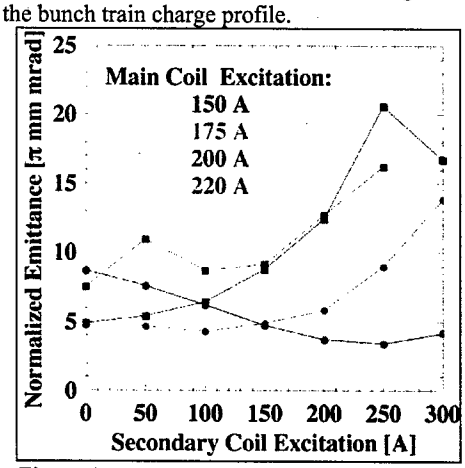


Figure 4: Measured vertical emittances of angular momentum-dominated beam at FNPL.

ACKNOWLEDGMENTS

The author would like to acknowledge the assistance of Kai Desler, James Santucci, and Yin-e Sun during the measurements, and to Helen Edwards for support for these studies.

REFERENCES

[1] J. Corlett, et.al., "A Recirculating Linac-Based Facility for Ultrafast X-ray Science", *Proceedings of the 2003 Particle Accelerator Conference*, Portland, 2003.

[2] R. Brinkmann, *et. al.*, 'A Flat Beam Electron Source for Linear Colliders', TESLA 99-09, DESY-Hamburg, 1999.

[3] B.E. Carlsten, Nucl. Instrum. Methods Phys. Res. A **285**, 313 (1989).

[4] L. Serafini and J.B. Rosenzweig, Phys. Rev. E, **55**, 7565 (1997).

[5] Martin Reiser, Theory and Design of Charged Particle Beams , Wiley, New York, 1994.

[6] M. Ferrario, *et. al.*, Part. Accel., **52**, 1 (1996).

[7] J.P. Carneiro, *et. al.*, 'Beam transport, acceleration and compression studies in the Fermilab high-brightness photoinjector', *Proceedings of the XIX International Linac Conference*, Chicago, 1998.

THE LBNL FEMTOSOURCE (LUX) 10 KHZ PHOTOINJECTOR *

John W. Staples, Steven M. Lidia, Steven P. Virostek, LBNL, Berkeley, California
Robert Rimmer, TJNAF, Newport News, Virginia

Abstract

The LBNL femtosecond-level X-ray source, now christened LUX, a source of hard X-rays with a pulse length in the 50–200 fsec range, will operate at a pulse rate of up to 10 kHz. The room-temperature 1.3 GHz photoinjector includes a modified re-entrant first-cell cavity which minimizes peak surface field, the addition of a third pi-mode acceleration cell, waveguide r.f. feeds to each cell, and an active energy removal procedure which reduces the wall power density of all four cells.

INTRODUCTION

The LUX [1] [2] RF gun will provide nominally a 1–3 nanocoulomb electron bunch, 20 psec long, at a 10 kHz repetition rate from a laser-illuminated Cs_2Te photocathode. The 20 psec beam will be compressed to 2 psec in the first 180 degree arc, and then accelerated to 2.5 GeV, and then through crabbing in the vertical plane, the X-ray pulse from each of a series of undulators will be further optically compressed by means of an asymmetric crystal to as short as 50 fsec.

The resulting photon flux of 10^6 photons per pulse per 0.1% bandwidth up to 12 keV from undulators from the "flat" beam injector to 10^{13} at 20–1000 eV from cascaded harmonic generation in FELs from a future off-axis "round" beam injector results in part from the high 10 kHz pulse rate, which presents a significant challenge for the room-temperature photoinjector. Table 1 lists the important parameters of the 3.5-cell photoinjector.

Table 1: 3.5-Cell Photoinjector Parameters

Parameter	Value	Unit
Frequency	1.3	GHz
Duty Factor	5	percent (equiv)
Cell 1 Q_0	21000	(pure Cu)
Cell 2–4 Q_0	29000	(pure Cu)
Rep Rate	10	kHz
Photocathode Field	64	MV/m
Axial Accel Cell Field	40	MV/m
Charge/bunch	1-3	ncoul
Output Energy	10	MeV

The photoinjector will be immersed in a solenoidal magnetic field to produce a magnetized beam at the photocathode, whose rotational angular momentum will subsequently be converted, through a series of skew quadrupoles, to a "flat" beam with a horizontal-to-vertical emittance ratio of at least 50 to 1. [3] The small vertical beam is then crabbed just before the photon radiators, and the transverse-longitudinal correlation is converted to a time-compressed photon pulse.

The selection of the 10 MeV output energy allows sufficient room for a beam transport system before a 110 MeV 1.3 GHz superconducting accelerator section to provide for emittance compensation solenoids and for the introduction of a septum magnet to combine a future 3.5-cell round-beam photoinjector for driving a future FEL.

Figure 1 shows the 3.5 cell photoinjector embedded in a series of five solenoids. The axial magnetic field at the photocathode is in the 1.0 to 1.5 kGauss range. For a round-beam photoinjector, the solenoids buck the axial B-field at the photocathode.

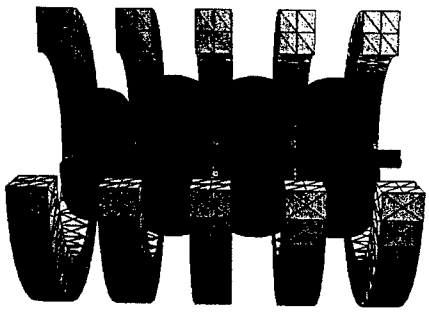


Figure 1: 3.5-Cell Photoinjector and Solenoids

CAVITY FIELD OPTIMIZATION

The first version of the gun was a 2.5-cell structure [4] and subsequently increased to 3.5 cell. With a peak field of 64 MV/m at the photocathode and a 5% duty factor, the peak electric field in the first cell should be held to as low a value as possible, even if it results in a decrease in shunt impedance of the first cell. Increasing radii of curvatures of the cell geometry brought the peak field down from 104 MV/m to 87 MV/m in the nosecone area opposite the photocathode: the ratio of peak to photocathode field was reduced from 1.62 to 1.36, while the peak RF wall current remained at 71 kA/m. The peak RF power demand increased from 580 to 750 kW with this modification.

Figure 2 shows the average wall power density around the surface of a 2-D URMEL calculation of the optimized first cell.

Cells 2 through 4 comprise the three accelerating cells in the photoinjector. The peak axial field in the $\pi/2$ structure

* This work supported by the US Department of Energy under Contract No. DE-AC03-76SF00098.

0-7803-7738-9/03/$17.00 © 2003 IEEE

is 40 MV/m, and the corresponding peak wall field is 46.7 MV/m. The walls are inclined at a 2 degree angle to the perpendicular, and the coupling iris radius is 1 cm.

The asymptotic RF power requirement (several filling times) is 1.35 MW for each cell, but as in the first cell, as described below, the peak available power will be 2.5 MW to fill each cell in 1.5 filling times. As in the first cell, the peak wall power density at the worst case, the outer radius edge of the iris in this case, is 82 W/cm^2.

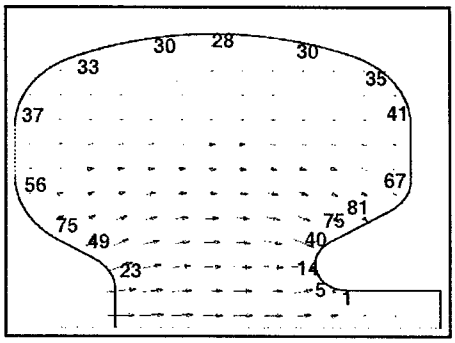


Figure 2: Average wall power density in cell 1 (W/cm^2)

POWER COUPLERS

Each of the four cells is driven by two symmetric iris-coupled waveguides from independent power sources. As described below, due to the 5 microsecond pulse relative to the 3.5 microsecond cavity filling time, the cavities will be overdriven, and then the stored energy will be actively removed to reduce the average power. This will increase the peak fields in the waveguides and iris couplers.

The coupling coefficient is optimized at approximately unity, so $Q_0 \approx Q_{ext}$ for each of the cavities. The dumbbell-shaped coupling iris area is calculated in the following way: The resonant frequency and Q_0 of the bare cavity are first determined. Using a MAFIA-4[5] half-cell mesh, the problem is set up using a waveguide port model and pinging the cavity with a "soft" packet near the 1.3 GHz resonant frequency. The field decrement is then measured and the iris dimensions are adjusted so that the field decrement per cycle is given by the loaded $Q_L = Q_0/2$ for unity coupling.

As the MAFIA-4 mesh is rectangular instead of conformal, fine adjustments will be made to the iris geometry using the *e-mag* module of ANSYS [6], which will also be used to confirm the details of the thermal model for the cavity, particularly in the iris region.

Figure 3 shows the MAFIA-4 half-model of the first cell with coupling port. The first $\lambda/4$ section of the waveguide is half-height, to make room for the solenoids, which straddle the intercell boundary regions.



Figure 3: MAFIA-4 Mesh of Cell1 and Waveguide Coupler

REDUCING AVERAGE WALL POWER

With unity coupling, the filling time of each cell is on the order of 3.5 microseconds. At a 10 kHz repetition rate and 5 microsecond pulse length, the macroscopic duty factor is 5%, and at 5 microseconds, only 1.5 filling times have occurred. For short RF pulse lengths, the "square pulse" analysis is inadequate to address the thermal dissipation. Extending the pulse length will further increase the already high duty factor, and overvolting the cavity will increase the average power dissipation, which would already be 75 kW per accelerating cell.

The field will rise to 77% of full at 1.5 filling times, so overpowering each cell by $1/0.77^2$, or about 2.5 MW, including a realistic value for the cavity Q_0 and waveguide and circulator losses will achieve operating gradient at 5 microseconds (the beam pulse is 20 psec). The average power may be reduced by about 40% by reversing the drive phase ("reverse SLEDding") and actively removing the stored energy to the circulator dummy load.

Figure 4 shows the cavity field level without and with active energy removal. The cavity is overdriven for 5 microseconds. Then the drive phase is reversed and drive power continues for about another 2 microseconds until the cavity is empty. (The beam loading is insignificant.)

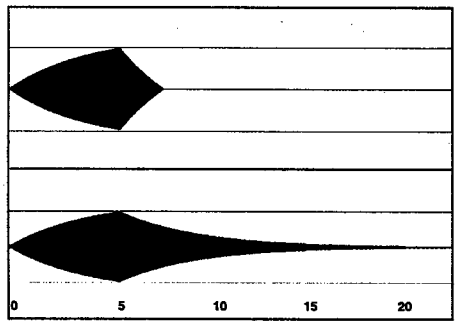


Figure 4: Fields in Cavity without and with phase flip at 5 microseconds. Horizontal scale: time in microseconds, Vertical scale: fields in cavity with and without active energy removal.

Peak Temperature Rise

Even though the peak wall power density approaches 82 W/cm^2 at one point, the average wall temperature will be less than 30 C above the wall temperature in the cooling channel (plus the film temperature difference). The Laplace thermal diffusion equation $k\nabla^2 T + \dot{Q} = \rho C_v \dot{T}$ is integrated in one dimension, with specific heat C_v, thermal conductivity k and target density ρ characteristic of copper for a 1 cm thickness between cavity surface and cooling channel. For a wall current density of 70 kA/m, 5 microsecond pulses at a 10 kHz rate, the asymptotic temperature rise is 30.3 C. Figure 5 shows the results of the beginning of the integration, before asymptopia, of the temperature rise for each 5 microsecond pulse of 0.6 C.

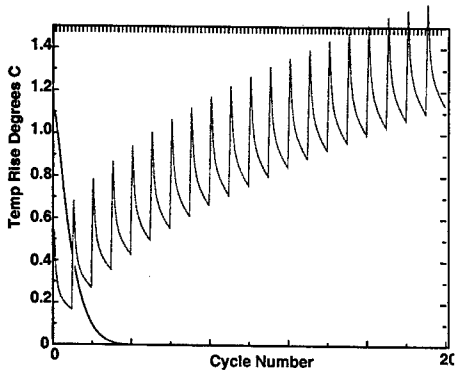


Figure 5: Temperature rise each cycle of worst-case wall power density, the first 20 cycles. Asymptote is 30.3 C

BEAM DYNAMICS

The proposed LUX photoinjector gun design will deliver a beam of quality similar to that of other operating RF guns. The brightness for the LUX RF gun is based upon a 1 nanocoulomb bunch with 3π mm-mrad normalized RMS emittance. This brightness is conservative, and is similar or less than that achieved at the same frequency from TTF and AFEL guns, for example.

The detailed beam dynamics in the RF gun and injector have been studied using the particle tracking code ASTRA [7]. For the flat beam injector, a magnetized cathode produces a finite canonical angular momentum carried by the beam. The 4D phase space, described in terms of horizontal and vertical coordinates and momenta is coupled. A decoupled description can be obtained if one is willing to use "drift" and "cyclotron" coordinates [8]. These normal mode coordinates each have an associated emittance. The product of the drift and cyclotron emittances is the total 4D emittance of the beam. For linear forces, the 4D emittance is preserved along the beamline. The variation of the different emittances through the RF gun and subsequent drift are shown in Figure 6. The photocathode is located at z = 0 meters. Shown are the cyclic mode (drift, cyclotron), total 4D, and usual radial RMS normalized emittances, along with the RMS horizontal spot size.

A discussion of injector optimization, emittance compensation, and dual-injector operation can be found in a companion paper at this conference [9].

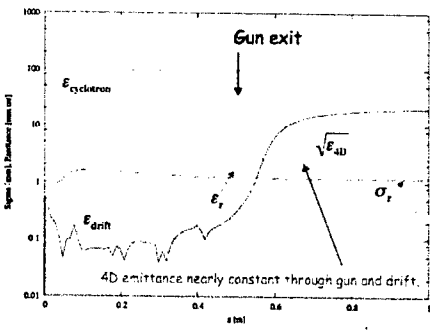


Figure 6: Evolution of Radial and Transverse Emittance

REFERENCES

[1] J. N. Corlett at al, "Feasibility Study for a Recirculating Linac-Based Facility for Femtosecond Dynamics", LBNL formal report LBNL-51766, Dec 2002.

[2] J. N. Corlett et al, "A Recirculating Linac-Based Facility for Ultrafast X-ray Science", this conference.

[3] D. Edwards et al., "The Flat Beam Experiment at the FNAL Photoinjector", Proc. XXth International Linac Conference, Monterey, 2000

[4] R. A. Rimmer, et al, "A High-Gradient High-Duty-Factor RF Photo-Cathode Electron Gun", 2002 EPAC, Paper TUPRI040, Paris, 2002

[5] Gesellshaft für Computer Simulationstechnik, Lauteschlägerstraße 38, D-64289 Darmstadt, Germany

[6] ANSYS Finite Element Analysis Code, Release 7.0, SAS IP, Inc., Canonsburg, PA.

[7] K. Flöttmann, ASTRA User Manual, DESY, 2000. The program and its documentation can be obtained at the web site www.desy.de/~mpyflo

[8] see, for example, A. Burov, S. Nagaitsev, and Y. Daroslav Phys. Rev. E 66, 016503 (2002)

[9] S. Lidia, et. al., An injector for the proposed Berkeley ultrafast x-ray light source, this conference,WPAB021

INITIAL TESTING OF A FIELD SYMMETRIZED DUAL FEED 2 MeV 17 GHz RF GUN

A. Kesar[1], J. Haimson[2], S. Korbly[1], I. Mastovsky[1], B. Mecklenburg[2], and R. J. Temkin[1]*
[1] MIT Plasma Science and Fusion Center, 167 Albany, Cambridge, MA 02139, USA
[2] Haimson Research Corporation, 3350 Scott Blvd., Building 60, Santa Clara, CA 95054-3104, USA

Abstract

A 3 cell 17.14 GHz RF gun designed and built by Haimson Research Corporation (HRC) [1] is being tested at the Plasma-Science and Fusion Center at MIT. The middle cavity consists of a racetrack design having dual-feed coupling holes for achieving highly symmetrical TM_{01} π-mode operation. The high symmetry is important for reducing the beam emittance. The power into the RF gun is supplied by an HRC 25 MW, 17 GHz relativistic klystron amplifier. A 1 MW, 100 ns input pulse is required to achieve a peak axial electric field of 150 MV/m in the cavities to provide the electron-bunch with a 1.6 MeV energy gain. A 2 ps, 20 μJ laser pulse is injected into the back of the first cell for emitting the electron bunch. The diagnostic setup consists of a YAG screen and a CCD camera for beam imaging, and a slit array, a magnetic spectrometer, and a Faraday Cup for emittance, energy, and bunch charge measurements, respectively. The RF gun is currently being fed by $\sim$ 0.7 MW, 100 ns pulses. Our next goals are to process the gun up to 1 MW and 100 ns pulses, to inject the laser pulse and synchronize it with the RF phase, and to measure the output bunch energy, brightness, and duration. The status of the experimental results is presented.

INTRODUCTION

RF guns, or photocathode injectors, are used to produce short bunches of high-energy high-brightness electron beams. Bunches in the order of sub-picoseconds having megawatt level energy are of interest for high-energy physics research and for sub-millimeter coherent sources. Frequency scaling in RF guns plays an important role in decreasing the bunch emittance and length while increasing its brightness and energy.

Future TeV linear colliders require high quality beams to produce an interaction point of sub-micrometer spot size having luminosities $> 10^{34}$ cm^{-2}s^{-1} [2]. RF accelerating cavities at frequencies $>$ 11 GHz may be very valuable in meeting this goal.

Free-electron lasers (FELs) are used to produce coherent sub-millimeter to sub-micron high-power microwaves that can be used for various applications such as material and biological studies. Low-emittance high-charge bunches are required for this purpose [3].

Reports on RF gun design and experimental study are described in Refs. [4, 5]. A high record of brightness, 80 A/(π mm mrad)^2, was reported in [6, 7]. Dual RF feeding ports can be used to increase the mode symmetry [8]. Dual coupling into a racetrack cavity profile (rather than circular) was suggested by Haimson in order to further increase the mode symmetry [9].

This paper presents the experimental status of the RF gun designed and built at HRC and tested at MIT. The objective of this experiment is to measure the brightness and output energy of the electron bunches. The results will be of importance for high-power short wavelength applications.

Table 1: RF gun operating parameters

Number of cells	3	
Cavity Q	4600	
Resonant frequency	17.142	GHz
Temperature sensitivity	280	kHz/°C
RF power	$\sim$ 1.5	MW
RF pulse duration	100	ns
Laser energy	10–20	μJ
Laser FWHM	2	ps

EXPERIMENTAL SETUP

The experimental setup for operating the RF gun consists of a high power RF system and a laser system. The operating parameters are described in Table 1. An HRC 25 MW, 68 dB gain, 17 GHz relativistic klystron amplifier supplies a $\sim$ 1 MW 100 ns pulse at 17.142 GHz to the RF gun (the excess power from the klystron is directed into a linear accelerator). A bidirectional coupler samples

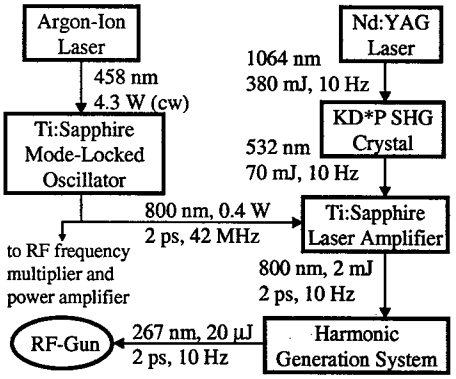


Figure 1: The laser system.

* temkin@psfc.mit.edu

0-7803-7738-9/03/$17.00 © 2003 IEEE

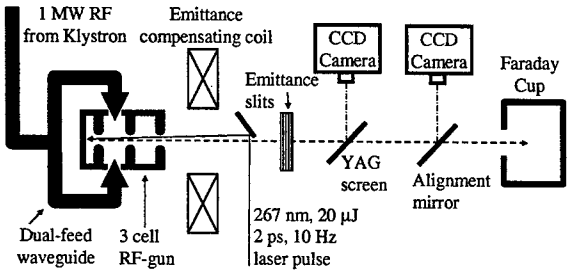


Figure 2: RF gun and diagnostic setup.

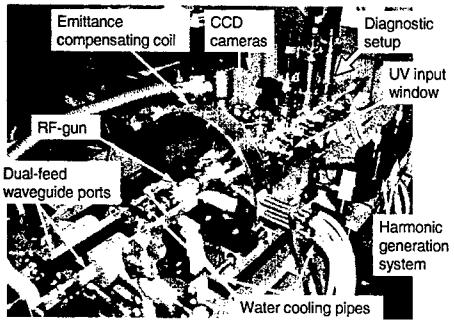


Figure 3: A picture of the RF gun and the diagnostic setup.

both the forward power into the RF gun, and the reflected power. The klystron is driven by a travelling-wave tube (TWT) amplifier where the input to the TWT is synchronized and phase-matched to the laser system.

The laser system is described in Fig. 1. It consists of a Ti:Sapphire laser amplifier that produces 2 ps 2 mJ pulses at 800 nm and 10 Hz. These pulses are tripled, by a harmonic generation system to UV light at 267 nm and are directed into the RF gun cathode. The laser amplifier is pumped by 532 nm 70 mJ pulses at 10 Hz repetition rate produced by an Nd:Yag laser and a KD*P second-harmonic generator crystal. The amplifier is seeded by 2 ps 800 nm pulses repetitive at 42 MHz from a Ti:Sapphire mode-locked laser oscillator. The oscillator is pumped by 4.3 W (cw) at 458 nm produced by an Argon-Ion laser. The Ti:Sapphire oscillator cavity is tuned around 42 MHz such that its mode-locking RF-frequency is multiplied by 408 to provide a synchronized 17.142 GHz signal that is subsequently phased-matched and amplified to stimulate electron emission from the RF gun.

The RF gun consists of a 3-cell water-cooled structure having radii of 0.2697", 0.2722", and 0.2713" for the first, second, and third cells, respectively. The middle cavity consists of a racetrack design having dual-feed coupling holes in order to achieve a highly symmetrical TM_{01} π-mode operation. The high symmetry is important for reducing the beam emittance. A water cooling system provides a frequency tuning ability of the RF gun cavity by 280 kHz/°C. A detailed description of the RF gun design is presented in Ref. [1].

The RF gun and its diagnostic setup are described in Fig. 2. A picture of our lab including the RF gun and the diagnostinc setup is presented in Fig. 3. The 1 MW input power from the klystron amplifier is injected into the second cavity through its dual ports. The laser pulse is directed through a UV mirror to the center of the copper end wall of the RF gun, the surface of which serves as a cathode. The electron-bunch emitted from the gun is focused by an emittance-compensating coil into a YAG screen. Steering coils are positioned along the beam-line in order to compensate for parasitic transverse magnetic fields. An image of the beam shape hitting the YAG screen is recorded by a CCD camera. A slit array can be lowered into the beam-line (or removed above it) in order to measure the beam emittance [6]. An alignment mirror can be lowered at the end of the beam-line in order to align the laser into the center of the RF gun cathode (in this case the YAG and slit array are removed up). The image is viewed by another CCD camera.

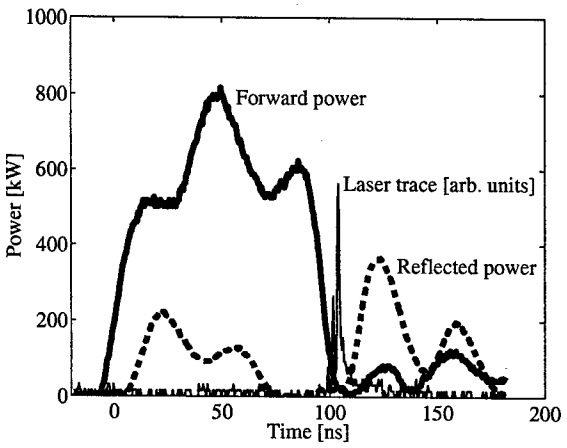


Figure 4: RF gun forward and reflected power traces (thick solid and dashed lines, respectively) and laser pulse trace (thin solid line).

EXPERIMENTAL STATUS

The RF gun is currently being RF processed up to a 1 MW power level. Scope traces of the 17.142 GHz forward and reflected power into and from the RF gun are shown in Fig. 4 in thick solid and dashed lines, respectively. It is seen that the forward pulse is $\sim$ 700 kW for 100 ns. After 80 ns of cavity filling time, the reflected power is close to zero and the laser pulse is injected into the cavity. The laser is detected by a photodiode, and its trace is shown in Fig. 4 as a thin-solid line. (Note: due to length differences in the setup, the laser-trace lags about 20 ns after the RF traces).

For the input power shown in Fig. 4, a white spot indicating dark current was detected on the YAG screen. This image appeared regardless of the laser pulse, and disappeared at lower RF input powers. Its shape was sensitive to

both the magnetic field strength of the emittance compensating coil and the steering coils. Its brightness, although not measured, appeared to be weak on the YAG screen.

FUTURE PLAN

Our future plan includes processing the RF gun up to a power level of 1.6 MW for 100 ns to achieve an electron beam energy of 2 MeV. We intend to measure the electron beam charge, emittance, and energy.

We might need also to improve a $\sim$ 3 ps phase jitter between the RF and the laser pulses. The jitter in our system, as studied in [7] is mostly related to our laser system, and is a source of an energy jitter of the output bunch. New laser technologies can reduce this jitter to sub-picosecond levels.

ACKNOWLEDGEMENT

This research is supported by the U.S. Department of Energy.

REFERENCES

[1] J. Haimson, B. Mecklenburg, and G. Stowell, "A field symmetrized dual feed 2 MeV RF gun for a 17 GHz electron linear accelerator", Advanced Accelerator Concepts, AIP Conference Proceedings, vol. 472, pp. 653–667, 1998.

[2] O. Napoly, "Luminosity stability, possible feedback, and background at future linear colliders". In Proceedings EPAC 2000, Vienna, Austria, pp. 53–57, 1998.

[3] R. Cee, M. Krassilnikov, S. Setzer, T. Weiland and A. Novokhatski, "Detailed numerical studies of space charge effects in an FEL RF gun", Nuclear Instruments and Methods in Physics Research A, vol. 483, pp. 321-325, 2002.

[4] D. T. Palmer, M. J. Hogan, M. Ferrario, L. Serafini, "A 90 GHz photoinjector". In Proceedings of the 1999 Particle Accelerator Conference, Piscataway, NJ, vol. 3, pp. 1997–1999, 1999.

[5] M. Uesaka, H. Iijima, K. Dobashi, J. Yang, S. Miyamoto, and A. Mizuno, "Review of Recent Development of Photoinjectors in Japan", AIP Conf. Proc., vol. 647, p. 839, 2002.

[6] W. J. Brown, S. E. Korbly, K. E. Kreischer, I. Mastovsky, R. J. Temkin, "Low emittance electron beam formation with a 17 GHz RF gun", Physical Review Special Topics - Accelerators and Beams, vol. 4, pp. 08351/1–8, 2001.

[7] W. J. Brown, "Low emittace electron beam production and characterization with a 17 GHz photocathode RF gun", PH.D. Thesis, Massachusetts Institute of Technology, 2001, and references therein.

[8] D. T. Palmer, X. J. Wang, I. Ben-Zvi, and R. H. Miller, "Beam dynamics enhancement due to accelerating field symmetrization in the BNL/SLAC/UCLA 1.6 cell S-band photocathode RF gun". In Proceedings of the 1997 Particle Accelerator Conference, Piscataway, NJ, vol. 3, pp. 2846–2848, 1998.

[9] J. Haimson, B. Mecklenburg, and E. L. Wright, "A racetrack geometry to avoid undesirable azimuthal variations of the electric field gradient in high power coupling cavities for TW structures", Advanced Accelerator Concepts, AIP Conference Proceedings, vol. 398, pp. 898–911, 1997.

CURRENT NANOPULSE GENERATION IN RF ELECTRON GUN WITH METAL-DIELECTRIC CATHODE

M.I. Ayzatsky, I.V. Khodak#, V.A. Kushnir, V.V. Mitrochenko, V.F. Zhiglo
National Science Center 'Kharkov Institute of Physics & Technology'
1, Academicheskaya St., NSC KIPT, 61108 Kharkov, Ukraine

Abstract

The RF gun operation with metal-dielectric cathode is reviewed in the paper. The beam is extracted from the plasma developed during the microwave flashover dielectric in vacuum. The cathode was designed and electron beam dynamics was computer simulated. Modes of the gun operation were researched experimentally on the linear resonance electron accelerator. The beam at the gun output has the pulse current of 3.5-4.5 A with the current pulse duration of 40-50 ns and with particle energy of 300 keV. Some treatments of the beam development and the gun cavity response to the flashover in high intensity RF fields are given.

1 INTRODUCTION

RF electron guns produce electron beams with extreme high brightness providing operation of free electron lasers and injector systems for linear colliders. Thermionic and photoemission RF guns are the most widely used now. Electron beam dynamics in such guns is well studied. The ways of beam brightness increasing are also defined.

The fundamentals of RF gun operation can be applied for the generation of intense high-energy bright beams with nanosecond current pulse duration. The main idea is in the total stored energy absorption in RF gun cavity. The generation of ultra-high current electron beams in thermionic RF guns is limited by the cathode emission current density that is not higher of 10 A/cm^2 for conventional dispenser cathodes. The operation of photoemission RF guns in nanosecond pulse duration mode is followed up by the cathode surface heating up that limits pulsed current value [1]. To provide the required current the plasma cathodes can be used. Such cathodes don't require complicated satellite equipment. Metal-dielectric cathodes with emission from the plasma developed during the microwave flashover dielectric in vacuum are somewhat more promising [2, 3] to be applied as electron sources. The source of the flashover is the metal-dielectric-vacuum contact. Application of metal-dielectric cathode in RF gun with high electric field strength will permit to extract high peak current due to bunched beam structure. Moreover, it's not excepted that the known electron back bombardment can contribute to the flashover development and self-maintenance.

The purpose of the work is to research experimentally S-band RF gun operation with metal-dielectric cathode.

2 EXPERIMENT APPROACH

Two-cavity S-band RF gun [4] was used for the research. The cathode was designed with taking into account RF gun properties and the flashover behaviour in vacuum. There is simplified RF gun design with metal-dielectric cathode and measurement layout on the Fig. 1.

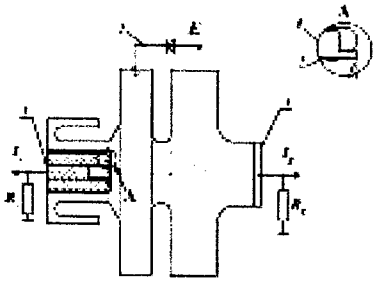


Fig. 1. The simplified RF gun design and measurement layout:
1-cathode; 2-detector; 3-beam current monitor; 4-dielectric cathode cylinder; 5-metalic cathode cylinder

The cathode 1 consists of inner copper cylinder 5 and outer polytetrafluorethylene cylinder 4 enclosed by the shielding tube. The cathode is placed in the quarter-wave line of the gun where the electric field has decreasing distribution along the discharge interval l. The copper cylinder has the curvature radius at the end face of ~ 20 μm to increase the electric field strength in the metal-dielectric contact. Besides, the small radius decreases discharge initiation field due to current density increasing through the emitting surface [5].

The flashover process in a spatial scale in S-band RF field is the same as in a pulse electric field [3] due to following the condition $l \ll \lambda_0$, where λ_0 is operating gun wave length. Defining l is the compromise between low initiation electric field strength and beam parameters at the gun output that is beam emittance. Thus, the computer simulation using SUPERFISH code [6] has defined that small values of l simplifies tuning of the gun cavity eliminating the dependence of the unloaded Q-factor Q_0, the operating frequency f_0 and longitudinal electric field distribution in the gun cavity on the dielectric properties. In particular, the relative variation of Q-factor and f_0 is 10^{-2} and 10^{-5} respectively for $l = 0.5...1.5$ mm and dielectric cylinder with diameters of 3 and 4 mm and with properties of $tg\delta = 10^{-4}...10^{-2}$ and $\varepsilon = 1...12$. Therefore,

#khiv@kipt.kharov.ua

0-7803-7738-9/03/$17.00 © 2003 IEEE

the discharge interval length was accepted of 1 mm that corresponds to the electric field strength ≅ 6.0 MV/m at the cathode plane with maximum axial electric field strength in the cavity of 30 Mv/m.

The hollow cathode design was used to take into account intense high current beam acceleration in RF gun. The extracted current density from plasma into vacuum follows up the thermo-field emission on the hypothesis that electron distribution in plasma spot follows Maxwell-Boltzmann statistics and is defined as following [7]:

$$j = en_e\left(\frac{kT_e}{2\pi m_e}\right)^{1/2}\exp\left(\frac{\sqrt{e^3E}}{kT_e}\right), \qquad (1)$$

where e is electron charge, m_e is electron mass; T_e is plasma temperature; n_e is plasma density; E is electric field strength; k is Boltzmann constant. The computed average current extracted from plasma spot in vacuum for the RF gun is 10.5 A. To accelerate this current and to keep the beam converged particles should meet high electric field strength. Beam dynamics simulation in approach of flat emitting surface using PARMELA code [8] shows that the maximum electric field ratio $\eta=E_1/E_2$ >1, where E_1 and E_2 is maximum of electric field strength in the gun first and second cavity respectively. Fig. 2 shows normalized beam emittance for 70 % of particles and transverse beam size vs η.

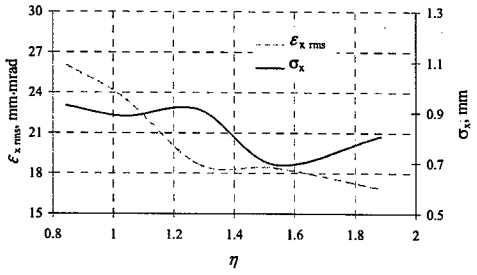


Fig. 2: Beam emittance and beam size vs maximum electric field ratio

For the input power value of 1.5 MW the energy spread (FWHM) and phase spread doesn't depend actually on the value η and is 32 % and 43 % respectively. The electron capture is increased in the range of 0.34..0.4 for the above (Fig. 2) values of η.

3 EXPERIMENTAL RESULT TREATMENTS

The RF gun operation was researched on the single-section linac LIC [9] having accelerating structure with phase velocity that is equal to the light velocity c. There was measured the current from metallic cylinder of the cathode I_c (Fig. 1), output gun current I_g and beam parameters at the linac output for different axial electric field strength E in the first cavity of the gun. For $E \le 25$ MV/m the current I_c is positive and is up to 1 A. The pulse shape follows up the shape of RF field E in this case. The measured I/E response in terms of the Fowler-Nordheim theory follows up the field emission mechanism in RF field [10]:

$$j = aE^{2.5}\exp(-b/E) \qquad (2)$$

where E is the surface electric field, a and b are constants (Fig. 3). There is no beam current I_g in this mode.

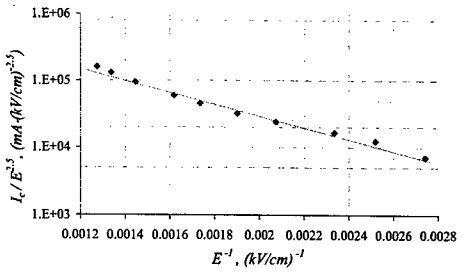


Fig. 3: Fowler-Nordheim plot for the pre-breakdown current

RF power increasing over the electric field strength of 25 MV/m causes the current increasing over than one order of magnitude ($I_c \approx 18$ A). The polarity of this signal is still positive. At the gun output the current pulse amplitude I_g and duration is 6-8 A and 30 ns respectively. During the pulse I_g duration RF field amplitude is decreased considerably (Fig. 4).

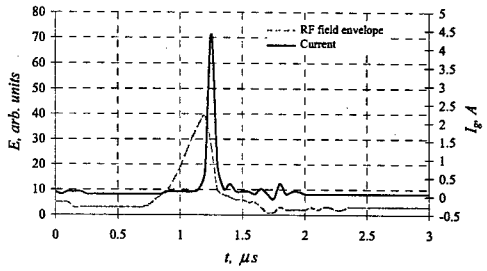


Fig. 4: RF field envelope in the gun cavity and the beam current at the gun output

The sharp current increasing due to beam loading indicates the flashover exciting. Thus, in the investigated RF gun the electric field strength of 25 MV/m is the threshold of the flashover development. Below the threshold the flashover is developed only in some points on the dielectric surface. Beam current at the gun output includes the field emission current from metallic surface and the current extracted from plasma spots. This is the feature of the first RF gun operating mode.

With a time ($\approx 8\cdot10^4$ pulses) the cathode operation is changed in another mode. The signal I_c is positive only up to the moment of the flashover exciting and the amplitude of this pre-breakdown current is not over of 1 A. The threshold electric field strength is decreased down to ~ 20 MV/m. After the moment of the flashover development the polarity of the signal I_c becomes negative and is kept in this state during the next time of RF power pulse. The beam current at the gun output I_g has the amplitude of 4.5 A and the current pulse duration of 40 ns in this mode (Fig 5).

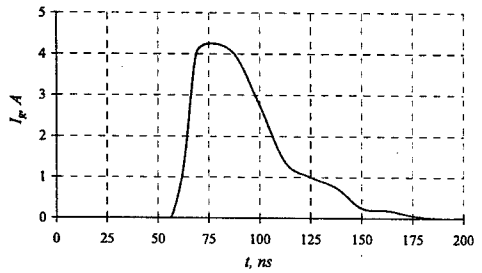


Fig. 5: The featured current pulse shape at the gun output

It's absolute evident that the dielectric is charged positively in points of plasma spots. The radial component of the electric field gets more strength. This causes the potential redistribution over the discharge surface and additional electric field amplifying in the metal-dielectric contact. Such positive feedback spreads plasma spots along the discharge interval. Finally, with the time required the charge distribution to be stable the dielectric surface is filled by plasma throughout the discharge interval. This provides the discharge self-maintenance and is the feature of the gun second operating mode. Some of secondary emission electrons reaches the metallic surface of the cathode and shunts field emission current. Beam current at the gun output is defined in this case only by the current from plasma spot.

The time to pass into the second operating mode can be reduced by the increasing of the pulse repetition frequency and by the electric field strength increasing over the threshold level.

The current amplitude instability is not over of 15 %. The time instability is defined by the time-position of output current relatively the RF power pulse duration and is in range of ± 5 ns during the rise time of the RF power pulse. The almost total stored RF power is absorbed during the flashover. The electric field amplitude falls down to near zero values and is kept in this state during the next time of RF power pulse (Fig. 4). The last fact with combination of the observed reflected RF power shape indicates the gun cavity detuning during the time of 2 μs that is much higher of the flashover duration time ~50 ns. The reasons of such detuning are not established and require further investigations. It's obviously that the gun operates in the stored energy mode because of the current pulse duration is $\tau << Q/\pi f_0$. The current pulse duration is defined by the flashover development rate and by the energy stored in gun cavities.

In the second gun operating mode beam current at the accelerator output has the amplitude over 2 A with the current pulse duration of 30 ns and electron energy of 13 MeV. Estimations of the electron capture into the linac accelerating waveguide shows that the electron energy at RF gun output is over 300 keV for the 50 % of particles.

The order of the above operating modes is saved after over 3600 s after the previous RF power switching off. The dielectric is discharged (due to dielectric conductivity and ions of the residual gas in the cavity) and the system state is changed into initial one.

4 CONCLUSION

Experiments have shown that metal dielectric cathode can be applied in S-band RF gun. The insertion of dielectric detunes resonance system of the gun in the range that is acceptable and doesn't change axial electric field distribution and cavity parameters significantly. For the electric field strength in the gun cavity of 25 - 30 MV/m there was obtained at RF gun output the stable beam current with amplitude of ≈ 3 - 4 A, current pulse duration of 30 - 40 ns and particle energy of over 300 keV.

Some questions concerning the emission mechanism in high intensity RF fields are still uncertain. In particular, the subject of interest is the role of back electrons, the effect of dielectric properties and dimensions on the flashover exciting and maintenance and resonance system optimization to extract higher beam currents. These questions are the subject of our further investigations.

REFERENCES

[1] M.I. Ayzatsky, A.N. Dovbnya, V.A. Kushnir et al. Photoemission from the Ba-Ni oxide cathode surface under intense ultraviolet laser irradiating, Journal of Kharkov National University, Ser.: "Nuclei, Particles, Fields", № 529, 3/15/, (2001), p.83-88. (in Russian)

[2] V.S. Balagura, B.G. Safronov, S.A. Cherenshchikov Short-pulse electron guns with unheated cathodes for linacs, Problems of Atomic Science and Technology. Ser.: Nuclear-physics research (theory and experiment), №4(25), (1992), p. 48-51. (in Russian)

[3] G. A. Mesyatz, D. I. Proskurovskiy, Pulse electric discharge in vacuum, Novosibirsk: Nauka, 1984, 256 p. (in Russian)

[4] N.I. Aizatsky, E.Z. Biller, A.N. Dovbnya et al. "Two-cell RF gun for a high-brightness linac" EPAC'96, Sitges, June 1996, p.1553.

[5] G. A. Mesyatz, About electron emission from ferroelectrics, Pisma v Zhurnal Technicheskoy Physiki, 20, №1, (1994), p.17-20. (in Russian)

[6] J.H. Billen and L.M. Young "POISSON / SUPERFISH on PC compatibles", PAC'93, Washington, 1993, p.790.

[7] G. A. Mesyatz, Ectons. Part 1, Ekaterinburg: Nauka, 1994, 184 p. (in Russian)

[8] L.M. Young, PARMELA, Los Alamos National Laboratory, LA-UR-96-1835 (preprint), Los Alamos, 1996, 93 p.

[9] M.I. Ayzatsky, V.A. Kushnir, V.V. Mitrochenko et al. "Operating Performances and Current Status of the Laser Injector Complex Facility (LIC)" LINAC'96, Geneva, 1996, p. 116.

[10] V.A. Teplyakov, About the criterion of RF breakdown for copper electrodes, Protvino, 1990, 10 p. (Prerpint/IHEP; 90-85). (in Russian)

AN ELECTRON SOURCE FOR A LASER ACCELERATOR*

C. D. Barnes, E. R. Colby, C. M. Sears, SLAC, 2575 Sand Hill Road,
Mail Stop 07, Menlo Park, CA 94025, USA

Abstract

Laser accelerators offer the promise of producing attosecond electron bunches from a compact accelerator. Electron source requirements for laser accelerators are challenging in several respects, but are achievable. We discuss these requirements, and propose an injector design. Simulation and design work for essential components for a laser accelerator electron source suitable for a high energy physics machine will be presented. Near-term plans to test key technical components of the laser injector will also be discussed.

INTRODUCTION

Laser performance has improved markedly in recent years, bringing the possibility of using lasers to accelerate charged particles closer to reality. Advances in power output though optical parametric chirped-pulse amplification, the mass production of inexpensive, highly efficient diode bars for laser pumping, and the production of very low quantum defect materials has already raised the wall-plug-to-light power efficiencies of high-power solid state lasers beyond 10% with theoretical limiting efficiencies of 30-40% possible. Advanced mode-locking and dispersion control techniques have led to lasers that are mode-locked and phase-locked at the optical carrier frequency, an essential step towards synchronizing many lasers to power a high energy accelerator.

Many laser acceleration mechanisms proposed for linear colliders rely on dielectric or metallic structures with beam tube apertures on the order of the accelerating wavelength, of the order of micrometers for laser-powered accelerators. Producing the required luminosity for high-energy physics applications will therefore require that high power beams be produced in spite of these tiny apertures. We offer an example here of how the demands for a linear collider can be met, and outline future experiments to test some of the key technical components.

A number of candidate structures with sufficiently high shunt impedance to give reasonable power efficiency for a laser linear collider have been proposed, and share in common accelerator apertures of order of the accelerating field wavelength. The example here is based on a structure proposed by Lin[1], and analyzed by Siemann[2].

The optimal beam loading bunch charge for the Lin photonic band gap structure (PBG) powered at a gradient of 1 GeV/m corresponds to ~1.5×10^5 electrons per laser pulse. Producing 10 MW of beam power at 0.5 TeV requires ~1.2×10^{14} electrons per second, or a bunch repetition rate of ~830 MHz at this population.

Obtaining this high repetition rate will require that the laser accelerator structures be embedded in resonant rings[3] with the driving laser amplifiers, together with suitable phase and dispersion control. Resonant recirculation of the laser power will not only reduce the average power required from the drive lasers by recycling the remaining laser power, but practical resonant ring dimensions (~1 m) will quite naturally lead to pulse spacings in the hundreds of megahertz.

Figure 1 illustrates the resonant enhancement of power coupling efficiency (power transferred to the beam in ratio to the total power input to the structure) against the recirculation Q of the resonant ring. The first curve at left corresponds to the η=5% power coupling efficiency of the Lin PBG structure, successive curves correspond to successively lower single-pass power efficiencies. It is clear that for very modest recirculation Q values (<10) the PBG structure power coupling efficiency approaches the power coupling efficiency of the NLC structures.

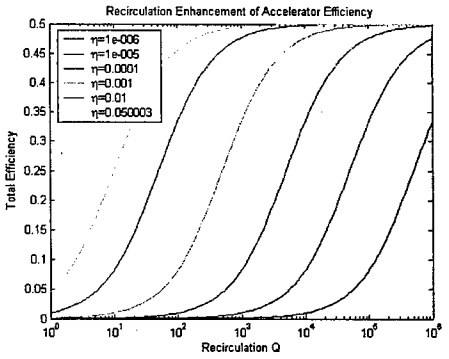


Figure 1: Enhancement of power efficiency through power recirculation.

Recirculation of the laser pulse offers a means to both increase power efficiency and to naturally obtain the high repetition rates needed to produce useful luminosities.

The micrometer-scale accelerator apertures naturally require very small normalized emittances for unintercepted beam transport. If the beam must maintain an n=5σ clearance from the accelerator (assumed to operate at 2 μm wavelength), which has an aperture a=1.2λ=2.4 μm, and focusing is carried out with permanent magnet quadrupoles of length L_q=1 cm with 0.1 mm apertures, K_q=2.5 kT/m gradients (2.5 kG pole tips fields), and a $\phi=\pi/4$ phase advance lattice is used, then the maximum normalized emittance is:

$$\varepsilon_N = \frac{a^2}{n^2}\frac{eK_qL_q}{2mc}\frac{\cos(\varphi)}{1+\sin(\varphi)} = 7\times10^{-4}\pi \text{ mm-mr}$$

*Work supported by Department of Energy contract DE-AC03-76SF00515 (SLAC).
†Corresponding author: ecolby@slac.stanford.edu.

0-7803-7738-9/03/$17.00 © 2003 IEEE

Although this is a very small normalized emittance, it is at very low charge ($5x10^5$ e/bunch or 80 fC/bunch). The transverse phase space density for this case is just $D=Q/e_N$~0.12 nC/π mm-mr, which is nearly an order of magnitude lower than the density sought for linac-based FELs, D~1 nC/π mm-mr, and is well within the current performance capabilities of rf guns.

INJECTOR CONCEPTUAL DESIGN

Obtaining very small transverse emittances from an rf gun requires aggressive control of the space charge and rf emittance growth. Space charge driven growth is naturally low given the small bunch charge. RF emittance growth is given by $\varepsilon_N=\alpha\, k_{rf}^3\, \sigma_x^2\sigma_z^2 2^{1/2}$, with α the dimensionless accelerating gradient, k_{rf} the rf wavenumber, σ_x the spot size, and σ_z the bunch length[4]. Suppressing transverse rf emittance growth therefore favors using the smallest possible bunch dimensions in a low gradient, low frequency rf gun. Further reduction in spot size, and hence transverse emittances, is possible by focusing the electron beam early on. A normal conducting rf gun, permitting a solenoid field to be introduced for focusing purposes, is therefore desirable. Additionally, thermal emittance contributions grow linearly with initial spot size, further motivating very small initial spot sizes.

Obtaining the required high repetition rate means the rf gun and booster accelerator must run CW with a bunch containing ~$5x10^5 e^-$ in every rf cycle. A normal conducting gun is required to permit solenoid focusing to keep the bunch (and hence the transverse emittances) small. Heat removal from a normal conducting rf gun operating CW is a daunting challenge, but one which has been largely met.

The Boeing APLE injector, built and operated in the early 1990s, demonstrated several essential aspects of the required technology[5]. The rf gun was a room-temperature, 433 MHz, 1.5 cell, solenoid-focused rf gun which demonstrated operation at 25% duty cycle, and used a high quantum-efficiency bi-alkali photocathode that could be rejuvenated in an attached preparation chamber. We have taken the frequency and operating gradient of this gun as our starting point for the following demonstration calculation.

Path length and collective effects would rapidly wash out optical bunching at low energies, so a booster linac must be used to accelerate the beam prior to optical bunching. For the example here, four TESLA-type 1.3 GHz, 9-cell superconducting cavities operating CW at 18 MeV/m gradient raise the beam energy to 61 MeV. It may prove advantageous to perform the optical bunching at still higher energies, an optimization that will be studied in the future. Since only one linac rf bucket in three is loaded, adding two more 433 MHz guns and interleaving the pulses would triple the current, and provide both for better gun failure tolerance and for continuous beam operation with two injectors while the third (for example) has its cathode reprocessed.

An IFEL buncher operating at the accelerator wavelength is used to produce the required optical bunching. Like the downstream laser accelerator structures, the IFEL will most likely be embedded in a resonant ring to reduce the average power required from the drive laser.

Plots of the transverse envelope and emittance evolution were calculated with Parmela through to the exit of the microwave injector and are shown in Figure 2. Evolution of the bunch length and energy spread are shown in Figure 3. Final electron bunch properties at the exit of the microwave linac are summarized in Table 1.

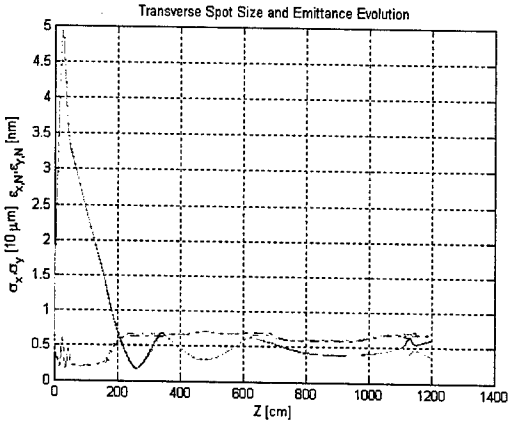


Figure 2. Transverse RMS beam sizes (solid curves, in units of 10 μm) and normalized (one-sigma) emittances (dashed curves, in units of nm) through the injector.

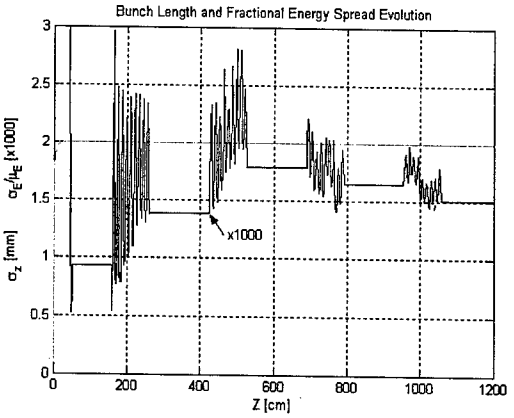


Figure 3. RMS bunch length and fraction energy spread (x1000) through the injector.

Optimization of the transverse emittance has been accomplished at the expense of significant increase in the longitudinal emittance, as can be seen in Table 1. The longitudinal emittance value (70 deg-keV), although for an 80 fC bunch, is more typical of an optimized 1 nC bunch. As the IFEL bunching process will induce significant energy spread beyond this value, this is not a serious issue.

Table 1: Beam Properties at Microwave Accelerator Exit

Property	Value	Units
Bunch Charge	5.8×10^5	e^-
Bunch Rep Rate	433	MHz
Energy	61.5	MeV
Transverse emittance	7.7×10^{-10}	m
Transverse emittance (65% collimated away)	3.6×10^{-10}	m
Transverse P.S. Density	0.12	nC/mm-mr
Bunch Length (rms)	6.7	ps
Fractional Energy Spread	0.0015	
Longitudinal Emittance	70	Deg-keV

Optical bunching of the resultant beam has been studied via numerical simulations in some detail, and will be tested experimentally at an optical wavelength of 800 nm in future experiments at SLAC.

LASER ACCELERATION AT THE NLCTA

Demonstration of optical bunch formation, capture, and subsequent acceleration at 10.6 μm wavelengths has already been demonstrated experimentally by the STELLA collaboration[6]. We are in the process of designing and constructing a facility at SLAC to produce pulse trains bunched at 0.8 μm for acceleration and wakefield experiments. This effort is part of experiment E-163, "Laser Acceleration at the NLCTA", approved in the summer of 2002. Facilities construction is underway now.

The NLCTA accelerator injector will be used to supply 60 MeV bunched beam similar to that simulated above, but at significantly higher charge and emittance. An rf gun will be installed at the position of the current thermionic gun, and 60 MeV beam extracted into a separate shielding enclosure. Simulations[7] show that very cold $\delta=2\times10^{-4}$, short σ_t=1-2ps, low charge q=50 pC beam can be produced for laser acceleration experiments. Detailed simulations of an IFEL optical buncher with magnetic chicane compressor using Genesis and Elegant are shown in Figure 4.

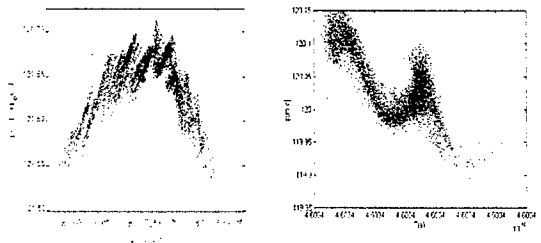


Figure 4. Unbunched (left) and optically bunched (right) longitudinal phase spaces. Entire time scale on left spans 1.5 psec, on the right: 3.3 fsec (one optical cycle).

The phase space plot on the right shows all ~450 optical pulses plotted one atop the other to show the degree of optical bunching over the entire ~1.2 psec long pulse.

The IFEL is a 3-period, 1.8 cm period, variable-gap permanent-magnet undulator (a_w=0.45) with half-period matching and mirror plates at the ends. NeFeB permanent magnets and vanadium permendur pole tips are employed. The chicane is a standard magnetic chicane, with $\theta=0.8^\circ$ rectangular bends of a hybrid permanent-magnet and coil excitation design. At optimal bunching, the correlated energy modulation induced for bunching is just 0.1 %. In principle, an IFEL alone could be used to bunch the electrons, however for the E163 experiment, a very small final energy spread is desired so that small energy gains (or losses) from short prototype laser accelerator structures can be clearly observed.

Once the IFEL and magnetic compressor are commissioned at the NLCTA, trains of optical bunches will be available for testing acceleration and wakefield properties of candidate laser accelerator structures.

CONCLUSION

We have presented a conceptual design for an electron injector, built from conventional technologies, which is a solution to the challenge of producing beam properties suitable for a laser-driven linear collider. Additional work to optimize the design, and explore options, such as the introduction of additional harmonic bunching stages to improve capture efficiency, will be explored in the future.

ACKOWLEDGEMENTS

The authors gratefully acknowledge the extensive contributions of Roger Carr, who has provided design, simulation, and fabrication expertise and the materials for the E-163 IFEL undulator, and R. H. Siemann, R. L. Byer, and L. Schächter for many stimulating discussions. This work was conducted under Department of Energy contract DE-AC03-76SF00515 (SLAC).

REFERENCES

[1] X. Lin, "Photonic Band Gap Fiber Accelerator", PRST-AB 4, 051301 (2001).

[2] R. Siemann, "Photonic Band Gap Fiber Accelerator Efficiency", ARDB-280, available as http://www.slac.stanford.edu/grp/arb/tn/arbvol3/ARDB280.pdf (2002).

[3] M. Tigner, "Near Field Linear Accelerators", in Proc. ECFA-RAL Conf., Oxford, U.K., p. 229ff, Sept. (1982).

[4] K.J. Kim, NIM, A275, 201, (1989).

[5] T. D. Hayward, et al, "A High Duty Factor Electron Linac for FEL", in Proc. IEEE PAC, Dallas, TX, p. 248ff, (1995).

[6] W. D. Kimura, et al, "Detailed Experimental Results for Laser Accelerator Staging", PRST-AB, 4, 101301, (2001).

[7] E. Colby, *et al*, http://www-project.slac.stanford.edu/E163/E163EndtoEndSimulation.pdf (2002).

ANALYSIS OF SLICE EMITTANCE MEASUREMENTS FOR THE SLAC GUN TEST FACILITY*

D. H. Dowell, P. R. Bolton, J. E. Clendenin, S. M. Gierman,
C. G. Limborg, B. F. Murphy, J. F. Schmerge
Stanford Linear Accelerator Center, Menlo Park, CA 94025, USA

Abstract

The Linac Coherent Light Source (LCLS) at SLAC requires the rf photo-injector to produce a beam with a normalized, projected emittance of 1 micron in a 10 ps long bunch with a charge of 1nC. In addition, a small longitudinal emittance is needed to attain the desired 3 kiloamperes peak current after compression in two chicane bunchers. To achieve this excellent beam quality, we are performing systematic studies of both the transverse and longitudinal beam properties from the rf photocathode gun at the SLAC Gun Test Facility (GTF). Time resolved emittances (slice) are determined by using a bunch with a linear energy chirp which is dispersed by a magnetic spectrometer. By varying the strength of a quadrupole lens upstream of the spectrometer allows measurement of the individual slice emittances. Spectrometer images at the various quadrupole settings are binned in small energy/time windows and analyzed for the slice parameters. Our measurements indicate a temporal resolution of approximately 100 femtoseconds. In addition, the longitudinal phase space distribution is determined by measuring the energy spectrum over a range of linac phases. The correlated and uncorrelated components of the phase space distribution are determined by fits to the energy spectra analogous to a quad scan in the transverse dimension. The combined analysis of the transverse and longitudinal data gives not only the slice and longitudinal emittances, but also any correlations due to wakefields or other effects.

INTRODUCTION

The first measurements of the slice emittance at GTF showed a large difference in value and behavior between the projected and slice emittances for low and high charge bunches [1,2]. At low charge they were in good agreement with each other and with thermal emittance measurements [3]. While it appeared obvious that most of the additional projected emittance was due to relative offsets between the slices, it had not be proven quantitatively. This paper describes further analysis of the data presented in ref [1] to quantify the slice offsets and their effect on the projected emittance.

EXPERIMENTAL TECHNIQUE

The SLAC Gun Test Facility consists of a 1.6 cell s-band gun with a copper cathode followed by a 3-meter SLAC section to produce beams at 30 MeV as shown in Figure 1. Details of this facility can be found in ref [4] and references therein. The slice emittance is measured using the chirped bunch technique, in which the linac is phased off crest to produce a bunch with a nearly linear energy-time correlation. The bunch is then dispersed by the energy spectrometer onto the spectrometer screen. The energy spectrometer is a vertical bend. The quadrupoles Quad1 and Quad2 are used to prepare the beam for a quadrupole scan determination of the slice emittance. In detail, the Quad1 is defocusing in the horizontal plane and focusing in the vertical. Therefore the beam in the vertical plane is small at Quad2 and the beam size on the spectrometer screen is only slightly affected by changes in Quad2. In the horizontal plane the beam is defocused by Quad1 making it large at Quad2. Thus changes in Quad2 strongly affect the beam size at the spectrometer screen. The result is that Quad2 can be varied to make large changes in the horizontal beam size on the spectrometer screen, while leaving the beam nearly unchanged in the spectrometer bend plane. This arrangement allows measurement of the slice emittance without disturbing the energy spectrum over the entire range of the quadrupole scan.

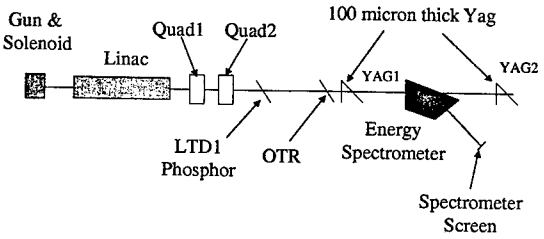


Figure 1: The SLAC/SSRL Gun Test Facility beam line components used for slice emittance experiments.

The emittance scan is done by varying Quad2 and collecting beam images on the spectrometer screen. The quadrupole range chosen includes the beam waist or minimum size on this screen. A typical image near the beam waist is shown in Figure 2. Each image is divided into 10 equal slices in energy/time, the transverse rms beam size is computed for the slices, averaged over 5 images at each quadrupole setting and then analyzed with the standard quadrupole scan technique to obtain the emittances transverse to the spectrometer bend plane. Additional energy spectra data are taken over a wide range of linac phases to obtain the longitudinal phase space. This is used to convert the energy scale to time[4]. The results of this analysis for three gun solenoid settings are shown in Figure 2.

0-7803-7738-9/03/$17.00 © 2003 IEEE

These data show the projected emittance is approximately twice the typical slice emittance, and results from a combination of twisting and offsets of the slices in transverse phase space. The emittance and Twiss parameters along the bunch are plotted in Figure 3.

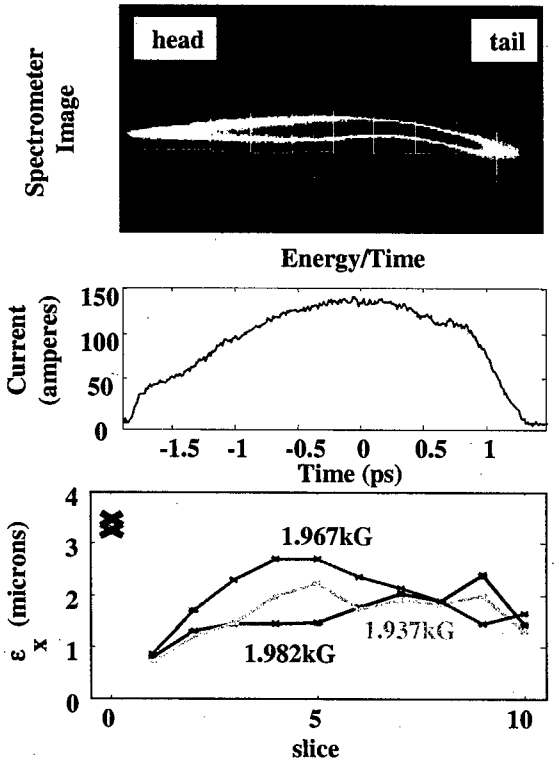


Figure 2: Slice emittance data from the GTF for three gun solenoid fields.

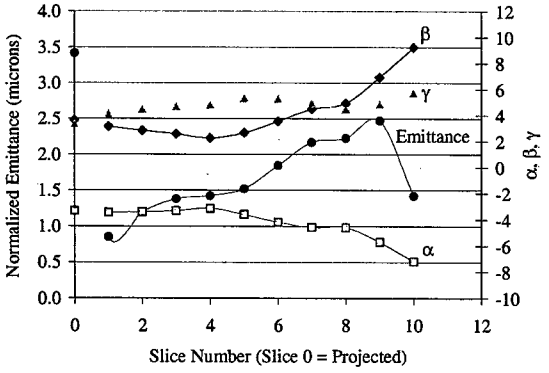


Figure 3: The slice emittance and Twiss parameters along the 300 pC bunch. The units for β and γ are meters and inverse meters, respectively.

DETERMINATION OF SLICE OFFSETS IN TRANSVERSE PHASE SPACE

In addition to the slice variation in Twiss parameters as given in Figure 3, there are also slice centroid offsets along the bunch due to wakefields and other effects. Experimentally, the slice ellipse offsets in transverse phase space are determined at the entrance to Quad1 by fitting the slice centroid as a function of the Quad2 strength. The slice centroids are computed relative to the full projected centroid. The basic concept is to determine the transverse position and angle of each slice by measuring the steering due to Quad2, similar to the standard method of beam-based alignment. The analysis includes the focusing properties of the spectrometer magnets. A typical fit to the centroid data is shown in Figure 4.

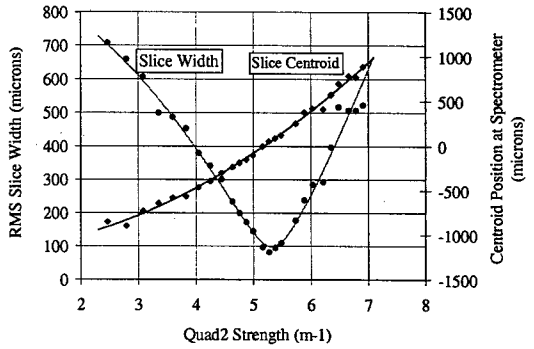


Figure 4: Rms width and centroid of a typical slice at the spectrometer screen as a function of Quad2 strength. The curves are fits to the data. The width fit gives the slice emittance and the centroid fit gives the slice offset in position and angle at the entrance to Quad1

The results of this analysis are summarized in Figure 5 where the emittance and slice position and angle offsets are given along the bunch. The X_0 and X_0' quantities are the position and angle offsets of each slice relative to the projected bunch center at the entrance to Quad1. The data show a significant oscillation of the slice offset from one side to the other near the tail of the bunch. The slices are offset by ~200 microns at Slice 6 and then shift to the other side of the bunch center to -700 microns at the tail. The position and angle offsets may be due to a single kick from the near-normal laser injection mirror located between the gun and linac section.

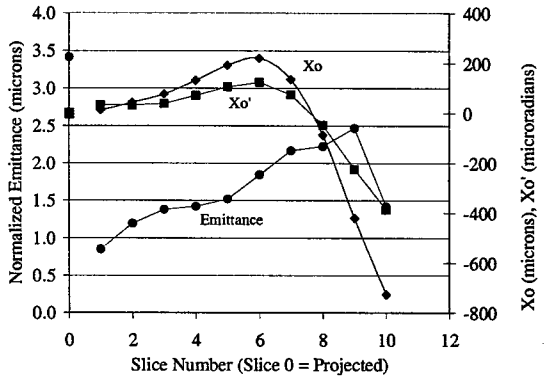


Figure 5: The slice offset in position and angle in front of the quadrupole doublet at 300 pC and a solenoid field of 1.982 kG. Slice 0 is the projected emittance and by definition the offset of the projected beam is 0.

SLICE ELLIPSES IN TRANSVERSE PHASE SPACE

With the slice ellipse parameters and offsets, their relative position can be plotted in transverse phase space, as is done in Figures 6 and 7. The figures clearly show the projected emittance is larger than the slice emittance not only due to variation in the Twiss parameters but also due to the position and angular offsets.

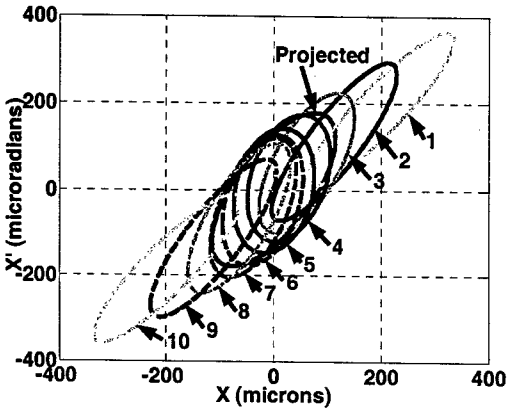


Figure 6: The slice rms emittance ellipses for slices labeled 1 to 10 in transverse phase space for 15 pC and a gun solenoid field of 1.669 kG. The projected emittance ellipse is shown in black.

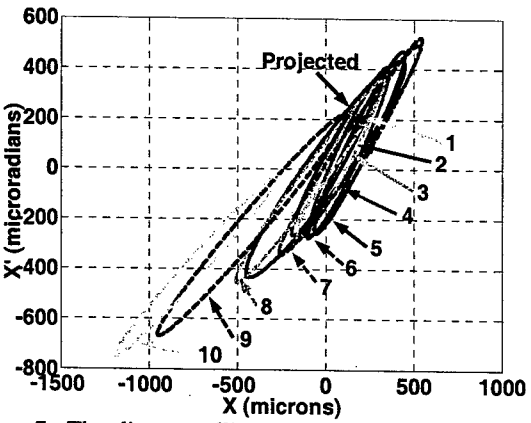


Figure 7: The slice rms ellipses in transverse phase space for 300 pC and a gun solenoid field of 1.982 kG. The projected emittance ellipse is shown in black.

In an attempt to separate these two effects, the rms Twiss parameters for each slice were used to construct Gaussian distributions in transverse phase space and the ten slices summed to produce an ensemble representing the total distribution. Computing the rms Twiss parameters for the total ensemble with and without offsets quantifies their effect.

For the case of the 15 pC data, the experimental projected emittance is 0.81 microns and the reconstructed emittance including the effect of offsets is 0.85 microns. If the offsets are artificially set to zero, the projected value becomes 0.65 microns. Since the emittance of the central slices is approximately 0.6 microns, the larger measured projected emittance is principally due to offsets.

For the 300 pC data, the experimental emittance is 3.4 microns and the reconstructed with offsets is 4.0 microns. This discrepancy is mostly likely due to an ideal Gaussian distribution used for each slice in the reconstruction while the real distribution is almost certainly not Gaussian. This is being investigated. In any case, the reconstituted emittance with no offsets is 2.5 microns. Implying ~44% of the projected emittance is due to the offsets. The average emittance of the central slices is 1.9 microns, suggesting that approximately 30% of the remaining projected emittance is due to slice misalignment. Even with the larger reconstructed projected emittance (4.0 microns vs 3.4 microns), it can still be concluded that more than half the the difference between slice and projected emittance is due to offsets with the remainder coming from slice misalignment.

ACKNOWLEDGEMENTS

*Work supported by Department of Energy contract DE-AC03-76SF00515

REFERENCES

[1] D. H. Dowell, P. R. Bolton, J.E. Clendenin, P. Emma, S.M. Gierman, W.S. Graves, C.G. Limborg, B.F. Murphy, J.F. Schmerge, "Slice emittance measurements at the SLAC Gun Test Facility", To be published in 2002 Free Electron Laser Conference Proceedings; SLAC-PUB-9540.

[2] D. H. Dowell, P. R. Bolton, J.E. Clendenin, P. Emma, S.M. Gierman, W.S. Graves, C.G. Limborg, B.F. Murphy, J.F. Schmerge, "Longitudinal measurements at the SLAC Gun Test Facility", To be published in 2002 Free Electron Laser Conference Proceedings; SLAC-PUB-9541.

[3] W. Graves et al., "Measurement of thermal emittance for a copper photocathode," Proceedings of the 2001 Particle Accelerator Conference, pp 2227-2229.

[4] J.F. Schmerge et al, "Transverse-emittance measurements on an S-band photocathode RF electron gun", NIM A483 (2002) 301-304.

EXPERIMENTAL MEASUREMENTS OF THE ORION PHOTOINJECTOR DRIVE LASER OSCILLATOR SUBSYSTEM*

Dennis T. Palmer, Ron Akre (SLAC), Stanford, CA, USA

Abstract

Timing jitter measurements have been conducted on the ORION photoinjector laser oscillator pulse train output with respect to a ultra low noise crystal rf oscillator running at 79 1/3 MHz, the 36th harmonic of S-Band. The ORION laser oscillator subsystem consists of a Spectra-Physics Tsunami ultra-fast tunable (750 – 850nm) laser pumped by a Diode pumped Spectra-Physics Millennia VsP 5W. Overall laser oscillator subsystem performance will be presented. These measurements consist of the laser oscillator generated noise and transfer function from the RF reference input of the laser to an external photodiode RF output. Timing jitter measurements of less than 500 fsec have been attained with the laser oscillator tuned to 800 nm. .

ORION LASER RF REQUIREMENTS

The ORION facility will use an S-Band photoinjector to inject into the X-Band accelerator at the NLCTA facility. The upgraded photoinjector will replace the present thermionic DC gun, this upgrade will allow for the use of the NLCTA as an Advanced Accelerator User Facility. The electron beam has the following beam characteristics: 0 – 1 nC, the transverse emittance at 0.25 nC has been simulated to be $\leq 2\times10^{-6}$ π mm mrad, and a beam energy of 67 MeV. The drive laser system is a commercial Ti:Sapphire 266 nm wavelength, 1 mJ output laser power. The stability requirement for the electron beam with respect to the RF is 500fS rms for the ORION[1] and the LCLS[2] projects.

The RF source used for the laser will be derived from the Main Drive Line (MDL) RF at SLAC. The timing system at SLAC is locked to a 1nS width fiducial pulse at 360Hz. This monopolar pulse is locked to, and transmitted with, the 476MHz RF on the MDL and causes a double height half cycle pulse which triggers counters. The 476MHz RF on the MDL is also used for PEP and is shifted in frequency and phase so the main linac can fill different buckets in PEP, figure 1.

Not only does the phase shifting cause a problem, but the phase noise of the RF at the ORION facility is to large to achieve timing jitter of less than 500fS rms. A phase locked oscillator must be used to reduce the phase noise and provide a stable signal for the laser to lock to, a signal which is also locked to the RF used by the existing timing system uses. Both the phase noise and transfer function of the laser oscillator are critical in understanding the RF to laser output timing jitter.

*Supported by the U.S. Department of Energy, contract DE-AC03-76SF00515: PAC2003 WPAB028: SLAC-PUB-9805

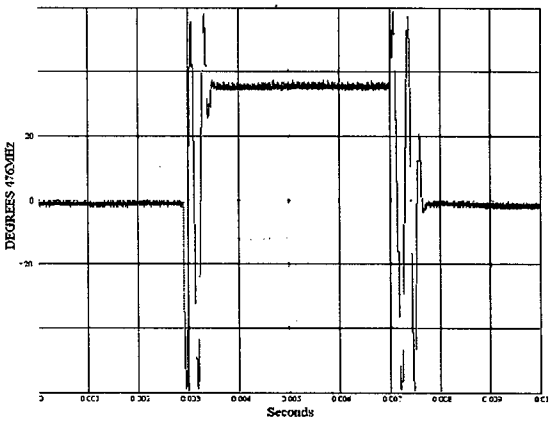


Figure 1: MDL Phase with phase shifts to fill buckets in the PEP storage rings.

PHASE NOISE MEASUREMENTS

Phase Noise Measurement System

The phase noise measurement system is shown in figure 2. An external photodiode detector was used to measure the phase noise of the Tsunami laser. A 79.3MHz Ultra Low Noise Oscillator was used as a reference oscillator for the laser. The same oscillator was used to power the LO of a mixer after being multiplied to 476MHz. A signal from a photodiode at the laser output was multiplied to 476MHz and used to drive the RF mixer port. The IF mixer port is amplified by 50dB, filtered, and digitized by a PC PCI scope card. The data are then collected at 40kHz and 20MHz. A 10kHz filter is used for collecting data at 40kHz and a 5MHz filter is used for collecting data at 20MHz. The 79.3MHz oscillator, multipliers, and low noise amplifiers were run off batteries to reduce the noise floor.

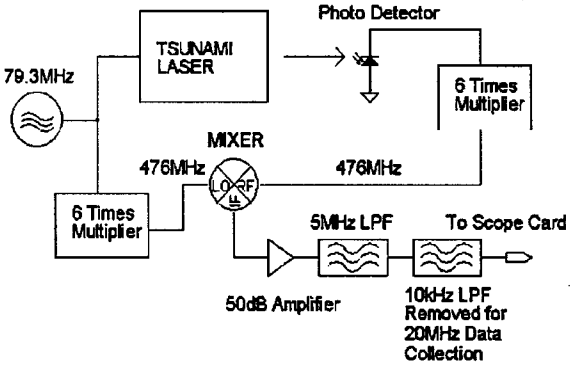
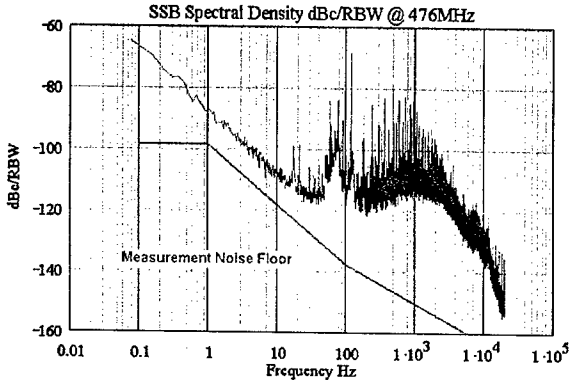


Figure 2: Phase Noise Measurement System.

Phase Noise Data

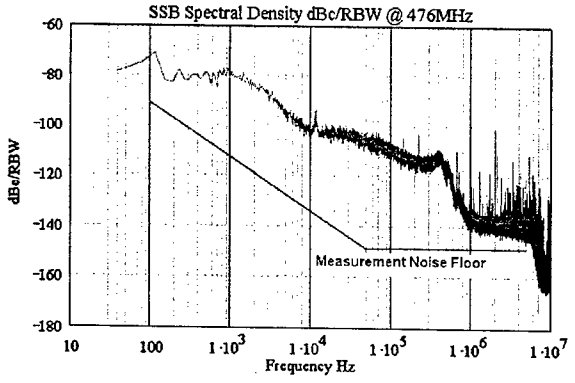
Phase noise data taken with the above system is seen in figures 3 and 4 with data sample rates of 40kHz and 20MHz respectively. The Resolution Band-Width, RBW, is listed below the frequency spectrums and is the frequency bandwidth the noise power is measured over.

The integrated phase noise plots, figures 5 and 6, are an integral from the frequency listed on the x axis to the Nyquist frequency of either 20kHz or 10MHz. The integration takes out much of the fluctuations of the fft, allowing one to see the frequencies which contribute most to the total noise. Since each point is an integral from an upper limit to the lower limit, the lower limit given by the horizontal axis, one can see how high in frequency a feedback system must go in order to reduce jitter to a value as read from the vertical axis.



RBW = 0.076

Figure 3: Laser Oscillator Noise Spectrum (40kHz)



RBW = 38.147

Figure 4: Laser Oscillator Noise Spectrum (20MHz)

Since jitter is the integral of noise, a system required to meet a jitter specification can only do so up to a certain frequency or band-width. The noise floor of the system will determine the maximum band-width for a given jitter level. To look at the effect on high frequency noise, we take a closer look at the noise floor of figure 4. The following numbers are from integration over the selected ranges of the data shown in figure 4.

Integration Range From Carrier	Noise Level Down From Carrier
1MHz to 2MHz	9.2e-10
2MHz to 3MHz	8.9e-10
3MHz to 4MHz	6.5e-10
4MHz to 5MHz	5.5e-10

The 5MHz low pass filter used to collect this data will cause the noise level to be 1dB lower at 5MHz and has a –3dB cutoff at 6MHz. From this data a conservative estimate of the noise floor is –90dBc/MHz. The timing jitter from this noise floor integrated out to 40MHz, 40X=16dB, would be –74dBc at 476MHz, or 69fS. The high frequency noise floor is not a significant source of jitter.

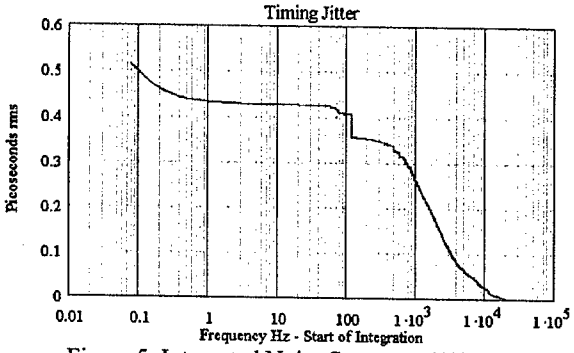


Figure 5: Integrated Noise Spectrum (40kHz)

The major contribution to jitter is a broad spectrum of noise from about 800Hz to about 3KHz. The noise source, which contributes the next highest amount to the jitter, is the sharp peak at 120Hz figures 3 and 5. Next in line would be the broad peak at about 400kHz, figures 4 and 6.

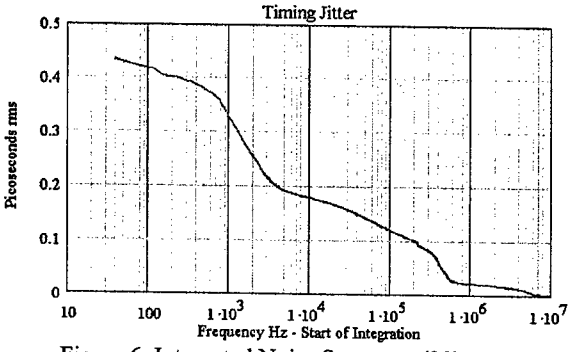


Figure 6: Integrated Noise Spectrum (20MHz)

From figure 5, the integrated noise from 1Hz to 10kHz is about 430fS. From figure 6, the integrated noise from 10kHz to 1Mhz is about 180fS. If we add up these two noise levels from 1Hz to 1MHz and add to that the 69fS from 1MHz to 40MHz, **the total integrated noise level from 1Hz to 40MHz is less than 480fS. This is the rms jitter at the laser oscillator output with respect to the input RF.**

TRANSFER FUNCTION MEASUREMENTS

A low frequency network analyzer was used to measure the transfer function from the locking input of the laser oscillator to the output of an external photodiode. The setup is shown in figure 7.

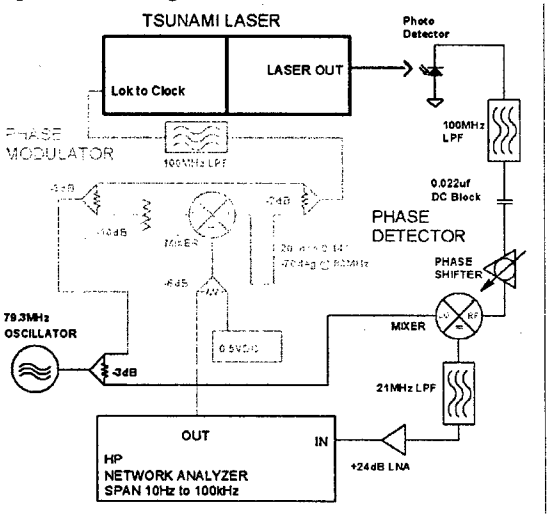


Figure 7: Transfer Function Measurement Test Setup.

The system was calibrated by connecting the cable from the Lok to Clock box input to the cable connected to the Photo Detector output. This bypassed the Tsunami Laser and the Photo Detector. The phase shifter was adjusted to zero the mixer IF output and the network analyzer normalized.

The output of the Phase Modulator was then connected to an HP8562A Spectrum Analyzer. The Network Analyzer output was set to an amplitude of 20mV and the Spectrum Analyzer showed sidebands at -63dBc.

The Phase Modulator output was then connected to the input of the Tsunami Laser Lok to Clock box. The Network Analyzer was set to 1kHz CW. The Photo Detector signal, before the RF port of the mixer was measured with the Spectrum Analyzer. The 1kHz sidebands were -60dBc which is consistent with the shape of the transfer function.

The calibration does not take out a gain offset in the system but 0dB gain is the level of the signal below 100Hz, as the output of the laser tracks the input very closely in this region.

The gain and phase data taken are shown in figure 8. The gain and phase are flat to about 1.5kHz. What looks like a resonance causes the gain to peak at about 3kHz and the phase to change by –90° from 1.5kHz to 4kHz. Beyond 10kHz the phase changes further which could cause a simple external feedback system with gain beyond 10kHz to go unstable.

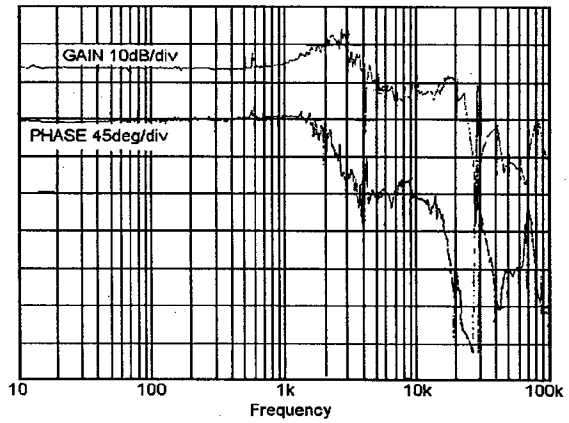


Figure 8: Transfer Function Data.

COMMENTS

The 120Hz peak in the noise, figures 3 and 5, has a magnitude of about 200fS. There could be many sources for this noise, likely sources would be DC power supplies for the electronics or pump laser. Since ORION and LCLS will be running at 120Hz or a sub-harmonic, this noise may not even be detected in the system.

The above transfer functions, figure 8, shows that a simple external feedback system could be used to control the phase if it has a cutoff frequency of about 1kHz. From the phase noise plots one might expect the jitter to be reduced by about 100fS with such a feedback. The total jitter in this case would be below 380fS.

By tuning the laser locking feedback and adding external feedback, one might be able to push the feedback limit to about 3kHz. A 3kHz feedback system might reduce the jitter level to about 240fS. To get much further below this level, noise floors in the electronics would have to be reduced and/or locking done at a harmonic of the laser frequency to further reduce noise levels.

The laser oscillator stability, as is, meets the requirements for the LCLS and ORION projects. At this time, work to further reduce the stability of the laser does not have a high priority.

ACKNOWLEDGEMENTS

The authors would like to thank Ben Cowan for his assistance in setup and operating the laser system. In addition, we are indebted to Spectra Physics Corp for providing engineering support for this work. The authors would also like to thank Bob Siemann and Eric Colby for their support of this work.

REFERENCES

[1] ORION Research Facility Technical Design Study, April 12, 2002, available at the ORION website http://www-project.slac.stanford.edu/orion/

[2] LCLS Design Study Report, SLAC-R-521 (1998) http://www-ssrl.slac.stanford.edu/lcls/

Proceedings of the 2003 Particle Accelerator Conference

STATUS OF THE UCLA PEGASUS LABORATORY*

G. Andonian, P. Frigola , S. Reiche, J.B. Rosenzweig, S.Telfer, G.Travish
UCLA, Los Angeles, California 90095

Abstract

The PEGASUS laboratory is a versatile radiation facility dedicated to the advancement of novel concepts in beam physics. The installation of a new LaB_6 cathode will allow for both thermionic emission and photoinjection operation. The PEGASUS plane wave transformer injector has been conditioned to 20 MW of RF power. Recent operations show a 15 MeV dark current beam that will be used for beam radiation studies. An upgrade to the drive laser system has been explored and will be realized shortly. This paper will describe and report the status of the various subsystems of the PEGASUS laboratory and outline the experiments underway, such as innovative beam instrumentation, surface effects in optical transition radiation, Thomson scattering, and waveguide SASE FEL.

INTRODUCTION

The PEGASUS (Photoelectron Generated Amplified Spontaneous Radiation Source) beam-radiation laboratory has been commisioned at UCLA. The long-term goal of PEGASUS is the study of SASE FEL physics and other beam-radiation interactions. The current experiment in progress at PEGASUS is the study and imaging of optical transition radiation from various surfaces. Thomson Scattering, and other radiative processes, will be examined at PEGASUS in the following months.

PEGASUS is a linac-based electron beam radiation laboratory. The present injector consists of the Plane Wave Transformer (PWT) Injector [1]. The existing design of the cathode supports the opertion of thermionic emission and photoinjection. Table 1 shows the relevant beam parameters for the photoinjection mode.

Table 1: Pegasus Design Parameters (Photoinjection mode)

Parameter	Value
Energy	12-18 MeV
Energy Spread	0.15%
Emittance	$\leq$ 4 mm-mrad
Bunch Charge	1 nC
Bunch Length	1 mm
Beam Size	150 μm
Undulator Parameter	1.05
Undulator Period	20.5 mm

* Work supported by DOE grant DE-FG03-98ER45693

LABORATORY DESCRIPTION

RF Injector

The PWT gun is a novel standing-wave S-band electron source that is designed to provide 1 nC, 17 MeV electron beams. The peak gradient is expected to be 60 MV/m. The PWT has a compact design, allowing a simple emittance compensation solenoid. At present, a LaB_6 cathode serves as the electron source via thermionic emission. Other cathodes to be tested at PEGASUS will include OHFC copper, single crystal copper, and Cs_2Te.

Thermionic Emitter The PWT allows for insertable and removable cathodes. The current cathode assembly entails a LaB_6 thermionic cathode heated conductively by a UHV substrate cartridge heater. Thermionic cathodes are desirable for high (accumulated) charge applications, such as transition radiation [2]. The thermionic cathode provides a quick and cost efficient method of generating beam charges up to the 1 nC level. Initial observations show that the heater has achieved operating temperatures between 1000°C - 1200°C, corresponding to an operating power of 5-6 Watts and an operating thermionic DC current of approximately 400 μA [3].

Photocathode Drive Laser

A drive laser system has been designed and will be procured from commercial sources in the near term. The laser is based on Ti:S to allow for femtosecond beam - laser interactions. A terawatt class amplifier is envisioned as an eventual extension for Thomson scattering and other radiative processes. The drive laser and terawatt system are further described in these proceedings [1].

RF Power System

The RF system is designed to supply 20 MW of power to the PWT injector. A small amount of the 89.25 MHz mode-locker RF from the laser oscillator is fed into a phase locked oscillator running at 2.856 GHz. Final amplification of the signal is made by a SLAC XK5 klystron. The 20 MW of RF power is transported to the PWT by a SF_6 filled Al waveguide system. Large reflected voltages, from the standing wave PWT structure, are absorbed by a high power ferromagnetic isolator [4].

Undulator

The PEGASUS undulator is available for FEL and undulator studies. The device a tapered, 2m long, planar magnet

0-7803-7738-9/03/$17.00 © 2003 IEEE

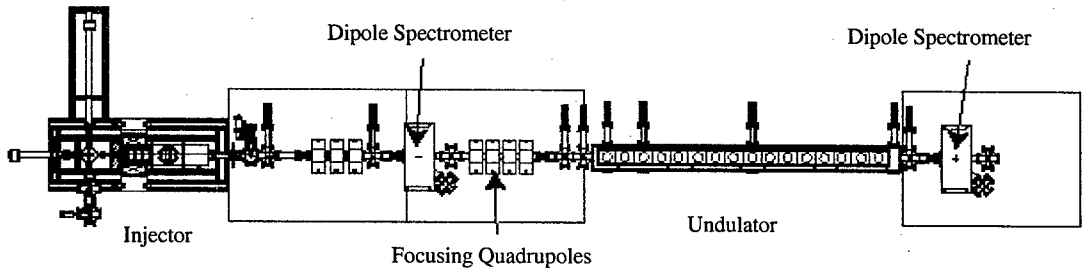


Figure 1: CAD Drawing of the PEGASUS Beamline.

undulator with a 20.5 mm period and K = 1.05. The undulator was constructed in collaboration with the Kurchatov Institute. SASE was first observed with it at LANL [5]. A pulsed wire apparatus developed at UCLA was used successfully in the UCLA/LANL experiment. This apparatus allows for multipole B-field measurements, and thereby facilitates alignment and quantification of the undulator parameter.

Experimental Diagnostics

Beam energy and energy spread are measured in the dispersive section after the dipole spectrometer. Beam charge is determined using impedance matched stripline sum-signals and Faraday cup beam dumps. Both charge and energy measurements are made in two locations, before and after the undulator. Throughout the beamline, beam position and size are monitored using YAG crystals imaged with CCD cameras. Intra-undulator measurements are conducted in a similar fashion. Emittance measurements are made via the quadrupole scanning technique. The focusing quadrupoles and dipole spectrometers were designed, fabricated and characterized at UCLA to meet laboratory specifications.

EXPERIMENTS

Optical Transition Radiation

An extended analytical model for optical transition radiation (OTR) has been developed [6]. Of particular interest is OTR from non-standard generic surfaces, which include arbitrary modulated surfaces in a limited plane. The results for a 17 MeV beam will be compared with the predicted analysis for parabolic, grating, and Fresnel surfaces. A thermioinic emitter is advantageous for this study since it provides the required high integrated charge beams to be intercepted by the various targets. A high resolution, color digital camera is used for spectral analysis. In the initial runs, rough ($\geq 2\lambda$) and smooth ($\lambda/4$) aluminum and copper surfaces were used to intercept the beam, where λ is the radiation wavelength ($\approx 1\mu$m) .

SASE FEL Physics

SASE FEL studies will revolve around the 2m IR FEL undulator. Although the beam provided by the PWT would not drive the FEL to saturation, GENESIS 1.3 simulations show that the addition of a 1 mm square waveguide will significantly enhance gain and reduce the saturation length by about 30 % [7]. Insertion of a commercially available waveguide in the undulator has been investigated. The waveguide will enhance FEL performance by compensating for diffractive effects, eventually yielding saturation. Of particular interest is the purity of the waveguide mode as well as the power losses of the proposed hollow glass waveguide [8].

Thomson Scattering

The installation of an upgraded drive laser system will facilitate the study of electron beam - laser beam interactions. Calculations show that with existing PEGASUS parameters, and a UV pulse length of 100 fs and peak power 1TW, the tunable x-ray pulse will have a photon flux of up to 10^8 photons per pulse (at 180° incident angle) and radiation wavelength of 2.2 Å[9].

REFERENCES

[1] G. Travish, et. al., WPAB031, These proceedings.

[2] J.M. Lafferty, Journal of Applied Physics, 22 3 (1951) 299.

[3] P.E. Frigola, et. al., FPAB015, These proceedings.

[4] S. Telfer, et. al., Proceedings of 2001 Particle Accelerator Conference, Chicago (2001) 2263.

[5] M. Hogan, et. al., Physical Review Letters, 81 22 (1998) 4867

[6] S. Reiche, et. al., Proceedings of 2001 Particle Accelerator Conference, Chicago (2001) 1282.

[7] S. Reiche, et. al., Presented at the 2000 International FEL Conference.

[8] Y. Matsuura, et. al., Applied Optics Vol. 35, No. 27 (1996) 5395.

[9] S. Reiche, et. al., MPPB058, These proceedings.

THE UCLA PEGASUS PLANE-WAVE TRANSFORMER PHOTOINJECTOR*

G. Travish, G. Andonian, P. Frigola, S. Reiche, J. Rosenzweig, and S. Telfer
UCLA Department of Physics & Astronomy, Los Angeles CA. USA.

Abstract

A photoinjector based on a multi-cell plane wave transformer accelerating structure has been commissioned at the UCLA Department of Physics' PEGASUS Laboratory. Design and construction of the novel structure have been previously reported [J. Rosenzweig, et al. PAC Proceedings 1997], and recent operation with a thermionic cathode is being presented at this conference [P. Frigola, et al. these proceedings]. This paper describes the planned operation of the PWT gun as a photoinjector, including design and construction details of the drive laser. Progress to date and future plans are discussed.

THE PHOTOINJECTOR STRUCTURE

The PEGASUS Photoinjector is a novel standing-wave S-band structure based on the Plane-Wave Transformer (PWT) design [1]. The injector consists of a replaceable cathode, an initial half-cell, and ten full cells, and a final half-cell for a total length of 60 cm [2]. Each cell is, in fact, a volume separated by disks of 4.2 cm diameter in a 12 cm diameter tank (see Figure 1). The RF structure features strong (0.3) cell-cell coupling to prevent mode overlap.

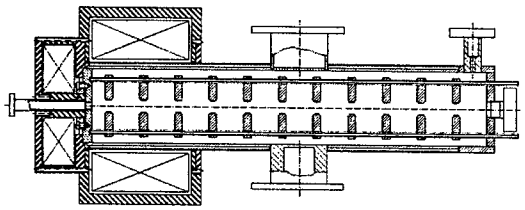


Figure 1: A cross section of the PEGASUS PWT Photoinjector showing the 11 discs forming the cells inside the tank and the solenoid surrounding the cathode region.

The peak field-gradient is designed to be 60 MV/m, and the nominal beam-energy is 17 MeV. The structure has a fill time of 2-3 μs, a shunt impedance of approximately 50 M/m, and a Q_L of roughly 6000.

Due to the compact and simple design of the gun, a simple solenoid can be used for emittance compensation. Simulations indicate that the design specifications of Table 1 should be readily achievable [3].

The interchangeable cathode design allows for a variety of cathode materials to be tested including the planned use of copper, magnesium, heated LaB_6, and conventional thermionic emitters.

* Work supported by DOE grant DE-FG03-98ER45693

Status

The status of the PEGASUS laboratory is reviewed elsewhere [4]. To date, the PWT linac structure has been conditioned at high power (20 MW) [5], and dark-current emission has been measured with a peak energy of 15 MeV over the 4 μs RF pulse [6]. An effort to retrofit a thermionic cathode has been underway [7] in order to deliver beam for testing and preliminary measurements until a drive laser can be procured.

Table 1: Photoinjector design beam specification.

Beam Parameter	Value
Energy	12-18 MeV
Energy Spread	0.15%
Emittance (norm. rms)	4 μm
Charge	1 nC
Bunch Length	1 mm

THE DRIVE LASER

The PEGASUS drive laser, as with all photoinjector drive-lasers, must provide a sufficient number of photons with an energy above the cathode workfunction, and within a pulse-length short relative to the RF period. In practice, this implies a UV (~266 nm) laser, with ≈200 μJ of energy at the cathode, and a pulse length adjustable from about 1 to 10 ps (see Table 2). The pointing stability, energy stability and reliability have been only qualitatively considered, but should be near state-of-the-art as the design calls for an all diode-pumped system. In addition to these general requirements, the drive laser needs to be operable by non-specialists (i.e. no dedicated laser operator), and be flexible enough to allow for reconfiguration to meet new research directions (i.e. addition of a pulse shaper, diagnostics, etc.).

Table 2: The design goals of the PEGASUS drive laser.

Laser Parameter	Value
Wavelength	266 nm
Energy	> 200μJ
Pulse length	1 – 10 ps
Repetition rate	500 - 1000 Hz

A future consideration for the laser system is to drive a terawatt class amplifier for short-pulse photon-electron interactions and to provide short-wavelength radiation. The above plan along with the desire to obtain as much of the laser from commercial vendors and to utilize proven technology, has lead to the selection of Ti:S as the laser medium.

0-7803-7738-9/03/$17.00 © 2003 IEEE

Drive Laser Design

Figure 2 shows a block diagram of the design for the PEGASUS drive laser. The majority of the components are commercially available. The salient components are the diode-pumped pump-lasers for both the oscillator and regenerative amplifier (regen), and the absence of any multi-pass amplifier which could degrade the beam quality and stability.

The ~100 fs pulses from the oscillator are grating stretched and then masked in order to produce a compressed pulse — after amplification — that has a minimum of residual chirp: as no pulse shaping techniques are to be employed initially, the full oscillator bandwidth is unnecessary.

The regen will likely operate at 500 Hz – 1Khz in order to improve stability, while the photoinjector RF-system will run between 1 and 10 Hz. The additional laser shots will simply hit the cathode, but not produce accelerated beam.

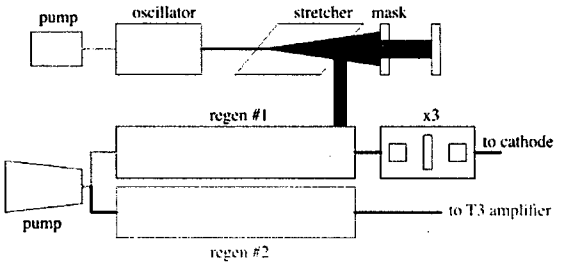


Figure 2: The design of the PEGASUS drive laser.

Future Work

Near term work on the PEGASUS drive laser includes preparation of the laser room, final selection of the oscillator and frequency conversion crystals, as well as engineering of the control system interfaces. Procurement of the laser system components should occur soon thereafter.

Selection of the oscillator between the various commercial offerings is complicated by limited data on performance of these lasers in general and specifically as mode locked seeds for photoinjectors.

The laser room requires facilities upgrades including construction of an inner dust-proof room, improvement of the thermal stability (HVAC system), and general "remodeling". While the room has previously supported a drive laser, changes to the building and age have created an environment that does not meet the requirements for reliable laser operation.

THE T^3 LASER

Beyond initial Photoinjector operation, beam studies, and near-term planned experiments, it is hoped to introduce a terawatt class laser into the PEGASUS lab for photon-electron interactions. One specific plan is for a Thomson source which provides modest x-ray fluxes for PEGASUS researchers and other on-campus studiers [8].

The head-on interaction of the electron beam focused to a 50 μm spot with a transversely matched laser of 1 TW (100 mJ) gives an x-ray flux of about 2 x 10^8 photons at about 2 Å. Increasing the laser power to 2 TW and focusing the beams to a difficult to achieve 25 μm spot size, yields more than an order of magnitude more x-ray photons and two orders of magnitude improvement in the brightness. However, the head-on scattering produces long x-ray pulses. To achieve shorter pulses, 90 degree scattering will be required, with the penalty being a substantial reduction in the photon flux (down to about 2 x 10^6 even in the aggressive case) [9].

As is indicated in Figure 2, room for a second regenerative-amplifier (regen #2) has been included in the design of the drive laser. The two regens are both pumped by the same laser, with the second regen allowing for amplification of unmasked stretched-pulses in order to produce femtosecond (~ 50 – 100 fs) pulses of sufficient energy to seed a multipass "bow-tie" amplifier. These short pulses would be transported in vacuum to near the interaction area where a vacuum compressor would be installed.

The nominal design goals for the PEGASUS T3 laser are given in Table 3, while a block diagram of the system is shown in Figure 3.

Table 3: The design goals of the PEGASUS T3 laser.

Laser Parameter	Value
Wavelength	800 nm
Energy	100 - 200 mJ
Pulse length	50 – 100 fs
Repetition rate	10 Hz

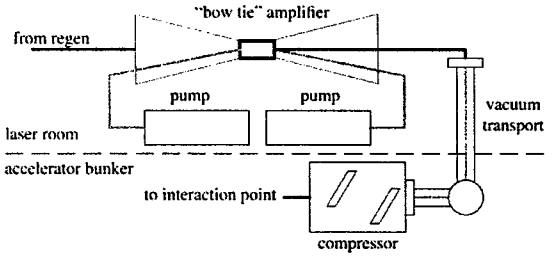


Figure 3: A simplified layout for the PEGASUS T3 laser.

REFERENCES

[1] R Zhang, C Pellegrini & R Cooper, NIM A 394 295 (1997).
[2] X. Ding et al., Proc. PAC Conf, pp 2021 (1999).
[3] J.B. Rosenzeig, *et al.*, Proc. PAC Conf. pp1968 (1997).
[4] G. Andonian, *et al.*, these proceedings.
[5] S. Telfer, *et al.*, Proc. of FEL Conf. (2002).
[6] G. Andonian, et al. Proc. of FEL Conf. (2002).
[7] P. Frigola, *et al.*, these proceedings.
[8] S. Reiche, *et al.*, these proceedings.
[9] O. Williams, PBPL internal note (2003. Unpublished).

EXPERIMENTAL CHARACTERIZATION OF THE ELECTRON SOURCE AT THE PHOTO INJECTOR TEST FACILITY AT DESY ZEUTHEN*

M.v. Hartrott, E. Jaeschke, D. Krämer, BESSY, 12489 Berlin, Germany
J.-P. Carneiro, K. Flöttmann, J. Roßbach, S. Schreiber, DESY, 22603 Hamburg, Germany
K. Abrahamyan[&], J. Bähr, I. Bohnet, U. Gensch, H.-J. Grabosch, J.H. Han, M. Krasilnikov[#],
D. Lipka, A. Oppelt, V. Miltchev, B. Petrossyan[&], F. Stephan, DESY, 15738 Zeuthen, Germany
P. Michelato, C. Pagani, D. Sertore, INFN Milano, 20090 Segrate, Italy
I. Tsakov, INRNE Sofia, 1784 Sofia, Bulgaria
H. Redlin, W. Sandner, R. Schumann, I. Will, Max-Born-Institute, 12489 Berlin, Germany
R. Cee, S. Setzer, T. Weiland, TU Darmstadt, 64289 Darmstadt, Germany

Abstract

The Photo Injector Test facility at DESY Zeuthen (PITZ) was built in order to study the production of high brightness electron beams, which are substantial for the successful operation of Free Electron Lasers (FEL) and linear colliders. The photoinjector at Zeuthen is based on a 1.5-cell L-band rf cavity with coaxial rf coupler equipped with emittance compensating solenoids, a laser capable to generate long pulse trains, an UHV photo cathode exchange system, and various diagnostics tools. The current goal of PITZ is a full characterization of the electron source, which will be installed at the TESLA Test Facility Free Electron Laser (TTF2-FEL) in autumn 2003. In the running periods before the gun is delivered to TTF2-FEL, the rf performance and the beam parameters will be measured in detail. The results presented in this contribution contain the measurements of dark current, driving laser parameters, beam charge, beam size along the facility, transverse emittance, momentum and momentum spread. The electron beam measurements will be presented in comparison with beam dynamics simulations.

INTRODUCTION

In January 2002 the first photoelectrons were produced at the photoinjector test facility at DESY Zeuthen [1]. The current near term goal of PITZ is to do a full characterization of the existing electron source and then to install it at the VUV-FEL at TTF2 in Hamburg in autumn 2003. The schematic overview is presented in Fig. 1.

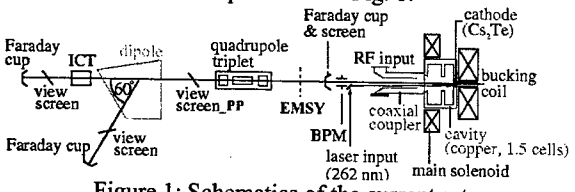


Figure 1: Schematics of the current set-up.

ACHIEVEMENTS ON RF COMMISSIONING

A smooth commissioning procedure, partially using an automatic conditioning program (ACP) [2], yields an operation with up to 900 μs long rf pulses at 10 Hz repetition rate and a gradient of about 40 MV/m. That corresponds to a maximum averaged power of 27 kW in the gun cavity with 0.9% duty cycle [3,4].

The dark current in the gun cavity has been measured as a function of the accelerating gradient, main solenoid and bucking magnet currents [4]. Measurements were performed using Mo and Cs_2Te cathodes (Fig. 2). With a rf electric field of ~40.5 MV/m and a main solenoid current of 200 A, the dark current for Cs_2Te is about 180 μA.

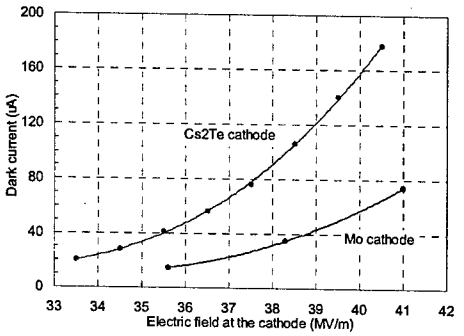


Figure 2: Maximum dark current measured as a function of the electric field at the cathode.

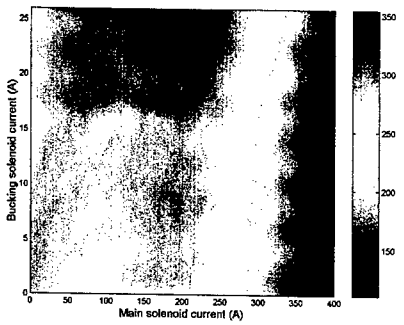


Figure 3: Contour plot of the dark current at 40 MV/m for the Cs_2Te cathode as a function of main solenoid and bucking solenoid currents.

Results of a detailed study of the dark current dependence on the magnetic field of main and bucking solenoids are presented in Fig.3.

* The project is funded partially by the HGF Vernetzungsfond.
# email: kras@ifh.de
& on leave from YERPHI, 375036 Yerevan, Armenia.

0-7803-7738-9/03/$17.00 © 2003 IEEE

PHASE SCAN

The PITZ driving laser is able to generate trains of micro pulses of up to 800 μs length. The actual temporal profile (gaussian shape) of the laser micro pulses in the UV was measured using a streak camera to be about (7±1)ps FWHM. The transverse profile of the laser beam can be varied and typical rms transverse sizes of ~0.5 mm can be obtained.

The laser shape determines significantly the photoelectron phase scan – the dependence of the number of accelerated photoelectrons on the rf launch phase. The beam charge measured by the first Faraday cup (0.78 m from the cathode) is shown in Fig. 4 for two different main solenoid currents.

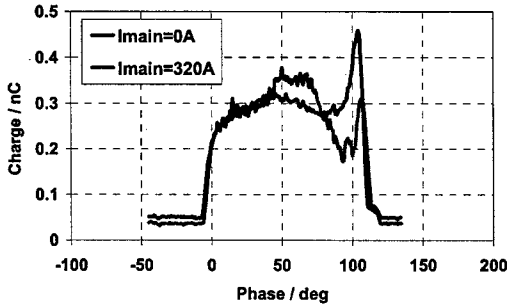


Figure 4: Measured beam charge as a function of rf phase. Gradient at the cathode 40 MV/m.

A two dimensional phase scan – measured beam charge as a function of rf phase and main solenoid current - is presented in Fig. 5.

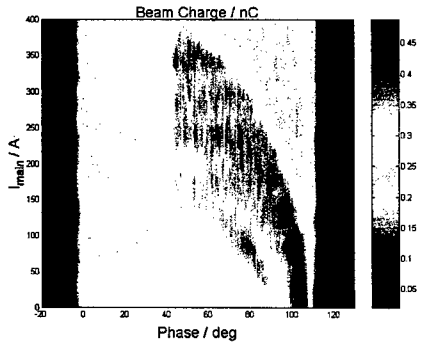


Figure 5: 2D phase scan - contour plot of the measured beam charge as a function of rf phase and main solenoid current. Gradient at the cathode 40 MV/m.

At zero solenoid field the peak at the right side of the phase scan (low beam energies) could be explained by focusing effects of the rf field. For increasing solenoid fields higher beam energy is needed to have a good transmission through the cavity. A particle tracking code ASTRA [5] was used to simulate the beam charge dependence. The result is shown in Fig. 6. According to simulations for the actual driving laser beam parameters and main solenoid longitudinal position, features of the phase scan are caused by particle loses at the photocathode (due to high space charge) or at cavity and beam line apertures.

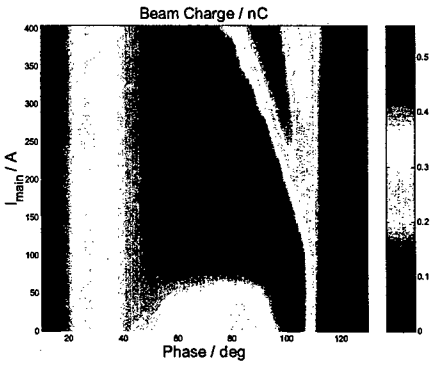


Figure 6: Simulated 2D phase scan - contour plot of the beam charge as a function of rf phase and main solenoid current. Gradient at the cathode 40 MV/m.

LONGITUDINAL MOMENTUM MEASUREMENT

The mean momentum and the momentum distribution of the electron beam were measured using the dipole spectrometer. The mean beam charge used was about 1 nC, the accelerating gradient at the cathode was 40.5 MV/m [6]. The dependence of the measured mean momentum and the momentum spread as a function of the rf phase compared to simulations is shown in Fig. 7.

The smallest momentum spread of 15 keV/c for 1 nC is measured at rf phase of ~ 15°.

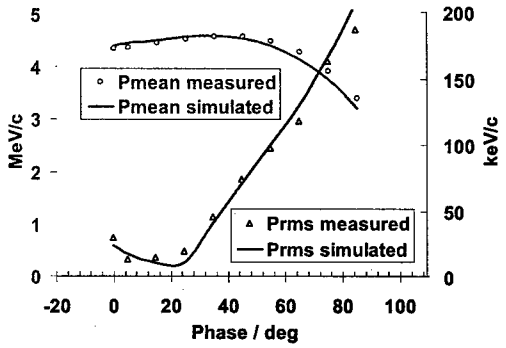


Figure 7: Mean momentum (left axis) and momentum spread (right axis) as function of the rf phase in comparison with simulation.

TRANSVERSE SIZE MEASUREMENTS

The rms size of the electron beam has been measured at different screens along the beam line. Dependences of the beam size at the screen of EMSY and screen_PP (1.62 m and 2.63 m from the cathode, respectively) on the main solenoid current are shown in Fig. 8. Rough estimations for the transverse emittance X/Y for main solenoid currents of 290A/292A yield normalized transverse emittances of (2.8±0.9) / (3.0±0.9) π-mm-mrad, respectively.

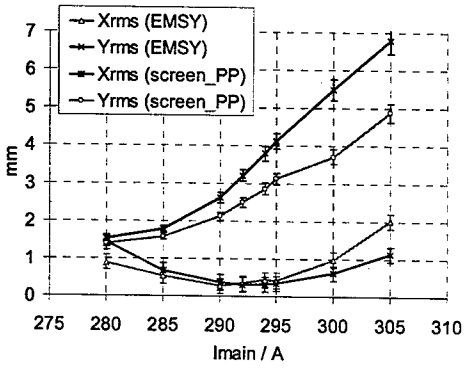


Figure 8: Measured beam spot sizes as function of the main solenoid current. Gradient at the cathode 40 MV/m, beam charge 0.5 nC.

The transverse beam size ($R_{rms} = \sqrt{X_{rms}^2 + Y_{rms}^2}$) measured at screen_PP as a function of the rf phase for different solenoid currents is shown in Fig. 9.

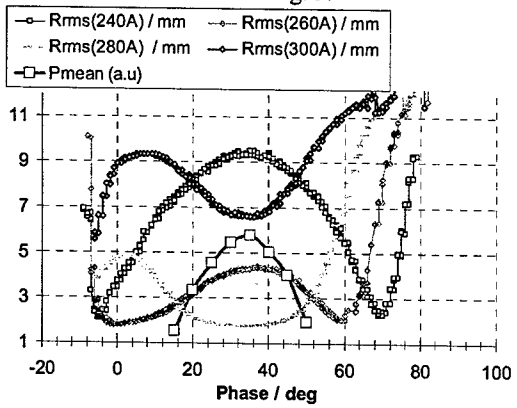


Figure 9: Measured beam spot sizes as function of the rf phase for different main solenoid currents. Gradient at the cathode 40 MV/m, beam charge 0.5 nC.

The longitudinal mean momentum dependence on the rf phase is shown on the same plot. It has a maximum at the phase of the local maximum of the beam spot size (minimum for higher solenoid currents). This is explained by the dependence of the solenoid focusing properties on the beam energy and was confirmed by corresponding simulations. Such a beam size phase scan can serve as an efficient tool for obtaining the phase of the maximal energy gain, since it is significantly faster than momentum measurements using dipole and dispersive arm.

TRANSVERSE EMITTANCE MEASUREMENTS

Measurements of the transverse emittance were performed using a single-slit diagnostics. Beamlet profiles were observed 1010 mm downstream of a single-slit mask (1 mm thick tungsten plate, 50 μm slit opening) at screen_PP [7]. The transverse emittance was measured as function of the main solenoid current. The results are shown in Fig. 10.

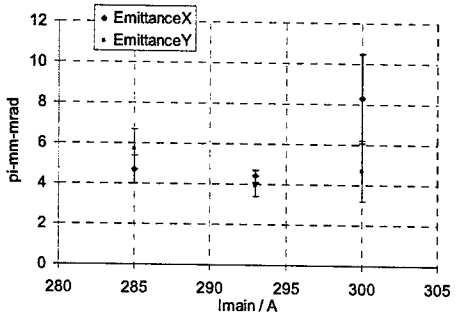


Figure 10: Measured transverse beam emittance as a function of the main solenoid current. Gradient at the cathode ~40 MV/m, beam charge ~0.5 nC.

The measured emittance values correspond to simulation predictions of the minimum achievable emittance of ~3 π-mm-mrad for the present short laser duration (7 ps FWHM). These values are different from the ones obtained earlier [8] because the laser beam parameters have been changed. Emittance improvement will be obtained by driving laser parameters optimization (temporal flat-top profile with short rise/fall times) as foreseen in the next months.

SUMMARY AND OUTLOOK

The experimental characterization of the electron source at the photoinjector test facility at DESY Zeuthen is ongoing. A maximum average power of 27 kW in the gun with a duty cycle of 0.9% has been achieved. Detailed measurements of dark current, beam longitudinal momentum and transverse phase space have been discussed.

REFERENCES

[1] F. Stephan et. al., "Photo Injector Test Facility under construction at DESY Zeuthen", Proc. FEL2000, Durham, August 2000.

[2] I. Bohnet et. al., "Photo Injector Test Facility in commissioning phase at DESY Zeuthen", Proc. EPAC2002, Paris, June 2002.

[3] J.-P. Carneiro, S. Schreiber, D. Edwards "Experimental Studies of RF Breakdowns in the Coupler of the TTF RF Gun", PAC2003

[4] J.H. Han et al. "Dark current measurements at the PITZ gun", Proc. DIPAC2003, Mainz, May 2003.

[5] K. Flöttmann, A Space Charge Tracking Algorithm (ASTRA), http:/www.desy.de/~mpyflo

[6] D. Lipka et al. "Measurements of the longitudinal phase space at PITZ", Proc. DIPAC2003, Mainz, May 2003.

[7] V. Miltchev et al. "Transverse emittance measurements at PITZ", Proc. DIPAC2003, Mainz, May 2003.

[8] R. Bakker et al. "First beam measurements at the photo injector test facility at DESY Zeuthen", Proc. FEL2002, Argonne.

Proceedings of the 2003 Particle Accelerator Conference

VELOCITY BUNCHING EXPERIMENT AT THE NEPTUNE LABORATORY

P. Musumeci, R. Yoder, J. B. Rosenzweig
Department of Physics and Astronomy, University of California at Los Angeles, CA 90095, USA

Abstract

In this paper we describe the rectilinear compression experiment at the Neptune photoinjector at UCLA. The electron bunches have been shortened to sub-ps pulse length by chirping the beam energy spectrum in a short S-band high gradient standing wave RF cavity and then letting the electrons undergo velocity compression in the following rectilinear drift. Using a standard Martin Puplett interferometer to characterize coherent transition radiation from the beam, we measured bunch lengths as short as 0.4 ps with compression ratio in excess of 10 for an electron beam of 7 MeV energy and charge up to 300 pC.

INTRODUCTION

In recent years electron beam users have increased their demands for high brightness beams in short sub-ps pulses. These beams find applications in the advanced accelerator community for injection into short wavelength high gradient accelerators [1], or as plasma wake-field drivers, and in the light source community for short wavelength SASE Free Electron Laser[2] and for Thompson-scattering generation of short X-ray pulses [3]. Recent designs of systems capable of delivering high brightness very short electron beams include the use of conventional photoinjectors in conjunction with magnetic compressors. While the magnetic compression scheme has been proved successful in increasing the beam current, the impact on the phase space has been shown to be quite dramatic [4]. An alternative scheme that could preserve the phase space quality while still shortening the beam to sub-ps bunch length has been recently proposed as an injector for X-ray Free Electron Laser, by Serafini and Ferrario [5]. This scheme, commonly known as "velocity bunching" is an elaboration of the old idea of RF rectilinear compression to the RF photoinjector system [6]. The idea is based on the weak synchrotron motion that the beam undergoes at moderate energies in the RF wave of a linac accelerating structure. The compression happens in a rectilinear section so that the damage suffered by going through bending trajectories is avoided. A main ingredient of the Serafini and Ferrario recipe to produce high brightness sub-ps electron beam is to integrate this compression section in the emittance compensation scheme, by keeping the transverse beam size under control through solenoidal magnetic field in the region where the bunch is compressing and the electron density is increasing.

A small variation inside this framework is the thin lens version of velocity bunching. Here the synchrotron motion of the electrons inside the RF structure is very limited. There is almost no phase advance inside the longitudinal lens and all the bunching happens in the drift following the linac. In this paper we describe an experimental study of the above configuration.

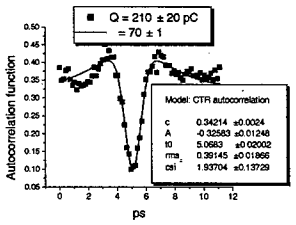


Figure 1: Results of Neptune ballistic compression experiment

EXPERIMENTAL SETUP

At the Neptune laboratory at UCLA [4] a 4 ps rms long laser pulse hits a single crystal copper cathode inside a 1.6 cell RF gun. The photoelectrons generated are then accelerated by the RF fields and go through the emittance compensation solenoid. At this point the beam can be energy chirped inside a 6+2 $\frac{1}{2}$ cell S-band PWT RF cavity. There is the capability of controlling and measuring independently the phases of the two accelerating structures allowing us to test the ballistic bunching scheme. Downstream of the linac an aluminum foil can be inserted and the transition radiation generated is collected by a parabolic mirror and reflected to a Martin Puplett autocorrelator for pulse length diagnostic [7]. There are also four chicane dipoles along the beamline and two of them can be turned on in a 45 degrees dipole mode. On the 45 degrees beam line there is a quadrupole lens and a Yag screen for emittance measurement via quad scan.

LONGITUDINAL DYNAMICS

Ballistic bunching can be viewed just as a thin lens version of the more general velocity compression mechanism. In this configuration, the phase advance of the electrons going through the longitudinal lens (the PWT linac) is few RF degrees and all the compression happens in the following drift. The important difference with the long RF-structure slow-wave version of velocity bunching is that the beam is

0-7803-7738-9/03/$17.00 © 2003 IEEE

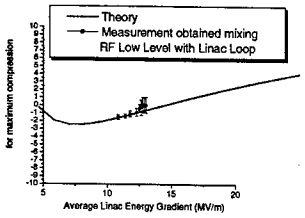


Figure 2: Phase of maximum bunching vs. Linac Accelerating gradient

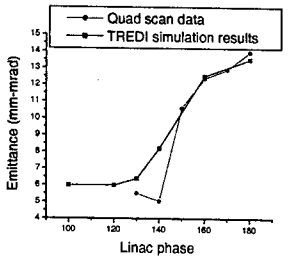


Figure 3: Emittance growth vs. PWT linac phase. Experimental results and simulations

extracted very close to the zero phase of the RF bucket and the RF non-linearities that in that case dominate the final bunch length are greatly reduced. One simple way to understand the ballistic bunching is to consider the time of arrival difference for particles having different velocities. When the time of arrival difference compensates the difference in the longitudinal position, the bunch length will be minimum and that is the maximum compression point. A relation between the parameters of ballistic compression valid to first order neglecting space charge and phase advance inside the PWT Linac can be written:

$$\frac{\Delta p}{p^3}L = \frac{E_{linac}\cdot\cos(\phi)\cdot k\cdot\Delta z}{(E_{gun}+E_{linac}\cdot\sin(\phi))^3}L = \Delta z \qquad (1)$$

where L is the distance from the RF structure, E_{linac} and E_{gun} are the energy gain of the PWT linac and the gun respectively, k is the RF wavenumber and ϕ is the Linac phase. We measured the pulse length in the frequency domain by Coherent Transition Radiation interferometry. For 210 pC of charge and 70 degrees off crest in the PWT cavity, we obtain the interferogram shown in fig.1. The data analysis yields a pulse length of 0.39 ps. The peak current of the bunched beam is in excess of 500 Amps. It is worth noticing the compressed beam is shorter than what was possible to get with magnetic compression for comparable beam charge, confirming the fact that in this case a more linear part of the RF wave is sampled. The predictions from the first order approximation given in (1) have been experimentally verified by measuring the compression phase changing the energy gradient in the Linac (fig. 2). The RF-cavity phase can be measured with a very small error by mixing the RF fields inside the structure with a reference RF-clock, at the same time the phase for maximum compression is easily determined by maximizing the Coherence Transition Radiation signal on the bolometer detectors. The agreement with the analytical formula is very good. Note that there is an important cancellation effect. As we decrease the energy gradient in the Linac, the beam is getting less energetic and less rigid to a rotation in the longitudinal phase space so that the adjustment of the phase to maintain the compression condition is minimal.

TRANSVERSE EMITTANCE MEASUREMENT

For optimal compression the beam runs through the high gradient structure far from the crest of the RF wave so that the energy spread at the exit of the Linac is very large. For example, for the case in which the focus of the longitudinal lens is 3 m downstream on the beamline, the RF phase was set 70 degrees off crest, resulting in a energy spectrum extending from 5 MeV to 9 MeV. This is a limitation to the determination of the transverse projected emittance because the energy spread translate to an angle spread and will appear to all measurement techniques (that are trace space measurements) as unphysical transverse emittance. On the other hand, the energy is correlated with the longitudinal position of the beam and with a small window of acceptance in energy, a longitudinal slice of the beam can be selected. Experimentally, we used the 45 degrees dispersing bending dipole configuration to select the central beam slice over which a vertical quad scan emittance measurement was performed. We measured the vertical phase space parameters of the electron beam varying the phase of the linac to understand the effect of the compression on the transverse dynamics of the beam.

ANOMALOUS VOLUME COMPRESSION

The experimental data show an increase in emittance even for phases for which the beam is not yet fully compressed. To completely understand this, it requires a deeper look into the dynamics of a chirped beam going through the bending magnet that we used as a slice selector in the measurement. For the vertical phase space, the bending magnet is in fact just a drift, but if we look at physical beam volume in x-s configuration space, we observe a strong compression if the beam is chirped in energy with particles with higher energy being in the tail of the beam. Note that a bending magnet has a negative R56 so that the compression is anomalous. The sizes of the projections of the beam density onto the curvilinear longitudinal axis s or onto the transverse dimension x and y increase as the beam bends, but the three-dimensional physical volume of the beam gets smaller. It is an effect that is ultimately due to the correla-

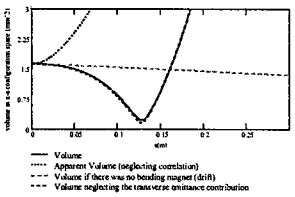


Figure 4: Anomalous compression for a beam chirped by phasing the PWT Linac 70 degrees off crest. The initial beam sizes at the entrance of the dipole magnetic field are $\sigma_x = 2.8mm, \sigma_s = 0.6mm$. The minimum volume point is 12 cm inside the magnet and the compression factor is 4.7.

tions in the configuration space introduced by the bending magnet. The effect of this electronic density spike at the cross-over point is dramatic for the electron beam quality especially at moderately relativistic energies where space charge forces are dominating the dynamics of the beam. A similar effect was observed in the Neptune magnetic compression experiment, where configuration space mixing was the origin of the observed emittance growth [4].

We analyze the problem of a chirped beam going through a bending magnet with a simple linear matrix calculation to illustrate the anomalous compression dynamics. The details of the calculation are given elsewhere. [9]. The result is that neglecting space charge forces and the contribution of the transverse emittance, we can write for the final configuration space volume the following:

$$V_f = \sqrt{\sigma_{xx}(\sigma_{ss}+2\sigma_{s\delta}R'_{56}+\sigma_{\delta\delta}R'^2_{56})+R^2_{16}\,(\sigma_{ss}\sigma_{\delta\delta}-\sigma^2_{s\delta})} \tag{2}$$

where s is the longitudinal coordinate along the beam path, R is the bending radius and γ is the design energy. R'_{56} can be written as:

$$R'_{56} = \frac{s}{\gamma^2} + R\cdot\sin\left(\frac{s}{R}\right) - s\cdot\cos\left(\frac{s}{R}\right) \tag{3}$$

a positive quantity increasing with distance (in the ultrarelativistic case, $\simeq s^3$), and R_{16} is the usual dispersion function, also an increasing function of the distance s. The volume at the beginning of the bend is $\sqrt{\sigma_{xx}\cdot\sigma_{ss}}$.

If the beam initially has a negative energy-position correlation ($\sigma_{s\delta} < 0$), somewhere along the beam-path the term multiplying σ_{xx} in (2) is zeroed and the volume goes through a minimum (fig. 4). This minimum volume point, the anomalous compression point, corresponds to the position along the beam line where the more energetic particles in the tail of the beam overtake *in the cartesian coordinate* z the less energetic ones. Not only the space charge effects become more significant because of an absolute increase in the total electron density, but more importantly this increase is localized to a region in the physical space in which a crossover happens. This implies a strong electric field gradient inside the bunch that is ultimately the cause for the quality degradation.

Full three-dimensional simulations with the particle tracking Lienard-Wiechert potential based code TREDI [8] confirm the validity of the linear analysis and, in fact, the results for the emittance growth match quite well the experimental data (fig. 3).

CONCLUSION

The Neptune ballistic bunching experiment demonstrated the efficiency of the rectilinear RF compression. A compression ratio in excess of 10 was achieved due to the strong suppression of the effect of the RF-non linearities. Experimental investigation of the transverse phase space quality showed emittance degradation. A deeper look into the beam dynamics shows that the technique used to select a small energy spread slice affects the beam quality in a serious way. A first order linear analysis is performed to quantify the anomalous beam compression of a chirped beam going through bending magnet. Three-dimensional simulations are in reasonable agreement with the experimental data.

The Neptune experiment points out the deleterious effect of crossovers in a space charge dominated beam dynamics, but because of the lack of post-acceleration we can not make conclusive statements on the quality of a beam compressed with a velocity bunching scheme. Future experiments are needed to investigate the full potential of the velocity bunching method for increasing the brightness of photoinjector beams, and the use of the magnetic solenoids to keep the beam phase spaces under control. One important point to be addressed is to investigate the difference between the thin lens version 'ballistic' bunching and the long version of the rectilinear compressor.

ACKNOWLEDGEMENTS

This work is supported by U.S. Dept. of Energy grant DE-FG03-92ER40693

REFERENCES

[1] C. E. Clayton,L. Serafini, IEEE Trans. On Plasma Science, 24, 400 (1996)

[2] Linac Coherent Light Source (LCLS) Design Report, Tech. Pub., SLAC-R-521 (1998).

[3] S. Anderson *et al.* these proceedings

[4] S. Anderson *et al.* Proc. of PAC 2001, p. 89 (2001)

[5] L. Serafini, M. Ferrario, AIP Conference Proceedings 581, 19th pp. 87 (2001)

[6] X. J. Wang *et al.*, Phys. Rev. E, 54, 3121 (1996)

[7] A. Murokh *et al.*, in AIP Conf. Proc. 472, 38 (1999)

[8] L. Giannessi et al., Nucl. Instr. Meth., 393, 434, 1997

[9] P. Musumeci *et al.*, Proceedings of 2nd ICFA High Brightness Beams Workshop, Chia Laguna, CA (2003)

Proceedings of the 2003 Particle Accelerator Conference

AN INTEGRATED TRAVELING-WAVE PHOTOINJECTOR

S. Telfer, Xgamma Corporation and UCLA, Los Angeles, CA 90095, USA

Abstract

Integrated photoinjectors have the potential to provide compact, low cost, high brightness electron beams, and are attractive for scaling to frequencies beyond S-band. Traditionally, they have been built as standing-wave devices. We are developing a novel high-brightness electron source that couples a two-cell standing wave cavity directly to a multi-cell traveling-wave structure. This configuration offers a number of advantages over the split standing-wave systems, most notably the almost complete removal of the reflected RF transient, and the absence of the bunch lengthening that occurs in the drift section of split systems. We will discuss these and other advantages, as well as provide results of our beam dynamics study.

BACKGROUND

The last fifteen years has seen a revolution in the production of high brightness electron beams due to the evolution of the RF photoinjector. This evolution derives its genesis from a multi-disciplinary approach to the difficult problems presented to the understanding of the behavior of a electron beam under the combined influence of large external applied electromagnetic fields and the self-induced space charge fields. Through these theoretical, computational, and experimental investigations, photoinjector physics has established itself at the confluence of a large number of disciplines, including accelerator beam dynamics, plasma physics, large-scale computational physics, surface studies, high-field RF physics and laser engineering. The manifest success of the RF photoinjector is a testament to this collective understanding.

The most prevalent photoinjector design in use today employs an arrangement of two accelerating structures split between a BNL/UCLA/SLAC-style 1.5/1.6 cell SW gun [1] and a post accelerating linac, separated by a ≈ 10 RF wavelength drift section. In these highly-optimized designs, the operating gradient in the gun is in excess of 100 MV/m. While extremely successful in providing ultra-high brightness beams for diverse applications, the split systems offer a number of obstacles in the path of the further evolution of the photoinjector. First, because of the photoinjector scaling laws, there is significant interest in the photoinjector community toward scaling existing designs to frequencies beyond S-band. However, because of the magnitude of the fields in the split system, scaling above s-band is greatly limited by RF breakdown. Second, all split systems exhibit bunch lengthening due to the presence of the drift section, which itself is essential for proper emittance compensation.

An alternative design, less popular yet perhaps even more successful, is exemplified by the LANL integrated L-band injector or the UCLA/DULY PWT Photoinjector [2], which integrates the gun and the linac and operates at lower overall gradient. While these systems do not exhibit pulse lengthening, the scaling of the designs, which initially seems promising is limited by the inherent difficulties in designing long SW structures, particularly at high frequencies. As a result, while these systems are compact, they are unable to provide beams with energies above 18 MeV.

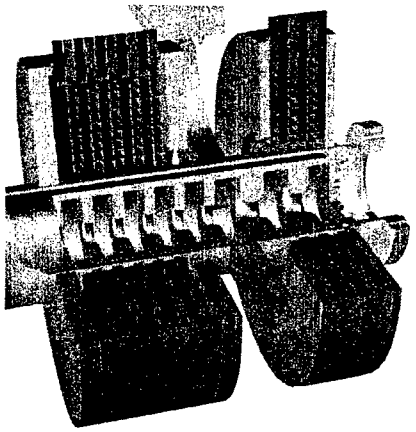


Figure 1: The first few cells of the hybrid photoinjector showing the emittance-compensating solenoid system.

In order to circumvent these and other limitations existing photoinjector designs we have studied a device which we call the "hybrid" photoinjector, whereby a relatively high-gradient two-cell standing wave structure is on-axis coupled directly to a long (≈ 2 m) $2\pi/3$ constant-impedance traveling wave accelerating section. The structure is coupled to the feed guide through the initial TW coupling cell. The first few cells of the hybrid photoinjector are shown in Figure 1. This design offers a number of advantages over both split and integrated existing designs, namely:

- Higher energies and better efficiency in power usage since most of the acceleration takes place in the TW section.
- Overall low gradients make it easier to hold RF voltages in cavities and improve vacuum.
- Robust accelerator dynamics, allowing flexibility in operating energy by simply changing RF power and laser injection parameters.
- Flexible emittance compensation beam optics because of the introduction of a dual-coil solenoid.
- Near complete removal of the transient RF reflected

0-7803-7738-9/03/$17.00 © 2003 IEEE

power since the structure is coupled to through the low Q TW cell. This feature is extremely important for scaling beyond s-band, where high-power isolators are expensive or non-existent.

- Simplifies the high power RF feed system required by split systems.
- Avoids the bunch lengthening observed after the exit of the 1.6 cell gun during the drift in a split system. The slow decrease in gradient enhances the emittance compensation process.
- Easier to fabricate, tune and operate than an integrated SW system of equivalent energy.

DESIGN OF THE DEVICE

The critical RF issue for the hybrid photoinjector is the design of the input coupling cell. The input cell connects both TW and SW sections to the feed guide, and so must provide an impedance match to two different structure impedances. To facilitate the coupler design process, we derived a circuit model which was solved numerically using a C program. The circuit model allows us derive a match condition by varying the Q, cell resonant frequency, and cell-to-cell coupling strength. To derive a match for the input cell, we first constructed a matched TW structure with no coupling to the SW section, and then slowly increased coupling while adjusting the input cell parameters to maintain a matched condition. In this way we were able to rapidly arrive at a set of matched coupler parameters.

The circuit model was also used to investigate the transient behavior of the device. Because the input coupling cell has a relatively low Q value ($\approx$ 600), the large initial reflected transient seen in SW structures such as the 1.6 cell gun, is suppressed in the hybrid structure. Circuit model results verified this characteristic. As a further check on these results, we used the time-domain finite-difference electromagnetic solver GdfidL [3]. Results from GdfidL qualitatively agreed with our circuit model.

For the design of the TW section we have chosen a long, $\approx$ 2 m, TW structure run at a nominal average gradient of eE_{ave} = 13.5 MV/m. For an optimized constant-impedance structure, this implies a power usage of roughly 17 MW. With an additional 3 MW for powering the 1.6 cell SW gun component of the structure, the total power needed is 23 MW, which is well within the reach of commercial S-band klystrons (¡30 MW standard). The 3 MW 1.6 cell power budget is chosen to yield a peak acceleration gradient on the cathode of E_0 = 70 MV/m (α = 1.1), which places notably higher in gradient than a SW integrated injector. This is again allowed by the separation of gradient levels allowed in the hybrid structure, as this higher gradient is confined to a very small part of the structure. Initial explorations of the beam dynamics with even higher gradients in the 1.6 cell part of the hybrid have yielded promising results, as is discussed below. The issue of allowable difference between the acceleration gradients in the 1.6 cell SW portion and the TW portion of the structure is of course a subject which ties the RF design to the beam dynamics.

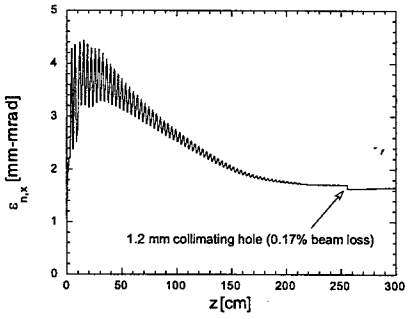


Figure 2: PARMELA results for the evolution of the transverse normalized rms emittance in hybrid injector. Effects of collimation (1.2 mm radius tube) of beam edge shown.

BEAM DYNAMICS

Studies of the beam dynamics in the injector were performed with UCLA PARMELA, multi-particle space-charge tracking code, as well as HOMDYN, a code which solves for the dynamics of the beam envelopes of the bunch associated with a large number of beam "slices". This slice-envelope model is indeed quite accurate in identifying the basic characteristics of a photoinjector working point, and is much faster than PARMELA. Once the working point is established with HOMDYN, one may proceed confidently to more detailed investigations with PARMELA. The field maps used in these dynamics simulations were obtained from magnetostatic POISSON and electromagnetic SUPERFISH modeling.

The higher gradient SW acceleration produces an energy of around 3.5 MeV, while the long TW section then brings the beam up to around 30.6 MeV (γ = 60). There is flexibility in choice of the final accelerating phase in the TW section, by adjusting the initial launch phase. This is akin to the case of the integrated injector, but unlike the split injector, where a large penalty is paid in induced "RF emittance" when one exits the gun at the incorrect phase. The choice of phasing allows tuning of the final longitudinal phase space for a given application, and enables operation at different RF field levels. The longitudinal beam evolution is noteworthy in that there is negligible bunch lengthening after the SW part of the structure. This allows the final bunch length to be 10% *shorter* than a standard 1 nC case with the split photoinjector. As peak current is even more important than emittance is many applications (*e.g.* wakefield acceleration driver, Thomson scattering), this is a significant advantage over existing devices.

The rms normalized emittance evolution for the nominal working point is displayed in Figure 2. The emittance compensates to a full value of 1.75 mm–mrad. This value is dominated by the tails, however, as collimation of only 0.17% of the beam charge lowers the emittance by a no-

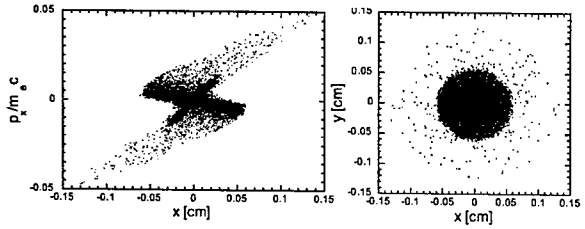


Figure 3: Final horizontal phase space, and transverse configuration space emitted from hybrid injector given by PARMELA

ticeable amount. Inspection of the transverse (horizontal) phase space, and configuration space shown in Figure 3 illustrates the reason for this sensitivity, as a fairly extensive halo which contains a very small amount of the beam charge surrounds the dense core of the beam. This halo exists mainly in the leading and trailing edge of the beam, where the beam slices do not come to a space-charge dominated waist. These components of the beam are typically ignored in applications, and in fact may be effectively collimated.

CONCLUSION

We have designed a hybrid SW to TW integrated photoinjector that shows significant promise for a compact, efficient 30 MeV source of high-brightness electrons. In further stages of this work we plan to further explore RF optimizations, particularly shaping of the peak field profiles in the TW section in order to optimize the results of our initial beam dynamics study. We also plan to perform a rigorous thermal and mechanical analysis before finally fabricating a prototype, which will be commissioned at the UCLA PEGASUS Laboratory.

REFERENCES

[1] D. T. Palmer, PhD Thesis, Stanford University, 1999.

[2] X. Ding, PhD Thesis, UCLA, 2000.

[3] W. Bruns, Proceedings of the 1997 Particle Accelerator Conference, 2018, 1997.

WEDGE-SHAPED, LARGE-APERTURE, DIPOLE MAGNET DESIGNS FOR THE JEFFERSON LAB FEL UPGRADE

D. Newsham, A. Smirnov, Y. Luo, D. Yu
DULY Research Inc., Rancho Palos Verdes, CA 90275
G. Biallas, *JLAB, Newport News, VA*

Abstract

Two types of dipole magnets were simulated and designed for the Thomas Jefferson National Accelerator Facility FEL upgrade. The magnets are to operate in series with a common power supply, and to provide ~0.01% accuracy of the field amplitude *and* field integral over a large aperture. The wedged magnets have quite different angles and effective length-to-aperture aspect ratios. The most difficult design problem was to provide high field quality in the magnet having a small aspect ratio ~2.7 and a 20° wedge angle. A design was developed which enabled small adjustments to be made before and after installation of the magnets. Trim coils, shims, and side sliders in the field clamps were introduced to compensate field gradients, non-uniformities, and parasitic fringe field effects. A number of design and adjustment issues are discussed.

INTRODUCTION

The upgrade project of a CW 1-kW infrared free-electron laser at the Thomas Jefferson National Accelerator Facility (JLab) [1] aims to produce higher power IR and shorter wavelength radiation, and includes two families of new extraction/injection dipole focusing magnets of different geometries (see Table 1).

Table 1. Specifications of GU and GV dipole magnets

Magnet family	GU	GV
Maximum beam energy E, MeV	160	11
Wedge angle α, degrees	4.87	20
Bend radius R, m	9.6	0.6
Maximum induction B, Tesla	0.0612	0.0612
Effective length L, mm	435	208
Vertical magnetic gap G, mm	76.2	≥76.2
Horizon. good field region, mm	≥76.2	≥76.2
Field non-uniformity ΔB/B along the horizon. Line of symmetry), %	±0.01	±0.01
Field integral non-uniformity over good field region ΔIB/IB, %	±0.01	±0.01

The need for high field quality (~10^{-4}) is driven by the requirement to suppress two main spurious effects: steering and focusing. Both are important for transport of a low-emittance beam having a large spot size and a halo (at maximum power). Compact design of the beam lattice requires usage of field clamps limiting the extent of the stray fields. An additional, important requirement is minimization of beam quality degradation caused by AC ripples. It implies the same current in both magnets, which are connected in series with a common power supply. Field non-uniformity is considered at the vertical plane of symmetry. Non-uniformity of the field integral is defined as the relative deviation with respect to an ideal model having the same effective length, wedge angle and uniform field B over the hard-edge trapezoidal volume. Field integral is defined along a straight line (theoretically for infinite particle energy) tangent to the beam centroid trajectory.

A 3D code Radia [2] was used in design simulations. In both models of the GU and GV magnets, equal angular dimension of each trapezoidal sub-segment was chosen in a fine mesh (up to 1 GB of RAM). Post-processing included trajectory analysis with calculation of end-field roll-off integral K_1 as defined in ref. [5], and focal length F.

GU MAGNET DESIGN

The GU magnet differs from an earlier prototype [3] in its wedged shape and field clamps. Some new design elements are the use of a Purcell gap, field clamps with adjustable longitudinal position, and non-magnetic gap. The Purcell gap consists of two thin layers: non-magnetic material and material with extremely high permeability up to 500,000 (see, e.g., CO-NETIC AA [4]). It was applied effectively for larger rectangular magnets with measured field flattening effect better than 5 times [5].

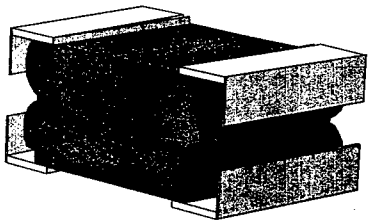


Figure 1: Radia schematic view of the GU magnet.

3D Radia modeling initially revealed significant numerical instability and slow convergence. These severe issues were caused by a high aspect ratio of the μ-metal plate (~250) with extremely high permeability. The problem was solved with a procedure of multi-parametric optimization of subdivision of the main objects.

During minimization of the field inhomogeneity we defined optimal dimensions of the μ-metal plate and field clamp configuration. The wave-like behavior of the field quality shown in Fig. 2 reflects in part the numerical effect of residual relaxation related to the large interaction

0-7803-7738-9/03/$17.00 © 2003 IEEE

matrix having many nearly equal elements. With some combinations of the segmentation parameters and number of elements, the curves can be smoothed. Fig. 3 illustrates the sensitivity to the horizontal displacement of the clamps with respect to vertical plane of symmetry.

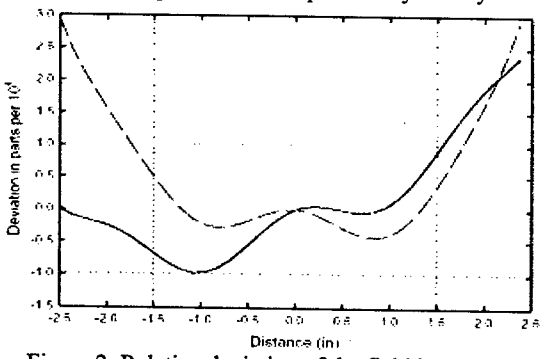


Figure 2: Relative deviation of the field integral (solid curve) and field (dashed) for the GU magnet.

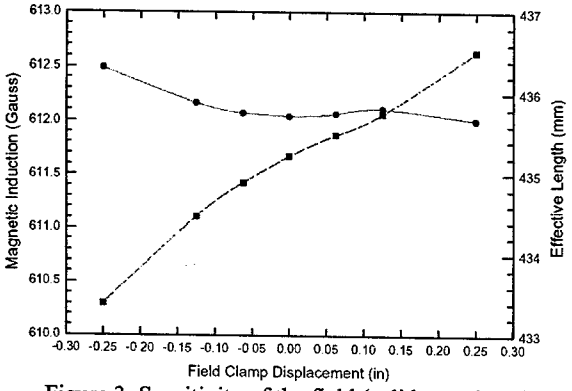


Figure 3: Sensitivity of the field (solid curve) and effective length (dashed) to symmetric shift of the clamps for the GU magnet.

GV MAGNET DESIGN

In designing the GV magnet two additional issues were addressed: suppression of the field gradient caused by a large wedge angle, and achievement of the parameters specified in Table 1 along with the same value of current found for GU magnet (2.1 kA). Unlike most conventional magnets, the GV magnet has a shorter length (with respect to the transverse gap) and a bigger wedge angle. It causes large non-uniformity of both the field and field integral, exceeding the nominal by more than one order. Also, unlike GU and other magnet designs [3,5,6], the Purcell gap turned out to be ineffective: the GV magnet is dominated by 3D effects of non-uniform fringe-field at shorter lengths. The sensitivity of the effective length of the GV magnet to the shift of the field clamps is almost twice as high as that for the GU magnet.

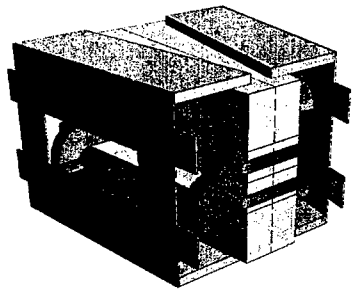


Figure 4: Schematic view of the GV magnetic design.

To provide field homogeneity in the GV design (see Fig. 4), three sets of additional elements were introduced. Trim coils on each of the return legs of the yoke suppress the field gradient. The coils on the opposite legs have the same current to provide increased magnetic flux for the smaller leg and decreased flux for the bigger one. Side sliders at the clamps provide adjustability of the field integral profile with tunable magnetic shortcut at the periphery of the window-framed aperture in the clamps. Finally, a set of shims, *i.e.* small pieces of μ-metal, are placed along the median line between the internal surface of horizontal clamps and the conductor. Thus trim coils provide the first-order (gradient) compensation of the field and field integral, μ-metal pieces provide the second-order compensation, and side sliders provide non-linear corrections for the field integral. In the mechanical design of the GU and GV magnets, we introduced an additional degree of freedom enabling compensation of the remnant slope of the field integral by a small angular shift of the clamps with respect to the yoke.

To provide the field required with the same current as it was computed for the GU magnet, we found numerically the optimized value of an enlarged vertical magnetic gap, along with other parameters of this final design. The GV magnet field quality in the median plane is depicted in Fig. 5.

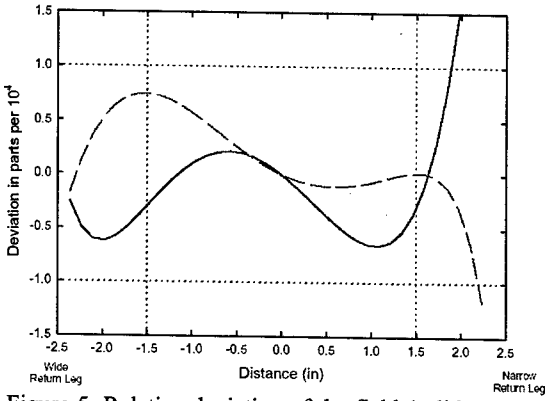


Figure 5: Relative deviation of the field (solid curve) and field integral (dashed) for the GV magnet.

Table 2: a) Computed sensitivities of the GV magnet parameters to the main adjustments

1GB-RAM Model with different conductor configuration	Not smoothed	Smoothed
Effective length to the symmetrical shift of all clamps along the trajectory, $\Delta L_{eff}/\Delta S_{clamp}$	0.295	0.271
Relative gradient of the field related to the relative trim coil current, $\Delta B/(\Delta x B_o)/\Delta I_{trim}/I_o$, averaged over central part of the good area, (%/m)	59	67.2
Gradient of relative field Integral to the angular position of the field clamp, $\left\|\Delta\int Bdz/(\Delta x B_o L_{eff})\right\|/\Delta\varphi_{clamp}$, averaged over the linearized part of good area, (%/m-mrad)	0.098	0.13

b) Computed optimal adjustments to provide specification parameters

Overlap of horiz. part of the field clamp with the body magnet along the central axis, (inches)	1.21-1.22	1.23-1.24
Trim coil current related to the main current, I_{trim}/I_o, (%)	4.99-5.1	4.9-5.1
Angular clamp position, (mrad)	-7.36	-5.1-2.77
Shift of wider-side slider towards the axis (from the nominal in mechanical drawings), (mm)	0-5	0

We studied the sensitivity of the main magnet parameters to the aforementioned tuning means. The results of this study are given in the Table 2 and implemented in the tolerances of the mechanical design. We noticed also a high sensitivity to the shape of the bent conductor parts (twisted arc-arc and bar-arc conjunctions).

CONCLUSION

Extensive studies of magnetic design demonstrated feasibility of the specified requirements. On the basis of these results, mechanical design of both magnets was made. The GU and GV magnets were manufactured and tested at Jlab GV magnet field measurements demonstrated ±0.01% deviation for the field, and ±0.02% for the field integral [7] over the good area. Note, only trim coils were used to adjust the field. In the real design, the field amplitude, field uniformity, and the effective length are affected by holes (for bolts, alignment pins, *etc.*) in the yoke and clamps, real shape of the main coil (especially conductor conjunctions), geometric tolerances and imperfections of magnetic materials. These features cannot be reproduced accurately in the numerical model, which has inherent numerical inaccuracy as well.

The key underlying concept of the cost-saving design of the GU and GV magnets is to provide flexibility with a number of adjustable elements. These elements include: field clamp longitudinal and angular positions, non-magnetic gap in the field clamps (GU only), side sliders in the clamps and μ-metal shims (GV only), trim coils and their adjustable current (GV only), and an adjustable common power supply.

The field and current differences between the GU and GV magnets can easily be compensated with a low-current (~a few Amperes), variable shunting resistors connected in parallel to main coils of the magnets.

REFERENCES

[1] D. Douglas *et al.*, in Proc. of the 2001 Part. Acc. Conf., Chicago (2001) 249.
[2] P. Elleaume *et al.*, Proc. of the IEEE Particle Accelerator Conference, May 1997, Vancouver, BC, Canada, p. 3509.
[3] G. Biallas *et al.*, Proc. of the 1999 Particle Accelerator Conference, New York, March-April 1999, p. 3306.
[4] http://magnetic-shield.com/graphics/perm-graph.jpg
[5] J. Karn *et al.*, Proc. of the IEEE Particle Accelerator Conference, May 1997, Vancouver, BC, Canada, p. 3333
[6] G. Biallas *et al.*, in Proc. of the IEEE Particle Accelerator Conference, New York, March-April 1999, p. 3312
[7] G. Biallas *et al.*, these proceedings.

PARMELA SIMULATIONS OF A PWT PHOTOINJECTOR*

Y. Luo, D. Newsham, D. Yu, *DULY Research Inc., Rancho Palos Verdes, CA 90275*
J. Clendenin, *Stanford Linear Accelerator Center, Menlo Park, CA 94025*

Abstract

Conventional rf guns such as the BNL/SLAC/UCLA 1.6-cell gun require a high operating peak field typically above 120 MV/m. By contrast, the PWT gun can operate at a much lower peak field with excellent beam properties. A 10+2(1/2)-cell PWT photoinjector can achieve an emittance of 0.56 mm-mrad for a 1 nC bunch charge at a peak field of 55 MV/m; and 1.04 mm-mrad for 2 nC at 60 MV/m. By operating the PWT gun at a low peak field, dark current production from back bombardment of electrons emitted elsewhere in the rf cavity is mitigated as the number of electrons which could back stream to hit the photocathode and the cathode holder is significantly curtailed. The quantum efficiency and lifetime of a semiconductor photocathode, such as GaAs are significantly improved if the surface of the cathode is subjected to a lower peak field

PWT PHOTOINJECTOR

A compact, 10-30 MeV, photoelectron linac using the Plane Wave Transformer (PWT) design (Figure 1) has been under development at DULY Research [1] for wide-ranging applications in research, medicine and industry. The PWT photoinjector integrates a photocathode directly into a multicell, standing-wave, π-mode linac, in which the open cells in a large vacuum tank are strongly coupled.

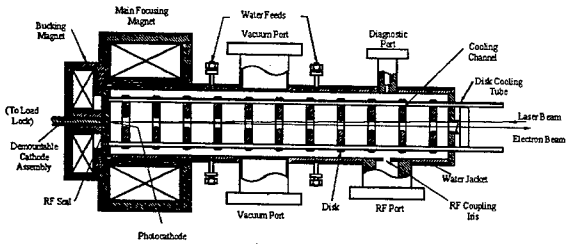


Figure 1: Schematic of a PWT photoinjector.

The beam is focused with emittance compensating solenoids or permanent magnets, and achieves high current with low emittance, producing extremely high brightness.

An S-band PWT prototype was fabricated by DULY Research and installed at UCLA [1]. A higher frequency (X-band) version of the PWT would produce an even brighter beam. In a current DULY/SLAC collaboration, an S-band PWT gun is being developed into a polarized rf gun capable of high vacuum in the 10^{-11} Torr range to support a long GaAs cathode life and a high quantum efficiency [2].

* Work supported by DOE SBIR grant no. DE-FG0398ER82566.

With an integrated photocathode, the PWT has a simple system design which eliminates a separate accelerating section with the associated focusing optics and additional rf feeds as required by a conventional 1.6-cell gun in order to achieve the same energy gain. In addition, the defocusing kick which the beam receives at the exit of the last cell occurs at a significantly higher energy than for a 1.6-cell gun, resulting in less emittance growth.

EMITTANCE CALCULATIONS

We have performed improved, detailed beam dynamics simulations of the PWT photoinjector using the Los Alamos gun code PARMELA, Version 3. With refined space charge mesh and careful optimization, the performance of the PWT gun was evaluated for three illustrative cases. Optimized results of the simulations are shown in Table 1, and in Figure 2.

Table1: Parameters of 0.1 nC, 1 nC and 2 nC operations.

Charge per Bunch (nC)	0.1	1.0	2.0
Frequency (MHz)	2856		
Energy (MeV)	8	17	17.5
Normalized RMS Emittance (mm-mrad, no thermal emit.)	0.36	0.56	1.04
Energy Spread (%)	1.4	1.0	1.3
Bunch Length (rms, ps)	2.2	3.6	3.2
Peak Current (A)	13	80	180
Linac Length (cm)	58		
Beam Size (rms, mm)	1.2	.85	1.62
Peak Magnetic Field (Gauss)	875	1694	1620
Peak Electric Field (MV/m)	27	55	60
Peak Brightness (10^{14} A/m^2-rad^2)	2.0	5.1	3.3

For a given charge per bunch, the initial beam size and bunch length (both flat top) are varied for each case and are optimized for space charge minimization. For a given peak field, the initial injection phase and the solenoidal field are adjusted to give the lowest normalized transverse emittance. A low field of 27 MV/m is sufficient for acceleration of a low emittance beam with a charge of 0.1 nC (see Table 1). The 1-nC case uses a peak field of 55 MV/m, and represents a typical FEL injector (Figure 2). The 2-nC case uses a peak field of 60 MV/m, and represents an injector under NLC-like conditions.

Shown in Table 1 are the calculated normalized emittance of 0.56 mm-mrad (1 nC) and 1.04 mm-mrad (2 nC), which are lower than earlier simulation results [1]. Thermal emittance is not included. From Figure 2, it is interesting to note that the energy spread and bunch length decrease with drift distance. It appears that a negative

chirp is introduced by the gun, in this case allowing for longitudinal focusing of the bunch. In all cases, the beam brightness, defined as twice the peak current divided by the transverse emittance squared, well exceeds 10^{14} A/(m-rad)^2. From Table 1 and Figure 2, it is clear that the integrated PWT design produces excellent beam quality over a wide range of input parameters.

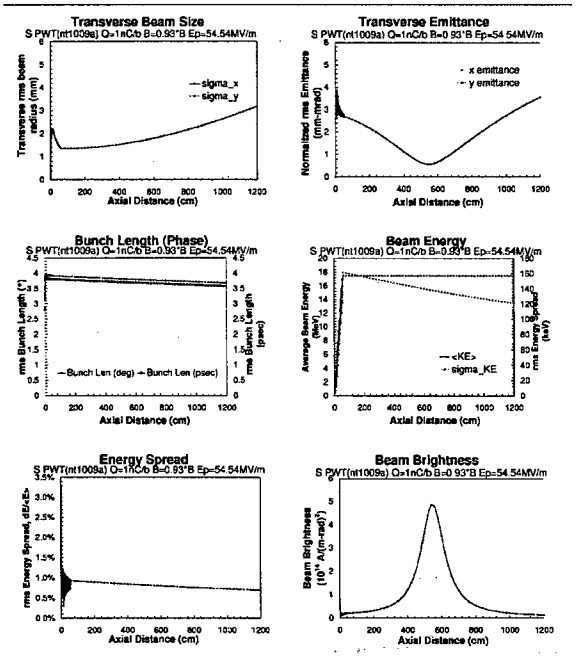


Figure 2: PWT beam parameters for 1 nC bunch charge.

Figure 2 indicates that the transverse emittance and beam size go through their respective minima and then grow as the beam continues on after leaving the PWT. This is a result of the energy (about 17 MeV) not being high enough to overcome space charge effects. The beam must be matched into an additional accelerator. The standard way to do this with a 1.6-cell gun is to position the input of the accelerator at a laminar beam waist. The emittance will then be preserved if the proper accelerating gradient is chosen. Two solutions have been found with 1.6-cell guns for achieving an emittance minimum after acceleration. The first is to adjust the gun solenoid so the waist coincides with the emittance minimum without the accelerator. Utilizing the fact that the emittance undergoes a plasma oscillation, the second solution is to adjust the solenoid so that the waist coincides with the immediately following emittance maximum. These strategies can also be applied to the PWT.

A peak field of 55 MV/m in an S-band PWT gun is considerably lower than an operating peak field of 120-140 MV/m in a conventional 1.6-cell gun. The lower peak field at the photocathode is particularly beneficial for the survivability of an activated GaAs cathode in a polarized rf gun, and also, as we shall see below, for mitigation of dark current and electrical breakdown due to field emission and electron back bombardment.

For comparison with the 1.6-cell gun [3], we also calculated the tranverse emittance for a PWT gun in which the length of the first cell is 0.625 of a normal cell of a half wavelength, instead of a 0.5 cell as in the present design. Figure 3 shows the normalized transverse emittance versus magnetic field (varying the injection phase at a given peak field) for these two cases.

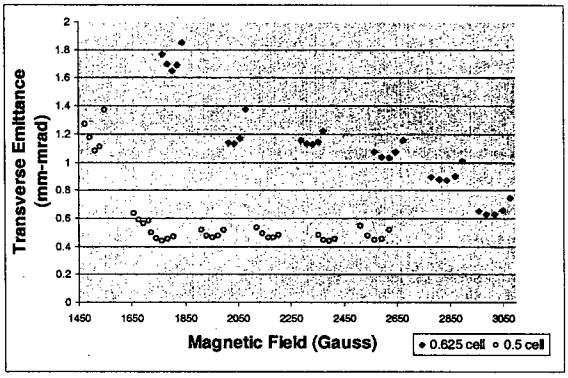


Figure 3: Emittance vs magnetic field for 1 nC bunch. The solid diamonds are for a 0.625 first cell at a peak field of 60, 80, 100, 120, 140 and 160 MV/m, and the open circles are for a 0.5 first cell at 45, 55, 73, 91, 109, 127 and 145 MV/m.

The simulations show that an S-band, π-mode, integrated PWT photoinjector with the first cavity of 0.5 cell is better than the first cavity of 0.625 cell. They both can achieve very low emittance. But performance is different for these two cases. For the 0.5 cell case, the normalized transverse emittance is 1.08 mm-mrad at 45 MV/m (Bz = 1.5 kG). It decreases to 0.56 mm-mrad as the peak field increases to 55 MV/m (Bz = 1.7 kG). From 73 to 145 MV/m, the emittance stays very close to 0.4 mm-mrad. For the 0.625 cell case, the emittance decreases as the field gradient increases, but always remains higher than the 0.5 cell case. The normalized transverse emittance is 1.6 mm-mrad at 60 MV/m (Bz = 1.8 kG) and is 0.63 mm-mrad at 160 MV/m (Bz = 3.0 kG). Unlike the BNL/SLAC/UCLA 1.6-cell gun, the PWT electron beam is only minimally affected by the exit rf kick.

ELECTRON BACKBOMBARDMENT SIMULATIONS

Electron Backstreaming from the PWT Iris to the Photocathode

A GaAs photocathode is prone to dark current emission when bombarded by electrons or ions. Since electrons have a smaller mass and are hence more mobile, field-emitted electrons in the rf cavity can potentially reach the cathode, damaging the activated layer. We have

performed PARMELA simulations to assess the effects of electron backstreaming from the first PWT iris to the photocathode. A thin ring electron bunch, initially with essentially zero velocity, is placed at a given location on the surface of the iris. The model includes a drift tube at the center of the endplate. The aperture of the drift tube is chosen to be that of the photocathode and its support plug (0.5 inch). Field emitted electrons move under the rf field and external magnetic field of the PWT. The number of electrons which can reach the photocathode depends on the initial location of the ring bunch, the rf phase and the peak rf field. At certain locations the rf field on the PWT iris surface may be as high as 1.17 times the maximum peak field on axis. The maximum number of electrons that can reach the cathode occurs at such locations when the rf field magnitude exceeds a threshold value and when the initial rf phase at the iris at the time the electrons are emitted is near zero. Figure 4 shows the dependence of the field threshold on the iris location at which electrons are emitted. Figure 5b is an example of snapshots of electrons emitted from the surface of the first iris and backstream toward the cathode plane under the rf and magnetic fields in the PWT. No electrons would reach the cathode below the field threshold. The beneficial effect of operating the PWT at a lower peak field (55 MV/m) than conventional rf guns (>120 MV/m) is evident from Figure 4.

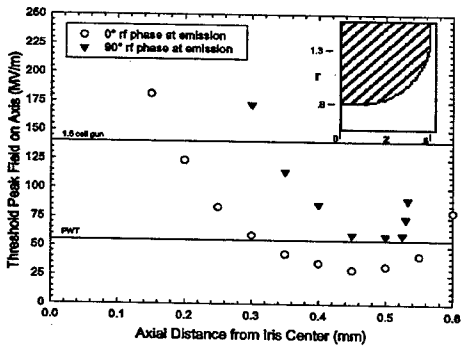


Figure 4: Threshold peak field for electrons emitted from the first PWT iris reaching the cathode surface. The insert shows the iris geometry.

In the PWT gun, backstreaming electrons emitted at an initial rf phase of 90° from the first iris never reach the cathode at a peak field (on axis) of 55 MV/m; and at an initial phase of 0°, only a small fraction of the electrons would reach the cathode. By contrast if the gun were to operate at a peak field (120MV/m) comparable to that in a conventional, BNL-type, 1.6-cell gun, then a large number of electrons emitted from the iris surface would hit the cathode. Since field emission is likely to be most abundant when the surface field is at its maximum (i.e. 90° rf phase); by operating the PWT at a peak field much lower than conventional rf guns, it is expected that dark current emission from the GaAs and its support structure would be considerably mitigated.

Back Bombardment of Electrons Emitted from the Cathode Holder

Another PARMELA simulation was performed to evaluate the possible back bombardment of electrons which were first emitted near the PWT end plate and cathode support. The model puts a ring of electrons initially around the cathode and tracks their trajectories under the rf field and the solenoidal field. At a sufficiently high peak electric field around 15 MV/m or higher, all electrons emitted near the cathode would either go through the first iris or hit the disk (see Figure 5a). At very low peak fields electrons would oscillate near the cathode surface. The low field resonance-like condition could send electrons back to the GaAs cathode surface and contaminate it. The lower the peak field, the longer the "trapped" electrons would stay near the cathode surface. Therefore in order to prevent electrons emitted from the cathode or the cathode holder from hitting the photocathode in an rf gun, the operating voltage should not be too low. The operating peak field chosen for the proposed polarized PWT gun appears to be optimum in that it is low enough to discourage back bombardment of electrons from the iris, and yet high enough to avoid back bombardment of electrons from the cathode holder. During rf conditioning, however, it is important that the GaAs cathode is not exposed to low fields. For that reason, we will be using a sacrificial cathode during rf conditioning and replacing it with a freshly activated cathode via the load lock.

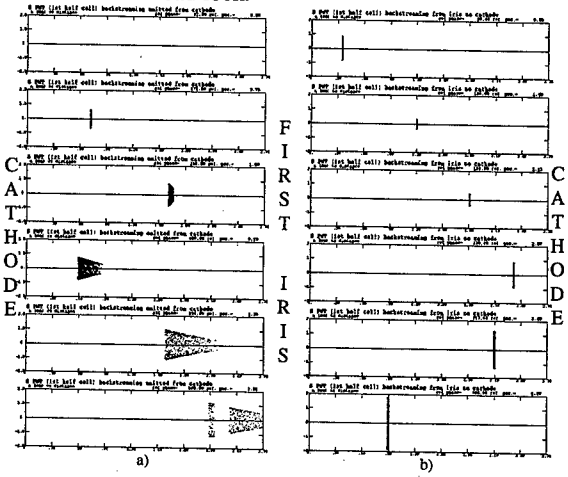


Figure 5: Examples of snapshots (projected onto an x-y plane) of backstreaming electrons emitted (a) from the cathode holder, and (b) from the first iris.

REFERENCES

[1] D. Yu, Proc. 2nd ICFA Adv. Accelerator Workshop on the Physics of High Brightness Beams, UCLA, November 9-12, 1999, p.585.

[2] D. Yu *et al.*, WPAB043 in these Proceedings.

[3] M. Ferrario et al., Proc. 2nd ICFA Adv. Accel. Workshop on the Physics of High Brightness Beams, Nov. 1999, p.534.

DEVELOPMENT OF A POLARIZED ELECTRON GUN BASED ON AN S-BAND PWT PHOTOINJECTOR*

D. Yu, D. Newsham, Y. Luo, A. Smirnov, *DULY Research Inc., Rancho Palos Verdes, CA 90275*
J. Clendenin, D. Schultz, *Stanford Linear Accelerator Center, Menlo Park, CA 94025*

Abstract

An RF polarized electron gun utilizing the unique features of an integrated, plane-wave-transformer (PWT) photoelectron injector [1] is being developed by DULY Research Inc. in collaboration with SLAC. Modifications to a DULY S-band device [2] include: a re-design of the photocathode/RF backplane interface to accommodate a GaAs cathode; change in the design of the vacuum ports to provide 10^{-11} Torr operation; the inclusion of a load-lock photocathode replacement system to allow for reactivation and cesiation of the GaAs photocathode in a vacuum; and alteration of the magnet field coils to make room for the load-lock. The use of a stainless steel outer tank and cooling rods without copper plating may also provide better vacuum performance at the expense of diminished Q-factor. The effectiveness of both the standard cooling rods and synthetic diamond heat sinks for disk cooling is investigated for future linear collider applications operating at a rep rate of 180 Hz and a bunch charge of 2 nC.

INTRODUCTION

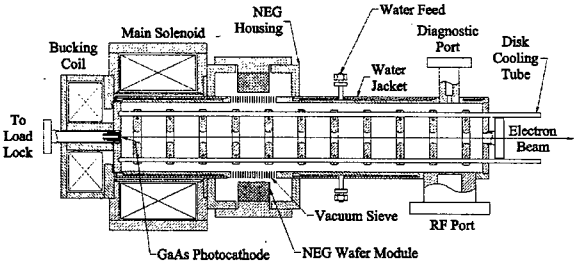


Figure 1: Schematic of the DULY S-band integrated PWT linac as modified for polarized electron production.

A polarized electron beam will be essential in future linear colliders for high-energy physics experiments to study the spin structure of fundamental particles. Important qualities required for a polarized electron source include large electron spin polarization (80%), high quantum efficiency (QE), long cathode life, high peak and average currents, and low beam emittance. An activated GaAs photocathode under extremely high vacuum can produce the required electron beam which is accelerated in an emittance-compensating rf cavity. The high vacuum conductance of the DULY S-band PWT [2], and its ability to provide excellent beam quality at low accelerating gradient make the PWT a good choice for a polarized electron gun. The new PWT design uses NEG pumps to achieve and maintain vacuum in the 10^{-11} Torr range. Figure 1 shows a schematic of the S-band PWT as modified for use as a polarized electron gun.

* Work supported by DOE SBIR grant no. DE-FG03-02ER83401.

VACUUM

The large vacuum conductance provided by the large annular region between the disk and the tank wall is an important feature of the PWT photoinjector. A fundamental change in the design is the incorporation of non-evaporable getter (NEG) pumps that have the unique advantage of maintaining their high pumping speed even at low vacuum pressures.

Vacuum Sieve

The S-band PWT installed at UCLA (DULY/UCLA PWT) uses a single vacuum port with a sieve consisting of 280 1/8" holes. This sieve, along with the associated piping, has a vacuum conductance that is comparable to (but less than) the conductance from the pumping port to the cathode. Two methods for increasing the effective pumping speed on the chamber exist. The first is to increase the number of identical pumping ports around the circumference of the tank, allowing for a conductance that is 3-4 times the single port value. The other option is particularly attractive if the tank is made from pure copper (not plated) and is depicted in Figure 2.

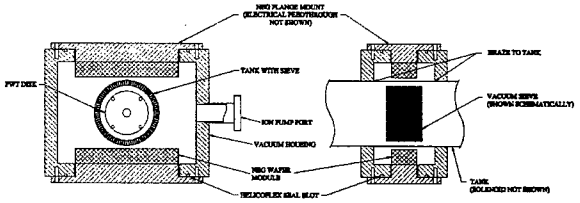


Figure 2: Schematic showing the circumferential sieve layout including the NEG modules and vacuum housing.

Instead of using several localized sieves, the holes can be drilled directly into the wall of the tank and can cover the entire circumference of the tank. This location would be surrounded by a chamber that is carefully brazed to the tank wall and contains standard NEG wafer modules capable of providing a pumping speed over 1000 l/s within the housing.

Pumping Location

The location of the pumping port can have a significant effect on the vacuum conductance from the cathode to the pumping port. The DULY/UCLA PWT has the pumping port at the 5th cell from the cathode. By moving the pumping port closer to the cathode, the vacuum conductance will increase. Table 1 shows the vacuum conductance to the photocathode of the accelerating

structure based on the number of cells away from the cathode that the pumping port is located. The size of the main solenoid prevents locating the pumping port any closer than 3 cells from the cathode.

Table 1: Vacuum conductance for the DULY/UCLA PWT calculated at various cell positions.

# of cells from cathode	Vacuum Conductance (l/s)
3	94
4	71
5 (DULY/UCLA PWT)	56

Despite the increase in the vacuum conductance of the accelerating structure, with either the multiple or the full circumferential sieve option, it still limits the overall conductance of the system. In addition to compensating for the degradation in Q caused by using stainless steel, increasing the tank diameter will also improve vacuum conductance. Figure 3 shows the vacuum pressure at the cathode as the diameter of the tank is increased, assuming a fully circumferential sieve and a NEG pump speed of 1000 l/s. The different data sets correspond to location of the pumping port in terms of the number of full cells from the cathode.

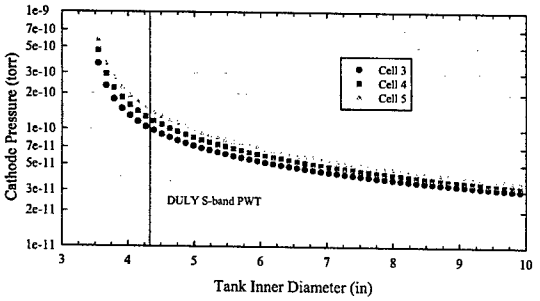


Figure 3: Pressure in the polarized PWT gun for increasing tank diameter and fully circumferential sieve.

Materials

The DULY/UCLA PWT used copper-plated 304 stainless steel for both the tank wall and the cooling/support rods. In general, clean stainless steel has an outgassing rate that is an order of magnitude lower than copper [3]. However, the increased rf losses at the tank and rods would result in an increased cooling requirement and a reduction in the Q of the structure. Thus, a higher power rf source would be required to maintain the same gradient in the 10+2(½) cell accelerating structure. Table 2 shows the Q values of a single cell without end plates when the walls and rods are made of 304 stainless steel instead of copper.

Table 2: Q-values for components made of stainless steel instead of copper, and for different tank diameters.

Stainless Steel Surface	Tank Diameter (in)			
	4.33	6.0	8.0	10.0
None	21,800	32,000	41,800	50,100
Tank wall only	8,980	14,900	21,500	27,600
Rods only	8,260	11,500	14,600	17,200
Wall and rods	5,360	8,160	11,000	13,400

The increase in Q that comes from increasing the tank diameter can compensate for the use of stainless steel walls. It is also possible to make the tank and rods from solid copper to reduce possible contamination from plating; however, the rod diameter would have to be increased to maintain strength.

CATHODE AND LOAD LOCK

An activated GaAs cathode requires a load lock system to maintain the high vacuum during the replacement or activation of the GaAs. Figure 4 shows a block diagram of the load lock system under design. In this design, the cathode puck is inserted into the vacuum system with the PWT gun isolated from the activation chamber. A magnetically coupled linear device brings the puck into the chamber through an all-metal gate valve, a wobble stick grabs the puck from the linear transporter which is then retracted, and the gate valve is closed. The wobble stick is used to lower the puck to a heater that is located inside the vacuum chamber, and is shown schematically in Figure 5. Heat cleaning of the cathode requires that the GaAs be held at 600°C for 1 hour, then rapidly cooled.

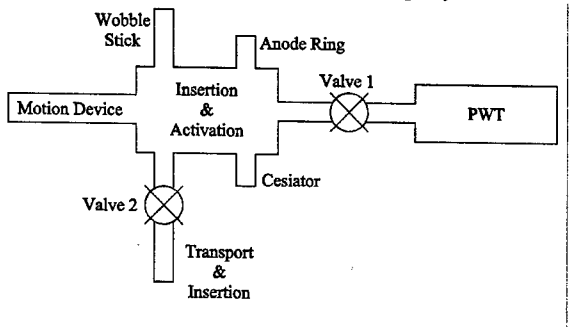


Figure 4: Block diagram of the load lock system.

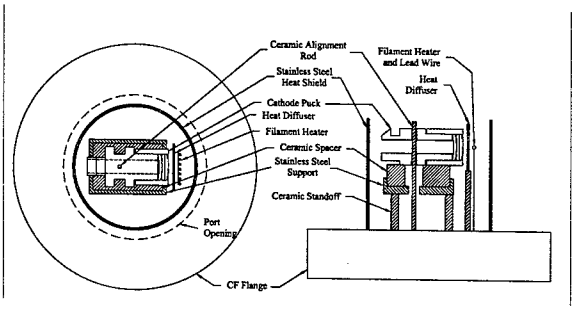


Figure 5: Schematic of the vacuum based heater used to activate the GaAs cathode.

After cleaning, the wobble stick is used to grab the cathode puck and maneuver it for mounting on the main magnetically coupled linear motion device that provides the axial transport of the puck. This linear device will place the puck in position for activation. Commercial cesium dispensers are arranged in a square pattern that will allow the puck to pass through the center. Driving current through the dispensers produces a cesium cloud that covers the surface of the GaAs. To activate the

GaAs, an oxidizing gas (O_2 or NF_3) is introduced during the cesiation process. The QE of the GaAs surface is monitored by illuminating the cathode with a laser and collecting the photoelectrons with a biased anode ring. The anode ring must be large enough for the cathode puck to pass through and is shown schematically in Figure 6.

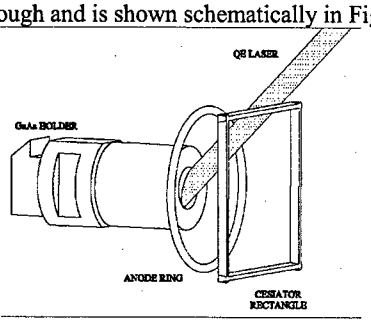


Figure 6: Schematic orientations of the anode ring, cesiator and QE diagnostic laser, showing that the laser clears the anode ring and the cesium dispensers.

After activation, the main motion device is used to move the cathode puck through a gate valve for mounting on the back plane of the PWT as shown in Figure 1. As the QE of the cathode drops, the puck is retracted back to the activation position where a new layer of cesium is deposited without the oxidizing gas.

In order to accommodate the larger size of the cathode puck, the back plane of the PWT is modified. The modifications include a larger beam pipe and flanges, as well as redesigned magnetic field coils. The rf seal at the cathode is provided by a watch-band style spring. Figure 7 shows both the axial and radial component of the magnetic field in the new solenoid design. The small radial magnetic field (Figure 7b) at the cathode of a few tens of Gauss is not expected to significantly change the longitudinal electron polarization.

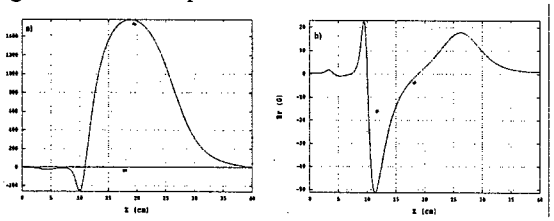


Figure 7: a) Axial and b) radial magnetic fields in the new PWT solenoid magnets. The radial field is taken near the edge of the electron beam envelope. The cathode plane is at z = 10.92 cm, where the axial field is null.

THERMAL SIMULATION

Steady-state thermal simulations of the S-band PWT have shown that for a 25 MW, 2.5 μs pulse width klystron operating at 10 Hz, the thermal gradient across each accelerating disk is ~0.25°C, and the coldest point on the disk is 1°C hotter than the cooling fluid. This model assumed a 1 l/s flow rate in the internal cooling channels of the PWT disk. In order to be of practical use in an advanced accelerator, the gun should operate at a higher repetition rate. Figure 8 shows the results of a finite element analysis (COSMOS/M) of a PWT operating at 180 Hz and a field gradient of 55 MV/m for increasing values of the fluid flow rate.

An alternative design for PWT cooling could eliminate the need for rods by providing support and heat transfer with synthetic diamond [4]. Thermal simulations indicate that the performance of the water cooled structure with a flow rate of 5 l/min is equivalent to cooling with a 1 mm thick diamond heat conductor. In both models, the thermal gradient across the disk is dominated by the thermal conductivity of the copper disk, not the efficiency of cooling. Because of the cost of producing synthetic diamond, the cooling/support rod design is preferable.

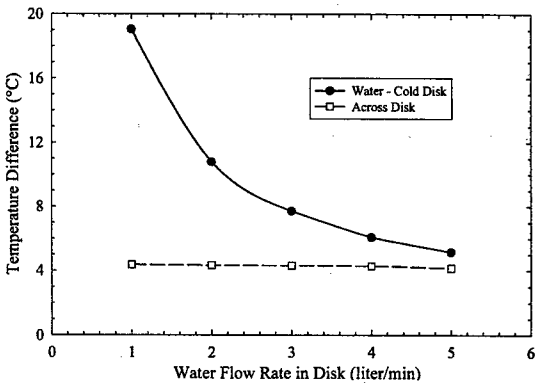


Figure 8: Temperature difference for the PWT disk as a function of flow rate. Solid line: temperature difference between the water and the coldest point on the disk; dashed line: thermal gradient across the disk.

CONCLUSION

The DULY S-band PWT integrated photoinjector has been carefully studied for use as an rf polarized electron source. The large vacuum conductance and good beam performance at low peak accelerating field make the PWT well suited for adaptation to activated GaAs use. The modifications required for the addition of a load locked activation chamber, and improved vacuum performance have been studied. Beam performance calculations, including the study of the potential problem of electron backstreaming into the cathode are discussed in a companion paper [5]. Additional advantages of operating the PWT at a low peak field (55 MV/m) are also discussed in the paper.

REFERENCES

[1] D. Yu, J. Clendenin, R. Kirby, US patent application no. 10/261831, 9/30/02.

[2] X. Ding *et al.*, PAC '99, p. 2021; D. Yu, in *The Physics of High Brightness Beams*, World Scientific (2000), p.585.

[3] R.B. Neil, ed., *The Stanford Two-Mile Accelerator*, p. 889.

[4] D.U.L. Yu, T. Lee, U.S. Patent No. 6,025,681.

[5] Y. Luo *et al.*, WPAB042 in these proceedings.

DESIGN OF A DC/RF PHOTOELECTRON GUN*

D. Yu, D. Newsham, Y. Luo, A. Smirnov, J. Yu
DULY Research Inc, Rancho Palos Verdes, CA 90275
J. Lewellen, *ANL, Argonne, IL*
J. Smedley, T. Srinivasan-Rao, *BNL, Upton, NY*
A. Zholents, *LBNL, Berkeley, CA*

Abstract

An integrated dc/rf photoelectron gun produces a low-emittance beam by first rapidly accelerating electrons at a high gradient during a short (~ 1 ns), high-voltage pulse, and then injecting the electrons into an rf cavity for subsequent acceleration. Simulations show that significant improvement of the emittance appears when a high field (~ 0.5 – 1 GV/m) is applied to the cathode surface. An adjustable dc gap (≤ 1 mm) which can be integrated with an rf cavity is designed for initial testing at the Injector Test Stand at Argonne National Laboratory using an existing 70-kV pulse generator. Plans for additional experiments of an integrated dc/rf gun with a 250-kV pulse generator are being made.

INTRODUCTION

The limitations on conventional electron rf photoinjectors are largely due to space charge induced emittance growth. This growth is particularly severe at low electron energies, i.e., near the cathode. To eject electrons from a photocathode source, a laser beam irradiates a photocathode embedded in an accelerating field. In an rf photoinjector, electrons released by the laser are accelerated by an rf field to relativistic velocities, thus reducing the emittance degradation during acceleration of a high intensity beam. The peak rf field in a photoinjector, however, is limited by the available rf power and by voltage breakdown. Recent work at Brookhaven National Lab (BNL) and elsewhere [1] suggests that using a short-pulse dc field that is much higher in amplitude than typical rf fields in a photoinjector can greatly suppress the space charge induced emittance.

In a dc/rf gun [2], a pulsed dc electric field quickly accelerates photoelectrons across a small gap between the photocathode and the backplane of an rf cavity. The electrons are then immediately injected into the rf cavity for further acceleration. Figure 1 shows a system schematic of the dc/rf gun, which consists of a high voltage (HV) pulse generator, an HV transmission line, a cathode/anode gap and rf cavities. The essential feature is the pulsed, high gradient field (~GV/m) that is created in the dc gap, since electrical breakdown occurs at larger fields for smaller pulse lengths. Recent advances in fast semiconductor switches have made possible short pulse, HV generator with high rep rate (> 10 kHz) [3], which can produce a large field in the dc gap. This would significantly improve the emittance while maintaining a high repetition rate, a high charge per electron bunch, and a small beam size.

In addition to the reduction of transverse emittance, another advantage of the proposed dc/rf photoelectron gun is the decrease of the work function of the photocathode due to the Schottky effect.

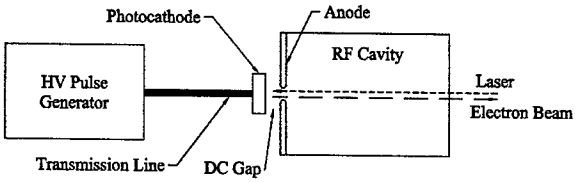


Figure 1: System schematic of the dc/rf gun.

DC GAP PERFORMANCE

Preliminary work was performed using the POISSON and PARMELA codes to simulate the performance of the dc gap first without the additional influence of the rf field. A simple geometry used in the simulations consisted of a flat cathode and anode with a 1 mm spacing and a circular aperture in the 1 mm thick anode plate that forms the backplane of the rf cavity. Figure 2 shows the normalized beam emittance through the gap with a 1 mm aperture as a function of the inverted dc voltage for several values of the bunch charge (0.1-1.0 nC). The initial bunch rms radius (.15-.35 mm) and bunch length (5-10 ps) were varied to obtain the minimum emittances. For the initial experiment, planned to be performed at the APS Injector Test Stand (ITS) at ANL a 70 kV pulser (on loan from LBNL), after voltage inversion, will accelerate a 0.1 nC bunch. The anticipated value of the emittance at the time of injection into the rf cavity is approximately 0.36 mm-mrad, not including thermal emittance.

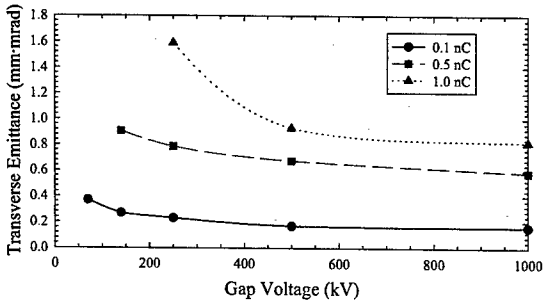


Figure 2: Emittance as a function of applied dc voltage for 0.1, 0.5, and 1.0 nC bunch charge.

* Work supported by DOE SBIR grant no. DE-FG03-02ER83402.

0-7803-7738-9/03/$17.00 © 2003 IEEE

From Figure 2, it is evident that an increase in the magnitude of the (inverted) dc voltage at the cathode will result in a reduction of the emittance. Increasing the gap voltage difference more than 500 kV does not improve the emittance, although it may improve subsequent rf acceleration. Figure 3 shows the PARMELA results as a function of axial distance for 70 kV and 1 MV dc acceleration of a 0.1 nC bunch charge. Our simulation results show a lower normalized transverse emittance when compared with the work at Eindhoven University of Technology in the Netherlands [2] which used a very short laser pulse (50 fs) compared to the standard S-band laser pulse (5-10 ps). The longer pulse at the same charge significantly mitigated space charge effects.

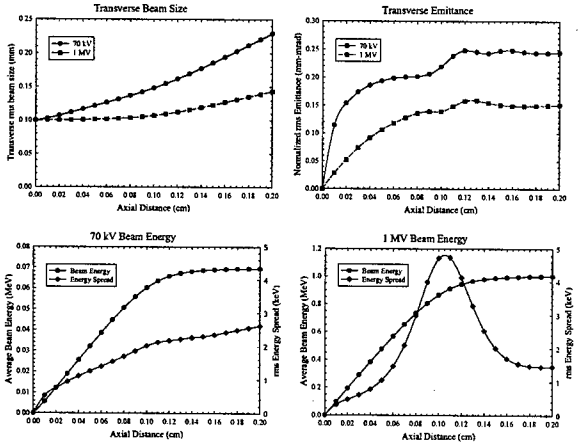


Figure 3: PARMELA results for the dc gap beam parameters with a gap voltage of -70 kV and -1 MV. Thermal emittance is not included in the calculation.

TIME DOMAIN SIMULATIONS OF DC GUN HEAD AND TRANSMISSION LINE

In preparation for initial testing with a 70 kV pulser, a dc head and transmission line were modeled using the 3D electromagnetic code CST Microwave Studio. The gun head consists of two pieces: a connector (Figure 4) and a terminated transmission line (Figure 6). The connector is the section that attaches to the pulser and transitions to the transmission line. The transmission line starts at the end of the tapered section of the connector, continues through a ceramic cone that forms the vacuum boundary, as well as providing mechanical support, and ends at the anode plate (backplane of the rf cavity) including the 1 mm gap.

Because of the space constraint at the ANL test facility, the transmission line was quite short so that the signal transit time is comparable to the pulse length. The two port device was designed with a characteristic waveguide impedance of 100 Ω, assuming the resistor termination is near the gun head. The impedance would of course be different if the resistor termination is placed inside the pulser instead. The end of the coaxial connector that attaches to the pulser is filled with teflon PTFE as a dielectric insulator. The other end of the connector transitions into an air filled coaxial transmission line that leads to a ceramic cone and the dc gap.

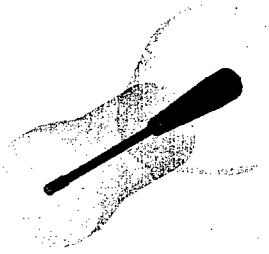


Figure 4: Model of the connector: the center conductor is connected to the pulser on the left, and slips into a precision hole on the large taper on the right.

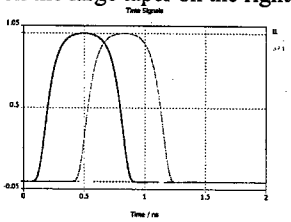


Figure 5: Transient simulation results of the connector: input (black), transmitted (gray), and reflected (light gray) signals of the 2-port device

The transmission line portion of the dc/rf gun has two parts separated by a ceramic cone. The section closer to the pulser is an air filled coaxial transmission line that matches the pulser connector and includes the resistor termination at the other end. The section on the other side of the ceramic cone is a vacuum filled transmission line encompassing and dc gap. Figures 6 and 7 show the model and the results of the simulation, respectively.

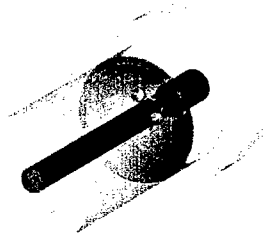


Figure 6: Model of the terminated transmission line and dc gap. The connector extends to the left of the figure.

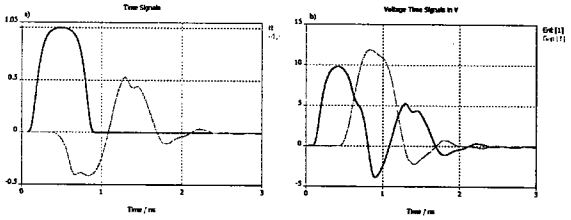


Figure 7: Transient simulation results of the transmission line/gap: a) input (black) and reflected (gray) time signals, b) inverted voltage at the dc gap (gray) and at the entrance of the transmission line (black) as a function of time.

The small, inverted reflection signal appears to come from the discontinuity presented by the ceramic cone. The large, upright reflection is expected from the capacitive nature of the transmission line termination at the dc gap, in addition to the indication of charging and discharging of a capacitor. The gap voltage (gray trace in Figure 7b) is about 15% higher than the applied voltage at the entrance of the transmission line because there is a mismatch with the combined impedances of the ceramic cone, terminating resistors and the gap, causing some reflection (gray trace in Figure 7a).

MECHANICAL DESIGN OF DC GUN HEAD

Figure 8 shows a preliminary design of the 70 keV dc gun head. The gun head was designed specifically for attachment to the BBC rf gun [4] at the APS/ITS (not shown, at left). The BBC gun backplane has a thin taper around the cathode hole, which should help reduce the beam transit time from the dc gun head to the rf cavity. The connector mounts to a stationary pulser which produces a –70 kV pulse of 1-2 ns (not shown, at right of Figure 8) using a teflon filled transmission line. The design will be modified with an oil filled transmission line later for a test with a 250 keV pulser.

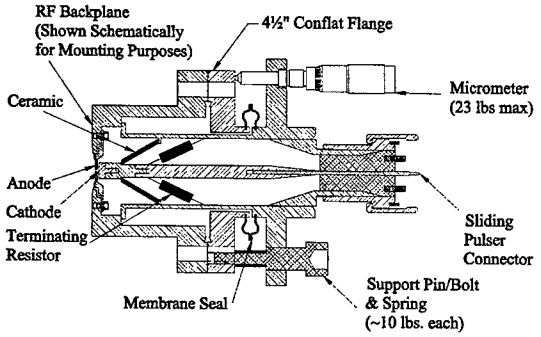


Figure 8: Schematic of the dc gun head for integration into the BBC gun at ANL/ITS.

The cathode/anode gap is adjustable using 3 precision micrometers. During the adjustment, the pulser/connector, the anode plate (rf backplane) and the vacuum flanges remain fixed. The thicker inner conductor on the gap side slides over the thinner inner conductor protruding from the connector; and the outer conductor moves along a sliding joint where the connector tapers from the teflon filled transmission line. A membrane seal allows axial motion of the outer conductor while maintaining the vacuum. Extension of the micrometers would result in an increase in the cathode/anode gap. Springs are added in the support pins to reduce the load on the micrometers due to the vacuum boundary.

HIGH ENERGY INJECTION

Several rf guns were simulated to see if the injection of high energy electrons would improve their performance. PARMELA simulations were compared for two different situations: a beam with a high initial kinetic energy as though it were from a dc gun (with negligible initial emittance and energy spread), and a beam injected from a photocathode in a normal rf gun. Figure 9 shows the simulation results for the AWA gun [5] with a 40 nC bunch charge and an initial injection energy of 1 MeV. Similar improvement (Figure 10) is seen for the BBC gun with a 0.8 nC charge and an injection energy of 1 MeV.

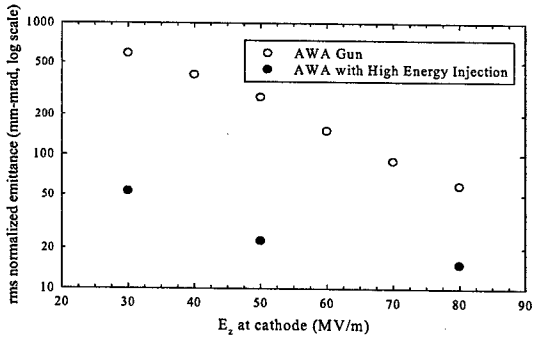


Figure 9: Transverse emittance calculated for the AWA gun with and without high energy injection.

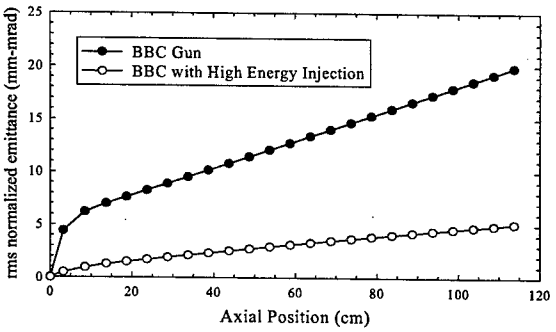


Figure 10: Emittance for the BBC gun running in π-mode with and without high energy injection.

CONCLUSIONS

A dc/rf gun head was designed and will be ready for testing with the BBC gun at ANL soon after the commissioning of the BBC gun. Simulations indicate that injecting high energy electrons into an rf cavity results in a significant decrease in the transverse emittance.

REFERENCES

[1] T. Srinivasan-Rao, *et al.*, J. Opt. Soc. Am. **B8**, p. 294, 1991; F. Villa, AAC96, Lake Tahoe, AIP 398, pp.739-746, 1997.

[2] M.J. van der Wiel, Proc. 2nd ICFA Advanced Accelerator Workshop, UCLA, Nov. 1999; S.B. van der Geer, *et al.*, Phys. Rev. E, Vol 65, 046501 (2002).

[3] See www.fidtechnology.com.

[4] J.W. Lewellen and S.V. Milton, SPIE Proceedings, Vol. 3154, pp.162-171, 1997; J.W. Lewellen, these proceedings.

[5] M. E. Conde, *et al.*, Proc. of PAC2001, p. 3957.

SHORT MULTIPOLE MAGNET DESIGNS FOR JLAB FEL UPGRADE

A. Smirnov, D. Newsham, Y. Luo, D. Yu
DULY Research Inc., Rancho Palos Verdes, CA 90275
G. Biallas, R. Wines, *JLAB, Newport News, VA*

Abstract

Novel designs for octupole and sextupole magnet families for the JLab 10kW IR FEL upgrade were developed and characterized. The designs were made with 3D simulations, and provided very short effective length that nearly equals the aperture radius, along with 1% accuracy of the field integral over 70% of a large aperture. The main feature is shaping of the cylindrical pole tips to provide high field quality dominated by fringe fields. Other features include magnetically isolated field clamps, usage of non-tapered coils of standard racetrack shape, and non-linear saturation effects (for sextupole magnets).

1 INTRODUCTION

Thomas Jefferson National Accelerator Facility (JLab) is upgrading a CW infrared FEL [1] to extend the IR power output to 10 kW and allow generation of UV radiation for industrial, defense, and scientific applications. The main requirement for the FEL beam optics is to avoid phase space dilution and to provide matched beam transport with high precision and brightness. This dilution is usually caused by beam lattice imperfections causing chromaticity and aberrations. Additional constraints on the beam lattice design result from the energy recovering system of the FEL, with an increased 6D phase space volume, and from an octupole component of the undulator field.

To meet the physics, performance and operational requirements [2], the octupoles and sextupoles should have specific parameters: field integral accuracy $\Delta IB_\perp/IB_\perp$ over 70-80% of the magnetic aperture radius to be better than 1%; and the aspect ratio $A= R/L_{eff}$, to be close to unity, where R is the magnetic aperture radius, and L_{eff} is the effective length.

Along with high variable magnet strength, power consumption limited by heating, and manufacturing cost, these requirements present challenging issues for both magnetic design and construction.

2 DESIGN APPROACH

Unlike traditional magnets having $A<<1$ it is impossible to provide comparable field quality with the same pole shaping when $A\sim1$. As the magnet length reduces, the fringe field effect grows because of contribution of parasitic azimuthal harmonics. In the first order, magnetic flux leakage at the magnet end faces reduces the effective magnetic strength. This fringe flux near the pole is higher for bigger azumuthal angles ϑ (ϑ=0 at the minimal radial coordinate of the pole) and radii because of higher partial side area of the pole and shorter magnetic path between adjacent poles. In the second order, it sharpens the field integral profile across the aperture, i.e. there is an effective increase of the equivalent parameter, $n_{equiv}= n(A\neq0) > n =integer$, which describes the pole shaping in a real magnet having a higher aspect ratio A, in terms of an equivalent long magnet with $A_0 \rightarrow 0$ (see (1)). To correct the field profile, we need to change the shape of the pole in such a way, that

$$r(\theta) = R/\sqrt[m]{\cos(m\theta)}, \text{ where } 2n\text{-}n_{equiv}\approx m<n. \quad (1)$$

In most cases we have $n\text{-}1\leq m<n$. The value n_{equiv} can be calculated using a standard procedure of parametric fitting of the given function (1) to approximate data for the field integral simulated (or measured) initially for a given value of A. An iterative procedure can be applied, i.e. for a calculated m from (2) we can find a new value n_{equiv} and so on (two iterations usually is enough). Another way to find m is direct optimization of the design over the generalized non-integer parameter m.

To implement this approach in magnetic design simulations, we used the 3D code Radia [3], a flexible tool enabling analytical programming of pre- and post-processing.

3 OCTUPOLE COMPACT MAGNET

The specifications for the family of octupole magnets [4] are given in the Table 1.

Table 1. Octupole magnet specification

Transverse field integral IB_r at r_g=12.5cm	5 T·mm
Field integral inaccuracy $\Delta IB_r/IB_r$ (r_g)	< 1%
Magnetic aperture radius R	15cm
Effective length L_{eff} at r_g=12.5cm	≤ 15cm
Geometric length	<25cm

In Fig. 2 we characterize several variants of the pole tip shaping with the following set of parameters:

- $\Delta IB_r/IB_r(\theta=0)$ is the maximum relative deviation of the transverse field integral with respect to an ideal octupole with the same field integral and for fixed angle (θ is angular position of the pole) in the "good field region" $r< r_g$;
- $\Delta IB_r/IB_r(r=r_g)$ is the maximum relative deviation of the transverse field integral with respect to an ideal octupole having the same field integral and for fixed radius over the circumference of good area at $r=r_g$;
- $|C_3|/|C_1|$ is the first unwanted harmonic C_3 related to the fundamental one (n=1) for the Fourier transform of

0-7803-7738-9/03/$17.00 © 2003 IEEE

the field integral at fixed radius $r = r_g$;

- $\Sigma|C_k|/|C_1|$ is the sum of spurious harmonics (25 or more odd harmonics) related to the fundamental one at fixed radius $r = r_g$.
- P is the total power consumption by the coils (copper wire with cooling channel) required to achieve the specified magnet strength.

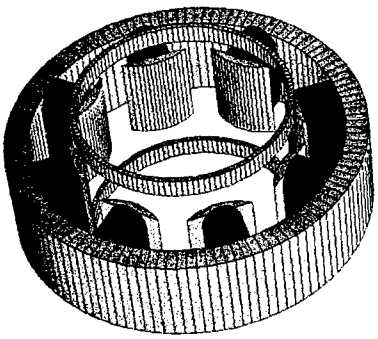


Figure 1. Magnetic design of a short octupole with ring field clamps, cylindrically shaped pole tip and standard racetrack coils.

Index n=1 corresponds here to octupole field component, n=3 corresponds to 24 -pole field component and so on. The main goal of the design under consideration (Fig. 1) is to satisfy field quality requirements: $max\{\Delta IB_r/IB_r(\theta=0), \Delta IB_r/IB_r(r=r_g), |C_3|/|C_1|\}<1\%$ for the given integrated magnet strength (which is 2.56T/m^2 in our example). Fig. 2 shows the explicit optimum achieved simultaneously for different field and field integral parameters in the vicinity of "sextupole-like" shaping (for fixed angular size and without field clamps). The optimal values found for this configuration (without clamps) are m=3.12 and $\Delta\theta$=32°. The corresponding parameters of this final variant #2 are given in Table 2.

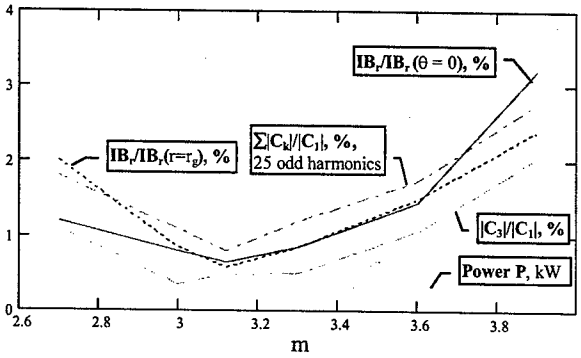


Figure 2. Octupole magnet parameters versus the order of tip shape m at fixed magnet strength 2.56T/m^2, $\Delta\theta$=38.6° (no clamps), r_g=12.5cm, and magnetic aperture radius r_{ap}=150mm.

One can see that the most dangerous first parasitic harmonic of the field integral is effectively suppressed by almost two orders compared to the initial design (without clamps). Introduction of field clamps (steel rings) to decrease the effective length, L_{eff}, adversely affects the field. To restore the field integral quality, a new optimization over the parameter m was undertaken with simple 3-point-parabola method. It resulted in further reduction of the key parameter m (see variant #3 in Table 2).

Thus the non-integer key parameter m in the extended formula (1) makes it possible to provide high quality field integral for multipole magnets with cylindrical pole tips of different lengths with/without field clamps. In addition, it gives enhancement of the magnet strength (or efficiency – *e.g.*, the power consumption is reduced by 33%, variant #2 vs. #1 in Table 2).

Table 2. Simulation results for octupole magnet with aperture r_{ap}=150mm and fixed magnet strength 2.56T/m^2: conventional (#1, n=4=m) and advanced designs (m<4).

#	Clamps	Tip $\Delta\theta$ (opt)	m	J, A/mm^2	ΣI, kA	P, W	L_{eff} mm	$\frac{\Delta IB_r}{IB_r}(0,r)$	$\frac{\Delta IB_r}{IB_r}(\vartheta,r_g)$	$\frac{C_3}{C_1}$, %	$\frac{\sum C_k}{C_1}$, %
1	no	36°	4	3.6	2.1	388	173	0.7, %	1.8 %	1.4	2.6
2	no	32°	3.12	2.93	1.71	261	173	0.58, %	0.42 %	0.018	0.75
3	yes	32°	2.9	3.49	2.04	370	146	0.64, %	0.79 %	0.31	1.6

4 SEXTUPOLE COMPACT MAGNET

Magnetic design of the sextupole magnet family for TJNAF Upgrade[5] is depicted in Fig. 3. Careful optimization of the pole shape was done to provide the highest field integral quality at nominal magnet strength. It led to the following value of the key parameter: m=2.67 (instead of standard value m=n=3 for a conventionally designed sextupole). The entire magnet operates far from saturation. However, unlike the octupole design above, high magnetization of some regions causes local non-linearities that can affect the field quality at different currents. We found such critical "hot spots" near the edge of the pole tip and in the vicinity of connection of the yoke and core. The magnet was optimized for a nominal strength ~2.15T/m. As a result the field quality is noticeably different for much smaller fields (see Fig. 4). Nevertheless, the magnetic design indicates high quality of the field integral for a wide range of coil currents: (0.4-1.4) with respect to nominal current.

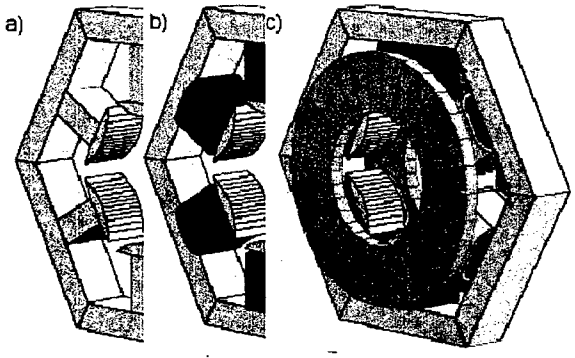


Fig. 3. Sextupole magnet design with conventional racetrack coils and circular disk clamp.

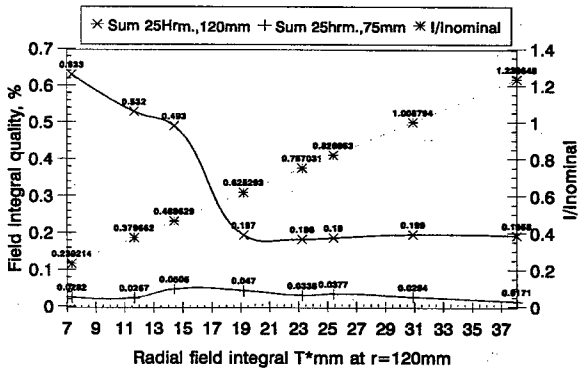


Fig. 4. Normalized sextupole field integral $I/I_{nominal}$ (right ordinate axis) and its quality $\Sigma|C_k|/|C_1|$ for 25 unwanted harmonics (on the left axis) vs field integral at r_g=120mm and r_g=75mm. Parameters: P_{max}=2.8kW, m=2.671, r_{ap}=150mm, pole tip angle $\Delta\theta$=44.9°.

Table 3. Sextupole design performance at different materials for the pole (tip+core) and constant (nominal) current

Material	Maximum magneti-zation M, T	Field strength $H\mu_o$, T at I·n=11668 A	Field quality at r=120mm, %	Estimated Power required, kW
RadMatXc06: Low Carbon Steel C<0.06% [AFNOR]	2.11	0.299	0.6 %	2.21
RadMatSteel37: Steel C<0.13%	2.052	0.286	0.7 %	2.065
RadMatSteel42: Steel C<0.19%.	2.06	0.282	0.67 %	2.092
RadMatAFK1: FeCo Alloy from MetalImphy (Fe : 74.2%, Co: 25%, Cr: 0.3%, Mn: 0.5%	2.35	0.297	0.87 %	1.85
RadMatAFK502: Vanadium Permendur from MetalImphy; (Fe : 49%, Co: 49%, V: 2%; similar to Vacoflux50)	2.34	0.318	0.92 %	1.72

Different geometries and materials were included in the study of saturation effects in local areas with maximum fields (see Table 3).

5 CONCLUSION

The design approach described here is applicable for any multipole magnet (i.e. quadrupole and higher). This type of shaping can be easily produced with programmable machinery tools. It simplifies the process of magnetic design of short multipole magnets and enhances its integrated moment. This is done by reducing the multi-parametrical, non-linear, complicated problem of 3D field optimization to a problem dominated by a main physical parameter variable in a well-defined range. One can also reduce the cost of the design with wider usage of simplified or standard elements like racetrack coils and disk clamps.

6 REFERENCES

[1] D. Douglas, S. V. Benson, G. Biallas et al., in Proc. of the 2001 Part. Acc. Conf., Chicago (2001) 249.
[2] D.R. Douglas, in Proc. of the 1997 Particle Accelerator Conf., Vancouver, Canada (1997), 1358.
[3] P. Elleaume, O. Chubar, J. Chavanne, ibid, p. 3509.
[4] R. Wines, Engineering Services Task Order #D2, FEL Upgrade, TJNAF 7/16/01.
[5] R. Wines, Engineering Services Task Order, #D4, FEL Upgrade, TJNAF 10/23/01.

BUILDING A FAMILY OF CORRECTOR MAGNETS FOR SNS FACILITY*

Sorin-Viorel Badea Ph.D, Nicholaos Tsoupas Ph. D, Joseph Tuozzolo PE, James Alduino,
Collider-Accelerator Department, Brookhaven National Laboratory, Upton NY 11973, USA

Abstract

The Spallation Neutron Source (SNS) in process to be built in Oak Ridge Tennessee includes an accumulator ring with a circumference of 248 meters, an injection line and an extraction line. The machine is designed to accumulate 2E+14, 1.0GeV kinetic-energy protons in 1ms, via a charge exchange injection of H.

This paper describes the concept behind the design and fabrication of five types of air cooled corrector magnets built in 15 functions totaling 80 magnets to be used in the above project.

INTRODUCTION

The main effort was aimed toward an original design to deliver the required magnetic field with cost effective solutions and easy installation, survey and convenient maintenance.

The list of magnets designed by the above constraints is shown in Table 1.

Table 1. List of Corrector Magnets for SNS

Magnet ID	Magnetic Field, for 1.0/1.3 GeV	Current Amps.
16CD20	Dipole, Intgr. field: 7.4/8.8KG*cm	9.0/10.8
27CDM30	Dipole Intgr Field: 6.26/8.6KG*cm Skew Quad, Intgr Grad: 0.208/0.270KG Skew Sextupole Intgr. Grad: 0.005/0.007KG/cm	10.0/13.0 10.0/13.0 10.0/13.0
27CD30	Dipole Intgr. Field: 8.06 /10.08KG*cm	10.0/13.0
36CDM30	Dipole, Intgr. Field 7.20/9.0 KG*cm Skew Quad, Intgr Grd: 0.266/0.333KG	10.2/12.7 10.2/12.7
41CDM30	Dipole Intgr. Field 7.50/9.40KG*cm Skew Quad,Intgr. Gr: 0.241/0.301 KG	10./12/7 10.2/12.7

Figure 1 shows the magnets from Table 1, already built and in the process of being delivered to Oak Ridge.

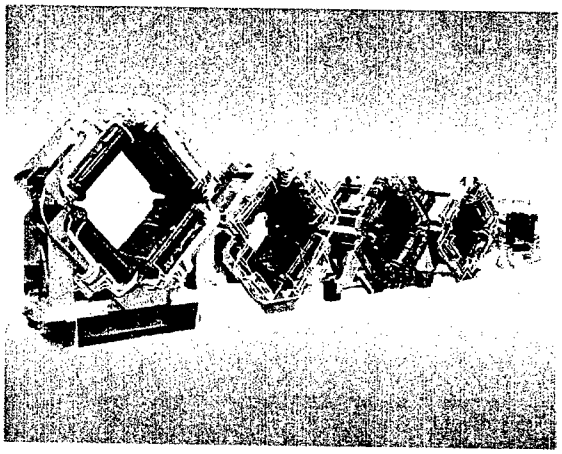


Figure 1. Actual picture of Corrector Magnets for SNS. (From left to right: 41CDM30, 36CDM30, 27CDM30, 27CD30, and 16CD20)

DIMENSIONAL MAGNETIC FIELD CALCULATIONS FOR THE 27CDM30 CORRECTOR MAGNET

The following 3Dimensional calculations performed for each of the corrector magnets provided information to be used in the mechanical design of the large aperture corrector magnets for the SNS accumulator ring.

a) The number of Amp-turns to produce the required dipole, sqew-quadrupole, and sqew-sextupole strength respectively.

b) The number of Amp-turns and the location of the "corrector coils" on the iron frame. These corrector coils (see figure 2) are required to minimize the sextupole strength produced by the main windings of the corrector dipole.

c) The number of Amp-turns of the coils which produce the sextupole corrector and also to determine the location of these coils on the iron.

The thickness of the iron core of the correctors was optimized to run well bellow the saturation when all

*SNS is managed by UT-Batelle, LLC under contract DE-AC0500Or22725 for the US Department of Energy. SNS is a partnership of six national laboratories: Argonne, Brookhaven, Jefferson, Lawrence Berkley, Los Alamos, and Oak Ridge.

0-7803-7738-9/03/$17.00 © 2003 IEEE

corrector windings (dipole, quadrupole, and sextupole) were powered simultaneously at full strength). This condition of "non saturation" of the iron allowed us to make use of the superposition principle and perform the 3D calculations and optimization for each corrector (dipole, quadrupole, and sextupole) separately.

3D Dipole Calculations

Figure 2 shows the placement of the coils, which produce the dipole field of the corrector. The coils consist of three layers of copper wire, which cover almost each side of the magnet frame. In addition to these three layers of copper we wound a few more layers of copper wire (corrector coils) at each corner of the iron frame. These corrector coils are shown in Figure 2, and are connected in series with the coils, which produce the dipole field. Their purpose is to minimize the integrated sextupole field produced by the dipole coils. The number of Amp turns of the corrector coils has been determined by performing 3D magnetic field calculations.

The reason that the square frame of the iron has been rotated 45^0 is to generate the skew-quadrupole when the quadrupole coils are powered.

The integrated dipole field ($\int B_{dip}dz$), when the coils are powered at maximum is 8600 Gauss.cm. This is plotted in Figure 3 as a function of distance from the center of the magnet and along the beam direction.The plot shows the radial components of only two of the allowed multipoles (B_{sext}), and (B_{deca}), which are generated when the dipole coils are powered. The quantities (B_{sext}), and (B_{deca}), are defined in the expression:

$B_r(r_0,z)=B_{dip}\sin(\theta)+B_{sext}\sin(3\theta)+ B_{dec}\sin(3\theta)+\ldots$

(Where r_0=12.78 cm). The integrated strength of the sextupole component ($\int B_{sext}dz$) has been minimized with the help of the corrector coils mentioned earlier, and its integrated strength is 20 Gauss.cm at a radius r_0=12.78 cm. The integrated strength of the decapole multipole ($\int B_{decat}dz$) is 4 Gauss.cm. The integrated strength of the sextupole and decapole multipoles are well below the limit which will affect the dynamics of the beam.

Duodecapole components are the first allowed multipoles. The number of layers of the coil have been chosen to obtain the required sqew-quadrupole integrated strength ($\int B_{deca}dz$) which has been calculated to be 3500 Gauss.cm at a radius r_0=12.78 cm . When the sqew-sextupole corrector is powered at full current, the integrated strength of the first three allowed multipoles (12,20,28) pole is 30 Gauss.cm 10 Gauss.cm and 0.3 Gauss.cm respectively. Similar calculations were developed for the Skew-Quad and Sextupole.

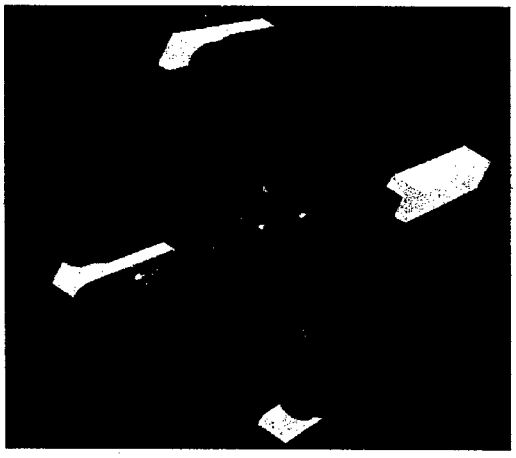


Figure 2. The windings of the dipole corrector.

The main windings cover almost each side of the iron core of the magnet and consist of three layers. The "corrector coils" which are powered in series with the dipole windings are placed symmetrically from each corner of the magnet.

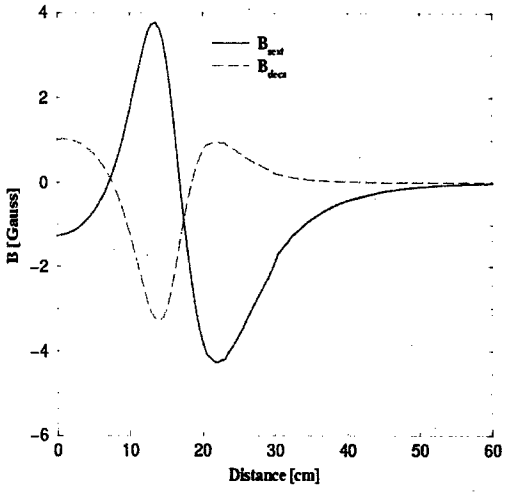


Figure 3: The calculated strength of the first two allowed multipoles (B_{sext}, and B_{deca}), of the dipole corrector magnet, plotted as a function of the distance from the center of the magnet and along the beam direction.

ENGINEERING CONCEPT AND CALCULATIONS

The entire family of magnets was designed with a standard approach as seen in Fig. 4.

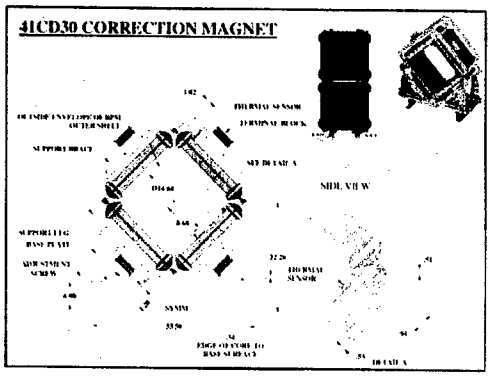


Fig. 4 Standard design of all corrector magnets

Based on aperture, length of magnet and magnetic field determined in the preceding chapter, the engineering part was developed as follows:

- Considering the number of ampere-turns the size of copper was determined (number of turns for dipole, quad or sextupole)
- All the cores and pole pieces were made of plain (non-laminated) steel 1006, because all the magnets are DC powered (no pulsed magnets included in this correctors category)
- The current density was kept under 100 Amps/cm²
- Calculations were performed using a finite element analysis program (ANSYS) to determine the stress, and maximum deflection under combinations of static loads and dynamic loads during transportation. Below in Fig. 5 is shown a typical result of stress analysis of a bracket, which holds the magnet true during split operations. Safety coefficient used for all the mechanical parts was 1.5.

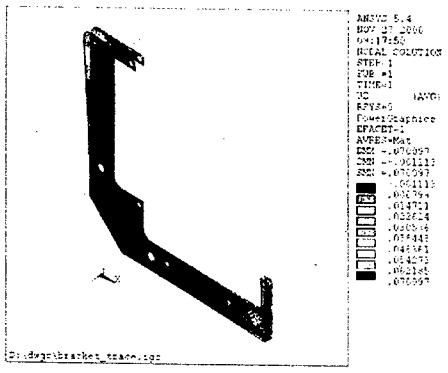


Fig. 5. Typical bracket deformed shape under maximum stress

ECONOMICAL CONSIDERATIONS

Based on actual prices of fabricated magnets we were able to plot the price variations as function of field values and weight.

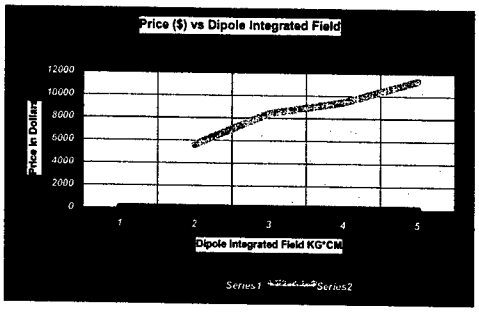


Fig.6 Price Variation Function of Dipole Field

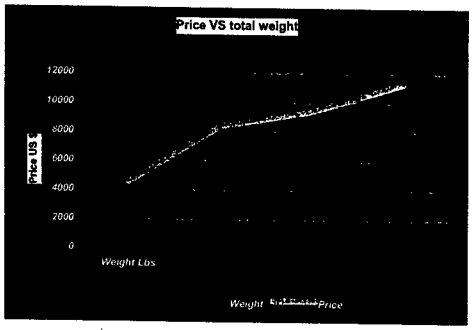


Fig. 7 Price Variation Function of Magnet Weight

As expected there is almost a linear variation of the two parameters despite the fact that different companies fabricated each type of magnet. (in USA or abroad)

CONCLUSIONS

As stated at the beginning of the paper, the effort was oriented towards designing a family of new corrector magnets under the given conceptual constrains, and to achieve all the above under very tight budget. The authors consider the task fulfilled and are confident that the reliability of the products will be proven during the years to come.

ACKNOWLEDGEMENTS

The authors would like to thank the following collaborators for their unconditional technical support in developing this family of magnets: Robert Lambiase, Ioannis Marneris, Jon Sandberg for the electrical design, Steve Bellavia, Anthony Arno, Richard Belkin, Cynthia Longo, Sam Mason, Gary Miglionico for the mechanical design.

DESIGN OF AN ULTRA HIGH VACUUM COMPATIBLE COPPER SEPTUM MAGNET*

M. Mapes, N. Tsoupas, Collider-Accelerator Department, BNL, Upton, NY 11973, USA

Abstract

An Ultra High Vacuum compatible thin copper septum magnet has been developed at Brookhaven National Laboratory. The solid core, single turn magnet is pulsed at 1500 amps and has a field of 0.6 KG. The 0.76 mm thick copper septum is water-cooled and is designed to run at a maximum power of 2 KW. A remote positioning system is used to optimize the septum position during various extracted beams. The cross section of the septum magnet was modeled and 2-dimensional magnetic field calculations were performed to compute the magnetic field uniformity in the main field region and in the field strength in the fringe field region. The calculated field uniformity as well as comparison of the calculated fields in the fringe field region with the measured fields in the same region will be presented. The design and construction techniques used to fabricate this magnet will also be described.

INTRODUCTION

A thin septum magnet, Figure 1, was designed, fabricated and installed as part of the beam extraction system for the NASA Space Research Laboratory (NSRL) at Brookhaven National Laboratory. The Magnet is installed in the Booster ring in the Collider-Accelerator complex. The Booster ring used to accelerate heavy ion and protons for various projects at Brookhaven.

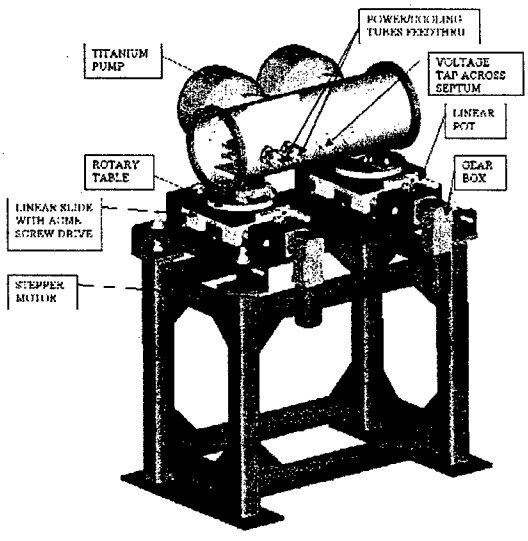


Figure 1. Isometric view of Thin Septum Magnet assembly

* Work Performed under the auspices of the U.S. Department of Energy

The Booster ring vacuum system is required to operate at a pressure of low 10^{-11} Torr, especially for gold heavy ions in order to reduce beam loss. The vacuum requirements of the system presented a challenge to design a magnet, which meets the vacuum criteria. Similar magnets were designed and built at Brookhaven but were not bakeable and contained organic materials used for electrical insulation.

The magnet was designed to run as a pulsed magnet, which typically runs at 7.5 pulses/sec at a nominal current of 1500 amps. However in order to test the magnet and especially cooling capacity of the monel cooling tubes the magnet was run at 2000 amps DC and was subsequently pulsed at a rep rate of 1 sec at 2000 amps for 1 million pulses. The cooling of the copper septum is of particular concern since the current density can be as high as 94 amps/mm^2.

DESIGN

The materials used for the internals of the vacuum system must meet outgassing rates of 5 x 10^{-13} Torr-l/s-cm^2 at 25° C. The vacuum vessel is fabricated with 316L stainless steel with 316LN stainless steel Conflat flanges with a 90° knife-edge. These special Conflat flanges are typically used throughout the Booster vacuum system since the knife-edges are less prone to rollover during repeated high temperature bakeouts. In addition all Conflat flange seals are copper seals with .05% silver impregnated to prevent crystallization of the copper during bakeout cycles.

The magnet core is fabricated from 1006 low carbon steel and is a solid c-shaped core 965mm in length. The magnet coil, which is a thin copper strip 0.73 mm thick, the back leg and the buss bar/cooling tube connections are all fabricated from OFHC copper. All other supports and brackets used inside the vacuum vessel are stainless steel. The fasteners are all silver-plated stainless steel and are vented whenever they are installed in blind tapped holes.

A key to designing a UHV compatible magnet was the use of porcelain enamel[1] to electrically isolate the power connections and the magnet coil from ground. Stainless steel parts were coated with 0.02mm of porcelain to clamp the septum against the magnet core and support the buss bar/cooling tubes inside the vacuum vessel. The edge of the core where the septum banks along the length of the magnet was also coated with porcelain to insulate the coil from the core. The thickness of the porcelain can be controlled very accurate to with +/-0.025mm of thickness with some practice.

0-7803-7738-9/03/$17.00 © 2003 IEEE

The porcelain is applied to parts with a paint sprayer allowed to air dry and then fired in a high temperature air furnace at 850° C. The result is a very durable glazed finish, which has an outgassing rate approaching that of stainless steel. In addition porcelain is radiation resistant and can be used at elevated temperatures.

The copper septum is cooled by two rectangular Monel cooling tubes as shown in Figure 2. These tubes were brazed to the septum with BAG 8 fluxless braze in a vacuum furnace with a partial pressure of 30 mtorr of Argon. Since it is desirable for most of the current to flow through the septum the material for the cooling tubes must have a much lower conductivity than copper. For this reason Monel 400 with a very thin wall was chosen to be a good material. A fixture was fabricated to clamp the tubes to the septum, which allowed longitudinal expansion during the brazing process.

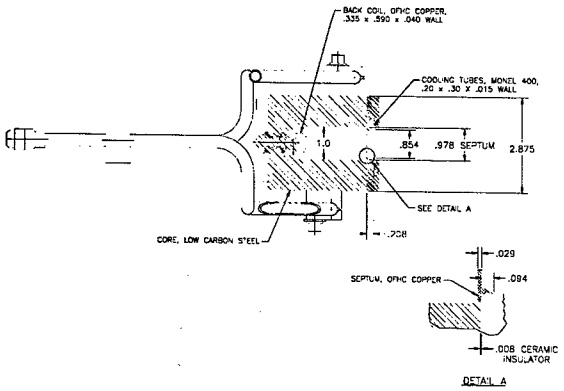


Figure 2. Cross section view of magnet core assembly

MOTION/DRIVE SYSTEM

The septum is required to move in and out of the beam in the horizontal plane as well as skew at any angle as shown in Figure 3. The upstream and downstream ends on the vacuum chamber can move independently of each other. This is accomplished by mounting each end of the vacuum chamber to a rotary table, which is mounted on a linear slide. Each linear slide is driven by an AC synchronous stepping motor coupled to a 50:1 gear reduction box. The output shaft of the gear reduction box is coupled to an ACME screw that moves the linear slide in the horizontal plane. The rotary tables allow the magnet to skew when the slides at each end are moved.

To accurately move the septum, linear potentiometers on each end of the vacuum chamber are coupled to a PC and indicate the exact position of the septum in the horizontal plane. The position system allows the septum assembly to move in and out of the beam with a repeatable accuracy of 0.025mm.

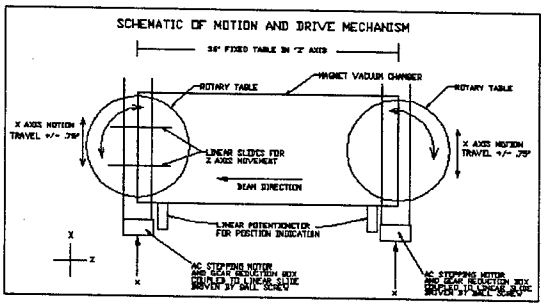


Figure 3. Schematic of motion and drive mechanism

MAGNETIC DESIGN/CALCULATIONS

The purpose of the magnetic field calculation was to twofold, first to calculate the field homogeneity of the magnet in the "Main Field Region" and second to calculate the strength of the fringe field at the "Fringe" region of the magnet where the beam is circulating.

Figure 4 shows a cross section of the magnet, with the "Magnet Iron" the "Septum" and "Return" conductors which both are made of copper, and the "Cooling Channel" which is made of material Monel 400.

In the calculations, which were performed with the 2D version of the code opera[2] the conductivity of both materials copper and Monel were taken into account by

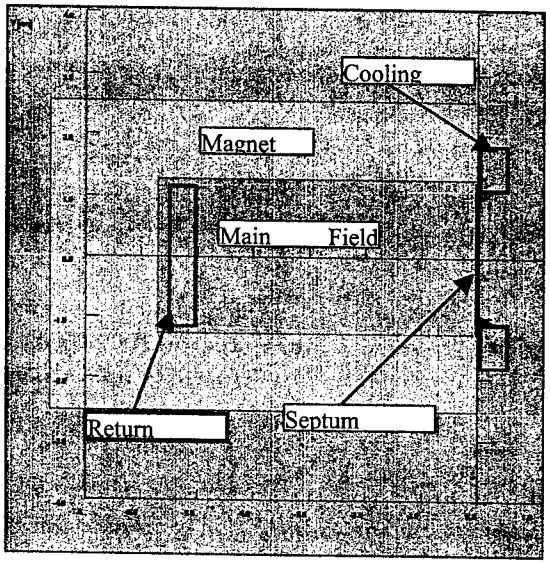


Figure 4. Cross-section of the Septum magnet showing the "Magnet Iron" the "Return" and "Septum" Conductors, the "Cooling Channel". The "Main Field Region" corresponds to the extracted beam, and the "Fringe" region to the circulating beam.

adjusting current densities in the "Septum" ($J=5.871x10^7$ A/m^2) and the "Cooling Channel" ($J=1.888x10^6$ A/m^2).

Figure 5 is a plot of the magnetic field homogeneity in the "Main Field Region" from the edge of the "septum" to a distance 4 cm inside the magnet. The maximum magnetic field in the "Main Field Region" is 462.5 Gauss.

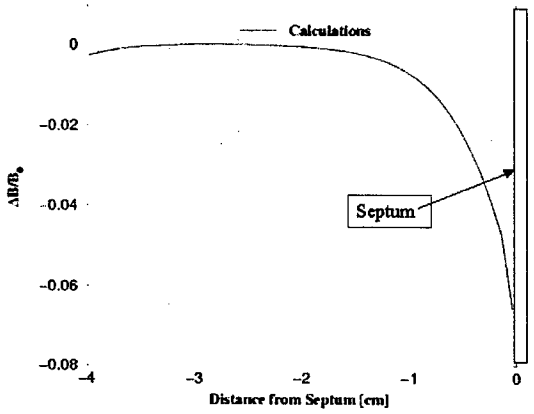


Figure 5. Field Homogeneity in the "Main Field Region" of the magnet

The magnetic field in the "Fringe" field region where the beam is circulating is plotted as function of distance from the edge of the septum. On the same plot the experimentally measured field is also plotted.

CONCLUSION

A successful UHV compatible Thin Septum Magnet has been designed, fabricated and installed in the Booster ring at Brookhaven. The magnet has been operational at a pressure of low 10^{-11} Torr and has been flawless.

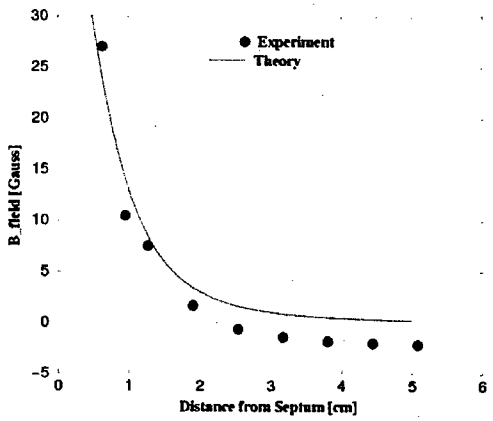


Figure 6. Experimental and Calculated values of magnetic field in the "Fringe" field region, plotted as a function of distance from the edge of the septum

REFERENCES

[1] J.Vac.Sci. Techno.A 18(4), Jul/Aug 2000 pg 1751
[2] Vector Fields Inc.

MECHANICAL DESIGN OF A FERRITE-BASED INJECTION KICKER FOR SNS ACCUMULATOR RING*

C. Pai#, N. Catalan-Lasheras, W. Eng, H. Hseuh, Y. Lee,
R. Lambiase, W. Meng, J Sandberg, S. Tepikian, J. Tuozzolo
Collider-Accelerator Department, Brookhaven National Laboratory, Upton, NY 11973

Abstract

Two sets of kickers, 4 pulsed dipoles in each set, will be used in the SNS accumulator ring to create a dynamic orbit bump for injection process. These kickers are designed as large aperture, window frame magnets. The design of these 8 kickers have been completed. The first article kicker has been assembled and is being tested. In this paper we discuss the mechanical design criteria for these kickers, the layout in the accumulator ring, the magnetic field requirements and the ferrite based magnet field analysis, the eddy current and thermal considerations in the choice of ceramic vacuum chamber and its implementation. Also we discuss a wedge shaped clamp which was designed to reduce the vibration in the coil when powered at the 60 Hz repetition rate.

1. INTRODUCTION

The injection of the SNS accumulator ring takes place in one of the straight sections of the ring. Two sets of kickers, two horizontal and two vertical in each set, are used to create dynamic orbit bumps to paint the phase space of the injected proton population [1].

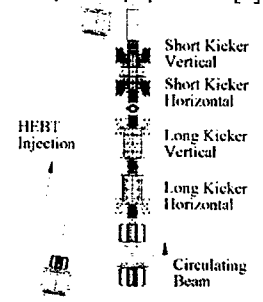


Figure 1: Upstream Set Of Injection Kickers

The injection kickers will be operated at a 60 Hz rate. The rise time and flat top time together are in the range of 2 to 3 ms. Ferrite is used as the core material for its high frequency response and low loss. The coils are wound with copper conductors and water-cooled. Since some heat will be generated in the ferrite and coil, the magnet is installed outside the vacuum system to prevent leaks from the water-cooling in the vacuum system. The vacuum chamber is made of alumina ceramic to avoid eddy currents induced by the pulsed magnetic field. The inner surface of the ceramic chamber will be coated with titanium nitride (TiN) to carry beam induced image current and reduce the secondary electron yield [2]. For simplicity, the horizontal magnets and vertical magnets are designed identically but oriented differently.

2. KICKER SPECIFICATIONS

Based on the beam dynamics, the eight kickers are designed as 4 long kickers and 4 short kickers. One set of 4 kickers is located upstream from the injection point. The sequence of kickers is long horizontal-long vertical-short horizontal-short vertical toward the injection point (Fig. 1). The other set of kicker is located down stream from the injection point with a mirrored sequence. The specifications of these kickers are listed in Table 1.

Table 1: Kicker Magnet Parameters.

	Long	Short
No. of Kickers	4	4
Ferrite Gap size: (cm)		
Height	19.55	21.55
Width	22.48	24.48
Length	64	21
Volume (cm^3)	81085	28313
Beam Pipe Material:	Ceramic	Ceramic
Inner Dia. (Aperture)	16 cm	18 cm
Turns per Coil	10	12
Max. Field (Gauss)	790	1000
Max Current (amps)	1230	1476
Ferrite Weight (lbs)	891	238
kicker assembly Weight (lbs)	1185	440

3. KICKER MAGNET

The fast kicker is designed as a ferrite core, rectangular window frame magnet (Fig. 2)

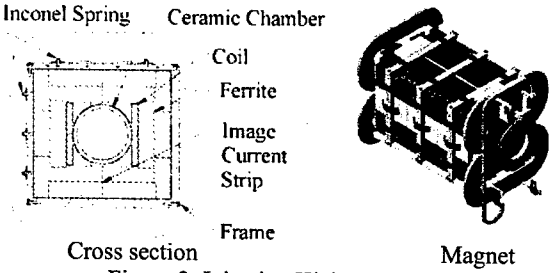


Figure 2: Injection Kicker Magnet

CMD 5005 Ni-Zn type ferrite is used for this magnet. This ferrite has high frequency response and very low eddy current loss. These properties are important for

*SNS is managed by UT-Battelle, LLC, under contract DE-AC05-00OR22725 for the U.S. Department of Energy. SNS is a partnership of six national laboratories: Argonne, Brookhaven, Jefferson, Lawrence Berkeley, Los Alamos, and Oak Ridge.
#pai@bnl.gov

0-7803-7738-9/03/$17.00 © 2003 IEEE

pulsed magnet operation. The ceramic chamber is centered in the gap and supported independently to the platform. The coil is installed outside the ceramic chamber. The coil is made of two identical 5 turn coils stacked together with one rotated 180 degrees. One jumper bus connects these two coils to form a single 10 turn coil. The window shape core is formed by stacks of ferrite blocks. Since ferrite is very brittle, these blocks are clamped by inconel springs to a metal frame. In the middle of the back leg is a copper strip that will carry beam image current to reduce beam impedance. The other purpose of the strips is to damper beam induced pulsed fields in the ferrite core. Pulsed power is fed through bus bars in the end of the ferrite core by 4 cables for each polarity. Two kickers, one horizontal and one vertical, are installed on a common platform. These two kickers are constructed identically except one is oriented 90 degrees with respect to the other (Fig. 3). On the platform, each kicker has its own adjusting screws, so they can be surveyed and aligned to each other. When installed in the ring, the platform will be final aligned to the beam line by sliding pads in the support stand. The kicker assembly is covered by a full length metal cover (not shown), which is grounded for shielding.

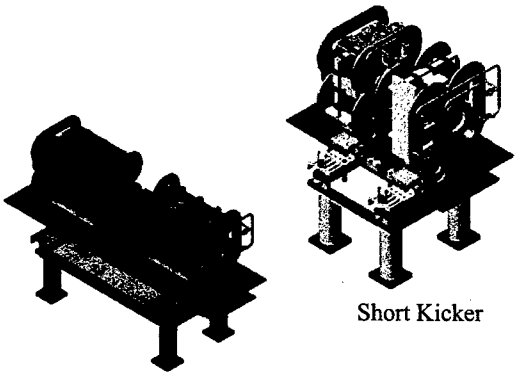


Figure 3: Injection Kicker Assembly

4. VACUUM COMPONENTS

The vacuum chamber is made of alumina ceramic with stainless steel flanges by metalized joints (Fig. 4). Helico-Flex type metal seals are used in the flange to protect the fragile joints. The number of bolts and required torque to tighten Helico-Flex seal are much less than for the conflat type. The inside surface of the ceramic chamber will be coated with copper and Titanium Nitride. Inconel spring fingers will be inserted and clamped in the two ends of the pipe to bridge the continuity between flange and inside coating. Low spring rate bellows will be used to connect ceramic pipe to other vacuum components in the system to compensate any misalignment and mechanical tolerances. These bellows are made of eight mil inconel sheets with a spring rate of 75 lb/in. All vacuum components will be cleaned and baked to 250 ^{0}C before assembled to meet the required vacuum quality of 1x10^{-8} torr range.

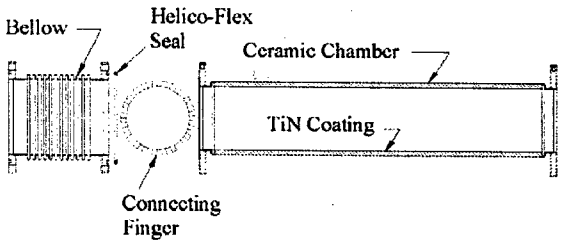


Figure 4: Vacuum Chamber Components

5. EDDY CURRENT HEATING

When operated at 60 Hz, the penetration of the magnetic field will induce eddy current in the inner coating of the ceramic chamber. The heat generated by this eddy current could reach around 100w/m along the center line. Calculation shows the maximum temperature rise in the chamber with a non-uniform distribution is about 46.8°C (Fig. 5).

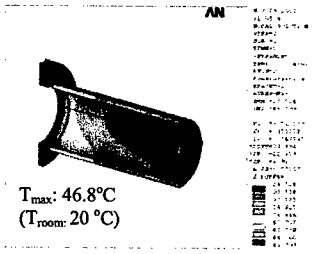


Figure 5: Eddy Current Heating In The Chamber

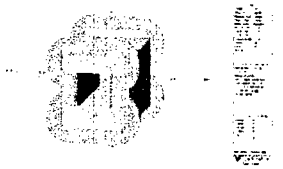
The induced thermal stresses in the transition joints are all in compression and are acceptable. Also, this ceramic vacuum chamber is specified to be baked to 450°C for high vacuum quality. The heat generated from eddy current is acceptable for this beam chamber.

6. MAGNETIC FIELD CALCULATION

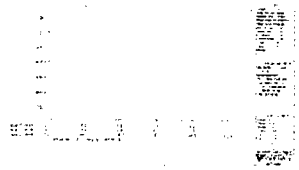
The injection kickers will create dynamic orbit bumps to paint the optimum phase space of the injected proton population. The required magnetic field quality for these kickers is the variation of integral field should be better than 1% [3]. An OPERA model was used to analyse its magnetic properties (Fig. 6). The results are listed in the table 2.

Table 2: Kicker Magnetic Properties

	Long	Short
Turns per Coil	10	12
Current (amps)	1230	1476
Center Field (gauss)	784.9	1006
Integral filed $\int$Bdl	65850.9	43505.0
Variation	+/- 1.00%	+/- 0.92%
Effective length	83.9	43.2
Inductance	158.0 x 10^{-6}(H).	149.0 x 10^{-6}(H).



Magnet Model



Center Field Along Beam Line

Figure 6: Magnetic Field Plot

7. DAMPER AND COIL SUPPORT

When the first article long kicker magnet was powered to full current, the Lorentz force caused the coil to start a vibration of 60 Hz. From an OPERA magnetic analysis and an ANSYS harmonic analysis (Fig. 8), the magnitude of the harmonic force is about 40 lb in the straight part of the coil. Von Mises stresses are 1507 psi in the copper and 1000 psi in the epoxy. These stresses are well below the yield strength of the materials, but in order to reduce this vibration, wedge clamps were designed and installed in the corner of the gap to push against the coils (Fig. 7). Each clamp provides more than 100 lb preload to each coil, which reduces the vibration. Test data of vibration in the coil when operated with and without wedge clamps are listed in the table 3. This data shows the total displacement of vibration is significantly reduced to a reasonable level for operation when wedge clamps are installed.

Table 3: Vibration Displacement

	Without wedges			With wedges		
	Vibration displacement			Vibration displacement		
Current	+ mm	- mm	Total	+ mm	- mm	Total
1050	0.088	-0.092	0.179	0.062	-0.046	0.108
1250	0.170	-0.125	0.295	0.101	-0.058	0.160

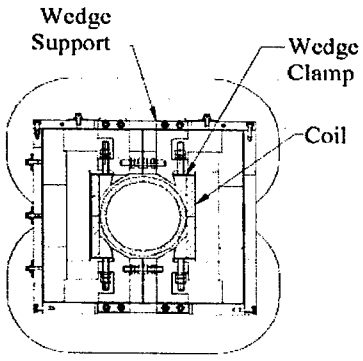
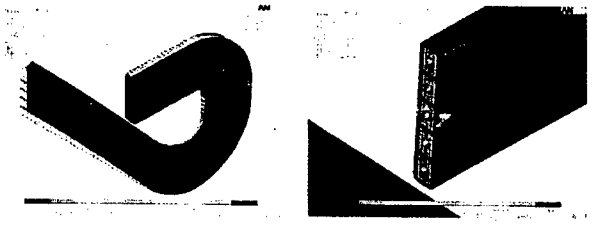


Figure 7: Wedge Clamps



Vibration Mode Shape Harmonic Stress

Figure 8: Harmonic Analysis of Coil

8. FIRST ARTICLE ASSEMBLY AND TEST

The first article long kicker magnet (without the ceramic chamber) was assembled (fig. 9) and used to test all design criteria. The coils have passed all mechanical, electrical and hydraulic tests. Ferrite blocks were accurately machined and formed a nice tight window frame. The magnet has gone through full power tests and magnetic measurements. From these tests, this magnet meets the design requirements. Four ceramic chambers have passed all mechanical tests and vacuum leak checks. They are being coated with TiN in the vacuum Lab. These beam pipes will be installed into the magnet soon.

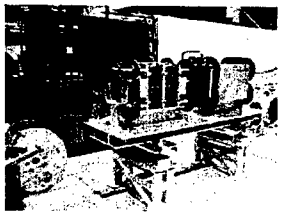


Figure 9: First Article Kicker Assembly

9. CONCLUSIONS

The first article injection kicker has been successfully assembled and tested. All components for the production kicker are in house except some ceramic pipes. Four of the 11 ceramic chambers are already in house and are being coated with TiN. The balance of the chambers will be delivered soon. The production kicker assembly work is in progress. The eight kicker assemblies will be completed in about six months.

10. ACKNOWLEDGEMENTS

The authors thank S. Henderson of ORNL for his valuable discussion on ceramic chamber coating .

REFERENCES

[1] J. Wei et al, "Low-loss design for the high-intensity accumulator ring of the Spallation Neutron Source" Phys. Rev. ST-AB 3, 080101 (2000).

[2] P.He, et.al. "Metallization of SNS Ring injection kicker ceramic chambers" Proc. of 2002 EPAC, Paris, France.

[3] J. Wei et al, Proc. of 2001PAC, Chicago, USA, pp. 2560.

MECHANICAL DESIGN OF FAST EXTRACTION KICKER AND PFN FOR SNS ACCUMULATOR RING*

C. Pai#, D. Davino, H. Hahn, H. Hseuh, Y. Lee, W. Meng, J. Mi,
J Sandberg, N. Tsoupas, J. Tuozzolo, D. Warburton, W. Zhang
Collider-Accelerator Department, Brookhaven National Laboratory, Upton, NY 11973

Abstract

Two kicker assemblies, seven pulsed magnet modules in each assembly, will be used in the SNS accumulator ring to kick the beam vertically to the extraction septum then to the target. These kickers are designed as window frame magnets housed inside a vacuum chamber. Fourteen Pulse Forming Networks (PFN) housed in separate silicon fluid containers are designed to power each kicker module. A single module prototype kicker magnet and PFN modulator have been successfully assembled and tested. In this paper we discuss the mechanical design criteria of these kicker assemblies, the installation layout in the accumulator ring, the structural analysis of the kicker chamber, the magnetic field analysis of the ferrite magnet, the high voltage feedthrough design, the structural design of the modulator container, the cooling and the thermal expansion considerations of the silicon fluids.

1. INTRODUCTION

The extraction from the SNS accumulating ring to Ring to Target Transport Line (RTBT) takes place in one of the accumulator ring's straight sections [1]. There are a total of fourteen kicker magnet modules to kick the circulating beam in a single bunch vertically into septum magnet (Fig.1). The septum then provides the large angle deflection to extract the beam into the RTBT line [2]. Seven kicker magnets in one assembly are located upstream of a quad-doublet, and seven magnets in another assembly are located downstream from the quad-doublet.

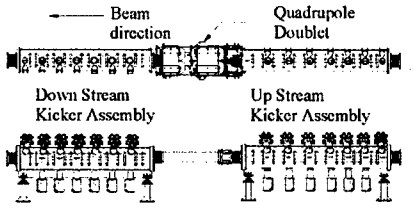


Figure 1. Extraction Kicker Layout

The extraction kicker will be operated at 60 Hz rate with a flat top of 750 ns and a rise time of 200 ns. Fourteen high voltage modulators installed in the modulator building will be used to power the 14 kicker magnets. Two coaxial cables connected in parallel from each modulator transfer current to each kicker magnet in the assembly. Since extraction from the accumulator ring has to have a high level of reliability, the large number of magnet modules, seven in each assembly, is to allow the full beam to be extracted within the acceptance of the RTBT line even when one of the modules in each assembly fails to function.

*SNS is managed by UT-Battelle, LLC, under contract DE-AC05-00OR22725 for the U.S. Department of Energy. SNS is a partnership of six national laboratories: Argonne, Brookhaven, Jefferson, Lawrence Berkeley, Los Alamos, and Oak Ridge.
#pai@bnl.gov

2. KICKER SPECIFICATIONS

Reflecting the beam acceptance and coupling impedance, the 14 kicker magnets have various apertures, lengths and relative heights to the beam [3]. To simplify the kicker design, the 14 magnets are grouped in 6 different types. The parameters of the kicker assembly with a typical magnet are listed in Table 1.

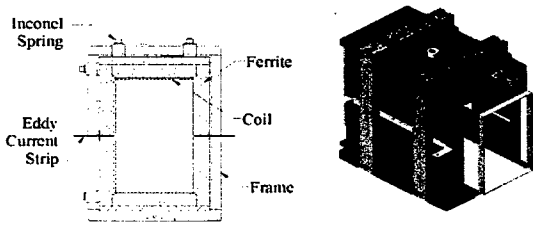
Table 1: Kicker Magnet Parameters.

Ferrite Gap (cm):	15.1(H), 24.3(V), 34.0 (L)
Ferrite Volume	11760 cm^3
Turns per Coil	1
Max. Field	251 G
Peak Current	2440 A
Peak Voltage	35 kV
Pulse Current Rise Time	200 ns
Current Pulse Flat Top Time	750 ns
Assembly Weight	4465 lb
(7 magnets in one chamber)	

3. KICKER DESIGN

3.1 Magnet

The fast kicker is designed as a ferrite core rectangle frame magnet (Fig. 2).



Cross Section Magnet

Figure 2. Extraction Kicker Magnet

CMD 5005 Ni-Zn type ferrite is used for this magnet. This ferrite provides high frequency response, low loss and low out gassing rate. These properties are important for pulsed power magnet in high vacuum application. Six ferrite blocks form a window shape frame. These ferrites

0-7803-7738-9/03/$17.00 © 2003 IEEE

blocks are clamped by inconel springs to a stainless steel structure. In the middle of the back leg, a copper strip is used to carry the beam–induced image current and help to reduce the eddy current heating caused by the beam induced magnetic field in the ferrite. The coil is made of a single-turn copper conductor. High voltage current is fed from one end of the ferrite core.

3.2 Support And Alignment

Seven magnet modules will be installed in a vacuum chamber in series (Fig. 3).

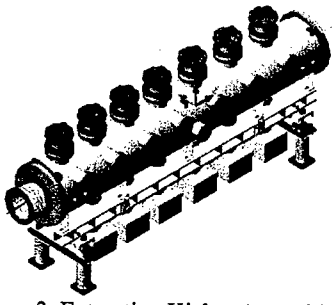


Figure 3. Extraction Kicker Assembly

A sliding fixture will be used to insert these seven modules into the chamber. After insertion, each magnet will be surveyed and supported independently to its final position as determined by the beam dynamics. The adjustments will be done through the access ports in the under side of the chamber (Fig. 4). All magnet supports provide sliding contact except the axial support in the feedthrough end, where the magnet is fixed in the support.

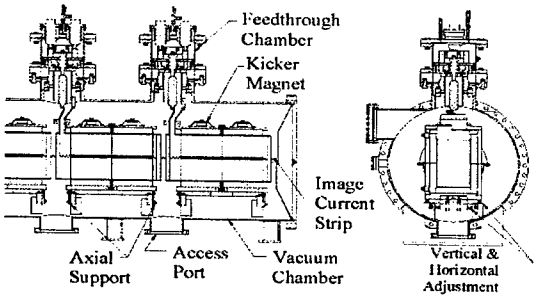


Figure 4. Cross Section Of Kicker Assembly

This design allows the magnet assembly to be baked in the ring. When various temperatures rise in the assembly, the connecting end of each magnet will stay with its ceramic feedthrough and will let the other end expand.

3.3 High Voltage Feedthrough Connection

Each magnet is powered by a modulator. Two high voltage cables from each modulator send the 35 KV pulse into each magnet in the vacuum chamber. Above each magnet, two high voltage connectors are jumped together then connected to the outside terminal of the coaxial HV feedthrough. Inside the vacuum chamber, two adapters are used to connect the terminals of the coil to the high voltage feedthrough. These adaptors can also be used to reverse the polarity of the magnet (Fig. 5). To provide better high voltage insulation, a feedthrough chamber is built around the outside of the HV feedthrough to house these high voltage connecting components. After installation, this chamber will be flushed clean and back filled with 1 atm of insulating dry nitrogen gas. A pressure relief valve will be used to safe guard the feedthrough chamber.

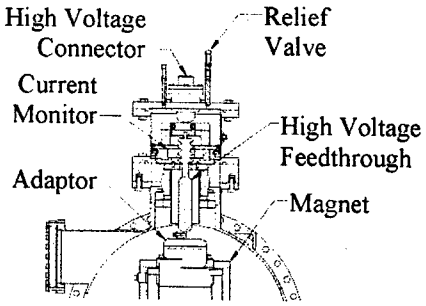


Figure 5. Feedthrough Chamber

3.4 Vacuum Quality Criteria

The required vacuum quality for extraction kicker is in the $1x10^{-8}$ Torr range. Since large quantities of ferrite are used in the system, to overcome the outgassing from these porous ceramics, six ion pumps are installed in the underside of the kicker assembly. The vacuum chamber and flanges are made of 304L stainless steel. End flanges are wire seal type with copper gaskets. All blind holes in machined parts are drilled with venting paths. All fasteners are high vacuum comparable silver plated hardware. Ferrite and all machined parts will be cleaned and baked to 250 ^{0}C before assembly. After installation, the whole assembly can be baked to 250 ^{0}C under vacuum in the storage ring.

4. STRUCTURAL STRENGTH

The total length of the kicker assembly is 170 inches and weights about 4500 lb. From finite element analysis (Fig. 6), the deflection of this structure under its own weight and a side load of 0.5 G is about .034". Maximum Von Mises stress in the chamber is 13052 psi, which is acceptable for SS304. Shims and support screws will compensate the small deflection to keep all magnets in alignment.

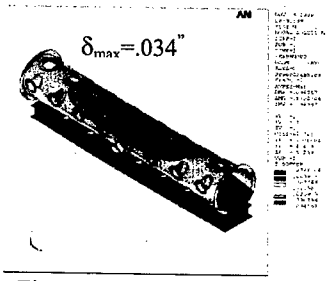


Figure 6. Structural Analysis

5. MAGNETIC PROPERTIES

An OPERA model was used to calculate the properties of the magnet (Fig. 7). When powered by 2000 A current, the center field of the magnet is 160 G. Maximum field in the ferrite is 2433 G, which is acceptable for CMD5005. Inductance of the magnet is .97 μH.



OPERA Model Field Contour Plot

Figure 7. Magnetic Analysis

6. MODULATOR ASSEMBLY

6.1 Design concept

The kicker magnets will be powered by 14 modulators [4][5]. Theses modulators are constructed as a large fluid container. All electric components are submersed in insulating silicon fluid (Fig. 8).

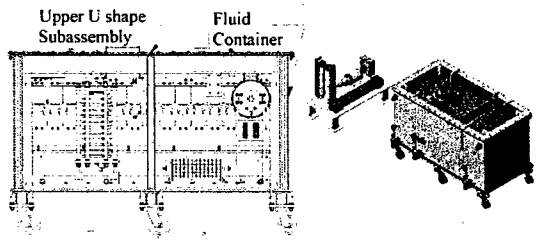


Figure 8. Pulse Forming Network (Modulator)

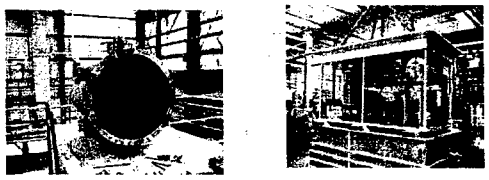
Since the modulator will be operated at 35 KV high voltage, the modulator is designed as a large fluid container to submerse all components into silicon fluid for insulation. The container assembly is a vented system to avoid internal pressure build up. A desiccant filter is installed in the vent pipe, which will keep the air dry and clean when it enters the system. The size of the container is 75"x38"x36" which can hold 400 gallons of silicon fluid. The upper part of the container is a U shape subassembly. A frame structure is built under the lower level of the U shape to house all modulator components. The shoulder of the U shape is the sealing flange. When assembled together, the fluid level will be kept just above the lower level and is enough to keep all components submersed in the fluid. The volume of the air space above the fluid level is 10 gallon. This space is designed as an expansion tank to compensate temperature fluctuation. The thermal expansion rate of the 400 gallons of fluid is about 0.23 gallon/°C. The 10 gallon space will allow 40 °C temperature fluctuations for operation. The U shape design has two advantages. One is the fluid level will be always below the sealing surface. The possibility of oil leak is greatly reduced. The other advantage is that all external fittings and components that mounted on the top are under the U shape. Any leaked oil will be contained in this U shape.

6.2 Modulator Cooling

The modulator will generate 10,000 watts of heat in total when operates at 60 Hz. Most of the heat is generated in the resistor pack. To remove this heat, a circulating pump will pump water-cooled oil into the tank in four inlets. Flow control valves and meters are installed in these inlets to keep flow rate equal. Oil from the three inlets in the bottom of the tank will flow across all electric components from bottom to the top. One of the inlets in the top of the upper flange will be connected to the bottom of the resistor pack. The resistor pack is designed with vertical cooling path in the center and radial cooling path in each of the copper disk. The warm oil will be pumped back from the three outlets in the upper flange to the pumping station where the warm oil will be cooled by a water cooled heat exchanger.

7. PROTOTYPE TEST

A single module kicker magnet and a full feature modulator (Fig. 9) were built to test all design criteria. Both, magnet and modulator have gone through various measurements and power tests. From test results, both magnet and modulator meet the design requirements.



Magnet Modulator

Figure 9. Prototype Magnet And Modulator

8. CONCLUSIONS

The design and test of the extraction kicker magnet and modulator are completed. The fabrication of the 14 modulators is already started by a contractor. The construction of the two kicker magnet assemblies will be following soon.

9. ACKNOWLEDGEMENTS

The authors thank K. Rust and R. Cutler of ORNL for their valuable discussions on modular construction.

REFERENCES

[1] J. Wei et al, Phys. Rev. ST-AB 3, 080101 (2000).
[2] J. Rank, et al, "SNS Extraction Lambertson Septum Magnet" prepared for PAC2003.
[3] N. Tsoupas et al, "Beam Extraction From The SNS Ring And Design Of Extraction Kickers" proceedings of EPAC 2000, Vienna, Austria
[4] W. Zhang et al, Proc. of 2001PAC, Chicago, USA, pp. 3714.
[5] J. Mi et al, "SNS Extraction Kicker System and First Article BPFN Test" Proc. of 2002 EPAC, Paris, France.

DESIGN CONSIDERATIONS FOR A LAMBERTSON SEPTUM MAGNET FOR THE SPALLATION NEUTRON SOURCE *

J. Rank, K. Malm, G. Miglionico, D. Raparia, N. Tsoupas, J. Tuozzolo, Y.Y. Lee
Collider-Accelerator Department, Brookhaven National Laboratory, Upton, NY 11973, USA

Abstract

Multiple-stage injections to an accumulator ring boost intensity until a final extraction delivers the full proton beam to a target transfer line. Kickers and an Extraction Lambertson Septum (ELS) magnet implement extraction.

Studied here are various concerns of the design of an ELS magnet, including: lattice geometry, beam dynamics and optics considerations; and vacuum, electromagnetic and mechanical design aspects. Reference datum and transformations are established and shown schematically. Coil, yoke, and shield design optimization is discussed.

1 INTRODUCTION

A Lambertson Septum Magnet intercepts and redirects the proton beam of the accumulator ring toward the target on extraction cycles, yet passes undisturbed the ring's circulating beam on accumulation cycles. The Extraction Region (ER), in a straight section of the accumulator ring (Fig. 1), consists of consecutively: A set of pulsed Kickers [1], each of which bump the beam at a downward "kick angle" in a vertical plane; the subject Lambertson Septum magnet; and finally the Quadrupole Doublets which refocus and correct beam projection to target.

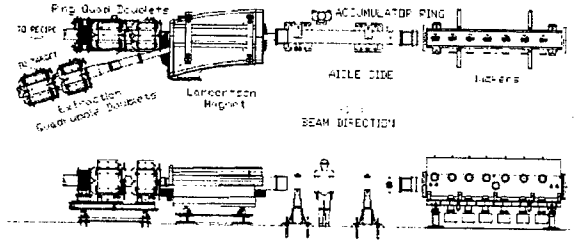
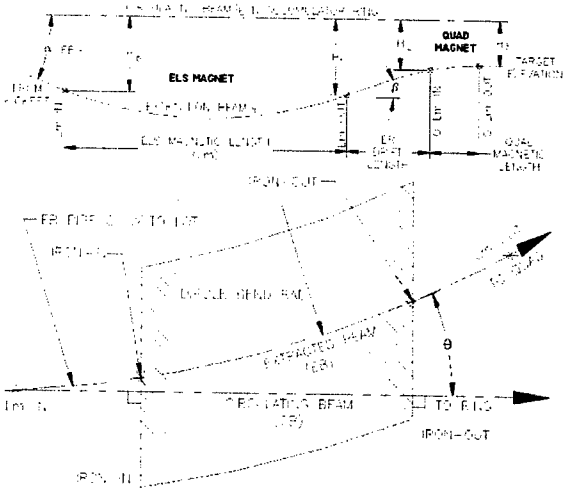


Figure 1: SNS Extraction Region plan and elevation views.

2 DESIGN CRITERIA

ELS design must satisfy constraints of the ER lattice specification: That the intercepted beam entering at the kicked angle ($a_{EB\,CL}$) finally exit to the transfer line on a path lying in a horizontal plane at the established target elevation (Fig. 2), and at an exit angle (Q) relative to the ring dictated by the lattice to-target projection (Fig. 3). To satisfy these, specifically for SNS with a committed target elevation, by design beam center is displaced vertically from magnet center at the first quadrupole; this introduces a small dipole component that corrects for a slight angular offset from the horizontal (b).

To avoid error magnification in 400 circulation passes per extraction cycle, we optimize electromagnetics for the circulating beam in the ring (CB). To this end, at beam



Figures 2 & 3: ER elevation (top) and plan view schematics.

entrance and exit, yoke design includes: iron squared to CB path, not the extracted beam (EB) path, to minimize quadrupole affects on CB; and allowance of space for "porch shielding" of the CB beyond the fringe field by tightening the bend radius to shorten iron length. Provision is also made to capture the CB within a shield assembly consisting of the "septum plate" and the "shield plate" (Fig.4). Between these plates "clamshells" the CB vacuum chamber wrapped in a thin non-magnetic copper shim to provide an effective impedance to flux to which the CB would be exposed. A narrow "shield cap" runs along CB axis, flush with the shield assembly. Total iron thickness (minus CB pipe OD) yields a flux density within iron saturation limits, even with inner-outer return path asymmetry as CB moves outboard of ELS center. Though ELS cross-section has near symmetry at the entrance saturation concerns persist in the thin septum.

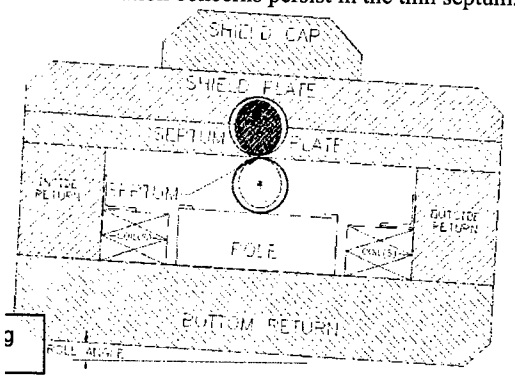


Figure 4: World x-y plane section at beam entrance to yoke.

0-7803-7738-9/03/$17.00 © 2003 IEEE

3 OPTICS AND GEOMETRY

Of four SNS operating modes, ELS design is based on physics parameters for the largest beams. In all modes the elliptical beam sections of both CB and EB diverge along both major and minor axes (y and x, respectively). The y-axis divergence of the EB, and the known kick angle of the EB centerline, ultimately determine ELS magnetic geometry. To maximize septum thickness each vacuum pipe remains always tangent to the major axes of the beam it contains; i.e., CB and EB points-of-tangency (POT) occur at 6 and 12 o'clock orientations respectively (Fig. 5). Thus pole (magnet yoke) geometry must be everywhere parallel to the EB pipe centerline. This pipes diameter is determined by the EB size at the exit, and thus fixes the magnetic gap; the distance between the primary pole and the septum quasi-pole (Fig. 6). Similarly, there exists an angular offset of the CB with respect to its vacuum pipe which determines the axis of the cut hole in the shield assembly. These angular offsets are corrected at both exit flanges with "skewed" bores which center the beam path in the downstream pipe. Bore angles are offset also at the upstream "crotched" entrance flange. The shim "air gap" runs the length of the magnet including shielding porches, but terminates at the "field clamp". The clamp, in contact with the magnetic CB pipe, closes the electromagnetic circuit at end of air gap for stray flux.

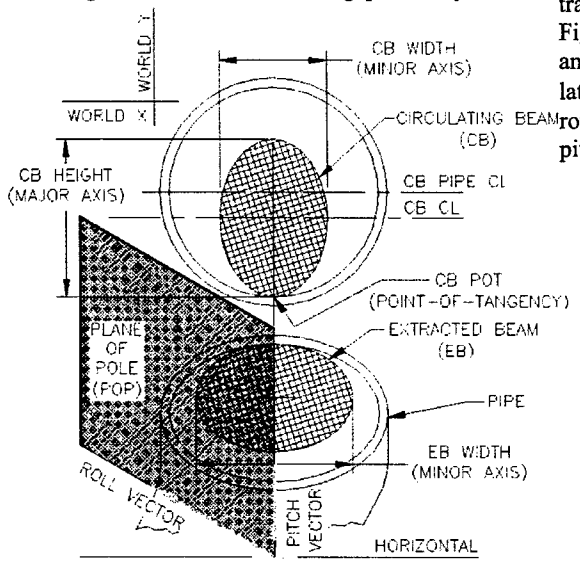


Figure 5: Schematic of world x-y section at beam entrance.

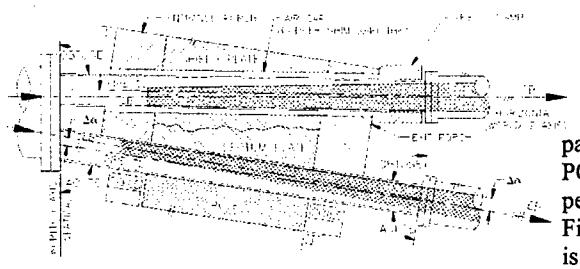


Figure 6: Schematic of world x-z section through pipe centers.

Recalling ELS design criteria, entering beam kicked downward relative to a world horizontal plane (WCS x-z) exits in that plane at a lattice-prescribed height and angle. Thus yoke geometry cannot be orthogonal to *any* WCS axis; i.e., the plane-of-pole (POP) first must lie tangent to an axis pitched about the world-x in order to receive the entering kicked beam, and second must be rolled about that pitch-axis in order to project the exiting beam at the given extracted angle, but parallel to the WCS x-z plane (or nearly; section 2). To gain pipe-to-diverging-beam tangency, pipe rotation about the world-x is by the kick angle ($a_{EB\,CL}$) less the EB y-radii divergence angle (Da).

$$\overrightarrow{V_{pop}} := \left(\overrightarrow{V_{wcs}}\cdot[T_{pitch}]\right)\cdot[T_{roll}] \text{ where } \overrightarrow{V_{pop}} := \left(V''_x\ V''_y\ V''_z\right) \text{ thus}$$

$$\frac{V''_x}{V_{wcs}} := \left[\sin(\gamma)\cdot\left[\frac{\tan(\theta)}{\tan(\gamma)} + \sin(\alpha)\cdot\left(1 - \frac{\tan(\beta)}{\tan(\alpha)\cdot\cos(\theta)}\right)\right]\right]$$

$$\frac{V''_y}{V_{wcs}} := \left[\cos(\gamma)\cdot\left[\tan(\gamma)\cdot\tan(\theta) - \sin(\alpha)\cdot\left(1 - \frac{\tan(\beta)}{\tan(\alpha)\cdot\cos(\theta)}\right)\right]\right]$$

$$\frac{V''_z}{V_{wcs}} := \left[\cos(\alpha)\cdot\left(1 + \frac{\tan(\alpha)\cdot\tan(\beta)}{\cos(\theta)}\right)\right] \text{ where } \begin{matrix}\alpha \text{ is pitch angle}\\ \gamma \text{ is roll angle}\end{matrix}$$

$$\text{Given } \left(V''_x\right)^2 + \left(V''_z\right)^2 := V_{wcs} \text{ and } V''_y := 0 \text{ solve for } \alpha,\gamma$$

Figure 7: POP to WCS coordinate transformation.

To relate ELS pole coordinate system (POP CS) to the customary perspective for a conventional dipole in the WCS, one must perform a series of two coordinate transformations. Mathematically, the matrix algebra of Fig. 7 is solved for both the divergence-corrected pitch angle (a_{LOT}) and the roll angle (g) given constraints on lattice geometry (b & Q of Fig. 2 & 3). Visually, we first rotate the viewing direction in Fig. 5 by the corrected pitch angle (Fig. 8), then by the roll angle (Fig. 9).

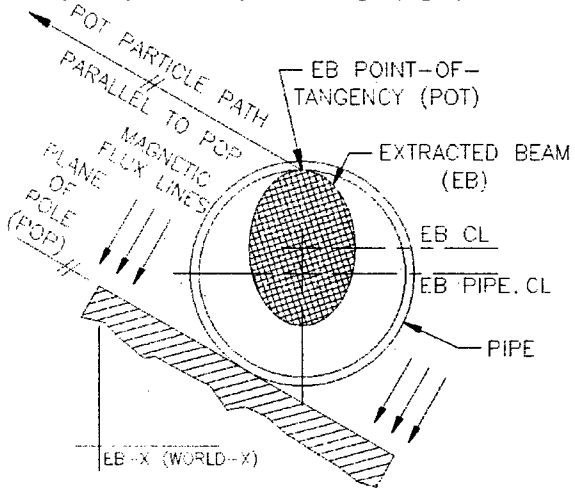


Figure 8: Pitch-corrected view of EB and pole.

We may resolve the velocity vector ***v*** of an arbitrary particle entering ELS field into components orthogonal to POP; i.e., aligned with the flux lines (POP-y axis, perpendicular to the pole), or lying in the POP (POP x-z). Fig. 10 depicts a particle on the LOT path. The vector ***v*** is resolved into components orthogonal to the POP CS. The resultant of vectors parallel to the POP is ***v // POP***.

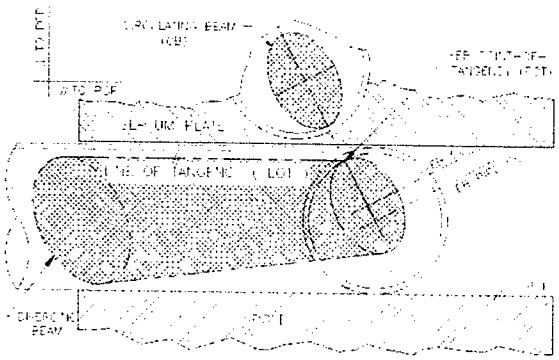


Figure 9: POP x-y plane section schematic at beam entrance.

Bend radius due to ELS field is proportional to ***v // POP*** ; but the component perpendicular to POP remains constant along the particle path. Thus only a particle positioned at the EB POT will travel on a circular arc always parallel to the POP; this line-of-tangency (LOT) arc shows in Fig. 9. All others, including those on beam center, have constant non-zero POP-y velocity component. Hence, the EB path through the ELS is a helix; the particle bunch appears as a "horn on a table" in contact on its LOT. This adds subtle complexities to 3D model development, lattice placement, and specification of survey and alignment at installation. A datum point used to place a conventional dipole, where entering and exiting centerlines intersect, does not exist.

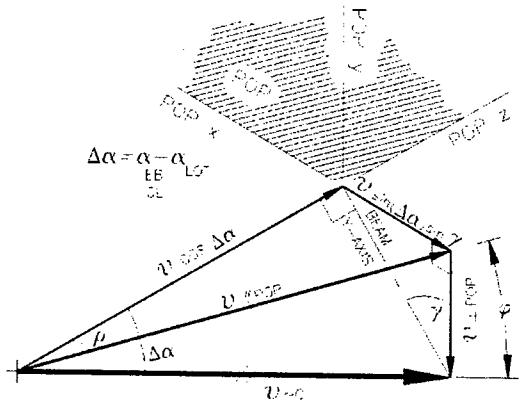


Figure 10: Velocity vector POP components for LOT particle.

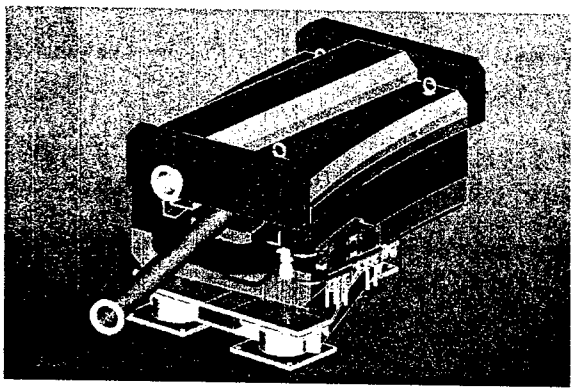


Figure 11: ELS magnet assembly view looking upstream.

4 ELS MAGNET ASSEMBLY

A discussion of design issues for the various components of the ELS magnet assembly (Fig. 11) is useful.

Coils

Water-cooled coils, sized for 1.3 GeV, have the following specifications: Allowable 20^{0}C rise, 70 psid max, 5-15 fps turbulent flow, and current density <1000 A/sq. cm. [2]. The resulting large cooling passage raises concerns about intermediate splice design, and "keystoning" at the bends. Radiation exposure of septa warrant "rad-hard" coils.

Vacuum Chamber

Chamber manufacture requires many stages. The CB pipe from ASTM A513 DOM tube for dimensional accuracy, is placed in an acid bath, vacuum fired, masked at the weld joints, and nickel plated inside and out. The tube is welded to 304L flanges of the now-formed EB weldment, including the delicate weld at the crotch. Care is taken here as the weld is compounded by: a thin base metal, a tight fit, dissimilar metals, a fragile nickel plating, and high stresses. Finally, the tube is TiN coated.

Shielding and Yoke

Kicker design limits septum thickness; as weighed against competing concerns of saturation and stress. A special convex cutter performs the final cut in both septum and shield plates. Close fit in the clamshell insures accurate location of CB tube. Allowable stack-up tolerance for this machining process, and for plate flatness and vacuum pipe geometrical tolerances, depends on beam emittance. Pole design is based on field uniformity requirement. The ELS pole has no square faces (Fig. 3). Porches from steel laminations shield the CB from local fringe field, and intercept any stray field away from the CB. A field clamp bolts to CB tube and to the porches; this reacts vacuum load on the chamber from the upstream ER bellows.

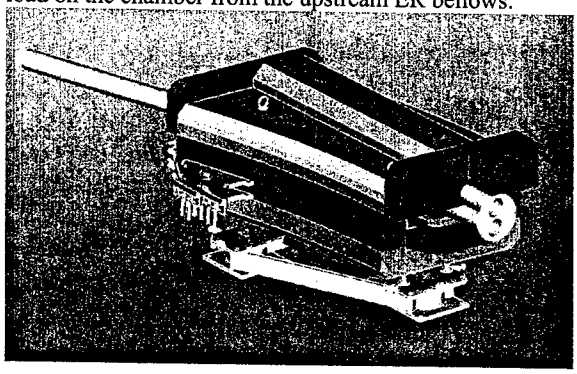


Figure 12: ELS magnet assembly view looking downstream.

REFERENCES

[1] C. Pai, et. al., "Mechanical Design of Fast Extraction Kicker and PFN for SNS Accumulator Ring", these proceedings.

[2] Jack Tanabe, SLAC, Accelerator Magnet Engineering, USPAS 2000.

MAGNETIC FIELD CALCULATIONS FOR A LARGE APERTURE NARROW QUADRUPOLE *

N. Tsoupas, J. Jackson, Y.Y. Lee, D. Raparia, J. Wei, BNL, Upton, NY 11973 USA

Abstract

In the design of high-intensity proton synchrotrons and accumulator rings, quadrupole magnets of narrower size in one of the transverse dimensions are often needed to accommodate the compact ring geometry, the various injection and extraction devices, and the large vacuum chamber aperture. The stringent limit on tolerable beam loss further demands a good magnetic field quality to minimize beam resonances caused by higher-order magneticmultipoles.

In this paper, we present results from magnetic field calculations performeed on 2D and 3D models of a large-aperture narrow-quadrupoles that is suitable for a high intensity, low beam-loss accumulator rings . The pole face of the quadrupole has been optimized to minimize the integrated field of the first three allowed multipoles (12pole,20pole and 28pole). The ratio of each integrated magnetic-multipole-strength to the integrated magnetic-quadrupole-strength at a radius of 85% of the quad's pole-tip-radius is less than $2x10^{-4}$. Results from the calculations performed on the two-dimensional and three-dimensional models of the narrow quad are presented.

1 INTRODUCTION

In a published paper[1] we provide detailed information about the design of a "narrow quadrupole" that has been built to be used in the SNS accumulator ring[2]. The transverse dimension of the quadrupole on the horizontal plane has helped accommodate the various devices which are located at the injection and extraction regions[1] of the SNS accumulator ring. The main requirements for the magnetic design of the narrow quadrupole was to minimize the integrated strength of the 12pole magnetic multipole down to $\int B_{12pole}dz/\int B_{4pole}dz < 2x10^{-4}$ at a radius of r=10 cm, and we did not regard the contributions from the 20pole and 28pole multipoles. Table I shows the integrated strength of these multipoles relative to the integrated quadrupole strength as were calculated by the 3-Dimentional model and also as were measured in the first built quadrupole.

In Table 1, $R_n = \int B_n(r,z)dz/\int B_1(r,z)dz$ where $B_n(r,z)$ is the n^{th} coefficient in the expansion of the radial field $B_r(r,z)$

$B_r(r,z) = \sum B_n(r,z)\cos[(n+1)\theta]$ {n=1 quad, n=3 oct ...} (1)

The $B_r(r,z)$ is calculated and measured at a radius r=10 cm and the coefficients $B_n(r,z)$ are integrated along the z-axis which is along the beam direction.

In Table 1, the 2nd row shows the calculated quantity R_n, and the 3rd and 4th rows the measured quantity R_n for the quadrupole as it was delivered by the manufacturer (3rd row) and with a minor modification (reduce the transverse pole length by 0.75 mm), (4th row). The modification resulted in reduction of the $R_{(12pole)}$ multipole strength down to $1.2x10^{-4}$. The error in the measurements of the harmonics was $\pm 0.02x10^{-4}$

Table 1: The Ratio R_n of few allowed multipoles. The quantity R_n is defined in the text.

	$R_{5\,(12pole)}$	$R_{9\,(20pole)}$	$R_{13\,(28pole)}$
CALC	$-4.2x10^{-4}$	$-5.2\,x10^{-4}$	$-1.5\,x10^{-4}$
MEAS#1	$+3.20x10^{-4}$	$-6.90\,x10^{-4}$	$-1.20\,x10^{-4}$
MEAS#2	$+1.20x10^{-4}$	$-6.81x10^{-4}$	$-0.92\,x10^{-4}$

Calculations performed on the SNS ring [3] showed that the measured strength of the (20 and 28)poles multipoles (see Table 1) of the narrow quadrupole are well below the limits that may bring the beam into resonance and cause significant beam emittance growth that will result in beam losses. Nevertheless we thought as a useful task to design a narrow quadrupole that minimizes the first three allowed multipoles (12,20,28)pole.The following sections are dealing with the design of such a narrow quadrupole.

2 THEORY FOR THE MAGNET DESIGN

Poisson's theorem states that the magnetic field vector **B** (or any vector, regular at infinity) can be expressed as:

$$\mathbf{B(x)}=(1/4\pi)\int\{[\nabla'(\nabla'\cdot\mathbf{B})-\nabla'\times(\nabla'\times\mathbf{B})]/|\mathbf{x}-\mathbf{x}'|\}\,d^3\mathbf{x}' \quad (1)$$

By defining the magnetization vector

$$\mathbf{M}=\mathbf{B}-\mu_0\mathbf{H} \quad (2)$$

and using the Maxwell equations $\nabla'\cdot\mathbf{B}=0$ and $\nabla'\times\mathbf{H}=\mathbf{J}$ equation (1) becomes:

$$\mathbf{B(x)}=(1/4\pi)\{\int[\mu_0\nabla'\times\mathbf{J}+\nabla'\times(\nabla'\times\mathbf{M})]/|\mathbf{x}-\mathbf{x}'|\}\,d^3\mathbf{x}' \quad (3)$$

Equation (3) expresses the magnetostatic field **B(x)** as the contribution of two terms; one term corresponding to the currents distribution **J** the other term to the magnetization **M** of the materials. With $\mathbf{J_M}=(1/\mu_0)(\nabla'\times\mathbf{M})$ equation (3) can also be written (see ref. [4]) as:

$$\mathbf{B(x)}=(\mu_0/4\pi)[\int\nabla'\times\mathbf{J}/|\mathbf{x}-\mathbf{x}'|]d^3\mathbf{x}'+\int\mathbf{J_M}\times\mathbf{r_u}/|\mathbf{x}-\mathbf{x}'|^2d^3\mathbf{x}'$$
$$+\int(\mathbf{M}\times\mathbf{n_{out}})\times\mathbf{r_u}/|\mathbf{x}-\mathbf{x}'|^2d^2\mathbf{x}' \quad (\mathbf{r_u}=\text{unit vector along } \mathbf{x}-\mathbf{x}') \quad (4)$$

In equation (4) the second integral extends over the interior of the finite volume of the magnetic material, and the third integral over the surface enclosing the volume of the magnetic material ($\mathbf{n_{out}}$=normal to the surface). It is the contribution of the third integral that can affect the strength of the various allowed multipoles by altering the contour of the pole face. We assume that the value of the permeability μ of the iron at the vicinity of the pole surface has a value $\mu>>1$ for the third integral to have an effect on the magnetic multipoles. It is therefore possible to affect the magnetic field in the space of the beam by

* SNS is managed by UT-Battelle, LLC, under contract DE-AC05-00OR22725 for the U.S. Department of Energy.

modifying the contour of the pole tip of the quadrupole. This approach [5] was followed in the design of narrow quadrupoles. In this paper we employ more sophisticated contour of the pole tip and we extend the calculations in three dimensions.

3 TWO-DIMENSIONAL MODELING

In this section we present the results of the two dimensional magnetic calculations as applied to three designs of the narrow quadrupole. The designs will be refered in the text as A,B and C. In each of the designs, discussed below, we provide enough information about the cross section of the narrow quadrupoles, for the reader to repeat the calculations using her/his preferred computer code for the elelectomagnetic design. In all three designs the strength of all allowed multipoles $B_{(12pole,20pole,28pole)}$ was calculated at r=10cm and the $B_{(12pole,20pole,28pole)}/B_{quad}$ ratio was reduced below the value of $1x10^{-4}$. The deviation of the narrow quad from the four fold symmetry, introduced multipoles like octupoles, 16poles etc. However the relative strength of each of the multipoles ($B_{(8pole,16pole,24pole)}/B_{quad}$) was below the value of $1x10^{-5}$ at r=10 cm. In each of the designs we kept intact both, the outside dimensions of the quadrupole (shown in Fig. 1) and the pole tip radius R_p and we only varied the width of the pole piece W, and the pole tip contour.
In order to keep the permeability of the iron at a reasonable large value $\mu>>1$, the quadrupole strength of each of the models was also kept at a value of ~4.2 [T/m]. All calculations were performed using the computer code for electomagnetics of Vector_Fields[6].

3.1 Narrow Quadrupole Design_A

The cross section of one of the pole pieces of the desisign_A quadrupole is shown in Fig 2. In this design we kept the contour of the pole tip similar to the contour of the narrow quad discussed in ref [1] but we increased the pole width (W) to a value of 19.8 cm, to achieve minimization of the 20pole and 28pole multipoles. The design was finally optimized by modifying the contour of the pole face, by varying the radii of curvature ρ_i ,ρ_o and the location of the inflection points P_1,P_2 ,shown in Fig 2. The optimization yielded a ratio B_n/B_{quad} of $<1x10^{-4}$ at a radius r=10 cm for the (12, 20, 28)pole multipoles.
The increase of the pole width (W) however reduced the area of the current conductor which has to run at a higher current density (J) to achieve the quadrupole strength of ~4.2 [T/m]. An alternative design which satisfies the requirements of low relative strength $B_{npole}/B_{4pole}<1x10^{-4}$, for the (12, 20, 28)pole multipoles, and also provides more conductor area, is discussed in the next subsection.

3.2 Narrow Quadrupole Design_B

The cross section of this alternative design of a narrow quadrupole is shown in Fig. 3. In this design the width of the pole piece has been reduced to 17.6 cm but the overall shape of the pole tip surface remained almost the same as in design_A with only small modifications of the location of the inflection points P_1,P_2 and radii of curvature ρ_i, ρ_o. These minor modifications reduced the relative strength B_{npole}/B_{4pole} of the (12, 20, 28)pole multipoles, below the required value of $1x10^{-4}$ at a radius r=10 cm.

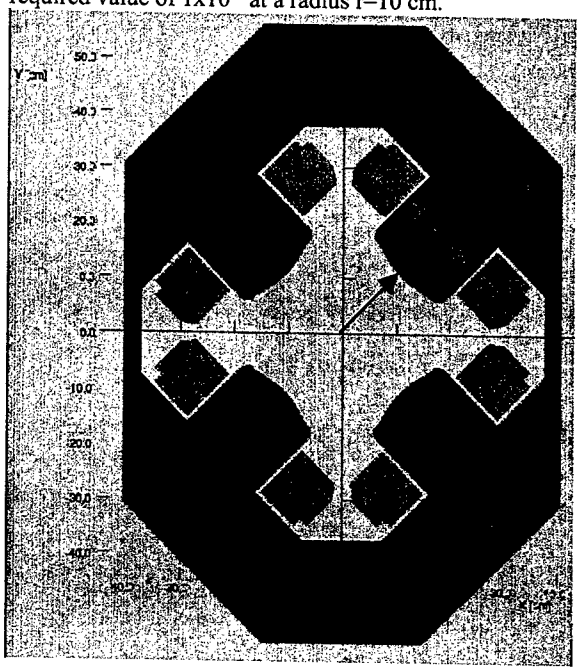


Figure 1: Cross section of the narrow quad. The outer dimensions were the same for all designs A,B, and C.

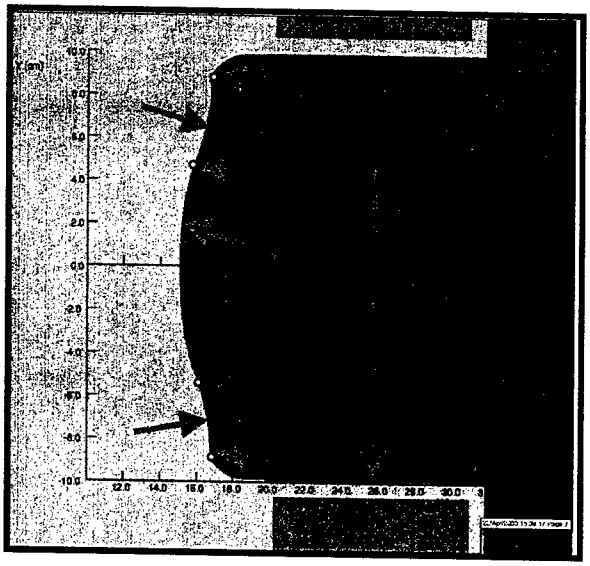


Figure 2. Cross section of pole piece corresponding to "design A" (see text). The inflection points P_1,P_2 , and the radii of curvature ρ_i , ρ_o were varied in order to minimize the strength of the (12,20,28)pole multipoles.

Compared with design A, this design allows for an increased cupper area and the required gradient of ~4.2 [T/m] is achieved at a reduced current density, but the magnetic field **B** inside the poles will be higher.

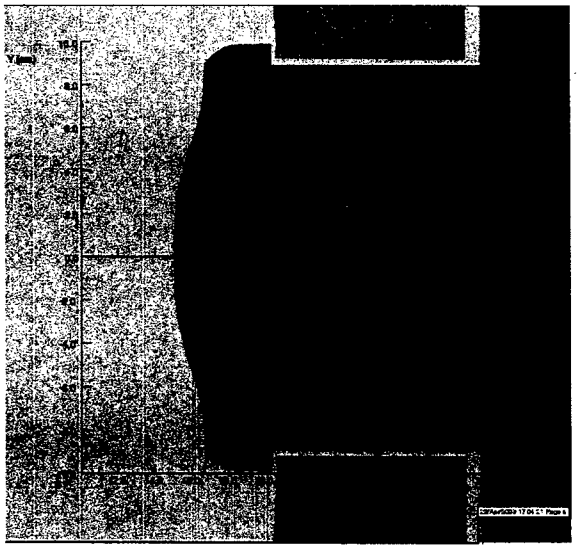


Figure 3. Cross section of pole piece for "design B".

3.3 Narrow Quadrupole Design_C

This design combines the features of the design_A and design_B namely larger conductor area (same as in design_B) and lower value of the magnetic flux density **B** in the pole pieces (as in design_A). The cross section is shown in figure 4. Tthe relative strength B_{npole}/B_{4pole} of the (12,20,28)pole is minimized to values < $1x10^{-4}$. Compare the contour shape of design_C with that of designs A or B.

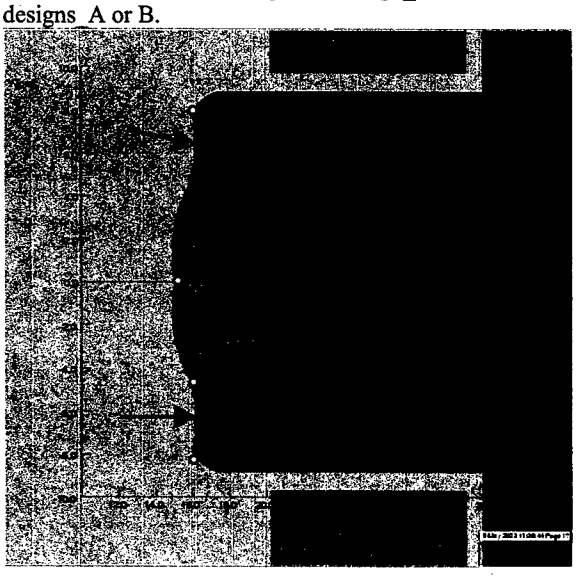


Figure 4. Cross section of the pole piece of "design_C".

4 THREE-DIMENSIONAL MODELING

Practical considerations lead us to perform the three dimensional magnetic field calculations on the "design_C". The goal was to minimize the relative integrated strength $\int B_{npole}dz/\int B_{4pole}dz$ of the (12,20, 28)pole multipoles. The method of optimization was to chamfer the edges of the pole pieces at both, the entrance and exit of the magnet [1] as shown in figure 6. The "pole chamfering" reduced the integrated strength of the 12pole multipole but introduced some strength in the 20pole and 28pole multipoles. This strength was reduced by reshaping slightly the contour of the pole tip inside the magnet. The optimization yielded the following results: $\int B_{12pole}dz/\int B_{4pole}dz=2x10^{-6}$ $\int B_{20pole}dz/\int B_{4pole}dz=4x10^{-5}$ $\int B_{28pole}dz/\int B_{4pole}dz=5x10^{-5}$ at r=10 cm.

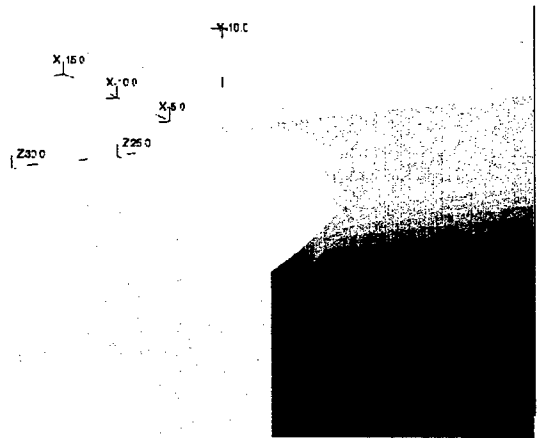


Figure 5 An isometric view of the chamfered ends of one of the pole-piece of the narrow quadrupole.

5 CONCLUSIONS

Two dimensional magnetic field calculations were performed on three models of a large aperture narrow quadrupole. Each of the models was optimized to minimize the relative strength B_{npole}/B_{4pole} of the (12, 20, 28)pole multipoles to values less than $1x10^{-4}$ at a radius r=10 cm. One of the models was optimized using 3D magnetic field calculations.

6 REFERENCES

[1] N. Tsoupas, et. al. "Large Aperture Narrow Quadrupole for the SNS Accumulator Ring" Proc. EPAC2002 p. 1106 Paris June 3-7 2002
[2] J. Wei, et. al. Phys. Rev. ST AB **3**, 080101 (2000)
[3] G.Parzen, A. Fedotov, BNL Private Communication
[4] N. Tsoupas et. al. Tech Note…
[5] G.T Danby and J. Jackson "Theory Design and Measurements of the Brookhaven Narrow Quadrupoles" Proceedings National Particle Accelerator Conf. Wash. DC March 1-3 1967
[6] Vector Fields Inc.

DESIGN AND MANUFACTURING OF THE SNS ACCUMULATOR RING AND TRANSPORT SYSTEM DC MAGNETS*

J. Tuozzolo, J. Alduino, V. Badea, J. Brodowski, G. Mahler, D. Raparia, S. Seberg, BNL, Upton, NY 11973

Abstract

The Spallation Neutron Source* Accumulator Ring requires large aperture dipole magnets, strong focusing quadrupole and sextupole magnets, and low field corrector dipole, quadrupole, sextupole, and octopole magnets. All of these magnets will provide a fixed magnetic field throughout the accumulator's fill/storage/extraction cycle. Similar fixed field magnets are also being built for the beam transport lines from the linac and to the target. Because of the high intensity in the accumulator, the magnets must be built with tight tolerances for optimum field quality. Because some of the magnets are powered in strings, those magnets must have tight tolerances and consistent material properties to provide the same integral field from magnet to magnet. Radiation resistance, maintainability, and cost were other major factors in determining the magnets' design.[1] The accumulator ring and transport line lattice design required 32 different magnet types out of the 312 magnets to be installed. This resulted in small quantity procurements that affected the cost of fabrication and testing of the magnets.

INTRODUCTION

The SNS physics group defined the detailed performance requirements, apertures, and lengths. High beam intensity and 60 Hz repetition rate[2] necessitated a design that was reliable and easy to maintain. The physics design required large aperture magnets for low loss and over 180 tons of collimation[3] will provide some protection from radiation damage for the magnets. As in any particle accelerator or accumulator there are many different magnets types to provide bending, focusing, steering adjustment, injection and extraction. The most common magnet types are provided in table 1. In addition to the types listed there are another 13 magnet types and a total of 312 magnets required.

MAGNET DESIGN

The 32 magnet types required were the biggest cost driver in the magnet development. Defining the parameters, doing the field analysis, providing a detailed design, and procurement all account for 1 man-year of cost per magnet type, some more. Where possible magnets were used in multiple areas. The ring 21Q40 and 30Q44/58 quadrupoles were used in the high-energy beam transfer line (HEBT) and ring to target beam transfer line (RTBT). This saved design and development effort, provided bulk savings in manufacturing, and reduced the requirements for spares.

Table 1: Magnet types used for the SNS Ring, HEBT, and RTBT lines. 21CS26 nomenclature provides: type - CS Corrector Sextupole, aperture – 21 cm, and core length – 26 cm.

Magnet Types	Aperture and Length in Cm.	Field/Grad T, m	Total Devices
Dipoles	17D120	.92 T	32
	8D533	.24 T	8
Quads	21Q40	5.6 T/m	59
	26Q40	5.3 T/m	8
	30Q44	5.4 T/m	11
	30Q58	5.0 T/m	11
	12Q45	7.2 T/m	32
Sextupoles	21S26	.86 T/m^2	12
	26S26	.86 T/m^2	8
Correctors	21CS26	.73 T/m^2	8
	21CO26	.129 T/m^3	8

An early decision was to manufacture the magnets with solid steel cores. Based on the constant beam energy, high field quality requirements, and cost savings considerations this was a good choice. The various vendors were able to provide high quality machined cores that met all of the dimensional requirements: mating surfaces flat to ±.025mm, pole tip profiles machined to ±.025mm, and apertures to .01mm. Unfortunately for the ring magnets that had to be powered in strings by a common power supply this turned out to be a difficult decision. The requirement for consistency exceeded the consistency of the steel used. Even though the steel was procured in common lots from the same "pour" the magnet to magnet variation was greater than the 1×10^{-4} integral transfer function requirement for the magnets powered in strings.[4] Magnets made from steel from different lots were significantly different. An advantage of the solid core design was that it was possible to shim the cores to achieve the required magnet to magnet uniformity. Even with the shimming and the additional magnetic measurement required for small procurements the solid steel cores were cost effective.

A major driver for the cost savings of solid cores was the use of serialized core components. The vendor was required to machine individual parts to ±.15mm tolerances. The final tolerance of the magnet aperture, which determined the field quality, was provided on a core drawing. The vendor could adjust the core component parts as necessary to achieve the final gap

*SNS is managedby UT-Batelle, LLC under contract DE-AC0500Or22725 for the US Department of Energy. SNS is a partnership of six national laboratories: Argonne, Brookhaven, Jefferson, Lawrence Berkley, Los Alamos, and Oak Ridge.

0-7803-7738-9/03/$17.00 © 2003 IEEE

tolerance by machining or positioning in the case of a quadrupole. The manufacturer then serialized the matched parts of the core so components could not be switched. The components were then pinned after alignment to allow magnet disassembly for vacuum chamber placement, future coil repairs, or as noted above shimming. Another cost savings was the use of 1006 steel for all of the magnet cores. It is cheap, easy to obtain, and easy to machine.

All of the high field magnets used conventional water-cooled copper bus with fiberglass epoxy resin systems applied. To provide an added degree of radiation resistance ½ lapped .005 Kapton was required around the conductor for turn-to-turn insulation. Other than added cost, the Kapton did not add any complications to the ring system magnets. On quadrupoles used for the Linac portion of the SNS project there was a problem. Because the kapton tape glue had been improperly cured by the manufacturer, coils from that particular batch had bubbles in them. The glue would outgas excessively when the coil was as the epoxy curing temperature causing the generation of the bubbles. Changing the tape eliminated the problem.

Table 2: Magnet Specifications

Magnet	Current (amps)	Coil Turns per pole	Current Density
17D120	5260	12	452
8D533	650	12	277
21Q40	870	28	558
26Q40	800	44	513
30Q44	1180	41	536
30Q58	1100	41	500
12Q45	520	20	401
21S26	200	21	342
26S26	330	23	564

After the physics group defined the field requirements and length, the mechanical engineer and the magnet design analyst defined the basic core design. 3D field analysis was done using the Opera 3D program. The results were used to define the pole shape (for quadrupoles and multipoles), pole longitudinal shims (for dipoles), and end chamfer (for quadrupoles). At this point there was a negotiation of trade-offs between the mechanical engineers and the electrical engineers (power supplies). The trade-offs were coil turns to achieve the required current density and matching the power supplies into matched groups that could be procured in large numbers.[5] The other trade-off was high current vs. low current for the mechanical engineer. High current magnets required large cross-section bus with a large cooling passage. The advantage was easy and efficient water flow, fewer turns for the coil winder, and more copper per given cross-section. The trade off is a lot of copper is required to get the current from the power supply house to the magnet. Therefore high current magnets were only used for the ring dipoles that were powered in series and the special injection and extraction magnets where the extra copper was needed to power otherwise tight magnet designs.

PROCUREMENT AND SCHEDULE

Multiple methods of magnet fabrication and procurement were employed depending on the magnet type. The majority of the large production magnets were built to specification with an accompanying detailed drawing package that defined in detail how the magnet was to be constructed. Most of the magnets were procured as complete assemblies that were shipped to BNL or ORNL for testing and magnetic measurement. The ring dipole (17D120) core and coils were purchased separately and then assembled and tested at BNL. This was done because core design iteration with steel was still on going while the project schedule was requiring fabrication of the magnet. The coils were sent out to bid while this testing continued. The cores followed four months later. The advantage of this was that the cores were bid to magnet manufacturers and large machine shops that specialized in machining heavy pieces. The large machine shops under bid the magnet manufacturers by 35% and did an excellent job delivering the magnets on time. Other effects on the magnet cost were the quantity purchased and the complexity of the design. Compare the table 3 with the quantities in table 1 and there is a significant effect. Also quadrupoles cost more than equivalent sized dipoles because of the complexity of the pole tip profile and more pieces have to be machined. Sextupoles have a step increase as well.

Table 3: Magnet Cost (This table does not include the first article magnet cost which was typically 50% higher).

Magnet Type	Total Weight	Unit Cost	Core $/lbs	Coil $/lbs
17D120	19500	$ 70,000	$ 1.59	$ 7.66
8D533	30400	$ 74,500	$ 2.33	$ 3.90
8D406	2600	$ 78,000	$ 2.84	$ 5.14
21Q40	4000	$ 29,400	$ 5.48	$ 4.00
26Q40	6000	$ 38,300	$ 7.39	$ 3.56
30Q44	6000	$ 33,000	$ 4.07	$ 7.74
30Q58	7300	$ 35,000	$ 2.97	$ 8.02
21S26	1200	$ 30,100	$ 6.48	$ 6.00
26S26	1400	$ 34,500	$ 8.63	$ 6.00

Each magnet procurement was competitively bid with the winning vendor being chosen based on lowest price without exceptions to the bid package. The bid package included the fabrication drawing package, three specifications (core steel, coil, and overall magnet assembly), and a statement of work (SOW). The SOW provided schedule information and project reporting requirements. After winning the low bid award, the technical team visited the vendor and all of the documentation was reviewed to clarify the requirements. What became clear at this point was that some vendors were not thorough in reading the specifications or the

SOW. They focused on the drawings and missed hardware and schedule requirements in the specifications and SOW. Scheduled weekly phone conferences were held to maintain contact and review progress.

Except for one of the kind magnets, all of the magnet contracts require that the vendor first build a 1st article magnet for inspection and magnetic measurement before proceeding with the rest of the production order. This allowed BNL to do detailed magnetic measurement to verify the field quality of the design and it gave BNL an option point where it could cancel an order if the vendor was not performing to specification. More important it allowed BNL to iterate on the magnetic design by modifying the steel. All of the ring quadrupole magnets required the procurement of additional pole tips so iterations could be done on the pole tip chamfers that added steel. Because the profile of the quadrupole pole tip was so critical to the magnetic performance, vendors also provided 1" thick samples to demonstrate the performance of their CNC machines before machining the full length 1st article pole tips. When tested all three of the ring quadrupoles magnet types that required the highest field quality went through at least two iterations of the pole tip shape or end chamfer before they were approved for production. These iterations required disassembly of the magnets to remove and remachine the pole tips or to remove and replace the pole tips. This required two to three months of testing time before a 1st article magnet could be approved for production.

Table 4: Time is in weeks after receipt of order.

Magnet Type	1st Article	Production Approval	1st Production	Order Complete
SOW	31	32	54	70
17D120	16	18	26	35
8D533	48	52	65	104
21Q40	39	43	56	100
26Q40	48	54	76	89
30Q58	36	53	83	95

Except for one of the kind magnets, all of the magnet contracts require that the vendor first build a 1st article magnet for inspection and magnetic measurement before proceeding with the rest of the production order. This allowed BNL to do detailed magnetic measurement to verify the field quality of the design and it gave BNL an option point where it could cancel an order if the vendor was not performing to specification. More important it allowed BNL to iterate on the magnetic design by modifying the steel. All of the ring quadrupole magnets required the procurement of additional pole tips so iterations could be done on the pole tip chamfers that added steel. Because the profile of the quadrupole pole tip was so critical to the magnetic performance, vendors also provided 1" thick samples to demonstrate the performance of their CNC machines before machining the full length 1st article pole tips. When tested all three of the ring quadrupoles magnet types that required the highest field quality went through at least two iterations of the pole tip shape or end chamfer before they were approved for production. These iterations required disassembly of the magnets to remove and remachine the pole tips or to remove and replace the pole tips. This required two to three months of testing time before a 1st article magnet could be approved for production.

Every production magnet received is high potted, leak checked, and magnetic measured. The magnetic measurement was used to verify the magnet matching and the requirement for shimming as discussed previously. If shimming was required, the magnets were magnetically measured again. Magnetic measurement results also were used to locate the magnets in the lattice.[6] Magnetic measurement was also used to verify the magnetic center of the multipole magnets.

CONCLUSIONS

The magnets for the SNS accumulator are conservatively designed for reliability in a high radiation environment, low cost, and ease of maintenance. Field quality has been a high priority because these magnets are part of a high intensity machine. Multiple steps have been taken to insure field quality and excellent matching from magnet to magnet. At this time of the 312 magnets required for the SNS ring systems, 182 have been delivered by the vendors, and 82 have been shipped to ORNL, tested, and are ready for installation.

REFERENCES

[1] J. Tuozzolo, et al, "Magnets For The National Spallation Neutron Source Accumulator Ring", PAC1999, New York.
[2] J. Wei, "Spallation Neutron Source Ring -- Status, Challenges, Issues, and Perspectives", (these proceedings).
[3] H. Ludewig, et al, "Integration of the Beam Scraper and Primary Collimator in the SNS Ring", (these proceedings).
[4] P. Wanderer, et al, "Final Test Results for the SNS Ring Dipoles", (these proceedings).
[5] R. Lambiase, J. Sandberg, "Designing and Implementing an Accelerator Power Supply System in a Multi-Laboratory Context", (these proceedings).
[6] S. Tepikian, et al, "SNS Ring and Transport System Magnet Acceptance and Installation Preparation", (these proceedings).

Abbott, S.R. 86
Abell, D. 1059
Aberle, O. 45, 878
Abeyta, E.O. 558
Ablett, J.M. 241
Abo-Bakr, M. 3020, 3023
Abrahamyan, K. 2114
Achard, C. 495
Ackermann, W. 3551, 3566
Adachi, T. 1679
Adams, D.J. 1527
Adelmann, A. 3524
Adolphsen, C. 668, 678, 1264, 2664, 2763
af Ugglas, M. 1590
Agarwal, D. 278
Agustsson, R. 944
Ahle, L. 989
Ahrens, L. 51, 405, 1542, 1545, 1640, 1685, 1697, 1706, 1715, 2441
Aiba, M. 1679, 3413, 3452
Aizatsky, N.I. 1107, 3303
Ajima, Y. 1978
Akai, K. 356
Akiyama, A. 2351
Akre, R. 235, 2107, 2285, 3141
Aladwan, A. 238
Alber, R. 983
Albrecht, C. 467
Al-Dmour, E. 238
Alduino, J. 2138, 2156
Aleksandrov, A. 65, 1524, 2598, 2706, 3536
Alekseev, I. 51
Alesini, D. 366, 2080, 2279, 2500, 2742, 3285
Alessandria, F. 2080, 3285
Alessi, J. 51, 89, 1637, 1715, 2793, 3282
Alexahin, Y. 1757
Alexandrov, V. 3536
Al-Khateeb, A. 2607
Allen, C.K. 2360, 3527
Allison, S. 235
Allison, T. 1485, 2379
Alsharo'a, M. 1792
Altmark, A. 1891, 1894, 1897
Alton, G.D. 995, 998, 1001
Ambrosio, G. 1966
Amemiya, Y. 530
Ames, F. 2869
Ammigan, K. 1452
Amundson, J. 2939, 3195
Anami, S. 1509
Anderberg, B. 2318, 2321
Anders, A. 98, 2622
Anders, W. 1186, 3020
Anderson, D. 3141
Anderson, D.E. 553
Anderson Jr., J. 1652
Anderson, R. 2390
Anderson, S.G. 95, 2957
Anderson, T.G. 1649, 3437
Andersson, A. 2318, 2321
Andler, G. 1590
Ando, L. 81
Andonian, G. 944, 947, 2110, 2112, 3321
Andreev, N. 1966
Andreoli, S. 470
Andresen, N. 869
Anerella, M. 164, 1939, 2162
Anferov, V. 699, 1563
Ang, Z. 1285
Anghel, A. 878
Angoletta, M.E. 2461
Ankenbrandt, C. 1792, 2936
Annala, G. 1730, 1972, 3062, 3359
Antokhin, E. 2198
Anzalone, E. 2382
Ao, H. 2826
Aoki, M. 1993, 2198
Aoki, N. 530, 713
Aoki, T. 2551
Apgar, S.E. 553
Arai, S. 1509
Arakida, Y. 568, 1512, 1784, 1807
Arduini, G. 307, 1718, 1727, 2240, 3038
Arkan, T. 1210
Arnold, N.D. 2327
Artoos, K. 1434
Aryshev, A.S. 2709
Asano, H. 1338
Asano, Y. 782
Aseev, V.N. 2875
Ashmanskas, W. 323
Asiri, F. 2748
Aspart, A. 1303
Assadi, S. 498, 1524, 1569, 2444, 2706
Assmann, R. 45, 665, 3494
Attal, M. 238
Autin, B. 444
Averboukh, I.I. 1074
Avilov, A. 1619
Ayvazyan, V. 467, 2342, 2730
Ayzatsky, M.I. 1605, 2098, 2878, 2969
Baartman, R. 1578, 1584
Baba, H. 3332
Baba, Y.H. 487
Baboi, N. 467, 1086, 1261, 1270
Babzien, M. 944, 1909
Baca, D. 312, 536, 553, 3294
Bacci, A. 2080, 3285, 3512
Bäcker, H.-J. 836
Badea, S.V. 2138, 2156
Bae, Y.S. 2539
Bagge, L. 1590
Baggett, K. 2183, 2186, 2189
Baglin, V. 307, 1727
Bähr, J. 2114
Bahrdt, J. 836
Bai, M. 51, 54, 405, 1697, 1706, 2204, 2207
Baichev, I. 3494
Bailey, C.P. 1527
Baishev, I. 45
Bajko, M. 1942
Bak, P. 3318
Bakker, R.J. 214

Balbekov, V. 1751, 2014, 2017
Balkcum, A. 1144
Ball, M.J. 1996
Balleyguier, P. 2053, 2458, 2601, 2799
Bandelmann, R. 467
Bandura, L. 1999
Bane, K. 126, 3126, 3252
Banna, S. 722, 1879
Bao, X. 2357
Baptiste, K. 869, 1240, 1252
Bär, R. 694
Barber, D.P. 372
Barletta, W.A. 186, 923
Barlow, D. 702, 1664
Barnard, J.J. 1521, 1990, 2658
Barnes, B. 1736
Barnes, C.D. 1530, 1933, 2101
Barnes, M.J. 1162
Barnes, P. 1309, 1323
Barni, D. 1341, 1506
Barov, N. 1870, 2682
Barr, D. 2512
Barr, G. 1987
Barstow, B. 192, 1317, 1320
Barsz, T. 2029
Bartolini, R. 914, 2077, 3285
Barton, D. 1637
Barty, C.P.J. 95
Baskiewicz, M. 302
Batchelor, K. 541
Batrakov, A. 250
Batygin, Y.K. 2751, 3548
Baudrenghien, P. 1718, 3050
Bauer, P. 1730, 1972, 3359
Bauer, S. 1410, 2887
Baum, D. 2527
Baynham, D.E. 1987
Bazarov, I. 192, 842, 848, 1201, 1317, 1323, 2062
Beard, K. 195, 332, 1104, 1575
Beaudoin, B. 426, 2312, 2571
Beche, J.-F. 2530
Bechstedt, U. 598, 3428
Bechtold, A. 1062
Beck, M. 2189
Beckert, K. 434
Beckman, L. 3389
Beczek, K. 2038
Beebe, E. 89
Beebe-Wang, J. 51, 1706
Beinhauer, W. 3551
Belgroune, M. 896
Bellavia, S. 1542
Bellenger, D.W.J. 1527
Beller, P. 434
Bellodi, G. 1527
Bellomo, P. 235
Bellucci, S. 917, 986
Beloglasov, V.I. 2878
Belohrad, D. 2461
Belomestnykh, S. 192, 1198, 1201, 1306, 1317, 1323, 1326, 1329, 1410, 1437, 2059, 3347
Beltran, C. 326, 3086
Bender, H. 558
Benedetti, G. 366, 2279, 2945
Benedetto, E. 1727, 3053
Benedikt, M. 1548
Bengtsson, J. 195
Benjamin, J. 1715
Bennett, J.R.J. 1527
Bennett, S.L. 189
Ben-Zvi, I. 39, 92, 944, 1300, 1909, 2005, 3186
Berden, G. 519
Berenc, T. 1736, 3362
Berg, J.S. 1804, 1816, 2002, 2210, 2213, 2216, 2219, 3413, 3485
Berg, S. 1416, 1422, 2029, 2038
Berg, W.J. 2417, 2420
Bergqvist, M. 2321
Berio, R. 989
Berkaev, D.E. 372
Berkvens, P. 854
Berman, L. 241
Bernal, S. 426, 1673, 1676, 2312, 2571, 2574, 2577, 2673
Bernard, A. 195
Bernardin, J. 1461
Bernaudin, P.-E. 2799
Bernstein, L. 989
Bertolucci, S. 3285
Bertrand, P. 2802, 3488
Bessonov, E. 1963
Bhashyam, S. 1966
Bhat, C.M. 514, 1769, 2345, 2348, 3180
Bhatt, R. 2643
Biagini, M. 366, 914, 2077, 2279, 2297, 2300, 2945, 3285
Biallas, G. 2123, 2135, 2183, 2186, 2189
Biarrotte, J.L. 1303, 2802
Biasci, J.C. 854
Bieler, T.R. 1359
Bieniosek, F.M. 98, 275, 312, 536, 1518, 2524, 2619, 3297
Bierwagen, J. 1353
Bilderback, D. 192
Bilheux, H. 998
Billen, J. 1461, 1515, 2844, 3518, 3521
Biller, E.Z. 1605, 2878
Billing, M. 3059
Binello, S. 1542, 1703
Bini, S. 917
Binkley, M.E. 2497
Biocca, A. 3374
Birkel, I. 893, 3273, 3276
Biryukov, V.M. 917, 986, 1655, 1691
Biscardi, R. 241
Biscari, C. 335, 366, 684, 2279, 2742, 2945, 3285
Bishofberger, K. 57, 1778, 1781
Bisognano, J.J. 3147
Bizen, T. 487
Björkhage, M. 1590

Bjorklund, E. 2354
Black, E. 983, 1792, 1834, 1999
Blair, G. 2739
Blanco-Vinuela, E. 1945
Blasche, K. 589
Blaskiewicz, M. 54, 135, 272, 394, 476, 797, 1195, 1569, 1706, 1715, 1816, 2595, 2598, 3026, 3029, 3035, 3344, 3419
Blind, B. 702, 1664, 2948
Bliss, N. 189, 1029
Blivet, S. 1303
Blokland, W. 1524, 2444, 2491, 2706
Blom, M. 1590
Blomqvist, I. 220
Blue, B.E. 731, 1530, 1864
Bluem, H. 92, 977
Bocchetta, C.J. 214
Boege, M. 3386
Boffo, C. 1210
Bogacz, A. 195
Böge, M. 291
Boggia, A. 3318
Bohl, T. 1718, 3050
Bohlen, H. 1144
Bohn, C.L. 2676
Bohnet, I. 2114
Boilot, D. 1332
Boimelshtein, Y. 3318
Boine-Frankenheim, O. 589, 2607
Bojtar, L. 2461
Boller, K.-J. 1900, 1903
Bolton, P.R. 2104, 2709, 3216
Bondarenco, N. 3329
Bondarev, B.I. 2679, 3002, 3530
Bongers, H. 2872
Bongers, N. 598
Boni, R. 366, 2279, 2742, 3285
Bookwalter, V. 1494
Borburgh, J. 1643
Borchard, P. 1113, 1116
Borden, M. 508, 2521, 3089, 3455
Bordry, F. 1945
Boriskin, V.N. 1107, 2878, 3303
Borissov, E. 1210
Borland, M. 247, 256, 283, 2330, 2417, 2420, 3138, 3461, 3470, 3473, 3476
Borovina, D.L. 553, 1168
Borrion, H. 2458
Bosch, R.A. 887, 929, 932, 935, 2373, 3147
Boscolo, I. 3285
Boscolo, M. 366, 914, 2077, 2279, 2945, 3285, 3548
Bosland, P. 878, 1332
Bosotti, A. 1341
Bossert, R. 1969
Bottura, L. 173, 1730, 1945
Bourcey, N. 1434
Bousson, S. 1303
Bowden, G. 1261, 1264
Bowler, M.A. 189
Boyce, J.R. 938, 941
Boyce, R. 235, 2174
Bozzini, D. 1945
Bradley III, J. 553, 1095, 1168, 1458
Brajuskovic, B. 830, 1017
Brarvar, S. 51
Braud, D. 1303
Braun, H. 495, 1156, 2721
Brautti, G. 3318
Bravin, E. 2464
Bredy, P. 878, 1332
Brelsford, B. 1542
Brenger, A. 2476
Brennan, J.M. 39, 51, 135, 394, 476, 1195, 1545, 1706, 1715, 3026, 3029, 3338, 3341, 3344
Bricault, P. 439, 1584, 1670
Bricker, S. 1353
Briddick, D. 2029, 2038
Bridges, F. 1092
Briggs, R. 3098
Brinkmann, A. 1374, 1395
Briscoe, B. 3282
Britvich, G.I. 917
Brodowski, J. 1195, 2156, 2444, 2598
Broemmelsiek, D. 3431
Broggi, F. 3285
Bromberek, D. 1416
Bross, A. 983, 1183
Broste, W. 558
Browdowski, J. 1428
Browman, A. 326, 508, 2521, 3086, 3089, 3455
Brown, B.C. 2165
Brown, C. 1446
Brown, K.A. 51, 405, 746, 1542, 1545, 1706, 1715, 2441, 2595, 3422
Brown, W. 95, 938, 2192, 2957
Browne, M. 2297
Bru, B. 2802
Brugger, M. 45, 3494
Bruhwiler, D.L. 719, 734
Brumwell, F.R. 592
Brunelle, P. 229, 896
Brunner, O. 473
Bruno, D. 743, 1700, 1706
Bruno, L. 45
Brüning, O.S. 42, 1748
Bui, T. 3560
Bukh, B. 2631, 2634
Bulfone, D. 3395
Bullard, D. 2183
Bultman, N. 1461, 2844
Bunce, G. 51
Burgazzi, L. 1506
Burgmer, R. 1948
Burke, D.L. 1264
Burkhardt, H. 45, 1721, 3041, 3044
Burns, M. 2354
Burov, A. 2020, 3062
Burrill, A. 39, 92
Burrows, P.N. 687
Busch, M. 2273
Bussmann, M. 112
Butler, C. 195

Butler, J. 1195
Büttner, T. 467
Byer, R. 722, 728, 1858
Bylinsky, I. 1285, 1584
Byrd, J. 863, 869, 1240, 2530
Cacciotti, L. 2476
Cadapan, L. 235
Cadorna, A. 2348
Cai, Y. 350, 2288, 2291, 2297, 2300, 3542
Calaga, R. 39, 272, 2207
Calatroni, S. 1309
Callahan, D.A. 2637
Calvet, O. 1434
Calzas-Rodriguez, C. 1945
Cameron, P. 54, 135, 394, 524, 1703, 1706, 2444, 2447, 2598, 2691, 2697, 3026, 3029
Campbell, L.P. 1909
Campisi, I. 457, 977, 1104, 1377
Cao, L. 2852
Capatina, O. 1434
Capista, D.P. 2165
Caporaso, G. 563
Cappi, R. 388, 2910, 2913
Carcagno, R. 1969, 1972
Cardona, J. 1059, 1706, 2901
Carey, D. 1446
Carli, W. 2872
Carlier, E. 1945
Carlson, C. (Bechtel) 558
Carlson, C. (BNL) 1715
Carlson, K. 2020
Carneiro, J.-P. 2065, 2068, 2114, 3548
Carr, G. 2354
Carr, G.L. 241, 1497
Carr, L. 329
Carroll, A. 1709, 3255
Carron, G. 1156
Carson, J. 1969
Carter, H. 1210, 1813
Cary, J.R. 719, 734, 1536, 1885, 1918, 2026
Casarin, K. 2309
Casey, B. 241
Casey, J.A. 547, 1500
Caspers, F. 1801, 2470, 2700, 3479
Caspi, S. 42, 170, 1984
Cassel, R. 235
Castellano, M. 2476, 3285
Castro, P. 198, 467, 1086, 2730
Catalan-Lasheras, N. 1428, 2144, 2225, 2598, 3026
Catani, L. 2476, 3285
Cattelino, M. 1144
Caudill, L. 558
Cederk€ll, J. 2869
Cee, R. 2114
Celata, C.M. 275, 536, 1518, 1521
Celona, L. 81
Cerniglia, P. 2444, 2697
Chacon-Golcher, E. 73, 3291, 3294
Chae, Y.-C. 3008, 3011, 3014, 3017
Chambers, F. 563, 2960
Champion, M. 1464, 3371, 3377
Chan, K.C.D. 558, 3210
Chang, C.H. 1041, 1044, 1047
Chang, C.K. 2376
Chang, H.P. 890, 1044
Chang, J.C. 1476, 1479, 1482, 2402, 2405
Chang, L.H. 1371, 2670
Chang, S.H. 2402, 2405
Chang, X. 39, 1300, 2005, 3186
Chao, A. 126
Chao, Y. 195, 294, 3243
Chao, Z. 487
Chapman, S. 167
Chaput, R. 229
Charrier, J.P. 1303
Chase, B. 1736, 1769
Chattopadhyay, S. 195
Chavanne, J. 253, 854
Chazot, G. 851
Cheever, D. 2324
Chel, S. 878, 1332
Chen, A. (FNAL) 623
Chen, A. (YY Labs) 2586
Chen, C. 1255, 1258, 2643, 2646, 2966
Chen, C.I. 3234
Chen, D. 1560, 3506, 3509
Chen, G. 2586
Chen, H. 467
Chen, J. 1044, 2376, 2554, 2557, 2580, 3237, 3392
Chen, J.R. 821, 1476, 1479, 1482, 2402, 2405
Chen, L. 2357
Chen, S. 1921
Chen, Y.-J. 558, 563, 2960, 3210
Chen, Z. 2844
Chen-Yao, L. 764
Cherbak, E. 1177
Chesnokov, Y. 917, 986, 1655, 1691
Cheung, H.W.K. 2488
Chevtsov, P. 2560
Chiadroni, E. 914, 3285
Chiaveri, E. 45, 878, 1309, 1332
Chiba, J. 1509
Chichili, D. 1969
Chien, Y.-C. 764, 767
Chiesa, L. 170, 1984
Chin, M. 869
Chin, Y.H. 479
Chiou, J. 764
Chishiro, E. 1338
Cho, Y.S. 1219, 1222, 2539, 2832, 2857, 2884
Choi, B. 235
Choi, B.H. 1219, 1222, 1602, 2539, 2832
Choi, J. 875, 3383
Choroba, S. 467
Chou, P.J. 1368, 3150
Chou, W. 604, 623, 1551, 1554, 1557, 2922, 2925, 2936

Chouhan, S. 899
Chrin, J. 291
Christensen, W. 2485
Christina, V. 920, 977, 2186
Christoph, M. 39
Chu, C. 2360, 2363, 3527
Chu, P. 2366
Chun, M.H. 1470, 2857
Chung, Y.C. 1479
Chupyra, A. 2769
Cialdi, S. 3285
Cianchi, A. 2476, 3285
Ciavola, G. 81
Cimino, R. 1727
Ciocci, F. 3285
Ciovati, G. 1362, 1374, 1395
Citver, G. 39, 92
Clark, G. 601
Clarke, D.G. 1029
Clarke, J.A. 189, 1029
Clarke-Gayther, M.A. 1473
Clauser, T. 3318
Clayton, C. 731, 1530, 1864, 1873, 1933
Clendenin, J. 2104, 2126, 2129, 3216
Clifft, B.E. 2426
Cline, D. 1787, 1876, 1909, 2008, 2709
Clozza, A. 366, 2279, 2742, 3285
Cobb, J.H. 1834
Codner, G. 2399
Cohen, R. 132, 312, 536
Colby, E. 722, 1858, 2101
Cole, J.M. 998
Cole, M. 92, 977, 2047, 2050
Coleman, J. 1485
Colestock, P. 977, 3086
Collier, M. 2844
Collier, P. 307, 1718, 1727
Collins, I. 1727
Collins, J. 699
Collins, S. 1661
Colocho, W. 2297
Compton, C. 1353, 1359, 1362
Conde, M.E. 2032
Coney, L. 1587
Congretel, G. 2799
Connolly, R. 135, 1706, 2444
Cook, E.G. 544
Coosemans, W. 665
Corbett, J. 2369, 2372
Corbett, W. 235
Corlett, J. 186, 812, 866, 923, 1246, 1249, 2086, 2408, 3198
Cornelis, K. 1718, 1727, 3038
Cornelis, M. 1942
Corniani, G. 1341
Corsini, R. 684, 2742
Courant, E.D. 405, 1697, 1816, 3485
Cousineau, S. 117, 259, 1428, 1569, 1572, 2598
Cowan, B. 722, 1855
Cox, L. 1144
Craddock, M.K. 1581
Craft, B. 1053, 2382
Craievich, P. 214, 878
Crandall, K. 1515, 2855
Crandall, K.R. 2889
Crane, J.K. 95
Crappell, A. 2382
Crawford, A. 1312
Crisp, J. 1781, 2348, 2491
Crittenden, J. 1023, 1954, 3425
Crofford, M. 3377
Cross, R.R. 95
Cui, Y. 426, 511, 3156
Cullerton, E. 3068
Cummings, K. 1095, 1237
Cummings, M.A. 1834
Cummings, M.A.C. 983, 1798, 1999
Cupolo, J. 524, 2444, 2697
Cusick, M. 1144
Cutler, R. 550, 617
Czyz, W.S. 592
Da¯l, A. 229
Dail, J. 2183
D'Alessio, C. 2500
Dallin, L. 220, 2195
Dalmas, D. 558
Daly, E. 457, 977, 1377, 2866
Danailov, M. 214, 2306
Danared, H. 1590
D'Angelo, A. 3285
Danilov, V. 117, 1569, 1572, 2598, 3032
Danilova, E. 2363
Daté, S. 250, 881
Datta, D. 3560
Datte, P. 2530
Dattoli, G. 914, 3285
D'Auria, G. 214
Davidson, R.C. 1667, 2655, 2658, 2661, 2975, 2978, 3117, 3120, 3123
Davino, D. 1428, 2147, 2598, 3035
Davis, G.K. 457, 1383
Davis, H. 120
Dawson, C. 2444, 2453, 2697, 3026
Dawson, W. 524
Day, L. 2429
De Baca, J.M. 1237
DeBarger, S. 3141
DeCarlo, A. 1467, 2706
De Conto, J.-M. 2802
Decker, F.-J. 423, 731, 1530, 1864, 1933, 2282, 2285, 2297, 2300, 2754, 3126, 3129
Decker, G. 833, 2688
Decking, W. 652
Decyk, V. 3174
DeFord, J.F. 3554
Degen, C. 524, 2444, 2697, 3026
Dehler, M. 3395
Dehning, B. 45, 2470
Deibele, C. 1524, 2706
Deitinghoff, H. 1335, 2942
de Jong, M. 220

Dejus, R.J. 1020
DeKamp, J.C. 161
Delaney, T. 690
Delayen, J. 92, 457, 992, 1098, 1291, 1380, 1383, 2379, 2860
DellaPenna, A. 524, 2444
Delle Monache, G. 366, 2279, 2742
Dell'Orco, D. 235, 2174
DeLong, J. 476, 1715, 3338, 3341, 3344
De Martinis, C. 2080, 3285
Demidov, N.V. 2878
Demirkan, M. 2318
Demma, Th. 2993, 2996, 2999
Demske, D. 1497
Denard, J.-C. 229, 2560
Denes, P. 2530
Deng, S. 1530, 1933
Den Hartog, P. 824, 830, 833, 1017
De Ninno, G. 214, 2306, 2309
Denz, R. 1945
Derbenev, Y. 941
Derenchuk, V.P. 1563
De Rijk, G. 1942
Deriy, B. 2261
Deryuga, V. 1619
De Santis, S. 186, 866, 2530, 2745, 3377
Deslandes, D. 2458
Desler, K. 2682
Devanz, G. 878, 1086
DeVoy, J. 2934
Devred, A. 42, 146, 173
Dewan, S. 770
Dey, J. 1204, 1769, 3353, 3356
Diao, C.Z. 968
Dickson, R. 2563
Diebele, C. 2444
Diep, A. 2312, 2571, 2577
Dierker, S. 241
Dietderich, D.R. 170, 1032, 1984
Dietrich, J. 598, 3428
Dilley, C.E. 1909
DiMarco, J. 1730, 1969, 1972
DiMauro, L. 217
Di Mitri, S. 214, 1050
Dimitrov, D.A. 734
Ding, Y. 2580
Di Pirro, G. 366, 2279, 2476, 3285
Di Salvo, R. 3285
Diviacco, B. 214, 1050, 2306
Diwan, M. 429, 1709, 3255
Dobbins, J. 2473, 3347
DÅbert, S. 495, 1156
Dodson, G. 1569
Doelling, D. 899
Dohan, D.A. 2327
Doleans, M. 1599
Dolgashev, V.A. 1264, 1267, 1276, 2763
Dolinskii, A. 434, 694
Dombsky, M. 439, 1584
Domning, E. 3374
Donald, M. 2288, 2297
Dong, H. 195
Dong, S. 758
Donley, L.I. 1159
Dooling, J.C. 592, 1159
Doolittle, L. 186, 1464, 2408, 3371, 3377
Doose, C. 1020
Doria, A. 3285
Dormiani, M. 3141
Dortwegt, R. 630, 2038
Doss, J.D. 553
D'Ottavio, T. 1715
Douglas, D. 195, 938, 977, 2183, 2186, 2189, 3243
Dovbnya, A.N. 1107, 2878, 3303
Dowell, D. 2104, 3216
Dowling, A. 439
Doyle, E. 644
Doyuran, A. 217, 241, 1192, 2455
Drago, A. 366, 2279, 2742, 3285
Dragt, A. 2772
Drees, A. 51, 54, 794, 797, 1685, 1688, 1691, 1706, 2691, 2904
Drees, K. 3026
Dris, S. 1204
Drozdoff, J. 638
Drozhdin, A. 1503, 1557, 1733, 1742, 2739, 2925, 2936
Drury, M. 457
Ducar, R. 1652
Ducimetiere, L. 1162
Dugan, G. 737
Duke, J.P. 2542
Du Mont, D. 1542
Dunkel, K. 2887
Duperrier, R. 2802, 2805
Durante, M. 1948
Durkin, A.P. 2679, 3002, 3530
DËrr, H.A. 836
DËrr, V. 836
Durtschi, G. 558
Duru, P. 854
Dutto, G. 601, 638, 1584
Dwinell, R.D. 86
Dykes, D.M. 189
Eberhardt, W. 836
Ebihara, K. 860, 1228
Ecklund, S. 2297, 2300
Edwards, D. 2068, 2682
Edwards, H. 447, 1213, 2682
Edwards, R.L. 1341, 1344
Efthimion, P. 98, 2622, 2655, 2661
Egawa, K. 1071, 1074
Ego, H. 250, 487
Ehrlich, R.D. 2399
Eichhorn, R. 598
Eickhoff, H. 694
Einfeld, D. 238
Eisen, E. 1122
Eisert, D.E. 887, 2373
Ekdahl, C. 558, 3210

Elioff, T. 235
Elleaume, P. 854
Ellis, S. 2841
Emamian, M. 2273
Emery, L. 256, 283, 833, 2261, 2330, 2423, 2438, 3461, 3464, 3470, 3473, 3476
Emhofer, S. 2869, 2872
Emma, P. 211, 423, 914, 926, 965, 1530, 1933, 3126, 3129, 3138
Endo, K. 1071, 1074
Eng, W. 743, 770, 1542, 2144
England, R.J. 3258
Enomoto, A. 2838
Erdelyi, B. 1760, 1772, 3542
Erdem, O. 1933
Eremeev, G. 1312
Erickson, R. 2297
Eriksson, L. 644
Eriksson, M. 2318, 2321
Ernst, D. 2174
Erokhin, A. 2769
Errede, D. 983, 1999
Esarey, E. 719, 734, 1885
Escallier, J. 164
Eschke, J. 467
Espinoza, C. 1664
Esposito, A. 3285
Esser, F.M. 598
Estrada, J. 1763
Evangelakis, G. 1709
Evans, I. 235
Evans, L.R. 19
Evans, R. 1485
Eversole, S. 558
Eylon, S. 98, 558, 1171, 2533, 2616, 2619, 2622, 2625, 2628, 2646, 3098
Ezura, E. 860, 1228
Faatz, B. 467
Fabbricatore, P. 1987
Fabris, A. 878
Facco, A. 470
Falabella, S. 563
Falce, L. 1113, 1116
Faltens, A. 536, 1990
Fan, L. 815
Fan, M. 1560, 3506, 3509
Fan, T.C. 1041, 1047
Fang, J.-M. 1882, 1924
Fang, S. 1285, 1404
Fang, Z. 1071, 1074
Fann, C.-S. 767
Fantini, A. 3285
Farinon, S. 1987
Farkhondeh, M. 956, 959, 980, 2324
Farrell, J.P. 541
Farrow, R.C. 189
Fartoukh, S. 2225
Farvacque, L. 854, 3189
Faucett, J. 2354
Faure, J. 1840
Faus-Golfe, A. 2240
Favale, A. 92
Fawley, W. 186, 558, 923, 959, 3098
Fedotov, A. 39, 117, 383, 1572, 2589, 2592, 2598, 3032
Fedurin, M. 1053, 2382, 2892
Feher, S. 1969
Feigerle, C.S. 617
Feikes, J. 845, 3023
Felden, O. 598
Feldman, D. 426, 3323
Feldman, R. 426
Fellenz, B. 2348, 2491
Ferguson, P. 1110
Ferianis, M. 214
Ferioli, G. 307
Fernow, R.C. 2002
Ferracin, P. 170, 1984
Ferrari, A. 45, 684
Ferrario, M. 467, 914, 2077, 2080, 2730, 3285, 3548
Fessenden, T.J. 2533
Fessia, P. 1942
Filhol, J.-M. 229, 1332
Filip, C.V. 1873
Findlay, A. 2461
Findlay, D.J.S. 2542
Finley, D. 1207, 1210, 1813
Fiorito, R. 1497, 2712
Fischer, R. 2476
Fischer, W. 51, 54, 135, 476, 794, 797, 1625, 1697, 1706, 1754, 2222, 2228, 3026, 3029
Fisher, A. 2285, 2297, 2300
Fisher, M. 887, 2303
Fittinghoff, D.N. 95
Fitzgerald, D. 508, 2521, 3089, 3455
Fitzgerald, J. 1781
Flanagan, J.W. 2503
Flanz, J. 690
Fliflet, A.W. 1128
Fliller III, R. 272, 1685, 1691, 1706, 2904
Floettmann, K. 965, 2114, 3500, 3548
Flora, F. 3285
Flora, R. 2491
Foley, M. 983, 1213
Folwell, N. 2664
Fong, K. 601, 1285, 1404, 1488
Fontenille, A. 2799
Fontus, R. 138
Forchi', V. 3395
Ford, R. 1652
Forest, E. 397, 1023, 2249
Foster, G.W. 323, 1649, 1766
Fox, B. 1688
Fox, J. 2297, 2300, 3141, 3389
Fox, W. 1461, 2841
Frak, B. 1715
Franchetti, G. 129, 589
Francis, V. 1029
Franczak, B. 589
Franklin, W.A. 2324
Franzke, B. 434
Frawczyk, F.L. 2083
Frayer, D. 558

Freyberger, A. 195, 2560, 2565, 3243
Friedlander, F. 1144
Friedman, A. 132, 275, 312, 536, 1518, 2673
Friesel, D.L. 699, 1065, 1563
Frigola, P. 947, 2110, 2112, 2192, 3321
Frisch, J. 644, 1279, 2545, 2548
Frischholz, H. 473
Froidefond, E. 2799, 2802
Fruneau, M. 2799
Fu, S. 1455, 1509
Fu, W. 1685
Fubiani, G. 719, 1885
Fuerst, J.D. 1291, 1294, 1297
Fujii, T. 1978
Fujita, T. 860, 3077, 3080, 3261
Fukami, K. 2551
Fukuda, S. 1509
Fukui, T. 250
Fukui, Y. (KEK) 1509
Fukui, Y. (UCLA) 1787, 1790, 2008, 2709
Fukuma, H. 860, 3056
Fuller, R. 235
Furman, M. 132, 297, 312, 350, 2598, 3219, 3222, 3524
Furukawa, K. (KEK) 533, 3368
Furukawa, K. (Osaka U) 755
Fusco, V. 914, 2077, 3285, 3548
Gagliano, J. 1416
Gai, W. 492, 1156, 1810, 1813, 1819, 1888, 1894, 2032
Galambos, J. 1569, 2360, 2363, 2366, 3527
Gallagher, R. 167
Gallardo, J.C. 1909, 2002, 3255
Gallegos, F. 2515, 2518
Gallegos, R. 558
Gallerano, G.P. 3285
Gallo, A. 366, 2080, 2279, 2742, 3285
Gamma, F.S. 3285
Gammino, S. 81
Ganetis, G. 164, 743, 1431, 1637, 1700, 1706, 2162
Gao, J. 3264, 3267
Gardner, C. 51, 1542, 1706, 1715
Gardner, I.S.K. 1527
Garnett, R.W. 2613
Garoby, R. 1724, 2336
Garrel, N. 1162
Garren, A.A. 1557, 1787, 1804, 1816, 2008, 2213, 2219, 3485
Gasser, Y. 1303
Gassner, D. 54, 794, 1425, 1542, 1691, 2444, 2447, 2450, 2694, 2904
Gattuso, C. 1649, 1766, 2931
Gaudreau, M.P.J. 547, 1500
Gaupp, A. 836
Gavrilov, N. 2273
Ge, L. 2664
Gebel, R. 598, 3428
Geddes, C.G.R. 1840
Geer, S. 983, 1183
Geisler, A. 899
Gelfand, N. 1557
Geng, R. 2580
Geng, R.L. 264, 1309, 1312, 1314, 1317, 1323, 2059
Genoni, T.C. 3165
Gensch, U. 2114
Genser, K. 1763
Gentzlinger, R. 1341, 2841
Gerigk, F. 1527
Geros, E. 73
Gerth, C. 189
Gerth, Ch. 911
Ghalam, A.Z. 3174
Ghigo, A. 366, 684, 1658, 2279, 2742, 3285
Ghiorso, W. 2524
Ghosh, A. 164, 2162
Giacone, R. 719, 1885
Giannessi, L. 914, 2077, 3285, 3548
Giannini, G. 917
Gibson, D.J. 95
Gibson, P. 2706
Gierman, S. 2104, 2667, 3216
Gillespie, W.A. 519
Gilpatrick, J.D. 2512, 3086
Gilson, E. 98, 2622, 2655, 2661
Giovannozzi, M. 129, 388, 2910, 2913, 2916
Giove, D. 2080, 3285
Giovenale, E. 3285
Girard, A. 81
Givens, M. 2029, 2038
Gjonaj, E. 3563
Glanzer, M. 426, 2571, 2577
Glass, H. 1766, 1969, 1972, 2168
Gl€Ùner, C. 1622
Glenn, J. 51, 405, 746, 1542, 1545, 1706, 1715, 2595, 3422
Gloor, W. 878
Gluckstern, R.L. 2592
Goddard, B. 45, 1646, 1721
Godlove, T. 426, 1673, 1676
Goeppner, G. 1416, 2029
Gold, S.H. 492, 1128, 1147
Goldin, F. 563
Golovko, N.G. 1605
Golub, Yu.Ya. 3101, 3103
Gomez, J. 1664
Gonin, I. 48, 1207, 1210, 1213, 2068
Gonzales, J.M. 553
Gonzalez, R. 2444
Goodzeit, C.L. 1996
Gopych, M. 3569
Gorbachev, A.M. 1147
Gordon, D.F. 716, 1846
Gordon, J. 2860

Gorelov, D. 2805, 2849, 2972
Gössel, A. 467, 1086, 1392
Gottschalk, S.C. 1909
Gould, H. 1837
Gould, O. 794, 3282
Gounder, K. 2928, 3434, 3437
Gourlay, S.A. 42, 170, 1032, 1984
Grabosch, H.J. 2114
Graef, H.-D. 3551, 3569
Graham, D. 89
Granata, V. 1945
Granatstein, V. 1140
Grau, M. 2444
Graves, W.S. 217, 329, 956, 959, 980, 1192
Gray, J.W. 1527
Green, M.A. (LBNL) 186, 1834, 1987
Green, M.A. (SRC) 887, 929
Greenwald, Z. 2056
Greenway, W. 1171
Grelick, A. 1416, 1422, 2029, 2038
Grenoble, C. 457
Gribble, R.F. 553
Grice, W. 1524, 2706
Griep, B. 2887
Grier, D. 1724
Griffin, J. 1554, 2922
Grimm, T. 1350, 1353, 1356, 1359, 1362, 1407, 2849, 2972
Grippo, A. 1485
Grisham, L. 2661, 3309
Grishin, V. 1007, 1010
Grote, D.P. 70, 275, 1518, 2637, 2673
Grote, H. 3497
Gruber, P. 1183, 1413
Gruner, S. 192
Gu, A. 2580
Guan, C.Y. 815
Guenzel, T. 854
Guerra, A. 195
Guethlein, G. 563
Guetz, A. 2664
Guidi, V. 917, 986, 1655
Guiducci, S. 366, 914, 2077, 2279, 2945, 3285
Guignard, G. 665
Guilhem, D. 2601
Guimbal, Ph. 2053, 2458
Gullotta, J. 54, 794, 1425, 2444, 2694
Gung, C. 1990
Gunther, K. 1113, 1116
Gupta, R. 42, 164, 1748, 1936, 1939
Guy, F.W. 2889
Gyr, M. 1646
Ha, K.M. 2857
Ha, W. 1861
Haase, M. 1724
Haber, I. 426, 511, 536, 1673, 2312, 2574, 2577, 2673, 3156, 3297
Haberer, Th. 694
Habs, D. 112, 2869, 2872
Hacker, K. 423
Hafalia, R.R. 170, 1984
Hafizi, B. 716, 1846
Hafz, N. 1849
Haga, K. 860
Hahn, A. 2488, 2491
Hahn, H. 39, 1625, 1706, 2147, 3035
Hahto, S.K. 3309
Hahto, S.T. 3309
Haimson, J. 2095
Hajima, R. 3443, 3446, 3449
Halaxa, E. 3297, 3300
Halbritter, J. 1374
Hall, R.P. 3300
Hamatsu, R. 2709
Hamm, R.W. 1563
Hammons, L. 1542, 1691
Han, J.H. 2114
Han, J.M. 1222, 2539, 2832, 2857, 2884
Han, S.H. 2539, 2832
Han, Y.J. 1470, 2857, 3114, 3383
Hanaki, H. 2838
Hanft, R. 1730, 1972
Hanna, B.M. 2497
Hanna, S.M. 1077
Hannink, R. 2625
Hannon, F.E. 1029
Hansen, R.W.C. 929
Hansen, S. 323
Hara, M. 250
Hara, T. 487
Harada, K. 857, 860, 3201
Hardek, T. 553, 1095, 1168, 1458, 1461
Hardekopf, R. 1461, 1661
Harding, D. 1730, 2168
Hardy, L. 854
Harkay, K. 508, 592, 2438, 3008, 3011, 3014, 3183
Harris, J. 426, 2312, 2571, 2577
Harrison, J. 558, 1237
Harrison, M. 39, 42, 164, 1748
Hartemann, F. 95, 938
Hartill, D. 1309, 2339
Hartline, R.E. 1792
Hartman, S. 752, 2270, 2273, 2482
Hartouni, E. 1446
Hartrott, M.v. 2114
Hartung, W. 1350, 1353, 1356, 1362, 1395, 2849, 2972
Harvey, M. 1715
Harwood, L. 586, 992, 1098
Hasegawa, K. 1509
Hashemi, H. 238
Hashiguchi, E. 1978
Hashiguchi, Y. 902, 3270
Hassanein, A. 1180
Hassanpour, N. 3389
Hassanzadegan, H. 238
Hassenzahl, W. 2162
Hatano, T. 1165
Hauviller, C. 1434
Hawkey, T. 547, 1500

Hawkins, S. 2533
Hayano, H. 530, 2545, 2548
Hayashizaki, N. 2826
Hayden, D. 2354
Hayes, M. 2231, 3494
Hayes, T. 476, 1706, 1715, 3338, 3341
He, D.H. 968
He, P. 54, 785, 788, 791, 1425, 2598
He, Y. 167, 2399
Hechler, M. 2706
Heese, R. 217, 241
Heidenreich, D.A. 553
Heifets, S. 2297, 2300, 3132, 3135
Heimann, P. 186, 1032
Heistermann, F. 3344
Held, B. 3554
Hemmer, M. 2390
Henderson, S. 117, 1467, 1569, 1572, 2598, 3416
Hendrickson, L. 423, 644, 662, 2545, 2757, 3126
Henestroza, E. 98, 558, 1171, 2616, 2619, 2622, 2625, 2628, 2637, 2646
Henn, K. 598, 3428
Henning, W. 16
Henrist, B. 1727
Henrist, H. 307
Henry, J. 1377, 2866
Heo, H. 3108
Heppner, G. 1685
Herbeaux, C. 229
Herr, A.D. 617
Herr, W. 3404
Hershcovitch, A. 39, 92
Hertel, I. 836
Herzog, R. 1945
Hess, M. 2643
Hettel, R. 235, 761
Hiatt, T. 2183, 2186, 2189
Hicks, J.D. 553
Hicks, R. 195, 2560
Hicks, W.R. 1377
Higashi, N. 1978
Higashi, Y. 2393, 2838
Hill, A. 235, 1273
Hill, C. 1029
Hilleret, N. 307, 788, 1727
Himel, T. 644, 2757
Hiramatsu, S. 2503
Hirashima, T. 1074
Hirata, K. 2996
Hirshfield, J.L. 725, 1128, 1131, 1147, 1150, 1882, 1924, 1927, 1930, 2881
Hitz, D. 81
Ho, D. 563
Ho, H.K. 1876
Ho, S. 620
Hobl, A. 899
Hock, J. 1542, 3422
Hoff, L. 1542, 2444
Hoffstaetter, G.H. 192, 369, 375, 842, 848
Höfle, W. 1718, 3038
Hofler, A. 195
Hofmann, I. 129, 589, 2592, 2607, 2954
Hogan, B. 1119
Hogan, G. 702
Hogan, J. 457, 1377, 2866
Hogan, M.J. 731, 1530, 1864, 1933
Holder, D.J. 189
Holldack, K. 836, 839, 2527, 3023
Holloway, M. 426, 2571
Holmes, J. 117, 1569, 1572, 3503
Holmes, R. 770
Holtkamp, N. 11
Holzscheiter, M. 558
Honkavaara, K. 467, 911, 2476
Hopkins, S. 1461
Horan, D. 1177
Hori, Y. 809, 860
Horioka, K. 1807
Horst, B. 467
Hosoda, N. 250, 2551
Hosokai, T. 2258
Houck, T. 558, 2628
Hourican, M. 1643
Hovater, C. 195, 1098, 2379
Howe, S. 705
Hseuh, H. 54, 785, 788, 791, 1425, 1715, 2144, 2147, 2390, 2598, 3419
Hsiao, F.Z. 2402, 2405
Hsiung, G.Y. 821
Hsu, K.T. 890, 1044, 2376, 2554, 2557, 3237, 3392
Hsu, S.-Y. 2376
Hsu, S.N. 821
Hu, K.H. 2376, 2554, 2557, 3237, 3392
Hu, M. 1649
Huang, C. 1530, 1864, 1933, 3174
Huang, H. (BNL) 51, 54, 405, 1697, 1706, 1712
Huang, H. (Yale U) 1688
Huang, J.Y. 875, 2539
Huang, M.H. 1047
Huang, Z. (ANL) 905
Huang, Z. (SLAC) 329, 3138, 3231
Hubbard, R.F. 716, 1846
Hubers, H.-W. 839
Huelsmann, P. 589
Huening, M. 467, 2074, 2682, 2730
Hughes, T. 120, 558, 3210
Huhn, A. 2444
Hulbert, S. 241
Hülsmann, P. 434
Humphries, S. 3557
Hung, D.S. 3234
Hunter, T. 2706
Huo, Y. 426, 2312
Hurh, P. 641, 1440, 1443, 1449, 1452
Hutchinson, E. 1542
Huttel, E. 893, 3273, 3276
Hutton, A. 195
Hwang, C.S. 821, 1041, 1044, 1047, 2376
Hwang, W.H. 2539, 2857
Iarocci, M. 1631
Iazzourene, F. 2306, 2309
Ieiri, T. 860, 3077, 3080

Igarashi, S. 568, 755, 1165, 1807, 2610
Igarashi, Y. 2838
Igarashi, Z. 1509
Igo, G. 51
Ihee, H. 420
Ihloff, E. 2324
Iida, K. 530
Iida, M. 1978
Iida, N. 2240
Ikeda, H. 2503
Ikeda, M. 3326
Ikegami, K. 1509
Ikegami, M. 1455, 1509, 2393, 2835
Ilg, T. 2841
Imai, T. 2829
Inagaki, S. 568, 1784
Inagaki, T. 487
Incurvati, M. 2279, 3285
Ingrassia, P. 1715
Irie, Y. 1512, 2509
Iriso-Ariz, U. 54, 794, 797, 1706, 1801, 3479
Isaev, V.A. 1147
Isagawa, S. 860, 1228
Ise, T. 755
Ishi, Y. 1512
Ishibashi, K. 1784
Ishikawa, T. 487
Ishimoto, S. 1834
Ishizuka, T. 3332
Ito, T. 1509, 2835
Ivanov, O. A. 1147
Ivanov, P.M. 3062
Ivanov, V. 1137, 2664, 3312, 3315
Ivanov, Yu.D. 3530
Ivanov, Yu.M. 917
Iversen, J. 467
Iverson, P. 1530
Iverson, R. 731, 1864, 1933, 2285, 2297
Ives, L. 269, 1110, 1113, 1116, 1119, 1125, 1127, 1137, 1140, 1142, 3312, 3560
Iwasaki, Y. 902, 2387, 3270
Iwashita, D. 1807
Iwashita, Y. 1993, 2198
Izawa, M. 3201
Jackson, A. 244
Jackson, G. 705, 3159, 3162
Jackson, J. 2153, 2159, 2390
Jacob, J. 854, 1332, 3192
Jacobs, K.D. 887, 929, 2303, 2373
Jacobson, E.G. 73
Jacobson, S. 3374
Jacques, E. 1303
Jacquez, E. 558
Jaeschke, E. 836, 2114
Jain, A. 39, 164, 1637, 2159, 2390
Jamilkowski, J. 1542
Jamison, S.P. 519
Jang, J.H. 1219, 2832, 2884
Jansma, W. 2029
Jansson, A. 1751, 1763
Jason, A. 702, 1664, 1966, 2948
Javanmard, M. 722, 1855
Jeanneret, J.-B. 45, 1682, 3494
Jenninger, B. 307, 1727
Jensch, K. 467
Jensen, A. 3315
Jensen, E. 2467, 2470
Jensen, J.-P. 749
Jensen, K.L. 3323
Jensen, L. 307
Jeon, D. 107, 1515, 2652, 2855
Jeong, K.K. 1222, 2832, 2884
Jeong, S.-H. 3114
Jia, L. 1431
Jia, Q.K. 968
Jian, X. 3506, 3509
Jiang, D. 2852
Jiang, H. 1359
Jimenez, J.M. 45, 307, 1727
Jin, L. 369
Jines, P. 2382, 2892
Jing, C. 492, 1810, 2032
Jing, D.M. 815
Jinnochi, O. 51
Jobe, K. 1279, 3141
Johnson, D. (Bechtel) 558
Johnson, D. (FNAL) 1649, 1766, 2931
Johnson, D. (UCLA) 1530, 1933
Johnson, E. 217, 241
Johnson, G. 2841
Johnson, J. 558
Johnson, M. 1350
Johnson, R.P. 1792
Johnstone, C. 983, 1446, 1557, 1649, 1831, 2216, 2931, 3413
Jones, F.W. 3404
Jones, J.K. 2243
Jones, K. 558
Jones, R.M. 1261, 1264, 1270, 2760, 2763
Jones, T. 716, 1846
Jones, W.P. 699, 1065, 1563
Jordan, K. 1485
Joshi, C. 731, 1530, 1858, 1864, 1873, 1933
Joshi, C.H. 1407
Joshi, P. 2162
Jowett, J.M. 1682
Julian, J. 1240
Julian, R.L. 929
Jung, J.Y. 3458
Jungwirth, H. 598, 2811
Junquera, T. 1303
Kabel, A.C. 2252, 3539, 3542, 3545
Kadokura, E. 1509
Kaertner, F.X. 959, 980
Kaganovich, D. 716
Kaganovich, I.D. 1667, 2975
Kageyama, T. 800, 803
Kahn, S.A. 1709, 3255, 3413
Kain, V. 45, 1685
Kaiser, H. 467
Kakihara, K. 2838
Kako, E. 1338

Kalantari, B. 238
Kalinichenko, A.I. 1080
Källberg, A. 1590
Kalnins, J.G. 1837, 2951
Kaltchev, D. 45, 1581, 3494
Kamikubota, N. 1509
Kamitani, T. 1225, 3288
Kamiya, Y. 530
Kammering, R. 467, 2730
Kanahara, T. 1978
Kanareykin, A. 1888, 1891, 1894, 1897
Kanazawa, K. 806, 2503
Kandaswamy, J. 167
Kaneko, N. 3326
Kang, H. 3180
Kang, H.S. 1470, 2857, 3383
Kao, C.C. 241
Kaplan, D.M. 1183, 1792, 1798, 1834
Kaplan, R. 1306, 1437, 3347
Karantzoulis, E. 2306, 2309
Karataev, P.V. 2709
Karl, F. 2390
Karmanenko, S. 1888
Karpov, G. 250
Kasemir, K. 3371, 3377
Kashikhin, V.S. 1966
Kashikhin, V.V. 1748, 1966, 1969, 1975
Kashiwagi, S. 3288
Kashtanov, E. 1781
Kaspar, K. 589
Kasper, P.H. 1503, 2936
Kasuga, T. 860, 1228, 3077, 3080, 3261
Kato, T. 1455, 1509, 2393, 2835
Katoh, T. 860, 2351
Katsouleas, T.C. 731, 1530, 1858, 1864, 1933, 3174
Katuin, J. 699, 1068
Kaugerts, J. 2162
Kawakubo, T. 1165, 1512
Kawamoto, T. 2351
Kawamura, M. 1509
Kawashima, Y. 250, 487
Kawata, H. 860
Kedzie, M. 1291, 1294, 1297
Keeley, D. 235, 2372
Keil, B. 3386
Keil, E. 414, 3413
Keil, R.G. 887
Kelez, N. 2527
Keller, L. 2739
Keller, R. 527, 3306
Kelley, J.P. 977, 1966
Kelly, J. 2706
Kelly, M.P. 1291, 1294, 1297
Kempkes, M.A. 547, 1500
Kephart, R. 1972
Kerby, J.S. 1745, 1969
Kersevan, R. 854
Kesar, A.S. 2095, 2536
Kesselman, M. 524, 2444, 2453
Kester, O. 2869, 2872
Kewisch, J. 39, 372, 1300, 1694, 1700, 2005, 2011, 3186
Khabiboulline, T. 48, 1207, 1210, 1213
Khachatryan, A.G. 1900, 1903
Khan, S. 836
Khodak, I.V. 2098
Kikuchi, M. 860, 3368
Kikuzawa, N. 3443, 3446, 3449
Kim, C. 1849, 1852, 1906, 1912, 2987
Kim, D.T. 1470, 2857
Kim, E.-S. 3105, 3108, 3111, 3114
Kim, G.H. 1849, 1852, 1906, 1912, 2987
Kim, J.B. 2984, 2987
Kim, J.U. 1849, 1852, 1906, 1912, 2987
Kim, K.-J. 905, 1813, 2682, 3138
Kim, K.R. 1602
Kim, M.G. 875, 3114
Kim, S.C. 2857, 3114
Kim, S.H. (ANL) 1020
Kim, S.-H. (ORNL) 1365, 1467, 1599
Kim, T.H. 1539
Kim, Y. (CHEP) 962, 965
Kim, Y. (DESY) 962, 965
Kim, Y.J. 2832, 2884
Kimura, N. 1978
Kimura, W.D. 1909
King, L. 457
King, Q. 1945
King, T.C. 2402, 2405
Kinkead, A.K. 492, 1128, 1147
Kinoshita, K. 2258
Kirchgessner, J. 1314
Kirk, H. 1628, 1631, 1634, 1709, 1787, 2008, 2213, 2219, 3255
Kishek, R.A. 426, 1673, 1676, 2574, 2577, 2673, 3156
Kishiro, J. 568, 1509, 1784, 1807
Kitamura, H. 487, 962, 965
Kitsuka, T. 902, 3270
Klein, H. 1335, 2942
Klein, H.-U. 1948
Klein, S.B. 699
Kleman, K.J. 887, 929, 2373, 3147
Klenov, V. 3282
Kling, N. 1542
Klotz, W.-D. 2360, 2363, 3527
Knapic, C. 1050
Kneisel, P. 92, 457, 1350, 1362, 1374, 1377, 1395, 1575, 2863
Knippels, G. 519
Knobloch, J. 1323
Ko, I.S. 1852, 2984
Ko, K. 2664
Koba, K. 1679, 1736
Kobayashi, H. 1509
Kobayashi, M. 860
Kobayashi, N. 713

Kobayashi, T. 1509
Kobayashi, Y. 857, 860, 2171, 3201, 3204
Kobilarcik, T. 1652, 2934
Koch, J.M. 851
Koda, S. 902, 2387, 3270
Kodera, M. 250
Koiso, H. 3368
Kokhanovski, S. 3282
Kolomiets, A.A. 2875
Komada, I. 2351
Kondaurov, M. 2769
Kondo, Y. 1509
Konecny, R. 492, 1156, 1810, 2032
Konkashbaev, I. 1180
Koop, I.A. 372, 2898
Koopman, J. 2470
Kooy, H. 690
Korbly, S. 2095, 2536
Korenev, I. 1013, 1611
Korenev, S. 1013, 1015, 1608, 1611, 1614
Koropsak, E. 3026
Korostelev, M. 2315
Koschik, A. 3044
Koscielniak, S. 1488, 1831, 3413
Koseki, K. 568, 1784, 1807
Koseki, T. 530, 857
Kostin, D. 467
Kostin, M. 1446
Kotlyar, Y. 1542
Kotov, V.I. 917, 1655
Kou, C.H. 1044
Kourbanis, I. 1736, 3353, 3356
Koutchouk, J.P. 2225
Kovach, P. 1939
Kozanecki, W. (CE Saclay) 2739
Kozanecki, W. (SLAC) 2297
Kozub, S. 1781
Kozyrev, E.V. 1128
Kponou, A. 89, 3282
Kraft, G.A. 192
Kramarenko, K. 1605, 2969
Krämer, A. 589
Krämer, D. 836, 1083, 2114
Kramer, S.L. 241
Kramper, B. 2020
Krasilnikov, M. 2114, 3551, 3566
Krasnogolovets, M.A. 1107, 3303
Krasnykh, A. 1137, 3312, 3315
Krause, S. 2324
Krawczyk, F.L. 1341, 1344
Krejcik, P. 423, 1530, 1933, 2297, 3126, 3129
Kreps, G. 467, 1392
Krinsky, S. 217, 3225
Krischel, D. 1948
Krishock, A. 1542
Kroc, T. 2020
Kroll, N.M. 1270
Kroyer, T. 2700
Krusche, A. 1724
Kuan, K.C. 821
Kuba, J. 95
Kubicki, T. 1204
Kubota, C. 1509
Kubota, T. 3335
Kubsky, S. 899
Kucharczyk, A. 2787
Kuchnir, M. 1792
Kudo, K. (AIST) 2387
Kudo, K. (KEK) 860, 2351
Kudo, T. 487
Kuehnel, K.-U. 1622, 2817
Kulikov, A. 2282, 2297
Kulinski, S. 2787
Kulipanov, G. 250
Kumada, M. 1993, 2198
Kumagai, N. 250, 782, 881, 884
Kumaran, R. 1285
Kuo, C.C. 890, 1044
Kuo, C.H. 764, 2376, 2554, 2557, 3234, 3237, 3392
Kuo, K.C. 1476
Kurennoy, S. 920, 977, 1661, 2083, 3515
Kurita, N. 235
Kusche, K.P. 1909
Kushnir, V.A. 1107, 1605, 2098, 2878, 3303
Kuske, P. 839, 1186, 3020, 3023
Kustom, R.L. 1020
Kuzikov, S. V. 1147
Kuzin, M. 250
Kuznetsov, A. 2769
Kuznetsov, G. 57, 1781
Kwan, J. 70, 3291, 3294, 3297, 3300, 3309
Kwiatkowski, S. 1240
Kwon, H.J. 1219, 1222, 2832, 2857, 2884
Kwon, S. 3371, 3377
Lach, J. 2769
Lackey, J.R. 1503, 2168, 2936
Ladd, P. 2706
Ladran, A. 1243, 2023
Lagniel, J.-M. 2601
Lai, S. 1763
Laier, U. 3569
Lamb, D. 426, 2571, 2574, 2577
Lambertson, G.R. 410, 1837
Lambiase, R.F. 550, 743, 770, 2144
Lamm, M. 42, 1730, 1969, 1972
Lamont, M. 45
Lange, R. 467
Langton, J. 235
LaPointe, M.A. 1131
Larbalestier, David C. 151
Larsson, JÅrgen 2321
Laskar, J. 378, 3189
Lau, T. 3563
Lau, W. 1243, 1834
Laurent, J.M. 307
Lauze, R. 195
Laverty, M. 1404
Lawson, Greg S. 288

Lawson, W. 1119, 1140
Lawton, D. 138
Laxdal, R.E. 601, 1488, 1584
Lazurik, V.M. 1616
Lazurik, V.T. 1080, 1616
Le, Tuong N. 3338, 3341
Lebedev, V.A. 29, 48, 1733, 1739, 1751, 2497, 3062
LeBlanc, G. 2318, 2321
Lebrun, P. 1739, 1754, 1763, 2703
Ledford, J.E. 1341
Lee, Demi 2376, 2554
Lee, E.P. 312, 1521, 2658, 2975
Lee, H.H. 2832
Lee, H.J. 1849, 1852, 1906, 1912, 2984, 2987
Lee, H.R. 1602
Lee, Jinhyung 2026
Lee, Peter J. 151
Lee, R.C. 54, 785, 794
Lee, S.Y. 1065, 3150, 3240
Lee, Soon-Hong 824
Lee, W.-T. 426, 2571, 2577
Lee, Y.-Y. 550, 571, 617, 1569, 1572, 1637, 2144, 2147, 2150, 2153, 2159, 2390, 2598, 3416
Leemans, W.P. 719, 734, 1840, 1885
Lefevre, T. 2464
Legg, R.A. 887
Lehrach, A. 598, 2811, 3428
Lei, S.C. 1476
Leibfritz, J. 2020
Leitner, D. 86
Leitner, M.A. 86, 1521, 1990
Lemaire, J.-L. 2601
Lemuet, F. 444
Lenci, S. 1122
Lenkszus, F. 283, 2435
Leone, S. 186
Leontiev, V.N. 553
Le Pimpec, F. 1279, 2748
LeSage, G.P. 95
Lessner, Eliane S. 3467
Letchford, A.P. 2542
Leung, K.N. 3309
Level, M.-P. 229, 1332
Leveling, A. 1440
Levi, D. 3285
Lewandowski, J.R. 1261, 1264
Lewellen, J.W. 905, 1813, 2029, 2035, 2038, 2132, 2333, 2417, 2420
Leyh, G.E. 235, 761, 1174
Li, C. 2357
Li, D. 186, 1183, 1243, 1246, 1249, 1389, 2023
Li, G. 968
Li, H. 426, 1673, 1676, 2574, 2577
Li, H.C. 2402, 2405
Li, J. 391, 2270, 2357, 2479
Li, Juexin 2715
Li, N. 2174
Li, R. 208, 941
Li, Shaoqing 2852
Li, Shiqui 1560
Li, W. 2357, 2715
Li, Xiaoguang 2852
Li, Y. (ANL) 905
Li, Y. (Cornell) 620, 2264, 2399
Li, Yuxiong 2715
Li, Z. 1264, 2664, 2760
Liaw, C.J. 617, 2444
Lidia, S.M. 186, 2086, 2089, 2092, 2682, 3198, 3500
Liebermann, H. 1335, 2820, 2942
Lien, M.K. 592
Liepe, M. 192, 467, 1201, 1317, 1320, 1323, 1326, 1329, 2059, 3347
Lietzke, A.F. 170, 1984, 1990
Ligi, C. 2279, 3285
Likhachev, S. 1010
Lill, Robert M. 2435
Lim, J. 2192
Lima, R.R. 2201
Limborg, C.G. 235, 329, 2077, 2104, 2667, 3216, 3548
Limon, P. 42
Lin, F.Y. 1047
Lin, M.C. 1371, 2402, 2670
Lin, Y.C. 1476
Lindgren, L.-J. 2318, 2321
Linnecar, T. 1718, 3050
Lipka, D. 2114
Litvinenko, V. 391, 752, 2273, 2479
Liu, C.Y. 1479, 1482
Liu, G. 2357
Liu, J.-F. 1341, 1344, 2083
Liu, J.Y. 968
Liu, Kuo-Bin 767
Liu, P. 1452
Liu, W. 492, 1156, 1810, 2032
Liu, Y. 998, 2607
Liu, Zuping 2715
Lo, Y.C. 3234
Lockey, R. 550, 1542
LoDestro, Vincent 3282
Loew, G.A. 647
Loewen, R. 1264
LÅfgren, P. 1590
Loftsdottir, A. 863
Logan, B.G. 1521, 2661
Logatchov, P. 3318
Loiacono, L. 3183
Longcoy, L. 2324
Longo, C. 1428
Lonza, M. 3395
Loos, H. 217, 241, 329, 908, 1192, 1497, 2455
Lopes, M.L. 1596, 2201
Lopez, A. 2029
Lorentz, B. 3428
Lorkiewicz, J. 467
Lorman, E. 2494, 3062
Losito, R. 878, 1309, 1332
Lou, G.H. 1044
Louie, W. 743, 1431, 1700
Loulergue, A. 229

Low, R. 1240
Lowe, D. 220, 2195
Lowenstein, D. 1715
Lu, J. 1285
Lu, W. 1870, 1933
Lucas, P. 2925
Luccio, A.U. 51, 272, 405, 1697, 1936
Ludewig, H. 1428, 1628, 1709, 2598, 2796
Ludvig, J. 2625
Ludwig, M. 2461
Lumpkin, A.H. 2411, 2414, 2417, 2420, 2423
Lund, S.M. 132, 312, 536, 1990, 2631, 2634
Luo, G.H. 890, 1041, 1371, 2670
Luo, Y. 2123, 2126, 2129, 2132, 2135, 2186
Luque, A. 3029
Lusk, M. 2354
Lyles, J.T.M. 1092
Lyn, L. 1240
Lynch, M.T. 553, 1095, 1168, 1458
Lyneis, C.M. 86
Lysenko, W.P. 2613
Ma, H. 1464, 3377
MacDonald, M.A. 189
Macek, R.J. 326, 508, 2521, 2598, 3086, 3089, 3419, 3455
MacGill, R. 1246
Machida, S. 1512, 1679, 3413, 3452
Machie, D. 1377, 2866
Macina, D. 1742
MacKay, W.W. 39, 51, 54, 164, 405, 1697, 1706, 1712, 1715, 1936
MacLachlan, J.A. 1554, 1736, 1769, 3180
MacLean, E.J. 708
MacLeod, A.M. 519
MacNair, D. 235
Madre, B. 1494
Maebara, S. 2829
Maesen, P. 1724
Magome, T. 250, 782
Mahler, G. 2156
Maier, R. 598, 2811, 2814, 3428
Maisheev, V.A. 917
Majeski, R. 2655
Makarov, O. 2261
Makita, Y. 1539
Malafronte, A.A. 2201
Malagu, C. 917, 1655
Malitsky, N. 272, 2919, 3482
Malm, K. 2150
Malmgren, L. 2321
Malo, J.F. 2470
Mammarella, F. 638
Mammosser, J. 457, 1104, 1386, 2860
Mansell, J. 1861
Mao, S. 779
Mapes, M. 785, 788, 1542, 2141
Marcellini, F. 366, 2080, 2279, 2742, 3141, 3285
Marchand, D. 2799
Marchand, P. 229, 878, 1332
Marchionni, A. 1649, 3440
Marcouill_, O. 229
Marechal, X. 487
Marhauser, F. 1189
Markiewicz, T. 644, 2739
Marks, S. 1032, 3458
Marlats, J.L. 229
Marneris, I. 746, 1542, 1637
Maroli, C. 3285, 3512
Marone, A. 164, 1939, 2162
Marque, S. 878
Marques, S.R. 2583, 3279
Marqversen, O. 2461
Marr, G. 1542, 1715
Marriner, J.P. 514, 2928, 3180, 3434, 3437
Marsden, D. 1110, 1119
Marsh, K.A. 731, 1530, 1864, 1873, 1933
Marshall, T.C. 1882, 1924, 1930
Marsi, M. 2306
Martens, M. (ANL) 2029
Martens, M. (FNAL) 1730, 1972, 3359
Marti, F. 138, 1353, 2649, 2849, 2972
Martin, D. 235
Martin, M.C. 863, 869
Martineau, R. 2841
Martinelli, G. 917, 1655
Martinez, D. 2512
Martini, M. 129, 388, 2913, 2916
Martins, M.N. 1593, 1596, 2201
Martovetsky, N. 1990
Marusic, A. 524, 1706
Maruyama, A. 1539
Maruyama, T. 2739
Masaki, M. 250, 881
Mastovsky, I. 2095
Masuda, T. 250
Masunov, E.S. 2640, 2963
Matheisen, A. 467
Matoba, M. 1679, 3452
Matsui, S. 250, 487, 884
Matsumoto, H. 487
Matsuoka, M. 1338
Mattioli, M. 3285
Matveev, Yu. 2273
Mauri, M. 2080
Mausner, L. 1628
Mavanur, A. 1407
Mazzitelli, G. 366, 1658, 2279
McCarrick, J. 563, 2533, 3557
McChesney, C.A. 2360, 3527
McCormick, D. 1279, 2545, 2548
McCrady, R. 2521, 3086, 3089, 3455
McCrea, M. 2183
McCuistian, B.T. 558
McDonald, J.L. 2385

McDonald, K.T. 1628, 1631, 1634, 1709
McGahern, W. 2390
McGee, M. 2020
McIntosh, P. 235, 1273, 3141
McInturff, A.D. 170, 1984
McIntyre, G. 39, 1691, 2904
McKinney, W. 869
McManamy, T. 1572
McMichael, G.E. 592, 1159
McNeil, B.W.J. 189, 950, 953
Mc Nerney, A. 746, 1542
Mead, J. 524, 2444, 2697
Mecklenburg, B. 2095
Medici, G. 3285
Medjidzade, V. 167, 2399
Medvedko, A. 2769
Medvedko, E. 235, 761
Meidinger, A. 558
Meinke, R.B. 1990, 1996
Meisner, K. 1736, 1769
Melin, G. 81
Meller, R.E. 2339
Meng, W. 1637, 2144, 2147, 2159, 2598
Meot, F. 444
Merl, R. 2354, 2515, 2518
Merminga, L. 192, 195, 332
Merrill, F. 702
Mertens, V. 1721
Mertins, H.-C. 836
Merz, W. 749
Messina, G. 3285
Meth, M. 1195
Métral, E. 129, 388, 2913, 2916, 3047
Métral, G. 388, 2913, 2916
Meyer, A. 1542
Meyer, B.J. 73
Meyer, F.W. 998
Meyer, T.S. 2491
Meyer Sr., R.E. 2485
Mezentsev, N. 250
Mezi, L. 914, 3285
Mi, C. 2447
Mi, J. 550, 1640, 2147
Michalek, W. 2029
Michelato, P. 1506, 2071, 2114
Michelotti, L. 1557
Michnoff, R. 1706, 2691, 3026
Miglionico, G. 2150
Migliorati, M. 2077, 3285
Mihalcea, D. 2682
Mihara, T. 2198
Mikado, T. 713, 971, 974
Mikhailichenko, A. 167, 1822, 1825, 1828, 1954, 1957, 1960, 1963, 2399, 2781, 2784, 3350
Mikhailov, S.F. 391, 752, 2273, 2276, 2482
Milani, D. 1945
Milardi, C. 366, 2279, 2742, 2945, 3285
Miles, J. 1942
Miller, R.H. 1264, 2760, 2763
Miller, T. 2382, 2892
Mills, G.D. 998
Milner, R. 956, 959, 980
Miltchev, V. 2114
Milton, S.V. 905, 1813
Minagawa, Y. 860, 3077, 3080, 3261
Minehara, E.J. 3443, 3446, 3449
Minervini, J. 1990
Miram, G. 1110, 1113, 1116, 1137, 1140, 1142, 3312
Mishra, C.S. 1, 1649, 1766, 2928, 3434, 3437, 3440
Mistry, N.B. 167, 2399
Mitchell, D. 1213
Mitra, A. 601
Mitrochenko, V.A. 1107, 3303
Mitrochenko, V.V. 1605, 2098, 2878
Mitsuhashi, T. 860, 2503, 2506, 3204, 3207
Miura, T. 2509, 2610
Miyajima, T. 860, 2171
Mizobata, M. 1071
Mizrahi, A. 722, 728
Mizuhara, A. 1142
Mizuhara, M. 1110, 1113, 1116, 1119
Modena, M. 1942
Moffitt, J.R. 2473
Mokhov, N.V. 42, 983, 1503, 1733, 1742, 1745, 1748, 2739, 2936
Möller, W.-D. 467
Molvik, A.W. 132, 312, 536
Monaco, L. 1506, 2071
Moncton, D.E. 959, 980
Monroe, J. 1587, 1652
Monroy, M. 1464, 3377
Montag, C. 51, 135, 1300, 1431, 1694, 1697, 1700, 1706, 2005, 2011, 2691, 2907, 3026, 3186
Montoya, D.I. 1341
Montoya, N. 558
Moog, E.R. 156, 1020
Moore, C. 1652, 2934
Moore, R. 1751, 1754, 2497
Moore, T. 167
Moraes, J.S. 2990
Morcombe, P. 752
Moretti, A. 1183, 1246, 1792, 2023
Morgan, G. 1936
Morgan, J. 641, 1443
Mori, W.B. 731, 1530, 1858, 1864, 1870, 1933, 3174
Mori, Y. 1231, 1234, 1679, 3413, 3452
Moricciani, D. 3285
Morishita, T. 2829
Moritz, G. 589, 2162
Moritz, L. 638
Morley, K. 702
Morris, C. 702
Morris, J. 746, 1542, 1715
Morris, W.A. 1527
Morse, E.C. 3291

Morvillo, M. 1724
Mosnier, A. 595
Mostacci, A. 1801, 2500, 3479
Mostrom, C. 558
Mottershead, T. 702, 1664
Mouat, M. 638
Moy, K. 558
Mueller, I. 2823
Mueller, N. 2823
Mueller, P.E. 1004
Muggli, P. 731, 1530, 1864, 1915, 1933
Muir, A.A. 1029
Mulholland, G. 1631
Mullany, B. 1428
Müller, A.-S. 388, 893, 2913, 3273, 3276
Mulvaney, J.M. 547, 1500
Murai, S. 1978
Murasugi, S. 1165
Muratore, J. 164, 2162
Muratori, B. 189
Murdoch, G. 1467, 2706
Murokh, A. 944, 2568
Murphy, B.F. 2104, 3216
Murphy, J.B. 176, 217, 241, 2455, 2808
Murray, S.N. 3306
Musser, S.E. 1356
Mustafin, E. 589
Musumeci, P. 1867, 1873, 2117, 2957, 3258
Muto, A. 1679, 3452
Muto, M. 755
Muto, T. 2709
Myakushko, L.K. 2878
Myneni, G. 1374
Na, J.H. 2832
Nadji, A. 229, 896
Nadolski, L. 229, 397, 896
Nagahashi, S. 860, 2171, 2351
Nagai, R. 3443, 3446, 3449
Nagaitsev, S. 2020
Nagaoka, R. 229
Naito, F. 1509, 2835
Nakai, H. 3326
Nakamoto, T. 1978
Nakamura, E. 568, 1165, 1784, 1807, 2610
Nakamura, N. 530, 857
Nakamura, S. 1539
Nakamura, T. 250, 881
Nakamura, T.T. 860, 2351
Nakanishi, H. 860, 1228
Nakanishi, T. 1539
Nakano, J. 1231, 1679, 3452
Nakashizu, T. 3326
Nakayama, K. 530
Nam, K.Y. 1602
Nam, S.H. 1470, 2539, 2857, 3108
Nantista, C.D. 482, 1276
Napoly, O. 2718, 2739
Narang, R. 1873
Nash, B. 126
Nassiri, A. 1416, 2038
Nath, S. 1461, 1515
Naumenko, G.A. 2709
Naylor, C. 1542
Naylor, G. 854
Nehring, T. 550
Neil, G.R. 181, 977
Neilson, J. 269, 1119, 1125, 1127
Nelson, J. 1279
Nelson, R. 1098
Nemesure, S. 1542
Nenasheva, E. 1888, 1894
Neri, F. 3086
Neumann, J. 1497
Newsham, D. 1153, 1156, 2123, 2126, 2129, 2132, 2135, 2186
Nexsen, W. 2533
Nezhevenko, O.A. 1128, 1131, 1147, 1150, 2881
Ng, C.-K. 235, 1264, 2664
Ng, K.Y. 1751, 2922, 3065
Nguyen, D. 977
Nicklaus, D. 323
Nicol, T. 1969
Nicolas, L.Y. 1733
Nielsen, K. 558
Nieter, C. 719, 1885, 1918
Nigorikawa, K. 1509
Nikitina, T.F. 2878
Nishimori, N. 3443, 3446, 3449
Nishimura, H. 244, 397, 1837, 2249, 2385
Noack, F. 836
Noble, R.J. 722, 1858
Noda, F. 1512
Noda, T. 250
Nogami, T. 809, 860
Noguchi, S. 1338, 1509
Nolden, F. 434
NÅlle, D. 2476
Nomura, M. 530
Norbrega, A. 1969
Nordberg, E. 2399
Norem, J. 1180, 1183, 1246, 1999
Norris, B. 983
Nosochkov, Y. 2288, 2291, 2300
Novati, M. 1506
Novokhatski, A. 315, 2294, 2297, 2300, 2981
Nusinovich, G. 1140
Nzeadibe, I. 235
Oakeley, O. 752
Obina, T. 860, 2351, 3077, 3080, 3201, 3207, 3261, 3365
Ochiai, Y. 902, 3270
O'Connell, C.L. 423, 731, 1530, 1864, 1933, 3126, 3129
Odagiri, J. 2351
Odajima, W. 1978
Oepts, D. 519
Oerter, B. 54, 1640
Ogata, A. 3335
Ogawa, H. 713, 971, 974
Ogawa, Y. 3368
Ogitsu, T. 1978, 3413
O'Hara, J.F. 2512
Ohashi, Y. 250

Ohgaki, H. 713, 902, 2387, 3270
Ohhata, H. 1978
Ohishi, M. 884
Ohkuma, H. 881
Ohmi, K. 345, 353, 3053, 3056, 3083, 3398
Ohmori, C. 1216, 1234, 1679, 3413, 3452
Ohnishi, Y. 3056, 3288
Ohnuma, S. 1557
Ohsawa, S. 2838, 3326
Ohsawa, Y. 860
Ohshima, T. 250, 782, 881, 2551
Ohuchi, N. 1978
Oide, K. 353, 2604
Oishi, M. 250, 782
Okada, M. 1509
Okamoto, H. 2592
Okamura, M. 164, 1936
Oleck, A.R. 1649
Olsen, J. 235, 761
Olson, C.L. 2685, 3165
Olson, M. 1781
Onishi, Y. 860
Onisto, H.J. 2583, 3279
Ono, M. 860, 1228
Onoe, K. 487, 3332
Oogoe, T. 2838
Oothoudt, M. 2354
Oppelt, A. 2114
Orikasa, T. 1978
Oro, D. 558
O'Rourke, S. 2975
Orris, D. 1969
Ortega, M. 235
Orzechowski, T. 3557
O'Shea, P.G. 426, 511, 1497, 1673, 1676, 2312, 2571, 2574, 2577, 2673, 2712, 3156, 3323
Österdahl, F. 1590
Ostiguy, J.-F. 2168, 2925, 3503
Ostojic, R. 42
Ostroumov, P.N. 400, 2426, 2790, 2875, 2963, 3467
Otboev, A.V. 372, 2898
Ott, K. 773, 776
Ottaviani, P.L. 3285
Ottavio, D. 2360
Owen, H.L. 189
Owens, T.L. 3344, 3380
Oz, E. 1530
Ozaki, T. 860
Ozelis, J.P. 1491, 1494
Paál, A. 1590
Padamsee, H. 192, 1201, 1309, 1312, 1314, 1317, 1320, 1323, 1410, 2059
Pagani, C. 467, 1300, 1341, 1506, 2114
Page, T. 1969
Pai, C. 550, 2144, 2147
Pakter, R. 1134, 2990
Palmer, D.T. 1858, 2107
Palmer, M.A. 2267, 2473
Palmer, R. 1816
Palmer, R.B. 1804, 1834, 1987, 2002, 3413
Palumbo, L. 944, 2500, 3285
Pantell, R.H. 1909
Paoluzzi, M. 1724
Papaphilippou, Y. 123, 851, 854, 1569, 2159, 3053, 3189
Paparella, R. 470
Pappas, C. 235
Paramonov, V. 2826
Pardo, R.C. 2426, 2875
Park, B.R. 1470
Park, B.S. 1602
Park, E.S. 875
Park, H.J. 3383
Park, J.H. 2539
Park, M.Y. 1219, 2832, 2884
Park, S. 235
Park, S.-S. 3114
Park, S.J. 2539
Parker, B. 372
Parkhomchuk, V. 2769
Parmigiani, F. 186
Parodi, R. 1395
Parsa, Z. 3005
Partridge, R. 644
Parzen, G. 2589
Pasky, S. 1419, 2038, 2333
Pasotti, C. 878
Pasquinelli, R.J. 3068, 3431
Pate, D. 39, 92
Pattengale, N. 2360
Pattengale, N.D. 3527
Patton, J. 2363
Paul, A.C. 2533, 2960
Paul, K. 2931
Paulon, R. 1506
Payet, J. 2718
Pearson, C. 1264
Peatman, W.B 836
Pedersen, F. 2461
Pedrozzi, M. 878
Peggs, S. 39, 42, 135, 278, 372, 797, 1059, 1691, 2204, 2901, 2904
Pei, Y.J. 818, 2852
Peiniger, M. 1410
Pekeler, M. 1410, 2887
Pelaia, T.A. 2360, 2363, 2366, 3527
Pellegrini, C. 211, 944, 1867, 1873
Pellegrino, L. 366, 2279, 3285
Pellico, W.A. 1587, 2936, 3177
Peñano, J.R. 716
Penco, G. 878
Penel, C. 253
Peng, Z.H. 601
Perevedentsev, E.A. 2898, 3398
Perez, F. 893, 3273, 3276
Perezhogin, S.A. 1605
Peschke, C. 434
Peters, H.-B. 467
Peterson, D. 3068
Peterson, E. 1294
Peterson, P.F. 2637
Peterson, T. 1966, 1969
Petra, M. 1020

Petracca, S. 2993, 2996, 2999
Petrillo, V. 3285, 3512
Petrossyan, B. 2114
Petrosyan, G. 470
Petrunin, A.A. 917
Petry, J.E. 1500
Peyrot, M. 1948
Pfeffer, H. 1781
Pfister, U. 598
Phillips, D. 1542
Phillips, L. 1401, 2860
Phinney, N. 678
Picardi, L. 3285
Pichoff, N. 2601, 2802, 3491
Pieck, M. 1168
Piekarz, H. 1649, 1981
Piel, C. 2887
Pierini, P. 1300, 1506
Pikalov, V.A. 917
Pikin, A. 89
Pilat, F. 42, 51, 1697, 1703, 1706, 1712, 2207
Pillai, C. 2515, 2518
Piller, M. 3377
Pinayev, I. 752, 2273
Pindak, R. 241
Piot, P. 911, 2682, 3500
Pirkl, W. 186
Pivi, M. 350, 2598, 3219, 3222
Pjerov, S. 241
Placidi, M. 186, 2530
Plan, B. 253
Planet, M. 2799
Plant, D. 2769
Plate, D. 1240
Plate, S. 164, 1939
Platz, M. 3569
Plawski, E. 467, 2787
Plawski, T. 195, 2379
Plettner, T. 722, 1861
Plouviez, E. 851, 854
Plum, M.A. 2429, 2444, 2485
Podlech, H. 1335, 2820, 2942
Podobedov, B. 241, 2808
Pogge, J. 1524, 2706
Pogorelsky, I.V. 1909
Poirier, R. 601, 1285, 1584
Polozov, S.M. 2963
Ponnaiyan, V. 54, 794
Pont, M. 893, 3273, 3276
Poole, M.W. 189, 950, 953
Popenko, V.A. 2878
Popov, G.F. 1080, 1616, 1619
Popov, V.G. 752, 2273
Popova, N. 1619
Popovic, M. 983, 1792
Pordes, S. 2491
Portmann, G. 890, 2369, 2372, 3213, 3374
Potter, J. 2354
Potter, K. 1467, 2706
Potylitsyn, A.P. 2709
Poupeau, J.P. 1303
Power, J. 1661, 2429, 3371, 3377
Power, J.G. 492, 1810, 1813, 1888, 1894, 2032, 2432, 2667
Power, K. 1936, 1939
Powers, T. 457, 2379
Pozdeyev, E. 138, 2649
Prasuhn, D. 598, 3428
Preble, J. 457, 977, 1104
Prebys, E.J. 1503, 1587, 1652, 2936
Preger, M.A. 366, 684, 1658, 2279, 2945, 3285
Preis, H. 1309
Prelec, K. 89
Prestemon, S. 1032
Prichard Jr., B.A. 73
Prior, C.R. 1527
Proch, D. 467
Prochnow, J. 2467
Prokop, M. 3371, 3377
Prom_, M. 2601
Prost, A. 1643
Prost, L.R. 275, 312, 536, 1518, 2524
Przeklasa, R.S. 1168
Ptitsyn, V. 51, 54, 135, 372, 405, 1697, 1703, 1706, 1712
Pu, Y. 1539
Puccio, B. 1945
Pugachev, G.D. 2878
Pugnat, P. 1942
Purcell, D. 2444, 2706
Pusina, J. 2086
Qian, B.L. 2646, 2966
Qian, Z. 1183, 1246
Qiang, J. 1509, 2613, 2954, 3401
Qin, B. 3506, 3509
Qin, H. 2655, 2658, 3117, 3120, 3123
Quan, S. 2580
Quast, T. 836
Quattromini, M. 914, 2077, 3285, 3548
Quigley, P. 1410, 1437
Quimby, D.C. 1909
Quinn, B. 426, 1673, 2312, 2571, 2574, 2577, 2673
Quinn, F.M. 189
Quirus, M. 2571, 2577
Rabedeau, T. 235
Rabehl, R. 1969
Radovinsky, A. 1990
Raguin, J.-Y. 2724
Raimondi, P. 366, 731, 2279, 2766, 2945, 3285
Raino, A. 3318
Raja, R. 1446
Raka, E. 2595
Rakhno, I.L. 983, 1742, 1745, 1748
Rakowsky, G. 217
Ranjbar, V. 3062
Rank, J. 39, 1467, 2150
Rao, Y.-N. 1578, 1584
Raparelli, M. 2476
Raparia, D. 571, 1428, 1467, 1569, 1572, 1637, 1709, 2150, 2153, 2156,

2390, 2598, 2793, 3282, 3416
Rarback, H. 235
Rathke, J.W. 92, 920, 977, 2186, 2790
Ratti, A. 186, 1464, 2530, 3371, 3377
Ratzinger, U. 1062, 1335, 2820, 2942
Raubenheimer, T.O. 662, 1038, 2739, 2754, 2757, 2760, 2775, 3219, 3231
Ravel, J.-C. 2799
Rawnsley, W. 601
Read, M.E. 1113, 1116, 1119, 1137, 1140, 1142
Reass, W.A. 553, 1168
Redaelli, S. 665
Redlin, H. 2114
Reece, C. 1377, 1398, 1494
Reece, K. 1569
Reed, C.A. 998
Rees, D.E. 553, 1095, 1168, 1458
Rees, G.H. 1527, 1557
Regan, A. 3371, 3377
Rehlich, K. 467, 2342, 2476
Reichardt, G. 836
Reiche, S. 211, 944, 947, 2110, 2112, 3153, 3321
Reich-Sprenger, H. 589
Reid, J. 48, 1204, 1213, 1769, 3353
Reilly, J. 1306
Reiser, M. 426, 511, 1673, 1676, 2312, 2571, 2574, 2577, 2673, 3156
Rej, D. 1461
Remondino, V. 173
Renieri, A. 3285
Rensfelt, K.-G. 1590
Repikhov, G.D. 2878
Reprintzev, L.V. 2878
Reschke, D. 467
Resende, X.R. 1056
Reshetnyak, N.G. 1107, 3303
Reuter, A. 92
Revol, F. 253
Revol, J.L. 851, 854
Rey, J.M. 1987
Reynolds, J. 2354
Rhee, S.J. 2177
Ricci, R. 366, 2279, 3285
Rice, D. 167, 278, 2399, 3425
Richards, D. 2844
Richardson, R. 563
Reiche, S. 203
Richichi, S. 167
Richter, A. 3551, 3569
Ries, T. 601, 1488
Rifflet, J.-M. 1948
Rimmer, R.A. 186, 977, 1104, 1183, 1243, 1246, 1389, 2023, 2092
Ringwall, A. 235
Rinn, J. 1942
Rinolfi, L. 684, 2742
Rios, P.B. 1593, 1596
Riot, V. 2530
Ritson, D. 1557
Ritter, J. 89, 3282
Rivetta, C. 3362
Rizzato, F.B. 2990
Robb, G.R.M. 950, 953
Robin, D. 224, 397, 2246, 2249, 3213
Robinson, K. 186
Robinson, T. 1119
Roblin, Y. 195
Robothom, W. 2168
Rock, B.Y. 2473
Rockford, J.H. 1987
Rode, C.H. 977, 2863
Rodrigiuez, M. 1237
Rodriguez, J. 138, 2649
Rodriguez, L. 558
Rodriguez, P. (LANL) 558
Rodriguez, P. (SLAC) 235
Rodriguez-Mateos, F. 1945
Rogers, G. 2303
Rogers, J.T. 375
Rogov, Yu.V. 1616
Rohlev, A. 2336
Rom, M. 3285
Romanov, G. 48, 1210
Romas'ko, V.G. 1107
Romè, M. 3285
Romero, D. 2354
Roncarolo, F. 2470
Ronsivalle, C. 914, 2077, 3285, 3548
Root, L. 1584
Ropert, A. 851, 854, 3189
Rose, C.R. 2485
Rose, D.V. 98, 2622, 2637, 2685, 3165
Rose, J. 217, 241, 1192, 2455, 2808
Roseberry, T. 1467
Rosenberg, R.A. 508, 3183
Rosenthal, S. 690
Rosenzweig, J.B. 95, 914, 944, 947, 1533, 1858, 1867, 1870, 1873, 2110, 2112, 2117, 2192, 2957, 3153, 3258, 3285, 3321
Roser, R. 1706
Roser, T. 24, 39, 51, 54, 405, 1545, 1637, 1697, 1715, 1936, 2204, 2793, 3026
Ross, I.N. 189
Ross, M.C. 503, 678, 1279, 2494, 2545, 2548, 2709
Rossbach, J. 2114
Rossen, P.v. 598
Rossi, A. 307, 1727
Rossi, C. 1724
Rossi, L. 42, 141
Rossmanith, R. 899, 3273
Rotela, E. 2790
Roth, I.S. 547, 1500
Rothgeb, T. 1377, 1386
Roudier, D. 1303
Rouleau, G. 73
Rowley, L. 2303
Rowton, L. 2841
Roy, P.K. 98, 2616, 2619, 2622, 2625, 2628
Roybal, R.J. 1341, 1661
Roybal, W. 1095, 1458
Royer, P. 684

Rubin, D.L. 1023, 2056, 2267, 3425
Rudolph, K. 2869, 2872
Rudychev, V. 1619
Ruegg, R. 638, 1584
Ruggiero, A.G. 1637, 2793, 2796
Ruggiero, F. 42, 45, 123, 1727
Ruggiero, R. 1748
Ruggles, S.C. 1168
Ruland, R. 2769
Rumolo, G. 123, 1727, 2234, 2607, 3038, 3041, 3044, 3053
Rusek, A. 1542
Rusnak, B. 989, 1347
Russell, A. 1652
Russell, S. 977
Russo, T. 1545, 3422
Rust, K. 550, 770
Rust, W.W. 635
Ruth, R.D. 1264
Ryan, J. 1542, 2595
Rybarcyk, L.J. 1092, 1566, 3086
Ryne, R.D. 1509, 2954, 3401
Saban, R. 1945
Sabbi, G. 42, 170, 536, 1032, 1521, 1984, 1990
Sabol, D. 2399
Saeki, H. 250
Saewert, G. 1781, 2020
Safranek, J. 235, 890, 3213
Sagan, D. 192, 848, 1023, 2267
Sahuquet, P. 1303
Saigusa, M. 2829
Saino, K. 487
Saito, K. 462
Sajaev, V. 417, 905
Sakai, H.R. 530, 857
Sakai, I. 1512, 1679, 3452
Sakamoto, Y. 860
Sakanaka, S. 860, 1228, 3207, 3365
Sakuda, M. 1807
Sakumi, A. 312
Saleh, N. 1921
Sanchez, B.J. 2515
Sanchez, M. 558
Sandberg, J. 550, 571, 743, 746, 770, 1640, 2144, 2147
Sanderson, D. 138
Sandner, W. 836, 2114
Sanelli, C. 366, 2279, 2742, 3285
Sanfilippo, S. 173
Sannibale, F. 863, 1658, 2527
Santucci, J. 2682
Sapozhnikov, L. 3389
Sarraf, R.H. 238
Sasaki, S. (ANL) 2261
Sasaki, S. (SPring-8) 250, 782
Sato, H. 568, 755, 1165, 1807, 1981
Sato, M. 860
Sato, Y. (IU) 3240
Sato, Y. (KEK) 1679, 2509, 3452
Satogata, T. 51, 54, 272, 278, 405, 1697, 1706, 1712, 1715, 2204, 2207, 2697, 2901, 3026, 3482
Satoh, M. 533, 860, 3368
Sauer, A. 1335, 2820, 2942
Saugnac, H. 1303
Saunders, A. 702
Saunders, J. 2860
Savage, R. 2390
Savalle, A. 2802
Savary, F. 1942
Savatteri, S. 746
Sawamura, M. 3443, 3446, 3449
Sazawa, S. 2829
Scaduto, J. 39, 92, 1631
Scandale, W. 173, 986, 1655
Scanlan, R.M. 170, 1032, 1984
Scarlett, C. 3255
Scarpine, V. 2414, 2494, 3062
Scarvie. T. 869, 2527, 3374
Schächter, L. 722, 728, 1879
Schaerf, C. 3285
Schaetz, T. 112
Schaller, S. 2354
Schamel, H. 3029
Schappert, W. 323, 2494
Schauer, M. 558
Scheer, M. 836
Scheidt, K. 854
Scheitrum, G. 3312, 3315
Schellong, B. 1948
Schempp, A. 598, 1062, 1622, 2817, 2823
Schilcher, T. 3386
Schimizu, J. 250
Schindl, K. 1682
Schirm, K.-M. 1948
Schlabach, P. 1730, 1969, 1972
Schlarb, H. 423, 467, 2074, 2730, 3126, 3129
Schlitt, B. 694, 1062
Schlott, V. 3386
Schlueter, R. 1032, 3458
Schmalzle, J. 1939, 2162
Schmekel, B.S. 375
Schmerge, J.F. 2104, 3216
Schmidt, C.W. 2020
Schmidt, F. 1754, 1757, 2207, 2228, 2231, 3494, 3497
Schmidt, P. 1948
Schmidt, R. 45, 1945
Schmidt-BÅcking, H. 1622
Schmidts, F. 1775
Schmor, P. 6, 439, 1584
Schnase, A. 598, 1216, 1234, 2817, 3428
Schneider, H. 598, 3428
Schneider, W.J. 2863
Schnitter, U. 2201
Schoenlein, R. 186, 2408, 2530
Schrage, D.L. 920, 977, 1341, 1344, 1661, 2083, 2790

Schramm, U. 112
Schreiber, S. 467, 911, 1086, 2068, 2071, 2114, 2730
Schreuder, A.N. 699
Schroeder, C.B. 1885
Schuett, P. 589
Schuh, P. 2297
Schulte, D. 657, 662, 665, 1727, 2721, 2727, 2733, 2736, 2739, 2757, 3053
Schultheiss, C. 524, 743
Schultheiss, T.J. 92, 920, 977, 2186, 2790
Schultz, D. 2129
Schultz, J. 1990
Schultz, R. 1443, 1449, 1452
Schulze, M. 3086
Schumann, R. 2114
Schussmann, G. 2664
Schwartz, H. 235
Schwarz, H. 1273, 2297, 3141
Scott, B. 235
Scott, D.J. 1029
Sears, C.M. 2101
Sears, J. 1309, 1312, 1314, 1323, 1410
Sebek, J. 235, 2494
Seberg, S. 2156
Seddon, E.A. 189
Seeman, J. 315, 2294, 2297, 2300
Sei, N. 713, 971, 974
Seidl, P.A. 275, 312, 536, 1518, 1990
Seifrid, P. 3068
Seike, T. 487
Sekachev, I. 601
Sekutowicz, J. 467, 977, 1086, 1300, 1374, 1377, 1392, 1395, 1575, 2730, 2866
Seletsky, S. 2020
Semenov, A. 323, 1781
Semertzidis, Y.K. 1625
Sen, T. 34, 42, 1754, 1757, 1760, 1772, 1775, 3401, 3542
Senf, F. 836
Senichev, Y. 598, 2814
Seo, J.-H. 3114
Seol, K.T. 2832, 2857
Serafini, L. 914, 2077, 2080, 3285, 3512
Serdobintsev, G.V. 2881
Sereno, N.S. 247, 827, 2420, 2435
Serio, L. 1945
Serio, M. 366, 2279, 2742, 3285
Serrano, J. 2336
Serriere, V. 3192
Sertore, D. 1506, 2071, 2114
Seryi, A. 657, 662, 2739, 2748, 2754, 2757, 2766, 2769
Sessler, A.M. 414, 3413
Setzer, S. 2114, 3566, 3569
Severino, F. 1195, 2441
Sezaki, K. 487
Sgamma, F. 366, 2279, 2742
Shaftan, T. 217, 241, 329, 908, 1192, 1497, 2455, 2808
Shang, H. 247, 283, 2330, 3461, 3470, 3473, 3476
Shang, J. 1452
Shao, L. 1876
Shapiro, A.H. 1341, 1344, 2083
Shapiro, M.A. 1255, 1258, 2536
Shapiro, S. 2796
Shaposhnikova, E. 1718, 3050
Sharamentov, S.I. 1291, 2426, 2790
Sharma, S. 2790
Sharp, W. 2622
Sharp, W.M. 98, 2637
Shatunov, P.Yu. 2898
Shatunov, Yu.M. 372, 2898
Shaw, R.W. 617
Shchelkunov, S.V. 1924
Shea, T.J. 1569, 2444, 2706
Sheehy, B. 217, 241, 329, 1192, 1497, 1819, 2455, 2808
Sheinman, I. 1888, 1891, 1897
Shelley, F. 2515, 2518
Shelley, Jr., F. 2354
Shemelin, V. 192, 1201, 1314, 1317, 2059
Shemyakin, A. 2020
Shen, J.L. 519
Shen, L. 2852
Shen, S. 1347
Shen, Y. 217, 2455
Shendrik, V.A. 2878
Shepard, K.W. 581, 1291, 1294, 1297
Shephard, M. 3560
Sheppard, J.C. 2751
Sherman, J. 73
Sherwood, R. 1661
Shi, J. 369
Shibata, K. 800, 803, 806
Shigaki, K. 1512
Shiho, M. 1807
Shiltsev, V. 48, 57, 1739, 1751, 1754, 1757, 1778, 1781, 2497, 2769, 3062
Shimada, T. 1512
Shimizu, N. 1165
Shimosaki, Y. 568, 1807, 2610
Shinoe, K. 530
Shintake, T. 487, 962, 965, 3332
Shintomi, T. 755, 1978
Shioya, T. 860
Shirakata, M. 568, 1807, 2610
Shishido, T. 1338
Shishlo, A. 117, 2360, 2363, 2366, 3527
Shkaruba, V. 250
Shkvarunets, A.G. 2712
Shoaee, H. 3371, 3377

Shoji, M. 250, 782, 2551
Shrey, T. 1542
Shubin, E. 2769
Shul'ga, N. 3329
Shumakov, I.V. 3530
Shuman, D. 98, 2625, 2628
Shurter, R.B. 2512
Shvedov, D. 2273
Shvets, G. 3117
Sibley, C. 607
Siddons, P. 241
Sideris, I.V. 2676
Sieber, T. 2869, 2872
Siemann, R.H. 722, 728, 731, 1530, 1855, 1858, 1864, 1879, 1933
Siemko, A. 1942
Sievers, P. 45
Sigler, F. 1664
Sikora, J. 1306, 3059
Sikora, R. 524, 2444
Silzer, M. 220
Simmons, D. 558
Simmons, L. 1213
Simoens, F. 1303
Simon, F. 1948
Simonsson, A. 1590
Simos, N. 1428, 1628, 1709, 3255
Simpson, J. 1813
Simrock, S. 467, 470, 2342, 2730
Sims, J. 2841
Sinclair, C.K. 76, 192, 1317, 2062
Singatulin, S. 2769
Singer, W. 467, 1374
Singer, X. 467
Singh, O. 283
Skarbo, B. 3318
Skaritka, J. 217, 1909, 2455
Skorobogatov, V.V. 917
Skrinsky, A. 250
Slaughter, D.R. 95
Slaughter, J. 1739, 1763
Smaluk, V. 214
Smart, L. 54, 785
Smedley, J. 541, 2132
Smirnov, A.V. 1153, 1156, 2123, 2129, 2132, 2135, 2186, 2640, 3171
Smirnova, E.I. 1255, 1258
Smith, B. 1210
Smith, E.N. 2399
Smith, G. 1715, 2444, 2453
Smith, H. 423
Smith, H.V. 558
Smith, J.C. 2267
Smith, K. 1377
Smith, K.S. 476, 1195, 1545, 1706, 1715, 2441, 3338, 3341, 3344, 3380
Smith, M. 2382
Smith, S. 235, 761
Smith, S.L. 189
Smith, T. 1279
Smith, T.L. 1416, 1422, 2038
Smolenski, K. 167, 1317, 2399
Snowel, M. 2574
Snydstrup, L. 1542
Soika, R. 2162
Soliday, R. 283, 1419, 2261, 3461, 3470, 3473, 3476
Solyak, N. 1207, 1210, 1213, 1781
Someya, H. 2509
Son, D. 962, 965
Song, L. 1110, 1142
Sonnad, K.G. 1536
Sorchetti, R. 2476
Soutome, K. 250, 782, 881
Spata, M. 195
Spataro, B. 914, 2500, 3285
Spataro, C. 2159
Spencer, C.M. 779, 2177
Spencer, J. 779, 1861, 2180
Spentzouris, P. 2939, 3195
Spickermann, T. 2521, 3086, 3089, 3455
Spiller, P. 589, 694
Spinka, H. 51
Spitz, R. 1195
Sprangle, P. 716, 1846
Sprehn, D. 3312
Springer, P.T. 95
Srinivasan-Rao, T. 39, 92, 541, 2047, 2132
Stanek, M. 423, 2297
Stanford, G. 601, 1488
Staples, J. 186, 1243, 1563, 2023, 2086, 2092, 2408, 3198
Starling, W.J. 2889
Startsev, E.A. 1667, 2975, 2978, 3120, 3123
Stascheck, A. 3569
Stassen, R. 598, 2814, 3428
Stecchi, A. 366, 2279, 2742, 3285
Steck, A. 2515
Steck, M. 434
Steerenberg, R. 388, 2913, 2916
Stefancich, M. 917, 1655
Stefanski, R. 1652
Steier, C. 397, 869, 2246, 2249, 3213, 3374
Steimel, J. 48, 1736, 3068, 3071, 3074, 3353, 3356, 3362
Stein, H.J. 3428
Stein, W. 2847
Steinhauer, L.C. 1909
Stella, A. 366, 2279, 2742, 3285
Stelzer, J.E. 73
Stenning, M. 1584
Stephan, F. 2114
Stephani, T. 1948
Stepin, D.L. 2878
Steski, D. 1715
Stettler, M. 2429, 2512, 3371, 3377
Stevens Jr., R.R. 73
Still, D. 1730
Stinson, G. 1584, 1670
Stirbet, M. 457
Stockhorst, H. 598, 3428
Stockli, M.P. 527, 3306
Stockwell, B. 1122, 1144
Stoltz, P. 132

Stott, J.P. 887, 2373
Stout, D. 2706
Stovall, J. 1515, 2652, 2855
Strait, J.B. 42, 1745, 1748, 1969, 1975
Straumann, T. 235, 761, 2494
Striganov, S.I. 1733
Strohman, C.R. 2473, 3347
Strohmer, S. 899
Studebaker, J. 558
Stulle, F. 3129
Stupakov, G.V. 102, 926, 1038, 3132, 3135, 3225, 3231
Sturgess, R. 558
Suetake, M. 860, 1228
Suetsugu, Y. 612, 800, 803, 806
Sugahara, R. 860
Sugai, I. 1512
Sugawara, S. 1978
Sugaya, M. 1231, 1679, 3452
Sugimoto, M. 2829
Sugimura, T. 3326
Sugita, K. 1978
Sugiyama, E. 1993
Suhring, S. 625
Suk, H. 1849, 1852, 1906, 1912, 2984, 2987
Suller, V.P. 189
Sullivan, G. 558
Sullivan, J. 2533
Sullivan, K. 2189
Sullivan, M. 340, 2282, 2294, 2297, 2300
Summers, D.J. 1804
Sun, D. 3068
Sun, X. 2688, 3008, 3011, 3014
Sun, Y. 2682
Sundelin, R. 1398, 1401
Suwada, T. 533, 1225, 3368
Suzuki, H. 1338
Svandrlik, M. 878
Svirida, D. 51
Swanson, C. 3371
Swenson, D.A. 2889
Swift, G. 2273
Swinney, C. 558
Swirsky, J. 2195
Sylvester, C. 1969
Symon, K.R. 452
Syphers, M. 1649, 1754, 2931
Syratchev, I. 495
Sytnik, V. 1781
Szott, Ph. 1303
Tabak, M. 2637
Taborelli, M. 495
Tada, J. 782
Tadano, M. 860, 2506
Tai, C.-Y. 1407
Tajima, T. 1341, 1344, 2083
Takagi, A. 1216, 1231, 1234, 1679, 2922, 3452
Takagi, T. 782
Takahashi, J. 1593, 1596, 2201
Takahashi, S. 487
Takahashi, T. 860, 1228
Takaki, H. 530, 857
Takala, B.E. 1168
Takano, S. 250, 881
Takao, M. 250, 782, 881
Takasaki, E. 1509, 2835
Takasaki, S. 860
Takashima, T. 250, 487
Takasu, Y. 487
Takayama, K. 568, 1784, 1807, 1981, 2610
Takayanagi, T. 1512
Takebe, H. 250
Takeda, H. 1515, 2855, 3518
Takeda, S. 487
Takeda, Y. 1512
Takeshita, K. 487
Takeuchi, H. 2829
Takeuchi, Y. 803, 860, 2351
Tallerico, P.J. 553, 1095, 1168, 1458, 1461
Talman, R. 192, 272, 848, 2919, 3482, 3485
Tamasaku, K. 487
Tamura, F. 1216, 1234
Tamura, K. 250, 881, 2551
Tan, C.Y. 1751, 2703, 3071, 3074
Tanabe, J. 2174
Tanabe, T. 235
Tanaka, H. (KEK) 1509, 2393, 2835
Tanaka, H. (Mitsubishi) 1539
Tanaka, H. (SPring-8) 250, 881
Tanaka, K. 1978
Tanaka, T. 487
Tang, C. 467
Tang, Z. 623
Tanimoto, Y. 809, 860
Taniuchi, T. 2838
Taniuchi, Y. 250
Tantawi, S.G. 482, 1125, 1127, 1261, 1264, 1270, 1276
Tarakanov, V.P. 1882
Tarasov, G.E. 2878
Tarawneh, H. 238, 2318, 2321
Tariq, S. 641, 1452
Tartaglia, M. 1730, 1969, 1972
Tateishi, T. 884
Tatum, B.A. 995
Tavakoli, K. 238
Tavares, P.F. 2583, 3279
Tawada, M. 353
Taylor, C. 86
Taylor, T. 42
Tazzari, S. 3285
Tazzioli, F. 3285
Tecker, F. 684
Tegenfeldt, F. 1945
Tejima, M. 860
Telfer, S. 947, 2110, 2112, 2120, 2192, 3321
Temkin, R.J. 1255, 1258, 2095, 2536
Temnykh, A. 167, 1026, 1954, 3425

Temple, R. 558
Tenenbaum, P. 657, 662, 681, 2739, 2757
Teng, L.C. 2895
ten Kate, H. 42
Tennant, C. 195, 2189, 3243
Tepikian, S. 51, 135, 405, 1706, 1712, 2144, 2159, 2390
Teramoto, A. 1071
Terashima, A. 1978
Terebilo, A. 235, 2255, 2369, 2372
Terekov, V. 1691
Terremoto, L.A.A. 1593
Tesarek, R. 2497
Teytelman, D. 318, 2297, 2300, 3141, 3389
Theobald, W. 1921
Thibus, J. 2823
Thieberger, P. 1628, 1634, 1715
Thiesen, H. 1945
Thikim, M. 2303
Thomas, C. 1575
Thomas, R. 164, 2162
Thomas-Madec, C. 1104, 1332
Thomason, J. 2542
Thompson, K.M. 1020
Thompson, M.C. 1870
Thompson, N.R. 189
Thomson, D. 3377
Thorndahl, L. 1156
Tiede, R. 2942
Tiefenback, M. 195, 3243
Tigner, M. 192, 1317
Tikhoplav, R. 2682
Timossi, C. 2385
Ting, A. 716, 1819, 1846
Tinsley, D. 3068
Titt, U. 690
Titus, P. 1631
Tiunov, M. 1781, 3318
Tkachenko, L. 1781
Tobiyama, M. 2709, 3141
Tochitsky, S.Ya. 1873
Todd, A. 977
Todd, R. 788, 791
Todesco, E. 173, 1942
Toelle, R. 598, 2811, 2814, 2817, 3428
Toellner, T. 2411
Togawa, K. 487, 3332
Tokuchi, A. 1165
Tollestrup, A.V. 48, 1733, 2491, 2497
Tolmachev, S. 1867
Tom, C.Y. 558
Tomàs, R. 2207, 2228, 2231, 2234, 2240, 2901
Tombolini, F. 917
Tomimasu, T. 902, 2387, 3270
Tomizawa, H. 2838
Tomizawa, M. 3083
Tomlin, R. 2936
Tompkins, J. 1730, 1966, 1969, 1972
Tordeux, M.A. 229
Torii, Y. 884
Torikai, K. 568, 1784, 1807
Torrez, P.A. 1237
Tortschanoff, T. 1948
Torun, Y. 1183, 1246, 1413, 1795
Tosi, L. 214, 1050, 2306, 2309
Totchisky, S. 1867
Toth, C. 1840
Touzzolo, J. 1428
Tovstiak, V.V. 1080
Towne, N. 241, 3168
Towns-Andrews, E. 708
Toyama, T. 568, 1784, 1807, 2610, 3083
Toyokawa, H. 195, 713, 902, 938, 974, 2387, 3270
Trakhtenberg, E. 824, 830, 1017
Trask, W. 167
Trautwein, A. 235
Travish, G. 944, 947, 1867, 1870, 2110, 2112, 2192, 3321
Trbojevic, D. 39, 51, 54, 135, 372, 794, 797, 1425, 1691, 1697, 1706, 1712, 1816, 2204, 2694, 2904, 3413, 3485
Tremaine, A.M. 95, 2192, 2957
Tromba, G. 2309
Trotman, J.V. 1527
Trovò, M. 2306
Trujillo, P.G. 553
Trzeciak, W. 887, 2303
Tsai, H.J. 890
Tsai, Z.D. 1479
Tsakov, I. 2114
Tsang, T. 541
Tschalaer, C. 372, 956, 959, 980, 2324
Tsentalovich, E. 2324
Tsoupas, N. 51, 405, 550, 1542, 1545, 1637, 1706, 1715, 2138, 2141, 2147, 2150, 2153, 2159
Tsuchiya, K. 860, 1978
Tsukishima, C. 1539
Tsumaki, K. 250, 782, 884
Tuckmantel, J. 1718, 3050
Tuozzolo, J. 550, 571, 1637, 2138, 2144, 2147, 2150, 2156, 2390, 2598
Tupikov, V. 2020
Tur, Yu.D. 2878
Turlington, L. 1350
Turner, J.L. 2297, 2754
Turner, W. 2530
Twarowski, K. 467
Uchiyama, T. 809, 860
Ueda, A. 860, 3201, 3204
Ueng, T.S. 3237
Ueno, A. 1509
Ueno, R. 1679
Uesaka, M. 2258
Uesugi, T. 1216, 1231, 1234, 1679, 3452
Ullrich, J. 1622
Umemori, K. 860, 1228
Umstadter, D. 1921
Underwood, D. 51
Urakawa, J. 2545, 2709

Uriot, D. 2802, 3491
Uvarov, V.L. 2878
Uythoven, J. 45, 1646
Vaccarezza, C. 366, 914, 2077, 2279, 2500, 2945, 3285
Valdiviez, R. 702, 1664
Valente, A.-M. 1401, 2860
Valente, P. 1658
Valentino, V. 3318
Valfells, A. 426, 1673, 2312, 2571, 2574, 2577, 3156
Valishev, A. 3398
Valuch, D. 473, 1089
van der Laan, J.B. 372, 956, 959, 980, 2324
van der Meer, A.F.G. 519
Vanenkov, I. 1951
van Goor, F.A. 1900, 1903
VanKuik, B. 1542
van Tilborg, J. 1840
van Weelderen, R. 1945
van Zeijts, J. 51, 135, 524, 1697, 1706, 1712
Varenne, F. 2802
Varfolomeev, A. 1867
Varfolomeev, Jr., A. 1867
Variale, V. 3318
Varnasery, S. 238
Vascotto, A. 2309
Vasserman, I. 2261
Vasyukhin, N. 2814
Vay, J.-L. 132, 312, 2673, 3297
Vaziri, K. 983
Velev, G. 1730, 1969, 1972
Veness, R. 1646
Venturini, M. 863, 2772, 3144
Venturini-Delsolaro, W. 1948
Verdier, A. 444, 2237
Vermare, C. 2464
Verzilov, V. 214
Vescovi, M. 366, 2279, 3285
Veshcherevich, V. 192, 1198, 1201, 1306, 1317
Vetter, K. 524, 2444, 2697
Vicario, C. 944, 3285
Vidal, R. 2497
Vignola, G. 1053, 1658
Vikharev, A.L. 1147
Vincenzi, D. 917, 1655
Vinogradov, N.E. 2790, 2963
Vinogradov, S.V. 3530
Vinokurov, N. 2273
Viren, B. 3255
Virgo, M. 3323
Virostek, S. 1243, 2023, 2092
Visentin, B. 1303
Vlachoudis, V. 45
Vlogaert, J. 1942
Vobly, P. 2273
Vogel, H. 1410, 2887
Vogel, V. 2545
Vogler, W. 269, 3560
Volk, J.T. 1766, 2180
Volkolupov, Yu.Ya. 1107, 3303
Volkov, V.N. 2041, 2044
Vollinger, C. 173, 1951
vom Stein, P. 1410, 2887
Vorobiev, L.G. 3533
Vos, L. 45, 1801
Wada, Y. 3335
Wahrer, B. 1032
Wait, G.D. 1162
Wake, M. 568, 1784, 1807, 1981
Waldron, W. 98, 536, 1171, 1521, 2628
Waldschmidt, G. 1422
Walker, N. 657, 2396, 2733, 2736, 2739
Walker, R.P. 232
Wallace, D.J. 2303
Wallace, P. 752, 2273
Wall_n, E. 2321
Wallig, J. 1246
Walstrom, P. 544, 1966
Walter, M. 426, 1673, 1676, 2312, 2571, 2574, 2577
Walz, D. 731, 1530, 1858, 1864, 1933
Wan, W. 186, 397, 2246, 2249
Wanderer, P. 164, 1637, 2159, 2162, 2390
Wang, B. 1032
Wang, C. 1927, 1930
Wang, C.J. 2554
Wang, C.X. 3407, 3410
Wang, Ch. 1041, 1371, 2402, 2670
Wang, D. 39, 1300, 2005, 3186, 3228
Wang, D.J. 890
Wang, F. 372, 956, 959, 980, 2324
Wang, H. (ANL) 1813, 2032
Wang, H. (TJNAF) 457, 1098, 1101, 1104, 1389
Wang, J.M. 241
Wang, J.P. 815, 2357
Wang, J.W. 1264, 2664, 2763
Wang, M.H. 890, 3150, 3240
Wang, P. 752, 2479
Wang, S. 1455, 1509
Wang, S.-H. 186, 2682, 3198
Wang, T. 1386, 1398, 2860
Wang, T.S. 508, 3092, 3095
Wang, X. 2174
Wang, X.J. 217, 241, 420, 1819, 2455, 2808
Wang, X.Z. 2586
Wang, Y. (CAMD) 2382, 2892
Wang, Y. (NSRL) 815
Wangler, T.P. 2613
Warburton, D. 550, 1625, 1640, 2147
Warner, A. 2020
Warner, D.K. 1237
Warnock, R. 3144
Warsop, C.M. 1527
Watanabe, Y. 1512
Watson, J.A. 2533, 2960
Wazlawik, S. 3569
Weathersby, S. 2981

Weaver, M. 2285
Webber, R.C. 1503, 2936
Weber, C. 1189
Weggel, R.J. 1628, 1631, 1634
Wei, J. 272, 394, 550, 571, 1569, 1572, 2153, 2159, 2390, 2598, 3029, 3032, 3416, 3419
Wei, W. 815
Weichert, G. 467
Weihreter, E. 1189
Weiland, T. 2114, 3249, 3252, 3551, 3563, 3566, 3569
Weiner, M. 2664
Weinrich, U. 694
Weir, J. 563, 2960
Weise, H. 673
Weiss, D. 785
Weiss, K. 307
Welch, D.R. 98, 2622, 2637, 2685, 3165
Welch, J. 3126
Wells, R.P. 186, 812
Welsch, C.P. 1622, 2817
Welton, R.F. 527, 3306
Wender, S.A. 1168
Wendt, M. 467, 1086, 2730
Weng, W.T. 429, 571, 1637, 1709, 2793
Wenhui, H. 467
Wenninger, J. 45, 1718
Werin, S. 2318, 2321
Werkema, S. 1554
Wermelskirchen, C. 235, 761
Wesling, S. 2029
Westenskow, G. 2533, 3297, 3300
Weterings, W. 1646
White, G.R. 2733, 2778
Whitlatch, T. 457, 977, 1377, 2866
Widger, D. 2399
Widjaja, C. 1921
Widmeyer, M. 235
Wiemerslage, G. 830
Wienands, U. 2297, 2300, 3141
Wilcox, R. 2408
Wildman, D. 323, 1781, 2922, 3177
Wildner, E. 173
Wilinski, M. 2441, 2444, 2691
Wilke, I. 519
Will, I. 836, 2114
Willen, E. 164, 1936, 1939
Williams, C.L. 998
Williams, E. 3374
Williams Jr., E.L. 288
Wilson, I. 495, 665, 1156, 2724
Wilson, K.M. 1377, 2866
Wilson, M. 426
Wilson, M.N. 2162
Wilson, P. 1264, 1282
Win, S.S. 3056
Wines, R. 2135, 2186
Wisdom, J. 1861
Wiseman, M. 457, 977, 1377
Witkover, R.L. 2444, 2447, 2450
Wittmer, W. 2237
Wojtkiewicz, G. 467
Wolf, M. 2664
Wolski, A. 186, 652, 657, 866, 2246, 2396, 2745, 2772, 2775, 3213
Wood, J. 51
Wood, R.L. 920, 977, 2083
Woodley, M. 657, 662, 2739, 2757, 2766, 2775, 3126, 3129
Woods, M. 2754
Wright, E. 1144
Wu, A.T. 1386, 2860
Wu, G. (NSRL) 815
Wu, G. (TJNAF) 1389, 1395, 1401, 1575
Wu, J. 126, 1035, 1038, 2775, 3228, 3231
Wu, J.K. 3294
Wu, K.C. 164
Wu, V. 1246, 1769
Wu, X. 2849, 2972
Wu, Y. 397
Wu, Y.K. 391, 752, 2249, 2270, 2273, 2479, 2482
Wu, Z. 217, 420, 1192, 1497, 1819, 2455
Wuensch, W. 495, 1156, 2467, 2724
WËstefeld, G. 836, 839, 845, 3020, 3023
Xiao, A. 2488
Xiao, M. 1730, 1757, 1760, 1772, 1775, 3401, 3542
Xie, M. 1843
Xiong, Y. 1560, 3506, 3509
Xu, H.L. 968
Xu, N. 2174
Xu, Z. (BNL) 1688
Xu, Z. (IMP) 1288
Yadav, S. 1748, 1969
Yakimenko, V. 944, 1909
Yakovlev, V.P. 1128, 1131, 1150, 1927, 2881
Yamada, K. 713, 971, 974
Yamada, R. 1981
Yamaguchi, S. 1509, 2838
Yamamoto, A. (IHI) 3326
Yamamoto, A. (KEK) 1978
Yamamoto, K. 1512
Yamamoto, M. 1216, 1234
Yamamoto, N. 860, 2351
Yamamoto, S. (KEK) 860
Yamamoto, S. (Mitsubishi) 1539
Yamanaka, S. 1165
Yamatsu, Y. 902, 3270
Yamazaki, A. 1679, 3452
Yamazaki, M. 1338
Yamazaki, Y. 576, 1509
Yan, X. (IAP) 1335
Yan, X. (UAD) 519
Yan, Y. 2297, 2300
Yang, B.X. 2411, 2423
Yang, J.S. 1470, 2857
Yang, M.J. 1649, 1766, 3440
Yang, S. 1243, 1834
Yang, X. 1288

Yanovsky, V. 1921
Yao, C. 758
Yao, C.Y. 2411, 2423, 2438
Yao, J. 2852
Yarovoi, T. 1867
Yasumoto, M. 713, 902, 971, 974, 3270
Yeh, M.K. 1371
Yin, Y. 2586
Yocky, J. 2297, 2754
Yoder, R. 1533, 1867, 1873, 2117, 3258
Yokoi, T. 1679, 3452
Yonehara, H. 250, 782, 884, 2551
Yonemura, Y. 1679, 3452
Yorita, T. 250, 782
York, R. 138, 1350, 1353, 1362, 2849, 2972, 3533
Yoshida, M. 487
Yoshii, M. 1216, 1234, 3452
Yoshikawa, H. 1509
Yoshimoto, M. 1679, 3452
Yoshimoto, S. 860, 1228
Yoshino, K. 1509, 2393
Yoshioka, M. 860
Yotam, R. 235
Young, A. 3141
Young, L.M. 60, 920, 977, 1461, 1515, 2844, 3515, 3521
Yu, D. 1153, 1156, 2123, 2126, 2129, 2132, 2135, 2186, 3171
Yu, I.H. 2857
Yu, J. 2132
Yu, L.H. 217, 241, 2455, 2808
Yu, S.S. 98, 558, 1171, 2616, 2619, 2622, 2625, 2628, 2637, 2646, 2661, 2685
Yu, T. 1560, 3506, 3509
Yuasa, Y. 1679, 3452
Yun, J.C. 1763
Yun, R. 426, 2571
Yunn, B. 332, 3246
Yusof, Z. 2032
Zadorozhny, V. 3005
Zagorodnov, I. 3249, 3252
Zahariou-Cohen, S. 1542
Zajic, V. 89
Zakutin, V.V. 1107, 3303
Zaltsman, A. 39, 476, 1195, 3344, 3380
Zambon, L. 3395
Zangrando, D. 1050
Zapfe, K. 467
Zaplatin, E. 598
Zaugg, T. 508, 2521, 3089, 3455
Zelenski, A. 51, 405, 3282
Zeller, A. 138, 161
Zeng, J. 770
Zeno, K. 51, 54, 794, 1542, 1545, 1715
Zhan, W. 1288
Zhang, B. 2580
Zhang, C. 250
Zhang, H. 818
Zhang, P. 1921
Zhang, P.F. 968
Zhang, S.C. 968
Zhang, S.Y. 51, 54, 785, 794, 1425, 1706, 1715, 2598, 2694, 3419
Zhang, W. (BNL) 550, 1640, 2147, 3255
Zhang, W. (IMP) 1288
Zhang, W. (YY Labs) 2586
Zhang, X.L. 57, 1754, 1757, 1778, 1781, 2703
Zhang, Y. (NSRL) 758
Zhang, Y. (ORNL) 995, 1001, 1004
Zhang, Y. (TJNAF) 941
Zhao, F.Y. 815
Zhao, H. 1288
Zhao, K. 2580
Zhao, Q. 92, 2047
Zhao, T. 2382, 2892
Zhao, Y. 39, 92, 1300, 2050
Zhavoronkov, N. 836
Zheng, H. 2922
Zheng, Q. 1404
Zheng, S. 467, 1392, 1395, 1575
Zhidkov, A. 2258
Zhiglo, V.F. 2098
Zholents, A. 186, 397, 812, 866, 872, 923, 2086, 2132, 2408, 3198
Zhou, F. 1876, 1909, 2709, 3186, 3228
Zhou, J. 2646, 2966
Zigler, A. 716
Zimmermann, F. 123, 307, 665, 1727, 1730, 1754, 1757, 1778, 2237, 2240, 2315, 2604, 2739, 3038, 3041, 3044, 3053, 3056
Zimmermann, H. 2823
Zink, R. 138
Zinkann, G.P. 2426, 2790
Zisman, M. 361, 1183, 1243, 1246, 2023, 2297
Zitelli, L. 1144
Zlobin, A.V. 42, 1748, 1966, 1969, 1975
Zobov, M. 366, 914, 2279, 2742, 2945, 3285
Zolfaghari, A. 956, 959, 980, 2324
Zolotorev, M. 2530
Zotter, B. 3044
Zou, Y. 426, 511, 1673, 2673, 3156
Zubets, V. 3282
Zuo, K. 235
Zviagintsev, V. 470
Zwart, T. 956, 959, 980, 2324